Heft 19
No. 19

Schriftenreihe Baustoffe und Massivbau
Structural Materials and Engineering Series

UNIKASSEL
VERSITÄT

Ultra-High Performance Concrete and Nanotechnology in Construction

Proceedings of Hipermat 2012
3rd International Symposium on UHPC and Nanotechnology for High Performance Construction Materials
Kassel, March 7–9, 2012

Edited by
M. Schmidt
E. Fehling
C. Glotzbach
S. Fröhlich
S. Piotrowski

kassel university press

Schriftenreihe Baustoffe und Massivbau
Structural Materials and Engineering Series

Heft 19
No. 19

Ultra-High PerformanceConcrete and Nanotechnology in Construction

Proceedings of Hipermat 2012
3rd International Symposium on UHPC and Nanotechnology for High Performance Construction Materials
Kassel, March 7–9, 2012

Edited by
M. Schmidt
E. Fehling
C. Glotzbach
S. Fröhlich
S. Piotrowski

kassel university press

Bibliografische Information Der Deutschen Nationalbibliothek

Die Deutsche Nationalbibliothek verzeichnet diese Publikation in der Deutschen Nationalbibliografie; detaillierte bibliografische Daten sind im Internet über http://dnb.d-nb.de abrufbar

ISBN print: 978-3-86219-264-9
ISBN online: 978-3-86219-265-6
URN urn:nbn:de:0002-32656

Herausgeber

Prof. Dr.-Ing. habil. M. Schmidt
Universität Kassel
Fachbereich Bauingenieur- und Umweltingenieurwesen
Institut für Konstruktiven Ingenieurbau
Fachgebiet Werkstoffe des Bauwesens und Bauchemie
Mönchebergstr. 7
D-34125 Kassel
Tel. +49 (561) 804 2601
Fax +49 (561) 804 2662
baustk@uni-kassel.de
www.uni-kassel.de/fb14/baustoffkunde

Prof. Dr.-Ing. E. Fehling
Universität Kassel
Fachbereich Bauingenieur- und Umweltingenieurwesen
Institut für Konstruktiven Ingenieurbau
Fachgebiet Massivbau
Kurt-Wolters-Str. 3
D-34125 Kassel
Tel. +49 (561) 804 2656
Fax +49 (561) 804 2803
bauing.massivbau@uni-kassel.de
www.uni-kassel.de/fb14/massivbau

Introduction

Ultra-High Performance Concrete (UHPC), one of the recent breakthroughs in concrete technology, impresses us with its high durability and a compressive strength comparable to that of steel. It permits the design of sustainable concrete structures such as wide-span bridges, filigree shells and high-rise towers and allows for spectacular architectural designs.

In 2004 and 2008, two International Symposia on UHPC took place at the University of Kassel, organized by the Department of Structural Materials and Construction Chemistry and the Department of Structural Engineering. Since then, the set of knowledge about the Ultra-High Performance Concrete has been substantially widened and its practical application has rapidly increased worldwide. New researchers and users of UHPC have joined the community and broadened the scope of its potential.

This conference as well has substantially grown since 2008. In 2012, about 130 speakers presented their impressions, research, and practical experience. It also attracted the attention of many international standardization bodies.

Even though the material is already highly developed, it is still possible to increase its potential even further using recent advancements in nanotechnology and colloidal chemistry. Nowadays, the reactions of binders can be studied at the nanoscale, synthetic nanoparticles of various oxides can significantly improve microstructure and reaction potential. This knowledge gives rise to many new possibilities that allow developing impregnable ceramics or multifunctional materials. They can, for example, carry agents for environmental protection, provide additional self-healing potential, and act as part of heating or cooling measures. As nanotechnology provides many new and auspicious approaches to improve the performance of construction materials and to open up new applications, the 3rd International Symposium on UHPC extended its focus towards nano-optimized construction materials and its recent advancements. This additional aspect led us to establish the new conference name **HiPerMat**, derived from **Hi**gh **Per**formance Construction **Mat**erials.

This volume thus contains more than 120 contributions from many research disciplines that are influenced by High Performance Materials and UHPC in particular: material sciences, structural engineering, environmental engineering, nanotechnology, chemistry, architecture, codification, and economy. A design adequate to the materials and to the construction of durable and sustainable high performance structures receives special attention.

We hope that our conference, Hipermat 2012, has once more contributed to the development of modern and progressive buildings and materials for construction and will continue to do so in the future.

Kassel, in January of 2012

Prof. Dr.-Ing. habil. Michael Schmidt

Prof. Dr.-Ing. Ekkehard Fehling

We thank our supporters

Scientific Committee for HiPerMat 2012

Chairmen

Prof. Michael Schmidt
Prof. Ekkehard Fehling
University of Kassel, D

Members

Prof. Tess Ahlborn
Michigan Tech Transportation Insitute, USA

Prof. Mouloud Behloul
Lafarge, F

Prof. Harald Budelmann
University of Braunschweig, D

Prof. Manfred Curbach
Dresden University of Technology, D

Prof. Françoise de Larrard
Lafarge, F

Prof. Marco di Prisco
Politecnico di Milano, I

Prof. Rüdiger Faust
University of Kassel, D

Dr. Xin Feng
Shanghai University, CN

Prof. Pietro Gambarova
Politecnico di Milano, I

Dr. Benjamin A. Graybeal
Federal Highway Administration, USA

Prof. Jürgen Grünberg
University of Hannover, D

Prof. Petr Hajek
Technical University Praque, CZ

Prof. Harianto Hardjasaputra
Universitas Pelita Harapan, Indonesia

Prof. Josef Hegger
RWTH Aachen University, D

Prof. Detlef Heinz
München Technical University, D

Prof. Maria Konsta-Gdoutos
University of Thrace, GR

Steve Kosmatka
Portland Cement Association, USA

Prof. Christian Meyer
Columbia University, USA

Prof. Bernhard Middendorf
University of Dortmund, D

Dr. Christoph Müller
German Cement Works Association (VDZ), D

Prof. Harald Müller
Karlsruhe University of Technology, D

Prof. Aurelio Muttoni
EPFL Lausanne. CH

Jacques Resplendino
Setec, F

Dr. Serge Rimlinger
CERIB, F

Prof. Liyi Shi
Shanghai University, CN

Alain Simon
Eiffage, F

Prof. Dietmar Stephan
Technical University Berlin, D

Prof. François Toutlemonde
IFSTTAR, F

Prof. Nguyen Tue
Graz University of Technology, A

Prof. Jan Vitek
Technical University Prague, CZ

Prof. Joost C. Walraven
Delft University of Technology, NL

Prof. Alphose Zingoni
University of Cape Town, ZA

Symposium organizers

Dipl.-Ing. Susanne Fröhlich
Dipl.-NanoSc. Christoph Glotzbach
Dipl.-Wirtsch.-Ing. Siemon Piotrowski

Table of Contents

Photocatalysis

MATERIALS

Raw Materials, Mixture Compositions and Fresh Concrete

Mechanical Behaviour of Hardened UHPC

Hydration and Early Age

Durability

STRUCTURAL BEHAVIOUR

Tension and Bending

Shear

Torsion and Bond

Fire and Impact

DESIGN AND CONSTRUCTION

Material Models

Composite Structures and Connection Technology

Structural Elements

APPLICATIONS

Special Concretes and Applications

Infrastructure

Architectural Elements

Off-shore Foundations

As part of the conference bag, you received a storage device containing the online version of this volume. You can access all the information in this book, skim through it via a fulltext search, filter the contributions, and get further information on the authors and the visitors of HiPerMat 2012.

To access the online proceedings, all you need is a recent web browser and a PDF viewer, you can use any operating system. Just plug the USB storage device into a compatible computer and open the file *start.html* in its root directory.

On the USB stick, you will find one additional contribution:

Part One

KEYNOTES

The Path to Ultra-High Performance Fiber Reinforced Concrete (UHP-FRC): Five Decades of Progress

Antoine E. Naaman[1], Kay Wille[2]

1: Department of Civil and Environmental Engineering, University of Michigan, Ann Arbor, Michigan, USA
2: Department of Civil & Environmental Engineering, University of Connecticut, Storrs, Connecticut, USA

Following the onset of modern developments of fiber reinforced concrete in the early 1960's, there has been a continuous search for its improved performance. One can thus follow such progress in milestones along four inter-related paths: one path for the cementitious matrix, another for the fiber, the third for the interface bond between fiber and matrix, and the forth for the composite itself. After identifying some key milestones for each path, over a period of five decades, leading to today's ultra-high performance fiber reinforced concretes (UHP-FRCs), the composition and key mechanical properties of newly designed UHP-FRC mixtures obtained without heat or pressure curing while using materials available on the US market are described. Record breaking performance in direct tension (in terms of strength, ductility, and fracture energy) is reported and sets limits to exceed in the future.

Keywords: bond strength, ductility, fiber reinforced concrete, fracture energy, high strength, high performance, steel fibers, tensile testing, ultra-high performance.

1 Introduction

The past five decades mark the modern development and broad expansion of fiber reinforced cement and concrete composites, which has led to today extensive applications and market penetration worldwide. Their success is due in part to significant advances in the fiber reinforcement, the cementitious matrix, the interface bond between fiber and matrix, fundamental understanding of the mechanics of the composite, and improved cost-effectiveness.

Ultra-high performance cement or concrete (UHPC) composites are very brittle and, as such, often compared to ceramics. Adding fibers to an UHPC matrix in order to improve its toughness and ductility, has led to the terminology used here, that is: "ultra high performance fiber reinforced cement or concrete composite" or UHP-FRC composite.

It is strongly believed that high performance and ultra-high performance fiber reinforced cement composites are emerging materials well suited for use in the next generation of infrastructure. There is real need to tailor-design these composites to satisfy certain demands on strength, toughness, durability, ductility, and fracture energy. These include demand for combined axial and bending resistance at the base of columns in high rise buildings, demand for high rotational capacity, demand for combined plastic shear and plastic bending deformations at the base of shear walls, high shear and bending resistance at the continuous supports in long-span bridges, and, blast and impact resistant structures. Clearly high performance mechanical properties are needed. UHP-FRC composites seem to be also particularly suitable in thin products applications, such as panels and cladding, where they could be used as stand-alone material. Enhanced durability properties could fulfill the need for structures with longer lifetime, less maintainance and repair.

Combined properties of interest to civil engineering applications include strength, toughness, energy absorption, stiffness, durability, freeze-thaw and corrosion resistance, fire resistance, tightness, appearance, stability, construct-ability, quality control, and last but not least, cost and user friendliness.

2 Definition and Characteristic Qualifications

High strength and high performance concrete, high performance fiber reinforced concrete (HPFRC), ultra-high performance concrete (UHPC), and ultra-high performance fiber reinforced concrete (UHP-FRC) have been addressed in numerous investigations in the US and abroad [1-52]. A recent review of their definitions, if available, can be found in Ref. [23]. For the purpose of this paper and with the intent of providing extremely brief definitions until technical committees working on these materials provide some, the following definitions are suggested:

- Ultra high performance concrete (UHPC) is a hydraulic cement-based concrete with a compressive strength at least equal to 150 MPa, etc.
- Ultra-high performance fiber reinforced concrete (UHP-FRC) is a UHPC with fibers added in order to significantly improve a particular mechanical property (or properties), etc.

The additive "etc…" suggests that these short definitions could be qualified by one or a combination of attributes, such as adopted by some researchers [19, 20]. For UHPC, these attributes include, for instance, a minimum water to binder ratio, a minimum cement content, a minimum packing density or a minimum level of durability performance. For UHP-FRC the composite can be qualified by whether it is strain-softening or strain-hardening in tension [12,13], or whether it is deflection-softening or deflection-hardening in bending, as well as by a minimum level of ductility, toughness or fracture energy. Other attributes may be imposed depending on particular applications; examples include permeability, electrical conductivity, resistance to chloride penetration, volume stability (shrinkage or expansion), etc.

How a recommended level of performance is achieved in practice should be of less interest to a general definition. Thus UHPC could be obtained using heat curing or pressure curing or none at all; it may necessitate the use of a particular mineral additive or a polymer additive, or a special mixing procedure.

Whether a single or multiple attributes are used, reference to broadly acceptable standard tests procedures and specimen dimensions is needed to help clearly identify a particular composite.

3 Chronological Developments: Five Decades of Progress

It is difficult to put specific limits at technical advances and progress on a particular subject, not only in terms of time but also geographic location. However, one can point out certain milestones that helped improve the performance of cement and concrete composites in general and somehow started a trend. For UHP-FRC, these milestones can be followed along four paths and their combination, namely, the cement matrix, the fiber, the bond at the interface between fiber and matrix, and the resulting composite.

3.1 Concrete Matrix and Fiber

In Table 1, the authors list in chronological order key advances related to the concrete matrix (2nd column) and the fiber (3rd column) since the 1960's, mostly as encountered in the Europe and the US. It is likely that a similar evolution took place elsewhere around the world, but with some slight delay (or advance) in adoption or implementation. Table 1 is self-explanatory.

3.2 Progress Leading to Ultra High Performance Fiber Reinforced Concrete

It has been a common aspiration for researchers dealing with cement and concrete composites to race for increasing compressive strength. In the early 1970's very high compressive strengths of up to 510 MPa were reported from testing small specimens prepared under special conditions with vacuum, heat and pressure curing [24, 25]. In the early 1980's the addition of special polymer and the use of very low water to cement ratios led to what was described as micro-defect-free cement with a compressive strength exceeding 200 MPa [26]; no pressure or

heat curing was needed. Such discoveries, however, while illustrating the potential of the material, did not translate into easily implemented applications. In Tables 2, the authors summarize various milestones related to numerous such composites developed since the 1970's. Widely used acronyms are highlighted. Table 2 covers the period from 1970 to 2011. It gives the approximate date of introduction, the range of compressive strength reported, the reference, the name and/or acronym used for the material developed, if any, and the special conditions applied to achieve the reported properties. Related references can be found in the reference list [24 to 49] Note that Table 2 is by no means exhaustive; it covers what the authors consider key developments in the US and Europe. The emphasis is on materials that have led to ultra-high performance concrete and ultra-high performance fiber reinforced concrete as understood at time of this writing.

Table 1: Chronological Advances in the matrix and fibers since the 1960's.

Decade	Cementitious Matrix and Concrete	Fiber
1970's	• Better understanding of hydration reactions; gel structure; • Better understanding shrinkage, creep, porosity, … • High strength concrete to 50 MPa in practice • Development of water reducers • Advances in concrete treatments and curing conditions	• Smooth steel fibers; normal strength • Glass fibers • Some synthetic fibers
1980's	• Increased development of chemical additives: HWRA, etc… • Increased utilization of fly ash and silica fume, and other mineral additives, etc… • Increased flowability (flowable concrete) • Reduction in W/C ratio; • High-Strength-Concrete terminology: up to 60 MPa; special high strength: up to 80 MPa; exotic high strength (special aggregate and curing): up to 120 MPa • High-Performance-Concrete terminology: high-strength-concrete with improved durability properties.	• Deformed steel fibers: normal and high strength • Low-modulus synthetic fibers (PP, nylon, etc..) • Increased use of glass fibers • Micro fibers • High performance polymer fibers (carbon, Spectra, Kevlar, etc..)
1990's	• Increased development in chemical additives: superplasticizers; viscosity agents; etc…. • Increased use of supplementary cementitious materials as cement replacement • UHPC: application of concept of high packing density; addition of fine particles; low porosity; lower water to cementitious ratio; • Self consolidating concrete; self compacting concrete;	• New steel fibers with a twist (untwist during pull-out) • PVA fibers with chemical bond to concrete • Improved availability of synthetic fibers
2000's	• Increased developments of proprietary and non-proprietary UHPC/UHP-FRC • UHPC: improved understanding of high packing density; application of nanotechnology concepts	• Ultra high strength steel fibers: smooth or deformed with diameters as low as 0.12 mm and strengths up to 3400 MPa • Carbon nano-tubes; carbon nano-fibers
2010's	• Increased understanding of the cementitious matrix at the nano-scale • …???...	• Carbon nano-fibers, graphene, … • …???...

Table 2: Developments in high strength high performance cement composites from the 1970's to date (in the US and Europe).

Year	f'_c [MPa]	Source/Ref.	Name	Special Conditions
1972	230	Yudenfreund, Skalny, et al.		Paste; vacuum mixing; low porosity; small specimens.
1972	510	Roy et al. (US)		Paste; high pressure and high heat; small specimens.
1981	200	Birchall et al. (UK)	MDF (Micro-Defect-Free)	Paste; addition of polymer; bending strength up to 150 MPa
1981-1983	120 to 250	Bache; Hjorth (Denmark)	DENSIT; COMPRESSIT	Mortar and concrete; normal curing; use of microsilica
1980' all	120 to 250	Bache; Young; Jennings; Aitcin (Denmark; US; Canada)	DSP (Densified Small Particles)	Improved particle packing; use of microsilica; use of superplasticizers;
1980's	Up to 120	Many researchers worldwide (Shah; Zia; Russell; Swamy; Malier; Konig; Aitcin; Malhotra)	High Strength Concrete; High Performance Concrete (HSC; HPC)	Concrete with special additives and aggregates for structural applications; use of superplasticizers; normal curing; better durability
1980's all	Up to 210	Lankard; Naaman (US)	SIFCON (Slurry Infiltrated Fiber Concrete)	Fine sand mortar with high volume fractions of steel fibers (8% to 15% by volume)
1987	Up to 140	Bache (Denmark)	CRC (Compact Reinforced Concrete)	Concrete with high volume of steel fibers used with reinforcing bars
1987	Open range	Naaman (US)	HPFRCC (High Performance Fiber Reinforced Cement Composites)	Mortar and concrete with fibers leading to strain-hardening response in tension
1991	Open range	Reinhardt and Naaman (Germany, US)	HPFRCC (First International Workshop)	Toward reducing the fiber content.
1992	Open range	Li and Wu (US)	ECC (Engineered Cementitious Composites)	Mostly mortar with synthetic fibers; strain-hardening behavior in tension
1994	In excess of 150	De Larrard (France)	Ultra-High Performance Concrete (UHPC)	Optimized material with dense particle packing and ultra fine particles
1995	Up to 800	Richard & Cheyrezy	RPC (Reactive Powder Concrete)	Paste and concrete; heat and pressure curing; particle packing
1998 and later	Up to 200	Lafarge; (Chanvilliard; Rigaud; Behloul) France	DUCTAL	90^{o}C heat curing for 3 days; steel fibers up to 6% (commercially available)
2000 and later	Up to 200	Rossi et al. LCPC (France)	CEMTEC; CEMTEC-multi-scale	Up to 9% fibers; hybrid combinations
Early 2000	Up to 200	Many researchers worldwide (Ulm, Graybeal, Rossi)	UHPC and UHP-FRC	Many formulations based on DUCTAL
2005	Up to 140	Karihaloo (UK)	CARDIFRC	Optimized particle packing and mixing procedure
2005	Up to 200	Jungwirth (Switzerland)	CERACEM	Formulation similar to DUCTAL, larger fibers, larger aggregates
2004	Open range >150	Fehling & Schmidt (Germany)	First International Symposium on UHPC	Many formulations similar to DUCTAL with and without heat curing; with and without fibers.
2005	Open	Schmidt et al. (Germany)	Sustainable Building with UHPC	German DFG funded broader initiative (2005-2012)
2008	Open range >150	Fehling & Schmidt (Germany)	Second International Symposium on UHPC	Many formulations similar to DUCTAL with and without heat curing; with and without fibers.
2011	>150	Accorsi & Meyer (US)	UHPC Workshop	First US Workshop
2011	Up to 290	Wille & Naaman (US-Germany)	UHP-FRC	No heat curing; optimized packing; record direct tensile strength
2011			ACI UHPC Committee 239	First meeting: Oct. 2011 Also: PCI working group
2012	Open range >150	Fehling & Schmidt (Germany)	Third International Symposium on UHPC	

German Research Program: Sustainable Building with UHPC

4 Summary of Key Mechanical Properties Achieved to Date

This section provides a summary of the composition, mixing procedure, and key mechanical properties achieved using particular UHP-FRC composites developed by the authors and their collaborators. Several references can be consulted for additional details [44 to 52].

4.1 Mixture Composition

Examples of mixture compositions for UHPC and UHP-FRC composites developed by the authors in prior investigations [45, 48] are provided in Table 3. The ratio for each material is given by weight of cement. The compressive and tensile strengths observed from tests are given in the last rows of the table. A typical composition of UHPC by volume is illustrated in Fig. 1 and is compared to a conventional normal concrete (NC) with the same air content. It can be observed that the paste phase in UHPC is more than 2.5 times that of NC while the inert particle phase is much smaller to essentially compensate for the difference. A description of the particle sizes of the various materials used and some of their recommended characteristics are shown in Fig. 2. The average particle size of each material is compared in Fig. 3 to the ideal theoretical particle sizes that would optimize packing density [44]; the theoretical particles sizes are shown as distribution functions around average diameters d_1, d_2, d_3, … where d_1 is assumed to be equal 0.5 mm, and the other diameters are derived for optimum packing.

Table 3: Examples of mixtures developed for UHPC and UHP-FRC.

Type	UHPC				UHP-FRC				
	A[d]	B[d]	C	D	A[d]	B[d]	C	D	SIFCON
Cement	1.00	1.00	1.00	1.00	1.00	1.00	1.00	1.00	1.00
Silica Fume	0.25	0.25	0.25	0.25	0.25	0.25	0.25	0.25	0.25
Glass Powder	0.25	0.25	0.25	0.25	0.25	0.25	0.25	0.25	0.25
Water	0.220	0.195	0.190	0.180	0.212	0.200	0.185-0.195	0.18-0.20	0.207
Superplasticizer[a]	0.0054	0.0108	0.0108	0.0114	0.0054	0.0108	0.0108	0.0108	0.0108
Sand A[b]	0.28	0.30	0.31	1.05	0.27	0.28	0.29	0.92	0.76
Sand B[c]	1.10	0.71	0.72	0.00	1.05	0.64	0.67	0.00	0.00
ratio Sand A/B	20/80	30/70	30/70	100/0	20/80	30/70	30/70	100/0	100/0
Fiber	0.00	0.00	0.00	0.00	0.15/0.25	0.22	0.18-0.27	0.22-0.31	0.71
Fiber Vol.%	0	0	0	0	1.5/2.5	2.5	2.0-3.0	2.5-3.5	5[e]/8[f]
$f'_c[cube,28d]$ MPa	194	207	220-240	232-246	207/213	219	227-261	251-291	270[e]/292[f]
$f_t[tension]$ MPa	6.1-7.4[g] ; 6.9-7.8[g]; 7.4-8.5[g]; 8.2-9.0[g]				8.2/14.2	15	16-20	20-30	37[e]

[a] solid content; [b] max. grain size 0.2 mm (1/128 in.); [c] max. grain size 0.8 mm (1/32 in.);
[d] non vibrated, non surface cut; [e] twisted (T) fiber; [f] straight (S) fiber; [g] at first cracking followed by immediate failure

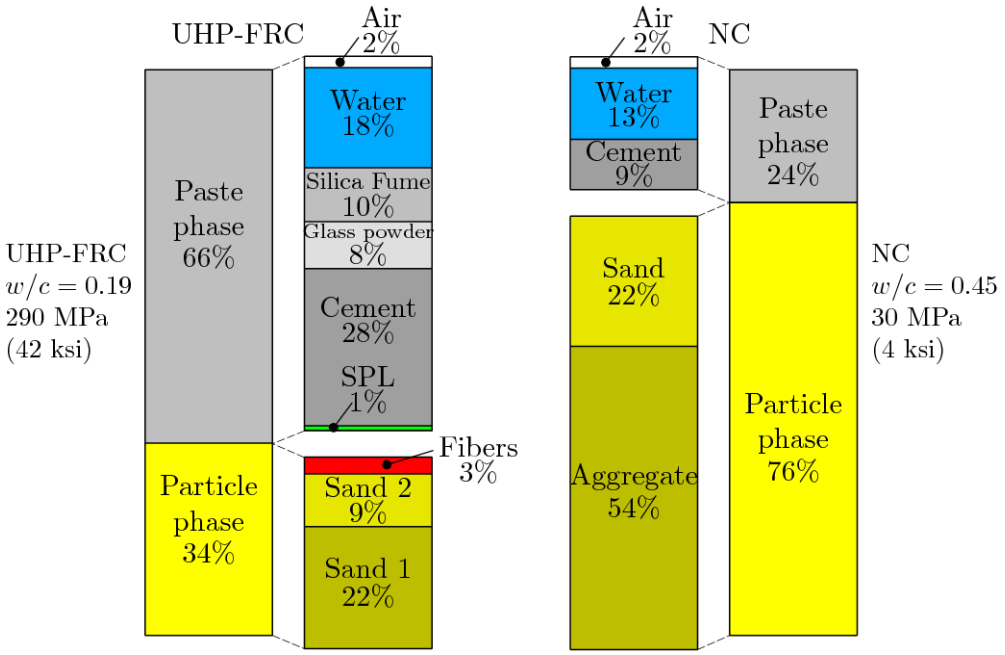

Figure 1: An example of mix proportions by volume comparing UHP-FRC with normal concrete (NC).

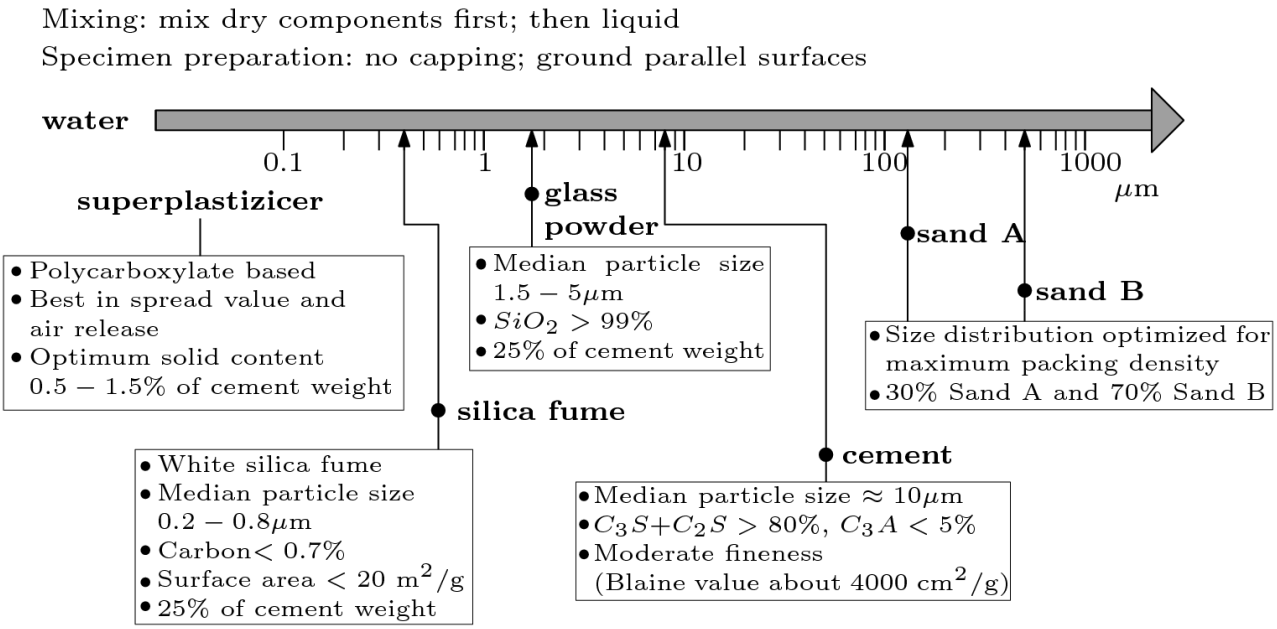

Figure 2: Materials used in the mixtures developed and their particular characteristics [Ref. 48].

4.2 Mixing Procedure

In UHPC, the number of ingredients is higher and the fineness of the particles is smaller compared to normal strength concretes. Therefore, it is important that all particles, especially the very fine ones, are uniformly distributed. Because very fine particles tend to agglomerate and form chunks, the minimal shear force for breaking these chunks can be reduced by keeping the particles dry; it is thus recommended to mix all dry particles first before adding the water and high–range water reducing (HRWR) additives.

In this investigation [45, 48], silica fume was first mixed with all the sand for about 5 minutes, similar to [40]. Afterwards, cement and glass powder were added and mixed dry for at least another 5 minutes before water was added. The whole amount of HRWR was added at once after the water. The UHPC became fluid after approximately 5 minutes of adding the water and HRWR. Fibers, if any, were then added during the following 5 min. A horizontal pan mixer

(capacity of around 60 Liter, 1.8 kW), with constant mixing speed (60 rpm), was sufficient for mixing the UHPC described in this research.

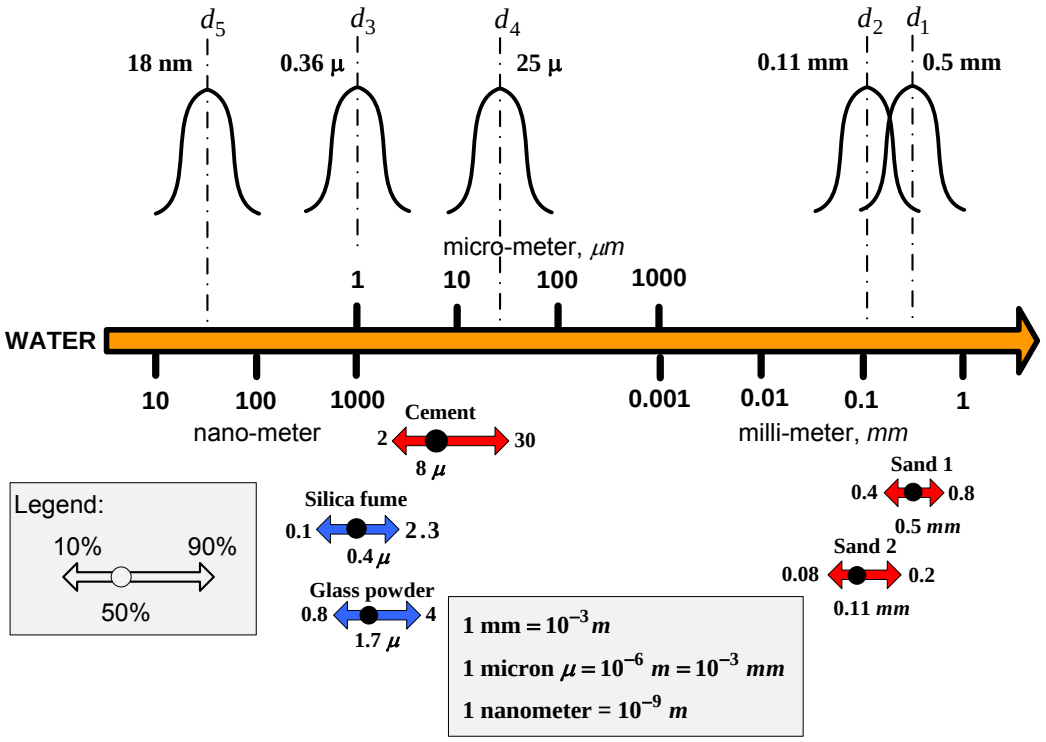

Figure 3: Comparison between particle sizes of materials used with theoretical sizes (di) obtained to optimize packing density [Ref. 44].

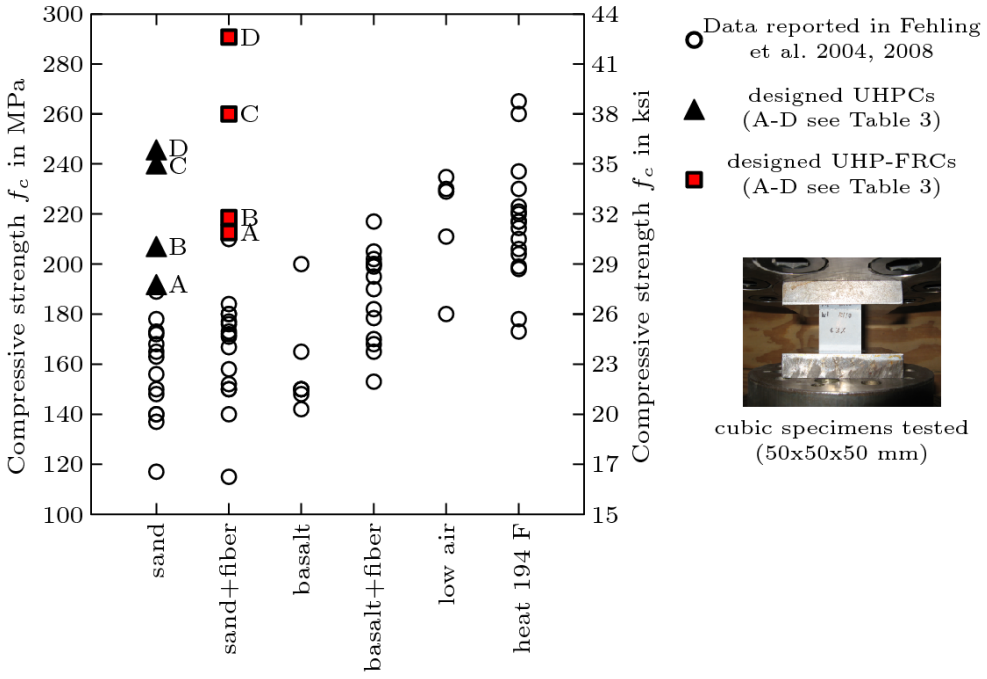

Figure 4: Comparison of compressive strength of UHPC and UHP-FRC mixtures developed versus existing data reported in the technical literature [Ref. 48].

4.3. Compressive Strength and Stress-Strain response

The average compressive strength at 28 days (using 50 mm cube specimens) of the various mixtures described in Table 4 is compared to equivalent cubic compressive strengths of various UHPC composites reported in the technical literature. It can be observed that they compare

very favorably to existing data, particularly given the fact that they were obtained with no heat treatment, no special mixer, and using materials commercially available on the US market. Details can be found in [45, 48].

4.4 Bond Stress-Slip at the Fiber-Matrix Interface

In order to optimize the response of UHP-FRC after first percolation cracking, that is, to essentially improve simultaneously its post-cracking tensile strength, the corresponding strain capacity, and its fracture energy, a thorough attempt was made to optimize the bond at the fiber to matrix interface, and to use deformed steel fibers of tensile strength as high as can be practically obtained from manufacturers of steel wires. The objective was to achieve the highest possible bond without failing the fiber. Extensive pull-out tests were then carried-out on single fibers with different characteristics [50, 51]. Examples of bond shear stress versus slip curves obtained using smooth brass-coated steel fibers embedded in various matrices are shown in Fig. 5. The shear stress was obtained from the pull-out load and the embedded length of fiber at the slip considered. It can be observed that even with smooth fibers, very high local shear stresses of up to 30 MPa can be obtained; unlike what is observed with conventional concrete, this behavior seems to be particular to UHPC and is likely due to the very dense transition zone around the fiber and the very fine particles it contains. Details of the study can be found in Ref. [50].

Figure 6 illustrates for a given fiber, the influence of the twist ratio on the pull-out load versus slip response. Thus the higher the twisted ratio, the higher the maximum pull-out load, up to a level where the fiber fails. Tensile stresses exceeding 3000 MPa are induced in the fiber. On the right side of Fig. 6, the photograph shows the damage on the surface of the fiber where the brass coating is abraded, likely due to the compactness of the zone around the fiber and the presence of glass powder.

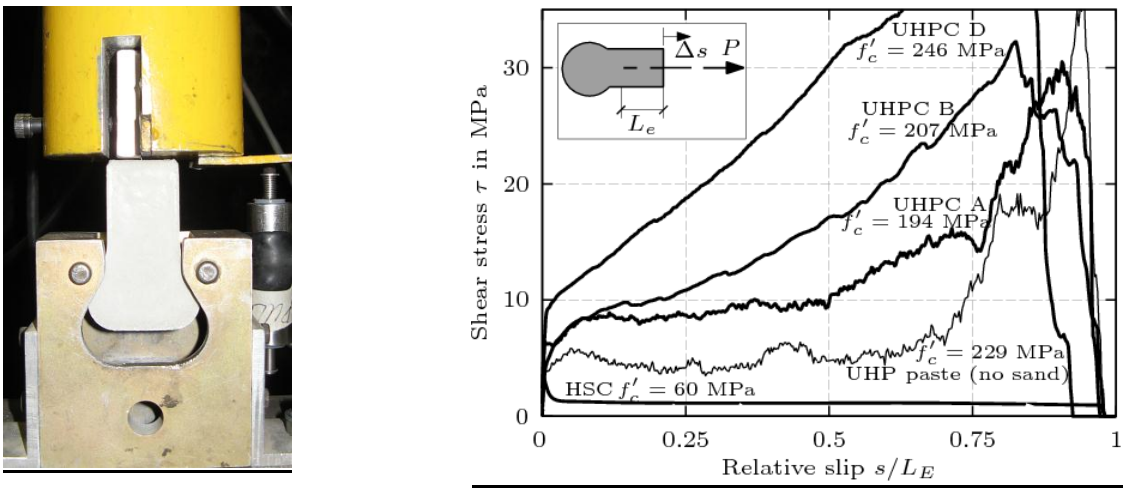

Figure 5: Typical bond stress versus relative slip relationships using different matrices [Ref. 50].

4.5 Tensile Response

Examples of stress-strain curves obtained from specimens tested in direct tension are shown in Figs.7 and 8. Figure 7 compares the tensile stress strain response of UHP-FRC composites using premixed twisted steel fibers with typical data reported in the literature from Ductal and Ceracem [16, 35, 36, 37, 41]. It can be observed that for about the same fiber content, the composite tensile strength is about doubled, and the strain at peak stress is about tripled. Note that, to the best of the authors knowledge, test series T12-1% (using high strength twisted steel fibers with an equivalent diameter of 0.12 mm) gives the highest tensile strength (15.9 MPa) per

unit volume of composite recorded to date in the technical literature and also the highest strain capacity, for any fiber reinforced cement composite using discontinuous fibers [49].

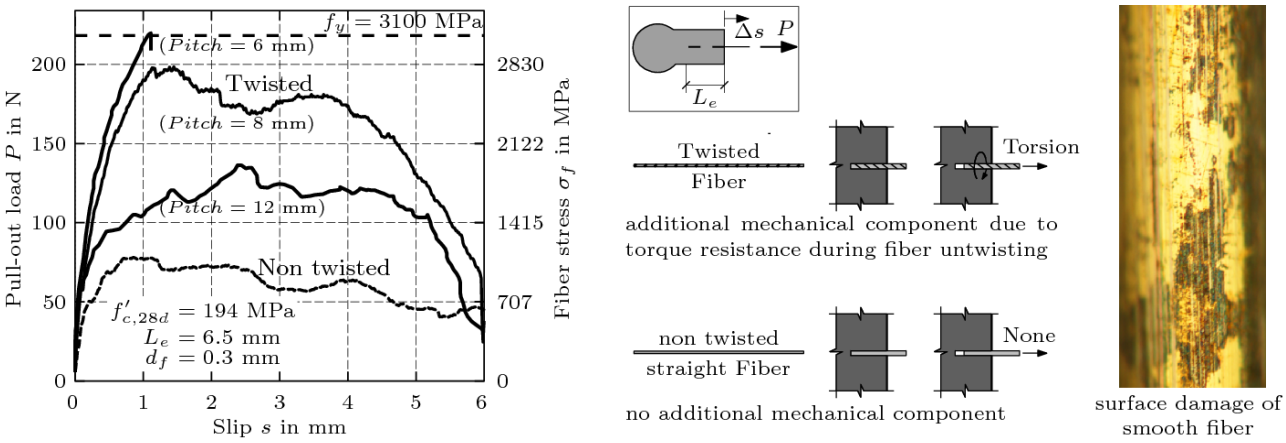

Figure 6: Typical effect of twist ratio of a steel fiber on its pull-out load versus slip response [Ref. 49].

Figure 8 also provides a comparison of the response of various UHP-FRC composites in tension. In particular, it shows the best results obtained in Ref. [49], for a composite using a Sifcon (slurry infiltrated fiber concrete) process, and an composite using a hybrid fiber mixture. Although the fiber content by volume is 5.5% and 6% respectively, to the best of the authors knowledge, the post-cracking tensile strength achieved (about 37 MPa) and its corresponding strain capacity are the highest so far reported in the technical literature for a fiber reinforced cementitious matrix subjected to direct tension. The tensile post-cracking strains at peak stress (Figs. 7 and 8) exceeding in some cases 1% are also the highest observed to date for steel fiber reinforced cement composites.

Similarly, to the best of the authors knowledge, the energy absorption capacity *g* obtained per 1% volume fraction of steel fibers for series T12 1% (Fig. 7) is the highest value (*g* = 128 kJ/m^3) achieved to date for a cement composite with discontinuous fibers. It exceeds at least 5 times the energy values reported by other researchers for UHP-FRC composites [49].

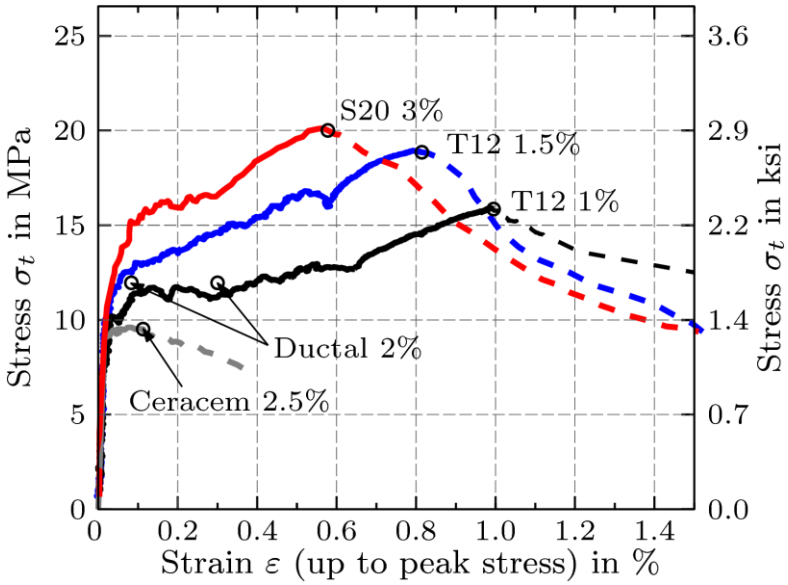

Figure 7: Comparison of tensile stress-strain response of UHP-FRCs developed with composites from other researchers [Ref. 49].

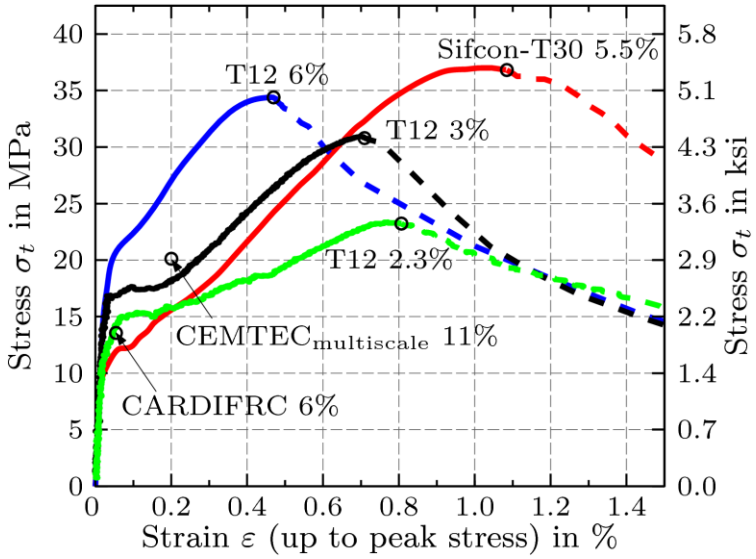

Figure 8: Tensile stress-strain response curves showing highest tensile strengths recorded to date [Ref. 49].

4.6 Fracture Energy

Figure 9 illustrates typical values of fracture energy obtained from direct tensile tests of different UHP-FRC-B (Table 3) varied by amount and type of fiber [47]. How the average fracture energy G_f (in kJ/in^2) of each test series was calculated is described in Ref. [47]. It comprises the dissipated energy per unit volume during strain hardening $g_{f,A}$, the dissipated energy per unit ligament area $G_{f,A}$ to open one crack up to δ_{pc} and the dissipated energy per unit ligament area $G_{f,B}$ to completely separate the critical (localized) crack during softening.

The values shown in Fig. 9 are among the highest reported in the technical literature and exceed the values of comparable UHP-FRC by a significant margin [47]. For instance, test series UHPFRC-T1-1.5 obtained with no heat curing shows G_f = 31 kJ/m^2, that is, G_f = 20.67 kJ/m^2 per 1% volume of fibers. In comparison, a fracture energy of 40 kJ/m^2 is reported by Richard and Cheyrezy (1995) for Reactive Powder Concrete using 2.5 % steel fibers with 90°C thermal treatment; that is equivalent to 16 kJ/m^2 per 1% volume of fiber.

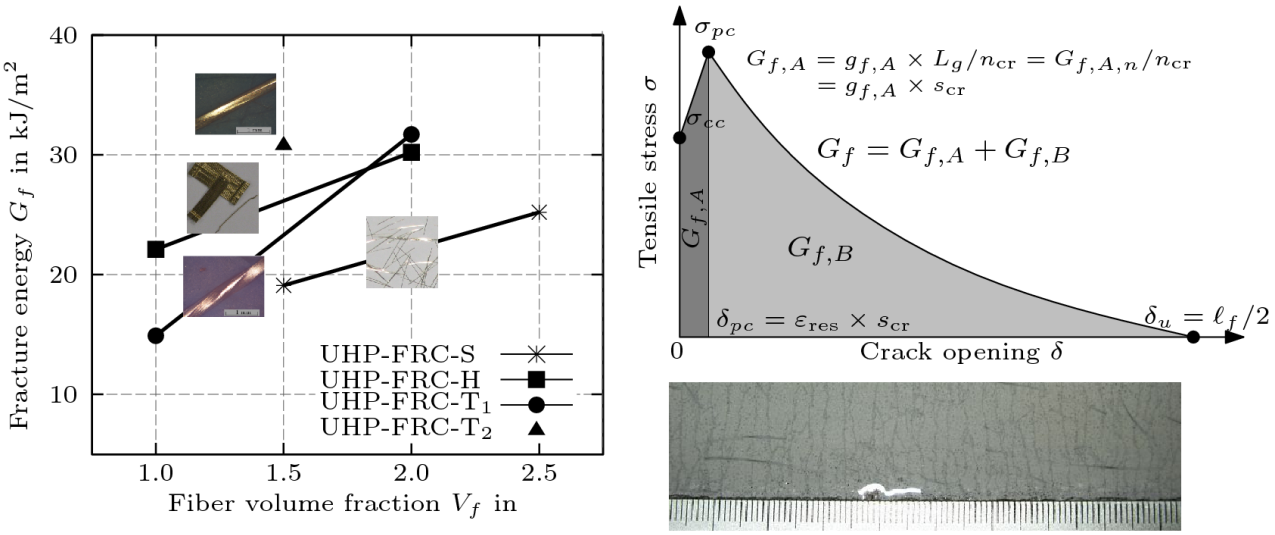

Figure 9: Examples of fracture energy values obtained for some of the UHP-FRC developed [Ref. 47].

5 Concluding Remark

This paper summarized in a first part some historical developments since the 1960's that led to ultra-high performance (UHPC) and ultra-high performance fiber reinforced concrete (UHP-FRC) as we understand them at time of this writing. The second half of the paper was devoted to describing key information on several UHPC and UHP-FRC mixtures that led to composites with record breaking tensile properties. Indeed by combining an ultra-high strength cementitous matrix and very high strength fine diameter steel fibers with tailored bond properties, tensile strength up to 37 Mpa, strain at maximum stress up to 1.1%, and energy absorption capacity prior to softening up to 304 kJ/m^3 were realized for the composite. These values exceed by a significant margin the current tensile properties of UHP-FRC reported in the technical literature. Multiple cracking with crack spacing as small as 1 mm and crack widths as small as 4 microns prior to localization of tension failure were observed.

Today the technical challenge for the use of ultra high performance fiber reinforced concrete in structural applications is not through increased compressive strength (which can easily be made to exceed 200 MPa) but rather through an increased combination of tensile strength, tensile ductility and energy absorption capacity. Moreover, on the practical side, the challenge is to achieve the desired properties for design, in both the fresh and hardened state, at least cost. Technically the record-breaking results mentioned above on tensile strength shall be exceeded in the future, but the real success of the composite in practice will greatly depend on its cost-benefit ratio in a given application.

References

The following list of references is very limited due to space limitation and does not do justice to the thousands of studies available at time of this writing.

[1] Russel, H.G., "ACI Defines High Performance Concrete," *Concrete International*, Feb. 1999, pp. 56-57.

[2] Naaman, A.E., and Reinhardt, H.W., "Proposed Classification of FRC Composites Based on their Tensile Response " *Materials and Structures*, Vol. 39, page 547-555, 2006.

[3] Naaman, A.E., "High performance fiber reinforced cement composites," Proceedings of the *IABSE Symposium on Concrete Structures for the Future,* Paris, France, September 1987, pp. 371-376.

[4] Reinhardt, H.W., and Naaman, A.E., Editors, *"High Performance Fiber Reinforced Cement Composites,"* RILEM, Vol. 15, E. & FN Spon, London, 1992, 565 pages.

[5] Naaman, A.E., and Reinhardt, H.W., Editors, "*High Performance Fiber Reinforced Cement Composites: HPFRCC 2,"* RILEM, No. 31, E. & FN Spon, London, 1996, 505 pages.

[6] Naaman, A.E., and Reinhardt, H.W., "Characterization of High Performance Fiber Reinforced Cement Composites," in "*High Performance Fiber Reinforced Cement Composites - HPFRCC 2*,' A.E. Naaman and F.W. Reinhardt, Editors, RILEM Pb. 31, E. and FN Spon, England, 1996; pp. 1-24.

[7] Reinhardt, H.W., and Naaman, A.E.,, Editors, *"High Performance Fiber Reinforced Cement Composites - HPFRCC 3,"* RILEM Proceedings, PRO 6, RILEM Pbs., S.A.R.L., Cachan, France, May 1999; 666 pages.

[8] Naaman, A.E., and Reinhardt, H.W., Editors, *"High Performance Fiber Reinforced Cement Composites - HPFRCC 4,"* RILEM Proc., PRO 30, RILEM Pbs., S.A.R.L., Cachan, France, June 2003; 546 pages.

[9] Reinhardt, H.W., and Naaman, A.E.,, Editors, *"High Performance Fiber Reinforced Cement Composites - HPFRCC 5,"* RILEM Proceedings, PRO 53, RILEM Pbs., S.A.R.L., Cachan, France, June 2007; 518 pages.

[10] Parra-Montessinos, G., Reinhardt, H.W., and Naaman, A.E., "*High Performance Fiber Reinforced Cement Composites, HPFRCC6*," Rilem Bookseries, Springer, 2011, 559 pages.

[11] Naaman, A.E., and Reinhardt, H.W., "Setting the Stage: toward Performance Based Classification of FRC Composites," in *High Performance Fiber Reinforced Cement Composites (HPFRCC-4*), A.E. Naaman and H.W. Reinhardt, Editors, RILEM Publications, Pro. 30, June 2003, pp. 1-4.

[12] Naaman, A.E., and Reinhardt, H.W., “High Performance Fiber Reinforced Cement Composites (HPFRCC-4): International RILEM Report,” *Materials and Structures*, Vol. 36, Dec. 2003, pp. 710-712. Also same in Cement and Concrete Composites, Vol. 26, 2004, pp. 757-759.
[13] de Larrard, F.; Sedran, T., 1994, “Optimization of ultra-high-performance concrete by the use of a packing model,” *Cement and Concrete Research*, Vol. 24, pp. 997 – 1009.
[14] Richard, P.; Cheyrezy, M., 1995, “Composition of reactive powder concretes,” *Cement and Concrete Research*, Vol. 25, No. 7, pp. 1501-1511.
[15] Richard, P., “Reactive powder concrete: a new ultra-high strength cementitious material,” Proceedings of the 4th International Symposium on *Ultilisation of High-Strength/High-Performance Concrete*, F. de Larrard and R. Lacroix, Editors, Presses des Ponts et Chaussees, Paris, France, 1996, pp. 1501-1511.
[16] Schmidt, M.; Fehling, E.; Geisenhanslüke, C. (Editors): "*Ultra High Performance Concrete (UHPC*)", Proceedings of the International Symposium on UHPC, Kassel University Press GmbH, Germany, September 2004, 868 pages.
[17] Fehling, E, Schmidt, M., and Sturwald, S., Editors, “*Ultra High Performance Concrete (UHPC)*”, Proceedings of Second International Symposium on Ultra High Performance Concrete, Kassel University Press, GmbH, Germany, May 2008, 902 pages.
[18] Rossi, P, 2000, “Ultra-high Performance Fibre Reinforced Concrete (UHPFRC): An Overview,” in Proceedings of Fifth RILEM Symposium in *Fibre-Reinforced Concretes (FRC) - BEFIB’ 2000*, pp. 87 – 100.
[19] Rossi, P., “Ultra High Performance Concretes – A Summary of the Current Knowledge,” *Concrete International*, February 2008, pp. 31-34.
[20] Naaman, A.E., "New Fiber Technology: Cement, Ceramic and Polymeric Composites," *Concrete International*, Vol. 20, No. 11, July 1998.
[21] Naaman, A.E., "Fibers with Slip-Hardening Bond," in *High Performance Fiber Reinforced Cement Composites - HPFRCC 3*,' H.W. Reinhardt and A.E. Naaman, Editors, RILEM Pro 6, RILEM Publisations S.A.R.L., Cachan, France, May 1999, pp. 371-385.
[22] Naaman, A.E., “Half a Century of Progress Leading to Ultra High Performance Fiber Reinforced Concrete,” Rilem Proceedings PRO 81, Strain Hardening Cementitious Composites (SHCC2-Rio), 2nd International Rilem Conference, Edited by R.D. Toledo Filho, F.A. Silva, E.A.B. Koenders, and E.M.R. Fairbrairn, December 2011, Parts I: Overall Review, Part II: Tensile Stress Strain Response, pp. 17-36.
[23] Yudenfreund, M.; Skalny, J.; Mikhail, R. S.; Brunauer, S., 1972, “Hardened Portland Cement Pastes of Low Porosity, II. Exploratory Studies. Dimensional Changes,” *Cement and Concrete Research*, Vol. 2, No. 3, May, pp 331-348.
[24] Roy, D. M.; Gouda, G. R.; Bobrowsky, A., 1972, “Very high strength cement pastes prepared by hot pressing and other high pressure techniques,” *Cement and Concrete Research*, Vol. 2, pp. 349 – 366.
[25] Birchall J.D.; Howard A.J., Kendall K., 1981, “Flexural strength and porosity of cements,” *Nature* 289, pp. 388 – 390.
[26] Bache, H. H., 1981, “Densified cement/ultrafine particle-based materials,” *2nd Int. Conference on Superplasticizers in Concrete*, Ottawa, Canada, 10-12 June.
[27] Hjorth, L., 1983, “Development and application of high-density cement-based materials,” *Phil. Trans. R. Lond.*, A 310, pp. 167 – 173.
[28] Bache, H.H., “Compact Reinforced Concrete: Basic Principles,” Aalborg Portland Cement-og Betonlaboratoriet, CBL Report No. 41, 1987.
[29] Lankard, D., “Slurry Infiltrated Fiber Concrete (SIFCON): Properties and Applications,” *Very High Strength Cement-Based Materials,* J. F. Young, Editor, Materials Research Society, Symposia Proceedings Volume 42, Pittsburgh, Pennsylvania, 1985, pp. 277-286.
[30] Homrich, J., and Naaman, A.E., "Stress-Strain Properties of SIFCON in Uniaxial Compression and Tension," Report No. UMCE 87-7, Department of Civil Engineering, University of Michigan, Ann Arbor, October 1987, 138 pp. Also published as AFWL-TR-87-115, August 1988.
[31] Naaman, A.E., and Homrich, J.R., "Tensile Stress-Strain Properties of SIFCON," *ACI Materials Journal*, Vol. 86, No. 3, May-June 1989, pp. 244-251.
[32] Naaman, A.E., "SIFCON: Tailored properties for structural performance," in *High Performance Fiber Reinforced Cement Composites,* RILEM Proceedings 15, E. and FN SPON, London, 1992, pp.18-38.

[33] Li, V.C., & H.C. Wu, "Conditions for pseudo strain-hardening in fiber reinforced brittle matrix composites," *J. Applied Mechanics Review*, V.45, No. 8, August, pp. 390-398, 1992.
[34] Behloul, M., "Tensile Behavior of Reactive Powder Concrete," 4th International Symposium on the *Utilization of High Strength High Performance Concrete*, Paris, France, 1996, pp. 1375-1381.
[35] Orange, G., Dugat, J., and Acker, P. "DUCTAL: New Ultra High Performance Concretes. Damage, Resistance and Micromechanical Analysis," BEFIB 2000, Fifth RILEM Symposium on *Fiber-Reinforced Concretes (FRC),* Ed. By P. Rossi and G. Chanvillard, Lyon, 2000, pp. 781-790.
[36] Chanvillard, G., and Rigaud, S., "Complete Characterization of Tensile Properties of Ductal UHPFRC According to the French Recommendations," in *High Performance Fiber Reinforced Cement Composites (HPFRCC-4),* A.E. Naaman and H.W. Reinhardt, Editors, RILEM Publications, Pro. 30, June 2003, pp. 95-113.
[37] Ulm, F.-J.; Acker, P., 2008, "Nanoengineering UHPC Materials and Structures," in Fehling, E, Schmidt, M., and Sturwald, S., Editors, "*Ultra High Performance Concrete (UHPC)*", Proceedings of Second International Symposium on Ultra High Performance Concrete, Kassel University Press, GmbH, Germany, May 2008, pp. 3-9.
[38] Graybeal, B.A. and Davis, M., "Cylinder or cube: strength testing of 80 to 200 MPa (11.6 to 29 ksi) ultra-high-performance fiber-reinforced concrete." *ACI Materials Journal*, Vol. 105, No. 6, 2008, pp. 603–609.
[39] Benson, D.S.P., and Karihaloo, B.L., "CARDIFRC – Development and Mechanical Properties," Part I, *Magazine of Concrete Research*, Vol. 57, 2005, pp. 347-352. See also Part III, Vol. 57, 2005, pp. 433-443.
[40] Jungwirth, J., 2006, "Zum Tragverhalten von zugbeanspruchten Bauteilen aus Ultra-Hochleistungs-Faserbeton," EPF Lausanne, Ph.D. thesis, 2006.
[41] Accorsi, M., and Meyer, C., „Ultra High Performance Concrete Workshop," Columbia University, New York, Jan. 2011; unpublished report.
[42] Kim, D.J., Naaman, A.E., and El-Tawil, S., "High Tensile Strength Strain-Hardening FRC Composites with Less Than 2% Fiber Content," in Proceedings of 2nd International Symposium, *Ultra High Performance Concrete (UHPC)*, Edited by E. Fehling, M. Schmidt and S. Sturwald, Universitat-Kassel, Germany, March 2008, pp. 169-176.
[43] Naaman, A.E., and Wille, K., "Some Correlation Between High Packing Density, Ultra-High Performance, Flow Ability, and Fiber Reinforcement of a Concrete Matrix; BAC2010 – 2nd Iberian Congress on Self Compacting Concrete, University of Minho – Guimaraes, Portugal. July 1-2, 2010 , Proceedings Edited by J. Barros, J. Sena-Cruz, R.M. Ferreira, and A. Camoes, pp. 3-18.
[44] Wille, K., Naaman, A.E., and Parra-Montesinos, G. "Ultra High Performance Concrete with Compressive Strength Exceeding 150 MPa: A Simpler Way," *ACI Materials Journal*, Vol. 108, No. No. 1, Jan.– Feb., 2011, pp. 46 – 54.
[45] Wille, K., Kim, D. and Naaman, A. E., "Strain-Hardening UHP-FRC with Low Fiber Contents", *Materials and Structures*, published online Aug. 4th 2010, in Journal Vol. 44, No. 3, 2011, pp. 583.
[46] Wille, K. and Naaman, A. E., "Fracture Energy of UHPFRC under Direct Tensile Loading", *FraMCoS-7* International Conference, Jeju, KOREA, May 23-28, 2010. Electronic Proceedings.
[47] Wille, K., Naaman, A.E., and El-Tawil, S., and Parra-Montesinos, G., "Ultra-high performance concrete and fiber reinforced concrete: achieving strength and ductility with no heat curing," *Materials and Structures*, accepted for publication. 2011.
[48] Wille, K., Naaman, A.E., and El-Tawil, S. "Optimizing Ultra-High Performance Fiber Reinforced Concrete: Mixtures with Twisted Fibers Exhibit Record Performance under Tensile Loading," *Concrete International*, Vol. 33, No. 9, Sept. 2011, pp. 35-41.
[49] Wille, K., and Naaman, A.E., "Bond-Slip Behavior of Steel Fibers Embedded in Ultra High Performance Concrete," Proceedings of 18 European Conference on Fracture and Damage of Advanced Fiber-Reinforced Cement-Based Materials, Contribution to ECF 18, Dresden, V. Mechtcherine & M. Kaliske (eds.), Aedificatio Publishers, Freiburg, September 2010, pp.99-111.
[50] Wille, K. and Naaman, A.E., "Pull-Out Behavior of High Strength Steel Fibers Embedded in UHPC," *ACI Materials Journal*, accepted for publication, in press.
[51] Wille, K., and Parra-Montesinos, G., "Effect of Beam Size, Casting Method and Support Conditions on the Flexural Behavior of Ultra High Performance Concrete," *ACI Materials Journal*, in press, 2012.
[52] Zia, P., Leming, M.L., and Ahmad, S.H., "High Performance Concretes, A State-of-the-Art Report," Strategic Highway Research Program, National Research Council, Report No. SHRP-C/FR-91-103, Washington, D.C., 1991.

Sustainable Building with Ultra-High-Performance Concrete (UHPC) – Coordinated Research Program in Germany

Michael Schmidt
Institute of Structural Engineering, University of Kassel, Germany

In Germany, a 12 Mio. € Research Program on UHPC has just been finished. It started in 2005, covering a wide range of topics related to UHPC. The program was funded by the German Research Foundation (DFG) and coordinated by the University of Kassel. More than 20 research institutes were involved. Its purpose was to elaborate the basic knowledge necessary to draft reliable Technical Standards covering materials, material adequate design principles and innovative construction and fitting technologies to make UHPC a reliable, commonly available, economically favorable, regularly applied material. This paper describes the intention and the background of the program, and it gives an overview over the topics being dealt with and the results recently available. It is part of a series of articles during this conference presenting some topics of the program in more detail.

Keywords: Ultra-High Performance Concrete, materials, design, construction, state-of-the-art

1 Introduction

In Germany, a comprehensive 12 Mio. € Research Program on UHPC is practically completed covering a wide range of topics related to UHPC. The program was funded by the German Research Foundation (DFG) and coordinated by the University of Kassel. More than 20 research institutes were involved, striving to elaborate the basic knowledge necessary to draft reliable technical standards covering both materials and design principles to make UHPC a reliable, commonly available, economically favorable, and regularly applied material. The fields of interest that the individual research projects concerned themselves with include the suitability and performance of raw materials including cements, inert or reactive mineral fillers, artificial nanoparticles, and improved plasticizers. Basic research on appropriate mix designs for different applications, the rheological specifics of the fresh concrete and its hydration were evaluated as well as the time dependent strength and deformation behavior of hardened UHPC with and without fibers. Also involved were scientists and engineers working on adequate design and construction procedures including new appropriate technologies to build high performance light and slender and thus sustainable structures.
The Program was subdivided in 8 main topics, each being coordinated by a working group combining several intertwined projects:

- Raw Materials and Rheology
- Hydration and Microstructure
- Time-Dependent Behavior (shrinkage, creep)
- Fiber Efficiency and Interaction with Conventional Reinforcement
- Failure and Fatigue Behavior
- Durability
- Design and Construction
- Testing

The paper will present the overall aims and visions of this project as well as the background aspects that led to its installation, and the main results elaborated from 2005 to 2011. In 2009, the last of three two-year-periods of research was started, primarily consisting of projects researching design and construction.

This contribution is a “keynote” introduction to a series of articles at this conference presenting some results of the last research period in more detail [10-16].

2 Objectives and technical background

The most notable characteristic of Ultra-High Performance Concrete (UHPC) is its extremely dense microstructure resulting in a steel-like compressive strength of about 180 to 250 MPa combined with a significantly improved durability. The structural density results primarily from a high packing density of fine and ultra-fine particles ≤ 125 µm in the cement matrix, and a comparatively low w/c-ratio of about just 0.20.

The technological basis was already laid by Bache [1] in Denmark in the 1980s. Among others, Okamura *et. al* contributed to the theoretical background of particle optimization [2,3,4].

The large scale practical application did not begin until the 1990s when new superplasticizers based on polycarboxylate ethers (PCE) with a significantly improved performance were developed. For about 10 years, dry mixed UHPC products have been commercially available and have already been successfully applied for bridges and other visually and technically appealing, spectacular structures in several countries.a, e.g. for the very first bridge made of UHPC in Sherbrook in Canada.

The first German large scale application was the “Gaertnerplatzbridge” in Kassel [5,6] built in 2007 (Figure 1). This very slender structure consists of a 3D steel truss in combination with longitudinal girders and deck slabs, both made of prefabricated, prestressed, fiber-reinforced UHPC elements. Due to the high adhesive tensile strength of the material, the slabs were glued to the girders with an epoxy resin without any additional mechanical fitting device [7]. The bridge has been intensively monitored since its construction. This data is used to validate the assumptions that had to be made concerning the mechanical behavior of the material, the design and the load-bearing behavior of the whole structure in practice. Up to now, the collected data comply with the expectations.

Figure 1: Gaertnerplatzbridge in Kassel, under construction (left) and in use (right) – a hybride bridge of 132 m span, longitudinal girders and deck plates fitted by gluing with an epoxy resin mortar. Slab thickness 85 mm only.

Apart from a small number of pilot projects, the application of UHPC has been restricted due to the fact that neither the material itself nor the material-specific design of the structures are covered by technical standards that already exist for ordinary or even high performance concrete, e.g. the European Standard EN 206 or the design codes for concrete structures. Thus, each application requires a single case approval from the Building Authorities.

In Germany, since about 1998, another strategy is pursued, which is to make UHPC a commonly available and standardized material based on individual regionally available raw materials. Each experienced and well-equipped producer of concrete or precast concrete elements shall be enabled to produce and apply UHPC on a sound basis of scientifically proven technical knowledge and on approved technical regulations covering both the material as well as the design and construction of structures made of UHPC.

Therefore, the primary objective of the priority program was to gather all information necessary to assure the long-time load-bearing capability and thus the structural safety structures consisting of UHPC elements. To promote the utilization of the material, other aspects have to be considered and approved as well, like the improved durability and the prolonged service-life, and also the challenge to make concrete structures more sustainable by designing them much more slender to reduce the raw materials needed. UHPC even inspires new fitting technologies like gluing of structural load-bearing members or – to spark an idea – to allow for new and modern industrialized construction technologies.

Trying to achieve the afore mentioned goals, the German Research Foundation initiated an extensive research program in 2005, coordinated by the University of Kassel, and funded with about 12 Mio. €. All together about 20 different research groups of universities and industrial research institutes worked on about 40 different projects. The projects covered fundamental research, e.g. on the interaction of fine particles due to surface forces, or the morphology of the cement phases in a dense microstructures, as well as more application-oriented problems, e.g. developing the appropriate mixing technology, or fitting slender UHPC elements by gluing or by small steel implants. The topics to be worked on had been identified in advance based upon a comprehensive survey [8] on recent research on and applications of UHPC, covering more than 200 papers, reports and other information available. A comprehensive list of all research projects, finished and still in progress, is given in abbreviated form in Table 1. It would break the mold by far to report on all the theoretical and experimental research and the information that has already been gathered. A more extensive survey on the research project being performed in the first two periods is given in the *Proceedings of the 2nd International Symposium on UHPC* [9], held in Kassel in 2008, being available on the internet.

3 Examples and points of interest

As can be seen from Table 1, the projects dealt with the main problems connected with the new material and its adequate application. The following examples shall shed some light on the wide field that was worked on, from micro- and nanostructures and the UHPC properties that differ from ordinary concrete to characteristics of whole building elements made of UHPC.

Raw materials, rheology and microstructure

Depending on the maximum grain size of the aggregates, UHPC contains between 550 and 1000 kg cement per m^3, up to about 250 kg/m^3 of microsilica and a significant amount of other mineral fillers to improve the packing density, and to increase the amount of cement phases densifying the microstructure. Thus, the autogenous shrinkage is much more pronounced than with ordinary concrete, and the high amount of fine and microfine particles dominates the rheological behavior due to interparticle forces and the significantly higher particle surface. The prevention of particle agglomerations by the addition of PCE superplasticizer and a material adequate high energy mixing technology are of great importance. As can be seen from Figure 2, one of the projects dealt with direct measurement of interparticle forces by using Atomic-Force-Microscopie (AFM) technology to evaluate the efficiency of superplasticizers. Figure 2 as an example shows the adhesion forces acting between microscaled SiO_2^- particles in water without and with PCE with differently designed structures of the polymers. In another project, it

was discovered that the real shape and the texture of the fine particles may significantly increase the “effective” surface of the particle mix. Considering this fact allows for a much better theoretical optimization of the packing density and gives a much better correlation between the packing density, the water demand, the flowability, and the viscosity of the fresh concrete compared to conventional models and algorithms merely based on spherical particles.

Table 1: Working groups inside the priority program and their individual research topic.

Working group	**# of projects 2005-2011**	**Topics of the individual projects**
Raw materials, rheology, processing, sustainability	4	- Influence of shape and texture of fine grains and of interparticle forces on packing density and rheology - Life cycle inventory on UHPC - UHPC with low-energy binders - Optimization of the mixing process
Hydration and microstructure	2	- Characterization of the microstructure - Micro- and nanostructure of UHPC with nanotubes and pyrogene SiO_2
Time-dependent behavior (shrinkage, creep, cracking)	6	- Early age behavior of UHPC - Reduction of crack formation by internal curing - Shrinkage-reducing chemical admixtures - Time-dependent stress-strain behavior - Early age cracking and durability - Autogenous shrinkage and microstructure
Fiber efficiency and interaction with conventional reinforcement	3	- Load-bearing capacity of elements reinforced with fibers and bars under tension and bending - Ductility of UHPC with fibers and nanoparticles - Self-compacting UHPC with fiber meshes
Strength and deformation	2	- Fatigue under uni- or multiaxial loads - Modelling of multiaxial strength
Durability	4	- Resistance to freezing and deicing agents - Resistance to chemical attacks (acid, sulphate) - Fire safety of UHPC under load - Corrosion of steel fibers and influence on the microstructure
Design, construction, and application	11	- Prestressed beams - Performance of steel fitting elements for hybrid structures (UHPC/steel) - Loadbearing of extensively loaded columns - Fitting of elements by gluing - Thin fiber-reinforced UHPC layers on conventional concrete structures - UHPC under transverse (biaxial) forces - Anchorage and overlapping joints of reinforcing bars - UHPC/steel pipes for truss structures - Thin-walled pipes - Structural connection of precast elements - Miniaturized fitting devices for slender slabs
Testing	2	- Adjusted test procedures for rheology and strength - Fiber distribution and orientation

Microstructure

Electron microscopy investigations by Möser [10] using a *NanoSEM* microscope confirmed that the hydrate phases in UHPC are significantly shorter owing to the high packing density, the low w/c ratio of about 0.20 only and the high superplasticizer content of UHPC. Figure 3 gives an image showing some unhydrated microsilica particles surrounded by dense CSH-phases.

Due to the dense matrix, the modulus of elasticity is significantly higher compared to ordinary concrete. As a rule, the UHPC matrix shows brittle rupture. To prevent uncontrolled cracking, steel fibers are of great importance for nearly all applications of UHPC. Usually, high strength steel fibers are used to provide the brittle material with sufficient ductility, and they improve its tension and bending tension strength up to about 15 to 40 MPa respectively. Thus UHPC members are able to carry tension forces even without additional reinforcing bars. For the realization of wide-span structures, fibers can be combined with non-prestressed or prestressed reinforcement in the tensile zone. As a result of the interaction of both types of reinforcement, the stiffness of tensile members with mixed reinforcement is significantly improved as exemplified in Figure 4.

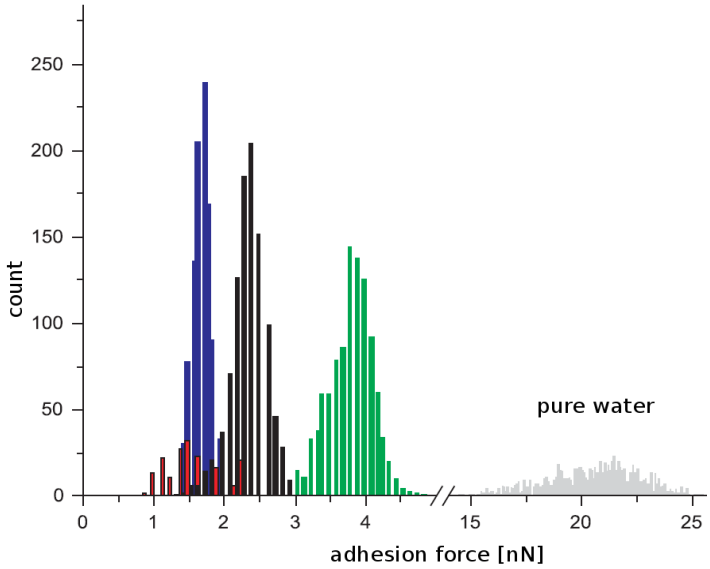

Figure 2: Interparticle forces between silica surfaces without (grey) and with four superplasticizers measured with AFM with different designed polymer-structures in nN [11].

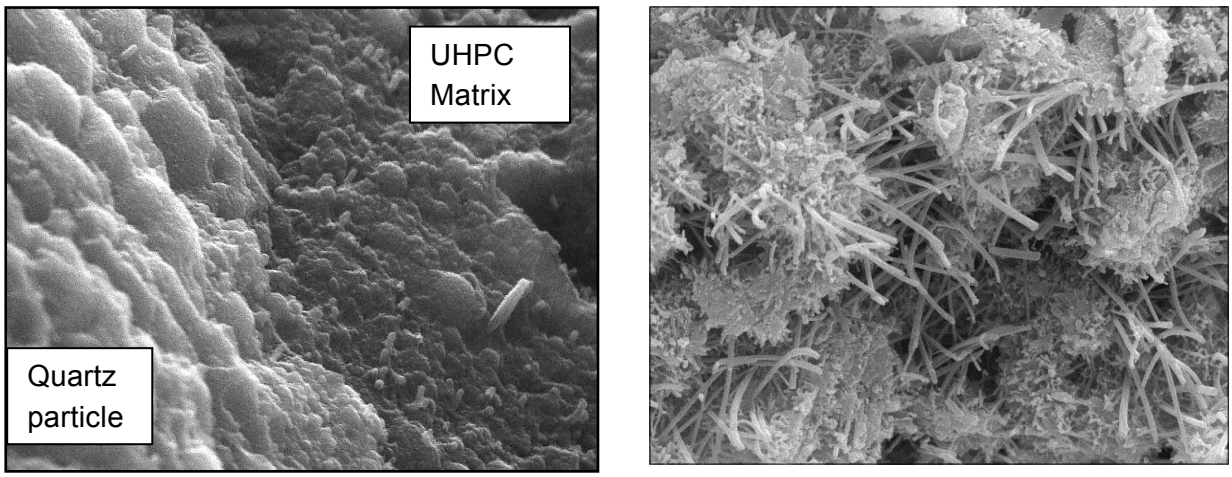

Figure 3: Matrix of UHPC, (left) compared to ordinary concrete (right). SEM pictures of same scale.

Leutbecher [12] developed a mechanical model, which combines the mechanical relationships of the crack formation of reinforced concrete and the stress-crack opening-behavior of the fiber-reinforced concrete considering the equilibrium of internal and external forces and the compatibility of deformations. Experimental results confirmed that crack distribution and thus the crack width can obviously be controlled much more effectively by a combination of fibers and rebars than exclusively by high fiber content.

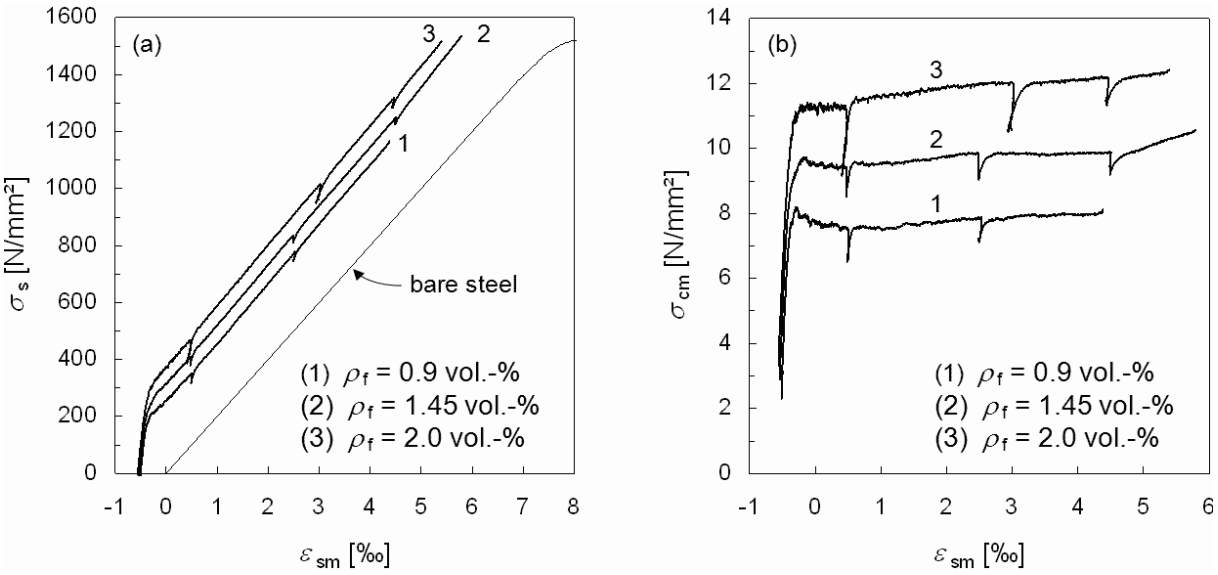

Figure 4: Load-deformation-behavior of tensile members (fibers high strength steel, diameter 0.15 mm, length 17 mm); (a) stress-strain-relationship, (b) contribution of fiber concrete [12].

Multiaxial strength

At the TU Dresden, behavior under multiaxial stress was examined [13]. The tests were performed in a triaxial test machine, as shown in Figure 5, which compressive or tensile forces can be introduced with in all three spatial directions independently. The results indicated that the multiaxial strength – related to the uniaxial strength – is considerably smaller than at normal concrete. There was, for example, no strength increase whatsoever in some stress ratios under biaxial compression, compared to the uniaxial strength (Figure 6). Despite a steel fiber content of up to 2.5 volume percent, UHPC exhibits very brittle behavior under uniaxial and biaxial compression. An all-side confinement due to increasing pressure components in both lateral directions works against the progressive crack growth and so it leads to increasing strength, to increasingly ductile behavior and to an early indication of failure (Figure 7). Related to the uniaxial strength the strength increase of UHPC under triaxial compression is smaller than for normal concrete.

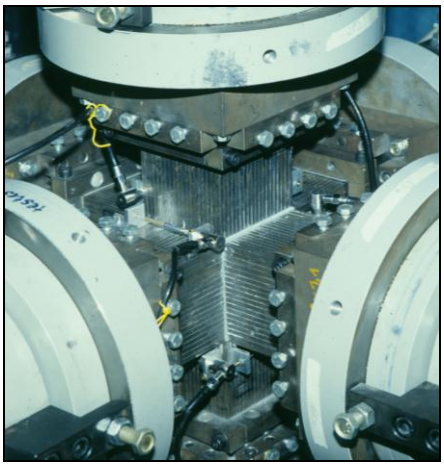

Figure 5: Triaxial experimental setup.

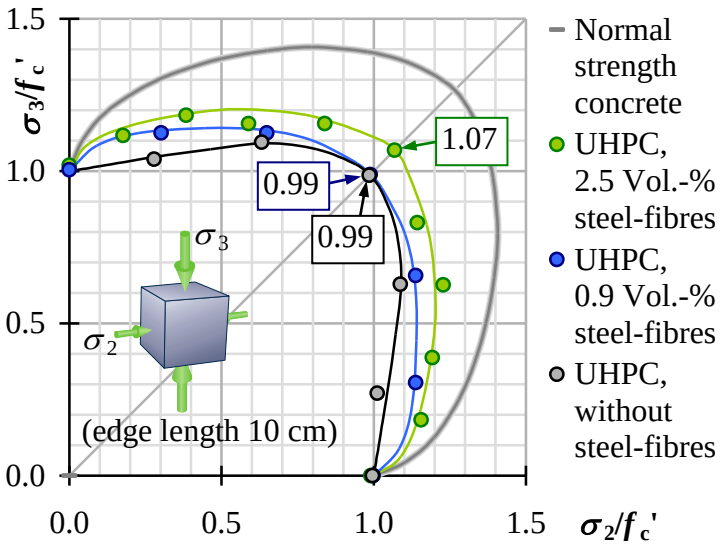

Figure 6: Strength under biaxial compression.[13]

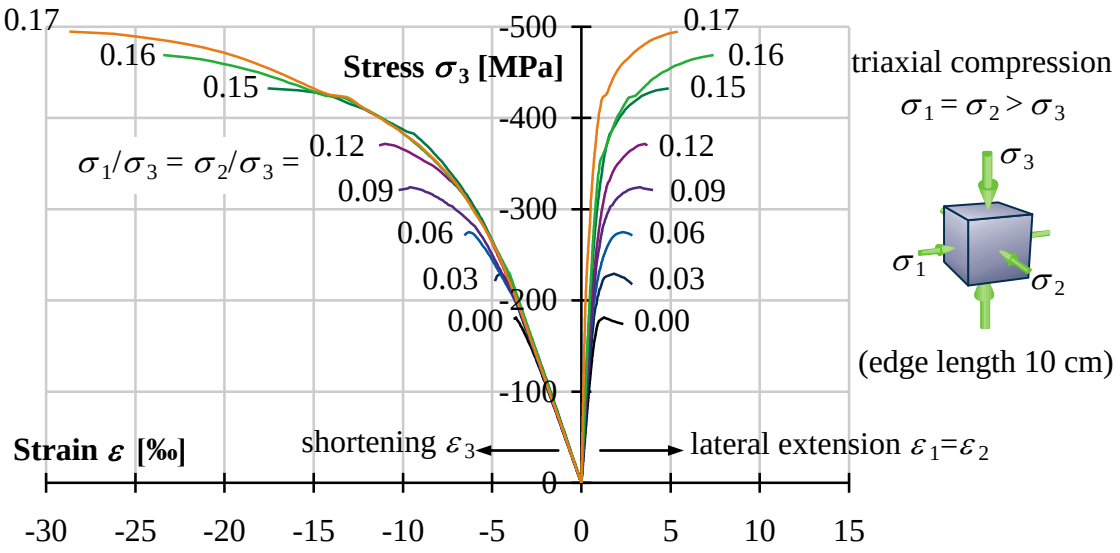

Figure 7: Stress-strain-behavior on compressive meridian ($\sigma_1 = \sigma_2 > \sigma_3$).[13]

Shear Capacity

In the following projects [14,15], special design aspects were investigated: the anchorage behavior of strands in UHPC, and the shear behavior. This knowledge is required basically for an economic and safe design of material adequate slender pretensioned beams. Due to the high tensile strength of fiber-reinforced UHPC, the height of such a beam can be reduced to approx. 50 %. The remaining dead load amounts about 1/3 compared to normal strength concrete and the steel fibers serve as shear reinforcement. The fiber action is illustrated in Figure 8 by the red tensile forces in the simplified shear model. Nevertheless additional shear reinforcement – in solid beams as well as in beams with openings – leads to further increase of the shear capacity.

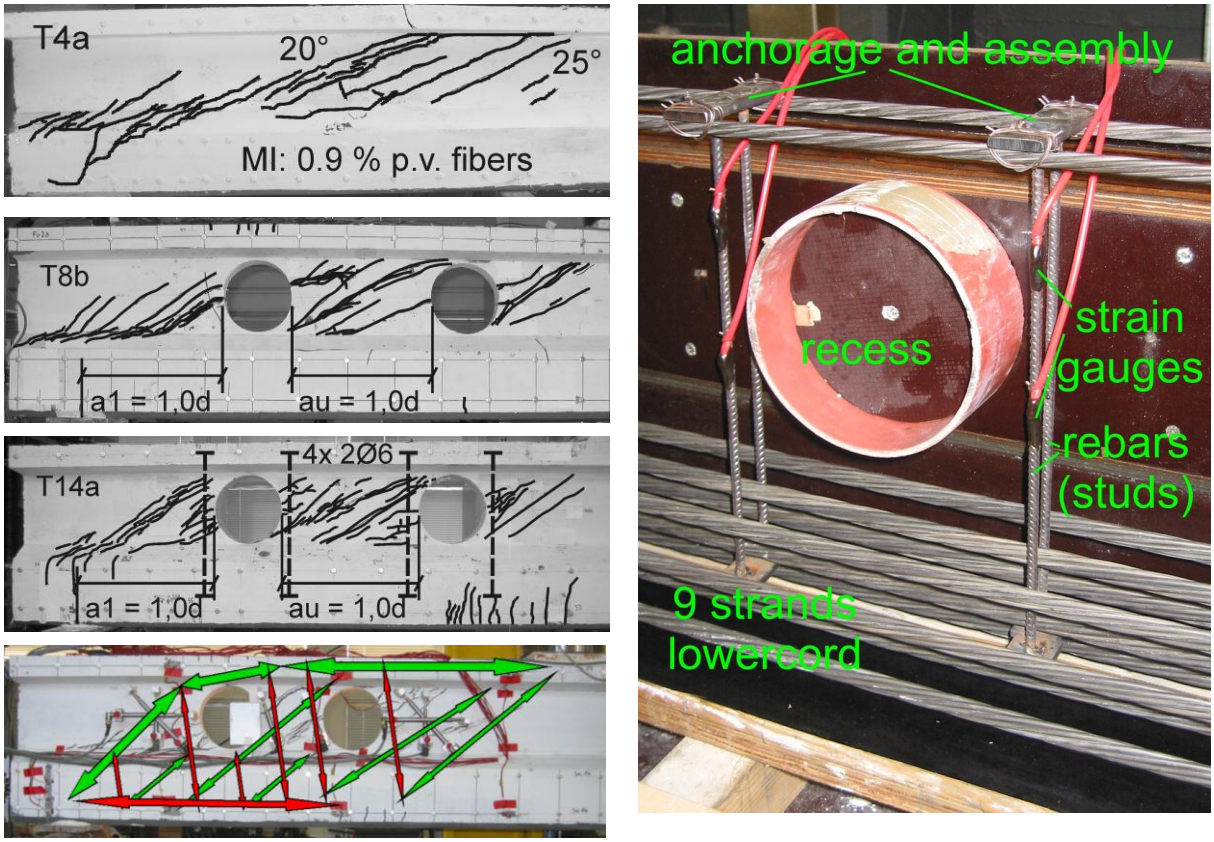

Figure 8: Crack pattern [14], simplified shear model and additional shear reinforcement [15].

4 Conclusions

Ultra-High Performance Concrete (UHPC) is a high performance material with steel-like compressive strength of about 200 MPa and – reinforced with steel fibers – significantly increased tensile, bending, and shear strength, therefore allowing for much lighter, longer lasting and even more economic concrete structures – it is sustainable material. To endorse widespread and regular use of this material, the German Research Foundation (DFG) funded an 12 Mio. € research program. About 20 research institutes were investigating in about 40 projects open scientific and technical questions covering the best fitting raw materials, their mixing and processing, rheological aspects and the specifics of the hydration process, as well as strength and deformation behavior of UHPC under uni- and multiaxial static and dynamic loads, and the resistance to chemical and frost attacks. The wide arc of topics ends in the load-bearing behavior of differently reinforced UHPC members and the development of new fitting technologies for slim precast elements. In the end, the research results provided a safe foundation to develop Technical Regulations for UHPC, enabling concrete producers to create mixtures and structural members using regionally available raw materials, and to allow designers and construction companies to build safe, long lasting, and economic UHPC structures.

References

[1] Bache, H. H., “Densified cement/ultra fine particle based materials”, 2nd International Conference on Superplasticizers in Concrete, Ottawa, Canada, June 10-12, 1981.

[2] Okamura, H., Kazumasa, O., “Mix Design of Self-Compacting Concrete”, Proc. of JSCE,V. 25, No. 6, 1995, pp. 107-120.

[3] Geisenhandlüke, C., Schmidt, M., “Methods for Modelling and Calculation of High Density Packing for Cement and Fillers in UHPC”, Proc. of the 1st International Symposium on UHPC, Sept. 2004, Kassel University Press, pp. 303-312.

[4] Teichmann, T., Schmidt, M., “Influence of the packing density of fine particles on structure, strength and durability of UHPC”, Proc. of the 1st International Symposium on UHPC, Sept. 2004, Kassel University Press, pp. 313-323.

[5] Fehling, E., Bunje, K., Schmidt, M., Schreiber, W., “The Gärtnerplatzbrücke, Design of First Hybrid UHPC-Steel Bridge across the River Fulda in Kassel, Germany”, Proc. of the 2nd Internat. Symp. on UHPC, March 05-07, 2008, Kassel, pp.581-588.

[6] Schmidt, M., Jerebic, D., “UHPC: Basis for Substainable Structures – the Gaertnerplatz Bridge in Kassel”, Proc. of the 2nd Internat. Symp. on UHPC, March 05-07, 2008, Kassel, pp. 619-625.

[7] Krelaus, R., Freisinger, S., Schmidt, M., “Adhesive Bonding of UHPC Structural Members at the Gaertnerplatz bridge in Kassel”, Proc. of the 2nd Internat. Symp. on UHPC, March 05-07, 2008, Kassel, pp. 597-604.

[8] Wiens, U., Schmidt, M., “State of the Art Report on Ultra High Performance Concrete of the German Committee for Structural Concrete (DAfStb)”. Proc. of the 2nd Internat. Symp. on UHPC, March 05-07, 2008, Kassel, pp. 629-637.

[9] Fehling, E., Schmidt, M., Stürwald, S. (eds.), „Ultra-High Performance Concrete – Proc. of the 2nd International Symposium on UHPC“, Structural Materials and Engineering Series, V. 10, Kassel University Press, March 2008 – available online under www.upress.uni-kassel.de/publi/abstract.php?978-3-89958-376-2

[10] Möser, B., Pfeiffer, C., “Microstructure and Durability of Ultra-High Performance Concrete”, Proc. of the 2nd Internat. Symp. on UHPC, March 2008, pp. 417-424.

[11] M. Schmidt, M., Stephan, D., Krelaus, R., Geisenhanslüke, C.: "The promising dimension in building and construction: Nanoparticles, nanoscopic structures and interface phenomena pt.1," Cement International, V. 5, 2007, pp. 86-100.

[12] Leutbecher, T., Fehling, E., "Crack Formation and Tensile Behaviour of UHPC Reinforced with a Combination of Rebars and Fibres", Proc. of the 2nd Internat. Symp. on UHPC, March 2008, pp. 497-504.

[13] Curbach, M., Speck, K., "Ultra-High Performance Concrete under Biaxial Compression", Proc. of the 2nd Internat. Symp. on UHPC, March 2008, pp. 477-484.

[14] Bertram, G., Hegger, J., "Anchorage Behavior of Strands in Ultra-High Performance Concrete, Proceedings", 8th International Symposium on Utilization of High-Strength and High-Performance Concrete, Tokyo, Japan in 2008, CD S3-3-6.

[15] Bertram, G., Hegger, J., "Pretensioned Concrete Beams made of Ultra-High Performance Concrete", Proceedings, International fib Symposium, London, The United Kingdom in 2009, CD (Mon 1600-1730 D2).

State of the art of design and construction of UHPFRC structures in France

Jacques Resplendino
Chief engineer, Chairman of the AFGC working group on UHPFRC, President of the AFGC Mediterraneen delegation, Director South Est SETEC TPI Vitrolles, France

After a fast reminder of the main caracteristics and compositions of UHPFRC, the paper makes a fast presentation of the new AFGC recommendations on UHPFRC by emphasizing the evolutions which benefit from experience feedback and from researches made on the last decade.The presentation continues by a general presentation of diverse recent realizations. Every project will be presented by trying to emphasize two essential points: the specific points of the design which justified the use of UHPFRC, the delicate points of the realization which bring out of the fields of traditional structures.
The article ends by a synthesis of the technological breaks engendered by these materials as long in the methods of conception than in the processes of implementation; breaks which impose on the engineers and the designers to go out of the reflexes attached to the traditional reinforced or prestressed concrete structures.

Keywords: AFGC recommendations, design method, construction process

1 Introduction – What is an Ultra High Performence Fiber-Reinforced Concrete (UHPRFC)

Ultra High Performance Fiber-Reinforced Concrete are materials with a cement matrix, and a characteristic compressive strength between 150 MPa and 250 MPa. They contain steel fibers, in order to achieve ductile behavior in tension and overcome if possible the use of passive reinforcement.

UHPFRC differ from high performance and very high performance concretes:

- the systematic use of fibres ensures that the material is not brittle and can allow to avoid any classical active or passive reinforcements,
- their compressive strength generally greater than 150 MPa,
- their composition with a high binder content that leads to the absence of any capillary porosity,
- their direct tensile strength of the matrix systematically higher than 7 MPa.

The aim of UHPFRC development is to achieve high tensile strenths through the participation of the fibres which provide tensile strength after the cement matrix has cracked. When the tensile strength is sufficiently high, it may be possible, depending on the way the structure works and the way the loads to which it is subject, to dispense with conventional reinforcement.

In general, one removes any traditional passive reinforcement cage in order to keep only the main passive or active reinforcement bars required when the resistance to major forces cannot be provided by the fibers.

2 Major research and feedback from the 2002 recommendations

Reinforcement in the need to produce proofs of convenience

To use UHPFRC structural material, the AFGC recommendations introduced in 2002 the concept of suitability tests to validate the methodologies of implementation. The principle of these tests was to perform a suitability test upstream of the actual structure: realize a specimen representative of the real structure, made of the same materials and following the same procedures as those proposed for the execution of the actual structure.

In the case of industrialized products, the process corresponds to the phase of development of industrial production processes. During completion of real structures, we were able to measure how this approach was valid and necessary, including when companies in charge of the construction were very experienced in the use of UHPFRC. Indeed, these suitability tests lead almost invariably to optimize implementation process initially planned, or to adapt the original design when technological and/or economical aspects prevent an adjustment of the process. Sometimes suitability tests lead to slightly change the formula to better control the rheology of the material.

Confirmation of the relevance of the K coefficient philosophy

The influence of the UHPFRC implementation on the tensile strength of the material in the actual structure is dealt with in the recommendations through a coefficient noted K that weights the theoretical behavior laws issu from laboratory tests. This coefficient is determined from the results of flexural tests performed on specimens sawn in the element built for suitability test described above. This notion of K coefficient validated though suitability test does not exist in Eurocodes but has been introduce in the last draft of the fib Model Code (MC2010 final draft september 2011, article 5.6.7). This notion is essential for UHPFRC, and shall be taken into account in any fiber-reinforced concrete in which the structural strength is provided by the fibers.

Fire behavior UHPFRC

Many recent tests [3] [4] (CERIB, CSTB) have determined for several UHPFRC materials all temperature mechanical properties in order to achieve numerical simulations of fire resistance (thermal conductivity, specific heat, thermal expansion, compression and tensile strength, Young's modulus). The new recommendations make a synthesis of these tests and provide values in order to make a first preliminary design of a UHPFRC structure subject to precise specifications of stability under fire.The UHPFRC behaviour under high tempatures depending strongly of the material, the recommandations remind that for a final design one must absolutely use the actual behaviour law of the material used to build the structure.

Punching resistance

Several recent research on punching [5] [6] [7] [8] allow to propose formulations in accordance with the philosophy of Eurocodes.

Abrasion

The new version of the recommendations provides the main results of abrasion tests (CNR test) made under the realization of hydraulic works. The results confirm the interest of UHPFRC used as a shield in case of strong mechanical stresses.

Shear resistance

In the context of drafting the new guidelines, a compilation of all existing international literature on shear testing was performed. In addition, LCPC performed 12 additional tests beams made with two different materials, with or without active and/or passive reinforcement.

The entire investigation on the reported results and additional testing campaign has allow to adjust and consolidate the formula proposed in the recommendations.

Tensile strength

Numerous tests were conducted to examine the tensile behavior of traditionnal reinforced UHPFRC (tension stiffening) [9] [10].

The new recommendations have been improved to better integrate the research results. These considerations have led to distinguish:

- UHPFRC with a hardening characterictic law in direct tension (only very few material are hardening in pure tension knowing that this requires a very high fiber content),
- UHPFRC with a hardening average law in direct tension, but with a softening characteristic law (the majority of UHPC available in the market),
- Softening material which have a softening average law in direct tension (UHPFRC with a low fiber content, which generally do not respect the non-brittleness criterion required for structural concrete).

3 Overview of recent applications

3.1. Structural applications in BCV

The PS34 is one of a the most remarkable structural applications made in BCV. It is an overpass on the A51 highway [22] [24] [25]. The structure is a single span road bridge 47m40 long made of a prestressed box beam. The deck is made of 22 UHPFRC match-cast pasted prefabricated segments. The geometry of the cross section is specially adapted to UHPFRC (Figure 1): Presence of curved surfaces to facilitate the implementation of concrete and fiber, removal of all geometric constraints related to the shaping of reinforcement frame which are found in traditional structures. This project demonstrated that it was possible to eliminate any watertight layer or carriageway on an UHPFRC structure, at the condition to work the roughness of the top surface to ensure adhesion of vehicles, and to wear special care to achieve joints between prefabricated components.

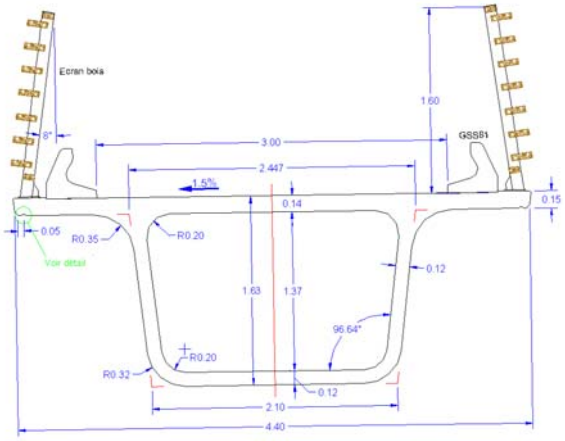

Figure 1: Cross section of PS34 (A51).

3.2. Structural ®applications in BSI / Ceracem

Since the important achievements of the beams of Civaux and Cattenom EDF power plant (1997-1998), the first global UHPC Highway Bridge in Bourg-lès-Valence (2000-2001) [11], [12], [13], [18] that served to support the development of the AFGC-SETRA recommendations on UHPFRC [1], the group Eiffage has conducted numerical structural applications made of BSI / Ceracem. We mention here only the most important.

The cover of Millau toll

This is a bulky structure, representing a total weight of 2300 tons implemented on site [20].

Figure 2: Overview of the coverage of Millau toll.

The structure measures 98m long and 28m wide (Figure 2). It is made of two thin slabs of 10cm thick souls connected by 12 prestressed beams. It was built using 53 match-cast pasted prefabricated segments assembled on a hanger with a longitudinal prestressing.
This project has highlighted the following points:

- The UHPC are able to produce complex shapes and thin membrane,
- The production of UHPFRC parts in high volume requires a perfect control of the rheology and a following-up by thermal metering method to apprehend the best internal thermal effects that develop in various parts of the structure during placement operations,

the realization of large prefabricated parts of structure needs special provisions for handling and assembly elements in order to control deflections and stresses during erection process,
UHPFRC materials are generaly hardened in pure bending, but softening in pure tension. Any design which occurs parts under tensile membrane behaviour requires prestressing or significant reserves compared to the tensile strength,

- The presence of shuttering increases thermal gradient effects on thin shells. Depending on weather conditions, and complexity of the design, it may be necessary to provide special thermal control devices to limit the effects of these gradients.

A canal bridge made of UHPFRC: a more economical and sustainable variant solution
During the completion of Lot 18 of the TGV Est (East High Speed Line), Eiffage built a canal bridge about 27 meters length made of BSI / Ceracem. This alternative solution was economically interesting and has given a very significant weight gain compared to the traditionnal reinforced concrete solution. The structure is a u-shaped beam made of three

Figure 3: View of the aqueduct.

longitudinal precast elements joint together in situ by a longitudinal post-tension presstressing (Figure 3). This solution has shown the ability of UHPFRC to assembly precast elements by prestressing without any match-casting during manufactory. This design needs only particular care to geometric tolerance and rigidity of the formwork masks used for precasting.

A new concept of pretensioning precast beams: the ITE beam

The ITE beam (poutre en I à Talon Elargi) [21] [23] is a prestressed precast inverted T-beam made of UHPFRC (Figure 4). This innovation received in 2009 the first prize category of large companies Innovation Awards from the French National Federation of Public Works (FNTP). Apart from the steel connection to the upper slab, the beam has no reinforcing steel.

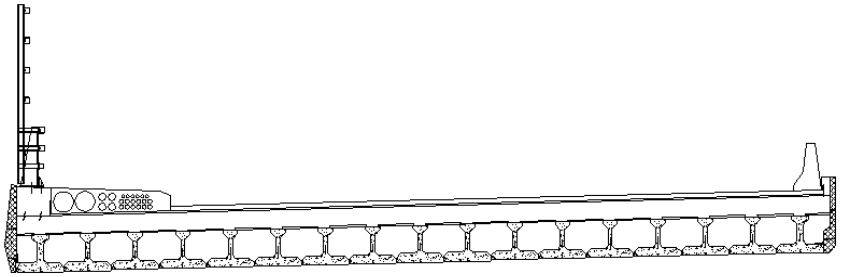

Figure 4: Cross section of the ITE ® beams deck.

The performance of ITE ® beams in terms of slenderness are identical to coated metal beams but their implementation has additional benefits:

- Significant reduction of the deck weight (reduction of 40 per cent),
- Shape and stiffness of the beams have a very insensitive behaviour to the phenomenon of lateral torsional buckling which significantly simplifies suggestions for implementation.

3.3. Bridges and footbridges made of Ductal ®

Several remarkable road bridges has been made of Ductal in the early 2000: Shepherds Bridge built in Australia [14], the bridge of Wapello, Iowa (USA) and the bridge of the expressway in Japan Kuyshu [26] and five pedestrian bridges: Sherbrooke in Canada, Korea Seonyu [15], Sermaises in France, Sakata Mirai and Akakura in Japan. More recently, a bridge was built in Calgary, Glenmore gateway and a road bridge in France, the Saint-Pierre-la-Cour bridge [22] [28] [29] .

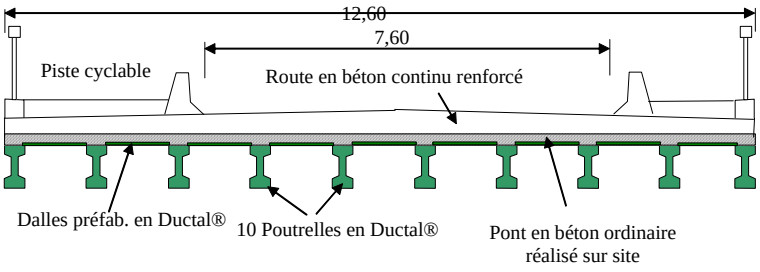

Figure 5: Cross section of the bridge.

The latter is a road bridge made of precast prestressed I-girder beams made of Ductal® , connected to a traditional reinforced concrete slab, poured in a second stage onto 83 precast panels in DUCTAL® of 25 mm thickness (Fig. 5).

In addition to the relief of the structure compared to a traditional solution (reduced weight of the deck by a factor of 2.2), the interest of the design is to fully utilize UHPFRC for its performance in terms of sustainability. Indeed, all surfaces of the deck in contact with ambient air are either made of UHPC (beams and underside of the slab) or protected by watertight layer (upper slab).

More recently, a footbridge with remarkable geometric characteristics and aesthetics was built in France. It is the Passerelle des Anges footbridge in the Herault [30]. It is an isostatic 67.5m span, 1.80 m in height representing a twinge of 1/38ème. It was built using 15 precast segments made of Ductal ® , prestressed by post tension (Figure 6).

As for the canal bridge presented in paragraph 3.2., the precast segments were performed without any match-casting during manufactory. The design fully utilizing the mechanical properties of UHPC has led to a slender structure requiring the implementation of a dynamic damper tuned to the first mode of vibration to avoid any risk of aeroelastic instability and to improve users comfort.

Figure 6: Overview of the Angels Gateway.

3.4 Use of UHPC for repair or strengthening work

Using CEMTECmultiscale ® in repair work

In the framework of European project SAMARIS, the Ecole Polytechnique de Lausanne (EPFL) studied with the help of LCPC the possibility of using UHPC to repair a reinforced or prestressed concrete deck.The study has been to implement a thin layer of UHPC on the upper surface of a slab to increase the rigidity of the structure, its mechanical strength and its durability, knowing that one of the interests of this repairing method is to remove and to avoid any waterproofing membrane on the structure.

These studies realized by the EPFL have shown the effectiveness of this method of strengthening that has been implemented since on several bridges using various UHPFRC formulations developed by the EPFL.

Using BSI for underpinning work of building

As part of the rehabilitation of the Credit Foncier building located rue Volney in Paris significant transformation of the building were carried out [16].

To accommodate larger interior volume, the project involved removal of columns and walls and their replacement by finer elements. The project included columns with metallic appearance, sharp corners, a 120x300mm section and an hour stability in fire.
Given these constraints, plus difficulties of a rehabilitation in situ (reduced access, delicate handling ...) a solution of columns made of fireproof UHPFRC cast inside a steel tube of 3 tenth of a millimeter thickness used as a lost formwork has proven advantageous. This solution has the advantage of being much lighter than the all-metal solution (the weight of the elements is approximately divided by 3) and allows to keep the demanded steel aspect (Figure 7).

Figure 7: Drilling of the facades and creation of new columns.

Using BSI to strengthen a "VIPP" bridge

The presence of the future tramway in the city of Le Mans has imposed to reinforced the Huisne bridge on the MANS. This bridge is a "VIPP" (Isostatic prestressed I-shaped beams) with two span of 31.60m built in 1976. The classical solution consisted of the implementation of external prestressing, supplemented by local reinforcements in flat carbon fiber. To find a more simple and powerful solution of strengthening, the idea was to use UHPFRC (BSI ® / Ceracem) to increase the inertia of the most sought side beams not only by increasing the section (Figures 8 and 9) [31] but also by taking advantage of the high value of Young's modulus of BSI ® / Ceracem which is twice than the value of conventional concrete (65 GPa).

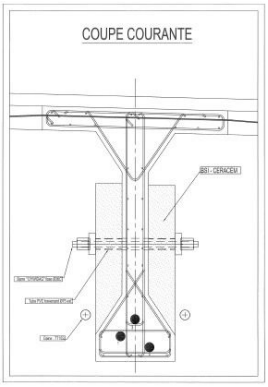

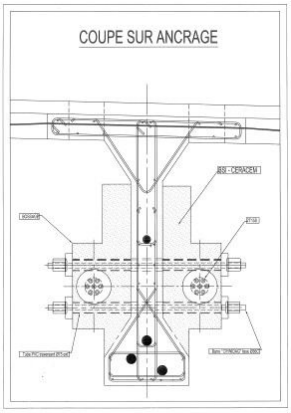

Figures 8 and 9: Cross-cut anchor and current building.

This principle of reinforcement avoids of course any passive reinforcement cage in the reinforcement braces, reinforcement cages which always cause some important issues du to the difficult access conditions and the difficulties to know and control the actual geometry of the elements to strengthening.

Using BSI for the repair and protection of structures subject to torrential flow

Repair and protection of structures subject to torrential flows are issues that can find very economical and efficient solutions using UHPFRC.

The effectiveness of UHPFRC towards these attacks can be quantified through "CNR" tests (CNR ie Compagnie Nationale du Rhône) which consist of comparing the fingerprint formed in the material subjected to a sandblasting projected under pressure. The results obtained for UHPFRC compared with values obtained for normal or HP concrete show the high interest of these solutions.

	C30/37	HPC	UHPFRC
CNR coefficient	4	2,8	1,1 à 1,3

The group Eiffage has used BSI / Ceracem to repair and protect footings and supports of the Valabres bridge. After removal of degraded concrete parts, a thin UHPFRC protective shell was cast in place against the existing structure (Figure 10 and 11).

Figure 10 and 11: Repair and protection of foundations and supports of the Valabres viaduct.

Uses of Ductal ® for repair, strengthening

Ductal ® was used in several applications focusing on the durability or fire such as beams and girders (over 2000) integrated into the cooling tower power plant of Cattenom in France, the anchor plates (more than 6000) to the island of Reunion and Ductal ®-AF used for the construction of composite columns of the Museum of Queen Sofia in Madrid (Spain). Ductal ® was used for making trenches of the treatment plant wastewater Gold Bar (Figure 12 & Fig. 13). Ductal ® was also used to build hydraulic structures (photo 8 - Repair of River Tunnel Hosokawa) [32]. The material allows for a very small building that does not cause significant decrease in the hydraulic opening. The solution is very interesting for its performance in terms of abrasion resistance and reduced the roughness to ensure a maintenance or an overall improvement of the hydraulic performance of the work.

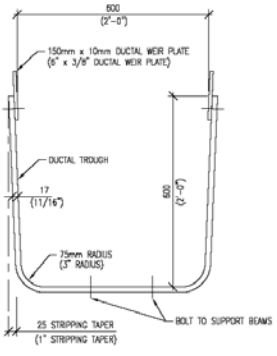

Figure 12: Cross section.

Photo 13: View from the trenches after installation.

Firgure.14: Using Ductal ® in the building of hydraulic structures.

3.5 Use of UHPC in the field of building equipment

In the areas of building equipment, UHPC have been the subject of numerous applications [33], which may include:

- Perforated panels to ensure cost-effective and sustainable structures with varied architectural forms (Figure 15-16). The UHPC interest in this area is clear, related to the finesse and variety of geometric shapes allowed by the absence of passive reinforcement Sunshades. In such structure, UHPC solutions competing with steel or aluminum alloy and can produce very slender, durable, aesthetic, and durable structures (Figure 17).

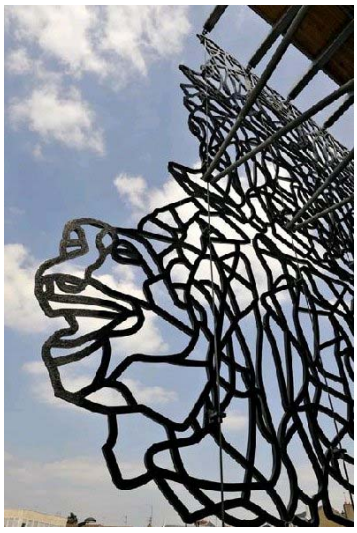

Figure 15-16: Examples of UHPFRC perforated panels.

Figure 17: Example of UHPFRC sunshade.

3.6 Major projects under way in Japan

The largest UHPFRC project underway in Japan is Haden Airport. It sees the construction on the sea of a huge slab of Ductal ® based on metal ferrules (Figure 18) [34]. This slab is carried out using precast elements, prestressed in both directions and built in a factory on site. Compared to a conventional solution, the material can significantly reduce the weight of the structure and ensures the sustainability of the structure subjected to a particularly aggressive atmosphere.

This achievement shows that the maritime sector is certainly one of the most relevant to the use of UHPFRC.

Indeed marine structures are generally subjected to considerable strain, and are located in environments chemically and mechanically very aggressive. Conventional solutions are very massive and pose significant maintenance problems associated with accelerated aging of traditional materials.

UHPFRC should allow to change significantly the design of these structures by providing much lighter solutions , mechanically efficient and sustainable. These solutions should present economical and environmental interest since the initial investment stage , and strengthen their interest in time through a significant reduction in maintenance costs.

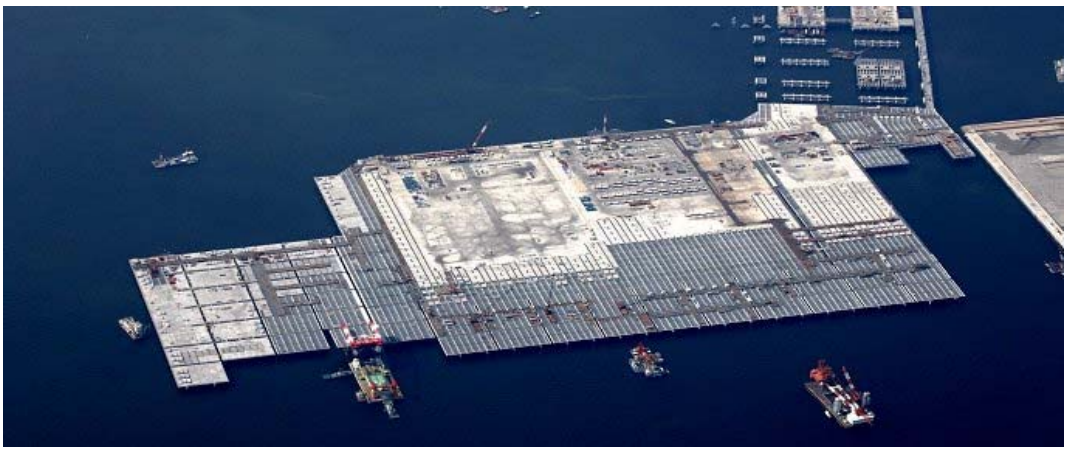

Figure 18 View of the construction of the structure of Ductal ® airport Haden.

3.7 Major projects under way in France

Some major UHPFRC projects are on the making in France: the MuCEM in Marseille, and the coverage of the Jean Bouin stadium in Paris.

The MuCEM (Museum of Mediterranean and Europeen Civilization) designed by the architect Rudy Ricciotti and the consulting firm SICA is being built by Dumez and Freyssinet [35].

The structure which is a cube of approximately 72x72m and more than 30m in height uses Ductal ® for all peripheric support structure made of treelike-shaped columns (Figure 19), for the perforated panels of the south-east and the south-west facades and above the roof, for the peripheric gateway and its support structure.

Ductal ® is also used to build the footbridge connecting the new museum and the Fort Saint-Jean. This three-span footbridge with a central span of more than 70m, has a similar design than the Passerelle des Anges footbridge presented in paragraph 3.3.

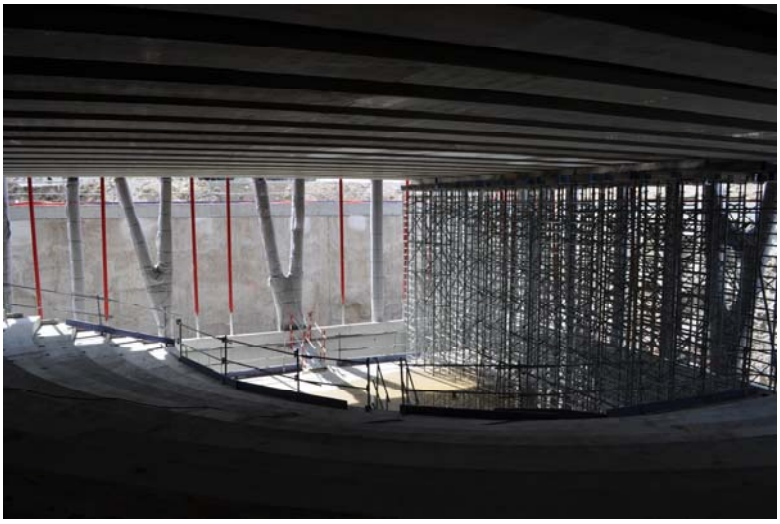

Figure 19: MuCEM – overview of the amphitheatre.

The coverage of the the Jean Bouin stadium in Paris designed by architect Rudy Ricciotti and engineer Romain Ricciotti is being implemented by the company Léon Grosse [36]. The structure is a three-dimensional shell made of large triangular ribbed slabs (up to 9m long) made of UHPFRC with glass inclusions (Figure 20). These elements are supported by a steel support structure.

This achievement has shown that the inclusion of glass panels in an UHPFRC slab imposes the implementation of flexible joints at the interface glass / UHPFRC to ensure sealing and avoid the risk of cracking of the glass panels as a result of contact pressures at the interfaces.

Figure 20: test specimen of the Jean-Bouin stadium coverage.

3.8 Research and development in progress on the material

Much research on UHPFRC has been conducted in recent years, with more or less fiber, armed or not, prestressed or not that led to better describe the combined effects of fiber and active or passive reinforcement , and to better define the conditions for obtaining a sufficient ductility.
Research should be continued on:

- Flow modeling during the implementation to optimize the process of implementation and the fibers orientation
- Optimization of formulations in order to control and / or limit the effects at the early age (autogenous shrinkage)
- The methods of evaluation and the development of global solutions towards sustainable development issues (CO2 balance, energy, recycling, life, overall cost investment and maintenance),
- The search for optimized structural solution.

4 Prospects and future of UHPC

4.1. UHPFRC interest vis-à-vis sustainable development issues

UHPFRC has a volume of about two times more cement than conventional concrete, and therefore produces twice as much CO2 and consumes twice as much energy to be produced. As against the experience of UHPFRC achievements shows that when used appropriately, it can divide the quantities of material used in a structure by two or three.

Compared to a conventional structure, a UHPFRC structure allows a slight gain in terms of CO2 and energy, but also offers a significant gain in terms of durability, lightness and an overall economy of material.

4.2. Areas of potential use of UHPC

As shown in the overview, UHPFRC are particularly suitable for precast structures, but their use on site is possible and can be completely relevant.
The preferred areas of application may include:

- Structures or parts of structures subjected to aggressive environments (abrasive effects, site works in marine chemical attack),
- Structures or structural parts for which weight gain is interesting (seismic zone, foundation problems, slender structures and far-reaching ...),
- Structures under shocks effects (waste storage container , shields, ...),

structures in which one seeks a high quality, finesse, and the possibility of forging sidings,

- Composite structures: the UHPC has a ratio strength on elastic modulus very interesting for use in combination with steel or carbon fiber. The near absence of delayed effects in the material (creep, drying shrinkage) makes their use in Composite structures particularly relevant,
- Structures or structural parts for which the complexity and density of the traditional passive reinforcement occur very difficult design and proper implementation (connecting to an existing structure with an uncontrolled geometry and difficulties to access, mechanical connection to a steel frame complex shape, ...).

4.3. UHPFRC: materials that are revolutionizing design and implementation methods

The design of UHPFRC structures requires to get out of reflex attached to traditional reinforced or prestressed concrete structures.

The volumes are further modified with thicknesses that can become very small, which can disturb uninitiated designers, but which is often very relevant : the thickness reduction tends to favor fibers orientation and increases material strength. The production of very slender parts

requires to be vigilant, to reduce and check geometric tolerances, to control stresses and distortions in transient phases of handling and assembly.

The shape of the forms must be completely reviewed. In a traditional structure one prefers angles allowing the shaping of the reinforcement frames. With UHPFRC one should avoid any corner and prefer curved surfaces that facilitate the implementation of the material and avoids discontinuities of flow.

The absence of reinforcement allows to consider all forms of structures as long as the geometry is consistent and relevant with the stresses in the structure, and compatible with a successful implementation of the concrete.

The perfect match of these materials with precasting often requires rethinking the overall design of a structure: for a large structure with a complex geometry a study should be conducted on how to achieve the overall structure from an assembly of reduced size elements which present a redundant geometrie, allowing an optimal resistance to external forces and an easy implementation. This requires an unconventional new way to design and build structures.
The development of precasting is consistent with researches on the design of the connections between elements to achieve most efficient forces transmission, sealing and durability of the assembly.

Formwork technology evolves. We see the development of 3D formwork solutions: molded plastic or polystyrene cut automatically to allow any three-dimensional shapes.
More performent the concrete is, more special care and controls for implementation are required:

-Validation of processes through suitability tests,

-Monitoring and control of the rheology depending on weather conditions,

-Strict respect of the material performance tolerances (consistency, strength...),

-Compliance with dimensional tolerances and geometric tracking.

Design methods differ from traditional use of reinforced and / or prestressed concrete well controlled by consultants: resistance calculations use theories developed for fiber-reinforced concrete that are little known (1997 AFREM recommendations for ordinary fiber reinforced concrete, 2002 AFGC-SETRA recommendations for UHPFRC).

Test methods for flexural tensile strength are not well known by laboratories and require specific numerical tools operating (inverse method).

One of the main obstacles to the current development of UHPFRC is thus related to the lack of specific skills in design offices, architects, laboratories and companies.

The material requires an important intellectual precondition investment. To date, the market was relatively small, and only a few number of offices has been involved.

Given that a certain taking off of these material can be observed (particularly in Japan, but also in Europe and in France) it is likely that a larger number of consulting firms and companies will form teams on these materials in order to meet demand. This should strengthen the development of material, knowing that it should lead to the emergence of a growing number of UHPFRC solutions in alternative to traditional structures.

5 Conclusion and outlook

The design and construction of UHPFRC structures require us to dispose of the reflexes attached to traditional reinforced or prestressed concrete.
UHPFRC are not revolutionary materials in the sense that their cost of production and implementation is still high and require a optimization to ensure a significant financial gain.
Niches exist and powerful applications tend to increasingly grow as far as durability, aesthetic, timeliness for erection, scalability, possible layouts, material gain are concerned.

These uses are growing and UHPFRC can bring real innovative responses.

Researches and important projects under way will further strengthen their development and contribute to demonstrate their structural and architectural potential

References

[1] « Bétons Fibrés à Ultra-Hautes Performances », Recommandations provisoires, Association Francaise de Genie Civil, Janvier 2002.

[2] P FRANCISCO, F BENBOUDJEMA, P ROUGEAU, JM TORRENTI Ultra High Performance Concrete for Prestressed elements – Intrest of creep prediction, colloque BFUP 2009, Marseille, 2009.

[3] M BEHLOUL, J ARSENAULT, “Ductal®: a durable material for durable structures”, 5th int. conf. On concrete under severe conditions, CONSEC’07, Tours (France), 2007, pp 951-958, Toutlemonde et al. (eds).

[4] J-C MINDEGUIA, P PIMIENTA, A SIMON, N ATIF “Experimental and numerical study of an UHPFRC at very high temperatures”, 5th int. conf. On concrete under severe conditions, CONSEC’07, Tours (France), 2007, pp 1659-1666, Toutlemonde et al. (eds).

[5 DK HARRIS, CL ROBERTS-WOLLMANN (2008) Characterization of punching shear capacity of thin ultra-high performance concrete slabs, Ultra High Performance Concrete (UHPC), 2nd int. symp. on Ultra High Performance Concrete, Kassel (Germany), March 05-07, Kassel University Press, Structural Materials & Engineering Series N°10, Fehling et al. eds, pp. 727-734.

[6] C JOH, H HWANG, E CHOI, J PARK, BS KIM (2008) Punching shear strength estimation of UHPC slabs, Ultra High Performance Concrete (UHPC), 2nd int. symp. on Ultra High Performance Concrete, Kassel (Germany), March 05-07, Kassel University Press, Structural Materials & Engineering Series N°10, Fehling et al. eds, pp. 719-726.

[7] A SPASOJEVIC (2008) Structural implications of ultra-high performance fibre-reinforced concrete in bridge design, Thèse de doctorat n°4051, Ecole Polytechnique Fédérale de Lausanne, Suisse.

[8] F TOUTLEMONDE, JC RENAUD, L LAUVIN, S BRISARD, J RESPLENDINO (2007) Local bending tests and punching failure of a ribbed UHPFRC bridge deck, 6th int. conf. On Fracture Mechanics of Concrete and Concrete Structures, FRAMCOS-6, Catania (Italy), 17-22 June, Carpinteri et al. (eds), Taylor & Francis, vol. 3 High-Performance Concrete, Brick-Masonry and Environmental Aspects, pp. 1481-1489.

[9] J JUNGWIRTH, Zum Tragverhalten von zugbeanspruchten Bauteilen aus Ultra-Hochleistungs-Faserbeton, Thèse de doctorat n°3429, Ecole Polytechnique Fédérale de Lausanne, Suisse.

[10] T LEUTBECHER, E FEHLING (2008) Crack formation and tensile behaviour of UHPC reinforced with a combination of rebars and fibres, Ultra High Performance Concrete (UHPC), 2nd int. symp. on Ultra High Performance Concrete, Kassel (Germany), March 05-07, Kassel University Press, Structural Materials & Engineering Series N°10, Fehling et al. eds, pp. 497-504.

[11] J Resplendino, JM Roy, J Petitjean, P Blondeau, Z Hajar, A Simon, T Thibaux, "Ouvrages innovants de Bourg-lès-Valence", Revue Travaux, No.783, pp. 42-47.

[12] T Thibaux , JA Tanner, "Construction des premiers ponts français en béton fibré à ultra hautes performances/construction of the first french road bridges in ultra high performance concrete", in La technique française du Béton, AFGC, The first fib congress 2002, Osaka 2002.

[13] Z Hajar, A Simon, D Lecointre, J Petitjean, "Construction of the first road bridges made of UHPC", 3rd International Symposium on HPC, Orlando 2003.

[14] B Cavill, G Chirgwin «The worlds first Ductal road bridge Shepherds gully creek bridge, NSW»; 21ème conférence biennale de l’institut du béton d’Australie, Brisbane, 2003.

[15] M Behloul, KC Lee «Ductal® Seonyu footbridge”. Structural Concrete 4 (4), 2003, 195-201.

[16] Genes P, Alexandre F, Novarin M, Simon A., "Restructuration d’un immeuble parisien", Revue Travaux Novembre 2004.

[17] J Resplendino « First recommendations for Ultra-High-Performance Concretes and examples of application », International Symposium on UHPC, Kassel 2004.

[18] Z Hajar, D Lecointre, A Simon, J Petitjean « Design and Construction of the world first Ultra-High Performance Concrete road bridges », International Symposium on UHPC, Kassel 2004.
[19] Z Hajar, D Lecointre, J Petitjean, J Resplendino, A Simon « UHPC – First recommendations and examples of application » fib Symposium: Concrete Structures: the Challenge of Creativity, Avignon (2004).
[20] Z Hajar, P Winiecki, A Simon, T Thibaux « Realization of an Ultra High Performance Fibre Reinforced Concrete thin shell structure covering the toll-gate station of MILLAU Viaduct. » fib Symposium: Concrete Structures: the Challenge of Creativity, Avignon (2004).
[21] Y El Gourari, N Fabry, Z Hajar, M Novarin, A Simon, T Thibaux, S Chanut, R Sale, D de Matteis, P Marchand, A Petel "La poutre ITE, une alternative aux poutrelles enrobées – Le triplement du pont Pinel à Rouen", Revue Travaux n°849 Février 2008.
[22] J Resplendino « Ultra-High Performance Concretes – recent realizations and research programs on UHPFRC bridges in France », International Symposium on UHPC, Kassel (2008).
[23] D de Matteis, M Novarin, P Marchand, N Fabry, A Petel, S Chanut « A fifth French bridge including UHPFRC components, the widening of the Pinel Bridge, in Rouen (France)», International Symposium on UHPC, Kassel (2008).
[24] J Resplendino, S Bouteille, O Delauzun, E Maleco, C Dumont, P Cantrelle, G Chanliaud, C Clergue, Y Lingard, A Capra, Ll Linger, J Martin, M Guilloud « Construction of an overpass on the A51 Motorway, made of a prestressed box beam built with UHPFRC », in the French technologie of concrete, AFGC, The second fib congress, Naples (2006).
[25] J Resplendino, S Bouteille, O Delauzun, E Maleco, C Dumont, P Cantrelle, G Chanliaud, C Clergue, Y Lingard, A Capra, L Linger, J Martin, M Guilloud «Construction d'un Passage supérieur sur l'autoroute A51, en caisson précontraint Réalisé en Béton Fibré ultra performant (BFUP)», congrès AFGC GC2007, Paris (2007).
[26] H Okuma et al : «The first highway bridge applying ultra high strength fibre reinforced concrete in Japan»; 7th conférence internationale sur les ponts de courte et moyenne portée, Montréal, Canada, 2006.
[27] J Hanoteau, M Behloul, O Bayard, J Resplendino , S Bouteille, L Boutonnet , S Vildaer, B Radiguet , S Bernhard, N Padovan « Ductal : a new material, the bridge of St Pierre La Cour », in the French technologie of concrete, AFGC, The second fib congress, Naples (2006).
[28] J Resplendino, S Bouteille « Les derniers développements dans l'utilisation des Bétons Fibrés Ultra Performants en France », congrès AFGC GC2005, Paris (2005).
[29] J Hanoteau, M Behloul, O Bayard, J Resplendino , S Bouteille, L Boutonnet , S Vildaer, B. Radiguet , S. Bernhard, N. Padovan « Ductal : a new material, the bridge of St Pierre La Cour », in the French technologie of concrete, AFGC, The second fib congress, Naples (2006).
[30] P Mazzacane, R Ricciotti, F Teply, "The Passerelle des Anges Footbridge", Designing and Building with UHPFRC – State of the Art and Developpement, ISTE Ltd 2011, chapter 9, pp. 111-124.
[31] T Thibaux, "Using UHPFRC for Structural Reinforcement of Buildings and Civil Works", Designing and Building with UHPFRC – State of the Art and Developpement, ISTE Ltd 2011, chapter 37, pp. 553 – 563.
[32] T Ono, "Application of UHSFRC for irrigation chanel repair works", Designing and Building with UHPFRC – State of the Art and Developpement, ISTE Ltd 2011, chapter 36, pp. 541 - 552
[33] D Stoeux, JF Batoz, L Jacques, L Guingot "A material for perforated panels and lattice work", Designing and Building with UHPFRC – State of the Art and Developpement, ISTE Ltd 2011, chapter 7, pp. 97 – 100.
[34] Y Tanaka and al, "The innovation and application of UHPFRC bridges in Japan", Designing and Building with UHPFRC – State of the Art and Developpement, ISTE Ltd 2011, chapter 12, pp. 149 - 187.
[35] G Gazon, R Ricciotti, J Portelatine, F Nicolas, P Rivillon, "The MuCEM", Designing and Building with UHPFRC – State of the Art and Developpemen, ISTE Ltd 2011, chapter 32 – 34, pp. 481 – 528.
[36] R Ricciotti, G Lamoureux, R Ricciotti "The Jean Bouin Stadium", Designing and Building with UHPFRC – State of the Art and Developpement, ISTE Ltd 2011, chapter 8 – 34, pp. 101 – 108.

An Overview of UHPC Efforts through the North American Working Group

Theresa (Tess) M. Ahlborn[1], Eric P. Steinberg[2]
1: Civil and Environmental Engineering Department, Michigan Technological University, USA
2: Department of Civil Engineering, Ohio University, USA

The North American UHPC Working Group (NA-WG) was established in June 2010 to provide a forum for UHPC experts to discuss and work toward implementation of UHPC in North America, along with the purpose to develop a design guide. Over 90 individuals are listed as members, with volunteer membership coming from academia, industry, and government sectors. The working group has identified numerous challenges to implementation and is working with several professional organizations to address these challenges. Recent efforts have also focused on disseminating information on UHPC. The co-chairs of this working group present herein the efforts of this working group as well as the recent efforts in North America.

Keywords: UHPC, implementation, challenges, North America

1 Introduction

All infrastructure, whether bridges, pipelines, or other critical lifeline systems, must be maintained for daily health to functionally perform in a major disaster. As such, it is imperative to significantly improve the resiliency of North America's infrastructure while investigating and developing protective systems for international security. The implementation of innovative materials such as ultra-high performance concrete (UHPC) will have a significant impact on the resiliency of the infrastructure.

Ultra-high performance concrete is a relatively new and advanced material to North America. First developed in France in the 1990's, the material was introduced on a very small scale in the United States and Canada about a decade or so ago. The advanced material has been shown to exhibit enhanced aesthetics, extreme strength and superior durability under a variety of loadings and exposures, lending itself to an assortment of potential applications.

Whether Mother Nature or non-natural hazards threaten these nations, proper implementation and enhanced performance of systems using UHPC can add robustness and longevity to the infrastructure. The material's toughness increases its ability to absorb environmental and man-made disturbances. And when properly designed in efficient systems, UHPC can contribute to global sustainability efforts through its lower life-cycle costs and reduced long-term impacts. Additional benefits of UHPC being widely used include added resiliency and improved security, not only post-disaster, but every day. From repair and replacement, to protection of the environment, UHPC provides the benefit of improving the resiliency of our infrastructure.

However, as promising as UHPC appears, the material has numerous challenges before widespread implementation in North America is possible. These challenges include:

- no commonly accepted standard definition of the material
- no commonly accepted test methods for material performance under varying environmental conditions in North America
- very few production standards for quality control in manufacturing facilities
- no design guides (e.g. buildings, bridges, blast protection systems) for engineers and owners to create confidence in system performance

- and only a handful of large scale projects in North America for owners to reference for lowering risk of implementation.

As with any new material, process, or application for use in the infrastructure within North America, there are challenges that need to be overcome before widespread usage is implemented. This paper summarizes the efforts of the North American UHPC Working Group (NA-WG) along with several activities within North America to promote the widespread usage of UHPC in the infrastructure and the efforts that are being undertaken to overcome the above challenges.

2 North American UHPC Working Group

The North American UHPC Working Group (NA-WG) was established on June 1, 2010 in Washington D.C., USA during the Third Congress & Exhibition of the Federation International du Beton (*fib*) and Precast/Prestressed Concrete Institute (PCI) 2010 Annual Convention. The first meeting was organized by Mr. Vic Perry of LaFarge - North America. The primary idea was to provide a forum for UHPC experts and users to discuss the implementation of UHPC in North America. The group agreed that

- development of a design guide was necessary,
- all applications of UHPC should be considered (buildings, bridges, etc),
- there was a need to develop a state-of-the-art report on UHPC along with a guide, and
- the group may need to be associated with another professional organization to publish guide specifications.

Drs. Tess Ahlborn and Eric Steinberg agreed to co-chair the efforts.

The group met again on September 24, 2010 in Chicago, Illinios, USA in conjunction with the PCI Committee Days. A master email list had been established and 76 members had joined. Presentations were provided by several members on possible professional organizations which could work with the working group. The presentations focused on the positive and negatives of each organization and the likelihood on being able to produce a recognized design guide in a timely fashion. There was also discussion on starting with a state of the practice report rather than detailed specifications so that the document could be produced in a timely practice and it would likely not require a host organization for the group.

The third meeting was held in Chicago, Illinios, USA on March 26, 2011, which coincided again with PCI Committee Days. Information on the activities of other organizations and upcoming events including UHPC were discussed. Steinberg reported on the results of a membership survey related to the preferred organization to work with the group. Based on these results and other information, it was proposed to pursue initial collaborations with

- the American Concrete Institute (ACI),
- the Precast/Prestressed Concrete Institute (PCI), and
- the Department of Homeland Security (DHS).

Because the membership of the group had grown to 86 members, it was proposed that group should have a Steering Committee of approximately ± 20 diverse and active members to lead the group. A Membership Selection subcommittee was established in order to develop membership criteria and to solicit or select people for the Steering Committee. A State of the Art Report subcommittee was also established to oversee development of a report within six months. A Design Guide subcommittee was created develop an outline and table of contents for a design guide.

The fourth meeting of the group occurred in Salt Lake City, UT on October 24, 2011 at the PCI Convention and National Bridge Conference. The total membership of the working group had grown to 96 members. Activities occurring related to UHPC were reported on by members

participating. The membership subcommittee reported reviewing the membership criteria for several other organizations. Proposed criteria would allow only one voting members from an organization and the voting member would have been required to attend three meetings either by being present or via conference call. For a diverse group of four classifications were established:

- Users,
- Producers,
- Owners,
- Designers and Academia.

The membership subcommittee is working on the issue of a Steering Group with the goal of establishing membership of the Steering Group by the next meeting in March 2011. Because of the group size and the evolving purpose of the group to host collaborative efforts and act as a clearinghouse for information, the group discussed the benefits of incorporating as a not-for-profit organization. This would require officers, bylaws, a charter, and an annual meeting. Membership dues could generate revenue and multi-tiered membership level could be used. This concept is currently being investigated in more detail. The State of the Art Report subcommittee has a rough outline for a document, but based on the activities of other organizations (see FHWA below) a temporary hold was requested before proceeding.

The NA-WG has continued to work with other professional organizations in North America. A summary of some of these efforts is described below.

3 American Concrete Institute (ACI)

To pursue collaborative efforts with the American Concrete Institute (ACI) as indentified by the North American UHPC Working Group, several avenues were taken, including approaching the Concrete Industry's Strategic Development Council (SDC) *www.concreteSDC.org* and presenting at the SDC meeting in Chicago, Illinios, USA on September 21-22, 2011. NA-WG members Ahlborn, Mr. Brian Green and Dr. C. Kennan Crane gave three general presentations on UHPC; one to introduce the material to those who were less familiar with UHPC (Green), one presentation to show current and potential applications for innovation in concrete (Crane), and one to present the challenges for widespread implementation in North America (Ahlborn). The meeting forum provided an opportunity for the leaders in the concrete industry, government, academia, and customers to discuss the key issues and challenges that impact the concrete industry. A well attended break-out session on UHPC indentified similar challenges to those indentified by the NA-WG (above). The SDC expressed support in establishing an ACI Technical Committee to begin to address these barriers to technology acceptance and implementation.

With progressive efforts from several NA-WG members, ACI formed *Technical Committee 239 – Ultra High Performance Concrete* in the summer of 2011. The first meeting of ACI 239 occurred on October 17, 2011 in Cincinnati, Ohio with 46 people in attendance. The committee mission is to develop and report information on Ultra-High Performance Concrete. The committee's scope is to:

- Develop the definition of UHPC
- Identify the current state of practice
- Identify gaps in knowledge
- Lay out long-term plans for addressing knowledge gaps

Three groups were formed within the committee to develop the following:

- A definition of UHPC (Eckart Buhler, Fred Meyer, Kay Willie, Mark Luther)
- An outline for a report on UHPC (Sue Lane, Karen O'Brian, Brooks Bucher, Jim Milligan)

- A long range plan for the committee (John Myers, Jim Hicks, Eric Steinberg, Kay Willie)

The next ACI 239 committee meeting is March 19, 2012 at the ACI Fall Convention in Dallas, TXexas, USA. More information on the committee activities can be found at: *www.concrete.org/committees*

There will be an upcoming session "UHPC Experience and Developments" during the Fall ACI Convention October 21-25, 2012 in Toronto, Ontario, Canada. The session is co-sponsored by ACI Committees 234 (Silica Fume in Concrete), 239 (Ultra High Performance Concrete), and 363 (High Strength Concrete).

4 Precast/Prestressed Concrete Institute (PCI)

The Precast/Prestressed Concrete Institute (PCI) is an organization dedicated to fostering greater understanding and use of precast and prestressed concrete *www.pci.org*, and has the potential to be a leader in the widespread use of UHPC. Collaborative efforts with PCI and the North American UHPC Working Group have begun as recommended by the NA-WG membership. Strategic planning discussions with the PCI Executive Committee and the PCI Foundation will begin to identify critical industry challenges and address these challenges for a variety of precast and prestressed concrete applications. Such support affords the ability of the PCI community to embrace the innovation opportunities of UHPC.

5 U.S. Department of Homeland Security (DHS)

The U.S. Department of Homeland Security (DHS) Science and Technology Directorate was identified by the NA-WG as a potential collaborator for UHPC implementation efforts. The Office of Infrastructure Protection within DHS in partnership with the Engineer Research and Development Center (ERDC) of the US Army Corps of Engineers has an effort to develop UHPC material that is affordable and competitive in the US market. The final goal is to provide a UHPC material that exhibits high performance standards for explosives and other natural hazards. It is expected that the material be easy to use when a hazard/integrated approach is required. The benefits of this product include high durability and less reinforcement requirements. ERDC is the lead of this project, and this effort will be significant in the protection of the US critical infrastructure. The main challenge of the project is to eliminate the barriers that are an impediment for the commercialization and decrease the cost of producing UHPC, a challenge similar tot hat identified by the NA-WG. In addition, DHS sponsored an *UHPC Critical Roadmap Workshop* on the campus of Columbia University in New York City, New York, USA on January 11-12, 2011. A report was published by DHS on the pathway to commercialization of UHPC and is available on-line:

http://www.dhs.gov/xlibrary/assets/ultra-high-performance-concrete-roadmap.pdf

DHS is also working through the National Institute of Building Sciences (NIBS) to form a UHPC committee to address and set forth the path that was developed as the critical roadmap.

6 Federal Highway Administration (FHWA)

The U.S. Federal Highway Administration showed interest in UHPC nearly two decades ago, and in 2002 sponsored a study tour of ultra-high performance concrete bridges in France [1]. The primary mission was to develop international relationships for future collaborative research efforts necessary to allow implementation of the virtually indestructible material into bridges throughout the United States. Since the tour, Drs. Joey Hartmann and Ben Graybeal have been involved in research of UHPC for FHWA at the Turner Fairbank Highway Research Center, McLean, Virginia, USA. The most recent project involves the use of UHPC in Connections for

Modular Concrete Bridge Components. This project involves the development and testing of connection details for facilitating the use of modular prefabricated concrete components in bridge construction. Other projects include the development of UHPC precast bridge deck elements, flexural behavior of minimally reinforced UHPC beams, and flexural fatigue behavior of UHPC beams. [2]

FHWA has also been supportive in bridge projects utilizing UHPC in the United States. The Mars Hill Bridge in Wapello County, Iowa was the first bridge in the U.S. to use UHPC. This 110-ft bridge opened to traffic in 2006 and included UHPC in modified Iowa Bulb-Tee Girders. The Cat Point Creek Bridge in Richmond County, Virginia was the second bridge in the U.S. to utilize UHPC. This ten-span bridge was constructed with UHPC in precast prestressed Bulb-Tee girders and opened to traffic in 2008. Both of these first two bridges eliminated the mild shear steel reinforcement by taking advantage of the tensile capacity of UHPC. The Jakway Park Bridge in Buchanan County, Iowa used UHPC in optimized pi-girders (shaped like the Greek letter π) to take advantage of the superior mechanical and durability properties of UHPC. The shape of the girders also allowed for accelerated construction of the bridge which opened to traffic in November 2008. Two bridges in New York State incorporated UHPC as cast-in-place joints between prefabricated bridge decks in 2009. The Route 31 Bridge over Canandaigua Outlet used UHPC as the closure material between decked Bulb-Tee elements. Straight epoxy coated bars protruded from the deck-bulb tees and were lapped into the connection. The deck of this bridge included a waterproofing membrane and an asphalt overlay. The Route 23 Bridge over Otego Creek in Oneonta, N.Y. included UHPC at the joints between 8-in thick precast concrete deck panels on steel stringers. UHPC was cast into the connections of the deck panels. The deck panels contained 180^{o} hooked bars that extended into the connection. NYSDOT also performed pullout tests of No. 4 through No. 6 steel reinforcement cast into cylinders of UHPC. Very minimal depths were used to determine the UHPC bond capacity. A UHPC waffle slab system has also been utilized recently in the Little Cedar Creek bridge of Wapello County, Iowa. The slabs were supported on Iowa Type B prestressed concrete girders spaced 7'4" on center. The 8" thick deck panels spanned from near the center of the bridge to one side and were supported by three girders. Each panel was 16' 2.5" wide by 8' long. This project was finishing up in late October of 2011.

The FHWA recently hired a consultant to develop a state of the art report on UHPC for the transportation industry in the United States (slated for completion in June 2012). The goal to is provide the state of current practice, looking nationally and internationally at work that has been done, consider codes that have been developed worldwide, research needed to be done, and to consider what else needs to be accomplished for innovative transportation applications.

7 Ministry of Transportation of Ontario, Canada

The Ministry of Transportation of Ontario (MTO) has recently implemented field-cast UHPC connection technology in nine bridges. Another seven bridges using UHPC connections were to be completed by the end of 2011. Some details of the bridges details are summarized below:

The Sunshine Creek Bridge, constructed in 2007 near Thunder Bay, Ontario, is a 34.5 ft. single span bridge containing 10 adjacent PC box beams with a 35^{o} skew. The beams are 23.62" deep by 46.8" wide and contain 30 – ½" grade 270 strands. The shear keys between the beams are diamond shaped with overlapping hairpin glass fiber reinforced polymer (GFRP) bars that extended from the boxes (see Appendix A Figure 2). Two longitudinal GFRP bars exist between the hairpin bars. No transverse tie rods or post-tensioning exist.

The Hawk Lake Bridge, constructed in 2008 between Kenora and Dryden, Ontario, is an 89.24 ft. single span bridge with 12 adjacent PC box beams. The beams are 31.5" deep by 45.2" wide and contain 30 – ½" grade 270 strands. The shear keys are diamond shaped with overlapping straight GFRP bars and one longitudinal GFRP bar between overlapping bars. No transverse tie rods or post-tensioning exist.

The Buller Creek Bridge, constructed in 2009 between Ear Falls and Vermillion Bay, Ontario, is a 92.26 ft. single span bridge with no skew. The bridge consists of 10 adjacent PC boxes that are 35.43" deep by 48.19" wide. The beams contain 36 - ½" grade 270 strands of which some are harped. The shear keys are diamond shaped with a 2-4" (5-10 mm) gap between beams. Straight GFRP bars extend into the shear keys that also contained one longitudinal GFRP bar. Transverse tie rod or post-tensioning did not exist.

The Wabigoon River Bridge, also constructed in 2009 between Ear Falls and Vermillion Bay, consists of three spans with the outer spans being 54.13ft and the center span being 90.22ft. Each span contains 10 adjacent PC box beams that are 35.43" deep by 48.19" wide. The beams contain 28 and 12 - ½" grade 270 strands for the center span and end span beams, respectively. The shear keys are diamond shaped with a 2-4" (5-10 mm) gap between beams. Straight GFRP bars extend into shear key that also contained one longitudinal GFRP bar. UHPC was also placed in connection over piers. The pier connection had both transverse and longitudinal GFRP bars in the top and threaded inserts in the bottom. The bridge did not contain any transverse tie rods or post-tensioning.

The Log River Bridge, constructed in 2009 between Fort Francis and Kendra, Ontario, is a 69.17 ft. single span bridge consisting of 8 adjacent PC box beams that are 24" deep by 50.39" wide. Each beam has 30 - ½" grade 270 strands some of which are harped. The shear keys are diamond shaped with little or no gap between beams. Straight transverse GFRP bars extend into shear key which also contains one longitudinal GFRP bar. No transverse tie rods or post-tensioning.

The Eagle River Bridge, constructed in 2009 and 2010 between Dryden and Vermillion Bay, Ontario, has three spans with outer spans of 86 ft. and a center span of 112 ft. Each span has 12 adjacent PC box beams that 43.31" deep. The shear keys are diamond shaped with a small gap between beams. The shear keys contain one longitudinal GFRP bar but transverse bars in shear key are unknown from drawings obtained. UHPC was also placed in connection over piers. The pier connection has both transverse and longitudinal GFRP bars in the top and threaded inserts in the bottom. No transverse tie rods or post-tensioning exist.

8 Other Efforts and Activities

National Precast Concrete Association (NPCA)

The National Precast Concrete Association (NPCA) *www.precast.org* has drafted guidelines for the NPCA Quality Control (QC) Manual on the architectural applications of UHPC. The Architectural subcommittee drafted several sections and intends that the sections be added at numerous locations throughout the QC Manual. The guidelines are currently under review by the NPCA Technical Committee.

ASTM International (ASTM)

As a part of addressing the identified challenges, NA-WG and ACI members worked to introduce the relevant challenges (e.g. material standards and tests) to ASTM. It was suggested that ASTM host a symposium at an upcoming ASTM meeting where the issues regarding UHPC testing could be discussed in open forum, thereby enabling ASTM to support the needs of the UHPC community in the best manner. A symposium is tentatively scheduled for June 2013.

Other Department of Transportations

Numerous State Department of Transportations have shown interest in using UHPC in some type of transportation application. Iowa, New York, Virginia, Michigan, Georgia and more have sponsored some type of research. For example, the New Mexico Department of Transportation has sponsored a research project entitled “A Feasibility Analysis of Ultra High Performance Concrete for Prestressed Concrete Bridge Applications.” (Information can be found on their respective state research web site).

Other Academic Institutions

Many universities are involved in some form of research on UHPC. Some of these universities and the faculty member(s) involved are listed below in Table 1. This list is not inclusive.

Table 1 – Some UHPC Research Universities in the United States

University	Faculty
Florida International University	Amir Mirmiran
Iowa State University	Sri Sritharan and Terry Wipf
Georgia Institute of Technology	Lawrence Khan and Kimberly Kurtis
Massachusetts Institute of Technology	Franz Ulm
Michigan Technological University	Tess Ahlborn and Devin Harris
Missouri University of Science and Tech.	John Myers
Ohio University	Eric Steinberg and Ken Walsh
University of Alberta	Adam Lubell and Sadegh Kazemi
University of Arkansas	Micah Hale
University of Calgary	El-Hacha Raafat and Thomas Brown
University of Central Florida	Kevin Mackie
University of Connecticut	Michael Accorsi and Kay Willie
University of Michigan	Antoine Naaman (Retired)
Virginia Tech University	Carin Roberts-Wollmann and Thomas Cousins

9 Conclusions

UHPC is growing in use and application in North America and the trend in the past few years has been increasing. Whether for bridges, buildings, water systems and pipelines, blast protection systems, or other innovative applications, many challenges must be addressed. The North American UHPC Working Group will continue its grass roots efforts to encourage UHPC experts and users to develop design guides, establish a broad definition, and collaborate on filling the research needs for UHPC implementation, while involving a variety of stakeholders with a broad perspective on widespread implementation of UHPC in North America.

10 Acknowledgements

The authors wish to thank the members of the North American UHPC Working Group for their hard work and continued dedication to supporting the implementation of UHPC in North America.

References

[1] Ahlborn, T.M., Steinberg, E.P., J. Hartmann, B. Graybeal, J. Volgi and J. Potter, “Ultra-High Performance Concrete –Study Tour 2002,” *3rd PCI / FHWA International Symposium On High Performance Concrete*, Precast/Prestressed Concrete Institute, Orlando Florida, October 19-22, 2003.

[2] Graybeal, B., *Technote – Ultra High Performance Concrete*, Federal Highway Administration, FHWA Publication No. FHWA-HRT-11-038, McLean, Virginia, USA, *www.fhwa.dot.gov/research*

On the way to international design recommendations for Ultra High Performance Fibre Reinforced Concrete

Joost Walraven
Delft University of Technology, The Netherlands

Ultra High Performance Fibre Reinforced Concrete is a material with a large potential for innovative structures. However, in order to enable large scale application of this material internationally recognized design codes are necessary. Such codes should take due notice of societal developments. In future the major design criteria for structures will not only be limited to structural safety and serviceability, but will regard as well durability. Moreover, a design recommendation for ultra high performance fibre reinforced concrete should not be edited as a "stand alone document", but should be harmonized in the field of fibre concrete design in general. Moreover harmonization with general code recommendations for structural concrete is required, in order to facilitate hybrid structures as well. In this paper the development of code recommendations for UHPFRC is shown, with different levels of sophistication.

Keywords: Ultra High Performance Fibre Reinforced Concrete Design Recommendation

1 General considerations about codes for structural design

Structural design codes have a history of centuries. They should guarantee that the buildings in which we live and work, and the bridges and tunnels that we use for transportation, are safe and serviceable. Experience gained during the last decades has convinced us, that not only the criteria safety and serviceability, but as well durability need adequate attention. Therefore a change in code objectives during the years is noticed. The newest codes differ from their predecessors, in that the aspect "time" has become an integral part of design: structures have to be designed for safety and serviceability *for a time span (service life).* In the new Model Code for Concrete Structures [1] this has been adopted as a leading principle. That means that more attention than before has to be given to material properties, especially those which determine the rate of deterioration. Another important influencing factor in the development of structural design codes is internationalisation. After a long period of national codes there is a development to international codes, like the Eurocode, but as well the ACI code and the Asian Model Code. International codes have to be written in such a way that they apply to a variety of conditions and cultures. It means as well, that compromises have to be reached between the countries involved, with different geographical conditions, climates and resources and different ideas with regard to structural design. During the discussions between the parties involved, it turned out that there are not only differences in view, which have to be discussed, but fortunately also common ideas. These ideas are [2]:

- *Codes should be well founded.*
  Codes should be based on clear and scientifically well-founded theories and models, corresponding to a good representation of the structural behaviour and the material physics.
- *Codes should be flexible*
  Code recommendations should not be limited to on one single model. Preferably a code should offer alternative models with different complexity. Simple models can be used in daily business and more complex models in cases that non-traditional structures have to be designed, or where large financial investments have to be made (e.g. production of large series of prestressed bridge beams).

- *The models used in a code should be transparent*
  This is necessary because in engineering practice a wide spectrum of complications can occur, which have to be solved based on understanding the phenomena and not by blind application of intransparent code rules.
- *The models should reflect the state of the art*
  New developments should be involved, but not on the cost of unnecessary complexity.
  The need for an integral approach to requirements such as service life design criteria should be respected.
- *Codes should allow as much as possible an integral approach*
  Combination of technologies offer special chances. Hybrid structures and hybrid material combinations are an example. Therefore harmonisation between structural design in different structural materials is a “must”.

2 Considerations about a design code for ultra high performance fibre reinforced concrete

The history of ultra high performance fibre reinforced concrete is remarkable. The development of its basis, conventional fibre reinforced concrete, goes back to about 1970. Many code committees have dealt with this material and have produced design rules. Even international codes have been edited, such as the recommendations developed by RILEM TC162-TDF. The focus of these recommendations is on concrete’s in the traditional strength classes to about C80. For reasons of workability the fibre content was seldomly larger than 80 kg/m^3. Contrary to most technical developments, which are characterized by a gradual progress, the development of fibre concrete was characterised by a remarkable jump. Publications on UHPFRC appeared from about 1990 and concentrated on concrete with cylinder strengths of about 180-200 MPa. The large difference in properties between conventional FRC and UHPFRC led initially to a treatment of those fibre concrete species in different study committees. An example is the work on fibre reinforced concrete in fib, where conventional fibre concrete (FRC) is treated in TG 8.3 and UHPFRC in TG 8.6. It was logic that soon the question of the scope of the two task groups came up. The initial idea, to limit the work of TG 8.3 to an *upper* strength class of C80 and to limit the work of TG 8.6 to a *lowe*r strength class of C180 appeared not to be a good solution, since then there would be no design recommendation for the range of intermediate strength classes, were many interesting applications are possible as well. Fig. 1 shows the difference in the focus of the two task groups in relation with some very interesting and actual applications in the intermediate range. Such an application is for instance the strengthening of old steel bridges with new fibre concrete reinforced bridge decks. Ultra high strength fibre concrete, which would lead to very thin overlays, would not be the best solution, since it would have the disadvantage of not sufficiently reducing the stress variations in the steel girders, which would not solve the problem of fatigue. Structural overlays in strength classes C120 - C140 yield the optimum solution between mass, durability, abrasion resistance and cost. Similar arguments apply for UHPFRC precast prestressed sheet piles as shown at the bottom right in Fig. 1, which are produced in a concrete strength class C130.

In order to solve the problem of the intermediate strength range it was suggested not to use a strength class criterion but to distinghuish two types of fibre reinforced concrete: one characterized by softening and one by hardening behaviour. However, also this distinction turned out to be unpractical, as evidenced by Fig. 2. Softening in uniaxial tension may correspond with harding in bending; moreover even softening in bending might go along with hardening on the level of the structural behaviour. Finally, softening in uniaxial tension loses its significance if fibres are combined with reinforcing bars.

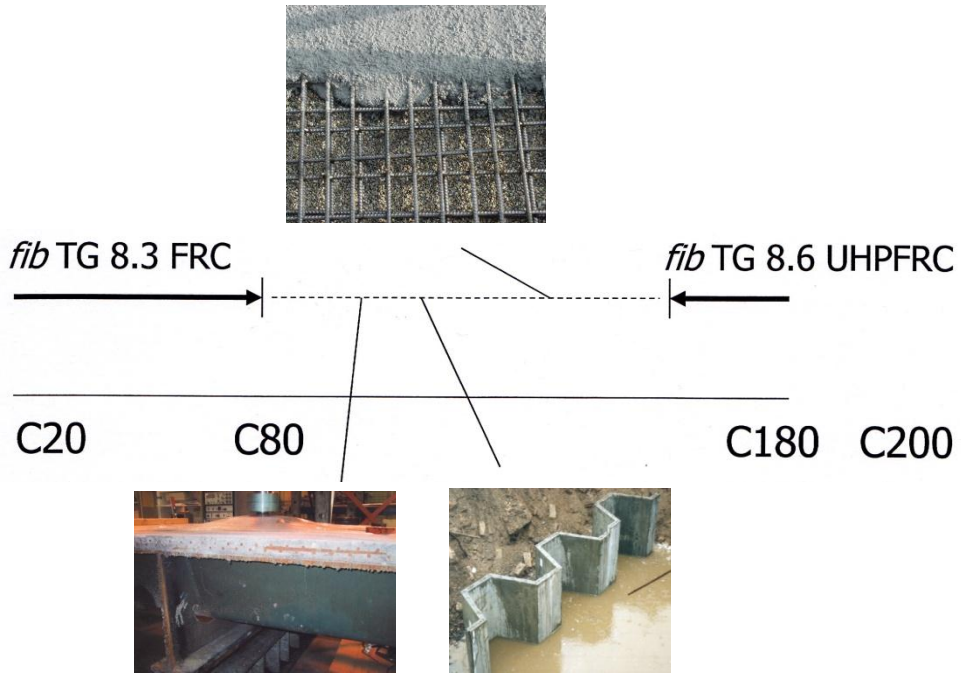

Figure 1: Scope of fib Task Groups 8.3 (conventional fibre reinforced concrete) and 8.6 (ultra high strength fibre reinforced concrete) with "lost applications" in the intermediate area like bridge decks (top picture and bottom left) and sheet piles (bottom right) in concrete strength classes C100 – C 150.

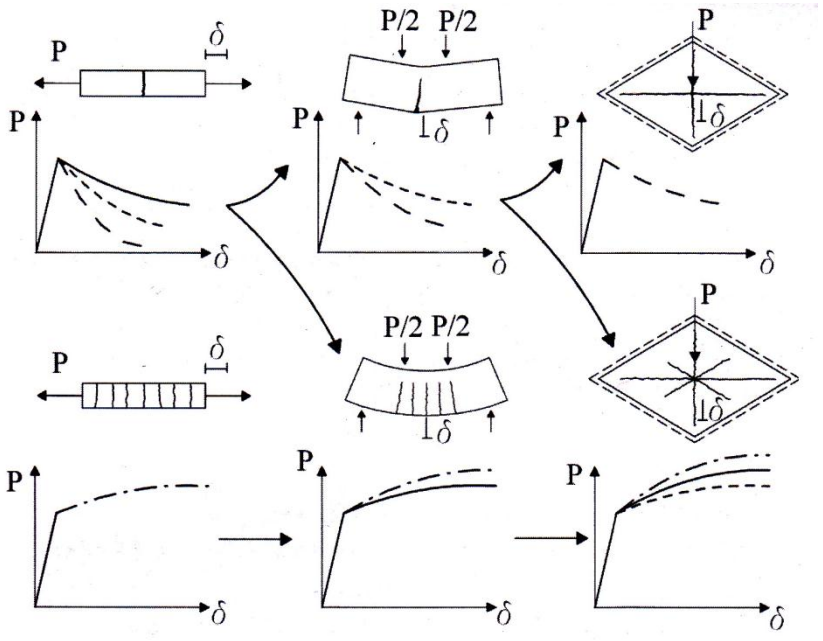

Figure 2: Softening versus hardening behaviour in uniaxial tension (left), bending (middle) and on a structural level (right) [1].

The next option considered was to develop one integral code for all types of fiber reinforced concrete in all strength classes, so valid from C20 to C200. This, however, was not acceptable to many members of both Task Groups, for different reasons. Members of TG 8.3 argued, that over many years considerable effort was invested in developing a reliable design code for conventional fibre reinforced concrete, with which meanwhile a lot of experience had been gained and which was already in a far stage of harmonization with the Eurocode for structural

concrete. Members of TG 8.6 argued that ultra high performance concrete differs substantially from conventional concrete, both in properties and in production technology. The high-tech properties and sensitive production procedures would not match well with the more “mass-type” character of conventional FRC. Moreover, it was feared that the harmonization of UHPFRC with all other types of fibre concrete would harm the market position, due to a conservative generalisation of properties.

In fib meanwhile the Model Code 2010 was produced, in which one of the principles was to offer different levels of sophistication in methods for design and analysis. Simple methods should be sufficient for simple daily applications, but more advanced methods should pay-off when, for instance, the analysis should lead to a decision whether considerable amounts of money should be invested in strengthening of a structure or not. The decision was therefore to develop a general design recommendation for all types of fibre concretes in Model Code 2010 and to develop additionally an approach tailored to UHPFRC in the TG 8.6 recommendation.

3 General recommendation for all fibre concrete types in Model Code 2010

In the fib Model Code for Concrete Structures 2010, the recommendation for fiber reinforced concrete is integrated in a more general code for “structural concrete”. So, fibers can be used as the only reinforcement, but also in combination with reinforcing or prestressing steel. Moreover the method applies to any concrete strength, so no difference is made between conventional fiber concrete, high performance and ultra high performance concrete. A new aspect is that fiber concrete is classified in a system of behavioural classes. As such, the designer can assume a certain design class and make the design calculations, based on the properties given for this class. As a part of the production, it should be proven by standardized control tests on the mixture used, that the mixture indeed satisfies the design assumptions. Basically, such a procedure is – for many years already - common practice in conventional concrete structures, where it should be demonstrated by cylinder or cube tests that the concrete satisfies the strength class assumed in the design. Fig. 3 shows the standard specimen used for the bending test on fibre reinforced concrete (according to EN 14651 (dimensions in mm). Fig. 4 shows the load-deflection relation obtained with a number of reference values (F_i,$CMOD_i$), where F_j is the force applied at a certain stage of loading, and $CMOD_i$ the corresponding value of the Crack Mouth Opening Displacement $CMOD_j$ (measured crack opening at notch A).

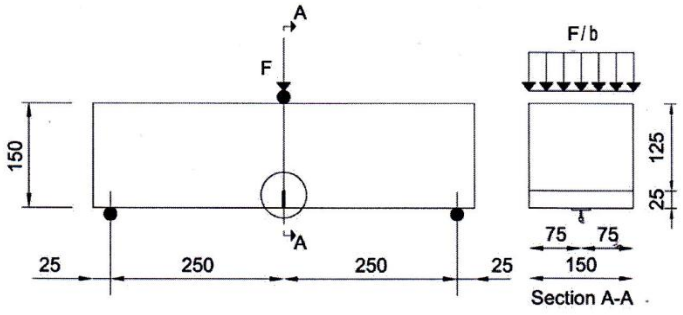

Figure 3: Standard bending test on a notched FRC beam.

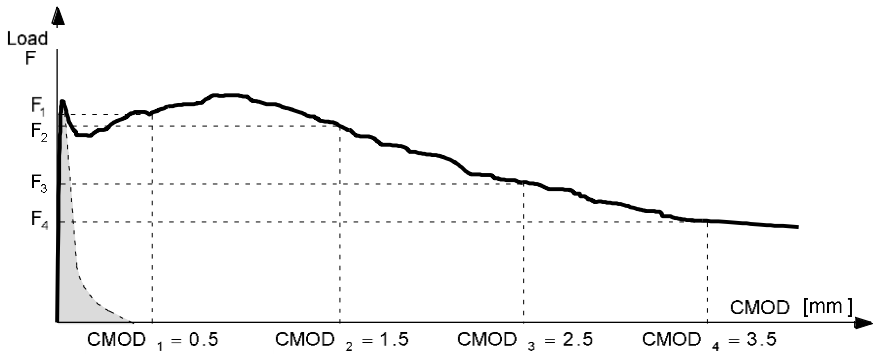

Figure 4: Typical load F – CMOD curve for FRC.

From the F – CMOD relation, flexural tensile strength values f_{Rj} are derived for a set of $CMOD_j$ values, according to:

$$f_{R,j} = \frac{3F_j l}{2bh_{sp}^2}$$

where $f_{R,j}$ *[MPa]* = residual flexural tensile strength corresponding to $CMOD = CMOD_j$, F_j [N] = load corresponding to $CMOD = CMOD_j$, l = span length in mm, b = specimen width in mm and h_{sp} distance between the notch tip and the top of the specimen (125 mm). The classification of fiber concrete is based on the values for $f_{R,j}$ obtained for $CMOD_1$ (= 0.5 mm) and $CMOD_3$ (= 2,5 mm).

In order to classify the post-cracking strength of FRC a linear elastic relation can be assumed, by considering the characteristic residual strengths for serviceability (f_{R1k}) and ultimate (f_{R3k}) conditions. In particular two parameters are relevant, namely f_{R1k} (representing the strength interval) and the letter a, b, c, d or e(representing the ratio f_{R3k}/f_{R1k}).

The strength interval is defined by two subsequent numbers in the series:

1.0, 1.5, 2.0, 2.5, 3.0, 4.0, 5.0, 6.0, 7.0, 8.0, … [MPa]

whereas the letters *a*, *b*, *c*, *d, e* correspond to the residual strength ratios:

a. If $0{,}5 \leq f_{R3k}/f_{R1k} \leq 0{,}7$
b. If $0{,}7 \leq f_{R3k}/f_{R1k} \leq 0{,}9$
c. If $0{,}9 \leq f_{R3k}/f_{R1k} \leq 1{,}1$
d. If $1{,}1 \leq f_{R3k}/f_{R1k} \leq 1{,}3$
e. If $1{,}3 \leq f_{R3k}/f_{R1k}$

For instance, a material denoted as “3b” has a tensile strength ranging between 3 and 4 MPa and a f_{R3k}/f_{R1k} ratio ranging between 0.7 and 0.9.

From the bending tests two simplified stress-crack opening laws can be deduced (Fig. 5): a rigid-plastic relation, or a linear post-cracking relation (hardening or softening) as schematically shown in Fig. 5, where f_{Fts} represents the serviceability residual strength, defined as the post-cracking strength for serviceability crack openings, and f_{Ftu} represents the ultimate residual strength. The solid and dashed lines refer to softening and hardening post-cracking behaviour respectively.

It is mentioned that the behaviour observed in standard tests can deviate substantially (in a beneficial and a non-beneficial way) from the behaviour of the corresponding FRC in the structural element. Thus the manufactoring method and the concrete consistency should be taken into account by the designer.

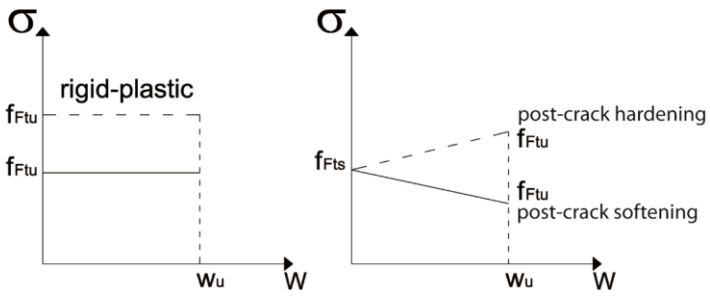

Figure 5: Simplified post-cracking constitutive laws: stress-crack opening.

If wished so, the stress – crack width relations can be converted to stress – strain relations by

$$\varepsilon = w / l_{cs}$$

where w = crack width and l_{cs} = "structural characteristic length" for the situation considered, defined as:

$$l_{cs} = \min\{s_{\min}, y\}$$

where s_{min} = mean distance between cracks and y = distance between neutral axis and tensile side of the cross section.

A special aspect considered is the orientation factor K, taking into account that due to the way of producing fibre reinforced concrete structural members a non homogeneous orientation of the fibres can occur, which has its influence on the mechanical properties of the material.

By providing simplified relations for the effect of fibres, as given before, it is not only possible to design structures with only fibres as reinforcement, but as well with combinations of fibres and conventional reinforcement. The equations are familiar to structural engineers and can also be used if fibres are combined with other reinforcing and/or structural materials, so that the promising area of hybrid structures invites for application. Additionally chapter 7.7 of Model Code 2010 "Verification of safety and serviceability of FRC structures" shows how the effect of fibres can be considered in a way harmonized with the design principles for structural concrete in general.

4 Recommendation for UHPFRC according to fib TG 8.6

Task Group 8.6 focuses on a recommendation tailored to the design of UHPFRC structures. Use is made of experience especially gained with this material. The draft document starts with extended information of the mechanical and physical properties of ultra high performance fibre reinforced concrete. Among these data, adequate attention is given to all aspects which give UHPFRC its credit for designing innovative structures. E.g. special attention is given to fatigue resistance, since it is expected that UHPFRC will be used in slender structures where the traffic load has a larger significance than in conventional reinforced concrete structures, for which the permanent load plays a more dominant role. Moreover special attention is given to aspects like porosity and pore size distribution, alkalinity, diffusion and permeability, carbonation and sulphur resistance and resistance to freezing and thawing, since it is expected that particularly thoses aspects may give UHPFRC additional chances in cases where life cycle criteria govern the design.

It is expected that the effect of fibre orientation, as a consequence of the rheological properties of UHPFRC, is stronger than for conventional fibre concrete's. This may particularly be expected to play a role in thin structures. For the determination of the properties of the

materials, and even the structural members, therefore a distinction is made between *thin* and *thick* structures. For thin structures, which are defined as structures with a cross-sectional height equal or smaller than 3 times the fibre length L_f , basically two methods exist:

a. Standard tests are carried out on thin standard specimens, as shown in Fig. 6. By carrying out this testing method, the stress - strain relations obtained are expected to include implicitely the effect of fibre alignement by the boundary conditions, which is expected to occur in the structural elements as well. This test is not regarded as "absolute truth": Therefore it is advised to apply a correction factor 1/K to the results obtained from a test on the actual structural element.
b. The structural member can be tested as a whole, according to the principle of "design by testing". This method has the advantage that the effect of casting and mechanical vibration is implicitely considered and even can be used to optimize the behaviour of the structural element. An example of such an approach is the design and testing of the precast slab elements for the platform, supporting the offshore runway of the new Haneda Airport inTokyo.

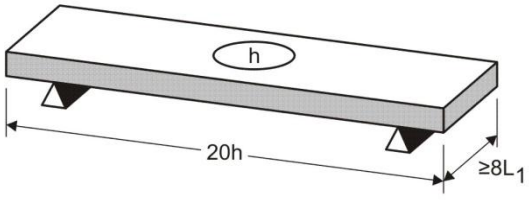

Figure 6: Standard test on thin element

Figure 7: Test on slab element for Haneda. Airport new Runway platform.

For the design of *thick* elements ($h \geq 3L_f$) the following procedure is advised: "Cast and notch a prism. Perform a flexural test. Conduct inverse analysis to determine a post-cracking stress – crack width (σ-w) relation. Correct this relation derived from this test as to integrate size and boundary effects associated with the specimen shape and casting method. Weight this law with a reduction coefficient 1/K representing the difference between a flexural test result for a cast prism and what is obtained on prisms sawn from an actual structural element. To determine an exact factor K for the particular application considered, make components that are representative for the actual geometry and manufacturing method used for the structure, and take specimens along the directions of principal stress".

For the stress-crack width relations and the stress–strain relations in tension, a bilinear descending curve is foreseen. Also in this case a harmonized implementation in structural design recommendations for conventional structural concrete are developed.

The table of contents for the fib TG 8.6 Recommendation for UHPFRC (draft version 2011) is given below:

1. Scope
2. Terminology and notations
3. Basis of design
   2.1 General
   2.2 Performance based design principles (SLS, ULS, Service Life, Sustainability)
   2.3 Reliability
   2.4 Quality control and management

4. Material properties
   4.1 Material components for UHPFRC mix design
   4.2 Behaviour in compression
   4.3 Behaviour in tension
   4.4 Behaviour under multi-axial loading conditions
   4.5 Behaviour under dynamic loads
   4.6 Time dependant effects
   4.7 Temperature effects
   4.8 Durability
   4.9 Interface properties
5. Design
   5.1 General requirements
   5.2 Safety concept
   5.3 Structural analysis
   5.4 Stress – strain relationships for UHPFRC
6. Design for structural safety (ULS)
   6.1 Bending with and without normal force
   6.2 Shear
   6.3 Torsion
   6.4 Punching
   6.5 Design with strut and tie models
   6.6 Design of interfaces in hybrid structures
   6.7 Fitting technology
7. Design for serviceability (ULS)
   7.1 Crack width control
   7.2 Deformation
8. Detailing
   8.1 Anchorage of reinforcing bars and prestressing strands and wires
   8.2 Splices
   8.3 Bar spacing
   8.4 Allowable bending radius in reinforcing steel
   8.5 Cover
9. Construction and quality management
10. References

5 Conclusions

International recommendations for UHPFRC are in a far state of development. In the fib Model Code for Concrete Structures 2010 a general method is given, valid for all types of fibre concrete, valid from C20 to C200. Simplified expressions are given which allow designers to use fibres as reinforcement in a way they are familiar with.

The fib task group TG 8.6 writes a recommendation especially for UHPFRC, which is a tailored approach in order to take, on the one hand, notice of the particularities of this material and take, on the other hand, full advantage of its superior mechanical and physical properties.

References

[1] fib Model Code for Concrete Structures: First complete draft. *fib Bulletins 55 and 56*, March 2010, International Federation of Concrete Structures, Lausanne.

Application of Nanoparticles

Surendra P. Shah[1], Shiho Kawashima[1], Pengkun Hou[1,2], David Corr[1]
1: Department of Civil and Environmental Engineering, Northwestern University, Evanston, IL, USA
2: College of Materials Science and Engineering, Chongqing University, Chongqing, P.R. China

This paper is a summary of recent work on the application of nanoparticles in cement-based materials. Through proper processing, nanoparticles can enhance many properties of concrete. Small additions of nanoclays can increase the fresh-state stiffness of self-consolidating concrete (SCC) with little compromise to initial flowability. Such properties make applications such as reduced SCC formwork pressure and slipform paving possible to increase efficiency in construction. Nanoparticles such as nanoSiO_2 and nano$CaCO_3$ can accelerate rate of hydration and improve the early-age mechanical properties of cementitious materials, including those with fly ash to lead to a more environmentally-friendly material. The future potential of concrete as a "smart" material will be discussed, as well. Carbon nanotubes can introduce piezoresistivy to concrete, making it a self-sensing material, and TiO_2 nanoparticles can introduce self-healing and smog-eating capabilities through photocatalysis.

Keywords: nanomodification, nanoparticles, clays, nanoSiO_2, nano$CaCO_3$, carbon nanotubes, TiO_2

1 Introduction

Due to the recent innovations in nanotechnology, nanomodification and nanocharacterization of cement-based materials has generated much research interest. The focus of this paper is on nanomodification: the manipulation of the structure at the nanoscale (less than 100nm) to develop cement composites that exhibit enhanced properties. Among the types of nanoparticles that have been studied are ZnO_2 [1], TiO_2 [2], $CaCO_3$ [3,4], clays [5], SiO_2 [6] and carbon nanotubes [7].

This paper is a summary of the current work being done on the application of nanoparticles in cementitious systems, highlighting those performed at the Center for Advanced Cement-Based Materials at Northwestern University (ACBM-NU). Small additions of nanoclays can significantly increase the fresh-state stiffness of self-consolidating concrete (SCC) with little compromise to initial flowability. Such properties make it possible to increase efficiency construction in applications such as reduced SCC formwork pressure and slipform paving. Through filler and/or seeding effects, nanoparticles can accelerate rate of hydration and improve early-age mechanical properties of cementitious materials, including those with fly ash to lead to a more environmentally-friendly material. The influence of the method of dispersion of nano$CaCO_3$ powder for this application will be evaluated. And an in-depth study on the mechanisms underlying the influence of nanoSiO_2 on the compressive strength gain of fly ash-cement systems will be explained.

Nanomodification can introduce novel properties and functions, as well. The future potential of nanomodification in making concrete a "smart" material will be discussed. Carbon nanotubes can introduce piezoresistivity to concrete and make it a self-sensing material, and TiO_2 nanoparticles can introduce self-healing and smog-eating capabilities through photocatalysis.

2 Highly thixotropic clay-modified cementitious materials

Work at ACBM has demonstrated that through proper proportioning of fly ash, superplasticizers, and a small addition of clays (<1% by mass of binder), it is possible to design an SCC mix that experiences high flowability during casting and high green strength immediately after placement [8-11]. Such properties can effectively reduce SCC formwork pressure. Fig. 1 shows the results of a study where a lab-scale formwork pressure device was used to simulate casting by

applying a vertical pressure and measure the lateral pressure of SCC over time [12]. Although both mixes had a slump flow of 60 ± 2cm, it is apparent that the SCC with a 0.33% nanoclay addition (NC0.33) exhibited significantly reduced lateral pressure compared to the SCC without nanoclays (NC0). (The nanoclay was a purified magnesium aluminosilicate with a rod-like shape – 1.75 μm in length, 3nm in diameter). This behavior has been tied to flocculation, where studies have shown that clays increase flocculation strength [13] and floc size [14].

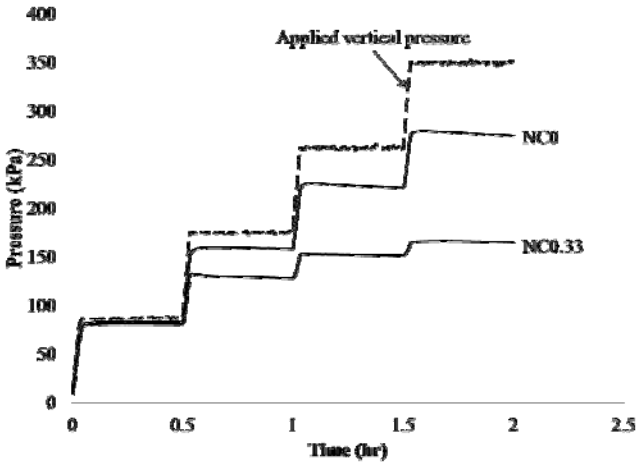

Figure 1: Formwork pressure response of SCC with (NC0.33) and without (NC0) 0.33% nanoclay addition [12].

In the most recent study, the contribution of water adsorption by the clays on stiffening was examined through a shear rheological approach. The nanoclays have a high water adsorption of 200% by mass, making it a possible governing factor. The water content of cement pastes with and without a 1% nanoclay addition were adjusted for clay water adsorption. The mix compositions are given in Table 1. Each mix was subjected to a constant applied shear rate of 300 s^{-1} for 60 min, during which the viscosity was recorded. Tests were performed in a temperature controlled rheometer, set at room temperature, with a coaxial cylinder geometry.

Table 1: Mix composition of pastes (200% water adsorption by mass assumed).

Mix	Cement (g)	Water (g)	Nanoclay (g)
NC0	500	215	0
NC1	500	217.6	5
NC1H	500	227.6	5
NC0H	500	205	0

Fig. 2a shows the viscosity evolution up to 5min, during which each mix reached equilibrium. If the loss of free water by clay water adsorption is a governing stiffening mechanism, mixes NC0 and NC1H and mixes NC1 and NC0H should exhibit similar viscosity evolutions. However, it is apparent that the viscosities of these mixes did not coincide – adjusting water content was not sufficient in negating the effect of the clays on stiffening. Also, both mixes with clays exhibited a significant decrease in viscosity upon the introduction of shear due to deflocculation. This shows that the clays had an immediate stiffening effect through flocculation, resulting in a highly thixotropic material.

After equilibrium, at which the flocs cannot be broken down any further under the given shear condition, each paste goes on to experience a similar increase in viscosity, as shown in Fig. 2b – the change in viscosity from equilibrium to final (60min) is 0.18 ± 0.001Pa-s for all mixes. This

indicates that although the clays have an immediate stiffening effect, they have little or no influence over time under a given constant shear condition.

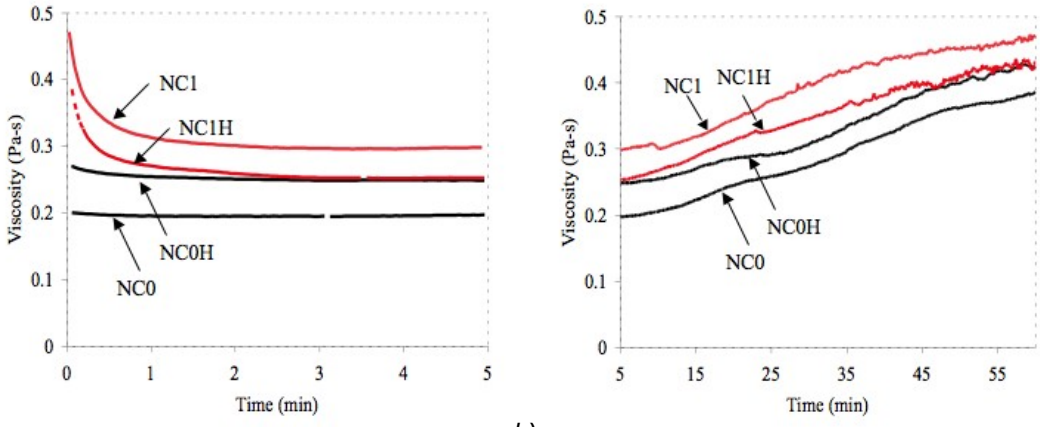

a) *b)*

Figure 2: Viscosity evolution of cement pastes a) before and b) after equilibrium.

3 Potential of nanomodification to facilitate cement replacement with fly ash

The use of fly ash in concrete introduces many advantages, namely increase in workability and later-age strength, and reduction in carbon footprint. However, its delayed rate of hydration, setting, and low early-age strength gain are major drawbacks. The potential of nanomodification as a strategy facilitate the use of fly ash is demonstrated in the following studies.

Nano-$CaCO_3$

Although limestone powder is typically considered to be inert, recent studies have found that they can accelerate rate of hydration when introduced as nanoparticles. However, few in-depth studies have been done thus far [3,4]. This study focuses on processing, where dry nano$CaCO_3$ powder is dispersed through ultrasonication. Through effective dispersion, the motivation is to enhance the effect of the nanoparticles and to decrease the addition level.

The effect of sonicated versus blended nano$CaCO_3$ on rate of hydration, setting time, and early-age compressive strength gain were compared in ordinary Portland cement (OPC) and type F fly ash-OPC pastes. Nano$CaCO_3$ was sonicated for 30 min in an aqueous solution at 15% concentration with a 0.06% polycarboxylate superplasticizer addition by weight of water. Blended suspensions were prepared in a household blender for 3min. The nano$CaCO_3$ had a particle size range of 15-40nm but were agglomerated to the micron scale as-received.

The rate of hydration of OPC pastes with and without a 5% nano$CaCO_3$ addition, measured through semi-adiabatic calorimetry, are shown in Fig. 3. It is apparent that for both samples with a nano$CaCO_3$ addition, there is an acceleration in rate of hydration. However, the effect is much more pronounced for the sonicated sample, where the peak is much higher and occurs earlier.

The setting time of 50% fly ash-OPC pastes and a plain OPC paste are shown in Fig. 4a. In both blended and sonicated samples, the addition of 5% nano$CaCO_3$ helped accelerate setting. Further, the sonicated nano$CaCO_3$ completely offset the delay caused by the 50% fly ash replacement, where it exhibited the same setting times as the plain OPC paste sample.

The compressive strength gain (1, 3, 7d) of 50mm cube samples of plain OPC paste and 30% fly ash-OPC pastes with and without a 5% nano$CaCO_3$ addition are shown in Fig. 4b. At 3 and 7d, the sonicated sample showed a greater improvement than the blended sample.

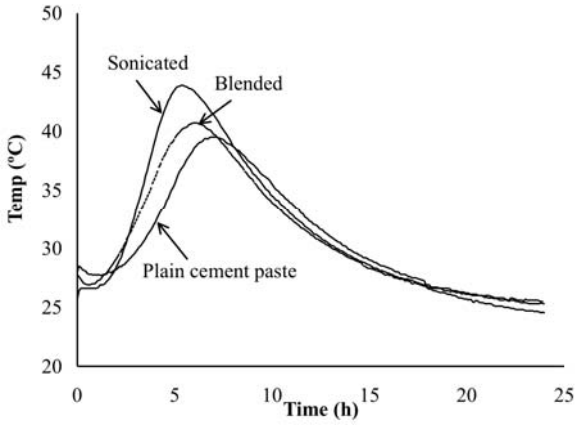

Figure 3: Rate of hydration of OPC pastes (w/c =0.4) with 5% nanoCaCO$_3$ addition,blended versus sonicated.

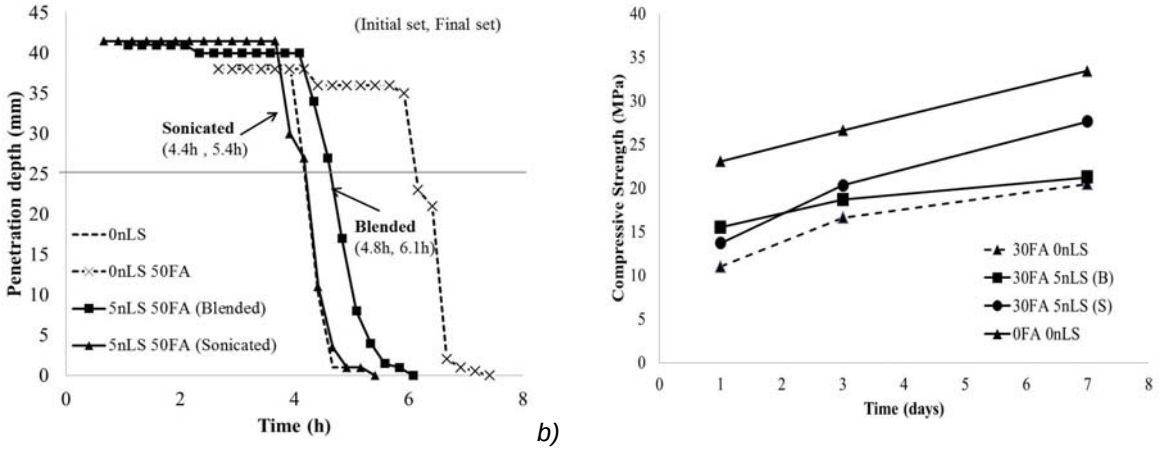

a) *b)*

Figure 4: a) Setting time of 50%FA-OPC pastes (w/b = 0.4) and b) compressive strength gain of 30%FA-OPC pastes (w/b = 0.43) with and without a blended (B) or sonicated (S) 5% nanoCaCO3 (nLS) addition

NanoSIO$_2$

With the incorporation of nanoSiO$_2$, the strength gain of cement-based materials can be improved due to its hydration seeding effect and high pozzolanic activity [15-18], which result in a higher amount of C-S-H gel and more densified bulk structure [19]. When considering the enhancing effect of nanoSiO$_2$ on strength gain, most studies thus far have focused on the early-age strength gain [17,20] and only a few contradicting results have been reported for the later-age strength development [21,22]. Thus, their effect on the later-age mechanical properties needs further investigation.

The compressive strength evolution of CNS-added cement-fly ash mortars is shown in Fig. 5. For the 40% fly ash-cement mortar, the addition of CNS significantly increased the strength gain early on. However, the enhancing effect decreased over time – after 3 months the strength of CNS-added mortar was equal to (CNS-20nm mortar) or less than (CNS-10nm mortar) the control fly ash-cement mortar. This implies that nanoSiO$_2$ has no positive effect on the strength gain of fly ash replaced cement-based material at later ages. To determine why, the hydration and morphology of CNS-modified fly ash-cement systems were closely examined.

Ca(OH)$_2$ content

For fly ash replaced cement-based materials, calcium hydroxide (CH) generated by cement hydration is critical for later-age pozzolanic reaction. It can be seen in Fig. 6 that CNS addition has a great influence on the CH content of fly ash-cement paste. At each age, the CH content of the 5% CNS-10nm paste was lower than that of the 0% CNS paste. This is due to the additional pozzolanic reaction by the CNS. Also, more CH was consumed in the 0% CNS paste

at later ages (28d-56d), indicating further pozzolanic reaction of fly ash. Although it has been reported that nanoSiO_2 is beneficial for the hydration of fly ash in the early age [22], a lack of CH prohibits the hydration of fly ash in the later age and is likely a contributing factor to the reduced rate in long-term compressive strength gain of CNS-modified fly ash – cement mortar.

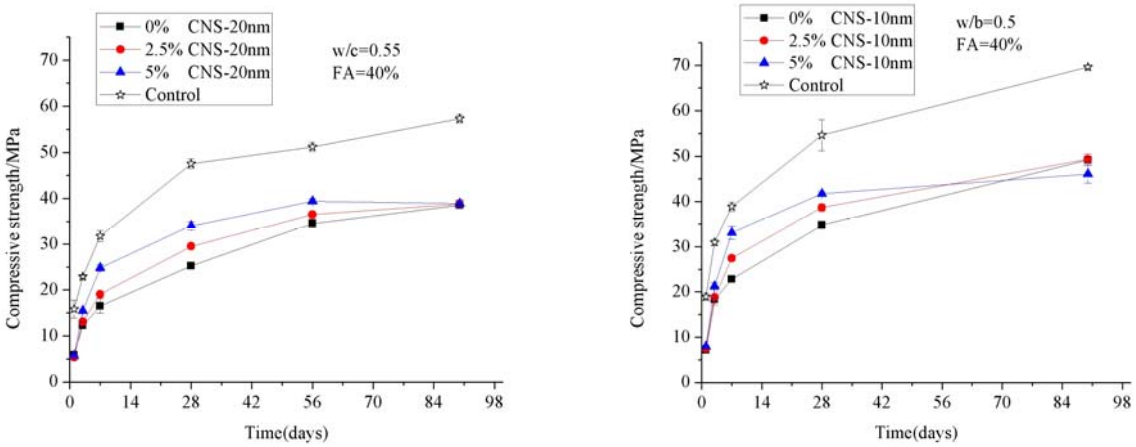

Figure 5: Effect of CNS on the compressive strength of fly ash mortar

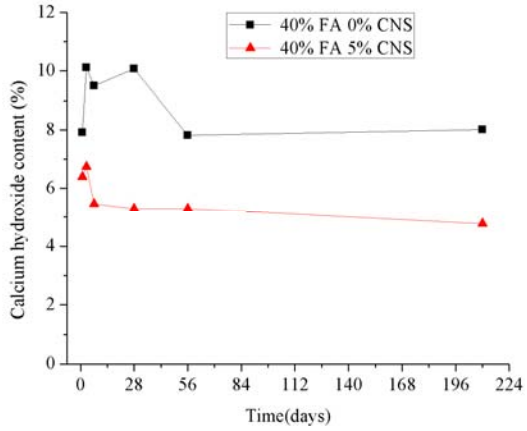

Figure 6: $Ca(OH)_2$ content vs. time (CNS-10nm)

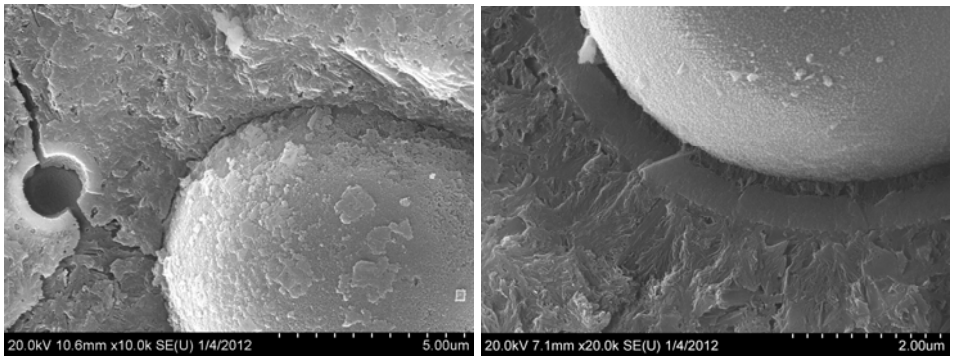

a) 0%CNS *b) 5%CNS-10nm*

Figure 7: Interface of cement paste and fly ash particle (7 month old) with a) 0% CNS and b) 5%CNS-10nm

Morphology

The effect of nanoSiO_2 on the hydration of fly ash particles and its interface with cement paste after 7 months is shown in Fig. 7. It is apparent that the fly ash particles in the control paste are severely eroded and an abundance of hydration products can be found coating the fly ash

particle surface. This implies that a high degree of pozzolanic reaction had occurred. For the CNS-added fly ash paste, the fly ash particles are smoother and featureless, indicating less pozzolanic activity. A distinct difference in morphology can be seen at the interface of the fly ash particle and cement paste between the two samples. For 0% CNS paste, the hydrates covering the fly ash surface are well-compacted rods and grains, which is typical for hydration products of mature cement pastes. However, for 5% CNS-10nm paste, there is a double-layer shell structure coating the fly ash particle. A close examination of the double-layer shell reveals that it is composed of an outer layer of finely compacted grains and a fibrous inner layer. The EDS results at 15 different areas of the compacted shell structure revealed an average Ca/Si ratio of 1.38, which is smaller than that of the adjacent C-S-H gel of 1.66. It has been reported that C-S-H gel with a low Ca/Si ratio is less permeable [23]. Thus, it can be deduced that the outer layer of compacted hydrates, which is formed by the pozzolanic reaction of CNS and CH, acts as an ion penetration barrier that hinders the hydration of fly ash particles. The inner fibrous hydrates can be formed by the pozzolanic reaction of fly ash.

4 Future of nanomodified concrete as a “smart” material

TiO_2 nanoparticles

Through photocatalysis, TiO_2 particles can introduce smog-eating capabilities to concrete and increase its environmental friendliness [24-26]. The reaction can introduce self-cleaning capabilities, as well, by helping to prevent bacteria and dust from sticking to the surface of the material – TIO_2 was used for the construction of the Jubilee Chruch (Rome, Italy) to keep its appearance white. More recently, it has been found that when introduced as nanoparticles, TiO_2 can help accelerate rate of hydration and improve compressive strength through filler effects. In a study by Jayapalyan et al., the rate of hydration of OPC pastes with nanoTiO_2 was found to be faster than OPC pastes with microTiO_2 [2,27]. Other work has observed some improvement in the compressive and flexural strength of concrete with nanoTiO2 additions, as well [28,29]. Such work demonstrates the possibility of a nanoTiO_2-modified cement composites with depolluting, self-cleaning capabilities and enhanced mechanical properties.

Carbon nanotubes (CNTs) and carbon nanofibers (CNFs)

The ability of CNTs and CNFs to control cracks at the nanoscale, induced by both flexure and autogenous shrinkage, brings researchers closer to achieving a crack-free cement composite. Konsta et al. demonstrated that highly-dispersed CNTs can significantly improve the flexural strength of cement pastes at dosages as low as 0.025%, Fig. 8 [7,30]. Other studies have found similar results [31-33]. And 0.048% CNT/CNF additions can lead to a substantial reduction in the autogenous shrinkage of low w/c ratio cement pastes (w/c = 0.3), Fig 9 [30]. In addition to having superior mechanical properties, CNTs are highly conductive and when subjected to stress/strain, their electrical properties change and express a linear, reversible piezoresistive response. Studies have demonstrated the potential of CNTs to introduce piezoresistivity to concrete [34-36]. Such properties can make applications such as health monitoring of concrete structures, damage evaluation and traffic monitoring possible. With proper processing, CNT-reinforced cement composites can exhibit not only superior mechanical properties but also self-sensing capabilities.

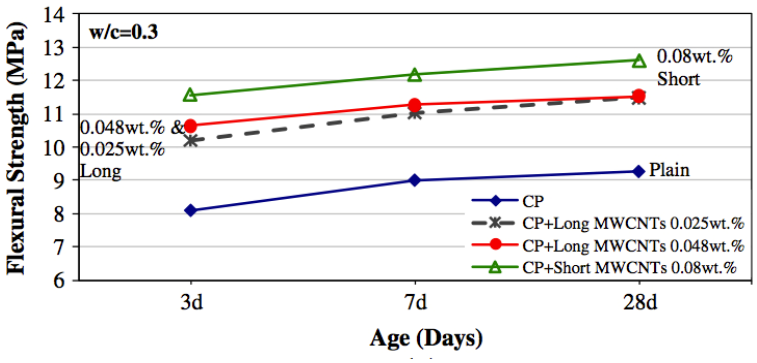

Figure 8: Flexural strength of highly-dispersed CNT-reinforced cement composites [30].

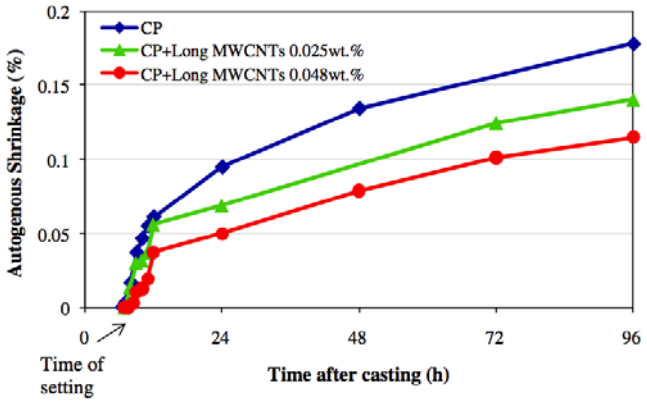

Figure 9: Autogenous shrinkage of highly-dispersed CNT-reinforced cement composites (w/c = 0.3) [30].

5 Conclusions

This paper is a summary of recent work on the application of nanoparticles in cementitious materials. Clays can help manipulate the properties of SCC to improve constructability. Well-dispersed nano$CaCO_3$ can enhance various early-age properties of fly ash-cement systems. NanoSiO_2 improves the early-age compressive strength of fly ash-cement materials but reduces the rate of later-age strength gain, due to their high CH consumption in the early age and the formation of a less-permeable gel coating on the fly ash particle surface, both of which can limit the hydration of fly ash. Although these studies demonstrate the potential of nanoparticles to enhance the properties of cement-based materials, continued investigation is needed. Similarly, more research can lead to the development of “smart“ concrete, where nanomodification introduces novel properties and functions. TiO_2 nanoparticles can improve mechanical properties while exhibiting depolluting and self-cleaning capabilities. And CNT-reinforced cement composites can potentially become a crack-free, self-sensing material.

Acknowledgements

The authors would like to acknowledge the financial support from both the Infrastructure Technology Institute at Northwestern University and Tennessee Valley Authority (TVA) and Oak Ridge Associated Universities (ORAU) (Award 105866). The third author would also like to thank the financial support from the China Scholarship Council.

References

[1] Nazari A and Riahi S (2011). "The effects of zinc dioxide nanoparticles on flexural strength of self-compacting concrete." Composites Part B: Engineering **42**(2): 167-175.

[2] Jayapalan AR, Lee BY and Kurtis KE (2009). Effect of Nano-sized Titanium Dioxide on Early Age Hydration of Portland Cement. Nanotechnology in Construction 3. Bittnar Z, PJM Bartos, J Němeček, V Šmilauer and J Zeman, Springer Berlin Heidelberg**:** 267-273.

[3] Sato T and Beaudoin JJ (2006). The effect of nano-sized $CaCO_3$ addition on the hydration of OPC containing high volumes of fly ash. In Proceedings of the 12th International Congress on the Chemistry of Cement. Montreal, Canada**:** pp 1-12.

[4] Sato T and Diallo F (2010). "Seeding effect of nano-$CaCO_3$ on the hydration of tricalcium silicate." Journal of the Transportation Research Board **2141**: pp 61-67.

[5] Chang T-P, Shih J-Y, Yang K-M and Hsiao T-C (2007). "Material properties of portland cement paste with nano-montmorillonite." Journal of Materials Science **42**(17): 7478-7487.

[6] Sobolev K, Flores I, Torres-Martinez LM, Valdez PL, Zarazua E and Cuellar EL (2009). Engineering of SiO2 Nanoparticles for Optimal Performance in Nano Cement-Based Materials. Nanotechnology in Construction 3. Bittnar Z, PJM Bartos, J Němeček, V Šmilauer and J Zeman, Springer Berlin Heidelberg**:** 139-148.

[7] Konsta-Gdoutos MS, Metaxa ZS and Shah SP (2010). "Highly dispersed carbon nanotube reinforced cement based materials." Cement and Concrete Research **40**(7): 1052-1059.

[8] Pekmezci BY, Voigt T, Kejin W and Shah SP (2007). "Low compaction energy concrete for improved slipform casting of concrete pavements." ACI Materials Journal **104**(Compendex): 251-258.

[9] Voigt T, Mbele J-J, Wang K and Shah SP (2010). "Using Fly Ash, Clay, and Fibers for Simultaneous Improvement of Concrete Green Strength and Consolidatability for Slip-Form Pavement." Journal of Materials in Civil Engineering **22**(2): 196-206.

[10] Tregger N. Tailoring the fresh state of concrete. PhD Thesis, Northwestern University, Evanston, IL, 2010.

[11] Tregger N, Voigt T and Shah S (2007). Improving the slipform process via material manipulation. Advances in Construction Materials 2007. Grosse CU, Springer Berlin Heidelberg**:** 539-546.

[12] Kim JH, Beacraft M and Shah SP (2010). "Effect of mineral admixtures on formwork pressure of self-consolidating concrete." Cement and Concrete Composites **32**(9): 665-671.

[13] Tregger NA, Pakula ME and Shah SP (2010). "Influence of clays on the rheology of cement pastes." Cement and Concrete Research **40**(Compendex): 384-391.

[14] Ferron R and Shah S (2010). "The Fresh State." Transportation Research Record: Journal of the Transportation Research Board **2141**(-1): 89-91.

[15] Nazari A and Riahi S (2011). "The effects of SiO2 nanoparticles on physical and mechanical properties of high strength compacting concrete." Composites Part B: Engineering **42**(3): 570-578.

[16] Shih J-Y, Chang T-P and Hsiao T-C (2006). "Effect of nanosilica on characterization of Portland cement composite." Materials Science and Engineering: A **424**(1,Äì2): 266-274.

[17] Li H, Xiao H-g, Yuan J and Ou J (2004). "Microstructure of cement mortar with nano-particles." Composites Part B: Engineering **35**(2): 185-189.

[18] Thomas JJ, Jennings HM and Chen JJ (2009). "Influence of Nucleation Seeding on the Hydration Mechanisms of Tricalcium Silicate and Cement." The Journal of Physical Chemistry C **113**(11): 4327-4334.

[19] Ji T (2005). "Preliminary study on the water permeability and microstructure of concrete incorporating nano-SiO2." Cement and Concrete Research **35**(10): 1943-1947.

[20] Jo B-W, Kim C-H, Tae G-h and Park J-B (2007). "Characteristics of cement mortar with nano-SiO2 particles." Construction and Building Materials **21**(6): 1351-1355.

[21] Gundogdu D, Pekmezci BY and Atahan HN. "Influence of nanosilica on the mechanical properties of mortars containing fly ash". International RILEM conference on materials science: Additions Improving Properties of Concrete (AdIPoC), vol. 3. pp. 345-354.

[22] Li G (2004). "Properties of high-volume fly ash concrete incorporating nano-SiO2." Cement and Concrete Research **34**(6): 1043-1049.

[23] Garrault S and Nonat A (2001). "Hydrated Layer Formation on Tricalcium and Dicalcium Silicate Surfaces: Experimental Study and Numerical Simulations." Langmuir **17**(26): 8131-8138.
[24] Khataee A, Amani-Ghadim A, Farajzade M and Ourang O (2011). "Photocatalytic activity of nanostructured TiO2-modified white cement." Journal of Experimental Nanoscience **6**(2): 138-148.
[25] Folli A, Pade C, Hansen TBk, De Marco T and Macphee DE "TiO2 photocatalysis in cementitious systems: Insights into self-cleaning and depollution chemistry." Cement and Concrete Research(0).
[26] Chen J and Poon C-s (2009). "Photocatalytic Cementitious Materials: Influence of the Microstructure of Cement Paste on Photocatalytic Pollution Degradation." Environmental Science & Technology **43**(23): 8948-8952.
[27] Jayapalan AR, Lee BY, Fredrich SM and Kurtis KE (2010). "Influence of additions of anatase TiO_2 nanoparticles on early-age properties of cement-based materials." Journal of the Transportation Research Board **2141**: pp 41-46.
[28] Meng T, Yu Y, Qian X, Zhan S and Qian K (2012). "Effect of nano-TiO2 on the mechanical properties of cement mortar." Construction and Building Materials **29**(0): 241-245.
[29] Xiong G, Deng M, Huang H and Tang M (2011). "Absorbing and mechanical properties of cement-based composites with nano-titanic oxide absorbent." Advanced Materials Research **177**(Dec): 558-561.
[30] Konsta-Gdoutos MS, Metaxa ZS and Shah SP (2010). "Multi-scale mechanical and fracture characteristics and early-age strain capacity of high performance carbon nanotube/cement nanocomposites." Cement and Concrete Composites **32**(2): 110-115.
[31] Collins F, Lambert J and Duan WH (2012). "The influences of admixtures on the dispersion, workability, and strength of carbon nanotube OPC paste mixtures." Cement and Concrete Composites **34**(2): 201-207.
[32] Chang L, Yue J and Sun Y (2012). "Experimental investigation of mechanical behavior of carbon-nanotube reinforced cement mortar." Applied Mechanics of Materials **142**(Nov): 217-220.
[33] Cwirzen A, Habermehl-Cwirzen K and Penttala V (2008). "Surface decoration of carbon nanotubes and mechanical properties of cement/carbon nanotube composites." Advances in Cement Research **20**(2): 65-73.
[34]. Yu X and Kwon E (2009). "A carbon nanotube/cement composite with piezoresistive properties." Smart Materials and Structures **18**(5): 055010.
[35] Liu ZG, Yang RL, Wei JC, Zhao BH and Feng XX (2011). "Piezoresistive properties of cement mortar with carbon nanotube." Advanced Materials Research **284-286**(July): 310-313.
[36] Coppola L, Buoso A and Corazza F (2011). "Electrical properties of carbon nanotubes cement composites for monitoring stress conditions in concrete structures." Applied Mechanics of Materials **82**(July): 118-123.

Part Two

NANOTECHNOLOGY

Optimization of UHPC by Adding Nanomaterials

Ehsan Ghafari[1], Hugo Costa[2], Eduardo Júlio[3], António Portugal[4], Luisa Durães[4]
1: ICIST & DEC - University of Coimbra, Portugal
2: ICIST & DEC ISEC - Polytechnic Institute of Coimbra, Portugal
3: ICIST& DECivil IST-Technical University of Lisbon, Portugal
4: Dept. of Chemical Engineering, University of Coimbra, Portugal

Ultra-high performance concrete (UHPC) is characterised by a dense microstructure, which presents both ultra-high compressive strength and ultra-high durability. Due to the growing interest in using nano-sized materials, the experimental study herein presented was conducted aiming to evaluate the influence of nano-SiO_2 addition on both mechanical and fluid transport properties of UHPC. The porosity and other parameters were assessed through different transport mechanisms and techniques. Mercury intrusion porosimetry (MIP) was performed to characterize the size distribution of capillary pores in the specimens' matrix. Moreover, the microstructures of the specimens were analysed by scanning electron microscopy (SEM). Results point out that the incorporation of nano-SiO_2 leads to a denser microstructure of UHPC, resulting in an enhancement of both mechanical and durability properties.

Keywords: UHPC, nano-SiO_2, transport properties

1 Introduction

Ultra-high performance concrete (UHPC) is one of the most promising types of concrete, which has been developed in the last decade. The efficiency of UHPC is particularly dependent on its density. This can be maximized by optimizing the particle packing, thus resulting in ultra-high consolidation of the concrete matrix. The optimized particle packing can be obtained through an almost 'perfect' grain size distribution, by incorporating a homogeneous gradient of fine and coarse particles in the mixture. In this scope, the use of nanomaterials, as pozzolanic additions, is highly effective. In fact, due to their extremely small size, nanomaterials can fill the voids between cement and silica fume particles, leading to higher packing level and also generating a denser binding matrix, with more calcium silicate hydrate (C-S-H). Thus, this causes a significant improvement on both durability and mechanical properties of concrete. In the following paragraph, conclusions from previous studies on this subject are presented.

Qing *et al.* [1] reported that the pozzolanic activity of nano-SiO_2 is much higher than that of silica fume. It was concluded that the bond strength of the paste-to-aggregate interface, incorporating nano-SiO_2, is higher than that of specimens with silica fume. Ji [2] also reported that nano-SiO_2 has pozzolanic effect, which can react with $Ca(OH)_2$ crystals, making the interfacial transition zone (ITZ), between the aggregates and the binding paste matrix, denser. Li *et al.* [3] showed that both the compressive and flexural strengths of concrete can be enhanced by incorporating nano-SiO_2 and nano-Fe_2O_3. A concrete with addition of silica fume, fly ash and nano-silica was studied by Collepardi et al [4]. It was concluded that concrete with this ternary combination has a better performance, in terms of both strength and durability, than those just with fly ash, but similar to those just with silica fume. Li [5] showed that the pozzolanic activity of fly ash significantly increased after incorporating nano-SiO_2. Li [5] also found that an addition of nano-SiO_2 resulted in an increase of both early-age strength and long-term strength. Moreover, the incorporation of nanomaterials also proved to improve the durability. He *et al.* [6] studied the chloride permeability and microstructure of Portland cement mortar with four different types of nanomaterials. This study confirmed that an addition of nano-SiO_2 and nano-clay significantly improved the chloride penetration resistance as well as the general ionic permeability of cementitious mortar. An experimental study performed by Ji [2]

showed that the addition of nano-SiO_2 to the mixture improved the water permeability resistance of concrete. The higher specific surface area of the nano-SiO_2 implies an increase in water demand of concrete mixture, which can somewhat affects the workability. However, Collepardi *et al* [7] studied the properties of self-compacting concrete with nano-SiO_2 and found out that the presence of nano-SiO2 makes the mixture more cohesive and reduces bleeding water and segregation, which finally improves the rheological behaviour of concrete in fresh state.

The present study aims to give a contribution in this field. In this scope, the mechanical properties of several UHPC mixtures were characterized, namely by measuring the compressive and flexural strengths. The evaluation of the fluid transport properties of concrete specimens, including the water absorption under vacuum, capillary water absorption, and water absorption by immersion, were also performed. Mercury intrusion porosimetry (MIP) tests were conducted to characterize the size distribution of capillary pores in the specimens. Moreover, the microstructures of the samples were analysed by scanning electron microscopy (SEM).

2 Experimental study

Materials and mixture proportion

The following main constituents were used to prepare the UHPC mixtures: ordinary Portland cement type I:52.5 R, silica fume (SF), quartz flour (P600), used as a micro filler (particle sizes less than 10 μm), siliceous sand, with maximum aggregate size of 0.6 *mm*, polycarboxylate ether based superplasticizers (SP), and two types of nano-SiO_2. The properties of nanoparticles are shown in Table 2. The SEM images of nano-SiO_2 particles are presented in Fig.1.

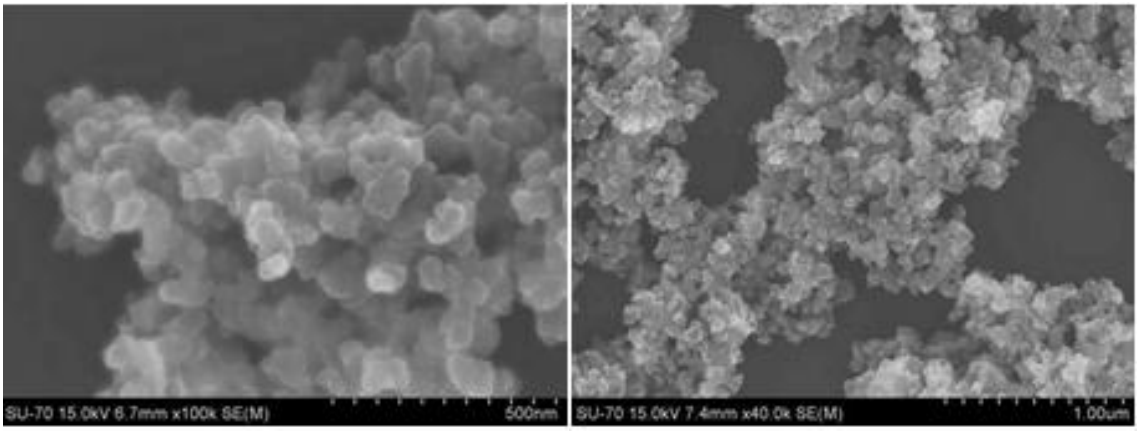

Figure 1: SEM micrograph of nano-SiO_2 particles with (left) and without (right) carbon coating.

From Fig. 1, it can be seen that both particles present a spherical shape. The particle coating is the main difference between the two types of nano-SiO_2 used in this study. One type of nano-SiO_2 particle was coated with a thin layer of carbon (NSC), which enables the particle to be dispersed easier in the mixture, while the other type was non-coated (NS). The mixture procedure involved several steps. First, in order to prevent agglomeration and also to promote uniform distribution of very fine particles, all powder and siliceous sand were mixed dry for 5 minutes at low speed. The Incorporation of dry nano-SiO_2 was not possible, since the particles were dispersed in the air due to its very low density. Therefore, the nano-SiO_2 was first dissolved in water, with the superplasticizer already diluted, and then gradually added to the mixture. After 5 minutes, the mixtures became fluid. After mixing, the concrete was poured in a mold and, 24 hours later, it was demolded. Then, the specimens were cured in water at 20 °C until the day of the test. The two types of nano-SiO_2 were incorporated as a cement replacement by 5 wt %. The large difference between the density of nano-SiO_2 and cement resulted in an increase in the paste volume. The total content of powder was kept in volumetric

constant. In addition, the water/powder ratio was kept constant for all mixtures and the dosage of SP was then adjusted for each mixture, in order to achieve the same consistency. Table 1 shows two series of mixtures, prepared with nano-SiO_2, and a reference mixture without nano-SiO_2.

Table 1: Proportion of UHPC mixture (by weight).

Materials	**Mixture**		
	UHPC	**UHPC-NSC**	**UHPC-NS**
cement	1.00	1.00	1.00
sand	1.40	1.40	1.40
silica fume	0.25	0.25	0.25
quartz flour	0.30	0.30	0.30
water	0.27	0.27	0.27
SP	0.03	0.05	0.03
nano-SiO_2	0.00	0.05	0.05

Experimental test

The axial compressive strength and flexural strength tests were performed at 7 and 28 days of age, using cubic (40×40×40 mm^3) and prismatic (40×40×160 mm^3) specimens, respectively.

The water sorptivity tests were performed according to the ASTM C-1585 standard [8]. At 28 days of age, three specimens, with standard dimensions of 100 mm diameter and 5 mm height were prepared. After that, the concrete specimens were dried in the oven, at 105 °C, until a constant mass was achieved, following the dry procedure described in ASTM C 642 –06 [9]. The specimens were sealed and placed on the support at the bottom of the board container. The water level was maintained 1 to 3 mm above the top of the support device. The mass increase of the specimens was measured at several times (0, 5, 10, 20, 30, 60, 180, 360, 1440 min), then the sorptivity coefficient was measured using expression (1):

$$I=A+Kt^{½} \quad (1)$$

where K [$mm/s^{1/2}$] is the water sorptivity coefficient, I [mm^3] is the total volume of water absorbed, A [cm^2] is the area of the specimen surface exposed to water. The initial rate of water absorption (mm/s) is defined as the slope of the line that best fits to I, plotted against the square root of time ($s^{1/2}$). The initial slope of the straight line is taken as the water absorption coefficient.

Table 2: Properties of nano-SiO_2.

Formula	**Colour**	**Purity**	**Crystal Phase**	**Morphology**	**Bulk density**	**BET**
SiO_2(NS)	White	>98.0 (%)	Amorphous	Spherical	0.05	64(m^2.g-1)
SiO_2(NSC)	Grey	>98.0(%)	Amorphous	Spherical	0.06	57(m^2.g-1)

The absorption of water was measured by immersion under vacuum of concrete specimens, using a test method similar to the one described in RILEM CPC-13 [10], which allows the calculation of a permeable porosity. For each mixture, three specimens with a diameter of 100 mm and a thickness of 50 mm were cut and dried to constant mass (<0.1% mass change within 24 h) at (105 ± 5 °C). The specimens were then placed, for at least 24 h, under 1 bar of vacuum pressure in a desiccator, which was filled with distilled water. The porosity was measured using expression (2).

$$P=\frac{M_2-M_1}{M_2-M_3} \quad (2)$$

in which P is the vacuum saturation porosity (%), M_1 is the weight of oven-dried specimen, and M_2 and M_3 stand for the mass under water and for the water saturated mass (after vacuum saturation), respectively.

Water absorptions of specimens were measured also by immersion procedure, according to the ASTM C-642 standard [9]. After conditioning the specimens to 105 ± 5 °C (mass A), the specimen was soaked until a constant mass in water (mass B) was reached. The water absorption corresponds to the difference in mass, expressed as a percentage of the mass of the dry specimen. Thus, the absorption after immersion, in %, is given by expression (3):

$$(B-A)/ (A) \times 100 \quad (3)$$

The volume of permeable voids (VPV), expressed as a percentage of the volume of the solid, was determined according to ASTM C-642 standard [9]. In this procedure, after boiling the specimens for 5 hours, these were allowed to cool with natural loss of heat for 14 hours until a final temperature of 20 to 25°C was reached. Then, the moisture of the specimen's surface was removed with a towel and the mass of the specimen was determined (mass C). Placing the specimen suspended in water, the apparent mass in water was determined (mass D). The volume of permeable voids is then obtained from expression (4):

$$VPV\ \% = [(C - A) / (C - D)] \times 100 \quad (4)$$

3 Results and discussion

Compressive and flexural strengths

The average values of compressive strength at 7 and 28 days are shown, for all the specimens, in Fig.2. It can be seen that the addition of nano-SiO_2 significantly increased the early-age compressive strength. The higher compressive strength might be due to larger specific surface area of nanoparticles, which can react more quickly with Ca $(OH)_2$, making the microstructure denser. At the age of 28 days, the highest compressive strength was obtained for the UHPC-NS. The effect of nano-SiO_2 coated with carbon was not as effective as not-coated silica, which may result from the fact that this coating reduces the activity of nanoparticle. From Fig. 3, it can be observed that the flexural strength was enhanced by incorporating nano-SiO2, at the ages of 7 and 28 days.

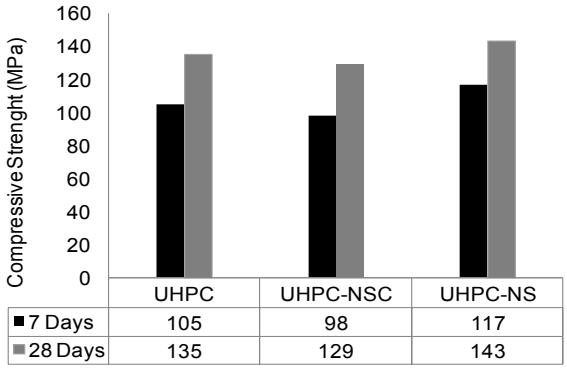

Figure 2: Compressive strength.

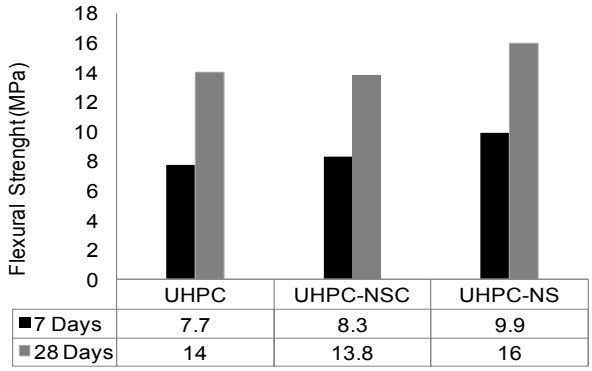

Figure 3: Flexural strength.

Transport properties

Most aspects of concrete durability are directly related with its porous structure, since capillary pores are responsible for fluids' migration in the concrete matrix. Different mechanisms of liquid transport in the concrete were evaluated in this study. The results obtained for water absorption and for volume of permeable voids (VPV) are presented in Table 3. Both types of nano-SiO_2

were found to be effective in reducing the volume of permeable voids as well as water absorption. It can be seen that an addition of nano-SiO_2 (NS) reduced VPV in 21 % and water absorption in 36 %. Table 3 also presents the results concerning the sorptivity coefficient and the porosity measured by vacuum saturation. The UHPC-NS specimen gave the lowest value of porosity (2.12%). This can be due to the discontinuity of capillary pores by formation of more C-S-H gel.

Table 3. Transport properties of UHPC mixtures.

	Water absorption		Sorptivity Test	Vacuum	MIP Test	
	absorption*	VPV*	Sorptivity Coef.**	Porosity*	Total porosity*	Capillary Pores*
UHPC	1.212	2.91	0.044	3.11	6.35	2.65
UHPC-NSC	1.110	2.75	0.041	2.94	4.74	2.56
UHPC-NS	0.808	2.28	0.038	2.12	4.3	1.72

* Percent (%) ; ** In unit $Kg/m^2/h^{0.5}$

In addition, the nano-sized particle acted as filler in the mixture design of UHPC, leading to an improvement in the pore structure. The sorptivity coefficients of all specimens were determined after 24 hours. The very low sorptivity coefficient of 0.044 ($Kg/m^2/h^{0.5}$) was obtained for the UHPC-NS mixtures, 14 % lower than the reference mixture coefficient. In Fig. 4, the water absorption versus the square root of time is plotted for all mixtures.

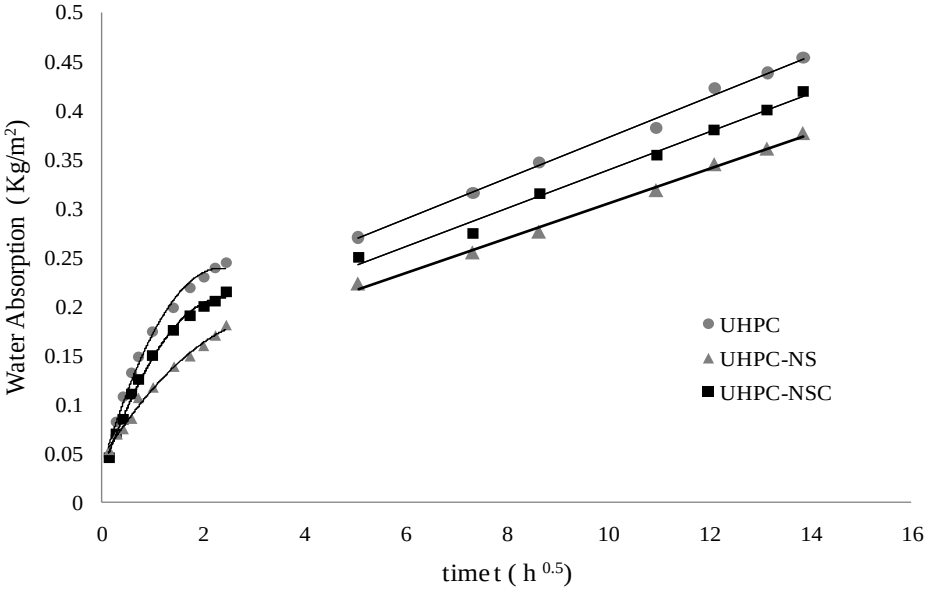

Figure 4: Water absorption of UHPC mixtures.

Table 4 presents two different regression equations, determined for the time 6 h before and the time 24 h after. A nonlinear correlation was used in the first case, while a linear correlation was determined for second one.

The pore size distribution of UHPC specimens is shown in Fig.5. Both MIP plots of UHPC containing NS and NSC stand slightly below the UHPC, particularly in the range 0.3-20 μm. Results show that pore structures of UHPC-NS and UHPC-NSC are finer than those of UHPC. All the specimens have much more pores ranging from 0.01 μm to 0.05 μm which correspond to the gel pores [11]. The incorporation of nano-SiO_2 resulted in a slightly lower amount of capillary pores. The UHPC-NS showed the lowest value of the capillary pores (1.7 vol.-%) which is 35% lower than the capillary pores content of UHPC mixture. The amount of total pore volume and capillary pores is also presented in Table 3.

Table 4. Regression equations for water absorption, of UHPC mixtures, before 6h and after 24h.

	Regression ≤ 6h Wa ($t^{0.5}$)	Regression > 24 h Wa ($t^{0.5}$)	correlation coefficient
UHPC	Wa ($t^{0.5}$) = -0.0365.t^2 + 0.1718.t + 0.0365	Wa ($t^{0.5}$) = 0.0209.t + 0.1633	R^2 = 0.99
UHPC-NSC	Wa ($t^{0.5}$) = -0.0299.t^2 + 0.1456.t + 0.0313	Wa ($t^{0.5}$) = 0.0196.t + 0.1422	R^2 = 0.99
UHPC-NS	Wa ($t^{0.5}$) = -0.0115.t^2 + 0.0817.t + 0.045	Wa ($t^{0.5}$) = 0.0178.t + 0.1272	R^2 = 0.99

The results obtained with the MIP test, presented in Fig. 5, are in good agreement with the porosity value measured by absorption under vacuum saturation method.

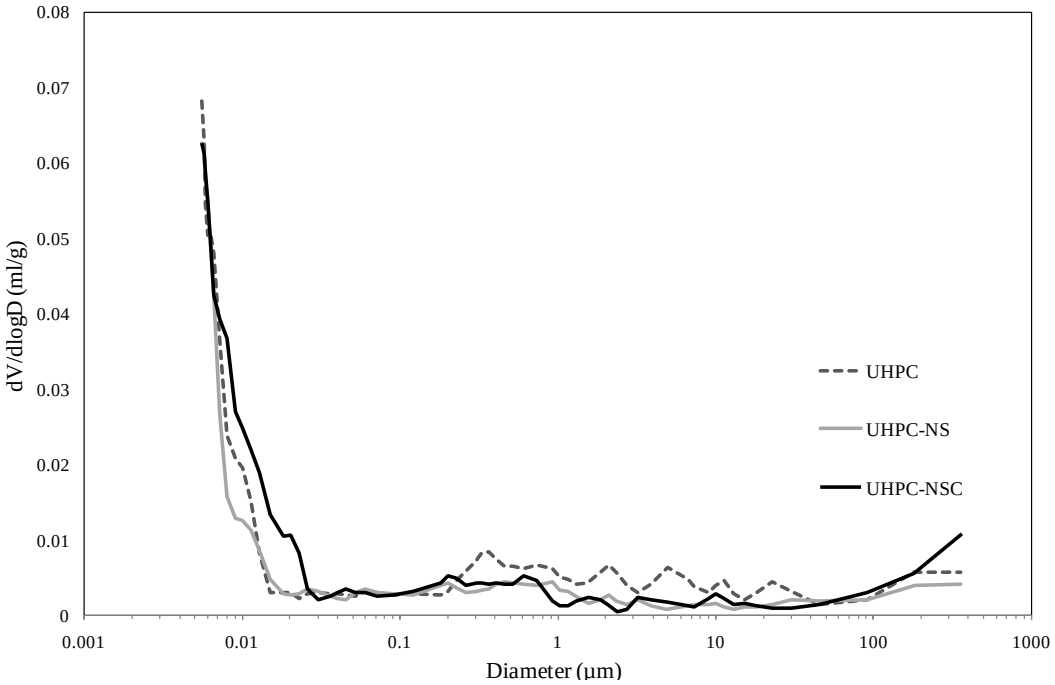

Figure 5: Mercury intrusion porosimetry results.

The microstructures of the specimens were analysed by scanning electron microscopy (SEM). Figures 6.(a) and 6.(b) show an overview of the microstructure of UHPC-NSC and UHPC using the same magnification. In general, the analysis of all images did not reveal any substantial differences in the microstructure of all specimens. However, it should be noted that the incorporation of nano-SiO_2 led to a further densification in the microstructure and to a concurrent reduction in capillary porosity of concrete mixtures. The SEM observation on the cement paste matrix, containing nano-SiO_2, revealed that the extreme fine particles of nano-SiO_2 acted not only as a filler, but also as an effective pozzolanic material to react with Ca $(OH)_2$ crystals, resulting in the formation of an additional C-S-H gel (Fig. 6(c)).

It is well know that portlandite, an oxide mineral, has a detrimental effect on bond strength of aggregates-paste [2], which causes a significant reduction in mechanical properties. Results showed that nano-SiO_2 can effectively reduce the amount of portlandite, leading to a denser microstructure of interfacial transition zone (ITZ), between aggregate and paste. Fig. 6(d) shows a perfect bond adhesion between the binding paste and the aggregates in UHPC-NS specimens.

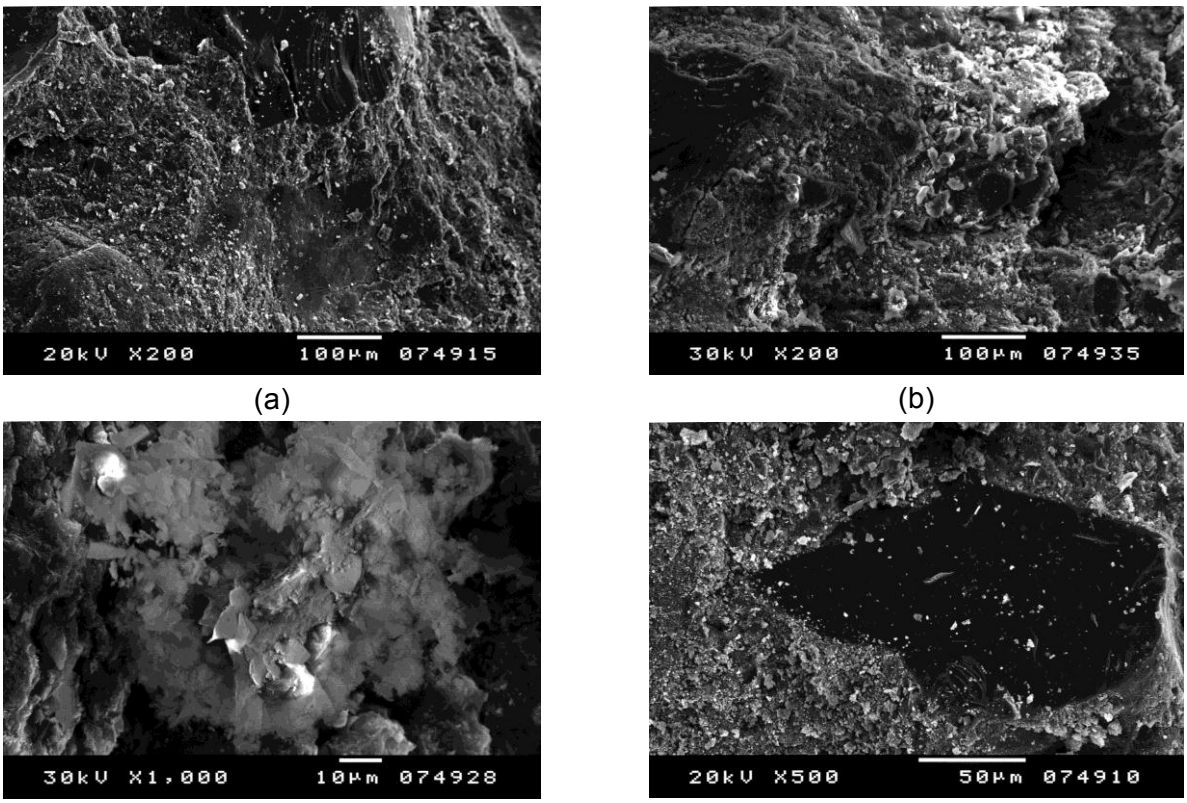

Figure 6: SEM micrograph of UHPC mixtures at age of 28 days: (a) microstructure of UHPC-NS; (b) microstructure of UHPC ; (c) formation of C-S-H gel in the cement and NS paste ; (d) interfacial transition zone (ITZ) microstructure between aggregate and paste in UHPC-NS specimen.

4 Conclusions

The effect of two types of nano-SiO_2 on the mechanical and water transport properties of UHPC was studied. The experimental results pointed out that the incorporation of nano-SiO_2 leads to a denser microstructure resulting in an enhancement of both mechanical and durability properties. MIP measurements revealed that the pore structure of UHPC can be effectively refined by adding nano-SiO_2. Scanning electron microscopy (SEM) proved that nano-SiO_2 can also efficiently improve the microstructure of the interfacial transition zone (ITZ) between the aggregates and the binding paste.

5 Acknowledgement

The authors thank the financial support of the Portuguese Science and Technology Foundation (FCT) for the project PTDC/ECM/098497/2008 entitled “Intelligent Super Skin (ISS)”.

References

[1] Ye Qing, Z.Z., Kong Deyu, Chen Rongshen, Influence of nano-SiO2 addition on properties of hardened cement paste as compared with silica fume. Construction and Building Materials, 2007. 21: p. 539–545.

[2] Ji, T., Preliminary study on the water permeability and microstructure of concrete incorporating nano-SiO2. Cement and Concrete Research 2005. 35: p. 1943 – 1947.

[3] Hui Li , H.-g.X., Jie Yuan, Jinping Ou, Microstructure of cement mortar with nano-particles. Composites: Part B 2004. 35: p. 185–189.

[4] M., C., S., Skarp, U., Troli, R. “Optimization of Silica Fume, Fly Ash and Amorphous Nano-Silica in Superplasticized High-Performance Concretes”,. in Proceedings of 8th CANMET/ACI International

Conference on Fly Ash, Silica Fume, Slag and Natural Pozzolans in Concrete. 2004. Las Vegas, USA.
[5] Li, G., Properties of high-volume fly ash concrete incorporating nano-SiO2. Cement and Concrete Research 2004. 34 p. 1043–1049.
[6] Shi, X.H.a.X., Chloride Permeability and Microstructure of Portland Cement Mortars Incorporating Nanomaterials. Journal of the Transportation Research Board,, 2008: p. 13-21.
[7] Collepardi, M., Ogoumah-Olagot, J.J., Skarp, U., Troli, R. Influence of Amorphous Colloidal Silica on the Properties of Self-Compacting Concretes, . in Proceedings of the International Conference"Challenges in Concrete Construction , Innovations and Developments in Concrete Materials and Construction,. 2002. Dundee, UK.
[8] ASTM, Standard Test Method for Measurement of Rate of Absorption of Water by HydraulicCement Concretes. 2004.
[9] ASTM, Standard Test Method for Density, Absorption, and Voids in Hardened Concrete 97.
[10] RILEM TC 14-CPC, C., Absorption of water by immersion under vacuum. Materials and Structures 1984(17): p. 391–394.

UHPC Containing Nanoparticles Synthesized by Sol-gel Method

Genady Shakhmenko[1], Aleksandrs Korjakins[1], Patricija Kara[1], Janis Justs[1], Inna Juhnevica[2]

1: Institute of Materials and Constructions, Riga Technical University, Latvia
2: Institute of Silicate Materials, Riga Technical University, Latvia

Sol-gel technology is an alternative method for producing nanoparticles. This paper deals with preparing UHPC mixes by using amorphous silicium dioxide nanoparticles specially synthesized by applying the sol-gel method. Grading of used micro and nano components was carried out by Dynamic Light Scattering (DLS) method. The studied micro and nanoparticles have dimensions in the range from 30 to 600 nm. Proportions of filler components were selected by taking into account optimal packing models. Experimental part of research includes preparation of the mix containing traditional UHPC ingredients (Portland cement, quartz filler, silica fume) and nanoparticles synthesized by sol-gel technology in amount up to 1% of cement. Influence of nanoparticles on concrete properties was studied. Mineralogical composition of UHPC matrix was examined by X-ray method. After summarizing the results it may be concluded that incorporation of the small amount of nano sized silicium dioxide nanoparticles synthesized by sol-gel technology slightly decreases compressive strength in early hardening period (7 days in normal conditions) and increases strength after intensive curing (+90 ºC for 3 days).

Keywords: UHPC, nanoparticle, sol-gel method

1 Introduction

It is necessary to ensure ultra-dense particle packing at macrostructure and microstructure levels in order to obtain the UHPC concrete. The concrete mix particles should be within a wide range of particle size distribution. Ground mineral materials and amorphous silica fume (as pozzolanic admixture) are normally used as micro fillers. Particle size of the commercially used silica fume is in range of 0.1 – 1 μm. A new generation of UHPC concrete provides the use of special nano sized amorphous nanoscale pozzolanic particles [1, 2] with the dimensions less than 100 nm. Nano silica allows achieving more dense structural packing and better physical and mechanical properties. Nowadays, pyrogenic nano silica products as an effective filling agent are commercially available.

Sol-gel technology is an alternative method for production of silica nanoparticles. The first silica sol-gel synthesis carried by J.J. Ebelmens was described 150 years ago. He proved that silicon esters are slowly hydrolyzed in the presence of hydrated silica. The term "sol-gel process" refers to chemical reactions between the colloidal particles and/or connections between the polymers in solution leading to a gelatine type structures. The liquid phase (or solvent) is removed by drying thereby obtaining a porous dry gel or xerogel, which can be sintered to a dense amorphous (or crystalline) solid. Metal alcoxides, which easily react with water, are often used as reagents for sol-gel chemistry. Silicate alcoxides, such as tetramethoxysilane (TMOS) and tetraethoxysilane (TEOS), are most widely used, as well as liquid glass - sodium hydrous. Sol-gel process is also used for other additives which provide the possibility to obtain particles with the required composition and structure [3, 4]. Sol-Gel synthesis is the chemical method carried out at a moderate temperature and by using moderate reagents. The method is based on molecular synthesis of nanoparticles [5]. The scheme of the used sintering method is shown in Figure 1. The synthesis of oxide nanoparticles in aqueous is based on the hydrolytic ion condensation process that leads to

formation of extremely small primary particles. The further aging process in nanodispersed system leads to a sol - gel or settlings formation.

Change of aging conditions (temperature, pH, constituent relations, their concentrations, etc.) allows regulating the phase compositions, created nanoparticle size and shape within a wide range [6].

2 Used Materials, Mix Composition and Methods

Raw Materials

Experimental UHPC concrete mixtures were produced by using commercially available binding agents, pozzolanic admixtures and local mineral fillers.

White, rapid hardening Portland cement CEM I 52.5 R was used as a binding agent. Undensified commercial silica fume product (SF) Elkem microsilica 971U was used as pozzolanic micro filler. Nanosilica (NS1) applied in reference mix is a high-purity pyrogenic silica industrial product in the form of powder with a high specific surface of 50 m^2/g.

Other silica materials were specially synthesized in the laboratory in accordance with the scheme shown in Figure 1. NS2 is synthesized non-calcined nano silica. NS3 material was calcined at the temperature 500^{o}C and additionally ground for 1 hour in a laboratory ball mill. NS4 material was calcined at the temperature 650°C and additionally ground for 1 hour. The last type of nanosilica NS4 was used in the form of sol (silicon dioxide particle concentration 25%). Nanosilica materials were incorporated in concrete as water suspension by mixing with water and superplasticiser. Characteristics of used pozzolanic materials are summarized in Table 1. Micro and nanoparticle size distribution were determined in water environment by the Dynamic Light Scattering (DLS) method, using Brookhaven Instrument (USA). Grading diagrams of used fillers and cement are shown in Figure 2.

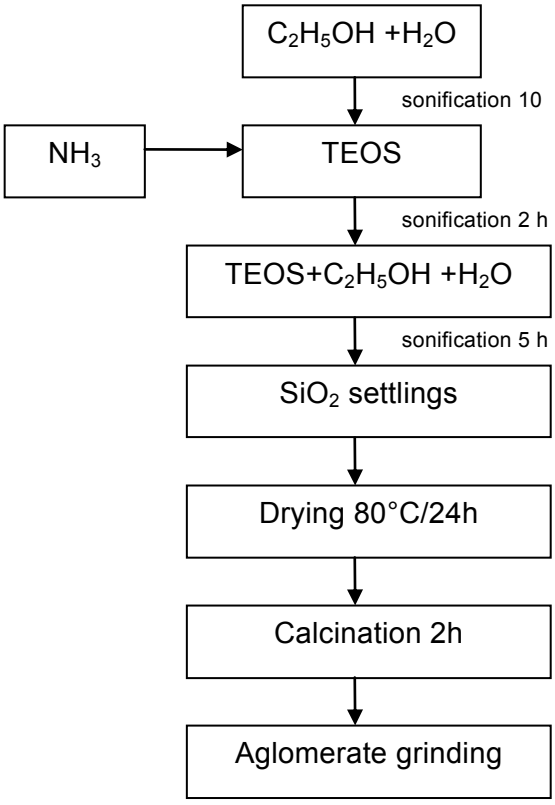

Figure 1: Method of synthesizing SiO_2 nanoparticle.

Table 1: Characteristics of cement, micro and nanosilica.

Parameter		CEM I 52.5 R	SF	NS1	NS2	NS3	NS4
Loss of ignition	%	<1	0.8	<0.01	<1	<1	<1
Particle effective diameter	μm	1-50	<1	0.184	0.099	0.600	
Density	kg/m³	3150	2200	2200	2200	2200	2200
Bulk density	kg/m³	1100	200	100	100-150	150-200	150-200
SiO_2 content	%		>97	99.9	99.9	99.9	99.9
Calcination temp.	°C				-	500	650

Three types of local fractionated quartz sand (fractions 0/0.5 mm, 0.3/0.8 mm and 0/0.3 mm as micro filler) act as mineral aggregate fillers. The content of quartz is about 97%.

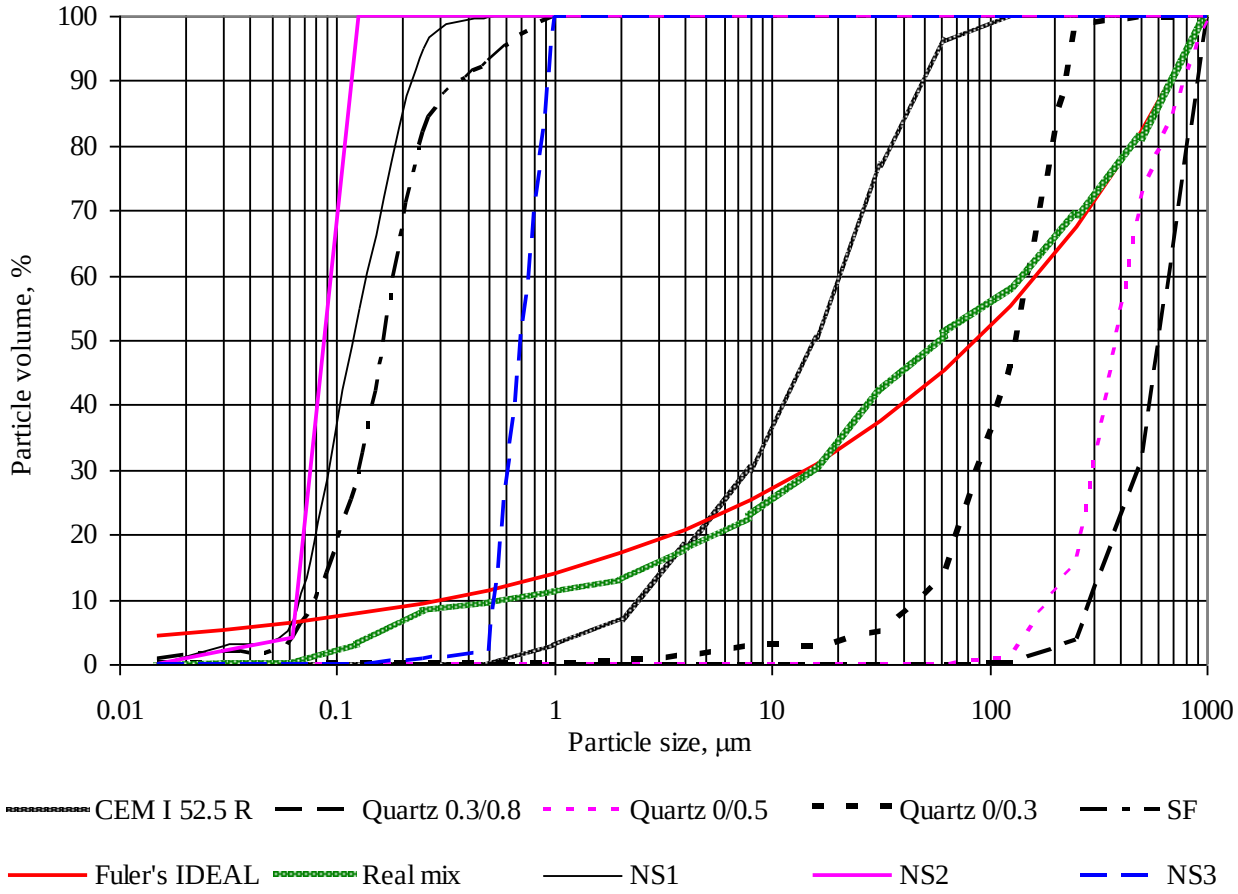

Figure 2: Particle size distribution.

Mix composition

Typical fine graded UHPC mix composition was selected as the basic (reference) mix. Proportions of the components are the same for all mixes, while the types of nanosilica vary. Cement content is 950 kg per cubic meter and nanosilica content of 10 kg/m^3 was assumed. Concrete mix compositions are summarized in Table 2. Water content and water/cement ratio (0.19) are kept constant for all mixes. The first mix (SF) was prepared without nanosilica (the corresponding amount was replaced by the additional content of microsilica). The second mix NS1 contains standard commercial nanosilica. The rest mixes were prepared by using specially synthesized nanosilica (NS2, NS3, NS4 and NS5 correspondingly).

Table 2: UHPC concrete mix compositions (kg/m^3).

Materials	SF	NS1	NS2	NS3	NS4	NS5
Portland cement CEM I 52.5 R	950	950	950	950	950	950
Quartz sand 0.3/0.8 mm	470	470	470	470	470	470
Quartz sand 0/0.5 mm	200	200	200	200	200	200
Quartz filler 0/0.3 mm	340	340	340	340	340	340
Silica fume 971U	150	140	140	140	140	140
Nanosilica Elkem	-	10	-	-	-	-
Nanosilica NS2 (non-calcined)	-	-	10	-	-	-
Nanosilica NS3 (500ºC)	-	-	-	10	-	-
Nanosilica NS4 (650ºC)	-	-	-	-	10	-
Nanosilica NS5 (sol)	-	-	-	-	-	10
Superplasticiser	30	30	30	30	30	30
Steel fibre 13 mm/0.16 mm	30	30	30	30	30	30
Water	180	180	180	180	180	180
Mix properties:						
Cylinder flow, mm	220	223	200	208	230	255
Concrete density, kg/m^3:	2400	2390	2370	2370	2370	2360

Methods

Concrete compositions were mixed in the high speed paddle mixer according to the following procedure: dry components were mixed for 1 minute, 2/3 of water amount was added and mixed for 1 minute. During the second step of mixing the remaining water was incorporated together with superplasticiser and nanosilica suspension. This mixing method was applied to achieve a more effective usage of the superplasticiser (otherwise superplasticiser can be absorbed by the dry aggregate thus reducing the plasticising effect). The mixing time was determined with the purpose to provide a homogenous mixture (approximately for 5 min).

Mix flowability was determined by means of cylinder flow test. Cylinder with the internal diameter 50 mm and height 100 mm was filled with UHPC concrete mix and lifted up. The diameter of the cylinder flow was measured after 1 minute.

Concrete cube specimens (10x10x10 cm) were made by using steel moulds. There were prepared 6 specimens for each composition. The specimens were cured in the water environment. The compressive strength was determined in accordance with the standard [7] at the age of 7 days in normal curing conditions (+20^{o}C), then additionally in accelerated curing conditions (in 90^{o}C hot water) for 3 days. Thus, the curing time of the specimen series are 7 and 10 days accordingly.

X-Ray analysis was carried out for hardened specimens by using the equipment with Rigaku Optima Plus diffractometer with $Cu_{K\alpha}$.

3 Results and discussions

It should be stressed that addition of nano silica into the mix has no particular effect on the flowability of the mix (Tab. 2); at the same time, mixes with nano silica were more plastic and homogeneous. The mixture with not calcined sol-gel nano silica N2 was with the lowest consistency.

Compressive strength results within the age of 7 days of the mixes with only silica fume and standard nano silica (NS1) were similar. The results for the mixes with nano silica that was synthesized by sol-gel method were even slightly lower.

It should be noted that the specimens with sol-gel nano silica were also marked by lower density (Table 2). It can be explained by insignificant air entraining effect, which can be caused

by residue of some organic solvents from sol-gel process. The lower strength results were registered by the mix NS5 containing nano silica sol. The mix had the highest cylinder flow (hence the amount of water could be reduced). Weak influence of this nanosilica sol may be explained by considerable amount of organic solvents.

After intensification of the hardening process (aging in hot water for 3 days) the results were completely different. Mixes with calcined sol-gel nano silica showed more increase in strength compared to the reference configurations SF and NS1. The highest result was for the mix with nano silica calcined at 500 °C. The hardening effect of these compositions may be explained by activation of the pozzolanic reactions between silica and calcium hydroxide. Superdisperse particles of sol-gel nanosilica could be as initiating centres of formation of new concrete minerals.

It must be emphasized that statistically proved effect of nano particles cannot be discussed taking into account the values of standard deviation. In spite of obtained tendencies of strength development, the differences between strength results are low (within 5%). In order to obtain objective results it is necessary to conduct further research with more amounts of nanoparticles as well as number of specimens.

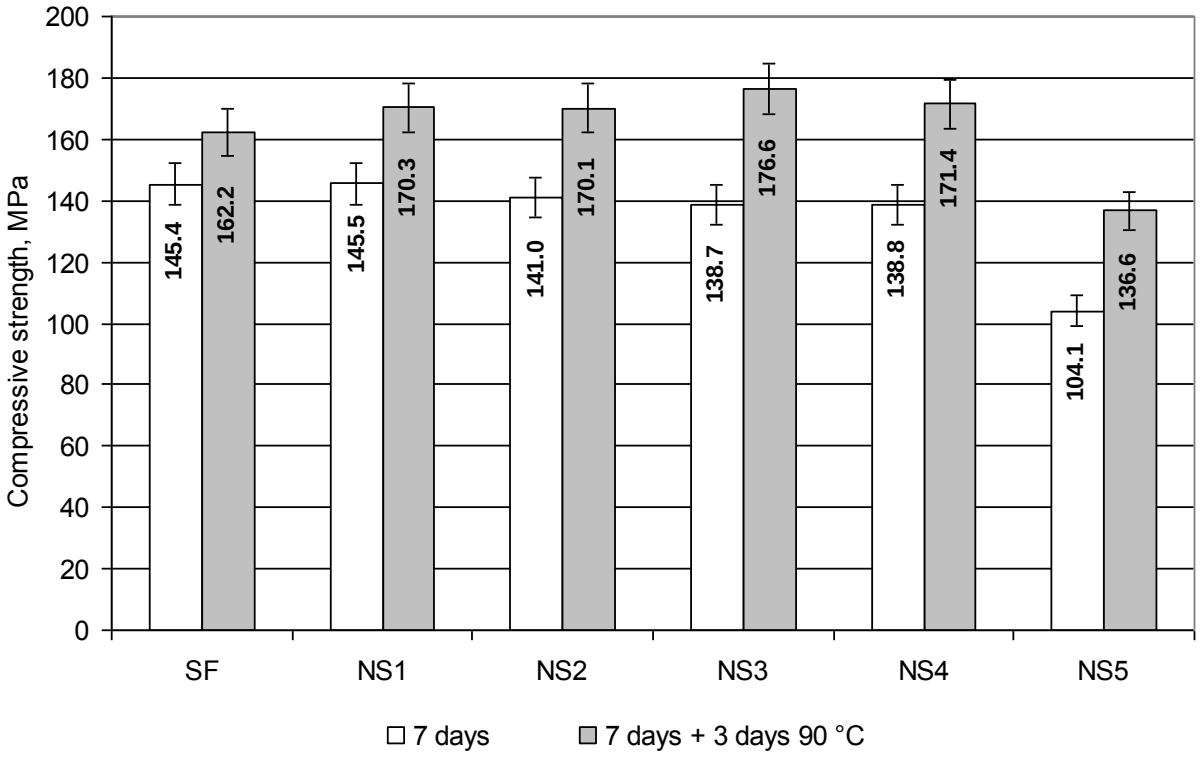

Figure 3: Compressive strength results.

X-Ray analysis was carried out for 3 mixes containing standard nanosilica (NS1), not calcined nanosilica (NS2) and calcined in 500°C nanosilica (NS3). Obtained results (Fig. 4) do not indicate any significant difference in mineralogical composition among those 3 specimens. The following minerals were recorded in the course of analysis of X-Ray diagrams. One of them is Quartz, which is the main component of aggregate. Minerals Hatrurite (also is known as Alite) and Larnite (also is known as Belite) are non-hydrated part of cement. The last recorded mineral is Portlandite (calcium hydrate) is the products of cement hardening. It should be mentioned that X-Ray analysis indicates only minerals in crystalline form while amorphous phases of material are not visible. It is possible to obtain more detailed results by using other methods of examination, for example SEM-microscopy.

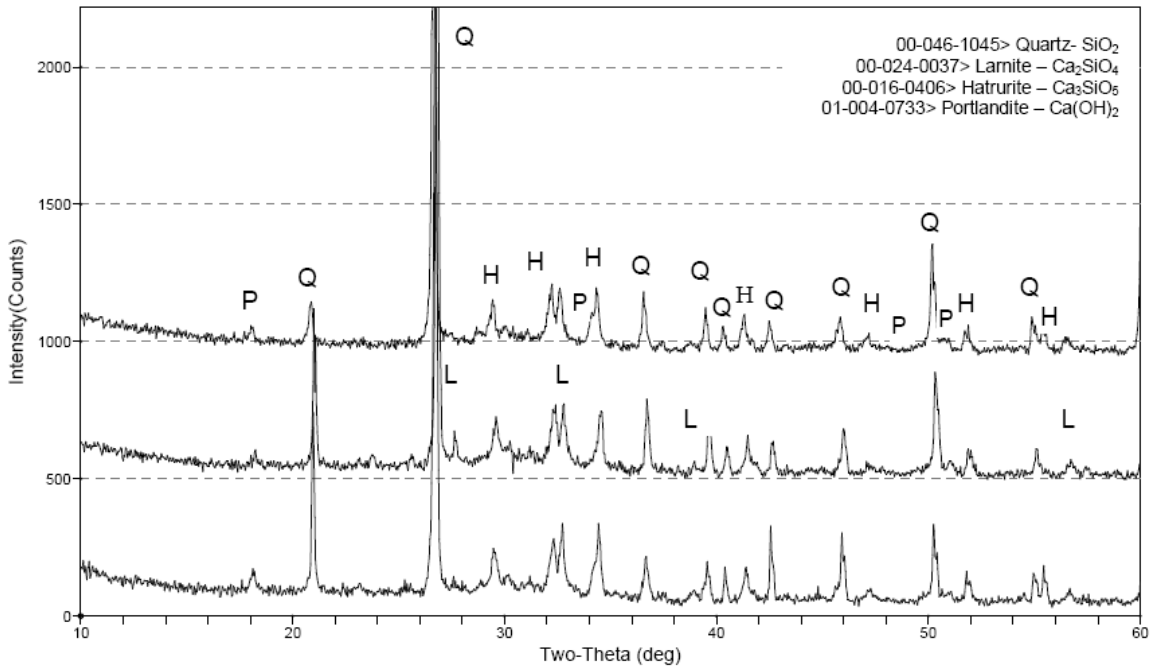

Figure 4: X-Ray analysis results (above: NS3, on the middle: NS2, below: NS1).

4 Conclusions

The effect of incorporation of nano silica particles synthesized by sol-gel method in UHPC mix has been examined in this study. Experimental results indicate that strength for mixes with synthesized nano silica was even slightly lower compared to the reference mix based on standard micro and nano silica in the early age concrete. It was found that mixes with sol-gel nano silica after accelerated hardening in hot water showed slightly increase in strength of up to 4 % compared to the reference mix. The highest result was achieved for the mix with calcined nano silica at 500°C. The hardening effect can be explained by activation of pozzolanic reactions between nanosilica and calcium hydroxide. It must be emphasised that effect of adding nano-particles, obtained by sol-gel method, is insignificant since strength characteristic of concrete mix differs only by some per cents (about 3-5 %). Ranges of standard deviation are overlap.

Synthesized nano silica produced by the sol-gel method may have some benefits compared to standard micro and nano silica:

1) the regulation of the parameters of sol-gel process makes it possible to provide the definite particle sizes in accordance with required the grading composition (thus, it becomes possible to achieve the optimum particle packing);

2) sol-gel technology can be implemented in a simple way since this process does not require very high temperatures compared to traditional pyrogenic nanosilica.

Initial investigation showed positive impact of non-traditional synthesised nano admixture by sol – gel method. In further studies it is worthwhile: 1) to synthesize particles with defined sizes; 2) to solve the problem of nano particles uniform dispersion and, 3) to perform detailed examination of microstructure and mineralogical composition of concrete specimens.

5 Acknowledgement

The financial support of the ERAF project Nr. 2010/0286/2DP/2.1.1.1.0/10/APIA/VIAA/033 „High efficiency nanoconcretes” is acknowledged.

References

[1] Korpa A., Reinhard T.: Ultra high performance cement-based composites with advanced properties containing nanoscale pozzolans. Proc. of the Second International Symposium on Ultra high performance concrete, Kassel, Germany, March 05-07, 2008, pp. 391-400.

[2] Ramezanianpour M., Moravej Jahromi M., Elmaili R.: Mechanical properties and durability of concrete incorporating nanosilica. Proc. of the 8th International Symposium on Utilization of High-Strength and High-Performance Concrete, Japan, 2008, pp. 252-256.

[3] Fallet M., Madhdjoub H., Gautier B., Bauer J.P.: Electrochemical behavior of ceramic sol-gel coatings on mild steel. *Non-Cryst. Solids*, 2001, 293, pp. 527–533.

[4] Mežinskis G.: Sola-gēla tehnoloģijas attīstība un perspektīvas Latvijā. *Latvijas ķīmijas žurnāls*, 1997, 2, pp. 72–81 (in Latvian).

[5] Silvia S.C.: Nanoparticles, and a method of sol-gel processing. Pat. EP 1971550 (24.09.2008).

[6] Popovs V.V., Shabanovs N.A., Sarkisov P.D.: Nanodispersal oxides chemistry and technology, Moscow, Akademkniga, 2007, pp. 309 (in Russian).

[7] LVS EN 12390-3:2002. Testing hardened concrete - Part 3: Compressive strength of test specimens. Riga, 2002. pp. 16.

Cavitation Treatment of Nano and Micro Filler and Its Effect on the Properties of UHPC

Janis Justs[1], Genady Shakhmenko[1], Viktors Mironovs[2], Patricija Kara[1]
1: Institute of Materials and Constructions, Riga Technical University, Latvia
2: Institute of Building Production, Riga Technical University, Latvia

The effect of cavitation treatment of micro and nano fillers in relation to ultra-high performance concrete (UHPC) was investigated in this paper. Specially designed and patented apparatus was applied to create turbulent flow and employ hydrodynamic cavitation process as a tool for silica fume micro and nano particle agglomerate disaggregation and surface activation. Silica fume/water slurry at the ratio 1 : 2 was subjected to the impact of the hydrodynamic cavitation process.
UHPC mixes with optimized particle packing were designed in order to evaluate effect of specially treated silica fume on the mechanical properties of the UHPC. Due to the cavitation treatment the agglomerates disaggregated into nano and micro particles and uniform suspension in water was obtained and incorporated into the UHPC mix.

Keywords: UHPC, microsilica dispersion, cavitation

1 Introduction

Pozzolanic additives are used in the concrete production to enhance mechanical properties and durability of the material. Silica fume, metakaolin, rice husk ash and nanosilica are some of the additives that can be beneficial and improve performance of the concrete. As pozzolanic additive particle sizes normally are less than those of cement (average silica fume particle size is around 0.15 μm), pozzolans in concrete can have dual effect – to improve physical particle packing and to react chemically with calcium hydroxide forming calcium silicate-hydrates [1].

However, sometimes desired effect is not reached due to the fact that smaller particles have increased surface energy and during the storage time aggregate more easily to secondary particles, having sizes on the order of hundreds of micrometres. It is not possible to break such agglomerates in conventional mixing process due to the low shear forces. As agglomerates can be bigger than cement particles, packing of the mix is not improved and chemical reaction is hindered due to the reduced active surface area of pozzolan. Moreover undispersed silica fume agglomerates can react as alkali–silica reactive aggregates in concrete [2] (See Figure 1).

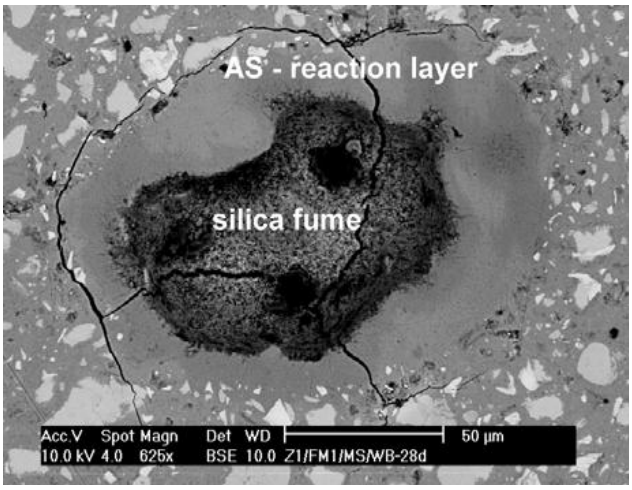

Figure 1: Silica fume agglomerate causing alkali-silica reaction [2].

Cavitation treatment of pozzolanic materials before concrete mixing is proposed in this paper in order to disaggregate agglomerated particles and therefore reach better particle dispersion in concrete mixture. A novel hydrodynamic dispersion method for fine particles was developed and patented in Germany (patent number 20 2007 914 913.1), Latvia (patent number 13592), Russia (patent number 2297876) and EU (patent application number P-11-67).

Hydrodynamic cavitation phenomena occur if the fast flowing liquid (e.g. water) encounters obstacles in its way. In some areas of disturbed flow continuity of water is broken and rapid pressure drop below the

water vapour pressure is encountered. Vapour cavities in the water are created. Source of cavitation nuclei is gas that is dissolved in the water. If the liquid pressure exterior to a bubble will be lower than the saturated vapour pressure, the nucleus will be activated and the radius of the bubble will increase. The increase of the liquid pressure results in the cavitation bubble collapse. Cavitation bubbles collapse violently generating either the micro-jets or shock pressure waves featured by high velocities, pressures and temperatures [3]. The temperature inside the cavitation bubble during collapse can reach 5075 K, but such extreme temperature exists for the very short time [4; 5]. Impacts of shock pressure waves and micro-jets are the source of the noise and the material damage. The impulse pressure might reach the pressure of approximately 1 GPa and impact velocity of 1000 m/s [6].

Cavitation is specifically avoided in the design of machines such as turbines or propellers because of possible damage risk. However, in this study it proved to be beneficial as a tool for silica fume agglomerate disjoining.

2 Materials and methods

Traditionally there are two types of UHPC mixtures - coarse grained with maximum aggregate size 4-8 mm and fine grained with maximum aggregate size 1-2 mm. To evaluate effect of silica fume cavitation treatment, fine-grained UHPC mixture was designed. Materials used in this study were the following:

- cement CEM I 52,5 R UHPC;
- silica fume;
- nanosilica;
- quartz sand 0 – 0.3 mm;
- quartz sand 0.3 – 0.8 mm;
- quartz sand 0 – 1 mm;
- polycarboxylat based superplasticizer;
- steel fibers Ø=0.6mm L= 13 mm;
- water.

The chemical composition of cementitious materials is presented in Table 1.

Table 1: Chemical composition of cementitious materials.

	SiO_2	Al_2O_3	Fe_2O_3	CaO	SO_3	MgO	Na_2O
CEM I 52.5R	25%	2.1%	3%	69%	2.3%	0.7%	0.2%
Silica fume	97.5%	0.4%	0.1%	0.2%	0.1%	0.1%	0.1%
Nanosilica	99.9%						

Specially designed and patented apparatus was applied to create turbulent flow and employ hydrodynamic cavitation process as a tool for silica fume micro and nano particle agglomerate disaggregation and surface activation (Figures 2, 3) [7].

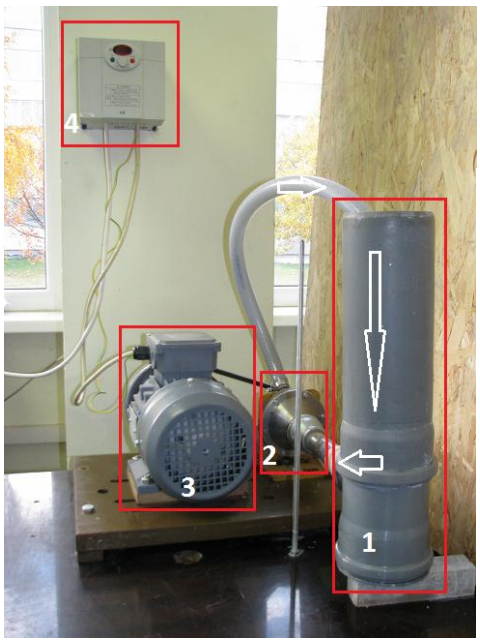

Figure 2: Setup for silica fume dispersion using cavitation phenomena. 1. reservoir, 2. cavitation chamber, 3. engine, 4. frequency converter.

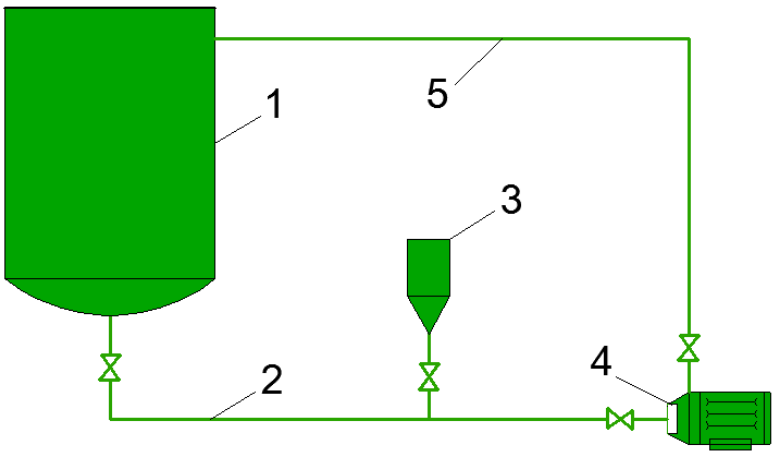

Figure 3: Silica fume suspension preparation scheme. 1. reservoir, 2. tube, 3. dispenser, 4. dispergator, 5. pipe.

The setup consists of four main components:

1) Cavitation chamber where high speed flow is created and cavitation phenomena occurs
2) The reservoir, where materials can be added and collected after treatment.
3) The electrical engine.
4) Frequency converter to adjust engine speed and choose most effective working regime.

The slurry was produced by adding silica fume and water in proportions 1:10 and 1:2. The volume of slurry was 3 liters and it was processed for 10 minutes. Device speed was 6000 rpm.

The concrete mixing procedure was organised in a following way: all dry materials were mixed for 1 minute in the high speed paddle mixer. Then silica fume slurry and 70% of total water amount were added. After 2 minutes of mixing rest of water and superplasticizer was added and mixing was continued for 5 minutes.

Mix consistency was determined by cylinder flow test. Cylinder with the internal diameter of 50 mm and height of 100 mm was filled with UHPC concrete mix and lifted up. The diameter of the flow was measured after 1 minute.

Specimens with dimensions 100x100x100 mm were cast and stored in climatic chamber (t=20°C, RH=90%) At the age of 1 day specimens were demoulded and stored in water bath (t=20°C). Specimens were tested according to standard [7] at the age of 7 days. The second testing was performed at the age of 12 days. Accelerated curing conditions (t=90°C) were applied for last 48 hours. Five concrete mixtures were produced. All mixtures had cement content of 950 kg/m^3. Two mixtures with silica fume content of 20 kg/m^3 were produced. One of them was reference mix (REF-1) without cavitation treatment and for second (CAV-1) cavitation treatment was applied. Three other mixtures had silica fume content of 100 kg/m^3. First was reference mix (REF-2) without treatment, second (CAV-2) was treated by cavitation and third (CAVNS-2) additionally to cavitation treatment had nanosilica addition 1% of cement mass. Prepared concrete mix compositions and cone flow values are summarized in the Table 2.

Table 2: UHPC mix compositions and cone flow values.

Materials	REF1	CAV-1	REF-2	CAV-2	CAVNS-2
Portland cement CEM I 52.5 R	950	950	950	950	950
Quartz sand 0.3/0.8 mm	470	470	470	470	470
Quartz sand 0/0.5 mm	200	200	200	200	200
Quartz filler 0/0.3 mm	400	400	340	340	340
Silica fume 971U	20	20	100	100	100
Nanosilica Elkem					9.5
Superplasticizer	25	25	25	25	25
Steel fibre 13 mm/0.16 mm	20	20	20	20	20
Water	200	200	200	200	200
Cavitation:	-	10 min	-	10 min	10 min
Cone flow, mm	226	260	260	250	255
Concrete density, kg/m^3:	2285	2285	2365	2365	2374.5

3 Results and discussion

The effect of cavitation treatment first can be evaluated visually. For untreated silica fume suspension larger agglomerates can be noticed even without microscope, while for processed suspension without microscope no visible particles are found. If untreated suspension (manually mixed) and cavitation treated suspension (silica fume/water ratio 1 : 10) is left undisturbed in the clear vessel, segregation can be observed for untreated suspension after 15 minutes, while processed suspension does not show any segregation (see Figure 4a). After two hours both suspensions are segregated (Figure 4b). And for untreated suspension large agglomerates are visible (Figure 4c).

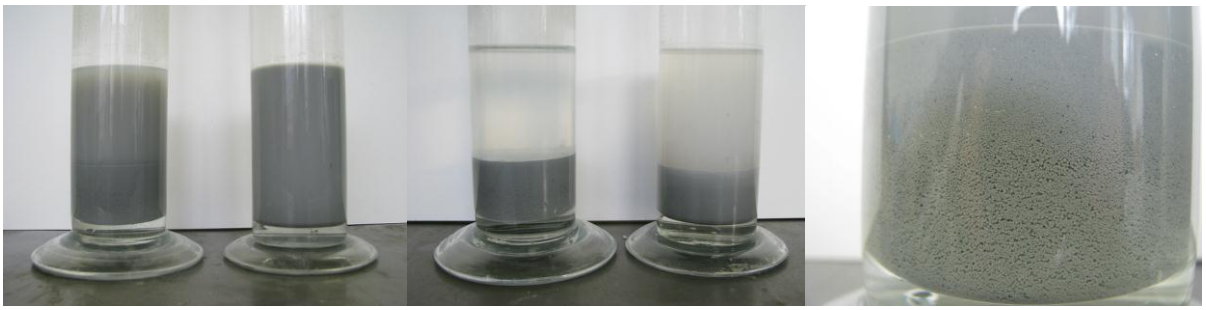

a) b) c)

Figure 4: a) Suspension segregation after 15 minutes. Left –untreated, right - cavitation treated. b) Suspension segregation after 2 hours. Left –untreated, right - cavitation treated. c) Agglomerates in untreated slurry after 2 hours.

Consistency was measured by means of cylinder flow test (see Figure 5). Results (see Table 2) have shown that cylinder flow increase from 226 to 260 mm after silica fume treatment for mixes with silica fume content of 20 kg/m^3. Reason could be better particle packing (that reduces necessary water amount and improves flowability of mixture. For mixes with silica

fume content of 100 kg/m^3 after cavitation treatment cylinder flow decreased from 260 to 255 and 250 mm. This effect could be explained by significantly increased silica fume surface area after agglomerate disaggregation that absorbs extra water and reduces flowability.

Compressive strength was tested at the age of 7 days (normal curing) and 12 days (10 days normal curing and 48 hours accelerated curing at the temperature of 90°C). For the mixtures with silica fume content 20 kg/m^3 results (see Figure 6) show compressive strength increase of 6% at the age of 7 days in normal curing regime and 4% increase at the age of 12 days in accelerated curing regime compared to those of reference mix.

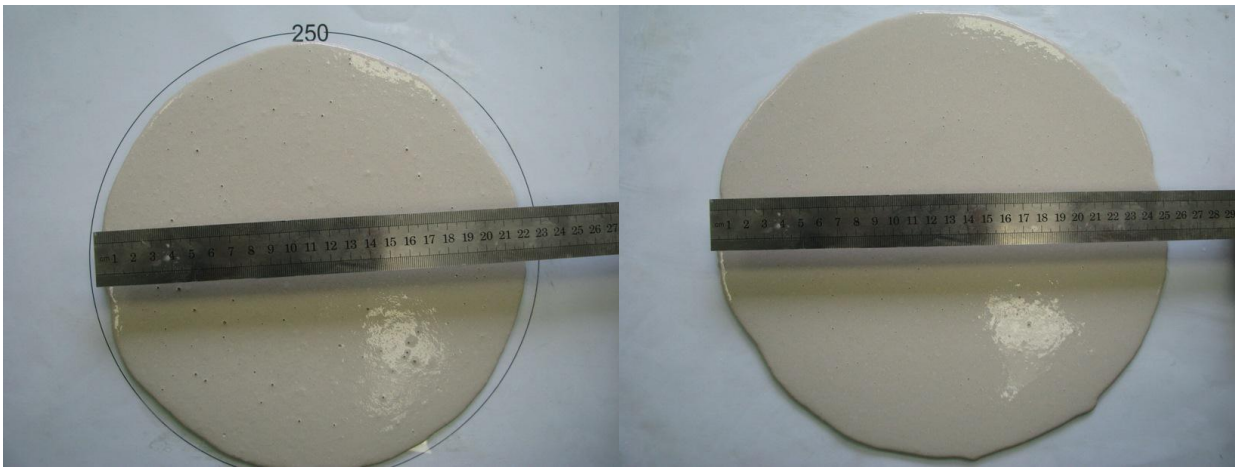

Figure 5: Cylinder flow test. Mix REF-1 (on the left), Mix CAV-1 (on the right).

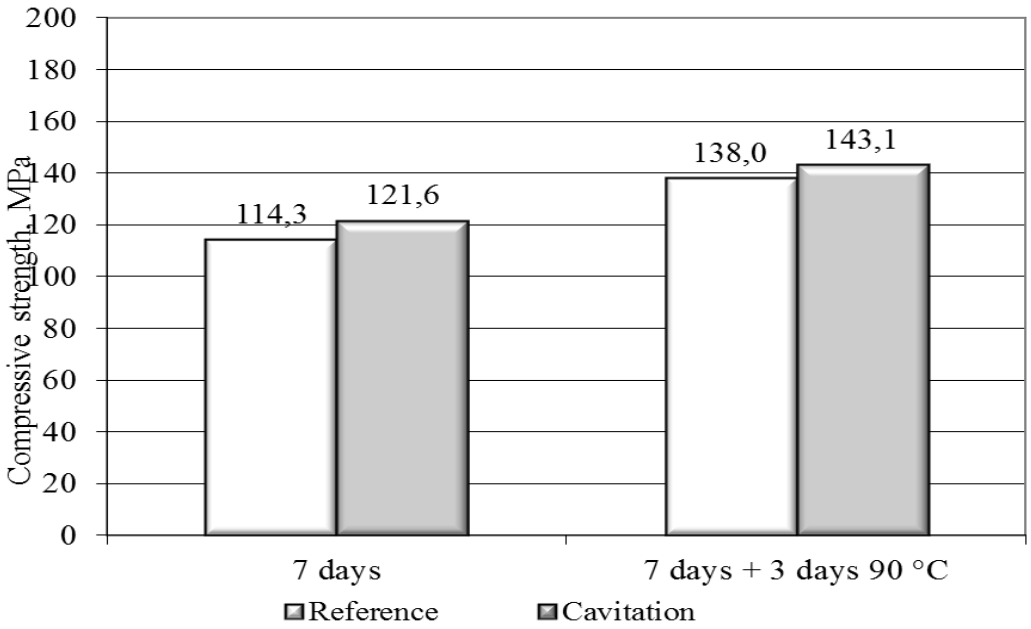

Figure 6: Compressive strength results for mix with silica fume content 20 kg/m^3.

Mixture with silica fume content 100 kg/m^3 show similar strength increase after silica fume cavitation treatment (see Figure 7). At the age of 7 days compressive strength increase is 4% and at the age of 12 days 5%. Mixture with the nanosilica addition shows best performance with the strength increase of 9% at the age of 7 and 12 days and reaches compressive strength of 164.5 MPa.

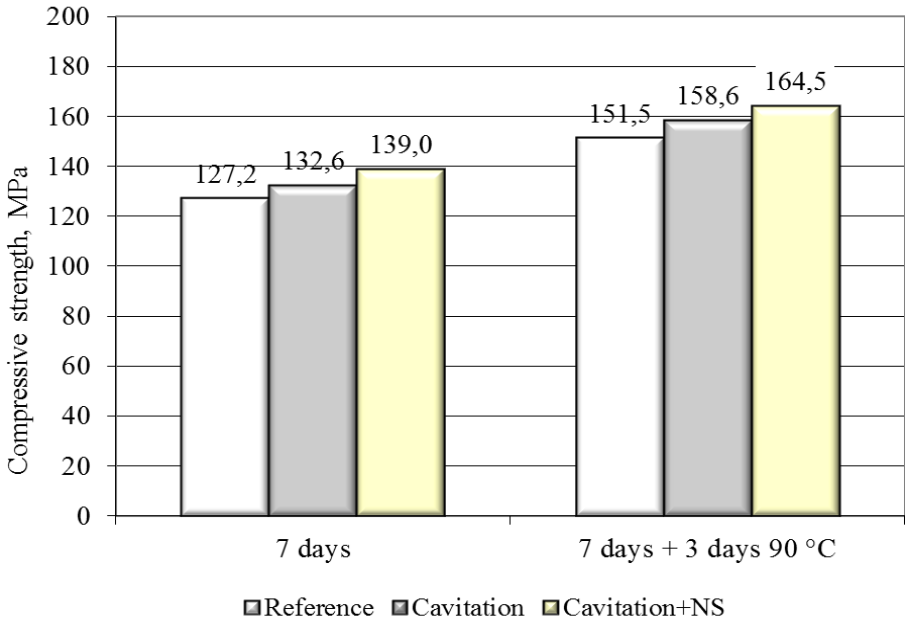

Figure 7: Compressive strength results for mix with silica fume content 100 kg/m^3.

4 Conclusions

Cavitation treatment of silica fume with the aim of agglomerate disaggregating and surface activating proved to be simple, fast and effective way to improve UHPC properties. Average compressive strength increase for both – normal and accelerated curing was 5%. In case of nanosilica addition compressive strength increased for 9%. Also risk of alkali – silica reaction due to silica fume agglomerates was minimized. Silica fume suspension in water (ratio 1:10) after cavitation treatment has shown higher stability. Cylinder flow value for higher silica fume amount decreased due to the higher cavitation treated particle surface area that can absorb more water.

The cavitation treatment apparatus can be easily upscaled for the purposes of industrial use.

5 Acknowledgement

The financial support of the ERAF project Nr. 2010/0286/2DP/2.1.1.1.0/10/APIA/VIAA/033 „High efficiency nanoconcretes” is acknowledged.

References

[1] Goldman A; Bentur A: Effects of pozzolanic and non-reactive fillers on the transition zone of high strength concrete. International Symposium on Interfaces in cementitious composites. Toulouse, 1992, Proceedings, E&FN SPON, London pp. 53–62, 1993.

[2] Möser B; Pfeifer C: Microstructure and Durability of Ultra-High Performance Concrete. Proceedings of the Second International Symposium on Ultra High Performance Concrete Kassel, Germany March 05-07, 2008.

[3] Krella A. K: The new parameter to assess cavitation erosion resistance of hard PVD coatings. Engineering Failure Analysis 18 p. 855–867 (2011),

[4] Knapp R.T; Daily J.W; Hammit F.G: Cavitation. New York: McGraw-Hill; 1970.

[5] Suslick K.S; Mdleleni M.M; Ries J.T: Chemistry induced by hydrodynamic cavitation. J Am. Chem. Soc.,119:9303–4, 1997.

[6] Bourne N.:. On the collapse of cavities. Shock Waves;11:447–55, 2002.

[7] LV 14364 B Int.cl.C01B33/00 RTU, 20.10.2011. Auth. V.Mironovs, A.Polakovs, A.Korjakins: Method and apparatus for suspension preparation.

[8] LVS EN 12390-3:2002. Testing of hardened concrete - Part 3: Compressive strength of test specimens. Riga, 2002. pp. 16.

Nanoparticles as accelerators for cement hydration

Gerrit Land, Dietmar Stephan
Dept. of Civil Engineering, Building Materials and Construction Chemistry, Technische Universität Berlin, Germany

Nanoparticles are known to have an influence on the kinetics of cement hydration. Therefore they have the potential to substitute conventional setting and hardening accelerators and their undesired side effects. There are two different approaches for nanoparticles as accelerators for cement hydration. Either stimulation of the nucleation processes during early cement hydration by nanoparticle addition or redundantize nucleation processes by direct addition of the nuclei to the cement paste. We have chosen one typical material for each method, nanosilica respectively C-S-H-seeds, to follow and compare their effect on the kinetics of cement hydration and the properties of the hardened cement paste. While nanosilica was found to be a hardening accelerator, C-S-H-seeds accelerate setting and hardening. Furthermore both kinds of nanoparticles result in enhanced mechanical properties of the hardened cement paste.

Keywords: nano-silica, nucleation seeding, cement hydration

1 Introduction

Within the last decade significant progress has been made in technologies for production of nanoparticles. Today a wide variety of nanoparticles of different materials, sizes or shapes can be produced in large quantities. Therefore these particles get more and more in focus for the use in construction materials, especially those who have a similar chemical composition as materials that are already common in construction. Nanosilica was one of the first nanomaterial that was used in cementitious systems and a lot of methods for the synthesis of nanosilica are known [1]. But also nanoparticles made of Al_2O_3, Fe_2O_3, TiO_2 or ZrO_2 were studied [2–6]. A large variety of effects was found when nanosilica is added to cementitious materials:

- Filler effect [7]
- Acceleration of cement hydration [8]
- Formation of additional C-S-H- by pozzolanic reaction [9]
- Denser microstructure [10]
- Higher compressive strength [11]
- Lower permeability [12]
- Reduced calcium leaching [13]

Another type of nanobased accelerators for cement hydration is C-S-H-seeds. In contrast to nanosilica and other nanoparticles they are not added to stimulate nucleation processes but to supersede the time-consuming nucleation processes because the seeds already are the nuclei for further crystal growth [14]. Significant acceleration effects could be found when C-S-H-seeds were added to pure C_3S or ordinary Portland cement [15] resulting in higher compressive strengths and denser microstructures [16]

The model on the influence of nanoparticles on cement hydration

Thomas et al. [17] introduced a model to describe the effects that occur when nanosilica or C-S-H-seeds are added to C_3S. They assume that in the case of nanosilica addition an early pozzolanic reaction with calcium hydroxide from C_3S hydration at the particles surface covers the particles with C-S-H-nuclei. In the middle period of cement hydration [18] these nuclei start to grow and form the C-S-H-gel as the main hydration product. Due to the early pozzolanic reaction of the silica particles more C-S-H-nuclei are present when this period of hydration starts resulting in an acceleration of the hydration processes (predominantly C_3S-hydration) in

this period. When C-S-H-nuclei are directly added to the cement paste as a seeding additive, nucleation reactions that form C-S-H-nuclei are not essential anymore and the added nuclei can instantly grow to form C-S-H-phases.

In pure cement lime the formation of C-S-H-gel is limited on the cement grain surface wherefrom it grows into the pore space. In contrast to this the model assumes that the C-S-H-gel may also be formed onto the nanoparticles, which are spread over the pore space as showed in figure 1. Therefore the cement paste should show a faster compressive strength development and less porosity when compared to pure hydrated cement.

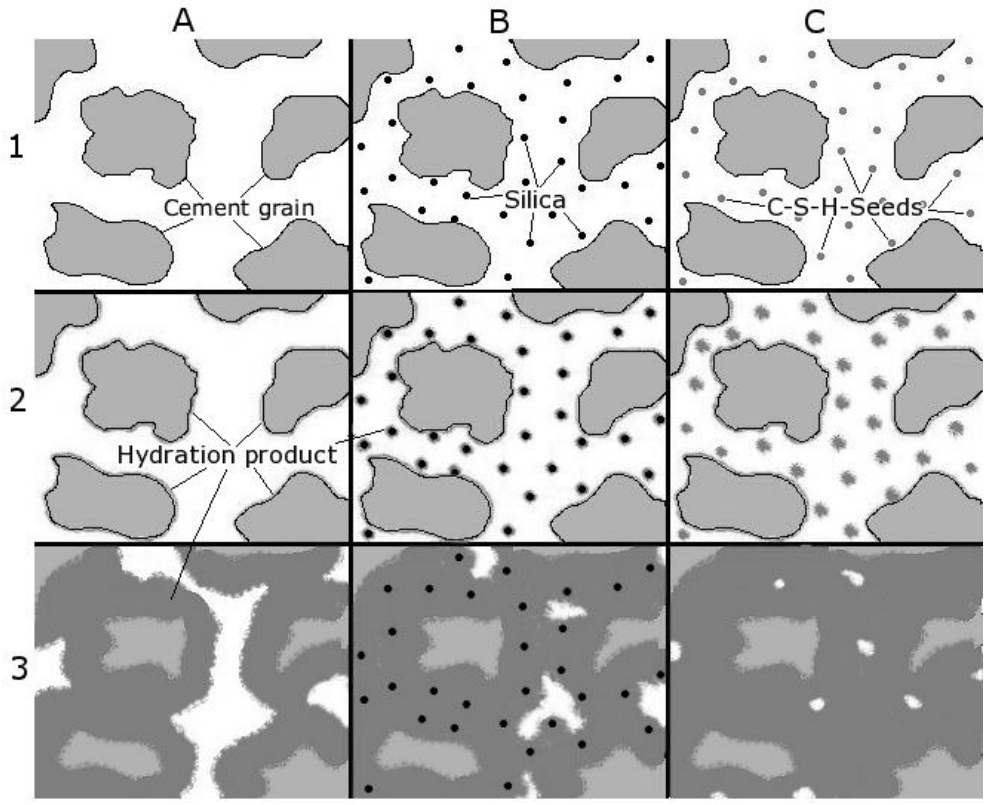

Figure 1: hydration of pure cement (A) and with addition of nanosilica (B) or C-S-H-seeds (C) at different times after mixing (1-3) according to [19].

If the assumption that the accelerating effects of nanosilica is based on an early pozzolanic reaction of the silica surface, the magnitude of the acceleration should depend on the total surface area of the added silica particles. Therefore we followed the accelerating effects of nanosilica of different size and dosage on the cement hydration. Furthermore commercial C-S-H-seeds were tested and compared to the nanosilica to evaluate which type of accelerating nanoparticles has the largest potential to substitute conventional accelerators for cement hydration.

2 Experimental procedure

White cement (Dyckerhoff white, CEM I 42.5 R) was used in all experiments. Nanosilica particles of four different sizes were used in the experiments. The larger ones (295 nm and 86 nm in diameter) were synthesized by the Stöber-method [19, 20] using tetraethyl orthosilicate (TES28, Wacker Chemie) as a precursor in an Ethanol/Ammonia solution. Furthermore the addition of commercial nanosilica particles of 18 nm (Köstrosol 1530) and 7 nm (Köstrosol 0730, both Chemiewerke Köstritz) in diameter was followed. X-Seed 100 (BASF) was used for experiments with C-S-H-seeds.

For heat flow calorimetry 4g of cement and a water-cement ratio of 0.5 were used. The nanoparticles were dispersed in the water before mixing. All samples were mixed for 90 seconds and then were put into the calorimeter (MC-CAL, C3 Prozess- und Analysentechnik). The hydration heat was followed for 7 days at 36°C (nanosilica) or 20°C (C-S-H-seeds) and was ensured by double determination.

Compressive strength tests were done on 2·2·2 cm cubes using a Z150 (Zwick/Roell) and were ensured by repeat determination (3x). The cubes were demoulded one day after mixing and then were stored at 20°C and 65% RH.

In the remains of compressive strength testing the hydration reactions were stopped by freeze drying. For SEM-pictures (XL30, Philips) pieces of this were sputtered with gold.

For mercury intrusion porosimetry (Poremaster 60GT, Quantachrome Instruments) the following classification of pores was used: gel pores 1-10nm, capillary pore 10nm-10µm, air voids >10µm.

3 Results and discussion

As mentioned above the model by Thomas et al. assume that the accelerating effect of nanosilica on the cement hydration is based on a reaction of the silica surface. Therefore the acceleration should be the more pronounced the larger the total surface area of the added particles is. Basically this total surface can be either controlled by the dosage of nanosilica in relation to the cement weight or by the addition of smaller particles that have much larger surfaces in relation to their weight.

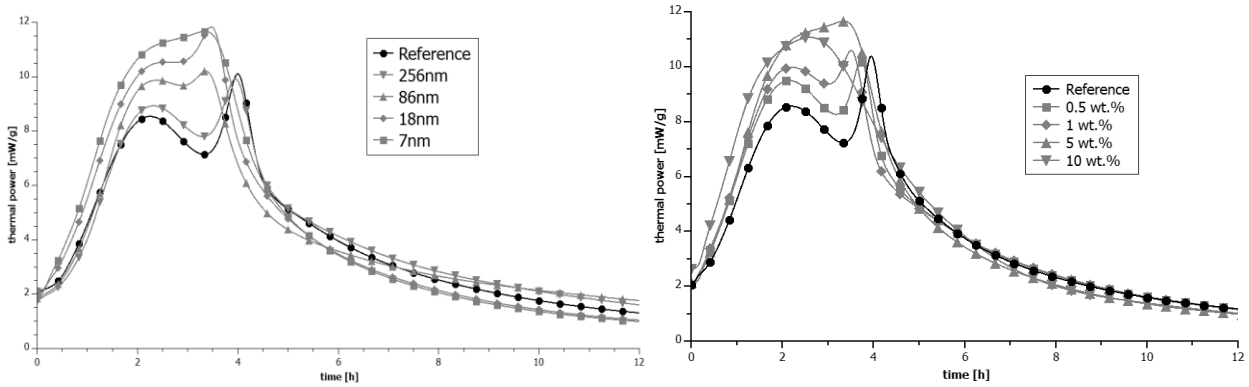

Figure 2: Calorimetry of cement at 36 °C when 5 wt.% of nanosilica are added (left) or different dosages of the 7nm nanosilica (right).

The effect of different particle sizes on the cement hydration is shown on the left side of figure 2 where 5 wt.% of nanosilica were added to the cement paste. The particles have diameters from 256nm down to 7nm and surface areas of 17m^2/g up to 285m^2/g. While the first intense heat output right after mixing can't be shown, since the samples were mixed outside the calorimeter, just the middle period of hydration is presented. There is a significant increase of hydration heat of the first peak (primarily C_3S-hydration) which can be determined when nanosilica is added. At the same time the second peak which is allocated to the formation of sulfate-type AFm shows a shift to earlier times. Both effects show a direct correlation to the particles diameters and surface areas respectively. Similar effects can be observed when the nanosilica dosage in the cement paste is changed instead of the particles diameter. This is shown on the right side in figure 2. The larger the nanosilica dosage is the more the thermal power during the middle period of cement hydration increases. The results indicate that there is a direct dependency of the nanosilica surface area and the magnitude of cement hydration acceleration. Whether this is an effect of an early pozzolanic reaction as described in the model or rather is caused by other

effects like the adsorption of ions from pore solution on the highly charged particles surface, cannot be answered here.

When C-S-H-nanoparticles are added to the cement paste instead of nanosilica, the first maximum of hydration heat in the middle period of cement hydration increases as it did under nanosilica addition. At the same time the maximum shifts to earlier times with increasing C-S-H-seed dosages. As seen in the case of nanosilica addition the maximum caused by the formation of sulphate type AFm also shifts in time with increasing C-S-H-seed addition (figure 3).

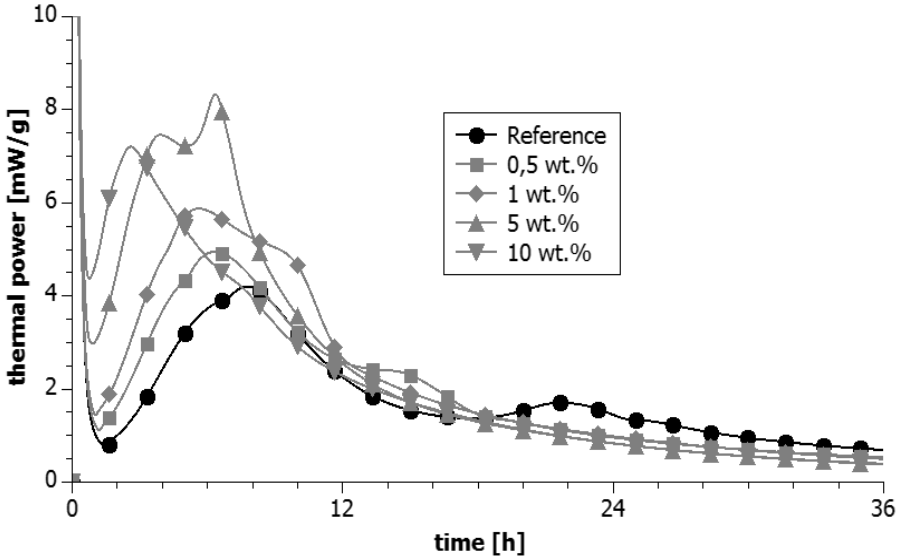

Figure 3: Acceleration of cement hydration by addition of C-S-H-seeds in different dosages.

All the results of the calorimetry are in accordance to the model described above. The larger the amount of nuclei, either by addition of C-S-H-seeds or by the formation on the silica surface, the higher the heat output during the middle period of hydration is, because all the nuclei can grow simultaneously to form the C-S-H-phase. In the case of C-S-H-nuclei addition the middle period also starts earlier, because the time consuming nucleation processes became redundant so that the dormant period before C_3S hydration shortens significantly the more C-S-H-seeds are present.

The acceleration of cement hydration which was found in the calorimetry should also result in faster development of the mechanical properties of the hardened cement pastes. The results of the compressive strength tests are shown in figure 4, where 5 wt.% of nanoparticles were added. In all samples the compressive strength was increased by nanoparticle addition. While samples with larger nanosilica particles doubles the compressive strength, when compared to pure cement paste, the smallest nanosilica results in a tripled and C-S-H-seeds in a quadrupled compressive strength after one day. After 3, 7 and 28 days the three larger silica particles still slightly enhance compressive strengths. At the same time samples with the smallest nanosilica show the best performance and even outperform the C-S-H-nanoparticles. Unlike the one-day results this improved strength development is not conform to the described hydration model, but we assume that it is a result of pozzolanic reaction of silica particles. Thereby additional C-S-H-phase is formed, giving additional compressive strength and less porosity. The 7nm particles might be more accessible for this reaction than the larger nanosilica particles because of a significantly increasing solubility of silicic acid in colloidal silica of sizes below 10 nm [21]. This is confirmed by a higher total heat of hydration after 7 days of the samples containing 7nm silica when compared to pure cement or C-S-H-seed addition.

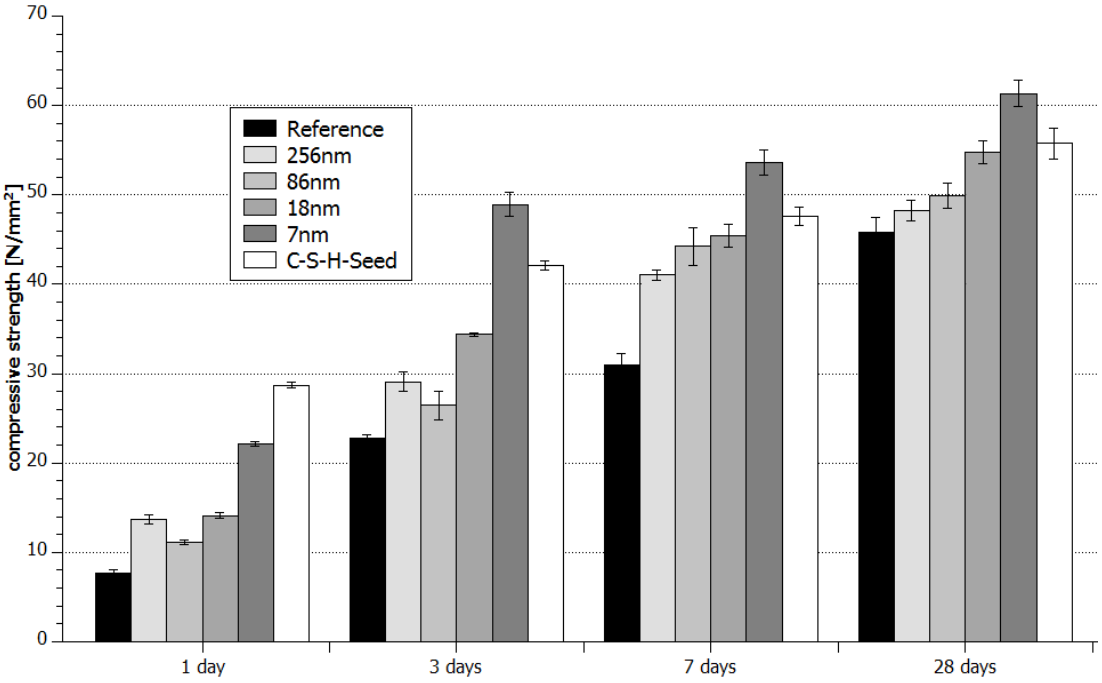

Figure 4: Compressive strength development within the first 28 days with 5 wt.% of nanoparticles added to the paste.

The results of the compressive strength test are also confirmed by mercury intrusion porosimetry, which is shown in table 1. In all samples containing nanoparticles the capillary porosity decreases for the benefit of gel pores, when compared to pure hardened cement paste. The results for 7nm silica and the C-S-H-particles hardly do not differ from each other. While C-S-H-seeds reduce capillary porosity slightly better after one day, it is reversed after 28 days. Since gel pores are unavoidable in hardened cement paste and have little effect on the mechanical properties of it (unlike capillary pores), the reduction of capillary porosity is a positive side effect of nanoparticle accelerators.

Table 1: Porosity of hardened cement paste compared to cement pastes with 5 wt.% nanoparticles added.

Sample	**Reference**		**Nanosilica 7nm**		**C-S-H-seeds**	
days	1	28	1	28	1	28
air voids [vol.%]	0.85	1.59	1.13	0.98	1.28	1.16
capillary pores [vol.%]	37.42	21.06	25.49	12.37	23.62	13.87
gel pores [vol.%]	9.02	12.19	13.18	18.96	14.98	17.69

The acceleration of cement hydration causes larger amounts of hydration phases at a certain time after mixing and therefore reduces capillary porosity of the hardened paste at this time. Furthermore the particles themselves may fill voids between the cement grains and the formation of hydration phases may take place on the particles in the pore space, whereby the pore space is faster filled out with the hydrated phases. SEM picture of four one-day old samples are shown in figure 6. Only little differences between pure cement and a sample containing 295nm silica can be seen (top left and right). The cement grains are covered with short C-S-H needles and long Ettringite needles which bridge the pore space. However cement paste containing 7nm nanosilica (bottom left) has a much denser structure and most of the pore space is already filled with hydration phase. This is even more pronounced in samples containing C-S-H-seeds. The structure of the hardened cement paste is very dense. Ettringite-

needles are not visible anymore because they are either overgrown by C-S-H-phase or are not formed in the typical needle-like shape.

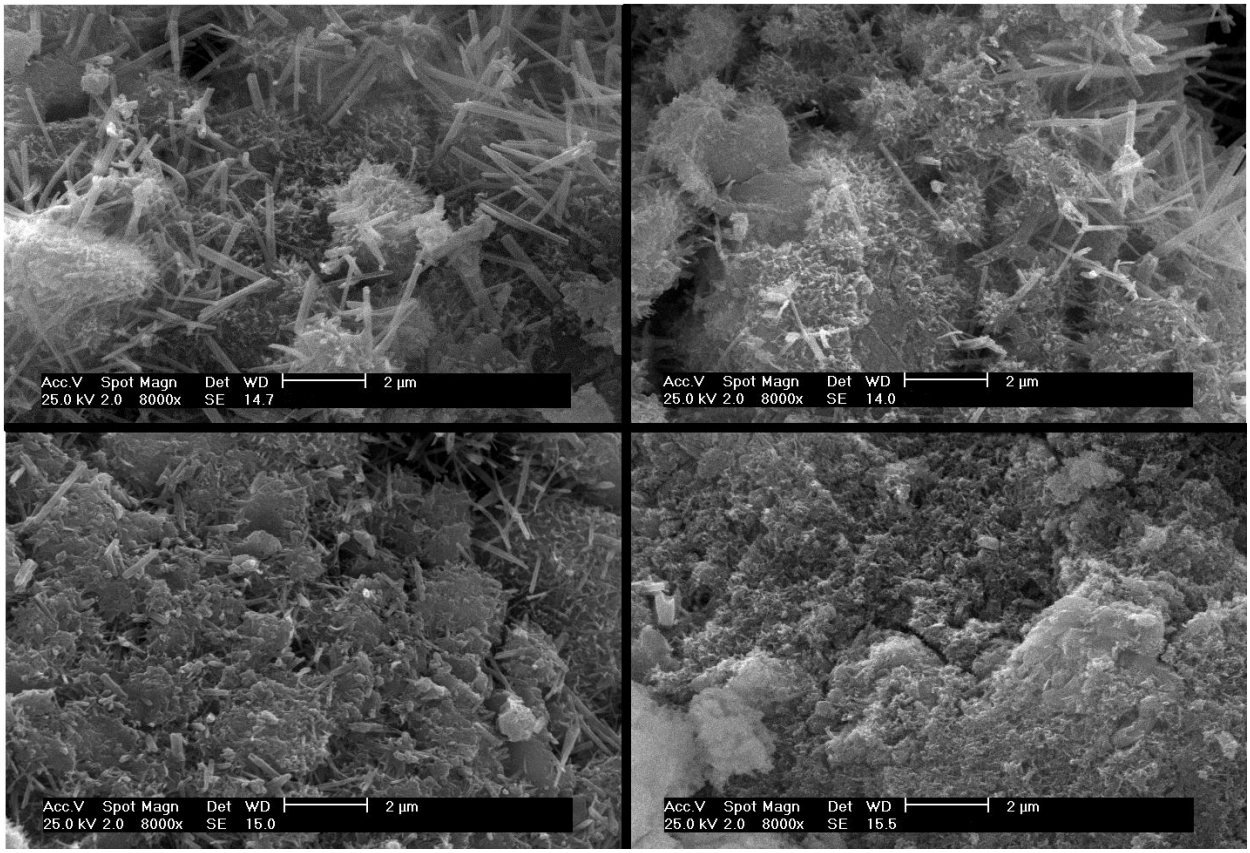

Figure 5: SEM –Image of cement stone after 1 day of cement hydration of pure white cement (top left) and with respectively 5 wt.% of nanosilica 295 nm (top right), nanosilica 7 nm (bottom left) and C-S-H-seeds (bottom right).

4 Conclusions

Two different ways of accelerating cement hydration by nanoparticles were explained, the addition of seeds or the addition of nucleation stimulating particles. The accelerating potential of C-S-H-seeds and nanosilica as typical representatives for one of these ways were respectively investigated. Nanosilica was found to be a hardening accelerator and it was shown that the acceleration is substantially dependent on the total surface area of the added particles. C-S-H-seeds, on the other hand, are both setting and hardening accelerators. They manifold early strength development when compared to pure cement but are outperformed by the nanosilica in late strength because of additional C-S-H-formation by pozzolanic reaction. Both nanoparticles reduce the capillary porosity of the hardened cement paste and result in much denser structures. Also here C-S-H-seeds show better performance during the early hydration while nanosilica give better results in the long term.

References

[1] Quercia G, Brouwers H. Application of nano-silica (nS) in concrete mixtures. In: *8th fib PhD Symposium in Kgs. Lyngby, Denmark*; 2010, p. 431–436.

[2] Jayapalan A, Lee B, Kurtis K. Effect of Nanosized Titanium Dioxide on Early Age Hydration of Portland Cement. In*: Nanotechnology in construction 3: Proceedings of the NICOM3* ; [with CD-ROM]. Berlin, Heidelberg: Springer; 2009, p. 267–273.

[3] Nazari A, Riahi S, Riahi S, Shamekhi SF, Khademno A. Mechanical properties of cement mortar with Al_2O_3 nanoparticles. *Journal of American Science* 6;2010(4):94–7.

[4] Nazari A, Riahi S, Riahi S, Shamekhi SF, Khademno A. The effects of incorporation Fe_2O_3 nanoparticles on tensile and flexural strength of concrete. *Journal of American Science* 2010;6(4):90–3.

[5] Nazari A, Riahi S, Riahi S, Shamekhi SF, Khademno A. An investigation on the Strength and workability of cement based concrete performance by using ZrO_2 nanoparticles*. Journal of American Science* 2010;6(4):29–33.

[6] Campillo I, Guerrero A, Dolado JS, Porro A, Ibanez J, Goni S. Improvement of initial mechanical strength by nanoalumina in belite cements. *Materials Letters* 2007;61(8-9):1889–92.

[7] Sobolev K, Amirjanov A. The development of a simulation model of the dense packing of large particulate assemblies. Powder Technol 2004;141:155–60.

[8] Björnström J, Martinelli A, Matic A, Börjesson L, Panas I. Accelerating effects of colloidal nano-silica for beneficial calcium–silicate–hydrate formation in cement*. Chemical Physics Letters* 2004;392(1-3):242–8.

[9] Belkowitz J, Armentrout D. The Investigation of Nano Silica in the Cement Hydration Process. In: *American Concrete Institute Special Publication* 2009; p. 87–100.

[10] Korpa A, Trettin R. Nanoscale pozzolans for improving ultra high performance cementitious binders. *Cement International* 2007;5(1):74–83.

[11] Shih J, Chang T, Hsiao T. Effect of nanosilica on characterization of Portaland cement composite. *Materials science & Engineering A* 2006;424:266–74.

[12] Ji T. Preliminary study on the water permeability and microstructure of concrete incorporating nano-SiO2. *Cement and Concrete Research* 2005;35(10):1943–7.

[13] Gaitero JJ, Sáez Ibarra Y de, Erkizia E, Campillo I. Silica nanoparticle addition to control the calcium-leaching in cement-based materials. *phys. stat. sol. (a)* 2006;203(6):1313–8.

[14] Ludwig H, Dressel F. Synthetische Calcium-Silikat-Hydrate in Fertigteilbetonen: Anwendungsspektren von Erhärtungsbeschleunigern. *BWI* 2011(05):46–50.

[15] Alizadeh R, Raki L, Makar JM, Beaudoin JJ, Moudrakovski I. Hydration of tricalcium silicate in the presence of synthetic calcium–silicate–hydrate. *J. Mater. Chem* 2009;19(42):7937.

[16] Alizadeh R, Beaudoin J, Raki L, Rakar J, Moudrakovski I. C-S-H seeding: an approach for the nanostructural tailoring of cement-based materials. In: *13th International Congress on the Chemistry of Cement*, Madrid, Spain. Madrid, Spain; 2011.

[17] Thomas JJ, Jennings HM, Chen JJ. Influence of Nucleation Seeding on the Hydration Mechanisms of Tricalcium Silicate and Cement. *J. Phys. Chem. C* 2009;113(11):4327–34.

[18] Taylor HFW. Cement Chemistry. 2nd ed. London: Thomas Telford Services Ltd; 1998.

[19] Land G, Stephan D. The influence of nano-silica on the hydration of ordinary Portland cement. *J Mater Sci* 2011, DOI:10.1007/s10853-011-5881-1.

[20] Stöber W, Fink A, Bohn E. Controlled Growth of Monodisperse Silica Spheres in the Micron Size Range. *J. Colloid Interface Sci*. 1968;26:62–9.

[21] Iler R. The Chemistry of Silica – Solubility, Polymerization, Colloid and Surface Properties, and Biochemistry. New York: Wiley-Interscience; 1979.

Using Atomic Force Microscopy to Evaluate Superplasticizers

Christoph Glotzbach[1], Dietmar Stephan[2], Michael Schmidt[1]
1: Dept. of Structural Materials and Construction Chemistry, University of Kassel, Germany
2: Berlin Institute of Technology, Germany

Recent concretes like UHPC can comprise large quantities of fines to fill the voids between coarser particles like the cement and displace water which positively influences the flowability. Together with a very low water-binder ratio of about 0.20, the density of the formed matrix prevents the migration of corrosive agents like chloride ions and results in compressive and tensile strength that supersedes that of traditional concrete by far. As the rheological properties of these fresh concretes depend mainly on the forces acting between the fines due to their high specific surface area, understanding of these forces has become crucial. At the University of Kassel, atomic force microscopy technique of colloidal probes have been used to study these forces, focusing on silica because these exhibit the largest fraction of inner surface in common UHPC mixtures. During these measurements, two individual silica particles were submerged in electrolyte solutions with added superplasticizer where they were approached and retracted from each other. The sum of the resulting forces that act between the particles while they were close could be measured with an accuracy of few nano-Newton. Using this technique and silica particles as a model system, several commercial superplasticizers could be evaluated regarding their influence on the interparticle forces and the range of interaction.

Keywords: aggregation, silica fume, surfactant, rheology, atomic force microscopy

1 Introduction

The rheological properties of highly concentrated suspensions are governed by the direct interaction of their particles. Under given boundary conditions, increased attractive forces between the particles lead to a higher viscosity and hinder the flowability of the paste. Regarding ultra-high performance concrete (UHPC), many of its raw materials have been characterized and the influence of their properties on flowability has been studied. While the effects of interparticle forces are usually visualized macroscopically by spread value and flowability, it is necessary to find more direct means to measure the acting forces in order to understand the basic mechanisms involved in the flow of cementitious pastes.

Atomic Force Microscopy (AFM) has now been used for two decades to study the forces between surfaces. Crystalline silicon dioxide surfaces belong to the most widely studied AFM samples as they are inert against a wide variety of conditions and as such permit easy handling of the samples. On the other hand, silica surfaces exhibit the largest surface in UHPC mortars. As can be seen in Table 1 [1], esp. silica fume, while only constituting about 6 wt.-% of all the solid materials in the mortar, is responsible for about 85 % of the surface of the solids. The interactions of these fines dominate the rheological behavior of the mortar at large. Because of this, we have focused our research on silica surfaces.

In our experiments, we have approached two spherical particles in a closed cell flooded with different additive solutions. The forces acting between the particles could be measured in a fluid environment that could be adapted to simulate a real mortar.

The flow behavior of suspensions like concrete depends mainly on the forces that act between individual particles. A wide range of superplasticizers has come to use in the recent decades which help disperse the particles by overcoming adhesive forces, and ease tangential movement of the particles by hindering contact between them. Understanding how these polymers adsorb onto different material surfaces and change the adhesive forces is therefore

important. It is understood that modern polycarboxylate esters mainly act via steric repulsion. Though limited to silica surfaces for the time being, our method allows analyzing these forces directly over a wide range of experimental conditions.

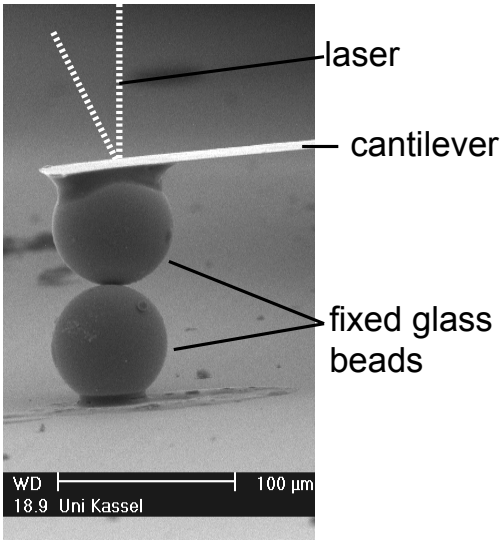

Figure 1. SEM model of the AFM test setup with glass beads of about 60 µm, larger than those used in the study. The laser path is shown for illustration purposes.

Table 1. Typical composition of ultra-high performance concrete [1]

	Mass fraction [%]	**Mass fraction [kg/m^3]**	**Surface area [m^2/m^3]**	**Surface fraction [%]**
Fine sand 0/0.5	45.4	975	–[a]	–[a]
Cement	38.7	832	386,880	12.2
Quartz powder	9.6	207	86,319	2.7
Silica fume	6.3	135	2,700,000	85.1

[a] value below measurement threshold

2 Experimental study

Materials

For the force measurements, the surfaces that are to be studied have to be of known geometry, asperities must be only minimal. Also, the particles have to be easy to handle for sample preparation. Therefore, glass beads (*SiLi 5210 S, Sigmund Lindner GmbH*, chemical composition see Table 2) with a typical diameter of 10 µm were used as a sample system for silica fume as depicted in Figure 1: For each measurement, one bead was fixed onto a glass substrate, another bead was fixed onto the tip of a tipless cantilever (*Mikromasch CSC-12 tipless/NoA*, typical spring constant k = 0.1 N/m) by means of a two-component methacrylate epoxy resin (*Uhu plus endfest 300*). All beads were subject to ultrasonic treatment to separate glass splinters from their surfaces. Before the tests, the smoothness of the surfaces was validated by measuring their topography over an area of 5 µm x 5 µm via contact mode AFM (see Figure 2 as an example). After fitting the surfaces to a second order polynom to accommodate for the surface curvature of the beads, the roughness was quantified as the root mean square of the height over the base plane (see Figure 2). All used beads had an rms

roughness of up to 6 nm (ref. Table 3). Beads with higher roughness or large asperities were rejected. The radius of the beads was measured by SEM imaging.

Table 2. Chemical Composition of the glass beads acc. to supplier

Component (oxide)	**wt.-%**
SiO_2	72.50
Na_2O	13.00
CaO	9.06
MgO	4.22
Al_2O_3	0.58

Four polymers were used in this study: a commercially available PCE superplasticizer ("PV", M_w = 81,000 kDa), a custom-synthesized polymer [2] ("CS", methacrylic acid and (ω-methoxypolyethylene glycol)-methacrylate with methallyl sulfonic acid as a chain transfer agent, M_w = 29,200 kDa, side chains 12 nm, backbone 13 nm), a melamine sulfonat ("MS"), and polyacrylate acid ("PAA") for comparison.

The test solutions were prepared with water purified by reversed osmosis and CDI (*VWR GPR Rectapur*). Polymer solutions as provided by the manufacturer were diluted to mass concentrations of 1, 0.1, 0.01, 0.001, and 0.0001 %, thus taking into account that only a small fraction of the polymer molecules in a mortar may be available for a given pair of particles.

Determination of cantilever spring constants

The spring constants were determined by the Cleveland method [3] and additionally taking further origins of errors into account. For this, the resonance frequency of the cantilevers was measured before and after modifying them with a bead, yielding the spring constant *k*. The inclination of the cantilever was measured to be 12°. Also, resulting spring constant after Cleveland would only be valid it the center of the bead was just beneath the outer end of the cantilever. As this could not be achieved, the distance *ΔL* by which the bead was off the end position of the cantilever was used to correct the spring constant by the terms similar [4] as described by Gibson [5], thus resulting in the effective spring constant k_{eff}.

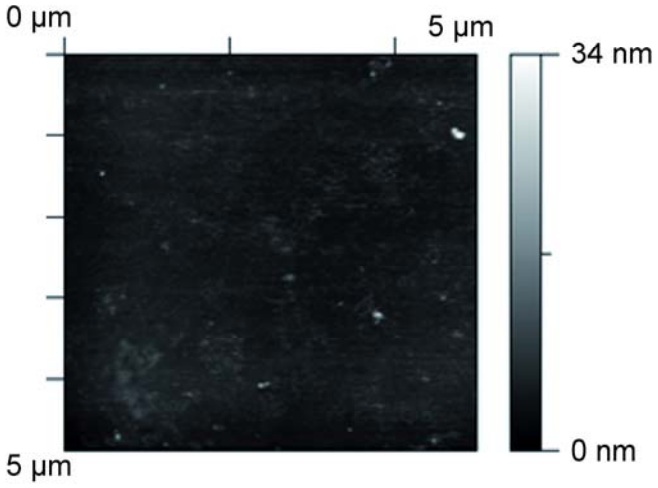

Figure 2. AFM image of a bead surface after fitting the curvature of the sphere to a polynom of 2nd order.

Force measurement

A glass substrate with a bead fixed onto it was inserted into the sample holder of the atomic force microscope (*Veeco MultiMode, Nanoscope IV*), a cantilever with another bead was put into the chip holder of the fluid cell. Both beads were placed atop each other (see Figure 1), but

were kept at distance at first. The fluid cell was sealed off with an o-ring. Then the test fluids were drawn into the cell using a syringe through tubing. This was repeated until no air bubbles were left in the fluid cell. The tubing was then removed from the fluid cell and replaced with two caps to prevent CO2 from the air diffusing into the test solution. The system was left for 5 minutes to reach an adsorption equilibrium. Afterwards, the beads were brought into contact at their outermost points, meaning that both centers as well as the contact point between them were in one straight line. Around this position, a matrix of 10 x 10 matrix points was defined in an area of 50 nm x 50 nm, resulting in a series of 100 measurements for one test solution. After moving the bottom bead to each of these matrix positions, the force was measured by pushing the beads together with a defined force of 42 nN and pulling them apart again. The measurement frequency was 0.5 Hz. This was repeated for all solutions of one polymer, starting with the lowest concentrations. Each pair of top bead and bottom bead was used for one polymer series only.

3 Results and discussion

During the force measurements, the deflection of the cantilever was measured while the distance between the particles was gradually changed. While the beads were apart from each other, the cantilever deflection was zero as no force was acting on the bead. The cantilever base was moved down along the *z* axis by piezo actuators. As soon as the beads contacted each other and were pushed together with a force of 42 nN, the cantilever was deflected. Then the cantilever was pulled away again. The two beads were then in contact and would not separate, deflecting the cantilever in the opposite direction. The cantilever was pulling the top bead away from the fixed bottom bead. Only if the pulling force exacted from the deflected cantilever was at least as large as the adhesive force between the beads, they could be separated again. This leads to a theoretical measurement cycle as depicted in Figure 3.

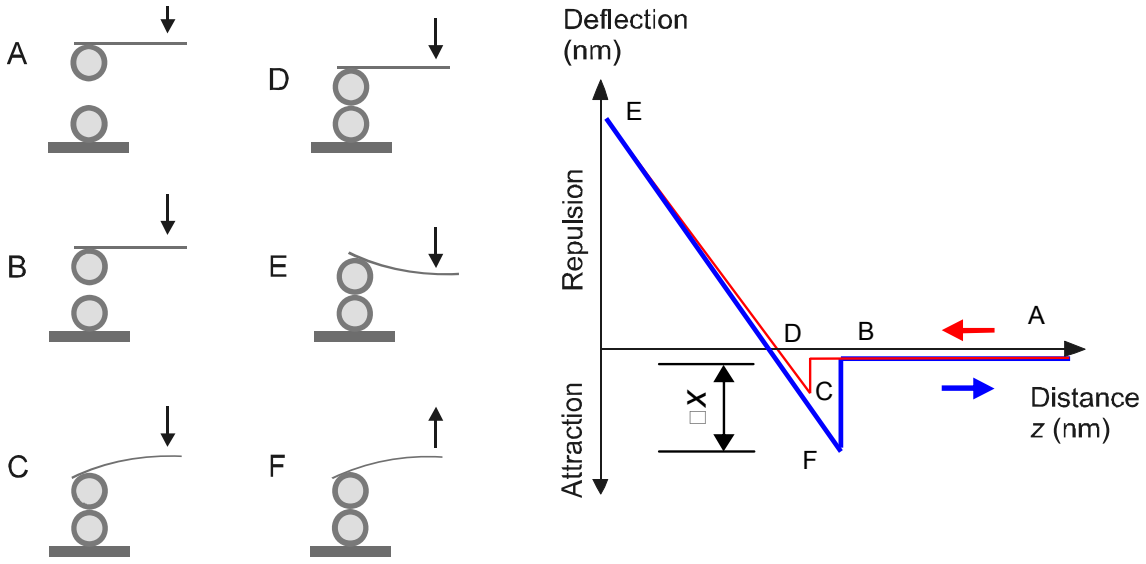

Figure 3. One optimal single force measurement cycle.

The adhesive force *F* between the beads is then calculated as the maximum deflection *x* multiplied by the effective spring constant k_{eff}.

F depends on the size of the conjoint areas of the beads. When the radii of the particles increase the resulting contact area between the two beads gets larger. As not all beads are of the same size, all resulting adhesive forces were normalized by division by the reduced radius

$$R' = \frac{R_1 R_2}{R_1 + R_2} \quad (1)$$

as described by Butt, Capella and Kappl [6], taking both individual bead radii R_1 and R_2 into account and yielding the normalized adhesive force

$$F' = \frac{F}{R'} \quad (2)$$

While evaluating the adhesive forces worked fine for saline solutions, polymer solutions could not be measured as there was often no single point of failure in the adhesion of the beads, but rather a gradual failure where the beads separated slowly away from each other. This was interpreted as the beads being held together by the chains of the polymers, only gradually desorbing from the silica surfaces. Thus, for evaluating the adhesion when polymer molecules were present in the solution, the force pulling the beads apart was integrated over the course of the separation of the beads:

$$E_A = \int_{z_e}^{z_i} F' dz \quad (3)$$

where z_i is the initial z position of the moving cantilever base at the beginning and also the end of the cycle (position A in Figure 3), and z_e is the z position when both beads are in contact, but no force is exacted on them by the cantilever (position D in Figure 3). dz is an infinitesimal movement of the cantilever base along the z axis. This yields the adhesion energy E_A that has to be overcome to separate the two beads, but normalized by the reduced radius R' as the normalized forces F' have been integrated. Therefore E_A is measured in $\frac{nN \cdot nm}{\mu m} = \frac{pJ}{m}$.

The indicated values are averaged over all 100 measurements for one sample and test solution.

Comparison of predictions and experimental results

Measuring the adhesive force between two beads in deionized water resulted in a normalized force of 11 nN/µm. Using the equation from [7]

$$A_H = -\frac{F}{R'} \times 12 D^2 \quad (4)$$

to calculate the Hamaker constant A_H for two silica particles in contact (distance between particles D = 0.2 nm when the particles are in direct contact) yields $A_H = 5.3 \cdot 10^{-21} J$, which is in accordance with the range of values for two silica surfaces in water in literature [7, 8]. This indicates that the resulting forces measured by this method are valid.

Experimental results and discussion

Though the adhesion forces showed the same tendency as the calculated adhesion energies, we evaluated the adhesion energies only, because the gradual failure of the adhesive bond between two beads did not show one single pull-off, but sometimes several. The normalized adhesion energy thus offers more substantial data.

The calculated adhesion energies that were normalized by the reduced radius of the used bead combinations show similar values for all used combinations when they were submerged in equal liquid environments, i.e. in pure water. This indicates that the results for all used bead

combinations are comparable, and that the screening of beads was appropriate and also successful.

Table 3. The bead combinations used for the polymers, and their characteristics

Additive	Cantilever spring constant [N/m]	Cant. bead size [µm]	Bottom bead size [µm]	Reduced radius [µm]
CS	0.14	13.1 (rms = 4.5 nm)	15.3 (rms = 2.2 nm)	7.06
PV	0.12	12.2 (rms = 5.8 nm)	14.2 (rms = 3.4 nm)	6.56
MS	0.15	16.8 (rms = 5.0 nm)	13.1 (rms = 3.7 nm)	7.36
PAA	0.14	14.4 (rms = 6.0 nm)	14.2 (rms = 5.7 nm)	7.15

rms values are the root mean square of surface height and indicate surface roughness

The normalized adhesion energies differ significantly between the studied polymers (see Figure 4). The rather large polymers PV did not reduce the energy necessary to separate the beads for a concentration of 10^{-4} wt.-%. The values rather show a slight increase in adhesion energy. But this small rise is not significant and can as well be attributed to statistical spread. Only after reaching a concentration of 0.1 wt.-%, the adhesion energy is reduced to a level that was reached with much lower concentrations for the other polymers.

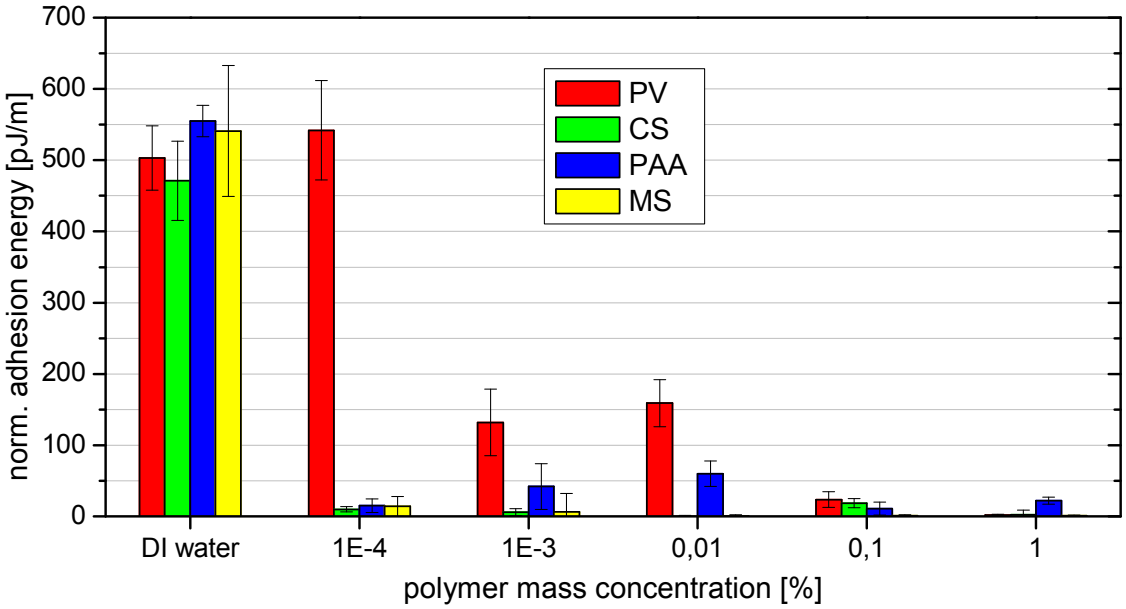

Figure 4. Normalized adhesion energy between two beads for four polymers in increasing concentration.

Polymer PV is a commercially available additive for concrete fluidization. It is rather large ($M_w \approx 80.000$ kDa) with long side chains in comparison with CS and its shorter side chains. The main difference between CS and PV is in architecture of the molecules. The latter shows a significant reduction in adhesion energy already at the lowest tested concentration, i.e. 10^{-4} wt.-%. Increasing the concentration does not lead to a further decrease in adhesion energy.

PAA and MS show a similar behavior like CS, i.e. a strong decrease in adhesion at small concentrations. PAA generally show higher adhesion. This polymer is in principle just the backbone of a superplasticizer with no ester groups as side chains. Therefore, there is only one functional group that can adsorb on a bead's surface, and this group is equally distributed along the whole chain of the polymer. When two beads are in contact, there are many polymer

molecules that are in contact with both beads and can therefore bridge them, leading to a more pronounced bond between them.
The large molecules of PV on the other hand have a long backbone together with long side chains. One would assume this to lead to a strong steric repulsion. But as can be seen in Figure 4, these molecules do not disperse the silica beads as well as the others. In fact there is still a pronounced adhesion energy that has to be overcome to separate the particles. This might be due to the protruding side chains strongly adsorbing to the surface of the adjacent bead, and thus bridging the particles and holding them together.

While shearing a suspension, many particles come into contact with each other throughout the suspension and have to be separated again for the motion to continue. If they are strongly bound to each other, this will hinder the suspension flow. This would mean that strong adhesion energies will lead to a worse workability. From the presented results, one can easily deduce that PV is not the perfect plasticizing agent for silica surfaces, e.g. silica fumes.

In concretes though, there are many chemically different surfaces that have to be dispersed, where these molecules might again prove more efficient. For the studied combination of two silica particles, PV seams the least efficient while CS and MS are more effective.

4 Conclusions

Based on the experiments and gathered results, the following conclusions can be drawn:

Atomic force microscopy can be used to measure the forces not only between specialized and custom made cantilever tips as they are common in the AFM community. Rather, real particles can be measured, though some obstacles have to be overcome. Well defined surfaces are of utmost importance to the success of the measurements.

Because of this, the measurements show a significant margin of error. Only small differences in adhesion energy cannot be resolved. But the studied polymers show significantly different behavior.

Adhesion energies describe the whole process of two contacted particles being completely separated again from each other. Gradual desorption of polymers is taken into account.

Large polymers may bridge the gap between two particles and bind them together if their constituents have a high affinity to the neighboring bead surfaces.

Acknowledgments

The presented study is part of a research project about UHPC generously supported by the DFG for which we are thankful. We would furthermore like to thank Wolfgang Peukert and Bettina Winzer from the University of Erlangen-Nürnberg, Germany, who helped us to set up the experiments. We also deeply appreciate the help and work of Sandra Schink [9] who carried out part of the shown AFM measurements, and Dr. Christof Schröfl [2] who provided us with custom superplasticizer polymers.

References

[1] Stephan, D., Krelaus, R., Schmidt, M.: Direct measurement of particle-particle interactions of fines for UHPC using AFM technology. Proceedings of the 2nd International Symposium on Ultra High Performance Concrete. S. 375-381. Kassel University Press, Kassel, Germany (2008).

[2] Schröfl, C.P.: Omega-Methoxypoly(ethylenoxid)-Methacrylsäureester-co-Methacrylsäure-co-Methallylsulfonsäure-Polycarboxylate als Fließmittel für ultra-hochfesten Beton: Synthese, Wirkmechanismus und Untersuchungen zum Synergismus von selektiv adsorbierenden Polymergemischen, (2010).

[3] Cleveland, J.P., Manne, S., Bocek, D., Hansma, P.K.: A nondestructive method for determining the spring constant of cantilevers for scanning force microscopy. Rev. Sci. Instrum. 64, 403-405 (1993).

[4] Glotzbach, C.: Interpartikuläre Wechselwirkungen in wässrigen Medien an einem Modellsystem für Feinstoffe (diploma thesis), (2008).
[5] Gibson, C., Smith, D., Roberts, C.: Calibration of silicon atomic force microscope cantilevers. Nanotechnology. 16, 234-238 (2005).
[6] Butt, H.-J., Cappella, B., Kappl, M.: Force measurements with the atomic force microscope: Technique, interpretation and applications. Surface Science Reports. 59, 1-152 (2005).
[7] Butt, H.-J., Graf, K., Kappl, M.: Physics and Chemistry of Interfaces. Wiley-VCH, Weinheim (2006).
[8] Lee, I.: Friction and adhesion of silica fibres in liquid media. Journal of Materials Science. 30, 6019-6022 (1995).
[9] Sandra Schink: Untersuchung der Veränderung der interpartikulären Kräfte zwischen silikatischen Modellpartikeln durch Betonfließmittel mit Hilfe der Rasterkraftmikroskopie, (2010).

Investigation the Effects of Nano-Silica Colloidal Solutions on Properties of Mortars

Aliakbar Ramezanianpour[1], Shabnam Firoozmakan[2], Hamed Bahrami Jovein[2]

1: Head of Concrete Technology and Durability Research Center, Amirkabir University of Technology, Tehran, Iran
2: Dept. of Civil Engineering, Amirkabir University of Technology, Tehran, Iran

Mechanical properties and durability of concrete may get improved using nano-silica as well as increasing the useful life of the structure. This study aimed to consider the impact of various kinds of nano-silica with different chemical and physical properties on compressive strength development and water absorption of concrete. The experiments were conducted in two stages. In the first stage, four mortar mixtures encompassing control and three mixtures containing three types of colloidal nano-silica were fabricated. In the second stage, to clarify the effect of nano-SiO_2 particle size, three mortar mixtures were made by silica powders with different size distributions. The nano-silica replacement level of all the mortars in the two stages was constant at 5%. It was found that the amount, particle size, colloidal potential and stability of SiO_2 particles in solution were effective factors in improvement of compressive strength and water capillary absorption.

Keywords: Mortar, Nano-sio2, compressive strength, Capillary water absorption,Zetasaizer

1 Introduction

Nanotechnology is a new method; in addition it is a novel scale in the technologies and a modern approach in all fields which makes the human able to improve the structure of materials. Nano-particles have been gaining increasing attention and been applied in many fields to fabricate new materials with novelty function due to their unique physical and chemical properties [1].

Recently, nano technology has attracted considerable scientific interest due to the new potential uses of particles in nanometer (10^{-9} m) scale. The nano scale-size of particles can result in dramatically improved properties from conventional grain-size materials of the same chemical composition. There are few reports on mixing nano-particles in cement-based building materials [2, 3]. Nano-particles of SiO_2 (nS) can fill the spaces between particles of C–S–H gel, acting as a nano-filler. Furthermore, by the pozzolanic reaction with calcium hydroxide, the amount of C–S–H increases. Thus, the size and amount of calcium hydroxide crystals are significantly decreased [1, 3, 4, 5, 7, 8, 9].

Nano-SiO_2 can behave as a nucleus to tightly bond with cement hydrates. The stable gel structures can be formed and the mechanical properties of hardened cement paste can be improved when a smaller amount of nano-SiO_2 is added [1, 3, 5, 6]. Higher densification of the matrix improves the strength and durability of the material when nano-silica is used in cement mortar. For constant w/c ratio and cement content, increasing nano-silica from 1 to 2 percent of cement weight improved the infiltration resistance [10]. It has been reported that the higher dosage of nano-SiO_2 lead to higher mechanical strength [3].

It can be concluded that the SiO_2 particles with average diameter of 15 nm can improve the early age strength of the concrete more than particles with 80 nm, however, after 90 days of moist curing the final strength of specimens made with 80 nm of SiO_2 particles was relatively enhanced [11].

In this paper, compressive strength and capillary water absorption of mortars incorporating different kinds of nano-silica with various chemical and physical characteristics are compared. The water/binder (w/b) ratio and slump flow of all the mortar mixtures were kept constant at 0.485 and 140±10 mm, respectively. The zetasizer test was used to analyses size of particles

and colloidal potential and XRF technique was used to determine chemical characteristic of colloidal solutions.

2 Experimental program

Material

ASTM C 150 type I Portland cement was used in all the mortar Mixtures. Four different types of nano-silica were used in this study. Type 1, 2 and 3 nano-silica denote Silica amorphous colloidal based solutions with a solid content of 12.5%, 15%, 30% respectively. The type 4 silica powders in three different particle sizes were used that 4-a, 4-b and 4-c refers to type 4 silica with particles with diameter lesser than 50 nm, between 300 up to 500 nm and between 700 up to 900 nm, respectively. The chemical constituent of these materials are, shown in Table 1. The physical characteristics of four types of nano-silica are indicated in Table 3. Aggregate is Standard packing sand and equivalent to DIN EN 196-1. The maximum size of sand particle is between 2 and 2.5 mm. Physical characteristics of sand are introduced in Table 2. Very fine size and high specific surface of nano-particles decrease the mortar workability. The superplasticizer (SP) admixture was a polycarboxylic acid based was employed to aid the dispersion of nano-particles in mortars and achieve proper workability of mortars.

Table 1: Chemical composition of cement and four types of nano-silica solutions.

Components	**SiO_2**	**MgO**	**CaO**	**SO_3**	**Fe_2O_3**	**Al_2O_3**	**Na_2O**	**K_2O**
Cement	19.9	2.07	64.1	4.09	4.1	3.83	<10ppm	0.79
Nano-SiO_2 (type 1)	63.9	0.15	0.087	0.39	0.038	0.15	17.3	4.3
Nano-SiO_2 (type 2)	91.5	0.085	0.065	0.26	0.021	0.085	0.97	0.013
Nano-SiO_2 (type 3)	94.06	0.09	0.1	0.026	0.037	0.13	1.13	0.002
Nano-SiO_2 (type 4)	92.1	0.076	0.192	0.185	0.093	0.066	1.07	0.08

Components	**Cl 2**	**TiO2**	**P2O5**	**MnO**	**LOI**	**C2S**	**C3S**	**C3A**	**C4AF**
Cement	0.008	0.47	0.064	0.23	0.04	6.92	66.45	3.21	12.47
Nano-silica (type 1)	0.18	0.047	0.019	0.009	13.27	-	-	-	-
Nano-silica (type 2)	0.045	0.04	0.008	0.003	6.79	-	-	-	-
Nano-SiO2 (type 3)	0.076	0.013	0.11	0.004	4.27	-	-	-	-
Nano-SiO2 (type 4)	0.044	0.064	0.129	0.006	5.88	-	-	-	-

Table 2: Physical characteristics of sand.

Characteristics	***Water absorption (%)***	***SSD Density(gr/cm3)***	***Fineness modulus***
Sand	*0.1*	*2.62*	*2.67*

Table 3: Physical characteristics of two types of nano-silica solutions.

Characteristics	Phase	Color	PH	Density (gr/cm3)	Viscosity (cps)	Solid particles (Percent)
Nano-silica (type 1)	liquid	transparent	13	1.05-1.4	<10	12.5
Nano-silica (type 2)	liquid	transparent	10	1.1	<10	15
Nano-SiO2 (type 3)	liquid	transparent	10.5	1.2-1.22	12.5-13	30
Nano-SiO2 (type 4)	poweder	white	10	1.05	-	-

Mix proportion

Seven mix proportions of mortars are presented in Table 4. The percentage of nano-silica in mortar specimens is 5% by weight of cement. Mortar mix proportions were selected according to ASTM-C109 with water/binder ratio (w/b) of 0.485 and aggregate/cement ratio of 2.75. The amount of superplasticizer was adjusted in nano-SiO_2 mortars to achieve similar slump flow as control mortar.

Table 4: Mix proportions of specimens (g/lit).

mixture no.	Cement (gr)	Water (gr)	Sand (gr)	w/b	Type of nano-silica	nano-SiO2 (gr)	SP (% binder)	Slump flow(mm)
OPC	1000	485	2750	0.485	-	-	-	138
NS1	950	485	2750	0.485	1	50	1.3	140
NS2	950	485	2750	0.485	2	50	4.2	141
NS3	950	485	2750	0.485	3	50	1.3	142
NS4-a	950	485	2750	0.485	4	50	1	140
NS4-b	950	485	2750	0.485	4	50	0.8	145
NS4-c	950	485	2750	0.485	4	50	0.5	149

Preparation of specimens

To fabricate mortar specimens, nano-silica, water and superplasticizer (if used) were mixed in Ultrasonic cleaner for the period of 15 minutes. Ultrasonic cleaner was used for uniformly disperse and prevent agglomeration silica nano-particles in colloidal based solutions and superplasticizer. To fabricate mortar specimens, after mixing cement and prepared solution in the mixer at low speed for about 30 seconds, the sand were added into the auto-stirred mixture afterwards mixing resumed at high speed for about 30 seconds. After ceasing the mixing process for 2 minutes, blending the mixture was started again for another 60 seconds. The slump flow of achieved mortar was measured by flow table test according to ASTM C-230. The well mixed Mortar was poured into molds to form the cubes of size 50×50×50 mm for all mixing proportion. The samples were demolded after 24h and then cured in lime-saturated water at 23 ± 2°C to prevent possible leaching of $Ca(OH)_2$ from these specimens for 7 and 28 days.

Test methods

Zetasizer System

The Zetasizer system determines the size by first measuring the Brownian motion of the particles in a sample using Dynamic Light Scattering (DLS) and then interpreting a size from

this using established theories. When a particle moves (e.g. due to gravity), ions within the liquid layer surrounding the particle (boundary) move with it, but any ions beyond the boundary do not travel with the particle. This boundary is called the surface of hydrodynamic shear or slipping plane. The potential that exists at this boundary is known as the zeta potential. The magnitude of the zeta potential gives an indication of the potential stability of the colloidal system. If all the particles in suspension have a large negative or positive zeta potential then they will tend to repel each other and there is no tendency to flocculate. However, if the particles have low zeta potential values then there is no force to prevent the particles coming together and flocculating.

Compressive strength

Mortar cubes of 50×50×50 mm dimension were cast for compressive strength using OPC and 5%nano-silica by weight of cement as replacement material. They were tested for compressive strength after 7 and 28 days of water curing and the average strength of three specimens was used as an index.

Capillary water absorption

The Capillary water absorption was measured on 50 mm mortar cubic specimens, which were dried in a 50°C oven for 10 days. After mass stabilization, the specimens were coated with the epoxy resin on their lateral surfaces only, in order to ensure uniaxial water absorption. The specimen was rested on rods to allow free access of water to the surface and the tap water level was kept no more than 5 mm above the base of the specimen. The masses of the specimens were measured after 0, 3, 6, 24 and 72 hours of absorption.

The Capillary water absorption coefficient (S) according to BS EN-480-5:1997 [12] was obtained using the following expression:

$$\frac{Q}{A} = c + S\sqrt{t} \qquad (1)$$

Where Q is the amount of water adsorbed; A is the cross section of specimen that was in contact with water; t is the time (second); c is the constant coefficient; and S is the Capillary water absorption coefficient of the specimen (m/s1/2). Density of water is 1 gr/cm3 hence this unit declared in $\frac{gr}{cm^2 hr^{0.5}}$ or $\frac{cm}{hr^{0.5}}$.

3 Results and Discussion

Zetasizer System

The general dividing line between stable and unstable suspensions is generally taken at either +30mV or -30mV. Particles with zeta potentials more positive than +30mV or more negative than -30mV are normally considered stable [13]. Colloidal based solutions containing silica particles of type1, 2 and 3 were measured by Zetasizer system. Moreover, for determining exact size of silica particles of type 4 which was uniformly dispersed in water by ultrasonic, Zetasizer system was used.

The results of size distribution showed that 90.4% of particles solutions type1in volume had 847 nm diameter, 99.8% of particles solutions type2 in volume had 1.97 nm diameter and whole particles of type 3 Colloidal solutions was with diameter of 78 nm. Also 100 % particles of type 4-a, 4-b and 4-c solutions in volume was with diameter 13.23, 390.3 and 829.2 nm, respectively.

Furthermore zeta potential of colloidal particles was determined by Zetasizer system. Zeta potential of colloidal particles in type 1, type 2 and type3 nano-silica solutions are -8.7 mV, -44

mV and -53.2 mV, respectively. To investigate the effects of zeta potential on the results of mortar tests, potential of type 4-a silica particles in water solution was measured and indicated Zeta potential of type 4-a silica particles was −18.8 mV.

Compressive strength

Figures 1 and 2 show strength development and Table 5 presents compressive strength of mortar specimens at 7 and 28 days.

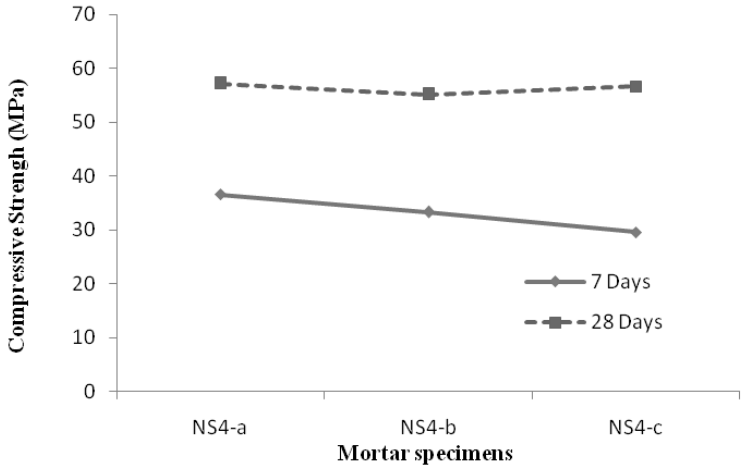

Figure 1: Compressive strength of type 4 nano-silica mortar specimens.

With the particle size reducing, there exist many uneven atom steps which increase chemical reaction area. For this reason, the nano-meter particles, such as NS, have high surface energy and atoms in the surface have a high activity, which leads the atoms to react on outer ones easily. Consequently, the pozzolanic activity of NS is high at early ages [8]. According to Figure 1, it can be concluded that the compressive strength progressively increases with decreasing the size of particles. As explained before, the reason of this increase is the more pozzolanic activity of finer particles. However with increase of samples' age, the difference will decrease in compressive strength. So that in type 4 nano-silica, the difference between earned strength in age 28 days limits just to 3.7% while the difference in age 7 days has been 21.3%. The reason can be attributed to the progress of pozzolanic reactions in each three samples at that age.

If all the particles in suspension have a large negative or positive zeta potential then they will tend to repel each other and there is no tendency to flocculate. However, if the particles have low zeta potential values then there is no force to prevent the particles coming together and flocculating [13]. Based on the results of compressive strength test between NS2 and NS4-a mortar specimens (see Table 5), considering the amount of silica and almost equal size of particles in both solutions, it can be said that the reason of higher earned strength in NS2 samples compare to NS4-a samples is the larger zeta potential and stability of particles according to ASTM D418-82 standard in the related solution and instability of particles in the type 4-a nano-silica solution which result in improper homogeneity silica particles in NS4-a mortar specimens compare to NS2 samples and making weak zones in that.

Table 5. Compressive strength test results.

Mixture Id	Compressive strength at 7 days		Compressive strength at 28 days	
	Target(MPa)	Improvement (%)	Target(MPa)	Improvement (%)
OPC	32.7	0	54.4	0
NS1	22	-32.7	31.8	-41.5
NS2	42.5	29.9	61.5	13
NS3	42.2	29	65.28	20
NS4-a	36.6	11.9	57.12	5
NS4-b	33.35	1.9	55.11	1.3
NS4-c	29.6	-9.4	56.67	4.1

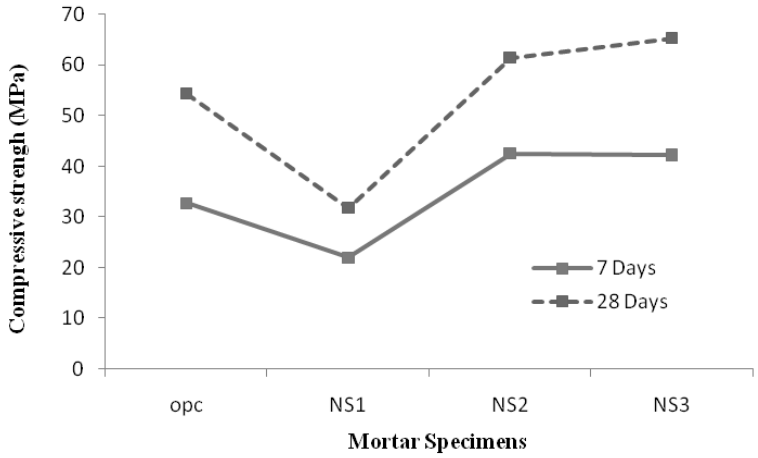

Figure 2: Compressive strength of type 1, 2 and 3 nano-silica mortar specimens as compared to OPC.

Nano-SiO_2 can behave as a nucleus to tightly bond with cement hydrates. The stable gel structures can be formed and the mechanical properties of hardened cement paste can be improved when nano-SiO_2 is added [1, 3, 5, 6]. Consequently, compressive strength of OPC is enhanced when nano-silica is added (see Figure 2). According to Figure 2 and Table 5, the maximum compressive strength in mortar specimens at 28 days was 62.3 MPa corresponding to the NS3 mixture and improved 20% when compared with samples without NS.

The nano-particles are more difficult to be dispersed uniformly in cement paste by increasing their content in the solution. The aggregation of nano-particles will form weak zones in cement paste. As a result, the enhanced extent of compressive strength of concrete decreases [3, 4, 5]. Regarding the zeta potential test results for NS1 specimens and unstable colloidal particles in related solution, homogeneity of nano-particles in mortar does not occur. Because of agglomeration of particles and creation of weak zone, compressive strength reduction is reduced. The minimum compressive strength in mortar specimens at 28 days was 31.8 MPa corresponding to the NS1 mixture and improvement was -41.5% when compared with samples without NS (see Figure 2 and Table 5). According to Zetasizer and XRF tests, the reduction in compressive strength is explained as the results of colloidal instability, lower amount and larger size of SiO_2 particles in related solution compare to others.

Capillary water absorption

Amount of absorbed water can be related to void capillary spaces form and its arrangement. High quantity of capillary water absorption can be alluded to weakness of structural cement

matrix, high permeability and destructive exposure of chloride diffusion. Capillary water absorption coefficient(s) are shown in Table 6.

Table 6: Assessment of capillary water absorption coefficient.

Mixture no	Capillary water absorption coefficient at 7 days		Capillary water absorption coefficient at 28 days	
	Target (mm/hr0.5)	Reduction (%)	Target (mm/hr0.5)	Reduction (%)
OPC	16.27	0	14.75	0
NS1	15.53	4.54	14.53	1.49
NS2	9.77	39.79	8.20	44.41
NS3	9.28	42.96	7.52	49.02
NS4-a	11.05	32.08	9.50	35.59
NS4-b	13.33	18.07	10.90	26.10
NS4-c	14.22	12.60	11.75	20.34

According to the result obtained for type 4 nano-silica mortar specimens (NS4), capillary water absorption decreased specially at 7 days, due to fineness, high pozzolanic activity of silica nano-particles and formation of dense hydration products at early ages. However difference between the capillary water absorption of specimens decrease at 28 days. This trend deals with pozzollanic activity of specimens containing silica more than nanometer scale in diameter, as the hydration progress.

Based on the results of capillary water absorption test between NS2 and NS4-a mortar specimens, considering the amount of silica and almost equal size of particles in both solutions , it can be said that the reason of lower water absorption in NS2 samples compare to NS4-a samples is the larger zeta potential (-44 mV) and stability of particles according to ASTM D418-82 standard in the related solution and instability of particles in the type 4-a nano-silica solution due to lower zeta potential (-18.8 mV) of related solution.

Nano-SiO_2 particles can react with calcium hydroxide $Ca(OH)_2$ crystals, which are mostly formed in the interfacial transition zone (ITZ) between hardened cement paste and aggregates and produce secondary C–S–H gel. Thus, the size and amount of calcium hydroxide crystals are significantly reduced, and more C-S-H fills the voids in interfacial transition zone (ITZ) to improve the density of matrix [3, 4, 5, 7, 8, 9]. Uniformly disperse of silica particles improve bonding between cement paste and aggregate and enhance compaction of mortar, hence capillary water absorption of specimens decrease due to capillary void reduction. Mortar specimens containing type 1 and type 3 solutions show maximum and minimum sorptivity coefficient, respectively. This issue is related to colloidal stability, amount and size of SiO_2 particles in solution.

4 Conclusions

From the results obtained in this study, the following conclusions can be drawn:

[1]. The result of compressive strength and capillary water absorption tests of mortar specimens containing silica type 4 (4-a, 4-b and 4-c) which have similar chemical characteristics and different particles size, show that compressive strength and sorptivity improved specially at 7 days due to fineness, high pozzolanic activity of nano-silica particles and formation of dense hydration products at early ages. However, difference between the tests results of specimens decrease at 28 days. This trend deals with pozzollanic activity of specimens containing silica more than nanometers scale in diameter, as the hydration progress.

[2]. According to the test results of mortar specimens containing two types of nano-silica considering the amount of silica and almost equal size of silica particles in both solutions, Colloidal potential can be recognized as effective factor on dispersion of silica particles in the mortar.

[3]. According to zetasizer and XRF tests, the reduction in compressive strength in all seven mixtures of mortars, NS3 has shown best performance in compressive strength and capillary water absorption tests. Some possible reasons have been represented to:

- More pozzolanic reaction of NS3 mortar specimens compare to other mixtures due to higher amount of SiO2 in type 3 silica solution than others.
- The fine silica particles accelerate the pozzolanic activity and act as a filler to enhance the density of mortar.
- The particles in suspension have a large negative zeta potential then they will tend to repel each other in mortar and there is no tendency to flocculate.

[4]. The minimum compressive strength and maximum capillary water absorption was observed in NS1 mixture specimens. This issue can be explained as the results of colloidal instability, lower amount and larger size of SiO2 particles in solution compare whit other mixtures.

References

[1] Ji T. Perliminary study on the water premeabiity and microstructure of concrete incoroporating nano-sio$_2$. Cement Concrete Research 2005; 35: 1943–47.

[2] Jo BW, Kim CH, Tae GH, Park JB. Characteristics of cement mortar with nano-SiO_2 particles. Construction and Building Materials 2007; 21: 1351–55.

[3] Li H, Xiano HG, Yuan J, Ou J. Microstructure of cement mortar with nano-particles. Composite Part B: Engineering 2004; 35: 185–189.

[4] Li H, Zhang MH, Ou JP. Abrasion resistance of concrete containing nano-particles for pavement, Wear 2006; 260: 1262-1266.

[5] Li H, Zhang MH, Ou, JP. Flexural fatigue performance of concrete containing nano-particles for pavement, International Journal of Fatigue 2007; 29: 1292-1301.

[6] Li G. Properties of high-volume fly ash concrete incorporating nano-SiO2. Cement Concrete Research 2004; 34: 1043–9.

[7] Björnström J, Martinelli A, Matic A, Panas I. Accelerating effects of colloidal nano-silica for beneficial calcium–silicate–hydrate formation in cement. Chemistry Physics Letters 2004; 392: 242–8.

[8] Qing Y, Zenan Z, Deyu K, Rongshen C. Influence of nano-SiO_2 addition on properties of hardened cement paste as compared with silica fume. Construction and Building Materials 2007; 21: 539–45.

[9] Collepardi M, Ogoumah Olagot JJ, Skarp U, Troli R. Influence of amorphous colloidal silica on the properties of self-compacting concretes. In: Proceedings of the international conference in concrete constructions – in novations and developments in concrete materials and constructions, Dundee, Scotland, UK; 9–11 September 2002. p. 473–83.

[10] Ji T, Mirzayee A, Zangeneh-Madar Z, Zangeneh-Madar E. Preliminary study on water infiltration of concrete containing nano-SiO_2 and silicone, In: 8th International Congress on Civil Engineering, Shiraz University, Shiraz, Iran, 11-13 May 2009.

[11] Naji Givi A, Abdul Rashid S, Nora Aziz F, Mohd Salleh MA. Experimental Investigation of the Size Effects of SiO_2 Nano-Pparticles on the Mechanical Properties of Binary Blended Concrete, Composites Part B: Engineering 2010; 43: 673-677.

[12] BS EN-480-5. Tests methods, determination of capillary absorption. British Standards Institution; 1997.

[13] Zetasizer Nano Series User Manual, Malvern Instruments Ltd., Man0317, Issue 1.1, Feb 2004.

Mechanical Properties and Durability of Self Consolidating Mortars containing Nano SiO_2

Ali Akbar Ramezanianpour, Mahdi Mahdikhani, S.Sina Yousefian Moghaddam, Morteza Nikravan, S.Rahimeh Mousavi

Concrete Technology and Durability Research Center, Dept. of Civil Engineering, AmirKabir University of Technology, Iran

The use of Nano particles in developing materials has gained its popularity and being applied in many fields. More specifically, such particles can lead to improvements in the nanostructure of building materials such as cement, mortar and concrete. On the other hand, it is well recognized that the use of mineral admixtures such as silica fume enhances the compressive strength of cementitious materials. In addition, self-consolidating concrete (SCC) and self-consolidating mortars (SCM) have been used increasingly over the last two decades, because of their ability to consolidate without vibration even in congested areas.

In this paper, the influence of Nano silica addition on mechanical properties cementitious materials as compared with silica fume has been studied. Four mortar mixtures are prepared containing zero to 6 percent Nano silica and silica fume. The rheological properties of fresh SCMs mixtures are investigated by mini-slump and mini V-funnel flow tests. In order to evaluate the static stability of the fresh mortar mixtures, the mini-column segregation test is also performed on all the mixtures. In addition, compressive strength of the hardened mixtures is determined. The results show that Nano silica can improve compressive strength of concrete. In addition, using Nano silica and silica fume increase stability of SCMs and decrease workability of fresh mixtures.

Keywords: self-consolidating mortars (SCM), Colloidal nano silica, Silica fume, Compressive strength, Fresh Mortar, Reology of Mortar

1 Introduction

Up to now, research performed over the years has been largely aimed at achieving high mechanical performance with cement replacement materials in micro size. Recently, nano technology has attracted considerable scientific interest due to the new potential uses of particles in nanometer scale. Due to the high specific surface area for the nano-meter sized particles, they constitute a highly reactive siliceous material. When ultra-fine particles are incorporated into Portlandcement paste, mortar or concrete, materials with different characteristics from conventional materials were obtained [1]. The performance of these cementitious based materials is strongly dependent on nanosized solid particles, such as particles of calcium–silicate–hydrates (C–S–H), or nano-sized porosity at the interfacial transition zone between cement and aggregate particles. Luciano Senff [2] reported that the addition of Nano-SiO2 modified the characteristics of fresh mortars. The addition of nano-SiO2 can shorten the setting time and also beneficial for the compressive strength of the mortar with different ash particle sizes [3]. The influence of nano-SiO2 on consistency and setting time are different. Nano-SiO2 makes cement paste thicker and accelerates the cement hydration process. It can be explained by the fact that, in formulations having fixed values of W/B, the presence of nano-SiO2 decreases the amount of lubricating water available in the mixture [4]. Bond strengths of paste–aggregate interface incorporating NS are higher than those of control sample and than those incorporating SF. With increasing the NS content, the rate of bond strength increase is more than that of their compressive strength increase [5]. SF belongs to the category of highly pozzolanic materials because it consists essentially of silica in non-crystalline form with a high specific surface, and thus exhibits great pozzolanic activity. But the activity of

SF at early ages is low according to the literature [6–9]. With additions of pozzolanic materials such as slag, fly-ash and silica fume added, the interface structure has been improved, especially in HPC [10–13]. Nano-silica decreased the setting time of mortar when compared with silica fume (SF) [4] and reduced bleeding water and segregation, while improving the cohesiveness of the mixtures in the fresh state [14]. The pozzolanic activity of nano-SiO2 is much greater than that of silica fume. Nano-SiO2 consumes CH crystals, decreases the orientation of CH crystals, reduces the size of CH crystals at the interface and improves the interface structure more effectively than silica fume [5]. In view of these advances, the aim of this study is to investigate the influences of silica particles in self-consolidating mortars (SCM). This work showed that by reducing the cement content in the presence of the silica particles, the mechanical properties of SCMs was improved. In view of this, it is concluded that both nano SiO2 and silica fume can be used to increase the mechanical properties of mortar mixtures.

2 Experimental Programs

The experimental program undertaken in this study aimed at the evaluation of stability and rheology of mortar mixtures reinforced with Nano silica and silica fume with different percentages. Therefore, in this study, four SCM mixtures have been designed by modifying the volume fraction of fiber.

Characterization of Materials

ASTM Type II, normal Portland cement and a type of local silica fume were used in all mixtures. The properties of cement and SF are shown in table 1. The colloidal Nano silica solution used contained 50 wt% of solid material. The Average particle size was 35 nm with 99.9% SiO2. Well-graded silica sand with specific gravity of 2.6, absorption value of 0.6% and maximum aggregate size of 2.36 mm, was employed in all mixtures. The aggregate size distributions are shown in Figure 1. A high range water reducing admixture (HRWRA) based on chains of modified polycarboxylic ether was used and had a specific gravity of 1.1. Optimum dosage of these admixtures is about 2% of cement weight as stated by the admixtures suppliers.

Table 1: Chemical and physical properties of cement and SF.

Items	Chemical composition (%)	
	Cement	Silica Fume
SiO_2	21.38	93.6
Al_2O_3	4.65	1.3
Fe_2O_3	3.51	0.9
CaO	63.06	0.5
MgO	3.2	1
SO_3	1.8	0.1
Physical properties		
Avg. particle size	10 µm	0.1µm
SSA(m^2/g)	0.33	20

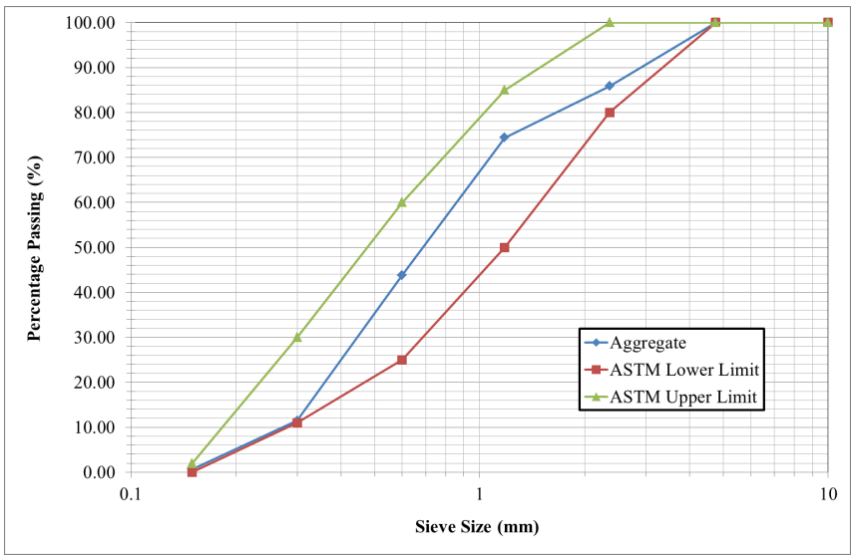

Figure 1: sand size distribution.

Test Methods

All specimens were fabricated according to ASTM C 192/C 192M-02, Standard Practice for Making and Curing Concrete Test Specimens in the Laboratory.

Spread measurement (mini-slump)

The mini-slump test is based on the measurement of the spread of mortar placed into a cone-shaped mould. The truncated cone (diameters: 100 and 70mm, height: 60mm) is placed on a smooth and non-absorbing plate, filled with paste and lifted. The resulting final diameter of the fresh paste sample is the mean value of two measurements made in two perpendicular directions as shown in Figure 2. [15].

Mini V-funnel test

This test consists of measuring the time required for a given volume of mortar (1 liter) to flow through the nozzle. This test is often used to measure the viscosity of the mortar which may be related to properties such as cohesiveness, pumpability and finishability. It should be noted that due to instability or inadequate flowability of mortars, the V-funnel values of some mixtures could not be measured. The instrument used in this test is shown in Figure 2.

Mini column segregation

As previously mentioned, static stability refers to the resistance of SCC to bleeding and segregation after the SCC is cast until it is hardened. Currently, the most commonly used methods to evaluate segregation resistance are the visual examination method, the column segregation test (ASTM C 1610). The internal diameter of cylinder is 75 mm (Figure 3). In the column segregation method, the contents of the top and bot-tom section of column are washed on No. 50 sieves after 15 minutes of casting. The remaining material on the sieve is dried in an oven and weighed. The static segregation (SI) is given by the following formula in percent. The induced bleeding is also measured after 5, 10 and 15 minutes. The acceptable segregation index for fresh concrete in most applications obtained from standard column segregation test is SI ≤ 15[13]. However, mortar mixture with SI≤30 that obtained from mini-column segregation test show satisfactory stability conditions. Mortars with a segregation index between 30-130 may exhibit segregation. Severe segregation is expected in mortar mixtures if the segregation index is above 130.

$$SSI = 2\left[\frac{(CA_B - CA_T)}{(CA_B + CA_T)}\right]\times 100 \qquad (1)$$

Where:
CA_B=Mass of aggregate retained on No. 50 sieve from bottom pipe section
CA_T= Mass of aggregate retained on No. 50 sieve from top pipe section

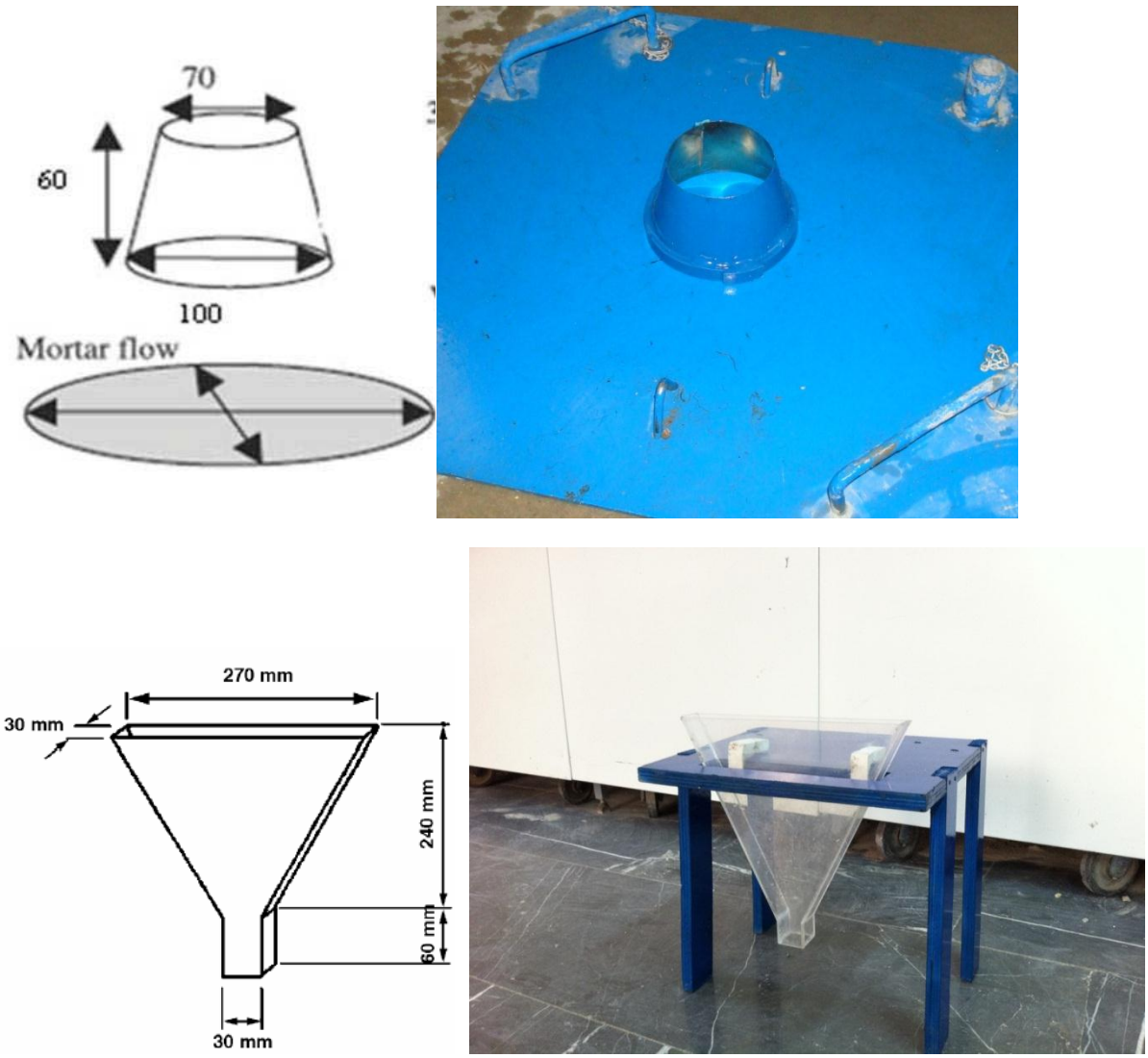

Figure 2: Configuration of mini-slump cone and mini V-funnel.

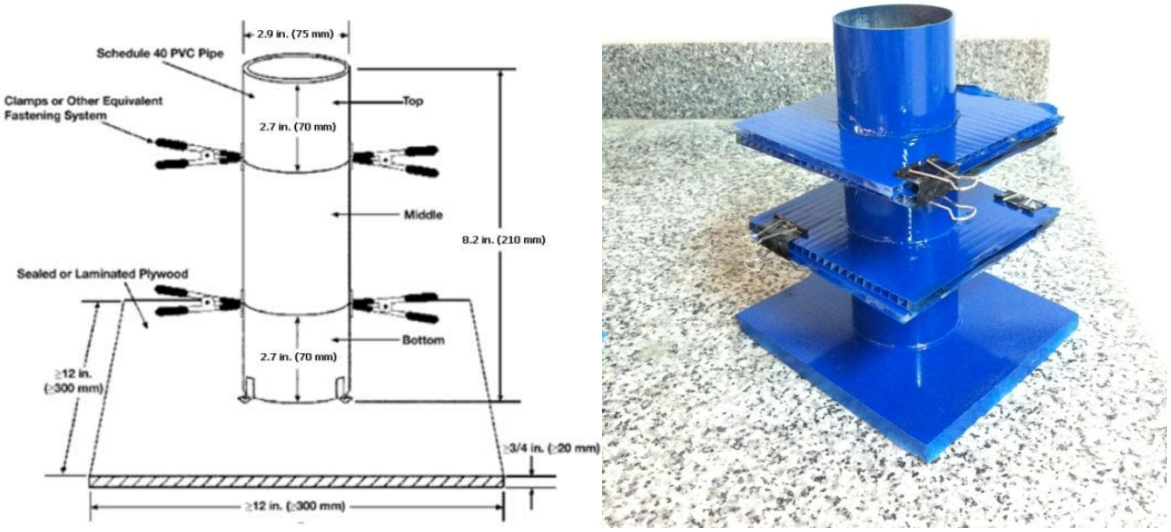

Figure 3: Dimensions of column segregation used in mortar experiments.

Mixture proportions

Four mixtures were prepared. In all mixtures water-cement ratios are 0.5. Mix proportions are summarized in Table 2.

Table 2: Mix proportions of Mortars.

	Nano silica (%)	Silica fume (%)	Cement (gr)	Nano silica (gr)	Silica fume (gr)	W/C	Water (gr)	Aggregate (gr)
Control (CTL)	0	0	1000	0.0	0	0.5	500	600.0
Nano silica	6	0	940	60	0	0.5	500	600.0
Silica fume	0	6	940	0.0	60	0.5	500	600.0

3 Results and Discussion

Fluidity

The results of mini-slump test are presented in Table 3. The control mixture achieved one of the highest slump flow values. As Nano silica and silica fume was added, slump values generally became lower. Bleeding is evaluated indirectly in the mini-slump flow test. This interesting finding can easily be validated by viewing the specimen under mini-slump flow test. The results clearly show that by using the Nano silica and silica fume bleeding of the mixtures was completely controlled.

Table 3: mini-slump test.

	Diameter 1 (cm)	Diameter 2 (cm)	Average (cm)
Control	28.5	28	28.25
Nano silica	28	28	28
Silica fume	24.5	23.5	24

Viscosity

The results of mini V-funnel test are presented in Table 4. In general, an increase in Nano silica and silica fume content increases the viscosity. Increasing the Nano silica from 0.0% to 6.0% increases the flow time by about 42% while increasing the silica fume from 0.0% to 6.0% resulted in 25% increment in the flow time. Obtained results clearly show that the effect of Nano silica on viscosity seems to be more significant than fluidity content.

Table 4: mini V-funnel test.

	flow time (sec)
Control	10
Nano silica	8
Silica fume	7

Stability

The required flowability of SCC, however, is difficult to achieve without decreasing the viscosity of the cement matrix, which reduces the ability of SCC to resist the segregation of large and dense coarse aggregate particles. In other words, both the yield stress and viscosity of the cement paste have direct bearing on the segregation of aggregate. For maximum segregation resistance, the yield stress and viscosity of the paste should be high. Nano silica and silica fume alter the rheological properties of the SCM such as viscosity and yield stress. The stability measurement consists of determining the segregation resistance of the mixtures and the resistance to bleeding when flowing across narrow sections.

The results of mini-column segregation test are summarized in Table 5. Based on these results, increasing Nano silica leads to a decrease in segregation index of the mixtures. For instance, control mixture with a W/C of 0.5 have a segregation index of 10.9%. The addition of Nano silica by 6% by weight leads to a decrease in segregation index to 2.7%. The results of the cylinder-segregation test agree well with the visually detectable distribution of coarse aggregate in hardened concrete.

Table 5: mini-column segregation test.

	SI
Control	10.9
Nano silica	7.6
Silica fume	2.7

Compressive Strength

Figure 6 demonstrates results of compressive strength at 3, 5, 7 and 28 days, for all mixtures. As can be seen the compressive strength of NS samples were higher than CTL samples, in all cases; the higher the NS content, the higher strength was achieved. With the same content of addition, NS samples had a higher compressive strength than SF samples. These results show that the compressive strength of HPC is enhanced with NS, even at early ages. After 28 days compressive strength of NS samples was about 37% higher than SF.

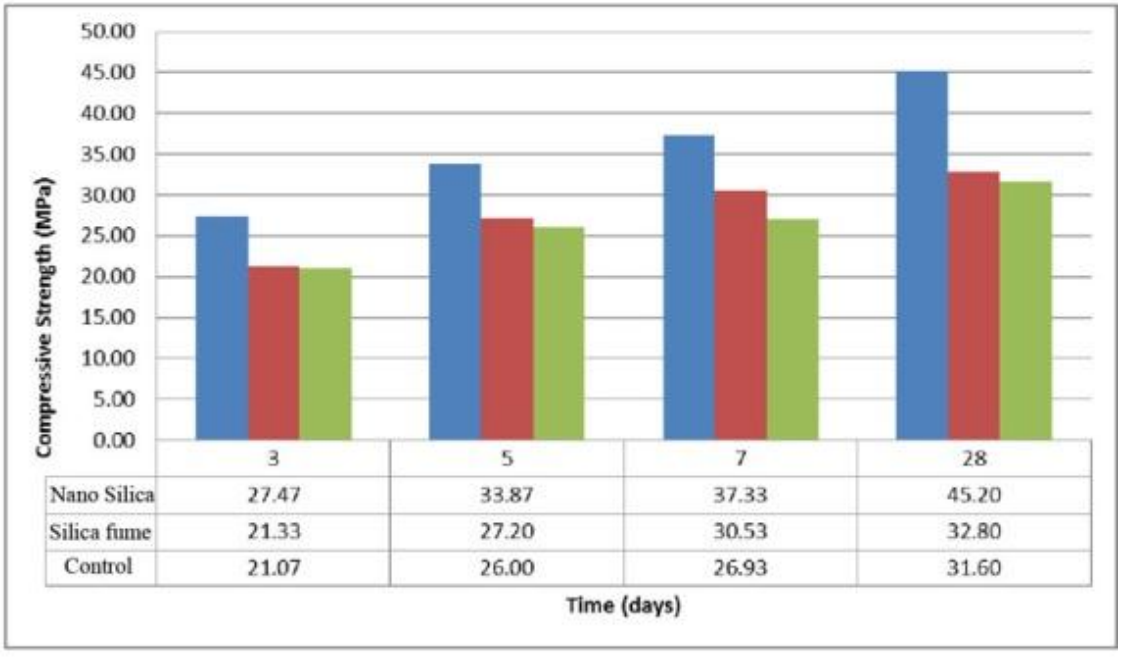

Figure 6: Strength improvement by time.

4 Conclusions:

The influence of Nano silica and silica fume on the workability and stability of fresh self-consolidating mortars (SCM) was investigated. Based on the results presented in this paper, the following conclusions can be drawn:

1. In constant water-cement ratio, increasing the Nano silica and silica fume causes rheological properties such as viscosity and yield stress to increase considerably.
2. Nano silica and silica fume can have rheological and mechanical synergistic effects and can better increase mechanical performance while maintaining adequate flow properties for self-compacting mortar. The results show that adding Nano silica to SCMs reduced its workability and ability to flow.
3. Compressive strength of SCM increases with increasing the NS content, especially at early ages.
4. Using nano-silica as an additive in concrete can improve the concrete microstructure and reduce the water permeability of concrete through filling pores and pozzolanic activity. Therefore, it is effective to add nano silica particles to concrete mixtures for making high-performance concrete.

Refrences

[1] Luciano Senff, João A. Labrincha, Victor M. Ferreira, Dachamir Hotza a, Wellington L. Repette. Effect of nano-silica on rheology and fresh properties of cement pastes and mortars. Construction and Building Materials 23, 2009, p 2487–2491.

[2] Luciano Senff, João A. Labrincha, Victor M. Ferreira, Dachamir Hotza, Wellington L. Repette, Effect of nano-silica on rheology and fresh properties of cement pastes and mortars, Construction and Building Materials, Volume 23, Issue 7, July 2009, Pages 2487-2491.

[3] K.L. Lin, W.C. Chang, D.F. Lin, H.L. Luo, M.C. Tsai ,Effects of nano-SiO2 and different ash particle sizes on sludge ash–cement mortar, Construction and Building Materials, Volume 23, Issue 7, July 2009, Pages 2487-2491.

[4] Mounir Ltifi, Achraf Guefrech, Pierre Mounangua, Abdelhafid Khelidj - Experimental study of the effect of addition of nano-silica on the behaviour of cement mortars. Science Direct Procedia Engineering , Vol. in press , pp , 2011.

[5] Y Qing, Z Zenan, K Deyu, C Rongshen, Influence of nano-SiO2 addition on properties of hardened cement paste as compared with silica fume, Construction and Building Materials (2007) Volume: 21, Issue: 3, Pages: 539-545.

[6] Mitchell DRG, Hinczak I, Day RA. Interaction of silica fume with calcium hydroxide solutions and hydrated cement pastes. Cem Concr Res 1998;28:1571–84.

[7] Larbi JJ, Fraay ALA, Bijen JM. The chemistry of the pore fluid of silica fume – blended cement systems. Cem Concr Res 1990;20:506.

[8] Papadakis Vagelis G. Experimental investigation and theoretical modeling of silica fume activity in concrete. Cem Concr Res 1999;29:79–86.

[9] Li S, Roy DM, Kumar A. Quantitative determination of pozzolanas in hydrated systems of cement or Ca(OH)2 with fly ash or silica fume. Cem Concr Res 1985;15:1079.

[10] Duval R, Kadri EH. Influence of silica fume on the workability and the compressive strength of high-performance concretes. Cem Concr Res 1998;28:533–47.

[11] Zhang MH, Lastra R, Malhotra VM. Rice-husk ash paste andconcrete: some aspects of hydration and the microstructure of the interfacial zone between the aggregate and paste. Cem Concr Res 1996;26:963–77.

[12] Bentur A, Cohen MD. Effect of condensed silica fume on the microstructure of the interfacial zone in Portland cement mortars. J Am Ceram Soc 1987;70:738–43.

[13] Taylor HFW. Cement chemistry. London, UK: Academic Press; 1990. p. 305–7, 374–8.

[14] Collepardi M, Ogoumah Olagot JJ, Skarp U, Troli R. Influence of amorphous colloidal silica on the properties of self-compacting concretes. In: Proceedings of the international conference in concrete constructions – innovations and developments in concrete materials and constructions, Dundee, Scotland, UK; 9–11 September 2002. p. 473–83.
[15] Roussel N, Stefani C, Leroy R (2005) From mini-cone test to Abrams cone-test: measurement of cement-based materials yield stress using slump test. Cem. Conc: 817-822.
[16] EFNARC (2002) Specification and Guidelines for Self-Compacting Concrete. 32 pp., http://www.efnarc.org.
[17] ASTM C 1610/C 1610M-06, Standard Test Method for Static Segregation of Self-Consolidating Concrete Using Column Technique. ASTM International.

A comparison between the pozzolanic reactivity of nanosilica sols and pyrogenic nanosilicas

Madani hesam[1], Bagheri Alireza[1], Parhizkar Tayebe[2]

1: Dept. of Civil Engineering, K.N.Toosi University of Technology, Tehran, Iran.
2: Building and Housing Research Center, Tehran, Iran.

Nanosilica sols which are manufactured through polymerization of silisic acid and pyrogenic nanosilicas are two kinds of synthetic amorphous nanosilicas which have in recent years attracted considerable research effort as super pozzolanic materials for enhancement of properties of cement based materials. These materials have high surface area due to their nanosize particles. Nanosilica sols which are produced through polymerization of silicic acid are almost monodispersed particles and don't form aggregates and agglomerates. However, in the production process of pyrogenic nanosilicas the particles fuse together and form aggregates up to a few hundred nanometers in length. The aggregates also bind together and form agglomerates up to about one hundred micrometers in length. Despite similar specific surface area of these two types of nanosilcas, their vastly different agglomeration state can influence their performance in cement based materials. This article presents the results of an investigation on the pozzolanic reactivity of the product Aerosil 200 (a pyrogenic nanosilica with surface area of 200 m^2/g) and Levasil 200/30 (a nanosilica sol with surface area of 200 m^2/g and concentration of 30%). The results show that despite the high agglomeration state of the pyrogenic silica its rate of pozzolanic reactivity with hydrated lime is higher than that of the silica sol. The 24 hour pozzolanic reactivity of the nanosilica sol is comparable with the 3.5 hour pozzolanic reactivity of the pyrogenic nanosilica in the lime-nanosilica mixtures. The pozzolanic reactivity of these materials in cement pastes also confirms the higher rate of reactivity of the pyrogenic nanosilica. The hydration degree of cement and the amount of hydrate water in the pastes containing the nanosilicas and the plain paste were also investigated.

Keywords: Pyrogenic nanosilica, nanosilica sol, pozzolanic reactivity, calcium hydroxide, Hydration degree.

1 Introduction

Pozzolanic materials have long been used as Portland cement replacement in concrete. Among these materials silica fume which is a by product of silicon and ferrosilicon industries has found a wide spread application in improving the durability and mechanical properties of cement based materials. In recent years by development of nano sience, a considerable research effort is attracted to the investigation of the influence of nanosilicas on the properties of cement based materials. These materials appear to have advantages over silica fume as super pozzolanic materilals for enhancement of properties of cement based materials. Some of these characteristics are finer particles, higher purity of silica and higher proportion of non-crystaline silica than silica fume.

Different types of nanosilicas are produced by a variety of methods. Two of the main kinds of these materials which have been used in the studies of cement based materials include the pyrogenic nanosilicas (also called fumed silica) and nanosilica aquasols. Pyrogenic nanosilicas are produced through reaction of silicon tetrachloride, hydrogen and oxygen in high temperature furnaces and are in powder form with specific surface area ranging from about 50 to 500 m^2/g. Monodisperse nanosilica aquasols are stable dispersion of discrete, amorphous silica nanoparticles in water and are mainly produced through nucleation and growth of silicic acid in the aqueous medium. Like pyrogenic nanosilicas, nanosilica sols have a wide range of specific surface areas. The different production process leads to differences in some characteristics of these materials. For instance, nanosilica sols are almost monodispersed particles and don't

form aggregates and agglomerates while, in the production process of pyrogenic nanosilicas the particles fuse together and form aggregates up to a few hundred nanometers in length. The aggregates also bind together and form agglomerates up to about one hundred micrometers in length. Despite similar specific surface area of these two types of nanosilcas, their different agglomeration state can influence their performance in cement based materials.

Some researches have studied the pozzolanic reactivity of the aformentioned nanosilicas. Chandra and Bergqvist 1997 reported the faster pozzolanic reactivity of nanosilica sols in the cement pastes compared to silica fume. Korpa et al 2008 and Wu and young 1984 also reported faster reaction of pyrogenic nanosilicas in contrast to silica fume. The higher degrees of hydration of C_3A and C_3S phases of cement by use the pyrogenic nanosilica was reported by Stein and Stevels 1964, Kurdowski et al 1982 and Beedle et al 1989.

Considering the different characteristics of the two aforementioned kinds of nanosilicas, particularly their vastly different agglomerated state, differences in the pozzolanic reactivity of these materials is expected. In this study, the pozzolanic reactivities of a pyrogenic nanosilica and a nanosilica sol with the same surface area of 200 m^2/g was studied. The hydration degree of cement and the amount of hydrate water in the pastes containing the nanosilicas and the plain paste were also investigated.

2 Materials and Methods

Materials and apparatus

In the current study Aerosil 200 and Levasil 200/30 were respectively utilized as representative of pryrogenic nanosilicas and nanosilica sols. Aerosil 200 was supplied by Degussa Corporation and according to manufacturer's data, has surface area of 200 m^2/g and mean particle size of 12 nm. To utilize Aerosil 200 in cement pastes, this material was mixed with water in mass concentration of 10%, the required amounts of NaOH for adjusting the pH of suspension to 10 was added, and the suspension was mixed for 1 hour with a high shear mixer. The aqueous suspension of Aerosil 200 prepared to utilize in lime pastes had a mass concentration of 15%

Table 1: the properties of materials.

Properties	cement	Levasil 200/30	Aerosil 200
SiO_2	21.85	30	99.8<
Fe_2O_3	4.6	0	-
Al_2O_3	4.55	0	-
CaO	60.36	0	-
MgO	3.8	0	-
SO_3	1.78	0	-
$Na_2O + .658K_2O$	0.8	0.15*	-
L.O.I	1.19	2.5>	1>
Moisture content	0.5	70	1.5>
Surface area(m^2/gr)	0.314	200	200
Density(gr/l)	3150	1205	50
pH	-	9	-

*According to manufacturer's data the additive includes only NaOH.

with adjusted pH of 10 and was mixed with a 3000rpm shear mixer for 1 hour. The silica aquasol, Levasil 200/30 with the surface area of 200 m^2/g and mean particle size of 15nm, was supplied by H.C.Stark GmbH & Co.KG Corporation in a mass concentration of 30%.

The cement used in this study was a PC equivalent to ASTM type II. The properties of the nanosilicas and cement are shown in table.1.

The thermal analyses (TGA/DSC) were conducted by a NETZCH STA449C instrument on 50-75 mg of paste samples in N_2 atmosphere. The samples were heated to 1005°C at a heating rate of 10°C/min.

Preperation of mixtures

Lime pastes were prepared by mixing of nanosilica and lime in mass ratio of 1.85 (molar ratio of 1.5) and water to solid ratio of 2. The pastes were mixed in a mechanical mortar mixer for 3 minutes followed by 1 minute stopping and further 3 minutes of mixing. The specimens were cast into plastic bottles which were sealed air tight and were allowed to react at a temperature of about 25 °C for designated periods of time. Prior to the test the specimens were washed by acetone and were dried under N_2 flow.

The cement pastes were prepared at a water to solids ratio (cement + nano silica) of 0.27 containing 3 percent nanosilica (Levasil 200/30 or Aerosil 200) as cement replacement. The higher replacement content was not reachable because of severe reduction of flowability. No dispersing agent or superplastisizer was used. The pastes were mixed in a mechanical mortar mixer for 3 minutes followed by 1 minute stopping and 4 minutes of further mixing. After casting into cubic 50×50×50 mm^3 steel molds, all specimens were vibrated on a vibration table and then covered to minimize water evaporation. The molds were stripped after 24 h, and the specimens immersed in water (CH-saturated) at 24°C until testing. At predetermined ages the specimens were crushed and the hydration was stopped by washing them with acetone and oven drying at 105°C for 18hours.

Determination of the pozzolanic reactivity of the nanosilicas in lime pastes

TGA/DSC was used to evaluate the pozzolanic reactivity of the nanosilicas in nanosilica-lime pastes. In this respect the pozzolanic reactivity is calculated through measuring the ratio of the consumed CH to the initial CH by considering the carbonation effect.

Determination of the degree of hydration of cement and calcium hydroxide content in cement pastes

TGA/DSC was used to determine the evolution of the nonevaporable water content $W_n(t)$ and the $Ca(OH)_2$ content in cement pastes during hydration. In this study it is assumed that amorphous silica do not consume water chemically to react with calcium hydroxide and the hydration of 1g cement produces about 0.23g non-evaporable water. The non-evaporable water content (W_n) was obtained as the difference in mass between the sample heated at 105°C and 1005 °C normalized by the mass after heating to 1005 °C. The non evaporeable water was corrected by considering the carbonation effect.

The following formula is used to calculate the hydration degree of cement:

$$Hydration\ \ \deg ree\ \ of\ \ cement = \frac{W_n(t)}{m_c.W_n(\infty)} \times 100 \qquad (1)$$

$W_n(t)$: the non evapoeable content of cement paste at any time t.

$W_n(\infty)$: the nonevaporable water content at $t \to \infty$ corresponding to full hydration of 1 g of cement.

m_c = the mass ratio of cement to cementitious materials

Weight loss due to Calcium Hydroxide (CH) decomposition is estimated by the TG graphs. The DSC graphs were used to determine the onset and the end of decomposition of CH. The normalized CH content was calculated by considering the carbonation effect, using the following formulas:

$$CH_{norm}(t) = \frac{CH(t)}{m_c \times CH_{plain\ paste}(t)} \quad (2)$$

m_c = the mass ratio of cement to cementitious materials
$CH_{plain\ paste}(t)$ = CH content of plain paste at any time t.
$CH(t)$: CH content of paste at time of t.

Determination of the hydrate water in cement pastes

Hydrate water content is the difference between the non-evaporable water content (w_n) and the water associated with CH (W_{CH}), both of which can be obtained from the TGA curves. Measuring the hydrate water can provide an indication of the amount of hydrated phases such as CSH other than CH. In the current study the carbonation effect is considered in calculating of the hydrate water.

3 The results

The pozzolanic reactivity of the nanosilicas in lime pastes

The pozzolanic reactivity of Aerosil 200, Levasil 200/30 are compared in fig.1. As shown, Aerosil 200 had faster reactivity compared to Levasil 200/30. Both products consume a considerable amount of lime in the first 3.5 hours. The pozzolanic reactivity of Aerosil 200 at 3.5 hour was more than 60%. This content is about 50% higher than pozzolanic reactivity of Levasil 200/30 that consumed less than 40% of lime at this age. At 24 hour the reactivity of Levasil 200/30 was comparable to 3.5 hour reactivity of Aerosil 200. At this time the consumed lime by Aerosil 200 was 82% which was 15% higher than the reactivity of Levasil 200/30. After 72 hour, both nanosilicas appear to have completed their reactivity and have consumed more than 90% of lime.

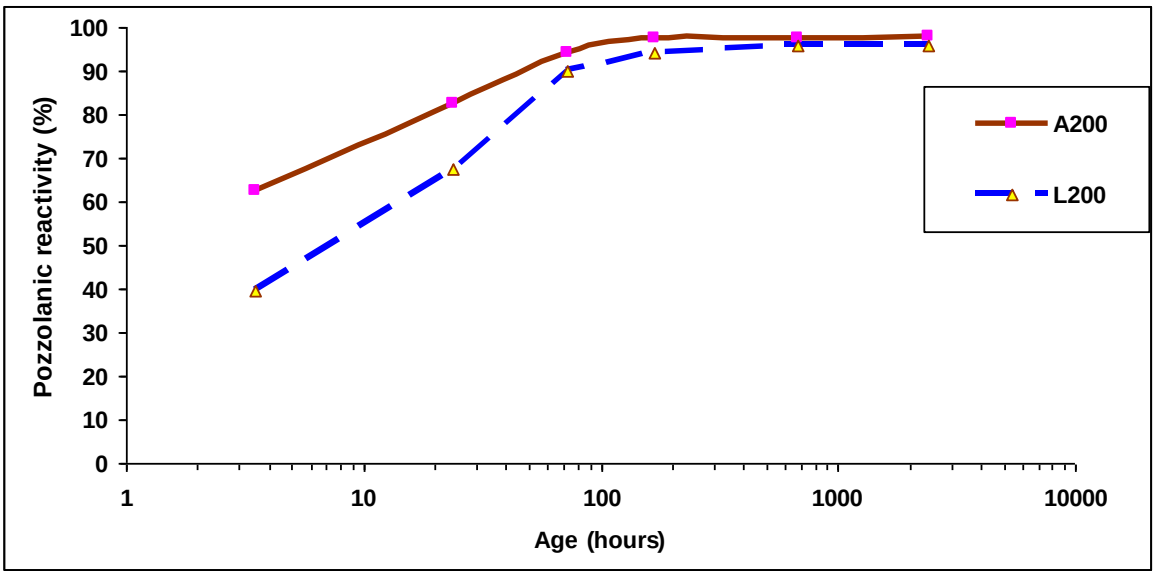

Figure 1: the pozzolanic reactivity of the nanosilicas in the lime pastes.

The pozzolanic reactivity of nanosilicas in cement pastes

The normalized calcium hydroxide contents of cement pastes containing the nanosilicas at different ages are presented in fig 2. As shown, the pyrogenic nanosilica consumed some of the lime at the first 24 hour. However, the considerable reduction of lime in cement paste containing Levasil200/30 was observed at 72 hour. This indicates that the pyrogenic nanosilica had a faster pozzolanic reactivity compared to the nanosilica sol and confirms the results of pozzolanic reactivity of the nanosilicas in the lime pastes. At all of the ages the cement paste containing Aerosil 200 had less lime than the cement paste containing Levasil 200/30, showing the higher pozzolanic reactivity of the pyrogenic nanosilica.

The difference between the amount of lime in the pastes containing the nanosilicas became smaller at the age of 100 days which indicates that Levasil 200/30 show more reactivity than Aerosil 200 between the ages of 28 and 100 days.

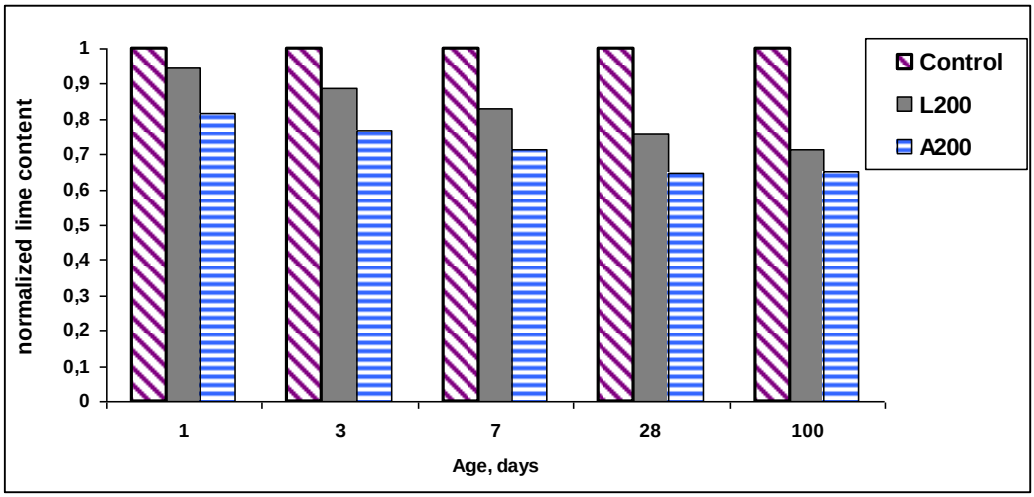

Figure 2: the normalized lime content of cement pastes.

The hydration degree of cement pastes

The hydration degrees of cement pastes at different ages are shown in fig 3. It is revealed that the pastes show considerable proportion of their hydration in the first day. The pastes containing Aerosil 200 and Levasil 200/30 have similar hydration degrees in 1, 3 and 100 days. However, the paste containing Aerosil 200 showed higher hydration degree than paste containing Levasil 200/30 in 7 and 28 days.

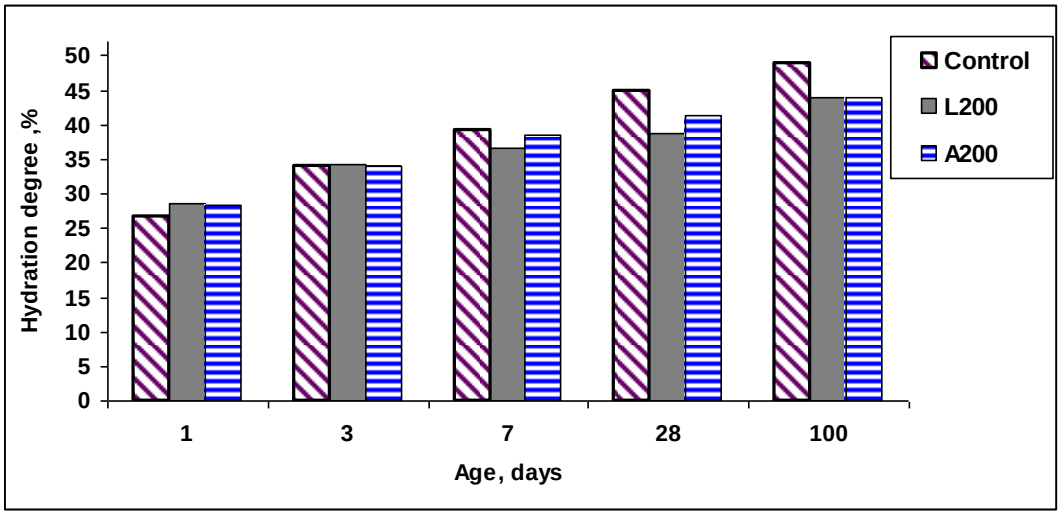

Figure 3: the hydration degree of cement in the cement pastes.

The pastes containing the nanosilicas had similar hydration degrees in the early ages of 1 and 3 days with the plain paste. After 7days, reduction in the hydration degree in contrast to the plain paste is observed. The less degree of hydration of cement pastes containing nanosilicas compared to plain paste may be due to the low water/cementitious materials, ie, nanosilicas adsorb a huge amount of water in their structure and consequently the reachable water to hydration of cement decreases. Therefore the degree of hydration of cement reduces.

The hydrate water of cement pastes

The hydrate water contents of pastes at different ages are presented in fig.4. As shown, the paste containing Aerosil 200 had higher amounts of hydrate water in contrast to plain paste until 28 days. At age of 100 days the reduction of hydrate water in this paste compared to plain paste was observed. The hydrate water amount of paste containing Levasil 200/30 was similar with the hydrate water content of the plain paste at ages of 1 and 3 days and was lower than the plain paste at the age of 7days and after this age. The higher or similar content of hydrate water of cement pastes containing the nanosilicas in the early ages is due to pozzolanic reactivity of these materials and similar hydration degrees of the cement of these pastes in contrast to plain paste which leads to higher contents of chemically bound water in the CSH phase. The reduction of hydrate water of pastes containing the nanosilicas at the later ages is due to lower hydration of these pastes compared to plain paste and inability of pozzolanic reactivity to produce enough CSH to compensating for lower hydration of cement.

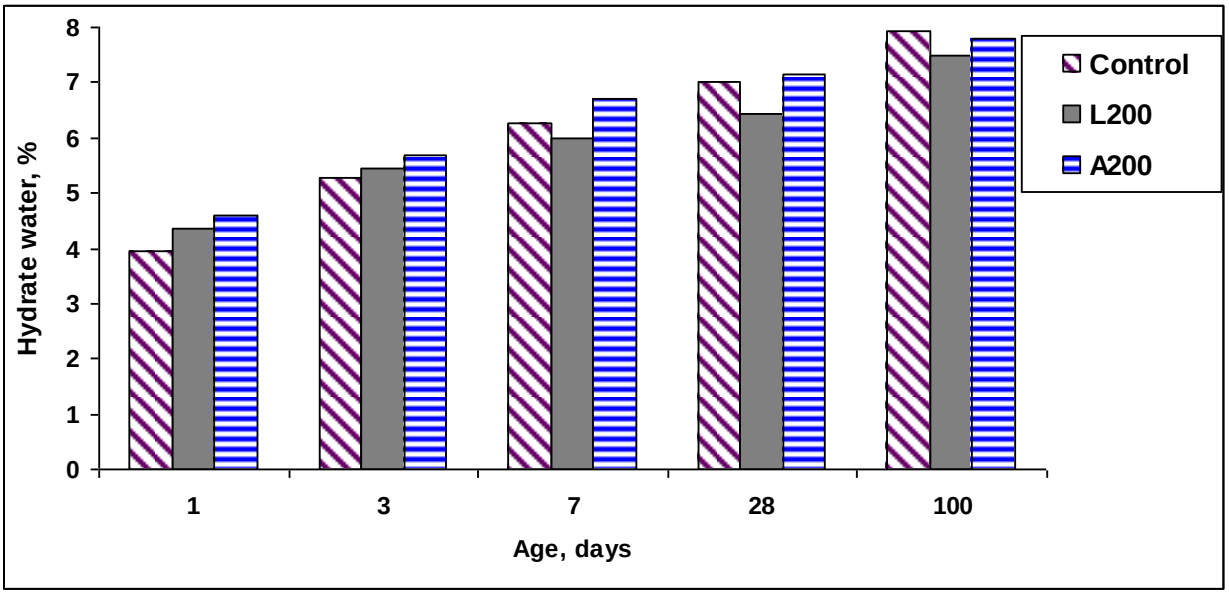

Figure 4: hydrate water contents of cement pastes.

4 Conclusions

Thermogravimetric analysis of nanosilica-lime pastes shows that despite the agglomerated state of the pyrogenic nanosilica, Aerosil 200, it has faster pozzolanic reactivity than Levasil200/30. This material also shows higher reactivity than the nanosilica sol in the cement pastes.

Replacing part of cement by both types of nanosilicas caused acceleration of cement hydration during the early ages up to three days. However, with the progress of hydration and from 7 days lower hydration of cement due to nanosilicas was observed.

5 Acknowledgments

Support from the building and housing research center (bhrc) is gratefully acknowledged. Authors also express their gratitude to Mrs jafarpoor and Mrs firoozyar for termogravimetric analysis of the samples.

References

[1] Chandra,S.; Maiti,S,C. :Improved properties of cement mortar and concrete with colloidal silica. Six'th NCB international seminar on cement and building materials,XII-58, 1998.

[3] Stein,H,N.; Stevels,J,M. :Influence of silica on the hydration of $3CaO.SiO_2$, Journal of Applied Chemistry 14, pp 338-346, 1964.

[4] Korpa,A.; Trettin,R.; Bottger,K,G.; Thieme,J.; Schmidt,C. :Pozzolanic reactivity of nanoscale pyrogene oxides and their strength contribution in cement-based systems, Advances in Cement Research 20, pp 35-46, 2008.

[5] Wu,Z,Q.; young,J,F. :The hydration of tricalcium silicate in presence of colloidal silica: , J. Mat. Sci 79, 1984.

[6] Kurdowski,W.; Nucun-Wczelik,W. :The tricalcium silicate hydration in the presence of active silica, Cement and Concrete Research 13, pp 341-348, 1983.

[7] Beedle,s,s.; Groves,G,W.; Rodger,S,A. :The effect of fine pozzolanic another particles on hydration of C_3S, Advances in Cement Research 2(5), pp 3-8, 1989.

Fluid Catalytic Cracking Residue additions such an alternative to Silica Fume in UHPFRC

Esteban Camacho[1], Juan Ángel López[1], Pedro Serna Ros[2]
1: PhD student, Universitat Politècnica de València, Spain
2: Professor, Universitat Politècnica de València, Spain

In UHPC some condensed silica fume (CSF) additions imply a remarkable decrease of the workability, requiring a high increase of water to reach selfcompacting properties. In some conditions the aglomerates doesn't disperse efficiently, even with an intensive mixing. In this cases, FC3R (Fluid Catalytic Cracking Catalyst Residue) can be a good alternative. This residue from the petrol industry has pozzolanic properties. Its particles are not condensed and the reduction on workability can be lower than with CSF. Its reactivity can be higher at short term and its white colour provides wider posibilites.
In this study different UHPFRC with these two additions are casted. The mixing process, the rheology, the time evolution of the compressive strength and the flexural strengh are contrasted. Microstructure is also observed to compare the size of the pozzolanic particles inside the concrete.

Keywords: Fluid Catalytic Cracking Catalyst Residue, condensed silica fume, compatibility, UHPFRC.

1 Introduction

Silica fume is a subproduct from industrial synthesis of silicon alloys considered nowadays necessary in every UHPC dosage. It provides stability in the fresh state, and higher compacity and compressive strength in hardened state. However, condensed silica fume (CSF) composition and particle distribution can significantly vary depending on the provider. Some CSF can strongly decrease the workability of the mixture, being sometimes impossible mix a dosage with low W/B content and the typical high content of CSF (15-30%) in UHPC.

The main parameters that vary depending on the CSF industrial origin are the degree of the particles condensation and the content of unburned carbon. This last parameter should be as low as possible due to its high water adsorption capacity. In previous works [9], the content of CSF with 4% of unborn carbon in the UHPC developed couldn't be higher than 10% over cement weight.

For this reason Fluid Catalytic Cracking Catalyst Residue (FC3R), a pozzolanic residue from petrol refinery processes, is suggested here such an alternative to CSF. This product is a zeolite type inorganic silica-alumina compound. The particles size range between 0.1 and 30 μm. Particles have a high degree of roughness with irregular shapes due to the previous process of grinding. Its special geometry implies a decrease in the workability of the mixtures if it substitutes Ordinary Portland Cement [4], but this effect is less marked than with some CSF.

FC3R has an activity index in the same range as CSF and it is commercialized in a not condensed state, what means that no intensive energy mixing is required to develop the potential efficiency of the addition. As CSF [3], FC3R could also produce a significant reduction of the thickness of the Interfacial Transition Zone (ITZ), improving the mechanical strength and durability [4]. Besides, its white colour can provide additional aesthetic possibilities.

The FC3R has not been used in concrete for structural applications. Only research has been developed adding it to Ordinary Concrete (OC) in laboratory conditions with successful results. As far as we know, this is the first experience of FR3R with UHPC-UHPFRC in any conditions.

On the other hand, fly Ash (FA) is a residue from thermoelectric power plants, and its particle morphology is spherical. This provides an enhancement of the workability of the fresh concrete when substitutes cement, and also reduces the bleeding risk. The costs are lower than the cement and the Activity Index is near to 1 when the W/B ratio is very low, as in UHPC. That's

why it's interesting to substitute cement such a second pozzolan. In some cases its combination with more active additions (CSF or probably with FC3R) can develop a very interesting synergy to reach higher mechanical strengths. The key point for FA suitability is that its particle size range complements the granulometric curve and that shows compatibility with the other binder.

2 Objectives

The main purpose of this paper is to study the possibilities of use FC3R as an alternative of CSF addition in UHPC, analyzing the effect on the rheological and mechanical differences. This effect was studied on concretes made with different cement types, additions and admixtures.

A secondary objective is to evaluate the effects of using a Fly Ash (FA) as secondary pozzolan with CSF or FC3R on the rheological and hardened state UHPC properties.

3 Experimental program

A two steps program was developed. The first one compare the FC3R effectiveness with other pozzolanics binders and its interaction with different cements, working with no fibers mortar mixtures. Flowability and compressive strengh are the analysed. The second fase study the effect of these admixtures in higher volumes of UHPFRC, adding also other CSF, and including in the analysed properties the concrete flexural behavior.

Binders effectiveness for UHPC analysis

In the first step the binder composition of on the UHPC was analysed. To do that a program of 50 different mortar dosages was composed modifying the binder proportions (considering as binder: cement, CSF, FC3R and FA). Mortars were prepared with 1:1 sand/binder weight ratio. The same 0-2 mm silica sand provided by Caolines Lapiedra was used for all mortars. PCE admixture Glenium ACE 32 (BASF) was used, keeping constant the content in 4.5% respect to binder, so fluidity suffered logic variations due to the binder proportions. This phase variables were: Two sulphate resistant cements were used: a "I - 42.5 R/SR" and a "I - 52.5 R/SR" from Lafarge, according with the Spanish standard [11]; and the pozzolanic additions: a CSF from Ferroatlántica S.A., a FA from Andorra Thermal Station, and a FC3R provided by Omya Clariana S.A. Chemical composition of the additions is shown in table.

Table 1: Chemical composition of the active additions used (: Guaranteed from the provider).*

Material	SiO_2	CaO	Al_2O_3	Fe_2O_3	Na_2O+K_2O	C	LOI
CSF*	>85%	<1%	<1%	-	-	<4%	-
FC3R [4]	48.2%	<0.01%	46%	0.95%	0.5%	-	1.5%
FA [6]	40.9%	9.8%	24.7%	13.6%	1.74%	-	-

25 of the dosages were done with cement I - 42.5 R/SR (W/B ratio fixed in 0.18) and the other 25 with cement I - 52.5 R/SR (W/B ratio of 0.2). This difference in the water binder ratio was established due to the higher specific surface of the 52.5, reaching with this change comparable fluidity for the same binder combinations. Table 2 shows the solids mix design of all mixes. Each dosage was done with both I-42.5 R/SR and I-52.5 R/SR cement.

1 litre of UHPC was cast with each dosage in a mortar mixer according to [10]. With the mixer working at the normal mixing speed all dry materials were mixed during 90 s., adding after the water with the half of the PCE. The mixing was stopped at the 3rd min. and restarted at the 4th min. with the addition of the remaining PCE. In general between the min. 5 and 8 the consistency changed from dry to plastic, and later to liquid. Only between the min. 8 and 9 high mixing speed was applied and the process finished at normal speed in the min. 10.

Table 2: Experimental program of the first phase. Solids mix proportions.

Dosage nº	Cement	Silica Fume	FC3R	Fly Ash	Sand
		% over total weight of solids, [% over cement weight]			
1	45	4.5 [10]	0	0	50
2	41.7	4.2 [10]	0	4.2 [10]	50
3	38.5	3.8 [10]	0	7.7 [20]	50
4	35.7	3.6 [10]	0	10.7 [30]	50
5	41.7	4.2 [10]	4.2 [10]	0	50
6	43.5	6.5 [15]	0	0	50
7	40	6 [15]	0	4 [10]	50
8	37	5.6 [15]	0	7.4 [20]	50
9	34.5	5.2 [15]	0	10.3 [30]	50
10	40	6 [15]	4 [10]	0	50
11	45.5	0	4.5 [10]	0	50
12	41.7	0	4.2 [10]	4.2 [10]	50
13	38.5	0	3.8 [10]	7.7 [20]	50
14	35.7	0	3.6 [10]	10.7 [30]	50
15	43.5	0	6.5 [15]	0	50
16	40	0	6 [15]	4 [10]	50
17	37	0	5.6 [15]	7.4 [20]	50
18	34.5	0	5.2 [15]	10.3 [30]	50
19	41.7	0	8.3 [20]	0	50
20	38.5	0	7.7 [20]	3.8 [10]	50
21	35.7	0	7.1 [20]	7.1 [20]	50
22	33.3	0	6.7 [20]	10 [30]	50
23	45.5	0	0	4.5 [10]	50
24	41.7	0	0	8.3 [20]	50
25	38.5	0	0	11.5 [30]	50

Fluidity was measured using the Mini-slump test [12] and 3 40x40x160 mm specimens were casted with no vibration. Curing process was at 20º C with RH 100%. Flexural and compressive strength were determined in one 40x40x160 mm prism at 2, 7 and 28 days according to [10].

UHPFRC dosages

16 mixtures of UHPFRC were casted in an intensive mixer (EIRICH R08 W). Variables modified in this phase were:

-Cement type as in previous phase and cement content (varied between 700-1000 Kg/m^3)

-Active addition type: The same as in the previous stage were used, adding another CSF (ELKEM 940-D) to compare the rheological and mechanical differences that can produce the use of a richer Si_2O product. Its composition was Si_2O>90%, LOI<3%.

-The active additions (CSF and FC3R) content of 10%-15%. 15% of FA was used in mix nº 14 as it seemed the optimum content in the previous step.

-Three different PCE were used (A: BASF SKY 575, B: BASF GLENIUM ACE 32, C: SIKA VSC 20 HE). According with previous studies PCE A was selected for mixes with cement I-52.5 R/SR as deduced the most efficient, while B,C were used with I-42.5 R/SR cement mixtures.

Different PCE were used for each cement. The % of each PCE was determined in previous study, providing all them similar workability to the same dosage. It is clear that effectivity depends on the admixture solid content, but also on its specifics properties and compatibility

with the binders. Only with ELKEM CSF the “B” PCE dosage was reduced as the low carbon content lead to a much more fluid concrete (mix. 13 and 16). W/B ratio was modified with the purpose of have similar workability except mixtures 10-11, where the W/B effect was analyzed.

Every mixture contained 2% in volume of high strength steel fibers: 1% of 13 mm straight fibers with a 0.16 mm diameter from Bekaert (Dramix® OL 13/0.16), and the other 1% of 30 mm length hooked end fibers an aspect ratio of 80 (Dramix® RC-80/30-BP).

The dosage of every mixture casted can be seen in table 3, except the sand content. The same 0-2 mm silica sand than in the first phase was used. Its dosage was adapted for each dosage to reach the cubic meter of UHPFRC volume.

Table 3: Experimental program of the second phase. (: Mixtures made with CSF ELKEM 940-D).*

Mix nº	Cement		CSF	FC3R	FA	W/B	PCE	
	Type	Kg/m^3	% over cement weight				Type	%
1	52.5 R/SR	700	10%	0	0	0.27	A	3%
2	52.5 R/SR	700	0	10%	0	0.27	A	3%
3	52.5 R/SR	850	10%	0	0	0.21	A	3%
4	52.5 R/SR	850	0	10%	0	0.21	A	3%
5	42.5 R/SR	850	10%	0	0	0.22	C	4.5%
6	42.5 R/SR	850	0	10%	0	0.21	C	4.5%
7	42.5 R/SR	1000	15%	0	0	0.21	B	3.5%
8	42.5 R/SR	1000	0	15%	0	0.2	B	3.5%
9 (x2)	42.5 R/SR	1000	15%	0	0	0.195	C	4.5%
10 (x2)	42.5 R/SR	1000	0	15%	0	0.19	C	4.5%
11	42.5 R/SR	1000	0	15%	0	0.18	C	4.5%
12	42.5 R/SR	1000	0	15%	0	0.175	B	3%
13	42.5 R/SR	1000	15%(*)	0	0	0.175	B	2.5%
14	42.5 R/SR	850	0	10%	15%	0.175	B	3%
15	42.5 R/SR	800	25%	0	0	0.22	C	4.5%
16	42.5 R/SR	800	25%(*)	0	0	0.19	B	2.5%

With every 50 litres batch were casted 16 specimens of 100x100x100 mm for compressive tests and 3 specimens of 100x100x500 mm for un-notched three point bending tests. For some batches slump-flow and T500 were measured according to ASTM C143.

4 Results and discussion

Binders effectiveness for UHPC analysis

Figure 1 shows the mixtures rheology. The mini-slump-flow decreased with the increasing quantity of FC3R or CSF as was expected. It was appreciated that for dosages with CSF the decrease of flowability is much stronger than for similar contents of FC3R. This effect is more significant when the mixture contain cement I-52.5 R/SR.

It was noticed that the amount of FC3R over cement weight can reach 20% without mixing problems unlike with CSF, which hardly decrease the workability with quantities over 10%. An addition of 20% of CSF was tried (as it was done with FC3R) but the decrease of flowability was so hard that it was impossible to reach a plastic-liquid mix even with longer mixing times.

It was also confirmed that increase the FA content implies an increase of flowability. This effect is stronger with I-52.5 R/SR cement, because in this case FA substitutes finer cement.

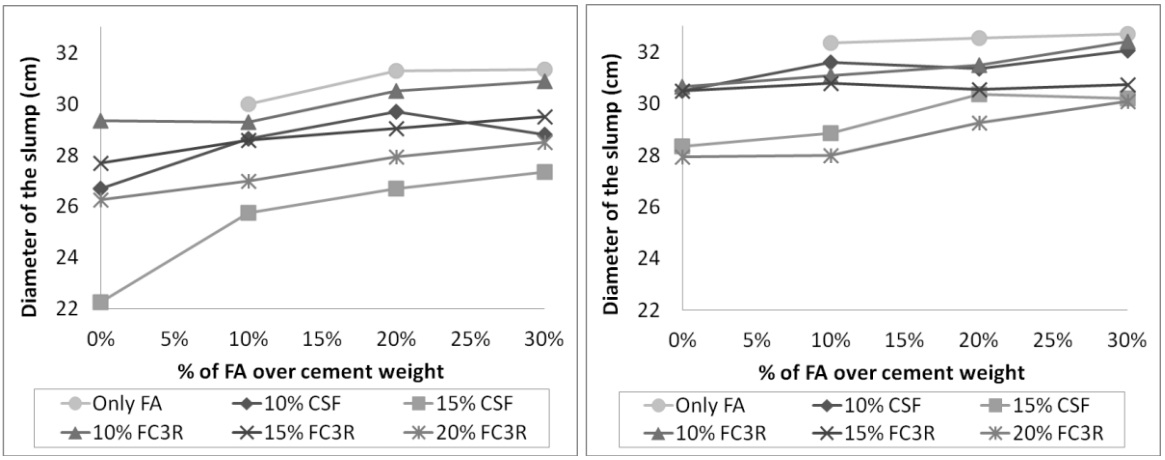

Figure 1: Mini-Slump-flow diameter for mixtures with cement I-52.5 R/SR (left) and I-42.5 R/SR (right).

Relatively to the hardened state, in the table 4 can be seen the 28 days compressive strength depending on the mixture composition. The absence of fibers produce a brittle failure which limits the strength. The value for 10% of FC3R mixtures is slightly higher (≈5%) than the ones with 10% of CSF. For 15% of content over cement weight, this difference turns more remarkable, being of 14% and 16% with I-52.5 R/SR and I-42.5 R/SR cements respectively. This difference is partly associated to the decrease of workability with 15% CSF content, which implies a more porous matrix because the air can't rise to the surface. The higher strengths with FC3R are also due to its higher FC3R activity and the incapacity of the mixer to disperse with total efficiency the CSF particles.

Table 4: 28 days compressive strength of the different dosages (MPa).

			CSF				FC3R					
	Only FA		10%		15%		10%		15%		20%	
	52.5	42.5	52.5	42.5	52.5	42.5	52.5	42.5	52.5	42.5	52.5	42.5
0% FA			127	127	109	128	139	131	123	142	146	147
10% FA	126	142	123	122	126	126	131	126	149	148	144	134
20% FA	127	128	134	122	124	125	131	125	144	139	144	153
30% FA	130	133	117	121	127	112	131	125	136	138	132	133
10% FC3R			125	132	123	123						

On the other hand, in general the effect of the FA didn't decrease the strength, showing even increases for some cases. This can be explained because a good activity but even more because of the fluidity that provides to the mix, which let the air to go out, creating then a more compact matrix. From other point of view, if the selfcompactability of a mixture is adequate, FA can be added and the W/B ratio reduced, for increase the strength maintaining the flowability.

It can be seen that combination of active additions with FA provides good results: Concretes with 711 Kg/m^3 of cement (mix. 22) reach similar strengths than others with 1000 Kg/m^3, as mix. 11, with advantages of less shrinkage, better compacity, lower costs and more sustainability. 20% of content of FA seemed to be the optimum one.

Compressive strength was also determined at 2 and 7 days. The first was 60%-70% of the 28 days strength, depending of the FA substitution but without noticeable differences between the FC3R and CSF mixes. At 7 days CSF mixes showed a strength ranged in 80-85% of the 28 days strength, while the FC3R mixes had between 87%-94%, depending on the FA content. This difference is due to the higher activity of the FC3R at short term, while the CSF develops

more its pozzolanic activity the following weeks. Increasing content of FA produced, in general, noticeable lower strengths at 2 days and slightly lower ones at 7 days.

As can be deduced from the results, the strength values with cement 42.5 R/SR and 52.5 R/SR are very similar, what means that the use of one or other cement would depend of each situation (prices, compatibility of materials, etc).

Finally, a study with Scanning Electron Microscope (SEM) was done to mixes 5, 8 and 24 with cement 52.5 R/SR 90 days after casting. Figure 2 shows the presence of an agglomerate powdered silica fume particle, what demonstrate that this CSF is not fully dispersed, so the potential of this active addition is only partially developed. Figure 3 shows the high degree of compacity of the mixtures. Active additions improved the interfacial transition zone, so the failure with compressive efforts is developed with a crack that breaks the silica arids.

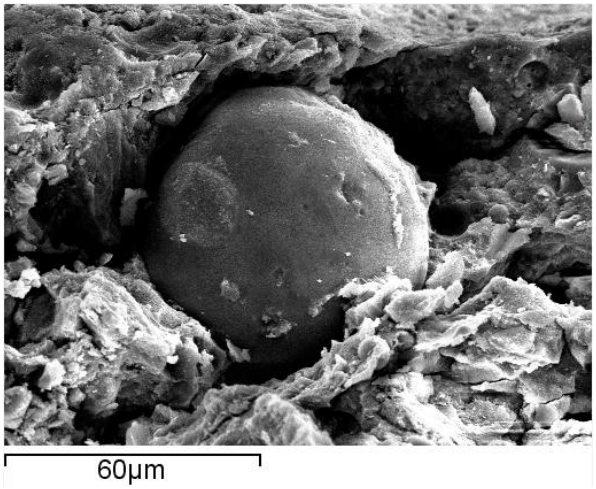

Figure 2: CSF particle, dosage 5.

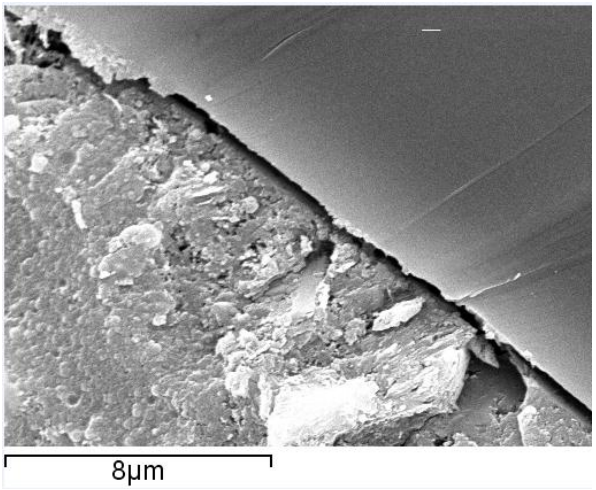

Figure 3: Interfacial Transition Zone (ITZ), dosage 5.

UHPFRC dosages

In the mixing process, some differences were noticed between concretes made with FC3R and those made with CSF. Concretes with FC3R needed longer times (9-11 min.) to change from a mass of solids to a suspension. At this moment the mixer required the maximum power to keep the programmed rotational speed. The stabilization time (time required until particles are homogeneously mixed) was also 2-3 minutes longer for FC3R than for CSF dosages.

The primary ettringite formation in the sulphate resistant cements is limited, because its low content of C3A. In the UHPFRC made with FC3R the primary ettringite formation may increase due to its high Al_2O_3 content. In an alkaline medium it changes to AlO_2^-, and forms ettringite crystals of seizes between 300 and 500 nm [2]. These are the first molecules of the Rapid Forming Ettringite. The admixture particles, with sizes 20 or 30 times smaller, are overgrown by these crystals or are chemically incorporated to these new formed hydration products, losing its efficiency. That is why FC3R needed longer mixing times than mixtures with CSF. To solve this problem part or all the PCE addition can be delayed, taking higher advantage of its properties, but requiring therefore higher mixing times.

Slight addition of water could reduce this time, but when the mass becomes a suspension fluidity increase radically showing a tendency to segregation. Then, FC3R seemed to be more sensible to the water addition than the CSF, which provided more stability. A qualitative measure of the segregation can be assigned to the mixtures by the Visual Stability Index (VSI) [5], based in a visual evaluation of the segregation of the UHPFRC during the slump flow test (0: high stable SCC, 3: Totally segregated SCC). VSI for mixtures with CSF was 0, while for

FC3R was 1. From a practical point of view this implies that the use of FC3R requires even more control of the humidity and water added to reach the desired fluidity in the mix.

Slump flow diameters and T500 were measured for some of the mixtures according to [1] (table 5). Most of them were SF3 according to the consistence classification of [8] –between 760 and 850 mm- having similar filling hability. Dosages with FC3R showed markedly higher values of T500, what means higher viscosity than similar mixtures with CSF. Probably this is due to the lower PCE efficiency in mixtures with FC3R previously discussed.

Its remarkable that mixtures 13 or 16, with ELKEM CSF has lower value of slump flow than the equivalent concretes made with other pozzolanes, but also a lower of T500, flowing fast when it is in movement, but with a short time slump increase. The lower water demand of the FC3R when compared with CSF is clear from results of the 9 and 10 mixtures.

Table 5: Slump flow diameters and T500 of some of the mixtures.

Test	5	6	9 (x2)	10 (x2)	12	13	15	16
Slump flow (mm)	830	763	744	790	820	743	No SCC	600
T500 (sec)	4,8	12,2	6,8	8,9	9,6	6,1	-	4,8

Relative to the hardened state, its noticeable the different effect of the active additions depending on the cement (figure 6). FC3R showed better compatibility with I-42.5 R/SR type and CSF with I-52.5 R/SR. The type of PCE used could also had affected to this compatibility. Its noticeable the strength increase respect to the previous phase due to the addition of 2% of fiber in volume, which sews the micro-crack evolution.

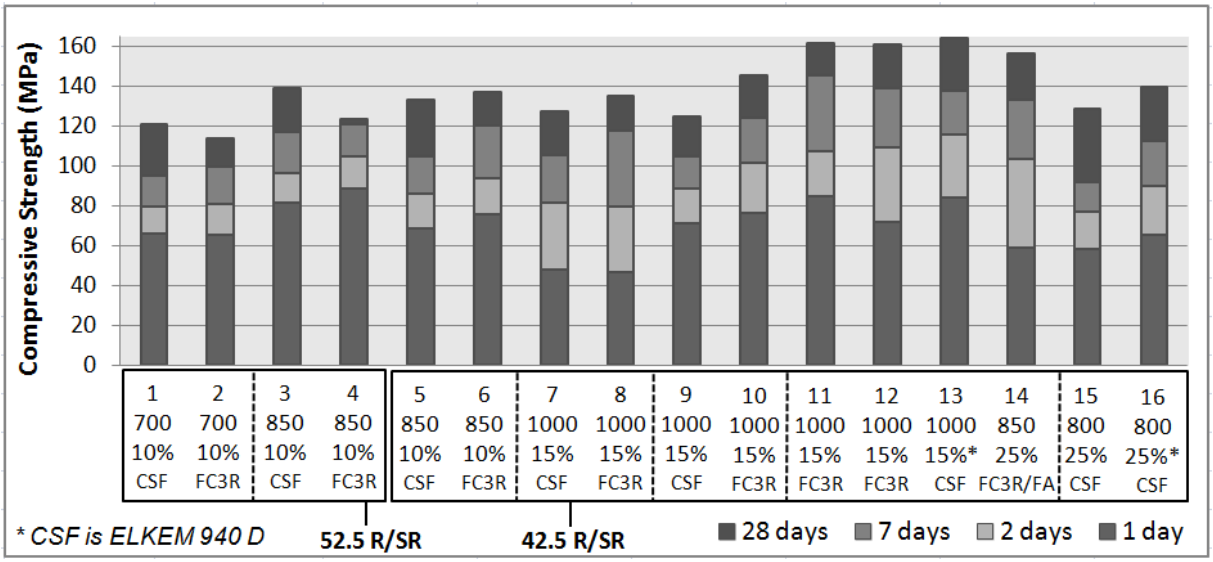

Figure 6: Compressive Strength evolution of the mixtures. Squares enclose comparable dosages.

It can be noticed that mixtures with FC3R develop more strength at 2-7 days because of the higher short term reactivity, while CSF is more active from second week. Dosage 14, with 15% of FA, had, as expected, slightly lower strength at 24 h, but the increase from this moment was marked, reaching 157 MPa at 28 days, 10 MPa more than the dosage 6, similar but without FA.

Mixtures 10 and 11 differed only in the W/B ratio, with 0.19 and 0.18 respectively. The slump-flow of both resulted higher than 750 mm, and the 28 days strength of the second was 9 MPa higher. On the other hand, mixture 13 was casted also (mixture 13 b) with W/B ratio of 0.162 instead of 0.175. The slump-flow was reduced to 650 mm, the T500 was 8.1 sec., and the 28 days compressive strength decreased from 165 MPa to 143 MPa. This showed the

importance of not to reduce too much the water content, because it can avoid the rise of the entrapped air and also its possible that the unhidrated binder quantity is too high. W/B should be as low as possible provided that selfcompactability is adequate.

Dosages made with ELKEM CSF provided the best performances. Mixture 13, 7 and 12 differed only in the active addition (ELKEM CSF, Ferroatlántica CSF and FC3R). Even though 3,5% of PCE was used in mixture 7, the W/B ratio required for good workability was 0.21, while for mixture 13 was 0.175. The only reason is the composition and microgranulometry of the CSF. For mixture 12, the W/B required was also 0.175 and the level of strength was very similar. This shows FC3R as a very efficient addition for UHPFRC.

In the mixes 15 and 16 typical contents of CSF in UHPFRC were added (25% with respect to cement). Ferroatlántica CSF was not selfcompacting even thought the 0.22 W/B ratio, and ELKEM CSF provided a suitable mixture with W/B of 0.19, generating consequently better strength results. In the case of mix 15, increase W/B ratio to reach high fluidity is unacceptable for produce a strong decrease of the performance, being out of the UHPC order. It was observed that 15% in respect to cement of any addition provides better properties than 25%.

Flexural strength was not markedly affected by the active addition type, depending mainly on the binder content. More information about flexural performance can be found in [7].

5 Conclusions

FC3R is an active addition that can be used successfully in UHPC-UHPFRC, providing more fluidity and mechanical strength comparing with some CSF. The % with respect to cement can be higher than 10% without that strong decrease of flowability. It seemed more active at short term (2 and 7 days) than CSF. Flexural strength performance is similar than with CSF dosages.

On the other hand, FC3R composition probably implies different chemical reactions during the mixing process, what can affect to the PCE efficiency, and this leads in higher mixing times. This effect should be considered if used. Delayed addition of the PCE can improve its efficiency. Results evidence that a good UHFRC mix design needs an important previous test program to optimise the components selection as its compatibility is not easily foreseeable.

References

[1] EN 12350-8. Testing fresh concrete-Part 8. Self-compacting concrete-Slump flow test.

[2] Schieβl, P.; Mazanec, O.; Lowke, D.; Plank, J.; Schröfl, C.; Gruber, M.; Schmidt, M.; Glotzbach, C.; Stephan, D.: Rheology of UHPC-Effect of superplasticizer and silica fume on mixing and workability of UHPC. 3rd fib International Congress, Washington D.C., USA, May-June 2010.

[3] Schie Rossignolo, J.A.: Effect of Silica Fume and SBR Latex on the Paste-aggregate Interfacial Transition Zone. *Materials Research. Vol 10, No. 1, 83-86, 2007*.

[4] Payá, J.; Monzó, J.; Borrachero, M.V.: FC3R: An excellent mineral by-product for improving early-strength development of cement mixtures. *Cement and Concrete Research* 29 (1999) 1773-1779.

[5] AASHTO TP 80-10. Standard Method of Test for VSI of Self-Consolidating Concrete (SCC).

[6] Soriano M., L.: Nuevas Aportaciones en el Desarrollo de Materiales Cementantes con Residuo de Catalizador de Craqueo Catalítico Usado. Doctoral Thesis. UPV, Valencia, 2007.

[7] Camacho , E.: Caracterización de HMAR: Estudio de las propiedades reológicas y mecánicas para dosificaciones de distintos niveles de rendimiento. Master Thesis, Valencia, February 2011.

[8] The European Guidelines for SCC: Specification, Production and Use. May 2005.

[9] Camacho, E.; Serna Ros, P.: Design and analysis of UHP-Hybrid-FRC ties for truss structures. 8th fib PhD Symposium in Civil Engineering. Denmark, June 2010.

[10] EN 196-1: Methods of testing cement. Part 1. Determination of strength.

[11] Aenor UNE 80303-1. Cementos con carac. adicionales. Parte 1: Cementos resistentes a sulfatos.

[12] Kantro, D.L.: Influence of water-reducing admixtures on properties of cement paste-a miniature slump test. *Cement, Concrete and Aggregates, Vol.2, Issue 2. Pp 95-102. 1980.*

Colloidal photocatalysts and their applications for air/water purification under UV or visible light irradiation

Shuai Yuan, Meihong Zhang, Jianping Zhang, Yin Zhao, Zhuyi Wang, Liyi Shi
Research Center of Nanoscience and Nanotechnology, Shanghai University, China

Based on our previous work, the visible-light (fluorescent lamp as light source) response colloidal photocatalysts with high dispersity and stability in aqueous solution were prepared by Cu^{2+} or Fe^{3+} ions doping. The samples were characterized by XRD and TEM. The absolute zeta potentials of the metal ion doped TiO_2/SiO_2 hydrosols were much higher than 50.0 mV in neutral condition. Methylene blue was taken as the simulated pollutants to study the adsorption and photocatalytic properties of the obtained hydrosols. The prepared hydrosols show high photocatalytic activity under the irradiation of visible light.

Keywords: Cu^{2+}, Fe^{3+}, TiO_2, hydrosol, visible-light photocatalysis

1 Introduction

Nanosized TiO_2 crystals of less than 10 nm show significant differences with bulk TiO_2 in many aspects due to the quantum size effect [1]. TiO_2 hydrosols consisting of highly crystallized nano-particles have been widely studied in the fields of photocatalytic degradation of pollutants and self-cleaning windows [2]. However, the pure TiO_2 hydrosol is usually adjusted to acidic conditions and stored at low temperature (~ 4°C) to avoid sedimentation [3].

Neutrality of the hydrosol is one of the important requirements as acidic or basic hydrosol is corrosive and harmful to the substrate materials. Recently, we investigated the preparation of TiO_2/SiO_2 hydrosols with small grain size (~10 nm). The prepared TiO_2/SiO_2 hydrosols are transparent, stable and show high photocatalytic activity in neutral range [4].

In this work, a chemical precipitation-peptization method was used to prepare organic-free TiO_2 hydrosols with $TiCl_4$ aqueous solution as a precursor. The hydrosols take advantage of both TiO_2 with high photocatalytic activity and SiO_2 with high stability in neutral condition. However, the TiO_2/SiO_2 hydrosol only shows high photocatalytic activity under UV light irradiation. To extend the light response to visible range, Cu^{2+} and Fe^{3+} ions were doped in the nanocomposites respectively. The photocatalytic properties of Cu^{2+} and Fe^{3+} ions doped TiO_2/SiO_2 were investigated by the degradation of dye solutions.

2 Experimental section

Materials:

All reagents used were of analytical grade purity. Aqueous $TiCl_4$ solution was provided from Sinopharm Chemical Reagent Co.Ltd. $NH_3 \cdot H_2O$, HCl, methylene blue, and oleic acid were obtained from Shanghai Reagent Ltd. SiO_2 sol (30wt %) were purchased from Shanghai Hengsheng Ltd.

Preparation of TiO_2 hydrosol.

The preparation process of Cu^{2+} and Fe^{3+} ions doped TiO_2/SiO_2 is similar to the process preparing TiO_2/SiO_2 reported in our previous work [4]. The metal ions were added to the reaction system during the acid-peptization stage.

Characterization

The powdered samples were prepared through rotatory evaporation of the colloids at 40°C. X-ray diffraction (XRD) was performed on a D/Max-2200 X-ray diffraction meter (Rigaku Corporation, Japan) at room temperature, operating at 30 kV and 30 mA, using Cu kα radiation

(λ=0.15418 nm). The crystal size was calculated by Scherrer's formula. UV-vis diffuse reflectance spectra were recorded with a UV-2501 PC spectrometer (Shimadzu, Japan) Spectrumlab. The samples for UV-vis spectra were obtained with the same solid content of 0.05wt % TiO_2.The zeta potential of the TiO_2 or SiO_2-modified TiO_2 nanoparticles was measured on a Zetasizer 3000HS (Malvern Instruments Ltd.UK.)

Evaluation of photocatalytic activity

The photocatalytic properties of the metal ions doped TiO_2/SiO_2 were evaluated by the degradation of methylene blue. Methylene blue is a cationic dye. For all the adsorption-desorption experiments and photocatalysis experiments, the initial concentration of methylene blue was 6.0 mg/L, equivalent to 1.0 g/L TiO_2 in aqueous solution. The adsorption-desorption experiment was operated by adding the photocatalyst to dye solution. The solution was constantly aerated and magnetically stirred in the dark. The dye concentration of the solution was measured every 10 min after removing colloids by centrifugation at 8000 rpm for 30 min. The remaining methylene blue was detected by a Visible Spectrometer at wavelength of 664 nm.

The photocatalytic activities of different samples were evaluated in a tube, equipped with a magnetic stirring bar. Before irradiation, the dye/sol mixture was magnetically stirred in dark for 30 min to establish an adsorption-desorption equilibrium, so the loss of the compound due to adsorption can be taken into account. During the photoreaction process, the colloid solution was irradiated by a fluorescent lamp (9 W, λ ≥ 400 nm) with constant aeration and magnetic stirring. The dye concentration of the solution was measured every 30 min after removing colloids by centrifugation at 8000 rpm for 30 min. The efficiency of degradation was calculated from the following formula:

$$D= (A_0-A)/A_0\times100\%$$

Where A_0 and A are the initial and final absorbance at 664 nm for methylene blue.

3 Results and discussion

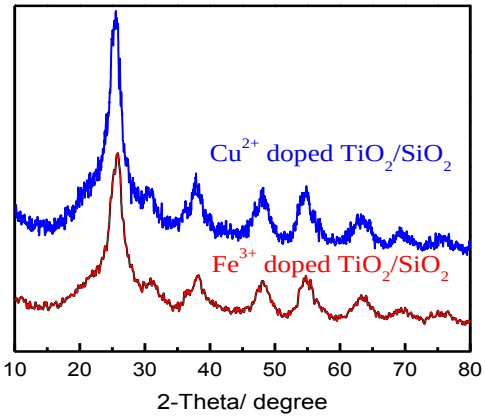

Figure 1: XRD patterns of Cu^{2+} and Fe^{3+} ion doped TiO_2/SiO_2.

XRD patterns of Cu2+ and Fe3+ ion doped TiO2/SiO2 are shown in Figure 1. For each sample, the peaks correspond to anatase phase according to PDF21-1276. There is no peak belonging to Fe_2O_3 or CuO, which may be due to the Fe^{3+} and Cu^{2+} doping in the anatase lattice. Compared to the undoped TiO_2/SiO_2, the crystal sizes of Fe^{3+} and Cu^{2+} doped TiO_2 nanocrystals are about 10 nm. The results indicate the metal ion doping didn't change the crystal phase and crystal size of TiO_2, due to the low dopant concentration.

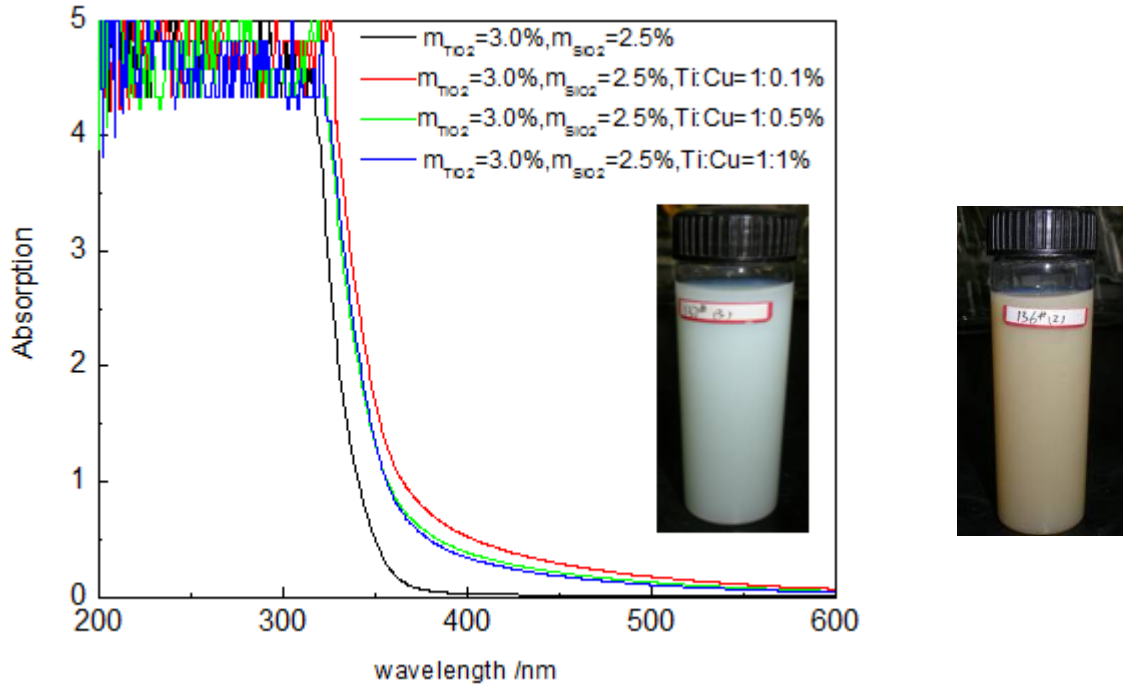

Figure 2: UV-vis spectra of Cu^{2+} and Fe^{3+} ion doped TiO_2/SiO_2 and photocatalytic degradation of methylene blue under the irradiation fluorescent lamp.

The light absorption property of photocatalyst in the UV-vis range is one key factor affecting the photocatalytic activity. From Figure 2, it can be observed that the absorption edge is around 365 nm. The Fe^{3+} and Cu^{2+} doping extend the response range to visible light. The absorption edge of Fe^{3+} doped TiO_2/SiO_2 is around 400 nm. Compared to Fe^{3+}, Cu^{2+} dopant can shift the absorption edge to longer wavelength. The ion radii of Fe^{3+} ion, Cu^{2+} ion are 0.064nm and 0.072nm, respectively, which are close to the radius of Ti^{4+} ion (0.680 nm) [5]. So Fe^{3+} and Cu^{2+} are easy to be doped in the TiO_2 lattice and replace partial Ti^{4+}. The acceptor doping can reduce the bandgap and make the visible-light excitation to be possible. Cu^{2+} doped TiO_2/SiO_2 shows higher photocatalytic activity than Fe^{3+} doped TiO_2/SiO_2, which may be due to the wider visible-light absorption range.

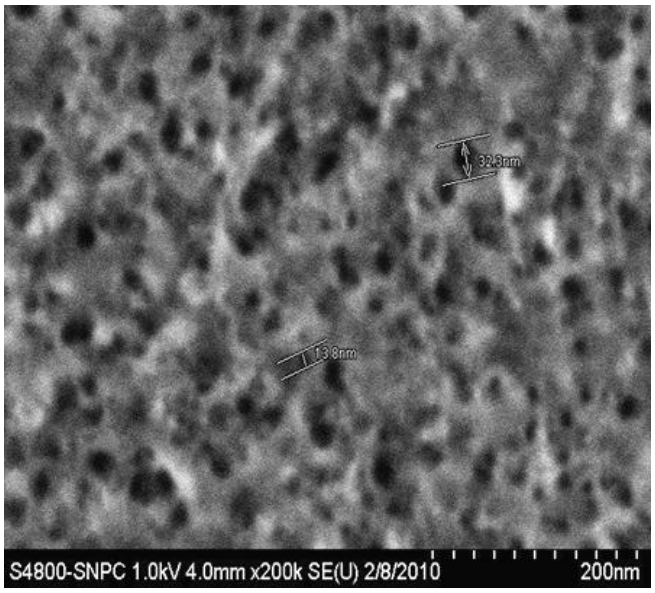

Figure 3: SEM image of Cu^{2+} doped TiO_2/SiO_2 coated stainless steel.

The Cu^{2+} doped TiO_2/SiO_2 colloid was coated on the stainless steel by spin-coating method. The SEM image shows the porous structure of photocatalytic film on stainless steel (Figure 3). This porous structure will benefit the adsorption and photocatalytic degradation of organic pollutants.

To evaluate the self-cleaning property of the photocatalytic film under visible light irradiation, we monitored the visible-light photocatalytic degradation of oleic acid adsorbed on the surface by measuring the contact angle of water on the film during different stages. As shown in Figure 4, the surface of Cu^{2+} doped TiO_2/SiO_2 coated stainless steel 15 are hydrophilic (contact angle 5.0°). The contact angle increased to 47.7°due to the adsorption of oleic acid. After irradiation by fluorescent lamp (9 W, $\lambda \geq 400$ nm) for 1h, 2h and 3h, the contact angle reduced to 30.7°, 21.4°, and 4.6 °, respectively, reflecting the gradual decomposition of oleic acid. After the complete removal of oleic acid, the surface property reverted to hydrophilic.

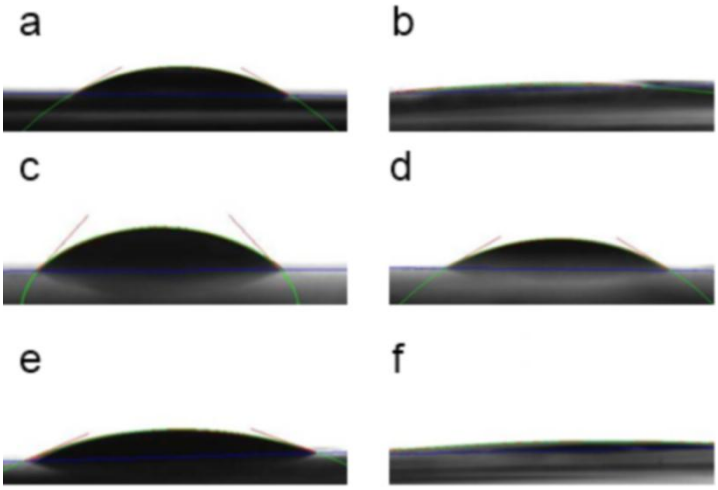

Figure 4 The contact angles of water on (a) stainless iron; (b) Cu^{2+} doped TiO_2/SiO_2 coated stainless iron; (c) Cu^{2+} doped TiO_2/SiO_2 coated stainless iron adsorbing oleic acid; (d) Cu^{2+} doped TiO_2/SiO_2 coated stainless iron adsorbing oleic acid after fluorescent lamp irradiated for 1h; (e) Cu^{2+} doped TiO_2/SiO_2 coated stainless iron adsorbing oleic acid after fluorescent lamp irradiated for 2h; (f) Cu^{2+} doped TiO_2/SiO_2 coated stainless iron adsorbing oleic acid after fluorescent lamp irradiated for 3h are 29.2°, 5.0°,47.7°,30.7°,21.4°,4.6°, respectively.

4 Conclusion

Based on our previous work, the visible-light (fluorescent lamp as light source) response colloidal photocatalysts with high dispersity and stability in aqueous solution were prepared by Cu^{2+} or Fe^{3+} ions doping. Furthermore, the colloidal photocatalysts with high dispersity and stability can be easily applied for air purification coating by spin-coating or spray-coating method.

5 Acknowledgement

The authors acknowledge the supports of Shanghai Leading Academic Discipline Project (S30107), International cooperation fund of Shanghai Science and Technology Committee (09520715400), and The Research & Innovation Projects of Shanghai Education Commission (11YZ22). Science Foundation for The Excellent Youth Scholars of Universities (Shanghai) and Innovative Foundation of Shanghai University.

Reference

[1] Y. Zhao, C. Li, X. Liu, F. Gu, H.L. Du, L. Shi. *Appl. Catal. B: Environ*. 79 (2008) 208.
[2] J Liao, L Shi, S Yuan, Y Zhao, J Fang. *J Phys. Chem. C*, 113(2009), 18778.
[3] T Liu, F Li, X Li. *J Hazard. Mater.* 152 (2008) 347.
[4] M Zhang, L Shi, S Yuan, Y Zhao, J Fang. *J Colloid Interf. Sci.*, 330(2009),113.
[5] L Yu, S Yuan, L Shi, Y Zhao, J Fang. *Micropor. Mesopor. Mater.*, 134(2010),108.

New Photocatalytic Cementitious Composites containing Modified Titanium Dioxide Nanoparticles

Vyacheslav Falikman[1], Alexander Vajner[2], Igor Zverev[3]

1: Moscow State University of Civil Engineering, Russia
2: Scientific Research Institute for Concrete and Reinforced Concrete, Moscow, Russia
3: Institute of Comprehensive Exploitation of Mineral Resources of the RAS, Moscow, Russia

Cementitious building materials containing TiO_2 nanoparticles find the increasing application in processes of organic and the inorganic compounds photomineralization representing a new resource of opposition to pollution. With use of a new synthesis procedure TiO_2 nanoparticles having anatase structure with high specific surface 300 m^2/g or so were prepared.
Photocatalytic cementitious composites were developed and tested (concrete, mortars, plasters, cement paints, etc.); relation was found between physical and chemical parameters and conversion processes occurring on their surface. The cement based matrix appeared to assist in conversion of the noxious pollutants and their removal from surrounding air. Influence of radiation intensity, relative humidity, and concentration of a contaminant and its stream speed on photocatalysis of nitrogen oxides, vapors of benzene and acetone was studied. It is established that efficiency of the composites with synthesized samples in 1,5 - 1,7 times higher that for known commercial samples.

Keywords: titanium dioxide, photocatalytic properties, cementiuos building materials, pollutants

1 Introduction

Nanodimensional titanium dioxide is widely used as a photocatalyst in photochemical decomposition reactions of many organic and non-organic pollutants by virtue of its high efficiency, biological and chemical inertness and relatively low cost [1, 2].

In the recent years one observes the increasing interest to application of cement composites comprising titanium dioxide nanoparticles. Building materials possessing photocatalytic properties allow noticeably reducing the environment polluting effect being particularly important in megalopolis conditions [3, 4]. Further achievements in their use expansion to a considerable extent depend on appreciable rise in nanocatalyst efficiency in decomposition reactions of the basic urban pollutants – nitrogen oxides, carbon monoxide, volatile organic substances, etc.

To date a variety of different methods to increase photocatalytic activity of nanodimensional titanium dioxide has been offered. In particular, recently it has been shown that higher activity is exemplary for mesoporous nanoparticles of TiO_2, which are characterized by predominance of the anatase phase, small sizes of crystals and high specific surface area [6].

The behavior of such nanocatalysts in cement systems may have certain peculiarities associated with high pore volume and high specific area. Such a research along with development of the simple and handy way of mesoporous anatase titanium dioxide synthesis has become the aim of this work.

2 Synthesis and characteristics of mesoporous nano-TiO_2

The synthesis of TiO_2 nanoparticles was carried out by adaptation of the previously described methods [7, 8]. As an initial titaniferous precursor the tetraisopropyltitanate (TTIP) was used. To inhibit the hydrolysis rate and subsequent condensation the 30% aqueous solution of H_2O_2 was introduced into the reaction mix. Cetyl trimethylammoniumbromide (CTMABr) was chosen as a template, a structure-forming and pore-forming agent. The initial sol-gel reaction of TiO_2 synthesis was conducted in the presence of tetramethylammonium hydroxide. The peroxytitanium acid solution obtained represented a clear and stable liquid with pH = 7. Then

this solution was subjected to autoclave crystallization under hydrothermal conditions at 80°C during 48 hours with subsequent air calcination of the product at 500°C during 4 hours, thereby resulting in formation of nano-TiO_2 with the anatase structure.

The analysis of TiO_2 nanoparticles obtained was made in conformance with established methods. For instance, the X-ray phase analysis of the specimens was made using DRON-3 diffractometer (Russia) with monochromatic Cu K_a emission. The dimensions of the anatase and rutile phase coherent-scattering region were determined by Sherrer formula [9] using half-widths of anatase (101) and rutile (110) diffraction reflections.

The total value of specific area S_{BET} was determined by the traditional method of argon thermal desorption according to four points of sorption equilibrium using "SORBI-M" instrument supplied by META Co. (Russia). The specimen porous structure was studied by the method of nitrogen low-temperature sorption at 77°K using DigiSorb-2600 Micromeritics unit (USA). Prior to this, the specimens were "trained" in 10^{-4} Torr vacuum at 200°C during 5 hours. Pore distribution by sizes was calculated by the stripping branch of nitrogen adsorption isotherm using the classical Barrett – Joyner – Halenda (BJH) method [10].

With the purpose to optimize structural-sorption characteristics of TiO_2 nanoparticles when being formed, the content of CTMABr template was varied in the initial reaction mixes. As is seen from Table 1, the test specimen of TiO_2-0 obtained in the absence of the template is characterized by the lower values of specific area and pore volume. The crystal grain sizes calculated by Sherrer formula are in the range of 6.7 to 7.6 nm, while with increase of CTMABr template content the crystal grain sizes decrease.

Table 1: Parameters of crystal grains, surfaces and pores of TiO_2 nanoparticles depending on CTMABr content in the reaction mixes.

Marking	CTMABr, mass.% TTIP	S_{BET}, m^2/g	Pore volume, V_{por}, cm^3/g	Pore size, nm	Crystal grain size, nm
TiO_2-0	0	145	0,275	3,8	7,6
TiO_2-10	10	218	0,299	4,2	6,8
TiO_2-20	20	230	0,300	4,8	6,7
TiO_2-30	30	267	0,298	5,1	6,4
TiO_2-45	45	284	0,314	5,6	6,1

It should be noted that all synthesized specimens including non-calcinated ones are characterized by the presence of only anatase modification of TiO_2, though the calcinated ones exhibit a more advanced crystalline structure. The nitrogen adsorption – desorption isotherms of synthesized TiO_2 nanoparticles correspond to the IV isotherm type with H2 hysteresis loop according to IUPAC classification [11], this being typical for mesoporous structures.

3 Preliminarily estimation of nano-TiO_2 photocatalytic efficiency

To preliminarily assess the photocatalytic efficiency of synthesized specimens in comparison with P 25 commercial product supplied by Evonic-Degussa GmbH (Germany) the methods [12] were used based on decomposition of rhodamine dye 6G aqueous solution (Table 2). When conducting photocatalytic decomposition, 0.1 g of TiO_2 was added to 40 ml of the dye solution with 10 mg/l concentration. The solution was exposed to polychromatic light of the Sylvania Par 38 100 W mercury vapor lamp The dye concentration was determined photometrically in the UV-range using Unicam 8700 spectrometer and absorption band λ = 539 nm. It is believed that photocatalytic decomposition of rhodamine 6G obeys the first-order chemical equation.

$$\ln\left(\frac{A_0}{A}\right) = kt \qquad (1)$$

where A_0 – initial dye absorption;
A - dye absorption in time t;
k - rate constant for first-order equation.

Table 2: Estimation of nano-TiO_2 efficiency.

Sample	Modification				S_{BET}, m^2/g	Pore volume, V_{por}, cm^3/g	Pore size, nm	k, min^{-1}
	Anatase		Rutile					
	Content, %	Crystal grain size, nm	Content, %	Crystal grain size, nm				
P 25	81	36	19	88	51	0,165	20	0017
TiO_2-45	100	6,1	0	-	284	0,314	5,6	0,029

The rate of rhodamine 6G photodecomposition using TiO_2-45 almost doubles that of its disappearance in the presence of P 25 photocatalyst. Thus, in the first case the dye in the experiment completely decomposes in 18 minutes, while in the second case – in 40 minutes.

4 Photocatalytic efficiency of nano-TiO_2 in cementitious composites

When studying cement compounds with titanium nanodioxide, the white cements of CEM I 52.5 class according to EN 197-1 from a number of manufacturers were used including those from Aalborg plants (Denmark), as well as the domestic ordinary Portland cement of CEM I 42.5 class according to GOST 31108 from the Belgorod Cement Plant with the standardized chemical composition (PC 500 D0). The actual activity of all cement samples conformed to the class and was more than 50 MPa during tests in the test mortars according to GOST 310.4. In a number of tests and compositions the Pikalyovo Portland cement PC 400 D20 was used according to GOST 31108-2003.

Gypsum and the second-grade air-setting hydrated high-calcium pulverized lime without additions were used in plastering and paint compounds according to GOST 9197.

Crushed granite stone from the igneous rock of the Lobskoye quarry (Republic of Karelia) with 5-20 mm fraction according to GOST 8267 was used as a coarse aggregate.

The quartz sand from the Mansurovsky deposit with M_f=2.5 (bulk density 1632 kg/m^3) was used as a fine aggregate for concrete and mortars according to the requirements of GOST 22263. In a number of compounds the quartz sand of 0.0-0.63 mm fraction with M_f=1.8 was used.

The efficiency of photocatalysts in cement systems was evaluated in relation to nitrogen oxide degradation as well as to volatile organic compounds – gasoline and acetone vapors. The concrete composition was assigned with account of the requirements of GOST 27006 and GOST 30459, that of cement mortars – according to GOST 28013, that of dry pack mortars – according to GOST 31357. TiO_2 proportioning, as a rule, was 5% of cement mass.

The studies of NO phototransformations in the presence of titanium nanoxide were conducted with consideration of recommendations of WG 33 ISO 206/SCN at 50% of air relative humidity, 25^{O}C and 3 l/min of air speed, while the initial content of nitrogen oxide in the air was 1 ppm, the photometric intensity was 10 W/m^2 under polychromatic exposure with wavebands 300-400 nm and the maximum emission of 365 nm. The exposure duration was 30 min. NO content in the air mixture was determined using adapted MX6 Multi-Gas Monitor supplied by ISC (USA).

The synthesized nanoparticles of mesoporous TiO_2 have demonstrated much higher efficiency of NO transformation as compared with P 25 commercial product (Table 3).

It is noteworthy that the phototransformation efficiency is somewhat decreases with the age of concrete specimens, this being rather connected with the course of hydration processes in

the cement matrix. The recent work [13] has established that introduction of TiO_2 nanoparticles with 15 nm average size into the concrete mix accelerates C – S – H gel formation and increases quantity of $Ca(OH)_2$. These products block up active centers on surfaces of TiO_2 nanoparticles, while calcium hydroxide can also react with titanium dioxide reducing its photocatalytic activity. With the initially higher photocatalytic activity the mesoporous TiO_2 specimens are seemed to be more affected, this being the cause of its more dramatic drop with the concrete age.

Table 3: Comparative assessment of TiO_2 photocatalytic efficiency in Portland cement concretes under NO conversion.

Sample of TiO_2	Concrete curing time, days	NO change ratio, %
P 25	3	25
	7	24
	28	23
TiO_2-45	3	42
	7	39
	28	35

Decorative elements from composite materials for architectural finish of building facades as well as landscaping elements and small architectural forms are more frequently used in modern construction practice. They shall answer architects' concepts and structural peculiarities of buildings. To improve their decorative properties, as a rule, white and color cements are used.

In this connection of interest is the assessment of TiO_2 photocatalytic activity in relation to the white cement whiteness (Table 4).

Table 4 – Effect of cement whiteness on NO conversion efficiency in concretes with TiO_2-45 nanoparticles (concrete age – 28 days).

Sample	Producer	Cement mark	Cement whiteness, %	NO change ratio, %
1.	Aalborg, Denmark	Aalborg White	95	52
2.	Aalborg, Egypt	Aalborg White	87	42
3.	Çimsa, Turkey	Super White Portland Cement	85,5	44
4.	Shchurovo Cement, Russia	PCB 1 500 D0	80	39

As it is seen from the table, NO conversion is most efficient in white Danish cement matrices characterized by the highest whiteness. The efficiency is somewhat decreases with Egyptian and Russian cements, this seems to be explained by "pollution" of these cements with transition metal ions Fe^{3+} and Mn^{3+} [14].

The high photocatalytic activity of synthesized mesoporous TiO_2 nanoparticles was confirmed in the course of decomposition of volatile organic compounds (VOC), while plastering mortars and cement paints were used as catalyst carriers.

In the course of measurements the kinetic characteristics of pollutant content variation in the air were determined under effect of the photocatalytic reaction on the specimen surface being exposed to soft ultra-violet radiation. Gasoline and acetone were used as VOC-pollutants of the air environment. The gas-air mixtures comprising the outdoor air and pollutant vapors with 5 x 10^{-4} g/l concentration were analyzed. The air stream speed was 1.1 l/min, relative humidity was 64%, duration of photocatalytic decomposition of VOC in each test – 6 hours. "Free" volume of

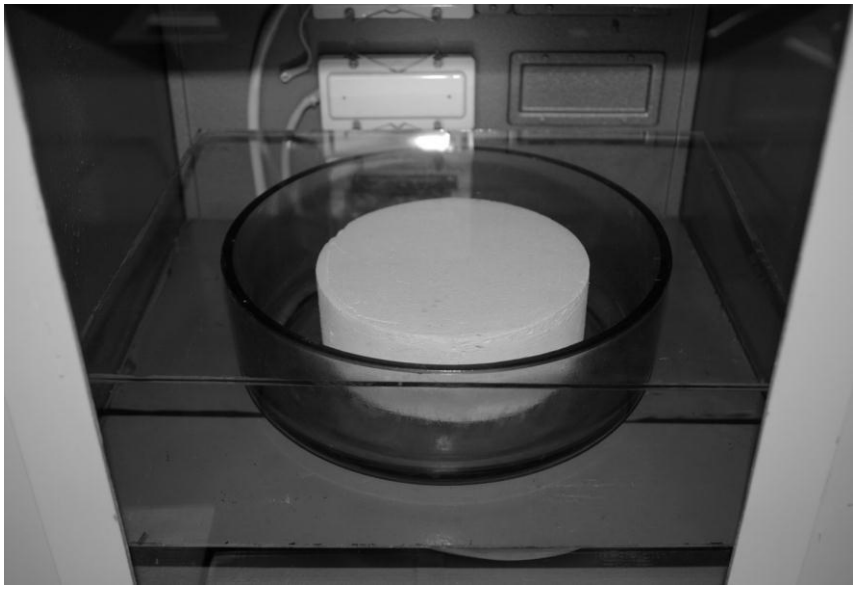

Figure 1: Specimen coated with cement paint with TiO_2-45 placed in the test box

the reaction chamber was 1.3 l. Exposure was conducted at illumination intensity of 10 W/m^2. The specimen surface temperature was 26^{o}C. The cylindrical specimens 15 cm in diameter and 5 cm high coated with cement dye or plastering mortar with TiO_2-45 content 1.9-3.3% were used (See Fig.1).

The preliminary tests for optimization of photocatalyst concentration in the specimens studied have shown that photocatalytic activity of TiO_2-45 nanoparticles grows with the rise of their content in cement composites up to 3.8%, after that it stabilizes. Thus, plastering mortar specimens with 1.9 and 3.8% content of TiO_2-45 nanoparticles allow in the above conditions implementing gasoline decomposition by 52.3 and 63.1% accordingly, while the gasoline concentration in the air decreases down to the values of 0.73 and 0.68 MAC, accordingly.

The photocatalytic activity of synthesized mesoporous TiO_2 nanoparticles is essentially reduced with the rise of relative humidity of the air environment (Table 5). Irrespective of the relative humidity value, replacement of mesoporous TiO_2 nanoparticles by P 25 commercial product reduces the photodecomposition rate by 1.5-1.7 times.

Table 5: Effect of relative humidity on photocatalytic activity of mesoporous TiO_2-45 nanoparticles in plastering mortars. TiO_2 content – 3.8%.

Duration of exposure, hours	Decomposition rate, %, under relative humidity, %	
	64	95
1	0	0
2	24,74	15,43
3	47,42	31,91
4	55,67	40,43
5	63,40	52,13
6	69,07	54,79

The gasoline photodecomposition rate increases with the exposure intensity growth, though the nature of this relationship varies depending on the exposure dose. For instance, in the range of exposure doses from 3.5 to 15 W/m^2 the gasoline decomposition extent increases non-linearly and only afterwards, in the range of 15 – 40 W/m^2 it acquires the linear nature.

It should be also emphasized that the gasoline decomposition rate in the presence of synthesized mesoporous TiO_2 nanoparticles depends on quite a number of other factors, e.g. pollutant concentration and its stream speed. Thus, with the double growth of gasoline content in the gar-air mixture its decomposition extent decreases by 22%. The double growth of gasoline vapor flow rate results in reduction of the pollutant decomposition extent by 17%.

As to acetone vapors in the air environment, the gypsum-cement plasters comprising 2.2% of mesoporous nano-TiO_2 provide 62% of conversion extent in two hours of exposure, this being 1.6 times higher than when using P 25.

5 Conclusions

Thus, the authors have developed the improved method of producing nanoparticles of anatase mesoporous TiO_2 with a high specific surface area in the order of 300 m^2/g and for the first time have shown an opportunity to use it as components of cement and gypsum composites as a highly efficient photocatalyst in the processes of nitrogen oxide and VOC conversion. The effect of structural parameters of nanoparticles and various physical and chemical factors on photocatalytic processes is considered. It is established that efficiency of synthesized mesoporous TiO_2 nanoparticles is 1.5-1.7 times higher than that of the titanium nanodioxide commercial specimen.

References

[1] Falikman, V.R., Vainer, A. Ya.: Photocatalytic active building materials with titanium dioxide nanoparticles - the new concept of ecology enhancement for megacities. *Application of nanotechnologies in construction.* M.: MSUCE, 2009. – 120 p., p.p. 35 – 49 (in Russian).

[2] Chen, J., Poon, C.-S.: Photocatalytic cementitious materials: influence of the microstructure of cement paste on photocatalytic pollution degradation. *Environ. Sci Technol*. 2009. V43. №23, p p. 8948-8952.

[3] Cassar, L., Beeldens, A., Pimpinelli, N., Guerrini, G. L.: Photocatalysis of cementitious materials *International RILEM Symposium on Photocatalysis, Environment and Construction Materials*. 2007, p.p. 131 – 145.

[4] Husken G., Hunger M., Brousvers H.G.H.: Experimental study of photocatalytic concrete products for air purification // Build Environ. 2009. V. 44. №12, p.p. 2463-2474.

[5] Chen, X., Mao, S.S.: Titanium dioxide nanomaterials: synthesis, properties, modifications and applications. *Chem Rev.* 2007 V. 107.№7. p.p. 2891-2959.

[6] Peng, J, Zhao, D., Dai, K. et al.: Synthesis of titanium dioxide nanoparticles with mesoporous anatase wall and high photocatalytic activity. *J. Phys. Chem.* B 2005. V. 109. №11. p.p. 4947-4952.

[7] Ichinose, H., Jerasaki, M., Katsuki, H.: Synthesis of peroxo-modified anatase sol flom peroxo titanic acid solution. *J. Ceram. Soc. Jpn.* 1996 v. 104. №8, p.p. 715-718.

[8] Cassiers, K., Linssen, T., Mathieu, M, et al.: Surfactant-directed synthesis of mesoporous titania with nanocrystalline anatase walls and remarkable thermal stability. *J. Phys. Chem* B 2004 V. 108. №12, p.p. 3713-3721.

[9] Li. X-L., Ishigaki. J.: Controlled one-step synthesis of nanocrystalline anatase and rutile TiO_2 powders by un-flight thermal plasma oxidation. *J. Phys Chem* B 2004 V 108 №40 p.p. 15536-15542.

[10] Barrett, E. P., Joyner, L. G., Halenda, P. P.: The determination of pore volume and area distributions in porous substances. Computation from nitrogen isotherms. *J. Am. Chem. Soc.* 1951 v. 73 p 373-80.

[11] Rouquerol, F., Rouquerol, J., Sing, K.: Adsorption by Powders and Porous Solid: Principles, Methodology, and Applications. Academic Press. San Diego, 1999.

[12] Beyers E., Cool P., Vansant E.E., Anatase formation during the synthesis of mesoporous titania and its photocatalytic effect. *J. Phys. Chem* B. 2005 V 109 №20 p.p. 10081-10086.

[13] Nazari, A., Riahi, S.: The effects of TiO_2 nanoparticles on physical, thermal and mechanical properties of concrete using ground granulated blast furnace slag as binder. *Mater Sci and Eng.* A. 2011 V.528 №4-5. p.p. 2085-2092.

[14] Lin, Z.-H., Tang, X., Zhang, C., Zhou, Q.: A novel TiO_2-pillared microporous manganese oxide. *Chem Letters.* 2005 v 34, №10, p.p.1312-1313.

Synthesis of Photoactive Silica Spheres with Titania Nano Coating as Potential Nano-Composites for Mortar and Concrete

Sameena Kamaruddin[1], Dietmar Stephan[2]
1: Institute of Structural Engineering, University of Kassel, Germany
2: Dept. of Civil Engineering, Technische Universität Berlin, Germany

In this work, monodisperse silica spheres around 440 nm in diameter, prepared via the "Stöber"-Process, were coated with a nano-scaled layer of titania via hydrolyzing tetrapropylorthotitanate (TPOT). This procedure yielded in a continuous layer of titania on the silica support. The success of the coating was verified via scanning and transmission electron microscopy (SEM/TEM) as well as via zeta-potential and X-ray fluorescence analysis (XRF). In order to evaluate the photoactivity of the samples, the degradation of an aqueous methylene blue solution and NO-gas under UV-A light were studied. The results showed that the composite particles consisted of only 4-5 wt.-% titania and their photocatalytic efficiency was close to that of P25.

Keywords: Photocatalysis, Nanomaterials, Sol-Gel-Method, Core-Shell-Particles, NO-Degradation

1 Introduction

Nano-crystalline TiO_2 is widely used for decomposing organic and inorganic substances [1-4]. It is already applied as an additive for paints, ceramics, roofing tiles and cement-containing products like plaster, paving stones or concrete for the decomposition of pollutants and green vegetation on their surfaces [5-8]. In addition to the photocatalytic properties, TiO_2 has also superhydrophilic characteristics. Decomposed material and dirt can therefore be very easily washed away by water [9-11].

However, nano-particles tend to agglomerate, which leads to a reduction of the active surface area and a higher dosage has to be employed to yield the mentioned effects. Composite materials consisting of a core and just a thin photoactive titania shell may be used as an alternative material to nanosized pure photocatalysts [12, 13]. Such systems can be tailored according to the purpose of their application, as the size of the particles, as well as the thickness of the shell can be altered. By using cores beyond the nanoscale, agglomeration can be reduced to a great extent.

There are different methods to encapsulate or modify the surface of a substrate. For instance, it is possible to use electrostatic attraction forces between the core and the shell component to combine them [14, 15]. The layer by layer (LBL) method also allows to apply multiphases on particles via electrostatic attraction forces by using polycations and polyanions respectively to adjust the surface charge [16, 17].

In this work, an organometallic titania precursor was directly hydrolysed and condensed on cores of monodisperse Stöber particles. A continuous titania shell was obtained via this method. In comparison with other research works in this field [18, 19] a more facile setup of preparing core-shell particles was used here, by mixing the titania precursor with the silica stock in a glass beaker instead of supplying the precursor into a reactor. However, gradual addition of the precursor was also studied. Additionally, photocatalytic activity was tested via the degradation of an aqueous methylene blue solution and also of NO_x in air. The degradation of methylene blue reflects the self cleaning properties of the composite materials. The degradation of NO_x represents their capability to degrade air pollutants and remarks their potential for the development of construction materials with environmentally beneficial properties.

2 Experimental

The spherical silica cores were synthesized by hydrolysing tetraethylorthosilicate (TEOS, Wacker silicones) in a solution of ethanol, ammonia and distilled water under continuous stirring at room temperature (20 °C) (Table 1). This method is well known as the “Stöber” procedure [20].

Table 1: Amounts of reactants used to prepare silica particles of 435 nm diameter

TEOS [ml]	Ethanol (99.9 Vol.-%) [ml]	Ammonia (29 wt. -%) [ml]	Water [ml]
44	1000	93	15

After 24 hours the precipitate was repeatedly centrifuged and washed with ethanol. In a glass beaker the washed precipitate was immediately redispersed in 270 ml of an ethanol/water mixture with a water content of 1 mol/L. To coat the silica particles with titania, 65 g of a solution of tetrapropylorthotitantate (TPOT) in ethanol with a concentration of 15 wt.-% were introduced to the silica sol under continuous stirring. The TPOT-solution was gradually supplied with a feed rate of 0.5 ml/min to obtain sample A and added all at once to obtain sample B. The preparation was stirred for 24 hours at room temperature (20 °C) and then centrifuged and washed with ethanol until the supernatant was clear. The coated particles were then dried at 40 °C and calcined at 650 °C.

3 Results and Discussion

Scanning and transmission electron microscopy

To characterize the morphology of the coated and uncoated particles SEM and TEM analysis were performed. Fig. 1 shows uncoated silica particles, which are spherical and have a smooth surface.

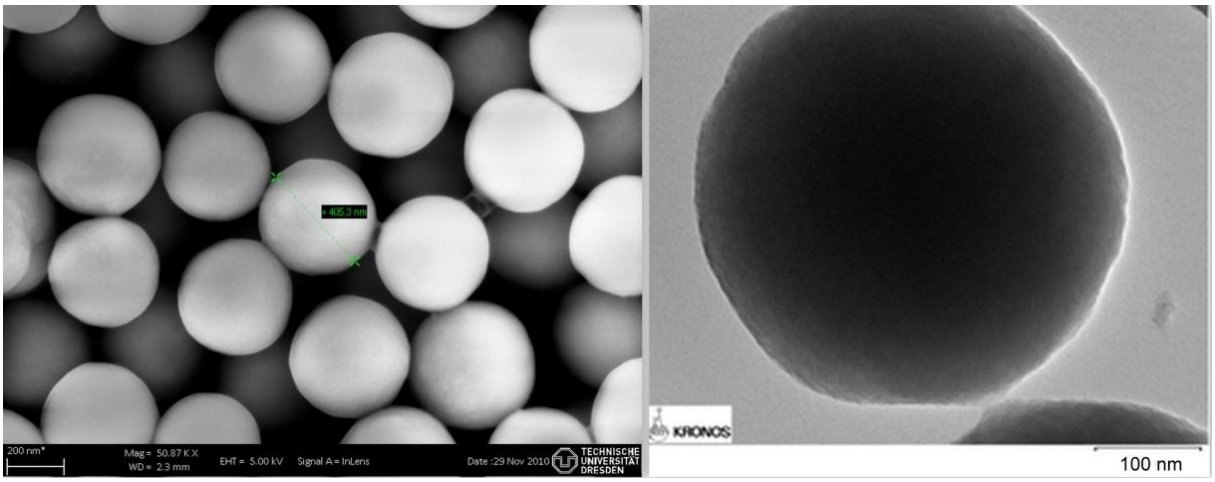

Figure 1: Uncoated silica particles. (Left: SEM-picture, right TEM picture).

In contrast to the uncoated ones a textured surface was observed for the coated particles (Fig. 2). The left micrograph in Fig. 2 was obtained on a sample prepared with a gold coating to enhance electric conductivity.

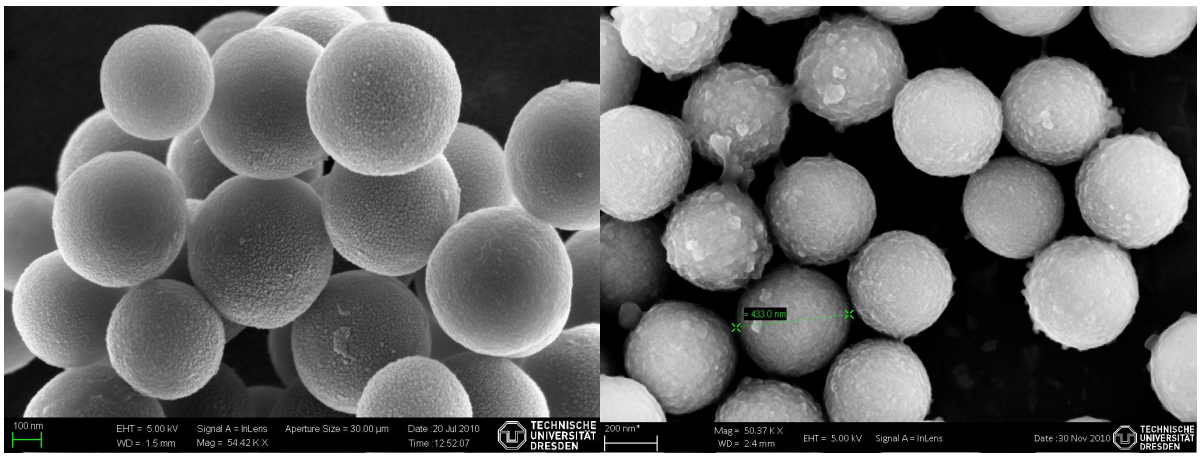

Figure 2: SEM image of coated particles. Left: sample A (with Au); Right: sample B (without Au).

In spite of the gold coating, the smoother coating of the particles generated with the slower field rate can be easily distinguished from the rougher coating of the particles, yielded when adding the precursor at once.

The analysis with the TEM allowed a closer look at the texture of the shell (Fig. 3). In the right picture of Fig. 3 a cristalline titania shell (sample A) can be observed on the particles in contrast to the uncoated particles in the left picture.The crystallinity of the shell was achieved by calcination at 650°C.

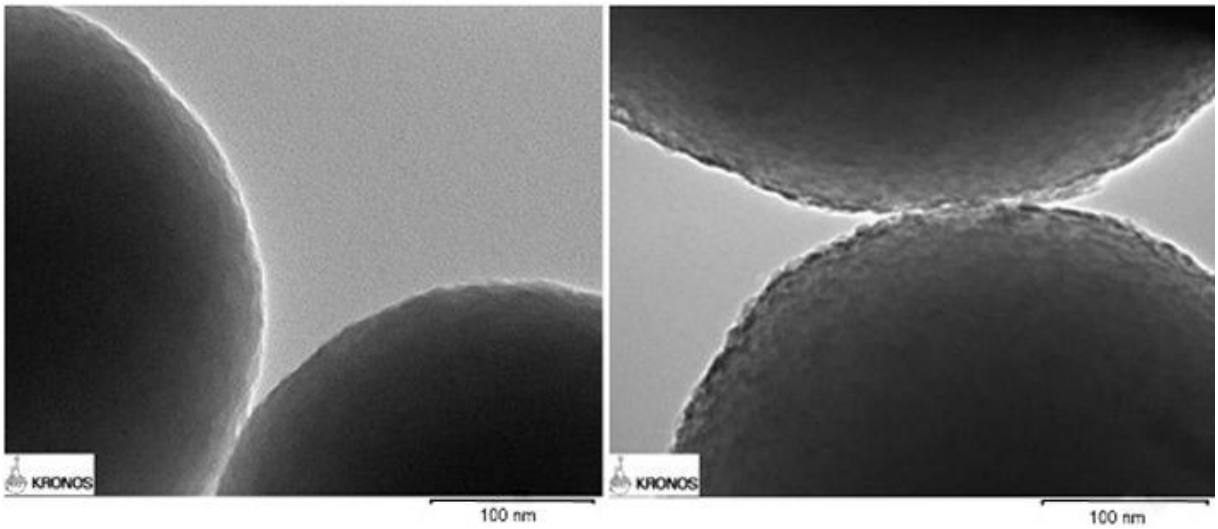

Figure 3: Left: uncoated particle; Right: coated particles (Sample A)

BET measurements

The water content and the feed rate are important factors, which can lead to secondary nucleation of the titania precursor. A slower feed rate leads to a lower concentration of the precursor in the silica sol and therefore to lower concentrations of titania monomers in the solution. It is more likely that titania monomers then bind to the core particles instead of forming individual titania particles which agglomerate and loosely precipitate on the silica to give a rough surface. This on the other hand causes a higher specific surface area as a more structured surface is obtained. BET values were analyzed, which are in agreement with the postulation given here. BET of sample A prepared with lower feed rate was 8.5 m²/g, BET of sample B was 25 m²/g.

Zeta potential measurements

Electro-acoustic zeta potential measurements showed a shift of the isoelectric point (IEP) towards higher pH values for the core-shell particles. According to the zeta potential measurements, pure silica had an IEP of 3.9, pure titania of 5.8 and the core-shell particles had IEP's of 5.8 (sample A) and 5.2 (sample B), see Fig. 4. Due to the fast addition of TPOT during the preparation of sample B, it is possible that the surface of the particles was not completely covered by titania. We suspect that the IEP of that sample was therefore between those of SiO_2 and TiO_2.

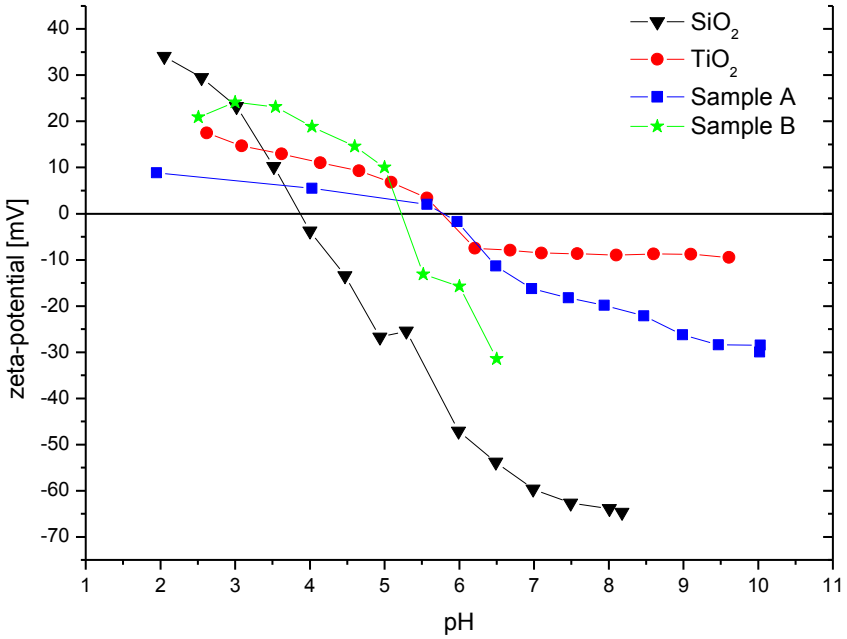

Figure 4 Profiles of the zeta potential with pH dependency of SiO_2, TiO_2 and the core-shell samples A and B.

X-ray fluorescence analysis

A quantitative analysis was performed via X-ray fluorescence analysis (XRF) to identify the quantity of titania in the entire sample. According to that, sample A consisted of 4 wt.-% TiO_2 and sample B consisted of 5 wt.- % TiO_2. During the synthesis an excess amount of TPOT was added, as loss of titania particles during the washing steps was expected as well as that not all particles bind to the core surface. In case of complete conversion to the oxides the amounts of titania and silica precursors used here equate to 80 wt.-% silica and 20 wt.-% titania.

Photocatalytic activity

For the evaluation of the photocatalytic activity of the samples the degradation of an aqueous methylene blue (MB) solution was examined. For this purpose an apparatus designed after DIN 52980 was used [21]. 30 mg of the sample sedimented in 40 ml of a 10 µmol/L MB-solution. The solutions were kept in the dark for two hours after which the samples were irradiated with UV-A light having an intensity of about 1.7 mW/cm² for another 18 hours. Illumination was provided by two 20 W UV-lamps (Philips Cleo).

The relative concentrations as functions of the irradiation time for sample A and B, calcined at 650°C are shown in Fig. 5. Both samples show similar degradation properties (rate constant $k = 46.9 \cdot 10^{-3} \cdot h^{-1}$). Fig. 6 shows exemplarily the discoloured MB-solution containing sample A in comparison with the sample containing the uncoated particles, after illumination with UV-light.

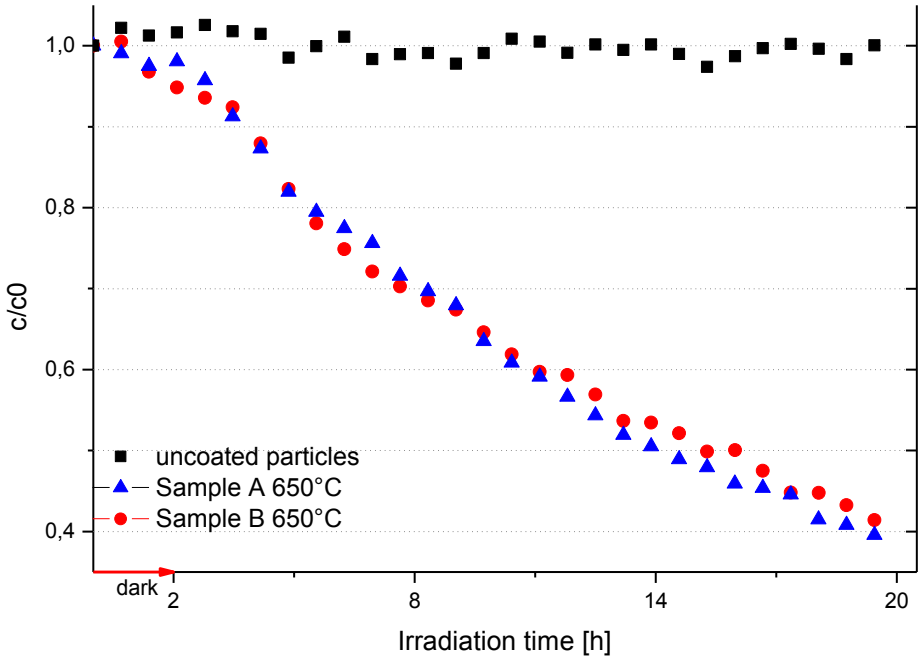

Figure 5: Comparison of MB degradation of samples A and B, calcined at 650°C.

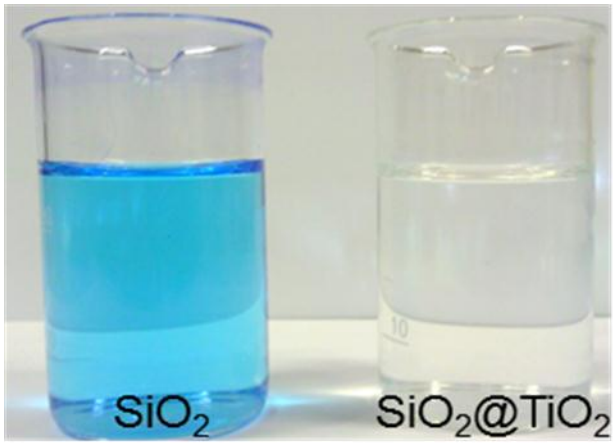

Figure 6: Methylene blue solutions containing uncoated particles (left) and sample A (right) after illumination with UV-light.

Additionally photonic efficiency was verified via degradation of NO-gas, based on ISO 22197-1 [22, 23]. For this purpose, a NO-gas stream with a concentration of about 1 ppm overflew a definite surface area covered by the core-shell samples (see Fig 7). Prior to the measurements, the samples were pre-exposed to UV-A light of 1 mW/cm² intensity over a time period of five hours. This ensured that pollutants, which were already on the sample, were degraded. NO degradation in the dark was analysed for one hour and under UV-light (1 mW/cm²) for another 5 hours. Exemplarily, the result of sample A is shown in Fig. 8. Photonic efficiencies were calculated according to Kandiel et al. [24]. In this case photonic efficiency was defined as the ratio of the NO degradation rate and the incident photon flux, for a mean irradiation wavelength of 350 nm. The photonic efficiency of sample A was 0.35 %, that of sample B 0.39 %. In comparison, the photonic efficiency of industrial P25 nano titania powder (Evonic), measured under the same conditions, was 0.50 %. In contrast, uncoated particles showed for this case negligible photonic efficiency of 0.02 %.

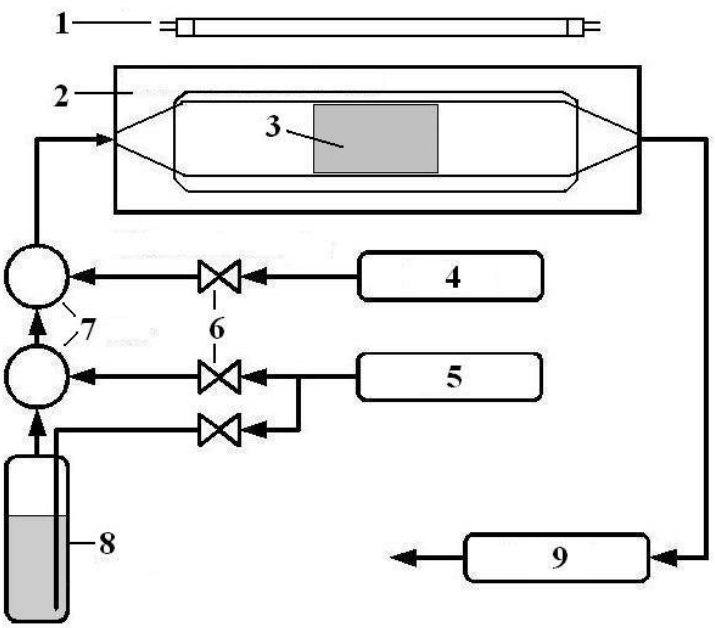

1 light source;
2 optical window;
3 test specimen;
4 gas containing the pollutant;
5 purified air;
6 mass-flow controllers;
7 gas mixers;
8 humidifier;
9 analyzer for pollutants

Figure 7: Schematic of the setup for analysis of NO degradation based on ISO 22197- 1 [22].

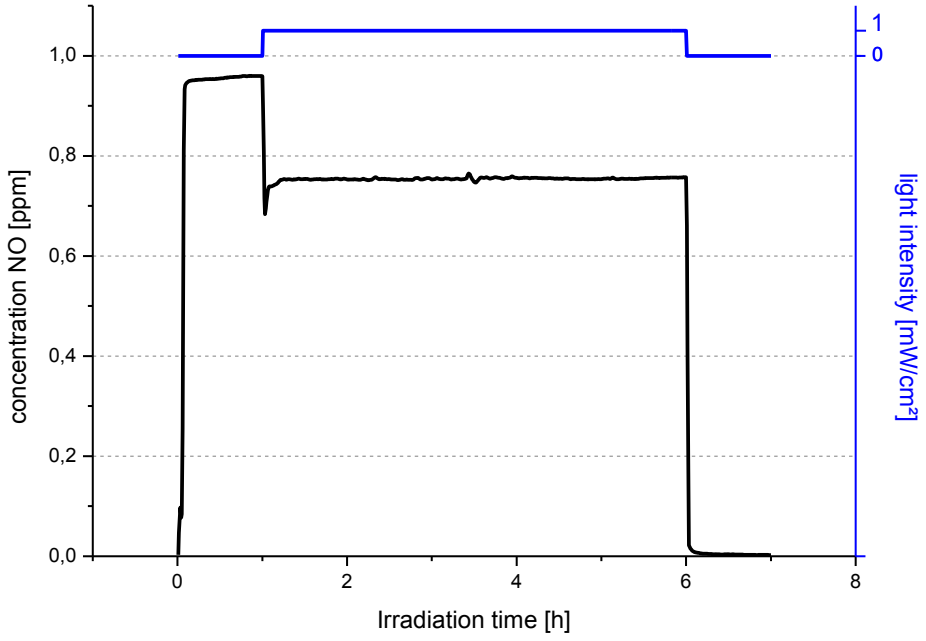

Figure 8: Profile of the NO degradation by sample A with the irradiation time.

4 Conclusions

Continuous titania shells in nanoscaled dimensions were successfully grown on silica particles prepared via the sol-gel method. A comparative study between two samples was performed, one prepared by gradual addition of the titania precursor and one by adding the precursor all at once. Differences in the surface morphology were evident, as characterized via SEM and TEM measurements. Sample A consisted of a smooth surface morphology, whereas particles of sample B were textured roughly. Interestingly, the feed rate did not affect the quantity of adsorbed titania significantly and therefore also not the photocatalytic activity.

TiO_2 quantities of just 4 wt. -% (sample A) and 5 wt.-% (sample B) were found. Photonic efficiencies were close to that of P25 (Evonik), which is frequently used as a benchmark in

photocatalysis and is worldwide applied for various photocatalytic products. The prepared core-shell samples are therefore promising photocatalysts, as the total amount of titania is very low. Further studies shall optimize this kind of composite material to make it applicable for different kind of photocatalytically modified products, such as mortar, concrete or paints.

5 Acknowledgements

The work is part of the project “HelioClean”. The authors greatly acknowledge the financial support of the German Bundesministerium für Bildung und Forschung (BMBF) in the program NanoTecture. We would like to thank KRONOS International, Inc. (Leverkusen) for performing the TEM measurements and Markus Günther at the Technical University of Dresden for performing the SEM measurements as well as Sylvia Heinemann at the University of Kassel for her assistance in the lab.

References

[1] D. Bahnemann: Current challenges in photocatalysis: Improved photocatalyst and appropriate photoreactor engineering. *Research on Chemical Intermediates* 2 (26), 207-220, 2000.

[2] W. Bahnemann, M. Muneer and M. M. Haque: Titanium dioxide-mediated photocatalysed degradation of few selected organic pollutants in aqueous suspensions. *Catalysis Today* 124 (3-4), 133-148, 2007.

[3] D. S. Bhatkhande, V. G. Pangarkar and A. A. C. M. Beenackers: Photocatalytic degradation for environmental applications - a review. *Journal of Chemical Technology and Biotechnology* 77 (1), 102-116, 2002.

[4] S. Devahasdin, C. Fan, K. Y. Li and D. H. Chen: TiO_2 photocatalytic oxidation of nitric oxide: transient behavior and reaction kinetics. *Journal of Photochemistry and Photobiology: A-Chemistry* 156 (1-3), 161-170, 2003.

[5] R. Benedix, F. Dehn, J. Quaas and M. Orgass: Application of Titanium Dioxide Photocatalysis to Create Self-Cleaning Building Materials. *Lacer* 157-168, 2000.

[6] M. Hunger, G. Hüsken and J. Brouwers: Photocatalysis applied to concrete products. *Materials Science* 61 77 - 85, 2008.

[7] A. Beeldens: An environmental friendly solution for air purification and self-cleaning effect: the application of TiO_2 as photocatalyst in concrete. *Proc. Transport Research Arena Europe, Gothenburg,* 2006.

[8] J. Auvinen and L. Wirtanen: The influence of photocatalytic interior paints on indoor air quality. *Atmospheric Environment* 42 (18), 4101-4112, 2008.

[9] A. Fujishima, K. Hashimoto and T. Watanabe: TiO_2 Photocatalysis - Fundamentals and Applications, 1999.

[10] K. Guan: Pelationship between photocatalytic activity, hydrophilicity and self-cleaning effect of TiO_2/SiO_2 films. *Surface & Coatings Technology* 191 155-160, 2005.

[11] M. Kaneko and I. Okura: Photocatalysis: science and technology, XVI, 356 S., 2002.

[12] S. Kamaruddin and D. Stephan: The preparation of silica-titania core-shell particles and their impact as an alternative material to pure nano-titania photocatalysts. *Catalysis Today* 161 (1), 53-58, 2011.

[13] D. Stephan: Nanomaterialien im Bauwesen - Stand der Technik, Herstellung, Anwendung und Zukunftsperspektiven. *Thesis*, 2011.

[14] P. Wilhelm and D. Stephan: On-line tracking of the coating of nanoscaled silica with titania nanoparticles via zeta-potential measurements. *Journal of Colloid and Interface Science* 293 (1), 88-92, 2006.

[15] S. T. Hwang, G. R. Jheong, Y. S. Lee, S. B. Ko and Y. S. Byoun: Preparation and characterization of SiO_2/TiO_2 core/shell composite particles using TiO_2 nanoparticles via heterocoagulation in a water system. *Journal of Industrial and Engineering Chemistry* 10 (6), 927-935, 2004.

[16] F. Caruso: Hollow inorganic capsules via colloid-templated layer-by-layer electrostatic assembly. *Topics in Current Chemistry* 227, 145-168, 2003.

[17] F. Caruso:Colloids and Colloid Assemblies - Synthesis, Modification, Organization and Utilization of Colloid Particles, 2003.
[18] S. H. Lim, N. Phonthammachai, S. S. Pramana and T. J. White: Simple Route to Monodispersed Silica-Titania Core-Shell Photocatalysts. *Langmuir* 24 (12), 6226-6231, 2008.
[19] J. Ida, T. Yoshikawa, T. Matsuyama and H. Yamamoto: TiO_2 coating on silica particles by deposition of sol-gel-derived nanoparticles. *Advanced Powder Technology* 18 (3), 329-348, 2007.
[20] W. Stöber, A. Fink and E. Bohn: Controlled Growth of Monodisperse Silica Spheres in the Micron Size Range. *Journal of Colloid and Interface Science* 26, 62-69, 1968.
[21] DIN 52980 Photokatalytische Aktivität von Oberflächen - Bestimmung der photokatalytischen Aktivität im wässrigen Medium durch Abbau von Methylenblau. *Legal Rule or Regulation* DIN 52980, 2008.
[22] International Standard ISO 22197-1 Fine ceramis (advanced ceramics, advanced technical ceramics) - Test method for air-prification performance of semiconducting photocatalytic materials, Part 1 - Removal of nitric oxide. 2001.
[23] K. Amrhein and D. Stephan: Principles and test methods for the determination of the activity of photocatalytic materials and their application to modified building materials. *Photochemical & Photobiological Sciences* 10 (3), 338-342, 2011.
[24] T. A. Kandiel, R. Dillert, A. Feldhoff and D. W. Bahnemann: Direct Synthesis of Photocatalytically Active Rutile TiO_2 Nanorods Partly Decorated with Anatase Nanoparticles. *The Journal of Physical Chemistry C* 114 (11), 4909-4915, 2010.

Photocatalytic Building Materials and Methods of Measurement

Kai Amrhein[1], Dietmar Stephan[2]
1: Institute of Structural Engineering, Universität Kassel, Germany
2: Building Materials and Construction Chemistry, Technische Universität Berlin, Germany

The introduction describes the basic concept of photocatalysis and shows the problem of air pollution in inner cities. One way to reduce the pollutants is the usage of photocatalytic building materials on huge surfaces, like facades, roofs, roads, and public places. To verify the aircleaning effect of these different materials dependable methods to determine the photocatalytic activity are necessary. Some measurement methods shall be presented in the second chapter, including international standards measuring air cleaning effects and national standards determining self cleaning properties of photocatalytic materials. In the end some examples and measurements are shown and problems using standards with porous materials are shown.

Keywords: TiO_2, titanium dioxide, photocatalyst, photocatalytic building materials, NO degradation, air cleaning, self cleaning

1 Introduction

The photocatalytic effect of TiO_2 was discovered 40 years ago by Fujishima in Japan [1] which resulted in increasing research activities in Asia, specially in Japan since then. But the last years photocatalysis became more and more popular in Europe too. The most common photocatalyst is crystalline titanium dioxide, to specify more precisely nanoparticles in rutile and anatas modifikation. Titanium dioxide can be explained as semiconductor with a bandgap of about 3.0 to 3.2 eV [2]. This complies with the wavelength of UV irradiation that enables TiO_2 to excite an electron from the valence bond to the higher energetic conducting bond. Organic and inorganic molecules can be decomposed directly or indirectly by the activated electrons and holes on the surface of the titanium dioxide now. Therefore the presence of oxygen and water is necessary [3]. These both components can react to very reactive OH or oxygen radicals which degrade for example air pollutants like nitrogen oxides [4]. Because reactions take place on the surface of the photocatalyst, a high specific surface is essential. Therefore smaller particles with a high ratio of surface to volume show the best effects. After full degradation of nitric oxide and nitrogen dioxide which are harmful air pollutants, nitric acid is formed, which reacts with alkaline constituents of the building surface, until only nitrates like $Ca(NOO_3)_2$ are left. In contrast to harmful NO and NO_2 which ere emitted by cars and combustion engines in general, nitrates are water-soluble and harmless in occurring concentrations. Legal limits concluded by the EU are regularly exceeded in German cities [5].

The problem are pollutants, mainly air pollutants like nitrogen oxides and small organic molecules like formaldehyde, toluene etc. which put the population at risk. One possibility to decrease the concentration of them is to ban cars with a high emission of pollutants in the inner city where the problem is the highest. Another way to reduce air pollutants is the use of great unused areas in the city area for photocatalytic aircleaning. Modified window glass that cleans itself and the air is already known. The next step is to use roads and parking areas. Research takes place in the modification of concrete road surfaces, paving stones, roof tiles and facade paintings [4, 6] .

But another problem results from the development of photocatalytically modified building materials. Dependable test methods to verify their activity are necessary because different

materials can hardly be compared with each other. Therefore some methods of measurement should be introduced in the next section.

2 Methods of Photocatalytic Measurements

Overview of some national and international standards on photocatalysis

A variety of products is already developed like eyeglasses, mirrors or glazed ceramic tiles with transparent TiO_2 coatings with a thickness of just a few nanometres. More and more construction materials with photocatalytic properties are developed. The modification of building materials like roof tiles, facade paints and concrete leads to some new properties like high porosities and higher pH values with cementitious materials. National and international standards are under development but most do not regard typical properties of different building materials like porosity but work fine for plain coated samples. An exception is the Italian UNI standard, specially created for cementitious systems.

Another effect of titanium dioxide which is prominent during irradiation with UV light is the superhydropilic property of the surface. This effect decreases the contact angle and spreads water, resulting in surfaces which are easy to clean [2]. Especially on flad surfaces like tiles or window glasses this so called self cleaning is successfully in service.

All methods and standards depend on the same principle. They all monitor the decomposition of various kinds of model pollutants. These may be gaseous like nitric oxide and toluene, liquid or dissolved in water like methylene blue or applied on the samples surface as solid film like rhodamine B or stearic acid. Table 1 shows an overview of existing standards as well as standards in concept phase.

Table 1: This table shows the different standards for proving photocatalytic activity of different kinds of modified materials, national and international standards are considered, some are still drafts (^{D}).

Measurement method	National / international standard	
Nitric oxide	JIS R1701-1 / ISO 22197-1 / BS ISO 22197-1	Gas
Acetaldehyde	JIS R1701-2 / ISO 22197-2 / BS ISO 22197-2	Gas
Toluene	JIS R1701-3 / ISO 22197-3 / BS ISO 22197-3	Gas
Formaldehyde	JIS R1701-4 / ISO/DIS 22197-4^D	Gas
Methylmercaptane	JIS R1701-5 / ISO/DIS 22197-5^D	Gas
NO / NO_2	UNI 11247	Gas
BTEX	UNI 11238	Gas
NO_x	XP B44-011	Gas
VOC / odour	XP B44-013	Gas
Methylene blue	DIN 52980 / ISO 10678 / BS ISO 10678	Dissolved in water
Rhodamine B	UNI 11259	Solid coating
Organic pollutant mixture	DIN EN 1096-5^D	Solid coating
Methyl stearate	Intended	Solid coating
Water contact angle	ISO 27448 / BS ISO 27448	Solid coating
Antimicrobial	ISO 27447	
Antifungal	ISO/DIS 13125^D	

International standards for gaseous air pollutants

The first standards to determine photocatalytic properties were established in Japan, were the research activities started. These are the JIS R 1701-1 to JIS R 1701-5, all standards for different degradation measurements in the gas phase. These were adapted for first international

standards. These are ISO 22197-1[7], ISO 22197-2 [8] and ISO 22197-3 [9]. Two further standards are still in concept status. These are ISO/DIS 22197-4 [10] and ISO/DIS 22197-5 [11]. The three valid standards are also adopted in Great Britain as national standards BS ISO 22197-1 to BS ISO 22197-3.

All these measurement methods, developed for ceramic materials, use gaseous pollutants and special flow through photo reactors with laminar flow shown in Figure 1. The sample has a surface of 5·10 cm² with a 5 mm thick channel for the gas flow above. Relativ humidity is set to 50 % and set by dividing the airflow into one dry flow and one flow humidified by a washing bottle. The concentration of the different pollutants is set to a constant value too. The active sample inside the photo reactor is irradiated through a quartz or borosilicate glas window with UVA light of 10 W/m². The first international standard, ISO 22197-1, uses synthetic air mixed with 1 ppm nitric oxide as inorganic pollutant and an air flow of 3.0 l/min [7]. The next two standards use acetaldehyde and toluene as widespread organic air pollutants. ISO 22197-4 and ISO 22197-5 which are still in concept phase track the decomposition of formaldehyde and methylmercaptan to determine the photocatalytic activity.

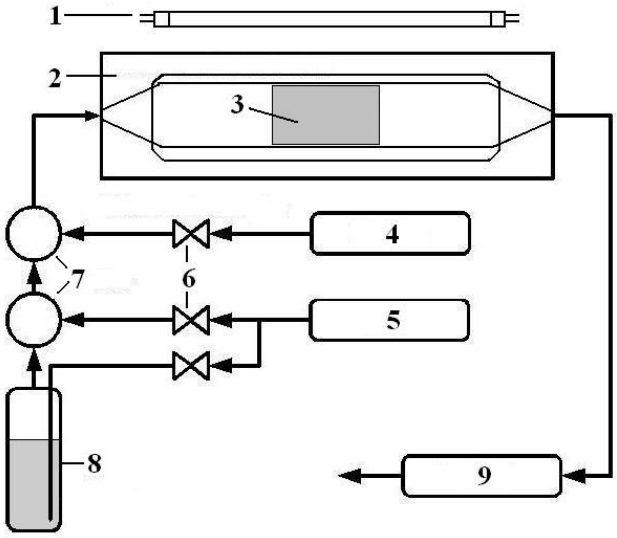

Figure 1: diagram of the assembly for measuring the photocatalytic decomposition of nitric oxide containing the following parts: UVA source (1), photo reactor (2), specimen (3), air pollutant in gas cylinder (4), synthetic air (5), mass flow controller (6), mixing chamber (7), humidifier (8) and NO analyser (9).

National standards for decomposing air pollutants

Besides Japanese and international standards there are some more national standards for determining the activity of photocatalytically modified materials to clean the air. As described above, Great Britain has adopted three valid ISO standards for degrading NO, acetaldehyde and toluene. France also has two national standards, XP B44-011 for decomposing nitrogen oxide mixtures (NO_x) [12] and XP B44-013 for decomposing volatile organic compounds and odours in closed rooms [13].

Italy has developed their standards for photocatalytic measurements specially for cementitious materials. Two of them use air pollutants in a bigger photo reactor than in ISO standards described above and more turbulent flow inside. UNI 11238 [14] uses a BTEX mixture as organic model. This is an acronym for a mixture of benzene, toluene, ethylbenzene and xylenes [15], which are some of the harmfull volatile organic compounds (VOC) that can be found in petrol for example.

UNI 11247 [16] is the second Italian standard for cementitious photocatalysts and uses a mixture of NO/NO_2 as pollutant which is decomposed in a photo reactor with turbulent flow. The

mixture consists of 0.4 ppm NO and 0.15 ppm NO_2 which are decomposed parallel by UVA irradiation with an intensity of 20 W/m².

Standards for decomposing organic dyes and self cleaning

The last of the three Italian standards for the determination of photocatalytical properties is the UNI 11259 [17]. The pollutant here is not gaseous but a solid coating on the surface of a cementitious specimen. The degradation of the red organic dye rhodamine B is visible as decrease of the color intensity and measured by a reflexion photometer. The big disadvantage of this method is, that it does not produce quantitative results but only qualitative information if the material is active or not. In contrast to the methods using gas as indicator for the activity, this method determines the ability of self cleaning.

Another way to show the self cleaning capability of materials is the only valid German standard DIN 52980 [18], which describes the decomposition of methylene blue dissolved in water by submerged material samples. The specimen is irradiated by UVA light with an intensity of 10 W/m² and the decrease in the methylene blue concentration is followed by a photometer and compared to a reference solution. This method is described in the international standard ISO 10678 [19] too.

A further standard for confirmation of the self cleaning effect is the ISO 27448 [20] which tracks the contact angle between water and a specimen that is coated with an organic hydrophobic substance. The coating causes a high contact angle of the droplet. After different periods of UVA irradiation and partly degradation of the organic material, the contact angle decreases and indicate the degradation of the organic film. This works for plane materials like coated glass etc. but results in complications with porous materials like most of the self cleaning standard procedures.

A draft of a German standard, DIN EN 1096-5, also tries to determine the effect of self cleaning behaviours by coating them with a mixture of organic pollutants and irradiating them after drying with UVA light and washing up the surface with water afterwards. Another method is to coat surfaces with another organic substance, methyl stearate, irradiating it and flushing it up with a defined amount of solvent and quantifying the remaining methyl stearat by gas chromatography.

Further standards

Other standards drafts as well as valid versions define how to measure the antimicrobial (ISO 27447 [21]) and antifungal (ISO/DIS 13125) effect of photocatalytic materials by decomposing defined bacteria and fungi strains under UVA irradiation, but should only be mentioned here, as well as standards for photocatalytic watercleaning (ISO 10676).

3 Applying different measurement methods to building materials

Some of the methods to measure different photocatalytic materials shall be explained and results and effects shall be shown in the following passages. For a better understanding the order will be analogue to the previous chapter. Some of the methods lead to problems when measuring building materials. These will be explained and the influence of factors like temperature and relative humidity to photocatalytic reactions will be illustrated.

Degradation of NO according to ISO 22197-1

ISO 22197-1 has turned out to be a good method to determine and compare the photocatalytic properties of modified materials. Therefore we built an assembly for measuring the degradation of nitric oxide which can be seen in Figure 2 on the left side. It works like described schematically in the diagram above Figure 1 and consists of the gas supply, the photo reactor and the analysator. On the right side of Figure 2 a graph of a NO degradation is shown. The

black line (NO) starts at about 0.9 ppm and decreases after turning on the irradiation after 1000 seconds. When turning off the UV light again, the concentration of NO flowing through the reactor rises again to the initial value. The graph shows the measured results of a modified mortar specimen Figure 3 containing titanium dioxide particles and a stable decomposing over a few hours.

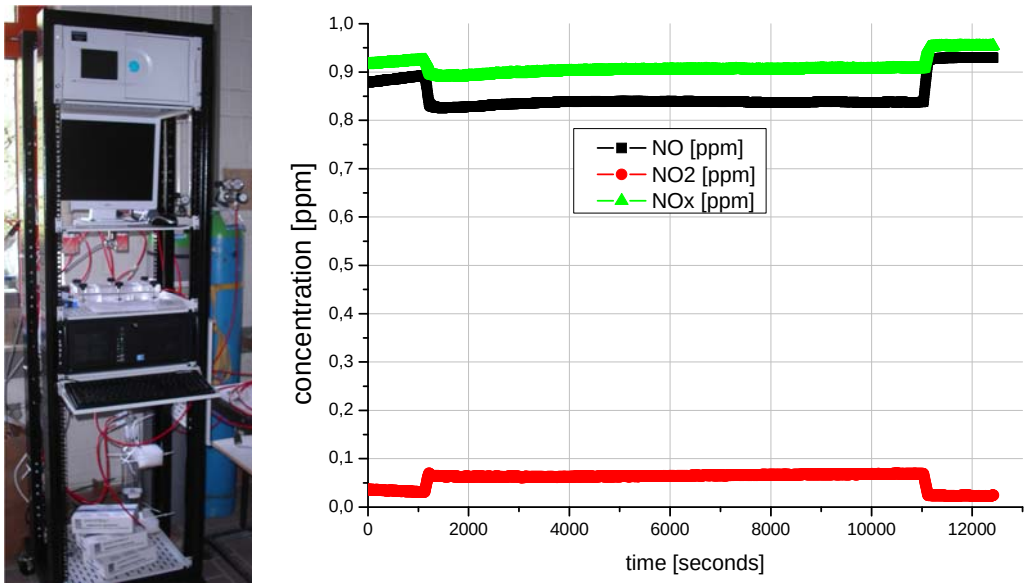

Figure 2: Assembly for measuring the degradation of nitric oxide by samples in a flow through reactor according to ISO 22197-1 and on the right side a graph of the degradation of nitric oxide (black line) by a modified mortar sample over a period of some hours. At the beginning without light and after approx. 1000 s with UV irradiation, which leads to a decrease of the pollutants concentration. After 11000 s the light was turned off again. Measurement according to ISO 22197-1.

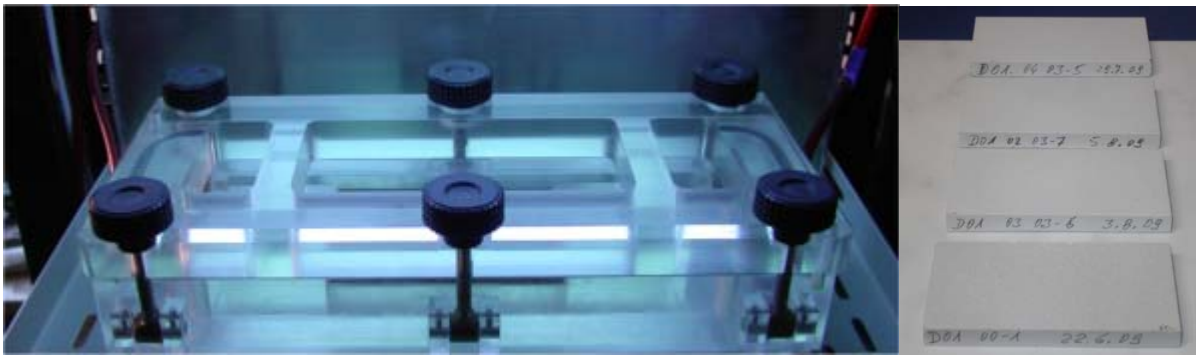

Figure 3: Photo reactor irradiated by UVA light on the left and photocatalytic mortar specimen on the right side.

Degradation of methylene blue according to DIN 52980

Samples measured according to DIN 52980 were thin films of facade paint, mortar samples, specimen out of roof tiles and coated glas. Except for the glas, measurements conforming to DIN standard could not be measured in most cases. Most samples were so porous, they adsorbed large amounts of the dye during the pretreatment in methylene blue solution with a higher concentration. After inserting them to the solution for measurement desorption occured and the concentration increased instead of decreasing like it is typical for photocatalytic degradation. Reducing the concentration of the dye solution for pretreatment to the normal concentration which is used during the test procedure avoided appreciable desorption phenomena during the measurement but now caused absorption as if no pretreatment was performed before. The only specimen with linear decrease in concentration were glas samples. Sorption phenomena predominate the changing of the concentration caused by photocatalytic

degradation which complicates adopting this standard to porous building materials. Roof tiles worked best out of the materials.

Degradation of rhodamine B according to UNI 11259

Thin film facade paint was coated with rhodamine B according to UNI 11259 as aqueos solution with a brush instead of dipcoating. A reflexion photometer was used to measure the color in the *L·a·b* color space [22] where *a* represents the intensity of red. The colour was measured after different times of UVA irradiation and is shown on the above half of Figure 5 on the right side for 25°C and 50 % relative humidity. Change of temperature and humidity influenced the degradation rate.

Figure 4: Specimen of facade painting coated with rhodamine B before irradiation with UVA light.

Influence of temperature and humidity on photocatalytic effects

This is illustrated in the four diagrams in Figure 5. The two diagrams on the top show the decrease in colour intensity of Rhodamin B coated thin film specimen of facade paint over 26 hours. Both show different temperature and humidity conditions. The two diagrams on the left side show behaviour at 50 % relative humidity and different temperatures. The other diagrams clarify that 50 % relative humidity stands for different absolute amounts of water in g/m³ at various temperatures. The right side of Figure 5 illustrates measurements at different temperatures and relative humidities but same absolute amounts of water in the air of about 10 g/m³. The left above graph suggests dependency to temperature at same relative humidity but the left graph shows identic decomposition rates at different temperatures and relative humidities. But a closer look shows that the absolute amount of water available is the same.

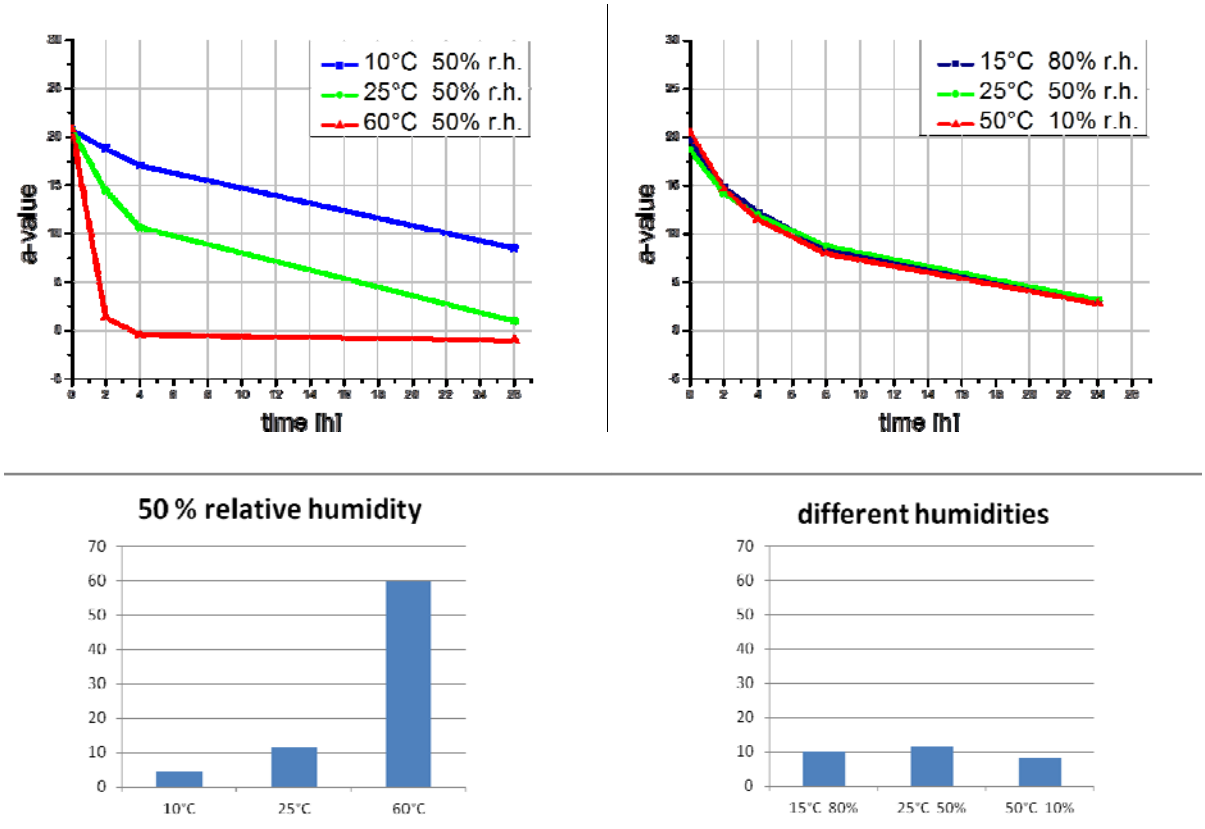

Figure 5: The two diagrams above show the decrease in colour intensity of rhodamine B coated thin film specimen of facade paint dependent to the irradiation time. The lower ones illustrate the total amount of water in the air at different temperatures in g/m³.

4 Conclusions

The development of more and more materials containing photocatalytic titanium dioxide including building materials increases the need of methods for measuring their activitiy to create possibilities to compare the materials to each other. Most standards are developed for ceramic materials without porosities and lead to difficulties measuring building materials. The mentioned Italian standards are specially designed for cementitious materials and therefore work. Although the decomposition of rhodamine B produces at best qualitative results about the material it can be used for building materials. Decomposing dissolved methylene blue however leads to some problems with thin film paints and the other materials tested, but this problems can be reduced by changing the pretreatment procedure. Measuring the photocatalytic decomposition of NO works well with different materials, when some time is given for equilibration before starting the UVA irradiation.

We thank the German Federal Ministry of Education and Research (BMBF) which funded the HelioClean project.

References

[1] Akira Fujishima and K. Honda: Electrochemical Photolysis of Water at a Semiconductor Electrode. Nature 238 (5358), 37-38, 1972.

[2] K. Hashimoto, H. Irie and A. Fujishima: Ti02 Photocatalysis: A Historical Overview and Future Prospects. Japanese Journal of Applied Physics 44 (12), 8269-8285, 2005.

[3] P. Wilhelm, C. Zetsch and D. Stephan: Titania coated silica nano-spheres as catalyst in the photodegradation of hydrocarbons. Progress in Colloid and Polymer Science 133 147–151, 2006.

[4] M. M. Ballari, Q. L. Yu and H. J. H. Brouwers: Experimental study of the NO and NO2 degradation by photocatalytically active concrete. Catalysis Today 161 175-180, 2011.

[5] Luftbelastungssituation 2010 - vorläufige Auswertung Report, 2011.

[6] J. Chen and C.-s. Poon: Photocatalytic construction and building materials: From fundamentals to applications. Building and Environment 44 1899 - 1906, 2009.

[7] ISO 22197-1:2007: Fine ceramics (advanced ceramics, advanced technical ceramics) - Test method for air-purification performance of semiconducting photocatalytic materials -- Part 1: Removal of nitric oxide.Legal Rule or Regulation ISO 22197-1, 2007.

[8] ISO 22197-2:2011: Fine ceramics (advanced ceramics, advanced technical ceramics) - Test method for air-purification performance of semiconducting photocatalytic materials - Part 2: Removal of acetaldehyde.Legal Rule or Regulation ISO 22197-2, 2011.

[9] ISO 22197-3:2011: Fine ceramics (advanced ceramics, advanced technical ceramics) - Test method for air-purification performance of semiconducting photocatalytic materials - Part 3: Removal of toluene.Legal Rule or Regulation ISO 22197-3, 2011.

[10] ISO/DIS 22197-4:2011: Fine ceramics (advanced ceramics, advanced technical ceramics) - Test method for air-purification performance of semiconducting photocatalytic materials - Part 4: Removal of formaldehyde.Legal Rule or Regulation ISO/DIS 22197-4, 2011.

[11] ISO/DIS 22197-5:2011: Fine ceramics (advanced ceramics, advanced technical ceramics) - Test method for air-purification performance of semiconducting photocatalytic materials - Part 5: Removal of methyl mercaptan.Legal Rule or Regulation ISO/DIS 22197-5, 2011.

[12] XP B44-011:2009: Photocatalysis - Test method for assessing photocatalytic materials with respect to NOx degradation - Tangential mode single pass process.Legal Rule or Regulation XP B44-011, 2009.

[13] XP B44-013:2009: Photocatalysis - Test and analysis method for determining the efficacy of photocatalytic systems for eliminating volatile organic compounds/odours in recirculating interior air - Confined chamber test.Legal Rule or Regulation XP B44-013, 2009.

[14] UNI 11238-1:2007: Determinazione dell'attività di degradazione catalitica di microinquinanti organici in aria - Parte 1: Materiali fotocatalitici cementizi per uso edile.Legal Rule or Regulation UNI 11238-1:2007, 2007.

[15] J. E. M. W.E. Wilson:Benzene, toluene, ethylbenzene, xylene.Book Section, 20, 1998.
[16] UNI 11247:2007: Determinazione dell'attività di degradazione di ossidi di azoto in aria da parte di materiali inorganici fotocatalitici. 2007.
[17] UNI 11259:2008: Determinazione dell'attività fotocatalitica di leganti idraulici - Metodo della rodammina. 2008.
[18] DIN 52980:2008-10: Photokatalytische Aktivität von Oberflächen - Bestimmung der photokatalytischen Aktivität durch Abbau von Methylenblau. 2008.
[19] ISO 10678:2010: Fine ceramics (advanced ceramics, advanced technical ceramics) - Determination of photocatalytic activity of surfaces in an aqueous medium by degradation of methylene blue.Legal Rule or Regulation ISO 10678, 2010.
[20] ISO 27448:2009: Fine ceramics (advanced ceramics, advanced technical ceramics) - Test method for self-cleaning performance of semiconducting photocatalytic materials - Measurement of water contact angle.Legal Rule or Regulation ISO 27448, 2009.
[21] ISO 27447:2009: Fine ceramics (advanced ceramics, advanced technical ceramics) - Test method for antibacterial activity of semiconducting photocatalytic materials.Legal Rule or Regulation ISO 27447, 2009.
[22] DIN 6174:2007-10: Farbmetrische Bestimmung von Farbmaßzahlen und Farbabständen im angenähert gleichförmigen CIELAB-Farbenraum. 2007.

Self-cleaning ultra-high performance concrete surfaces

Jeffrey Chen, Matthieu Horgnies
Lafarge Central Research, Saint Quentin Fallavier, France

Ultra-High Performance Concrete (UHPC) such as Ductal® offers an attractive mineral surface that is particularly valued in design elements, building facades, and other architectural applications. A technical challenge for these applications is how to keep the surface durably clean from the deposition of stains, micro-particles, and micro-organisms. Our research has demonstrated two different fabrication strategies to impart self-cleaning properties to a UHPC surface. The first approach, inspired by the Lotus effect found in plants, uses a microtextured UHPC surface that is post-treated with a silicone compound to create a superhydrophobic surface with water contact angles > 160° and contact angle hysteresis < 8°. These properties cause water drops to slide off the surface, carrying debris away. The second approach uses a thin photocatalytic coating on a smooth UHPC surface. Upon UV-irradiation, water drops spread completely on the superhydrophilic surface, thereby creating water films that flush debris away. Both of the above strategies open up exciting new avenues for self-cleaning UHPC surfaces.

Keywords: aesthetic, self-cleaning, Lotus effect, photocatalytic, surface functionalization

1 Introduction

The deposition of stains, micro-particles, and micro-organisms on ultra-high performance concrete (UHPC) leads to premature degradation of surface aesthetics. These phenomena can have particularly damaging consequences to architectural applications such as façades, where aesthetics have a major impact on the perception of a structure. To ensure a durably clean surface, it is most desirable to have a self-cleaning surface—that is, a surface that stays clean without the need for human intervention. There are myriad examples in Nature that can do this, such as certain plants leaves, bird feathers, and insect exoskeletons [1].

This paper outlines two different strategies that can impart self-cleaning properties to a UHPC surface. The first one mimics the superhydrophobic effect found in plants, whereby a microtextured and hydrophobic surface causes water drops to roll off the surface, while carrying particulate debris away. This phenomena is called the Lotus effect. A superhydrophobic surface is characterized by water contact angles that exceed approximately 150° [2,3]. Numerous synthetic routes to creating superhydrophobic surfaces have been developed over the past two decades [4-6].

The second strategy of imparting self-cleaning properties exploits the use of photocatalytic coatings [7-9] applied on a smooth UHPC substrate. After exposure to UV radiation, the water contact angles can reach extremely low values close to 0°, thereby creating a superhydrophilic surface. On these surfaces, drops of water spontaneously spread on the surface to create films of water that flush debris off inclined surfaces.

This paper demonstrates how a careful control of particle packing, mold-concrete interactions, and chemical functionalization can carry out the above strategies to create self-cleaning UHPC surfaces.

2 Materials and methods

Concrete mix-designs

Two mix-designs were prepared in order to compare the surface properties of an ordinary concrete (OC) and an ultra high performance concrete (UHPC). The OC samples were prepared by pouring a fresh mix (water/cement ratio, *w*/*c*, of 0.4) comprised of ordinary Portland cement (CEM I 52.5), limestone filler, sand (0–4 mm) and gravel (5–10 mm) into formwork

(15×12×1.5 cm) made of polyvinylchloride (PVC) or polydimethylsiloxane (PDMS). The UHPC samples were prepared by using a fresh mix (w/c = 0.26) comprised of Portland cement (CEM I 52.5), limestone filler, silica fume, fine sand, and superplasticizer. All the UHPC and OC samples were removed from their formworks after 20 hours. They were cured for 28 days under ambient conditions (20 °C, 50% relative humidity) before being coated and characterized.

Coatings

Two coatings were applied by spray-gun on UHPC surfaces: i) a hydrophobic coating based on a polysilane and ii) a photocatalytic coating using anatase titanium dioxide as a photocatalyst.

Surface characterization

The surfaces of concrete samples were characterized directly after demolding, as well as after being coated. The topography of the concrete samples were examined in a scanning electron microscope (SEM), using a high-resolution field-emission gun scanning electron microscope (FEG–SEM Quanta 400 from FEI Company) operating at an accelerating voltage of 15 keV. Images of the cross-sections were obtained in back scattered electron (BSE) mode after being impregnated and polished.

The roughness and microtexture of selected samples were studied by optical profilometry (Micromesure full-field 3D confocal profilometer) with a spot size of 2.0 µm, a working distance of 4.5 mm and a sensor equipped with a 350 µm light pen. The arithmetic mean of the profile deviations from the mean line (R_a) were measured, as well as the 3D topographical profile.

The composition of the surface was characterized with a Fourier Transform-Infrared (FTIR) spectrometer (Nicolet iS10 from Thermo Fisher Scientific Inc.). Attenuated Total Reflexion (ATR) mode was used to analyze the samples over an area of approximately 1 mm². The crystal used was made of diamond, and 32 scans were routinely recorded over the range 4000–650 cm^{-1} with a spectral resolution of 4 cm^{-1}.

The wetting properties of the functionalized surfaces were studied by using the sessile drop method with a Drop Shape Analysis DSA-100 from Kruss. This technique provides information on the static water contact angle (WCA). The drop volume of distilled water was 2.5 µl and the contact angle was measured after 5 s. The contact angle hysteresis (CAH) was calculated from the difference between the measured advancing and receding contact angles. For each sample, the value was determined by averaging the data obtained on 10 different locations on the surface. All the measurements were performed under 20°C and 50 % relative humidity.

3 Impact of particle packing and molding conditions on surface microstructure and wettability

SEM images of Figure 1 compare the surfaces as a function of mix-design (UHPC and OC) and of mold type (PVC and PDMS). As shown in Figure 1a, the OC/PDMS sample showed a micro-textured surface with rounded asperities, as well as large open pores. As shown in Figure 1b, the UHPC/PDMS surface showed a similar micro-textured surface with rounded asperities, but with a reduced open porosity. The UHPC/PVC induced a flat, smooth, and non-porous UHPC surface (as shown by Figure 1c). The only defects notable on the surface were due to the scratches on the PVC mold, which were subsequently transferred to the UHPC surface. The differences in morphology between the PDMS and PVC molded samples were due to the differences in textures of the molds themselves: the PDMS molds possessed an undulating surface (presumably due to wear), while the PVC mold possessed a flat surface. Both of these textures were accurately replicated in the UHPC surface, by a mechanism described below.

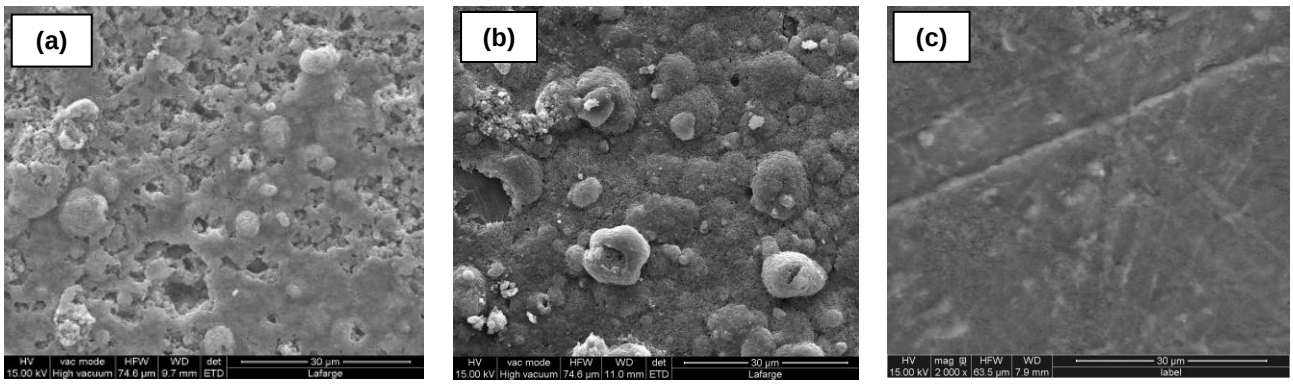

Figure 1: SEM images of the concrete surfaces: (a) OC/PDMS; (b) UHPC/PDMS; (c) UHPC/PVC.

Cross-sections of UHPC samples cast in PVC and PDMS molds were also characterized by SEM in BSE mode. Figure 2a illustrates the undulating surface as seen in Figure 1, giving a closer view of the rounded asperities that have a height of 5 μm and an approximately regular spacing of 30 μm. Figure 2b shows that within these rounded asperities, there is a high concentration of ultrafine particles, mostly silica fume, with particle sizes less than several micrometers. In contrast, the UHPC/PVC sample (in Figure 2c) showed a flat, smooth surface, with a considerably lower concentration of silica fume at the surface. Optical profilometry results confirmed these observations by giving R_a values of 2.0 μm (± 0.3) and 0.8 μm (± 0.2) for UHPC cast with PDMS and PVC mold, respectively.

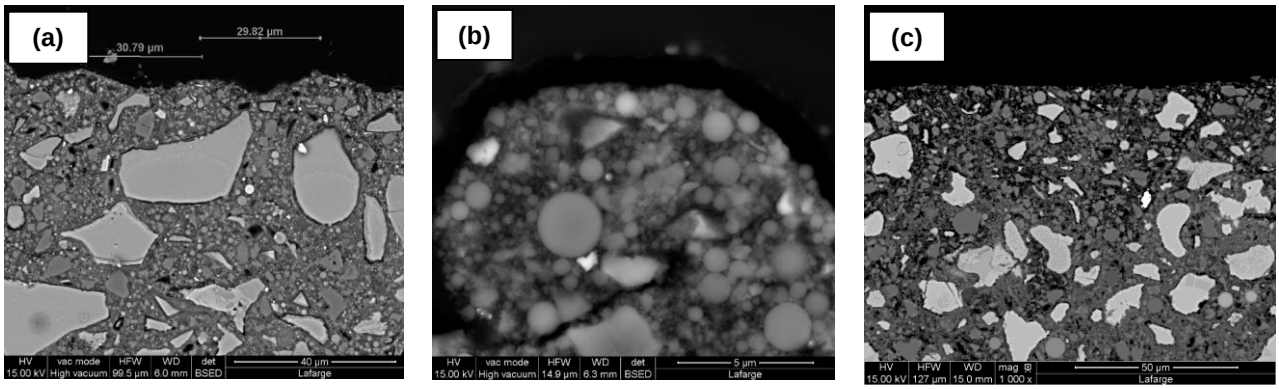

Figure 2: SEM images in BSE mode of: (a, b) UHPC/PDMS cross-sections with micro-asperities enriched in silica fume particles; (c) UHPC/PVC cross-section that shows a flat and smooth surface.

The different surface morphologies in Figures 1 and 2 between the OC and UHPC mixes can be explained in terms of differences in particle packing in the cementitious matrix. It is well-known, for example, that the particle packing at a hard surface is decreased due to the restricted motion of the particles adjacent to the surface [10]. The porosity of this perturbed interfacial zone will subsequently be higher than in the bulk. For monodispersed particulate systems, the thickness of this zone is roughly equal to half the diameter of the grain [10]. Thus, for the OC system, which lacks ultrafines and is characterized by a high *w*/*c*, we see a relatively porous surface in Figure 1a. This high porosity is amplified in the PDMS mold, since the OC sample lacks the small particles that can fit in the 5-μm sized rounded asperities. In contrast to the OC, the UHPC system, which possesses abundant ultrafine particles in the mix, has a dense surface in Figures 1b and 1c due to the filling of the perturbed surface volume with ultrafine particles. Moreover, fine surface details such as the 5-μm asperities in the PDMS mold and the surface scratches in the PVC mold can be accurately replicated by UHPC mixes.

The surface chemistry and properties of the UHPC surfaces were characterized by FTIR and WCA measurements. As shown in Table 1, portlandite was strongly detected by FTIR (at 3640 cm^{-1}) in the UHPC/PVC sample. Other strong FTIR bands were assigned to the presence of $CaCO_3$ (at 1410, 870 and 710 cm^{-1}) and silicates/silica (at 1080 cm^{-1}). The WCA measurements performed on the UHPC/PVC surface showed moderately hydrophilic values of 42° (±3). Concerning the UHPC/PDMS surface, FTIR showed no portlandite, but revealed small peaks assigned to Si-O-CH_3 (at 2970, 1260 and 780 cm^{-1}), which can be attributed to the transfer of silicone oligomers. These silicone residues were not homogenously transferred across the entire surface (as indicated by the presence of other strong FTIR bands assigned to $CaCO_3$ and silicates/silica). However, the transfer was sufficient to induce a strongly hydrophobic surface with WCA value of 144° (± 3) and contact angle hysteresis of 37°. In contrast, the WCA measurements performed on the OC/PDMS sample showed hydrophilic values (15° ± 4), presumably due to imbibition of the drop by the porous OC substrate.

Table 1: FTIR bands and water contact angles measured on UHPC surfaces cast in PVC or PDMS molds.

Wavelength and assignment of FTIR bands (cm^{-1})	**UHPC/PVC**	**UHPC/PDMS**
3640: O-H, $Ca(OH)_2$	+++	No
2950–2850: CH_3/CH_2, methyl units	No	+
1450: CH_3/CH_2, methyl units	No	No
1410, 872, 710: C=O, $CaCO_3$	+++	+++
1270, 780: Si-CH_3, Si-O-CH_3	No	+
1100–970: Si-O, silicates, C–S–H	++	+++
Water contact angle (°)	42	144

The above SEM observations, FTIR analyses, and WCA measurements clearly indicate that the chemistry and the microstructure of the UHPC surface are influenced by the nature and texture of the mold. Figure 3 summarizes the mechanisms involved in these processes. Figure 3a compares the interface between the fresh concrete mix and the mold, while Figure 3b details the different microstructures of hardened UHPC surfaces obtained after demolding. Due to the prevalence of portlandite crystals at the surface of the UHPC/PVC mix (as detected by FT-IR and SEM), it is believed that a film of water was present between the hydrophilic PVC mold and the fresh UHPC mix. This water film would allow the precipitation of portlandite via a through-solution mechanism, as is known to occur during the hydration of cement [11]. The presence of portlandite and calcium carbonate (formed by carbonation) on the UHPC/PVC surface would also explain the hydrophilic nature of this surface [12]. In contrast to the UHPC/PVC interface, a film of water would not be expected between the hydrophobic PDMS mold and the fresh UHPC mix. This absence of a water film would suppress the formation of portlandite at the surface, which is consistent with the FT-IR and SEM results. The UHPC/PDMS surface was furthermore altered and made more hydrophobic by the transfer of siloxane residues from the PDMS mold to the UHPC surface as noted above.

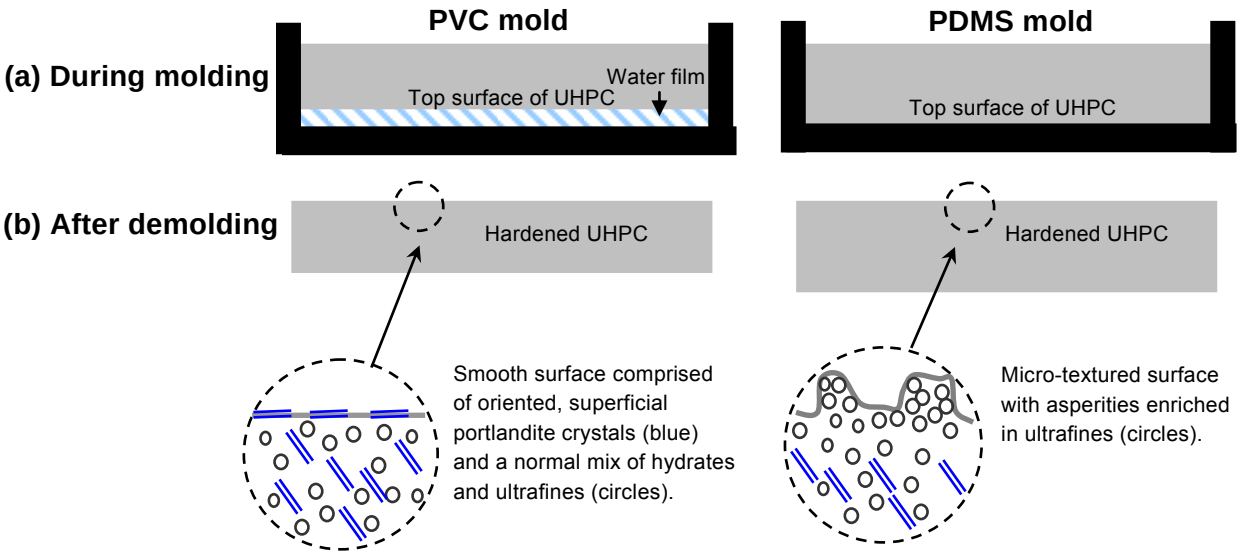

Figure 3: Influence of mold type (a) on the nature of the UHPC/mold interface during molding and (b) on the surface microstructure after demolding.

4 Self-cleaning properties obtained after chemical functionalization

Super-hydrophobicity after using micro-pillared mold and hydrophobic coating

In order to enhance the superhydrophobic properties of UHPC, a homogeneous micro-pillared PDMS mold (Ra: 4 µm, pillars of 10 µm high, spaced by 100 µm) was specifically manufactured. A UHPC mix was cast in this mold, and subsequently post-treated with a hydrophobic siloxane coating 28 days after demolding. The resulting surface showed a WCA value of 160° (as shown by Figure 4a) and a contact angle hysteresis (CAH) of 8°. These properties induced a dramatic water-repellant effect, whereby water drops would instantaneously slide off a slightly inclined surface. This superhydrophobic effect is the first reported instance for a concrete surface with an integrated microtexture. The high contact WCA and low CAH can be interpreted by the Cassie and Baxter mechanism of superhydrophobicity, whereby drops of water sit on solid asperities and over pockets of air. For comparison, the WCA values measured on UHPC/PVC sample coated by the same hydrophobic coating noted above only reached a value of 130°.

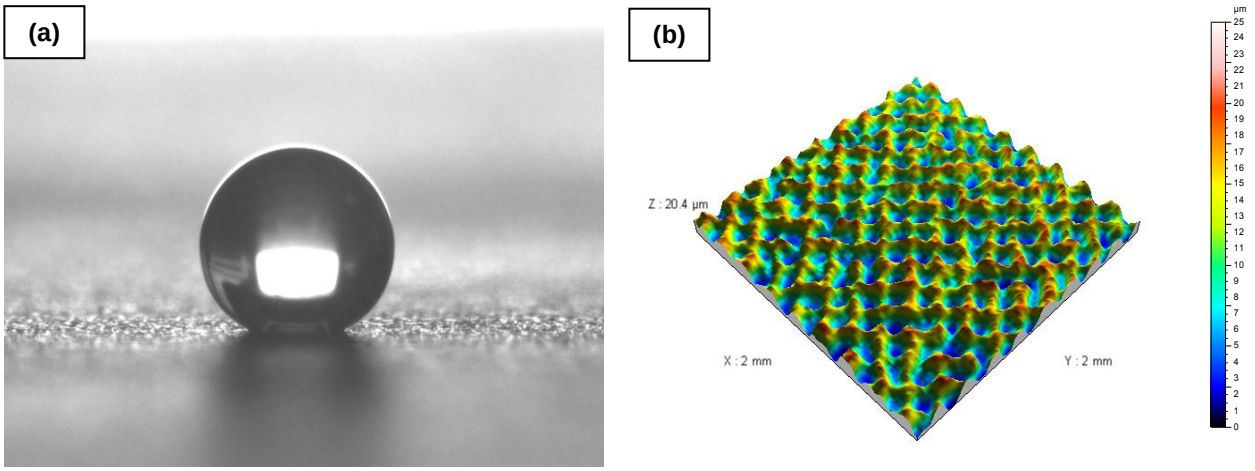

Figure 4: Image of a drop of water (a) deposited on a microtextured UHPC surface (b).

Characterization of the hardened UHPC by optical profilometry confirmed that a microtexture can be accurately transferred from a micro-pillared PDMS mold to the UHPC surface (Figure

4b). This ability to replicate fine surface features is due to the abundance of ultrafines in the UHPC mix. The integrated concrete microtexture shown here is believed to be mechanically more robust compared to superhydrophobic, microtextured coatings, which suffer from weak abrasion resistance and thus poor durability. Further research is ongoing in this area.

Super-hydrophilicity obtained through photocatalytic coatings

To exploit the smooth surface obtained by casting a UHPC mix in a PVC mold, we applied a photocatalytic coating 28 days after demolding. A spray-gun application enabled a very smooth coating (R_a of 0.5 µm ± 0.2). Table 2 compares the different WCA measurements performed on three UHPC/PVC samples: i) without coating, ii) with coating, but not exposed to UV, and iii) with coating and exposure to UV for 1 hr (wavelength of 365 nm). The results show that UV irradiation of the photocatalytic coating can indeed induce superhydrophilic properties, causing drops of water to spread spontaneously over the surface.

Table 2: Water contact angles and images of water drops on UHPC surfaces without a coating, with a photocatalytic coating but no UV irradiation, and with a photocatalytic coating with UV irradiation.

	UHPC/PVC sample without coating	**UHPC/PVC sample + photocatalytic coating, without UV exposure**	**UHPC/PVC sample + photocatalytic coating, after 1h of UV exposure**
Image recorded just after deposition			
Image recorded 2s after deposition			
WCA measured 5s after deposition	42	16	0

As a test of the self-cleaning mechanism, UHPC samples covered with a photocatalytic coating were stained with various solutions (e.g., wine, coffee, lemon juice, methylene blue, and oil). As shown in Figure 5, after 10 days of exposure to sun and light rain, all of the stains were eliminated from the surface. These results confirm the interest of using photocatalytic coatings on UHPC to obtain self-cleaning facades.

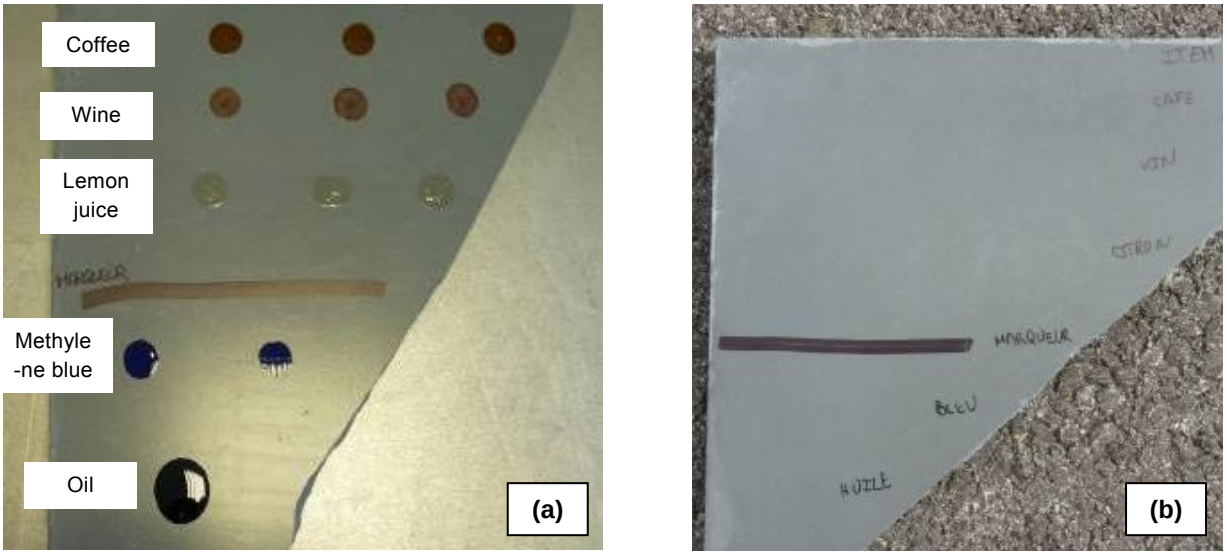

Figure 5: UHPC (PVC) sample covered by a photocatalytic coating: (a) after staining; (b) after 10 days of external weathering (sun + rain exposure).

5 Conclusions

Self-cleaning UHPC surfaces can be designed through a deliberate manipulation of particle packing, mold-concrete interactions, and chemical functionalization. Two distinct strategies were demonstrated. The first strategy produced a superhydrophobic surface (water contact angle, 160º) through the use of a micro-pillared PDMS template to fabricate a micro-textured surface that was post-treated with a siloxane coating. As far as the authors are aware, this is the first reported instance of a superhydrophobic concrete surface with an integrated microtexture. The second strategy applied a photocatalytic coating on a smooth UHPC surface cast in a PVC mold. Superhydrophilic behavior (water contact angle of 0º) was confirmed after UV irradiation. External aging tests confirm the efficacy of the self-cleaning mechanism.

6 Acknowledgement

The authors would like to thank S. Lombard, C. Bouillon, S. Brun and M. Dykman for their help in sample preparation, SEM observations, profilometry, and wetting measurements.

References

[1] Benyus J.M.: Biomimicry—Innovation inspired by Nature. HarperCollins Publishers Inc, New York, USA, 2002.

[2] Neinhuis, C.; Barthlott, W.: Characterization and distribution of water-repellent, self-cleaning plant surfaces. Annals of Botany 79, pp. 667–677, 1997.

[3] Cassie, A.B.D.; Baxter S.: Wettability of porous surfaces. Transactions of the Faraday Society 40, pp. 546–551, 1944.

[4] De Gennes, P.-G. ; Brochard-Wyart, F.; Quéré, D.: Capillarity and wetting phenomena: Drops, Bubbles, Pearls, Waves. Springer-Verlag, USA, 2004.

[5] Furstner, R.; Barthlott, W.: Wetting and self-cleaning properties of artificial superhydrophobic surfaces. Langmuir 21, pp. 956–961, 2005.

[6] Callies, M.; Chen, Y.; Marty, F.; Pépin, A.; Quéré D.: Micro-fabricated textured surfaces for super-hydrophobicity investigations. Microelectronic Engineering 78–79, pp. 100–105, 2005.

[7] Fujishima, A.; Honda, K.: Electrochemical photolysis of water at a semiconductor. Nature 238, pp. 37–38, 1972.

[8] Fujishima, A.; Zhang, X.; Tryk, D.A.: TiO2 photocatalysis and related surface phenomena. Surface Science Report 63, pp. 515–582, 2008.

[9] Beeldens, A., Van Gemert, D.: Experimental investigation of efficiency of TiO2-cement coating for self-cleaning and air-purification. Cement and Concrete Research 34, pp. 2223–2236, 2004.

[10] De Larrard, F.: Concrete mixture proportioning. E & FN Spon, London, United Kingdom, 1999.

[11] Gartner, E.M.; Gaidis, J.M.; Grace W.R.: Hydration mechanisms I. Materials Science of Concrete, pp. 95–125, 1989.

[12] Gueit, E.; Darque-Ceretti, E.; Tintillier, P.; Horgnies, M.: Surfactant-induced growth of a calcium hydroxide coating at the concrete surface. Journal of Coating Technology and Research, DOI: 10.1007/s11998-011-9368-4.

Efficient Photocatalysis in the Visible with TiO_2/Phthalocyanine-Hybrid Particles

Andreas Winzenburg, Rüdiger Faust
Institute of Chemistry and CINSaT – Center for Interdisciplinary Nanostructure Science and Technology, University of Kassel, Germany

In efforts to extend the activity of TiO2-based photocatalysts into the visible we present a hybrid material consisting of TiO2 that is surface-modified with a functional phthalocyanine (Pc). We reveal that the hybrid particles photosensitise the formation of singlet oxgen and demonstrate that they exhibit a significantly enhanced photocatalytic activity in NO photodegradation experiments with visible light.

Keywords: Visible-light photocatalysis, titanium dioxide, phthalocyanine, hybrid, nitric oxide degradation

1 Introduction

The continuing industrialisation in large parts of the world poses increasing environmental burdens on Nature and its inhabitants. Water and air pollution by noxious substances often reach levels that effect the well-being of life in many of its forms. Some of the major pollutants in air are carbon monoxide (CO), sulphur dioxide (SO_2), nitrogen oxides (NO_x), volatile organic compounds (VOCs) and fine particulate matter. In Europe, the EU has regularly issued increasingly strict directives with limiting concentrations for these pollutants [1] and EU member states are obliged to adopt the directives and transform them into national environmental law. Frequently, however, the communities struggle to comply with the regulations, a particular problem in case of combustion-generated pollutants such as fine particulate matter and nitrogen oxides (NO_x) [2-4]. Hence, effective measures are sought that significantly reduce pollution levels. One such measure makes use of the well-documented photocatalytic properties of TiO_2, i.e. the UV-triggered generation of oxidising species on the surface of TiO_2 in the presence of water and oxygen, which leads to substantial reductions of air- and waterborne pollutants [5-10]. Due to the electronic band-gap of semiconducting titanium dioxide, photocatalysis is only efficient when initiated with UV light. However, for many applications (shady areas, seasonal sunlight fluctuations, indoors) an extention of the photocatalytic activity into the visible is highly desireable. Immense efforts are therefore underway to establish Vis-active photocatalysts by either doping the titanium dioxide crystal lattice or by modifiying the surface of TiO_2 [11-13].

We present here a surface modification of TiO_2 particles with organic phthalocyanine dyes. Phthalocyanines have intense absorptions throughout the visible spectrum and – most importantly – sensitise the generation of singlet oxygen as an efficient oxidising species. Using NO-photodegradation as a reference reaction, we will demonstrate that the hybrid material derived from the irreversible attachment of phthalocyanines onto TiO_2 particles shows an enhanced photocatalytic activity when irradiated with visible light.

2 Background

Titanium Dioxide Photocatalysis

The term “photocatalysis” has first been mentioned in the 1930s and is now usually interpreted as “the acceleration of a photoreaction by the action of a catalyst” [14]. The prime example of a photocatalyst is titanium dioxide, whose properties have been intensely investigated [5-9,11].

Titanium dioxide occurs in the three crystalline forms brookite, rutile and anatase. Besides slightly varying band gap energies (E_g), these modifications exhibit different photocatalytic

activities. While anatas (E_g = 3.2 eV) is known to be highly active, brookite (E_g = 3.13 eV) and rutile (E_g = 3.0 eV) are generally not efficient photocatalysts [12,15, but also see 16].

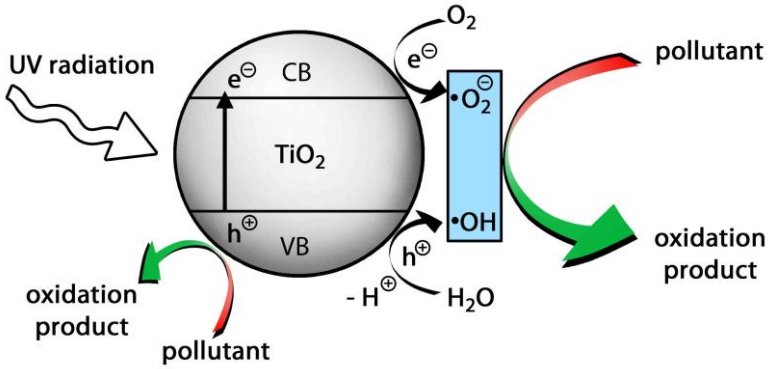

Figure 1: Simplified photocatalysis mechanism of pure TiO_2 (anatase) upon UV irradiation.

The simplified mechanism of TiO_2 photocatalysis is visualised in Figure 1. UV irradiation promotes an electron into the conduction band (CB) of TiO_2, leaving a vacancy in the valence band (VB). The photocatalytical degradation of pollutants by TiO_2 is usually an oxidative process brought about by oxidising radical species, such as hydroxyl radicals (·OH) and superoxide radicals ($\cdot O_2^-$) derived from the reaction of water with electron holes and oxygen with electrons, respectively. Secondary oxidising agents may also be involved [5-7,9,12].

Phthalocyanine Photosensitisation

Phthalocyanines (Pc) are chemically and photophysically robust organic dyes with strong absorptions in the visible. Peripheral Pc-substitution and coordination of various metal ions in the central Pc-core allow the tuning of the electronic, optical and photophysical properties of the phthalocyanines, as well as a control over their aggregation and binding behaviour [17,18]. Most important in the context of photocatalysis is the fact that diamagnetic Pc-derivatives act as efficient photosensitisers in the conversion of triplet oxygen ($^3O_2$, ground state) into singlet oxygen ($^1O_2$, excited state), as shown in Figure 2 [19].

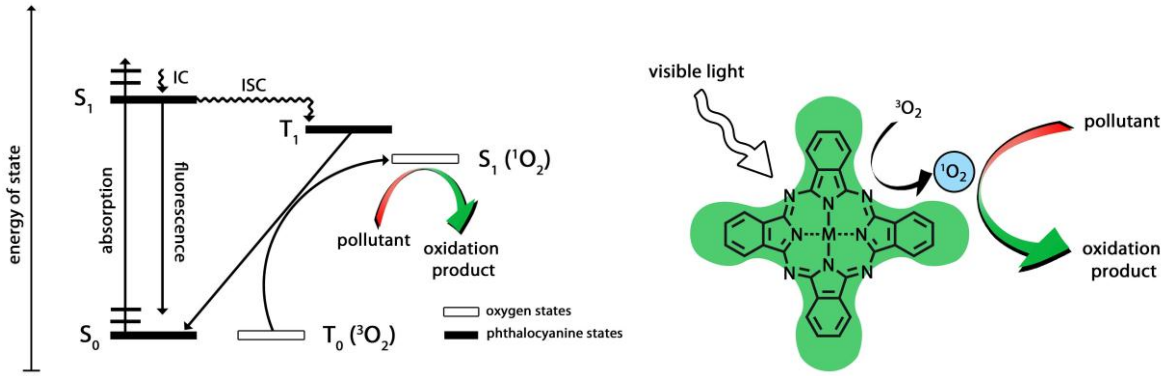

Figure 2: Simplified Jablonski-diagram (left) and a schematic drawing of Pc photosensitisation (right).

As an electronic prerequisite, phthalocyanines need to access the excited triplet state (T_1) to transfer energy onto molecular oxygen in the triplet ground state ($^3O_2$). Oxygen thereby is excited into its singlet state ($^1O_2$) and referred to as singlet oxygen. Singlet oxygen is a highly energetic and reactive species. It is able to oxidise a variety of organic [12,20] and inorganic compounds [12]. Moreover, singlet oxygen is known to degrade efficiently biologic material [21,22], such as proteins [23], viruses [24] and bacteria [25]. Diagnostic for singlet oxygen formation is its NIR-emission at 1270 nm.

Visible Light Photocatalysis

The solar irradiance has significant intensities in the visible. For this reason, efficient photocatalysis applications relying on solar irradiance require vis-responsive photocatalysts. This requirement is even more significant for indoor photocatalysis applications. The two principle modes by which the activity of TiO_2-based photocatalysts can be extended into the visible are doping and surface modifications [12].

Doping generally means the insertion of atoms, or group of atoms or ions into a host's crystal lattice, in dopand concentrations ranging typically from ppms to percent. Doping of TiO_2 with suitable metal ions [12,27] such as chromium, iron or tin or with non-metallic atoms like sulphur [28], nitrogen [29] or carbon [30] induces interband states (Figure 3). Hence, additional absorptions of lower energy (i.e. longer wavelengths) lead to the promotion of electrons into the conduction band of TiO_2 [12,26]. In addition, the energy gap of doped TiO_2 can be slightly reduced by crystal lattice deformations.

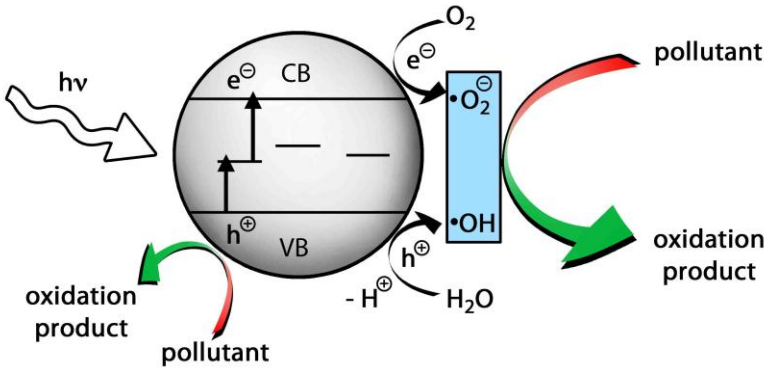

Figure 3: Simplified photocatalysis mechanism of doped TiO_2 (anatase) upon irradiation with visible light.

Surface modifications are a valuable alternative to obtain Vis-active photocatalysts. Suitable modifyers for the TiO_2 surface are secondary semiconductors (SC) such as CdS or Bi_2S_3 [31] or organic dyes such as erythrosin B, Rose Bengal, or corbocyanines [32] (not shown in *Figure 4*). Both semiconductor and surface-bound dyes can act as electron donors, if the energy of their excited state matches that of the conducting band of TiO_2 [12].

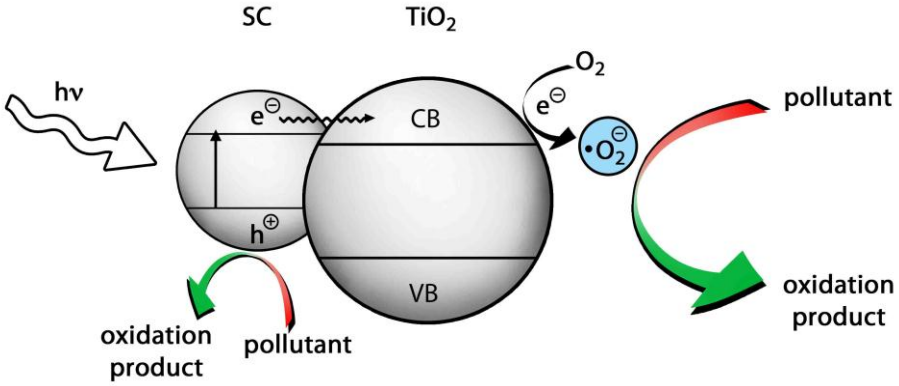

Figure 4: Simplified photocatalysis mechanism of sensitised TiO_2 (anatase) upon irradiation with visible light.

Our approach delineated herein relies on a surface modification that benefits from the independent action of a photosensitising dye irreversibly attached to the TiO_2 surface. TiO_2 surface modifications with organic dyes often bear the risk of dye photodegradation [12]. Due to their chemical inertness, the phthalocyanines will resist photodegradations for extended periods of time. We can therefore demonstrate that the hybrids derived from phthalocyanines and TiO_2 are vis-active photocatalysts that use singlet oxygen and can photodegrade NO as a reference chemical for noxious airborne pollutants.

3 Experimental

Electronic absorption spectra were recorded on a Perkin-Elmer *Lambda 40* spectrophotometer. Singlet oxygen quantum yields of phthalocyanines were determined using the singlet oxygen luminescence at 1270 nm. The irradiation with visible light was performed with a 100 W QTH lamp from Newport Physics light using appropriate optical filters (*KG1* and *OG570* from Merck). The samples wer held in a temperature-controlled cuvette holder with integrated magnetic stirrer from OceanOptics (*CUV-QPOD*). The detection system consisted of the monochromator *Cornerstone* ™ 260i 1/4m from Newport Physics with 600 lines/mm grating blazed at 1250 nm, a cooled InGaAs single diode detector, a chopper-system and the *Oriel Merlin*™ digital lock-in radiometry system from Newport Physics. Higher-order fluorescence around 1270 nm was eliminated by a suitable filter system (780 nm cut-on, range: 800-2700 nm). More detailed information is available upon request. The NO_x degradation experiments were performed in photoreactor systems provided by D-TOX in Hannover, Germany and by the Institute of Construction Materials (Prof. Dietmar Stephan) at the University of Kassel. The synthesis of the phthalocyanines and the preparation of the phthalocyanine/TiO_2 hybrid materials will be published elsewhere.

4 Results and Discussion

A novel hybrid material consisting of TiO_2 (P25 from Degussa/Evonik) and phthalocyanines (3 weight %) was prepared by adding a solution of the appropriately functionalised phthalocyanine to a suspension of TiO_2. In contrast to structurally simple dyes that have been used in other studies [32-35], the phthalocyanines investigated here have specific anchoring groups for the attachment onto the metal oxide surface. We therefore expected that the photocatalytic activity of the hybrid system in the visible should be enhanced compared to that of pure TiO_2 and that photosensitisation of oxygen should produce oxidising species in addition to those formed by standard TiO_2. As discussed below, these expectations were met.

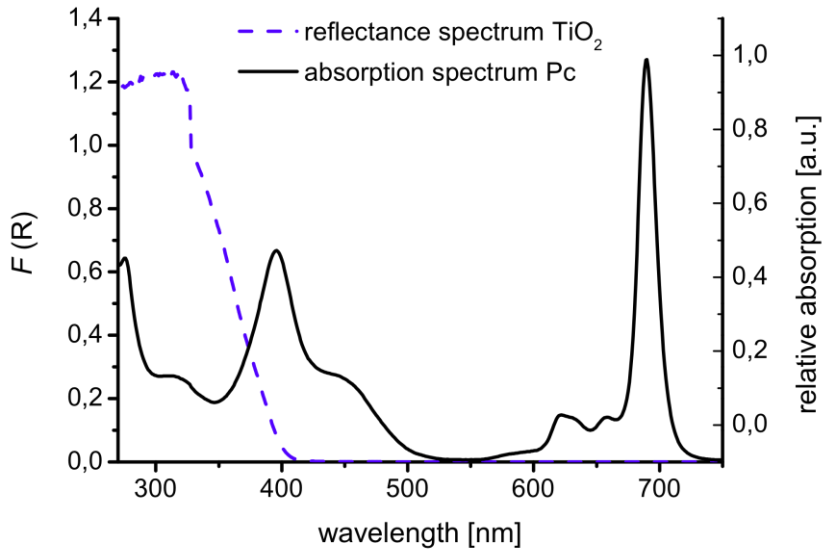

Figure 5: Diffuse reflectance spectrum of TiO_2 in $BaSO_4$ at room temperature (left scale, dashed line); electronic absorption spectrum of a Pc in dichloromethane at room temperature (right scale, straight line).

As the overlay of the phthalocyanine electronic absorption spectrum and the TiO_2 diffuse reflectance spectrum reveals (Figure 5), there is significant overlap in the region around 400 nm that allows the hybrid material made up of these two components to extend its photocatalytic

activity well into the visible range. In addition, there are intense Pc-absorptions at the far red end of the visible spectrum (around 700 nm) that can be used to trigger the photosensitisation of singlet oxygen.

The use of phthalocyanines equipped with anchouring groups leads to an irreversible binding of the Pc on the surface of TiO_2. Figure 6 illustrates that a reextraction of the dye from the hybrid material by organic solvents was not possible. In contrast, loosely adsorbed phthalocyanines that lack peripheral binding groups, can be easily reextracted into solution.

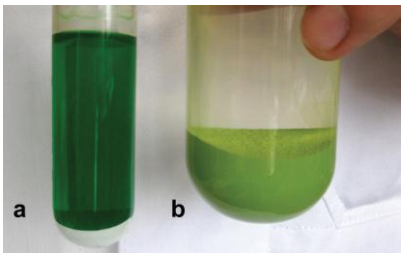

*Figure 6: Photograph of Pc/TiO_2 suspensions in THF after 4 hours of centrifugation at 3000 rpm (**a**: Pc without anchouring group and **b**: Pc with anchouring group).*

The preparation and the photocatalytic activities of a range of Pc/TiO_2 composites are described in the literature [32-35]. In these contributions, the role of the Pc is primarly described as that of an electron donor for TiO_2 (i.e. the mechanism illustrated in Figure 4). Contrastingly, a role for the Pc/TiO_2 hybrids as a photosensitiser for singlet oxygen appearence was either declared to be unprobable under the experimental conditions [33,34] or could simple not be verified [34,35]. We can now reveal for the first time that the Pc/TiO_2 hybrids investigated in this study, produce $^1O_2$ when irradiated with visible light. Experimental proof is depicted in Figure 7 in form of a diagnostic $^1O_2$ emission signal at 1270 nm that is oberserved upon irradiation of suspensions of the hybrid material in deuterated methanol (CH_3OD). While the hybrid suspension exhibits a strong $^1O_2$ luminescence signal, the control sample (the centrifuged liquid) showed no emission.

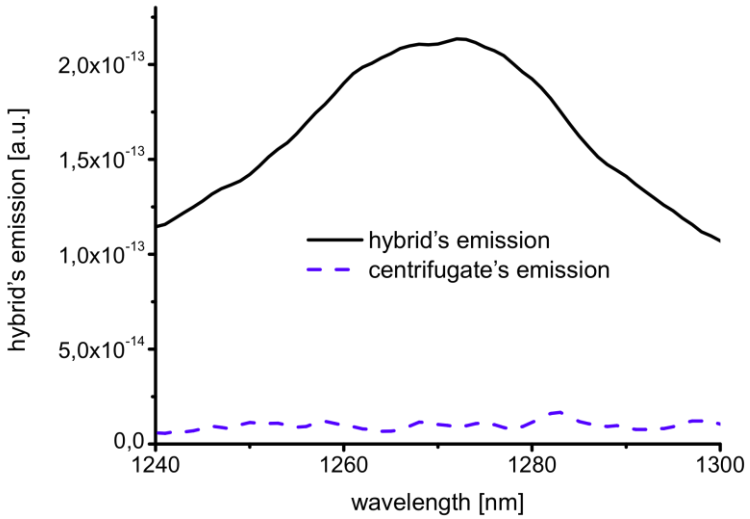

Figure 7: NIR emission spectra of a hybrid suspension in d-methanol (straigth line) and its supernatant liquid after centrifugation (dashed line) at room temperature upon irradiation with light of 700 nm wavelength.

The photocatalytic activity of the Pc/TiO_2 hybrid material in the visible was studied by NO_x degradation measurements using a 455 nm LED-array. Figure 8 shows the photon efficiencies (ξ) with which nitrogen oxides (NO_x) are photochemically converted by either commercial TiO_2

or by the Pc/TiO_2 hybrids investigated here. It is evident that the photocatalytic activity of the Pc/TiO_2 hybrids in the visible is significantly enhanced by about 50 % compared to that of TiO_2 (P25). A more detailed analysis (not shown) reveals that the photodegradation of NO by the hybrids is not accompanied by a substantial rise in NO_2-levels, a fact that is usually oberved with unmodified TiO_2. It can therefore be assumed that $^1O_2$ formed by Pc/TiO_2 hybrid material contributes to the photodegradation process.

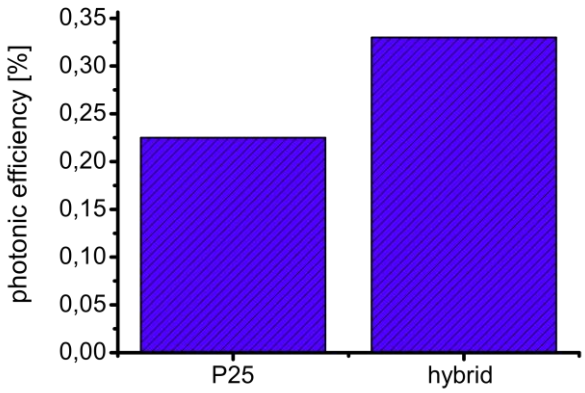

Figure 8: Photonic efficiencies (ξ) of the NO-degradation by P25 (TiO_2) and by Pc/TiO_2 hybrid material at room temperature upon irradiation with light of 455 nm wavelength.

5 Conclusions

We developed a modified phthalocyanine (Pc) suitable for irreversible binding to the TiO_2-surface. The corresponding Pc/TiO_2 hybrid material has absorptions in the visible region. As a result, the photocatalytic activity of the hybrid material upon irradiation with visible light is enhanced. Furthermore, we present evidence for singlet oxygen ($^1O_2$) generation by Pc/TiO_2 hybrids and thus assume that oxygen photosensitisation by the phthalocyanine is an additional pathway in the photocatalysis process.

6 Acknowledgements

We thank the German Federal Ministry of Education and Research (BMBF) for financial support and Prof. Dietmar Stephan and his team as well as all our partners in the HelioClean consortium for a fruitful collaboration.

References

[1] European Parliament and Council: Directive 2008/50/EC of 21 May 2008 on ambient air and cleaner air for Europe, *OJ L* 152, p. 1-44, 2008.

[2] Bundesanstalt für Straßenwesen (BASt): Bericht über die Messungen der Luftqualität an BAB durch die Bundesanstalt für Straßenwesen - Kalenderjahr 2010 -, Bergisch Gladbach, 2011.

[3] Rauterberg-Wulff, A.; LUTZ, M.: Impact Assessment of the Low Emission Zone Berlin, *UMID: Umwelt und Mensch – Informationsdienst* (4), p. 11-18, 2011.

[4] Lorenz, J.: Particulate Matter: Immission Control Concerns Us All – Experience with Low Emission Zones in Munich, *UMID: Umwelt und Mensch – Informationsdienst,* (4), p. 19-26, 2011.

[5] Carp, O.; Huisman, C.L.; Reller, A.: Photoinduced reactivity of titanium dioxide, *Progress in Solid State Chemistry* (32), p. 33-177, 2004.

[6] Chen, X.; Mao, S.S.: Titanium Dioxide Nanomaterials: Synthesis, Properties, Modifications and Applications, *Chemical Reviews* (107), p. 2891-2959, 2007.

[7] Fujishima, A.; Rao, T.N.; Tryk, D.A.: Titanium dioxide Photocatalysis, *Journal of Photochemistry and Photobiology C* (1), p. 1-21, 2000.

[8] Robertson, P.K.J.; Bahnemann, D.W.; Robertson, J.M.C.; Wood, F.: Photocatalytic Detoxification of Water and Air, *The Handbook of Environmental Chemistry*, Vol. 2, Part M, Springer, Berlin, 2005.
[9] Hoffmann, R.M.; Scot, T.M.; Choi, W.; Bahnemann, D.W.: Environmental Applications of Semiconductor Photocatalysis, *Chemical Reviews* (95), p. 69-96, 1995.
[10] Dalton, J.S.; Janes, P.A.; Jones N.G.; Nicholson, J.A.; Hallam; K.R.; Allen, G.C.: Photocatalytic oxidation of NO_x gases using TiO_2: a surface spectroscopic approach, *Environmental Pollution* 120, p. 415-422, 2002.
[11] Linsebigler, A.L.; Lu, G.; Yates, J.T.Jr.: Photocatalysis on TiO_2 Surfaces: Principles, Mechanisms, and selected Results, *Chemical Reviews* (95), p. 735-758, 1995.
[12] Chatterjee, D.; Dasgupta, S.: Visible light induced photocatalytic degradation of organic pollutants, *Journal of Photochemistry and Photobiology C* (6), p. 186-205, 2005.
[13] Rehmann, S.; Ullah, R.; Butt, A.M.; Gohar, N.D.: Strategies of making TiO_2 and ZnO visible light active, *Journal of Hazardous Materials* (170), p. 560-569, 2009.
[14] Serpone, N.; Emiline, A.V., Suggested terms and definitions in photocatalysis and radiolysis, *International Journal of Photoenergy* (4), p. 91-131, 2002.
[15] Reyes-Coronado, D.; Rodríguez-Gattorno, G.; Espinosa-Pesqueira, M.E.; Cab, C.; de Coss, R.; Oskam, G., Phase-pure TiO_2 nanoparticles: anatase, brookite and rutile, *Nanotechnology* 1(19), p. 1-10, 2008.
[16] Ismail, A.A.; Kandiel, T.A.; Bahnemann, D.W.; Novel (and better?) titania-based photocatalysts: Brookite nanorods and mesoporous structures, *Journal of Photochemistry and Photobiology A* (216), p. 183-193, 2010.
[17] Leznoff, C.C; Lever, A.B.P.: *Phthalocyanines: Properties and Applications* (Volume 1-4), Wiley-VCH, New York, 1989-1996.
[18] Kadish, K.M.; Smith, K.M.; Guilard, R.: *The Porphyrin Handbook – Phthalocyanines: Synthesis* (Volume 15), Elsevier, San Diego, 2003.
[19] DeRosa, M.C.; Crutchley, R.J.: Photosensitized singlet oxygen and ist applications, *Coordination Chemistry Review* 223-224, p. 351-371, 2002.
[20] Xu, H.; Chan, W.-K.; Ng, D.K.P.: Efficient and Recycable Pthalocyanine-Based Sensitizers for Photooxygenation Reactions, *Synthesis* (11), p. 1791-1796, 2009.
[21] Glaeser, J.;Nuss, A.M.; Berghoff, B.A.; Klug, G.: Singlet Oxygen Stress in Microorganisms, *Advances in Microbial Physiology* (58), p. 141-173, 2011.
[22] Jori, G.; Brown, S.B.: Photosensitized inactivation of microorganisms, Photochemical and Photobiological Sciences 3, p. 403-405, 2004.
[23] Pattison, D.I., Rahmanto, A.S., Davies, M.J.: Photo-oxidation of proteins, *Photochemical and Photobiological Sciences* 11, p. 38-53, 2012.
[24] Wainwright, M.: Photoinactivation of viruses, *Photochemical and Photobiological Sciences* 3, p. 406-411, 2004.
[25] Chen, J.; Cesario, T.C.; Rentzepis, P.M.: Time resolved spectroscopic studies of methylene blue and phenothiazine derivatives used for bacteria inactivation, *Chemical Physics Letter* 489, p. 81-85, 2010.
[26] Asahi, R.; Morikawa, T.; Ohwaki, T.; Aoki, K.; Taga, Y.: Visible-Light Photocatalysis in Nitrogen-Doped Titanium Oxides, *Science* 13, p. 269-271, 2001.
[27] Lin, Y.-M; Tseng, Y.-H.; Huang, J.-H.; Chao, C.C.; Chen, C.C.; Wang, I.: Photocatalytic Degradation of Nitrogen Oxides over Visible Light Responsive Titania-Based Photocatalysts, *Environmental Science and Technology* (40), p. 1616-1621.
[28] Ohno, T.; Mitsui, T.; Matsumura, M.: Photocatalytic activity of S-doped TiO_2 photocatalyst under visible light, *Chemistry Letters* 32, p. 364-365, 2003.
[29] Asahi, R.; Morikawa, T.: Nitrogen complex species and ist chemical nature in TiO_2 for visible-light sensitized photocatalysis, *Chemical Physics* 339, p. 57-63, 2007.
[30] Sakthivel, S.; Kisch, H.: Daylight Photocatalysis by Carbon-Modified Titanium Dioxide, *Angewandte Chemie International Edition* 42 (40), p. 4908-4911, 2003.

[31] Bessekhouard, Y.; Robert, D.; Weber, J.V.: Bi_2S_3/TiO_2 and CdS/TiO_2 heterojunctions as an available configuration for photocatalytically degradation of organic pollutant, *Journal of Photochemistry and Photobiology A* 163 (3), p. 569-580, 2004.
[32] Chen, F.; Deng, Z.; Li, X.; Zhang, J.; Zhao, J.: Visible light detoxification by 2,9,16,23-tetracarboxyl phthalocyanine copper modified amorphous titania, *Chemical Physics Letters* 415, p. 85-88, 2005.
[33] Hodak, J.; Quinteros, C.; Litter, M.I.; San Román, E.: Sensitization of TiO_2 with phthalocyanines, *Journal of Chemical Society, Faraday Transactions* 92 (24), p. 5081-5088, 1996.
[34] Machado, A.E.H.; Franca, D.M.; Velani, V.; Magnino, G.A.; Velani, H.M.M.; Freitas, F.S., Müller, P.S.Jr.; Sattler, C.; Schmücker, M.: Characterization and Evaluation of the Efficiency of TiO_2/Zinc Phthalocyanine Nanocomposites as Photocatalysts for Wastewater Treatment Using Solar Irradiation, *International Journal of Photoenergy* , p. 1-12, 2008.
[35] Mele, G.; Garcìa-Lòpez, E.; Palmisano, L.; Dyrda, G.; Slota, R.: Photocatalytic Degradation of 4-Nitrophenol in Aqueous Suspension by Using Polycrystalline TiO_2 Impregnated with Lanthanide Double-Decker Phthalocyanine Complex, *Journal of Physical Chemistry C* 111, p. 6581-6588, 2007.

Part Three

MATERIALS

Synergistic Effect of Rice Husk Ash and Fly Ash on Properties of Self-Compacting High Performance Concrete

Le Thanh Ha[1,2], Karsten Siewert[1], Horst-Michael Ludwig[1]

1: Institute for Building Materials Science, Department of Civil Engineering, Bauhaus-Universität Weimar, Germany
2: University of Transport and Communications, Hanoi, Vietnam

In this study, the effect of rice husk ash (RHA) on properties of fresh and hardened self-compacting high performance concrete (SCHPC) containing fly ash (FA) was investigated, and compared to that of silicafume (SF). SCHPC mixtures were designed with ternary binders from cement and mineral admixtures such as FA, RHA, SF. Filling ability, passing ability, segregation resistance, viscosity, air content and compressive strength at 3, 7, 28 and 56 days were tested. The results show that an economical SCHPC with very high compressive strength of about 130 MPa close to that of ultra high performance concrete was successfully developed by combining RHA and FA. The combination of RHA and FA improved not only self-compactability but also compressive strength of SCHPC. The increase in RHA content led to lower filling ability and higher viscosity and then better segregation resistance. The SCHPC containing RHA had similar self-compactability, but higher compressive strength than SCHPC containing SF.

Keywords: Self-compacting high performance concrete, rice husk ash, silicafume, self-compactability, compressive strength.

1 Introduction

Self-compacting high performance concrete (SCHPC) is considered as a new type of concrete, which is defined based on the concept of self-compacting concrete (SCC) and high performance concrete (HPC). As a result, SCHPC possesses adequate self-compactability (filling ability, passing ability, segregation resistance) of SCC and high strength and good durability of HPC [1]. Segregation resistance of SCHPC is controlled by using viscosity modifying agents (VMA) or high amounts of powder or their combination [2]. At the same time, mineral admixtures, such as silica fume (SF), are utilized to fulfil its high strength and durability requirements [3, 1]. However, these admixtures are very expensive, and one of the main reasons for the high cost of SCHPC, especially in developing countries. Therefore the limitation of using VMA and the substitution for SF by less expensive mineral admixture such as RHA or its combination with other admixtures, such as FA are necessary.

RHA is the residue of incinerating rice husk under controlled temperature conditions. Rice husk is an agricultural waste from the milling process of paddy rice in developing countries i.e. Vietnam. Similar to SF, RHA possesses high content of amorphous silica, and large specific surface area. However, RHA has angular and highly porous particles with the average mean size from 5μm to 10μm, and a very high BET surface area (even more than 250 m^2/g). Meanwhile SF particles are spherical with mean size of 0,1 μm, and a BET surface area of about 20m^2/g [4, 5]. RHA is a very good replacement for SF in respect of compressive strength and durability of concrete [5, 1]. In SCC, RHA is used to modify viscosity for good segregation resistance [6]. Another mineral admixture, FA, is commonly used to produce SCC. Generally, SCC incorporating FA has an increase in workability-slump flow, but a decrease in compressive strength compared with those of the control concrete containing only cement as binder [3, 7]. However, the use of RHA combined with FA as a partial cement replacement, also as a mineral admixture to modify viscosity, and to improve compressive strength of SCHPC has not yet been studied.

In this study, the combination of RHA and FA was used in a ternary binder to develop SCHPC with adequate self-compactability and very high compressive strength close to that of ultra high performance concrete. The effect of RHA on filling ability, passing ability, viscosity, segregation resistance and compressive strength of SCHPC was investigated to find out the optimal RHA content in combination with FA. Besides, the effect of RHA on these properties was compared to that of SF.

2 Experimental program

Materials

An ordinary Portland cement (PC - CEM I 52.5R), FA, SF and RHA were used. The PC, FA, SF complied with DIN EN 197-1, DIN EN 450-1, DIN EN 13263-1, respectively. The rice husk was burnt under controlled temperature conditions in a simple incinerator in Vietnam. The obtained ash was ground in a ball mill. Crushed Basalt stone was used as coarse aggregate with a maximum size of 16mm. Natural sand was used as fine aggregate with a maximum size of 2 mm. The physical properties and the chemical composition of cement and mineral admixtures are summarized in Table 1. The sieve analysis and the physical properties of fine and coarse aggregate are presented in Table 2. In addition, a polycarboxylate based super plasticizer with specific gravity of 1.08 and 40% solid content by weight was used. The Fig.1 shows the Scanning Electron Microscopic (SEM) images of RHA before and after grinding, SF and FA. It can be found that particles of RHA are angular and still have porous surface structure after grinding.

Table 1: Chemical composition and physical properties of cement and mineral admixtures.

Chemical analyses,%	Cement	RHA	SF	FA
SiO_2	19.40	87.00	96.20	56.60
Al_2O_3	5.30	0.80	0.70	25.80
Fe_2O_3	2.50	0.40	0.30	6.40
CaO	61.20	1.20	0.00	2.50
MgO	1.20	0.60	0.10	1.30
SO_3	3.20	0.40	0.10	0.60
Na_2O	0.07	0.40	0.06	0.62
K_2O	0.61	2.63	0.37	2.08
L.O.I	4.90	3.70	1.60	2.90
Density, g/cm^3	3.09	2.27	2.26	2.27
Mean particle size, μm	7.07	5.70	0.29	16.39
BET (Blaine), m^2/g	2.07 (0.595)	25.21	26.43	2.14(0.405)

Table 2: Sieve analysis and physical properties of the fine and coarse aggregate.

Agg**	Sieve size, mm									Fineness modulus	Density, g/cm^3	Abs*, %
	0.125	0.25	0.5	1	2	4	8	16	22			
Fine	3.0	20.1	66.2	84.7	93.9	100	100	100	100	2.32	2.65	0.08
Coarse	0.0	0.0	0.8	1.4	26.2	60.9	79.3	96.7	100	6.14	3.05	0.80

** Water absorption; ** Aggregate.*

Mixture proportions

The mixtures were designed based on the absolute volume of the constituent materials. Proportions of aggregate blend were calculated relying on the theory of Funk and Dinger with the factor of 0.25, as mentioned by the author [**8**], to reach the highest packing density. The minimum paste volume for filling ability was computed from the void content in the compacted aggregate blend. The superplasticizer (SP) dosages for the concretes were set based on the SP saturation dosages of their own mortars, and fixed at 2.5% binder. The proportion of water

was calculated based on the water-binder (w/b) ratio, the absorption of fine and coarse aggregates and the water contribution of SP [9]. In this research, eight mixtures were designed with a constant w/b ratio of 0.26, constant paste volume of 38,5 % (which includes 2% of air) and constant fine and coarse aggregate contents. Mixture proportions are shown in Table 3 in which mixture types were designated based on the type and the percentage of mineral admixtures replacement cement by weight. For instance, in the ''FA20R10'' mixture, 30% cement content was replaced by 20% FA, and 10% RHA.

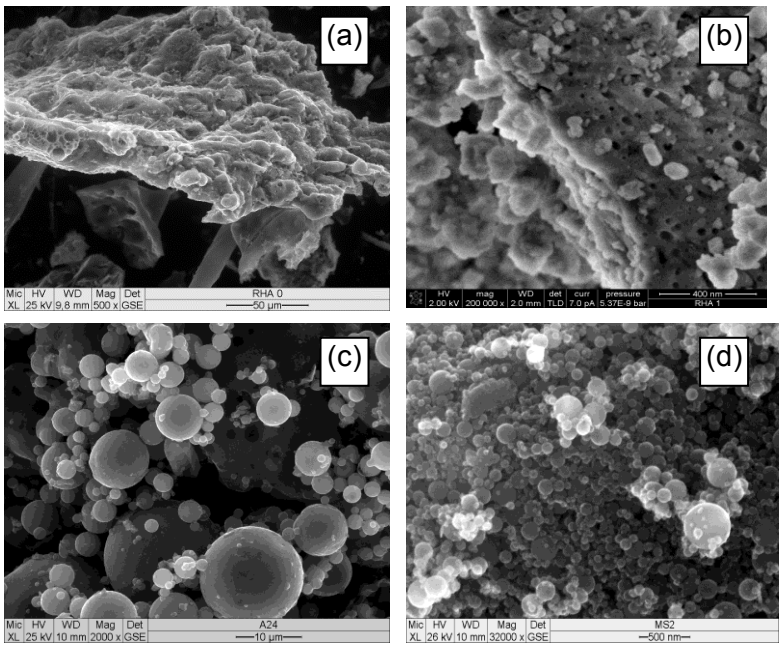

Figure 1: SEM images of RHA before grinding (a); RHA after grinding (b); FA (c); SF (d).

Table 3: SCHPC mixture proportions.

Mixture	w/b	Water, kg/m^3	PC, kg/m^3	FA, kg/m^3	RHA kg/m^3	SF, kg/m^3	FA*, kg/m^3	CA**, kg/m^3	SP, %B
FA0R0	0.26	163	625	0	0	0	790	966	2.5
FA20R0	0.26	156	481	120	0	0	790	966	2.5
FA40R0	0.26	151	347	232	0	0	790	966	2.5
FA20R5	0.26	155	447	119	30	0	790	966	2.5
FA20R10	0.26	153	413	118	59	0	790	966	2.5
FA20R15	0.26	152	380	117	88	0	790	966	2.5
FA20R20	0.26	151	347	116	116	0	790	966	2.5
FA20SF10	0.26	153	413	118	0	59	790	966	2.5

** Fine aggregate, ** Coarse aggregate.*

Experimental methods

All mixtures were prepared in a Zyklos rotating pan compulsory mixer with total mixing time of 13 minutes. The mixing procedure was shown in Fig.2.

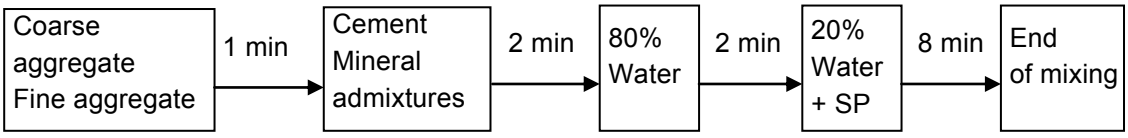

Figure 2: Mixing procedure.

The slump flow, slump flow time (T_{50}), V-funnel, sieve segregation and J-ring tests were conducted to evaluate filling ability, viscosity, segregation resistance and passing ability of SCHPC according to DIN EN 12350-8, DIN EN 12350-9; DIN EN 12350-11; DIN EN 12350-12,

respectively. The air content in fresh concretes was determined in accordance with DIN EN 12350-7. Cubic specimens of 150x150x150mm for compressive strength were cast without vibration and compaction. After 1 day, the specimens were demoulded, stored in water at 20 ±2 ^{o}C for further 6 days, and then cured in controlled room at 20 ±2 ^{o}C and 65±5% relative humidity until testing at 7, 28, and 56 days according to DIN EN 12390-2. Compressive strength of concrete was determined under DIN EN 12390-3.

3 Results and discussion

The effect of the content of cement replacement by FA on self–compactability of SCHPC

1) Filling ability and Viscosity

Fig.3 shows that the mixture containing 20% FA had the highest slump flow (indicating filling ability) of 820mm, and the lowest V-funnel flow time (indicating viscosity) of 12.1s, compared to the control, and 40% FA mixtures. Especially, the mixture containing 40% FA had lower slump flow, and higher flow time than those of control mixture.

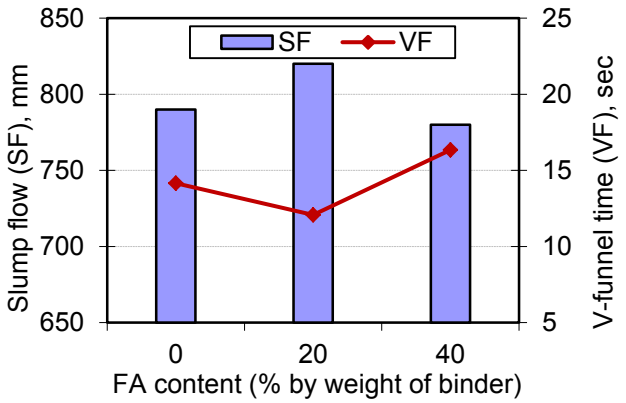

Figure 3: Slump flow and V-funnel time of SCHPC mixtures containing FA with various contents.

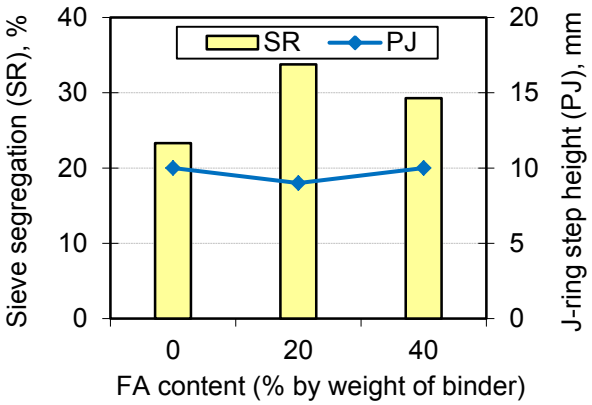

Figure 4: J-ring step and sieve segregation of SCHPC mixtures containing FA with various contents.

Previous research indicated that compared to control mixture containing only PC as binder, the mixtures containing FA has higher slump flow and the increase in the FA content results in increasing slump flow, when the binder content by weight and SP dosage are kept constant. It can be explained that, firstly, the spherical shape of FA can help to disperse agglomeration of cement particles. Secondly, the surface area of binder decreases because of spherical and coarse FA particles. Finally, the partial cement content replaced by FA in weight leads to increased paste volume because of its lower density [10]. The increase in paste volume yields increased workability due to a reduction in the friction between aggregate particles [11, 1].

The self-compactability of fresh SCC is dependent on characteristics of aggregate, the paste volume, the paste composition [12]. In this study, the aggregates and the paste volume were kept constant, therefore the paste composition significantly affects on slump flow and viscosity of concrete. On the one hand, the replacement of cement by FA with spherical shape and coarser size of the particles decreases water demand due to the decrease in surface area, ball-bearing effect and hence increases the slump flow when w/b is kept constant. On the other hand, the increase in FA content results in a decrease in binder content by weight, and the water content due to the constant w/b ratio of concrete, see in table 3. The reduction in water content contributes to increased friction between the solids in the paste and hence leads to higher viscosity and lower slump flow of concrete. The replacement of cement by 20% FA might give the optimal composition of paste to reduce the viscosity and hence increase the slump flow of concrete.

2) Segregation resistance and passing ability

Fig.4 shows that the control and FA mixtures also passed through the bars of J-ring easily and were not blocked. The 20% FA mixture flowed through the spacing bars easier than the control and the 40% FA mixtures did. However, the resistance of this mixture to segregation was lowest with sieve segregation index of over 30%. It is well known that filling ability, in terms of slump flow, is correlated to passing ability, increasing filling ability yields good passing ability. And for a given coarse aggregate particle size, segregation resistance or static stability of SCC depends on the difference between the relative densities of aggregate and matrix, yield stress and viscosity of mixture [1]. The results, here, agree with previous conclusion. The 20%FA mixture, which possesses higher slump flow, lower V-funnel flow time, would have lower J-ring step height, indicating better passing ability, and poor segregation resistance.

Based on higher slump flowability and passing ability, lower viscosity and segregation resistance, the mixture containing 20% FA was chosen to investigate effect of RHA combined with FA on properties of SCHPC, especially the viscous role of RHA.

Effect of the combination of RHA and FA on self-compactability of SCHPC

1) Filling ability and Viscosity

Fig.5 shows the effect of RHA content on slump flow and V-funnel time of SCHPC when the content of cement replacement by FA was fixed at 20%, and compared to that of SF. It can be seen that the increase in RHA content led to lower slump flow, and higher V-funnel flow time. The mixture containing 10% RHA had minor higher slump flow, and higher flow time than those of mixture containing 10% SF.

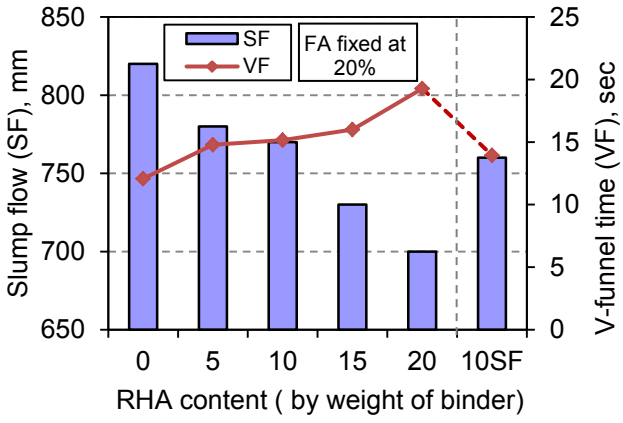

Figure 5: Slump flow and V-funnel time of various SCHPCs.

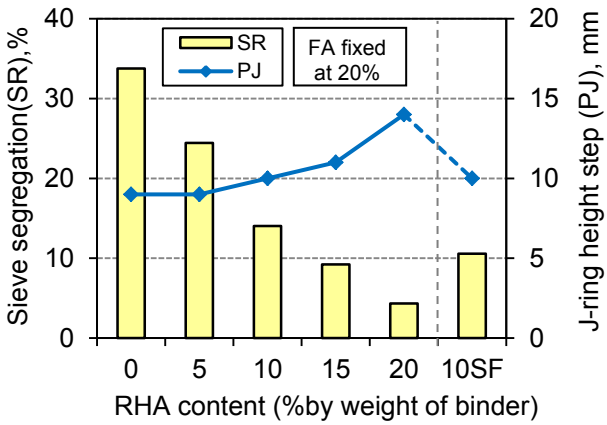

Figure 6: Sieve segregation and J-ring height step of various SCHPCs.

The result from the work [1] shows that with various w/b ratios of 0.30; 0.35; 0.40 and 0.50, the slump flow and the Orimet and the inverted slump cone flow times (indicating viscosity) of SCC mixtures increase with an increase in RHA content replacing cement in weight. This replacement leads to an increased paste volume, due to lower density of RHA, hence to the increased slump flow. Whereas the reasons for the increased flow time are mostly the reduction in the amount of free water available in the paste due to the higher volume content and the larger specific surface area of the binder. On contrary, in another study [6], the addition of 0%, 25%, 50% RHA to the mixture proportion of SCC leads to a decrease in the w/b ratio from 0.4, to 0.38, and to 0.36, respectively. As the amount of RHA increases, the V-funnel time increases, and the slump flow decreases with the same dosage of SP. Here, it is unclear whether the increased V-funnel time, and the decreased slump flow is due to reduced w/b ratio or higher RHA content resulting in the reduction in free water in the concrete.

In the present study, the w/b ratio and paste volume of mixtures were kept constant. It is evident that the replacement of cement by RHA having particles with porous structure and large

specific surface area leads to a reduction in free water, an increase in plastic viscosity of paste, and hence an increase in V-funnel time of concrete. Consequently, the slump flow of these concretes decreases simultaneously.

2) Segregation resistance and passing ability

Fig.6 shows the effect of RHA content on segregation resistance, and passing ability of SCHPC when the content of cement replacement by FA was fixed at 20%, and compared to that of SF. The mixture with SF had the same passing ability in terms of J-ring height step, and minor better segregation resistance compared to those of the mixture with RHA. The increase in cement content replaced by RHA resulted in higher segregation resistance (lower sieve segregation), and lower passing ability (higher J-ring height step) simultaneously. These results totally correlated to results of slump flow, and V-funnel flow time. The increase in RHA yields lower slump flow, and hence lower passing ability. The resistance of mixtures with higher RHA content to segregation are better because of their higher viscosity, in spite of the reduction in paste density compared to that of aggregate, see in Fig.7.

Effect of the combination of RHA and FA on air content and unit weight of SCHPC

The air content and unit weight of SCHPC containing RHA with various contents and fixed 20%FA are presented in Fig.7. The more cement content was replaced by RHA, the lower was unit weight and generally the higher was air content in fresh concrete. All mixtures had an air content lower than 2% that was suitable for non–air entrained concrete as designed. In the case of the constant aggregate weight, the unit weight decreased with increasing RHA content, because of the lower RHA density and the increase in air content.

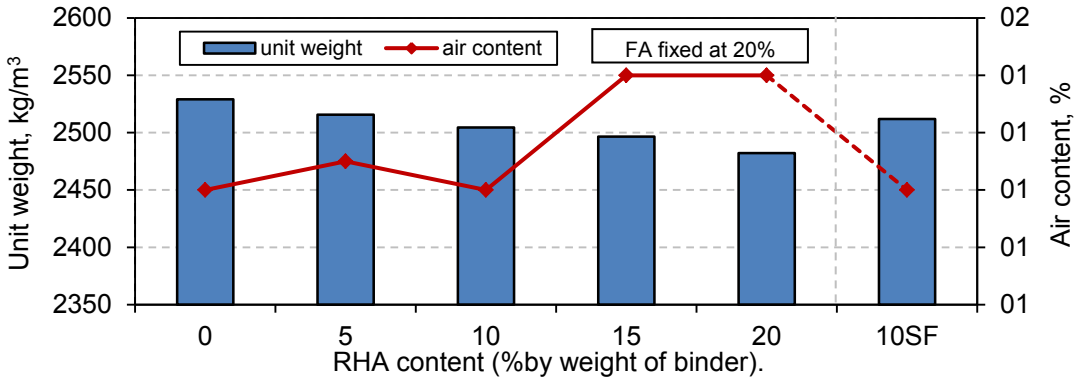

Figure 7: Unit weight and air content of various SCHPCs.

Effect of the combination of RHA and FA on compressive strength of SCHPC

It can be seen in Fig.8 that the compressive strength of SCHPCs containing only FA at early ages (3, 7days) decreased with higher FA content, except for 20% mixture at 7 days. The results were different at late ages (28, 56 days). With the cement content replaced by FA up to 40%, the compressive strength of concrete was still similar to that of control concrete containing only cement as binder. It can be explained that the amorphous silica content in FA reacts with calcium hydroxide generated from the hydration of cement to form additional C-S-H gel and results in the improvement of strength [13]. Moreover, from the mixture proportions in table 3, it can be seen that in spite of the constant w/b ratio, the water content decreases with higher FA content because of the reduction in binder weight due to the lower FA density and the constant paste volume. It might be another reason for improving compressive strength.

For the ternary binder SCHPCs with fixed 20% FA, the inclusion of RHA decreased compressive strength at 3 and 7days, except for mixtures containing 5% and 10% RHA. Compressive strength of these mixtures at 7 days was similar to that of mixture incorporating 20%FA. At later ages, concrete using ternary binder, irrespective of the RHA content, possessed similar or higher compressive strength than that of control and 20% FA concrete.

Moreover, the compressive strength increased with increase in RHA content. The positive effect of RHA on compressive strength are explained thoroughly in previous works [14, 1]. RHA is a very reactive pozzolanic material with very large specific surface area, and high silica content. RHA reacts intensively with water and calcium hydroxide generated from the hydration of cement to produce additional C-S-H. The additional C-S-H itself is the main strength-contributing compound, and also fills in the capillary pores to improve microstructure of paste matrix and transition zone in concrete resulting in improvement of compressive strength. Another reason is that the finer RHA particles can fill the pores within cement particles leading high density of paste matrix. Moreover, the increase in compressive strength of concrete with RHA at the late period is also due to the internal curing of RHA in the cement paste. RHA with porous structure may absorb free water during mixing leading to lower w/b ratios of RHA mixtures. This amount of water is released from the pores at late ages, when the relative humidity in paste reduces because of cement hydration, and therefore keeps the hydration of blended cement continuous [5].

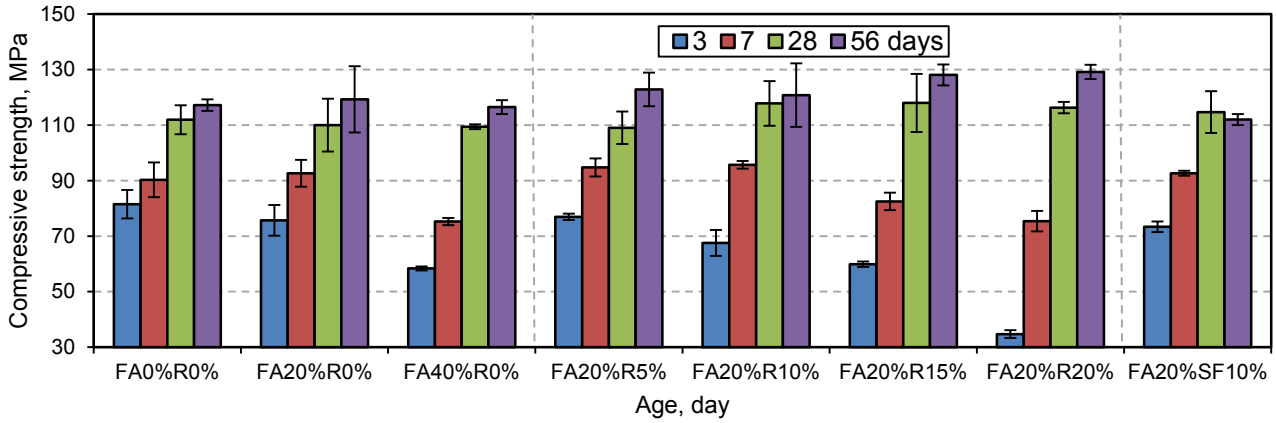

Figure 8: Compressive strength of various SCHPCs at various ages

Compared to 10% SF mixture, the compressive strength of 10% RHA mixture was lower at 3 days, however it became higher at later ages of 7, 28, 56 days. It can be explained that Although SF possesses much finer particle and higher silica content than those of RHA, RHA in concrete can enhance the cement hydration due to internal curing especially in long term. Besides, RHA with porous structure absorbs certain amount of free water resulting in the lower w/b ratio of RHA mixture compared to that of SF mixture, as mentioned previously.

4 Conclusions

It is well known that one of the main disadvantages of SCC is its cost, because of the use of chemical admixtures, in terms of super plasticizer and viscosity modifying admixtures and/or use of high volumes of Portland cement. Consequently, the cost of SCHPC is even higher due to the addition of expensive mineral admixture, such as SF in mixture, especially in developing countries, i.e. Vietnam. Using less-expensive and locally available RHA, produced from rice husk, an agricultural waste, to modify viscosity of concrete, to replace SF and partly cement brings a lot of benefits to the cost, the technical properties of concrete and the environment as well. Based on the experimental results in this study, the following conclusions can be drawn:

- It is possible to produce relatively low cost SCHPC containing RHA and FA with very high filling ability, adequate passing ability, segregation resistance and very high compressive strength close to that of UHPC, especially in the long term.
- The replacement of cement by 20% FA results in higher filling ability, lower segregation resistance and minor higher long term compressive strength of SCHPC than that by 40% FA when w/b ratio and paste volume of concrete are kept constant.

- The increase in RHA as a replacement of cement increases the plastic viscosity and hence improves segregation resistance of SCHPC, regardless of the reduction in density of paste due to lower density of RHA. RHA can be considered as viscosity modifying agent.
- The increase in RHA as a replacement of cement increases compressive strength of concrete in long term. At the age of 56 day, SCHPC containing 20%RHA and 20%FA partial replacement cement has significantly higher compressive strength than that of SCHPC with only cement as binder.
- The combination of RHA and FA improves not only self-compactability but also compressive strength of SCHPC. The SCHPC containing 20% FA and 10% RHA as a partial replacement of cement has better self-compactability in terms of segregation resistance and higher compressive strength than those of control concrete containing only cement as binder.
- With this particle size of RHA (5,7µm), the SCHPC mixture containing 20% FA and 10%RHA as a partial replacement of cement has similar self-compactability and higher long term compressive strength compared to corresponding mixture containing SF and FA.

5 Acknowledgements

The principal author would like to express thanks to Ministry of Education and Training of Viet Nam, F.A. Finger-Institute for Building Material Science (FIB) and German Academic Exchange Service (DAAD). The authors are also grateful to Dr. Bui, D.D.; Dipl.-Ing. Flohr, A.; Dipl.-Ing. Müller, M.; Dipl.-Ing. Ehrhardt, D.; Dipl.-Ing. Giese, A. for helpful discussions.

References

[1] Safiuddin, M.: Development of self-consolidating high performance concrete incorporating rice husk ash, PhD thesis, University of Waterloo, Canada, 2008.
[2] EFNARC.: Guidelines for viscosity modifying admixtures for concrete, 2006.
[3] Gesoglu, M.; Güneyisi, E.; Özbay, E.: Properties of self-compacting concretes made with binary, ternary, and quaternary cementitious blends of fly ash, blast furnace slag, and silica fume, *Contruction and Building materials* 23(5), pp. 1847-1854, 2009.
[4] Bui, D. D.: Rice husk ash as a mineral admixture for high performance concrete, PhD thesis, Delft University, The Netherlands, 2001.
[5] Nguyen, V.T.; Ye, G.; Breugel, K.V.; Fraaij, A.L.A.; Bui, D.D.: The study of using rice husk ash to produce ultra high performance concrete. *Construction and Building Materials* 25(4), pp. 2030-2035, 2011.
[6] Memon, S.A.; Shaikh, M.A.; Akbar, H.: Utilization of rice husk ash as viscosity modifying agent in self-compacting concrete, *Construction and Building Materials* 25 (2), pp. 1044-1048, 2011.
[7] Khatib, J. M.: Performance of self-compacting concrete containing fly ash, *Construction and Building Materials* 22(9), pp. 1963-1971, 2008.
[8] Brouwers, H.J.H.; Radix, H.J.: Self-compacting concrete: Theoretical and experimental study, *Cement and Concrete Research* 35 (11), pp. 2116-2136, 2005.
[9] Le, T. H.; Siewert, K.; Ludwig, H.M.: The modified mix design for self-compacting high performance concrete containing various mineral admixtures, Proc. 3rd symposium on Ultra high performance concrete and Nanotechnology for High performance construction materials, Kassel 2012. under preparation.
[10] Uysal, M.; Sumer, M.: Performance of self-compacting concrete containing different mineral admixtures, *Construction and Building Materials* 25 (11), pp. 4112-4120, 2011.
[11] Okamura, H.; Ouchi, M.: Self-compacting concrete, Journal of advanced concrete technology, pp. 5-15, 2003.
[12] Koehler, E.P.; Fowler, D.W.: Aggregates in self-consolidating concrete, International Center for Aggregates Research, Austin, 2007.

[13] Barbhuiya, S.: Effects of fly ash and dolomite powder on the properties of self-compacting concrete, *Construction and Building Materials* 25 (8), pp. 3301-3305, 2011.

[14] Yu, Q.; Sawayama, K.; Sugita, S.; Shoya, M.; Isojima, Y.: The reaction between rice husk ash and $Ca(OH)_2$ solution and the nature of its product, *Cement and Concrete Research*, pp. 37-43, 1999.

Proportioning Optimization of UHPC Containing Rice Husk Ash and Ground Granulated Blast-furnace Slag

Van Viet Thien An[1,2], Horst-Michael Ludwig[1]
1: Institute for Building Materials Science, Bauhaus-University Weimar, Germany
2: Building Materials Technology Department, National University of Civil Engineering, Hanoi, Vietnam

The suitable fineness of rice husk ash (RHA) to completely replace silica fume (SF) in producing economical UHPC was chosen by study on the effect of different finenesses of RHA on workability and compressive strength. The optimum RHA content partial replacement cement was proposed. Furthermore, mini-cone slump flow and compressive strength of 28 statistically designed mixtures with four variables, namely cement, RHA, ground granulated blast-furnace slag (GGBS) and superplasticizer (SP) dosage, have been experimentally determined. These mixtures were designed by the D-optimal design of the Design-Expert 8 software. Using the statistical technique, two complete models of the flowability and compressive strength were proposed. Their 3D response surface and contour plots clearly showed how the ingredients of UHPC affect its workability and compressive strength. A ternary binder composed of cement, RHA and GGBS, and a dosage of SP were chosen for the highest strength.

Keywords: UHPC, proportioning optimization, RHA, GGBS, superplasticizer

1 Introduction

Previous study [1] indicated that the combination of rice husk ash (RHA) and ground granulated blast-furnace slag (GGBS) enhances not only workability but also compressive strength of ultra high performance concrete (UHPC). When dosage of the used superplasticizer (SP) is higher than the saturation dosage, it reduces slump flow, increases air content and hence decreases the compressive strength of UHPC. Furthermore, RHA used to produce UHPC in studies [1-3] are very fine, with mean particle size about 5.5 μm. It needs high energy consumption and suitable equipment to grind. The finer RHA not only possesses a lower specific surface area, water or SP demand, but also reduces compressive strength of standard mortar [4]. Therefore, the influence of different finenesses of RHA, RHA content, and synergic effect of combination of RHA, GGBS and SP dosage on properties of UHPC need more detail investigations.

Concrete is a multivariate system and normally needs more than one important objective function. The classical method for optimizing mixture proportions is trial and error, or changing one ingredient and studying the effect of the ingredient on the response. It will be inefficient and costly. More importantly, they may not provide the economical mixture. Standard response surface designs, such as factorial designs or central composite design can use for optimizing concrete mixture in which the n mixture components have to be reduced to n-1 independent factors by taking the ratio of two components [5]. However, changing the proportion of one ingredient immediately influences the proportion of the others because the mix proportions are limited to sum to 100%. Moreover, some processing factors have strong effect on the responses. Hence, different method is required for choosing appropriate experimental design and analyzing final results for all variables. The combined mixture-process model is appropriate for these problems [5-7]. User can evaluate both of all n dependent mixture components and process variables such as mixing time, vibration time, SP dosage… which can be varied independently of others and of mixture components.

The aim of this study was to investigate the effect of different fineness of RHA on workability and compressive strength of UHPC to choose the suitable RHA for UHPC production in terms of economic, technical validity and realization. With the selected RHA, the optimized RHA content to partially replace cement in UHPC has been proposed. In addition, the effect of the

combination of RHA and GGBS to partially replace cement, and SP dosage on workability and compressive strength of UHPC has been statistically analyzed by D-optimal criterion of the Design-Expert 8 software. Using the optimization tool of the program, the optimal proportions of UHPC containing RHA and GGBS in contribution with a suitable SP dosage for the highest compressive strength were also proposed.

2 Experimental design

Materials and test methods

An ordinary portland cement sample, CEM I 52.5 R-HS/NA conforming to DIN EN 1164-10, and the following additives, aggregates were used: RHA, GGBS, quartz powder, quartz sand (0.125/0.5 mm). The polycarboxylate ether superplasticizer with 40% of solid content was selected in previous study [1]. This SP is highly compatible with the UHPC containing RHA. The chemical compositions and properties of the materials can be taken in elsewhere [1].

Five different fineness rice husk ashes were used to investigate the effect of fineness of RHA on workability and compressive strength of UHPC. This RHA is a mesoporous amorphous siliceous material with more than 85 wt.-% SiO_2 and 97.4 wt.-% amorphous phase (Figs.1 and 2) [4]. Time of grinding in a ball mill, mean particle size and specific surface area (SSA) of RHA are given in Table 1. The particle size distribution of materials is shown in Fig. 3. For more details of these RHA, it can be found in elsewhere [4].

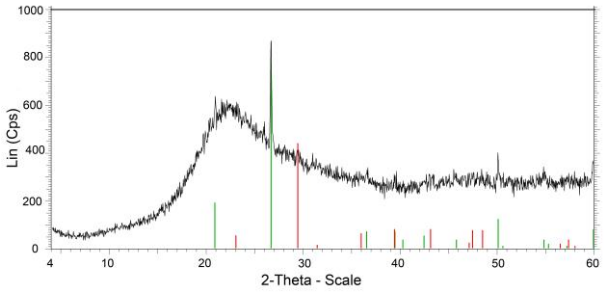

Figure 1: XRD patterns of RHA sample.

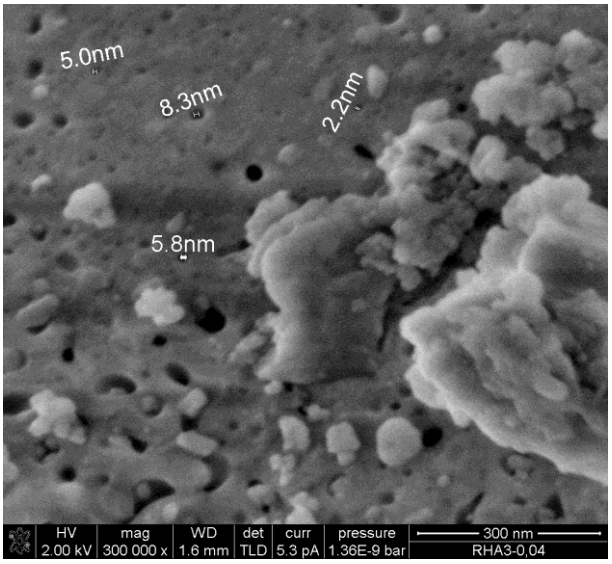

Figure 2: Surface structure of ground RHA particle.

Table 1: Grinding time, mean particle size and specific surface area of RHA.

Rice husk ash	RHA-45	RHA-120	RHA-240	RHA-360	RHA-540
Grinding time [min]	45	120	240	360	540
Mean particle size [µm]	9.65	7.41	6.22	5.78	5.34
SSA (BET) [m^2/g]	59.42	52.28	47.78	44.02	43.69

Principles of mix design, mixing procedure, casting and test methods of UHPC are found in elsewhere [1]. Typical UHPC mixtures are given in Table 2. Volume of water to volume of fine materials ratio (W/F_v) of UHPC is 0.55. The paste volume is 61 vol.-% of UHPC. Quartz powder is 20 vol.-% of fine materials. These values were chosen based on previous studies [1, 8-9].

The pozzolanic admixtures partially replace cement in volume. Mini-cone slump flow of UHPC mixtures was determined 15 minutes after water addition.

The slump flow values were measured after further 2 minutes without shocking. Samples 40 x 40 x 160 mm3 were formed with 30 seconds vibration, kept in moulds at 20°C, 95% relative humidity (RH) for 48h and followed by storing at 20°C, 100% RH until examination. Compressive strength of samples was tested at the age of 28 days in accordance to DIN EN 196-1.

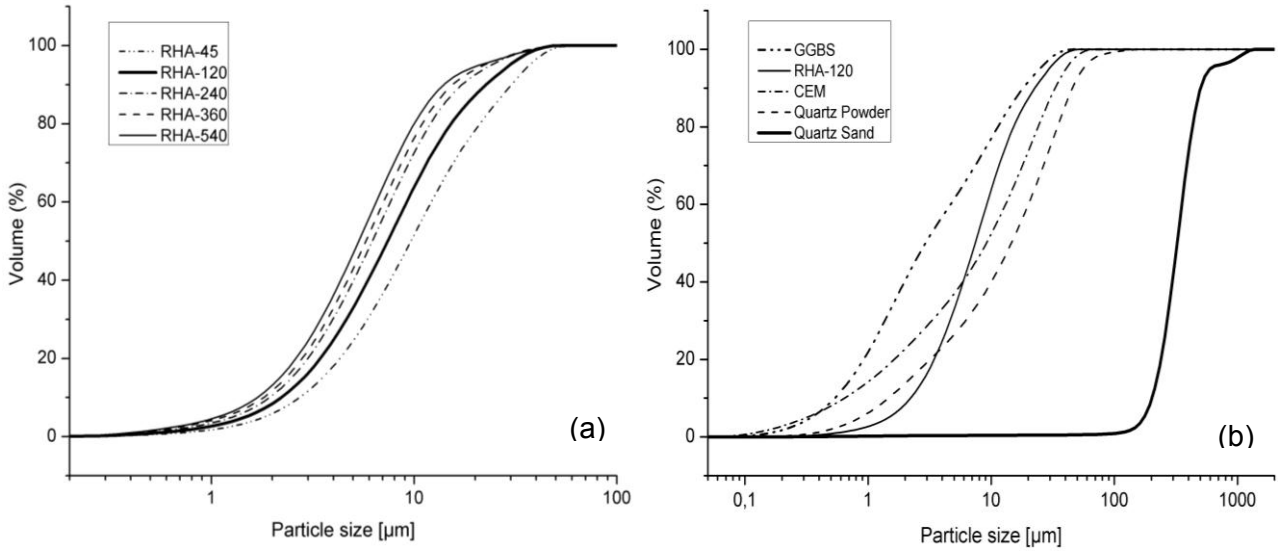

Figure 3: Particle size distribution of materials: a) RHA; b) UHPC.

Table 2: Typical mix proportions of UHPC mixtures.

UHPC mixture	Cement [kg/m^3]	Q. sand [kg/m^3]	Q. powder [kg/m^3]	RHA [kg/m^3]	GGBS [kg/m^3]	Water * [kg/m^3]	w/b	W/F$_v$
UHPC-22.5%RHA	780.8	1029.6	207.8	155.1	-	216.5	0.231	0.55
UHPC-15%RHA -10% GGBS	755.6	1029.6	207.8	103.4	91.6	216.5	0.228	0.55
UHPC-15%RHA -20%GGBS	654.9	1029.6	207.8	103.4	183.2	216.5	0.230	0.55
UHPC-22.5%RHA -20%GGBS	579.3	1029.6	207.8	155.1	183.2	216.5	0.236	0.55

(*)- The total water content

Design of combined mixture-process model

Three cementitious materials: cement, RHA-120 and GGBS in volume content as mixture components of binder and superplasticizer dosage in dry mass content of cementitious materials as process variable were chosen to investigate their effect on workability and compressive strength of UHPC. Three binder components are designated as A, B, C, respectively. Process variable is D. And the predicted responses, namely flowability and compressive strength are designated as R_1 and R_2, respectively. All the other components of UHPC, mixing procedure, casting, treatment, and test methods were kept in constant for all mixtures. Based on preliminary tests, the range of process variable, 0.8% ≤ D ≤ 1.2% was selected. The mixture constraints for the binder components were also chosen:

$$A + B + C = 100\%$$

$47.5\% \le A \le 82.5\%$
$7.5\% \le B \le 22.5\%$
$10\% \le C \le 30\%$

Because the SP dosage and the change of SP dosage were very small, it was ignored in calculation of mix proportions. Hence, it was a three-component mixture combined with one process variable experiment. The D-optimal design was chosen and assumed that a combined quadratic x quadratic model should be satisfactory to represent the effect of the mixture components and process variable on both the predicted responses. The complete combined model is in Equation (1). The designing experiments produced by the Design-Expert 8 are shown in Fig. 4 and Table 3. They are the actual mixture components and process variable levels. The complete model has 28 runs including 23 points at three levels of process variable D (0.8%, 1.0%, 1.2%) with 5 replicated runs to provide an estimate of error, 5 points at D = 0.9% and 1.1% to estimate the lack of fit. The typical mix proportions of mixtures can be found in Table 2.

$$R = f(A, B, C, D) = \beta_1 A + \beta_2 B + \beta_3 C + \beta_{12} AB + \beta_{13} AC + \beta_{23} BC + \alpha_{11} AD + \alpha_{21} BD + \alpha_{31} AD + \alpha_{121} ABD + \alpha_{131} ACD + \alpha_{231} BCD + \delta_{111} AD^2 + \delta_{211} BD^2 + \delta_{311} CD^2 + \delta_{1211} ABD^2 + \delta_{1311} ACD^2 + \delta_{2311} BCD^2 \quad (1)$$

Where: β_1, β_2, β_3 are linear coefficients; β_{12}, β_{13}, β_{23} are cross product coefficients; α_{11}, α_{21}, α_{31}, α_{121}, α_{131}, α_{231} are linear process variable coefficients; and δ_{111}, δ_{211}, δ_{311}, δ_{1211}, δ_{1311}, δ_{2311} are quadratic process variable coefficients.

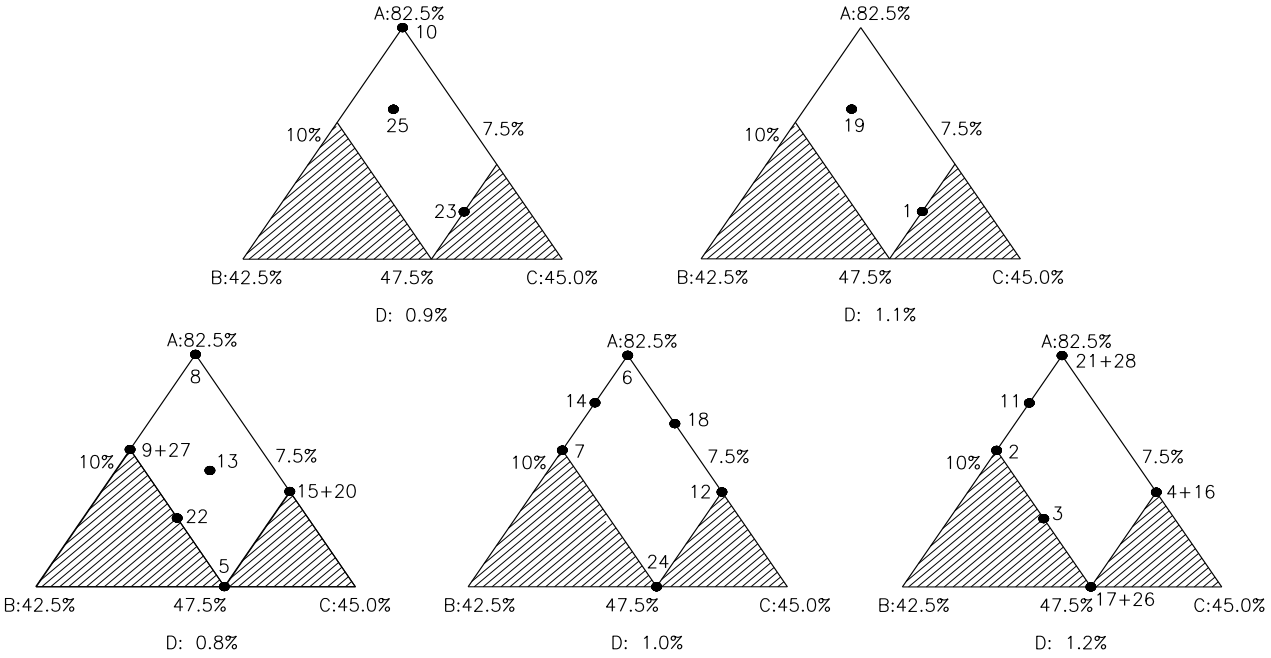

Figure 4: Twenty-eight-run D-optimal design. Points with a (+) indicate replicates.

3 Results and discussion

Effect of fineness of RHA on properties of UHPC

UHPC-15%RHA-10%GGBS mixture given in Table 2 with 1 wt.-% SP was used to investigate the effect of different finenesses of RHA on the properties of UHPC.

The results in Fig. 5 show that UHPC containing RHA-45 takes about 20 minutes of mixing to get fluidity and possesses low slump flow. All the other RHA can allow producing UHPC

mixtures within 15 minutes of mixing. They have a slump flow over 300 mm. In generally, the finer the RHA gives the higher the flowability of concrete. UHPC containing RHA-360 has the highest compressive strength. The slump flow and strength of UHPC containing RHA-120 are similar to those of RHA-240. With the aims to produce UHPC in terms of economic, technical validity and realization, RHA with mean particle size of 7.41 μm (RHA-120) was chosen to produce UHPC in further researches.

Influence of RHA content on properties of UHPC containing RHA

With selected RHA, different content of RHA was used to study how it influences on workability and compressive strength of UHPC. GGBS was not used in this test. The SP dosage was 1 wt.-% of binder. Typical UHPC mixture (UHPC-22.5%RHA) can be found in Table 2. The results are shown in Fig. 6. When RHA content increases, both flowability and strength of UHPC increase initially and then decrease. There is no significant difference of slump flow and compressive strength between UHPC-15%RHA and UHPC-22.5%RHA. When 1 vol.-% steel fibers with a length of 9 mm and a diameter of 0.15 mm was used, the compressive strength of both UHPC obtained 169.5 MPa. Therefore, 22.5% RHA in volume partial replacement cement can be considered as optimal content in UHPC containing RHA in this study.

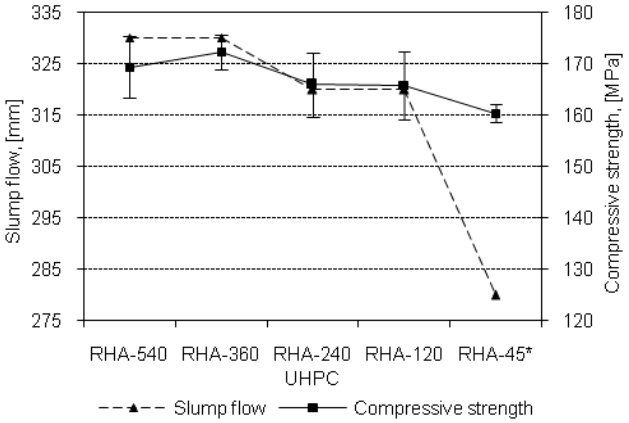

*- Mixing time is 20 minutes

Figure 5: Effect of different finenesses of RHA on properties of UHPC.

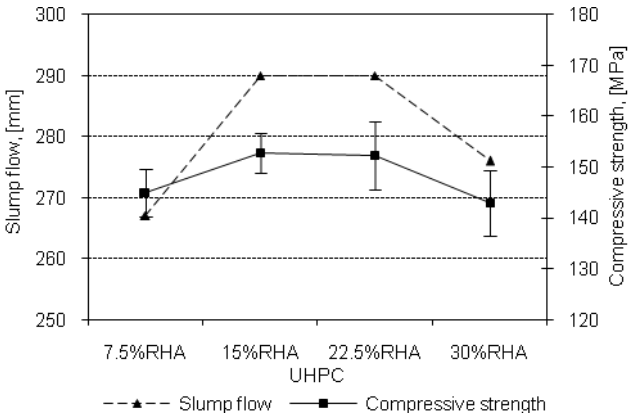

Figure 6: Effect of RHA-120 content on properties of UHPC.

Optimization of mix proportions of UHPC incorporating RHA and GGBS

The 28 designed mixtures of UHPC in Table 3 were carried out and tested the slump flow and compressive strength. The 28-run design result was run and analyzed with the Design-Expert 8 software. With the input data, the software suggested the combined quadratic x quadratic model against other models such as quadratic x linear, quadratic x cubic… for both of the responses. Thus the models chosen to design the experiment were good. Both of the predicted models were significant. Their lacks of fit were not significant. The adjusted R-squared and the predicted R-squared were 0.9671 and 0.8206 with the slump flow response; and 0.9301 and 0.8204 with the compressive strength response, respectively. Several techniques in diagnostic tool of the program have been also used to check the model's adequacy. The complete fitted models with the actual mixture components and process factor are given in equation 2 and 3. Some of the coefficients in the models are insignificant and could be eliminated. In this case, there is no advantage to reduced model because the adjusted R-squared is changed not so much. Moreover, the interactions should not be removed in the combination of mixture and process model, especially with the combined quadratic x quadratic model [5, 10]. Therefore, the complete models should be used. The predicted data calculated from Equations (2), (3) and the

ratio between predicted and experimental data are also given in Table 3. It shows that the fitness of the selected models is good and these models could be used for further navigations.

Table 3: Twenty-eight-run D-optimal design with data.

Run	Cement A [%]	RHA-120 B [%]	GGBS C [%]	SP D [%]	Experimental		Predicted		Ratio	
					R_1 [mm]	R_2 [MPa]	R_1* [mm]	R_2* [MPa]	R_1*/R_1	R_2*/R_2
1	55.0	15.0	30.0	1.1	347	159.9	347.1	158.9	1.0004	0.9934
2	67.5	22.5	10.0	1.2	324	149.4	324.6	149.5	1.0018	1.0004
3	57.5	22.5	20.0	1.2	336	152.3	335.0	151.9	0.9969	0.9973
4	62.5	7.5	30.0	1.2	341	156.8	339.5	155.5	0.9955	0.9918
5	47.5	22.5	30.0	0.8	343	154.2	342.4	154.0	0.9981	0.9989
6	82.5	7.5	10.0	1.0	321	158.7	318.6	158.6	0.9927	0.9996
7	67.5	22.5	10.0	1.0	316	161.5	316.7	161.3	1.0021	0.9987
8	82.5	7.5	10.0	0.8	295	158.3	294.4	158.3	0.9978	1.0000
9	67.5	22.5	10.0	0.8	306	154.8	303.7	155.3	0.9923	1.0030
10	82.5	7.5	10.0	0.9	307	159.8	310.0	160.0	1.0097	1.0011
11	75.0	15.0	10.0	1.2	320	155.8	318.8	155.7	0.9964	0.9992
12	62.5	7.5	30.0	1.0	349	156.8	347.6	157.3	0.9959	1.0032
13	65.0	15.0	20.0	0.8	338	165.2	339.2	165.3	1.0037	1.0005
14	75.0	15.0	10.0	1.0	320	164.6	320.3	164.5	1.0008	0.9991
15	62.5	7.5	30.0	0.8	351	161.2	349.8	161.1	0.9965	0.9991
16	62.5	7.5	30.0	1.2	338	154.4	339.5	155.5	1.0044	1.0092
17	47.5	22.5	30.0	1.2	346	141.0	348.7	142.0	1.0079	1.0073
18	72.5	7.5	20.0	1.0	329	155.1	330.6	154.5	1.0048	0.9963
19	70.0	15.0	15.0	1.1	323	159.0	325.1	160.3	1.0065	1.0084
20	62.5	7.5	30.0	0.8	349	161.0	349.8	161.1	1.0022	1.0003
21	82.5	7.5	10.0	1.2	314	150.0	315.2	147.0	1.0039	0.9803
22	57.5	22.5	20.0	0.8	330	157.0	330.3	157.1	1.0010	1.0009
23	55.0	15.0	30.0	0.9	351	162.1	353.3	162.3	1.0066	1.0014
24	47.5	22.5	30.0	1.0	349	155.3	348.3	155.5	0.9981	1.0014
25	70.0	15.0	15.0	0.9	331	162.7	326.1	162.4	0.9852	0.9979
26	47.5	22.5	30.0	1.2	351	142.7	348.7	142.0	0.9935	0.9953
27	67.5	22.5	10.0	0.8	301	155.7	303.7	155.3	1.0088	0.9972
28	82.5	7.5	10.0	1.2	316	144.2	315.2	147.0	0.9975	1.0197

$$R_1 \text{ (flowability)} = -11.54A - 66.55B - 76.76C + 1.21AB + 1.54AC + 1.68BC + 26.72AD + 98.73BD + 154.33CD - 1.85ABD - 2.90ACD - 2.75BCD - 12.12AD^2 - 32.59BD^2 - 71.62CD^2 + 0.70ABD^2 + 1.34ACD^2 + 1.10BCD^2 \quad (2)$$

$$R_2 \text{ (strength)} = -7.22A - 72.13B - 105.33C + 0.90AB + 1.81AC + 2.34BC + 18.43AD + 141.45BD + 222.87CD - 1.72ABD - 3.79ACD - 4.69BCD - 9.67AD^2 - 73.05BD^2 - 113.89CD^2 + 0.90ABD^2 + 1.94ACD^2 + 2.38BCD^2 \quad (3)$$

Influence of cementitious materials and SP dosage on the flowability of UHPC

To interpret the influence of the components of binder and SP dosage on flowability of UHPC, 3D response surface and contour plots of the workability versus the mixture components at three levels of the SP dosage have been produced (Fig. 7). It would be seen clearly that GGBS strongly improves the workability of UHPC at all levels of SP dosage. The effect of RHA depends on the dosage of SP used. At low SP dosages, flowability of UHPC increases initially and then decreases when RHA content increases. But at high SP dosage (D = 1.2 wt.-%), the more the RHA content the higher the flowability of UHPC. The impact of the different cementitious materials at the different dosages of SP is illustrated by how the shape and the pace of the contours change.

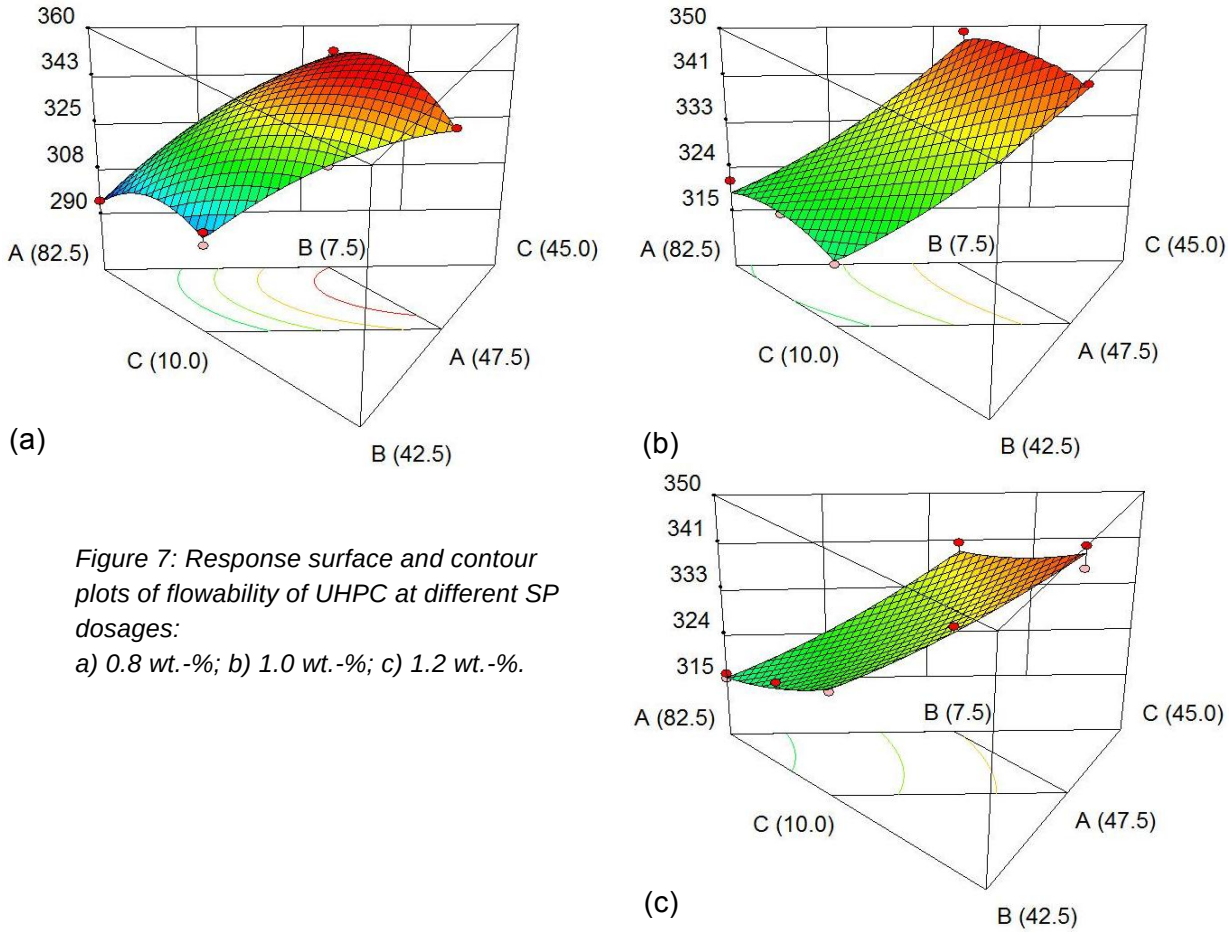

Figure 7: Response surface and contour plots of flowability of UHPC at different SP dosages:
a) 0.8 wt.-%; b) 1.0 wt.-%; c) 1.2 wt.-%.

The behavior of SP in UHPC is mainly influenced by GGBS and RHA content replacement cement. At low GGBS and RHA content, the flowability of UHPC increases initially and then decreases when SP dosage increases. At low GGBS and high RHA content, the dosage of SP improves the workability of UHPC. But when GGBS content is increased, the high dosage of SP makes workability of UHPC reduce with low RHA content and slightly increase with high RHA content. These results assume that GGBS decreases and RHA increases the saturation dosage of SP of UHPC mixture. The slump flow of UHPC reduces when SP dosage is higher than saturation dosage. It is consistent with results of previous study [1]. With the aim to get maximum slump flow, we will want to adjust the variables to high content of GGBS, low dosage of SP in combination with a content of RHA.

Influence of cementitious materials and SP dosage on the strength of UHPC

Similar to the workability response, 3D response surface and contour plots of compressive strength versus the mixture components at three levels of the process factor are found in Fig. 8

These response surface and contour plots illustrate that there is an optimized content of RHA which enables UHPC mixture obtain the highest compressive strength at all levels of GGBS and SP. The effect of GGBS on compressive strength is affected by SP dosage. At SP dosage of 0.8 wt.-% and 1.2 wt.-%, the compressive strength initially increases but decreases afterward when GGBS increases. This change is contrary at SP dosage of 1 wt.-%. The reason for the difference in the effect of GGBS on strength of UHPC at 1 wt.-% superplasticizer is unclear. The maximum compressive strength comes from a ternary binder composed of cement, RHA and GGBS, and a low dosage of SP.

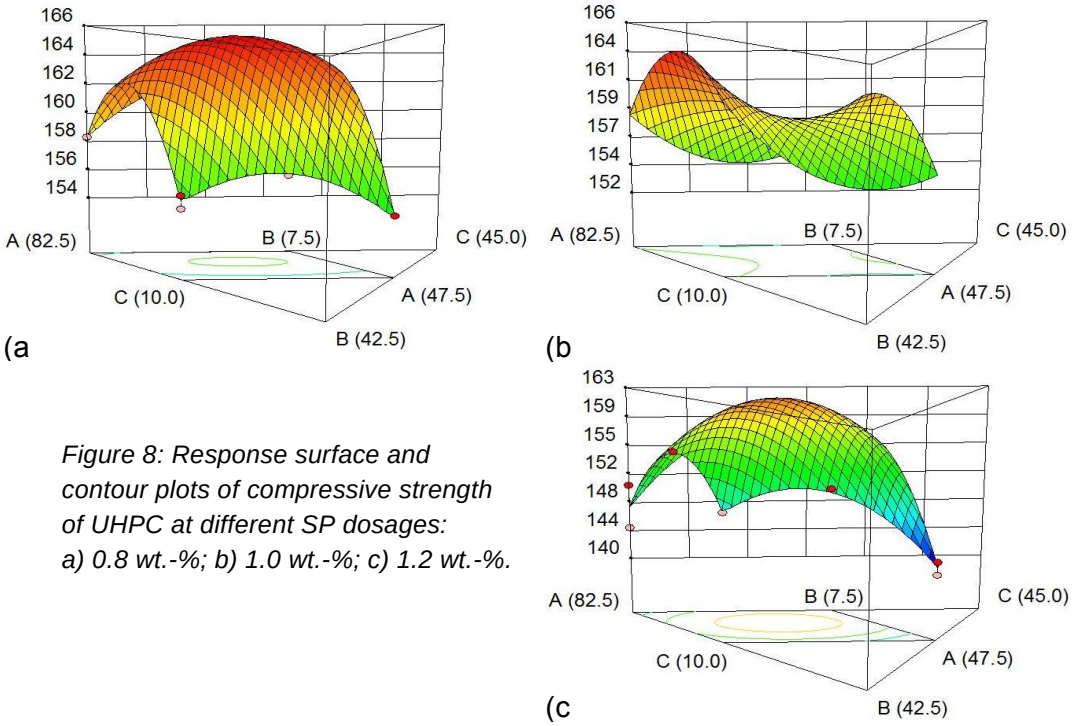

Figure 8: Response surface and contour plots of compressive strength of UHPC at different SP dosages: a) 0.8 wt.-%; b) 1.0 wt.-%; c) 1.2 wt.-%.

Proportioning optimization of UHPC containing RHA and GGBS

The optimization tool of the program was used to find the optimal proportions of UHPC containing RHA, GGBS, and a suitable dosage of SP. The input criteria are: A (Cement), B (RHA), C (GGBS), D (SP): in range; R_1 (workability): in range; R_2 (strength): maximum. The program gave some solutions. The best solution was chosen in Table 4 in terms of highest compressive strength, low cement content and SP dosage to produce UHPC more sustainable.

Table 4: Experimental proportions versus optimized proportions.

Material	Variable	Unit	The mix proportions having the highest strength	
			Experimental	Optimized by Design-Expert
Cement	A	[vol.-%]	65	63.8
RHA	B	[vol.-%]	15	13.3
GGBS	C	[vol.-%]	20	22.9
SP	D	[wt.-%]	0.8	0.8
Slump flow		[mm]	338	345
Compressive strength at 28d		[MPa]	165.2	165.4

The results of slump flow, compressive strength of the experimental mixture and Design-Expert's mixture are similar (Table 3). Thus, the UHPC with 65 vol.-% cement, 15 vol.-% RHA, 20 vol.-% GGBS of binder and 0.8 wt.-% SP of cementitious material is selected as optimal mix proportions. The weight of materials for 1 m^3 concrete are given at UHPC-15%RHA-20%GGBS

mixture in Table 2. When 1 vol.-% steel fibers with a length of 9 mm and a diameter of 0.15 mm was used, the compressive strength of this UHPC obtained 196 MPa at the age of 28 days.

4 Conclusions

The following conclusions can be drawn from the results of this study:

RHA with mean particle size of 7.41 µm is suitable for producing economical UHPC by complete replacement silica fume. When this RHA is used to partially replace cement, 22.5 vol.-% is considered as the optimum content.

The mixture-process models of workability and compressive strength of UHPC with three mixture components and a process variable built based on 28 designed experiments by the D-optimal design of Design-Expert software fitted well with the experimental data. The influence of the variables on the workability and compressive strength was also interpreted clearly by using 3D response surface and contour plots.

The ternary binder composed of 65 vol.-% cement, 15 vol.-% RHA and 20 vol.-% GGBS combining with a dosage of 0.8 wt.-% SP in solid content of the binder is the optimum mixture proportions for the highest compressive strength of the sustainable UHPC in this study.

5 Acknowledgments

The principal author would like to thank for the PhD scholarship sponsored by Ministry of Education and Training of Vietnam, F.A. Finger-Institute for Building Material Science (FIB)-Bauhaus-University Weimar and German Academic Exchange Service (DAAD). The authors also gratefully acknowledge helpful discussions from Dr. Bui Danh Dai, Dipl. -Ing. Simone Peters, Dipl. -Min. Claudia Pfeifer and Dipl. -Ing. Christin Pflug during this study.

References

[1] Van, V.T.A.; Ludwig, H.-M.: Using rice husk ash and ground granulated blast-furnace slag to replace silica fume in UHPC. Workshop on Performance-based Specifications for Concrete, Leipzig 2011.

[2] Nguyen, V.T.; Ye, G.; Van Breugel, K.; Fraaij, A.L.A.; Bui, D.D.: The study of using rice husk ash to produce ultra high performance concrete. Construction and Building Materials, 25(4), pp. 2030-2035, 2011.

[3] Nguyen, V.T.; Ye, G.; Van Breugel, K.; Copuroglu, O.: Hydration and microstructure of ultra high performance concrete incorporating rice husk ash. Cement and Concrete Research, 41(11), pp. 1104-1111, 2011.

[4] Van, V.T.A.; Ludwig, H.-M.: Study on pozzolanic reactivity of rice husk ash in cement system. Workshop on Performance-based Specifications for Concrete, Leipzig 2011.

[5] Myers, R.H.; Montgomery, D.C.; Anderson-Cook, C.M.: Response surface methodology: process and product optimization using designed experiments, Wiley, 2009.

[6] Anderson-Cook, C.M., et al.: Mixture and mixture–process variable experiments for pharmaceutical applications. Pharmaceutical Statistics 3(4), pp. 247-260, 2004.

[7] Duineveld, C.A.A.; Smilde, A.K.; Doornbos, D.A.: Comparison of experimental designs combining process and mixture variables: Part I. Design construction and theoretical evaluation. Chemometrics and Intelligent Laboratory Systems 19(3), pp. 295-308, 1993.

[8] Richard, P.; Cheyrezy, M.: Composition of reactive powder concretes. Cement and Concrete Research, 25(7), pp. 1501-1511, 1995.

[9] Park, J.J.; Kang, S.T.; Koh, K.T.; Kim, S.W.: Influence of the ingredients on the compressive strength of UHPC as a fundamental study to optimize the mixing proportion. Proceedings of the Second international Symposium on Ultra High Performance Concrete, Kassel 2008.

[10] Anderson, M.J.; Whitcomb, P.J.: Designing Experiments that Combine Mixture Components with Process Factors. Chemical Engineering Progress, December, 2000.

Making UHPC with Local Materials - The Way Forward

Per Fidjestol[1,2], Rein Terje Thorsteinsen[2], Paul Svennevig[2]
1: Elkem AS Silicon Materials, Kristiansand, Norway
2: University of Agder, Grimstad, Norway

Commercially available UHPC is frequently based on prepackaged dry materials. Logistics and handling then become an important part of the cost picture compared to what would be the case if more conventional, locally available, materials were used. The paper presents work done with particle packing software for the successful use of locally available materials in the production of Ultra High Performance Concrete (UHPC).

Keywords: ultra high performance, uhpc, silica fume, microsilica, local materials

1 Introduction

Ultra High performance Concrete (UHPC) has been around for three decades and Elkem has been involved since the early days; first with Densit® and later with Elkem's proprietary brand, Ceramite®, based on CA cement. In order to benefit from the concept on a larger scale, local raw materials should be used. The project described investigated this option for the University location in Southern Norway. With the concept proven, this opens the door for future development based on this technology and intended for the local industry.

Figure 1: UHPC bridge Kg. Linsum Motorway Bridge, Negeri Sembilan, Malaysia, Picture: Courtesy of Dr Voo Yen Lei, Dura Technology Sdn Bhd.

Wide scale use of UHPC is challenged by the availability of raw materials. Much of the more publicized reference projects with UHPC, from the early Densit® and onwards, have been made using prebagged materials, introducing costs and logistic issues. The need to use local materials is significant in order to make the use of this material more economical and generally available.

The project referenced here was to investigate the possibility of making UHPC with more readily available materials and more conventional processing tools. The development used sieving and particle packing software to develop the optimum material for this locality. .

2 Use of local materials

The task of the main project [1] was to select from locally available materials in order to produce UHPC in the lab. The local materials are sands from typical suppliers in the locality of Agder University, cement from the national producer, fly ash from the closest supplier (in Denmark) (who also supplies the cement company) and admixtures from one of the large suppliers in Norway.

Three water/binder ratios were used, and curing was done at 20 and 90 degrees centigrade.

Table 1: Materials

Aggregates	Natural granite and gneiss based : Reddal, Tveit , Årdal sand (10, 50 and 250 km away) Crushed: Dura-Splitt® (from 250 km away) The sands were sieved on sieves 4mm – 2mm – 1mm – 0,5mm – 0,250mm – 0,125mm – 0,063mm (approximately US sieves 4, 10, 18, 35, 60, 120, 230) An additional test was made with high strength crushed sand from Dura-Splitt 0-2mm, fractioned as the natural sands.
Cement	Industri (Rapid hardening Portland Cement) Blaine 550 m^2/kg, 7 % C3A, EN CEM1-42.5 Anlegg (High strength Portland Cement) Blaine 360 m^2/kg, 7% C3A, EN CEM 1-52.5 (Both from Norcem as, 100 km away)
Additions	Undensified silica fume (940U) (EN 13263/ASTM C1240) Fly ash (EN450/ASTMC618, type F) (Silica Fume from Elkem, 50 km away, Fly Ash from Denmark, 500 km away)
Admixtures	Suppliers were Rescon Mapei, BASF and Sika
Steel Fibers	Bekaert 6mm and 13mm (imports)
W/B-ratios	0.16, 0.18 and 0.20

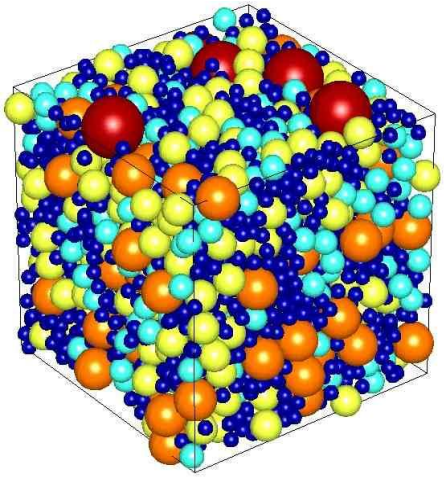

Figure 2: Packing of particles.

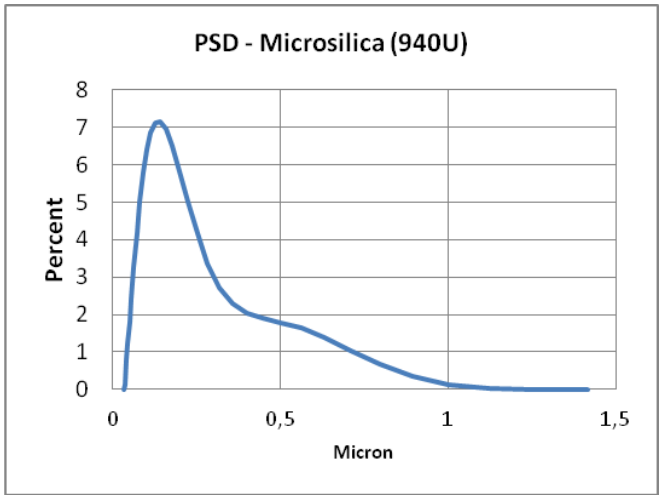

Figure 3: Particle Size Distribution of typical microsilica.

To achieve the optimal mix design for UHPC, maximum packing of the particulate materials are required. The smaller particles fill the gaps between the bigger ones (Fig. 2).

The aggregates were sieved into a number of fractions in order to allow the fine tuning of the particle size distribution (PSD). The mixtures were assembled using EMMA (Elkem Materials Mix Analyzer) [2]. EMMA is based on the Andreassen model [3] for particle packing, and helps design a mixture with a minimum of voids. The "ideal" mix is represented by a straight line in a cumulative double-log particle

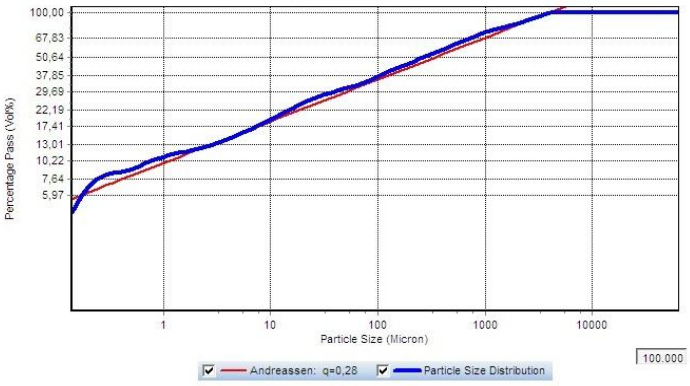

Figure 4: EMMA diagram, good fit, good flow.

size/volume fraction diagram, The inclination of this line, “q”, influences the rheological properties of the mixture; a low q (<0.28) give a composition containing more fine material, thus increased likelihood of good flow. A q-value of 0.36, which gives a very stiff mixture, has been applied with success for roller compacted concrete mixtures. (With q>0.36, optimum packing is not possible.) 0.30 is the program default value. Figure 4 shows a typical (good) EMMA-plot, with the q-line in red and the cumulative PSD in blue. If the proportions are selected so that the blue line matches the red, optimum packing is obtained.

3 Batching and mixing procedures

A Hobarth mixer was used, and the mixing procedure was based on recommendation in ASTM and EN standards for testing silica fume with suitable modifications, both for batching sequence and mixing time. The mixing sequence below was found to give the best results.

Curing

Curing involved both standard curing and heat curing:

- Standard: 20°C in water tank
- Heat curing: 48 hours between day 1 and 3 at 90°C and 100% RH. By wrapping wet burlap and plastic around the specimens appropriate moisture conditions were ensured.

Table 2: Batching and mixing procedure

What	Time	Mixing speed
Mix water, aggregate and 2/3 of additive	30 sec	1
Add cement	30 sec	2*
Add microsilica	30 sec	2*
1/3 of additive	15 sec	2
Add fly ash	30 sec	2*
Fiber dosing	30 sec	2
Move mortar from rim into bowl	30 sec	0
Final mix	135 sec	2
SUM	5 min 30sec	

4 Tests and results

The tests made on the mortar were

- Flow table test, ASTM C230
- Compressive strength, 50 mm cubes; 1, 3, 7 and 28 days
- Bending tensile strength, 40X40X160 mm beams, 28 days
- Chloride permeability, Modified NTBuild 492, 14 days
- Density.

Compressive strength

The specimens were tested for compressive strength after 1, 3, 7 and 28 days.

The results show that aggregates from Reddal, Tveit and Årdal are all able to give ultra high performance concrete, with heat cured strengths in the range of 160 to 190 MPa.

Table 3: Mix compositions (kg/m3) and flow (mix 27 deleted due to failure of curing container).

Mix	W/B	Aggregate	Cement		Microsilica	FA	Water	Admixture/dry content			Fiber		Sand [kg/m³]					Flow
			Anlegg	Industri				1 22%	2 40%	3 16.5%	[liter/m³]	diameter/ length	0.0063-0.125mm	0.125-0.25mm	0.25-0.5mm	0.5-1mm	Total	mm
13	0.30	Reddal		437	297.22	156.31	252.56			17.47	20.0	0.6/16	264.68	264.68	264.68	264.68	1059	147
14-1	0.18	Reddal		674	252.61	168.34	112.65			101.03	20.0	0.6/16	50.44	336.89	339.89	336.89	1064	172
14-2	0.16	Reddal		576	329.88	274.79	116.76			86.37	20.0	0.6/16	58.12	302.33	314.05	314.05	989	159
15	0.20	Reddal		550	315.00	262.40	156.58			82.48	20.0	0.6/16	55.50	288.70	299.89	299.89	944	217
16	0.20	Reddal		526	376.67	301.26	196.87			52.61	20.0	0.6/16	63.83	382.37	382.37		829	183
17	0.18	Reddal		538	385.44	308.27	167.83			64.60	20.0	0.6/16	65.31	391.27	391.27		848	173
19	0.20	Reddal	660		264.16	220.06	151.70			92.42	20.0	0.6/16	55.12	286.20	297.23	297.23	935.78	218
20	0.18	Reddal	675		270.11	225.02	126.08			101.26	20.0	0.6/16	56.36	292.66	303.93	303.93	956.88	188
22	0.20	Reddal	724		289.68	263.33	182.84			86.87	20.0	0.6/16	65.88	342.18	342.18		750.24	230
23	0.18	Reddal	740		296.16	269.21	136.11			118.41	20.0	0.6/16	67.36	349.83	349.83		767.02	197
24	0.20	Reddal		655	245.57	163.64	131.08	105			20.0	0.6/16	49.03	327.50	327.50	327.50	1032	156
25	0.18	Reddal		666	249.70	166.39	90.88	133			20.0	0.6/16	49.85	333.00	333.00	333.00	1049	139
26	0.20	Reddal		696	278.55	227.91	142.80	125			20.0	0.6/16	63.41	379.85	379.85		823.11	172
28	0.18	Reddal	718		287.39	261.25	154.77		122		20.0	0.6/16	65.36	339.48	339.48		744.32	200
29	0.18	Reddal		718	287.39	261.25	154.77		122		20.0	0.6/16	65.36	339.48	339.48		744.32	193
30	0.18	Reddal	674		269.62	224.61	114.61			114.59	20.0	0.6/16	56.26	292.13	303.38	303.38	955.15	193
31	0.18	Tveit	673		269.16	224.23	103.18			127.85	20.0	0.6/16	56.16	291.63	302.86	302.86	953.51	201
32	0.18	Tveit	739		295.60	268.71	123.52			132.97	20.0	0.6/16	67.23	349.18	349.18		765.59	206
33	0.18	Tveit		739	295.60	268.71	123.52			132.97	20.0	0.6/16	67.23	349.18	349.18		765.59	153
34	0.18	Tveit	718		287.39	261.25	154.77		122		20.0	0.6/16	65.36	339.48	339.48		744.32	202
35	0.18	Tveit		718	287.39	261.25	154.77		122		20.0	0.6/16	65.36	339.48	339.48		744.32	184
36	0.18	Årdal	673		269.16	224.23	103.18			127.85	20.0	0.6/16	56.16	291.63	302.86	302.86	953.51	182
37	0.18	Reddal	673		269.16	224.23	103.18			127.85	20.0	0.13/20	56.16	291.63	302.86	302.86	953.51	191
38	0.18	Årdal	739		295.60	268.71	123.52			132.97	20.0	0.6/16	67.23	349.18	349.18		765.59	216
39	0.18	Årdal		739	295.60	268.71	123.52			132.97	20.0	0.6/16	67.23	349.18	349.18		765.59	128
40	0.18	Årdal	716		286.65	260.57	150.07		128		20.0	0.6/16	65.19	338.60	338.60		742.39	209
41	0.18	Årdal		718	287.39	261.25	154.77		122		20.0	0.6/16	65.36	339.48	339.48		744.32	192
42	0.20	Årdal	658		263.28	219.33	129.22			118.44	20.0	0.13/20	54.94	285.25	296.24	296.24	932.67	216
43	0.20	Årdal	658		263.28	219.33	129.22			118.44	20.0	0.6/16	54.94	285.25	296.24	296.24	932.67	224
44	0.20	Durasplitt	719		287.57	261.41	133.51			143.72	20.0	0.6/16	65.40	339.69	339.69		744.78	222

Table 4: Compressive strength results (some low early strengths because of retardation by admixture)

Mixture	Compressive strength [Mpa]							Flexural strength[Mpa]	
	1	3		7		28		28 days	
	Curing temperature day 2 and 3							Curing	
	20°C	20°C	90°C	20°C	90°C	20°C	90°C	20°C	90°C
13	22.2	49.3	122.6	73.9	123.4	99.9	128.9	15.2	19.4
14-1	45.1	80.2	170.0	101.7	166.0		172.8	16.9	15.6
14-2	48.4	86.8	181.3		170.3		177.2	19.5	20.5
15	24.8	79.0	159.5	100.7	159.9	140.6	173.4	18.6	20.8
16	45.2	79.1	161.2	97.9	171.9	132.1	167.3	17.5	22.5
17	46.7	83.6	175.7	103.0	177.7	140.6	180.2	18.0	20.6
19	51.8	84.3	166.8	111.8	163.6	127.2	171.5	21.2	22.8
20	46.9	87.9	170.2	108.2	176.7	133.5	170.4	20.6	22.6
22	42.2	82.3	175.1	107.3	145.8	142.0	174.8	18.4	17.8
23	38.4	64.2	118.1	109.1	178.6	134.8	177.6	19.6	16.6
24	14.3	64.3	162.6	88.9	171.1	120.2	169.4	18.7	18.1
25	1.0	64.3	129.2	80.1	138.3	118.6	134.0	16.0	17.9
26	0.6	63.1	74.3	83.2	113.9	119.4	154.7	11.3	10.4
28	0.2	28.8	120.4	46.2	142.4	63.5	146.1	13.6	19.9
29	0.6	34.4	96.2	51.2	93.0	110.4	107.1	14.1	15.0
30	58.8	87.1	185.5	112.0	184.5	154.2	185.8	21.2	20.4
31	52.3	80.7	181.2	103.5	181.6	146.2	174.3	21.5	19.5
32	40.5	82.1	183.6	107.0	182.4	147.1	176.8	20.1	22.9
33	36.3	75.2	174.5	99.2	175.7	127.5	160.2	15.3	21.9
34		2.4	137.2	56.8	152.3	103.9	153.2	14.1	18.4
35		3.6	136.2	68.8	148.4	101.6	139.0	12.3	17.3
36	49.7	87.0	185.4	111.6	175.5	147.3	187.9	20.4	20.3
37	44.3	81.8	175.2	103.8	184.5	146.3	187.4	19.7	21.8
38	44.3	80.9	179.5	108.4	168.2	140.6	184.6	22.1	23.2
39	59.6	78.7	168.0	109.2	160.7	117.8	160.8	17.2	22.7
40		33.0		53.4	157.1	101.0	112.4	22.1	23.2
41		24.6		52.6	144.5	109.6	143.8	16.3	15.6
42	49.0	88.3	179.2	105.5	168.3	142.6	170.7	18.9	21.6
43	45.7	84.7	174.0	104.4	171.8	141.7	167.9	19.1	21.7
44	38.5	73.3	168.4	103.6	176.4	132.6	176.7	19.8	22.6

Chloride resistance

1. Modifications made to make "Nordtest method NTBuild 492" suit UHPC

Figure 5: Cylinder form for chloride penetration measurement

This is a description of the modifications made to NTBuild 492 method to make it applicable to UHPC. The modifications were made using a diamond saw or a diamond grinder.

The standard is complied with, except section 6.3 "Preparation of the test specimen":

In place of the more common ø100* 200 mm cylindrical form, the UHPC specimens were cast in cylindrical forms of 50mm high and 100mm width.

The purpose was to eliminate the need of using a diamond saw to produce samples of the correct length, since the saw would in all likelihood have been damaged by the high strength sample.

By making the specimens in the correct thickness from the beginning, the only preparation necessary was to use a grinder to roughen the surface of the specimen, so as to eliminate as much as possible of a surface skin effect.

Figure 6: Grinding head.

2. Results of chloride penetration measurement

Chloride penetration was measured after 14 days of curing. The results show a very small chloride penetration and large temperature efffect. For series 38 the 90°C thermally treated specimen had a coefficient= 0,0131 x 10^{-12} m²/s while the specimen that was kept outside the thermally steam treatment had a coefficient=0,274 x 10^{-12} m²/s.

Table 5: Chloride transport coefficients

Mixture	**Chloride coeffisient [m²/s] * 10^{-12}**	
Curing temp.→	20°C	90°C
20	.015	
23	.044	
28		.036
29		.021
32	.22	.032
33	.036	
34		0.11
35		0.019
38	0.27	0.013
39	0.093	0.022
42	0.36	
Conventional technology, 20 degrees		
High strength concrete (100 MPa):	0.48	
45 MPa (cement only):	8.18	

5 Brief discussion of tests

Cement type

The two cements are quite different: Where everything else was kept constant, a comparison between mixes 32 and 33 in term of strength is shown in fig. 7, and in terms of chloride resistance in fig 8. The effect of cement fineness is shown in 1 day strength, in flow and in chloride resistance for samples cured at 20 degrees. The lower Cl-resistance of the coarser Anlegg cement at room temperature is very clear.

Effect of curing Temperature

The beneficial effect of heat curing is interesting. Traditionally (e.g. Hooton et al [4]) , high temperature during early curing would be expected to result in a coarser microstructure with higher chloride diffusivity. Here, however, there is a huge positive effect of the heat curing. This is interesting in light of the observations by Pfeifer et al [5] in whose experiments only about 10% of the silica fume had reacted after 56 days at room temperature (almost none at 14 days), while in the temperature accelerated situation around 50% was reacted. They also report from SEM investigations that CSH phases form a very dense binder matrix surrounding the microsilica particles. This increased pozzolanic reaction can then be assumed as the reason for the difference between heat cured and conventionally cured material – both for strength and for permeability.

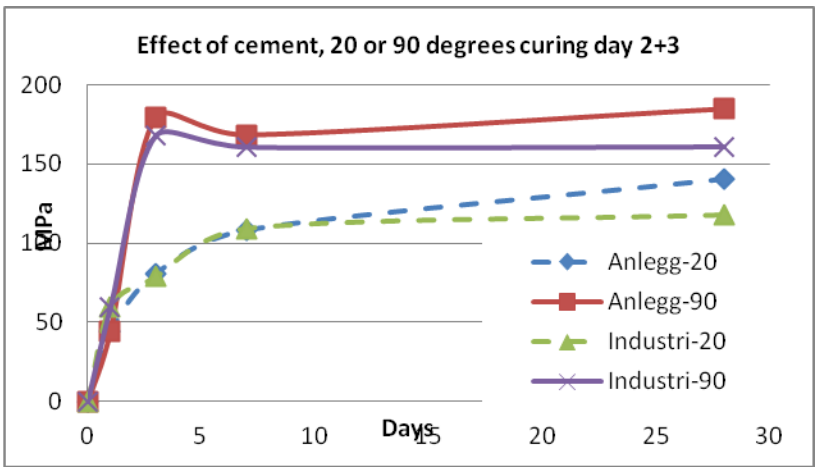

Figure 7. Effect of cement and temperature on strength.

Effects of mixture parameters

There is an effect of superplastiziser type on strength. The recommendation is, however, to test with the cement and SCM that is used, since formulations are changing and development of admixtures is rapid

Aggregate source appears to have a minor impact, as does the maximum size of the aggregate (0.5 or 1.0 mm). All sands are mainly gneiss and/or granite with small quantities of quartzite.

On the balance, for workability versus strength, w/cm of 0.18 was found to be the best compromise. The “Anlegg” cement, being the coarser and higher strength, showed the best results. Dmax: using less tha 2mm had, in this case, no real effect on strength, and would be detrimental to flow. There was no real difference between 6 and 13 mm fiber lengths.

High temperature curing on day 2 and 3 contributed significantly to performance.

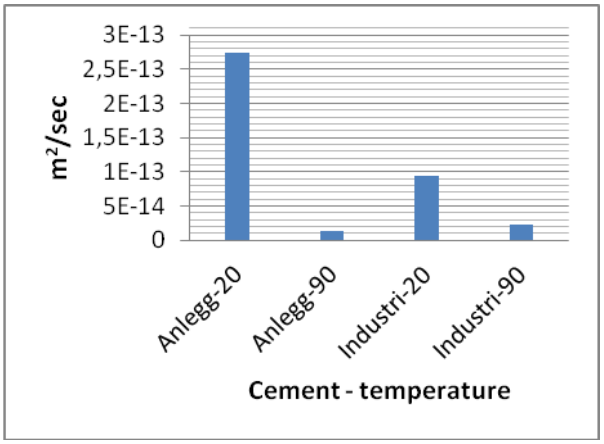

Figure 8. Effect of cement and temperature on Chloride transport

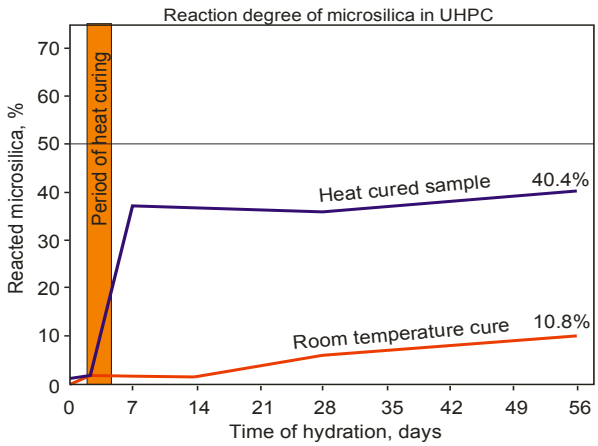

Figure 9. Effect of temperature on hydration of microsilica in UHPC (Pfeifer et al)

6 Conclusions

In this project it is found that at this location, producing UHPC is possible using materials easily available locally. The compressive strength varied between 160-190 MPa, depending on the recipe.

The high compressive strength, combined with 2 vol% fibers gives UHPC large flexural strengths, more than 20 MPa in most most mixtures made here.

The excellent chloride resistance of the UHPC, especially when cured at high temperatures, also makes it a very attractive material for durability and long service life under such conditions. The optimal UHPC recipe in this project has the following contents (from among the tested materials);

- **Anlegg** cement over Industri because of its better flow.
- **Aggregate** could be any of the three tested types. (Reddal, Tveit and Årdal)
- **Water/binder ratio**=0,18 which gives a combination of good flow and good strength
- $\mathbf{D_{max}}$: 1 or 0,5 mm does not give difference in compressive strength.

The Software program EMMA was found to be a very useful implementation of the Andreassen model in the optimization of particle packing

The content of water reducing agent seems high, but at only about 16% dry content, the dosage is typically about 2.5% dry by weight of cement and 1.3% by weight of total binder. HRWRA is an important cost factor, and more development is needed.

7 Closing words

The ability to make UHPC using locally available material has the potential of broadening the use of this material.

The availability of ultra high strength concrete makes possible new concepts in the use of concrete. Such opportunities as insulating sandwich elements, sandwich floor slabs with lightweight concrete as the core, very slender horizontal structures, “impermeable” UHPC as permanent formwork etc. Opportunities are many-fold; combine for example the properties of UHPC with ADAPA’s technique [6] for shaping thin concrete slabs – exiting possibilities open for dramatic, organically shaped, structures. Dura-Con’s highway bridge and beam elements [7] show another way of new technology with UHPC.

An important contribution to the economical use of UHPC, and thereby groth in the use, is to minimize logistics cost, so that locally available materials can be used. Particle packing is an important tool for this work.

8 Acknowledgement

The contribution of our bachelor students is gratefully acknowledged: Tom Erik Dahl Dyrseth, Stian Berge, Alexander Rosenborg-Johnsen

References

[1] Berge,S; Rosenborg-Johnsen,A and Dahl Dyrseth,TE. Developing Ultra High Performance Concrete with local materials. Bachelor project in construction design. University of Agder. Grimstad 2010

[2] Available from http://www.concrete.elkem.com

[3] Andreasse,n A.H.M. and Andersen, J.: Kolloid Z. 50 (1930) 217-228

[4] Hooton,R.D., Pun,P, Kojundic,T, Fidjestøl,P. Influence of silica fume on chloride resistance of concrete.. Proc. PC/FHWA Internationa Symposium on High Performance Concrete. New Orleans, Lousiana, October 1997

[5] Pfeifer, C; Möser,B; Weber,C and Stark,J. Investigations of the pozzolanic reaction of silica fume in ultra high performance concrete. Proc. International RILEM Conference on Materials Science – MATSCI, Aachen 2010

[6] http://adapa.dk

[7] http:// http://www.dura.com.my/

Control of Rheology, Strength and Fibre Bond of UHPC with Additions – Effect of Packing Density and Addition Type

Dirk Lowke[1], Thorsten Stengel[2], Peter Schießl[2], Christoph Gehlen[1]
1: Center for Building Materials, Technische Universität München, Germany
2: Ingenieurbüro Schießl – Gehlen – Sodeikat GmbH, Germany

This contribution illustrates the effect of additions different in type and fineness and maximum packing density on the macroscopic properties, rheology and bond of steel fibres of UHPC. The results show that the properties of the UHPC investigated were decisively affected by the particle size distribution of the additions rather than the type of material. A new packing density test for fine materials (< 125 µm) was developed to provide calibrated input parameters for the calculation of the maximum packing density of UHPC with different additions. The rheological properties, and therefore fresh concrete workability, were affected by the maximum packing density of the UHPC bulk matrix. The bond strength of steel fibres in a straight pull-out test was affected by addition exchange too. Again, this is explained by packing density effects. Based on packing density calculations as well as SEM and EDX investigations, higher fibre bond strength is explained by a larger proportion of very fine particles in the matrix adjacent to the fibre ITZ which leads to a decrease in the maximum packing density of the fibre ITZ.

Keywords: rheology, fibre bond, ITZ, packing density

1 Introduction

Ultra high performance concrete (UHPC) consists of a combination of cement with reactive and inert additions optimized to obtain the specified properties of the fresh and hardened concrete. The low water-to-fines ratio and high particle packing density of UHPC compared with regular concrete produces a dense microstructure with almost no capillary porosity. Depending on composition and production method, compressive strengths are reached between 180 and 250 MPa.

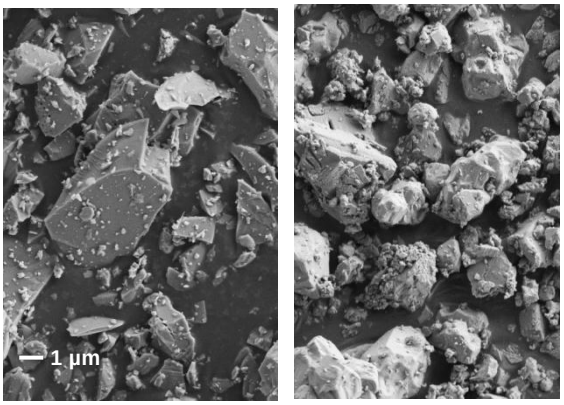

Figure 1: SEM image, 2,500x, quartz flour (c) (left) and ground limestone (f) (right).

As well as the hardened concrete properties, the rheological behaviour of fresh UHPC can be controlled by appropriate choice of mineral additions. Usually silica fume and quartz flour are added to the mix, but fly ash and ground granulated blast-furnace slag are also used [1]. The additions vary in granulometry, particle shape and specific surface. These parameters can modify the properties of the fresh and hardened concrete. For example, crushed particles possess a higher surface area than round particles of the same diameter which leads to lower packing densities. The type of crushed material affect packing density too. Investigations by Geisenhanslüke [2] have shown that the circularity of quartz flour particles is less than for limestone particles, but limestone particles possess a rougher surface structure, Fig. 1. Circularity and surface roughness affect packing density and consequently the rheological behaviour of UHPC.

In this study, the effect of quartz and limestone flour additions of varied fineness on the rheological behaviour and properties of hardened UHPC was considered. Fibre pull-out tests were carried out to investigate the effect of the additions on matrix/fibre bonding.

2 Investigations

The tests performed aimed at covering the essential aspects of the application of UHPC in building practice, in particular, workability and the mechanical performance of the material. Workability and de-aeration were characterized by rheological measurements. Mechanical performance was assessed based on the strength of the UHPC without fibres and the bond behaviour of single fibres. Furthermore, packing density tests and calculations were carried out to investigate the effect of particle sizes on fresh concrete rheology and fibre bonding, the latter determined in single fibre pull-out tests. The surface of the steel fibres was examined before testing using a confocal microscope. SEM and EDX were used to examine the fibre ITZ after fibre pull-out.

Table 1 shows the composition of the UHPC considered. Portland cement (d_{50} = 14.3 µm) was used with quartz sand (d_{max} = 0.5 mm) and silica fume (d_{50} = 0.2 µm). The additions were either fine Q(f) or coarse Q(c) quartz flour or limestone flour in three grades of fineness: L(c), L(f) or L(ff). Fig. 2 shows the particle size distributions of the dry mixture of cement and additions (without sand) in the UHPC investigated. The additions were exchanged volumetrically keeping the volumetric ratio of water to fines (V_W/V_F) constant. The fluidity of the mix was adjusted with a polycarboxylate superplasticizer whereby the dosage was set to yield a slump flow of 285 ± 15 mm measured with the mini-cone (test without jolting). This permitted direct assessment of the ability of the superplasticizer to fluidify the mix for each addition.

Table 1: Concrete compositions and particle size of addition.

Addition type / mix notation	**Q(c)**	**Q(f)**	**L(c)**	**L(f)**	**L(ff)**
Material			**[kg/m³]**		
CEM I 42,5 N	680	680	680	680	680
Silica fume	138	138	138	138	138
Quartz powder (c, f)	360	360	-	-	-
Lime stone powder (c, f, ff)	-	-	371	371	371
Water	164	170	165	171	165
Quartz sand 0/0.5 mm	990	990	989	990	990
Superplasticizer	35.0	31.0	37.0	29.5	36.0
Particle size of addition	14.7	4.4	8.2	5.5	1.9
w/c-ratio			0.28		
V_w/V_F [1)]			0.46		

[1)] volumetric water / fines-ratio (< 125 µm)

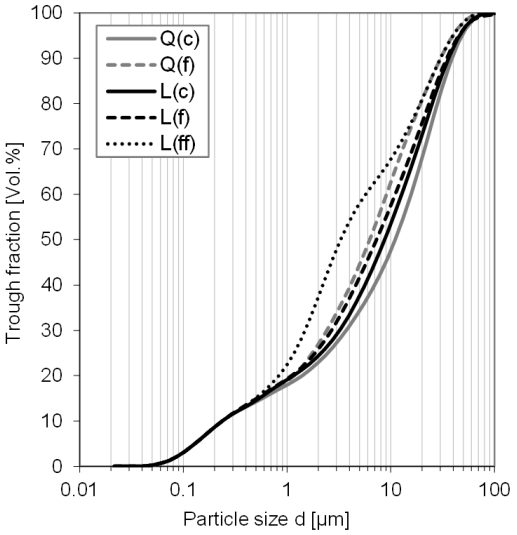

Figure 2: Particle size distribution of dry UHPC mixes without sand.

A high shear vacuum mixer with an inclined drum (Eirich R02-Vac) was used to prepare the concretes. After homogenizing the dry materials for 60s, the water was added with 40% of the superplasticizer within the first 10 s of wet mixing. The mix was then blended for a further 80 s after which the remaining superplasticizer was added within 10 s. Finally, a reduced pressure of 50 mbar was applied and mixing ended after a total time of 180 s. Specimens for the determination of hardened concrete properties and the fibre pull-out tests were produced immediately at the end of mixing, stored for 24 h in a humidity chamber at 20°C/95% RH, demoulded and returned to the chamber for a further four days. At an age of five days, the specimens were heat treated at 90°C for 48 h in a humid environment above water. At an age of seven days, the properties of the hardened concretes were determined and the fibre pull-out tests performed.

3 Maximum Packing Density – Calculation and Experimental Results

The compaction test according to de Larrard [3] was used to determine the maximum packing density of the sand. However, this test is not suitable for the determination of the maximum packing density of cement and additions. For this reason a packing density test based on the idea of Flatt [4] was developed to determine experimentally the maximum packing density of the fines (d < 125 µm). Firstly, the material in question was mixed with water to produce a suspension of cement or cement with additions equivalent to the proportions in UHPC. To produce the same degree of dispersion of solids as in the UHPC, superplasticizer was added at a quantity equivalent to the dosage in UHPC. Roughly 100 to 150 ml of the suspension was poured into a cylindrical extraction device (d = 80 mm, Fig. 3) and compacted in a defined manner at constant pressure until equilibrium was reached, i.e. a compaction rate below 0.002 mm/min. Surplus pore solution was expressed during the compaction process. The pore solution volume remaining in the suspension corresponds to volume of voids in the mixture of particles for the particular pressure used. Thus the voids content was determined by drying the compacted suspension at 105°C and an ambient pressure of 100 mbar. This test was carried out with separate suspensions each at pressures of 2, 4, 10, 20 and 40 MPa. Following Flatt [4], the experimental maximum packing density $\Phi_{m,exp}$ of the particles was obtained by fitting the data and extrapolating back to zero, see Fig. 4.

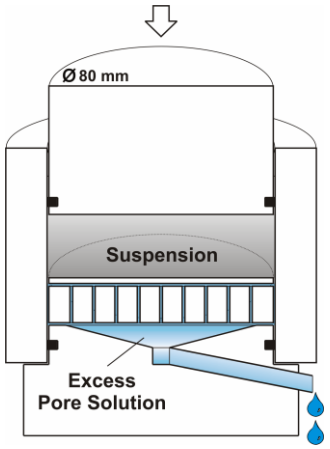

Figure 3: Compression device to compact particle suspensions.

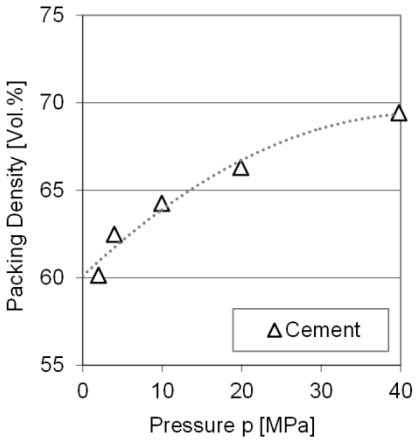

Figure 4: Packing density Φ_{exp} of cement in dependence of applied pressure p.

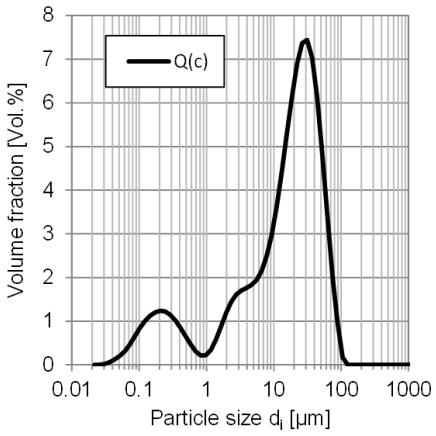

Figure 5: Experimentally determined particle size distribution of freshly mixed UHPC Q(c) without sand.

The experimental maximum packing densities $\Phi_{m,exp}$ are shown in Tab. 2. The new packing density test was found to perform very well with cement, quartz flour and limestone powder as well as the mixtures of these components. However, the experimental determination of the maximum packing density of a mixture of cement, addition and silica fume was unsuccessful owing the high impermeability of the compacted suspension. For this reason, the maximum packing densities Φ_m of the UHPC mixes (including high amounts of silica fume) were calculated with a linear packing model (LPM) according to Larrard [3], Equation 1, using the experimentally determined maximum packing densities $\Phi_{m,exp}$ of the individual components to calibrate the calculations.

$$\Phi_m = \min \Phi_i = \frac{\beta_i}{1 - \sum_{j=1}^{i-1} \left[1 - \beta_i + b_{ij}\beta_i\left(1 - 1/\beta_j\right)\right] y_i - \sum_{j=i+1}^{n} \left[1 - a_{ij}\beta_i / \beta_j\right] y_i} \qquad (1)$$

The LPM was calibrated with maximum packing densities $\Phi_{m,exp}$ determined experimentally for the individual materials cement and sand as well as for mixtures of cement, quartz flour (f) and limestone flour (ff). These materials cover a wide range of the particle sizes of UHPC. In a first step, mean residual packing density β_i values used by the LPM for a defined number of particle sizes groups d_i of a particular material (cement, addition, sand) were calculated from the experimental maximum packing density $\Phi_{m,exp}$ using Equation 1, see Table 2. In a second step, the residual packing densities β_i determined for the individual components in this manner may now be used as calibrated input parameters for the LPM to calculate the maximum packing density of different mixtures of these components, i.e. the UHPC variations considered.

It was found that the mean residual packing density β_i in the particle size region of the cement particles at 43.7 % is almost the same as for finer mixtures of cement and quartz flour (f) at 43.7 % or limestone flour (ff) at 44.2 %, respectively. For sake of ease, a value of 43.7 % was used in the calculations for the β_i of all particles smaller than 125 µm. Due to the very high amount of superplasticizer, it was assumed that cement, addition and silica fume particles disperse completely in fresh concrete without agglomeration. This was confirmed by laser granulometric measurements with freshly mixed UHPC pastes in which the cement, addition and in particular silica fume particles were observed to be well dispersed, Fig. 5. For particle size groups above 125 µm, a value of 55.0 % was used for β_i, see Table 2.

Table 2: Experimental determined maximum packing density $\Phi_{m,exp}$ and resulting residual packing density β_i of sand, cement and mixtures of cement and quartz flour (f) and limestone flour (ff) respectively.

	Cement	Cement/ quartz flour (f)	Cement/ limestone flour (ff)	Sand
Particle groups, *i* d(10%) / d(90%)	40-24	42-25	44-25	15-10
Particle size d_i [µm] ($d_i = 2^{(-0{,}25 \cdot i + 1{,}25)} \cdot 10^3$ [µm])	2.3/37	1.6-31	1.2/31	177/420
Maximum packing density (experimental) $\Phi_{m,exp}$ [%]	60.1	61.2	63.8	60.2
Mean residual packing density of one particle group (calculated) β_i [%]	43.7	43.7	44.2	55.0

The maximum packing densities for the UHPC variations calculated with the calibrated LPM are shown in Table 3. As well as the maximum packing density of the total particle distribution of UHPC $\Phi_{m,bulk}$, representing the bulk matrix, the maximum packing density of particles below 125 µm $\Phi_{m,ITZ}$ was calculated. As will be shown later, the maximum packing density of particles below 125 µm $\Phi_{m,ITZ}$ is decisive for properties of the ITZ between the matrix and fibres.

Table 3: Calculated max. packing density of bulk matrix $\Phi_{m,bulk}$ and ITZ $\Phi_{m,ITZ}$ for the different UHPC variations.

	Addition type / mix notation	Q(c)	Q(f)	L(c)	L(f)	L(ff)
Max. packing density of bulk matrix	$\Phi_{m,bulk}$ [%] d_{max} = 500 µm	79.3	79.9	80.1	80.8	80.6
Max. packing density of ITZ	$\Phi_{m,ITZ}$ [%] d_{max} = 125 µm	69.1	68.6	69.5	70.1	68.8

4 Rheology

The slump flow and the plastic viscosity η were determined 5 min after water addition. The rheological measurements were performed with a double annular gap cell [5] in a rotation rheometer (Schleibinger, Viskomat NT) at the low rates of shear which occur when concrete flows. The double annular gap cell is, according to [5], particularly suitable for the determination of the rheological properties of highly flowable mortar. The inner rigid sensor is a fine grid which produces approximately fluid-fluid shear. This has the advantage that the adhesive bond between the suspension and the surface of the cell, which is critical for suspensions, is replaced by a cohesive bond thus avoiding wall slippage. The UHPC specimens were placed in the cell immediately after mixing (180 s).

At the beginning of the measurement, the specimen was subjected to shear at $\dot{\gamma}$ = 2.5 s^{-1} for 30 s in order to break up the dormant structure. Afterwards, the rheological properties were determined by controlling the rotational speed in 10 s steps $\dot{\gamma}$ = 2.5, 1.0, 0.5, 0.25, 0.10 and 0.05 s^{-1}. Viscosity was calculated by applying the Bingham model over the range 0.5 to 0.05 s^{-1}.

The UHPC with the coarsest additions, Q(c) and L(c), required the highest dosage of superplasticizer, 35.0 and 37.0 kg/m^3, respectively, to achieve the target slump flow of 285 ± 15 mm. Despite the increase in specific surface of the mixture of particles, exchanging the coarse additions for the finer materials Q(f) and L(f) reduced the necessary superplasticizer dosage considerably to 31.0 and 29.5 kg/m^3, respectively. This can be explained primarily by an increase in maximum packing density $\Phi_{m,bulk}$ of the UHPC mixes made with finer additions (f), see Table 3. By reducing the voids content more rheologically active water is available to coat the particle surfaces. However, on further increasing fineness by adding limestone flour (ff), it was necessary to increase the superplasticizer dosage. In this case the positive effects of a higher maximum packing density outweigh the negative effect of the larger specific surface.

Table 4: Rheological properties of the UHPC mixes.

			Q(c)	Q(f)	L(c)	L(f)	L(ff)
Slump	[mm]	a	290	297	292	298	270
Viscosity	[Pa·s]	η	60.3	28.8	44.9	33.1	35.4

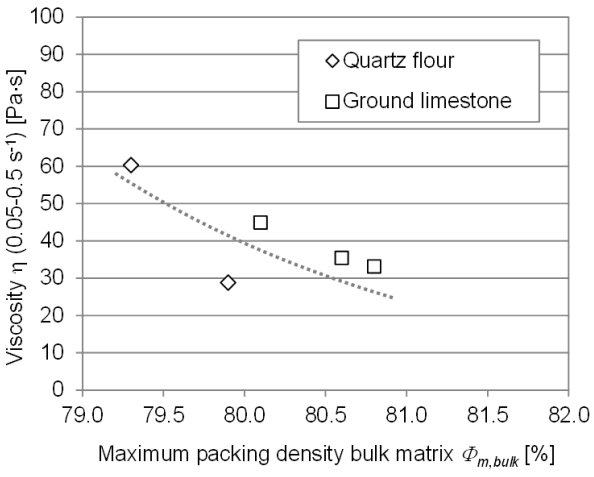

Figure 6: Plastic viscosity η in dependence of maximum packing density of the bulk matrix $\Phi_{m,bulk}$ (d < 500 µm) 5 min after addition of water.

The UHPC with the coarse additions Q(c) and L(c) exhibit the highest viscosities, Tab. 4. This means a very stiff consistency and unfavourable workability during concrete production in practice. It is possible that the required mechanical properties are not achieved owing to insufficient de-aeration or an uneven distribution of fibres. By replacing the coarse with the finer additions, Q(f), L(f) and L(ff), viscosity is reduced considerably which is accompanied by a corresponding improvement in workability. Accordingly, the viscosity of UHPC is also markedly affected by the maximum packing density of the particle mixture, Table 3 and Fig. 6. Higher maximum packing densities $\Phi_{m,bulk}$ lower viscosity considerably. This, again, is due to the reduction in voids content with maximum packing density. The excess water is available for the layer of water around the particles. It is interesting that this effect seems to be more pronounced for

UHPC with quartz flour Q(c) and Q(f) than for UHPC with limestone L(c), L(f), L(ff). This could be due to the higher surface roughness of the limestone particles, Fig. 1.

5 Compressive and Splitting Tensile Strength, Young's Modulus

The compressive (f_c) and splitting tensile (f_{sp}) strength of the investigated UHPC were measured using cylinders (Ø 50 mm, height 50 mm and 100 mm, respectively) for each mix; Table 5 shows the resulting mean values. In addition, the static Young's moduli were measured with concrete cylinders (Ø 50 mm, height 100 mm).

The compressive strengths lie within a narrow range of 225 MPa ± 10% with coefficients of variation ranging from 1 to 10%. Based on the scatter of the results, it is concluded that replacing quartz flour by lime-stone flour had no detrimental effect on the compressive strength of UHPC, which also was not affected by the fineness of the limestone flour. The use of fine quartz flour Q(f) led to compressive strengths which were somewhat higher. The splitting tensile strength of UHPC varied around approximately 10.9 MPa with coefficients of variation which, at 11 to 20%, were clearly higher than for the compressive strength. The splitting tensile strength of UHPC with Q(f) and L(ff) were, however, about 10% outside the range of scatter. The Young's moduli of the concretes with Q(c) and L(f) were 49.8 and 48.0 GPa, respectively. In short, the mechanical properties of the concretes were roughly equivalent and therefore independent of the addition used.

Table 5: Mean compressive (f_c) and splitting tensile (f_{sp}) strength [MPa] of the UHPC mixtures.

	Q(c)	Q(f)	L(c)	L(f)	L(ff)
f_c	212.5	253.6	221.7	203.4	226.3
f_{sp}	11.6	14.4	10.3	10.0	8.2

6 Single Fibre Pull-Out Behaviour

On account of its brittle failure behaviour, UHPC commonly used in construction is reinforced with steel fibres. Single fibre pull-out tests were carried out with the UHPC considered to quantify effect of addition exchange on bonding and thus the effectiveness of the steel fibres.

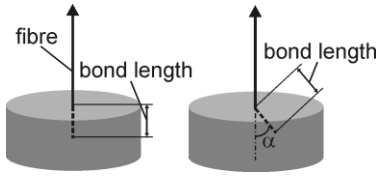

Figure 7: Specimen used for single fibre pull-out tests

Table 6: Bond strength τ_b [MPa] of the mixtures for different angles between load and fibre axis

α	Q(c)	Q(f)	L(c)	L(f)	L(ff)
0°	15.0	16.5	13.9	11.1	14.3
45°	24.4	24.3	25.4	24.6	28.5

Smooth steel wires 0.48 mm in diameter, $Ø_F$, with a bonding length l_b of 5 mm were used in the investigations. The angle α between the fibre axis and the direction of applied load was set to 0 or 45°, Fig. 7. The pull-out tests were performed using a spindle-driven machine with a 500 N load cell controlled at a speed of 1.8 mm/min. The pull-out load and displacement of the machine were recorded continuously. The bond strength $\tau_b = F_{max} / (l_b \cdot Ø_F \cdot \pi)$ was calculated from the maximum load. Table 6 summarises the bond strengths (at least four individual specimens per variation) for each angle and UHPC composition investigated.

In the case of the straight pull-out ($\alpha = 0$), the mean bonding strength of all UHPC was 14.2 MPa with coefficients of variation ranging from 7.4 to 14.7%. A significantly different in mean bond strength was observed for the mixtures Q(f) and L(f). While L(f) exhibited a

considerably lower bond strength at 11 MPa (-22 %), the UHPC Q(f) exceeded the mean by 17 %. A weak correlation was found between bond and compressive strengths of the mixtures considered here. Indeed, earlier investigations have shown that compressive strength is only of secondary importance for fibre bonding in UHPC (investigated range 175 MPa to 250 MPa), [6,7].

Hence, the observed difference between L(f), Q(f) and the remaining mixtures cannot fully be explained by the strength of the concretes. Fig. 8 shows how the maximum packing density of the ITZ $\Phi_{m,ITZ}$ affects bonding strength. Here, the maximum packing density was calculated without considering the sand particles (>125 µm) – as opposed to the calculation for the rheological properties of the bulk mix. The sand particles >125 µm were omitted because the granular structure is disturbed at the fibre surface and the particles become smaller as the fibre surface is approached, see e.g. Stroeven [8]. Limitation to particles smaller than 125 µm also appears sensible in view of the hydration reactions in the bonding zone. Investigations by Lawrence [9] have shown that inert particles > 60 µm have no significant effect on the hydration reactions whereas small inert particles provide nucleation centres increasing the growth rate of C-S-H.

It was found that a higher maximum packing density of the ITZ $\Phi_{m,ITZ}$ results in a reduction of bond strength, Fig. 8. An increase in maximum packing density of the fine particles (which are decisive for the bonding zone) appears therefore to affect the area of contact unfavourably; the friction between the fibre and the concrete matrix during pull-out is reduced. The fibre/concrete contact zone is examined in more detail in Section 7 in order to explain the effect of maximum packing density of ITZ on bond strength.

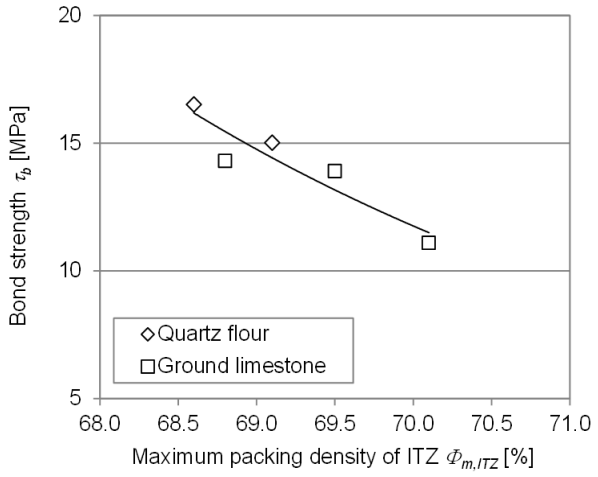

Figure 8: Bond strength τ_b versus maximum packing density of ITZ $\Phi_{m,ITZ}$ (d_{max} < 125 µm).

If the fibres are subjected to load at an inclined angle, the fibre deformation at the kink and the macroscopic properties of the UHPC matrix specify bonding behaviour. Besides bond failure, i.e. destruction of the adhesive and sliding friction bond, UHPC spalling and bursting occur. In contrast to straight pull-out, bond strength increases if the fibre is pulled at an inclined angle. Since the mechanical properties of the investigated UHPC are approximately equivalent, the difference in the bond strengths for an inclination of 45° vary by only 10% around the mean value of 25.5 MPa. Consequently, the investigated concretes may be regarded as roughly equivalent in the case of fibre pull-out at an inclined angle.

7 Effect of ITZ Microstructure on Bond Strength

Additional investigations on the fibre surface and bonding zone were performed to reveal a possible effect of particle size distribution and packing density on bonding behaviour during straight fibre pull-out. The characteristic surface of a macroscopically smooth steel wire is shown in Fig. 9. The grooves in the surface originate in the process of wire drawing. Using a confocal microscope, the fibre roughness parallel to the fibre axis was characterized by a maximum total height difference of the surface R_z of approximately 0.1 to 0.5 µm. The grooves were typically up to about 3 µm wide.

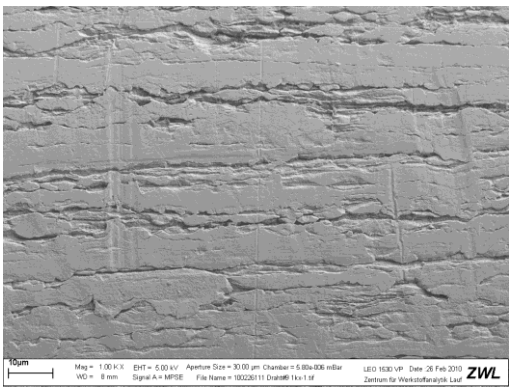

Figure 9: SEM image of a fibre surface.

After the pull-out tests, the specimens were split to permit SEM and EDX investigations in the fibre channel. No significant difference in the topology of the UHPC surface in contact with the fibres was observed for the different UHPC compositions. None of the SEM images revealed a duplex layer containing portlandite as typically occurring in regular concrete. Moreover, investigations on the degree of hydration of cement and silica fume in the bulk matrix (^{29}Si-NMR) showed that portlandite was completely consumed by the pozzolanic reaction with silica fume.

The EDX analysis (size of backscattered SEM image: 220 × 150 μm², acceleration voltage: 15 kV) yielded values for calcium, silicon and iron content. The results in Table 7 are based on 20 individual measurements.

The Ca/Si ratios of the bulk matrix for mixtures of the same chemical composition vary over 0.08. Thus, differences in Ca/Si ratio between the bonding zone and the matrix which are over 0.08 are significant. Therefore the composition of bonding zone in UHPC Q(c) is similar to that of the matrix. Opposed to this, the Ca/Si ratio of the UHPC Q(f) indicates that the bonding zone contains somewhat more silicon than the matrix. In analogy, zhis applies to calcium in UHPC L(f) too where, apparently, less calcium is in the bonding zone.

In contrast, the bonding zones of the UHPC L(c) and L(ff) possess significantly higher Ca/Si ratios and therefore higher calcium contents than the matrix. In the case of UHPC with limestone flour, the higher calcium content of the ITZ compared with the matrix indicates that the cement content is lower within the ITZ. This is equivalent to a larger separation of the cement particles. Since the rather coarse cement particles at 680 kg/m³ dominate the particle packing of the mix, only much finer particles can fill the space between the cement particles at the fibre surface. The size of the finer particles was estimated by following Kessler [10] and, in addition, taking the wall-effect into account as ½·(0.315·d_i). With a mean particle size of 14.3 μm for the cement, these space filling particles are about 2.3 μm in size. Particles of this size were abundant in all the limestone flour grades used, Fig. 2. It is concluded that the very fine limestone particles accumulate at the fibre surface within aforementioned space. Due to the narrow particle size distribution, these space filling limestone particles exhibit a low maximum packing density. Thus a larger proportion of the very fine limestone

Table 7: Mean calcium content and Ca/Si-ratio of ITZ and bulk matrix.

		Q(c)	Q(f)	L(c)	L(f)	L(ff)
Ca/Si	bulk [-]	0.76	0.81	1.70	1.69	1.77
Ca/Si	ITZ [-]	0.76	0.55	1.86	1.55	2.56
Ca	ITZ [wt.%]	18.4	15.8	27.9	21.6	31.1

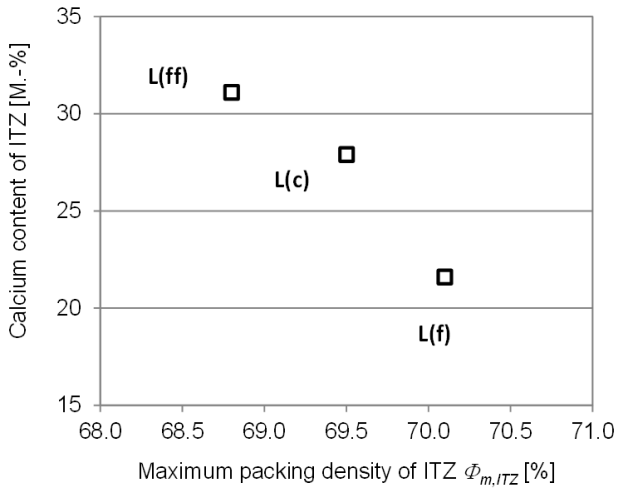

Figure 10: Calcium content of ITZ versus maximum packing density of ITZ $\Phi_{m,ITZ}$ (d_{max} < 125 μm) of ground limestone UHPC.

particles in the ITZ results in a lower maximum packing density of ITZ $\Phi_{m,ITZ}$. This hypothesis is supported by the correlation between the calculated maximum packing density of the ITZ $\Phi_{m,ITZ}$ and the experimentally determined calcium content of the ITZ, Fig. 10. This shows that a decrease in maximum packing density of the ITZ $\Phi_{m,ITZ}$ is connected with an increase in the content of limestone particles.

This behaviour is also apparent for UHPC with fine quartz flour Q(f), but to a lesser degree. In the case of quartz flour UHPC the space filling particles are the very fine quartz flour particles. Therefore the Ca/Si ratio of the ITZ of UHPC Q(f) is lowered somewhat which indicates a higher silicon content of the ITZ, Tab. 6. However, the effect is not observed for UHPC with coarse quartz flour Q(c) because the particle size distribution of cement (d_{50} = 14.3 µm) and coarse quartz flour (d_{50} = 14.7 µm) are, in the present case, almost identical. The quartz flour (c) has no effect on the maximum packing density of the ITZ $\Phi_{m,ITZ}$.

By applying aforementioned interactions, it is possible to describe the decisive mechanisms concerning the effect of ITZ microstructure on bond strength. A reduction in maximum packing density of the ITZ $\Phi_{m,ITZ}$, which corresponds to an increase in the amount of very fine particles (around < 2.3 µm) in the bonding zone, results in an increase in the number of contact points, i.e. the area of contact between the fibre and the bonding zone. Consequently the friction during pull-out is larger. Since the very fine particles are similar in size to the surface roughness (< 3 µm) of the fibres, micro interlocking is promoted. It is also possible that hydration is promoted by additional growth at the additional surface nucleation sites provided by the very fine particles, see [9,11]. This explains why fibre bonding strength is enhanced by a reduction in maximum packing density in the bonding zone as is evident in Fig. 8.

The increased real area of contact and the enhanced interlocking between fibres and matrix, was verified by the EDX investigations in which the amount of iron in the bonding zone after fibre extraction was above the bulk matrix value. This was produced by fibre wear. With the exception of UHPC with L(f), the amount of iron was, in general, larger than in the matrix.

8 Conclusions

In order to understand more about the mechanisms governing the rheological and mechanical properties of UHPC, concretes were prepared with mineral additions of different fineness and type at a constant volume in the mix. A new test method was developed to determine the maximum packing density of the fine materials (< 125 µm) in order to calibrate the linear packing model by de Larrard [3]. With this calibrated linear packing model it was possible to calculate the maximum packing density of different UHPC mixtures. In addition, the ITZ between the fibres and the concrete matrix was examined with SEM and EDX. As well as rheology, compressive and tensile splitting strength, the pull-out strength of single steel fibres was investigated.

The rheological properties, and therefore fresh concrete workability, were decisively affected by the particle size distribution of the additions rather than the type of material. Coarser additions increased superplasticizer demand and mix viscosity. This effect can be explained in terms of the maximum packing density of the UHPC bulk matrix. Higher maximum packing densities lead to a reduction in the viscosity of UHPC. Besides packing density, superplasticizer demand also depends on the fineness of the additions. The favourable effect of an increase in maximum packing density competes with the unfavourable effect of an increase in specific surface.

Exchange of the additions had little effect on compressive and tensile splitting strength as well as static Young's modulus. Compressive strengths around 225 MPa were obtained with all additions. The static Young's moduli were near 49 GPa.

However, the bond strength of steel fibres at straight pull-out was considerably affected by addition fineness which is also explained by packing density effects. Packing density calculations and EDX analysis of the fibre bonding zone show that depending on the particle size distribution more fine particles, about 2 µm in diameter, are present in the zone. This results in more contact points between the matrix and the fibre therefore enhancing friction during fibre pull-out. Abrasion during fibre pull-out produced a larger amount of iron in the fibre ITZ as was observed by EDX after fibre extraction. Further positive effects on bond strength may be due to enhanced hydration, i.e. additional growth of C-S-H at the surface nucleation sites provided by the very fine particles at the fibre ITZ.

In contrast, no significant effect of addition type and fineness was observed for fibres pulled out at an inclined angle. In this case, spalling and bursting of surface material around the fibres occurred indicating that the macroscopic properties of the concrete as a whole are decisive. In this case, quartz and limestone flour additions affect the mechanical properties of UHPC similarly - irrespective of fineness.

References

[1] Gerlicher, T.; Heinz, D.; Urbonas, L.: Effect of Finely Ground Blast Furnace Slag on the Properties of Fresh and Hardened UHPC, 2nd Int. Symposium on UHPC, March 2008, pp. 367-374.

[2] Geisenhanslüke, C.: Einfluss der Granulometrie von Feinstoffen auf die Rheologie von Feinstoffleimen. Universität Kassel, Dissertation 2008.

[3] De Larrard, F.: Concrete Mixture Proportioning, A Scientific Approach. London (1999) Spon

[4] Flatt; J.R.; Bowen, P.: Yodel: A Yield Stress Model for Suspensions. *J. Am. Ceram. Soc.*, 89(2006)4, pp. 1244–1256.

[5] R. Vogel: Eine Messzelle für Spezialmörtel. www.vogel-labor.de.

[6] Stengel, T.: Optimization of steel fibre bonding in UHPC, in: Breit, W.; Kurz, W.; Schnell, J.; Kohlmeyer, C.: 51. Forschungskolloquium des DAfStb, p. 589-600, Kaiserslautern 2010 (in German).

[7] Stengel, T.; Schießl, P.; Gehlen, C.: Steel fibre reinforced UHPC – An alternativ to micro steel fibres, in: Proceedings Neuntes Münchener Baustoffseminar, München, 2011 (in German).

[8] Stroeven, P.; Stroeven, M.: SPACE approach to concrete´s space structure and its mechanical properties, in: HERON, Vol. 46, No. 4, ISSN: 0046-7316, 2001.

[9] Lawrence, P.; Cyr, M.; Ringot, E.: Mineral admixtures in mortars, Effect of inert materials on short-term hydration. *Cement and Concrete Research* 33(2003), pp. 1939-1947.

[10] Kessler, H.-G.: Kugelmodell für Ausfallkörnungen dichter Betone. Betonwerk + Fertigteil-Technik 60 (1994) 11, pp. 63-76.

[11] Stark, J.; Möser, B.; Bellmann, F.: Quantitative Characterisation of Cement Hydration. In: Transport in Concrete: Nano- to Macrostructure (Tanscon 07), Freiberg (2007) Aedificatio Pub., pp.161-179.

Influences on Repeatability and Reproducibility of Testing Methods for Fresh UHPC

Susanne Fröhlich, Michael Schmidt
Institute of Structural Engineering, University of Kassel, Germany

From the very beginning, the fresh concrete properties of standard mixtures applied in all 34 projects of the German Priority Research Program "Sustainable Building with Ultra High Perfomance Concrete" were investigated using the flow table test and the test for air content according to the European Standard EN 12350. The statistical evaluation of the test results showed that the values scattered widely and did not permit a accurate prediction of the quality of fresh and also of hardened UHPC. Considering the very special rheological behaviour of fresh UHPC characterised by a high viscosity and a pronounced thixotropy, these results revealed that it was necessary to specify the test methods more precisely than in the current European standards. Based on this specification, the repeatability and the reproducibility of fresh UHPC properties were examined in comprehensive test series and finally in a round robin test with several institutes.

Keywords: Fresh concrete, slump flow, air void content, rheological behaviour

1 Introduction

Fresh Ultra High Performance Concrete (UHPC) is normally characterised by a high viscosity and a pronounced thixotropy. This effect is trace back to the packing-optimized microstructure of UHPC. Because of the low water/cement-ratio and the high amount of fine materials, a flowable consistency is only possible with a high content of superplasticizers (SP) [1]. As a result, the consistency of UHPC reacts more sensitive to inaccuracy of dosing, environmental conditions like temperature and the mixing process in general compared to ordinary concrete. Furthermore, the effective period and the efficiency of the different SP varied significantly. Therefore, the time-depending behaviour of the UHPC-consistency must be considered, if different mixtures will be compared among each other.

The analysis of different test values have shown that the mechanical behaviour of UHPC can be improved when the air void content is minimized and the fibres are uniformly distributed in the mixture [2]. These two features can be achieved by a very flowable consistency comparable with self-compacting-concrete (SCC). The properties that could be used to describe the concrete flow are the yield stress and the viscosity [3]. The determination of these factors is possible with a rheometer in laboratory. Because the tests are very time-consuming, easier tests are applied to control and assess the flowability of SCC or UHPC on construction side. Properties of fresh concrete can be measured as described in the European Standard EN 12350 [4-7] or the approaches for fresh SCC as described in the German guideline for SCC [8]. In more detail, but also more time consuming, rheometer tests are used to measure properties of fresh concrete.

In the project "Testing of UHPC", Subproject of the German Priority Research Program "Sustainable Building with Ultra High Performance Concrete" (SPP), different standard test methods for fresh and hardened concrete were examined, in order to find out if they are suitable for UHCP. In case these methods were not suitable, they had to be specified more precisely for the purpose of applying the methods on UHPC.

In the research projects of the SPP, two mixtures (M3Q and B5Q) were used as references with the aim that the institutes are able to compare the gained data by their specific research with those of other projects. To harmonize the procedures of specimen preparation and testing, three round robin tests were performed to identify and evaluate the main influence factors on

compressive strength and also on flexural tensile strength [2]. For quality assurance the fresh properties were measured by using the flow table test and the test for the air void content according to the European Standard EN 12350 for each production during the tests. The statistical evaluation of the test results showed that the values scattered widely and did not permit an accurate prediction of the quality of fresh and also of hardened UHPC [2]. Therefore, in the third period of SPP the standard test methods for flow properties and the air void content were analysed more precisely combined with investigations on the rheological behaviour of UHPC.

2 Mixtures

Two reference mixtures M3Q and B5Q, which were developed at University of Kassel [6], were used within these investigations. Both mixtures have a very flowable consistency independent of the maximum grain size. The first one is a UHPC with a maximum grain size of 0.5 mm denoted as M3Q. The second one, B5Q, contains basalt with particles up to 8 mm grain size. The M3Q is the further development of M2Q [9], which was used in the first two periods of the SPP.

In M3Q a new superplasticizer, which was specifically designed for UHPC, was used to improve the processing time of the mix. Also type and amount of silica fume were changed. By default, M3Q was mixed in an intensive mixer to avoid that the fine materials agglomerate. Comparable to [1], all dry materials were mixed for two minutes with low mixing intensity. Subsequently the water-superplasticizer-mix was added and the mixing intensity was increased. Two minutes later the mixer was stopped for two minutes. Afterwards, the process was continued by low mixing intensity and the fibre addition was started. In total, the mixing process takes 15 minutes.

Table 1: UHPC-mixes with 2.5 % by volume fibres

Raw materials		**M3Q**	**B5Q**
CEM I 52,5R HS-NA	kg/m³	775	650
Silica Fume	kg/m³	164	177
Quartz I	kg/m³	193	325
Quartz II	kg/m³	-	135
Sand 0.125/0.5	kg/m³	946	354
Basalt 2/8	kg/m³	-	598
Steel fibres	% b.vol.	2.5	2.5
Water	kg/m³	183	158
Superplasticizer	kg/m³	23.5	30.3
w/c-ration*		0.255	0.28
w/(c+s)-ratio*		0.21	0.22

* including the water content of the superplasticizer

The B5Q was mixed in all tests with a compulsion mixer with a high-speed-whirler, because of the coarse aggregate. The mixing intensity of the compulsion cannot be changed. Therefore, the whirler was switched on at the time of liquefaction. Apart from that, the mixing process was identical to M3Q.

In the conducted test series, micro steel-fibres with a diameter of 0.19 mm and a length of 9 respectively 17mm were used to measure the influence of fibres on the fresh properties of UHPC. The fibre content was varied between 0, 1.0, and 2.5% by volume.

3 Test Methods

Consistency

In the first period of the SPP 1182 the consistency of UHPC was measured after the entire mixing procedure with a truncated metal cone according to EN 12350-5 [4], which was filled with flowable UHPC and then lifted quickly. Deviating from EN 12350, the metal sheet wasn't

lifted and dropped after the cone was lifted. When UHPC stopped flowing, the spread was measured and noted.

A comparison of spread values gained at different institutes [2] showed that the test procedure isn't sufficient for quality control. The test results scattered widely and did not permit an accurate prediction of the quality of fresh and also of hardened UHPC. Based on this specification, the repeatability and the reproducibility of fresh UHPC properties were examined with an optimized test methods in different test series.

With the previous test method of consistency, only one rheological value respectively factor, yield stress or viscosity, could be examined. Therefore, additional test methods were used, where both rheological factors describing the consistency can be determined: The slump- flow test according to EN 12350-8 [6] and the V-funnel test acc. to EN 12350-9 [7].

In the slump flow test, two factors were measured: the t_{500}-*time* and the slump flow *SF* as final spread. Therefore, UHPC was filled in a tall metal cone, which was sitting on a horizontal metal plate with the smaller open end. The cone was lifted 30 sec after filling and was held over the plate until UHPC was flowed out completely. After that, the adhering residues on the cone were removed with a scraper and then the cone was removed. The time period from lifting the cone until UHPC achieved a diameter of 500 mm on the plate was measured (t_{500}-time). The maximum slump flow was determined after UHPC stopped flowing.

In slump tests, the concrete will slump or move only if the yield stress is exceeded and will stop when the stress (or weight of the concrete per unit area) is below the yield stress. Therefore, the slump, respectively the slump flow in this test, is related to the yield stress [3]. The t_{500}-value as well as the time of the V-funnel test t_V are useful factors describing the viscosity. But, the correlation between the measured values and the two fundamental rhelogical parameters (yield stress and viscosity) is not obvious. In most cases, the fundamental parameter cannot be calculated from the factor measured, but can only be assumed to be related [3].

Air void content

By default, the air void content of UHPC was measured according to EN 12350-7 [5] respectively EN 1015-7 [11]. The evaluation of different test values of the SPP has shown that there were no correlation between the flow properties and the air void content identifiable of UHPC (cf. Figs. 1 and 2). Especially the air void content of fine-grained mixture M2Q scattered significantly between 0.9 and 6.2 % by. vol. independent of the flowability. This can be attributed to the special rhelogical behaviour and the formation of a surface layer of UHPC during spreading. In contrast, a correlation between the flowability and the air void content of B5Q was discernible. (Fig. 2).

As a result of these test values the test method must be specified more precisely than described in the standards. Therefore, in a first step the filling process was optimized described in the following. The pot was fixed on a vibration table and filled by means of a funnel. UHPC was poured directly after the mixing process into the funnel. To guarantee a continuous flow of UHPC, the funnel was adjusted above the pot. Then a vent at the bottom was opened and the UHPC flowed evenly through a hose into the pot. The outflow speed was adjusted to the consistency of UHPC.

In the next step, the influence of different factors on the test result was investigated. Therefore, the point of measurement and the period and frequency of compaction were varied. First test results have shown that the compaction time and frequency depend on the viscosity of the mixture must be determined for each mixture. By numerous repititions of this process, one could deduce that the standard deviation of the air void content could be minimized, when the

filling process was optimized and the measurements were conducted at a specific time after end of mixing [12].

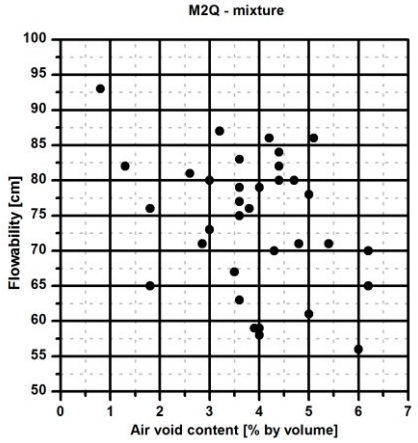

Figure 1: Correlation of flowability and air-void-content of the M2Q

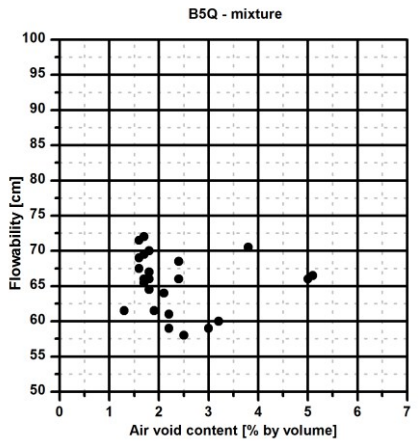

Figure 2: Correlation of flowability and air-void-content of the B5Q

4 Realization of the test series

The aim of the tests was to improve the significance of the measurements of flow properties of UHPC. Usually, many different factors may contribute to the variability of results from a measurement method, including: the operator, the equipment used, the calibration of the equipment, the environment (temperature, humidity, etc.), and the time elapsed between measurements [10]. In the following test series with UHPC, the point of measurement as well as the laboratory and material temperatures were varied and measured, respectively (Tab. 2). Because of the high amount of fine materials and the usage of PCE-Superplasticizer, the consistency of UHPC-mixtures can differ significantly by using different batches of raw materials.

Table 2: Influence factors of the test series

Influence factors	**Quantity**	**Test Series**			
		1	**2**	**3**	**4**
Water/binder-ratio	3	**variable**	constant	constant	constant
Operator	2	constant	constant	constant	**variable**
Mixing equipment	2	**variable**	constant	constant	**variable**
Laboratory temperature	3	constant	constant	constant	**variable**
Water temperature	1	constant	constant	constant	constant
Time of measurement	2	constant	constant	constant	constant
Batches of the materials	3	**Batch 1**	**Batch 1**	**Batch 2**	**Batch 3**

In [10], the precision is described as the general term of variability between repeated measurements. Two conditions of precision, termed repeatability and reproducibility conditions, have been found necessary and, for many practical cases, useful for describing the variability of a measurement method. Under repeatability conditions, factors like mentioned above (Tab. 2) are considered constants and do not contribute to the variability, while under reproducibility conditions and do constribute to the variability of the test results [10].

In the following two test series the values of the slump flow and the V-funnel-tests were examined and the precision of the test methods was evaluated depending on the influence

factors. The precision in the test series were expressed as the standard deviations of the slump flow *SF*, the t_{500}-time and the t_V-time.

First test series: Reproducibility of M3Q

In the first test series, the change of consistency of M3Q was investigated regarding two factors: the water-binder ratio and the mixing equipment. The water-binder ratio was varied in the range of 0.20 to 0.22. As mixing equipment, a 40L-intensive and also a 150L-compulsion mixer were used. An optimal water-binder ratio resulting in a sufficiently stable consistency of the mixture was the aim of these experiments.

In Fig. 3, the test results of the slump flow test of M3Q with variable water-binder ratio are depicted. The consistency was measured directly after the mixing process at 20 min and was repeated 10 min later. Between these two times UHPC was remixed for 30 sec.

In this short period, it was recognized that the consistency increased significantly independent of the mix condition. On average, the *SF*-values were 12 cm higher at the point of 30 min than at 20 min. This means that the time of measurement is important for the quality control of an UHPC, and should be specified individually for every mixture. Furthermore, it was noticed that the influence of the mixer on the consistency was reduced by increasing the water-binder ratio. The flow properties of the M3Q-mix were reproducible when the water-binder ratio exceeds a certain point.

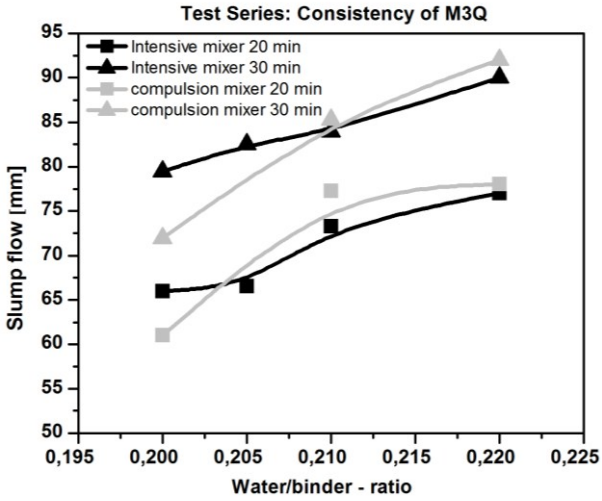

Figure 3: Influence of the water/binder-ratio and the mixing equipment on the slump flow.

Second test series: Repeatability of M3Q and B5Q

In this test series, the repeatability of the flow properties was tested by using the two reference mixtures. As described in Paragraph 2, different mixers were used for each. Therefore, the testing procedures had to be adapted to the maximum mixing volume.

M3Q was always produced in an intensive mixer in 25 litre batches and was investigated with four different fibre combinations and a constant water-binder ratio of 0.21. Every combination of fibres was mixed four times per test series in order to ensure that every value was determined at least twice per operator. In table 3 the procedure of the flowability test is given.

Tab. 3 specifies the procedure of the flowability tests: In the first iteration, the slump flow was tested by two operators 20 min after start of mixing, and the t_V after 30 min. In the second one, the procedure was changed. The third one was focussed on t_V-time and the last one on slump flow values at different points of measurement.

In Fig. 2, the test values of the slump flow as mean values (average of four measurements) and standard deviations respectively the values of the t_{500}-time are depicted.

Like in test series 1, the test values of all mixes were influenced by the point of measurement. Independently of fibre content and fibre length, the slump flow 30 min after start of mixing was always higher than the value after 20 min.

Table 3: Test procedure of the M3Q-mix per combination.

Number of mixture	Time of measurement	SF [mm]		t_{500} [sec]		t_V [sec]
Operator	[min]	1	2	1	2	1
1	20					
	30					
2	20					
	30					
3	20					
	30					
4	20					
	30					

Also the t_{500}-time, representing viscosity, was reduced over time. Furthermore, it was noticed that the fibre content influenced the consistency more than the fibre length, as can be seen in Figs. 4 and 5. With higher fibre content, the test values scattered strongly, which made an exact specification of consistency impossible. To improve the significance of the test, an increase of the number of repetitions may lead to better results for UHPC mixtures with high fibre contents.

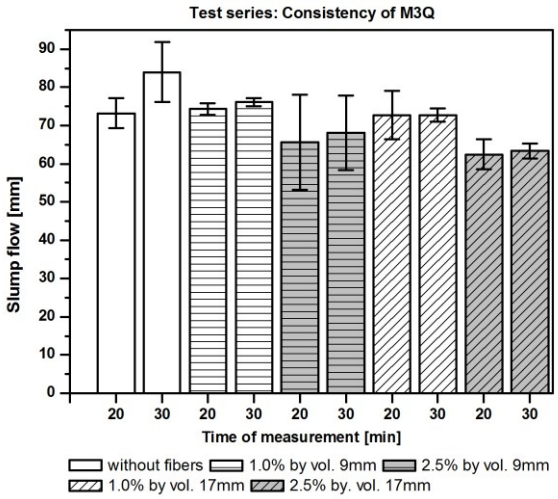

Figure 4: Slump flow of M3Q

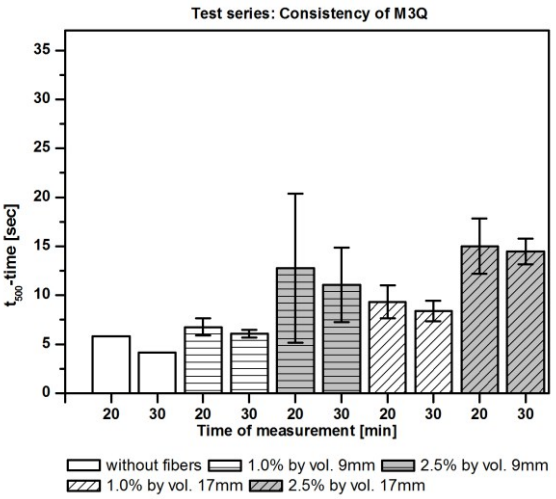

Figure 5: t_{500}-value of M3Q

B5Q was produced in this test series in a consumption mixer as described before. The water-binder ratio was constant, only fibre type and fibre content were varied comparable to M3Q. Because of the higher mixing volume in this case, every combination was only mixed twice per test series. In contrast to the M3Q test series, the slump flow test and the V-funnel-test could be conducted at both times of measurement.

In Figs. 6 and 7, the values of slump flow and t_{500}-time are presented. Although, B5Q was produced by using another superplasticizer. The consistency showed a time-depending behaviour as well. In comparison to M3Q, the maximum slump flows of B5Q were lower and the t_{500} values increased from 14 to 35 sec.

As can be seen in Fig. 6, the precision, described as the standard deviation of the slump flow was very low for the first three combinations, but the significance of the t_{500}-values were not sufficient in these tests. Due to the coarse aggregate in the mix, the flow properties were influenced significantly by the fibres. With the mix containing 2.5% by vol. of 17mm long fibres a limit was exceeded, where the chosen test methods are no longer suitable and the table-test should be preferred to describe the fresh concrete properties.

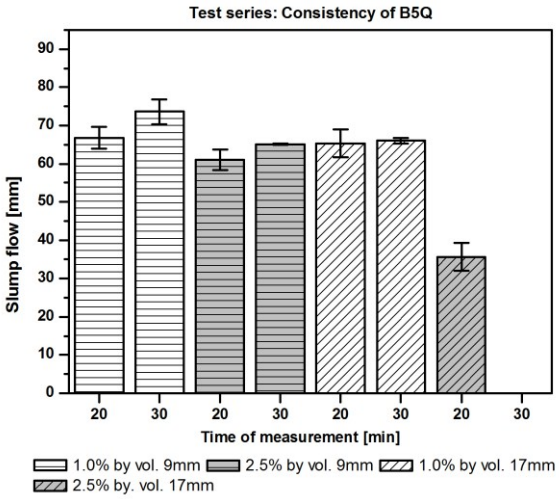

Figure 6: Slump flow of B5Q

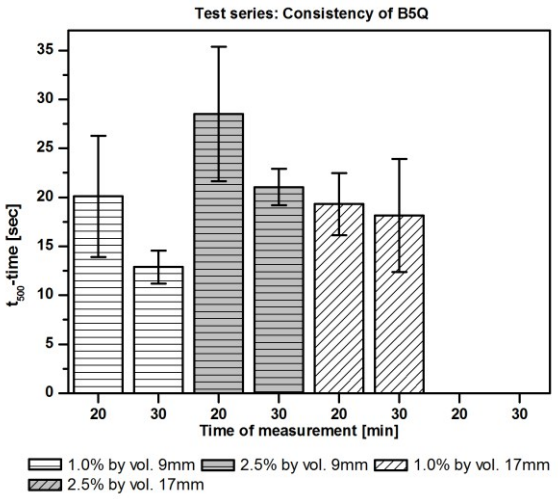

Figure 7: t_{500}-value of B5Q

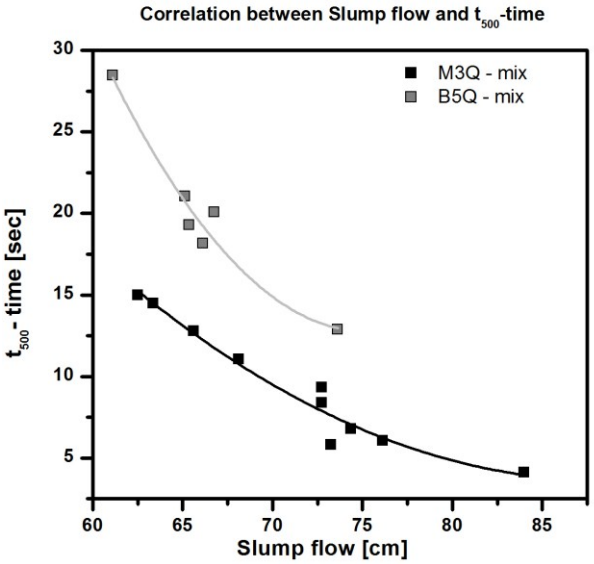

Figure 8: Curve shapes of the flow properties

In Fig. 8, the correlation of slump flow and t_{-500} of the second test series is presented. The values of each measurement can be described with a curve independent of fibre type and content. Both mixtures show a typical curve shape, which can be used as standard for quality control in further test series.

Outlook

In a third test series, the repeatability of the second test series will be investigated. In this case only new batches of material will be used to identify the influence of the raw materials, the test procedure and the laboratory conditions will be comparable to test series 2 (Tab. 2). Finally, a round robin test (Test series 4 in Tab.2) with other institutes will be performed to analyse the influence of different operators and laboratory conditions.

5 Conclusions

The fresh properties of UHPC were influenced significantly by different factors like the point of measurement, the mixing equipment, the laboratory conditions, the operator and especially the air-void content by the filling process.

Furthermore, the methods for ordinary concrete and self-compacting-concrete can be applied to UHPC with some specifications. Especially the point of measurement must be defined exactly

to compare different test values. Due to the different effective period of the superplasticizer in UHPC and due to the different duration of mixing, the quality control should be optimal performed 30 min after start of mixing. UHPC with flowable consistency should be tested with the slump flow test. In different test series a good correlation between the *SF*-value and the t_{500}-time was identified, which allows to describe the special rheological characteristic of each mixture. A correlation between the V-funnel value and the t_{500}-time wasn't found, so far. More tests and a higher number of values are necessary to analysed the qualification of the V-funnel-test to UHPC.

6 Acknowledgement

This project is part of the priority programme "Sustainable Building with Ultra High Performance Concrete" currently under way in Germany. The authors thank the "Deutsche Forschungsgemeinschaft (DFG)" for the financial support of this research work.

References

[1] Schmidt, M. (Hrsg.) et al.: Sachstandsbericht Ultrahochfester Beton. Deutscher Ausschuss für Stahlbeton (DAfStb) Heft 561, Berlin, 2008.
[2] Schmidt, M.; Fröhlich, S.: Testing of UHPC. Proc. 3rd international fib congress Washington, 2010
[3] Ferraris, C.: Measurement of Rheological Properties of High Performance Concrete: State of the Art report. Journal of Research of National Institute of Standards and Technology 104 (5), p. 461-478, 1999
[4] DIN EN 12350-5: Testing fresh concrete – Part 5: Flow table test; German version EN 12350-7:2009
[5] DIN EN 12350-7: Testing fresh concrete – Part 7: Air content – Pressure methods; German version EN 12350-7:2009
[6] DIN EN 12350-8: Testing fresh concrete – Part 8: Self compacting concrete – Slump-flow test; German version EN 12350-8:2010
[7] DIN EN 12350-9: Testing fresh concrete – Part 9: Self-compacting concrete - V-funnel test; German version EN 12350-9:2010
[8] Deutscher Ausschuss für Stahlbeton (DAfStb): DAfStb-Richtlinie Selbstverdichtender Beton (SVB-Richtlinie). Teil 1-3. Ausgabe November 2003.
[9] Bornemann, R.; Schmidt, M.; Fehling, E.; Middendorf, B.: Ultra-Hochleistungsbeton UHPC – Herstellung, Eigenschaften und Anwendungsmöglichkeiten. Beton- und Stahlbetonbau 96 (7), p. 458-467, 2001.
[10] ISO 5725-1: 1994-12: Accuracy (trueness and preceision) of measurement methods and results – Part 1: general principles and definitions. Beuth Verlag, Berlin.
[11] DIN EN 1015-7: Methods of test mortar for masonry – Part 7: Determination of air content of fresh mortar. German version EN 1015-7:1998
[12] Glotzbach, C.: Fröhlich, S.; Schmidt, M.: Measuring Air Content and Rheological Characteristics of UHPC Mortars, Proc. fib symposium, Stockholm, 2012

Hybrid Intensive Mixer with integrated Rheometer for High Performance Concrete

Harald Garrecht, Christian Baumert, Andreas Karden
Chair of Building Materials, Technische Universität Darmstadt, Germany

High-performance concretes with high amounts of fine particles, such as ultra-high performance concrete (UHPC) are due to its composition expensive in practice, as well as technically complex in the production process. This article presents a new comprehensive concept which is based on a three-step principle of the ecological and economic optimization for concrete production. Moreover these steps allow reproducibility with minimal variations of fresh and hardened concrete properties. Theoretical-numerical calculations define initially the mix design and determine relevant rheological parameters, such as yield stress and viscosity. The second step involves the mixing process. The mixer also acts as a rotational rheometer and can also carry out oscillatory measurements. Within the third step and on the basis of the obtained data, including an evaluation of thixotropy, mix design or mixing regime can be optimised.

Keywords: mix design, (suspension) mixing techniques, rheology, in-mixer oscillatory measurement, controlled dose and mixing process, workability

1 Problem Statement

Requirements of a modern concrete include, in addition to the classical properties of hardened concrete, aspects of durability and increasingly preservation of resources. Concrete-technological methods are the reduction of the cement clinker content, a partial substitution of cement by low-emission and cheap substitutes, the increase of the packing density and a reduction of the w/b-value. Due to a low water content suitable high-performance superplasticizers are compulsory up to an amount depending on the fine materials, to achieve a workable consistency until self-compaction.

The significantly modified mix design for high performance concretes, e.g. UHPC is characterised in comparison to normal concretes by considerably longer mixing times and a higher consumption of electrical energy [1, 2]. Mix design and mixing technique are well-known, while their practical and coupled application is seldom used. For the fresh concrete characterisation test methods according to the national standards, e.g. DIN EN 12350-8:2010-12 are used, whereas rheological measurements are rarely performed, because most adequate devices are expensive and the use is time-consuming.

2 State of the Art

Concrete Mix Design

UHPC is characterised by compressive strengths above 150 MPa and an excellent durability. This can be achieved by using very high amounts of cement and puzzolanic nano materials. Thus the demand of water increases, which must be compensated by using superplasticizer. From an ecological point of view UHPC is expensive due to its raw materials and the required high energy input during the mixing process. [3]

High-volume fly ash (HVFA) concrete contains at least 50 M.-% fly ash by weight of cement, but less than 200 kg/m³ of the cement itself. The water content is lower than 130 kg/m³. HVFA concretes show a comparable high durability to UHPC. Additionally it is a low cost material with a low degree of shrinkage and low CO_2 emissions. [4].

Mixing Technique

In practice, the mixing process is completed after the so-called stabilisation time. Thereby, the energy consumption of the electric motors approximates asymptotically to a minimum, according to [5]. The results obtained in the fresh concrete properties are dependent on the type and size of the mixer and the mixing regime. Large mixers [6] and those with higher agitator speeds [1] enable lower values for the yield stress and in particular for the viscosity of the therein produced concretes. While the electrical input rating of the agitator is to be increased significantly by an increasing agitator speed, the energy required to produce a concrete batch is reduced due to shorter mixing times [1]. Concretes with superplasticizer-addition, which are produced in a two-stage mixing process, achieve higher compressive strengths by 8-17 %, up to 52 MPa [7]. Furthermore in [2] slump flow and the maintaining of the consistency of a self compacting concrete (SCC), UHPC and HVFA concrete were significantly increased by applying a two-stage mixing process with a suspension mixer in the first step.

Rheological measurements in the cone mixer

The usage of the current and power consumption of drive motors has been proved as suitable for the evaluation of usual consistency classes of concretes. In addition, the individual mixing stages and thus the end of mixing can be derived from the development of the power consumption over the mixing time [8]. According to [9], this procedure is inappropriate for the rheological evaluation of SCC. Alternatively, the speed shall be lowered within this method in 5 steps with a frequency converter in the final mixing stage. The pairs of values speed/torque of the individual stages are used to calculate the rheometric parameters by linear regression and hence deriving the slump flow. The Viscoprobe^{TM}, by Skako Concrete, measures the resistance to motion of a steel ball immersed in concrete, which is attached via a rod to a torque sensor. To calculate the relative rheometric parameters, two pairs of values (speed and associated torque) are required. The data collection and analysis is in real time, parallel to the mixing process and therefore does not lead to longer mixing times.

3 Methodology

In the context of research projects, conducted by the authors it was the aim to develop a production process for high performance concretes which considers all effects of the mix design, mixing technique and -regime towards the fresh and hardened concrete properties. The underlying optimization process allows to decrease costs of raw materials and the production process, by keeping fresh concrete properties constant or even improving them. It also increases the environmental quality of designed concretes by the purposeful selection of sustainable starting materials. Furthermore, the appropriate choice of the mixing technique enables to deagglomerate fine materials, which are especially used in UHPC and to a certain amount in a HVFA concrete. In the present article the comprehensive obtained results of an developed high-performance concrete with an high content of fly ash will be presented. The determined compressive strength of 120 MPa at 90 days can be allocated towards a lower UHPC range even with a low amount of cement and without silica, while still featuring quality characteristics such as good workability (despite a significantly reduced water content), excellent durability, low costs, low emissions and low shrinkage. Higher Compressive strengths up to 150 MPa can be achieved for a HVFA concrete through the use of fine limestone fillers, a further reduction of the water-binder ratio and a moderate increase of the superplasticizer amount. The production of the HVFA concrete was carried out in one- and two-stages mixing processes in a modified cone mixer. In the one-stage mixing process all dry starting materials were homogenised for ten seconds, before water was added. Within the two-stage mixing the mortar was produced first, followed by the addition of coarse aggregates. In both methods, the

detected electrical energy of the mixer motor, the tool speed and the timing of the superplasticizer addition were varied.

Concrete Mix Design

This contribution presents an example of an high-strength concrete, with which the results were verified. The concrete mix design is based on a concept of [4], with the aim to substitute a high amount of the cement by fly ash, to increase the durability and to minimise the stabilisation time. An optimisation of the concrete was carried out by theoretical calculations with BétonlabPro. The software was developed at the Laboratoire Central des Ponts et Chaussées (LCPC) to create concrete mix designs and allows the calculation of the stabilisation time, as well as the estimation of values of the fresh and hardened concrete properties. A low relative solid concentration is in this context associated with a short stabilisation time [5]. BétonlabPro can also be used as a tool box to adjust the mix design in an iterative process to an optimum.

In order to identify in advance which addition sequences of the starting materials are useful, calculations were performed with BétonlabPro, see Table 1. Firstly, the packing density of the reference concrete was optimised by the change of the volume fractions of the aggregates, and secondly the possible stabilisation time was determined at a minimum. The stabilisation times for subsets of the mixtures without some starting materials are given and are depending on the relative solid concentration.

Table 1: Mix design for the Reference concrete (R. c.) and with BétonlabPro optimised mix designs (O1 until O6) with the stabilisation times; SP stands for superplasticizer.

		Concretes						
		R. c.	**O1**	**O2**	**O3**	**O4**	**O5**	**O6**
CEM I 52,5 N HS/NA	kg/m³	180	180	180	180	180	180	180
Fly Ash KM/C	kg/m³	309	309	309	309	309	309	-
SP Sika 20 HE	kg/m³	6	4	4	4	4	4	4
Water	kg/m³	112	113	113	113	113	113	113
Sand 0/2	kg/m³	640	577	577	289	-	-	577
Coarse Aggregate 2/8	kg/m³	746	245	-	-	245	-	245
Coarse Aggregate 8/16	kg/m³	391	955	-	-	-	955	-
Stabilisation time	sec	-	210	166	143	122	178	235

Production – mixer, mixing technique, mixing regime

The investigated concretes were produced in a cone mixer from Kniele, in one- and two-stage mixing processes. A speed-variable drive is installed in the mixer for adjustable speed with higher torque. The measurement of rheometric parameters, which are described below, requires for maximum efficiency of the inverter. Therefore the so-called direct torque control method can cope with this requirement, due to the fact that the engine can be accelerated speed-controlled from a standstill and enables the operation with lowest speeds. Another advantage is the ability for torque-controlled operations, as it is usual for rheological measurements [10]. Due to the possibility of having access to the data of the converter, there is no need for additional components such as torque sensors. To avoid gear reduction and the associated disadvantages to achieve high speed performance, a high torque permanent magnet synchronous motor was used, which allows a direct drive of the internal agitator. The so-obtained stiffness of the drive train allows oscillatory measurements in the mixer. Additionally dosage units are installed, which operate very precisely.

Determined Parameters

For the aim to use the mixer for rheometric measurements, a calibration was required. Therefore the gauging vane of the rheometer was firstly attached with an adapter to the mixer shaft to measure concrete – produced in an additional mixer – directly in the mixer. In a second step the measurements of the same concrete were carried out after a short period of time with a portable rheometer in a cone having equivalent dimensions as the cone mixer, see Figure 1.

Figure 1: ICAR Rheometer in a cone form with equivalent dimensions of the cone mixer for calibration of the mixer.

After the calibration of the mixer an optimised agitator was installed onto the mixer shaft to produce concrete. Additionally is possible to perform rheometric analysis with the aim to determine relative values, due to the fact that the agitator does not show defined geometries. To determine the flow curve the concrete is pre-sheared for 10 seconds. Then the agitator rotates in 9 steps with speeds of 21.8 rpm to 1.7 rpm, each over 4 seconds. For the evaluation, the data from the pre-sheared phase and from the first second of each step are not considered. During each phase of measurement with predefined constant speed, the actual speed and the associated torque is recorded at intervals of 100 msec. From the measured data in turn pairs of values are averaged and logged for each speed step. The calculation of the rheometric parameters is proceeded in the Programmable Logic Controller (PLC) of the mixer according to the method of least squares. To determine the dynamic and static yield stress, the torque is increased continuously until the agitator starts to rotate.

Another possibility to characterise viscoelastic substances are oscillatory measurements, where the shear stress is changed harmonic-periodically over the time. Oscillation measurements can be illustrated by the Two-Plate Model, see Figure 2.

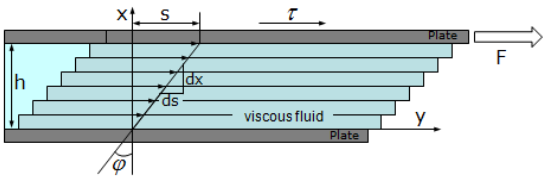

Figure 2: Two-Plate Model.

While the lower plate is stationary, the deflection ± s of the top plate occurs with the deflection angle ± φ according to the sine curve by a force ± F. This results in the shear stress ± τ (Pa) = ± F/A and the deformation ± γ = ± s/h.

The complex shear modulus G* describes the viscoelastic properties and consists of the storage modulus G' (elastic component) and the loss modulus G'' (viscous component). From the relative values of the engine torque M and the position value POS of the agitator shaft REL' and REL'' can be determined analogously.

$$G' = \frac{\tau_{Amplitude}}{\gamma_{Amplitude}} \cdot cos\delta \qquad REL' = \frac{M_{Amplitude}}{POS_{Amplitude}} \cdot cos\delta \qquad (1)$$

$$G'' = \frac{\tau_{Amplitude}}{\gamma_{Amplitude}} \cdot sin\delta \qquad REL'' = \frac{M_{Amplitude}}{POS_{Amplitude}} \cdot sin\delta \qquad (2)$$

To characterise the flow behaviour of concrete an undisturbed flow of a homogeneous material needs to be assumed, by a sample height of at least 5 times of the largest grain diameter is required at the outer edge of the sample [11]. To get both values of the actual yield stress and viscosity, the LCPC box method was modified. To get an evidence for the viscosity the time can be measured until the concrete overflows a line at 700 mm. The filling of the LCPC box can be carried out reproducible at one end of the box with the flow cone, see Figure 3.

The Vicat test according to DIN EN 196-3 and DIN EN 480-2 allows the determination of the final setting time only for pastes and mortars. Since a realistic strength development can only be detected in the concrete itself, the BEUS system was used (BEtonUltraSchall - concrete ultrasonic, developed at the Chair of Building Materials, TU Darmstadt).

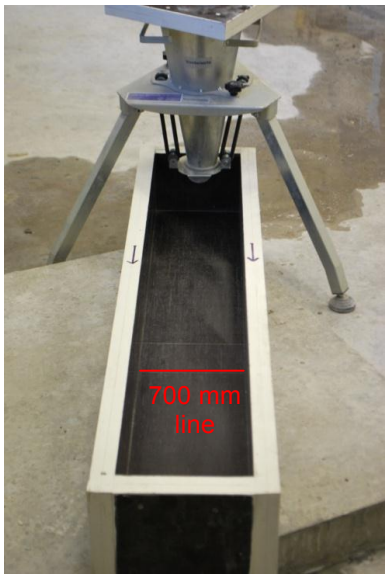

Figure 3: LCPC box (length = 120 cm, width = 20 cm, depth = 15 cm) with flow cone (volume = 6 l)

4 Results

Flow curves – Calibration

The measured flow curves by the cone mixer and the ICAR Rheometer present a good correlation, see Figure 4. So it is possible to detect significant rheometric results with the mixer motor in combination with the inverter.

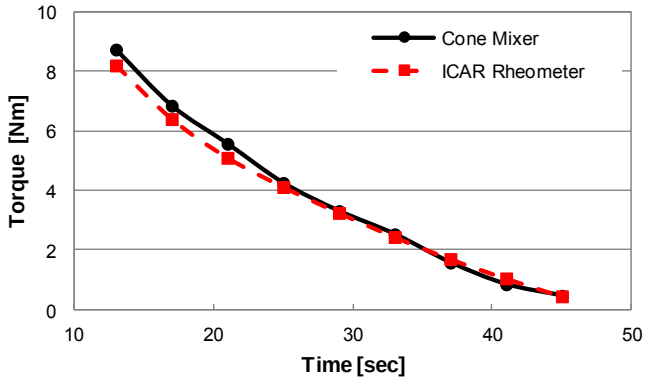

Figure 4: Flow curves, measured inside the cone mixer with the gauging vane of the remoter and the ICAR Rheometer in a cone form with equivalent dimensions of the cone mixer.

Flow curve measured in the mixer

Figure 5 shows measured flow curves of the reference concrete mix design with the cone mixer immediately after mixing and 30 min after addition of water and a two-stage addition of the superplasticizer. 60 % of the superplasticizer was added with the water after a dry mixing phase of ten seconds. The remaining super-plasticizer of 40 % was added after two-thirds of the total mixing time. Test 1 was carried out in one-stage with a agitator speed of 400 rpm. In test 2 the mixing process was operated with 600 rpm for the mortar in the first stage and with 150 rpm during the second stage with addition of the coarse aggregates.

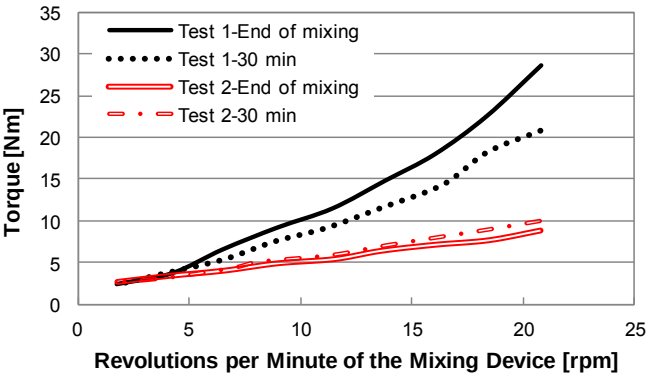

Figure 5: Measured flow curves with the cone mixer of the reference mix design with different mixing regimes.

The superplasticizer was likewise added, 60 % with the water and 40 % near completion of the first stage of the mixing process. Although the introduced mixing energy is equal, the viscosity of the fresh concrete in test 2 is significantly lower and less variable.

Yield stress

The torque was increased linearly from zero starting and the response was monitored with the rotary encoder. Once the angular velocity, which is measured with the rotary decoder, deviates from the linear trend the intersection point – the yield point – is determined with the tangent method. An actual yield point value is identified, in comparison to a extrapolated model value, see Figure 6.

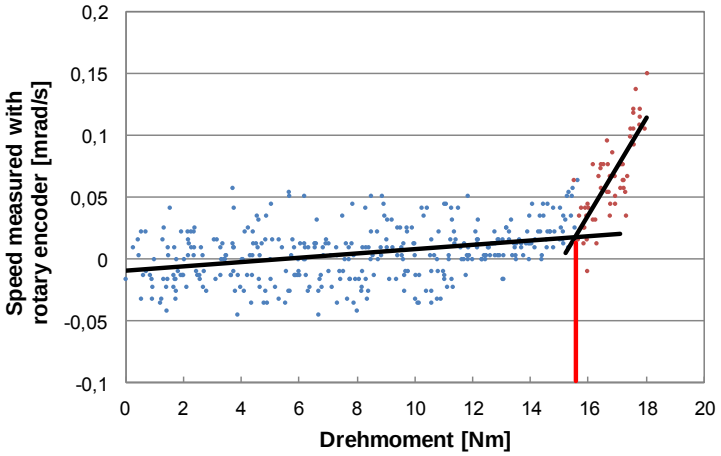

Figure 6: Determination of the yield stress in the mixer; linearly increasing torque input and measurement of the angular velocity with rotary encoders; analysis of the intersection point (= yield stress) by using the tangent method.

Thixotropy

Using the method to determine the yield stress, an further analysis of the detected data can give back the static and dynamic yield stress. Directly after mixing the measurement of the static yield stress corresponds to the dynamic yield stress. Only in test 2 the amount of superplasticizer was 6 kg/m³ concrete. All other test were carried out with 4,5 kg/m³ concrete. The results show that the test which were carried out in two-stages show lower dynamic and static yield stresses, see Figure 7. Although test 2 contains a higher amount of superplasticizer, the results of the torque do not reach the low values of the results achieved by mixed in two-stages.

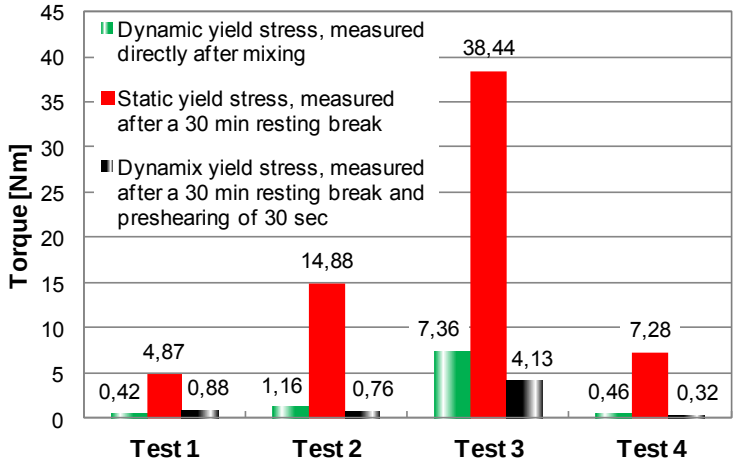

Figure 7: Measured torque values indicating dynamic and static yield stress depending on the time of measurement; directly after mixing, after a resting break (30 min) and after a resting break with a preshearing period of 30 sec.

Oscillations test – Amplitude sweep in the mixer

With specification of the torque, it is – while maintaining the frequency – increased steadily. The measured results in the amplitude test allow a characterisation of the viscoelastic material behaviour, dependent of the applied load. The limit value of the torque $M_{y,relativ}$ (yield point), which leads to exceed the linear-viscous range is described as yielding-limit. Only at the inter-section of REL' with REL'' a change takes place towards liquid characterisation, see Figure 8.

This point defines in terms of concrete rheology the conventional yield stress $M_{f,relativ}$ (flow point). According to [10], the values $M_{y,relativ}$ and $M_{f,relativ}$ differ significantly from each other and can affect the corresponding shear rate by more than a factor of 10. Consequently, the bandwidth of the analysed results depends on the method of determination and varies significantly.

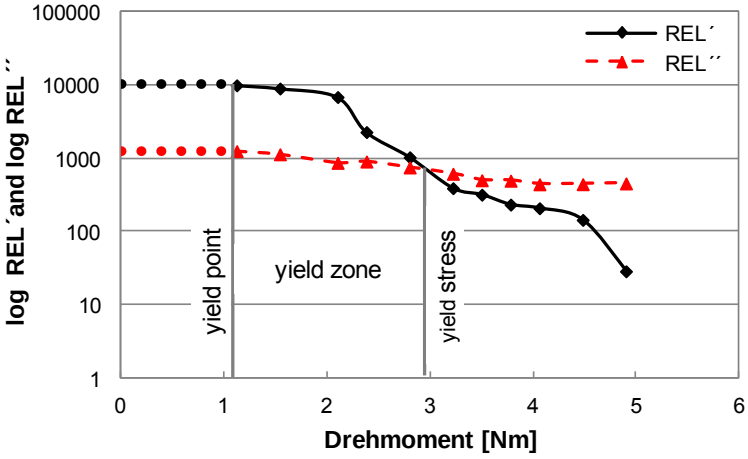

Figure 8: Determined REL' and REL''-curves by measuring the amplitude sweep in the mixer, with the yield point, yield zone and intersection point (= yield stress).

LCPC-box

In the modified LCPC Box the time between the opening of the funnel-cap and the overflow of the 700 mm line in the box by the concrete is measured to evaluate the viscosity. An indication for the viscosity is given by the measured times T_{700} with the LCPC box. Two-stage mixing regimes have the effect of a lower mixing energy demand and reduce the viscosity of fresh concrete significantly, see Table 2.

Table 2: Investigated mixing regimes for test 1 until 4 with measured values of the modified LCPC box.

		Test 1	Test 2	Test 3	Test 4
Number of Stages	-	2	1	1	2
Mixing Energy	kWh/m³	5,25	5,25	3,45	3,45
Agitator speed	rpm	1000/150	250	250	1000/150
T_{700} LCPC Box	sec	29	43	51	37
Spread Length LCPC	cm	111,5	111	110	106

BEUS

The determination of the final setting of the concrete was measured with the BEUS method. As expected, the final setting affects the early strength. However, depending on the mixing regime significant differences exist. Concrete, produced in two stages shows a tendency of a later setting along with a reduced early strength, see Figure 9. Due to a reduction of the superplasticizer amount a better early strength can be reached by keeping the same rheological behaviour.

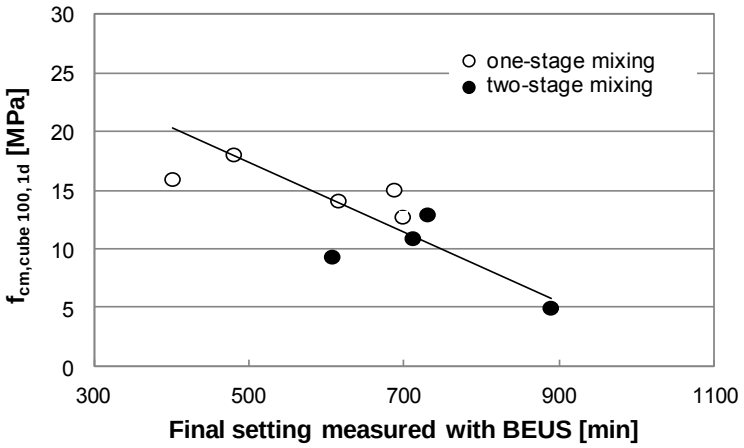

Figure 9: Early strength $f_{cm,cube\ 100,\ 1d}$ and final setting measured with BEUS; results in dependence of a one- or two-stage mixing regime.

5 Conclusion

The production of high performance concretes, e.g. HVFA or UHPC requires concepts to ensure projected qualitative requirements. To fulfill these demands first results of a three-step principle are presented. Within this concept it is possible to create mix designs with further data for the mixing. An improved mixing process can be performed with a higher drive capacity and automatic control technique to measure rheometric parameters reproducibly and directly in the mixer with the agitator to evaluate the concrete more comprehensive. The effects on the rheology due to a modified mixing regime are so recognizable and can specifically optimised in an integral process towards a particular application by adjusting the mix design. For the determination of viscosity and absolute values for yield stress, the LCPC box was modified for high viscosity concretes. Further improvements are the reduction of the mixing time and the energy consumption up to 50 % and a lower amount of superplasticizer is required.

References

[1] Baumert, Ch.: Rheologische Mischprozessführung (working title). Dissertation in preparation, TU Darmstadt, 2012.

[2] Baumert, Ch.; Garrecht, H.: Mischen von Hochleistungsbetonen. *Beton- und Stahlbetonbau* 105 (6), p. 371-378, 2010.

[3] Deutscher Ausschuss für Stahlbeton: Sachstandsbericht Ultrahochfester Beton. DAfStb 561, Berlin, 2008.

[4] Malhotra, V.M.; Mehta, P.K.: High-Performance, High-Volume Fly Ash Concrete for Building Sustainable and Durable Structures, 3rd edition, Ottawa (Canada): Supplementary cementing Materials for Sustainable Development Inc., 2008.

[5] Chopin, D.; Larrad, F. de; Cazacliu, B.: Why do HPC and SCC require a longer mixing time? *Cement and Concrete Research* 34 (12), p. 2237-2243, 2004.

[6] Wallevik, O.H.; Wallevik, J.E.: Rheology as a tool in concrete science: The use of rheographs and workability boxes. *Cement and Concrete Research* 41 (12), p. 1279-1288, 2011.

[7] Rejeb, S. K.: Improving compressive strength of concrete by a two-step mixing method. *Cement and Concrete Research* 26 (4), p. 585-592, 1996.

[8] Cazacliu, B.; Roquet, N.: Concrete mixing kinetics by means of power measurement. *Cement and Concrete Research* 39 (3), p. 182-194, 2009.

[9] Nordenswan, E.; Käppi, A.: A new online method of measuring the workability of self-compacting concrete. Proc. 5th RILEM Symposium on SCC, Ghent 2007.

[10] Mezger, Th. G.: Das Rheologie Handbuch, 3rd edition, Hannover: Vincentz Network, 2010

[11] Roussel, N.: The LCPC Box: a cheap and simple technique for yield stress measurements of SCC. *Materials and Structures* 40 (9), p. 889-896, 2007.

Influence of vacuum mixing on the mechanical properties of UHPC

Jeroen Dils[1], Geert De Schutter[1], Veerle Boel[1,2],Egon Braem[1]

1: Magnel Laboratory for Concrete Research, Ghent University, Belgium
2: Departement of Construction, Faculty of Applied Engineering Sciences, University College Ghent, Belgium

The influence of vacuum mixing of UHPC on the compressive and tensile strength, and Young's modulus is examined. These mechanical properties are influenced by the microstructure and the pore system. Classical models predicting these properties based on the water-to-cement ratio do not consider the effect of vacuum mixing, which is quite new. This will be even more important in the case of UHPC because of the extremely low water-to-cement ratio and the larger influence of changes in air content. In this research, two different mixer sizes are considered: a vacuum paste mixer (capacity of 5 liter) and a vacuum concrete mixer (capacity of 75 liter). For each mixer, three different pressure levels are examined: vacuum (100 mbar), semi-vacuum (500 mbar) and atmospheric pressure (1013 mbar). The influence of heat treatment (90°C) in coMParison or combination with vacuum mixing is evaluated by means of the compressive strength on concrete cubes 100 mm.

Keywords: UHPC, vacuum mixing, compressive & tensile strength, Young's modulus

1 Introduction

UHPC mixtures often contain a high amount of air voids which have an influence on the mechanical and rheological properties [1]. Especially the air voids between 0.1 and 1 mm can be seen as considerable defects in the concrete which can initiate failure at high loads [2]. The airvoids in UHPC can not as easily escape from the mass as in the case of self-coMPacting concrete. The consistency of UHPC is typically higher than of SCC, so the air bubbles are not able to escape. A possible way to remove the air is to apply external or internal energy as with traditional vibrated concrete. According to Bresson [3] the vibration speed for concrete with a water-to-cement ratio lower than 0.3 should be around 0.2 m/s. Chiocchio et. al. [4] state that the aggregate sizes affect the optimum vibration frequency. The best coMPaction should be reached when the vibration frequency corresponds to the resonant frequency of the mean grain size. Unfortunately such vibrators are not common in concrete production. The high internal vibration can also cause fibre orientation or even sedimentation of the fibres.

A new way to facilitate the removal of entrapped air is the use of a mixer that can control the air pressure in the mixing pan. In the past, tests were done with mixers having a content of maximal 5 liter of UHPC [1]. The compressive strength increased from 150 to 230 MPa with a heat treatment and a lowered air pressure during the last 60 s of the mixing procedure. In this research a 5 liter paste mixer will be used, as well as a 75 liter concrete mixer.

2 Materials and mix composition

The chemical and mineralogical composition as well as the standard compressive strength of the Portland cement, used in this research, is given in Table 1. CEM I 52.5 R (HSR) had a particle size distribution with a d_{50} of 14.5 µm and a Blaine fineness of 4392 cm²/g. A cement with a low C_3A content was used due to their low water demand [5].

Table 1: Chemical and mineralogical composition and the standard compressive strength of the cement.

chemical composition	**SiO_2**	**Al_2O_3**	**CaO**	**Fe_2O_3**	**K_2O**	**MgO**	**Na_2O**	**Na equivalent**	**SO_3**
[%]	21.48	3.61	63.37	4.2	0.56	1.64	0.17	0.54	2.54
mineralogical composition	**C3S**	**C2S**	**C3A**	**C4AF**					
[%]	57.16	18.55	2.47	7.72					
Standard compressive strength (NBN EN 197)	**2d**	**7d**	**28d**						
[MPa]	28.1	42.4	59.1						

A polycarboxylic ether was used as a superplastisizer with a molecular weight of approximately 40000 g/mol and 35% of solids. The compacted silica fume contained 95.6% SiO2, had a N_2-BET specific surface of 17,77 m²/g and a d_{50} of 0.16 µm. The quartz sand had a density of 2650 kg/m³ and a mean particle size of 389 µm. The composition of the concrete with a water to binder ratio of 0.15 is given in Table 2. The particle size distribution can be seen in Fig. 1.

Table 2: Composition of UHPC.

materials	**[kg/m³]**
CEM I 52,5 R (HSR)	925.61
silica fume	231.40
sand M31 (150-600µm)	1018.17
superplasticizer	42.31
water	173.55

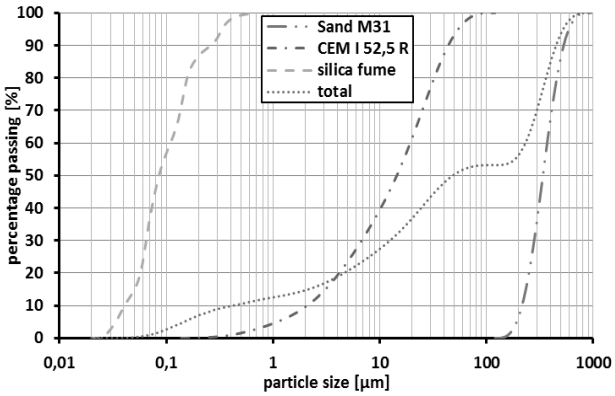

Figure 1: Particle size distribution.

The composition in table 2 is based on the work by Richard and Cherezy[6]. As the materials used in present study are not exactly the same as in [6], some preliminary test were performed with and without heat treatment in order to verify the mix design. The results, as shown in (Fig. 2). Indicate a good correlation with the results given in [6] in the case of no heat treatment. Different results are obtained when a heat treatment is performed. This difference is probably due to the way of curing. In the present research the cubes were steam cured at ±90°C during 48 h. No specific information was found on the heat treatment in the paper of Richard and Cherezy [6].

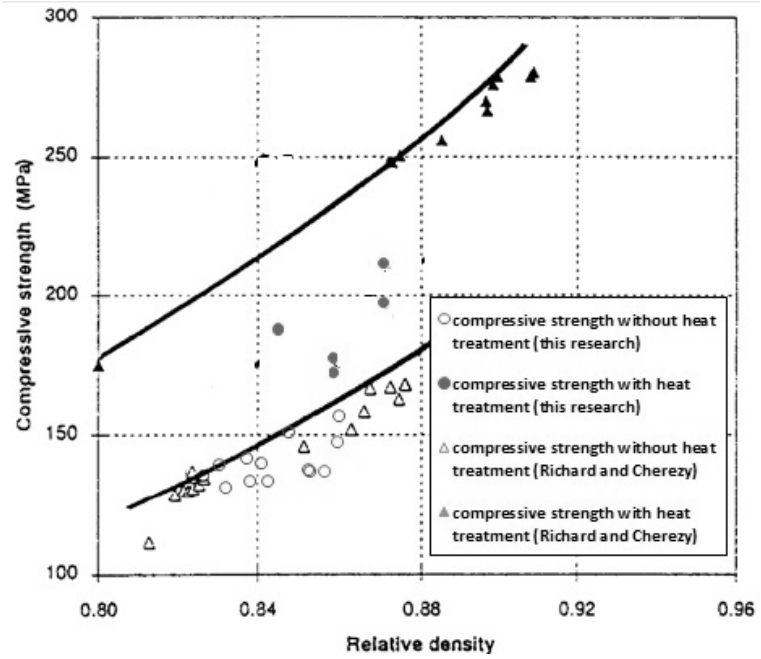

Figure 2: Comparison of the mix design with results by Richard and Cherez.($f_{c,28d}$) [6].

3 Mixing procedure

Small batches were were made in a 5 liter intensive paste mixer while larger batches were prepared in a 75 liter intensive concrete mixer. A star mixing tool was used to mix intensively and the mixing procedure was the same for both mixers. To eliminate the influence of mixingenergy, the same circumferential speed at the extremity of the vanes of the mixing tool, is used in both mixers. First, cement, silica fume and sand are weighed in a mobile scale and all these powders are introuced in the mixer simultaneously. The dry powders were mixed during 15 s. The superplastisizer was added together with the water within 20 s at a mixing speed of 1.6 m/s. This is followed by an intensive mixing period. The duration was determined based on the powercurve (see Fig. 3). The stabilisation time was considered to be reached when the curve reached a gradient of -0,0006 [7]. The authors have chosen for a hybride mixing procedure, consisting of an intensive phase for 135 s at a speed of 6 m/s until the maximal power is reached and a slow phase for 120 s at a speed of 1.6 m/s until stabilistation. At this point, the optimal workability (slumpflow and V-funnel) is obtained. The effect of the air pressure is at three levels: 1013 mbar (atmospherical), 500 mbar (semi-vacuum) and 50 mbar (vacuum). The vacuum phase lasted 70 s, during the slow mixing phase. The effect of vacuum mixing on strength is also combined and coMPared with the effect of a heat treatment.

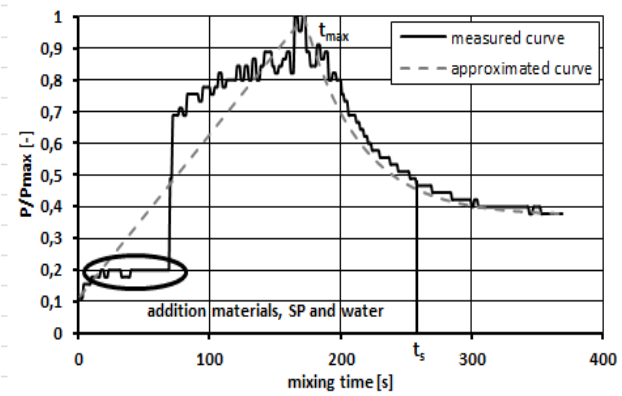

Figure 3: Normalised power curve of the mixing process to determine the stabilisation time t_s.

4 Results and discussion

Influence of vacuum mixing on the mechanical properties of UHPC (paste mixer)

After completion of the mixing procedure as described in section 3, the air content of the fresh paste was determined according to the water column method (EN 12350 part7: aircontent). Two batches of 5 liter were made from which six prisms with dimensions 40x40x160 mm were moulded per age (2 d, 7 d and 28 d). The prisms were stored for 1day in the climate room (20°C±2°C and RH= 90%±5%) and than kept under water, until the age of testing was reached. On each prism the flexural bending strength was determined. On the two remaining halfs a compressive test was performed. This implies that the values, given in Fig. 4, are an average of 12 compressive test results. The standard deviation is also included in the graph. Besides the prisms, a cube of side 100 mm is made in order to perform an air void analysis on the hardened concrete. Fig. 5 gives the air content of the fresh as well as the hardened concrete.

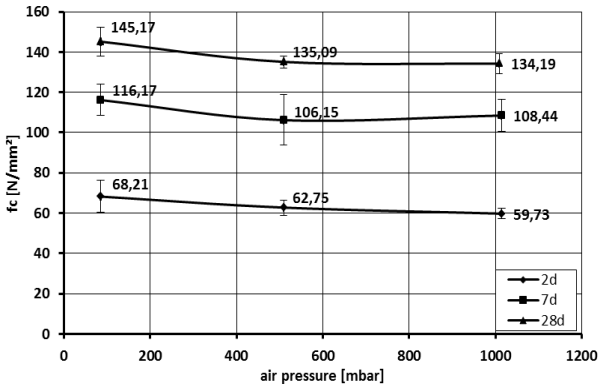

Figure 4: Compressive strength paste in function of the applied pressure in the mixing pan.

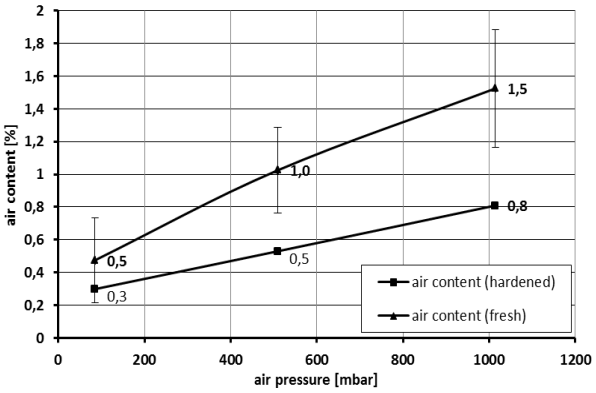

Figure 5: Air content in function of the applied pressure in the mixing pan.

The results of the bending tests are omitted, because no clear trend could be seen. The compressive strength clearly increases with a decreasing mixing pressure. The lowered pressure causes a decrease in air content of the fresh and hardened concrete. Therefor a higher homogeneity is obtained and less defects, which can initiate cracks and failure, are caused. These phenoma explain the higher compressive strength when the vacuum condition is applied. This is in agreement with the results of [1] and [2].

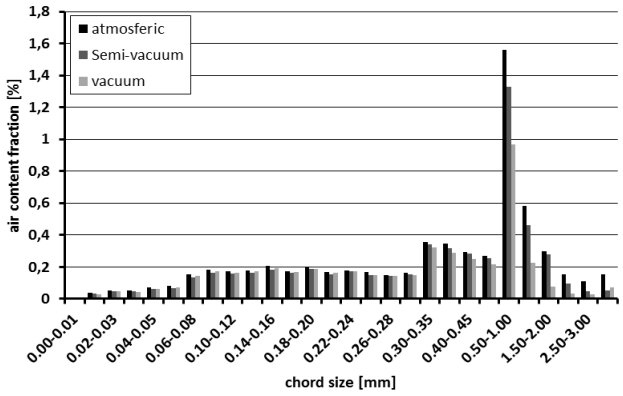

Figure 6: Air void distribution of UHPC (paste mixer).

The airvoid distribution shows on which type of air cavities [8] the vacuum mixing technique has the most pronounced influence. The lowered air pressure during mixing has a rather big iMPact

on the chord sizes between 0.06 mm and 1 mm. For smaller and larger sizes the lowered pressure gives a higher amount of air cavities. An air void analysis only gives the effect on the air cavities (10 µm-1 mm) and not on the capillary cavities (5 nm-10 µm). In order to gather this kind of information further research, with other techniques, is planned.

Influence of vacuum mixing on the mechanical properties of UHPC (concrete mixer)

The compressive strength on concrete was determined on 7 d, 28 d and 3 months on cubes with size 150 mm. Two batches of 50 liter were made, so that five cubes per age could be tested. In Fig. 8 the cylindrical compressive strength is also shown, as obtained on the samples on which the Young's modulus is determined.

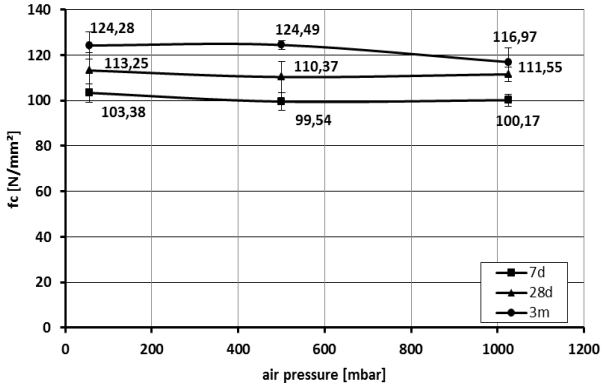

Figure 7: Compressive strength concrete in function of the applied pressure in the mixing pan.

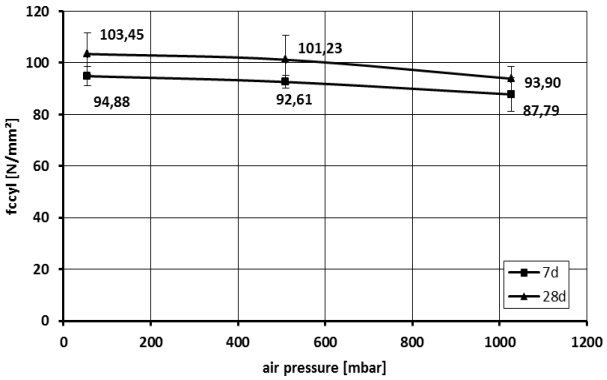

Figure 8: Cylindrical compressive strength in function of the applied pressure in the mixing pan.

Fig. 7 and Fig. 8 give the same increasing trend when the air pressure is lowered in the mixing pan. The increase is however less pronounced on concrete level than on paste level. Considering the variation on the results, the increase is not significant for concrete. Two differences can be notified with the results in Fig.2. The mixtures are made with a larger mixer (75 liter) and the tests were performed on cubes 150 mm. The first difference may be a reason for the insignificant increase in compressive strength when the pressure is reduced. The latter gives an explanation for the lower values of the compressive strength in coMParison with those in Fig. 2.

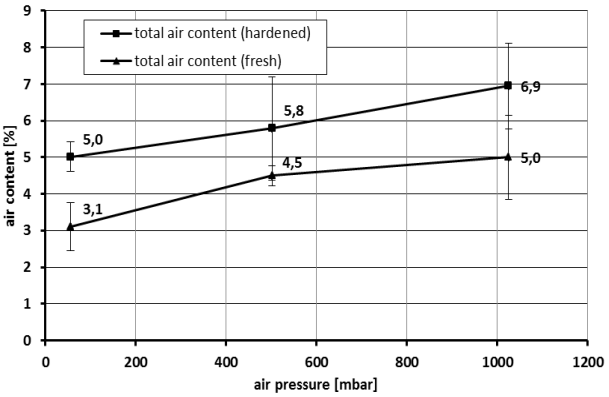

Figure 9: Fresh and hardened air content in function of the applied pressure in the mixing pan.

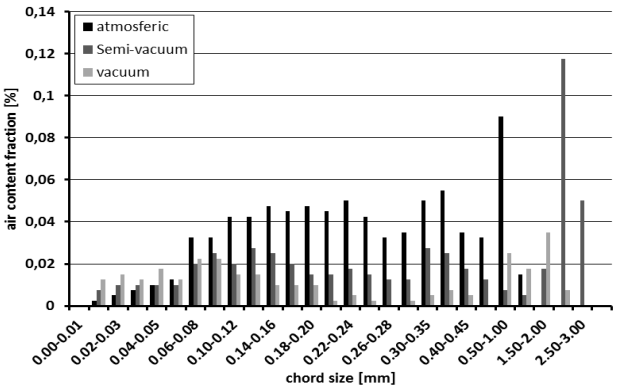

Figure 10: Air void distribution of ultra high performance concrete.

The hardened air content in Fig.9 is the average of seven air void analyses. The reduction of the air content by vacuum mixing in the mixer of 75 liter is only 2/7 of the content under atmospheric conditions, in coMParison with a reduction of 2/3 in the case of vacuum mixing in

th mixer of 5 liter. The airvoid distribution of Fig. 10 shows the largest reduction of air content in the range of air cavities with a chord size of 1 mm to 3 mm. The influence window of the vacuum mixer is clearly smaller for the concrete mixer (75 liter) than the paste mixer (5 liter) when the same duration of vacuum conditions (70 s) are applied.

In the case of ultra high performance co ncrete the splitting tensile strength and Young's modulus are also determined on 7 d and 28d. The results can be seen in Fig. 11 and Fig. 12.

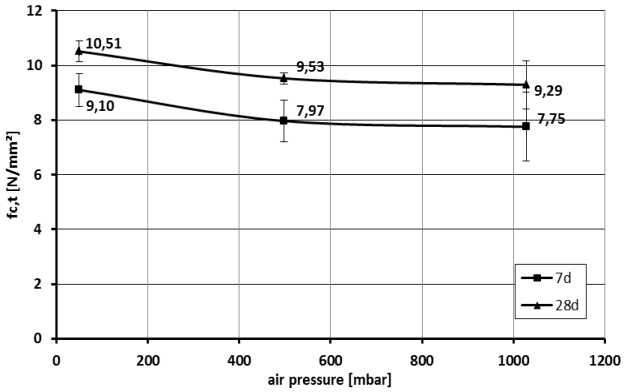

Figure 11: Splitting tensile strength concrete in function of the applied pressure in the mixing pan.

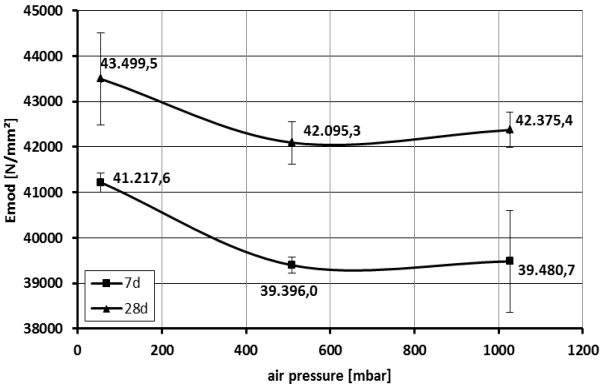

Figure 12: Young's modulus in function of the applied pressure in the mixing pan.

The influence on the splitting tensile strength, also determined on cubes with size 150 mm, is more significant than on the compressive strength. One possible explanation is the fact that for concrete the influence of vacuum mixing is more pronounced for the larger cavities (see Fig. 10). These type of cavities are large defects where cracks will initiate more frequently. The cube will fail in a zone with the most defects, near the line load. If these defects are less prominent, a large splitting tensile strength can be obtained. The Young's modulus, determined according to NBN B 15-203, also shows an improvement when vacuum conditions are applied. Concrete with less air and more specific with a smaller amount of larger air cavities exhibits a higher modulus. However more tests should be done, to study the level of significance.

Comparison between and combination of vacuum mixing and heat treatment

Different influences were studied, in order to increase the compressive strength of UHPC:

- Sieving off the larger sand grains
- Vacuum mixing
- Reduction of the water content, compensating the water content of the SP
- Heat treatment during 48 h at 90°C

Some typical strength results are shown in Fig. 13.

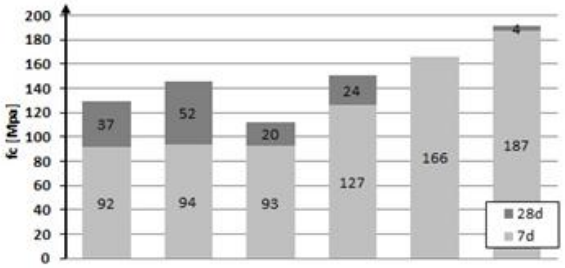

seven between150µm-500µm		X	X	X	X	X
vacuum (100mbar)				X		X
heattreatment (48h & 90°C)					X	X
compensation water SP			X			

Figure 13: Influence of acts to increase the compressive strength of UHPC (h=100 mm).

When the sand is sieved and a lower pressure is applied during the mixing procedure, an increase of the compressive strength of the ultra high performance concrete is achieved. However, the increase is not enough to match the increase obtained by heat treatment.

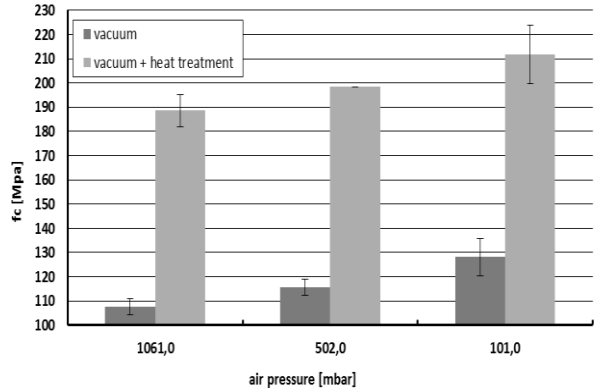

Figure 14: Influence of vacuum mixing & heat treatment on the 7 d compressive strength (h=100 mm).

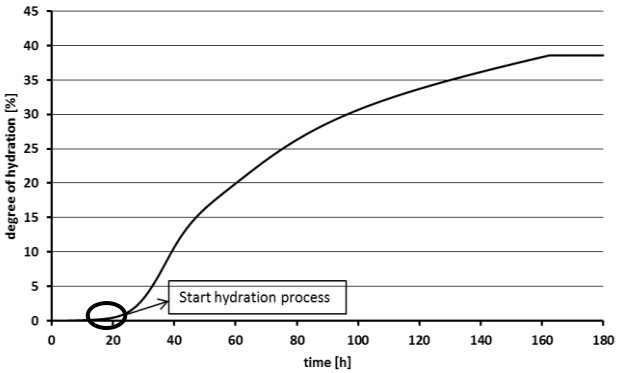

Figure 15: Degree of hydration of ultra high performance paste (W/B=0,15).

The difference between the two techniques is clearly illustrated in Fig. 14. The increase that is obtained with a heat treatment is about 80 MPa, while the reduced air pressure only brings up 20 MPa. A possible explanation for the high strength increase due to heat treatment can be seen on Fig. 15. The composition of UHPC in this paper has a very low water-to-binder ratio (W/B=0.15), which lead to a very low degree of hydration. A heat treatment, accelerates the hydration process and refines the pore structure, making the concrete stronger. The strength gain due to vacuum mixing is lower, as the reduction in air content is having less influence than the improved hydration and the pore refinement in case of a heat treatment.

5 Conclusions

In this study the effect of vacuum mixing on the mechanical properties of UHPC has been studied by means of a vacuum paste mixer (5 liter) and a vacuum concrete mixer (75 liter). The following conclusions have been obtained:

- It was possible to make UHPC with a compressive strength coMParable to the results of Richard and Cherezy [6].
- In the case of the vacuum paste mixer, vacuum mixing of UHPC lowers the air content significantly. Especially the amount of air cavities with a chord size between 0.06 and 1 mm decreases. This effect improves the compressive strength with 10 MPa.
- In the case of the vacuum concrete mixer, the air content of UHPC decreases less. The largest effect is seen on air cavities of size 1 mm to 3 mm. This leads to an insignificant increase in compressive strength but a significant rise of the splitting tensile strength and the Young's modulus.
- For the considered mix design and mixing procedure, the effect of vacuum mixing is less pronounced than the effect of heat treatment.

6 Acknowledgements

The financial support of the Hercules Foundation and of the Fund for Scientific Research Flanders is greatly acknowledged.

References

[1] Mazanec O. and Schiessl P.: Improvement of UHPC properties through an optimized mixing procedure. Proc. 8th International Symposium on utilization of High-Strength and High-Performance Concrete,Tokyo, Japan 2008.

[2] Schachinger I., Schubert J. and Mazanec O.: effect of mixing and placement methods on fresh and hardened Ultra High Performance Concrete (UHPC).International Symposium on Ultra-High Performance Concrete, Kassel, Germany 2004.

[3] Bresson J.: Mixing and CoMPacting Techniques for the Production of Very High Performance Precast Concrete Products. Proc. Of the 4th International Symposium on Utilization of High-strength/High-performance concrete, Paris 1996.

[4] Chiocchio, G., Mangialardi, T. and Paolini, A.E.: Effects of Addition Time of Superplasticizers on Workability of Portland Cement Pastes with different Mineralogical Composition. Il Cemento, Heft 2 1986.

[5] Siebel, E., Müller, C.: Geeignete Zemente für die Herstellung von UHFB. Ultrahochfester Beton. Innovationen im Bauwesen. Beiträge aus Praxis und Wissenschaft S. 13-24. Berlin. 2003.

[6] Richard, P., Cheyrezy, M.: Composition of reactive powder concretes. Cement and concrete research vol. 25 No. 7 p. 1501-1511, 1995.

[7] Mazanec, O., Lowke, D., Schiessl, P.: Mixing of high performance concrete: effect of concrete composition and mixing intensity on mixing time. Materials and Structures vol. 43 nr. 3 . 357-365, 2010.

[8] Boel, V.: Microstructure of self-coMPacting concrete and relation with gas permeability and durability (in Dutch). Doctoral thesis, Magnel Laboratory for Concrete Research. Ghent University, Belgium pp.144, 2007.

Definition of three levels of performance for UHPFRC-VHPFRC with available materials

Esteban Camacho, Juan Ángel López, Pedro Serna Ros
Universitat Politècnica de València, Spain

In this document three dosages of VHPFRC-UHPFRC are proposed and characterized. Each one corresponds to basic, medium and high level of flexural and compressive strength exigence. Some alternative materials were introduced, as limestone coarse aggregates, normal strength fibers or fluid catalytic cracking catalyst residue (FC3R). Also the content of cement, the compacity theory adopted and mixer type were modified in order to study the effect of simplify the dosages, methods and processes.
The evolution of the mechanical properties was studied, obtaining the compressive strength in 100 mm size cubic specimens at different ages and the flexural strength. The mixture rehology was analyzed by means of the flow test and in some cases rehometer.

Keywords: VHPFRC, UHPFRC, normal strength steel fibers, coarse aggregates, mixer efficiency

1 Introduction

The UHPC-UHPFRC common families have properties coming from three concrete technologies to a greater or lesser extent: Self-compacting concretes (SCC), fiber reinforced concretes (FRC) and high strength concretes (HSC) taken to the extreme.

UHPFRC dosages normally require very exclusive materials: Selected and reduced diameter aggregates because micro-cracks are proportional to their size; high strength steel fibers, 3rd generation superplasticizers and high content of active additions. Also intensive mixers, steam curing and high control to guarantee the thickness of the slender elements are very common.

Till this moment, the most frequent way to build UHPFRC structures is by means of precast elements using concrete made with one of the few patents existent in the world market (Ductal®, CERACEM®, BCV®…), calculated and designed according to the French or Japanese recommendations [3, 4]. The great majority of the UHPC-UHPFRC experiences have been developed in Japan, France, USA, Germany and Denmark. Table 1 shows the dosages of some of these products.

Table 1: Dosages and properties of the most common commercial UHPFRC.

	Ductal®		**BSI®**		**CRC®**		**CEMTEC$_{multiscale}$®**		**BCV®**	
	Type	**kg/m^3**	**Type**	**kg/m^3**	**Type**	**kg/m^3**	**Type**	**kg/m^3**	**Type**	**kg/m^3**
Cement	Portl.	746	-	1114			CEM I 52.5	1050		↑
Silica fume	-	242	-	169	Binder	930	-	275		2115
Quartz flour	-	224	-	-			-	-		premix
Sand (mm)	0,1-0,6	1066	0-6	1072	0-5	1325	<0,5	730	2-3	↓
Water	W/C	0,19	W/C	0,19	W/B	0,16	W/C	0,181	W/C	0,25
Admixture	Chryso	9	SIKA	40	-	-	Chryso	35	-	21.5
Fiber	13/0.2	161	20/0.3	234	12/0.4	150-300	10/0.2	470	$20_{2/3}13_{1/3}$	156
SlumpFlow(mm)		700		640		-		-		750
$f_{ct,28}$ (MPa)		8		8.8		-		-		8
$f_{cm,7}$ (Mpa)	20º	101	20º	165		-	20º	-	20º	98
$f_{cm,28}$ (Mpa)	20º/90º	124/198	20º	199	20º/90º	150/400	20º	168	20º/90º	130-150

The development of variety and amount of applications are limited because high cost of the material and precasting process. The development of generic VHPFRC-UHPFRC with accessible materials from every region would decrease the cost, and different levels of performance in the UHPFRCs adapted to every application exigencies may increase the

development of the potential uses. The future of the material depends also on the appearance of an International Recommendation, which is already under development [5].

2 Objectives

The objective of this work is the development of UHPFRC-VHPFRC mixtures able to be produced in precast company with no adaption of mixing/curing processes and using local materials, normally used to cast ordinary concrete (no exclusive). Coarse limestone aggregate, low binder content, medium strength fibers, national active additions and a simple compacity theory are proposed. Also mixing in a tilting mixer (according with the [7] nomenclature) typically used for in-situ concrete casting has been studied. With these materials, three different levels of performance have been conceived, analizing their reology, flexural strength and compressive strength evolution.

3 Analyzed variables justification

In many applications very high compressive strengh is not essential. Much more important is flexural strength, ductility and durability. Because of that, in the mixtures proposed fines content is lower than for comercial UHPFRC: The aggregate size is higher than 2 mm, quartz flour is not used as it's not a very common material, the content of active addition is <=15%, and in some cases coarse aggregate is added. This produces that compressive strength is not always extremely high. Heat curing process is avoided. Variables modified were:

Cement

Its increase in the dosage let decrease the W/B ratio and consequently, establish the performance of the concrete. To propose the three levels of performance the main difference was the content of cement per cubic meter of mortar: 700 Kg/m^3 for the basic, 850 for the medium and 1000 for the high level. Two sulphate resistant cements were used: a "I - 42.5 R/SR" and a "I - 52.5 R/SR" from Lafarge, according with the Spanish standard [11]. The three compositions suggested here come from a previous process of mixture optimization, where the material proportions and the mixing process were modified [2].

-Three different active additions are used, because available products in the Spanish market would be preferently used if the performance provided is adequate. Condensed silica fume provided from the Spanish provider Ferroatlántica (named SF A), condensed silica fume ELKEM® 940 D (SF B) and Residue of Catalytic Cracking Catalyst Residue (FC3R). More information about the use of FC3R in UHPFRC can be found in [13].

Compacity

One of the key points in UHPFRC mixture design is reach a high compacity. Some methods have been developed to adjust microgranulometry, searching the higher compacity and then decreasing the water demand of the compose (De Larrard, Andreasen and Andersen (A&A), Dinguer and Funk). However, reach a simple satisfactory method for UHPFRC granulometry is still a challenge. A simple way to deduce the granulometric curve that suggest a high compacity was the proposed by Dinger and Funk, denoted as A&A$_{MOD}$ as it was modified from the A&A method. Spherical particles are supposed, and the cumulative percent finer than a diameter "D" (CPFT) is obtained (1). It depends on the minimum and maximum diameter of the aggregates.

$$CPFT/100=(D^q-D^q_{min})/(D^q_{max}-D^q_{min}) \quad (1)$$

A&A proposed a q value of 0.37. It has been proved that, the lower the value of D_{max}, lower is the q value that should be used to obtain higher compacity. In this work granulometry of some

mixtures was adjusted with the A&A_{MOD} theory. For them was adopted q=0.2, 0.25 y 0.3 depending if the level of performance of the concrete was high, medium or basic respectively.
In other dosages, the theory used to distribute the silica sands was called Compacity Ternary Diagram (CTD), and developed by our group. This method is based in combine the three sands (0-0.6 mm, 0-2 mm y 2-3 mm in our case) in different proportions, generating 21 mixtures. A recipy with constant volume was filled with each one and its weight obtained with no compaction. The bulk densities are represented in a ternary diagram, and the combination with the higher one was chosen as the best between this sands, and in this case were 30% de 0-0.6 mm and 70% 0-2 mm. The CTD provided a thicker granulometry than the A&A_{MOD} method. This could derive in more flowability, but also in higher segregation risks and in lower compressive strength due to the higher D_{max} of the aggregate, which increase the size of the micro-cracks that generate the compressive failure.

Coarse aggregates

Its use in UHPFRC is scarce. Only in some cases basalt, bauxite or granite are used [6]. Despite of that, add it to a mortar or micro-concrete is interesting to reduce the cement content and then the autogeneous shrinkage and the price. The use of this aggregate is possible if the elements have much higher thickness than the aggregates.

In this project 600 Kg/m^3 of 4/7 mm limestone coarse aggregate were added to the basic, medium and high performance mixtures, implying a proportional reduction of cement/m^3 of concrete (in basic dosage from 700 to 522 Kg, in medium from 850 to 635 Kg, and in high from 1000 to 747 Kg). Even though this aggregate is used to cast ordinary concrete, its very attainable and its strength theoretically enough to be used in VHPFRC. Previus tests were done to quantify the water demanded by the adsorption and absorption phenomena. A 4% of water with respect to coarse aggregate weight was obtained. The aggregates mixed with the water were wet but didnt drop, and their addition to the UHPFRC in the middle of the mixing didn't produce noticeable variations of the workability, as desired. The cracking of the coarse particles due to the intensive mixing was minored with the late addition.

With this addition granulometry was not continue, and as the coarse aggregate content was not hight the system could be considered semi-diluted [12]. This didn't produce a segregation tendence because of the similar density of mortar and aggregate.

Steel Fibers

Medium strength fibers with hooked ends (>1200 MPa) costs approximately half of the price of high strength fibers (>2000 MPa). It is proved [Van Gysel, 2000] that the last provides 50-100% much pull-out force than the firsts in FRC. In the case of UHPFRC the high compacity and active additions improve the Interfacial Transition Zone (ITZ), developing a higher pull-out force and then probably deriving in a brittle failure of the medium strength fibers. This limit the use of medium strength fibers, but deeper research is required in this field. This must be checked for a certain type of fiber geometry, matrix composition and fiber orientation. In this work 2% over volume of total steel fiber content was used. Every concrete contained 1% in volume of Dramix® OL 13/0.16 mm straight fibers and 1% in volume of, depending on the dosage, high strength fibers Dramix® RC-80/30-BP (>2000 MPa) or normal strength fibers Dramix® RC-65/35-BN (>1200 MPa). The slenderness of the normal strength fibers was smaller than for high strength fibers to reduce the tendence to brittle failure, assuming lower performance in the flexural strength.

Mixer

Intensive mixers (IM) are the most convenient to be more energic, efficient and develop an homogeneous UHPFRC, improving the dispersion of the CSF and admixture. The lack of this

mixer type in most of precast company and the impossibility to use them in in-situ applications is a problem for the UHPFRC market developement. In this study a 50 liters IM EIRICH R-08W was used, comparing its performance with a 30 l. tilting mixer (TM), wich represented the low energy mixers. Intensive and low energy mixing differences should be evaluated. The first has a rotor that can was used between 50 and 300 r.p.m., and the second works without relative movement, drum mixing takes place by lifting part of the material and then letting it fall [7].

Admixture

The admixture (PCE) type was chosen according to previous compatibility tests developed with the binder. In the mixtures without coarse aggregates, the water content was modified to reach the same workability aspect at the end of the mixing process. The W/B ratio in coarse aggregate mixtures is higher because the water added with the coarse aggregate is considered.

4 Experimental Program

Table 2: Table of the 28 VHPFRC-UHPFRC mixtures designed. % o.c.w.: Over Cement weight.

Mix	Cement		Active addition		PCE	W/B	Coarse Agreg.	Long Fibers	Mixer	Comp. Theory	Compr. strength
Nº	Type	Kg/m^3	Type*	%o.c.w.	Type	Ratio		Type**	Type		MPa
1	52.5	700	FC3R	10%	A	0,27	NO	BP	IM	CTD	113
2	52.5	700	SF A	10%	A	0,27	NO	BP	IM	CTD	121
3	42.5	522	SF A	10%	B	0,37	SI	BN	IM	A&A$_{MOD.}$	113
4	42.5	522	SF A	10%	C	0,36	SI	BN	IM	A&A$_{MOD.}$	103
5	42.5	522	SF A	10%	C	0,33	SI	BN	IM	A&A$_{MOD.}$	121
6	42.5	700	SF A	10%	C	0,31	NO	BN	TM	A&A$_{MOD.}$	101
7	42.5	700	SF A	10%	C	0,28	NO	BN	IM	A&A$_{MOD.}$	113
8	42.5	700	SF B	15%	B	0,25	NO	BP	IM	CTD	126
9	52.5	850	FC3R	10%	A	0,21	NO	BP	IM	A&A$_{MOD.}$	127
10	52.5	850	FC3R	10%	A	0,23	NO	BP	TM	A&A$_{MOD.}$	123
11	52.5	635	FC3R	10%	A	0,25	SI	BP	TM	A&A$_{MOD.}$	122
12	52.5	850	SF A	10%	A	0,21	NO	BP	IM	A&A$_{MOD.}$	139
13	52.5	850	SF A	10%	A	0,23	NO	BP	TM	A&A$_{MOD.}$	132
14	52.5	635	SF A	10%	A	0,25	SI	BP	TM	A&A$_{MOD.}$	124
15	42.5	850	FC3R	10%	C	0,21	NO	BP	IM	A&A$_{MOD.}$	137
16	42.5	850	FC3R	10%	C	0,24	NO	BP	TM	A&A$_{MOD.}$	128
17	42.5	635	FC3R	10%	C	0,27	SI	BP	TM	A&A$_{MOD.}$	120
18	42.5	850	SF A	10%	C	0,22	NO	BP	IM	A&A$_{MOD.}$	134
19	42.5	635	SF A	10%	B	0,26	SI	BP	IM	A&A$_{MOD.}$	136
20	42.5	635	SF A	10%	C	0,26	SI	BP	IM	A&A$_{MOD.}$	127
21	42.5	850	SF B	15%	B	0,21	NO	BP	IM	CTD	138
22	42.5	800	SF A	25%	C	0,22	NO	BP	IM	CTD	129
23	42.5	800	FC3R	25%	B	0,21	NO	BP	IM	CTD	142
24	42.5	800	SF B	25%	B	0,21	NO	BP	IM	CTD	133
25	42.5	1000	FC3R	15%	B	0,18	NO	BP	IM	CTD	161
26	42.5	1000	FC3R	15%	C	0,19	NO	BP	IM	A&A$_{MOD.}$	149
27	42.5	747	FC3R	15%	C	0,22	SI	BP	IM	A&A$_{MOD.}$	141
28	42.5	1000	SF B	15%	B	0,18	NO	BP	IM	CTD	165

* SF A: Ferroatlántica CSF, SF B: 940 D ELKEM CSF.

** *Long fibers used: Dramix® RC-80/30-BP and RC-65/35-BN*

28 mixtures from a wider program are studied (table 2). In every mixing the process started observing the mixing of the product. Mixing process toke 28-30 min in the TM (batch of 25 liters) and 13-17 min for the IM (batch of 30 liters).

To characterize the reological state the maximum slump flow and the T_{500} was also obtained, and for some mixtures a 4C-Rehometer (Danish Technological Institute) provided the graphic diameter-time of the slump.

Compressive strength was characterized with 12 cubes of 100 mm size, obtaining the 1, 2, 7 and 28 days strength according to UNE-EN 12390-3. Two 100x100x500 mm unnotched prisms were used to obtain the 28 days flexural behaviour ($f_{ct,fl}$), measuring the load and center displacement δ from three point bending tests. From them the flexural strength and energy until δ=3 mm (MPa*mm) were obtained. These beams were opened to make a visual study of the fiber orientation, its breaking-slipping behaviour, possible segregation of them and coarse aggregate and the section homogeneity.

5 Results

Cement

Logically, the cement content influenced markedly both in compression and flexion, leading to the three levels of performance. Difference between dosages 8, 21 and 28 (refered with the abbreviation D8, D21, D28) was only the cement content and the W/B ratio to reach approximately similar workability in the mixes. In figures 1 and 2 can be appreciated the rehology and compressive strength evolution compared for this dosages.

Even though the aspect during the mixing of these three dosages was very similar, only the 1000 and 850 Kg/m^3 dosages had similar flowability and viscosity behaviour. 700 Kg/m^3 dosage had higher content of water and lower of fines, so the growth of the slump stopped earlier. The higher sand content implied also more influence of the fibers in the workability [12].

Summarizing, the 700 Kg/m^3 behaviour was more similar to conventional SCC. The filling hability of the dosages was enough to many applications, and the high workability was proved because beams were not vibrated and the compressive performance obtained (figure 2) was the expected.

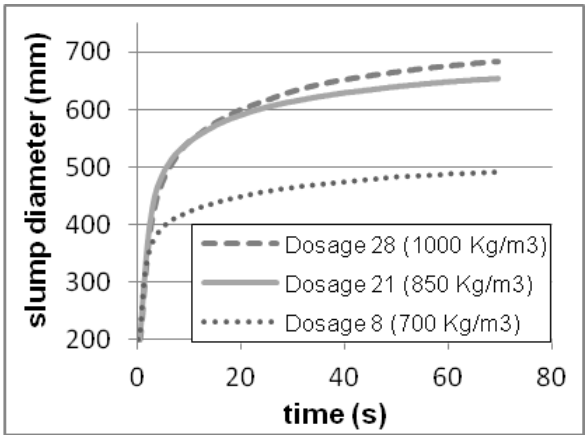

Figure 1:Slump-flow evolution with the time.

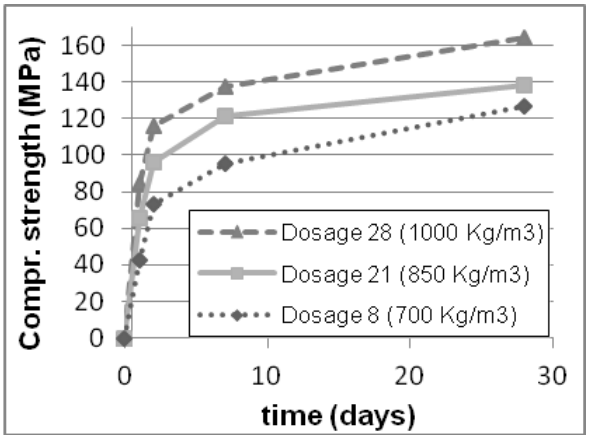

Figure 2: Compressive strength time evolution.

Active additions

Higher contents of active additions didn't provide better rheological and mechanical results. Dosages 22, 23 and 24, wtih 25% of active addition in respect to cement, reached 128, 142 and 133 MPa, similar than dosage 21 (138 MPa), which contains only 15%.

Compacity theory

Dosages 25 and 26 differ only in the sands proportion due to the compacity theory. The content of fine sand was 30% and 65-70% with the CTD and the A&A$_{MOD}$ method respectively.

This implied that the first had lower specific surface and W/B ratio could be reduced from 0.185 to 0.175 with the same workability. No segregation was observed in any of the mixtures, and the compressive strength improved the compressive strength in from 148 MPa to 161 MPa. Besides, the T500 value for the CTD mixtures was lower than the value of A&A_{MOD} mixtures. With all this can be remarked that, even though A&A_{MOD} method doesn't provide insatisfactory results, the simple method developed here, named CTD, provided better results.

Coarse aggregate

Coarse aggregate showed lower value of slump, because in absence of movement aggregates and fibers tend to form a mass in the center of the cone. Despite of that, the no segregation of the products was checked cutting the flexural beams, as the mixture flowed homogeneously in dynamic conditions. In figure 3, strengths remarked together in squares can be compared as their diference is only the coarse aggregate addition with 4% in its weight of water. Compressive strength differences decrease with the time because the weakest section in coarse aggregates UHPFRC is the aggregate-mortar interphase, and the active additions improve with the time this union.

Despite of the slightly higher W/B ratio of the coarse aggregate mixtures, 28 days compressive strengths were very similar. Flexural results didn`t show neither lower performance. This showed surprisingly how conventional limestone coarse aggregates are very interesting to make cheaper-lower cement VHPFRC-UHPFRC. Until now almost every coarse aggregates used for UHPC had higher strength requirements, i.e. basalt, granite, etc.

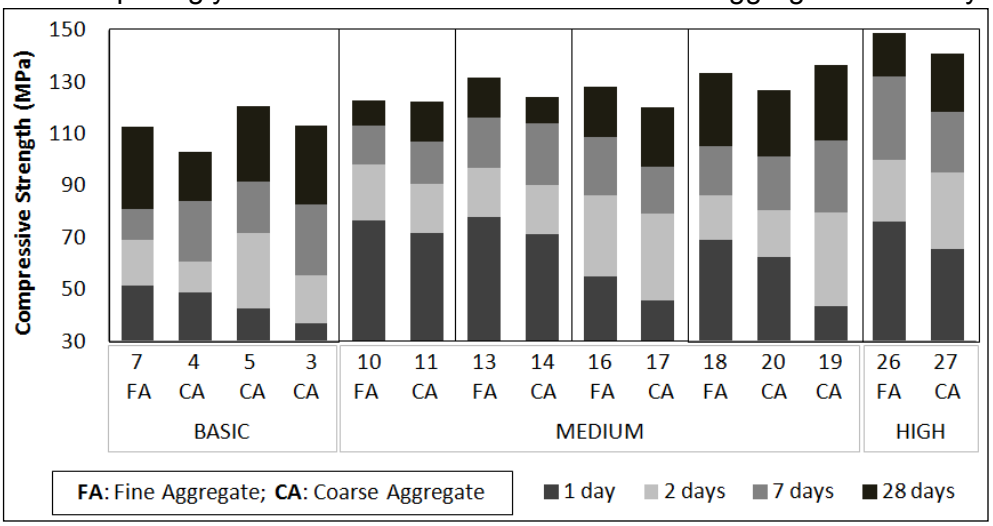

Figure 3: Evolution of the compressive strengths of mixtures with and without coarse aggregates.

Mixer type

Soon was noticed that due to the much lower mixing energy, longer times and higher W/B ratio were required to induce the change from solid to fluid state. Time needed to reach selfcompactability could be decreased increasing even more the W/B ratio, but then at the end of the mixing segregation of the self-compacting product would happened. If W/B is not increased more, mixing times of 30 minutes are required, but the final product is suitable.

Construction mixer didn't show as good separation of the fiber bundles than the intensive mixer. The low W/B ratio and mixing energy implies a slow dissolving of the glue between the single fibers. Mixing of coarse aggregates dosages in the TM required slightly shorter time, because the aggregate broke up faster the solid slumps with the knocking. Disperssion of the compressive strength results were very similar, lower than 6% between cubes of every batch. Table 3 compares the reological and mechanical properties of these mixtures.

Table 3: Data of couples of similar dosages casted with intensive (IM) and construction mixers (CM).

Nº mix-Mixer type	**8 -IM**	**7 -TM**	**10-IM**	**11-TM**	**13-IM**	**14-TM**	**16-IM**	**17-TM**
W/B ratio	0.28	0.31	0.21	0.23	0.21	0.23	0.21	0.24
28 d strength (MPa)	113	101	127	123	139	132	139	128
Mixing time (min)	17	35	16	28	15	29	17	30
Slump flow (mm)	850	712	770	850	<500	757	762	840

Dosages

Dosages with 1% of normal strength fiber showed, as expected [10], less flexural performance than mixtures with high strength fibers. However, the failure was totally ductile as fibers pull out, with a plastic deformation of the fibre hooks. No tensile failure of the fibers was observed. This could be explained with the following reasons:

- The pullout process of a hooked end fibre is based in the debonding and the plastic deformations of the hook. The last phenomena is the most dominant phracture mechanism for the hooked end fibers [10]. The two possible fiber behaviour are the plastic deformation of the hooks and the tensile failure of the fiber. Both are lineary proportional to the fiber tensile strength.
- The slenderness of the normal strength fiber used was 65, and for the high strength fibers was 80. This reduces the ratio specific surface/sectional area, so the debonding process is less marked and consequently the tendency to brittle failure.
- Inclined fibers with respect to the direction of the main tensile stresses have to be partly bent, what generally increases the total frictional resistance during the pull out. Highest forces needed to pull the fibers out were with inclination angle of 15º [10]. In linear elements with self-compacting UHPFRC, as in this research, fibers were preferently aligned in the direction of the forces, increasing the tendence to ductile failure. Figure 5 shows lower flexural performance, but similar bending behaviour, as the flexural failure mechanism is based in the same principles, as can be also observed in figure 6.

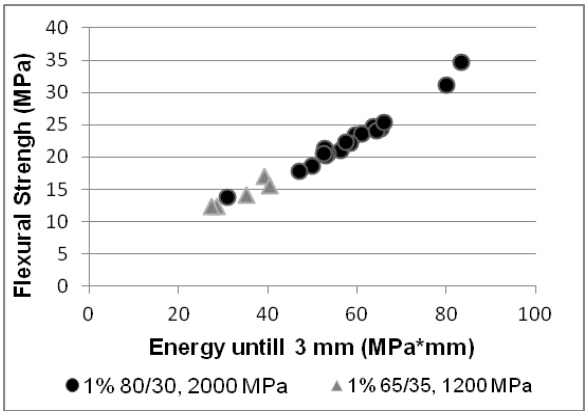

Figure 5: Relationship between the maximum flexural strength obtained and the energy developed until 3 mm of deflection in the concretes with both types of fibers.

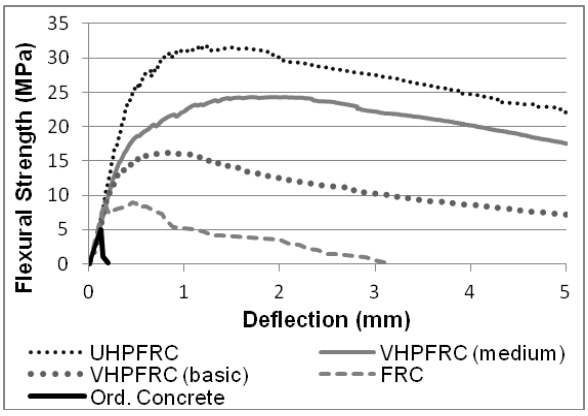

Figure 6: Graphics Flexural Strength-Deflection of three mixtures of UHPFRC and VHPFRC from this research compared with OC and FRC.

The change of the long fiber didn't produce compressive strength differences, and the flexural performance observed was intermedium between the provided by FRC and UHPFRC. This expand the viability of this VHPFRC for many other applications, as the price of normal strength fibers is over half of the high tensile strength fibers.

According to the results, dosages of the three levels of performance for VHPFRC-UHPFRC are proposed in table 4.

Table 4: Dosage of three different performance VHPFRC-UHPFRC.

Type	Cement	Addition	W/B	Coarse Aggregate	Long Fibers	Mixer	Compr-Flex strength expected
Level	Kg/m^3	%o.c.w.	Ratio	Kg/m^3	Tensile strengh	Type	MPa-MPa equiv.
Basic	522	10%	0,27	600	>1200	Low Energy	120-15
Medium	850-635	10%	0.21	0-600	2000	LE-Intensive	135-28
High	1000	15%	0.175	0	2000	Intensive	160-35

6 Conclusions

It should be remarked the suitability of the limestone coarse aggregate to reduce the price of the VHPFRC-UHPFRC keeping the level of performance, and the ductility of VHPFRC with normal tensile strengh fibers. Conventional mixers can be used to cast this concretes accepting a longer mixing time. No steam curing is needed to reach 160 MPa at 28 days and more than 70 MPa at 24 hours.

Results obtained showed that UHPFRC-VHPFRC processes can be simplified, being able use non exclusive materials to reach aceptable very high performance concretes, which are valid to many applications between FRC and UHPFRC.

7 Acknowledgements

The authors of this document would like to express their gratitude to the Spanish Science and Innovation Ministery and to the “Plan E”, for the financial support of the project BIA 2009-12722, and also to the Spanish Science and Innovation Ministery and the FEDER funds for the financial support of the project IPT-2011-1242-380000, included under the National Plan of Scientific Reseach, Developement and Technological Innogation 2008-2011.

References

[1] Camacho, E.; Serna Ros, P.: Design and analisis of UHP-Hybrid-FRC ties for truss structures, 8th fib International PhD Symposium in Civil Engineering, Denmark, June 20-23, 2010.

[2] Camacho, E.; Serna Ros, P.: Optimización de dosificaciones de Hormigón Autocompactante de Muy Alto Rendimiento Reforzado con Fibras Híbrido. 2º Congreso Ibérico sobre Hormigón Autocompactante. July 1-2, 2010.

[3] SETRA-AFGC, UHPFRC. Interim Recommendations, AFGC. Groupe de travail BFUP, January 2002.

[4] JSCE, Guidelines for the Design and Construction of UHSFRC (draft), 2004.

[5] Walraven, J.C.: HPFRC: Progress in knowledge and design codes. Materials and Structures, pp 1247-1260, Vol. 42, 2009.

[6] Ma, J.; Orgass, M.: Comparative investigations on UHPC with and without coarse aggregates. LACER nº9, 2004.

[7] Beitzel, H.; Charonnat, Y.: Assessment and classification of performance mixers. RILEM TC 150-ECM: Efficiency of Concrete Mixers. Materials and Structures, pp 250-264, Vol. 36, May 2003.

[8] Andreasen, A.H.M.; Andersen, J.: Über die Beziehung zwischen Kornabstufung und Zwischenraum in Producten aus losen Körnern (mit einigen Experimenten), 1930.

[9] Droll, K.: Influence of Additions on UHPC-grain size optimisation. International Symposium on UHPC, pp.285-301, Kassel, September 13-15, 2004.

[10] Markovic, I: HP-Hybrid-FC. Development and Utilisation. PhD, Delft University. 2006.

[11] Aenor UNE 80303-1. Cementos con carac. adicionales. Parte 1: Cementos resistentes a sulfatos.

[12] Martinie, L.; Rossi, P.; Roussel, N.: Rheology of fiber reinforced cementitious materials: classification and prediction. Cement and Concrete Research 40 (2010) 226-234.

[13] Camacho, E.; López J.A.; Serna, P.: Fluid Catalytic Cracking Residue additions such an alternative to Silica Fume in UHPFRC. 3º International Symposium on UHPC, Kassel, March 7-9, 2012.

Characteristics of Mechanical Properties and Durability of Ultra-High Performance Concrete Incorporating Coarse Aggregate

Juan Yang[1], Gai-Fei Peng[1], Yu-Xin Gao[2], Hui Zhang[1]
1: Faculty of Civil Engineering & Architecture, Beijing Jiaotong University, Beijing, 100044, China
2: Chengdu China Construction Ready Mixed Concrete Co., Ltd., Sichuan, 61000, China

Ultra-high performance concrete (UHPC) incorporating coarse aggregate was prepared with common raw materials. Fresh concrete had excellent good workability with slump of 265 mm and slump spread of 673 mm. Compressive strength of UHPC at 56 d reached 150 MPa. However, UHPC exhibited high brittleness in terms of spalling failure which occurred during compression loading.The ratio of splitting tensile strength to compressive strength of about 1/18 and the ratio of flexural strength to compressive strength of about 1/14 at 56 d were also associated with the brittleness of UHPC in this research. Mineral admixtures and fluidity of fresh concrete influenced compressive strength of UHPC significantly. Moreover, UHPC had excellent permeation-related durability but considerable shrinkage. Autogenous shrinkage of UHPC was less than half of free shrinkage, for which the reason is unknown and needs further research.

Keywords: Ultra-high performance concrete, coarse aggregate, strength, durability, brittleness.

1 Introduction

With the development of high-rise buildings and constructional elements with small section, ultra-high performance concrete (UHPC) has been increasingly researched and shows a very promising future in practical engineering due to its excellent properties, i.e. ultra-high strength and super-high durability. Normally, UHPC may include two types, reactive power concrete (RPC) and concrete incorporating coarse aggregate with the compressive strength of more than 100 MPa [1]. In this investigation, UHPC incorporating coarse aggregate was focused on.

More and more research attention has been paid to UHPC recently [2-3]. In Japan, a 59-story residential tower was the first engineering structure of the UHPC about 150 MPa [4]. In China, Pu X.C. et al conducted earlier researches on the UHPC [5, 6]. UHPC about 100 MPa was successfully applied in construction of the Guangzhou International Finance Centre [7]. However, UHPC with compressive strength over 100 MPa still needs research for practical construction. Furthermore, UHPC is potentially threatened by explosive spalling when subjected to high temperature. Therefore, for more application of UHPC in China, research on mechanical properties of the UHPC is needed and can be regard as the first step of research for improving fire resistance of UHPC.

In this paper, UHPC incorporating coarse aggregate was researched. Mechanical properties including compressive strength, splitting tensile strength, flexural strength and static elastic modulus were investigated, and related parameters of the toughness of UHPC such as the ratio of splitting tensile strength to compressive strength, the ratio of flexural strength to compressive strength were measured. Furthermore, durability tests were conducted, including water permeability test, resistance to chloride ion penetration, and shrinkage test.

2 Experimental details

General

UHPC was prepared with normal materials and ordinary technology. Limestone was used as coarse aggregate with the two particle size range of 5～10 mm and 10～20 mm, the calculation

mass proportion of which was 3:7. Its crushing index is 4.0 %. Artificial sand was used as Fine aggregate, physical properties of which are showed in Table 1. Physical properties of mineral admixtures including fly ash (FA), silica fume (SF), ground granulated blast furnace slag (GGBS) were determined in accordance with GB/T 18046-2008, which is in agreement with ASTM C311-07. The results are presented in Table 2. Polycarboxylate superplasticizer labelled "SPC" and Polyacrylate superplasticizer labelled "SPA" in Table 3 were used.

Table 1: Physical properties of artificial sand.

Fineness modulus	Apparent density (Kg/m^3)	Packing density(Kg/m^3)	Mud content (%)	Clay pieces content (%)	MB value	Stone power content (%)
2.2	2730	1590	4.6	0.5	0.5	4.6

Table 2: Properties of mineral admixtures.

Mineral materials	Density (g/cm^3)	Specific surface (cm^2/g)	Loss on ignition (%)	Compressive strength (MPa)		Activity index (%)	
				7d	28d	7d	28d
SF	2.09	251000	2.8	34.8	52.4	94	121
FA	2.48	7850	2.1	26.6	41.6	72	96
GGBS	2.90	7460	0.5	31.8	49.5	82	109

Table 3: Solid content and dosage of superplasticizer.

Type of superplasticizer	Polycarboxylate				Polyacrylate
	SPC-1	SPC-2	SPC-3	SPC-4	SPA
Solid content (%)	20	20	24	24	20
Dosage (wt. %)	4	4	4	4	2

Specimens of six types of UHPC denoted by 0.21UHPC-S, 0.22UHPC-S, 0.23UHPC-S, 0.24UHPC-S, 0.18UHPC-S-F and 0.18UHPC-S-F-G respectively were prepared, using "SPC-1" except for those specified specially. The mixture proportions are listed in Table 4.

Table 4: Mix proportions of UHPC.

Mix No.	Type	W/B	Binding materials (Kg/m^3)				Sand (Kg/m^3)	Coarse aggregate (Kg/m^3)
			C	SF	FA	GGBS		
1	0.21UHPC-S	0.21	810	90	0	0	620	930
2	0.22UHPC-S	0.22	810	90	0	0	620	930
3	0.23UHPC-S	0.23	810	90	0	0	620	930
4	0.24UHPC-S	0.24	810	90	0	0	620	930
5	0.18UHPC-S-F	0.18	630	90	180	0	620	930
6	0.18UHPC-S-F-G	0.18	540	90	180	90	620	930

After mixing, the slump and the slump spread were measured for the evaluation of workability. After casting, each specimen was covered with plastic film and stored at room temperature for 24 hours, then demoulded and stored at standard curing room with temperature of (20±2) °C and relatively humidity above 95%, until being tested. Compressive strength test of all types of UHPC was conducted, but only 0.22UHPC-S and 0.18UHPC-S-F-G were for all the other mechanical property test and durability test.

Determination of mechanical properties

Tests for mechanical properties including compressive strength, splitting tensile strength, flexural strength and static elastic modulus were conducted according to GB/T 50081-2002 of China, i.e. Standard for test method of mechanical properties on ordinary concrete.

100 mm cube specimens were prepared for compressive strength test. The loading rate was 10 KN/s, i.e. about 1 MPa/s and the load had to be as uniformly as possible due to the brittle performance of UHPC. The loading rate of splitting tensile test with the 100 mm cube specimens was 0.1 MPa. Flexural strength tests were performed employing the specimens of 100 mm×100 mm×400 mm by the method of three-point bending. Specimens of 100 mm×100 mm×300 mm were employed for the static elastic modulus test under compressive loading.

All the mechanical properties of the UHPC were investigated at four ages, i.e. 3 days (d), 7 d, 28 d and 56 d. The experimental result was the average value of three specimens tested.

Determination of durability

Determination of durability including water permeability, resistance to chloride ion penetration, shrinkage test, were carried out in accordance with GB/T 50082-2009 of China, i.e. Standard for test methods of long-term performance and durability of ordinary concrete.

For the water permeability test, avoiding water to seep through specimen circum is the most important procedure for achieving successful results. Test method for the Coulomb Electric Flux for Chloride ion penetration test was applied. Specimens with the length, wide and height of 100 mm, 100 mm and 515 mm respectively for shrinkage test were placed in curing room with the temperature of (20 ± 2) °C and the relative humidity of (60 ± 5) %. Autogenous shrinkage and free shrinkage were measured. The difference between the two was only that, specimens for autogenous shrinkage were sealed hermetically. Within the initial three days, shrinkage test apparatus can collect and process data automatically. For the later days, outside micrometer was used to measure the shrinkage manually.

3 Results and discussion

Workability

Workability of UHPC was determined in terms of the slump and the slump spread measured for two times, immediately after mixing for the first time, then after one hour for the second time. The results in Figure 1 showed that, UHPC had excellent workability, the slump of exceeding 250 mm and the slump spread of above 600 mm measured one hour after mixing can be obtained. This indicated that, these UHPC can be applied as pumpable concrete for high-rise building construction. In addition, the fluidity of 0.18UHPC-S-F-G was superior to that of 0.22UHPC-S, the fluidity loss of which within one hour was more than that of 0.18UHPC-S-F-G. The reasons may be that,mix of 0.18UHPC-S-F-G had better water-retention than 0.22UHPC-S.

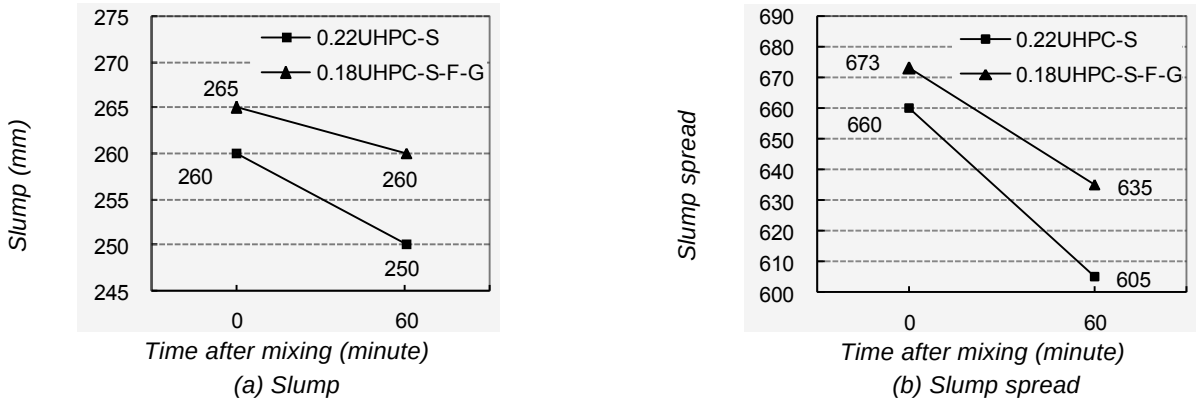

Figure 1: Workability of UHPC incorporating the superplasticizer "PC-4" measured at different time.

Mechanical properties

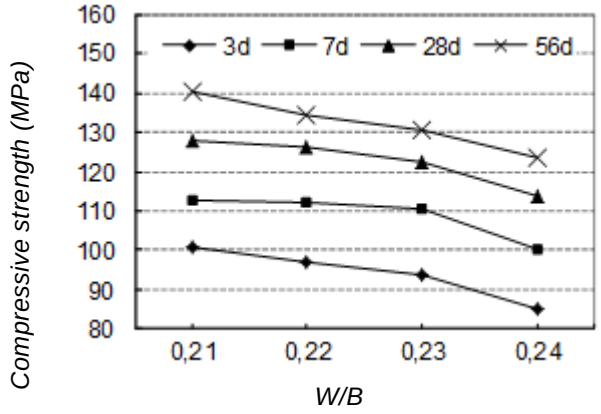

Figure 2: effect of W/B on compressive strength of UHPC-S at different ways.

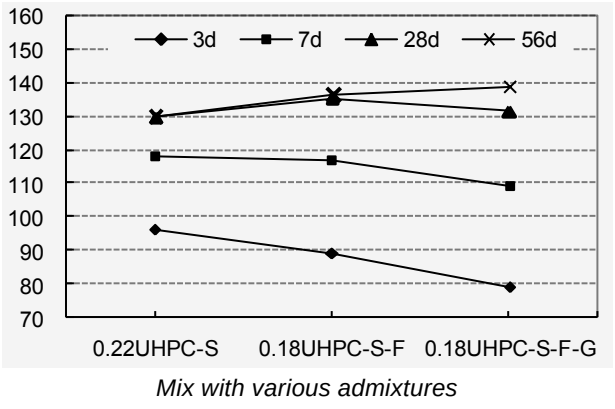

Figure 3: Influence of different mineral admixtures on compressive strength of UHPC.

1) Compressive strength

A series of compressive strength test on six types of the UHPC (in Table 4) were conducted. The influencing factors on compressive strength, including water to binder ratio (W/B) and different types of mineral admixtures as well as fluidity of fresh concrete 0 minute after mixing were determined. During loading process for all the compression tests, spalling failure of specimen occurred with loudcracking.

For the UHPC with only SF, the effect of W/B on its compressive strength was determined. The results in Figure 2 indicated that, compressive strength of the UHPC decreased with the increasing W/B at all ages, which affected the compressive strength of the UHPC significantly.

The influence of different types of mineral admixtures on compressive strength of the UHPC was showed in Figure 3. The results indicated that, FA and BBGS reduced the early compressive strength, but improved the long-term compressive strength. The reducing of cement content and the "filling effect" of mineral admixtures with different particle sizes can be attributed to that.

The results of influencing of fluidity of fresh concrete with different superplasticizers (SP) on compressive strength at 56 d in Table 5 showed that, fluidity of fresh concrete affected the compressive strength of the UHPC significantly, better fluidity, higher compressive strength. When the maximum slump of 265 mm and the slump spread of exceeding 660 mm were attained, UHPC reached to 151 MPa at 56 d. Fluidity was directly affected by SP. In this research, "SPA" exhibited the best effect and had the similar result with "SPC-4". Furthermore, with "SPA", the compressive strength of 0.22UHPC-S at 56 d was 139.5 MPa, less than that of

0.18UHPC-S-F-G. It demonstrated that compound mineral admixtures may be beneficial to preparation of UHPC. Therefore, high fluidity was an important factor for the preparation of UHPC.

Table 5: Effect of fluidity of fresh concrete with different superplasticizers on compressive strength at 56 d.

Type of UHPC	SP	Fluidity (mm)		Compressive strength (MPa)
		Slump	Slump spread	
0.22UHPC-S	PC-1	245	475	130.4
	PA	260	660	139.5
0.18UHPC-S-F-G	PC-1	240	520	138
	PC-2	235	490	131
	PC-3	250	550	142.3
	PC-4	265	660	150.7
	PA	265	673	151

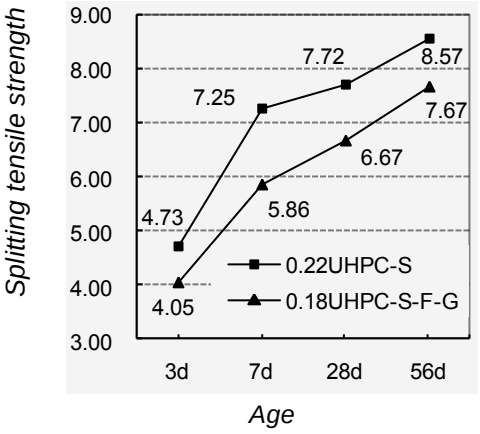

Figure 4: Splitting tensile strength of UHPC at different agesSplitting tensile strength.

2) Splitting tensile strength

The results in Figure 4 indicated that, splitting tensile strength increased with age. Splitting tensile strength of 0.22UHPC-S was higher than that of 0.18UHPC-S-F-G at all ages. From Figure 5, the ratio of splitting tensile strength to compressive strength of 0.22UHPC-S and 0.18UHPC-S-F-G at 56 d was 1/16 and 1/18 respectively. Compared with that of HSC, about 1/14～1/16, UHPC presented more brittleness. The results on HPC indicate that, at 300℃, vapour pressure is about 8 MPa, above 300℃, the pressure can reach to 17 MPa, if inner vapour pressure of concrete is at or higher than the splitting tensile strength of concrete per se, the explosive spalling will occur [8]. While the splitting tensile strength of the UHPC was less than 9 MPa, it is more possible to explosive spalling for the UHPC subjected to high temperature. Therefore, avoiding the occurrence of explosive spalling for UHPC in fire is very important and needs further research.

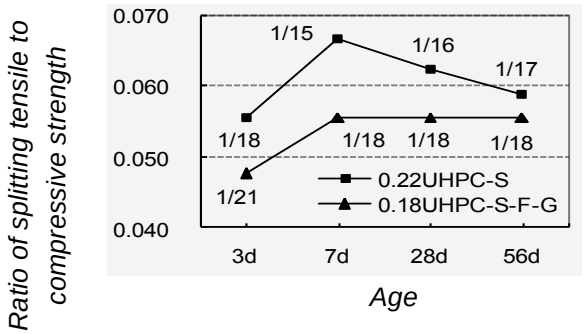

Figure 5: Ratio of splitting tensile strength to compressive strength of UHPC at different ages.

Figure 6: Observation of fractured surface of 0.18UHPC-S-F-G after splitting tensile strength test.

It was observed that the specimen in the splitting tensile test was split into two parts and each of them was unbroken in this research, as shown in Figure 6. From the fractured surfaces, it can be found that most of coarse aggregates in UHPC were fractured into two parts. The

reason can be that, since interfacial bond strength was quite high, when the loading damage occurred, cracking passed across coarse aggregates.

3) Flexural strength

The results from flexural strength tests in Figure 7 showed that, flexural strength of the UHPC increased with age and reached to about 10 MPa at 56 d. The ratio of flexural strength to compressive strength of the UHPC at all ages showed in Figure 8 was lower than 1/13. The UHPC may be regarded as more brittle since that of HSC is about 1/11～1/9.

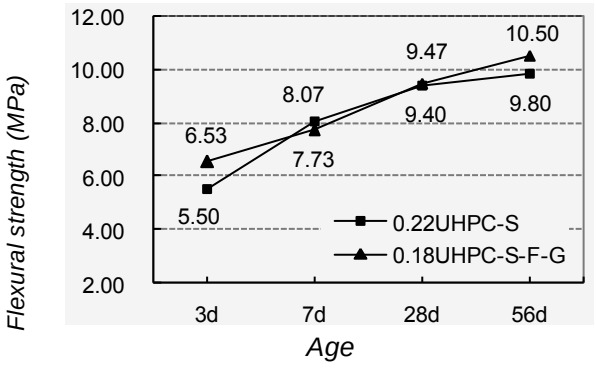

Figure 7: Flexural strength of UHPC at different ages.

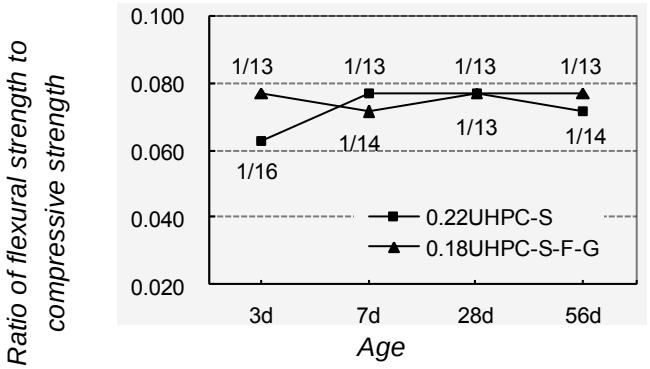

Figure 8: Ratio of flexural strength to compressive strength of UHPC at different ages.

4) Static elastic modulus

The results of static elastic modulus under compression shown in Figure 9 indicate that elastic modulus of UHPC increased with age, and that of 0.18UHPC-S-F-G was higher than that of 0.22UHPC-S at all ages. At 56 d, elastic modulus of 0.22UHPC-S and 0.18UHPC-S-F-G was 45.6 GPa and 48.0 GPa respectively, which indicated that UHPC had high stiffness.

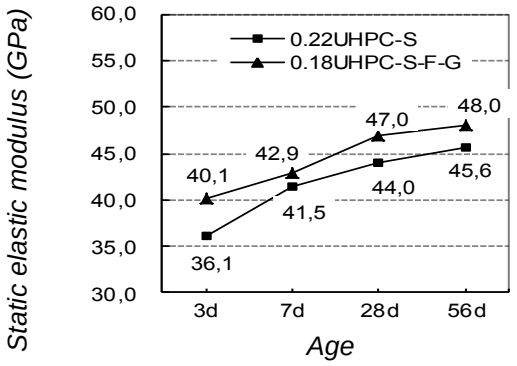

Figure 9: Static elastic modulus of UHPC at different ages.

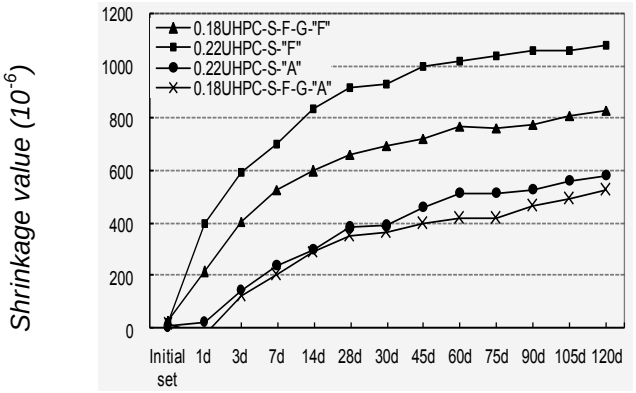

Figure 10: Shrinkage of UHPC at different ages.

Durability

In water permeability test, water pressure reached 4.0 MPa and was then maintained for seven days. No water was observed in the top surfaces of all specimens. Therefore, UHPC had quite high resistance to water permeation.

The electric flux of 0.18UHPC-S-F-G and 0.22UHPC-S at 56 d was 69 C and 94 C, respectively. Therefore, UHPC presented excellent resistance to chloride ion penetration.

The results of shrinkage test were showed in Figure 10. “F” means “free shrinkage”, “A” means “autogenous shrinkage”. The results indicate that, whether 0.22UHPC-S or 0.18UHPC-S-F-G, free shrinkage was much higher than autogenous shrinkage. Furthermore, free shrinkage and autogenous of 0.22UHPC-S was higher than that of 0.18UHPC-S-F-G. The

reason may be attributed to that, the blended mineral admixtures (SF, FA and GGBS) can be beneficial to minimizing shrinkage, although different results were also reported when the mineral admixtures SF or GGBS was used lonely [9, 10]. It was reported that, as to concrete at low water-binder ratio, autogenous shrinkage would be the most part of shrinkage [11]. However, in this research, autogenous shrinkage of UHPC was less than half of free shrinkage, for which the reason is unknown and needs further research.

4 Conclusions

Based on the experimental results in this research, following conclusions may be drawn.

(1) UHPC with compressive strength of 150 MPa were prepared with excellent workability with slump of 260 mm and slump spread of 635 mm at one hour after mixing. Mineral admixtures and fluidity of fresh concrete influenced compressive strength of UHPC significantly.

(2) UHPC had high stiffness and ultra-high permeation-related durability. UHPC had not only high resistance to water permeation, but also excellent resistance to chloride ion penetration, with the electric flux as low as less than 100 C.

(3) UHPC exhibited considerable shrinkage. However, autogenous shrinkage of UHPC was less than half of free shrinkage, for which the reason is unknown and needs further research.

5 Acknowledgements

The authors gratefully acknowledge the financial support of the National Natural Scientific Foundation of China (Project No: 50978026) and the China Ministry of Education (Project No: 20100009110014).

References

[1] Rahman, S.; Molyneaux, T.; Patnaikuni, I.: Ultra high performance concrete: recent applications and research. Australian Journal of Civil Engineering, Vol. 2, pp. 13-20, 2005.

[2] Watanabe, S.; Jinnai, H.; Kuroiwa, S.; Teraushi, R.: Development and Application of Quality Control System Based on Careful Selection of Coarse Aggregate for High-Strength Concrete. Proceedings of 8th International Symposium on Utilization of High-Strength and High-Performance Concrete, Japan, pp. 1127-1132, 2008.

[3] Koizumi, S.; Imoto, H.; Sugamata, T.; Ohta, A.: A Study on Potential Strength Development and the Hydration Reaction of Ultra-High-Strength Concrete. Proceedings of 8th International Symposium on Utilization of High-Strength and High-Performance Concrete, Japan, pp. 489-496, 2008.

[4] Kojima, M.; Mitsui, K.; Wachi, M.; Sato, T.: Application of 150N/mm^2 Advanced Performance Composites to High-rise R/C Building. Proceedings of 8th International Symposium on Utilization of High-Strength and High-Performance Concrete, Japan, pp. 1199-1206, 2008.

[5] Pu, X.C.: Super High-Strength /High-Performance Concrete [M] (In Chinese). Chongqing University Press, Chongqing, China, 2004.

[6] Wang, C.; Yang, C.H.; Liu, F.; Wan, Z.J.; Pu, X.C.: Preparation of Ultra-High Performance Concrete with common technology and materials. Cement Concrete Composites, doi:10.1016/j.cemconcomp.2011.11.005., 2011.

[7] Gao, Y.X.; Wu, Y.J.; Wang, M.Y.: Research and application of ultra-high strength high performance concrete in China (In Chinese). Ready-mixed Concrete, Vol. 12, pp. 30-31, 47, 2009.

[8] Kodur, V.K.R.: Fiber reinforcement for minimizing spalling in High Strength Concrete structural members exposed to fire. ACI SP 216-14, pp. 221-236, 2003.

[9] Zhang, M.H.; Tam, C.T.; Leow, M.P.: Effect of Water-Cementitious Materials Ratio and Silica Fume on the Autogenous Shrinkage of Concrete. Cement and Concrete Research, Vol. 33, pp. 1687-1694, 2003.

[10] Lee, K.M.; Lee, S.H.; Kim, G.Y.: Autogenous Shrinkage of Concrete Containing Granulated Blast-Furnace Slag. Cement and Concrete Research, Vol. 36, pp. 1279-1285, 2006.
[11] Tam, C.M.; Tam, V.W.Y.; Ng, K.M.: Assessing drying shrinkage and water permeability of reactive powder concrete produced in Hong Kong. Constr Build Mater, doi: 10.1016/j.conbuildmat. 2011. 05. 06., 2011.

UHPC composites based on glass fibers with high fluidity, ductility, and durability

Jeffrey Chen, Gilles Chanvillard
Lafarge Central Research, Saint Quentin Fallavier, France

There is a growing interest in the use of ultra-high performance concrete (UHPC) for architectural applications. As these applications often call for slender structural elements with complex geometry and a white color, a new UHPC has been developed based on the use of pozzolanic ultrafines and glass fibers. Through an optimization of particle packing and matrix/fiber interactions, this glass-reinforced UHPC (GF-UHPC) shows an unprecedented combination of self-placing behavior, deflection-hardening behavior in bending of thin plates, excellent resistance to wet aging, and a very low permeable matrix. A back analysis of the flexural data to extract the tensile strength of the GF-UHPC shows a highly efficient use of the 2.2 vol. % glass fibers to achieve tensile strengths of 9–11 MPa in the post-cracking regime. Microstructure characterization by scanning-electron microscopy (SEM) and mercury-intrusion porosimetry (MIP) furthermore point to the high durability of the GF-UHPC.

Keywords: UHPC, architectural, glass fibers, tensile strength, microstructure

1 Introduction

The unique combination of high compressive strength, self-placing properties, extreme durability, ductility, and aesthetics make Ductal® a truly revolutionary construction material. In the past 10 years, it has been shown that these properties have allowed designers to exploit elegant architectural designs that would otherwise have been only accessible to high-strength steel or to complex materials systems. Figure 1 shows several architectural projects in Ductal®, highlighting applications in thin shells and perforated panels; others examples can be found in Ref. [1].

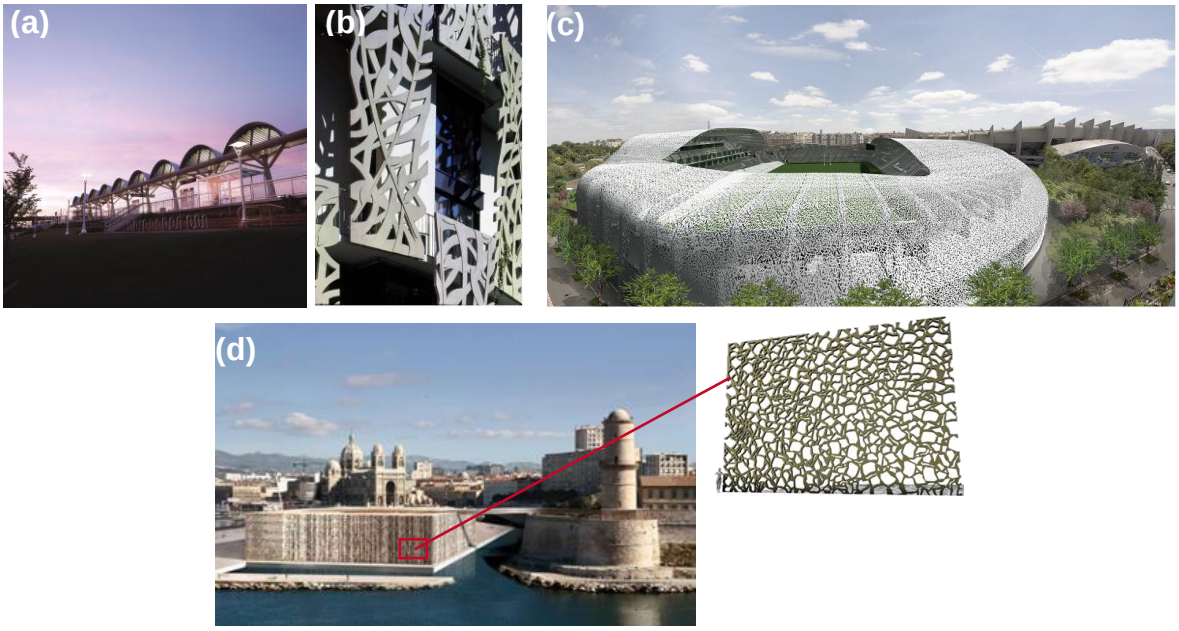

Figure 1: Examples of architectural applications in Ductal®: a) thin-shelled canopies at Shawnessy LRT station in Calgary (2004); b) perforated façade panels in the ZAC apartment building in Paris; c) perforated roof and envelope of the future Jean Bouin Stadium near Paris (model, Ref. [2]); d) perforated façade panels and footbridge at the MuCEM in Marseille (under construction).

We have recently developed a self-placing UHPC based on glass fibers for architectural applications. The interest of using glass fibers is its higher tensile strength (approximately 1700 MPa) compared to organic fibers, lower cost compared to steel fibers, and that it does not show rust stains at the concrete surface—a major aesthetic impediment to using steel fibers in white UHPC. In a previous study [3], it was demonstrated that a deflection-hardening behavior can be achieved on 20-mm plates with glass fiber dosages as low as 2.0 vol. %—a substantial reduction over the typical 3 to 4 vol. % dosages used in cast and sprayed glass reinforced concrete (GRC) formulations, respectively. Reverse analysis of the flexural curves show that the direct tensile strength of the composite was between 9–11 MPa. It was furthermore shown that the composite maintained its ductile performance in wet conditions (submerged in 50 °C water for 3 months). This property is not associated with normal glass-reinforced composites (GRC), which generally suffer from embrittlement with wet aging [4]. Collectively, these mechanical properties for our glass fiber-reinforced UHPC (GF-UHPC) should allow for greater freedom in structural design of architectural applications.

Although the use of glass fibers in concrete is well-known, there are few reported GF-UHPC in the literature. For example, Roth et al. [5] have also shown a deflection-hardening GF-UHPC with a matrix containing silica fume and fiber dosages of 3.0%. A large dispersion in flexural results was observed, presumably due to the continuous, gravity-loading process of adding the fibers to the UHPC. Neither aging tests, nor flow properties were reported.

In this study, we will report on new developments of our GF-UHPC composite, where the silica fume ultrafines normally present in the UHPC matrix have been partially or wholly replaced by metakaolin pozzolanic ultrafines. A characterization of the mechanical properties and of the microstructure of the composite will be discussed.

2 Experimental Procedure

Mix Design

The UHPC matrix contained a fine sand (0–1 mm), a white cement, and a mix of ultrafines, which included varying amounts silica fume, metakaolin, and limestone filler. The quantity of silica fume was 5 wt. % with respect to cement in the example shown in the current study. A superplasticizer was also used.

The composite contained alkali resistant (AR) glass fibers with a length of 12 mm and a dosage of 2.2 vol. %. Fibers were added to the UHPC mix in the mixer after a homogeneous cementitious matrix was obtained.

Spread flow test

Spread flow tests were taken at various times after mixing with a cylindrical ring of 70 mm height and 100 mm diameter. After filling the mold with the GF-UHPC, the mold was carefully lifted, and the horizontal spread was measured approximately 2 min after lifting. No additional shocks were used.

Curing conditions and Flexural tests

Each GF-UHPC mix was cast in 2 separate 550×550×20 mm plate molds. Care was taken to pour the mixes at one end of the mold to encourage optimal fiber orientation. After demolding at 24 hours, 2 plate specimens measuring 450*145*20 mm were cut from each of the large plates. The resulting 4 plates were then placed in a curing chamber at 20 °C and 100% RH. At 7d, 2 of these plates were placed over a closed vessel over 50 °C water for an additional 21 d to simulate an accelerated aging. The other 2 plates were left in the original curing chamber at 20 °C and 100% RH. Changing the aging period to 1 month at 20 °C, followed by an additional 1 month at 50 °C over water showed no significant difference to the conditions described above.

At 28 days, all 4 plates were tested in four-point bending, with an inner span of 140 mm, and an outer span of 420 mm. With the use of an attached LVDT sensor, the flexural tests were deflection controlled at a constant rate of 0.1 mm/min.

Microstructural characterization

A field-emission gun scanning-electron microscope (FEG-SEM) was used to image the microstructure of the GF-UHPC. After being cut, epoxy impregnated, and polished, cross sections of the composite were imaged in back-scattered electron (BSE) mode, operating at 15 keV and a current intensity of 1 nA.

Mercury intrusion porosimetry (MIP) was performed on samples without fibers. At 28 days, samples were crushed, dried at 45 ºC for 2 days at 20 mbar, then submitted for testing.

3 Results and Discussion

Spread flow

As shown in Figure 2, the GF-UHPC with 2.2 vol. % glass fibers is a truly self-placing material. Horizontal spreading of the GF-UHPC reached over 240 mm (starting from an initial cylinder diameter of 100 mm). This value can be maintained over a period of at least 90 min at 20 °C.

The self-placing behavior of the mix can be attributed to the high particle packing of the matrix and the relatively low fiber dosage. High fluidity enables casting of complex or textured elements, which is impossible for traditional GRC that contain 3 vol. % fiber or more. The fluidity furthermore aids in proper fiber orientation of the composite.

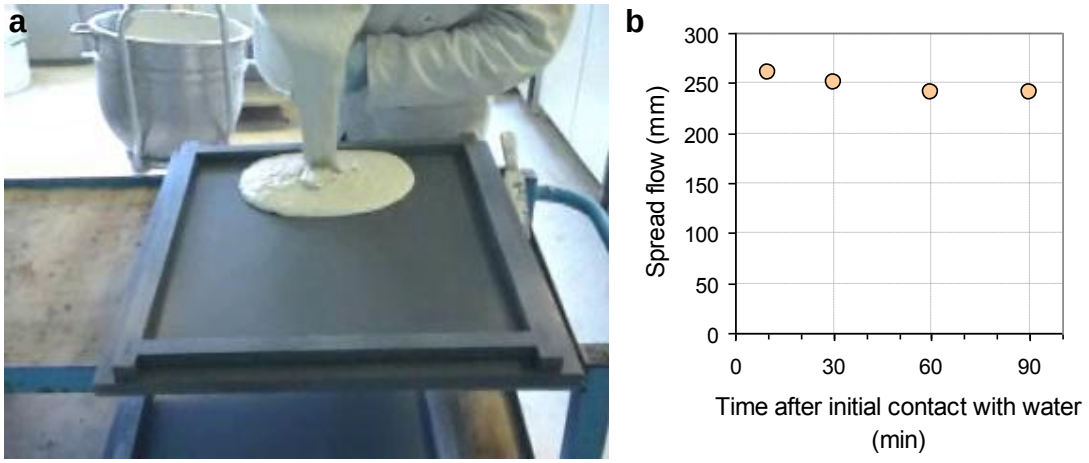

Figure 2: (a) Self-placing behaviour of the GF-UHPC. (b) Spread flow measured as a function of time after initial contact with water.

Mechanical properties

Flexural results on thin plates.—Figure 3a shows the flexural results of the GF-UHPC composite with 2.2 vol. % glass fibers measured at 28 d after normal curing (20 °C) and after accelerated wet aging (50 °C). All samples, including those subjected to aging, illustrate deflection hardening: after the limit of proportionality was reached, the load was effectively transferred to the fibers, without a drop in stress, and continually increased until failure of the fibers. The limit of proportionality (LOP) is 13–14 MPa at 20 °C and 16–17 MPa at 50 °C; these are values notably higher than traditional GRC with values between 6–10 MPa [4]. The ultimate deflections were 5.5–6 mm at 20 °C (6mm being the limit of the setup) and 3–3.3 mm to 50 °C. The Young's Modulus was approximately 48 GPa, both before and after aging. As discussed in more detail in ensuing sections, these properties, along with the fine microcracking pattern along the tensile face of a tested plate (Figure 3b), demonstrate a highly efficient use of the glass fibers in the GF-UHPC composite.

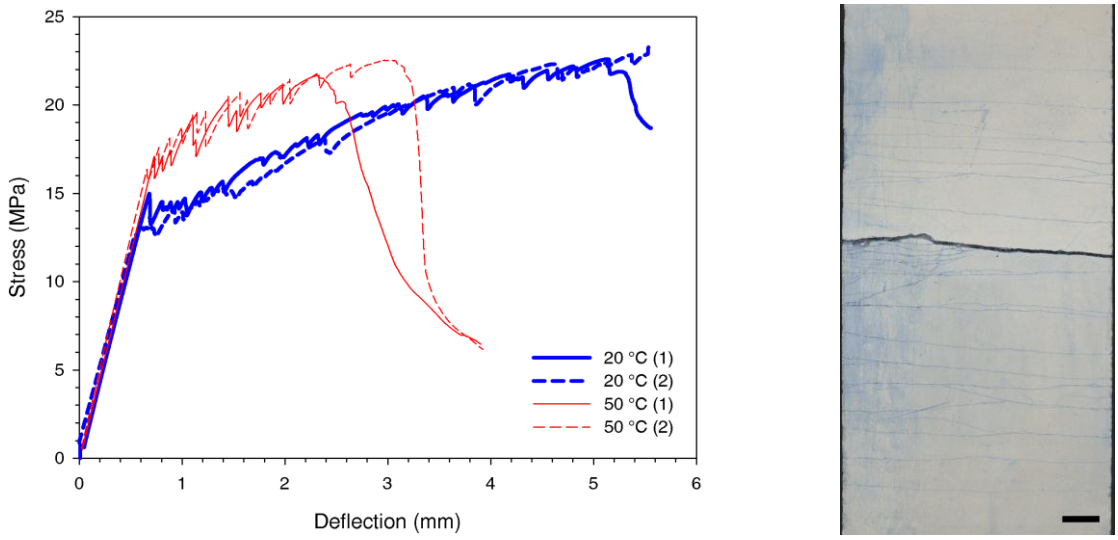

Figure 3: (a) Flexural results on 28-d GF-UHPC plate, after normal curing at 20 °C (blue, thick lines) and after accelerated aging (red, thin lines). (b) Multi-cracking pattern observed on the tensile face of plate after a flexural test; scale bar, 2 cm.

Tensile strength from back analysis of flexural results.—The potential contribution of the fibers to the tensile strength of the composite can be estimated by a simplified analysis, as well as by a back analysis of the flexural results.

A simplified approach to estimating the upper bound of the contribution of the fibers, σ_p, to the tensile strength of the composite is:

$$\sigma_p = v_f \sigma_f k \omega \quad (1)$$

were v_f is the volume content of the fibres, σ_f is the direct tensile strength of the fibres (~1700 MPa), k is a coefficient taking into account the effect of the fibres orientation in the matrix (typically 0.5, $2/\pi$ or 1 for a 3D, 2D or 1D distribution, respectively), and ω is a coefficient representing the effectiveness of the fibre/matrix couple (depending on the statistical anchoring length of the fibre with respect to a crack). Assuming k = 0.64 (2D), ω = 0.5 (optimised fibre/matrix anchoring length) and for v_f around 2.2%, the estimated upper bound tensile strength of the composite is approximately 12 MPa.

To see if the experimental flexural results were consistent with the estimates of the fiber potential outlined above, a back analysis was performed on the flexural data. The methodology for the calculation applied to plates was given in Ref. [3]. Considering the relatively homogeneous distribution of cracks along the tensile face in the central section of the specimen (Figure 3b), we assume a non-linear homogeneous material, which allows us to define a stress versus strain constitutive equation. Figure 4 shows that the reinforcement provided by glass fibers is close to a constant post-crack strength until a certain level of ultimate strain. This post-crack strength is approximately 9 MPa and 11 MPa for the samples at 20 °C and 50 °C, respectively. Note that irregularities on the curves come from numerical treatments of experimental curves.

The results of the back analysis highlight two important points. First, the calculated tensile stresses in the post-cracking regime (9–11 MPa) are consistent with the upper bound fiber potential (12 MPa) calculated from eq. (1). Second, aging at 50 °C appears to increase the tensile strength of the composite. These observations are believed to be linked to the particular microstructure of the glass fiber and its interface with the cementitious matrix.

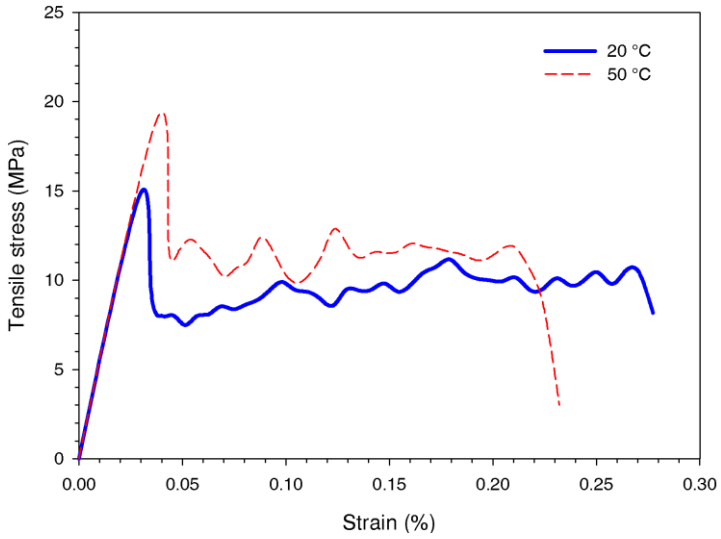

Figure 4: Tensile stress versus strain calculated from a back analysis of the flexural curves.

Materials design criteria for deflection-hardening fiber-reinforced plates.—The ultimate objective in designing a thin plate element subject to bending is to ensure a 'structural ductility' of the element—that is, the ability of a element to safely deflect under loads without failing in a brittle manner. The ideal load-deflection behaviour of a material is thus a deflection-hardening response with sufficient ultimate deflection. An analysis presented below outlines a simple criteria based on the materials properties of the composite to ensure a deflection-hardening response in bending.

It should be noted that, in addition to materials properties, the size of the specimen is also important in determining the ductility of a structural element. For example, increasing the length of a plate element increases the zone where multicracking can occur, thereby increasing the opportunity for a deflection hardening response. Roughly, under the same loading conditions, and for a given plate thickness, the ultimate deflection scales with the square of the span.

To derive a criteria for deflection hardening, consider a rectangular section of height, h, subject to bending. Figure 5 shows the stress distribution of the section at the moment a crack has formed and propagated to a height, αh. Three zones are created in the plate: i) an elastic, compressive zone above the neutral axis at $\alpha_n h$; ii) an elastic tensile zone, below the neutral axis and above the crack, with a maximum tensile stress, σ_t ; and iii) a damaged zone with a uniform tensile stress of σ_f distributed along the face of the crack.

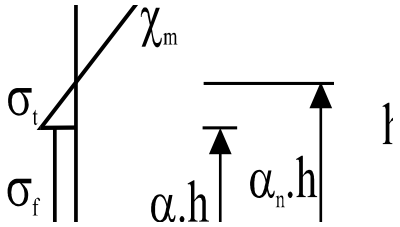

Figure 5: Stress distribution in a cracked section subject to bending.

Considering mechanical equilibrium, it can be shown that the load-deflection response will exhibit a deflection hardening behaviour if the fiber potential at the onset of cracking σ_f (i.e., the contribution of the fibers to the tensile strength of the composite) exceeds half of the tensile strength of the matrix σ_t [6].

Therefore, considering the results obtained from back analysis, it is not surprising to get a deflection hardening behaviour in flexion (Figure 3), even after having a drop in stress after the LOP in direct tension (Figure 5). More precisely, at 20°C, the ratio between the post-crack

tensile strength and the LOP is close to 0.5, which thus explains the small plateau on the flexural curve (Figure 3a). At 50°C, the ratio is higher than 0.5 (Figure 5), thereby resulting in an immediate deflection hardening after cracking (Figure 3a). This analysis thus illustrates that a non-strain hardening in tension can give a deflection hardening response in flexion.

Effect of glass strand microstructure on post-cracking behavior

A central characteristic of the glass fiber is that it is, in fact, a bundle of hundreds of microfilaments (~ 14 μm wide) comprising a strand. Zhu and Bartos [6] showed, through direct microindentation tests on a glass fiber, that the resistance of the individual microfilaments to sliding was heterogeneous across the cross section of the fiber strand. The microfilaments at the periphery of the fiber were most resistant to sliding, as they were bound firmly with the cementitious matrix, while the microfilaments in the interior of the fiber were more free to slide during pull-out. With this heterogeneous microstructure of the strand, it follows that a higher proportion of interior fibers participating in pull-out relative to exterior fibers participating in load transfer would decrease the contribution of the fibers to the tensile strength of the composite. This phenomenon could explain why the experimental tensile strengths in the post-cracking regime were lower than the upper bound fiber potential (12 MPa) calculated from eq. (1), which assumes a (homogeneous) monofilament structure for the fiber.

In the same microindentation study [6], it was also shown that the resistance to sliding of the interior microfilaments gradually increases with wet aging (ultimately exceeding the values of the exterior microfilaments in certain matrix formulations). This phenomenon is attributed to the gradual precipitation of hydration products within the interstices of the strand. The impact of this phenomenon on the tensile performance of the composite is that, with increasing cohesion of the microfilaments, the strand gradually increases its potential for load transfer and thus approaches the behavior of a monofilament-type fiber. This conclusion would explain the observed increase in tensile strength of the GF-UHPC composite after aging from 9 to 11 MPa, as well as the close correspondence between the experimental tensile strength and estimated value from eq. (1).

Microstructure and Durability

Embrittlement of normal GRCs is a major deterrent to the use of GRCs in load-bearing applications. Two main mechanistic pathways for embrittlement have been proposed: i) chemical degradation of the glass fibers and ii) densification of the strand (as discussed above) and of the strand/matrix interface. As discussed below, both of these mechanistic pathways are significantly impeded in the current GF-UHPC, thereby significantly retarding embrittlement.

Dissolution of glass fibers in the alkaline pore solution of cementitious systems was particularly a problem with E-glass fibers used in early GRC composites, but much less so in today's alkali-resistant (AR) glass (containing 16% ZrO_2). Nevertheless, AR glass can be susceptible to some attack after very long periods of time (30–50 years) [4]. In the current GF-UHPC composite, glass dissolution is impeded for several reasons: i) the pH of the pore solution is low due to the use of low alkali cements and reactive pozzolanic ultrafines; ii) the composite has a very low water/cement ratio, so little mix water would be available for glass dissolution; and iii) the composite has an exceptionally low porosity and permeability. Figure 6 shows the porosity and pore size distribution of the GF-UHPC as measured by MIP. Total porosity is very low, being 5%. The breakthrough radius (or the pore size of the principal percolated path) is 10–15 nm, indicating that the capillary pores are depercolated (and virtually eliminated). Transport of water and other species must therefore pass through the fine gel pore

network of the UHPC matrix, where flow is severely impeded. This allows the GF-UHPC to create water-tight elements, suitable for façade applications.

The second mechanism for embrittlement of GRC has been associated with the precipitation of calcium hydroxide either within the interstices of the glass strand or at the interface of the strand and the cementitious matrix. The filling of the strand interstices with portlandite is thought to encourage fracture of the fiber, especially when it bridges cracks at inclined (i.e., non-orthogonal) angles [4]. The densification of the strand/matrix interface is also believed to encourage fracture either through excessive bond [4] or through the propagation of surface flaws mediated by the nucleation of portlandite on the surface of the strand [8]. Regardless of the precise mechanism, the evidence from the GRC studies show that, to promote resistance to embrittlement, the formation of portlandite should be avoided at the glass fiber interface.

Our SEM observations of wet aged GF-UHPC formulations support this above strategy (Figure 7). For example, in the UHPC mix containing metakaolin ultrafines, no portlandite was found at the strand/matrix interface, and, instead, the interface was enriched with C–S–H (Figure 7a). This is due to the pozzolanic reaction of the metakaolin and silica fume ultrafines in the matrix. As shown in Figure 3a, the C–S–H-rich interfacial structure led to good ductility retention after aging. On the other hand, if the UHPC mix lacked pozzolanic ultrafines, abundant portlandite was found at the strand/matrix interface, thereby resulting in a brittle post-cracking regime after aging. Infilling of strand interstices by hydrates was less apparent in both samples. However, when present, the metakaolin-based sample showed C–S–H in the strand interstices, while the non-pozzolanic sample showed portlandite. The presence of C–S–H within the strand could cause an increase in fiber cohesion of the strand, which was hypothesized above to explain the increased tensile strength of the composite observed after aging. Note that, unlike with portlandite, infilling strand interstices with C–S–H does not cause embrittlement [4,8].

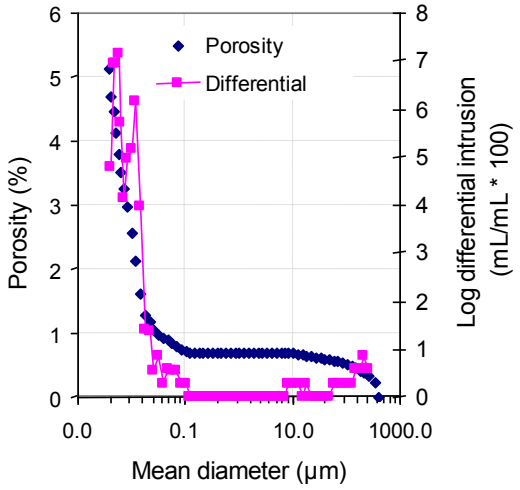

Figure 6: MIP results on the GF-UHPC showing the low porosity and fine pore structure of the composite.

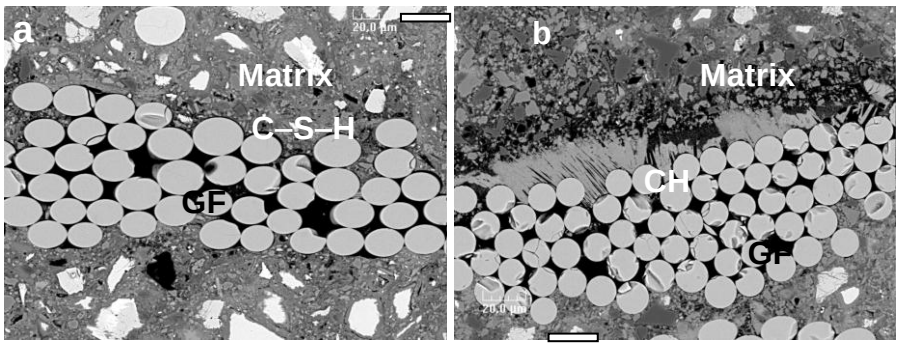

Figure 7: SEM images of the glass fiber strand in different UHPC matrices either a) based on metakaolin ultrafines or b) lacking pozzolanic ultrafines (GF = glass fibers; CH = portlandite; scale bar = 20 µm).

4 Conclusion

The glass-fiber reinforced UHPC (GF-UHPC) presented here has an unprecedented combination of self-placing behavior, deflection hardening behaviour in bending, and excellent durability. These properties, along with the aesthetic properties of the material (white color, without the risk of rust), make the material particularly well-suited to slender, complex-shaped, and waterproofed structural elements for architectural applications (e.g., facades).

The unique properties of the GF-UHPC are a result of an optimized combination of the UHPC matrix and of the fibers. For example, by coupling a UHPC matrix containing metakaolin ultrafines and only 2–2.2% glass fibers, it was possible to have a high LOP (14–18 MPa) and a deflection hardening response, even after wet aging. Back analysis of the flexural data show that the tensile strengths in the post-cracking regime (9–11 MPa) are close to the maximum expected from a random 2D distribution. SEM investigations confirm that the aging resistance is due to the pozzolanic reaction of the ultrafines, which promote the formation of C–S–H (instead of portlandite) at the glass strand/matrix interface. It is also suggested that the precipitation of C–S–H within the glass strands after aging increased the observed post-cracking tensile strength, due to an enhanced cohesion and load-transfer capacity of the interior microfilaments. Lastly, MIP showed the GF-UHPC to have a very low porosity (5%), with an associated breakthrough diameter of 10–15 nm. Transport of water and of deleterious species will thus be severely impeded in this durable GF-UHPC.

References

[1] Batoz, J.-F.; Behloul, M.: UHPFRC development: Experience with Ductal® over the last two decades. Proceedings of Designing and Building with UHPFRC, State of the Art and Development, Marseille, France, pp. 43–62, 2009.

[2] Ricciotti, R.; Lamoureux, G.; Ricciotti, R.: The Jean-Bouin stadium. Proceedings of Designing and Building with UHPFRC, State of the Art and Development. Marseille, France, pp. 101–108, 2009.

[3] Rigaud, S.; Chanvillard, G.; Chen, J. J.: Characterization of bending and tensile behaviors of ultra-high performance concrete containing glass fibers. Proceedings of High Performance Fiber Reinforced Cement Composites 6, Ann Arbor, MI, USA, 2011.

[4] Bentur, A.;Mindess, S.: Fibre reinforced cementitious composites, 2nd ed. Taylor & Francis, Oxon, England, 2007.

[5] Roth, M. J.; Eamon, C. D.; Slawson, T. R.; Tonyan, T. D.; Dubey, A.: Ultra-high strength, glass fiber-reinforced concrete: Mechanical behavior and numerical modeling. ACI Materials Journal, 107(2), pp. 185–194, 2010.

[6] Chanvillard, G.: Characterization of fibre reinforced concrete mechanical properties : A review, plenary conference, Fifth International Rilem Symposium on Fibre Reinforced Concretes, BEFIB'2000, Ed. P. Rossi and G. Chanvillard, Lyon, France, pp. 29–50, 2000.

[7] Zhu, W.; Bartos, P. J. M.: Assessment of interfacial microstructure and bond properties in aged grc using a novel microindentation method. Cement and Concrete Research., 27(11), pp. 1701–1711,1997.

[8] Purnell, P.; Short, N. R.; Page, C. L.;Majumdar, A. J.: Microstructural observations in new matrix glass fibre reinforced cement. Cement and Concrete Research., 30(11), pp. 1747–1753, 2000.

Energy Dissipation and Strength Evolution of Ultra-High-Performance Fiber-Reinforced Concrete (UHPFRC)

Brett Ellis[1], Min Zhou[1,2], David L. McDowell[1,2]

1: Woodruff School of Mechanical Engineering, Georgia Institute of Technology, Atlanta, USA
2: School of Material Science and Engineering, Georgia Institute of Technology, Atlanta, USA

A fully dynamic 3D mesoscale model was developed to quantify the energy dissipation and load-carrying capabilities of Ultra-High-Performance Fiber-Reinforced Concrete (UHPFRC) subjected to compression at strain rates of 500 - 1,000 s-1 under conditions of nominal plane strain. This model accounts for three constituents: porosity, fibers, and cementitious matrix. Microstructure instantiations encompass a range of pore volume fraction (1-10%), pore diameter (0.2-0.4 mm), fiber volume fraction (0-4%), and fiber-matrix interfacial bonding strength (1-2 MPa). Calculations delineate and characterize the evolution of kinetic energy, strain energy, work expended on interfacial damage and failure, frictional dissipation along interfaces, and bulk dissipation through granular flow as functions of microstructure (constituent spatial distributions), loading, and constituent properties.

Keywords: Modeling, Fiber-Reinforced, Concrete, Explicit Microstructure

1 Introduction

Ultra-High-Performance Fiber-Reinforced Concretes (UHPFRCs) are a class of promising cementitious materials that have been slow to transition to commercialization. One reason is the scarcity of data concerning the mechanical responses of UHPFRCs subjected to dynamic loading. The literature on dynamically loaded UHPFRCs is predominantly concerned with the structural length scale (i.e., order of 1 m). Results of experiments on blast-loaded UHPFRC slabs were published by Zhou et al. [1], Wu et al. [2], Rebentrost and Wight [3], and Schenker et al. [4]. Numerical simulations reported in the literature were obtained via either hydrocodes utilizing homogenized equations of state (e.g., Zhou et al. [1], Schenker et al. [4]) or modified single degree-of-freedom approaches (e.g., Wu et al. [2]). These approaches cannot resolve the effects of microstructure, material heterogeneity, or interfacial interactions.

In contrast, this paper presents a novel approach that explicitly accounts for the distributions of fibers, voids, and matrix in a UHPFRC. This new approach allows the load-carrying and energy-dissipation capabilities of the materials to be quantified as functions of microstructure heterogeneity and constituent properties, thereby providing an important tool to support the multiscale design of UHPFRCs.

2 Framework of Analysis and Constitutive Models

Constitutive Relation: Matrix

No constitutive relation is employed for pores, which are assumed empty. The matrix is represented by an extended Drucker-Prager constitutive relation included in Abaqus/Explicit v6.10 [5] that is pressure and strain-rate sensitive. Specifically, the yield condition is

$$F = \frac{1}{2} q \left[1 + \frac{1}{K} - \left(1 - \frac{1}{K} \right) \left(\frac{r}{q} \right)^3 \right] - p \tan(\beta) - d \leq 0 \quad , \tag{1}$$

where

$q = \sqrt{\frac{3}{2}(\mathbf{S}:\mathbf{S})}$ is the Mises equivalent stress,

$\mathbf{S} = \boldsymbol{\sigma} + p\mathbf{I}$ is the deviatoric stress,

$\boldsymbol{\sigma}$ is the Cauchy stress,

$p = -\frac{1}{3}\mathrm{tr}(\boldsymbol{\sigma})$ is the pressure defined in terms of the trace of $\boldsymbol{\sigma}$,

$\mathbf{I}$ is the second rank identity tensor,

K is the ratio of yield strengths in triaxial tension to triaxial compression (must be in the range $0.778 \le K \le 1.0$),

$r = \left(\frac{9}{2}\mathbf{S}\cdot\mathbf{S}:\mathbf{S}\right)^{\frac{1}{3}}$ is the third invariant of deviatoric stress,

β is the internal friction angle in the meridional stress plane, and

d is the cohesion of the material under pure shear.

When the yield condition is satisfied (i.e., $F = 0$), the material follows the non-associative flow rule

$$\mathbf{D}^p = \frac{\dot{\bar{\varepsilon}}^p}{c}\frac{\partial G}{\partial \boldsymbol{\sigma}}, \tag{2}$$

where

$\mathbf{D}^p$ is the plastic part of the rate of deformation tensor,

$\dot{\bar{\varepsilon}}^p = \sqrt{\frac{2}{3}\mathbf{D}^p:\mathbf{D}^p}$ is the equivalent plastic strain rate,

$c = 1 - \frac{1}{3}\tan(\psi)$ is a constant,

$G = \frac{1}{2}q\left[1 + \frac{1}{K} - \left(1 - \frac{1}{K}\right)\left(\frac{r}{q}\right)^3\right] - p\tan(\psi)$ is the flow potential, and ψ is the dilation angle.

Strain-rate sensitivity is incorporated using the Compression Dynamic Inflation Factor (CDIF) given by

$$\mathrm{CDIF} = \frac{\bar{\sigma}_c}{\sigma_o} = \begin{cases} \left(\dot{\varepsilon}_\mathrm{d} \big/ \dot{\varepsilon}_\mathrm{cs}\right)^{1.026\alpha}, & 30\times10^{-6}\ \mathrm{s}^{-1} \le \dot{\varepsilon}_\mathrm{d} \le 30\ \mathrm{s}^{-1}; \\ \left(\dot{\varepsilon}_\mathrm{d}\right)^{1/3} e^{6.156\alpha - 0.49}, & 30\ \mathrm{s}^{-1} < \dot{\varepsilon}_\mathrm{d} \le 1{,}000\ \mathrm{s}^{-1}; \end{cases} \tag{3}$$

as recommended by Zhou et al. [1]. In Eq.(3),

$\bar{\sigma}_c$ is the compressive yield strength at the dynamic strain rate $\dot{\varepsilon}_\mathrm{d}$,

σ_o is the compressive yield strength at the quasi-static strain rate $\dot{\varepsilon}_\mathrm{cs} = 30\times10^{-6}s^{-1}$, and

$\alpha = (5 + 3f_c' / 4)^{-1}$ is a factor based on quasi-static unconfined compressive strength f_c'.

For $\dot{\varepsilon}_\mathrm{d} > 1{,}000$ s^{-1}, a conservative rate sensitivity level is assumed by setting $\mathrm{CDIF} = (1{,}000)^{1/3} e^{6.156\alpha - 0.49}$.

Table 1 lists the mass density ρ_m, unconfined compressive yield strength f_c', elastic stiffness E_m, Poisson's ratio ν_m, ratio of yield strengths in triaxial tension to triaxial compression K, internal friction angle β, and dilation angle ψ. A conservative estimate of elastic stiffness is

$$E_m = \left(3{,}320\sqrt{f_c} + 6{,}895\right)\left(\frac{\rho_m}{2.32}\right)^{1.5}, \tag{4}$$

as recommended by Nawy [6]. The values of K, β, and ψ are taken from the experimental results of Park, Xia, and Zhou [7].

Table 1: Cementitious matrix material parameters.

ρm (g/cm3)	fc (MPa)	Em (GPa)	vm	K	β	ψ
2.4	100	42.1	0.2	0.8	28°	20°

Constitutive Relation: Fiber

The fibers are assumed to be elastic-viscoplastic. Yielding of the fibers is assumed to follow the Von Mises yield criterion (i.e.,

$$F(\boldsymbol{\sigma}, \tilde{\varepsilon}^{pl}, \dot{\tilde{\varepsilon}}^{pl}) = \tfrac{1}{2}\mathbf{S}:\mathbf{S} - \frac{\left(\sigma^o(\tilde{\varepsilon}^{pl}, \dot{\tilde{\varepsilon}}^{pl})\right)^2}{3} \le 0, \tag{5}$$

where $\tilde{\varepsilon}^{pl}$ and $\dot{\tilde{\varepsilon}}^{pl}$ are the equivalent plastic strain and equivalent plastic strain rate, respectively). The Johnson-Cook model [8],

$$\sigma^o\left(\tilde{\varepsilon}^{pl}, \dot{\tilde{\varepsilon}}^{pl}\right) = \left[A + B\left(\tilde{\varepsilon}^{pl}\right)^n\right]\left[1 + C\log_{10}\left(\frac{\dot{\tilde{\varepsilon}}^{pl}}{\dot{\varepsilon}_0}\right)\right], \tag{6}$$

defines the yield stress with material parameters $A, B, n, C,$ and $\dot{\varepsilon}_0$. Because the fiber material is assumed to be associative, the evolution equation for plastic strain is

$$\dot{\boldsymbol{\varepsilon}}^{pl} = \dot{\lambda}\frac{\partial F}{\partial \boldsymbol{\sigma}} \tag{7}$$

when $F = 0$, with $\dot{\lambda}$ being the plastic multiplier obtained from the consistency condition.

The material parameters shown in Table 2 are representative of 4340 steel [1]. From left to right, Table 2 lists the mass density ρ_f, elastic stiffness E_f, Poisson's ratio v_f, and the Johnson-Cook model parameters $A, B, n, C,$ and $\dot{\varepsilon}_0$.

Table 2: Fiber material parameters.

ρ_f (g/cm^3)	E_f (GPa)	v_f	A (MPa)	B (MPa)	n	C	$\dot{\varepsilon}_0$ (s^{-1})
7.85	200	0.3	792	510	0.26	0.014	1

Constitutive Relation: Fiber-Matrix Interface

The interfacial debonding between fibers and matrix is modeled through the use of zero-thickness cohesive elements. The bilinear traction-separation relation shown in Fig. 1 defines the relation between normal separation δ_n and normal traction t_n, as well as the relation between tangential displacements $\delta_{s,t}$ and tangential tractions $t_{s,t}$. In Fig. 1, G^c is the work of

separation defined as the total area under the bilinear separation relation. Interpenetration (i.e., negative normal separation) is strongly discouraged through a numerical penalty algorithm.

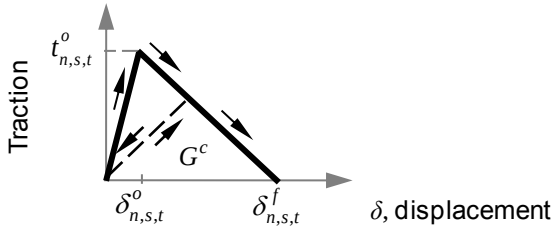

Figure 1. Traction-separation constitutive responses of the fiber-matrix interface.

The initial linear-elastic portion in Fig. 1 is decoupled in the normal and tangential directions (i.e., $t_i = K_i \delta_i$ where $i = n,s,t$ without summation implied, and K_i is the stiffness in the i^{th} direction).

Damage initiation (peak traction in Fig. 1) leads to coupling between the normal and tangential directions and is governed by the quadratic initiation criterion

$$\left(\frac{\langle t_n \rangle}{t_n^0}\right)^2 + \left(\frac{t_s}{t_s^0}\right)^2 + \left(\frac{t_t}{t_t^0}\right)^2 = 1 \tag{8}$$

where t_n^o, t_s^o, and t_t^o are critical traction values in the corresponding directions and $\langle\ \rangle$ are MacCaulay brackets defined by $\langle \chi \rangle = \frac{1}{2}\left(|\chi| + \chi\right)$.

Mixed-mode damage evolution is considered using the Benzeggagh and Kenane [9] criterion in the form of

$$G_n^c + \left(G_s^c - G_n^c\right)\left(\frac{G_s + G_t}{G_n + G_s + G_t}\right)^\eta = G^c \tag{9}$$

where G_n^c, G_s^c, and G_t^c are critical fracture energies in the normal and tangential directions, respectively; η is a material parameter; and G_n, G_s, and G_t represent work done by t_n, t_s, and t_t, respectively.

The response of the matrix-fiber interface is assumed to be strain-rate insensitive in light of the work of Kim, El-Tawil, and Naaman [10] that showed minimal dependence on strain rates between $0.0001\ \text{s}^{-1} \le \dot{\varepsilon} \le 0.1\ \text{s}^{-1}$. Table 3 lists two different sets of Cohesive Element Material Properties (*CEMPs*). For the remainder of this paper, these two sets will be referred to as $CEMP_1$ and $CEMP_2$, respectively.

Table 3. Cohesive element material properties.

Name	$\boldsymbol{K_{n,s,t}}$ (GPa)	$\boldsymbol{t^o_{n,s,t}}$ (MPa)	$\boldsymbol{G^c_{n,s,t}}$ (J/m^2)	η
$CEMP_1$	200	1	52.5	1.45
$CEMP_2$	200	2	110	1.45

Constitutive Relation: Friction

The matrix constitutive relation is used to reflect frictional flow of the granular matrix. For explicit contact situations (i.e., failed fiber-matrix interfaces and collapsed pores), a friction model is employed. The friction model used is a rate-independent, isotropic Coulomb friction model. In this model, the relative motion between two surfaces is allowed only when the equivalent friction stress $\tau_{eq} = \sqrt{\tau_1^2 + \tau_2^2}$ meets or exceeds the critical stress $\tau_{crit} = \mu p_{contact}$, where τ_1 and τ_2 are mutually orthogonal shear stresses at the interface, μ is the coefficient of friction, and $p_{contact}$ is the normal contact stress between the two surfaces.

Because the model is assumed to be isotropic, the magnitudes of the shearing rates $\dot{\gamma}_1 = \sqrt{\dot{\gamma}_1^2 + \dot{\gamma}_2^2}\,\frac{\tau_1}{\tau_{eq}}$ and $\dot{\gamma}_2 = \sqrt{\dot{\gamma}_1^2 + \dot{\gamma}_2^2}\,\frac{\tau_2}{\tau_{eq}}$ are proportional to the shear stresses τ_1 and τ_2, respectively. In this work, a pressure-independent coefficient of coulomb friction of 0.30 is used in light of the work of Baltay and Gjelsvik [11].

3 Model Description

The model at the scale of multiple fibers consists of a 3D periodic microstructure containing fibers, pores, and matrix. Figure 2 shows a typical microstructure instantiation with the fibers shaded in dark grey, the matrix in light grey, and the pores in medium grey.

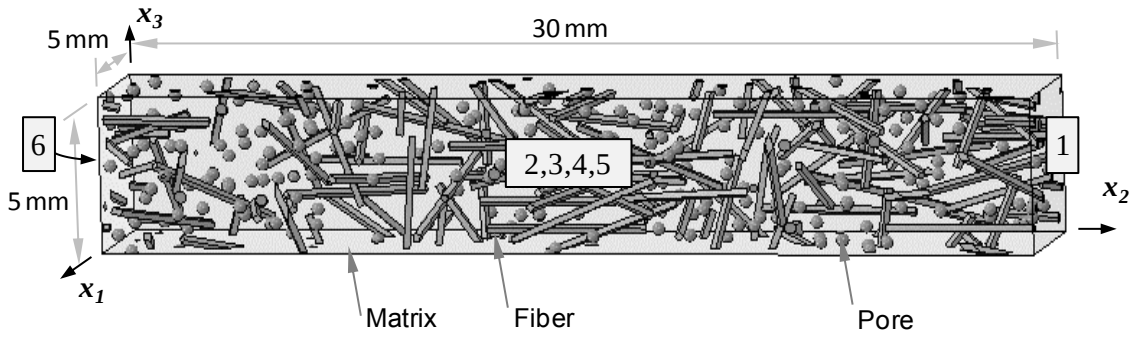

Figure 2: Sample microstructure instantiation at the scale of multiple fibers showing matrix, fiber, and pore phases. The fiber volume fraction V_{fiber}, pore volume fraction V_{pore}, and pore diameter ϕ_{pore} shown are 2%, 1%, and 0.4 mm, respectively.

The six faces of the sample microstructure are identified by the face numbers shown within light grey rectangles. It is assumed that each microstructure instantiation is sufficiently large to constitute a statistical Representative Volume Element (sRVE) [12].

Microstructure Instantiation

Periodic microstructure instantiations are generated from an initially homogeneous matrix. The 5-mm-long fibers are straight and smooth and have square cross sections of width 0.2 mm. A Random Sequential Absorption (RSA) algorithm places fibers in the matrix until the desired fiber volume fraction, V_{fiber}, is reached. During fiber placement, the RSA ensures a 0.1-mm minimum standoff distance between the edges of any two fibers. After all the fibers are placed, the spherical pores are placed in the microstructure. First, solid spheres are placed into the fiber-matrix microstructure via a second RSA algorithm until the desired pore volume fraction, V_{pore}, is reached. Within a given instantiation, all spheres are characterized by a pore diameter, ϕ_{pore}, of either 0.2 mm or 0.4 mm. A 0.1-mm minimum standoff distance is enforced between the surfaces of any two spheres as well as between the surface of any sphere and the edge of any fiber. Should a portion of a placed fiber or sphere be outside the matrix, the outside portion is separated from the placed portion and translated to the opposite face of the matrix to ensure

the 3D periodicity of the microstructure. Once all the spheres are placed, the matrix material within each sphere is removed, thus creating the porosity.

The Abaqus meshing algorithm [5] is subsequently used to create an unstructured mesh for each instantiation. The matrix domain is meshed with 4-node type C3D4 tetrahedral elements. The domains that represent fibers are meshed with 8-node type C3D8R reduced integration hexahedral elements. The fiber-matrix interfaces are meshed with 8-node type COH3D8 zero-thickness cohesive elements. The spherical pores are not meshed.

At a characteristic matrix element size of 0.1 mm, an instantiation with V_{fiber} = 2%, V_{pore} = 1%, and ϕ_{pore} = 0.4 mm contains approximately 170,000 fiber elements, 340,000 cohesive elements, and 4,300,000 matrix elements. As V_{fiber} increases to 4% and ϕ_{pore} decreases to 0.2 mm, the number of matrix elements increases to approximately 10,000,000. Depending on the number of elements, the computation time per instantiation varies from 6 to 60 hr using 48 parallel AMD 2350QC processing cores. A mesh sensitivity study indicates a negligible effect on the calculated load-carrying capability and dissipated energy density of this change in the number of elements.

Boundary Conditions

Boundary conditions are chosen to achieve high-strain-rate loading with lateral confinement. In Fig. 2, nodes on Faces 2-6 have roller supports that permit nodal displacements within the plane defined by the face. Nodal displacements normal to the plane are prohibited. Loading is applied on Face 1 through the imposition of a velocity of 15 m/s or 30 m/s in the negative x_2 direction. The velocity is applied as a step function that starts at 0 μs and remains constant thereafter. The imposed velocities of 15 m/s and 30 m/s give rise to overall strain rates of 500 s^{-1} and 1,000 s^{-1}, respectively. All simulations concern the first 18 μs of material response, resulting in nominal compressive strains of 0.9% and 1.8% in the x_2 direction for the 15 m/s and 30 m/s cases, respectively.

4 Results and Discussion

The analysis focuses on the effects of fiber volume fraction V_{fiber}, pore volume fraction V_{pore}, pore diameter ϕ_{pore}, the cohesive element material properties $CEMPs$, and overall strain rate $\dot{\varepsilon}$. Fourty-four cases with different combinations of microstructure and material parameters shown in Table 4 are simulated.

Table 4: Variables and levels.

Variable		Level 1	Level 2	Level 3
V_{fiber}	%	0	2	4
ϕ_{pore}	mm	0.2	0.4	
V_{pore}	%	1	5	10
$CEMPs$		$CEMP_1$	$CEMP_2$	
$\dot{\varepsilon}$	s^{-1}	500	1,000	

Figure 3a shows the evolution of the traction T_{22} on Face 1 of a sample microstructure instantiation as a function of the overall engineering strain ε_{22} for $\dot{\varepsilon}$ = 1,000 s^{-1}. Here, ε_{22} is calculated as the absolute value of the displacement of Face 1 divided by the total length in the x_2 direction. Since it represents the actual force per unit area sustained by the material in the loading direction, T_{22} is used as a measure of the evolving load-carrying capability of the material. Following an initial rapid increase to 35 MPa, T_{22} gradually decreases to 31 MPa at

ε_{22} = 14 mm/m due to plastic deformation of the matrix around the voids. The first evidence of plastic deformation is observed at a pressure below 250 MPa. This is reasonable when compared to the 93 MPa initial compaction pressure used by Zhou et al. [1] for an f_c = 170 MPa UHPFRC under static loading conditions. Solid compaction (i.e., complete compaction of pores) is not observed or expected, as the 600 MPa maximum observed pressure is less than the 6,000 MPa solid compaction pressure used by Zhou et al. [1]. Note that at ε_{22} = 14 mm/m, T_{22} increases rapidly from 31 MPa to approximately 85 MPa. This increase is due to the arrival at the loading surface of the stress wave reflected from the other end of the microstructure.

Figure 3b decomposes the total energy density into the strain energy density, kinetic energy density, and the total dissipated component. The maximum value of the kinetic energy density at ε_{22} = 7.5 mm/m marks the point at which the compressive wave reflects from Face 6. For the remainder of this paper, the dissipated energy density at 7.5 μs is taken as a measure for the energy dissipation capability of the materials during the initial passage of the compressive wave.

The total dissipated energy density shown in Fig. 3b is further decomposed in Fig. 3c into three parts: (1) the plastic work density due to the granular flow of the matrix and the plastic deformation of the metal fibers, (2) the density of work associated with frictional dissipation at interfaces, and (3) the density of work associated with cohesive damage (i.e., separation of the fiber-matrix interfaces).

The average traction $\bar{T}_{22}$ is defined as the time-averaged value of T_{22} from 0 μs to 7.5 μs. This value provides a measure of the load-carrying capability as the initial stress wave tranverses the material.

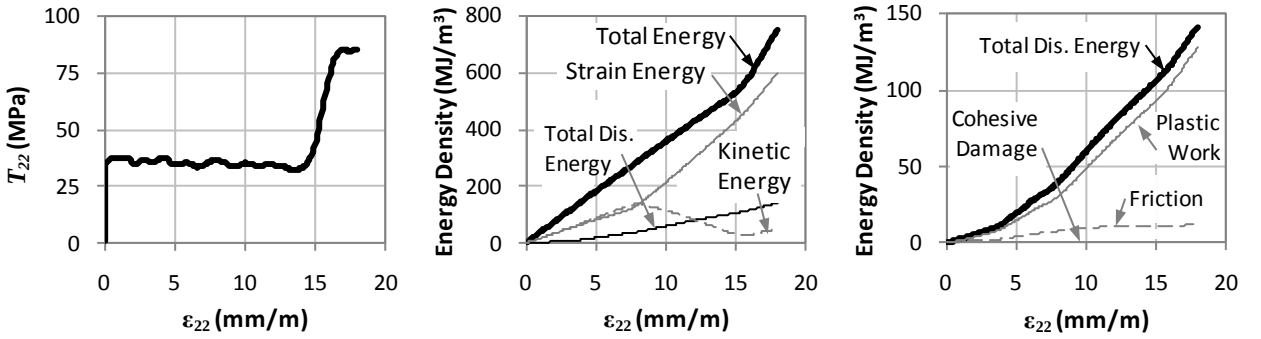

(a) Load-carrying capability. *(b) Total energy density.* *(c) Total dissipated energy density.*

Figure 3: Evolution of (a) load-carrying capability, (b) total energy density, and (c) density of total energy dissipated for V_{fiber} = 2%, ϕ_{pore} = 0.4 mm, V_{pore} = 5%, $CEMP_1$, and $\dot{\varepsilon}$ = 1,000 s^{-1}.

Figures 4 and 5 summarize the results of the simulations. Figures 4a and 5a show the average traction for the strain rates of 500 and 1,000 s^{-1}, respectively. Figures 4b and 5b show the density of the total energy dissipated for the strain rates of 500 and 1,000 s^{-1}, respectively. All four figures use the same markers for the different combinations of V_{fiber} and ϕ_{pore}.

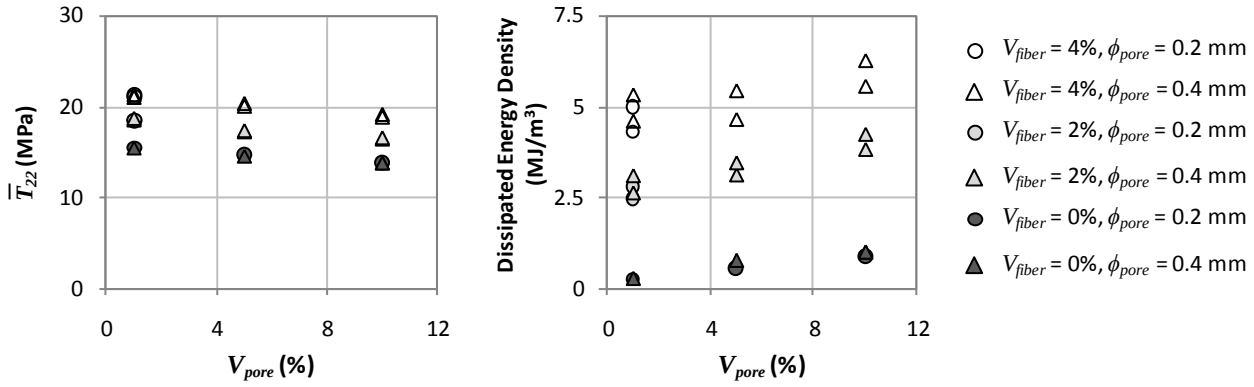

(a) Average traction. *(b) Density of total energy dissipated.*

Figure 4: (a) Average traction and (b) total energy dissipated as functions of V_{pore} ($\dot{\varepsilon}$ = 500 s^{-1}).

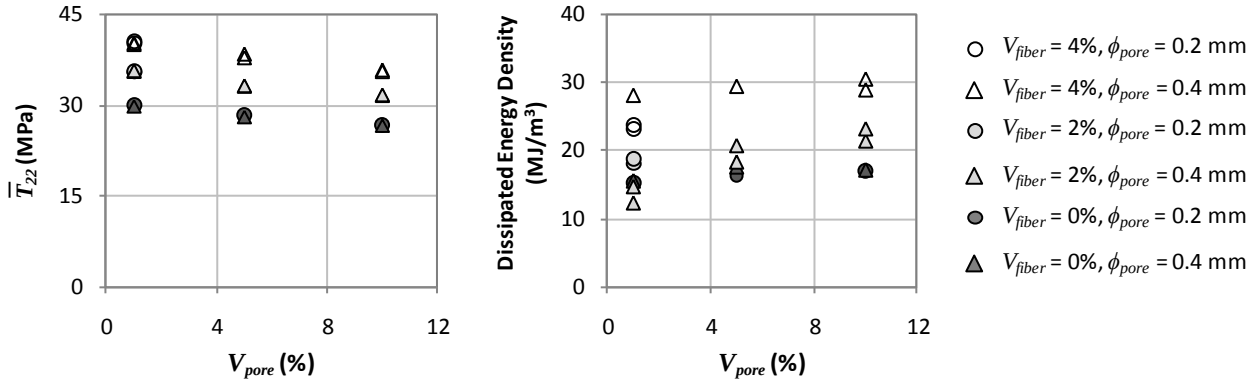

(a) Average traction. *(b) Density of total energy dissipated.*

Figure 5: (a) Average traction and (b) total energy dissipated as functions of V_{pore} ($\dot{\varepsilon}$ = 1,000 s^{-1}).

Four significant observations can be made from Figs. 4 and 5:

1) For the conditions studied, $\bar{T}_{22}$ is strongly influenced by V_{fiber}, V_{pore}, and $\dot{\varepsilon}$ and weakly influenced by ϕ_{pore} and $CEMPs$. As expected, UHPFRC designs with higher V_{fiber} and lower V_{pore} are preferred for enhanced load-carrying capability. Even if V_{pore} is held constant, there is evidence of diminishing improvements in $\bar{T}_{22}$ as V_{fiber} increases. For example, as V_{fiber} is increased from 0% to 2% and from 2% to 4%, $\bar{T}_{22}$ increases by 19% and 13%, respectively.
2) For $\dot{\varepsilon}$ = 500 s^{-1}, V_{fiber} is the primary factor influencing dissipation. Dissipation increases by 110% for every 1% increase in V_{fiber}. The second order effects of $CEMPs$, ϕ_{pore}, and V_{pore} are also evident. For example, the stronger fiber-matrix interface $CEMP_2$ dissipates 14% more energy than the weaker interface $CEMP_1$. Microstructure instantiations with 0.4-mm-diameter pores dissipate 10% more energy than similar instantiations with 0.2-mm-diameter pores. Furthermore, for every 1% increase in V_{pore}, dissipation increases by 10%.
3) At $\dot{\varepsilon}$ = 1,000 s^{-1}, the amount of energy dissipated is 6 times the energy dissipated at $\dot{\varepsilon}$ = 500 s^{-1}. Although V_{fiber} is the primary factor influencing dissipation, the second order effects of ϕ_{pore}, V_{pore}, and $CEMPs$ are still appreciable.
4) While energy dissipation is strongly influenced by microstructure composition and phase distribution, the load-carrying capability as measured by the average reaction traction at the loading face is relatively insensitive to microstructure level heterogeneity and microstructural changes over the range analyzed.

5 Conclusions

Cohesive Finite Element Model (CFEM) simulations under nominally plane strain conditions at strain rates of 500 and 1,000 s^{-1} allowed the dynamic response of UHFRPC at the length scale of multiple fibers to be analyzed. The results yielded the following findings.

1) At constant pore volume fraction values, an increase in fiber volume fraction from 0% to 2% and from 2% to 4% increases the average load-carrying capability of the material by 19% and 13%, respectively, for dynamic loading.
2) The energy dissipated during such dynamic loading is strongly influenced by V_{fiber} and $\dot{\varepsilon}$ and weakly influenced by V_{pore}, ϕ_{pore}, and $CEMPs$. The influences of these factors on energy dissipation are quantified for the strain rate levels of 500 and 1,000 s^{-1}.

This approach has successfully identified and will continue to identify avenues of improving the response of UHPFRC microstructures to dynamic loading. Structures containing these tailored UHPFRC microstructures are expected to have improved dynamic loading responses.

6 Acknowledgement

This work was sponsored by the U.S. Department of Homeland Security, Science and Technology Directorate, Infrastructure Protection and Disaster Management Division: Ms. Mila Kennett, Program Manager. The research was performed under the direction of Dr. Beverly P. DiPaolo, Engineer Research and Development Center, U.S. Army Corps of Engineers. Permission to publish was granted by the Director, Geotechnical and Structures Laboratory, ERDC. Approved for public release; distribution is unlimited.

References

[1] Zhou, X.Q.; Kuznetsov, V.A.; Hao, H.; Waschl, J.: Numerical prediction of concrete slab response to blast loading. International Journal of Impact Engineering. 35 (10), p. 1186-1200, 2008.
[2] Wu, C.; Oehlers, D.J.; Rebentrost, M.; Leach, J.; Whittaker, A.S.: Blast testing of ultra-high performance fibre and FRP-retrofitted concrete slabs. Engineering Structures. 31 (9), p. 2060-2069, 2009.
[3] Rebentrost, M.; Wight, G.: Behaviour and resistance of ultra high performance concrete to blast effects. Ultra High Performance Concrete (UHPC), Proceedings of the Second International Symposium on Ultra High Performance Concrete, 05-07 March 2008, Kassel, Germany. Eds. E. Fehling, M. Schmidt, S. Stürwald. Kassel: University of Kassel, p. 735-742, 2008.
[4] Schenker, A.; Anteby, I.; Gal, E.; Kivity, Y.; Nizri, E.; Sadot, O.; Michaelis, R.; Levintant, O; Ben-Dor, G.: Full-scale field tests of concrete slabs subjected to blast loads. International Journal of Impact Engineering. 35 (3), p. 184-198, 2008.
[5] Abaqus v6.10 Theory Manual, Dassault Systèmes, 2010.
[6] Nawy, E.G.: Fundamentals of high strength high performance concrete. Harlow: Longman, 1996.
[7] Park, S.W.; Xia, Q.; Zhou, M.: Dynamic behavior of concrete at high strain rates and pressures: II. numerical simulation. International Journal of Impact Engineering. 25 (9), p. 887-910, 2001.
[8] Johnson, G.R.; Cook, W.H.: Fracture characteristics of three metals subjected to various strains, strain rates, temperatures and pressures. Engineering Fracture Mechanics. 21 (1), p. 31-48, 1985.
[9] Benzeggagh, M.L.; Kenane, M.: Measurement of mixed-mode delamination fracture toughness of unidirectional glass/epoxy composites with mixed-mode bending apparatus. Composites Science and Technology. 56 (4), p. 439-449, 1996.
[10] Kim, D.J.; El-Tawil, S.; Naaman, A.E.: Rate-dependent tensile behavior of high performance fiber reinforced cementitious composites. Materials and Structures. 42 (3), p. 399-414, 2009.
[11] Baltay, P.; Gjelsvik, A.: Coefficient of friction for steel on concrete at high normal stress. Journal Materials in Civil Engineering. 2 (1), p. 46-49, 1990.
[12] McDowell, D.L.: A perspective on trends in multiscale plasticity. International Journal of Plasticity. 26 (9), p. 1280-1309, 2010.

Effect of Heat Treatment Method on the Properties of UHPC

Detlef Heinz, Liudvikas Urbonas, Tobias Gerlicher
cbm Centre for Building Materials, Technische Universität München, Germany

Heat treatment of UHPC enables the production of very high strengths in short time periods. However, heat treatment conditions must be optimized for a particular UHPC composition. In the present study, the effect of heat treatment method on the properties of UHPC with different compositions was investigated. Specimens of a typical UHPC and UHPC with clinker content reduced by replacement with fly ash (FA) or ground granulated blast-furnace slag (GGBS) were cured under different conditions. Concrete age at the beginning of heat treatment and the duration and temperature of the treatment were varied. Heat treatment was performed in water, air or air saturated with water vapour. The ultrasonic pulse velocity was monitored in situ to assess changes in concrete microstructure at early hydration times and during heat treatment. X-ray diffraction analysis was used to characterize the hydration products. Compressive strengths of the typical UHPC over 200 MPa were achieved at an age of 24 h after 8 h initial storage at 20 °C followed by 8 h heat treatment at 90°C in water. Higher concrete age at the beginning of treatment or prolonged heat treatment had a positive effect on compressive strength of UHPC with GGBS. The highest strengths of UHPC with fly ash were obtained after 8 h heat treatment in an autoclave at 150°C.

Keywords: UHPC, Heat treatment, mix design

1 Introduction

Accelerated strength development of UHPC and a high final strength may be achieved by heat treatment at temperatures up to 90°C combined with a high relative humidity at an age of just a few days. Heat treatment at 90°C accelerates the hydration of clinker phases and the reaction of silica fume and quartz flour completely binding portlandite while increasing the amount of C-S-H phases [1-4] and their chain length [2]. However, few systematic investigations exist in the current literature on the effect of different heat treatment regimes on the hydration and microstructural development of UHPC. Usually treatment temperatures ranging from 90 to 450°C and times between 24 h and 7 d are chosen following an initial storage period between 24 and 48 h [1-6]. According to [6] initial storage periods of 70 h, 10 d or 24 d before heat treatment at 90°C for 48 h have no significant effect on strength, Young's modulus and the durability of UHPC. According to Schachinger et al. [7], initial storage periods of 3 or 5 d are necessary to achieve of the highest strength of Portland cement UHPC. Higher heat treatment temperatures usually enhance the strength measured immediately after heat treatment [3, 7, 8]. The actual conditions of heat treatment affect strength and its development after treatment [8, 9]. Sometimes the dry conditions during heat treatment lead to loss of strength during storage following the treatment [9]. The present investigations aimed at determining the effect of different heat treatment regimes on the strength of UHPC with different compositions. Portland cement concretes were considered as well as concretes with clinker replaced by fly ash or ground granulated blast-furnace slag.

2 Materials and Methods

The concretes were prepared with a Portland cement CEM I 52.5 R-HS/NA, silica fume (grade 983 produced by Wörmann), quartz flour (d_{50} = 14.7 µm), quartz sand (d_{50} = 291.3 µm), fly ash (d_{50} = 15.2 µm) and GGBS (d_{50} = 13.1 µm). A superplasticizer Glenium 51 based on polycarboxylate ether was used. The UHPC mix compositions considered are listed in Table 1.

Table 1: Compositions of UHPC investigated.

Component		***M2Q***	***H75***	***M2F***
Cement	kg/m³	875.6	222.5	571.9
GGBS	kg/m³	-	602.9	-
Fly ash	kg/m³	-	-	487
Silica fume	kg/m³	142.1	144.4	144.1
Quartz flour	kg/m³	217.9	221.4	-
Quartz sand	kg/m³	984.9	1000.9	871.4
Water	kg/m³	186.6	179.5	186.6
Superplast.	kg/m³	16.7	13.3	16.7

The fresh concrete mixes were prepared in an intensive mixer with an inclined drum (EIRICH R02 Vac.) which enabled the production of homogeneous mixes after short mixing times. A vacuum unit attached to the mixer was applied to remove air from the fresh concrete thus keeping the air content at about 0.5 vol.%. An optimized mixing procedure was used which was based on earlier work performed at the cbm in Munich [12]. After mixing, the concrete was poured into cylindrical moulds with a diameter of 50 mm and a height of 50 mm. The specimens were stored at 20°C/95% RH before demoulding. Immediately after demoulding the specimens were subjected to different heat treatment procedures. The compressive strength of the specimens was measured immediately after treatment and the mineralogical composition determined using XRD with the Rietveld refinement. The variation in ultrasonic pulse velocity during heat treatment was monitored *in situ* with the FreshCon system (SMART MOTE). This system was developed especially for these investigations.

3 Heat Treatment at Temperatures ≤ 90 °C

In earlier investigations [9-11] on the optimization of UHPC composition by replacing cement with fly ash or GGBS to reduce the amount of clinker, the specimens were stored for 24 h at 20°C and a relative humidity of at least 95% RH before demoulding and heat treatment in water at 90°C. The specimens were heated to 90°C over one hour, kept at this temperature for 24 h and then cooled down to room temperature within 12 h. This is taken as the reference treatment in this contribution. Companion specimens, not subjected to heat treatment, were stored at 20°C in water after demoulding. Table 2 shows the strengths of the concretes subjected to the reference heat treatment or stored at 20°C.

Table 2: Properties of UHPC. Effect of the reference heat treatment on compressive strength after treatment (age 3 d) and subsequent storage at 20°C/65% RH up to an age of 28 d.

Mix		***M2Q***	***H75***	***M2F***
Temperature of fresh concrete	[°C]	27	25	26
Bulk density	[kg/m³]	2.46	2.40	2.29
Air content	[%]	0.6	0.5	0.6
Spread	[cm]	24	29	25
Begin of setting	[h:min]	5:50	17:00	8:20
End of setting	[h:min]	6:10	19:20	8:40
Compressive strength				
3 d	[MPa]	136.3	47.5	103.6
28 d	[MPa]	216.1	144.3	181.6
3 d, heat treated	[MPa]	232.5	164.5	199.9
28 d, heat treated	[MPa]	232.8	163.2	199.1

Effect of Initial Storage Time

It is well known that the mechanical properties of UHPC can be affected significantly by the length of the initial storage period prior to heat treatment. Efficient production of prefabricated UHPC components in practice requires the optimization of the mechanical properties of UHPC by using a heat treatment process which is as short as possible thereby saving energy and increasing turnover. For this purpose, the mechanical properties of the UHPC mixes were investigated for the initial storage period shortened from 24 h to the time of setting or lengthened to ages of 2, 3 and 5 days.

In the case of the shortened initial storage period, the specimens were demoulded immediately after setting. Thus the heat treatment of M2Q and M2F commenced at ages of 8 and 9 h, respectively. Owing to the high GGBS content of the H75 mix setting and hardening were slow. It was not possible to demould this mix before 1 d.

By monitoring the ultrasonic pulse velocity *in situ* during heat treatment with the FreshCon system, it was possible to investigate the effect of the shortened initial storage on the hardening process of mixes M2Q and M2F. The ultrasonic pulse velocity is related to the dynamic Young's modulus of concrete. Shortening the initial storage period resulted in a faster increase in pulse velocity which reached a maximum after 4 h and 6 h for mixes M2Q and M2F, respectively, thereafter changing little. Unfortunately, concrete strength cannot be determined from ultrasonic pulse velocity alone. Lower strengths were measured immediately after heat treatment of specimens with shortened initial storage, Figure 2, although the corresponding ultrasonic velocities were almost the same, Figure 1. Hydration continued during the storage of the specimens at 20°C and 65% RH after heat treatment. This resulted in strength gains of 6.6 and 14.7% for the mixes M2Q (8h-HT) and M2F (9h-HT), respectively. At an age of 28 d, concrete M2F (9h-HT) even reached a higher strength than obtained with the reference heat treatment (1d-HT). The XRD investigations confirm that hydration also continues during storage after heat treatment. The amount of C-S-H phases (amorphous contribution) increases while the amount of silicate phases from the clinker decreases, Figure 3.

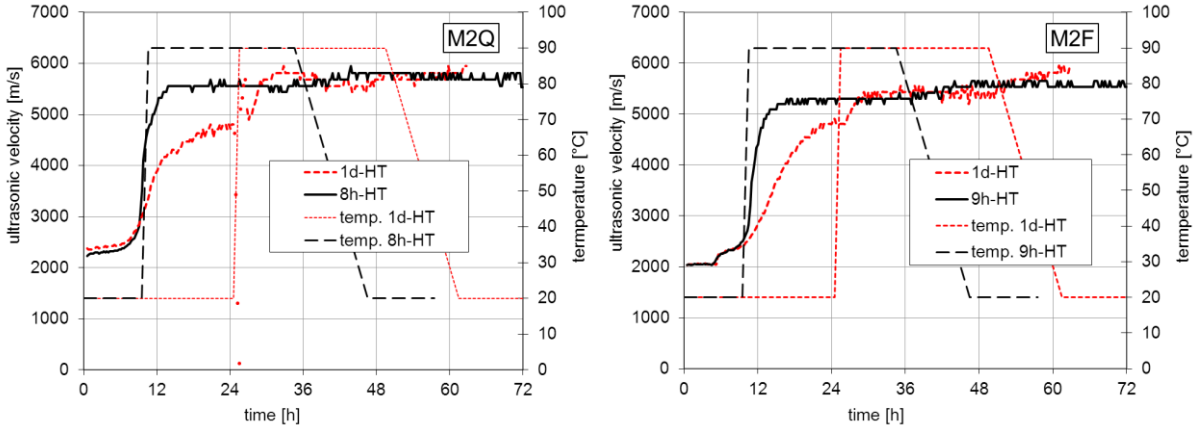

Figure 1: Ultrasonic pulse velocity und storage temperature for the UHPC mix M2Q (left) and M2F (right).

Prolonging the initial storage period for the mixes M2Q and M2F did not produce an increase in strength immediately after heat treatment, Figure 2. Apart from concrete M2Q with an initial storage period of 2 d, the strengths increased slightly during subsequent storage up to an age of 28 d. In the case of the mix H75 with GGBS, the strength of the concrete immediately after heat treatment increased with the duration of initial storage up to 3 d. A further slight increase in strength up to an age of 28 d was observed. Prolonging the initial storage period to 5 d produced no significant additional strength increase.

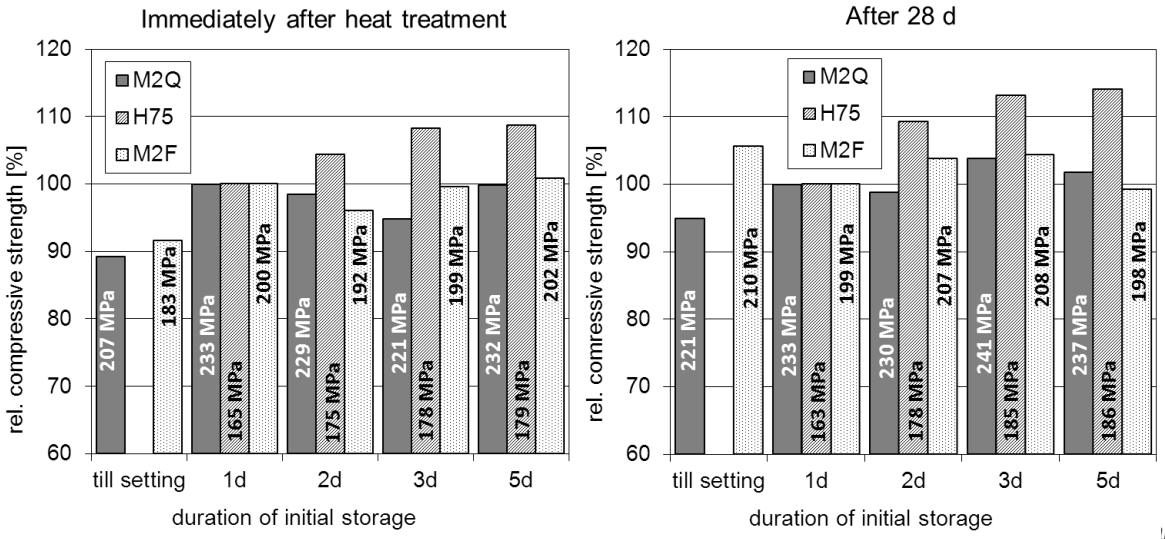

an initial storage period of 1 d. The compressive strengths are shown in the columns. Left, strengths immediately after heat treatment, right, at an age of 28 d.

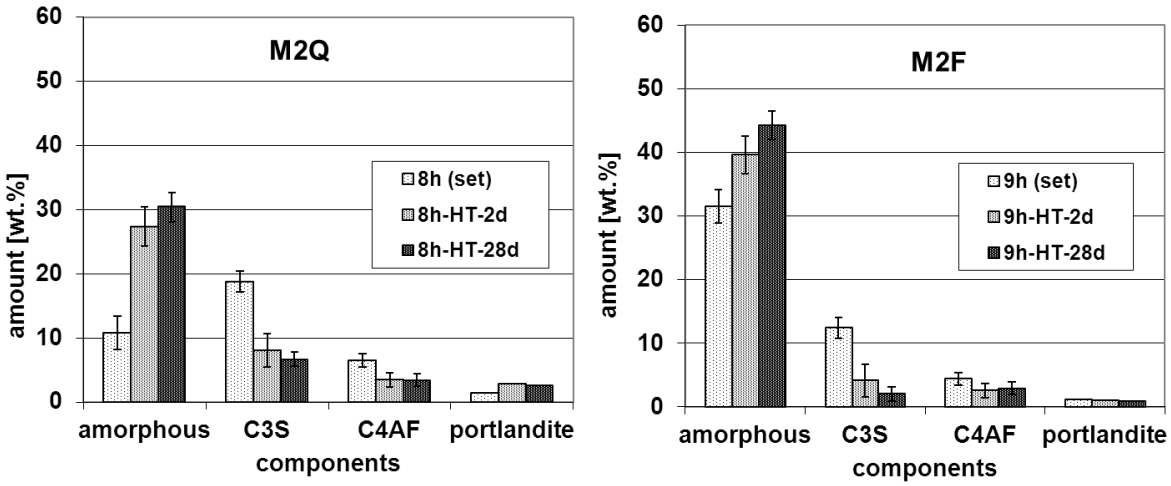

Figure 3: Mineralogical composition of the binder for UHPC concretes M2Q and M2F after setting and at ages of 2 and 28 d after heat treatment.

Effect of Heat Treatment Duration

In order to investigate the effect of heat treatment duration, specimens were stored initially for 24 h at 20°C before heat treatment for periods of 8, 12, 24 (reference) and 48 h at 90°C. In an addition tests with the mixes M2Q and M2F, the heat treatment was performed directly after setting, i.e. after 8 and 9 h, respectively.

The short 8 h heat treatment of the Portland cement mix M2Q led to somewhat lower strengths of around 220 MPa immediately after heat treatment, but a 28 d strength corresponding to the reference concrete M2Q-24h, Figure 4. The longer 48 h treatment did not increase strength. It is possible that recrystallization of the hydrate phases occurs during long hydration periods at high temperatures which result in loss in strength [13]. Variation of treatment time affected the strength of the GGBS mix H75 to a great extent. The strength immediately after heat treatment increased with the duration of heat treatment. Moreover, the strength continued to increase during subsequent storage up to an age of 28 d. The strength of the fly ash concrete M2F also increased with the duration of heat treatment. This behaviour is explained by the slow hydration of GGBS and the slow pozzolanic reaction of fly ash.

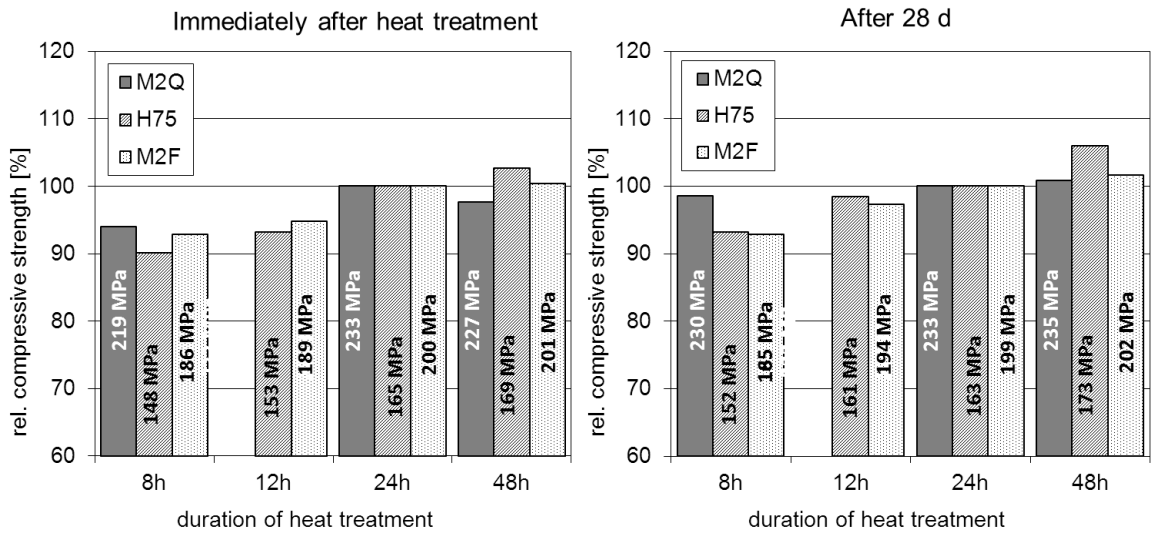

Figure 4: Effect of duration of heat treatment on compressive strength with respect to the values for heat treatment of 1 d for UHPC with different compositions. The compressive strengths are shown in the columns. Left, strengths immediately after heat treatment, right, at an age of 28 d.

Shortening the duration of heat treatment from 24 to 8 h had little effect on the strength of M2Q specimens which were heat treated immediately after setting, Figure 5. However, much lower strengths of UHPC containing fly ash M2F were obtained when these specimens were heat treated after setting. Afterwards the strengths increased considerably, after 28 d almost reaching those of the specimens subjected to the reference treatment.

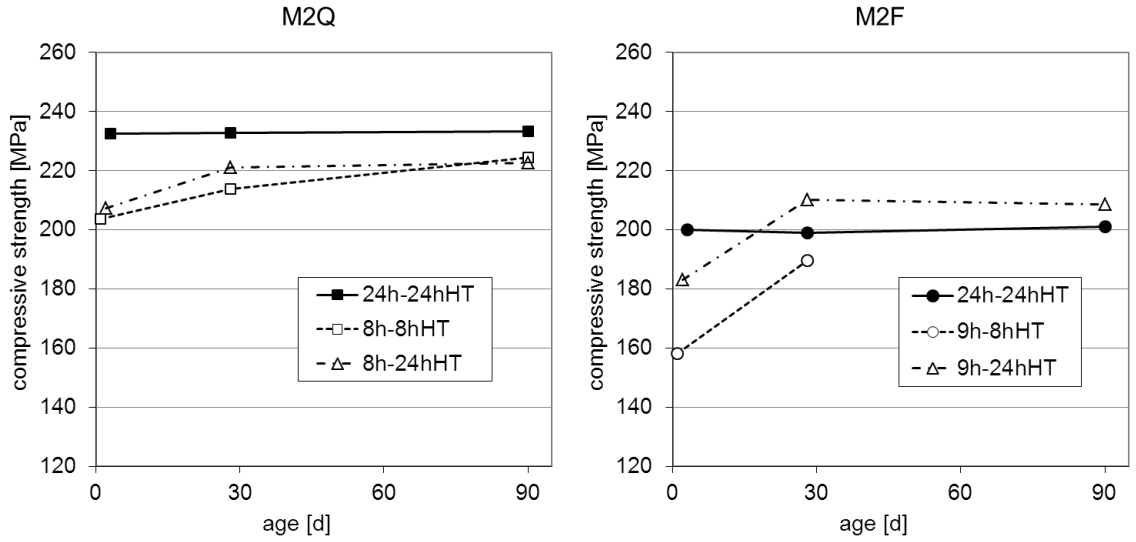

Figure 5: Effect of duration of initial storage and heat treatment on compressive strength of UHPC M2Q and M2F.

Effect of Heat Treatment Temperature

The effect of lower heat treatment temperatures of 75 and 50°C on compressive strength was investigated taking heat treatment at 90°C as a reference. As expected, lower treatment temperatures led to lower strengths. However, lower temperatures resulted in a much larger degree of hardening during storage after heat treatment. At an age of 90 d the specimens treated at 75°C almost achieved the strength of the reference specimen, Figure 6. The large increase in strength up to an age of 28 d after heat treatment at 50°C is explained by the

ongoing hydration of the calcium silicates and the reaction between portlandite and silica fume. Less water is bound during treatment at lower temperatures. Consequently, sufficient pore water is available to enable the reaction of silica fume with portlandite and the hydration of the clinker minerals.

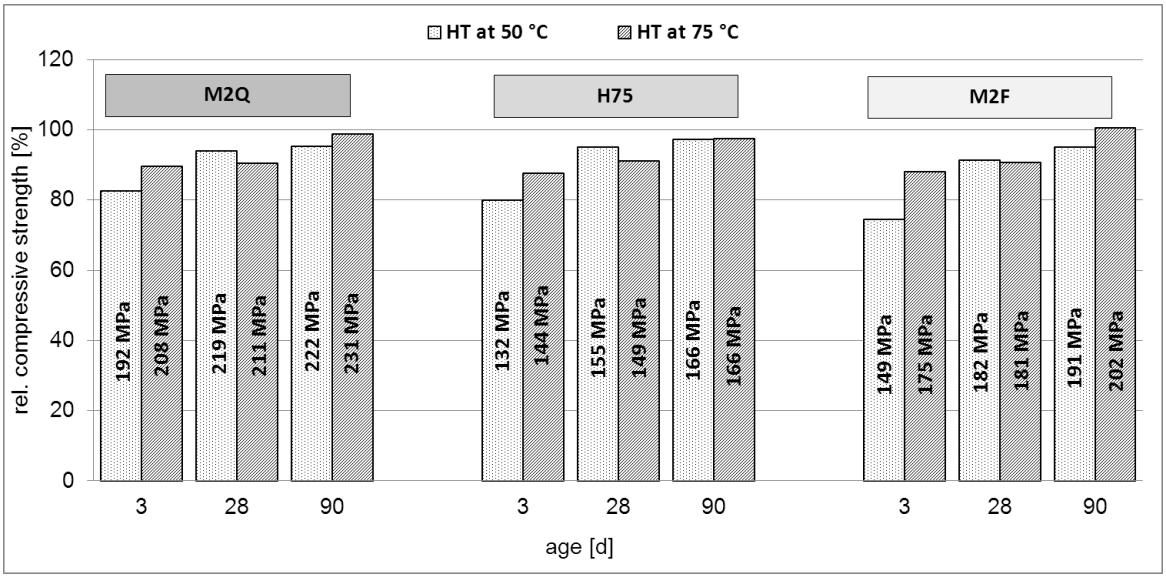

Figure 6: Effect of heat treatment temperature on compressive strength with respect to the values for heat treatment at 90°C for UHPC with different compositions. The compressive strengths are shown in the columns.

4 Heat Treatment at Temperatures > 90 °C

Specimens were heat treated at 150°C either exposed to air in an oven or exposed to air saturated with water vapour at 5 bars in an autoclave. At an age of 24 h the specimens were heated at 35 K/h to a temperature of 150°C which was then kept constant for 8 h. The specimens were then cooled down to room temperature within 11 h. After heat treatment, the specimens were stored at 20°C and 65% RH until testing. As opposed to treatment in the autoclave in which the mass of the specimens increased, heat treatment in air led to loss of moisture from the specimens.

The strength of the concrete H75 prepared using GGBS and heat treated in air reached the level obtained by the reference heat treatment whereas the strengths of the concretes M2Q and M2F fell below it, Figure 7. During subsequent storage in standard climate 20°C / 65% RH, the mass of all specimens increased due to the uptake of water vapour from the atmosphere; at the same time the strength decreased. This effect has been observed previously for specimens treated in air at 90°C [9] and is probably due to the redistribution of water in the hardened cement paste matrix during the uptake of moisture. Immediately after heat treatment the strengths of the autoclaved specimens M2Q and H75 were lower than those of the specimens subjected to the reference treatment, but increased during subsequent storage exceeding after 28 d the strengths of the reference specimens, Figure 7. Autoclaving had a particularly positive effect on specimens made with fly ash M2F.

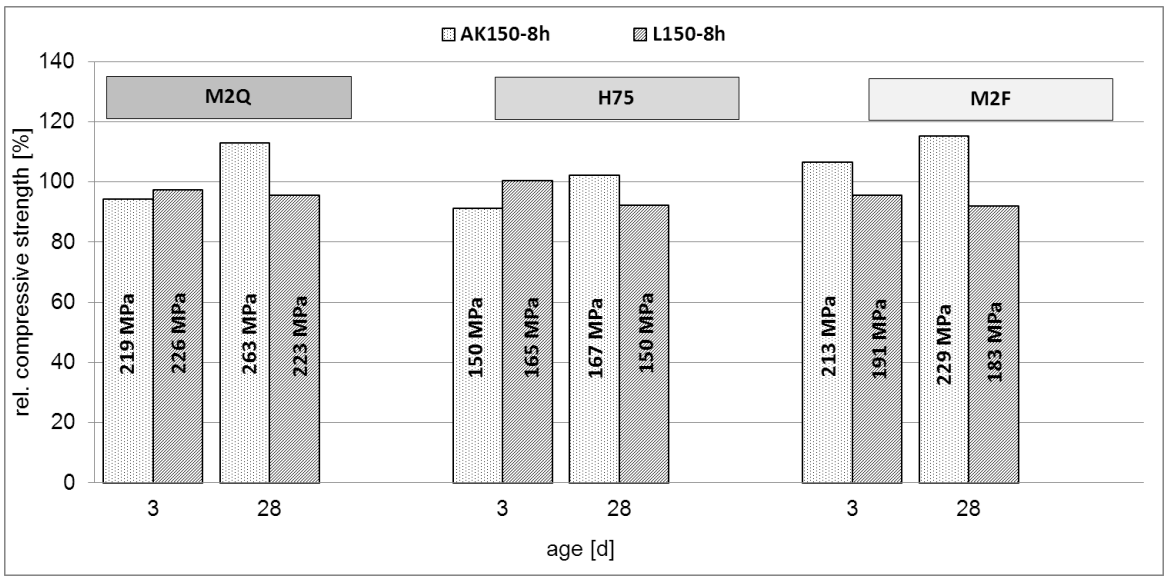

Figure 7: Effect of heat treatment type at 150°C (AK150-8h – treatment in autoclave; L150-8h – treatment in air) on compressive strength with respect to the values for heat treatment at 90°C for UHPC with different compositions. The compressive strengths are shown in the columns.

The X-ray diffraction investigations revealed that the clinker phases in the specimens M2Q and M2F continued to react with water forming X-ray amorphous phases and portlandite during treatment in the autoclave. The silica fume reacted with portlandite to form additional C-S-H phases. No appreciable reaction of the quartz flour was observed, most likely, owing to the presence of silica fume which reacts readily with portlandite. Although expected for these treatment conditions, crystalline hydrogarnet or tobermorite were not detected. During storage after heat treatment the hydration of the calcium silicates in the clinker phases as well as the pozzolanic reaction of the silica fume both continued resulting in considerable further hardening of the concrete specimens.

In addition, specimens were treated in air at 250°C. This type of treatment led to a considerable increase in strength immediately after heat treatment, but loss of strength during subsequent storage of the specimens. The results of these investigations will be presented elsewhere.

5 Conclusions

The present results show that an optimum heat treatment for UHPC depends on concrete composition. With an initial storage period (8 h) shortened to the setting time and a shortened heat treatment (8 h at 90°C) very high strengths >200 MPa may also be obtained for Portland cement concrete mixes M2Q after 30 h. Heat treatment for 8 h at 150°C in an autoclave enables a gain in strength up to 260 MPa at an age of 28 d. The fly ash concretes M2F also reached their highest strengths of 230 MPa after autoclaving. The strengths of concretes immediately after the shortened heat treatment are at 160 MPa relatively low, but nevertheless the concretes harden during subsequent storage at 20°C/65% RH to reach 190 MPa at an age of 28 d. To obtain higher strengths, the mix H75 containing GGBS requires a longer initial storage period (3 d) or a longer heat treatment (48 h) at 90°C.

6 Acknowledgement

The authors thank the German Research Foundation (DFG) for financial support within the priority programme SPP 1182.

References

[1] Philipp, U., Dehn, F., Schreiter, P.: Temperatureinfluss auf die Phasen- und Gefügebildung in UHFB. In: Ultrahochfester Beton. Innovationen im Bauwesen, Beiträge aus Praxis und Wissenschaft, Bauwerk, 2003, S. 79-88.

[2] Zanni, H., Cheyrezy, M., Maret, V., Philippot, S., Nieto, P.: Investigation of hydration and pozzolanic reaction in reactive powder concrete (RPC) using 29Si NMR. Cem. Concr. Res., Vol. 26, 1996, pp. 93-100.

[3] Heinz, D., Ludwig, H.-M.: Heat treatment and the risk of DEF delayed ettringite formation in UHPC. In: Proc. of Int. Symp. on Ultra High Performance Concrete, Kassel, September 13-15, , 2004, pp. 717-730.

[4] Reda, M., Shrive, N. G, Gillott, J. E.: Microstructural investigations of innovative UHPC. Cem. Concr. Res. Vol. 25, 1999, pp. 323 – 329.

[5] Cwirzen, A.: The effect of the heat treatment regime on the properties of RPC. Advances in Cement Research, Vol. 19, 2007, pp. 25-33.

[6] Ahlborn, T. M., Misson, D. L., Peuse, E. J., Gilbertson, c. G.: Durability and strength characterization of ultra-high performance concrete under variable curing regimes. Proceedings of Second International Symposium on Ultra High Performance Concrete, Kassel, March 05-07, 2008, pp. 197-204.

[7] Schachinger, I., Hilbig, H., Stengel, T. Effect of curing temperature at an early age on long-term strength development of UHPC. Proceedings of Second International Symposium on Ultra High Performance Concrete, Kassel, March 05-07, 2008, pp. 205 – 212.

[8] Müller, U., Meng, B., Kühne, H.-C., Nemecek, J., Fontana, P.: Micro texture and mechanical properties of heat treated and autoclaved ultra high performance concrete (UHPC). Proceedings of Second International Symposium on Ultra High Performance Concrete, Kassel, March 05-07, 2008, pp. 213 – 220.

[9] Gerlicher, T., Heinz, D., Urbonas, L.: Effect of ground blast furnace slag on the properties of fresh and hardened UHPC. Proceedings of Second International Symposium on Ultra High Performance Concrete, Kassel, March 05-07, 2008, pp. 367 – 371.

[10] Gerlicher, T., Hilbig, H., Urbonas, L., Heinz, D.: Effect of silica fume replacement by fine fly ash on the properties of fresh and hardened UHPC. XIII International Congress on the Chemistry of Cement, Madrid, 2011, p. 47.

[11] Gerlicher, T., Leonhardt, S., Heinz, D., Urbonas L.: Einfluss des Steinkohlenflugascheeinsatzes auf die Frisch- und Festbetoneigenschaften von ultrahochfestem Beton. Ibausil, 17. Internationale Baustofftagung, 23.-26. September 2009, Weimar, S. 1-1091 – 1-1098.

[12] Schachinger, I., Schubert, J,. Mazanec, O.: Effect of mixing and placement methods on fresh and hardened ultra high performance concrete (UHPC) Proceedings of International Symposium on Ultra High Performance Concrete, Kassel, September 13-15, 2004, pp. 575-586.

[13] Altner, W., Reichel, W.: Betonschnellhärtung. VEB Verlag für Bauwesen, Berlin, 1982.

Modeling Cement Hydration Kinetics Using the Equivalent Age Concept

Xueyu Pang[1], Dale P. Bentz[2], Christian Meyer[1]

1: Dept. of Civil Engineering and Engineering Mechanics, Columbia University, USA
2: Engineering Laboratory, National Institute of Standards and Technology, USA

In this study the hydration kinetics of four different types of cements during early ages were investigated by both chemical shrinkage and isothermal calorimetry tests. Chemical shrinkage tests were performed at both different temperatures and pressures while isothermal calorimetry tests were conducted only at different temperatures. The hydration kinetics curves at different curing conditions converged reasonably well if properly transformed with a set of scaling factors. Therefore, the experimental hydration kinetics curve at one curing condition can be used to predict that of another curing condition using a single scale factor. The scale factor is similar to the coefficient used to compute the equivalent age of a specified curing condition when applying the maturity method to estimate concrete strength. Its dependence on curing temperature and curing pressure can be modeled by the activation energy and the activation volume of the cement, respectively.

Keywords: hydration kinetics, temperature, pressure, chemical shrinkage, heat evolution, oil well cement

1 Introduction

Cement hydration is a complex chemical process that involves a number of different reactions. Although many detailed features of the process are still not clearly understood today, the general hydration kinetics can be approximately represented by the overall degree of hydration as a function of time. This overall degree of cement hydration, defined as the total weight fraction of cement reacted, is directly related to many different physical and mechanical properties of cement-based materials, such as viscosity [1], setting time [2-4], autogenous shrinkage [5], compressive strength [6, 7], tensile strength [8], and modulus of elasticity [5, 8]. It is arguably the most important parameter that can be used to model the time-dependent characteristics of cement-based materials [9]. Since Portland cement mainly consists of four clinker phases, its overall degree of hydration can be written as [10]:

$$\alpha(t) = p_{C_3S}\alpha_{C_3S}(t) + p_{C_2S}\alpha_{C_2S}(t) + p_{C_3A}\alpha_{C_3A}(t) + p_{C_4AF}\alpha_{C_4AF}(t) \quad (1)$$

where p_i is the original weight fraction of *Phase i* in the anhydrous cement and $\alpha_i(t)$ is the degree of hydration of *Phase i* at time *t*. Direct determination of $\alpha_i(t)$ can be made by using quantitative X-ray diffraction analysis [10, 11], but the method is rarely used in practice due to complex test procedures and high equipment cost.

Some properties of a hydrating cement paste, such as the cumulative heat evolution, the total chemical shrinkage, and the non-evaporable water content, have been shown to have approximately linear relationships with each other and the overall degree of hydration [4, 10, 12, 13]. These properties therefore provide indirect ways of determining $\alpha(t)$. As a matter of fact, α is more commonly determined by these indirect methods due to their simplicity. The following equation may be used to convert experimental results to the degree of hydration of cement:

$$\alpha(t) = \frac{H(t)}{H^0} = \frac{CS(t)}{CS^0} = \frac{w_n(t)}{w_n^0} \quad (2)$$

where $H(t)$ and H^0 are the amounts of cumulative heat evolution at time *t* and at complete hydration, respectively (typically in J/g cement); $CS(t)$ and CS^0 are the amounts of chemical shrinkage at time *t* and at complete hydration, respectively (typically in mL/g cement); while $w_n(t)$ and w_n^0 are the non-evaporable water contents at time *t* and at complete hydration,

respectively (typically in g/g cement). It should be pointed out that the hydration reactions of different phases in Portland cement have different contributions toward the overall parameters (i.e. $H(t)$, $CS(t)$, and $w_n(t)$). Since these reactions progress at different rates (that also vary with time), the indirect methods only give a gross approximation to the total hydration kinetics.

Among the different methods of evaluating cement hydration kinetics, heat evolution measured by isothermal calorimetry tests used to be the only ones that give continuous test results (i.e. hydration kinetics curves). In recent years, several new chemical shrinkage test methods have been developed, which also give continuous test results [14-17]. Hydration kinetics curves are most commonly represented by two types of curves: total degree of hydration vs. time (defined here as the integral curve) and rate of hydration vs. time (defined here as the derivative curve). According to Eq. (2), estimating the parameters at the complete hydration condition (i.e. H^0 and CS^0) is essential for converting experimental data to degree of hydration. The cumulative heat evolution of cement at complete hydration mainly depends on the cement compound composition and may be estimated in units of J/g cement by the following equation [17],

$$H^0 = 510\,p_{C_3S} + 247\,p_{C_2S} + 1356\,p_{C_3A} + 427\,p_{C_4AF} + 239\,p_{C_2F} \quad (3)$$

The total chemical shrinkage at complete hydration is more difficult to estimate because it depends on both cement composition and curing condition. By studying the correlations between chemical shrinkage and non-evaporable water content, the following equations were proposed to estimate the total chemical shrinkage at complete hydration [17]:

$$CS^0 = w_n^0 \left(v_w - v_n \right) \quad (4)$$

$$w_n^0 = 0.257\,p_{C_3S} + 0.217\,p_{C_2S} + 0.56\,p_{C_3A} + 0.202\,p_{C_4AF} + 0.113\,p_{C_2F} \quad (5)$$

where v_w and v_n are the specific volumes (cm^3/g) of capillary water and non-evaporable water in cement pastes, respectively, both of which depend on curing condition. For the ambient condition (25 °C, 0.101 MPa), it was estimated that v_w = 0.988 cm^3/g and v_n = 0.752 cm^3/g.

2 Experimental materials and methods

Four different classes of oil well cements (American Petroleum Institute (API) Specification 10A [18]), namely Class A, C, G, and H cements, were used here to study hydration kinetics. The main potential compound compositions of the different types of cement (derived from the oxide analysis test results using the Bogue calculation method) are listed in Table 1. The specific surface areas of Class A, C, G, and H cements calculated from the PSD data (assuming spherical cement particles with a density of 3150 m^3/kg) were 356.2 m^2/kg, 564.9 m^2/kg, 326.5 m^2/kg, and 393.9 m^2/kg, respectively. It is obvious that Class C cement was ground much finer than the other classes to achieve a higher specific surface area. Neat cement slurries were prepared with standard water-to-cement (*w/c*) ratios for each class of cement, as defined in API Specification 10A [18]. More detailed information about the properties of these cements as well as cement slurry preparation procedures is given in [17]. Note that only one type (premium) of Class H cement is used in this study.

Table 1: Estimated main compound compositions of the different types of cements (mass %).

Cement	C_3S	C_2S	C_3A	C_4AF	C_2F	$CaSO_4$	Free Lime
A	61.66	12.01	8.36	9.41	0	4.67	1.43
C	72.24	5.21	2.16	11.82	0	4.74	0.23
G	62.62	15.90	4.80	10.87	0	3.84	0.21
H	47.91	27.46	0	16.17	1.97	4.21	0.30

Two main test series will be discussed. In test series I, hydration kinetics of the cements is measured by isothermal calorimetry tests using an isothermal calorimeter according to standard test procedures [19]. Tests were conducted at atmospheric pressure and three different curing temperatures. Table 2 shows the test scheme for this test series. The temperatures of isothermal calorimetry tests can be controlled precisely due to the small sample size (4 ~ 5 g). For this technique, the average absolute difference between replicate specimens of cement paste is 2.4×10^{-5} W/g (cement), with a maximum absolute difference of 0.00011 W/g (cement), for measurements conducted between 1 h and 7 d after mixing [20].

Table 2: Isothermal calorimetry tests (test series I, test age = 168 hours).

Curing Temperature (°C)		25	40	60
Cement	w/c	-	-	-
A	0.46	A-25	A-40	A-60
C	0.56	C-25	C-40	C-60
G	0.44	G-25	G-40	G-60
H	0.38	H-25	H-40	H-60

In test series II, hydration kinetics of the cements is measured by chemical shrinkage tests using an innovative test apparatus consisting of pressure cells and syringe pumps. Detailed descriptions of the test apparatus and test procedures are given in [17]. Chemical shrinkage tests were performed under both different curing temperatures and pressures. The test scheme is shown in Table 3. The advantages of the new test apparatus are that it allows easy application of hydrostatic pressure and that it appears to eliminate the dependence of test results on specimen thickness. The main shortcoming of the new apparatus is the lack of precise temperature control. Test data oscillation seems to be dramatically increased when heat controllers are used to control the temperature of the specimens, which usually prevents reliable derivative curves to be directly obtained from experimental data. As shown in Table 3, a majority of the tests in this test series were conducted at lab temperatures without using the heat controllers such that derivative curves could be obtained. Due to lab temperature fluctuations, it is very difficult to produce exact replicate specimens at ambient temperatures. The lab temperatures at the beginning of each test were recorded for later calibrations (temperature fluctuations during the period of a single test were typically within ±1.1 °C). Uncertainties in test results caused by factors other than temperature fluctuations are estimated to be less than 3% at the end of 3 days. More detailed uncertainty analysis of this experimental technique is given in [17].

Table 3: Chemical shrinkage tests (test series II, test age = 72 hours).

Curing Temperature (°C)		Ambient[a]				40.6[b]	60[b]
Curing Pressure (MPa)		0.69	17.2	34.5	51.7	0.69	0.69
Cement	w/c	-	-	-	-	-	-
A	0.46	A-1	A-2	A-3	A-4	A-5	A-6
C	0.56	C-1	C-2	C-3	C-4	C-5	C-6
G	0.44	G-1	G-2	G-3	G-4	G-5	G-6
H	0.38	H-1	H-2	H-3	H-4	H-5	H-6

[a]: Lab temperature (~24 °C±2.8 °C).

[b]: Estimated cement specimen temperature.

3 Model formulation

In ASTM standard 1074 [7], maturity is defined as the extent of the development of a property of a cementitious mixture and equivalent age is defined as the number of days or hours at a specified temperature required to produce a maturity equal to the maturity achieved by a curing period at temperatures different from the specified temperature. The maturity function used to compute the equivalent age at a specified (reference) temperature is as follows [7],

$$t_r = \sum \exp\left(-\frac{E_a}{R}\left(\frac{1}{T}-\frac{1}{T_r}\right)\right)\cdot \Delta t \tag{6}$$

where t_r (h) is the equivalent (reference) age at the reference temperature T_r (K); E_a (J/mol) is the activation energy of the cement; R is the gas constant; and T (K) is the average temperature during time interval Δt (h). For isothermal curing conditions (T is constant over time), Eq. (6) becomes,

$$t_r = \exp\left(\frac{E_a}{R}\left(\frac{1}{T_r}-\frac{1}{T}\right)\right)\cdot t = C\cdot t \tag{7}$$

where t is the actual age at temperature T; C is a scale factor, which is a function of T_r and T. Eq. (7) means that the maturity achieved at age t at curing temperature T is the same as that achieved at age Ct at curing temperature T_r. For the purpose of modeling cement hydration kinetics, maturity can be interpreted here as the degree of hydration of cement. Therefore, if the hydration kinetics at the reference temperature T_r is represented by the following unknown functions

$$\text{Integral curve}:\ \alpha = f(t),\ \text{Derivative curve}:\ d\alpha/dt = f'(t) \tag{8}$$

then the hydration kinetics at temperature T can be represented by

$$\text{Integral curve}:\ \alpha = f(Ct),\ \text{Derivative curve}:\ d\alpha/dt = C\cdot f'(Ct) \tag{9}$$

The maturity function (Eq. (6)) is developed based on the Arrhenius equation, which is one of the basic chemical kinetics laws describing the temperature dependence of the reaction rate constant. Therefore, the results shown in Eqs. (8) and (9) are the same as those derived from chemical kinetics theories [17]. When the pressure dependence of the reaction rate constant is also taken into account, the scale factor should be written as [17],

$$C = \exp\left(\frac{E_a}{R}\left(\frac{1}{T_r}-\frac{1}{T}\right)+\frac{\Delta V^{\ddagger}}{R}\left(\frac{P_r}{T}-\frac{P}{T}\right)\right) \tag{10}$$

where $\Delta V^{\ddagger}$ is the activation volume of the cement; P is the actual curing pressure; and P_r is the specified (reference) curing pressure.

4 Test results and discussion

To convert heat evolution and chemical shrinkage test results to degree of hydration data, the conversion factors (i.e. H^0 and CS^0) for different cements must be estimated. H^0 can be obtained by substituting the cement composition data listed in Table 1 into Eq. (3). The total heat evolution at complete hydration (H^0) of the Class A, C, G, and H cements used in this study are determined to be 497.7 J/g, 461.1 J/g, 470.1 J/g, and 385.9 J/g, respectively. For ambient curing temperature (25 °C), CS^0 can be estimated by substituting the cement composition data into Eqs. (4) and (5). The variations of v_w and v_n with pressure can be estimated by assuming that capillary water has the same bulk modulus as fresh water and that non-evaporable water has a bulk modulus of 10.6 GPa [17]. The variation of v_n with curing

temperature is still uncertain, making it difficult to estimate CS^0 at different temperatures. However, within the range studied here, CS^0 may be assumed to decrease approximately linearly with increasing temperature. The linear reduction rate varies slightly with cement composition and is estimated to be 0.63 %, 0.66 %, 0.59 %, and 0.75 % per °C for the Class A, C, G, and H cements, respectively [17]. The calculated values of CS^0 at different curing conditions are listed in Table 4. Figure 1 and Figure 2 show some representative hydration kinetics test results measured by isothermal calorimetry and chemical shrinkage tests, respectively. It is obvious that hydration rate increases with both increasing curing temperature and increasing curing pressure, especially at early ages. Figure 2 also suggests that a relatively large pressure increase is comparable to only a small temperature increase, in terms of its effect on the rate of hydration. For tests conducted at ambient temperatures (Table 3), hydration kinetics test results reflect both the effect of curing pressure and temperature since the lab temperatures of these tests are not exactly the same.

Table 4: Total chemical shrinkage at complete hydration (mL/100g).

Temperature (°C)	25	25	25	25	25	40.6	60
Relative Pressure (Mpa)	0	0.69	17.2	34.5	51.7	0.69	0.69
A	5.914	5.906	5.756	5.606	5.468	5.326	4.604
C	5.505	5.498	5.358	5.218	5.090	4.932	4.228
G	5.771	5.763	5.617	5.470	5.335	5.233	4.573
H	5.140	5.133	5.003	4.872	4.752	4.533	3.786

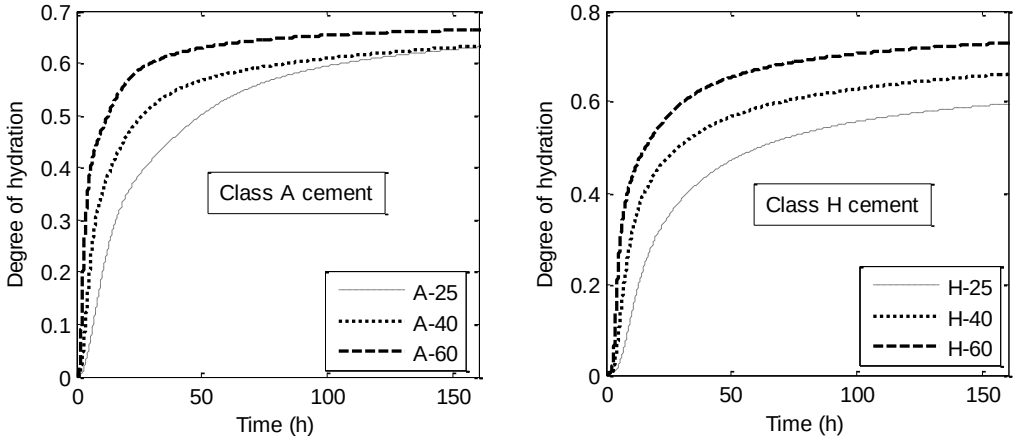

Figure 1: Representative hydration kinetics test results measured by isothermal calorimetry.

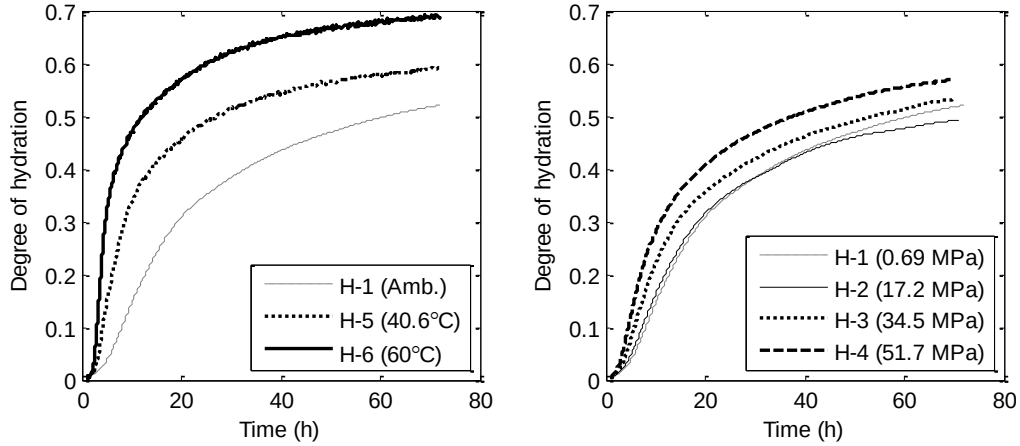

Figure 2: Representative hydration kinetics test results measured by chemical shrinkage.

Theoretically, based on the analysis in Section 3, the hydration kinetics curves at different curing conditions should converge when they are normalized by plotting the degree of hydration as a function of the equivalent age using the same reference curing condition. Therefore, the scale factor *C* associated with a particular curing condition may be estimated by trial and error such that its normalized hydration kinetics curve has the best agreement with the reference curve. Due to the fact that Portland cement is essentially a mixture of several different compounds, which hydrate at different rates and have different sensitivities to curing temperatures and pressures, the normalized hydration kinetics curves for different curing conditions usually do not converge perfectly. In addition, it is often necessary to slightly offset the curve to achieve the best agreement. In other words, a more accurate representation of Eq. (9) is as follows,

$$\text{Integral curve: } \alpha = f(C(t-t_0)),\ \text{Derivative curve: } d\alpha/dt = C\cdot f'(C(t-t_0)) \qquad (11)$$

where t_0 is the offset time. Such offset is primarily due to the variation of the induction period between different tests, which are affected by many different factors and hence very difficult to model. In this study, the induction period (and the obtained offset value) is also affected by experimental artifacts because cement pastes are not mixed in-situ and it takes time for their temperatures to reach equilibirum. Therefore, for practical purposes, the small offset may be accepted as experimental errors and Eq. (9) should be used to predict hydration kinetics. Table 5 shows the scale factors and offset time obtained for isothermal calorimetry tests. The activation energies of different cements can be calculated using linear regression analyses according to Eq. (10). The values obtained for Class A, C, G, and H cements are 40.3 kJ/mol, 36.9 kJ/mol, 40.1 kJ/mol, and 35.4 kJ/mol, respectively. Table 6 shows the scale factors and offset time obtained for chemical shrinkage tests. The correspondingly determined activation energies of Class A, C, G, and H cements are 43.2 kJ/mol, 40.1 kJ/mol, 40.1 kJ/mol, and 44.1 kJ/mol, respectively. These values are less accurate than those calculated from isothermal calorimetry tests due to the relatively poor temperature control scheme of chemical shrinkage tests. It appears that offset is not necessary for tests conducted at different curing pressures (i.e. t_0 = 0). As the ambient (lab) temperatures of the tests conducted at different pressures are not exactly the same, it is important to separate the temperature influences when calculating the activation volumes of the cements. After calibrating for the ambient temperature fluctuations (Table 6) according to Eq. (10), the activation volumes of Class A, C, G, and H cements are estimated to be -20.8 cm^3/mol, -27.5 cm^3/mol, -20.1 cm^3/mol, and -24.5 cm^3/mol, respectively.

Table 5: Best-fit scale factors (C) and offset time (t_0) for test series I (: reference tests).*

Test	**A-25***	**A-40**	**A-60**	**C-25***	**C-40**	**C-60**	**G-25***	**G-40**	**G-60**	**H-25***	**H-40**	**H-60**
t_0 (h)	0	0.4	0.8	0	0.75	1	0	0.9	1	0	1	1.5
C	1	2.1	5.5	1	2.18	4.8	1	2.3	5.5	1	2.15	4.5

Table 6: Ambient temperatures, best-fit scale factors (C) and offset time (t_0) for test series II (: reference tests).*

Test	**A-1***	**A-2**	**A-3**	**A-4**	**A-5**	**A-6**	**C-1***	**C-2**	**C-3**	**C-4**	**C-5**	**C-6**
$T_{amb.}$ (°C)	24.4	22.8	25	24.4	-	-	26.9	27.5	25	25.6	-	-
t_0 (h)	0	0	0	0	0.7	1	0	0	0	0	0.6	1.2
C	1	1	1.4	1.5	2.7	6.5	1	1.18	1.38	1.6	2.2	5
Test	**G-1***	**G-2**	**G-3**	**G-4**	**G-5**	**G-6**	**H-1***	**H-2**	**H-3**	**H-4**	**H-5**	**H-6**
$T_{amb.}$ (°C)	25	24.7	23.1	25	-	-	25.6	22.2	23.9	26.1	-	-
t_0 (h)	0	0	0	0	1	1	0	0	0	0	1	1.7
C	1	1.2	1.18	1.55	2.4	5.5	1	1.02	1.3	1.7	2.5	6.3

As shown in Figures 3, 4, and 5, the normalized hydration kinetics curves at different curing temperatures and pressures converge reasonably well for each type of cement (after offset). The error associated with the offset (which ranges from 0 to 1.7 hours) is only signifincant during early stages of hydration and becomes negligible when long-term properties are concerned. Test results of different pressures (Figure 5) seem to have better convergences than those of different temperatures (Figures 3 and 4), probably because curing pressure has relatively small effect on hydration kinetics compared to curing temperature for the range studied here. The convergences of the curves suggest that the hydration kinetics curves at various curing conditions can be approximately predicted from that of a reference curing condition using a simple scale factor of *C*, which can be estimated from Eq. (10). Examples of such predictions are given in [17].

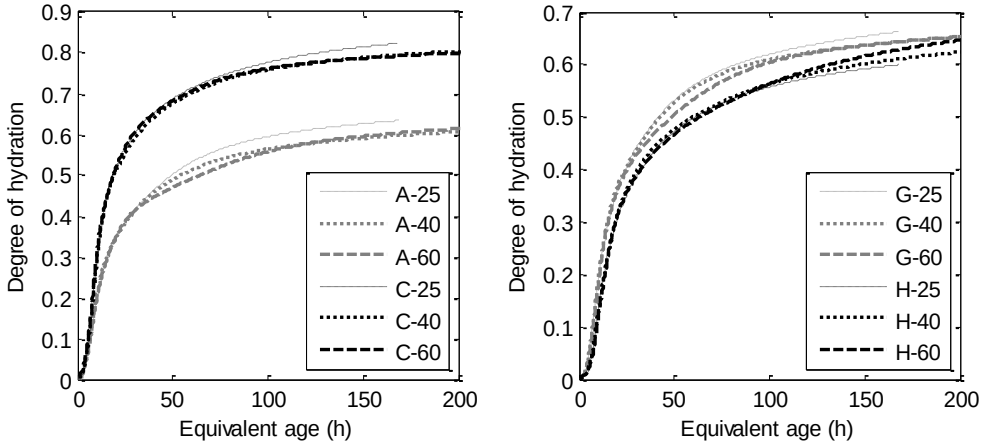

Figure 3: Normalized hydration kinetics curves of different tests (test series I).

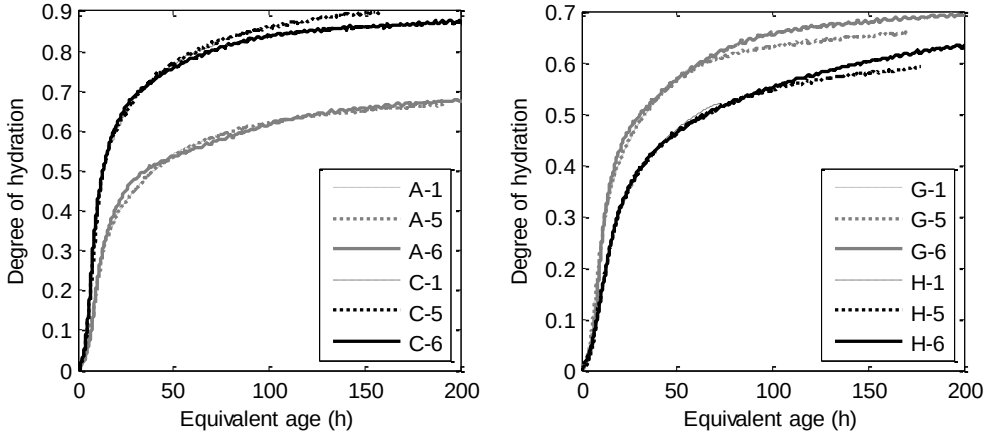

Figure 4: Normalized hydration kinetics curves of different tests (test series II).

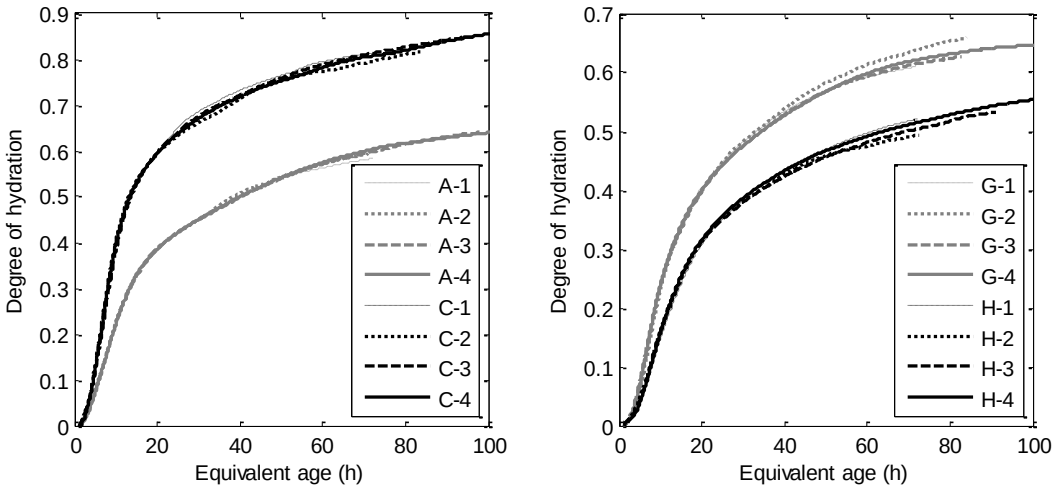

Figure 5: Normalized hydration kinetics curves of different tests (test series II).

5 Conclusions

A simple mathematical model is proposed in this study to model the effect of curing temperature and pressure on cement hydration kinetics. The model is developed based on a similar principle as the equivalent age concept used to compute the maturity of cement-based materials. The model suggests that the hydration kinetics of a given cement at various curing conditions can be approximately predicted from an experimental curve obtained for a reference curing condition using a simple scale factor related to the chemical properties of the cement. However, since the induction period can not be predicted accurately, sometimes a slight offset in the time axis between the predicted curve and the actual experimental curve may be observed.

References

[1] Scherer, G.W., G.P. Funkhouser, S. Peethamparan, Effect of pressure on early hydration of class H and white cement, Cement and Concrete Research, V. 40, pp. 845-850, 2010.

[2] Pinto, R.C.A. and K.C. Hover, Application of maturity approach to setting times, ACI Materials Journal 96, pp. 686–691, 1999.

[3] García, Á., D. Castro-Fresno, and J.A. Polanco, Maturity approach applied to concrete by means of Vicat tests, ACI Materials Journal 105 (5), pp. 445-450, 2008.

[4] Zhang, J., E.A. Weissinger, S. Peethamparan, G.W. Scherer, Early hydration and setting of oil well cement, Cement and Concrete Research 40, pp. 1023-1033, 2010.

[5] Lin, F., Modeling of Hydration Kinetics and Shrinkage of Portland Cement Paste, Ph.D. Dissertation, Columbia University, 2006.

[6] Kjellsen, K.O., R.J. Detwiler, and O.E. Gjørv, Development of microstructures in plain cement pastes hydrated at different temperatures, Cement and Concrete Research 21, pp. 179-189, 1991.

[7] ASTM C1074, Standard Practice for Estimating Concrete Strength by the Maturity Method, ASTM International, West Conshohocken, PA, 2010.

[8] Krauss, M. and H. Karim, Determination of initial degree of hydration for improvement of early-age properties of concrete using ultrasonic wave propagation, Cement & Concrete Composites 28, pp. 299-306, 2006.

[9] Pane, I. and W. Hansen, Concrete hydration and mechanical properties under nonisothermal conditions, ACI Materials Journal 99 (6), pp. 534-542, 2002.

[10] Parrott, L.J., M. Geiker, W.A. Gutteridge and D. Killoh, Monitoring Portland cement hydration: comparison of methods, Cement and Concrete Research 20, pp. 919-926, 1990.

[11] Escalante-Garcia, J.I. and J.H. Sharp, Effect of temperature on the hydration of the main clinker phases in Portland cements: Part I, neat cements, Cement and Concrete Research 28 (9), pp. 1245-1257, 1998.

[12] Bentz, D.P., A three-dimensional cement hydration and microstructure program: I. hydration rate, heat of hydration, and chemical shrinkage, NISTIR 5756, U.S. Department of Commerce, Washington DC, 1995.
[13] Escalante-Garcia, J.I., Nonevaporable water from neat OPC and replacement materials in composite cements hydrated at different temperatures, Cement and Concrete Research 33 (11), pp. 1883-1888, 2003.
[14] Geiker, M., Studies of Portland cement hydration: measurements of chemical shrinkage and a systematic evaluation of hydration curves by means of the dispersion model, Ph.D. Thesis, Technical University of Denmark, 1983.
[15] Mounanga, P., V. Baroghel-Bouny, A. Loukili, A. Khelidj, Autogenous deformations of cement pastes: Part I. Temperature effects at early age and micro-macro correlations, Cement and Concrete Research 36 (2006) 110-122.
[16] Peethamparan, S., E. Weissinger, J. Vocaturo, J. Zhang, and G. Scherer, Monitoring chemical shrinkage using pressure sensors, Advances in the Material Science of Concrete, ACI SP-270, Vol. 7 (2010), 77-88.
[17] Pang, X., Effects of curing temperature and pressure on the chemical, physical, and mechanical properties of Portland cement, Ph.D. Dissertation, Columbia University, 2011.
[18] API Specification 10A, Specification for Cements and Materials for Well Cementing, American Petroleum Institute, 2010.
[19] ASTM C1679, Standard Practice for Measuring Hydration Kinetics of Hydraulic Cementitious Mixtures Using Isothermal Calorimetry, ASTM International, West Conshohocken, PA, 2009.
[20] Bentz, D.P., and Ferraris, C.F., Rheology and setting of high volume fly ash mixtures. Cement and Concrete Composites 32 (4), pp. 265-270, 2010.

Mechanical Properties of Ultra-High Performance Concrete (UHPC) at Early Age

Harald Budelmann, Jens Ewert
Institute of Building Materials, Concrete Construction and Fire Protection (Building Materials and Reinforced Concrete Construction Department), Technische Universität Braunschweig, Germany

Although ultra-high performance concrete (UHPC) is a promising construction material with outstanding mechanical properties the utilisation of this high efficient material in practice is still in the beginning since its characteristics are not yet completely established. This is particularly true for the early age development of mechanical properties and shrinkage deformations. In this paper it is shown, that existing approaches, valid for high performanche concrete or normal strength concrete, may be adapted on UHPC. A significant difference is the progress of hardening and the development of mechanical properties, due to the low water-cement ratios, which are typical for UHPC. Such low water-cement ratios cause an incomplete hydration, which is considered by means of a limited ultimate degree of hydration α_U.

Keywords: UHPC, degree of hydration, effective age, shrinkage.

1 Introduction

The Institute of Building Materials, Concrete Construction and Fire Protection (iBMB) participated for six years in the priority program “Sustainable Building with Ultra-high performance concrete” funded by the Deutsche Forschungsgemeinschaft (DFG). UHPC is especially suited for applications, where its properties, like the high compressive strength or the outstanding durability offer advantages to normal strength concrete. For a broader application of UHPC in practice it is necessary to have constitutive laws of the time-dependant mechanical properties, especially at early age. The european standards DIN EN 1992-1 [1] define constitutive laws for concrete up to a compressive strength class of C100/115. To evaluate and, if necessary, to modify those well established material laws for UHPC was the major goal of the research project, reported here.

As an universal state variable the degree of hydration α or the effective age t_e is used. The degree of hydration is measured directly from the adiabatic heat release in calorimetric tests. Due to the low water-cement ratio the degree of hydration is limited to an ultimate degree of hydration α_U, much lower than 1.0.

For the validation of the material laws valid for normal strength concrete a broad data basis of mechanical properties had to be created. Therefore several tests of the compressive strength f_{cc}, the tensile strength f_{ct}, the Young’s modulus for compression E_{cc} and the Young’s modulus for tension E_{ct} were carried out. The first tests were started at the earliest possible age, but not before 12 hours after mixing.

Another aim of this project was to determine deformations caused by autogenous shrinkage, which were measured in temperature-stress-testing machines (TSTM) under different isothermal temperatures.

2 Experimental procedures

Mixtures

The experimental studies were based on two different UHPC mixtures. The first one was a fine grain UHPC (FG) with a maximum grain size of 0.500 mm. The second mixture was a coarse grain UHPC (CG), which additionally contained crushed basalt aggregate with a grading in the range of 2/8 mm. An optimised particle packing was ensured using two different quartz flours

and a silica fume as a microfiller. The quartz flour I had a maximum grain size of 60 µm and the quartz flour II of 300 µm. The steel fibers used for both mixtures had a length of 9 mm and a diameter of 0.15 mm. Table 1 gives a general survey of the mix proportions.

Table 1: UHPC-mixture proportions.

base material	**unit**	**FG**	**CG**
cement	kg/m³	832.00	650.00
quartzsand (0.125 – 0.500 mm)	kg/m³	975.00	354.00
crushed basalt aggregate	kg/m³	-	597.00
microsilica fume	kg/m³	135.00	177.00
steel fibres	kg/m³	192.00	192.00
quartz flour I	kg/m³	207.00	325.00
quartz flour II	kg/m³	-	131.00
superplasticiser	kg/m³	35.28	36.48
additional water	kg/m³	162.47	154.35
water-cement ratio	-	0.22	0.27
water-binder ratio	-	0.19	0.21

Fresh concrete properties

Generally the fresh concrete temperature, the fresh concrete density and the flow diameter were measured. Table 2 shows the average values $\bar{x}$ and the mean square error σ of all parameters. In general it can be asserted, that the fine grain concrete is easier to produce and has a better robustness against variations during mixing.

Table 2: Statistic fresh concrete properties.

parameter	**unit**	**FC**		**CG**	
number of tests	-	40		25	
statistical parameter		$\bar{x}$	σ	$\bar{x}$	σ
fresh concrete temperature	°C	21.87	2.777	21.02	1.017
fresh concrete density	kg/m³	2475	21.1	2536	42.6
flow diameter	cm	63.50	3.245	50.00	8.214
air void content	%	4.17	0.689	3.51	0.992

Degree of hydration

In this paper the degree of hydration α and the equivilant age t_e are used to describe the hardening process. State of the art is to calculate α directly from the adiabatic heat release in calorimetric tests. Usually the degree of hydration of normal strength concrete, with water-cement ratios of 0.40 or more, increases up to values from 0.8 to 1.0, if there is enough water to react with the admixed portland cement and enough space in the matrix for the C-S-H phases to grow inside. In fact that UHPC mixtures are produced with water-cement ratios of 0.30 or less and the hardening matrix is very dense, the hydration reaction stops, before the added cement has hydrated completely. The not hydrated amount of cement remains within the matrix as a microfine filler, being a characteristic feature of UHPC. A later continuation of the hydration reaction may be excluded, since the dense and free of capillary pores material prevents a transport of external water or moisture. In order to describe the uncompleted hydration reaction in this paper the ultimate degree of hydration α_U is used. It can be calculated with equation 1, according to the research of Mills [2]. With equation 1 and the water-cement ratios given in

table 1 the ultimate degree of hydration is 0.55 for the fine grain UHPC and 0.60 for the coarse grain UHPC.

$$\alpha_U = \frac{1.031 \cdot w/z}{0.194 \cdot w/z} \quad (1)$$

The application of the activation energy concept and the degree of hydration were tested in several adiabatic calorimetric tests. For each test two specimen (ca. 10 liters) for the calorimetric test and 18 cylindric specimen (∅ = 80 mm, h = 160 mm) for compressive strength tests were prepared. The compressive strength tests were carried out in the age of 1, 2, 3, 7, 14 and 28 days at 3 specimens each. To determine the activation energy E_A the fresh concrete temperature was varied from 5°C to 40°C. The specimens were stored at isothermal conditions corresponding to the fresh concrete temperature. As described before the degree of hydration can be calculated from the adiabatic heat release in calorimetric tests with equation 2.

$$\alpha(t) = \frac{Q_{ad}(t)}{Q_{pot}} \quad (2)$$

In this equation $Q_{ad}(t)$ is the adiabatic heat release measured in the calorimeter and Q_{pot} is the maximum heat release. Q_{pot} can be calculated dependent of the masses of the used ingredients according to [3]. In opposition to [3] the maximum heat release has to be limited with respect to the ultimate degree of hydration. In the literature several approaches to calculate the degree of hydration are existing [4] and [5]. Krauß [6] proved that the two parametric approach according to [7] based on the research of Jonasson [5] is a suited approach to calculate the degree of hydration with equation 3.

$$\alpha(t_e, t_{k,I}, c_{1,I}) = exp\left[-\left(ln\left(1 + \frac{t_e}{t_{k,I}}\right)\right)^{c_{1,I}}\right] \quad (3)$$

In this equation t_e is the effective age and $t_{k,I}$ and $c_{1,k}$ are variables. The effective age t_e indicates the time span for an arbitrary temperature history during which the same degree of hydration is reached as for a constant temperature of 20°C. This approach is based on the Arrhenius equation which was transferred into a maturity concept for concrete (cf. equation 4) by Freiesleben Hansen and Pedersen.

$$t_{e,j} = \int_0^t exp\frac{E_A}{R}\left[\frac{1}{293} - \frac{1}{273+T_j(t')}\right]dt' \quad (4)$$

Besides the temperature $T_j(t')$ the activation energy E_A is the main influencing parameter in this equation. It is well known that the hydration of concrete is a temperature dependant chemical reaction, starting immediately after exceeding an activation energy barrier. The value of this barrier is depending on the chemical composition and the particle size distribution of the reactive ingredients. The determination of E_A is still in the focus of international research, so that several approaches to detect E_A are existing. In this paper the activation energy is calculated with equation 5. This approach is temperature dependant and was established by Jonasson [5].

$$E_A = \Theta_{\mathrm{ref}} \cdot \left(\frac{30}{\mathrm{T}+10}\right)^{\kappa} \quad (5)$$

Jonasson created in his doctoral thesis [5] a broad data basis for CEM I cements and obtained good results for E_A with Θ_{ref} = 47.39 kJ/mol and κ = 0.54. Figure 1 and 2 show the measured values for α of the tests carried out with different fresh concrete temperatures and the degree of hydration calculated with equation 3. The data of the regression analysis $t_{k,I}$ = 14.52 and $c_{1,I}$ = -

2.15 for the FG and $t_{k,I}$ = 25.64 and $c_{1,I}$ = -1.91 for the CG. In figure 1 the ordinate is limited to 0.55 respectively 0.60 in figure 2 according to α_U calculated with equation 1.

The comparison between figure 1 and 2 show what could be deduced of the differences of the tested mixtures. The hydration reaction and the development of mechanical properties of the FG begins earlier compared to the CG mixture. The low water-cement ratio of the FG initializes a higher osmotic pressure, so that the on-going reaction after the dormant phase starts at an equivilant age of approximate 10 – 12 h, respectively at 16 – 18 h for the CG. This point of time matches with the calculated α_0, which indicates the beginning of the development of mechanical properties. The acceleration of both mixtures is nearly identical, because the amount of reactive materials (cement and microsilica in combination with the ultimate degree of hydration) is almost equal.

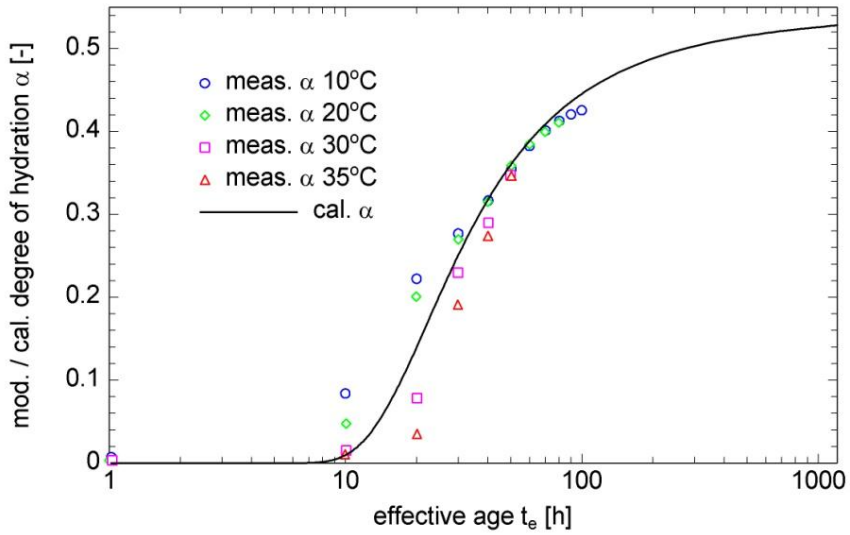

Figure 1: Measured and calculated degree of hydration (FG).

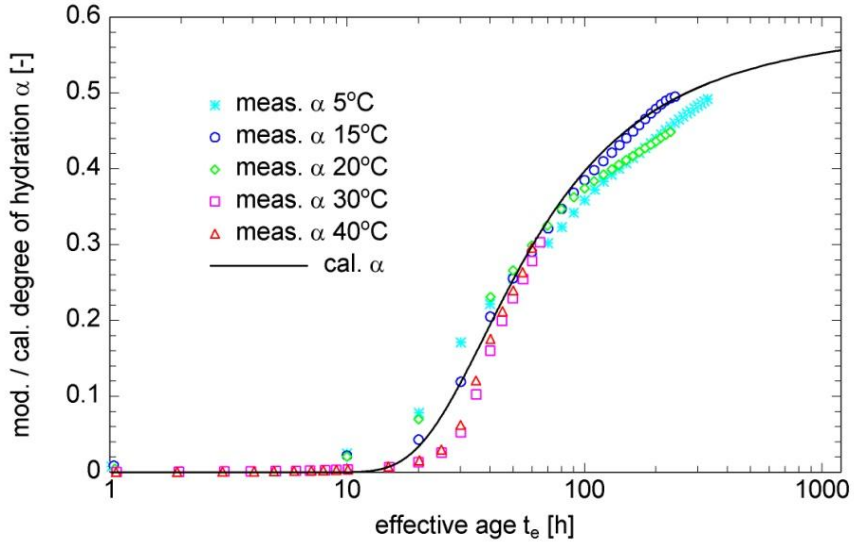

Figure 2: Measured and calculated degree of hydration (CG).

Mechanical properties

A comprehensive material model has to include the time dependant development of mechanical properties. In this paper the degree of hydration, respectively the equivilant age t_e is used as an universal parameter. For normal strength and high strength concrete several approaches are

existing to calculate mechanical properties as a function of α [8] and [9]. The general approach of a mathematical calculation is shown in equation 6, in which Z indicates the mechanical property regarded, α is the degree of hydration and b, c and d are parameters to describe the development of Z.

$$f_Z^{(R)}(\alpha, b, c, d) = d \cdot \left(\frac{\alpha - b}{1 - b}\right)^c \tag{6}$$

This equation assumes a degree of hydration of 1, respectively 100%, but as described before the degree of hydration of UHPC is limited to α_U, due to the low water-cement ratio. Therefore this value is substituted by α_U in the equations 7, 8 and 9 to take the incomplete hydration into account. The equations 7, 8 and 9 are functions to calculate the relative tensile strength, the relative compressive strength and the relative Young's Modulus. In this case relative material property means the strength at a time t in relation to maximum strength at 28 days. A main influencing value in these equations is α_0, which describes the time when the concrete begins to obtain properties like a solid material. In this paper α_0 is extrapolated linear from the measured values for the tensile strength. The values obtained for α_0 are 0.01435 for the FG and 0.01951 for the CG, resulting to 10.5 h respectively 17.5 h after mixing.

$$\bar{f}_{ct} = \frac{f_{ct}(\alpha)}{f_{ct}(\alpha_U)} = \frac{f_{ct}(\alpha)}{f_{ctU}} = \frac{\alpha - \alpha_0}{\alpha_U - \alpha_0} \tag{7}$$

$$\bar{f}_{cc} = \frac{f_{cc}(\alpha)}{f_{cc}(\alpha_U)} = \frac{f_{cc}(\alpha)}{f_{ccU}} = \left[\frac{\alpha - \alpha_0}{\alpha_U - \alpha_0}\right]^{3/2} \tag{8}$$

$$\bar{E} = \frac{E(\alpha)}{E(\alpha_U)} = \frac{E(\alpha)}{E_U} = \left[\frac{\alpha - \alpha_0}{\alpha_U - \alpha_0}\right]^{1/2} \tag{9}$$

For a reliable validation of equation 7 to 9 a broad data basis of experimental results (tensile strength, compressive strength and Young's modulus) has been created. The compressive strength and Young's modulus for compression were determined using specimen with a diameter of 80 mm and a height of 160 mm. The tensile strength and Youngs modulus for tension were measured using specimen with a diameter of 80 mm and a height of 300 mm. An overview over the tests carried out is shown in [10]. Figure 3 and 4 show the comparision between measured and calculated mechanical properties (see equation 7 to 9) versus the degree of hydration calculated with equation 3.

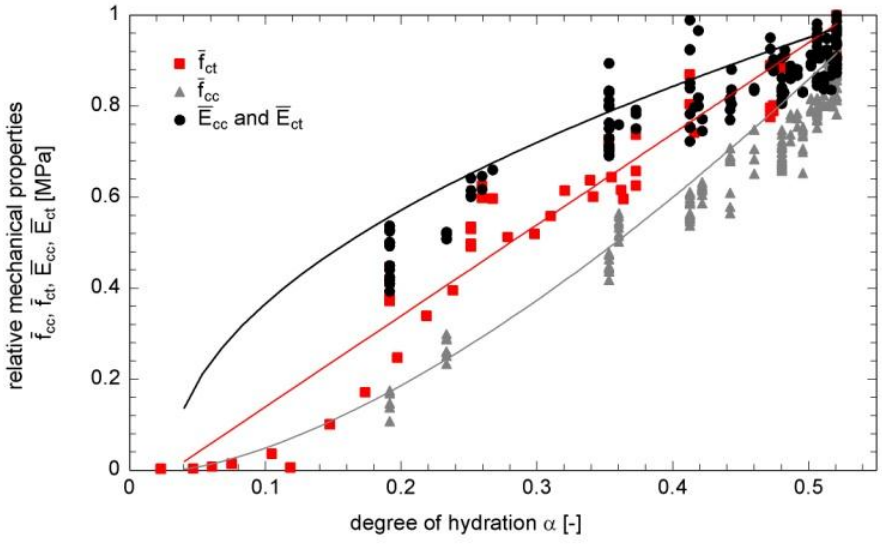

Figure 3: Relative measured and calculated mechanical properties vs. degree of hydration (FG).

The development of mechanical properties starts 12.5 h after mixing for the FG and 17.5 h for the CG. The time delay between the beginning of the hardening was already mentioned before, when the progress of α was explained. Certainly the development of mechanical properties begins earlier, but usually tests carried out on concrete specimen before α_0 are quite imprecise. The calculated results of the applicated material models show a sufficient correlation to the measured values, except for lower degrees of hydration, which also can be explained with the difficulty to test young concrete specimen.

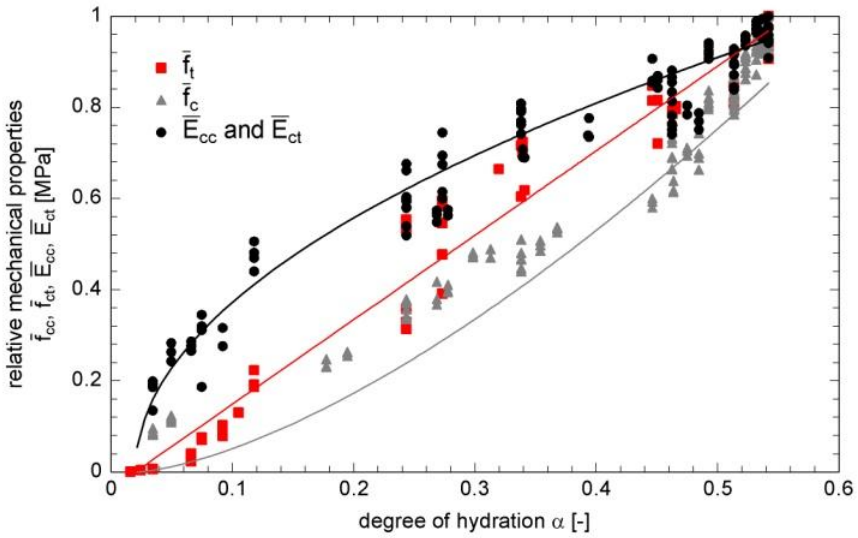

Figure 4: Relative measured and calculated mechanical properties vs. degree of hydration (CG).

Shrinkage

Shrinkage tests are carried out using horizontal temperature-stress-testing machines (TSTM), each containing two different specimen. One specimen is unrestraint and may deform free, so that deformations due to shrinkage or temperature could be measured. The specimen for shrinkage observation has a length of 60 cm and a cross-section of 10 cm x 10 cm. The other specimen is dog-bone shaped with a total length of 100 cm and a cross-section 10 cm x 10 cm and can be loaded with a defined tensile stress to measure tensile creep deformations additionally. Both specimen can be cooled and heated from 5°C to 50°C. The deformations are measured by a strain gauge protected by a plastic casing. The measurement system PMFL-60-2LT manufactured by Tokyo Kenkyujo Co. Ltd. has a total length of 70 mm. The system is placed in the cross-section of the fresh concrete, so that deformations could be measured from the beginning. All tests were carried out under isothermal temperature conditions. A quite good approach to calculate the total autogenous shrinkage is equation 10 according to the material model by Gutsch [9].

$$\varepsilon_{as}(t_e - t_{e0}) = \varepsilon_{as0} \cdot \beta_t \cdot \beta_T \tag{10}$$

In this equation ε_{as0} is the maximum shrinkage value stored under sealed isothermal conditions, β_t considers the time-dependant progress of shrinkage and β_T is a factor for a concrete storage at higher temperature. The maximum shrinkage ε_{as0} is calculated with equation 11, which is temperature independent, but mainly influenced by the water-binder ratio, which is shown in table 1. Best results are obtained with the factor F = 3.5.

$$\varepsilon_{as0} \approx 1.3 \cdot 10^{-3} \cdot exp\left(-F \cdot \frac{W}{B}\right) \tag{11}$$

The time dependant development of shrinkage is calculated with equation 12. In this equation t_e is the effective age and a_{as} and b_{as} are concrete specific coefficients.

$$\beta_t \approx 1 - exp\left[-a_{as} \cdot \left(\frac{t_e - t_{e0}}{t_1}\right)^{b_{as}}\right] \quad (12)$$

Other temperature during hardening are considered by β_T in equation 10. For storage temperatures of 20°C, 30°C and 40°C β_T is 1.0. By applying all values in equation 10 the calculated maximum shrinkage ε_{as0} is 0.669 mm/m for the fine grain mixture and 0.623 mm/m for the coarse grain mixture. The figures 5 and 6 show the measured shrinkage deformations and the calculated shrinkage deformations for isothermal conditions of 20°C, 30°C and 40°C versus the effective age t_e. The measurement of shrinkage deformations starts approximately 8 h after mixing. After a short period in which only small deformations could be measured, the shrinkage is accelerating and after 28 days the final value is nearly reached. The maximum shrinkage value is a little higher for the fine grain mixture caused by the slightly higher content of reactives in the mixture. The acceleration of the shrinkage is nearly equal, due to the marginal differences in the water-cement ratios.

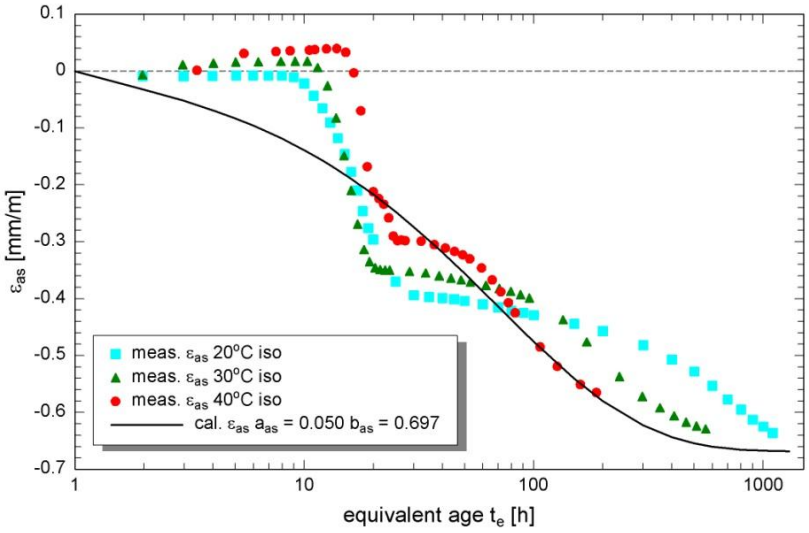

Figure 5: Measured and calculated shrinkage deformations vs. effective age t_e for the fine grain mixture.

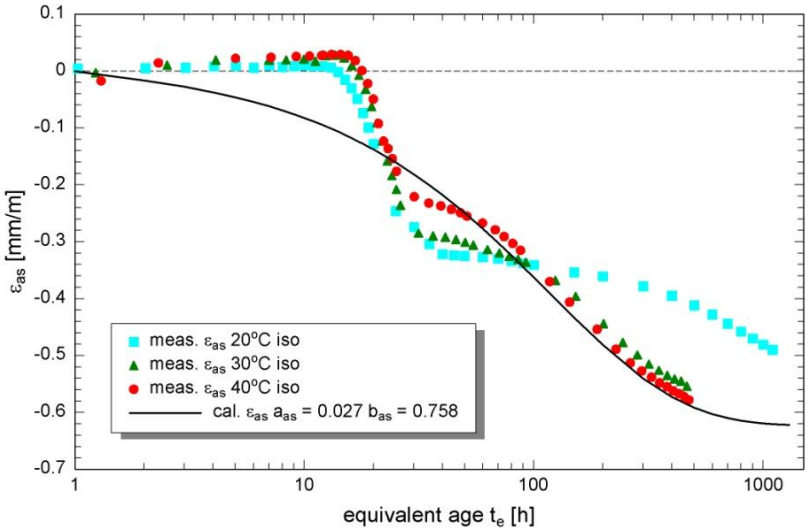

Figure 6: Measured and calculated shrinkage deformations vs. effective age t_e for the coarse grain mixture.

3 Conclusions

The implication of material laws for UHPC in standards and design codes is obvious. A broad data basis and reliable laws for the calculation of material properties have to be established. In this paper the application of constitutive laws, usually valid for normal strength concrete, on ultra-high performance concrete is shown. With these equations calculations of the time dependant mechanical properties, the degree of hydration and autogenous shrinkage are possible. As an universal state variable the degree of hydration was used. The degree of hydration was determined in adiabatic calorimetric tests. A specific characteristic of UHPC is the incomplete hydration, which is taken into account with the limitation of the hydration reaction by α_U. Furthermore the application of the activation energy concept on UHPC was shown.

References

[1] Deutsches Institut für Normung e.V.: DIN EN 1992-1-1. Eurocode 2: Bemessung und Konstruktion von Stahlbeton- und Spannbetontragwerken - Teil 1-1: Allgemeine Bemessungsregeln und Regeln für den Hochbau; Deutsche Fassung EN 1992-1-1: 2004 + AC: 2110. Ausgabe Januar 2011. Beuth Verlag GmbH, 10772 Berlin.

[2] Mills, R. H.: Factors Influencing Cessation of Hydration in Water Cured Cement Pastes. In: Proceedings of the Symposium on the Structure of Portland Cement Paste and Concrete. Highway Research Board. Special Report No. 90. Page 406 – 424. Washington D.C. 1966.

[3] Rostásy, F. S., Krauß, M.: Frühe Risse in massigen Betonbauteilen – Ingenieurmodelle für die Planung von Gegenmaßnahmen. Deutscher Ausschuss für Stahlbetonbau. Heft 520 (2001). Beuth Verlag GmbH, 10772 Berlin.

[4] Freiesleben Hansen, P., Pedersen, E. J.: Måleinstrument til control af betons hærdning. Nordisk Betong 1-1977. Stockholm.

[5] Jonasson, J.-E.: Modelling of temperature, moisture and stresses in young concrete. Doctoral Thesis. University of Technology Luleå, Sweden. Division of Structural Engineering. Luleå, Sweden, 1994.

[6] Krauß, M.: Probabilistischer Nachweis der Wirksamkeit von Maßnahmen gegen frühe Trennrisse in massigen Betonbauteilen. Dissertation. TU Braunschweig. Institut für Baustoffe, Massivbau und Brandschutz. Braunschweig 2004.

[7] IPACS: “Improved Production of Advanced Concrete Structures”, Brite-EuRam Project BRPR-CT97-0437, Juni 1997 – Mai 2001. Koordinator Dr. M. Emborg; H.-E. Gram; M. Øberg. Edt.: Elfgren, L. Luleå University of Technology, Department of Civil & Mining Engineering, Division of Structural Engineering, Sweden.

[8] Laube, M.: Werkstoffmodell zur Berechnung von Temperaturspannungen in massigen Betonbauteilen im jungen Alter. Dissertation. TU Braunschweig. Institut für Baustoffe, Massivbau und Brandschutz. Braunschweig 1990.

[9] Gutsch, A.-W.: Stoffeigenschaften jungen Betons – Versuche und Modelle. Dissertation. TU Braunschweig. Institut für Baustoffe, Massivbau und Brandschutz. Braunschweig 1998.

[10] Budelmann, H., Krauß, M., Ewert, J.: BU 730/16-1+BU730/16-2: Werkstoffverhalten von Ultrahochfestem Beton im frühen Alter. Abschlussbericht DFG Schwerpunktprogramm SPP 1182 „Nachhaltiges Bauen mit Ultra-Hochfestem Beton“. 2010.

Early Age Creep and Shrinkage of High Performance Concrete

Andina Sprince[1], Aleksandrs Korjakins[2], Leonids Pakrastinsh[1], Genadijs Shakhmenko[2], Girts Bumanis[2]

1: Department of Structural Engineering, Riga Technical University, Latvia
2: Institute of Materials and Structures, Riga Technical University, Latvia

This research deals with elastic and time-dependent deformations of high performance concrete reinforced with polyvinyl alcohol (PVA) fibers. The early age drying creep in compression and shrinkage were experimentally studied. Three concrete mixes with a different amount of fibers were developed and prepared. The concrete specimens were tested in a controlled constant temperature and with a constant level of moisture. The compression strength and modulus of elasticity were determined and compared with those of the reference concrete. The results indicate that in the early age the creep of concrete with PVA fibers reduces the deformation, but after a longer time of hardening it exhibits higher creep deformation than the reference concrete without fibers.

Keywords: PVA fibers, creep, shrinkage, creep coefficient, compression strength, modulus of elasticity

1 Introduction

Concrete is an important structural material used in every country of the world. Moreover, the complexity of structures and their size have continued to increase, and this has resulted in a greater importance of their strength and deformation characteristics in more serious consequences of their behavior [1].

Last three decades scientists and concrete technologists have been working on the development of new types of concrete. One of the most perspective products is fiber-reinforced high performance concrete (FRHPC). Fibers in concrete provide improved mechanical and physical properties of the material. For example, the obtained fiber-reinforced concrete has higher resistance to cracking. This is very important for high performance concrete, which usually has high amount of cement and low water/cement ratio. This type of concrete is sensitive to cracking, especially in the early age. The deformation characteristics of concrete are important in the design of sustainable structures [1]. Creep and shrinkage of concrete are a complex problem, especially at very early ages, due to the complexity of the material [2]. Creep deformation of concrete is often responsible for excessive deflection at service loads, which can compromise the performance of elements within a structure [3].

Nowadays construction at site demands rapid concrete strength development to minimize the building time, and that is why concrete deformations at early age are an important issue to concrete technologists and scientists.

Time-dependent deformations like creep and shrinkage should be tested to characterize those concretes.

2 Materials and methods

The experimental work included the preparation of two fiber-reinforced high performance concrete (FRHPC) mixes with different amounts of polyvinyl alcohol (PVA) fibers — 0.6% and 0.8% from the total amount of cement — and one reference mix without fibers for comparison. The mix compositions are given in Table 1. PVA fiber properties are listed in Table 2.

Table 1: Concrete mix composition.

Component		Reference	PVA-0,6	PVA-0,8
Cement *Kunda* CEM I 42,5 N	kg/m³	675	675	675
Cement *Aalborg white* CEM I 52,5 N	kg/m³	225	225	225
Quartz sand 0/1mm	kg/m³	300	300	300
Quartz sand 0.3/2.5mm	kg/m³	300	300	300
Diabase 0/5mm	kg/m³	200	200	200
Diabase 2/5mm	kg/m³	200	200	200
Ground quartz sand 8 min.	kg/m³	100	100	100
Silica fume *Elkem* 920 D	kg/m³	100	100	100
Water	kg/m³	200	200	200
Superplasticizer HE-30	kg/m³	24	24	24
PVA fibers	kg/m³	0	5,4	7,2
W/C		0,22	0,22	0,22

Table 2 : Properties of PVA fibers.

Fiber type	Ø [µm]	L [mm]	f_t [GPa]	E [GPa]
MC 40/8	40	8	1,6	42

Concrete components were measured out and then mixed in a laboratory conic rotation mixer for 4 minutes. For the investigation of properties of the material prismatic specimens 40x40x160 mm were produced. Concrete mixtures were cast into oiled steel moulds without vibrating because this is a self-compacting UHPC concrete. After one day specimens were de-moulded. Standard ageing conditions (temperature 20±2ºC, RH > 95±5%) were provided during hardening until certain concrete ages were reached.

Prismatic compressive strength, modulus of elasticity, drying creep and shrinkage tests were performed on early age concrete. The tests were performed after 1, 4, 7 and 14 days of concrete hardening in standard conditions. A compression testing machine with accuracy of ±1% was used, the rate of loading was 0.7 MPa/sec (according to LVS EN 12390-3:2002 standard). The modulus of elasticity was obtained from sample loading during creep tests. The creep was measured for hardened concrete specimens subjected to a uniform compressive load which was kept constant over a long period of time, and shrinkage was measured for the same specimens without loading [4, 5].

At the beginning of the test, the stress level of all mixes was 25% of the maximum strength of the concrete, which had been determined during destructive tests carried out on prismatic specimens. The load was applied gradually in four steps and as fast as possible. Specimens were kept under a constant load for 28 days, and for recoverable creep they were kept without load for 7 days. Four aluminium plates had been centrally and symmetrically glued onto two sides of the creep specimens in order to provide a basis for the strain gauges. The distance between the centers of the two plates was 50 mm. Two ±0.001 mm precision strain gauges were symmetrically connected to each specimen and then the specimens were put into a creep lever test stand and loaded (see Fig. 1). Two aluminium plates had been centrally and symmetrically glued onto ends of the shrinkage specimens and strains were measured with a shrinkage clamp. All specimens were kept in a dry atmosphere of controlled relative humidity in standard conditions: temperature 23±1ºC and relative humidity 25±3% [6]. After creep and shrinkage tests, the prismatic compressive strength of the specimens was determined.

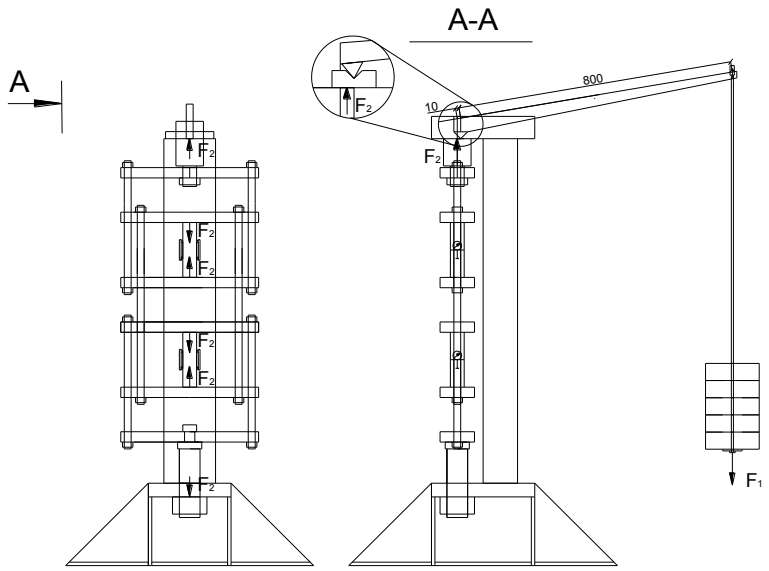

Figure 1: Creep lever test stand.

The instantaneous strain that occurs immediately upon application of stress may be considered to be elastic at low stress levels, and therefore:

$$\varepsilon_{e(t)} = \sigma_{c0} / E_{c(\tau 0)} \tag{1}$$

where $E_{c(\tau 0)}$ is the elastic modulus of concrete at time τ_0
$\varepsilon_{e(t)}$ is the instantaneous strain
σ_{c0} is the compressive stress applied at time τ_0

The capacity of concrete to creep is usually measured in terms of creep coefficient, $\varphi_{(t,\tau)}$. In a concrete specimen subjected to a constant sustained compressive stress, $\sigma_{c(\tau)}$, first applied at age τ, the creep coefficient at time t is the ratio of the creep strain to the instantaneous strain and is given by:

$$\varphi_{(t,\tau)} = \varepsilon_{cr(t,\tau)} / \varepsilon_{e(\tau)} \tag{3}$$

where $\varphi_{(t,\tau)}$ is the creep coefficient, $\varepsilon_{cr(t,\tau)}$ is the creep strain [7].

3 Results and discussion

High cement content and low water/cement ratio provides rapid concrete hardening process with high strength gain even at an early age. All concrete compressive test results are given in Figure 2. High prismatic compressive strength had developed after 24 hours of hardening, and continuous prismatic compressive strength growth was observed. After 14 days it had reached 90 MPa. The obtained results show similar compressive strength development for all mixes. A slightly (about 7% and 2%) higher prismatic compressive strength is exhibited by the reference mix after the 1st and 14th day respectively. The prismatic compressive strength after one day was 42 MPa, after 4 days of hardening — 64 MPa, after 7 days of hardening — 80 MPa and after 14 days of hardening the prismatic compressive strength reached 94 MPa. The obtained compression strength results were used to determine the necessary stress level for creep tests.

Compression strengths were tested after the creep test (35 days later). It had grown significantly for early age specimens. The highest strength gain was exhibited by specimens tested after 1 day of hardening — 90 MPa. Specimens hardened for a longer period of time in standard hardening conditions developed higher prismatic compressive strength after 35 days

of creep test. The highest prismatic compressive strength was obtained in the PVA-0,6 specimens, and it was 118 MPa. The lowest final prismatic compressive strength was developed by the reference specimens —110 MPa.

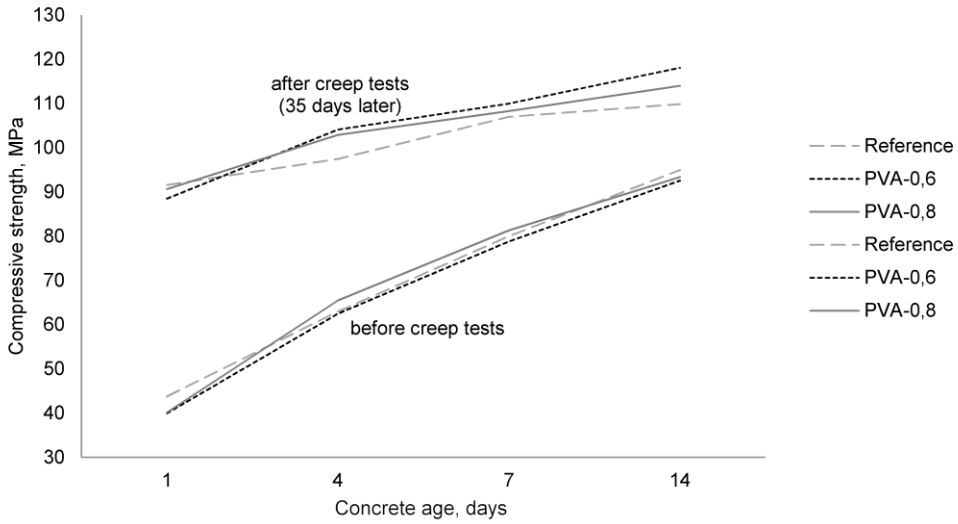

Figure 2: Prismatic compressive strength of high strength concrete specimens before and after creep tests.

During concrete specimen loading, the modulus of elasticity was obtained. The modulus of elasticity increases with the concrete hardening time and strength gain in the similar way for all mixes (see Fig.3) from 28 to 40 GPa.

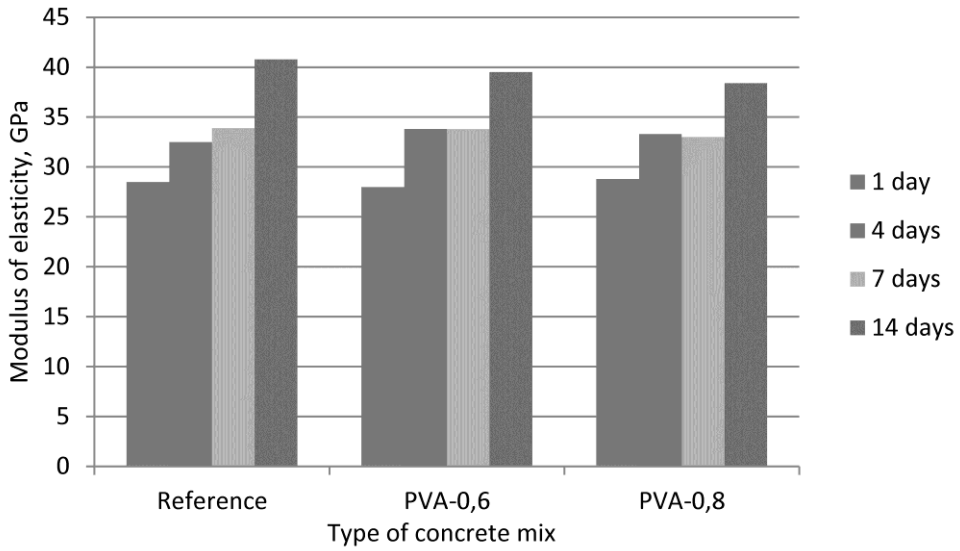

Figure 3: The modulus of elasticity for high strength concrete specimens.

The results of drying creep tested at an early age of the FRHPC and reference specimens indicate that the highest creep deformations were observed after the application of load on the 1st day (see Fig. 4). The highest deformation response was exhibited by the reference concrete specimens. After 4 days, the highest creep deformations had developed in the PVA-0.8 specimens, but in specimens with a fiber amount of 0.6% the deformation level was the lowest. After 7 days of hardening, the reference concrete specimens showed the lowest deformation response. Specimens hardened for 14 days exhibited a much lower deformation response than previously. The lowest creep deformations were observed in the reference concrete specimens.

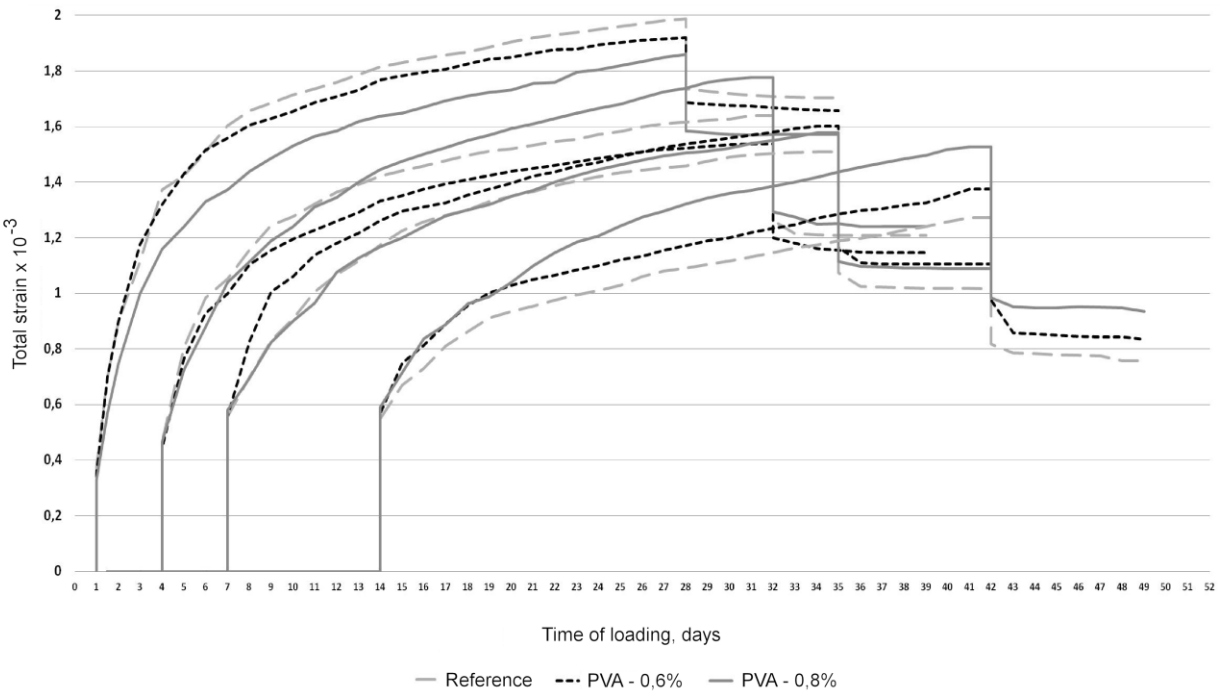

Figure 4: Drying creep and recoverable, irrecoverable creep and shrinkage strains.

The total creep and shrinkage strains are given in Figure 4. After 28 days of loading, the load was removed. The creep recovery was measured 7 days after the loading period. The highest residual creep strains were observed in 1 and 4 days old reference concrete specimens. Concrete specimens hardened for 7 and 14 days provided lower creep strains, and the smallest deformations were exhibited by the reference specimens. The highest creep strains had developed in concrete specimens with a fiber amount of 0.8%. The final creep strains were $0{,}76 \cdot 10^{-5}$ for the reference concrete, $0{,}83 \cdot 10^{-5}$ for PVA-0.6 and $0{,}93 \cdot 10^{-5}$ for PVA-0,8 specimens.

The final stress level was obtained after the creep tests. It was calculated as a ratio of the applied load and the prismatic compressive strength after the creep test. The gained prismatic compressive strength and the final stress ratio of the specimens were lower at early ages. In specimens loaded after 1 day of hardening the stress level varied from 0,10 to 0,12, and for specimens loaded after 14 days of hardening the stress level varied from 0,19 to 0,20. Despite the fact that the final stress level was higher in the reference concrete mix specimens, the creep deformations were lower in the specimens with PVA fibers.

The creep coefficient increases with time at an ever-decreasing rate. The final creep coefficient is a useful measure of the creeping capacity of concrete (see Fig. 5). The highest creep coefficients were established for concrete specimens loaded after one day of hardening, and it was for specimens with fibers. Specimens that were loaded after one day of hardening produced creep coefficients from 4.2 to 4.8. The creep coefficient reduces significantly with the growth of the concrete strength. They decreased considerably already after the 4th day and ranged from 2.6 to 3.0. The lowest creep coefficients were determined in specimens that had been loaded for 14 days, and these ranged from 1.5 to 1.7. The lowest creep coefficient was exhibited by the reference concrete specimens.

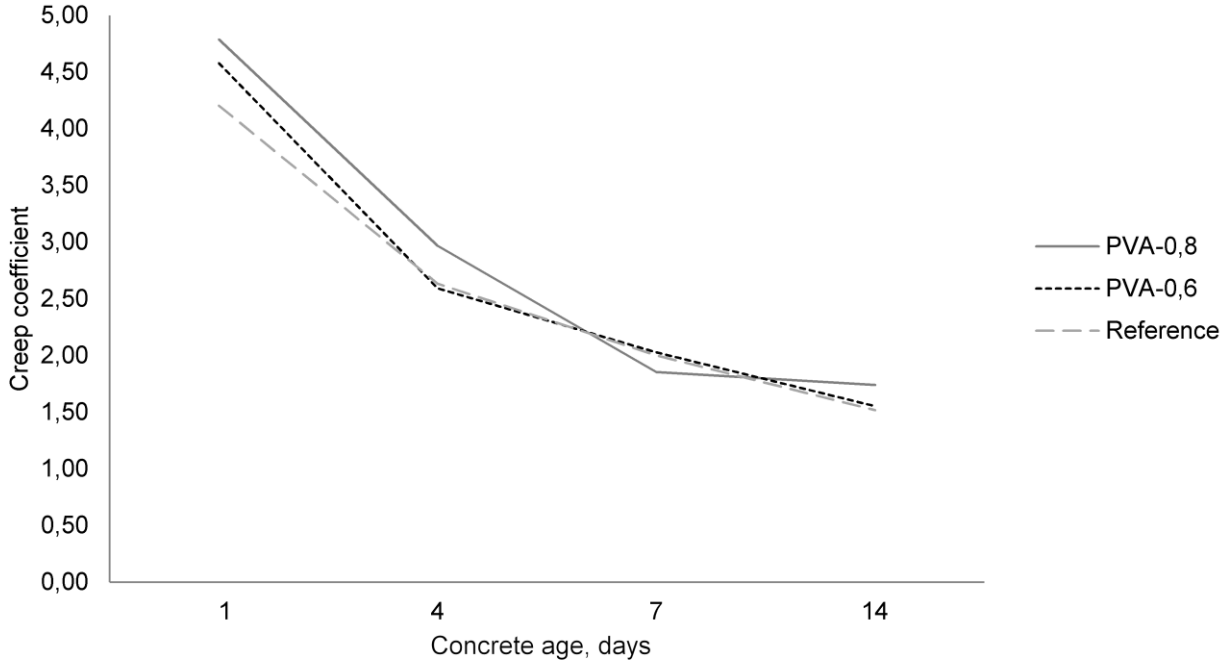

Figure 5: Creep coefficient of high strength concrete specimens.

Drying shrinkage results (see Fig. 6) were obtained from the same shape and concrete mix specimens as the creep specimens [4], and the strains were measured during creep tests. Figure 6 shows that the drying shrinkage deformations are decreasing with time. In specimens hardened for a prolonged period of time in standard hardening conditions the drying shrinkage strains were lower. The lowest shrinkage deformations were observed in concrete specimens with fibers.

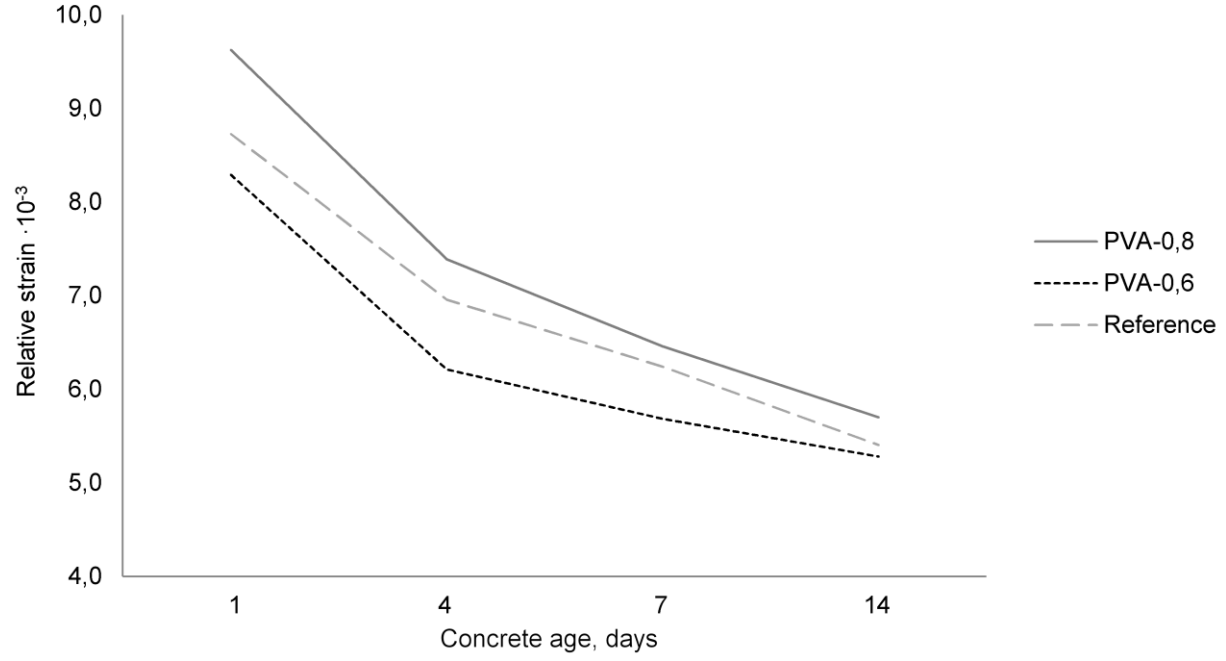

Figure 6: Drying shrinkage strains of high strength concrete.

4 Conclusions

Two fiber-reinforced high performance concrete (FRHPC) mixes with polyvinyl alcohol fibers (PVA) were prepared for a laboratory examination of processes ongoing in concretes at an early age, and the results were compared with those of a reference concrete mix without fibers. Two fiber contents were chosen for comparison — 0.6% and 0.8% of fibers from the total amount of cement.

Concrete specimens were tested at an early age after 1, 4, 7 and 14 days of hardening. The prismatic compressive strength, modulus of elasticity, drying creep and shrinkage were determined.

The compression strengths after the creep test (35 days later) were established. In the early age it had grown significantly. The highest prismatic compressive strength was developed by the fiber-reinforced specimens and it reached 118 MPa.

During concrete specimen loading the modulus of elasticity was obtained. The modulus of elasticity increases with the concrete hardening time and strength gain in the similar way for all mixes.

Concrete specimens were tested for an early age drying creep. All specimens were loaded with an equal stress level 0.25. The load was applied for 28 days and the long-term deformation responses were measured. The creep recovery was observed over a time period of 7 days. The creep deformations were found to decrease with concrete aging and time.

Drying shrinkage results were obtained from the same shape and concrete mix specimens as the creep specimens, and the strains were measured during creep tests. In specimens hardened for a prolonged period of time in standard hardening conditions the drying shrinkage strains were lower. The lowest shrinkage deformations were observed in the PVA fiber-reinforced concrete specimens.

5 Acknowledgement

This work has been supported by the European Social Fund within the scope of the project “Support for the Implementation of Doctoral Studies at Riga Technical University”.

References

[1] Neville A. M., Dilger W. H., Brooks J. J. Creep of Plain and Structural Concrete. *Construction Press*, London and New York, 1983.

[2] Kangvanpanich K. Early Age Creep of Self-Compacting Concrete Using Low Heat Cement at Different Stress/Strength Ratios. *A dissertation submitted to Kochi University of Technology in partial fulfillment of the requirements for the Degree of Master of Engineering*, Kochi, 2002

[3] Fanourakis G. and Ballim Y. Predicting Creep Deformation of Concrete: *A Comparison of Results From Different Investigations, Proceedings, 11th FIG Symposium on Deformation Measurements*, Santorini, Greece, 2003.

[4] Rilem TC 107-CSP: Creep and Shrinkage Prediction Models: Principles of Their Formation. Measurement of Time-dependent Strains of Concrete*. Materials and Structure, RILEM* Publications SARL, 1998.

[5] ACI Committee 209, Report on Factors Affecting Shrinkage and Creep of Hardened Concrete (ACI 209.1R-05) *American Concrete Institute*, Farmington Hills, Michigan, USA, 2005.

[6] Sprince A., Pakrastinsh L., Korjakins A., Shakhmenko G. Effect of Montmorillonite Nano Admixture on Long-term Deformations of Concrete. *Scientific Journal of Riga Technical University, Construction Science*, Vol.12, Riga Technical University, Riga, Latvia, 2011.

[7] Gilbert R.I., Ranzi G. Time-Dependent Behaviour of Concrete Structures. *Span Press*, London and New York, England and USA, 2011.

Shrinkage Behavior of Ultra High Performance Concrete at the Manufacturing Stage

Sungwook Kim[1], Jungjun Park[1], Dooyeol Yoo[2], Youngsoo Yoon[2]
1: Structural Eng. and Bridge Research Division, Korea Institute of Construction Technology, Korea
2: School of Civil, Environmental and Architectural Engineering, Korea University, Korea

Ultra High Performance Concrete (UHPC) is subject to large amount of shrinkage due to its low water-to-binder ratio and large content of binders. The large amount of autogenous shrinkage in the UHPC member at the manufacturing stage can induce confined stress, and cracks can be developed when the confined stress becomes higher than the early tensile strength of UHPC. Since the most important issue in the manufacturing process of UHPC structural members is to control cracks at early age, this study focuses on the early age shrinkage behavior. The shrinkage of UHPC in plastic state is not generating confining stress, which is the main cause of initial crack. However, the current test and analysis methods dedicated to autogenous shrinkage are involving plastic shrinkage. Therefore, this study carries out autogenous shrinkage test, setting time test and ring test in order to pick up and re-estimate the shrinkage behavior of UHPC at the manufacturing stage in concern the crack-inducing stress.

Keywords: ultra high performance concrete, shrinkage behavior, early crack.

1 Introduction

Ultra-high performance concrete (UHPC), characterized by a high strength and high ductility, is also very vulnerable to premature shrinkage cracking because of its low water-to-binder ratio (W/B) and its large content in high fineness silica fume (SF) and silica power as filler without coarse aggregate. Accordingly, the shrinkage behavior of UHPC should be assessed precisely to derive countermeasures for the reduction of shrinkage.

Active research has been conducted on the usage of expansive admixture (EA) and shrinkage reducing agent (SRA) in order to reduce shrinkage of UHPC. EA expands the volume of concrete and catalyzes hydration at early age by generating massively ettringite from C_4A_3S clinker. SRA, essentially a non-ionic surfactant based on ether, reduces shrinkage by diminishing the surface tension and increasing the viscosity of pore water in the hydrated cement paste [1-2].

An ordinary concrete structural member with large stiffness and low confining stress can endure crack at the manufacturing step without the admixing of EA and SRA. Besides, a UHPC structural member presents generally slim cross section, which requires the adoption of EA and SRA to prevent cracking at the manufacturing step.

This study considers two types of mix proportion of which one contains EA and SRA and the other without EA and SRA. The shrinkage behavior is analyzed by means of non-restrained shrinkage test, restrained shrinkage test, and ring test for the two mix proportions. Furthermore, the setting time of UHPC is studied to estimate precisely the autogenous shrinkage.

2 Mechanical properties of UHPC

Mix proportions

Table 1 lists the mix proportions used for the two types of UHPC specimens. The UHPC specimens basically contain cement, SF and filler. Two types of mix are considered: Mix A indicates the mix without EA and SRA, and Mix B the mix adopting EA and SRA. Steel fibers with an average length of 13 mm are introduced at volume fraction of 2% in all specimens, but

are discarded for the specimens to be used for setting time test. In Table 1, SP stands for superplasticizer.

Table 1: Mix proportions of UHPC (by weight except for fibers).

Type	W/B	Cement	Silica fume	Sand	Filling powder	SP	SRA	EA	Steel Fiber (vf)
Mix A	0.2	1	0.25	1.1	0.3	0.016	-	-	2%
Mix B	0.2	1	0.25	1.1	0.3	0.016	0.01	0.075	2%

Test Method

Flow was determined in compliance with ASTM C 1437. The compressive strength was measured with respect to ASTM C 39 on cylindrical specimens of Φ100 mm × 200 mm using a universal testing machine (UTM) with capacity of 3,000 kN. The elastic modulus was computed using a compressometer measuring the average compressive strain based on the measurements of three linear voltage differential transformers (LVDTs). The flexural strength was estimated by 4-point loading test.

Basic properties

Table 2 arranges the resulting an average flow and strength properties of the two mixes for 3 batches each mix. It can be noted that the flowability is practically not affected by the admixture of both EA and SRA. The development of the compressive and flexural strengths is slightly delayed by EA and SRA at early age but this delaying effect vanishes after 7 days. The secant elastic modulus listed in Table 2 was calculated by Eq. (1).

$$E_c = \frac{0.4 f_{ck} - f_1}{\varepsilon_2 - 0.00005} \quad (1)$$

where f_{ck} is the ultimate compressive strength (MPa); f_1 is the stress corresponding to a longitudinal strain of 50 με (MPa); and, ε_2 is the longitudinal strain produced by a stress corresponding to 40% of f_{ck} (με).

Table 2: Properties of UHPC at 1, 3, 7 and 28 days.

Designation	Flow (mm)	f_{ck} (MPa)				f_{ft} (MPa)				E_c (GPa)			
		1	3	7	28	1	3	7	28	1	3	7	28
Mix A	235	78.8	105.6	126.2	152.4	26.3	28.7	33.8	34.1	28.2	40.3	41.2	43.3
Mix B	240	70.7	98.7	127.3	152.2	24.1	25.1	32.5	33.4	30.9	41.1	44.6	46.0

The test results indicate that Mix B has slightly higher elastic modulus than Mix A. The elastic modulus increases rapidly until approximately 3 days to experience small change thereafter. Since the experimental results were measured at discrete times, a regression function was formulated to obtain the time-dependent material properties and free elastic tensile stresses of UHPC at any ages. The elastic modulus can be calculated by Eq. (2) using the regression coefficients shown in Table 3 [3].

Table 3: Regression coefficients.

Designation	*a*	*b*	R^2
Mix. A	0.389	0.001	0.9948
Mix. B	0.381	0.001	0.9985

$$E_c(t) = E_{c28} \exp\left(\frac{a}{b-t}\right) \quad (2)$$

where E_{c28} is the 28-day elastic modulus (GPa); and, a and b are the regression coefficients.

3 Setting property of UHPC

Fig. 1 illustrates the setting time test of UHPC conducted in compliance with ASTM C 403. A penetration time of 10 seconds and depth of 25 mm were applied to measure the setting time. When the Vicat spindle penetrated to a depth of 25 mm within 10 seconds, the setting time after casting UHPC in a test bowl was recorded. Generally, measurement of the initial setting time starts when the stress inside the matrix by Vicat spindle reaches 3.5 N/mm^2. The final setting time is measured when the internal stress of matrix reaches 28.5 N/mm^2. This procedure was applied for UHPC in this study.

Figure 1: Setting time test of UHPC.

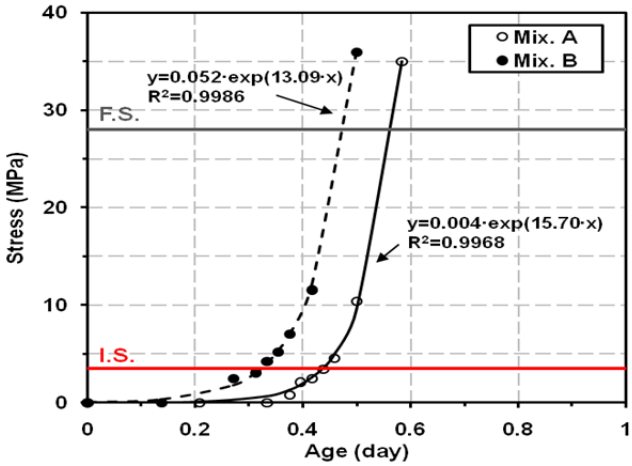

Figure 1: Results of setting time test of UHPC.

Fig.2 plots the results of the setting time test of UHPC. The initial and final setting times of Mix A are 11 h and 13.5 h after casting. For Mix B containing EA and SRA, the initial and final setting times occurred earlier than Mix A by 2.5 h and 4 h at 7.5 h and 11.5 h, respectively. The earlier setting time of Mix B can be explained by the presence of ettringite generated by EA. The resistance stress of UHPC is proportional to the exponential of time.

4 Non-restrained Shrinkage of UHPC

Test setup

The test of non-restrained shrinkage was carried out on UHPC using the method recommended by the Japan Concrete Institute (JCI). Only the upper side of the specimen was exposed to the air (Fig. 3), since structural members such as beam, girder, and slab are generally exposed on their upper side. UHPC being adopting massive quantities of binders, shrinkage occurs mainly through autogenous shrinkage while drying shrinkage has very poor contribution.

A thermocouple was embedded to evaluate the thermal strain. A Teflon sheet was introduced between UHPC and the steel mould to reduce friction. The non-restrained shrinkage was measured using a strain gauge embedded at the center of the

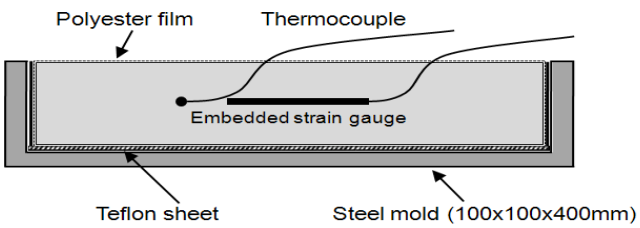

Figure 2: Layout of non-restrained shrinkage test.

specimen. This means that the measured non-restrained shrinkage is the result of both autogenous shrinkage and drying shrinkage from the exposed upper side.

Test results

Fig. 4 plots the results of the non-restrained shrinkage test of UHPC at 28 days. The results are calibrated with the thermo-strain. The non-restrained shrinkage of Mix A and Mix B converge respectively to 800 με and 400 με after 91 days with a smaller shrinkage for Mix B. This difference can be explained by the swelling of Mix B between 0.7 day and 1.2 days due to the generation of ettringite by EA in the matrix. The shrinkage of Mix A increases continuously while Mix B shows stabilized shrinkage after 7 days. Fig. 5 shows a zoom up of Fig. 4 for the 4 first days. It can be seen that, during this period, the shrinkage of Mix B with EA and SRA contents is larger than that of Mix A. This implies that the shrinkage stress developed in UHPC at the manufacturing stage may provoke cracking in Mix B.

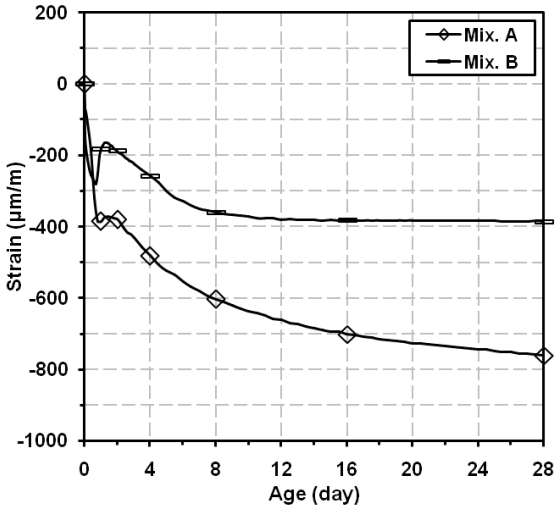

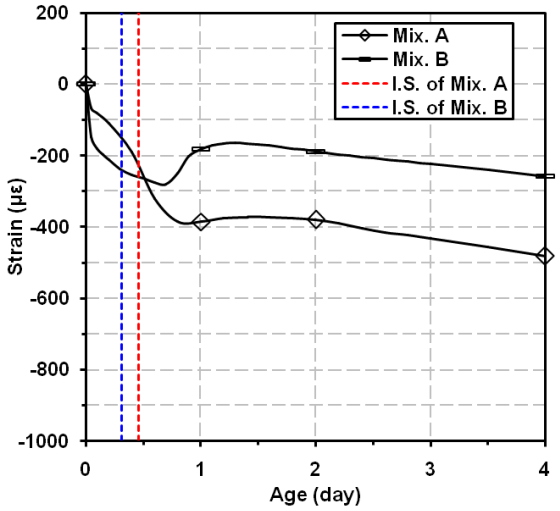

Figure 3: Non-restrained shrinkage of UHPC (28 days). Figure 4: Non-restrained shrinkage of UHPC (4 days).

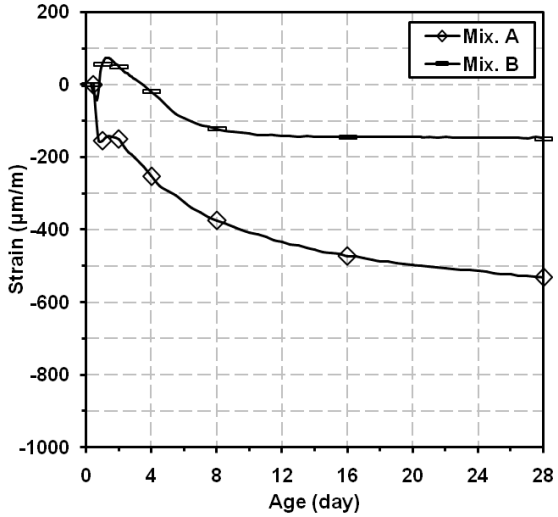

Figure 6: Non-restrained shrinkage after initial setting.

The dotted lines in Fig. 5 indicate the initial setting times of Mix A and Mix B. According to the research results of JCI, shrinkage occurring prior to the initial setting time can be assumed as plastic deformation in normal concrete. Recalling that shrinkage of UHPC in plastic state is not generating confining stress, which is the main cause of initial crack, this statement can be applied to UHPC. Generally, cracks initiate when internal stress is higher than the strength in the hydrated matter like concrete. In terms of crack control, shrinkage prior to the initial setting can be discarded from the non-restrained shrinkage of UHPC.

Fig. 6 plots the non-restrained shrinkage from which shrinkage before initial setting has been removed. Here, the corrected shrinkage of Mix A and Mix B converge to approximately 150 με and 550 με, respectively. The shrinkage value of 250 με before initial setting can be ignored with regard to internal stress. However, this may not be acceptable in terms of crack control. Since the previous test results are not

sufficient to confirm this assumption, further study is required to estimate accurately the inner stress of UHPC at very early age.

5 Restrained Shrinkage of UHPC

Test setup

The restrained shrinkage test was conducted in accordance with AASHTO PP34-98. The details of the specimens are depicted in Fig. 7. A Teflon sheet was applied to prevent restraint induced by the friction between concrete and the wooden base. Concrete was casted between the inner and outer steel rings and the ring specimens were placed in a room maintained at temperature of 23±1°C and humidity of 60±5%. After 24 hours, the outer ring mold was removed and the upper side of the concrete ring was sealed using a silicone-rubber sealer. Therefore, drying was allowed only from the outer circumferential surface as shown in Fig. 7(b). Four strain gauges were attached inside the steel ring to monitor steel strain. Two different thicknesses of 35 and 76 mm were used for the concrete ring, and the corresponding designation is explained in Fig. 8.

(a) Molds

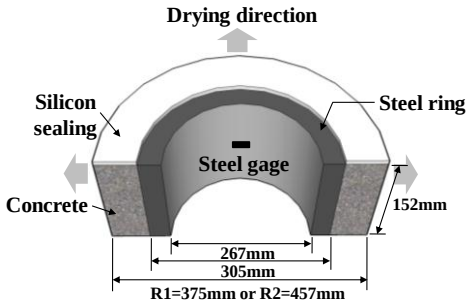

(b) Geometry of ring specimens

Figure 7: Description of ring-type restrained specimens.

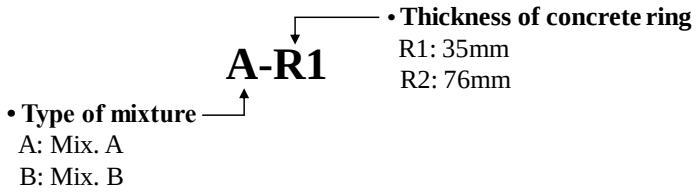

Figure 8: Designation for restrained shrinkage specimens.

Prismatic molds with 150 mm square cross section and length of 550 mm were prepared and UHPC was placed to heights of 35 and 76 mm to create cross sections identical to specimens R1 and R2. A strain gage was embedded in the middle of each specimen to measure shrinkage strain and a Teflon sheet was placed between concrete and the mold to reduce friction. Shrinkage strain was measured immediately after concrete casting in a room with constant temperature and humidity equal to those of the restrained shrinkage test. All specimens were demolded after 24 hours and sealed with aluminum adhesive tape so as to obtain a ratio of exposed surface area to volume (S/V) identical to that of the concrete ring specimens.

Restrained shrinkage

Fig. 9 presents the strains of the inner steel ring of specimens R1 and R2. As shown in Fig. 9(a), the steel strain of specimens R1 at 28 days reaches -123 and -79 με for Mix A and Mix B, respectively. The smaller steel strain of Mix B-R1 can be explained by the shrinkage compensation effect of EA and SRA. After 8 days, the steel strain of Mix B-R1 decreases slightly due to the tensile creep effect caused by insignificant free shrinkage. For specimens R2, the steel strain at 28 days reaches -158 and -104 με, which is about 28% and 32% larger than specimens R1 despite of identical inner steel ring and exposed condition (Fig. 9(b)). The larger decrease of steel strain in Mix B-R2 caused by tensile creep than in Mix B-R1 is originated from

the increase of the amount of shrinkage and internal pressure caused by the use of a thicker concrete ring.

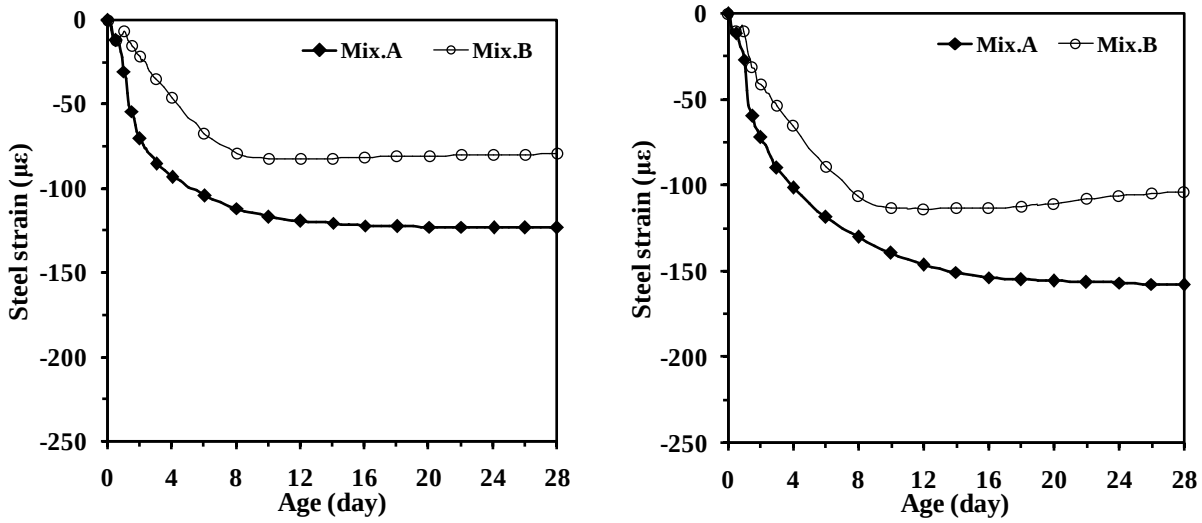

(a) Specimen R1 (b) Specimen R2

Figure 9: Average steel ring strain measurements for Mix A and Mix B.

6 Tensile stress by ring-test

The internal pressure, which is caused by the combined effect of concrete shrinkage and restraint of the inner steel ring, is calculated by Eq. (3). If shrinkage occurs uniformly all over the cross section, the maximum residual tensile stress of concrete develops at the inner surface of the concrete ring. Accordingly, the maximum residual tensile stress can be expressed as Eq. (4) assuming that r is r_{ic}, based on elasticity theory [4].

$$P_i = \frac{(r_{os}^2 - r_{is}^2)}{2r_{os}^2} E_{st}\varepsilon_{st} \tag{3}$$

$$\sigma_{t\max} = \frac{(r_{os}^2 - r_{is}^2)}{2r_{os}^2}\frac{(r_{ic}^2 + r_{oc}^2)}{(r_{oc}^2 - r_{ic}^2)} E_{st}\varepsilon_{st} \tag{4}$$

where P_i is the internal pressure (MPa); r_{is} and r_{os} are the inner and outer radius of steel ring (mm); E_{st} is the elastic modulus of the steel ring (GPa); ε_{st} is the steel strain (με); and, r_{ic} and r_{oc} are the inner and outer radius of concrete ring (mm).

Fig. 10 compares the elastic tensile stresses ($\sigma = E_c \cdot \varepsilon_{sh}$) caused only by shrinkage and the residual tensile stresses of specimen R1 calculated by Eq. (4). In this case, the elastic modulus was predicted using Eq. (2). In Fig. 10, the solid and dotted lines represent the elastic and residual tensile stresses, respectively. The tensile stresses of UHPC caused by the steel restraint were reduced by stress relaxation. The residual tensile stresses of Mix A and B-R1 were relaxed and reached 14.1 and 9.1 MPa at 28 days, which correspond to about 61 and 64% of the elastic stresses, respectively. The tensile strength being higher than the residual tensile stress, shrinkage cracking did not occur.

Interface pressure depends on the geometric properties, modulus of elasticity and strain of the inner steel ring. In this study, comparison of the maximum interface pressure is performed for ring specimens with two mixtures and thickness of concrete ring while applying an identical

inner steel ring (Fig. 11). Test results indicate that the interface pressure of Mix A-R1 is 1.4~1.5 times larger than that of Mix B-R1 and increases with larger S/V and thickness of concrete ring.

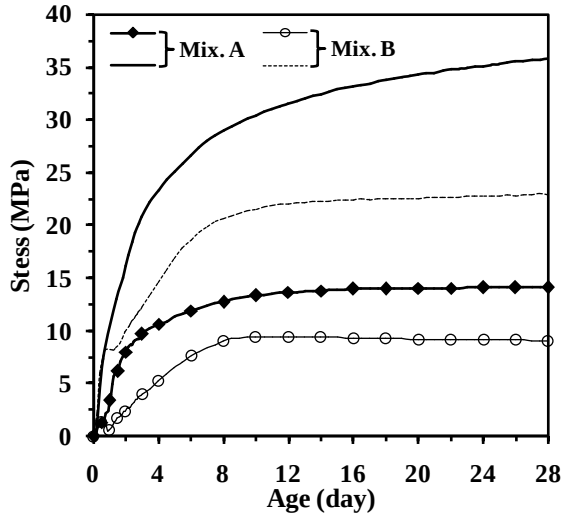

Figure 10: Comparison of elastic and residual tensile stresses of R1 specimen.

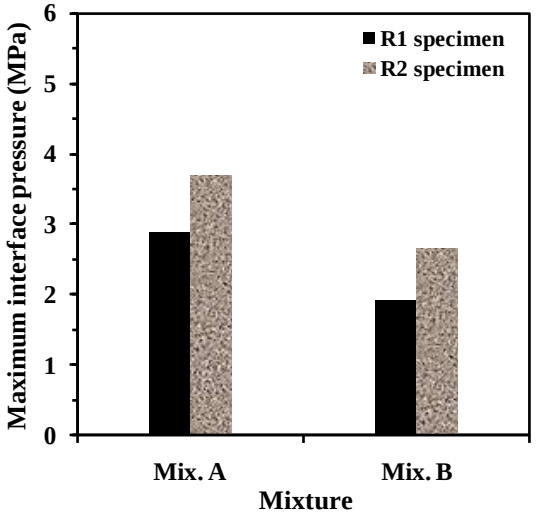

Figure 11: Calculated maximum interface pressures of R1 and R2 specimens.

The restrained strain, $\varepsilon_r(t)$, is equal to the total non-restrained shrinkage when concrete is perfectly restrained. However, the inner steel ring is deformed by concrete shrinkage as shown in Fig. 9. Thus, the restrained strain is calculated using Eq. (5) by subtracting the steel strain from the total free shrinkage.

$$\varepsilon_r(t) = \varepsilon_{sh}(t) - \varepsilon_{st}(t) = \varepsilon_e(t) + \varepsilon_{cr}(t) \tag{5}$$

7 Relationship between setting time and stress

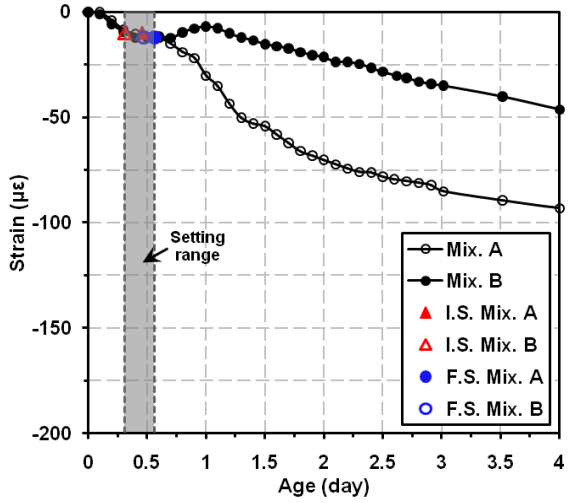

Figure 12: Comparison of setting time and stress of UHPC.

Fig. 12 compares the setting time and strain of the steel ring at early age. The strain of Mix A increases rapidly after final setting time, whereas Mix B experiences expansive behavior after final setting time. In general, the development of strength in UHPC can be assumed to start after final setting time. However, the results of ring test revealed that the inner steel ring was deformed before initial setting time. This implies that tensile stress occurred in UHPC. Accordingly, thorough conclusion cannot be drawn on the initiation of tensile stress in UHPC.

Future study should conduct restrained shrinkage test of UHPC without steel fiber and setting test under identical conditions to clarify this problem.

8 Conclusions

UHPC requires massive quantities of binders, which generate significant autogenous shrinkage in the structural member at very early age of the manufacturing stage. This study, as part of a research for the control of cracks that may occur in UHPC structural members due to the restraint of forms, investigated experimentally the shrinkage behavior of UHPC at very early age and the corresponding stresses developed in UHPC.

Differently from the common acceptation, results revealed the occurrence of confining stresses in UHPC even in its visco-plastic state prior to early setting. This implies that the sole evaluation of the non-restrained shrinkage behavior is insufficient for the control of cracks in UHPC at very early age and stresses the necessity to provide solutions enabling to evaluate the shrinkage behavior under restrained state. In addition, the mix adopting EA was seen to experience relatively large autogenous shrinkage strain at early age, which increases the risk of occurrence of internal cracks before early setting. Ring tests also verified the possibility to compute the confining tensile stress and strain according to the shrinkage of UHPC at very early age.

Further studies will investigate solutions enabling to simulate the cross-sectional stiffness and restraint of the form according to the thickness of the UHPC structural member, and verify these solutions experimentally. It is expected that the results of this study will contribute to the advancement of crack control at the manufacturing stage of UHPC structural members presenting cross-sectional shapes slimmer than conventional concrete members.

9 Acknowledgement

This work is the result of the research project, the Super Bridge 200 of Korea Institute of Construction Technology. The authors hereby express their appreciation for the support.

References

[1] Maltese, C., Pistolesi, C., Lolli, A., Bravo, A., Cerulli, T. and Salvioni, D., 'Combined effect of expansive and shrinkage reducing admixtures to obtain stable and durable mortars', *Cem. Con. Res.*, **35** (12) (2005) 2244-2251.

[2] Bentz, D. P., 'Influence of shrinkage-reducing admixtures on early-age properties of cement pastes', *J. Adv. Concr. Tech.*, **4** (3) (2006) 423-429.

[3] Cha, S. W., Kim, K. H., Kim, S. W., Park, J. J. and Bae, S. G., 'Models for hydration heat evelopment and mechanical properties of ultra high performance concrete', *J. KCI*, **22** (3) (2010) 389-397.

[4] Hossain, A. B., Weiss, W. J., 'Assessing residual stress development and stress relaxation in restrained concrete ring specimens,' *Cem. Con. Comp.*, **26** (5) (2004) 531-540.

Creep and shrinkage prediction for a heat-treated Ultra High Performance Fibre-Reinforced Concrete

Philippe Francisco[1], Farid Benboudjema[2], Patrick Rougeau[1], Jean-Michel Torrenti[3]

1: CERIB (Study and Research for the French Concrete Industry), France
2: LMT–Cachan (ENS Cachan/CNRS UMR8535/UPMC/PRES UniverSud Paris), France
3: IFSTTAR (Institut français des sciences et technologies des transports, de l'aménagement et des réseaux), France

This paper is a contribution for the state of knowledge on the time-dependent strains of Ultra-High Performance Fiber-Reinforced Concrete (UHPFRC) undergoing a heat treatment at a moderate temperature. This type of heat treatment is applied under factory's conditions, just after the placement of the concrete in its mould, in order to accelerate during few hours the hardening of an intended product to be seen applying a prestressing to the early age. In order to develop the use of UHPFRC for this application, it is suitable to have adapted design models which take into account the influence of these heat treatments when they are a part of the industrial process. Adapted analytical models, taking as a starting point those presented in Eurocode 2, are proposed to consider the time-dependent strains of UHPFRC. Moreover, modeling and simulations reveal that it is possible to predict correctly the behavior of these UHPFRC as well on the change of internal temperatures as on the change of the time-dependent strains.

Keywords: UHPFRC, ultra-high performance fiber-reinforced concrete, heat treatment, shrinkage, creep, time-dependent strains, prestressed

1 Introduction

UHPFRC (Ultra High Performance Fibre Reinforced Concrete) mechanical properties allow manufacturing slimmer and even more durable prestressed concrete elements limiting the use of reinforcements. In order to develop the use of UHPFRC for this application, it is suitable to have adapted design analytical models which take into account the influence of heat treatments when they are a part of the industrial process. Two types of heat treatments can be distinguished. The first type, called heat treatment at moderate temperature (around 65°C maximum), aims to accelerate UHPFRC hardening in the first hours after moulding. The second type around 90°C is applied to the hardened concrete with the intention of developing new hydrates to increase concrete mechanical resistance and to limit time-dependent strains.

The heat treatment duration is a key parameter which determines the production cadences. Previous works [1] had optimized mixes and heating characteristics to accelerate the UHPFRC hardening so as to apply prestressing before 24 hours. Compressive strengths over 120 MPa are obtained no more than 20 hours after moulding with a heat treatment at moderate temperature (50°C). The tests carried out by Loukili [2] were used in particular for the development of the French Recommendations on UHPFRC [3]. The analytical models for creep and shrinkage selected distinguish heat-treated UHPFRC from non heat-treated UHPFRC. The heat treatment used during Loukili [2] works consisted of a curing at 90°C during several days applied to hardened concrete specimens.

This paper proposes adapted analytical models based on Eurocode 2-2 standard taking into account the experimental data in order to calculate the UHPFRC time-dependent strains after a submission to a heat treatment at moderate temperature. The concrete characteristics and the standards selected for analysis are presented. This study is under a more global project including numerical simulations of UHPFRC creep and shrinkage with a prediction based on the methodology worked out by Benboudjema [4] and taking into account the effects of heat treatments at moderate temperature.

2 Experiments

Concrete mixes

The UHPFRC mixes studied are presented in table 1. UHPFRC A and B differ by the supplier and the amount of superplasticizer added and by the kind of mixer used. Both superplasticizers are carboxylate-based admixtures. The binder contains CEM I 52,5 N cement according to EN 197-1 standard and silica fume.

These concretes are mixed in laboratory. Dry constituents are homogenised before adding water and superplasticizer. The mixing duration and methodology depend on the device used. UHPFRC A was mixed using a usual planetary mixer with vertical axis and UHPFRC B using a new generation mixer with a rotating mixing pan. UHPFRC A and B have a selfcompacting behavior.

Table 1: UHPFRC mixes studied.

Constituents	Mass proportions (kg)	
	UHPFRC A	UHPFRC B
Cement	900	900
Silica fume	180	180
Siliceous sands	1160	1160
Metallic fibres	157	157
Superplasticizer A	15	0
Superplasticizer B	0	45
Effective water/cement ratio	0.2	0.2

Heat treatments

Concrete specimens underwent a heat treatment in wet conditions after being demoulded and protected from drying. Two moderate heat treatments were studied, both having for objective to accelerate the hardening of UHPFRC during the very first hours. UHPFRC A underwent a heat treatment at 50°C. UHPFRC B underwent two different heat treatments simultaneously: the same used for UHPFRC A at 50°C and a second with a lower duration at 65°C (see Fig. 1: the chamber temperature corresponds to the external temperature imposed to the specimen). In both cases, the concretes have sufficient mechanical resistances to sustain prestressing prior to 24 hours of age.

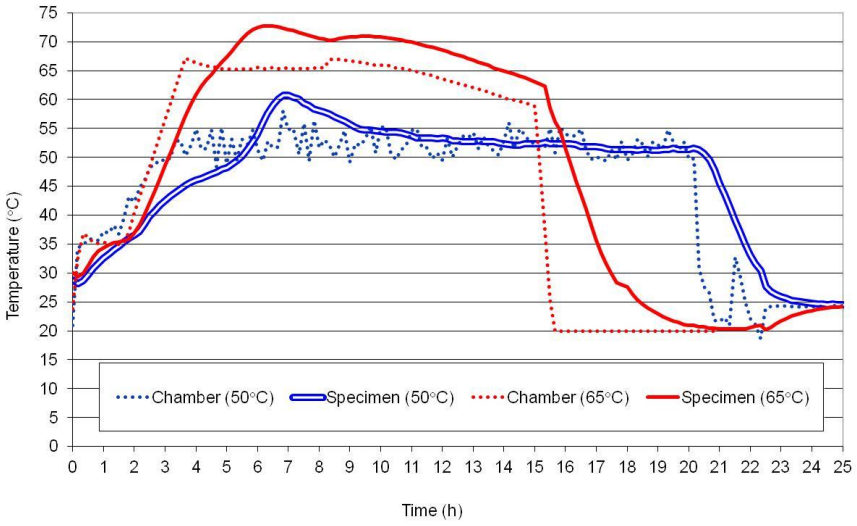

Figure 1: Temperature evolutions during the heat treatments.

Mechanical properties

The UHPFRC A mechanical characteristics after heat treatment are presented in table 2 (UHPFRC B properties are similar to UHPFRC A).

Table 2: UHPFRC A mechanical properties [1].

Mechanical properties on specimens of 40 x 40 x 160 mm (20 ± 2°C / storage in water)	UHPFRC A (50°C)
Average compressive strength at 20 hours (MPa)	152
Average compressive strength at 28 days (MPa)	188
Average flexural strength at 28 days (MPa)	29

Under standardized storage conditions, between 20 hours and 28 days, the compressive strength of UHPFRC A increases approximately by 24%. The moderate heat treatments imposed on the UHPFRC studied lead to materials likely to undergo significant autogenous strains (at 20 hours the concrete have a temperature adjusted concrete age lower than 5 days taking into account the accelerated hydration by heat treatment).

Evolution of the hydration degree

The evolution of the hydratation degree determined by mass loss at 550°C was measured after a storage of the specimens at 20 ± 2°C in autogenous conditions. The results (see. Table 3) show an accordance between the evolution of the hydration and the compressive strength until 28 days and probably after. The autogenous time-dependent strains after the heat treatments used are also in accordance with these results (see Fig. 3 and 4 respectively for the curves of autogenous shrinkage and basic creep experimental results).

Table 3: Evolution of the hydration degree.

Concrete age (days)	Temperature adjusted concrete age* (days)	Hydration degree (%)	
		UHPFRC B 50°C	UHPFRC B 65°C
2	5	34	34
7	10	35	36
28	31	47	46

* the temperature adjusted concrete is an equivalent age taking into account the acceleration of hydration induced by the heat treatment. It was calculated according to the NF EN 1992-1-1 standard

Time-dependent strain measurements

The tests were carried out on Ø 70 x 220 mm cylinders stored in a room at 20 ± 2°C and 50 ± 5% of relative humidity to obtain drying data. To obtain autogenous data, the specimens intended to be protected from the drying were coated with two layers of aluminium adhesive tape. Two metallic balls per axe of measurement (2 axes for UHPFRC A and 4 axes for UHPFRC B) are vertically glued on each cylindrical specimen tested and separated by 150 mm. The strains are measured using a hand ball-micrometer that measures the evolution of the distance between two metallic balls. It is calibrated before each series of measurements.

For each test named UHPFRC A 50°C, UHPFRC B 50°C and UHPFRC B 65°C, three specimens were used to quantify the autogenous shrinkage, the shrinkage under drying conditions, the creep strain under loading in drying conditions and the creep strain under loading in autogenous conditions. Drying shrinkage is equal to total shrinkage minus autogenous shrinkage, basic creep is equal to the total strain under loading in autogenous conditions minus autogenous shrinkage and drying creep is equal to strain under loading in drying conditions minus the total shrinkage and the elastic strains. Experimental results are

similar for UHPFRC A 50°C, UHPFRC B 50°C and UHPFRC B 65°C, they have similar temperature adjusted concrete age. Next part presents experimental data for UHPFRC A 50°C.

Effect of the stress level

For the creep tests, a constant load was applied 2 days after the mixing corresponding to 40% of the compressive strength measured at 2 days: 133 MPa. The elastic modulus measured during the stress application is equal to 43 GPa. A second constant stress level was also considered corresponding to 25% of the compressive strength. The results (see Fig. 2) show that the difference is not significant.

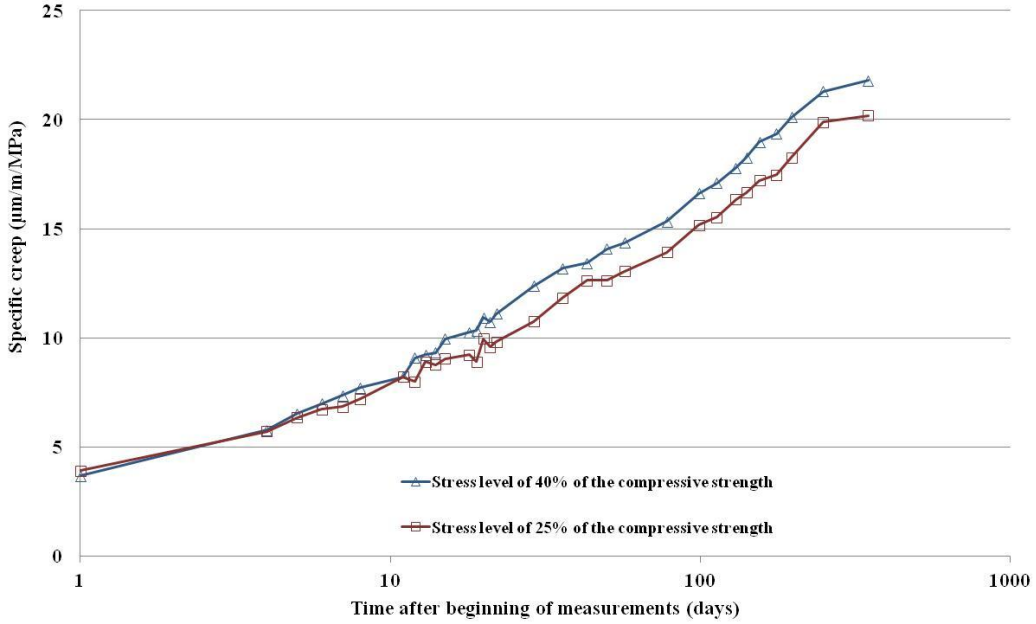

Figure 2: Impact of the stress level on the UHPFRC A specific creep.

3 Analytical models

Available guidelines and standards

The UHPFRC French Recommandations document was requested by the Scientific and Technical Committee of the AFGC (French Association of Civil Engineering) and was elaborate by the AFGC/SETRA working group on UHPFRC. The new version of this document will be published in 2012. The recommendations and analytical models selected for creep and shrinkage distinguished the UHPFRC with or without heat treatments. However heat treatments at moderate temperature were not plainly taking into account. For example, it was considered that no further shrinkage occurred after heat treatment and a guideline value of 550 µm/m was given if nothing were known at the preliminary design stages.

NF EN 1992-1-1 (EC2-1-1) and NF EN 1992-2 (EC2-2) standards of Eurocode 2 [5], [6], [7], [8] were not worked out to design UHPFRC structures. The highest strength class corresponds to C90/105 in France and the French annex of EC2-1-1 standard requires to refers to EC2-2 standard for high performance concretes of strength class higher than C50/60, with or without silica fume and using a Class R cement (according to Eurocode 2, cements of Class R includes cements having the following strength classes: 42,5 R, 52,5 N and 52,5 R). Three main benefits of this standard must be noticed:

- when a heat treatment is applied, the concept of “temperature adjusted concrete age” for temperatures varying between 0°C and 80°C may be taken into account;
- for drying creep and shrinkage, the relative humidity level and the concrete shape are taken into account;

- to evaluate time-dependent strains with greater precision, it is possible to identify the parameters in the models describing creep and shrinkage from experimental measurements and following a described procedure in EC2-2 (see OPT-EC2-2 in figures 3 and 4).

Adapted models suggested

The experimental results of time-dependent strains were compared with the output of the analytical models taken from the 2002 UHPFRC Interim Recommendations and Eurocode 2 standards). For all analytical models selected, the temperature adjusted concrete age was taking into account and for EC2-2 standard, the selected equations concerned high performance concretes using silica fume.

According to EC2-2 standard, the annex B may be used for calculating creep and shrinkage, including development with time. However, typical experimental values can exhibit a scatter of ± 30% around the values of creep and shrinkage predicted in accordance with this annex. Consequently, where greater accuracy is required, an experimental assessment should be undertaken following the annex B guidelines for the experimental determination of creep and shrinkage coefficients.

In addition, some parameters were included in these models to adjust the estimation. These parameters were chosen in order to minimise the sum of the squares (least square method) of the differences between the model estimation and the experimental results. The minimisation methodology respects the requirements of the procedure described in the informative annex B of EC2-2 standard.

Taking into account the differences observed between experimental results and models or adjusted models, this paper suggests models based on NF EN 1992-2 standard (named OPT-EC2-2 in figures 3 and 4) to calculate creep and shrinkage of UHPFRC undergoing a moderate heat treatment (for long term time-dependent strain estimation, see EC2-2 standard).

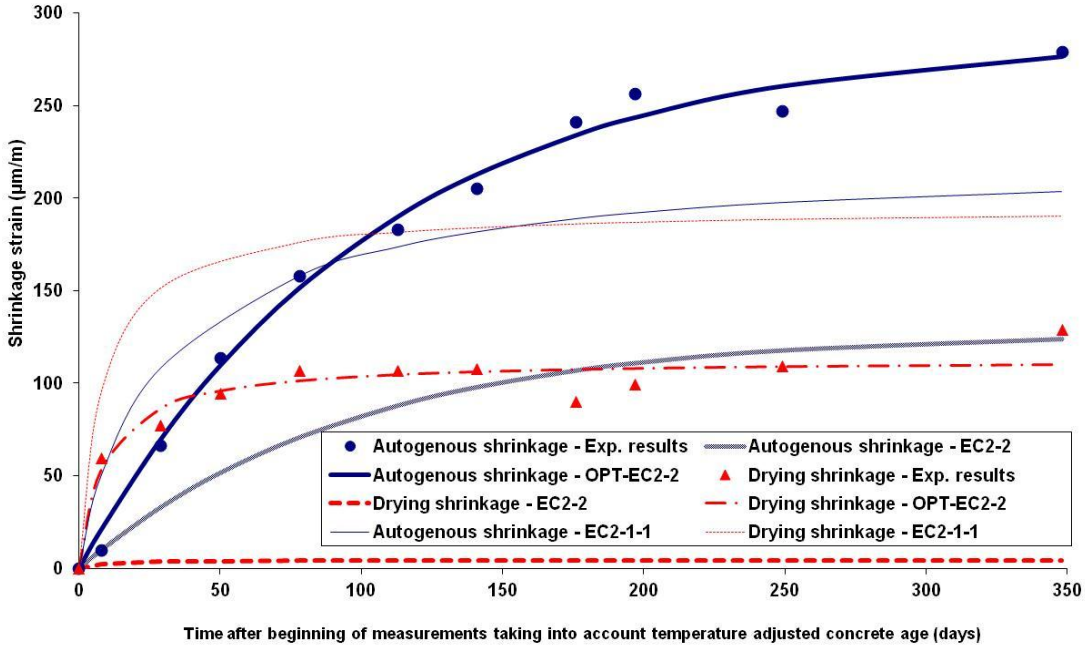

Figure 3: Shrinkage analytical models of EC2-2 suggested based on experimental results obtained with UHPFRC A 50°C (each point is the average of three measurements).

As illustration, the equation (1) suggested for the calculation of the autogenous shrinkage by EC2-2 standard is the following one (for t > 28 days):

$$\varepsilon_{ca}(t) = \beta_{ca1}(f_{ck} - 20)\left[\beta_{ca2} - \beta_{ca3}\exp\left(-t/\beta_{ca4}\right)\right]10^{-6} \quad (1)$$

(where t is the time in days, f_{ck} is the characteristic compressive strength at 28 days and β_{cai} with *i* between 1 and 4 are the coefficients identified using the method presented above).

For the example showed in figure 4, the optimisation is not necessary for drying creep because drying creep – EC2-2 curve is closed to the drying creep – OPT-EC2-2 curve.

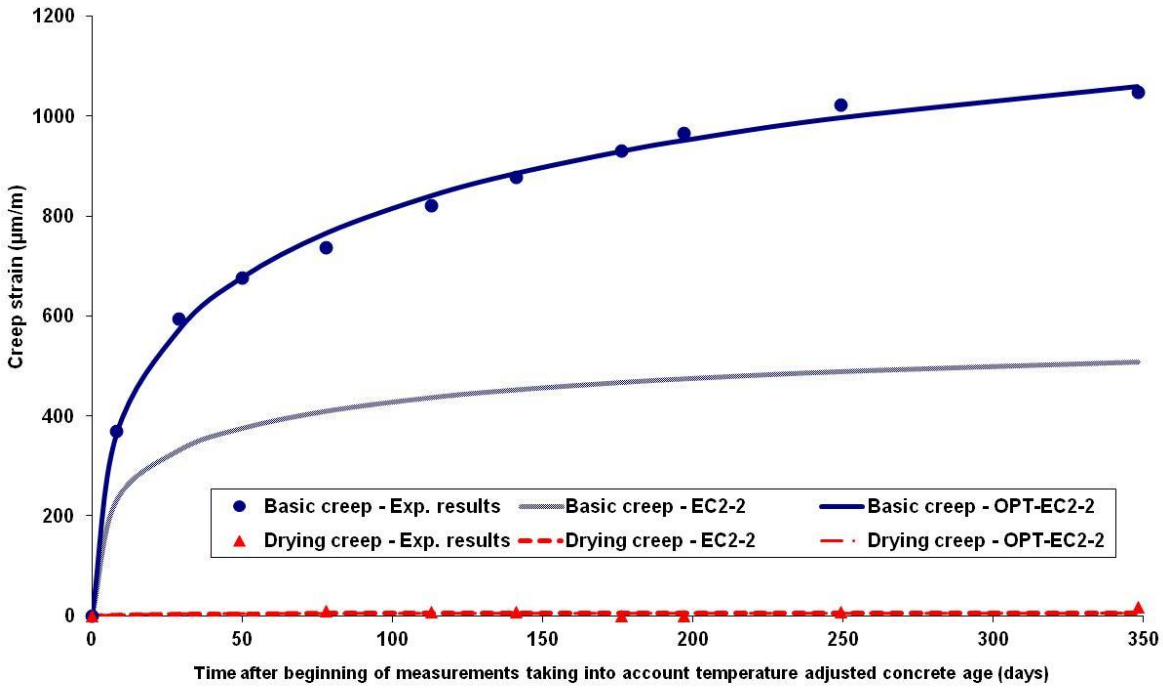

Figure 4: Creep analytical models of EC2-2 suggested based on experimental results obtained with UHPFRC A 50°C (each point is the average of three measurements).

4 Conclusions

The work presented is a contribution for the state of knowledge on the time-dependent strains of Ultra-High Performance Fiber-Reinforced Concrete (UHPFRC) undergoing a heat treatment at a moderate temperature. The results confirm the significance of the effect of the type of heat treatment used for UHPFRC regarding the time-dependent stains as shrinkage and creep. It is well documented that heat treatments at 90°C applied to the hardened concrete for almost two days increases concrete mechanical resistance and limit time-dependent strains. The heat treatments at moderate temperature studied here were applied just after mixing the UHPFRC with the aim to accelerate during few hours the hardening process.

For UHPFRC undergoing a moderate heat treatment, experimental results show that autogenous shrinkage must be taken into account for the calculation of the time-dependent strains. The French Interim Recommendations on UHPFRC (AFGC/SETRA, 2002) distinguished the UHPFRC with or without heat treatments. The new version of this document will be published in 2012 and would integrate plainly the impact of heat treatments on creep and shrinkage distinguishing heat treatments at moderate temperature applied during few hours after moulding from heat treatments at around 90°C applied to the hardened concrete.

NF EN 1992-1-1 and NF EN 1992-2 standards of Eurocode 2 were not worked out to design UHPFRC structures. Nevertheless, with the help of some adaptations using the methodology described in the annex B of EC2-2 standard, these analytical models allow to calculate creep and shrinkage of UHPFRC when a moderate heat treatment is used. Moreover, Eurocode 2

already take into account the concept of “temperature adjusted concrete age” for temperatures varying between 0°C and 80°C.

A better prediction of the evolution of the properties of the prestressed UHPFRC products according to the nature of the heating applied should allow the optimization of the production cadences and the energy used for the heat treatments.

References

[1] Rougeau, P.; Francisco, P.: Accélération du durcissement des BFUP – Exemples de produits réalisés en BFUP. CERIB report, France, 2003.

[2] Loukili, A.: Etude du retrait et du fluage de Bétons à Ultra-Hautes Performances, thèse de doctorat. Ecole Centrale de Nantes, France, 1996.

[3] AFGC / SETRA : Ultra High Performance Fibre-Reinforced Concretes – Interim Recommendations. AFGC / SETRA, France, 2002.

[4] Bendoudjema, F.: Modélisation des déformations différées du béton sous sollicitations biaxiales. Application aux enceintes de confinement de bâtiments réacteurs des centrales nucléaires, thèse de doctorat. Université de Marne-la-Vallée, France, 2002.

[5] NF EN 1992-1-1 standard: Eurocode 2 – Design of concrete structures – Part 1-1: General rules and rules for buildings. AFNOR, France, 2005.

[6] NF EN 1992-1-1/NA standard: Eurocode 2 – Design of concrete structures – Part 1-1: General rules and rules for buildings – National annex to NF EN 1992-1-1:2005 – General rules and rules for buildings. AFNOR, France, 2007.

[7] NF EN 1992-2 standard: Eurocode 2 – Design of concrete structures – Part 2: Concrete bridges – Design and detailing rules. AFNOR, France, 2006.

[8] NF EN 1992-2/NA standard: Eurocode 2 – Design of concrete structures – Part 2: Concrete bridges – Design and detailing rules – National annex to NF EN 1992-2 – Concrete bridges – Design and detailing rules. AFNOR, France, 2007.

Creep Behaviour of UHPC under Compressive Loading with Varying Curing Regimes

Jason Flietstra, Theresa M. Ahlborn, Devin K. Harris, Henrique de Melo e Silva
Civil and Environmental Engineering Department, Michigan Technological University, USA

This Ultra High Performance Concrete research involves observing the early age creep and shrinkage under a compressive load throughout multiple thermally treated curing regimes. The goal is to mimic the conditions that would be expected of a precast/prestressing plant in the United States, where UHPC beams would be produced quickly to maximize a manufacturing plant's output. The practice of steam curing green concrete to accelerate compressive strengths for early release of the prestressing tendons is utilized (60oC [140oF], 95% RH, 12 hrs), in addition to the full thermal treatment (90oC [195oF], 95% RH, 48 hrs) while the specimens are under compressive loading. Michigan Tech has three moveable creep frames to accommodate two loading criteria per frame of 0.2f'c and 0.6f'c. Specimens are loaded and moved into a custom build curing chamber at different times, mimicking a rapid precast plant producing This paper will present the effects of creep strain (minus the companion shrinkage strain) due to the varying curing regimes.

Keywords: compressive creep, creep coefficient, creep strains, curing, UHPC

1 Background and Motivation

The compressive creep and shrinkage behaviour of UHPC while undergoing varying onset thermal curing treatments is presented herein. While previous research has measured compressive creep and shrinkage strains on UHPC, the creep strain measurements were only observed on ambient cured specimens or after a recommended thermal treatment. The goal of this research was to mimic curing procedures that would be expected of a common precast/prestress plant in the United States. As such, this research considered five unique curing regimes, where creep specimens were under a compressive load during a thermal treatment. Table 1 defines the curing regimes. The composition of all the mixed, cast and tested UHPC was completed with procedures similar to previous work at Michigan Technological University (Michigan Tech), [1], [2], [3], [4], and all research reported herein was conducted using Ductal, a UHPC supplied by Lafarge North America.

Table 1: Curing regimes defined.

Abbreviation	Description of Curing Regime
AMC	Ambient cure for 70 hrs, then loaded in compression, continue ambient cure
SST	Ambient cure for 70 hrs, loaded, standard thermal cure applied
PST	Pre-steam cure for 14 hrs, loaded, standard thermal cure applied
PSD	Pre-steam cure for 14 hrs, loaded, ambient conditions for 72 hrs, standard thermal cure applied
PDD	Pre-steam cure for 14 hrs, loaded, ambient conditions for 11 days, standard thermal cure applied

Loading of the test specimens was done once the specimens reached the recommended compressive strength for the release of prestress of 96.5 MPa (14 ksi), [5]. This required early-age compressive testing for both ambient and pre-steam cured specimens to locate the time, from batching, when specimens reached a compressive strength of 96.5 MPa.

Nine 75-mm (3.0-in) diameter by 300-mm (12.0-in) long cylinders were required for each curing regime. Three cylindrical specimens were loaded in compression at the high stress level

of 0.6$f`_{ci}$ (58 MPa [8.4 ksi]), and three specimens were loaded at the low stress level of 0.2$f`_{ci}$ (19.3 MPa [2.8 ksi]). The final three specimens were used as companion shrinkage specimens and were subjected to the same curing regimes, but not the load. Three specimens, 100-mm (6.0-in) in length were tested to determine the compressive strength of the UHPC at the time of loading.

Compressive strength gain studies were conducted prior to creep loading to locate the time at which UHPC reached a target compressive strength of 96.5 MPa. These studies determined the age at which the creep specimens would be loaded in compression using an ambient cure time, and a pre-steam treatment to accelerate the compressive strength of the UHPC. The curing scenarios of the UHPC while undergoing a compressive creep load are listed in Table 1. Prior to compressive creep loading, specimens attained a compressive strength of 96.5 MPa by either an ambient cure or pre-steam cure. Once the specimens reached this compressive strength, standard dimensional measurements were recorded and the specimens were subjected to the compressive creep loading. Once loaded in constant compression, specimens were left in the ambient cure condition and only removed from the ambient cure room to undergo the thermal treatment at varying times, which would best mimic precast production facilities. [1]

2 Experimental Plan

One goal of this research was to mimic conditions selective to UHPC creep and shrinkage procedures of current precast/prestressed plants in the U.S. to allow for a clear understanding of these conditions and impacts on future design codes. The use of a steam cure immediately after concrete is placed in the prestressing beds is commonly used in precast/prestressed plants around the U.S. The steam cure will accelerate the concrete compressive strength gain and therefore allow the release of the prestressing strands earlier, which reduces cycle time of the prestressing beds. From interviews with precast/prestress facilities using normal strength concrete (NSC) and high strength concrete (HSC) it was determined that (regardless of climate) cure temperatures prior to prestress release are maintained between 24-35°C (75-95^{o}F) for approximately 3 hours immediately following casting; the cure temperature is then slowly raised, over a period of 2-3 hours, to a maximum temperature between 49-65°C (120-150^{o}F), where it is maintained until the forms are stripped and the prestress is released (at approximatley 12-15 hours from casting), [2]. This information was used a basis for the pre-steam cure.

The five curing regimes chosen for this research aimed to mimic several scenarios expected at precast/prestressed plants. Four curing scenarios involved the use of a standard thermal treatment (90^{o}C [194^{o}F] at 95% relative humidity (RH) for 48 hours) while maintaining a compressive load. The fifth curing regime remained at ambient conditions (23^{o}C [73^{o}F] at 50% RH) and was used as a baseline for comparison, [1].

A pre-steam cure (60^{o}C [140^{o}F] at 95% RH) was administered to accelerate the compressive strength of the specimens for three curing regimes, while the remaining curing regimes were ambient cured, until a compressive strength of 96.5 MPa (14 ksi) was reached. The time in which all the specimens of a single batch were placed into the curing chamber for the pre-steam treatment or placed in the ambient conditions, was the reference “zero” starting point for the tests. This pre-stream treatment consisted of raising the chamber temperature to 60^{o}C over a three hour period and then holding at 60^{o}C for the next 14 hours.

In order for UHPC to “lock in” its high compressive strength and durability characteristics, a thermal treatment was required, [4]. In all cases the thermal treatment occurred *after* the creep loading was applied to the specimens. The thermal treatment required moving the creep

frames (while maintaining a compressive load on the specimens) into a custom built curing chamber, as seen in Figure 1 where the temperature was increased to 90°C (194°F) over a 6 hour period, holding at 90°C for 48 hours before the specimens cooled to ambient conditions.

Figure 2 provides a graphical representation of the PSD specimens using two vertical axis against a common time dependent axis. The left axis is the temperature that the PSD specimens are subjected to throughout the experiment represented against time by the solid line. The hatched lines correspond to the right axis, which represents the high and low stress level scenarios. This curing regime employs the use of the pre-steam treatment immediately following casting then loading the specimens in compression following the 14 hour pre-steam treatment. A delay of 72 hours occurs before the PSD specimens are finally subjected to the standard thermal treatment, while constantly being subjected to a compressive load, [1].

Figure 1: Michigan Tech's custom creep frame curing chamber.

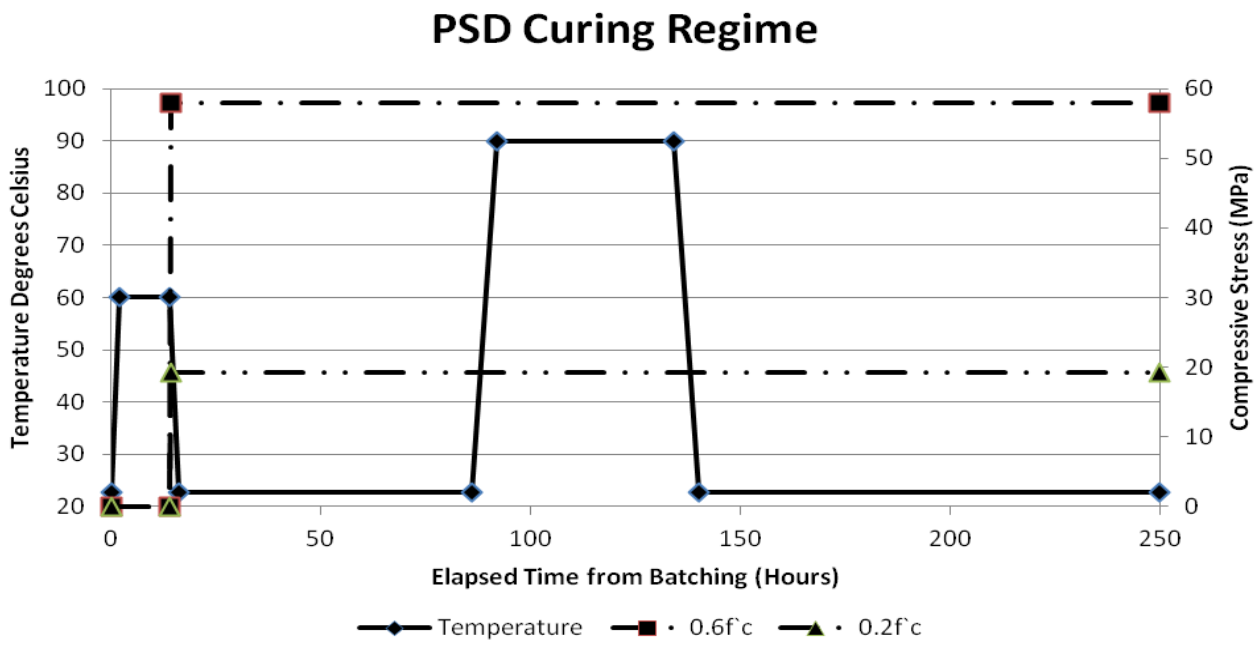

Figure 2: PSD applied creep stress level and cure temperature variation with respect to specimen age.

3 Results

The data collected covered the initial findings of the early-age creep effects of UHPC under a compressive load through varying curing regimes. To isolate the creep strains for each curing scenario, the elastic strain and the shrinkage strains must be removed from the total measured strain. For example, the total measured strain for the ambient cured specimens under the high load level, $0.6f`_{ci}$, at 28 days was 2707με, the elastic strain was 1269με, and the shrinkage strain was 380με. Therefore, the creep strain at 28 days for this scenario was 1058με. Table 2 lists the average initial elastic strain, shrinkage strain, and creep strain for each curing regime and compressive creep load level at 24-28 days. (Because of the testing timeline, two creep frames were used for multiple curing regimes. Therefore the standard thermal cured (SST) specimens and the pre-steam standard thermal cured (PST) specimens were unloaded at 24 days). The creep coefficients are calculated in Table 2 by dividing the measured 28 day creep strains by the initial creep strain ($\epsilon_{28d}/\epsilon_{initial}$) found for each curing regime. The average creep coefficient (C_{ct}) for specimens subjected to a thermal treatment was 1.12 for the $0.6f`_{ci}$ stress level and 0.76 for the $0.2f`_{ci}$ stress level, [1].

Table 2: Average initial elastic and 24-28 day strain values for each curing regime.

Curing Regime	$f`_{ci}/f`_c$	Elastic Strain, $\epsilon_{initial}$	Shrinkage Strain	24-28 day Creep Strain Measurement, ϵ_{28d}	C_{ct}
AMC	0.60	1269	380	1058	0.83 (1.27)*
	0.20	579		313	0.54 (0.80)*
SST	0.63	1494	172	1678	1.12
	0.21	496		442	0.89
PST	0.60	1316	158	1653	1.26
	0.20	573		309	0.54
PSD	0.60	1542	212	1727	1.12
	0.20	526		491	0.93
PDD	0.60	1543	305	1537	1.00
	0.20	591		404	0.68

*predicted values at one year

Effects of ambient cure

The isolated creep strains collected for the ambient cured specimens were fit to a logarithmic function for the high stress level and low stress level specimens. The models can be seen in Figure 3. The logarithmic functions are plotted along with curves for each data series only looking at the creep strains in excess of the elastic strain due to loading, and the shrinkage strains removed. This type of function best fit the data produced in this research and the function reaches an asymptotic value, as would be expected due to sustained loading, which can be used to predict a one year creep coefficient for the AMC specimens.

Equation 1 is the logarithmic relationship that best fit the ambient cured specimens subjected to the high stress level of $0.6f`_{ci}$. This relationship fits the early-age compressive creep strains closely, and predicts creep strain at 360 days of 1610με. The creep strains rapidly increase in the first week of applied loading and the rate of creep decreases in the following weeks. This prediction is almost identical to Graybeal's calculated 1600με, even though Graybeal used 100mm dia. (4.0-in.) by 200mm (8.0-in.) long specimens and loaded the specimens in compression at 28 days after demolding, [6].

$$\varepsilon_x = 213.7 * ln(x) + 352.5 \quad (1)$$

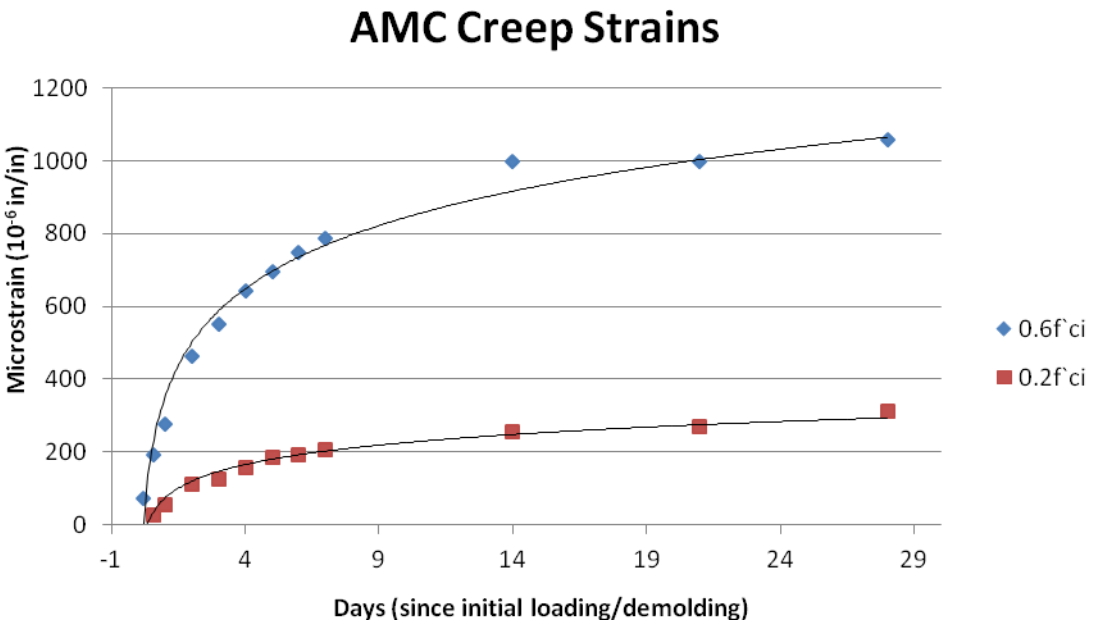

Figure 3: Creep strain results for the ambient cured (AMC) specimens.

Equation 2 is similar to equation 1, but represents the best fit logarithmic relationship for the lower $0.2f`_{ci}$ stress level. Using this equation, the predicted 360 day ultimate creep strain for the $0.2f`_{ci}$ load level best yields a value of 468με, [1].

$$\varepsilon_x = 65.88 * ln(x) + 74.1 \quad (2)$$

Using the predicted values for the one year creep strains on the ambient cured (AMC) specimens, creep coefficient of 1.27 and 0.80 were calculated for the $0.6f`_{ci}$ and $0.2f`_{ci}$ stress levels, respectively. The higher stress level creep coefficient is comparable to previous research found by Graybeal at 0.78, [6], SETRA 0.80, [7], JSCE 1.20, [8], and UNSW 1.20, [9]. No research to date has subjected UHPC to a compressive stress as low as $0.2f`_{ci}$ to compare the validity of the predicted relationship.

Effects of the pre-steam treatment

The administration of a pre-steam cure (60°C at 95% RH) was used in this research to mimic what would be expected at a precast/prestress plant in the U.S. conforming to current practices. This pre-stream treatment accelerates the compressive strength of UHPC to the target compressive strength of 96.5 MPa (14 ksi) five times faster than an ambient cure. The pre-steam treatment, independent of when a standard thermal treatment was applied, had no affect effect on the 28 day creep coefficients for the curing regimes in this research, [1].

Effects of the thermal treatment

The effects of the thermal treatment on specimens under a compressive load were an important goal in this research. The following figures (Figure 4 and Figure 5) plot the average increasing creep strain against time for the three specimens tested in each curing regime. In these graphs, the initial elastic strain is neglected, and the shrinkage strains have been subtracted to plot only the creep strain measured in this research, [1].

The creep data shown in Figure 4 for the specimens subjected to the $0.6f`_{ci}$ stress level reveals that after a thermal treatment was applied to the specimens, the strain increased up to

approximately 1650με, with no significant additional strain occurring thereafter. Specimens subjected to an immediate thermal treatment (SST and PST) saw a rapid average increase of

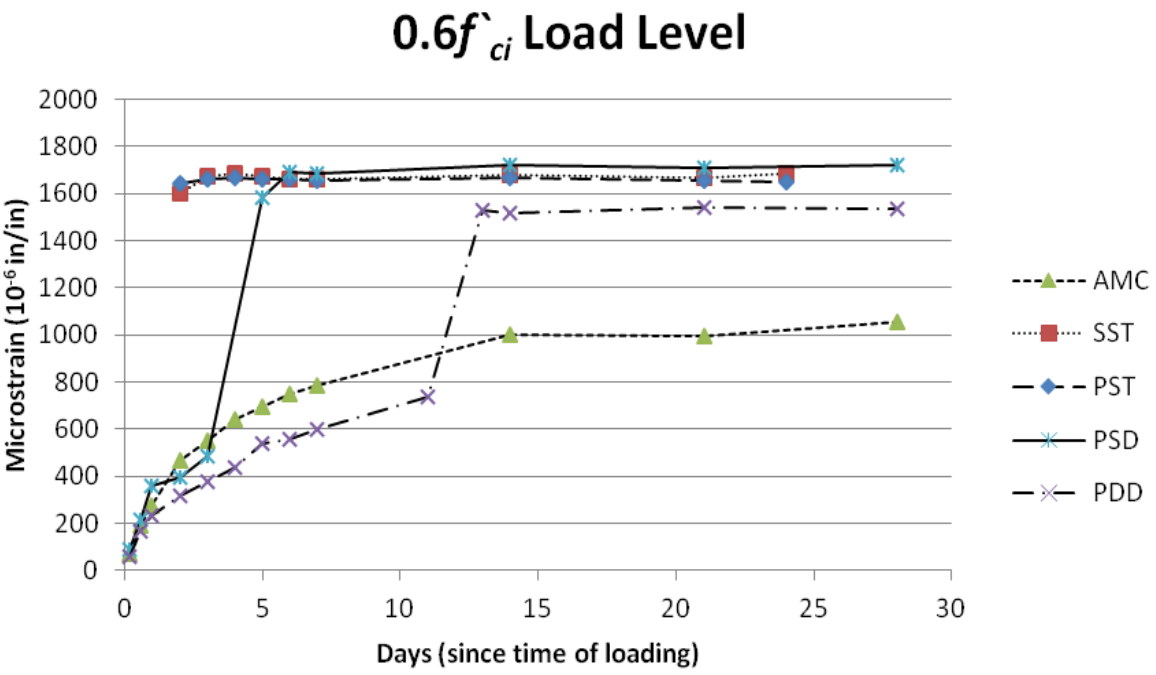

Figure 4: Average creep strain values for the 0.6f`$_{ci}$ load level, [1].

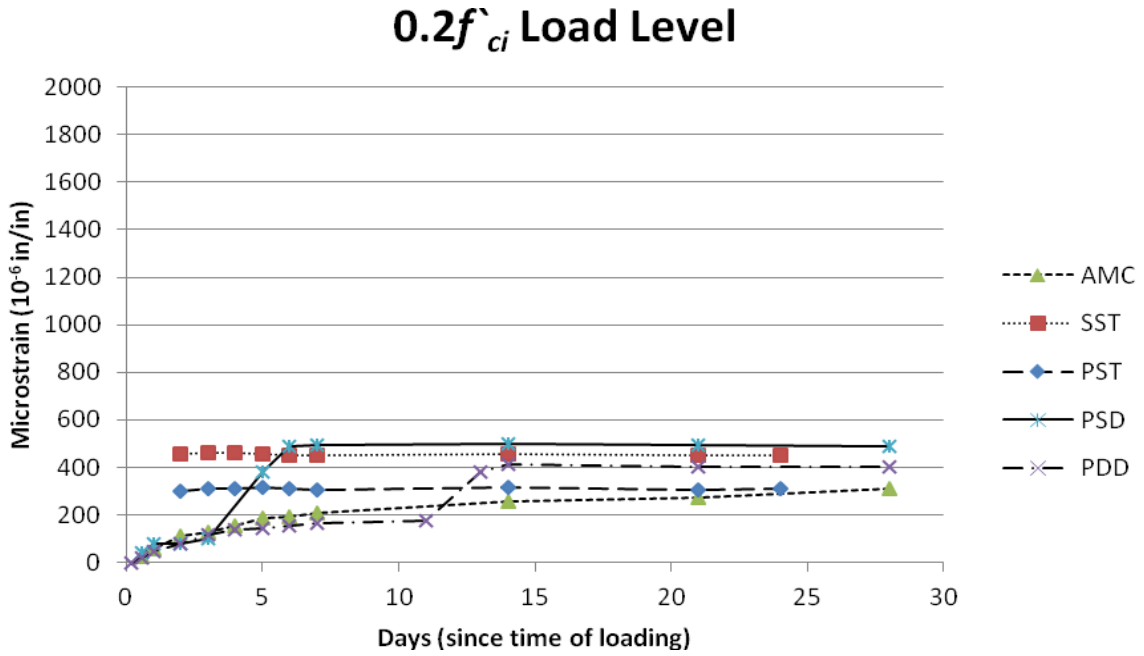

Figure 5: Average creep strain values for the 0.2f`$_{ci}$ load level, [1].

1655με after removal from the custom built curing chamber. Specimens subjected to delayed treatments saw increases of 1593με and 1527με for the PSD and PDD curing regimes, respectively. In all curing regimes subjected to the thermal treatment, the application of the thermal treatment "locked in" the creep strains in the UHPC. Prior to the application of the thermal treatment on the PSD and PDD specimens, the creep strains followed ambient cure (AMC) baseline. But following the thermal treatment, creep strains were "locked in" to approximately 1550-1650με, with minimal changes in creep strains occurring thereafter, [1].

Looking at specimen data for the lower stress level for each of the curing regimes (Figure 5), more scatter in the results is observed. Similar to the higher stress level, the strains occurring during the thermal treatment decreases as the specimens subjected to the delayed treatment increases (PSD and PDD curing regimes). The specimens with delayed onset of a thermal treatment show increasing strains following the pattern of the ambient cured specimens before the thermal treatment is administered. In general, and independent of any pre-steam treatment, specimens that were thermally cured reach creep strains of 300-500με, and this strain was "locked in" and stable. The scatter in data is attributed to the low stress level chosen for this research; the higher stress level produced more consistent creep data for UHPC, [1].

For each curing scenario subjected to a thermal treatment, Table 3 shows the creep strains (excluding the elastic strains) for the high and low stress levels due to the thermal treatment, as well as the companion shrinkage strains before during, and after a thermal treatment. The standard thermal treatment (SST) and pre-steam standard thermal treatment (PST) specimens were immediately demolded, loaded in the creep frames and subjected to the thermal treatment, therefore the strains induced on the specimens before the thermal treatment are negligible. However, the pre-steam delayed (PSD) and pre-steam double delayed (PDD) specimens were demolded, loaded in the creep frames and delayed the onset of the thermal treatment. Delaying the thermal treatment allowed the PSD and PDD specimens to undergo creep and shinkage strains before the applying the thermal treatment. Table 3 introduces the creep strains (neglecting the elastic and companion shrinkage strains) before and during the thermal treatment for each curing scenario, the companion shrinkage strains are also listed for each curing regime, [1].

Table 3: Measured creep and shrinkage strain before, during and after thermal treatment (μin/in), [1].

		AMC	SST	PST	PSD	PDD
Compressive Creep Level 0.6f`ci	*Before TT*	--	0	0	472	737
	During TT	--	1666	1644	1121	790
	After TT	--	1666	1644	1593	1527
Compressive Creep Level 0.2f`ci	*Before TT*	--	0	0	103	176
	During TT	--	520	459	348	203
	After TT	--	520	459	384	355
Shrinkage Specimens	*Before TT*	--	0	0	147	253
	During TT	--	172	158	65	52
	After TT	--	172	158	212	305

4 Conclusions

The data presented in this research provides the beginning framework for a more expansive compressive creep study on UHPC specimens under a thermal treatment. The importance of this research was to characterize the early-age (28 day) creep characteristics of UHPC as it is thermally treated, under a compressive load. By doing so, this research found that the effects of the thermal treatment "locked in" the creep strains independent of when the thermal treatment was administered. In general, precast/prestressed plants would be able to produce several prestressed UHPC elements on differing timelines, then administer the thermal treatment to all the elements together to save on energy costs, without having any significant effects on the "locked in" creep coefficient for thermally cured elements.

The following specific conclusions have been determined based on the data collected for specimens subjected to creep loading at a compressive strength of 96.5 MPa (14 ksi). The

creep coefficient was found to be greater on specimens under a compressive load during a thermal treatment, as opposed to previous research of being thermally cured prior to loading. Average creep coefficient values of 1.12 and 0.76 were observed on specimens subjected to a thermal treatment under $0.6f`_{ci}$ and $0.2f`_{ci}$ stress levels, respectively. The application of the thermal treatment "locked in" the creep coefficient, as minimal strain changes were measured following the thermal treatment. Specimens subjected to delayed onset thermal treatments followed the ambient cured increase in strains until the thermal treatment was applied.

Future work would include determining the impact of creep prior to thermal treatment for various scenarios that may be expected in the U.S. precast plant. This impact would be towards prestress losses, camber and deflections.

References

[1] Flietstra JC. 2011. Creep and Shrinkage Behavior of Ultra High Performance Concrete under Compressive Loading with Varying Curing Regimes. [Houghton, MI]: Michigan Technological University. p. 149.

[2] Nyland EM. 2009. Early-Age Creep and Shrinkage Behavior of Ultra-High Performance Concrete for Precast/Prestressed Concrete Applications. [Houghton, MI]: Michigan Technological University. p. 113.

[3] Kollmorgen, GA. 2004. Impact of Age and Size on the Mechanical Behavior of an Ultra-High Performance Concrete. [Houghton, MI]: Michigan Technological University. p. 125.

[4] Peuse EJ. 2008. Impact of Age at Thermal Treatment on the Mechanical Properties of an Ultra-High Performance Concrete. [Houghton, MI]: Michigan Technological University. p. 150.

[5] Larfarge North America. "Ductal Reference." Calgary, Canada, 2003.

[6] Graybeal, BA. 2006. Material Property Characterization of Ultra-high Performance Concrete. Federal Highway Administration, Office of Research, Development and Technology, Turner-Fairbank Highway Research Center: 2006: McLean, VA.

[7] Association Française de Génie Civil-Service D'études Techniques des Routes et Autoroutes (AFGC/SETRA). "Ultra-High Performance Fiber-Reinforced Concrete Interim Recommendations." 2002.

[8] Japanese Society of Civil Engineers (JSCE). Recommendations for Design and Construction of Ultra High Strength Fiber Reinforced Concrete Structures (Draft). Subcommittee on Research of Ultra High Strength Fiber Reinforced Concrete-Japan Society of Civil Engineers. 2006: Tokyo, Japan.

[9] N Gowripalan and R I Gilbert School of Civil and Environmental Engineering-The University of New South Wales (UNSW). 2000. Design Guidelines for RPC Prestressed Concrete Beams. VSL (Aust) Pty Ltd.

Mitigation of early age shrinkage of Ultra High Performance Concrete by using Rice Husk Ash

Nguyen Van Tuan[1,2], Guang Ye[3], Klaas van Breugel[1]

1: Faculty of Civil Engineering and Geosciences, Delft University of Technology, Delft, the Netherlands
2: Department of Building Materials, Hanoi University of Civil Engineering, Hanoi, Vietnam
3: Magnel Laboratory for Concrete research, Department of Structural engineering, Ghent University, Belgium

Ultra high performance concrete (UHPC) has become one of promising concretes in the last decade because of its excellent performance, such as high strength, low permeability and very good durability. However, like high performance concrete, UHPC is also subjected to high autogenous shrinkage due to high amount of cement and silica fume used. Seeking the ways to reduce the autogenous shrinkage is a very important task in the field of cement and concrete research. In this paper, the Rice husk ash, an agriculture waste, is explored to mitigate the autogenous shrinkage of UHPC. With high amorphous SiO_2 content and special porous structure, the RHA shows not only reduce the cost and improve the early age properties of the UHPC but also increase the environmental benefits.

Keywords: ultra high performance concrete, rice husk ash, autogenous shrinkage

1 Introduction

Ultra high performance concrete and autogenous shrinkage

Ultra high performance concrete (UHPC) is a family of concretes offering a combination of materials and performance characteristics. It made of Portland cement, silica fume (SF), quartz flour, fine silica sand, high-range water reducer, water, and steel or organic fibers. The UHPC shows some excellent performances on the ductility, ultra high compressive strength, and extreme durability. However, it can experience large shrinkage values. A very high autogenous shrinkage already found in the first one or two days after mixing, which causes a considerable cracking potential at early ages. The early age cracking due to restrained autogenous shrinkage could affect the numerous advantageous properties of UHPC and significantly restrict its prospective utilization in construction. The high autogenous shrinkage of UHPC is due to the low w/b ratio and a greatamount of SF used in UHPC, which causes a significant decrease in the internal relative humidity (RH) in the cement paste during the hardening, and a self-desiccation occurs in the absence of an external source of water [1].

Seeking the ways to reduce or to limit the autogenous shrinkage of UHPC is becoming very important for both research and engineering practice. A work reported that mitigation of autogenous shrinkage using external curing is not effective, due to the fact that the dense microstructure of UHPC could result in penetrating water rather slowly into the interior of concrete members [2]. As a result, internal water curing is considered as an effective solution to the problem of counteracting self-desiccation and autogenous shrinkage for the low permeability of the low w/b ratio cementitious system, thereby reducing the likelihood of early-age cracking. The most popular methods of internal curing for concrete are to use water-saturated aggregates and super-absorbent polymers (SAPs) [2]. Unfortunately, he SAPs have been proposed to be used as an internal curing agent to mitigate the autogenous shrinkage of UHPC due to the strict requirements on mechanical behaviours and the maximum size of aggregate. This technology is also used in engineering [3]. However, SAPs may easily make the concrete heterogeneous, because it will leave voids even as big as 600 μm [4], equal to the maximum sand size in concrete during hydration, which might negatively influence the properties of UHPC. Searching for the internal curing method of UHPC still remains a motivation for researchers to explore in this field. One of the very interesting questions is that

whether one material can play 'a duplex role' to replaces both SF and SAPs to make UHPC. If possible, it will give a big advantage in both technology and sustainability. This paper will explore the possibility by using rice husk ash (RHA) to mitigate autogenous shrinkage of UHPC.

Properties of Rice Husk Ask

Rice husk ash (RHA) is produced by burning rice husk as an agricultural waste. When the husk is incinerated completely under controlled conditions, the residue as RHA contains 90-96% silica in amorphous form. The average particle size of RHA ranges in general from 5 μm to 10 μm with a very high specific surface area (even more than 250 m^2/g) [5]. This high surface area comes from the porous structure of RHA as shown in Figure 1. Similar to SF, the RHA is considered as ‘‘highly active pozzolans’’ [6]. When incorporated in cement, the RHA affect the rate and the extent of hydration [7,8]. The addition of RHA in concrete, like SF, can lead to reduced porosity and $Ca(OH)_2$ content in the interfacial transition zone (ITZ) between the aggregate and the cement paste.

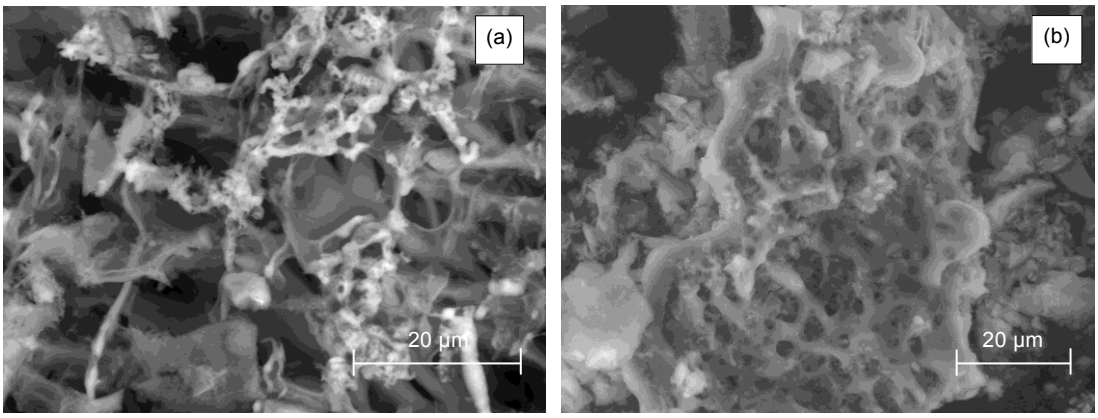

Figure 1: SEM images of RHA before grinding (a) and RHA after grinding (b.)

2 Materials and Method

Materials and mix composition

The materials used in this study were silica sand with a mean particle size of 225 μm, Portland cement (CEM I 52.5N) with a Blaine specific surface area of 4500 cm^2/g, condensed silica fume, rice husk ash, and polycarboxylate based superplasticizer with 30% solid content by weight. The SF has an amorphous SiO_2 content of 97.2% and its mean particle size is about 0.1–0.15 μm. The particle size distribution and the mean particle size of materials in this study were determined by laser diffraction. Rice husk, from Vietnam, was burnt in a drum incinerator developed by Pakistan Council of Scientific & Industrial Research [9] under uncontrolled combustion conditions. Details of the oven and rice husk combustion process were described elsewhere [5]. The obtained ash was ground in a vibrating ball mill for 90 min. The ash contains 87.96% amorphous SiO_2, 3.81% loss on ignition and its mean particle size ($d_{RHAmean}$) is from 3.6 μm to 9.0 μm. The particle size distribution of these materials is shown in Figure 2. Table 1 gives the mix compositions used to evaluate autogenous shrinkage of UHPC. It has to be mentioned that no additional water was added in the mixture.

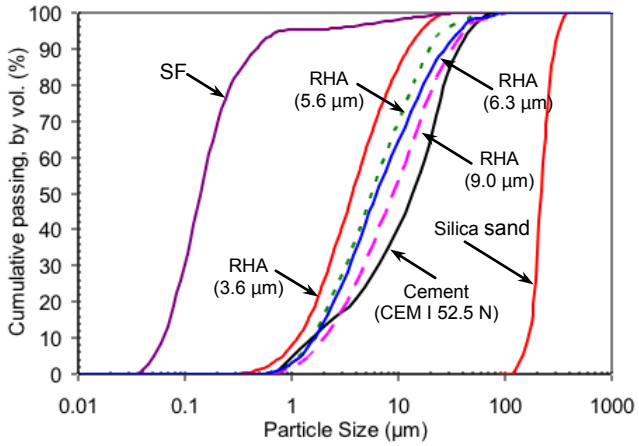

Figure 2: Particle size distribution of materials used in this study.

Table 1: Mix compositions of UHPC used to study autogenous shrinkage (% weight to cement).

Mixture	cement, (kg/m^3)	w/b ratio (by weight)	Sand/binder ratio	RHA (%weight)	SF (%weight)	Mean particle size of RHA (µm)
REF	1140	0.18	1	0	0	
RHA10(5.6)	1010	0.18	1	10	0	5.6
RHA20(5.6)	885	0.18	1	20	0	5.6
SF10	1010	0.18	1	0	10	-
SF20	885	0.18	1	0	20	-
RHA20(9.0)	885	0.18	1	20	0	9.0
RHA20(3.6)	885	0.18	1	20	0	3.6

Autogenous shrinkage measurement

The autogenous shrinkage of UHPC mixtures was measured based on the ASTM C1698 standard [10], in which three sealed corrugated moulds of 440 mm Ø28.5 mm were determined for each mix composition. After preparing and mixing, each mixture was carefully filled into three sealed corrugated tubes. Figure 3 shows the apparatus used to measure the autogenous shrinkage. According to this standard, the length of samples is started measuring at the time of final setting of the mixture. All samples and the dilatometer were kept in a thermostatically controlled room during the whole test. The surrounding temperature was maintained at 23±1°C.

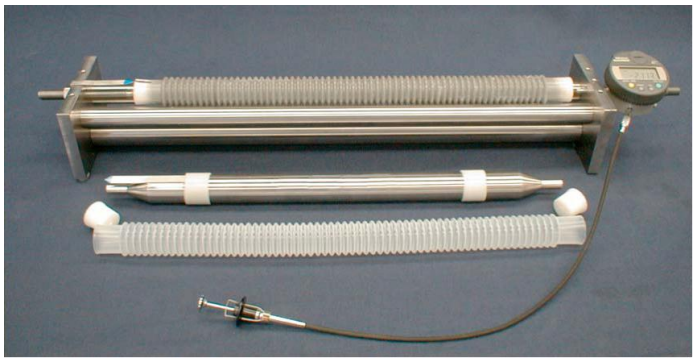

Figure 3: The dilatometer bench with accessories used to determine autogenous shrinkage.

3 Results and Discussion

Effect of RHA replacement

Figure 4 and Fifure 5 show the development of autogenous shrinkage of UHPC incorporating different amounts of RHA and compare to the samples made by same amount of SF. In general, the autogenous shrinkage of all samples is very high at a very early age, particularly in the first 12 hours from the final set time, and then remains more or less constant afterwards.

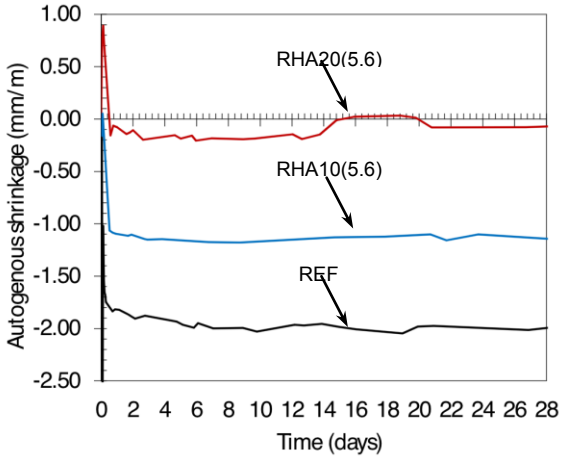

Figure 4: Autogenous shrinkage of UHPC mixtures containing different amounts of RHA measured from the final setting time, $d_{RHAmean}$ = 5.6 µm, w/b = 0.18.

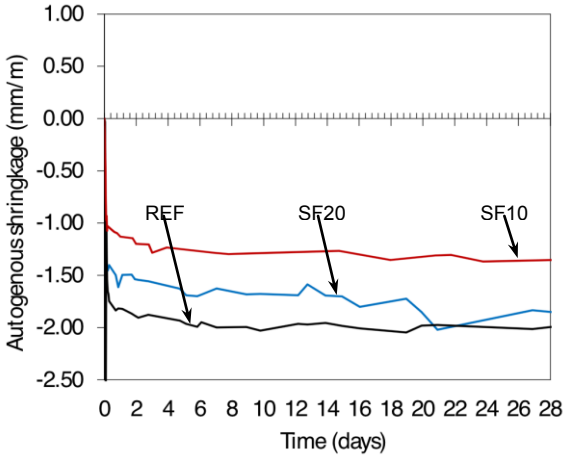

Figure 5: Autogenous shrinkage of UHPC mixtures containing different amounts of SF measured from the final setting time, w/b = 0.18.

When a higher amount of RHA is added, i.e. 20%, the autogenous shrinkage of UHPC was reduced compared to the control sample without RHA. After the first 12 hours from the final set, the RHA modified samples show only a very small increase in autogenous shrinkage. In addition, after reaching the age of 10 days, the autogenous shrinkage of the RHA modified samples was further mitigated. Especially the autogenous shrinkage of the 20% RHA sample was even completely eliminated after 15 days. However, the autogenous shrinkage of SF samples increases with increasing of SF content.

Effect of fineness of RHA

The effect of the fineness of RHA on autogenous shrinkage is depicted in Figure 6. It is clear that RHA particles are particularly effective in mitigating the autogenous shrinkage of UHPC when the mean size of RHA particles ranges between 5.6 µm and 9.0 µm. The sample containing the RHA with a smaller particle size, i.e. 3.6 µm, shows a higher autogenous shrinkage. This may be caused by the collapse of the porous structure which reduces the amount of absorbed water in RHA. The less absorbed water will reduces the positive effect of RHA particles to mitigate the autogenous shrinkage of UHPC. This result implies that the benefit of RHA on reducing the autogenous shrinkage can be achieved when the mean particle size is bigger than 5.6 µm.

4 Discussion

The results above show a positive effect of using RHA on the mitigation of autogenous shrinkage of UHPC. Besides, the reduction of autogenous shrinkage of UHPC by using RHA is due to the effectiveness of internal water curing and become a potential in the practical application.

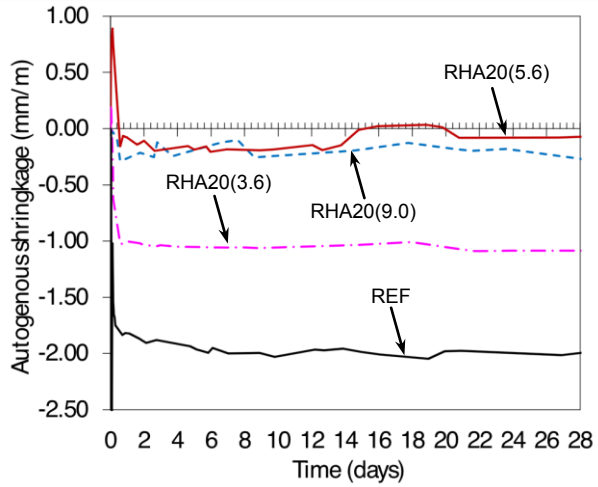

Figure 6: Autogenous shrinkage of UHPC mixtures containing RHA with different mean particle sizes measured from the final setting time, w/b = 0.18.

At low water/binder ratio, the water will be consumed rapidly (i.e., a few days), and water from the RHA will then be thought to be consumed. In the other studies [11, 3], the water is stored in particles, i.e. LWAs and SAPs, which are several orders of magnitude larger, and might be expected to retain water over a significant time-scale. In the case of RHA, with such a small particle size, the water from RHA will probably be available very quickly, and may also become exhausted in a few days. However, in fact, the experimental results provided evidence that the internal water curing of RHA still remains effective at later ages. This can be caused by several reasons as discussion below.

The specific pore volume of ground RHA with a mean particle size of 5.6 µm is approximately 0.086 cm^3/g. It is assumed that the water will fill all these pores. Theoretically because 20% RHA was added corresponding to about 220 kg RHA/m^3 concrete, the total absorbed water by RHA is about 18.9 l/m^3 UHPC. The extra water for internal curing of UHPC by super-absorbent polymers (SAP) ranges from 33 - 64 l/m^3 UHPC [3]. Thus, the absorbed water in RHA in UHPC is also significant. In addition, the distribution of water reservoirs also plays an important role for internal curing because it relates to the effective distance for transporting water to the vicinity of these water reservoirs [2]. With a lower w/b ratio in particular for UHPC, the microstructure of cement paste is very dense which constrains the water from reservoirs to migrate to the surroundings. This means that the water reservoirs should be separated into smaller ones to enhance the effectiveness of using internal curing agents in the system. In this respect, RHA is an appropriate candidate.

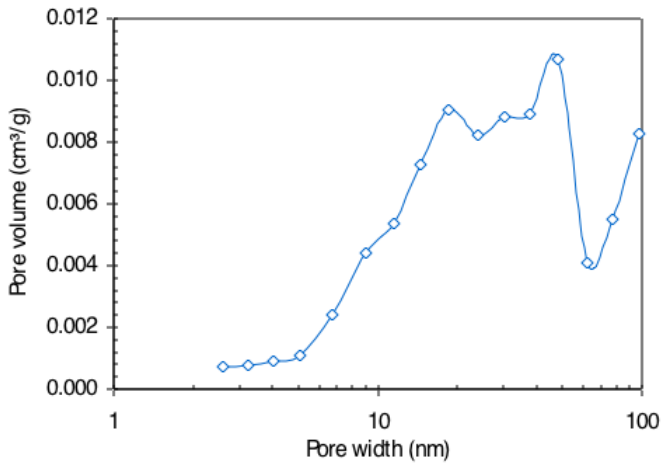

Figure 7: Pore size distribution of the RHA powder, $d_{RHAmean}$ = 5.6 µm [15].

The size of pores in RHA particles, i.e. from 5 to 60 nm in diameter (see Figure 7), is much smaller than that of SAP particles which is about 450 µm [3] and that of LWAs (about 10-20 µm [11]). Figure 8 shows the pore size distribution of UHPC made by RHA at different curing age [15]. According to Kelvin's equation [12], this size range of pores in RHA particles corresponds to the change of relative humidity (RH) in the cement matrix from 81.9 to 98.0%. The effectiveness of water released from inside of the pores of RHA particles to the surrounding cement matrix depends on the suction force, which in turn depends on the porosity and RH in cement paste [2]. At early ages, the RH in the cement paste with a w/c ratio of 0.25 is still higher than 87%, which corresponds to the diameter of 8.5 µm, before 7 days [13]. Thus only water in the big pores, i.e. about 8.5 nm in diameter, of RHA particles can be released. A certain amount of water still remains in the smaller pores and gradually releases at later ages, even after 28 days at which the RH decreases to 78% [13]. This process is illustrated in Figure 9.

Furthermore, small pores i.e. smaller than 8.5 nm in diameter, in the RHA particles remain water-filled for a longer period of time, and the small pore in their saturated state are available to be filled with hydration products, resulting in the absence of these empty pores surrounding the residual cement grains. This effect in combination with the higher degree of hydration could contribute to the higher compressive strength achieved at later ages of the RHA modified sample. Bentz, et al also observed this phenomenonwhen pre-wetted lightweight aggregates were used for high performance mortar [14].

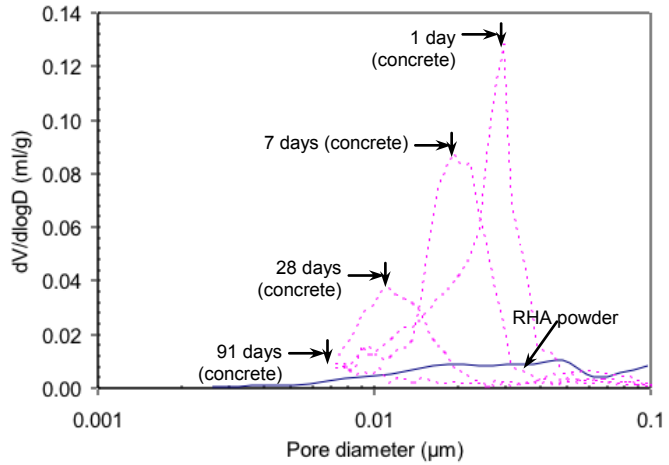

Figure 8: Pore size distribution of UHPC made with RHA at (a) 1 day, (b) 7 days, (c) 28 days and (d) 91 days, and of the RHA powder, dRHAmean = 5.6 µm.

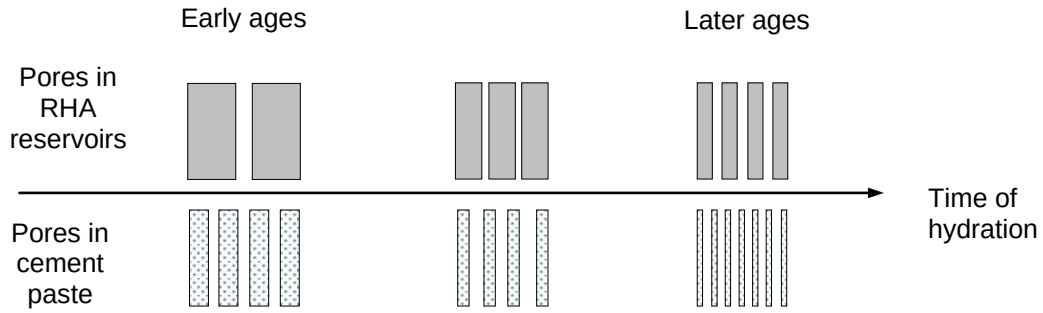

Figure 9: Illustration of the potential for internal curing of RHA with time of hydration; dots indicate water-filled pores within the hydrating cement paste whereas grey indicates empty pore [15].

5 Conclusions

From this study, when RHA is used in UHPC, the RHA shows a “duplex” function: in the one hand its high silica content shows good pozzolanic properties like SF; in the other hand, its special porous structure significantly reduces the shrinkage of UHPC. When the particle size of 5.6 µm and 20% of RHA is used, the shrinkage of UHPC is almost eliminated after 15 days curing. To be concluded, such an agriculture waste material use in UHPC not only reduce the cost and improve the early age properties of the UHPC but also increase the environmental benefits.

References

[1] Jensen O.M., Hansen P.F. (2001). Water-entrained cement-based materials: I. Principles and theoretical background. Cement and Concrete Research 31(4):647-654.

[2] Kovler K., Jensen O.M. (2007). Internal Curing of Concrete, State-of-the-art Report of RILEM Technical Committee 196-ICC.

[3] Mechtcherine V., Dudziak L., Hempel S. (2008). Mitigating early age shrinkage of Ultra-High Performance Concrete by using Super Absorbent Polymers (SAP). In: Creep, Shrinkage and Durability Mechanics of Concrete and Concrete Structures: Taylor & Francis, pp. 847-853.

[4] Dudziak L., Mechtcherine V. (2008). Mitigation of volume changes of Ultra-High Performance Concrete (UHPC) by using Super Absorbent Polymers. Proc. of the Second International Symposium on Ultra High Performance Concrete, . Kassel University, Kassel, Germany, pp. 425-432.

[5] Bui D.D. (2001). Rice husk ash as a mineral admixture for high performance concrete. PhD thesis, Delft University of Technology, Delft, The Netherlands.
[6] Mehta P.K. (1983). Pozzolanic and cementitious by-products as mineral admixtures for concrete. ACI SP-79 1–46.
[7] Huang C., Feldman R.F. (1985). Hydration reactions in Portland cement–silica fume blends. Cem Concr Res 15(4):585–92.
[8] Qingge F., Hirohito Y., Masami S., Sugita S. (2003). Efficiency of highly active rice husk ash on the high-strength concrete. In: Proceedings of the 11th international congress on the chemistry of cement (ICCC), Durban, South Africa; p. 816–22.
[9] UNIDO (United nations industrial development organization), (1984). Vienna. Rice husk ash cement: its development and application; p. 100.
[10] ASTM Standard (2009). ASTM C1698-09, Test Method for Autogenous Strain of Cement Paste and Mortar. Vol. 04.02, West Conshohocken, PA.
[11] Zhutovsky S., Kovler K., Bentur A. (2004). Influence of cement paste matrix properties on the autogenous curing of high-performance concrete. Cement and Concrete Composites 26(5):499-507.
[12] Lura P., Jensen O.M., van Breugel K. (2003). Autogenous shrinkage in high-performance cement paste: An evaluation of basic mechanisms. Cement and Concrete Research 33(2):223-232.
[13] Wittmann F.H. (1969). Physikalische Messungen an Zementstein, Habilitationsarbeit, TU München
[14] Bentz D.P., Stutzman P.E. (2008). Internal Curing and Microstructure of High-Performance Mortars. Internal Curing of High Performance Concrete: Lab and Field Experiences, ACI SP256-07, Detroit: American Concrete Institute, pp. 81-90.
[15] Nguyen van T. (2011). Rice husk ash as a mineral admixture for ultra high performance concrete, PhD thesis, Delft University of Technology, Delft, The Netherlands

Microstructure of Ultra High Performance Concrete (UHPC) and its Impact on Durability

Jennifer C. Scheydt[1], Harald S. Müller[2]

1: Materials Testing and Research Institute (MPA Karlsruhe), Karlsruhe Institute of Technology (KIT), Germany
2: Institute of Concrete Structures and Building Materials, Karlsruhe Institute of Technology (KIT), Germany

The structure of ultra high performance concrete (UHPC) is very dense compared to normal or high strength concrete. Thus, UHPC shows a high resistance against corrosion. Nevertheless there are some factors that strongly can affect its durability. On the one hand, microcracks resulting from heat treatment or autogenous shrinkage can enhance the ingress of attacking media. Besides, the interfacial transition zone of UHPC (that was considered very dense and thus negligible for transport processes so far) can lower the penetration resistance. Within the following paper, the results of an extensive experimental program on the microstructure and durability of UHPC are summarised.

Keywords: microstructure, porosity, interfacial transition zone (ITZ), microcracks, durability

1 Introduction

The experience in ultra high performance concrete (UHPC) obtained within international research projects shows that the durability of UHPC is very high compared to conventional concrete [1]. Nevertheless, there are some factors related to UHPC that can strongly influence its durability. Above all, microcracks due to the high rate of autogenous shrinkage or resulting from a thermal treatment can significantly reduce the concretes resistance against penetrating media. Furthermore, the interfacial transition zone (ITZ) between cement paste and steel fibre reinforcement or coarse aggregates can cause a decrease in durability. Subsequently, the results on the microstructure of UHPC and its impact on durability gained at the Karlsruhe Institute of Technology (KIT), Germany, within the framework of a research project supported by the Deutsche Forschungsgemeinschaft (DFG) are presented.

2 Characteristics of the microstructure of UHPC

Porosity and microstructure

Due to its low water-binder-ratio, UHPC shows a very low porosity compared to normal or high strength concrete and thus a high resistance against penetrating corrosives. For the pore structure characterisation of a coarse aggregate UHPC (d_{max} = 8 mm), measurements by the mercury intrusion method (MIP) were performed on small cores (d/h = 15/20 mm) drilled out of the interior of cylindric specimens (d/h = 150/300 mm). The maximum pressure used for MIP was about 420 MPa. A contact angle of 141° and the recommended surface tension value of mercury of 0.485 N/m were used to calculate the pore size distribution.

The mixing composition of the investigated concretes UHPC (water cured for 28 days), $UHPC_{90\,°C}$ (heat treated at 90 °C for 3 days) and $UHPC_{n.\,f.}$ (water cured for 28 days, no steel fibres) is given in Table 1, the mechanical characteristics are reported in [2].

Table 1:Mixing composition [kg/m³] and water-binder-ratio w/b [-] of the investigated concretes UHPC, $UHPC_{90\,°C}$ and $UHPC_{n.\,f.}$ (the concrete $UHPC_{n.\,f.}$ does not contain steel fibres).

CEM I 52,5 R-HS/NA	silica fume	quartz sand	quartz powder	basalt (2/8 mm)	steel fibres (l/d = 8/0.175 mm)	super-plasticiser	mixing water	w/b
582	178	355	458	714	196	28	138	0.21

The results of the MIP measurements at a concrete age of 28 days are given in Figure 1. For a better comparability of the different concretes, the porosity is given in % by volume of hardened cement paste (hcp, consisting of cement, microsilica and water).

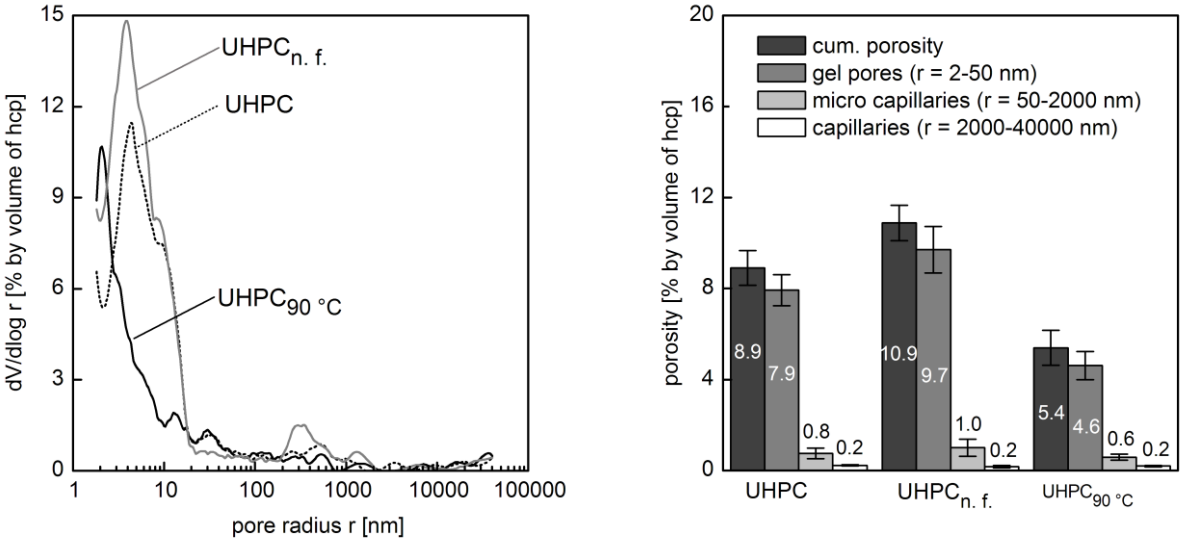

Figure 1: Pore size distribution dV/dlog r (left) and porosity (right) of the concretes UHPC, UHPC$_{n.\ f.}$ and UHPC$_{90\ °C}$.

Due to the heat treatment, the concrete is densified not only in the range of capillary pores (r = 50-40000 nm) but especially in the range of gel pores (r = 2-50 nm), see Figure 1.

The UHPC without steel fibres (UHPC$_{n.\ f.}$) shows a higher gel porosity – probably resulting from a lower mixing energy due to the lack of fibres – and a higher porosity in the range of micro capillaries.

As a result of their high binder content, ultra high performance concretes show strong deformations due to autogenous shrinkage leading to microcracks. By the use of steel fibres, microcracks are prevented or reduced, e. g. [3]. As the main reason for the higher capillary content in the fibreless concrete UHPC$_{n.\ f.}$, microcracks with a crack width between 0.5 and 2 µm were detected by using the Environmental Scanning Electron Microscope (ESEM). The cracks were mainly running alongside the quartz grains (see Figure 2, left).

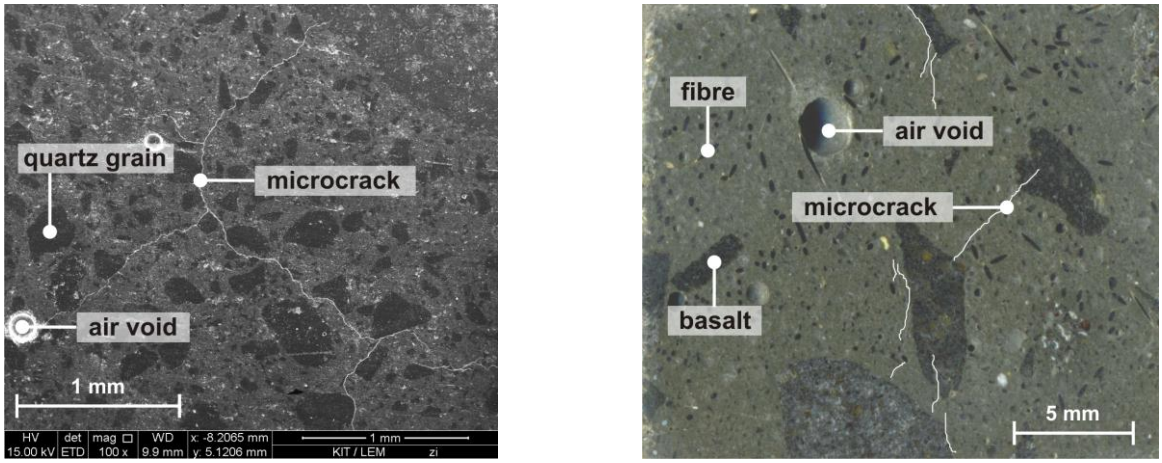

Figure 2: Microstructure of cracked concrete (left: UHPC$_{n.\ f.}$, ESEM – right: UHPC$_{90\ °C}$, reflecting microscope, cracks retraced).

But also the densified structure of heat treated concretes can strongly be affected by microcracks. Even though a low heating (0.2 K/min) and cooling rate (0.1 K/min) was chosen, some samples of the heat treated concrete $UHPC_{90\,°C}$ showed cracks visible without the need of microscopy (crack width 30 to 100 µm, see Figure 2, right).

Interfacial Transition Zone (ITZ)

The interfacial transition zone (ITZ) of ultra high performance concrete is supposed to be as dense, that it can be neglected considering transport processes. However, most investigations published (e. g. [4]) only take into account the ITZ of heat treated concretes.

Thus, an experimental program applying the MIP method was carried out to characterise the ITZ of UHPC. The experimental conditions are described above. Different samples were made only consisting of cement paste and the concerning component (quartz sand and quartz powder, fibres, basalt). The mixing proportions of the underlying mixing composition (see Table 1) were kept in each case.

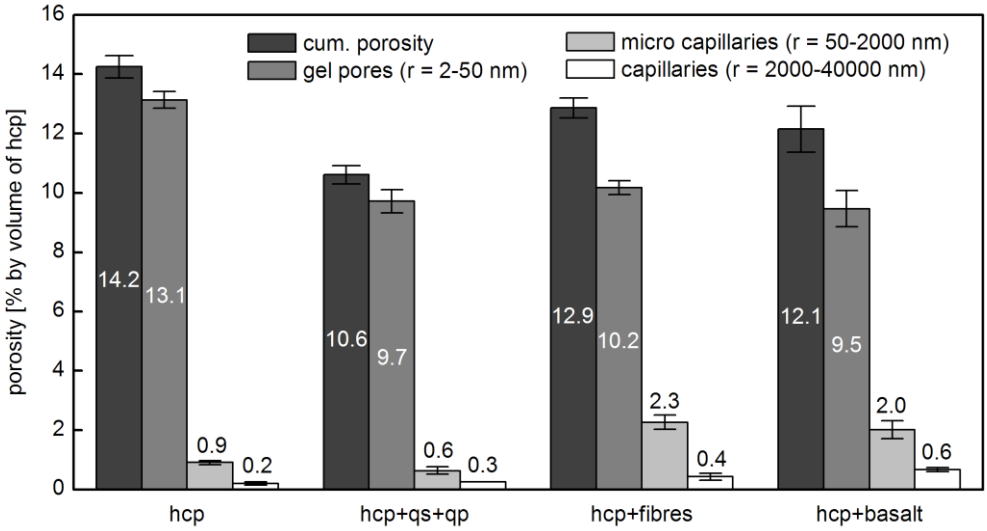

Figure 3: Porosity of hardened cement paste (hcp) depending on its composition (qs: quartz sand, qp: quartz powder).

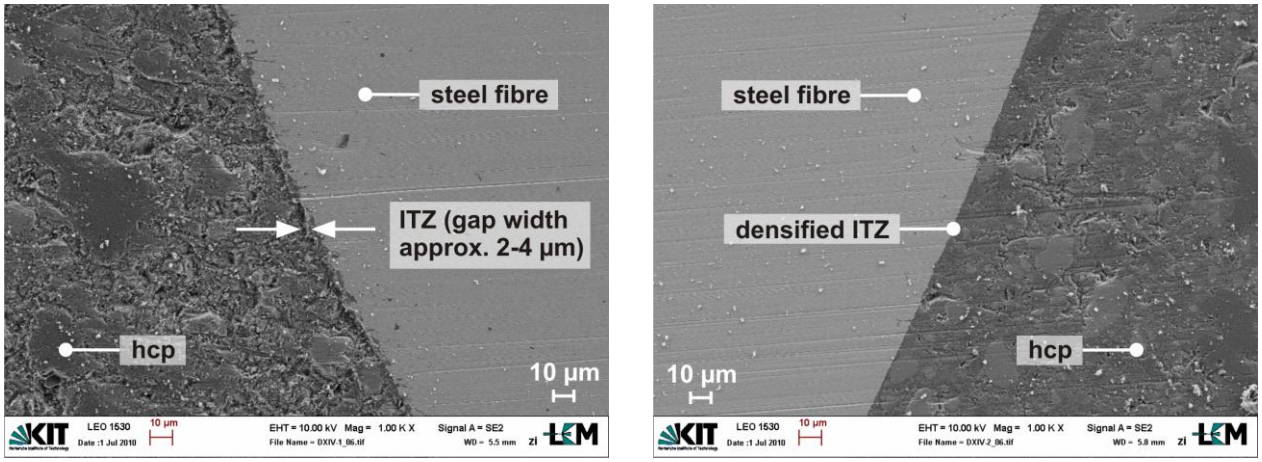

Figure 4: ITZ between hardened cement paste (hcp) and a steel fibre in UHPC (left) and in $UHPC_{90\,°C}$ (right), SEM.

The results of the MIP measurements are shown in Figure 3. The higher gel porosity of hcp compared to the other samples can mainly be attributed to the lack of components (e. g. quartz powder) acting as initial nuclei for the growth of CSH phases, see e. g. [5]. A higher amount of

micro capillaries (r = 50-2000 nm) as well as capillaries (r = 2000-40000 nm) indicates a higher porosity of the ITZ. According to Figure 3, especially the ITZ between hcp and steel fibres or basalt, respectively, shows an increased porosity. This increased porosity in the vicinity of the fibres was confirmed by investigations using the Scanning Electron Microscope (SEM), see Figure 4 (left). In heat treated samples, the hcp and particularly the ITZ was significantly densified (Figure 4, right).

3 Influence of the mirostructure on the durability of UHPC

The very dense structure of ultra high performance concrete complicates the avoidance of microcracks in fibreless UHPC. Even though intensive water curing, no water uptake takes place into the inner concrete structure to reduce autogenous shrinkage.

Concrete structures made from heat treated, fibre reinforced UHPC not necessarily show microcracks. Microcracks mostly can be minimised or avoided by combining very slow heating and cooling rates with slim structure dimensions. Furthermore, desiccation of the concrete surface during the heat treatment must be avoided.

As will be shown below, UHPC without microcracks shows a very high resistance against ingressing media, while the resistance of cracked concrete is significantly lowered.

Permeability and water absorption

In uncracked concrete, the densitiy and thus the transport resistance R_t of ultra high performance concrete diminishes in the following way due to a decrease in the structure density and an increase in the influence of ITZ:

$$R_t\,(UHPC_{90\,°C}) > R_t\,(UHPC_{n.\,f.}) > R_t\,(UHPC)$$

This is demonstrated by permeability measurements carried out according to [6] on uncracked slices with a diameter of 150 mm and a height of 20 mm and 25 mm, respectively. Before testing, the slices were ovendried at 40 °C for three weeks. For further details see [2]. The results of the measurements are presented in Table 2.

Table 2: Specific permeability coefficient, standard deviation and number of examined specimens of the investigated concretes.

Concrete	spec. permeability coefficient [10^{-18} m²]	standard deviation [10^{-18} m²]	number of examined specimens [-]
UHPC	4.70	0.86	15
$UHPC_{n.\,F.}$	2.57	0.47	6
$UHPC_{90\,°C}$	2.49	0.23	6

Due to microcracks of the concrete structure, the density of UHPC is strongly affected. Within the experiments carried out in [2], the heat treated concretes showed the maximum crack width (30-100 µm) followed by the crack width of the fibreless concretes (0.5-2 µm). Thus, in cracked UHPC the transport resistance R_t decreases vice versa compared to uncracked UHPC (see above):

$$R_t\,(UHPC) > R_t\,(UHPC_{n.\,f.}) > R_t\,(UHPC_{90\,°C})$$

Experiments on the water absorption of cylindrical specimens (d/h = 150/75 mm) under atmospheric pressure and 150 bar did confirm this correlation [2]. The specimens were sealed at the sawn front surfaces so that the water absorption took place from the casted surface. The results are shown in Figure 5. Due to the microcracks within the ultra high performance concretes, an increase in water absorption up to 90 % ($UHPC_{90\ °C}$ under atmospheric pressure) was determined.

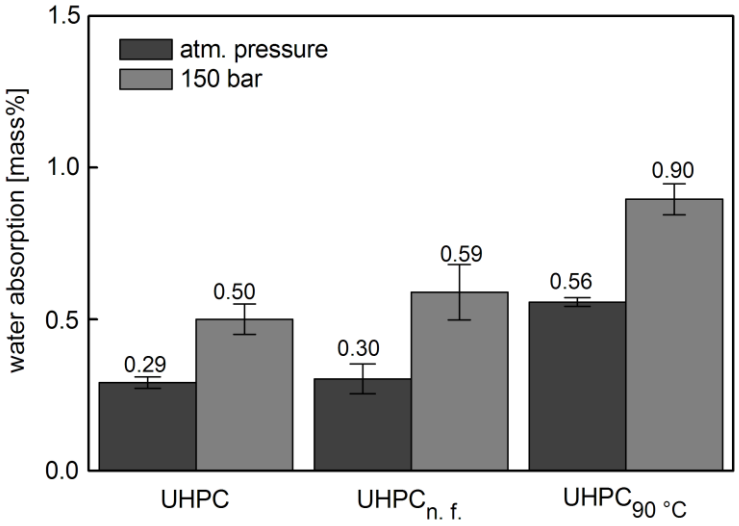

Figure 5: Water absorption of the concretes UHPC, $UHPC_{n.\ f.}$ and $UHPC_{90\ °C}$.

While the fine microcracks of the fibreless $UHPC_{n.\ f.}$ only filled under an increased pressure of 150 bar, the wider cracks of the heat treated concrete $UHPC_{90\ °C}$ already filled under atmospheric conditions, compare Figure 5.

Chloride ingress and chemical attack

The lowered resistance of microcracked UHPC also showed within durability experiments on the capillary suction of a NaCl solution (3 %) and on the chemical attack of hydrochloric acid (HCl). For experimental details see [2].

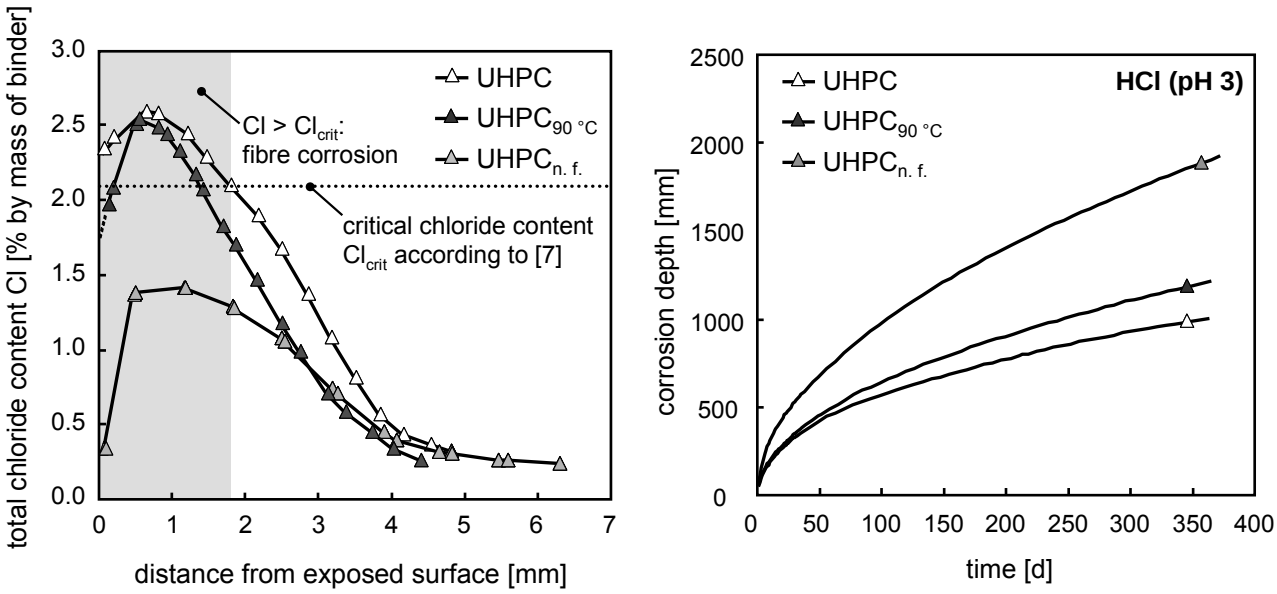

Figure 6: Chloride profiles after NaCl suction (left, exposure time 16 months) and time-dependent corrosion depth after chemical attack (right, HCl, pH 3) of the concretes UHPC, $UHPC_{n.\ f.}$ and $UHPC_{90\ °C}$.

In Figure 6 (left), the chloride profiles after the NaCl suction are exemplarily shown for an exposure time of 16 months. Within the edge zone of the specimens, an increase of the chloride content up to a maximum value was observed for all investigated concretes (also for normal and high strength concrete, see [2]). This could be ascribed to the leaching of the edge zone due to the NaCl solution and an associated reduction in chloride binding. Regarding the steel fibre corrosion, the critical chloride content Cl_{crit} for fibre reinforced concretes according to [7] was confirmed (compare Figure 6, left and Figure 7). Mainly pitting corrosion of the steel fibres was detected (Figure 7). For a detailed description of the results see [2].

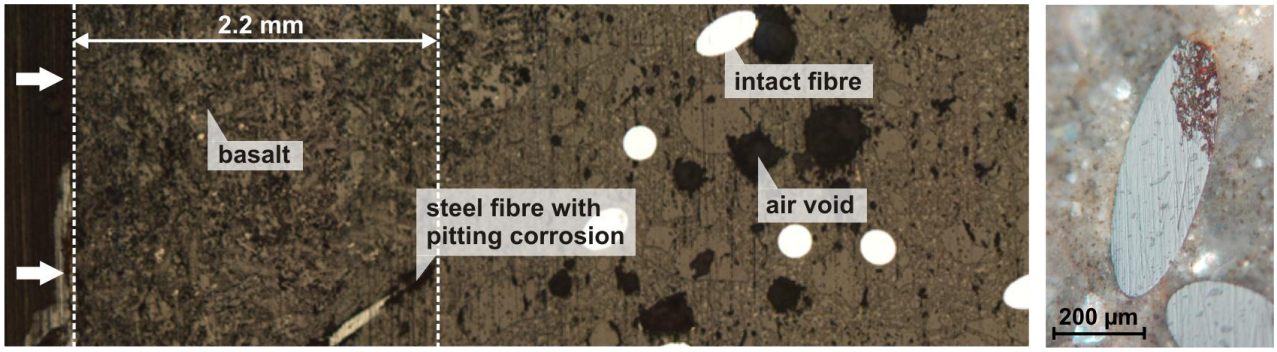

Figure 7: Cross section through an ultra high performance concrete after 16 months of NaCl attack (left, image analysis, dashed lines: fibre corrosion zone ($Cl > Cl_{crit}$), arrows: direction of NaCl attack) and fibre with pitting corrosion after NaCl attack (right, reflecting microscope).

The penetration depth of the chloride front is not significantly affected by the absence of fibres or the thermal treatment (see Figure 6, left). However, the maximum chloride content for the fibreless $UHPC_{n.f.}$ is distinctly lower than for the heat treated ($UHPC_{90\,°C}$) or water cured (UHPC) concretes. The most possible explanation for this effect is that the chloride ingress is locally pushed by the fibres due to the increased porosity of the ITZ between fibres and hcp and due to a local potential difference.

Besides, particularly the resistance of the heat treated and thus densified concrete against the chloride ingress is lowered by microcracks. Hence, the maximum chloride content of the heat treated and the water cured concretes is comparable (Figure 6, left).

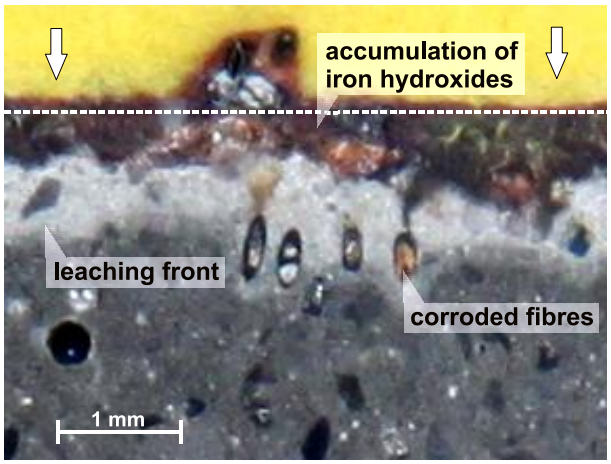

Figure 8: Cross section through an ultra high performance concrete after 80 weeks of chemical attack (HCl, pH 5, reflecting microscope); dashed line: origin surface of the specimen, arrows: direction of acid attack.

Within the experiments on chemical attack, the fibres also turned out to accelerate the acid ingress. As can be seen in Figure 8, the leaching front deeper penetrated the concrete in the vicinity of the fibres. However, the higher corrosion rate of the steel fibres compared to the

chloride attack caused an accumulation of iron hydroxides within the leaching front and on the exposed surface, see figure 8. This accumulation densifies the leaching zone and acts as a protective coating decelerating the corrosion process (compare Figure 6, right). Therefore – differently from the chloride attack – the resistance of the fibre reinforced concretes was approximately twice as high as the resistance of the fibreless concrete (see Figure 6, right). Furthermore – due to the microcracks after heat treatment – the concrete $UHPC_{90\ °C}$ showed less resistance against the acid attack than the concrete UHPC.

Carbonation

The increased porosity of the ITZ between fibres and hcp also affects the resitstance against carbonation of ultra high performance concretes. On thin slices prepared from prisms (40 x 40 x 160 mm³) after storing for three years at 20 °C and 65 % r. h. or outside protected from direct weathering, respectively, only a marginal carbonation front of maximum 180 µm thickness was detected.

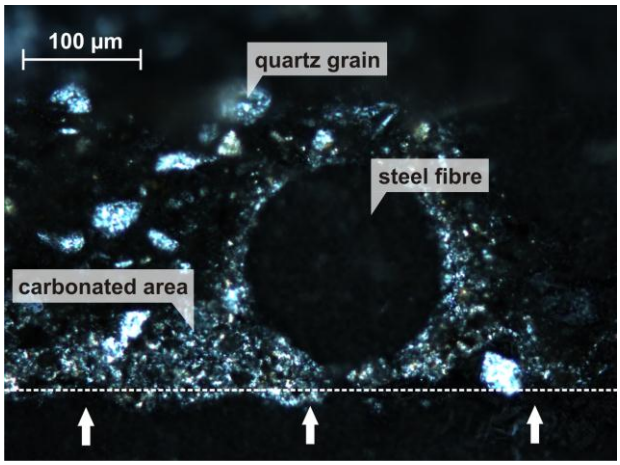

Figure 9: Carbonation of ultra high performance concrete in the vicinity of a steel fibre located near the attacked surface (exposure time: 6 months, storage: outside, protected from direct weathering); dashed line: origin surface of the specimen, arrows: direction of CO_2-attack.

However, in the surrounding area of fibres located near the surface, an increased ingress of CO_2 and thus an accelerated progress of the carbonation front takes place even for a shorter exposure time, as can be seen in Figure 9.

4 Conclusions

Ultra high performance concrete shows a very high resistance against attacking media due to its low porosity compared to conventional concretes. However, it was demonstrated that some factors essentially can reduce the durability of UHPC.

On the one hand, microcracks resulting from thermal treatment or autogenous shrinkage of fibreless UHPC significantly can lower the penetration resistance of the concrete. Furthermore, the interfacial transition zone (ITZ) formerly supposed to be negligible in ultra high performance concretes was proved to weaken the dense concrete structure. Thus, it is possible that the resistance of UHPC without fibre reinforcement or densified by heat treatment is equal or even lower than the resistance of undensified, fibre reinforced UHPC. This was proved by experiments on the water absorption, the chloride ingress and the chemical attack.

Anyway, it must be differentiated between the particular exposure conditions. While the steel fibres lower the resistance against chloride attack, they significantly enhance the resistance against the attack of acid solutions.

Especially in ultra high performance concretes without fibre reinforcement, it is hard to avoid microcracks resulting from autogenous shrinkage. While a reduction of the autogenous shrinkage strains by careful curing is nearly impossible due to the dense structure of UHPC, one possible way to fight this problem is inner curing as presented in [8]. Microcracks due to heat treatment can be minimised or avoided by very slow heating and cooling rates and slender concrete structures.

In either case, planning an UHPC construction must include preliminary tests to estimate the formation of microcracks. This is indispensable for a realistic durability evaluation.

References

[1] Müller, H. S., Scheydt, J. C.: Dauerhaftigkeit und Nachhaltigkeit von ultrahochfestem Beton. Ergebnisse von Laboruntersuchungen. In: beton 9 (2011), pp. 336-343.

[2] Scheydt, J. C.: Mechanismen des Korrosionswiderstands von Beton unter besonderer Berücksichtigung ultrahochfester Betone (working title). Karlsruhe Institute of Technology (KIT), Institute of Concrete Structures and Building Materials, doctoral thesis, in progress.

[3] Eppers, S., Müller, C.: Autogenous Shrinkage Strain of Ultra-High-Performance Concrete (UHPC). In: Proceedings of the 2nd International Symposium on Ultra High Performance Concrete, Fehling, E., Schmidt, M., Stürwald, S. (Eds.), kassel university press, Kassel, 2008, pp. 433-441.

[4] Sorelli, L., Constantinides, G., Ulm, F.-J., Toutlemonde, F.: The nano-mechanical signature of Ultra High Performance Concrete by statistical nanoindentation techniques. In: Cement and Concrete Research 38 (2008), No. 12, pp.1447-1456.

[5] Stark, J., Möser, B., Bellmann, F.: Nucleation and growth of C-S-H phases on mineral admixtures. In: Advances in Construction Materials 2007, Grosse, C. U. (Ed.), Springer Verlag, Berlin, 2007, pp. 531-538.

[6] Bunke, N.: Prüfung von Beton. Empfehlungen und Hinweise als Ergänzung zu DIN 1048. Heft Nr. 422, Deutscher Ausschuss für Stahlbeton (Ed.), Beuth Verlag, Berlin, 1991.

[7] Dauberschmidt, C.: Untersuchungen zu den Korrosionsmechanismen von Stahlfasern in chloridhaltigem Beton. RWTH Aachen University, Institute of Building Materials Research, PhD thesis, 2006.

[8] Dudziak, L., Mechtcherine, V.: Mitigation of volume changes of Ultra-High Performance Concrete (UHPC) by using Super Absorbent Polymers. In: Proceedings of the 2nd International Symposium on Ultra High Performance Concrete, Fehling, E., Schmidt, M., Stürwald, S. (Eds.), kassel university press, Kassel, 2008, pp. 425-432.

Computer Modeling and Investigation on the Chloride Induced Steel Corrosion in Cracked UHPC

Alireza Rafiee, Michael Schmidt
Department of Structural Materials and Construction Chemistry, University of Kassel, Germany

Ultra High Performance Concrete (UHPC) has been developed as a solution for corrosion problem in reinforced infrastructures, due to the packing density of fine particles through the rigid skeleton of hydration products with fairly negligible capillary pores. It is demonstrated that Coexistence between concrete matrix and micro crack is an unavoidable fact. In other hand the deterioration causing factors could easily pass through the cracks and tragically accelerate the rate of steel corrosion embedded in concrete. In this research, it has been tried to propose a computational scheme, which could predict the time history of cross section loss of steel bar as well as steel fiber caused by chloride induced macrocell corrosion in cracked UHPC. In this way, a series of laboratory experiments have been designed to determine and compare the steel corrosion behavior as well as penetration potential of water and chloride ion within UHPC. Finally, the developed computer model has been certified by an individual validation test.

Keywords: Chloride, Computational Scheme, Crack, Steel Corrosion, UHPC

1 Introduction

The chloride-induced corrosion of steel reinforcement is known as the main cause of deterioration in different types of concrete structures. Generally, sources of chloride ions are the seawater at the offshore platforms and salts used at bridges and parking garages for deicing during winter. The corrosion of steel reinforcement leads to concrete deterioration through cracking, delamination and spalling of the concrete cover, reduction of reinforcement cross section, decrease of bond between the steel and concrete, and consequently reduction in strength and ductility of membrane [1].

The rate of steel corrosion depends on the accessibility of oxygen and water near the steel-concrete interface, and is accordingly a function of the concrete permeability. In order to get the durability of a concrete structure better, it should be tried to increase the resistance of concrete against permeation of factors causing deterioration such as chloride ions, oxygen and water [2]. Ultra High Performance Concrete (UHPC) as the packing density of fine particles, rigid skeleton of the hydration products and negligible capillary pores is developed and investigated as the solution for corrosion problems in reinforced concrete [3]. Although, when a crack forms in the cover of concrete, deterioration causing factors can easily pass through the crack and accelerate the rate of steel corrosion embedded in concrete element [4].

The main objective of this research is to develop a multi-scale modeling of steel corrosion in cracked Ultra High Performance Concretes and to create a computer lifespan simulator, which could predict the reinforcement section loss as well as the electro potential behavior of steel corrosion in concrete. The concrete lifetime estimation is influenced by their characteristics such as concrete microstructure properties, environmental exposure conditions, crack width, crack depth and et cetera. In this article, it is tried to explain briefly the corrosion modeling as well as validation test applied in the project. It should be mentioned that the comprehensive numerical model including water, oxygen and chloride ingress will be found in the PhD thesis written by the Author.

2 Corrosion Model

Assumptions

Steel corrosion in concrete has been recognized as a complicated phenomenon, whose analysis depends on several known and unknown factors. In order to simplify this complexity, the following assumptions have been made by the Author.

1- As this model has been developed and specialized for cracked UHPC, the main cause of steel corrosion initiation is the breakdown of protective oxide film at the crack area as a result of concrete shield absence or high chloride concentration.
2- Carbonation induced corrosion is ignored in this model, owing to the high resistance of UHPC against carbonation.
3- In the case of steel fiber reinforced concrete, due to the unknown distribution and direction of steel fibers in concrete member and complexity of corrosion analysis for each fiber, the analysis is carried out only for an individual steel fiber placed among the crack with a specified concrete cover thickness. It should be mentioned that in the reality, the corrosion electrochemical potential around of steel fibers influence on each other, which is ignored in this study.
4- The pH value of the concrete is constant during the time.
5- Type of steel corrosion is macro cell, in which the anodic and cathodic regions of steel are obviously separated from each other.
6- The corrosion starts, when either the concentration of chloride ions on the steel surface becomes higher than the chloride threshold value or the anode would directly be exposed to the water.
7- The most severe corrosion section is located directly in the crack area.
8- Steel corrosion is considered to be a cathodically controlled process, during which greater polarization takes place at the cathodic sites far from the crack.
9- Polarization at the steel-concrete interface is expressed by the Butler-Volmer kinetics.
10- The cathodic and anodic equilibrium potential will remain constant through the corrosion.
11- There are not considerable capillary pores or porous zone around the steel-concrete interface in UHPC. Therefore the corrosion rust could not diffuse into these voids, but should accumulate among the crack.

Applied Equations

The rate of steel corrosion at the anode in crack zone is related to the current density, which is calculated from the surrounding electrochemical potential distribution. In this situation, the current density at any point on the steel surface could be determined by [6]:

$$i = -\frac{1}{r}\frac{\partial \phi}{\partial n} \tag{1}$$

Where, i denotes the current density at the steel surface [A/cm^2], is the electrochemical potential [V], r is the concrete resistivity [Ω.cm], and n is the direction normal to the steel surface. According to [7], the formation of corrosion products at the steel surface decreases the diffusion rate of iron ions away from the steel surface. For that reason, the corrosion current reduces with time and should be modified at each time step as follows:

$$i_{modified} = i \times \left(\frac{t}{t_0}\right)^{-0.29} \tag{2}$$

Where, $i_{modified}$ is the modified corrosion current, t is the time since start of corrosion, and t_0 is the first time step of analysis. If the current density is known, then the rate of rust production as well as steel damage at the anode area could be estimated by the Faraday's law, as follows [6]:

$$J_{Fe} = 55.845\times10^{-3}\frac{i_a}{z\,F} = 2.894\times10^{-7}\times i_a \tag{3}$$

Where, J_{Fe} is the rate of steel damage at the anode [kg/cm^{2}s], i_a is the anodic current density [A/cm^2], F is the Faraday's constant [9.65×10^4 C/mol], and z is the number of exchanged electrons in the reaction (for iron =2). If it is assumed that the efficiency of anodic current for steel dissolution would be approximately 100% and uniform corrosion products are formed on the steel surface, then the percentage of steel cross section loss ($S_{corrosion}$ [%]) during the corrosion process could be calculated using equation (3), as follows:

$$S_{corrosion} = \frac{2.894\times10^{-7}\times I_a\times\Delta t}{l_c\times\rho_s\times S_0\times10^{-6}}\times100 \tag{4}$$

Where, I_a is the corrosion current at the anode [A], Δt is the elapsed time after initiation of steel corrosion [s], l_c is the length of anodic area on the reinforcement [mm], ρ_s is the density of steel [≈7800 kg/m^3], and S_0 is the area of steel cross section before corrosion [mm^2]. Considering the Equation (1), the computation of current densities around the steel surface requires knowledge of the electrochemical potential distribution in concrete member. Assuming isotropic conductivity, the three dimensional potential distribution is expressed by the following Laplace's equation [6]:

$$\frac{\partial^2\phi}{\partial x^2}+\frac{\partial^2\phi}{\partial y^2}+\frac{\partial^2\phi}{\partial z^2}=0 \tag{5}$$

The boundary conditions for the anodic and cathodic regions on the steel surface could be defined as:

$$\text{Anodic regions:}\quad \phi=\phi_a \tag{6}$$

$$\text{Cathodic regions:}\quad \phi=\phi_c \tag{7}$$

Where, ϕ_a and ϕ_c are the anodic and cathodic potentials, which are calculated by means of the polarization phenomena, as follows:

$$\phi_a = \phi_{a0}+\beta_a\log\frac{i_a}{i_{a0}} \tag{8}$$

$$\phi_c = \phi_{c0}-\beta_c\log\frac{i_c}{i_{c0}}-\frac{RT}{4F}\ln\frac{i_L^{O_2}}{i_L^{O_2}-i_c}-\frac{RT}{2F}\ln\frac{i_L^{H_2O}}{i_L^{H_2O}-i_c}\approx\phi_{c0}-\beta_c\log\frac{i_c}{i_{c0}}-\frac{RT}{4F}\ln\frac{i_L^{O_2}}{i_L^{O_2}-i_c} \tag{9}$$

Where, ϕ_{a0} and ϕ_{c0} are the equivalent potential of the anodes and cathodes [mV], β_a and β_c are the anodic and cathodic Tafel slope [mV/decades], i_a and i_c are the anodic and cathodic current density [A/mm^2], i_{a0} and i_{c0} are the exchange current density of the anodic and cathodic reaction [A/mm^2], R is the universal gas constant [=8.314 J/K mol], T is the absolute temperature [K], and $i_L^{O_2}$ is the limiting current density of oxygen consumption. The exchange current density is a temperature dependent parameter which would follow the Arrhenius equation [8]:

$$i_0^2 = i_0^1\exp\left(\frac{E_a}{R}\left[\frac{1}{T_1}-\frac{1}{T_2}\right]\right) \tag{10}$$

Where, i_0^1 and i_0^2 are exchange current densities at two different temperature of T_1 and T_2 respectively, R have its usual significance, and E_a is the activation energy which has been reported 19 kJ/mol [9]. The limiting current density of oxygen, which the model considers, is the minimum value of the following equations. Herein, the first one is calculated from the concentration of oxygen on the steel surface when the oxygen supply is adequately high, but the latter is calculated from the limited supply of oxygen through the concrete cover [10,6,11].

$$i_{L_1}^{O_2} = 4F\frac{D_{O_2}^S C_{O_2}^S}{\delta t}\times 10^6 \quad (11)$$

$$i_{L_2}^{O_2} = 4FJ_{O_2}^{max} = 4F\frac{D_{O_2}^{avg} C_{O_2}^{max}}{d}\times 10^6 \quad (12)$$

Where, $D_{O_2}^S$ is the oxygen diffusion coefficient next to the steel surface [mm^2/s], $D_{O_2}^{avg}$ is the average oxygen diffusion coefficient along the concrete cover of d [mm/s], $C_{O_2}^S$ is the concentration of dissolved oxygen adjacent steel surface [mol/lit], $C_{O_2}^{avg}$ is the average concentration of dissolved oxygen along the concrete cover of d [mol/lit], $J_{O_2}^{max}$ is the maximum supply of oxygen on the steel surface [mol/mm^{2}s], δ is the stagnant layer thickness of electrolyte next to the steel surface (≈0.5 mm for an unstirred solution [11]), t is the transference number of all ions in solution except the reduced ion (=1 when many other ions are present [11]), F is the Faraday's constant [9.65×10^4 C/mol], and d is the thickness of concrete cover on the steel [mm], through which the concentration of oxygen varies from the maximum amount to approximately zero at the steel surface (due to the rapid reduction of oxygen in the case of limited oxygen supply). It has already been confirmed that concretes with high saturation levels follow the Equation (12), but otherwise the Equation (11) governs the limitation current density in the concentration polarization [10].

In the model, the consumption of oxygen molecules in the cathodic regions along the steel surface is considered as an internal boundary condition for oxygen ingress through the concrete member. It is expressed as follows [6]:

$$\frac{\partial C_{O_2}}{\partial n} = \frac{i_c}{4FD_{O_2}} \quad (13)$$

Where, C_{O2} is the concentration of dissolved oxygen in concrete, D_{O2} is the diffusion coefficient of oxygen, and n is the direction normal to the steel surface.

Solution Strategy

According to the mentioned equations in the previous section, the solution algorithm for computer modeling of the phenomenon has been considered as follows:

1- Firstly, it is assumed that the initial distribution of potential in concrete is zero and the electrical potential of steel surface at the anode and cathode regions is equal to the user/model defined anodic and cathodic equivalent potential, respectively.
2- Limiting current density of the cathodic reaction is determined for each grid point of the mode; along the steel surface from the Equation (11) or (12).
3- Corrosion current densities for anodic and cathodic reactions could be calculated by substituting the electrical potential of each point at the steel surface in the Equations (8) and (9). It should be noted that the anodic current density can be obtained directly from the Equation (8), while iteration is applied to find the cathodic current density from the Equation (9).

4- Electrical potential flux ($\partial\varphi/\partial n$) is calculated by substituting the corrosion current density in the Equation (1).
5- Distribution of electrical potential in the concrete is determined by solving the Equation (5), using finite difference method.
6- In order to improve the analysis precision, steps 2 to 5 should be repeated several times.
7- From the anodic current density, the percentage of steel cross section loss at each time step is estimated by the Equation (4).
8- Finally, after the corrosion analysis, the boundary conditions are applied to the oxygen movement analysis, using the Equation (13).

3 Experimental Programs

Ultra High Performance Concrete, due to the improved density of the grain structure of the matrix and hydration products, could be recognized as an impermeable material. Therefore, each laboratory experiment related to permeability on UHPC, takes a long time to become complete and time plays an important role in design of tests. In the other side, the precision of laboratory instruments applied for UHPC specimens should be adequate to guarantee accuracy of test results. In this project, a comprehensive experimental program was designed to obtain essential parameters which are required as an input data in numerical model. These parameters include chloride diffusion coefficient, water diffusion coefficient, water sorption coefficient, concrete resistivity, Tafel slope, compressive strength and porosity. The comprehensive finite difference numerical model, test methods as well as experimental results have already been written by the author and will be presented as PhD Thesis.

4 Validation Test

In order to simulate the macro cell steel corrosion in cracked concrete, three reinforced UHPC beams of 700×150×150 mm in dimension were casted. The artificial cracks were made by plastic plates, which were placed exactly in the middle of steel bar during the specimen preparation process. The potentially cathodic reinforcement next to crack section was simulated by adding six reinforcing steel sections with different lengths on each side of the crack, allowing generated current to be determined as a function of crack distance [12]. The steel sections had been connected by non-resistance copper wires, end of which were kept exterior side of the concrete body, in order to be able to measure the generated current between the sections during the steel corrosion in concrete; see Figure (1).

Figure 1: Assembled reinforcement (Left) and final specimen (Right) used in the validation test.

The rods diameters were 10 mm, which were embedded in three different concrete cover depths of 10, 20 and 30 mm for each case of specimen. The concrete beams were covered with plastic foil kept wet for 48 hours after casting. Thereafter, the plastic plates were removed and the specimens were soaked in water saturated with calcium hydroxide for 28 days. After the

curing time, the beams were taken out and the side faces of them were coated to prevent rapid drying of the concretes from these areas. As well, the bottom sides of the beams were soaked in water.

In order to accelerate the macrocell corrosion of steel in the crack area, a salt water reservoir was placed exactly above the crack zone for each beam. After the preparation process, all specimens were stored in climate room at 20°C and 65% relative humidity. The corrosion currents were then measured regularly by the multimeter in the different time durations to validate the results obtained by the numerical model. The schematic set up of the experiment is shown in Figure (2). Furthermore, comparisons have been made between the corrosion current measured by multimeter during one year and outputs of numerical model which has briefly been described in the previous sections. These comparisons are illustrated in Figure (3) to Figure (5).

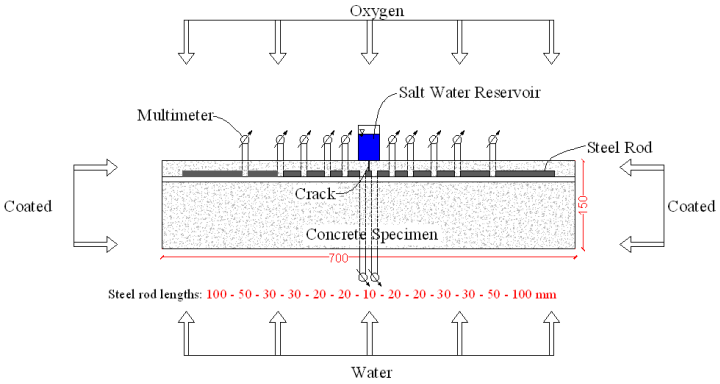

Figure 2: The schematic set up of the validation test.

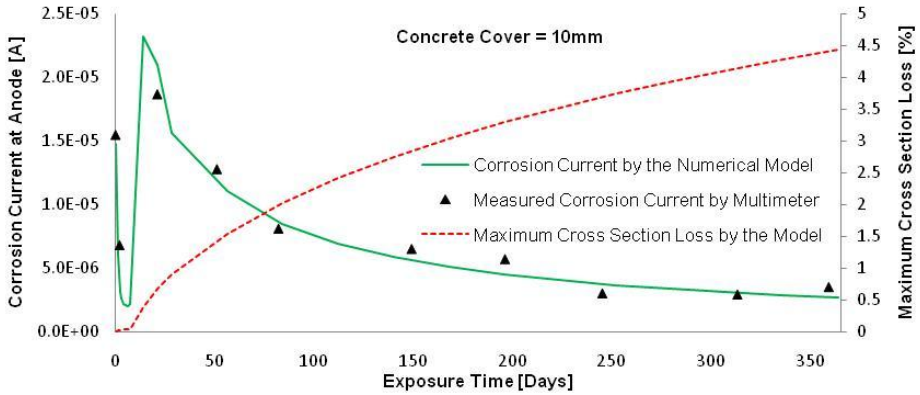

Figure 3: Comparison between the reality and model for UHPC specimen with 10mm concrete cover.

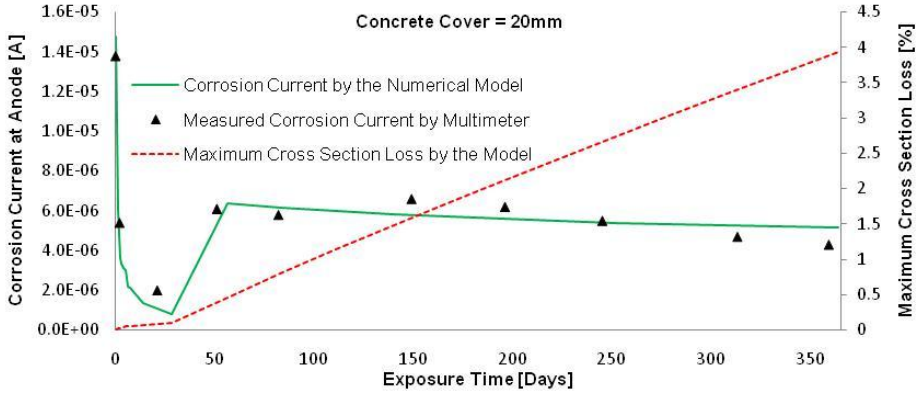

Figure 4: Comparison between the reality and model for UHPC specimen with 20mm concrete cover.

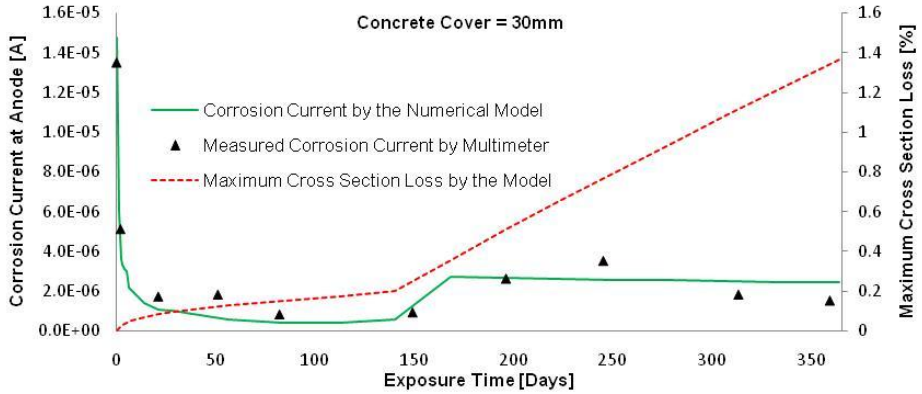

Figure 5: Comparison between the reality and model for UHPC specimen with 30mm concrete cover.

5 Summary and Conclusions

A comprehensive finite difference model for predicting the corrosion current as well as steel cross section loss in cracked concrete exposed to chloride ions has been developed. The model includes the effects of changes in exposure conditions, temperature, concrete age, crack width, concrete microstructure, and concrete cover on the corrosion behavior. The significant agents that contribute to the rate and amount of steel corrosion such as temperature, moisture, chloride, oxygen movement and distribution, have been modeled by the second order explicit finite difference method. The corrosion current and steel dissolution amount are predicted based on the potential distribution around the concrete-steel interface, which is obtained by solving the Laplace's equation. The polarization characteristics of the steel surface impose the boundary conditions for current densities along the concrete-steel interface. The model results have been validated by the self-designed laboratory experiments on beam specimens with different concrete types and concrete covers. The reasonable compatibility between the model prediction and the measured test data confirms that despite ignoring many complexities of corrosion process, the current theories could well satisfy the realities.

6 Acknowledgements

This research was supported by a grant from the Department of Structural Materials and Construction Chemistry of University of Kassel in Germany, which is thankfully acknowledged.

References

[1] Jieying Z.; Zoubir L.: Sensitivity analysis of simplified diffusion-based corrosion initiation model of concrete structures exposed to chlorides. Cement and Concrete Research, 36, pp.1312–1323, 2006.

[2] Gowripalan, N.; Mohamed, H.M.: CHLORIDE-ION INDUCED CORROSION OF GALVANIZED AND ORDINARY STEEL REINFORCEMENT IN HIGH-PERFORMANCE CONCRETE. Cement and Concrete Research, 28(8), pp.1119–1131, 1998.

[3] Schmidt, M.; Teichmann, T.: New development in Ultra High Performance Concrete non corrosive PVA-fibers and glueing of structural elements. 2nd fib congress, pp. 326-337, Neapel 2006.

[4] Ema K.; Yoshitaka, K.; Taketo, U.: Development of simulation model of chloride ion transportation in cracked concrete. Journal of advanced concrete technology, 3(1), pp.85-94, 2005.

[5] Yu, W.; Long-yuan, L.; Page, C.L.: Modelling of chloride ingress into concrete from a saline environment. Building and Environment, 40, pp.1573–1582, 2005.

[6] Burkan Isgor, O.; Ghani Razaqpur, A.: Modeling steel corrosion in concrete structures. Materials and Structures, 39, pp.291-302, 2006.

[7] Kim Anh, T.V.; Stewart, M.G.: Structural reliability of concrete bridges including improved chloride-induced corrosion models. Structural Safety, 22(4), pp.313-333, 2000.

[8] Zhang, J.: PEM Fuel Cell Electrocatalysts and Catalyst Layers, Fundamentals and Applications. Springer-Verlag London, p. 93, ISBN 978-1-84800-935-6, 2008.

[9] Youping, L.: Modeling the Time-to-Corrosion Cracking of the Cover Concrete in Chloride Contaminated Reinforced Concrete Structures. Doctor thesis of philosophy in civil engineering, Virginia Polytechnic Institute, P.5, Blacksburg, Virginia. 1996.
[10] Markeset, G.; Myrdal, R.: Modeling of reinforcement corrosion in concrete - State of the art. COIN P4 Operational service life design, SP 4.1 F Service life modeling and prediction, 2008.
[11] Winston, R.R.; Herbert, H. U.: Corrosion and Corrosion Control. Hoboken New Jersey, John Wiley & Sons, Inc.
[12] Raupach, M.: Chloride-induced macrocell corrosion of steel in concrete-theoretical background and practical consequences. Construction and Building Materials, 10(5), pp.329-338, 1996.

Marine Performance of UHPC at Treat Island

Michael Thomas[1], Brian Green[2], Ed O'Neal[2], Vic Perry[3], Sean Hayman[1], Ashlee Hossack[1]
1: University of New Brunswick, Fredericton, NB, Canada
2: U.S. Army Corps of Engineers, Vicksburg, MS, USA
2: Lafarge North America, Calgary, AB, Canada

Three series of ultra-high performance concrete mixtures have been placed at the mid-tide level of the marine exposure site at Treat Island, Maine, over the past 15 years. The exposure conditions at Treat Island are considered to be very severe with 6-metre tides and more than 100 freeze-thaw cycles per year. Specimens from each of the three series of mixes were retrieved in 2009 and 2010 for laboratory testing. The testing included measurements of strength and stiffness, electrical properties, chloride profiling, corrosion activity of reinforcing steel (if present) and microstructural evaluation. No visible deterioration was evident after exposure periods of 5 to 15 years and there was no evidence of any degradation of mechanical properties after more than 1500 freeze-thaw samples in some cases. The depth of chloride penetration was extremely low, much lower than observed for typical high-performance concrete in the same environment.

Keywords: UHPC, durability, marine performance, chloride resistance, freeze-thaw resistance

1 Introduction

Since 1995 three series of ultra-high performance concretes (UHPC) have been placed at the mid-tide level of a marine exposure site at Treat Island, Maine. The first was a series of fibre-reinforced very-high strength concrete (VHSC) beams that were produced at the laboratory of the U.S. Army Corps of Engineers (USACE) in 1995 using locally-available materials. In 1996 the USACE also produced reactive powder concrete (RPC) beams containing steel reinforcing bars at cover depths of 25, 19 and 10 mm. In 2004, specimens of RPC were produced at the University of New Brunswick (UNB) using either steel or plastic fibres; some of these specimens were pre-cracked prior to installation. The exposure conditions at Treat Island are very aggressive for concrete with tides in excess of 6 m and an average of 100 cycles of freezing and thawing per year. At yearly intervals concrete specimens were subjected to a visual inspection and measurement of resonant frequency and pulse velocity. Samples from each series were retrieved after between 5 to 15 years of exposure for testing in the laboratory at the University of New Brunswick (UNB). The testing consisted of compressive and flexural strength, static modulus of elasticity, electrical properties, chloride profiling, corrosion activity of reinforcing steel (if present) and microstructural evaluation of the concrete.

2 Details of UHPC Mixtures

RPC (USACE)

This series of concrete mixtures were produced at the U.S. Army Corps of Engineers' (USACE) Waterways Experiment Station (WES) as part of an evaluation of reactive powder concrete (RPC) for producing sewer, culvert and pressure pipes [1]. Materials and proportions were selected based on criteria established by Bouygues, and details of the "wet mixture" used in this study are given in Table 1. The cement was a Class H oil well cement, the sand was a silica sand with a maximum particle size of 0.6 mm, metallic fibres were 0.16 mm diameter x13 mm long, and the high-range water-reducing admixture was a naphthalene sulfonate sodium salt. Concrete specimens were cured for 1 day in the forms, 6 days in limewater, 4 days in hot water at 90°C, and 2 days in air at 90°C.

To evaluate corrosion protection three concrete beams (152 x 152 x 533 mm) containing 13-mm diameter steel reinforcing bars with cover depths of 25, 19 and 10 mm were placed on the mid-tide deck at the Treat Island exposure site in 1996. These beams were reportedly [1] stored in limewater for 28 days prior to being shipped to the exposure site. Two beams were retrieved in 2009 at an age of 13 years for testing at UNB.

Table 1: Mixture Proportions (kg/m^3) of UHPC.

Material	USACE		Ductal RPC[1]
	RPC 200	VHSC	
Cement	942	796	712
Silica Fume	236	199	231
Silica Flour	-	110	211
Fine aggregate	1036	897	1020
Fibres	160	235	156
Water	136	207	109

"Typical composition" reported by Graybeal for Ductal [2]

VHSC (USACE)

The VHSC series of mixtures (Table 1) were also produced at WES and beams (152 x 152 x 533 mm) were placed at Treat Island in 1995. Sand with a maximum particle size of 4.75 mm and hooked-ended steel fibres 30 mm in length and 0.5 mm in diameter were used in these mixtures. Four beams were retrieved in 2010 at an age of 15 years.

RPC (UNB)

Two series of concrete mixtures were produced at UNB using a premixed RPC formulation produced by Lafarge and marketed under the name Ductal®. The premixed material contains cement, silica fume, silica flour and fine sand; although the precise composition material is not provided a "typical composition" of RPC produced using this product is given by Graybeal [2] and is presented in Table 1. The two series produced at UNB differed in the type of fibre used, metallic (FM) or PVA (FO) and in the water content; the mixture proportions are given in Table 2. The metallic fibres had a diameter of 0.2 mm and a length of 12.7 mm, the maximum particle size of the sand was 0.6 mm and the HRWRA was a polycarboxylate. FM and FO specimens were cured for 2 days in the forms at 20°C and were then wrapped in pre-soaked burlap and plastic. FM specimens were then cured for a further 2 days at 90°C and FO specimens for 3 days at 60°C.

Table 2: Mixture Proportions (kg/m^3) of RPC (UNB).

Material	FM	FO
Ductal Premix	2195	2195
Metallic Fibres (2%)	156	-
PVA Fibres (4%)	-	50.4
Water	130	167

Six concrete beams (152 x 152 x 533 mm) were produced from each mixture. Three beams were loaded in flexure until the first crack appeared. All six specimens were then placed on the mid-tide deck at Treat Island in 1994 and one cracked and uncracked specimen was retrieved from each mixture in 2009 (at an age of 5 years). Cylindrical specimens were also cast for compressive strength tests and for the determination of the chloride diffusion coefficient using a bulk diffusion test (ASTM C 1556).

3 Experimental Methods

Beam samples were collected from Treat Island in 2009 and 2010, and were subsequently tested at UNB. Beams were first broken in flexure (VHSC and UNB test series only) and then cores (75-mm diameter) were cut to determine the compressive strength, static modulus of elasticity and chloride profile. Additional 100-mm cores were cut from the 15-year-old VHSC series to determine the "chloride permeability" using ASTM C 1202 and the bulk-diffusion coefficient (ASTM C 1556), but these data are not reported here. Samples of the UNB concretes were also tested for strength, chloride permeability and bulk diffusion prior to placing the beams at Treat Island.

Chloride profiles were measured by grinding cores and collecting powder samples in 1-mm increments from the surface to a depth of at least 15 mm. The chloride content of the samples was determined by extraction in nitric acid and subsequent titration of the solution.

4 Results

All specimens retrieved from Treat Island were in excellent condition with no evidence of surface scaling, mass loss or cracking. The beams that were pre-cracked prior to exposure were still intact and the cracks did not appear to have widened significantly, having a maximum crack width of just 2.5 mm. This is somewhat surprising as it was expected that the multiple freeze-thaw cycles (approximately 500 over the 5-year period) would have widened the crack significantly. A piece of embedded reinforcing steel with nominally 10-mm cover was extracted from one of the beams was found to be in pristine condition.

Table 3 shows results from strength tests on cores cut from the beam samples after marine exposure and cylinders stored under laboratory conditions for 28 days. The strength data for the cores extracted from the beams appears to be highly variable and the reason for this is not known. However, in many cases the core strengths after marine exposure exceed the strength of laboratory-stored, cast cylinders determined prior to exposure of the beams. Overall the results would indicate that there has not been any regression in the mechanical properties due to marine exposure.

Table 3: Results of Strength Tests before and after Marine Exposure.

Property, Study	Exposure period (y)	Strength (MPa)	
		Before	After
Compressive strength, RPC-USACE	13	214 [ref 1]	160, 224
Compressive strength, VHSC	15	157 [ref 3]	173, 188, 194, 183
*Flexural strength, VHSC			21.7, 23.1, 19.9, 27.4
Compressive strength, UNB-FM	5	209, 206	175, 192, 203, 256
Compressive strength, UNB-FO	5	129, 121	119, 134, 123, 120
*Flexural strength, UNB-FM	5	20.3	21.9
*Flexural strength, UNB-FO	5	10.1	9.4

*Load at first crack

Fig. 1 shows the chloride profiles for the various UHPC specimens collected from Treat Island. The maximum depth of penetration of chlorides for all specimens ranges from approximately 7 to 12 mm after between 5 to 15 years exposure to the marine environment.

Only one profile was measured for the RPC specimens from USACE and UNB, and these appear to be similar despite the different durations of exposure (5 versus 13 years). Profiles were measured for all four VHSC specimens and these data show a considerable amount of

scatter. In addition, the shape of the profiles for the VHSC specimens is different as the chloride contents in the increments closest to the surface (0-1 and 1-2 mm) are reduced compared to the maximum values that occur in the third increment (2-3 mm). This shape of profile is often observed in concretes that are exposed to chlorides intermittently, such as highway structures exposed to deicing salts and concrete in the splash zone (above high tide level), but is not typical for concrete in the tidal zone. It is possible that reactions between the seawater and the hydrates led to densification of the surface layers in these samples; for example, the production of brucite or magnesium silicates is known to occur in concrete exposed to seawater. Microstructural analysis of the samples is currently underway.

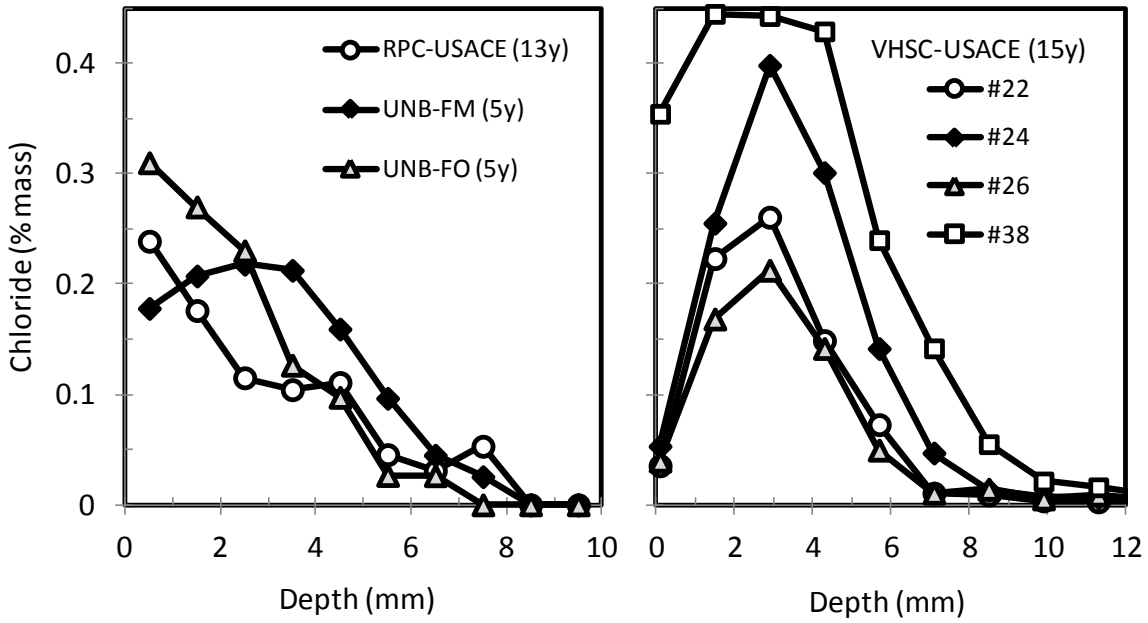

Figure 1: Chloride Profiles for UHPC.

The bulk diffusion test (ASTM C 1556) conducted on laboratory-cured samples of RPC (without fibres) produced at UNB yielded a diffusion coefficient of D = 1.3 x 10^{-13} m^2/s after 63 days exposure to NaCl solution (165 g/L). The "chloride permeability" (ASTM C 1012) was measured on two samples and the charge passed after 6 hours was 0 and 19 coulombs.

5 Discussion

Regardless of the shape of the profiles, all of the concretes show a very high resistance to chloride-ion penetration as can be seen in Fig. 2 which compares the profiles for the UHPC after 5 to 15 years with the profiles for high-performance concrete (HPC) with 8.5% silica fume and w/cm = 0.33 after 12 years at the mid-tide level at Treat Island [4]. Also shown in Fig. 2 is the range of chloride threshold, C_t, often used in service-life modelling (0.05 to 0.10% total chloride by mass of concrete). The depth of penetration, d_t, of the threshold, C_t, of UHPC ranges from 4 to 8 mm after 5 to 15 years marine exposure whereas d_t ranges from 17 to 23 mm after 12 years. Assuming diffusion to be the dominant chloride transport mechanism for concrete at mid-tide and assuming the diffusion coefficient to be constant with time (reasonable assumption for mature heat-cured concrete with very low w/cm?) then the rate of penetration of the threshold concentration, C_t, can be expected to be proportional to the square-root of time; in other words: $d_t = k \cdot \sqrt{t}$.

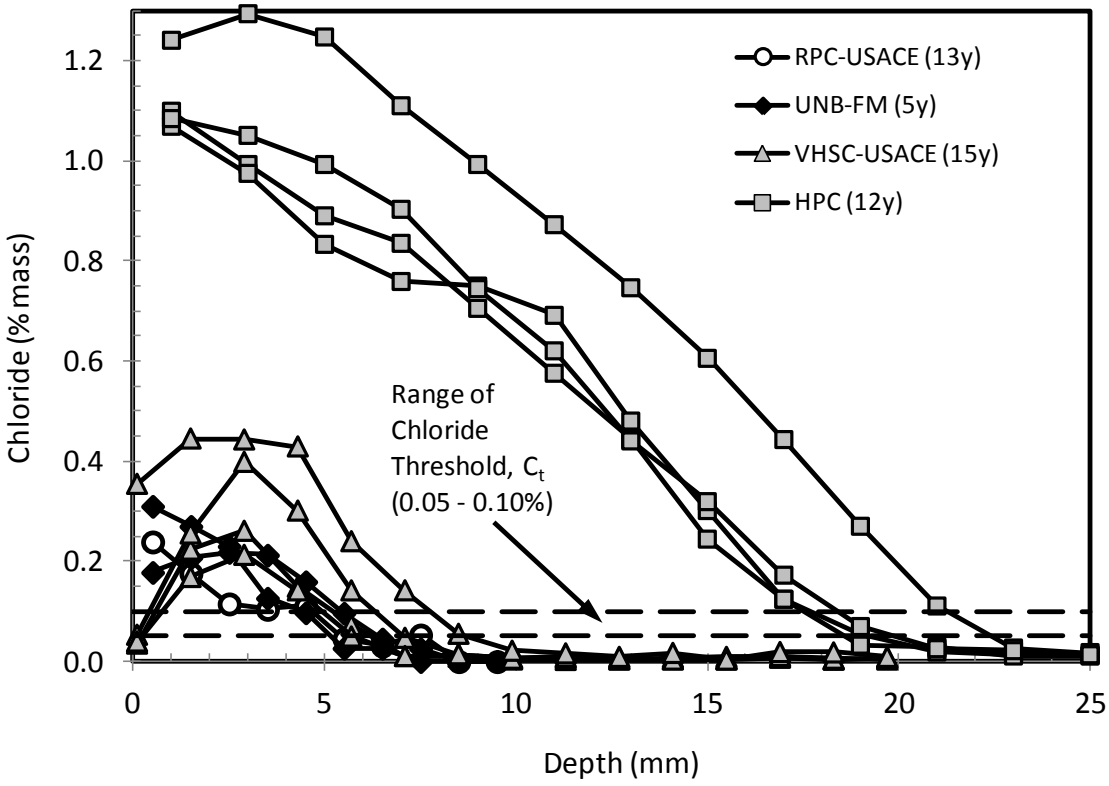

Figure 2: Comparison of Chloride Profiles for UHPC and HPC.

Fig. 3 shows the depth, d_c, of the chloride threshold for C_t = 0.05 and 0.10% plotted against the age of the concrete for the UHPC concrete tested in this study and for the HPC (8.5% silica fume and w/cm = 0.33) tested in a previous study [4]. Also shown is extrapolation of the data assuming $d_t = k \cdot \sqrt{t}$. This indicates that the UHPC can be expected to provide considerably greater protection to embedded steel reinforcement than typical HPC.

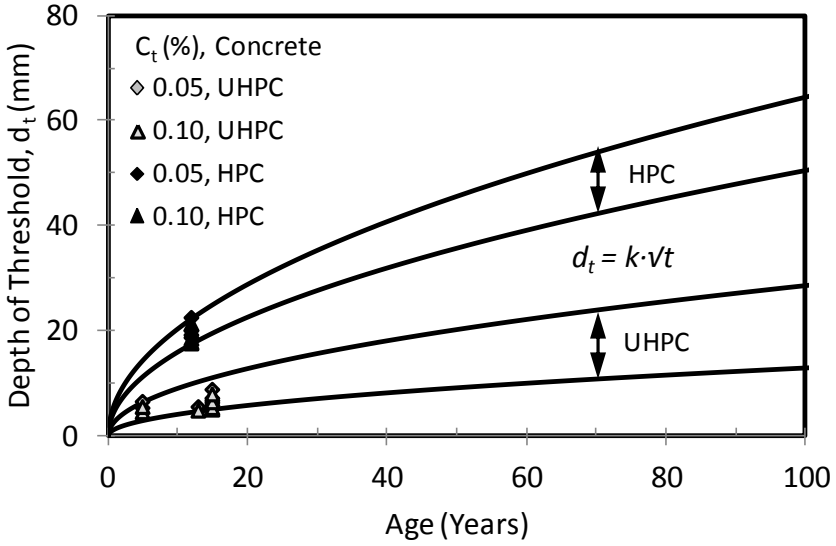

Figure 3: Rate of Penetration of Chloride Threshold for UHPC and HPC.

Table 4 shows the results of the bulk diffusion and rapid chloride permeability tests conducted on the laboratory-stored RPC produced at UNB compared with data for typical HPC samples with w/cm = 0.35 to 0.40 and with various levels of supplementary cementing materials (SCM)

tested at UNB at ages between 28 and 91 days. The data shows that typical HPC containing SCM and with w/cm ≤ 0.40 is significantly more resistant to chlorides than the minimum quality of Portland cement concrete (PCC) generally specified for chloride environments (e.g. w/cm ≤ 0.40 in ACI 318), but that UHPC is more than an order of magnitude more resistant than HPC.

Table 4: Comparison of "Chloride Permeability" and Chloride Diffusion Test Results for UHPC and HPC.

Type of concrete (w/cm, SCM)	Age (days)	RCPT (Coulombs)	Diffusion Coeff, *D* (x 10^{-13} m^2/s)
RPC (produced at UNB)	28	0 - 19	1.3
PCC (0.40, no SCM)	91	2200	80
HPC # 1 (0.35, 8% SF)	28	975	-
HPC # 1 (0.35, 8% SF)	56	850	13
HPC # 2 (0.40, 4% SF + 22% SG)	91	500	19
HPC # 3 (0.35, 5% SF + 20% FA)	91	450	17

RCPT = rapid chloride permeability test (ASTM C 1202), SF = silica fume, FA = fly ash, SG = slag
PCC = Portland cement concrete without SCM

It is encouraging that the piece of embedded steel reinforcement with nominally 10-mm cover which was retrieved from one of the RPC samples was in pristine condition after 13 years exposure. However, it has been found in previous studies at Treat Island that there is insufficient oxygen in concrete at the mid-tide level to sustain corrosion even in PCC. Consequently, one of the remaining steel-reinforced RPC specimens was relocated to the high-tide level to ensure that oxygen would be available. The corrosion activity of the steel bars in this specimen will be monitored periodically.

6 Conclusions

UHPC beams produced in three separate studies were placed at the mid-tide level of the marine exposure site at Treat Island, ME. After periods of exposure ranging from 5 to 15 years, with approximately 100 freeze-thaw cycles per year, the beams appear to be in excellent condition. The depth of chloride penetration is very low being approximately 1/3 of that of typical high-performance concrete (HPC) with 8.5% silica fume and w/cm = 0.33 after 12 years exposure to the same conditions.

References

[1] Campbell, R.L., O'Neil, E.F., Dowd, W.M. and Dauriac, C.E. Reactive Powder Concrete for Producing Sewer, Culvert, and Pressure Pipes. U.S. Corps of Engineers, Technical Report CPAR SL-98-3, 1998.

[2] Graybeal, B.A. Material Property Characterization of Ultra-High Performance Concrete. Federal Highways Administration, Report FHWA-HRT-06-103, 2006.

[3] O'Neil, E.F., Neeley, B.B. and Cargile, J.D. Tensile Properties of Very-High-Strength Concrete for Penetration-Resistant Structures. *Shock and Vibration,* 6, 1999, pp. 237-245.

[4] Thomas, M.D.A. and Bremner, T. Performance of Lightweight Aggregate Concrete after 25 Years in a Harsh Marine Environment. *Cement and Concrete Research,* 2011.

Evaluation of Durability Parameters of UHPC Using Accelerated Lab Tests

Julie Piérard, Bram Dooms, Niki Cauberg
Belgian Building Research Institute (BBRI), Limelette, Belgium

Ultra-High Performance Concrete (UHPC) mixes are characterized by a very low water-to-cement (w/c) ratio and high powder contents. A compressive strength of 130 MPa or more can be obtained without heat treatment or other special measures. Apart from high strength, extremely high durability is generally recognized to be one of the distinctive features of UHPC, even when exposed to severe environments. This paper aims to quantify some durability parameters of UHPC using typical lab tests such as accelerated carbonation, chloride penetration, sulphate attack and freeze-thaw cycling with and without de-icing salt. Compared to normal strength concrete, the duration of the tests has been prolonged several times in order to get measurable results. In addition, the durability results are linked to porosity measurements (microstructure) and probabilistic models are used to predict the service life of structural elements or structures made of UHPC.

Keywords: Ultra-high performance concrete (UHPC), porosity, permeability, durability, carbonation, chloride diffusion, sulphate attack, freeze-thaw attack.

1 Introduction

Ultra-high performance concrete (UHPC), a family of concretes with compressive strengths exceeding 130 N/mm², offers the possibility to design exciting and innovative structures. Because this concrete type is relatively new in Belgium, some properties have still to be validated for mixes made of local materials.

In order to evaluate the performances of UHPC exposed to different aggressive environments, the water porosity and the gas permeability of the concrete were measured and the following accelerated tests were performed: carbonation, chloride diffusion, sulphate attack and freeze-thaw cycling with and without de-icing salt.

The performances were compared to those of normal strength concrete and high performance concrete (HPC). In addition, probabilistic models were used to evaluate the benefit in the lifetime of the structure and the possible need to review some design rules related to durability.

2 Materials and curing

Three concrete mixes were subjected to the test program. The UHPC types M1, M2 and M3 represent different approaches of UHPC-design, ranging from compositions with larger aggregate size and minimal cement content (M1) to reactive powder concrete with high powder contents and complete removal of coarse aggregates (M3). The mix proportions and the properties of the fresh concrete mixes are given in table 1. In some cases, 2 vol.% (i.e. 156 kg/m³) steel microfibres of 6 mm length are added to the mix (in this case, for carbonation test only). Silica fume slurry and quartz powder are used to densify the matrix. The addition of high dosages of polycarboxylate based superplasticizer ensures a suitable fluidity, close to that of a self-compacting concrete.

All concrete specimens were demoulded 24 hours after casting and then stored at 20 ± 2°C and more than 95% RH until testing (up to an age of 90 days for the specimens used for durability testing). No heat treatment was applied.

Table 1: Mix design of M1, M2 and M3 and properties of the fresh concrete mixes.

		M1	M2	M3
Quartz sand 0/0.5 mm	kg/m³	786	335	1060
Quartz powder (d_{50} = 12 µm)	kg/m³	50	83	211
Basalt 1/3 mm	kg/m³	510	0	0
Basalt 5/8 mm	kg/m³	386	0	0
Porphyry 2/4 mm	kg/m³	0	776	0
CEM I 42.5 R HSR LA (c)	kg/m³	500	830	777
Silica fume (sf)	kg/m³	100	166	156
Mixing water (w)	kg/m³	150	178	162
Superplasticizer (SP, con. 30%)	kg/m³	15	24	28
(w/c)-ratio (SP included)		0.32	0.23	0.23
(sf/c)-ratio		0.20	0.20	0.20
Slumpflow	mm	750	750	800
Fresh density	kg/m³	2490	2420	2430
Air content	vol.%	2.5	2.0	3.5

3 Mechanical properties and microstructure

The compressive strength was obtained by testing cubes with an edge length of 100 mm (see table 2). Other mechanical properties of the three mixes are provided in [1] and [2].

The total water absorption was measured by immersing concrete cores. A water porosity ratio was calculated (see table 2) using the following expression:

$$P = \frac{m_{ssd} - m_d}{m_{ssd} - m_{susp}} \times 100 \, (vol.\%) \quad (1)$$

where m_{ssd} is the mass of water saturated surface dry concrete (in g), m_d is the mass of concrete oven-dried at 105°C (in g) and m_{susp} is the mass of concrete suspended in water (in g). Typical values for normal strength concrete range from 12 to 16 vol.% [3, 4].

As a supplemental durability indicator, the oxygen permeability was also measured by using the AFREM recommendation entitled “Gas permeability of hardened concrete” [3]. The test involves measuring the steady-state volumic flowrate of gases passing through a sample under a constant pressure gradient, and then deducing its permeability to gas (in this case, oxygen) using Darcy’s law. The results given in table 2, corresponding to the material in its dry state, are very close to the detection limit of the method (10^{-19} m²) and seem to be in accordance with the French Guidelines for UHPC [4]. Typical values for normal strength concrete range from 10^{-15} to 10^{-16} m² [3, 4].

Table 2: Compressive strength and porosity of the tested UHPC mixes.

		M1	M2	M3
28-day compressive strength	MPa	130 - 140	140 - 160 (*)	140 - 160 (*)
Water porosity ratio (P)	vol.%	*N.D.*	6	5
Oxygen permeability (k_{app})	10^{-19} m²	2	9	*N.D.*

(*) up to 200 MPa for heat treated specimens.

4 Durability properties

Accelerated carbonation test

The resistance against carbonation was determined on prisms having a cross-section of 100×100 mm². Prior to the test, the prisms were oven-dried at 50°C during 14 days and then placed in a climate chamber at 20 ± 2°C and 60 ± 5% RH during 7 days. The prisms were then stored under a 1%-CO_2 atmosphere for accelerated aging and the carbonation front was regularly analyzed by spraying a phenolphtaleine acid/base indicator solution on a fresh fracture. It should be noted that the carbonation front is sometines difficult to observe due to the darker colour of UHPC compared to concrete without silica fume.

The results of these measurements are plotted in figure 1. After a one-year exposure to 1%-CO_2 atmosphere (duration of this test is generally limited to 56 days), a carbonation depth of only 1.5 to 2 mm was reached. A coefficient of carbonation can be calculated (see fig.1 and table 3) using the following equation:

$$x_c = k_c \cdot \sqrt{t} \qquad (2)$$

where x_c is the carbonation depth at time t (in mm); k_c is the coefficient of carbonation which represents the carbonation rate (in mm/√day) and t is the exposure period (in days).

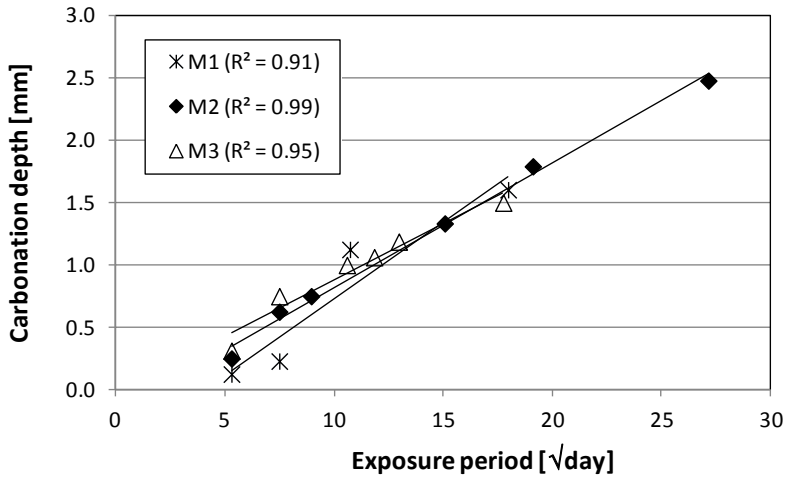

Figure 1: Carbonation depth vs. exposure period to 1%-CO_2 atmosphere for fibre reinforced UHPC mixes.

From a practical point of view, this coefficient can be used as input data in predictive approaches like the DuraCrete Model [6] to estimate the carbonation depth in real conditions as a function of time. In order to compare the performances of an ordinary concrete (k_c = 1.5 mm/√day), a HPC (k_c = 0.6 mm/√day) and a UHPC (k_c = 0.1 mm/√day) in the same conditions (see also [1]), we can for example calculate the minimum concrete cover needed to reach a lifetime (towards carbonation induced rebar corrosion) of 100 years. We obtain values of 65 mm for ordinary concrete, 25 mm for HPC and less than 5 mm for UHPC.

Accelerated chloride diffusion test

The resistance against chloride diffusion was determined on drilled cores of 90 mm diameter by accelerated testing in non-steady state conditions, according to the Nordtest method NT Build 443 (1995). In this test, a $Ca(OH)_2$ saturated surface is exposed to a chloride solution, obtained by dissolving 165 g of dry NaCl in one litre of water, while the other surfaces are coated with epoxy resin. After an exposure period of at least 35 days (in this case extended to 90 days),

thin successive layers (1 mm thick) are ground off parallel to the exposed surface. The acid-soluble chloride content of each layer is then determined by potentiometric titration.

According to the test results (see chloride ingress profile in fig.2), the chloride penetration after 90 days of accelerated testing is restricted to the outer 2 to 3 mm. Similar intrusion depths were observed by Scheydt et al. [7] for UHPC subjected to real-time testing. A chloride diffusion coefficient (D_{app}) can be calculated using a mathematical model based on the Fick's second law of diffusion. This coefficient is found to be as low as 0.2×10^{-12} m²/s (see table 3), while typical values for normal strength concrete are in the range from 5×10^{-12} to 50×10^{-12} m²/s [3, 4].

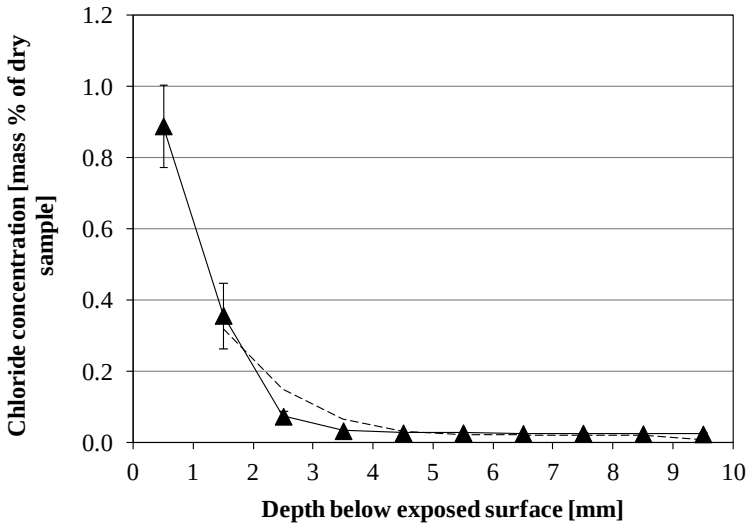

Figure 2: Chloride ingress profile of UHPC-type M2 after 90 days of exposure to a saline solution. The dotted line represents the regression analysis according to the mathematical model (1st experimental point excluded).

Freeze-thaw attack

The frost resistance of UHPC was tested according to the reference method (Slab Test) described in the technical specification CEN/TS 12390-9 (Freeze-thaw Resistance – Scaling, 2006). In this test, four concrete cores (diameter 113 mm, height 50 mm) are subjected to freeze-thaw attack in presence of a 5±2 mm deep layer of de-ionised water or 3% sodium chloride (NaCl) solution. All surfaces of the specimens except the test surface are coated and insulated according to the test set-up in figure 3. The freeze-thaw resistance is generally evaluated by the measurement of the mass of material (in kg/m²) which is scaled from the concrete slab after 56 freeze-thaw cycles (i.e. 56 days). In this case, the duration of the test was extended to 112 cycles.

The results indicate that the mass losses of the specimens (i.e. the masses of scaled material) after 112 cycles are extremely low, even with NaCl solution. The values are limited to 0.3 kg/m² (see table 3) and seem to be in good agreement with those obtained by Cwirzen et al. [8]. For comparison, values up to 2 kg/m² after 30 cycles are generally accepted for road applications.

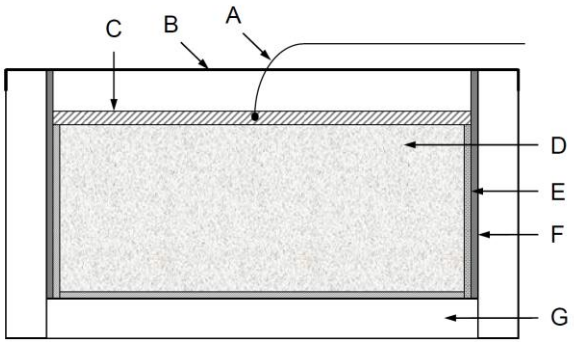

Figure 3: Slab Test set-up. A = Temperature measuring device, B = Evaporation protection, C = Freezing medium, D = Concrete specimen, E = Epoxy resin, F = PVC tube, G = Thermal insulation.

Sulphate attack

The sulphate resistance was evaluated based on the CUR Recommendation 48 (The Netherlands, 1999). Prisms of 40x40x160 mm³ are immersed in a sodium sulphate solution (Na_2SO_4, 16g SO_4^{2-} per litre) and the length variation is regularly measured. The results indicate no expansion nor deterioration, even after 500 days of immersion.

Table 3: Durability results for M1, M2 and M3.

		M1	M2	M3
Coefficient of carbonation by 1% CO_2 (k_c)	mm/√day	0.12	0.10	0.09
Apparent chloride diffusion coefficient (D_{app})	10^{-12} m²/s	0.23	0.23	*N.D.*
Surface scaling after 56 cycles with de-ionised water	kg/m²	0.16	0.02	0.04
112 cycles	kg/m²	0.22	0.03	N.D.
Surface scaling after 56 cycles with NaCl solution	kg/m²	0.17	0.10	0.06
112 cycles	kg/m²	0.27	0.12	N.D.
Length variation after 365 days in a sulphate solution	%	0	0	0

5 Conclusions

This study investigated the durability parameters of three concrete mixes, covering a broad range of UHPC types. The results indicate a spectacular improvement in durability compared to normal strength concrete and even HPC. No significant difference was observed between the tested UHPC mixes since the mix M1 with a rather limited powder content and a (w/c)-ratio above 0.30 gives results of the same order of magnitude. The influence of the fibre reinforcement was not investigated here.

The resistance to carbonation of the UHPC mixes being very high, steel rebars and reinforcing fibres are much longer protected from carbonation induced corrosion then in ordinary concrete mixes. However, the possible corrosion of some steel fibres directly at the concrete surface could be a problem for aesthetic considerations. UHPC mixes also show a very strong resistance against ingress of aggressive materials such as chloride ions and sulphate water. Moreover, the deterioration caused by freeze-thaw attack is negligible. These results are in good agreement with previous studies and existing recommendations [4, 5].

The highly dense hardened state of UHPC, caused by a very low w/c-ratio and high powder contents, is the primary reason for this enhanced durability. The porosity could be reduced even more by applying a specific heat treatment, especially for the mixes M2 and M3 (for example, curing the concrete at 2 days for about 4 days at 90°C).

From a practical point of view, the mechanical and durability properties of UHPC allow for the design of slimline concrete structures and components with high structural capacities and a very

long life span. The minimum requirements for the concrete cover with regard to durability for reinforcement steel, as specified today in the Eurocode 2 (EN 1992-1-1 and national annexes), are however not adapted for UHPC structures. Such a study could be used as an impulse to review this aspect of said standard.

6 Acknowledgements

The authors gratefully acknowledge the project partner Vrije Universiteit Brussel (VUB) and the financial support of IWT, the Flanders Agency for Innovation by Science and Technology.

References

[1] Piérard, J.; Cauberg, N.; Remy, O.: Evaluation of Durability and Cracking Tendency of Ultra-High Performance Concrete. Proceedings of the 8th International Conference on Creep, Shrinkage and Durability of Concrete and Concrete Structures (CONCREEP 8), Ise-Shima, Japan, 2008, p.695-700.

[2] Cauberg, N.; Remy, O.; Parmentier, B.; Piérard, J.; Van Itterbeeck P.: Shrinkage Behavior and Cracking Tendency of UHPC. Proceedings of the 9th International Symposium on High Performance Concrete – Design, Verification and Utilization, Rotorua, New Zealand, 2011.

[3] Baroghel-Bouny, V. & al.: Conception des bétons pour une durée de vie donnée des ouvrages – Maîtrise de la durabilité vis-à-vis de la corrosion des armatures et de l'alcali-réaction – Etat de l'Art et Guide pour la mise en oeuvre d'une approche performantielle et prédictive sur la base d'indicateurs de durabilité (in French). Association Française de Génie Civil (AFGC), France, July 2004, 252p.

[4] Ultra-High Performance Fibre-Reinforced Concretes: Interim Recommendations. AFGC/SETRA, France, January 2002.

[5] Uchida, Y & al.: Review of Japanese Recommendations on Design and Construction of Different Classes of Fiber Reinforced Concrete and Application Examples. Proceedings of the 8th Symposium on Utilization of High-Strength and High-Performance Concrete, Tokyo, Japan, 2008, p.92-100.

[6] DuraCrete: General Guidelines for Durability Design and Redesign, EU-Project (Brite EuRam III), 109 p., 2000.

[7] Scheydt, J.C.; Herold, G.; Müller, H.S.: Long Term Behaviour of Ultra High Performance Concrete Under the Attack of Chlorides and Aggressive Waters. Proceedings of the 2nd International Symposium on Ultra High Performance Concrete, Kassel, Germany, 2008, p.231-239.

[8] Cwirzen, A.; Habemehl-Cwirzen, K.; Penttala V.: The effect of heat treatment on the salt freeze-thaw durability of UHSC. Proceedings of the 2nd International Symposium on Ultra High Performance Concrete, Kassel, Germany, 2008, p.221-230.

Bond Strength between UHPC and Normal Strength Concrete (NSC) in accordance with Split Prism and Freeze-Thaw Cycling Tests.

Miguel A. Carbonell[1,2], Devin K. Harris[1], Ph.D. , Sarah V. Shann[1], Theresa M Ahlborn[1]
1: Michigan Technological University, USA
2: Polytechnic University of Valencia, Spain

An experimental study was performed to assess the bond performance of UHPC for overlay applications. Pre-wetting conditions, surface preparation, freeze-thaw cycling and indirect tensile strength were variables taken into account to study such performance. A total of 60 composite and 7 monolithic concrete specimens, 102x76x394 mm, were cast to test in indirect tension. Experimental results showed that samples subjected to 300 freeze-thaw cycles present greater bond strength than samples of the same age without freeze-thaw cycles, and all samples in which the moisture condition of the substrate is saturated before placing UHPC achieves excellent bond strength which amply satisfies the range specified in the ACI Concrete Repair Guide.

Keywords: UHPC, bond, concrete repair, splitting tensile test, freeze-thaw cycles, roughness, surface treatment.

1 Introduction

Bridge deck protection

The rehabilitation of concrete structures, particularly within the transportation infrastructure network, is a major challenge for transportation agencies in the United States. This is especially true for concrete bridge decks, which are frequently subjected to severe operating conditions, both environmental and man-made. Often, the most appropriate strategy to preserve or rehabilitate these structures is to provide some form of a protective coating or barrier. These surface treatments have typically been some form of polymer, asphalt, or low-permeability concrete, but the application of Ultra-High Performance Concrete (UHPC) has shown promise for this application mainly due to its negligible permeability, but also as a result of its excellent mechanical properties, self-consolidating nature, rapid gain strength, and minimal creep and shrinkage characteristics. However, for widespread acceptance, durability and performance of the composite system must be fully understood, specifically the bond between UHPC and Normal Strength Concrete (NSC) often used in bridge decks. It is essential that the bond offers enough strength to resist the stress due to mechanical loading or thermal effects, while also maintaining an extended service-life performance [1].

Literature review

The bond strength between two different concrete materials is influenced by many factors, such as substrate surface (wetting conditions, roughness, presence of microcracks, cleanliness), compaction method, curing process, concrete substrate (strength and aggregate gradation), use of bonding agents, age of the bond, and overlay material (strength and thickness) [2 - 4]. There is a broad consensus among research of how some of these factors influence the bond, for example, hydrodemolition followed by power washing has been shown to be the best unsound concrete removal and surface preparation technique. The impact methods (scabbling, milling, scarifying) present the advantage of being the most economical treatment to remove the damaged concrete, but one major shortcoming is that they fracture the remaining concrete surface, causing a low fracture tensile strength. Substrate surfaces prepared by these methods usually achieve half of the bond strength of that prepared by hydrodemolition method [3, 5 - 7].

On the other hand, there are conflicting opinions between engineers about how other factors affect the bond. The moisture condition of the substrate material is one example. It is hard to draw a general conclusion about how the saturated concrete substrate helps to improve the bond strength because it depends on the sorptivity and porosity characteristics of the substrate material. A large porosity could produce a weak interface zone due to the lack of water for proper hydration, but in contrast a low porosity could reduce the mechanical interlock between the substrate and overlay materials [4].

Freeze-thaw cycling is one of the most common causes of repair failure in a bridge deck; therefore, a proper performance evaluation of the bond between concrete materials should include this effect. Li and Geissert [8, 9] presented a new method based on the ASTM C 666 [10] and a modification of ASTM C 496 [11] to study how freeze-thaw cycling influences the bond strength between the old and repair concretes because there are currently no ASTM standard tests for assessing this. The method consisted of casting composite specimens, 102x76x406 mm, that fit within the freeze-thaw apparatus. The specimens were cut into four small prisms, 102x76x76 mm, after being subjected to 300 freeze-thaw cycles according to ASTM C 666. Finite element analysis and experimental results showed that small prisms, 102x76x76 mm, had a more uniform distribution along the bond surface than that of large prisms, 76x102x178 mm, due to the width-height ratio. They concluded that four cast specimens, which produced 16 test prism samples, provided a reasonable estimation of the indirect tensile strength. Previously, Ramey [12] studied the splitting tensile strength between two different materials using composite cylinders instead of monolithic ones. Wall [13] and Momayez [2] used composite splitting prisms, 102x102x102 and 150x150x150 mm respectively, to assess indirect tensile strength between concrete substrate and repair materials, without including freeze-thaw cycles as made by Li and Geissert [8, 9]. The splitting tensile results obtained in these different studies were consistent, verifying that the splitting tensile test is an appropriate method to assess the bond strength between overlay and substrate materials. All these studies used Eq. (1), based on elasticity theory, to estimate the indirect tensile strength:

$$f_{sp} = \frac{2 \times P}{A \times p} \tag{1}$$

where f_{sp} is the splitting tensile strength, P is the maximum applied load and A is the area of the bonding plane.

2 Experimental work

To assess how different surface treatments, substrate moisture conditions and freeze-thaw cycles affect the splitting tensile bond strength, 60 composite and 7 monolithic specimens were cast and tested. The composite specimens, with a nominal dimension of 102x76x394 mm, were made up of NSC and UHPC layers of 38 mm each. Ductal® brand UHPC manufactured by Lafarge North America was used as overlay material. Graybeal [14] presented an extensive mechanical and durability characterization of this material. NSC mixes were designed to satisfy the requirements given by Michigan Department of Transportation Bridge Design Manual [15]. These requirements consist of a 28-day compressive strength greater than 31 MPa, a minimum cement content of 390 kg/m^3, an entrained air of 4.5±1.5 %, and a slump of 25–150 mm. The maximum size for the coarse aggregate used in the NSC mixes was 9.5 mm to avoid compaction problems. Table 1 lists the number of composite specimens assigned to each case study. Four composite prisms were obtained from each beam for testing under indirect tension.

Preparation of concrete substrates

The first and second of a total of three NSC mixes of NSC were used to cast substrates for the composite samples. A third mix was used to cast monolithic specimens with the same size as those of composite specimens. All concrete substrate samples were demoulded 24 hours after casting and cured in a lime water tank.

Table 1: Composite specimens distribution for each case study.

Dry Substrate		Saturated Substrate	
With freeze-thaw cycling	**Without freeze-thaw cycling**	**With freeze-thaw cycling**	**Without freeze-thaw cycling**
3 specimens per each surface treatment	3 specimens per each surface treatment	3 specimens per each surface treatment	3 specimens per each surface treatment

When the concrete substrates reached 28 days of age, the surface preparation was carried out. Smooth, chipped, grooved, brushed and sandblasted surfaces were chosen in order to cover a broad range of different roughness profiles and to represent some of the most widespread surface preparation techniques [3, 16]. Figure 1 shows these different surfaces. The grooves had dimensions at approximately 6-11 mm wide by 7-11 mm deep. It is necessary to mention that at first the smooth surface was considered to be without any surface treatment and the chipped surface to be only with small holes produced by a hand drill, but after casting the UHPC for the samples in the dry moisture condition, all the composite specimens where the concrete surface was chipped or smooth failed prematurely after demoulding. This was due to the fact that no dust removal method was applied to these surfaces; therefore, no bond was achieved between new and old materials. These samples were slightly brushed, and a new layer of UHPC was poured on them, obtaining composite specimens that did not split after demoulding.

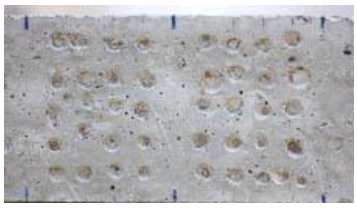

(a) Chipped surface, slightly brushed.

(b) Smooth surface, slightly brushed.

(c) Smooth surface, no dust removal treatment applied.

(d) Sandblasted surface.

(e) Brushed surface.

(f) Grooved surface.

Figure 1: Different NSC substrate surfaces.

Roughness measurement

Two methods were used to evaluate the degree of roughness obtained by each surface treatment: the macrotexture depth test [17] and the Concrete Surface Preparation index (CSP) given by [7]. The macrotexture depth determines the area covered by a known volume of glass spheres spread on the concrete surface. The volume of the glass beads used in the test was 2 ml, although the minimum value specified in [17] is 25 ml, because the size of the samples were not large enough. The test was repeated four times in each concrete specimen. The CSP index provides 9 different rubber profiles that replicate different degress of roughness. The resuts of both tests are summarized in the Table 2.

Table 2: Results of the macrotexture depth test and classification of the surfaces according to CSP.

Surface treatment	ICRI Profile	Macrotexture Depth (mm)
Smooth	1, 2	0.64-0.74
Brushed	1, 3	0.67-0.88
Chipped	No applicable	0.86-1.05
Sandblasted	4, 5	0.92-1.29
Grooved	No applicable	No applicable

Placing overlay material

The loose particles on the concrete substrate were removed by high-pressure air before placing the overlay material. As mentioned previously, two different moisture conditions were used. Dry concrete substrate is considered as the concrete substrate that was kept in environmental conditions for a period longer than 28 days. Saturated concrete substrate is defined as the concrete substrate that was submerged in a water tank for a period of at least 24 hours, and then covered by a damp cloth to keep the moisture until placing the overlay material, as shown in Figure 2(d). The surface was wet, but with no free water on it. After pouring the overlay material, the composite specimens were covered by plastic sheets for three days before demoulding.

Freeze-thaw cycling

Those samples which were subjected to 300 freeze-thaw cycles, Figure 2(b), were cured in ambient air for at least 14 days prior to testing according to ASTM C 666, Procedure B [10]. Once the freeze-thaw test was completed, each specimen was cut into four small prisms, 102x76x76 mm, discarding approximately 46 mm of each end, as described in [8, 9].

(a) The set-up for the splitting tensile test.

(b) Composite samples in the chamber.

(c) Composite specimen.

(d) Wet cloths covering the concrete substrate.

Figure 2: Several steps of the experimental work.

Loading test

Compression loading was applied at a constant rate of 8 kN/min until the sample was split, Figure 2(a). All samples were exposured to the same environmental conditions and tested approximately at the same age. Therefore, the differential shrinkage between samples was kept constant, avoiding the introduction of a new variable into the test matrix [16]. To estimate the indirect tensile stress along the bond interface, Eq. (1) was applied despite the fact that the prisms were made up of two different materials. The nominal area, 102x76 mm, was used.

Results

Table 3 gives the compressive strength of the repair and old layers on the same day as the splitting test was carried to have a measure of the quality of both materials.

Table 3: Age and compressive strength of overlay and substrate materials on the day indirect tension test.

	Composite UHPC/NSC Samples						Monolithic concrete samples		
	Dry Substrate			Saturated Substrate					
Material	N°	Age	Strength	N°	Age	Strength	N°	Age	Strength
NSC	5	270-278	46.8	4	278-280	44.5	4	227-228	59.4
UHPC	10	221-231	154.9	6	185-186	152.7			

Note: N°: number of cylinders. Age in days. Strength in MPa.

A number of the composite specimens cast, with the old substrate being dry, failed during the cutting process, indicating a general failure of the bond from construction. Table 4 shows the percentage of prisms that split before the loading test. Only those specimens with a grooved substrate surface were fully successful, due to the fact that the bond was achieved by fitting UHPC in the grooves rather than any adhesive mechanism since no dust removal treatment was applied in the grooved surface, as shown in Figure 1(f). The tensile strength of prisms with grooved substrate surface and the coefficient of variation (COV) in % are given in the Table 5.

Table 4: Percentage of prisms that failed prematurely under dry concrete substrate condition.

Case	Percentage of failure (%)	Case	Percentage of failure (%)
Sb FT	50	Sm FT	50
Sb W/o	16.7	Sm W/o	75
Br FT	83.3	Ch FT	100
Br W/o	66.7	Ch W/o	100

Note: Sb: sandblasted, Br: brushed, Sm: smooth, Ch: chipped, FT: 300 freeze-thaw cycles, W/o: without freeze-thaw cycles.

Table 5: Results of grooved surface under dry concrete substrate condition.

		Prism (strength+failure mode)								Average strength, specimen	COV, specimen	Average strength, case study	COV, case study
	N	A		B		C		D					
Gr FT	1	4.4	G	5.8	G	6.8	G	6.0	G	5.7	17.2	5.3	24.4
	2	5.1	G/C	4.6	G/C	7.2	G	6.0	G	5.8	19.8		
	3	5.0	G	5.1	G	5.0	G	2.2	G	4.3	32.8		
Gr W/o	1	5.3	G	4.9	G	5.3	G	5.7	G	5.3	5.9	5.0	11.2
	2	4.2	G/C	5.2	G	4.3	G/C	3.8	G	4.4	12.8		
	3	5.0	G/C	5.4	G	5.2	G	5.3	G	5.2	3.0		

Note: N: number of the specimen, Gr: grooved, FT: 300 freeze-thaw cycles, W/o: without freeze-thaw cycles, G: failure in the grooves, G/C:mixture failure between bond and concrete. Strength in MPa.

However, excellent bond performance was achieved under saturated concrete substrate, with the exception of a specimen of sandblasted surface that presented scattered results. The test results for the saturated substate samples are presented in Table 6 along with descriptions of the failure modes. The rest of the samples widely satisfied the range of 1.7 to 2 MPa at 28 days specified in the ACI Concrete Repair Guide [18] for an acceptable bond strength and 2.1 MPa that Sprinkel [19] defined as an excellent bond. These values refer to direct tensile bond. This comparison with indirect tensile strength is based on results from Momayez [2] that demonstrated the bond strength obtained with the pull-off test (direct tensile strength) to be equal or slightly lower than that of the splitting test (indirect tensile strength).

Table 6: Summary of indirect tensile strength composite sample results under saturated concrete substrate.

		Prism (strength+failure mode)								Average strength, specimen	COV, specimen	Average strength, case study	COV, case study
	N	A		B		C		D					
Sb FT	1	5.3	C	3.2	C	3.4	C	3.9	C	4.0	24.4	4.2	17.9
	2	3.0	B/C	4.0	B/C	4.7	C	4.4	C	4.0	18.9		
	3	4.9	C	4.6	C	4.3	C	5.1	C	4.7	7.2		
Sb W/o	1	4.0		3.8	B	2.5	B	2.3	B	3.2	27.9	3.1	45.8
	2	4.5	C	4.4	B	4.2	B/C	3.5	B	4.2	10.8		
	3	3.8	B/C	2.9	B	1.0	B	0	B	1.9	90.0		
Br FT	1	4.8	C	4.9	C	3.9	C	4.8	C	4.6	10.2	4.2	10.5
	2	3.6	C	4.3	C	3.9	C	4.6	C	4.1	11.3		
	3	4.1	C	3.9	C	3.9	C	4.0	C	4.0	2.0		
Br W/o	1	4.2	C	3.8	C	4.2	C	4.7	C	4.2	8.4	4.1	8.3
	2	3.9	C	4.2	C	3.8	C	4.4	C	4.1	7.0		
	3	4.4	C	3.6	C	4.5	C	3.8	C	4.1	11.0		
Sm FT	1	4.4	C	4.3	B/C	3.6	C	4.3	B/C	4.2	8.3	4.2	11.7
	2	3.6	B/C	4.1	B/C	5.0	C	3.8	B/C	4.1	15.0		
	3	4.5	C	4.6	C	5.0	B/C	3.6	B/C	4.4	13.0		
Sm W/o	1	2.6	B	3.4	B	2.8	B	3.3	B	3.0	12.0	3.6	16.9
	2	3.3	B/C	4.4	C	4.0	C	3.5	C	3.8	13.0		
	3	4.5	C	4.4	C	4.1	C	3.6	B/C	4.1	9.7		
Ch FT	1	5.2	C	4.6	C	4.8	C	4.3	C	4.7	8.4	4.5	7.8
	2	4.5	C	3.9	C	4.4	C	4.7	C	4.4	8.6		
	3	4.7	C	4.4	C	4.2	C	4.3	C	4.4	4.3		
Ch W/o	1	3.7	C	4.3	C	3.3	C	4.2	B/C	3.9	11.1	4.1	10.1
	2	3.6	B/C	3.9	B/C	4.2	C	4.2	C	4.0	6.7		
	3	3.9	B/C	4.6	C	4.8	C	3.9	B/C	4.3	10.8		
Gr FT	1	6.8	G	5.2	C	4.5	C	3.2	C	4.9	30.4	5.7	25.8
	2	5.9	G/C	4.9	G/C	5.5	G/C	5.3	G/C	5.4	7.3		
	3	6.2	G	5.0	G	6.4	G/C	9.2	G	6.7	26.5		
Gr W/o	1	5.0	G	4.4	G	4.3	G	5.3	G	4.8	10.2	4.8	18.1
	2	4.0	G	4.4	G	3.9	G/C	4.2	G/C	4.1	4.8		
	3	5.1	G/C	5.1	G/C	4.7	G/C	7.1	G/C	5.5	20.1		

Note: N:number of the specimen, Sb: sandblasted, Br: brushed, Sm: smooth, Ch: chipped, Gr: grooved, FT: 300 freeze-thaw cycles, W/o: without freeze-thaw cycles, C: failure in the concrete, B: failure in the bond, B/C: mixture failure between bond and concrete, G: failure in the grooves, G/C: mixture failure between bond and grooves. In Sb W/o, N 1, prism A, the load was removed before splitting of the prism. Strength in MPa.

Table 7 shows the results of 7 monolithic NSC specimens that were cast for use as a benchmark to assess the quality of the bond. These samples were subjected to the same conditions as those of the composite specimens.

Table 7: Summary of indirect tensile strength monolithic NSC sample results.

	N	Average strength, specimen	COV, specimen	Average strength, case study	COV, case study		N	Average strength, specimen	COV, specimen	Average strength, case study	COV, case study
FT	1	4.9	6.4	4.9	6.7	W/o	1	4.7	8.6	4.5	12.9
	2	5.2	2.9				2	4.5	14.3		
	3	4.6	4.8				3	4.2	16.9		
	4	4.9	6.8								

Note: N:number of the specimen, FT: 300 freeze-thaw cycles, W/o: without freeze-thaw cycles. Strength in MPa.

In the splitting tensile test, the bond interface is subjected to the greatest tensile stress in the specimen. It should be emphasized that when the failure of the composite prism takes place in the concrete substrate, the bond strength is considered greater than the failure stress of the sample. Only in the cases in which failure occurred fully in the bond that stress value can be taken as the bond strength. Figure 3 shows the different failure modes considered in this study.

(a) G/C: groove-concrete.

(b) G: grooved.

(c) B/C: bond-concrete.

(d) C: concrete.

(e) B: bond.

(f) Failed prism samples.

Figure 3: Representive failure modes of composite specimens.

3 Conclusions and discussion

The results from this study highlight that the moisture condition of the concrete substrate is a critical factor for achieving good bond performance. The bond between UHPC and NSC gives excellent results under indirect tensile stress if the moisture condition of the concrete substrate is saturated before placing the overlay material, regardless of the surface treatment applied. In contrast, a general premature failure occurred with those samples cast on a concrete susbstrate with a dry moisture condition. Smooth, sandblasted, brushed and chipped surfaces presented similar strengths which indicates that the surface treatment is not a critical factor, at least under this loading configuration. Additional testing under different states of stress will be used to further study the effect of surface roughness, with more appropriate testing configurations [1, 2]. Macrotexture depths equal or greater than 1.5 mm are often related with good bond strength based on field experience [5], but in this research, the different substrate surfaces had macrotexture depths between 0.64 and 1.29 mm, and all of them presented outstanding strengths. Therefore, it can be concluded that when UHPC is used as overlay material on a saturated substrate, a simple surface treatment that removes the dust from the concrete surface is enough to achieve a good bond that satisfies the bond strength ranges given by [18, 19]. In all cases, 300 freeze-thaw cycles have a benefitial effect on the bond strength.

The low COV for the monolithic samples confirms the consistency of the splitting tensile test. Whereas the COV for the composite specimens with brushed, smooth or chipped substrate surfaces was acceptable. The COV for grooved samples is slightly greater due to the variation in the size of grooves. The COV for sandblasted samples was higher due to the fact that two prisms had strengths significantly below the mean strength. The latter might be due to an error in some stage of the prism preparation. For the composite specimens with a smooth, brushed or chipped substrate surface, the average strengths attained were about 81% to 92% of the strength of monolithic samples. For sandblasted substrate surface, this range varied from 69% to 87% due to those two outlier prisms previously mentioned. The grooved surface obtained better results, between 107% and 117%, approximately. This was due to the fact that in the plane in which the force was applied, the UHPC that filled the grooves was bearing most of the indirect tensile stress.

4 Futher research and acknowledgment

Future work will include the evaluation of more composite samples subjected to 600 and 900 freeze-thaw cycles and slant shear and pull-off tests to evaluate behavior of the bond under different states of stress. The rise of freeze-thaw cycles will assess if the increase of bond strength stabilizes or if there is a turning point from which the bond strength decreases. The slant shear is more sensitive to the surface preparation [1, 2]. The pull-off test can be carried out in situ or in the laboratory giving the opportunity of correlation among the others tests. The authors thank Lafarge North America for their support of the highlighted research activities.

References

[1] Harris, D.K.; Sarkar, J.; Ahlborn, T.M.: Interface Bond Characterization of Ultra High Performance Concrete Overlays. *Transportation Research Board (TRB) 90th Annual Meeting*, Transportation Research Board, Washington, D.C., 2011.

[2] Momayez, A.; Ehsani, M. R.: Comparison of methods for evaluating bond strength between concrete substrate and repair materials. *Cement and Concrete Research* 35 (4), p. 748-757, 2005.

[3] Silfwerbrand, J.: Improving concrete bond in repaired bridge decks. *Concrete International* 12, p. 61-66, 1990.

[4] Beushausen, H.: The influence of concrete substrate preparation on overlay bond strength. *Magazine of Concrete Research* 62, p. 845-852, 2010.

[5] Sprinkel, M. M.: Preparing bridge decks for overlays. *Aberdeen's Concrete Repair Digest* 8, p 242-247, 1997.

[6] Hindo, K. R.: In-place bond testing and surface preparation of concrete. *Concrete International* 12, p. 46-48, 1990.

[7] ICRI Guideline. No. 03732. Selecting and Specifying Concrete Surface Preparation for Sealers, Coatings, and Polymer Overlays. International Concrete Repair Institute, IL., USA, 1997.

[8] Li, S. E.; Geissert D. G.: Freeze-thaw bond durability of rapid-setting concrete repair materials. ACI Materials Journal 96, p. 242-249, 1999.

[9] Geissert, D. G.; Li, S. E.: Splitting prism test method to evaluate concrete-to-concrete bond strength. ACI Materials Journal 96, p. 359-366, 1999.

[10] ASTM C666 / C666M - 03. Standard Test Method for Resistance of Concrete to Rapid Freezing and Thawing. West Conshohocken, PA., 2008.

[11] ASTM C496/C496M. Standard Test Method for Splitting Tensile Strength of Cylindrical Concrete Specimens. West Conshohocken, PA., 2004.

[12] Ramey, G.E.; Strickland, A.M.: An experimental evaluation of rapid-setting patching materials used in the repair of concrete bridges and pavements. Alabama Highway Research, Project 930-103, Part II, pp. 48– 56, 1984.

[13] Wall, J. S.; Shrive, N. G.: Testing of Bond between Fresh and Hardened Concrete. Adhesion Between Polymers and Concrete, Proceedings of an International Symposium, France, 1986.

[14] Graybeal, B.: Material Property Characterization of Ultra High Performance Concrete, FHWA-HRT-06-103, Federal Highway Administration, U.S Department of Transportation, Washington,D.C., 2006.

[15] Michigan Department of Transportation. MDOT Bridge Design Manual. Lansing, MI., 2009.

[16] Julio, E. N. B. S.; Branco, F. A. B.: Concrete-to-concrete bond strength: Influence of an epoxy-based bonding agent on a roughened substrate surface. Magazine of Concrete Research 57, p. 463-468, 2005.

[17] ASTM Standard E965-96. Standard Test Method for Measuring Pavement Macrotexture Depth Using a Volumetric Technique. West Conshohocken, PA., 2006.

[18] Concrete Repair Guide (546R-04). American Concrete Institute. Farmington Hills, MI., 2004.

[19] Sprinkel, M. M; Ozyildirim, C.: Evaluation of high performance concrete overlays placed on route 60 over Lynnhaven inlet in Virginia. VTRC 01-R1. Virginia Transportation Research Council, VA., 2000.

Alkali-Activated Ground Granulated Blast Furnace Slag Binders for High Performance Concretes with Improved Acid Resistance

Ricarda Tänzer[1], Dietmar Stephan[2], Michael Schmidt[1]
1: Institute of Structural Engineering, University of Kassel, Germany
2: Building Materials and Construction Chemistry, Berlin Institute of Technology, Germany

This paper presents the approach from fundamental investigations of alkali-activated GGBFS with different types of alkali silicates as activators to mortars and concretes that can be used for sewage pipes with improved acid resistance. Methods such as flow-table test, compressive strength or scanning electron microscopy and mercury intrusion porosity as well as the examination of the acid resistance are used to characterise the properties of the binders, mortars and concretes in fresh and hardened state. Finally the production of a pipe in laboratory scale is represented.

Keywords: ground granulated blast-furnace slag, alkali silicate binders, sewage pipes

1 Introduction and background

The item “High and Ultra High Performance Concrete” is usually defined by a high compressive strength [1] and dense microstructure. Derived from this, other performance criteria like improved chemical resistance can be mentioned. Currently used concrete pipes that form part of sewer systems are increasingly exposed to aggressive fluids. Concretes based on conventional cements have a restricted resistance especially to acid attack even if they fulfill the structural and strength requirements for HPC or UHPC. Because of that plastic or ceramic materials with a higher acid resistance are preferably used.

Therefore, alternative binders with an improved acid resistant attract more and more attention. One opportunity is based on alkali-activated ground granulated blast-furnace slag (GGBFS) and fly ash, also referred to as “cold ceramics”. Activating agents such as alkali salts (carbonates, sulfates), alkali hydroxides or alkali silicates, also known as waterglass, can be used for producing binders which harden at temperatures lower than 100°C and also provide a high degree of chemical and mechanical resistance.

One requirement for the activator is to attack and dissolve the glass network of the GGBFS or fly ash [2]. The basic mechanism of these reactions was described by Glukhovsky [3] in three steps: destroying glass network of the raw material and precipitation; precipitation and condensation as well as condensation and crystallization. According to the CaO-content in the raw materials different reaction products are formed. At high CaO-contents mainly C-S-H and C-A-H phases can be found in the binders. With decreasing CaO-content this proportion is reduced and the proportion of zeolite-like phases is rising [4]. If blast-furnace slag is mixed with solids low or free in calcium such as fly ash or metakaolin, reaction products of both C-S-H and C-A-H phases and an aluminosilicate network are formed [5-8].

In particular, the application of waterglass as activator results in a consistent silicification of the material structure, because of the high amount of silicate in the liquid. This reaction has a significant influence on the pore structure and thus on the impermeability and physical resistance of the binder.

In the following paper the whole development from binder investigations over mortar to the concrete mixing design and finally the production of a pipe in laboratory scale is represented.

2 Materials and methods

Ground granulated blast furnace slag and alkaline activators

The used GGBFS had a glass content of 99.9 wt.-% and a Blaine fineness of 4150 cm²/g. The chemical composition is shown in Table 1.

Table 1: Chemical composition of the industrial GGBFS in wt.-%.

wt.-%	SiO_2	Al_2O_3	FeO	TiO_2	MnO	CaO	MgO	Na_2O	K_2O	S^{2-}
GGBFS	37.4	10.0	0.25	0.80	0.23	38.7	10.3	0.27	0.62	1.14

As alkaline activators several sodium and potassium silicates were used, which differ in their modules (defined as molar ratio SiO_2/Me_2O). Table 2 shows the abbreviations and explanations of the activators used in this investigation. Furthermore, for all binders a water to slag ratio of 0.35 was defined, to allow a comparability of all binders, because of the different solids contents of the waterglasses.

Table 2: Composition of the alkaline activators.

abbreviation		waterglass	molar ratio SiO_2/Me_2O	alkali concentration in mol/kg	solid content
Na-WG-0.5	2 mol/kg Na	sodium waterglass	0.5	2.0	9.2
Na-WG-1.0	2 mol/kg Na	sodium waterglass	1.0	2.0	12.2
Na-WG-2.0	2 mol/kg Na	sodium waterglass	2.0	2.0	18.2
K-WG-0.5	2 mol/kg K	potassium waterglass	0.5	2.0	12.4
K-WG-1.0	2 mol/kg K	potassium waterglass	1.0	2.0	15.4
K-WG-2.0	2 mol/kg K	potassium waterglass	2.0	2.0	21.5

Experimental Investigation

At first sample specimen (2·2·2 cm³) of alkali-activated slags were prepared for investigating the characteristics of the hardened binders. They were kept in moulds at 20 °C and 65 % RH for one day. After demoulding the hardened binders were stored at 20 °C and 100 % RH until testing the compressive strength after 1, 7, 28 and 180 d, respectively. In order to analyze the pore size distribution and microstructure of the binders the hydration of some specimen was stopped by means of vacuum drying 28 d after the preparation. For these investigations a mercury intrusion porosimeter (Poremaster 60 GT, Quantachrome) and a scanning electron microscope (XL 30, Phillips) were used. The setting time of the binders was detected with an automatic Vicat apparatus according to DIN EN 196-3.

The mortars were prepared with a mortar mixer according to DIN EN 196-1. To determine the workability in dependence of the time, the slump was measured in accordance with DIN EN 1015-3 4 minutes after zero time as well as 10, 20, 30 minutes, and if possible 40 minutes after zero time. In addition the acid resistance of mortars were checked. At the age of 28 d, prism (4·4·16 cm³) were exposed to sulfuric acid, nitric acid and lactic acid (each pH-value 4 and 2) and for comparison in water and air. After 14 days, the specimens were removed from the solution, and stored two more days under standard conditions before testing their flexural and compressive strength.

For the concrete two quartz gravels (2/8 and 8/16) were used as aggregates. It was prepared with a concrete mixer ZZ 150 HE by Zyklos company with 150 l of usable volume. First the dry ingredients were pre-mixed to homogenize them for two minutes. Subsequently, the liquid component, consisting of the waterglass K-WG-0.75 and water were added and the concrete was mixed 4 more minutes.

3 Results and discussions

Binder

The compressive strength of the binders in Figure 1 depict several findings. After 1 d, the binders containing waterglasses with low SiO_2/Me_2O-ratios show slightly higher strength compared to the binders containing waterglasses with higher SiO_2/Me_2O-ratios. But from a reaction time of 7 d the strength is increasing with increasing module. This effect becomes more obvious when taking a closer look at the binders with sodium silicates.

High compressive strengths were achieved with potassium waterglasses, in particular K-WG-1.0. This binder reached already after 1 d a strength of nearly 40 N/mm², which increases over time up to 120 N/mm² after 180 d.

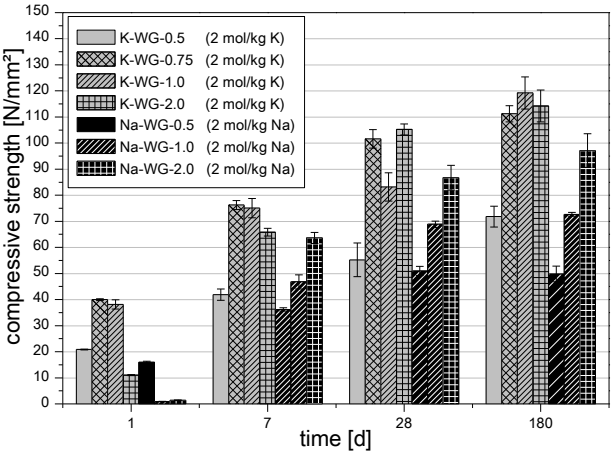

Figure 1: Effect of the SiO_2/Me_2O-ratio of the waterglass activators on the compressive strength of the activated GGBFS.

The porosity of alkali activated binders depend on the modulus of the waterglass used and can be very low. Figure 2 shows the pore size distribution of selected binders with potassium waterglas with moduli of 0.5, 1.0 and 2.0 compared to a hardened cement paste made from CEM I 42.5 R (water to cement ratio 0.35). After 28 d of hydration the hardened cement paste had a broad pore size distribution between 2 and 300 nm with a total porosity of 21.4 vol-%, where of 5.4 vol-% are in the range of gel pores. The total porosities of the alkaline-activated binders are all lower compared to cement paste sample. The majority of this porosity is formed from gel pores. The binder with K-WG-0.5 had the highest porosity with 15.2 vol-%. The lowest porosity had the binder with potassium waterglass with molar SiO_2/Me_2O-ratio of 1.0.

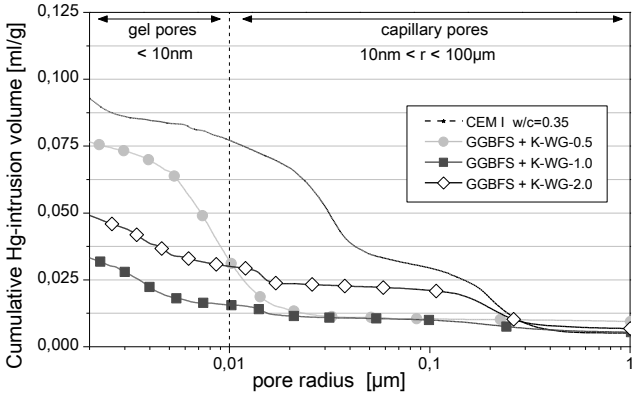

Figure 2: Pore size distribution of alkali-activated GGBFS with different potassium water-glasses as activator compared to a hardened cement paste (CEM I 42.5 R, water to cement ratio= 0.35).

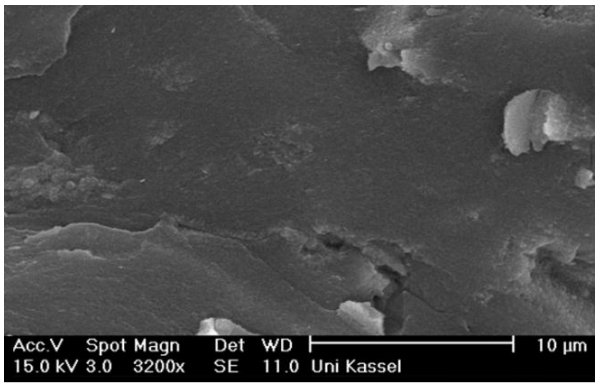

Figure 3: SEM photomicrographs of a binder after 28 d of reaction (GGBFS with K-WG-1.0).

In Figure 3 scanning electron microscopy (SEM) images of the binder with K-WG-1.0 is represented. The selected specimen shows an extremely dense and obviously closed surface without visible pores. It is assumed that gel structures are formed during the hardening process, that cross-linked the slag particles. In contrast to CEM cements no distinct network of capillary pores is formed, which explains the density of the binder [9]. The high density is assumed to

have a positive effect on the performance of these binder systems, especially regarding the high mechanical strength and the resistance against chemical attack, caused by the exposition to aggressive liquids and gases.

For the evaluation of the workability times of these alkali-activated binders the setting times were measured twice with an automatic Vicat needle apparatus. Figure 4 presents the setting times of the alkali activated binder pastes with sodium and potassium waterglasses. The clear dependency of the waterglass modulus becomes obvious. With rising SiO_2/Me_2O-ratio the setting times decrease. A possible explanation for this behavior could be a condensation of the colloidal silica oligomers of the waterglass resulting in a stiffening of the binder [9, 10]. The ratio of SiO_2/Me_2O, has a high impact on the resulting setting times, which is shorter with a rising content of SiO_2.

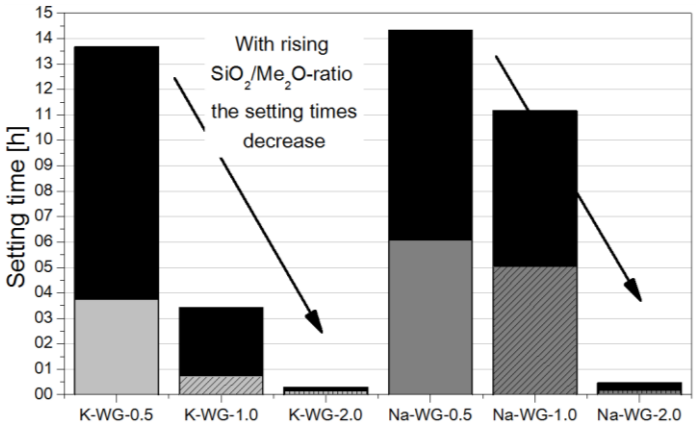

Figure 4: Setting times of alkali activated binders with GGBFS and waterglasses with different molar ratios of SiO_2/Me_2O (black part of the bar: time between the initial set and end set).

Mortar

The consistency and the workability time are important practically relevant properties of mortars and concretes. For practical use, it is specially necessary to influence the consistency, hence not only thin liquid mortar for coatings but also stiff concretes for pipes can be manufactured. For the investigation of consistency and processing time first a mix design for mortar was formulated which consists of GGBFS (Table 1) and a quartz sand 0/2 as well as waterglass and water as the activator. According to the calculation algorithm of Schwanda and Reschke [11, 12] to optimize packing density of broken material, GGBFS (40.8 wt.-%) and quartz sand 0/2 (59.2 wt.-%) were selected, resulting in mixtures with a low content of voids, and hence a maximum space filling of 0.799. The ratio of granulated slag and waterglass was the same as in the binder pastes. The water contents had to be adjusted because of the different solid contents of the waterglasses and the selected water to binder value.

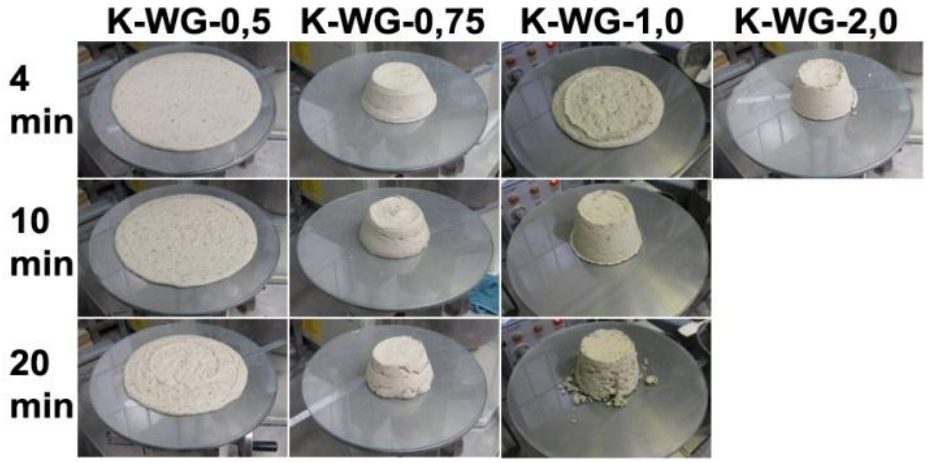

Figure 5: Value of flow table test of different mortars with alkali activated GGBFS (flow table Ø 30 cm).

The mortar with K-WG-0.5 as activator has the softest consistency (see Figure 5), and remains fluid and workable for a certain time after mixing. In contrast to that the mortar with K-WG-1.0

has a soft and fluid consistency at the beginning, but after 20 minutes it began to stiffen very fast resulting in a total loss of workability. The mortar with K-WG-2.0 stiffens even faster and the slump cone could not be filled for a second test after 10 min. Therefore, another activator was required, combining the high slump and long workability of K-WG-0.5 with the high strength of the binder with K-WG-1.0. All the advantages can be combined in the waterglas K-WG-0.75. As can be seen in Figure 1 the compressive strength after 1 d is around the same level like the binder with K-WG-1.0. The mortar with K-WG-0.75 shows a pronounced thixotropic behaviour. The slump is not as fluid as with K-WG-0.5, but the workability of mortar is good. With low mixing energy it is possible to stir up a plastic consistency again and keep it for more than 40 minutes.

This mortar was chosen for testing the acid resistance. Figure 6 on the left side represents the strength (relative to the residual cross-section) of the mortar with GGBFS and K-WG-0.75 after 14 d of storage in various media. The compressive strength of the prism embedded in sulfuric acid (pH=4 and pH=2), nitric acid and lactic acid (each pH=4) are comparable to the strength of the references in air or water. A loss in compressive strength could be observed in consideration of the specimens that have been exposed to nitric acid and lactic acid (pH=2).

On the right side of Figure 6 photomicrographs of two prism after 14 d storage in lactic acid (pH=2) are represented. The mortar above contains alkali-activated GGBFS as a binder, the mortar below is based on Portland cement. The latter is attacked until complete destruction. It was not possible to measure a compressive strength on these deformed specimens. This comparison shows that alkali-activated systems have great potential for acid resistance mortars in the case of sulfuric acid attack, als well as in the case of exposure to organic acids.

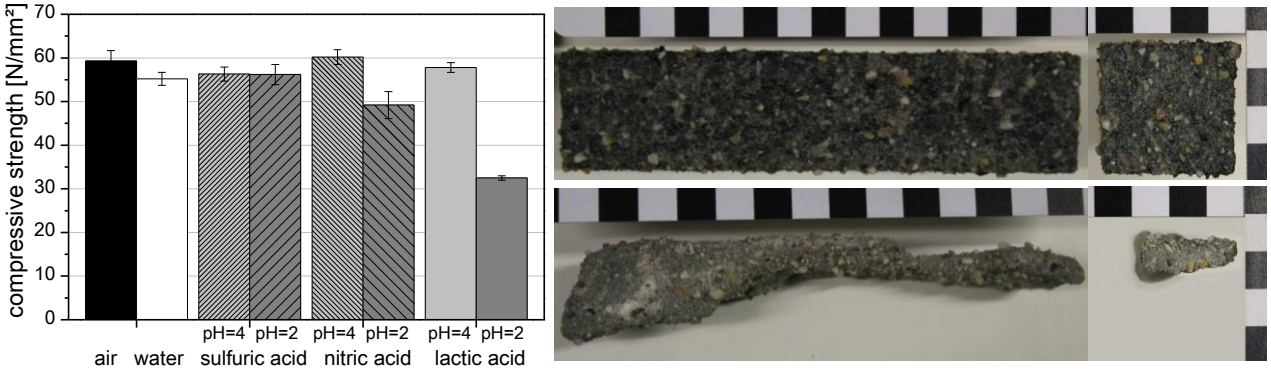

Figure 6: left side: Strength of mortar with K-WG-0.75 activated GGBFS after 14 d storage in various media; right side: Comparison of two prism after 14 d storage in lactic acid (pH=2); above: alkaline-activated mortar with K-WG-0.75, below: cementitious mortar.

Concrete

The final step was the transfer from mortar to concrete scale and the production of an prototype. For the concrete products industry characteristics such as high green strength, good properties for demoulding and a high dimensional stability are necessary. These properties can be achieved with earth-moist concrete, which has a very stiff consistency and a high proportion of aggregates. The used binder paste or mortar must have a flowable consistency to allow a complete coating of the aggregate. For this reason, the mortar with K-WG-0.75 (water to binder value 0.45) was chosen. In order to achieve an immediate demoulding property, a high dimensional stability and a closed surface of the manufactured cylinders, it was necessary to find the optimum mortar to aggregate proportion. In Table 3 the concrete compostions depending on the ratio of mortar to aggregate are listed.

The specimens from earth-moist concrete (cylinder diameter 20 cm) were produced under load (27.5 kg) while compressing on the vibrating table. The proportion of mortar rises from 35 up to 50 vol-%. It was possible to produce green stable cylinders with high contour accuracy. As illustrated in Figure 7 the surface becomes denser with increasing binder content. Because the specimens with 45 and 50 vol-% do not differ so much, the concrete with a ratio mortar to aggregates of 45 : 55 was used for the prototype pipe for the lower content of waterglass.

Table 3: Concrete composition based on mortar with GGBFS and K-WG-0.75 with different mortar to aggregate ratios (water to binder value 0.45).

		Weight for 1 m³ concrete [kg]			
Ratio Mortar (M) to Aggregates (A) [vol-%]		**M : A 35 : 65**	**M : A 40 : 60**	**M : A 45 : 55**	**M : A 50 : 50**
Mortar	GGBFS	259	296	333	370
	K-WG-0.75	100	114	128	143
	Water	31	35	39	44
	Quartz sand 0-2	375	429	482	536
Aggregates	Gravel 2/8	984	909	833	757
	Gravel 8/16	738	681	625	568
Amount of paste [vol-%] Paste = GGBFS + WG + H_2O		21	24	27	30

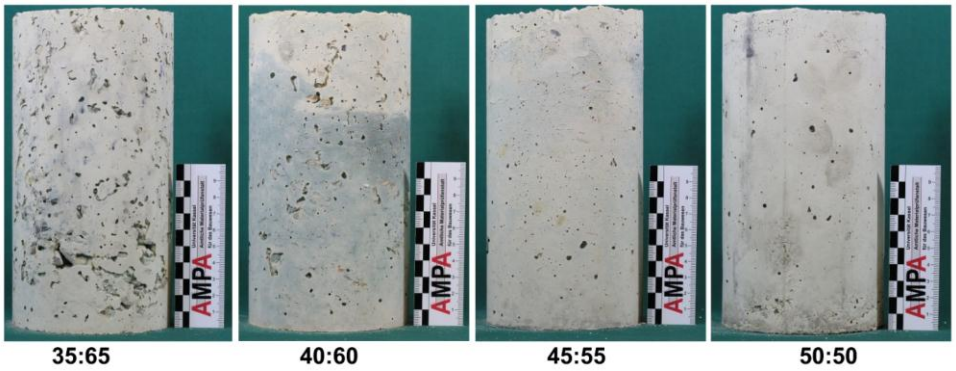

Figure 7: Dimensional stability and surface appearance of concrete specimens with different ratios of mortar to aggregate

At first a formwork was prepared for a 1 m long pipeline with a wall thickness of 5 cm (inner diameter 20 cm, outer diameter 30 cm). After mixing the concrete it was poured in layers in the formwork, which was fixed on a vibrating table. To simulate the industrial manufacturing process the pipe was demoulded immediately. Figure 8 shows the described production process of the pipe demonstrator as well as the finished pipe, a sectional area and the surface of the hardend tube. Due to the mechanical treatment after demoulding a largely non-porous surface could be achieved on the inside and outside of the tube. This rework of the surface is quite commen in concrete factories e.g. in pipe manufacturing.

Figure 8: Production process of the pipe demonstrator (filling the formwork and demoulding), the finished pipe (iner diameter 20 cm, wall thickness 5 cm, height 1 m) as well as the sectional area and the surface of the hardend tube.

4 Conclusions

In this paper the development from binder over mortar and concrete to a prototype pipe was represented. Key finding of the investigation is that the specific choice of the waterglass is a dominant control variable to influence the binder, fresh and hardened mortar and concrete properties. With the decision whether a sodium or potassium waterglass is used with a high or low waterglass module (molar ratio SiO_2/Me_2O), the processing properties (consistency and processing time), the solidification and hardening and solid-state properties can be controlled in general. As a consequence mortar and concrete recipes can be developed that are adapted to application requirements. Furthermore, the production of the demonstrator shows that with these binders it is possible to produce concrete which is suitable for the concrete industry and has a good resistance to aggressive external conditions.

Acknowledgements

The authors thank the Bundesministerium für Bildung und Forschung for financial support. Thanks are also expressed to Mr. Ehrenberg (FEhS) and Mr. Krakehl (Woellner) for supply of materials.

References

[1] DAfStb: Sachstandsbericht Ultrahochfester Beton, Heft 561. 1. Auflage, Beuth Verlag, Berlin, (2008).
[2] Shi, C., Krivenko, P. V. and Roy, D.: Alkali-Activated Cements and Concrete. Taylor and Francis, New York, (2006).
[3] Glukhovsky, V. D.: Soil silicates. Their properties, technology and manufacturing and fields of aplication, Doct Tech Sc. Degree thesis, Civil Engineering Institute. Kiev, (1965).
[4] Škvára, F.: Alkali activated material - Geopolymer, Proc. International Conference Alkali Activated Materials (Prague, 2007), pp. 661-676.
[5] Buchwald, A., Hilbig, H. and Kaps, C.: Alkali-activated metakaolin-slag blends - performance and structure in dependence of their composition, Journal of Materials Science, vol. 42, no. 9, pp. 3024-3032 (2007).
[6] Buchwald, A.: Geopolymer binders - Part 1: What are geopolymers?, ZKG International, vol. 60, no. 12, pp. 78-84 (2007).
[7] Yip, C. K., Lukey, G. C. and van Deventer, J. S. J.: The coexistence of geopolymeric gel and calcium silicate hydrate at the early stage of alkaline activation, Cement and Concrete Research, vol. 35, no. 9, pp. 1688-1697 (2005).
[8] Yip, C. K. and van Deventer, J. S. J.: Microanalysis of calcium silicate hydrate gel formed within a geopolymeric binder, Journal of Materials Science, vol. 38, no. 18, pp. 3851-3860 (2003).
[9] Zellmann, H.-D.: Metaphosphat - modifizierte Silikatbinder als Basis säurebeständiger Beschichtungsmaterialien, doctoral thesis, Bauhaus-Universität, (2008).

[10] Goberis, S. and Antonovich, V.: Influence of sodium silicate amount on the setting time and EXO temperature of a complex binder consisting of high-aluminate cement, liquid glass and metallurgical slag, Cement and Concrete Research, vol. 34, no. 10, pp. 1939-1941 (2004).
[11] Schwanda, F.: Der Hohlraumgehalt von Korngemischen, beton, vol. 9, no. 1, pp. 12-17 (1959).
[12] Reschke, T.: Der Einfluss der Granulometrie der Feinstoffe auf die Gefügeentwicklung und die Festigkeit von Beton. Verlag Bau und Technik GmbH, Düsseldorf, (2000).

Part Four

STRUCTURAL BEHAVIOUR

Direct and Flexural Tension Test Methods for Determination of the Tensile Stress-Strain Response of UHPFRC

Benjamin A. Graybeal[1], Florent Baby[2], Pierre Marchand[2], François Toutlemonde[2]
1: Federal Highway Administration, TFHRC, McLean (VA), United States of America
2: Paris-Est University - IFSTTAR, Bridges and Structures Department, Paris, France

The tensile stress-strain response of Ultra-High Performance Fiber Reinforced Concrete (UHPFRC) is a fundamental mechanical behavior, and knowledge of this response is necessary for appropriate use of the concrete. To date, direct tension test methods aimed at assessing this property have generally found limited application due to their complexity and impracticality when considered in terms of a commercial testing environment. A joint research effort recently completed by the U.S. Federal Highway Administration and the French IFSTTAR (formerly LCPC) has succeeded both in further advancing the field of flexure testing as well as in developing a novel, practical direct tension test method. The direct tension test can be considered as a reference method as it directly reports the uniaxial tensile stress-strain response of the concrete both pre- and post-cracking without requiring the use of any complex stress or strain transformations. Moreover, it can be completed relatively quickly through the use of commercially available mechanical testing equipment on cast or extracted specimens of cross-sectional dimension up 51 mm square. The flexural test remains easier to perform, while data processing requires special care. The paper describes the direct tension and flexure test methods, as well as results obtained from applying these tests to multiple UHPFRC-class materials.

Keywords: Ultra-High Performance Fiber Reinforced Concrete, UHPFRC, UHPC, direct tension test, flexure test, uniaxial stress-strain response, inverse analysis

1 Introduction

The tensile stress-strain response of Ultra-High Performance Fiber Reinforced Concrete (UHPFRC) is a fundamental mechanical behavior, and knowledge of this response is necessary for appropriate use of the material. However, accurate assessment of this mechanical property is quite difficult in general due to the brittle, discontinuous nature of the response of cementitious materials. To date, this property has primarily been either indirectly assessed via flexure or biaxial tension-compression, or directly assessed through cumbersome, time-consuming test methods. A joint research effort recently completed by the U.S. Federal Highway Administration and the French IFSTTAR (formerly LCPC) has succeeded both in further advancing the validation and analysis of flexure testing as well as in developing a novel, practical direct tension test method.

The direct tension test can be considered as a reference method as it directly reports the uniaxial tensile stress-strain response of the concrete both pre- and post-cracking without requiring the use of any complex stress or strain transformations. Additionally, the method can be completed relatively quickly through the use of commercially available mechanical testing equipment on cast or extracted specimens of cross-sectional dimension up to 51 mm square.

The flexure test method provides for a potentially more robust capture of the specimen response. The associated inverse analysis method is presented and compared with results from direct tensile tests. Advantages and limitations of the experimental and analysis methods are derived.

2 Test Program

The test program was designed to allow for the development and assessment of a novel direct tension test method. In order to assess the applicability of the test method, two different

commercially available UHPFRCs were engaged along with two different steel fiber reinforcement contents. The curing regime applied to the UHPFRC was also a variable, with one of the UHPCs being used to create both steam treated and ambient laboratory cured specimen sets. The direct tension test specimens, prism flexure specimens, and associated compression test specimens in each set were all fabricated simultaneously from a single UHPFRC mix.

The UHPFRCs engaged in this test program all had compressive strengths ranging from 190 to 237 MPa, modulus of elasticity ranging from 59 to 65 GPa, and density ranging from 2560 to 2690 kg/m^3. The fiber reinforcement for one of the UHPFRCs was 13 mm long, 0.2 mm diameter, straight steel fibers. These fibers were included at either 2 percent or 2.5 percent by volume. The other UHPFRC contained 20 mm long, 0.3 mm diameter, straight steel fibers included at 2.5 percent by volume.

Sets of test specimens nominally included at least 10 identical prisms, with five allocated for the direct tension test and five for the prism flexure test. All prisms had a 51 mm by 51 mm cross section. Prisms were cast in open-top steel forms by pouring the UHPC into the form at one end then allowing it to flow toward the other end. Tests were completed after the UHPC has been allowed to cure for at least 3 months.

3 Direct Tension Test

The development of this direct tension test was necessitated by the need for a standardized test method which is applicable to a wide variety of UHPC-class materials in either cast or extracted form. As such, the requirements for the test method included: 1) applicability to cast or extracted (i.e., cut) specimens as opposed specifically-made dogbone specimens [1-2], 2) capability of being conducted on commercially available testing equipment, 3) minimization of flexure stresses on test specimen, 4) test duration allowing at least 6 tests to be completed in four hours, and 5) high likelihood of any individual test being completed successfully.

The direct tension test developed in this test program builds on work completed previously in this topic area as well as on tensile testing commonly completed on alternate structural materials. Much of the previous direct tensile test work on concrete, fiber reinforced concrete, and UHPFRC has focused along two paths. The first engaged unique dog-bone shaped specimens specially cast or milled for the test. The second engaged adhesives to glue the ends of a specimen to the cross-heads of a testing machine. Although both paths present the possibility of producing reliable test results, neither is conducive to the rapid completion of multiple tests on cast or extracted specimens. References [3-4] provide a representation of the work that has been completed in this area.

ASTM E8 Standard Test Methods of Tensile Testing of Metallic Materials [5] presents a set of standardized tests for metals. One particular test, the tension test for plate-type specimens, allows for the uniaxial tensile testing of a prismatic metal specimen in a commonly available computer controlled, closed-loop hydraulic uniaxial testing machine. In practice, hydraulic-actuated wedge grips are used to grasp the enlarged grip length of the dogbone-shaped metallic specimen. Developing a test which engages the existing metals testing infrastructure thus enhances the broad applicability of the UHPFRC direct tension test proposed herein.

The direct tension test demonstrated herein involves the fixed-end, uniaxial tensile testing of 51 mm by 51 mm by 431.8 mm prismatic specimens. The basic test setup is illustrated in Figure 1, along with a photograph of a specimen under test. The prismatic specimen has tapered aluminium transfer plates epoxied to two parallel faces at each end. These full width plates have a constant thickness of 4.8 mm for 108 mm then a linear transition to a 1 mm thick tip over 50.8 mm. The plates are glued to the specimen with a thin layer of high strength, high

stiffness structural epoxy. The testing machine hydraulic wedge grips then apply a clamping stress of approximately 40 MPa which facilitates the uniaxial loading of the specimen.

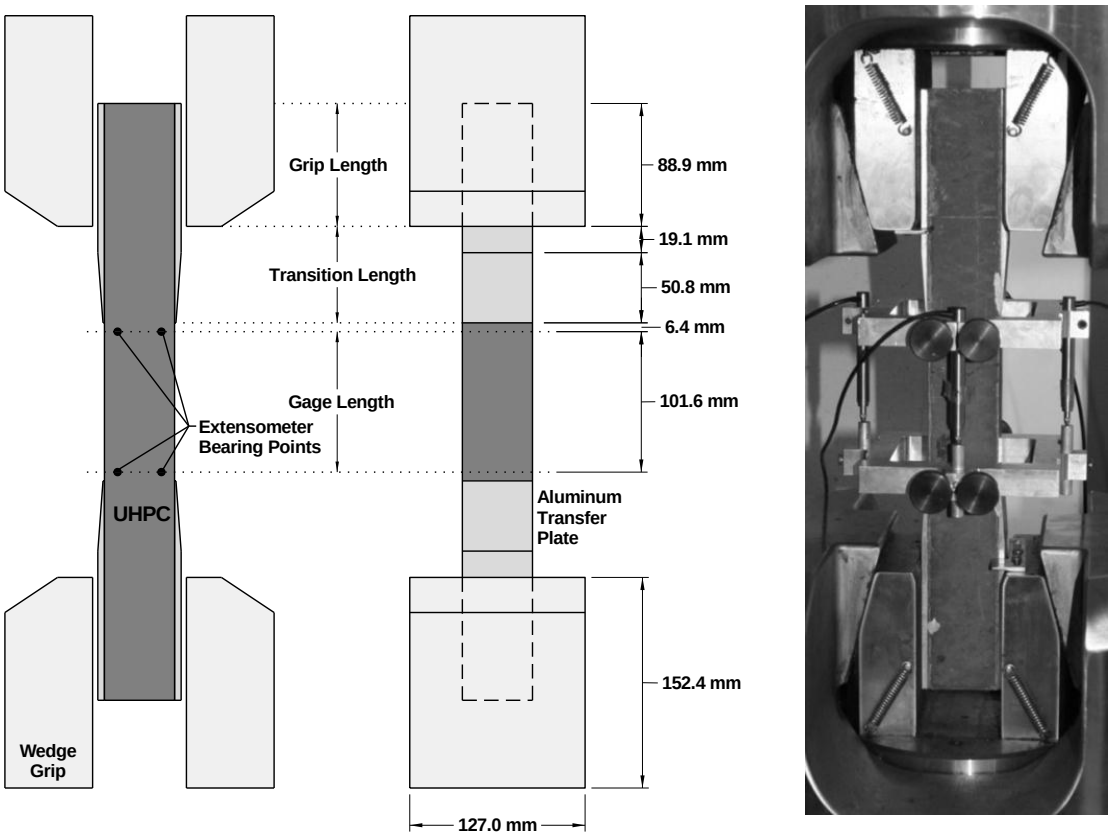

Figure 1: UHPC direct tensile test setup with a 51 mm by 51 mm by 431.8 mm prism.

The test is completed under cross-head displacement control at a rate of 0.00254 mm/sec. Initially, the specimen is loaded in compression to a stress of approximately 7 MPa, and then is loaded in tension through tensile failure. The strain within the 101.6 mm gage length is measured via a 4 LVDT parallel ring extensometer as shown in the photograph in Figure 1. This extensometer design both provides a simple, reusable measurement system, while simultaneously providing a clear means of capturing both the average response and any bending response that might be applied to the specimen.

Figure 2 provides a sample of the results obtained from the direct tension testing. Three out of six specimens were successfully tested within this series, with success being defined as capture of the full tensile stress-strain response of the UHPFRC including strain localization within the instrumented gage length. The stresses from these three responses at each strain increment were then averaged to create the average response for this set of specimens. Qualitative assessment of the response of the UHPFRC can also be obtained by mapping the cracking observed on the test specimen. Figure 3 shows the cracks observed on the surface of one of these test specimens after the conclusion of the test.

The overall results observed throughout the direct tension test program implemented herein indicate that the conceptual UHPFRC tensile mechanical response can be described as illustrated in Figure 4. This idealized representation includes four distinct phases, namely I: Elastic, II: Multi-Cracking, III: Crack Straining, and IV: Localized. As their names suggest, these phases refer to specific performance states which occur through the uniaxial straining of the UHPC. Note that this conceptual response is highly dependent on the efficiency of the fiber

reinforcement and may not be observed in practice if appropriate fiber reinforcement dosage, dispersion, or orientation are not achieved.

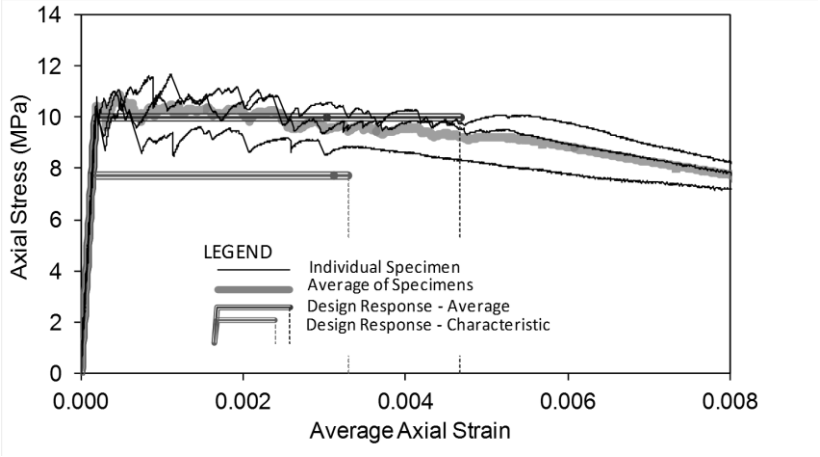

Figure 2: Analyzed direct tension stress-strain results from a set of test specimens.

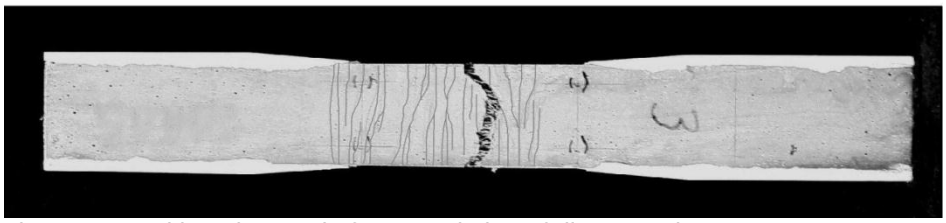

Figure 3: Cracking observed after completion of direct tension test.

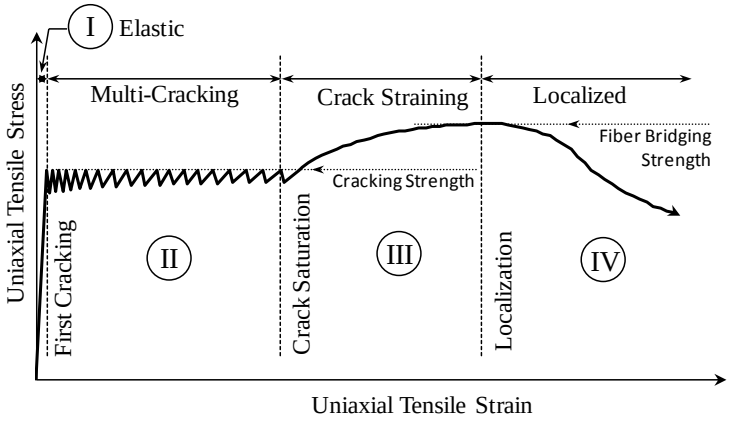

Figure 4: Idealized tensile mechanical response of UHPFRC.

Phase I, the elastic phase, generally continues through first cracking of the section which occurs at the tensile strength of the cementitious composite. Phase II, the multiple cracking phase, refers to the portion of the behavior wherein the cementitious matrix repeatedly cracks within the gage length. Given that the post-cracking strength of each cracked section, as afforded by the steel fiber reinforcement, is greater than the cementitious matrix cracking strength, the specimen accumulates elastic strain both within cracks and in the uncracked sections of the cementitious matrix between cracks, but does not experience significant widening of individual cracks. Also note that this phase is characterized by a nearly constant stress level, which is attributed to the homogeneity of the cementitious matrix. Phase III, the crack straining phase, is the portion of the behavior characterized by the accumulation of strain within the existing set of cracks. At the start of this phase, the crack density, which is a function of the fiber reinforcement dispersion, orientation, geometry, and bond properties, is such that the generation of additional cracks is unlikely. The increasing strain is thus predominantly due to an increasing crack opening as opposed to further crack initiation. In the crack straining phase, a degrading increase in stress capacity is observed as the fiber reinforcement

undergoes a combination of elastic straining and interface debonding. The phase ends when the fiber bridging strength is reached leading to crack localization. The final phase, localization, is characterized by a widening of an individual crack as the fibers bridging that crack fully debond and pull-out of the matrix. The remainder of the specimen elastically unloads in this phase, meaning that the behavior in this phase is based on crack-opening, not strain. The specimen stress continually decreases throughout this phase.

A key goal in the development of the tensile test method is to allow for the creation of a characteristic design response applicable to a particular UHPC under a particular set of casting and curing conditions. As such, the obtained results from each set of test specimens were analyzed to determine an average and a characteristic design response. An elastic-plastic uniaxial stress-strain model was assumed. One set of results is shown in Figure 2. The key performance indicator in this model is the average stress observed during the multicracking phase. For the average design response, this phase begins at the intersection with the elastic response as defined by the modulus of elasticity and concludes at the start of crack localization. The key parameter in the characteristic response is again the stress during the multicracking phase, defined as the average stress minus the t-Student coefficient times the standard deviation. This plastic portion of the response extends from the elastic response through the minimum last cracking strain observed in any of the specimens within the set.

4 Prism Flexure Test

Analytical inverse analyses for four point flexural tests on UHPFRC or HPFRCC have been developed by many researchers ([6-10]) with some success. The focus of this research was to optimize an analysis method for deriving the tensile stress-strain response of UHPFRC from four point flexural tests ensuring consistency with the direct tension determination. The midspan strain measurement on the specimen tensile face, as captured by two staggered extensometers, is used to obtain the experimental curve “Bending moment – Midspan Strain on Tensile Face” and also to determine the crack localization. Then a point-by-point inverse analysis is used to derive the tensile stress-strain relationships. Thus, the UHPFRC tensile stress-strain relationship is derived through a method which reduces the reliance on assumed behaviours.

Determination of crack localization

The use of a pair of staggered LVDTs allows for simplified identification of crack localization. It helps distinguish the onset of bifurcation of the cracking process, with crack localization over one of the gauge lengths while cracking remains diffuse over the other gauge length (Figure 5). In some cases, two localized cracks can occur before reaching the main failure crack, or the localized crack can be detected by both LVDTs (case (c) in Figure 5). For these latter cases, the crack localization is assumed to correspond to the maximum bending stress. In case (a) three steps can be observed: (1) elongations measured by both LVDTs increase, (2) one elongation stops increasing, and (3) an unloading branch occurs with a decreasing value for one elongation. In this case, the “Bending Moment – Midspan Strain on Tensile Face” curve can exhibit a long plateau with little increase of the load before reaching the maximum load. During this step, the elongation rate reported by one elongation stops increasing. This step could be explained by a very low stress decrease in the “localized crack” combined with the bending configuration which allows stabilization of or a small increase in the load.

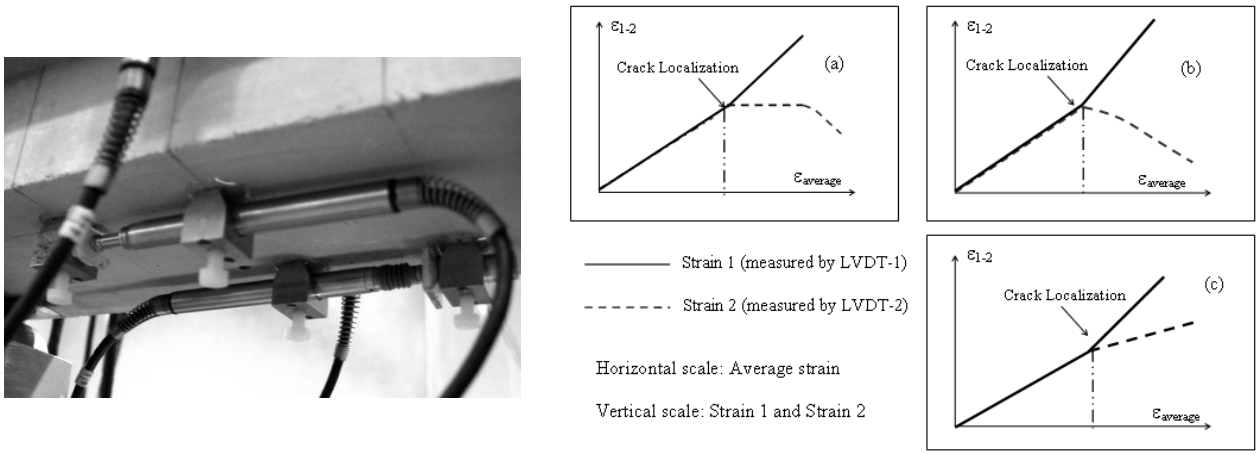

Figure 5: Midspan strain measurement including staggered extensometers on the tensile face (at left) and proposed method to detect the crack localization with identification of the elastic unloading (at right).

Point-By-Point Inverse Analysis

The experimental curve "Bending Moment – Midspan Strain on Tensile Face" is converted into a tensile stress–strain curve through an inverse method applicable from elastic loading through crack localization. The stress-strain curve is derived from the equilibrium of moments and forces in a sectional analysis for each value of midspan strain on the tension face and the corresponding bending moment. This approach, based on the method described in [7], does not need to assume the profile of the tensile stress-strain relationship. The main difference with [7] is the fact that the experimental midspan strain at the extreme tension fiber is directly measured, not derived from a global measurement. The strain and stress distributions in the compressed zone are considered as linear. For each strain measurement, the position of the neutral axis and correspondingly the depth of section in tension are determined via the inverse analysis, as detailed from Eq.1 to Eq. 13. The width and the height of the specimen are noted *b* and *h*. *E* is the elastic modulus, $\alpha_n h$ is the height under tension and Φ the curvature. Compressive stresses and strains are considered as negative and tensile stresses and strains as positive. Thus, in the zone under compression:

$$N_c = -b \cdot E \cdot \phi \cdot (\alpha_n - 1)^2 \cdot \frac{h^2}{2} \quad (1) \qquad \text{and } M_c = -b \cdot E \cdot \phi \cdot \left(2 + \alpha_n{}^3 - 3\alpha_n\right) \cdot \frac{h^3}{6} \quad (2)$$

In the zone under tension: $\varepsilon_t = \varepsilon_t(z) = \phi \cdot (\alpha_n h - z)$ (3)

At the extreme tension fiber, ε_t is equal to ε_{tf} and at the neutral axis, ε_t is equal to zero.

$$N_t = \int_0^{\alpha_n h} b \cdot \sigma_t(\varepsilon_t) \cdot dz = b \cdot \int_0^{\varepsilon_{tf}} \frac{\sigma_t(\varepsilon_t)}{\phi} \cdot d\varepsilon \quad (4) \text{ and } M_t = \alpha_n h \cdot N_t - b \cdot \int_0^{\varepsilon_{tf}} \frac{\sigma_t(\varepsilon_t) \cdot \varepsilon_t}{\phi^2} \cdot d\varepsilon \quad (5)$$

The tensile stress-strain relationship $(\varepsilon_{t,i}, \sigma_{t,i})$ is discretized considering successive loading steps *i* and *i+1*. Between these two loading steps, the strain at the extreme tension fiber increases from $\varepsilon_{tf,i}$ to $\varepsilon_{tf,i+1}$ and the corresponding stress changes from $\sigma_{t,i}$ to $\sigma_{t,i+1}$. For these two steps, there are two different curvatures and two neutral axis positions. Therefore, at the loading step *i*:

$$N_{t,i} = b \cdot \int_0^{\varepsilon_{tf,i}} \frac{\sigma_t(\varepsilon_t)}{\phi_i} \cdot d\varepsilon \quad (6) \text{ and } M_{t,i} = \alpha_{n,i} h \cdot N_{t,i} - b \cdot \int_0^{\varepsilon_{tf,i}} \sigma_t(\varepsilon_t) \cdot \left(\frac{\varepsilon_t}{\phi_i^2}\right) \cdot d\varepsilon \quad (7)$$

At the loading step *i+1*: $N_{t,i+1} = b \cdot \int_0^{\varepsilon_{tf,i+1}} \frac{\sigma_t(\varepsilon_t)}{\phi_{i+1}} \cdot d\varepsilon = \frac{\phi_i}{\phi_{i+1}} \cdot N_{t,i} + b \cdot \int_{\varepsilon_{tf,i}}^{\varepsilon_{tf,i+1}} \frac{\sigma_t(\varepsilon_t)}{\phi_{i+1}} \cdot d\varepsilon \quad (8)$

$$M_{t,i+1} = \alpha_{n,i+1} h \cdot N_{t,i+1} + \frac{\phi_i^2}{\phi_{i+1}^2} \cdot \left(M_{t,i} - \alpha_{n,i} h \cdot N_{t,i}\right) - b \cdot \int_{\varepsilon_{tf,i}}^{\varepsilon_{tf,i+1}} \sigma_t(\varepsilon_t) \cdot \left(\frac{\varepsilon_t}{\phi_{i+1}^2}\right) \cdot d\varepsilon \quad (9)$$

For both previous equations, the last term can be expressed in discrete form using the trapezoidal method for integral computation, so that $N_{t,i+1}$ and $M_{t,i+1}$ read:

$$N_{t,i+1} = \frac{\phi_i}{\phi_{i+1}} \cdot N_{t,i} + b \cdot \frac{1}{\phi_{i+1}} \cdot \frac{\sigma_{t,i+1} + \sigma_{t,i}}{2} \cdot \left(\varepsilon_{tf,i+1} - \varepsilon_{tf,i}\right) \quad (10)$$

$$M_{t,i+1} = \alpha_{n,i+1} h \cdot N_{t,i+1} + \frac{\phi_i^2}{\phi_{i+1}^2} \cdot \left(M_{t,i} - \alpha_{n,i} h \cdot N_{t,i}\right) - b \cdot \frac{\sigma_{t,i+1} \cdot \varepsilon_{tf,i+1} + \sigma_{t,i} \cdot \varepsilon_{tf,i}}{2 \cdot \phi_{i+1}^2} \cdot \left(\varepsilon_{tf,i+1} - \varepsilon_{tf,i}\right) \quad (11)$$

All parameters at loading step *i* are considered as already determined. Thus, solving this inverse problem consists in determining the parameters $\alpha_{n,i+1}$ and $\sigma_{t,i+1}$ in order to satisfy the mechanical equilibrium in the section:

$N_{t,i+1} + N_{c,i+1} = 0$ (12) and $M_{c,i+1} + M_{t,i+1} = M_{i+1-\text{experimental}}$ (13)

The validation of the proposed model has been established using a simple self-consistency case which consists of generating a curve “Bending Moment – Strain” by a direct calculation and then verifying that the result obtained with the inverse analysis is similar to the tensile stress-strain relationship used in the direct calculation. Moreover, in Figure 6, the average tensile stress-strain relationships obtained from the proposed point-by-point inverse analysis method and the average experimental curves obtained from the direct tensile tests are presented for two specimens groups.

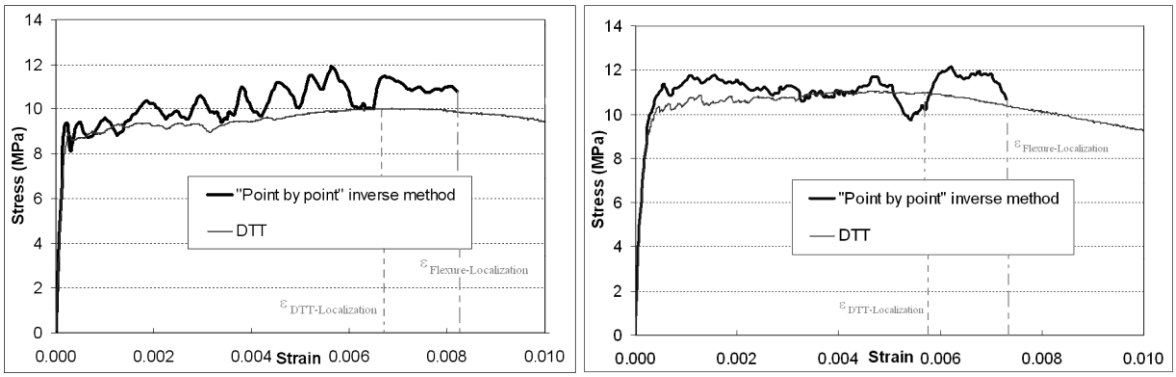

Figure 6: Average tensile stress-strain curves for two specimens groups: “Point by point” inverse analysis method and direct tension test (DTT) method.

In terms of strain, the proposed point-by-point inverse analysis method overestimates the strain capacity when considering average curves and characteristic curves. Indeed, the flexural tests involve an overestimation of the strain capacity due to the fact that the side under higher tension corresponds to the zone where the preferential orientation of fibers is optimal. This phenomenon has already been observed on hardening UHPFRC [11]. Completing the tests on larger prisms would minimize the strain gradient effect and thus allow the results to be closer to the DTT results. In terms of strength, the comparison between both methods differs when considering the average or the characteristic curves, due to a “statistical scale effect”. For the flexural tests, the tensile area is smaller than in the direct tensile tests. As a consequence, the average results are better for flexural tests, but the impact of an eventual composite (matrix and fibers) flaw is greater and the standard deviation is more important. Thus the characteristic strength can be inferior for flexural tests.

5 Conclusions

This joint US-French research effort has succeeded in advancing the practice and analysis of tensile testing of UHPFRC. Specifically:

1. The developed direct tension test method presents a reliable, practical method to directly capture the uniaxial tensile stress-strain response of UHPFRC.
2. The developed direct tension test method facilitates the creation of strain-based structural design criteria representative of the direct tensile response of UHPFRC.
3. An improved testing and processing method based on flexural tests has been developed to determine the tensile stress-strain response of UHPFRC.
4. The average tensile stress-strain response of UHPFRC derived from flexural tests is slightly higher in terms of strength and strain capacity when compared to curves obtained from direct tensile tests. This results from a smaller tested tensile zone for flexure tests. Coincidently, the characteristic values can be inferior for flexural tests due to a larger standard deviation. This conclusion has been demonstrated through the use of an inverse method (for flexural tests analysis) which reduces the reliance on assumed behaviours, thus providing more realistic and reliable results.

6 Acknowledgements

This research was jointly funded by the U.S. Federal Highway Administration and IFSTTAR (formerly LCPC). The authors gratefully acknowledge the support for this international collaboration provided by Henri Van Damme, Sylvie Proeschel, and Patrick Malléjacq from IFSTTAR, and by Debra Elston and Ian Saunders from FHWA.

References

[1] Behloul, M., “Analyse et modélisation du comportement d’un matériau à matrice cimentaire fibrée à ultra hautes performances”, E.N.S. Cachan, France, PhD Thesis, in French, December 1996, 182 p.

[2] Jungwirth J., “Zum Tragverhalten von zugbeanspruchten Bauteilen aus Ultra-Hochleistungs-Faserbeton”, École Polytechnique Fédérale de Lausanne (EPFL), Thesis No. 3429, Lausanne, Switzerland, 2006, 214 p.

[3] Boulay, C.; Rossi, P.; Tailhan, J.-L.: Uniaxial Tensile Test on a New Cement Composite Having a Hardening Behaviour. Fiber Reinforced Concretes – BEFIB 2004, Proceedings of the Sixth International RILEM Symposium, 2004, pp. 61-68.

[4] RILEM, TC 162-TDF: Test and Design Methods for Steel Fibre Reinforced Concrete – Recommendations: Uni-axial Tension Test for Steel Fibre Reinforced Concrete. *Materials and Structures*, 34(1), 2001, pp. 3-6.

[5] ASTM E8: Standard Test Method for Tension Testing of Metallic Materials. American Society for Testing and Materials Standard Practice E8, Philadelphia, PA, 2009.

[6] AFGC-SETRA, 2002, “Ultra High Performance Fibre-Reinforced Concretes,” Interim Recommendations, SETRA, Bagneux, France.

[7] Ostergaard, L., Walter, R., and Olesen, J.F., 2005, “Method for Determination of Tensile Properties of Engineered Cementitious Composites (ECC),” Proceedings of ConMat'05, Vancouver, Canada.

[8] Chanvillard, G., 2006, Report on “Méthode inverse appliquée au comportement des plaques en BFUP .”(in French), PN MIKTI, France.

[9] Kanakubo, T., 2006, “Tensile characteristics evaluation Method for DFRCC,” Journal of Advanced Concrete Technology, Vol. 4(1), pp. 3-17.

[10] Qian, S., and Li, V.C., 2008, “Simplified inverse method for determining the tensile properties of SHCCs,” Journal of Advanced Concrete Technology, Vol. 6(2), pp. 353-363.

[11] Tailhan, J.-L., Rossi, P., and Parant, E., 2004, “Inverse Numerical Approach to Determine the Uniaxial Tensile Behaviour of a Stress Hardening Cement Composite From Its Bending Behaviour,” Proceedings of the Sixth International RILEM Symposium, 2004, pp. 913-922.

Experimental and Analytical Analysis of the Flexural Behavior of UHPC Beams

Eric T. Visage, K. D. S. Ranga Perera, Brad D. Weldon, David V. Jauregui, Craig. M. Newtson, Lucas Guaderrama
New Mexico State University, United States of America

Scaled beams are designed using ultra-high performance concrete (UHPC) and tested to investigate the flexural (moment-curvature) behavior of the beams. Design parameters are varied including compressive strength of concrete, main steel reinforcement, and percent by volume of steel fibers in the concrete mixture proportions. The test results are compared to traditional methods of estimating moment-curvature relationships.

Keywords: moment curvature, flexure, UHPC, fiber reinforced

1 Introduction

Ultra-high performance concrete (UHPC) has the potential to influence many applications in structural design. However, due to the lack of design codes and analytical tools for UHPC there has been limited use of this material, particularly within the United States. To expand the use of UHPC in structural design, there is a need for cost effective mixture proportions and simplified but reliable analytical tools and design procedures capable of predicting the flexural behavior of UHPC prestressed and reinforced concrete members. Thus, this research looks to investigate the behavior of an UHPC that consists of materials local to New Mexico, USA through an experimental program examining the moment-curvature relationship of scaled reinforced concrete beams under four-point bending.

The fundamental requirement in predicting the moment-curvature behavior of a flexural member is the understanding of the behavior of its constituents. With UHPC, the constituents have changed from typical normal strength and high strength concretes. In order to achieve the high compressive strength, a lower water-to-cementitious material (w/cm) ratio is used. Coarse aggregates are removed and steel fibers are added. In addition to the increase in compressive strength, adding steel fibers to the mixture proportions improve the tensile strength and ductility. This in turn changes the typical flexural and shear behavior of UHPC beams. To investigate the behavior of UHPC in structural members, moment-curvature data was collected on several beam test specimen. Beams parameters varied included: concrete compressive strength, percent volume of fibers, reinforcement ratio, and beam length. The results are also compared to moment-curvature estimations based on traditional methods to examine the influence of UHPC and the various parameters on the behavior of the flexural beams.

2 Mixture Proportion and Curing Regimen

The UHPC mixture proportions used a water-to-cementitious material (w/cm) ratio of 0.15. To improve workability, a high range water reducing admixture was used. Silica fume was used in the mixture proportions to improve the thermal properties of UHPC. Class F Fly Ash was used to help minimize the amount Silica fume required and angular sand with a specific gravity of 2.58 from Placitas, New Mexico, USA passing through a No. 30 sieve (0.595 mm nominal sieve opening) was used. Prior to sieving, the sand was oven-dried to remove moisture. It was then washed over a No. 200 sieve (0.074 mm nominal sieve opening) to remove dust particles and oven-dried again. The steel fibers used were 13 mm in length, continuously deformed (wavy)

with an aspect ratio of 24, and had a yield strength of 344 MPa. Type I/II portland cement and water are the additional constituents used.

Once mixing was completed the concrete was poured into steel molds and consolidated on a vibrating table. Once the specimens were cast they were covered with plastic sheeting to prevent bleeding. Following casting, the specimens were allowed to cure in an ambient environment for 24 hours until removed from their molds. After demolding, the specimens underwent a combined steam and dry heat curing regimen. Finally, the specimens were removed from their curing environment and tested.

Test Specimens

Beam test specimens measuring 152 mm x 152 mm x 610 mm and 152 mm x 152 mm x 762 mm were constructed for testing (see Figure 1). Two to four specimens were constructed for each batch of concrete. Cubes measuring 100 mm were prepared at the same time to test for the compressive strength of the concrete. Parameters varied for the test specimens included: compressive strength, amount of reinforcement, percent volume of steel fibers; and beam length. Tensile mild steel reinforcement (if present) was placed at an effective depth of 127 mm. The reinforcement ratio, ρ varied between 0 and 0.013. The percent volume of fibers was varied between 0% and 2.0%. Table 1 shows the parameters for each of the beam specimens.

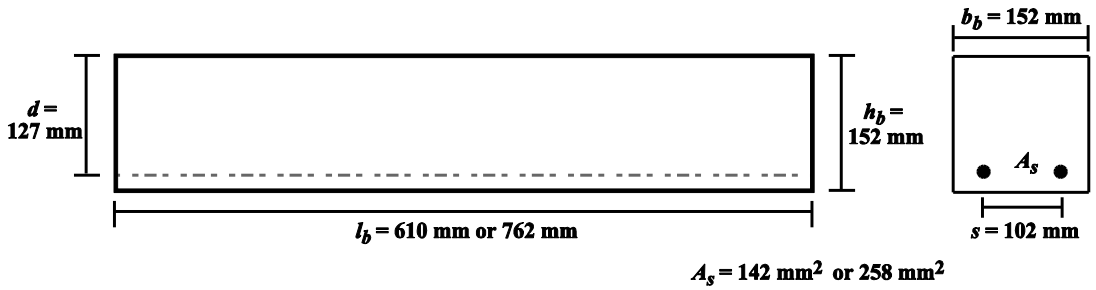

Figure 1: Beam dimensions.

On the day the beam specimens were tested, 100 mm cube specimens were tested following British Standard (BS) 1881: Part 116 standard methods for the compressive strength of the UHPC. The loading rate was modified to achieve failure in an adequate period of time. Graybeal's [1] research concluded a load rate of 62 MPa/minute was acceptable for cube specimens. Typically, it is expected that higher load rates will result in higher compressive strength. However, Graybeal [1] conducted compressive strength tests with varying load rates on 24 cylinders with a 76 mm diameter. The results indicated that there was no significant change in the compressive strength, the modulus of elasticity, or Poisson's ratio. Thus, it was determined that an increased rate of loading would be beneficial to reduce the overall testing time while having negligible effect on the material characteristics.

Two material samples for each batch of reinforcing bars used in the beams were tested monotonically in tension using an Instron 5882 universal testing machine with an 89 kN capacity. The strains were measured using an Instron extensometer with a 25 mm gauge length. The specimens were approximately 200 mm long. Figure 2 shows a photograph of a No. 10 bar being tested and the measured monotonic tensile stress-strain relationship for the two batches of No. 10 bars used. Table 2 summarizes the material properties of the reinforcing bars. The yield strength was determined as the lower yield point on the measured stress-strain relationship. The yield strain can be determined by dividing the yield strength with the measured Young's modulus, which was determined based on the slope from two points on the linear-elastic portion of the measured stress-strain relationship.

Table 1: Beam Properties and Test Results.

Type	Batch	ρ	Compressive Strength		Fibers (% by volume)	Beam Length (in)	Measured Strength	
			Age (days)	f'c (MPa)			Vu (kN)	Mu (kN-mm)
Normal Strength (w/cm=0.5)	4	0.007	43	67.6	0	610	77.20	11770 (F)
							78.44	11950 (F)
	5	0.007	45	82.84	1	610	87.83	13390 (F)
							80.76	12310 (F)
	7	0.007	35	84.43	1.5	610	87.05	13270 (F)
							77.02	11740 (F)
	9	0.007	35	85.81	2	610	82.81	12620 (F)
							79.04	12050 (F)
	11	0.013	28	66.53	1.5	610	51.32	7320 (S)
							59.07	9000 (S)
High Strength (w/cm=0.35)	8	0	28	66.86	1	610	52.88	8060 (F)
							54.78	8350 (F)
	12	0.013	28	79.29	1	610	45.70	8440 (S)
							45.70	6960 (S)
	13	0.007	43	67.60	0	610	56.88	8670 (F)
							58.67	8940 (F)
	15	0.007	35	84.43	1.5	762	48.05	7320 (F)
							44.19	6730 (F)
UHPC (w/cm=0.15)	21	0.013	7	149.2	0	610	28.42	4330 (S)
							25.98	3960 (S)
	22	0	7	138.6	1.5	610	21.36	3250 (F)
							19.12	2910 (F)
	23	0.007	5	137.2	1.5	610	22.30	3260 (F/S)
							20.30	2920 (S/F)
	24	0.007	5	145.5	1.42	610	83.20	12300 (S/F)
							130.3	14900 (S/F)
	25	0.007	5	131.7	1.5	610	98.80	14400 (S/F)
						762	94.80	13100 (-)
	26	0.007	14	143.0	1	610	72.25	11010 (F)
							73.28	11170 (F)
		0.007	14	137.7	1	762	44.53	6790 (F/S)
							42.01	6400 (F/S)
	27	0.007	12	141.1	1.5	610	78.20	11920 (F)
							77.79	11860 (F)
		0.007	12	140.3	1.5	762	43.05	6560 (F/S)
							45.67	6960 (F/S)
	28	0.007	14	142.3	2	610	66.51	10140 (F)
							67.97	10360 (F)

Table 2: Reinforcement Material Properties.

Reinforcement	No. 10 – Batch 2	No. 10 – Batch 3	No. 13 – Batch 1
E (GPa)	189.7	203.5	160.9
Yield (MPa)	473.5	327.1	379.2
Ultimate (MPa)	775.9	476.9	530.9

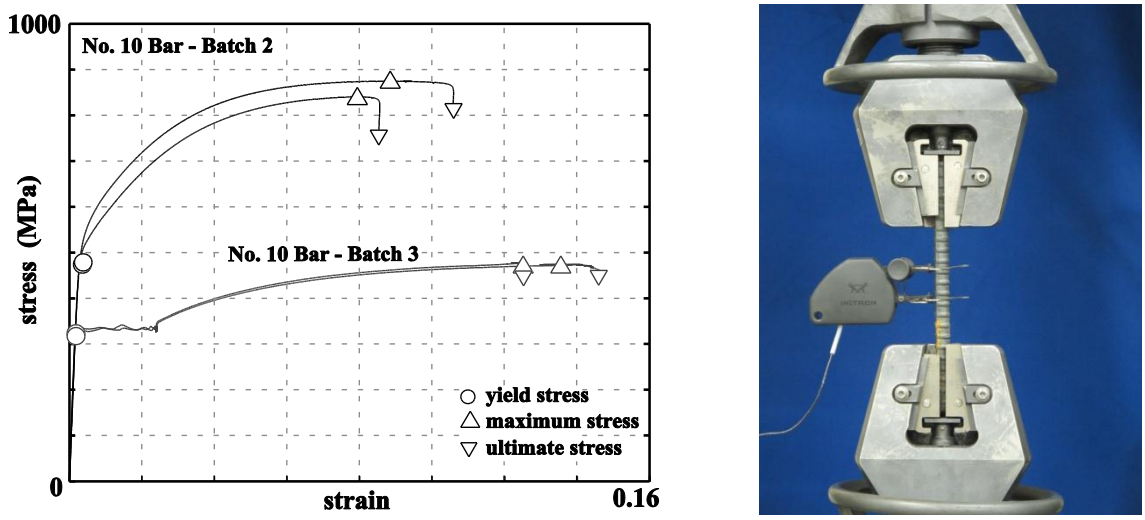

(a) (b)

Figure 2: No. 10 bar material test: (a) No. 10 bar stress vs. strain relationship, (b) tension test.

3 Test Procedure

Each beam was loaded under four-point flexure to create a pure moment region spanning 152 mm at the center of the beam. The load was applied at a rate 10 MPa/minute up to initial cracking of the beam. After cracking, the load was applied in displacement control at the same displacement rate at which first cracking occurred. The beam was loaded to failure at this rate. These load rates are based off the load rates required for the ASTM Standard C 38-02 for the modulus of rupture measurement. The testing apparatus used in this research was a Tinius Olsen compressive machine that has a maximum capacity of 1780 kN.

4 Instrumentation

Each beam is instrumented with load cells and displacement transducers. A load cell is placed under each support to measure the load applied to the beam. A string potentiometer (not shown) is attached to the top of the beam at the centerline to measure the vertical displacement as the beam is loaded. Linear Variable Displacement Transducers (LVDTs) are placed on the east side of the beam at a distance of 25 mm from the top and bottom of the beam (see Figure 3) directly below the vertical point load on the north end of the beam. Reaction plates are placed directly under the point load on the south end of the beam. This allows for deformation measurements to be read over the pure moment region on the beam and capture the opening of flexural cracks within this region. Figure 3(a) shows the placement of the instrumentation on the beam, and Figure 3(b) shows the exaggerated displaced shape of the beam under load. The instrumentation and test set-up can be seen in Figure 4.

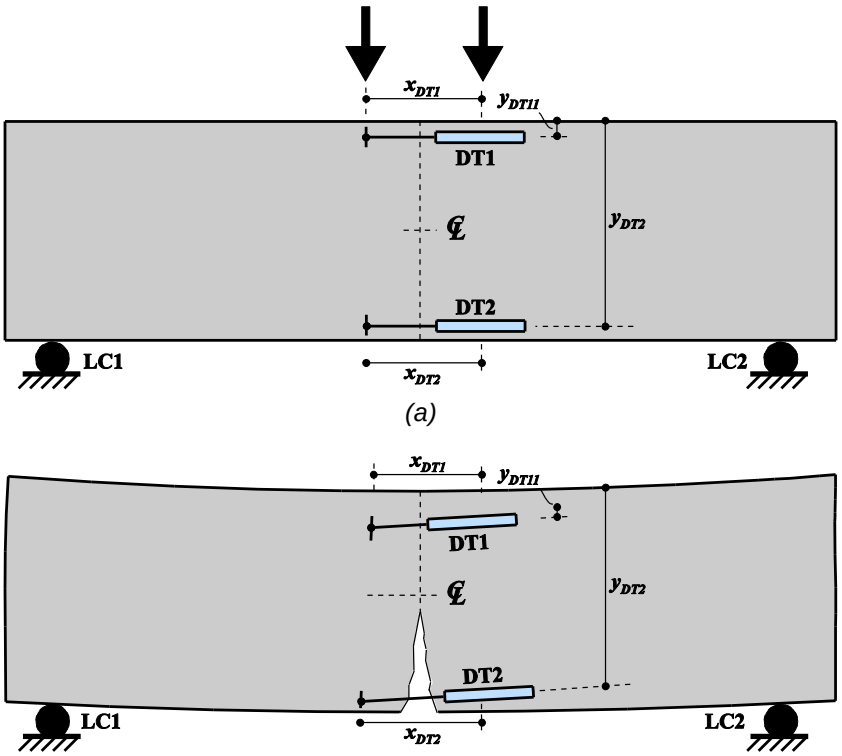

Figure 3: Beam test set-up – (a) instrumentation; (b) exaggerated displaced configuration.

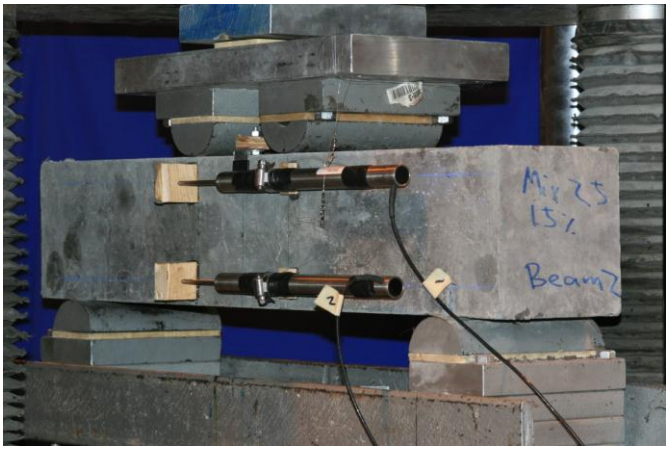

Figure 4: Beam test setup.

5 Results and Preliminary Conclusions

The results from the experimental program are compared using estimations of the moment-curvature behavior based off of kinematics, constitutive relationships, and equilibrium. To verify the procedure, a normal strength concrete baseline beam and two high strength concrete beams were tested. The beams use similar geometry and reinforcement ratios as the UHPC beams. The design compressive strengths for the normal strength and high strength concrete were 41.3 MPa and 67.6 MPa, respectively. The stress-strain curves from the reinforcement material tests were used to model the reinforcement behavior and a uniform stress block was used for the concrete. Figure 5 shows the test results (solid line) compared to the estimations (dashed line), which predict the behavior very well. In addition, several additional normal strength and high strength beams with varying reinforcement ratios, percent volume of fibers, and compressive strength have been tested and the measured strengths are presented in Table 1.

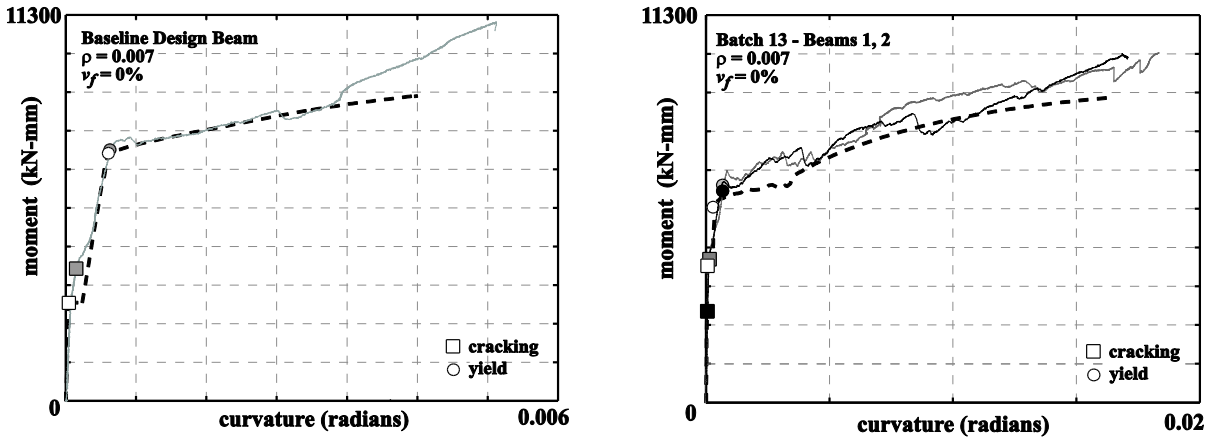

(a) *(b)*

Figure 5: (a) Baseline design beam, (b)Batch 13.

A similar procedure was used to estimate the behavior of the UHPC beams. To account for the difference in concrete behavior, a triangular distribution was used for UHPC. In addition, a uniform stress distribution was used to estimate the contribution of the fibers to the UHPC beams. This stress was assumed to act over a depth from the neutral axis to the effective depth of the reinforcement once yield was reached. Due to the cracks remaining small and both the concrete and reinforcement remaining linear-elastic, it was assumed that the fibers did not contribute until the nonlinear region was reached. The nonlinear estimations used an iterative procedure to predict the moment-curvature behavior. For the UHPC, the modulus of rupture was based off the results of the beam tests (Batch 22) with no mild steel reinforcement [see Figure 6(a)] and the modulus of elasticity was estimated using the equation developed by Graybeal [1].

Eight UHPC batches of beams were constructed for testing. All batches used the same UHPC mixture proportions. Batch 22 had no mild steel reinforcement. Batch 21 had a reinforcement ratio of 0.013 and remaining batches had a reinforcement ratio of 0.007. Batches 23, 25, and 27 have a volume of fibers, v_f of 1.5%. Batch 24 has a slightly lower v_f at 1.42%. Batch 26 and 28 had a v_f of 1.0% and 2.0%, respectively. Up to four beams were constructed for each batch. Each batch had beam specimens measuring 152 mm x 152 mm x 610 mm. Batches 25, 26, and 27 also included specimens with an increased beam length of 762 mm. Two dashed line in Figures 6(b) – 6(f) show the predicted behavior of the beams. (Please note that not all specimens are shown in Figure 6.) The upper bound includes the effect of the fibers on the moment capacity, while the lower bound does not include any fiber contribution. It is expected that the behavior would fall within this range or above the upper bound.

Table 1 lists the measured strength for all beams tested. In addition, the failure type is shown following the measured moment (S = shear, F = flexure, F/S = flexure-shear; S/F = shear with flexural cracks). In the case of a shear failure, yielding of the reinforcement did not occur.

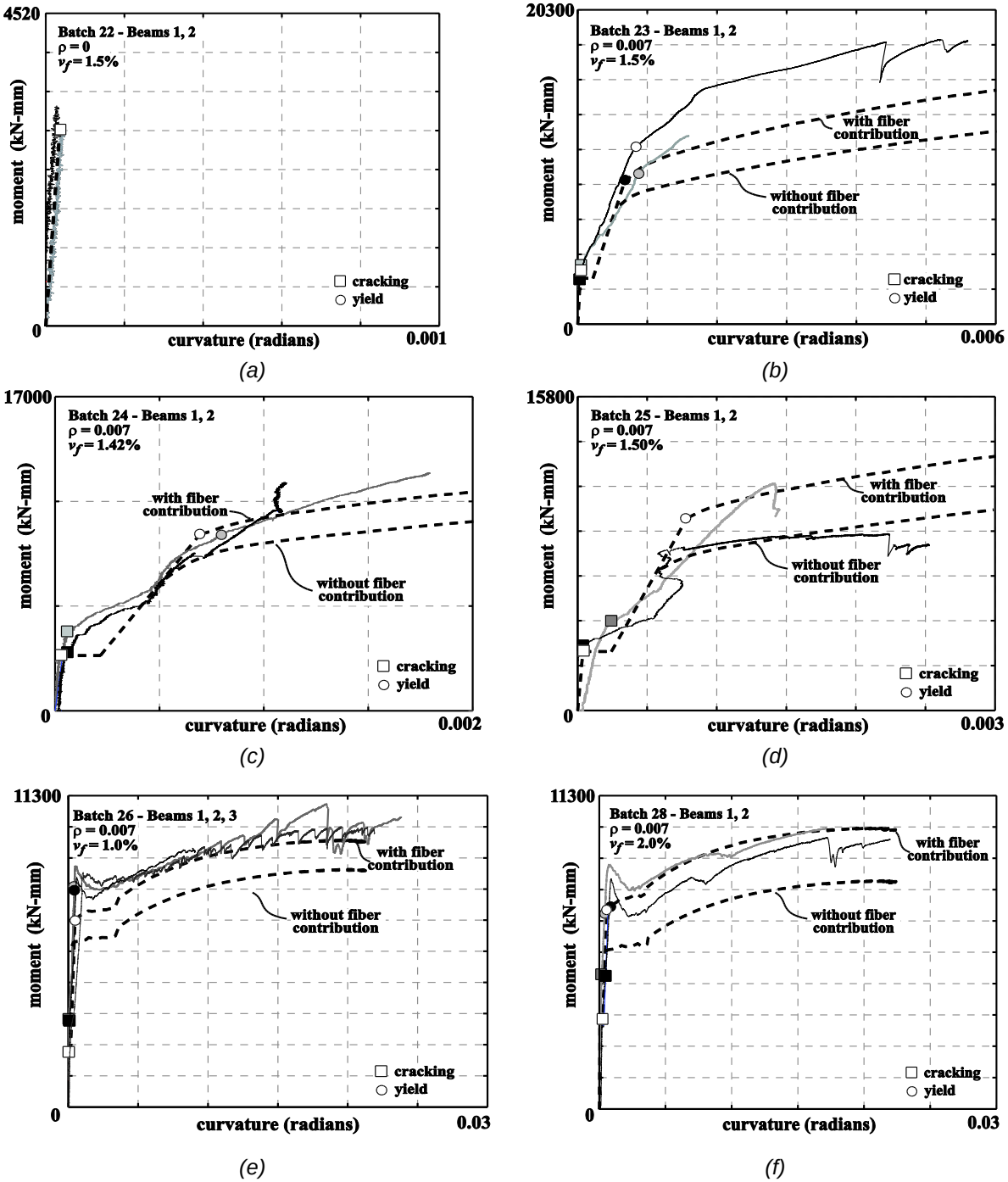

Figure 6: Beam test results-(a) Batch 22,(b) Batch 23,(c) Batch 24,(d) Batch 25,(e) Batch 26,(f) Batch 28

The results of the batches 23 - 25 show some variability in the behavior of the beams. Batch 23 beam 1 failed in flexure but also suffered significant shear damage [see Figure 7(a)]. Batch 23 beam 2 failed in shear; however, the failure was not a typical catastrophic failure. Rather, it had a gradual loss in strength as the crack propagated. Both capacities fell above the upper bound of the estimations shown. This could be due to variation in fibers (orientation and amount) within the beam.

Both beams of batch 24 as well as beam 1 of batch 25 failed in shear as shown in Figures 6(c) and 6(d). Significant flexural cracks were observed during these tests; however, the beams ultimately failed in shear [see Figure 7(a)]. A decrease in curvature observed in Figure 6(c) is due to the LVDTs capturing some of the shear behavior. However, the moment capacities are close to the estimations up to failure of the test specimens.

Batch 25 beam 2 experienced longitudinal splitting of the concrete at the location of the mild steel reinforcement. This led to unsymmetrical behavior. The moment capacity of this beam is closer to the lower bound of the predicted results (i.e., more similar to a beam without fibers). This is most likely due to the splitting of the concrete reducing the effect the fibers had on the behavior.

Batches 26 and 28 showed more consistent flexural failure as shown in Figures 6(e) and 6(f). Beam 3 of batch 26 had an increased length. It is noted that beams with increased beam lengths also developed significant shear cracks. The estimations are similar to the measured behavior during the tests.

(a) *(b)*

Figure 7: Typical failures (a) flexure-shear; and (b) flexure.

Based on the results of the experiments that have been conducted and comparisons made with the moment-curvature estimations, the following observations were made:

- The fibers have a large effect on the moment capacity of the beams.
- Due to the variation in the results, including failure mode, the distribution and orientation of the fibers could play a role in the behavior and capacity of the beams. This large variation in behavior could potentially be attributed to the small scale of the beams.
- The moment capacity of the beams was significantly increased with UHPC. Flexural failure was often accompanied by significant shear damage or the beam failed in shear.
- Shear failure was more ductile due to the crack bridging fibers. However, there was variation in the behavior, which could depend on the distribution and orientation of the fibers.
- The modeled behavior provided good estimations of the initial stiffness, cracking moment, post-crack stiffness, and yield point. Due to the variable results, the post-yield behavior needs further investigation and will be refined as this study progresses.

This research is currently ongoing and continues to investigate the moment-curvature behavior of UHPC beam. Work is currently investigating the effect the fibers play in the behavior of the beams. Beams with varied percentages of fibers will be tested, as well as different types of fibers. In addition, to help investigate the size effect on the variability of the behavior of the beam, different beam geometries will be tested.

In addition to the experimental work, a companion analytical program is underway. Based on the experimental results, a finite element model and a fiber beam column analytical model are being developed to further investigate the behavior of the UHPC beams under various loads and varied design parameters. These models will be used as a basis to develop full scale models of UHPC beams.

References

[1] Graybeal, B. Material Property Characterization of Ultra High Performance Concrete. FHWA-HRT-06-103, McLean, VA, 2006

Characterization of the Fracture Behavior of UHPC under Flexural Loading

Eric L. Kreiger, Theresa M. Ahlborn, Devin K. Harris, Henrique A. de Melo e Silva
Department of Civil and Environmental Engineering, Michigan Technological University, USA

Currently, in the United States, UHPC is not readily used, since the understanding and knowledge base has yet to be properly developed. One of the key aspects of UHPC, which enables it to have improved properties under tension/flexure, is its intrinsic composite nature due to the dispersion of discontinuous fibers. These improved properties include strength (before and after cracking), anelasticity ("ductility"), and fracture energy. In order to develop a model to describe the fracture behavior of this material, a series of three point notched prism tests were performed. This study tested the effects of variables, such as age of curing, span-to-depth ratio, and prism cross section on the fracture behavior of a Ductal® brand UHPC with steel fibers at 2% by volume. The results of these tests were used to determine material properties and develop a model to describe the fracture behavior of UHPC.

.

Keywords: Ultra High Performance Concrete, UHPC, Flexure, Fracture Modeling, Weibull

1 Introduction

Perhaps the most intriguing aspect of Ultra-High Performance Concrete (UHPC) is its ability to resist fracture, due to the inclusion of randomly dispersed discontinuous fibers within a cementitious matrix, commonly referred to as a fiber reinforced cementitious composite (FRCC). The matrix in UHPC is typically termed as being densified, which is achieved through the omission of large aggregates and optimization of small particulates (fine aggregates, silica fume, fly ash, cement)[1]. This densification leads to improved compressive strengths, and can be referred to as DSP (Densified Small Particulate) Concrete, but may go by other names [2]. Fibers can come in many different varieties, but one of the more frequently used materials is steel, due to its high strength and ductility.

In a FRCC such as UHPC, the fracture behavior is dependent upon the material properties of the matrix, the fibers, and the way in which they interact or bond [3, 4]. The bond and the strength of the fibers are the primary mechanisms which drive a FRCC's ability to resist fracture [4]. For UHPC, the dense matrix leads to improved bonding because of low porosity reducing the size of the weak interfacial transition zone [5]. In short, UHPC can be defined as a composite material consisting of a densified cementitious matrix reinforced by randomly dispersed fibers with improved strength and ability to resist fracture.

The purpose of this study was to develop a model based upon preliminary tests, which describes the fracture behavior of steel fiber reinforced UHPC under flexural loading. This model could be used by designers to determine design parameters, by inspectors to determine the expected capacity of a cracked structure, or by researchers to predict the behavior of tested specimens beyond normal testing ranges. The type of tests performed were 3-point bending tests conducted on a single-edge notched prisms (SNP) using a crack mouth opening displacement (CMOD) controlled system. This test method was chosen over other fracture tests due to its simplicity, commonality, and relevance to actual applications.

Currently, the tensile behavior of UHPC is based on a multi-linear model [6], which tends to be overly conservative. It was proposed that a model based on either a Modified Weibull probability distribution function (PDF) or a Modified Lognormal PDF could be used to describe the post cracking tensile behavior of UHPC under flexural loading. This paper focuses on the

modelling of a Load-CMOD (P-w) curve, which is one step in the progression towards the greater research project-goal to develop a model for the Stress-CMOD (σ-w) curve.

2 Testing

Parameters

As part of the larger initiative, it was decided that five parameters would be tested to study their effect on UHPC's fracture behavior. These are fiber content, curing regime, prism aspect ratio, prism cross sectional area, and age of specimen. For the sake of brevity, all results that appear in this study are based on ambient cured specimens with a 2% by volume fiber content (see Table 1).

Table 1: Test Matrix.

Age	Prisms Height x Length (mm x mm)				
days	51x229	51x343	51x457	76x343	51x699
3	X	X	X	X	X
7	X	X	X	X	X
28	X	X	X	X	X
56	X	X	X	X	-

As shown, five square prism sizes (51x229, 51x343, 51x457, 76x343, 51x699) were tested, where each specimen is named for its depth/width (mm/mm) by span (mm). The control specimen was the 51x229 having an aspect ratio of 4.5, and a cross sectional area of 2580 mm^2. From this, the length was increased, which increased the aspect ratios to 6.75, 9, and on the long range 13.75. The cross sectional area was tested by increasing the depth and width of the prism to 76 mm, while maintaining a 4.5 aspect ratio. All specimens except for the 51x699, which was only tested at 3-, 7-, 28-days, were tested at ages of 3-, 7-, 28-, and 56-days.

Mixing and Testing

For this research a Ductal® brand UHPC was used, consisting of a Ductal® premix, ASTM 820 grade 14 mm x 0.185 mm straight steel fibers, superplastisizer, and water. The mix procedure was done according to recommendations from LaFarge North America. Based on previous research [7, 8], prisms were cast by filling the mold from one end, which due to UHPC's flowable rheology allowed the mix to travel to the opposite side. This procedure was performed in two equal volume lifts, after each lift the mix was vibrated for a short amount of time to release any entrapped air. A vibration time of 0-to-10 seconds was used, because during preliminary mixing it was noticed that if the vibration exceeded 10 seconds the fibers would settle and their distribution in the matrix would favor the bottom edge of the prism. Casting was done in this manner in an attempt to align the fibers in a one dimensional orientation along the length of the prism.

Testing of each specimen was performed using a CMOD controlled closed-loop system connected to a MTS 318.25 810 Material Testing System (250 kN) test machine, which recorded measurements of time, applied force, crosshead deflection, and CMOD. The UHPC prisms were tested using the 3-point flexure test as recommended by RILEM TC 162-TDF for FRCCs [9]. However, the testing procedure was based on the SETRA recommendations for UHPC [6]. Since the purpose of this study was to model the fracture behaviour, testing was continued well beyond the typical range to a CMOD value of 10 mm. As such, a rate of 0.00045 mm/s was used until the CMOD reached a value of 1.2 mm, which was chosen because it was

far from the peak load. At this point the rate switched to 0.2 mm/min until the end of the test. A data acquisition rate of 5 Hz was used throughout the entirety of the test. The increased length of testing limited the number of prisms that could be tested, since all testing was performed with respect to the ASTM time tolerances specified for compressive testing of concrete [10]. The number of prisms that were tested at 3-, 7-, 28-, and 56-days was limited to 2, 4, 6, and 12, respectfully

CMOD was measured perpendicular to the face of the prism using an Epsilon-Technology 3541 Fracture Mechanics Clip-on Gage. This set up (see Figure 1) was chosen as opposed to mounting the gauge directly under the specimen to protect the gauge from being harmed during testing and to obtain a direct measurement of the CMOD. This was only possible due to the rigidity of the gauge arms in the direction perpendicular to the face of the prism. One day prior to testing, all specimens were notched using an adjustable circular saw with a diamond tipped blade to a depth of 10% the specimen height, which is the minimum depth recommended by SETRA [6], and clips used to hold the clip-on gauge were adhered to the bottom edge of the prism using a 5-minute epoxy.

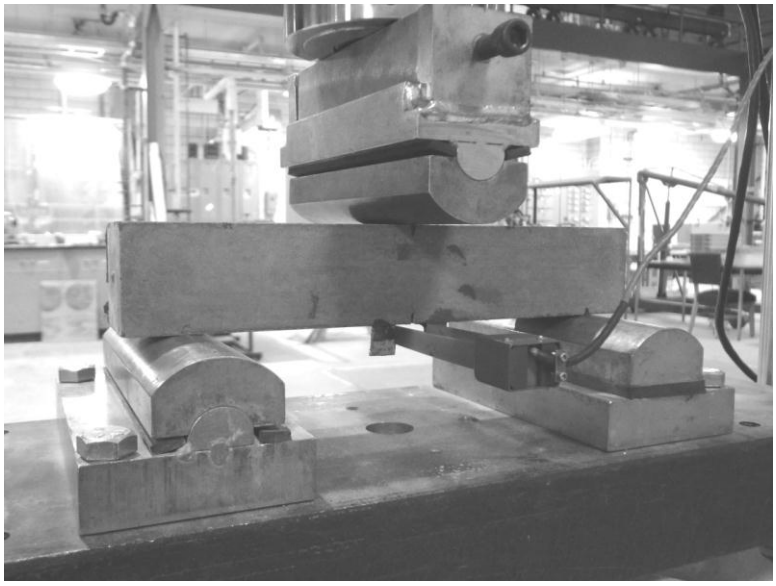

Figure 1: Fracture Test Configuration.

3 Results

Testing Data

The test results were used to develop mean P-w curves for prisms of similar parameters. Due to the limited number of samples this was done by performing an arithmetic mean of P and w values at each data point. A curve comparison as parameters are varied could then be performed. An example of such a comparison is the variation in load for the ambient curing age of 76x343 prisms (see Figure 2), which, as expected, shows that as age increases the strength does as well.

From these plots, values for CMOD (w), load (P), and stress (σ) were determined for the elastic limit or first crack (w_f, P_f, σ_f) and plastic limit (w_p, P_p, σ_p), as well as the fracture energy required to reach 40% of the maximum load on the descending branch ($G_{f,40}$). The first crack load was determined as the point where the data diverted from a linear path.

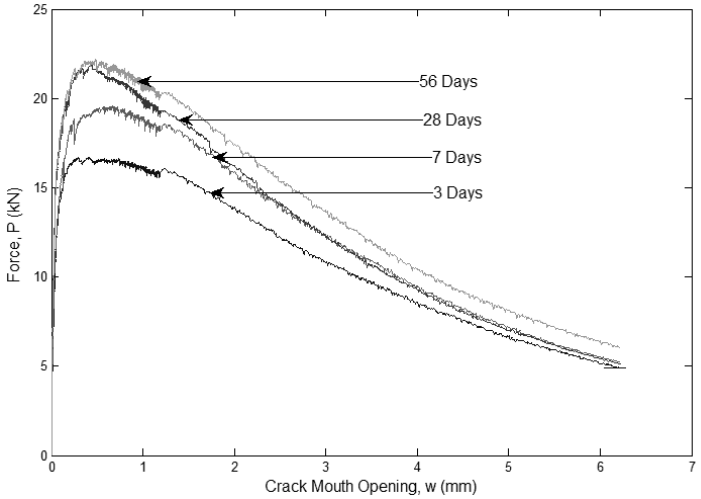

Figure 2: P-w curve for 76x343 specimens, ambient cure and variable age.

After which the corresponding w_f was found and σ_f was calculated using the expression (1) given by RILEM [9] for a 3-point bend test.

$$\sigma = \frac{3PL}{2bd^2} \tag{1}$$

In this equation P is the applied load, L is the span of the prism, and bd^2 is the unfractured area multiplied by the midspan depth of the prism (d), where b is the prism width and d is the total depth of the prism subtracted by the crack depth.

Following the elastic limit, the prisms undergo deflection hardening until the plastic limit is reached, after which the prism undergoes a considerable amount of deflection softening. The plastic limit load and CMOD were found by determining the maximum load of the data and the corresponding CMOD value. The stress was estimated using equation (1), as recommended by RILEM [9]. It is important to note that this stress value is an underestimate of the actual stress, because the effective area is reduced due to fracturing of the specimen.

Introduced by Hilleborg [11], the fracture energy (G_f) is a commonly used parameter to describe the behavior of concrete under fracture. The fracture energy is defined as the area under the stress–CMOD curve. This was estimated by dividing the area under the curve, calculated using the trapezium rule, by the unfractured area (bd) of the prism. Due to the limited amount of data for some of the specimens, the fracture energy was only calculated up to a 60% reduction in force ($G_{f,40}$). This value is reasonable because if a structure fails to 40% of the design load it would be thought of as unsafe and not fit for its intended purpose.

It has been well documented that brittle materials, such as the UHPC matrix, undergo reductions in stress when size is increased, due to an increased probability of flaws in the material [12]. This is commonly referred to as the scale effect and for UHPC has been shown to conform to the following expression (2) used as a multiplier [14], which is referenced to a 100 mm deep prism. This expression was applied to the calculated stresses and fracture energy, in order to normalize the size change between the 51 mm and 76 mm deep specimens.

$$S_t = S_f \frac{2\left(h/h_o\right)^{0.7}}{\left(1+2\left(h/h_o\right)\right)^{0.7}} \tag{2}$$

Here the scale effect is used to relate the direct tensile strength (S_t) to the flexural strength (S_f), where h is the height of the specimen and h_0 is the reference height of 100 mm.

For comparison purposes w_f, P_f, σ_f , w_p, P_p, σ_p , and G_f for each prism have been tabulated (see Table 2). From this data, it can be concluded, that as the age of the specimen increases all values except for plastic limit location, which only shows a possible slight increase, exhibit an obvious increase. The values for the CMODs and stresses at each age of curing tend to be fairly constant. The fracture energy decreases as the length of the prism increases, which is understandable because the ability to resist fracture should decrease due to an increase in moment for any given load. Increasing the cross sectional area, however, shows inconclusive results. For 3- and 7-day samples their fracture energy is similar as area is increased, but appears to decrease at 28 days and increase at 56 days. It should be noted that the values obtained for the first crack strength for ambient cured 28-day specimens agree with values obtained by others [13, 14], therefore the research presented should be applicable for general UHPC applications and are not just specific to this research.

Table 2: Fracture Data.

Curing Days	Prisms	L/d	Samples #	w_f mm	P_f kN	σ_f MPa	w_p mm	P_p kN	σ_p MPa	$G_{f,40}$ kJ/m^2
3	51x229	4.5	2	0.012	2.78	4.81	0.4303	7.97	13.80	6.31
	51x343	6.75	3	0.0116	1.59	4.13	0.348	4.42	11.48	3.49
	51x457	9	3	0.0139	0.94	3.26	0.4492	3.82	13.24	2.85
	51x699	13.75	1	0.0118	0.86	4.53	0.4815	2.8	14.87	2.38
	76X343	4.5	3	0.0100	4.94	4.35	0.4707	17.12	14.88	6.91
7	51x229	4.5	3	0.0118	2.93	5.06	0.4913	9.99	17.30	8.05
	51x343	6.75	3	0.0135	1.83	4.76	0.4254	6.05	15.7	4.78
	51x457	9	3	0.0132	1.31	4.54	0.581	4.36	15.08	3.67
	51x699	13.75	2	0.0136	0.76	3.89	0.3225	2.94	15.54	2.24
	76X343	4.5	2	0.0106	5.67	4.93	0.4672	20.23	17.59	7.56
28	51x229	4.5	12	0.0327	5.66	9.81	0.519	10.66	18.47	9.05
	51x343	6.75	2	0.0274	3.87	10.04	0.512	7.63	19.82	5.63
	51x457	9	4	0.0390	2.72	9.44	0.437	5.07	17.55	3.86
	51x699	13.75	1	0.0276	1.80	9.51	0.288	3.41	18.04	2.47
	76X343	4.5	2	0.0230	10.74	9.33	0.446	21.95	19.08	7.51
56	51x229	4.5	3	0.0651	6.8	11.77	0.4028	10.09	17.29	6.85
	51x343	6.75	4	0.0358	4.35	11.31	0.5543	8.13	21.12	6.44
	51x457	9	2	0.0387	3.28	11.35	0.479	5.4	18.71	3.98
	76X343	4.5	2	0.0335	12.96	11.27	0.5198	22.42	19.49	8.47
Modified Weibull				0.0000	5.67	9.81	0.501	10.37	17.95	8.72

Modeling

The two models proposed in this study to describe the fracture process were based on common probability distribution functions (PDFs). The lognormal function is frequently used in reliability analysis [15] and the Weibull function [16] has been well established to describe the strength of brittle materials [12, 17] and in some research has been used to describe the fracture process [18]. The following expressions (3) and (4), respectfully, are modified versions of these distributions and are used to describe the applied load as a function of w during the fracture process.

$$P(w)=\left(\frac{A}{w-w_f}\right)\exp\left[-\frac{1}{2}\ln\left(\frac{(w-w_f)-\lambda}{\zeta}\right)\right] \quad (3)$$

In the case of the modified lognormal PDF, A is the equation modifier, λ and ς are the lognormal mean and variance, respectively, w is the measured CMOD, and w_f is the experimentally determined first crack CMOD.

$$P(w) = \beta\left(\frac{w-w_f}{w_o}\right)^{m-1}\exp\left[-\left(\frac{w-w_f}{w_o}\right)^{m}\right] \quad (4)$$

The Modified Weibull PDF has a shape parameter m, a skewness parameter w_0, β is the distribution modifier, where w and w_f are the measured CMOD and first crack CMOD.

These parameters were estimated by limiting the curve so that it underestimated or equated the strength and CMOD values, while minimizing the value of the χ^2 goodness of fit test. The χ^2 test is one of many possible methods that could be used to estimate these parameters [19, 20] and can be explained using the following.

$$\sum_{i=1}^{n}\left[\frac{(n_i-e_i)^2}{e_i}\right]<c_{1-\alpha,f} \quad (5)$$

where n_i is the observed frequency of n number of values within a certain range of values, e_i is the theoretical frequency estimated for that same range, $c_{1-\alpha,f}$ is the critical χ^2 value at cumulative probability of 1-α, and f degrees of freedom, and can be found using a χ^2 table. The values α, and f can further be explained, respectively, as the significance level and the number of samples subtracted by the number of unknown parameters.

This procedure is demonstrated for a 28-day 51x229 specimen. The best fit of the modified Lognormal PDF and the modified Weibull PDF were graphically compared to the fracture curve for a 51x229 prism undergoing 28 days of curing (see Figure 3). The Modified Weibull achieved a better fit than the Modified Lognormal, suggesting that UHPC follows a Modified Weibull distribution.

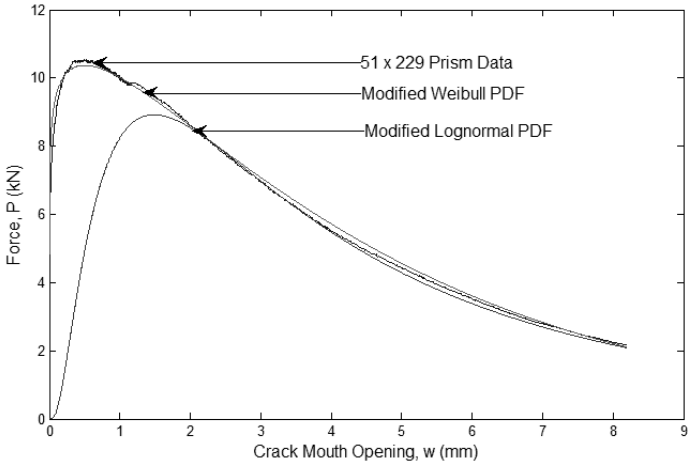

Figure 3: Curve Fitting of 51x229 Prism Fracture Curve.

The best fit was tested only for values of force above 2 kN, because the data collected during the fracture process never dropped below this value. The force ranges were in increments of 0.5 kN until values above 10 kN (see Table 3), which lead to an n of 18. For both models the f

value would be 13, because there are four unknown parameters. If a confidence level (α) of 0.05 was chosen the corresponding χ^2 reference value ($c_{1-\alpha,f}$) would be 23.7 [20]. Based on this analysis it can be concluded that the Modified Weibull distribution passes and the Modified Lognormal fails the χ^2 test.

Table 3: χ^2 Goodness of Fit Test.

Force kN	n_i 51x229	e_i Weibull	e_i Lognormal	$(n_i-e_i)^2/e_i$ Weibull	$(n_i-e_i)^2/e_i$ Lognormal
<2.0	59	0	596	NA	NA
2-2.5	227	232	363	0.11	50.95
2.5-3.0	288	250	357	5.78	13.34
3.0-3.5	218	215	303	0.04	23.84
3.5-4.0	196	189	273	0.26	21.72
4.0-4.5	170	170	250	0.00	25.60
4.5-5.0	164	214	238	11.68	23.01
5.0-5.5	149	143	230	0.25	28.53
5.5-6.0	136	135	228	0.01	37.12
6.0-6.5	129	128	235	0.01	47.81
6.5-7.0	132	124	247	0.52	53.54
7.0-7.5	123	123	272	0.00	81.62
7.5-8.0	129	127	322	0.03	115.68
8.0-8.5	149	140	432	0.58	185.39
8.5-9.0	157	166	456	0.49	196.05
9.0-9.5	199	214	0	1.05	NA
9.5-10.0	560	565	0	0.04	NA
>10.0	1617	1667	0	1.50	NA
Sum	4802	4802	4802	22.34	NA

Based upon this analysis the parameters A, λ, ς for the Modified Lognormal and those of β, m, and w_0 for the Modified Weibull were determined to be 21.95, 1.4, 1 and 230.6, 4.45, 1.1, respectively.

From the above plot and the passing of the χ^2 test, it can be determined that the Modified Weibull distribution is better for describing the fracture process of UHPC prisms. The values calculated from the fracture curves in the previous section were also calculated for the modified Weibull (see Table 2). This model tends to underestimate or agree with the values for the actual 51x229 28-day cured specimen. It is for these reasons that the Modified Weibull distribution will be used in the greater research to describe and model the variations in fracture data from the previously mentioned parameters.

4 Conclusions

The results of the fracture tests show that as age increases the parameters describing the fracture behavior of UHPC, even after 28 days, show some amount of increase. The stress and crack opening for the elastic and plastic limit are fairly constant for any size prism at a given curing age. As the length of the prisms increases the fracture energy decreases. In addition, the results from the 28-day tests reaffirm previously determined 28-day first crack stress values for UHPC.

Furthermore, it has been shown that the fracture curve obtained from performing these tests can be modelled using a Modified Weibull distribution. This model will be subject to further study, and will be fit to all tested UHPC prisms. The final model will incorporate the variables of fiber content, prism aspect ratio, prism cross sectional area, curing regime, and age of curing. It is proposed that this model can be utilized in the design of future UHPC structures, UHPC research, and inspection of damaged UHPC structures.

5 Acknowledgements

The researchers would like to acknowledge the members of the Michigan Tech UHPC group, the staff at Benedict Laboratory, Epsilon Technology, MTS Systems, and LaFarge North America for all their help during this research.

References

[1] Richard, P.; Cheyrezy, M.: Composition of Reactive Powder Concretes. Cement and Concrete Research 25(7), p. 1501-1511, 1995.

[2] Rossi, P.: Development of New Cement Composite Materials for Construction. Proceedings of the Institution of Mechanical Engineers, Part L, Journal of Materials, Design and Applications, Paris 2005.

[3] Bentur, A.; Diamond, S.; Mindess, S.: The Microstructure of Steel Fibre-Cement Interface. Journal of Materials Science 20, p. 3610-3620, 1985.

[4] Bentur, A.; Mindess, S.: Fibre Reinforced Cementitious Composites. New York, NY, Taylor and Francis, 2007.

[5] Reda, M.M.; Shrive, N. G.; Gillott, J.E.: Microstructural Investigation of Innovative UHPC. Cement and Concrete Research 29, p. 323-329, 1999.

[6] SETRA; AFGC: Ultra High Performance Fiber Reinforced Concrete-Interim Recommendations. France, 2002.

[7] Peuse, E.J.: Impact of Age at Thermal Treatment on the Mechanical Properties of an Ultra-High Performance Concrete, Department of Civil and Environmental Engineering, Michigan Technological University: Houghton, MI. 2008.

[8] Kollmorgen, G.A.: Impact of Age and Size on the Mechanical Behavior of Ultra High Performance Concrete, Department of Civil and Environmental Engineering, Michigan Technological University: Houghton, MI. 2004.

[9] RILEM TC162-TDF: Bending test Final Recommendation. Materials and Structures 35(November 2002), p. 579-582, 2002.

[10] ASTM International: Annual Book of ASTM Standards. C-39 Standard Test Method for Compressive Strength of Cylinders, 2005.

[11] Hillerborg, A.: Existing Methods to Determine and Evaluate Fracture Toughness of Aggregative Materials: RILEM Recomendations on Concrete, Fracture Toughness and Fracture Energy. Test Methods for Concrete and Rock, ed. Mihashi, H., et. al, p. 145-151, Balkema, Rotterdam 1989.

[12] Bažant, Z. P.; Planas J.: Fracture and Size Effect in Concrete and Other Quisibrittle Materials. CRC Press, Boca Raton, FL 1998.

[13] Graybeal, B.A.: Characterization of the Behavior of Ultra-High Performance Concrete, Department of Civil and Environmental Engineering, University of Maryland: College Park, MD 2005.

[14] Chanvillard, G.;Rigaud, S.: Complete Characterisation of Tensile Properties of Ductal® UHPFRC According to the French Recommendations. International Workshop High Performance Fiber Reinforced Cement Composites, p. 21-34, 2003.

[15] Steinberg, E.: Structural Reliability of Prestressed UHPC Flexure Models for Bridge Girders. Journal of Bridge Engineering 15(1), p. 65-72, 2010.

[16] Weibull, W. A.: A statistical distribution function of wide applicability, Journal of Applied Mechanics 18, p. 292-297, 1951.

[17] Chawla, K. K.: Ceramic Matrix Composites. Chapman and Hall, London, UK 1993.

[18] Chen B.; Liu, J.: Experimental study on AE characteristics of three-point-bending concrete beams. Cement and Concrete Research 34, p. 391-397, 2004.

[19] Leon, M.; Kittl, P.: On the Estimation of Weibull's Parameters in Brittle Materials. Journal of Materials Science 20, p. 3778-3782,1985.

[20] Ang, A. H. S.; Tang, W. H.: Probability Concepts in Engineering: Emphasis on Applications to Civil and Environmental Engineering. Wiley, 2007.

Bending Behaviour and Variation of flexural Parameters of UHPFRC

Johannes Gröger[1], Nguyen Viet Tue[1], Kay Wille[2]
1: Institute for Structural Concrete, Graz University of Technology, Austria
2: Dept. of Civil and Environmental Engineering, University of Connecticut, USA

A series of 60 four-point-bending tests was carried out in order to study the bending behaviour and the variation of bending parameters of ultra-high performance fibre reinforced concrete. Five different types of ultra-high performance fibre reinforced concretes have been included in this research, which have been altered by the length and the amount of steel fibers. In order to investigate the variation of bending parameters each series of three beams was carried out four times.The research show that the length and the amount of fibers influences the variability, which might need to be considered in design guidelines of ultra-high performance fiber reinforced concrete for future application.
In order to facilitate the quantification of the material tensile stress-strain relationship, needed for the design, the second part of this research has been emphasized on the development of a numerical model to back calculate the tensile stress-strain-relationship of ultra-high performance fibre reinforced concrete from bending tests without using Finite Element Method.

Keywords: UHPFRC, steel fibre, fibre content, deflection hardening/softening, stress-strain-relationship

1 Introduction

Superior mechanical and durability properties of ultra-high performance fibre reinforced concrete (UHPFRC) have attracted many researchers, agencies and contractors worldwide. Previous experiences show that influences of fibres on the mechanical behaviour are not easy to determine, particularly for development of design rules [1-4]. The variability of the mechanical properties especially regarding the tensile performance of UHPFRC can be seen as one reason holding back the broad application of UHPFRC.

The first part of the paper is focused on the investigation of the variability of the bending behavior of UHPFRC. In the second part the development of a numerical model to back calculate the tensile stress-strain-relationship of UHPFRC from bending tests without using finite element method is emphasized. The success of accelerating the development of design guidelines and the application of UHPFRC in the construction market depends on the simplicity and reliability of methods to characterize the design strength of UHPFRC.

2 Experimental Program

A series of 60 four-point-bending tests was carried out in order to study the bending behaviour and the variation of bending parameters of UHPFRC. Five different types of ultra-high performance fibre reinforced concretes have been included in this research, which have been altered by the fibre length (6.0 mm, 12.7 mm) and the volumetric amount of steel fibers (0 %, 0.75 %, 1.5 %).

Materials and specimen preparation

The mix composition of the five different materials used in this research is shown in Table 1. The fibre volume fraction was varied from 0, 0.75 to 1.5 percent by replacing the equivalent volume of sand. Two types of straight steel fibres were used in this research. Fibre type I and II are characterized by a diameter of 0.15 mm and a tensile strength of 2100 N/mm². The length of fibre type I and II is 6.0 mm and 12.7 mm, respectively.

Table 1: UHPC / UHPFRC mixture [kg/m³].

Component	UHPC	UHPFRC			
		1	2	3	4
CEM I 42,5 R-HS	725	725	725	725	725
Silica fume	131	131	131	131	131
Quarz powder	391	391	391	391	391
Water[a]	159	159	159	159	159
Superplasticizer[b]	32	32	32	32	32
Steel fibre	-	58.5	117	58.5	117
	-	Type I	Type I	Type II	Type II
Quarz sand	922	902	882	902	882

[a]water to cement ratio = 0.25, [b]solid content 30 %

For each of the five series three bending beams were cast. In order to investigate the variation of bending parameters each series of three beams was carried out four times (four different days), thus 60 specimens in total. In addition to the bending beams at least three cylinders (d = 100 mm, h = 200 mm) were cast with each series. The mixing procedure and the casting method were not varied throughout the research for consistency.

All beams have been cast from one end of the formwork. Due to the flowability (spread value ≈ 730 mm) of the concrete, self-consolidating and good release of entrapped air was maintained without compacting. This ensures a uniform fibre distribution in the centre region of the beams.

Subsequent to casting the free concrete surface was covered with plastic sheet for two days. Afterwards the specimens were demolded and cured under standard climate conditions for 26 days.

Cylindrical specimens were used to determine the compressive strength as well as the elastic modulus for each type of concrete. As expected the different fractions of steel fibres did not have a significant influence on the material strength. The compressive strength has been tested in excess of f_c = 160 N/mm² for all series. The elastic modulus has been tested to E_c = 48000 N/mm².

Test setup and procedure

All 12 beams of each type of concrete have been tested at a concrete age of 28 days. The four point bending test setup corresponding to the guideline ‘Faserbeton (Fibre Reinforced Concrete)’ [5] by the German Committee for Structural Concrete was used in this research. The test setup is illustrated in Figure 1. The specimens were rotated by 90 ° so that the top surface during casting faced sideways during testing. It should be noted that the specimens have been supported by steel bars to ensure low horizontal forces due to support friction (see [6]).

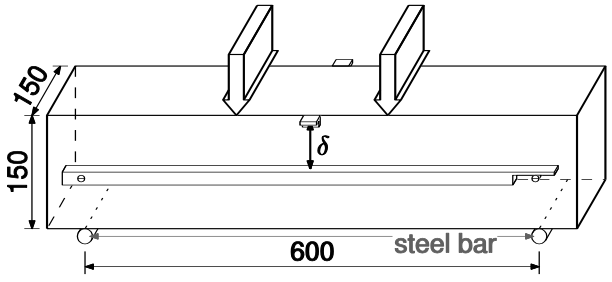

Figure 1: bending test specimen and setup.

The specimens have been tested accordingly to the guideline 'Faserbeton' [5]. The load was applied displacement controlled by the test equipment (accuracy class 1 to DIN 51220 [7]) at a rate of 0.1 mm/min up to peak load. The descending branch was performed at a higher displacement rate of 0.25 mm/min at begin of descending and at 0.5 mm/min when the load became smaller than 50 percent of the peak load. The mid-span deflection δ was measured by displacement transducers at both sides of the beam.

3 Results & Discussion

The equivalent bending stress – mid-span deflection relationship for all concrete mixes with steel fibres are given in Figure 2 and 3. Figure 2 illustrates test results of UHPFRC1 and UHPFRC2 including 6.0 mm fibres at a volume fraction of 0.75 % and 1.5 %, respectively.

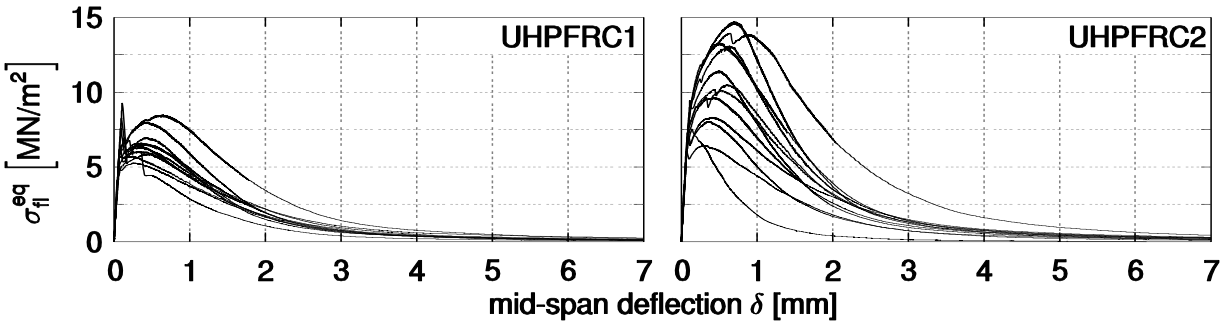

Figure 2: bending stress – mid span deflection of UHPFRC1/2 (Fibre 6.0 mm).

The addition of 6mm long steel fibres of 0.75 % volume fraction results in deflection softening behaviour. After the tensile strength of the concrete matrix is reached the material tensile resistance decreases considerably which results in a reduction of the equivalent bending stress up to 40 percent at a deflection of $\delta \approx 0.1$ mm. After the stress drop a slight increase of bending stress is observed, which is followed by deflection softening.

If the content of steel fibres is raised up to 1.5 volume percent, deflection hardening of UHPFRC2 is observed. However, nearly 50 percent of the tested specimens also show a decrease in bending stress after the tensile strength of the concrete matrix ($\sigma_t \approx 7.5$ MN/m^2) was exceeded. Figure 2 illustrates that the equivalent bending strength and also its variation is increased by a higher fibre volume fraction.

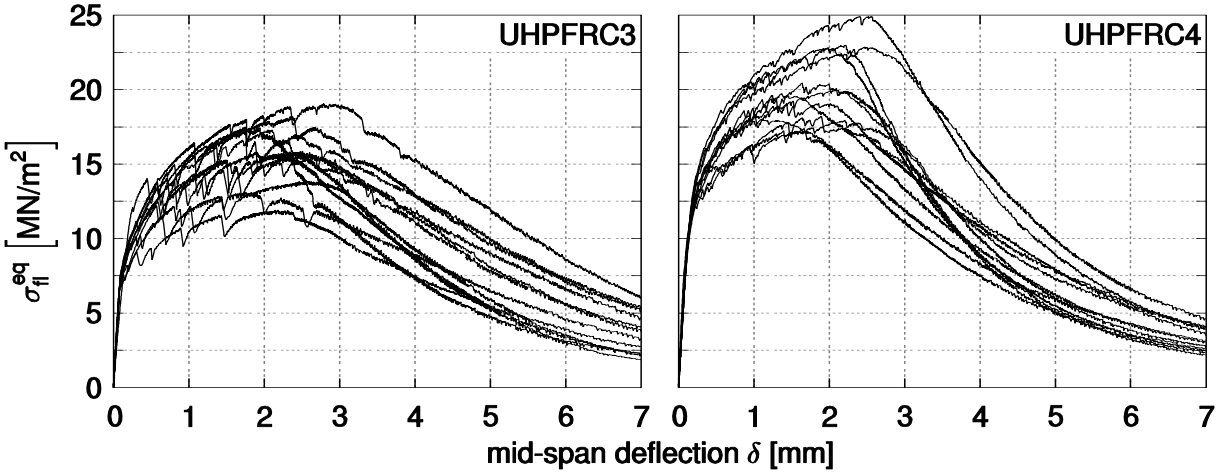

Figure 3: bending stress - mid-span deflection of UHPFRC3/4 (Fibre 12.7 mm).

Figure 3 summarizes test results of UHPFRC3 and UHPFRC4 including 12.7 mm long fibres at a volume fraction of 0.75 % and 1.5 %, respectively.

The addition of 12.7 mm long steel fibres results in a more uniform bending behaviour. Deflection hardening was observed for all 24 specimens with 0.75 as well as 1.5 volume percent steel fibres (supercritical fibre content). According to the test results of UHPFRC1+2 the increase of fibre content results in a higher equivalent bending strength. An increase in variation of bending strength with increase of fibre volume fraction was not observed by using 12.7 mm long steel fibres.

Table 2 summarises the variation of the investigated flexural parameters of UHPC and UHPFRC1-4. The average value $\bar{\chi}$ and the coefficient of variation ν are shown for the equivalent bending strength σ^{eq}_{fl} and for the deflection at load maximum δ_{Peak} for each of the five different concretes.

Table 2: statistical analysis.

Fibre	UHPC	UHPFRC			
		1	2	3	4
σeqfl [N/mm²]					
$\bar{\chi}$	6.56	6.53	10.59	15.92	20.30
ν	0.285	0.142	0.259	0.135	0.121
δPeak [mm]					
$\bar{\chi}$	0.08	0.37	0.48	2.25	1.88
ν	0.02	0.306	0.329	0.164	0.206

The statistical analysis points out the strong distinctions between the five different concretes. Using steel fibres improves the brittle load bearing behaviour of UHPC considerably, as it can be seen by the high values of δ_{Peak} for UHPFRC1-4, e.g. UHPFRC1/2 (6.0 mm fibre length) results in a more than four times higher deflection at load maximum compared to UHPC, which is further increased up to over 20 times for UHPFRC 3/4 (12.7 mm fibre length). Based on these results the value of δ_{Peak} is primarily influenced by the length of the fibre. In summary Table 2 points out that longer fibre leads to higher equivalent bending strength, higher values of δ_{Peak} and lower coefficient of variation. Note, that this conclusion is only valid as long the failure mechanism is primarily controlled by fibre pull-out.

4 A model to formulate stress-strain-relationship of UHPFRC

A numerical model has been developed to analyse four-point-bending tests corresponding to the guideline ‘Faserbeton’ [5]. The model considers Euler-Bernoulli beam theory and formulates the stress-strain-relationship for structural design of UHPFRC. In comparison to simulations based on finite elements the computational time of the numerical model is decreased, and thus leading to a more efficient analysis.

The numerical model is able to take into account deflection hardening and softening behaviour. Therefore the development of multiple cracking up to peak load as well as localisation of macro-crack opening during softening is considered. Required input parameters to calculate the polygonal tensile stress-strain relationship are the experimental load-deflection curve, the UHPFRC compressive stress-strain relationship and the position of the macro-crack.

Basic Concept of the Model

The numerical model bases on dividing the beam in a finite number of sections along the beam axis. By strain-level iteration the rotation angle of the cross-section is calculated according to the associated bending moment. Hereby the tensile forces, determined by the selected stress-strain relationship, equilibrate the compressive forces, defined by materials uniaxial compressive behaviour. Along the beam axis the moment distribution is divided in parts and the rotation at every section based on the strain distribution over beam height is determined. The mid-span deflection is calculated by double integration of the rotation values. After load maximum the kinematics of the bending beams changes due to the development of a macro-crack, this initiates the softening behaviour. Given the location of the opening crack the numerical model predicts the descending load-deflection branch and allows for the back calculation of the complete tensile material behaviour of UHPFRC.

Backward Calculation

To demonstrate the quality of the developed model two characteristic bending tests were analysed representing the behaviour of UHPFRC2+4. UHPFRC4, reinforced with 12.7 mm long fibres, shows a highly deflection hardening behaviour in comparison to UHPFRC2.

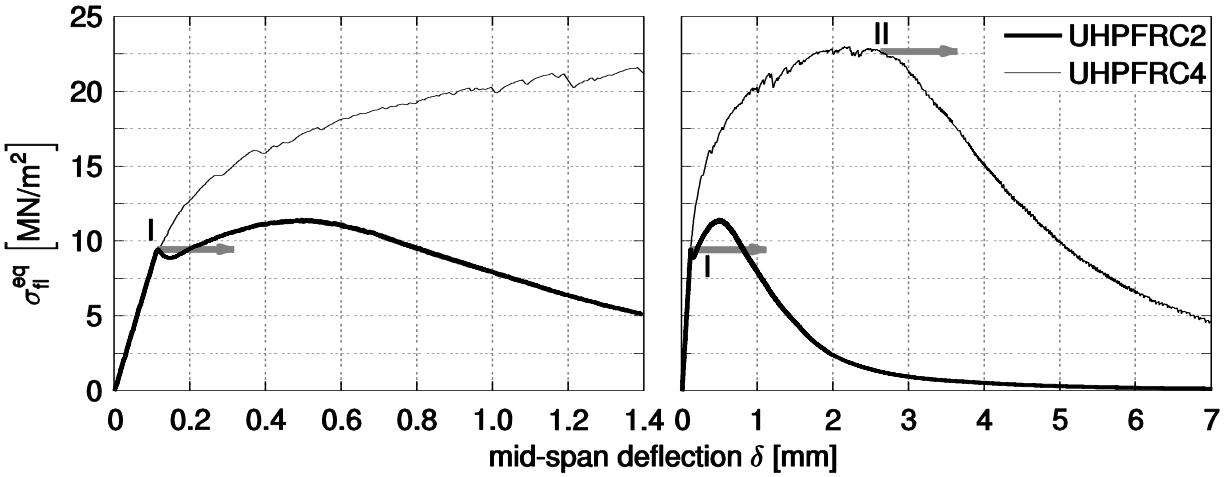

Figure 4: bending stress - mid-span deflection (1.50 Vol.-%) – UHPFRC 2/4.

The label **I** in Figure 4 marks the load level when concrete matrix fails. If short fibres are used this point nearly equals to the state when macro-crack starts to open (signed by arrow). If long fibres are used the matrix fails at nearly the same level. If the load bearing capacity of fibres is higher than matrix strength, the equivalent bending stress increases until point **II** is reached. Label **II** marks the state when multiple cracking ends and macro-crack starts. The bending behaviour during opening of the macro-crack depends strongly on fibre length. The beam with the short fibres shows a small increasing range after the concrete matrix failed, followed by the deflection softening. Both, the hardening as well as the softening range, are resulting from one macro-crack.

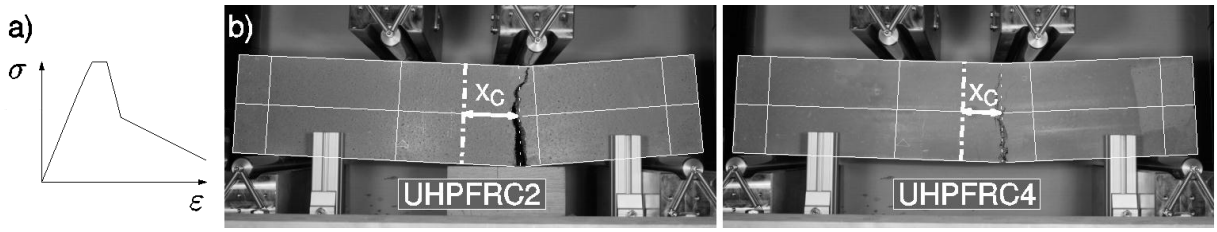

Figure 5: required input parameters: a) material behaviour under compression, b) position of macro-crack.

The developed model is able to consider these different bending behaviours. Controlled by the different characteristics of the tensile stress-strain relation (user input) the model is able to calculate every possible bending state.

Three input parameters are required for the numerical model as follows:

1) the equivalent bending stress – mid-span deflection curve of the bending test (Fig. 4)
2) the compressive stress – strain relationship determined in this research with 100 x 200 mm cylindrical specimen (Fig. 5a)
3) the position of the macro-crack in relation to the centre axis (Fig. 5b)

In this example the macro-crack position for the beam reinforced with 6.0 mm fibres is at x_C = 0.08 m and for the beam reinforced with 12.7 mm fibres at x_C = 0.06 m (see Figure 5).

Results

On a step-by-step basis a backward analysis was performed considering piece-wise linear material uniaxial tensile behaviour, also called poly-linear approximation method. This method is described and has been used in [6, 8-10].

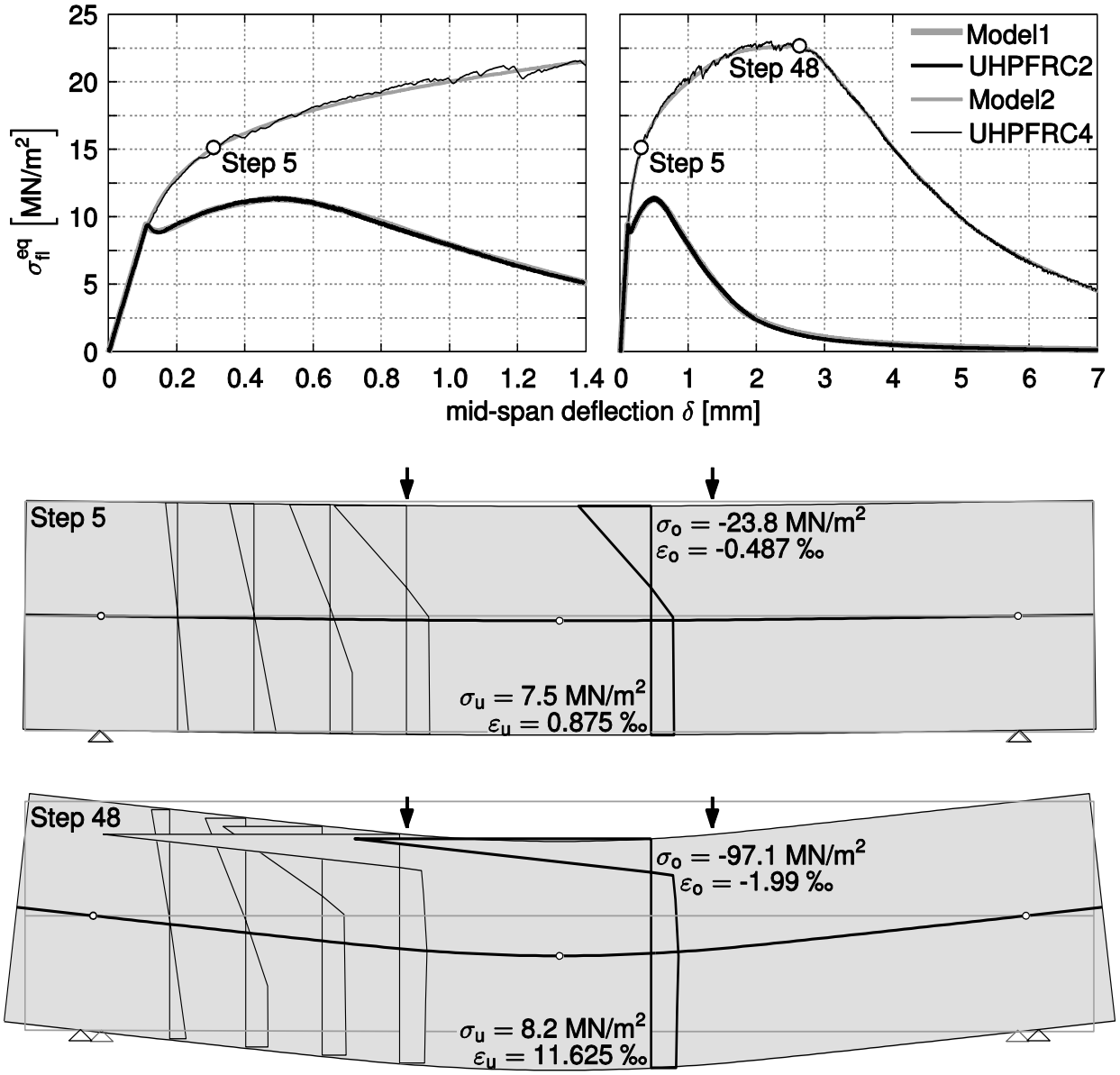

Figure 6: results of bending test compared with simulation results.

For the tested beams a good correlation between the simulations results and the bending test response was obtained. The model allows accurately following the experimental bending stress – mid-span deflection curves. Figure 6 illustrates that deflection hardening as well as softening and even combined macro-crack opening behaviour can be simulated with the model.
With a distance of 5.0 mm between the sections of the model the maximum tensile strain $\varepsilon_{t,fat}$ (1) an d the corresponding crack opening w_c (2) can be calculated.

$$\varepsilon_{t,fat} = \frac{l_F}{2 \cdot 5.0\,mm} \quad (1)$$

$$w_c = (\varepsilon_t - \varepsilon_{elast}) \cdot 5.0\,mm \quad (2)$$

The backward calculated polygonal stress-strain relationships are shown in Figure 7. The beam reinforced with 6.0 mm fibres is simulated with the stress-strain relation labelled ‘Model 1’. After an elastic branch up to 9.0 N/mm² the tensile stress is reduced to 3.5 N/mm² and then increases slightly before the softening starts with a tensile strain higher 85 ‰.

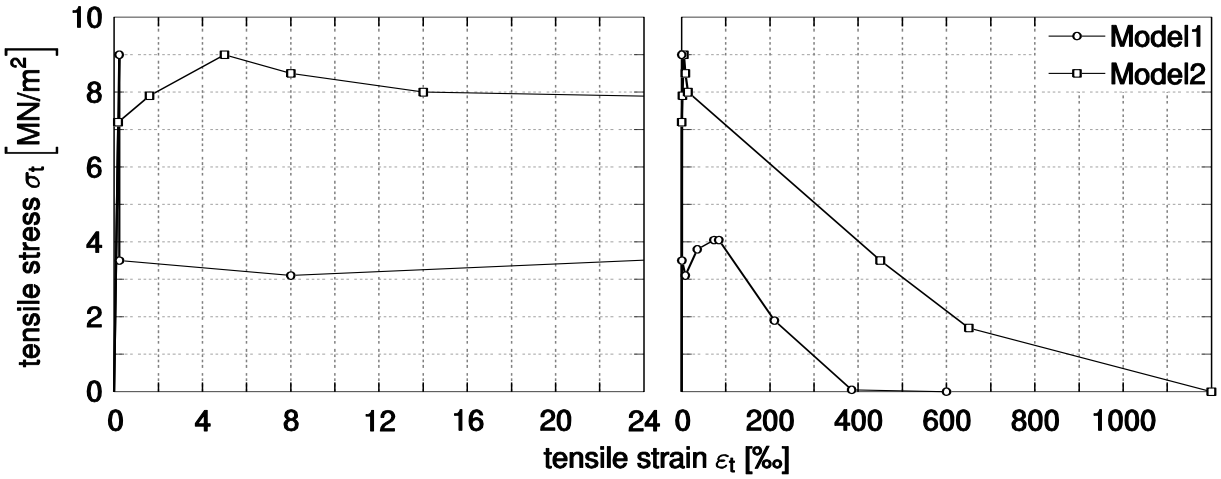

Figure 7: backward calculated stress-strain relationship.

Contrary to the stress-strain relation of the short fibres (Model 1) the Model 2 shows hardening after the tensile strength of the concrete matrix is exceeded. The maximum tensile strength of σ_t = 9.0 N/mm² is reached at a strain of 5.0 ‰. Because of the fibre length of 12.7 mm the softening branch must be defined up to 1200 ‰ (see equation 1). Up to this strain or equal to a maximum crack opening of about 6.0 mm (l_F / 2) fibres can bridge a gap.

5 Conclusions

This study investigated the bending behaviour of UHPFRC compared to UHPC and the variation of flexural parameters. The results can be summarised as follows:

- The variation of flexural parameters like equivalent bending strength or displacement at peak load can be reduced by adding steel fibres.
- Longer fibres not only increase flexural strength at same fibre volume fraction, they also decrease the variation of flexural parameters.
- A new numerical model has been developed to effectively back calculate the tensile stress-strain relationship from four-point-bending tests. The results show that the numerical model is able consider deflection hardening, softening and macro-crack opening.

References

[1] Leutbecher, T.: Rissbildung und Zugtragverhalten von mit Stabstahl und Fasern bewehrtem Ultrahochfesten Beton (UHPC); Dissertation, Kassel 2007.

[2] Jungwirth, J.: Zum Tragverhalten von Zugbeanspruchten Bauteilen aus Ultra-Hochleistungs-Faserbeton; Dissertation, Lausanne 2006.

[3] Lappa, E.S.: High Strength Fibre Reinforced Concrete, Static and fatigue behaviour in bending; Dissertation, Delft 2007.

[4] Grünewald, S.: Performance-based design of self-compacting fibre reinforced concrete; Dissertation, Delft 2004.

[5] Deutscher Ausschuss für Stahlbeton: Richtlinie – Stahlfaserbeton. DAfStb, Berlin, 2010-03.

[6] Wille, K., and Parra-Montesinos, G., “Effect of Beam Size, Casting Method and Support Conditions on the Flexural Behaviour of Ultra High Performance Concrete,” ACI Materials Journal, in press, 2012.

[7] DIN standard: Werkstoffprüfmaschinen – Allgemeines zu Anforderungen an Werkstoffprüfmaschinen und zu deren Prüfung und Kalibrierung. DIN 51220, Beuth Verlag, Berlin, 2003-08.

[8] Uchida, Y., Kurihara, N., Rokugo, K., Koyanagi, W., 1995 “Determination of tension softening diagrams of various kinds of concrete by means of numerical analysis,” FRAMCOS-2, Germany, AEDIFICATION, pp. 17 – 30.

[9] Kitsutaka, Y., 1995 “Fracture parameters for concrete based on poly-linear approximation analysis of tension softening diagram,” FRAMCOS-2, Germany, AEDIFICATION, pp. 199 – 208.

[10] Hong, K.N., Kang, S.T., Kim, S.W., Park, J.J., Han, S.H., 2010 “Material properties of air-cured ultra-high-performance steel-fiber-reinforced concrete at early ages,” International Journal of the Physical Sciences, Vol. 5, No. 17, pp. 2622 – 2634.

Tests on the Flexural Tensile Strength of a UHPFRC subjected to Cycling and Reversed Loading

Björn Frettlöhr[1], Dominique Corvez[2], Emmanuel Chatoux[3] ,Karl – Heinz Reineck[1]
1: ILEK – Institute for Lightweight Structures Conceptual and Structural Design, University of Stuttgart, Germany
2: Lafarge, Paris, France
3: École des Ponts, ParisTech, France

The paper presents the results of tests on the flexural tensile strength under cycling and reversed loading up to 250 cycles on prisms out of Ductal® of Lafarge with a compressive strength of 211 MPa.
In a first phase the following test were performed on prisms with h = 50 mm: 6 cycling tests and 12 tests under reversed cycling loading. The upper load was set at 2,25-times the elastic limit of the flexural stress respectively 71 or 76 % of the flexural tensile strength. It could be shown that for cycling and reversed loading the flexural tensile stresses can be utilized up to 2-times the elastic limit respectively 70 % of the flexural tensile strength.
In a second phase additional 7 displacement controlled bending tests were performed of prisms h = 50 mm and b/h = 3 under reversed cycling loading. Different levels for the displacement amplitude were selected and were increased until failure occurred. The evaluations of the results comprised the development of the stiffness and ductility as well as the energy dissipation.

Keywords: flexural tensile strength, cycling loading, reversed loading, UHPC, seismic

1 Aim of test program and test set-up

Aim of test program

The aim of the test program was to assess whether flexural stresses higher than the elastic limit can be utilized in design of UHPFRC members subjected to cycling and reversed cycling loading. In this range of micro-cracks appear before localization occurs, and the question is whether this range can be utilized in the design. If this would have to be avoided only stresses up to the elastic limit could be tolerated and this could be uneconomical. This is especially relevant for containments, like e.g. hot-water tanks for the utilization of solar heat [1]. For such tanks reversed bending moments occur due to temperature differences in the wall which are stresses in tension. Since this loading occurs seasonally the number of loading cycles is not high and for the tests up to 250 cycles were run. This is also critical for seismic design of structures where material properties should be assessed with symmetric reversed cyclic loading before making any equivalent static analysis, through modal pushover analysis for instance. The range of 250 cycles appears to be also convenient based on statistical analysis of the number of cycles observed during the El Centro ground motion [2].

The paper presents the results of tests on the flexural tensile strength under cycling and reversed loading up to 250 cycles. Full details are reported in [3]. All tests were performed with the UHPFRC Ductal® of Lafarge with a compressive strength of 211 MPa and a modulus of elasticity of 53.071 MPa. The fibre content of the material was 2 Vol-% with fibres of 13 mm length and 0,175 mm diameter. The axial tensile strength was about 14,5 MPa and the flexural tensile strength of prisms 40·40 mm was on average 42,3 MPa. The testing program consisted of 2 phases which are reported separately in Chapter 2 (phase 1) and Chapter 3 (phase 2).

1.2 Test set-up

The test set-up for all the to cycling and reversed cycling bending tests was designed by the first author and is shown in Fig. 1 and Fig. 2. In this test set-up prisms with a height of 50 and 75 mm and a maximum width of 250 mm could be tested, and the span was 450 or 675 mm. Special considerations were paid to the kinematic support conditions shown in Fig. 3. The two

upper and lower roller supports were in a distance of Δh = 10 mm in order to avoid any clamping effects and account for tolerances. The deflection at midspan was measured by 2 ERS- gauges as shown in Fig. 2.

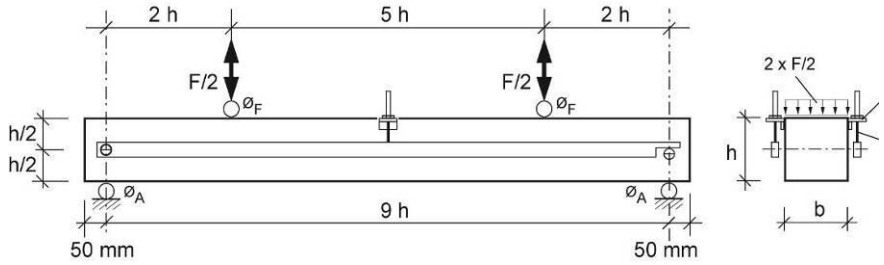

Figure 1: Test specimens.

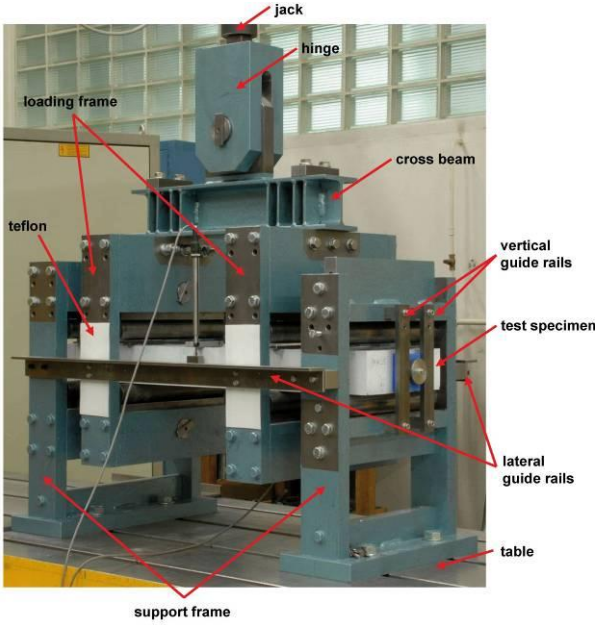

Figure 2: Foto of test set-up.

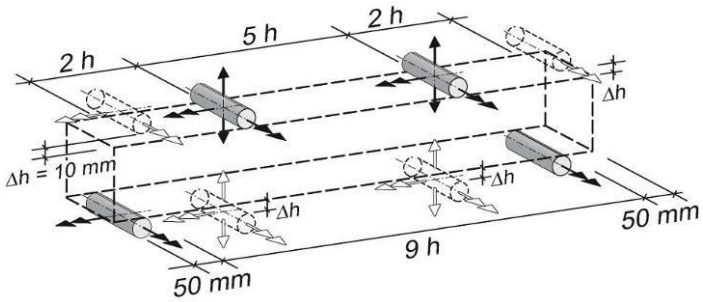

Figure 3: Kinematic support conditions.

2 Test program and test results for phase 1

In phase 1 the following test were performed:

- 3 cycling tests each on prisms with h = 50 mm and ratios of b/h = 1 and 5; altogether 6 tests.
- 3 tests each under reversed cycling loading on prisms with h = 50 mm and ratios of b/h = 1, 3 and 5, as well as 3 tests on prisms with h = 75 mm and b/h = 3; altogether 12 tests.

The upper loads were determined from the relevant static tests and was set at 2,25-times the elastic limit $f_{ct,el}$ of the flexural stress respectively, which is about 71 to 76 % of the flexural tensile strength. At 1,75-times the elastic limit 50 cycles were performed, and after that the load increased to the value of 2,25 · $f_{ct,el}$ and the remaining 200 cycles applied. After that the flexural tensile strength was determined, unless a prior failure had occurred under cycling loading. The lower load of the cycling tests was set at 0,10·$f_{ct,el}$. For the reversed cycling tests the lower load was set at 1,75-times the elastic limit for the lower side, which was lower than that determined for the upper side with the due to the reversed moment causing tension on the rough top side of the specimen at casting.

The results of the cycling test on one of the specimens with b = h = 50 mm is shown in Fig. 4a, where the applied flexural tensile stress is plotted versus the deflection at midspan. For comparison also the 3 curves of the static tests are plotted. It can be seen that this specimen did not attain the 200 cyles at the higher load level but it failed after 122 cycles. This was the only specimen of the cycling test which exhibited a premature failure due to cycling. All other

specimens survived all cycles and could be tested up to failure under static loading, as shown in Fig. 4b for a specimen with b = 3·h and h = 50 mm, which attained the flexural tensile strength of the 3 static tests.

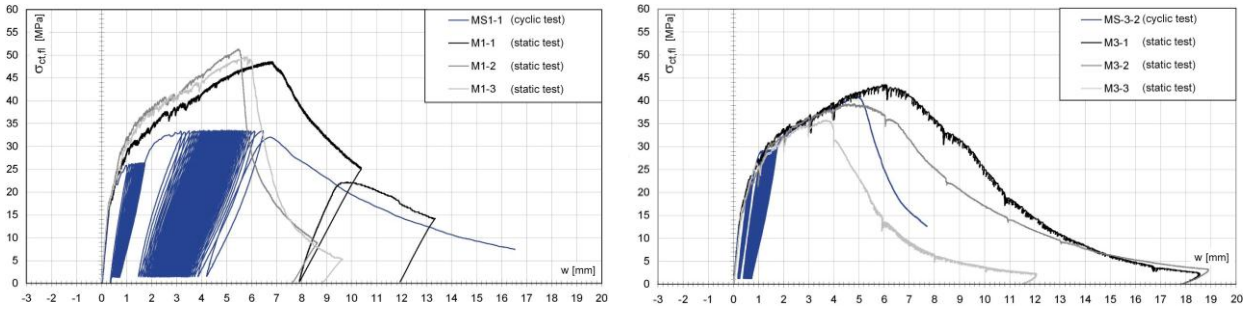

a) prism with b=h=50 mm (failure after 122 cycles) *b) prism with b=5·h and h=50 mm (static test after 200 cyles)*

Figure 4: Flexural tensile stress versus deflection at midspan for cycling test of two prisms.

For the tests under reversed cycling loading 4 out of the 12 specimens did not survive 250 cyles. Fig. 5 shows the flexural tensile stress plotted versus the deflection at midspan for two prisms with h = 50 mm and b=5·h. In case of the prism shown in Fig. 5a localisation and failure occurred after 137 cycles, whereas the prism in Fig. 5b could be tested up to failure after 250 cycles had been applied.

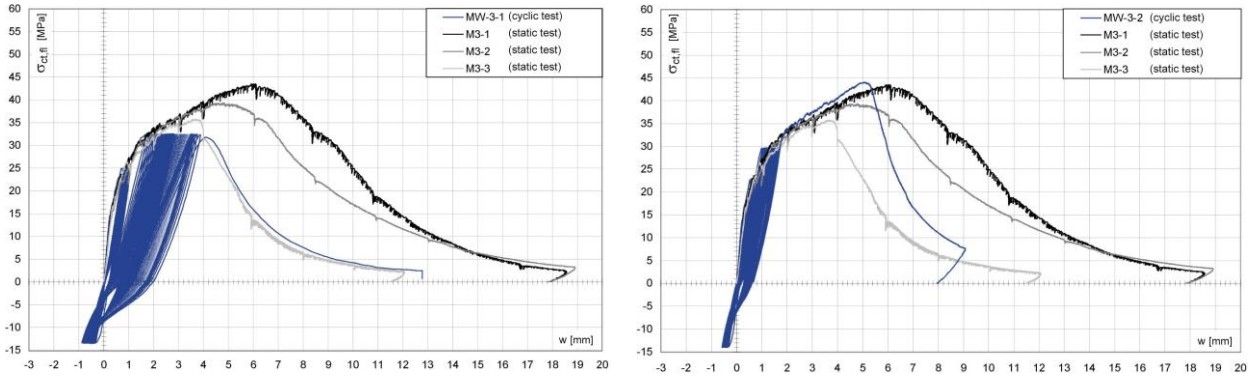

a) prism with failure after 137 cycles *b) prism with static test after 205 cycles*

Figure 5: Flexural tensile stress versus deflection at midspan for reversed cycling tests of two prisms with h=50 mm and b = 5·h.

In concluding, it could be shown that in a design for cycling and reversed cycling loading the flexural tensile stresses can be utilized up to 2-times the elastic limit respectively 70 % of the flexural tensile strength.

3 Test program and test results for phase 2

In phase two, the experimental approach remains with the program testing a series of displacement controlled 4 points bending reversed cyclic on similar plates with a focus on displacement behaviours. The idea is to focus on stiffness degradation, ductility and energy dissipation. The loading is realized by “trains” of cycles (that is to say a series of a given number of cycles at a given displacement amplitude) with an increasing displacement (see Fig. 6), at a loading rate near to the maximal force reached under static loading.

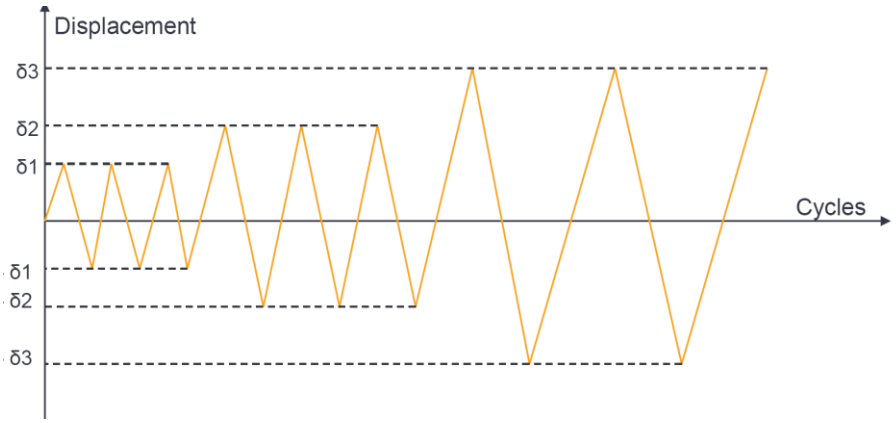

Displacement [mm]	0,2	0,5	1	1,5	2	2,5	3	3,5	4
Number of cycles	10	20	20	40	20	20	40	40	40

Figure. 6: Displacement levels and associated number of cycles.

During the casting of the 7 tested samples (L = 550 mm, b = 150 mm, h = 50 mm), the priority was to cast two similar faces since they would be sollicitated symmetrically and it was necessary to apply the same load on both sides to reach similar displacements with same damage. The UHPC was then poured softly from one side of a vertical formwork to make it flows itself to the other side. The flexural tensile stress versus deflection results are presented in Fig. 7 with a comparison with monotone static loading.

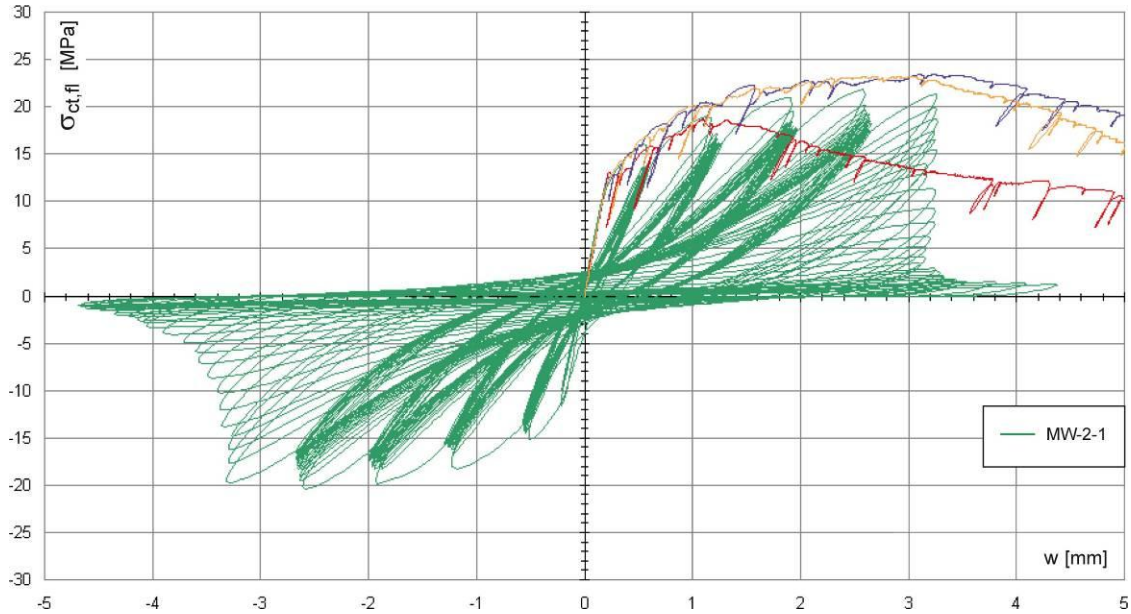

Figure 7: Flexural tensile stress versus deflection for a given specimen subjected to cyclic displacement levels (green) compared to static behaviour (in yellow, red and blue)

After 10 cycles in the linear elastic, first micro-cracking is observed on the second cycle train which corresponds to a change of stiffness (damage) in the hysteretic. The muli-cracking phase would continue with the crack propagating through the width of the sample in direction of the casted side. The stiffness measured on the linear part of the curves between 20% and 80%

flexural tensile stress is gradually decreasing with cyclic trains corresponding to an increasing plasticization with an increasing displacement.

It has been observed also that for a given displacement, the sample would damage at each cycle reaching an asymptotic hysteretic curve (see Fig 7). In Fig 8, the initial response (n°1 in Fig. 8b) and the ultimate (n°2 in Fig. 8b) are presented. The average loss of strength is between 10% - 20% (last cycle excluded). A the end, for large displacements, two localized cracks are observed on each side. Concrete splits along the crack when it re-enters in compression. Fibres “buckling” can even be noticed.

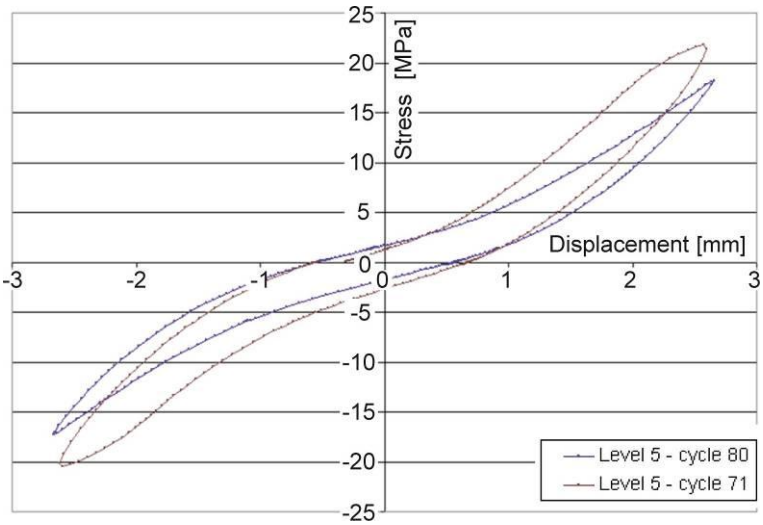

a) Initial and intermediate curves for a given cyclic train

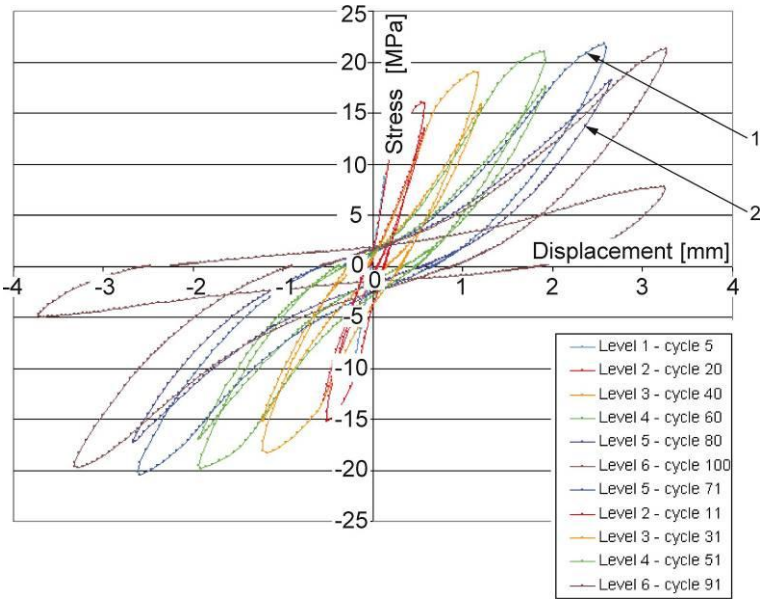

b) First and last cycle curves of the "trains"

Figure 8: Flexural tensile stress versus deflection for a given specimen subjected to cyclic displacement levels (green) compared to static behaviour (in yellow, red and blue).

4 Discussion

The first observation is that, after cracking, for a given displacement, a loss of strength that is limited to 20% is observed. The intermediate curves converge to an asymptotic curve.

Second observation, the initial curve in Fig. 8a corresponding to the opening of the crack and the intermediate curves have a different shape, with a remaining hysteretic area which is lower. The energy dissipation in initial cycles of each train combined cracking and other phenomenon

as matrix fibre friction, thermal dissipation etc. In intermediate cycles, the crack is already opened. It could be then possible to extract the energy dissipation provided by the material after cracking energy dissipation. A “post cracking viscous energy dissipation” can be introduced.

A third observation is that a “ductility” remains in reversed cyclic loading. An energetic approach from Chopra based on an elasto plastic model is used to define a “pseudo ductility factor” (see Fig. 9). On that geometry, an average remaining “pseudo ductility factor” equal to 6 is observerd for reversed cyclic loading compared to a “pseudo ductility factor” equal to 8 for the corresponding monotone loading. The material ductility in cyclic loading still exists after cracking but has carefully to be lowered by a factor 0,75.

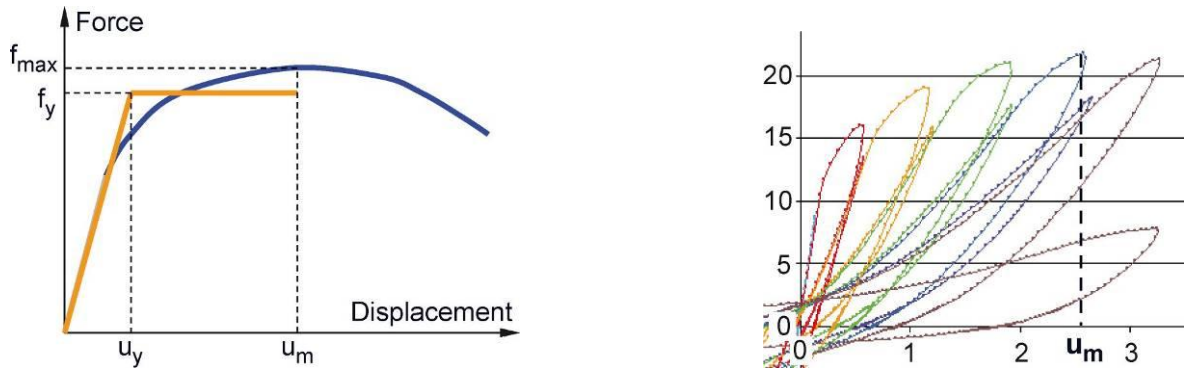

a) Elastoplastic approach for building “pseudo ductility factor” b) Application on reversed cyclic curves

Figure 9: Definition of a pseudo ductility factor.

Last, it has been tempted to plot “Stiffness” versus “Pseudo Ductility factor” (see Fig. 10). A correlation close to a hyperbolic law can be established. This simple relation could be helpful in calibrating a numerical material model in term of energy (trough ductility) and stiffness in future research combining UHPC and reinforcements.

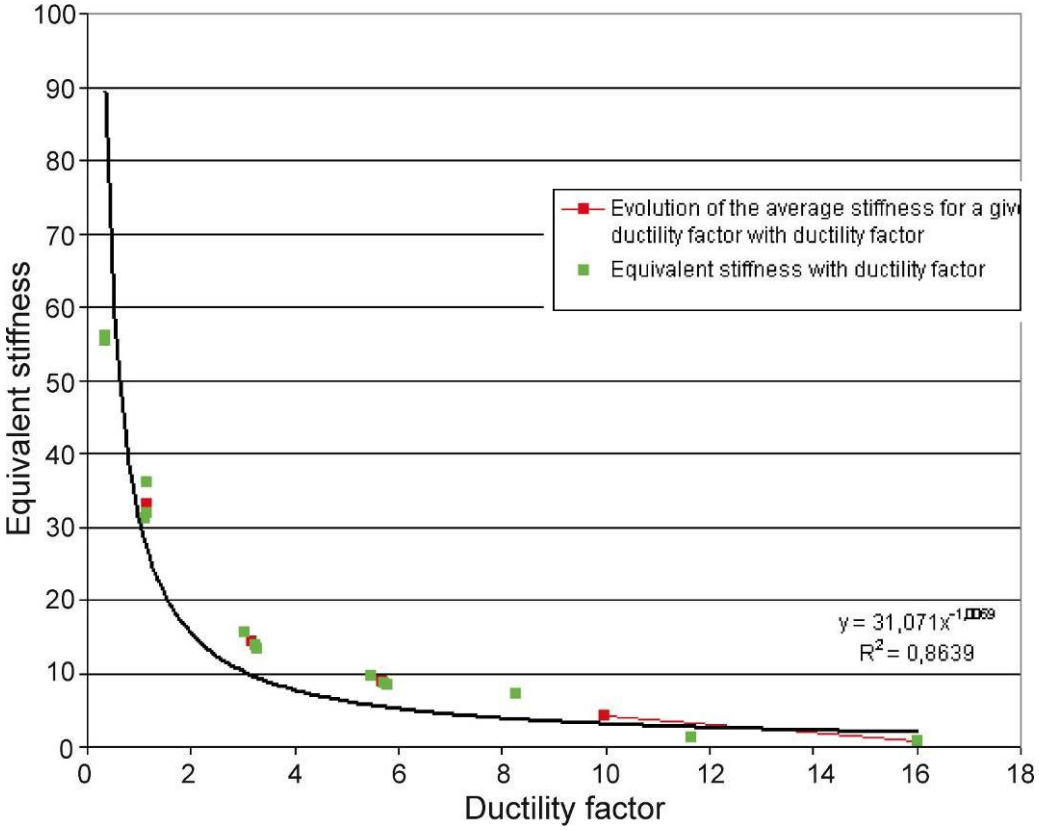

Figure 10: Stiffness versus ductility factor following a hyperbolic law.

In conclusion of this part, it has been observed, through those symetric reversed cyclic testings, on 50 mm plates that:

- Flexural strength in the hardening phase remains with a convergent and limited loss of strength of around 20% at a same level of imposed deformation (for the specimen geometry tested);
- Energy dissipation could be split with this testing between “cracking energy” and a “post cracking viscous energy dissipation”;
- A pseudo ductility factor can be introduced with a decreased value in case of reversed and cyclic loading compared to monotone static loading;
- A correlation between “stiffness” and “pseudo ductility factor” can be made with an hyperbolic law which could be helpful in numerical analysis.

5 Conclusions

Reversed cyclic loadings results were presented in this study. In phase 1 it has been shown that the material was able to endure reversed cyclic loading at a constant load corresponding to 70% of the flexural strength for around 250 cycles. In a design for cycling and reversed cycling loading the flexural tensile stresses can be utilized up to 2-times the elastic limit respectively 70 % of the flexural tensile strength.

A limit of the study in phase 1, was that the two faces were not sollicitated symmetrically like in case of seismic solicitations. A second experimental approach that consists in 4 points bending reversed cycle trains was developed in phase 2 which allowed us to test the deformation capacity of the material by proceeding with displacement steps for a given plate geometry.

A “pseudo ductility factor” was introduced for Ductal samples, which should apply with no consideration of the number of cycles to be applied. A ductility factor decreased by 25%, in average, compared to the one in monotone loading was observed with a limited loss of strength of around 20%. This has to be investigated for different geometries. One should pay attention that after crack localization, the stiffness is decreasing quickly. Before localization an hyperbolic law is proposed to link “stiffness” and “pseudo ductility factor”. Finally the study of samples’ energy dissipation shows us that, during the hardening phase, a large energy is being dissipated through cracking but also through friction and viscosity phenomenon as a “post-cracking viscous energy dissipation”

The following step corresponding to that observation, would be to evaluate , with the same protocol, the energy dissipation of a reinforced UHPC elements to asses the energy dissipation that could be provided by the fibre content. This could open the way to dedicated fibre content, UHPC formulation and reinforcement for critical structural details like plastic hinges in seimic design.

References

[1] Reineck, K.-H.; Lichtenfels, A.; Greiner, S.; (2004): Hochfester und ultrahochfester Beton für Heißwasser-Wärmespeicher. Beton Werk International 7 (2004), H. 2, April, 66 - 80

[2] Chopra, A K; (2007). *Dynamics of structures*. New Jersey : Pearson Prentice Hall, 2007, 876 p

[3] Frettlöhr, B; Reineck, K.-H. (2009). Versuche zum Maßstabseinfluss bei kombinierter Beanspruchung aus Biegung und Längskraft von dünnen Bauteilen aus ultrahochfestem Faserfeinkornbeton. (Tests on the size effect of thin members out of Ultra-High-Performance fibre reinforced concrete subjected to combined bending and axial forces). Abschlussbericht zum Forschungsvorhaben RE 813/6-1 der Deutschen Forschungsgemeinschaft (DFG). Universität Stuttgart, Institut für Leichtbau Entwerfen und Konstruieren (ILEK). September 2009

Flexural Model of Doubly Reinforced Concrete Beams Using Ultra High Performance Fiber Reinforced Concrete

Chuchai Sujivorakul
Dept. of Civil Technology Education, King Mongkut's University of Tech. Thonburi, Thailand

This paper presented a flexural model to predict the relationship between moment and curvature of doubly reinforced concrete beams using ultra high performance fiber reinforced concrete (UHPFRC).The model was developed from linear strain compatibility, stress-strain relationship of UHPFRC in compression and tension, and equilibrium of forces. Muli-linear relationship was assumed in both ascending and descending parts of the stress-strain relationship of UHPFRC under Tension. Some parametric studies also presented in this paper, such as effect of different volume fractions of fibers (V_f), effect of different positive reinforcement ratios (ρ_s), and comparison between the use of UHPFRC and ordinary performance fiber reinforced concrete (OPFRC). The results from this model showed that the use of UHPFRC in doubly reinforced concrete beams led to a significant increase in rigidity and nominal moment resistance of beams.

Keywords: reinforced concrete beams, ultra high performance concrete, UHPFRC

1 Introduction

The addition of discontinuous fibers to concrete, resulting in fiber reinforced concrete (FRC), enhances the ductility and the tensile strength (post-cracking strength) of concrete due to the fibers bridging the cracks through bond between fibers and concrete. The ductility and the post-cracking strength of FRC is dependent on volume fraction of fiber, length of fiber, tensile strength of fiber, and compressive strength of concrete [Oluokun and Malak (1999), Sujivorakul and Naaman (2003)]. It is currently reported that the use of high-strength deformed steel fibers (hooked or twisted steel fibers with tensile strength of 2800 MPa) at volume fraction of 1.5%-2.0% with ultra high performance concrete (UHPC) with compressive strength of 150-200 MPa could lead to ultra high performance fiber reinforced concrete (UHPFRC), which shows the strain hardening and multiple cracking behavior [Frettlöhr et al. (2011), Wille et al. (2011), Kim et al. (2011), and Park et al. (2012)]. They reported good tensile performance of UHPFRC with strain capacity about 0.5% and the post-cracking strength up to 18 MPa.

Reinforced concrete (RC) is a type of composite materials, which are the most widely used in building structures and infrastructures. It is the combination of steel reinforcing bars and concrete, because concrete is good under compression, while steel reinforcing bars is good under tension. RC beam is the structural member used in carrying moment and shear. It is generally known that the nominal moment resistance of RC beam is mainly dependent on the amount of positive reinforcing bars, while an increase in compressive strength of concrete enhances slightly nominal moment resistance. Thus, the only use of ultra high strength concrete in RC beams does not seem to improve their flexural properties. This paper presents the flexural behavior of doubly reinforced concrete beams using UHPFRC through the analytical model developed in this study, it is showed a significant improvement in flexural strength and behavior of RC beams when UHPFRC is used instead of ordinary performance concrete (OPC) and UHPC.

2 Objective and Research Significance

The main objective of this research is to develop an analytical model for predicting resisting moment and curvature of doubly reinforced concrete beams using ultra high performance fiber

reinforced concrete. The model is based on strain compatibility and equilibrium of forces over the cross section of beams. This research also investigates some parameters such as volume fraction of fibers and positive reinforcement ratio on the flexural performance of RC beam. This model would help structural engineers to predict the nominal resistance of flexural RC members as well as their behavior when UHPFRC is used.

3 Flexural Model of Doubly RC Beam Using UHFRC

Basic Concept and Assumptions

The flexural model of doubly reinforced concrete beams using UHPFRC developed here is based on the equilibrium of forces obtained from strain compatibility. The model is based on the following assumptions.

1. The stress-strain relationship of UHFRC in compression is assumed to be a parabola relationship in ascending part and a linear relationship in descending part (Figure 1(a)). Multi-linear relationship is assumed in ascending and descending parts of the stress-strain relationship of UHPFRC in tension (Figure 1(a)).
2. When moment is applied to a reinforced concrete beam, it is assumed that plane section of the beam remains plane, and the strain throughout the cross section of the beam is linearly from the neutral axis (N.A.) as shown in Figure 2(b).
3. Prefect bonding between UHPFRC and steel reinforcing bars is assumed.
4. The stress-strain relationship of reinforcing bars is linear equal to the elastic modulus of steel, until the steel is yielding. After that the relationship becomes a constant equal to the yield strength of steel.
5. Pure concrete is not able to carry load in tension, while UHPFRC is able to carry load in tension and its ability is dependent on the type of fibers, volume fraction of fibers and compressive strength of concrete.

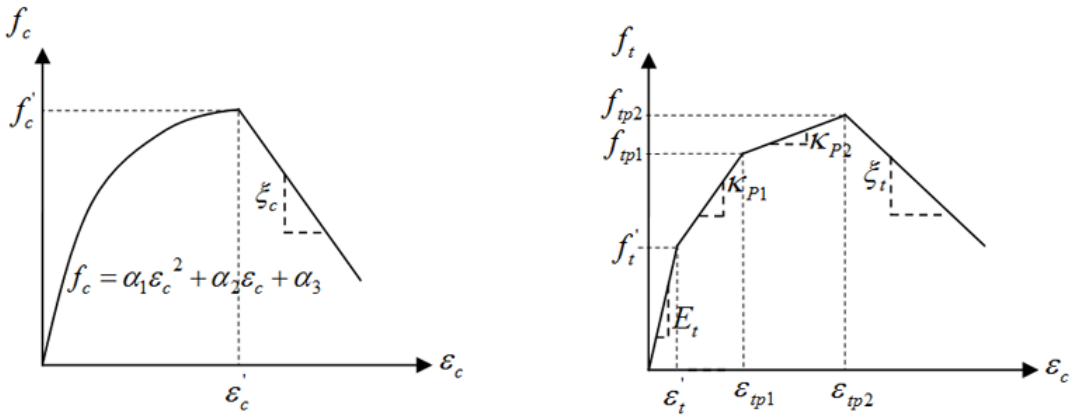

(a) Stress-Strain Relationship in Compression (b) Stress-Strain Relationship in Tension

Figure 1: Assumed Stress-Strain Relationship of UHPFRC under Compression and Tension

Definition of Symbols

A_s, A_s' = cross sectional area of positive and negative steel reinforcing bars

b, h = the size of beam section

d, d' = effective depth of bottom and top steel reinforcing bars

E_s = elastic modulus of bottom and top steel reinforcing bars

E_t = elastic modulus of UHPFRC in tension

$f_c^{'}, \varepsilon_c^{'}$ = compressive strength of UHPFRC and corresponding strain

$f_s, f_s^{'}$ = actual tensile stress of positive and negative steel reinforcing bars

$f_t^{'}$ = tensile strength of UHPFRC at first crack

f_y = yield strength of steel reinforcing bars

$f_t^{'}, \varepsilon_t^{'}$ = tensile stress and strain of UHPFRC at bottom surface of beam

$f_{tp1}, \varepsilon_{tp1}$ = tensile strength of UHPFRC at post crack 1 and corresponding strain

$f_{tp2}, \varepsilon_{tp2}$ = tensile strength of UHPFRC at post crack 2 and corresponding strain

ε_c = compressive strain of UHPFRC at top surface of beam

κ_{p1}, κ_{p2} = ascending modulus of UHPFRC in tension after first crack

ξ_c = descending modulus of UHPFRC under compression

ξ_t = descending modulus of UHPFRC under tension

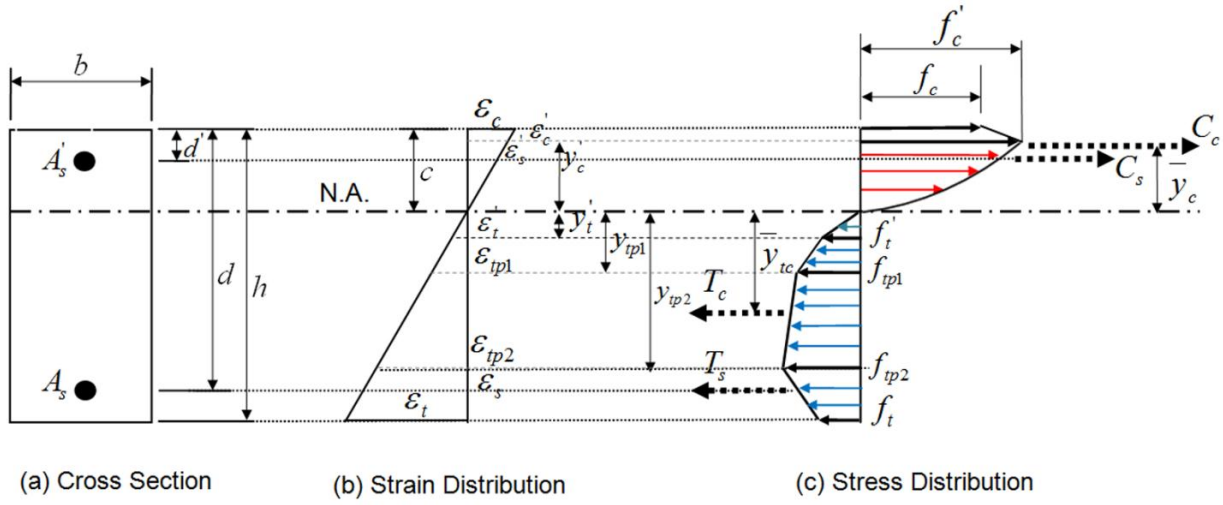

Figure 2: Strain and Stress Distribution throughout the Section of Beam using UHPFRC

Analytical Formulation

From the parabola relationship in ascending part of UHPFRC under compression (Fig. 1a) when $\varepsilon_c \le \varepsilon_c^{'}$, the following relationship can be expressed as follows:

$$f_c = \alpha_1 \varepsilon_c^{\ 2} + \alpha_2 \varepsilon_c + \alpha_3 \tag{1}$$

Find the constants α_1, α_2 and α_3 from 3 boundary conditions: i.e. (a) $f_c = 0, \varepsilon_c = 0$; (b) $f_c = f_c^{'}, \varepsilon_c = \varepsilon_c^{'}$; (c) $\frac{df_c}{d\varepsilon_c} = 0, \varepsilon_c = \varepsilon_c^{'}$. Thus, it leads to

$$\alpha_1 = -\frac{f_c^{'}}{\left(\varepsilon_c^{'}\right)^2}; \alpha_2 = \frac{2 f_c^{'}}{\varepsilon_c^{'}}; \text{and } \alpha_3 = 0 \tag{2}$$

Substituting Eq. (2) into Eq. (1), we will obtain

$$f_c = -\left(\frac{f_c^{'}}{\left(\varepsilon_c^{'}\right)^2}\right)\varepsilon_c^2 + \left(\frac{2 f_c^{'}}{\varepsilon_c^{'}}\right)\varepsilon_c \qquad \text{when} \quad \varepsilon_c \le \varepsilon_c^{'} \tag{3}$$

The descending part of UHPFRC under compression can be expressed as follows:

$$f_c = f_c^{'} + \xi_c\left(\varepsilon_c - \varepsilon_c^{'}\right) \qquad \text{when} \quad \varepsilon_c > \varepsilon_c^{'} \tag{4}$$

It is noted that ξ_c has a negative value. Tensile stresses in the reinforcing bars can be obtained from stress-strain relationship as follows:

$$f_s = E_s\varepsilon_s \le f_y \tag{5}$$

$$f_s^{'} = E_s\varepsilon_s^{'} \le f_y \tag{6}$$

where $\varepsilon_s = \frac{\varepsilon_c}{c}(d-c)$ and $\varepsilon_s^{'} = \varepsilon_c\left(\frac{c-d^{'}}{c}\right)$ (7)

The tensile stress calculated in Eqs. (5), (6) and (7) must not be higher than the yield strength of steel, f_y .Two equilibrium equations at any section of beam (Figure 2(b)) are:

$$\sum F_x = 0 \quad \text{or} \quad C_c + C_s = T_s + T_c \tag{8}$$

$$\sum M = 0 \quad \text{or} \quad M = T_s\left(d-c+\bar{y}_c\right)+T_c\left(\bar{y}_c+\bar{y}_{tc}\right)-C_s\left(\bar{y}_c-c+d^{'}\right) \tag{9}$$

The correct value of c obtained by trial and error in Eq. (8), and moment resistance at any ε_c can be calculated from Eq. (9). The value of C_c, C_s, T_s, T_c and $\bar{y}_c, \bar{y}_{tc}$ can be calculated as follows:

(i) In case of $\varepsilon_c \le \varepsilon_c^{'}$

$$C_c = \frac{2}{3}f_c(cb);\ C_s = A_s^{'}f_s^{'};\ \bar{y}_c = \frac{5c}{8} \tag{10a,b,c}$$

(ii) In case of $\varepsilon_c > \varepsilon_c^{'}$

$$C_c = \frac{2}{3}y_c^{'}f_c^{'}b+\left(\frac{f_c+f_c^{'}}{2}\right)\left(c-y_c^{'}\right)b;\ C_s = A_s^{'}f_s^{'} \tag{11a,b,c}$$

$$\bar{y}_c = \frac{\left(\frac{2}{3}f_c^{'}y_c^{'}\right)\left(\frac{5y_c^{'}}{8}\right)+\left(f_c\left(c-y_c^{'}\right)\right)\left(y_c^{'}+\left(\frac{c-y_c^{'}}{2}\right)\right)+\left(\frac{1}{2}\left(f_c^{'}-f_c\right)\left(c-y_c^{'}\right)\right)\left(y_c^{'}+\left(\frac{c-y_c^{'}}{3}\right)\right)}{\frac{2}{3}y_c^{'}f_c^{'}+\left(\frac{f_c+f_c^{'}}{2}\right)\left(c-y_c^{'}\right)}$$

where $y_c^{'} = \frac{\varepsilon_c^{'}c}{\varepsilon_c}$

(iii) In case of $\varepsilon_t \le \varepsilon_t^{'}$

$$\varepsilon_t = \frac{\varepsilon_c}{c}(h-c) \tag{12}$$

$$T_c = \frac{1}{2}f_t(h-c)b;\ T_s = A_s f_s;\ \bar{y}_{tc} = \frac{2}{3}(h-c) \tag{13a,b,c}$$

where $f_t = E_t\varepsilon_t$

(iv) In case of $\varepsilon_t^{'} < \varepsilon_t \le \varepsilon_{tp1}$

$$T_c = \frac{1}{2}f_t^{'}y_t^{'}b+\left(\frac{f_t^{'}+f_t}{2}\right)\left(\left(h-c-y_t^{'}\right)b\right);\ T_s = A_s f_s \tag{14a,b,c}$$

$$\bar{y}_{tc} = \frac{\left(\frac{1}{2}f_t^{'}y_t^{'}\right)\left(\frac{2}{3}y_t^{'}\right)+\left(f_t^{'}\left(h-c-y_t^{'}\right)\right)\left(\frac{h-c-y_t^{'}}{2}+y_t^{'}\right)+\left(\frac{1}{2}\left(f_t-f_t^{'}\right)\left(h-c-y_t^{'}\right)\right)\left(\left(\frac{2}{3}(h-c-y_t^{'})\right)+y_t^{'}\right)}{\frac{1}{2}f_t^{'}y_t^{'}+\left(\frac{f_t^{'}+f_t}{2}\right)\left(h-c-y_t^{'}\right)}$$

where ε_t is expressed in Eq. (12), $y_t^{'} = \frac{c\varepsilon_t^{'}}{\varepsilon_c}$, and $f_t = f_t^{'}+\kappa_{p1}\left(\varepsilon_t-\varepsilon_t^{'}\right)$

(v) In case of $\varepsilon_{tp1} < \varepsilon_t \le \varepsilon_{tp2}$

$$T_c = \frac{1}{2} f_t^{'} y_t^{'} b + \left(\frac{f_t^{'} + f_{tp1}}{2} \right) \left(\left(y_{tp1} - y_t^{'} \right) b \right) + \left(\frac{f_{tp1} + f_t}{2} \right) \left(\left(h - c - y_{tp1} \right) b \right); \quad T_s = A_s f_s$$

(15a,b,c)

$$\bar{y}_{tc} = \frac{\left(\frac{1}{2} f_t^{'} y_t^{'} \right) \left(\frac{2}{3} y_t^{'} \right) + \left(f_t^{'} \left(y_{tp1} - y_t^{'} \right) \right) \left(\frac{y_{tp1} - y_t^{'}}{2} + y_t^{'} \right) + \left(\frac{1}{2} \left(f_{tp1} - f_t^{'} \right) \left(y_{tp1} - y_t^{'} \right) \right) \left(\left(\frac{2}{3} \left(y_{tp1} - y_t^{'} \right) \right) + y_t^{'} \right)}{+ \left(f_{tp1} \left(h - c - y_{tp1} \right) \right) \left(\frac{h - c - y_{tp1}}{2} + y_{tp1} \right) + \left(\frac{1}{2} \left(f_t - f_{tp1} \right) \left(h - c - y_{tp1} \right) \right) \left(\left(\frac{2}{3} \left(h - c - y_{tp1} \right) \right) + y_{tp1} \right)}$$
$$\frac{}{\frac{1}{2} f_t^{'} y_t^{'} + \left(\frac{f_t^{'} + f_{tp1}}{2} \right) \left(y_{tp1} - y_t^{'} \right) + \left(\frac{f_{tp1} + f_t}{2} \right) \left(h - c - y_{tp1} \right)}$$

where ε_t is expressed in Eq. (12), $y_t^{'} = \frac{c \varepsilon_t^{'}}{\varepsilon_c}$, $y_{tp1} = \frac{c \varepsilon_{tp1}}{\varepsilon_c}$, and $f_t = f_{tp1} + \kappa_{p2} \left(\varepsilon_t - \varepsilon_{tp1} \right)$

(vi) In case of $\varepsilon_t > \varepsilon_{tp2}$

$$T_c = \left(\frac{1}{2} f_t^{'} y_t^{'} b \right) + \left(\frac{f_t^{'} + f_{tp1}}{2} \right) \left(\left(y_{tp1} - y_t^{'} \right) b \right) + \left(\left(\frac{f_{tp1} + f_{tp2}}{2} \right) \left(\left(y_{tp2} - y_{tp1} \right) b \right) \right) + + \left(\frac{f_{tp2} + f_t}{2} \right) \left(\left(h - c - y_{tp2} \right) b \right)$$

$$T_s = A_s f_s \qquad \text{(16a,b,c)}$$

$$\bar{y}_{tc} = \frac{\left(\frac{1}{2} f_t^{'} y_t^{'} \right) \left(\frac{2}{3} y_t^{'} \right) + \left(f_t^{'} \left(y_{tp1} - y_t^{'} \right) \right) \left(\frac{y_{tp1} - y_t^{'}}{2} + y_t^{'} \right) + \left(\frac{1}{2} \left(f_{tp1} - f_t^{'} \right) \left(y_{tp1} - y_t^{'} \right) \right) \left(\left(\frac{2}{3} \left(y_{tp1} - y_t^{'} \right) \right) + y_t^{'} \right)}{+ \left(f_{tp1} \left(y_{tp2} - y_{tp1} \right) \right) \left(\frac{y_{tp2} - y_{tp1}}{2} + y_{tp1} \right) + \left(\frac{1}{2} \left(f_{tp2} - f_{tp1} \right) \left(y_{tp2} - y_{tp1} \right) \right) \left(\left(\frac{2}{3} \left(y_{tp2} - y_{tp1} \right) \right) + y_{tp1} \right)}$$
$$\frac{+ \left(f_t \left(h - c - y_{tp2} \right) \right) \left(\frac{h - c - y_{tp2}}{2} + y_{tp2} \right) + \left(\frac{1}{2} \left(f_{tp2} - f_t \right) \left(h - c - y_{tp2} \right) \right) \left(\left(\frac{1}{3} \left(h - c - y_{tp2} \right) \right) + y_{tp2} \right)}{\frac{1}{2} f_t^{'} y_t^{'} + \left(\frac{f_t^{'} + f_{tp1}}{2} \right) \left(y_{tp1} - y_t^{'} \right) + \left(\frac{f_{tp1} + f_{tp2}}{2} \right) \left(y_{tp2} - y_{tp1} \right) + \left(\frac{f_{tp2} + f_t}{2} \right) \left(h - c - y_{tp2} \right)}$$

where ε_t is expressed in Eq. (12), $y_t^{'} = \frac{c \varepsilon_t^{'}}{\varepsilon_c}$, $y_{tp1} = \frac{c \varepsilon_{tp1}}{\varepsilon_c}$, $y_{tp2} = \frac{c \varepsilon_{tp2}}{\varepsilon_c}$ and $f_t = f_{tp2} + \xi_t \left(\varepsilon_t - \varepsilon_{tp2} \right)$

The curvature of beam at any ε_c can be obtained as follows:

$$\theta = \frac{\varepsilon_c}{c} \qquad (17)$$

Fig. 3 summarizes the procedure to obtain the relationship between resisting moment (M) and curvature (θ) of RC beam using UHPFRC.

4 Results and Discussion from Parametric Study

In this parametric study, the size of RC beams is assumed to be 0.2 m x 0.4 m, the effective depth is fixed as d = 0.35 m and d' = 0.05 m, and yield strength and elastic modulus of reinforcing bars are 400 MPa and 200,000 MPa, respectively. Table 1 summarized parameters investigated here, i.e. ρ_s = 0%, 0.5%, 1.0%, and 1.5%; ρ'_s = 0%, and 0.5%, and the compressive strength of UHPFRC is 170 MPa with coefficients under compression and tension as given in Table 1.

Table 1: Parameters and Properties of UHPFRC used in this study

ρ_s [%]	ρ'_s [%]	V_f [%]	Properties of UHPFRC									
			Compression			Tension						
			f'_c [MPa]	ε'_c	ξ_c	f'_t [MPa]	f_{tp1} [MPa]	f_{tp2} [MPa]	ε'_t	ε_{tp1}	ε_{tp2}	ξ_t
0 to 1.5	0 & 0.5	0	170	0.0025	-113333	8	0	0	0.0002	0	0	0
		1			-85000	8	9	10	0.0002	0.0012	0.005	-2000
		1.5			-68000	9	12	14	0.0002	0.0012	0.005	-2800
		2.0			-56667	10	15	18	0.0002	0.0012	0.005	-3600

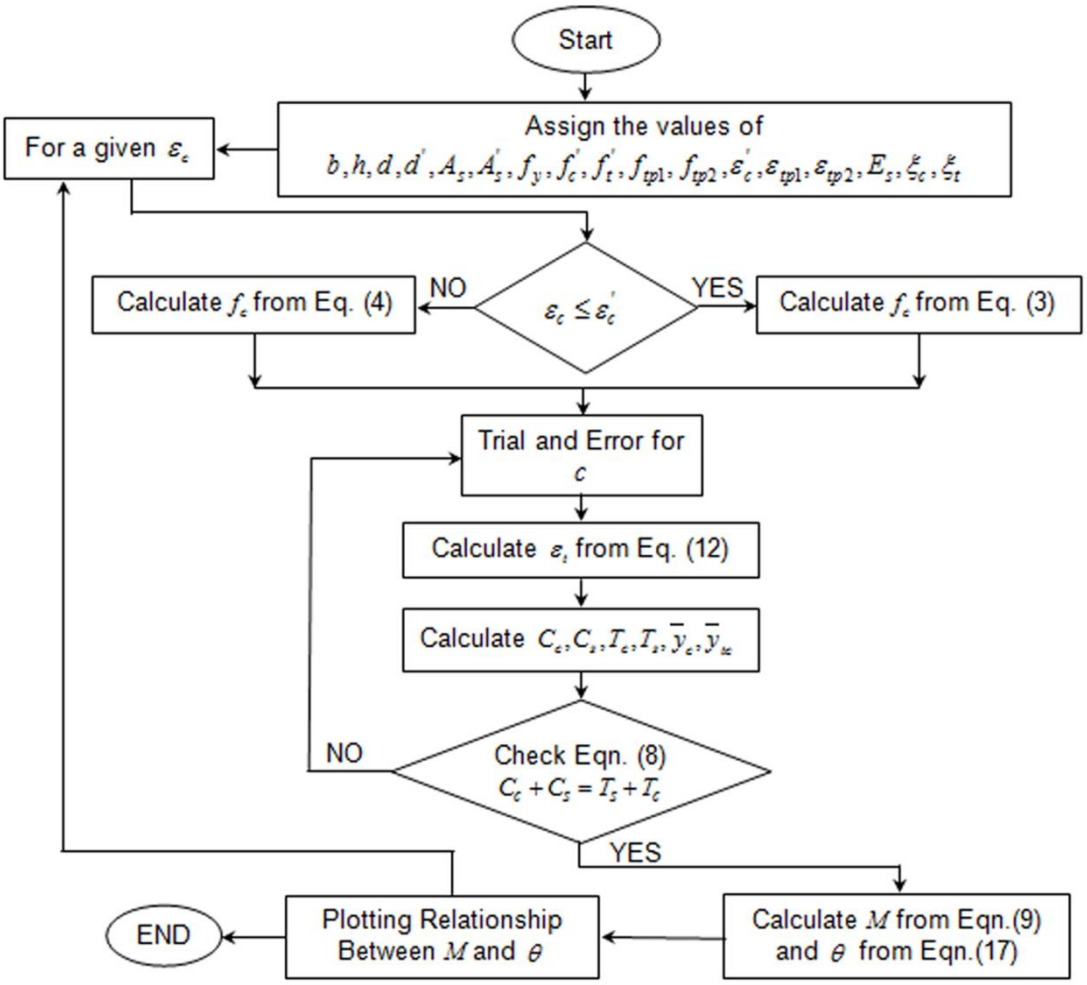

Figure 3: Procedure for Obtaining Moment and Curvature Relationship of RC Beam Using UHPFRC

For performance comparison, some parametric studies of ordinary performance concrete reinforced with steel fibers (OPFRC) and steel reinforcing bars are also investigated and then compared the results with those of UHPFRC. OPC used here has the compressive strength of 50 MPa, and the tensile strength of steel fibers is 1100 MPa.

Fig.4 presents moment and curvature relationship of RC beams using UHPFRC obtained from the model developed in this study. It is observed in Fig.4 (left) that when there is no steel fibers (V_f = 0), the resisting moment of beams depends on the amount of steel reinforcing bars (ρ_s). An increase in the amount of reinforcing bars increases the nominal moment resistance as well as flexural behavior. When the steel fibers are added in UHPC, the nominal moment resistance as well as flexural behavior is significantly improved. Moreover, it is observed that resisting moment and rigidity of RC beams increase with an increase in volume fraction of steel

fibers. Fig. 4 (right) expresses the contribution of resisting moment, which consists of two components: resisting moment from steel reinforcing bars (M_s) and resisting moment from UHPFRC or OPFRC (M_c). It is seen that the contribution due to M_s from UHPFRC is nearly the same as those from OPFRC, while the contribution due to M_c from UHPFRC is significantly higher than those of OPFRC. Thus, the nominal moment resistance, rigidity, and flexural behavior of UHPFRC are much better than those of OPFRC.

Fig. 5 shows the effect of volume fraction of fibers on nominal moment resistance (M_n), the curvature at M_n, the strain ε_c at M_n, and the distance c at M_n of RC beam using UHPFRC. It is clearly seen that an increase in volume fraction of fibers leads to an increase in M_n, and the distance c at M_n due to the contribution of fibers in tension zone of the beam section. As a result, the compression zone (related to the distance c) increases with an increase in volume fraction of fibers. Furthermore, when V_f = 1.0% to 2.0%, the curvature at M_n is slightly increase with an increase in volume fraction of fibers. This means the ductility of RC beams enhances with an increase in volume fraction of fibers. However, without using of steel fibers in UHPC and OPC, the large curvature of beams would be attained due to the yielding behavior of steel reinforcing bars. Finally, it is seen that the maximum strain of concrete at M_n (ε_c) decrease significantly with the use of steel fibers in UHPC or OPC due to the contribution of steel fibers in tension zone as mentioned before. However, when V_f = 1.0% to 2.0%, the strain ε_c at M_n increases slightly with an increase in volume fraction of fibers.

5 Conclusions

In this research, the flexural model of doubly reinforced concrete beams using ultra high performance fiber reinforced concrete is developed to predict the relationship between moment and curvatute of beams. Some parameters such as volume fraction of fibers and positive reinforcement ratio are investigated in order to study the effect of these parameters on the nominal moment resistance and rigidity of beams. The results show that an increase in volume fraction of fiber leads to an increase in nominal moment resistance, rigidity, and flexural behavior of beams due to the contribution of fibers in tension zone of the beam section. This model could be applied for any high performance concrete structures reinforced with steel reinforcing bars and different types of fibers. However, before using this model, it is recommended firstly to determine the stress-strain relationship of the high performance fiber reinforced concrete. Moreover, it should be reminded that the size of the tensile specimen and interaction between UHPFRC and reinforcing during loading affect the strain capacity of UHPFRC, therefore the standard size of tensile specimens and some correction coefficients should be determined in the future research.

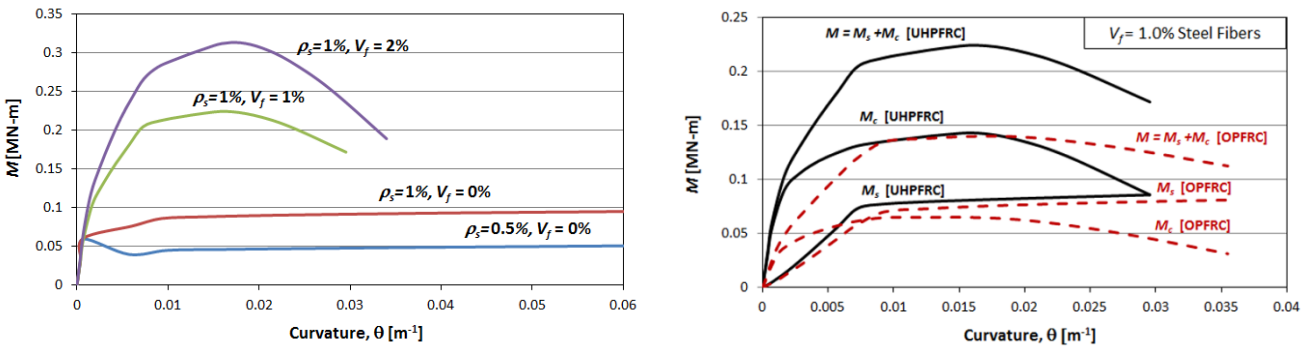

Figure 4: Moment and Curvature Relationship of RC Beam Using UHPFRC: Left Figure - Comparison of Different V_f; Right Figure - Contribution of Resisting Moment from UHPFRC or OPFRC and Reinforcing Bars.

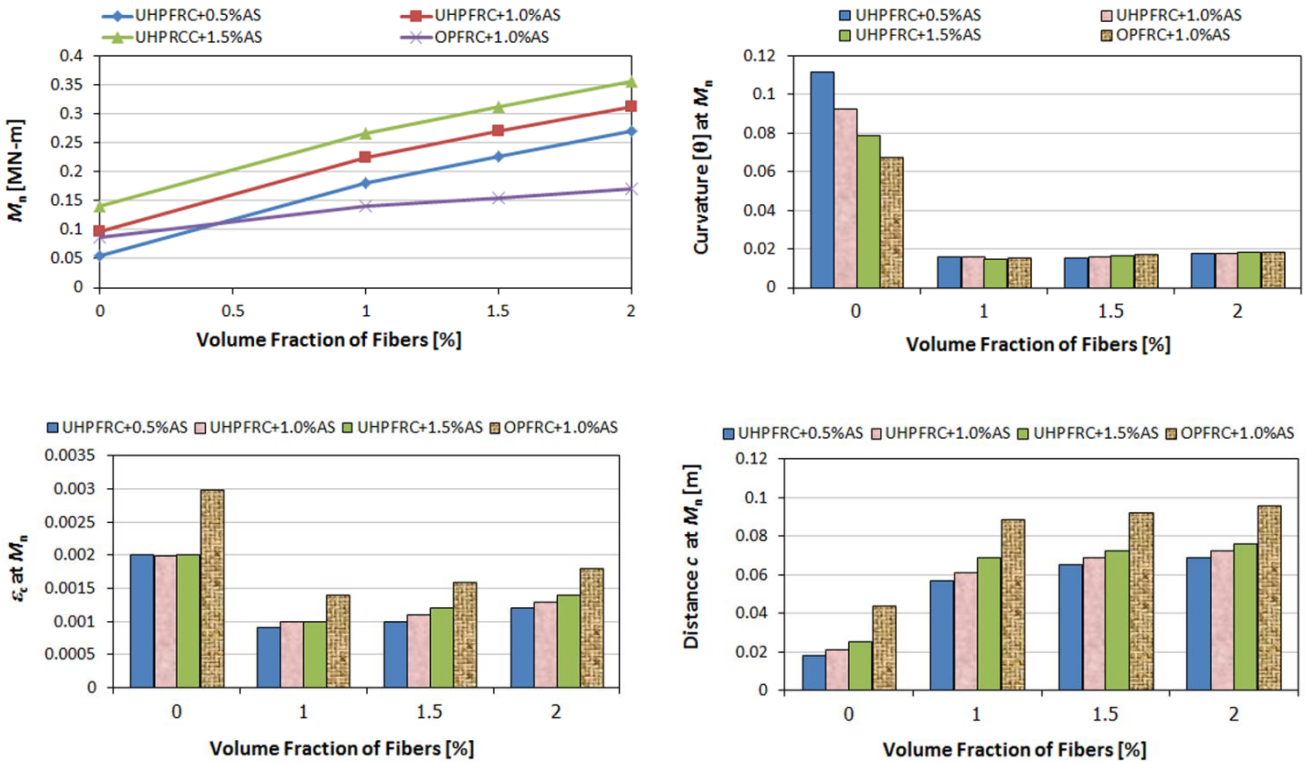

Figure 5: Effect of V_f on M_n, Curvature at M_n, ε_c at M_n, and Distance c at M_n of RC Beam Using UHPFRC.

References

[1] Oluokun, A. F., and Malak, S. A. J., "Some Parametric Investigations of the Tensile Behavior of Slurry Infiltrated Mat Concrete (SIMCON)," *High Performance Fiber Reinforced Cement Composites - HPFRCC 3.* H. W. Reinhardt and A. E. Naaman, Editors, RILEM Pro 6, RILEM Publications S.A.R.L., Cachan, France, pp.271-297, 1999.

[2] Sujivorakul, C. and Naaman, A. E., "Tensile Response of HPFRC Composites Using Twisted Polygonal Steel Fibers," *ACI-Special Publication on Innovations in FRC for Value (SP216-11)*, edited by N. Banthia, M. Criswell, P. Tatnall, and K. Folliard, 2003.

[3] *Frettlöhr, B., Reineck, K. -H., Reinhardt, H. W., "*Size and Shape Effect of UHPFRC Prisms Tested Under Axial Tension and Bending," *High Performance Fiber Reinforced Cement Composites - HPFRCC 6.* G. J. Parra-Montesinos, H. W. Reinhardt and A. E. Naaman, Editors, RILEM Pro 6, RILEM Publications S.A.R.L., Cachan, France, pp.351-358, 2011.

[4] *Wille, K., El-Tawil, S., Naaman, A. E., "*Strain Rate Dependent Tensile Behavior of Ultra-High Performance Fiber Reinforced Concrete," *High Performance Fiber Reinforced Cement Composites - HPFRCC 6.* G. J. Parra-Montesinos, H. W. Reinhardt and A. E. Naaman, Editors, RILEM Pro 6, RILEM Publications S.A.R.L., Cachan, France, pp.367-373, 2011.

[5] Kim, D. J., Wille, K., Naaman A. E., El-Tawil, S., "Composite Properties in the Fresh and Hardened States; 1 Strength Dependent Tensile Behavior of Strain Hardening Fiber Reinforced Concrete," *High Performance Fiber Reinforced Cement Composites - HPFRCC 6.* G. J. Parra-Montesinos, H. W. Reinhardt and A. E. Naaman, Editors, RILEM Pro 6, RILEM Publications S.A.R.L., Cachan, France, pp.2-9, 2011.

[6] Park, H. P., Kim, D. J., Ryu, G. S., and Koh, K. T., "Tensile Behavior of Ultra High Performance Hybrid Fiber Reinforced Concrete," *Cement & Concrete Composites*, 34, pp.172-184, 2012.

Design of Reinforced UHPFRC in Flexure

Simone Stürwald[1], Ekkehard Fehling[2]
1: Institute for Construction and the Environment, HSR Hochschule Rapperswil, Switzerland
2: Institute of Structural Engineering, University of Kassel, Germany

Ultra High Performance Concrete (UHPC) is a smart and innovative material because of its high compressive strength and its durability. In order to carry flexural tension of bending members effectively, fibres are combined with conventional bar reinforcement even for economical reasons. Thereby, the structural and deformation behaviour is affected significantly.
For flexural loading, a mechanical model based on equilibrium and compatibility is proposed. It includes the development of the largest crack width as well as the estimation of the load capacity.
The mechanical model is verified by bending tests of prismatic beams. Theoretical and experimental results demonstrated that positive influences of fibres, rebars and bond stiffness on the cracks in SLS lead to the negative effect of reduced ductility in ULS. However, the tests showed that a small amount of fibres fits well structural and economical requirements.

Keywords: UHPC, UHPFRC, Flexion, Fibres, Rebars, Design

1 Introduction

A family of Ultra High Performance Concretes (UHPC) with a compressive strength of about 180 N/mm² was developed at the University of Kassel. The high compressive strength of the material is attended by an extremely brittle behaviour, which is prevalently improved by adding fibre reinforcement. For economical and ecological reasons, it is recommended to keep the fibre content as low as possible. However, to attain long-span beams under systematical utilisation of the high compressive strength of the UHPC-matrix, additional bar reinforcement in the tensile area is required. This also reduces the effects of scattering in fibre orientation and distribution.

Modelling of the combined action of two reinforcement types has to take into account differences of the structural behaviour to ensure a safe application of such structures. For the design in serviceability and ultimate limit state the equilibrium as well as the compatibility of deformations have to be considered. The reinforcement configuration primarily influences stiffness and cracking process. Bearing capacity and ductility are significantly affected as well.

Within the research project the flexural behaviour of structural members made of Ultra High Performance Concrete (UHPC) having a combined reinforcement of steel fibres and conventional bars was investigated. First, an experimental program was carried out. Material and bond properties were tested to get realistic input values and four-point bending tests on prismatic beams were performed. The aim of this study is to obtain more information about the interaction of both reinforcement types in variable load ranges. Parameters like the beams' height, the fibre content, the type of rebars and the bar reinforcement ratio were varied.

Second, mechanical approaches for the calculation of the structural behaviour in the critical cracked section have been developed. Based on theoretical and experimental results, a simplified model for an efficient design in ultimate limit state was invented.

2 Material and Bond Properties

An experimental programme [6] was carried out to determine the material properties, the tensile behaviour of UHPC with fibre reinforcement and the bond properties of steel bars in UHPC.

Materials

Within the research project a fine aggregate UHPC-mixture named M3Q was used, which was developed at the University of Kassel [1], [2].

Table 1: Properties of UHPC-matrix, range of test results.

UHPC matrix	**Unit**	**M3Q**
compressive strength $f_{c,cyl}$	MPa	180 - 200
tensile strength f_{ct}	MPa	5 - 8
elastic modulus E_c	MPa	45000 - 50000

The UHPC-matrix itself has a low tensile strength in comparison to its compressive strength and a very brittle failure mode. The improvement by smooth micro fibres depends on the fibres' type, content, geometry and orientation. The geometrical parameters (length l_f / diameter d_f in mm) of the applied steel fibres were 20/0.25. The applied fibre dosage was varied (0.0; 0.5 and 1.5 % by volume). Within the test series, conventional rebars BSt 500 and ribbed high strength steel bars St 1375/1570 were used.

Tensile behaviour of UHPFRC

The tensile behaviour of fibre reinforced UHPC was derived from tension tests on notched prisms and presented as a stress crack opening relationship. For a fibre content of 0.5 % by vol., a maximum stress carried by fibres - the fibre efficiency - of σ_{cf0} = 4.0 N/mm² and for 1.5 % by vol. a fibre efficiency of σ_{cf0} = 10.3 N/mm² could be determined experimentally.

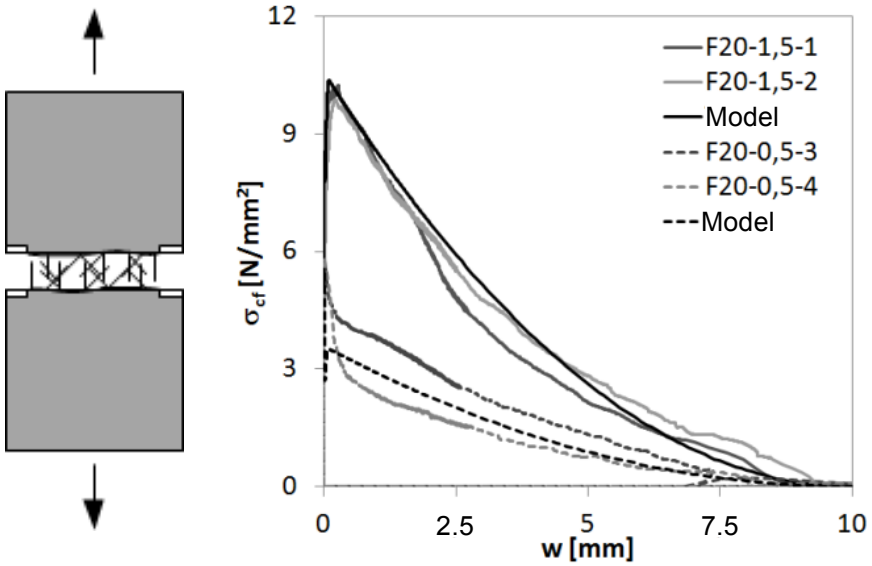

Figure 1: Tensile test on notched prism (left), mean test results and model (right).

Based on the fibre efficiency, the characteristic stress - crack opening relationship can be formulated by the model given by Leutbecher [3].

Bond of rebars

To investigate the bond behaviour at large slips and the influence of the steel stress or strain, pullout tests were carried out. The relative displacement was measured at the unloaded end of the bars.

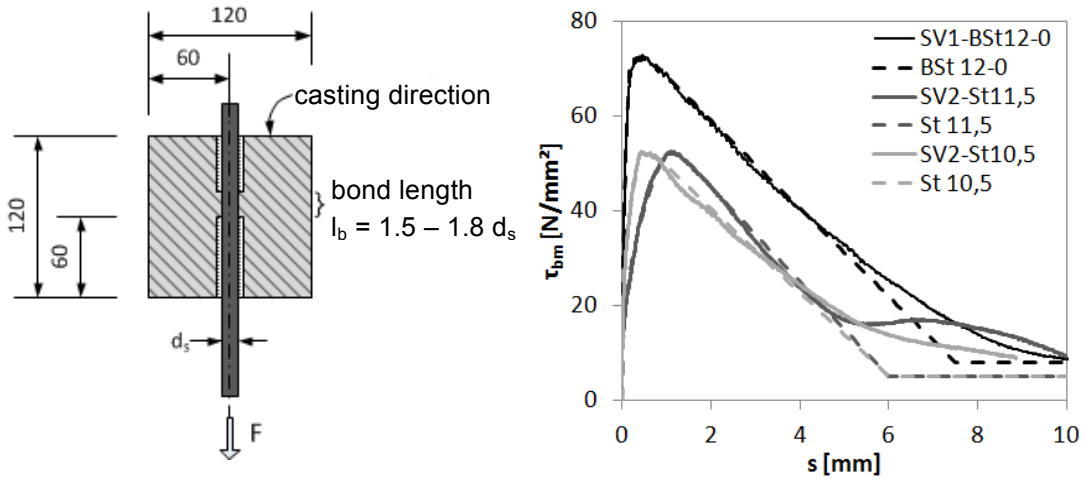

Figure 2: Test setup with specimen (left), mean test results and derived bond law (right).

For rebars BSt 500, d_s = 12 mm, the bond strength (maximum average value along bond length) was $\tau_{b,max}$ = 73 N/mm². Compared to the results of Leutbecher [3] ($\tau_{b,max}$ = 55 N/mm²) and Oesterlee [4] ($\tau_{b,max}$ = 40 N/mm²), a much higher bond strength could be observed because of a higher compressive strength of the concrete. The bond strength of high strength steel bars St 1375/1570 was lower ($\tau_{b,max}$ = 52 N/mm²) due to a smaller relative rib area. The proposed bond law is based on the relationships given in MC 2010 [5].

3 Bending Tests

Test setup and test procedure

The experimental work focused on the investigation of the flexural behaviour of combined reinforced UHPC members subjected to four point bending tests. A total of ten beams were examined. Detailed information for all beams is given in [6]. Below, the results of three beams with different fibre dosages are compared. The beams' geometry and the test setup are shown in principle in Fig. 3.

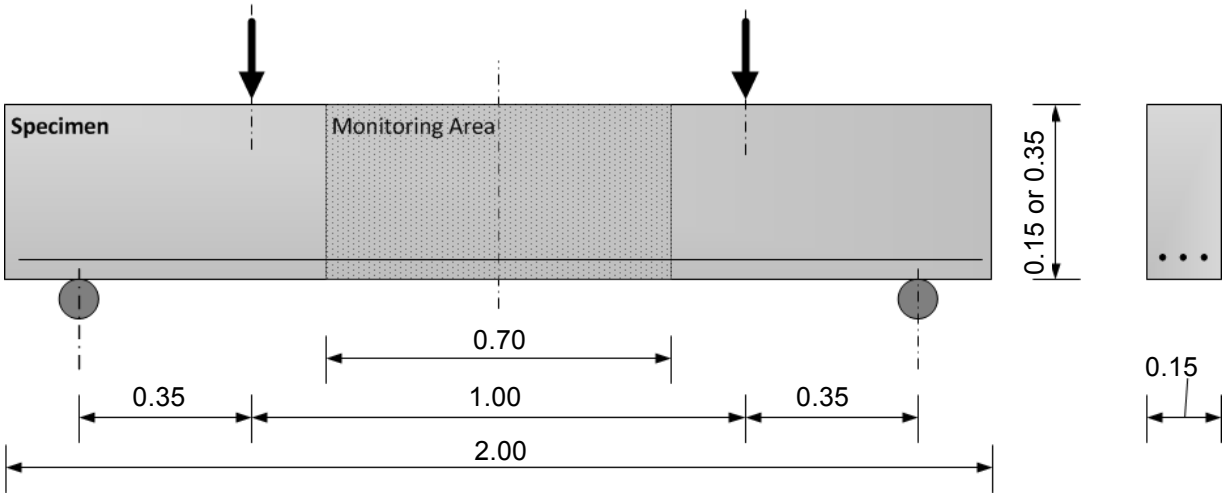

Figure 3: Test setup with specimen, 4 LVDTs and load cell on top (left) and both halves of a specimen after pullout test (right).

The tests were performed deformation controlled. Deflection and rotation angles at the beams' ends were measured continuously by LVDTs. Integral deformations at the top and bottom of specimens were detected over the total length of monitoring area to determine average strains.

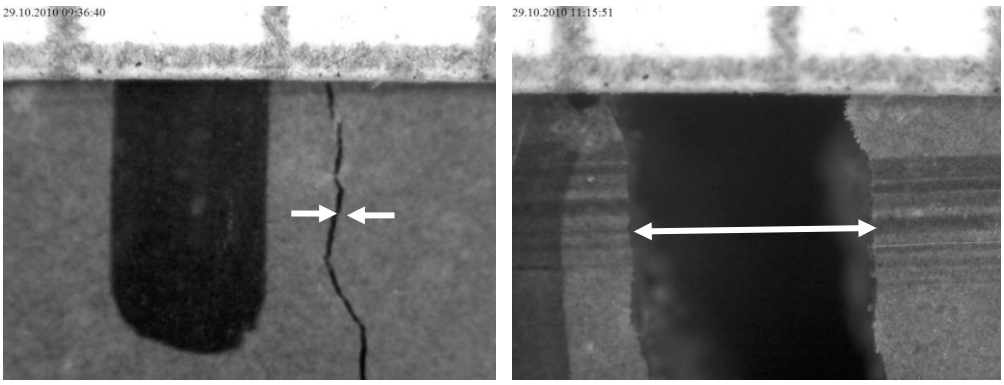

Figure 4: Exemplary pictures of the cracks: 0.04 mm (left) and 1.1 mm (right).

During several stops at certain average strain rates, cracks were marked within the monitoring area the bottom of the beam and pictures of the cracks were taken. After the tests, crack spacings were measured and crack widths were determined by analysing the pictures (see the example pictures of the cracks in Fig. 4).

Test results

The influence of the fibre dosage was very significant. In the following, three beams with different fibre content (0 % by vol., 0.5 % by vol., 1.5 % by vol.) were compared. The beams' height was 35 cm and the ribbed bar reinforcement was 3 Ø 11.5 mm with a type of high strength steel St 1375/1570.

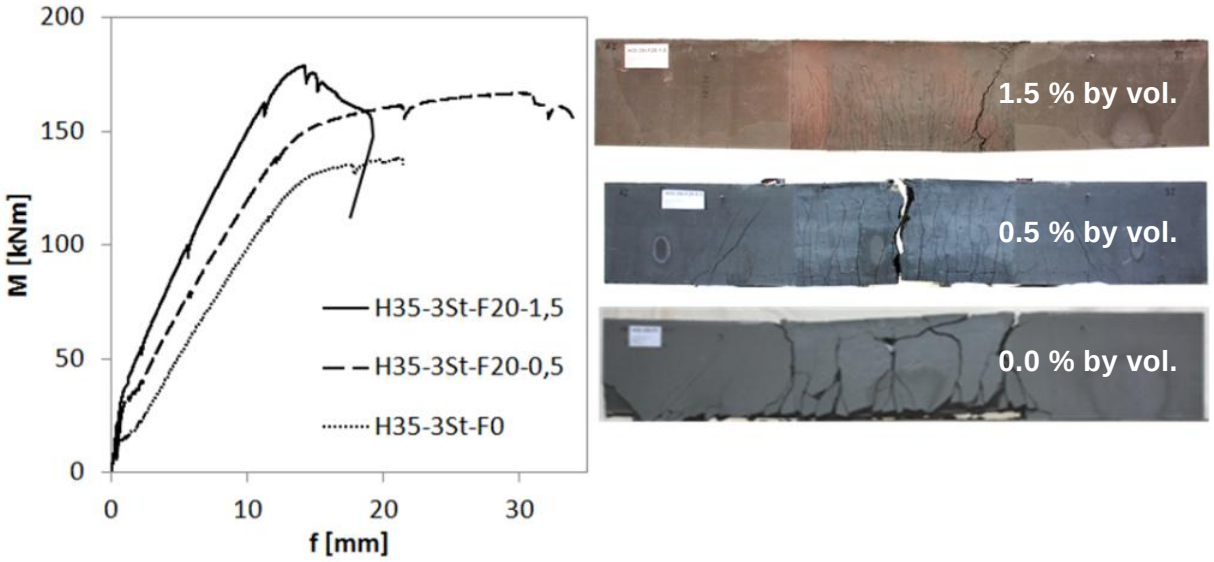

Figure 5: Moment versus mid span deflection (left) and failure pattern (right).

The influence of the fibres on the beams' stiffness, load bearing capacity as well as on the failure pattern is very obvious. The failure of the beam H35-3St-F20-1,5, which had a high fibre dosage, occurred due to localisation of deformation in one crack. Accordingly, its rotation capacity and ductility was reduced.

Beam H35-3St-F0 without fibre reinforcement failed in a brittle manner by spalling of the concrete cover and crushing in the compressive zone. The observed crack spacings and crack widths were significantly higher. Although ductile behaviour in tension could be expected, it was limited by the brittle concrete compression failure.

Beam H35-3St-F20-0,5, with a medium fibre dosage of 0.5 % by vol., failed by rupture of the bar reinforcement. The localisation of deformation in about five cracks within the monitoring area began when the rebars were already in the plastic range. The crack widths were limited

and brittle failure could be avoided. No localisation of deformation in a single crack was observed.

As well known, a higher bar reinforcement ratio increased the stiffness of the test beams in the elastic state of bar reinforcement as well as the load bearing capacity. However, it could also be confirmed that a higher bar reinforcement ratio reduces the beams' rotation capacity if concrete failure in the compression zone of the beam becomes decisive.

During the tests, it was observed, that the beams' compression zone became very small and most of the beams were damaged in the top layers. Due to the very high concrete stress, surface defects like small blisters or pores could lead to premature failure at the top layer.

4 Mechanical Model

Leutbecher [3] has developed a mechanical model to describe the crack development and deformations of tensile members with combined reinforcement in the elastic range of steel bars. Based on this, the model was adopted to flexural loadings and extended to the plastic range of steel bars.

Flexural crack element

The basis of the model is a flexural crack element, which is a beam segment with a length s_r equal to the crack spacing (see Fig. 6).

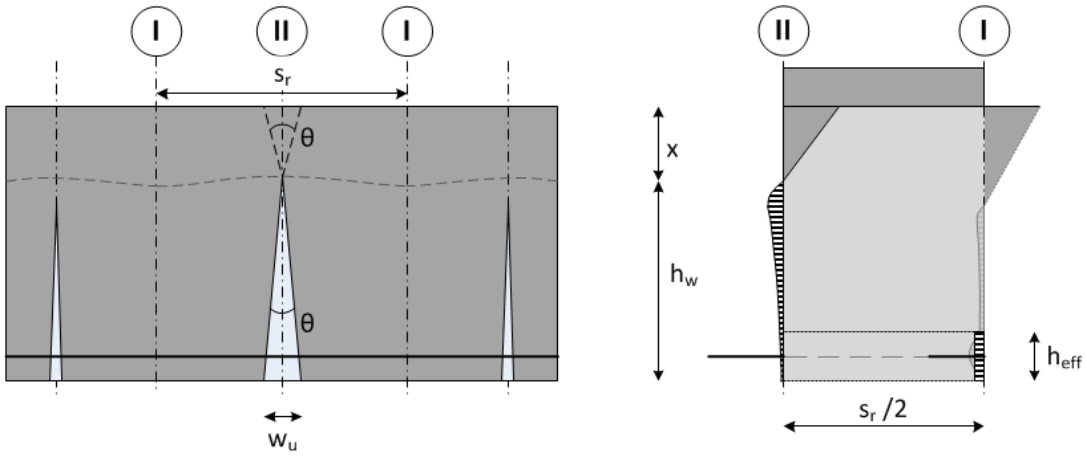

Figure 6: Model of a critical flexural crack element and the assumed stress distribution.

For the calculation of stresses and crack widths, the following assumptions are made. A beam is divided into crack elements which are independent from each other. Within the crack, tensile loads are transferred by steel bars and by fibre reinforcement but not by the UHPC-matrix. The compressive stress-strain relationship of UHPC is assumed to be linear. Crack surfaces as well as the integral flexural crack element remain plain. Tensile stress, transferred by steel fibres, depends on the crack width and follows the determined stress crack opening relationship. Hence, for the calculation, the equilibrium as well as the compatibility have to be considered. The bond behaviour is defined nonlinear according to the determined bond law.

Within the bond length, forces are transmitted from the rebars to the surrounding concrete – the effective tension zone. If the stress in cross section I in the effective tension zone reaches the fracture stress f_{ctf}, a new crack will form.

Effectiveness of the fibre dispersion

The fibre efficiency is a scattering size. The scatter depends on numerous factors such as geometry, casting conditions, compaction method or the consistency of the concrete, which are difficult to quantify. However, the cross section with the lowest fibre efficiency defines the critical

crack with the maximum crack width. There, the bearing capacity is reached. Based on current design codes the characteristic fibre efficiency was estimated as 70 % of the average value.

Maximum crack spacing

The largest possible crack width occurs where the lowest fibre efficiency and the largest crack spacing merge. The largest possible crack spacing is obtained if the tensile stress in the effective tension zone approaches the fracture stress between two cracks.

Within the model, the maximum crack spacing and the moment is calculated for a certain crack width. While increasing the assumed value of crack width stepwise, the critical crack element can be calculated. The maximum bending moment thus correspond to the load capacity of the cross section.

5 Validation of the Models by Experimental Results

The influence of the fibre dosage was very significant. The theoretical and test results of the previously presented three beams are shown.

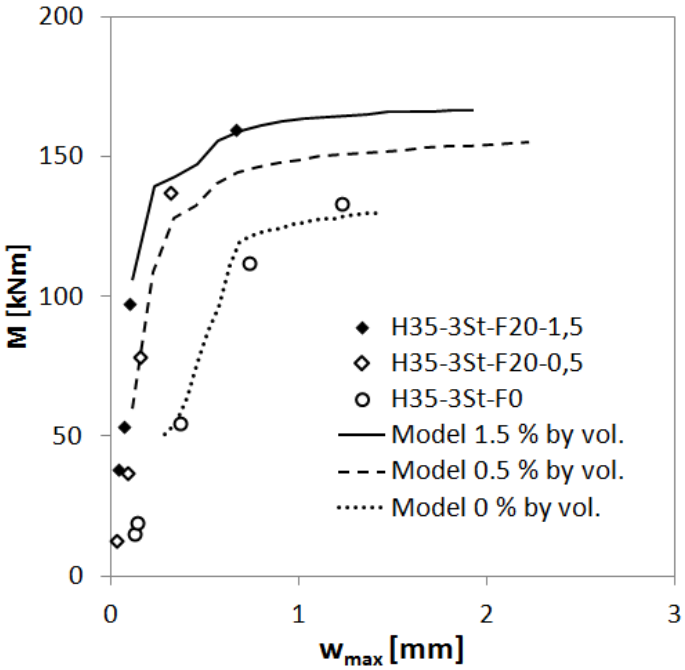

Figure 7: Moment versus maximum crack width of test results and calculation.

Figure 7 presents the measured maximum crack widths of the tests and the results of the model for the critical crack. The comparison demonstrates that the curves are covered well. The maximum difference between measured and calculated crack widths amounts to 4 %. The crack width development of the critical crack can thus be understood well.

6 Simplified Design Model in ULS

For the practical design in ultimate limit state, a simplified approach can be used. Based on the assumptions that the fibre efficiency is reached when the behaviour of rebars gets plastic and that the subsequent softening of the fibre concrete is dominant, the maximum moment can be estimated. Tensile stress transferred by fibres in the cracked cross section is represented by a stress block, which gives the quantity and position of the resultant in this case well. Parameter studies on prismatic beams have shown that the parameters of the stress block can be assumed to k = 0.9 and χ = 0.9. For UHPC, the stress distribution in the compression zone can assumed to be linear even in ULS.

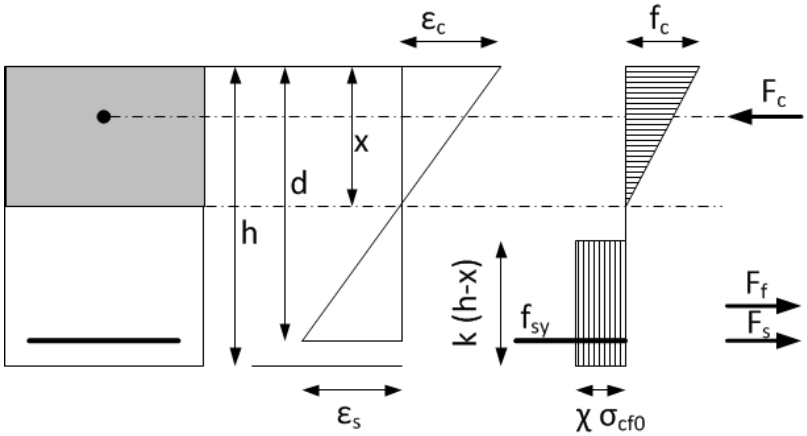

Figure 8: Moment versus mid span deflection (left) mean and failure pattern (right).

For the recalculation of the load capacity of the presented beams, the fibre efficiency in the critical crack is assumed with 70 % of the average value. The results are compared with experimental results in Table 1. The design model shows a good agreement with the experimental results. The maximum deviation of 5 % was observed for beam H35-3St-F20-0,5, because of hardening in the plastic range.

Table 2: This is the table description.

Specimen	$\sigma_{cf0;0,7}$ [N/mm²]	Test max M [kNm]	Model max M [kNm]
H35-3St-0	0	137	140
H35-3St-F20-0,5	2.45	167	158
H35-3St-F20-1,5	6.32	179	183

7 Conclusions

The flexural behaviour of UHPC beams with combined reinforcement was investigated. First the material behaviour of UHPC was determined. The stress-crack opening behaviour of fibre reinforced UHPC could be characterized by tensile tests on notched prisms. Pull out tests of the applied bar reinforcement in UHPC led to a bond law (stress-slip relationship) according to MC 2010 [5]. Bond tests showed very stiff bond behaviour between bar reinforcement and UHPC-matrix.

Flexural tests on beams made of UHPC with combined reinforcement of bars and steel fibres were performed to investigate the development of cracking as well as the load bearing capacity.

Results of the test series demonstrate that additional fibre reinforcement has positive effects to reduce crack widths, crack spacings and to improve the stiffness in SLS as well as to improve the load bearing capacity in ULS. Nevertheless a high fibre dosage limits the rotation capacity because of crack localisation. To avoid this in the plastic range of rebars, the hardening effect of bar reinforcement has to be more dominant in comparison to the softening of fibre reinforcement. Hence, the higher the fibre dosage, the more bar reinforcement is needed to achieve a ductile behaviour.

Decisive for the load capacity is the behaviour of the critical crack, where the fibre efficiency has a minimum and the crack spacing is maximal. For representation of the critical crack, a mechanical model has been formulated. In addition to the equilibrium conditions, the compatibility conditions in the cracked cross section are considered. A comparison with experimental results like measured crack widths and crack spacing's shows good agreement.

The mechanical model allows to estimate the load capacity and the associated maximum crack if the scatter of fibre efficiency was known.

On this basis, a simplified design model was derived, in which it is assumed that the load capacity is reached when the yield strength of bar reinforcement is attained. For small crack widths, the stresses transferred by fibres are represented by a simplified stress block. The comparison with experimental results verifies the approach. For the design of structural elements, a suitable safety concept has to be considered.

8 Acknowledgements

This project was part of the Priority Programme SPP 1182 “Building Sustainable with Ultra-High-Performance Concrete (UHPC)” and supported by the German Research Foundation (DFG). All support is gratefully acknowledged.

References

[1] Fehling, E. et al.: Entwicklung, Dauerhaftigkeit und Berechnung Ultra-Hochfester Betone (UHPC), Forschungsbericht DFG FE 497/1-1“, Structural Materials and Engineering Series, No. 1, Kassel University, 2005.

[2] Stürwald, S.: Bending Behaviour of UHPFRC combined with Rebars, 8th fib PhD Symposium Copenhagen, Denmark, June 2010.

[3] Leutbecher, T.: “Rissbildung und Zugtragverhalten von mit Stabstahl und Fasern bewehrtem ultrahochfesten Beton (UHPC)“, PhD Thesis, University of Kassel, Germany, 2008.

[4] Oesterlee, C.: Tragverhalten von Verbundbauteilen aus bewehrtem UHFB und Stahlbeton, *Beton- und Stahlbeton 104*, Heft 8, pp. 462, 2009.

[5] fib Bulletin 56: Model Code 2010, First complete draft, 2010.

[6] Stürwald, S.: Versuche zum Biegetragverhalten von UHPC mit kombinierter Bewehrung, Forschungsbericht (technical report), Fachgebiet Massivbau, Fachbereich Bauingenieurwesen, Universität Kassel, 2011.

Shear Capacity of UHPC – Beam Tests

Niki Cauberg[1], Julie Piérard[1], Benoit Parmentier[1], Olivier Remy[2]
1: Belgian Building Research Institute, Belgium
2: Vrije Universiteit Brussel, Belgium

Ultra-high-performance concrete (UHPC), a very high performance concrete with usually a compressive strength of 130 N/mm^2 or more, is obtained with a number of mix design modifications compared to HPC. These modifications include, among others, the use of high quantities of cement and superplasticizers and the addition of fillers and microfillers (often silica fume) combined with rather specific granular distributions and sometimes a post-treatment. Altogether, this gives the wanted low porosity and high performance of the concrete, with an influence on all concrete properties compared to HPC or normal strength concrete for which the Eurocode 2 describes material properties and design rules. Research illustrates that UHPC sometimes shows a different material behavior, consequently resulting in the requirement for a case-by-case specification and material check. This paper focuses on a general check of the material behavior and the comparison with Eurocode 2. More specifically, the paper describes the research on the shear capacity of UHPC, which has been tested with a set of 45 beams. The research used three mix designs to cover a broad range of UHPC (dmax from 0.5 mm to 8 mm), without heat curing (f_{cm} between 130 and 180 N/mm^2). UHPC with and without fibres have been used (up to 2 %), and two a/d-ratios have been studied.

Keywords: UHPC, shear, beam

1 Introduction

Problem description

Due to its specific mix design, questions arise about the shear capacity of ultra-high performance. Mainly the absence of coarse aggregates might have a negative influence on the shear capacity. Secondly, the large amounts of cement, fillers and microfillers might have a negative effect as well. On the other hand, the mechanical performance of UHPC, for instance the compressive and tensile strength, might indicate a good behaviour for shear capacity.
Eurocode 2 (EN 1992-1-1:2004, EC2) allows for the calculation of a design strength for shear capacity, and Model Code 2010 gives a proposition to include (steel) fibre reinforcement. This paper presents some empirical results, comparing these calculations and test results on medium scaled beams (2.3 meter length, 0.16 meter height and 0.25 meter width).

Test set-up

A simple test set-up has been used, as can be seen in Figure 1: An isostatic configuration, with a span of 2 meters in between the supports. The detailed beam and longitudinal reinforcement configuration can be found in Figure 3. An important reinforcement ratio was needed to avoid flexural rupture. For some beams, additional shear reinforcement has been placed: stirrups diameter 8 mm, with an interspace of 180 mm. The force has been applied in four loading steps. This allowed for an inspection of the cracks in the middle part of the beams. The analysis of the evolution of these crack width measurements will be studied as a seperate project.

Three parameters have been varied in this study: the a/d-ratio (2 ratios), the fibre reinforcement dosage (4 fibre dosages) and the mix design of the UHPC (3 compositions M1, M2 and M3). The force has been applied with an a/d-ratio of 1.8 and 3, in order to study different types of rupture (compression and shear, as described in literature or reference works, see Figure 2 and [1]). Some details about the mix design and fibre reinforcement are given in the next chapter. For each situation, three beam tests have been performed.

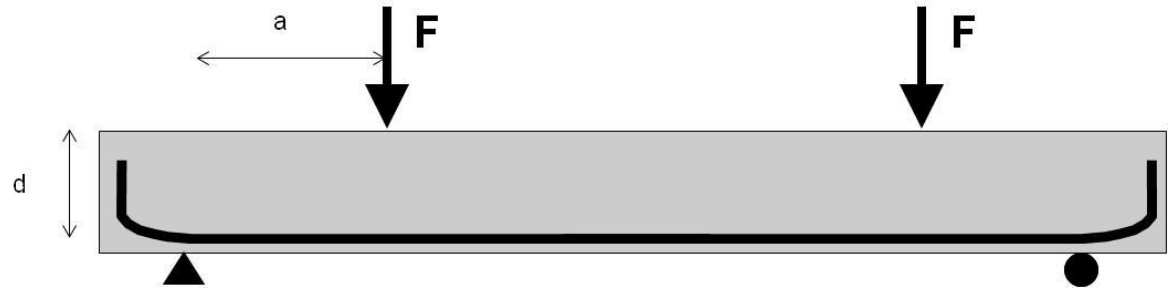

Figure 1: Simple test set-up.

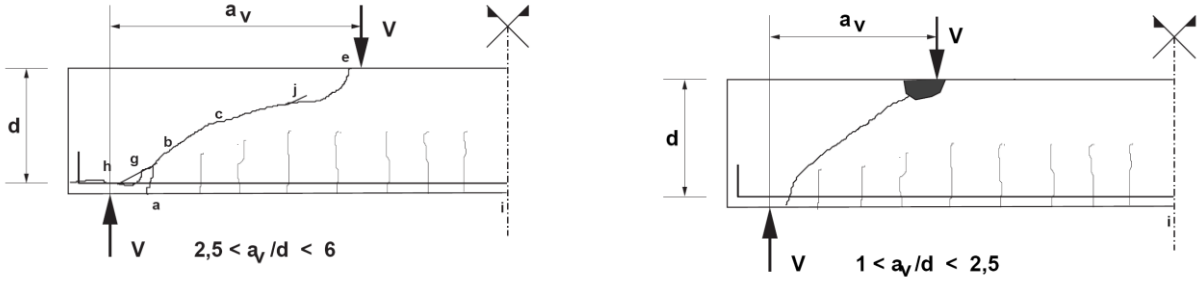

Figure 2: Different situations for shear rupture, according to [1].

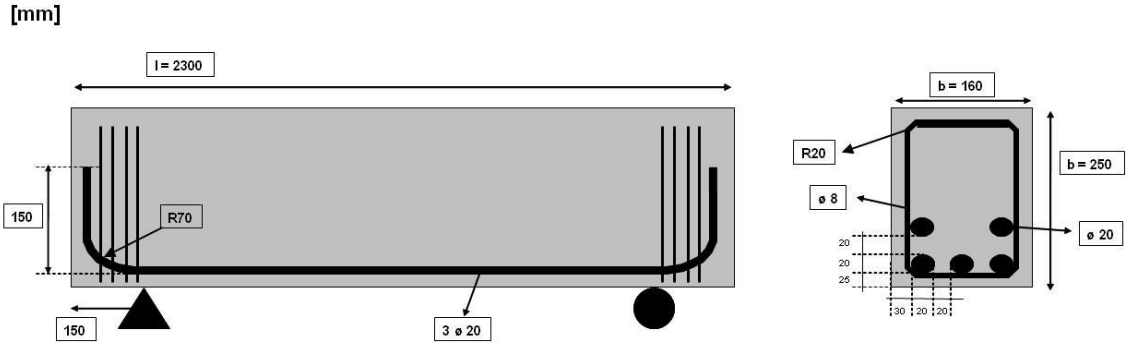

Figure 3: Beam configuration for testing.

Mix design

The used UHPC-types M1, M2 and M3 represent different approaches of UHPC-design, ranging from compositions with larger aggregate size and minimal cement quantity (M1), to reactive powder concrete with large powder quantities and complete removal of coarse aggregates (M3). Table 1 gives the detailed mix compositions and some basic material parameters as tested in this research. Two fibre reinforcement types have been used, at dosage from 0 % to 2 % in volume: only short fibres (6 mm length, Ø 0.16 mm), or a fibre mix (70 % short fibres and 30 % longer fibres 30 mm length and Ø 0.38 mm).

Table 1: Mix design and basic material parameters of the tested UHPC-compositions.

		UHPC compositions		
Component	**Type**	**M1 [kg/m³]**	**M2 [kg/m³]**	**M3 [kg/m³]**
Cement CEM I (C)	42.5 R HSR LA	500	830	777
Quartz powder	d_{av} = 7µm	50	83	211
Quartz sand	0/0.5	786	335	1007
Porphyry	1/4	0	723	0
Basalt	1/3	510	0	0
Basalt	5/8	327	0	0
Silica fume (SF)	powder fraction	100	166	156
Water		150	178	162
Fibres	6 mm and/or 30 mm	(up to 2%)	(up to 2%)	(up to 2%)
Superplasticizer (SP)	polycarboxylate, 30%	15	24	28
Average density [kg/m³]		2498	2392	2393
W/C (SP included)		0.32	0.23	0.23
W/Binder		0.27	0.20	0.19
Basic material parameters (28 days)				
Slumpflow, without fibres [mm]			600 - 800	
Compressive strength (cubes 100 mm side) [N/mm²]		130	160	150
Compressive strength, thermal treatment [N/mm²] *(1)*		145	190 - 210	
Splitting tensile strength [N/mm²]		7.4	8.0	9.9
Tensile strength (from splitting test) [N/mm²]		6.7	7.2	8.9
Uniaxial tensile strength (measured) [N/mm²]		> 6	> 5	> 5
Max. flexural tensile strength, 2% fibres [N/mm²] *(2)*		19.8	25.0	18.5
f_Ftsm / f_Ftum with w = 1.5 mm [N/mm²] *(3)*		8.5 / 5.0	10.3 / 6.7	7.8 / 5.1

(1) Thermal treatment at 90°C, started 48h after casting, during 96h.

(2) 3-point bending test with notch according to EN 14651.

(3) According to Rilem TC 162 TDF or draft fib Model Code 2010.

Shear capacity of fibre reinforced UHPC

Draft Model Code 2010 provisions [2] have been used to predict the shear capacity of fibre reinforced UHPC (equation 1). To simplify the design equations, the contribution of the fibres to the shear resistance is mainly based on the improvement due to pull-out mechanism. The analytical expression for the calculation of the shear capacity is rearranged from the EC2 expression by adding a term $7.5 \cdot f_{Ftuk}/f_{ctk}$ to the longitudinal reinforcement ratio. For this study, safety coefficients have been set to 1, in order to obtain a realistic estimation of the ultimate strength. Furthermore, average values have been used, for instance for the ultimate residual tensile strength and the tensile strength for the concrete matrix, rather than characteristic values.

$$V_{\mathrm{Rd,F}} = \left\{ \frac{0.18}{\gamma_c} \cdot k \cdot \left[100 \cdot \rho_1 \cdot \left(1 + 7.5 \cdot \frac{f_{\mathrm{Ftuk}}}{f_{\mathrm{ctk}}} \right) \cdot f_{\mathrm{ck}} \right]^{1/3} + 0.15 \cdot \sigma_{\mathrm{cp}} \right\} \cdot b_w \cdot d \qquad (1)$$

with:

- γ_C is the partial safety factor for the concrete without fibres (1,5) ;
- k is a factor taking the effect of the depth of the cross-section into account :

  $k = 1 + \sqrt{\frac{200}{d}} \leq 2{,}0$ with d in mm, as defined before;

- ρ_l the longitudinal reinforcement ratio :
  $\rho_l = \frac{A_{sl}}{b_w.d}$
- f_{Ftuk} is the characteristic value of the ultimate flexural residual tensile strength of the fibre reinforced concrete by considering wu=1.5 mm [MPa] ;
- f_{ctk} is the characteristic value of the tensile strength for the concrete matrix [MPa] ;
- σ_{cp} is the average stress acting on the cross-section due to an axial force (loading or prestressing action);
- b_w is the smallest width of the cross-section in the tensile area.

To determine the value of f_{Ftuk} in the above equation, two approaches can be followed to describe the post-peak behaviour of the fibre reinforced concrete. These approaches are based on two distinctive stress-crack opening constitutive laws in tension: the linear elastic model and the rigid-plastic model (see Figure 5).

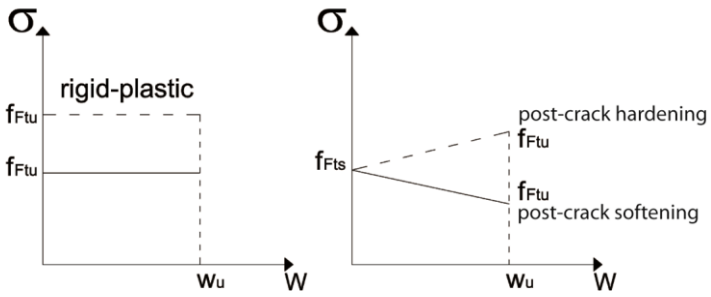

Figure 4: Simplified post-cracking constitutive laws: stress-crack opening (continuous and dashed lines refer to softening and hardening post-cracking behaviour respectively).

The linear elastic model is used for the analysis of this test results, and defines the residual strength significant at ultimate limit state f_{Ftu} by:

$$f_{FTu} = f_{Fts} - \frac{w_u}{CMOD_3}(f_{FTs} - 0.5f_{R3} + 0.2f_{R1}) \geq 0 \quad (2)$$

With f_{Rj} is the residual flexural tensile strength corresponding with CMOD = $CMOD_j$:

$$f_{R,j} = \frac{3F_j l}{2b h_{sp}^2} \quad (3)$$

- F_j is the load corresponding with CMOD = $CMOD_j$;
- l is the span length [mm] ;
- b is the width of the specimen [mm] ;
- h_{sp} is the distance between the notch tip and the top of the specimen [mm], 125 mm ;
- f_{FTs} corresponds the serviceability residual strength given by:

$$f_{Fts} = 0.45\ f_{R1} \quad (4)$$

- w_u is the crack opening corresponding to the ultimate limit state. A value of w_u = 1.5 used in the following, is considered on the safe side.

For the rigid-plastic model, it is assumed that the whole compressive force is concentrated in the top fibre of the section and the static equivalence is taken into account. So, the following relationship can be applied:

$$f_{Ftu} = \frac{f_{R3}}{3} \quad (5)$$

Testing of basic parameters

A number of basic material parameters have been determined, such as compressive strength, tensile strength and residual flexural strength. Compressive tests are performed on cubes with side 100 mm. Uni-axial tensile tests have been performed on cylinders with diameter 150 mm and heigth 300 mm. Residual flexural strength has been determined based on Rilem recommandations and testing standard EN 14651, based on notched beams of 150 mm width and 600 mm length.

2 Test results

A 2 % fibre mix (70 % short fibres and 30 % longer fibres 30 mm length and Ø 0.38 mm) has been applied for all three UHPC mix compositions and two a/d-ratios, resulting in six test series, for which Figure 5 shows the average test results. The horizontal lines are the minimum and maximum predictions for the six test series.

For UHPC type M2 a large range of situations has been studied. The average results for the test situations given in Table 2 can be found in Figure (a/d = 1.8) and Figure 7 (a/d = 3.0). These graphs compare the predicted shear forces, based on EC2 and MC'10, with the actually measured shear forces. In Figure (a/d = 1.8), all test results show an underestimation

Table 2: Different test specimens and failure mode (beam1/beam2/beam3).

Test specimens	**a/d = 1.8**	**a/d = 3.0**
UHPC beam without fibre reinforcement or stirrups *(indicated on the figure as $V_{Rd,c}$)*	**A/A/A**	**B/B/B**
UHPC beam without fibre reinforcement, with stirrups *($V_{Rd,s}$)*	**A/A/A**	**A/A/A**
UHPC beam with 0.5 % fibre reinforcement, a fibre mix of 6 mm and 30 mm length *($V_{Rd,F}$ (0.5 % mix))*	**B/B/A**	**A/B/A**
UHPC beam with 2 % fibre reinforcement, fibres 6 mm length *($V_{Rd,F}$ (2 % 6 mm))*	*****	**A/C/C**
UHPC beam with 2 % fibre reinforcement, a fibre mix of 6 mm and 30 mm length *($V_{Rd,F}$ (2 % mix))*	*****	**B/B/B**

Failure modes: (A) shear compression failure.
(B) shear bond failure.
(C) flexural failure.
* no detailed description available.

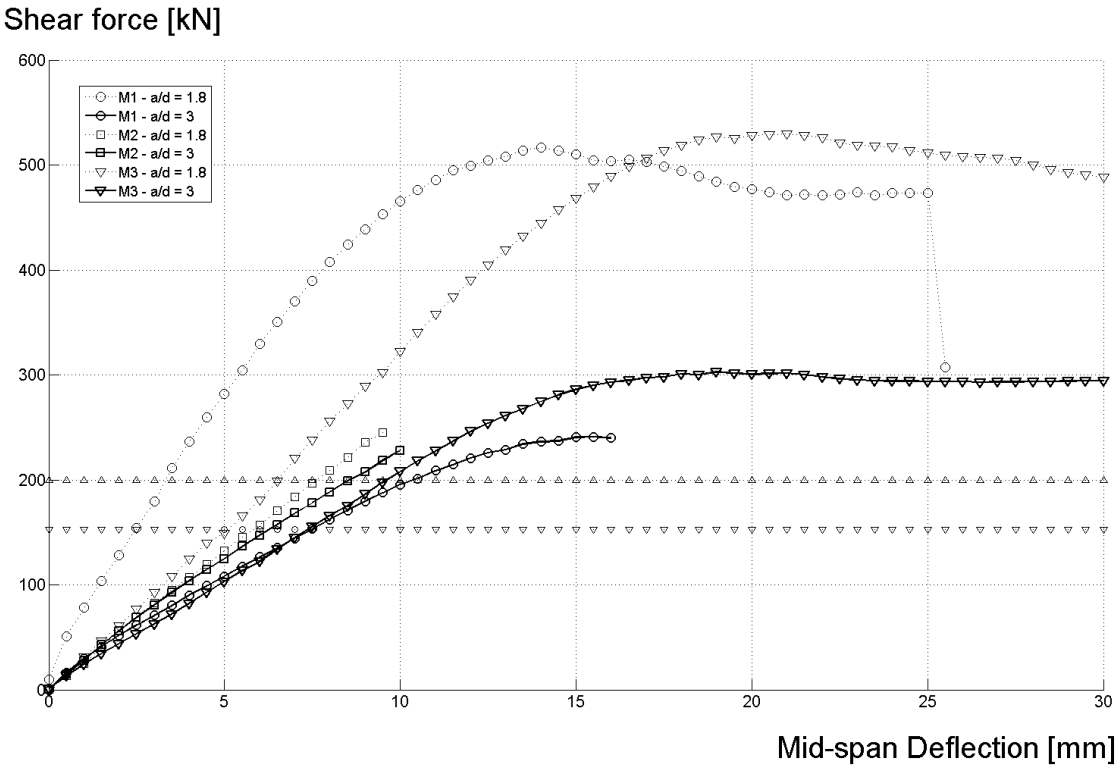

Figure 5: Average test results for all tests situations with 2 % fibre mix (70 % short fibres and 30 % longer fibres 30 mm length and Ø 0.38 mm), for three UHPC mix compositions and 2 a/d-ratios.

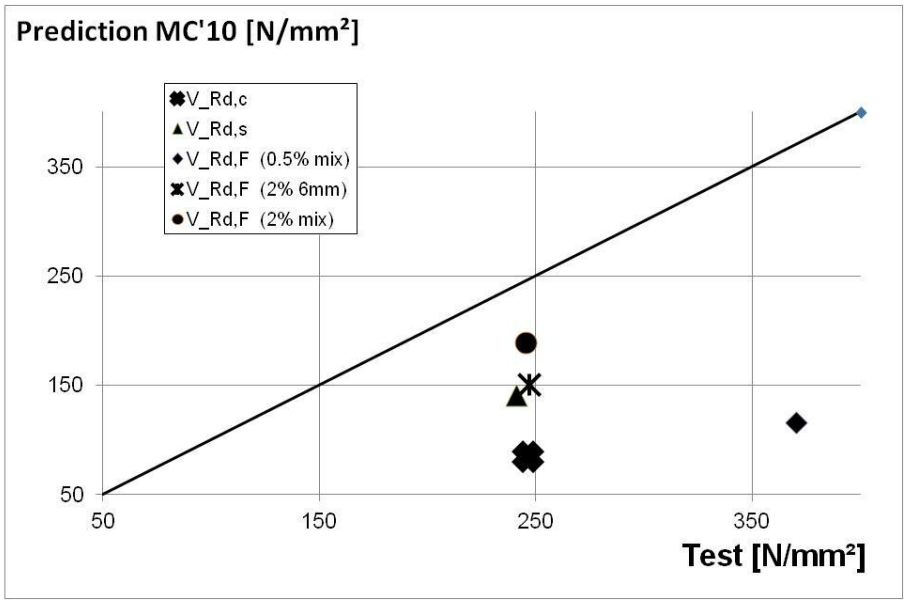

Figure 6: Test results for mix design M2, a/d-ratio = 1.8, with different fibre dosages or stirrup shear reinforcement.

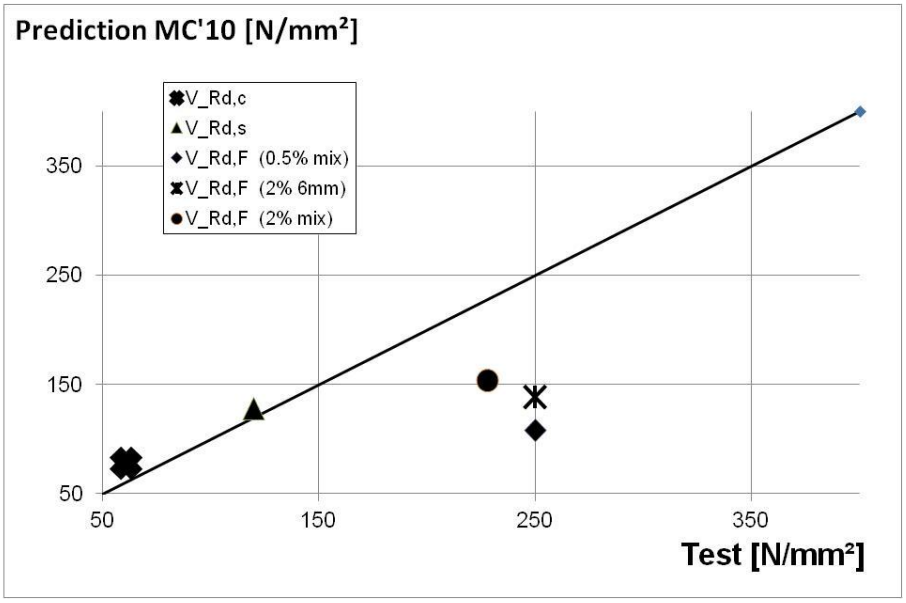

Figure 7: Test results for mix design M2, a/d-ratio = 3.0, with different fibre dosages or stirrup shear reinforcement.

3 Conclusions

First conclusions based on the beam tests with different a/d-ratios, mix compositions and shear reinforcement types (stirrups and fibre reinforcement):

- The shear capacity of the studied fibre reinforced UHPC is much higher than predicted by draft Model Code 2010 if we take into account the contribution of the fibres. The most important difference between test and prediction can be noted for a/d = 3. Design of fibre reinforced beams without additional stirrup reinforcement seems feasable with sufficient security.
- The shear capacity of UHPC without fibres is rather low, and in some cases an extrapolation of EC2 provides even an overestimation of the shear capacity, creating an unsafe prediction. This situation has been noted for mix design M2, with a/d-ratio = 3, with and without stirrups as shear reinforcement (capacity overestimation up to 30%). Some similar results can be found in literature, where this lower shear capacity is attributed to the lower aggregate volume and the resulting decreased aggregate interlocking.
- Although preliminary test on notched beams show the highest residual flexural strengths for mix composition M2, the large beam tests show a better performance, both for a/d = 3 and a/d = 1.8.
- Further research should demonstrate if these conclusions remain valid for pretensioned beams as well.

4 Acknowledgements

The authors acknowledge gratefully the financial support of the IWT, Flanders agency for innovation by Science and Technology.

References

[1] Cap J.-F., Calcul Organique du Béton Armé, 2002.
[2] CEB – Fib, Bulletin 55, Model Code 2010 – First complete draft, 2010..
[3] Minelli F. and Plizzari G.A.: Shear design of FRC members with little or no conventional shear reinforcement, Proc. Fib-symposium Tailor Made Concrete Structures, Amsterdam, 2008.

Interface Shear Capacity of Small UHPC / HPC Composite T-Beams

Charles Kennan Crane[1], Lawrence F. Kahn[2]

1: United States Army Engineer Research and Development Center, Vicksburg, MS, USA
2: Dept. of Civil and Environmental Engineering, Georgia Institute of Technology, Atlanta, GA, USA

The purpose of this research study was to evaluate AASHTO LRFD and ACI interface shear requirements for composite T-beams having a "precast" ultra-high performance concrete (UHPC) web and a cast-in-place high performance concrete (HPC) deck. Five T-beams were cast using UHPC (200 MPa compressive strength) for the rectangular web and HPC (83 MPa compressive strength) for the deck. For each beam, the surface roughness and reinforcement ratio were varied. The beams were tested in three-point bending with a span length of 2.90 m. Both the ACI and the AASHTO shear friction equations conservatively predicted the performance of those beams with fluted interfaces. The AASHTO shear friction equation, however, was unconservative in predicting shear strength of smooth interfaces even with relatively high levels of reinforcement. Based on the results of these tests, it was recommended that a fluted surface be created at any cold-joint between UHPC and HPC.

Keywords: UHPC, HPC, shear friction, interface shear, composite beams, surface roughness

1 Introduction

The purpose of this research was to evaluate American Association of State Highway and Transportation Officials (AASHTO) Load and Resistance Factor Design (LRFD) and American Concrete Institute (ACI) interface shear requirements for composite T-beams with a "precast" ultra-high performance concrete (UHPC) web and a cast-in-place high performance concrete (HPC) deck. The goals were to compare the results obtained with current code provisions and to determine if the current codes can be used to satisfy strength and serviceability requirements in precast UHPC girders with HPC decks.

The scope of the research was restricted to five T-beams cast using UHPC for the web with a compressive strength of 200 MPa and HPC for the deck with a design compressive strength of 55 MPa, which yielded an actual strength of 83 MPa. Each beam was constructed with either a smooth interface (no roughening), burlap roughened, or a fluted form liner (6 mm roughened) interface between the web and the deck slab. The transverse reinforcement ratio ranged between zero and 0.286 percent for all beams.

2 Significance and Background

Ultra high performance concretes (UHPCs) are being considered for construction of precast pretensioned highway bridge girders. These concretes have self-consolidating properties, include steel fiber reinforcement, and use a maximum size aggregate of less than 2mm. These properties create a smooth surface upon placement and also prevent the concrete surface from being roughened by raking. Therefore, it is not possible to create, in the usual manner, the 6 mm surface roughness specified by ACI 318 [1] and AASHTO LRFD [2]. The interface properties between UHPC girder and cast-in-place concrete deck must be investigated to determine if current shear friction concepts can be utilized in design with UHPC.

AASHTO LRFD [2] provides an equation for shear friction along an interface between two concretes cast at different times. As long as minimum transverse reinforcement requirements are met, the nominal shear resistance of the interface plane is given in Eq. (1):

$$V_n = cA_{cv} + \mu[A_v f_y + P_c] \quad (1)$$

not greater than the smaller of

$K_1 f'_c A_{cv}$

or $K_2 A_{cv}$

ACI 318 [1] gives a similar equation for shear friction along an interface with minimum transverse reinforcement. This equation is given in Eq. (2):

$$V_n = \left(1.8 + 0.6\rho_v f_y\right)\lambda b_v d \le 3.4 b_v d \quad (2)$$

Furthermore, both AASHTO LRFD [2] and ACI [1] permit the shear friction equation given in Eq. (3) to be used when evaluating interface shear strength:

$$V_n = \mu A_v f_y \quad (3)$$

not greater than the smaller of:

$0.2 f_c' A_{cv}$,

$(3.3 + 0.08 f_c') A_{cv}$,

or $11 A_{cv}$

Neither Eq. (1) nor Eq. (2) takes into account the concrete compressive strength (f_c'), and Eq. (3) only uses compressive strength as an upper boundary. Yet several authors have investigated the influence of f_c' on nominal shear strength of beams. Loov and Patnaik (1994) performed tests on 16 composite beams with varying concrete strengths, web widths, stirrup spacing and two different flange lengths. They also made sure that the surface between the flange and web was roughened and that the coarse aggregates were protruding at the concrete surface. Loov and Patnaik [3] proposed Eq. (4), which calculates nominal shear stress capacity and takes into account the roughed surface as well as f_c':

$$v_n = k\lambda\sqrt{(0.1 + \rho_v f_y) f_c'} \quad (4)$$

where k = roughness constant equal to 0.6 for rough surfaces and 0.5 for smooth surfaces.

Loov and Patnaik concluded that the stirrups did not contribute to shear resistance until the horizontal shear stress reached 1.5 to 2 MPa, suggesting that the roughened surface provided adequate shear resistance before this stress range.

Fifty push-off specimens were tested by Kahn and Mitchell [4] to determine if current design standards may be used for high strength concretes. Concrete compressive strengths ranged between 47 and 123 MPa, and transverse reinforcing ratios ranged between 0.0037 and 0.0147. Testing concluded that both AASHTO and ACI methods yielded conservative estimates for shear resistance when using high strength concretes. Kahn and Mitchell introduced Eq. (5) that is applicable for both monolithic concrete and as-cast cold joints, with a friction coefficient equal to 1.4:

$$v_n = 0.05 f_c' + 1.4\rho_v f_y \le 0.2 f_c' \quad (5)$$

Kahn and Slapkus [5] tested 6 composite beams with precast, high strength concrete webs with compressive strengths of 83.6 MPa, and cast-in-place decks with compressive strengths of either 50.2 or 77.8 MPa. The tests concluded that both AASHTO and ACI provisions were a conservative estimate for interface shear resistance of composite beams with high strength concrete made with an intentionally roughed interface with protruding coarse aggregate.

3 Test Setup

The five composite beams were constructed to replicate the tests run by Kahn and Slapkus [5]. Each beam was 3.05 m long with 2.90 m span between supports. The cast-in-place deck slab had a reduced length of 2.24 m in order to force an interface shear failure. The “precast” web

had a depth of 254 mm and a width of 152 mm, while the slab depth was 140 mm deep by 419 mm wide as shown in Figures 1 and 2. The confined area under the compressive load was not assumed to resist interface shear, so the interface area, A_{cv}, of each beam was calculated to be 0.298 m^2.

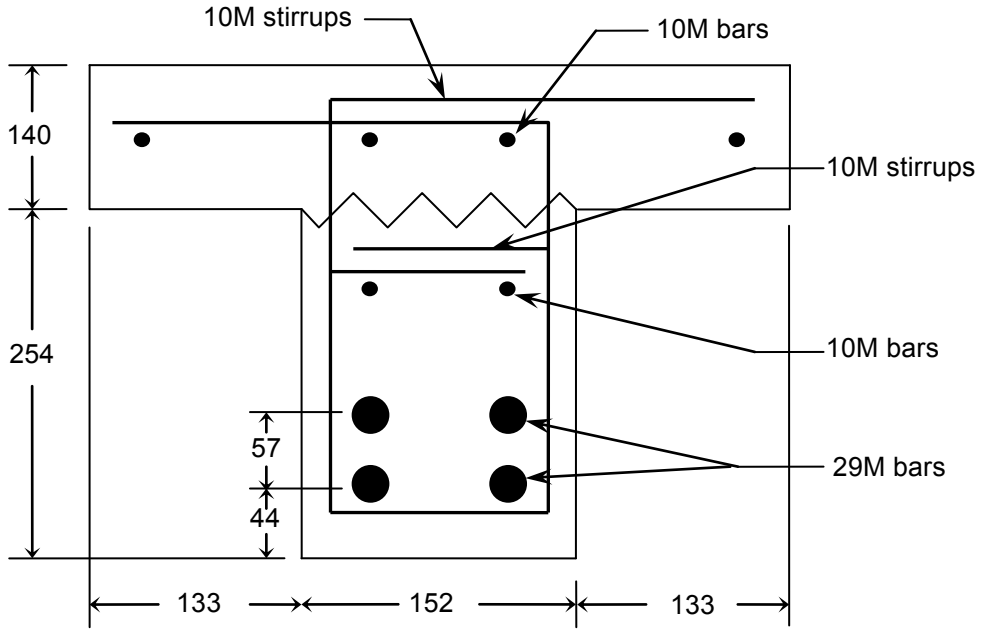

Figure 1: Typical T-beam cross section. All dimensions in mm.

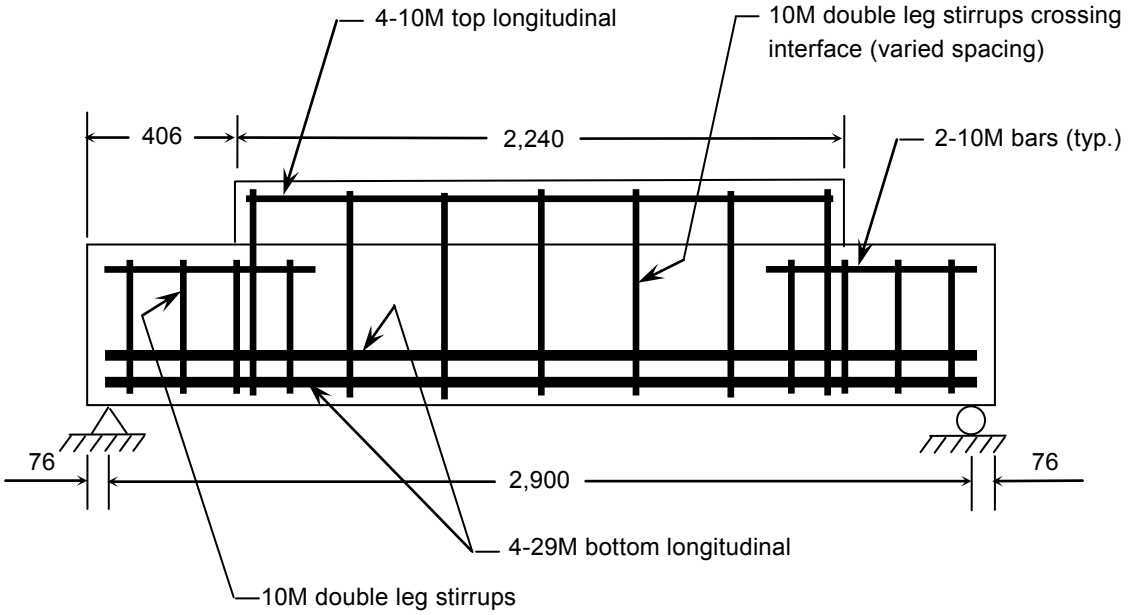

Figure 2: Typical reinforcement for all beams. All dimensions in mm.

The web was cast using UHPC at a precast concrete plant operated by Tindall Corporation, Conley, GA, USA. Two days after casting, the web was thermally treated at 90°C for 48 hours. The UHPC was Lafarge Ductal® using 2% by volume steel fiber reinforcement. The 28-day mean compressive strength was 199.5 MPa (the strength was not significantly different at time of testing). Three hundred forty-two days after casting the web, the deck was placed using conventional high performance concrete (HPC) (19 mm maximum size aggregate) delivered by ready-mix. The HPC had a mean compressive strength at the time of testing of 83.9 MPa. All

reinforcement was ASTM A615, Grade 60 (415 MPa). The elastic modulus for both the 29 M and 10 M bars was taken as 200 GPa.

The main variation between each composite beam was the interface between the web and the flange and the number of stirrups. The top surface of the UHPC beams proved impossible to roughen by raking, brooming, or cutting with a trowel. To make a rough interface, a form liner was used to create 6 mm flutes analogous to the roughness amplitude required by codes. The variations between all five of the beams tested can be seen in Table 1. Burlap was placed atop the interface of one beam containing no reinforcement. The goal of including burlap was to create a textured surface, which would provide an improved bond to the deck slab. The burlap proved difficult to remove from the surface after the initial 48-hour cure, and significant wire brushing was required. Further, while moving a sixth beam that contained a smooth interface and no reinforcement, the deck fell off, indicating that there was little bond between the web and slab. The latter beam was not included in any tables, but data for the non-composite UHPC section by itself are included in load-deflection results.

Table 1: Summary of Experimental Results.

Beam	ρ_v (percent)	Clamping Stress (kPa)	Maximum Load (kN)	Load at slip (kN)	Number of Stirrups	Type of Interface
0-B	0.000	0	281	61	0	Smooth
4-S	0.190	786	288	65	4	Smooth
7-S	0.286	1179	316	80	7	Smooth
0-FL	0.000	0	297	219	0	Fluted
7-FL	0.286	1179	415	415	7	Fluted

The beams were designated using the following convention X-Y where the first term indicates the number of double-legged 10 M stirrups crossing the interface, and the second term indicates the type of interface between the web and the flange. B denotes a burlap interface, S denotes a smooth cold joint interface, and FL denotes a form liner interface with 6 mm deep by 13 mm wide flutes.

Each beam was tested between 697-703 days after web casting and 355-361 days after deck casting. Each beam was loaded in three-point bending. Four mechanical strain gauges made with linear variable displacement transducers (LVDTs) were placed at the midspan of the beam on both sides near the bottom and top of the web. Each had a gauge length of 406 mm. Along with the strain gauges, two LVDT slip gauges were placed on one side of the beam. The body of the LVDT was attached to the web, while the extension portion of the LVDT was attached to the underside of the cast-in-place deck to measure slip between the beam and deck. Finally, the midspan deflection was measured using a string potentiometer.

4 Experimental Results and Discussion

For all five beams, the primary failure mode was cracking and slipping between the web and the flange – an interface shear failure. Figure 3 compares the load deflection curves for all five composite beams plus a plain beam without a deck. Interface failure was assumed to occur when there was a significant decrease in flexural stiffness and a sudden jump in the slip between web and flange. This interface failure is denoted on Figure 3 with a circle on each load deflection curve.

Even prior to the noted interface slip, there were distinct differences in the slopes of the load-deflection (P-Δ) curves for each specimen. Table 2 gives the stiffnesses for each specimen prior to the interface slip marked in Figure 3. Based on these values, it is clear that even prior to loss of full composite action or gross slipping of the deck, only partial composite action was attained in the beams with smooth interfaces. Among these beams, the preliminary stiffness increased as the reinforcement ratio increased. This trend suggests that larger amounts of interface steel do reduce initial slippage. The two beams with fluted interfaces showed the highest stiffnesses initially. This shows that the fluted surface creates a more fully composite connection than does a smooth surface.

There was a drastic difference between the slip load for beams that had a smooth or burlap interface and the beams that had fluted interfaces. It was observed that the greatest interface shear capacity was obtained from the beam that contained a form liner interface along with seven stirrups crossing the interface. The beam with a burlap-roughened interface and no stirrups had the least interface shear capacity. After composite action was lost, the beams behaved similarly to the plain beam as can be seen in Figure 3.

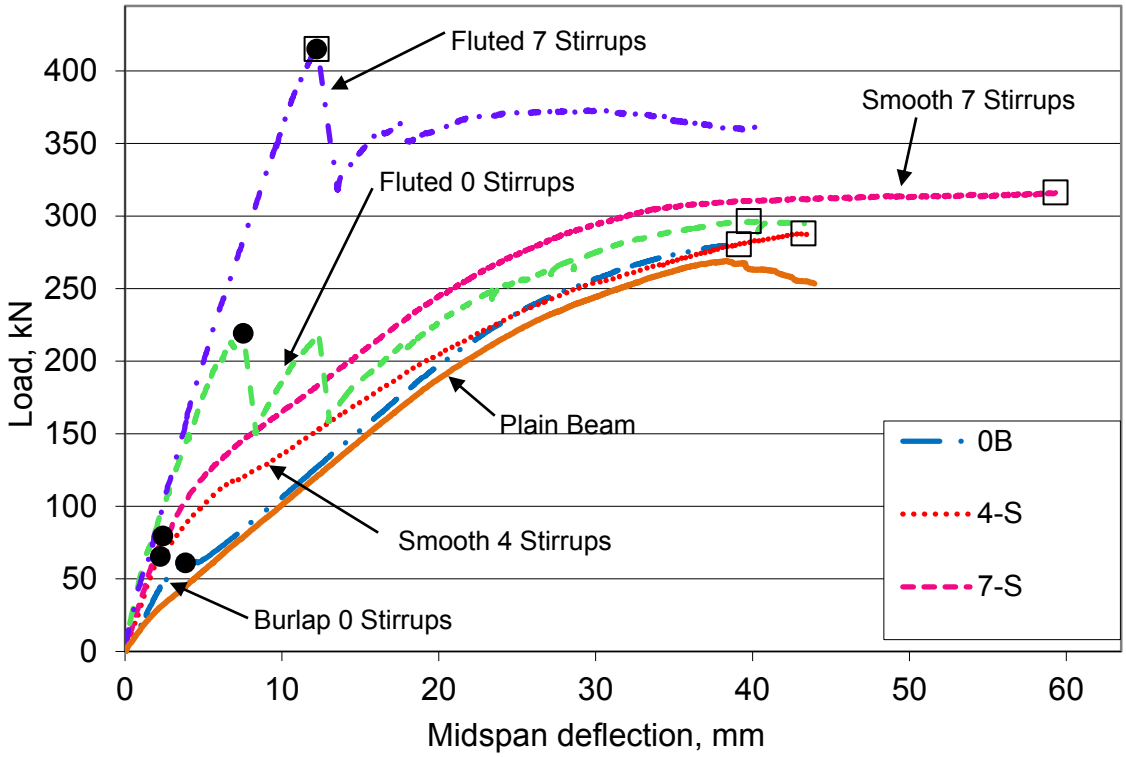

Figure 3: Load-deflection plots for beams with slip and max load denoted.

Table 2: Initial stiffnesses of composite t-beams.

Beam	Interface Surface Preparation	Interface Reinforcement Ratio, ρ_v, percent	Initial Slope of Load-Deflection Curves, kN/m	Initial Composite Stiffness [EI], kN*m^2
Plain Beam	N/A	N/A	15.6	7,700
0-B	Smooth	0.000	19.4	9,800
4-S	Smooth	0.190	31.3	15,800
7-S	Smooth	0.286	34.5	17,500
0-FL	Fluted	0.000	50.1	25,300
7-FL	Fluted	0.286	47.5	24,000

Figure 4 compares the moment-curvature diagrams for four of the composite beams and the plain beam to the theoretical moment curvature calculated using the computer program Response 2000 developed by Bentz [6]. The beam designated 0-FL is not included, because there was insufficient data to calculate an experimental curvature. Initially stiffer behavior in experimental beams than predicted by Response 2000 can be explained by the non-negligible tensile capacity of the UHPC. After slipping of the deck, Response 2000 showed a strain hardening response, where strain softening was observed in the test. It was unclear what modeling assumptions created this discrepancy.

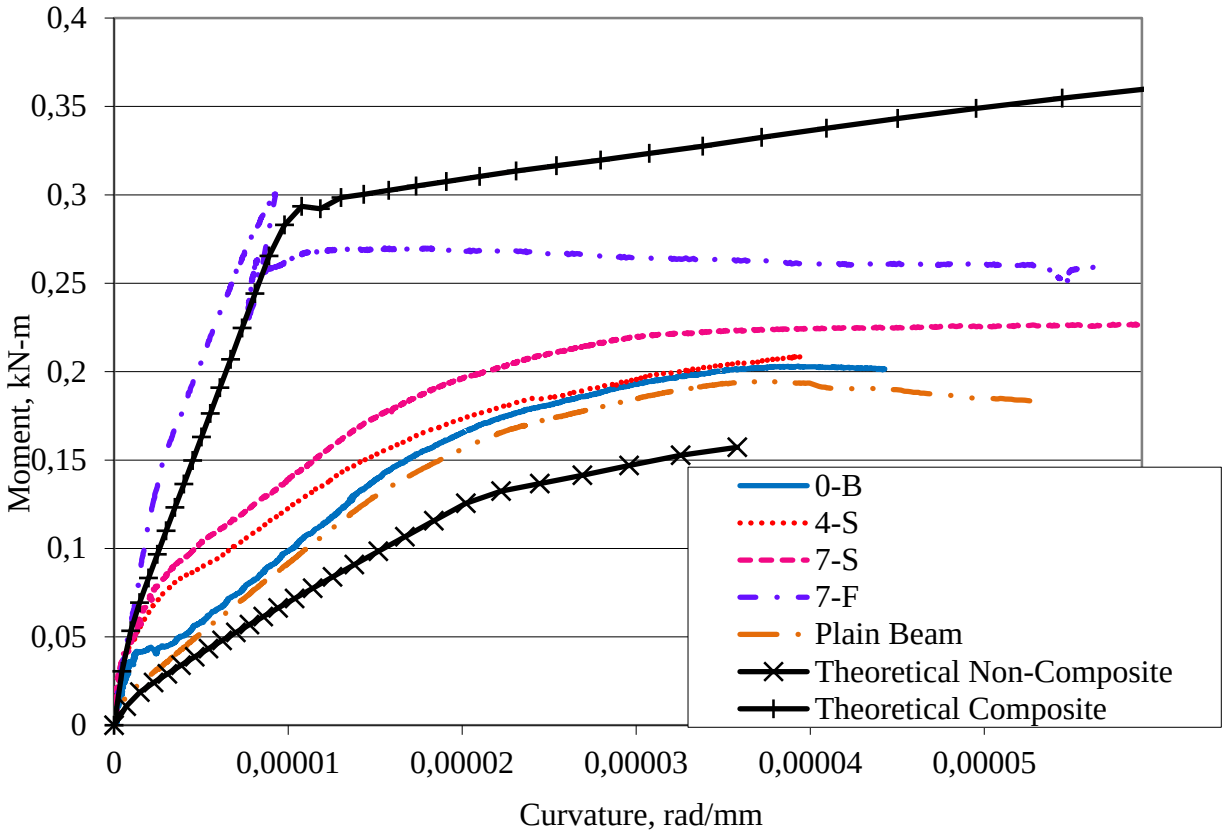

Figure 4: Moment-curvature plots for beams with theoretical moment-curvature curves plotted.

The grooves made with the form liner were the key component in providing composite strength. The beams that did not use the form liner failed at an average load of 68.7 kN, while the beams that did use the form liner failed at an average load of 317.1 kN. For the beam containing both stirrups and form liner, the maximum load was the load at interface failure; therefore, this combination provided the greatest composite interface shear capacity.

Table 3 compares the experimental interface shear stress based on two loads: the load at interface failure and the maximum load. These two criteria were chosen because, while there is still a substantial amount of strength remaining in the beam once the interface has failed, the stiffness has been substantially reduced. The experimental interface shear stress was obtained using ACI interface stress from Equation (2):

$$v_{\exp} = \frac{V_u}{b_v d} \tag{6}$$

Along with the experimental interface shear stress, Table 3 contains the interface shear stress capacities calculated using the Equations 1 through 5.

Table 3: Experimental and predicted interface shear stresses, MPa.

Beam	Experimental (Max) v_{exp}	Experimental (Slip) v_{exp}	ACI Shear Friction Eq. (3)	Kahn and Mitchell Eq. (5)	Loov and Patnaik Eq. (4)	AASHTO LRFD Eq. (1)	ACI Eq. (2)
0-B**	2.87	0.59	0	4.19*	1.48*	0.52	1.79*
4-S	2.94	0.67	0.47	5.30*	4.32*	0.99	2.26*
7-S	3.23	0.81	0.71	5.85*	5.19*	1.23	2.50*
0-FL	3.03	2.24	0	4.19	1.48	1.93	1.79
7-FL	4.25	4.25	1.18	5.85	5.19	3.11	2.50

*These equations assume a roughened interface that was not provided.

**0-B assumed unroughened surface because ¼ in. amplitude was not achieved with the burlap interface.

Tables 4 and 5 give the ratio of the experimental interface shear stress (both maximum and slip loads) to the theoretical interface shear stress calculated using the Equations 1 through 5 above. It was observed that the ACI equation (2) provided the best conservative estimate for stress along the interface when compared to the experimental interface shear stress due to maximum loads. At the experimental interface shear stress due to slip loads, the ACI interface shear equation (3) was the only equation to provide consistently conservative performance estimates. It should be noted that ACI equation (2) assumes a roughened surface and was conservative for specimens with fluted surfaces.

Table 4: Ratio of $v_{exp\ max}$, observed interface shear stress at max load, to predicted interface shear stress.

Beam	$v_{exp\ max}$ / ACI Shear Friction Eq. (3)	$v_{exp\ max}$ / Kahn and Mitchell Eq. (5)	$v_{exp\ max}$ / Loov and Patnaik Eq. (4)	$v_{exp\ max}$ / AASHTO LRFD Eq. (1)	$v_{exp\ max}$ / ACI Eq. (2)
0-B**	-	0.68*	1.94*	5.55	1.60*
4-S	6.28	0.56*	0.68*	2.99	1.30*
7-S	4.55	0.55*	0.62*	2.63	1.29*
0-FL	-	0.72	2.06	1.57	1.69
7-FL	3.60	0.73	0.82	1.37	1.70
Mean	4.81	0.65	1.22	2.82	1.52
Standard Deviation	1.36	0.08	0.64	1.49	0.18
Coefficient of Variation	28.2%	12.1%	52.0%	53.0%	12.0 %

*These equations assume a roughened interface that was not provided.

**0-B assumed unroughened surface because ¼ in. amplitude was not achieved with the burlap interface.

Table 5: Ratio of $v_{exp\ slip}$, observed interface shear stress at slip load, to predicted interface shear stress.

Beam	$v_{exp\ slip}$ /ACI Shear Friction Eq. (3)	$v_{exp\ slip}$ /Kahn and Mitchell Eq. (5)	$v_{exp\ slip}$ /Loov and Patnaik Eq. (4)	$v_{exp\ slip}$ / AASHTO LRFD Eq. (1)	$v_{exp\ slip}$ / ACI Eq. (2)
0-B**	-	0.14*	0.40*	1.15	0.33*
4-S	1.43	0.13*	0.15*	0.68	0.30*
7-S	1.14	0.14*	0.16*	0.66	0.32*
0-FL	-	0.53	1.52	1.16	1.25
7-FL	3.60	0.73	0.82	1.37	1.70
Mean	2.05	0.33	0.61	1.00	0.78
Standard Deviation	1.35	0.25	0.52	0.28	0.58
Coefficient of Variation	65.6%	75.0%	84.4%	28.3%	75.0 %

*These equations assume a roughened interface that was not provided.

**0-B assumed unroughened surface because ¼ in. amplitude was not achieved with the burlap interface.

5 Conclusions and Recommendations

It is evident that a smooth UHPC interface, even when reinforcement is present, does not provide the interface shear capacity anticipated by equation 1 (AASHTO LRFD). Based on these small beam tests, Equation 2 (ACI) was a close indicator of performance of smooth interfaces in composite beams but is not recommended for use in design due to the high variability of smooth interface performance. Smooth interfaces were also shown to create only quasi-composite action even prior to full slip . Therefore, it is recommended that any cold-joint between UHPC and HPC use a form liner or other technique to create a fluted surface which provides strong mechanical interlock between the adjacent placements of concrete. Under these conditions, both Equations 1 and 2 with constants based on roughened interfaces can be used to conservatively design UHPC-HPC interfaces.

6 Acknowledgements

This research was funded by the Georgia Department of Transportation (GDOT) research project No. 2043, Task Order No. 02-08 and project No. 07-05, Task Order No. 02-37. Jeremy Mitchell, Kate Howard, Roshanak Gharaat, Danielle Simpson, and John Bennett assisted in performing this research. Their support is gratefully acknowledged. Permission to publish was granted by the Director, Geotechnical & Structures Laboratory. The opinions, conclusions, and recommendations presented herein are those of the author and do not necessarily represent the opinions and recommendations of the cooperating organizations.

7 Notation

A_{cv} = area of concrete considered to be engaged in interface shear transfer ($b_{vi}d_v$)
A_v = area of interface shear reinforcement crossing the shear plane within the area A_{cv}
b_v = interface width considered to be engaged in shear transfer
b_{vi}= interface width considered to be engaged in shear transfer
c = cohesion factor,
0.52 MPa for a clean concrete surface, not roughened,

1.9 MPa for a roughened surface with a 6 mm amplitude,
2.8 MPa for concrete cast monolithically
d = distance from top of slab to centroid of bottom tensile reinforcement (note difference from d_v in AASHTO equation).
d_v= the distance between the centroid of the tension steel and the mid-thickness of the slab to compute a factored interface shear stress.
f_c' = unconfined 28-day compressive strength (taken as weaker of deck or girder for Equation 1, 3-5)
f_y = yield stress of transverse reinforcement
P_c = permanent net compressive force normal to the shear plane
K_1 = concrete cohesion term that is related to strength,

0.3 for cast in place slab cast against roughened girder

0.25 for normalweight concrete placed monolithically, normalweight and lightweight concrete with a roughened surface,

0.2 for normal weight concrete placed against non-roughened surface or cast against studded steel girders

K_2 = maximum allowable interface stress

12.4 MPa for normal-weight concrete deck cast against roughened girder,

10.3 MPa for normal-weight concrete cast against roughened concrete or placed monolithically

9.0 MPa for lightweight concrete deck cast against roughened girder,
6.9 MPa for lightweight concrete cast against roughened concrete or placed monolithically
5.5 MPa for concrete cast against studded steel girders
s = spacing of transverse reinforcement
v_n = nominal shear stress
V_n = nominal shear strength
μ = friction factor
1.0 for a roughened surface with a 6 mm amplitude
0.6 for a not intentionally roughened surface
1.4 for concrete cast monolithically
ρ_v = transverse reinforcement ratio, $\frac{A_v}{b_v s}$

References

[1] ACI Committee 318 (2008). Building code requirements for structural concrete: (ACI 318-08); and commentary (ACI 318R-08). Farmington Hills, Mich., American Concrete Institute.

[2] AASHTO (2010). AASHTO LRFD Bridge Design Specifications. Washington, D.C., American Association of State Highway and Transportation Officials.

[3] Loov, R. E. and A. K. Patnaik (1994). "Horizontal Shear Strength of Composite Concrete Beams." PCI Journal 39(1): 48-67.

[4] Kahn, L. F. and A. D. Mitchell (2002). "Shear Friction Tests with High-Strength Concrete." ACI Structural Journal 99(1): 98-103.

[5] Kahn, L. F. and A. Slapkus (2004). "Interface Shear in High Strength Composite T-Beams." PCI Journal 49(4): 102-110.

[6] Bentz, E. C. (2000). Sectional Analysis of Reinforced Concrete Members. Civil Engineering. Doctor of Philosophy Thesis. University of Toronto, Toronto.

Numerical Study on the Shear Behavior of Micro-Reinforced UHPC Beams

Martina Schnellenbach-Held, Melanie Prager
Institute of Structural Concrete, University of Duisburg-Essen, Germany

To ensure ductility of the inherently brittle Ultra High Performance Concrete (UHPC), usually micro steel fibers are added. This paper presents an alternative to these steel fibers – the utilization of an innovative micro-reinforcement. The main focus here is the affected shear bearing behavior due to a targeted orientation of this micro-reinforcement. Based on the main findings of the current research concerning the structural behavior of micro-reinforced UHPC, in the paper the results of physical nonlinear finite element analyses referring to the shear capacity of beams with different steel volume fractions of micro-reinforcement, varying longitudinal reinforcement and shear-span/depth ratios will be presented. Material models applied herein are obtained from experimental studies. In addition, the findings are compared to steel fiber-reinforced UHPC beams without stirrups and finally evaluated.

Keywords: UHPC, micro-reinforcement, shear behavior, nonlinear finite element analyses

1 Introduction

Background

Because of its dense structure, Ultra High Performance Concrete (UHPC) shows extremely high compressive strength and excellent durability properties. Beside these advantages UHPC is completely brittle. To ensure sufficient ductility, usually fibers are mixed into the fresh concrete. However, the random distribution and orientation inside the matrix cause fibers to be an incalculable factor. Additionally, steel fibers along untreated surfaces are predicted to leave displeasing rusty spots. An alternative for the application of fibers provides the micro-reinforcement, constructed of spot welded thin wires (see Fig. 1a). Concerning the mechanical properties, the utilization of micro-reinforcement in UHPC leads to at least comparable compressive, tensile and flexural strength [1]. Because of the grid-structure and therefore improved bond characteristics, the material behavior after cracking is even stiffer.

An experimental study on the orientation of the micro-reinforcement mats in UHPC beams showed, that sensible integration of the mats into the structure has a decisive influence on the shear loading capacity. Due to the grid-structure of the micro-reinforcement, there are wires in and perpendicular to the load bearing direction (see Fig. 1b). The vertical wires act as stirrups by carrying the vertical stresses. In the following chapters, results of numerical investigations are presented to demonstrate, that these additional vertical components improve the deformation and load bearing behavior, so that stirrups can be reduced or even omitted.

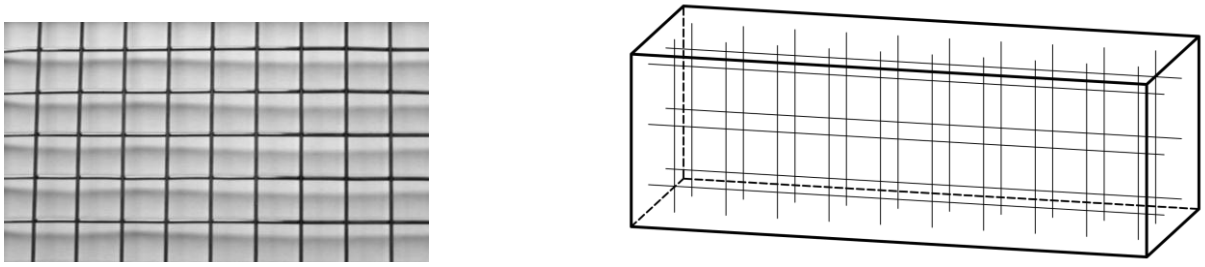

Figure 1: (a) Micro-reinforcement (Ø 1mm, mesh 10mm). (b) targeted orientation of the micro-reinforcement.

Numerical Test Program

Reliable design of new composite structures require combinations of theoretical and experimental studies. Within this article the theoretical investigations on shear resistance of micro-reinforced UHPC beams are presented. In general, for numerical modeling it is appropriate to simulate already conducted experiments (or setups taken from the literature). On the one hand this procedure provides a verification of basic parameters for the calculation, on the other hand it offers a direct comparison e. g. between different materials or reinforcement types.

The results of the finite element analyses shown in this paper are mainly based on the experimental setup published by Fehling and Thiemicke [2] (see Fig. 2). To study the effect of fibers on the shear resistance of UHPC, a 3-point beam, composed of 2 different cross-sections – a rectangle and an I-section – was chosen. The studies of [2] were focused on the profiled part of the beam, which was supposed to fail in shear. To clarify the influence of fibers, a variation of the shear reinforcement in the web was conducted. The following shear reinforcement types were varied: (i) vertical bars (Ø5/10.5), (ii) steel fibers (Ø/L = 0.175/13 mm), (iii) combination of vertical bars and fibers. As reference, a beam without reinforcement/steel in the profiled region was checked.

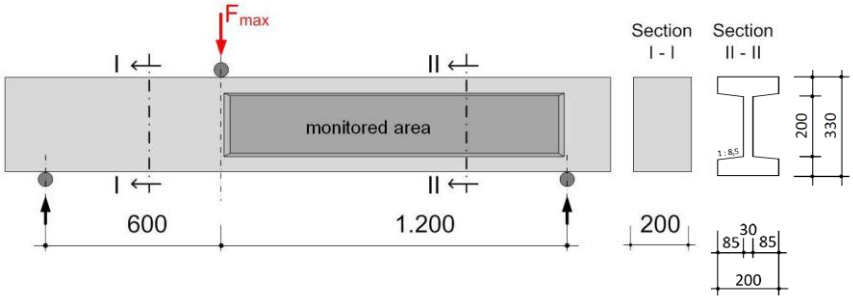

Figure 2: Geometry and test setup of the specimen [2].

In this paper the effect and efficiency of the micro-reinforcement on the shear capacity is evaluated by performing numerical simulations. Within these calculations the properties of the beam are varied according table 1. Additionally, calculations with vertical bars (Ø5/10.5, arranged in the I-girder) and those without shear reinforcement in the I-shaped cross-section are conducted as references.

The shear-span/depth ratio of 4.0 results from the setup given in [2]. Furthermore a quotient of a/d = 2.5 is chosen, to consider the investigations by Kani [3]. The shear-slenderness of 2.5 is realized by moving the right support towards the loading point.

Three flexural reinforcement ratios were defined with respect to their effect on the shear capacity of the studied beam: (i) a minimum reinforcement according to DIN 1045-1 [4] for the profiled cross-section (ρ_l = 2.45 %), (ii) a high reinforcement ratio (ρ_l = 21.82 %, represents the main reinforcement given by [2]) and (iii) an average reinforcement ratio (ρ_l = 12.13 %). It should be noted, that the horizontal wires of the micro-reinforcement are ignored here.

The variation of the micro-reinforcement in the web of the I-girder is performed as follows: (i) 0.5 % by volume steel (1 mat), (ii) 1.0 % (to draw a comparison to fiber reinforced I-girders, as this is a typical fiber content), (iiI) 2.5 % by volume steel (results in an equivalent shear resistance of vertical bars Ø5/10.5, whereas different yield values of the stirrups and the micro-reinforcement are considered), (iv) 5,0 % by volume steel and (v) 7.85 % by volume steel (maximum value for geometric reasons with a concrete cover of 3 mm and closest positioning of the mats like Ferrocement [5] or Ducon [6]).

Table 1: Calculation matrix.

shear-span/depth ratio	2.5 / 4.0
longitudinal reinforcement ratio $\rho_l=A_{sl}/(b_w \cdot d)$ [%]	2.45 / 12.13 / 21.82
micro-reinforcement content (% by vol. steel)	0.5 / 1.0 / 2.5 / 5.0 / 7.85

2 Nonlinear finite element analyses

General

The finite element analyses are performed with the software DIANA. Because of the failure mechanisms of the beams are expected to be mainly influenced by cracking of the concrete in tension, yielding of the reinforcement/micro-reinforcement or crushing of the concrete, physically nonlinear analyses are performed.

Material models

For the concrete the smeared crack concept is applied. In detail, a total strain based crack model is adopted, which describes the tensile and compressive behavior of concrete with one stress-strain relationship. Beside the definition of basic properties like the Young's modulus (here: 52.500 MPa), the total strain crack model requires the input of the material behavior in tension, shear and compression. Material properties, taken from conducted experiments ensure, that the real structural behavior is simulated. In the case of unreinforced UHPC, direct tension tests and uniaxial compression tests lead to a quasi brittle failure with negligible fracture energy. DIANA offers predefined stress-strain functions, which need to be completed by appropriate parameters. As a consequence of the brittleness, the function "brittle" is chosen in tension (see Fig. 3a) with a measured peak stress f_t = 10 MPa. In compression, a brittle behavior leads to unstable calculations, thus the function according to Thorenfeldt [7] (see Fig. 3b) with a peak-stress of f_c = -150 MPa is employed. Lateral influences (cracking and confinement) are neglected.

The ability of diagonally cracked concrete to transmit tension and shear is considered. Figure 3c presents the shear stress (τ) over the corresponding shear strain (γ). The shear retention factor β reduces the shear stiffness (G) after cracking: G_{cr} = β *G. For normal strength concrete [8] recommends β = 0.1. Because of the fine grain and therefore smoother roughness of the cracked surface, the transmission in UHPC is expected to be less, so that a value of β = 0.075 is assumed.

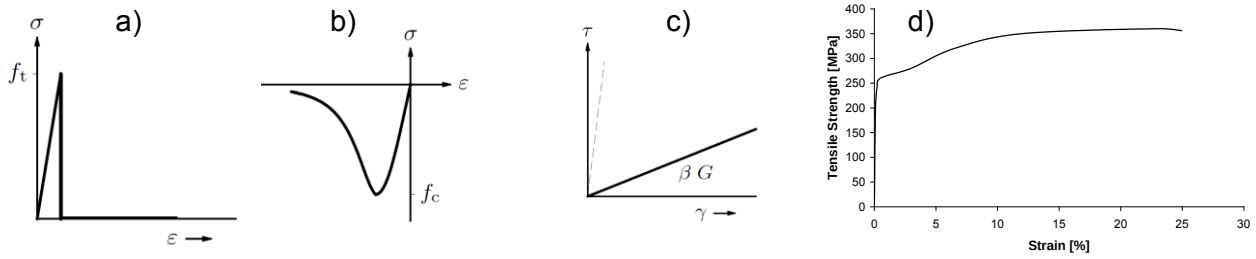

Figure 3: Stress-strain relationship for concrete in a) tension, b) compression, c) shear and d) for micro-reinforcement.

The main reinforcement as well as the stirrups are embedded and 'smeared' to the corresponding concrete elements. This reinforcement is defined by the yield condition/criterion of Von Mises with a yield value of 500 MPa.

A material law for the discrete modeled micro-reinforcement results from direct tension tests of the micro-reinforcement. The resulting stress-strain relationship (Fig. 3d) serves as an direct input for the calculation.

Elements and meshing

Two-dimensional quadrilateral plane-stress elements based on quadratic and Gauss integration are chosen to model the concrete structure. The main bars and stirrups are modeled as smeared reinforcement, while the micro-reinforcement is modeled discrete by applying three-node beam elements, which are also based on Gauss integration. To ensure a load transfer from concrete to micro-reinforcement, the welded intersections of the wires are directly linked to the closest concrete node.

To prevent singularity evoked by discontinuity of the cross-section, the transitions from the full cross-section to the I-shaped one is smoothed. This is also performed for the area web/flange.

Due to the parametric study there are three main models with a shear slenderness a/d = 4.0 (Fig. 4) and three ones more with a ratio of 2.5.

a) web without shear reinforcement b) web with vertical bars c) web with micro-reinforcement

Figure 4: Finite-element models a/d = 4.0.

Analysis options

Load increments are applied as deformations and vary after cracking between 0.01 mm and 0.005 mm.

For the analysis of the structural system the Regular Newton-Raphson method is applied. To determine the iterative increment (deformation), the tangential stiffness matrix is evaluated in every iteration. The tolerance for convergence (here: energy norm) is set to be 0.0001 and the maximum number of iterations is set to 35. Convergence behavior is observed carefully to exclude incorrect results due to consecutive problems of convergence and stability.

3 Results and discussions

General Behavior

To compare and evaluate the results of the conducted calculations, 14 load-deflection diagrams are presented (see Fig. 5), separated by the type and amount of shear reinforcement. Every diagram contains three curves, which differ in the main reinforcement ratio (minimum, average, high). The shear force of the I-girder is given on the y-axis over the corresponding deflection under the loading point on the x-axis. A dropout of single curves means that the convergence criterion was not fulfilled five load steps in a row.

In all diagrams, three distinct stages can be observed: As the first stage, a linear elastic response is plotted. Depending on the main reinforcement ratio (and the micro-reinforcement content), the drop resulting from first flexural crack describes the second stage. The third part differs substantially by the type of shear reinforcement, amount of longitudinal reinforcement and failure of the beam.

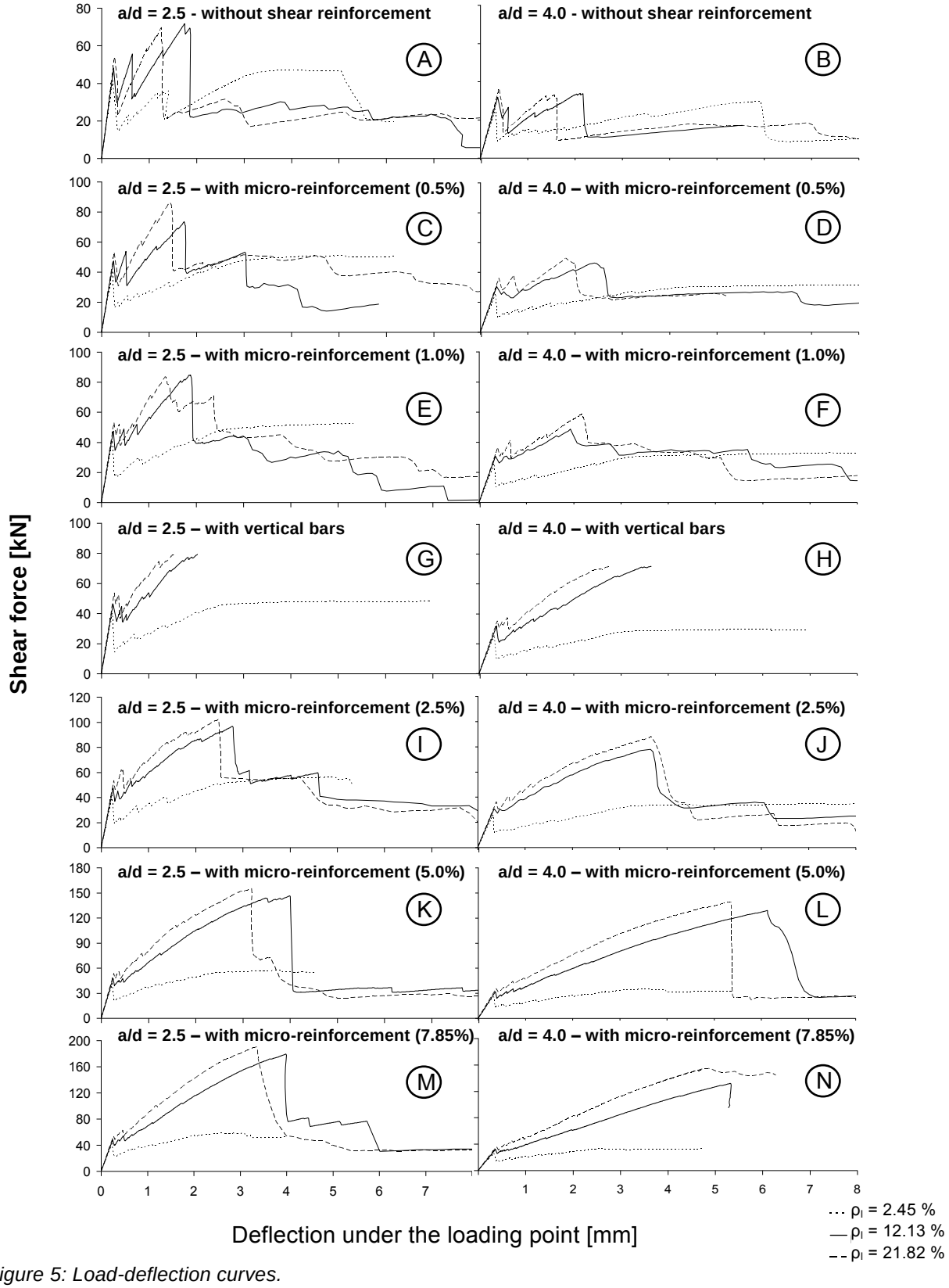

Figure 5: Load-deflection curves.

Variation of the main reinforcement

Independent of the shear slenderness a minimum main reinforcement ratio leads, with the exception of beams without shear reinforcement, to a flexural failure mode, which is initiated by one of the vertical cracks widening. The location of the major crack is influenced by the micro-reinforcement content. Due to its grid structure, the micro-reinforcement contains not only wires in vertical direction, but also in longitudinal direction, affecting the load bearing behavior. Micro-

reinforcement contents from 2.5 % by volume steel for a/d = 4.0 and from 5.0 % by volume steel for a/d = 2.5 respectively cause a flexural failure of the beam in the rectangular cross-section (see Fig. 6, left) with cracks propagating towards the top flange. Lower contents lead to a failure under the loading point. Omitting vertical reinforcement in the profiled section yields in a shear failure, with a diagonal crack emanating in the web from the loading point, propagating to the bottom flange and a final tearing crack (see Fig. 6, right).

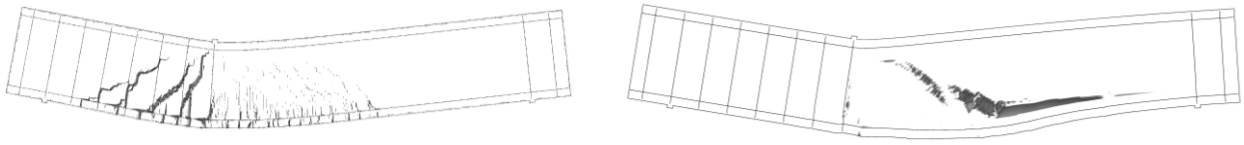

Figure 6: a/d= 4.0, minimum main reinforcement, principal strains, micro-reinforced with 7.85% by vol.steel (left), without shear reinforcement (right).

For average and high reinforcement ratios, the load bearing behavior (see Fig. 5) and failure is almost indistinguishable. Higher deflections solely follow from the lower stiffness of the beams with average longitudinal reinforcement ratios.

Variation of shear slenderness (a/d)

Figure 5 explains, that the load bearing capacity increases with decreasing shear slenderness. Beams with a/d = 4.0 show an extended shear span of the I-girder (60 % longer) in comparison to beams with a/d = 2.5. Comparing the curves with a minimum main reinforcement and therefore failure in bending, it comes clear, that ratios of a/d = 2.5 lead to 60 % higher bending capacities. The shear capacity also rises with a shear slenderness of a/d = 2.5, whereas an influence of the shear reinforcement must be mentioned here. While beams with low shear reinforcement ratios (0, 0.5 and 1.0 % by vol. steel micro-reinforcement content) show an high dependence of the shear slenderness, beams with vertical bars or micro-reinforcement contents above 1.0 % by vol. steel are less affected by the shear slenderness.

Variation of the micro-reinforcement content

Independent from the shear slenderness, low micro-reinforcement contents (0.5 % and 1.0 % by vol. steel) lead to primarily web reinforcement failure. One dominant shear crack in the web starting at the loading point proceeds to the bottom flange (similar to beams without shear reinforcement) and causes debonding of the bottom flange with yielding of the vertical wires of the micro-reinforcement. In contrast to beams without shear reinforcement, this process is followed by debonding of the top flange and a second dominant diagonal crack at the support. A parallelogram-shaped area of the web (see Fig. 7, left) is separated by cracks from the surrounding concrete. At post peak load, the top flange of the girder is rotated at distinct locations. Subsequent failure occurs due to high compressive strength in the strut connecting the loading point and the support of the beam (see Fig. 7, right).

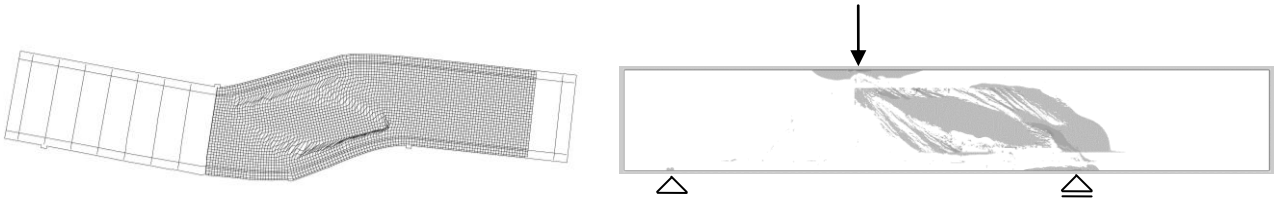

Figure 7: a/d = 2.5, micro-reinforced 1.0 % by vol. steel, shaped beam (left) and principal stresses (right).

Micro-reinforcement contents above 1.0 % by vol. steel show with increasing load finely distributed shear cracks across the span of the profiled section (see Fig. 8, left). After yielding of

the vertical wires of the micro-reinforcement, at peak load many fine cracks occur in the web and thin struts in steep angles finally fail in compression (see Fig. 8, right). High micro-reinforcement contents (5.0 and 7.85 % by vol. steel) even cause yielding of the stirrups in the rectangular cross-section.

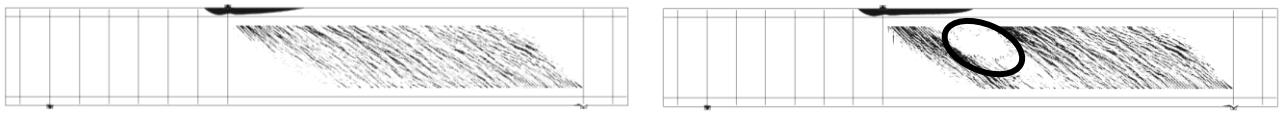

Figure 8: a/d = 4.0, micro-reinforced 5.0 % by vol. steel, principal strains (left) and principal stresses (right).

Comparison of vertical bars versus micro-reinforcement

Consecutively, the behavior of beams with vertical bars is compared to the behavior of beams with a micro-reinforcement content of 2.5 % by vol. steel (equivalent shear resistance under consideration of different yield values) in the profiled section. In general, it can be seen, that the first drop down after the first crack is less (see Fig. 5 G-J) resulting from the additional longitudinal wires of the micro-reinforcement and therefore enhanced bearing capacity. Replacing vertical bars by micro-reinforcement leads to an average increase in shear force of 20 % and distinct deformation capacity (see Fig. 5 G-J). Crack formation differs substantially due to uniformly distributed vertical wires of the micro-reinforcement in the web. Failure differs likewise: while the close distance of the micro-reinforcement wires results in steep struts, failing (after yielding of the wires) in compression (see Fig. 9, right), beams with vertical bars fail due to yielding of these bars and formation of one dominant diagonal flat crack, emanating from the loading point to the support (see Fig. 9, left)).

Figure 9: a/d = 2.5, left: vertical bars, principal strains; right: micro-reinforced 2.5 % by vol. steel, principal stresses.

Comparison of the experimental and numerical results

Investigations conducted by [2] lead to the load-deflection curves presented in Figure 10 (left). The calculated beam without shear reinforcement (1) as well as that one with vertical bars (2) behaves more stiff. Peak load is therefore reached at less deflection (compare Fig. 6 B, H). Due to the failure of the bars and subsequent concrete spalling, the numerical results for the beams with vertical bars are only available till peak load. A comparison of the maximum values of the shear force shows good correlation – the behavior is simulated reliably.

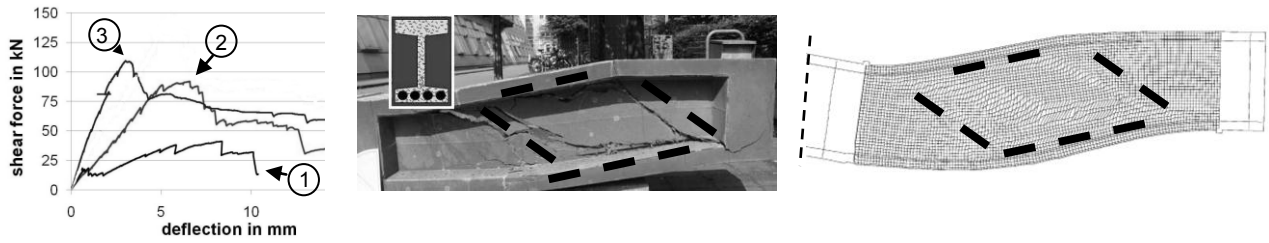

Figure 10: Load deflection curve [2], beam with fibers after test [2], beam with micro-reinforcement at failure.

A comparison of the fiber reinforced (Figure 10 (left 3)) and the micro-reinforced beam (Figure 5 (F, high main reinforcement ratio)) reveals, that the maximum shear force of the fiber reinforced beam is twice that of the micro-reinforced beam. This fact is due to the production of fiber reinforced structures. In [2], the complete beam contains fibers with an amount of 1 % by vol. steel. Micro-reinforced beams presented within this paper are only strengthened in the I-shaped section, so that a direct comparison leads to a disadvantage of the micro-reinforcement. Additionally, the compressive strength, which is set for the calculations to be f_c = 150 MPa, fits to experiments conducted in [1], but probably underestimates the UHPC-mixture of [2]. Nevertheless, the deformation capacities are comparable, although the steel content of the micro-reinforced beam is less. Further investigations are required, to draw direct comparison between these two shear reinforcement types.

4 Conclusions

This paper reports on an investigation of the shear resistance of micro-reinforced UHPC beams. A total of 42 UHPC beams were calculated with varying ratio of longitudinal reinforcement, type of shear reinforcement, amount of micro-reinforcement and shear slenderness.

Based on the numerical results, the following conclusions have been drawn:

1. The shear strength increases with a decreasing shear slenderness and an increasing amount of micro-reinforcement, whereas significantly increase in strength can be observed for contents of micro-reinforcement as from 2.5 % by vol. steel.
2. All beams containing micro-reinforcement developed numerous cracks before failure, vertical cracks in flexural zone and diagonal cracks in shear span.
3. Increasing micro-reinforcement content leads to increasing angles of the struts.
4. Adding micro-reinforcement leads, with rotating of the top flange before tearing of the bottom flange occurs, to a more ductile failure in contrast to beams without shear reinforcement.
5. Considering beams without shear reinforcement as reference, the bearing capacity of beams with micro-reinforcement (especially contents as from 2.5 % by vol. steel) is more affected with increasing shear slenderness (a/d = 4.0).

As the presented results are based on numerical calculations only, experimental tests are required to validate the results for the micro-reinforced beams. Further research will focus on a design concept for micro-reinforced UHPC structures.

References

[1] Schnellenbach-Held. M; Prager, M.: Mikrobewehrter Ultrahochleistungsbeton – Trag- und Verformungsverhalten. *Beton- und Stahlbetonbau* 106 (11), pp. 770-779, 2011.

[2] Fehling, E.; Thiemicke, J.: Shear Bearing Behavior of Ultra High Performance Concrete. Poster presented at fib symposium 2011, Prague.

[3] Kani, N. J.: The Riddle of Shear Failure and its Solution. *ACI Journal*, April 1964, pp. 441-466.

[4] DIN 1045-1: Tragwerke aus Beton, Stahlbeton und Spannbeton - Teil 1: Bemessung und Konstruktion, Ausgabe: 08/2008, Berlin, Beuth Verlag.

[5] ACI Committee 549: Guide for the Design, Construction, and Repair of Ferrocement. ACI 549.1R-88. *ACI Structural Journal* 85 (1988), pp. 325-351.

[6] Wörner, J.-D., Hauser, S.: DUCON, ein innovativer Hochleistungsbeton. *Beton- und Stahlbetonbau* 94 (2), pp. 66-75, 1999.

[7] Thorenfeldt, E., Tomaszewicz, A. and Jensen, J. J.: Mechanical properties of high-strength concrete and applications in design. In: Symposium on Utilization of High-Strength Concrete, Stavanger, Norway, 1987.

[8] Kotsovos, M. D.; Pavlović M. N.: Structural Concrete: Finite-Element Analysis for Limit-State Design. Thomas Telford Publications, 1995.

Experimental Investigations on I-Shaped UHPC-Beams with Combined Reinforcement under Shear Load

Ekkehard Fehling, Jenny Thiemicke
Institute of Structural Engineering, University of Kassel, Germany

The shear bearing behaviour of UHPC-beams with combined shear reinforcement of stirrups and fibres is investigated in this paper. Eight beams with an I-shaped monitoring area and a shear slenderness of a/d = 4 were tested in 3-point-bending tests; all of them failed in shear. To show the influence of fibres on the shear bearing behaviour, different shear reinforcement was arranged:stirrups with a diameter of 5 mm and a distance of 105 mm, a steel fibre content of 1 % by volume, a combination of these two shear reinforcements, and no shear reinforcement at all. During the tests, the crack initiation and propagation, the inclination of the compression strut, and the shear load bearing capacity were identified. The results confirm the increase of the bearing capacity, the stiffness and the inclination of the crack angles when steel fibres are added. This paper describes the experiments and its observed phenomena.

Keywords: shear, UHPC with combined shear reinforcement, stirrups, steel fibres, shear crack

1 Introduction

The shear bearing behaviour of beams, subject to research for more than 100 years, is described in various models as a function of existing or non-existing shear reinforcement.

For members without shear reinforcement ZINK [1] developed a mechanical model. Here, the main bearing capacity is attributed mainly to the capability of the compression zone to carry shear stresses. Additional capacities are provided by the dowel effect of the bending reinforcement, the aggregate interlock and in the compression damage zone (fig. 1a). ZINKS's approach leads to identical results like the semi-mechanical approach on which the DIN 1045-1 (08.08) [2] is based.

For members with shear reinforcement made of rebars different models exist since many years. These models describe the load transfer with struts and ties (fig. 1b) and account for variable inclination of struts [2].

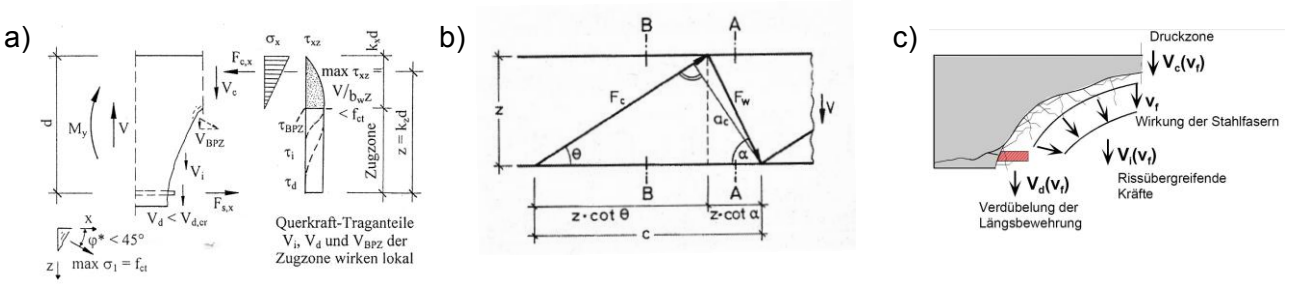

Figure 1: Models of shear bearing behaviour [1], [2], [3].

The development of high (HPC) and ultra high performance concretes (UHPC) with their pronounced non-ductile behaviour demands for the addition of fibres. These fibres increase the deformation capacity of members made of HPC and UHPC. At the same time, they influence the load bearing behaviour of these members. ROSENBUSCH [3] describes this increasing influence of fibre reinforcement on the shear bearing capacities based on the compression zone, the dowel effect of the bending reinforcement, and on the aggregate interlock (fig. 1c).

A testing programme on UHPC-beams was carried out to identify the influence of fibres on the shear bearing behaviour. The tests presented in this paper show the influence of a variation of shear reinforcement on in other respects identical beams.

2 Test specimens

UHPC-beams with two different cross sections and different shear reinforcement were fabricated. To determine the material properties Young's modulus, compressive strength, and bending tensile strength, cylinders and prisms of every mixture were produced accompanyingly.

Materials

The test specimens of this research project were produced using the mixture *M3Q*, which was designed by the department of building materials at the University of Kassel as a standard mixture in the priority programme SPP 1182 of the German Research Foundation [4] and is a fine aggregate concrete. Because of the specimen's shape, it was necessary to get a free flowing fresh concrete. Therefore, the w/c-value was set at an upper limit of 0.255.

Rebars made of BSt500S (f_y = 500 N/mm²) were used. The bending reinforcement consisted of 4Ø25. Outside the monitoring area stirrups with a diameter of 8 mm at a spacing of 100 mm were placed. Transverse reinforcement was added in the chords (fig. 2, fig. 3 left).

The very strong bending reinforcement resulted from the requirement, that a bending failure must be avoided even for the specimens with combined shear reinforcement.

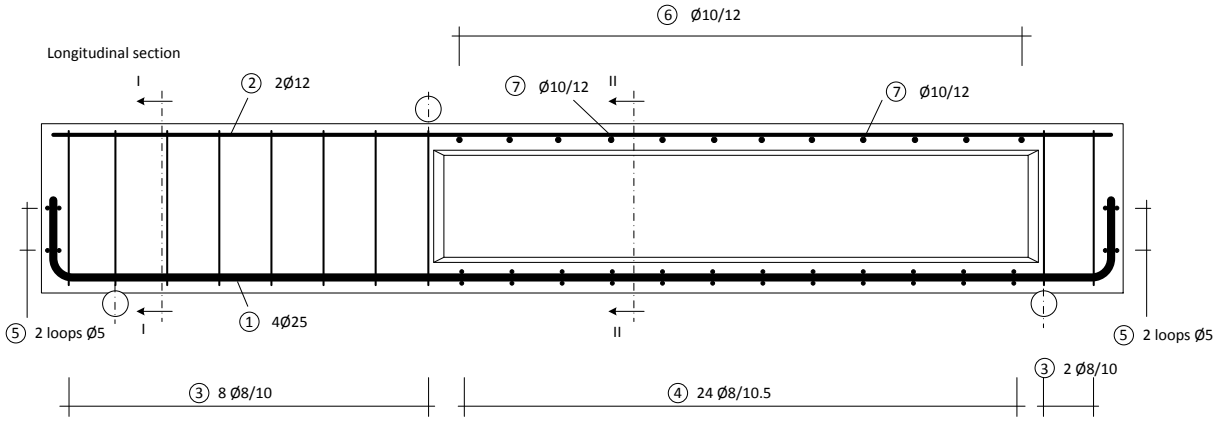

Figure 2: Standard reinforcement.

Steel fibres with a tensile strength of 2,500 N/mm² were added. They had a length of 13 mm and a diameter of 0.175 mm (fig. 3 right). The fraction of the mixture was 1.0 % by volume.

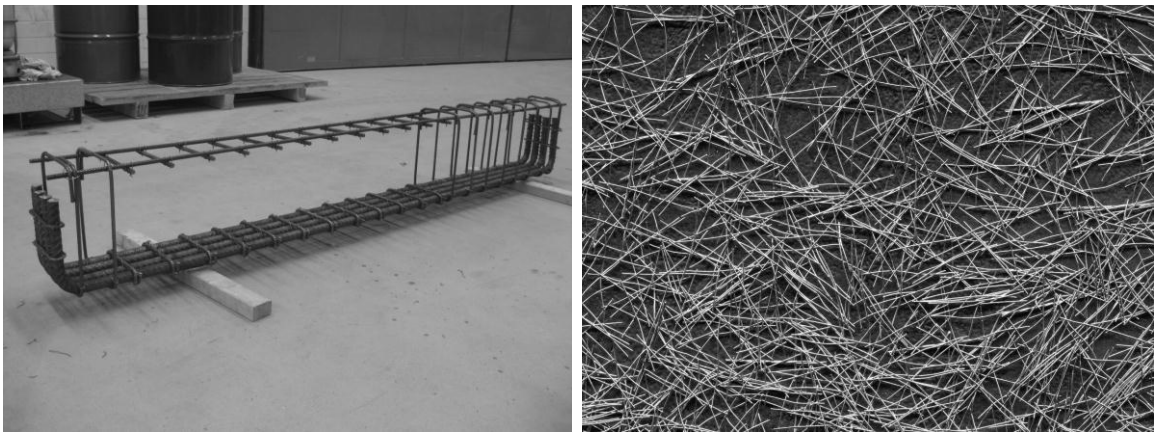

Figure 3, left: Reinforcement cage; right: Used fibres.

Dimensions

The specimens were 210 cm long. They had two different cross sections; outside the monitoring area, it was rectangular with a width/height of 20/32 cm. In the monitoring area, it was I-shaped with a web thickness of 3 cm as well as top and bottom chords with a medium height of 5,5 cm. The monitoring area was 120 cm long and 20 cm high. There is a different shaped ending for

the beam named Q2-F1-1. Instead of arranging the monitoring area like shown in fig. 5, in this beam the I-shaped cross section is continued until the end of the beam.

Variation of shear reinforcement

To identify the influence of the fibres on the shear bearing capacity, UHPC-beams with different shear reinforcement were produced. Table 1 shows the variation.

Table 1: Variation of shear reinforcement.

Shear reinforcement	Q	Q-B1	Q-F1	Q-F1-B1
Stirrups Ø 5 mm, spacing: 10.5 cm	-	+	-	+
Fibres Ø 0.175 mm, length: 13 mm, 1.0 % by volume	-	-	+	+

Fabrication of the beams

Following the recommendations of the priority programme [4], the concrete was produced and inserted into the form work, where it stayed for 48 hours. To get the ultimate strength, the specimens were heat-cured for another 48 hours at a temperature of 90°C.

Till the day of testing, the beams and references were stored under in-door-conditions. All in all eight specimens were produced.

Pre-damage due to residual stress behaviour and shrinkage

The first four beams were produced in the winter season of 2010. When hardening in the form work, the specimens were exposed to very low temperatures during the night. Due to the difference in temperature and shrinkage, residual stresses occured at an early concrete age which caused cracking.

The specimens without fibres showed wider cracks in this context than beams with fibres. Cracks occurred in the web and chords near to reinforcement bars (fig. 4), with partially crack width of about 250 µm. To reduce or eliminate this effect, the next four beams were stored under in-door-conditions during hardening.

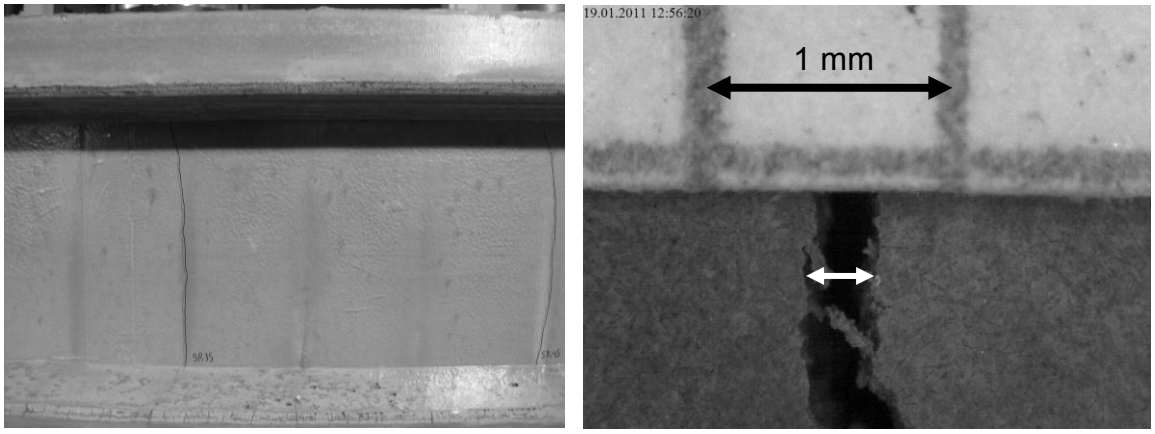

Figure 4, left: Detail view of monitoring area - crack due to shrinkage, right: Pre-damage crack width approx. 250 µm.

Material properties

To determine the material properties, cylinders with a diameter of 100 mm and a height of 200 mm as well as prisms with the dimensions of width and height of 40 mm and a length of 160 mm were produced from every mixture. Testing the reference cylinders and prisms provided the following material properties (table 2).

Table 2: Material properties.

Specimen	Young's modulus of cylinders	Compression strength of cylinders	Bending tensile strength of prisms
	N/mm²	N/mm²	N/mm²
Q-1 (without shear reinforcement)	48,162	212.9	7.4
Q-B1-1 (stirrups only)	48,240	224.3	9.6
Q-B1-2 (stirrups only)	46,488	195.3	-
Q-F1-2 (fibres only)	45,873	201.2	23.2
Q-F1-3 (fibres only)	48,528	207.9	-
Q2-F1-1 (fibres only)	49,611	185.6	-
Q-F1-B1-1 (combined reinforcement)	45,717	197.8	23.6
Q-F1-B1-2 (combined reinforcement)	46,386	197.4	-

3 Test setup

Test setup

The tests were carried out as 3-point-bending tests on UHPC-beams with indentical shape but varying shear reinforcement [5] (fig. 5). The reduced thickness in the monitoring area made sure that the failure occurred there. The dimensions of the test setup resulted in a shear slenderness of 4. The supporting points allowed the horizontal movement of the test specimens.

The load was applied over a load application plate with a spherical hinge. The applied load was controlled by a load cell. Displacement transducers measured the deflection under the load application point, the horizontal deformation of the chords near the application point, and the shear deformations on three places in the monitoring area (fig. 6).

Testing

The test was executed by displacement control. The loading velocity started with a value of 0.01 mm/s. During the test, the velocity was raised up to 0.1 mm/s. On some selected loading points, the test was stopped and the crack initiation and propagation was documented.

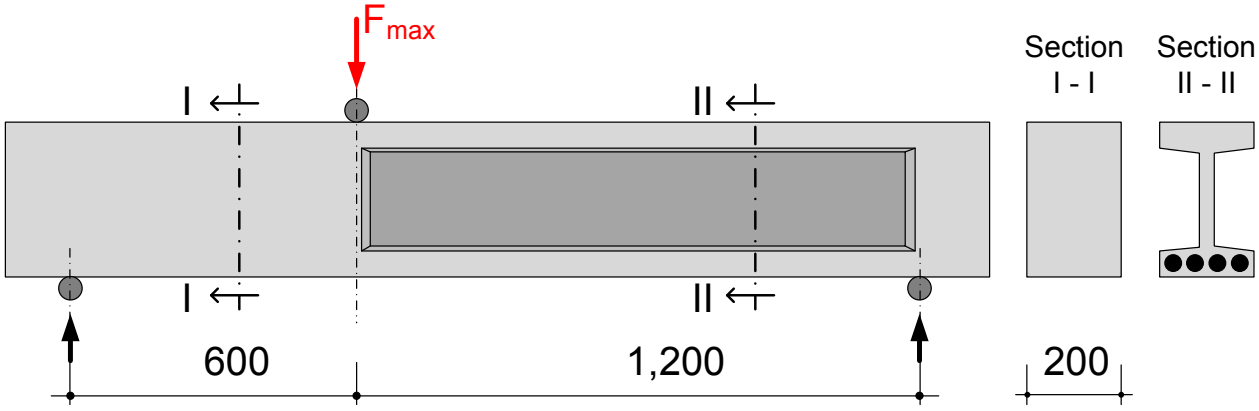

Figure 5: Test setup [5].

4 Test results

All tested beams showed a shear tension failure. In the beams with stirrup reinforcement, the stirrups ruptured. Failure cracks occurred in the web of the monitoring area. After reaching the ultimate load and during further deformation, these cracks either snapped through the compression zone or grew along the bending reinforcement in the direction of the support.

In general, it could be observed, that except for the beam without shear reinforcement the increase of load led to an increase of the number of cracks, but during further testing all

deformation concentrated in a few cracks, which developed large widths while the other cracks reduced their width.

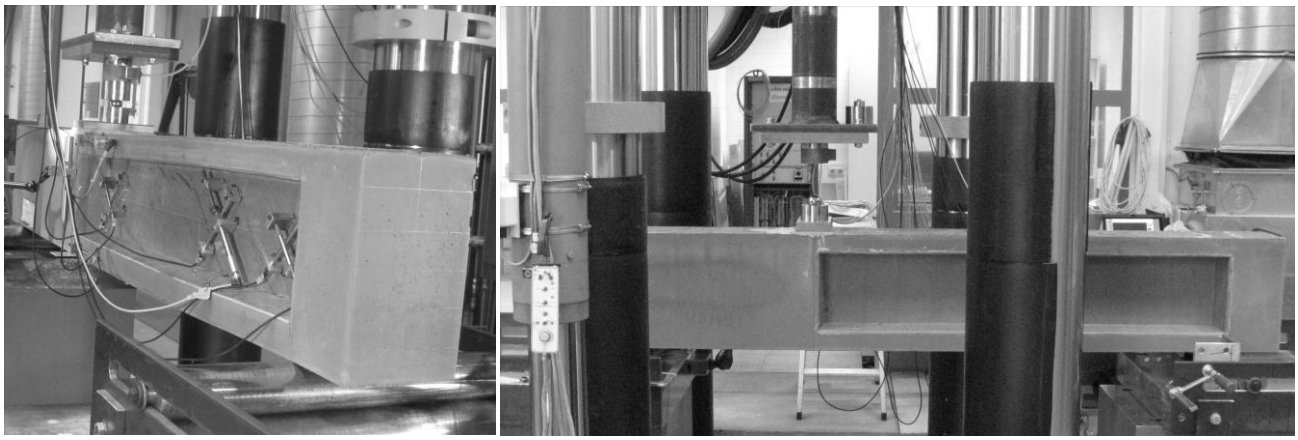

Figure 6, left: Instrumentation with measuring devices; right: Test setup (left support not visible).

Beam without shear reinforcement

In the UHPC-beam without shear reinforcement (no fibres, no stirrups) shear cracks developed already at a low load level (fig. 9 left) with an inclination of approximately 30° (fig. 7). These shear cracks were initiated by the cracks due to shrinkage (fig. 8 left) and crossed them. When all shear cracks were developed, further increasing of the load was possible due to the dowel effect of the bending reinforcement.

The snap through of the failure cracks into the compression zone induced a blast off of the compression chord (fig. 8 right). Even though this beam didn't possess shear reinforcement, the very strong bending reinforcement made sure that the failure came with preliminary signs.

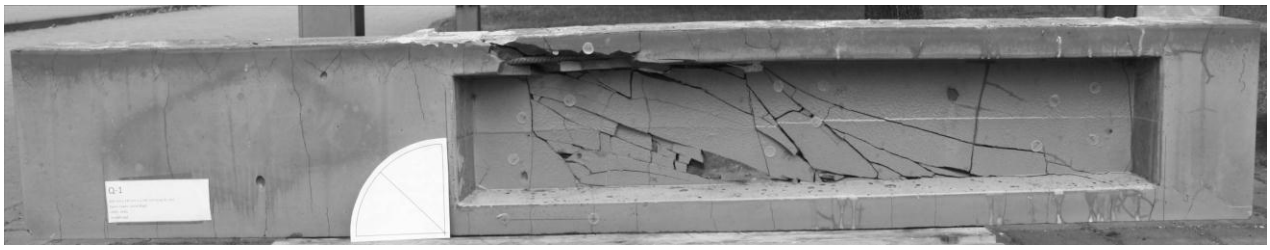

Figure 7: Crack pattern of UHPC-beam with no shear reinforcement (Q-1).

Figure 8, left: Shear cracks starting from a crack due to shrinkage; right: Blast off of the compression chord.

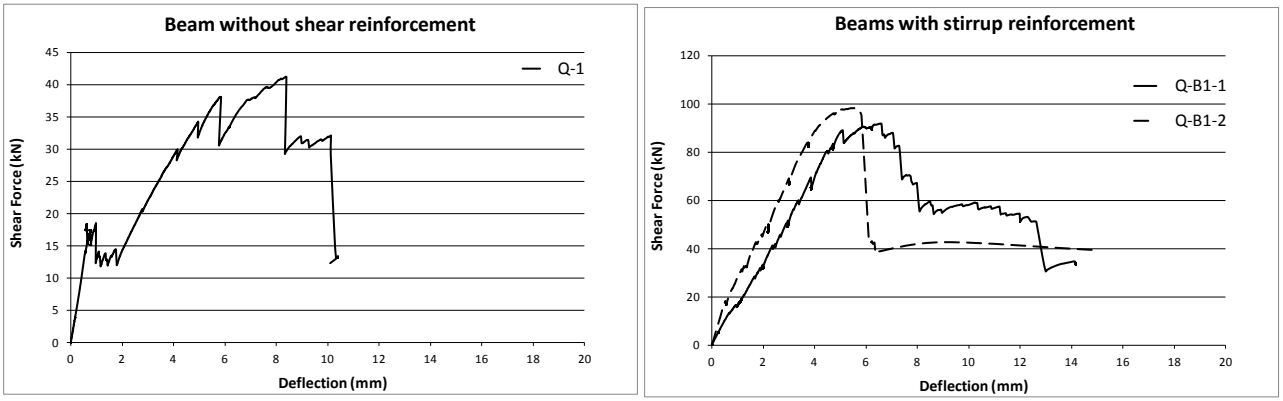

Figure 9, left: Beam without shear reinforcement; right: Beams with stirrup reinforcement.

Beams with stirrup reinforcement

Two UHPC-beams with stirrup reinforcement were tested. The shear cracks in the pre-damaged beam (Q-B1-1) were also initiated by the cracks due to shrinkage and temperature and crossed them. Hence, the beam without pre-cracking (Q-B1-2) developed a higher bending stiffness, however not a significantly higher bearing load (fig. 9 right).

After reaching the ultimate load, further deformation was applied, which led to localisation in two failure cracks (fig. 10). The stirrups crossing these cracks ruptured. One of the cracks snapped through into the compression zone and led to a blast off of a part of the chord. The inclination of the shear cracks amounted to 40°.

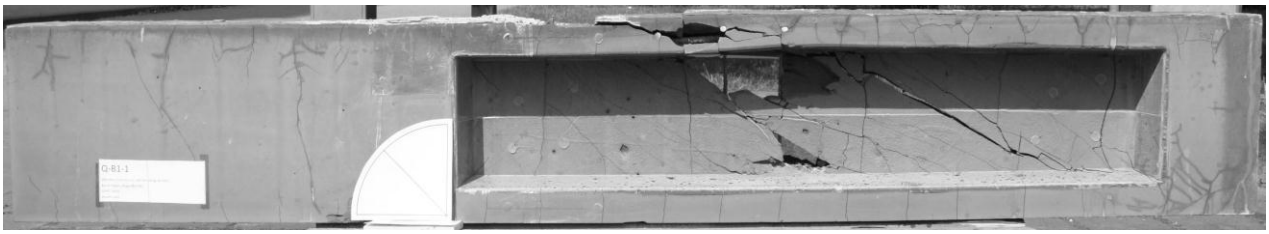

Figure 10: Crack pattern of UHPC-beam with stirrup reinforcement (Q-B1).

Beams with fibre reinforcement

Three UHPC-beams with fibre reinforcement were produced. These UHPC-beams showed a higher amount of cracks in the monitoring zone compared to the beams without fibres. These cracks showed a more narrow spacing and smaller crack width than cracks in the beams without fibres. The inclination of the cracks was between 30° and 45°.

Two failure cracks occurred. One of them grew along the bending reinforcement in the direction of the support and beyond, as well as into the compression zone but not with a blast (fig. 11).

Figure 11: Crack pattern of UHPC-beams with fibre reinforcement (Q-F1).

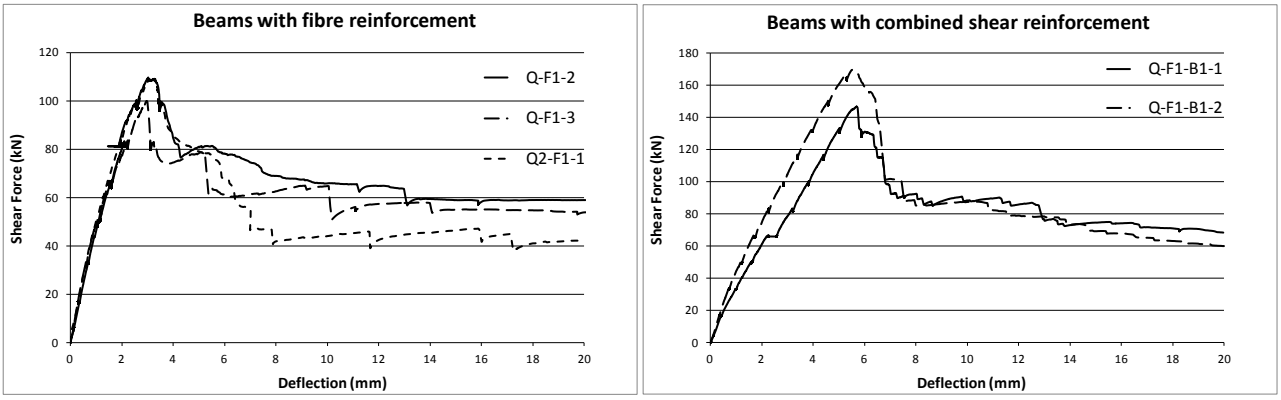

Figure 12, left: Beams with fibre reinforcement; right: Beams with a combined shear reinforcement.

Beams with a combined shear reinforcement

Two beams with combined shear reinforcement were tested. They showed a similar crack initiation and propagation like the beams with fibre reinforcement only, but with a steeper inclination of the cracks of about 50° (fig 13). When reaching the ultimate load, the stirrups crossing the failure cracks ruptured. One failure crack grew along the bending reinforcement in the direction of the support and beyond. The most significant difference was seen in the higher ultimate load (fig. 12 right).

Figure 13: Crack pattern of UHPC-beams with combined shear reinforcement (Q-F1-B1).

5 Discussion / conclusion

Failure mode

All tested beams showed a shear tension failure in the web of the monitoring area. Shear cracks occurred in the monitoring area, which were initiated by already developed cracks due to shrinkage and temperature. When stirrups were arranged, they ruptured. After reaching the ultimate load, the load bearing capacity dropped to a plateau, reflecting the strong influence of the bending reinforcement on the shear bearing capacity. The end of the test was either characterised by a damage of the compression chord (in case of no fibre reinforcement) or the damage of the bond of the bending reinforcement near the support (in case of fibre reinforcement). The pre-damage due to shrinkage and temperature of the first four members had no influence on the failure mode.

Shear bearing capacity

As figure 14 shows, the graph of the beam without shear reinforcement presents a different behaviour compared to the beams with shear reinforcement. Due to pre-damages this beam was developing shear cracks already at the shear load level of less than 20 kN. Further increase of the load is related to the strong bending reinforcement. The shear bearing capacity of the beams with stirrups or fibres reached approximately 90 kN and 110 kN, respectively. In contrast the load bearing capacity of the beam with combined shear reinforcement added up to 145 kN. As figure 9 and 12 show, there is no significant influence of the pre-damage due to shrinkage and temperature.

Force-deformation behaviour

In comparison to the beams without shear reinforcement, a smaller stiffness of the beams with stirrups is obvious. This may be explained by the the reduced effective web thickness and therefore a reduced stiffness after onset of cracking. In the post peak rage, a level of reduced bearing capacity can be observed, even for substantial levels of deformation. This residual bearing capacity can be attributed to the dowel effect of the strong bending reinforcement a swell as on a Vierendeel type of frame action.

After reaching the ultimate load, the load-deformation graphs fall down to a level which because of the strong bending reinforcement represents mailnly the dowel effect. For members with either fibre or stirrup reinforcement the level was about 60 kN, for member with combined reinforcement it reached about 90 kN. Here again, the influence of the fibres can be seen.

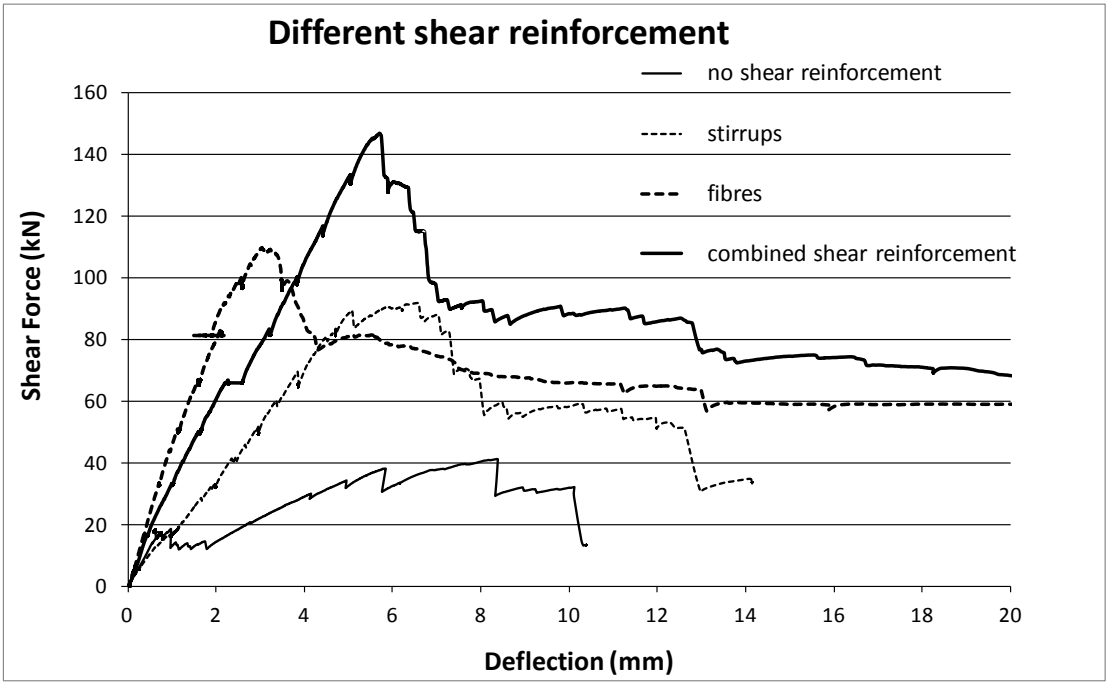

Figure 14: Shear Force-Deformation of beams with different shear reinforcement.

Adding fibres increases the shear bearing capacity and stiffness. Now, analytical examination and further detailed tests are recommended in order to describe how a combined reinforcement acts together and to verify the results.

6 Acknowledgement

This research project is funded by the German Research Foundation in the priority programme SPP 1182.

References

[1] Zink, M.: „Zum Biegeschubversagen schlanker Bauteile aus Hochleistungsbeton mit und ohne Vorspannung“, Dissertation, B.G.Teubner Verlag, Stuttgart, 2000.

[2] DIN 1045-1 (08.08.) „Tragwerke aus Beton, Stahlbeton und Spannbeton - Teil 1: Bemessung und Konstruktion“, Beuth Verlag, Berlin, 2008.

[3] Rosenbusch, J.: „Zur Querkrafttragfähigkeit von Balken aus stahlfaserverstärktem Stahlbeton“, Dissertation, TU Braunschweig, 2003.

[4] DFG-Schwerpunktprogramm „Nachhaltiges Bauen mit Ultrahochfestem Beton“ SPP 1182.

[5] Fehling, E.; Thiemicke, J.: “Shear Bearing Behaviour of UHPC”, proceedings of the fib Symposium Prague 2011.

Ultimate Shear Strength of Ultra High Performance Fibre Reinforced Concrete Beams

Florent Baby, Joël Billo, Jean-Claude Renaud, Cyril Massotte, Pierre Marchand, François Toutlemonde

Paris-Est University - IFSTTAR, Bridges and Structures Department, Paris, France

In order to quantify the safety margin of shear design provisions for UHPFRC, an experimental campaign has been carried out. In a Four-Point Bending configuration, shear tests have been conducted on eleven 3m-long I-shaped girders with varied types of shear reinforcement (links, fibers and both) or without shear reinforcement, combined with longitudinal prestressing or passive reinforcement. These shear tests have been analyzed thanks to a complete materials characterization. Moreover, in order to identify the contribution of the fibers in the ultimate shear strength, prisms have been cut horizontally, vertically, at 30° and at 45° in both extremities of the beams, to determine the effective "orientation factor". A detailed analysis has been carried out based on these experimental results both at the material and structural scale. This analysis helps validate the safety of the shear design AFGC provisions at the Ultimate Limit State (ULS).

Keywords: UHPFRC, UHPC, steel fibers, shear, stirrups, links, Ultimate Limit State.

1 Introduction

Many parameters such as the properties of concrete used, the slenderness, the presence or absence of shear reinforcement, the tension reinforcement ratio and the cross section influence the shear capacity of beams. For fiber reinforced concrete properties, main parameters are the fiber content, their shape, their dimensions, the quality of cementitious matrix and the actual fiber orientation ([1]). Many previous programs have indicated the major positive effect of fiber content and presence of stirrups on shear behavior of beams and have shown the synergetic effect of both factors (beyond a minimum shear reinforcement ratio) in the case of "normal" fiber reinforced concrete ([2]). Concerning UHPFRC, previous researches have studied the shear behaviour of reinforced or prestressed beams made of UHPFRC ([3-5]). AFGC provisions on UHPFRC ([6]) had been based on careful extrapolation of FRC ([1]) and HPC ([7]) provisions, yet verified on a limited number of test configurations. Nevertheless, in these experimental campaigns, the real orientation of fibres in the tested structures had not been identified. Thus, an experimental program was defined to analyse the shear behaviour of reinforced and prestressed beams made of UHPFRC taking into account the actual orientation of fibres.

2 Shear Tests

Specimens and parameters

All specimens were fabricated in a precast factory (Veldhoven, the Netherlands), using four concrete mixes (A, A-NF, B and B-OF), with main features presented in Table 1. During the manufacturing of beams made of concrete A, the prestressed beam with stirrups was not satisfactorily cast. An additional casting was decided for both prestressed beams. Consequently two batches exist for the first concrete mix: A and A(2). Two days after casting, the beams made of concrete B were placed during 48 hours in a climate-conditioned box at 90°C with a relative humidity of about 100 %. The intent of this step is to increase the mechanical characteristics of concrete and to complete maturation: the total further shrinkage is zero and the creep is significantly reduced after the heat treatment. The main parameters studied in this experimental program were the UHPFRC mix, the active or passive longitudinal reinforcement

and the presence of shear reinforcement (none, fibers, links, both) in the specimens. Eleven beams of I-shaped cross section were tested. An overview of beams characteristics is given in Table 2.

Table 1: UHP(FR)C mix characteristics.

Concrete Mix	f_c cube 28 days (MPa)	f_c cylinders About 11 months (MPa)	Young's Modulus About 11 months (GPa)	Steel straight fibers $L_f - \Phi_f$ (mm)	Organic straight fibers $L_f - \Phi_f$ (mm)	V_f (%)
A	195	203	60.7	20 – 0.3	--	2.5
A(2)	202	202	60.8	20 – 0.3	--	2.5
A-NF	170	187	58.6	--	--	--
B	212	205	56.0	13 – 0.2	--	2
B-OF	150	157	46.5	--	proprietary information	4.7

Table 2: Parameters of the shear tests.

Specimen	Concrete Mix	Reinforced / Prestressed	Links
UHPFRC-A-PC-NS	A	Prestressed	No
UHPFRC-A(2)-PC-NS	A(2)	Prestressed	No
UHPFRC-B-PC-NS	B	Prestressed	No
UHPFRC-A(2)-PC-WS	A(2)	Prestressed	Yes
UHPFRC-B-PC-WS	B	Prestressed	Yes
UHPFRC-A-RC-NS	A	Reinforced	No
UHPFRC-B-RC-NS	B	Reinforced	No
UHPFRC-A-RC-WS	A	Reinforced	Yes
UHPFRC-B-RC-WS	B	Reinforced	Yes
UHPC-A-NF-RC-NS	A-NF	Reinforced	No
UHPFRC-B-OF-RC-NS	B-OF	Reinforced	No

The beams got a total length of 3 meters having a span of 2.0 meters and a total depth of 380 mm. The effective depth was 305 mm for all beams. The web was designed as a thin membrane 65 mm-thick. The top flange was 270 mm wide and the bottom flange 230 mm. For prestressed beams, the lower chord was pretensioned with six rectilinear T15S tendons, each with a prestressing force of 170 kN. For other specimens, the passive longitudinal reinforcement was realized with five #20 and one #25 rebar. The shear reinforcement consisted in #6 links and was installed in four specimens with 75 mm spacing. The shear reinforcement ratio was 0.6 %. This value has been chosen to represent the ratio existing in real structures made of UHPFRC (in which stirrups are generally used just as a local help for shear capacity) and to produce a significant contribution of transversal steel reinforcement (approximately 20 % of the total ultimate shear resistance). Only specimens with shear reinforcement had an upper steel rebar (#10) for stability of the reinforcing "frame". In order to get homogeneously distributed fibers throughout the whole specimen, the distance between reinforcements or between formwork and steel reinforcing bars was fixed higher than 30 mm (= the Maximum Fiber Length). Indeed the combination of fibers and shear reinforcement could have shown a negative effect due to fibre blockage if enough space for concrete flow into the mold could not have been provided. The full details of dimensions and arrangement of reinforcement are shown in Figure 1.

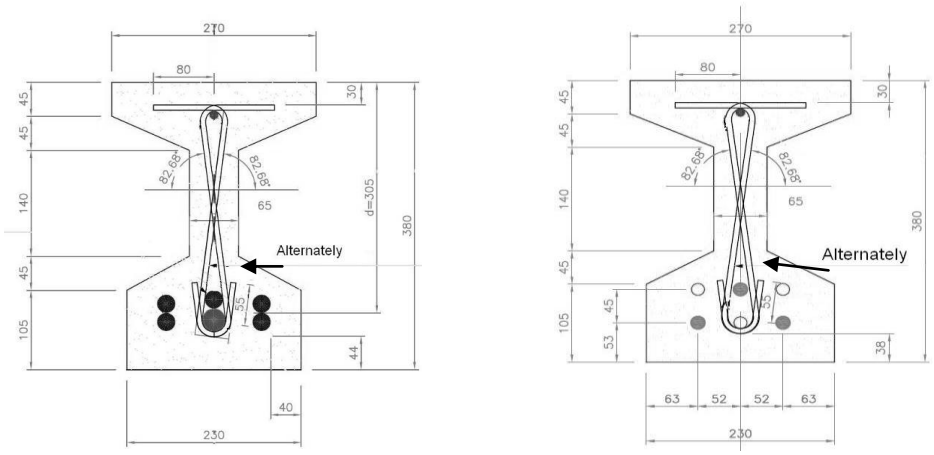

Figure 1: Cross section of prestressed beams with links (Left side) and reinforced beams with links (Right side) – Dimensions in mm.

All beam specimens were tested in a four point bending configuration. The span was 2 meters and the shear span ratio was 2.5 in order to avoid an important arching action. More details are provided in [8].

Experimental results

Figure 2 shows the experimental load-deflection curves for prestressed and reinforced beams, respectively. Although they were fabricated with a different batch, the behaviour of beams UHPFRC-A-PC-NS and UHPFRC-A(2)-PC-NS were very similar with approximately the same ultime load. Except beams with passive longitudinal reinforcement and with stirrups, all specimens have failed in shear, exhibiting a largely opened diagonal tension crack. Beams UHPFRC-A-RC-WS and UHPFRC-B-RC-WS failed in bending but with large openings of diagonal cracks which indicate that the maximum load applied was close to the ultimate shear capacity. More details are provided in [8].

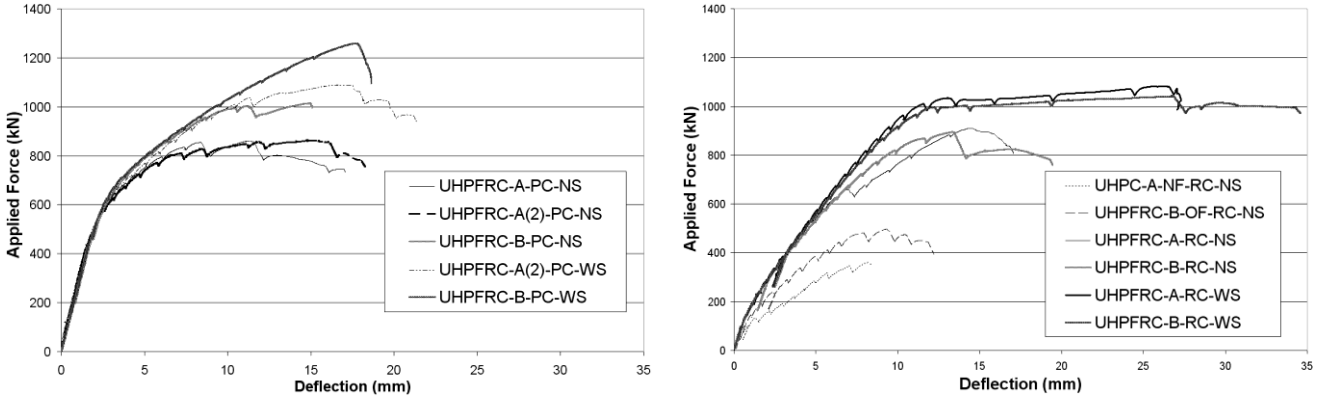

Figure 2: Load-deflection curves of prestressed beams (at left) and reinforced beams (at right).

3 Materials Characterization

Fibres orientation

In order to identify the contribution of the fibers in the ultimate shear strength as detailed in AFGC provisions [6], prisms have been cut in both undamaged extremities of the beams, at different inclinations to determine the real “coefficient of orientation”. The chosen angles for each material are (Figure 3):

- 0°, 45°, 90° for the UHPFRC-B and 0°, 45°, 60°, 90° for the UHPFRC-A (an additional inclination has been tested in reason of a bigger number of specimens).
- 0°, 45° for the UHPFRC-B-OF: only one beam had been cast.

Except for the UHPFRC-B-OF, for each considered inclination, six prisms 7cm*6.5cm*L (L > 26 cm) have been extracted, notched (the un-notched height is equal to 6.1 cm) and tested in 3 point bending configuration.

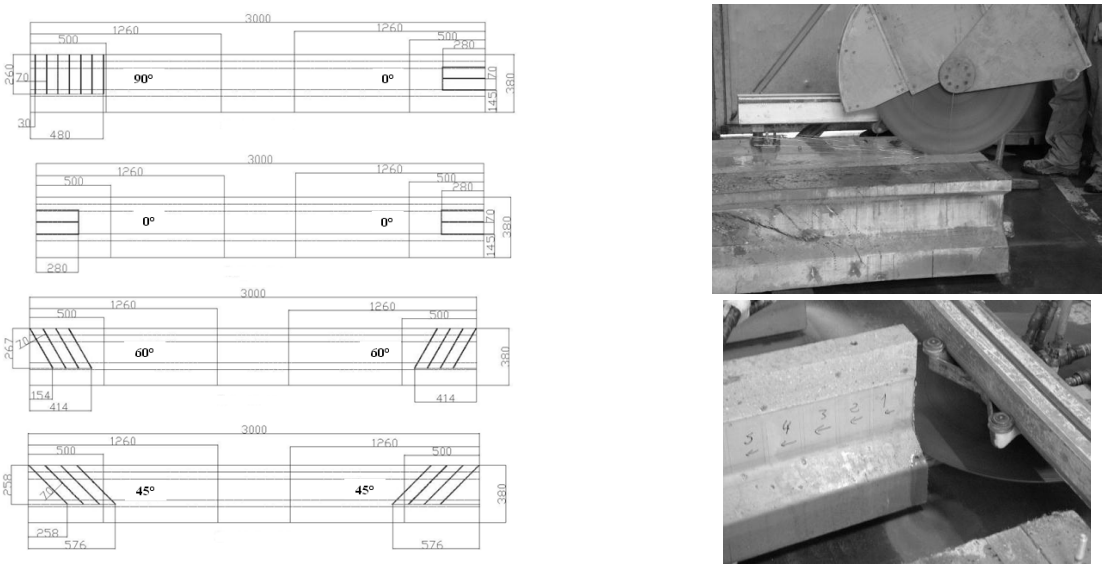

Figure 3: Prisms extraction for the UHPFRC-A (length in mm).

For both UHPFRC-A and –B Mixes, from the average curves "Bending Stress (BS) – Measured crack opening ($w_{measured}$)" corresponding to the different inclinations, an average curve has been constructed in order to determine an orientation factor (1) for each angle [Figure 4] (as recommended in [6]):

$$Orientation\ \ factor\ \alpha° = \frac{Max("BS - w"-\alpha°)}{Max\left[\ Average("BS - w"\ \ 0°;"BS - w"\ \ 45°;"BS - w"\ \ 90°)\ \right]} \quad (1)$$

For the UHPFRC-A [UHPFRC-A(2)], in order to keep the symmetry for the construction of the average curve, the results corresponding with the angle 60° are not taken into account.

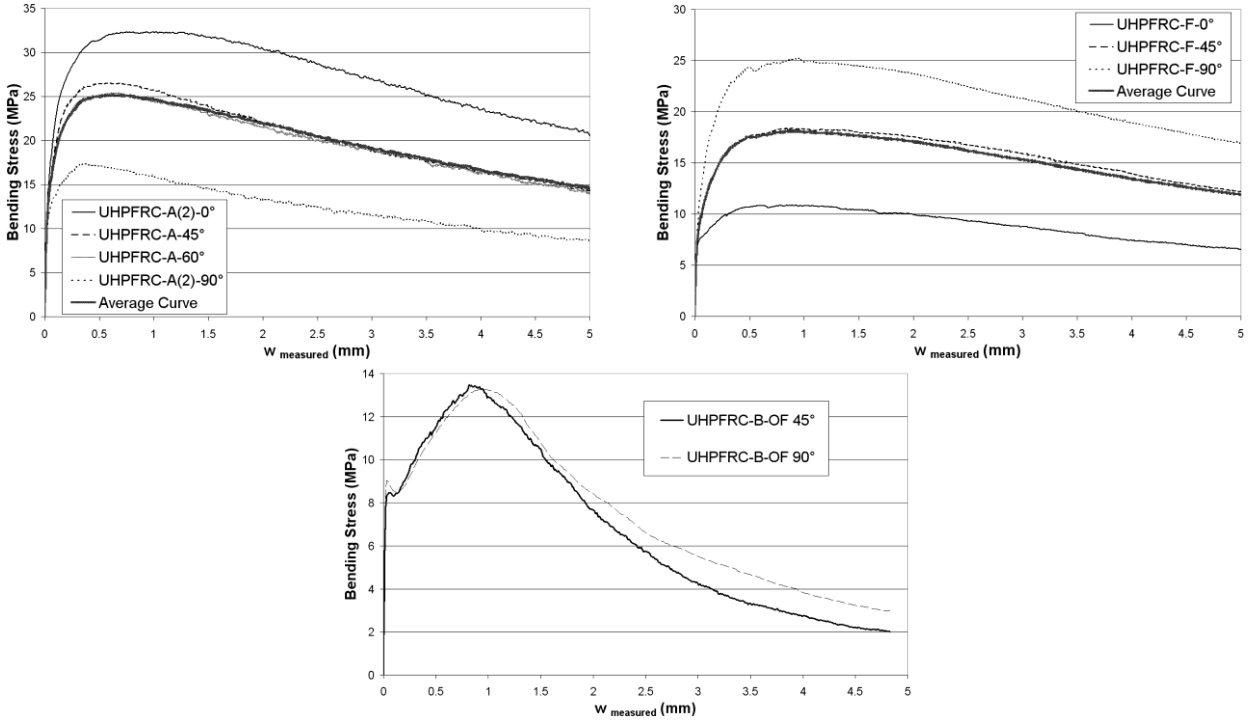

Figure 4: For each UHPFRC : Curves "Equivalent Bending Stress (EBS) – Measured crack opening (w)" obtained from the 3 point bending tests on sawn and notched prisms with different inclinations equal to 0°, 45°, 60° and 90° : corresponding average curve (without taking into account the results for 60°).

Table 3: "Orientation factor" for each inclination and for each UHPFRC.

Concrete	Inclination (°)	Max "BS-w" at α° (MPa)	Max Average Curve ("BS-w"-0°-45°-90°) (MPa)	Orientation factor
UHPFRC-A UHPFRC-A(2)	0	32.3	25.1	0.78
	45	26.5	25.1	0.95
	60	25.4	25.1	0.99
	90	17.4	25.1	**1.45**
UHPFRC-B	0	10.9	18.1	**1.67**
	45	18.4	18.1	0.99
	90	25.2	18.1	0.72
UHPFRC-B-OF	45	13.5	-	-
	90	13.3	**-**	-

Reference "Stress – crack opening" ("σ-*w*") relationship

For each UHPFRC, the reference "σ-*w*" relationship is obtained from the average curve "Bending Stress (BS) – Measured crack opening ($w_{measured}$)" derived from the average curves "BS – $w_{measured}$" corresponding to the inclinations 0°, 45° and 90°. The inverse method described in [6] is applied to average curves "BS-$w_{measured}$" for each UHPFRC. The obtained "σ-w" curves are then corrected concerning the limit of linearity. Indeed the notch realised for the third point bending tests induces a stress concentration which can disturb the behaviour of the cementitious matrix. Thus the value of the limit of linearity obtained from the four point bending tests on un-notched prisms (7cm*7cm*28cm) is chosen ([6]) : f_t is equal to 9.2 for UHPFRC-A-A(2), 9.8 for UHPFRC-B and 9.0 for UHPFRC-B-OF. In the case of a soft-hardening behaviour, the post-peak value is obtained by lopping at the maximum value post-peak. The "σ-*w*" curves are also smoothed in using a third degree polynomial interpolation with an interval on the crack opening equal to 0.05 mm (Figure 5).

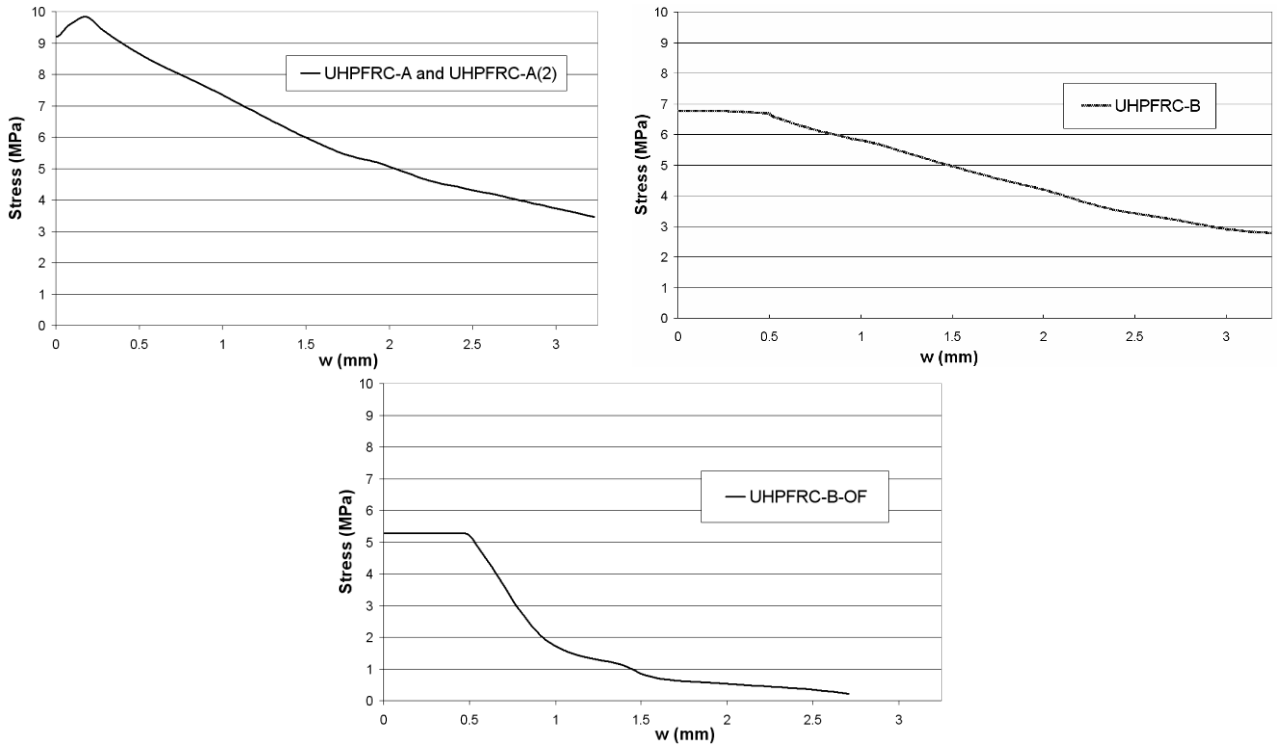

Figure 5: Reference "σ-w" relationships obtained with inverse analysis for each UHPFRC.

Properties of passive and active steel reinforcements

The "σ-ε" relationship has been experimentally determined for both passive and active reinforcement (Table 4).

Table 4: Characteristics of the "σ-ε" relationship for each kind of reinforcement.

Steel Reinforcement	Young's Modulus (GPa)	σ at 0.1% (MPa)	σ at 0.2% (MPa)	Ultimate Stress (MPa)	Ultimate Strain (‰)
Tendons T15S	195	1728	1772	1918	48
#20 and #25 rebars	199	-	551	618	53
#6 rebars	176	-	561	594	24

The prestress losses have been estimated from experimental results with assumption on strand relaxation (initial prestressing force for each tendon equal to 170 kN):

- 30.5 % of prestress losses for beams made of UHPFRC-A[(2)] (σ_x = 12.55 MPa)
- 32.5 % of prestress losses for beams made of UHPFRC-B (σ_x = 12.3 MPa)

The important percentage of prestress losses is in particularly due to a low initial pretension.

4 Comparison with theoretical shear strength predictions

From the designer's point of view, all the results are compared (Table 5) to the theoretical shear strength prediction according to [6]:

$$V_{ult} = V_{rb} + V_a + V_f \quad (2)$$

V_{rb} represents the contribution of the concrete, V_a is the term for the contribution of the stirrups and V_f the contribution of the fibers.

For reinforced concrete (without axial force):

- $V_{rb} = 0.21 \cdot \sqrt{f_{cj}} \cdot b_0 \cdot d$
- $V_a = 0.9 \cdot d \cdot \frac{A_t}{s_t} \cdot f_y$ and $V_f = 0.9 \cdot d \cdot b_0 \cdot \sigma_p$ with $\sigma_p = \frac{1}{K} \cdot \frac{1}{w_{\lim}} \times \int_0^{w_{\lim}} \sigma(w) \cdot dw$

For prestressed concrete:

- $V_{rb} = 0.24 \cdot \sqrt{f_{cj}} \cdot b_0 \cdot z$
- $V_a = z \times \frac{A_t}{s_t} \times f_y \times \cot an\beta_u$, with $\tan \beta_u = \frac{2 \cdot \tau_u}{\sigma_{cd}}$ and $V_f = b_0 \cdot z \cdot \sigma_p \cdot \cot an\beta_u$

With :

- b_0 web width and d effective depth of the longitudinal reinforcement
- z lever arm of internal forces.
- f_{cj} compressive strength and τ_u ultimate shear stress
- σ_{cd} design value of the normal concrete stress in the centre line.
- σ_p concrete post cracking tensile strength, f_y yield strength of stirrups, A_t cross sectional area of the stirrups and s_t spacing of shear reinforcement.
- w_{lim} = max (w_u; w_{max}) w_u being the crack opening at the bottom side, under the bending moment exerted in the section and w_{max} the crack opening corresponding to an irreversible decrease of the stress in the reference "σ-*w*" relationship (w_{max} = 0.20 mm for UHPFRC-A[(2)], w_{max} = 0.50 mm for UHPFRC-B and w_{max} = 0.47 mm for UHPFRC-B-OF)

All material safety factors have been taken equal to 1 for the purpose of design provision validation. The French AFGC-Sétra Recommendations on UHPFRC consider that the crack opening which has to be taken into account for the calculation of the fibres contribution (for ultimate shear strength) is determined from the bending moment related to the ultimate shear force. Thus, in the case of our study, two options are possible :

- The crack opening corresponding to the ultimate shear strength is determined from the calculated curve “Bending Moment – Crack Opening” and the bending moment corresponding to the ultimate shear force obtained experimentally.
- The experimental results are not considered in the calculations. The crack opening corresponding to the ultimate shear strength and the compressive struts angle θ is determined by iteration.

Both options have been studied in order to quantify their deviation.

Concerning the consideration of real fibers orientation inside specimens, the tensile residual strength σ_p is divided by an “orientation factor” depending on the compressive struts angle :

- Reinforced beams : “orientation factor” corresponding to 45 °.
- Prestressed beams : “orientation factor” corresponding to θ° with θ the inclination of compressive struts with respect to the beam axis.

The “orientation factor” is assumed to be linearly variable with θ, thus derived from a linear interpolation between the experimental points obtained for 0°, 45° and 90°. In the realistic direction of the struts, this factor will be comprised between 0.92 and 0.99. For design purpose, it is recommended ([6]) to take the most unfavourable value of “orientation factor” : 1.45 for UHPFRC-A-A(2) and 1.67 for UHPFRC-B. It should provide a significant safety margin.

Table 5: Comparison of experimental and theoretical results according to [6].

	Type of Failure	Experimental results not used (With Iteration)				Experimental results used (No Iteration)			
		Predicted Force (kN)	Exp / Theory	Struts Angle (°)	w_{lim} (mm)	Predicted Force (kN)	Exp / Theory	Struts Angle (°)	w_{lim} (mm)
UHPFRC-A-PC-NS	Shear	632	1.36	35.1	0.2	587	1.47	37.6	0.4
UHPFRC-A(2)-PC-NS	Shear	632	1.36	35.1	0.2	587	1.47	37.6	0.4
UHPFRC-B-PC-NS	Shear	527	1.92	33.5	0.5	433	2.34	38.8	0.99
UHPFRC-A(2)-PC-WS	Shear	771	1.41	36.8	0.22	683	1.59	39.1	1.02
UHPFRC-B-PC-WS	Shear	663	1.90	35.7	0.5	532	2.37	40.0	2.02
UHPFRC-A-RC-NS	Shear	479	1.90	45	0.28	454	2.00	45	0.81
UHPFRC-B-RC-NS	Shear	362	2.47	45	0.5	356	2.51	45	0.85
UHPFRC-A-RC-WS	Flexure	596	1.82	45	0.42	528	2.05	45	1.76
UHPFRC-B-RC-WS	Flexure	484	2.15	45	0.5	416	2.50	45	3.2
UHPC-A-NF-RC-NS	Shear	114	3.17	45	-	114	3.17	45	-
UHPFRC-B-OF-RC-NS	Shear	295	1.68	45	0.47	295	1.68	45	0.47

Given these experimental results, the approach proposed by the French recommendations is conservative in all cases. The safety factor on the maximum applied load ranges from 1.36 to 2.37 for prestressed UHPFRC beams and from 1.82 to 2.50 for reinforced UHPFRC beams.

Concerning the specimens UHPFRC-A-RC-WS and UHPFRC-B-RC-WS, the theoretical shear strength predictions obtained without iteration are underlined because they correspond to a flexural failure. The predicted strength is thus a lower bond value.

The average deviation between the shear strength predictions obtained with and without iteration is equal to 12.6% for the prestressed beams (with a maximum close to 20%) and 8.1% for reinforced beams made of UHPFRC with steel fibers (the maximum being close to 15%). Due to the influence of the compressive struts angle, the deviation is more important in the case of prestressed beams.

5 Conclusions

Shear tests have been realized in a Four-Point Bending configuration on eleven prestressed or reinforced UHPFRC I-shaped beams with different types of shear reinforcement: fibers or no fibers and combination of links and fibers. In order to identify the contribution of the fibers in the ultimate shear strength, prisms have been cut in the beams, at different inclinations to determine the real “orientation factor”. This is very useful to analyse the experimental results in particularly to identify the real contribution of fibres in the ultimate limit state. According to this analysis, the approach proposed by the French recommendations is conservative in all cases.

6 Acknowledgement

This experimental program has been supervised by a committee chaired by J. Resplendino (SETEC), also chairman of the French mirror group of fib TG8.6. Eiffage (A. Simon and T. Thibaux) and Lafarge (L. Jacques and G. Molines) are gratefully acknowledged for their sponsoring and contribution in the specimen preparation.

References

[1] Casanova, P., Rossi, P. 1996. Analysis of metallic fibre-reinforced concrete beams submitted to bending. Materials and Structures, vol 29, July 1996, pp.354-361.

[2] Swamy R.N., Jones R., Chiam A.T.P. 1993. Influence of steel fibers on the shear resistance of lightweight concrete I-beams, ACI Structural Journal, vol 90, n°1, pp. 103-114.

[3] Graybeal, B. 2006. “Structural Behavior of Ultra-High Performance Concrete Prestressed I-Girders,” U.S. Department of Transportation, Federal Highway Administration, FHWA-HRT-06-115, Aug. 2006,104 pp.

[4] Sato Y., Pansuk W., Den Uijl J.A., Walraven J.C. 2008. Shear Capacity of high performance fiber reinforced concrete I-beams, 8th International Symposium on Utilization of High-Strength and High-Performance Concrete, pp. 369-376.

[5] Bertram, G., and Hegger, J. 2010. “Pretensioned UHPC beams with and without openings”, Proceedings of 3rd fib International Congress, Washington DC, USA, May 2010.

[6] AFGC-Sétra. 2002. “Ultra High Performance Fibre-Reinforced Concretes”. Interim Recommendations, Bagneux: SETRA.

[7] Toutlemonde, F., Fouré, B., de Larrard, F. 2003. “Vérifications concernant la prise en compte réglementaire de certaines propriétés des bétons à hautes et très hautes performances”. BLPC, Vol. 246-247, pp. 73-100.

[8] Baby, F., Billo, J., Renaud, J.C., Massotte, C., Marchand, P., Toutlemonde, F. 2010. “Shear resistance of ultra high performance fibre-reinforced concrete I-beams,” FraMCoS7, B.H. Oh et al. eds, Jeju (Korea), 23-28 May, pp. 1411-1417.

Shear Behavior of Pretensioned UHPC Beams – Tests and Design

Guido Bertram, Josef Hegger
Institute of Structural Engineering, RWTH Aachen University, Germany

Ultra High-Performance Concrete (UHPC) is a high-tech material opening new opportunities especially for slender constructions. Within the priority program [1] supported by the German Research Foundation (Deutsche Forschungsgemeinschaft DFG) sixty shear tests on prestensioned beams have been carried out at the Institute of Structural Concrete at RWTH Aachen University. Different amounts of steel fibers have been added to the concrete to ensure a sufficient ductility and also to serve as shear reinforcement. Further main parameters were the prestressing, the shear slenderness, the number and position of web openings, the opening diameter and additional shear reinforcement. The latest tests were focused on the size effect. Generally, the effective depth is the most used influencing factor for size effects in shear models. In case of fiber reinforced concrete, a further size effect due to the web thickness may occur, which is based on different fiber orientations and distributions close to the formwork surface.
The investigations, which were carried out between 2006 and 2011, have been presented amongst others in Kassel (UHPC 2008), Amsterdam (fib 2008), Tokyo (HPC/HSC 2008), London (fib 2009), Washington DC (fib 2010), Rotorua (HPC 2011) and Salt Lake City (PCI 2011). An overview of shear tests on beams with a height of 40 cm is given in the SCC2010 proceedings [6].

Keywords: Ultra-high Performance Concrete, fibers, shear, pretensioning, openings

1 Introduction

A priority program [1] on UHPC with over 20 projects in Germany started in 2005. The shear behavior of pretensioned beams made of UHPC as well as the bond behavior of strands in UHPC have been investigated in one of these projects at the Institute of Structural Concrete at RWTH Aachen University. The bond behaviour is published in [8,9] and another paper at the Hipermat [10].

The compressive strength of UHPC is about five times the strength of conventional normal strength concrete. Therefore, a high degree of prestressing can be applied and thus, more slender structures are feasible. This leads to significant savings in dead load and transportation costs which is an important issue especially for precast members. The stringent production requirements for UHPC restrict the main field of application to precast members, e.g. roof girders of large span. Adding steel fibers to the concrete contributes to the shear resistance and improves the post-cracking behavior. Thus, steel fibers eliminate the need for conventional shear reinforcement. Generally, this is allowed in Germany according to the guideline for steel fiber reinforced concrete [11], which contains additions to the German Design Code [12]. Prestressed members are not included in [11] due to the lack of basical knowledge. Web openings influencing the ultimate shear carrying capacity are frequently arranged in the girders to accommodate building utilities.

In order to investigate the shear strength of pretensioned UHPC beams with and without web openings, an extensive experimental program consisting of a total of sixty shear tests was carried out.The investigated test parameters were the fiber content, the grade of prestressing applied, the shear slenderness, the location and number of web openings in the beams as well as size effects. Furthermore, different shapes of additional shear reinforcement close to the openings were investigated and compared to the bearing capacity of beams without such reinforcement.

2 Experimental Investigations

Materials

The UHPC used in this study is flowable and nearly self compacting. No concrete vibrators were used, merely a little poking to avoid air entrapments in the lower cord due to the lateral covering formwork and the density of strands. All specimens were cast with the concrete composition presented in Table 1. Merely the fiber type and ratio were varied. All fibers were straight – without hooks – and of high strength steel. Two fiber ratios (0.9 % and 2.5 % per volume) were investigated. The diameter of 0.15 mm is specified by the manufacturer and the margin is ±0.02 mm. In several spot tests the diameter was about 0.17 mm in average. The steel fibers had a length between 9 mm and 17.5 mm and a strength f_y^f > 2200 N/mm². In some tests on size effects, the fibers were enlarged in beams with a higher cross section (M1a, f_y^f > 1400 N/mm²). The reference composition MR contained no fibers. Due to the slenderness of the fibers and the short anchorage length (half of the fiber length), no tensile failure of the fibers is possible but rather a fiber pull-out. This results in a more ductile tensile behavior of the UHPC affecting the shear behavior of the beams as well. The slump flow spread of the concrete mixtures M0 as well as M1 ranges between 66 and 72 cm. In mixture MR without fibers the slump flow spread was increased to 75 to 80 cm, which has led to a partial settlement of the basalt. In mixtures with fibres, no segregation was observed.

Table 1: Concrete composition with different fiber contents.

Mix/fiber ratio / Material		M0	M1	M1a	MR
		2.5% p.v.	0.9% p.v.	0.9% p.v.	w/out
Cement CEM I	[kg/m³]	650	660	660	666
Silica fume	[kg/m³]	177	180	180	181
Quartz powder	[kg/m³]	456	463	463	467
Sand 0.125-0.5mm	[kg/m³]	354	360	359	363
Basalt 2-8mm	[kg/m³]	598	606	606	612
Steel fibers 9.0/0.15	[kg/m³]	194	-	-	-
Steel fibers 17.5/0.15	[kg/m³]	-	70	-	-
Steel fibers 30/0.40	[kg/m³]	-	-	70	-
Water	[kg/m³]	158	161	160	162
Superplasticizer	[kg/m³]	31	32	32	32

Testing Program, Specimens and Setup

An overview of the conducted shear test program is given in the Tables 2 and 3. On each beam with h = 40 and 70 cm, two shear tests were carried out (Fig. 1). The first test is denoted by “a” and the second by “b”. On beams with h = 100 cm only one test was carried out due to the restricted member size in the lab. Overall, there are five main groups of pretensioned beams:

- beams without openings,
- beams with single web openings,
- beams with several web openings,
- beams with additional shear reinforcement near the web openings,
- and beams with varied height and web width (size effects).

For beams without openings, the fiber content, the prestressing and the shear slenderness were varied ($3.5 \leq a/d \leq 4.4$). The clearance between the first opening and the support line as well as the clearance between the openings were varied between $0.5d$ (150 mm) and $2.0d$ (600 mm). The diameter of the openings was $0.5d$ for all beams except for beam T13, in which

the diameter of the opening was reduced to 0.33*d* (100 mm). The web openings were not fabricated by sawing but by recesses in the formwork.

The material properties were determined at the day of the release as well as before the shear tests. The compressive strength was determined with 100 mm cubes and the flexural strength in a three point bending test on prisms 16 cm x 4 cm x 4 cm. In the last column, the ultimate shear force V_u at the support including the dead load is given.

Table 2: Testing parameters and main results of beams with h = 40 cm and b_w = 6 cm.

Test	Mix	a/d	0.5'' strands		Ø [mm]				Openings no./a_1/a_2	$f_{c,cube100}$ [MPa]		$f_{ct,fl}$ [MPa]		V_u
					Studs	Stirrups	Ring	Hook		Release	Shear test	Release	Shear test	[kN]
T1a	M1	3.8	7	without opening	-				- / - / -	88.9	151	-	22.7	234
T1b	M1	3.8	9								174		21.2	267
T2a	MR	3.8	7							86.8	134	8.9	10.7	134
T2b	MR	3.8	9								134		12.3	147
T3a	M0	3.8	7							103.2	170	22.1	23.1	***
T3b	M0	3.8	9								162		24.1	408
T4a	M1	3.8	9							100.3	176	16.5	19.1	347
T4b	M1	4.4	9								183		20.2	292
T5a	M1	3.8	9							102.6	177	14.6	-	326
T5b	M1	3.8	9								179		20.1	296
T18a	M1	4.1	9							116.4	185	27.9	34.1	301
T19b	M1	3.5	9							105.9	174	20.5	24.3	324
T21b	M1	3.8	9		6					113.3	187	19.8	22.6	358
T6a	M1	3.8	9	single opening					1 / 0.5*d* / -	89.0	142	18.8	22.8	266
T6b	M1	3.8	9						1 / 1.0*d* / -		155		23.0	226
T7a	M1	3.8	9						1 / 1.5*d* / -	112.8	192	16.9	26.0	234
T7b	M1	3.8	9						1 / 2.0*d* / -		183		24.7	232
T9a	MR	3.8	9						1 / 0.5*d* / -	108.7	162	8.3	12.8	116
T9b	MR	3.8	9						1 / 1.5*d* / -		157		15.4	101
T10a	M1*	3.8	9						1 / 0.5*d* / -	120.5	202	31.5	35.9	257
T10b	M1*	3.8	9						1 / 1.5*d* / -		201		36.3	241
T12a	M0	3.8	9						1 / 1.0*d* / -	123.6	181	24.6	30.0	323
T8a	M1	3.8	9	several openings					2 / 1.0*d* / 0.5*d*	110.7	175	-	-	169
T8b	M1	3.8	9						2 / 1.0*d* / 1.0*d*		177		-	192
T11a	M1	3.8	9						2 / 1.0*d* / 1.5*d*	110.8	181	22.0	27.8	230
T11b	M1	3.8	9						2 / 0.5*d* / 2.0*d*		181		31.0	250
T12b	M0	3.8	9						2 / 1.0*d* / 1.0*d*	123.6	185	24.6	26.8	216
T13a	M1	3.8	9						4 / 0.5*d* / 0.5*d***	104.1	181	20.1	25.0	184
T13b	M1	3.8	9						2 / 1.0*d* / 1.0*d***		176		27.7	235
T14a	M1	3.8	9	two openings with additional rebars	6				2 / 1.0*d* / 1.0*d*	113.4	178	15.1	21.8	242
T14b	M1	3.8	9		8				2 / 1.0*d* / 1.0*d*		175		22.2	287
T15a	M1	3.8	9		6				2 / 1.0*d* / 1.5*d*	114.3	186	16.7	24.7	269
T15b	M1	3.8	9		8				2 / 1.0*d* / 1.5*d*		186		20.6	304
T16a	M1	3.8	9			6			2 / 1.0*d* / 1.0*d*	122.2	189	28.0	31.0	274
T16b	M1	3.8	9			8			2 / 1.0*d* / 1.0*d*		184		30.0	281
T17a	M1	3.8	9				6		2 / 1.0*d* / 1.0*d*	103.0	162	18.6	23.2	208
T17b	M1	3.8	9				8		2 / 1.0*d* / 1.0*d*		161		25.6	202
T18b	M1	4.4	9		8				2 / 1.0*d* / 1.0*d*	116.4	186	27.9	34.4	275
T19a	M1	3.8	9		10				2 / 1.0*d* / 1.0*d*	105.9	178	20.5	25.2	301
T20a	M1	3.8	9					6	2 / 1.0*d* / 1.0*d*	100.4	164	18.2	23.8	270
T20b	M1	3.8	9					8	2 / 1.0*d* / 1.0*d*		166		-	291
T21a	M1	4.4	9		6				2 / 1.0*d* / 1.0*d*	113.3	174	19.8	25.0	251

* fiber content increased to 1.5 % p.v.

** diameter of the web openings reduced to *d*/3 = 10 cm (*d*/2 = 15 cm in all other tests)

*** test abort due to bending failure

Table 3: Testing parameters and main results on size effects.

Test	Mix	a [m]	h [cm]	b_w [cm]	0,5'' strands	Ø/s [mm] studs		Openings no./a_1/a_2	$f_{c,cube100}$ [MPa] Release	$f_{c,cube100}$ [MPa] Shear test	$f_{ct,fl}$ [MPa] Release	$f_{ct,fl}$ [MPa] Shear test	V_u [kN]
T22b	M1	1,20	40	4	6	-	without opening	- / - / -	112.3	189	26.2	25.6	174
T23b	M1	1,20	40	8	12	-			124.0	184	23.0	-	454*
T24b	M1	2,35	70	4	12	-			102.8	178	23.8	29.6	316
T25b	M1	2,35	70	6	18	-			103.2	169	20.9	23.7	465
T26b	M0	2,35	70	6	18	-			109.7	172	26.4	31.5	521
T27b	M1	2,35	70	6	18	8/30			120.1	189	21.5	30.2	610
T28b	M1	2,35	70	6	18	8/45			123.6	176	22.4	-	512
T29b	M1a	2,35	70	6	18	-			117.9	183	21.0	25.1	476
T30	M1	3,50	100	4	18	-			118.4	184	20.6	23.0	371
T31	M1a	3,50	100	4	18	-					coming	soon	
T22a	M1	1,20	40	4	6	-	single opening	1 / 1,0d / -	112.3	187	26.2	31.9	210
T23a	M1	1,20	40	8	12	-		1 / 1,0d / -	124.0	178	23.0	25.2	361
T24a	M1	2,35	70	4	12	-		1 / 0,5d / -	102.8	179	23.8	29.6	319
T25a	M1	2,35	70	6	18	-		1 / 1,0d / -	103.2	172	20.9	24.9	344
T26a	M0	2,35	70	6	18	-		1 / 1,0d / -	109.7	178	26.4	36.8	368
T27a	M1	2,35	70	6	18	8/30		1 / 1,0d / -	120.1	180	21.5	25.5	567
T29a	M1a	2,35	70	6	18	-		1 / 1,0d / -	117.9	181	21.0	24.3	386
T28a	M1	2,35	70	6	18	8/30	2 Op.	2 / 1,0d / 1,0d	123.6	176	22.4	-	534

* unexpected shear failure occurred on the second beam side due to a predamage of the first test

In tests on size effects the web thickness was varied between 4 and 8 cm, the height between 40 and 100 cm. Here, the shear slenderness a/d = 3.8 and the pressing stresses were kept constant. Due to the limited length of the paper, only the beams with h = 40 cm and b_w = 6 cm are illustrated in Figure 1. Further details are given in [5,7]. Additionally, tests with openings and shear reinforcement in the higher beams were carried out in selected cases. Because of a more brittle failure of the higher beams, further tests with longer fibers (mix M1a) were added.

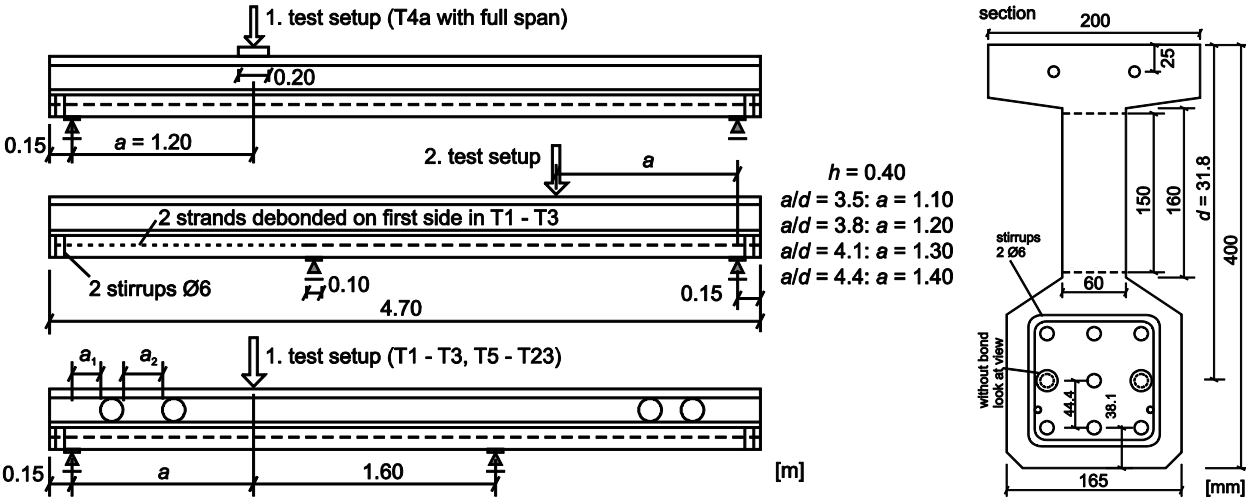

Figure 1: Test setup, side view and cross-section of the beams with h = 40 cm and b_w = 6 cm.

The specific concrete cover was taken as $c/Ø_p$ = 2.5 according to the previous small scale beam tests [8-10] ($Ø_p$: diameter of the prestressing strands). In order to avoid an anchorage failure, two stirrups Ø6 were arranged in the vicinity of the support.

The beams were fabricated in a prestressing bed. The 0.5'' prestressing strands were tensioned to a maximum value of $0.9 \cdot f_{pk}$ = 0.9·1500 MPa = 1350 MPa according to the German

Standard DIN 1045-1 [12], resulting in an initial strain ε_0 of 1350/200000 = 6.75 ‰ and a maximum prestressing force of 125 kN per strand. The prestressing was released gradually three days after casting with the concrete strength about 100 MPa. Before the shear tests, the longitudinal concrete strain was measured. This way, the prestressing losses due to elastic shortening as well as creep and shrinkage were estimated and the effective prestressing force acting on the beam was determined.

The concrete strain in the lower chord was 0.9-1.0 ‰ after the release of prestressing. Until the shear tests at the age of about four weeks, the concrete strain increased to 1.45 to 1.6 ‰ due to creep and shrinkage. As a consequence, the loss of prestressing - time dependent and the elastic part – ranged between 1 – (6.75 –1.45)/6.75 = 21 % and 24 %, where 6.75 ‰ is the initial steel strain inside the prestressing bed. In beams with seven strands, the concrete stresses due to prestress were less, which led to 18 % losses.

The shear tests were carried out when the compressive strength was between about $f_{c,cube100}$ = 160 MPa and 200 MPa (Tables 2 and 3). The deflection was measured with a LVTD under the loading point.

3 Test Results

Effect of fiber ratio in case of solid beams

Generally, the shear tests showed a very stiff load bearing behavior due to the high prestressing. In Figure 2 (left) the load-deflection curves for three beam tests without openings and with different fiber ratios are presented. The comparison of the load-deflection curves of T2b, T5a and T3b as well as the ultimate shear forces in Table 2 indicate the effectiveness of the steel fibers as shear reinforcement. A steel fiber ratio of 0.9 % p.v. led to a substantial increase of 119 % in the failure load (T5a: 326 kN) and an amount of 2.5 % p.v. increased the failure load by 177 % (T3b: 409 kN) compared to T2b without fibers (149 kN). Figure 2 (right) illustrates the ultimate shear force as a function of the fiber ratio and indicates the significant effect of the steel fiber ratio on the shear resistance. The scatter for the beams of 0.9 % fiber ratio and 9 prestressing strands may be related to the different casting method used for T1, while test T4a forms the upper range of the scatter respectively. For the following comparisons test T5a (326 kN) will be used as average reference.

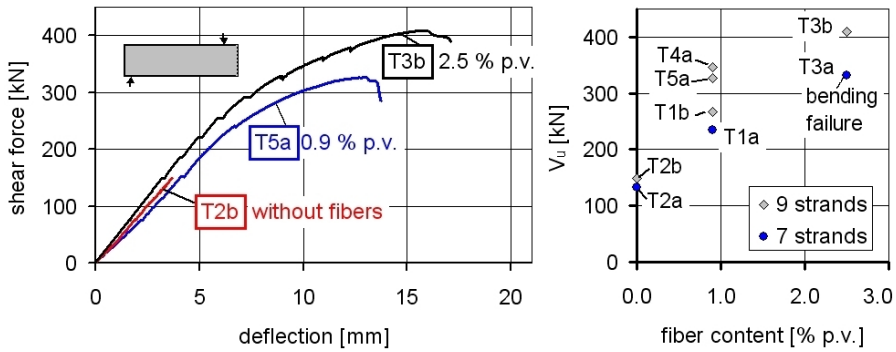

Figure 2: Left: Load-deflection curves of solid beams with different fiber contents, Right: Ultimate shear force versus fiber content.

Effect of degree of prestressing

The effect of the degree of prestressing on the shear resistance can be investigated by comparing tests T1a, T2a and T3a (7 strands) with tests T1b, T2b and T3b (9 strands). The effective depth remains the same because the centre of reinforcement was not varied (Fig. 1). The effective prestressing force at the time of testing can be calculated from the concrete strain

measurements. As previously discussed, this results in an effective prestressing force of 857 kN for 9 strands and 717 kN for 7 strands. Increasing the effective prestressing from 717 kN to 857 kN by 20 % resulted in an increase in the shear capacity from 134 kN to 149 kN by 12 % for beam T2 without fibers and from 234 kN to 268 kN by 14 % for beam T1 with 0.9 % p.v. fibers (Fig. 2, right). In beam T3a with 2.5 % p.v. fibers the shear capacity exceeded the bending capacity with seven strands and hence the failure load is not comparable.

Effect of the shear slenderness

The effect of the shear slenderness on the shear strength is shown in Figure 3. An increase in the shear slenderness from *a*/*d* = 3.5 (T19b) to *a*/*d* = 4.4 (T4b) resulted in a decrease in the shear resistance from 324 kN to 292 kN (10 %). Test T4a seems to be in the upper range of scatter (*a*/*d* = 3.8, V_u = 347 kN). The different stiffnesses in these tests were due to the different spans (1.6 m + *a*). Generally, a significant influence of the shear slenderness was not expected when the slenderness exceeds *a*/*d* = 3.5, even in prestressed members, nevertheless a slight influence was observed.

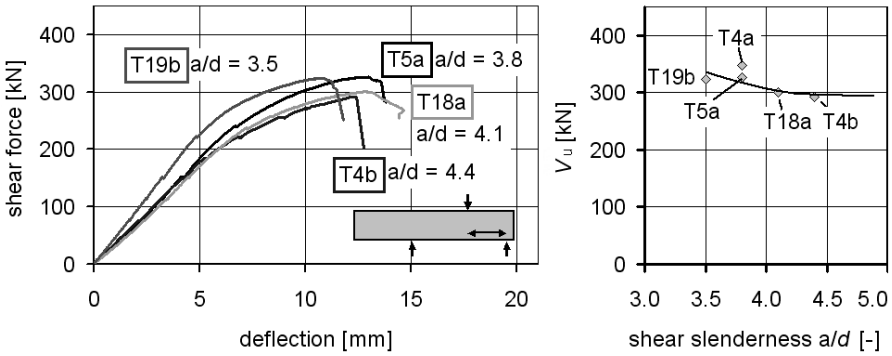

Figure 3: Left: Load-deflection curves of beams with different shear slendernesses (0.9 % p.v.), Right: Ultimate shear force versus shear slenderness.

Effect of single web openings

Single openings were arranged at a clearance to the support between 0.5*d* and 2.0*d*. In Figure 4 (left), the load-deflection curves for beams T6 and T7 are plotted. The beams were identical except for the location of the opening. The fact is interesting that in test T6a the distance was 0.5*d* and the shear carrying capacity reached a high value of 266 kN. It seems that, due to the small distance of the opening in T6a, the arch action to the support was capable to develop underneath the opening. When the distance was enlarged, the ultimate shear force was 234 kN (T7a) and 232 kN (T7b). In Fig. 4 (right) the ratio $V_{Test\text{-}Ø}/V_{Test\text{-}without\ Ø}$ is drawn as a function of the relative distance a_1/d from the face of the opening to the support. $V_{Test\text{-}Ø}$ is the failure shear force of beams with an opening, while $V_{Test\text{-}without\ Ø}$ is the failure shear force of the corresponding beam without opening (T2b, T5a, T3b). For example, the ratio 234/326 = 0.72 (T7a/T5a) shows the remaining shear resistance with 0.9 % p.v. fibers and one opening in a distance a_1 = 1.5d.

Effect of two openings

The effect of two openings on the shear behavior can be studied using the test results of beams T8 and T11. The beam tests T8a, T8b and T11a were identical with the first opening being located at a distance a_1 = 0.5*d* from the support. The distance between the second and the first opening a_2 varied between 0.5*d* and 2.0*d*. In Figure 5 (left), the load-deflection curves are illustrated. The location of the second opening seems not to have a significant impact on the initial stiffness of the beams. In Figure 5 (right), the ratio $V_{Test\text{-}2Ø}/V_{Test\text{-}without\ Ø}$ is drawn as a function of the relative distance a_2/d between the openings. It can be concluded that the capacity of beams with two openings is in the same range of beams with single openings (Fig.

4), if the spacing exceeds 1.5*d*. When the openings are closer to each other, the capacity was decreased down to 50 % (T8a).

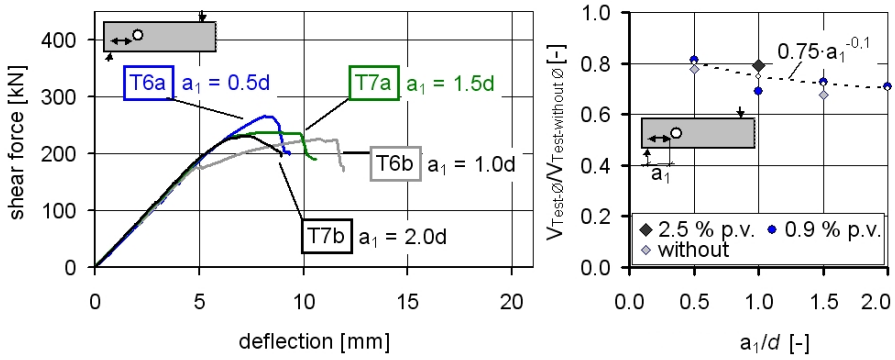

Figure 4: Left: Load-deflection curves of beams with one opening with a different distance to the support (0.9 % p.v.), Right: Specific ultimate shear force versus distance to support a_1/d.

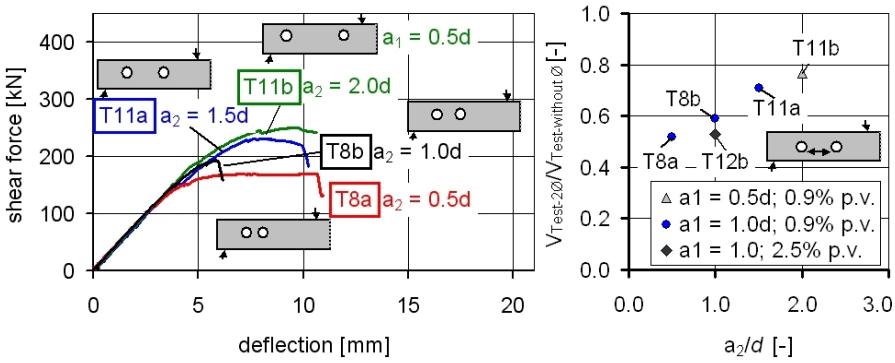

Figure 5: Left: Load-deflection curves of beams with a different spacing between two openings (0.9 % p.v.), Right: Specific ultimate shear force versus spacing a_2/d.

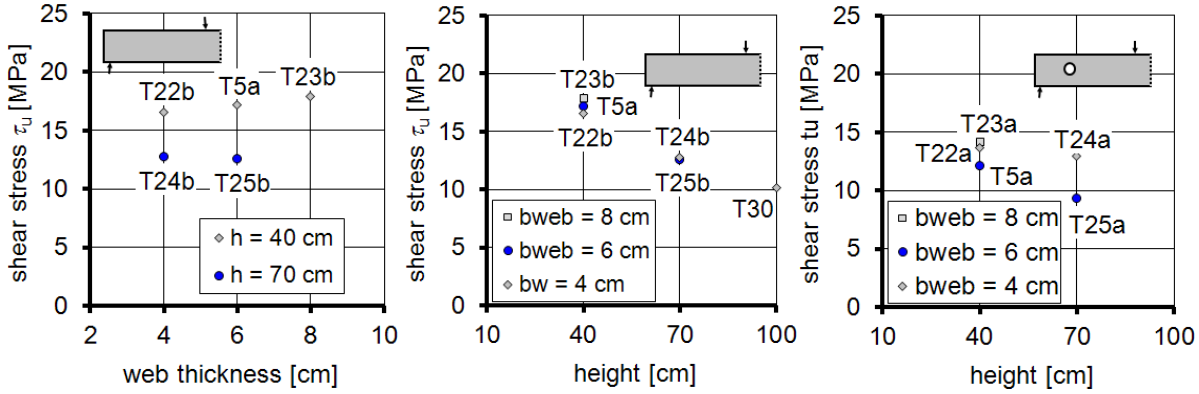

Figure 6: Influence of the web thickness and the beam height on the ultimate shear stresses of beams without openings.

Size effects

To compare the results with different cross sections, the shear forces were normalized on the shear stress $\tau_u = V_u/(b_{web} \cdot d)$ where d = 31,7 cm for h = 40 cm, d = 61,7 cm for h = 70 cm and d = 91,7 cm for h = 100 cm. These shear stresses are plotted for the beams without openings against the web thickness as well as the height of the beams in Figure 6. While the web thickness seems to have a minor impact on the shear stresses, the beam height shows a significant effect. The shear stresses of the 70 cm high cross sections were decreased down to about 70 % compared to the values of 40 cm height and in test T30 even to 60 %. The ultimate shear stresses of beams with single openings had a larger scatter than the beams without

openings. Nevertheless, the tendencies are similar. Beam T29 with longer fibers did not result in significantly higher capacities, but the cracking and failure behavior was improved. Test T31 with longer fibers will be tested soon and presented at the conference.

4 Summary and Outlook

Within the priority program funded by the German Research Foundation a total of sixty shear tests were carried out. The effectiveness of the fibers was evident in beams 40 cm high and the effect decreased with rising height. Further parameters like shear slenderness, prestressing, openings or additional reinforcement were tested. The height and the web thickness were varied in the last period, where a heavy impact of height was observed.

All tests were accompanied with finite element simulations to predict and to verify the test results. The experimental and calculated results form the base for a calculation model for pre-tensioned UHPC beams with and without openings. The model will be presented at the conference.

5 Acknowledgements

The authors acknowledge the funding of the German Research Foundation.

References

[1] German Research Foundation, priority program (DFG SPP 1182), Nachhaltig Bauen mit UHPC (Sustainable Construction with UHPC).

[2] Hegger, J.; Bertram, G.: Shear carrying capacity of steel fiber reinforced UHPC. Proceedings, 2nd International Symposium on UHPC, Kassel, Germany in 2008, S. 513 – 520.

[3] Hegger, J.; Bertram, G.: Shear Carrying Capacity of Ultra-High Performance Concrete Beams. Proceedings, International fib Symposium, Amsterdam, The Netherlands in 2008, S. 96.

[4] Bertram, G.; Hegger, J.: Shear Carrying Capacity of Ultra-High Performance Concrete Beams. Proceedings, 8th International Symposium on Utilization of High-Strength and High-Performance Concrete, Tokyo, Japan in 2008, CD S3-3-5.

[5] Bertram, G.; Hegger, J.: Pretensioned Concrete Beams made of Ultra-High Performance Concrete. Proceedings, International fib Symposium, London, The United Kingdom in 2009, CD (Mon 1600-1730 D2).

[6] Bertram, G.; Hegger, J.: Pretensioned UHPC Beams with and without Openings. Proceedings, SCC2010, Montreal, Canada, USB Stick: 1111-1118.

[7] Bertram, G.; Hegger, J.: Size Effects of Pretensioned Ultra-High Performance Concrete Beams. Proceedings, 57th annual PCI convention and national bridge conference, Salt Lake City, US in 2011, in progress.

[8] Hegger, J.; Bertram, G.: Verbundverhalten von vorgespannten Litzen in UHPC - Teil 1: Versuche zur Verbundfestigkeit und zur Übertragungslänge (bond behavior of strands in UHPC – part 1: tests on bond strength and transfer length). In: Beton- und Stahlbeton 105 (2010), issue 6, p. 379 - 389.

[9] Bertram, G.; Hegger, J.: Verbundverhalten von vorgespannten Litzen in UHPC - Teil 2: Ableitung eines Verbundmodells zur Berechnung der Übertragungslänge (bond behavior of strands in UHPC – part 2: bond model derivation for the calculation of transfer lengths). In: Beton- und Stahlbeton 107 (2012), issue 1, print in progress.

[10] Bertram, G.; Hegger, J.: Bond Behavior of Strands in UHPC – Tests and Design. Proceedings, 3rd International Symposium on UHPC, Kassel, Germany in 2012, in progress.

[11] DAfStb-Richtlinie Stahlfaserbeton (guideline steel fiber reinforced concrete): Addition of DIN 1045-1 (German Design Code) and DIN EN 206-1. Scheduled for publishing in 2010.

[12] DIN 1045-1, German Design Code: Concrete, reinforced and prestressed concrete structures. Berlin/Germany, 08.2008.

Experimental Investigations on UHPC Structural Elements Subject to Pure Torsion

Ekkehard Fehling, Mohammed Ismail
Institute of Structural Engineering, University of Kassel, Germany

In this paper, twelve UHPC beams with different combinations of steel fibers and traditional reinforcement were experimentally investigated under pure torsion. Two types of steel fibers having 17mm length and 0.15mm diameter with volumetric ratios of (0.0, 0.5 and 0.9%) were used. The average compressive strength of the reference UHPC standard cylinders was about 200 MPa.
The plain UHPC beams showed very brittle behavior. Meanwhile, the UHPC beams with steel fibers showed a ductile behavior. It was found that the addition of longitudinal reinforcement alone to the steel-fiber UHPC beams added much to the ductility and very little to the ultimate strength. The steel fibers beyond a volumetric ratio of 0.9% together with the longitudinal reinforcement accomplished an effective load carrying mechanism after cracking. Only the case of longitudinal and web reinforcement in addition to steel fibers provided a very high increase both in ultimate torsion capacity and ductility.

Keywords: UHPC, torsion, steel fibers, ductility

1 Introduction:

Torsion appears in structural elements when the line of action of the shearing force does not coincide with the shear center of the element. It appears, for example, in bridges, curved structural elements and spandrel beams in buildings.

Ultra High Performance Concrete (UHPC) is characterized by a very high compressive strength which may reach more than 200 MPa. The behavior of this material under tension and compression actions has been established to be very brittle in nature. Discontinuous fibers (normally steel fibers) are usually added to UHPC mix to introduce ductility.

UHPC attracted a lot of researchers in the last two decades to investigate its performance under different load actions such as: tension [1], shear [2], [3], punching shear [4], bending moment [5], biaxial loading [6], [7], biaxial compression [8], and multi-axial and fatigue [9]. However, until recently, almost no tests data about the performance of UHPC under torsion are at hand.

As many UHPC structures - including bridges - have been already constructed worldwide, this urges research to be done on this important field in order to understand the behavior of this new structural material under torsion.

2 Experimental Program

Principally, the deformation behavior and ultimate capacity of twelve UHPC beams with/out steel fibers and with/out traditional reinforcement under pure torsion were investigated. The detailed experimental plan is shown in table 1.

The test beams had square cross section and dimensions of (18cm×18cm×240cm) as shown in figure 1, with extra enlarged reinforced ends of dimensions (28cm×28cm) in cross section in order to withstand the concentrated stresses due to load application at these areas and to gradually transfer the stresses to the main tested part of the specimen. The tested part of the beams had a length of 170 cm, see figure 1, except for the two beams UL(1.4)T(1.68)F1(0.5) and UL(2.48)T(2.53)F1(0.5) where the tested part was reduced to a length of 95 cm because of the limited deformation capability of the test setup. Reinforcement details for cross section A-A for different beams are shown in table 1.

The parameters studied during the experimental program were: steel fiber type, steel fiber volume, longitudinal reinforcement ratio and web reinforcement ratio. The varied steel fiber volumetric ratios were (0.0, 0.5 and 0.9 %) and the varied longitudinal and web reinforcement volumetric ratios were (0.0, 1.4, 2.48 %) and (0.0, 1.68 and 2.53 %) respectively.

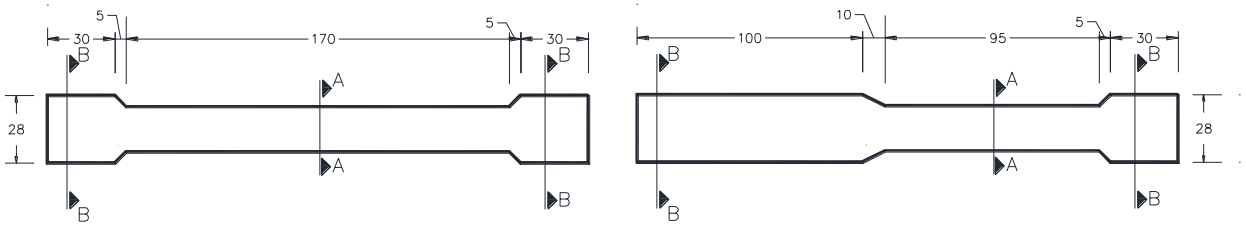

Figure1: The original test beam (left), the modified test beam (right) (dimensions are in cms).

Table 1: The experimental program.

Group	No. of beams	Fiber vol. %	Long. reinft. ρ_L	Web reinft. ρ_T	Code	Cross section (A-A)
1	2	-	-	-	UP	
2	2	0.5	-	-	UPF1(0.5), UPF2(0.5)	
	1	0.9	-	-	UPF1(0.9)	
3	1	0.5	4Ø12 mm, 1.4%	-	UL(1.4)F2(0.5)	
	1	0.5	4Ø16mm, 2.48%	-	UL(2.48)F1(0.5)	
	1	0.9	4Ø16mm, 2.48%	-	UL(2.48)F1(0.9)	
4	1	0.5	4Ø12 mm, 1.4%	-	UL(1.4)F1(0.5)m	
5	1	0.5	4Ø12 mm, 1.4%	Ø8mm@45mm, 1.68%	UL(1.4)T(1.68)F1(0.5)	
	1	0.5	4Ø16mm, 2.48%	Ø8mm@45mm, 1.68%	UL(2.48)T(1.68)F1(0.5)	
	1	0.5	4Ø16mm, 2.48%	Ø8mm@30mm, 2.53%	UL(2.48)T(2.53)F1(0.5)	

Legend: U=UHPC, P=Plain concrete, L=Longitudinal reinforcement, T=Transverse reinforcement, F1,F2=Steel fibers types, m=Longitudinal reinforcement in the middle of the cross sections' sides, ( )=Volumetric ratio in %.

3 Materials

A fine-grained (maximum grain size of 0.5 mm) UHPC mix (M3Q) was used. This mix was developed at the University of Kassel and was used as the reference mix in the priority program (Sustainable construction with UHPC, SPP1182) of the German Research Foundation (Deutsche Forschungsgemeinschaft DFG). It is considered as a further development of the (M2Q) UHPC mix which is described in detail in (Feh, 2005). The (M3Q) mix proportions are shown in table 2.

The consistency of the fresh UHPC was determined by slump tests executed immediately after mixing. The resulted slump ranged between (70-80) cm.

For all the test beams, the average cylinder compressive strength was 205.37 MPa and the average modulus of elasticity was 48000 MPa.

The reinforcing steel used was of the type Bst IV S with a yield strength of 570 MPa and an ultimate strength of 630 MPa.

Two types of steel fibers (F1 and F2) having tensile strength of 2500 MPa and the same dimensions, but different bond properties were used. The fiber length and diameter were 17mm and 0.15mm respectively. To distinguish between the behavior of the steel fibers in the hardened UHPC, axial tensile tests of notched UHPC prisms according to [1] having steel fiber volumetric ratio of 0.5% and 0.9% have been conducted. Figure 2 shows the average stress-crack width diagrams for these tests, where it can be seen that the fracture energy of the steel fibers F1 measured by the area under the stress crack width diagram is greater than that of the other type F2. Hence, it can be concluded that the bond between the steel fiber F1 and the UHPC is stronger than that between the steel fiber F2 and the UHPC.

Table 2: The used UHPC mix proportions (M3Q.)

Component	Volume (dm^3)	Mass (kg)
Water	175	175
Cement	266.13	825.00
Silica fume	79.55	175.00
Superplasticizer	25.70	27.50
Ground Quartz	75.47	200.00
Sand 0.125/0.50	367.92	975.00
Water/Binder (0.19)		
Steel fibers (0.9 - 2.5 Vol. %)		
$f_{c,cyl}$ (200 MPa)		

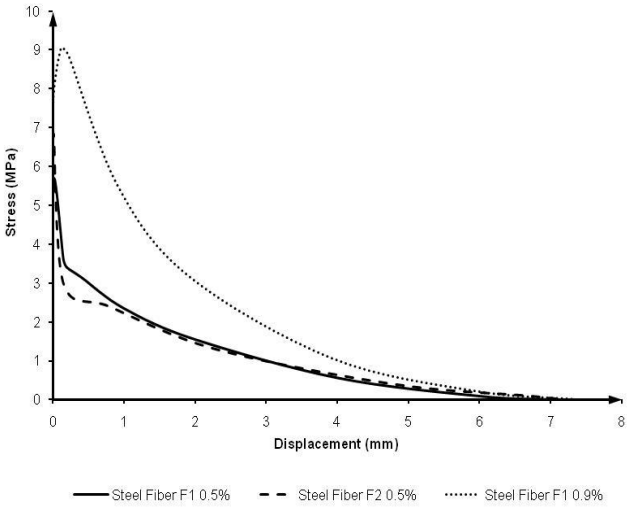

Figure 2: Average axial tensile tests of notched prisms for fibers F1 and F2.

4 Casting and treatment of the beams

The beams were cast in pairs together with the reference test specimens for the compression and tension tests. A mixer with 400 l UHPC capacity was used, where the coarser materials were added first followed by the finer materials. Steel fibers were added to the mix through a sieve to insure that the fibers will not accumulate in bundles in the mix. The beams were compacted using a vibrating table in order to keep the normal distribution of the fibers within the mix. The room temperature of the laboratory and the temperature of the UHPC mix were measured directly after mixing and were found to be between (17-20 and 26-30 degrees, respectively) for all beams. After casting, the beams were left in forms for two days to harden, then the forms were removed and the specimens were heat treated under 90 degrees Celsius for two days.

5 The test setup

The test setup shown in figure (3) consists of several steel U-profiles connected together in a way to facilitate the implementation of the torsion tests. It consists of four main components: 1- the rotating hinge at "End 1" of the beam, which is composed of two semi-circular UHPC parts with a specific radius in cross section to allow for rotation about the cross sectional center of the UHPC beams, 2- the fixed support at "End 2" and 3- the hydraulic cylinder which is

connected to the test setup by hinge connections, and 4- the strong floor of the laboratory to which the whole setup was fixed.

6 The test procedure

As it is shown in figure 3, the load was applied at one end of the beam (End 1) by a manually controlled hydraulic cylinder, while the other end (End 2) was fixed. The center of the beams cross section at End 1 (point C) was fixed against movement but free in rotation by means of a steel box profile attached horizontally to point C at one end and to a very stiff steel frame at the other end. This fixing mechanism of point C prevented the introduction of any bending moment to the beam. During the load application, the vertical position of the hydraulic cylinder was monitored and maintained by means of a steel vice that was fixed below the hydraulic cylinder.

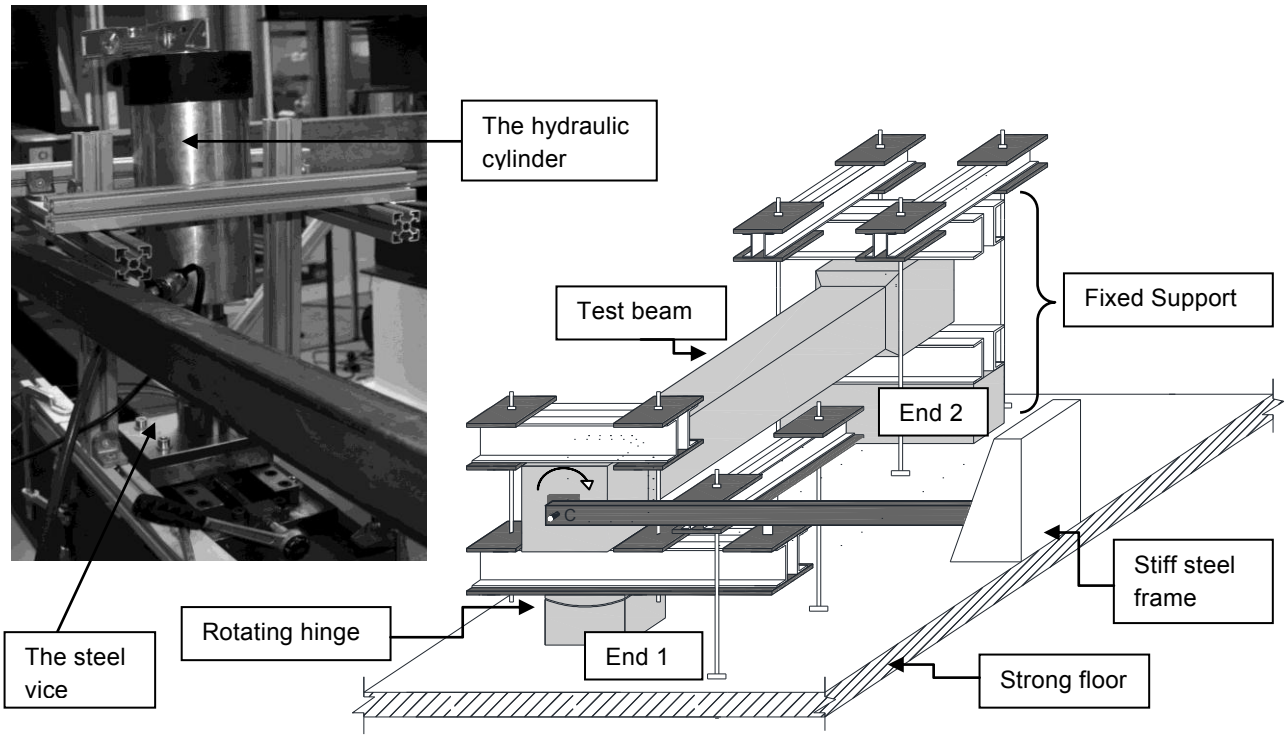

Figure 3: The test setup for torsion.

The tests were conducted displacement controlled so as to get the full Load-Displacement diagram including the post peak region. The tests were stopped at certain deformation stages (angles of twist) to document the cracking behavior of the beams. These stages correspond to angles of twist of (0.35, 0.85 Deg/m) for the second, the third and the fourth groups and (0.54, 1.32 and 3.37 Deg/m) for the fifth group of beams. The cracks pattern, their development, lengths and widths were measured and documented.

7 Tests results

UHPC with/out steel fibers

Figure 4 shows the Load-Deflection diagrams of these beams, where the plain UHPC beams (UP1 and UP2) showed very brittle behavior. They failed abruptly at the moment of reaching their maximum tensile strength. No cracks were formed before failure.

The failure of the steel fiber UHPC beams: UPF1(0.5), UPF2(0.5) and UPF1(0.9) was initiated by continuous widening of a single crack due to fiber pull out from the UHPC matrix. The steel fiber UHPC beams UPF1(0.5) and UPF1(0.9) showed a different cracking behavior than that of the plain UHPC beams. After reaching the UHPC tensile strength, few cracks

developed before a localized failure at one crack location happened. As for all the tested beams, the cracks were initiated at the middle of the cross sectional walls, then propagated inclined to the longitudinal axis of the beam to circulate around the beam walls. The initial cracks were very narrow in widths, where they begun at widths of about (0.03-0.05) mm. Table 3 shows a summary of the cracking behavior of the steel fiber UHPC beams at the aforementioned deformation stages. While the UHPC beam UPF1(0.9) showed more cracks before failure than the UPF1(0.5) beam, the UHPC beam UPF2(0.5) however, did not show cracking before failure. This can be attributed to the weaker bond strength of this type of steel fibers (F2) in comparison with the other type (F1), which in turn affects the crack bridging mechanism of the fibers. The UPF1(0.9) beam showed smaller average crack widths than the other beams in this group.

Figure 4 shows that for the same type of steel fibers, the higher the steel fibers volumetric ratio in the mix, the higher the cracking torsion, the ultimate torsion, the stiffness after cracking, the toughness and the ductility of the Load-Deflection diagram.

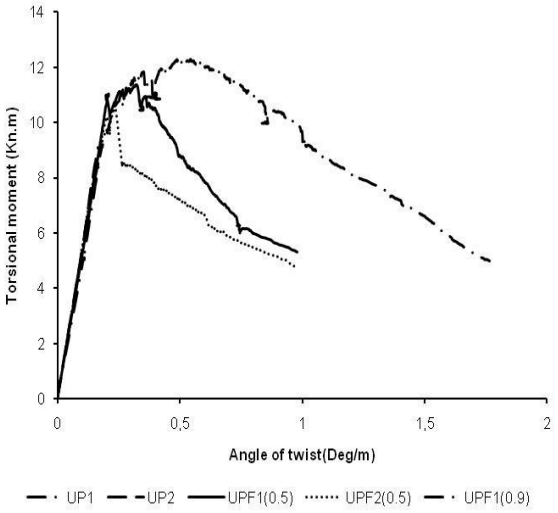

Figure 4: Torsion tests results for UHPC beams with/out fibers.

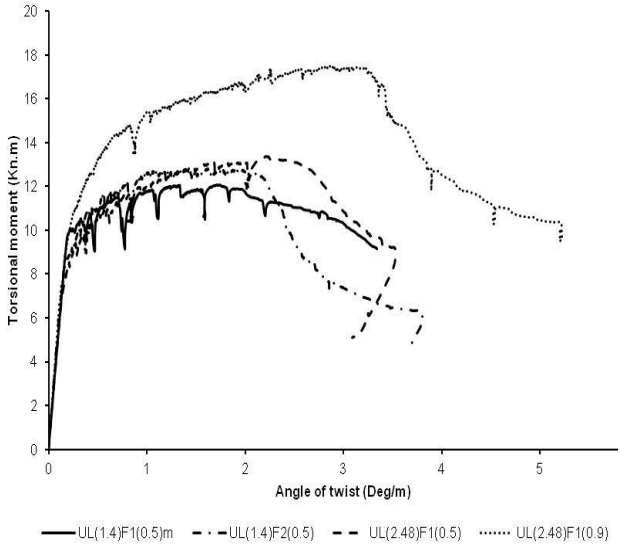

Figure 5: Torsion tests results for UHPC beams with steel fibers and longitudinal bars.

Table 3: Cracking behavior of the steel fiber UHPC beams.

Beam Code	Average No. of cracks/m	Crack width (mm)			Crack angle (Degrees)		
		Min	Max	Average	Min	Max	Average
Beam deformation stage 1: Angle of twist = 0.35 Deg/m							
UPF1(0.5)	2	0.05	0.15	0.081	43	50	46.4
UPF1(0.9)	3	0.03	0.12	0.065	40	57	46.4
UPF2(0.5)	Only one crack was developed						44
Beam deformation stage 2: Angle of twist = 0.85 Deg/m							
UPF1(0.5)	3	0.05	3	0.54	43	52	46.65
UPF1(0.9)	5	0.04	2.3	0.22	43	57	46.82
UPF2(0.5)	Only one crack was developed						44

Table 3 shows that the addition of steel fibers did not cause much deviation of the cracking angles from 45 degrees, where their values ranged between 40-57 degrees, but the average values of these angles were around 45 degrees. This may be due to the random distribution of

the steel fibers within the mix. Addition of the steel fibers had essentially no influence on the elastic torsional stiffness.

UHPC beams with steel fibers and longitudinal bars

This group of beams showed much ductile failure than the steel fibers UHPC beams as shown in figure 5. Failure of these beams was initiated by the continuous widening of more than one crack, where the final failure was due to yielding of the longitudinal reinforcement and pull out of the steel fibers from the UHPC matrix.

These beams showed in general intensive cracking before failure as shown in table 4. The intensity of cracks was directly proportional to the volumetric ratios of the steel fibers and the longitudinal reinforcement. The cracks were uniformly distributed along the length of the beams and closely spaced, while those of the steel fibers UHPC beams were non-uniformly distributed but rather congested in a cracking zone. This may be attributed to the different load resistance mechanisms of the two types of reinforcements: the fibers act locally, while the bar reinforcements behave globally.

In comparison with the steel fiber UHPC beams, the addition of longitudinal reinforcement alone with little steel fiber content (0.5%) added much to the torsional ductility and very little to the ultimate torsional capacity. Only beyond a steel fiber content of (0.9%), the increase in the ultimate torsion was significant as shown in the results of the UL(2.48)F1(0.9) beam. This reflects the ability of the steel fibers beyond a certain volumetric ratio to accomplish an effective load carrying mechanism together with the longitudinal bar reinforcement after cracking.

The UL(1.4)F2(0.5) beam showed better performance than that of the UL(1.4)F1(0.5)m. It is to be concluded that placing the longitudinal bar reinforcement at the corners of the cross section provides more efficient arrangement and enhances the behavior of the beam under both the serviceability and ultimate limit states. This arrangement is shown to provide better confinement to the UHPC core and hence prevents excessive cracking and loss of stiffness.

Table 4: Cracking behavior of the UHPC beams with steel fibers and longitudinal reinforcement.

Beam Code	Average No. of cracks/m	Crack width (mm)			Crack angle (Degrees)		
		Min	Max	Average	Min	Max	Average
		Beam deformation stage 1: Angle of twist = 0.35 Deg/m					
UL(1.40)F1(0.5)m	4	0.03	0.15	0.076	40	60	51.00
UL(1.40)F2(0.5)	5	0.05	0.30	0.080	45	72	55.13
UL(2.48)F1(0.5)	5	0.03	0.18	0.050	43	75	56.30
UL(2.48)F1(0.9)	7	0.03	0.12	0.040	43	62	51.54
		Beam deformation stage 2: Angle of twist = 0.85 Deg/m					
UL(1.40)F1(0.5)m	12	0.03	0.53	0.094	38	65	50.46
UL(1.40)F2(0.5)	8	0.05	0.35	0.085	45	72	52.20
UL(2.48)F1(0.5)	12	0.03	0.18	0.075	41	75	53.60
UL(2.48)F1(0.9)	14	0.03	0.19	0.065	40	62	47.93
		Beam deformation stage 3: Angle of twist = 2.00 Deg/m					
UL(1.40)F1(0.5)m	16	0.01	1.94	0.154	33	65	49,67
UL(1.40)F2(0.5)	16	0.05	1.80	0.122	35	72	48.97
UL(2.48)F1(0.5)	24	0.03	1.50	0.128	33	75	49.56
UL(2.48)F1(0.9)	32	0.03	0.67	0.094	35	62	45.12

UHPC beams with steel fibers, longitudinal and web reinforcement

The Load-Deformation diagrams of the UHPC beams in this group are shown in figure 6. Unlike that for all other beams, the increase in the ultimate torsion and ductility for this group of beams was significant. Failure occurred after very intensive cracking by continuous widening of more than one crack. The cracking behavior and pattern of these beams are documented in table 5. The cracking documentation was carried out at the following deformation stages: (0.54, 1.32 and 3.37 Deg/m) in order to cover a wide range of the beams deformations.

The average number of cracks per meter, the minimum, maximum and average crack widths and the minimum, maximum and average cracking angles in the three stage of deformation for the beams in this group show very close values. This means that while the steel fiber volumetric ratio is constant, increasing the reinforcement ratios in the beams beyond certain values has very little effect on the cracking behavior and pattern.

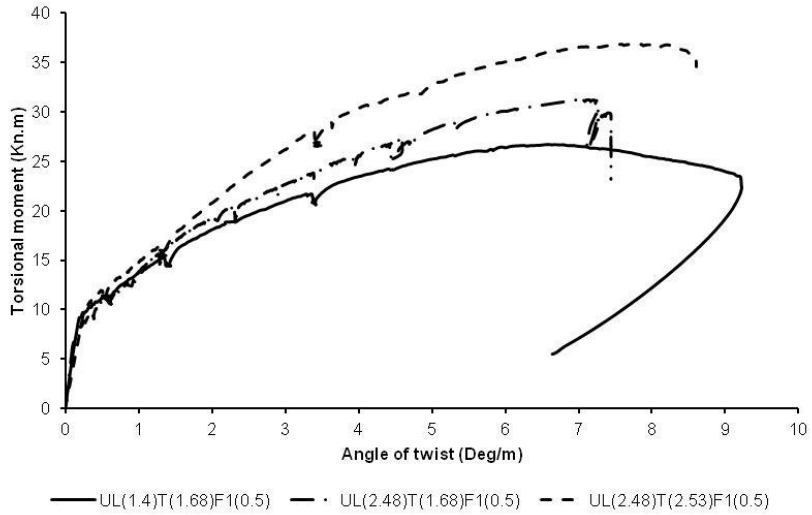

Figure 6: Torsion tests results for UHPC beams with steel fibers longitudinal and web reinforcements.

Table 5: Cracking behavior of the UHPC beams with steel fibers, longitudinal and web reinforcement.

Beam Code	Average No. of cracks/m	Crack width (mm)			Crack angle (Degrees)		
		Min	Max	Average	Min	Max	Average
	Beam deformation stage 1: Angle of twist = 0.54 Deg/m						
UL(1.40)T(1.68)F1(0.5)	13	0.01	0.13	0.049	34	69	50.21
UL(2.48)T(1.68)F1(0.5)	11	0.01	0.11	0.045	27	63	46.70
UL(2.48)T(2.53)F1(0.5)	6	0.03	0.10	0.054	29	70	46.76
	Beam deformation stage 2: Angle of twist = 1.32 Deg/m						
UL(1.40)T(1.68)F1(0.5)	25	0.01	0.17	0.054	34	69	48.17
UL(2.48)T(1.68)F1(0.5)	25	0.02	0.15	0.050	27	63	45.35
UL(2.48)T(2.53)F1(0.5)	26	0.03	0.21	0.064	29	70	46.17
	Beam deformation stage 3: Angle of twist = 3.37 Deg/m						
UL(1.40)T(1.68)F1(0.5)	45	0.02	0.48	0.128	31	70	47.39
UL(2.48)T(1.68)F1(0.5)	47	0.02	0.46	0.120	27	63	44.37
UL(2.48)T(2.53)F1(0.5)	47	0.03	0.45	0.122	29	70	44.92

The absolute maximum and the maximum of the average crack widths for the first, second and third stages of deformation for these beams are 0.13, 0.21, 0.48 mm and 0.054, 0.064, 0.128 mm respectively. So, at about 70% of the ultimate torsion, the maximum and average crack widths are about 0.48 and 0.128 mm respectively. This confirms the high durability of the reinforced steel fiber UHPC.

Figure 6 shows that increasing the steel reinforcement ratio of any type, whether longitudinal or transverse, increases the ductility, toughness and post cracking stiffness, but the maximum increase of these factors happens only when both the longitudinal and transverse reinforcement have been increased together.

8 Conclusions

1. Addition of steel fibers to the plain UHPC beams increased both the cracking and ultimate torsion capacity and added torsional ductility, post cracking stiffness and toughness to the beams.
2. As the steel fiber volumetric ratio in the mix increases, the average number of cracks per meter increases as well, yet having smaller average crack widths. The initial cracks were very small in width, they begun at widths of about (0.01- 0.05) mm.
3. The addition of longitudinal reinforcement to the steel fiber UHPC beams with little steel fiber volume enhanced very much the stiffness after cracking, the toughness and the ductility of the beams but the resulted increase in the ultimate torsion was marginal. The most significant increase of these factors happens only when both the longitudinal and transverse reinforcement increased together.
4. The distribution and orientation of the steel fibers within the UHPC matrix when combined with traditional reinforcement may influence the average inclination of cracks.

References

[1] Leutbecher, T.: Rissbildung und Zugtragverhalten von mit Fasern und Stabstahl bewehrtem Ultrahochfesten Beton (UHPC), PhD Dissertation, Kassel 2008.

[2 Fehling, E.; Schmidt, M.; Teichmann, T.; Bunje, K.; Bornemann, R.; Middendorf, B.: Entwicklung, Dauerhaftigkeit und Berechnung Ultra-Hochfester Betone (UHPC)“, Research report (DFG FE 497/1-1), Kassel 2005.

[3] Fehling, E.; Thiemicke, J.: Shear bearing behavior of ultra high performance concrete (UHPC), fib Symposium, Prague 2011.

[4] Harris, D. K.; Roberts-Wollmann, C. L.: Characterization of Punching Shear Capacity of Thin Ultra-High Performance Concrete Slabs. Proc. Second International Symposium on Ultra High Performance Concrete P. 727- 734, Kassel 2008.

[5] Fehling, E.; Stürwald, S.: Zum Tragverhalten von UHPC mit einer Kombination aus Faser- und Stabstahlbewehrung unter Biegebeanspruchung“, Arbeitsbericht zum Forschungsvorhaben Fe 497/4-2. 2009.

[6] Fehling, E.; Leutbecher, T.; Röder, F.-K.: Structural behaviour of normal strength and ultra high strength reinforced concrete with and without fibres under biaxial loading; Recent Developments in Structural Engineering, Mechanics and Computation. P. 557-558, Rotterdam 2007.

[7] Fehling, E.; Leutbecher, T.; Röder, F.-K.; Stürwald, S.: Structural behavior of UHPC under biaxial loading. Proc. Second International Symposium on Ultra High Performance Concrete. P. 569-576, Kassel 2008.

[8] Curbach, M.; Speck, K.: Ultra High Performance Concrete under Biaxial Compression. Proc. Second International Symposium on Ultra High Performance Concrete. P. 477-484, Kassel 2008.

[9] Grünberg, J.; Lohaus, L.; Ertel, C.; Wefer, M.: Multi-Axial and Fatigue Behaviour of ultra-high-performance concrete (UHPC). Proc. Second International Symposium on Ultra High Performance Concrete, Kassel 2008.

Torsional Test of Ultra High Performance Fiber-Reinforced Concrete Square Members

Changbin Joh[1], Jungwoo Lee[1], In-Hwan Yang[2], Byung-Suk Kim[1]
1: Structural Engineering Research Division, Korea Institute of Construction Technology, Korea
2: Dept. of Civil Engineering, Kunsan National University, Korea

The torsional behavior of Ultra High Performance Fiber-Reinforced Concrete (UHPFRC) members has not been fully investigated yet. As a result, UHPFRC design recommendations of AFGC/SETRA and JSCE recommend a designer to use the torsional design method of reinforced concrete, so-called thin-walled tube theory that does not consider the contribution of concrete in tension after cracking. This paper reports the torsional test of UHPFRC square members with different reinforcement details. The results showed that the UHPFRC member even with no rebar did not lose its torsional strength after cracking due to the ductility of UHPFRC, and others also showed ductile behavior. Comparison of test results with the modified thin-walled tube theory that considers the tensile strength of UHPFRC showed that the modified theory seems to be reasonable to estimate the cracking torque and torsional strength of UHPFRC members.

Keywords: ultra high performance fiber-reinforced concrete, torsional strength, skew bending theory

1 Introduction

Ultra High Performance Fiber-Reinforced Concrete (UHPFRC) has higher tensile strength and ductility than normal concrete, which makes it possible to design UHPFRC members with reduced amount of reinforcement. The studies on the flexural and shear behavior of UHPFRC show that the UHPFRC girder can be designed without conventional stirrups in the web [1] and the longitudinal reinforcement required to resist the flexural moment can be reduced remarkably [2]. As a result, together with very high compressive strength, it is possible to design slender, light and economical UHPFRC structures. However, this advantage might pale into significance due to the little studies on torsional behavior of UHPFRC.

UHPFRC design recommendations by AFGC/SETRA and JSCE have no torsional design method that considers the high tensile strength and ductility of UHPFRC [3, 4]. Instead, they recommend a designer to use the torsional design method of reinforced concrete, so-called thin-walled tube theory that does not consider the contribution of concrete in tension after cracking [5]. Therefore, if the applied torque is greater than a quarter of the cracking torque of a member, all the tension from the applied torque should be resisted by the stirrups and longitudinal rebars. This probably requires unnecessary stirrups and longitudinal rebars for the UHPFRC members, which diminishes the advantage of UHPFRC.

Thus, a different design procedure is required to estimate the torsional behavior of UHPFRC members. The torsional resistance of the UHPFRC member will not drop suddenly after initial cracking. It will increase or at least maintain the strength even after cracking due to the ductility from the bridging action of steel fibers. Consequently, the torsional strength of the UHPFRC member will be higher than the strength estimated by the thin-walled tube theory based on the behavior of reinforced concrete members.

This paper reports the currently finished part of torsional test of UHPFRC square members to understand their torsional behavior. Three UHPFRC square members with same cross section but with different reinforcement details were subjected to pure torsion. The cracking torque and torsional strength were investigated experimentally. The different torsional behavior compared to the reinforced concrete member was carefully observed. In addition, this paper modified the

thin-walled tube theory to incorporate the tensile strength of UHPFRC and examines its applicability to the torsional design of UHPFRC members.

2 Torsional test of UHPFRC members

UHPFRC composition and material properties

The UHPFRC composition developed by KICT (Table 1) was used for all UHPFRC test specimens. The steel fibers differ only in length (L= 19.5 mm and 16.3 mm) were used 1% each. The diameter of steel fibers was 0.2 mm and the tensile strength of the steel fiber was 2500 MPa. All UHPFRC specimens were steam cured for 72 hours at 90 degree after 24-hour curing at room temperature.

Table 1: UHPFRC composition developed by KICT (by weight except for fibers).

W/B	Cement	Silica fume	Sand	Filling powder	Super plasticizer	Steel Fiber (ρ_f)
0.2	1	0.25	1.1	0.3	0.016	1% (L=16.3 mm)+ 1% (L=19.5 mm)

Material tests were done to understand the compressive and tensile behaviors of UHPFRC itself. Cylindrical specimens (diameter = 100 mm, height = 200 mm) were used for compression tests. The UHPFRC tensile specimens (Fig. 1) with notches were tested using the UTM with the capacity of 250 kN (Fig. 2). Clip gauges were attached to the notches to measure the crack opening.

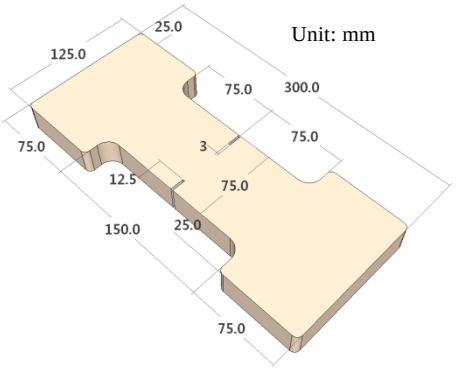

Figure 1: Tensile test specimen with notches.

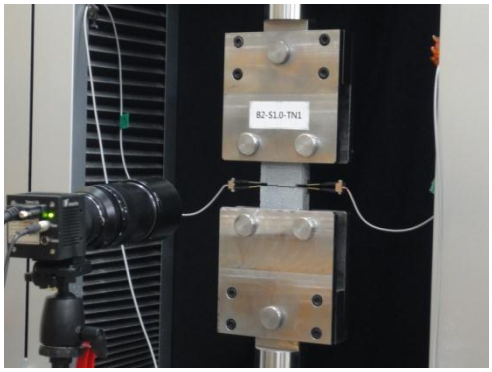

Figure 2: Tensile test setup for UHPFRC.

Table 2 shows test results of compressive and tensile strengths for each specimen. Compressive strength is 184 MPa in average and tensile strength is 14.1 MPa in average.

UHPFRC specimems

All test specimens were 3.0 m long to accommodate the test setup in the laboratory, having a square cross section of 300 mm by 300 mm (Table 2, Fig. 3). The cover thickness of 35 mm was used considering the length of the longer fiber. Test specimen was composed of 3 regions; a test region (1,600 mm) and two end regions (700 mm each). The end regions were reinforced with additional stirrups to allow for failure to occur in the test region.

Test parameters were stirrups and longitudinal rebars. The specimen SS-F2-L00-S00 was to investigate the torsional behavior of UHPFRC only. There was no reinforcement in the test region. The other two specimens had reinforcement. The specimen SS-F2-L88-S00 had 4 longitudinal rebars at each corner of the cross section. D16 bars were used. This specimen was

to represent the reinforced UHPFRC girders without stirrups. The specimen SS-F2-L88-S35 had both longitudinal rebars and torsional stirrups. D16 and D10 bars were used for longitudinal rebars and stirrups respectively. The spacing of the torsional stirrups was chosen in such a way that at least one of the stirrups passes through the assumed inclined cracks of 45 degree. The yield strength of rebars was 450 MPa for all specimens

Each specimen was made from a different mixing with same composition. The average compressive and tensile strengths measured from the material tests explained in the previous section are shown in Table 2.

Table 2: UHPFRC specimens for torsional test.

Specimen	Longitudinal reinforcement		Torsional stirrups		Compressive strength in Avg. (MPa)	Ultimate tensile strength in Avg. (MPa)
	Rebar	A_s (%)	Rebar	A_s (%)		
SS-F2-L00-S00	-	0.00	-	0.00	192	14.6
SS-F2-L88-S00	4×D16	0.88	-	0.00	178	13.3
SS-F2-L88-S35	4×D16	0.88	D10@200mm	0.35	184	14.3

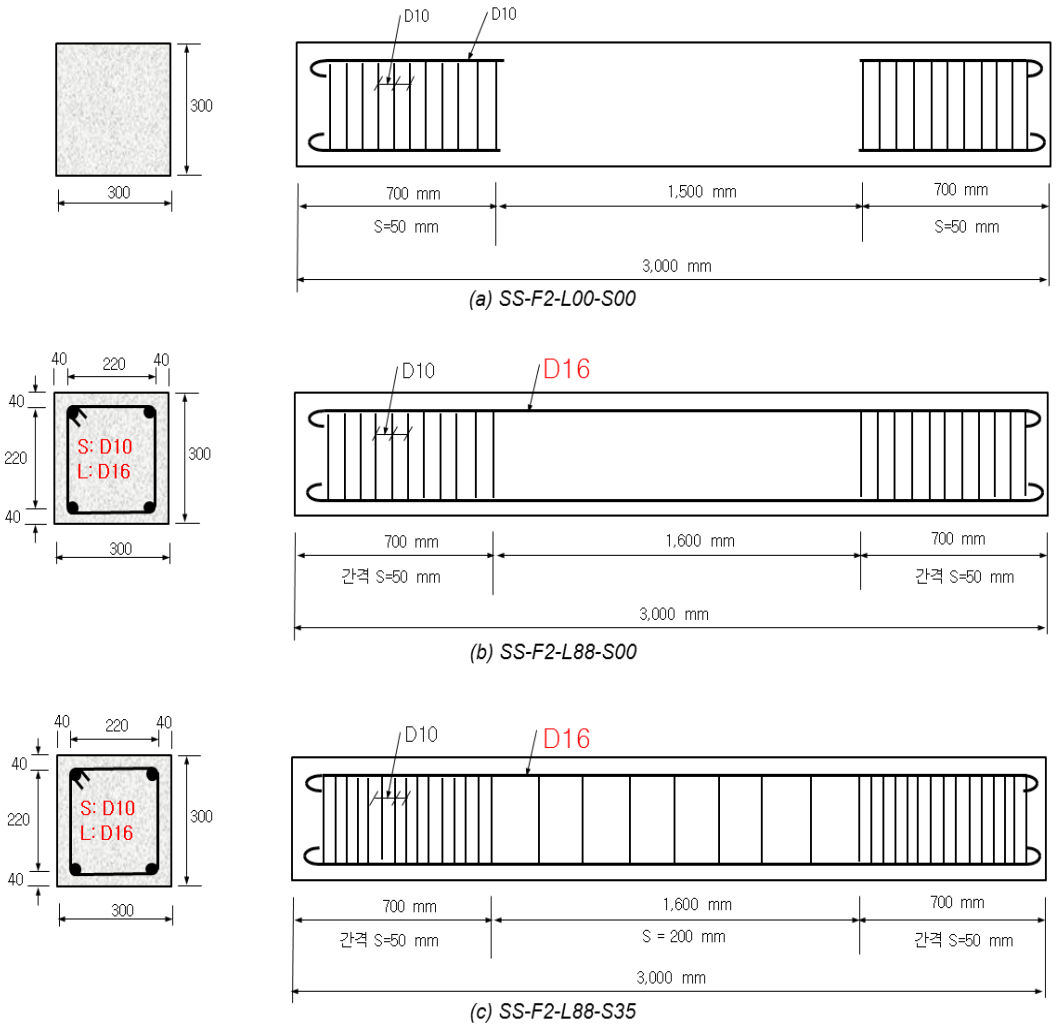

Figure 3: Test specimens and reinforcement details.

Test setup

Details of the test setup for pure torsion are shown in Fig. 4. One of the ends was a rotational one with axially movable arc bearing (Fig. 4 (b)) and the other was a fixed one (Fig. 4(c)). The test specimen was clamped at both ends against rotation using steel frames. The arc bearing allowed axial deformation of the specimen during the test.

A 1,000 kN hydraulic actuator was used to apply the load near the rotational end. The load had an 800 mm lever arm from the centroidal axis of the specimen. The length of the lever arm was chosen as same with the radius of rotation (800 mm). The load was introduced in displacement control mode (0.1 mm/sec).

An aluminium frame was attached to the end of test region with a displacement transducer to measure the rotation of the cross section of the specimen. At the rotational end, a tiltmeter was also installed to measure rotation. In addition, to measure axial deformation, two displacement transducers were installed at both ends of the specimen (Fig. 4(b) and 4(c)). The electric strain gages were mounted on the stirrups and longitudinal rebars.

(a) Test setup for pure torsion *(b) Rotational end.* *(c) Fixed end.*

Figure 4: Test setup.

3 Test results and analysis

Torsional Behavior

Fig. 5 shows the applied torque-rotation relationship of three tested specimens. Initial torsional stiffness and cracking torque were similar in each test, but, after initial cracking, the specimens showed different behaviors according to their reinforcement details.

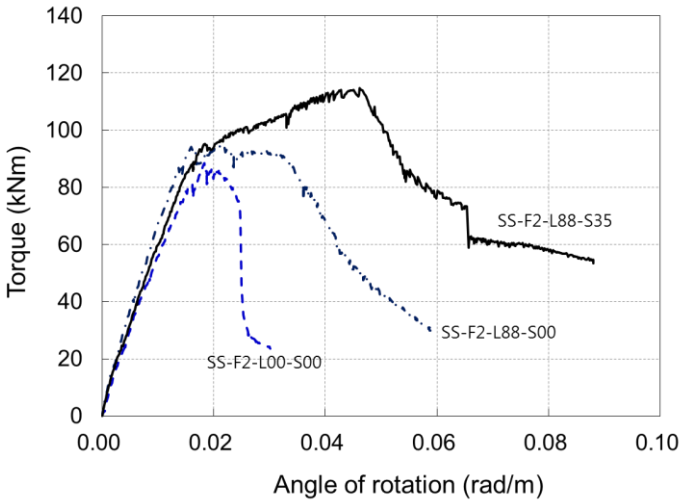

Figure 5:. Torque-angle of rotation relationship.

The crack pattern and failure of the SS-F2-L00-S00 that had no reinforcement are shown in Fig. 6. Initial cracks occurred near 79.1 kNm with the rotation of 0.0153 rad/m (Fig. 6(a)). After initial cracks, additional cracks near the initial cracks were formed and, in spite of no reinforcement, the specimen could take additional torque up to 88.5 kNm with the rotation of 0.0183 rad/m. After exceeding ultimate torque, the specimen begun to soften as one of cracks started to open (Fig. 6(b)). At the 0.025 rad/m, the specimen lost its torsional strength abruptly.

It should be noted that the torsional behavior of the SS-F2-L00-S00 is quite different from the typical torsional behavior of unreinforced concrete members. It did not fail abruptly after initial cracks as expected from the unreinforced concrete member.

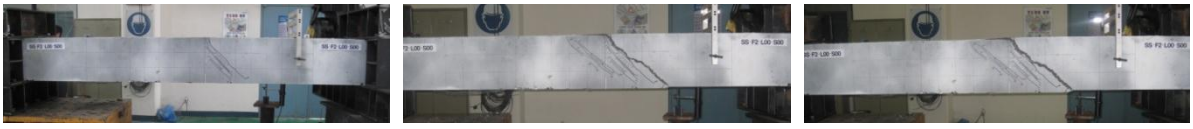

(a) at the peak (79.1 kNm) *(b) at 0.025 rad/m (44.8 kNm)* *(c) at the ultimate rotation (0.03 rad/m)*

Figure 6: Crack pattern and failure of SS-F2-L00-S00.

Fig. 7 illustrates the crack pattern and failure of the SS-F2-L88-S00 that had longitudinal rebars only. Initial cracks occurred at 87.2 kNm with the rotation of 0.0137 near the end zone, instead of the designated test zone (Fig. 7(a)). However, as the load increased, additional cracks started to form around the test zone (Fig. 7(b)). The torsional strength was about 95.1 kNm with rotation of 0.016 rad/m, and the strength was maintained until the rotation reached 0.0315 rad/m. After the rotation of 0.0315 rad/m, the specimen showed softening behavior with additional crack formations and opening one of cracks (Fig. 7(c)).

(a) at the initial crack (87.2 kNm) *(b) at 0.015 rad/m (90.4 kNm)* *(c) at 0.036 rad/m (opposite side)*

Figure 7: Crack pattern and failure of SS-F2-L88-S00.

Similar to the SS-F2-L88-S00, the initial cracks of the SS-F2-L88-S35 occurred at 88 kNm with the rotation of 0.0162 in the end zone (Fig. 8(a)). However, different from the specimen with longitudinal rebars only (SS-F2-L88-S00), this specimen that had longitudinal rebars and stirrups showed hardening with multiple cracks as the load increased (Fig. 8(b)). The torsional strength was about 114.7 kNm with rotation of 0.046 rad/m. After exceeding ultimate torque, a softening behavior followed with additional crack formations and opening of the leading crack similar to the other specimens. (Fig. 8(c)).

(a) at the initial crack (88.0 kNm). *(b) at 0.031 rad/m (104 kNm).* *(c) at 0.054 rad/m.*

Figure 8: Crack pattern and failure of SS-F2-L88-S35.

Modified thin-walled tube theory to consider the tensile strength of UHPFRC

To apply the thin-walled tube theory to UHPFRC members with a solid cross section, it is necessary to define the equivalent thin-walled tube. Similarly to the thin-walled tube theory of reinforced concrete beams [5], after cracking, an UHPFRC rectangular beam subjected to pure torsion can be idealized as shown in Fig. 9. The resistance to torsion comes from outer

UHPFRC skin, stirrups and longitudinal rebars. The UHPFRC diagonals are at an angle θ, generally taken as 45 degree for non prestressed beams. The applied torque (T) is divided into four shear forces along the wall (V_1, V_2, V_3 and V_4). The area enclosed by a line around the equivalent tube at the mid thickness of the wall ($A_0 = x_1 y_1$) can be decided empirically.

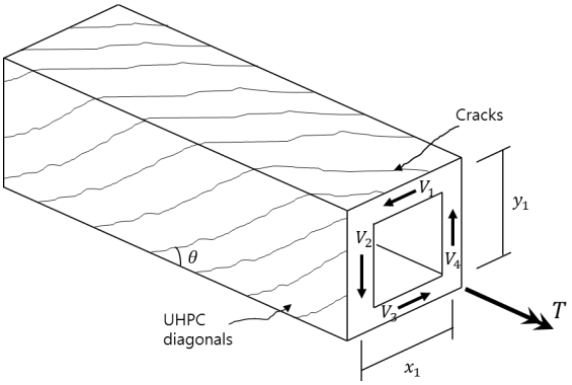

Figure: Thin-walled tube analogy for UHPFRC rectangular beams.

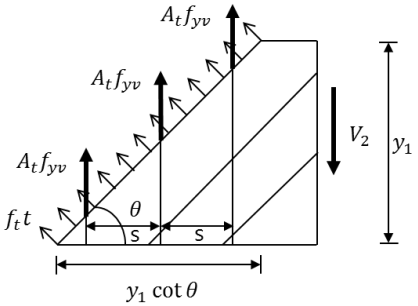

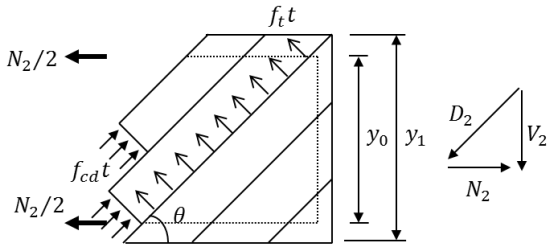

Figure 10: Portion of vertical side of space truss. Figure 11: Resolution of shear force in side 2 of space truss.

Nominal torsional strength (T_n) can be derived from the equilibrium of forces in the idealized thin-walled tube (Fig. 9). The shear force due to the torque in a vertical side of tube, V_2 is

$$V_2 = \frac{T}{2A_0} y_1 \tag{1}$$

The portion of torque, V_2 can be resisted by the forces of stirrups and the vertical component of tensile force at the cracked UHPFRC surface. Assuming all the stirrups yield and UHPFRC reaches tensile strength at the ultimate limit state (Fig. 10), the force equilibrium in the vertical direction gives

$$V_2 = \frac{A_t f_{yv} y_1}{s} cot\,\theta + f_t y_1 t\, cot\,\theta \tag{2}$$

where f_t is the tensile strength of UHPFRC, t is the thickness of the idealized thin-walled tube, s is the stirrups spacing, and A_t and f_{yv} are the area and yield strength of stirrups respectively. Substituting the value of V_2 from Eq. (2) and taking T equals to T_n, the nominal torsional strength is

$$T_n = T_s + T_{UHPC} = \frac{2A_0 A_t f_{yv}}{s} cot\,\theta + 2A_0 f_t t\, cot\,\theta \tag{3}$$

where T_s and T_{UHPC} are nominal torsional strengths resisted by stirrups and UHPFRC respectively.

It is worthy to note that Eq. (3) becomes the nominal torsional strength for reinforced concrete members if the tensile strength of UHPFRC is not considered (T_{UHPC}=0). This theory

incorporates the tensile strength of UHPFRC in the torsional strength, which reduces the amount of shear stirrups required to resist the applied torque.

The area of longitudinal rebars required to resist T_n, A_l can be calculated by considering the equilibrium of horizontal forces on all four sides of the tube (Fig. 11). The detailed derivation is omitted because similar derivation is in the reference [5]. As a result, A_l is given by Eq. (4).

$$A_l = \frac{T_n P_h}{2A_0 f_{yl}} cot\,\theta - \frac{f_t t}{f_{yl}} p_h \quad (4)$$

where, P_h is the perimeter of A_0, and f_{yl} is the yield strength of longitudinal rebars.

Again similarly to the thin-walled tube theory of reinforced concrete beams, although the tube analogy is less obvious before cracking, Eq. (5) is used to predict the cracking torque (T_{cr}) to maintain the consistency of the theory.

$$T_{cr} = 2 f_{cr} A_0 t \quad (5)$$

where, f_{cr} is the cracking strength of UHPFRC.

Table 3 and 4 provide the comparison of the cracking torque and torsional strength of tested specimens with the estimation based on the modified theory. In the estimation, similarly to the ACI code, θ is assumed to be 45 degree, and the thickness of idealized tube (t) and A_0 are assumed to be $3A_{cp}/4P_{cp}$ and $2A_{cp}/3$ respectively (A_{cp} and P_{cp} are the area and perimeter of the uncracked UHPFRC section). Considering the ductile behavior of UHPFRC and simplicity, the same t and A_0 are used for the estimation of both cracking torque and torsional strength, although the ACI code recommends different t and A_0 for each. Little research is available for the effect of biaxial stress tension-compression condition on the tensile behavior of UHPFRC. But similar research on steel fiber reinforced concrete showed that this effect is negligible [6]. Based on this result, the biaxial effect is ignored.

Table 3: Comparison of test results with the estimated cracking torque based on the modified theory.

Specimen	A_0	t	f_{cr}	$T_{cr,cal}$	$T_{cr,test}$	$T_{cr,cal}/T_{cr,test}$
	mm^2	mm	MPa	kNm	kNm	
SS-F2-L00-S00	60000	56.25	13.5	91.1	79.1	1.15
SS-F2-L88-S00	60000	56.25	11.2	75.6	87.2	0.87
SS-F2-L88-S35	60000	56.25	11.7	79.0	88.0	0.90
Avg.						0.97

Table 4: Comparison of test results with the estimated torsional strength based on the modified theory.

Specimen θ= 45°	A_0	t	f_t	A_t	s	f_{yv}	Calculated		$T_{u,test}$	$T_{n,cal}/T_{u,test}$
							T_s	T_{UHPFRC}		
	mm^2	mm	MPa	mm^2	Mm	MPa	kNm	kNm	kNm	
SS-F2-L00-S00	60000	56.25	14.6	0.0	N/A	450	0.0	98.2	88.5	1.11
SS-F2-L88-S00	60000	56.25	13.3	0.0	N/A	450	0.0	89.8	95.1	0.94
SS-F2-L88-S35	60000	56.25	14.3	71.3	200	450	19.3	96.8	114.7	1.01
Avg.										1.02

For cracking torque, the modified theory returns reasonable values between 115.0% and 87% of the actual cracking torque (in average, 97%). For torsional strength, this theory returns a little bit more accurate values between 111% and 94% of the actual strength (in average, 102%) compared to the estimation of the cracking torque. This result also indicates that the thin-walled tube theory for reinforced concrete members cannot be applied to the UHPFRC members (see

T_s). It is should be noted that considering the tensile strength of UHPFRC makes the modified theory applicable to the UHPFRC members even with no reinforcement or stirrups.

The area of required longitudinal rebars (A_l) is estimated using Eq. (4). The result shows that the specimens without stirrups (SS-F2-L00-S00 and SS-F2-L88-S00) do not need torsional longitudinal rebars, and the specimen with stirrups (SS-F2-L88-S35) needs longitudinal reinforcement of 350 mm^2 (only 44% of the actually used in the specimen).

As a result, although the result of only three tests is not enough to reach a definite conclusion, the modified theory seems to work reasonably to estimate the torsional behavior of UHPFRC members. Additional tests in progress will be used to verify this theory thoroughly and to find more reasonable t and A_0.

4 Conclusion

This paper studied the torsional test of UHPFRC square members to understand their torsional behavior. Based on the result, the following conclusions may be drawn.

The UHPFRC specimens with no reinforcement did not lose its torsional strength after cracking due to the ductility of UHPFRC, and the UHPFRC specimen with longitudinal rebars only also showed a ductile behavior. Those are different from the behavior of ordinary reinforced concrete members. The UHPFRC specimens with longitudinal rebars and stirrups showed hardening after cracking.

Comparison of test results with the modified thin-walled tube theory that considers the tensile strength of UHPFRC showed that the modified theory seems to be reasonable to estimate the cracking torque and torsional strength of UHPFRC members with/without torsional reinforcement. Since the number of tests is limited and more analyses on many parameters are required, additional tests in progress will be used to verify the modified theory more completely.

5 Acknowledgement

This work is the result of the research project, the Super Bridge 200 of Korea Institute of Construction Technology. The authors hereby express their appreciation for the support.

References

[1] Joh, C.; Lee, W; Yang, I. H.; Kim, B.: Shear test of Ultra High Performance Concrete girders without stirrups. Proc. 9th International Symposium on High Performance Concrete, Rotorua, New Zealand 2011.

[2] Yang, I. H.; Joh, C.; Kim, B.: Structural behavior of Ultra High Performance Concrete beams subjected to bending. *Engineering Structures 32*, pp.3478-3487, 2010.

[3] AFGC/SETRA: Ultra High Performance Fibre-Reinforced Concretes Interim Recommendations. AFGC/SETRA, 2002.

[4] Japan Society of Civil Engineers (JSCE): Recommendations for design and construction of ultra-high strength fiber reinforced concrete structures (draft). JSCE, 2004.

[5] MacGregor, J. G.; Ghoneim, M. G.: Design for torsion. *ACI Structural Journal* 92 (2), pp.211-218, 1995.

[6] Demeke, A.; Tegos, I. A.: Steel fiber reinforced concrete in biaxial stress tension-compression conditions. *ACI Structural Journal* 91 (5), pp.579-584, 1994.

UHPFRC Box Girders under Torsion

Martin Empelmann, Vincent Oettel
Institute for Building Materials, Concrete Construction and Fire Protection (iBMB), TU Braunschweig, Germany

The following paper will give an overview of torsion tests carried out on seven box girders constructed with Ultra-High Performance Fibre Reinforced Concrete (UHPFRC). The bearing and cracking behaviour of the box girders were investigated to understand the performance of this members under pure torsion and under the combined loading of torsion moments and normal forces. Additionally, the experimental results were compared with design equations for conventional reinforced concrete box girders based on the space truss model.

Keywords: UHPFRC box girdes, torsion, steel fibers, space truss model, tension strut, concrete strut

1 Introduction

The achievable compression strength of UHPFRC as well as the enormous durability gives engineers the possibility to design and construct innovative thin-walled elements, which are weight-optimized and advantageous in regard to transport and installation on site. Under loadings such components are not only stressed by bending and shear, but also torsion. In this context, box girders are more favourable than rectangular or I-shaped cross sections with regard to the torsional stiffness.

Currently, the design check for the torsional bearing capacity of UHPFRC components is neither regulated in DAfStb-Heft 561 „Sachstandsbericht – Ultrahochfester Beton“ [1] nor in DAfStb-Richtlinie „Stahlfaserbeton“ [2]. Therefore, experimental and theoretical studies on monolithic and segmental UHPFRC box girders were conducted at the iBMB of the TU Braunschweig within the third funding period of the priority program SPP 1182 of the German Research Society (DFG) [3].

2 Materials

The concrete mix used for the test specimens is based on the concrete composition called M3Q of the priority programm [3] and summarized in Table 1. In order to ascertain the influence of the steel fibers on the loading capacity the percentage volume fraction of steel fibers was varied.

Table 1: Concrete composition M3Q.

Material [kg/m³]	M3Q (0.00 vol.-%)	M3Q (1.25 vol.-%)	M3Q (2.50 vol.-%)
cement CEM I 52,5R HS-NA	795	785	775
silica fume	169	166	164
superplasticizer	24	24	23
quartz flour	198	196	193
quarz sand 0.125/0.5	971	959	946
straight steel fiber 13.0/0.19	0	98	196
water	188	186	183

The test specimens were reinforced with longitudinal and transverse reinforcement, composed of deformed bars with diameters 8 mm and 12 mm of steel grade BSt 500 S.

3 Test Specimens and Test Setup

The geometry of the test specimens is shown in Figure 1. Each girder was sized 50 cm x 50 cm x 335 cm with a wall thickness of 5 cm in the mid span. At the ends of the girders the wall thickness was increased to 12 cm in order to reduce the effects of local stresses from the supports and the loading equipment and to produce the torsional failure modes in the middle region. Additionally, a higher percentage of longitudinal and transverse reinforcement was placed at the girders ends. Table 2 gives the details of the chosen longitudinal and transversal reinforcement in the middle region. To secure the concrete cover of 1.0 cm, selfmade UHPFRC spacers were used.

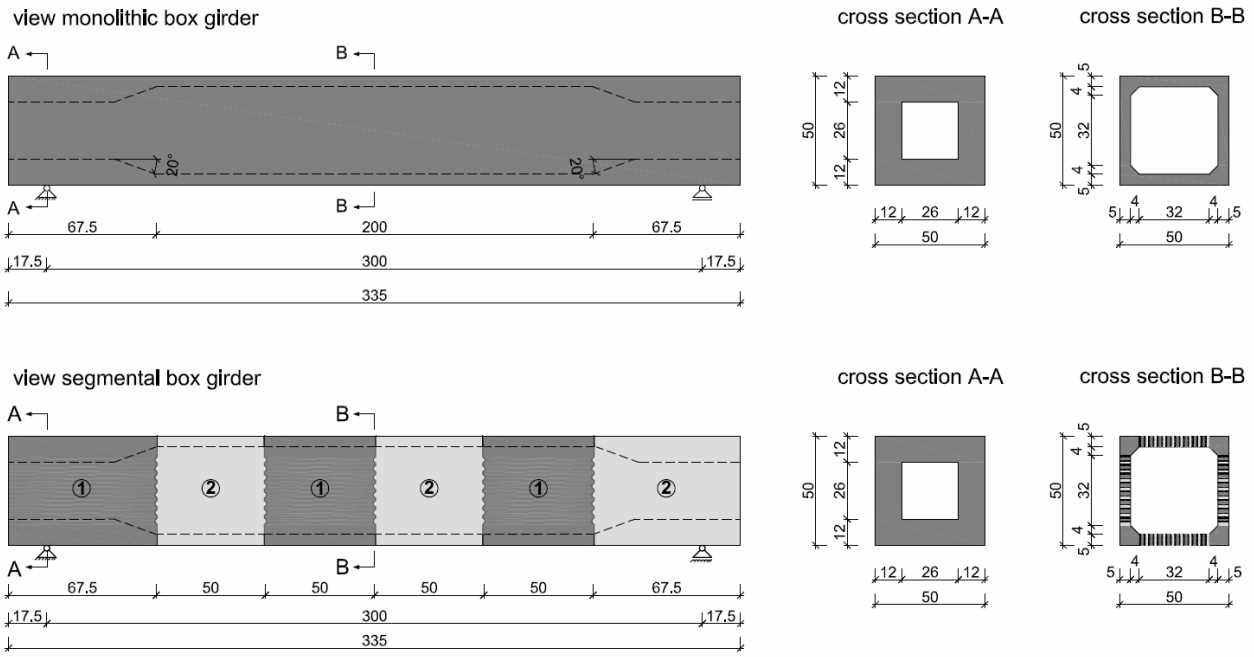

Figure 1: Plan and section view of box girder specimens.

Test specimen V8 was constructed as a segmental girder using the concept of match casting in order to study the effects of a prestressed dry joint. In order to compare the test results, V8 was reinforced just as test specimens V6 and V7, with the difference that the longitudinal reinforcement (ø 8 mm in each corner) could not cross the joints.

Table 2: Box girder specimen details.

Specimen	type	longitudinal reinforcement	transverse reinforcenment	fiber content [vol.-%]	concrete cover [cm]
V1	monolithic	-	-	2.50	-
V2	monolithic	-	-	1.25	-
V3	monolithic	12 ø12	ø12 / 21	1.25	1.0
V4	monolithic	12 ø12	ø12 / 21	0.00	1.0
V6	monolithic	4 ø8	ø12d / 11	1.25	1.0
V7	monolithic	4 ø8	ø12d / 11	1.25	1.0
V8	segmental	4 ø8 *)	ø12d / 11	1.25	1.0

*) each segment.

Figure 2: Overall test setup.

All specimens were tested with both ends of the girder being rotated by stiff twist arms as illustrated in Figure 2 and 3. Special torsion bearings were used to ensure free rotation around the center line of the box girder. The load was recorded by means of a measuring box fixed upon the hydraulic cylinder. The rotation was measured by inductive displacement transducers under the girders. Furthermore, a grid sized 12.5 cm x 12.5 cm was drawn on the front, back and upper side of the test specimens to facilitate the crack measurements. The box girders were tested at incremental load stages so that the cracking could be observed in detail for each load stage. The direction of the principal stresses was measured with sixteen 3-element rosette strain gauges placed on the four sides of the specimen. Furthermore, strain gauges were applied on the longitudinal and transverse reinforcement.

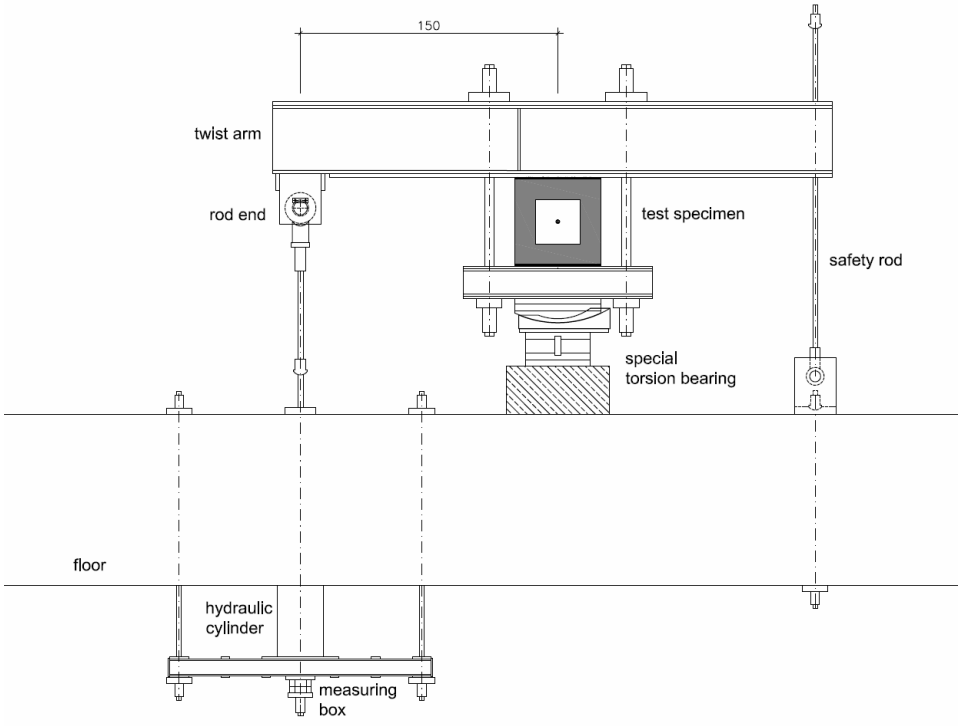

Figure 3: Test setup – section view.

The test specimens V1 – V4 were loaded with a torsion moment purely; V6 – V8 received a combined loading of torsion moment and normal force. The normal force was applied with a unbounded tendon, which was installed in the center line of the girders and fixed at the end of the girders. To assure that the tendon is not participating in the load transfer, axial spherical plain bearings were arranged. The normal force was measured using strain gauges on the tendon.

4 Investigations on the Tension Strut

Test Results

As explained in Chapter 3, the test specimens V1 – V4 were loaded with pure torsion. The test specimens V1 and V2 without reinforcement, but different fiber content, showed linear-elastic torque-twist-curves and both failed after a few, single cracks which occurred nearly at the same ultimate load. In contrast, the test specimens V3 and V4 presented a further load increase after the first cracks and an announced failure mode. Figure 4 shows the torque-twist-responses and the cracking patterns of the specimens V2 – V4.

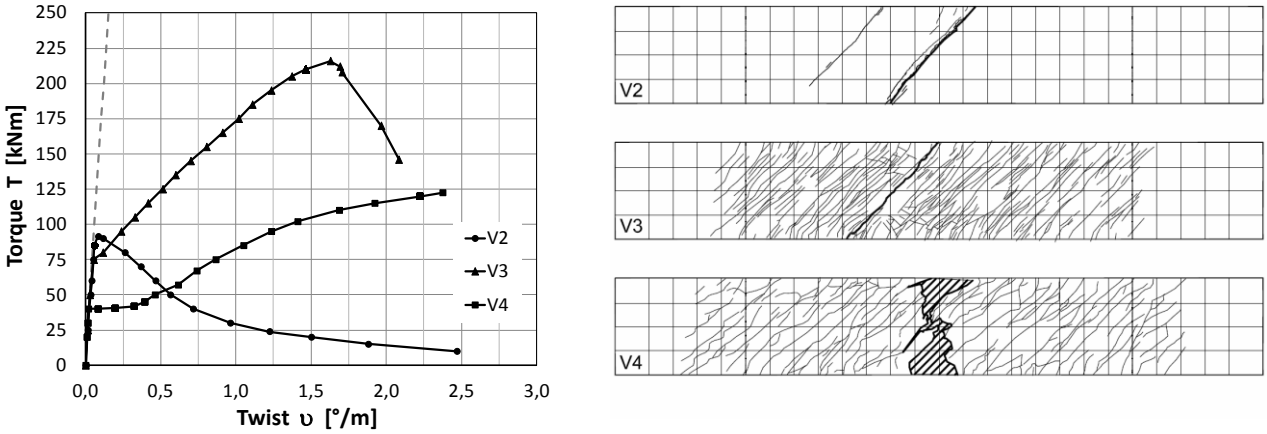

Figure 4: Torque-twist-response (left) and cracking patterns upper side (right) of the test specimens V2 – V4.

The detailed investigation of the torque-twist-response of test specimen V4 (conventionally reinforced with fiber content 0.00 vol.-%) shows three distinct phases: pre-cracking phase, transition phase and post-cracking phase, which is quite similar to a torque-twist-response of a normal strength concrete box girder without fibers. Although specimen V4 was designed for transverse reinforcement failure and the transverse reinforcenment started to yield in the last load stage, the concrete failed suddenly and separated the box girder into two pieces.

In comparison, test specimen V3 (same longitunal and transverse reinforcement as V4, but fiber content of 1.25 vol.-%) shows a different torque-twist-behaviour. Here, only two characteristic phases can be observed: pre-cracking phase and a combination of transition phase and post-cracking phase. Furthermore, V3 reached a higher ultimate torsional strength, which was induced by the failure of the transverse reinforcement. This follows to the conclusion that the addition of fibers improved the stiffness after cracking and the ultimate torque. It can also be observed, that the cracking torque is influenced by the addition of fibers.

For all test specimens V1 – V4 the inclination angle of the cracks was about 45°. The addition of steel fibres resulted into smaller crack widths and a higher number of cracks in V3 compared to V4 (Table 3). Futhermore, due to the presence of steel fibres no spalling of the concrete cover was obtained during the testing of V1, V2 and V3.

Table 3: Test results of tested box girders V1 – V4.

Specimen	cracking torque [kNm]	ultimate torque [kNm]	failure [-]	crack width *) [mm]	crack spacing [cm]
V1	95.0	100.9	fibers	-	-
V2	87.5	91.6	fibers	-	-
V3	75.0	216.0	stirrup	≤ 0.3	1 – 7
V4	37.5	122.5	concrete	≤ 0.8	3 – 13

*) crack width at T = 120 kNm.

Theoretical Investigation

As shown in Figure 4, the fiber-reinforced test specimens V1 and V2 could only be stressed up to the cracking torsion moment. The maximum principal tensile stress is equal to the axial tensile strength f_{ctm}, respectively to the shear stress resulting from the torsion (Figure 5). For such box girders the torsional resistance can be determined with the following equation:

$$T_{Rk,sy,f} = f_{ctm} \cdot t_{eff} \cdot 2 \cdot A_k \quad (1)$$

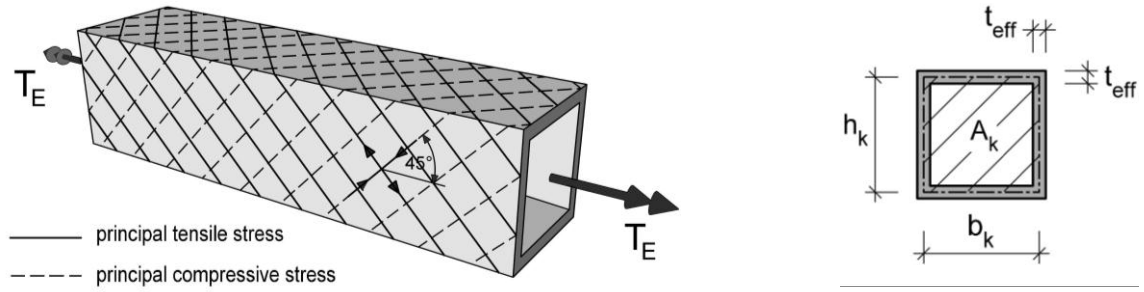

Figure 5: Pattern of principal stresses in pre-cracking phase (left) and cross section (right).

For the reinforced box girders V3 and V4 a load increase beyond the single-cracking phase was possible. The observed spiral cracking leads off to the known space truss model with the coaction of reinforcement and concrete trusses (Figure 6). Additionally, Figure 6 shows for one side a modified plane truss model considering the fibre effect, which results into a “sewing” of the crack edges between the concrete struts.

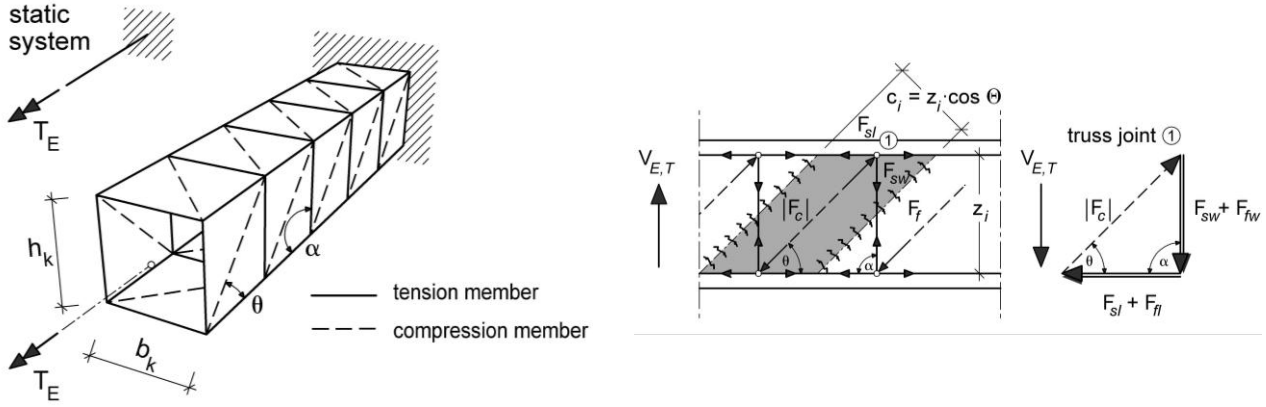

Figure 6: Space truss model (left) and modified plane truss model for one side wall (right).

As the fibers are involved in the load transfer the torsion resistance has to consider the loading capacity of the fibers. This can be done with the summation approach in equation (2) for the longitudinal tension strut using the resistance capacity of the fibres in longitudinal direction with equation (3) and the resistance capacity of the longitudinal reinforcement (according to DIN 1045-1 [4]) in equation (4). Accordingly, the summation approach for the vertical tension strut results from the formulas (5) to (7). In the formulas (3) and (6), $f_{ct,f}$ represents the post cracking axial tensile strength of the fiber-reinforced UHPC.

$$T_{Rk,sy,l} = T_{Rk,sy,fl} + T_{Rk,sy,sl} \quad (2)$$

with

$$T_{Rk,sy,fl} = f_{ct,f} \cdot t_{eff} \cdot 2 \cdot A_k \cdot \tan\theta \quad (3)$$

$$T_{Rk,sy,sl} = a_{sl} \cdot f_y \cdot 2 \cdot A_k \cdot \tan\theta \quad (4)$$

$$T_{Rk,sy,w} = T_{Rk,sy,fw} + T_{Rk,sy,sw} \quad (5)$$

with $$T_{Rk,sy,fw} = f_{ct,f} \cdot t_{eff} \cdot 2 \cdot A_k \cdot \cot \theta \quad (6)$$

$$T_{Rk,sy,sw} = a_{sw} \cdot f_y \cdot 2 \cdot A_k \cdot \cot \theta \quad (7)$$

Figure 7 illustrates the torque-twist-response and the theoretical results calculated with the equations specified above. Comparing the experimental and theoretical torsional resistance, V2 and V4 show a good correlation. For test V3 an upper and lower range of torsional resistance is presented, calculated with the post cracking axial tensile strength $f_{ct,f,L1}$ and $f_{ct,f,L2}$ according to [2]. The final determination of the value for the applying post cracking axial tensile strength requires further investigations.

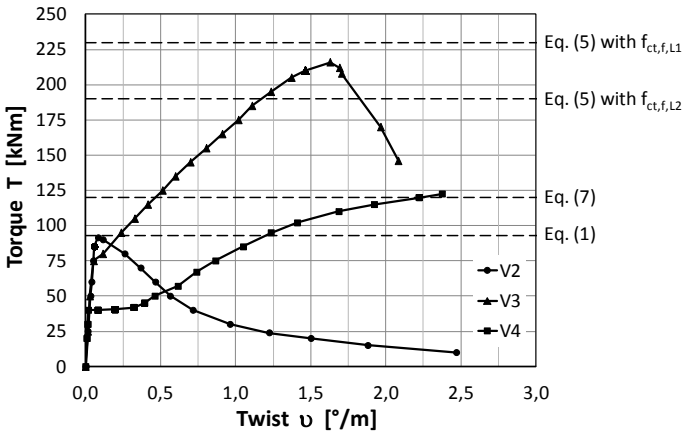

Figure 7: Torque-twist-response (left) and theoretical results (right) of the test specimens V2 – V4.

5 Investigations on the Concrete Compression Strut

Test Results

The test specimens V6 – V8 were loaded with a combined loading of torsion moments and normal forces in order to investigate the bearing capacity of the concrete compression strut. Test specimen V7 was tested with a higher normal force to examine the influence of the concrete strut angle θ. Furthermore, the influence of the prestressed dry joint of the segmental box girder V8 should be compared with the monolithic box girder V6. Figure 8 gives the torque-twist-responses and the cracking patterns of the test specimens V6 – V8.

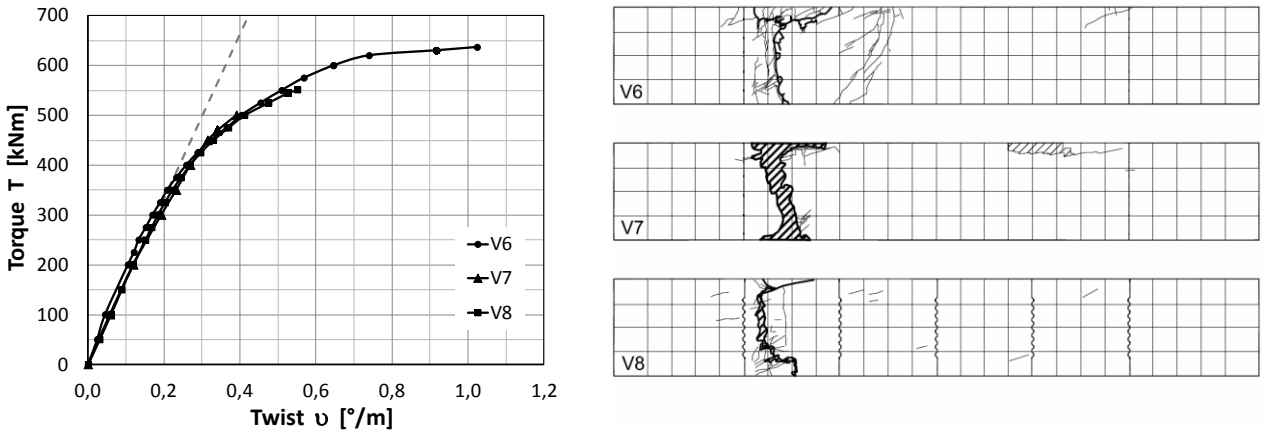

Figure 8: Torque-twist-response (left) and cracking patterns front side (right) of the test specimens V6 – V8.

The torque-twist-responses show for all specimens V6 – V8 a linear-elastic behaviour up to a torque of around 400 kNm and a similar nonlinearty up to the torsional failure, which is corresponding to the torque-twist-curves of prestressed normal strength concrete box girders without fibers. Although the concrete failures occured suddenly and the tested box girders got separated into two pieces, no spalling of concrete cover could be observed up to the ultimate torque. Table 4 presents the results of specimens V6 – V8.

Table 4: Test results of tested box girders V6 – V8.

Specimen	ultimate torque [kNm]	normal force [kN]	failure [-]	angle θ [°]	$f_{c,cyl}$ [N/mm²]
V6	636.7	5249	concrete	29.4	156.4
V7	500.7	5944	concrete	15.7	169.4
V8	551.4	5040	concrete	22.3	160.9

The torque-twist-responses of the monolithic box girder V6 and the segmental box girder V8, which were tested with nearly the same normal forces, show no difference. In conclusion, a prestressed dry joint does not disturb the torsional load transfer, in case the box girder, respectively the joint, is completely under compression up to the failure stage.

Theoretical Investigation

According to the mathematical fomula in DIN 1045-1 [4], which is based on the space truss model (Figure 6, left), the torsional resistance of the concrete strut can be determined by the following equation (8).

$$T_{Rk,max} = \alpha_{c,red} \cdot f_{c,cyl} \cdot 2 \cdot A_k \cdot t_{eff} / (\cot \theta + \tan \theta) \quad (8)$$

Because of cracking, transverse stresses due to reinforcement, strut deflection at the cross section corner and bending stress of the wall due to twisting, the compressive strength $f_{c,cyl}$ has to be attenuated with the reduction factor $\alpha_{c,red}$. For normal strength concrete (NSC) this factor is assumed to 0.525. If high strength concrete (HSC) is applied, the compressive strength additionally has to be reduced by the safety factor $1/\gamma'_c$. Since DIN 1045-1 regulates only concrete up to concrete strength class C100/115, a proposal for the safety factor for UHPC with fibers and UHPC without fibers can be found in [1]. Figure 9 on the left-hand side gives an overview of the safety factor $1/\gamma'_c$ for the different concrete strength classes.

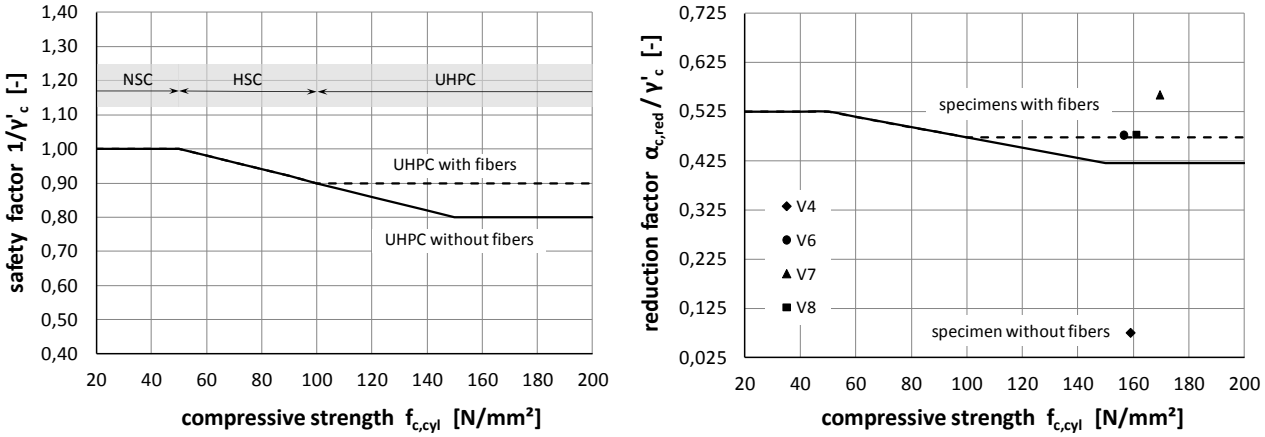

Figure 9: Safety factor $1/\gamma'_c$ (left) and reduction factor $\alpha_{c,red}/\gamma'_c$ (right) in relation to the compressive strength.

Figure 9 on the right-hand side shows the reduction factor divided by the safety factor in relation to the concrete compressive strength and the experimental results. The results of the tested box

girders V6 – V8 (UHPC with fibers) show a good correlation with the reduction factors of UHPC with fibers. In contrast, the sudden failure of test specimen V4 (UHPC without fibers) indicates a considerable deviation from the value of UHPC without fibers. Here, further investigations have to be undertaken.

6 Conclusion

UHPFRC box girders have been examined to investigate the cracking and loading bearing as well as to determine the capacity of the tension strut of the steel fibres under pure torsion and the bearing capacity of the compression strut under combined loading by torsion moments and normal forces.

Due to the results of the four torsion tests in regard to the tension strut the following conclusions can be drawn:

The addition of steel fibers

- causes smaller crack widths and more cracks,
- increases the cracking torque,
- improves the torsional stiffness after cracking and
- increases the ultimate torque.

The tests on two monolithic and one segmental box girder in regard to the concrete compression strut can be summarized as follows:

- All test specimens showed no ductility and failed suddenly.
- The prestressed dry joint does not disturb the load transfer, in case the segmental box girder, respectively the joint, is completely under compression at the stage of failure.

Furthermore, mathematical equations have been developed from the space truss model to determine the loading capacity of the tension strut of the fibers, which show a good correlation with regard to the experimental torsional resistance. In regard to the bearing capacity of the concrete strut a proposal for the reduction factor of the compressive strength of UHPC with and without fibers has been presented.

7 Acknowledgement

This research project is part of the priority programm SPP 1182 which is founded by the DFG (German Research Foundtation). The authors acknowledge the financial support.

References

[1] Deutscher Ausschuss für Stahlbeton: Sachstandsbericht – Ultrahochfester Beton. DAfStb 561, Berlin, 2008.

[2] Deutscher Ausschuss für Stahlbeton: DAfStb-Richtlinie – Stahlfaserbeton. Berlin, 2009.

[3] German Research Society (DFG), Priority Program SPP 1182, Nachhaltig Bauen mit UHPC (Sustainable Building with UHPC).

[4] DIN 1045-1: Tragwerke aus Beton, Stahlbeton und Spannbeton – Teil 1: Bemessung und Konstruktion, August 2008.

Bond Behavior of Strands in UHPC – Tests and Design

Guido Bertram, Josef Hegger
Institute of Structural Engineering, RWTH Aachen University, Germany

Ultra-High Performance Concrete (UHPC) is an appropriate construction material for pretensioned girders. To ensure an economic and safe design, a detailed knowledge of the behavior of pretensioned strands in the anchorage zone is essential. The dimension of the bond anchorage zone favors the cost-effective design of pretensioned girders, especially when the shear resistance is decisive. However, a minimum concrete cover is required to avoid splitting cracks in the transfer zone, since they lead to an uncontrolled increase in transfer length and may cause a premature anchorage failure.
Within a priority program [1] supported by the German Research Foundation (Deutsche Forschungsgemeinschaft DFG) experimental and theoretical investigations on the bond behavior of strands in UHPC were carried out at the Institute of Structural Concrete at RWTH Aachen University. The influence of the Hoyer-effect [2-6] and the concrete cover were systematically investigated by pull-out-tests. Additionally, small scale beam tests were carried out to determine the transfer length and the end slip. Furthermore, the experimental as well as the theoretical results were verified on full scale beams. The detailed test results were published in [7] and the calculation model in [8]. The bond model was derived based on the test results and will be presented at the conference.

Keywords: Ultra-high Performance Concrete, fibers, Strands, bond, pretensioning, transfer length

1 Introduction

Generally, the number of strands in pretensioned girders results from the bending design. In addition, the prestressing force above the support is essential to calculate the shear resistance. A decisive part of the shear carrying capacity arises from arch action as presented in Figure 1. When the anchorage length is shorter than the support overhang, the full prestressing force is available to intensify arch action. The vertical support reaction corresponds with the prestressing force and the arch action.

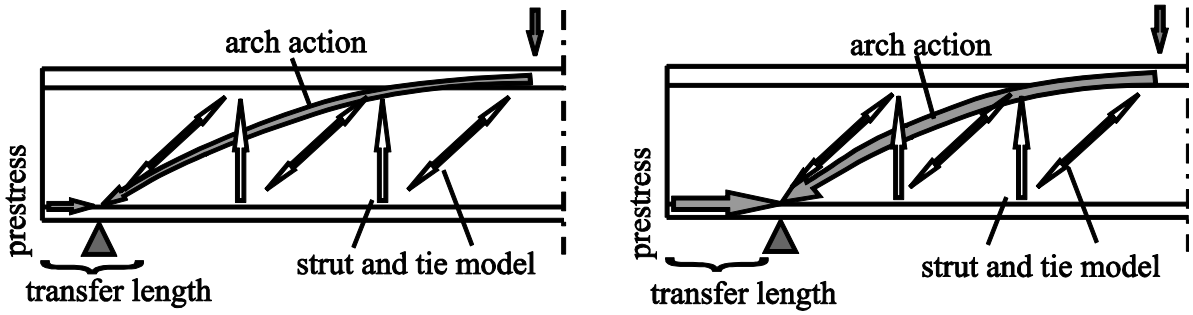

Figure 1: Principle of arch action with corresponding prestressing force.

The higher the bond stresses are between strands and concrete the shorter is the transfer length. On the other hand, higher bond stresses lead to increased tensile stresses in the concrete cover around the strands. Therefore, the minimum concrete cover for strands in UHPC has to be determined. The compressive strength of UHPC is about five times higher than normal strength concrete. The bond strength and the compressive strength, however, show no linear coherence. Nevertheless, the concrete compressive strength is normally used in design methods. To ensure a safe design, constitutive design rules to calculate the anchorage and transfer length of strands in UHPC are required. The gradient of the bond forces is influenced by the slip, the Hoyer-effect, the material properties and the concrete cover. With an adequate

theoretical method derived from test results, the transfer length can be determined merely knowing the end slip, the compressive strength and the concrete cover.

2 Bond behavior of strands

While ribbed rebars rely on a direct load transfer between the ribs and the supporting concrete under each rib, strands depend on friction to a greater extent. Hence, the stress-slip relation of strands has a plastic branch after exceeding the ultimate bond strength. So far, several investigations have been performed on the bond behavior of strands [2-6]. Generally, the bond stresses can be described with three parts (Figure 2):

- a constant part caused by the basic friction, also called the rigid-plastic bond behavior;
- a stress dependent part which is based on the Hoyer-effect and which increases with the transfer of pretensioning;
- and a slip dependent part which is also independent of the prestressing. This effect can be explained by the “lack of fit” which results from the geometry of the strands which is not completely uniform.

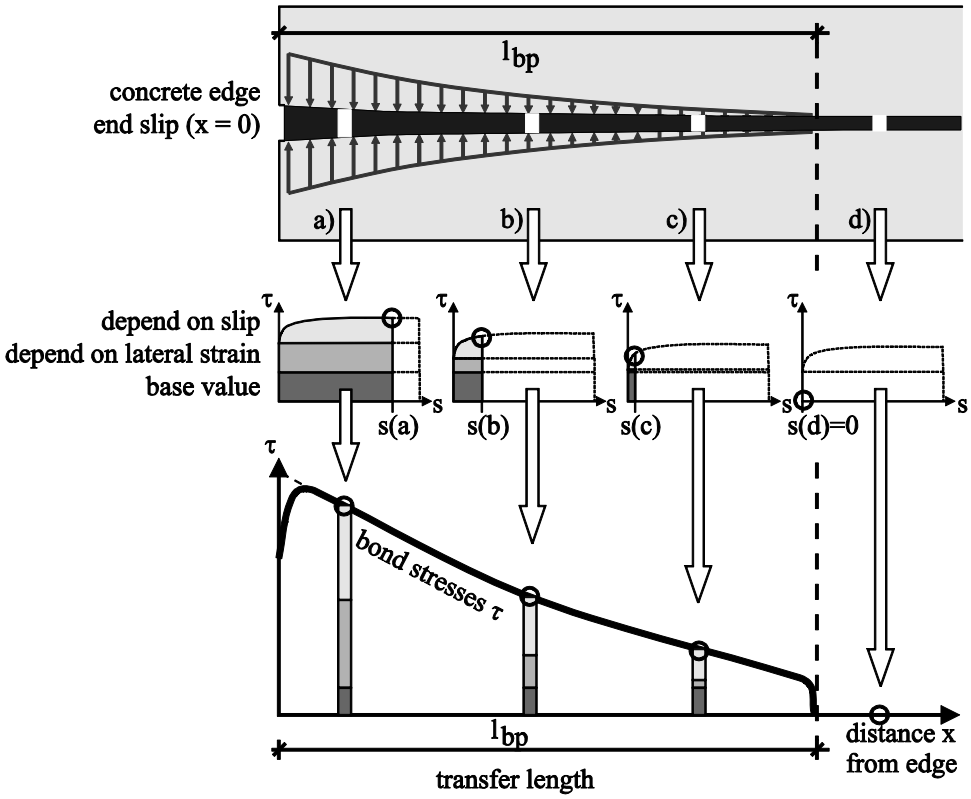

Figure 2: Schematical stress distribution along the transfer length of strands.

Due to the dependency on slip and lateral strain, the bond stresses are not constant along the transfer length (Figure 2). The slip as well as the lateral stresses rise from the difference between steel and concrete strain while the pretensioning is released. At the end of the member, the slip has the highest value and the longitudinal steel stress is zero. All three bond parts are fully activated ((a) in Figure 2). In the middle of the transfer zone, the slip as well as the lateral stresses are decreased. Hence, the bond stresses are on a lower level (b). At the end of the transfer length, most stresses already have been transferred from steel to concrete. Here the lateral stresses and the slip are very low and the bond is mainly established by the base value of the bond (c). Outside the transfer length, there are neither bond nor lateral stresses nor slip due to pretensioning (d).

To determine the bond stresses along the transfer length and to investigate the bond behavior, pull-out tests with different steel stresses, which means different lateral strain, were performed. In the next step, small scale beam tests were carried out to measure the transfer length and to investigate the influence of the concrete cover. Finally, the results are used for dimensioning the pretensioned I-beams [7-9]. The end slip and the transfer lengths of the I-beams were measured to verify the results.

3 Experimental Investigations

Concrete mixtures, fibers and strands

All specimens were fabricated with the concrete mix presented in Table 1. Merely the fiber ratio was varied. All fibers were straight – without hooks – and of high strength steel (f_y^f > 2,200 MPa (320,000 psi)). The diameter of 0.15 mm (0.06 in) is specified by the manufacturer and the margin is ±0.02 mm. In several spot measurements the diameter was about 0.17 mm in average. The steel fibers had a length between 9 mm (M0 with 2.5 %) and 17.5 mm (M1 with 0.9 %). In the M7 mix a fiber cocktail with 6 and 13 mm long fibers was added and the reference composition MR contained no fibers. The 7 wire strands with a cross section A_p = 93 mm² (diameter 0.5'') respectively A_p = 140 mm² (0.6'') had an E-Modulus of 200,000 MPa and f_{py} = 1500 MPa (218,000 psi).

Table 1: Concrete mix.

Material \ Mix/fiber ratio		M0	M1	M7	MR
		2.5% p.v.	0.9% p.v.	1.04% p.v.	w/out
Cement CEM I	[kg/m³]	650	660	660	666
Silica fume	[kg/m³]	177	180	180	181
Quartz powder	[kg/m³]	456	463	463	467
Sand 0.125-0.5mm	[kg/m³]	354	360	359	363
Basalt 2-8mm	[kg/m³]	598	606	606	612
Steel fibers 9.0/0.15	[kg/m³]	194	-	-	-
Steel fibers 17.5/0.15	[kg/m³]	-	70	-	-
Steel fibers 13.0/0.16	[kg/m³]	-	-	39	-
Steel fibers 6.0/0.15	[kg/m³]	-	-	42	-
Water	[kg/m³]	158	161	160	162
Superplasticizer	[kg/m³]	31	32	32	32

Pull-out-tests

A total of 72 tests were performed (Table 2). The main test parameters were the fiber ratio, the specific concrete cover and the concrete strength (age). Because of the high bond stresses, short embedment lengths between 25 and 50 mm (0.98-1.97 in) were chosen. Each test batch consisting of a total of 9 tests included three times three tests with different lateral strain stages (0 %, 50 %, 100 %), where 100 % means a change of prestressing stress Δf_p = 1200 MPa (174,000 psi), 50 % means Δf_p = 600 MPa (87,000 psi) and 0 % without a change. In the test batches PO10-PO15, one test was carried out for each concrete cover and change of prestressing. Figure 3 shows the sequences of the pull-out tests. Three strands have been prestressed inside a rig before casting with the maximum allowed initial prestressing stress 0.9·1500 = 1350 MPa ($P_0 = 1350 \cdot A_p$) according to the German design code [10]. After three

days, the first three tests were carried out. Afterwards, the prestressing force was decreased about 50 % (600 MPa) and the next three tests were performed. Finally, the last tests were carried out with full release (100 %, 1200 MPa), which means nearly full lateral strain of the strand. The remaining f_p = 150 MPa were needed to avoid total relaxing of the strands on one side while increasing the bond forces (P_b/2 on each side in Fig. 3, phase IV).

Table 2: Parameters of the pull-out tests (72 tests).

test batch	concrete mix / age	concrete cover *c*/d_p [-]	strands d_p [in]	bond length l_b [mm (in)]	number 0 %/ 50 %/100 %	$f_{c.cube100}$ [MPa]
PO1-PO3	M1 / 3d	4.4	0.6	30 (1.18)	3 / 3 / 3	116
PO4-PO6	M0 / 3d	4.4	0.6	30 (1.18)	3 / 3 / 3	118
PO7-PO9	M7 / 3d	4.4	0.6	30 (1.18)	3 / 3 / 3	111
PO10-PO12	M1 / 3d	1.5/2.0/2.5	0.6	30 (1.18)	1 / 1 / 1	113
PO13-PO15	M1 / 3d	1.5/2.0/2.5	0.6	50 (1.97)	1 / 1 / 1	112
PO16-PO18	M1 / 3d	5.5	0.5	25 (0.98)	3 / 3 / 3	107
PO19-PO21	M1 / 14d	4.4	0.6	30 (1.18)	3 / 3 / 3	154
PO22-PO24	MR / 3d	4.4	0.6	30 (1.18)	3 / 3 / 3	105

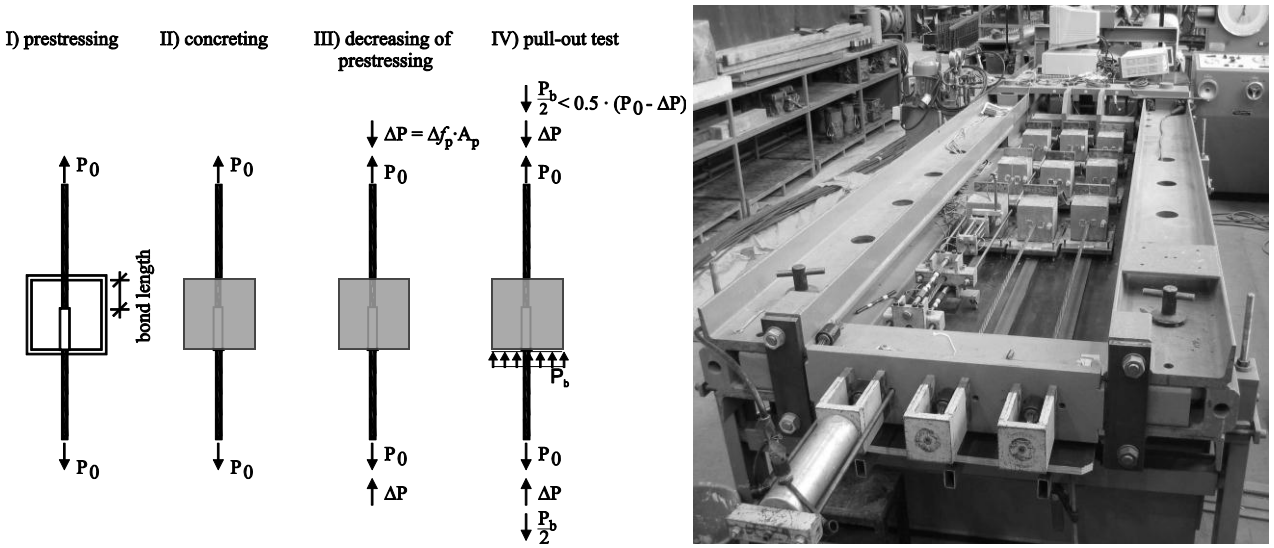

Figure 3: Fabrication and test sequences of the pull-out tests and test rig.

The diagrams in Figure 4 indicate, that the fiber ratio had no significant influence within the tested range. With a concrete compressive strength of app. 100-115 MPa (≈ 15,000 psi) at an age of three days a bond strength of 30 MPa (≈ 4,350 psi) was achieved with full lateral strain (100 % release of prestressing), 20 MPa (≈ 2,900 psi) with 50 % release and about 12 to 14 MPa (≈ 1,900 psi) without a change of the prestressing force. The bond stresses f_{pb} were calculated with the nominal diameter d_p.

$$f_{pb} = P_b/(l_b \cdot \pi \cdot d_p) \quad \text{with} \quad \begin{array}{l} f_{pb}\text{: bond stress} \\ P_b\text{: bond force} \\ l_b\text{: bond length} \end{array}$$

The variation of the concrete cover showed no effect on the bond strength when the prestressing remains unchanged as presented in Figure 5 (left diagram). A release of 50 % (middle diagram in Fig. 5), however, led to a reduction of the bond stresses of about 10 to 15 %. When the full lateral strain was preset, visible splitting cracks appeared below a specific

concrete cover of c/d_p = 2.5. Hence, the transferred bond stresses were reduced for 10 to 30 % according to the existing concrete cover (right diagram in Fig. 5).

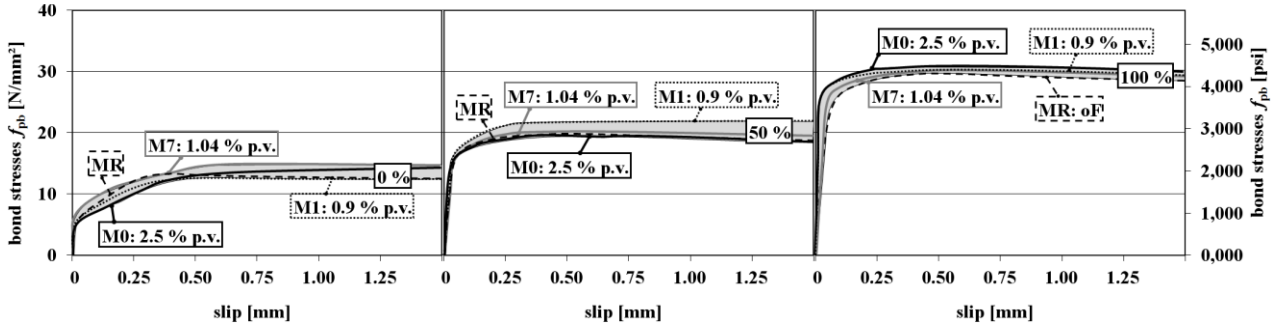

Figure 4: Influence of the fiber ratio and the prestressing (0 %, 50 %, 100 %) on the bond slip behavior of the test batches PO1 to PO9, PO22 to PO24.

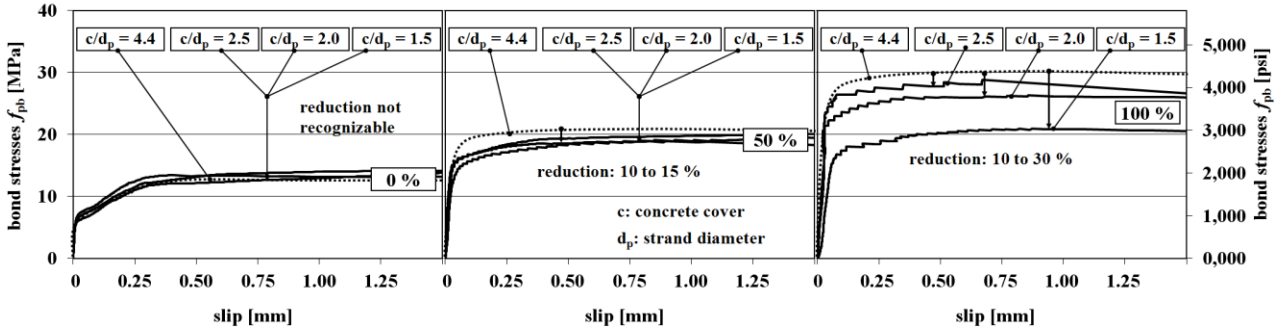

Figure 5: Influence of the concrete cover on the bond slip behavior of the test batches PO10 to PO12.

In further tests, the concrete age, the bond length and the strand diameter were varied. The strand diameter had no effect on the bond stresses. The tests with a bond length l_b = 50 mm (PO13-PO15) confirm the tests with 30 mm (PO10-PO12), when the change of prestress was 0 or 600 MPa (0 %, 50 %). After full release (100 %), the bond forces were too high (up to 40 kN) with l_b = 50 mm. Hence, splitting cracks were intensified and the change of strain inside the bond length might have influenced the results as well. More detailed test data is given in [8].

Small Scale Beam Tests

The main targets of these 14 tests were to determine the minimum dimensions of the concrete cross section to avoid splitting cracks and the transfer length of the specimens which remained uncracked. Furthermore, the corresponding end slip is important. Specimens with two strands were chosen to investigate the minimum concrete cover (Figure 6). Four strands were required to test the minimum spacing between the strands. The test parameters and the main results are listed in Table 3. The concrete cross section $b \cdot h$ results from the specific concrete cover c/d_p and the spacing s/d_p horizontal as well as vertical.

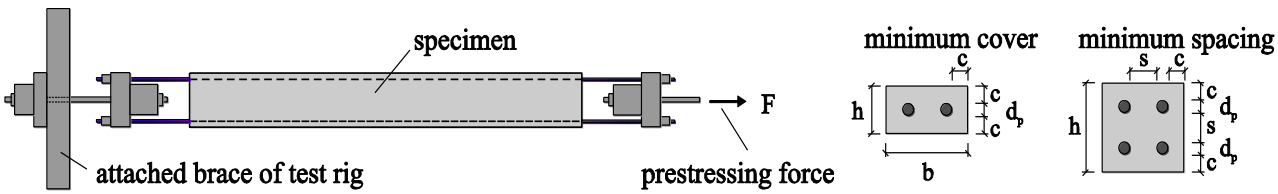

Figure 6: Test setup of the small scale beam tests.

Similar to the pull-out tests, the specimens were fabricated in a rig. The 0.5'' strands were already prestressed at the time of concreting. After three days the prestressing was gradually released in five steps of 20 %. At each load stage the concrete strains were measured along

the longitudinal axis of the specimen. This way, the transfer of prestressing could be derived from the strain differences. In addition, the slip at the end of the specimen was measured continuously with displacement transducers.

Table 3: Parameters and main results of the small beam tests.

	mix/ stirrups	*b*	*h*	c/d_p	s/d_p [-]		0.5'' number		cracked		$f_{c.cube100}$	$f_{ct.fl}$	end slip [mm]	transfer length [mm]	
test		mm	mm	[-]	hor.	vert.	2	4	left	right	MPa	MPa	min – max	left	right
SE1	M1	101.6	50.8	1.5	3.0		x		x	x	106	19.3	0.70 – 0.89	*	*
SE2	M1	114.3	63.5	2.0	3.0		x		x	x	106	19.3	0.53 – 0.67	*	*
SE3	M1	120.7	120.7	2.5	2.5	2.5		x	-	-	99	21.3	0.39 – 0.56	206	210
SE4	M1	127.0	127.0	2.5	3.0	3.0		x	-	-	99	21.3	0.42 – 0.56	205	206
SE5#	M1	127.0	76.2	2.5	3.0		x		-	-	115	23.6	0.48 – 0.63	193**	195**
SE6#	M1+Ø6	127.0	76.2	2.5	3.0		x		x	-	115	23.6	0.63 – 0.71	*	239**
SE7	M1	108.0	108.0	2.0	2.5	2.5		x	x	o	100	20.9	0.54 – 0.87	*	*
SE8	M1	108.0	101.6	2.0	2.5	2.0		x	x	x	100	20.9	0.59 – 0.75	*	*
SE9	M1	120.7	120.7	2.0	3.5	3.5		x	-	x	108	20.5	0.44 – 0.63	204	*
SE10	M1	114.3	114.3	2.0	3.0	3.0		x	x	x	108	20.5	0.44 – 0.88	*	*
SE11	M1	225.0	150.0	5.4	4.9		x		-	-	106	23.7	0.44 – 0.60	228	243
SE12	M1	158.8	101.6	3.5	3.5		x		-	-	110	20.6	0.43 – 0.53	213	219
SE13	M0	114.3	63.5	2.0	3.0		x		-	-	112	26.3	0.46 – 0.48	205	183
SE14	M0	127.0	76.2	2.5	3.0		x		-	-	107	23.4	0.44 – 0.56	225	205

* Transfer zone cracked / transfer length not evaluable

** Concrete strain measured with strain gauges (no manual measuring with gauge points)

o Crack not observable visually, but concrete strain indicates cracks

\# Test carried out after 5 days

The specimen SE1 with a specific concrete cover c/d_p = 1.5 started cracking when 70 % of the prestressing was induced. Due to the splitting crack the stress depending part (Hoyer-effect) diminished leading to a higher slip. SE2 with c/d_p = 2.0 cracked at 95 %. The transfer lengths were evaluated by a German method [11]. They become shorter compared to tests with high strength concrete (HSC) or even normal strength concrete (NSC)[3] when cracks were avoided. In these cases the measured transfer length in UHPC was about 20 to 24 cm (7.9 to 9.4 in). Further data is given in [8].

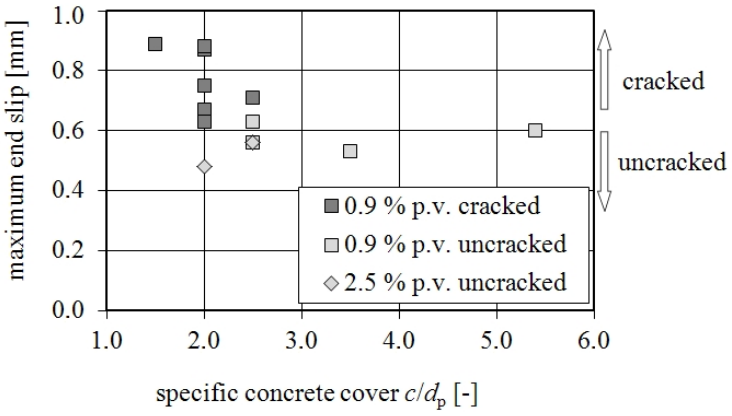

Figure 7: Influence of specific concrete cover and fiber content on end slip and cracking.

The influence of the concrete cover and the fiber content on end slip and cracking is illustrated in Figure 7. An end slip of app. 0.5 to 0.6 mm (0.20 to 0.24 in) indicates a transfer without cracks. Compared to HSC a reduction of the minimum concrete cover c/d_p = 2.5 could not be accomplished. Most likely, the splitting stresses arose simultaneously due to the higher bond stresses. Only when the specific concrete cover was at least c/d_p = 2.5 the full prestressing was feasible without visible cracks. With higher fiber content, a reduction to c/d_p = 2.0 seems possible.

Transfer length and end slip of the full Scale Beams

According to the small scale beam tests the specific concrete cover of the girders was always c/d_p = 2.5 (Fig. 8) and the prestressing was released after three days in the same way. The right diagram shows the transfer lengths of 21 beams. The transfer length was slightly increased to 22 to 28 cm (8.7 to 11 in). There seems to be a slight coherence to the end slip, but splitting cracks were not observed. The middle diagram in Figure 8 shows the average values of 362 measurements on the end slip. The end slip values of the middle and the lower strands did not indicate any cracks as well. They are comparable to the small scale beam tests without cracks. But it is remarkable, that the values of the upper strands are increased. There seems to be a decreased bond strength due to the covering lateral form work.

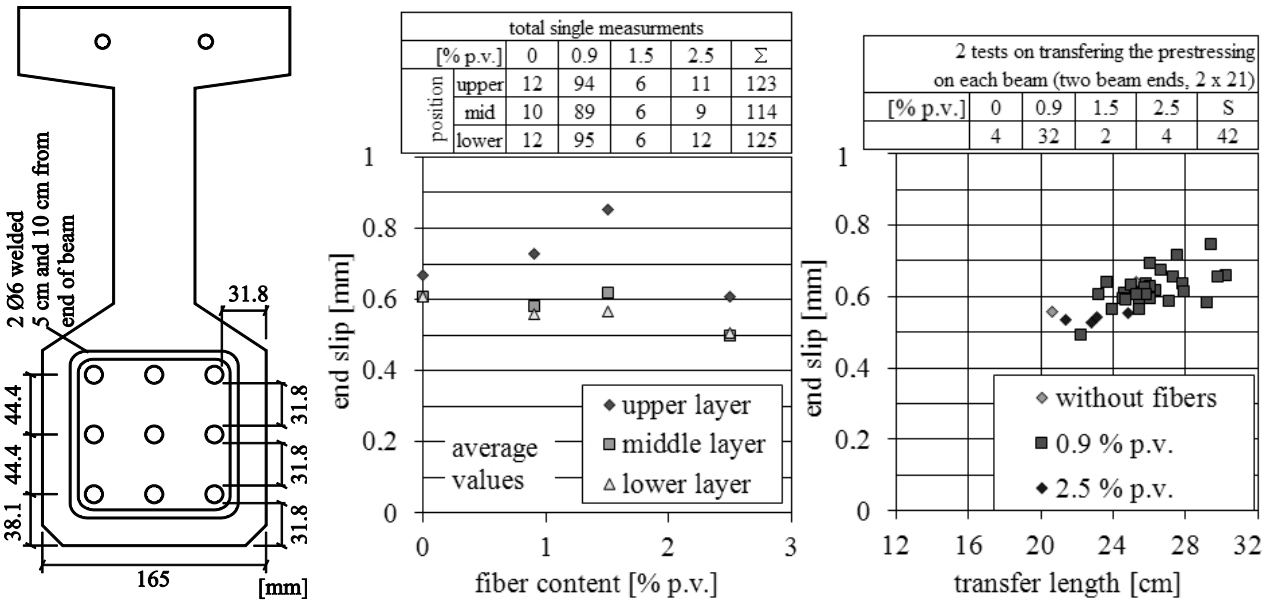

Figure 8: Cross section of the beams and evaluation of the influence of the fiber content and strand position on end slip and transfer length.

4 Conclusions and Outlook

The bond strength of strands in UHPC amounts app. 30 MPa (≈ 4,350 psi) with full release, 20 MPa (≈ 2,900 psi) with 50 % and 12 to 14 MPa (≈ 1,900 psi) without release. The local bond stresses are affected by the concrete cover, when the specific concrete cover is reduced to c/d_p = 2.5 or more. The transfer length in the I-beams ranged between 22 and 28 cm (8.7 to 11 in), primarily affected by the concrete cover and the strand density. Therefor a minimum specific concrete cover c/d_p = 2.5 as well as a minimum clearance s/d_p = 2.5 is required. With 2.5 % p.v fibers the concrete cover seems to be reducible to c/d_p = 2.0.

Further details of the model are not described in this paper. The bond model as well as the calculation method are published in [8] and will be presented at the conference. An English Version of [8] will follow soon.

5 Acknowledgements

The authors acknowledge the funding of the German Research Foundation.

References

[1] German Research Foundation, priority project (DFG SPP 1182): Nachhaltig Bauen mit UHPC (Sustainable Construction with UHPC).
[2] Hoyer, E.: Der Stahlsaitenbeton. Otto Elsner Verlagsgesellschaft, 1939, Berlin Wien Leipzig.
[3] Nitsch, A.: Spannbetonfertigteile mit teilweiser Vorspannung aus hochfestem Beton. Dissertation, Aachen, Germany, 2001.
[4] Stocker, M.F.; Sozen, M.A.: Bond characteristics of prestressed strand. Investigations of prestressed reinforced concrete of Highway bridges. University Illinois, Structural Research, 1969, Series No. 344.
[5] den Uijl, J.: Bond and splitting action of prestressing strand. Proceedings, Bond in Concrete, Riga, 1992, S. 2/79-2/88.
[6] Bülte, S.: Zum Verbundverhalten von Spannstahllitzen unter Betriebsbeanspruchung (bond behavior of strands under cyclic loading). Dissertation, Aachen, Germany, 2008.
[7] Hegger, J.; Bertram, G.: Verbundverhalten von vorgespannten Litzen in UHPC - Teil 1: Versuche zur Verbundfestigkeit und zur Übertragungslänge (bond behavior of strands in UHPC – part 1: tests on bond strength and transfer length). In: Beton- und Stahlbeton 105 (2010), Journal 6, p. 379 - 389.
[8] Bertram, G.; Hegger, J.: Verbundverhalten von vorgespannten Litzen in UHPC - Teil 2: Ableitung eines Verbundmodells zur Berechnung der Übertragungslänge (bond behavior of strands in UHPC – part 2: bond model derivation for the calculation of transfer lengths). In: Beton- und Stahlbeton 107 (2012), Journal 1, p. 23 - 31.
[9] Bertram, G.; Hegger, J.: Pretensioned UHPC Beams with and without Openings. Proceedings, 3rd International fib Congress & PCI Convention, Washington DC, USA in 2010, DVD ID: 236.
[10] DIN 1045-1, Tragwerke aus Beton, Stahlbeton und Spannbeton (German design code, Concrete, reinforced and prestressed concrete structures). Berlin, 2008.
[10] Bertram, G.; Hegger, J.: Anchorage Behavior of Strands in Ultra-High Performance Concrete. Proceedings, 8th International Symposium on Utilization of High-Strength and High-Performance Concrete, Tokyo, Japan in 2008, CD S3-3-6.
[11] Deutsches Institut für Bautechnik (German Building Authorities): Richtlinie für die Prüfung von Spannstählen auf ihre Eignung zur Verankerung durch sofortigen Verbund (Guideline for testing pretensioned strands on their suitability for anchorage). Berlin, Germany, Juni 1980.

Experimental Investigations on Anchorage of Rebars in UHPC

Ekkehard Fehling, Paul Lorenz, Torsten Leutbecher
Institute of Structural Engineering, University of Kassel, Germany

Designing reinforced UHPC concrete structures requires information about the bond-behavior of non-prestressed rebars. Determining the influence of the main parameters in test series is necessary, especially in order to acquire the basic information needed to develop design-regulations. Because of the high compression strength, UHPC-structures are often filigree. Therefore the concrete cover and the failure mode are the main parameters in these investigations. If fibers are used, it is important to know how they influence the bond behavior or if they can replace a transverse reinforcement. Further important parameters are the bar diameter, rib geometry, pouring direction of concrete and load direction. In the building practice, the relevant influences of the aforementioned parameters are important. The main intention is to find out the necessary bond length and concrete cover of non-prestressed rebars in UHPC under these parameters.

Keywords: anchorage, bond, UHPC, UHPFRC, Rebars

1 Introduction

The material UHPC exhibits compression strengths near those of construction steel, which enables a reduction of cross sections and the use of fewer resources. In terms of reinforcement corrosion, the high packing density and the high resistance against ingress of fluids and gases allows markedly smaller concrete covers. At the same time, minimum concrete cover requirements must be observed in order to ensure a secure anchorage. For this purpose, the differences in bond behavior in comparison with NSC must be explored. Through the load transfer from the deformed bar along the ribs in the concrete, struts are formed, which are balanced by a tensile ring. A failure of the tensile ring results in the formation of splitting cracks, which negatively affect the multiaxial state of stress on the ribs. Due to the fact that the increase in tensile strength in comparison with that of NSC is disproportionately lower than the increase in compression strength, the focus must be placed on tensile failure. It is known that fibers have positive effects on the tensile failure characteristics.

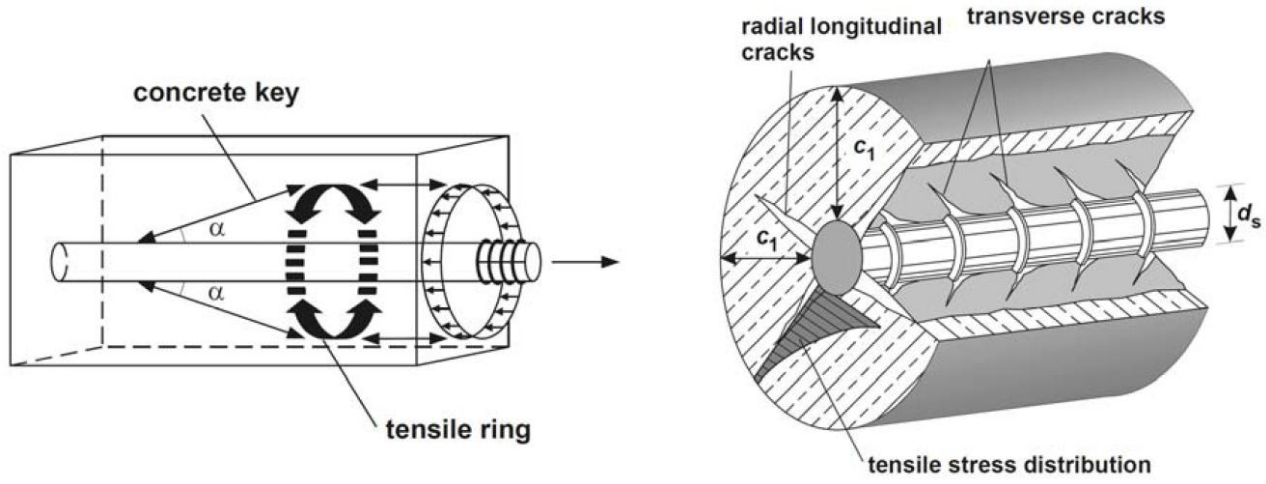

Figure 1: Spatial strut and tie model (left) and crack formation and concrete stresses (right) [7], [6].

Eligehausen et al. [8] examined various anchorage failure modes for NSC including pull-out, pry-out, splitting as well as combinations of these individual modes. Each mode was influenced by different parameters, for example confinement, the addition of fibers, relative rib area, concrete cover, casting direction etc. For this reason, the relevant parameters must be determined in order to assess anchorages for the ULS. These will be examined within the framework of a project funded by the German Research Foundation.

2 Current State of Research

From NSC to UHPC

Rehm [10] made one of the most fundamental contributions to questions concerning the bond between steel and concrete. In his work, he proposed to make initially all observations on a very short reinforcement element and established the differential relationship of bond.

Martin [12] provided, among others, approximations for the differential relationship of bond.

Fehling [1] developed a bond model, which worked with rheological, spring and friction elements [11] for both monotonic and cyclic loading.

Eligehausen et al. [8] examined anchorages in NSC. The obtained engineering models were introduced in the ETAG 001 [9]. Further studies for NSC are shown in [14].

Aarup et al. [4] examined the bond behavior of CRC (Compact Reinforced Concrete) on pull-out tests. Fiber contents of between 3 and 6 % by vol. were used. The concrete cover was 1.7 d_s (d_s = 8 mm) at a compression strength of 165 MN/m². A bond length of 6.3 d_s was sufficient to cause steel rupture prior to bond failure. In the case of smaller embedded lengths, pull-out failure with splitting cracks was observed. In addition he found that transverse reinforcement or lateral pressure is capable of causing a shortening of the bond length by 40 %. A lateral pressure of 5 % of the compression strength is sufficient to increase the bond strength by 60 %.

Based on fiber-reinforced fine-grained UHPC (DUCTAL®), Reineck and Greiner [5] determined a bond strength of between 43 and 51 MN/m² on ribbed bars with d_s = 4 mm and a concrete cover of 4.5 d_s. The bond length was 2 d_s. Pull-out tests were conducted on fiber-free fine-grained UHPC with a bond length of 3.3 d_s. This resulted in bond strengths of between 46 and 49 MN/m². Thereby no negative impact from failing fibers could be established. No splitting was observed.

Jungwirth [3] conducted pull-out tests on coarse-grained UHPC (CERACEM®) with threaded bars. The compression strength of the concrete was 190 MN/m² and the steel fiber content was 2 % by vol. (l_f/d_f = 20 mm/0.3 mm = 66.7). The slip was measured at the unloaded end. The result was an average bond strength of 59 MN/m² (see Fig. 1 and Tab. 1). He observed splitting failure at d_s = 20 mm with a concrete cover ratio of 3.5 d_s and showed that after splitting the load droped sharper in the post failure stage than without splitting.

Leutbecher [2] conducted tests to examine the bond behavior of reinforcement steel and high-strength steel in UHPC as well as in UHPFRC using the M1Q mixture [15]. Here, a total of 27 specimens were tested varying type of steel, the bar diameter, the concrete cover, and the casting direction. Additionally, a fiber content of 1 % by vol. was examined. It turned out that for high-strength steel and a concrete cover of 2.5 d_s the maximum bond stress, that means for high slip values, can be doubled by a addition of fibres i.e. a fiber content of 1 % by vol. in case of splitting crack formation. An increase of bond stress for values under 0.2 mm, however, is also achieved. Fiber addition showed no effect on the bond behavior if splitting crack formation could be excluded.

3 Own Tests on Anchorage of Rebars in UHPC

Experimental Program

The specimens consisted of a panel with constant length and width (see Fig. 2). The ribbed bar on which the bond behavior was to be observed was BSt 500 S with a diamameter of d_s = 12 mm. The embedded length l_b and the concrete cover c of this bar was modified. The casting direction was orthogonal to this bar and the concrete cover. The embedded length of the other bar (d_s =14 mm) was constant. In transverse direction to this bar, wire stirrups were used in order to avoid bond failure. To avoid a tensile failure between the two bars mentioned first, two additional bars with a diameter of d_s = 10 mm were arranged. The fine-grained UHPC M3Q with a fiber content of 1.5 % by vol. (l_f/d_f = 13 mm/0.19 mm = 68.4) and a compression strength of 170 MN/m² was used for all specimens. The formwork was stripped after 48 hours. Afterwards heat treatment at a temperature of 90 °C was applied to the specimens for 48 hours. An overview of the test program is presented in Tab 1. The investigated parameters were the bond length and the concrete cover.

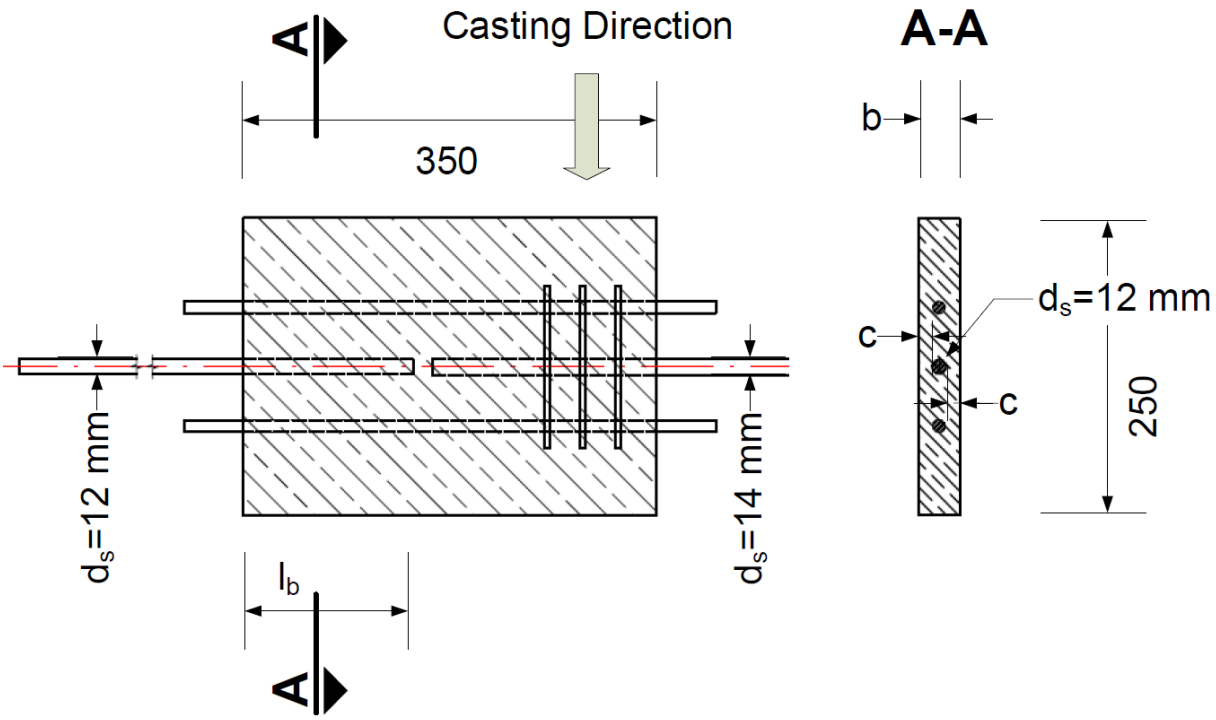

Figure 2: Specimen principle for ribbed bar Pull-Out with varying embedded lengths and concrete covers.

Table 1: Investigated parameters.

Name of the specimen		V12/1/4 V12/1/6 V12/1/8 V12/1/10 V12/1/12	V12/1.5/4 V12/1.5/5 V12/1.5/6 V12/1.5/8 V12/1.5/10	V12/2/2 V12/2/4 V12/2/5 V12/2/6 V12/2/8	V12/2.5/2 V12/2.5/3 V12/2.5/4 V12/2.5/5 V12/2.5/7
Concrete cover	c_{nom} / d_s	1	1.5	2	2.5
Bond length	l_b / d_s	4, 6, 8, 10, 12	4, 5, 6, 8, 10	2, 4, 5, 6, 8	2, 3, 4, 5, 7

Test Set-Up and Test Procedure

At first, the specimen was installed in the machine and the LVDT´s were applied. The ribbed bar on which the bond behavior was to be observed was free and not loaded at this time. After starting the measurement, this bar was pinched in the machine and the load-application was

started in a displacement-controlled way with a velocity of 0.1 mm/sec. The steel strain on this bar was obtained from the elongation Δl_b as measured by the LVDT-Group B with a measurement length l_b (see Fig. 3). The slip between the steel and the concrete was measured indirectly by the LVDT Group A. Here the measurement-length was l_a and the measured elongation was Δl_a. The slip was calculated from the measured values (see Eq. 3) using the assumption that the strains within l_a and l_b are identical. This assumption is valid for elastic behavior but not after onset of yielding.

$$\varepsilon_s = \Delta l_b / l_b \quad (1)$$

$$s + l_a \cdot \varepsilon_s = \Delta l_a \quad (2)$$

$$s = \Delta l_a - l_a \cdot \Delta l_b / l_b \quad (3)$$

Additionally, perpendicular to the direction of tensile force, splitting cracks were monitored on the concrete. Using three LVDT rows at the front side and three at the back of the specimen, information about the opening of the splitting crack could be obtained.

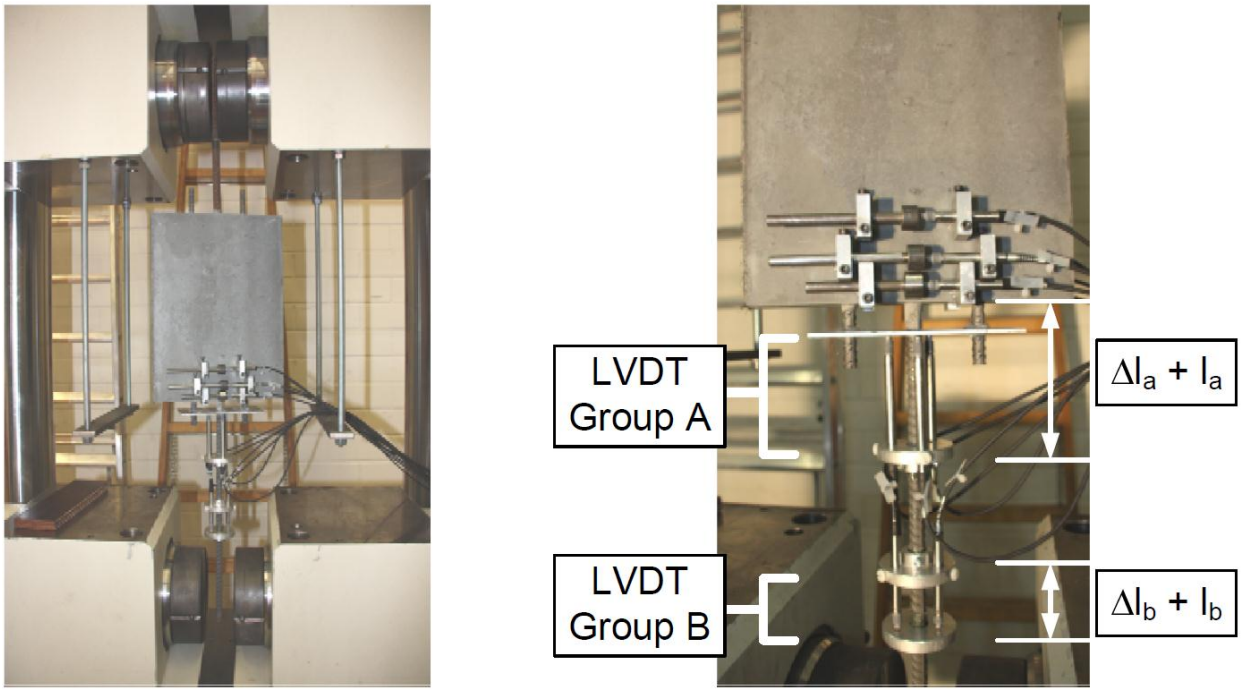

Figure 3: Specimen in testing machine (left), LVDT´s arrangement (right).

Results

During the test, various concrete failure modes could be observed and recorded. The major modes are illustrated in Fig. 4 and 5. In most cases, mixed failure modes developed. For this reason, failure modes were evaluated on the basis of the failure pattern and the remaining crack width. The results of the observations are depicted in Fig. 5. Here, especially the transition between concrete cone failure and V-type splitting can be seen to be very smooth. The overlap between V-type splitting and splitting means that V-type splitting occurred, in particular, near the load application, while splitting took place across the rest of the bond length. The yielding failure mode was observed when the reinforcement reached the yield plateau in the force-strain relationship.

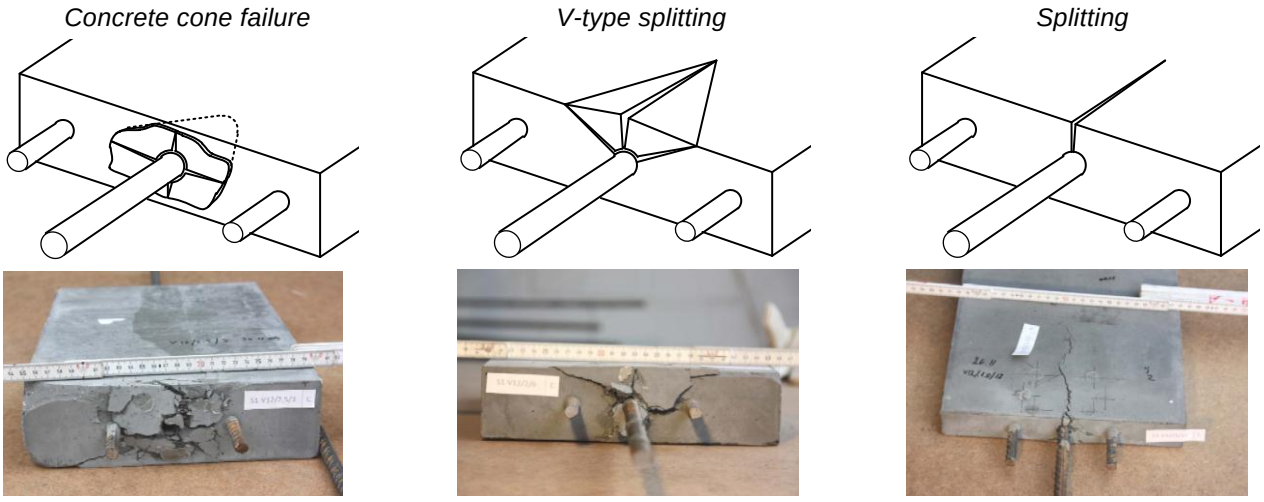

Figure 4: Concrete failure modes.

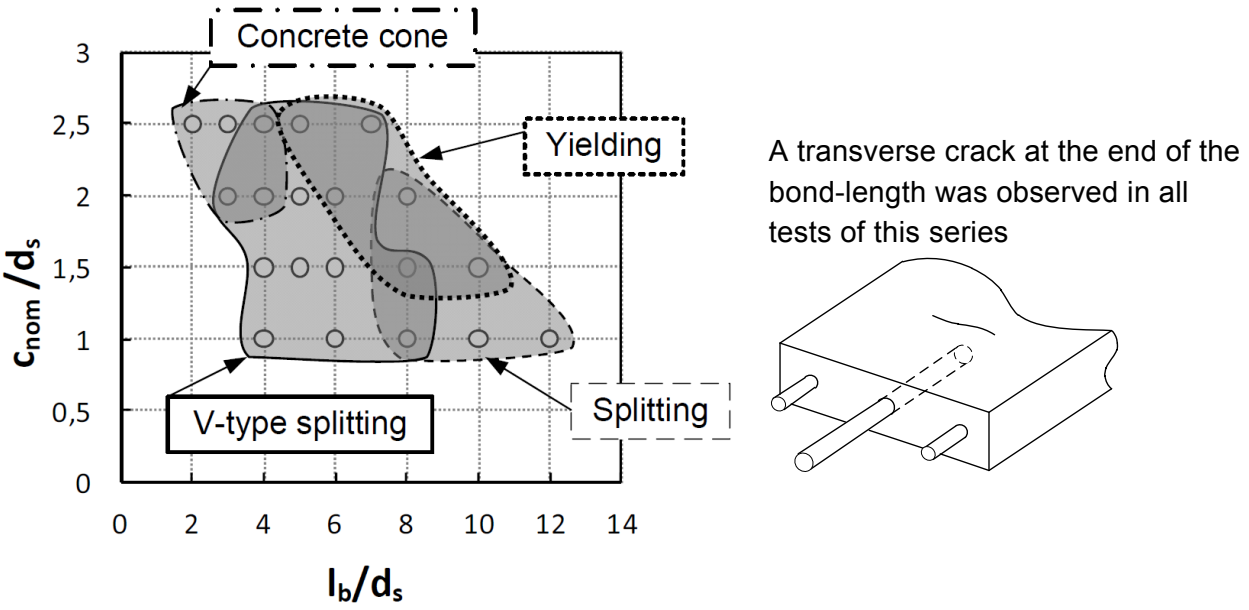

Figure 5: Major failure modes of the test specimens.

The steel stress-slip relationships of the individual tests are shown in Fig. 6 and Fig. 7. After reaching the yield plateau (two-point-dash line), the slip could be determined only qualitatively and should therefore be regarded with caution. The main parameters can be derived from the test denomination. „V12“ represents an anchorage of a bar diameter of 12 mm. The two-digit number without a decimal point after the letter “C” indicates the concrete cover ratio and the number after “L” the anchorage ratio.

With a concrete cover of c = 1 d_s and anchorage lengths of less than l_b = 8 d_s, increases in the maximum steel stress could be achieved by increasing the anchorage length (see Fig. 6). The failure mode observed here was V-type splitting. Increased anchorage lengths did not result in increasing failure load. The steel stress-slip relationships for the anchorage lengths 8 d_s, 10 d_s and 12 d_s are quite identical, even for slip values up to 14 mm (see Fig. 7). At the end of the test, the residual steel stress was between 50 and 100 N/mm². In the process of the test the steel stress remained below the yield plateau and the concrete failed due to splitting. This may be caused by a zipper-effect.

With a concrete cover ratio of 1.5 d_s, the steel stresses for $l_b \leq 6\ d_s$ remained below the yield stress. By increasing l_b until l_b = 6 d_s the maximum steel stresses increased (see Fig. 6). The

descending branch of the curves is almost identical for slip values between 4 mm and 15 mm (see Fig. 7). After reaching a slip value of 15 mm, a residual steel stress level of between 80 or 100 N/mm² could be observed and the test was aborted then. For $l_b = 8\ d_s$, a maximum steel stress (in the hardening stage) of 640 N/mm² was reached. Subsequently, the stress diminished with increasing slip. For $l_b = 10\ d_s$, the maximum steel stress was 670 N/mm². Here, the concrete failure switched from v-type splitting to splitting. For larger concrete covers, the concrete cone failure mode was observed more frequently. Nevertheless, predominantly mixed failure modes combining concrete cone and V-type splitting were observed (see Fig. 5).

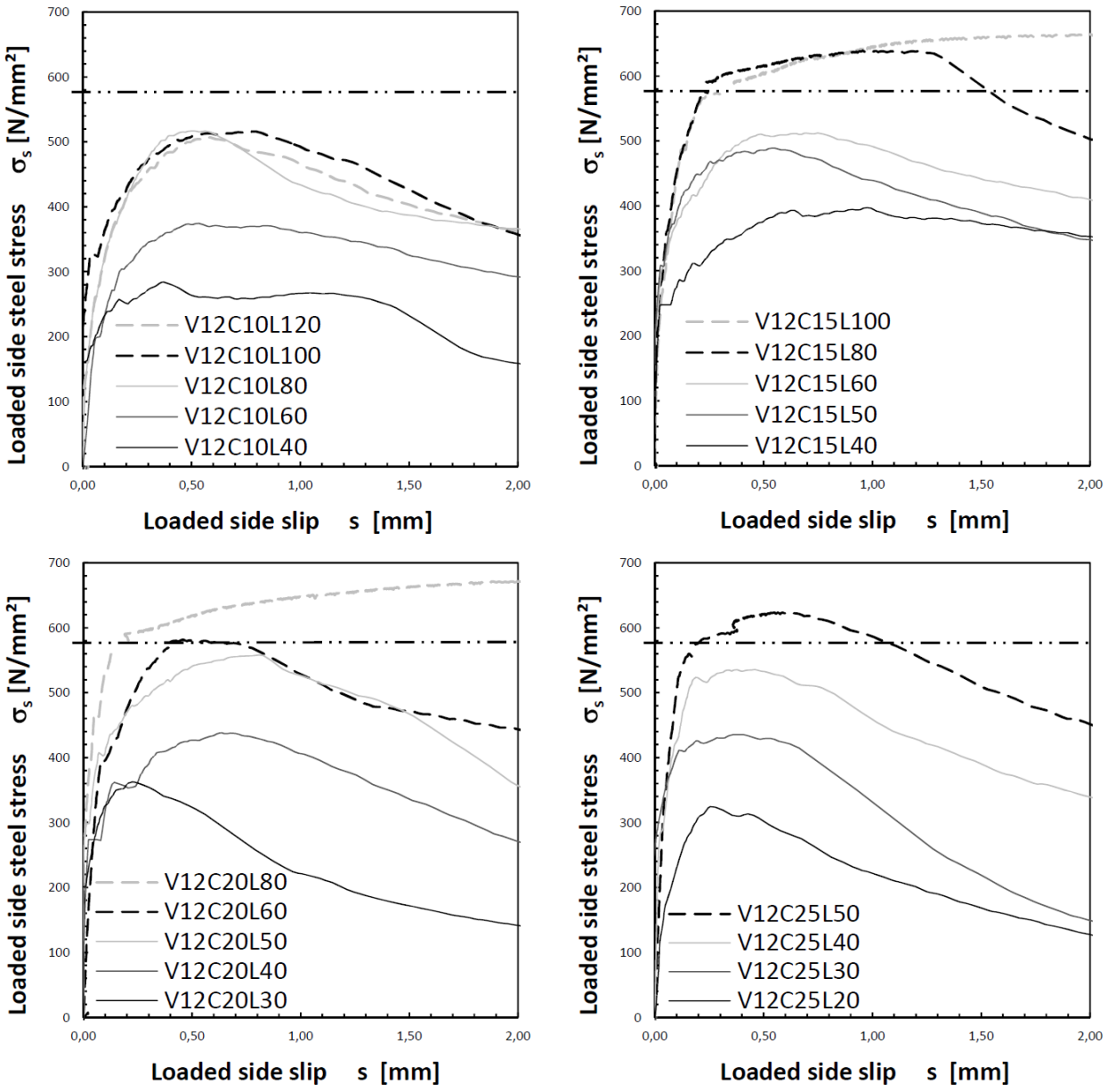

Figure 6: Steel stress-slip relationships for s ≤ 2,0 mm.

For $c = 2\ d_s$ and $l_b \leq 5\ d_s$, the steel stresses generally remained below the yield point. The yield point was exactly reached for $l_b = 6\ d_s$ whereas a steel stress in the hardening regime of 680 N/mm² was reached for $l_b = 8\ d_s$. The maximum steel stresses for $c = 2.5\ d_s$ and $l_b \leq 4\ d_s$ correspond approximately to those of $c = 2\ d_s$ and $l_b \leq 5\ d_s$. Here, the effect of the stiffer tensile ring from the larger concrete cover becomes obvious. This allows for an anchorage length of one diameter less and causes concrete cone failure.

For c = 2.5 d_s, $l_b \leq 3\ d_s$, pure concrete cone failure was observed. This type of failure resulted in a rapid decrease of the steel stress after reaching the peak load. At a slip value of 8 mm, the steel stress was almost zero.

For the concrete cover c = 2.5 d_s and the anchorage length $l_b = 5\ d_s$, it was possible to apply a steel stress of 620 N/mm². Due to a malfunction of the instrumentation, no slip values could be measured for the anchorage length $l_b = 7\ d_s$. However, a steel stress of 620 N/mm² was reached also for this specimen and the V-type splitting failure mode with yielding was observed (see Fig. 5).

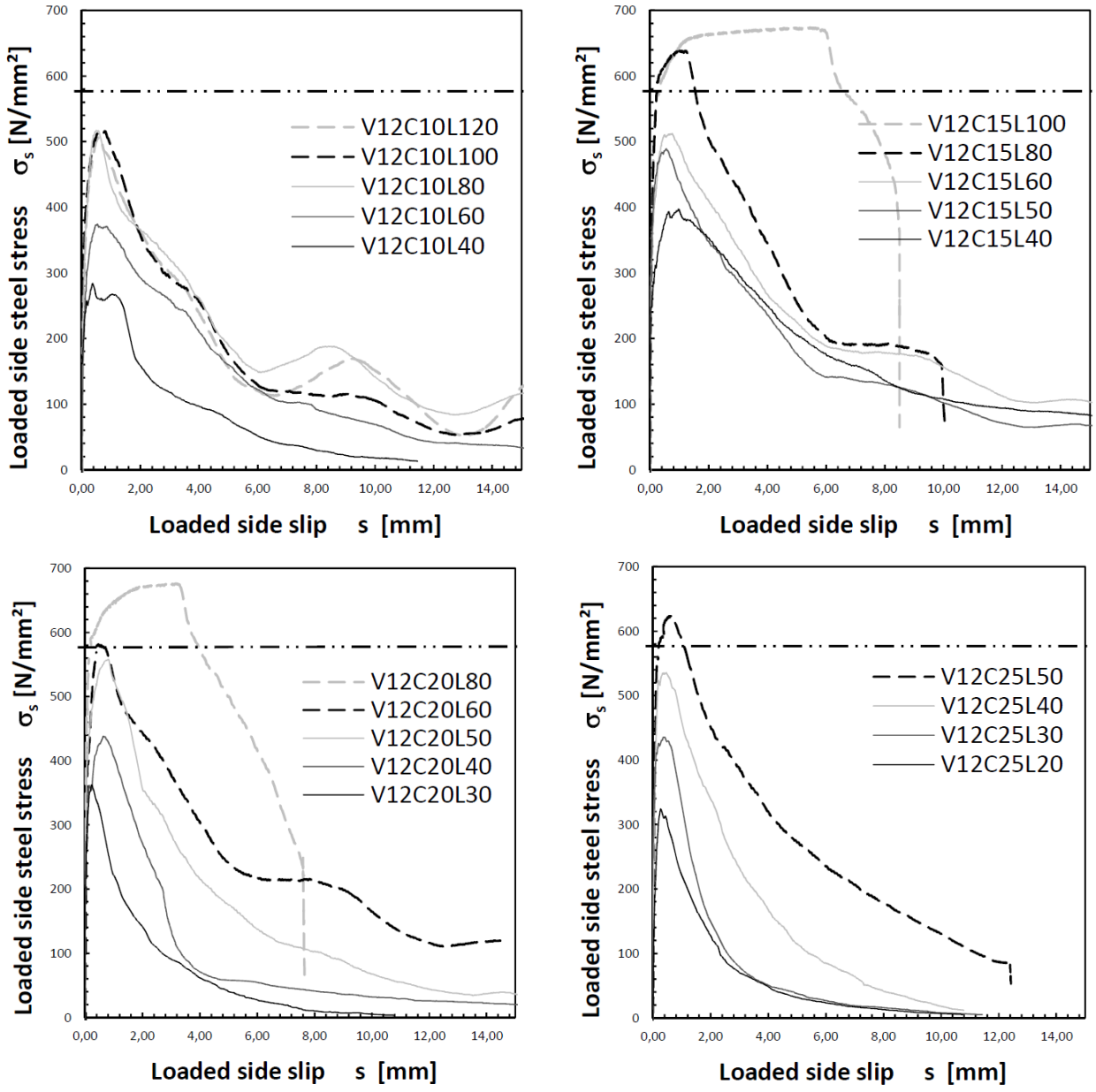

Figure 7: Steel stress-slip relationships for s ≤ 15,0 mm.

4 Conclusions and Outlook

In the case of concrete cone failure, the post failure behavior is rather brittle. Based on the assumption that the slip arises only from the opening of the cone shaped crack, it becomes evident that no or only very small forces can be transferred at a slip of $l_f /2 \approx 7$ mm. This is the reason why the steel stress diminishes so rapidly in this case. This type of failure, which is frequently seen with dowel connections, should be avoided. In the case of splitting and V-type

splitting, a more ductile post failure behavior can be obtained, which results from the crack direction and the formation of multiple cracks. Due to the activation of the fibers in the splitting crack, a certain confinement effect is preserved. Therefore, this post failure behavior is significantly influenced by the stress-crack opening behavior of the fiber-reinforced concrete.

Further questions require more detailed examination:

- How are the obtained relations between geometrical parameters and failure modes influenced by the diameter and the relative rib area of the rebar?
- How much transverse reinforcement is required in order to achieve a shortening of bond length at constant fiber contents?
- To what extent do fibers and transverse reinforcement ratio compliment each other?

To answer these questions further investigations should be made by varying the transverse reinforcement ratio, the diameter and the relative rib area of the bar.

References

[1] Fehling, E.: Zur Energiedissipation und Steifigkeit von Stahlbetonbauteilen unter besonderer Berücksichtigung von Rißbildung und verschieblichem Verbund. Dissertation, Darmstadt, 1990.

[2] Leutbecher, T.: Rissbildung und Zugtragverhalten von mit Stabstahl und Fasern bewehrtem Ultrahochfesten Beton (UHPC). Dissertation, Schriftenreihe Baustoffe und Massivbau, Heft 9, kassel university press GmbH, Kassel, 2008.

[3] Jungwirth, J.: Zum Tragverhalten von zugbeanspruchten Bauteilen aus ultra-hochleistungs-Faserbeton. Thèse N° 3429, Faculté Environment Naturel, Architectural et Construit, Ècole Polytechnique Fédérale de Lausanne, 2006.

[4] Aarup, B.; Karlsen, J.; Lindström, G.: Fiber reinforced high performance concrete for in-situ cast joints. Proceedings of International Symposium on High Performance Concrete, Orlando, Florida, USA, September 2000.

[5] Reineck, K.-H., Greiner, S.: Tests on ultra-high performance fibre reinforced concrete designing hot-water tanks and UHPFRC-shells. Ultra High Performance Concrete (UHPC), Proceedings of the Inernational Symposium on Ultra-High Performance Concrete, Schriftenreihe Baustoffe und Massivbau, Heft 3, kassel university press GmbH, Kassel, 2004.

[6] Holschemacher, K.; Weiße, D.; Klotz, S.: Bond of Reinforcement in Ultra High Strength Concrete. Proceedings of the International Symposium on Ultra High Performance Concrete, Kassel, 2004.

[7] Tepfers, R.: A Theory of bond applied to overlapped tensile reinforcement splices of deformed bars. Report 73-2, Chalmers University of Technology, Göteborg, 1973.

[8] Eligehausen, R.; Mallée R.; Silva, J.F.: Anchorage in Concrete Construction. Ernst&Sohn, Berlin, 2006.

[9] EOTA: ETAG 001. Guideline for european technical approval of metal anchors for use in concrete. 2007 -2011.

[10] Rehm, G.: Über die Grundlagen des Verbundes zwischen Stahl und Beton. DAfStb, Heft 138, 1961.

[11] Tue, N.: zur Spanungsumlagerung im Spannbeton bei der Rißbildung unter statischer und wiederholter Belastung. DAfStb, Heft 435, 1993.

[12] Martin, H.: Zusammenhang zwischen Oberflächenbeschaffenheit, Verbund und Sprengwirkung von Bewehrungsstählen unter Kurzzeitbelastung. DAfStb, Heft 228, 1973.

[13] fib Bulletin 55: Model Code 2010. First complete draft-Volume 1.

[14] Kurz, W.: Ein mechanisches Modell zur Beschreibung des Verbundes zwischen Stahl und Beton. Dissertation, Darmstadt, 1997.

[15] DFG SPP 1182: DFG Schwerpunktprogramm, Nachhaltiges Bauen mit ultra-hochfestem Beton.

Effect of adding micro fibers on the pullout behavior of high strength steel fibers in UHPC matrix

Seung Hun Park[1], Dong Joo Kim[1], Gum Sung Ryu[2], Kyung Taek Koh[2]
1: Dept. of Civil Engineering, Sejong University, Korea
2: Korea Institute of Construction Technology, Korea

The effect of adding micro fibers on the interfacial bond properties of four high strength steel macro fibers embedded in Ultra High Performance Concrete has been investigated. The four macro fibers (d_f≥0.3mm & L_f≥30mm) are longer smooth fiber, two types of hooked fiber, and twisted fiber while shorter smooth (d_f=0.2mm & L_f=12mm) fibers were added as micro fibers. The volume content of micro fiber added in the UHPC matrix varied between 0.0% and 1.5%. The addition of micro fibers in the UHPC matrix produces various effects, according to the types of macro fiber, on the pullout load versus slip curves macro fiber. Twisted steel macro fibers produced the highest interfacial bond strength in the UHPC matrix albeit twisted fibers showed slip softening behavior unlike the slip hardening pullout behavior usually available in mortar matrices.

Keywords: macro fiber, micro fiber, maximum bond strength, equivalent bond strength, pullout mechanism.

1 Introduction

Much research has been carried out to remedy the brittle behavior of Ultra High Performance Concrete (UHPC) and moreover to produce tensile strain hardening behavior by blending macro and micro fibers. The blending micro and macro fibers in UHPC produced favorable effects on the strain hardening behavior Ultra High Performance Hybrid Fiber Reinforced Concrete (UHP-HFRC) [Kim et al. (2011), Park et al. (2011)]. They have different roles in UHPC: macro fibers are effective in increasing ductility while micro fibers contribute more in enhancing tensile strength. However, little information is available for the pullout load versus slip response of high strength steel deformed macro fibers especially in UHPC matrices reinforced with micro fibers albeit the bond strength at the interface between fiber and the matrix is the most important information in the development of Ultra High Performance Fiber Reinforced Concrete [UHPFRC] with tensile strain hardening and multiple cracking behavior.

Only a few references reported the pullout resistance of high strength steel fibers in UHPC matrices as follows: Orange et al. (1999) carried out single fiber pullout tests of high strength smooth steel fibers in DUCTAL and pointed out that the fiber-matrix adhesion is mainly due to the compressive hydrostatic pressure developed around the fiber by the shrinkage of the matrix. Chan and Chu (2004) performed fiber pullout experiments by using pullout specimens with nine high strength (2600MPa) smooth steel fibers in Reactive Powder Concrete [RPC], one type of UHPC, and reported that the incorporation of silica fume in a matrix considerably enhanced interfacial bond properties especially in fiber pullout energy. They concluded that the optimum silica fume content is between 20% and 30%.

Shannag et al. (1997) inspected the effect of adding micro steel fibers (d_f=0.15mm & L_f=6mm) by 3.0% to 6.0% fiber as volume content on the pullout behavior of hardened stainless steel piano wire in a Densified Small Particle [DSP] matrix. They reported that the addition of 6.0% micro fibers in DSP generated a 20% increase in peak pullout load and pullout energy. Markovich and van Mier (2001) also reported that the addition of 4.0% micro steel fibers in matrices enhanced the pullout resistance of high strength hooked steel fiber in high strength mortar matrices having 70-120MPa compressive strength.

Based on the few references mentioned ahead, it has been found that the densification, by applying silica fume, of the interfacial transition zone of UHPC matrices enhances the interfacial bond properties. Besides, the addition of micro fibers in a UHPC matrix also improves the interfacial bond properties of macro steel fibers in a UHPC pullout medium. However, most previous studies reported have focused on the pullout behavior of smooth steel fibers in a UHPC matrix and the amounts of micro fiber added in a UHPC are quite small, although more than 1.5%, ranging between 3% and 6% as volume content. Thus, there is still not enough information about the pullout behavior of high strength deformed steel fibers particularly in a UHPC matrix reinforced with small amounts of micro fibers lower than 1.5%.

The main purpose of this study is to determine the interfacial bond strength of high strength steel macro fibers in a UHPC matrix reinforced with small amounts of micro fiber lower than 1.5%. The detailed objectives are 1) to investigate the pullout load versus slip response of high strength deformed steel fibers in UHPC, 2) to estimate the effect of adding micro fibers on the interfacial bond properties of macro fiber, and 3) to discover whether the slip hardening behavior of deformed steel fibers is still available in UHPC with compressive strength about 200MPa.

2 Pullout behavior and bond strength of high strength steel fibers

Typical pullout load versus slip behavior of smooth, hooked and twisted steel fibers embedded in mortar matrices with normal strength lower than 84MPa are illustrated in Fig. 1. Smooth fibers usually show the slip softening pullout behavior, i.e. the pullout load resistance rapidly decreases subsequent to the interfacial debonding while hooked and twisted fibers produce slip hardening behavior as shown in Fig. 1. To obtain the slip hardening behavior during fiber pullout, the pullout load resistance following debonding should be higher than the debonding pullout load. Kim et al. (2010) reported the typical slip hardening behavior of deformed steel fibers, hooked and twisted, in a mortar matrix with 84MPa compressive strength as shown in Fig. 1.

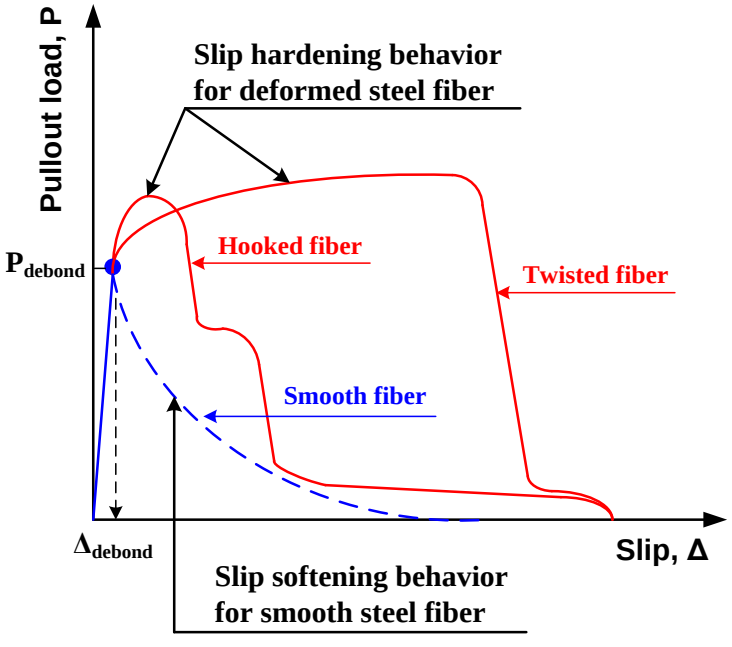

Figure. 1: Typical slip hardening and softening pullout behavior of high strength steel fibers. [Kim et al. (2010)].

However, it is not clear yet whether the slip hardening behavior of the deformed steel fibers is available in UHPC due to the very high adhesional bond [Orange et al. (1999)]. The very high adhesional bond in a UHPC matrix significantly increases the fiber pullout load at debonding and makes it more difficult to generate the slip hardening behavior during fiber pullout. Moreover, it is in question whether the high slip capacity of twisted fiber shown in Fig. 1 is still available in UHPC because the amount of pullout energy is influenced a lot by the slip capacity as well as the magnitude of the pullout load.

Thus, the pullout resistance of high strength deformed steel fibers in UHPC was investigated, in this study, by performing single fiber pullout tests. Based on the test results, two different interfacial bond strengths were estimated: 1) maximum bond strength $\tau_{\max}$ based on the maximum pullout load; and, 2) equivalent bond strength $\tau_{equiv.}$ based on the pullout energy.

The maximum bond strength $\tau_{\max}$ was calculated by using Eq. [1] while the equivalent bond strength $\tau_{equiv.}$ was estimated by using Eq. [2].

$$\tau_{\max} = \frac{P_{\max}}{\pi d_f \times L_{embed.}} \qquad [1]$$

$$\tau_{equiv.} = \frac{2E_{pullout}}{\pi d_f L_{embed.}^2} \qquad [2]$$

where $P_{\max}$ is the maximum pullout load, $E_{pullout}$ is the complete pullout energy, d_f is the diameter of the fiber, and $L_{embed.}$ is the embedment length.

3 Experimental program

The matrix composition of the UHPC matrix used and its average compressive strength are provided in Table 1. The detailed information regarding the matrix composition and mixing procedure can be found in Park et al. (2008) and Ryu et al. (2010).

Table 1: Composition of matrix mixtures by weight ratio and compressive strength [Park et al. (2008), and Ryu et al. (2010)].

Cement (Type I)	Silica fume	Silica sand	Glass powder	Super plasticizer	Water	Compressive strength(MPa)
1.00	0.25	1.10	0.30	0.067	0.20	200

Four types of macro fibers were embedded in UHPC matrices mixed with short smooth steel micro fibers and their pullout resistance were investigated by performing single fiber pullout tests. The four macro fibers include longer smooth (LS-), hooked type A (HA-), hooked type B (HB-), and twisted (T-) steel fibers. The volume contents of the shorter smooth steel fibers (SS-) mixed in the UHPC matrix varied between 0.0% and 1.5%. The properties of the fibers used in this study are provided in Table 2. T- fibers, investigated in this study, have a triangular section and six ribs within 30mm fiber length.

An electro-mechanical universal testing machine, with a capacity of 500kgf, running in displacement control was used to conduct the single fiber pullout tests. The pullout speed was 1.0mm/min. The combination of the four macro fibers and four volume content of micro fibers leads to sixteen series of pullout tests. Three to five specimens per series were investigated for all test series.

Table 2: Properties of fibers.

Fiber type	Name (notation)	Diameter (mm)	Length (mm)	Density (g/cc)	Tensile strength (MPa)	Elastic modulus (GPa)
Macro	Long smooth (LS-)	0.3	30	7.9	2580	200
	Hooked A (HA-)	0.375	30	7.9	2311	200
	Hooked B (HB-)	0.775	62	7.9	1891	200
	Twisted (T-)	0.3	30	7.9	2428	200
Micro	Short smooth (SS-)	0.2	13	7.9	2788	200

Materials and specimen preparation

Before mixing a mortar matrix, the fibers were pre-installed in the device to firmly hold the pre-determined embedment length of fibers within the pullout medium during casting. Then, the devices were placed in the pullout molds. A Hobart type laboratory mixer with a twenty liter capacity was used to prepare the mix. The UHPC mixture mixed with micro fibers was poured into the molds by using a beaker. The specimens were covered with plastic sheets and stored at room temperature for 48 hours prior to demolding. Water curing at high temperature (90 ± 2°C) for 3 days after demolding was carried out. All specimens were tested in a dry condition at the age of 14 days.

Test setup and procedure

The single fiber pullout test set-up is shown in Fig. 2. The section of pullout test specimens used was 25×25mm (1×1in.), and the embedment length of fiber was 15mm for LS-, HA- and HB- fibers while the embedment length of T- fiber was 5.5mm. Because all previous pullout test results of T- fiber with 15mm embedment length in UHPC matrix showed fiber breakage during pullout, the embedment length of T- fiber was adjusted to estimate the bond properties of the fiber in a UHPC matrix by avoiding fiber breakage. The slip of embedded fiber during the test was measured from a LVDT attached to the specimen as shown in Fig. 2 while the load signal was measured from a load cell directly attached to the bottom of the cross head. The capacity of the load cell used in measuring pullout resistance was 500kgf.

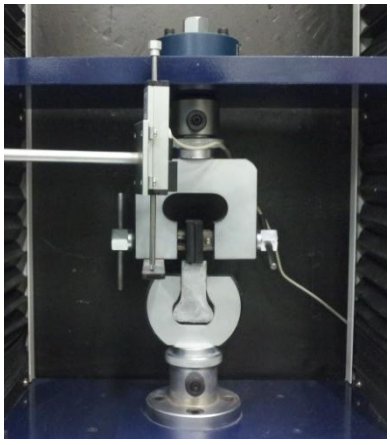

Figure. 2: Test set-up for single fiber pullout test.

Test results

The influence of adding micro fibers on the pullout behavior of the macro fibers (LS-, HA-, HB- and T-) in the UHPC matrix is provided in Fig. 3. The pullout load (stress) versus slip curves in Fig. 3 were averaged at least from three specimens. The embedment length of LS-, HA- and

HB- fibers was 15mm while that of T- fiber was 5.5mm in pullout specimens as mentioned before.

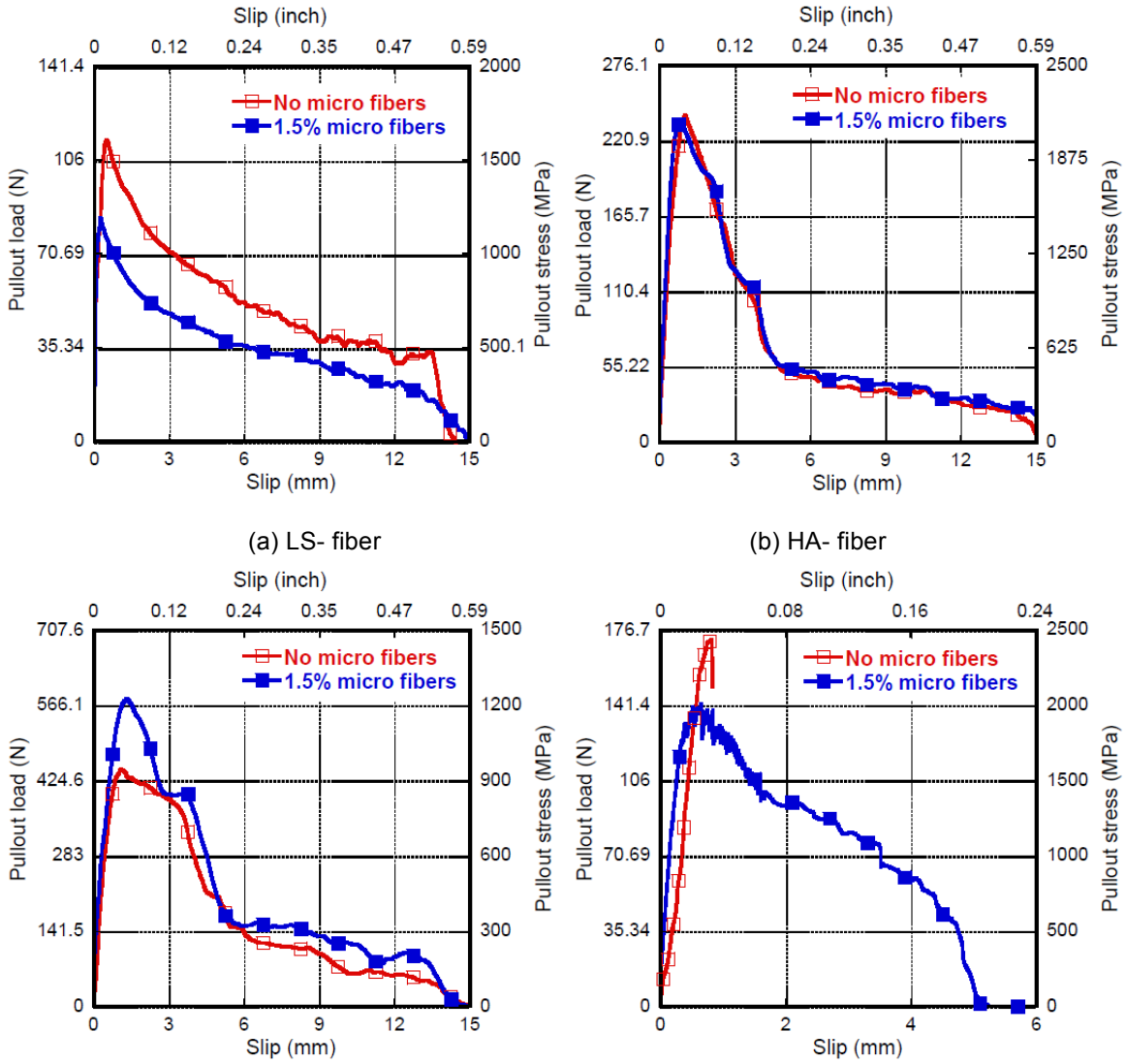

Figure. 3: Pullout load versus slip response of macro fibers.

As demonstrated in Fig. 3a to 3d, the effect of adding micro fibers on the pullout behavior of the macro fibers is various according to the types of macro fiber. Fig. 3a describes the different pullout behavior of LS- fiber in a UHPC matrix according to the addition of micro fibers: the maximum pullout load and the pullout energy were reduced by adding 1.5% micro fibers to a UHPC matrix. LS- fiber maintained its typical slip softening behavior in UHPC as well.

However, there is no clear difference in the pullout behavior of HA- fiber regardless of the addition of the micro fibers in the UHPC matrix as provided in Fig. 3b. Unlike HA- fiber, although HB- fiber has similar geometry but different size, HB- fiber showed a clear enhancement in both maximum pullout load and pullout energy when 1.5% micro fibers were mixed in a UHPC matrix as shown in Fig. 3c: the maximum pullout stress of HB- fiber in a UHPC matrix with no micro fibers is 992.0MPa while that in a UHPC matrix with 1.5% micro fibers is 1273.4MPa. The pullout test results of LS- and HB- fibers are provided as well in Fig. 4 and Fig. 5 respectively to show the consistency of the test results.

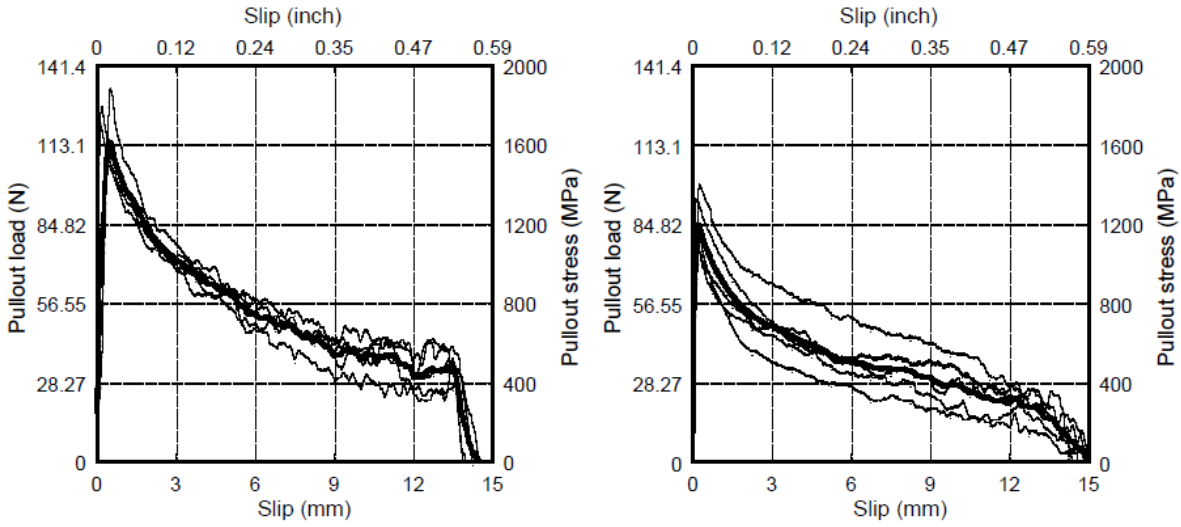

(a) No micro fibers (b) 1.5% micro fibers

Figure. 4: Pullout load versus slip response of LS- fiber.

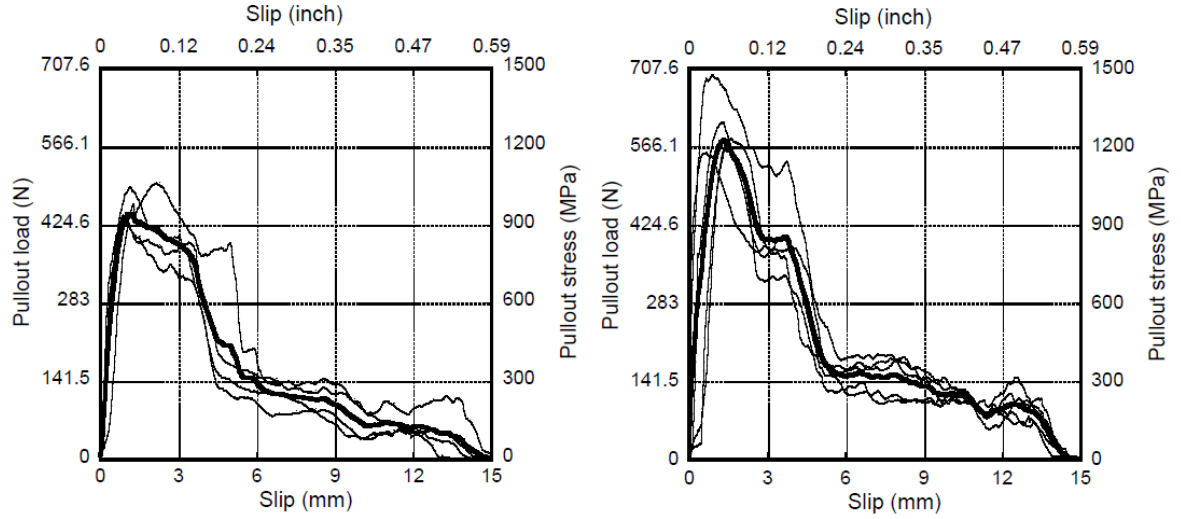

(a) No micro fibers (b) 1.5% micro fibers

Figure. 5: Pullout load versus slip response of HB- fiber.

The pullout resistance of T- fiber, similar to LS- fiber, in a UHPC matrix was reduced by adding micro fibers, i.e., T- fiber in a UHPC matrix with no micro fibers showed fiber breakage while T- fibers in a UHPC matrix mixed with micro fibers maintained fiber pullout with no fiber breakage. Thus, the addition of micro fibers in a UHPC matrix reduced the adhesional bond strength of T- fiber. Regarding the pullout behavior of the macro fibers, T- fiber in a UHPC matrix showed slip softening behavior unlike the typical slip hardening behavior reported. This slip softening behavior of T- fiber in UHPC matrix is due to the highly densified matrix structure of UHPC. The densified interfacial zone of UHPC, by incorporating very fine fillers and silicafume, significantly enhanced the debonding pullout load. Thus, it is more difficult to produce higher pullout load resistance after debonding, which is mainly based on a mechanical bond from the interaction between the fiber and matrix. Since the pullout load based on the mechanical bond is dependent upon the size and shape of T- fiber, further investigation is needed to obtain the slip hardening behavior in a UHPC matrix by adjusting the interfacial properties and changing the geometry of T- fibers. However, the slope of the softening part in the T- fiber pullout versus slip curve, shown in Fig. 3d, is more gradual in comparison with other macro fibers.

Discussion on the test results

The influence of adding micro fibers to a UHPC matrix on the interfacial bond strength of macro fibers is estimated by quantifying maximum bond strength and equivalent bond strength as shown in Fig. 6a and 6b.

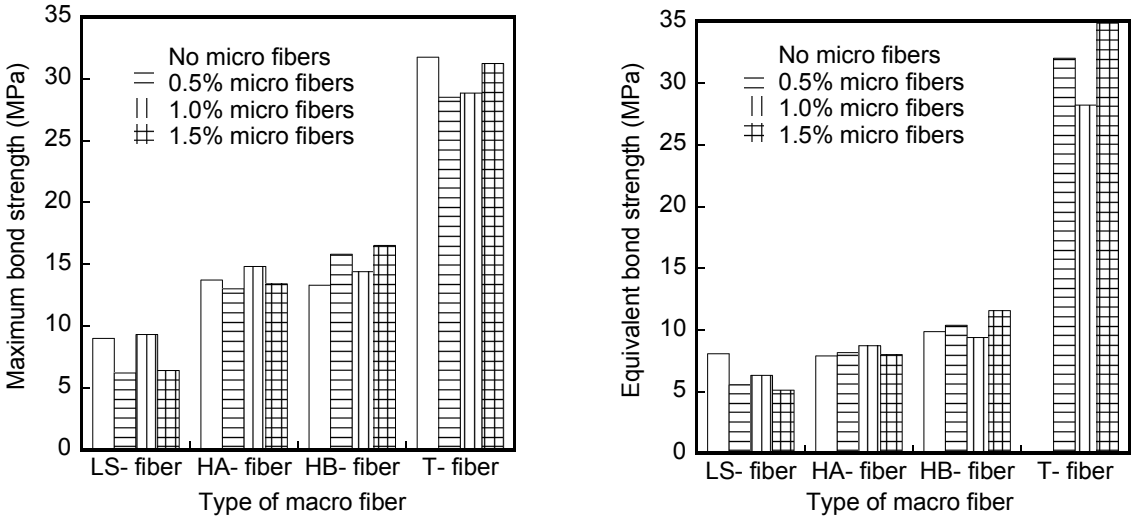

(a) Maximum bond strength (b) Equivalent bond strength

Figure. 6: Influence of adding micro fibers on interfacial bond strength.

First of all, it is clear that the bond strength of T-fiber in UHPC is significantly higher than other macro fibers: e.g., the equivalent bond strength of T- fiber is 24-34MPa while those of other macro fibers is 5-12MPa as shown in Figure 6.

However, the influence of adding micro fibers on the interfacial bond strength of macro steel fibers in a UHPC matrix is quite different, as shown in Fig. 6, according to the types of macro steel fiber. As the amount of micro fiber increased, the bond strength of HB- fiber improved while those of LS- fiber showed a clear reduction. However, there is no clear tendency in the pullout behavior of HA- fiber according to the addition of micro fibers. And, it is also difficult to find any trend for T- fiber since T- fiber in a UHPC matrix with no micro fibers showed fiber breakage at the initial stage of fiber pullout during the test.

This different tendency originated from the different pullout mechanisms and relative size ratio between macro and micro fibers. The bond components of LS- fiber are mainly composed of adhesional (before debonding) and frictional (after debonding) bond strength. Both adhesional and frictional bonds are strongly influenced by the amount of matrix shrinkage and the stiffness of interfacial transition zone between fiber and matrix [Shannag et al. (1997)]. Although the high shrinkage of a UHPC matrix is favorable for the bond strength of LS- fiber, the effect of matrix shrinkage on LS- macro fiber is diluted by adding the micro fibers. Unlike LS- fiber, the main bond component of deformed steel macro fibers is the mechanical bond which is a function of geometry and material properties of macro fibers. Those deformed steel macro fibers are though to be a little sensitive to the matrix shrinkage although the mechanical bond strength also can be influenced by the interfacial pressure generated from the matrix shrinkage besides the mechanical interaction between fiber and matrix.

Among the deformed steel macro fibers, HB- fiber, of which the diameter is 0.775mm, showed clear enhancements in bond strength unlike other macro fibers with 0.3mm to 0.375mm diameter in this study. Thus, the relative diameter of macro fiber in comparison with that of micro fiber is also an important parameter on the influence of adding micro fibers.

4 Conclusions

This research investigated the influence of adding micro fibers to a UHPC matrix on the pullout behavior of macro steel fibers: long smooth (LS-), two types of hooked (HA- and HB-) and twisted (T-) fiber. The amount of micro fiber varied between 0.0% and 1.5%. The following conclusions can be drawn from this experimental study.

The effect of adding micro fibers on the pullout behavior of macro fibers in a UHPC matrix is quite different according to the type of macro fiber: LS- fiber showed a clear reduction in pullout resistance while HB- fiber produced a noticeable enhancement by adding micro fibers in the UHPC matrix. And, HA- fiber produced no difference according to the addition of micro fibers while it is hard to find any trend for T- fiber.

T- fiber in the UHPC matrix produced slip softening pullout behavior unlike the typical slip hardening pullout behavior of the fiber in mortar matrices. Nevertheless, T- fiber, among the macro fibers investigated in this study, produced the highest values in both maximum and equivalent bond strength.

5 Acknowledgements

The research described herein was supported by Super Bridge 200 in the Korea Institute of Construction Technology and by the Human Resourses Development of the Korea Institute of Energy Technology Evaluation and Planning (KETEP) grant funded by the Korea government's Ministry of Knowledge Economy (No. 20104010100520). The opinions expressed in this paper are those of the authors and do not necessarily reflect the views of the sponsors.

References

[1] Chan Y.-W.; Chu S.-H.: Effect of silica fume on steel fiber bond characteristics in reactive powder concrete. Cement and Concrete Research 34, 2004, PP. 1167-1172.

[2] Kim D.J..; El-Tawil S.; Naaman A.E.: Effect of matrix strength on pullout behavior of high strength deformed steel fibers. In ACI special publication 2010; SP 72, Antoine E. Naaman Symposium – Four Decades of Progress in Prestressed Concrete, Fiber Reinforced Concete, and Thin Laminate Composites, Edited by G.J. Parra-Montesinos and P. Balaguru, pp. 135-150.

[3] Kim D.J.; Park S.H.; Ryu G.S.; Koh G.T.: Comparative flexural behavior of Hybrid Ultra High Performance Fiber Reinforced Concrete with different macro fibers. Construction and Building Materials 25. 2011; pp. 4144-4155.

[4] Markovich I.; Van Mier J.G.M.; Waliraven J.C.: Single fiber pullout form hybrid fiber reinforced concrete, Heron, Vol. 46, No. 3, 2001, pp. 191-200.

[5] Orange G.; Acker P.; Vernet C.: A new generation of UHP Concrete: DUCTAL damage resistance and micromechanical analysis, HPFRCC3, Mainz, Germany, 1999, pp. 101-111.

[6] Park J.J.; Kang S.T.; Koh K.T.; Kim S.W.: Influence of the ingredients on the compressive strength of UHPC as a fundamental study to optimize the mixing proportion. In: Proceeding of Second International Symposium on Ultra High Performance Concrete, Germany, E. Fehling, M. Schmidt and S. Stűrwald, Co-Editor, Kassel University, Germany, 2008, pp. 105-112.

[7] Park S.H.; Kim D.J.; Ryu G.S.; Koh G.T.: Tensile behavior of Ultra High Performance Hybrid Fiber Reinforced Concrete. Cement and Concrete Composites 34. 2012; pp. 172-184.

[8] Ryu G.S.; Kang S.T.; Park J.J.; Koh G.T.: Evaluation of flexural performance in UHPC (Ultra High Performance Concrete) according to placement methods. Key Engineering Materials 2010; 417-418: 581-584.

[9] Shannag M.J.; Brincker R.; Hansen W.: Pullout behavior of steel fibers from cement-based composites. Cement and Concrete Research, Vol. 27, No. 6, pp. 925-936, 1997.

Literature Review on the Behaviour of UHPFRC at High Temperature

Pierre Pimienta[1], Jean-Christophe Mindeguia[2], Alain Simon[3], Mouloud Behloul[4], Roberto Felicetti[5], Patrick Bamonte[5], Pietro G. Gambarova[5]

1: University of Paris-Est, Centre Scientifique et Technique du Bâtiment, Marne La Vallée, France
2: University of Bordeaux, 12M Laboratory (Mechanics Institute of Bordeaux), Bordeaux, France
3: Eiffage TP, Bridge Engineering Service (STOA), Neuilly sur Marne, France
4: Lafarge Ciment, Paris, France
5: Politecnico di Milano, Dept. of Structural Engineering, Milan, Italy

The results of several experimental campaigns concerning eight Ultra High-Performance Fibre-Reinforced Concretes (UHPFRCs) carried out in different European industrial and university laboratories are presented and compared in this paper. In the temperature range from 20°C to 850°C the results concerning the compressive strength, the elastic modulus and the thermal strain are presented and analysed. The influence of the testing procedures is discussed as well (for instance, with/without pre-loading during the heating phase). Comparisons are made with the decay curves provided by EC 2, for both ordinary and high-performance concrete. The presentation of the mechanical properties is accompanied by suitable observations made during several fire-resistance tests on small structural members (slabs, columns and beams). The temperature-time curves adopted in the tests were the well-known curves ISO 834 and the Increased Hydrocarbon Temperature Curve (HC_{inc}). Once more, the effectiveness of polypropylene fibres against the risk of spalling is confirmed by the rather extended family of UHPFRCs and by the various geometries of the specimens considered in this paper.

Keywords: Ultra High-Performance Concrete, high temperature, compressive strength, elastic modulus, thermal strain, fire resistance, ISO fire curve, Increased Hydrocarbon Temperature Curve, concrete spalling, polypropylene fibers.

1 Introduction

Structures made of UHPFRC (Ultra High-Performance Fibre-Reinforced Concrete) are at a risk of fire even more than ordinary-concrete structures, since UHPFRC is generally used in rather severe environments, where its higher durability and strength can be fully exploited. Fire-induced heating affects the structural behaviour because of the following factors:

- mechanical decay of the material;
- changes in the thermal properties; and
- thermal expansion (that is generally constrained and brings in thermal stresses).

The complex behaviour of concrete at high temperature depends on its rather high heat sensitivity and can in principle cause a sizable damage to the structure, followed - in the worst circumstances - by the collapse of the most exposed members and even by the collapse of the whole structure [1]. Among the various forms of damage, concrete “spalling” is the most evident, since it involves the partial destruction of the concrete member, or even its total destruction. This phenomenon occurs both in ordinary concrete and in high-performance/ultra high-performance concrete [2]. The spalling risk, however, is generally considered to be more severe in compact concretes, such as high-performance and self-compacting concretes. In most cases, concrete spalling brings in severe sectional reductions, that can be repaired at a considerable cost [3,4,5].

For its excellent mechanical and physical properties, UHPFRC has been increasingly used in the last ten years. UHPFRC, however, is still a rather new material, which most structural designers are little familiar with. For this reason, some countries have recently decided to prepare and publish guidelines on how to use UHPFRC. For instance, the French Association

of Civil Engineering (AFGC) has recently published (2011) an updated version of its recommendations on the use of UHPFRC [21], where a chapter on UHPFRC's behaviour at high temperature and in fire is included.

In this paper, a literature review is presented about several experimental campaigns carried on eight different UHPFRCs tested in a number of European industrial and university laboratories located in France, Italy, Germany and Denmark [6-14]. Such parameters as compressive strength, elastic modulus and thermal strain were investigated as a function of the temperature between 20°C and 850°C. Quasi-steady tests were carried out during or after the exposure to high temperature (hot and residual tests). Though the results are somewhat dispersed – because of the differences among the mixes – there are clear trends, that yield useful information for the pre-design phase of the structures to be made of UHPFRC. The results obtained by the different teams are systematically compared with the decay curves provided by EC 2 [15] for high-performance concrete.

Some observations on HPFRC's behaviour under highly-unsteady heating (as in fire) are presented as well, since physical testing is still the only reliable support for a correct design – or verification – of any fire-exposed structure. In such situations, the spalling risk is high, but calculations aimed to predict this risk are still hardly possible.

Two fire curves (ISO 834 "standard" curve and Increased Hydrocarbon Temperature Curve - HC_{inc}) and three geometries (slabs, columns and beams) have been studied. Polypropylene (pp) fibres are shown to be – once more - very effective in reducing or even zeroing the risk of spalling.

2 Mix designs and main properties

University and industrial laboratories are often very reluctant to provide information about the mix design of their UHPFRCs, since these materials are still considered as "innovative" products. In Table 1 the mix designs of the 8 UHPFRCs investigated in this study are given, even if some data were not available. In Table 2 the main mechanical properties are presented, with their literature references.

3 Experimental setting

The main features of the experimental procedures are presented in the following. For more details reference should be made to the literature.

Tests in quasi-steady thermal conditions

Most of the tests reported in this study were carried out in accordance with RILEM's recommendations [16], whose use is strongly suggested whenever testing be required to provide suitable input data in the design of a HPFRC structure. These recommendations specify different procedures, depending on the purpose of each test. For example, the compressive strength can be evaluated by testing at high temperature or after cooling to room temperature (hot or residual tests), with/without any pre-loading in compression applied to the specimen during the heating phase (stressed/unstressed specimens). Having the specimen pre-loaded in compression during the heating phase (stressed specimens) improves the mechanical properties at any temperature and gives a realistic picture of the static situation of R/C columns, that are mainly subjected to permanent loads. For lightly-loaded members, however, reference should be made to the tests without pre-loading (unstressed specimens).

The main test parameters of the studies examined in this paper are summarized in Table 3.

Table 1: mix design of the UHPFRCs considered in this study.

UHPFRC	Binder (kg/m3)	Aggregates (kg/m3)	Water (kg/m3)	W/ binder ratio	Steel fibres (kg/m3) (length / diameter in mm)	Polypropylene fibres (kg/m3) (length / diameter in mm)
BSI®- fire *	2355 (Commercial premix)		216	0.19	195 (20 / 0.3)	3 (12 / 0.018)
DUCTAL®- AF **	2192 (Commercial premix)		168	0.14	146 (13 / 0.2)	4.2
Politecnico-Italcementi	635	1480	200	0.31	0	5.2 (20 / 0.2) & 1.1 (6 / 0.04)
CERIB UHPC_I	/	Basalt & sand	/	/	79 (13 / 0.16)	3 (12 / 0.018)
CERIB UHPC_II	/	Sand	/	/	133 (13 / 0.16)	3 (12 / 0.018)
BCV®	2086 (Commercial premix)		216	/	158 (12.7 / 0.175)	0
Rostock_1	/	Quartz, Diabase & sand	/	0.219	0	/
Rostock_3	/	Quartz & sand	/	0.2	0	/

** Eiffage (French construction firm) ** Lafarge-Bouygues-Rhodia / Unavailable data*

Table 2: mechanical properties and references of the UHPFRCs considered in this study.

UHPFRC	Compressive strength (MPa)	Modulus of elasticity (GPa)	Literature reference
BSI®- fire	148 – 165	50 – 55	[6], [7]
DUCTAL®- AF	160 (200 with thermal treatment)	45 (50 with thermal treatment)	[8]
Politecnico-Italcementi	121	42	[9] to [10]
CERIB UHPC_I	170	/	[11], [12]
CERIB UHPC_II	200	/	[11], [12]
BCV®	155	45	[13]
Rostock_1	160 - 180	/	[14]
Rostock_3	160 - 180	/	[14]

Table 3: Main parameters of the compression tests (quasi-steady heating).

UHPFRC	Sample geometry	Heating rate	Mechanical pre loading (regarding to 20 °C compressive strength)	Type of measure
BSI®- fire	Ø 104 x h 300 mm cyl.	1 °C/min	0 %	Hot
DUCTAL®- AF	Ø 70 x h 140 mm cyl.	2 °C/min	0 % & 20 %	Hot & residual*
Politecnico	Ø 36 x h 110 mm cyl.	0.5 °C/min	0 %	Hot & residual*
CERIB UHPC_I & CERIB UHPC_II	Ø 100 x h 300 mm cyl.	1 °C/min	20 %	Hot
BCV®	Ø 40 x h 60 mm cyl.	3.3 °C/min	0 %	Hot
Rostock_1 & Rostock_3	Ø 70 x h 200 mm cyl.	3 °C/min	0 %	Hot

** In this paper, only the results obtained via hot tests are presented*

Tests in fire

The main observations coming from the tests carried out at high temperature in unsteady thermal conditions (i.e. in fire) on BSI®- fire, Ductal®- AF and CERIB-UHPFRC are presented in the following. In parallel the same mixes were tested without polypropylene fibres in order to verify the effectiveness of the fibrous reinforcement against the risk of spalling.

Various geometries were adopted for the specimens to be tested (slabs, columns and beams, as well as prismatic “research” specimens with various sections). Some specimens were tested in compression; other specimens were tested in 4-point bending.

As previously mentioned, in the tests characterised by unsteady thermal conditions the standard ISO 834 Curve and the Increased Hydrocarbon Temperature Curve were adopted, the former representing current fires, and the latter violent fires typical of tunnels.

The ISO 834 temperature-time curve is defined by Eq.1; temperatures as high as 600, 800 and 1000°C are reached in 6, 24 and 90 minutes, respectively. The HC_{inc} curve (Eq.2) is much more severe, since 1000°C are reached in only 2 minutes and 1250-1300°C in 15 minutes.

$$T = 345 \log (8\,t + 1) + 20 \quad (1)$$

$$T = 1280\,(1 - 0.325\,e^{(-0.167\,t)} - 0.67\,e^{(-2.5\,t)}) + 20 \quad (2)$$

where T is in °C and t in minutes.

4 Tests in quasi-steady thermal conditions (low heating rate)

Compressive strength

The normalised compressive strength of the eight concretes is plotted in Figure 1 as a function of the temperature. (The normalising factor is the strength of the unheated material, at room temperature, i.e. in virgin conditions, see Table2).

At first glance, the test data exhibit a considerable scattering, that can be explained in two different ways. The first reason lies in the different mix designs and initial properties. A second reason is the effect of the test procedure. For instance, in the tests on stressed specimens (i.e. pre-loaded in compression during the heating phase) the compressive strength at any temperature tends to be larger than in unstressed specimens. The design implications are immediate: in the case of R/C columns mostly subjected to permanent loads reference should be made to the strength measured on stressed specimens, while the strength measured on unstressed specimens should be adopted in the case of lightly-loaded members. However, when only one protocol can be applied, the most conservative choice is recommended (i.e., the strength obtained by testing unstressed specimens).

In general the relationship between the compressive strength and the temperature is nonlinear and in some cases even highly nonlinear. A general decrease with the temperature can be observed. In some cases, however, there is an increase up to 350-400°C or – in preloaded specimens - a sort of stabilisation up to 600°C, around values close to the original strength. Values higher than the original strength have been observed also in ordinary and high-performance concretes [17,18, 19].

Some comments are required by the heat sensitivity of the three “weakest” concretes (between 300 and 600°C), namely BSI, Politecnico and Rostock 1: the rather small difference between BSI and Politecnico may be explained with the lack of steel fibres in the latter case, while the greater heat sensitivity of Rostock has another probable explanation in the highly-siliceous aggregate (quartz and diabase), rather unstable at high temperature, contrary – for instance – to basalt aggregate [19].

Finally, it is worth noting that Rostock 1 (no pre-loading and no steel fibres) exhibits a mechanical decay similar to that given by EC 2 for Class 3 concrete (C90/105 MPa).

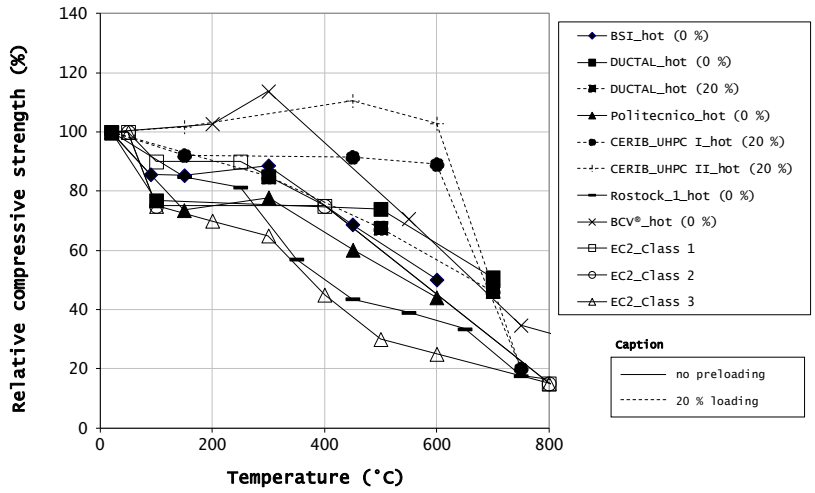

Figure 1: plots of the normalised compressive strength as a function of the temperature, and comparison with EC 2 provisions.

Modulus of elasticity

The normalised elastic modulus of six of the eight concretes is plotted in Figure 2 as a function of the temperature. (The normalising factor is the elastic modulus of the unheated material, at room temperature, see Table 2). As in the case of compressive strength, the scattering is huge indeed, and the causes are the same as those mentioned earlier, i.e. different mix designs and different initial properties on the one hand, and different test procedures on the other hand. A third cause, however, should be added, i.e. the different ways to define the modulus (at the origin of the stress-strain curve, secant, stabilised, static, dynamic, including inelastic strains, …). Anyway, pre-loading the specimen during the heating phase brings in a 20% increase in the elastic modulus with respect to unstressed specimens.

In general, the relationship between the modulus and the temperature is more regular than in the case of compressive strength, and in some cases there is a sort of linearity, at least between 200 and 600°C.

The normalised values of the elastic modulus are definitely higher than those suggested by EC 2. EC 2, however, takes care implicitly of the so-called transient thermal strain – TTS, which is rather similar to creep, even if there is no time dependence. TTS occurs in compression during the first load cycle and causes a relaxation of the self-stresses due to the kinematic incompatibility between the aggregate and the cement paste.

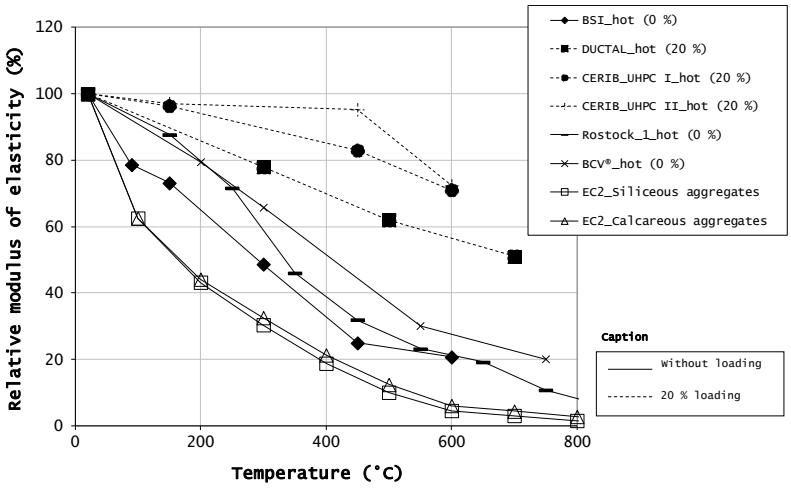

Figure 2: plots of the normalised elastic modulus as a function of the temperature and comparison with EC 2 provisions.

Thermal strain

The thermal strain of three UHPFRC is plotted as a function of the temperature in Figure 3, where the curves provided by EC 2 are reported as a reference. The thermal strain is highly variable, depending on the mix design. The two extremes are represented by Ductal (whose thermal strain continuously increases up to 600°C following closely the values given by EC 2 for siliceous aggregates, and then flattens off) and BSI (whose thermal strain increases up to 200°C, then flattens off up to 300-400°C and starts decreasing to zero between 600 and 700°C). The behaviour of Rostock 3 is intermediate and closer to the second one. Above 700°C Rostock 3 starts decreasing and exhibits negative values (shrinkage). Summing up, it is fair to say that the differences among the various behaviours are still not well understood.

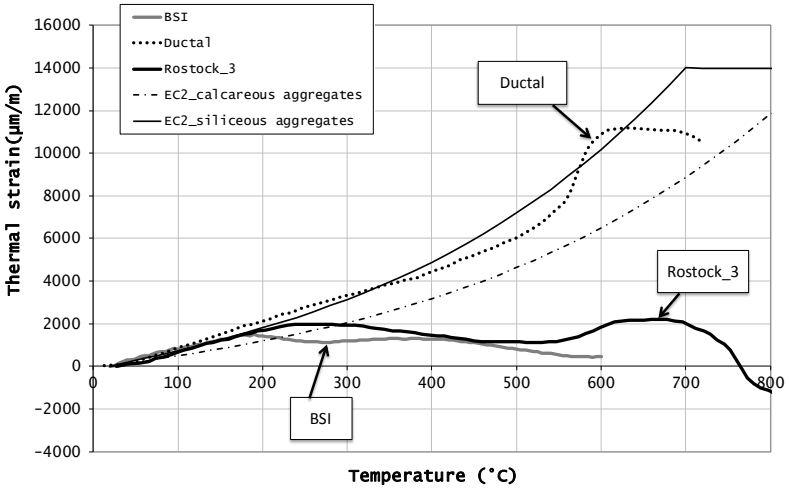

Figure 3: plots of the thermal strain for three mixes and comparison with EC 2 provisions.

5 Tests in fire (highly unsteady thermal conditions)

The main features of the tests performed in highly unsteady conditions are reported in Table 4, in terms of specimen geometry, thermal treatment, fire curve and applied load.

As an example of the tests performed on small structures, several Ductal® columns exposed to ISO 834 fire is reported. Two mixes were tested: Ductal®-fire and the same mix but without polypropylene fibres. Another example is reported in Figure 4, where two small slabs are shown after being subjected to the ISO 834 fire. Also in this case, two mixes were tested: CERIB – UHPC – II (Table 1) and the same mix but without polypropylene fibres.

These tests results (Table 4 and Figure 4) confirm the good effectiveness of the polypropylene fibres against concrete spalling.

Figure 4: Slabs made of CERIB – UHPC - II (right, with pp fibres) and reference mix (left, no pp fibres); extensive spalling can be observed in the slab without pp fibres (left).

Table 4: details of the tests in fire performed on Ductal® [20], BSI [6] and CERIB-UHPC [11].

Specimen geometry	UHPFRC	Thermal treatment	Fire curve	Applied load	Observation
Slabs 400 x 400 x 25 mm3	Ductal®-AF	Yes ***	ISO 834	Unloaded	No spalling
		No			
	Ductal®-FM *	Yes			Spalling
	Ductal®-FO **	Yes			
Columns 900 x 200 x 200 mm3	Ductal®-AF	Yes	ISO 834	Unloaded	No spalling
		No			Minor spalling
700 x 300 x 300 mm3	Ductal®-FO **	Yes			Severe spalling
I shape beam Span = 6,15 m	Ductal®-AF	Yes	ISO 834	Loaded (4 points bending)	Minor spalling
		No			No spalling
Cubes 100 x 100 x 100 mm^3 Cylinders Ø 110 mm x h 220 mm	BSI®-fire	Yes ****	HC_{inc}	Unloaded	No spalling
		No			
U shape sample 1 500 mm [11	CERIB UHPC I et II without pp fibres	No	ISO 834	Unloaded	Severe spalling
U shape sample 1 500 mm [11]	CERIB UHPC I et II with pp fibre	No	ISO 834	Unloaded	No spalling

(*) No pp fibres; (**) no pp fibres, with organic fibres; (***) 48 hours at 90°C; (****) 48 hours at 80°C, in sat. vapour.

6 Conclusions

The aim of this paper is to provide useful information for structural designers on the evolution that the mechanical properties of UHPFRC undergo at high temperature. This evolution is documented through a concise examination of the results of a number of experimental campaigns on eight UHPFRCs.

Though the UHPFRCs examined in this study belong to a rather small group within the very extended family of cementitious composites, their thermal and mechanical properties at high temperature are very dispersed in terms of compressive strength, elastic modulus and thermal strain, just to cite the parameters considered in this study. This dispersion is mainly due to the mix design and to the test procedures.

As commonly found in normal-strength and high-performance concrete, the compressive strength is a nonlinear or even highly nonlinear decreasing function of the temperature. The compressive strength appears to be dependent on the aggregate type and on the state of stress during the heating phase. Also the elastic modulus is a decreasing function of the temperature, but its evolution is more regular than that of the compressive strength. As for the thermal strain, there are huge differences among the different materials examined in this study.

Polypropylene fibres appear to be very effective in limiting or preventing concrete spalling.

Because of the complexity of UHPFRC's behaviour at high temperature, the updated version of the French AFG-SETRA guidelines (by the French Association of Civil Engineering, 2012) considers the information gathered so far – and the order of magnitude of the various parameters - as a useful tool in the pre-design phase of UHPFRC structures. In the final phase of the design, however, it is strongly recommended to assess experimentally the properties of the UHPFRC to be used, especially if the structure is expected to be exposed to fire.

References

[1] Schrefler B.A., Khoury G.A., Gawin D., Majorana C.E.: Thermo-hydro-mechanical modelling of high performance concrete at high temperatures. Engineering Computations 19(7-8): 787-819, 2002.

[2] Kodur V.K.R.: Spalling in High Strength Concrete Exposed to Fire – Concerns, Causes, Critical Parameters and Cures, Proceedings of Structures Congress, Advanced Technology in Structural Engineering, Philadelphia, USA, May 8-10, 2000.

[3] Khoury G.A., Anderberg Y., Concrete spalling - Review, Fire Safety Design, 2000.

[4] Franssen J.M., Hanus F., Dotreppe J.C.: Numerical evaluation of the fire behaviour of a concrete tunnel integrating the effects of spalling. fib task group 4.3 workshop "Fire design o concrete structures - from materials modelling to structural performance". Coimbra, Portugal, 2007.

[5] Haack, A.: Catastrophic Tunnel Fires - What have we learnt? International symposium on catastrophic tunnel fires (CTF). Boras, Sweden, Haukur Ingason, 2003.

[6] Mindeguia J.C., Pimienta P., Simon A., Atif N.: Experimental and numerical study of an UHPFRC at very high temperature. Concrete under severe conditions: environment and loading. Consec'07, vol 2, p. 1659-1674, Tours, June 4-6 2007.

[7] Brekelmans J.W.P.M., Breunese A.: CERACEM split-tensile and compressive strength at high temperatures in comparison with B105 concrete. TNO Report 2006-D-R0223, Mars 2006.

[8] Behloul M., Chanvillard G., Casanova P., Orange G.: “Fire resistance of Ductal® ultra high performance concrete”. Proceedings of the 1st fib congress - Concrete Structures in the 21st Century, Osaka, 2002, pp. 105 -122.

[9] Bamonte P., Cangiano S.: High-Temperature Performance of a HPFRC for Heavy-Duty Road Pavements, Proc. Int. Workshop “Fire Design of Concrete Structures: What now? What next?”, fib TG 4.3 “Fire Design of Concrete Structures”, Milan, Italy, December 2004, pp.63-67.

[10] Bamonte P., Gambarova P.G.: Thermal and Mechanical Properties at High Temperature of a Very High-Strength Durable Concrete, ASCE-J. of Materials in Civil Eng., V.22, No.6, 2010,pp. 545-555.

[11] De Chefdebien A., Robert F., Collignon C.: Performance of Ultra High Strength Concrete subjected to fire. CONSEC'07, 5th international conference CONSEC., Vol 2, Tours June 4-6, 2007, FRA, 2007.

[12] De Chefdebien A., Robert F.: Mechanical properties of Ultra High-Performance Fibre-Reinforced Concrete at high temperature, 7th Int. Conf. “Concrete: Construction’s Sustainable Option”, V. 5, Dundee, U.K., July 2008, pp.139-148.

[13] Missemer L.: Etude du comportement sous très hautes températures des Bétons Fibrés à Ultra Performances : application au BCV®. PhD Grenoble University. May, 23rd 2011.

[14] U. Diedrichs, O. Mertzsch, Behaviour of Ultra High Strength Concrete at High Temperatures. 2nd International Symposium on Ultra High Performance Concrete, Kassel, Mars 2008.

[15] EN 1992-1-2, Eurocode 2: Design of concrete structures, Part 1.2 Structural fire design, December 2004.

[16] RILEM, "Compressive strength for service and accident conditions", Materials and structures. 28, p.410-414, 1995.

[17] Phan L.T., High-Strength Concrete at High Temperature: An Overview. Utilization of High Strength/High Performance Concrete, 6th International Symposium. Leipzig, Germany, 2002.

[18] Pimienta P., Propriétés des BHP à hautes températures. Etude bibliographique (HPC properties at high temperatures. A state of the art). Cahiers du CSTB. July-August 2001.

[19] Bamonte P., Gambarova P.G., Cangiano S.: Mechanical and thermal properties of NSCs and HPCs exposed to high temperature: cement and aggregate roles, 7th Int. Conf. “Concrete: Construction’s Sustainable Option”, V. 5, Dundee, U.K., July 2008, pp.103-114.

[20] Cesmat E., Pardon D. Pestana J., CSTB Tests report about the fire resistance of concrete samples, Centre Scientifique et Technique du Bâtiment, Marne la Vallée, France, n° RS00-023, 2000.

[21] SETRA – AFGC Ultra High Performance Fiber-Reinforced Concretes. Interim Recommendations, UHPFRC task group of the French Association of Civil Engineering, January 2002.

Thermal properties of Mortar with Ceramic Microspheres

Sung-Gul Hong[1], Sung-Hoon Kang[1], Eo-Jin Lee[1], Soo-Min Jeong[2]
1: Dept of Architecture, Seoul National University, Korea
2: Samsung Construction Co., Seoul, Korea

For the development of a new fire resistant mortar mixed with microspheres on the surface of concrete structures, this study investigates the thermal properties of the mortars for the insulation performance. Microspheres known as insulation material are used to delay heat transfer to the concrete. Heat transfer in the microspheres themselves consists of three important heat exchange mechanisms: (1) heat conduction by the solid state, (2) heat conduction by the residual gas, and (3) heat transfer by radiation. The experimental program in this study investigates how microspheres affect the thermal conductivity of the cement mortar. The main parameters of the program are types of microspheres, the volume ratio of the microspheres and the relative humidity of the curing conditions. The residual flexural and compressive strengths of mortar with microshperes after heating and the delays in temperature-rise of the mortar specimens are discussed by analyzing the experimental result. When heat passes through a cement paste, the vacuum properties of microspheres are generally supposed to block the heat and lower the thermal conductivity. However, the experimental results show that the thermal conductivity of the specimens slightly increases. The temperature-rise of the specimens, on the other hands, is delayed due to the mixed microspheres.

Keywords: mortar with microspheres, explosive spalling, thermal property of concrete, heat resistance mortar, microstructure of concrete

1 Introduction

Use of high performance concrete has been increasing due to the demand of new construction materials and durability to save construction resources. High Performance Concrete (HPC) has shown high performances and excellent durabilty in the structures.

In general, the fire resistance of reinforced concrete structures has been known to be excellent to fire compared to steel structures. However, HPC whose compressive strength is high, has the disadvantage related to safety due to the explosive spalling phenomenon. This phenomenon is related to the lost of surface concrete because it cannot exhaust the water vapor generated during a fire.

The prevalence of the fire resistance method is urgent for the direct block against heat of the concrete with prevention explosive spalling and easy maintenance in case of fire. As a way to compensate for former shortcomings of HPC, the most popular methods of using organic fibers mixed in the concrete by reducing the internal vapor pressure has a point of difficult installation and problems in terms of maintenance after the fire. Also common methods of the anti-falling effect of concrete or mortar by wire-mesh or metal lath need the physical mock-up test. Thus, the methods reducing or delaying temperature elevation are simple, economical, and adequate to take the various thermal performances.However, it is difficult to conduct such a large-scale test.

To determine the role of the microspheres in cement-based composites, various phenomena in macro and micro-sized units have been investigated. Although, some studies on the mortar mixed with microspheres investigated thermal properties and strength, researches on the micro-sized thermal properties are still necessary.

The purpose of this paper is first to review the theoretical backround of thermal insulation of microsphere for the development of the fire resistant mortar to protect and maintain HPC by mixing microspheres. The mortar is expected to improve the durability and fire resistance of

structural members. Forming the hybrid layer of the mortar on the surface of concrete structures, the explosion protection and the excellent insulation performance secure the structure from the flames. As the core material for insulation, microspheres are used to delay heat transfer to the concrete. To develop the thermal microstructure for cement mortar, the micro structural properties of concrete and mortar are analyzed as the basic material. To this end, the effects of microspheres in the mortar are investigated to examine various perspectives.

2 Thermal properties of Microspheres

What is Microsphere?

About thirty years ago, the insulation phenomena of microspheres was attracted by many researchers with considerable interest as a new type of cryogenic thermal insulation. It has been qualified as a type of well-known vacuum-powder insulation. Owing to some advantages, it can replace the classical multilayer super insulation (the latter having better thermal properties). The basic advantages of microsphere insulation are: the large resistivity to microsphere destruction caused by compressive forces of order 106 – 107 Nm^{-2} ; the lack of thermal conductivity anisotropy ; the simplicity of application ; and the good reproducibility of the thermal parameters. The apparent coefficient of thermal conductivity involved lies in the limits 2– 8×10^{-4} $Wm^{-1}\cdot K^{-1}$.

The research groups in US have shown the greatest interest in microsphere insulation. Also Poland and German have tried to apply this insulation method to practical cases. In particular, microsphere insulation in Poland is widely used in the building and heating industry.

The microsphere insulation can be considered as a special case of the porous media. Hollow glass spheres, typically 20 to 150 μm wall thickness, provide the thermal resistance to radiation and conduction transport. Thin coatings of a highly reflective nature can be applied to the exterior surface of each sphere to reduce radiative heat transfer even further, or a mixture of coated and uncoated spheres can be used in a fashion similar to the opacification of powders by the addition of metallic particles. Compared to solid spheres, hollow spheres substantially increase the conduction thermal resistances and reduce heat capacity and weight.

Effective Coefficient of Thermal Conductivity

The heat transfer in the microsphere insulation is due principally to the three fundamental heat exchange mechanisms: (1) heat conduction by the solid state material, (2) heat conduction by a residual gas, (3) heat transfer by radiation. The effective thermal conductivity coefficient $k(T)$ may be expressed as the sum of the corresponding components:

$$k_{eff}(T,p) = k_c(T,p) + k_r(T) = k_{ss}(T) + k_{gc}(T,p) + k_r(T) \quad (1)$$

where, k_c is the component of the heat transfer by conduction, k_r is the component of the heat transfer by radiation, k_{ss} is the component of the heat conduction by the solid state, and k_{gc} is the component of the heat conduction by gas.

Chan and Tien have considered a situation in which a pressure p acts on a layered medium of regularly packed solid or thick-walled spheres. In this case, the relations for thermal conductivity through a solid body such as this medium have the following equations:

$$k_{ss}(T) = S_p\left(\frac{1-\mu^2}{E}P\right)^{1/3}\cdot k_s(T) \quad \text{for } P>0 \quad (2)$$

and

$$k_{ss}(T) = S_N \left(\frac{(1-\mu^2) Q_s V_s L}{E r_0^3} P \right)^{1/3} \cdot k_s(T) \quad \text{for} \quad P = 0 \tag{3}$$

where μ : Poisson's ratio, S_p and S_N : parameters depending on the mode of sphere packing, L : thickness of layer of spheres, E : Young's modulus for sphere material, P : externally applied pressure, Q_s: heat flux flowing through one sphere, r_o: sphere radius, T : temperature, V_s : volume of sphere.

Based on the equations (2) and (3), two important results are evident. First, in both cases of loading, the thermal conductivity of microsphere layers does not depend on the microsphere diameter *d*, but depends on the ratio of the wall thickness (*t)* to the microsphere radius r_o. Second, microsphere insulation is directly proportional to the thermal conductivity of the microsphere materials (*T*).

Assuming that the thermal conductivity coefficient of the material is a linear function of temperature and that the radiation component $k_r(T)$ is proportional to T^3 then using Stefan-Boltzmann's law, one may write:

$$K(T) = AT + BT^3 \tag{4}$$

where, A and B are constants.

The dependence expressed by the equation was proved by experiment performed on a sample of microspheres characterized in next part of this paper.

Applying the model of two heat fluxes transferred by radiation, Klein considered the radiation scattering on uniform diameter spheres and obtained an expression for the dependence of the radiation component of heat transfer:

$$k_r(T) = \frac{4\sigma d}{\delta_s} \left(\frac{\varepsilon}{2 - \varepsilon_p} \right) T^3 \tag{5}$$

where, σ: Stefan-Boltzmann constant, d : diameter of microspheres, δ : solid fraction, ε_p : emissivity coefficient of microspheres.

Based on equation (5), the diameter of microspheres is proportional to k_r value. Actual diameter of microspheres used in the experiments is small, thus small thermal conductivities can be expected.

The component of heat transfer by gas, $k_{gc}(T,p)$, in microsphere insulation is a function of the gas thermal conductivity k_g, the thermal conductivity of the spheres k_{gr}, the average local distance between the surfaces of contacting microspheres δ_a and the mean free path of the gas particles *L*. The equation for the thermal conductivity of a gas in a porous granular material is as follows :

$$k_{gc}(T,p) = k_g \left[\frac{5.8\delta_s}{K} \left(\frac{1}{K} \ln \frac{k_{gr}}{k_g} - 1 - \frac{K}{2} \right) + 1 \right] \tag{6}$$

where

$$K = 1 - \frac{k_{gr}}{k_g}; k_g = \frac{k_{g0}}{1 + \frac{19}{6} \frac{2-\alpha}{2} K_n}$$

where k_g: modified gas thermal conductivity under atmospheric pressure, k_{gc} : component of the heat conduction by gas, k_{g0} : gas thermal conductivity under atmospheric pressure, k_{gr}: sphere effective conductivity, K : 1-(k_g/k_{gr}), K_n : Knudsen number, δ_s : solid fraction, α : accommodation coefficient. The conduction of component is proportional to the internal gas pressure.

3 Experimental Program

In order to investigate the thermal properties of mortar with microsphere, specimens were prepared in which the water-cement ratio and sand proportion were fixed at 0.50 and 0.33 respectively. The microsphere of 5, 10 and 20% to the total mortar volume were mixed to compare the heat performance under the same conditions.

Experimental parameters are types of microspheres, volume ratio of the microspheres and the relative humidity during curing periods. The properties of microspheres are listed in Table 1.

Table 1: Propertities of Microsphere.

Type	Diameter (μm)	Internal gas	Density (g/cm^3)	Thermal conductivity
M100	100	Vacuum	0.7	0.1~0.2
M80	80	Vacuum	0.38	0.127
M35	35	Vacuum	0.2	0.05
M70	70	Vacuum	0.1~0.13	-
M50	50~70	Vacuum	0.1~0.14	-
M12	12	Atmosphere	2.5	-

Table 2: Mixing Plan.

Spec.	Curing condition		W/C (wt.%)	C/S (wt.%)	Mixing				
	Temp (℃)	Humidity (%)			W	C	S	Microspheres content, V_m	
						(g)		(vol.%)	(g)
5M0B	20	50	50	33	225	450	1350	-	0.0
5M70S					201	402	1350	5	2.7
5M70M					177	354	1350	10	5.4
5M50S					225	450	1350	5	3.0
5M50M					225	450	1350	10	6.1
5M12S					225	450	1350	5	48.0
5M12M					225	450	1350	10	96.0
9M0B					225	450	1350	-	0.0
9M100M					200	400	1201	10	49.6
9M100L					179	358	1074	20	92.0
9M80M	20	90			211	423	1268	10	27.4
9M80L					199	398	1195	20	51.7
9M35M					225	450	1350	10	15.4
9M35L					211	421	1264	20	28.8

** AMBC (A: relative humidity of the curing condition- 5 and 9 for 50% and 90%, respectively, B: diameter of microspheres, C: amount of microspheres .*

Before heating, the flexural and tensile strengths, microstructures and thermal conductivities of the cement mortars are investigated and compared to the result of microstructure after heating. This helps the effect of microspheres to the cement before and after heating to be seen. In addition, heating temperature change of each cement mortar is investigated. The size of specimens is different to each experiment as noted the standard developed by KS. The mixing and curing plan for the specimens are listed in Table 2.

Strength

The fire resistance mortar made in this study is supposed to be used for exterior finishing rather than structural components to transfer stresses. However, some minimum strength is required for practical use. The tensile and compressive strengths are measured by flexural test and uniaxial compressive strength by cube specimens. Figure 1 shows the results of the tests. The yellow ones indicate the stength of the mortar without microsphere. As the amount of microsphere increases, the tensile and compressive strength decrease due to the void spaces in the mortar. The curing temperature also influenced the degree of strength reduction.

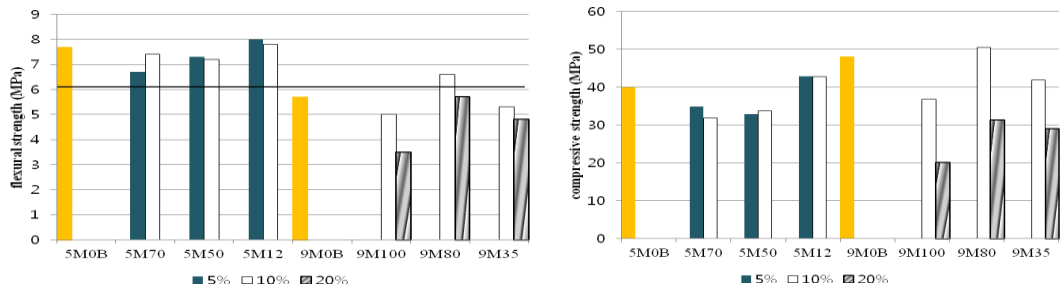

Figure 1: Flexural tensile strength and compressive strength of mortar with microspheres.

Thermal Conductivity Test

The thermal conductivity test was performed according to the direct plate method of KS L 9016 (Korean Industrial Standard) at the condition of the temperature, 20℃. The direct plate method estimates the thermal conductivity by measuring the differences of the specimen temperature directly and electrically when heat passes the specimens. A main heating plate is equipped with supplementary heating plate to make heat from the main heating plate pass the test specimens in one direction (Figure 2).

Figure 3 shows the result of thermal conductivity test. The thermal conductivity of the specimens rises by adding microspheres, especially, small sized microspheres are added. However, the thermal conductivity of the specimens mixed 10 % of microspheres is low compared to that of the specimens mixed 5% of microspheres. The summary of detailed result is listed in Table 3.

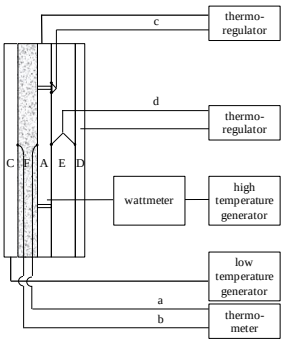

A : Main heating plate
C : low heating plate
D : supplementary heating plate
E : warm plate
F : specimen

a : thermocouple for high temperature
b : thermocouple for low temperature
c : thermocouple for difference of warm plates
d : thermocouple for difference of supplementary plates

Figure 2: Test set-up for thermal conductivity.

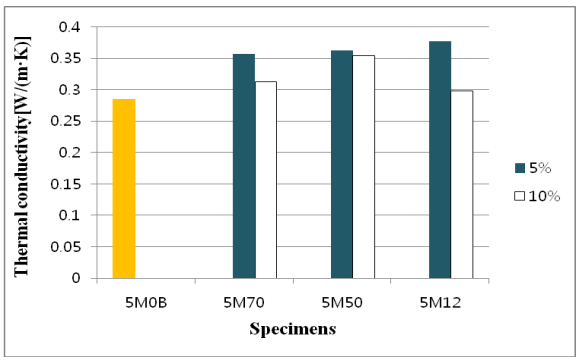

Figure 3: Thermal conductivity results.

To compare the theory of microsphere on thermal conductivity with the exerimental results, the state of mixture with mortar should be considered.

Table 3: Test Results

Curing Humidity	50%	90%
Spalling	No spalling	All specimens except M100
Heating Rate	M12 < M70 = M50	M100 < M35 < M 80
Thermal Conductivity	M12 < M70 < M50	-

Fire Resistance

Generally, real heating temperature is slightly below the standard temperature in the condition of an electric furnace because electric furnace cannot raise the temperature rapidly in a short time. Figure 4 shows the electric furnace and the test set-up for fire resistance test.

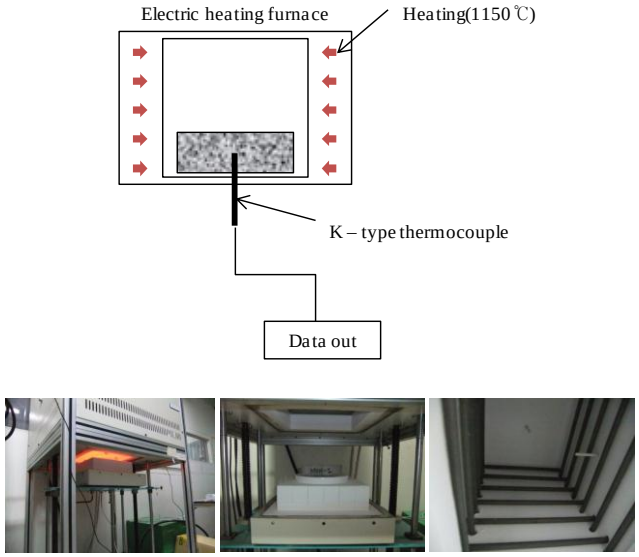

Figure 4: Fire resistance test set-up.

The temperature of the mortar is lower than heating temperature because of its own general physical characteristics. The rate of temperature increase of the 5M series specimens, cured on 50% humidity conditions, was lower than that of 9M series specimens because 5M series specimens, have relatively small amount of water compared to 9M series specimens.
Figure 5 shows a typical fre resitance test results by the time of explosion due to spalling.

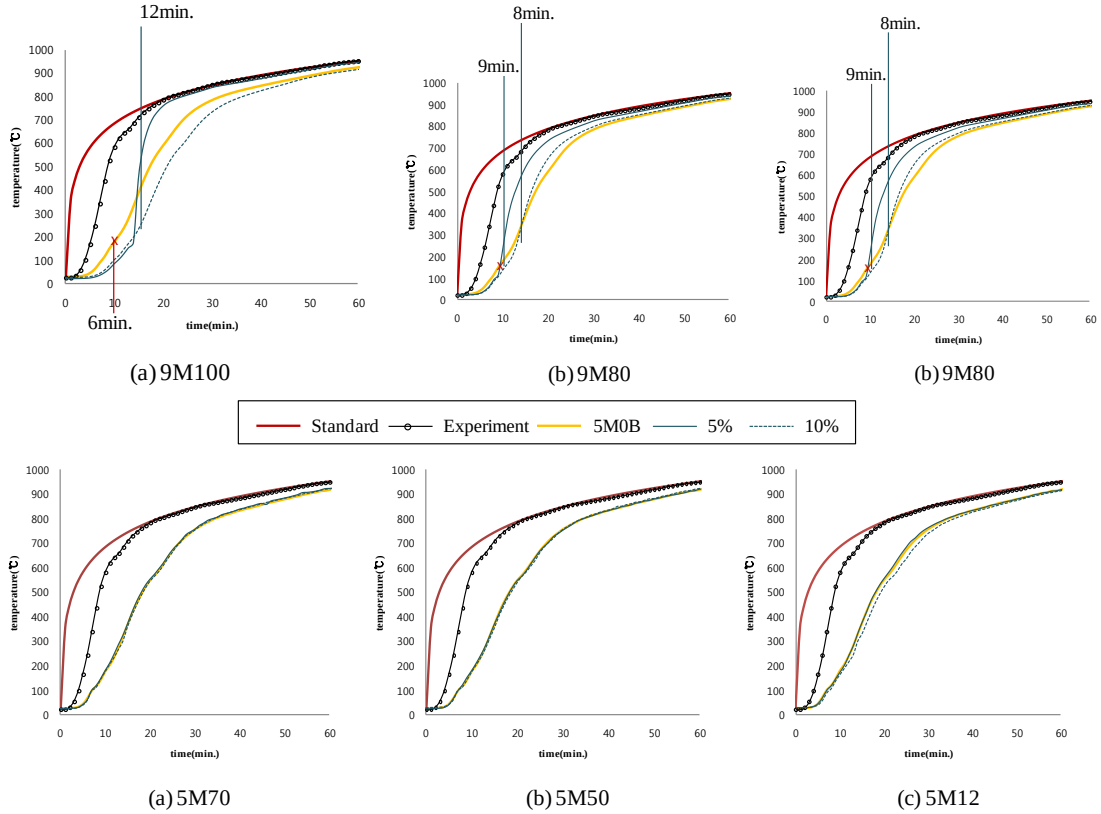

Figure 5: Fire resistance test results for explosion failure.

SEM

The term macrostructure is generally used for the gross microstructure visible to human eyes; the limit of resolution of the unaided human eye is approximately one-fifth of a millimeter (200 μm). The term microstructure is used for the microscopically magnified portion of a macrostructure. The magnification capability of modern electron microscopes is of the order of 105 times. Therefore, application of transmission and scanning electron microscopy techniques has made it possible to resolve the microstructure of materials to a fraction of one micrometer. To investigate microstructure of the cement mortar, Field Emission Scanning Electron Microscope (FE-SEM) is used (S-4800, HITACHI Ltd., Japan).

Because SEM images show only the surface of the target material, we cannot get a lot of information of the material. Nevertheless, it is possible to confirm how the microspheres exist in cement paste. Figure 6 and 7 show the SEM images of 9M 100-20% mortar before and after heating, respectively. In Figue 6, the microspheres are located between cement pastes. An important result is observed in Figure 7. Unlike other fire resistant material, e.g. PP fiber, the microspheres are not melted at temperatures of more than 1000 degrees Celsius. This result contributes to the insulation performance of a new fire resistant mortar.

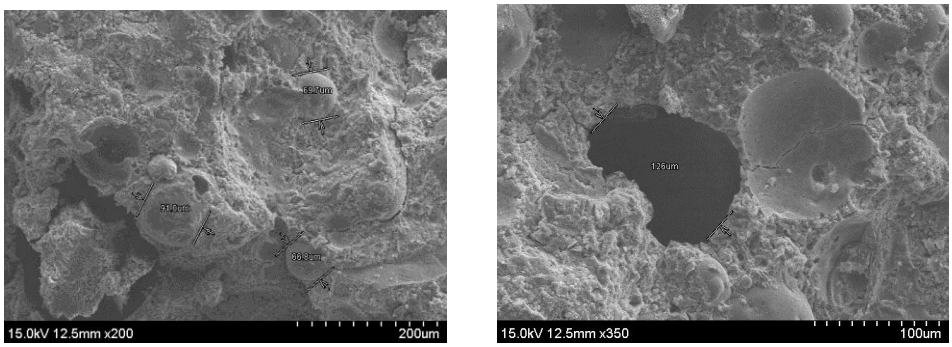

*Figure 6: SEM images of 9M100-20% mortar before heating (*200) and (*350).*

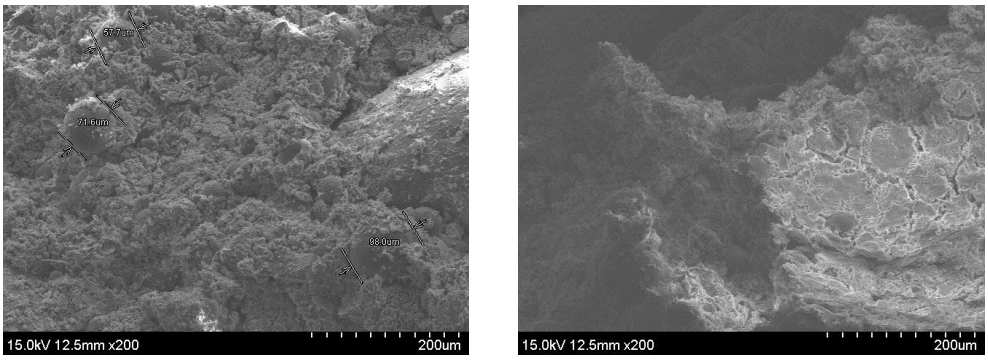

*Figure 7: SEM images of 9M100-20% mortar after heating (*200).*

4 Conclusion

This paper based on the theory of thermal insulation materials has investigated the mortar with high-performance microspheres for the developlmnet of the mortar on the surface of concrete structures.

From the experimental program in this study, the following results can be drawn.

1. The size of microspheres effects on thermal properties slightly.
2. Temperature increases differently depending on density of microspheres, the volume of microspheres, and the mixing condition - humidity.
3. The mortar with low thermal conductivity has low heating rate.

According to the experiments, the smaller diameter of microspheres, the lower mortar internal vapor pressure. The smaller amount of microspheres temperature showed a lower temperature-rise rate. The equation in the section 2.2 to obtain the thermal conductivity of the substance is influenced by the variables - K_{ss}: density of the wall of microspheres material, k_r: the diameter of microspheres. In the heating experiment, the variables included the volume ratio of microspheres (0, 5, 10, 20% volume percent) and the diameter of microspheres. To predict the thermal conductivity of mortar by the equation, it is required more investigation of the thermal properties of fire resistance mortar.

5 Acknowledgement

This study was supported by Brain Korea Program 2.

References

[1] Sarvaranta, L. & P.Raivio. (1994). Microstructure of fibre mortar composites under fire impact effect of polypropylene and polyacrylonitrile fibres. “Cement and Concrete Research”, 24(5), 896-906.

[2] Rafalowicz, R. w. (1988). Heat transfer in microsphere insulation. Journal of Thermal Analysis, 34, 249-527.

[3] Tien, C. L., & Cunnington, G. R. (1976, October). Glass microsphere cryogenic insulation. CRYOGENICS, 583-586.

[4] Toshifumi Sugama, E. w. (1994). Microsphere-filled lightweight calcium phosphate cements. Journal of Materials science, 29, 5165-5176.

[5] Wawryk, R., Rafalowicz, J., & Balcerek, K. (1983, August). The influence of microsphere diameter on the coefficient of thermal conductivity of microsphere insulation. CRYOGENICS, 441-443

[6] Chan, C. K., & Tien, C. L. (1973). Conductance of packed spheres in vacuum. Journal of Heat Transfer, 95, 3, 302-308.

Material Characterization of an Ultra High-Performance-Fibre Reinforced Concrete under Elevated Temperatures

Richard Way, Kay Wille
Dept. of Civil and Environmental Engineering, University of Connecticut, United States

Concrete's resistance to fire is a widely investigated topic. In this research, a new approach for investigating the residual compressive strength and elastic modulus of a commercially available ultra-high performance concrete is used to determine the effects of chemical and material degradation. The material known as Ductal® was provided by LaFarge North America. This mix was cast into cylindrical specimens of 76.3 x 152.4 mm, dried at 135ºC for four weeks, and then heated from 135º to 900ºC. A heating rate of less than 0.2ºC/min was used in order to minimize the risk of spalling and harmful thermal gradients. Prior to heating the specimens, a DSC/TGA analysis was carried out on powdered concrete material to obtain the areas of interest in the heating range.Residual compressive strength and elastic modulus were then tested.

Keywords: UHPC, Ductal, Thermal Testing, Fire, DSC, DTG, Compressive Strength, Elastic Modulus

1 Introduction

Fire or sources of high temperature continue to be serious threats to structures constructed of concrete. This area of research has been investigated in many different capacities over the years from investigations into the effect of fire on the mechanical properties of normal strength concretes [1] to the investigations of fibre-reinforced composites exposed to high temperatures [2], to the recent investigations in High and Ultra High Performance Concretes (HPC, UHPC) under thermal loading [3-5]. Research has shown that increasing the temperature rapidly can lead to the risk of explosive spalling. This is especially true in concretes with low porosity such as HPC and UHPC [5-6], in which the vapour pressure cannot be released easily. However, the use of steel and polypropylene fibres has been shown to mitigate this problem [5-6]. The damaging effects resulting from vapour pressure and thermal gradient are defined as physical degradation.

Additional strength loss in concrete at elevated temperatures is found to come from a wide range of chemical decompositions [7-8]. These include the dehydration of cement gel at temperatures greater than 100ºC and the chemical dehydration of Portlandite, $Ca(OH)_2$, at temperatures greater than 450ºC [9-10]. Beyond 570ºC quartz aggregate undergoes an alpha-beta phase change resulting in an expansion of the quartz molecules [8-9]. These are only two of many chemical and molecular changes that occur due to heating. The damaging effects resulting from dehydration and decomposition of the composite materials are defined as chemical degradation.

There have been extensive efforts to develop empirical relationships between the mechanical properties and temperature of the concrete [8] considering the combination of physical and chemical degradation. In laboratory tests, concrete was reported to lose only a small fraction of its compressive strength below 400ºC. However, after this point the concrete loses around 40% of its strength [11]. By the time concrete reaches 1000ºC, it has typically lost most of its compressive strength. Similarly, as the temperature of exposure climbs the elastic modulus decreases dramatically [2, 7]. This results in a decreased stiffness and a decreased resistance to bending, shear, torsion and axial loading.

While there have been a large number of tests conducted on the effects of heat on concrete residual strength, there have been very few tests performed that stray away from standardized

heating curves such as ASTM E-119-11a [12]. These heating curves are used to mimic the heating rate and intensity of a model fire for the purposes of testing. This rate of heating as discussed above can result in a build-up of vapour pressure, caused by evaporating free and physically or chemically bound water. This is widely thought to be the cause of spalling. [6] The effect of chemistry alone has not been extensively researched for UHPC.

Research presented here is performed under very slow heating conditions to investigate the relationship between chemical degradation of UHPFRC and residual mechanical properties.

2 Procedure

Mixing

In this research the commercially available ultra-high performance fibre-reinforced concrete Ductal® has been used. LaFarge North America provided the constituent materials, mix design and mixing regiment. Further information about the material can be found in [13-14]. The water to cement ratio was found to be 0.183. [14] A concrete mixer from Eirich has been used with variable speed control for pan and rotor. During the mix, the mixer was stopped for a few moments to allow air to escape, which decreases the air void content in final concrete samples [15]. Additionally the bowl walls and mixing tools were scraped to prevent introduction of dry materials at the end of mixing. Specimens were cast into 76.3 x 152.4mm (3 x 6 in) metal cylindrical moulds using vibratory compaction and a circular pouring pattern in an attempt to disperse the fibres randomly throughout the mix. After cylinders were cast, they were allowed to sit on the vibration table for one minute and then were removed. After casting was complete specimens were covered in plastic sheet to prevent water loss.

In order to ensure an acceptable thermal gradient, several specimens were cast with two type K thermally shielded thermocouples embedded. The first thermocouple was embedded at the centre of the specimen and the other was placed immediately below the surface of the sample (see Fig. 1).

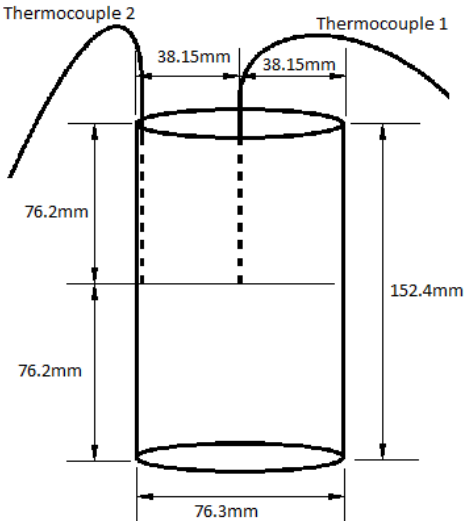

Figure 1: Thermocouple Placement.

Specimen Preparation

Specimens were allowed to sit for 24 hours in the moulds and then steam cured at 95% humidity and 90ºC for roughly 44 hours. After the curing was complete, specimens were cooled to room temperature and ground to within 0.2º of end planeness. This was tested with a dilatometer to locate the high and low point of the specimen's ends then a distance was measured between the two to ensure the criteria were not exceeded.

Once the specimens were ground, they were placed into a convection oven and slowly heated to 135ºC and were held there for a period of four weeks. This was used to drive off as much free water as possible before the specimens underwent the heating.

3 Testing

DSC/TGA

Prior to heating the specimens, a Differential Scanning Calorimetry/ Differential Thermogravimetry analysis (DSC/DTG) was conducted using a Netzsch STA 449 F3 Jupiter Simultaneous TGA/DSC. Samples of the concrete without fibres were ground to a powder using a ceramic mortar and pestle. This powder was then loaded into an aluminium oxide holder for testing. The DSC/DTG tests were completed in order to determine critical points in the heating process. They were carried out in an argon atmosphere with temperatures ranging from 20ºC to 1000ºC. Argon was chosen because of its inert characteristics.

Temperature Testing

Ten temperature steps were chosen to investigate the effect of change in chemistry on the residual compressive strength and elastic modulus. For each temperature step, three specimens were tested in compression. In order to ensure the thermal gradient in the concrete did not lead to an uneven thermal expansion, specimens were tested at a ramp rate of less than 0.2ºC per minute or approximately 12ºC per hour. This slow heating rate was also used to allow slow elimination of any remaining free water or water liberated by chemical dehydration. It also allowed time for equilibration of temperature between the surface and core of sample, which was constantly monitored by the thermocouples in a dummy specimen. Once the specimens reached their target temperature they remained there for at least two hours. Some specimens remained at the target temperature longer as research has suggested that beyond one hour at a temperature, the change in compressive strength was not statistically significant [4]. After heating, specimens were cooled to room temperature at the same rate. For this research, specimens heated to 90ºC are considered to be the control specimens.

Compressive Strength

Compressive strength tests were carried out using a Satec 1800kN load frame with a MTS controller. While ASTM C39-10 prescribes a loading rate of approximately 0.25 MPa/s, the ultra-high compressive strength of UHPFRC necessitates a quicker load rate [14]. The compressive tests were performed machine displacement controlled with a loading rate of 0.5mm/min. Specimens were loaded, carefully centred, and pre-stressed with approximately 4.5 kN of force before beginning the test.

Elastic Modulus

The elastic modulus was measured as the slope of the linear stress versus strain curve. The strain was measured by three LVDTs held in place using a three armed LVDT holder pictured in Figure 2. The cross piece is mounted with thumb screws at approximately 2.5 cm from each end of the specimen. The distance between the thumb screws has been measured prior to each test for strain calculation.

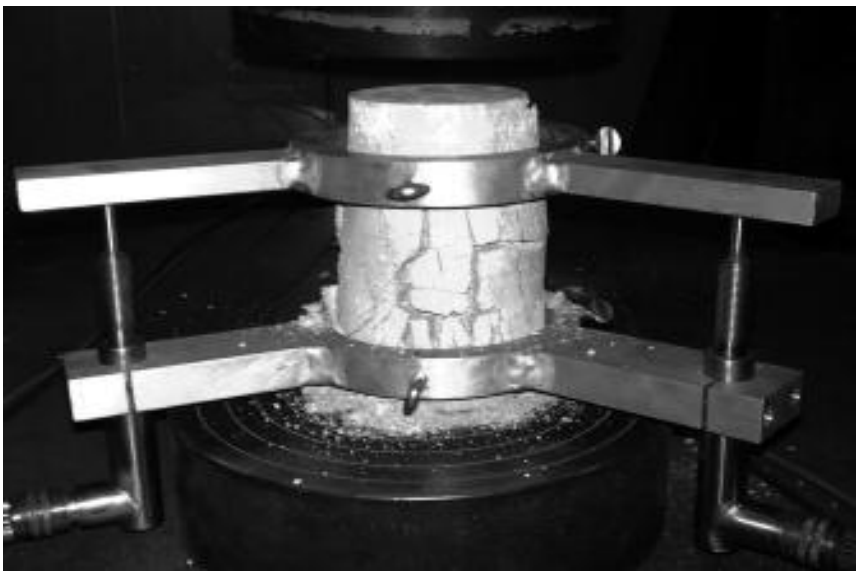

Figure 2: Test setup for compression tests.

4 Results and Discussion

In order to better understand the temperature ranges that powdered UHPC is undergoing specific phase changes or chemical decompositions, a DSC/DTG test was carried out. The results for this test can be seen in Figures 3 and 4. The TGA was used to determine the percentage mass loss of the concrete with an increase in temperature. As the overall output is very smooth, the derivative of the graph was taken in order accentuate the changes in slope that would correspond to rapid change in mass loss.

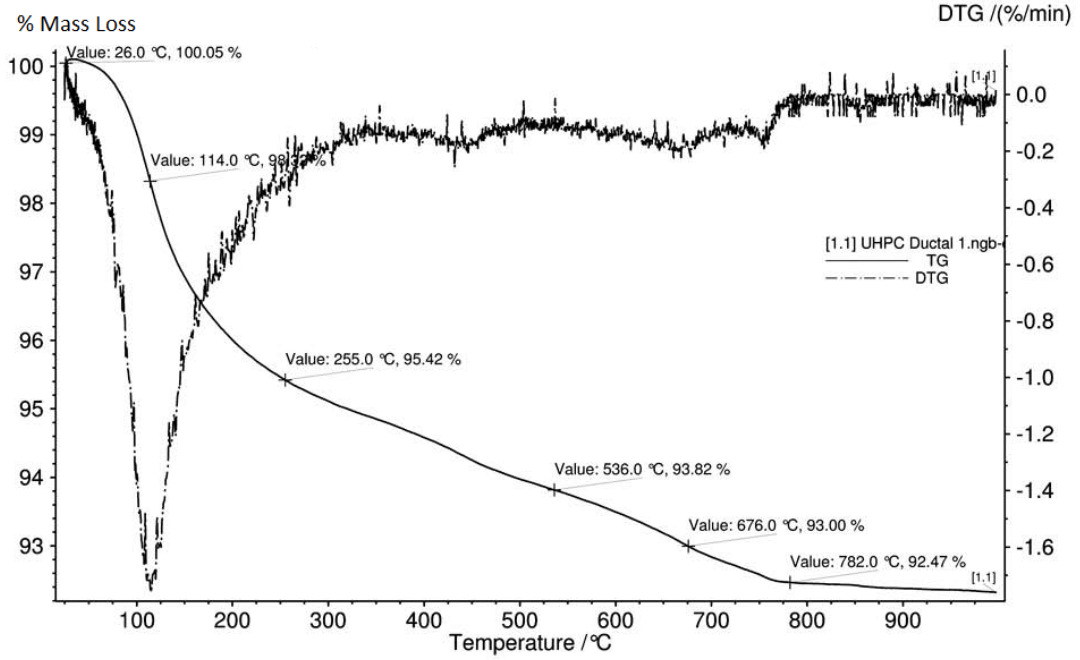

Figure 3: % Mass Loss and Derivative % Mass Loss plot vs. Temperature.

The first spike in the DTG plot occurs at roughly 114ºC. This point most certainly corresponds to the evaporation of free water from the concrete powder. Between 420ºC and 500ºC, another dip occurs. In this temperature range, typically the $Ca(OH)_2$ dehydrates into Lime (CaO) and water [16]. Around 770ºC, the graph takes a final dip where tobermorite and xonotlite dehydrate in wollastonite. [17]

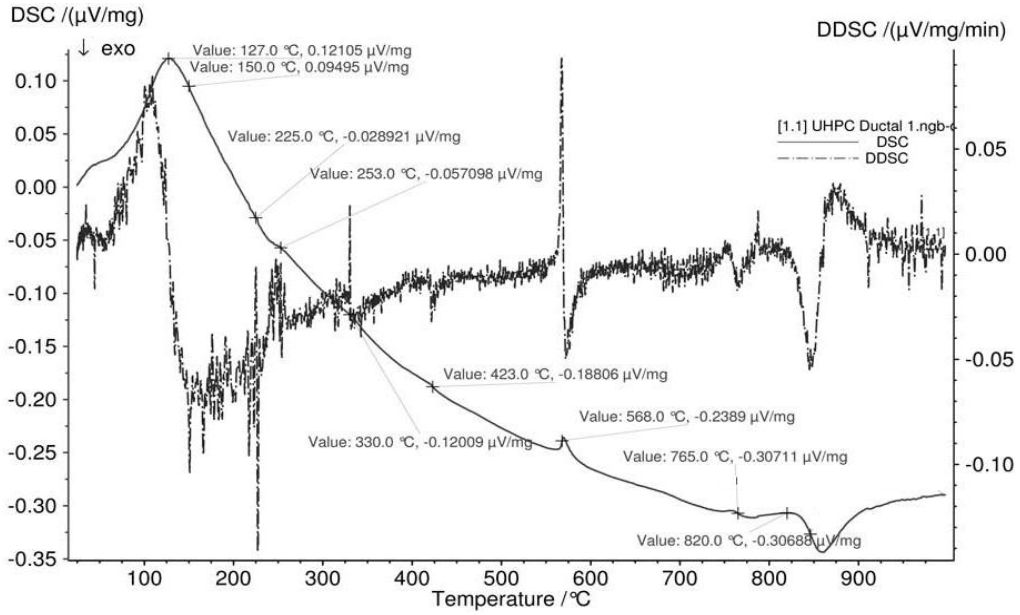

Figure 4: DSC and DDSC plot vs. Temperature.

Similar to the DTG plots, the DDSC shows a peak around 100ºC which most likely corresponded to evaporating free water from the system. The peaks in the DDSC around 250ºC most likely align with the reorientation and dehydration of tobermorite which takes place between 250ºC and 300ºC. [18] At around 570ºC, phase transition from alpha to beta phase quartz can be seen which leads to an increase in volume of the quartz molecule. [2, 8-9, 16] Between 700ºC and 800ºC there is another dip which most likely coincides with the dehydration of xonotlite and tobermorite to low T-wollastonite. [17]

Figure 5 shows the residual compressive strength of Ductal® exposed to ten different maximum temperatures (90ºC, 135ºC, 200ºC - 900ºC). Results are presented as individual test values with an average trend overlaid. All specimens exposed to 135º up to 900ºC were oven-dried for about 4 weeks prior to exposing them to higher temperatures. An increase in compressive strength of 32% and 43% over the control specimens at 90ºC have been obtained for the specimens heated up to 135ºC and 200ºC, respectively. This increase might be attributed to the dehydration and reorientation of tobermorite in the cement paste as well as the lack of free water in the specimen. [17-18] The continual decrease in compressive strength after 500ºC is most likely linked to the dehydration of the calcium silicate hydrate products and thermal expansion damage of the cement paste. The second sudden drop after 700ºC is likely attributed to the dehydration of xonotlite and tobermorite into T-wollastonite. [17]

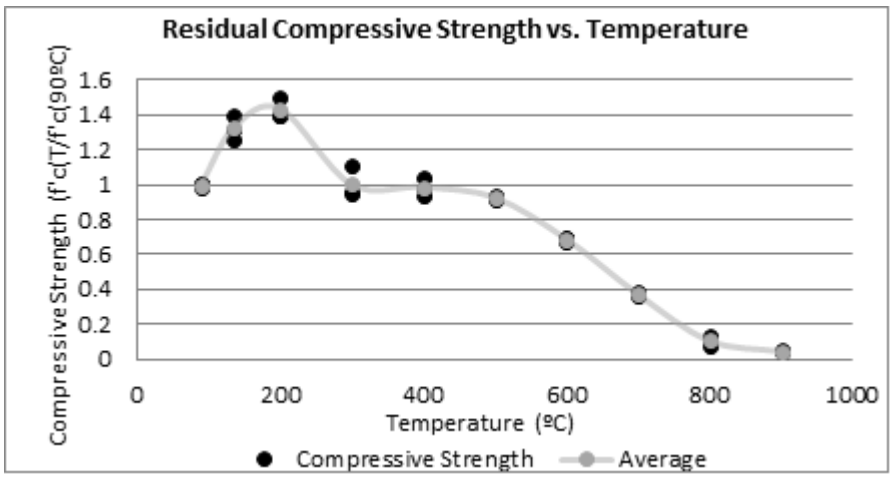

Figure 5: Compressive Strength vs. Temperature.

The residual elastic modulus versus temperature (Fig. 6) follows a similar trend to the residual compressive strength plot. However, the elastic modulus only increased by about 5% for the specimens which were oven dried in comparison to the control values. For samples heated to 200ºC, the compressive strength increased but the modulus of elasticity actually decreased reaching a value of only 1% higher than the control specimens.

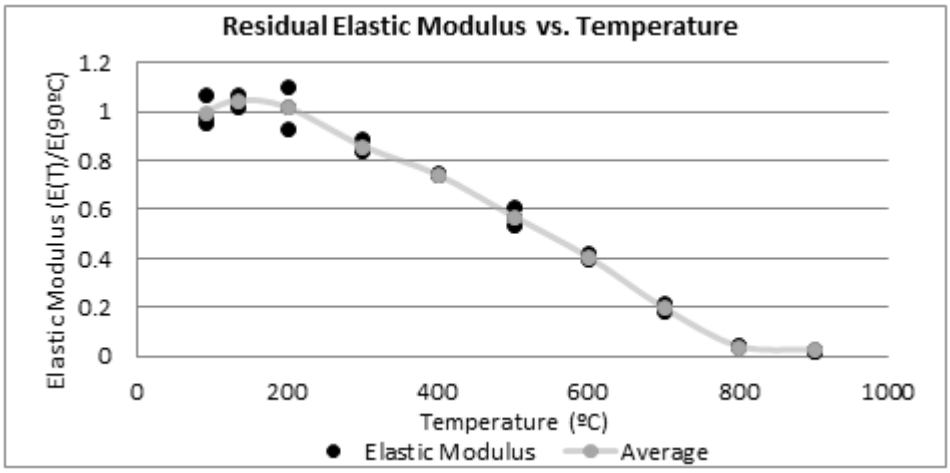

Figure 6: Modulus of Elasticity vs. Temperature.

The results of the residual compressive strength and elastic modulus suggests that oven dried specimens have a better mechanical behaviour than the control specimens, steam cured at 90ºC. The increase in compressive strength and modulus up to 200ºC is followed by a progressive decrease of mechanical properties with the increase in temperature. This indicates changes to and deterioration of the chemical structure of the concrete.

Through the course of testing, specimens failed suddenly with low ductility. This could be attributed to excessive drying and fibre settling observed along the height of the specimens. More investigations are needed to characterize the ductility of dried specimens. Specimens heated to 300ºC and 400ºC after drying showed a marked increase in ductility over those from other thermal ranges. However, despite having comparable residual compressive strength, specimens heated to 500ºC failed to show this same ductility. It is worth noting the specimens heated to 500ºC still had a compressive strength of 93% of the control value. Beyond 500ºC, the mechanical properties significantly degraded. For specimens heated to 900ºC, the compressive strength and the elastic modulus dropped to just 5% and 3%, respectively. Table 1 shows the residual compressive strength and elastic modulus in terms of a percentage of the control.

Table 1: Residual Compressive Strength and Elastic Modulus.

Temperature (ºC)	f'c(T)/f'c(90)	E(T)/E(90)
90	1.00	1.00
135	1.32	1.05
200	1.43	1.02
300	1.00	0.86
400	0.99	0.74
500	0.93	0.57
600	0.69	0.41
700	0.37	0.20
800	0.11	0.04
900	0.05	0.03

Figure 7 illustrates failed specimens at different temperatures. The specimen on the left only underwent the drying treatment. During failure it maintained its physical shape and showed no signs of thermal decay. On the right is a specimen heated to 900ºC. The specimen broke in half while testing revealing a deteriorated matrix more closely resembling dried sand than concrete. The fibres had degraded to the point where they were no longer distinguishable from the concrete beyond small black dots on the failed surface. Here, it becomes visible how the chemical deterioration of concrete and fibres can affect the mechanical properties of UHPFRC.

Figure 7: Failed specimens under different temperatures (left 135ºC, right 900ºC).

5 Conclusions

The research focused on the investigation of the residual mechanical properties of Ductal® UHPFRC under elevated temperatures. Special emphasis was placed on specimen preparation and curing conditions in order to not damage the specimen due to vapour pressure or unequal thermal gradient.

1. Oven dried specimens performed better than those un-dried. This is most likely due to accelerated hydration and the reduction of incompressible water in the pore structure. Compressive strength and elastic modulus increased up to 200ºC and significantly decreased over 500ºC. The rapid downward trend after 500ºC is in agreement with most current research on the topic.
2. As the temperature of the concrete approaches 900ºC, the concrete deteriorated beyond usability. At 900ºC the compressive strength and modulus of elasticity of the concrete had dropped to less than 5% of their original values. This can be attributed to the chemical degradation and excessive cracking due to thermal stresses despite slow heating rate.

3. Beyond 700ºC, the steel fibres had degraded to the point where they were no longer distinguishable from the concrete itself. This loss of strength is most likely attributed to the slow cooling process which did not allow the steel to quench and regain its strength.
4. Ductility was shown to increase for specimens heated to 300ºC and 400ºC. The exact reasons for the increase in ductility were not readily discernible and require addition investigation. It was also seen that specimens heated below 400ºC did not show cracking due to thermal gradients.

References

[1] M. S. Abrams: Compressive Strength of Concrete at Temperatures up to 1600ºF. PCA Research and Developement Bulletin, RD016. 1973.

[2] Lau, A.; Anson, M.: Effect of high temperatures on high performance steel fibre reinforced concrete. Cement and Concrete Research 36, pp 1698-1707, 2006.

[3] Khalig, W.; Kodur, V.K.R.: Effect of High Temperature on Tensile Strength of Different Types of High Strength Concrete. ACI Materials Journal V 108, pp. 394-402. July-August 2011.

[4] Burke, B.T: Residual Strength of Ultra-High Performance Concrete After Exposure to Elevated Temperatures. Master's Theses Paper 44, 2011.

[5] Heinz, D.; Dehn, F.; Urbonas, L.: Fire Resistance of Ultra High Performance Concrete (UHPC) – Testing of Laboratory Samples and Columns under Load. International Symposium on Ultra High-Performance Concrete, pp. 703-715, Kessel 2004.

[6] Wille, K.; Dehn, F.: Micro analytical investigations on the effect of polypropylene fibres in fire exposed high-performance concrete (HPC). 6th International RILEM Symposium on Fibre Reinforced Concretes, pp. 659-668 2004.

[7] Odelson, J.B.; Kerr, E.A.; Vichit-Vadakan, W.: Young's Modulus of Cement Paste At Elevated Temperature. Cement and Concrete Research 37, pp. 258-263 2007.

[8] Alarcon-Ruiz, L.; Platret, B.; Massieu, E.; Ehrlacher, A.: The Use of Thermal Analysis in Assessing the Effect of Temperature on a Cement Paste. Cement and Concrete Research 35, pp. 609-613 2005.

[9] William, K,; Rhee, I.: Thermal Degradation of Heterogeneous Concrete Materials. Journal of Materials in Civil Engineering 17 (3), pp.276-285 2005.

[10] Jonaitis, B.; Papingis, V.: Effect of Long-Term Loading and Fire Temperatures on Mechanical Properties of Concrete. Journal of Civil Engineering and Management 11 (4), pp. 283-288 2005.

[11] Joongwon, L.; Choi, K.; Hong, K.: The Effect of High Temperature on Color and Residual Compressive Strength of Concrete. Fracture Mechanics of Concrete and Concrete Structures 7, pp. 1772-1775, 2010.

[12] ASTM E-119-11a: Standard Test Methods for Fire Tests of Building Construction and Materials. American Society of Testing and Materials. 2011.

[13] Ahlborn, T.M.; Peuse, E.J.; Misson, D.L.: Ultra-High-Performance-Concrete for Michigan Bridges Material Performance – Phase I. Michigan Technical University, Michigan Department of Transportation. 2008.

[14] Graybeal, B. A.: Material Property Characterization of Ultra-High Performance Concrete. PSI, Inc. Federal Highway Administration. 2006.

[15] Schachinger, I.; Schubert, J.; Mazanec, O.: Effect of Mixing and Placement Methods on Fresh and Hardened Ultra High Performance Concrete (UHPC). International Symposium on Ultra High Performance Concrete pp.575-586, Kassel, 2004.

[16] Mendes, A.; Sanjayan, J.; Collins, F.: Phase transformations and mechanical strength of OPC/ Slag pastes submitted to high temperatures. Materials and Structures 41, pp. 345–350, 2008.

[17] Shaw, S.; Henderson, C.M.B.; Komanschek, B.U.: Dehydration/Recrystallization mechanisms, energetics, and kinetics of hydrated calcium silicate minerals: an in situ TGA/DSC and synchrotron radiation SAXS/WAXS study. Chemical Geology 167, pp.141-159, 2000.

[18] Taylor, H.F.W.: The Dehydration of Tobermorite. Clays and Clay Materials 6, pp.101-109, 1957.

Behavior of Ultra High Performance Concrete (UHPC) in Case of Fire

Dietmar Hosser, Björn Kampmeier, Dirk Hollmann
Institute of Building Materials, Concrete Construction and Fire Protection (iBMB), Technische Universität Braunschweig, Germany

The use of UHPC for building constructions requires design models for fire resistance according to Eurocode 2 part 1-2. For these design models the thermal properties and the mechanical properties of UHPC have to be determined as functions of temperature. In addition, it is important to predict the distinctive explosive spalling behavior of UHPC which can lead to an early collapse of building members. Thermal conductivity and thermal diffusivity have been analyzed using the TPS method (Transient Plane Source). In addition, the specific heat has been determined by DSC (Differential Scanning Calorimeter) and the mass loss by TGA (Thermo Gravimetric Analysis). The test data show that the thermal conductivity of UHPC is somewhat higher than for normal strength concrete. Steady state tests and unsteady-state tests have been performed to derive temperature-dependent stress-strain relationships which also contain high temperature creep.

Keywords: UHPC, fire, thermal properties, thermo-mechanical properties, explosive spalling

1 Introduction

The current priority program 1182 „Nachhaltiges Bauen mit ultrahochfestem Beton (UHPC)“ (`Sustainable building with ultra-high performance concrete`) of the German Research Foundation (DFG) pursues the goal of creating a reliable scientific data base for building with UHPC from source material up to the finished building component.

The priority program consists of 34 research projects, some of which are already completed and others are still running until 2012. In the research project “Theoretische und experimentelle Untersuchungen zur Ermittlung und Optimierung des Brandverhaltens von ultra-hochfestem Beton“ (`Theoretical and experimental investigation for determination and optimization of ultra-high performance concrete’s fire behavior`) iBMB is investigating the necessary fundamentals for structural fire design of structural members and systems with fire protection requirements. Currently, there are significant knowledge gaps regarding the thermal as well as the mechanical material properties of UHPC under fire exposure. Furthermore explosive spalling of UHPC in case of fire seems to be very critical and suitable solutions need to be found to avoid failure of structural members.

In this report interim results of the research project are presented. Particular attention is paid to i) the thermal material properties which are used to calculate the temperature rise in cross sections due to fire exposure and ii) the thermo-mechanical material properties which are needed for calculating the load-bearing capacity using simplified or general calculation methods according to Eurocode 2 part 1-2 (in the following: EC 2-1-2) [1]. Based on the experimental results, numericals models for calculating the behavior of UHPC structures regarding to temperature rise, load bearing and deformation behavior will be developed. The models will be validated with the help of large scale fire tests of loaded columns under standard fire exposure.

Two representative mixtures of UHPC which were developed in another project of the priority program have been examined: a mortar with indication M3Q and a concrete with indication B5Q (see table 1).

Table 1 Typical mixtures for 1 m³ volume of UHPC M3Q (mortar) and B5Q (concrete).

Base material	M3Q Mass [kg]	B5Q Mass [kg]
Water	175	155
CEM I 52,5 R HS/NA	825	650
Microsilica	175	170
Liquifier	27,5	34,5
Quartz powder	200	456
Quartz sand 0,125/0,5	975	354
Basalt 2/5	0	298,5
Basalt 5/8	0	298,5
Steel fibers 0,19/9 mm	80 (1 Vol.-%)	201 (up to 2,5 Vol.-%)
PP-fibers	up to 2,5 kg/m³ (0,27 Vol.-%) *	up to 2,5 kg/m³ (0,27 Vol.-%) *

* optimal fiber addition is still object of research

2 Influencing Factors

When using UHCP in building constructions, requirements concering load capacity and durability and on the other side on fire protection have to be fulfilled. The latter refer to reaction to fire and fire resistance time. According to the German standard DIN 4102-4 [2] UHPC can be classified as building material class A (non-combustible) without any further proofing. Since the structural fire design rules for normal strength concrete are not valid for UHCP, the behavior under fire exposure is still an open question, especially the temperature-dependent strength and deformation. In addition, the temperature of the reinforcing steel bars is important for the fire resistance of reinforced concrete members. Therefore it is necessary to calculate the temperature profile inside the cross-section in case of fire. For this purpose the thermal material properties λ, ρ *and* c_p are needed which are temperature-dependent, too. Knowing the thermal and the thermo-mechanical properties, the fire resistance time can be calculated. It has to be ensured that the concrete cover which protects the reinforcing steel is not seriously damaged due to fire exposure, i. e. explosive concrete spalling has to be avoided or at least limited. Otherwise one cannot rule out that reinforcing steel bars or tendons become directly exposed to the fire, leading to a rapid loss of load capacity.

3 Spalling and heating behavior

To examine the spalling and heating behavior, 20 specimens with a cross section of 20 x 20 cm² and a length of 60 cm were made of M3Q and B5Q. They were examined unloaded under fire exposure according to the standard fire curve (SFC). The endings of the specimens were protected by vermiculite panels, therefore a two-dimensional heating input can be assumed (see Fig. 1).

The objective of these experiments was to show which combination of fire protecting lining and PP fibers content (polypropylene) is able to minimize concrete spalling under SFC exposure. Therefore varying amounts of PP fibers were added to the concrete mixtures and different linings and coatings were applied to protect the specimens against heating. Table 2 shows the different combinations of PP fibers content and protective coating.

Figure 1: Test set-up for investigating the spalling and heating behavior of UHCP specimens exposed to SFC.

Table 2: List of examined combinations of PP fibers content and lining.

Formula	PP fibers content [kg/m³] ([Vol.-%])	Protective coating / lining
B5Q	0 (0)	----------
	0,75 (0,08)	----------
		High performance fire protection coating
		Mineral wool 10 mm
		Mineral wool 20 mm
		Ablation coating
		Intumescent paint
	1,50 (0,16)	----------
	2,25 (0,25)	----------
M3Q	0 (0)	----------
	0,75 (0,08)	----------
		High performance fire protection coating
		Mineral wool 10 mm
		Mineral wool 20 mm
		Ablation coating
		Intumescent paint
	1,50 (0,16)	----------
	2,25 (0,25)	----------

Each combination is examined with both concrete mixtures B5Q and M3Q. Hereby PP fibers content varies in the range of 0 to 2,25 kg/m³ (0 to 0,25 Vol.-%). Mineral wool panels (thickness 10 mm and 20 mm), a high performance fire protection coating (originally developed for wooden building components), an ablation coating and a costumary intumescent paint are used as protection systems. To examine the influence of PP fibers on concrete spalling separately as

well as for comparison reasons, specimens without protection are examined, too. Thermocouples are attached halfway level of the specimen´s concrete surface as well as in a depth of 10 mm, 20 mm, 30 mm, 40 mm and 50 mm to measure the temperature inside the cross-section. The behavior of the test specimens under fire exposure (especially temporal alterations of the protection system and spalling process) is documented and analyzed by video recording. Additionally, the specimens are weighed before and after the experiments to get an objective valuation.

Figure 2 shows for the specimens without lining decisive dependencies between the spalled concrete mass, the concrete mix and the PP fibers content. If the concrete does not contain any PP fibers the test specimens of the M3Q mixture are completely destroyed. The concrete with the B5Q mixture shows considerably less tendency of spalling: without addition of PP fibers this kind of concrete has only limited surface spallings. Increasing the fibers content of both concrete mixtures up to 1,5 kg/m³ (0,16 Vol.-%) and more, there is practically no destructive spalling, as far as unloaded situation is concerned.

Figure 2: Spalling tests under SFC exposure on prisms 20/20/60 [cm³] with different PP fibers contents and UHPC mixtures M3Q (above) and B5Q (below).

To study the heating behavior of reinforcing bars of the specimens with lining or coating,, temperature development at the lateral surface in 3 cm depth of B5Q specimens is measured. Figure 3 shows the temperatures as a function of fire duration. For comparison temperature development without coating systems is pictured, too.

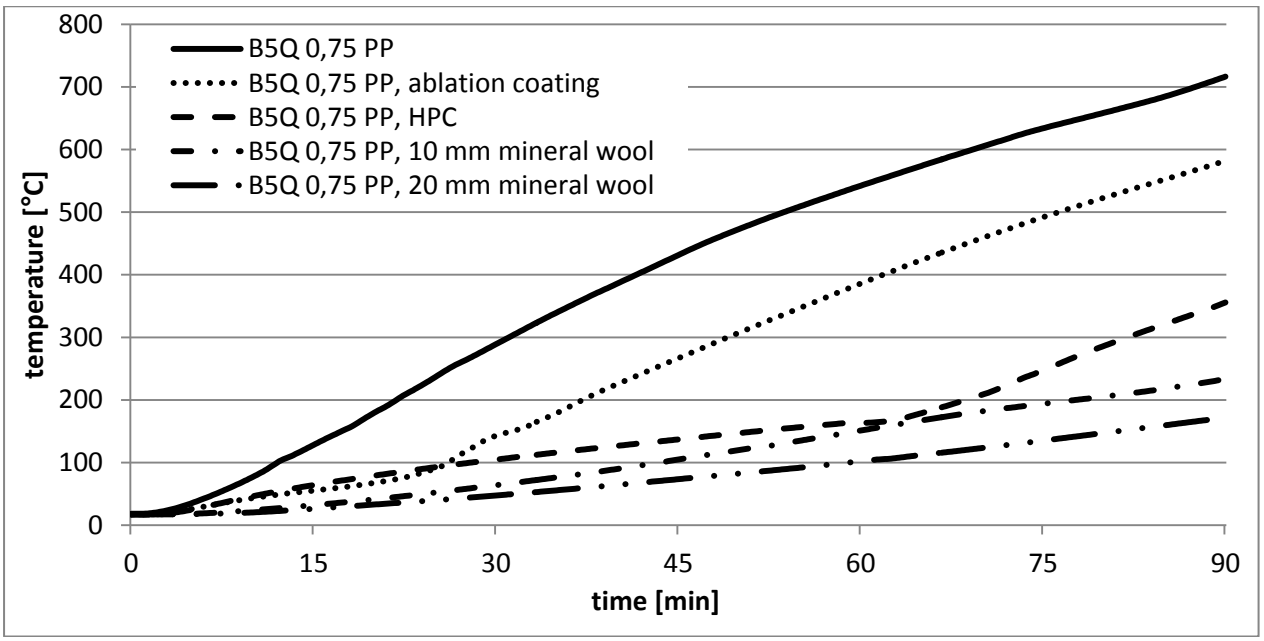

Figure 3: Temperature development at 3 cm depth of B5Q with fibers content 0,75 kg/m³ (0,08 Vol.-%) specimens with different lining or coating during 90 minutes of SFC exposure

Remarkably, the temperature of the unprotected specimen at the position in question exceeds 700 °C after 90 minutes fire exposure. A thermal analysis according to EC 2-1-2 [1] with thermal material properties for normal strength concrete results in temperatures of only 615 °C. Reasons for the rapid temperature rise can be found in the high thermal conductivity of UHPC which is explained in the next chapter.

With the help of the examined ablation coating temperatures are reduced by about 120 °C compared to the unprotected specimen. The high performance fire protection coating even yields a reduction by about 350 °C. The available coating systems are therefore suitable to prevent heating of inserted reinforcement, even with very architecturally-complex cross-sections. Mineral wool lining, which was examined for comparison, only provides final temperatures of about 200 °C, which is even another advantage for this protection option.

4 Thermal material properties

In the following, the laboratory tests to determine the thermal material properties thermal conductivity λ and specific heat c_p of UHPC and the related results for the concrete mixes B5Q and M3Q are presented. All experimental studies include test specimens at an age of 100 days at least which were stored at indoor temperature after 28 days. The expected moisture content varies in a range of 2,5 to 3,2 M.-%.

Transient Test Procedure

The temperature-dependent volumetric specific heat capacity $\rho \cdot c_p$ and the heat conductivity λ can be analyzed simultaneously with the aid of the so-called TPS method (Transient Plane Source) according to DIN EN ISO 22007-2 [3]. The TPS method is a transient process in which a sensor is clamped between two halves of one specimen. The sensor serves as heating element and temperature sensor at the same time. The measured data provide a basis for the determination of the heat conductivity λ and the thermal diffusity $D = \lambda/(\rho \cdot c_p)$. The quotient of both provides the volumetric specific heat capacity $\rho \cdot c_p$. With the help of a bulk density model the needed mass-related specific heat capacity c_p is derived. For more detailed theory see [7]. The TPS method is hardly used in Germany, whereas the applicability to building materials has been proven by *SP Fire Technology* [4].

Thermal conductivity

Temperature-dependent thermal conductivity λ of UHPC mixtures B5Q and M3Q with 0,75 kg/³ (0,08 Vol.-%) fibers content is shown in figure 4. The design model of the upper limit according to EC 2-1-2 [1], which is shown for comparison, gives lower values. At *SP Fire Technology* [4] high strength concrete was examined with the TPS device and the results were even higher as for B5Q and M3Q. The great density of UHPC´s structure is supposed to be the reason for the higher thermal conductivity.

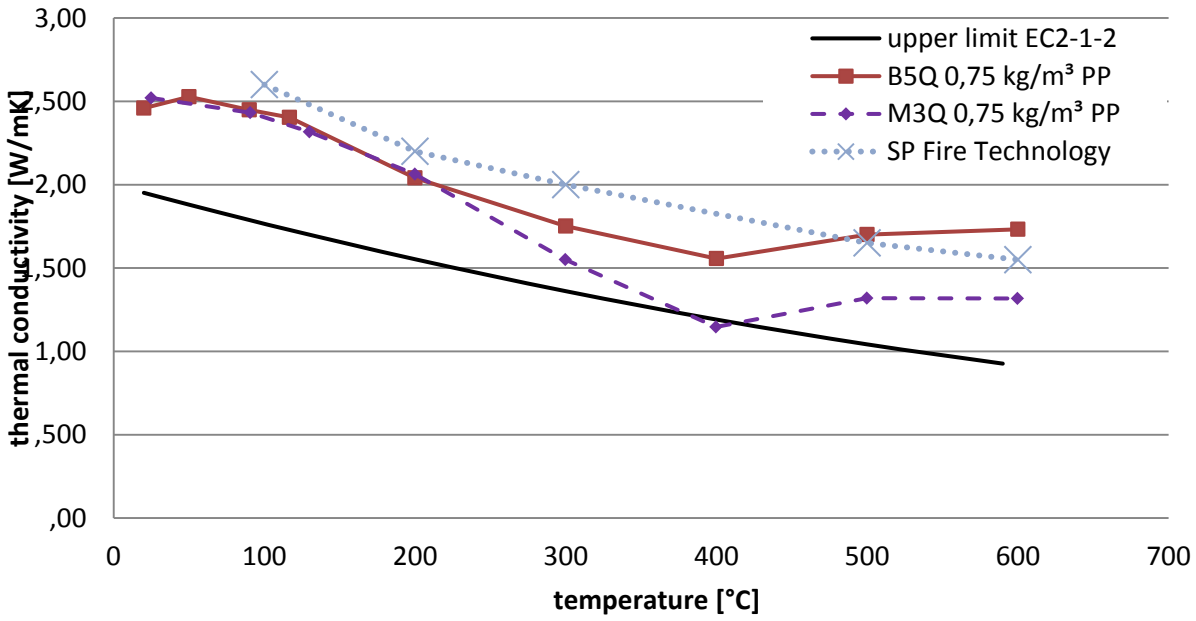

Figure 4: TPS measurements: temperature-dependent thermal conductivity of B5Q and M3Q with fibers content 0,75 kg/m³ (0,08 Vol.-%); for comparison upper limit for normal strength concrete according to EC 2-1-2 [1] and measurements at SP Fire Technology [4] for high strength concrete.

Specific heat capacity

When using the TPS method, it is necessary to stabilize the temperature exactly within the specimen and the sensor. Due to the resulting dwell time the energetic effects of the chemical reaction or evaporation of free and bonded water are not detected. In addition to the TPS method, DSC measurements (dynamical difference calorimetry) are carried out according to DIN 51007 [5]. In this context the so-called Saphir method is used which enables the determination of the specific heat capacity up to temperatures of 600 °C. In the following the results of the DSC measurement concerning B5Q and M3Q with PP fibers content 0,75 kg/m³ (Vol.-%) are depicted and discussed (see figure 5).

Reaching a temperature of 100 °C, a distinctive heat capacity peak becomes evident resulting from the free and physically bound water. The peak at 450 °C is based on the decomposition of portlandit and the smaller one at 570 °C on the quartz' lattice changes [6].

The data dimensions in EC 2-1-2 [1] are comparable, although they contain the peaks of the physical and chemical processes in a simplified way in form of calculation values.

The temperature-dependent mass loss of UHPC can be measured by thermogravimetric analysis (TGA) according to DIN 51006 [7]. By neglecting the change of volume under temperature exposure, the TGA values can directly be transferred into a model for the mass per unit volume. Figure 6 shows the related mass per unit volume of B5Q und M3Q with 1,50 kg/m³ (0,16 Vol.-%) fibers content in comparison with normal concrete of EC 2-1-2 [1]. At the age of around 100 days B5Q has an absolute mass per unit volume of 2500 up to 2600 kg/m³ and M3Q of 2300 up to 2400 kg/m³. In EC 2-1-2 [1] a somewhat lower mass per unit volume of 2300 kg/m³ is used for concrete with silicious aggregate.

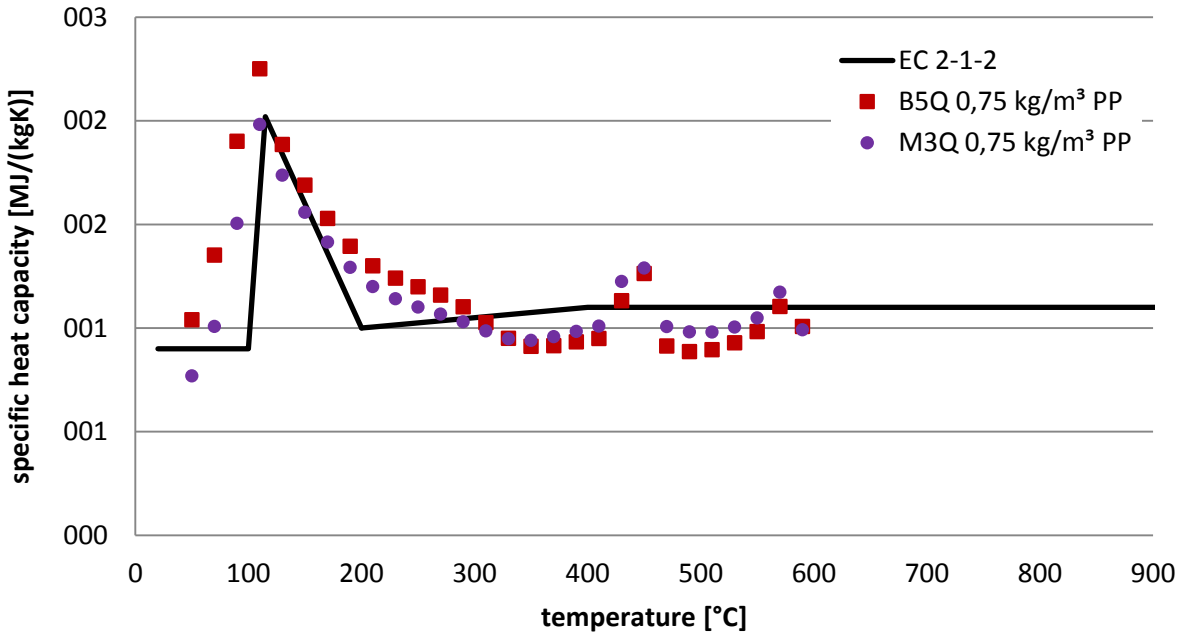

Figure 5: DSC measurements: specific heat capacity of UHPC; B5Q and M3Q mixtures with 0,75 kg/m³ (0,08 Vol.-%) fibers content.

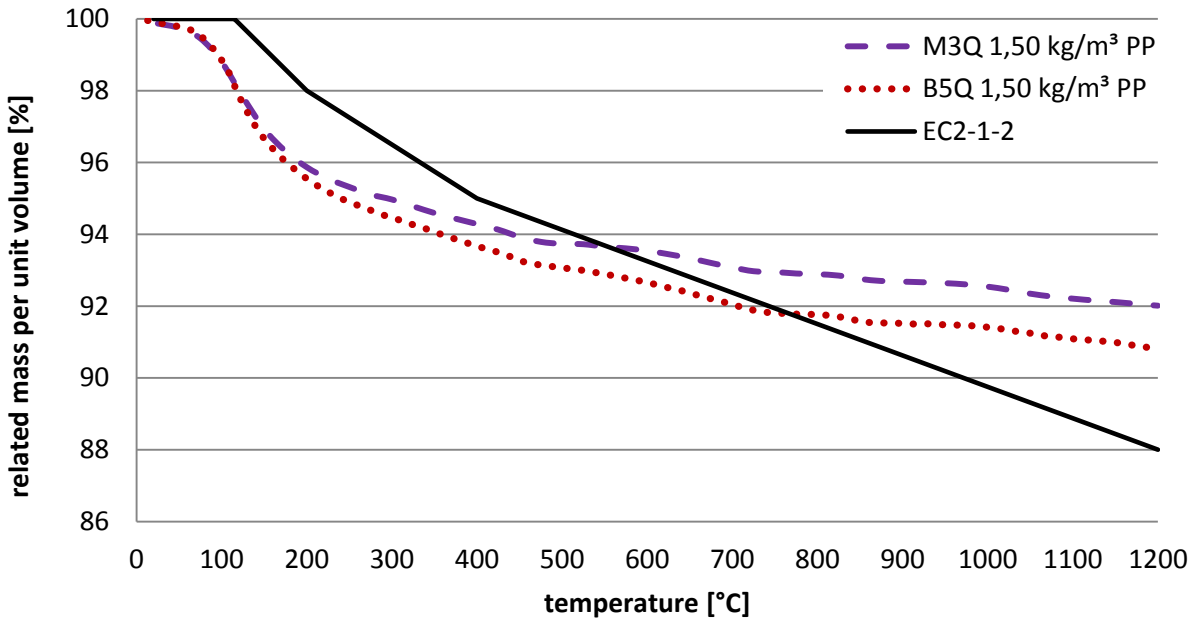

Figure 6: TGA measurements: related mass per unit volume of UHPC; B5Q and M3Q mixtures with 0,75 kg/m³ (0,08 Vol.-%) fibers content.

5 Mechanical material properties

In order to determine the temperature-dependent mechanical material properties, three different test types in accordance with [8] are used. At test type I, the steady-state test, specimens are analyzed at constant temperature and increasing load until failure occurs. This is followed by strain measurement. In regard to test type II, specimens are under constraint concerning their strain. The constraint forces are measured during heating up. The so-called unsteady-state high temperature creep tests form test type III. Here specimens are heated up at a constant load until failure occurs, again followed by deformation measurement. This test type has a major importance for fire behavior of structural elements because it reflects the real load situation best. The steady-state tests must not be used directly for calculating the components

deformation in case of fire, because they do not consider the high temperature creep. For this purpose, the unsteady-state tests according to test type III are stringently required.

Test execution

At first, steady-state tests were run (test type I) to obtain information about strength reduction with increasing temperature. Concrete specimens were heated up with a constant heating rate of 4 K/min up to test temperatures of 50, 100, 150, 200, 300, 400, 500, 600, 700 and 800 °C. After reaching the test temperature, the concrete specimens were loaded three times force-controlled with a loading rate of about 0,5 N/mm^2s^{-1} up to a maximum of about 30 % of the expected temperature-dependent strength. After this, loading was increased deformation-controlled until failiure. By the use of the deformation-controlled loading it was possible to examine the beginning of post-cracking behavior, too.

The illustration in figure 7 shows that strength decreases until 100 °C, then increases again until 300 °C before decreasing continuously at temperatures higher than 400 °C. This figure shows UHPC's maximum strength in comparison with measured data on high strength concrete and the calculation values according to EC 2-1-2 [1] for normal strength concrete and for high strength concrete C90/105. It is recognizable that strength decrease until 100 °C of UHPC happens faster, whilst the calculation values for the strength of normal strength concrete, remain constant at this level. The strength loss between 20 °C and 200 °C is similar for high strength concrete, both in standardized calculation values according to EC 2-1-2 [1] and in experimental results according to [9]. Whereas strength of both normal strength concrete and high strength concrete decreases continuously, UHPC's strength remains on baseline value up to a temperature of 400 °C and decreases just at higher temperatures.

In this context it is important that the strength model according to EC 2-1-2 [1] gives calculation values, which do not have to coincide absolutely with the actually measured values. Especially at temperatures above 400°C the measured strength reduction of UHPC is considerably less than strength reduction of normal strength concrete and high strength concrete. For example, the strength of UHPC at 600 °C is still 90 % of the strength at normal temperature whereas the strength of normal strength concrete has already decreased to less than 50 %.

With regard to the strength determined by steady-state tests at 20 °C, the unsteady-state tests are implemented with load levels of 0 %, 10 %, 20 %, 30 %, 40 %, 50 %, 60 % und 70 %. The test specimens are installed in the testing device. Then, the load is increased deformation-controlled to the requested load level. Holding this level constant, the temperature in the furnace is increased with a heating rate of 4 K/min until specimen's failure. During the test strain and compression are measured and documented continuously. The test results for the UHCP mixture B5Q are depicted in figure 8. The temperature-elongation curve with load level 0 % displays the temperature-dependent thermal elongation. The other curves in figure 8 show that the thermal elongation is compressed to some extent at higher load levels. As already mentioned, these data are the main base for the formulation of stress-strain relationships including thermal creep.

The comparison with the calculation values for normal strength concrete in figure 9 makes clear that thermal strain of UHPC is considerably smaller. As a consequence, the internal stress of UHPC resulting from different thermal elongations is less in areas near the cross-section edges and the inner cross-section as comparable to normal strength concrete.

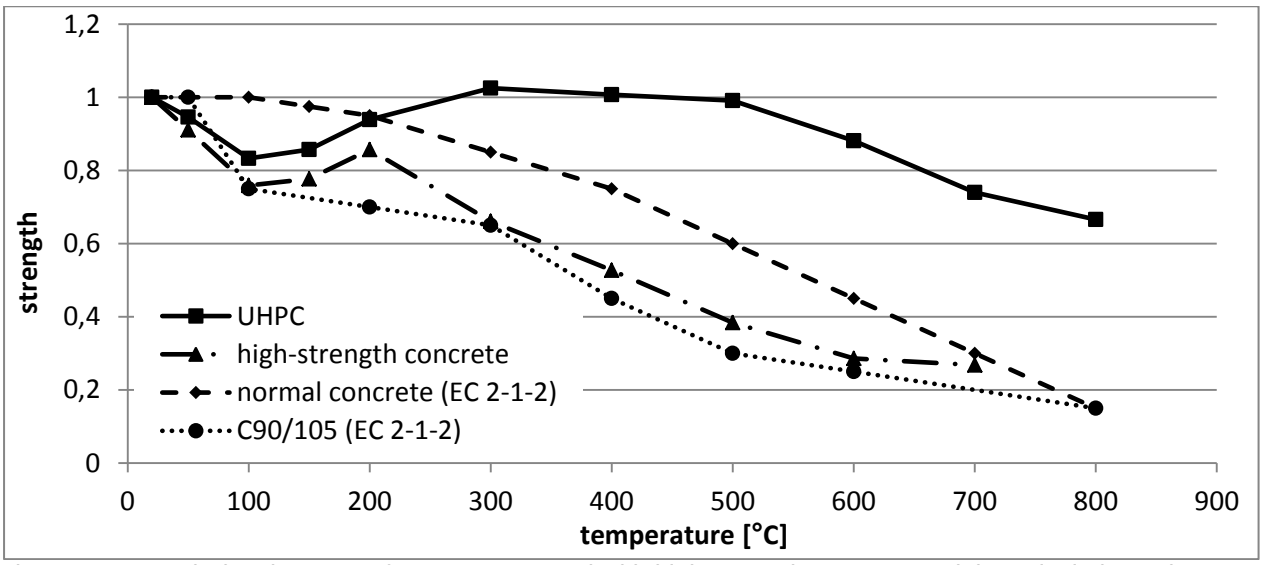

Figure 7: Strength development of UHPC compared with high strength concrete and the calculation values according to EC 2-1-2 [1].

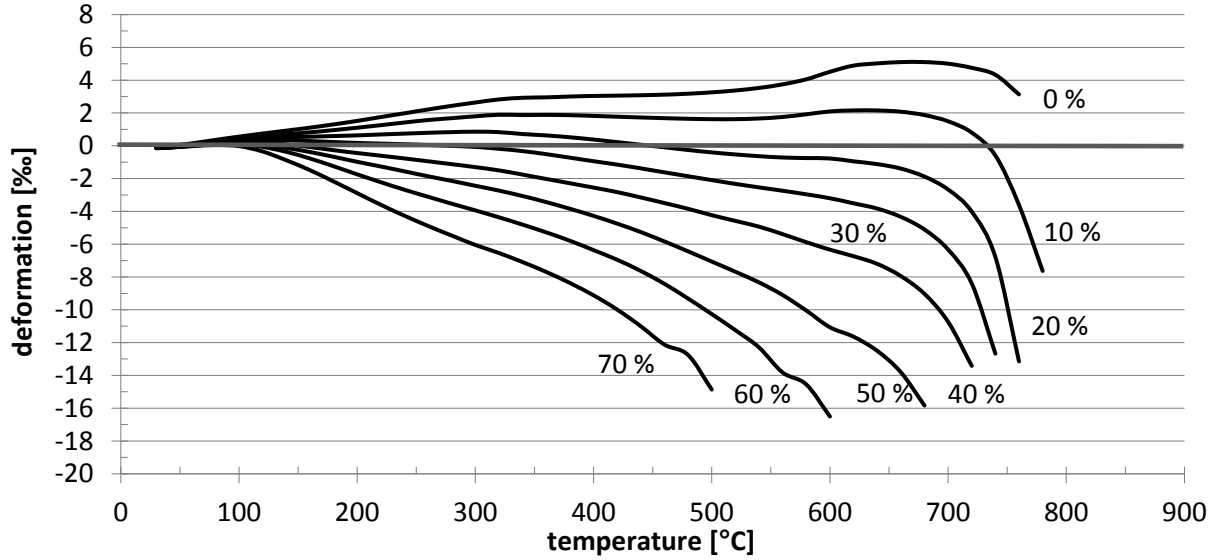

Figure 8: Related total deformation of the test specimens in unsteady-state tests using B5Q.

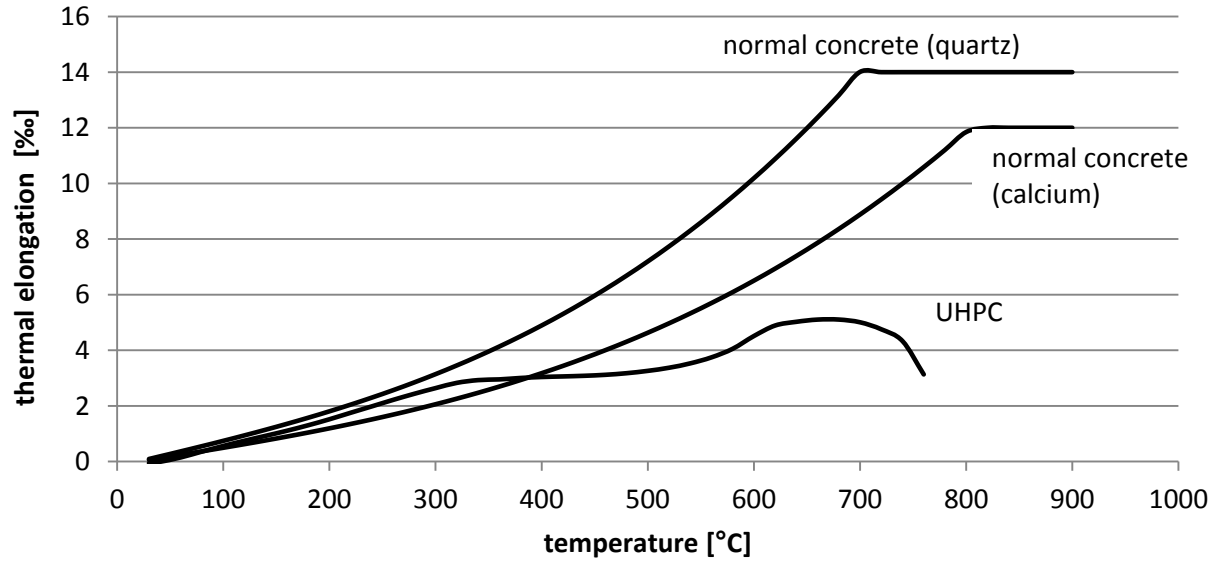

Figure 9: Comparison of measured thermal elongation of B5Q with calculation values according to EC 2-1-2 [1].

6 Outlook

The experimental studies concerning thermal and mechanical material properties of UHPC will be finished in the first half of 2012. Based on the experimental results calculation models for the temperature-dependent thermal and mechanical material properties will be derived. The thermo-mechanical material behavior of UHPC will be described by temperature-dependent stress-stain curves analogously to Eurocode 2 part 1-2, which can be implemented easily in so-called general caluculation methods, i. e. common finite element computer programs for the simulation of the load and deformation behavior of structural members and systems exposed to fire. With such a computer program enhanced by the developed models for thermal and thermo-mechanical material behavior of UHPC a column will be designed for a fire resistance rating of R 90. Afterwards real scale standard fire tests will be performed with such columns in order to check and validate the calculation models as well as the computer program.

7 Special Thanks

The authors would like to acknowledge the German Research Foundation (DFG) for the support of the research project „Theoretische und experimentelle Untersuchungen zur Ermittlung und Optimierung des Brandverhaltens von ultra-hochfestem Beton“(`Theoretical and experimental studies for determining and optimizing the fire behavior of ultra high performance concrete`) in the priority program 1182.

References

[1] DIN EN 1992-1-2:2010-12 – Eurocode 2: Design of concrete structures – Part 1-2: General rules – Structural fire design; German version EN 1992-1-2:2004 + AC:2008.

[2] DIN 4102-4:1994-03 – Brandverhalten von Baustoffen und Bauteilen (engl.: fire behavior of building materials and structural members) – Teil 4: Zusammenstellung und Anwendung klassifizierter Baustoffe, Bauteile und Sonderbauteile.

[3] DIN EN ISO 22007-2: Plastics – Determination of thermal conductivity and thermal diffusivity – Part 2: Transient plane heat source (hot disc) method.

[4] Jannsson, R.: Measurement of thermal properties at elevated temperatures – Brandforsk project 328-031. SP Fire Technology, SP Report 2004:46.

[5] DIN 51007:1994-06 – Thermische Analyse (engl.: thermal analysis) (TA); Differenzthermoanalyse (engl.: differential thermal analysis) (DTA); Grundlagen.

[6] Diederichs, U.; Jumppanen, U.-M.; Penttala, V.: Behaviour of high strength concrete at high temperatures. Helsinki University of Technology, Department of Structural Engineering, Report 92.

[7] DIN 51006:2005-07 – Produktabbildung – Thermische Analyse (TA) (engl.: picture of the product – thermal analysis) – Thermogravimetrie (TG) (engl.: thermogravimetric analysis) – Grundlagen.

[8] Kordina, K.; Meyer-Ottens, C: Beton Brandschutz-Handbuch (engl.: handbook of fire protection for concrete structure); 1. Auflage; Beton-Verlag GmbH; 1981.

[9] Huismann, S.: Materialverhalten von hochfestem Beton unter thermomechanischer Beanspruchung (engl.: material properties of high strength concrete under thermo mechanical exposure); Dissertation Technische Universität Wien; 2010.

Failure Mechanisms of UHPC Components under Explosive Loading

Oliver Millon, Werner Riedel, Christoph Mayrhofer, Klaus Thoma
Fraunhofer-Institute for High-Speed Dynamics, Ernst-Mach-Institut, EMI, Freiburg, Germany

The paper reports about the material behavior of ultra-high performance concrete (UHPC) at extreme loads. Dynamic properties are analyzed and compared to standardized concretes. Moreover, the failure behavior of a UHPC with low fiber content is investigated under different strain rates analyzing the macroscopic and microscopic damage. Hopkinson-Bar experiments enable to determine dynamic properties at strain rates up to 180 1/s. High values for the tensile strength and the fracture energy can be observed with a strong strain rate effect for the tensile strength. The dynamic fracture energy increases with 10000 N/m around 26 times compared to conventional concrete and shows a considerable higher resistance under detonative loads with extended micro-cracking and reduced global damage. The paper provides both a short characterization of UHPC tensile properties and failure analysis of UHPC and conventional concrete slabs and columns under blast loads and contact detonations.

Keywords: ultra-high performance concrete, Hopkinson-Bar, dynamic tension, failure mechanisms

1 Introduction

Future buildings tend to be higher and more filigree constructions. Especially buildings of economic, political and societal importance buildings have to be designed against extraordinary load-cases, coming from explosions or impacts from terrorist attacks or accidents. In this focus not only building materials with high static loading capacity, but also with high dynamic resistance are needed to allow sufficient resilience.

Ultra-high performance concrete (UHPC) is one of the youngest materials within concrete research and hence still under investigation concerning static, dynamic and long-time behavior. First results are reported in [1], [2]. The dynamic behavior is rarely described in the literature [3], [4], [8], [9] until today. Its investigation not only offers new applications in the construction of, e.g., high-rise buildings, long-span bridges and constructions in aggressive media but also an application as a protective material. This paper focuses on the behavior at high strain rates of shock induced load-cases.

1.1. Mixture and static reference properties of UHPC

Ultra-high performance concrete is a cement-based material, which uses high strength cement, high strength aggregates and a large portion of fine aggregates (
Table 1).

The low water-cement ratio (0.2) leads to a very compact matrix. The well aligned grain-sizes of the aggregates down to the nanoscale result in a high packing density with a low porosity and a low permeability. The addition of high strength and ductile fibers to the otherwise brittle plain material increases its ductility significantly.

Table 2 shows the essential static properties for three UHPC mixtures with different fiber content (0.0 Vol.-%, 1.0-Vol.-% and 2.5 Vol.-%). These mixtures of the applied coarse-aggregate UHPC have been established and statically tested by the University of Kassel, Department of Civil Engineering [1]

All investigated mixtures show a static compressive strength far above 100 MPa. The growing fiber content leads to an increase of all resistance parameters with the most significant effect on

the fracture energy. A low fiber-content of 1.0 Vol.-% is sufficient to bring a strong enhancement. As for any concrete, the tensile strength is low compared to the compressive strength, however reaches higher values for UHPC compared to standardized mixtures.

Table 1: Concrete Mixture of UHPC B4Q with 1.0 Vol.-% steel fibers.

Components	**UHPC 1.0 Vol.-%**
	Mass [kg*m^{-3}]
Cement CEM I 52.5 R	660
Water	162
Basalt-split	612
Quartz-sand	363
Fine quartz	463
Silica fume	180
Superplasticizer	30
Steel-fibers	78

Table 2: Static material properties of UHPC with various steel-fiber content.

	Young's modulus [MPa]	**Compression strength [MPa]**	**Tensile strength [MPa]**	**Fracture energy [N*m-1]**
UHPC 0.0 Vol.-%	52700	153	5.9	100
UHPC 1.0 Vol.-%	53000	166	6.6	10300
UHPC 2.5 Vol.-%	59600	208	10.3	13900

2 Dynamic investigation of low fiber reinforced UHPC

Concretes are highly strain rate-dependent. Many researchers reported about different failure-mechanisms and increasing strength values in case of dynamic loads on conventional and high-performance concrete [5], [6] and [7]. An investigation of the stain rate dependency of UHPC is required as well, to understand the material behavior under extreme loads. For that, a complete analysis of the material is required. The following passages describe laboratory experiments and scaled experiments on structural elements to determine the essential dynamic tensile properties, carried out by Nöldgen and Millon [3], [4], [8] and to investigate the material behavior depending on different extreme load-cases.

2.1. Dynamic properties of UHPC

One possibility to determine dynamic material properties at high strain rates is the application of Hopkinson-Bar tests. In different testing configurations the most essential properties can be determined with high accuracy. The tensile properties are of highest interest, because the tensile strength is the weakest of the material which include the highest failure-potential. Spall experiments, are a well-based and accepted method investigating tensile behavior of brittle materials [5], [6], [7] at high strain rates.

Test-configuration

To investigate the cracking process of concrete under dynamic loads the spallation configuration, published in [5] and further established by Schuler [6], [7], makes it possible to observe the cracking process and to determine dynamic tensile parameters like Young's

modulus, tensile strength and fracture energy (Figure 1). Nöldgen and Millon [3], [4] investigated the dynamic tensile properties of the UHPC in a former study. For detailed information is referred to them.

Testing procedure and evaluation

The specimen is fixed on the end of the bar. A striker is shot on the other end, generating a loading pulse which propagates towards the sample. The loading pulse is transmitted into the specimen, propagates through it and reflected as release wave running back. Tensile stresses are generated in the specimen due to superimposition of the release wave from the free ends of the sample and the striker, leading to tensile states up to fragmentation (spallation). The determination of the dynamic Young's modulus (Equation 2) is based on the theory of wave-propagation in elastic materials.

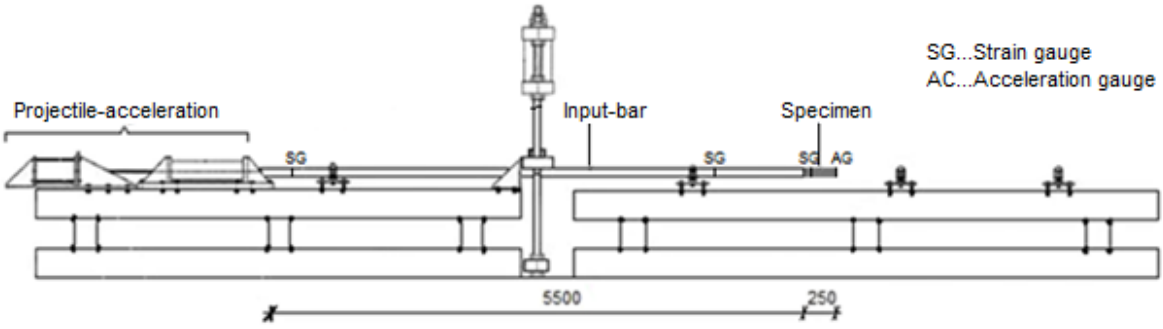

Figure 1 Schematic setup of the Hopkinson-Bar, spallation configuration.

$$C_L = \sqrt{\frac{E}{\rho}} \quad (1)$$

$$E_{dyn} = C_L^2 * \rho \quad (2)$$

C_L is the longitudinal wave-propagation velocity. ρ describes the material density.
Using the momentum conservation and the free surface approximation for the particle velocity, the tensile strength of a brittle material can be calculated as Equation 3.

$$f_{t,dyn} = \frac{1}{2} * \rho * C_L * \Delta u_{pb} \quad (3)$$

Additional to the parameters of the Young's modulus, the pull-back velocity Δu_{pb}, the velocity of the free surface, is required for its calculation.The dynamic fracture energy is required to lead the material to failure. It is calculated from the energy dissipation during spallation.

$$G_f = \int F d\delta = \int \frac{dI}{dt} * \delta' dt \quad (4)$$

$$G_f = \Delta v * m * \delta' \quad (5)$$

The determination of the fracture energy bases on the momentum transfer from one fragment to the other. The fragment velocities at the time of crack initiation are determined analytically by using the elastic wave theory. The velocities of the fragments during crack-opening are measured optically. Equation 5 calculates the fracture energy using the crack-opening velocity. δ' and the velocity reduction Δv of fragment 2 between crack initiation and total opening of the crack. The results of the dynamic experiments on the Hopkinson-Bar are shown in Table 3.
Table 3 shows that all dynamic material properties increase with growing fiber-content. A moderate increase from 50.6 to 56.6 GPa was found for the Young's modulus. No difference

was observed between static and dynamic values. The tensile strength shows a relevant increase for higher fiber-contents (1.0 Vol.-%: 42.7 MPa, 2.5 Vol.-%: 55.3 MPa). The fracture energy reveals a very strong rise by the addition of a low amount of steel-fibers (0.0 Vol.-%: 360 N/m, 1.0 Vol.-%: 10070 N/m) and a slower increase with further growing fiber-content. For unreinforced UHPC the fracture energy is, similarly to all concretes, very low. A very brittle behavior after reaching the ultimate load is the result, excluding an application of this material.

Table 3: Dynamic material properties for all analyzed ultra-high performance concretes.

	Density [kg*dm^{-3}]	Young's modulus [MPa]	Tensile strength [MPa]	Strain rate [s^{-1}]	Fracture energy [N*m^{-1}]
UHPC 0.0 Vol.-%	2374	50600	40.7	100 – 110	360
UHPC 1.0 Vol.-%	2456	53100	42.7	120 – 150	10070
UHPC 2.5 Vol.-%	2592	56600	55.3	130 – 150	11290

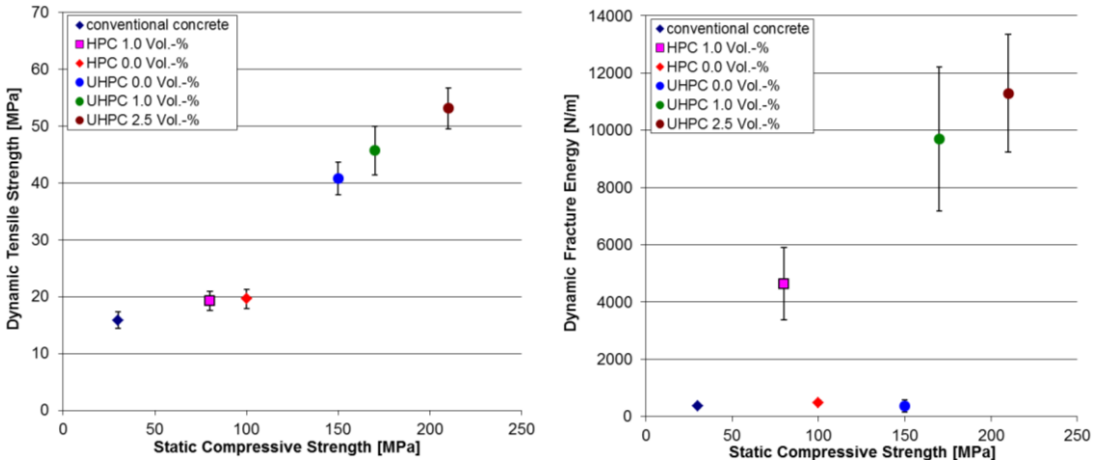

Figure 2: Development of the tensile strength and the fracture energy for different concrete qualities.

Figure 2 displays the development of the dynamic tensile strength (left) and the dynamic fracture energy (right) of UHPC compared to conventional and high performance concretes.

The Hopkinson-Bar experiments showed that all investigated properties of UHPC reach higher values than those of conventional concrete and high-performance concrete (

Table 4). The dynamic tensile strength is of special interest. UHPC shows a high dynamic tensile strength already for the plain material. A strong increase of the low fiber-reinforced UHPC compared to the HPC with the same degree and type of fiber reinforcement was observed.

The tensile strength of UHPC rises by more than the factor 2 up to 43 MPa. An increase in the fiber-portion up to 2.5 Vol.-% leads to a further and stronger rise. Compared to the conventional concrete the tensile strength of UHPC increases up to 3.5 times. The fracture energy of UHPC shows high values for any fiber-reinforced mixture. In comparison to HPC the mixture with low fiber-content shows similar behavior. A significant increase by the addition of steel fibers was found, although with 10070 N/m the value of UHPC is about 2 times higher.

The experiments pointed out that fiber-reinforced UHPC shows a higher resistance against dynamic loads (strain rates up to 1.8*10^2 1/s) than standardized concretes. The addition of high

strength and ductile fibers does not only lead to an increase of the ductility, but also to an increase of the strength and the fracture energy under static and dynamic loading.

*Table 4: Dynamic material properties of UHPC, HPC and conventional concrete (strain rate range: 2.0*101 - 1.8*102 1/s [3], [4]).*

Concrete	Young's modulus [MPa]	Tensile strength [MPa]	Fracture energy [N*m^{-1}]
Convent. concrete C 30/37	39600	15.5	380
HPC C 80/95–1.0 Vol.-%	43000	20.3	2600
HPC C 100/115–0.0 Vol.%	51400	19.8	480
UHPC 0.0 Vol.-%	50600	40.7	360
UHPC 1.0 Vol.-%	53100	42.7	10070
UHPC 2.5 Vol.-%	56600	55.3	11290

2.2. Dynamic experiments on scaled structural elements

To understand the behavior of the material under different loading conditions, it is important to know essential material properties, as shown in the previous section. However it is of the same importance to know the failure and to understand its mechanisms for the overall material description. Experiments on structural elements with the focus on comparative investigation of structural damage complete the extensive analysis begun in [3] and [4]. This chapter reports about scaled experiments on structural elements in three relevant dynamic loading configurations. First statements about failure mechanisms at high strain rates were given by the evaluation of the Hopkinson-Bar experiments [3], [4]. A multiple failure with the damage of the matrix, the aggregates and the bond between matrix and aggregates as well as between matrix and fibers can be observed. Figure 3 shows the corresponding computer-tomographic image of a UHPC fragment with its fracture surface.

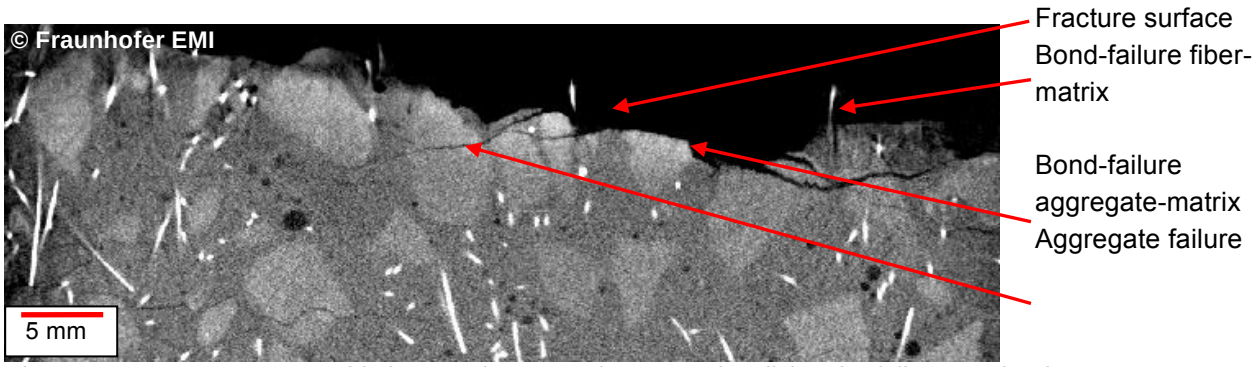

Figure 3: Computer-tomographic image of a UHPC fragment visualizing the failure mechanisms.

Contact detonation on concrete columns

Contact detonations lead to strong local damage. Components with a diameter of 150 mm and a length of 1500 mm were tested in the first series. Not only the macroscopic and microscopic damage of the compressive and the tensile failure zone, but also the residual strength after the dynamic load was analyzed.

Figure 4 shows the typical strong local damage of the element due to the contact detonation for UHPC and conventional concrete. On the loading side (

Figure 4, left), compressive failure through fragmentation and cratering occurs. Vertically oriented fractures with a large crack-width are visible. On the element's rear surface (

Figure 4, middle), tensile damage is shown. It is caused by the reflection of loading pulse on the element's free surface leading to tensile stresses. Fragmentation does not occur, however a large cracking-zone with some vertical macro-cracks and many arbitrarily oriented micro-cracks can be seen. A comparison to conventional concrete in Figure 4, right shows the advantage of UHPC. The element is strongly damaged – no remaining load-carrying cross-section is visible. The reduced damage of the UHPC column leads to a remaining cross section of 45 percent.
A quantitative analysis shows a significant higher residual strength of UHPC element compared to the elements in standardized concretes. In a static compression tests, the ultimate loads of the damaged and not damaged element are correlated, leading to the residual strength for UHPC of 26%, for HPC of 10% and for conventional concrete of 5% of the material specific undamaged compressive strength.

The computer-tomographic analysis in Figure 5 of fragments visualizes the failure mechanisms, which occur in this loading situation.

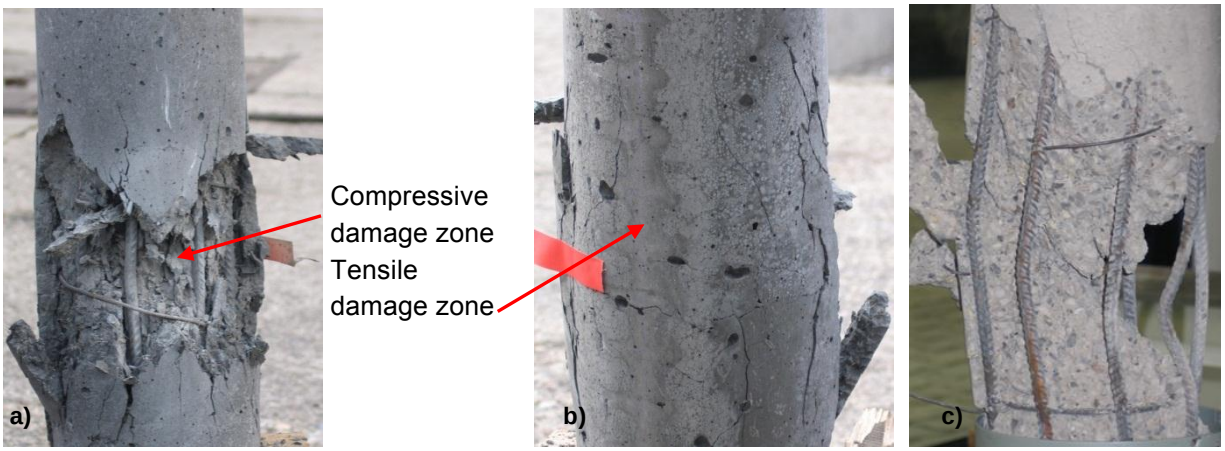

Figure 4: Damage of column in UHPC after contact detonation: a) loading side, b) rear side, c) damage of the column in conventional concrete.

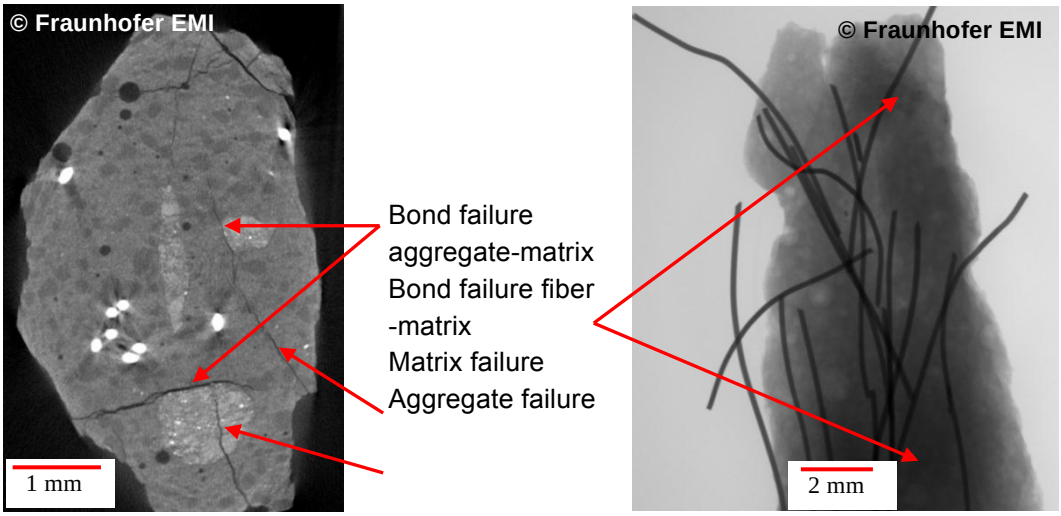

Figure 5: Computer-tomography image of UHPC fragments visualizing material failure.

Similar to the Hopkinson-Bar experiments multiple failure of the material is found under contact detonation as well. The detonative load leads to cracks in the matrix and in the aggregates. The bond between aggregate and matrix as well as between fiber and matrix is damaged. This

failure process consumes a large portion of loading energy, leading to higher resistance and lower global damages. The fibers transmit the forces across the cracks between the fragments. The extended micro-cracking is evidence for the positive influence of the fibers.

Close-in detonation on façade elements and blast loading on walls

The close-in detonation (1000 g PETN at 30 cm clear distance) causes a combined damage of local destruction (contact detonation) and bending (blast loading). Tensile stresses occur at the rear side of the element, as shown in Figure 6 for conventional concrete without fiber reinforcement (right) and UHPC (left and middle).

In conventional concrete the load leads to complete failure of the element. A much better resistance under the same loading shows the element in UHPC. Only cracks with a maximal crack-width of 0.5 millimeters (highlighted) are observed. An extended micro-cracking over the whole element appears, however fragmentation is avoided, concluding that the protective function of the element remains.

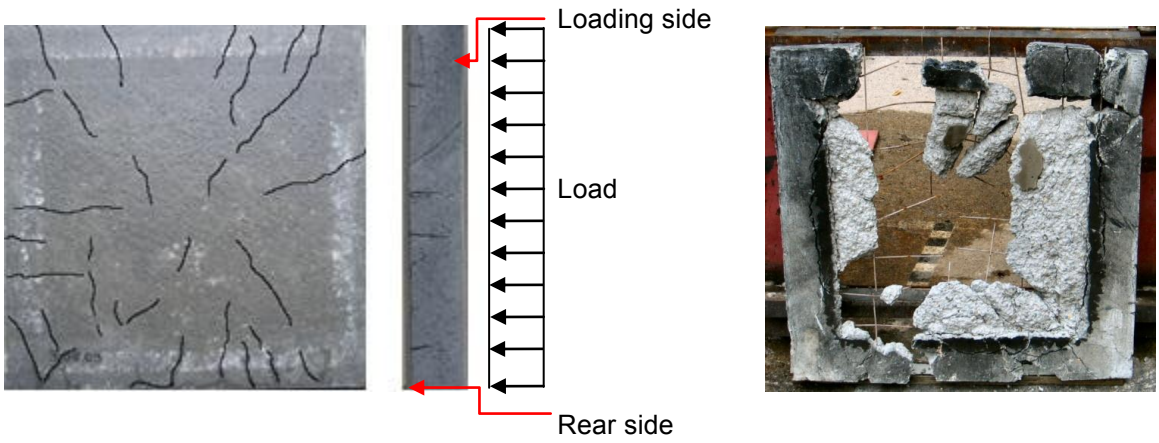

Figure 6: Damage of facade-elements after close-in detonation; left, middle: UHPC, right: conventional concrete. (constructive reinforcement (steel mat) with low degree of reinforcement for both elements)

Blast loads lead (p_{max}= 230 kPa, t_+=40 ms) to bending failure (bending crack in places of maximal deflection) of the structural elements. The behavior of UHPC walls against blast loads was investigated with shock tube tests. Figure 7 shows the damage of wall elements in UHPC (left) and conventional concrete (right) at the ultimate loading of the conventional concrete.

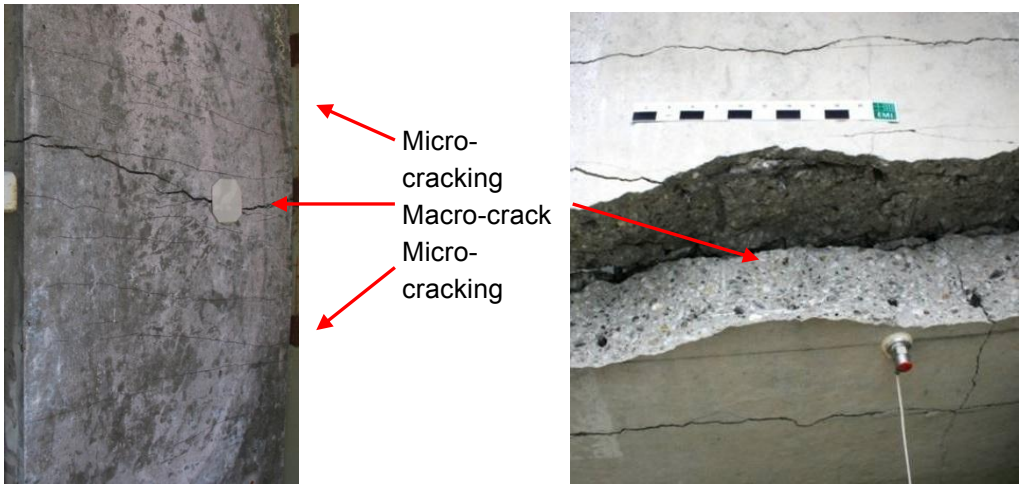

Figure 7: Damage of concrete elements after blast loading; left: UHPC, right: conventional concrete without fiber-reinforcement. (equal steel-bar reinforcement for both elements).

The primary crack opens in the element in conventional concrete on the place of the largest deflection. This leads to full destruction of the concrete and the reinforcing bars. The UHPC element shows a significantly lower damage. A primary crack and a large zone of horizontally oriented micro-cracks occur. The fibers show also in this load case a positive effect on the material behavior. Figure 8 shows a computer tomographic image of the primary crack and the corresponding fracture-surfaces for the determination of failure-modes in the micro-structure. Under blast loading multiple failure modes are observed again. Cracking of matrix and aggregates occurs. Bond failure between fibers and matrix and between aggregate and matrix is identified. Pulled out fibers and corresponding fiber channels were visualized in Figure 8. In a microscopic analysis the fibers appear to be intact, no non-reversible deformation or break occurs. Bond failure occurs confirming static analyses and the assumptions from the Hopkinson-Bar-Tests [3,4].

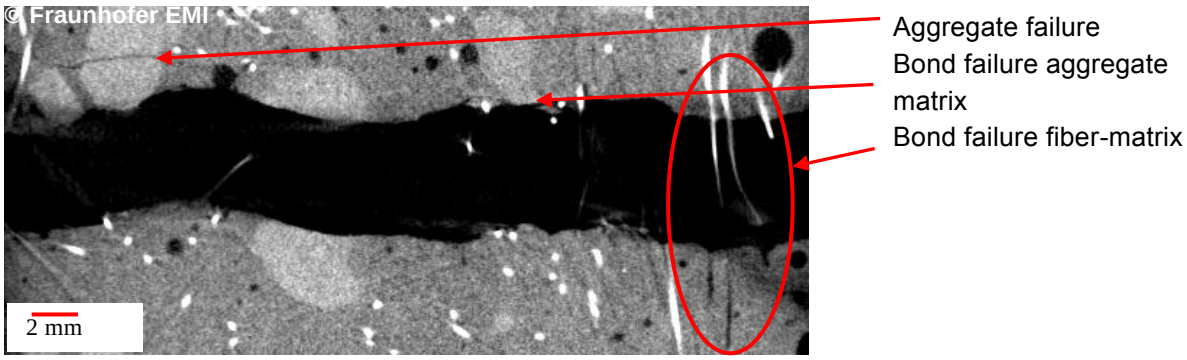

Figure 8: Computer-tomography: detail of macro-crack (due to bending in blast load).

Results of the experiments on structural elements

The experiments on structural elements in UHPC and their comparison to lower-strength concretes show a remarkable increase in resistance of UHPC against relevant shock induced loads. A low fiber-content is sufficient to reach the positive effects stated above. Lower material-damages (crack-width and crack-depth) and higher residual strength are the main results in all analyzed dynamic load-cases. The extent of local compressive and tensile damages in case of contact detonation is reduced. Instead of macro-cracking, a large zone of micro-cracks was observed. In close-in detonation and under blast loading a large micro-cracking occurs as well, leading to reduced global damage of the elements. This positive behavior is due to the addition of high strength fibers, increasing the energy-absorption and improving ductility and coherence of the material.

UHPC shows multiple failure mechanisms, a significant difference to conventional concrete. The most important and high energy consuming failure mode is the bond failure between fibers and matrix. As well failure of the matrix, of the bond between aggregate and matrix and the failure of aggregates are found. A good bond between aggregates and fibers with the matrix, the reason for the good behavior, results from the use of fine and high strength aggregates and a reduced water-cement ratio, leading to a dense and high strength matrix.

3 Discussion and Summary

The article reports about dynamic investigations on fiber reinforced UHPC. Results of the essential dynamic tensile properties, former investigated in Hopkinson-Bar tests, were stated. With growing fiber-content, the investigated material parameters Young's modulus, tensile strength and fracture energy increase – moderate for the Young's modulus (50.6 to 56.6 GPa) and significant for the fracture energy (360 to 11290 N/m). The tensile strength of the non-

reinforced mixture is up to 2.7 times higher than that for conventional concrete under dynamic load and reaches for UHPC 41 MPa. In comparison to high-performance concrete, the tensile strength raises by the factor 2.1 times up to 43 MPa for low fiber reinforced mixtures and up to 55 MPa for highly reinforced UHPC. The fracture energy rises significantly by an addition of a low fiber portion for both HPC and UHPC. However UHPC reaches up to 2 times higher values compared to HPC.

The qualitative analysis showed that the addition of steel-fibers leads to a higher ductility. Furthermore, the structural damage is reduced, which increases the resistance of UHPC in all analyzed load-cases. The addition of steel-fibers is responsible for the improved resistance. Extended micro-cracking and a reduction of macro-cracks is the consequence leading to larger zones of lower damage. Low fiber-reinforced UHPC shows reduced damage with no fragmentation under contact detonation. Multiple failure mechanisms of UHPC are found in all shock induced load-cases. Fiber pull-out was proven and identified as an important failure-mode, consuming large amounts of deformation energy.

Resulting from these investigations UHPC is a material with an improved resistance which shows a strong potential for protecting buildings against extreme loads.

References

[1] Fehling E. et al.: Entwicklung, Dauerhaftigkeit und Berechnung Ultra-Hochfester Betone (UHPC). Schriftreihe Baustoffe und Massivbau, Heft 1, Kassel: Universität Kassel, 2005, ISBN 3-89958-108-3

[2] Schmidt M. et al.: Sachstandsbericht Ultrahochfester Beton. Berlin: DAfStb Heft 561 (2008), ISBN 3-410-65045-4

[3] Nöldgen, M.: Modeling of Ultra High Performance Concrete (UHPC) under Impact Loading – Design of a High Rise Building Core against Aircraft Impact, Forschungsergebnisse aus der Kurzzeitdynamik, Fraunhofer Verlag, Heft 19, ISBN 978-3-8396-0286-7, 2011

[4] Millon O., Riedel W., Thoma K., Nöldgen M., Fehling E.: Fiber-reinforced ultra-high performance concrete under tensile loads. 9th International Conference on the Mechanical and Physical Behavior of Materials under Dynamic Loading DYMAT, conference proceedings, Brussels, 2009

[5] Klepaczko J.R., Brara A.: An experimental method for dynamic tensile testing of concrete by spalling. IJIE 25 (2001): 387 – 409

[6] Schuler H.: Experimentelle und numerische Untersuchungen zur Schädigung von stoßbeanspruchtem Beton. epsilon – Forschungsergebnisse aus der Kurzzeitdynamik, Heft 6, Freiburg i. Br.: Fraunhofer-Institut für Kurzzeitdynamik, EMI, 2004, ISBN 3-8167-6463-0

[7] Schuler H., Mayrhofer C., Thoma K.: Spall experiments for the measurement of the tensile strength and fracture energy at high strain rates. IJIE 32 (2006) 10: 1635 – 1650

[8] Nöldgen, M., Millon, O. Thoma, K., Fehling, E.: Hochdynamische Eigenschaften von Ultrahochleistungsbeton (UHPC), Beton und Stahlbetonbau 104 (2009) 11

[9] Rebentrost M., Gavin W.: Behaviour and Resistance of Ultra High Performance Concrete to Blast Effects, Structural Materials and Engineering Series, Vol. 10, Proceedings Second International Symposium on UHPC, March, 05-07, 2008, University of Kassel, 2008

Ultra High Performance Concrete Structures under Aircraft Engine Missile Impact

Markus Nöldgen[1], Ekkehard Fehling[2] ,Werner Riedel[3], Klaus Thoma[3]

1: Schüßler-Plan Engineering, Düsseldorf / Cologne University of Applied Sciences (CUAS), Germany
2: Institute of Structural Engineering, University of Kassel, Germany
3: Fraunhofer Institute for High-Speed Dynamics, Ernst-Mach-Institute, Freiburg, Germany

The impact of an aircraft engine missile causes high stresses, deformations and a severe local damage to conventional reinforced concrete. As a consequence the design of R/C protective structural elements results in components with rather large dimensions.
Fiber reinforced Ultra High Performance Concrete (UHPC) combines an ultra high strength and an improved ductility with a significantly increased energy dissipation capacity due to the addition of fiber reinforcement. With those attributes the material is potentially suitable for improved protective structural elements with reduced dimensions and reduced need for material resources.
The submitted paper presents the results of a series of scaled aircraft engine impact experiments with reinforced UHPC panels. The investigations are focused on the material behavior and the damage intensity in comparison to conventional concrete. The fundamental work of Sugano et al. [12] with R/C elements is taken as reference for the evaluation of the results. The impactor model of a Phantom F4 GE-J79 engine developed and validated by Sugano et al. is used as defined in the original work. In order to achieve best comparability, the experimental configuration and method are adapted for the UHPC experiments. With 'penetration', 'scabbing' and 'perforation' all relevant damage modes are investigated so that a full set of results is provided for representative UHPC structural configurations applicable for example in secure high-rise buildings or nuclear facilities.

Keywords: UHPC, Aircraft Impact, Ballistic Limit, Dynamic Behavior, Steel Fibres

1 Introduction

In the early 1990s an extensive experimental series of reinforced concrete panels subjected to aircraft engine impact was conducted and published by Sugano et al [12]. Motivated by a full scale aircraft impact test the authors systematically investigated the engine impact separately as it had caused the deepest local penetration of all aircraft components in the massive concrete target. In order to be able to investigate a large variety of parameters of protective reinforced concrete structures it was necessary to find an appropriate model for the aircraft engine. Against this background the development of a deformable lumped mass-spring model in full scale engine impact tests was an important achievement as it provided the possibility to properly account for the energy dissipation capacity of the missile. The experiments with the new model led to appropriate results with respect to the energy balance and local damage of the structural panels. In addition to full scale tests an extensive series of engine impact tests was conducted in scales 1:2,5 and 1:7,5. It was shown that scaled impact tests lead to satisfying quantitative results as long as physical scaling laws are considered properly. This important finding enabled the authors to extend their investigations on smaller testing facilities in laboratories to vary more parameters of protective structural elements.

The variations in [12] included bending and shear reinforcement ratio, panel thickness, additional steel liners and the concrete´s compressive strength. The latter parameter was varied from 23.5 MPa to 35.3 MPa. In the past 20 years concrete technology has improved significantly in various directions such as self-compacting concrete, ductile concrete and high-strength concrete. Fiber reinforced Ultra High Performance Concrete (UHPC) potentially provides decisive improvements as a material for protective structural elements as it combines an ultra high strength, an improved durability and a high energy dissipation capacity –

increased by two orders of magnitude - with the well known advantages of R/C-materials in pre-fabricated and on-site construction applications (see table 1).

Table 1: UHPC material properties [1,3].

Material Parameter	Concrete		UHPC	
Compressive Strength	35	[MPa]	180 -200	[MPa]
Tensile Strength	3,5	[MPa]	9-13	[MPa]
Fracture Energy	100	[N/m]	10000-12000	[N/m]
Dyn. Tensile Strength*	18-21	[MPa]	41-55	[MPa]
Dyn. Fracture Energy*	300	[N/m]	10000-12000	[N/m]

Note: * Dynamical material properties at a strain rate ~10^2 1/s [4,10]

Based on these promising material parameters of UHPC a series of experiments was conducted to substantiate recent developments in structural safety concepts for high-rise buildings and nuclear power plants.

2 UHPC under Aircraft Engine impact - Experimental Series

A gas gun with 90mm caliber, shown in figure 1 right, is used to accelerate the missile. A laser sensor barrier is located immediately behind the barrel to measure the impact velocity (see figure 1 left). The impact process of the missile on the front side of the panel is recorded by a high-speed camera so that the deformation of the missile is documented by several high resolution pictures (see figure 2).

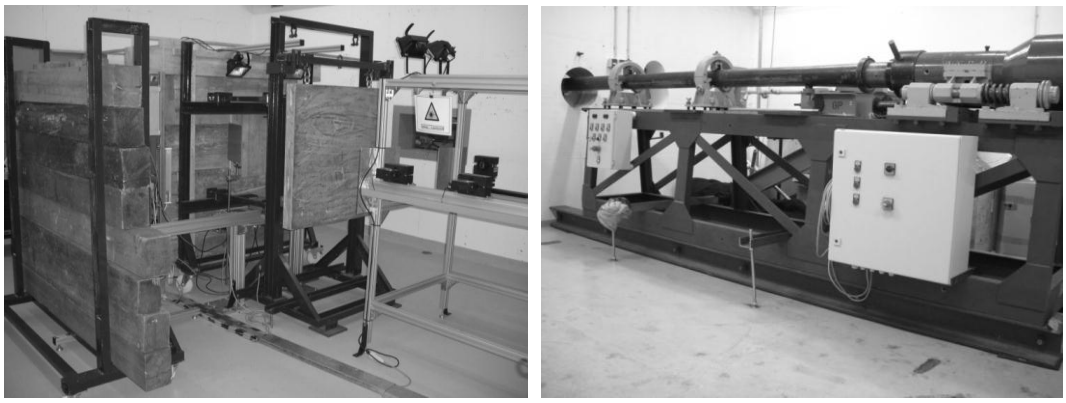

Figure 1: Impact test facility; left: UHPC Structure and Laser Sensor Barrier, Right: Compressive Air Launcher, Barrel Caliber 90mm [5,6].

A second high-speed camera records the rear side deformation and local damage of the panel. In case of a missile perforation the second camera is used to determine the residual velocity of missile parts as well as the velocity of concrete debris ejected from the rear surface. A “split view” allows for the examination of the panel rear side in a parallel and orthogonal view respectively.

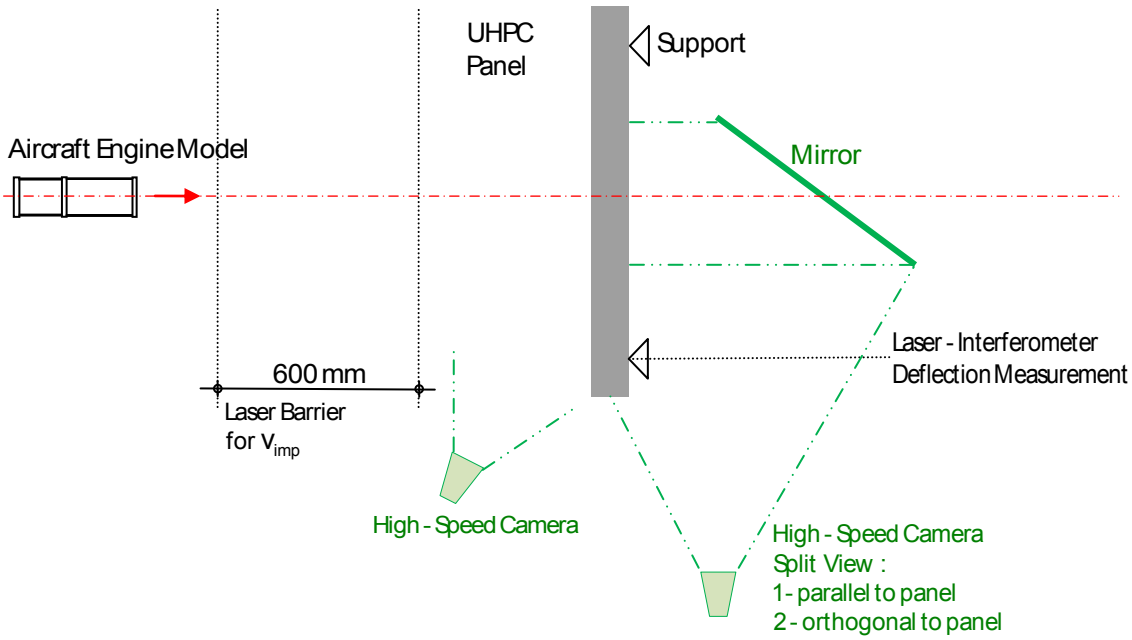

Figure 2: Experimental configuration: Scaled aircraft engine impact experiments on scaled reinforced UHPC panels (thickness 100mm) - measurement configuration.

Experimental Results

The experimental results are summarized in table 2 according to the terminology defined by Sugano et al. [12]. The “Penetration Mode” (C) is characterized by a front side penetration of the projectile and rear side hairline cracks in radial direction from the impact axes towards the outer edges of the panel. The “Scabbing Mode” (S) describes a front side missile penetration with concrete debris ejected from the rear side. The “Just Scabbing Mode” (JS) is a transition stage between “Penetration” and “Scabbing”. The “Just Perforation Mode” (JP) describes the state when the panel just prevents the missile from perforation while the “Perforation Mode” (P) finally defines the shear failure of the panel and the persistent missile motion with a measurable residual velocity. The last two damage modes define states immediately above and below the perforation of the panel characterized by a significant change in energy state.

Table 2: Summary of test results [8].

Exp.	Impact Velocity	Residual Velocity	Mode	Front Depth	Damage Width	Damage Height	Rear Side Remark	Rear Side Mode	Deformation Length
No.		[m/s]	[-]	[mm]	[mm]	[mm]	[-]	[-]	[mm]
1	194.7	-8.6 (Rebound)	C	<0.2	220	220	Hairline Cracks	Buckled	83
2	258.7	-7.3 (Rebound)	JS	7-12	260	260	Hairline Cracks	Buckled	56
3	320.0	0.0	JP	55	310	270	Concrete Debris	Crushed	28
4	332.0	11.1	P	-	250	310	Perforation	Crushed	28
5	248.9	-9.42 (Rebound)	JS	0.7	240	240	Hairline Cracks	Buckled	58
6	368.6	16.1	P	-	280	290	Perforation	Crushed	28

Note: * C: Penetration Mode, JS: Just Scabbing Mode, S: Scabbing Mode, JP: Just Perforation Mode, P: Perforation mode

The fiber reinforced Ultra High Performance Concrete panels show a reduced damage and penetration depth on the panel front side in comparison to normal strength concrete. Especially in Mode C and JS the missile leaves only but a “footprint” on the UHPC surface with local concrete surface damages ranging from 0.2 – 10mm depth. Beyond the footprint, there is no damage or cracking observed on the front side.

The local damage on the rear side of the UHPC panels is significantly different to normal strength concrete for all damage modes. In the Experiments 1, 2 and 5 a formation of radial hairline cracks with a maximum crack width of <0.2mm is observed. A limited area around the impact axes undergoes inelastic deformation normal to the panel surface of 2mm up to 12mm with increasing crack opening. However, the cracks are connected by intact steel fibers suppressing noticeable concrete debris and scabbing. In comparable damage modes for normal strength concrete scabbing occurs at a far lower stage of impact velocity.

With increasing impact velocity the inelastic shear deformation on the rear side of the panel increases until finally the fibers are completely pulled out at velocity 320m/s. The rear side bending reinforcement is subsequently activated as a membrane preventing the missile from perforating the panel as shown in figure 3 left. This mechanical effect was observed in the reference experiments as well but it occurred for conventional concrete at a far lower impact velocity of 219 m/s. Apart from the more than doubled energy dissipation capacity of the UHPC panel the damaged area is significantly smaller with UHPC (25%) as shown in figure 3 (middle and right).

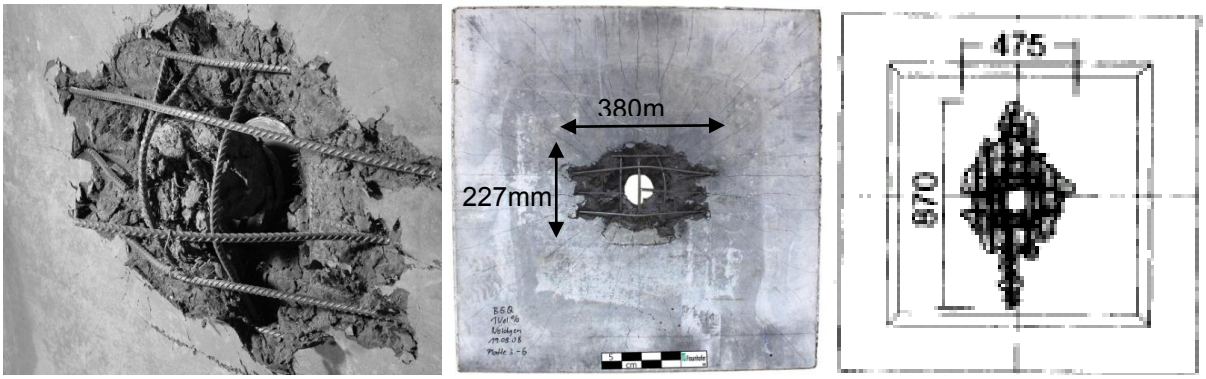

Figure 3: “Just Perforation Mode”: Left: Damage Modes of UHPC Panel vimpact=320 m/s [8], Middle: Missile stuck in UHPC Panel with highly deformed rear reinforcement (Scaled 1/10) [8], Right: Comparison to normal strength concrete panels (Scaled 1/7.5) in JP Mode vimpact=219 m/s [12].

The progress of missile deformation and residual velocity after perforation are studied in high-speed recordings of experiments No. 4 and No. 6. Figure 4 shows four sequences of the deformation process and the motion of a missile slice.

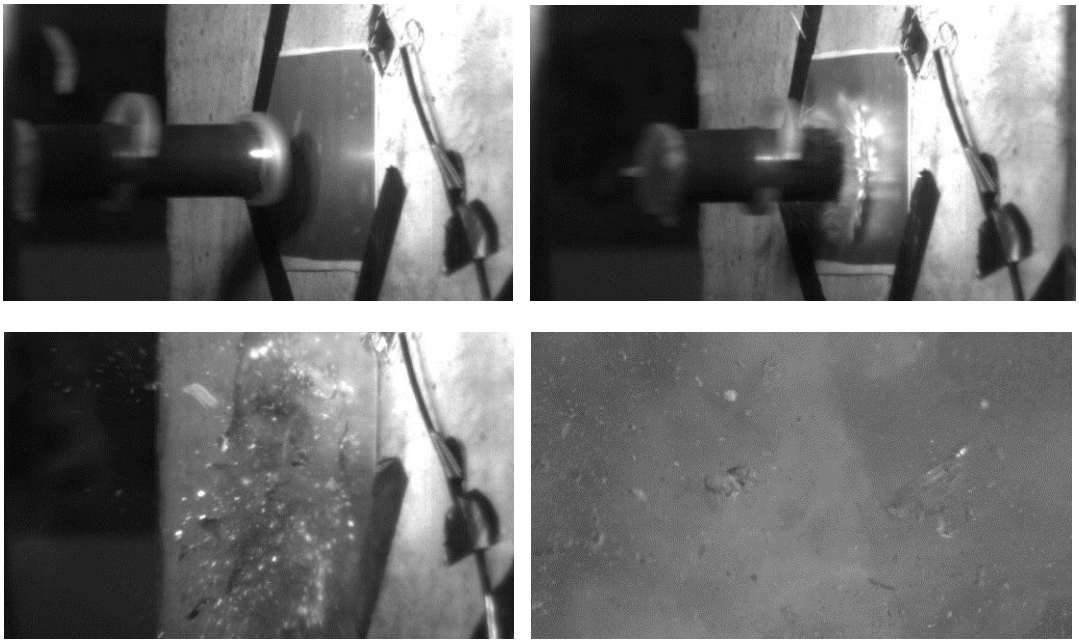

Figure 4: Sequences from the high-speed cameras on the panel front (1-3) and rear side (4) in experiment No. 4, "Perforation Mode" [8].

The analysis of the rear side rebars after the perforation in experiments No. 4 and No. 6 shows distinctive cross-section constriction of the rebars caused by yielding. Perforation finally occurs when the rear reinforcement fails with the exceedance of the maximum strain deformation of the rebars. Hence the observations in the reference experiments and theoretical failure analysis conducted by Schlüter [9] can be confirmed also for UHPC. The total shear resistance behavior of a reinforced concrete panel can be separated into a serial connection consisting of the material´s shear strength at low deformation stages and the reinforcement´s tensile strength thereafter up to ultimate perforation.

Ballistic Limit

In experiment No. 3 the ballistic limit of the UHPC panel against missile perforation is obviously just reached at an impact velocity of 320 m/s. A further increase of this velocity leads to a perforation of the panel in experiment No. 4. Figure 5 shows that there is a discrete jump in energy state around the area limited by the two stages JP and P. Small variations and deviations in material and panel properties usually lead to significantly different results as investigations with other materials and specimens show [11]. Hence this area is often called the Zone of Mixed Results (ZMR). In this zone the v_{50}-velocity is usually derived if a significant number of limit experiments is available. It denotes the velocity for which 50% of the experiments perforate and 50% of the projectiles are stopped. Another method to determine the state at which the panel just prevents a projectile from perforation is the ballistic limit formulated by Lambert and Jonas [2]. This method takes into account for at least two experiments with a perforation and according measured residual velocity of the missile. Through minimization of α in the parabolic equation (1) across the experimental results the ballistic limit v_{BL} can be determined. Even if the accuracy of the result increases with an increasing number of experiments K satisfying approximations have already been achieved with a number of two experimental values [11].

$$v_{res} = \begin{cases} 0 < v_{imp} < v_{BL} \\ \alpha \left(v_{imp}^{K} - v_{BL}^{K} \right)^{1/K}; v_{imp} \geq v_{BL} \end{cases} \quad (1)$$

Hence the presented experimental series provides two experiments with a missile perforation and the according measured residual velocity (see table 2). Despite the limited experimental basis, the limiting impact velocity v_{BL} in equation 5 results to 320,5 m/s which can be confirmed by the experimentally observed value in experiment No. 3. Figure 5 illustrates the function for the UHPC panels including the six individual results in the experiments.

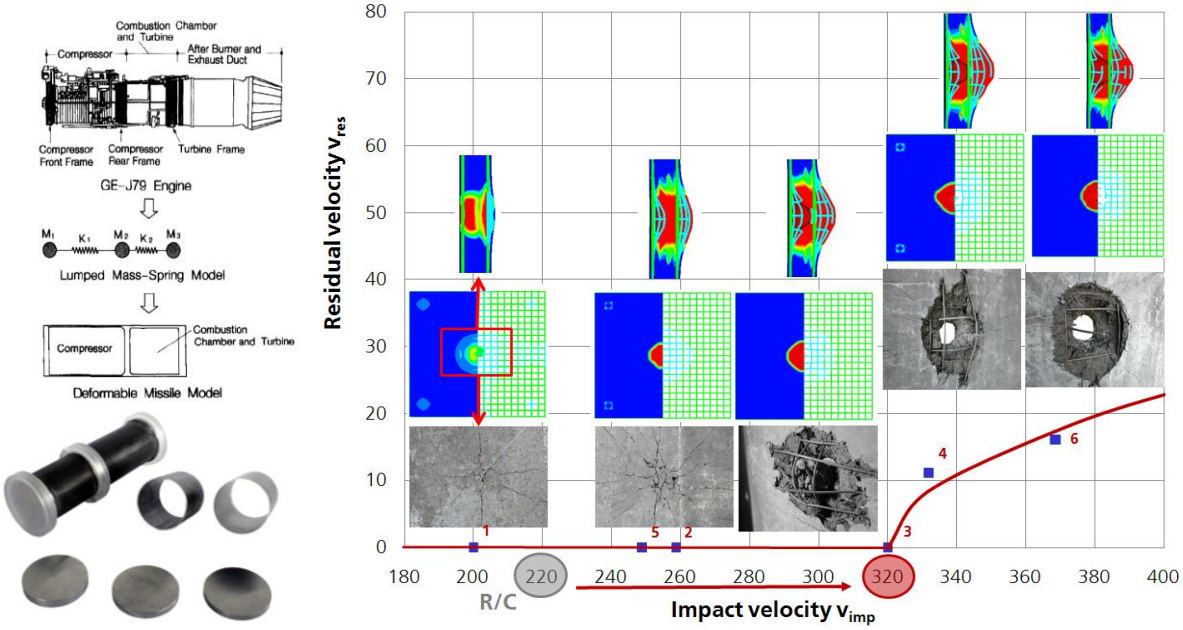

Figure 5: Engine impact model based on Sugano [12]; increased ballistic limit from 219 m/s for conventional concrete to 320 m/s ±10 m/s in own UHPC tests and FE validation [5,6].

The reference experiments with normal strength concrete derived a limit velocity of max. 219m/s for perforation. The residual velocities are not given in these experiments so that the ballistic limit function cannot be used in the same way. However, the difference to UHPC is remarkable. The UHPC panels absorbe at the limit state 110% more kinetic energy than the same configuration made of conventional concrete.

3 Application of UHPC in new building safety concepts

Aircraft impact and subsequent kerosene fire has to be considered as realistic threat against critical infrastructure. Typical examples are high-rise buildings in the range of several hundred meters altitude, potentially as part of a large scale urban development, housing several ten thousands of occupants in office and/or residential space. The largest of these buildings worldwide carry symbolic value making them susceptible to attacks. Furthermore, major nuclear facilities have to be considered, especially those designed about 2-3 decades ago without or with low protection requirements against accidental aircraft impact. Especially early designs of boiling water reactor housings with a large control area are principally more vulnerable than pressurized reactors with very localized and often strongly covered reactors. The authors were involved in two recently developed comprehensive and innovative concepts of these building types, based on high and ultra high performance concretes (HPC, UHPC). The ‘Security Scraper’, designed in [5,6] and illustrated in Figure 6, is a concept for a high-rise building with 500m altitude and more consisting of:

- a UHPC safety and security core shown in blue, providing resistance against the complete aircraft and the most localized penetration loading by the engines
- escape and rescue routes (green) and key installations for fire protection placed inside the security core to remain functional during an impact and the associated fire

- alternate load paths compensating larger scale local failure of columns by outrigger constructions redirecting the static loading forces around the damaged area

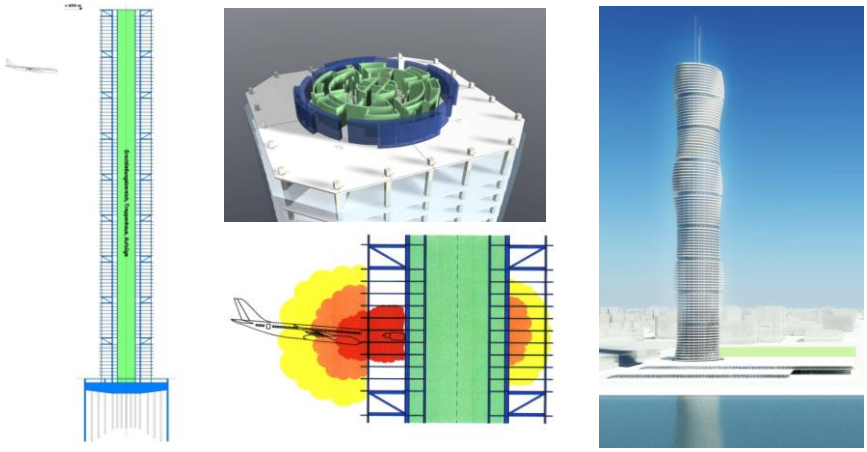

Figure 6: Security Scraper concept with protective ultra high performance concrete core (blue) housing escape and rescue routes (green); design impression by Dissing + Weitling Architects.

The second concept describes a superstructure for existing boiling reactor type nuclear power (Figure 7) plants with:

- a box girder construction spanning contact free across the plant structure to leave the existing operation license virtually untouched
- a structural design, such that the superstructure can absorb momentum and energy of the global impact forces
- an outer UHPC hull as local penetration protection (red in Figure 7) to keep all burning kerosene out of the superstructure and the security zone
- sufficiently low transmission of impact induced vibrations from the superstructure, through the foundations into the existing plant building, to achieve acceptable floor response spectra for critical components

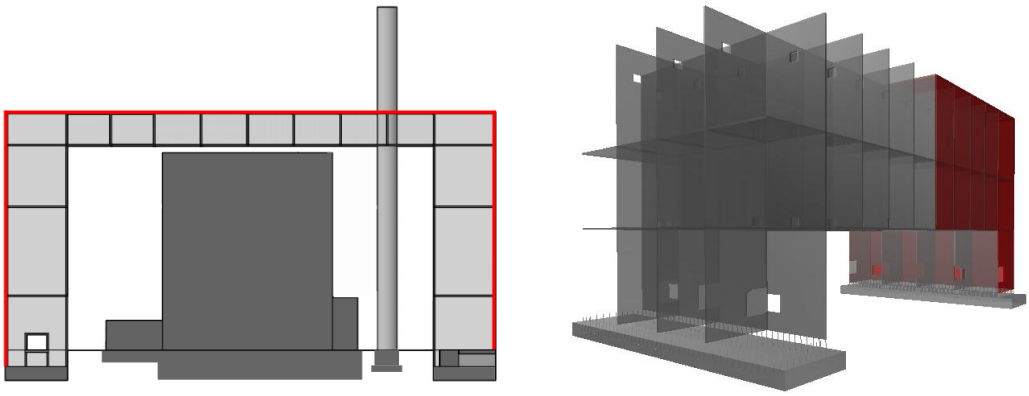

Figure 7: Power plant superstructure concept: Free-spanning protection of a boiling water reactor type against civilian and military aircraft; right: partly opened 3D view of the HPC security hull (red) onto the bracing structures [7].

The design of these structures involves the analysis of global integrity, such that the building can absorb the overall momentum and kinetic energy of all impacting aircraft components. In order to protect the security cores from failure caused by kerosene fire, the local penetration resistance must be dimensioned appropriately. The design methods on these two scales have been analysed and detailed in recent studies to quantify the benefit of ultra high performance concretes in innovative concepts [6,7,8].

4 Conclusions

An experimental series on UHPC panels subjected to aircraft engine impact has been conducted with reference to a test series on normal strength concrete. The experimental investigation was focused on the specific material behavior of the ultra high strength and fiber reinforced ductile material UHPC. The results of the six scaled impact tests were sufficient to cover experimentally all major damage modes at different stages of impact velocity.

In all damage modes significant improvements of UHPC panels to conventional concrete panels could be observed. The material´s high compressive strength reduced the effect of the front side missile penetration to a “footprint” without significant spalling. On the panel rear side the fibers connected the opening cracks up to a crack width of half their length and thus widely prevented the matrix from scabbing. While the fibers were gradually pulled out of the UHPC matrix with increasing impact intensity the material was still able to carry loads at a high level of inelastic deformation. These mechanical effects reduce damage to the panel rear side and increase the ballistic limit by more than 100m/s up to 320m/s approximately. The higher ballistic limit velocity corresponds to an increase of 110% of absorbed kinetic energy.

Based on these experimental results recent concepts for structures to resist aircraft impact are substantiated.

References

[1] Fehling, E.; Schmidt, M., Teichmann, T.; Bunje, K.; Bornemann, R.; Middendorf, B., 2005. Entwicklung, Dauerhaftigkeit und Berechnung Ultra-Hochfester Betone (UHPC), Forschungsbericht DFG FE 497/1-1, Schriftenreihe Baustoffe und Massivbau der Universität Kassel, kassel university press, Heft 1.

[2] Lambert, J.P. and Jonas, G.H., 1976. Ballistic Res. Lab., Rep. BRL-R-1852, Aberdyn, USA.

[3] Leutbecher, T. and Fehling, E., 2009. Rissbildung und Zugtragverhalten von mit Stahlfasern verstärktem Stahlbeton am Beispiel des Ultrahochfesten Betons, Teil 1: Rissmechanische Zusammenhänge, Beton- und Stahlbetonbau 104, Heft 6, Ernst&Sohn, 357-367.

[4] Nöldgen, M.; Millon, O.; Thoma, K.; Fehling, E., 2009. Hochdynamische Eigenschaften von Ultrahochfestem Beton (UHPC), Beton- und Stahlbetonbau 104, Heft 11, Ernst & Sohn.

[5] Nöldgen, M., 2010. Modellierung von Ultrahochfestem Beton (UHPC) unter Impaktbelastung, Auslegung eines Hochhauskerns gegen Flugzeuganprall, Schriftenreihe Baustoffe und Massivbau der Universität Kassel, kassel university press, Heft 12.

[6] Nöldgen, M., 2011 *Modeling of Ultra High Performance Concrete (UHPC) under Impact Loading – Design of a High Rise Building Core against Aircraft Impact*, Forschungsergebnisse aus der Kurzzeitdynamik, Fraunhofer Verlag, Heft 19.

[7] Nöldgen, M., Laubach, A.; Lukaschek, F.; Riedel, W.; Stolz, A.; Roller, C.; and Pattberg, G., 2011 *Impact Resistant Superstructure for Power Plants Part II: Structural Concept and Global Response*, Int. Conf. Structural Mechanics in Reactor Technology - SMIRT, New Dheli, India.

[8] Riedel, W.; Nöldgen, M.; Thoma, K. & Fehling, E. (2010), Local Damage to Ultra High Performance Concrete Structures caused by an Impact of Aircraft Engine Missiles, Nuclear Engineering and Design 240, pp. 2633-2642, DOI 10.1016/j.nucengdes.2010.07.036.

[9] Schlüter, F.H., 1987 Dicke Stahlbetonplatten unter stoßartiger Belastung – Flugzeugabsturz, Dissertation, TH Karlsruhe, Heft 3.

[10] Schuler, H.; Hanson, H., 2006. Fracture behavior of High Performance Concrete (HPC) investigated with a Hopkinson Bar, Journal de Physique IV, France (134), 1145-1151.

[11] Straßburger, E., 2004. Beitrag zum Seminar WB 2.05 “Kleinkalibrige Rohrwaffen und Splitter-Wirkung und Schutz” der CCG, Efringen-Kirchen, Germany.

[12] Sugano et al., 1993a. Local damage to reinforced concrete structures caused by impact of aircraft engine missiles, Part 1. Test program, method, results, Nucl. Eng. Des. 140, 387-405.

Part Five

DESIGN AND CONSTRUCTION

A Triaxial Fatigue Failure Model for Ultra-High-Performance Concrete (UHPC)

Jürgen Grünberg[1], Christian Ertel[2]
1: G+S Planungsgesellschaft mbH, Hamburg, Germany
2: Institute for Concrete Construction, Leibniz University of Hannover, Germany

The "three phases model" developed at the Leibniz University Hannover describes the anisotropic triaxial fatigue failure of concrete. This failure model is based on characteristic failure curves along the principal stress meridians of the fracture surface, in particular along the compressive meridian. Triaxial static as well as dynamic experiments are performed both in a especially made dynamic tri-axial cell and in a "real" triaxial experimental setup in order to calibrate the three phases model with respect to the failure characteristics of ultra-high-performance concrete. This extension of the three phases model with respect to fatigue failure is derived from experimental results of dynamic loading along the compressive meridians using different loading amplitudes and determining the associated numbers of load cycles. Finally, uni-axial as well as "multi-axial" S-N-curves related to arbitrary triaxial stress proportions are derived from the different damage surfaces intersected them by proportional load paths.

Keywords: Triaxial Fatigue, Fatigue Failure Model, UHPC, Dynamic Tiaxial Cell

1 Introduction

The outstanding characteristics of Ultra-High-Performance Concrete (UHPC) require the development of a triaxial mechanical model for numerical investigations. The three phases model allows for describing the behaviour of concrete in the range from extremely brittle to more ductile by using the characteristic developments of the principal meridians of the fracture surface in particular the compressive meridian. Furthermore, the anisotropic damage due to fatigue is considered in the principal-stress space deriving different grades of damage in relation to the tensile and the compressive meridian.

The necessary parameters are determined in experimental investigations in order to calibrate the three phases model for UHPC by specifying the failure curve of static and dynamic loading on the compressive meridian.

2 Three phases model for Ultra-High-Performance Concrete

The general shape of a failure surface in the three-dimensional stress space can be described by its failure curves in the principal meridians sections and its cross-sectional shapes in the deviator sections (figure 1). The surface in the 60 degree sectors between the principal meridians are generated by means of elliptic interpolation. There are numerous multiaxial failure models (e.g. Drucker-Prager or Willam-Warnke) in literature to be used for normal-strength concrete. But these traditional failure criteria are not applicable for UHPC.

The failure of UHPC under uniaxial loading is brittle, in both, tension and compression. Therefore, the three phases model [1] has been modified to take into account these characteristic material properties of UHPC.

The compressive meridians of the three phases model (figure 1) are described by two straight lines with different slope which are connected by a parabolic curve. The change-over range of UHPC is short and near to the uniaxial strength. The cross section on the deviator plane changes from nearly triangular (brittle fracture) to more and more circular with increasing hydrostatic pressure (sliding fracture).

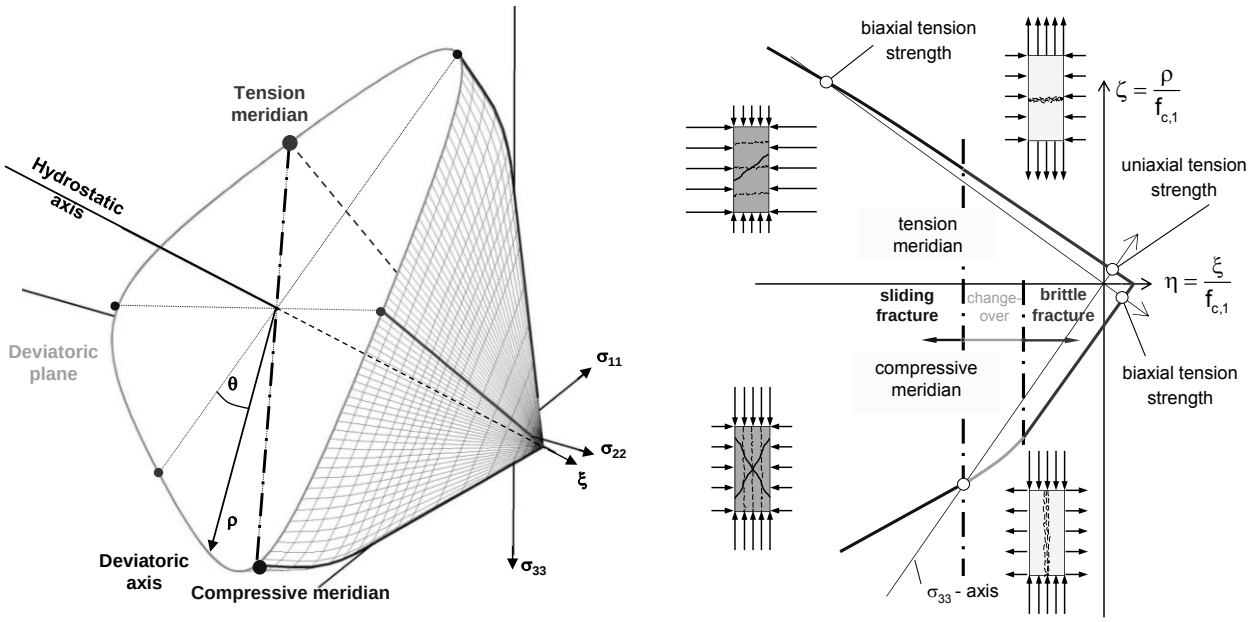

Figure 1: Definitions in the three-dimensional stress space (left) and Principal meridians section of the failure surface due to three phases model (right).

Extended three-phase model to describe dynamic loads

Based on the fracture curves on the principal meridians for static stress, the three-phases model can be applied to dynamic fatigue stress by appropriately modifying these curves. This involves triaxial dynamic testing of various stress states along the compressive meridian (different radial stress levels).

Test results are taken to establish S-N curves, i.e. one curve for each radial stress level, which are selectively transferred to the principal meridian section in order to obtain curves of equivalent stress reversal cycles before failure. The resulting set of curves characterises the fatigue strength along the compressive meridian.

In order to verify the basic parameters of the three-phases model both static and dynamic triaxial experimental investigations are performed.

3 EXPERIMENTAL INVESTIGATIONS

Information about the fibre reinforced ultra high performance concrete mixtures “M2Q” examined in the Priority Programme 1182 “Building Suitable with Ultra-High Performance Concrete” can be found in [2] and [3]. This paper focuses on static and dynamic triaxial investigations. For a discussion of uniaxial dynamic investigations – carried out in cooperation with the Institute of Building Materials Science (Leibniz University Hannover) – see [3], [4] and another paper in this conference proceedings [5].

3.1 Triaxial static Loading

3.1.1 Compressive Meridian

The characteristics of the failure curve on the compressive meridian depend on specific loading conditions (figure 2). These are states of stress composed of predominantly axial compression and rotation-symmetric transverse stress, either tension or compression.

One point on the compressive meridian – the uniaxial compressive strength – is already known and can be found on σ_{33}-axis ($\sigma_{11} = \sigma_{22} = 0$). The uniaxial compressive strength divides the failure curve into two parts, axial compression below compressive strength combined with transverse tension and axial compression above compressive strength combined with transverse compression.

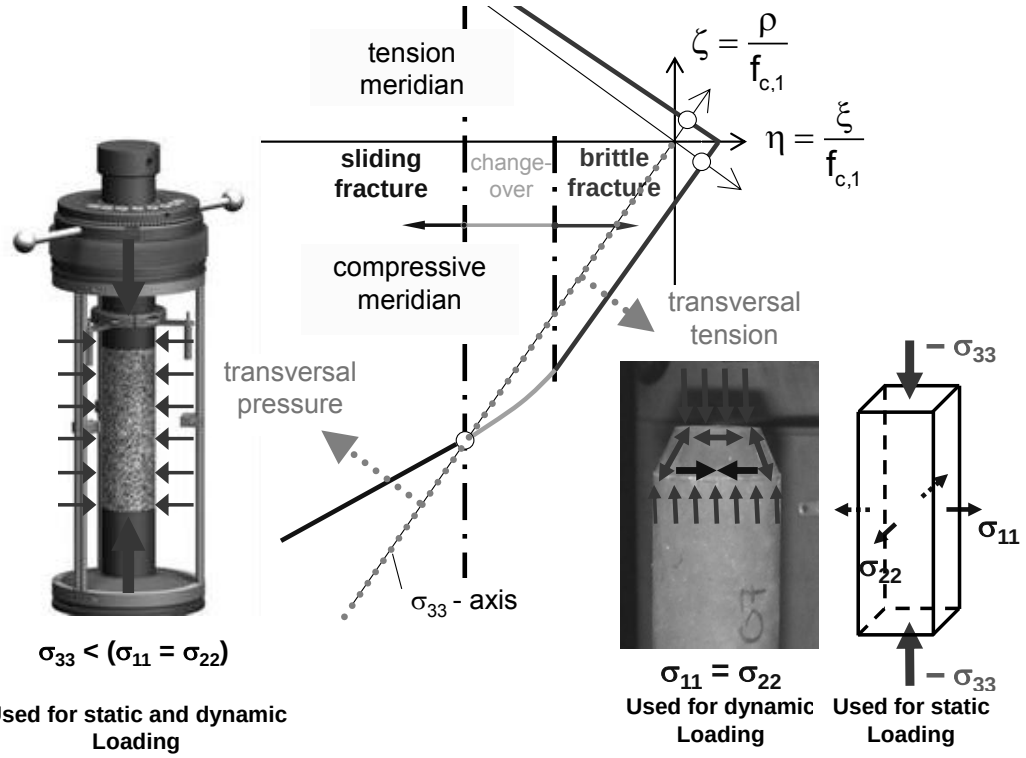

Figure 2: Loading conditions of compressive meridian section on the failure surface due to three phases model for ultra high performance concrete.

3.1.2 Transverse tensile stress

A special test array for a prismatic test body (40*40*160mm³) was developed for "realistic" transverse tensile strength testing, see figure 2. In this array, a hydraulic cylinder directly applies the axial load. Aluminium brushes glued on transversely are intended to prevent the required transverse tensile forces from constraining axial elongation. An appropriate deflection allows both transverse directions to be separately controlled by two hydraulic cylinders. The prisms were cut from a cube in order to prevent marginal disturbance. In this experimental set-up, the results of two sets of three tests were averaged to determine axial stability under two transverse tensile stresses (4 MPa, 6 MPa). Experiments showed (see table 1) that these high transverse stress levels hardly reduced axial stability. Uniaxial tensile strength ($f_{ct,1}$ = 9.37 MPa) had been previously determined using a "Bochum test rig" [6].

Table 1: Results uniaxial compression combined with transverse tension.

Transverse tension = 4 MPa	σ_{33} **[MPa]**	$\sigma_{11} = \sigma_{22}$ **[MPa]**	$\sigma_{33} / f_{c,1}$	$\sigma_{c,r} / f_{c,1}$
Specimen M045_01	-190.7	4.0	1.014	-0.021
Specimen M045_02	-184.5	4.0	0.981	-0.021
Specimen M045_03	-173.1	4.0	0.920	-0.021
$f_{c,1,M045}$ = - 188.0 MPa	**-182.8**	**4.0**	**0.972**	**-0.021**
Transverse tension = 6 MPa	σ_{33} **[MPa]**	$\sigma_{11} = \sigma_{22}$ **[MPa]**	$\sigma_{33} / f_{c,1}$	$\sigma_{c,r} / f_{c,1}$
Specimen M045_05	-162.0	6.0	0.862	-0.032
Specimen M045_21	-170.0	6.0	0.904	-0.032
Specimen M045_23	-162.4	6.0	0.864	-0.032
Specimen M045_24	-167.1	6.0	0.889	-0.032
$f_{c,1,M045}$ = - 188.0 MPa	**-165.4**	**6.0**	**0.879**	**-0.032**

The design with the glued brushes proved to be unsuitable for dynamic loads. Therefore, a different test array was designed for later dynamic compressive meridian testing. This alternative design uses flat top face and a flat bottom cylinders, specifically to accommodate high frequency load reversals under later dynamic loads. Diverting the axial pressure trajectories generates radial and tangential tensile stresses combined with axial loading, see internal force vectors in figure 2. Because of the conical shape, longitudinal compression occur in combination with transverse tension already under linearelastic condition, i.e. before fracture. Although a rotation-symmetric state of stress ensues, this set-up fails to produce a state of meridian stress across the entire cross-section. This is due to radial stresses diminishing along the cross-section and turning zero at the edge. Since the state of meridian stress is not retained across the entire cross-section, the failure states obtained are located a little outside the expected failure area.

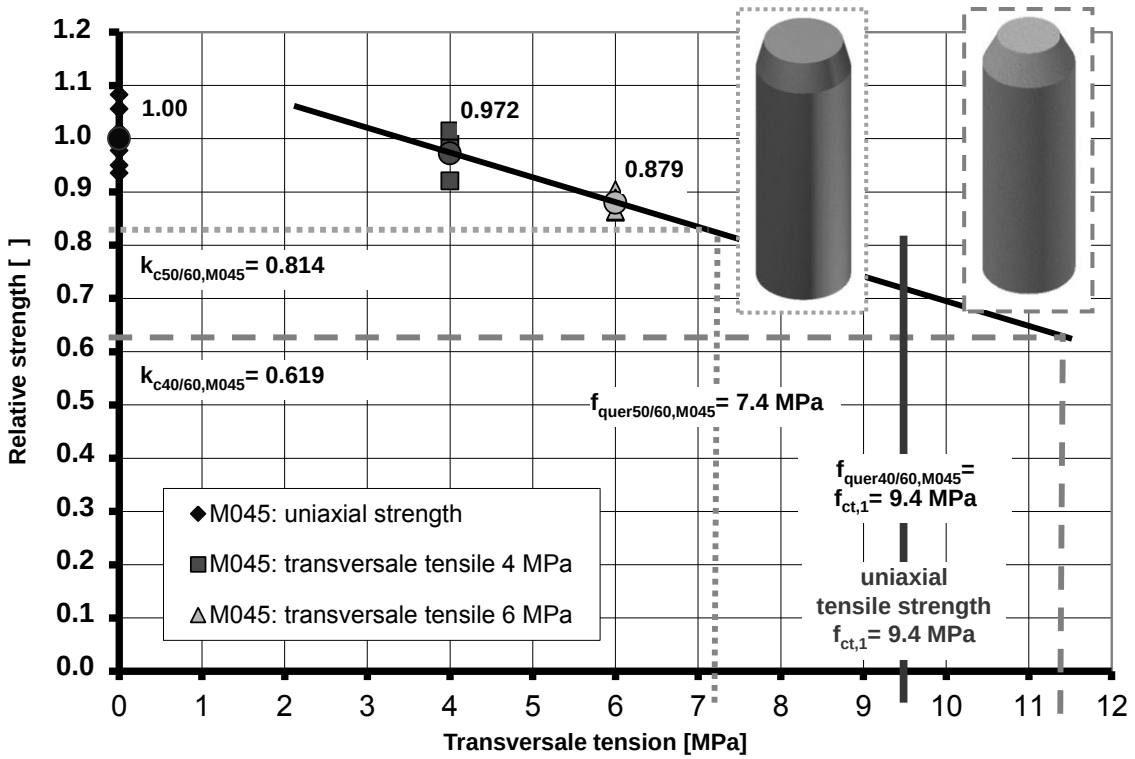

Figure 3: „realistic" transverse tensile strength testing and alternative design.

Calibration tests carried out under static load after the flat face cylinder tests and before the "realistic" radial tensile strength tests were taken to determine the radial tensile stress equivalent to both flat face geometries. The equivalent radial tension for the first flat face specimen is $f_{ct,50/60}$ = 7.4 MPa. The radial tension of the less slope one is limited to the uniaxial tensile strength $f_{ct,40/60}$ = $f_{ct,1}$ = 9.37 MPa.

3.1.3 Triaxial testing cell for uniaxial compression combined with transverse pressure

Different test arrangements (e.g. rings, coil) have been tested, but all these experiments did not produce suitable results [3]. Finally, a special designed triaxial testing cell was bought, see figure 2. This experimental setup allows controlling different rotation-symmetric transverse compression states in combination with axial compression. The pressure tank is used for carrying out triaxial stress-deformation tests on cylindrical specimens with a confining pressure of up to 100 MPa [7]. The specimen geometry (cylinder d/h = 60/180 [mm]) is the same as used for uniaxial fatigue investigations.

3.2. Triaxial dynamic loading

Dynamic investigations of the compressive meridian are a consistent continuation of previous static tests. Again the different test arrays distinguish between axial pressure combined with rotation-symmetric transverse stress, either pressure or tension.

3.2.1 Radial tension

Dynamic investigations into this type of stress are carried out using flat top face cylinders of a total height of 180 mm. The cylindrical section is 160 mm high at a 60 mm diameter which tapers from 60 mm to 40 mm along the remaining 20 mm of height. The resulting tilt is 1:2 (∅40). Due to the geometry of the chosen test body, the radial tensile stress immediately results from the axial stress.

Testing so far involved 4 test bodies at each of three load levels. Further tests will follow. The table below itemises the number of stress reversal cycles before failure. Compared to the radial pressure tests, there is an obvious greater spread in the number of cycles before failure this time.

Table 2: Results uniaxial compression combined with radial tensile (see also [8]).

Specimen	upper-stress level (*)	lower-stress level	load cycle [N]	load cycle [log N]	average value [log N]
M044_16	0.85 (0.553)	0.05	4990	3.70	
M044_08	0.85 (0.553)	0.05	4310	3.63	**3.27**
M044_18	0.85 (0.553)	0.05	317	2.50	
M044_07	0.85 (0.553)	0.05	1720	3.24	
M044_17	0.75 (0.486)	0.05	11595	4.06	
M044_09	0.75 (0.486)	0.05	26511	4.42	**4.42**
M044_12	0.75 (0.486)	0.05	61905	4.79	
M044_06	0.75 (0.486)	0.05	25111	4.40	
M044_05	0.70 (0.455)	0.05	33145	4.52	
M044_15	0.70 (0.455)	0.05	127806	5.11	**5.07**
M044_19	0.70 (0.455)	0.05	394081	5.60	
M044_04	0.70 (0.455)	0.05	2942	3.47	

(*) in relation to triaxial strength $f_{c,40/60}$ (as well as to *uniaxial strength* $f_{c,1m}$)

3.2.2 Radial compression

The triaxial cell especially was designed for dynamic investigations. The oil filled chamber volume of triaxial testing cell can be minimized by packing from about 8.0 litre down to 1.5 litre. Therefore, a dynamic loading frequency up to 5 Hertz is possible. In combination with the digital multi-channel control system axial force and oil pressure can be controlled in phase.

For this project, dynamic test series are performed for two steps of lateral pressure (– 20 MPa, – 40 MPa). At the beginning of each dynamic triaxial test series three uniaxial specimens and two specimens with a constant transverse pressure were tested statically. The uniaxial strength f_{cm} is needed to compare the triaxial and uniaxial S-N-curves. The triaxial static failure stress (e.g. $f_{c,20MPa}$) is the reference to specify the upper-stress levels. The lower-stress level always is 5 %. Table 3 shows the results of triaxial fatigue investigations for two levels of a lateral pressure – 20 MPa (series M043) and – 40 MPa (series M042). For comparison, upper stress levels are normalized with respect to uniaxial compression strength (f_{cm}) additionally.

Figure 4 shows the results of all executed triaxial dynamic investigations. The upper stress levels are normalized to the triaxial static compression strength ($f_{c3,xxMPa}$) of each series. That is why an intersection point for all lines can be found at low load cycles. In comparison to the uniaxial S-N-curves, the slope of the regression line signifying the triaxial dynamic

investigations obviously is steeper. There is also a difference in steepness of the S-N curves for different levels of transverse compression (series E and series F). That means the static increase as a result of transverse pressure (e.g. $f_{c,20MPa}/f_{c,1}$= 1.60) will decrease for higher number load cycles, but it is always higer than 1. The dynamic investigations for the conical specimens still are running. All S-N-curves have to cut off at a upper stress level S_o = 1.0.

Table 3: Results of triaxial fatigue investigations.

Series M043:				**Series M042:**			
uniaxial strength:	$f_{c,1}$ =	-194.6 MPa		uniaxial strength:	$f_{c,1}$ =	-202.0 MPa	
triaxial strength:	$f_{c11,-20MPa}$ =	-311.6 MPa		triaxial strength:	$f_{c11,-40MPa}$ =	-371.3 MPa	
	$\sigma_{c22} = \sigma_{c33}$ =	-20.0 MPa			$\sigma_{c22} = \sigma_{c33}$ =	-40.0 MPa	
	$f_{c,20MPa}/f_{c,1}$=	1.60			$f_{c,40MPa}/f_{c,1}$=	1.84	
	$\sigma_{c11}/\sigma_{c22}=\sigma_{c11}/\sigma_{c33}$=	0.064			$\sigma_{c11}/\sigma_{c22}=\sigma_{c11}/\sigma_{c33}$=	0.108	
stress level (*) ratio [ ]	**load cycle [N]**	**load cycle [log N]**	**average value [log N]**	**stress level (**) ratio [ ]**	**load cycle [N]**	**load cycle [log N]**	**average value [log N]**
0.80 ; 0.05 (1.28 ; 0.08)	112 2352 713 5291	2.05 3.37 2.85 3.72	**3.00**	**0.80 ; 0.05** (1.47 ; 0.09)	Stress level not available in dynamic triaxial cell in Hannover		
0.70 ; 0.05 (1.12 ; 0.08)	8685 11357 18176 12732 14966 5393	3.94 4.06 4.26 4.10 4.18 3.73	**4.04**	**0.70 ; 0.05** (1.29 ; 0.09)	4910 3380 5158 2727 5083 5314	3.69 3.53 3.71 3.44 3.71 3.73	**3.63**
0.60 ; 0.05 (0.96 ; 0.08)	29103 47383 157565 42741 11501 28019	4.46 4.68 5.20 4.63 4.06 4.45	**4.58**	**0.60 ; 0.05** (1.10 ; 0.09)	15509 14330 24079 12858 26519 15132	4.19 4.16 4.38 4.11 4.42 4.18	**4.24**
0.50 ; 0.05 (0.80 ; 0.08)	270916 310767 719815 469009 216426 326960	5.43 5.49 5.86 5.67 5.34 5.51	**5.55**	**0.50 ; 0.05** (0.92 ; 0.09)	134499 183879 102092 106721 127457 103136	5.13 5.26 5.01 5.03 5.11 5.01	**5.09**

(*) in relation to triaxial strength $f_{c.20MPa}$ (as well as to *uniaxial strength* $f_{c.1}$)

(**) in relation to triaxial strength $f_{c.40MPa}$ (as well as to *uniaxial strength* $f_{c.1}$)

4 Extension of three phases model with respect to fatigue

Now the fatigue strength, associated to each load cycle number, is taken from the experimental S-N-curves to be transformed into the principal meridians section.

The ultimate numbers of stress cycles until failure according to the uniaxial S-N-curve are attached to the σ_{33}-axis (see triangular symbols in figure 5). In a similar manner the triaxial S-N-curves for different ratios of deviator versus hydrostatic stress (ρ/ξ = 0.064 and accordingly ρ/ξ = 0.108) are transferred in each case to the straight load path defined by this ratio.

Fatigue failure curves connecting equal cycle numbers can be derived. You can see these lines for numbers of cycles to failure log N = 3, 4 and 5 in figure 5.

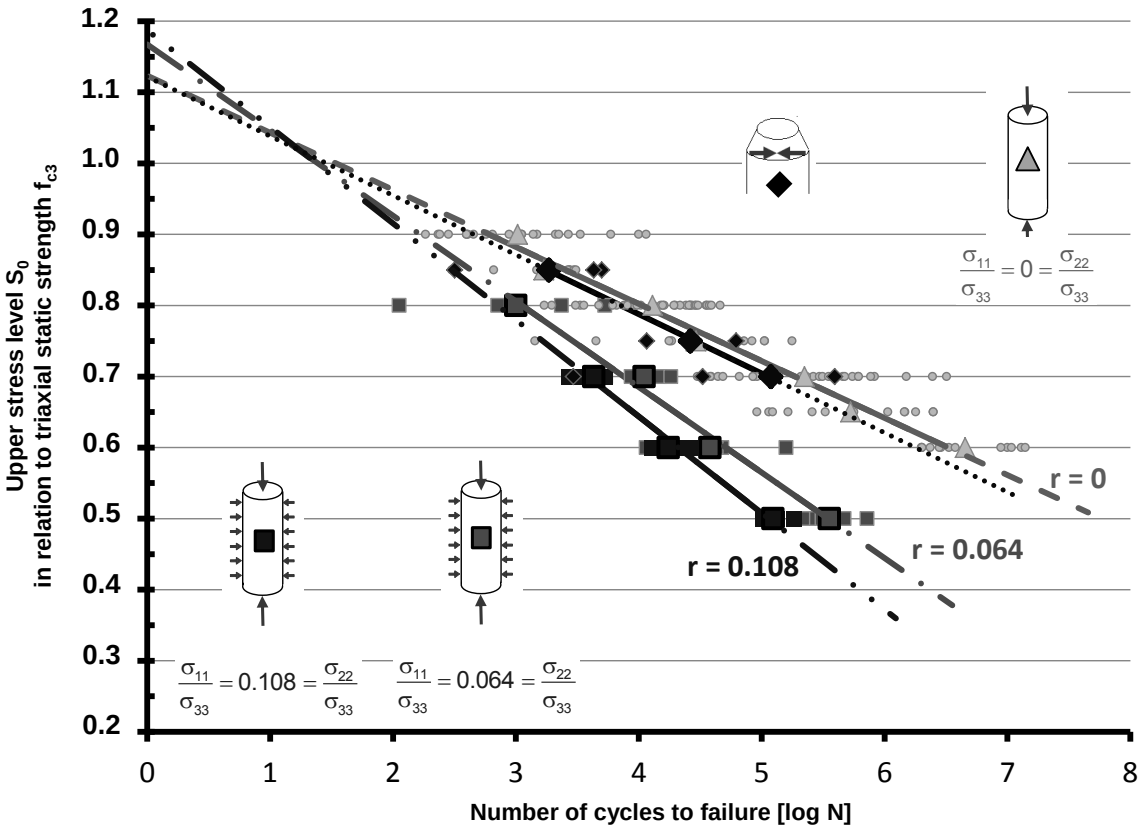

Figure 4: Triaxial- and uniaxial S-N-curves for UHPC.

Thereby, the three phases failure model is extended to a three phases fatigue failure model.

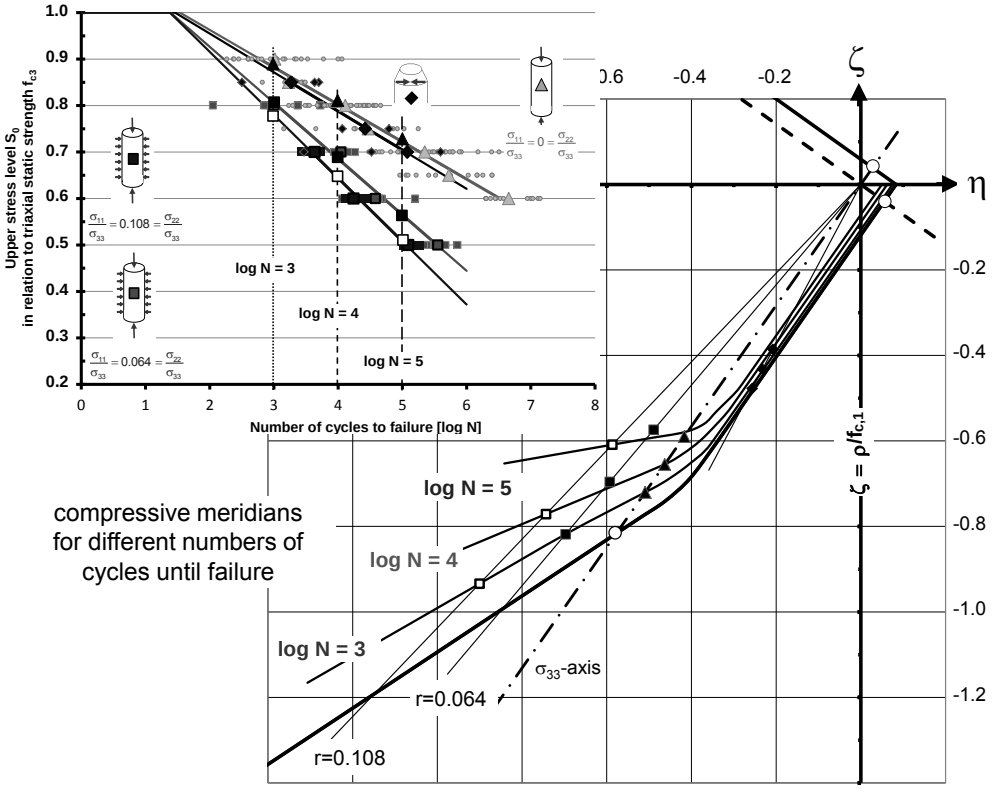

Figure 5: Extension of Three phases model for fatigue loading.

5 Conclusions

The test setups designed and built by the Institute of Concrete Construction at the Leibniz University of Hannover can be used for the experimental investigation of the failure curves on the compressive meridian with respect to both, static as well as dynamic stresses. The triaxial test cell allows a dynamic in-phase investigation of triaxial compression conditions above uniaxial strength limits. Flat point cylinders can be basically used for dynamic strength tests under axial compression combined with transverse tension, but require appropriate calibration tests to be performed first.

The findings of triaxial meridian tests show that the advanced three-phase model is a good means of describing the compressive meridian of the stress to failure. A radial pressure load causes UHPC to be more ductile than the brittle response obtained from uniaxial stress.

The steeper S-N curves attached to triaxial compression in comparison to the uniaxial S-N-curves suggest that the increase of fatigue strength due to lateral compression is consumed with rising load cycles.

6 Acknowledgement

This project is part of the priority programme “Sustainable Building with Ultra High Performance Concrete” currently under way in Germany. The authors thank the “Deutsche Forschungsgemeinschaft (DFG)” for the financial support of this research work.

References

[1] Ertel C.; Grünberg J.: “Triaxial Fatigue Behaviour of Ultra High Performance Concrete”; 3rd fib International Congress; May 29 – June 2, 2010, Washington, D.C.

[2] Schmidt, M.; Fehling, E.: Entwicklung, Dauerhaftigkeit und Berechnung Ultrahochfester Betone (UHPC), Kassel, 2005

[3] Grünberg, J.; Lohaus, L.; Ertel, C.; Wefer, M.: “Mehraxiales mechanisches Ermüdungsmodell von Ultra-Hochfestem Beton – Experimentelle und analytische Untersuchungen”, Beton- und Stahlbetonbau, V. 102, No. 6, Jun. 2007, pp. 388-398.

[4] Wefer, M.: Materialverhalten und Bemessungswerte von ultrahochfestem Beton unter einaxialer Ermüdungsbeanspruchung. Dissertation, Leibniz Universität Hannover, Institut für Baustoffe, 2010

[5] Ludger, L.; Oneschkow, N: New fatigue design model for all concrete strengths; HiPerMat 2012, Kassel

[6] Lohaus, L; Wefer, M.; Gerlach, J.: Zentrisches Zugtragverhalten von Ultrahochfestem Beton (UHPC), Internationale Baustofftagung 17th ibausil, 23.-26.09.2009, Weimar

[7] GL Test-Systems: Dynamic triaxial testing cell, Operating manual, Heiligenstadt, 2009

[8] Lohaus, L.; Elsmeier, K: Fatigue Behaviour of plain and fibre reinforced Ultra-High Performance Concrete; HiPerMat 2012, Kassel

New fatigue design model for all concrete strengths

Ludger Lohaus, Nadja Oneschkow
Institute of Building Materials Science, Leibniz Universität Hannover, Germany

At the Institute of Building Materials Science, Leibniz Universität Hannover, a new design model for compressive fatigue loading was developed. This design model is mainly based on investigations conducted on two ultra-high strength concretes. It is also applicable to normal strength and high strength concretes. This model was further integrated into the design concept of CEB-FIP Model Code 90 [1] to ensure an easy practical application. In this paper, the new design model is presented and its capabilities shall be demonstrated. The effects of the changes compared to the current standard design model are also shown. Thereby, the ensured safety level is particularly analysed. This analysis shows that the required safety level is maintained. Furthermore, the new model enables an economic fatigue design.

Keywords: Fatigue design, Model Code, safety level, ultra-high strength concrete

1 Introduction

In recent years concretes with high compressive strengths of 100 MPa up to 200 MPa have been developed and used in different building constructions. On the one hand, these high compressive strengths lead to light and slender structures which are increasingly susceptible to non-static loading. As a consequence the influence of cyclic stresses increases. On the other hand, there are building structures which are typically exposed to high fatigue relevant stresses, e.g. wind turbines. In both cases fatigue loading is relevant for design. However, the concrete grades considered in CEB-FIP Model Code 1990 [1] are limited to C 80. Furthermore, the definition of the fatigue reference compressive strength as stated in [1] is not applicable to concrete grades above C120. Considering the current developments, design rules for fatigue should also be applicable to concretes with higher compressive strengths.

At the Institute of Building Materials Science, Leibniz Universität Hannover, experimental investigations on the fatigue behaviour of normal strength, high strength and ultra-high strength concretes have been carried out, applying ultimate numbers of cycles to failure up to log N = 7. Based on these investigations, a material model was developed for concretes with enhanced compressive strength under uniaxial compressive fatigue loading [2] and further developed subsequently [3], [4]. The material model was integrated into the design concept of CEB-FIP Model Code 90 [1]. Therefore, a new approach for the determination of the fatigue reference compressive strength was developed. The new design model with its capabilities is presented in this paper. Relevant aspects with regard to safety are also analysed and presented.

2 New fatigue design model

Experimental tests

The following results were attained based on experimental investigations on two ultra-high strength concretes (UHPC) [2], [5]. The ultra-high strength fine-grained concrete (M2Q) and coarse-grained concrete (B4Q) had 28-day compressive strengths of $f_{c,cube,100}$ = 160 MPa and $f_{c,cube,100}$ = 180 MPa respectively, both after storage under water. Both mixtures contained 2.5 Vol.-% of high strength smooth steel fibres with a length of 9.0 mm and l/d-ratio of 60. Cylindrical heat-treated test specimens with dimension d/h = 60 mm/180 mm were used. Before testing, the loaded surfaces of the specimens were plane-parallel grinded and finally polished. No significant differences in the regression lines were deduced from the test results for UHPCs with different grain compositions. Therefore the two UHPC-mixtures were analysed together [2].

In Figure 1 the experimental test results and the resulting regression lines, purely based on these test results, for UHPC are shown.

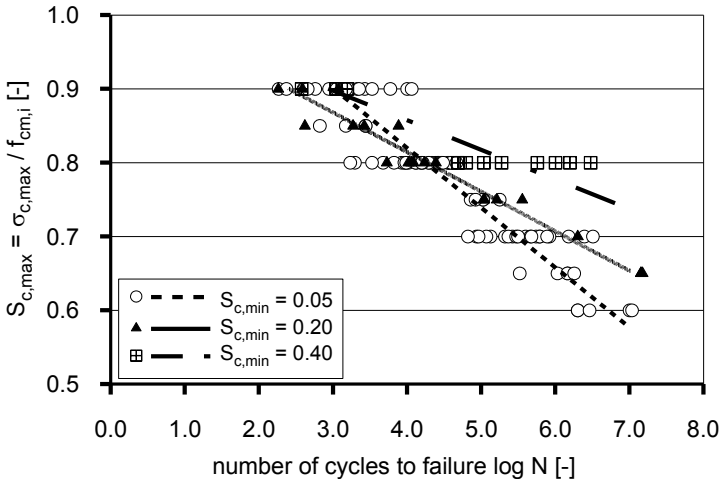

Figure 1: Experimental test results and regression lines [2].

Woehler curves

Combining Woehler- and Goodman-diagrams, a parameterized failure surface for uniaxial compressive fatigue is defined in a three-dimensional coordinate system with axes $S_{c,max}$, $S_{c,min}$ and log N [2], [3]. The derivation is based on the experimental test results (Figure 1) taking the following requirements into consideration:

- Intersection with the ordinate at $S_{c,max}$ = 1.0 [6],
- Linear approximation, at least for the range up to log N = 7 [7],
- Deviation from test results that are on the safe side,
- Connection to high numbers of load cycles (N > 10^7) and thus continuous description for all maximum stress levels $S_{c,max,i}$,
- For high numbers of load cycles, asymptotic approach for the respective minimum stress levels [1].

Four input parameters, $P_{1,fat}$, $P_{2,fat}$, $P_{3,fat}$ and $P_{4,fat}$, were used to generate this failure surface [2], [3]. These parameters represent four fatigue strengths determined for a number of cycles to failure of log N_2 = 8. $P_{1,fat}$, $P_{2,fat}$ and $P_{3,fat}$ are deduced by extrapolation of the regression lines, which intersect the ordinate at $S_{c,max}$ = 1.0, up to a number of cycles to failure of log N_2 = 8. $P_{4,fat}$ corresponds to the sustained static load $S_{c,min} = S_{c,max}$ = 0.85. Up to log N = 8, the Woehler curves are straight lines as expressed by equation (1). For log N > 8, a monotonic decreasing exponential function is defined, which approaches the respective minimum stress level $S_{c,min,i}$ asymptotically (cf. equation (2)).

For log N ≤ 8

$$\log N = \frac{8}{(Y-1)} \cdot (S_{c,max} - 1) \tag{1}$$

For log N > 8

$$\log N = 8 + \frac{8 \cdot \ln(10)}{(Y-1)} \cdot (Y - S_{c,min}) \cdot \log\left(\frac{S_{c,max} - S_{c,min}}{Y - S_{c,min}}\right) \tag{2}$$

where: $$Y = \frac{0.45 + 1.8 \cdot S_{c,min}}{1 + 1.8 \cdot S_{c,min} - 0.3 \cdot S_{c,min}^2}$$

The new Woehler curves are displayed as the failure surface in Figure 2.

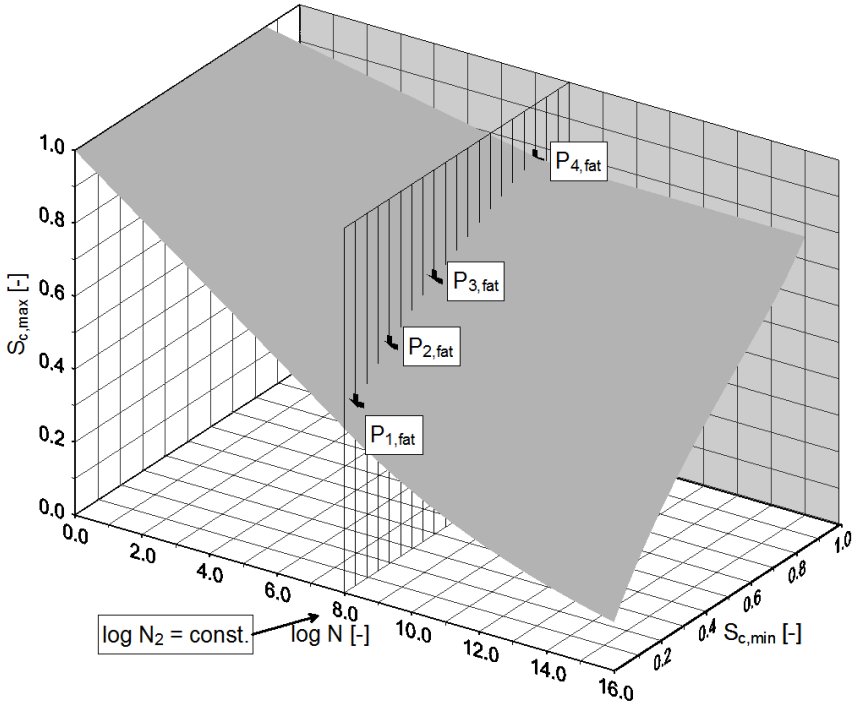

Figure 2: New Woehler curves displayed as the failure surface [3].

Comparison with own test results and test results and models documented in literatures has demonstrated the applicability of these Woehler curves to normal strength, high strength and ultra-high strength concretes [3].

Fatigue reference strength

According to CEB-FIP Model Code 90 [1], the design fatigue reference strength $f_{cd,fat}$ is determined based on the static compressive strength's design value f_{cd} which is reduced by a term, here referred to as α_{fat}:

$$f_{cd,fat} = \underbrace{0.85 \cdot \beta_{cc}(t_0) \cdot \frac{f_{ck}}{\gamma_c}}_{f_{cd}} \cdot \underbrace{\left(1 - \frac{f_{ck}}{25 f_{ck0}}\right)}_{\alpha_{fat}} \qquad \text{[1], section 6.7.3} \qquad (3)$$

where: f_{ck0} = 10 MPa (reference strength)

The term α_{fat} depends on the characteristic static compressive strength and it decreases with increasing concrete strength. Equation (3) is usable for concrete grades of up to C120. Applying equation (3) to concretes with strengths above f_{ck} = 125 MPa would lead to decreasing values of $f_{cd,fat}$. Thus, the function has to be modified for higher concrete grades. Accordingly, the design fatigue reference strength (equation (3)) was modified taking into account an extreme loading condition [2]. For this purpose, the regression line for a minimum stress level of $S_{c,min}$ = 0.05 (cf. Figure 1) was considered. The linear extrapolation of this regression line up to a number of cycles to failure of $N = 10^8$ leads to a corresponding compressive stress level of $S_{c,max} \approx 0.5$, which accounts for a loss in bearing capacity by 50 %. Hence, the term α_{fat} was modified in such a way that for concretes with f_{ck} = 200 MPa, the design fatigue reference strength $f_{cd,fat}$ amounts to 50 % of the static strength's design value f_{cd}. The new design fatigue reference strength is calculated according to equation (4):

$$f_{cd,fat,Hannover} = \underbrace{0.85 \cdot \beta_{cc}(t_0) \cdot \frac{f_{ck}}{\gamma_c}}_{f_{cd}} \cdot \underbrace{\left(1 - \frac{f_{ck}}{40 f_{ck0}}\right)}_{\alpha_{fat}} \quad (4)$$

where: f_{ck0} = 10 MPa (reference strength)

In [2] a partial safety factor of γ_c = 1.5 is derived for UHPC. Similarly, the same partial safety factor is applicable for all normal strength, high strength and ultra-high strength concretes.

Integration into the design concept of Model Code

In order to ensure an easy practical application, the new design model was integrated into the design concept of CEB-FIP Model Code 90 [3], [4]. The design concept according to Model Code includes three levels of approximation. The new Woehler curves and the modified fatigue reference strength can easily be integrated by substituting the currently standard equations for pure compressive fatigue loading:

"Level 1 Approximation":

Detailed fatigue design is not necessary if the following requirement for concretes under compressive fatigue loading is met.

$$\gamma_{Sd} \cdot \sigma_{c,max} \cdot \eta_c \le 0.45 \cdot f_{cd,fat,Hannover} \quad (5)$$

where: $f_{cd,fat,Hannover} = \underbrace{0.85 \cdot \beta_{cc}(t_0) \cdot \frac{f_{ck}}{\gamma_c}}_{f_{cd}} \cdot \underbrace{\left(1 - \frac{f_{ck}}{40 f_{ck0}}\right)}_{\alpha_{fat}}$

f_{ck0} = 10 MPa (reference strength)

In such cases, a number of cycles to failure of N ≈ 10^8 is reached for a minimum stress level of $S_{cd,min}$ = 0.

"Level 2 Approximation":

If the requirement of level 1 is not met, then the verification refers to a single load level including the dominant fatigue loading. The requirements are considered to be met if the number of acting load cycles n is less than the number of resisting cycles N:

$$n \le N \quad (6)$$

For $S_{cd,max}$ < 0.90, 0 ≤ $S_{cd,min}$ ≤ 0.80 and frequencies f > 0.1 Hz the number of resisting load cycles N is calculated using the following equations (7) and (8). In cases where $S_{cd,min}$ > 0.80, the minimum compressive stress level's design value can be taken as $S_{cd,min}$ = 0.80.

For log N ≤ 8:

$$\log N = \frac{8}{(Y-1)} \cdot (S_{cd,max} - 1) \quad (7)$$

For log N > 8:

$$\log N = 8 + \frac{8 \cdot \ln(10)}{(Y-1)} \cdot (Y - S_{cd,min}) \cdot \log\left(\frac{S_{cd,max} - S_{cd,min}}{Y - S_{cd,min}}\right) \quad (8)$$

where: $S_{cd,min} = \gamma_{Sd} \cdot \sigma_{c,min} \cdot \eta_c / f_{cd,fat,Hannover}$ $S_{cd,max} = \gamma_{Sd} \cdot \sigma_{c,max} \cdot \eta_c / f_{cd,fat,Hannover}$

γ_{Sd} = 1.1 or rather 1.0 in accordance with [1], section 1.6.6.4

η_c in accordance with [1], equation (6.7-2)

$$Y = \frac{0.45 + 1.8 \cdot S_{cd,min}}{1 + 1.8 \cdot S_{cd,min} - 0.3 \cdot S_{cd,min}^2}; \; f_{cd,fat,Hannover} = 0.85 \cdot \beta_{cc}(t_0) \cdot \frac{f_{ck}}{\gamma_c} \cdot \left(1 - \frac{f_{ck}}{40 f_{ck0}}\right)$$

Level 3:
If the requirement of level 2 is not met, then the whole spectrum of load levels has to be known. As explained in CEB-FIP Model Code 90 [1], it is recommended to verify the fatigue requirements in accordance with the Palmgren-Miner summation. The limiting fatigue damage has to be met.

$$D = \sum_{i=1}^{j} \frac{n_{Si}}{N_{Ri}} \le D_{lim} \qquad \text{in accordance with [1], section 6.7.5} \qquad (9)$$

The numbers of resisting load cycles N_{Ri} are to be calculated using equations (7) and (8). In [1], it is stated that failure occurs if D = 1.0.

The new design model, comprising the new Woehler curves and the modified value of fatigue reference strength, is included in the new fib-Model Code 2010.

3 Analysis of safety

Woehler curves

In Figure 3, the new Woehler curves [3], [4] and the current standard ones [1] are compared. For high maximum stress levels the new Woehler curves lead to higher numbers of cycles to failure (resistance). However, for low maximum stress levels in the range of log N > 8, depending on the minimum stress level, the new Woehler curves lead to lower numbers of cycles to failure. Generally, only a few experimental test results are available in this range. For this reason, the approximation was done on the safe side.

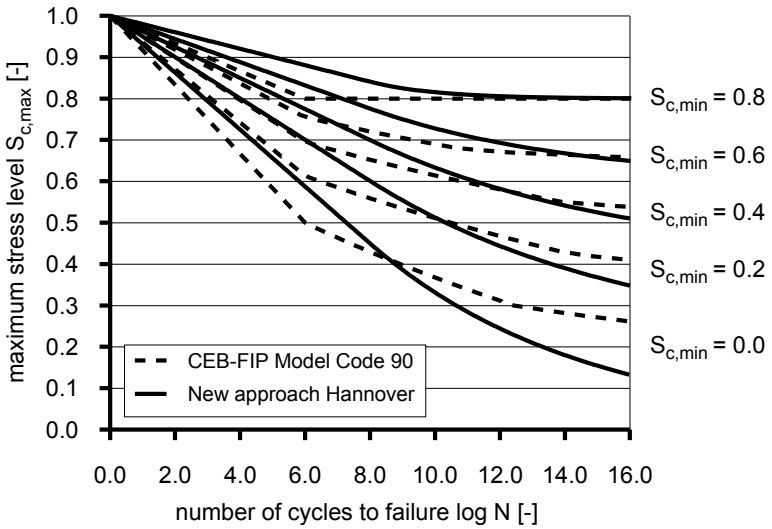

Figure 3: Comparison of new and current standard Woehler curves [3].

Fatigue reference strength

As previously mentioned, the fatigue reference strength includes an additional reduction term α_{fat} taking account of fatigue loading. Higher compressive strengths f_{ck} lead to higher amounts of additional reduction. This was generally justified by the increasing brittleness of the material and also due to the lack of knowledge concerning high strength concretes in the 1990s, when the CEB-FIP Model Code 90 [1] was published. However, an analysis of this reduction term shows, that for a concrete grade C80 this reduction is already higher than the reduction due to

the partial safety factor $\gamma_c = 1.50$. For concretes with a static compressive strength $f_{ck} = 120$ MPa, the corresponding reduction term is $\alpha_{fat} = 0.52$. That means, the design fatigue reference strength $f_{cd,fat}$ only amounts to 52 % of the static strength's design value f_{cd}.
In Figure 4, the correlations between the compressive strength and the design fatigue reference strength, according to the new approach and CEB-FIP Model Code 90 [1] are shown. In addition, the correlations for constant values of $\alpha_{fat} = 1.0$, which implies no additional reduction ($f_{cd,fat} = f_{cd}$), and $\alpha_{fat} = 0.7$ are analysed.

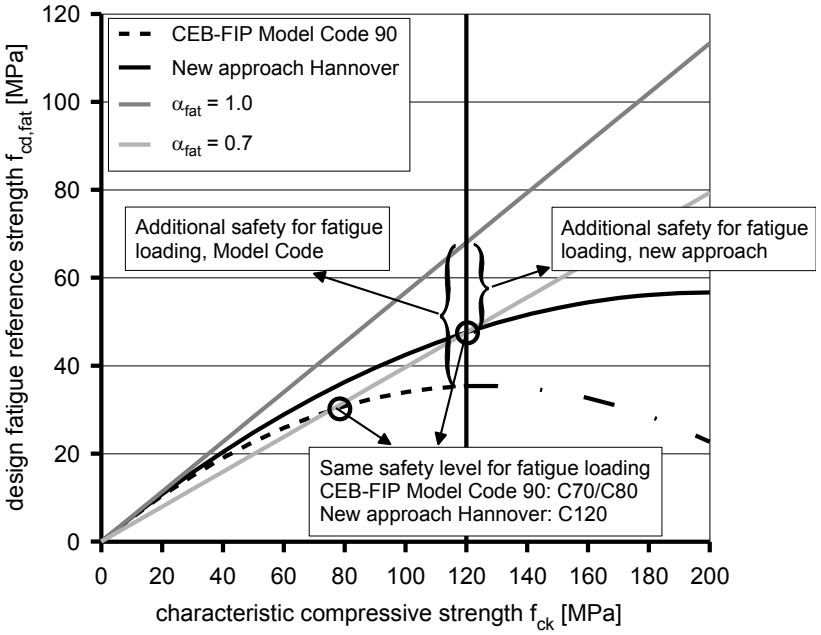

Figure 4: Comparison of the new approach for $f_{cd,fat}$ with the approach of CEB-FIP Model Code 90 [3].

It is obvious that the application of the design fatigue reference strength $f_{cd,fat}$ according to CEB-FIP Model Code 90 [1] to concretes with compressive strengths of $f_{ck} > 125$ MPa would lead to decreasing values of $f_{cd,fat}$. On the contrary, the new approach (equation (4)) gives an increasing function and, therefore, it is applicable up to a compressive strength of $f_{ck} = 200$ MPa. Moreover, applying the modified fatigue reference strength leads to $\alpha_{fat} = 0.70$ for a concrete grade C120. That means the same safety level is ensured for a C120 using the new approach as it was specified for a concrete in the range between C70 and C80 according to CEB-FIP Model Code 90 [1] in the early 1990s. Meanwhile existing extensive scientific research works on high strength concretes justifies this adjustment in the safety level. Thus, the required safety is ensured for all concrete grades of up to $f_{ck} = 200$ MPa.

Complete design model

Evaluating fatigue design of concrete structures, both Woehler curves and fatigue reference strength need to be analysed together. However, the required safety level is ensured by the definition of the design fatigue reference strength, which is the reference value of $S_{cd,max}$ and $S_{cd,min}$, or rather by the amount of reduction in characteristic static compressive strength. Modifying the design fatigue reference strength, leads to a change in the correlation between the design stresses $\sigma_{cd,max}$ and $\sigma_{cd,min}$ and the numbers of cycles to failure N. Because of the non-linear correlation between $S_{cd,max}$ and $S_{cd,min}$ and N, small changes in $f_{cd,fat}$ lead to disproportional changes in numbers of cycles to failure. Of course, with increasing concrete grades, this influence increases. In Figure 5, the effect of different reference values is exemplarily presented for the concrete grades C30 and C120. For this purpose, the characteristic static strength f_{ck}, the static strength's design value f_{cd} and the design fatigue

reference strength $f_{cd,fat,Hannover}$ are used as reference values. For this, the new Woehler curve is used. In addition, the dashed curve is calculated using the Woehler curve and the design fatigue reference strength $f_{cd,fat}$ of CEB-FIP Model Code 90 [1]. For simplicity the minimum stress $\sigma_{ci,min}$ = 0.05 is kept constant.

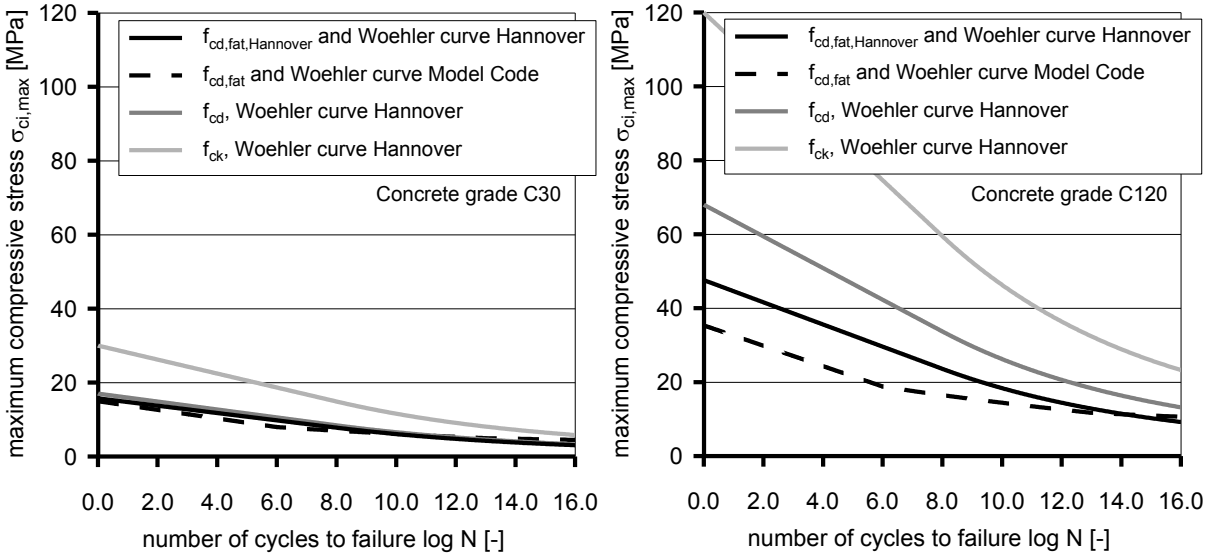

Figure 5: Analysis of the effect of reference values f_{ck}, f_{cd}, $f_{cd,fat}$ and $f_{cd,fat,Hannover}$ (C30 and C120).

In Figure 5 it is shown that the new approach permits higher numbers of cycles to failure for the same maximum compressive stress than [1]. But the differences in load cycles between the new and the current standard curves are significantly smaller than the total difference when f_{ck} is used as reference strength. It is obvious that the effect of the new design model is greater for normal strength concretes than for higher concrete grades (see also Figure 4). For a concrete C30 both approaches lead to quite similar maximum compressive stresses $\sigma_{cd,max}$ ($f_{cd,fat}$ or $f_{cd,fat,Hannover}$ as reference strength). Comparing the curves for reference values $f_{cd,fat,Hannover}$ and f_{ck}, it is obvious that a huge reduction in numbers of cycles to failure exists, especially for a C120. This reduction is also observable by comparing the maximum stresses for the same number of cycles to failure log N. For a concrete class C120, the ratio of $\sigma_{c,max}(f_{cd,fat,Hannover}) / \sigma_{c,max}(f_{cd})$ = 0.7 (see also Figure 4).

For the evaluation of the safety level, further aspects have to be considered. Generally and different from both design approaches, the determination of the stress levels in experimental tests refers to mean values of the static strength. This means, even without any safety factors and additional reduction terms taking account of fatigue loading, there is an additional safety included in the design concept since f_{ck} refers to the 5%-quantile and not to the mean value of static strength. This additional reduction in the number of cycles to failure is not shown in Figure 5. Another aspect is that the fatigue reference strength refers to 28-days compressive strengths. However, subsequent concrete hardening, which is not considered in the design concept, normally leads to a better fatigue bearing capacity, thereby providing additional safety. Two further positive influences regarding fatigue strength are the redistribution of stresses in damaged zones and the combined bearing capacity of reinforced concrete. On the contrary, there are influences like preliminary damage, overloads and the combination of different load levels, which might reduce the fatigue strength of structures. The effect of redistribution, preliminary damage and overloads can hardly be quantified in a general valid way for all concrete structures, yet. All together, the new approach does not lead to significant changes in the fatigue design results for normal strength concretes. For higher strength concretes, there is

still a huge reduction in numbers of cycles to failure representing safety. Taking this into account, and additionally considering both the previously described “hidden” safety factors and the new research results concerning fatigue of higher strength concretes, it can be stated that the required safety level is ensured.

4 Conclusions

In this paper a new design model for compressive fatigue loading is presented. This design model was developed based on extensive research on normal strength, high strength and ultra-high strength concretes [2], [3]. It comprises new Woehler curves and a modified design fatigue reference strength. To ensure an easy practical application, the new design model was integrated into the design concept according to CEB-FIP Model Code. The applicability of the Woehler curves for normal strength, high strength and ultra-high strength concretes is verified [3]. The modified fatigue reference strength ensures the same safety level for a C120 as for a concrete in the range of C70/C80 according to [1]. In addition, the ensured safety of the new design model is analysed exemplarily for two concretes having normal strength and high strength grades. It is shown that the new design model leads to higher numbers of resisting cycles to failure, especially for high strength concretes. These improvements are absolutely crucial for practical application taking the increasing fatigue relevant loads into consideration. According to meanwhile existing experimental test results for high-strength concretes, this modification is justified. Simultaneously and most important, it is demonstrated that the required safety is still assured. Altogether, the new design model enables a safe and economic fatigue design of concrete structures. Furthermore, it enables a prospective extension of application for ultra-high strength concretes up to f_{ck} = 200 MPa. The presented design model is included in the new fib-Model Code 2010 whereby the concrete grades are limited to C120. Background information will also be included in [8].

References

[1] CEB – Comité Euro-international du Béton: „CEB-FIP Model Code 90“. Bulletin d’Information, No. 213/214, Thomas Telford Ltd., London, 1993.

[2] Wefer, M.: Materialverhalten und Bemessungswerte von ultrahochfestem Beton unter einaxialer Ermüdungsbeanspruchung. Dissertation, Leibniz Universität Hannover, Institut für Baustoffe, 2010

[3] Lohaus, L.; Wefer, M.; Oneschkow, N.: Ermüdungsbemessungsmodell für normal-, hoch- und ultrahochfeste Betone. In: Beton- und Stahlbetonbau, Jahrgang 106, Heft 12, S. 836 - 846, Ernst & Sohn, 2011.

[4] Lohaus, L., Wefer, M., Oneschkow, N.: High Performance Concrete – How do deal with fatigue? In: Proceedings of the fib Symposium Prague, June 2011.

[5] Grünberg, J.; Lohaus, L.; Ertel, Ch.; Wefer, M.: Mehraxiales mechanisches Ermüdungsmodell von Ultra-Hochfestem Beton (Experimentelle und analytische Untersuchungen). In: Beton- und Stahlbetonbau, Jahrgang 102, Heft 6, Ernst & Sohn, 2007.

[6] Petković, G.; Stemland, H.; Rosseland, S.: High Strength Concrete SP 3 - Fatigue, Report 3.2 Fatigue of High Strength Concrete. SINTEF Structures and Concrete, Trondheim, August 1992

[7] Klausen, D.: Festigkeit und Schädigung von Beton bei häufig wiederholter Beanspruchung. Dissertation, TU Darmstadt, 1978.

[8] fib – International Federation for Structural Concrete: fib-Bulletin: Constitutive Modelling of Concrete Behaviour according to Model Code 2010. (in Process).

This research project was part of the priority program 1182 “Sustainable Building with Ultra-High Performance Concrete (UHPC)” funded by the German Research Foundation (DFG).

Mechanical Behaviour of Ultra High-Performance Fibrous-Concrete Beams Reinforced by Internal FRP Bars

Emmanuel Ferrier[1], Laurent Michel[1], Philippe Lussou[2], Bruno Zuber[2]
1: LGCIE Site Bohr, Université Claude Bernard Lyon I, Domaine scientifique de la DOUA, France
2: Lafarge, LCR, Saint Quentin Fallavier, France

The main objective of the research project reported in this paper is to develop a new type of high performance light beams that will increase the performance of usual beams (timber steel or RC beams) by combining FRP rebars cast in a ultra-high-performance concrete with short fibre reinforcement (UHPC-SFR). The beam is obtained to get a light beam with a high compressive and tensile capacity to sustain high bending moment and to be also shear resistant. The hybrid beam thus obtained possesses a lower bending stiffness than a glulam beam or steel beam of similar overall dimensions but a higher ultimate load capacity. One model is developed to validate this concept is presented in this paper. It is an analytical model based on the usual force equilibrium hypotheses. The load-displacement and moment-curvature relationships are compared to experimental results obtained from 5 large scales specimens. The results show good correlation between analytical and experimental results, and illustrate the potential interest of such composite beam configurations for civil engineering structures.

Keywords: CFRP bars, ultra-high-performance concrete, Reinforced concrete, beams

1 Introduction

Construction with ultra high performance short fibers has increased significantly in Europe and all over the world in recent years. Since the materials strength are very high in compression and very interesting in tension combined with a capacity to mitigate the effects of environemental exposure thanks to a low permeability, its increased use is predictable when sustainable development principles are taken in consideration [1, 2]. Use of this technology enables the designer to create thinner sections and longer spans that are lighter, more graceful and innovative in geometry and form, with improved durability and impermeability against corrosion, abrasion and impact [3]. The material technology permits it to be used without passive reinforcing (rebar) and reductions in formwork, labor and maintenance further add to economy [4]. The elimination of shear stirrups framework improves safety, the reduction of weight speeds construction, and the improved durability reduces maintenance and extends the usage-life. As a consequence, the consumption of UHPC has increased significantly for construction all over the world, to such a level that new ways to optimize its use are now necessary [5, 6]. This paper presents the analytical and experimental results of an investigation on a new type of hybrid beam. On the one hand, as shown in Figure 1, the hybrid beam is obtained by casting FRP rebars in the bottom of a beam made of ultra-high-performance concrete with short fibre (UHPC-SFR). The high performance concrete, with a compressive strength of 150 MPa and a tensile strength of 15 MPa, are cast in mould to get the lighter beam as possible. The Young modulus of UHPC- SFR is approximately 50 000 MPa [1, 2]. The UHPC-SFR beams are reinforced with 1, 2 or 3 FRP bars embedded in the concrete in order to increase the tensile strength of the bottom portion of the hybrid beam [7]. On the other hand, the objective of the modelling was to develop a modelling wich consider concrete cracking and post pic behaviour and then allowing to optimize the configuration of the section, by selecting the most appropriate thickness of UHPC for shear and flexure, FPR properties (rebars area, Young modulus), thus increasing the bending stiffness and the ultimate load capacity. The experimental testing was done on beams with a 2- or 4-meter span. The performance of this innovative hybrid structural configuration is confirmed in this paper. We

consider a type of I section. The objective is to develop different failure modes; the geometry of the section has been adapted to each case study. The objective was either to reach the tensile FRP reinforcement failure (beam with a 4 meter span) or to reach the compressive strength failure (beam with a 4 meters span) or by retaining a smaller span length (2 meters) to get a shear failure.

2 Experimental program

Test specimens

A typical hybrid beam such as the one described above is shown in Fig. 1. The beam of length Lw has a width b_w and height h_w. The tensile bottom of the beam has a thickness of h_{w1} which is reinforced with FRP. At the top of the section, the compressive part of the beam has a thickness of h_{w1}. For the sake of comparison, the total depth of the specimen is selected to be identical for all the beams. In order to evaluate the efficiency of this beam, a limited number of parameters was retained. Obviously, geometrical and material parameters such as beam length, depth and span, depth-to-width ratio, volume percentage of concrete versus short steel fibers, volume ratio of the tensile rebars and their mechanical properties including axial stiffness of rebars, and mechanical properties of concrete and FRP are all significant. In this study, the parameters that were investigated are the beam span, depth-to-width ratio, and the tensile strength of the rebars incorporated in the lower part (Fig. 1).

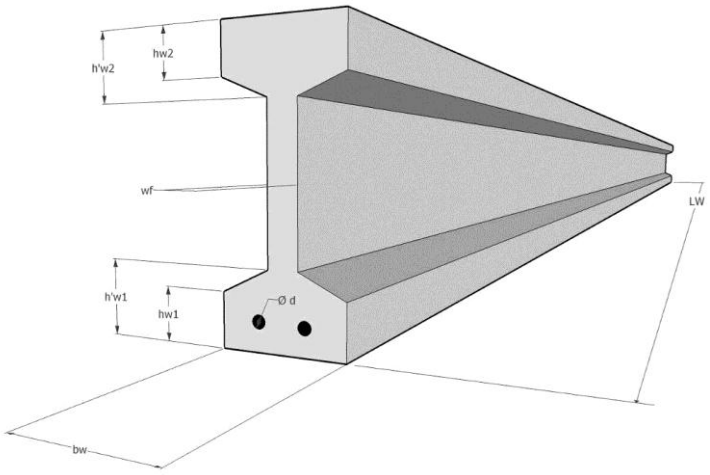

Figure 1 : Geometrical parameters of beams.

The geometrical properties of the five beams studied are given in Table 1. For the five beams the volume percentage of short metalic fibers is 2 % and the axial stiffness E_rA_r of the rebars was fixed to range from 20 MN to 30 MN for carbon FRP rebars and to range from 9 to 18 MN for glass FRP rebars. The material properties of the rebars, made of, glass (G) or carbon (C) fiber-reinforced polymers, are given in table 1 and 2.

Table 1 : Parameters of mechanical behaviour law.

Material		Parameters	Value
Ultra high performance concrete	Tension	f_{ctj} [MPa]	9
		ε_e [%]	0.02
		f_{ct} [MPa]	17
		$\varepsilon_{0.3\%}$ [%]	0.3
		$\varepsilon_{1\%}$ [%]	1
		ε_{lim} [%]	10
	Compression	ε_{bc} [%]	0.3
		f_{cc} [MPa]	150
	Young's modulus	E_c [MPa]	50000
FRP Rebars	Tension	$f_{FRP\ r}$ [MPa]	1900
		ε_{re} [%]	1.35
	Young's Modulus	E_r [MPa]	140000

The depth-to-width ratio h/b_w was fixed to range from 8 to 9.7 to obtain the wanted failure modes. The beam span-to-depth ratio L_w/h_w was taken as 9 for the four 2-metre beams to get a shear failure and 20 to 22 for the four 4-metre beams to obtain a flexural failure. The highest value for this ratio is anticipated to favor the flexural behavior rather than the shear behavior more likely to control the shorter beams. The L_{span}/h value of 20 corresponds to the standard value proposed by ASTM D3737 [8] test procedure used forglulam beams. The short span beam 5 has been lighten thanks to 50 mm diagonal void in the flange (Fig. 2).

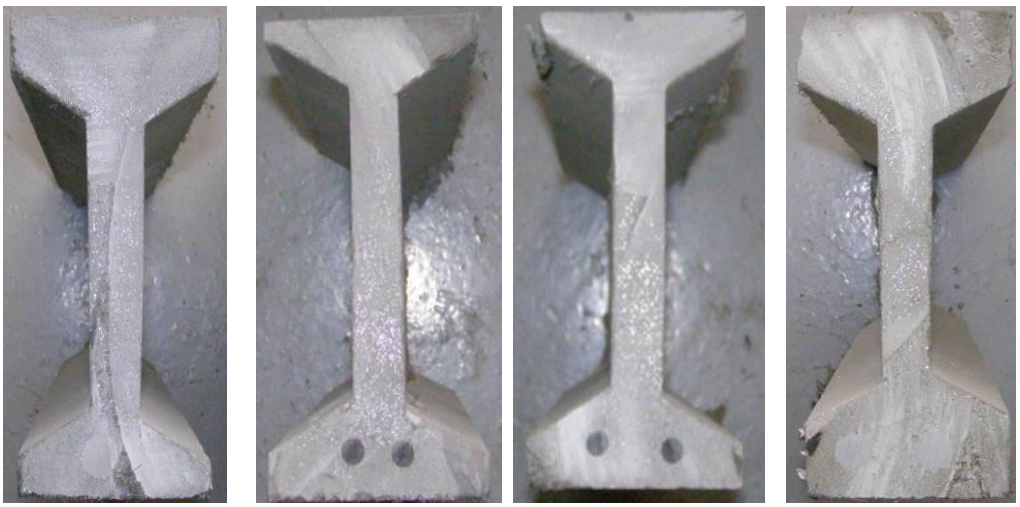

Beam 1 Beam 2 Beam 3 Beam 4 -5

Figure 2 : Beams section after testing.

Material

As described above, the hybrid beam is made of an ultra high performance concrete. The UHP concrete is a Ductal® F1 premix. In order to evaluate the mechanical properties, mechanical tests were performed on each concrete batch. The 5 beams were cast in two different batches.

Table 2: Materials and geometrical parameter definitions.

	h_{w1}	h'_{w1}	h_{w2}	h'_{w2}	b_w	b_f	h_w	L_w	FRP TYPE	Diameter	number	Area
	[mm]	[mm]	[mm]	[mm]	[mm]	[mm]	[mm]	[m]	CF/GF	[mm]	[u.]	[mm^2]
Beam 1	23	40	32	48	90	22	200	4	Glass	16	1	201
Beam 2	17	33	10	21	90	22	176	4	Carbon	9.6	3	217
Beam 3	17	33	10	21	90	22	192	4	Carbon	9.6	2	144
Beam 4	38	55	35	50	90	22	215	2	Glass	16	2	402
Beam 5	38	55	35	50	90	22	215	2	Glass	16	2	402

Nine cylindrical concrete specimens were tested under compression 90 days after casting, according to the specifications of UHPC standart [9, 10]. A mean compressive strength f_c of 174 ± 7.4 MPa was found. For FRP rebars, we did not perform specific mechanical testing in the laboratory and we used the properties provided by the suppliers in our calculations (Table 1).

Specimen preparation

The FRP-concrete composite beams used in this research were fabricated using casting as mentioned earlier. FRP rebars were fixed in the mould because of their low density. The beams were cast vertically.

3 Experimental result

Mechanical testing

The tests done in order to obtain the bending stiffness and the load bearing capacity of the composite beam and moment-curvature relation are illustrated in Fig. 3. The beams specimens prepared according to the above detailed procedure were subjected to a four-point loading test according to ASTM standards D 3737-04 and D 4761-05 [11]. The distance between support and applied load was higher than twice the depth of the beam, as required by the standard. For the 2.0-metre beams, this distance is 0.7 m while for the 4.0-metre beams, it is 1.3 m. The loading was displacement-controlled and, as requested by the standard ASTM D4761-05, the total test duration was always between 10 s and 10 min. The exact speed rate was 9 mm/min for the beam with a span/depth ratio of 20 and 1 mm/min for the beams with a span/depth ratio of 9. The loads and displacements were recorded at 1 s intervals by data logger using load cells and LVDT transducers. In order to obtain strain distribution in the mid-span section, four strain gauges were bonded on the lateral face of the beam. Rebar strains were also measured during the loading with gauges bonded before the beams were cast. Before the tests, the beams were conditioned to a mean value of about 12 % for the moisture content and a temperature of 20° C.

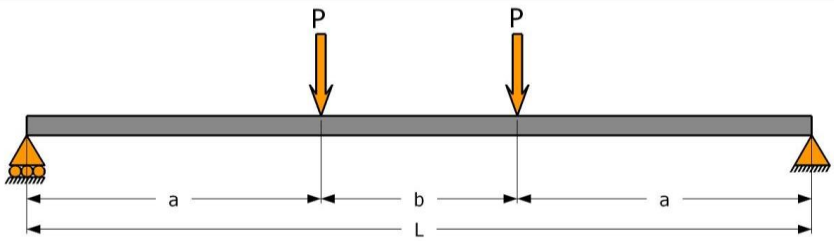

Figure 3 : Testing device.

Load-deflection response of composite beams

The analysis of the load-displacement curves indicates that there are two or three stages of distinct behavior during the test, corresponding to the progressive damages in the constitutive materials (concrete, rebars). The curves showing the load-displacement relationship for the three 4.0-metre beams are given in Fig. 4 and, for the two 2-metre beams, in Fig. 5.

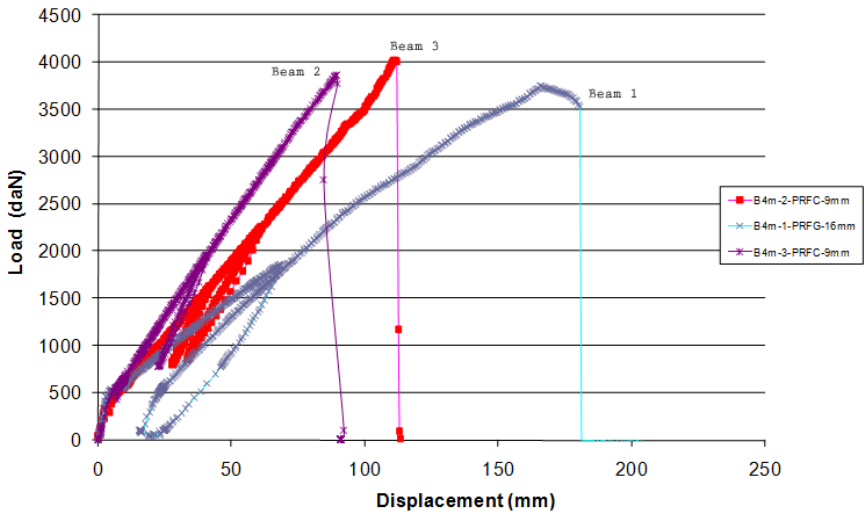

Figure 4 : Load –displacement curve Beam 1 to 3.

For all beams with UHPC reinforced with GFRP or CFRP, the first stage of behavior corresponds to that of the uncracked section and the beam exhibits an important bending stiffness. The second stage of behavior is attained when the load reaches about 11 kN for the 2.0-metre span beams and for a load of 5 kN in the case of the 4-

metre span beams. At this point, the bottom UHPC of the beam begins to crack, and a reduction of the bending stiffness is observed.

Table 3: Experimental results.

			Elastic limit load	Displacement at elastic load	Load at failure	Displacement at failure
			[kN]	[mm]	[kN]	[mm]
Beam	1	B4m-1-PRFG-16 mm	5.20	5.29	37.42	166
Beam	2	B4m-3-PRFC-9 mm	5.50	5.12	38.62	90
Beam	3	B4m-2-PRFC-9 mm	4.57	3.21	40.15	112
Beam	4	B2m-2-PRFG-16 mm	13.62	1.20	85.55	24.13
Beam	5	B2m-A-2-PRFG-16mm	10.62	1.35	21.62	9

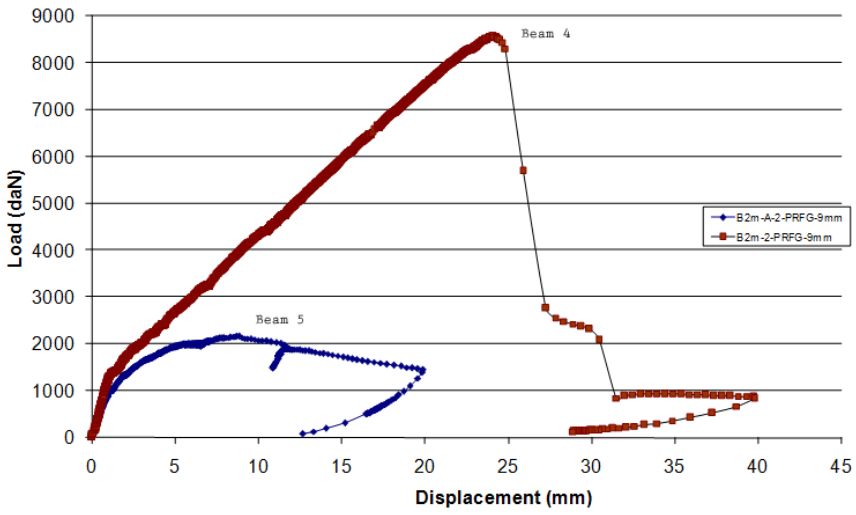

Figure 5 : Load –displacement curve, Beam 4 to 5.

The behavior of the composite beam remains linear but with a reduced stiffness until the third stage of behavior may occurs (beam 1). This corresponds to the yielding of tensile steel short fibers that occurs at loads of about 35 kN for the beam 1. After the cracking load the behavior remains elastic with a constant stiffness until failure. This emphasizes the interest of using FRP rebars to allow an increase of the tensile capacity of the lower beam part and to increase the ultimate capacity of the beam (Table 3). But shear failure should be carrefully avoid like for beam 5 where the ultimate load is reduced due to shear failure.

Behaviour at failure

Using the mid section strain measurements, an evaluation of the mechanical behavior of the composite beams and of the efficiency of the hybrid solution at failure can be performed. For the upper UHPC section in compression, the strain rate at failure was higher than 2500 μm / m for beam 3 and nearby 2300 μm/m for beam 1. For FRP rebars, ultimate strength was attained in beam 1 with GFRP bars while 80 % of the CFRP strength was reached at failure for Beam 3. For 2-meter beams, the range of tensile stress in CFRP or GFRP varied from 20 to 50 % of the ultimate FRP strength due to the premature shear failure of the beam (Table 3). From this observation, it was concluded that this new innovative hybrid beams allows to get higher stress at failure in each material at failure and increase then the performances of the beam. It can be stated that the hybrid configuration of the beam allows each material to reach a high strain at failure in the concrete in compression; this confirms the interest of this approach. At the ultimate load level, various failure modes were observed, depending on the span and characteristics of the beam.

The 2.0-metre beams failed in shear (Fig. 6c and d), while the 4-metre beams exhibited compressive (Fig. 6b) or tensile failure (Fig. 6a). The failure load of the hybrid beams occurred between 18 kN (beam 1) and 85 kN (beam 5) (Table 3). It is important to note that there was no debonding of the FRP rebars from UHPC from any of the beams. The use of Carbon composite rebars seems to be the most appropriate in relation to reduce span displacement. This can be explained by the fact that Carbon FRP Young modulus is higher than GFRP Young Modulus (Table 1). For structure design purpose, the main design criterion will be related to service condition (deflection criterion) as for glulam or steel beams. The design properties should consider the axial stiffness of FRP rebars.

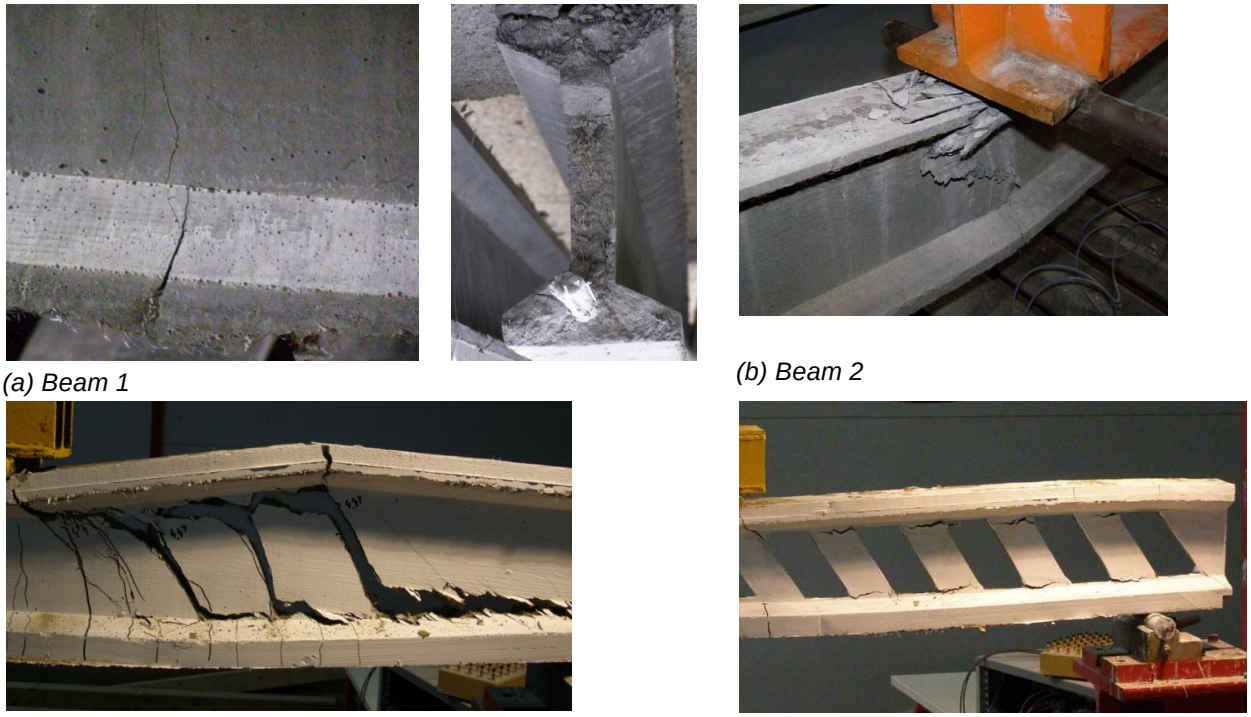

(a) Beam 1

(b) Beam 2

(c) Beam 4

(d) Beam 5

Figure 6 : Failure modes.

4 Analytical modelling

In this study, a nonlinear material analytical modelling of the hybrid beams was undertaken. A sectional analysis was used initially to develop an appropriate moment–curvature relationship for the composite sections. This modelling was preferred to a FEM analysis because of concrete cracking wich need a high number of elements necessary to reduce numerical instabilities caused by the size of the finite element mesh for a full 3-D analysis [12]. The method developed in this study to predict the strength and the stiffness of the multi-material hybrid beam is based on an iterative procedure. This analytical model, based on strain compatibility and equilibrium of internal forces in the section, can simulate the multi-material beam behaviour and take into account the non-linearity of the constituent materials [413]. Causes of non-linearity in the section include tensile cracking of concrete and post tensioning, plastic behaviour of concrete in compression, and yielding of the internal short metalic fibers reinforcement.

Material properties

To model the mechanical behaviour of UHPC-SFR concrete, an elastic, multilinear stress-strain relationship proposed by Habel *et al*. [14] and AFGC [3] for UHPC-SFR was used. For concrete, the values of strains corresponding to critical levels on the stress-strain curve are

given by the following equations. The tensile stress corresponding to first cracking is f_{ctj} with a strain value given by $\varepsilon_{0.3\%}$. The maximal point of the tensile stress/strain relation is given by the stress corresponding to f_{ct} and the strain to $\varepsilon_{1\%}$.

$$\varepsilon_{0.3} = \frac{w_{O.3}}{l_c} + \frac{f_{c_{tj}}}{E_{cj}} \quad (1)$$

$$\varepsilon_{1\%} = \frac{0.01h}{\frac{2}{3}h} + \frac{f_{c_{tj}}}{E_{cj}} \quad (2)$$

$$\varepsilon_{\lim} = \frac{15}{4h} + \frac{f_{c_{tj}}}{E_{cj}} \quad (3)$$

where h is the depth of the section; $f_{ctj,}$ the ultimate tensile elastic strength and f_{ct} the ultimate tensile strength of UHPC; E_{cj}, are the elastic Young moduli of the UHPC.

The stress-strain relationship for wood, CFRP or GFRP can be considered elastic. Table 1 gives the parameter values of the mechanical behaviour law of each material.

Calculation procedure

The stress-strain relationships for UHPC, FRP reinforcements are combined with the section and span information to obtain the load-deflection and moment-curvature relationships of the beam [13]. Relevant data include the height and width of the beams, depth and amount of FRP reinforcement, geometries of the UHPC-SFR section, span length and position of the external loads. To initiate the calculation procedure, a value for the strain in the top concrete (□sup) and a position for the depth of the neutral (zg) are assigned arbitrarily. The depth of the beam is divided into 200 slices. The strain profile along the height of the RC beam is obtained from the following equations.

$$\varepsilon_c(\mathrm{i}) = \frac{(\mathrm{d_c(i)} - \mathrm{z_g})}{\mathrm{d_c(i)}}\varepsilon_{\sup} \quad (4)$$

and

$$\varepsilon_r = \frac{(d_r - z_g)}{d_r}\varepsilon_{\sup} \quad (5)$$

where ε_w(i) is the strain in UHPC layer i; d_r is the depth of the rebars, and ε_r is the strain in the reinforcing bars.

An average strain is calculated for each slice, and the corresponding compressive and tensile stresses are found using the stress-strain relationship for each material. Multiplying the stress by the area of the slice gives the compressive and tensile forces. The following equations are used for this purpose.

$$\sigma_c = \sum_{i=1}^{n} E_c \varepsilon_c(i) \quad (6)$$

$$F_c = \sum_{i=1}^{n} A_c(i) E_c \varepsilon_c(i) \quad (7)$$

$$\sigma_r = E_r \varepsilon_r \tag{8}$$

$$F_r = A_r E_r \varepsilon_r \tag{9}$$

where A_r is the area of the rebars, A_c is the area of the concrete section. Once all forces are calculated, equilibrium of the section is verified with the next equation.

$$\sum \mathrm{F} = 0 = \mathrm{A_r E_r \varepsilon_r} + \sum_{\mathrm{i=1}}^{\mathrm{n}} \mathrm{A_c(i) E_c \varepsilon_c(i)} \tag{10}$$

If equilibrium conditions are not satisfied, the position of the neutral axis (z_g) is moved to a different location and the process is repeated until the sum of the compressive forces in the section balances the sum of the tensile forces. Once the iterative procedure has converged to equilibrium, the internal moment and the curvature are determined, taking into consideration the load and location of the material splice (Equations 11 to 13).

$$\sum m = m_{ext} = m_r + m_c \tag{11}$$

with

$$m_r = A_r E_r \varepsilon_r (d_r - z_g) \tag{12}$$

$$m_c = \sum_{1}^{i} A_c(i) E_c \varepsilon_c(i) (d_c(i) - z_g) \tag{13}$$

In determining the theoretical moment–curvature relationship for the composite section in flexure, it is assumed that plane sections remain plane and that the longitudinal strain is directly proportional to the distance from the neutral axis.

A finite difference model is used to calculate the deflection of the beam. Taking advantage of the symmetry of the loaded beam, the finite difference calculation is performed with one half of the beam, cut into five sections. A flow chart of the calculation procedure is shown in Figure 10. The computation is done in a Visual Basic environment. The moment-curvature and load-displacement curves are calculated and, at any level of loading, strains and stresses in each constituent material are obtained.

Failure criteria

The calculation continues by incrementation of the applied load, until the maximum strength of one of the materials is reached. Possible failure modes in compression that must be taken into account include crushing of the topmost fibers in the UHPC-SFR. In tension, failure of the hybrid beam may occur in the FRP, of in the bottommost fiber of the beam; tensile failure of concrete in the lower UHPC-SFR is also consider thanks to the UHPC equivalent mechanical law.

In RC beams, shear controls design when flange width is small. It is necessary to check the shear strength. According to AFGC standart [5], the maximum shear stress of composite beams can be assessed as follows:

$$V_f \leq V_u \tag{14}$$

The horizontal shear stress at the neutral axis is:

$$V_f = \frac{S \cdot \sigma_p}{\gamma_{bf} \cdot \tan(\beta_u)} \tag{15}$$

where V_u= applied shear force (N)

σ_p = UHPC concrete strength (MPa)

S = concrete shear area (mm^2)

γ_{bf}= safety factor for concrete (equal to 1 here).

β_u = cracks angle (45°)

This method allows us to calculate the maximum shear stress in the beam and then to compare this value to the UHPC shear strength [14, 15, 16, 17]. Here, S =b_0z is the resistance area of fibers calculated by multiplying the width of web b_0 by the lever arm z between the tensile and compressive resultant forces. It is assumed that z=0.9d for rectangular sections [4], and that this is a conservative assumption for T-sections. Parameter ß$_u$ represents the angle of the struts of compressed concrete from the neutral fiber of the beam. Partial safety factor γ_{bf} was introduced to account for any manufacturer defects that influence the tensile property of UHPC. It equals 1.3 for the case of fundamental combinations and 1.05 for the case of accidental combinations.

The average post-crack residual tensile strength σ_P can be calculated as

$$\sigma_p = \frac{1}{K} \cdot \frac{1}{w_{\lim}} \int_0^{w_{\lim}} \sigma(w) dw \qquad (16)$$

Variable σ_P is determined by the maximum crack width w_{lim} and the stress versus crack width relation σ(w). The maximum crack width limit of 0.3 mm is recommended in the French code. If it is assumed that the stress versus crack width relation is linear up to the maximum crack width of 0.3 mm, then σ_P can be approximately estimated as the average of the stress level corresponding to zero crack width and a crack width limit of 0.3 mm. The anisotropy of fiber orientation distribution is not considered (K=1).

The results are summarized in Table 7, based on the following assumptions. The design safety factors γ_{bf} were set to 1.0, and the angle ß$_u$ was assumed to be 45°. A linear stress versus crack width response was assumed for crack widths up to 0.3 mm. Therefore, the average post-crack strength can be estimated as σ_P=9 MPa, based on the Xia et al. [18].

The shear strength prediction from the French code at a maximum crack width equal to 0.3 mm were significantly lower (-25 %) than the test results for the beam 4 and 5. The reason for the underestimation is because the predicted shear strength was actually corresponding to the shear crack width of 0.3 mm and thus it cannot consider the secondary contribution. The shear resistance contribution from this secondary effect is considerable for a UHPC beam with passive high strength reinforcement.

Experimental/theoretical comparison

In order to evaluate the validity of the modelling, the experimental program performed on five hybrid beams is used. Experimental load-displacement and moment-curvature curves obtained experimentally from the 2-meter spans and 4-meter spans were compared to the analytical model. The changes in the position of the neutral axis between the analytical procedure and the experimental results, as the applied load increased, were also compared (Fig. 7).

Bending stiffness and deflection comparison

The modelling of the load-displacement relationship is compared to experimental results in Figure 8. It can be observed that the typical moment–curvature relation for the hybrid section can be idealized as a bi_linear relation (Figure 7). In the first portion of the curve, all materials remain elastic; the concrete starts to crack in tension during the second stage, and steel yielding occurs during the third stage. For the 4-meter beams, the load-displacement modeling

results are compared to the experimental data in Figure 7. The experimental load-deflection curves exhibit the same three stages of behaviour predicted by the analytical modelling. The comparison between theoretical and experimental data generally indicates a good correlation. The stages of behaviour are well represented and the slope of the curve is obtained with an accuracy of more than 95%.

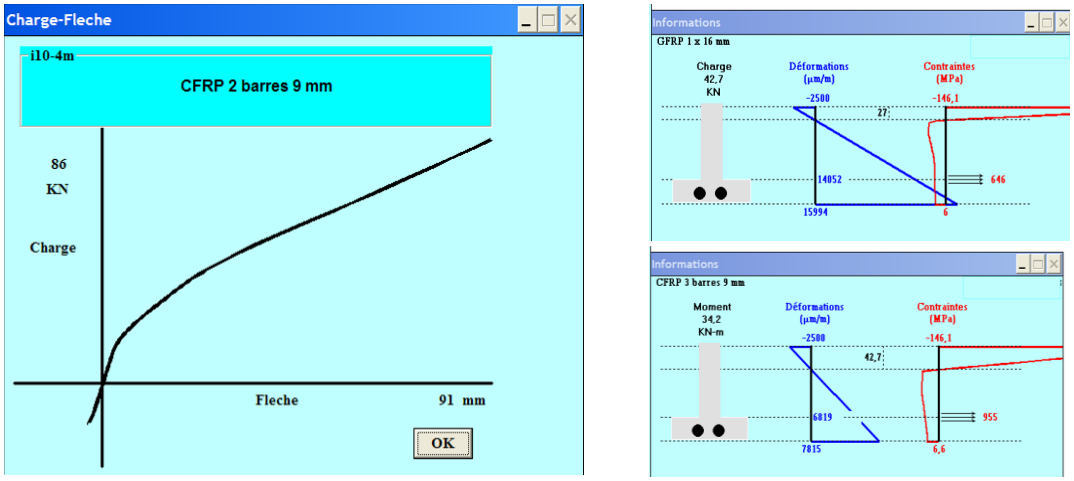

Load displacement curve *Strain profil*

Figure 6 : Examples of results.

Comparison at failure

Table 4 and 5 compares the ultimate load and displacement at failure, as well as predicted and observed failure modes. It can be readily observed that the prediction of the ultimate load is not as accurate as the general bending behavior discussed in the preceding section. For the 4-meter span beams, for which the predominant failure mode was in tension or in compression, the prediction of the ultimate load is satisfactory with a value that differs from the experimental values by about 7 to 17%. For the beams with small dimensions, predictions are also quite close with a predicted failure load ranging from 0.96 to 1.18 of the experimental results. The scattering of experimental results can be explained by the presence of defects in Short metallic fibers distribution in concrete when beams are casting.

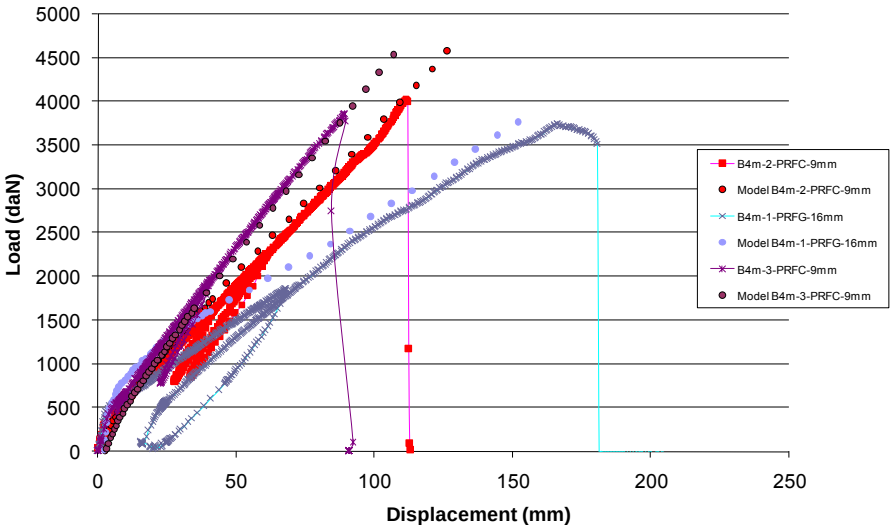

Figure 7: Comparison between experimental and numerical result for load and displacement curve.

Table 4: Comparison of theoretical and experimental load and displacement.

	Load at failure	Displacement at failure	theoretical load at failure	Theoretical displacement at failure	Normalised load	Failure mode
	[kN]	[mm]	[kN]	[mm]		
Beam 1	37.42	166	39.8	176	1.06	FRP in tension
Beam 2	38.62	90	48.9	113	1.26	UHPC in Comp.
Beam 3	40.15	112	50.3	140	1.25	UHPC in Comp.

Table 5: Comparison of theoretical and experimental load for shear.

	b_f	h_w	S	V_f (Theo)	Vu_{exp}	Failure mode
	[mm]	[mm]	[mm2]	[kN]	[kN]	
Beam 1	22	200	3564	32,1	18,7	flexure
Beam 2	22	176	3136	28,2	19,3	flexure
Beam 3	22	192	3421	30,8	20,1	flexure
Beam 4	22	215	3831	34,5	42,8	shear
Beam 5	22	50	891	8,0	10,8	shear

5 Conclusions

This study presents an innovative hybrid beam constructed of ultra-high performance concrete with short fibres and FRP reinforcing bars. Results from an analytical procedure are compared to a preliminary experimental study. The bending stiffness and the ultimate load of the hybrid beam investigated are improved over those of conventional beams of similar dimensions. The combination of materials allows a control of the ultimate load and ductility. The results of this study should be confirmed by an extensive experimental program with large-scale beams and more specimens. Fatigue and also creeping behaviour are extensive research to study.

6 Acknowledgements

This research has been done thanks tot he financial support of LAFARGE, LCR, FRANCE. Authors thanks Lafarge for supling Ductal® and Pulltral for supling FRP rebars.

Reference

[1] In Hwan Yang, Changbin Joh, Byung-Suk Kim, Structural behavior of ultra high perform ance concrete beams subjected to bending Engineering Structures, Volume 32, Issue 11, November 2010, Pages 3478-3487.

[2] Behloul, M., et al. 'The Sherbrooke Footbridge: The First Reactive Powder Concrete Structure',Structural Engineering International February 1998, 140-144.

[3] AFGC (Association Francaise de Genie Civil) Interim Recommendations 'Ultra-High performance, Fiber-Reinforced Concretes', AFGC Publication, France, January 2002.

[4] Acker, P., and Behloul, M., 'Ductal® Technology: A Large Spectrum of Properties, A Wide Range of Applications', FIB Symposium, Avignon, France, April 2004.

[5] Perry, V., Royce, M., "Innovative Field-Cast UHPC Joints for Precast Bridge Decks (Side-by-Side Deck Bulb-Tees), Village of Lyons, NY – Design, Protoyping Testing and Construction", 2007 Concrete Bridge Conference, USA, 2007.

[6] Amin Kamal Akhnoukh, Haiyan Xie, Welded wire reinforcement versus random steel fibers in precast/prestressed ultra-high performance concrete I-girders, Construction and Building Materials, Volume 24, Issue 11, November 2010, Pages 2200-2207.
[7] R. El-Hacha, D.Chen Behaviour of hybrid FRP–UHPC beams subjected to static flexural loading Original Research Article Composites Part B: Engineering, In Press, Corrected Proof, Available online 13 July 2011.
[8] ASTM D3737 – 08,. Standard practice for establishing allowable properties for structural glued laminated timber (glulam). ASTM International, 10.1520/D3737-08, (2008) 1-28.
[9] Japan Society of Civil Engineers, “Recommendations for Design and Construction of Ultra-High Strength Fiber Reinforced Concrete Structures”, September 2006.
[10] U.S. Dept. of Transportation - Federal Highways Administration “Material Property Characterization of Ultra-High Performance Concrete Prestressed I-Girders”, (Publication No. FHWA-HRT-06-103), August, 2006.
[11] ASTM D 4761-05, ASTM D4761 - 05 Standard Test Methods for Mechanical Properties of Lumber and Wood Base Structural Material, ASTM International, 10.1520/D4761-05, (2002), 1-10.
[12] Ranzi G., Bradford M.A. Direct stiffness analysis of a composite beam-column element with partial interaction Computers & Structures; August 2007; 85(15-16):1206-1214.
[13] Hyo-Gyoung Kwak, Sun-Pil Kim, Nonlinear Analysis of RC Beams Based on Moment–Curvature Relation, Computers and Structures; 2002; 80:615–628.
[14] Katrin Habel, Marco Viviani, Emmanuel Denarié and Eugen Brühwiler, Development of the Mechanical Properties of an Ultra-High Performance Fiber Reinforced Concrete (UHPFRC), Cement and Concrete Research; July 2006; 36(7):1362-1370.
[15] Raafat El-Hacha, Hani Abdelazeem, Ignacio Cariaga, Effect of casting method and shear span-to-depth ratio on the behaviour of Ultra-High Performance Concrete cross arms for high voltage transmission lines Engineering Structures, Volume 32, Issue 8, August 2010, Pages 2210-2220
[16] Su-Tae Kang, Yun Lee, Yon-Dong Park, Jin-Keun Kim, Tensile fracture properties of an Ultra High Performance Fiber Reinforced Concrete (UHPFRC) with steel fiber Composite Structures, Volume 92, Issue 1, January 2010, Pages 61-71.
[17] Rammer, Douglas R.; McLean, David I.; Cofer, William F, In-Place Shear Strength of Wood Beams, Proc 5th World Conference on Timber Engineering; August 17-20, 1998, Montreux, Switzerland, 207-214.
[18] J. Xia, K. R. Mackie, M. A. Saleem , A.Mirmiran, Shear failure analysis on ultra-high performance beams reinforced with concrete high strength steel, Engineering structures, available online on march 2011.

Fatigue Behaviour of plain and fibre reinforced Ultra-High Performance Concrete

Ludger Lohaus, Kerstin Elsmeier
Institute of Building Materials Science, Leibniz Universität Hannover, Germany

Higher concrete strengths lead to the possibility of building light, filigree bearing structural elements. However, these structures are more susceptible to dynamic loading and as a consequence the importance of material fatigue increases. At the Institute of Building Materials Science, Leibniz Universität Hannover, extensive experimental investigations on the fatigue behaviour of ultra-high performance concrete have been carried out [1], [2]. This paper describes the conducted experimental and theoretical investigations on the fatigue behaviour of plain and fibre reinforced concretes. Results of the experimental tests and the observed effects of fibre reinforcement on the strain development and the ultimate number of cycles to failure will also be presented.

Keywords: Ultra-High Performance Concrete, Fatigue, Fibre Reinforcement

1 Introduction

In the course of the priority program “Sustainable Building with Ultra-High Performance Concrete”, extensive investigations regarding the fatigue behaviour of ultra-high performance concretes have been carried out [1], [2]. A partial aspect of these investigations was to determine the influence of fibre reinforcement on the fatigue behaviour. For this purpose, cylindrical specimens of plain and fibre reinforced ultra-high performance concrete were examined under compression fatigue loading with different loading amplitudes. In addition, special specimen geometries, which cause a passive transverse tension to maximize the influence of the fibre reinforcement, were investigated. The effect of fibre reinforcement on the fatigue behaviour is examined on the basis of the ultimate number of load cycles to failure and the strain development. In the following sections, the test results are presented and the fatigue behaviour of plain and fibre reinforced ultra-high performance concrete shall be compared in order to quantify the effect of fibre reinforcement on static and fatigue behaviour.

2 Test program

Tested Concrete and Specimen Geometry

The examined concrete mixture belongs to the standard mixtures in the German Research Foundation (DFG) priority program 1182 “Sustainable Building with Ultra-High Performance Concrete (UHPC)” [1]. The ultra-high strength fine grain concrete M2Q has a maximum grain size of 0.5 mm and a 28 day compressive strength of $f_{c,cube,100}$ = 160 MPa, following storage in water. This mixture contains 2.5 Vol.-% of 9 mm long, smooth, high-strength steel fibres with a l/d ratio of 60.

The formwork of the specimens was removed after 48 hours. Then all the specimens were subjected to a two-day heat treatment of 120° C. The mean value of the static compressive strength of the cylindrical specimens after heat treatment was $f_{c,cyl}$ = 185 MPa. Afterwards, the specimens were stored at standard climate (20° C / 65% r.H.). Before testing, the top surfaces of the specimens were plane-parallel grinded and polished. The experimental tests were carried out primarily on cylindrical specimens with dimensions of d/h = 60/180 [mm/mm], see Figure 1. Furthermore, a variation in geometry, also shown in Figure 1, has been developed in cooperation with the Institute for Concrete Constructions, Leibniz Universität Hannover [3].

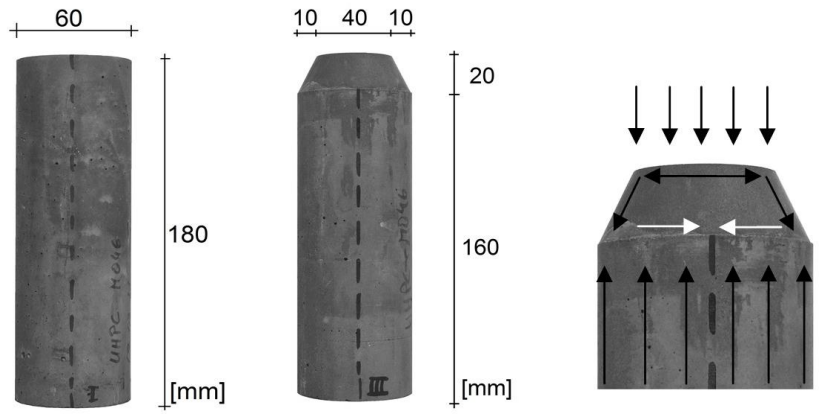

Figure 1: Specimen geometries and schematically shown force flux of the truncated cone.

Due to the newly developed specimen geometry, it was possible to generate a transverse tension, which normally is difficult to realize. Hence, the influence of the fibre reinforcement on the fatigue behaviour can be investigated more exactly. The truncated cone enables testing with combined loadings of uniaxial pressure and transverse tension. This passive transverse tension occurs in the transition area between the cylinder and the truncated cone.

Experimental Setup and Testing Program

The experimental investigations have been carried out in collaboration with the Institut for Concrete Construction, Leibniz Universität Hannover [4]. These tests have been performed with a servo-hydraulic universal testing machine with a 1 MN-Actuator. The experimental setup is shown in Figure 2.

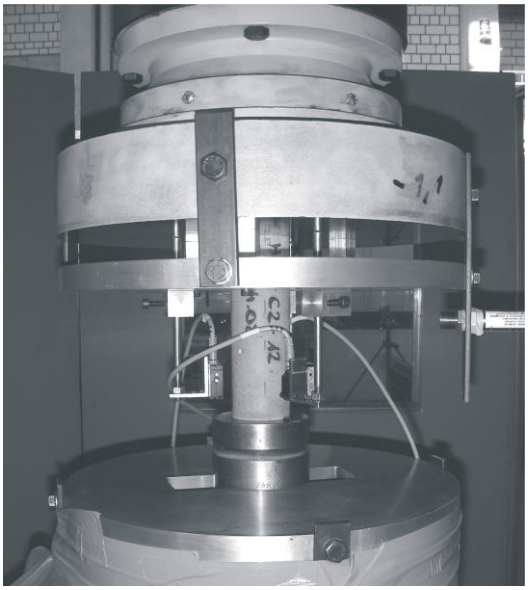

Figure 2: Experimental Setup.

During the investigations, the axial deformation of the test specimens was measured using three laser distance sensors which are positioned at 120° around the specimen. In addition, the surface temperature of the specimens was measured using a temperature sensor. Furthermore, the force applied by the machine and the corresponding displacement were recorded.

The static uniaxial compressive tests were carried out right before the dynamic investigations. The static compressive strength was determined based on the mean value of three specimens and serves as the reference strength for the dynamic tests. The static investigations were carried out displacement-controlled with a rate of v = 0.2 mm/min.

The dynamic investigations were carried out under pure compression loading. At first, the mean load was applied using force-controlled-method. Then, the sinusoidal force-controlled fatigue load was applied with a transient oscillation of 100 load cycles.

The dynamic investigations using cylindrical specimen geometry were carried out by [1]. Single level tests (Woehler tests) have been conducted using three different load levels. The maximum and minimum compressive stress level for these investigations was calculated according to the mean values of static compressive strength. The minimum compressive stress level was $S_{c,min} = 0.05$. The cylindrical specimens with fibre reinforcement were investigated using a maximum compressive stress level $S_{c,max}$ between 70 % and 90 % of the static compressive strength. These tests make use of eight to eleven specimens per stress level. On the other hand, the cylindrical specimens without steel fibres were examined with a maximum stress level of $S_{c,max} = 0.70$ and $S_{c,max} = 0.80$ and make use of six to seven specimen per stress level. The investigations on the truncated cones were as well carried out with a minimum stress level of $S_{c,min} = 0.05$. The maximum stress level was between 70 % and 90 % of the static compressive strength. For these dynamic investigations on the truncated cones without fibres, six specimens were used for each stress level. As can be seen in Table 1, the tests with a maximum stress level of 70 % only make use of three specimens. These investigations were cancelled after reaching a number of cycles of $N = 2*10^6$. The investigated truncated cones with fibre reinforcement were categorized into two different test series (M035 and M044). These investigations make use of two to four specimens per stress level. The maximum stress level varies between $S_{c,max} = 0.70$ and $S_{c,max} = 0.85$. The frequency used in all dynamic investigations had a magnitude of $f = 10$ Hz. An overview of the performed dynamic investigations is given in Table 1.

Table 1: Overview of the dynamic investigations.

	$S_{c,max} = 0.70$	$S_{c,max} = 0.75$	$S_{c,max} = 0.80$	$S_{c,max} = 0.85$	$S_{c,max} = 0.90$
cylinder without fibre reinforcement	7	-	6	-	-
cylinder with fibre reinforcement	8	-	11	-	9
truncated cone without fibre reinforcement	3	6	6	6	6
truncated cone with fibre reinforcement (M035)	2	3	3	-	-
truncated cone with fibre reinforcement (M044)	4	4	-	4	-

3 Test Results

Static Investigations

The static compressive strength's mean values of the different specimen geometries with and without fibre reinforcement are summarized in Table 2. Furthermore, the ratio between the results with and without fibre reinforcement as well as the ratio between the static compressive strength of the different specimen geometries is presented. It can be clearly seen that the truncated cones achieve a larger increase of the static compressive strength according to the fibre reinforcement than cylindrical specimens. Furthermore, the difference in the static strength's values between the different specimen geometries is higher for the specimens without steel fibres.

Table 2: Comparison of static strength for different specimen geometries with and without fibre reinforcement.

	cylinder [kN]	truncated cone [kN]	ratio [-]
with fibre reinforcement	551	388	1.4
without fibre reinforcement	489	246	2.0
ratio	1.1	1.6	

Figure 3 shows the stress-strain curves of four selected truncated cones with and without steel fibres. The compressive strength is calculated based on the larger base area. Here, the static strength's values of the truncated cones without fibre reinforcement could only reach about 60 % of the static compressive strength of the specimens with steel fibres. Furthermore, it can be observed that the fibre reinforced test specimens show a certain advance notice of the failure whereas the failure of the plain UHPC occurs abruptly.

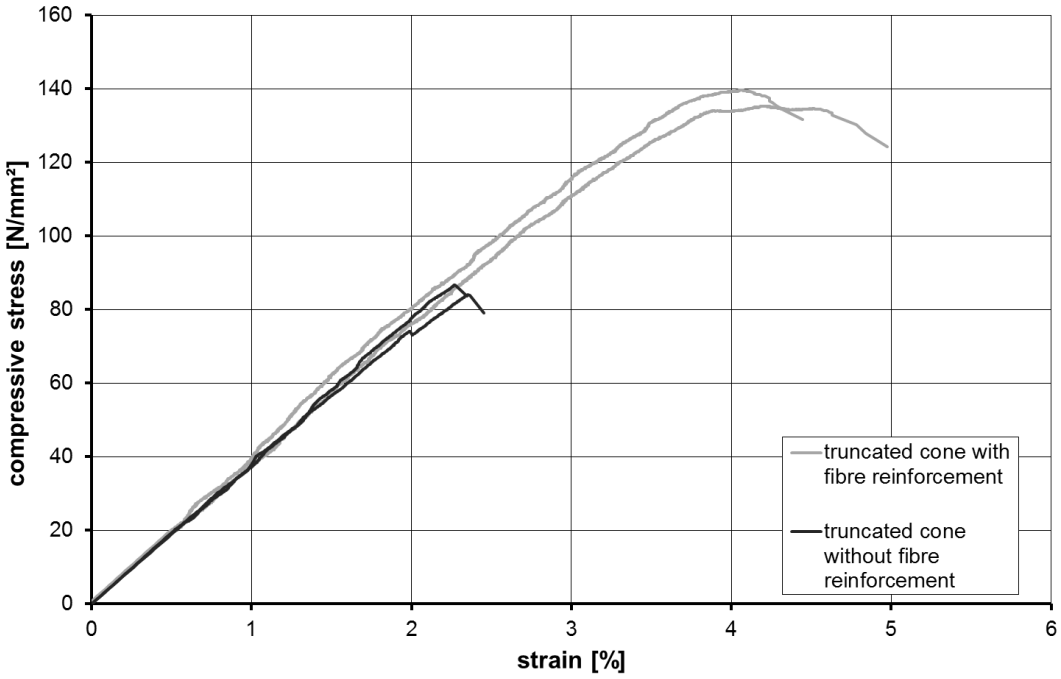

Figure 3: Comparison of the stress-strain relation of the truncated cones with and without fibre reinforcement.

Dynamic investigations

The results of the dynamic investigations are shown in the following illustrations. Figure 4 shows the mean values of the ultimate numbers of cycles to failure N of the cylindrical specimens with and without fibre reinforcement. The S/N-curve of the CEB-FIP Model Code 90 [5] is also presented. The results show, that the ultimate numbers of cycles to failure of the specimens without as well as with fibre reinforcement are considerably higher than the requirements of [5]. As can be seen in Figure 4 the test results of the cylindrical specimens have more or less the same inclination as that of the S-N curves. Admittedly, the ultra-high strength concrete without steel fibres reaches slightly higher ultimate numbers of cycles to failure.

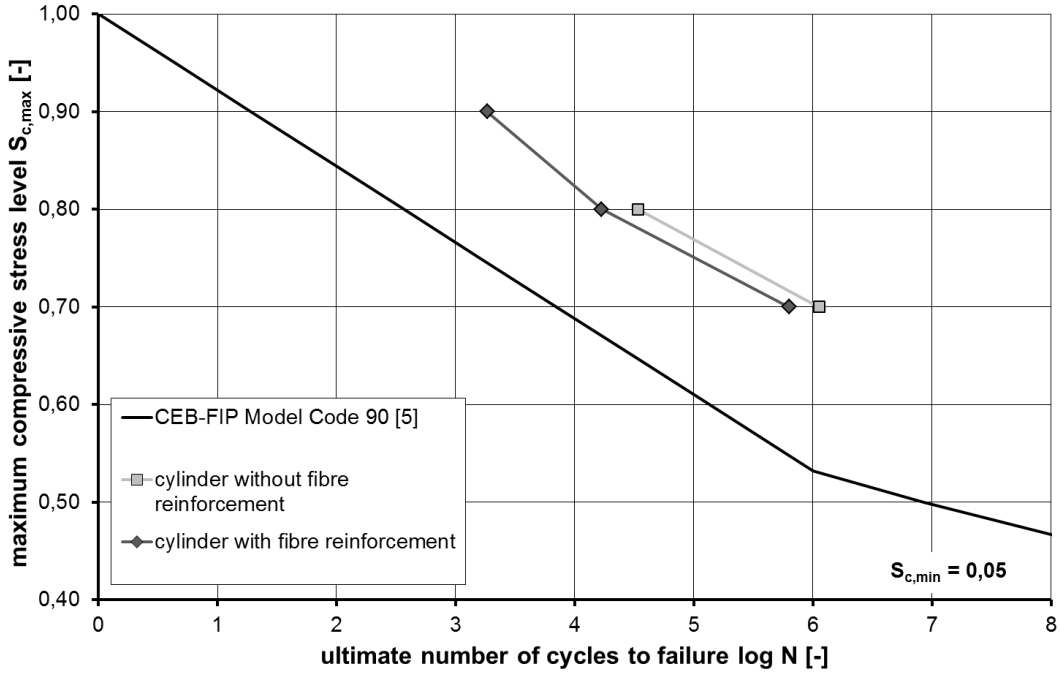

Figure 4: Ultimate numbers of cycles to failure of cylindrical specimens.

In Figure 5 the results of the dynamic investigations on the truncated cones with and without fibre reinforcement as well as the S/N-curve according to CEB-FIP Model Code 90 [5] are presented. The difference concerning the ultimate numbers of cycles to failure between the ultra-high strength concrete with and without fibre reinforcement, which was already observed on the basis of the cylindrical specimens, becomes clearer based on the results of the truncated cones. Here, the mean values of the ultimate numbers of cycles to failure of both test series with steel fibres are lower than the values of the specimens without fibre reinforcement. Furthermore the results of the test series M035 have generally lower numbers of cycles to failure than the recommended values according to CEB-FIP Model Code 90 [5]. Similar to the results of the cylindrical specimens, the incline of the truncated cones with and without fibres have more or less the same inclination.

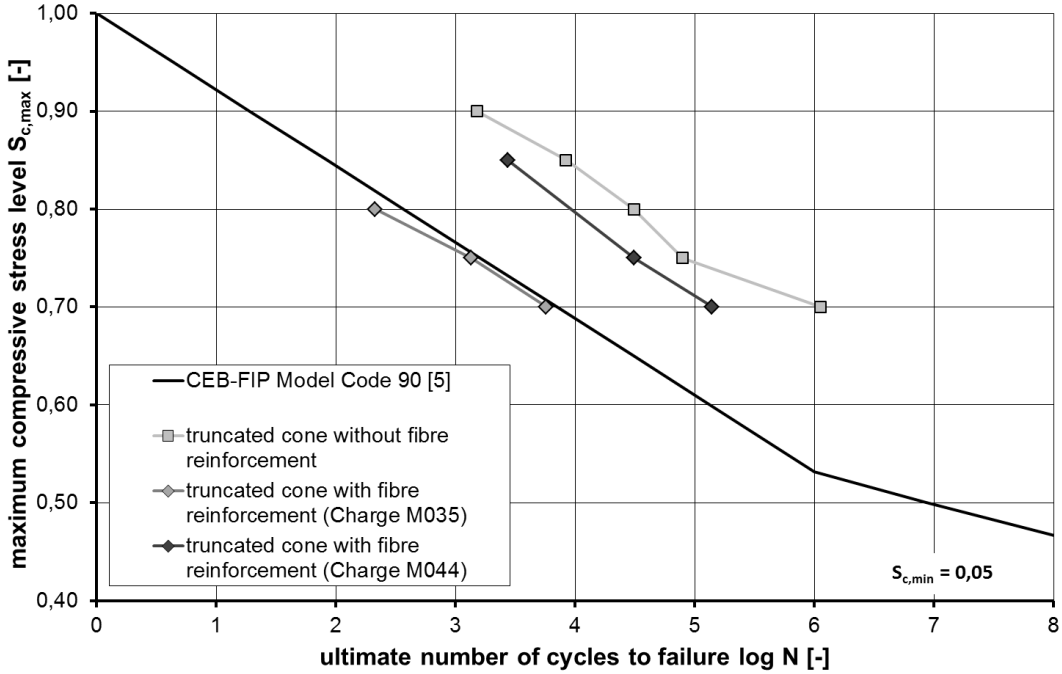

Figure 5: Ultimate numbers of cycles to failure of the truncated cones.

The influence of the fibre reinforcement on the fatigue behaviour is visibly demonstrated for both specimen geometries. The mean ultimate numbers of cycles to failure of all fibre reinforced specimens are lower than the corresponding results of the plain UHPC. According to these results, an assumption can be made that the crack initiating mechanism of the steel fibre reinforcement is dominant and therefore the failure of the specimen is accompanied by an accelerated fatigue fracture.

According to the results presented above, an assumption can be made that the crack initiating mechanism of the steel fibre reinforcement is dominant and therefore the failure of the specimen is accompanied by an accelerated fatigue fracture.

In addition to the investigations regarding the influence of fibre reinforcements on the ultimate number of cycles to failure, the effect of the fibres on the strain development during the dynamic loading has been investigated. In Figure 6, the strain development is exemplarily presented on the basis of two tests on fibre reinforced concrete (left) and two specimens without fibre reinforcement (right). The minimum stress level of this investigations was $S_{c,min}$ = 0.05, the maximum stress level was $S_{c,max}$ = 0.80. The course of the strain is presented for the maximum and minimum stress level. Comparison of the strain development of the specimens with and without fibre reinforcement show obvious differences. The specimens with fibre reinforcement show a steeper growth in the second phase of the strain development. The third range of the strain development of the UHPC with steel fibres is more distinctive. The failure of the specimen does not appear to be abrupt, it rather occurs with a certain advance notice. The course of the strain development of the specimens without fibre reinforcement shows a nearly straight-line development in the second phase. The failure of the plain UHPC occurs abruptly. The strain development does not indicate any pattern with respect to failure.

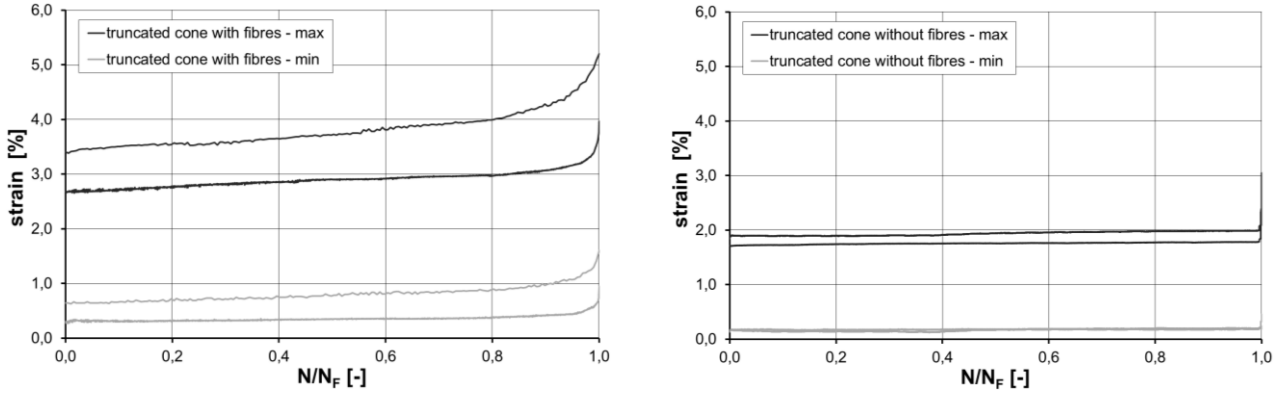

Figure 6: Comparison of the strain development of specimens with fibres (left) and without fibres (right).

In comparison with the results of the ultimate number of cycles to failure N, the strain development indicates a positive influence of the fibre reinforcement. The steel fibres lead to a certain advance notice of the failure.

The investigated truncated cones with and without fibre reinforcement exhibit a similar fractured surface. In Figure 7, the fracture surface of a truncated cone of high-strength concrete without fibre reinforcement (right) is presented. These investigations on high-strength concrete were carried out by [6]. Additionally, the fractured surface of ultra-high performance concrete with steel fibres (left) is presented. It is visible that a conical fragment breaks out of the truncated cone, whose base area corresponds to the reduced cross-sectional area at the top. The angles between the surface line and the axis of the cone generally lie between 15° and 25°.

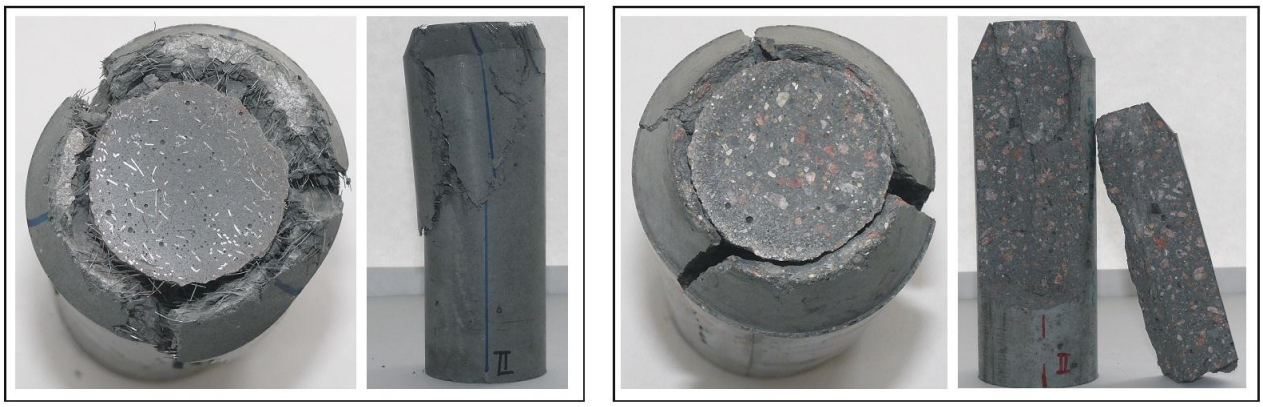

Figure 7: Fracture surface of the truncated cones of UHPC with fibres (left) and HPC without fibres (right).

4 Conclusions

In this paper, the results of experimental investigations on the influence of fibre reinforcement on the static strength and the fatigue behaviour of ultra-high performance concrete carried out in course of the priority program “Sustainable Building with Ultra-High Performance Concrete” are presented. The results of the investigations showed that the static compressive strength of the fibre reinforced ultra-high performance concretes are considerably higher than that of plain concretes. It should be noted that this increment in strength occurred as a consequence of using steel fibres. The dynamic investigations show positive as well as negative influences in relation to fibre reinforcements. On the one hand, the steel fibres reduce the ultimate numbers of cycles to failure. That means, the specimens without reinforcement endure a higher number of load cycles until failure occurs. On the other hand, fibre reinforcements have a positive effect with regard to strain development and ultimately damage development. Due to the addition of fibre reinforcement, the failure of the specimens occurs with a certain advance notice. However, further investigations would be required in order to make a clear assertion regarding the influence of steel fibres on the fatigue behaviour of ultra-high performance concretes.

References

[1] Wefer, M.: Materialverhalten und Bemessungswerte von ultrahochfestem Beton unter einaxialer Ermüdungsbeanspruchung. Dissertation, Leibniz Universität Hannover, Institut für Baustoffe, 2010.

[2] Lohaus, L.; Wefer, M.; Oneschkow, N.: Ermüdungsbemessungsmodell für normal-, hoch- und ultrahochfeste Betone. In: Beton- und Stahlbetonbau, Jahrgang 106, Heft 12, Ernst & Sohn, 2011.

[3] Ertel, C.; Grünberg, J.: Triaxial Fatigue Behaviour of Ultra High Performance Concrete (UHPC). 3rd fib International Congress, Washington D.C., May 29 – June 2, 2010.

[4] Grünberg, J.; Lohaus, L.; Ertel, Ch.; Wefer, M: Mehraxiales mechanisches Ermüdungsmodell von Ultra-Hochfestem Beton (Experimentelle und analytische Untersuchungen). In: Beton- und Stahlbetonbau, Jahrgang 102, Heft 6, Ernst & Sohn, 2007.

[5] CEB – Comité Euro-international du Béton: “CEB-FIP Model Code 90“. Bulletin d’Information, No. 213/214, Thomas Telford Ltd., London, 1993.

[6] Grünberg, J.; Oneschkow, N.: Gründung von Offshore-Windenergieanlagen aus filigranen Betonkonstruktionen unter besonderer Beachtung des Ermüdungsverhaltens von hochfestem Beton. Abschlussbericht zum BMU-Verbundforschungsprojekt, Leibniz Universität Hannover, 2011.

This research project was part of the priority program 1182 “Sustainable Building with Ultra-High Performance Concrete (UHPC)” funded by the German Research Foundation (DFG).

Moment Redistribution Capacity in Ultra-High Performance Concrete

Kenneth K. Walsh, Eric P. Steinberg
Department of Civil Engineering, Ohio University, USA

Increasing the utilization of ultra-high performance concrete (UHPC) in the US bridge construction industry will require evaluating its behavior according to current AASHTO bridge design standards. One important characteristic of continuously supported bridges is moment redistribution capacity, or the amount of moment that can be transmitted between sections of the bridge at ultimate capacity. The objective of the current research is to examine moment redistribution capacity of UHPC lab specimens. Experiments were conducted on small-scale continuously supported two-span UHPC beams. Equal concentrated loads were simultaneously applied to each span until failure occurred. Load and strain measurements were used to calculate the moment redistribution capacity based on moment and load from the yield to ultimate stage. Results suggest that the moment redistribution capacity of UHPC is comparable to that outlined in the AASHTO LRFD Bridge Design Specifications.

Keywords: UHPC, moment redistribution, laboratory testing, AASHTO

1 Introduction

The improved mechanical properties of Ultra-High Performance Concrete (UHPC) make it an attractive alternative to conventional concrete for the construction of highway bridges in the US. Replacing conventional concrete with UHPC results in smaller members, thereby reducing transportation, formwork, labor, and maintenance costs. However, current design specifications based on conventional concrete require members to have certain minimum dimensions. Using these specifications with UHPC will result in overly designed members, and an unnecessary increase in cost due to the relatively high cost of UHPC constituents. The lack of design specifications for UHPC has resulted in only a limited number of applications for highway bridges in the US. They include bridges in Wapello County, Iowa (2006), Richmond County, Virginia (2008), and Buchanan County, Iowa (2008). In order to increase the utilization of UHPC in the US bridge construction industry, design specifications need to be developed that account for its unique mechanical and material properties. To develop such specifications, additional knowledge about the behavior of UHPC in highway bridges is required.

Past research in UHPC has centered on its behavior and performance in various structural applications [1]. Vicenzino et al. [2] detail the first application of UHPC for the roof shell of a Canadian light rail train station. Bruhwiler and Denarie [3, 4] investigated UHPC for rehabilitating conventional structural concrete structures by hardening those zones subject to high environmental and mechanical loading. Applications included a road bridge, bridge pier, crash barrier wall, and an industrial floor. UHPC has also been explored for use in highway bridge girders. The Federal Highway Administration (FHWA) has investigated UHPC Type II American Association of Highway and Transportation Officials (AASHTO) girders [5], and is studying a unique bulb-double-tee girder [6]. Almansour and Lounis [7] evaluated UHPC for the case of a simply supported cast-in-place concrete slab on precast/prestressed UHPC girder bridges. In a later study, the same researchers proposed a simplified design approach of concrete slab on UHPFRC girders using the Canadian Highway Bridge Design Code [8]. Steinberg and Lubbers [9] investigated bond performance between UHPC and 1.27 cm diameter prestressing strands. It was concluded that the bond between UHPC and prestressing strands will develop in 30.5 cm of embedment. The flexural behavior at the ultimate limit state for an UHPC girder has also been examined analytically [10]. Results show that using typical

AASHTO procedures, acceptable levels of reliability can be achieved while allowing the use of familiar and non-complex equations.

While UHPC has received significant attention over the last two decades, its widespread utilization in the U.S. bridge construction industry will require evaluating its behavior according to current AASHTO bridge design specifications. Doing so can lead to the adoption of current standards, or may lead to the development of new standards tailored to UHPC's superior mechanical and material properties. In either case, additional research is needed to understand the behavior of UHPC for application in highway bridges. To date, UHPC research for highway bridges has focused primarily on the behavior of simply-supported spans. However, many bridges are continuously supported, and exhibit different behavior under load. One important characteristic of continuously supported bridges is moment redistribution capacity, or the amount of moment that can be transmitted between sections of the bridge at ultimate capacity. Moment redistribution capacity is taken into consideration in the design of continuously supported bridges in the US. The AASHTO LRFD specification adopts a 20% limit on the redistribution of negative moment. The objective of the current research is to examine the moment redistribution capacity of continuously supported UHPC lab specimens, and compare the results to current AASHTO standards.

2 Background

Linear elastic analysis can be utilized for predicting the bending moment in a beam up to a point where the elastic limit of any constituent material is exceeded. Beyond the material's elastic limit, the bending moment diagram deviates from that determined by linear elastic analysis, and approaches the diagram obtained using plastic analysis under increasing loads. Thus, the bending moment determined by means of linear elastic analysis is different than actual bending moment after the elastic limit of material is exceeded. The difference between the two is referred to as redistribution of moment.

Maximum moments are usually concentrated over short segments of the beam causing yielding and plastic hinge formation. Plastic hinges rotate due to increasing load but can transmit a small amount of increased moment up to failure. After a plastic hinge is formed at a particular location, increased moment at the section due to increased load is very small. Therefore, increased moment due to increased load redistributes to other sections that are still in the elastic range. Subsequently, the moment in another section reaches the ultimate moment of resistance causing the formation of another plastic hinge. The process of plastic hinge formation continues until a plastic mechanism is formed. At this stage, the member is no longer able to support additional load and fails.

Redistribution of moment can be full, partial, or none. If both sections reach their ultimate capacity, full redistribution is attained. On the other hand, when failure occurs with maximum positive and maximum negative moments equal to those in the elastic case, no redistribution has taken place. For a two-span continuous beam with a concentrated load in the middle of each span, cracking will occur first at the middle support section if the negative moment is larger than the positive moment. When yielding occurs at the middle support section, moment starts to redistribute into the spans. If the beam fails before moment at the middle support has reached the ultimate capacity, the redistribution is said to be partial. In this case, plastic hinges have not formed in the maximum positive moment sections, and the only plastic hinge formed would be the maximum negative moment section.

AASHTO LRFD Limits

The AASHTO LRFD specification adopts limits on the redistribution of moment from ACI 318-08 [11, 12]. Article 5.7.3.5 states the following: "In lieu of more refined analysis, where bonded

reinforcement that satisfies the provision of Article 5.11 is provided at the internal supports of continuous reinforced concrete beams, negative moments determined by elastic theory at strength limit states may be increased or decreased by not more than $1000\varepsilon_t$ percent, with a maximum of 20 percent. Redistribution of negative moments shall be made only when ε_t is equal to or greater than 0.0075 at the section at which moment is reduced". It also states that positive moments shall be adjusted to account for the changes in negative moments to maintain equilibrium of loads and force effects [11].

3 Moment Redistribution

For a two-span continuous beam in which negative moment is larger than positive moment, yielding will occur first at the interior support, and negative moment is redistributed to the span. The amount of moment redistribution is limited by the yield capacity of the beam in the span, which may be assumed to be equal to that at the support. As a result, the yield moment in the span may be calculated from:

$$M_y^+ = \frac{P_y^- \cdot a \cdot b}{2 \cdot L^2}(L+a), \tag{1}$$

where P_y^- is the load acting on the span immediately before yielding occurs at the support, L is the span length, and a and b are the distances between the exterior support and the load, and the interior support and the load, respectively. The onset of yielding in the span results in redistribution of moment back to the interior support. When the beam reaches its ultimate capacity at this location, moment is again redistributed to the span. Once the span ultimate capacity is reached, a plastic mechanism is formed, and the beam fails. The ultimate limit state is important in the design of structures, and the moment distribution of members at the ultimate stage should be investigated.

Once yielding of the beam at the interior support has occurred, the two-span continuous beam may be idealized as two side-by-side beams. A schematic of the idealized beam model is shown in Figure 1. As previously discussed, yielding of the span results in redistribution of the moment back to the interior support. The ultimate moment at the interior support may now be calculated from equilibrium using the load acting on the span when span yielding occurs P_y^+:

$$M_u^- = P_y^+ \cdot b - R_{ext} \cdot L, \tag{2}$$

where

$$R_{ext} = \frac{M_y^+}{a}, \tag{3}$$

Once the ultimate capacity of the beam at the interior support has been reached, moment is redistributed back to the span. If it is assumed that the moment in the span increases the same as that at the support before the ultimate moment is reached, then the ultimate moment in the span may be calculated from:

$$M_u^+ = M_y^+ + \left(M_u^- - M_y^+\right) = M_u^-. \tag{4}$$

Moment redistribution corresponding to the ultimate limit state is then calculated from [13]:

$$\beta_p = \left(\frac{M_u^+ - M_y^+}{M_y^+}\right) \times 100. \tag{5}$$

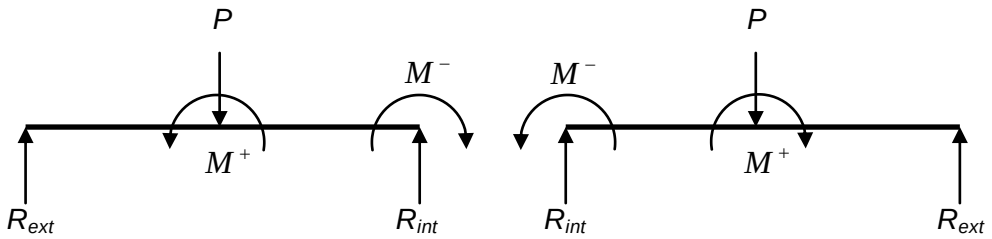

Figure 1: Idealized beam model after yielding has occurred at the interior support.

4 Laboratory Testing

In order to study the moment redistribution in ultra-high performance concrete, four beams were tested. The beam dimensions are presented in Table 1. The UHPC used in the samples was a premix commercially available in North America. Table 2 provides information about the mix design. The premix packages included Portland cement, silica fume, quartz powder and sand. The beams in this test were supported at three points: the middle and two ends. Loads were applied on each span at a distance of 29.21 cm from the support. This created a negative moment approximately 20 to 30 percent larger than the positive moment produced in the spans under the load. This was done in the interest of obtaining full moment redistribution. Application of the loading was achieved using a small frame and MTS machine. Figure 2 shows the loading apparatus. Six strain gages per beam were used to record the strains during testing. Strain gages were installed along the side of the beam about 1.27 cm from the extreme compression fiber to avoid load effects on the gage grids. Strain gages were installed on both sides of the beam in case out-of-plane bending occurred. A schematic showing the location of the applied loads and strain gages is shown in Figure 3. Data on load and strain was recorded using a MEGADAC data acquisition system.

Table 1: Dimensions of Tested Beams.

Beam No. (1)	Beam Length (cm) (2)	Span Length (cm) (3)	Depth ± 0.25 (cm) (4)	Width ± 0.25 (cm) (5)
1	119.63	57.15	9.53	9.14
2	119.38	57.15	7.62	7.37
3	121.92	57.15	10.16	8.41
4	119.38	57.15	9.04	8.89

Table 2: Mix Design for Tested UHPC Specimens (Lubbers 2003).

Mix Component (1)	Weight (kN/m^3) (2)	Percent by Weight (%) (3)
Premix	21.49	87.22
Water	1.32	5.36
3000NS	0.30	1.22
Steel Fibers	1.53	6.21

Figure 2: Picture of testing apparatus.

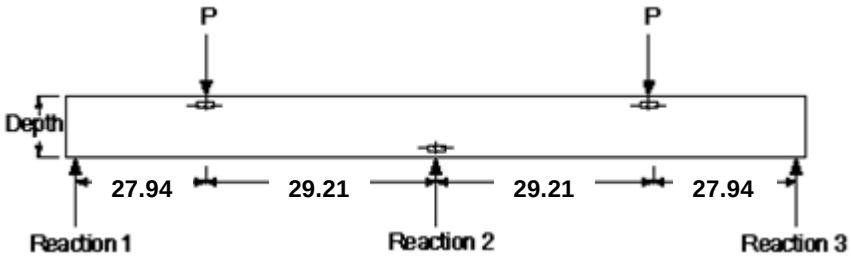

Figure 3: Load and strain gage location.

5 Results

During testing, data was recorded at a rate of 1,000 scans per second as each specimen was loaded to failure. The total load (2*P*) was plotted versus strain for each gage. From the load vs. strain curves, the yield and ultimate loads for each specimen were determined based on major changes in the slope of the load versus strain curves. Figure 4 shows the total load plotted against strain on either side of beam 1 at the middle support. The curve was linear up to a total load of 22.24 kN (5000 lb). At this load, the curve deviated from linearity designating the onset of cracking. The fibers likely started to yield or slip and the strain value began to decrease when the total load reached 28.91 kN (6500 lb). As it can be seen from Figure 4, the strain values on both sides of the beam showed similar behavior. Finally, the ultimate load was determined to be 80.07 kN (18000 lb). This stage of loading has been intentionally omitted from the load versus strain curves in Figure 4 in order to distinguish concrete cracking and fiber yielding. Figure 5 shows the total load versus strain in a span of beam 1. A very small amount of strain was recorded up to a total load of about 31.14 kN (7000 lb), at which time cracking occurred in the concrete. The load increased to 60.50 kN (13600 lb) before the fibers in the span yielded. Finally, the ultimate load in the span was 80.07 kN (18000 lb). All three stages of loading can be observed in Figure 5.

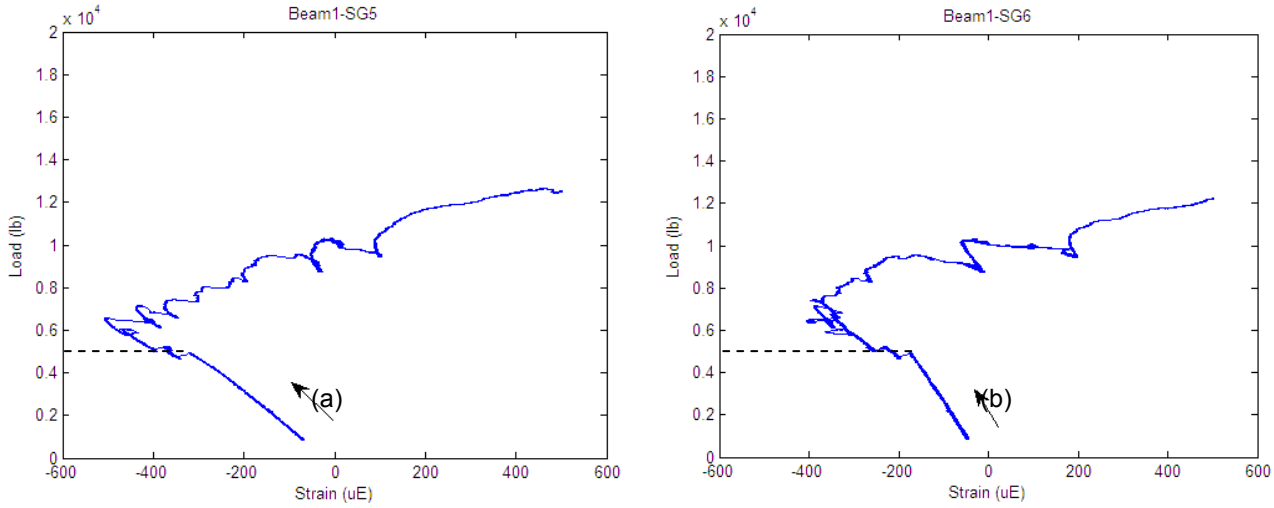

Figure 4: Total load versus strain on each side of beam one at middle support.

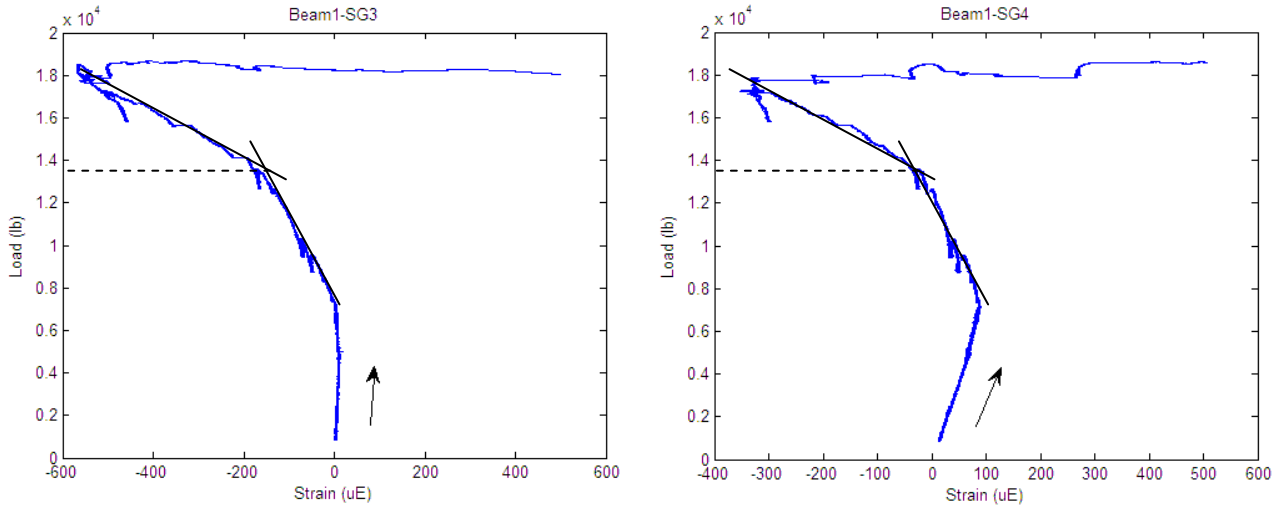

(a) (b)

Figure 5: Total load versus strain on each side of beam one in span.

The results presented in Figures 4 and 5 are for beam 1. The yield and ultimate loads for all 4 beams are provided in Table 3. The values are used with Equations (1)-(4) to calculate the moments in the span for span yielding and at the ultimate stage (rows 3 and 4, Table 3). The moments in the span at the yield and ultimate stage are then used with Equation (5) to calculate the moment redistribution in each beam (row 5, Table 3). The data for only one span of each beam is included. Comparison of columns 3, 5, 7, and 9 in Table 3 shows that beam 2 had a smaller ratio of ultimate moment to yield moment in the span than the other three beams resulting in significantly lower moment redistribution. Inspection of beam 2 revealed premature failure due to a weak section located 15.24 cm from the exterior support. As a result, the data for beam 2 is not considered representative of the moment redistribution behavior of UHPC, and beam 2 is excluded from further discussion. A picture of beam 2 after testing is shown in Figure 6.

Columns 3, 7, and 9 show that the moment redistribution in the remaining 3 beams was 200 % or greater, with beam 1 achieving a redistribution as much as 270 %. The variation in moment redistribution between beams is attributed to irregularities in their geometry that may have caused various degrees of out-of-plane bending during testing. The moment redistributions determined from the present analysis show that redistribution between the yield

and ultimate stage in UHPC far exceeds the AASHTO LRFD limit of 20 %. However, it should be noted that calculation of the moments in the span at the various stages of loading is based on the assumption that the yield capacity, and the ultimate capacity, of the beams is the same in the span and at the interior support. This assumption is necesary due to the difficulty in directly measuring the moments in the beam. An alternate measure of the beams redistribution behavior is calculated as the percent increase in the load from the yield to ultimate stage. While this may not be a direct measure of moment redistribution, it is an indication of the moment redistribution mechanism in the beam. That is, the amount of load increase from the yield to ultimate stage is dependent on the redistribution of the bending moment from the span to the support, and then back to the span. For comparison sake, the percent increase in the load is also included in Table 3. The results show that the percent increases in the load for the three beams is consistent with that of the moment redistribution, with beam 1 being the largest, followed by beams 4 and 3. From the data in Table 3, it can be seen that the percent increases in load from the yield to ultimate stages are more aligned with the 20 % limit as specified by AASHTO LRFD.

Table 3: Moment redistribution in laboratory specimens.

Stage	**Beam 1**		**Beam 2**		**Beam 3**		**Beam 4**	
(1)	**Support (2)**	**Span (3)**	**Support (4)**	**Span (5)**	**Support (6)**	**Span (7)**	**Support (8)**	**Span (9)**
Yield Load (kN)	28.91	60.50	21.80	25.93	36.92	67.61	18.68	35.59
Ultimate Load (kN)	80.07	80.07	28.29	28.29	77.84	77.84	43.15	43.15
Span Yields (kN-m)	-5.69	1.53	-1.42	1.15	-5.86	1.97	-3.17	0.99
Span Ultimate (kN-m)	-0.05	5.69	-1.23	1.42	0.62	5.86	0.18	3.17
Moment Redistribution (%)	-	270	-	22	-	199	-	219
Change in Load (%)	-	32	-	-	-	15	-	21

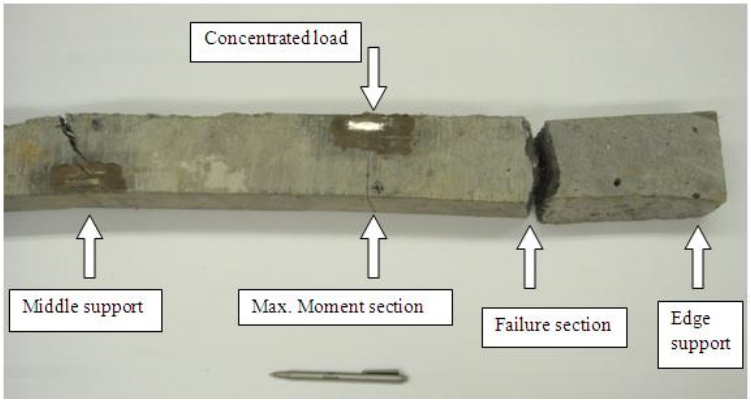

Figure 6: Premature failure of beam 2 due to defect 15.24 cm from exterior support.

6 Conclusions

Laboratory testing was conducted to investigate moment redistribution capacity in UHPC lab specimens. Preliminary results indicate the redistribution capacity based on moments far exceeded the 20 % limit specified in AASHTO LRFD, indicating that an increase on moment

redistribution for UHPC may be possible. However, the moments were calculated based on assumptions about the behavior of the beam specimens under load, and additional research is necessary to validate the results. An alternate measure of moment redistribution capacity was calculated as the percent increase in load from the yield to ultimate stage. The results yielded values that were more aligned with the 20 % limit specified by AASHTO LRFD. However, there was variation in the results and further research should be conducted using a larger number of beam specimens.

References

[1] Walraven, J. C.: High performance fiber reinforced concrete: progress in knowledge and design codes. *Materials and Structures* 42 (9), pp. 1247–1260, 2009.

[2] Vicenzino, E.; Culham, G.; Perry, V. H.; Zakariasen, D.; Chow, T. S.: First use of UHPFRC in thin precast concrete roof shell for Canadian LRT station, *PCI Journal* 50 (5), pp. 50-67, 2005.

[3] Brühwiler, E.; Denarié, E.: Rehabilitation of concrete structures using Ultra-High Performance Fibre Reinforced Concrete. The Second International Symposium on Ultra High Performance Concrete, Kassel 2008.

[4] Denariè, E.; BrÜhwiler, E.: Tailored composite UHPFRC-concrete structures. *Measuring, Monitoring and Modeling Concrete Properties* Part 1, pp. 69-75, 2006.

[5] Graybeal, B. A.: Material property characterization of ultra-high performance concrete. Rep. No. FHWA-HRT-06-103, Federal Highway Administration, McLean, VA. 2006.

[6] Graybeal, B. A.; Hartmann, J. L.: Ultra-high performance concrete material properties. Transportation Research Board Conference, Washington 2003.

[7] Almansour, H.; Lounis, Z.: Structural performance of precast prestressed bridge girders built with ultra high performance concrete. *Second International Symposium on Ultra High Performance Concrete*, Kassel 2008.

[8] Almansour, H.; Lounis, Z.: Design of prestressed UHPFRC girder bridges according to Canadian Highway Bridge Design Code. NRC Institute for Research in Construction; National Research Council Canada, NRCC-53296, pp. 1-15, 2010.

[9] Steinberg, E.; Lubbers, A.: Bond of Prestressing Strands in UHPC. International Symposium on High Performance Concrete, Orlando 2003.

[10] Steinberg, P: Structural Reliability of Prestressed UHPC Flexure Models for Bridge Girders. *Journal of Bridge Engineering* 15 (1), pp. 65-72, 2010.

[11] AASHTO LRFD (2007). “AASHTO LRFD Bridge Design Specifications.” American Association of State Highway and Transportation Officials, Washington, DC.

[12] ACI 318 – 08 (2008). “Building code requirements for reinforced concrete.” American Concrete Institute, Detroit, MI.

[13] Rebentrost, M.: Deformation capacity and moment redistribution of partially prestressed concrete beams. Ph.D. Dissertation, Adelaide University 2003.

Design Models for Composite Beams with Puzzle Strip Shear Connector and UHPC

Joerg Gallwoszus, Josef Hegger, Sabine Heinemeyer
Institute of Structural Concrete, RWTH Aachen University, Germany

The outstanding mechanical properties of ultra-high performance concrete (UHPC) in combination with high strength steel offer new opportunities to design elegant and slender structures. The challenging task with high performance materials is their adequate application to utilize the structural benefits. Due to the ideal interaction of UHPC and high strength steel, composite systems are very appropriate.
To account for the high performance of the respective materials, the local interconnection has to be guaranteed, which calls for appropriate shear connectors capable of transferring high shear forces across the composite joint. Therefore, a series of push-out tests were carried out to evaluate the mechanisms of shear connectors in UHPC. By means of the test results and accompanying numerical simulations and the evaluation of a database design models for continuous shear connectors were derived.
The behavior of the composite joint and the global load carrying capacity were investigated in beam tests under positive bending. Not only conventional composite beams were tested, but also filigree composite girders with the shear connectors directly cut into the web of the steel girder. A parametric study was performed to develop a design model which enables a safe and economic plastic design of composite beams with UHPC.

Keywords: Composite Construction, Design Model, Ultra High Performance Concrete, High Strength Steel, Puzzle-strip Shear Connector, Composite Beams

1 Introduction

The present paper summarizes the results of a research program involving the testing of push-out specimens with the innovative puzzle-strip shear connectors in ultra-high performance concrete (UHPC). Based on the push-out tests performed to investigate the load carrying behavior design models were derived for concrete and steel failure. By means of the beam tests and a parametrical study a safe plastic design model for high performance materials was developed.

The outstanding mechanical properties of ultra-high performance concrete (UHPC) in combination with high strength steel offer engineers new opportunities to design elegant and slender structures. Fig. 1 shows two examples of composite bridge systems with an UHPC deck.

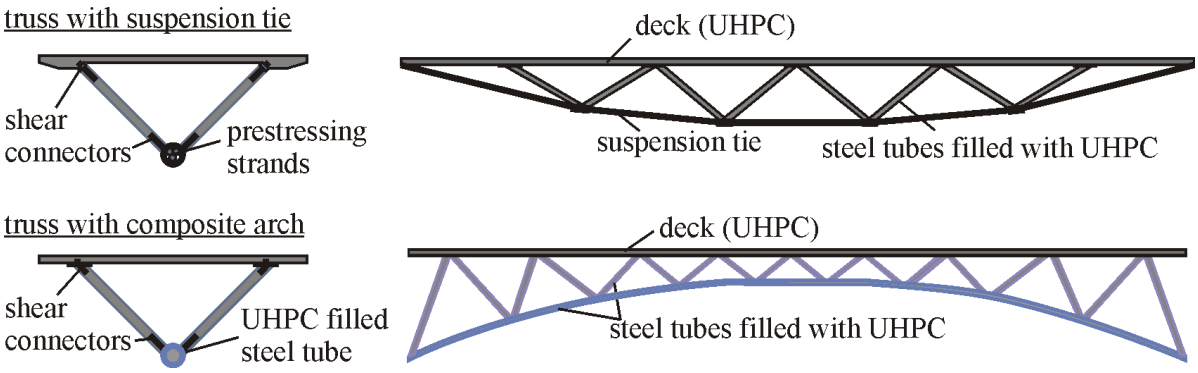

Figure 1: Composite bridge systems with UHPC.

The challenging task using high performance materials is their adequate application to utilize the structural benefits. Composite structures are very appropriate due to the efficient interaction of the two components concrete and steel. Taking into account the material properties, the steel carries the tensile forces and the concrete is arranged in the compression zone. To account for the high performance and the interaction of the respective materials, the local interconnection has to be guaranteed, which calls for appropriate shear connectors capable of transferring high shear forces across the composite joint like continuous shear connectors [1] e.g. the puzzle strip (Fig. 2a) or the saw tooth (Fig. 2b). Therefore, a series of push-out tests was carried out to determine the load carrying capacity and the ductility of the composite joint between high strength steel and ultra-high performance concrete.

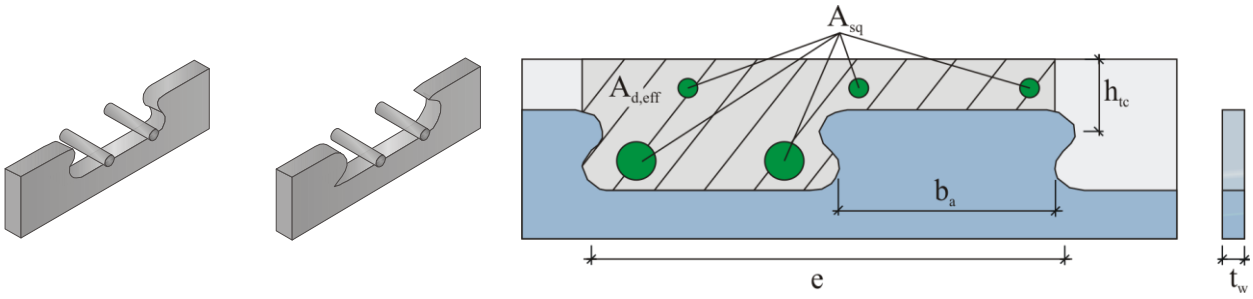

a) puzzle strip b) saw tooth c) notation

Figure 2: Shear connectors.

In beam tests the performance of the puzzle strip shear connector was investigated and the global load carrying capacity of composite beams with high performance materials was examined.

For all tests a UHPC mixture based on B5Q which was developed for the SPP1182 [6] was used. Details on the concrete mixes can be found in [2].

2 Puzzle strip shear connector

Continuous shear connectors general

Continuous shear connectors have been used for about 30 years. The most common one is the perfobond strip [3], where the shear forces between the steel beam and the concrete slab are transferred by vertical steel plates with holes. In [1] the so-called puzzle strip, an innovative shear connector, is introduced. Its main advantage is the symmetrical geometry. This way two shear connector strips can be manufactured with one cut and no material is wasted, leading to significant savings in production costs. If the cut is performed in the web of a steel I-beam, two composite beams can be produced.

Basically, the innovative shear connectors act as a conventional concrete dowel. So far, their load carrying behavior has been investigated by several researchers [1], [2], [4], [5]. Five failure modes have to be considered (Fig. 3), splitting, local concrete failure in front of the shear connector, concrete pry-out failure, shear failure of the concrete and steel failure due to the moment and shear stresses acting onto the steel strip.

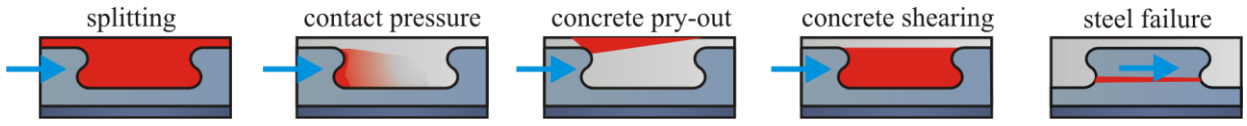

Figure 3: Failure modes of continuous shear connectors.

Push-Out tests

The test parameters were designed to achieve both concrete and steel failure. Concrete failure is mainly governed by the concrete cover between the shear connector and the concrete surface, the fiber content and the degree of transverse reinforcement. Steel failure can be controlled by the thickness of the shear connector. All these parameters were varied within an extensive research program [2], [6], [8]. This paper presents two test series with UHPC and HSC. The tests were performed as a reference for the beam tests. The test specimen is shown in Fig. 4, left. It consists of two halves of an IPE600 profile where the puzzle shape is cut into the web. The concrete slab was poured and later the flanges have been welded together in the middle. The specimens were reinforced with 2∅12 in each opening and ∅10/10 at the concrete surface.

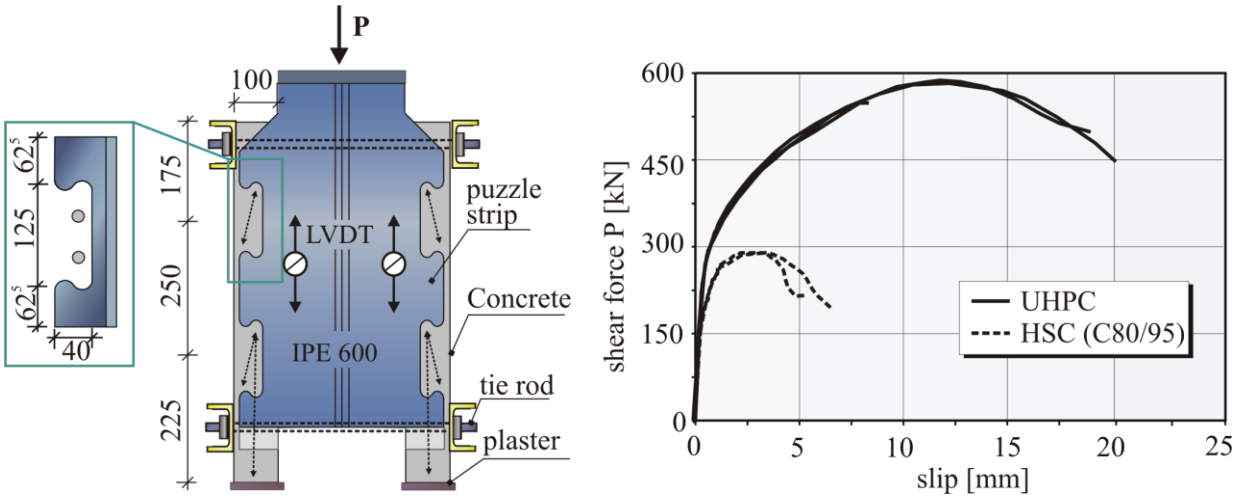

Figure 4: Push-Out Standard Test POST and load slip curve.

Test results

The material properties (concrete strength $f_{c,cube100}$ and f_y) as well as the test results (mean maximum load $P_{max,mean}$, characteristic load P_{Rk} and relative displacement in the plastic range $\delta_{uk,pl}$) are presented in Table 1.

Table 1: Test results.

Series -	$f_{c,cube}$ N/mm²	f_y N/mm²	$P_{max,mean}$ kN	P_{Rk} kN	$\delta_{uk,pl}$ mm
UHPC	179.1	472	587.0	495.0	8.4
HSC	92.6	472	297.5	267.1	2.7

The load-slip diagram in Fig. 4, right, shows that the load carrying capacity of the puzzle strip in UHPC is about twice as high as in HSC and the ductility was also increased significantly. However, the load-deformation behavior was more flexible compared to the push-out test with HSC and its ultimate load was reached after a fairly large slip of about 10 mm. Steel failure occurred with a horizontal crack in the puzzle strip. On the outer surface there were signs of concrete pry-out failure. However, on the inside of the concrete surface no cracks were visible.

Design model – puzzle strip shear connector

Based on the results of the total test program, design models have been derived in [2]. Three different failure modes occurred in the tests: splitting, concrete pry-out and steel failure.

Splitting failure

Splitting failure only occurred in specimens without transverse reinforcement. In order to prevent splitting failure, a minimum transverse reinforcement is to be applied:

$$A_{sq} = 1/2 \frac{P}{f_{yd}} \tag{1}$$

Where A_{sq} is the required transverse reinforcement to prevent spalling, P is the shear force and f_{yd} is the design value of the steel yield strength.

Pry-out failure

During pry-out failure a cone develops which peels off when the ultimate load of the shear connector is reached. The failure load can be calculated as follows:

$$P_{pryout} = \frac{1}{\eta} \cdot 20{,}15 \cdot h_{tc}^{1,5} \cdot f_{ck}^{1/2} \cdot (1 + \frac{E_s A_{sq}}{E_{cm} A_{d,eff}}) \cdot \frac{1}{\gamma_v} \tag{2}$$

$$\eta = 0{,}4 - 0{,}001 \cdot f_c \tag{3}$$

Where P_{pryout} is the design load for pry-out failure, f_{ck} is the characteristic value of the concrete compressive strength, E_s and E_{cm} are the young's moduli of steel and concrete, A_{sq} is the transverse reinforcement and A_d is the effective concrete area of the shear connector according to Fig. 2c. The safety factor γ_v equals 1.25.

Steel failure

The steel part of the shear connectors is under combined shear and bending stresses. The derived model is based on the equivalent stress criterion taking into account the interaction of moment and shear stresses onto the steel strip:

$$P_{y,steel} = \frac{1}{\sqrt{3}} \cdot \Gamma \cdot t_w \cdot b_a \cdot f_{yd} \tag{3}$$

$$\Gamma = \begin{cases} 1{,}0 \\ 1.6 - M / M_{pl} \end{cases} \quad \text{for} \quad \begin{matrix} 0 \le M / M_{pl} \le 0.6 \\ M / M_{pl} > 0.6 \end{matrix} \tag{4}$$

Where $P_{y,steel}$ is the design load for steel failure, Γ is the correction factor according to eq. (4) taking into account the interaction, t_w and b_a are the dimensions according to Fig. 2c and f_{yd} is the design value of the steel yield strength. M and M_{pl} are the actual and the theoretical plastic moment of the cross section of the steel strip.

3 Composite beams

Plastic design according to EC4

According to EC4 a plastic design may be carried out when:

- the steel profile can be classified into a class 1 or class 2 cross section;
- The effective area of the structural steel member is stressed to its design yield strength f_{yd} in tension or compression;
- The effective area of concrete in compression resists a stress of $0.85 \cdot f_{cd}$, constant over the whole depth between the plastic neutral axis and the most compressed fiber of the concrete.

Under positive bending moments it has to be verified that the plastic theory is applicable, i.e. the steel profile plasticizes before the concrete compression zone fails. Using high performance materials this becomes even more vital since the high strength steel requires a higher yield strain to plasticize and for concrete the strain at failure decreases with increasing strength (Fig. 5).

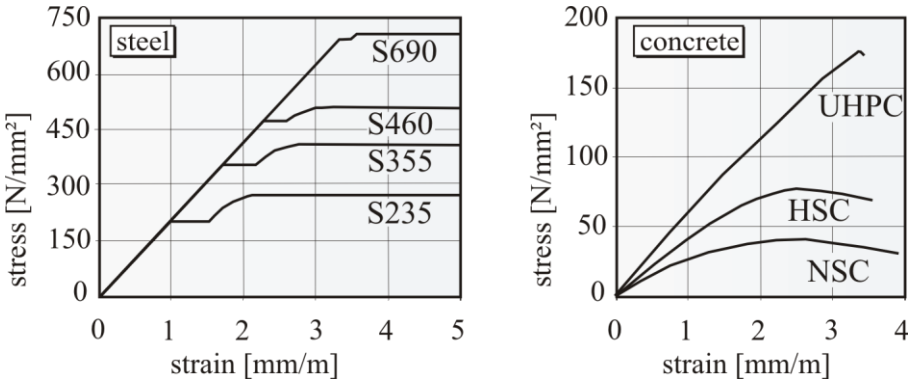

Figure 5: Stress-strain behavior of steel and concrete.

Beam tests

Within several beam tests the plastic moment carrying capacity of composite beams was investigated. In the following the results from a test with a conventional composite beam are compared to the results of a filigree beam.. Both beams were made of UHPC with a steel fiber content of 0.9 % p.v. and high strength steel S460. Fig. 6 presents the test set-up and the cross section of the tested beam.

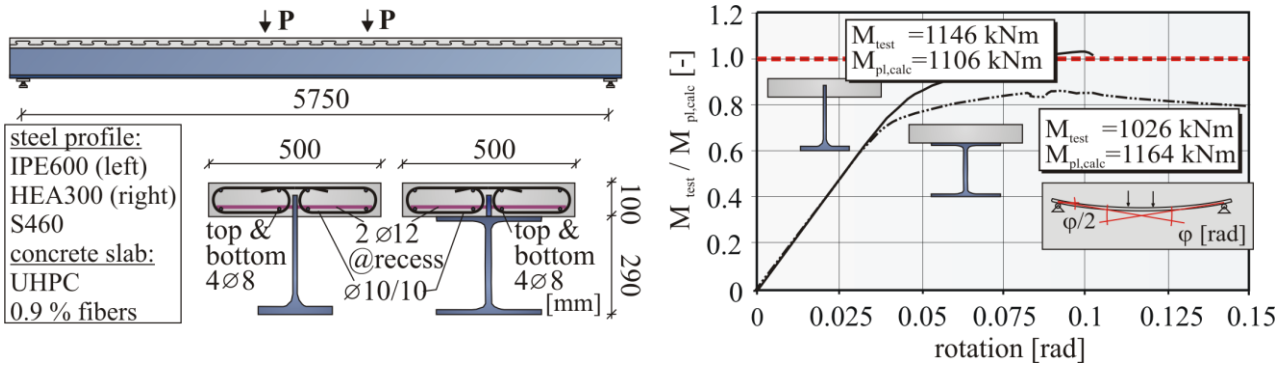

Figure 6: Beam tests under positive bending and moment-rotation behavior.

The tests were performed under positive four-point bending. Principally, the two beams had the same cross section. One consisted of a compact I-beam (conventional composite beam) and one of an I-beam where the puzzle strip was directly cut into the steel web (filigree composite beam). The profiles were chosen in order to achieve a comparable moment carrying capacity. Taking into account the load-slip behavior achieved in the push-out tests (Fig. 4), the beams were fully shear connected. Along the shear joint between the steel profile and the concrete slab, LVDT's were attached to measure the slip. At midspan, strain gauges were fixed across the cross section to investigate the strain distribution. The characteristics of the tested beams are presented in Table 2, where the concrete compressive strength $f_{c,cube}$ the medium yield strength of the steel flange $f_{y,flange}$, the ultimate moment in the tests M_{test} and the calculated plastic moment $M_{pl,calc}$ under consideration of the actual material properties (safety factors γ_i set to unity) and the ultimate concrete strain at failure $\varepsilon_{c,ult}$ are listed.

Table 2: Beam characteristics.

Series -	$f_{c,cube}$ N/mm²	$f_{y,flange}$ N/mm²	M_{test} kNm	$M_{pl,calc}$ N/mm²	ε_{ult} ‰	$M_{test}/M_{pl,calc}$ mm
Filigree beam	191.0	510	179.5	499	-3.9	1.04
Conventional beam	177.9	537	176.1	499	-3.7	0.88

In both tests a failure of the compression zone was observed when the ultimate strain of the concrete was exceeded. Fig. 5 shows the moment-rotation curves of the tested beams. The angle φ represents the rotation of the cross section at midspan and is determined by the tangent angles of the rotation at the supports. The specific flexural capacity, which is the ratio of the experimental and the calculated plastic moment, is plotted against the rotation. The EC4 regulation ($M_{test}/M_{pl,calc} \geq 1$) was reached for the filigree beam. The conventional composite beam, however, failed at approximately 90 % of the theoretical plastic moment. In this case, the upper flange of the HEA 300 profile, which is close to the neutral axis, does not yield in the ultimate limit state. Hence, the plastic design according to EC4 overestimates the resistance achieved by plastic stress blocks.

For full and rigid shear connection between steel and concrete there is a continuous strain distribution with no considerable slip between the two components. However, due to the flexible puzzle strip there is a slight step in the strain distribution in the composite joint. Fig. 7 shows the strain distribution at the ultimate load level for the cross sections of the two beams at midspan. The neutral axis is in the concrete slab and the steel profile is almost completely under tension. Basically, there is hardly any difference in strain distribution between the two cross sections. However, when the areas where the steel profile does not reach the yield strength are compared for the filigree and conventional beam. It is evident, that the area is larger for the conventional beam since there is an upper flange. The error made in the plastic design increases and thus, the plastic moment carrying capacity is overestimated for the conventional composite beam.

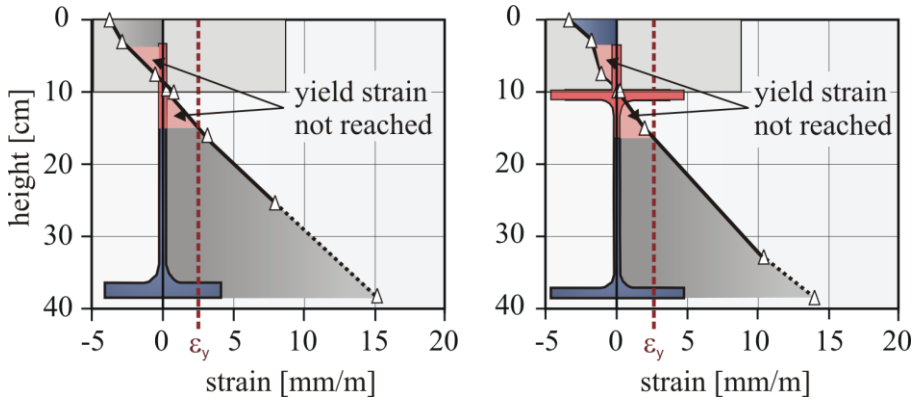

a) Filigree beam b) Conventional beam

Figure 7: Strain distribution.

After testing, the concrete slabs were removed and the shear connectors in the composite joint were investigated. No cracks were found in the shear connectors or the concrete. Thus, the plastic moment was limited by the rotation capacity of the cross section rather than by the shear connection.

Plastic design model

A parametrical study was carried out with different geometries as well as steel and concrete grades where the plastic moment carrying capacity according to EC4 is compared to the elastic-plastic moment carrying capacity. The elastic-plastic moment carrying capacity was determined iteratively since realistic non-linear material laws had to be implemented.

For high strength steel the plastic design according to EC4 overestimates the actual moment carrying capacity of the composite beams (Fig. 8, $M_u/M_{pl} < 1$). The failure increases with enhancing concrete strength.

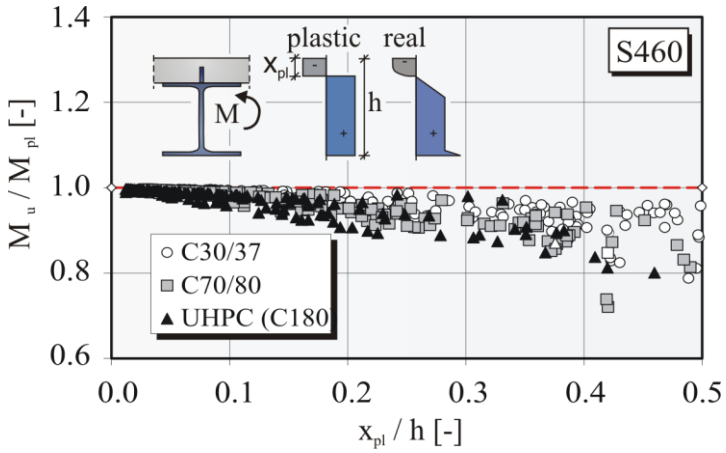

Figure 8: Ratio M_u/M_{pl} without reduction factors.

The results in Fig. 8 illustrate that the application range of EC4 cannot be transferred to high strength materials without additional notice.

Therefore, the factor β stated in EC4 when using high strength steel S460 is expanded for different relations h_c/h, where h_c is the thickness of the concrete slab and h is the height of the whole cross section (Factor β_1, Fig. 9, left). For high strength concretes over C60/70 the factor α_{new} is proposed taking into account their characteristic stress-strain behavior of the concrete (Fig. 9, right).

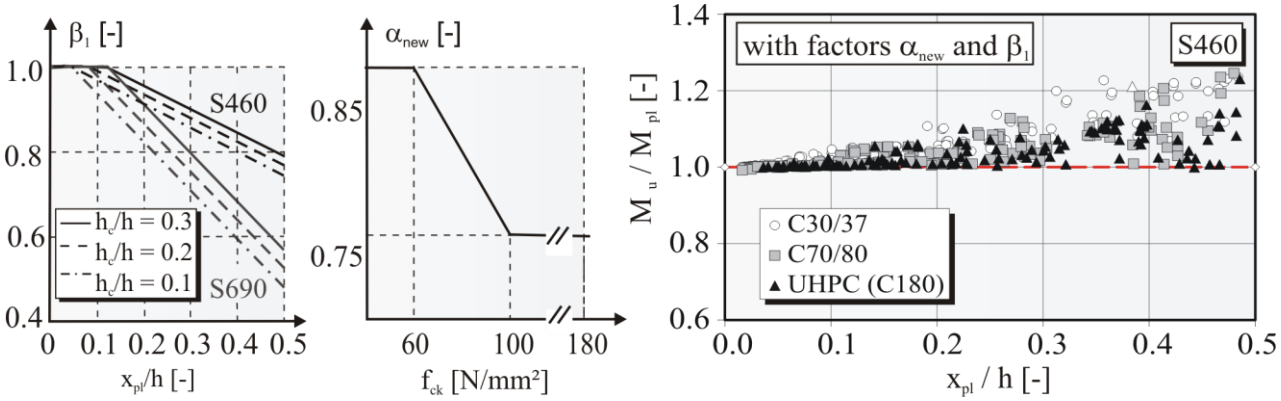

Figure 9: Reduction factors β_1 and αnew and Ratio M_u/M_{pl} with reduction factors.

The plastic moment carrying capacity can be calculated as:

$$M_{pl,new} = \beta_1 \cdot M_{pl,EC4}(\alpha_{new}) \qquad (1)$$

Applying these factors in the new stress block model leads to values $M_u/M_{pl} \geq 1$ (Fig. 9), which means a safe plastic design can be performed.

4 Conclusions

In push-out tests the influencing factors for the load carrying capacity of shear connectors were investigated. Two types of shear connectors made of high strength steel S460 were tested, the puzzle strip and the saw tooth. The parameters were the geometry and the thickness of the shear connector as well as the steel fiber amount and orientation and the transverse reinforcement. The results can be summarized as follows:

- Continuous shear connectors are capable of transferring high shear forces in UHPC. Due to its symmetry, the puzzle strip is a very appropriate shear connector.
- Depending on the thickness of the steel strip a rigid shear connection can be established.
- A minimum amount of steel fibers is required to achieve a ductile behavior. The own tests showed a minimum percentage of 0.9.
- Arranging transverse reinforcement leads to an increase in ultimate load of up to 30 % and an improved ductility.
- Design models were developed which are capable of predicting the load carrying capacity of the puzzle strip shear connector and enable a safe plastic design of composite beams with high performance materials.

Especially for bridges with traffic loads the cyclic performance of the shear connectors is of major interest. Experimental investigations concerning the cyclic behavior of the puzzle strip are presented in [8].

References

[1] Feldmann, M.; Hechler, O.; Hegger, J.; Rauscher, S.: Untersuchungen zum Trag- und Verformungsverhalten von Verbundmitteln unter ruhender und nicht ruhender Belastung bei Verwendung hochfester Werkstoffe, FOSTA-Final Report P621, Aachen, 2007 (in german).

[2] Heinemeyer, S.: Zum Trag- und Verformungsverhalten von Verbundträgern aus ultrahochfestem Beton mit Verbundleisten, PhD thesis, Institute of Structural Concrete, RWTH Aachen University, 2011 (in german).

[3] Leonhardt, F.; Andrä, W.; Harre, W.: Neues, vorteilhaftes Verbundmittel für Stahlverbund-Tragwerke mit hoher Dauerhaftigkeit, Beton- und Stahlbetonbau; 82(12): 325-331, 1987 (in german).

[4] Wurzer, O.: Zur Tragfähigkeit von Betondübel, PhD thesis, Institut für Konstruktiven Ingenieurbau, Universität der Bundeswehr, München, Juni 1997 (in german).

[5] Zapfe, C.: Trag- und Verformungsverhalten von Verbundträgern mit Betondübeln zur Übertragung der Längsschubkräfte, PhD thesis, Institut für Konstruktiven Ingenieurbau, Universität der Bundeswehr, München, Juni 2001 (in german).

[6] Priority program SPP 1182, Subproject "Shear Connectors in UHPC". SPP 1182 - Sustainable building with ultra high performance concrete (UHPC), German research foundation (DFG), 2008.

[7] EC 4, prEN 1994-1-1. 2004. Design of composite steel and concrete structures Part 1.1 – General rules and rules for buildings. Brussels, Belgium.

[8] Hegger, J.; Rauscher, S.: UHPC in composite construction. In “Ultra high performance concrete”, 2nd Int’l Symposium on Ultra High Performance Concrete, March 05-07, 2008, ISBN: 978-3-89958-376-2, pp. 545-552.

[9] Gallwoszus, J.; Hegger, J.; Heinemeyer, S.: Cyclic Behaviour of Puzzle-strips in UHPC, HiPerMAt 2012, Kassel, Germany, 2012.

Connections of Precast UHPC Elements

Josef Hegger[1], Nguyen Viet Tue[2], Janna Schoening[1], Martina Winkler[2]
1: Institute of Structural Concrete, RWTH Aachen University, Germany
2: Institute of Structural Concrete, Graz University of Technology, Austria

At the Institutes of Structural Concrete at RWTH Aachen University and Graz University of Technology the authors investigate connections of precast ultra-high performance concrete (UHPC) elements. Modified established connections will be tested to derive design concepts for UHPC elements based on the existing design concepts for normal and high-strength concrete. Connections under compressive, tensile as well as shear loads will be investigated. The new design approach will take advantage of the high performance properties of the concrete. The research work comprises theoretical and experimental investigations. Further variation of certain parameters as well as the verification of the test results and the implementation in design concepts will be accomplished using non-linear FE computation.

Keywords: ultra-high performance concrete, prefabrication, connection, joint, shear-compression loading, anchorage, lapped splice, column

1 Introduction

The development of economical connections for pre-fabricated concrete elements is of great importance to the global applicability of UHPC. Feasible design concepts are in demand that support the core characteristics of UHPC like its high compressive strength, its high durability and the possibility of creating filigree constructions, but also its high demands on fabrication. For the development of design models the bearing behaviour of such connections will be investigated in detail by a cooperation project within the priority programme 1182 of the German Research Foundation (Deutsche Forschungsgemeinschaft DFG) at the Institutes of Structural Concrete of the RWTH Aachen University and the Graz University of Technology.

For plain compression and shear tests, joints with direct contact of the end faces and with end faces connected by mortar are investigated. Besides, the influence of surface treatment of the end faces will be examined. The transfer of plain compressive forces will be tested by two columns linked either by butt joints, joint layers or by variously reinforced wet/glued end faces.

The experimental set-up of the combined shear-compression loading is based on a standard push-out test, using a horizontal testing cylinder for a variable lateral compressive loading. At each test, the load bearing and deformation behaviour of two joints will be tested to evaluate the coefficient of friction.

For concepts dealing with tensile forces, tests on the required lap length of reinforcement bars will be performed. With lapped splices in coarse-grained UHPC and anchorage in ducts subsequently grouted with fine-grained UHPC, two different types for the transfer of tensile forces will be investigated.

2 Shear Compression

Test Programme

Specimens with dry and wet joints under variation of the contact surface, the glue material and the level of the compression forces have been tested.

The test set up is shown in Figure 1. Three UHPC slabs are laterally compressed by a constant load and charged vertically displacement-controlled with 0,01 mm/sec. The displacement is measured using four displacement transducers. The slabs used in the tests had a dimension of 300 mm x 200 mm x 80 mm and were made of coarse-grained UHPC reinforced

by 1 % p.v. steel fibres. The compressive strength of the used UHPC is about 150 N/mm²; the modulus of elasticity is about 47.500 N/mm².

Untreated, grinded (for consistent load distribution) and profiled surfaces were analysed in the test series. The untreated surfaces were defined by the used wooden multilayer formwork of the type Dokaplex. Grinded surfaces were treated by a CNC-machine using two different speeds of propulsion, 500 and 1000 revolutions per minute. For producing profiled surfaces, the formwork used was covered by Zemdrain liners.

Figure 1: Test configuration for combined compression-shear testsunder variation of the load levels.

Two different high performance adhesives were used for gluing the UHPC slabs, epoxy resin Sikadur 30 and reactive powder concrete (RPC). As RPC a fibreless fine-grained UHPC was used. Different levels of compressive stress on joints were simulated by varying the level of lateral compression force. A load variation of 500, 450, 300 and 150 kN was applied to the dry joints. Joints glued by RPC were loaded with 450 and 300 kN for even surfaces and 150 kN for profiled surfaces. Joints glued by epoxy resin Sikadur 30 were stressed with 10 kN only.

Table 1: Test programme, coefficient of friction m and ultimate load related to the analysed parameters.

Test type	Number of tests	Pre-tension					Dry joint				Wet joint					
		Level of pre-stress					Contact Surface				Glue		Contact surface		Coefficient of friction μ	Failure load [kN]
		N1 = 500kN	N2 = 450 kN	N3 = 300 kN	N4 = 150kN	N5 = 10 kN	even	polished / fibres	polished / no fibres	profiled	RPC	Epoxy resins	even	profiled		
Q1	2	x					x								0,88	-
Q2	2		x				x								0,9	-
Q3	2			x			x								0,91	-
Q4	2		x					x							0,75	-
Q5	2		x						x							-
Q6	2		x							x						-
Q7	2		x								x		x		-	950
Q8	2					x						x	x		-	985
Q9	2				x						x			x	-	750
Q10	2					x						x		x	-	-
Σ							12 Tests				8 Tests					

Results

To evaluate the test results and compare tests with different levels of compressive stresses the Mohr-Coulomb failure criterion was used. The Mohr-Coulomb criterion describes a linear relationship between normal and shear forces at failure. This relationship is defined as the coefficient of friction μ. The results are stated in Figure 2.

For joints with untreated and profiled surfaces high coefficients of friction μ between 0,75 and 0,85 were reached within the first 0,2 mm of displacement, whereas joints with grinded surfaces achieved considerably lower values of about 0,6 to 0,75. For untreated surfaces μ increased according to the displacement. For grinded surfaces the shape of the curve depended on the propulsion of grinding. The curves of the majority of grinded surfaces showed a significant decrease of μ at a displacement of approximately 2 mm. Average test results for dry joints are stated in Figure 2.

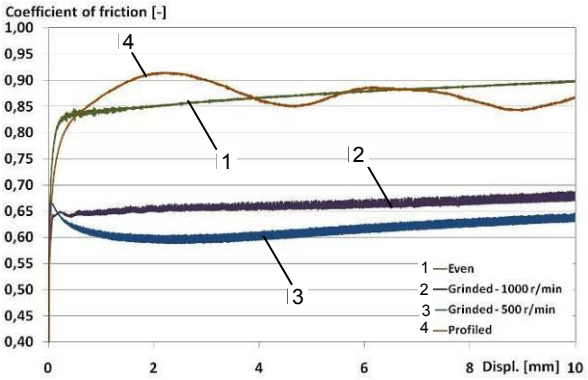

Selected curves of each surface type

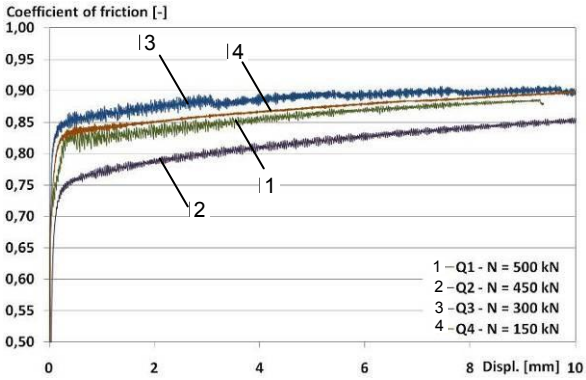

Coefficients of friction for even surfaces

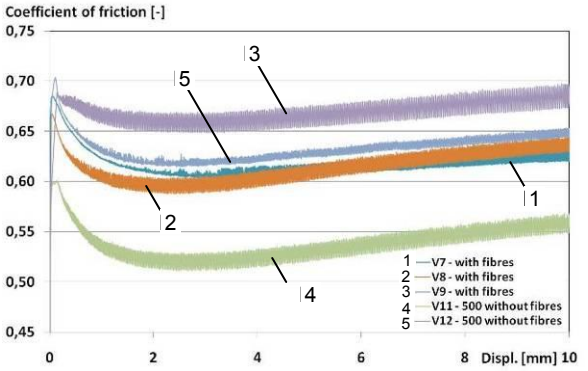

Coefficients of friction for grinded surfaces
Speed of propulsion of grind = 500 U/min.

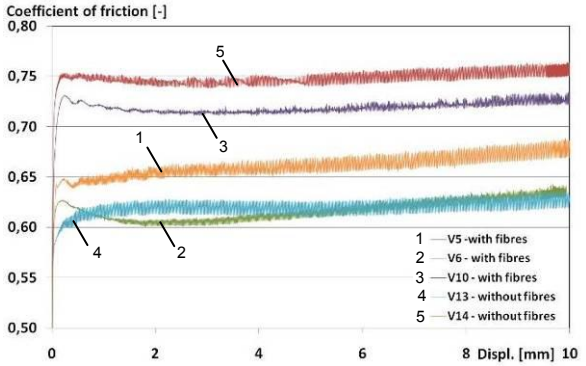

Coefficients of friction for grinded surfaces
Speed of propulsion of grind = 1000 U/min.

Figure 2: Average coefficient of friction for tests on dry joints.

The ultimate load of glued joints depends largely on the applied compressive stress. Joints with untreated surfaces glued by fine-grained UHPC reached a failure load of 950 kN by using a compression force of 450 kN. Joints with profiled surfaces glued by fine-grained UHPC reached a failure load of 750 kN at a compression force of 150 kN. Joints glued by epoxy resins with untreated surfaces had a failure load of 985 kN by using a compression force of only 10 kN whereas the same joints with profiled surfaces did not fail by achieving a shear load of 1 MN.

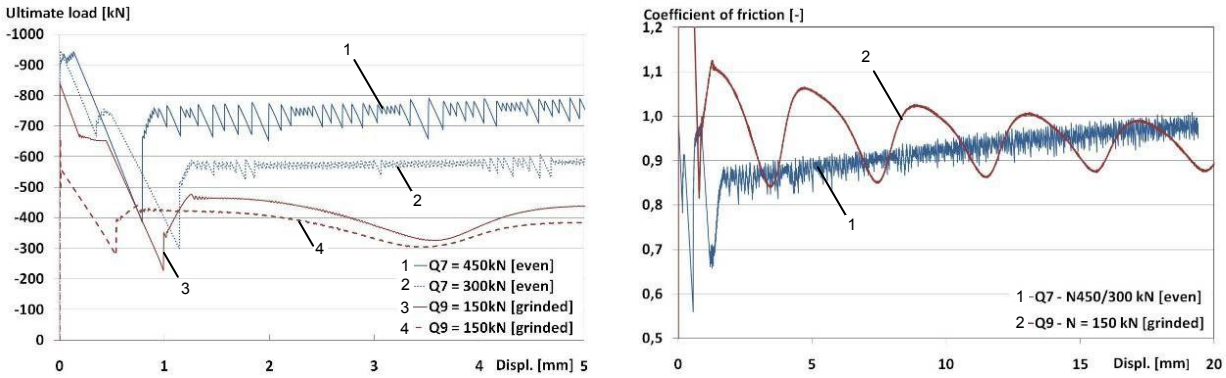

Relative displacement v = 5 mm *Relative displacement v = 20 mm*

Figure 3: Average failure load and coefficient of friction for tests on wet joints.

Joints glued by epoxy resins failed brittle after the bond strength was exceeded whereas for the tests with joints glued by fine-grained UHPC a friction coefficient of 0,85 to 1 could be reached due to the applied normal forces after the bond failure of the mortar. For joints with profiled surfaces the profile had great influence on the coefficient of friction-displacement curve which results in a sinusoidal curve of decaying amplitude. The test results are shown in Figure 3.

Discussion of the results

Henze [1] already showed that joints with untreated surfaces feature a higher coefficient of friction than joints with post treated surfaces like sandblasting. Treating causes macroscopic cones and rills which allow only a punctual contact between the two partners and leads to local plastic deformation under compressive normal stress.

Also in the peformed test this effect was observed. Apart from the macroscopic rills, the surfaces where very smooth by the polishing of the grinding head. This polishing effect was already observed by Turmo at al. [2] in 2006. The increase after the low point at approximately 2 mm can be explained by the formation of new and deeper rills caused by the quartz sand grains with progression of the test. The rills are caused by abrasion.

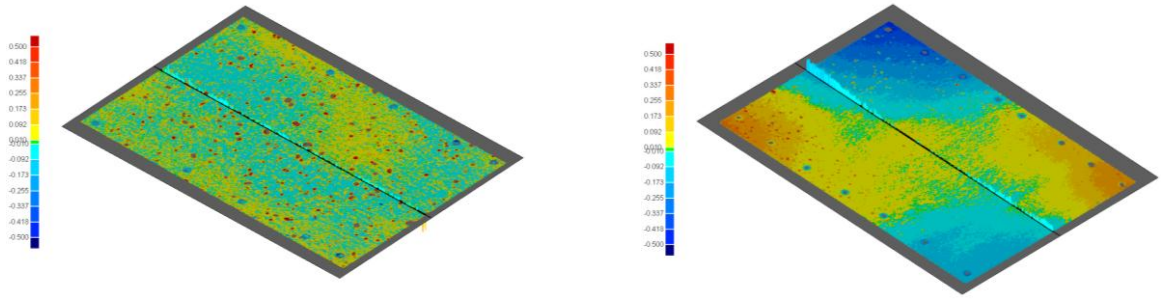

Grinded surface *Untreated surface*

Figure 4: Planarity in dependence of surface post-treatment.

In the performed test series the joints with grinded surfaces show a smaller coefficient of friction than the joints with untreated surfaces, while the planarity of the treated surfaces is considerably better as shown in Figure 4. The planarity of the surfaces was measured in advance to the tests with the GOM – ATOS 3 photogrammetrical system. Thereby, it was possible to quantify the deviation of the surfaces to a reference plane. For untreated surfaces the deviation to the plane laid within a range of 0,5 mm whereas for grained surfaces the deviation laid within 0,1 mm, as shown in Figure 4.

3 Compression test programme

Test Programme

The scope of the work programme is to investigate how the joint and the adjacent pre-fabricated columns have to be designed to appropriately take advantage of the characteristics of UHPC. The decisive parameters for the bearing capacity of the compressive joint are being determined to develop a design recommendation. The test programme is summarized in Table 2 (each test will be conducted twice).

Table 2: Test programme and failure loads for compression tests.

test	joint type	longitudinal reinforce-ment ratio		steel-fiber ratio		end face surface			mortar bed thickness		wire mesh diameter		thickness of steel plate		Failure loads [MN]
		1 %	2,7-%	0.75 % p.v.	1.0 % p.v.	formed	blasted	ground	10 mm	20 mm	Ø 6 mm	Ø 10 mm	5 mm	10 mm	
D0	dry	x		continuous reference column											8,14/8,20
D1		x			x	x									7,43/7,52
D2		x			x			x							6,98/6,95
D3		x			x			x							7,38/7,09
D4			x	favorite D1 to D3											6,72/7,16
D6	wet		x		x	x			x		x				7,30/6,78
D7			x		x	x			x			x			6,82/6,81
D8			x		x	x				x	x				6,55/6,48
D9			x		x		x				x				7,43/6,78
D10			x		x	x			x				x		7,89/7,57
D11			x		x	x			x					x	7,70/7,25
D12			x		x	continuous reference column									7,46/7,50

Two basic categories for the connection of compressive members are being investigated; wet and dry joints. In combination with dry joints, the longitudinal reinforcement ratio and the surface treatment of the column end faces are being investigated. Wet joints have been tested with varying thicknesses of the mortar bed and different transverse reinforcement ratios with welded wire meshes and steel plates (Figure 5).

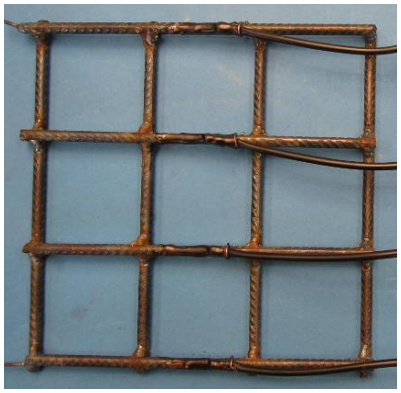

Figure 5: wire mesh.

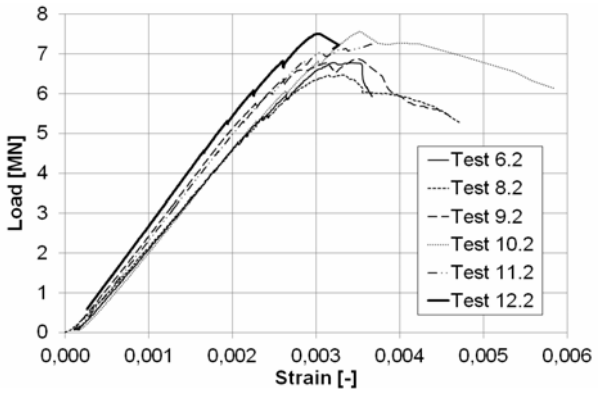

Figure 6: load-strain diagramme.

All specimens have been tested displacement-controlled without eccentricity. Before loading the specimens up to their failure load, 10 load cycles between 40 % and 60 % of the failure load have been applied. The ultimate load and length has been restricted by the 10 MN testing machine in use, which allowed a total length of 120 cm. Hence, 22 x 22 cm square UHPC columns with four reinforcement bars were feasible for the tests, as illustrated in Figure 7. The length of 80 cm for the bottom compression member allowed the formation of a shear band to study the bearing capacity of columns without joints, while the top compression member had a length of 40 cm. The transverse reinforcement ratio in the joint area was conforming to the design of high-strength concrete columns.

To avoid failure at the loading points, the cross-section in these points was increased by 25 %. During the tests, the longitudinal and transverse deformations of the column and especially the joint area have been recorded by strain gauges and displacement transducers. Additionally, the strain in the joint area has been measured and evaluated with Aramis, a digital image correlation system.

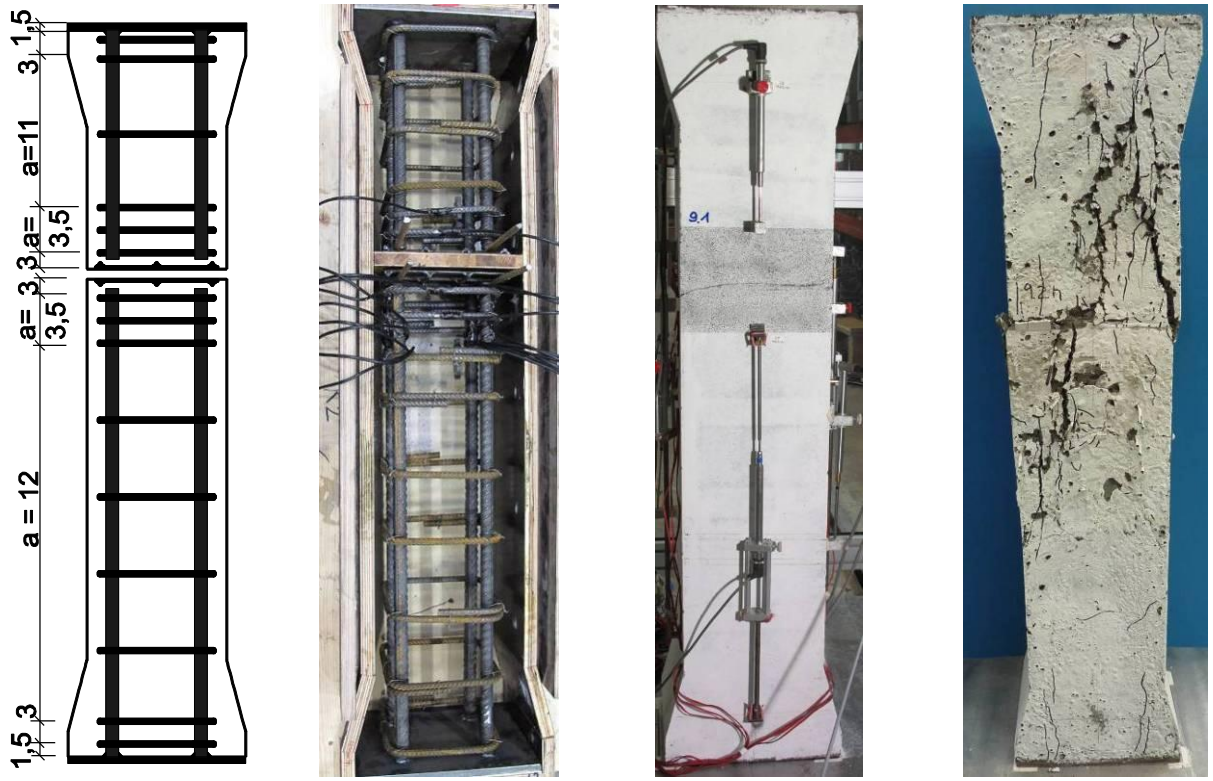

Figure 7: Compression test reinforcement and crack formation.

Results

The continuous reference column had a load bearing capacity of 7,48 MN and a compression failure in the section size transition. The columns with wire meshes in the wet joint had a bearing capacity of 92 % of the reference column and the cracks developped beginning from the joint. The columns with steel plates in the wet joint had a bearing capacity of 97 % of the reference column and either diagonal shear cracks or a failure in the change of section size transition developped. All test specimens failed abruptly, but due to the steel fibre reinforcement, the concrete cover did not spall off.

Since the longitudinal reinforcement only contributes 10 % to the whole bearing capacity, only a minor excess of the uniaxial concrete compressive strength occurs. Furthermore, a RPC mortar with the same stiffness as the column material has been used in the joint, so the transverse strain differences and the splitting tensile forces in the end face have been small.

The longitudinal reinforcement ends just outside the joint, and the part of the longitudinal force in the reinforcement has to be transferred into the concrete either by point pressure or by bond stress. In all tests, the longitudinal reinforcement strain at the end of the rebar has been recorded. By comparing the strain in the end of the reinforcement to the strain at defined distances from the end, it was clearly visible, that up to 75 % of the force in the reinforcement are transmitted into the concrete by point pressure. Only 25 % of the reinforcement force is transmitted over the anchorage length of the reinforcement.

Further variations of parameters as well as more detailed interpretations of the test results will be accomplished by non-linear FE computation using Abaqus/CAE. Based on the experimental and theoretical investigations, design and construction rules will be derived.

4 Tensile Tests

For the transfer of tensile loads, lapped splices in UHPC joints are investigated. Directly lapped splices (Figure 8) as well as bars lapped with bars in subsequently grouted ducts (Figure 9) are tested. For the directly lapped splices, the reinforcement diameter d_s, the lap length l_0, the steel fibre percentage per volume in the joint area, and the transverse reinforcement ratio A_{tr}/A_l are being investigated. Joints with grouted lapped splices are tested with different transverse reinforcement ratios A_{tr}/A_l and different concrete covers c. The test programme is summarized in Table 3 (each test will be conducted twice).

Table 3: Test programme for tensile tests.

	Rebar diameter	**Lap length**	**Steel fibre ratio**	**Transverse reinf. ratio**	**Concrete cover**
Test	d_s [mm]	l_0 [mm]	% p.V.	A_{tr}/A_l [-]	c [mm]
Z1	20	100	1	0,63	30
Z2	20	140	1	0,63	30
Z3	14	110	1	0,63	21
Z4	20	210	2	0,63	30
Z5	20	140	2	0,63	30
Z6	14	110	2	0,63	21
Z7	20	140		0,96	30
Z8	20	140		0,96	30
Z9	14	140		0,96	21
Z13	20	140	favourite	0,63	30
Z14	20	210		0,63	30
Z15	20	140		0,63	45
Z16	20	210		0,63	45

To select the lap length, the bond strength of the UHPC in use has been determined in 30 previous Pull-Out-Tests. Four lapped splices are tested in each test specimen. Depending on the diameter, 28 cm or 21 cm square UHPC elements with four reinforcement bars are used for the tests, as illustrated in Figure 12. The precast elements have a length of 70 cm each, while the joint length depends on the lap length and varies between 11 to 24 cm (Figure 10 and Figure 11).

Figure 8: directly lapped splice.

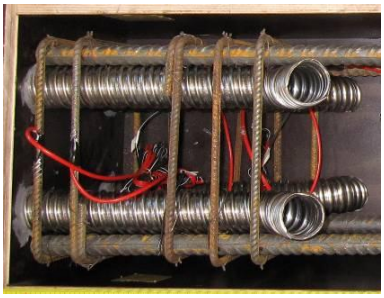

Figure 9: lapped splices with grouted steel ducts.

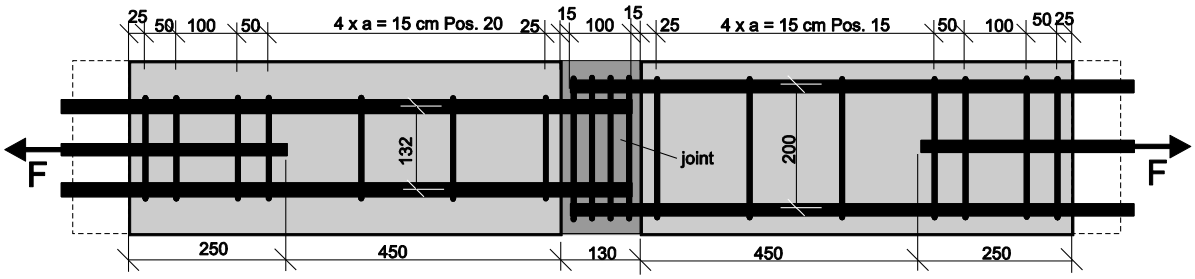

Figure 10: Reinforcement test Z1.

Figure 11: Joint area after failure test Z1.

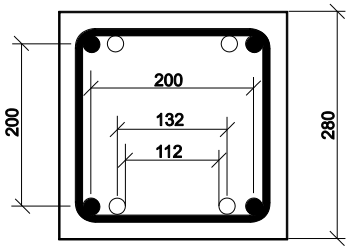

Figure 12: Cross section joint are test Z1.

Results

It was visible during the first tests, that the joint between the precast UHPC element and the UHPC joint opens from the beginning of the load application. The lapped splices in the tests Z1 and Z2 failed due to splitting of the concrete cover, while the bond strength was not exceeded.

5 Conclusions

The bearing behaviour of connections of precast UHPC elements has been investigated at the Institutes of Structural Concrete of the RWTH Aachen University and the Graz University of Technology. Tests on nodes for the transfer of plain compressive, shear-compressive and tensile loads have been conducted.

Tests on shear-compression joints showed, that surfaces of precast elements feature high coefficients of friction within the first 0.2 mm of deformation. A design security is given, since the coefficient of friction rises during further deformation.

The tested column joints indicate that the load bearing capacity of correctly designed precast UHPC elements in the joint area equals the load bearing capacity of continuous columns.

Joints of precast UHPC elements for the transfer of tensile loads can be designed with short lap lengths, when the concrete cover and transverse reinforcement is chosen adequately.

References

[1] Henze S., “Entwicklung und Beschreibung des Tragverhaltens einer modularen Fachwerkkonstruktion aus Hochleistungsbeton”, The Universität Leipzig, dissertation, 2009.

[2] Turmo J., Ramos G., Aparicio A.C., “Shear strength of dry joints of concrete panels with and without steel fibres”, Engineering Structures 28 (2006), p.23-33.

UHPFRC for Prefabricated Bridge Component Connections

Benjamin A. Graybeal[1], Matthew Swenty[2]
1: Federal Highway Administration, United States of America
2: Virginia Military Institute, USA (formerly of PSI, Inc. in Herndon, Virginia, USA)

Construction of highway bridges using precast concrete components normally requires the field placement of connections with a high quality grout or concrete. Many shortcomings have been documented with the standard materials used in these connections, therefore as part of the Federal Highway Administration's ongoing research program, ultra-high performance fiber reinforced concrete (UHPFRC) has been investigated as an alternative material. This multiphase investigation has focused on developing appropriate connections details through assessing the global and local structural performance of the connected component systems. The full-scale cyclic structural testing of UHPFRC connections between precast deck panels indicated that non-contact lap-splice reinforcing bar connections were capable of emulating cast-in-place bridge deck performance. The full-scale cyclic structural testing of UHPFRC composite connections between precast girders and precast decks indicated that UHPFRC was capable of meeting the fatigue design requirements for the connection while allowing for a significantly simplified construction process as compared to standard practice. This test program has demonstrated that UHPFRC is a material capable of ensuring appropriate performance of simplified structural connections, thus facilitating the use of prefabricated concrete bridge elements.

Keywords: Ultra-High Performance Fiber Reinforced Concrete, UHPFRC, UHPC, Bridge Design, Prefabricated Elements, Precast Concrete, Connections

1 Introduction

The use of modular prefabricated components has the potential to produce higher quality, more durable infrastructure systems. However, the required connections have often proved lacking, resulting in less than desirable overall system performance. Advanced cementitious composite materials, whose mechanical and durability properties far exceed those of conventional concretes, present an opportunity to significantly enhance the performance of field-cast connections, thus facilitating the wider use of modular prefabricated systems. UHPFRC represents a class of such advanced cementitious composite materials. Of particular interest here, UHPFRCs can significantly shorten the development length of embedded discrete steel reinforcement and can exhibit exceptional bond when cast against previously cast concrete. These properties allow for a redesign of the modular component connection to facilitate accelerated construction and enhanced long-term system performance.

The two fundamental differences between the field-cast UHPFRC connection concept and conventional construction concepts are simplicity and performance. The UHPFRC connection concept allows for small, simple connections without requiring the use of post-tensioning or the use of large volumes of field-cast concrete. The performance of the connection exceeds that normally anticipated from a field-cast connection, thus allowing the joined components to emulate or surpass the behavior of monolithic construction.

A research, development, and deployment effort focused on UHPFRC connections is being conducted by the U.S. Federal Highway Administration. This program is building on a decade of experience with UHPFRC applications [1] along with past efforts specifically focused on UHPFRC connections [2-3] to create practical solutions which address clear needs within the American highway transportation system. FHWA's efforts have included conducting fundamental research into UHPFRC structural behaviours, constructing and testing full-scale component connection systems, developing appropriate mechanical and durability testing

methods for UHPFRC, developing advanced computational modelling capabilities, and working with State-level partners to begin deployment of UHPFRC systems within the public infrastructure.

2 Component to Component Deck-Level Connections

The concept of using the advanced properties of UHPFRC to significantly modify the design of connections between prefabricated concrete components is gaining interest in the United States and Canada. For the most part, the connections on which these efforts have focused have been deck-level connections. As of late 2011, field-cast UHPFRC connections between prefabricated bridge components have been implemented in approximately two dozen roadway bridges in North America. These bridges use a range of details to connect a variety of different precast concrete modular bridge components, including adjacent box beams, full-depth precast deck panels, and deck-bulb-tee girders. The connection designs deployed to date have tended to mimic non-contact lap splice connections with a female-female shear key profile. Figure 1 shows a bridge with UHPFRC longitudinal connections between the top flanges of deck-bulb-tee girders. This bridge, constructed by the New York State Department of Transportation (NYSDOT), opened to traffic in 2009. The embedded illustration provides an overview of the connection detail.

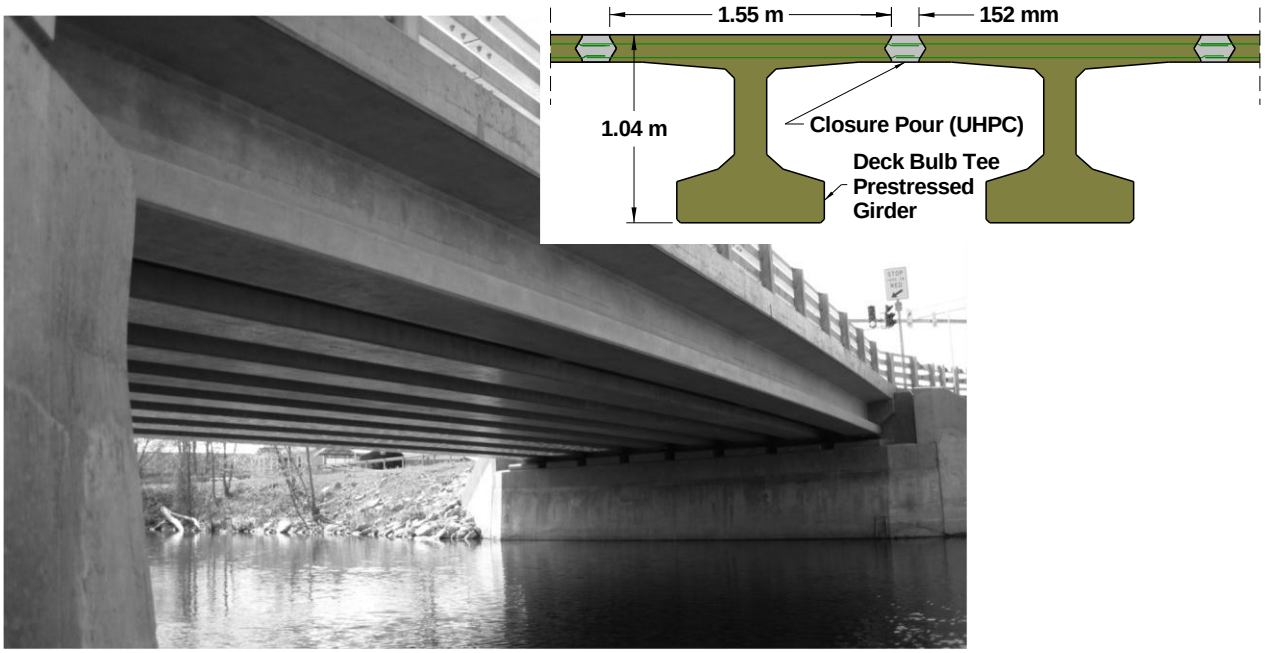

Figure 1: Deck-bulb-tee girder bridge with non-contact lap splice connection detail, including illustration of cross section.

In support of the efforts by State Departments of Transportation in the U.S. to begin using UHPFRC connections in bridges, the Federal Highway Administration has expanded its UHPFRC research program to include a significant focus on UHPFRC connections. This work, which began in 2009, included a phase wherein cyclic and static tests were completed on full-scale longitudinal and transverse deck-level connection subcomponents. Figure 2 shows the cyclic flexural testing of a longitudinal connection which simulates the connection between the top flanges of two deck-bulb-tee girders. Full results of this test program can be found in [4-5].

In summary, this testing program demonstrated that UHPFRC connections can emulate or exceed the performance expected from monolithic reinforced concrete. The tests of transverse connections demonstrated favourable cracking behaviours with no interface debonding. The static loadings to failure resulted in global flexural failure of the simply-supported panels, with

behaviors progressing through cracking, rebar yielding, and eventual concrete crushing. The tests of longitudinal connections focused greater emphasis on the development and bonding performance of the reinforcement embedded in the connections. In the most severe test, a large structural overload followed by over 11.5 million cycles of structural loading did not result in any debonding of the 16M (#5) rebar embedded 150 mm (5.9 inch) in the non-contact lap splice connection.

These tests demonstrated that UHPFRC presents a viable solution for creating robust constructible deck-level connections between prefabricated bridge elements. Even under the one-way bending, simply supported loading scenarios engaged herein, the performance of the connections emulated the performance of monolithic concrete.

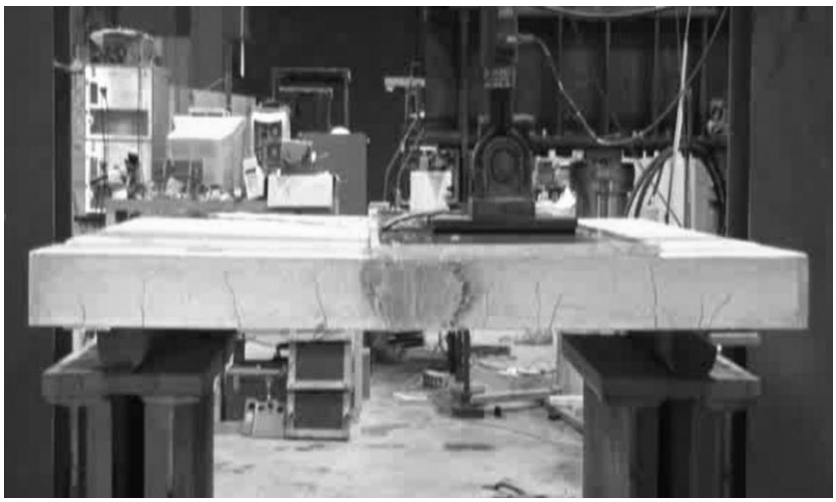

Figure 2: Cyclic structural load test setup for a field-cast UHPFRC bridge deck connection.

3 Deck to Girder Composite Connection

The connection between a bridge deck and the bridge girders, commonly referred to as the composite connection, is also critically important to the long-term performance of a bridge. In the U.S., the use of prefabricated bridge deck elements has been hindered by types of details required for these connections and the constructability thereof. Standard practice requires that the spacing of the connectors emanating from the girder cannot be greater than 0.6 m (2 feet), resulting in clusters of connectors at a 0.6 m (2 foot) spacing. These connector clusters pass into pockets in the deck panels, frequently resulting in significant constructability issues due to misalignment of the intersecting rebar, studs, and/or stirrups.

Ongoing research by FHWA and the NYSDOT is investigating the possibility of completely redesiging the composite connection to simplify the detail and eliminate interference between connected elements. The new connection relies on UHPFRC to facilitate the creation of a continuous connection running the entire length of each girder. As such, the need for intermittent pockets is eliminated. Additionally, the UHPFRC is engaged to transfer the horizontal shear and tension forces between the bottom mat of deck reinforcement and the composite connectors emanating from the girder. A conceptual illustration is provided in Figure 3. Views of two actual connections are shown in Figure 4, with a steel girder connection shown on the left and a concrete girder connection shown on the right. The bottom mat of 13M (#4) rebar spaced at 200 mm (7.9 inch) can be seen toward the top of each photo, with approximately 75 mm (3 inch) clear space between this mat of reinforcement and the composite connectors below.

Full scale physical testing of this concept was recently completed at FHWA. The testing included constructing a 1.31 m (51.5 inch) deep, 12.2 m (40 foot) long precast beam and

precast bridge deck system connected with the novel UHPFRC connection. This test specimen was subjected to four-point bending loads which generated horizontal shear forces in the composite connection. These shear forces, applied cyclically for more than 11 million cycles, were initially commensurate with the infinite fatigue life service load range which would occur in a two-span steel plate girder bridge with 64 m (209 ft) spans and 2 m (79 inch) deep girders. During later cycles the magnitude of the load range was increased until the final 5 million cycles were completed at two times the initial load range. This final cyclic stage amounted to an average of 0.40 kN/mm (2.28 kips/inch) of shear being repeatedly transferred through the connection along each shear span. Following the cyclic loading, the test specimen was statically loaded to failure. The global failure of the specimen occurred when the prestressed girder failed in shear at a vertical shear load of 2200 kN (495 kips). Thus, the connection was demonstrated to be capable of carrying at least 2.1 kN/mm (12 kip/inch) of horizontal shear force after being subjected to over 11 million cycles of severe cyclic shear loading. The horizontal shear stress in the field-cast UHPC connection along the minimum shear plane averaged 1.16 MPa (168 psi) during the final cyclic loading stage and 5.44 MPa (789 psi) at the peak static load. Throughout this loading, no damage was observed within the UHPFRC connection. The report detailing the full results of this test program will be published in early 2012.

The demonstrated performance of this connection concept opens new avenues toward wider use of UHPFRC in prefabricated system connections. The NYSDOT is looking to deploy this concept in the near future on an upcoming project which engages precast deck panels. More broadly, the concept of using the inherent UHPFRC tensile strength to provide shear resistance across an “unreinforced plane” could greatly increase the constructability of a variety of structural systems.

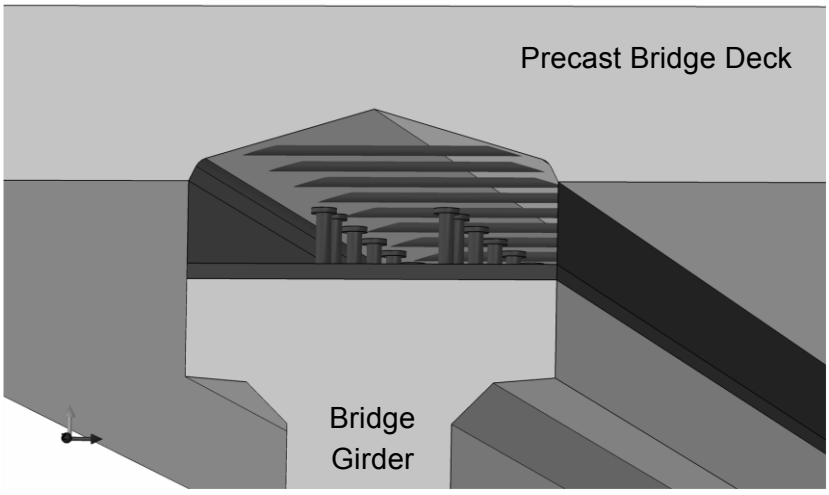

Figure 3: Conceptual illustration of composite connection between bridge girder and precast deck.

Figure 4: Photographs of UHPFRC connection at bridge girder to precast deck interface. Steel girder connection is on left; concrete girder connection is on right.

4 Other Applications of UHPFRC Connection Concepts

The topics presented above demonstrate the viability of UHPFRC connections, but also point toward far broader application of this concept. Within the highway bridge construction field, a number of other applications are being considered for deployment. These include:

- adjacent box beams,
- pre-topped steel girders,
- substructure column, pier caps, and abutments,
- barrier rails to bridge decks,
- spliced girder splices,
- continuous for live-load interior support connections,
- closure pours between cast-in-place staged construction,
- approach slab connections,
- secondary concrete pours at expansion joints, and
- connections for prefabricated systems for seismic regions.

Many of these connection concepts are currently being investigated via research programs in the U.S. Some of these applications, such as connections between adjacent box beams, are already being deployed by progressive departments of transportations in local regions of the U.S. and Canada.

5 Future Direction

FHWA efforts in the field of UHPFRC technology continue to delivery results which open doors toward new applications. While recognizing the need to develop the technological applications, there is also a lower profile effort underway to determine the fundamental UHPFRC mechanical behaviours as appropriate for inclusion within existing structural design frameworks. This design provision development effort, focused on provisions of greatest applicability to near-term deployable concepts, will continue for the foreseeable future as UHPFRCs become more prevalent and demand for their use grows.

6 Conclusions

The concept of using field-cast UHPFRC to complete connections between prefabricated structural components is gaining momentum. The inherent mechanical, durability, and rheological properties of UHPFRC make it an ideal candidate for facilitating the “strong connection” concept wherein the connections between concrete components cease to be weak points within the structure. Combining these facts with the recognition that the connections themselves can be simplified thus facilitating easier prefabrication and greater constructability, there is growing recognition that UHPFRC connections are a means to advance the state-of-the-art in infrastructure construction.

7 Acknowledgements

The research which is the subject of this paper was funded by the U.S. Federal Highway Administration. The authors gratefully acknowledge this support. The publication of this article does not necessarily indicate approval or endorsement of the findings, opinions, conclusions, or recommendations either inferred or specifically expressed herein by the Federal Highway Administration or the United States Government.

References

[1] Graybeal, B.: Ultra-High Performance Concrete, FHWA Report HRT-11-038, March 2011, 8 pp.

[2] Aarup, B.; Karlsen, J.; and Lindström, G.: Fiber Reinforced High Performance Concrete for In-Situ Cast Joints, Proceedings of the PCI/FHWA/FIB International Symposium on High Performance Concrete, Orlando, Florida, September 2000, 9 pp.

[3] Hansen, L.; and Jensen, B.: A New Building System Using Joints of Ultra High-Strength Fibre Reinforced Concrete, *Innovation in Concrete Structures: Design and Construction*, 1999, pp. 543-552, Dundee.

[4] Graybeal, B.: Behavior of Field-Cast Ultra-High Performance Concrete Bridge Deck Connections Under Cyclic and Static Structural Loading, NTIS Report No. PB2011-101995, Nov. 2010, 106 pp.

[5] Graybeal, B.: Fatigue Response of an Ultra-High Performance Concrete Field-Cast Bridge Deck Connection, Proceedings of the 2011 Transportation Research Board Conference, Washington D.C., January 2011, 12 pp.

Field Cast UHPC Connections for Precast Bridge Elements and Systems

Vic Perry[1] and Peter Seibert[2]
1: Vice-President & General Manager, Ductal®, Lafarge North America Inc., Calgary, AB, Canada
2: Technical Director, Ductal®, Lafarge North America Inc., Calgary, AB, Canada

Bridge owners are often faced with the need to replace critical bridge components during limited or overnight road closure periods. Previous papers [4, 5] have presented the development, testing and installation of high performance precast concrete bridge elements connected with field cast ultra-high performance concrete (UHPC) Joint Fill, for the replacement of deteriorated bridge decks in the USA and Canada. This paper presents current and promising applications for field cast UHPC connections (precast bridge parapet to decks, precast pile cap to piles, thin bonded overlays for repairs and high early strength UHPC for accelerated bridge construction). By utilizing UHPC's combination of superior properties in conjunction with precast bridge elements, benefits include: reduced joint size and complexity, improved durability and continuity, speed of construction, elimination of post-tensioning and extended usage life. With UHPC Joint Fill, the connections in precast bridge systems can now become the "strongest link".

Keywords: UHPC, connections, joints, connections, abrasion, composite, ductile, durability, fatigue, fiber-reinforced, impermeability, field casting

1 Introduction

Every day, engineers face the challenge of increasing traffic volume and loadings on aging bridge infrastructure with reduced budgets and public demand for less inconvenience during maintenance or repairs. As well, transportation authorities are faced with replacing or repairing these critical bridge components during strictly limited or overnight road closures. The result of not being able to meet these challenges is demonstrated by the USA Federal Highway Administration (FHWA) data which rates 150,000$^+$ bridges as structurally deficient or obsolete. [1]

One of the largest challenges facing bridge authorities is the long-term durability and resiliency of bridge decks which receive continuous impact loading from trucks and changing environmental conditions. Years of continuous flexural and thermal stresses create long-term deterioration and maintenance issues for bridge decks. While Cast-In-Place (CIP) concrete decks with High-Performance Concrete (HPC) and corrosion resistant reinforcing can significantly extend deck life, it creates high user inconvenience and is problematic for bridge deck replacement in high traffic areas or in remote areas with limited access of ready-mix concrete. The use of HPC precast deck panels is a common method to speed construction and alleviate user inconvenience; however the jointing of the precast system is a source of potential maintenance.

While it is recognized that precast bridge components can provide high durability, conventional joints are often the weakest link in the system. The introduction of new methodologies and innovative material technologies facilitates the implementation of new solutions. One new technology helping to solve the problem with deteriorating bridges is an ultra-high performance, fiber reinforced cement composite material ("Ductal®") by Lafarge North America [2,3] which offers superior technical characteristics including ductility, strength and durability while providing highly moldable products with a high quality surface aspect and a short bond development length. Ultra-high performance concrete (UHPC), used as a jointing

material in conjunction with reinforced high performance concrete (HPC) panels provides a synergistic, new approach for reconstruction of bridge superstructures.

Since 2005, several US state [4] and Canadian provincial highway departments [5] have implemented the use of UHPC joint fill with full precast bridge decks for the replacement of deteriorating highway bridges. The solution is to use a precast concrete deck with field cast UHPC joints to develop the continuity in the deck. Utilizing the superior characteristics of the material technology enables the simplification of the precast panel fabrication and installation processes. This simplified design provides the owner with improved tolerances, reduced risk, increased speed of construction, an overall cost savings in construction and a more resilient/durable, longer lasting bridge deck solution.

2 Characteristics and Supply of the UHPC Jointing Material Technology

The UHPC technology utilized for the joints is an ultra-high-strength, ductile material formulation made with constituent ingredients such as: Portland cement, silica fume, quartz flour, fine silica sand, high-range water reducer, water and steel fibers. The family of products utilized for this application, is Ductal® JSXX00, and is covered by one of many patents in a range of ultra-high performance concretes, all under trademark (Ductal®). Compressive strengths for bridge applications can range from 120 to 200 MPa and flexural strengths range from 15 to 40 MPa.

The material's high mechanical properties are a result of proportioning the constituent ingredients to produce a modified compact grading with a nominal maximum coarse aggregate size of 400 μm, and a fibre geometry of 12 mm x 0.2 mm. The ratio of maximum coarse aggregate size to fibre is important to facilitate random orientation of fibres and a ductile behavior. These performance characteristics result in improved micro-structural properties of the mineral matrix, especially toughness and control of the bond between the matrix and fibre. The material has superior durability characteristics due to low porosity from a combination of fine powders, selected for their relative grain size (maximum 0.5 mm) and chemical reactivity. The net effect is a maximum compactness and a small, disconnected pore structure. The ultra-high strength properties (see Table 1) and low permeability also provide excellent protection of the rebar against corrosion and improved bond.

Table 1: Range of material characteristics for Ductal® JS1000.[6]

Strength		**Durability**	
Compressive (28 days)	140 MPa	Freeze/thaw (after 300 cycles)	100%
Compressive (48 hours)	100 MPa	Salt-scaling (loss of residue)	<0.10 g/m^2
Flexural	30 MPa	Carbonation depth	0.5 mm
Young's Modulus (E)	50 GPa		

The materials are supplied to the site in a three-component premix (pre-blended powders in 22 kg bags or 1100 kg super-sacs plus superplasticizer and fibres), along with portable mixers (see Fig. 1) and technical support from the supplier. The mixers are set up in pairs to provide a continuous supply of material for the joint filling operation. The mixers are normally set up at the end of the bridge to provide direct access to the bridge deck.

IMER Mortarman 750 mixers are capable of batching 0.23m^3 per 20 minute batch cycle time for a volume of 1.36 m^3/hour per pair of mixers. The number of mixers delivered to the site is determined based on the contractor's schedule. Larger, Ryan Industries 2500 mixers of 0.5 m^3 batches (20m^3/ day capacity) are also available. For even higher volume supply, ready-mix truck batches of 6 m^3 are available. The UHPC joint material is transported to the joints by

power buggy or wheel barrow then placed directly into the joints (see Fig. 2). The UHPC material was batched with a mini-slump of 200mm to 250mm (self consolidating and self-leveling). The rheology of material permitted the UHPC to be poured directly into the joints without any vibration.

Figure 1: UHPC Portable Mixers

Figure 2: Filling the Joints with UHPC.

The joints are covered with form grade plywood strips and allowed to cure until reaching 100 MPa before opening to traffic. The time to reach 100 MPa will vary, depending on ambient and curing temperatures. At ambient temperatures (20°C) without accelerators, this would be approximately 3 days or reduced with accelerator and heat or use of a rapid strength product.

3 Full Scale Testing of UHPC Joints

In 2008, the owner (NYSDOT), material supplier (Lafarge), precaster (The Fort Miller Co.) and the FHWA agreed to undertake a prototyping and testing program to validate the full depth precast panel and UHPC joint design. The prototypes to be cast and tested were pairs of precast panels with joint fill (see Fig. 3) and small samples of UHPC with rebars for direct pullout tests. [7]

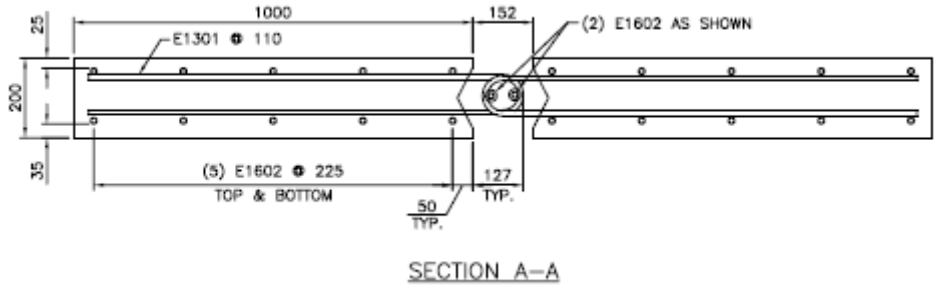

Figure 3: Prototype Panel (Pairs) for Testing Joint Fill Performance [7].

The precast panel pairs were manufactured with three rebar joint configurations (straight bars, hairpins, stud heads) and three types of rebar (epoxy coated, galvanized and black) and for a total of nine configurations. Note, Figure 3 shows only the hairpin joint configuration. Pullout test specimens were manufactured with 13mm, 16mm and 19mm bar sizes in epoxy coated and black steel bars. Embedment lengths were 75mm for the 13mm Ø bar; 100mm for the 16mm Ø bar; and 125 mm for the 19mm Ø bar. Failure behavior of the pullout tests conducted on all samples was rebar failure. To validate the joints' ability to remain water tight during the life of the bridge, the precast panel pairs were loaded with a simulated wheel impact loading while water was ponded on the joint (see Fig. 4). The pairs of panels were simply-supported with the

joint arrangement in both a parallel and perpendicular direction in order to simulate both a transverse joint and a longitudinal joint.

The test panels manufactured at The Fort Miller Co., NY were shipped to the FHWA Turner-Fairbanks laboratory for fatigue testing in a field simulated, wet condition. [8] The HPC precast deck panels (see Fig. 4) with the UHPC Joint fill showed no signs of leakage or degradation at 9 million cycles of a simulated wheel loading (cycling from one ton to 8 tons).

Fig. 4 Bridge deck panels with water ponding under fatigue loading Courtesy of FHWA).

4 Previous Experience with UHPC Field Cast Joints

Full Depth Precast Deck Panels

The Rainy Lake Bridge, Ontario (see Fig. 5) constructed in 2006 was the first UHPC Joint Fill ("JS1000") project; part of an innovative field cast joint solution for a bridge superstructure/precast deck panel system developed for the Ministry of Transportation of Ontario [5]. UHPC was used for all joints including shear pockets and haunches. Through design, testing and construction, it validated a precast bridge deck (slab thickness 235 mm) with a 200 mm wide joint and led the way to other, repetitive joint fill projects.

Figure 5: Rainy Lake, Ontario Bridge Deck prior to receiving asphalt wearing surface

The Oneonta Bridge in New York, USA constructed in 2009, has 22 precast slabs jointed on top of 5 steel girders (slab thickness: 200 mm). The bridge was 38.8 m in length, with a deck surface area of 504 m^2 and the joint cross-section was 152 mm wide by 200 mm thick. The deck was reinforced with galvanized bars and received a bonded concrete overlay riding surface.

The Chukuni River Bridge**,** Ontario**,** (see Fig. 6) - completed in 2010, has 4 – 3.7 m deep steel beams and 54 precast concrete deck panels (slab thickness 225 mm). UHPC joint fill was used to interconnect the precast concrete panels to each other as well as provide the shear connection to the steel structure. This bridge is 101 m long with a clear span of 83.5 m (the longest single span bridge in Canada).

Figure 6: Chukuni River Bridge, Ontario.

Side-by-Side Box Girders

During the period from 2007 to 2010, seven bridge projects *(Sunshine Creek, Hawk Lake, Buller Creek, Log River, Eagle River, LaVallee River and Wabigoon River)* have been competed with UHPC joint fill (see Fig. 7) between side-by-side box girders (varying depths from 600 mm to 1150 mm). The projects ranged in length from 21 m to 87 m and from single to three span continuous (see Fig. 8). For all of these bridges, lateral connections was with UHPC only (no post-tensioning was applied).

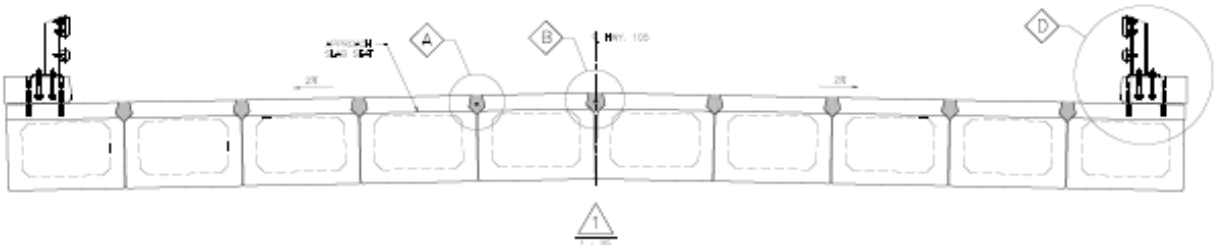

Figure 7: Typical cross section of side-by-side box girders with UHPC Joint Fill (depth 600 to 1150 mm).

Side-by-Side Deck Bulb-Tees

The Village of Lyons Bridge, NY, USA built in 2009, is a side by side, single bulb-tee girder project consisting of 8 – 26 m long, side by side single bulb-tee girders (see Fig. 9) with UHPC Joint Fill connecting the flanges between the bulb-tees. The deck has an asphalt overlay/ riding surface.

Figure 8: Eagle River Bridge, Ontario - a multiple span side-by-side box girder bridge.

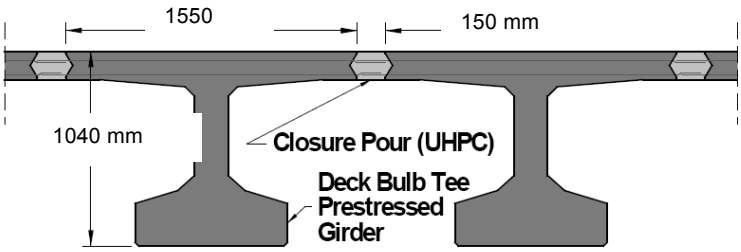

Figure 9: Section showing Side-by-side Bulb-Tees with UHPC Joint Fill connecting the flanges [9].

Field Cast Joint Fill for Live-load Continuity

During 2010, two bridge projects (Eagle River @1100mm deep box-girders [see Fig. 10] and Wabigoon River, ON @ 900 mm deep box-girders) utilized UHPC field cast joints for live-load continuity over internal piers in precast bridges. This joint design (see Fig. 11) completely eliminated the need for post-tensioning and provided fast, simple field connections of precast bridge elements.

Figure 10: Wabigoon River Bridge, Ontario, Canada joint.

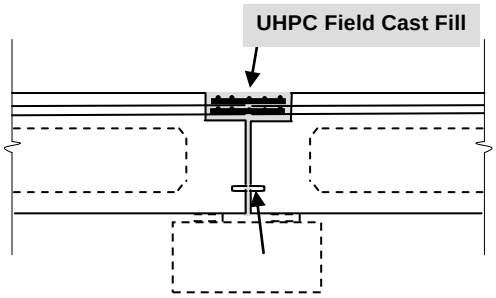

Figure 11: Section through a live-load continuity.

Field Cast Joint Fill for Precast Approach Slabs

To date, ten precast bridges have utilized UHPC field cast joints for precast approach slabs (typically 250 mm thick). The use of UHPC field cast joints completely eliminate the need for post-tensioning, contribute to further reductions in construction time and provide a more durable solution.

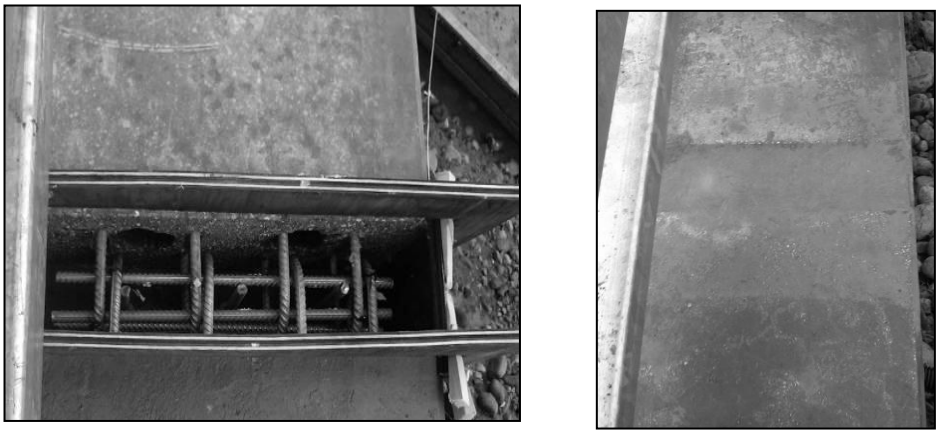

Figure 12: Forming and finished view of UHPC curb joints.

Field Cast Connections for Precast Curbs

UHPC field cast joints for precast curbs (typically 260 mm thick) were used on 8 bridge projects between 2007-2010, The use of UHPC connections ensures that continuity in the curb-deck system simplifies the deck precasting operations and contributes to speed of construction (see Fig. 12).

5 Promising New Applications for UHPC Field Cast Joints

The use of UHPC field cast connections is a relatively new solution, only have been implemented since 2006 and used in fewer than 20 bridges. However, this early adoption has provided excellent field experience and validation of the methodology. It has also provided exposure and confidence in the technology which has led to innovations for the use of UHPC for other types of field connections for precast bridge systems. The following are examples where this material has been recently (2011) used on a limited basis.

Field Cast Connections for Precast Waffle Deck Panels and Hidden Shear Pockets

The use of UHPC for Precast Waffle Deck Panels (see Fig. 13) provides a light weight durable bridge deck system suitable for new or the rehabilitation of bridges. Installing UHPC joint fill (see Fig. 14) between the 205 mm thick UHPC Waffle Deck panels provides an entire deck made from UHPC. To further reduce dead load and improve the deck durability the waterproofing and wearing surface are removed, thereby leaving the entire UHPC deck exposed in order to provide the highest durability, where it is most needed, at the riding surface.

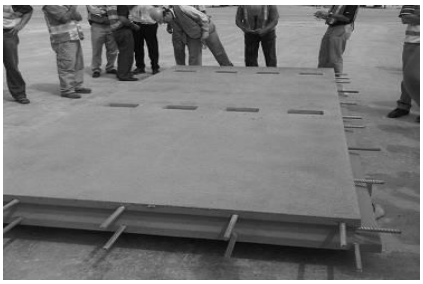

Figure 13: Waffle Deck Panels for Wapello County Bridge, Iowa, USA.

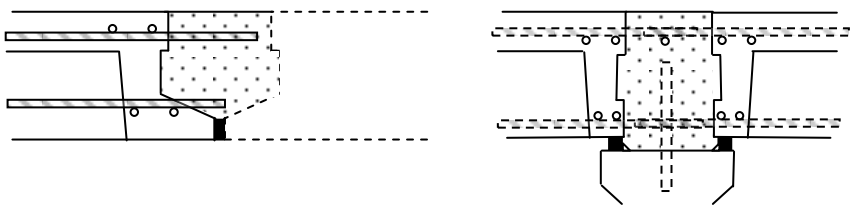

Figure 14: Jointing Details between Waffle Deck Panels.

Removing the wearing surface and membrane not only exposes the deck panels, but also the field cast joint fill and shear pocket openings. Obtaining a high quality riding surface on exposed field cast UHPC requires additional field work. One option is to reduce the quantity of exposed fields cast joint fill. To further minimize the exposed surface of joint fill, hidden shear pockets maybe introduced into the precast panel. The UHPC filled hidden or conventional shear pockets and haunches provide a fully composite action with the supporting beams.

Field Cast Connections for Precast Parapets / Barrier Walls

As an alternative to cast-in-place, precast parapets or barrier walls maybe supplied to the bridge already integral (Fig 15) with the deck or as separate units to be field attached. In both cases the precast parapet units need to become fully composite with the bridge deck system in order to carry the traffic barrier loadings.

Figure 15: Integral Deck and Parapets.

Field cast UHPC connections for precast parapets and barriers provides the integral continuity and further aids in speeding the construction of the bridge.

Field Cast Connections for Piles to Abutments

As bridge engineers look for more innovative methods to further speed bridge construction, precast abutments placed on piling and connected with UHPC [10] provides a further reduction in construction time. The Whiteman Creek project (Fig. 16) was under completed in August, 2011.

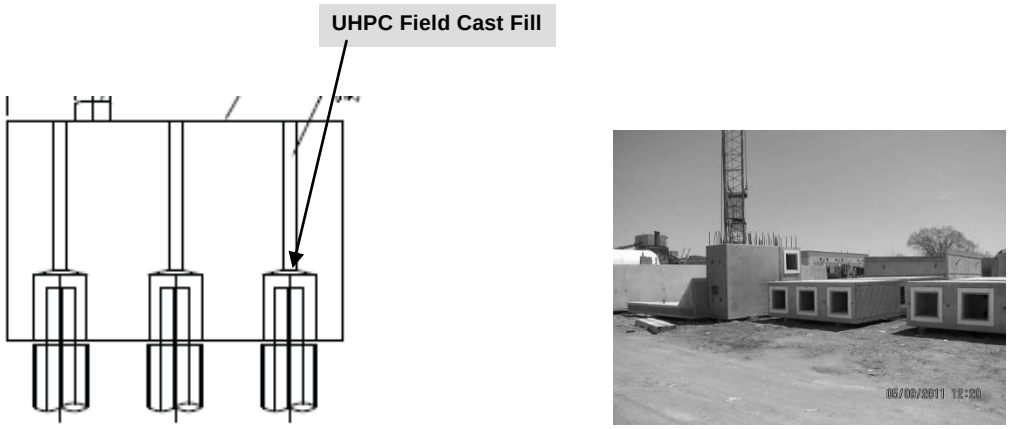

Figure 16: Precast Abutment for Whiteman Creek, ON [10].

Field Cast UHPC for Expansion Joints

UHPC field cast expansion joints (see Fig. 17) provide strong and durable solutions to solve the durability problems with freeze/thaw, deicing, the constant impact/abuse from trucks and snow ploughs crossing the expansion joints. The use of UHPC for expansion joints eliminates the need for embedded steel edges or casting of field concrete between the precast deck and steel embed. The expansion joint is formed (see Fig. 18) and the UHPC is cast through a chimney in order to maintain a constant head on the filled portion of the joint. Once the UHPC has gained 80 MPa, it is ground (see Fig. 19) to exact grade and profile to match the asphalt wearing surface. This type of UHPC expansion joint has been used on several bridge projects in the province of Ontario.

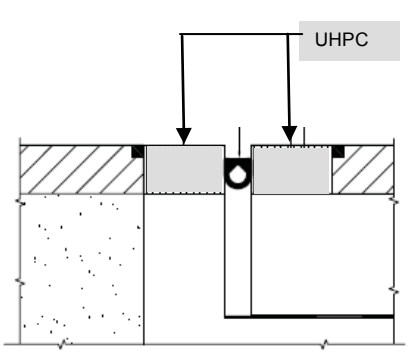

Figure 17: Section through expansion joint.

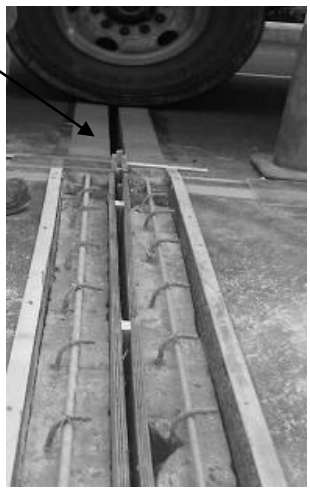

Figure 18: Expansion Joint ready for UHPC.

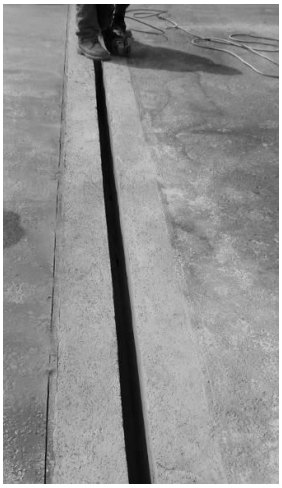

Figure 19: Finished Joint.

Field Cast UHPC for Thin bonded Overlays

Another promising use for UHPC field cast rehabilitation is thin bonded overlays (or "Hybrid") to re-strengthen deteriorating bridge decks (see Fig. 20). Several State DOTs, cooperatively with Universities, are investigating the use of UHPC as a cost effective method to significantly extend the life of bridge decks approaching their service life. Early research work undertaken by several universities [11,12] has shown that the inter-facial bond between post cast UHPC onto hardened HPC has provide excellent bond. In all testing conducted to date the failure has always occurred in the base HPC material and not in the interface between the UHPC and HPC. This ongoing research is a further validation of the fatigue testing conducted by the FHWA [8] on the pairs of precast slabs with UHPC joint fill, where the joints did not fail or leak after 10,000,000 load cycles.

Figure 20: Thin Bonded UHPC Overlay [11].

The use of this system is being investigated as both a field cast topping for in-situ deck repairs and as a precast system. The precast "Hybrid" would be cast top surface down where the UHPC is first cast in a textured form liner and then the HPC as a structural back-up. Then panels would be cured, flipped and ready for delivery to site. The precast "Hybrid" panels would be connected with field cast UHPC. Hidden shear pockets may also be used with this system.

Field Cast UHPC for Accelerated Bridge Construction

UHPC is a family of products where the mix designs can be formulated to provide a wide range of slump flows, hardened mechanical properties and rate of strength gain. One UHPC product formulated specifically for ABC construction is Ductal JS1100RS, which provides a high early strength of 55MPa in 12 hours at normal ambient temperatures (Figure 21). The product has similar fluid workability to other UHPCs. This UHPC rapid strength product is designed for ABC projects executed during weekend closures or other time limited type repairs.

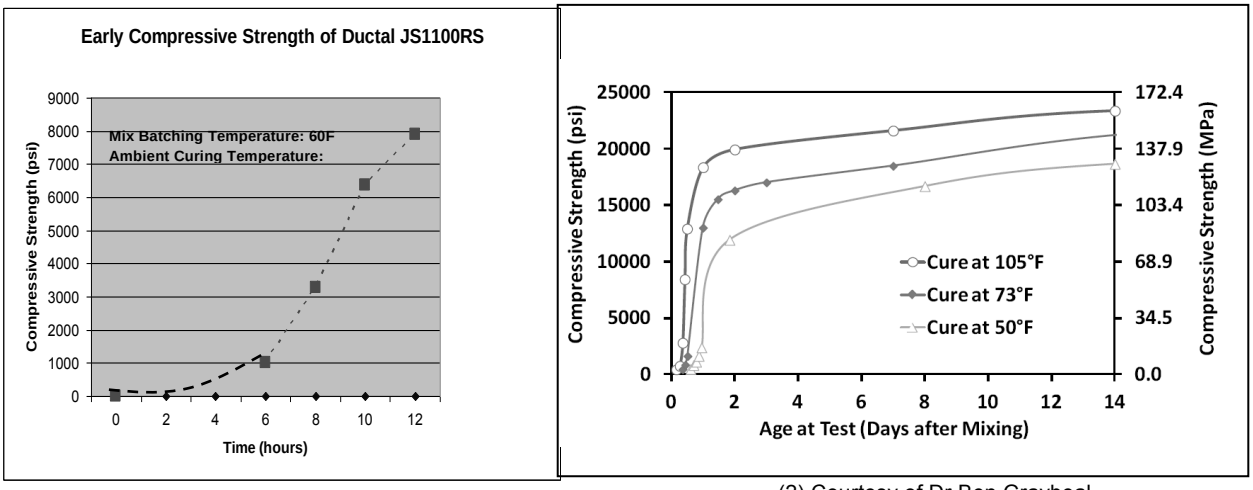

(1) Courtesy of Rutgers

(2) Courtesy of Dr Ben Graybeal,

Figure 21: High Early Strength UHPC for Accelerated Bridge Construction.

6 Conclusions

The UHPC material's combination of superior properties including strength, durability, resiliency, fluidity and increased bond capacity, in conjunction with reinforced precast panels, provides engineers with the ability to create new, optimized and innovative solutions for bridge construction, repair and rehabilitation. Direct benefits may include: improved bridge deck performance through the reduction of joint size and complexity; improved continuity and speed of construction and; elimination of field post-tensioning, while indirect benefits include: improved durability; lower maintenance, reduced user inconvenience and; extended usage life.

Examples were highlighted and testing presented from several DOTs and universities currently involved in precast bridge decks and UHPC programs. The early testing to date indicates that rebar in UHPC has a much shorter bond development length and that the interface bond between UHPC and HPC is stronger than the base HPC. This provides opportunities for bridge engineers to design narrower joint widths for precast deck systems without the use of post-tensioning, improved jointing between precast bridge deck systems, improved horizontal shear transfer systems for fully composite decks, and improved rehabilitations for bridges near their design service life. The use of UHPC for field connection between precast bridge elements has shown promising results and opportunities for expanding its usage. Full scale laboratory testing and early field perusals have indicated that to date the results of using this technology is providing improved bridge systems; however the authors also recognize that 5 years of performance it rather short compared to the desired service life of 100's of years. While the feedback from bridge owners using this system has been very positive with respect to performance, the authors plan to conduct an in depth field study of the joint performances and publish a future paper detailing the results.

The projects presented indicate that this material can be successfully batched on site in a range of batch sizes and provide high early strengths during typical field curing conditions. This experience also shows that local contractors can easily adapt to using UHPC material in bridge projects. While there are still challenges when implementing new material technologies on a wide scale basis, the real challenge ahead is to identify the optimized shapes for precast decks, shear pockets, joints for various deck arrangements and to disseminate on a wide basis the 'know-how' to the engineering community.

References

[1] Bhide, S.: *Material Usage & Condition of Existing Bridges in the USA,* PCA, Skokie, Illinois, USA, 2008.

[2] Graybeal, B.A.: Fabrication of an Optimized UHPC Bridge. PCI National Bridge Conference, Atlanta, GA, USA, 2004.

[3] Bierwagen, D; Moore, B; Perry, V.: Revolutionary Concrete Solutions, *Construction Specifier,* USA, 2006.

[4] Perry, V.; Royce, M.: Innovative Field Cast UHPC Joints for Precast Decks (Side-by-side single Bulb Tees),Village of Lyons, NY– Design, Prototyping, Testing and Construction. Third Congress of the International Federation for Structural Concrete (*fib*), Washington, DC, USA, 2010.

[5] Perry, V.; Scalzo, P.; Weiss, G.: Innovative Field Cast UHPC Joints for Precast Deck Panel Bridge Superstructures – CN Overhead Bridge at Rainy Lake, Ontario. Concrete Bridge Conference, USA, 2007

[6] Lafarge North America, Product Data Sheet: Ductal® JS1000, www.lafarge-ductal.com, 2009.

[7] Shop Drawings: Ductal® UHPC Joint Test", The Fort Miller Co., Inc., 2008.

[8] Federal Highway Administration, Tech Brief, FHWA Publication No. FHWA-HRT-11-022, 2010.

[9] Drawings: Bridge Rehabilitation – Route 31 Over Canadaigua Outlet, SH 8028, Route 31, NYSDOT, 2008.

[10] Young, W.; Boparai, J.: Whiteman Creek Bridge – A Synthesis of ABC, UHPC and FRP. PCI/NBC, Salt Lake, UT, USA, 2011.

[11] Harris, D.; Sarkar; J., Ahlborn, T.: Interface Bond Characterization of UHPC Overlays. Transportation Research Board Annual Conference, Washington, DC, USA, 2010.

[12] Wift, T.; et al: Iowa's UHPC Implementation. Bureau of Research & Technology, *Iowa Department of Transportation News,* April 2011, Iowa, USA, 2011.

Timber – UHPC composite floor structures – environmental study

Petr Hajek, Magdalena Kynclova, Ctislav Fiala
Faculty of Civil Engineering, Czech Technical University in Prague, Czech Republic

The experimental investigation performed at Czech Technical University in Prague verified the possibilities of using ultra high performance concrete (UHPC) in timber-concrete composites. Timber-concrete composite floor structures benefit from lower weight of UHPC deck while improving acoustic parameters and fire safety of the structure. One of the key problems is the connection between timber beam and UHPC deck. Wet process is not suitable due to the effect on wood and slim UHPC deck does not provide space for mechanical joint. The results of the experiments have showed that this can be solved by gluing.
A complex life cycle analysis (LCA) of four alternatives of RC floor structures is presented and environmental impacts are compared and discussed in the article. The results show that the high quality of mechanical and environmental performance creates the potential for wider application of UHPC in building construction in the future.

Keywords: timber-UHPC composites, glued connections, environmental study

1 Introduction

Optimization of concrete structures can contribute to the needed reduction of global environmental impacts. One possible way is utilizing of ultra high performance concrete in optimized structural shapes. Mechanical properties of these materials such as high compressive strength, durability, water tightness etc. create conditions for designing subtle structures that leads to saving up to 70% of material in comparison with ordinary concrete, and consequently to reduction of embodied CO_2 emissions.

The composite structures based on high performance silicates and wood represent a advantageous alternative to the timber floor structures. The timber structures have problems to achieve sufficient stiffness; the lack of mass causes troubles with acoustics, inflammability of wood limits their use because of issues with fire safety. These disadvantages can be reduced by employing timber-silicate composites.

Timber-concrete composite floor structures benefit from lower weight of UHPC deck in comparison to deck from OPC (ordinary Portland cement concrete) while improving acoustic parameters and fire safety of the structure. The combination of a thin silicate slab and a timber beam represents an effective cross-section from the perspective of bending stress. One of the key problems is the means of connection between timber beam and UHPC deck. Wet process is not suitable due to the effect on wood and slim UHPC deck does not provide space for mechanical joint. The experimental results have showed that this can be solved by gluing.

A complex life cycle analysis (LCA) of various alternatives of RC floor structures is presented, and environmental impacts are compared and discussed in the article. Relevant complex LCA is based on local environmental data collected during the inventory phase of the LCA procedure. The results show that the high quality of mechanical and environmental performance creates a potential for wider application of UHPC in building construction in the future.

2 Experimental verification of timber-concrete glued connections

The primary research focuses on developing UHPC mixture from materials available in the Czech Republic. A broad spectrum of cements, superplasticizers, microsilicas and sands from

various producers were tested. Only Stratec fibres were imported from Germany. The mixture used in these experiments has a compressive strength of 160 MPa tested on cubes a=100 mm. The optimalization of UHPC mixture is still in progress.

The first step in the research of the timber-concrete composite floor structures was to verify the performance of glued connection and for this,the shear test was selected. Both sides of concrete prism 100/100/400 were glued to two timber prisms 80/160/320. The arrangement of the test is apparent from figure 1.

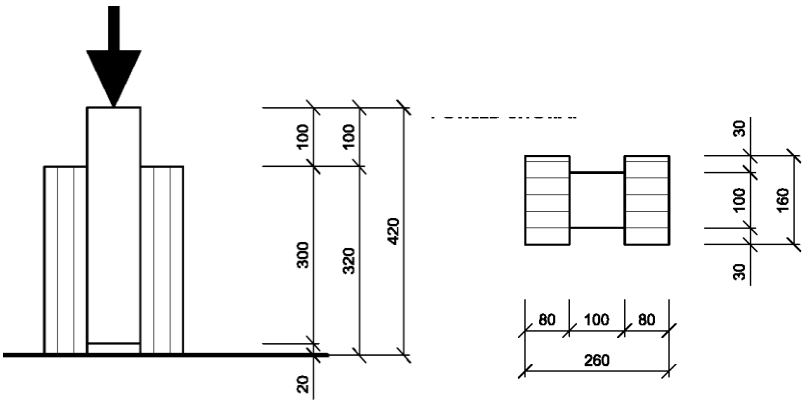

Figure 1: Shear test arrangement of timber - concrete composite.

Two types of concrete (OPC – ordinary Portland cement concrete and UHPC – ultra high performance concrete) and three various glues (Sikadur 30, Sikadur 330, SikaFloor 156) were used and tested in the first set of experiments. Timber prisms were from glued laminated wood. Even though, there were quite high variances in the results, the trend was obvious. The difference between OPC and UHPC timber composites was in the kind of a failure – the rapture in timber-OPC composites was mainly in concrete while in UHPC-timber composite the rapture was in the timber (figure 2). The best results were achieved with SikaFloor 156 although it has the worst workability as this type of glue is too liquid for such a purpose. Therefore, for the second set of experiments specific filler (3% and 5% by mass) was introduced into the SikaFloor 156. The glue with 5% of filler performed well both from the point of workability and shear strength.

Figure 2: Shear failure of timber - OPC composite and timber-UHPC composite.

Large scale experiments are now under preparation. Slender UHPC deck 1200x2400 mm with thickness of only 30 mm is to be glued to two timber beams. The results of the experiment will be presented at the conference.

3 LCA of four various concrete floor structures

Description of floor structures variants

The analysis was performed with four various RC floor structures, that were designed for four-storey residential building with ground plan 14.2 x 22.3 m. This analysis focuses mainly on floor structures and does not include concrete beams and supporting structures. The analysis covers all significant life cycle stages: transport of the raw material to the concrete plant, concrete production, and transport to the building site, pumping of fresh concrete, formwork and demolition of structures. All assessed variants V1-V4 were designed for following conditions: theoretical span 4.4 m (simply supported), dead load (excluding self weight of the floor structure) g_k = 4.0 kN/m^2 and live load q_k = 2.0 kN/m^2. Variants V1, V2 and V4 were designed as one way slabs, variant V3 as two way slab then. The variants considered in the study are shown in the Figure 3.

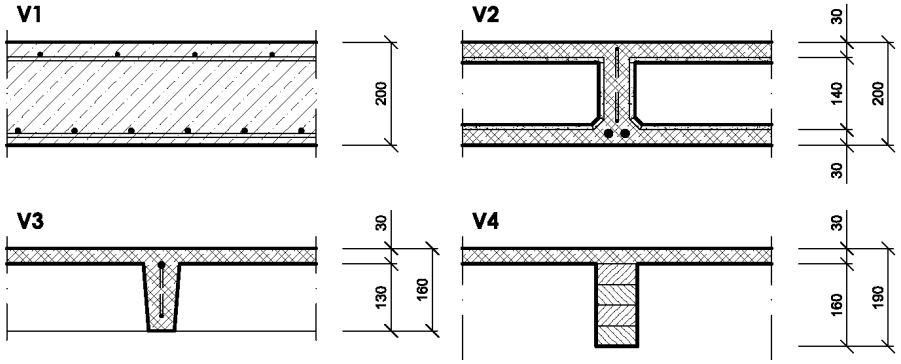

Figure 3: Schematic sections of floor structures alternatives.

V1 full RC slab C30/37 – thickness 200 mm, main reinforcement R10 ā 110 mm at the bottom surface, distributive reinforcement R8 ā 200 mm and reinforcing mesh W8/150/150 at the upper surface, ring beams reinforced by 4 R12 with stirrups R6 ā 200 mm.

V2 prefab concrete panels HPC105 with fillers from recycled laminated drink cartons - thickness 200 mm, high performance fibre concrete with compressive strength of 105MPa, upper and bottom deck 30 mm without conventional reinforcement, reinforced only by fibres Fibrex A1 1% by volume, width of ribs 50 mm, ribs spacing 500 mm, main reinforcement 2 R16 ā 500 mm, filigree shear reinforcement R5 ā 250 mm, ring beams from C30/37 on external walls reinforced by 4 R12 with stirrups R6 ā 200 mm, ring beams on inner walls reinforced by 2 R12 with stirrups R6 ā 200 mm.

V3 waffle floor structure HPC105 – thickness 160 mm, upper deck 30 mm, width of ribs in both directions 50-70 mm, rib's spacing 600 mm, rib's reinforcement at the bottom surface R8 and R14 at upper surface in both directions, filigree shear reinforcement R5 ā 200 mm and R5 ā 180 mm, ring beams from HPC105 on external walls reinforced by 4 R12 with stirrups R6 ā 200 mm, ring beams on inner walls reinforced by 2 R12 with stirrups R6 ā 200 mm.

V4 timber-concrete composite floor structure - thickness 190 mm, upper deck 30 mm from UHPC160 reinforced by steel microfibers 13 mm long, timber beam 80/160, timber-concrete connection by gluing, ring beams from C30/37 on external walls reinforced by 4 R12 with stirrups R6 ā 200 mm, ring beams on inner walls were reinforced by 2 R12 with stirrups.

The four alternatives were designed from three different concrete mixtures – ordinary concrete C30/37, high performance fibre concrete HPC105 and UHPC160. The HPC105 mixture was fibre concrete with 25 mm long steel fibres Fibrex A1. These fibres have tensile strength of only 350 MPa. The UHPC160 mixture was designed as fine-grained with 13 mm long steel microfibres. The tensile strength of these fibres is 2400 MPa. The amount of steel

fibres in both mixtures was 1% by volume. As suggested in designation, HPC105 has compressive strength of 105 MPa, UHPC160 has 160 MPa then.

Table 1: Concrete mixtures.

Concrete mixture		C30/37	HPC 105	UHPC 160
CEM I 42.5R	kg/m^3	350	480	-
CEM I 52.5R	kg/m^3	-	-	717
sand 0-4	kg/m^3	785	925	-
crushed gravel 4-8	kg/m^3	350	-	-
crushed gravel 8-16	kg/m^3	650	-	-
basalt 4-8	kg/m^3	-	830	-
microsilica	kg/m^3	-	24	225
sand 01/06	kg/m^3	-	-	985
micro milled sand ST9	kg/m^3	-	-	179
steel fibres Fibrex A1	kg/m^3	-	80	-
steel fibres Stratec 0.15/13	kg/m^3	-	-	80
superplasticizer	kg/m^3	2.7	8.8	32.6
water	kg/m^3	183	150	176

Input data for the analysis

A set of environmental information data on concrete components and related processes has been collected and determined during the research performed at the CIDEAS centre of the Czech Technical University in Prague [1]. These data are based on regionally available materials and on source data provided by companies producing and/or selling their products mainly on the Czech market. Energy and emission factors were taken from GEMIS [2].

In the following analysis the expected life span of concrete floor structures was considered for all alternatives equally 100 years. Two major repairs of 10% of the concrete surface were considered for reference alternative V1 from ordinary concrete C30/37. The two floor alternatives from HPC105 (V2, V3) are planned to have a repair of 30% of balcony surfaces, one in a life span. No repair is considered in the case of the alternative V4 from UHPC160, due to the significantly better surface quality and density of the concrete matrix.

The location of the analysed building is in the city of Kladno, Czech Republic. The concrete mix will be transported from a company 4 km away, concrete prefab panels from a precast concrete plant 23 km away and the demolition waste will be transported 26 km to the recycling plant. Analysis does not cover the extra energy necessary for demoliton of ultra high performance concrete due to a lack of data.

Analysis results and discussion

Two alternatives of floor structures from HPC V2, V3 and one from UHPC V4 were analyzed and compared with reference solid RC slab from standard concrete C30/37 – V1. Graphs in Figures 5, 6 and 7 show aggregated environmental data achieved by detailed LCA analysis of all four variants of floor structures.

The graph in Figure 4 shows for all four alternatives primary energy flows associated with particular material components, transport and construction processes. It is evident that the highest energy consumption is associated with cement production and steel use. The best results shows alternative V4 – composite timber- UHPC floor structure, due to the use of timber beams with significantly lower primary energy demands. Top slab was made of very thin UHPC160 slab precast elements. Variants V2 and V3 from HPC105 show lower primary energy

consumption in comparison with reference solid slab (V1) due to more effective optimized hollow core and ribbed shape of floor cross section.

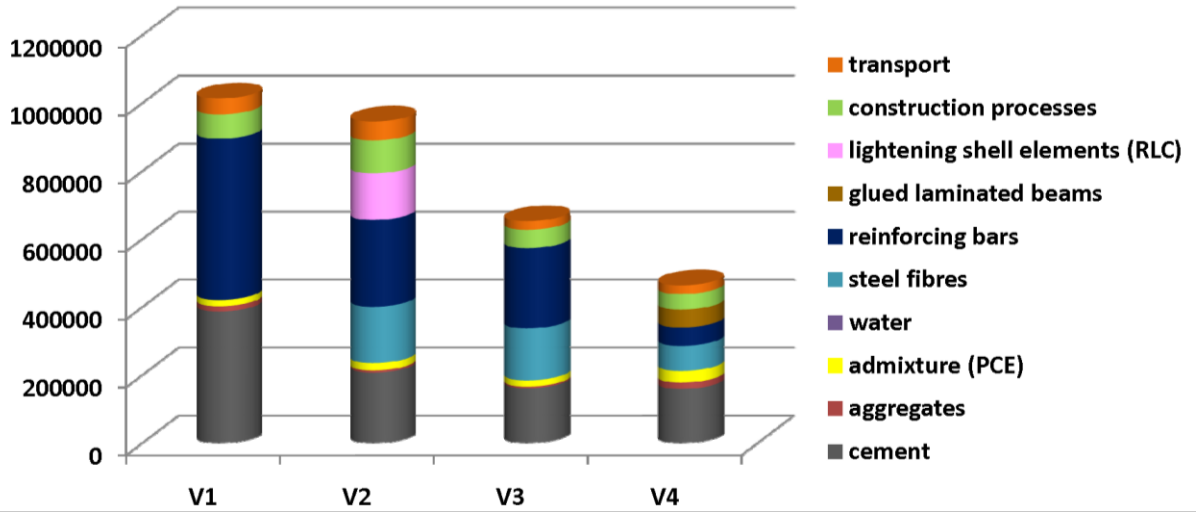

Figure 4: Aggregated data – primary energy consumption in MJ.

The graph in Figure 5 shows similar results for global warming potential (GWP). Again variant V4 – timber-UHPC shows the lowest GWP environmental impact. Both HPC105 alternatives V2 and V3 are again better than reference solid RC slab. The reason is the same as for primary energy consumption – more structurally efficient cross section shapes in the case V2 – hollow core precast pannel and in the case V3 – light ribbed structure.

The graph in Figure 6 shows relative comparison of selected aggregated LCA data – GWP – global warming potential, AP – acidification potential, POCP – photochemical ozone creation potential, raw material consumption, water use and primary energy consumption. 100% represents solid RC slab from ordinary concrete (variant V1). All optimized alternatives have lower environmental impacts in all assessed environmental criteria. The best one is variant V4 – timber-UHPC composite ribbed structure.

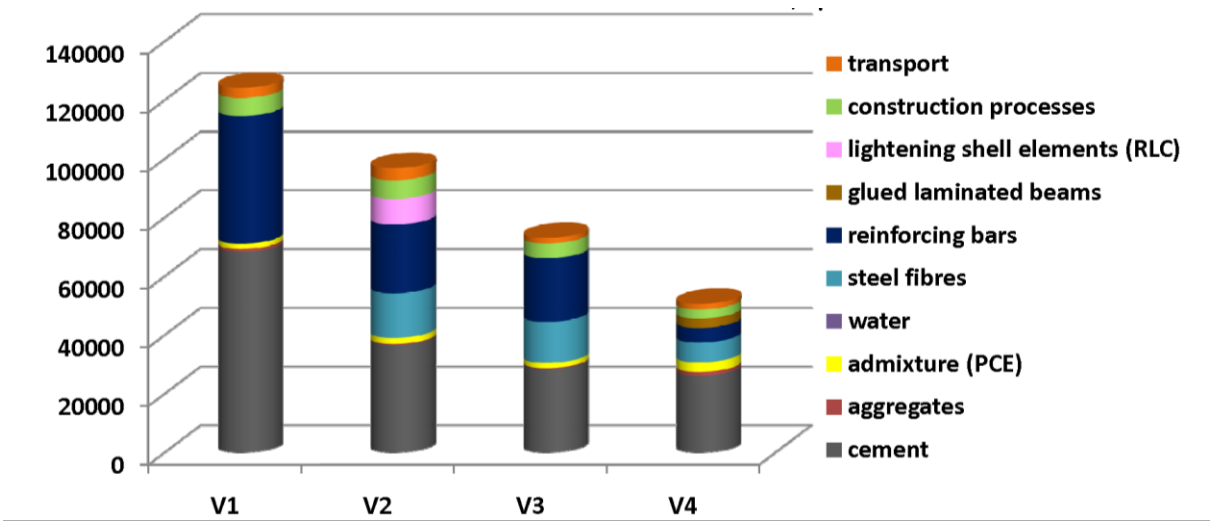

Figure 5: Aggregated data – global warming potential (GWP) in kg $CO_{2,\ equiv.}$

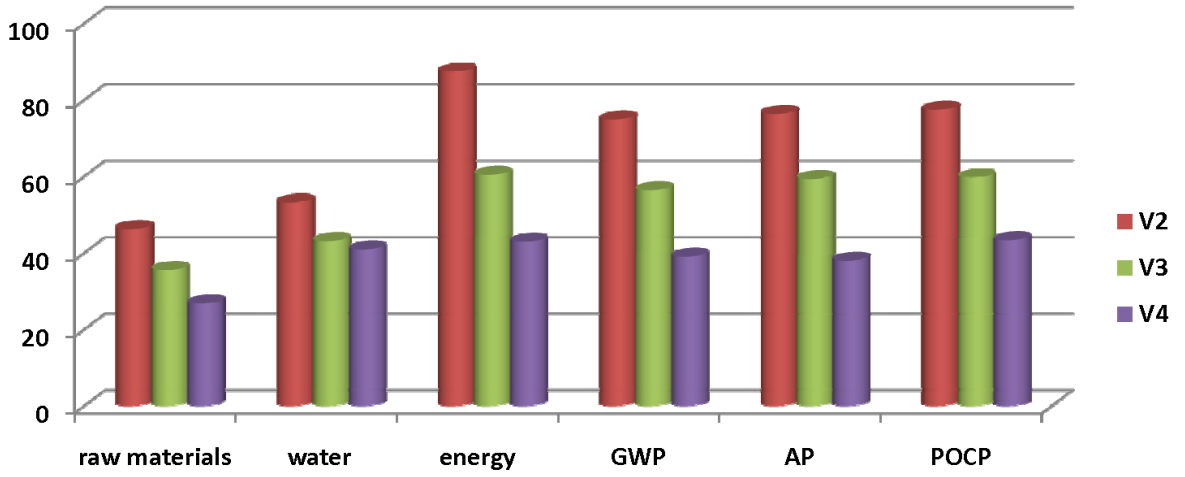

Figure 6: Aggregated data of assessed variants for whole life cycle (GWP – global warming potential, AP – acidification potential, POCP – photochemical ozone creation potential), 100% is represented by V1 – solid RC slab.

4 Conclusions

New types of high performance silicate composites enable design of ultra thin decks with thickness less than 30 mm. Some applications use even 15 – 20 mm thin UHPC decks [3, 4]. However, at such thickness ordinary mechanical kinds of connection cannot be used. Glued connection represents a possible and effective option.

Presented experimental results of timber-concrete composite shear test proved the potential of timber-concrete glued connection. Therefore, there is a possibility to design the timber-concrete composite with HPC or UHPC slender deck with thickness of only 30 mm or less. Environmental efficiency of such composite structure has been shown in the LCA case study. The research of timber-concrete composite floor structures is continuing with the large scale bending tests of composite beams with UHPC slender slab.

This outcome has been achieved with the financial support of the research project granted by Czech Grant Agency GACR P104/10/2153. All support is gratefully acknowledged.

References

[1] Hájek, P., Fiala, C., Kynčlová, M.: Life cycle assessments of concrete structures – a step towards environmental savings, Structural Concrete, Journal of the fib, Vol 12/1, March 2011, ISSN 1464-4177, pp. 13-22, 2011.

[2] GEMIS (Global Emission Model for Integrated Systems) - version 4.6, database CZ, D 2010, www.oeko.de/service/gemis/, 2010.

[3] Perry, V.H., Zakariasen, D.: First Use of Ultra High Performance Concrete for an Innovative Train Station Canopy, Concrete Technology Today / August 2004, http://www.cement.org.

[4] Ductal® technical library, www.ductal-lafarge.com.

Special Nodes in Ultra High Performance Concrete

Hasan Han[1], Steffen Grünewald[2], Joost Walraven[2], Jeroen Coenders[2,3], Pierre Hoogenboom[2]

1: Royal BAM Group n.v., Bunnik, The Netherlands
2: Faculty of Civil Engineering and Geosciences, Delft University of Technology, Delft/The Netherlands
3: Arup BV Amsterdam, The Netherlands

A study was carried out on the technical feasibility of creating Special Nodes using UPHC with fiber reinforcement and to establish a new practical application for UHPC. A 'Special Node' is a structural node element that connects incoming members in a frame structure, has a complex 3D geometry and contains geometrical distortions in the form of holes. In order to create Special Nodes the computational structural design tool 'VisionNode' was developed, which uses a Genetic Algorithm for computational optimization. VisionNode starts the structural optimization process by exchanging data between a geometric-modeler, which creates the geometry, and a Finite-Element-Model, which determines the structural feasibility during each cycle. Special Nodes created by VisionNode have a unique design, a 3D geometry and contain holes. This is achieved with a minimum of material used while satisfying all structural checks. Case studies demonstrate the potential of this innovative design approach.

Keywords: Special Nodes, Ultra High Performance Concrete, Fibers, Computational Optimization, Structural Optimization, Genetic Algorithm

1 Introduction

The number of unique and innovative structures is rapidly increasing. Advances in design software, material science and manufacture methods in the last decades seem to have removed the boundaries between the imaginable and what is actually constructible. Examples are structures with complex 3D-geometrical properties like double-curved surfaces, varying angles between members and changing cross-sectional dimensions. The structural challenges with such designs, can be dealt with more efficiently today due to the advanced resources available to engineers, such as stronger construction materials, improved manufacture methods and increased computational power. However, advancements in material science do not automatically result in new possibilities and applications for design and construction. It is up to the designers and engineers to acknowledge the advanced and new materials and to come up with new practical applications and possibilities for the building industry. A lot of research is being conducted today to develop new materials and structural applications supported by computational power.

This study aimed at developing a new and innovative application for Ultra High Performance Concrete (UHPC) with fiber reinforcement and without passive reinforcement, applied to structural nodes. Structural nodes are elements that are used in a structure to connect separate structural elements. UHPC and a new manufacture method were considered for the development Special Nodes. In context of this research, a 'Special Node' is defined as a structural element that connects incoming members in a frame structure, has a complex 3D-geometry and has geometrical distortions in the form of holes. The purpose of the holes in the node is to intentionally disturb the natural flow of forces thus introducing a structural inefficiency. This way, the optimization tool demonstrates the ability to combine material properties and structural efficiency. A complex 3D geometry can be defined as a combination of double curved surfaces, multiple sub-elements with varying angles between and continuously varying dimensions. See Figure 1 for an impression of a Special Node; the element placed in the center is the Special Node and the rectangles represent the incoming structural elements.

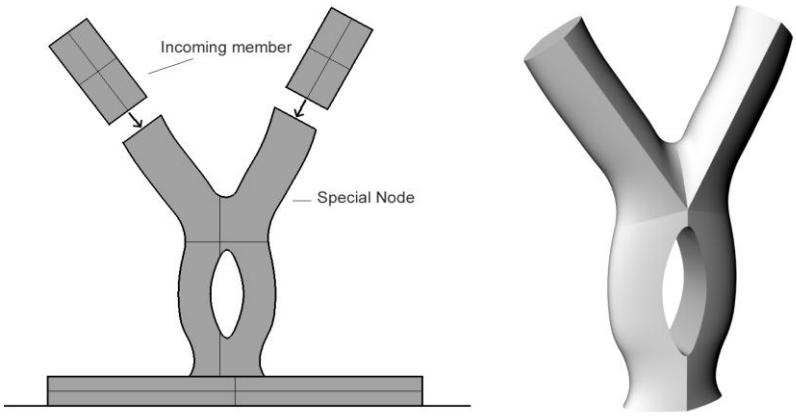

Figure 1: Special Node; 2D- and 3D impression.

UHPC with fiber reinforcement is a material that has a very high compressive strength and a relatively high tensile strength when compared to conventional concrete. For this reason, it is a promising material chosen for particular application. As the compressive strength of UHPC is much higher than the tensile strength, this research has focused on Special Nodes exposed to mainly compressive forces and limited bending forces.

The objective of this study was to determine whether it is technically feasible to design Special Nodes in UHPC without passive reinforcement. A computational structural design tool that uses computational optimization was developed which can create and structurally check the Special Nodes. The goal of the optimization process was to determine the most efficient solution for the structural problem.

2 UHPC

Ultra High Performance Concrete (UHPC) with fiber reinforcement is a type of concrete that has material properties superior to normal strength concrete. The main characteristics of UHPC are a compressive strength up to 250 MPa, a much higher ductility, tensile strength and a better durability compared to traditional concrete. In combination with a sufficiently high amount of steel fibers it is possible to design sustainable lightweight concrete constructions without any additional reinforcement [1]. The superior mechanical properties are obtained because of:

1. Homogeneity of the mixture that allows for better stress distribution
2. A high packing density and a lower water-cement-ratio
3. An improved microstructure obtained through post-set heat-treatment of the concrete
4. Addition of fiber reinforcement

Several commercial UHPC mixtures are available on the market today. In this research, material characteristics of the UHPC mixture Ductal C170/200, developed by LaFarge, Bouygens and Rhodia, are assumed [2]. Design and calculations were executed according to the French recommendations for UHPC [3].

The most important characteristic of UHPC for the design of Special Nodes is the high compressive strength. Since Special Nodes are primarily loaded by high compressive forces, the high compressive strength of the material would be used to full potential. Even though a Special Node is not directly loaded in tension, the presence of holes and a complex 3D-geometry will cause tensile stresses to occur within the node.

The relatively high tensile strength is mainly attributed to the presence of fiber reinforcement in the UHPC mixture; the fibers also increase the ductility of the material. Ductility of a structural

node is very important since small deformations and displacements are bound to occur. For this reason, adequate ductility is required and is provided by UHPC. Next to the material strength properties of UHPC in Special Nodes, a high workability is required for manufacturing the Special Nodes. The self-compacting property of UHPC facilitates the casting process.

3 VisionNode in Design Optimization

VisionNode is a Windows-application that enables users to create Special Nodes using UHPC as a construction material. At the core of the computational optimization in VisionNode is a mathematical optimization algorithm that is controlled by the tool. The algorithm is called a Genetic Algorithm (GA) and is essentially a continuous cycle of iterations in which a pre-determined objective-function is continuously changed and evaluated after each iteration. The goal is to minimize the objective function, which minimizes the volume of concrete, while satisfying other boundary conditions. The algorithm generates a new geometry every iteration step, performs a structural check and evaluates the volume of the concrete. Every iteration solution that complies with the structural boundary conditions is considered a feasible solution. The best feasible solution of the optimization process contains the data for the final design of the structural node.

The optimization process starts by creating a new 2D-geometry every iteration-step. For the geometry modeling, VisionNode uses the 3D modeling program ‘Rhinoceros’ by McNeel [4]. Through the geometric modeler, VisionNode calculates the location of the design-variables and uploads the information to the optimization algorithm. For every geometry, the stresses in the node are calculated with a Finite-Element-Analysis (FEA) through ‘Ansys’ [5]. The results of the FEA are evaluated by VisionNode and checked according to the structural boundary conditions that are based on the mechanical properties of the material.

If the optimum of the objective function has been obtained, the Special Node is created. When this is not the case and the optimum has not been obtained, the previous steps are performed again with different parameters. This process is displayed in Figure 2. Before the optimization starts, the user defines the following parameters:

- The coordinates and the dimensional properties of the incoming structural members that are connected to the Special Node
- The forces transferred from the incoming members to the Special Node
- Concrete characteristics
- Specification where material must or must not be used in the geometry, in order to create the holes

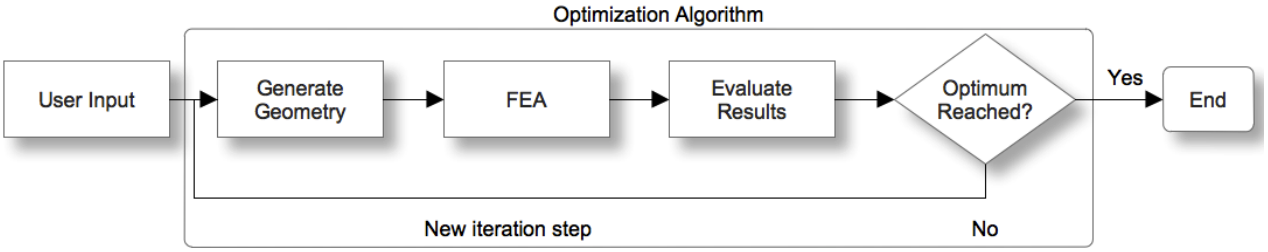

Figure 2: VisionNode optimization process.

Genetic Algorithm

The Genetic Algorithm (GA) is an evolutionary algorithm which mimics the evolutionary process of natural selection, reproduction, mutation and survival of the fittest. The GA is a mathematical

stochastic search method that was first devised by Holland [6] and later extended by Goldberg [7]. Before the GA starts the iteration process, it is first supplied with an objective function, a set of design variables and algorithm constraints. The aim of the GA is to find the minimum value of the objective function in the search space (the space in which all the feasible solutions are located). During its operation, the algorithm searches for solutions for the objective function that minimize its value and consequently the volume of the Special Node. The solutions have to be feasible to be accepted by the algorithm. A solution is considered feasible when it satisfies the predetermined algorithm constraints. When a solution does not satisfy the constraint, it is considered infeasible and it is omitted from the search space.

By continuously changing the design variables every iteration step and repeating this process, the algorithm searches for the best possible feasible solution that is called the optimum solution. The design variables represent coordinates in the XY-plane and are needed to create the geometry of the Special Node for every iteration.

The constraints for the optimization process consist of a structural failure-check in the form of a Mohr-Coulomb-Failure-Check (Equation 1). This is a failure-check that can be used for brittle materials such as concrete exposed to internal compressive and tensile stresses. The nonlinear-inequality constraint in VisionNode is 0,6-1,0.

$$\frac{\sigma_1}{\sigma_t} + \frac{\sigma_3}{\sigma_c} \leq 1 \qquad (1)$$

σ_1 = largest principal tensile stress in structural element
σ_3 = largest principal compressive stress in structural element
σ_t = tensile capacity of material
σ_c =compressive capacity of material

Only a solution that satisfies these boundary conditions is considered feasible. The goal is to get as close as possible to the upper boundary condition while maintaining a minimum volume of the Special Node.

Finite Element Analysis

The geometry of the Special Node is the output of the geometric modeler that calculates the location of the design-variables in the XY-plane. These coordinates are used to create NURBS-curves from the design variables. All the NURBS-curves are uploaded to Ansys that in return creates the Finite-Element-Model needed for the structural calculation. VisionNode instructs Ansys to create two different geometries of a Special Node, a 2D-geometry and a 3D-geometry. This step is displayed in Figure 3.

Next to the geometric properties, the material properties and loads on the node are also input to Ansys. As mentioned before, a mixture with characteristics of Ductal is applied for the Special Nodes. The mechanical properties of Ductal are entered into the FEM prior to the calculation. The loads on a Special Node consist of an axial compressive force, a bending moment and a shear-force. These forces act from the surrounding structure on the Special Node through a contact surface.

The goal of the optimization with VisionNode is to generate a 3D geometry of a Special Node with a sculptural quality. Because such a 3D geometry takes a lot of calculation time during the FEA, optimization times of up to a day can be expected. To shorten the optimization run, VisionNode switches between a 2D- and a 3D geometry during the FEM calculations.

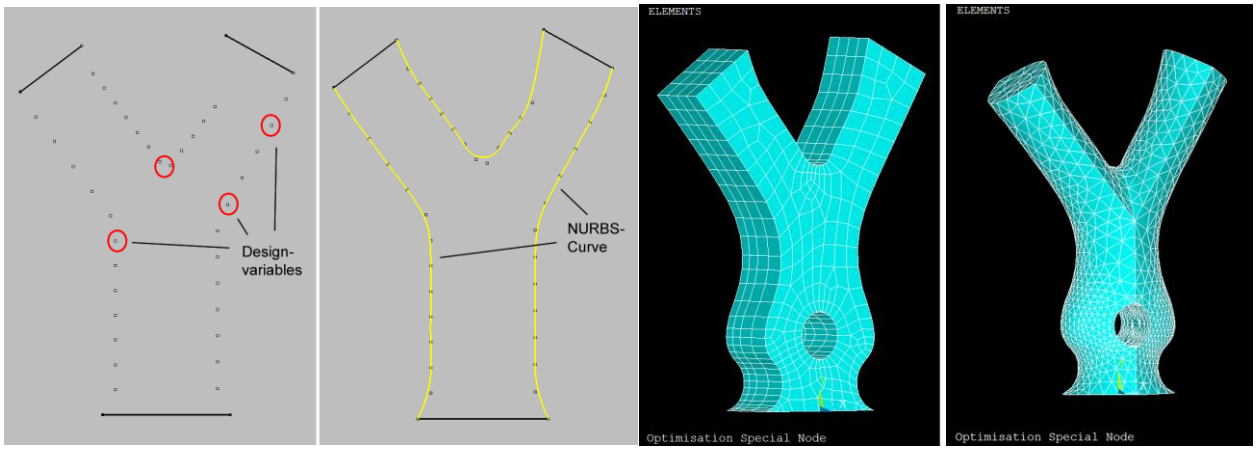

Figure 3: Geometric NURBS model and the corresponding Finite-Element-Model.

In essence, when the solutions of the objective function are far from the optimum, VisionNode uses a 2D-geometry of the Special Node during the FEM calculations. A 2D-geometry calculation in the FEM takes between 10-30 seconds. This way, the optimization process can work fast when the solutions have not converged yet. Whenever a solution becomes feasible, VisionNode switches to the 3D geometry and requests a 3D Special Node. The FEM calculation of a 3D-geometry takes about 1-10 minutes depending on the complexity of the shape. When considering that during the entire optimization process almost 95% of all solutions are likely to be infeasible, the advantage of 2D- to 3D-switching becomes evident. Because of this feature of VisionNode, optimizations to create Special Node take several hours instead of an entire day to be completed. After the FEM calculations are completed, VisionNode checks whether a solution is feasible.

4 Results

A case study was performed with an existing structure to design Special Nodes and to test the program. The Yas-Hotel structure in Abu Dhabi was considered suitable for this purpose and is displayed in Figure 4. In order to obtain realistic geometrical and structural boundary conditions for the optimization algorithm, the structure itself was modeled in a finite-element-program and exposed to realistic loads. The resulting force distribution in the structure was transferred to VisionNode before starting the optimization.

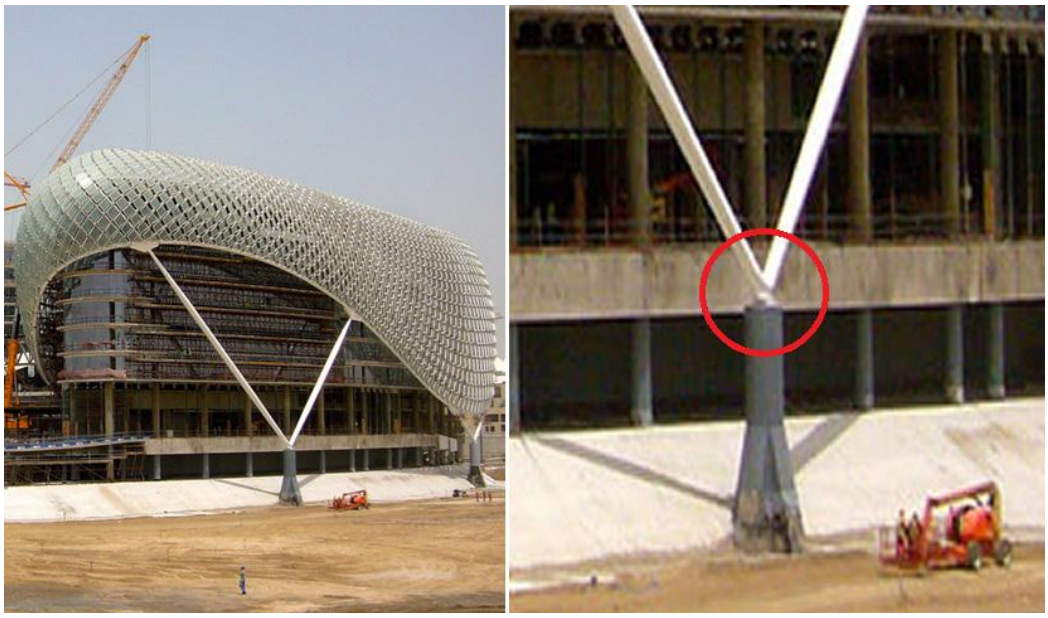

Figure 4: Yas-Hotel in Abu Dhabi [8].

The results of the optimization process for a Special Node with a height of 2,9 m and two holes in the center, are displayed in Figure 5 and Table 1. VisionNode generated a Special Node after 5 hours of optimization. The resulting node has the smallest possible volume based on the geometrical and structural boundary conditions.

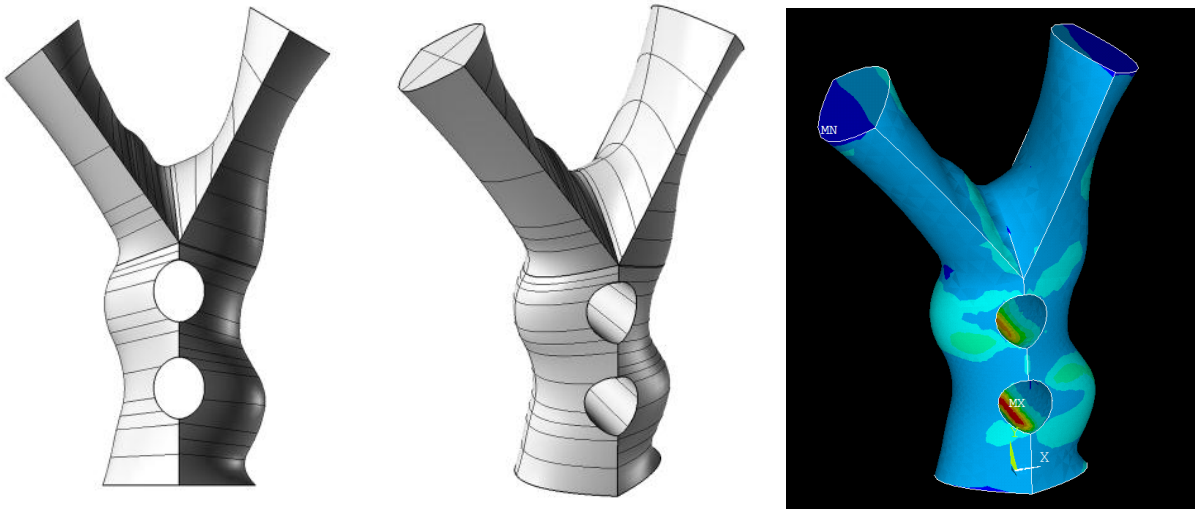

Figure 5: Special Node created by VisionNode; left and center: the resulting 3D geometry; right: the same 3D geometry after structural analysis by Ansys.

Table 1: Numerical results of optimization process.

Property		**Value**
Volume of Special Node	m^3	1,464257380
Maximum tensile stress	MPa	7,266
Maximum compressive stress	MPa	-37,67
Mohr-Coulomb-Failure-Check		1,000082
Optimization time	Hours	5

Figure 6 shows the history of how the algorithm obtains a Mohr-Coulomb value of 1,000082 after almost 1400 iterations. The algorithm was searching for the most efficient solution while reducing the volume of the node and keeping the Mohr-Coulomb value close to 1,0.

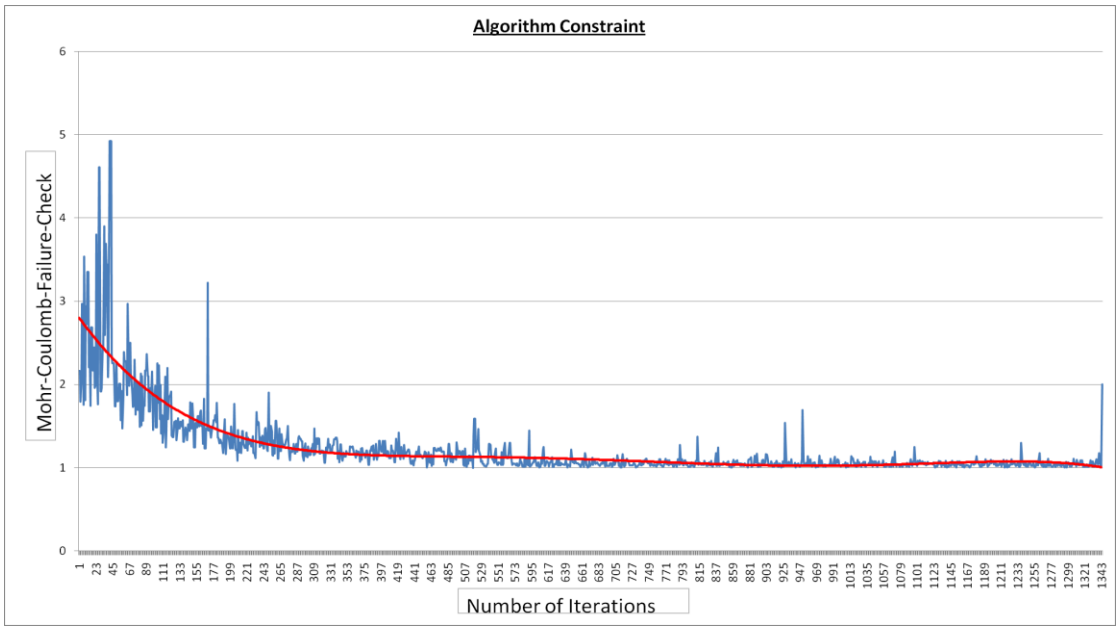

Figure 6: Mohr-Coulomb-Failure-Check during optimization process.

To determine the effect of different tensile strengths on the node structure, tensile strengths of respectively 11, 15 and 30 MPa were assumed. Figure 7 shows the results of the optimization process with different tensile strengths. It can be seen that with a higher tensile strength the concrete volume decreased with more slender Special Nodes as a result.

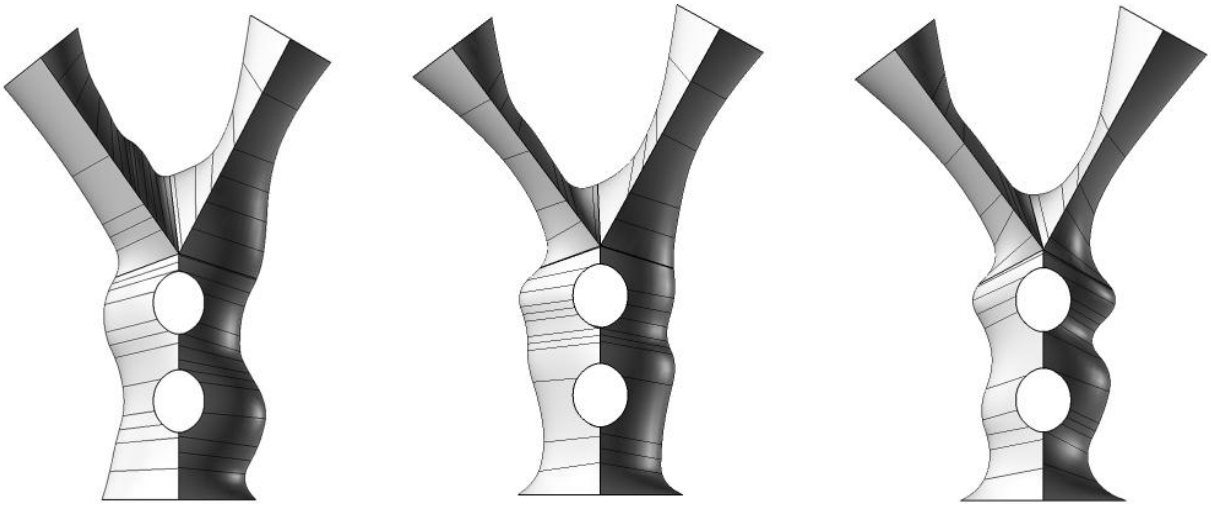

Figure 7: Geometrical results with different tensile strengths 11; 15; 30 respectively.

Table 2: Numerical results with different tensile strengths.

Tensile Strength	**MPa**	**11,0**	**15,0**	**30,0**
Volume of Special Node	m^3	1,464257380	1,368151684	1,184695894
Maximum tensile stress	MPa	7,266	9,976	16,6
Maximum compressive stress	MPa	-37,67	-33,87	-45,64
Mohr-Coulomb-Failure-Check		1,000082	0,966	0,961

Special Nodes can be manufactured using an advanced manufacture method that creates a concrete mould with a complex 3D geometry. This manufacture method is a fully automated 3D milling of polystyrene where computer controlled milling is applied on a block of polystyrene. In order the produce a Special Node, two moulds have to be milled. The moulds are shown in Figure 8.

VisionNode stores the resulting geometry of the Special Node in a 3DM-file format and the 3D milling machine supports this file format. This means that based on the output of VisionNode, the Special Node can actually be produced. A Special Node can be connected by two methods with the incoming members of the frame structure: a) welding of metal plates or b) concrete connection reinforced with rebars.

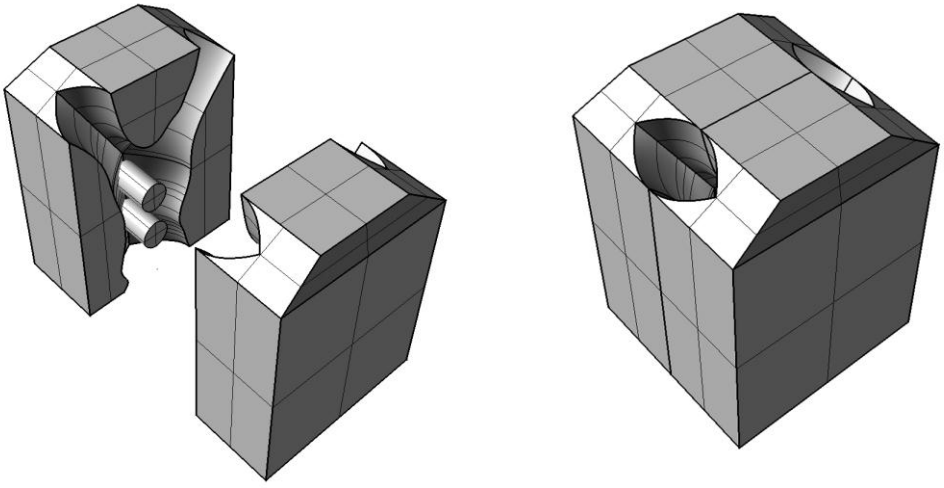

Figure 8: Special Node mould manufacture.

5 Conclusions

By developing and applying the structural design tool called VisionNode, it was possible to create technically feasible Special Nodes with a complex 3D geometry in UHPC without passive reinforcement. The tool was applied for the case study of the Yas-Hotel structure. Even though the efficiency of the structural node was intentionally disrupted by the introduction of geometrical distortions in the form of holes, VisionNode was able to create the desired Special Nodes. This was mainly possible because of the excellent mechanical properties of UHPC with fiber reinforcement.

Additionally, the optimization process controlled by the Genetic Algorithm provided the computational power that was needed to create the most material efficient structural node for a set of boundary conditions. With computational optimization unique structural nodes, that seem illogical and inefficient in the beginning, can be created and are technically feasible at the same time.

New manufacture methods such as fully automated 3D milling of polystyrene can be applied to produce Special Nodes with a complex 3D geometry.

References

[1] Schmidt, M., Fehling, E.: Ultra-High-Performance Concrete: Research, Development and Application in Europe. 10 Years of research and development at the University of Kassel, pp. 194-221. 2007.

[2] Acker, P., Behloul, M.: Ductal® Technology: A Large Spectrum of Properties, A Wide Range of Applications. Fib Symposium, Avignon, France. 2004.

[3] AFGC / SETRA: Ultra High Performance Fibre-Reinforced Concretes: Interim Recommendations. 2002.

[4] Robert McNeel & Associates. http://www.mcneel.com; May 2010.

[5] Ansys inc. http://www.ansys.com; May 2010.

[6] Holland, John H: Adaptation in Natural and Artificial Systems, University of Michigan Press, Ann Arbor. 1975.

[7] Goldberg, David E: Genetic Algorithms in Search, Optimization and Machine Learning, Kluwer Academic Publishers, Boston, MA. 1989.

[8] Yas Hotel Press Release, Retrieved August 2009: http://www.asymptote-architecture.com. 2009

[9] Beasley, D et al.: An overview of Genetic Algorithms, part 1: Fundamentals, University Computing, pp. 58-69. 1993.

[10] Veenendaal, D., Preliminary study on Evolutionary Optimization of Fabric Formed Structural Elements, Delft University of Technology. 2007.

[11] Makhanov, S.S., Anotaipaiboon,W., Advanced Numerical Methods to Optimize Cutting Operations of Five Axis Milling Machines, Springer, 206p. 2007.

Cyclic Behaviour of Puzzle strips in UHPC

Joerg Gallwoszus, Josef Hegger, Sabine Heinemeyer
Institute of Structural Concrete, RWTH Aachen University, Germany

It is well known that composite structures feature a high load carrying capacity due to the efficient interconnection of concrete and steel, where steel carries the tensile forces and concrete is under compression. High performance materials, e.g. ultra-high performance concrete (UHPC, 150-250 MPa without thermal treatment), high strength steel, contribute to the load carrying capacity, as well as to a significantly increased sustainability of the structure. Due to its high compressive strength very slender and attractive structures are feasible, provided that the deflections under service loads are limited.
At the Institute of Structural Concrete at RWTH Aachen University the load carrying behaviour of shear connectors under static loading was investigated within a collaborative research project [1]. Design models were derived and guidelines for the static design of composite beams under positive bending moments were developed [2], [3].
For bridge and industrial constructions the cyclic behaviour is of great importance, since a premature failure of the structure can occur. Hence, the scope of the investigations presented in this paper is the fatigue behaviour of shear connectors. Therefore, cyclic single tension tests and push-out tests were carried out to investigate the local behaviour of composite constructions with high and ultra high performance materials.

Keywords: Composite Construction, Ultra High Performance Concrete, High Strength Steel, Puzzle strip shear connector, fatigue

1 Introduction

The combination of ultra-high performance concrete (UHPC) and high strength steel in composite constructions allows elegant and slender structures [4]. These constructions are much more susceptible to dynamic excitation and fatigue loading than conventional concrete structures. Especially for composite bridge constructions with traffic loads and low dead load, the cyclic performance of shear connectors in UHPC is of major interest.

The operational stability of steel connectors is mainly controlled by the stress amplitude, whereas fatigue of concrete depends on the load level [5]. The behaviour of a novel and innovative shear connector, the so called puzzle strip (Fig. 3), should be investigated by small-scale and beam tests in UHPC under cyclic loads to investigate applicability in composite constructions.

In composite beams, shear forces occur between the concrete slab and the steel beam. The behaviour under static loading has been analysed in various research projects. To analyse this behaviour under cyclic loading, Push-Out Tests (POT) according to Eurocode 4 [6] have been carried out. Furthermore, tension forces occur due to the exentricity of the struts according to the strut-and-tie-model of a beam presented in Fig. 1. Therefore, the Single-Tension-Test (STT) has been developed for static loads [4] and can be extended for cyclic loads. To verify these results, at the end of the current period of SPP 1182 [1] full-scale beam tests will be conducted under cyclic loading.

The first experimental investigations of continuous shear connectors under cyclic loading have been carried out in 1987 [7]. The researchers detected only a little slip evolution during the load cycles for the perfobond strip with small and mainly closed holes. However, continuous shear connectors with openings showed a significant higher slip evolution [8].

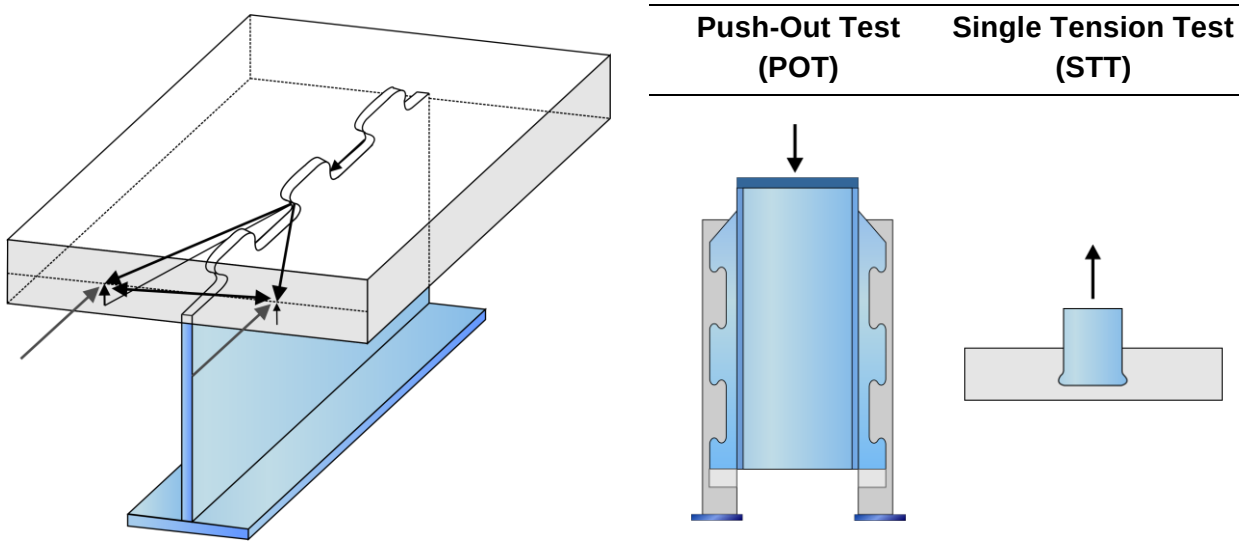

Figure 1: Strut-and-tie-model of a composite beam (left) and small-scale tests (right).

2 Ultra High Performance Concrete (UHPC)

Behaviour under static loading

The composition of ultra high performance concrete (UHPC) differs fundamentally from conventional concrete such as normal strength concrete (NSC) or high strength concrete (HSC) and is presented in [2].

To ensure a sufficient ductility thin micro steel fibres are added. Due to the steel fibres, UHPC exhibits a high compressive strength as well as a linear-elastic behaviour until about 90 % of its compressive strength which is achieved at a strain rate of about 4.5 ‰ (Fig. 2, left). Conventional concrete (NSC and HSC) shows a distinctive nonlinear behaviour due to microcracks which develop at a stress level of about 40 % of the compressive strength.

Behaviour under cyclic loading

The UHPC used for the tests under cyclic loading is the same as for the static tests [2].

Cyclic tests in the compression-compression regime of UHPC show, that concrete with a high compression strength generally exhibits a more sensitive behaviour under cyclic loading compared to normal strength concrete (NSC) [9]. Furthermore, the load level has an influence on the fatigue behaviour. The fatigue strength of UHPC with rising load ranges is higher than for high strength concrete [9]. The fibres showed no significant influence on the fatigue behaviour.

Fig. 1 (right) shows the increase of compression strain in a cyclic compression-compression test with an upper load of $0.8 \cdot f_{ck}$ and a lower load of $0.2 \cdot f_{ck}$ of UHPC [10] in comparison to NSC.

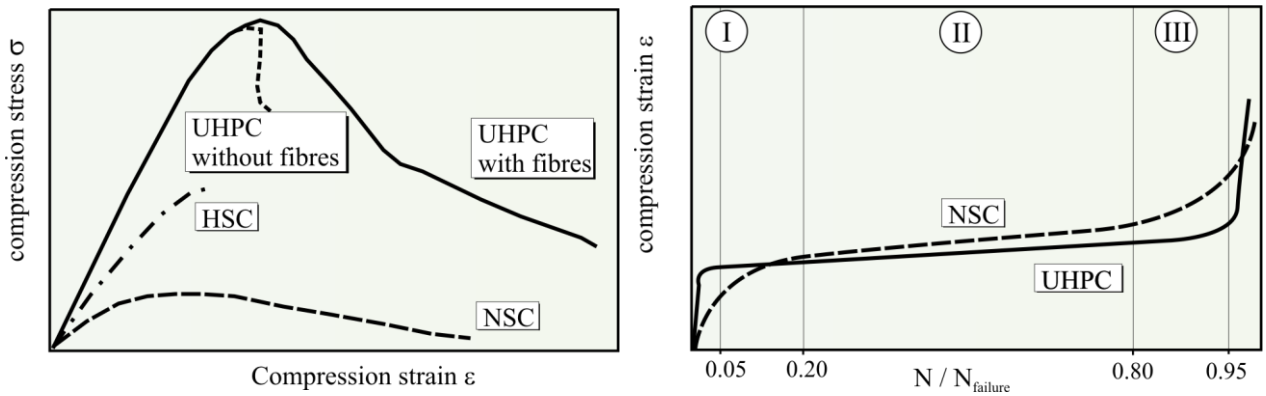

Figure 2: Static (left) and cyclic (right) behaviour of Ultra-High-Performance-Concrete.

The already known 3-phase-shape of NSC can be confirmed for UHPC; however, the length of each phase differs. In the first phase, the irreversible strain increases due to a significant development of microcracks. The second phase is characterized by a continuous crack growth, whereas in the third phase, an instable crack growth with a significant increase in strain and decrease in stiffness occurs. The results in [10] suggest a strong reduction of phase I and III for UHPC. In NSC, the first and the third phase capture about 20% of cycles based on the number of cycles to failure. Due to the dense packing and the associated embrittlement of UHPC, the first and the third phase capture only about 3%-5% of the cycles to failure. A brittle failure occurs, despite of the steel fibres.

3 Test program

The tests under shear loading were tested in the Push-Out Test (POT). The set-up of the POT (Fig. 3, left) according to [6] is described exactly in [2].

For tests with one puzzle under tension, a new set-up has been developed, the Single-Tension-Test (STT) (Fig. 3, right). All specimens for these tests consist of one steel puzzle with a thickness of 20 mm in a 500x500x100mm UHPC-plate. The measuring program contained the global deformation of the UHPC-plate, the deformation of the steel puzzle relative to the concrete and the strain distribution in the middle of the concrete-plate (Fig. 3, right). The tests were designed for concrete breakout and a bending failure was prevented by short spans (a=200mm). All specimen were tested with an upper concrete cover of c_o=60mm.

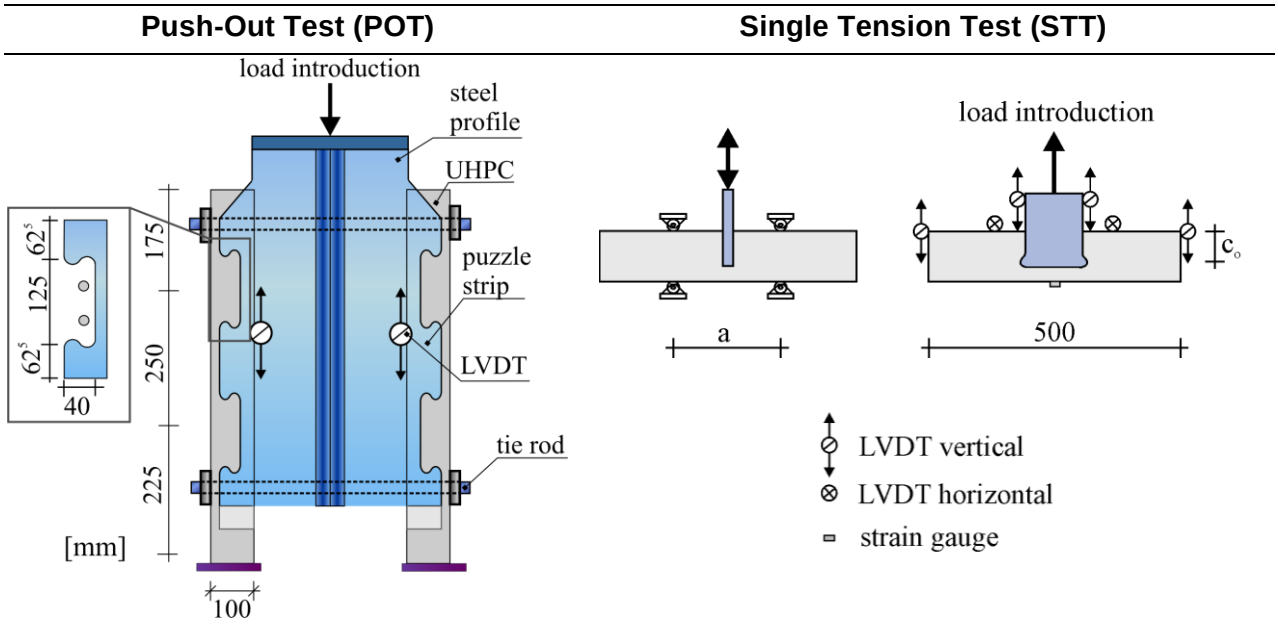

Figure 3: Test set-up of POT (left) and STT (right).

In Push-Out Tests the upper load and the load amplitude have been varied. Table 1 shows the varied loads, which are ratios of the maximum load (P_{stat}=2500 kN) investigated in a static reference test.

In this paper, five Single-Tension-Tests are presented. In the tests STT-E3 and E4 the influence of a cyclic preloading on the residual strength was developed. Furthermore, a cyclic concrete failure was forced by high upper loads. Because of the scattering, three tests were carried out with the same load level (STT-E5, E7, E8). All specimen were tested with the same upper load of 25% of the static capacity.

Table 1: Test program.

set-up	Series	P_{up}/P_{stat} [-]	P_{low}/P_{stat} [-]	$\Delta P/P_{stat}$ [-]	f [Hz]	describtion
POT	PP-I-E1	0.55	0.30	0.25	4.6	low amplitude, low upper load
	PP-I-E2	0.55	0.05	0.50	4.6	high amplitude, low upper load
	PP-I-E3	0.75	0.50	0.25	5.1	low amplitude, high upper load
	PP-I-E4	0.75	0.25	0.50	5.1	high amplitude, high upper load
STT	E3	0.55	0.25	0.30	4.0	residual strength
	E4	0.75	0.25	0.50	4.0	residual strength
	E5	0.85	0.25	0.60	4.0	cyclic concrete failure
	E7	0.85	0.25	0.60	4.0	cyclic concrete failure
	E8	0.85	0.25	0.60	4.0	cyclic concrete failure

4 Results of cyclic Push-Out Tests

The concrete compression strength for a 100-mm-cube $f_{c,cube}$, and the test results (initial stiffness C at 50% of maximal static load $P_{u,0}$, the mean maximum slip at the end of the tests separated for upper and lower load $\delta_{max,mean}$, load cycles N) of the cyclic push-out-tests are summarized in table 2.

All steel profiles were made from the same steel charge (material properties of the web: f_y=467 MPa, f_u=569 MPa, E_a=200.600 MPa)

I.a. due to the different concrete strengths and material related effects (e.g. fibre orientation, inhomogeneities of concrete), the initial stiffnesses C of the specimens PP-I-E1, E2 and PP-I-E3, E4 diverge. Therefore, the specimens PP-I-E3 and E4 showed a less pronounced crack pattern during the initial loading.

In the following, the test results are described separately for specimens with the same amplitude (PP-I-E1, PP-I-E3 and PP-I-E2, PP-I-E4).

Table 2: Test results of cyclic Push-Out Tests.

Set-up	Series	$f_{c,cube,100}$ [MPa]	C [kN/mm]	$\delta_{max,mean,up}$ [mm]	$\delta_{max,mean,low}$ [mm]	N [-]
POT	PP-I-E1	174.5	3043	4.1	3.9	2,000,000
	PP-I-E2	174.5	2823	5.9	5.4	103,500
	PP-I-E3	185.4	4076	4.4	2.3	2,000,000
	PP-I-E4	185.4	3921	8.4	8.1	128,500

The tests are evaluated in dependence of the slip range $\Delta\delta$, which describes the difference of slip under upper and lower load. Changes in slip range are a good dedicator to show changes in stiffness of the specimens, whereas the slip under upper load grows constantly because of the force controlled tests.

The specimens PP-I-E1 and PP-I-E3 were tested with the same load range (25% of $P_{u,0}$), but with variable load levels. It could be presumed, that with increasing upper load a larger damage and consequential a higher slip evolution occurs, which was not the case in these two tests (Fig. 4, left). Due to the lower stiffness of specimen PP-I-E1 more cracks occurred in the concrete slabs. Additionally, the slip range between the connector and the concrete slab is of higher level compared to PP-I-E3. On top of this, a crack in the lower puzzle occurred at about 1.6 million load cycles and the slip range increased abruptly. In the lower puzzle of PP-I-E3 only

a small crack could be detected and the cracks in the concrete slab were not as pronounced as in specimen PP-I-E1.

The specimens with a higher load range (50% of P_{max}) failed due to the cyclic loading after 103.500 (PP-I-E2) and 128.500 (PP-I-E4) load cycles. Both tests showed a similar behaviour with only a slight increase of the slip range up to about 25.000 load cycles. From this point on, the test with the higher upper load (PP-I-E4) showed a significant loss of stiffness indicated by a higher angle in the slip range-load cycle curve, which was the initiation of the failure.

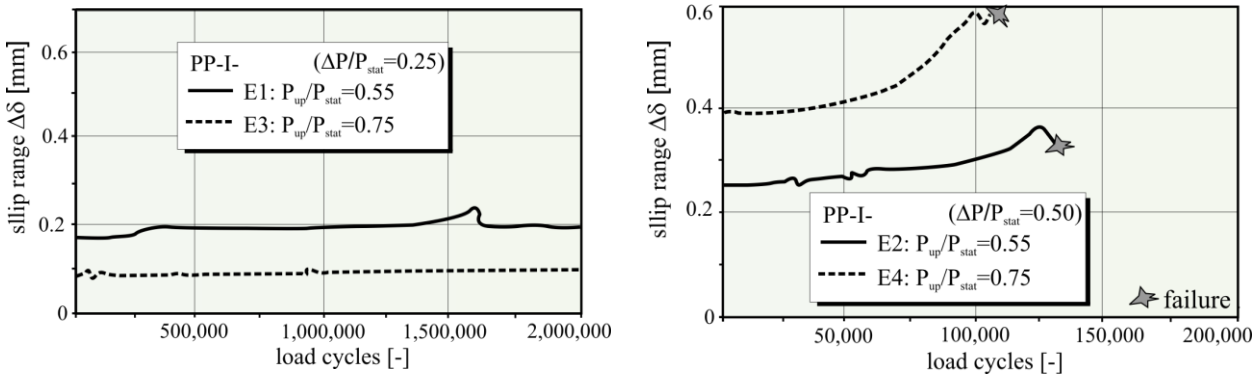

Figure 4: Slip range-load cycles-diagrams of specimens PP-I-E1, E3 (left) and PP-I-E2, E4 (right).

In specimens E1 and E3, the cracks started at the bottom of the shear connector (Fig. 5). After crack initiation, the crack proceeded in an angle of about 45°. This responds the direction of the main stresses.

However, both specimens achieved the predefined 2 million load cycles without a complete failure.

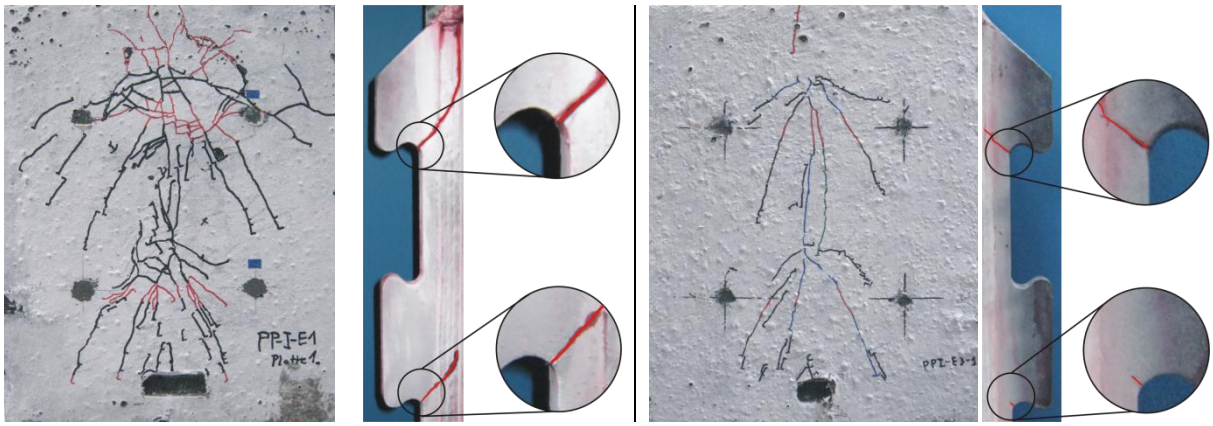

Figure 5: Crack patterns of specimens PP-I-E1 (left) and PP-I-E3 (right).

The failure of PP-I-E2 and E4 was initiated by a concrete pry out cone. After cutting the specimens next to the puzzle strip, a large crack in the upper puzzle with the same angle like PP-I-E1 and E3 as well as cracks in the concrete have been detected similar to the failure mode “concrete pry-out” in the static tests [3] (Fig. 6).

The failure mode can be described as a combination of steel and concrete failure. Calculations with the “Local Concept” [11] showed a crack in the steel in the area when the slip range $\Delta\delta$ during the test changed its direction. Afterwards, cracks in the concrete slab occur and the total failure can be seen as interaction between the two parts, steel and concrete.

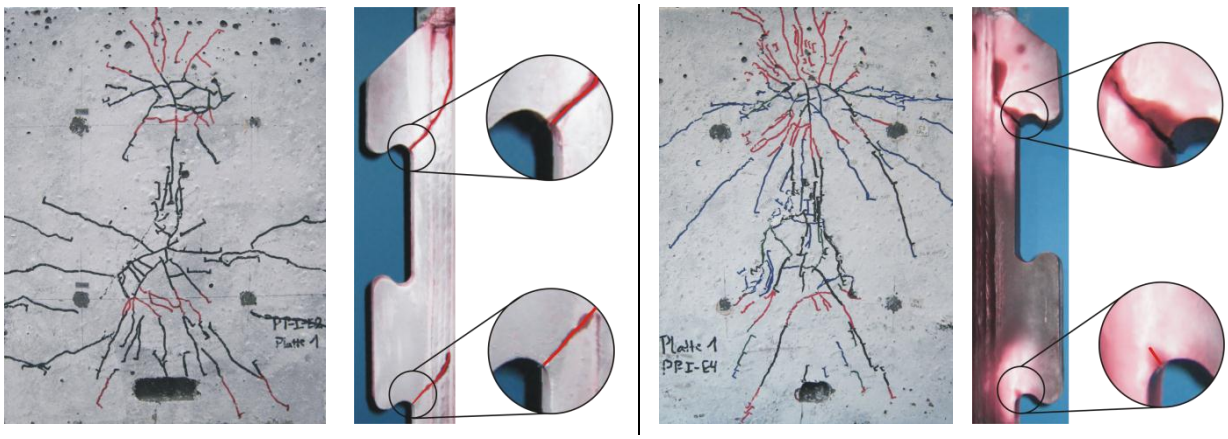

Figure 6: Crack patterns of specimens PP-I-E2 (left) and PP-I-E4 (right).

5 Results of cyclic Single Tension Tests

Table 3 shows the evaluation of the cyclic tension tests (concrete strength $f_{c,cube,100}$, load cycles N). If no failure occurred under cyclic loading, the result of the residual strength is given by a ratio related to the static reference test (P_{stat}=129.4 kN). The last column shows the failure mode under cyclic loading.

Table 3: Test results of cyclic Single Tension Tests.

Set-up	Series	$f_{c,cube,100}$ [MPa]	N [-]	$P_{max,rs}$ /P_{stat} [-]	cyclic failure
	E3	187.4	2,500,000	1.23	-
	E4	183.7	4,250,000	1.19	-
STT	E5	194.4	1,679,000	-	break-out cone
	E7	180.6	229,441	-	break-out cone
	E8	185.6	272,274	-	break-out cone

Residual strength

The slip development of the specimen STT-E3 and E4 showed only a slight increase during the load cycles (Fig. 7, left). Because of the higher upper load, STT-E4 started with a higher slip. However, both specimens showed no indications for cyclic failure and the residual strength was tested.

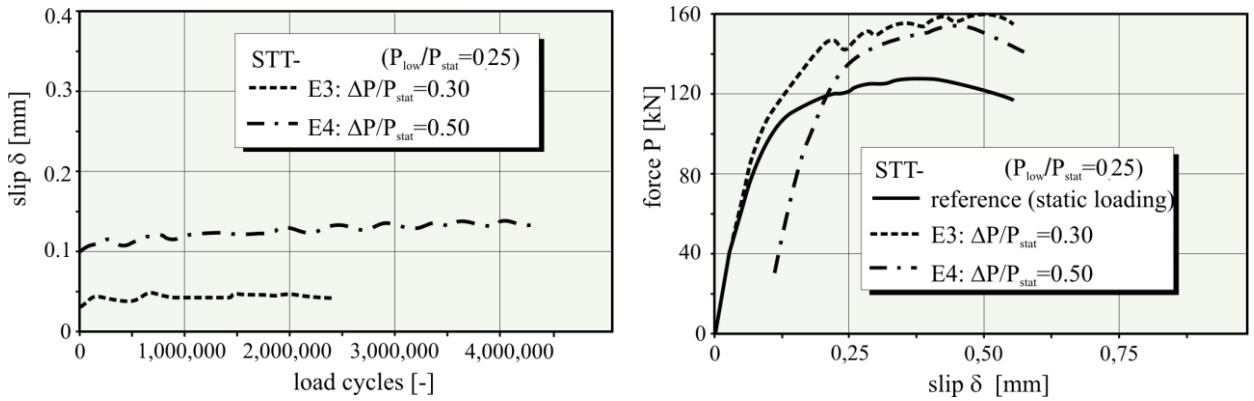

Figure 7: Slip development of specimens STT-E3, E4 (left) and test of residual strength (right).

Surprisingly, the residual strength of both specimens was about 20% higher than the maximum force in the static reference tests (Fig. 7, right). A reason might be the multiaxial stress area in the recess, where the concrete matrix is destroyed. The concrete powder acts as a pillow and less stress-peaks occur.

Cyclic behaviour

The slip-load cycle-curve of specimen STT-E8 with a load range of 60% is shown in Fig. 8. STT-E5 and E7 showed a comparative behaviour during their lifetime.

Three phases are clearly visible. In Phase I there is a strong compression of the concrete in the area of the recess. This fact could be seen after the test, when a highly compressed piece of concrete with a light color appeared in the rounding of the puzzle recess (Fig. 8, Phase I). In Phase II, the concrete compression proceeds and a diagonal crack occurs. This crack grows continuously and there is only a slight slip-growth (Fig. 8. Phase II). In Phase III the crack opens and the slip rises disproportionately. A concrete break-out cone appeared (Fig. 8, Phase III).

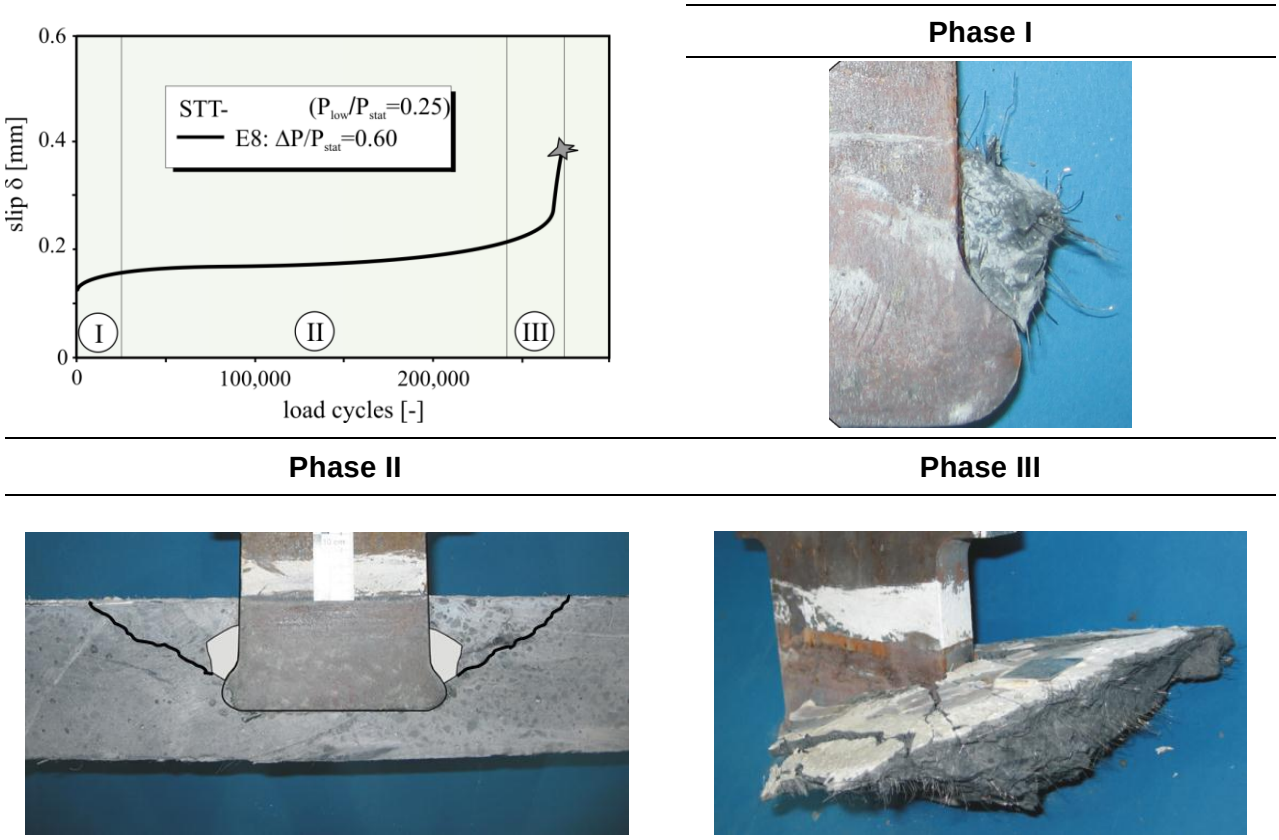

Figure 8: Cyclic behaviour of a break-out cone at the example of STT-E8.

6 Conclusions

Four cyclic Push-Out Tests and five Single-Tension-Tests with the puzzle strip shear connector are presented in this paper. Two different load amplitudes and upper loads have been investigated in the POT. In the STT, three different load levels with constant upper load have been carried out and a three-phase-model could be detected for a cyclic break-out cone.

The results from these tests can be summarized as follows:

- Generally, the puzzle strip shear connector is capable of carrying high fatigue loads under shear and tension forces.

- The puzzle strip in UHPC under cyclic loading with high load amplitude of $0.5 \cdot P_{max}$ shows a combined failure resulting in cracks in steel and cracks in concrete.
- The direction of the crack in the puzzle strip under cyclic loading differs from the crack under static loading.
- The initial stiffness is a major factor to evaluate the lifetime of the puzzle strip in UHPC.
- In the presented tests, the load amplitude played a more significant role than the upper load.
- The residual strength of the puzzle strip in the tension tests is not reduced. Rather, an increase of 20% could be determinded.
- The cyclic behaviour under pure tension can be idealized in three phases.

Advanced push-out-tests with changing load levels, based on the results presented in this paper, are planned. Furthermore, cyclic beams tests will be carried out in the near future.
Finally, numerical simulations and the comparison of the test results with theoretical concepts for steel and concrete failure will be carried out.
This research project is part of the SPP 1182 which is founded by the DFG (German Research Foundation). The authors acknowledge the funding through the DFG and express their thanks for the support of Arcelor S.A. and FA. Neuman Anlagentechnik, Eschweiler for the excellent prefabrication of the puzzle strip.

References

[1] Priority program SPP 1182: Subproject "Shear Connectors in UHPC". SPP 1182 - Sustainable building with ultra high performance concrete (UHPC), German research foundation (DFG), 2008.
[2] Heinemeyer, S, „Zum Trag- und Verformungsverhalten von Verbundträgern aus ultrahochfestem Beton mit Verbundleisten”, PhD thesis, Institut of Structural Concrete, RWTH Aachen University, 2011.
[3] Gallwoszus, J.; Hegger, J.; J Heinemeyer, S.: Design Models for Composite Beams with Puzzle Strip Shear Connector and UHPC. Hipermat 2012 - 3rd International Symposium on Ultra-High Performance Concrete and Nanotechnology for Construction Materials, Kassel, 2012.
[4] Hegger, J.; Rauscher, S.; Gallwoszus, J.: Modern hybrid structures made of UHPC and high strength steel. Proc. 3rd fib International Congress, Washington, 2010.
[5] Hohberg, R.: Zum Ermüdungsverhalten von Beton, phD thesis, Fakultät Bauingenieurwesen und Angewandte Geowissenschaften, TU Berlin, 2004.
[6] EC 4, prEN 1994-1-1. 2004. Design of composite steel and concrete structures Part 1.1 – General rules and rules for buildings. Brussels, Belgium.
[7] Leonhardt, F.; Andrä, W.; Harre, W.: Neues, vorteilhaftes Verbundmittel für Stahlverbund-Tragwerke mit hoher Dauerhaftigkeit, *Beton- und Stahlbetonbau 82 (12)*, pp. 325-331, 1987.
[8] Burger, S.: Untersuchungen zum Ermüdungsverhalten von Betondübeln im Verbundbau, PhD thesis, Institut für Konstruktiven Ingenieurbau, Universität der Bundeswehr München, 2009.
[9] Wefer, M.: Materialverhalten und Bemessungswerte von ultrahochfestem Beton unter einaxialer Ermüdungsbeanspruchung, PhD thesis, Institut für Baustoffe, Leibniz Universität Hannover, 2010.
[10] Grünberg, L. et. al.: Mehraxiales mechanisches Ermüdungsmodell von Ultra-Hochfestem Beton, *Beton- und Stahlbetonbau 102 (6)*, pp. 388-398, 2007.
[11] Song, J.: Untersuchung der Anrißlebensdauer von Betondübeln mit Hilfe des örtlichen Konzepts, phD thesis, Technische Universität Darmstadt, 2002.

Application of Steel Shares as Shear Connectors in Slender Composite Structures

Wolfgang Kurz[1], Jürgen Schnell[2], Susanne Wiese[1]
1: Institute of Steel Structures, University of Kaiserslautern (TU), Germany
2: Institute of Concrete Structures and Structural Design, University of Kaiserslautern (TU), Germany

An application of ultra high performance concrete, which satisfies the material properties and economic demands, requires hybrid constructions with minimized cross sections. These constructions are characterised by very thin concrete slabs and slender steel webs. A main challenge of such structures is the design of the connection between the concrete and steel parts.
A new developed shear connector called steel share is analysed in the scope of a research project. The strains of a steel share, that occur in the fabrication process, were determined with optical strain measurements and recalculated by numerical simulations. The push-out-tests with 30 mm thin concrete slabs showed high load bearing capacities for longitudinal forces in combination with good deformability. Girder tests verified the applicability of the shares in composite girders. FE-Models of the push-out-tests are the base for considerations about the load bearing mechanisms.

Keywords: composite structures,shear connector

1 Shear Connectors

The longitudinal shear forces in composite girders have to be transferred by shear connectors between concrete and steel. Conventional shear connectors are headed studs or concrete dowels for example. Concrete dowels are formed by cuts in the steel sections, which are filled with concrete. The forces are transmitted by the concrete into the offcut cross sections of the steel web. The openings can have different forms and dimensions. In the past two decades intensive research work was done on the load bearing behaviour of concrete dowels in normal and high strength concrete [1], [2], [3], [4], [5], [6]. For the application in thin concrete plates headed studs and concrete dowels are not suitable respectively have limitations by their height. So a new shear connector was developed by arranging rectangular steel teeth at the upper edge of the steel plate and distorting them about 90° at their tops (see Fig. 1). The so called "steel shares" are capable of transferring longitudinal shear forces as well as tension forces perpendicular to the concrete slab. It was expected, that the load is transferred by the concrete mainly into the base of the share similar to concrete dowels.

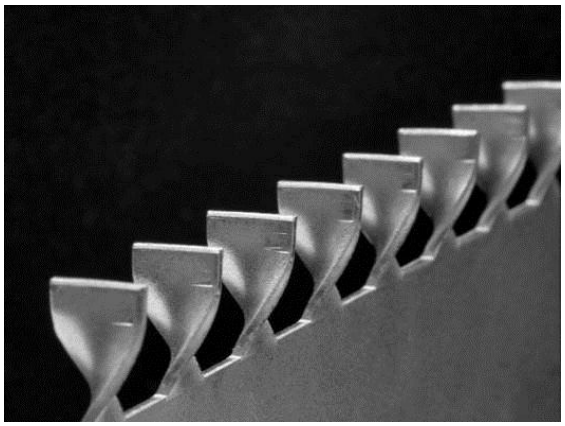

Figure 1: shear connectors steel shares.

2 Strains of the Fabrication Process

In order to get realistic information about the strains of the steel share during the fabrication process, strain measurements by means of the digital image correlation were carried out. The method of digital image correlation belongs to the non-contact measurement methods. It is suited for the measurement of three-dimensional deformations and tangential strains of structural members in the range of 0,05% up to several 100% [7]. For the existing field sizes a strain resolution of 0,1% was achieved. The following figure (Fig. 2) shows the principal strains, that were measured after the torsion process.

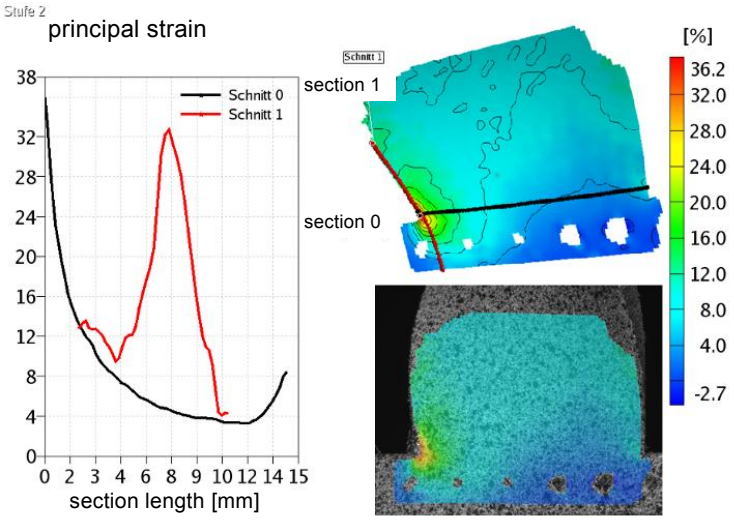

Figure 2: Measured first principal strains.

The maximum strains occur at the corner at the bottom of the share with up to 40%, but decrease rapidly over the plate thickness. These high local strains indicate the location where failure begins, as it could be seen in the push-out-tests. They also imply that the steel shares are not suited for dynamic loads.

The fabrication process was also simulated with the FE-program ANSYS. Therefore an undistorted share with u-shaped clamps was modelled, where the clamp at the bottom was fixed and the upper clamp was charged with the distortion (see Fig. 3).

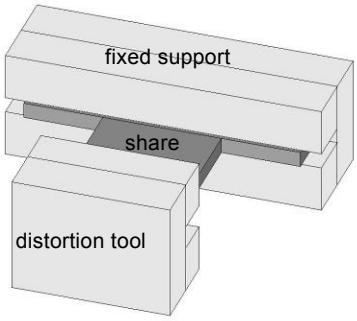

Figure 3: volume model for simulation of distortion.

The resulting strains showed a satisfying correlation with the optical measurements (see Fig. 4). The computed strains were used to determine the increased yield strength at the base of the share for the subsequent FE-models of the shares in concrete.

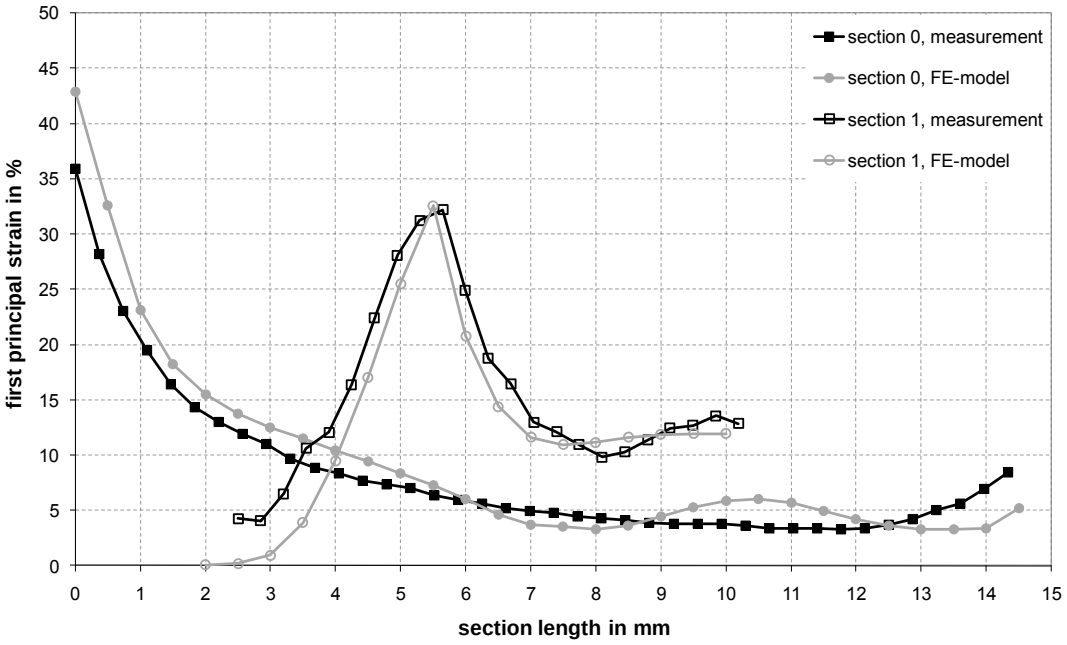

Figure 4: Comparison of simulation and measurement of the fabrication process.

3 Push-out-tests

For the series of push-out-tests a concrete mixture of the DFG research programme SPP 1182 with 1.5 vol% steel fibres and a maximum grain size of 2 mm was used. The concrete had a compressive strength of about 135 N/mm² at the time of testing measured with cubes of 100 mm edge length. Fig. 5 shows a typical test specimen. Geometry and test procedure referred to Eurocode 4 [8]. The test specimens were concreted in an upright standing position.

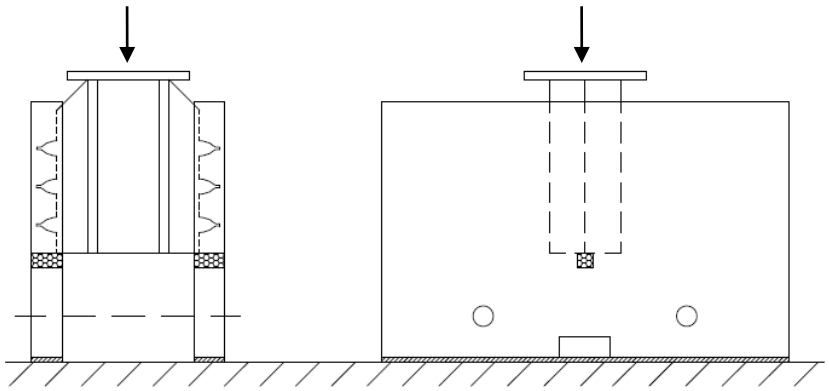

Figure 5: drawing of test specimen for push-out-test.

For the reference tests a steel plate of the grade S320 with a thickness of 2mm was used. The plates were provided with 3 shares per side with a certain dictance. The reference dimensions of a share were 15mm/20mm (length/height) with a distance of 15mm. The concrete slabs of the push-out-tests had a thickness of 30mm. In the tests different parameters as the share geometry, the distances and the steel grade were investigated. The applied load was measured as well as the vertical slip between steel and concrete in order to analyze the deformation characteristic. The diagram (Fig. 6) shows the load-slip-behaviour of some selected push-out-tests with different parameters.

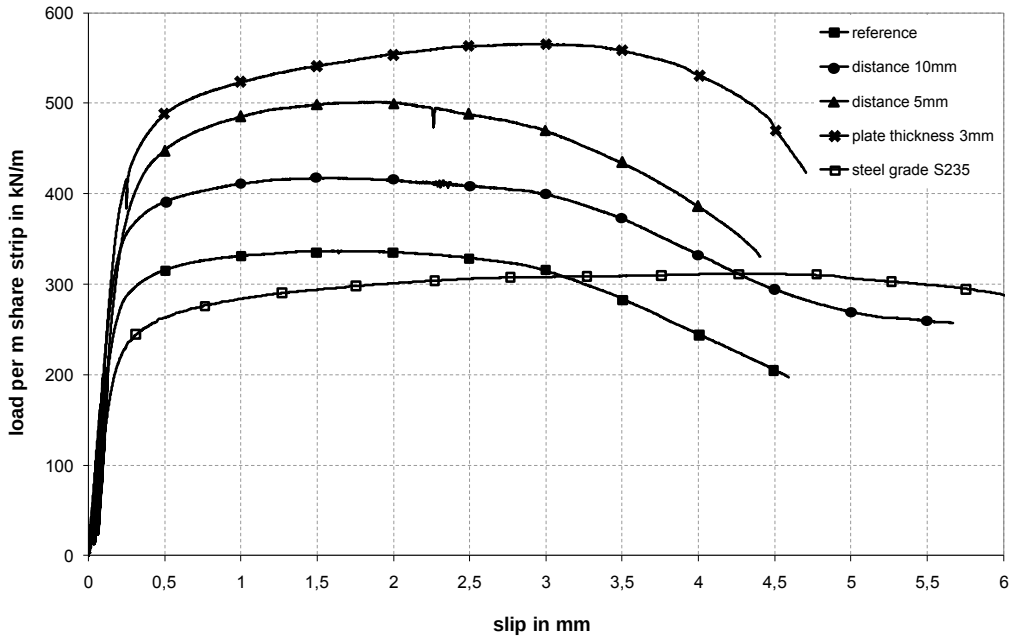

Figure 6: load-slip-curves of push-out-tests.

It is obvious, that smaller distances between the shares increase the maximum load of about 350kN/m steel share strip for the reference configuration up to 515kN/m. Tests with a higher plate thickness also show higher loads of about 540kN/m. Test specimens with a lower steel grade correspondingly reached a lower load bearing capacity, but with an increased deformability. This steel had a greater failure strain in tension tests and therefore offers a better deformation capability in the push-out-tests.

The reason for failure in the presented tests was steel failure by shearing off of the steel shares at their bases. The incipient crack occurs at the base of the share and develops until complete break (see Fig. 7).

Figure 7: sheared off steel share.

The table lists the achieved average loads for the tested parameters per share as well as per m steel share strip.

Table 1: parameters and results of push-out-tests.

test description	share geometry (width/height/ thickness) [mm]	distance [mm]	steel grade	maximum load per m strip [kN/m]	maximum load per share [kN]
reference configuration	15/20/2	15	S320	352.0	10.56
smaller distance 10mm	15/20/2	10	S320	430.7	10.77
smaller distance 5mm	15/20/2	5	S320	514.8	10.30
higher width of share	20/20/2	15	S320	391.0	13.68
higher plate thickness	15/20/3	15	S320	541.3	16.24
lower steel grade	15/20/2	15	S235	299.4	8.98

This array shows, that for the same share geometry the load bearing capacities per share differ only little. This was expected for steel failure, but the values exceed the pure bearing capacity of the steel section. This increase is attributed to frictional effects, which are currently being studied in detail by means of the numerical models (see chapter 5).

Push-out-tests with further parameter variations demonstrated, that also concrete failure is possible. In tests with a plate thickness of 4mm longitudinal cracks occurred along the steel web (see Fig. 8). The further opening of these cracks was avoided by the arrangement of a reinforcement rebar below the shares, so that the loading could be increased. Final failure happened by shearing off of the shares again.

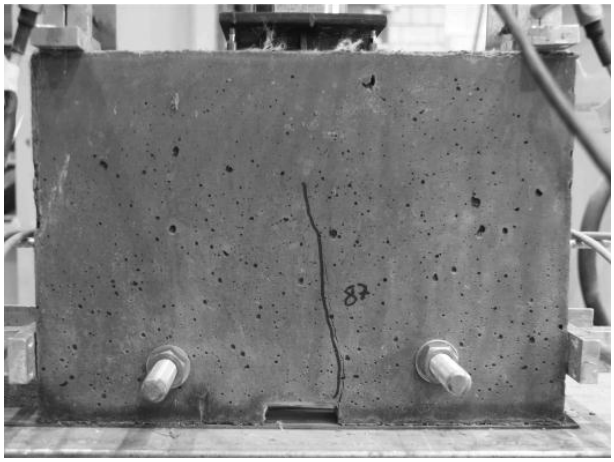

Figure 8: longitudinal crack.

Tests with concrete slabs made of normal strength concrete also cracked in longitudinal direction, but in the end concrete pry-outs occurred at the inner and outer sides of the concrete plates (see Fig. 9).

Figure 9: concrete pry-outs at the outer (left side) and inner side (right side).

4 Girder Tests

The applicability of the steel shares in large scaled composite girders was analyzed in 6 girder tests. The girders had a total length of 2m and were tested in 4-point-bending tests with a span of 1,85m. The steel sections had a height of about 200mm and had a profiling in order to avoid buckling. The concrete plate had a thickness of 30mm and a width of 500mm. The test setup and the cross section of a girder is shown in Fig. 10.

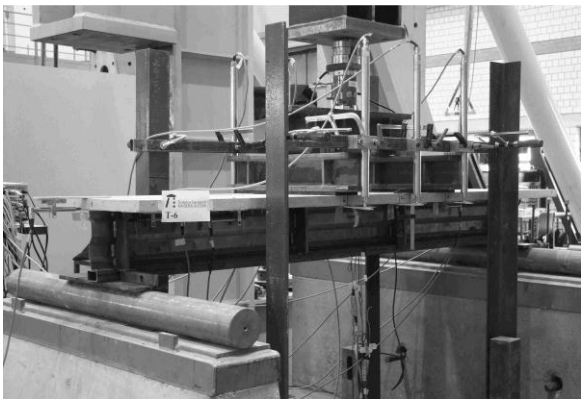
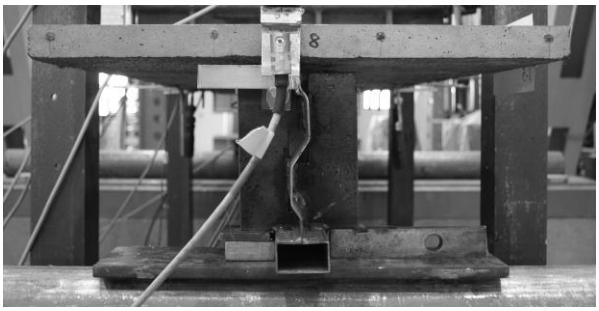

Figure 10: test setup (left side) and cross section (right side) of girder tests.

The girders differed in the grade of shear connection, steel plate thickness and concrete grade. The achieved bending moments reached respectively exceeded the theoretical possible bending moments. The middle deflection as well as the slip along the shear length and the strains over the height of the cross section were measured and provide information about the load bearing behaviour of the composite girders.

5 Numerical Simulations

By means of the FE-program ANSYS numerical models of the push-out-tests were built up in order to recalculate the tests and to identify the load bearing mechanisms. Therefore one half of the push-out-tests, that means 3 shares in a concrete slab, were modelled. For the steel shares, hexahedral elements and a multilinear material model were used. The pre-strains of the fabrication process were considered by an increased yield strength at the base of the share (see chapter 2). The concrete was discretisized with tetrahedral elements and provided with the implemented Extended-Drucker-Prager model. For the contact zone a coefficient of friction of $\mu = 0.44$ was used, which was determined by friction tests before. The load was applied by a

displacement of the steel plate and the concrete slab was supported in the corresponding direction.

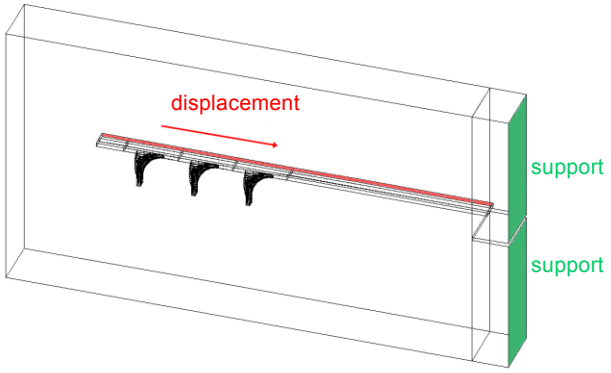

Figure 11: volume model of push-out-test.

The model shows, that for small slip load is induced over a large part of the shares height, but with increasing slip the load introduction is shifted towards the base corner of the share. Due to the multiaxial stress high local compressive stresses occur in the concrete in front of a share. Transverse tensile stresses occur between the steel shares and may cause longitudinal cracking for certain geometries and concrete properties.

The analysis of the load-slip-behaviour of the reference configuration showed a sufficient correlation with the reference tests (see Fig. 12).

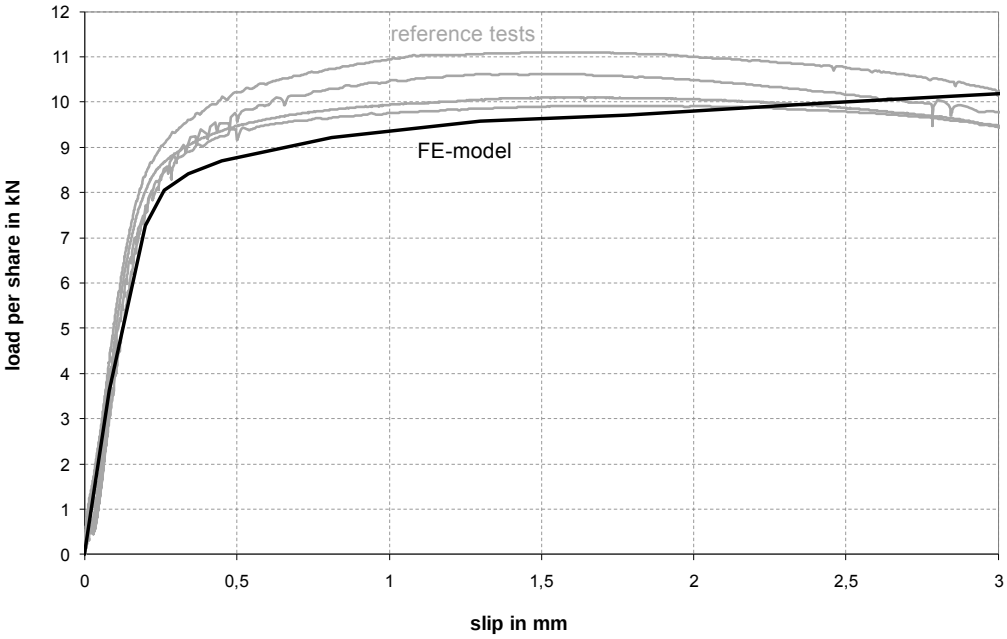

Figure 12: load-slip-curves of test and FE-model.

An exact determination of the maximum load is not possible with the numerical model, as no damage model for the steel is included. Therefore no cracks can occur and the load continuously increases due to the effects of friction [9]. The share is quasi fixed in the concrete slab and so mainly stressed by shearing in the ultimate limit state (about 90%). The different load bearing mechanisms can be identified by comparison with the same model using a coefficient of friction of $\mu = 0$. Here it could be seen, that the shares are able to transmit a load

of about the shear bearing capacity of the share cross section. On the base of the reference model a parameter study is being carried out. Considering the results of the tests and the simulations a design approach for the load bearing capacity of the shares will be developed.

6 Conclusions

The presented novel shear connectors show high load bearing capacities with sufficient deformability in push-out-tests. Steel failure occurs as well as concrete failure for certain geometries and concrete properties. The applicability of steel shares in slender composite girders was demonstrated in large scaled girder tests. The numerical simulations contribute to the identification of load bearing mechanisms and so to the development of a design concept. The analyses and tests demonstrate the fitness of the steel shares for slender composite structures. Such structures can be used as waterproof roof elements, filigree facade panels or hollow walls with integrated HVAC components.

7 Acknowledgements

The presented results have been achieved thanks to the financial support of the Deutsche Forschungsgemeinschaft DFG within the scope of the project Schn 771/5-1 in the course of the research programme SPP 1182.

References

[1] Wurzer, O.: Zur Tragfähigkeit von Betondübeln. Dissertation, Universität der Bundeswehr München, Neubiberg 1997.

[2] Zapfe, C.: Trag- und Verformungsverhalten von Verbundträgern mit Betondübeln zur Übertragung der Längsschubkräfte. Dissertation, Universität der Bundeswehr München, Neubiberg 2001.

[3] Tue, N. V.; Küchler, M.; Hegger, J.; Rauscher, S.: Arbeitsbericht – Zur Wirkungsweise von Verbundmitteln in Verbundkonstruktionen aus ultrahochfestem Beton. Berichtsnr. IMB 183/2007, RWTH Aachen 2007.

[4] Tue, N. V.; Küchler, M.; Hegger, J.; Rauscher, S.: Arbeitsbericht – Zur Wirkungsweise von Verbundmitteln in Verbundkonstruktionen aus ultrahochfestem Beton. Berichtsnr. IMB 229/2009, RWTH Aachen 2009.

[5] Berthellemy, J.; Lorenc, W.; Mensinger, M.; Rauscher, S.; Seidl, G.: Zum Tragverhalten von Verbunddübeln – Teil 1: Tragverhalten unter statischer Belastung. Stahlbau 80 (2011), S. 172-184.

[6] Feldmann, M.; Hegger, J.; Hechler, O.; Rauscher, S.: Abschlussbericht – Untersuchungen zum Trag- und Verformungsverhalten von Verbundmitteln unter ruhender und nichtruhender Belastung bei Verwendung hochfester Werkstoffe (FOSTA P 621 / AiF-Nr. 13867). RWTH Aachen 2007.

[7] Stelzer, G.; Renz, R.: Berührungslose optische und thermische Messverfahren und deren Anwendung bei der Untersuchung von Werkstoffen und Bauteilen aus Kunststoff. DVM-congress, Berlin, 2008.

[8] DIN EN 1994 (Eurocode 4): Design of composite steel and concrete structures, Part 1-1: General rules and rules for buildings. Beuth publishing Berlin, 2004.

[9] Wies,S.; Schnell, J.; Kurz, W.: Innovative Verbundmittel in Ultrahochleistungsbeton. Beton- und Stahlbetonbau 106 (2011), S. 694-699.

Structural Behaviour and Load-Bearing Capacity of Reinforced Glued Joints of UHPC-Elements

Daniel Wingenfeld, Christian Muehlbauer, Konrad Zilch
Dept. of Concrete Structures, Technische Universitaet Muenchen, Germany

The use of structural elements made of ultra-high performance concrete (UHPC) in construction projects requires the development of appropriate techniques for joining them. Gluing UHPC elements produced in a precast factory on site to a structural element or structure would constitute an ideal joining method. At the Department of Concrete Structures of the Technische Universitaet Muenchen a high-strength mineral mortar – an RPC-adhesive – was developed. Experiments have proven that the glue is highly performant and very durable when used in joining UHPC elements. In order to increase resistance of the "pure" glued joint and to also achieve ductile failure behaviour another innovative joining technique was developed based on the glued joint: the reinforced glued joint. In this paper the results from fundamental experimental investigations to the structural behaviour and the load-bearing capacity of reinforced glued joints will be presented. The influence of the diameter and percentage of the reinforcement, use of high-strength reinforcement steel, reinforcement anchorage and the spacing of the keyways on reinforced glued joints was investigated on composite specimens.

Keywords: Ultra-High Performance Concrete (UHPC), joining, gluing, Reactive Powder Concrete (RPC) adhesive, reinforcement

1 Introduction

Ultra-high performance concrete (UHPC) allows the production of extremely slender and high-strength elements. Manufacturing of those structural elements will predominantly take place in factories. Transport on public roads and on-site erection cause limitations to the dimension of these precast elements. Therefore it is necessary to create durable and high-strength design solutions for joining UHPC precast elements under construction site conditions.

At the Department of Concrete Structures of the Technische Universitaet Muenchen two innovative joining techniques are being developed, the "pure" and the reinforced glued joint. Figure 1 exemplary shows both connections in a combined use for a T-shaped girder. For the reinforced glued joint stirrups are cast into the girder of the T-beam. The UHPC slabs have keyways at these locations where the stirrups can be cast into the slab. On site, girder and slabs are then joined using RPC-adhesion and the keyways filled in so that a force-transmitting connection is created. The stirrups form the girder can also be used as shear reinforcement if necessary.

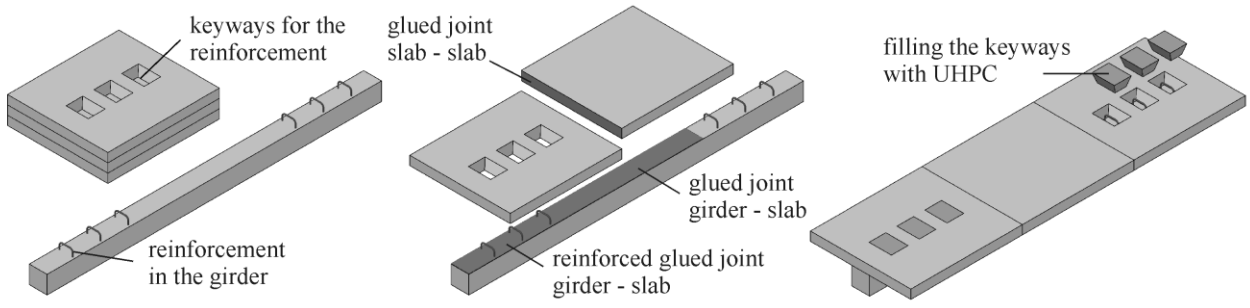

Figure 1: Joining principle for "pure" and reinforced glued joints.

2 Structural Behaviour of Glued Joints

The inherent structural behaviour of "pure" and reinforced glued joints of UHPC structural elements corresponds to the structural behaviour of shear joints of subsequently added concrete elements (refer e.g. to [1]). The load-bearing behaviour of the joint is made up of three partially independently acting structural mechanisms: adhesion, friction and reinforcement (Figure 2).

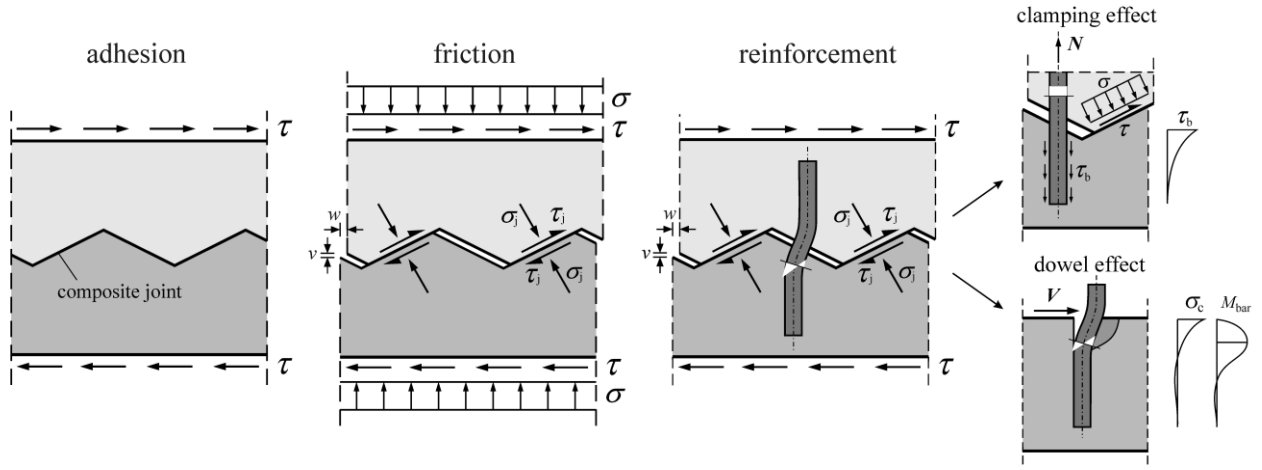

Figure 2: Structural mechanisms of composite joints.

Adhesion has both a chemical and a mechanical component. As long as the applied shear is lower than the adhesive bond the test specimen act quasi-monolithically (refer to Table 2). If the shear overcomes the strength of this bond then adhesive failure occurs i.e. it results in the brittle failure of the joint. If an external normal force acts on the joint then shear forces can still be transferred through friction even after the bond's adhesion has failed. The amount of shear is then dependent on the roughness of the joint surface and the applied normal force. If reinforcement crosses the joint then shear forces can be transmitted by the clamping and dowel behaviour of the bars after the bond has failed. Through a joint longitudinal displacement, the joint begins to open and the reinforcement is extended longitudinally. The resulting tensile force in the bars is in equilibrium with the compressive force acting on the joint. Similarly to when an external normal force is applied, friction effects occur. Furthermore because of the longitudinal displacement, the reinforcement embedded inside the concrete acts analogous to a laterally loaded dowel where the shear load is transferred via bending and corresponding concrete compression. Clamping effects cause axial forces in the reinforcement while dowel action causes bending. The superimposed stress distribution of both components at the location of maximum stress is shown in Figure 3. With increasing displacement the reinforcement plasticizes and a plastic zone is formed. From this point, the shear stress is transferred via diagonal pull effect of the reinforcement.

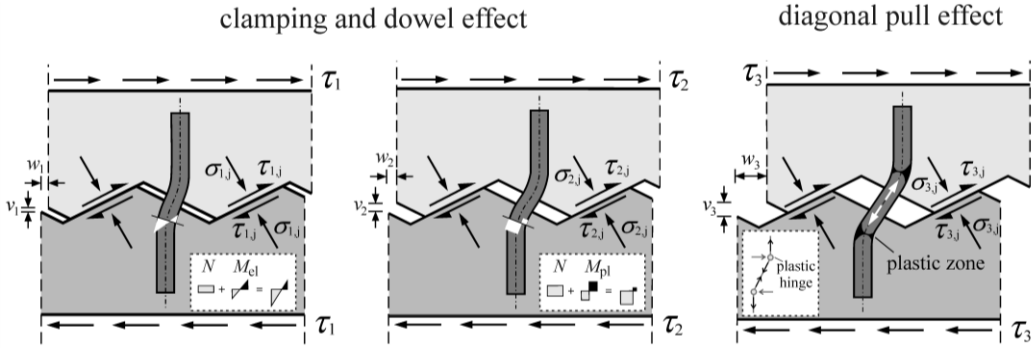

Figure 3: Bearing effect of the reinforcement.

3 Experimental Investigation

Test Specimen

In order to investigate the effects of the governing parameters of the shear loading behaviour of reinforced glued joints two test specimen were conceived. Test specimen Type I (Figure 4) has a joint length of 50 cm and Type II (Figure 5) of 100 cm.

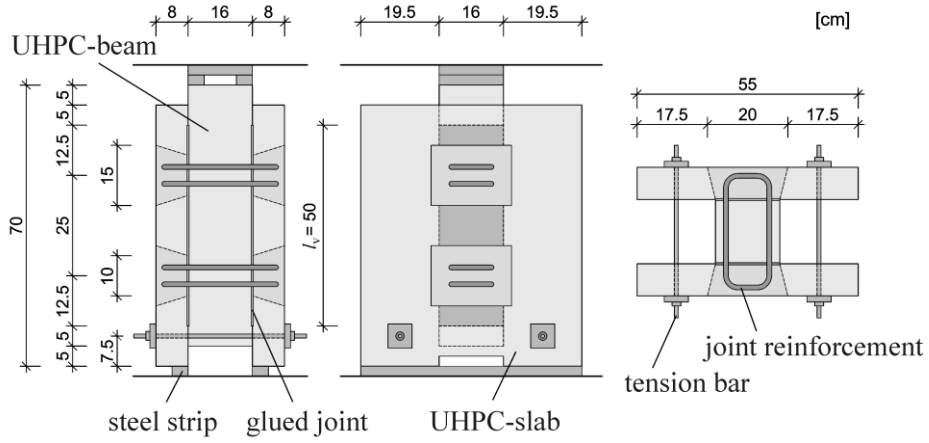

Figure 4: Composite specimen Type I, joint length l_v = 50 cm.

Test specimen Type I was used to investigate various reinforcement parameters and Type II to understand the influence of the length of the joint and the reinforcement content as well the spacing of the keyways. For both test specimens a slab were glued to each of the two sides of a beam-shaped joining element with RPC adhesive and the openings filled in.

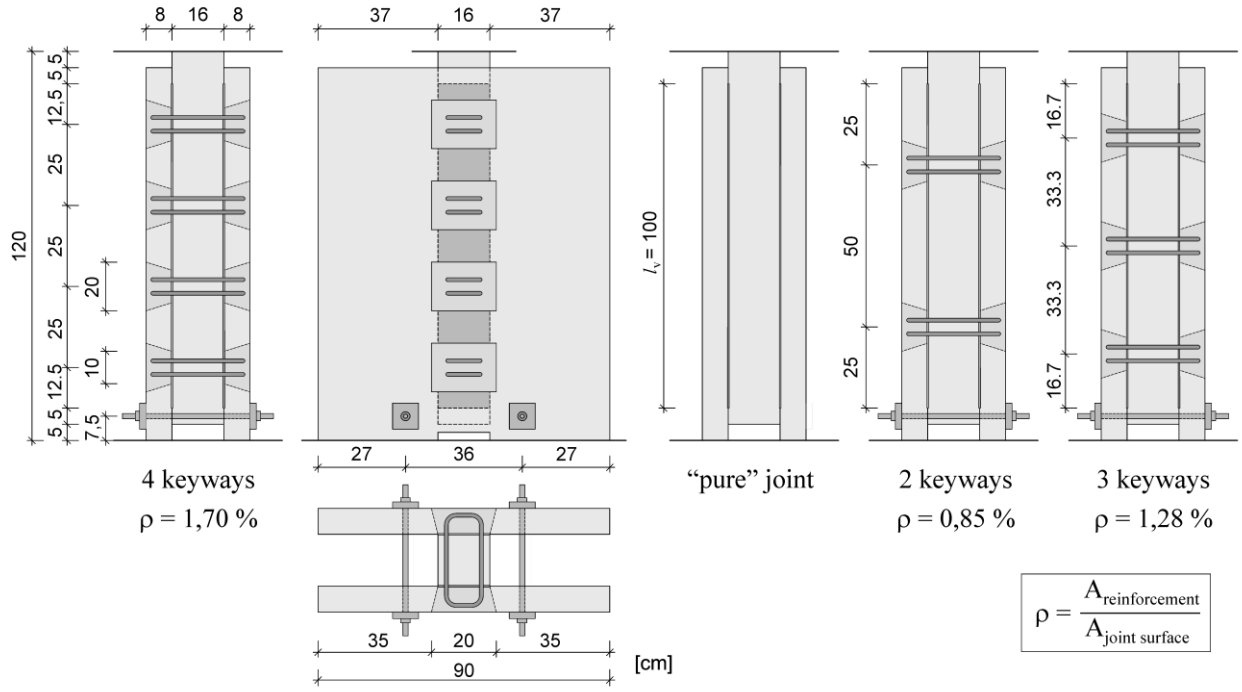

Figure 5: Composite specimen Type II, joint length l_v = 100 cm.

For the UHPC joining elements the coarse-grained UHPC mix B5Q without heat treatment and a 2.5 vol.% of fibres developped in the SPP 1182 research programme of the Deutsche Forschungsgemeinschaft (DFG) was used. The exact mixture of the UHPC's B5Q mix can be found in [2], those of the RPC adhesive as well as further details regarding the test specimen, test setup and measuring technique are given in [3].

Test Programme

Nine test series were done to determine the governing parameters (Table 1). Figure 6 shows the reinforcement types used in the tests. The first series with "pure" adhesion served as reference to the tests carried out in the research project "Joining UHPC Structural Elements by Gluing". The second to fifth series were used to investigate the influence of bar diameters, bar shape, steel grade and reinforcement content. For Series 6 a Teflon foil was inserted into the joint in order to assess the dowel effect. The influence of joint length and spacing of the keyways as well as the reinforcement content was investigated with Series 7 and 8. In Series 9 RPC adhesive without fibres was used to fill in the openings.

Table 1: Test Programme.

series	name of specimen	type	no. of tests	no. key-ways	material filling	reinforcement ∅ [mm]	reinforcement type	reinforcement content [%]	reinforcement quality
1	1.1	I	5	-	-	-	-	-	-
	1.2	I	3	2					
2	2.1	I	6	2	B5Q mF oWB	12	B2	1,13	B500B
	2.2	I	3	2		14	C1	1,15	B500B
	2.3	I	2	2		20	B1	1,57	B500B
3	3.1	I	3	2		12	A2	1,13	B500B
4	4.1	I	3	2		15	C1	1,33	St 900/1100
5	5.1	I	6	2		12	C2	1,70	B500B
6	6.1	I	3	2		12	B2	1,13	B500B
	6.2	I	1	2		20	B1	1,57	B500B
7	7.1	II	3	-		-	-	-	-
8	8.1	II	3	2		12	C2	0,85	B500B
	8.2	II	3	3		12	C2	1,27	B500B
	8.3	II	3	4		12	C2	1,70	B500B
9	9.1	I	3	2	RPC, oF	12	B2	1,13	B500B

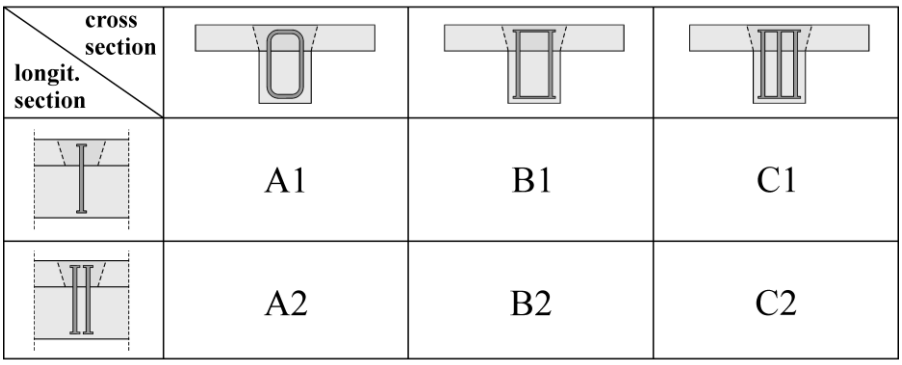

Figure 6: Reinforcement type.

4 Test Results

The results of the composite specimen tests are summarized in Table 2 which includes the average values for the UHPC cylinder compressive strength (150 x 300 mm², f_c) on the day of testing of the respective test specimen and keyway in-fills, the average yield strength (R_{eH}), ultimate tensile strength (R_m) and uniform strain (A_{gt}) of the reinforcement bars, the average values of test slips between beam and slab (w) and test loads per joint (F). The indices *ad, pl* and *fa* stand for the slip or load at adhesive failure, plasticization of reinforcement and failure of reinforcement, respectively.

Table 2: Test Results.

speci-men	concrete		steel			test results					
	$f_{c,specimen}$	$f_{c,keyways}$	R_{eH}	R_m	A_{gt}	w_{ad}	w_{pl}	w_{fa}	F_{ad}	F_{pl}	F_{fa}
	[N/mm²]	[N/mm²]	[N/mm²]	[N/mm²]	[%]	[mm]	[mm]	[mm]	[kN]	[kN]	[kN]
1.1	164,4	-	-	-	-	0,014	-	-	349	-	-
1.2	168,0	158,6	-	-	-	0,014	-	-	351	-	-
2.1a,c	178,5	164,4	598	686	10,2	0,028	0,30	6,26	463	669	513
2.1d-f [1)]	181,7	158,8	598	686	10,2	-	0,41	6,36	-	461	471
2.2	169,2	138,1	558	669	10,3	0,023	0,37	7,26	361	489	483
2.3 [1)]	170,1	158,8	514	617	11,4	-	0,46	11,18	-	517	588
3.1 [1)]	175,6	163,1	598	686	10,2	-	0,39	7,10	-	499	483
4.1 [1)]	178,1	163,1	960 ($R_{p0,2}$)	1170	4,07	-	1,73	8,46	-	776	807
5.1a-c	176,1	158,6	598	686	10,2	0,024	0,43	6,40	419	828	720
5.1d-f [1)]	180,2	158,8	598	686	10,2	-	0,51	6,09	-	655	685
6.1	165,3	138,1	598	686	10,2	-	0,40	7,37	-	301	475
6.2	170,1	158,8	514	617	11,4	-	0,50	12,82	-	368	608
7.1	188,1	-	-	-	-	0,023	-	-	473 (3) [2)]	-	-
8.1	187,0	144,4	598	686	10,2	0,026	0,45	5,66	469 (1) [2)]	895	767
8.2	181,1	142,9	598	686	10,2	0,030	0,52	6,06	476 (3) [2)]	1257	1201
8.3	184,9	142,9	598	686	10,2	0,032	0,70	5,84	436 (4) [2)]	1600	1540
9.1	174,5	107,8	598	686	10,2	0,028	0,41	8,63	344	535	481

[1)] joint surfaces treated with separating agent

[2)] ( ) no. of evaluated joints, only joint bearing capacities with nearly central load introduction were evaluated

Load-slip Behaviour

Figure 7 shows the load-slip curves of Test Specimen 2.1 (glued joint, continuous line) and 6.1 (Teflon foil inside joint, dashed line). For the qualitative comparison of the test results the average values from three tests are shown. The joint reinforcement content of both test specimen was the same.

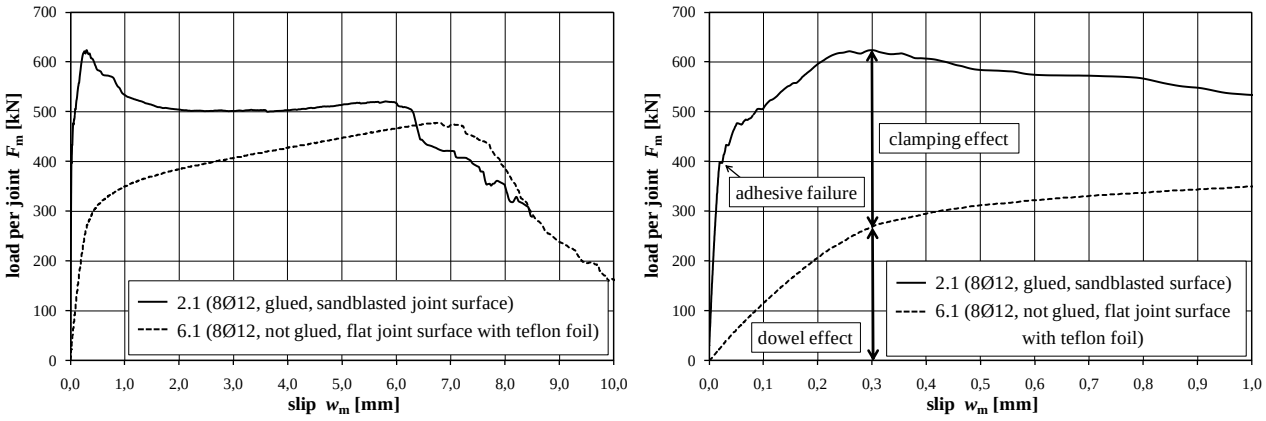

Figure 7: Load-slip diagrams of Test Specimen 2.1 & 6.1.

The test specimen with the glued joint showed a much stiffer structural behaviour and was able to bear a much higher maximum load F_{pl} (ca. 120 % higher). The test specimen with the Teflon foil inside the joint had a slightly greater maximum slip w_{fa}. Its structural behaviour resulted in a displacement of w_{pl} = 0.3 mm from dowel action alone beyond which a plastic zone formed in the reinforcing that activated diagonal tension. Adhesive failure of Test Specimen 2.1 occurred at a displacement of w_{ad} = 0.03 mm resulting in even larger displacement and thus activation of the reinforcement.

With a greater reinforcement content it is also possible – as the load-slip diagrams in Figure 8 illustrate – to increase of the joint's load-bearing capacity further. The structural behaviour of the test specimens with ρ = 1.13 % and ρ = 1.70 % is similar.

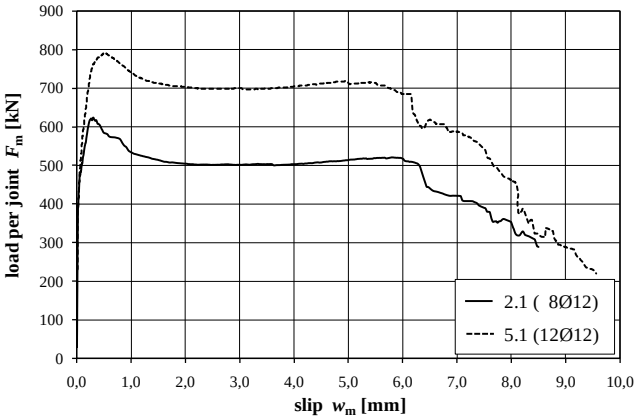

Figure 8: Load-slip diagram of Specimen 2.1 & 5.1.

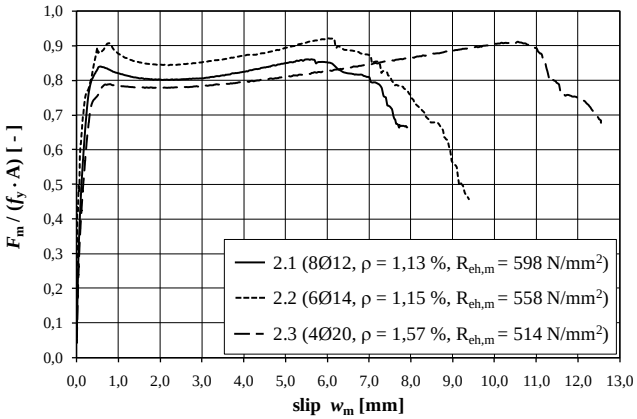

Figure 9: Load-slip diagram of Specimen 2.1, 2.2, 2.3.

In all test specimen adhesive failure was observed at the interface between RPC adhesive and the UHPC surface [3]. Furthermore, reinforced glued joints showed two typical failure patterns (Figure 10): a) failure of the joint in a single plane and b) in two planes. The latter resulted in a stiffer structural behaviour and thus larger bearing capacity of the joint because of the interlock between the in-fill and adhesive materials. In order to improve comparability of the results, the beams of test specimen 2.1d-f, 2.3, 3.1, 4.1 & 5.1d-f were treated with a separating agent to force failure in a single plane.

Figure 9 shows the load-slip curves of Series 2 with different reinforcement bar diameters. The maximum test load there is put into relation to the yield strength and the reinforcement area. With increasing bar diameters the relative displacement w_{fa} increases along with ductility. The relative bearing capacity of the test specimen with Ø 20 is roughly 6 % smaller than with Ø 12. For Test Specimen 2.2 no separating agent was used but joint failure still occurred in a single plane (Figure 10 a)).

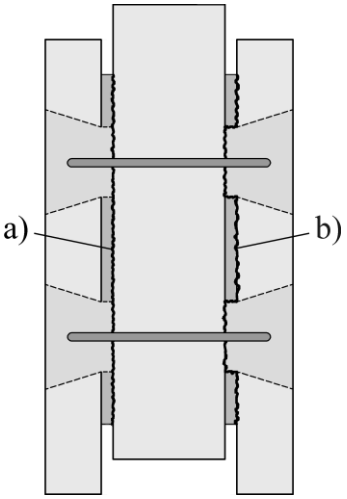

Figure 10: Fracture Pattern: a) joint failure in a single plan b) joint failure in two planes.

The results for Series 6 with Teflon foil and smooth joint surfaces as well as the test results by Randl [4] with normal-strength concrete and foil between smooth joint surfaces are shown in Figure 11. For the UHPC tests the relative displacement is much greater for the larger diameters as has already been remarked for Series 2. The shape of the curves for Ø 12 and Ø 20 is similar. In comparison to normal-strength concrete the structural behaviour of reinforcement bars inside UHPC is much stiffer and the dowel effect significantly larger.

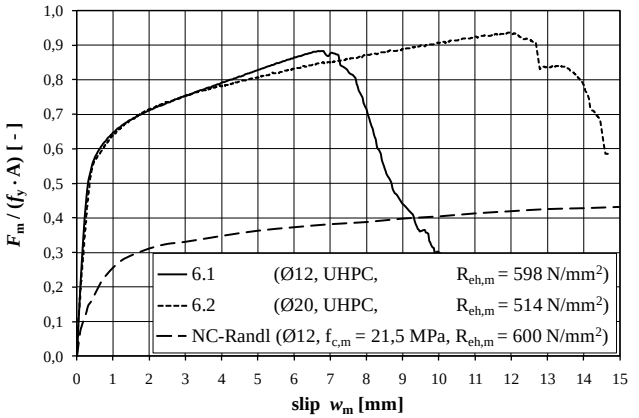

Figure 11: Load-slip diagram of Series 6 & NC.

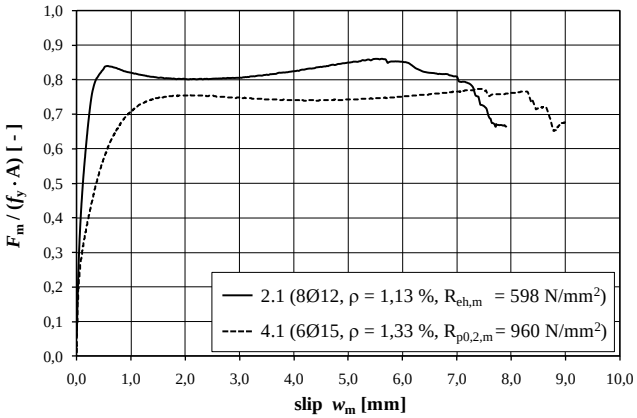

Figure 12: Load-slip diagram of Specimen 2.1 & 4.1.

How the reinforcement bar strength influences the structural behaviour was investigated with Series 4. In this series, form ties Ø 15 with a yield strength of 960 N/mm^2 were used. When comparing the load-slip curves (Figure 12) of the test specimens with high and normal strength reinforcement it becomes clear that the structural behaviour of the normal strength reinforcement is much stiffer and its load-bearing capacity is roughly 10% greater. This is due to the fact that the concrete's plastification zone and thus the corresponding bending moment is higher in high-strength steels when compared to steels of normal strength.

Using test specimen of Type II (Series 7 and 8) the influence of the joint length, the keyway spacing and the reinforcement conctent on the structural behaviour of the "pure" and reinforced glued joint was investigated. With increasing joining length the shear stresses (ratio of load F_{ad} to the joint surface A_{js}) at adhesive failure actually decrease. This means that the shear stress is not constant across the joint length. Maximum shear stresses must have occurred in the area where the upper load was applied, because joint failure began there. The keyways as well as their spacing do not have influence on the adhesive structural behaviour in comparison to pure adherence. The typical load-slip behaviour of the test specimen of Series 8 is shown in Figure 13 (Test 8.1a). Adhesive failure begins as aforementioned from the top and then continues downward so that the reinforcing is activated successively. A regression anaylsis showed that a proportional increase of the joint's bearing capacity is possible with an increasing reinforcement content (Figure 15).

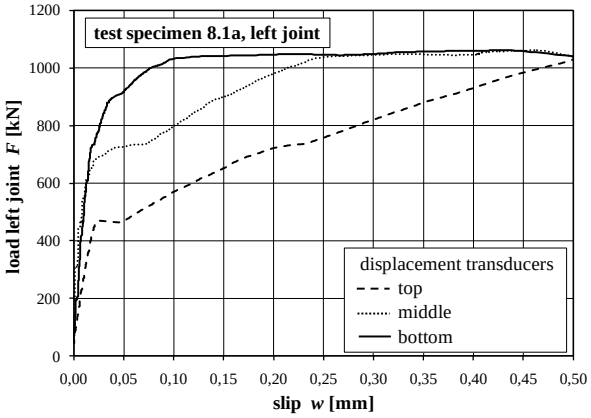

Figure 13: Load-slip diagram of Test Specimen 8.1a.

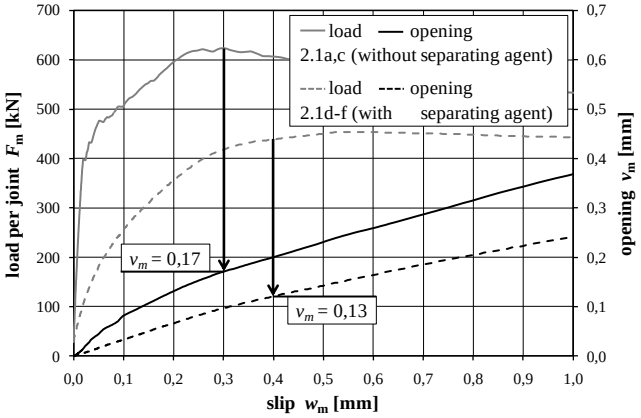

Figure 14: Joint opening of Test Specimen 2.1.

Joint Opening

For test specimens where the beam surface was treated with a seperating agent a smaller joint opening v was observed than for those specimens without the agent. Because of the smaller joint opening the longitudinal expansion of the reinforcement is smaller and so the friction component of the clamping effect resulting in a 27% lower load-bearing capacity of the test specimen. Figure 14 shows the relationship of the joint openings using Test Specimen 2.1a-c (without separating agent) and 2.1d-f (with the agent) as an example. The adhesion without separating agent resulted in joint openings at maximum load (F_{pl}) of v = 0.17 mm, those with agent opened to v = 0.13 mm. The larger joint opening are on one hand the result of the interlock between infill and adhesive described in Section 4.1 and the rougher surface created by the adhesive failure.

Very high bond stresses can be transferred between ribbed reinforcement bars and UHPC. The pull-out tests in [5] on ribbed bars embedded in the coarse-grained UHPC mix B5Q showed that the maximum bond stress can already be reached for very small displacements of roughly 0.2 mm. Thus the relatively small joint openings observed above are sufficient to activate a relatively high friction component through clamping effect (see also Figure 7).

Friction coefficients

The friction coefficients were determined using a regression analysis. The maximum shear stress τ_{max} (F_{pl} over the joint's surface) is shown in Figure 15 in relation to the reinforcement content ρ multiplied by the yield strength f_y. When assuming that for a reinforcement content ρ = 0 the shear stress is τ = 0 then for a joint length of l = 50 cm one obtains for ρ = 1.13 % (Test 2.1a-c) a friction coefficient of μ = 1.24. For a reinforcement content of ρ = 1.7 % (Test 5.1a-c) the coefficient is μ = 1,02, i.e. for increasing of the reinforcement content the friction coefficient decreases. For better comparability of the individual series a separating agent was applied to the joint surfaces of some of the test specimens as explained in Section 4.1. This decreases the friction coefficient but the scatter of the coefficients was also decreased and the comparability of the test results was improved. For ρ = 1.13 % and ρ = 1.7 % the friction coefficient is now μ = 0.85. For Series 8 with a joint length of l = 100 cm the adhesive load-bearing capacity was significantly reduced vis-à-vis the reinforcement's capacity (see also Table 2). For this test series the friction coefficient is constant regardless of the reinforcement content at μ = 1.02 and corresponds to the friction coefficient of Test Specimen 5.1.

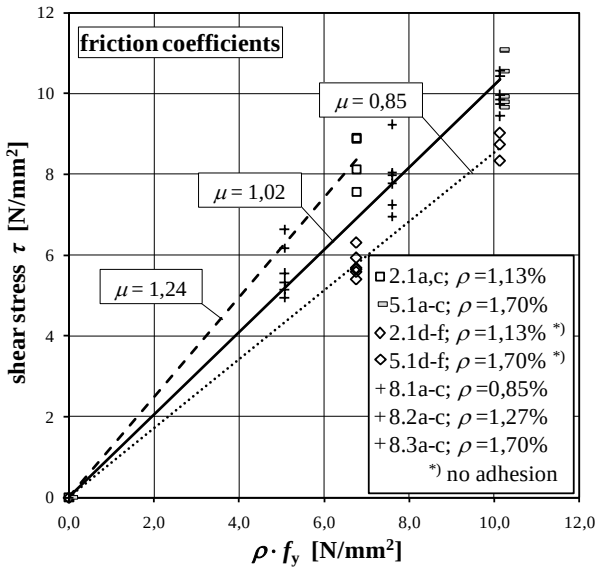

Figure 15: Friction coefficients.

5 Summary and Outlook

With this series of tests on composite specimens it was possible to investigate the structural behaviour and load-bearing capacity of reinforced glued joints of elements made of UHPC. The tests showed that the joining method with reinforced glued joints offers a high load-bearing capacity and ductility and thus presents an adequate connection between UHPC elements.

Based on the test results presented above a generally applicable design approach for reinforced glued joint will be deduced for UHPC elements. This approach will then be verified empirically using structural elements (e.g. T-shaped girder) in order to describe the structural behaviour accurately. Once accomplished, the initial constructive solutions and design equations for the practical application of reinforced glued joint will then be available for structural elements made of UHPC.

References

[1] Zilch, K.; Lenz, P.: Beton-Beton-Verbund – Potenziale für Neubau und Ertüchtigung. In: Bauingenieur 84 (2009), Heft 11, S. 466 – 471.

[2] Muehlbauer, C.; Zilch, K.: Glued Joints of Ultra High Performance Concrete Structures. In: Proceedings of the Third International fib Congress, May 29 - June 2, 2010, Washington D.C., U.S.

[3] Zilch, K.; Muehlbauer, C.; Wingenfeld, D.: Experimental investigation of reinforced glued joints of UHPC elements. In: M. Khrapko und S. Chair (Hg.): Proceedings of the 9th International Symposium on HPC, 9 - 11 August 2011, Rotorua, New Zealand, 2011, ISBN: 978-0-473-19028-6.

[4] Randl, N.: Untersuchungen zur Kraftübertragung zwischen Alt- und Neubeton bei unterschiedlichen Fugenrauigkeiten, Universität Innsbruck, Dissertation, 1997.

[5] Gehrlein, S.: Experimentelle Untersuchungen zum Verbundverhalten von Bewehrungsstäben in UHPC unter statischer Zugbeanspruchung, TU Muenchen, Bachelor Thesis, 2011.

Adhesion of fine-grained HPC and UHPC to Steel and Glass

Joachim Juhart[1], Bernhard Freytag[2], Gerhard Santner[2], Erwin Baumgartner [3]
1: Institute of Technology and Testing of Building Materials, Graz University of Technology, Austria
2: Laboratory for Structural Engineering, Graz University of Technology, Austria
3: School of Civil Engineering and Architecture, Carinthia University of Applied Sciences, Austria

The adhesive bonding capacity of ultra high performance concrete with construction materials is exceptional. Due to the numerous chemical, physical and geometrical influences and their complex interaction, the adhesive strength has been hard to predict until now.
The outlined paper presents the results of a multi-disciplinary research project in which the adhesion of fine-grained HPC and UHPC with steel and glass was explored. An extensive research program comprised investigations on the theoretical value of specific adhesion, on the technical adhesion under shear and tensile loading, enforcements in the interface due to restrained shrinkage and even more.
With the parameters found out to be decisive and an introduced failure criterion, the bond strength of a smooth joint of fine-grained HPC/UHPC and steel or glass can be calculated. Based on the findings also the effectiveness of rough surfaces for the bond can be explained from a geometrical point of view.

Keywords: fine-grained HPC and UHPC, steel, glass, specific/technical adhesion, tensile bond strength, shear bond strength, surface energy

1 Introduction

The adhesion of fine grained high performance and ultra high performance concrete – in this paper subsequently referred to as “UHPC” – to smoothly polished steel can principally be strong to an extent that tensile loading leads to fracture of the concrete and not of the interface (fig. 6). With slightly roughened steel and glass surfaces UHPC shows also such a high adhesive bonding capacity so that new flat-spread connections and composite construction technologies become possible [1], [2]. The adhesion is influenced by numerous chemical, physical and geometrical factors and their complex interaction and therefore the adhesive strength has not been predictable until now.

To provide the basis for calculations of the adhesive bond strength a multi-disciplinary research project was carried out with the aim to identify the decisive factors in the adhesion and to describe their interaction. To study the phenomenon comparatively two chemical distinct materials, steel and glass, were chosen as partner materials for UHPC, being non-porous materials relevant in building practice. Their surfaces were treated to realize smooth and differently roughened faces. They were brought in contact with two different fine grained mixtures as adhesive. A comprehensive description of the research can be found in [3].

The outlined paper focuses on a smooth joint of UHPC with steel or glass. It shows how the bond strength can be calculated with parameters found out to be decisive and a newly introduced failure criterion.

2 Adhesion of UHPC - Basic Principles

Specific Adhesion Mechanical Adhesion

According to Bischof [4] and Habenicht [5] bond can be distinguished in the form of specific and mechanical adhesion. Mechanical adhesion describes the bond in the contact surface through form fitting, mechanical interlock on a microscopic scale respectively. It is not focused on in the presented paper. Specific adhesion includes strong chemical bond between atoms – covalent and ionic bonds for example – as well as intermolecular forces – weak chemical bonds based

on electrostatic forces like van der Waals forces and hydrogen bonds, which are permanent or induced electrostatic forces.

Strong chemical bonds need sufficient chemical affinity between the bonding elements, sufficient mobility of the atoms and activation energy. Between UHPC and the materials glass and steel no strong chemical bonds are expected under normal conditions, because the above mentioned preconditions are not fulfilled. The authors conclude that only intermolecular forces between the investigated materials are responsible for specific adhesion.

Intermolecular Forces Inducing Adhesion and Thermodynamic Approach

Intermolecular forces are closely related to the surface energies of the materials used. Energy states at all times of the concrete hardening process affect the adhesion phenomena. Thus the surface tension, surface energies respectively, of fresh until finally hardened UHPC as well as of steel and glass surfaces are determined as pointed out in detail in [6].

To activate these intermolecular forces, the interacting molecules need to be as close as 0,2-1,0 nm [5]. Therefore at least one of the components needs flexible molecules, which is provided in case of liquid or at least flowable substances.

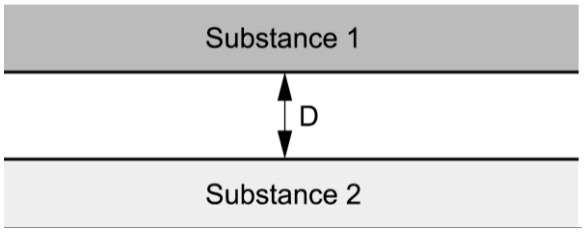

Fig. 1: Geometry of interacting bodies.

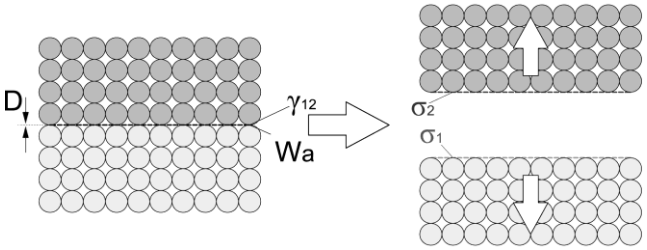

Fig.2: Definition of the thermodynamic work of adhesion Wa

The theoretical adhesive force acting between two materials can be calculated by differentiating the potential energy of interaction $W_{(D)}$ between two bodies with respect to their distance D [8]. The potential energy of interaction $W_{(D)}$ depends on the geometry of the two bodies. In the case of two infinitely extended surfaces (fig. 1) we get an interacting force F according to equation (1) as pointed out in detail in [6].

$$F = \frac{2 \cdot W_{(D)}}{D} = \frac{2 \cdot Wa}{D} \qquad (1)$$

According to the thermodynamic approach the reachable adhesion can be related to the proportion of surface energies of the participating materials. In the thermodynamic approach the potential energy of interaction $W_{(D)}$ is called work of adhesion W_a. If two different materials are interacting, an additional interaction energy γ_{12} exists. When disjoining the two parts, two new surfaces with surface energies σ_1 and σ_2 are created, and neither work of adhesion nor interaction energy exist any longer (fig. 2). For detailed information the surface energy is usually divided into dispersive and polar parts, according to the method of Owens, Wendt, Rabl and Kaelble (OWRK).

Technical Adhesion

Theoretically determined material strength, as well as adhesion strength, is always much higher than the real measured strength [9], in particular when brittle materials are dealt with. The UHPC-matrix, which is assumed to be responsible for bond, is very brittle and has a rather heterogeneous structure. Thus a considerable difference between theoretical and technical adhesion is expected in the investigated case. It is defined by the ratio g of the theoretical to the technical adhesion strength.

Influence of Hindered Shrinkage

Differential shrinkage between an applied coating and the substrate causes restraints, which can cause delamination or cracks [10]. Hindered shrinkage is the reason why horizontal tensile stresses are transferred into the overlay (thickness t_c) by shear in the interface over a defined bond length l_e (l_e~$4xt_c$, [10]). In addition to that vertical tensile stresses at the free edge occur in the interface. Hindered shrinkage reduces the reachable bond strength, because constraint stresses in the interface have to be added to loading stresses.

3 Material Properties and Methods

Fine Grained HPC and UHPC as Adhesive

Two different mixtures are used, an own mix (OM) and a commercially available premix for UHPC (PM). The mixtures are produced in a way that they establish very similar fresh concrete properties, as this influence shall be kept constant. As a consequence the two types of concrete show almost the same compressive and tensional strengths. To keep the complexity in limits, the concrete is made without heat treatment and without addition of fibers which is unusual for UHPC. Strictly speaking OM shall be classified as fine grained HPC, whereas PM is an UHPC. Probably because of its optimized packing density, the latter develops higher compressive strength when made with fibers and after heat treatment. See table 1.

Table 1: mix composition and concrete properties.

mix composition		**OM**	**PM**	**concrete properties**		**OM**	**PM**
cement	kg/m³	1062	premix 2260,4	slump flow, mortar cone EN 1015-3 without shocks	mm	235	246
microsilica	kg/m³	133					
quartzsand	kg/m³	959		flow time to Ø 200 mm	sec	14	26
water addition	kg/m³	160	113,9	air content	%	3,8	5,3
superplasticizer	kg/m³	38	31,2	compressive strength f_{cm}, cube 100mm, 28d, n≥4	N/mm²	127	128
w/b-ratio	[-]	0,15	0,15				
remark: f_{cm}, cube 100mm, 28d, with heat treatment and 2% steel fibers					N/mm²	-	*184*

The significant relevance of shrinkage on the development of the adhesive strength requires the knowledge of the shrinking behaviour from the very beginning of the hardening process. Measurements are carried out with a shrinking trough. They start 4 hours after water addition to the mix before the initial setting of the concrete. To study the influence of extreme limits of the shrinkage deformation two curing methods of the concrete are introduced: with full dehydration protection (DP) and without dehydration protection (NDP). In the case of DP the autogenous shrinkage is measured. In the case of NDP the UHPC is exposed to drying immediately after the casting and an enormous plastic shrinkage during the first hours occurs. Early age cracks can be observed in parallel microscopic investigations in the glass-UHPC interface corresponding to the setting time of the UHPC, showing that significant stresses arise at a critical time of strength development. Low humidity (NDP) yields a 2,3-fold shrinking deformation compared to high humidity (DP). Results in detail can be found in [3].

Steel and Glass as Adherent

To determine the specific adhesion, plain glass and polished steel surfaces are used. Observations of the polished steel and plain glass surfaces with a scanning electron microscope show that the remaining microscopic roughness is unlikely to provide any mechanical adhesion [3].

Surface Tension and Surface Energies

The surface tension of the viscous suspension of the fresh UHPC cannot be obtained by means of known methods for liquids. As described in detail in [6] a range of the surface tension of UHPC could be estimated with a maximum of 50 mJ/m² by capillary rise tests and taking into account other published results.

The surface energies of hardened UHPC, plain glass and steel were determined by contact angle measurements using the sessile drop method with four liquids [6]. Mean values for surface energies of UHPC, for glass and for polished steel – which was put in an alkaline substance (pH=12,5) to passivate its surface – are shown in table 2.

Table 2: Measured surface energies SE [mJ/m²] of hardened UHPC, plain glass and passivated steel.

substrate	**dispersive-**	**polar part**	**total SE**	UHPC	**dispersive-**	**polar part**	**total SE**
Glass	32,9	24,7	57,6	**OM**	34,9	30,7	65,6
Steel	35,3	11,7	47,0	**PM**	35,1	29,6	64,7

Tensile and Shear Adhesion Tests

To determine the real, so-called technical adhesive tensile and shear strength, direct tension and torsional shear tests are performed. Symmetric cylindrical sandwich specimens (diameter d=100 mm) are fabricated with a horizontal position of a thin concrete layer (thickness t_c=2,5 mm). The arrangement with a high d/t_c-ratio of the layer (“thin layer”) ensures a minimized area of the interface influenced by stresses due to shrinkage and a nearly constant pressure on both interfaces of the specimen. The thickness of the concrete is ensured by the use of a hanging spacer, which is removed when the first setting occurs. Thus shrinking in direction of thickness can freely take place. See figure 3 and 4.

Tests are performed on various combinations of UHPC OM or PM with steel or glass and with the above mentioned two different curing methods (DP/NDP) with at least 4 specimens each. On the rule the concrete age is 28 days.

Fig. 3: Fabrication of composite sandwich specimens.

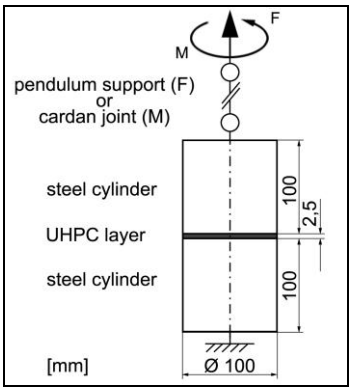

Fig. 4: schematic test set-ups.

4 Results and Discussion

Wetting of Steel and Glass by UHPC

The wetting process provides the necessary close contact between the initially liquid concrete and the solid substrate so that intermolecular forces can come into being. Combining the specified value of the surface tension of fresh UHPC (50 mJ/m²) and the determined surface energies of steel and glass it can be concluded that fresh UHPC wets the glass surface totally and better than the steel surface. Parallel spread flow tests on plain surfaces of the two different materials show also that UHPC wets glass better than polished steel.

Calculation of Theoretical Specific Adhesive Strength

With the knowledge of the surface energies of all materials in the composite system, as well as their polar and dispersive fractions, the specific work of adhesion W_a and out of it the theoretical specific adhesive strength $f_{ad,spez,0}$, specific interacting adhesion force F respectively, can be calculated according to equation (1). For a typical intermolecular distance at equilibrium of intermolecular forces of 0,5 nm [7] values of about 500 N/mm² are obtained [6]; $f_{ad,spez,0}$ is slightly stronger for glass than for passivated steel, but no significant difference between the UHPC OM and PM is detected.

Technical Tensile Adhesion and Shear Adhesion

Figure 5 gives an overview of the results gathered from series of the described direct tension and torsional shear tests of UHPC OM and PM in combination with plain steel or glass surfaces. The adhesive tensile strength values f_{ad} are calculated from the measured testing force F divided through the real contact area A of the interface. A is smaller than the geometrical area A_g, because of an annular gap in the interface, that occurs already before the testing date. This means, that the contact is lost in the interface in a small outer ring area (zone “I” in fig. 6) due to initial movements and shear stresses and probably further influences. This area shows a bare plain fracture surface and does not participate in the bond. In an analogous way the diameter d is reduced to calculate the effective section modulus of torsion W_T. The torsional shear strength values τ_{ad} are calculated by dividing the measured torsional moment M through W_T with $W_T=\pi/16d^3$ assuming a linear torsional stress distribution.

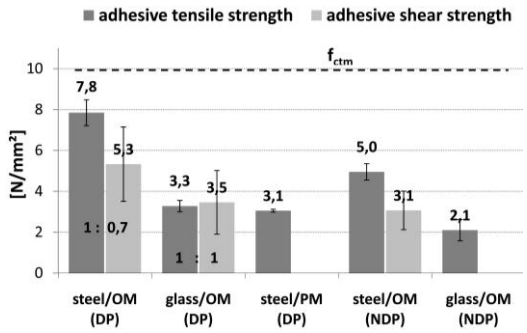

Fig. 5: results of direct tension and torsional shear tests, UHPC with plain steel and glass.

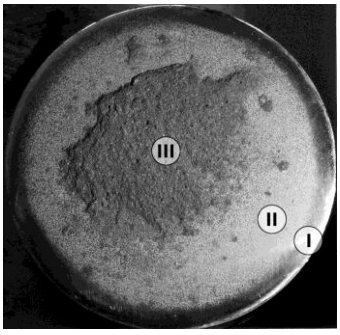

Fig. 6: Failure surface of polished steel/UHPC-PM(DP)

Fig. 7:Crack pattern, layer of UHPC-OM/glass(NDP).

When using dehydration protected specimens (DP), the adhesive tensile strength of 7,8 N/mm² is reached in the combination “steel/OM”. The value corresponds nearly to the tensile strength f_{ctm} of the concrete, which is about 10 N/mm² for both types of UHPC. f_{ctm} is obtained by direct tension tests with roughened surfaces (DP) where the fracture completely goes through the concrete layer. In the combination “glass/OM” the adhesive tensile strength is 2,4-fold less than in “steel/OM”.

As expected, the tensile strength achieved in the bond system is far less than the theoretically calculated adhesive strength. However, the technical adhesive strength is higher for UHPC/steel than for UHPC/glass in contradiction to the theoretical values mentioned above.

Regarding the described thermodynamic approach, a serious difference in the theoretical adhesive strengths that corresponds to the technical adhesion strength values will exist only, if the respective intermolecular distances arise to unequal levels and are higher for glass than for steel. As the specific intermolecular distances D of the material combinations are not known, they can only be estimated as shown in [3] and [6]. There values of 0,26 nm for steel/UHPC and 0,74 nm for glass are calculated which correspond to a theoretical adhesive strength of 800 N/mm² for steel/UHPC and 330 N/mm² for glass/UHPC (factor again 2,4). It is plausible,

that the different wetting behavior – glass is wetted better than steel – causes a larger intermolecular distance in the material combination UHPC/glass and therefore is responsible for a smaller theoretical and technical adhesive strength.

The adhesive tensile strength is 2,5-fold less in the combination steel/PM than in the combination steel/OM (DP). The differences may be related to different characteristics of the interfacial zones. Comparing the fracture surfaces shows that OM breaks predominantly in the concrete (50-90%) whereas PM shows the failure in the interfacial zone (concrete failure only 0-30%). The interfacial zone of UHPC PM seems to be more weakened than the one of UHPC OM in comparison to the regular concrete. The optimal dense packing of the fine grains in UHPC is disturbed by a geometrical effect at a plain interface. The effect is similar to the “wall effect” of normal concrete [11]. In addition to that a better wetting can lead to water segregation and a locally higher w/b-ratio. UHPC PM seems to be more affected by this phenomenon than UHPC OM, which is plausible as its packing density is more optimized in the regular concrete and it has a lower binder-content, higher amount of inert ultrafines respectively. OM therefore offers probably a higher capacity of filling voids or consuming water at the interface by CSH-growth than PM. A different wetting behavior, lower surface tension respectively of PM, has to be proved in further investigations.

Results of the torsion tests on smooth surfaces point out that shear adhesion works in another way than tensile adhesion (fig. 5). The ratio between tension and shear is 0,7 for steel and 1,0 for glass.

Failure Surfaces, Crack Pattern

The failure surface appears in three different forms. I) Totally bare surfaces occur if the loading of the interface is dominated by shear. That is in the above mentioned outer ring of all specimens and to a major part in the fracture surfaces of torsion test specimens. II) A thin film of cementitious matrix (~5 µm) adhering to the steel or glass surface represents a tensile fracture through the interfacial zone. III) Pure concrete fracture. See figure 6.

If no curing is applied on the specimen (NDP), the shrinkage that is hindered by the bond becomes so strong that cracks occur in a typical pattern (fig. 7) that agrees very well with calculated stresses in the UHPC layer. As each crack is an origin for stresses in the interface, the reachable tensile adhesion strength is reduced in correlation with the total crack length.

Enforcements due to Hindered Shrinkage

Finite element calculations show that the stress distribution of constraint stresses in the interfaces due to hindered shrinkage depends highly on the diameter/thickness-ratio (d/t_c-ratio) of the UHPC-layer within the stiff composite specimen. Assuming rigid bond, the bond length l_e over which maximum horizontal tensile constraint stresses are introduced into the UHPC-layer through shear stresses is $l_e \sim 5 x t_c$. When the horizontal stress reaches the tensile strength of the concrete, vertical cracks divide the UHPC layer into cracking cells with a new, smaller d/t_c-ratio. If the ratio becomes smaller than 10:1, the bond lengths of opposed edges overlap, shear stresses extend to the whole interface and lifting-off, vertical tensile stresses increase strongly at the edges. The stress distributions for two cases, a “thin” uncracked layer and a “compact” crack cell are shown in figure 8.

5 Conclusion and Findings

Adhesion on Smooth Surfaces

The discovered ratio between the shear adhesion and the tensile adhesion allows for developing the hypotheses that shear adhesion works like friction in a micro scale and a new failure criterion can be introduced (fig. 9). The intermolecular forces act perpendicular to the

surface and are permanently active forces. They represent the contact pressure of classical friction. The friction coefficient at the micro level for steel/UHPC ($\mu_{micro,steel/UHPC}$=0,7) is the same as in the macro scale, determined by own friction tests [not published].

The following parameters were found to provide a comprehensive description of the adhesive capacity of UHPC:

- The theoretical value of specific adhesive strength $f_{ad,spec,0}$, in a thermo-dynamical approach.
- The factor $g=f_{ad,spec,0}/f_{ad,spec}$, assumed to be material-specific for each UHPC (for OM: $g \approx 100$).
- The technical specific adhesive strength under shear- ($\tau_{ad,spec}$) and tensile-loading ($f_{ad,spec}$). The values can be determined approximately by testing of composite specimens (DP) with thin layers (e.g.: d/t_c=40/1) of UHPC between smooth surfaces as constraint stresses in the interface due to shrinkage are small in such cases.
- The ratio of $\tau_{ad,spec}$ / $f_{ad,spec}$, referred to as micro-friction coefficient μ_{micro}.
- The distribution of the constraint shear (τ_e) and tensile ($\sigma_{z,e}$) stresses in the interface due to restrained shrinkage (time development, creep and relaxation have to be considered). Therefore the d/t_c-ratio or geometry of the UHPC layer or the crack cell – crack spacing respectively – and its tensile strength at the critical time of cracking have to be known.

A smooth surface (area A_g) can bear a tensile adhesive strength f_{ad} perpendicular to its plane:

$$f_{ad} = \frac{F}{A_g} = \frac{1}{A_g} \cdot \int_{A_g} (\sigma_z)\,dA = \int_{A_g} \left(f_{ad,spec} - \frac{\tau_e}{\mu_{micro}} - \sigma_{z,e} \right) dA \qquad (2)$$

f_{ad} in equation (2) corresponds to the tested values F/A. All relevant parameters and their orders of magnitude are described in detail in [3].

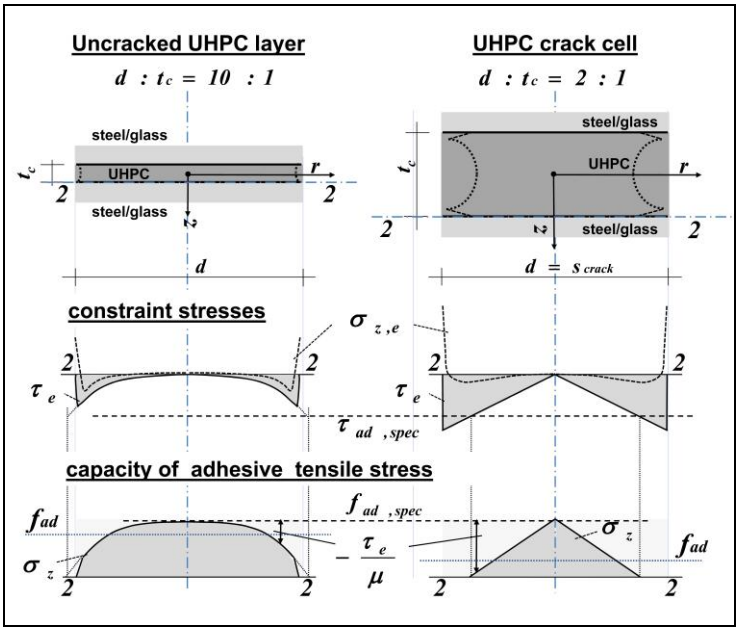

Fig. 8: stress distributions in the interface.

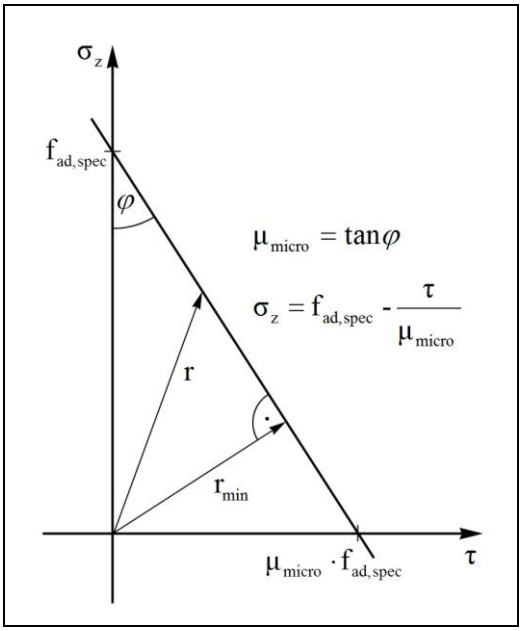

Fig. 9: failure criterion of adhesion.

Adhesion on Rough Surfaces

Based on the findings the effectiveness of rough surfaces for the bond can be explained from a physical and geometrical point of view. If the new failure criterion is applied to surfaces inclined to the loading direction with an angle α, the adhesive strength depends on μ_{micro} and α. At certain angles it decreases! The least effective inclination is ($\alpha = (45°-\varphi)/2$) as shown in [3].

6 Outlook

With the presented work only a first step to new scientific ground is made. An open question is how to determine the different, material specific intermolecular distances D, which account for the real theoretical value of specific adhesive strengths to the authors' opinion.

Further efforts have to be made to determine the surface tension of fresh concrete. The described effects at the interface due to the wetting behavior shall be verified subsequently.

In fresh concrete or mortar with a "high" water/binder ratio (> 0,4), there is always an excess of water, that is not taken up by the cement hydration. Therefore the expectable total wetting will cause a local accumulation of water in the interface to construction materials like steel or glass and lead to a weak interface. It can be concluded and may be proved experimentally, that with such concretes as adhesives to non-porous materials the technical adhesive tensile strength will never reach the tensile strength of the concrete in difference to the results shown for fine grained HPC/UHPC.

Regarding rough surfaces a parameter, which specifies the (mean) flank-inclination angle of the roughened surface, shall be developed to apply the proposed model. Of course mechanical adhesion has to run into a comprehensive model additionally.

Even slightly rough surfaces of all material combinations (DP) show such a high tensile adhesive strength, that the tensile strength of the concrete limits the results. Thus new flat-spread connections, for example with sand-blasted glass or steel surfaces and new connectors can be developed.

Systematic long-term investigations on the durability of the adhesive power are suggested.

7 Acknowledgements

The research was carried out in cooperation of Carinthia University of Applied Sciences and Graz University of Technology, Austria and funded by the Austrian Science Fund FWF (project L 412-N14 "Adhesive Bond between UHPFRC and other Construction Materials). The thesis [3] was written during employment at the Carinthia University of Applied Sciences. Thanks to the Institute of Physics, University of Leoben, for carrying out the contact angle measurements.

References

[1] Freytag, B.; Juhart, J.; Sparowitz, L.; Baumgartner, E.: The Use of UHPC in Composites – Ideas and Realisations. *Proc. 1st International Symposium on Ultra High Performance Concrete, Kassel 2004.*

[2] Freytag, B.: Glass-Concrete Composite Technology. *Structural Engineering International* 14 (2), p.111–117, 2004.

[3] Juhart, J.: Adhäsion von UHPC an Stahl und Glas. Dissertation, Technische Universität Graz 2011. *https://online.tugraz.at/tug_online/voe_main2.getVollText?pDocumentNr=222707&pCurrPk=60273*

[4] Bischof, C.; Possart, W.: Adhäsion. Berlin, Akademie-Verlag, 1983.

[5] Habenicht, G.: Kleben - Grundlagen, Technologie, Anwendungen. 4th ed., Springer, Berlin 2002.

[6] Santner, G.; Freytag, B.; Juhart, J.; Baumgartner, E.: Adhesive Power of UHPC from a Thermodynamic Point of View. *ASCE Journal of Materials in Civil Engineering*, submitted.

[7] Nardin, M.; Schultz, J.: Relationship between Work of Adhesion and Equilibrium Interatomic Distance at the Interface. *Langmuir*, p. 4238–4242. 1996

[8] Israelachvili, J. N.: Intermolecular and Surface Forces. 2nd ed., Acad. Press., London 1991

[9] Griffith, A.: The phenomenon of rupture and flow in solids. *Phil. Transaction of the Royal Society, series A,* Vol. 221, p. 163-198, 1921

[10] Haardt, P.: Zementgebundene und kunststoffvergütete Beschichtungen auf Beton. *Heft 13, Schriftenreihe des Institutes für Massivbau und Baustofftechnologie*. Universität Karlsruhe 1991.

[11] Maso, J. C.: Interfacial transition zone in concrete: State-of-the-art report. London: E & FN Spon, *(RILEM report, 11)*, 1996.

Probabilistic Modelling of UHPC Slender Columns

Martin Heimann, Holger Schmidt, Carl-Alexander Graubner
Technische Universität Darmstadt, Institut für Massivbau, Germany

Ultrahigh-performance concrete (UHPC) has been used successfully since the early 1990s. Meanwhile concrete-technological developments have allowed production of UHPC with a compressive strength of more than 150 N/mm². Thus, the field of application of reinforced concrete constructions currently in use can be extended. In particular, the cross-sectional dimensions required for highly stressed compression members can be reduced. However, in many cases this positive development increased the trend to even more slender and therefore likelier to buckle structural systems. Hence, it is to be expected that under certain conditions the safety level of such construction elements decreases. Because of this, the reliability of slender UHPC structural members is being investigated in a research project, supported by the Deutsche Forschungsgemeinschaft (DFG), at the Technische Universität Darmstadt. The purpose of this project is the calibration of safety factors in order to achieve the target reliability for safe and efficient design. Realistic modelling of the load-bearing behaviour of slender UHPC columns requires material and geometric nonlinearities to be considered. Material nonlinearity describes stiffness reduction with increasing load intensity while geometric nonlinearity results from second order effects. Due to the load-dependent material behaviour, a sudden stability failure may occur long before the material's strength is exceeded. An adequate analysis of this phenomenon calls for realistic material laws. As a first step, calculation results at cross-sectional level can be used to identify the sensitivity of the parameters. Therefore, specific moment-axial force-diagrams and moment-curvature-diagrams, which are based on stochastic simulation methods, are being developed to identify the influence of compressive strength on the load-carrying behaviour of a structural member with rectangular cross-section. Moreover, the calculations are verified by experimental test series of slender columns. On the basis of the results of this research project, innovation potentials and limits of application of UHPC will be discovered.

Keywords: ultrahigh-performance concrete, probabilistic design, slender columns, safety, reliability

1 Modelling of slender UHPC columns

General

Realistic modelling of the load-bearing behaviour of slender reinforced concrete columns requires material and geometric nonlinearities to be considered. Material nonlinearity describes stiffness reduction with increasing load intensity while geometric nonlinearity results from second order effects. Due to the load-dependent material behaviour (moment-curvature-relationship) a sudden stability failure may occur long before the material's strength is exceeded. In this case, we talk about stability failure due to load-dependent stiffness reduction. Correct analysis of this phenomenon calls for realistic material laws both for the stress-strain-relationships of concrete and reinforcing steel as well as for the variation of the modulus of elasticity. The stochastic finite element program developed by Heimann&Tran takes this phenomenon accurately into account and has been checked by comparison of numerical and experimental results.

Concrete

Concerning the probabilistic model of ultrahigh-performance concrete it has to be mentioned that in the past statistical information about the scatter of compressive strength was rarely available. A former study by Tue et. al. [1] delivered interesting findings about the standard deviation of concrete compressive strength. One important finding was that the standard deviation of concrete compressive strength of UHPC compared to high-strength concrete (HSC)

is not as high as expected. Compared to earlier studies (e.g. Rüsch [2]) it was possible to see that the standard deviation of concrete compressive strength of HSC has decreased by about 1.2 MPa because of the use of ready-mixed concrete instead of in-situ concrete. Furthermore the standard deviation of concrete compressive strength of HSC is only marginally higher than that of normal strength concrete (NSC) with 5 N/mm². Investigations of several experimental test series at the research laboratory for concrete structures at the Technische Universität Darmstadt confirm these results. Based on the results of the experimental test series, idealized stress-strain-relationships were formulated for two different mixtures of UHPC (cp. Fig. 1). The scatter in the area of increasing stress-strain-relationship can be neglected, but in the area of decreasing stress-strain-relationship the scatter is distinctive. Therefore, mean stress-strain-relationships were formulated with limit points σ_{cu}/σ_{c1}=0,125 and $\varepsilon_{cu}/\varepsilon_{c1}$=2,305 for UHPC with fine grain aggregate and σ_{cu}/σ_{c1}=0,183 and $\varepsilon_{cu}/\varepsilon_{c1}$=2,136 for UHPC with basalt aggregate.

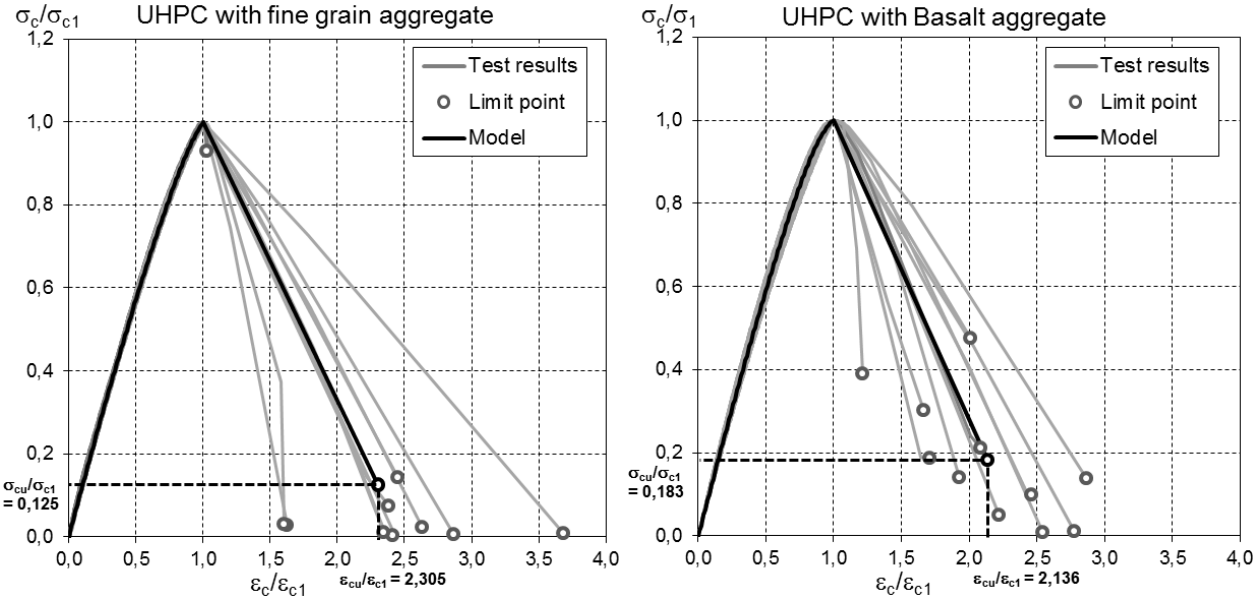

Figure 1: normed stress-strain-relationship of UHPC with fine grain aggregate and with basalt aggregate.

In addition to this assumption, the following relationship between the secant modulus of elasticity E_c at approximately ~0.4·f_c and compressive strength f_c has been used

$$E_c = \alpha_E \cdot f_c^{1/3} \qquad (1)$$

The mean value of the parameter α_E was set to 9.350 [-] for both concrete mixtures. A lognormal distribution with a coefficient of variation of $v_{\alpha E}$ = 0.05 [-] for UHPC with fine grain aggregate and $v_{\alpha E}$ = 0.045 [-] for UHPC with basalt aggregate was used to fit the test results. The basic variable α_E thus represents the scatter of modulus of elasticity E_c independent of compressive strength f_c.

Reinforcing steel

The yield strength of reinforcing steel f_y is described by a lognormal distribution with a coefficient of variation of v_{fy} = 0.06 [-]. The mean value for steel grade S500 amounts to μ_{fy} = 550 [MPa]. The scatter of the steel modulus of elasticity E_s is very small and is thus neglected in subsequent investigations. The scatter of the geometric dimensions of the reinforcing bars is small as well. Its mean value complies with the nominal value μ_{As} = nom A_s and the coefficient of variation is taken to be v_{As} = 0.02 [-]. The distribution type is normal according to the recommendation of the JCSS Probabilistic Model Code P.3 [3].

Geometric dimensions

The nominal cross-sectional dimensions h_{nom}/b_{nom} correspond to their mean values $\mu_{h,b}$. The standard deviation depends on the size of the cross-sectional dimensions and is assumed to be $\sigma_{h,b}$ = 5 [mm]. The effective depth d depends on the specific cross-sectional height h and the concrete cover c. A normal distribution with a mean value equal to the nominal value and a standard deviation of 5 [mm] was used as stochastic model for the concrete cover c. The column height is assumed to be deterministic, because slenderness λ is formulated as constant in the investigations.

Stochastic parameters

Table 1 shows the statistical parameters and adopted probabilistic density functions of the basic variables. UHPC-specific parameters were determined by experimental testing. All remaining parameters have been modelled according to the Probabilistic Model Code [3]. In this study only the influence of material and geometry were investigated. The model uncertainty is one of the most important influence parameter, but will only effect the overall reliability of the structural system and not the relation between the scattering of material and geometry parameters.

Table 1: Statistical parameters of the basic variables.

class	Variable	distribution	Mean value	Std.-deviation	Var.-coefficient
concrete	f_c^{fine}	LN	>150 N/mm²	-	0,060
	f_c^{basalt}	LN	>150 N/mm²	-	0,113
	ε_{c1}^{fine}	LN	-3,80 ‰	-	0,100
	$\varepsilon_{c1}^{basalt}$	LN	-3,92 ‰	-	0,075
	ε_{c1u}^{fine}	LN	-8,79 ‰	-	0,326
	$\varepsilon_{c1u}^{basalt}$	LN	-8,40 ‰	-	0,258
	α_{ct}	LN	0,30	-	0,300
	α_E^{fine}	LN	9.350	-	0,049
	α_E^{basalt}	LN	9.350	-	0,045
reinforcement	f_y	LN	550 N/mm²	-	0,060
	A_s	N	$A_{s,nom}$	-	0,020
geometry	h	N	h_{nom}	5 mm	-
	b	N	b_{nom}	5 mm	-
	c	N	a_{nom}	5 mm	-
load	G	N	G_m	-	0,100
	Q	Gumbel	Q_k/1,746	-	0,400
model uncertainty	ξ	under development, based on experimental test results			

2 Identification of important basic variables

Preliminary remark

In order to identify the sensitivity of important variables, a parametric study was carried out at cross-section level. The study was split into three parts. In part 1 specific moment-axial force diagrams were constructed to analyze the scatter of m-n-interaction. In part 2 moment-curvature-relationships were calculated to identify important variables for structural members made of UHPC. At least, the calculation results were compared with results based on material laws according to EC-2 Part 1-1 [4]. The study was carried out for structural members with rectangular cross-section. UHPC-specific parameters were determined by experimental testing.

Parametric study at cross-section level

As previously described, part 1 of the study focuses on the calculation of moment-axial force-combinations to analyze the scatter of the m-n-interaction. Therefore, stochastic simulations were carried out for different types of concrete. An example for a specific moment-axial force-diagram is given in Fig. 2, using normalized moments μ and forces ν. The following variables have been modeled as random: concrete strength, yield and tensile strength of reinforcement, section height, cross sectional-width, concrete cover, diameter of reinforcing bar, maximum concrete strain and the modulus of elasticity of concrete.

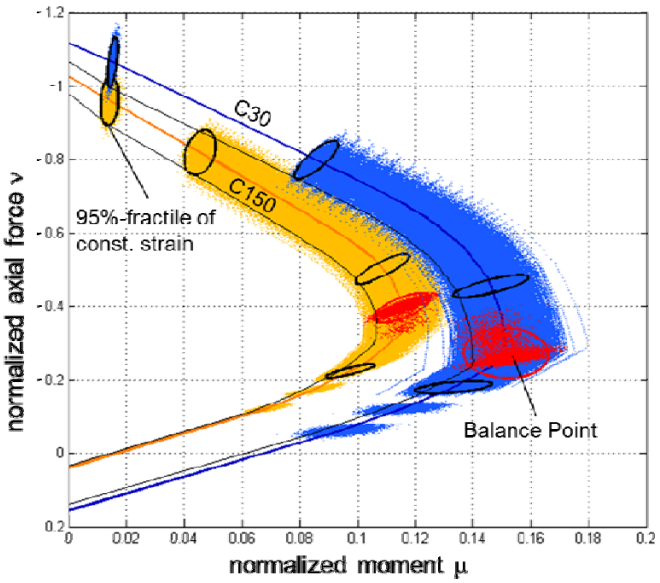

Figure 2: Specific moment-axial force-diagram.

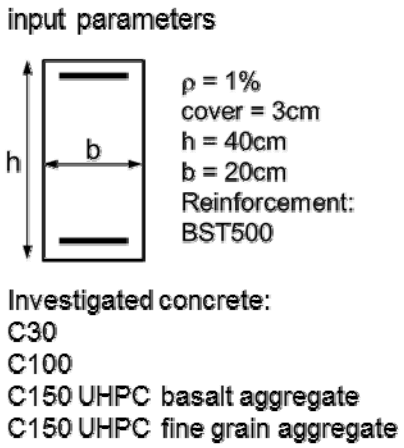

Figure 3: Input parameters for the study.

The normalized axial force is defined by $\nu = N / (h_m \cdot b_m \cdot f_{cm})$ and the normalized moment by $\mu = M / (h_m^2 \cdot b_m \cdot f_{cm})$. The black ellipses represent the 95%-fractile of a specific strain state. The solid lines represent the m-n-combinations, calculated for two different concrete types on basis of the mean values of the variables. The diagram illustrates that the m-n-interaction of UHPC is comparable to normal concrete (NSC). The scattering balance point of UHPC is also comparable to the balance point of NSC. The range of application of slender columns can be found between a normalized normal force of $-0.2 \leq \nu \leq -1.0$. Therefore, the following studies focus only on this range of application.

The intention of part 2 was to identify important variables on the m-κ-behaviour of structural UHPC members. For this purpose, a calculation of scattering moment-curvature-diagrams was carried out with the help of stochastic finite element calculations. Fig. 4 exemplarily illustrates such a diagram based on the input parameters according to Fig. 3. The diagram has been drawn for $\nu = -0.4$. The solid line ellipses around the characteristic points (compressive yield point, concrete crack point, yield point, bearing capacity limit) define the 95%-fractiles. To start with, only one basic variable per sample was considered as random and different scattering diagrams were calculated for each variable.

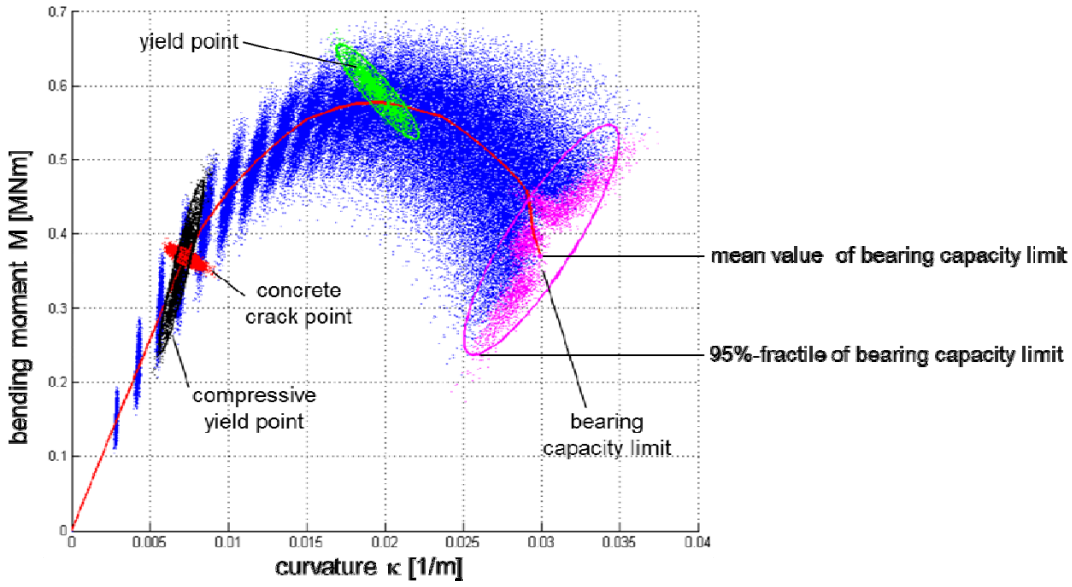

Figure 4: Scattering moment-curvature-diagram (ν = -0.4).

In order to compare these results and estimate the influencing variables, two parameters were calculated. The first parameter (V_{Rmax}) is the coefficient of variation of the bearing capacity limit. The second parameter (V_{Mmax}) is the coefficient of variation of the maximum moment. Fig. 5 shows the results for the parameters V_{Rmax} and V_{Mmax} calculated for a rectangular cross-section and two different UHPC mixtures.

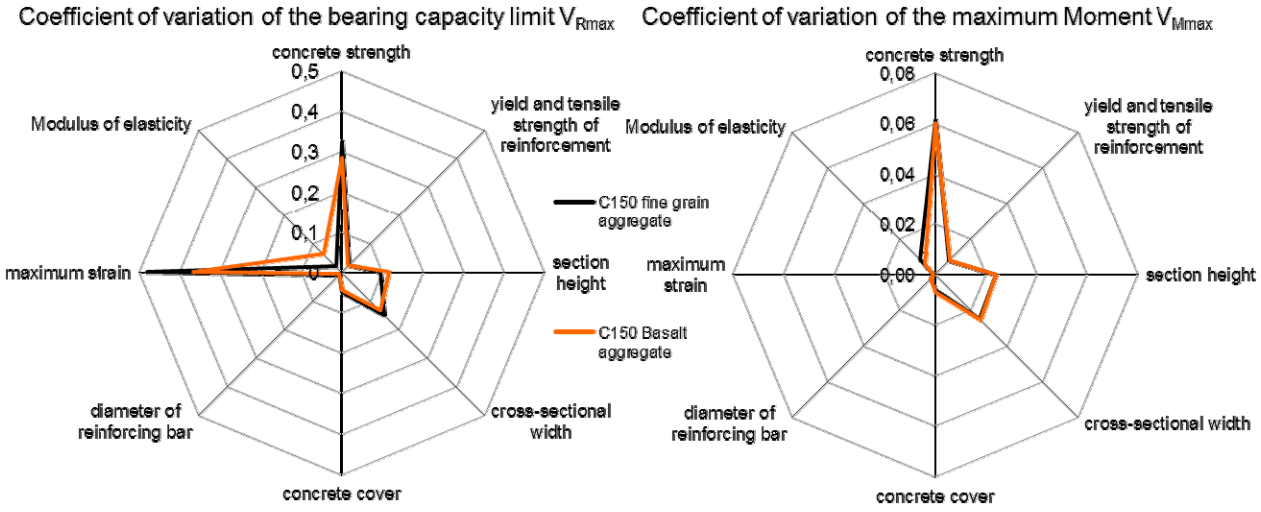

Figure 5: V_{Rmax} (lhs) and V_{Mmax} (rhs) for UHPC.

It is obvious, that in the area of the maximum moment (V_{Mmax}), the maximum concrete strain is nearly insignificant compared to V_{Rmax}. Furthermore, the variables regarding the reinforcement are of minor importance, both for V_{Rmax} and V_{Mmax}. The modulus of elasticity has also a low influence due to the calculation at cross-section level. The modulus of elasticity is taken into account only in the stress-strain-relationship of the concrete model; a more significant influence is to be expected at system level. Figure 6 illustrates the coefficient of variation of the bearing capacity limit V_{Rmax} for NSC, HSC and UHPC. It can be seen, that at cross-sectional level the variations of concrete strength, concrete cover, cross-sectional width and section height are much more significant with UHPC compared to NSC and HPC. Considering all variables as random emphasizes the importance of concrete strength, because V_{Rmax} is approximately the same when all variables or concrete strength alone are taken as random.

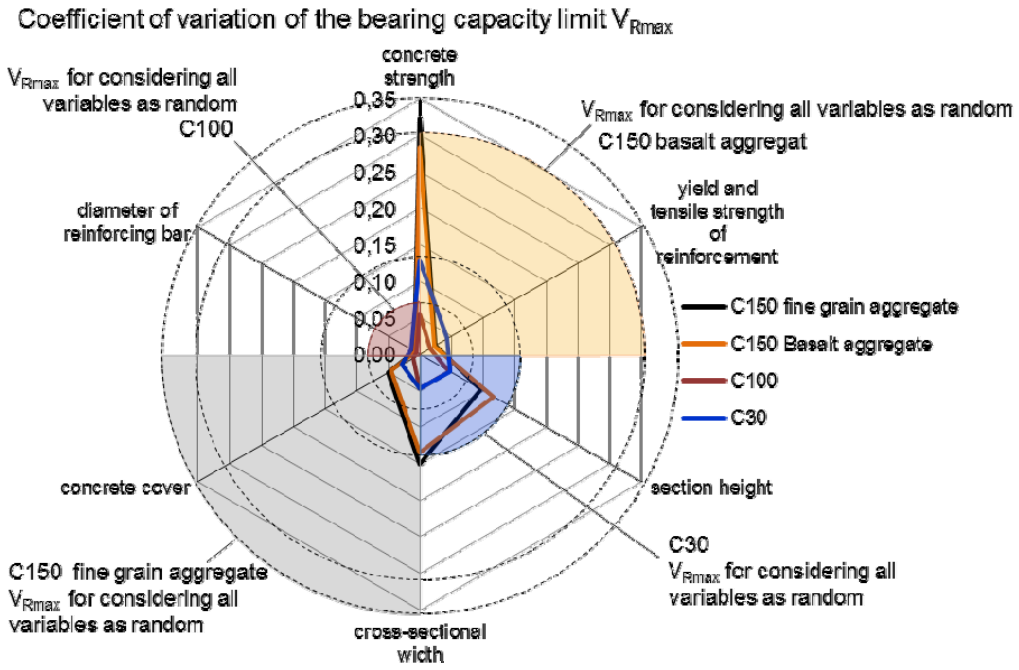

Figure 6: V_{Rmax} for NSC, HSC and UHPC.

3 Reliability analysis

General

As previously described, it has to be expected that the load-dependent material behaviour of UHPC may cause a sudden stability failure long before the material's strength is exceeded. Because of this phenomenon, reduced reliability is to be expected as already shown by Schmidt/Six [5] for HSC. This case of failure is not considered in the current design concept for concrete columns. In order to identify the reliability level, stochastic analyses at system level will be carried out considering the characteristics of UHPC. The reliability analysis will concentrate on short (slenderness ratio $\lambda = 0$) and slender (slenderness ratio $\lambda \geq 80$) UHPC columns with a nominal compression strength of f_{ck} = 150 MPa. The cross-sectional dimensions will be chosen according to common fields of application, such as rectangular and circular cross-sections, but innovative concepts such as hollow columns will also be considered. In a first step, the total reinforcement ratio will be defined as ρ_{tot} = 1%. Further parameters are the eccentricity ratio e/h of the applied axial load as well as the ratio of characteristic live to dead load Q_k/G_k.

First of all, the design value of bearing capacity is calculated for each column type according to the safety format of Eurocode 2 [4]. Taking an economical design approach, the design value of bearing capacity is equal to the design value of the applied load combination:

$$R_d = E_d = \gamma_G \cdot G_k + \gamma_Q \cdot Q_k \qquad (2)$$

If the ratio of characteristic live load to characteristic dead load Q_k/G_k is known, the mean value of the dead load can be calculated as

$$\mu_G = G_k = \frac{R_d}{\gamma_G + Q_k / G_k \cdot \gamma_Q} \qquad (3)$$

As a first step, the coefficient of variation is taken to be v_G = 0.10 [-]. The mean value of the live load μ_Q is given by the annual 95%-fractile of the extreme value distribution I (Gumbel) assuming a coefficient of variation of v_Q = 0.40 [-]:

$$\mu_Q = \frac{Q_k}{1-(\gamma + \ln(-\ln 0{,}95)) \cdot \sqrt{6} \cdot v_Q / \pi} = \frac{Q_k}{1{,}746} = \frac{Q_k / G_k}{1{,}746} \cdot \mu_G \qquad (4)$$

The ratio of characteristic live load to dead load Q_k/G_k is determined to be either 0.25 or 1.00. The calculation of failure probabilities p_f and safety index β for a reference period of 50 years as well as the sensitivity factors α^2 (influence of each basic variable on the probability of failure) is carried out with the help of a variance-reduction based sampling method (AIS).

Stochastic analysis of UHPC columns

The main focus of stochastic simulations is the implementation of a numerical model for UHPC columns. Realistic modelling of load bearing behaviour requires consideration of material and geometric nonlinearities, such as effects of second order theory or tensile strength of concrete and reinforcement (tension stiffening effect). The previously developed numerical method at cross-sectional level is based on an optimized Gaussian-Integral cross-section calculation. The finite element method used at system level is adapted by the procedure of field transfer matrices (Tran [6]) and is still under development. The calculation results will be verified by experimental test rersults of slender NSC, HSC and UHPC columns.

4 Experimental tests on slender columns

General

Accompanying the numerical calculations, experimental tests were carried out on slender columns. In order to test columns with a high ratio of slenderness ($\lambda \geq 80$) the cross-setional dimensions have to be relatively small (h/b/l = 12cm/12cm/278cm) due to the capacity of the laboratory's mechanical equipment. The columns are loaded in a position-controlled component test by a hydraulic cylinder. During the test, deflections and compressions of reinforcement, concrete and structural system are measured with strain gauges and displacement sensors at more than 20 measuring points. In addition to these tests, investigations on compressive strength, flexural strength and modulus of elasticity of UHPC were carried out.

Test results

In order to adequately estimate the model uncertainties, the number of samples should be maximized. Because of this, more than 10 columns were tested at TU Darmstadt. Figure 7 illustrates a slender column in different loading states of 300, 518 and 330 kN as well as the force-deflection-relationship of the experimental test.

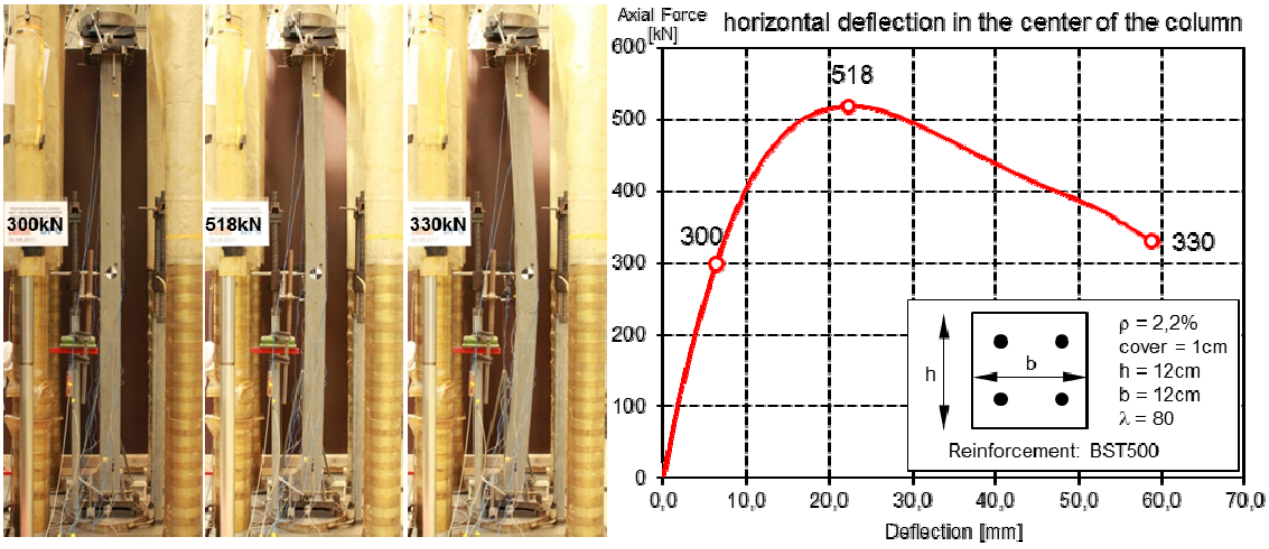

Figure 7: Slender UHPC column in different loading states.

Figure 8 illustrates the axial force of the hydraulic cylinder dependent on axial compression of the column for NSC and UHPC. It is obvious that the maximum axial force of the UHPC column is higher than that of the same column type made of NSC. Much more interesting is that, also in the case of fiber-reinforced UHPC, system behaviour can be characterized as brittle. Hence, the nearly linear trend of the axial force-compression-relationship confirms the doubts about an increasing risk of failure due to less ductile system behaviour.

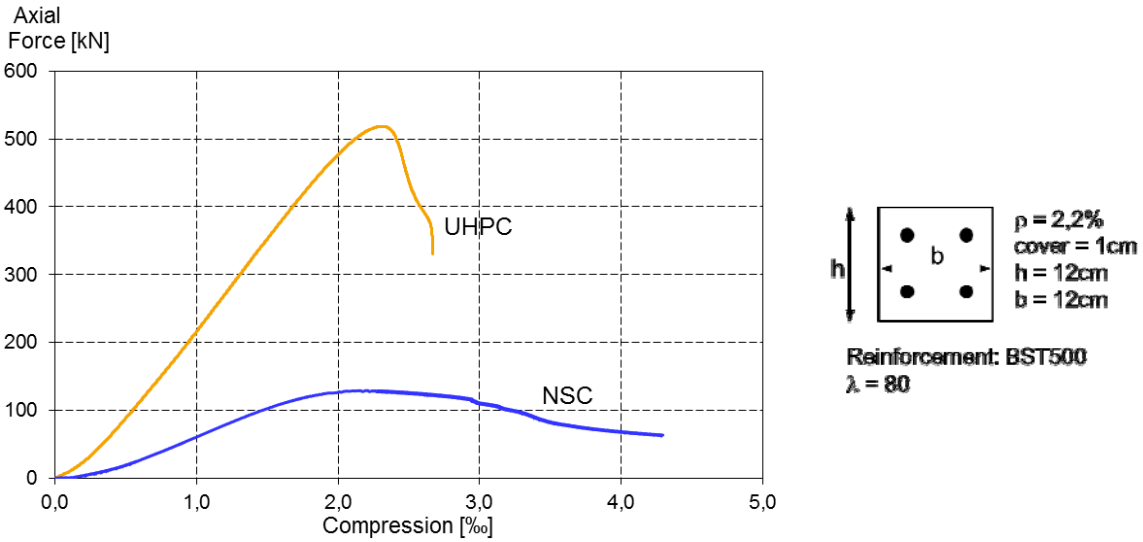

Figure 8: Behaviour of NSC and UHPC column.

5 Conclusions and Outlook

This paper deals with probabilistic modelling and experimental testing of UHPC columns. The reliability analysis of slender UHPC columns considered new statistical parameters concerning UHPC compressive strength and concrete strain, as well as the modulus of elasticity. Stochastic simulations were carried out, taking into account the special characteristics of UHPC at cross-sectional level. As expected, the results of the parametric studies identified concrete strength as highly sensitive, while the variables of reinforcement are insignificant. After that, a concept for extending the results from cross-sectional to system level is presented. The appropriate stochastic finite element tool is still under development, but first comparisons of numerical and experimental results on slender NSC, HPC and UHPC columns show very good coincidences. After completion and verification of the stochastic model at system level, the relevant influencing factors will be identified and a proposal for the design of slender UHPC columns will be presented.

References

[1] Tue N.V., Schenk G., Schwarz J.: Eine kritische Betrachtung des zusätzlichen Sicherheitsbeiwertes für hochfesten Beton. Bauingenieur, Band 82, Januar 2007.

[2] Rüsch H.: Statistische Analyse der Betonfestigkeit. Band 206 des Deutschen Ausschusses für Stahlbeton DAfStb. Berlin: Ernst & Sohn, 1969.

[3] JCSS Probabilistic Model Code Part 3 Resistance Models, Joint Committee of Structural Safety, 2001.

[4] EN 1992-1-1 EUROCODE 2: Design of concrete structures - Part 1-1: General rules and rules for buildings, European Committee for Standardization, 2012.

[5] Six M., Schmidt H.: Probabilistic Modelling of HSC Slender Columns in High-Rise Buildings, IABSE Symposium 2008, Creating and Renewing Urban Structures, Chicago, USA, 2008.

[6] Tran N.L.: Berechnungsmodell zur vereinfachten Abschätzung des Ermüdungsverhaltens von Federplatten bei Fertigträgerbrücken, Dissertation Heft 20, Technische Universität Darmstadt – Institut für Massivbau, Mai 2011.

Ultra-High Performance Spun Concrete Columns with High-Strength Reinforcement

Corinna Müller[1], Martin Empelmann[1], Helmut Lieb[2], Florian Hude[3]

1: Institute for Building Materials, Concrete Construction and Fire Protection (iBMB), Concrete Construction Department, TU Braunschweig, Germany
2: Europoles GmbH & Co. KG, Neumarkt, Germany
3: Stahlwerk Annahütte, Hammerau, Germany

Slender columns are frequently used construction elements within modern architectural buildings. Beside of the light and filigree appearance the effective rental area and flexibility of buildings can be increased by downsizing of the columns cross section. Nowadays such columns are usually made off steel or steel composite. The competitiveness of reinforced concrete can be increased considerably with the use of high performance materials such as ultra-high performance concrete and high-strength reinforcement steel combined in spun concrete columns. The paper will give an overview of the experimental research work which included short- and long-term material analyses of ultra-high performance concrete and high-strength reinforcment steel, pull-out test to investigate the bond behavior and full-scale column tests under eccentric normal forces.

Keywords: highly reinforced spun concrete columns, ultra-high performance concrete, high-strength reinforcement

1 Introduction

Within a ZIM (Zentrales Innovationsprogramm Mittelstand) research project, founded by the BMWi, the iBMB of the TU Braunschweig and the companies Europoles and Stahlwerk Annahütte investigated an innovative concrete column construction for very slender columns (Fig. 1), which is based on the special production process of the spun concrete. In this connection the advantages of spun concrete should be further increased with the use of cost-optimized ultra-high performance concrete (UHPC) and high-strength reinforcement SAS 670 resulting in a technically and economically comparable alternative to steel-composite columns.

Figure 1: Examples for slender spun concrete columns made by Europoles (left to right: Haus der Ärzteschaft, Düsseldorf (© A. M. van Treeck); IKEA, Dresden; Department for Foreign Affairs, Berlin).

2 Production process of spun concrete columns

The production process of spun concrete columns is characterised by the rotation of a pipe-shaped steel form with a speed of up to 600 rpm around its longitudinal axis (Fig. 2). The induced radial acceleration forces press the concrete mass with a centrifugal force of 20 G against the walls of the form and thus are compacting the concrete. The special production process results into concrete elements with an absolutely smooth concrete surface, a dense concrete structure, which is free of visible pores, and a high concrete compressive strength, even with very small cross-sections.

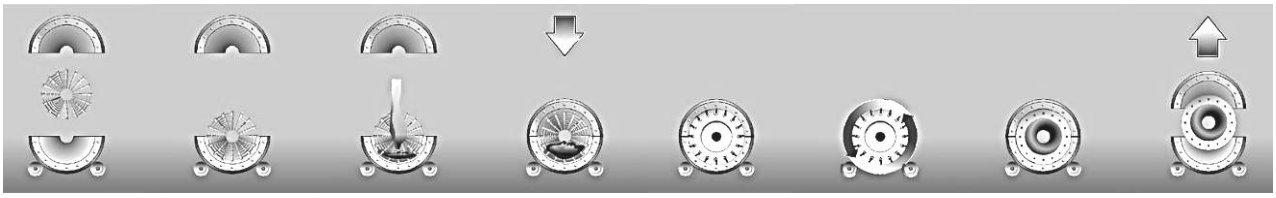

Figure 2: Production process of spun concrete columns.

3 Material properties

As both used materials, UHPC and SAS 670, are currently not standardized, the material properties had to be investigated for the theoretical assessment of the experimental full-scale column tests and for the definition of characteristic material and design values.

Short-term behaviour of ultra-high performance spun concrete

For the determination of the material properties of UHPC a lot of drilling cores (Ø55 mm, slenderness ratio ≥ 2) were removed from vibrated concrete and spun concrete specimens. Tables 1 and 2 contain an abstract of the experimental results. The compressive strength tests were performed with a force controlled loading with a speed of 0.6 N/mm²/s according to [1].

Table 1: Material properties of vibrated concrete drilling cores (concrete age: 28d ± 1d) – abstract.

Concreting No.	f_{cm} [N/mm²]	Var(f_{cm}) [%]	f_{ctm} [N/mm²]	Var(f_{ctm}) [%]	E_{cm} [N/mm²]	Var(E_{cm}) [%]
1 (03/08/11)	141.5	2.7	7.9	1.1	57 800	9.6
2 (18/08/11)	141.4	4.7	-	-	-	-
3 (25/08/11)	140.8	3.1	-	-	54 100	1.8

Table 2: Material properties of spun concrete drilling cores (concrete age: 28d ± 1d) – abstract.

No.	f_{cm} [N/mm²]	Var(f_{cm}) [%]	f_{ctm} [N/mm²]	Var(f_{ctm}) [%]	E_{cm} [N/mm²]	Var(E_{cm}) [%]
1 (03/08/11)	143.1	1.5	8.7	4.2	59 600	2.9
2 (18/08/11)	156.3	2.9	-	-	68 700	1.6
3 (25/08/11)	151.9	1.8	-	-	56 700	1.0

The variation coefficient of the concrete strength within the three casting series amount to 4 % approximately. For the vibrated ultra high performance concrete (UHPC) the statistical evaluation of the compressive strength resulted in a short-term characteristic value (5 % quantile for a normal distribution) of 130 N/mm²; for the ultra high performance spun concrete (UHPSC) in 140 N/mm² respectively. Hence, the influence of the producing process on the concrete strength of UHPSC was determined to 8 % approximately.

Fig. 3 shows the stress-strain relationship of the spun concrete determined on drilling cores from two different castings under a displacement controlled loading with a speed of 0.001 mm/s.

The plasticity coefficient k (relation between tangent and secant elasticity modulus) ranges between 1.1 and 1.35 and characterizes, beside the maximum compression stress f_{cm} and the failure strain ε_{c1} (approximately 3.0 ‰), the stress-strain relationship under compression. In conclusion, the tests results allow the application and modification of the mathematical formulation for non-linear calculations according to [2] (Eq. 1) for the UHPSC.

$$\frac{\sigma_c}{f_{cm}} = \frac{k \cdot \frac{\varepsilon_c}{\varepsilon_{c1}} - \left(\frac{\varepsilon_c}{\varepsilon_{c1}}\right)^2}{1 + (k-2) \cdot \frac{\varepsilon_c}{\varepsilon_{c1}}} \qquad (1)$$

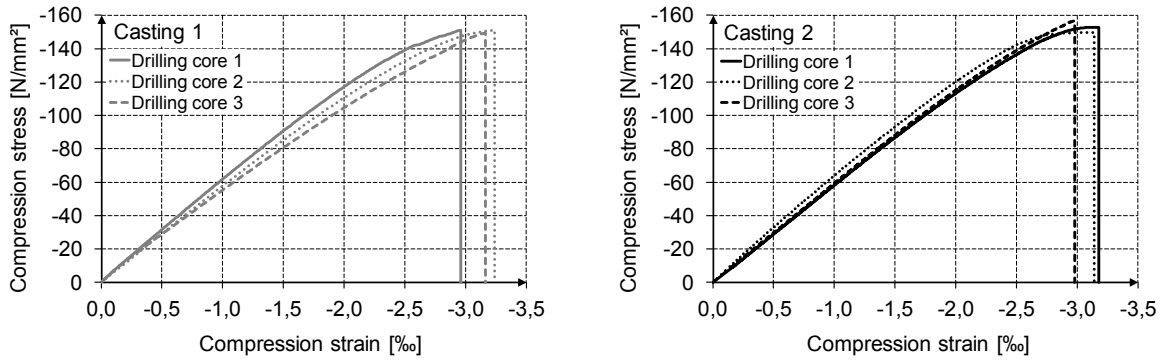

Figure 3: Stress-strain relationship of the ultra high performance spun concrete (UHPSC).

Long-term behaviour of ultra-high performance spun concrete

The design value of the concrete strength is obtained from the short-term characteristic concrete strength with the consideration of the material safety factor of concrete and the long-term coefficient α_{cc}. Eurocode 2 [2] recommends a value of α_{cc} = 1.0, the German annexe to Eurocode 2 [3] defines a value of α_{cc} = 0.85. In Fig. 4 the development of the compression strain and the creep coefficient of the spun concrete for a compression level of approximately 90 % of the mean value of the compressive strength are given. A comparable long-term behavior for UHPC under high compression is presented in [4]. As the developed UHPSC showed a favourable long-term behaviour compared to those of normal strength concrete, the value of α_{cc} = 0.85 is expected to be on the conservative side [4].

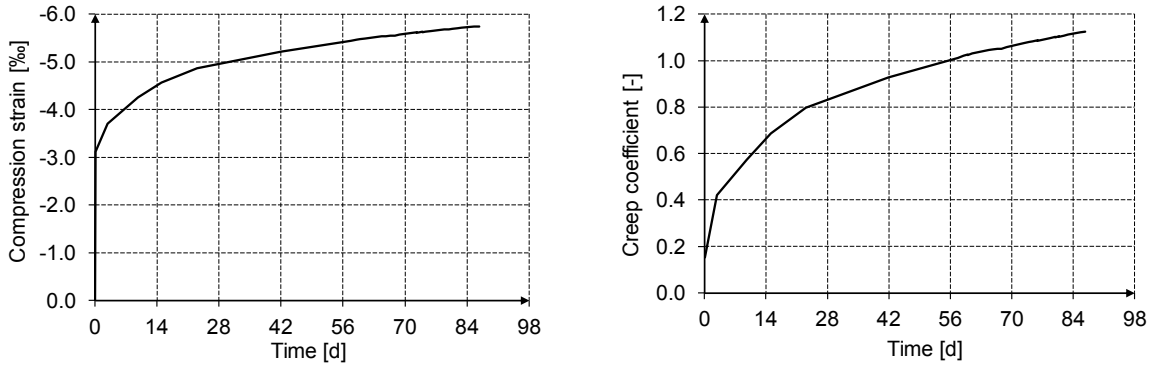

Figure 4: Development of the compression strain (left) and the creep coefficient (right) (21°C, 50 % RH, $f_c = 0.9 \cdot f_{cm}$).

High-strength reinforcement

High strength steel can either be microalloyed or water tempered. The advantages of water tempering are lower costs and a sufficient tensile strength to yield strength ratio. The advantage of microalloying is a higher tensile strength to yield strength ratio. High strength reinforcement

SAS 670 is water tempered and has a not well defined yield point (Fig. 5 (left)). Under compression stress the high-strength reinforcement SAS 670 has a linear-elastic stress-strain relationship up to a strain of approximately 2.5 ‰. Beside the higher strength of SAS 670 the key differentiator to normal strength reinforcement is the shape of the ribs, which allow to continuously screw the bar (Fig. 5 (middle)). Accessories, like couplers and end bearing anchorages, help to improve the reinforcement detailing by reducing the anchorage and overlapping length and increasing the clear spacing between the single bars. The available bar diameters of the high strength reinforcement SAS 670 are given in Fig. 5 (right).

The other material properties have the same characteristics as known from normal strength reinforcement. In detail these are: ductility, bend- and weldability, sufficient bond behaviour and a sufficient resistance against stress corrosion.

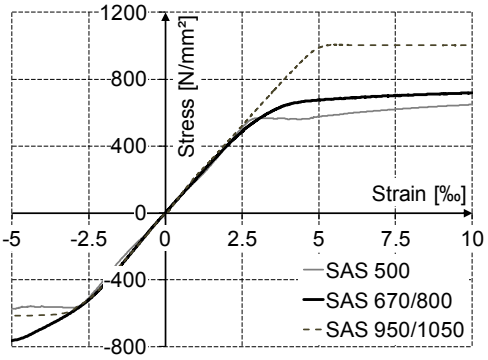

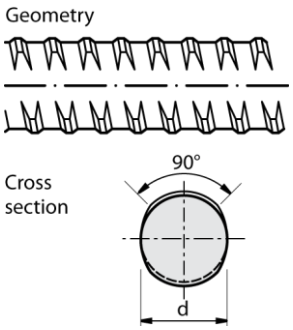

Nominal diameter	Mass	Nominal cross section
d_s [mm]	M [kg/m]	A_s [mm²]
18	2,00	254
22	2,98	380
25	3,85	491
28	4,83	616
30	5,55	707
35	7,55	962
43	11,40	1.452
57[5]	20,38	2.597
63[5]	24,86	3.167
75	34,68	4.418

Figure 5: left: Stress-strain relationship for different steel grades; middle: Geometry of bars; right: Nominal values for grade SAS 670.

4 Bond behaviour

For the specifcation of the bond behaviour of SAS 670 with UHPSC pull-out tests with different reinforcement diameters, concrete covers, concrete grades and test specimen geomentry (spun concrete segments (Table 3) and cubes) were carried out according to [5].

Table 3: Variation parameters of pull-out tests (∅18 mm).

No.	Description	Spun concrete segment
P1	according to [6]	
P2	UHPC and SAS 670, cube specimen (side length 190 mm) incl. spiral reinforcement	
P3	C 50/60 and SAS 670, cube specimen (side length 190 mm) incl. spiral reinforcement	
P4-1	UHPC and SAS 670, spun concrete pie piece, concrete cover $1d_s$	
P4-2	UHPC and SAS 670, spun concrete pie piece, concrete cover $2d_s$	

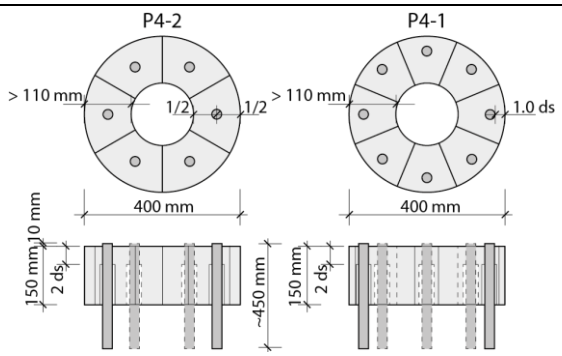

Due to the ultra-high strength of the spun concrete and the production process the layout of the test specimens has to be modified. In [5] a bond length of $5 \cdot d_s$ is recommended. Previous pull-out tests from literature were performed with a bond length between $1 \cdot d_s$ and $2 \cdot d_s$. In this connection a short bond length induces a wide scatter of the bondstress-slip curve; a long bond length induces an early splitting failure of the test specimens. Based on the conclusions in the literature a bond length of $2 \cdot d_s$ was chosen. The parameter variation of the pull-out tests with a bar diameter of 18 mm are given in Table 3.

The results for bars ∅18 mm are summarised in Fig. 6 (left). The bond strength of UHPSC is remarkable higher than for normal strength concrete. The relative bond stress (bond stress over concrete strength) (Fig. 5 (right)) at a slip of 0.1 mm is lower due to the higher splitting effects of UHPSC.

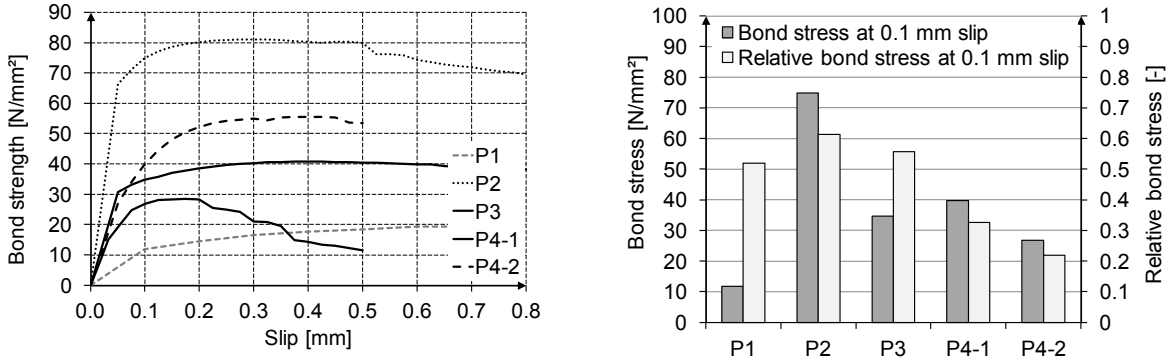

Figure 6: left: Experimental bond stress-slip curve; right: Bond and relative bond stress at 0.1 mm slip.

5 Full-scale column tests

Experimental program and test set-up

In total, 16 spun concrete column tests were conducted under an eccentric normal force loading (Fig. 7). In order to investigate the ultimate load level and the post failure modes all columns were tested under a displacement controlled loading. Beyond a load level of approximately 60 % of the ultimate load a loading speed of 0.001 mm/s was chosen. The concrete strains were determined by strain gauges in five points over the longitudinal axis in the bending direction as well as in lateral direction. The bending deflection was measured by displacement transducer (DT) in three points arranged oppositely in the bending axis.

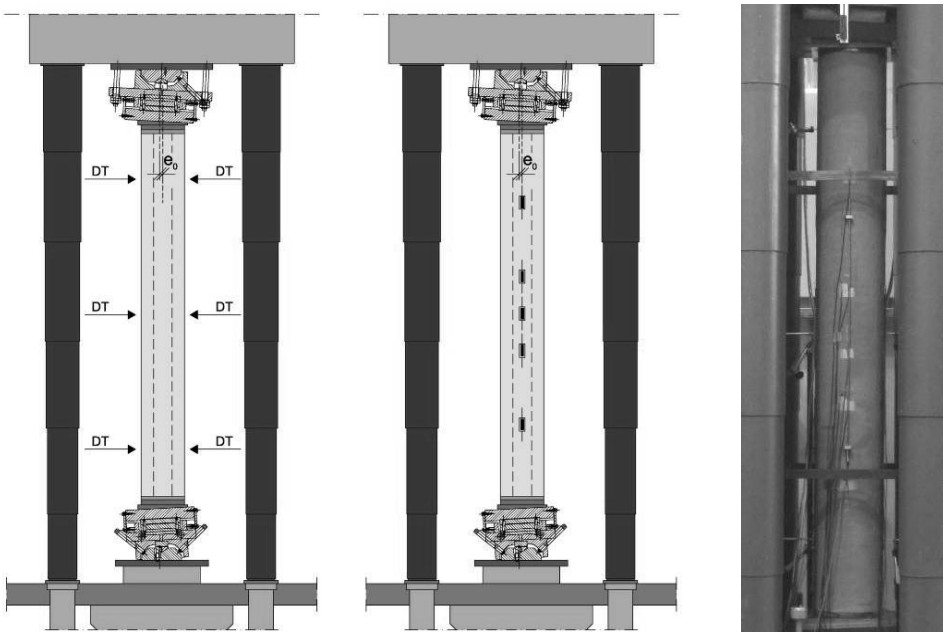

Figure 7: Test set-up (Arrangement of displacement transducer and strain gauges; built-in test specimen).

The varied parameters in the full-scale column tests were the outer column diameter, the column length, the initial eccentricity (e_0), the concrete strength and steel grade as well as the longitudinal and spiral reinforcement content (ρ_l, ρ_q). This paper presents only an abstract of the experimental investigations (Table 4).

Table 4: Variation parameters full-scale column tests – abstract.

No.	Diameter / Length [cm]	Longitudinal reinforcement SAS 670	ρ_l [%]	Spiral reinforcement BSt500S	ρ_q [%]	e_o [mm]
V3-1	25 / 200	6∅25	7	∅5/5[5]	0.6	10
V3-2	25 / 200	6∅25	7	∅5/3	0.9	10
V4-1	25 / 200	6∅25	7	∅5/5[5]	0.6	25
V4-2	25 / 200	6∅25	7	∅5/3	0.9	25
V5-2	35 / 300	12∅18	4	∅8/5	1.0	35
V6-2	35 / 300	12∅35	15	∅8/5	1.0	35

Experimental results

Table 5 summarizes the results of the 6 column tests in regard to the failure normal force N_u, the eccentricity at the end of the test e_{tot} (= e_o + e_2), the compression strain at the higher compressed cross section side in the middle of the column (ε_{c1}) and at the opposite side (ε_{c0}) as well as the description of the main failure mode.

Table 5: Overview of the experimental results – full-scale column tests.

No.	N_u [kN]	e_{tot} [mm]	ε_{c1} [‰]	ε_{c0} [‰]	Main failure mode
V3-1	4545	16.0	-2.92	-0.77	[1) 2) 3)]
V3-2	5038	19.0	-3.50	-0.76	[1) 2) 3)]
V4-1	4030	35.9	-3.37	-0.05	[1)]
V4-2	4271	37.3	-3.84	0.08	[1)]
V5-2	6658	49.2	-3.03	0.09	[1) 2) 3)]
V6-2	9628	51.6	-3.31	-0.03	[1)]

[1)] concrete cover spalling; [2)] buckling longitudinal reinforcement; [3)] rupture spiral reinforcement

The comparison of the test specimens V3-1 with V3-2 and V4-1 with V4-2 (equal longitudinal reinforcement content and eccentricity e_0, but different spiral reinforcement content) indicates that an increase of the spiral reinforcement content results into an increase of the ultimate compressive strain of approximately 0.5 ‰. In consequence, the columns with higher spiral reinforcement obtained a higher ultimate load level caused by the increased utilization of the concrete cross-section and of the longitudinal reinforcement.

Fig. 8 (left) shows the comparison of the load-deflection relationship of the test specimens indicating firstly a linear-elastic increase and then only a slight non-linearity up to maximum load level. The post-peak behaviour beyond the maximum load level of the columns is presented in Fig. 8 (right).

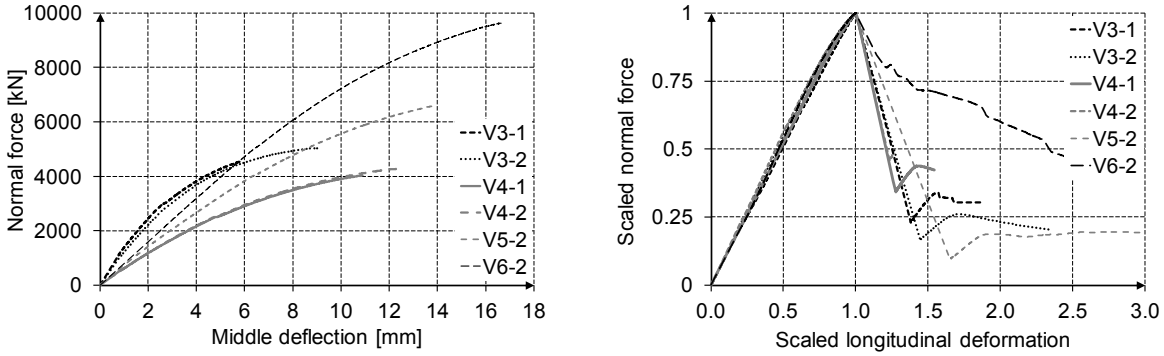

Figure 8: left: Load-middle deflection relationship; right: Scaled load-longitudinal deformation relationship.

In order to compare the different column configurations the normal force is scaled to the maximum load and the longitudinal deformation to the longitudinal deformation at the maximum load level showing that the post-fracture behavior of the test specimen improves with increased longitudinal reinforcement ratio. In case the longitudinal reinforcement content is kept constant a more robust failure mode could be observed with increasing eccentricity and the possibility of stress rearrangement within the cross section.

In all tests the exceedance of the bearing capacity was characterized by an explosive spalling of the concrete cover. In consequence and depending on the strain gradient over the cross section as well as the longitudinal reinforcement content some test specimens showed a buckling of the longitudinal reinforcement and a rupture of spiral reinforcement (Fig. 9 and Table 5).

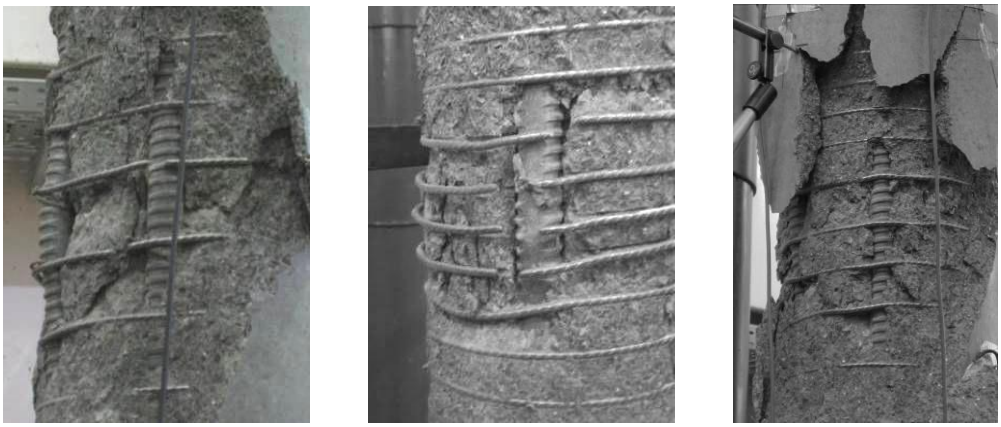

Figure 9: Pictures of the test specimen directly after failure (left: V3-1; middle: V3-2; right: V4-1).

Comparison of experimental and theoretical results

The theoretical investigations were performed on the system level using a non-linear calculation program [7]. For the theoretical analysis the mean value of the materials properties and the stress-strain relationship for the UHPSC according to [2] (Eq. 1) were used. Table 6 and Fig. 10 summarize the theoretical results for the test specimens V3-1 and V4-1. The theoretical investigations of the other test specimen are in process.

Table 6: Comparison of experimental and theoretical results – abstract.

No.	k [-]	$N_{u,cal}$ / $N_{u,exp}$	$e_{2,cal}$ / $e_{2,exp}$
V3-1	1.0	1,03	0.93
V3-1	1.1	1.07	0.96
V4-1	1.1	0.95	1.02
V4-1	1.4	1.0	1.01

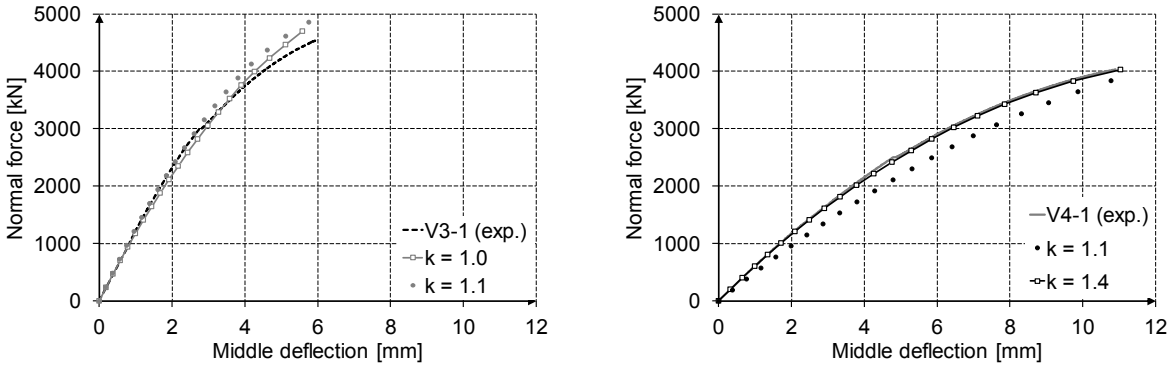

Figure 10: Comparison of experimental and theoretical load-middle deflection behaviour (left: V3-1; right: V4-1)

In case the lower value of the experimentally observed plasticity factor k = 1.1 is used for the determination of the theoretical stress-strain curve of the UHPSC, the theoretical load-deflection curve of V3-1 shows a satisfying agreement with the experimental load-deflection curve. For the test specimen V4-1 a very good agreement can be found using k = 1.4.

6 Conclusions

In order to assure the practical application of innovative ultra-high performance spun concrete columns with high-strength reinforcement experimental and theoretical investigations were carried out at the iBMB of the TU Braunschweig (long- and short-term material properties of UHPSC, full-scale column tests), at Europoles (cost-optimized UHPSC, production process) as well as at Stahlwerk Annahütte (material properties SAS 670, bond behaviour). The main results are:

- The developed UHPSC reached in the production process - without any additional measures - a characteristic compressive strength of 140 N/mm² with a low statistical spread of the mean value. The advantages of the spun concrete technology (smooth surface and dense concrete structure) are maintained using this concrete mixture, also in combination with high longitudinal and spiral reinforcement contents. The definition of the long-term coefficient and the material safety factor for the UHPSC in accordance with the current standards of normal respectively high strength concrete is expected to be on the conservative side.
- The compression stress-strain relationship of the high-strength reinforcement SAS 670 is comparable to those under tension.
- The experimental results of the pull-out tests showed for common concrete covers no negative effects (early splitting), so that the coaction of the UHPSC and the high-strength reinforcement SAS 670 is secured.
- Due to a failure strain of the UHPSC of approximately 3.0 ‰ the higher compressive strength of the SAS 670 compared to those of normal strength reinforcement BSt 500S can be activated in a composite member.
- The results of the present theoretical investigations show that the high bearing loads and the load-deformation behaviour of the experimental column tests can be described in good accordance with adapted state-of-the-art theoretical constitutive laws.

In summary, with the combination of UHPSC and high-strength reinforcement SAS 670 very slender and innovative spun concrete columns can be constructed which achieve high load bearing capacities comparable to those of steel-composite columns with equal cross section.

References

[1] DIN EN 12390-3: Prüfung von Festbeton – Teil 3: Druckfestigkeit von Probekörpern, 2002.

[2] DIN EN 1992-1-1: Eurocode 2: Bemessung und Konstruktion von Stahlbeton- und Spannbeton-tragwerken – Teil1-1: Allgemeine Bemessungsregeln und Regeln für den Hochbau, 2011.

[3] DIN EN 1992-1-1/NA: Nationaler Anhang – Nationale Parameter - Eurocode 2: Bemessung und Konstruktion von Stahlbeton- und Spannbetontragwerken – Teil1-1: Allgemeine Bemessungsregeln und Regeln für den Hochbau, 2011.

[4] Schmidt, M. et al.: Ultahochfester Beton – Sachstandsbericht. DAStb Heft 561, Berlin, 2008.

[5] RILEM RC 6: Bond test for reinforcement steel. 2. Pull-out test, 1983.

[6] Hegger J. et al.: Untersuchungen an Pfählen aus Stahl S670: Versuchsergebnisse der durchgeführten Pull-Out Versuche nach der RILEM/CEB/FIP Recommendation RC 6, 1978(1), 2004.

[7] Quast, U.; Pfeifer, U.: INCA2 (Interactive Nonlinear Cross Section Analysis Biaxial) und STAB2DNL. www.tu-harburg.de/mb.

Experimental analysis and numerical simulation of Ultra-High-Performance Concrete tube columns with a steel sheet wrapping for large sized truss structures

Ludger Lohaus[1], Jürgen Grünberg[2], Nick Lindschulte[1], Sven Kromminga[3]

1: Institute of Building Materials Science, Leibniz Universität Hannover, Germany
2: G+S Planungsgesellschaft mbH, Germany
3: Institute of Concrete Construction, Leibniz Universität Hannover, Germany

The compressive strength of ultra-high performance concrete (UHPC) is comparable to structural steel and can be advantageously used in thin construction elements. Because of its extreme brittle fracture behavior innovative concepts for design and casting procedure are necessary which are different from traditional concrete engineering. Slight UHPC-tubes, which are covered by thin steel sheets, should be designed as compressive struts for large-scale frameworks. Experimental tests with tubular columns (hollow profiles) were made in addition to numerical simulations and will be presented in this paper. In opposite to the composite or sandwich engineering the axial load bearing capacity should be generated prior by the pure concrete cross section. The steel cover is designed to serve as minimum circumferential reinforcement, therefore its thickness is to be minimized to achieve an economic optimum but still ensure ductile fracture behavior.

Keywords: Concrete, Ultra-High-Performance Concrete, Tube Columns, Truss, Compression Member, Ductility, Steel Fibers, Steel Sheet Wrapping, Finite Element Simulation, Experimental Analysis

1 Motivation

The high compressive strength of Ultra-High-Performance Concrete (UHPC) allows new, innovative fields of application. Considering the extreme brittleness of UHPC, a useful application of this material requires a sufficient ductility for the applied construction component. Particularly, the increase in ductility through the addition of steel fibres to the matrix of UHPC is in the focus of actual research. Experimental investigations in the context of the comprehensive research program „Sustainable Building With Ultra-High-Performance Concrete“ by the German Research Foundation (DFG) show that an exclusive addition of steel fibres does not guarantee any reliable increase in ductility in case of high compressive loads. This is for example caused by the arbitrary orientation of the steel fibres. Otherwise, a high contingent of steel fibres makes the casting process difficult. Especially, this applies to components with filigree dimensions.

To take advantage of the high compressive strength of UHPC with simultaneous consideration of economical and sustainable aspects, an effective utilisation of UHPC is required for slender compression members. The aim of this research-project (DFG SPP1182) is to develop a new structural element: a slender and light tube made from UHPC. These UHPC-tubes are to be used as compressive members in large-sized truss structures. The necessary increase in ductility of the UHPC-tube is achieved by a wrapping with a thin steel sheet. This wrapping is comparable to a minimum reinforcement required, together with the effect of circumferential tension. Furthermore, the steel sheet is used as a lost formwork. In this research project “UHPC-Rohr” the experimental tests has been performed by the Institute of Building Materials Science while the numerical analysis has been done by the Institute of Concrete Construction of Leibniz Universität Hannover.

2 Experimental Investigations

Small as well as large specimens of UHPC-tubes are loaded statically in their longitudinal direction. This experimental analysis shall show the mechanical mode of action of the steel sheet wrapping and the mode of failure of the structural element as a whole.

Experimental Setup

The tube specimens were made by using the inner and outer steel-sheet as a formwork, which have been fixed by a construction during the casting procedure. The fine grained ultra high performance concrete (UHPC) was filled in by using a funnel (type 1) and a small mortar pump (type 2). All specimens have been heat treated at 90°C for 48 hours [1]. Variations of steel wall thickness, tube diameter and concrete wall thickness are executed in small scaled series R-001 to R-008. Additionally large-scaled tests G-001 to G-003 have been performed with selected geometry values (Figure 1). The ratio of (length)/(mean diameter) approx. belongs to 3/1. The specimens end in stiff cover-plates, fixed by UHPC, to form the load application. These cover-plates refer to a possible type of joints in frameworks and compensate geometric conditional weakness on the pipe heads at the same time.

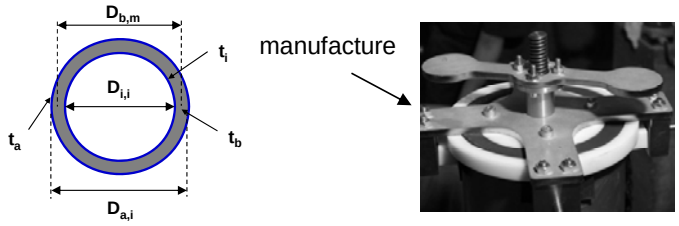

series	number specimen [pcs]	steel external ta [mm]	Da,i [mm]	concrete tb [mm]	Db/tb [-]	steel internal ti [mm]	Di,i [mm]	perc. Aa / Ab [%]
R- 001	3	0,8	166,4	10,8	14,4	0,7	143,4	8,0
R- 002	3	0,8	166,4	10,8	14,4	0,7	143,4	8,0
R- 003	3	1,5	180,0	20,0	8,0	1,0	138,0	8,5
R- 004	3	1,0	180,0	20,0	8,0	1,0	138,0	5,7
R- 005	3	0,8	180,0	20,0	8,0	1,0	138,0	4,2
R- 006	3	1,5	180,0	15,0	11,0	1,0	148,0	11,0
R- 007	3	1,0	180,0	15,0	11,0	1,0	148,0	7,3
R- 008	3	0,8	180,0	15,0	11,0	1,0	148,0	5,5
G- 001	1	2,0	356,0	28,0	11,7	2,0	296,0	7,8
G- 002	1	2,0	356,0	28,0	11,7	2,0	296,0	7,8
G- 003	1	2,0	356,0	28,0	11,7	2,0	296,0	7,8

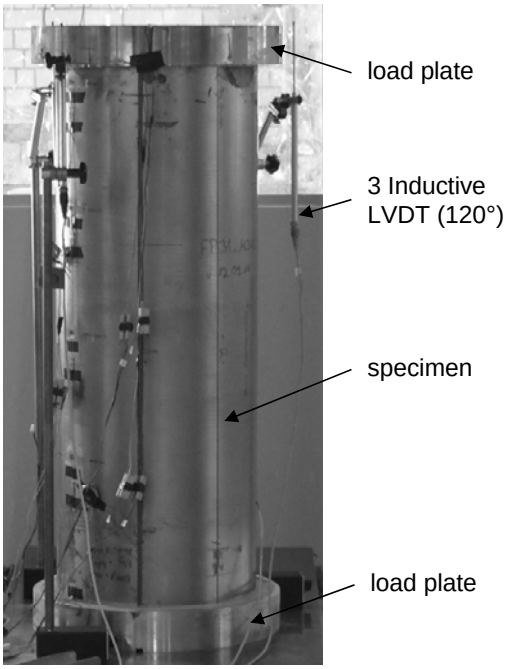

Figure 1: Experimental setup and overview of the tube tests.

Test results

By using a small mortar pump the flow ability and the compressive strength were increased due to the compacting effect of the worm shaft. The UHPC M3Q+ achieved a compressive strength up to 200 N/mm², while in case of the pump the compressive strength reached 230 N/mm² performed on heat treated cubes with a side length of 100 mm. The conversion factor to the axial compressive strength for the thin geometry was nearly founded to 0.8 and will be further analyzed in additional investigations (Table 1). The E-Modul has been performed on cylindrical specimens which were fabricated similar to the tube filling process.

Table 1: test results – material specimens.

UHPC					steel sheet				
material	$f_{c,cube,100}$ [N/mm²]	$f_{c,axial}$ [N/mm²]	E-Modul [N/mm²]	$\varepsilon_{,u}$ [%]	material	$R_{p0,2\%}$ [N/mm²]	R_m [N/mm²]	E-Modul [N/mm²]	$\varepsilon_{,u}$ [%]
M3Q+	200	160	36000	0,50	type 1	252	418	213000	25
M3Q_P+	230	185	36000	0,58	type 2	171	305	195000	20

The test results of the tube specimens show a great scatter within the series (Table 1). This is caused by the filigree cross-section and the quite complex behaviour between steel and concrete under axial compression.

Table 2: Overview of test results – tube specimens.

series	geometry				concrete	steel	experiment			theory	
	A-ø [mm]	$t_{s,o}$ [mm]	t_c [mm]	L [mm]	$f_{c,axial}$ [N/mm²]	$R_{p0,2\%}$ [-]	Fu (ultimate load) [kN]	Fres (residual load) [kN]	Fres/Fu [%]	Fcal [kN]	Fcal/Fu
R- 001 - 1	166,40	0,80	10,80	500	160,00	252,0	858,50	330,00	38,4%	1035,4	120,6%
R- 001 - 2							751,80	320,00	42,6%	1036,9	137,9%
R- 001 - 3							797,40	360,00	45,1%	1038,8	130,3%
R- 002 - 1							842,40	244,00	29,0%	1036,9	123,1%
R- 002 - 2							853,50	460,00	53,9%	1036,9	121,5%
R- 002 - 3							979,50	300,00	30,6%	1035,4	105,7%
R- 003 - 1	180,00	1,50	20,00		185,00	171,0	1604,55	750,00	46,7%	2085,5	130,0%
R- 003 - 2							1586,41	705,00	44,4%	2085,3	131,4%
R- 003 - 3							1555,74	835,00	53,7%	2070,8	133,1%
R- 004 - 1		1,00					1794,65	-	< 20 %	2029,6	113,1%
R- 004 - 2							2199,75	-	< 20 %	2025,6	92,1%
R- 004 - 3							1954,25	-	< 20 %	2074,7	106,2%
R- 005 - 1		0,75					1465,60	560,00	38,2%	1990,7	135,8%
R- 005 - 2							1757,85	540,00	30,7%	1998,4	113,7%
R- 005 - 3							2118,32	-	< 20 %	1995,2	94,2%
R- 006 - 1		1,50	15,00				1556,78	690,00	44,3%	1649,2	105,9%
R- 006 - 2							1601,33	490,00	30,6%	1656,1	103,4%
R- 006 - 3							1699,54	450,00	26,5%	1659,8	97,7%
R- 007 - 1		1,00					1707,83	400,00	23,4%	1616,3	94,6%
R- 007 - 2							1152,09	550,00	47,7%	1608,3	139,6%
R- 007 - 3							1301,13	460,00	35,4%	1615,5	124,2%
R- 008 - 1		0,75					1588,89	-	< 20 %	1595,1	100,4%
R- 008 - 2							1384,58	400,00	28,9%	1585,2	114,5%
R- 008 - 3							1379,38	340,00	24,6%	1585,2	114,9%
G- 001 - 1	356,00	2,00	28,00	1000	185,00	171,00	3769,00	2240,00	59,4%	6042,5	160,3%
G- 001 - 1							4646,00	1440,00	31,0%	6042,5	130,1%
G- 001 - 1							in the planning				

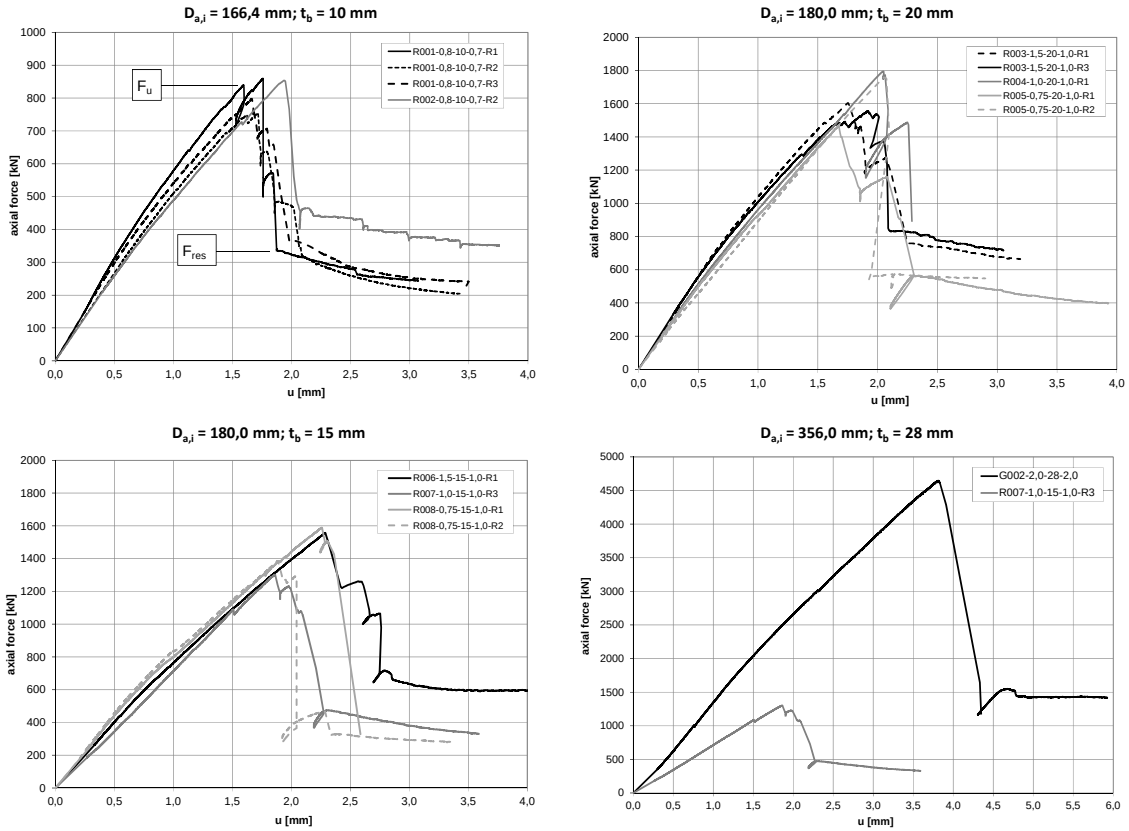

Figure 2: force-displacement-behaviour of tube specimens with different cross-section geometries.

The load bearing behaviour of selected specimens is illustrated in the force-displacement diagrams, shown in Figure 2. At the beginning a linear elastic behaviour is given which nearly remains until the ultimate load (F_U). After reaching a displacement of approx. 0.5 mm for the small series and 1.0 mm for the big series the stiffness is decreased because of exceeding the yield strength of the steel sheets. The area of the remaining fracture is firstly characterized by a step like gradient behaviour with abrupt parts and ends finally in a ductile residual load bearing capacity (F_{res}) depending on the steel sheet thickness (Figure 2). An area-ratio of the outer steel to the concrete core of lower than 7% (series R004, R005 and R008 cf. Figure 1 and Figure 2) seems not to be reliable for a residual strength level of minimal 20%.

The fracture appearance shows that the concrete core breaks splintered in local areas of the tube length and gets supported by the steel sheets which buckle in each case to the outside (Figure 3). Depending on the radial stiffness of the steel sheets the concrete is still able to transfer loads by its residual shear forces.

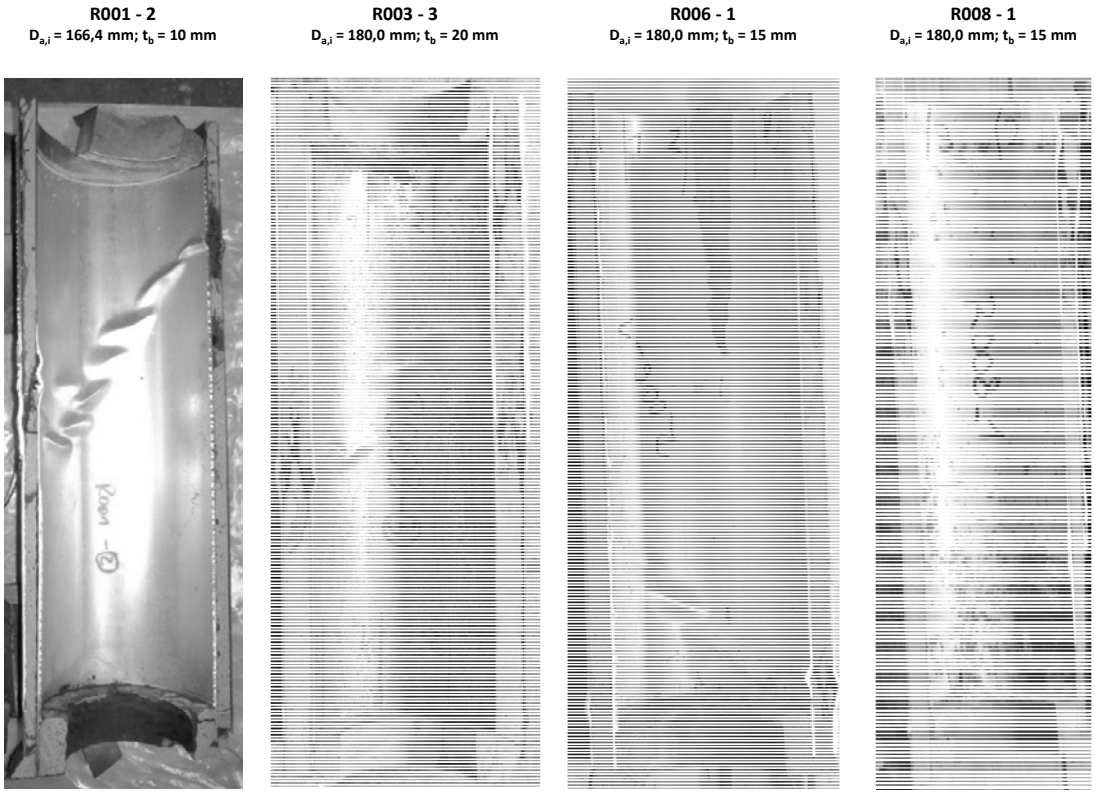

Figure 3: fracture appearance of selected specimens.

3 Numerical Analysis

A finite element model will be developed for an accompanying numerical investigation. Finite element simulations shall verify the results of the experimental investigations described above. The FE model used for these simulations has to be calibrated and experimentally verified. A parameter study of geometrical and structural parameters has to be carried out to identify the parameters with the largest influence on the mechanical mode of failure and on the load capacity of the UHPC-tube.

Later this model can be used to simulate the realistic performance of the UHPC-tubes as compression members in frameworks.

Description of the numerical model

The numerical simulation of the UHPC-Tubes under longitudinal compression is carried out with the non-linear FE program ABAQUS. The specimens will be modelled as a spatial system formed of 8-node brick elements with linear isoparametric shape-functions.

The input-files for the calculation with ABAQUS will be generated by a self-implemented tool which has its own meshing routines and, therefore, allows a complete parameterization of the geometrical and structural properties of the FE model. The use of an own implementation has the advantage of the possibility for a flexible extension of the FE model. The direct control over the FE meshing of the structure allows to model geometrically meaningful imperfections in the steel sheets as well as their impact on the inner UHPC-core, by reason of the use of the steel sheets as lost formwork. Also the imperfection of the weld seam can be modelled. Other scopes for a flexible extension are the statistical dispersion of material properties and the effect of concrete shrinkage.

For the finite element model the steel sheets and the UHPC-core itself are meshed independently (Figure 4). Then contact is defined between the steel sheets and the UHPC-core. Therefore ABAQUS offers the possibility to combine elements of a structure to "contact surfaces". Between a steel sheet and the UHPC-core a coulomb friction will be assumed tangentially which allows the transmission of shear. In the normal direction a hard contact will be defined which allows opposite FE nodes to touch each other as well as their separation but no penetration.

To model the constraints imposed by the stiff cover-plates at the end of the tube specimen all FE nodes at the ends are tied in all three degrees of freedom. For the simulation of the longitudinal deformation all FE nodes at the top of the structure are translated about 3.5 mm.

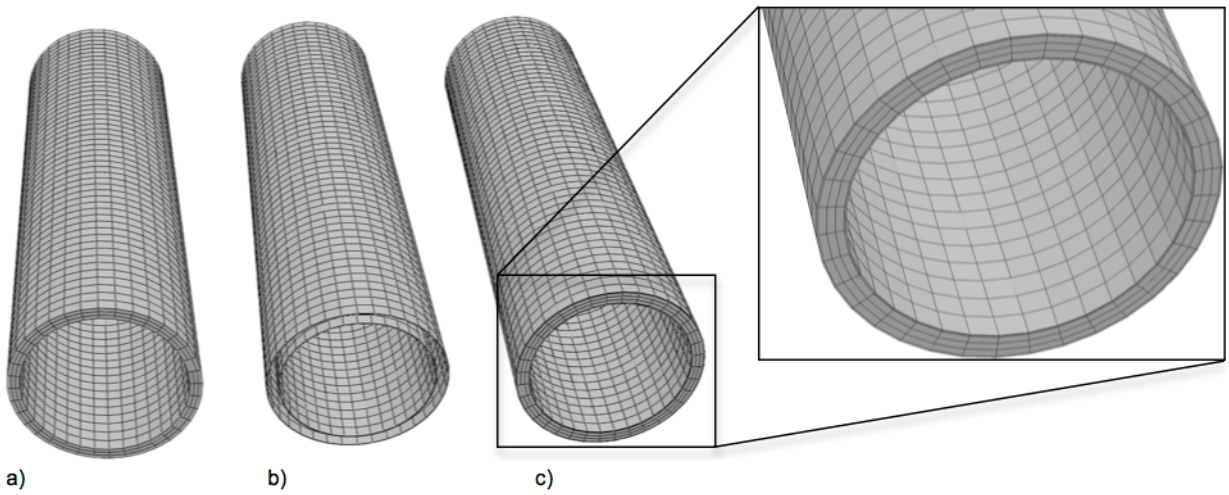

Figure 4: Finite-Element Model of the UHPC-tube.
a) inner UHPC-core, b) steel sheets, c) combined UHPC-tube.

Material Models

For both of the materials, UHPC and steel, nonlinear material models are used. At present the behaviour of the steel is modelled by a bilinear stress-strain curve.

The most important part of the realistic numerical simulation of the mechanical mode of action of the UHPC-tube is the material law used for the UHPC.

For the UHPC the uniaxial and triaxial material behaviour is described in [1], [2] and [3]. For the numerical simulation of this material behaviour the material model "CONCRETE DAMAGED PLASTICITY" (“CDP”) in ABAQUS will be used (see [4]). It bases on the plastic material model proposed in [5] and extended in [6]. The material behaviour under compression as well as under tension is described by a plasticity formulation and controlled in compression and tension by total stress vs. inelastic strain curves. Cracks in the concrete manifest themselves as positive inelastic strains. A modified cone describes the yield surface. The shape of the yield surface in a deviatoric section (Figure 5) can be modified by a parameter K_c. For normal concrete $K_c = 2/3$ is the default value. However own investigations have shown that for UHPC a value $K_c = 0{,}695$ gives more accurate results.

In “CDP” also the ratio between uniaxial and biaxial compression strength can be calibrated. The default value for concrete here is $f_{b0}/f_{c0} = 1{,}16$ based on the investigations from [7]. In [3] it is shown that this ratio is significantly lower for UHPC, and so $f_{b0}/f_{c0} = 1{,}05$ is used to model an UHPC without fibres.

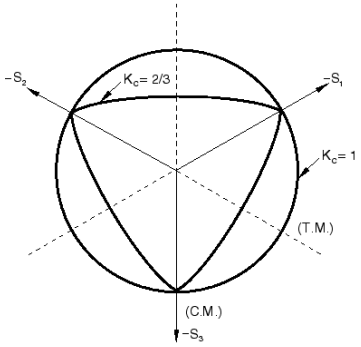

Figure 5: yield surface in the deviatoric plane, corresponding to different values of K_c (from [4]).

At present the numerical investigation focuses on the experiment series R-001 and R-002 (Figure 1). The first numerical results of the numerical investigation are shown as axial force over deformation compared to the experimental results in Figure 6. The FE calculation of the specimen results in a lower load bearing capacity (about 80-90%) compared to the experiments. At first the total stiffness of the FE-model is higher compared to the experiments. In the experiments the total stiffness decreases after reaching a displacement of approx. 0,5 mm because of exceeding the yield strength of the steel sheets. This effect is also seen in the FE simulation after reaching a displacement of approx. 0,6 mm. The remaining total stiffness is significantly lower compared to those in the experiments. The reason for this effect is still under investigation. In the experiments the specimens reach their load bearing capacity at a displacement from 1,6 to 1,7 mm, approximately. In the FE simulation this point is reached at approx. 1,5 mm. Then the curve falls down steeply as in the experiments. The residual load capacity in the simulation corresponds roughly to those of the experiments.

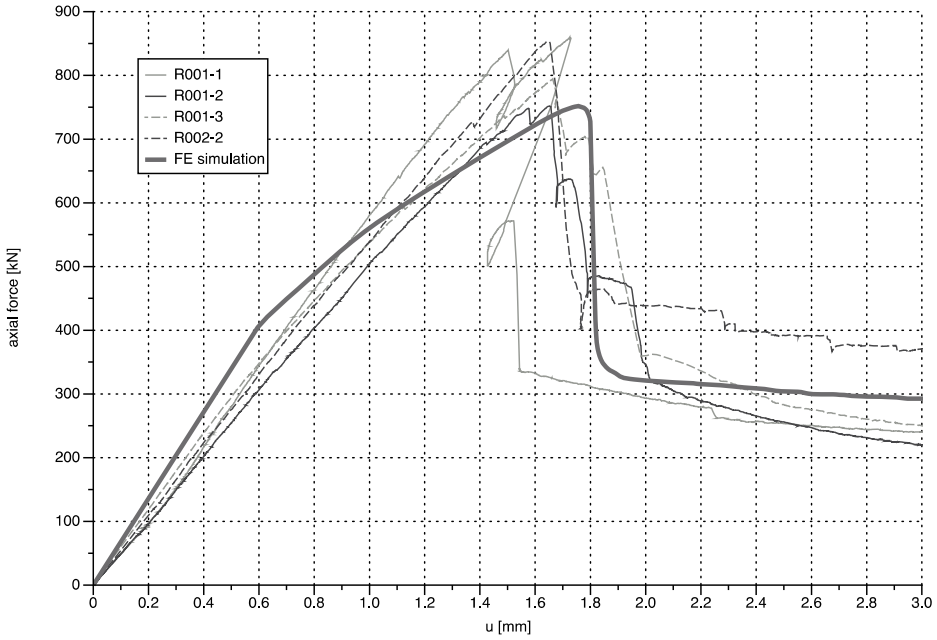

Figure 6: comparison of the experimental results with the FE simulation.

Figure 7 shows the FE model after the failure of the specimen. The left figure shows the longitudinal deformation at the whole specimen. The middle figure shows the longitudinal

deformation at the inner and outer steel sheet. The buckling of the steel sheets is clearly visible. The right figure shows the inelastic positive strains at the UHPC-core, which indicates cracks. It can be seen that the UHPC-core fails by shear fracture.

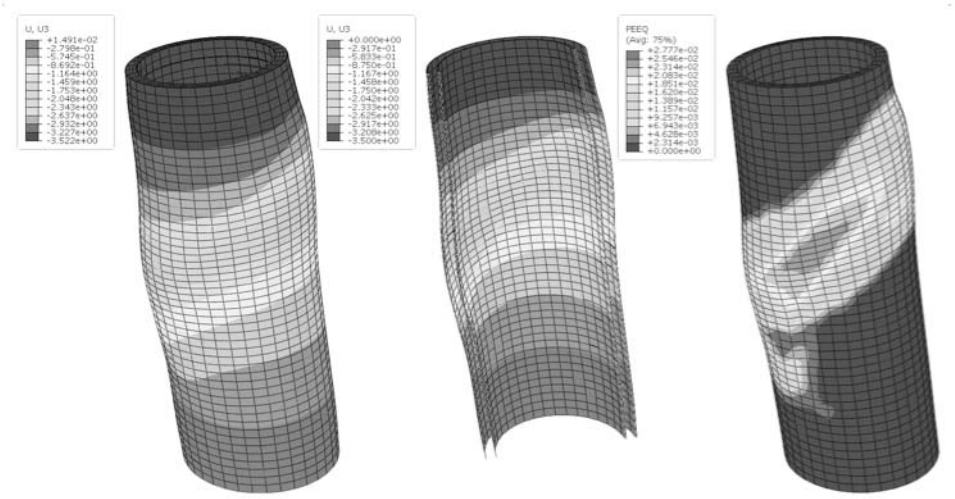

Figure 7: FE simulation - deformation of the specimen.

4 Conclusions

In the context of the research project experimental investigations were carried out. The results show that the remaining fracture ends in a ductile residual load bearing capacity depending on the steel sheet thickness.

Up to now the results of the numerical investigation are not fully satisfying. The FE simulation of the specimen results in a lower load bearing capacity compared to the experiments. After the steel-sheets exceed their yield strength the remaining total stiffness in the FE simulation is too low. Further investigations on this effect have to be performed.
If the results of advanced FE-simulations are closer to those of the experiments in the series R001 and R002, the remaining experiments (Figure 1) shall be simulated for further calibration of the FE model. After that a parameter study shall be carried out to identify sensitive geometrical and structural parameters.

References

[1] Deutscher Ausschuss für Stahlbeton: Ultrahochfester Beton – Sachstandsbericht. DAfStb 561, Berlin, 2008.

[2] Grünberg, J. ; Lohaus, L. ; Wefer, M. ; Ertel, Chr.: Mehraxiales mechanisches Ermüdungsmodell von Ultra-Hochfestem Beton - Experimentelle und analytische Untersuchungen. In: Beton- und Stahlbetonbau 102 (2007), pp. 388–398.

[3] Curbach, M. ; Speck, K.: Versuchstechnische Ermittlung und mathematische Beschreibung der mehraxialen Festigkeit von Ultra- Hochfestem Beton (UHPC) - Zweiaxiale Druckfestigkeit / Technische Universität Dresden - Institut für Massivbau. 2007 (DFG CU 37/6-1). – technical report.

[4] Systèmes, Dassault: ABAQUS Documentation, Version 6.10. Dassault Systèmes, 2010.

[5] Lubliner, J. ; Oliver, J. ; Oller, S. ; Onate, E.: A plastic-damage model for concrete. In: International Journal of Solids Structures Vol. 25, No. 3 (1989), pp. 299–326.

[6] Lee, J. ; Fenves, G.L.: Plastic-Damage Model for Cyclic Loading of Concrete Structures. In: Journal of Engineering Mechanics (1998), pp. 892–900.

[7] Kupfer, H.: Das Verhalten des Betons unter mehrachsiger Kurzzeitbelastung unter besonderer Berücksichtigung der zweiachsigen Beanspruchung. DAfStb 229, Berlin, 1973.

Shear and flexural strength of thin UHPC slabs

Lionel Moreillon, Joanna Nseir, René Suter
Institute of Construction & Environement iCEN, University of Applied Sciences Fribourg, Switzerland

This paper presents several results of an experimental campaign carried out at the University of Applied Sciences (HES-SO), Fribourg, on thin UHPC slabs with and without conventional steel reinforcement. The experimental studies included load tests on one and two-ways slabs. The principal aim of this research was to analyze the interaction between the thickness, the reinforcement ratio and the fibre volume ratio on Serviceability Limit State (SLS) and Ultimate Limit State (ULS). The tests have highlighted the beneficial contribution of UHPC combined with steel reinforcement on flexural and shear capacity. They have also shown that increasing the fibre content tends to decrease the strain capacity at ultimate load by locating the plastic strains of the rebars on a single macro-crack. The casting method and its repeatability have a great influence on the tensile strength. For thin slabs the SLS is often the design criterion, particularly in terms of the deflections.

Keywords: thin slabs, reinforced-UHPC, flexural behaviour, punching shear strength, full scale tests, design methods

1 Introduction

Ultra-High Performance Concrete (UHPC) exhibits significantly higher mechanical properties and very low permeability compared to plain concrete. Thanks to their exceptional properties, UHPC has undeniable potential to allow innovative design and to improve durability of structures [1] [2]. With its high tensile toughness, elements subjected to moderate stress or having complex shape can be realized without conventional steel reinforcement. Furthermore, structural elements with less complicated shapes, such as slabs, decks or facade panels, can be achieved with a combination of UHPC, a lower fibre volume ratio and steel reinforcement.

Since 2007, the UAS Fribourg performs a large research program on UHPC structures. The principal aim of this project is to analyze the behaviour of UHPC structures with and without reinforcement and to propose design models. Several experimental studies on structural elements, beams and slabs, were undertaken for this purpose. The test specimens were made with Béton Composite Vicat BCV®. The BCV is developed by Vicat and belongs to the family of UHPC as defined in the interim recommendations of the French Civil Engineering Association (AFGC) [3]. The fibre content is adjusted to the desired tensile properties. The BCV offered particular potential in innovative achievements such as the Chabotte bridge on the highway A51 in France.

2 Material properties

As part of the various experimental studies, the BCV has been used with different volume ratios and types of fibers. The four following compositions with their respective names were analyzed:

- BCV-1%A short steel fibres 13/0.18 mm, V_f = 1% (79 kg/m^3)
- BCV-1%B mix steel fibres 13/0.18 and 20/0.30 mm, V_f = 1% (79 kg/m^3)
- BCV-2% mix steel fibres 13/0.18 and 20/0.30 mm, V_f = 2% (158 kg/m^3)

The BCV has an average compressive strength f_{cm28} of 130 MPa and a f_{cm90} of 150 MPa on cylinder, produced without heat treatment. The Young's modulus is 45 GPa. In order to define the tensile behaviour, a large number of sawed prisms with a 700 mm length, 200 mm wide and with a thickness varying between 30 and 80 mm, casted like the one-way loaded and the two-ways loaded slabs, were tested in 3-points bending on a 500 mm span (fig. 1).

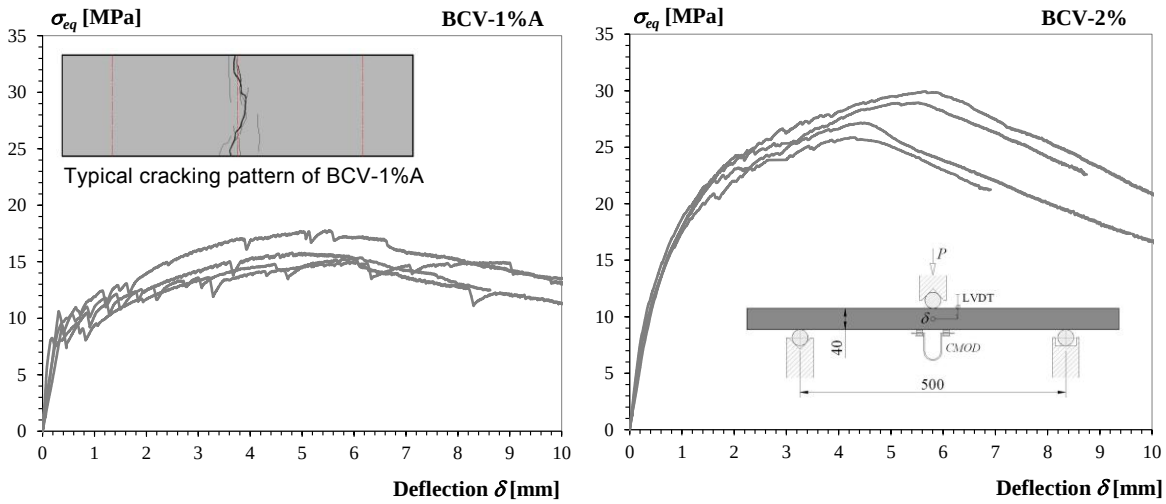

Figure 1: Some results of 3-points bending tests on prisms in relation with the two-ways loaded slabs.

The thin slabs are particularly influenced by the preferential orientation of fibres due to the casting method and wall effects. Therefore, the characterization tests must demonstrate the potential anisotropy. The prisms in BCV 1% and 2% exhibited a hardening behaviour in bending with the formation of multiple cracks. The interim recommendations of the AFGC [3] assumed a constitutive law in tension expressed in a bilinear relationship $\sigma(\varepsilon)$ for a thin element. In these studies, we assumed an elastic perfectly plastic tensile law.

3 One-way loaded slabs

Description of the experimental study

In order to analyze the flexural behaviour of thin UHPC slabs with and without reinforcement, the UAS Fribourg has performed a large experimental campaign. The experimental study was conducted on twenty stripes slabs of 1400 mm length each and 400 mm wide. The varying parameters among the specimens are: the thickness h, the fibre volume ratio V_f and the reinforcement ratio ρ (tab. 1). All specimens were casted in a similar manner. The UHPC flow was oriented in the longitudinal direction.

Table 1: Properties of the specimen.

Series	Thickness h [mm]	Reinforcement ρ [%] / [mm]	Fibre volume ratio V_f [%]	Effective depth d [mm]
BCV-V_f_30_ρ	30	0	1A / 1B / 2	-
BCV-V_f_40_ρ	40	0 1.13 / 4 ϕ6 2.01 / 4 ϕ8	1A / 1B / 2 0 / 1A / 1B / 2 0 / 1A / 1B	25
BCV-V_f_60_ρ	60	0 1.12 / 4 ϕ8 2.13 / 2 ϕ10; 2ϕ12	1A / 1B / 2 0 / 1A / 1B / 2 0 / 1A / 1B	45
BCV-V_f_80_ρ	80	0 0.98 / 4 ϕ9 2.05 / 4 ϕ14	1A / 1B / 2 0 / 1A / 1B / 2 0 / 1A / 1B	65

The load tests were performed in the Structural laboratory of UAS Fribourg. The slabs were tested on 4-points bending on 1200 mm span. The load was applied at extremities in order to obtain inverse bending. The displacement of the actuators was monitored by a servo-electronic

system. Recorded data included: applied forces, deflections, top strains, cracking pattern and the corresponding openings (fig. 2).

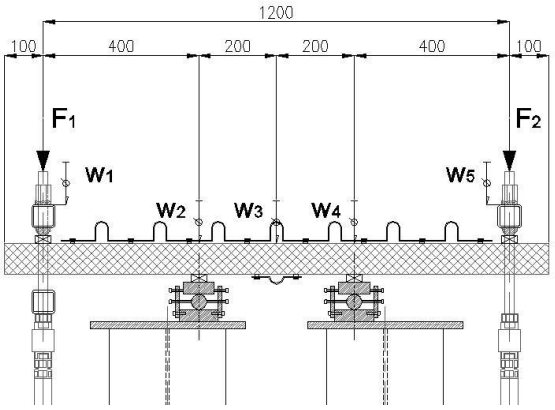

Figure 2: Test set-up and the instrumental configuration.

Tests results and analysis

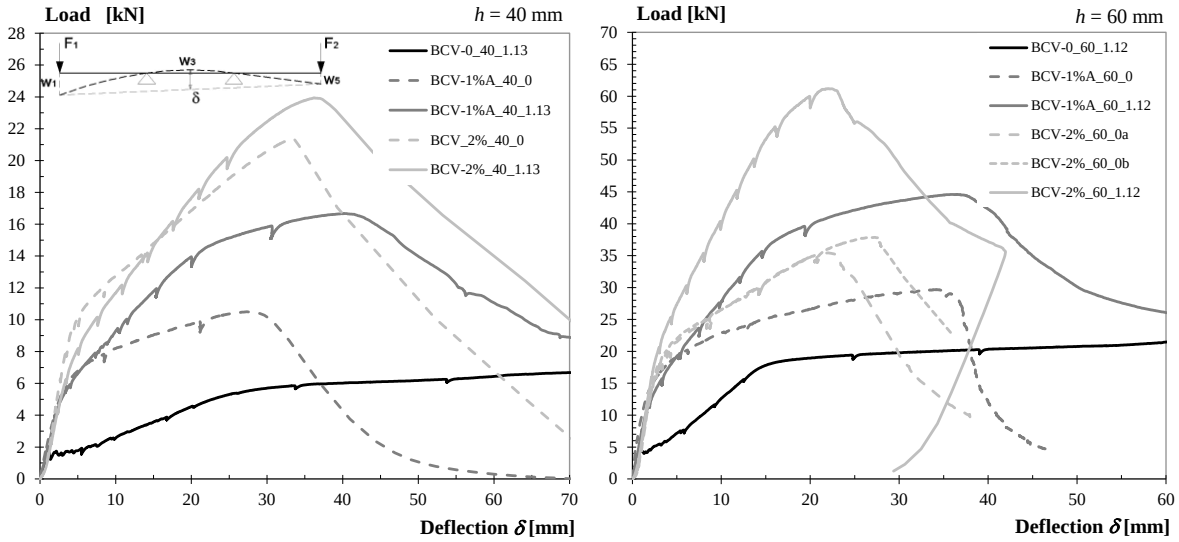

Figure 3: Some load V – deflection at centre δ curves of one-way loaded slabs according to the corresponding thicknesses.

The stiffness and the strength of UHPC slabs with and without conventional steel reinforcement were higher compared to the reinforced slabs without fibres BCV-0. However, the deformation capacity of UHPC slabs diminished largely with the increasing fibre volume ratio; For a fibre volume ratio of 2%, the deflection at ultimate load was similar between slabs with and without reinforcement. The reinforced slabs BCV-1% exhibited larger deflection at ultimate load than the slabs without reinforcement. Once the steel reinforcement reached the yielding limit, the deformations were localized on a single macrocrack for UHPC reinforced slabs.

The flexural strength was calculated using a simplified model. The model assumed an elastic perfectly plastic tensile law up to an ultimate strain ε_u. The parameters (f_{ctf} and ε_u) were defined on the prisms. This simplified model showed a good agreement with tests results of slabs with and without conventional steel reinforcement.

For thin slabs, the deformation criteria at SLS could become the design criteria compared to the strength. In this study, a deformation criteria of L/300 was considered and the service load was assumed as following: $P_{serv} = P_u / \gamma_{global}$ with $\gamma_{global} = 2.14$. The test results analysis highlighted that the deformation criteria at SLS was determinant for the UHPC-reinforced slabs. Whereas the flexural strength was the design criteria for the UHPC slabs without reinforcement.

4 Two-ways loaded slabs [4]

Description of the experimental study

In order to analyze the flexural behaviour and the punching shear strength of thin UHPC slabs with and without reinforcement, the UAS Fribourg have performed a large experimental campaign. The experimental study was conducted on twenty square slabs with a 960 mm side. The varying parameters among the specimens were: the thickness *h*, the fibre volume ratio V_f and the reinforcement ratio ρ (tab. 2). One serie, called BCV-2%_*h*_0, was composed of UHPC with a fibre volume ratio of 2% and without reinforcement. All slabs were casted in a similar manner. The UHPC was poured at the centre of the slabs.

Table 2: Properties of the specimen with reinforcement.

Series	Thickness *h* [mm]	Reinforcement ρ [%] / [mm]	Fibre volume ratio V_f [%]	Effective depth *d* [mm]
BCV-Vf_30_ρ	30	1.31 / ϕ5 #100 2.57 / ϕ7 #100	1A 1 / 2	15
BCV-Vf_40_ρ	40	0.98 / ϕ5 #100 1.92 / ϕ7 #100	1A 1A / 2	20
BCV-Vf_60_ρ	60	0.96 / ϕ7 #100 1.96 / ϕ10 #100	1A 1A / 2	40
BCV-Vf_80_ρ	80	1.06 / ϕ9 #100 1.88 / ϕ12 #100	1A 1A / 2	60

The load tests have been carried out in the Structural laboratory of UAS Fribourg, on a punching test set-up which was specially designed for this study. The load was applied with an actuator located at the centre point of the slab through a 80 mm diameter punch. The displacement of the actuator was monitored by a servo-electronic system. The slab was supported by eight steel rods, anchored to a steel frame. The support system described a circle with a diameter of 878 mm and spherical plain thrust bearings allowed free rotations. Recorded data included: applied forces, deflections, top strains, cracking pattern and the corresponding openings (fig. 4).

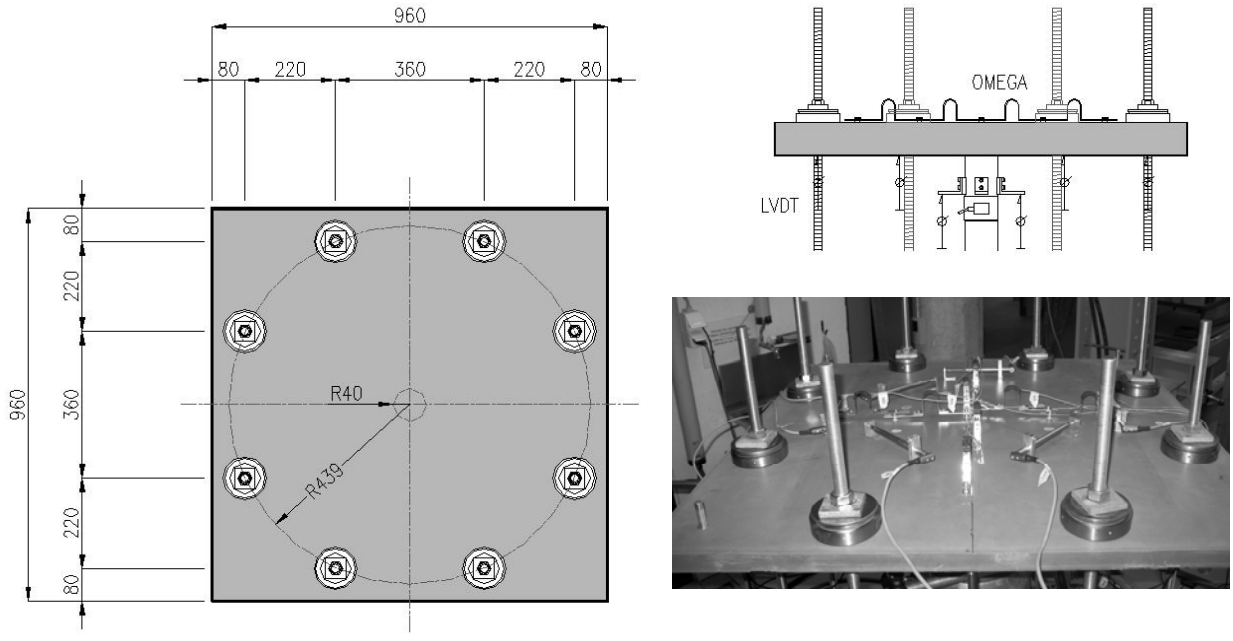

Figure 4: Punching test set-up and the instrumental configuration.

Tests results and analysis

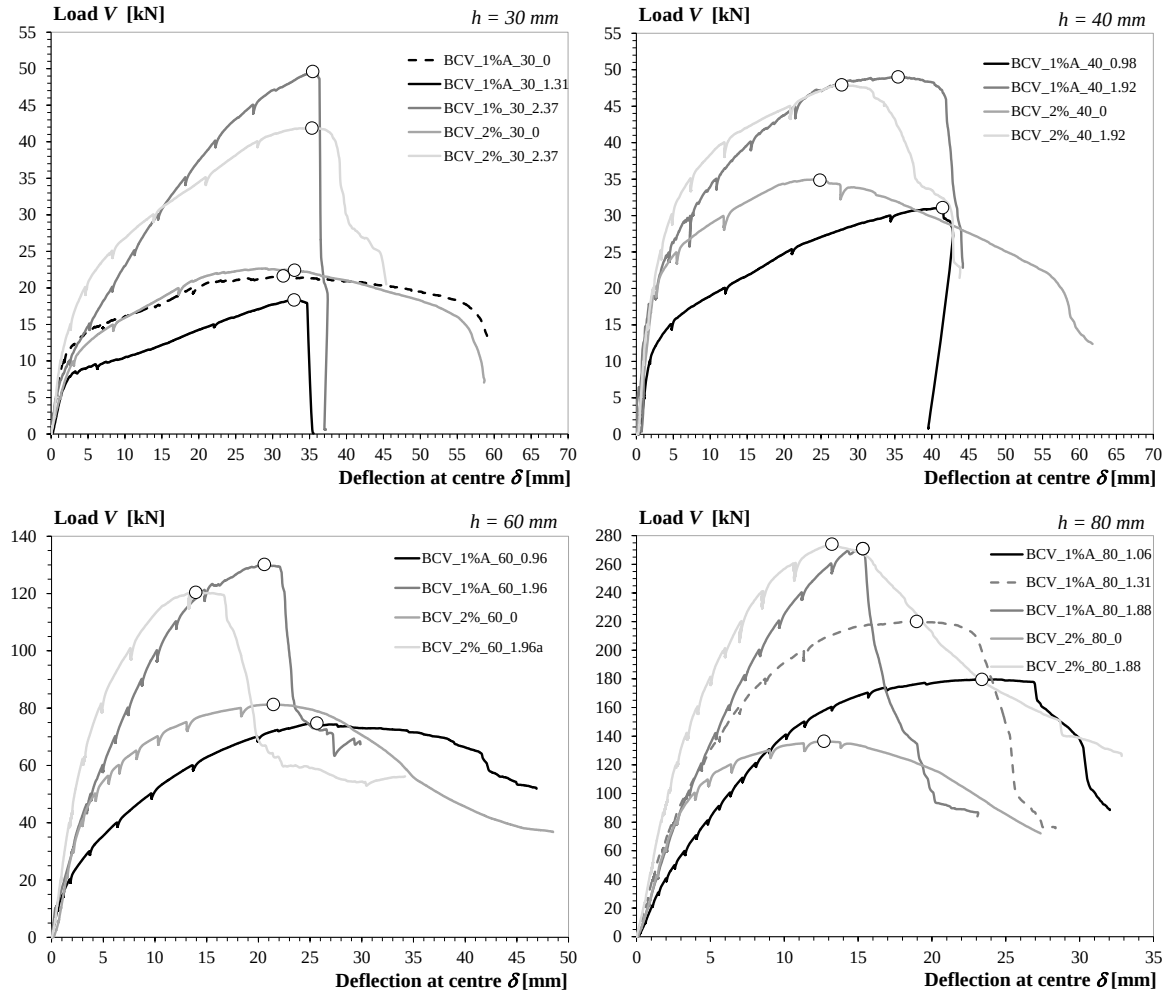

Figure 5: Load V – deflection at centre δ curves of the slabs according to the corresponding thicknesses.

For conventional reinforced-concrete slabs without transversal reinforcement, several experimental studies highlighted that the punching shear strength was inversely proportional to the deflection capacity. In other words, for similar RC slabs in terms of concrete compressive strength, thickness and statical system, as the reinforcement ratio increases, the punching shear strength increases as well, but the deformation capacity diminishes. Based on the experimental observations and results, this established fact was similar for the UHPC slabs [5].

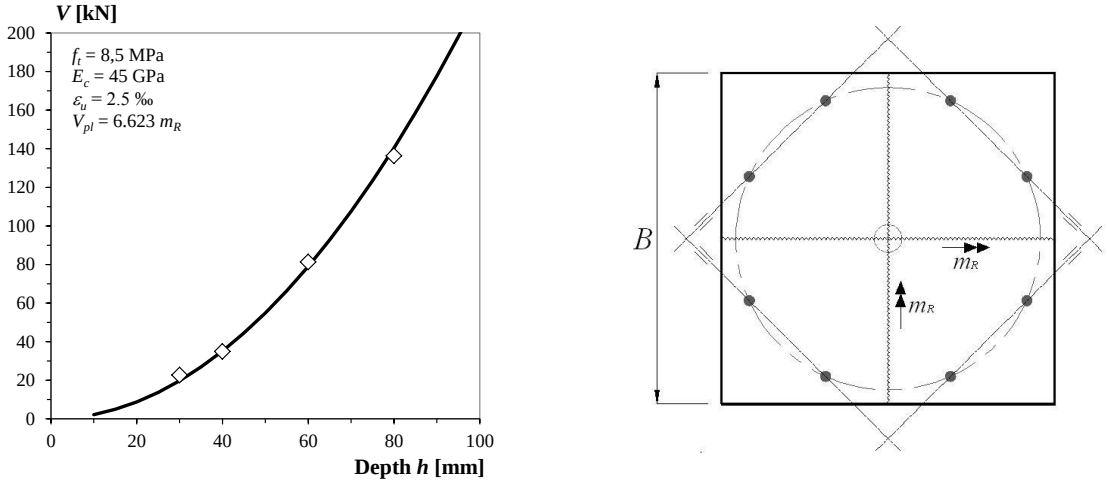

Figure 6: Plastic strength V_{pl} according to the assumed mechanism and experimental results of the slabs without reinforcement.

The slabs without reinforcement exhibited a flexural failure with the development of yield lines. However, the distribution of the yield lines was random compared to the considered yield mechanism (fig. 6). The slabs were sawed in half. After the internal cracking analysis, no punching shear cones were developed for the elements without reinforcement. The flexural strength of these slabs was moderate, therefore the punching shear strength was not determining in this studied case.

All slabs with reinforcement reached the yielding limit of the steel reinforcement followed by a short plastic plateau. The drop of strength was relatively high or not, according to the thickness and the reinforcement ratio. For the given reinforcement arrangement, we distinguished two types of failure mechanisms; The first type was when the critical shear crack intercepts the rebars, resulting in the development of a punching cone and thus the load capacity was high. As for the second type of failure, the critical shear crack didn't intercept the rebars,resulting in a development of yield lines, with a concentrated punching cone and thus a lower load capacity.

The slabs called BCV-2%_40_1.92 and BCV-2%_60_1.96 showed a smaller failure load compared to the slabs with a fibre volume ratio of 1%. The cracking pattern analysis highlighted a more accentuated stress localization with the BCV-2% reinforced slabs. Therefore, the centre rebars were more stressed and reached their yielding limit in a quicker way resulting in a punching shear failure. The internal cracking analysis is still in process in order to confirm this assumption.

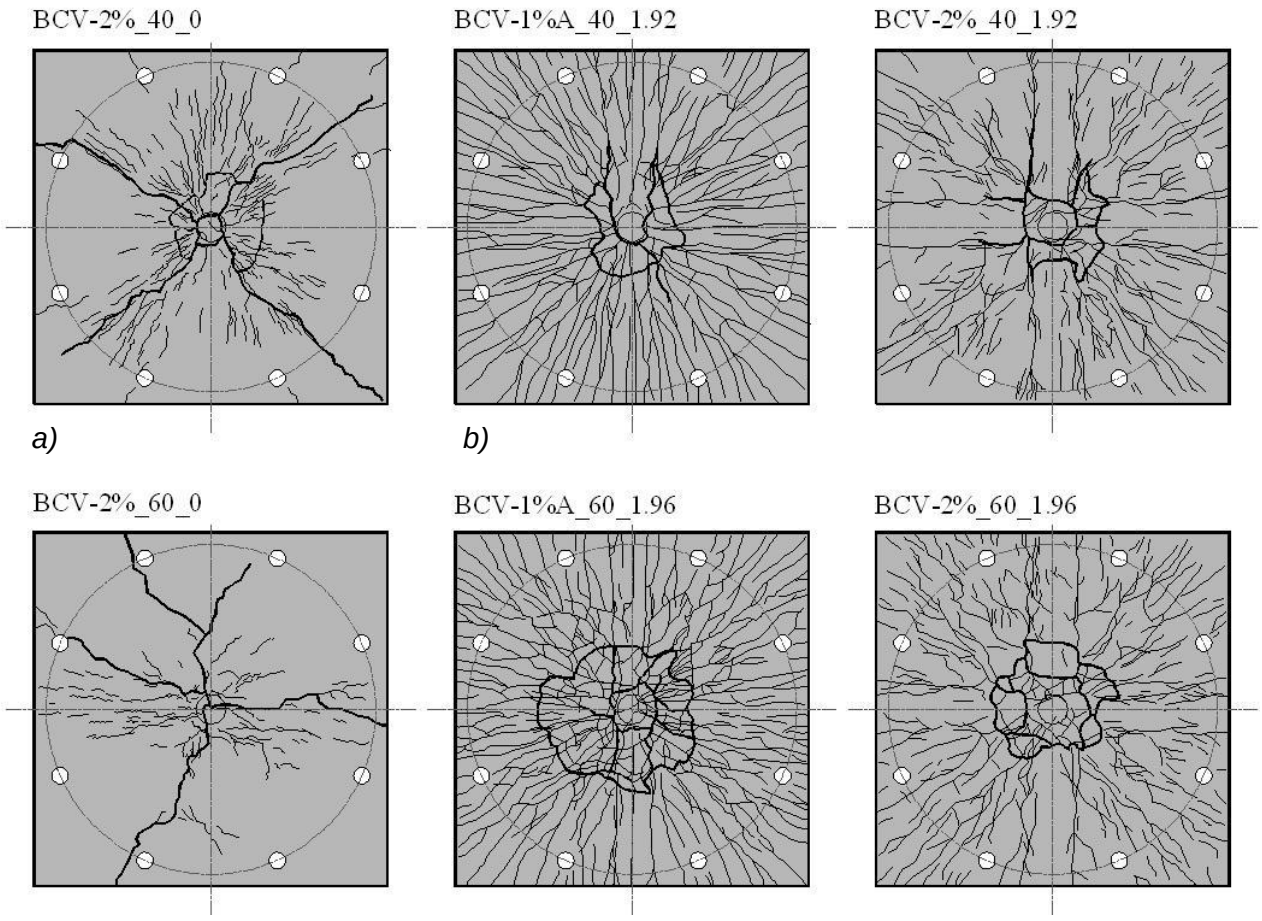

Figure 7: Cracking pattern, a) slabs without reinforcement, b) slabs with reinforcement.

On the basis of the Critical Shear Crack Theory (CSCT) and a proposal for fibre reinforced concrete developped by Muttoni and Fernandez [5] [7], the punching shear strength model have been adapted to the UHPC. The developed punching shear model involves the contributions of the matrix $V_{R,c}$ and the fibres $V_{R,f}$. For the matrix contribution, it is assumed that the punching shear strength is carried by the shear friction and is a function of the critical crack opening. The critical crack opening is assumed to be proportional to the product of the effective depth d with the slab rotation ψ. Based on these assumptions, the failure criterion is defined as the following:

$$\frac{V_{R,c}}{b_0 \cdot d \cdot \sqrt{f_c}} = \frac{3/4}{1+15 \cdot \frac{\psi \cdot d}{16+d_g}} \tag{1}$$

Where b_0 is the control perimeter, located at $d/2$ of the edges of the loading support, d_g is the diameter of the biggest aggregate, for UHPC d_g = 0.

The fibres contribution correspond to the vertical component of the integration of the tensile stresses across the punching shear plan A_p *(fig. 8)*. The distribution of the crack opening is assumed to be linear along the failure plan. With the tensile stress – opening law $\sigma(w)$, the distribution of the tensile stresses is defined along the failure plan. In order to not consider two times the tensile strength of the matrix, the softening tensile law of the matrix is substracted from the tensile relationship. The factor K takes account of the fibres orientation.

$$V_{R,f} = \frac{1}{K} \cdot \int_{A_p} \sigma_f(w) \cdot dA_p \tag{2}$$

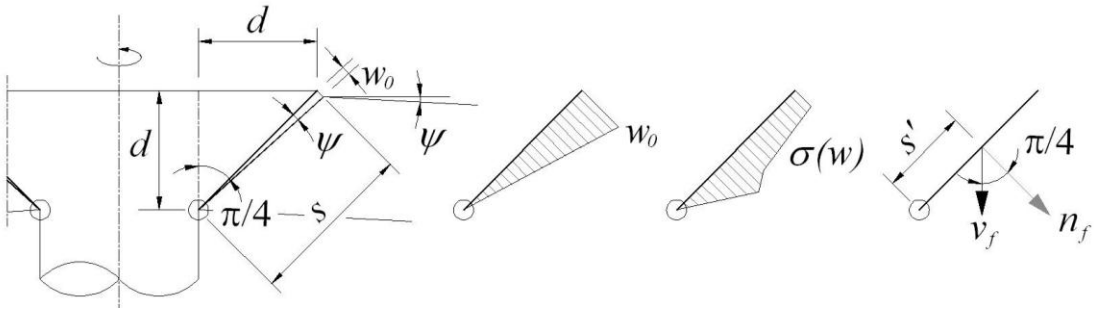

Figure 8: Mechanical model of the fibres' contribution.

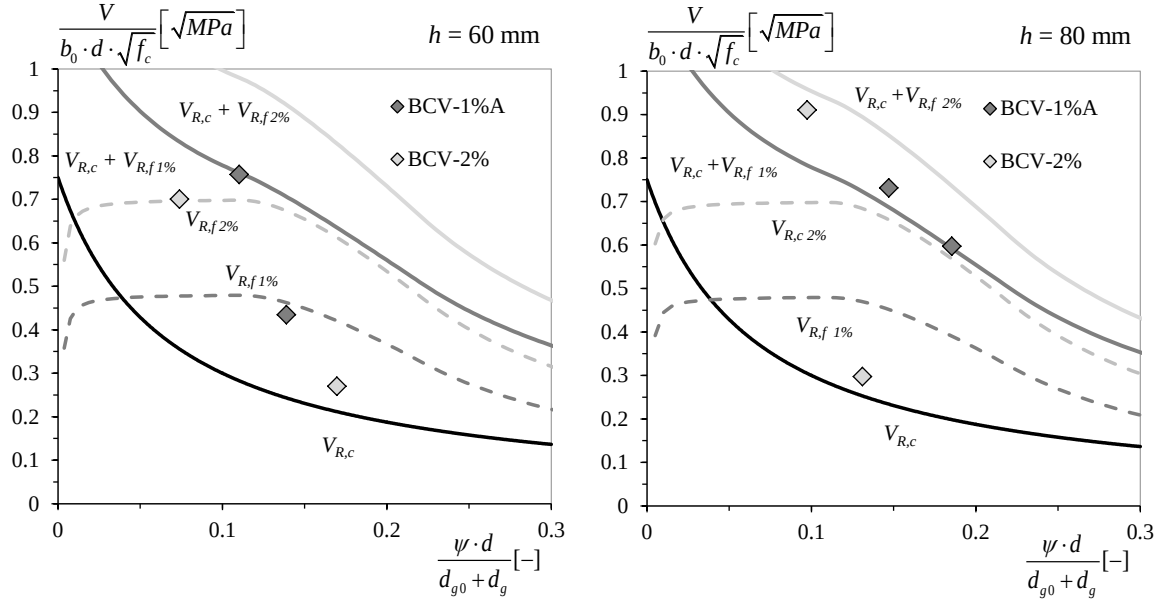

Figure 10: Punching shear failure criterion and tests results.

For determining the punching strength, the load – rotation curve must be prealabely calculated. The relationship $V(\psi)$ can be modelized by finite difference or finite element methods [7]. The intersection between this curve and the failure criteria corresponds to the punching shear strength. If the curve does not cut the criteria, the flexural strength is determining. In the graphics of figure 10, the dotted curves represent the fibres contribution along the thickness *h* and the plain curves represent the sum of the matrix and fibres contribution on the effective depth *d*. The different criterion show a good correlation with the tests results and the observed mechanisms. However, the punching shear is a local phenomenon and thus the variability due to fibres orientation can affect the strength in a non-negligible manner.

5 Conclusions

Since 2007, the University of Applied Sciences Fribourg has conducted a large research program on UHPC structures. The principal aim of this project was to analyze the behaviour of UHPC structures with and without reinforcement and to propose design models. Several experimental studies on structural elements, beams and slabs, were undertaken for this purpose. The experimental studies performed in the structural laboratory of UAS Fribourg have highlighted the following points:

- UHPC slabs showed a high punching shear strength. Their high tensile strength allowed an effective control of the punching critical shear crack.
- The tensile strength of UHPC depended on the casting method. The determination of the material's tensile law must take into account an eventual anisotropy.
- The flexural strength of UHPC slabs without reinforcement was moderate, therefore the punching shear strength was not determining.
- The cracking pattern analysis highlighted a stress localization which was more important for the reinforced BCV-2% slabs. Therefore, their punching shear loads were smaller than those with a 1% fibre volume ratio (BCV 1%)
- On the basis of the Critical Shear Crack Theory the authors propose an harmonized model for the punching shear strength of UHPC slabs. Therefore, this model must be validated and simplified to be operational for practitioners [8].

References

[1] Toutlemonde F., Resplendino J. Designing and Building with UHPFRC: State of the Art and Development, Proceedings of UHPFRC symposium in Marseille (France), November 17-18, 2009, London, 2011, 814 pp.

[2] Brühwiler E., Moreillon L., Suter R. Bétons fibrés ultra-performants, Proceedings of UHPC symposium in Fribourg (Switerland), October 26, 2011, Fribourg, 2011, 207 pp.

[3] AFGC-SETRA. Interim recommandations, Ultra High Performance Fibre-Reinforced Concretes. Paris, 2002.

[4] Nseir J., Moreillon L., Suter R. Flexural and punching shear strength of thin UHPFRC slabs, Tests report, Ecole d'ingénieurs et d'architectes de Fribourg, 2011.

[5] Fédération Internationale du Béton (*fib*). Shear and punching shear in RC and FRC elements – Workshop October 15-16, 2010, Salò. Bulletin 57, Lausanne, 2010.

[6] Fédération Internationale du Béton (fib). Model Code 2010 – First complete draft. Bulletin 56, Lausanne, 2010.

[7] Muttoni, Aurelio. "Punching Shear Strength of Reinforced Concrete Slabs without transverse Reinforcement", ACI Structural Journal, 2008, V.105, No 4, pp. 440 à 450.

[8] Moreillon, Lionel. Shear and punching shear strength of high performance fibre reinforced concrete structures. Thesis Université Paris-Est SIE, Champs-sur-Marne, 2012. (in redaction)

Modelling Flexural Tests on UHPFRC Thin-Walled Structures

Pierre Marchand, Florent Baby, Waël Al Khayer, Mohammed Attrach, François Toutlemonde
Department for Bridges and Structures, IFSTTAR, Paris-Est University, Paris, France

The paper presents the results of analytical and numerical simulation of flexural tests under concentrated load carried out on waffle UHPFRC slabs developed in the frame of the French Mikti national R & D project and thin-walled UHPFRC box-cells representative of these slabs. While the failure on UHPFRC slabs was a punching failure, the box cells showed a ductile failure mode in flexion. Typical yield lines pattern has been observed, which typically illustrates the ductile bending failure mode of clamped UHPFRC thin plates.
The experimental results have been compared with the results of non linear finite element models and with a simpler approach based on the yields line theory. These two methods have enabled to better understand the failure mechanisms and the behaviour of the 5 cm-thick UHPFRC plate during the tests.

Keywords: UHPFRC, thin element, thin plate, yields line theory, finite element method

1 Experimental program and test results

Between 2004 and 2007, the French R & D National Project MIKTI studied different innovative solutions concerning steel-concrete composite bridges. In this framework, a prototype of composite bridge with a UHPFRC waffle deck, was designed by the Bridges Division of CETE de Lyon (cf. figure 1) and some elements were tested at LCPC (now IFSTTAR) Structures Laboratory [1] [2] [3] and [4]. Elements were made with two different UHPFRCs, that we will call UHPFRC A (with heat treatment) and UPFRC B (with no heat treatment), corresponding to similar main design properties. The mean compressive strength is about 190 MPa for both materials, mean tensile strength is 9.8 MPa for UHPFRC A and 9.3 MPa for UHPFRC B, and Young's modulus is 55 GPa for UHPFRC A and 65 GPa for UHPFRC B.

The waffle deck was prestressed in the transversal direction by pre-tensioning and prestressed in longitudinal direction by external post-tensioning. Transversal pre-tensioning is ensured by 2 T15.7 strands by rib with initial tensioning at 0.8 f_{pk} (characteristic tensile strength of tensile elements: 1860 MPa) leading to a permanent compressive stress of 2.98 MPa in top side, and 18.59 MPa in bottom side (3.86 MPa for mean stress in top deck). External tendons made of T12.5 strands (f_{pk} = 1860 MPa) ensure longitudinal post-tensioning. The tendons are approximately at the neutral axis, resulting in a quasi-homogeneous compressive stress of 4.35 MPa in the section.

Experiments concerned the fatigue resistance under intense traffic loadings, anchoring of the safety barrier, connection between steel beams and waffle UHPFRC deck, and resistance of waffle deck under localized traffic load [5].

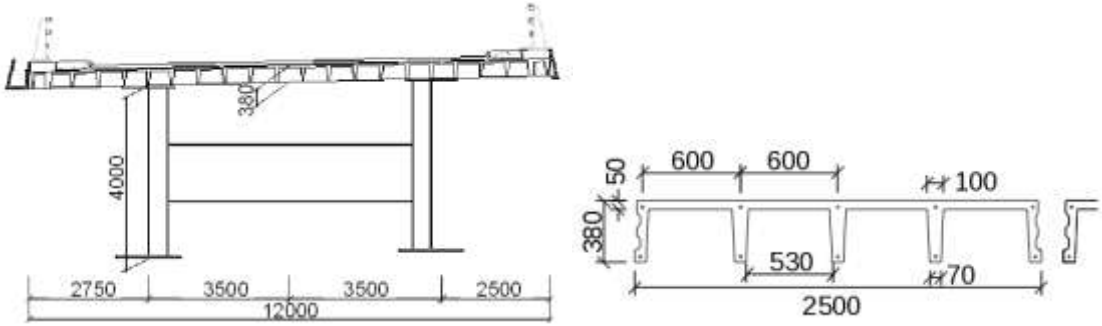

Figure 1: Transverse profile of composite bridge deck (left); longitudinal segments cross-section, waffle slab dimensions (right) - dimensions in mm.

Punching shear tests on the whole waffle deck

To assess resistance of UHPFRC deck under concentrated wheel load generated by traffic, a localized rectangular loading has been applied on the UHPFRC waffle deck to check the safety with respect to punching shear failure mechanism (cf. figure 2).

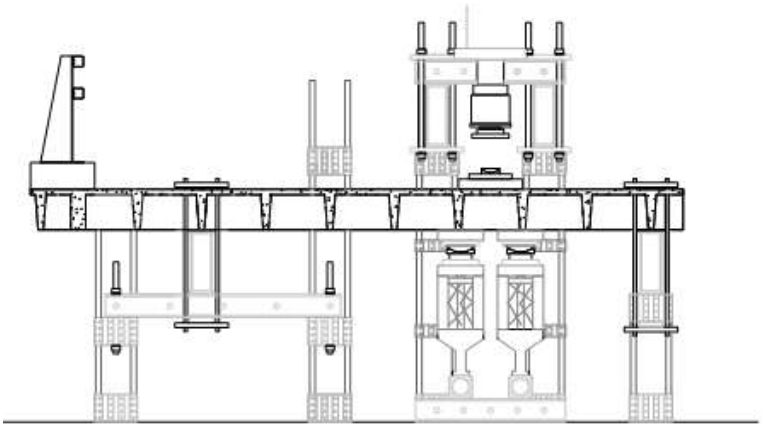

Figure 2: Punching test on the UHPFRC waffle deck.

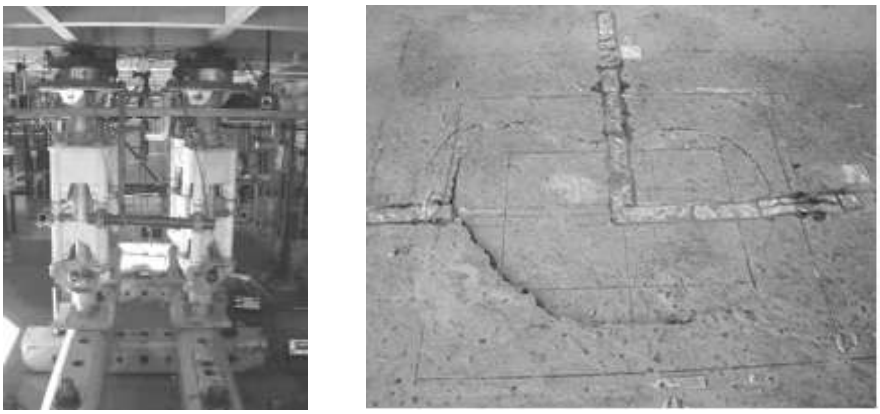

Figure 3: Supporting stays under corners of the loaded box cell (left), punching failure (right).

The load was applied directly at the center of the box while 4 supporting stays were placed on the 4 corners of the loaded cell box, to limit transverse deflection. These supporting stays were adjusted in such a way that they took 90% of the dead weight effect before applying the load by the actuator.

The load was applied following four successive configurations, to represent the effect of a wheel load and the bituminous concrete layer. Indeed, the bituminous concrete layer enables to enlarge the loaded zone through a distribution phenomenon in its depth. Here, ®Ertalon material was used because of its stiffness very close to bituminous concrete (Young's Modulus about 2.5 to 3 GPa).

1 : steel plate dimensions 400x400x40 mm, on a 90 mm thick ®Ertalon plate

2 : steel plate dimensions 400x400x40 mm, on a 3 mm sand layer

3 : steel plate dimensions 260x190x40 mm (with corners cut at 20 mm), on a 90 mm thick ®Ertalon plate

4 : steel plate dimensions 260x190x40 mm (with corners cut at 20 mm), on a on a 3 mm sand layer.

Only the fourth configuration enabled the punching failure before reaching the capacity of the stays (around 700 kN). The first three configurations only create cracks less than 0.2 mm wide. Failure loads were between 352 and 417 kN corresponding to punching shear (cf. figure 3).

Local bending tests on isolated box cells

Loading configurations 1, 2 and 4 have also been applied directly on two isolated box cells, (cf. figure 4), fabricated with the same UHPFRC batches as the waffle decks. The ribs height and deck depth were the same, but the rib thickness was increased. One box cell was made of UHPFRC A and the other one is made with UHPFRC B. The box cells were supported by four roll bearings located at the corners under the ribs.

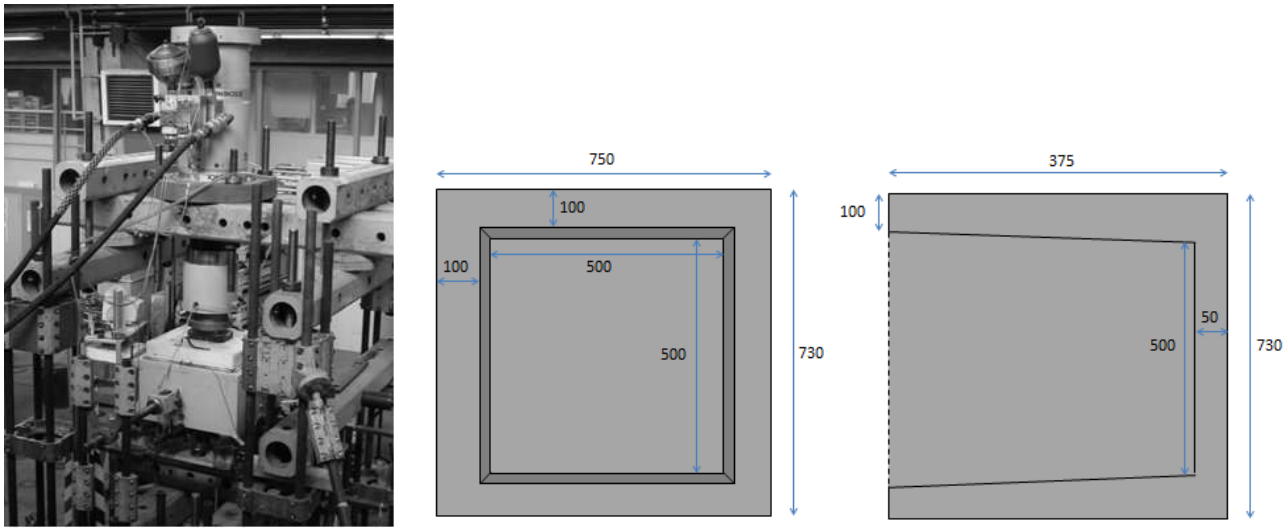

Figure 4: Local bending test on isolated box cell (loading configuration number 1), cell box geometry (dimensions in mm).

Under configurations 1 and 2, cracks developed in the ribs without reaching failure (even under about 800 kN). Under configuration 4, failure was reached, but the failure mechanism was not punching failure but local bending failure, with the development of yield lines in the deck as shown on figure 5. The failure load was 382 kN for UHPFRC A and 390 kN for UHPFRC B.

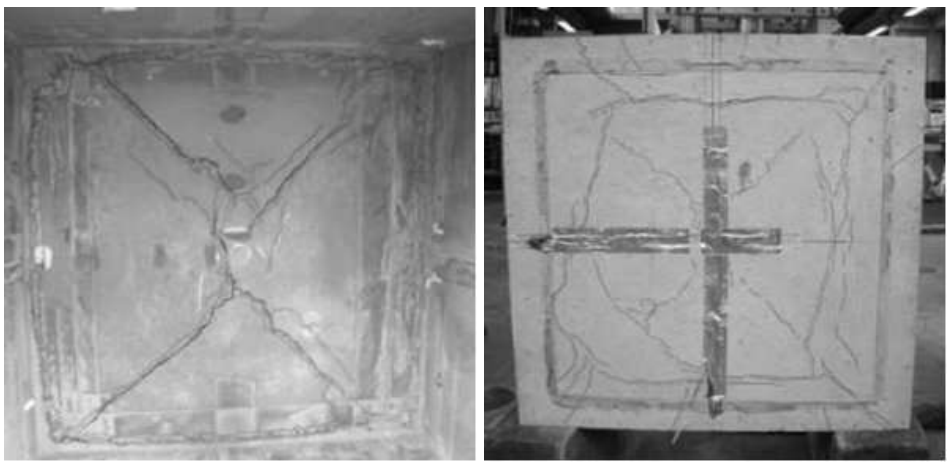

Figure 5: Yield lines after failure at bottom side (left) and top side (right).

2 Analysis using yield lines theory

Theory and application on single cell boxes

The yield lines method consists in using the mechanism which leads to the failure of the structure to predict the failure load. We consider that the structure turns progressively into a multi-hinges mechanism. These hinges are created by the material yielding along lines between plates supposed perfectly rigid. Equalling internal forces work and external forces leads to the

maximum force determination. Here the yield lines are directly known from the experimental results. We will hence apply this method with the observed yield lines and no minimum energy solution is to be computed.

To apply this method, we need to determine the law between bending moment M and concentrated rotation angle θ. We use the law provided by French AFGC-BFUP recommendations for UHPFRC [6] with parameters consistent with mechanical characteristics determined during the study (cf. figure 6) [2]. We consider here the constitutive law for thick elements σ-w, rather than the law for thin elements σ-ε. This latter assumes that multi-cracking occurs due to the good fibre orientation because of the thin depth. We are obviously beyond this step here. The values of elastic tensile strength and post-cracking peak stress have been slightly increased to take into account the fibres favourable orientation in thin elements.

We have here considered the following behaviour law for both materials:

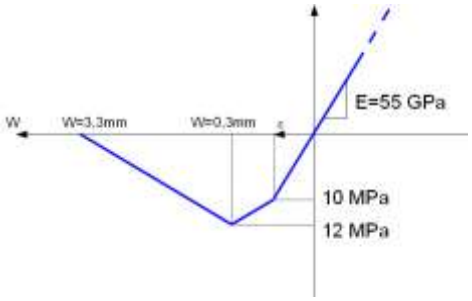

Figure 6 : constitutive law for both UHPFRC materials

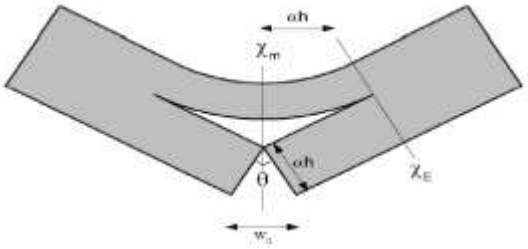

Figure 7 : kinematic hypothesis for UHPFRC.

The M-θ law is determined using the kinematic assumption proposed by [7] (cf. figure 7) which stipulates that the deformed shape has a parabolic variation of curvature between χ_m and χ_E:

$$\chi = \chi_E + (\chi_m - \chi_E)\left(1 - \frac{x}{\alpha h}\right)^2 \quad (1)$$

Which leads to

$$\theta = \frac{w_0}{\alpha h} = \left[\chi_m + 2\chi_E\right]\frac{2}{3}\alpha h \quad (2)$$

Using this latter equation as well as the axial force and bending moment equation, we can deduce the M-θ law (cf. figure 8). We assume here that the axial force is equal to zero which is the case for the isolated box cells.

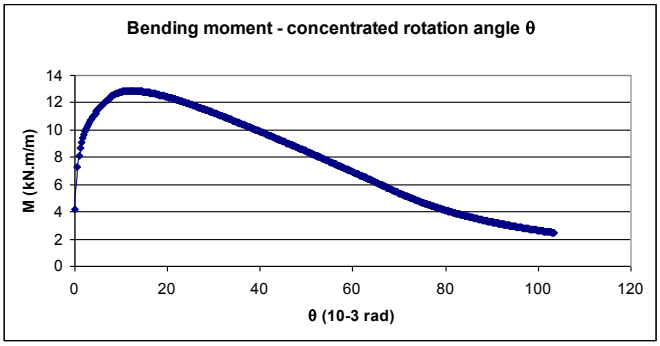

Figure 8 : M-θ law.

The mechanism is shown in figure 9 for load configuration n°4. We assume that the load is applied only on the perimeter of the steel rectangular plate (we neglect the 2 cm cut corners). Indeed, we consider that the load is equally distributed under the rectangular steel plate when the test starts, but the contact pressure becomes non uniform when the load increases and the

deflection of the specimen increases. When the deflection is rather high, the contact pressure only applies at the periphery of the rectangular steel plate. We suppose that the 3 cm sand layer is not sufficient to distribute load when the deflection increases.

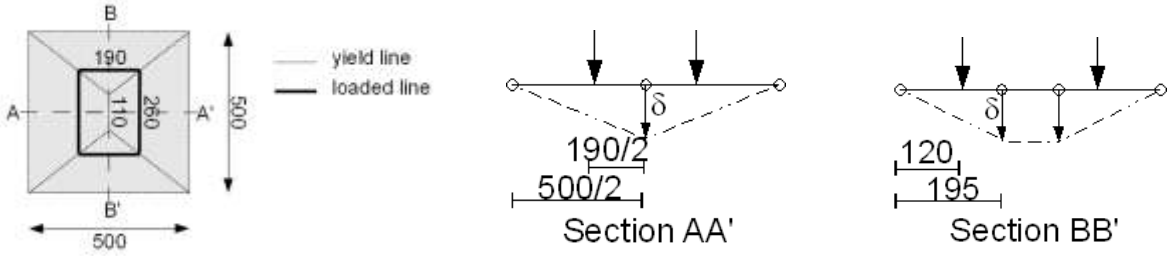

Figure 9 : mechanism with yield lines.

We can write the virtual power of internal forces only in function of the angles between the undeformable plates and their derivatives. For example, considering a yield line, with a length L between two plates having an angle θ and a virtual speed angle $\hat{\theta}$, the virtual power of internal forces for this yield line is :

$$P_{\text{int}} = L.\hat{\theta}.M(\theta) \tag{3}$$

As all these angles depend on the deflection δ, the virtual power of internal forces can be written as :

$$P_{\text{int}} = \hat{\delta}.f(\delta) \tag{4}$$

The virtual power of external forces is (cf. figure 9):

$$P_{ext} \approx \frac{500-190}{500}\hat{\delta}.F \approx \frac{120}{195}\hat{\delta}.F \tag{5}$$

Where F is the force exerted by the actuator.

Equalling virtual power of internal forces and virtual power of external forces enables to obtain the force in function of the deflection δ.

Results on single box cells in configuration 4

For a single box cell, the force function of deflection δ is shown in figure 10 and table 1.

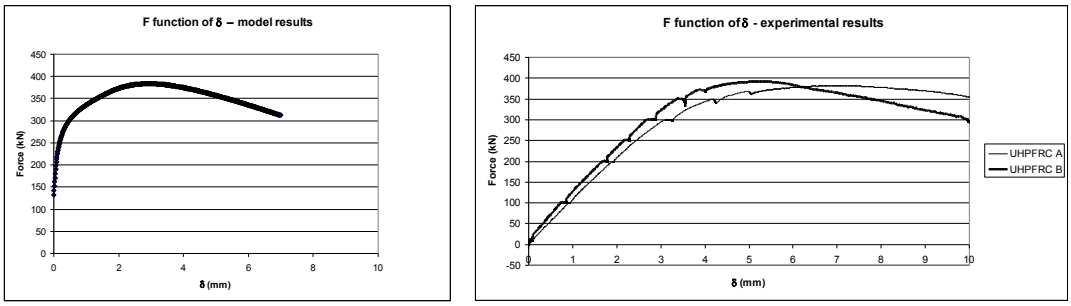

Figure 10 : comparison between analytical model and experimental results.

While the computed vs experimental maximum force is comparable, the predicted deflection is rather far from experimental results. First the deflection is not only caused by the breaking angle between plates supposed undeformable but also by continuous deformation of these plates, where cracks have appeared during the first two configurations of load. Moreover, several cracks have occurred in some yield lines, leading to a bigger rotation angle for a same bending moment.

Table 1: comparison between analytical model and experimental results.

	Maximal force	Deflection at max force
Yield lines model	378 kN	2.2 mm
UHPFRC A	382 kN	6.8 mm
UHPFRC B	391 kN	5.3 mm

Results on UHPFRC waffle slab

The main difference with the single box comes from the effect of prestressing on the upper deck. The resulting compressive stress is about 3.86 MPa in transversal direction and 4.35 MPa in longitudinal direction (cf. part 1) (on figure 8, AA' axis is in transverse direction). This compressive stress has an influence on the M-θ curve as can be seen in figure 11. The two curves in figure 11 are obtained using the same method than the one described in part 2 but with an axial force not equal to zero but corresponding to the mean stress obtained in both transversal and longitudinal direction.

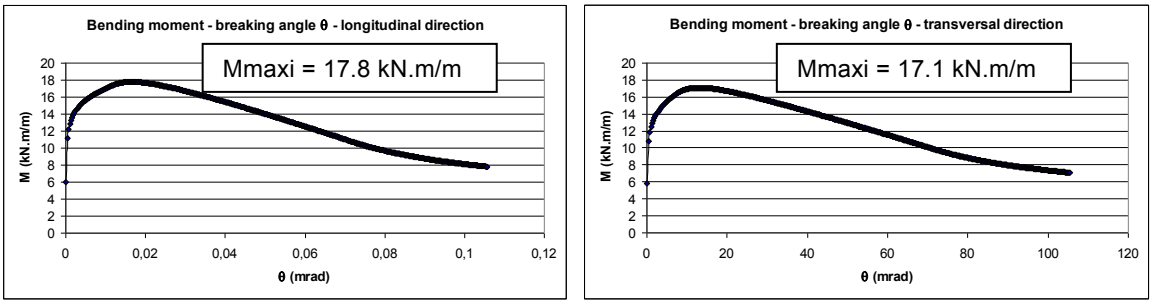

Figure 11: M-θ law for longitudinal (left) and transversal direction (right).

This leads to a maximum force equal to 523 kN. Figure 12 shows the force-deflection curve obtained with this method. The force obtained is much higher than the experimental failure load (maximum force between 352 and 417 kN with punching failure). This is perfectly consistent with the fact that shear failure occurred before local bending failure.

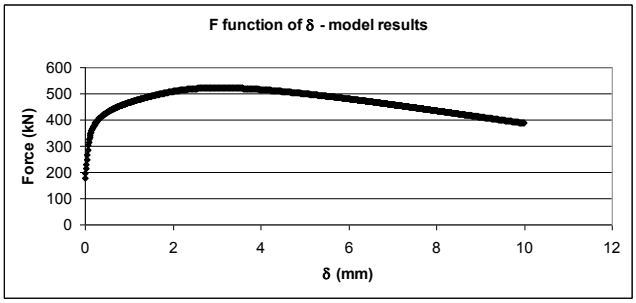

Figure 12 : Force versus deflection for local bending failure mode on prestressed waffle slab.

3 Finite element method

In order to better understand the behaviour of the single box cell including the formation of cracks, we have modelled it using CESAR-LCPC® F.E. software.

The model contains 3D hexaedric elements with quadratic interpolation. Figure 13 shows the geometry of the model.

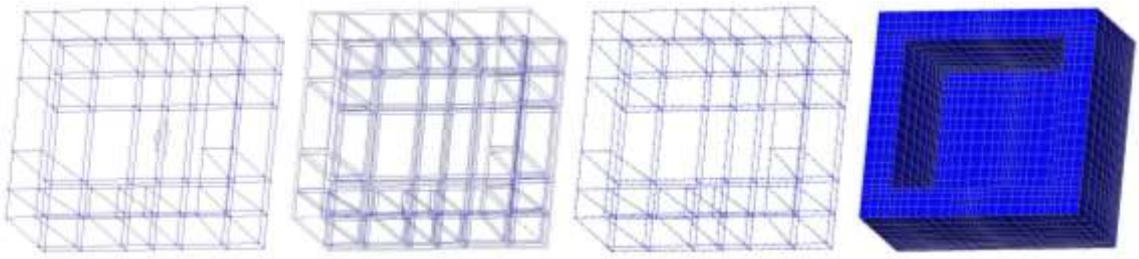

Figure 13 : Model geometry.

To take into account the non linear behaviour of UHPFRC in tension, we used the William Warnke plasticity criteria [8] with a compressive strength of 190 MPa and a tensile strength of 9 MPa.

Results

The maximum force computed is about 420 kN, that is slightly higher than the experimental results, despite the relatively low tensile strength taken into account.

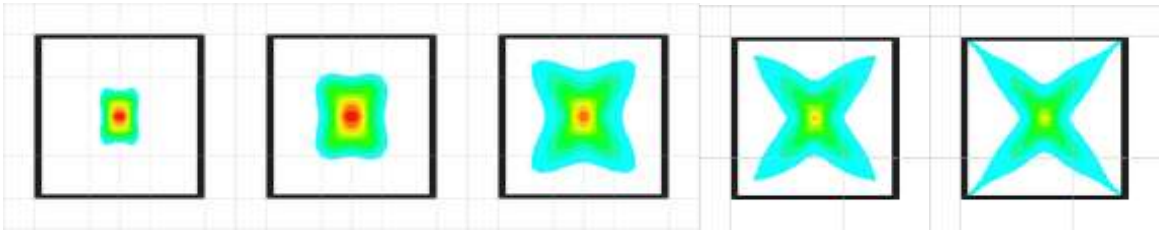

Figure 14 : Visualisation of plastic strain at bottom side of plate when increasing the load up to 382 kN.

Figure 14 shows the plastic strain at bottom side under increasing load. We can notice that the yield lines shapes appear under heavy load. Figure 15 shows the force-deflection curve for a FEM elastic model, a FEM non linear model (as described above), and experimental results with UHPFRC A and B. As observed with the yield lines analytical method, the maximum deflection is significantly underestimated in the model. Moreover, the predicted initial stiffness is much higher. A possible explanation is the pre-cracked state when applying the load in configuration n°4 (due to previous loading in configurations n°1 and 2). This hypothesis has been confirmed by comparing the experimental results of the first loading with configuration n°1 and FEM model results (cf. figure 16).

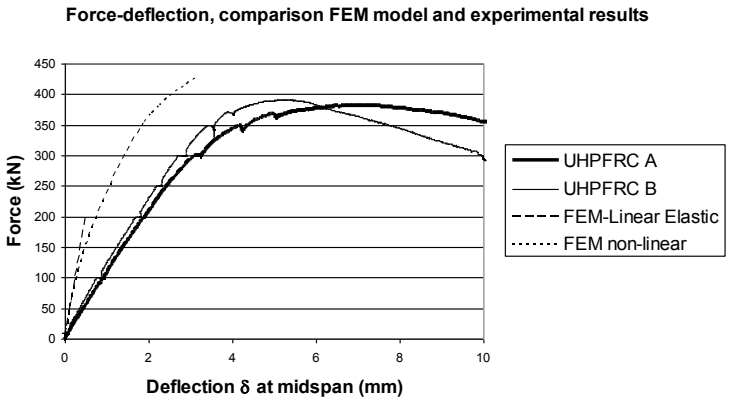

Figure 15: Force-deflection curve, comparison between FEM model and experimental results for load configuration n°4.

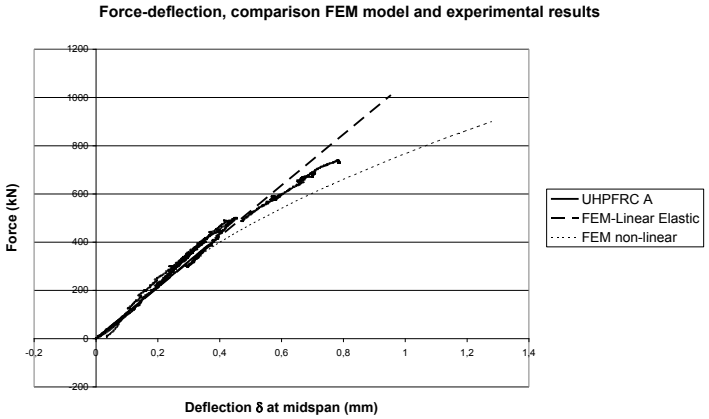

Figure 16: Force-deflection curve, comparison between FEM model and experimental results for load configuration n°1.

4 Conclusions

This paper highlights the possibility of using the yield lines method for assessing the resistance of thin UHPFRC plates under local loads.

FEM methods can be used to determine the directions of the yield lines in the mechanism and estimate roughly the resistance. It still needs to be improved for deflection prediction of complex UHPFRC structures.

References

[1] Chabrolin B., Kretz T., Laravoire J., Ponts mixtes acier-béton, un guide pour des ouvrages innovants – Projet national Mikti, Presses de l'école nationale des ponts et chaussées (2010).

[2] Toutlemonde F., Resplendino J., Sorelli L., Bouteille S., Brisard S. (2005) Innovative design of Ultra-high Performance Fiber–reinforced Concrete ribbed slab : experimental validation and preliminary detailed analyses, 7th International Symposium on Utilization of High Strength / High Performance Concrete, Washington D.C. (USA), june 20-22, 2005, ACI SP-228, *H. Russel ed., SP 228--76*, pp. 1187-1206.

[3] Toutlemonde, F. : Synthèse des études et résultats de validation d'un prototype de dalle gaufrée en BFUP, rapport d'essais experimentaux réalisés de 2004 à 2007 dans le cadre du projet national Mikti. *Imprimerie du laboratoire national des ponts et chaussées*, 2009.

[4] Toutlemonde, F., Renaud J.C., Lauvin L., Simon A., Behloul M., Bouteille S., Resplendino J. : Experimental validation of ribbed UHPFRC bridge deck. Proc. 2nd International Symposium on UHPC 2008, p771.

[5] Toutlemonde, F. et al : Local bending tests and punching failure of a ribbed UHPFRC deck. In proc FRAMCOS-6, Catania (Italy), 2007.

[6] AFGC-Sétra : Ultra-high performance Fiber-Reinforced Concretes, Interim Recommendations. Bagneux, France. 2002.

[7] Casanova, P., Rossi, P.: Analysis of metallic fibre-reinforced concrete beams submitted to bending. *Materials and Structures*, vol29, July 1996, pp354-361.

[8] Ulm, F.J. : Un modèle d'endommagement plastique : applications aux bétons de structure. Thèse de doctorat de l'ENPC,1994, *Presses du laboratoire des Ponts et Chaussées*, ERLPC, OA19.

Buckling Behaviour of UHPFRC-Panels under Compression

Bernhard Freytag[1], Martha Escobar[1], Werner Guggenberger[2], Linder Josef[1], Lutz Sparowitz[3]

1: Laboratory for Structural Engineering, Graz University of Technology, Austria
2: Institute of Steel Structures, Graz University of Technology, Austria
3: Institute of Structural Concrete, Graz University of Technology, Austria

14 Laboratory tests on 25 mm thick UHPFRC-panels demonstrate that the buckling behaviour is strongly influenced by early lateral cracking. Nevertheless a typical bifurcation behaviour appears. This paper briefly summarises the experimental investigation but mainly explain the results by means of theoretical exploration. It is shown that an orthotropic linear buckling theory describes simply and appropriately the bifurcation load in the cracked state obtained in the experiments. In order to investigate the field of plastic buckling, three uniaxial compressive material laws for UHPFRC are developed and applied to the Engesser-Karman-Shanley theory. The solutions obtained represent the plastic buckling of cracked but geometrically perfect plates and is hence the upper limit of plastic buckling capacity. In terms of an exploration of the entire buckling problem in the n-m plot (axial force - bending moment) it is clearly shown how the imperfections of real plates affect the respective buckling load and how the theories presented have to be extended.

Keywords: plate buckling, UHPFRC, buckling experiments, orthotropic buckling theory

1 Introduction

Plate buckling is a failure mode of plates that are mainly loaded in plane through compression or shear or both. The more slender a structure, the more likely is a buckling failure. Using the II. order theory the critical load can be calculated according to the theory of Euler. The buckling criterion is a point of bifurcation. It is valid for perfect plates with linear elastic materials. If theories of higher order are used, large deformations are taken into account, what leads to carrying capacities higher than the bifurcation load. Due to lateral tensile membrane stress the loading compression relocates from freely buckling regions to stabilised regions at the supported edges. This is a well known phenomenon in the field of steel structures and is called hypercritical capacity. In order to get a comprehensive theory covering the entire variety of slenderness the non linear material behaviour must finally be considered.

Conventionally reinforced concrete structures are rather thick and do not often show a buckling risk. Thanks to the high compressive strength of UHPFRC modern structures are designed light and slender and therefore require careful structural analyses including a buckling verification. In order to deepen the understanding in this field, an experimental program has been performed in the scope of the translational research project UHPC-Panels (L280-N07), funded by the Austrian Science Fund. This paper focuses on the analytical exploration of the experimental and numerical results which are briefly summarised in the following chapter. More detailed information about the experimental program is given in [1].

2 Experimental and Numerical Investigation

Specimens

The program consists of 14 specimens and covers 5 levels of slenderness. The buckle specimens under investigation have an I-cross section in the plan view. The flanges at the vertical edges of the plate ensure sufficient fixation of the edges during the tests. Rotations of the edges are possible to an extent which depends on the torsional stiffness of the flanges. The concave edges are rounded out in order to avoid notch stress as well as local disturbances in

fibre orientation. The specimens are cast with ductal®, a product of Lafarge. It is a fine aggregate UHPC reinforced with 2 vol.-% steel fibres. The high specimens have significant tolerances in thickness caused by the high casting pressure due to the highly flowable mix. Thus, the real distribution of thickness is measured for the subsequent consideration in numerical as well as analytical analyses. The most important properties of the material and the specimens are given in table 1.

Table 1: Specimens, material.

lable	b [cm]	h [cm]	a [cm]	average at the buckling region t [cm]	area of the corss section A [cm²]	$d = \frac{b}{1,34}$ d [cm]	slenderness d/t [-]	tested on prisms 4/4/16 E_c [N/mm²]	poisson ν [-]	tested on cubes 10/10/10 $f_{c,cube}$ [N/mm²]	$=f_{c,cube}\cdot 0{,}87$ $f_{c,shell}$ [N/mm²]	bifur-cation load [kN]	ultimate load [kN]	related ultimate load [-]	related bifurcation load [-]
50-01	50	10	80	2,5	172,3	37,3	**14,9**	57.300	0,15	198,1	172,3	-	2540	**0,86**	-
50-02	50	10	80	2,55	175,7	37,3	**14,6**	58.100	0,15	198,1	172,3	-	2817	**0,93**	-
75-01	75	15	120	2,6	263,5	56,0	**21,5**	57.300	0,15	198,1	172,3	-	3950	**0,87**	-
75-02	75	15	120	2,6	263,5	56,0	**21,5**	58.100	0,15	198,1	172,3	-	2856	**0,63**	-
75-04	75	15	120	2,55	259,9	56,0	**21,9**	56.700	0,15	180,9	157,4	-	2021	**0,49**	-
100-01	108	22	172	2,7	399,6	80,2	**29,7**	56.400	0,15	207,6	180,6	3982	3982	**0,55**	**0,55**
100-02	108	21	172	2,6	385,4	80,2	**30,9**	56.400	0,15	196,9	171,3	3957	3957	**0,60**	**0,60**
100-03	108	22	172	2,5	374,3	80,2	**32,1**	52.800	0,15	178,4	155,2	3395	3395	**0,58**	**0,58**
150-01	153	30	240	2,8	571,3	113,8	**40,6**	55.000	0,15	182,2	158,5	3500	3501	**0,39**	**0,39**
150-02	153	30	240	2,7	557,0	113,8	**42,2**	55.800	0,15	180,4	156,9	3500	3652	**0,42**	**0,40**
200-01	198	40	305	3	818,1	147,4	**49,1**	60.100	0,15	190,6	165,8	3600	3645	**0,27**	**0,27**
200-02	198	40	308	2,9	731,4	147,4	**50,8**	56.400	0,15	182,2	158,5	3300	3617	**0,31**	**0,28**

Experimental Set-up

The upper and lower edges are totally fixed in terms of well fitting compression contact between the specimen and the testing machine. A layer of ultra high strength mortar and a 1m deep steel element ensure uniform load distribution. The geometric dependencies between width and height as well as the flange depth are chosen in a way that the load-buckling behaviour of the specimen is nearly the same as that from an all-around simply supported quadratic plate (d/d in Fig. 1). This geometric coordination offers the possibility of comparisons to simple analytical solutions. 32 sensors record the deformations and strains as well as the load during the test. Detailed information about the measuring setup is also given in [1].

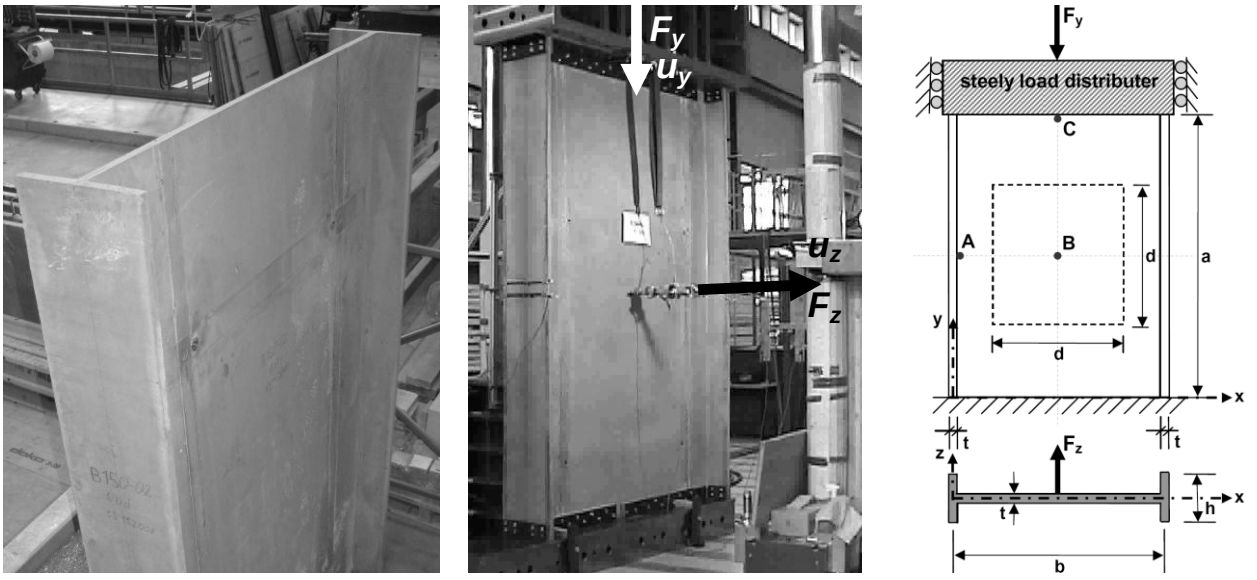

Figure 1: Specimen, experimental set-up.

Experimental procedure

Buckling is generally a spontaneous failure where lateral displacements suddenly increase without further load increase. In order to avoid that kind of collapse, the experiments presented here are controlled by the use of a new hybrid type of control. The sum of the vertical machine way $\mathbf{u_y}$ and the lateral displacement $\mathbf{u_z}$ (buckle) is increased steadily with a rate of 5μm/s. This method allows for remaining the measuring instruments on the specimen until the very end of the experiment. The decreasing part of the load-buckling curves can be observed and the crack pattern can be evaluated. A trouble free test procedure can only be assured if the direction of the buckle is known. FE simulations show, that a 1mm imperfection in the middle of the plate is small enough for getting load-buckle curves with a typical course to find the bifurcation load. Since the 1 mm imperfection cannot be manufactured, the initial buckle is imposed by means of a lateral single load $\mathbf{F_z}$. This load causes an elastically deformed buckle which must be kept up throughout the experiment. Thus, also the load must be constant throughout the test, which is realised by means of a deviated weight of ballast. Numerical investigation verified that the buckling behaviour of a non perfect specimen and that of the laterally preloaded specimen are similar.

The final test procedure consists of three steps. Firstly, the specimen is vertically loaded up to 300 kN. This assures that a certain lateral load can be transferred over the contact joint by means of friction. Secondly, the lateral load is applied and increased until the initial buckle amounts to 1 mm. Thirdly, the intrinsic load is applied.

Results and Findings

The key evaluation of the experiments is performed in the n-m diagram (Fig. 2). The specific development of axial force and bending moment is plotted for the three critical points A, B and C (marked in Fig. 1) and can comfortably be compared with the cross-sectional failure criterion and the crack criterion. Since section forces can not be measured directly, the curves are taken from carefully modelled numerical simulations. These consider non perfect, real wall thickness as well as actual strength and Young's modulus.

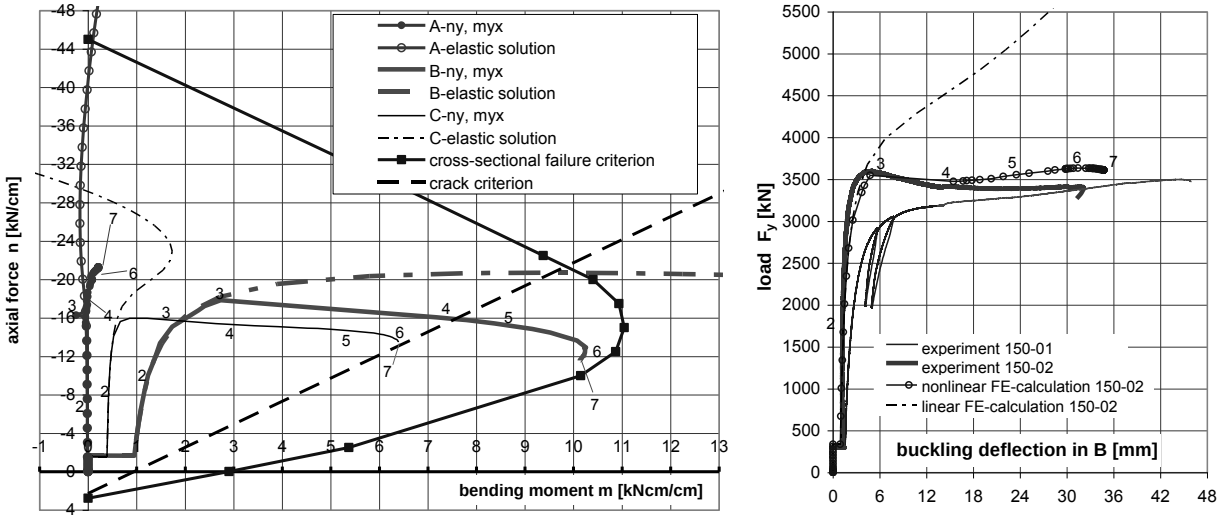

Figure 2: Experimental results of series 150.

The experiment 150-02 represents the classical case of bifurcation (Fig. 2 right). This is because the laterally imposed deflection obviously only compensates for a real lateral imperfection. It results in a loading with almost no bending until buckling occurs. Thanks to the special loading control the plateau of bifurcation is also nicely realised. At the end of the experiment some further load increase takes place. This is made possible by the formation of

horizontal cracks as can be seen in Fig. 2 (left) where the development of axial force and bending moment crosses the crack criterion at point 4. Axial forces relocate from the buckle to the fixed edges (see line A-n_y, m_{yx} point 7). As explained in the introduction this is a matter of hypercritical behaviour. At the more slender series 200 it is more distinct.

The above mentioned typical bifurcation load can be seen in several experiments of the series 100, 150 and 200. It is indicated through a peak in the n_y-m_{yx} development in the middle of the plates (point B). These lines are summarised in Fig. 3 and compared to their physically linear equivalent, one of each slenderness. The experimental bifurcation loads are always lower than the ideal critical Euler solution. This is due to the loss of lateral bending stiffness caused by vertical cracking or even by exceeding the lateral bending capacity. Finally it must be noticed, that the results of the more compact types (especially series 75) scatter significantly. The reason for that could not be reliably detected. It is most likely that an unintended weakness in the load introducing joint accounts for that. Since the real compressive stress is very high in these cases, it is very likely that the mortar layer plastifies and thus permits rotation.

3 Analytical approach

The following treatise is limited to the all around simply supported quadratic plate. This fundamental case leads to simple equations which can easily be extended for other edge relations or other supporting conditions later on. Experiments are compared with theory by means of the adequate quadratic plate ((d/d) in Fig. 1).

The buckling behaviour is highly affected by the crack formation in UHPFRC. It is important to distinguish between cracks in the lateral carrying system (vertical cracks) and in the longitudinal one (horizontal cracks). So it is advisable to specify different terms. In the following text, state II refers to cracks parallel to the loading direction, which always occur before transversal cracking. Cracks in both directions are referred to as state III. Nothing has been changed in the use of the term state I (uncracked) (see Fig. 4).

The hyper-critical behaviour, especially observed at the specimens 200, is not subject of the following treatise.

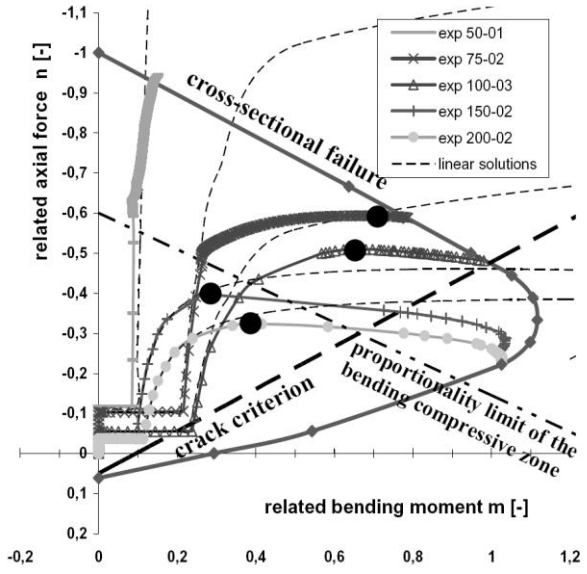

Figure 3: Overview of experimental results.

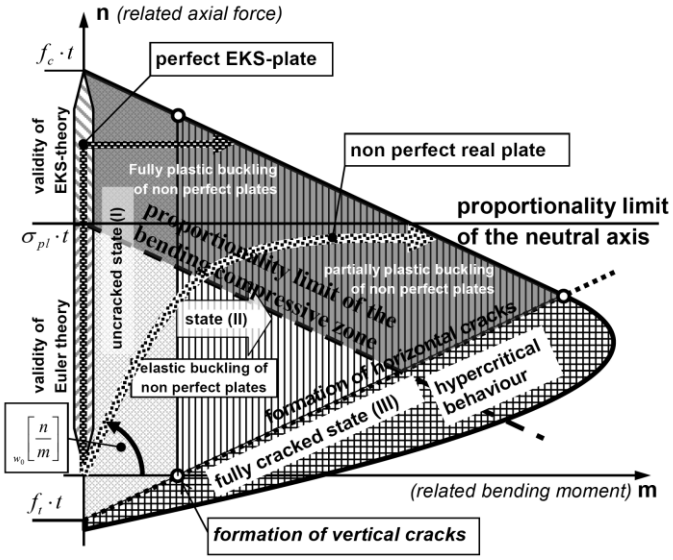

Figure 4: Theoretical principles in the n-m plot.

Elastic buckling under cracked conditions (state II)

State II represents reduced flexural stiffness orthogonal to the loading direction. The buckling load shall be calculated in form of the elastic bifurcation load of an orthotropic plate and subsequently be compared to the experimental results. The universally valid solution for short rectangular plates (one wave) is given in equation (1).

$$N_{buck,I} = \frac{E \cdot \pi^2}{12 \cdot (1-\nu^2)} \left(\frac{t}{d}\right)^2 \cdot \frac{1}{4} \left[k_y + 2\alpha^2 k_{yx} + \alpha^4 k_x\right] \quad (1)$$

$\alpha = \frac{c}{d}$ ..... width-to-height ratio

$k_y = \frac{K_y}{K_y}$, $k_x = \frac{K_x}{K_y}$ ..... related flexural stiffnesses, y=longitudinal, x=lateral

$k_{xy} = \frac{K_\nu + 2K_{yx}}{K_y} = \frac{K_y \cdot \nu + 2 \cdot G \frac{t^3}{12}}{K_y} = 1$ ..... related twisting stiffness

In the case of the quadratic plate α becomes 1 and as a consequence a simple partitioning of the buckling resistance arises: longitudinal bending 25%, lateral bending 25%, twisting 50%.

The experiments have shown, that the transversal bending resistance has either already been exceeded before the buckling takes place or it is reached at the same time. So it makes sense to calculate the lateral bending stiffness at the ultimate limit state (beginning of the pulling out of fibres). Doing this according to [2], the loss of lateral bending stiffness amounts to more than 90%. To simplify matters, a total loss of lateral bending stiffness is assumed for further calculations. Since the experiments do not show diagonal cracks, the twisting stiffness is considered to be still existent. Consequently, the elastic bifurcation load of cracked plates (state II) can be described by the following equation.

$$N_{buck,II} = \frac{E \cdot \pi^2}{12 \cdot (1-\nu^2)} \left(\frac{t}{d}\right)^2 \cdot \frac{3}{4} \quad (2)$$

In the field of metal structures a non-dimensional notation has been established. Its key advantage is that the relationship between slenderness and buckling load can be separated from material effects such as the real strength and stiffness of the plate. Doing so, the comparison between experimental results and analytical models is free from unintended errors. In order to benefit from that method, the slenderness (d/t), which is commonly used in structural concrete, must be multiplied by a material based constant. The so obtained related slenderness will be denoted as $\bar{\lambda}$:

$$\bar{\lambda} = \frac{d}{t} \sqrt{\frac{f_c \cdot 12\left(1-\nu^2\right)}{E \cdot \pi^2}} \quad (3)$$

f_c ..... compression strength

The buckling capacity is related to the cross-sectional ultimate capacity $N_u = f_c \cdot A$. Thus, the equation of the hyperbola of Euler (equations (1) and (2)) simplifies to equation (4) wherein the right part (partitions of buckling resistance) is substituted by the constant κ, which indicates the state of cracking ($\kappa_I = 1$ for state I, $\kappa_{II} = \frac{3}{4}$ for state II)

$$\frac{N_{buck}}{N_u} = \kappa_i \frac{1}{\bar{\lambda}^2} = \bar{\sigma}_e \quad (4)$$

These theoretical results as well as the experimental results are illustrated in Fig. 5 (right). The agreement between the observations from experiments and the theoretical results is very satisfactory. In particular the test results of series 150, which has been identified as the classical bifurcation case, verify the theoretical approach impressively. The bifurcation loads obtained in the experiments of series 200 are also in good accordance to the “orthotropic hyperbola”. The existence of hyper-critical capacity in series 200 is also confirmed in theory. The less slender experiments (series 100), which also buckled far from cross-sectional material failure (see Fig. 3), do not fully agree with the linear orthotropic theory. They indicate a small deviating trend. The reason for this will be disclosed in the following chapter.

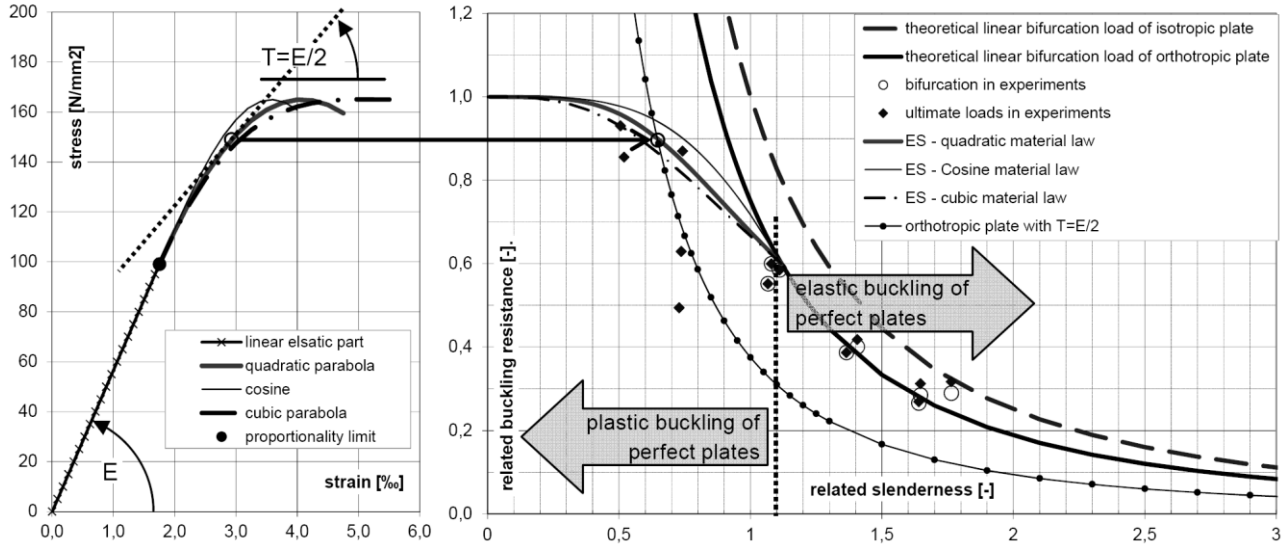

Figure 5: Elastic and plastic theory of bifurcation for state II in comparison to experimental results.

Plastic Buckling under Cracked Conditions (state II)

The linear elastic theory presented above loses its validity once the occurring stress exceeds the proportionality limit. In the cracked state (II) the Hook´s law is given up any way, but this fact has already been considered in terms of the orthotropic behaviour. Thus, the following discussion about stress and plastic material behaviour relates only to the longitudinal direction and concerns only compression.

Generally, a bifurcation theory is based on the indifferent equilibrium of a structure in an infinitesimal laterally deflected state. The resetting effects come from the three parts of buckling resistance shown in equation (1). Assuming that the twisting stiffness is not affected if the longitudinal stress exceeds the proportionality limit, the theory of Engesser, Karman and Shanley (EKS) should be well applicable for plastic buckling of UHPFRC plates. The theory has initially been developed for buckling of columns but it became also part of the DIN 4114A concerning buckling of rectangular steel plates [3].

In particular the theory contains a mechanically consistent reduction of the flexural stiffness if the compressive stress is beyond the proportionality limit. The stiffness is proportional to the actual slope of the material law; the tangent modulus T_c at the stress level of bifurcation.

$$\overline{\sigma}_{EKS} = \frac{T_c(\overline{\sigma}_{EKS})}{E_c} \cdot \overline{\sigma}_e \qquad (4)$$

E_c ..... Elastic modulus of UHPFRC

$T_c(\overline{\sigma}_{EKS})$ ..... Tangent modulus of UHPFRC dependent on $\overline{\sigma}_{EKS}$

How to find the solution of $\bar{\sigma}_{EKS}$ for a given material law is illustrated in Fig. 5 by means of one example point $T_c = E_c / 2$. Three types of uniaxial material laws are developed (Fig. 5 left). Simple and practicable, explicit solutions can be found with a quadratic parabola and a cosine approach. The constitutive laws are given in table 2, line 1. Line 2 shows the fracture strain for a given proportionality limit σ_{pl}. It is a matter of course, that it is also possible to specify the fracture strain and calculate the proportionality limit. The final explicit solution of plastic bifurcation is written in non-dimensional notation in line 3 of table 2 without further derivation. The third approach is a cubic parabola, which offers one more free parameter and hence allows for specification of both material parameters, ε_u and σ_{pl}. Its complicated solution is not provided in terms of a formula but it is illustrated graphically together with the others in Fig. 5.

Table 2: Explicit solutions for plastic bifurcation.

		Quadratic parabola	Cosine approach
1	material law	$\sigma = f_c - (\varepsilon_u - \varepsilon)^2 \cdot \left[\frac{E^2}{4 \cdot (f_c - \sigma_{pl})} \right]$	$\sigma = \sigma_{pl} + (\sigma_{pl} - f_c) \cdot \cos\left[\frac{E \cdot (\varepsilon - 1)}{f_c - \sigma_{pl}} + \frac{\pi}{2} \right]$
2	strain at ultimate stress	$\varepsilon_u = \frac{2 f_c - \sigma_{pl}}{E}$	$\varepsilon_u = \frac{\sigma_{pl}}{E} \cdot \left[1 - \frac{\pi}{2} \left(1 - \frac{f_c}{\sigma_{pl}} \right) \right]$
3	plastic buckling load	$\bar{\sigma}_{EKS} = \frac{-1 + \sqrt{(1 + 2p \cdot \bar{\lambda}^4)}}{p \cdot \bar{\lambda}^4}$ with $p = \frac{32}{9}(1 - \bar{\sigma}_{pl})$	$\bar{\sigma}_{EKS} = \frac{\bar{\sigma}_{pl} + \sqrt{\bar{\sigma}_{pl}^2 - (1 + p \cdot \bar{\lambda}^4) \cdot (2\bar{\sigma}_{pl} - 1)}}{1 + p \cdot \bar{\lambda}^4}$ with $p = \frac{16}{9}(\bar{\sigma}_{pl} - 1)^2$

The knowledge about the real uniaxial material law of the specimens is unfortunately bad. Only the compressive strength and the E-modulus are determined from tests on cubes and prisms respectively. As already mentioned in chapter 2 there is a strong scatter of the results in series 75. These two facts preclude a reputable comparison between experiments and plastic theory. In any case the theoretical treatment is very helpful to gain a fundamental understanding and experience about the key effects on buckling behaviour. The illustration of the theoretic values in fig. 5 is based on a proportionality limit of 60% of the strength, taken from former compression tests on samples of the same material. The fracture strain ε_u varies with the choice of the function from 3,6‰ to 4,1‰. In the case of the cubic approach ε_u is chosen as being 5,5‰ in order to learn about the sensitivity of the plastic bifurcation load to the material law. Special attention is drawn to the comparison between the series 100 experiments and the plastic as well as the elastic buckling theory. Since these experiments are fully reliable the deviation from the theory must be explained. The EKS-theory as well as the Euler-theory deal only with perfect plates which are loaded absolutely axially until the bifurcation load is reached. At this point the actual tangent stiffness works against buckling. This circumstance can be comprehended in the n-m diagram (see Fig. 4). If the slenderness is between $\bar{\lambda} = 0$ and $\bar{\lambda} = \bar{\lambda}_{pl} = 1{,}12$ (Fig. 5), the stress will reach the plastic part of the material law. Finally, an infinite imperfection suffices to buckle the plate and the bending moments will grow exorbitantly without any further increase of axial force. The point of buckling is situated at the ordinate. It is obvious, that the area of validity of bifurcation theories is limited to the n-axis. In order to get better understanding of all cases of buckling off the n-axis, the n-m area will be subdivided through

two additional criterions: the proportionality limit of the neutral axis and the proportionality limit of the bending compression zone. In the upper area the cross-section is fully plastifying, in the lower area only parts of the bending compression zone exceed the proportionality limit. According to the bifurcation theory, the specimen 100 would buckle elastically (Fig. 5), but the n-m plot (Fig. 3) clarifies, that in fact the buckling takes place in the area of partial plasticity. At this n-m point the neutral axis is still elastic but the bending compression zone already behaves nonlinear which results in a certain reduction of flexural stiffness. This also needs consideration in the theory. The magnitude of additional reduction of the buckling capacity due to partial plastification depends on the lateral imperfection or on lateral loads. These induce pre buckling bending moments which make the n-m path run to the fully plastic or to the partially plastic area. The final location of the buckling point depends on the magnitude of the imperfection w_0 which correlates with the initial slope of the n-m curve (Fig. 4). Improved solutions are expected if the relationship between axial force and lateral deflection, the decisive flexural stiffness and the classical buckling criterion are brought together.

4 Conclusions

The proposed orthotropic bifurcation theory captures the crack formation of UHPFRC very well. If changing conditions also lead to a drop of the twisting stiffness the theory can be easily extended. At high slenderness where the material remains elastic until buckling the theoretic bifurcation load represents also the real ultimate capacity, because there is no reduction due to imperfections [3]. Further increase of slenderness leads to hypercritical bearing behaviour which is not theoretically treated here. The theory of Engesser et al. represents a strict solution for plastic bifurcation of less slender plates. It only covers perfect plates and is hence just an upper limit of the buckling capacity. The exploration of buckling in the interaction plot (axial force – bending moment) points out how the present theories must be advanced in order to cover imperfections. A large area of partial plastification which is beneath the uniaxial proportionality limit clearly demonstrates that the border between elastic and plastic buckling (Fig. 5 right) will shift to the right (higher slenderness) if imperfections are considered. At the opposite end of the slenderness scale the interaction plot says that imperfections even affect the ultimate bearing capacity of compact structures. Here further tests are needed to compensate for the actually unreliable data. Finally, the small area of state I (Fig. 4) theoretically exists indeed, but a practical exploitation of it is absolutely unadvisable, because lateral cracking can also be initiated by shrinkage, temperature or other unintended loads.

5 Acknowledgements

This research is part of the translational research project UHPC-Panels (L280-N07) which is funded by the Austrian Science Fund. The material of the specimens is sponsored by Lafarge (Paris and Vienna) prepared with a special mixer, sponsored by the Gustav Eirich GmbH and tested at FH-Kärnten. The authors are deeply grateful for this support.

References

[1] Escobar, M.; Freytag, B.; Linder, J.; Sparowitz, L.: Experimentelle und numerische Untersuchungen zum Beulen von dünnen Scheiben aus UHPFRC unter Druckbeanspruchung. *Beton- und Stahlbetonbau* 107 (1), 2012.

[2] Heinzle, G.; Freytag, B.; Linder, J.; Sparowitz, L.: Rissbildung von biegebeanspruchten Bauteilen aus ultrahochfestem Faserbeton. *Beton- und Stahlbetonbau* 104 (3), p.134-144, 2009.

[3] Petersen, C.: *Statik und Stabilität der Baukonstruktionen: elasto- u. plasto-stat. Berechnungsverfahren druckbeanspruchter Tragwerke; Nachweisformen gegen Knicken, Kippen, Beulen*; Vieweg, Braunschweig, Wiesbaden 1980.

Analytical and experimental investigations on the introduction of compressive loads in thin walled elements made of UHPFRC by the use of implants

Jan Mittelstädt[1], Werner Sobek[1,2]
1: Institute for Lightweight Structures and Conceptual Design (ILEK), University of Stuttgart, Germany
2: IIT College of Architecture, Illinois Institute of Technology (IIT) Chicago, USA

Ultra-High-Performance Fiber Reinforced Concrete (UHPFRC) has advantageous structural and aesthetical properties that enable a wide range of practical applications [1]. Its given high compressive strength, almost free formability and potential application without any traditional reinforcement allows for the design of thin walled structural elements. Connecting these elements on site requires the development of new construction techniques. The authors are developing a construction method which allows thin walled elements to be point connected by means of so called implants. Design basis for the implants so far is the transfer of high local compressive loads. Thus, the utilization of bearing capacity in the connecting point by a homogeneous introduction of stresses becomes the main design issue. Based on a first implant design [2,5], further analytical and experimental investigations were carried out. Different effects on the stiffness, size, form and geometry of implant components were analysed and are presented in this paper.

Keywords: Ultra-high-performance concrete, Fiber reinforced concrete, Joining/Fitting, Prefabricated elements, Composite construction method, Implant

1 Introduction

Advantageous properties of Ultra-High-Performance Fibre Reinforced Concrete (UHPFRC) are its given high compressive strength, almost free formability, potential application without any traditional reinforcement and its excellent surface quality. Prefabrication of structural elements made of UHPFRC allows for a consistent high material quality [1]. However, requirements for the assembly, disassembly and recyclability as well as the compensation of tolerances and the accessibility of the gap between joined structural elements have to be taken into account for joining prefabricated elements on site [2]. New tendencies for the structural and architectural design by the use of UHPFRC elements arise. A reduction in weight, consumption of material, resources and energy as well as the creation of aesthetical surface impressions could go along. Practical applications for thin walled elements made of UHPFRC are for example shell structures, roofing's or facade elements. Considering the basic necessity for a prefabrication of structural elements made of UHPFRC, the development of a construction method moves into the center of attention for practical applications. The authors are developing a construction method for thin walled elements made of UHPRFC by the use of implants. Basis for the construction method are considerations of essential requirements coming from the design for assembly, disassembly, flexibility and the general transfer of high forces, thus, enhancing the material utilization. Connecting prefabricated structural elements by point connections meet these essential requirements for a joining technology on site. To avoid stress concentrations in the connecting area, the implant consists of two components. Compressive stresses are transferred by a longitudinal tooth bar and a thin tie element, a so called „fan", is designed to cover the lateral tension.

2 Joining structural elements

General aspects

Essential for the appropriate design process of joining, fitting, connecting and assembling structural elements are considerations related to the material involved. By categorising connections into a differential-, integral-, composite- and integrating construction method, constructive qualities and properties, characteristics for the assembly, disassembly and the recyclability are possible to evaluate [3]. The general function of a construction technology is primarily the structural connection of elements, in detail the transfer of loads. Secondary, aspects of coupling thermal and acoustic influences as well as deformations between connected elements are typical characteristics to be considered for the joining technology.

Connection types for structural elements

Connections of structural elements can be categorized in continuous and point connections. Continuous connections of structural elements allow for a continuous load transfer in the connecting area. Therefore the joint construction requires a sufficient bearing capacity for compressive, tensile and shear stresses. Point connections on the other hand result typically in stress concentrations in the connected area. A concentrated introduction of forces causes stress peaks that may affect local material failure and reduce the bearing capacity. Stress peaks caused by a concentrated load introduction, as shown in Fig. 1 for a compressive load, result in tensile stresses (σ1) perpendicular to the minimal principal stress (σ2). Fig. 1 shows exemplarily the stress trajectories caused by a concentrated load introduction in an isotropic shell element. The homogenisation (θP=0°) of stresses for isotropic materials can generally be achieved within a distance of ~d from the point of loading. The length in anisotropic materials may increase.

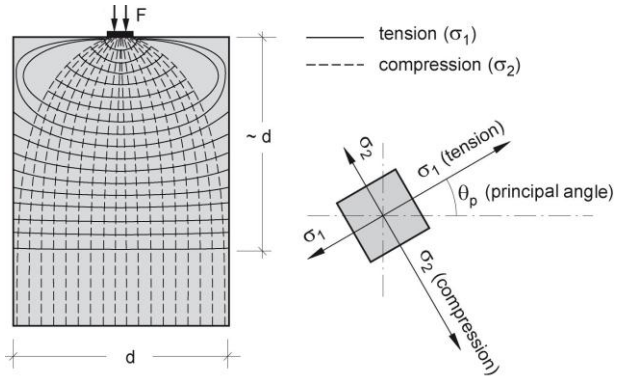

Figure 1: Stress trajectories using an example of a shell with isotropic material under concentrated load introduction (left); Definition of principal stress directions (right) [4].

The focus in this paper is on thin walled structural elements. Typical solutions for connecting those structural elements are: a) bonding due to glue, b) overlapping of thin reinforcement in the joint between elements with filling the joint afterwards, c) mechanically fastening of elements by means of prestressing. Drawbacks of aforementioned solutions are mainly caused by the required construction effort, precision, durability and the environmental influences as for instance temperature dependencies. A technique, focussed on in this paper, is a point connection of structural elements by the use of a built in part, a so called implant [2,4,5]. Advantageous properties are a minimized construction effort, a possible design for assembly and disassembly as well as for recyclability, possibilities for balancing tolerances, the prefabrication of joining elements and an optimized solution for the transfer of loads.

3 Implant design

General design issues

Basis for the implant design is the stress field caused by the introduction of a concentrated load in a thin walled element (Fig. 1). Reduction of the stress peaks, homogenization of the stresses and maximization of the applicable load introduction are the driving design issues for the component design of the implant. Based on a preliminary design carried out at the Institute for Lightweight Structures and Conceptual Design (ILEK), University of Stuttgart [2,5], a detailed investigation of the implant components for the concentrated load introduction is being carried out by the authors [4]. For the time being the compressive load introduction is the leading design parameter. The general focus in the design of the implant is on the analytical description of the mechanisms acting on the implant components. Developing a design concept for the practical application of implants as part of a construction method is designated by the authors. The mode of action of the implant for the introduction of concentrated loads in thin walled elements is based on two components [2]. First, a longitudinal tooth bar for the homogeneous introduction of forces into structural elements [5,6,7]. Secondly, a thin tie element, so called „fan“, designed to cover the lateral tension in the connecting area. Different parameters for the geometrical design of the implant components, influencing the structural behaviour, have been investigated and are presented in this paper.

Analytical investigations

Based on first developments [5], further analytical investigations on the implant design have been carried out for a detailed understanding of the general mode of action of the components. The main parameters, influencing the design of the implant are the size, length, material, construction, tip pressure, grade of toothing at the toothing bar and the differing stiffness of elements. As a start a numerical analysis on a linear elastic basis was carried out to firstly analyse the general behaviour of the toothing bar. At this stage of the design the influence of the load introduction, especially the design of the toothing bar, is in the centre of attention.

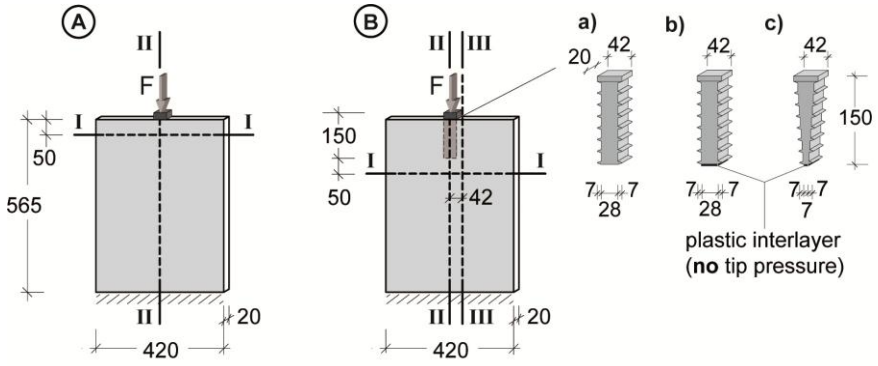

Figure 2: Numerically analysed geometries and variants of toothing bar.

Fig. 2 and Fig. 3 show the numerical results of a parameter study where the geometry of the toothing bar was varied (block form (type B_a)) vs. wedge form (type B_c))) and the tip pressure of the toothing bar (with (type B_a)) and without tip pressure (type B_b))). First, the design issue of a homogenization of stresses was looked at. Fig. 3 shows the compressive load distribution in a shell element by a concentrated load introduction. In comparison to the variants with an implant (type B)), results for a plain shell element (type A)) are also presented. A homogenization of compressive stress in the shell element by the use of a toothing bar is shown in Fig. 3. The ratio of stress peak to basic stress by using a toothing bar for the load introduction can be reduced from 4.6 to 1.5 using a wedge geometry for the toothing bar (type B_c)) or by using a block geometry with no tip pressure (type B_b)). Beside a homogenization

of compressive stress, also the tensile stress distribution in the element is in the focus of interest. For elements made of UHPFRC, the tensile strength of the material is about 1/16 of the compressive strength (Tab.1) and therefore relevant for the practical design of unreinforced elements.

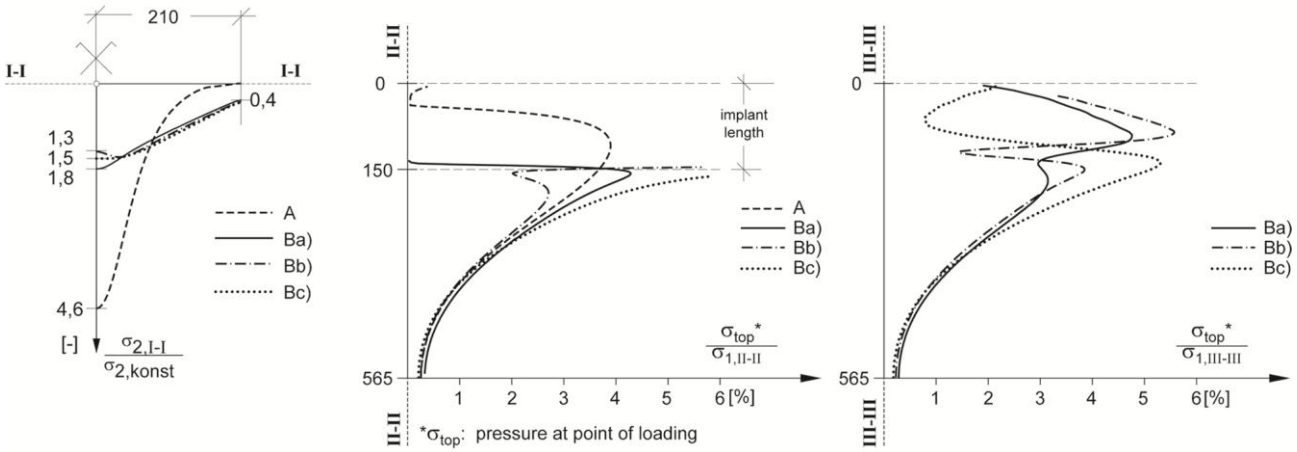

Figure 3: Distribution of principal stress (σ_2) in section 1-1 in relation to constant stress at the basis (left); Tensile stress (σ_1) in section 2-2 (middle) and 3-3 (right) in relation to the stress at point of loading.

In general, a shell element with an implant can geometrically be divided in two parts. Part one is the area beginning at elements top and vertically limited by the implant length. In this area the „fan“, working as reinforcement, is designed to cover exceeding tensile stresses in the UHPFRC material. In the area below the implant, only the tensile strength of the material is relevant for design. Fig. 3 presents the tensile stress distribution in the elastic stage (uncracked) for a shell element with a use of aforementioned different implant variants. It is shown, using the toothing bar for the load introduction, that the tensile stress distribution in both areas, above and beneath the implant, is strongly linked to the geometrical design of the toothing element. Conclusions from this numerical study are the basis for the following experimental investigations.

4 Experimental investigations

Programme

The test programme, according to afore investigated implant variants, consisted of 15 test specimen that were tested by a concentrated load introduction. 12 specimens were tested with an implant and 3 specimens without implants, loaded by a partial area pressure at specimens top. Investigated parameter on the implants design were the form of the toothing bar (type B_a) and B_c)) and the construction with and without tip pressure (type B_a) and B_b)). Additionally, the construction of the “fan” was varied and tested by using welded armature plates in comparison to a perforated „fan“ (type B_a) and B_d)). See Fig. 4 for the different construction types and tested implant variants. Each parameter has been tested by three specimens. A series of three specimens without an implant (type A)) was also tested for reference purposes.

Test specimen

The test specimens were 20mm thin shell elements made of UHPFRC. The geometrical ratio of loading area to specimen’s basis was 0.1 (42mm/420mm). Ratio of height to width was 1.3 (~560mm/420mm). The material used for the specimens was the UHPFRC Ductal®FM with 2 Vol.-% steel fibres. The construction of the implants consisted of high strength steel. Tab. 1 summarizes the material properties for the UHPFRC and the used high strength steel. The

components of the implant geometry have been prefabricated by a laser (toothing bar) and a high pressure water jet (“fan”), providing production accuracy. The construction of single parts then is based on fittings (Fig. 4). For the investigation of the effectiveness of the components by itself, especially the toothing bar, a mechanical separation of the components was considered for this test series. A long hole in the “fan” (Fig. 4) combined with a plastic interlayer between loading plate and “fan” enabled sliding between toothing bar and “fan”. Though, the compressive load introduction was only carried out by the toothing bar. The “fan” only carried tensile stresses. Six specimens were manufactured in one charge (Fig. 5). After striking, the specimens were put in a water tank for heat treatment. The water temperature was slowly increased to 90°C and kept constant for 48 hours.

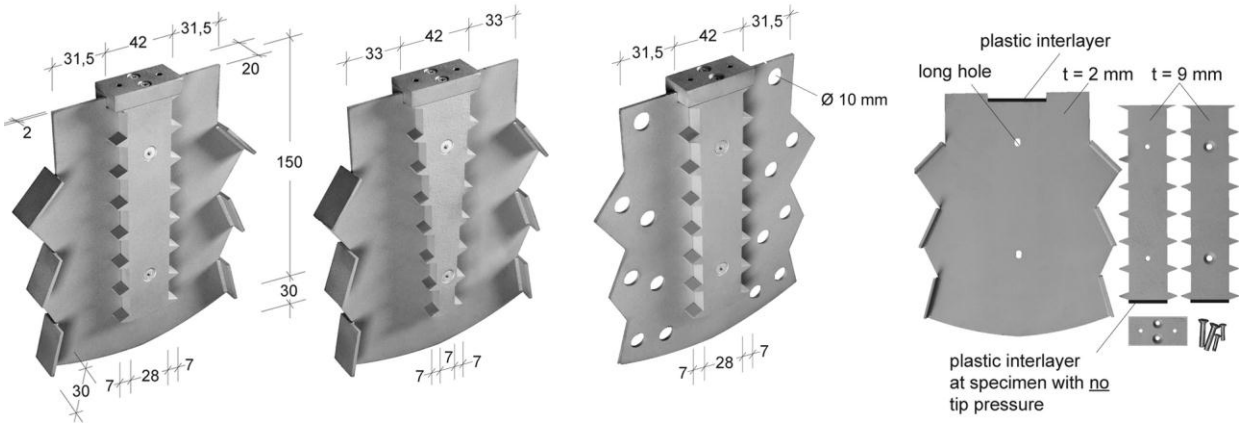

Figure 4: Tested variants of implant components: Type B_a), B_c), B_d) (from left); General implant construction (right).

Table 1: Material properties.

element	material	producer	compressive strength [MPa]	elastic tensile strength [MPa]	ultimate tensile strength [MPa]	modulus of elasticity [MPa]
shell	Ductal®FM	Lafarge	245[1)]	10,0[2)]	14,5[2)]	59.364[3)]
toothing bar	S960QL	Thyssen Krupp	960	-	960	210.000
„fan“	SZSM1200	Salzgitter Flachstahl	1200-1450	-	1200-1450	210.000

1) Mean value of tested control cylinder (h=200mm, Ø=100mm), 2) [9], cross section of test specimen 75mmx75mm, 3) [9], control cylinder h=200mm, Ø=100mm

Test setup

Fig. 5 shows the test setup at a 3MN universal testing machine. The tests were carried out displacement controlled at a test speed of 0,05 m/s. Two LVDT’s were diametrically positioned at the specimen’s top, measuring the displacement between specimen and loading plate. A further measurement by strain gauges was carried out at separated specimen [4]. The load introduction was carried out vertically with a high strength steel plate at specimens top. Specimen basis was linear supported in vertical directions and also horizontally to avoid influences due to stability effects.

Results

In Tab. 2 are the test results summarized regarding the mean values of the cracking force and the maximum compressive force. The coefficient of variation shows a largely consistent behavior for each implant type. Fig. 7 to Fig. 9 present the load displacement curves of the tested specimens. The different behavior and structural effects of the various parameters could be investigated. The failure mechanisms were basically equal in all cases. After reaching the cracking force, almost no loss in stiffness could be observed. First vertical cracks were observed below the implant. The crack width varied between maximal 0.1mm-0.4mm. Close to

the maximum force, splitting at the toothing bar started and was followed by a failure of the compression struts at the toothing flanks. Only a little residual strength could be observed after the specimen reached their maximal load. Some specimens failed explosively. Fig. 6 shows the toothing bar after maximum loading for the tested implant variants. A consistent behavior for the cause of failure could be observed for the different implants, although the cracking and maximum force were influenced by the design of the implant components. General observations regarding the structural behavior can be summarized as follows:

- the stress in the loading area increased nearly linear up to the maximum load, although cracking of the specimens occurred at an early stage.
- the partial area pressure for the specimens of series C3, without implants, only reaches a value of $1.1f_c$.
- the wedge form of the toothing bar caused a homogenization regarding the stress distribution along the toothing flank (Fig. 3), but resulted in an early cracking of the element and a general reduction of load carrying capacity.
- considered tip pressure decreased the stress at the flanks of the toothing bar and increased therefore the load carrying capacity. Further influences by the ratio of length and tip pressure have to be investigated.
- the stiffness of the “fan”, firstly analyzed by a perforated and armatured “fan”, had its influence on the maximum loading capacity. Further investigations on the influence and for the optimization have to be carried out.
- failure occurred by the loss of material strength at the toothing bar. The grade of toothing as well as the size has to be analyzed to optimize the load carrying behavior.
- the failure was largely not ductile for the investigated implant construction. By connecting the working mechanism of toothing bar and “fan” the post failure behavior is assumed to be more ductile. Further investigations on this are in progress.
-

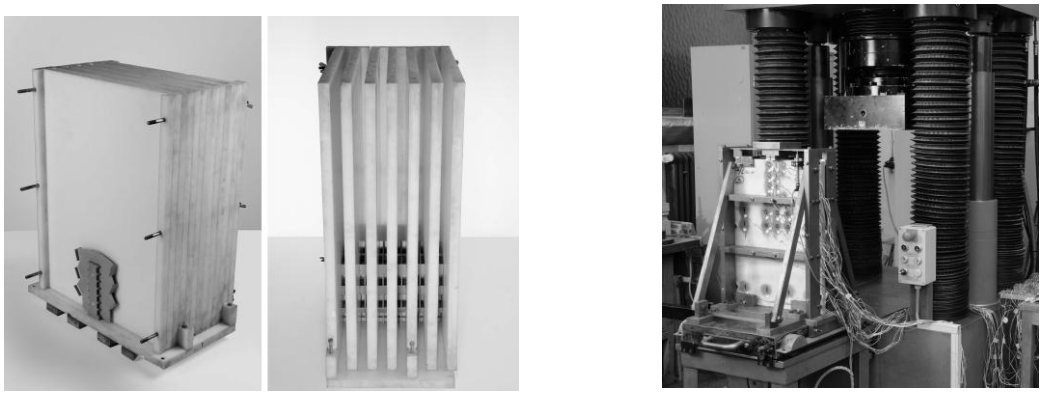

Figure 5: Casing of the test specimen with applied implants (left); test setup (right).

5 Conclusions

The numerical and experimental results presented in this paper summarize the development of a construction technique for thin walled elements made of UHPFRC by the use of implants. The assessment of the structural behaviour and the influence of the various parameters on the component design of the implants were the basis of investigations. The compressive load introduction was investigated so far, while further investigations regarding the introduction of tensile and shear loading are still in progress. The results presented illustrate the possible introduction of high local forces which are three times higher than without using implants. The need for further investigations on the implant size, construction and grade of toothing arises from presented investigations and will be carried out by the authors for a detailed understanding

of working mechanisms of the implant components and the development of a design concept. This process is accompanied by further tests and numerical nonlinear analyses.

Figure 6: Structural failure at toothing bar C5-2 (B_a)), C5-5 (B_b)), C6-1 (B_c)), C6-2 (B_d)) (test specimens backside).

Table 2: Summary of test results.

specimen	type	mean value FCrack [kN]	coefficient of variation [%]	mean value FMax [kN]	coefficient of variation [%]	mean value of partial area pressure at specimens top [MPa]
C3-1,2,3	A	163	12,5	218	15,6	260
C5-1,2,3	B_a)	182	9,3	550	5,7	655
C5-4,5,6	B_b)	253	2,3	655	1,8	780
C6-1,3,6	B_c)	114	35,3	524	6,5	624
C6-2,4,5	B_d)	181	6,3	493	1,9	587

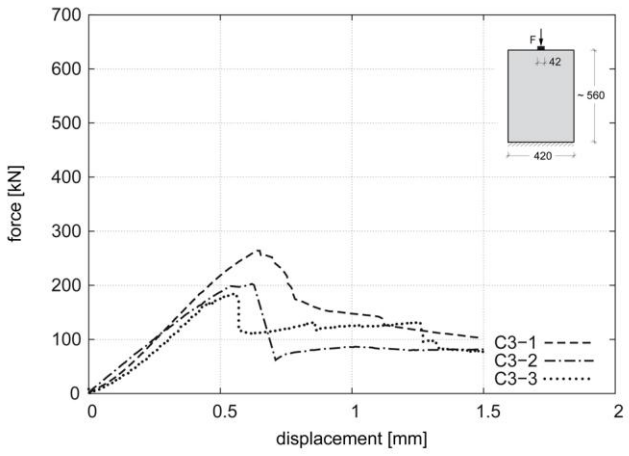

Figure 7: Force displacement curve for the test specimens type A)

6 Acknowledgement

The authors gratefully acknowledge financial support from the Deutsche Forschungsgemeinschaft (DFG) and express their thanks to Lafarge, Paris, for the support of the UHPFRC material Ductal®FM.

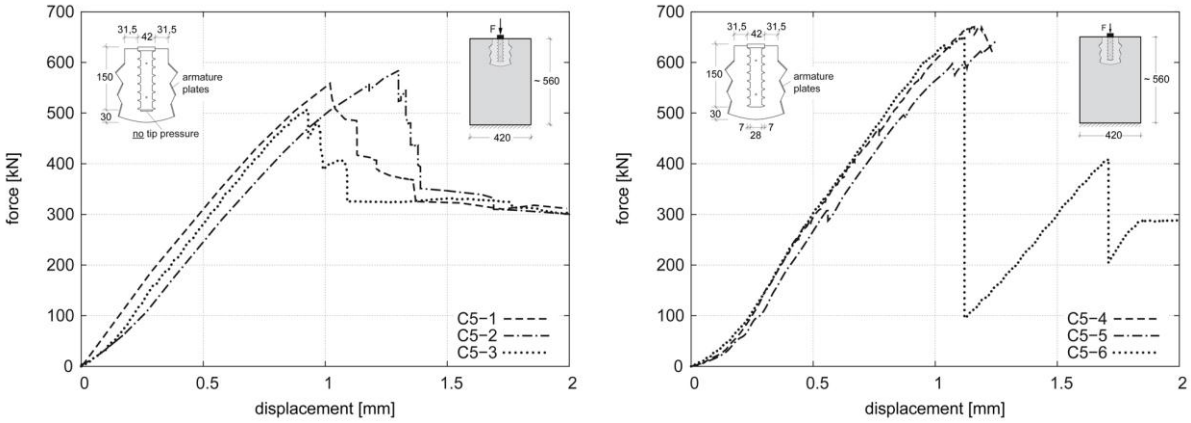

Figure 8: Force displacement curve for the test specimens type B_a) (left) and type B_b) (right).

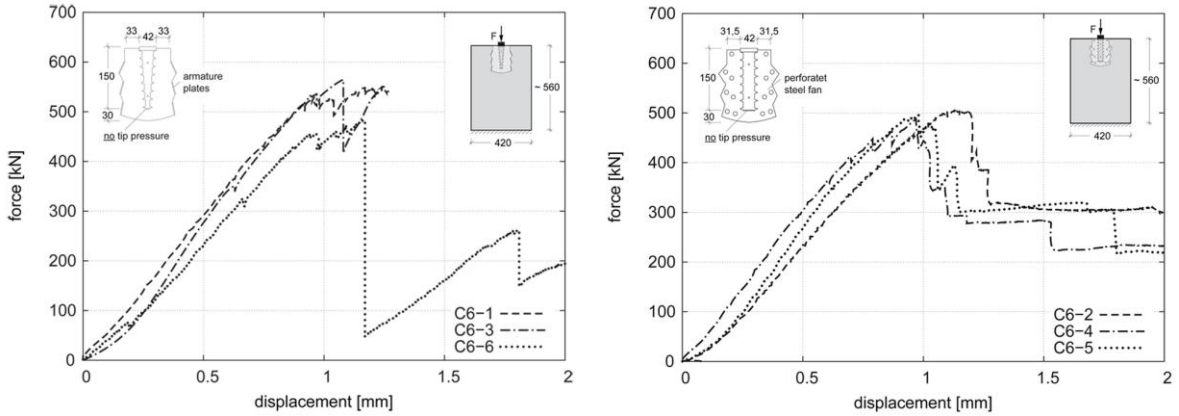

Figure 9: Force displacement curve for the test specimens type B_c) (left) and type B_d) (right).

References

[1] Deutscher Ausschuss für Stahlbeton: Ultrahochfester Beton – Sachstandsbericht. DAfStb 561, Berlin, 2008.

[2] Sobek, W., Mittelstädt, J., Kobler, M.: Fügen schlanker Bauteile - Untersuchungen zur Einleitung von Druckkräften mittels Implantaten. *Beton- und Stahlbetonbau* 106 (2011) 11, pp. 779-784.

[3] Sobek, W. (1995): Zum Entwerfen im Leichtbau. Bauingenieur, 70/1995, pp. 323–329.

[4] Mittelstädt, J; Sobek, W. (2012 in preparation): Lokale Lasteinleitung von Druck-, Zug- und Querkraftbeanspruchungen mit Implantaten in Bauteile aus ultrahochfestem Beton. Abschlussbericht zum Forschungsvorhaben SO 365/9-1 der Deutschen Forschungsgemeinschaft (DFG); Antragsteller: Prof. Dr.-Ing. Dr.-Ing. E.h. Werner Sobek, Institute for Lightweight Structures and Conceptual Design (ILEK), University of Stuttgart, Germany.

[5] Kobler, M.; Sobek, W. (2008): The introduction of High Forces into Thin-Walled UHPC Elements by the use of Implants. P. 683-690 in: Ultra High Performance Concrete. Proceedings of the Second International Symposium on Ultra High Performance Concrete. Schmidt, M.; Fehling, E.; Stürwald, S. (Hrsg.). University of Kassel, Schriftenreihe Baustoffe und Massivbau, Heft 10.

[6] Wiedemann, J. (1989): Leichtbau Band – 2: Konstruktionen. Berlin, Springer Verlag.

[7] Schmid, V. (2000): Hochbelastete Verbindungen mit Zahnleisten in Hybridtragwerken aus Konstruktionsbeton und Stahl. PhD, Institute for Structural Design II, Univ. of Stuttgart, Germany.

[8] Dehlinger, C. (2004): Stählerne Verzahnungen für Stahlbetonkonstruktionen. PhD, Institute for Lightweight Structures and Conceptual Design (ILEK), University of Stuttgart, Germany.

[9] Sobek, W., Frettlöhr, B., Plank, M., Quappen, J.(2010): Strukturoptimierte Türme für Offshore-Windenergieanlagen aus UHFFB in Segmentbauweise. Zwischenbericht zum Forschungsvorhaben FD-Nr.: SF-10.08.18-7-09.25; II3-F20-09-43. Bundesamt für Bauwesen und Raumordnung -BBR-, Bundesinstitut für Bau-, Stadt- und Raumforschung -BBSR-, Forschungsinitiative "Zukunft Bau", Bonn (Förderer); Antragsteller: Prof. Dr.-Ing. Dr.-Ing. E.h. Werner Sobek, Institute for Lightweight Structures and Conceptual Design (ILEK), University of Stuttgart, Germany.

Load-Bearing Behaviour of Sandwich Strips with XPS-Core and Reinforced HPC-Facings

Frank Müller, Christian Kohlmeyer, Jürgen Schnell
Institute of Concrete Structures and Structural Engineering, Technische Universität Kaiserslautern, Germany

In order to examine the load-bearing behaviour and the failure modes of sandwich strips with an extruded polystyrene foam (XPS) core and thin high performance concrete (HPC) facings, four different test series with a total number of 37 bending tests were carried out. A distinctive feature of this type of sandwich elements is the bond between the layers, which was only achieved by adhesion between the concrete and the XPS. No additional mechanical connecting devices were used. In the four test series, the manufacturing process, the type of reinforcement, the density of the XPS-core, as well as the layer thicknesses of the facings and the cores were varied. The influence of this variation on the load-bearing behaviour and the failure modes was investigated and compared. The results of this analysis are described in detail in the following paper.

Keywords: sandwich panels, high performance concrete, extruded polystyrene foam

1 Introduction

The primary aim of the research project “Sandwich Wall Panels with HPC-Facings” is the development of innovative three-layered sandwich wall panels which consist of two thin high performance concrete (HPC) facings and an extruded polystyrene foam (XPS) core. The dimensions of the concrete and the polystyrene foam layers can be chosen due to mechanical and thermal requirements. The necessary adhesion between the concrete and the XPS was achieved with an imprinted diamond-shaped texture of the XPS-surface (see Fig. 1) and without any additional mechanical connecting devices, comparable to the common sandwich panels with metal skins [1, 2].

In order to set up design recommendations for the practical application of the sandwich elements, extensive experimental investigations were carried out. The test programme consisted of four series of bending tests. In each test series, a particular parameter or property of the sandwich specimens was varied. In this way, the influence on the load-bearing behaviour and load-bearing capacity, as well as on the failure mode was investigated.

2 Specimens and test set-up

For the manufacturing of the sandwich specimens a fine-grained, self-compacting concrete was used (see Table 4). The mechanical properties of the concrete at 28 days were as follows: mean compressive strength $f_{cm,cube}$ = 125 N/mm², mean elastic modulus E_{cm} = 35390 N/mm² and mean flexural tensile strength $f_{ctm,fl}$ = 10.5 N/mm². For the XPS-core, insulating panels Styrodur® C with imprinted texture, supplied by the chemical company BASF SE, were used.

Similar to the recommendations given in standard EN14509 for “self-supporting double skin metal faced insulating panels” [3], a set-up for the testing of the sandwich strips was developed. The span and width of all tested specimens was 1150 mm and 200 mm, respectively. The

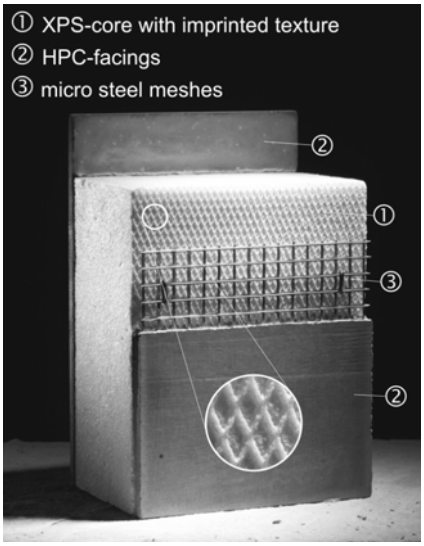

Figure 1: Arrangement of a sandwich panel reinforced with micro steel meshes.

facings of the specimens had a thickness of 10 - 20 mm and the core a thickness of 120 - 140 mm.

To achieve different moment to shear force ratios, 4-point and 3-point bending tests were carried out (see Fig. 2). During the tests, the deflections and strains on top of the concrete surface as well as the applied load were measured.

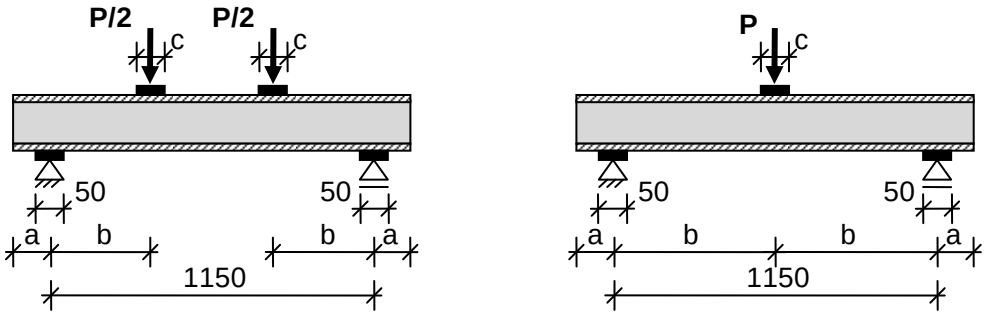

Figure 2: Schematic test set-up of the 4-point bending tests (left) and the 3-point bending tests (right).

3 Test programme

In the test programme, the parameters which were expected to have the greatest influence on the load bearing-behaviour and capacity were investigated. These parameters were as follows: (i) the manufacturing process, (ii) the type of reinforcement, (iii) the density of XPS and (iv) the layer thicknesses.

A summary of the four test series, with the varied parameters and all tested specimens is given in Table 1. The names of the specimens indicate the properties and parameters of each specimen, i.e. type of reinforcement, the batch of XPS and the layer thicknesses (see Fig. 3).

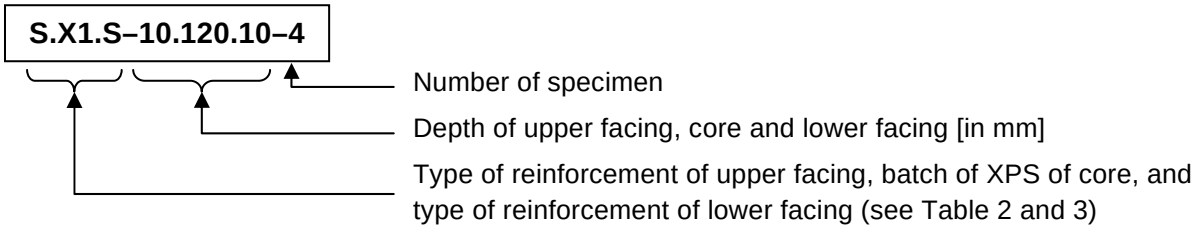

Figure 3: Description of the names of the specimens.

Manufacturing process

In the first testing series, the influence of the manufacturing process on the bond between the concrete and the XPS was investigated. Two different methods were used. In the first set, the XPS-core was pushed into the wet concrete. In the second set of tests, the concrete was cast on top of the XPS-core. In the following three series, the former method was used.

Type of reinforcement

In order to examine the influence of the reinforcement material on the load-bearing behaviour and failure modes, three different types of reinforcement, i.e. micro steel meshes [4] as well as glass and carbon fibre grids [5] were used. The material properties provided by the manufactures of the reinforcement are summarized in Table 2. In the case of the steel meshes and the glass fibre grids, 3 layers of reinforcement were used. Due to the high tensile strength and large cross section of the carbon fibre grid, one layer was sufficient.

Table 1: Test programme and varied parameters.

Varied parameters	Specimen	BTS[1]	a[2] [mm]	b[3] [mm]	c[4] [mm]	Failure mode[5]
Manufacturing process:						
XPS core pushed into wet concrete	S.X0.S–10.120.10–1[6]	4-PBT	100	350	50	E
	S.X0.S–10.120.10–2	4-PBT	50	400	50	F
	S.X0.S–10.120.10–3	4-PBT	50	400	50	F
	S.X0.S–10.120.10–4	4-PBT	50	400	50	F
	S.X0.S–10.120.10–5	3-BPT	50	575	50	A
	S.X0.S–10.120.10–6	3-PBT	50	575	50	A
concrete cast on top of XPS core	S.X0.S–10.120.10–7	4-PBT	50	400	50	F
	S.X0.S–10.120.10–8	4-PBT	50	400	50	G
	S.X0.S–10.120.10–9	4-PBT	50	400	50	F
Type of reinforcement:						
3 layers of glass fibre grids	**G**.X1.**G**–10.120.10–1	3-PBT	50	575	60	A
	G.X1.**G**–10.120.10–2	3-PBT	50	575	60	A
	G.X1.**G**–10.120.10–3	3-PBT	50	575	150	A
	G.X1.**G**–10.120.10–4	3-PBT	50	575	150	A
1 layer of carbon fibre grids	**C**.X1.**C** –10.120.10–1	3-PBT	50	575	60	B, C
	C.X1.**C**–10.120.10–2	3-PBT	50	575	60	B, D
	C.X1.**C**–10.120.10–3	3-PBT	50	575	150	C
	C.X1.**C**–10.120.10–4	3-PBT	50	575	150	E
3 layers of micro steel meshes	**S**.X1.**S**–10.120.10–1	3-PBT	50	575	60	A
	S.X1.**S**–10.120.10–2	3-PBT	50	575	60	A
	S.X1.**S**–10.120.10–3	3-PBT	50	575	60	A
Density of XPS:						
X2, density = 36.6 kg/m³	S.**X2**.S–10.120.10–1	4-PBT	35	400	50	A
	S.**X2**.S–10.120.10–2	4-PBT	85	350	50	A
	S.**X2**.S–10.120.10–3	4-PBT	35	200	50	F
	S.**X2**.S–10.120.10–4	4-PBT	35	200	50	F
	S.**X2**.S–10.120.10–5	4-PBT	35	200	50	F, G
X3, density = 45.8 kg/m³	S.**X3**.S–10.120.10–1	4-PBT	35	200	50	F
	S.**X3**.S–10.120.10–2	4-PBT	35	200	50	F
	S.**X3**.S–10.120.10–3	4-PBT	35	200	50	F
Layer thickness:						
facings = 10 mm, core = 140 mm	S.X4.S–10.**140**.10–1	4-PBT	50	400	50	A
	S.X4.S–10.**140**.10–2	4-PBT	50	400	50	E
	S.X4.S–10.**140**.10–3	4-PBT	50	400	50	A
facings = 15 mm, core = 120 mm	S.X5.S–**15**.120.**15**–1	4-PBT	50	400	50	F
	S.X5.S–**15**.120.**15**–2	4-PBT	50	400	50	F, G
	S.X5.S–**15**.120.**15**–3	4-PBT	50	400	50	F
facings = 20 mm, core = 120 mm	S.X5.S–**20**.120.**20**–1	4-PBT	50	400	50	F, G
	S.X5.S–**20**.120.**20**–2	4-PBT	50	400	50	F
	S.X5.S–**20**.120.**20**–3	4-PBT	50	400	50	G

[1] Bending test set-up, 3-PBT: 3-point bending test, 4-PBT: 4-point bending test
[2] Excess lengths at the supports (see Fig. 2)
[3] Distance between the supports and the point of load application (see Fig. 2)
[4] Width of the load distribution plate (see Fig. 2)
[5] Explanation of the failure modes see Table 5
[6] Span = 1050 mm

Density of XPS

In previous publications [6-8], it was established that the load-bearing behaviour and capacity of the sandwich elements strongly depend on the shear modulus and shear strength of the XPS. Furthermore, shear modulus and shear strength both correlate with the density of the XPS. The higher the density, the higher the shear modulus and shear strength. Because of this, the density of the XPS-cores was varied in an additional test series. Two types of XPS, i.e. X2 and X3, with an increased density of 36.6 and 45.8 kg/m³ were applied.

Table 2: Material properties of the reinforcement.

No.	Type of reinforcement	Material properties	
S	micro steel meshes (3 layers)	wire diameter = 1 mm grid spacing = 12.6 mm elastic modulus = 210,000 N/mm² tensile strength of wire = 400 N/mm²	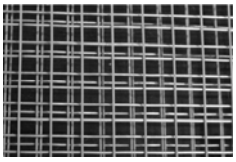
G	glass fibre grids (3 layers)	fineness of yarn = 620 tex grid spacing = 10.0 mm elastic modulus of filaments = 74,000 N/mm² tensile strength of filaments = 1,400 N/mm²	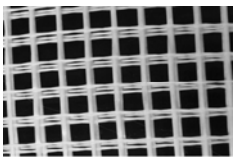
C	carbon fibre grid (1 layer)	fineness of yarn = 3,300 tex grid spacing = 18.0 mm / 10.8 mm elastic modulus of filaments = 240,000 N/mm² tensile strength of filaments = 4,000 N/mm²	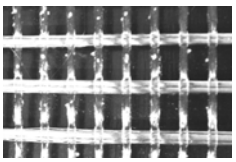

For all other specimens a XPS-type with an in average lower density was used. However, due to the manufacturing process of the material, the properties vary from batch to batch to some extent. Consequently, it was necessary to determine for each batch of XPS the shear properties. The results are summarized in Table 3.

Table 3: Material properties of the XPS.

No.	Density [kg/m³]	Shear strength [kN/m²]	Shear modulus [kN/m²]
X0	32.0	-	-
X1	36.7	220	8,700
X2	37.7	250	8,400
X3	46.9	297	10,500
X4	36.0	168	9,300
X5	31.4	182	6,900

Table 4: Concrete mix.

Raw material	[kg/m³]
cement CEM I 42,5 R	831,6
water	73,8
coarse sand (d_{max} < 2 mm)	694,0
fine sand (d_{max} < 0.5 mm)	223,9
quartz powder	205,4
silica suspension (incl. 50% water)	249,5
superplasticizer (PCE)	35,8

Layer thickness

The load-bearing behaviour is dependent on the bending and shear stiffness of the sandwich panels. The bending stiffness consists partly of the bending stiffnesses of the three layers and partly of the bending stiffness caused by the sandwich effect, which is dependent on the distance between the neutral axes of the two facing and the elastic moduli of the facings. The shear stiffness is dependent on the shear modulus and also on the distance between the neutral axes of the two facings and the thickness of the core [1].

Because the bending and shear stiffness both depend on the layer thicknesses of the facings and the cores, the ratio of the thicknesses were varied. In addition to the ratio of all other

specimens of 10 / 120 mm, three further configurations, i.e. 10 / 140 mm, 15 / 120 mm, 20 / 120 mm, were tested. All three configurations were reinforced with micro steel meshes. Instead of 3 layers of reinforcement, 4.5 and 6 layers were used for the specimens with a 15 and 20 mm facing thickness to keep the percentage of reinforcement constant.

Table 5: Failure modes.

No.	Failure mode		
A	tension failure of the reinforcement	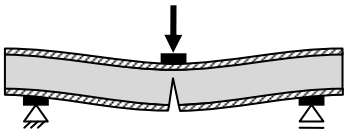	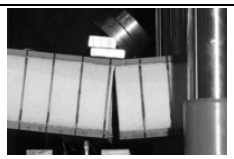
B	compression failure of the core at the point of load application	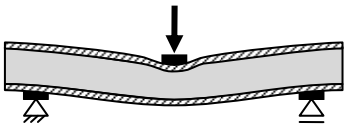	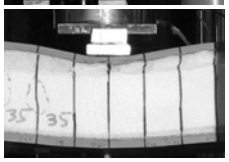
C	local bending failure of the upper facing	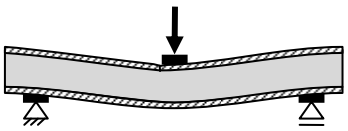	
D	local shear failure of the upper facing	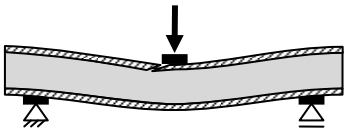	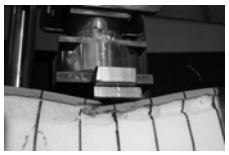
E	shear failure of the core and delamination of core and facings	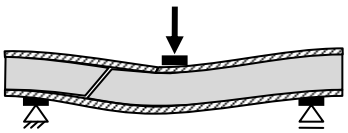	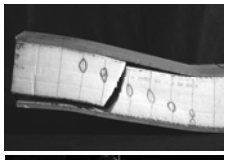
F	longitudinal shear failure of the bond between the core and the upper facing (at one or both ends)	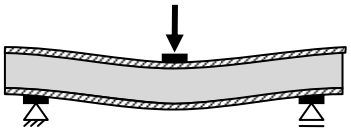	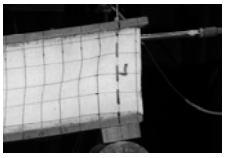
G	compression failure of the core at the supports (at one or both ends)	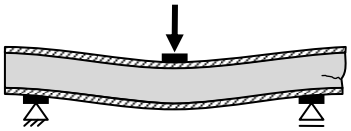	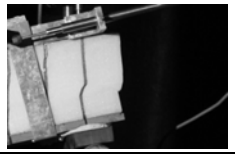

4 Test results

Failure modes

In the experiments, seven different failure modes were determined (see Table 5). The failure mode of each tested specimen can be found in Table 1.

The tension failure of the reinforcement (see Table 5, No. A) occurred mainly in the 3-point bending tests, due to the fact that this set-up has the highest moment to shear force ratio. However, in case of the experiments with the higher XPS-density, tension failure occurred also in two 4-point bending tests.

In case of the specimens with steel meshes, the tension failure of the reinforcement was indicated by a widening of the cracks, which was caused by the yielding of the steel. However, the specimens reinforced with glass fibre grids failed in all tests without any prior indication. In a fatigue test with cylic loading, the glass fibre reinforcement of specimen G.X1.G–10.120.10–3

failed after about 60 cycles of a deflection from 4.1 mm to 15.5 mm. In test G.X1.G-10.120.10-1, the failure occurred after 20 cycles of a loading from 0.5 kN to 7.5 kN. Because of its high tensile strength and its large cross section, it was not possible to achieve a tension failure of the specimens reinforced with carbon fibre grids.
In case of the 4-point bending tests, the majority of specimens failed due to a longitudinal shear failure of the bond between the core and the upper facing. This shear failure of the bond occurred either on the right or left side of the specimens, in some tests at both sides.

In the experiments with carbon fibre grids, the compressive strength of the XPS was exceeded at the point of load application. This failure resulted in a compression of the core (see Table 5, no. B). Along with these deformations, secondary failures of the facing occurred, which were either a local bending failure (see Table 5, no. C) or a local shear failure (see Table 5, no. D), both were located directly next to the point of load application. Another local compression failure of the core caused by an application of a concentrated load occurred at the supports. The core was crushed and a sharp bend developed at the end of the core (see Table 5, no. G).

A shear failure of the core along with a delamination of core and facing occurred in three tests of different testing series. By examining the specimens after testing, it was determined that there was a void between the concrete and the XPS, because the core had not touched the wet concrete in this area. Due to the void, the shear force could not be transferred continuously. As a result, the shear force concentrated at the edges of the void and caused the core to crack.

General load-bearing behaviour

The diagrams Fig. 4-7 show the moment at midspan as well as the shear force between the points of load application and the supports printed over the deflection at midspan, whereas the moment is represented on the left y-axis and the shear force on the right y-axis. As the deflection of the sandwich elements is caused partly by moment and partly by shear force, it is necessary to consider both effects in the analysis.

In general, the load-deflection behaviour of all specimens was up to a deflection of about 10 mm almost linear. After this linear part, the load-deflection curves developed differently. In case of the specimens which failed due to a longitudinal shear failure of the bond, i.e. failure mode F, and a compression failure of the core at the supports, i.e. failure mode G, the load-bearing behaviour was very ductile and a large yield plateau developed (see Fig. 4 and 7). No brittle failure occurred. In the majority of these tests, the experiments were stopped due to large deflections, although the applied load was still being transferred by the sandwich strips.

The load-bearing behaviour in case of the failure mode A, i.e. tension failure of the reinforcement, did not show large plastic deformations. Caused by the yielding of the micro steel meshes the load-deflection curves flattened slightly before the failure. In the tests of the specimens reinforced with glass fibre grids, failure occurred even in the linear part of the load-deflection curves (see Fig. 5).

The specimens which failed due to a compression at the point of load application, i.e. failure no. B, with the subsequent secondary failures C and D did not show a ductile behaviour (see Fig. 5). In case of a shear failure of the core, i.e. failure no. E, the cracking of the core led to a rapid drop of the load. However, the load deflection-behaviour of these specimens before the failure was similar to the specimens with the same parameter set and undamaged bond.

Load-bearing behaviour of the different test series

By analysing the curves of the test series “manufacturing process” (see Fig. 4), it can be seen that there was a minor difference in the load-bearing behaviour of the specimens with different manufacturing methods. The load-deflection curves of the specimens which were manufactured by casting the concrete on top were slightly stiffer than the specimens which were produced by

pushing the core into the wet concrete. Furthermore, the maximum moment of the former was in average about 2.4% higher.

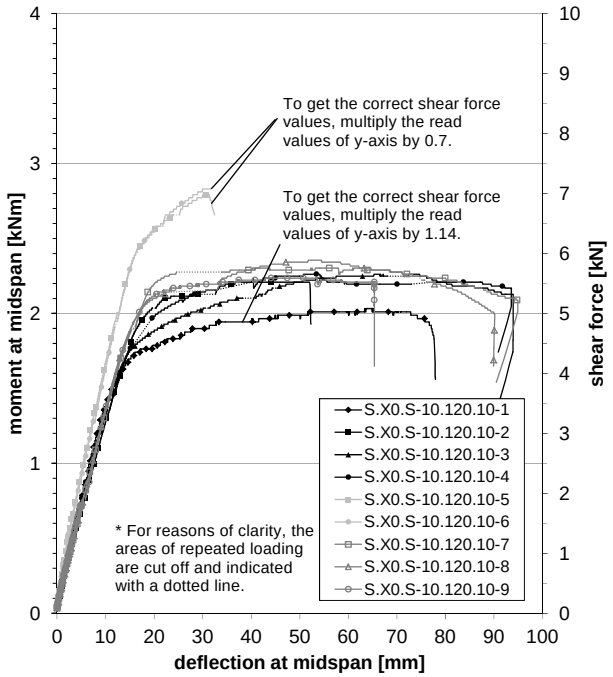

Figure 4: Load-deflection curves of test series "manufacturing process".

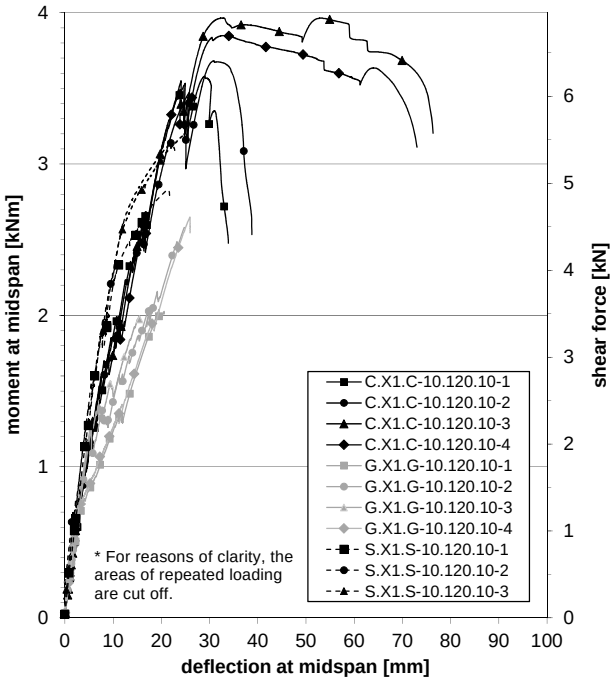

Figure 5: Load-deflection curves of test series "type of reinforcement".

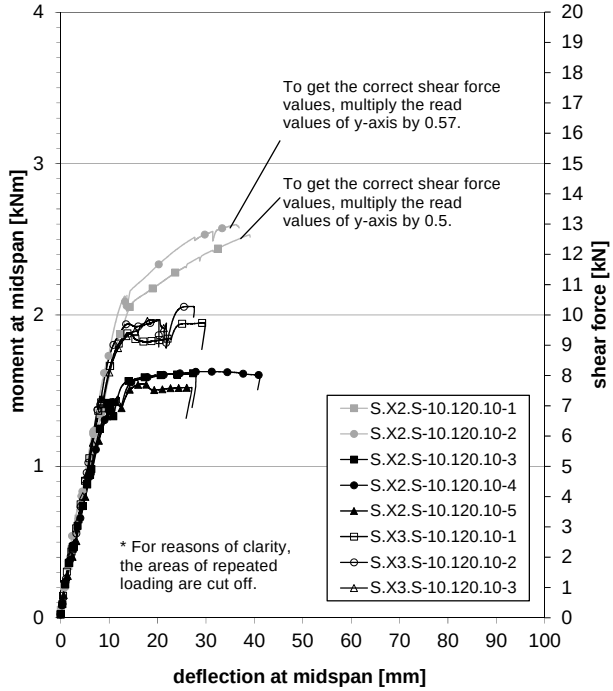

Figure 6: Load-deflection curves of test series "density of XPS".

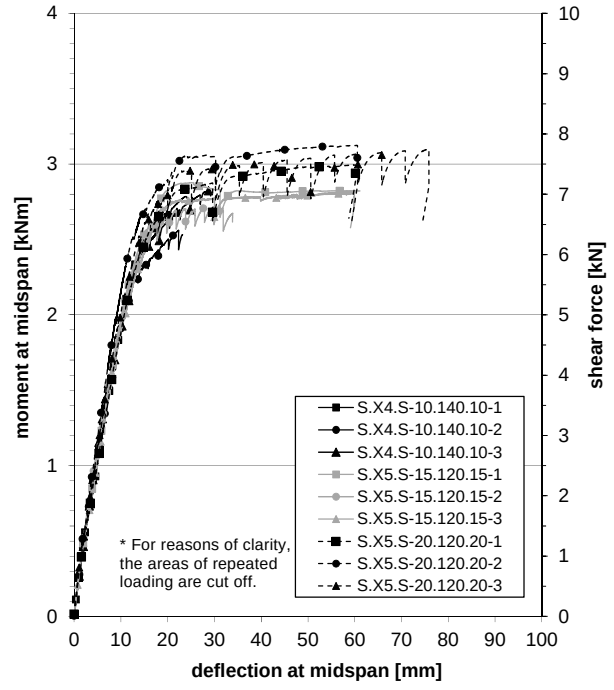

Figure 7: Load-deflection curves of test series "layer thickness".

In case of the test series "type of reinforcement", the load-deflection curves of the specimens were identical up to an applied moment of approximately 0.6 kNm. At this load level, the first cracks occurred in the lower facing. The load-deflection behaviour in this area of the curve was dependent on the tensile stiffness of the reinforcement. In the tests, the specimens reinforced

with micro steel meshes were the stiffest, followed by the specimens reinforced with carbon fibre grids. The specimens reinforced with glass fibre grids were the least stiff.
By comparing the curves of the test series “density of XPS” (see Fig. 6), it can be determined that the specimens with XPS-type X3 were slightly stiffer than the specimens with type X2. This difference in the stiffness resulted from the different shear moduli of the XPS. The maximum shear force which could be transferred was approximately 25% higher in case of the specimens with XPS X3. This fact can be explained by the higher shear strength.

When analysing the test series “layer thickness” (see Fig. 7), it needs to be considered that two different batches of XPS were used, i.e. the batch X4 for the specimens with 120 mm core and the batch X5 for the specimens with 140 mm cores. The densities of the two batches vary to some extent so that the specimens with the layer thickness ratio 10/140 mm cannot directly be compared with the specimens with the ratio 15/120 and 20/120 mm.

The specimens with the ratio 20/120 mm were slightly stiffer than the specimen with 15/120 mm. However, in general the influence of the layer thickness ratio on the load-deflection behaviour was not considerably large. This can be explained by the fact that the cracking of the concrete reduces significantly the stiffness of the facings.

5 Conclusions

With the help of the described experimental investigations, the load-bearing behaviour and the failure modes of the sandwich strips were analysed in detail. Due to the variation of the parameters and properties, different failure modes were achieved. Depending on the failure modes, the load-bearing behaviour of the sandwich strips was in some tests very ductile, e.g. failure mode F and G, and in other tests brittle, e.g. failure mode D.

In addition to this experimental investigation, a numerical investigation with the help of a finite element (FE) model has been undertaken. The FE-model is being calibrated and verified with the results of the described experiments. Based on the findings of this experimental investigation and the numerical investigations, recommendations for the design of the sandwich panels at the ultimate limit and serviceability limit state will be set-up.

This research project is financially supported by the “Ministerium für Bildung, Wissenschaft, Jugend und Kultur des Landes Rheinland-Pfalz” (Ministry for Education, Science, Young Persons, and Culture of Rhineland-Palatinate), the “European Regional Development Fund” and the companies “RETT GmbH” and “BASF SE”. All support is gratefully acknowledged.

References

[1] Stamm, K.; Witte, H.: Sandwichkonstruktionen. Berechnung, Fertigung, Ausführung. Wien, 1974
[2] Davies, J. M.: Lightweight Sandwich Construction. Oxford, 2001
[3] European Committee for Standardization: EN 14509 – Self-supporting double skin metal faced insulating panels, 2007.
[4] Hauser, S.; Wörner, J. D.: DUCON, ein innovativer Hochleistungsbeton. *Beton- und Stahlbetonbau* 94 (2), pp. 66-75, (3), pp. 141-145, 1999.
[5] Jesse, F.; Curbach M.: Verstärken mit Textilbeton. Beton-Kalender 2010: Brücken – Betonbau im Wasser, Berlin, 2010.
[6] Horstmann, M.: Zum Tragverhalten von Sandwichkonstruktionen aus textilbewehrtem Beton, Aachen, 2010.
[7] Müller F.; Kohlmeyer, C.; Schnell, J.: From research to practice - development of UHPC-sandwich wall panels. Proc. Current Scientific Challenges in Concrete and Steel Structures and Concrete Technology, p. 113–120, Gdansk, 2011.
[8] Kohlmeyer, C.; Schnell, J.; Müller, F.: Sandwich wall panels with UHPC facings. Proc. fib Symposium Prague 2011, p. 1209–1212, Prague, 2011.

Part Six

APPLICATIONS

Microstructural Optimization of High-Strength Performance Air Hardened Foam Concrete

Bernhard Middendorf, Armin Just
Department of Building Materials, TU Dortmund University, Germany

A new type of foam concrete was developed by combination of chemical foaming with aluminum powder and air hardening. Compared to autoclaved aerated foam concretes the manufacturing of this new type of foam concrete consumes less energy and the production is not stationary. The main advantage of this foam concrete is the combination of high thermal insulating properties with high compressive strength. The microstructural optimization of the matrix is based on the same approaches which were already developed for HPC and UHPC. The above mentioned properties are the results of a high density of the cement paste matrix combined with a dedicated pore size distribution of the macropores. The preparation of target-oriented properties are fulfilled by using a combination of ordinary portland cement, foaming agent, admixtures as well as additives.

Keywords: high performance foam concrete, chemically expanded, air hardened

1 Introduction

Buildings require energy during any period of their life cycle. The need for energy starts with the production of the building materials and the construction of the buildings. After that the use and operation of buildings need energy as well. Finally there is also energy required for the deconstruction of a building.

The paper deals with the benefits of multifunctional building materials. With present-day construction, any building material fulfills its specific task. Steel and concrete are used for load transfer but they do not achieve thermal insulation properties. For heat insulation, highly porous materials like foams are necessary. Such constructions have energetic disadvantages because several different building materials and components must be produced, assembled and also, finally, have to be disposed of or recycled. One advantage of multifunctional building materials is that one component and of course one material can fulfill different tasks in a modern building.

Mineral-bound foam is one such multifunctional building material. These fine-grained concretes have a density ≤ 2.0 g/cm^3 and are classified as lightweight concretes. Some of them are applicable for load bearing constructions with thermal insulation properties at the same time. Thereby the use of this class of building materials requires less energy and supports the establishment of sustainable construction.

Figure 1 shows the classification of mineral-bound foams according to the manufacturing process. The process of forming air voids in the fresh cement paste is significant. The methods of chemical expansion, as well as physical or mechanical foaming are well known and state-of-the-art. Autoclaved aerated concrete can be based on a mortar with finely grounded, quartzitic sand, cement and/or lime and water where a foaming agent, commonly aluminum powder, is added. The stable material is cured after being removed from its mould in a saturated steam atmosphere in autoclaves at high pressure within a few hours and thereby receives its final properties [1, 2].

Foam concretes are given their structure by using foam generators or stirring up the cement paste using foaming agents and fast rotating pug mill mixers. The paste consists of the binder, usually cement, finely grounded quartzitic sand, water and foam generating admixtures. After moulding the foam, the concrete hardens under normal atmospheric conditions.

During the mechanical foaming procedure, a foam agent is added to the mortar. Numerous voids are mechanically introduced by high speed mixers. A relatively unstable foam develops with an irregular structure and undefined void structures [3].

In practice, a more usual manufacturing method is physical foaming. A pre-manufactured foam consisting of water and chemical admixture is mixed with the additional components. Under these conditions, a more stable mortar with a fine pore structure can be created [3].

In addition to the two established representatives of mineral-bound foams, the possibility to produce chemically expanded, air cured, mineral-bound foams, with mechanical properties which allow their use as construction material has been established recently [4 - 7]. The physical-mechanical properties of these air cured foams - like density, compressive strength and thermal conductivity - are partially superior to the conventional cellular concretes hardened in autoclaves. This type of foam concrete hardens without using an autoclave and therefore without the need of additional production energy. Thus it makes the further development of this innovative foam concrete ecologically worthwhile.

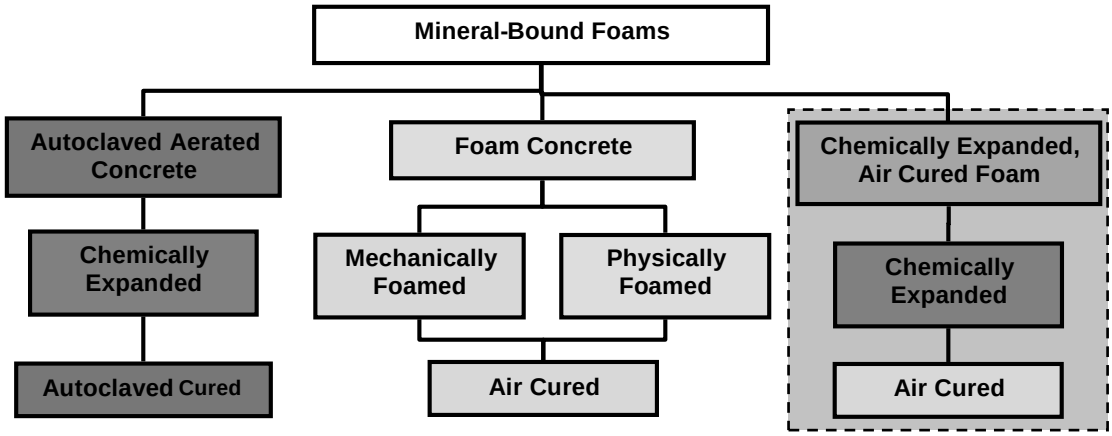

Figure 1: Classification of mineral-bound foams according to the manufacturing process.

2 Materials and Methods

The studies on foam concretes were made by using a cement paste without aggregates. In part, admixtures and additives were added. In Table 1 the materials used to produce the paste mixtures are listed.

Table 1: Basic materials used.

Binder	
cement	CEM I 42.5 R
Additives	
aluminum powder	I (average. ∅ 60 - 70 µm)
	II (average. ∅ 20 - 30 µm)
	III (average. ∅ 15 - 20 µm)
	IV(average ∅ 15 µm)
plasticizer	PCE
Admixtures	
microsilica	suspension

CEM I 42.5 R according to EN 197-1 [8] was used as binder. By using different grain sizes of the aluminum powder, the air void distribution in the hardened material was controllable, whereas the air void volume was adjusted by the total quantity of the aluminum powder.

The water/cement ratio (w/c) has a crucial influence on the increase of volume of the cement paste during expansion. In order to ensure an expansion in cement pastes with a low water volume, the introduction of superplasticizers on the basis of polycarboxylatether was necessary.

The structure of the hardened cement paste matrix was also optimized using a reactive microsilica suspension.

The samples were examined by means of light microscopy with an associated digital image analysis, scanning electron microscopy as well as by mercury intrusion porosity. The methods of investigation are described briefly in the following.

Digital image analysis:
For structural examination of foam concrete using digital image analysis, for detecting the pores it is essential that the sample is first saturated with coloured epoxy resin. When the epoxy resin is hardened the surface of the cross section was ground and polished. The digital image analysis detects air voids by means of differences of contrast between the cement paste matrix and the air voids which are filled with coloured epoxy resin. The properties of the air voids are determined by analysing polished cross sections by means of light microscopy for each individual air void.

For the investigations the digital image analising software Omnimet by Buehler GmbH and a light microscope by Zeiss were used.

Scanning electron microscopy:
SEM images were acquired using a Philips XL30i scanning electron microscope. Imaging was performed in high vacuum with the application of a conductive coating. The samples were made conductive with a carbon and gold layer. The accelerating voltage of the scanning electron microscope was 15 kV.

Mercury intrusion porosity:
For the determination of the porosity and the pore size distribution a mercury intrusion porosimeter was used. Therefore the samples were first dried. After this the samples were put into a dilatometer which was afterwards filled with mercury up to a pressure of 200 MPa. Therewith pore radii to 4 nm could be determined.

A mercury intrusion porosimeter type Pascal 140-240 by Porotec was used for the investigations.

3 Results and Discussion

Microstructure
The structure of the hardened cement paste implies the spatial arrangement of the reaction products and the partly unfilled or filled areas with an aqueous solution: the pores. The pore area is composed in its entirety by the gel pores, the capillary pores and the air voids. The existing gel porosity and capillary porosity are primarily responsible for the characteristics of the microstructure. Regarding the optimization of this structure of air hardened foam concretes, the same basic approaches maintain their validity for mineral-bound foams, as they were already developed in [9-13] for high performance concrete (HPC) or even for ultra high performance concrete (UHPC).

The influence of the reduction of the w/c ratio and the simultaneous use of microsilica solidify and consolidate the microstructure of the hardened cement paste matrix. In Figure 2 a hardened cement paste is represented on the left side, which was manufactured without additives and admixtures and with a w/c ratio of 0.60. The right side of Figure 2 illustrates a foam concrete, which is manufactured with the w/c ratio of 0.35 and the use of superplasticizers and microsilica. A clearly more consolidated and thus firmer structure is identifiable. This

structure of the foam concretes´ cement paste matrix is comparable with the structure of a HPC. Usual for UHPCs are w/c ratios less than 0.20. This low w/c ratio is not applicable for mineral-bound foams. The approach taken by UHPC technology for improving the hardened cement paste structure often make the generation of an arranged air void area more difficult even by using superplasticizers. The lower limit for w/c ratio of chemically expanded, air hardened, mineral-bound foams is 0.28, in the authors´ opinion [4]. Of course this sets limits to the properties of the structural optimized foams.

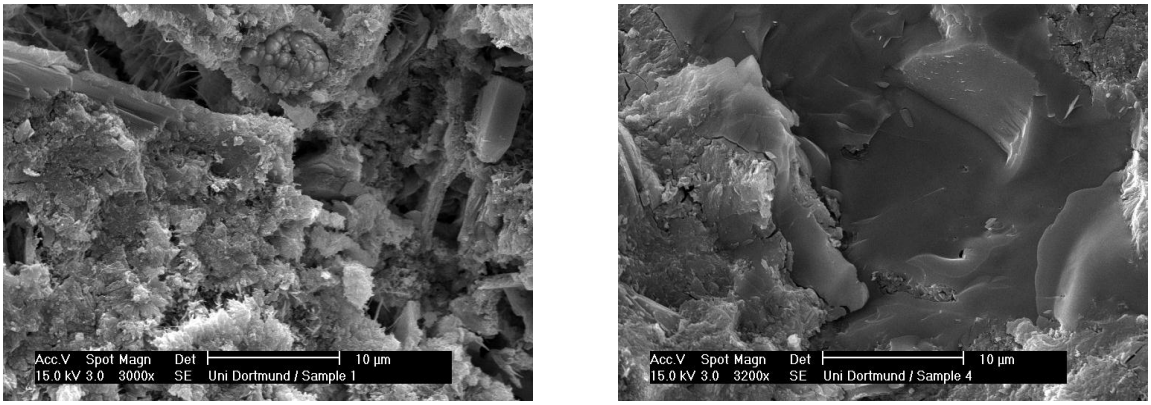

Figure 2: Microstructure of two foam concretes; left: w/c ratio = 0.60, without microsilica; right: w/c ratio = 0.35, microsilica content = 10 wt.%.

Figure 3 clearly shows the influence of the selected structure optimizing methods by comparing more than 100 foam concretes which differ in their compositions. The exponential trend lines, with numeric values of $R^2 = 0.979$ and $R^2 = 0.888$, agree nearly congruently with the measured individual values. The trend line of the foam concretes, which were prepared by using additives and admixtures, is clearly above the trend line of the foam concrete mixtures which were produced only with cement, water and aluminum. The increase in compressive strength depends on the mass density which is illustrated in Figure 3. The use of admixtures and additives increase the compressive strength by approximately 20 %.

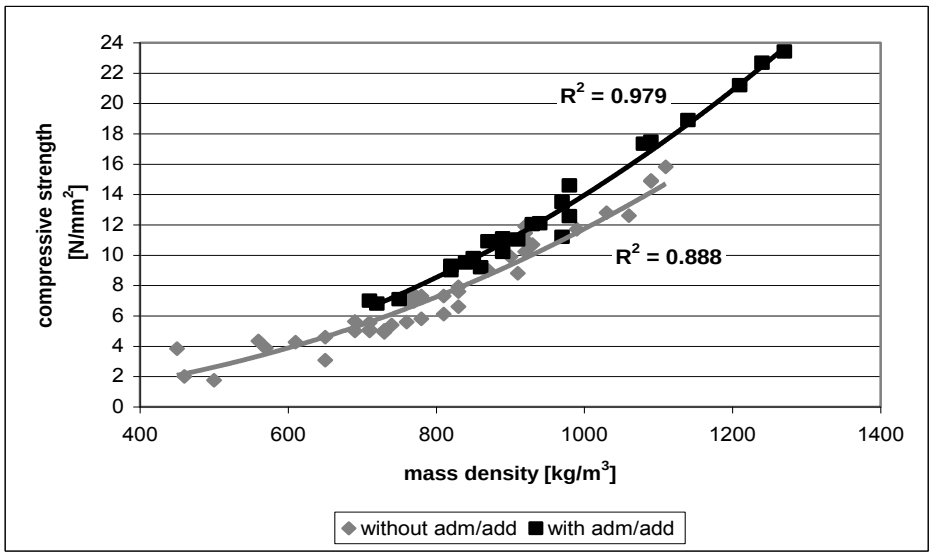

Figure 3: Compressive strengths as a function of the mass density with and without the usage of admixtures (adm) and additives (add).

The same methods for the improvement of the structure have a significantly larger influence on the properties of pure hardened cement pastes, which were manufactured without foaming agents. Comparative measurements of reference samples R0 to R9, according to Table 2, show an increase in compressive strength with decreasing w/c ratio and increasing content of

microsilica. The reference samples correspond, apart by the exclusion of the foaming agent, in their composition to the mixtures of the foam concretes, whose characteristics are represented in Figure 3. The compressive strength, of 48.0 N/mm^2, is the lowest of all reference samples. A reduction of the w/c ratio to 0.35 and the simultaneous addition of superplasticizer and 10 wt.% microsilica at the same time increases the compressive strength of the reference sample R9 to 105.7 N/mm^2 (Δ= + 120 %) which is conform to the compressive strength of a HPC.

The strength increase in the corresponding foam concretes is lower, as shown in Figure 3.

Table 2: Compositions and strengths of the reference samples.

Specimen	Cement	w/c ratio	Microsilica	Superplasticizer	Compressive strength
			[wt.%]	[wt.%]	[N/mm^2]
R0	CEM I 42,5 R	0.60	0	0	48.0
R1		0.45	0	0.25	77.5
R2		0.45	5	0.75	86.8
R3		0.45	10	1.10	87.2
R4		0.40	0	0.06	67.2
R5		0.40	5	0.40	81.9
R6		0.40	10	0.73	78.3
R7		0.35	0	0.20	93.2
R8		0.35	5	0.56	102.4
R9		0.35	10	1.00	105.7

The comparison of the microstructure of foam concretes and reference samples, whose compositions (Table 3) do not contain aluminum powder, results in comparable characteristics. The cumulative pore volumes of the investigated samples are comparable (Figure 4). The pore size distribution of foam concretes and non foamed cement pastes is also largely comparable. An influence of the foaming agent on the pore sizes < 5 µm cannot be determined. That means that the optimized microstructure of air hardened foam concretes is comparable with the microstructure of high performance concrete. The phenomenom of bottle neck pores limits the informational value of mercury intrusion porosimetry regarding to foam concretes. This is the reason why in this case only pores < 5 µm can be analyzed.

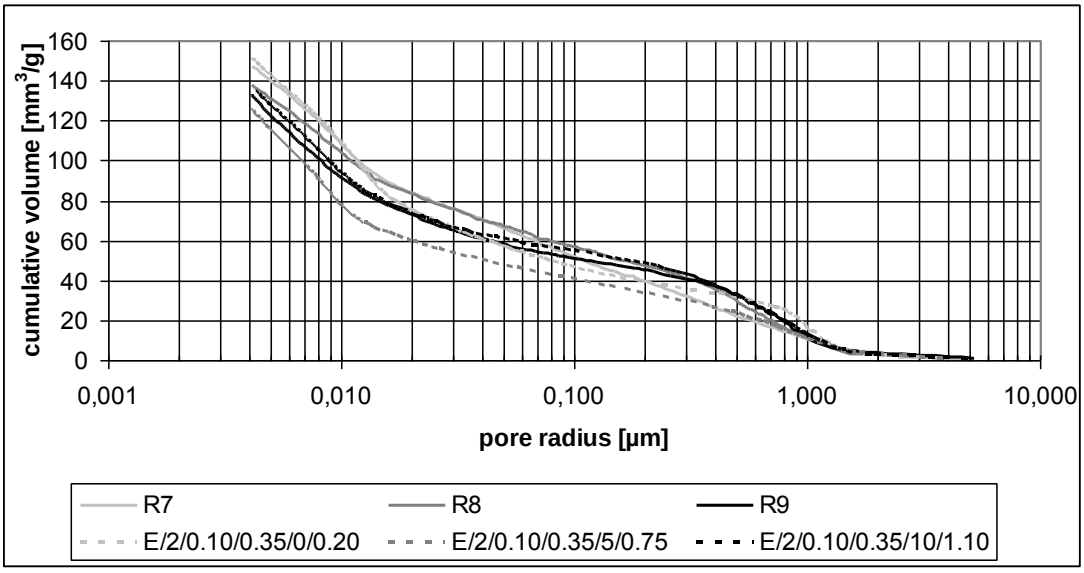

Figure 5: Cumulative pore volume of foams (E/…) and reference samples (R…)with a w/c ratio of 0.35 determined by mercury intrusion porosity

Structure of Air Voids

The air voids must be responsible for the slight increase of compressive strength on air hardened foam concretes, because the optimization of the microstructure leads to the expectation of a higher strength increase.

Getting a detailed view of the structure of the porosity of the air voids, the results of 3 selected sample mixtures are examined and compared to each other. The sample A does solely consist of water, cement and aluminum powder. This three-substance-system is extended by a superplasticizer in sample B. In sample C the mineral-bound foam represents a five-substance-system consisting of water, cement, aluminum powder, superplasticizer and microsilica. Thereby the microstructure of the hardened cement paste of specimen C is comparable with the microstructure of HPC.

Although the composition of the single samples differentiate extremely, density and compressive strength are very similar. The compressive strength has values between 10.9 and 12.0 N/mm^2 with densities of 0.92 and 0.93 kg/dm^3. The compositions and the properties of the selected mixtures are shown in Table 3.

Table 3: Recipes and properties of three selected sample mixtures.

Specimen	w/c ratio	Aluminum powder	Microsilica	Super-plasticizer	Density	Compressive strength
		[wt.%]	[wt.%]	[wt.%]	[kg/dm^3]	[N/mm^2]
A	0.60	0.05	0	0	0.92	11.9
B	0.40	0.08	0	0.04	0.92	10.9
C	0.40	0.10	10	0.85	0.93	12.0

The shape and the size distribution of the air voids are responsible for the properties of the hardened foam concrete. The structural differences within the air voids become clear when examining the roundness of the pores. The roundness of all examined samples tends to decrease with rising pore sizes (Figure 6).

For all samples the roundness of the pores with a surface < 0.1 mm^2 is very similar. The roundness has values from 0.74 to 0.78 and has the least deviation from the cross section of all classes. Since these pores develop in all cases similarly, their influence on compressive strength must take place via the pores with an area larger than 1.0 mm2. The roundness of the air voids of the class >1.0 mm2 ranges between 0.50 for sample A to 0.27 for sample B. These differences are justified in the consistency of the fresh paste. The high water content of the sample A permits the production of a foam with the dry bulk density of 0.92 kg/dm3 when using an aluminum powder content of 0.05 wt.%. The remaining samples represented here reach this dry bulk density only with an accordingly higher aluminum ratio of 0.08 and 0.10 wt.%. This means that the roundness of the air voids decreases when the generation of gas bubbles is obstructed by stiffer fresh paste consistency.

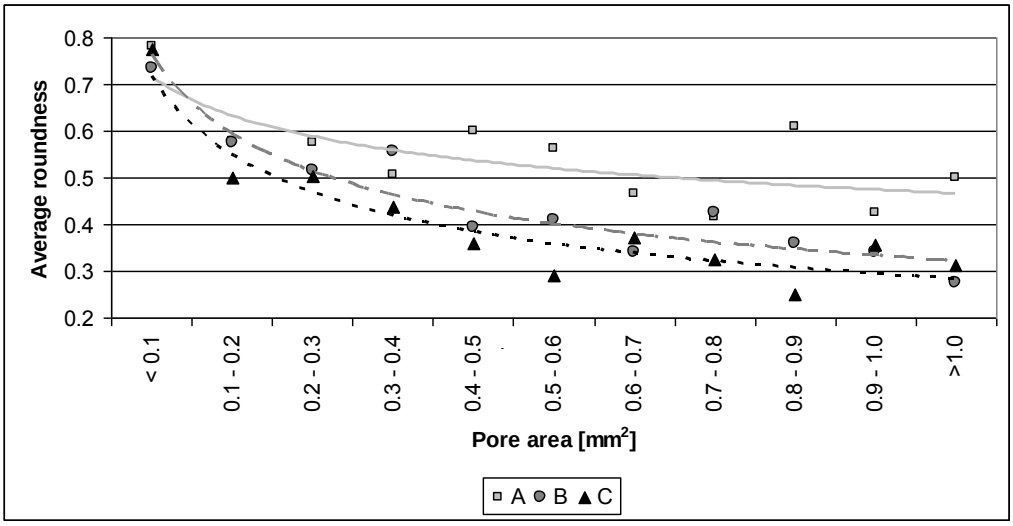

Figure 6: Average roundness of different air void classes of the three selected specimens.

This change to the air voids finally results in a reduction of the compressive strength when comparing the samples A with B and C because the hardened cement paste matrix solidified due to the reduced w/c ratio and due to the use of admixtures and additives, as shown in [5].

The most important results can also be derived qualitatively from Figure 7. With a high performance microstructure, that means with decreasing w/c ratios and simultaneous use of microsilica and superplasticizer, the average diameter of the air voids decreases and the number of inconsistently formed pores increases. This is because a stiffer fresh paste consistence requires a higher amount of aluminum for the same densities compared with less stiff consistences. Furthermore, the quantity of irregularly formed pores increases considerably. The smaller the diameter of the pores are, the more regularly they are formed. Regularly formed air voids, however, increase the compressive strength with comparable densities.

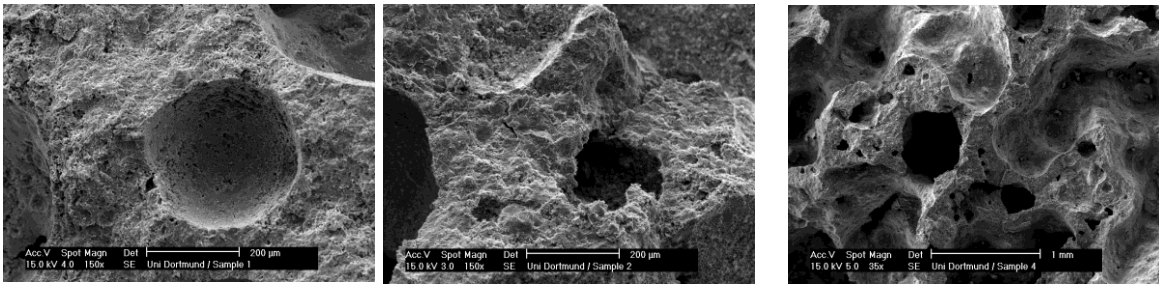

Figure 7: SEM pictures (different magnifications) of air voids in three foam concretes:
left: w/c ratio = 0.60, no microsilica, no superplasticizer.
middle: w/c ratio = 0.40, no microsilica, superplasticizer content = 0.04 wt.%.
right: w/c ratio = 0.40, microsilica content = 10 wt.%, superplasticizer content = 0.85 wt.%.

4 Conclusions

It is technically possible to manufacture chemically expanded, air cured, high performance mineral-bound foams, which can be used for load bearing structures. These foams are sustainable and multifunctional because of the combination of high strength and high thermal insulating properties.

The properties of HPC mineral-bound foams can be improved by the specific use of microsilica as well as superplasticizer. The reduction of the w/c ratio and the simultaneous use of microsilica lead to a optimized cement paste matrix and a stiffer consistency. To get a processible consistency the use of a PCE superplasticizer is necessary. The microstructure of

high performance foam concretes is largely comparable with the microstructure of HPCs. Furthermore the consistency of the stiff paste is influenced by the use of superplasticizer in such a way, that the growing of unequally shaped air voids, which occur during the chemical expansion, is encouraged. These unequally shaped air voids negatively affect the properties (e.g. compressive strength) of the hardened foam concrete, because the load transmission within the cement paste matrix is disturbed. The more superplasticizer is used the more irregularly formed air voids occur. It was observed that the size of the air voids plays a decisive role. The bigger the air voids the more irregularities occur.

It can be stated that optimized air hardened foam concretes, which should have increased compressive strengths, must be adjusted in such a way that they preferably possess as few air voids as possible, with a cross section area of > 1.0 mm^2. Independent of the paste composition, air voids with a cross section area < 0.1 mm^2 are consistently formed.

References

[1] Verein Deutscher Zementwerke e.V.: Zementtaschenbuch. 50. Ausgabe Verlag Bau + Technik GmbH, 2002.

[2] Homann, M.: Porenbeton Handbuch. 6. Auflage, Bauverlag, 2008.

[3] Readymix: Sonderdruck 37, Fließfähiger Porenbeton. Transportbeton Beratungsgesellschaft, 1978.

[4] Just, A.: Untersuchungen zur Weiterentwicklung von chemisch aufgetriebenen, lufthärtenden, mineralisch gebundenen Schäumen. Dissertation, Shaker Verlag, ISBN 978-3-8322-6905-0, 2008.

[5] Just, A., Middendorf, B.: Microstructure of High-Strength Foam Concrete. Materials Characterization, 07/2009, pp. 741-748, Elsevier, 2009.

[6] Just, A., Middendorf, B: Influence of PCE on the Macro- and Microstructure of Air Hardened Foam Concrete. 13th International Congress on Polymers in Concrete, Proceedings pp. 473 - 479, ISBN 972-99179-4-3, 2010.

[7] Just, A., Middendorf, B., Klein, D.: Structural Optimization of High Strength Air Hardened Foam Concrete. fib Symposium 2011, Prague, Proceedings pp. 337 - 340, ISBN 978-80-87158-29-6, 2011.

[8] EN 197-1, Cement - Part 1: Composition, specifications and conformity criteria for common cements. German version EN 197-1:2000 + A1, 2004.

[9] Bornemann, R., Schmidt, M., Fehling, E., Middendorf, B.: Ultra-Hochleistungsbeton UHPC - Herstellung, Eigenschaften und Anwendungsmöglichkeiten, Beton- und Stahlbetonbau 96, Nr. 7, S. 458-467, Verlag Ernst & Sohn GmbH & Co. KG, Berlin 2001.

[10] de Larrard, F., Sedran, T.: Mixture proportioning of high-prformance concrete: Cement and Concrete Research, Volume 32, Issue 11, Pages 1699-1704, 2002.

[11] de Larrard, F.: Ultrafine particles for the making of very high strength concrete. Cement and Concrete Research, Volume 19, Issue 2, Pages 161-172, 1989.

[12] Richter, T.: Hochfester Beton – Hochleistungsbeton. Verlag Bau + Technik GmbH, Düsseldorf, 1999.

[13] Cwirzen, A., Penttala, V., Vornanen, C.: Reactive powder based concretes: Mechanical properties, durability and hybrid use with OPC. Cement and Concrete Research, Volume 38, Issue 10, Pages 1217-1226, 2008.

UHPC Under Intensive Autoclave Cycles for Energy Storage Water Tanks

Mohamed Abd Elrahman[1,2] Bernd Hillemeier[1]

1: Dept. of Building Materials and Chemistry, Institute of Civil Engineering, TU Berlin, Germany.
2: Structural Eng. Dept., Faculty of Engineering, Mansoura University, Egypt.

This paper presents a new ultra high performance concrete for solar energy storage concrete tanks to store water and steam at a temperature above 100 °C. The modified Fuller &Thompson curve has been used for proportioning the aggregate and fines. Rene LCPC software has been used to measure the porosity and dense packing of dry mixture. The autoclave technique has been used to load the concrete specimens with a temperature of 200 °C and a pressure of 15,5 bars for repeated cycles with heating/cooling rates of about 1/0,5 °C/min respectively. Experimental investigation involving the measurements of porosity, permeability and strength will be presented. The results indicated that optimization of the concrete mixture can effectively reduce the total porosity and permeability of concrete as well as increase the compressive strength. After hydrothermal exposure, the optimized concrete showed very stable properties with regarding to durability and strength.

Keywords: concrete optimization, durability, hydrothermal attack

1 Introduction

Storage of solar thermal energy or of waste heat from heat and power cogeneration plants can significantly contribute to substitute fossil fuels in future energy systems. Some solar energy storage tanks have been built in the last few years [1], but these tanks were limited with maximum temperature of 95 °C and the stored energy is used for heating only. Normal concrete can not be used alone as a construction material for these tanks because of the high porosity which gets higher with increasing the temperature [2 and 3]. The construction costs are very high because these tanks need stainless steel liner to prevent water leakage [1]. In recent years, some tanks without liner have been built with high performance concrete to store hot water at 95 °C [4]. However, to make a practical use of the stored energy such as industrial processes and steam generation, the storing temperature must be increased above 100 °C.

The present paper is a part of an extensive investigation on ”Hot water concrete tank to store solar generated energy”. The purpose of this article is to optimize a low porosity/high durability concrete mixture to be used in the construction of the closed energy storage tank to store water and steam at a temperature of 200 °C and a pressure of about 15,5 bars.

2 Concrete Mixture Optimization

When a concrete wall subjected to hydrothermal cycles, water and vapour try to penetrate the wall. The penetration rate depends mainly on the temperature and pressure of the water and vapour as well as on the microstructure, durability and porosity of concrete. The aggregate, the matrix, and the bond between them affect concrete porosity, microstructure and durability. The matrix depends not only on the w/c ratio but also on the granulometry and reactivity of the cementitious material. Therefore, in this research, concrete mixture optimization is primarily based on three fundamental mechanisms:

1- Enhancing packing density of solid particles
2- Designing of dense cement matrix
3- Optimization of water/cement ratio

Enhancing packing density of solid particles

The production of extremely dense concrete to resist hydrothermal conditions is based on the designing of a system with highly compatible well graded components. Uniform grading with proper amount of each size results in mixture with high packing density [5] and in concrete with minimum binder content and low water demand. As a result, the concrete will have less durability problems such as permeability, shrinkage, and thermal degradation. An additional object is to block and lengthen the access path of contaminants to the concrete.

Fuller [6] stated that if the aggregate is graded according to Equation 1, the resulting mix requires less cement and gives higher compressive strength. The Fuller curve despite its historical value is still the base for proportioning of the aggregate in many national concrete standards [7]. The problems of applying this curve are the low workability and probability of segregation in fresh state. To overcome these problems, some modifications have been done to achieve better workability and mix stability and have better particle packing [8] (see figure 1).

$$P = \left(\frac{d}{D_{max}}\right)^n \quad (1)$$

Where P: cumulative percent finer than d, d: particle size, D_{max}: maximum particle size, n ≈ 0,5. In this research, the mixture components proportioning has been calculated according to the modified Fuller curve (figure 1). For the maximum aggregate size of 16 mm (D_{max}), the aggregate volume (d > 125 μm) is 85,1%, while the cementitious materials (d< 63 μm) is 12,9% by volume. Quartz powder (63 < d < 125 μm) (QP) and quartz sand (QS) have been used to fill the gap between cement and aggregate.

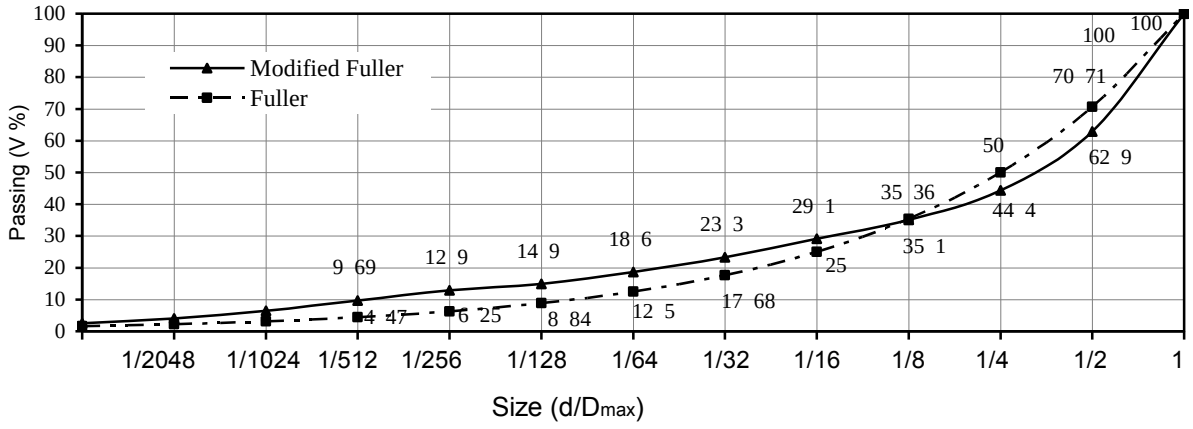

Figure 1: The grading curve for aggregate and binder according to modified Fuller & Thompson.

Designing of dense cement matrix

All transport processes depend primarily on the structure of the hydrated cement paste [9]. During the hydration process, the size and the continuity of the pores would control the permeability of the hardening concrete. If the hydration process of cement is too fast, large amounts of hydration products with capillary pores are generated on the surface of cement particles at early age and the microstructure is not dense as desired. In contrast, if the hydration rate is slow, a denser microstructure is formed [10]. In addition, Portland cement hydration produces about one-third of its mass of calcium hydroxide (CH), which is associated with greater permeability and lower durability. The use of pozzolans improves the durability through the pore refinement and the reduction in the CH [11].

Concrete durability can be improved significantly by using cements containing blast furnace slag. These cements, in contrast to ordinary Portland cement(OPC), show lower permeability,

lower hydration heat, lower effective alkali content, and lower steel corrosion. The beneficial effects of blast furnace slag arise from the low CH content and making the pore space being filled with CSH. The slag retains the alkali and CH in its hydration products (i.e. CSH). This results in a hardened cement paste with denser microstructure and smaller pore sizes than equivalent OPC paste, thus permeability and ionic diffusivity are reduced [12]. Due to their pozzolanic reactivity, using pozzolanic materials with slag cement enhances the concrete impermeability by the formation of additional CSH phases. In this research, the amount of cementitious materials is about 312 kg/m3 (12.9% by volume). CEM III/B 32,5, fly ash, fine fly ash (M10 and M20) and silica fume were used as cementitious materials.

Optimization of water/cement ratio

The durability of concrete cannot be characterized with a uniform value, but the impermeability of concrete against water and gases is always of the most crucial aspects. The transport of liquids and gases, which can be harmful to concrete, occur exclusively through the capillary pore system of the cement matrix. Accordingly, the minimization of the fraction of capillary pores is of vital importance for concrete impermeability and durability. It is theoretically known that, capillary pores begin to form at a water/cement ratio higher than 0,42. However, there is a physical limit to how low the w/c ratio can be. This is because the water added must be at least sufficient to fill up the voids between solid particles [13]. Because of the low cement content, small increase in the water content may lead to high increase in w/c ratio [14].

In this research, the water/cement ratio was 0,42 (mixing water) for all mixes with k factor of 0,4 and 1 for fly ash and silica fume respectively. The water required to fill the voids between solid particles (required water) has been calculated by the help of Rene LCPC software [15].

3 Rene LCPC Software

Rene LCPC software which is based on the compressible packing model developed by Larrard [15] was used to calculate the porosity of the dry mixture. This model is based on the concept of virtual packing density and compaction index. Two interaction effects should be considered in this calculation: the wall effect exerted by coarser grains, and the loosening effect, exerted by the finer particles. This model aims to predict the packing density and porosity of polydisperse mix, from the knowledge of three types of parameters: packing density of monosized classes, size distribution of the mix and compaction index (K). The compaction index (K) depends mainly on the type of compacting (see table 1). The calculated porosity was used to determine the required water assuming the air content of concrete is 1%.

$$\text{required water} = \text{calculated porosity} - \text{air content} \quad (2)$$

Table 1: K values for different compaction methods according to [15].

Implementation	Loose	Striking with a rod	vibration	Wet packing	Vibration with Comp. 10 KPa	Virtual
K	4,1	4,5	4,75	6,7	9	infinity

4 Materials and methods

Materials and concrete mixes

In the experimental work, CEM III/B 32,5 N-LH/HS/NA with slag content of 68,8 % according to DIN EN 197-4, fly ash according to DIN EN 450-1, and silica fume (SF) according to DIN EN 13263-1 have been employed as cementitious materials. Three types of fly ash have been used; normal (FA) and fine fly ash (M20 and M10). Figure 2 shows the particle size distribution of fine materials. Superplasticizer (Muraplast FK63.30) has been used to achieve a desirable

consistency (class F4) according to DIN EN 206-1. Table 1 shows the physical properties of the used materials. Ten mixes have been prepared and tested (table 2). The autoclave technique was used to load the concrete specimens with repeated cycles of high pressure (15 bars) and temperature (200 °C) with heating and cooling rates of 1 K/min and 0,5 K/min respectively.

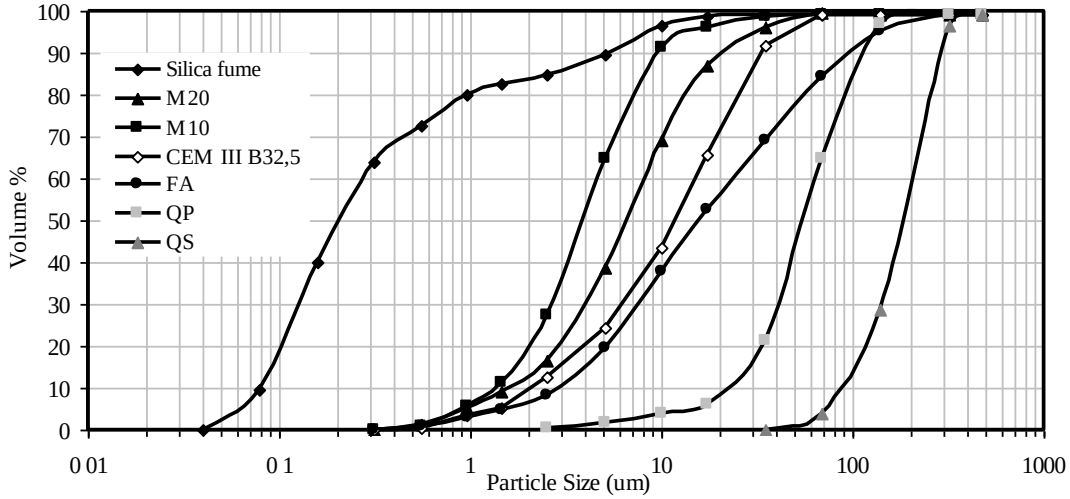

Figure 2: Particle size distribution of fine materials by Laser granulometry.

Table 1: Physical properties of the used materials.

Material	CEMIII/B	FA	M 10	M20	SF	QP	QS	Aggregate
Density (t/m^3)	2,96	2,29	2,49	2,45	2,2	2,69	2,67	2,61
Surface area cm^2/gm*	4156	2877	6400	6000	200000	2683	760	-
Water demand [15]	22,6	18,5	23	21,6	49,9	24,4	-	-

*The surface area of all materials were measured by Blaine method except Silica fume which measured by BET.

Table 2: Mixes composition and fresh properties of concrete.

Mix	Composition of cementitious materials(wt.%)					SP (wt.%)	Aggregate Kg/m^3	QS Kg/m^3	QP Kg/m^3	Flow Diameter (cm)	Air Content (V %)
	Cement	FA	M20	M10	SF						
1	100	-	-			0,7	1854	84	46	53	1,5
2	70	30	-			1	1854	84	46	52	1,3
3	70	-	30			1	1854	84	46	48	1,6
4	70	-	-	30		1	1854	84	46	51	1,4
5	70	-	15	15		1	1854	84	46	51	1,3
6	70	20	5	5		0,9	1854	84	46	54	1,3
7	90				10	0,7	1854	84	46	48	2,3
8	65	25			10	1,1	1854	84	46	50	2,0
9	65		12,5	12,5	10	1	1854	84	46	50	2,2
10	65	15	5	5	10	1	1854	84	46	50	2,0

Mixing Sequences

In order to enhance the distribution of all particles and make the mixture more homogenous, the following diagram shows the sequence of the addition of concrete constituents in the mixer.

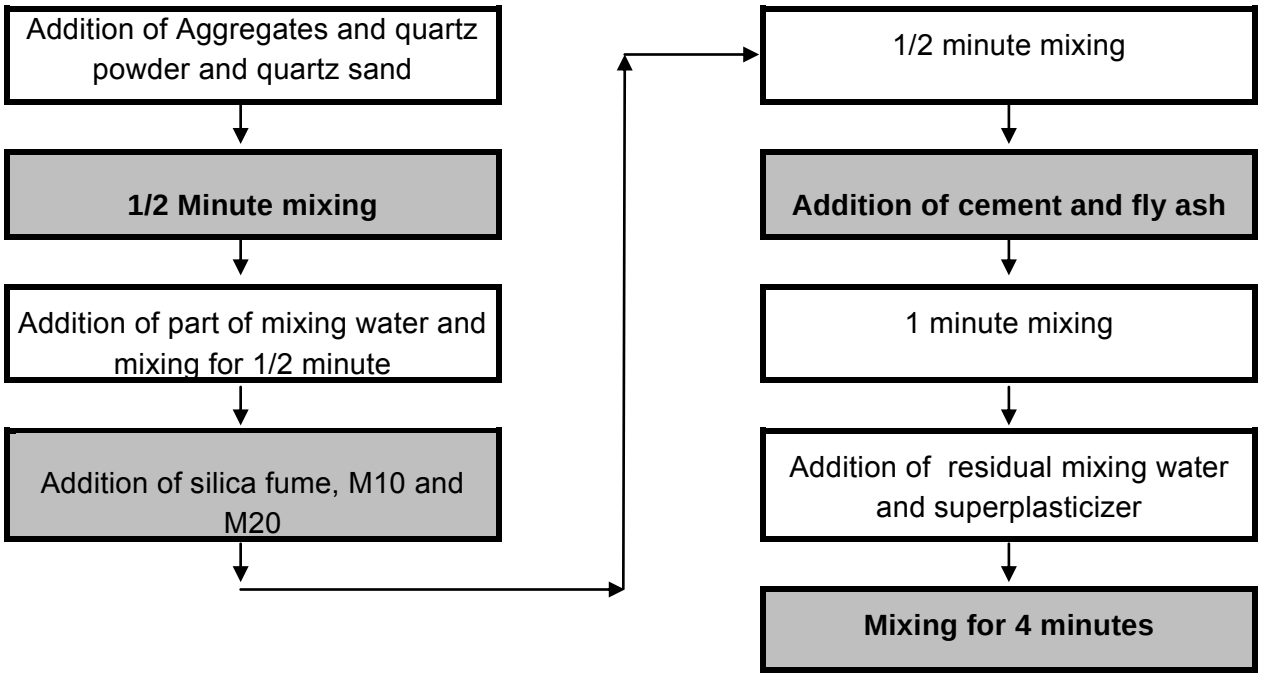

Figure 3: The sequence of addition of concrete constituents in the mixer.

Test procedures

In this experimental work, the porosity of dry mixture have been measured using Rene LCPC software. The porosity of hardened concrete was measured using Helium Pycnometer. The air permeability of concrete according to TGL 21094-12 (Equation 3) has been measured on cylindrical samples with diameter of 50 mm and height of 20 mm. The compressive strength of concrete specimens according to DIN EN 206-1 for 100 mm cubes has been tested. All tests of hardened concrete have been made after 56 days in two cases; in normal conditions and after autoclaving for 15 cycles. Flow diameter and air content have been measured according to DIN EN 12390.

$$K = \frac{V.h.\eta}{A.t.p} \qquad (3)$$

Where: K = gas permeability coefficient (cm^2), V: flow volume (cm^3), t: passing time (seconds), h: height (cm), A: cross section area (cm^2), p: pressure N/cm^2, η: dynamic viscosity of the air N/cm^2.

5 Results and Discussion

Water requirement

The mixing water (w/c = 0,42) and required water (Equation 2) contents of all mixes are given in table 3. For mixes 8, 9, and 10, the required water is higher than the mixing water which means that the voids between solid particles are not fully filled with water. In contrast, mixes 1, 2, 6, and 7, the mixing water is more than the required water; the volume of the added water is larger than the available volume between solid particles. While mixes (3, 4, and 5), the mixing and required water are approximately the same; little escape as free water, and no voids is still empty.

Table 3: Mixing and required water content of mixes.

Mix	1	2	3	4	5	6	7	8	9	10
mixing water	131,3	107,7	107,7	107,7	107,7	107,7	131,3	111,6	111,6	111,6
required water	110,7	105,8	107,3	107,3	107,2	106,1	119,8	112,8	116,6	115,4

Porosity

The test results showed that optimizing concrete mixture results in reducing the porosity of all mixes as seen in figure 3. In dry mixture, fly ash with its spherical shape enhances the packing density and reduces the water demand. The packing density of mixes with silica fume is lower than other mixes because the ultra fine nature and lower density of silica fume particles which makes the particle dispersion inhomogeneous and reduces the packing density [16]. In hardened concrete, fine fly ash (M10 and M20) enhance the packing density and reduce the porosity to less than 6% (mix 5). After autoclaving for 15 cycles a slight increase in porosity for all mixes can be observed. Due to the hydrothermal conditions, contrary to heating alone, the volume of fine pores tend to increase and the volume of big pores decreases. This phenomena is due to the autoclaving effect, which is associated with a decrease in the phases (C3S +β-C2S) and in an increase in CH content [3].

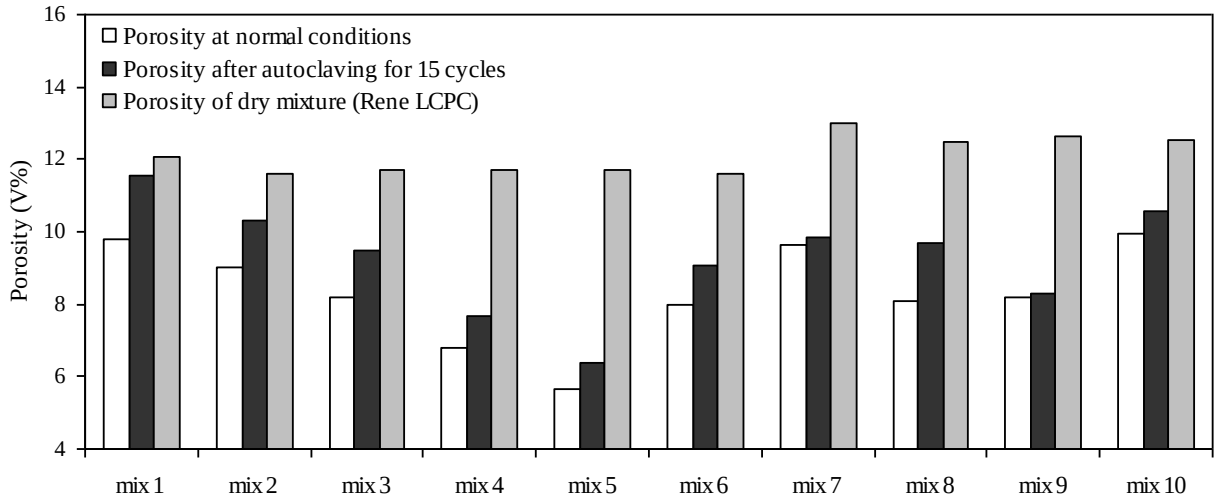

Figure 3: Porosity of normal and autoclaved concrete at age 56 days.

Air permeability

It can be seen from figure 4 that optimization of concrete mixture can significantly reduce the air permeability for all mixes. This can be due to the higher packing density of the mixture which reduces the porosity and the required cement paste. In the same time, the high content of aggregate lengthens the flow paths and makes them unconnected. Mixes containing fine fly ash exhibited lower air permeability. It reacts with CH to form CSH, which fills large capillary voids and disrupts their continuity. By autoclaving for 15 cycles, the air permeability of concrete reduced to $1.8*10^{-17}$ m^2 (mix 5). The hydrothermal process increases the reaction of fine fly ash with calcium hydroxide and this reaction leads to two important effects. First, the volume of calcium hydroxide is reduced because it is substituted by CSH product which makes the microstructure denser and as a result the permeability is reduced. Secondly, the hydration products of this reaction fill the voids and reduce its size and connectivity and consequently the permeability is reduced also.

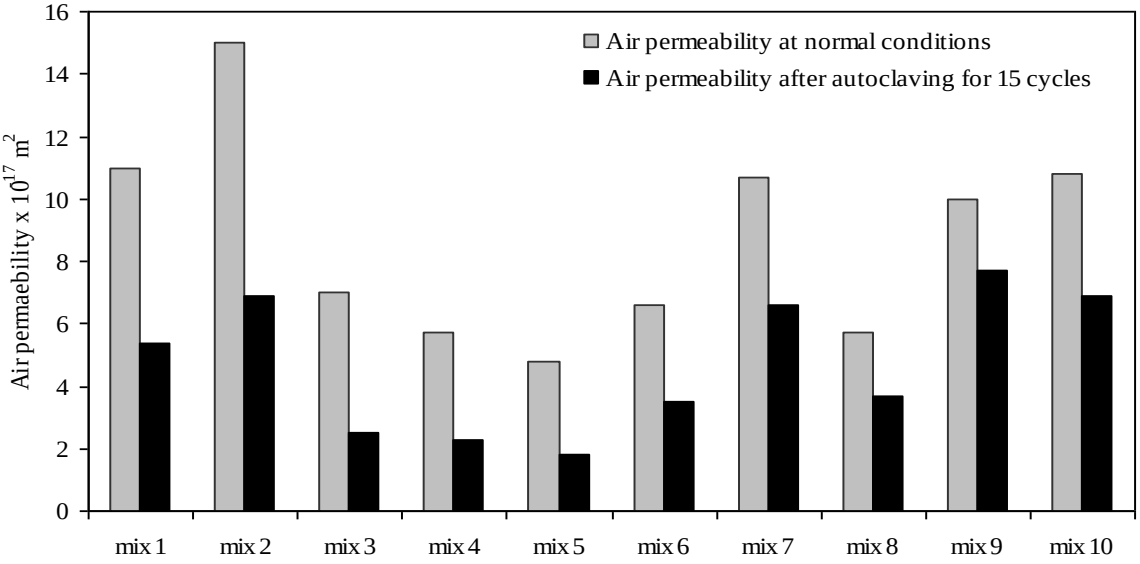

Figure 4: Air permeability of normal and autoclaved concrete at 56 days.

Compressive strength

Results of compressive strength at 56 days are given in figure 5. For mixes with pozzolanic materials, hydrothermal process improves concrete strength because this process accelerates the reaction of cement components with water as well as the pozzolanic reactions between fly ash and silica fume with CH. As seen from figure 5, the increase of strength in the first stage of autoclaving (5 cycles) is more noticeable, while in the later stages of autoclaving (10 and 15 cycles) the compressive strength is approximately constant.

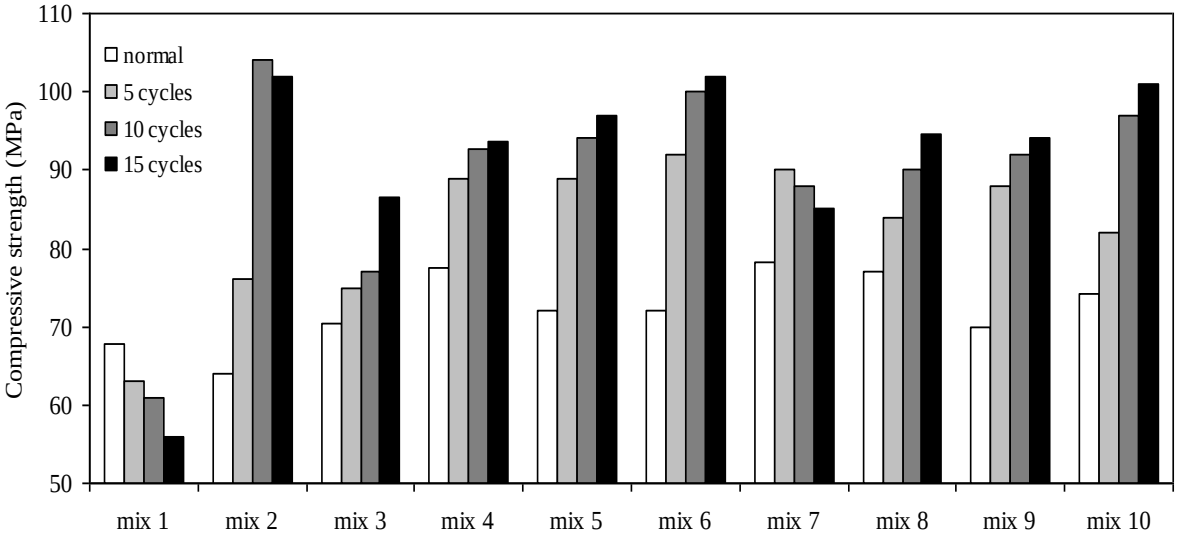

Figure 5: compressive strength of normal and autoclaved concrete at 56 days.

6 Conclusions

The following conclusions can be drawn from the present investigation:

1 With optimization of concrete mixture, it is possible to produce low porosity, highly durable concrete with desirable workability and strength by using a low cement content.

2 Incorporation of fine fly ash enhances the packing density and reduces the water requirement as well as it reduces the concrete porosity and permeability.

3 After hydrothermal treatment, the optimized concrete showed very stable properties with regarding to durability. The changes in the matrix morphology, microstructure, mineral

and chemical composition were limited and can be neglected in the applied hydrothermal conditions.

References

[1] Schmidt, T. and Mangold D., “New steps in seasonal energy storage in Germany”, Proceedings of Ecostock 2006: 10th International Conference on Thermal Energy Storage, May31-June2, 2006, Pomona, USA.

[2] Djaknoun S., Ahmed Benyahia A., Ouedraogo E., ”Porosity and permeability of mortar exposed to elevated temperature”, Journal of Applied Science Research, 4(3), 2008, pp 231-240.

[3] M. Schekarchi, G. Debicki, L. Granger, Y. Billard, “Study of leaktightness integrity of containment wall without liner in high performance concrete under accidential conditions – I. Experimental”, Nuclear Engineering and Design 213 (2002), pp 1-9.

[4] Jooß M., “Dichtheit von heißwasser-langzeitspeichern aus hochleistungsbeton”, Ph.D. Thesis, Institut für Werkstoffe im Bauwessen, Universität Stuttgart, 2001.

[5] Geisenhanslüke, C. and M. Schmidt, ," Methods for modelling and calculation of high density packing for cement and fillers in UHPC", International Symposium on Ultra High Performance Concrete. 2004, Kassel.

[6] Fuller, W.B. and Thompson, S.E. (1907), “The laws of proportioning concrete”, ASCE J. Transport, Vol. 59. pp. 67-143.

[7] Vogt, C. (2010), “Ultrafine particles in concrete; influence of ultrafine particles on concrete properties and application to concrete mix design”, School of Architecture and the Built Environment, Division of Concrete Structure, Stockholm: Royal Institute of Technology.

[8] Hillemeier BHA. “High performance concrete specialized for acid resistance”, 1st International conference on Concrete & Development, 30 April-2 May, Tehran, Iran, 2001.

[9] Neville A. M.,” Properties of concrete”, Fourth and Final Edition, Standards updated to 2002, 844 P.

[10] Tongsheq Zhang, Qijun Yu, Jianngiong Wei, Peng Gao, Pingping Zhang, “Study on optimization of hydration process of blended cement”, Journal of thermal analysis and calorimetry. DOI. 10.1007/s10973-011-1531-8.

[11] P. Chindaprasirt, S. Homwuttiwong, V. Sirivivatnanon, “Influence of fly ash fineness on strength, drying shrinkage and sulphate resistance of blended cement mortar”, Cement and Concrete Research 34 (2004), pp 1087-1092.

[12] ACI Committee 233 R, ”Ground Granulated Blast Furance Slag as a cementitious constituent in concrete” American Concrete Institute, Farmington Hills, Mich. 1995.

[13] A.K.H.Kwan, H. H. C. Wong," Packing density of cementitious materials: part 2 packing and flow of OPC + PFA + CSF", Materials and Structures (2008), 41:773-784, DOI 10.1617/s11527-007-9281-6.

[14] S.A.A.M. Fennis, “Design of ecological concrete by particle packing optimization”, PhD Thesis, Design and Construction Department, Faculty of Civil Engineering and Geosciences, TU Delft, 2011.

[15] Sedran, T. and Larrard, F. de. (2000) "Rene LCPC user manual", (in French).

[16] Reschke T., “Einfluß der Granulometrie der Feinstoffe auf die Gefügeentwicklung und die Festigkeit von Beton”, Schriftenreihe der Zementindustrie Vol. 62, Düsseldorf, 2001.

Ultra High Performance Concrete for Drill Bits in Special Foundation Engineering

Hursit Ibuk, Karsten Beckhaus
BAUER Spezialtiefbau GmbH, Germany

The strength properties of Ultra High Performance Concrete (UHPC) allow it to be used for research applications in special foundation engineering. In this regard, UHPC generally competes with steel. In many special foundation applications, steel is used as the common material. For the successful market penetration of applications made of UHPC, however, it is not only mechanical aspects that are decisive, but also economical and – nowadays additionally – ecological aspects.
The research presented here is supported by the Federal Ministry of Education and Research (BMBF, Germany, FKZ: 13N10456) and is mainly focused on the use of UHPC in special foundation engineering. So far, drill bits for constructing full displacement piles made of UHPC have been researched. Initial field tests have been carried out with great success.

Keywords: UHPC, special foundation engineering, drill bits

1 Introduction

BAUER Group and UHPC Research

The BAUER Group is an international construction and machinery manufacturing corporation based in Schrobenhausen, Germany. The Group markets its products and services all over the world. The operations of the Group are divided into three segments: Construction, Equipment and Resources.

The company BAUER Spezialtiefbau GmbH (abbr. BST – construction segment) performs special foundation works for excavation pits, foundations, cut-off walls and ground improvement worldwide. The company BAUER Maschinen GmbH (abbr. BMA – equipment segment) develops and manufactures equipment and tools for specialist foundation engineering applications and mining. In the third segment BAUER Resources GmbH focuses on products and services in the fields of water, energy, mineral resources and environmental technology.

Especially for the fields of activity of BST and BMA, applications made of UHPC may lead to research into economical and ecological products. Here, the commonly used building material steel is the reference for UHPC.

Within the framework of the collaborative research project “UHPC in Special Foundation Engineering” run jointly by BST and the cbm (Centrum Baustoffe und Materialprüfung, Technische Universität München), the application of drill bits made by UHPC was researched and verified. The research presented here is supported by the Federal Ministry of Education and Research (BMBF, Germany, FKZ: 13N10456).

Execution of bored piles in full displacement method with the lost bit technique

The specific construction method of bored piles made of reinforced concrete must be chosen from a number of special foundation methods dependant on the present soil conditions and economical aspects. In particular in soft to stiff, loose to medium-dense soils, the execution of bored piles in the full displacement method with the lost bit technique is becoming increasingly relevant.

With this method, a drill bit is used. A drilling rig equipped for the displacement pile method provides the required power (force and torque) (Fig. 1). First the present soil is drilled by the drill bit at the toe of the drill string and the soil is loosened. Then, the drill string enlarges the borehole in its final diameter by displacing the loosened soil radially into the surrounding soil.

The drill bit performs its task only once, until the final depth of the bored pile is reached. Afterwards the drill bit remains in the soil. In this way, a borehole for placing the reinforced concrete pile is constructed. Following this, the reinforcement and the concrete are installed in the hollow of the drill string in order to ensure a proper result of the bored pile (Fig. 1, Fig. 2).

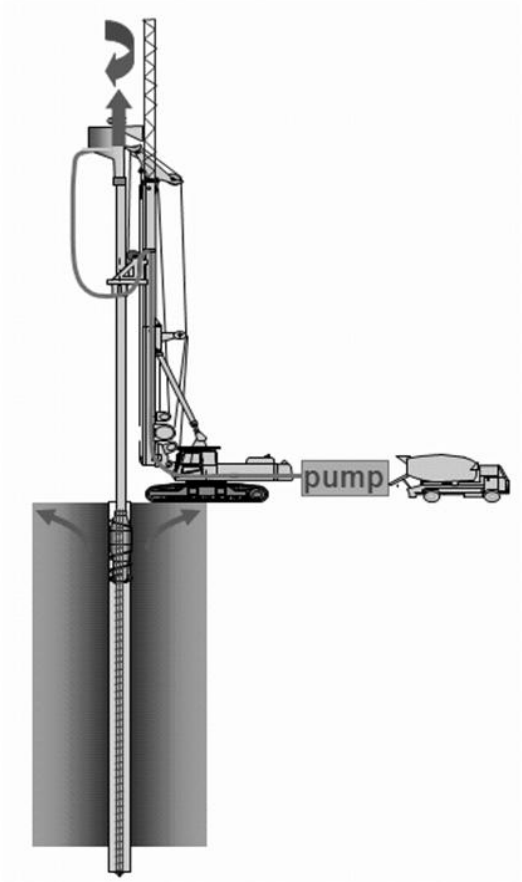

Figure 1: Full displacement method with lost bit technique.

2 Bits made of Ultra High Performance Concrete

The common material for drill bits is steel (Fig. 2). Steel is the reference material for possible special foundation applications made of Ultra High Performance Concrete (UHPC).

Figure 2: Common steel bit (bottom left) and the drill string (hollow).

There are several fields of special foundation engineering in which steel could be replaced in the future by UHPC. UHPC is characterised by its dense structure, which gives UHPC excellent durability properties. Furthermore, the very high compression strength of UHPC, which is about 5 times higher than the compression strength of common concrete in special foundation engineering, is an important UHPC property. Within the bored pile construction, the drill bits are not only applied by compression forces rather by torque additionally. This makes the shear resistance and shear strength of UHPC extremely important (Fig. 3).

Figure 3: Shear strength test of an UHPC specimen.

For this reason, shear strength was examined in separate test series. Furthermore, the large-scale production of UHPC applications was researched. The mixing technique of UHPC and the material handling characteristics of UHPC were also considered in the test program. The influences on product quality were researched.

The use of steel fibres in UHPC compositions leads to greater ductility characteristics for the final UHPC product. For this reason, steel fibres are also unavoidable for “one-way” drill bits made of UHPC. A total failure of the drill bit after reaching its strength is prevented by steel fibres limiting the crack width (Fig. 4).

Figure 4: UHPC drill bit.

Drill bits made of UHPC – with embedded steel fibres – can be characterised by extremely high corrosion-resistance. This durability aspect represents a huge advantage for UHPC drill bits (Fig. 4) over steel bits.

UHPC drill bits were successfully tested at a number of special foundation job sites in Italy and Switzerland. Bored piles with a diameter of 620 mm were constructed by using UHPC drill bits in the full displacement method, including in difficult soil conditions for drilling. After the drilling process, UHPC drill bits were still fully functional and were free of any cracks (Fig. 5). In addition, the essential sealing system between the UHPC drill bit and the drill string remains active so that groundwater from outside cannot flow into the drill string (hollow). The following concreting process can thus be properly carried out. An equivalent drilling performance between UHPC and steel bits was also verified by practical tests. Mechanical abrasion due to drilling at the surface of the UHPC drill bit cannot be avoided, but is not relevant for the drilling process (Fig. 5).

Figure 5: UHPC drill bit after the drilling process.

3 Conclusions

With the researched drill bit for full displacement piles, a first product made of UHPC (Ultra High Performance Concrete) is now available. This product may have good market opportunities because of its high quality and proper realisation standard. At the same time, UHPC drill bits are cheaper to produce than steel bits.

Technically, UHPC drill bits are not inferior to steel bits. Moreover, the carbon footprint of UHPC drill bits is comparatively small.

In future, products made of UHPC may become increasingly important because the price of steel is set to increase in the medium term, as well as in the long term – significantly more than the price of UHPC.

The UHPC drill bit was taken from the research project “UHPC in Special Foundation Engineering”. The basic understanding of UHPC up to this point was obtained in collaborative research work (BST and cbm). In the future, further product developments (e.g. economical optimisation in steel fibre content, form and strength improvement) will be started separately in order to achieve market readiness.

Effect of Fibres on Impact Resistance of Ultra High Performance Concrete

Sandy Leonhardt, Dirk Lowke, Christoph Gehlen
Centre for Building Materials, Technische Universität München, Germany

The suitability of ultra high performance concrete (UHPC) as a material for driven piles is demonstrated in this contribution. The effect of fibre content and type on the impact resistance of UHPC was investigated. Impact resistance increased with the amount of micro steel fibres 0.16 mm in diameter. Replacement of the micro steel fibres by crimped fibres with a larger diameter reduced the impact resistance of UHPC. It was shown that fibre orientation and distribution affect the impact resistance of UHPC.

Keywords: UHPC, impact resistance, steel fibres, fibre content, fibre orientation

1 Introduction

Driven piles are employed to improve the load bearing capacity of the construction ground. While being driven the piles are continuously subjected to impact and therefore require appropriate high resistance (Fig. 1). Thus up to now piles were mainly made of ductile cast iron [1].

Figure 1: pile driving in operation.

Because of increasing environmental awareness as well as economic considerations and availability of raw materials the replacement of cast iron by a new material for driven piles would help reduce the amount of steel used in construction and thus the environmental impact of steel production as a whole. Ultra high performance concrete possesses excellent properties with regard to compressive strength, but fails in a brittle manner if steel fibres are not included in the mix. Usually 1.5 to 3.0 vol.% steel fibres are added [2], [3] to counteract the explosive failure which otherwise occurs on reaching maximum strength. The higher ductility also improves the impact resistance of UHPC whereby knowledge of optimum fibre content and orientation is vitally important. Consequently, the present investigations focus on the effect of steel fibre content and orientation on the impact resistance of UHPC. The impact resistance of fibre-

reinforced regular concrete has been investigated in the past [4], [5], [6]. Bonzel and Dahms [5], [4] showed that impact resistance could be increased by more than a factor of 20 by adding 3 vol.% steel fibres with dimensions of l/d = 25/0.4 mm to the mix. The increase in deformation energy of steel fibre concrete was attributed to the high degree of friction between the fibres and the concrete. The authors noted that the distribution and orientation of the fibres affected impact resistance; an uneven distribution of fibres with a preferred alignment originating from the manufacturing process led to more scatter of the measurements [4].

Fibre orientation also affects concrete strength significantly for other types of mechanical loading. Empelmann and Teutsch [7] investigated the effect of the production-related orientation of fibres on flexural strength after crack initiation using beams concreted in either a horizontal or vertical position. The post-cracking flexural strength of vertically concreted beams was found to be at most only 70% of the value for the horizontally concreted beams. According to the state-of-the-art report published in 2008 [8], the direction of concreting and thus the preferred alignment of the fibres in the flow direction of fresh concrete affects tensile strength greatly. In the case of a flexural load, the fibres should preferably be aligned in the direction of tensile force because then all the fibres will contribute to stress transfer in the crack [9]. Consequently, load direction and fibre orientation affect decisively the strength of concrete reinforced with steel fibres.

2 Investigations

The investigations were carried out using three UHPC which differed in fibre content and type, Table 1. Micro steel fibres were used which were 6 mm long and 0.16 mm in diameter as well as crimped fibres 6 mm long and 0.50 mm in diameter. The concrete mixes were prepared using Portland cement of strength class 42.5 N, silica fume with a mean grain size of 0.15 µm, quartz flour and sand with a maximum grain size of 0.5 mm. A superplasticizer based on polycarboxylate ether was added to fluidize the mix. To investigate possible sedimentation effects during concreting concrete specimens were produced by pouring as well as the conventional pumping method.

Table 1: UHPC compositions.

Materials		**UHPC 1**	**UHPC 2**	**UHPC 3**
Cement	kg/m³	680	675	680
Silica fume	kg/m³	138	138	138
Quartz flour	kg/m³	360	356	360
Quartz sand	kg/m³	990	982	990
Steel fibres l/d = 6/0,16 mm	kg/m³	118	236	39
6/0,50 mm crimped	kg/m³	-	-	79
Total steel fibre content	vol.%	1.5	3.0	1.5
Superplasticizer	kg/m³	21	21	21
Water	kg/m³	179	170	179
w/b[1)]	-	0.24	0.24	0.24
Slump flow	mm	901	780	865

[1)] including silica fume and water in superplasticizer

The concretes were prepared in a high performance mixer in which the mineral materials and steel fibres were homogenized before adding the water and 40% of the superplasticizer. The remaining superplasticizer was added after mixing for two minutes. After a total mixing time of 3.5 minutes the fresh concrete was fed into a receptacle fitted with a screw pump. A total of six

standing (vertical) cylindrical moulds were used with dimensions near ø/h = 100/200 mm. At first, fresh concrete specimens were scooped directly out of the receptacle for slump flow measurements, Table 1, and to fill three of the moulds. Fresh concrete was then pumped out of the receptacle into the remaining three moulds. The fresh concrete was not compacted externally. After demoulding and storing in standard climate 20°C/65% RH until an age of five days, the cylinders were heat treated for 48 h in water at 90°C. Finally, the cylinder ends were ground parallel to height of 200±2 mm.

Impact Resistance

The impact resistance of the specimens was investigated in an impact test device according to DIN 1097-2 [10], Fig. 2. Each specimen was positioned between a hydraulic cylinder and a die and then preloaded with 1000 N. A 50 kg weight falling from 600 mm onto the die produced the impact. After a series of five consecutive impacts the specimens were removed from the device and the ultrasonic pulse velocity measured between transducers mounted on the ends of the cylinders [11]. The specimens were then returned to the testing device and the procedure repeated until the pulse velocities decreased by 10% of the initial value. The number of impacts needed to reach this velocity was designated as the impact failure number. It was used to characterize the impact resistance of the cylinders. Mostly cracks parallel to the direction of impact appeared during testing (longitudinal cracks, Fig. 3) indicting that the main load was in the horizontal direction (transverse tensile load).

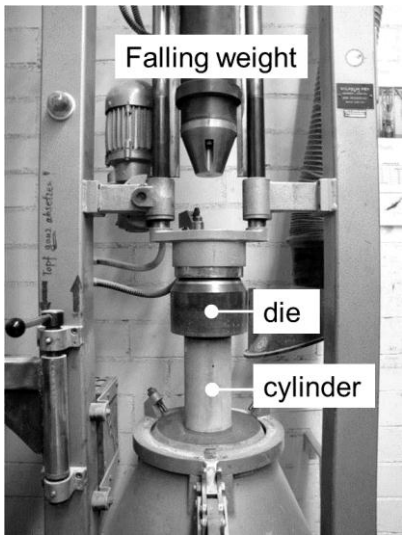

Figure 2: Impact resistance tester.

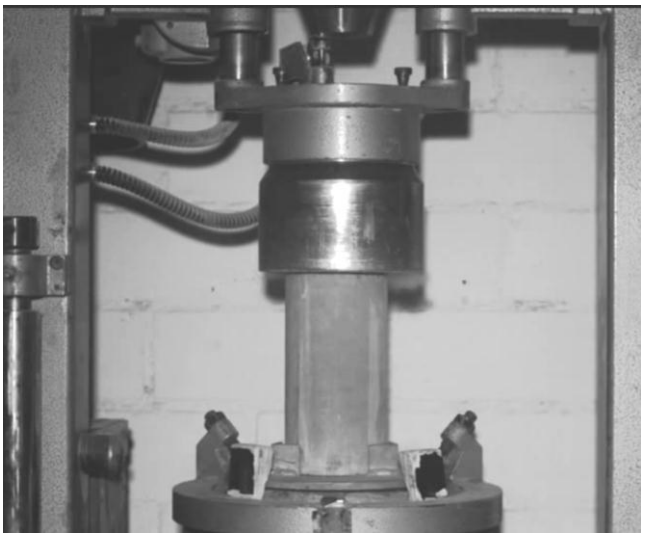

Figure 3: Specimen during impact.

Fibre Content and Orientation

After impact testing, the amount and orientation of the fibres in the cylinders were determined. Fibre segregation in the fresh concrete was investigated by cutting the cylinders into three sections (top, middle, bottom) each 67 mm in height as shown in Fig. 4 enabling the determination of the orientation of the fibres at different concrete heights. In particular, alignment of the fibres along the base of the mould was reckoned with.

The amount and orientation of the fibres was determined using inductive measuring equipment, Fig. 5, in which the ferromagnetic steel fibres acted as the core coil. Excitation and induction coils were used to measure the induced voltage [12], [13]. High voltages corresponded to high fibre contents.

At first, the ferromagnetic properties of the steel fibres were characterized by calibration measurements for each fibre type, Table 1. A container having the same dimensions as the cylinder sections was filled with a mixture of fibres and 0/4 mm sand. Calibration measurements

were carried out for different amounts of fibres in the mixture [13]. In this manner, fibre “profiles” were entered in the database of the device for each fibre type in UHPC and the mix of fibre types in UHPC 3. The cylinder sections could then be measured using the appropriate calibration for the fibres used.

By measuring the voltage once along the cylinder axis and at four different angles in the transverse direction it was possible to determine the orientation of the fibres as well as the percentages V_x, V_y and V_z ($V_x+V_y+V_z$ = 100%) lying in the *x*, *y* and *z* (vertical) directions. The results for the *x* and *y* directions were added to yield the orientation in the horizontal direction. An accuracy of 5% is stated by the manufacturer for the measurement, but it may be as much as 7% according to [12].

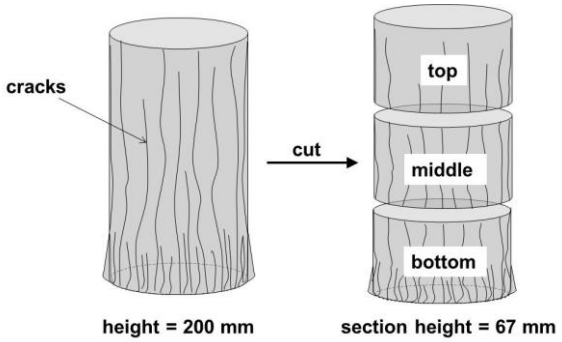

Figure 4: Cylinder cut in three sections for the inductive measurement.

Figure 5: Inductive measuring equipment with specimen.

3 Results and Discussion

Impact Resistance

Table 2: Impact failure numbers measured for the cylinders.

Series	Cylinder no.	1	2	3	4	5	6	Average
		Poured			Pumped			
		Impact failure number [-]						
UHPC 1		51	27	25	50	54	x	41
UHPC 2		55	150	x	110	48	128	98
UHPC 3		5	6	9	15	35	4	12

x - impact failure number not determined

The impact failure number of the cylinder with 1.5 and 3 vol.% micro steel fibres, UHPC 1 and UHPC 2, were on average 41 and 98, respectively, i.e. doubling the micro steel fibre content doubled on average the number of impacts to failure. Replacement of 1.0 vol.% micro steel fibres in UHPC 1 with crimped fibres, 0.50 mm in diameter (UHPC 3), reduced the mean impact failure number to 12.

Fibre Content and Orientation

Fibre contents and orientations in vertical and horizontal directions measured in the top, middle and bottom sections and as an average for the whole cylinder are compiled in Table 3. Values are shown for the horizontal and vertical contributions. The mean fibre contents for series UHPC 1 and UHPC 2 of 1.8 and 3.3 vol.%, respectively, were both above the calculated designed values in Table 1.

Table 3: Fibre contents (T: top, M: middle, B: bottom) and orientations (H: horizontal, V: vertical) in top, middle and bottom sections as well as averages for cylinders as a whole.

Series	Cyl.	Fibre content [vol.%]				Fibre orientation [%]							
	No.	T	M	B	Mean	Top		Middle		Bottom		Mean	
						H	V	H	V	H	V	H	V
UHPC 1	1	1.6	x	1.9	**1.7**	49	51	x	x	64	36	**56**	**44**
	2	1.6	1.8	1.8	**1.7**	50	50	46	54	64	36	**53**	**47**
	3	1.7	1.7	1.8	**1.7**	46	54	49	51	66	34	**54**	**46**
	4	1.9	1.8	2.0	**1.9**	53	47	54	46	66	34	**58**	**42**
	5	1.8	1.8	2.0	**1.9**	53	47	55	45	62	38	**56**	**44**
UHPC 2	1	2.5	3.1	3.2	**2.9**	58	42	66	34	74	26	**66**	**34**
	2	3.0	3.1	3.7	**3.3**	62	38	70	30	71	29	**68**	**32**
	4	3.2	3.6	3.9	**3.6**	69	31	69	31	74	26	**71**	**29**
	5	3.3	3.2	3.6	**3.4**	69	31	72	28	73	27	**72**	**28**
UHPC 3	1	1.4	1.3	1.4	**1.3**	62	38	68	32	73	27	**67**	**33**
	5	1.5	1.7	1.8	**1.7**	55	45	62	38	62	38	**60**	**40**
	6	1.5	1.6	1.7	**1.6**	55	45	60	40	61	39	**59**	**41**

x – not measured

In the case of UHPC 3, the designed content was measured. It was apparent that the fibre content in the bottom section of the cylinders was generally higher than in the middle and top sections, indicating sedimentation of fibres in the cylinders. Notwithstanding the slump flow of the concrete of series UHPC 2 which was lowest, fibre sedimentation was largest; up to 0.7 vol.% more fibres were in the bottom section, cf. Table 1. Furthermore it is noticeable that the fibre content of cylinders (No. 1 to 3) which were not filled by pumping the concrete tended to be less than for the cylinders (No. 4 to 6) filled by pumping. This is explained by sedimentation of the fibres in the bottom of the pumping receptacle because the cylinders were filled using the pump last and therefore the fresh concrete in the bottom of the receptacle contained more fibres. In general, the fibres in the bottom section of the cylinders possessed a higher orientation in the horizontal direction, Table 3, indicating a tendency to parallel alignment to the bottom of the moulds.

Most of the fibres (53 to 72%) in concretes UHPC 1 and UHPC 2 reinforced with micro steel fibres were aligned horizontally. The degree of horizontal alignment was observed to increase with the content of steel fibres, Fig. 6.

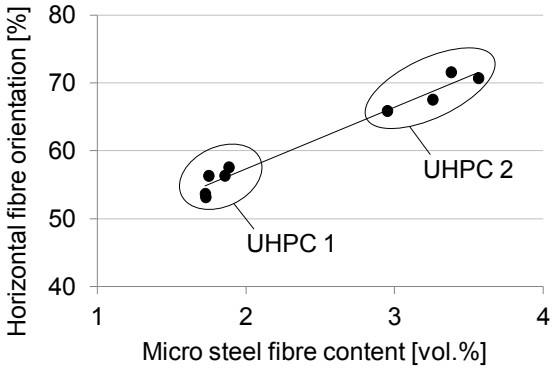

Figure 6: Horizontally orientated fibres as a function of micro steel fibre content.

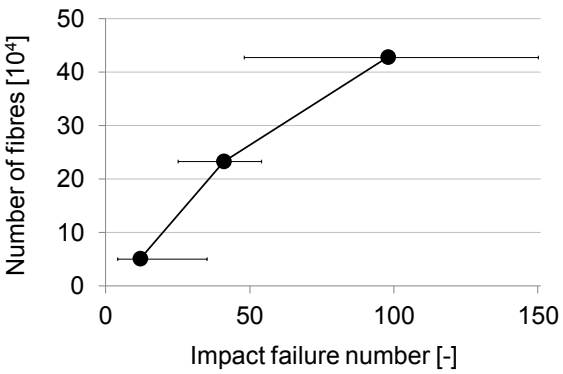

Figure 7: Relationship between impact failure number and number of fibres (determined according to a single fibre volume and density).

On replacing 1.0 vol.% micro steel fibres 0.16 mm in diameter (UHPC 1) with crimped fibres 0.50 mm in diameter (UHPC 3), the mean impact failure number decreased from 41 to 12. Although the volume of fibres was the same in the cylinders UHPC 1 and UHPC 3, the latter contained less fibres owing to the larger dimensions of the crimped fibres. Apparently, this resulted in faster cracking. Fig. 7 shows how the impact failure number increases when the cylinders contain more fibres. This behaviour can be explained by a larger friction surface between the fibres and the concrete [5], [6]. More fibres increase surface friction and therefore the energy of deformation. Owing to the transverse load the more pronounced horizontal orientation of the fibres in the series UHPC 2 (Fig. 6) appears to have a favourable effect on impact resistance.

Owing to high degree of fibre sedimentation in the cylinders of series UHPC 2, the fibres are very unevenly distributed over cylinder height, Table 3. This could explain the high scatter of the impact failure number for series UHPC 2. Dahms [4] noted a larger degree of scatter in test results for an uneven fibre distribution.

The results of the investigations show that it was possible to increase the failure impact number and thus impact resistance by increasing the horizontal orientation of the fibres and the number of fibres in the concrete. Further investigations are necessary using specimens with different fibre contents and types to provide a larger database to confirm the results.

4 Conclusions

In specialist foundation engineering, ductile cast iron is mainly used for the production of driven piles. However, this material is often subject to large variations in price and requires large amounts of energy for its production. Fibre-reinforced ultra high performance concrete is presented as a new material for driven piles in this contribution. Concretes were investigated which were made with 1.5 and 3.0 vol.% micro steel fibres 0.16 mm in diameter or crimped steel fibres 0.50 mm in diameter. Impact resistance was tested using cylinders with dimensions of ø/h = 100/200 mm. Impact resistance was characterized by the impact failure number, i.e. the number of impacts leading to a reduction in ultrasonic pulse velocity of 10%. After impact testing, the cylinders were cut into three sections and the content and orientation of the fibres determined using an inductive measuring device. It was thus possible to measure the effect of fibre content on fibre segregation over the height of the concrete specimens.

The results showed that impact resistance increased with the amount of micro steel fibres. Doubling the fibre content from 1.5 to 3.0 vol.% increased the impact failure number from 41 to 98. Replacement of 1.0 vol.% the former micro steel fibre content by crimped fibres with a larger diameter reduced the impact failure number from 41 to 12. This was due to the reduced number of fibres in the mix and therefore smaller deformation energy of the concrete. Higher fibre alignment in the horizontal direction appears to affect impact resistance favourably.

The measured steel fibre contents and orientations revealed distinct differences over the height of the UHPC cylinders. As observed for the series with 3 vol.% micro steel fibres, a large variation in fibre content over height indicates a high degree of sedimentation of fibres. The high scatter in impact failure number for this series is primarily due to an uneven distribution of fibres caused by fibre segregation.

5 Acknowledgements

The authors would like to thank the Federal Ministry of Education and Research for providing financial support.

References

[1] Schmidt H. G., Seitz, J. M.: Grundbau. Beton-Kalender 1998, Teil 2, Verlag Ernst und Sohn, Berlin, 1998.

[2] Fehling, E., Schmidt, M., Teichmann, T., Bunje, K., Bornemann, R., Middendorf, B.: Entwicklung, Dauerhaftigkeit und Berechnung Ultra-Hochfester Betone (UHPC). Forschungsbericht DFG FE 497/1-1, Schriftenreihe Baustoffe und Massivbau der Universität Kassel, Heft 1, 2005.

[3] Stengel, T., Schießl, P.: Sustainable Construction with UHPC – from Life Cycle Inventory Data Collection to Environmental Impact Assessment. Proceedings of the 2nd Int. Symposium on UHPC, Kassel, 2008.

[4] Dahms, J.: Herstellung und Eigenschaften von Faserbeton. Beton 19 (4), Betontechnische Berichte, pp. 139-143, 1979.

[5] Bonzel, J., Dahms, J.: Schlagfestigkeit von faserbewehrtem Beton. Beton 31 (3), Betontechnische Berichte (3), pp. 97-101, 136-142, 1980/81.

[6] Stangenberg, F.: Stahlfaserbeton als hervorragender Baustoff für stoßbeanspruchte Bauteile. Bauingenieur 61 , pp. 339-345, 1986.

[7] Empelmann, M., Teutsch, M.: Faserorientierung und Leistungsfähigkeit von Stahlfaser- sowie Kunststofffaserbeton. Beton 6, pp. 254-259, 2009.

[8] Schmidt, M., Bunje, K., Dehn, F., Droll, K., Fehling, E., Greiner, S., Horvath, J., Kleen, E., Müller, C., Reineck, K.-H., Schachinger, I., Teichmann, T., Teutsch, M., Thiel, R., Tue, N. V.: Sachstandsbericht Ultrahochfester Beton. Deutscher Ausschuss für Stahlbeton, Heft 561, Beuth Verlag, 2008.

[9] Bergmeister, K.; Fingerloos, F.; Wörner, J.-D. (Hrsg.): Faserbeton, Beton-Kalender 2011, Band 2, Berlin, Ernst & Sohn, 2010.

[10] DIN EN 1097-2: Tests for mechanical and physical properties of aggregates - Part 2: Methods for the determination of resistance to fragmentation. Beuth Verlag, Berlin, 2009.

[11] Leonhardt, S., Lowke, D., Stengel, T., Gehlen, C.: Schlagversuche an ultrahochfestem Beton – Charakterisierung der Dehnungen und der Ultraschallgeschwindigkeiten, accepted for publication, Materials Testing 53 (11-12), 2011.

[12] Breitenbücher, R., Rahm, H.: Zerstörungsfreie Bestimmung des Stahlfasergehalts und der Stahlfaserorientierung im Frisch- und Festbeton. Beton 3, pp. 88-93, 2009.

[13] Schuler, F., Sych, T.: Analyse der Faserorientierung in Betonen mit Hilfe der Computer-Tomographie, Technische Universität Kaiserslautern, Fraunhofer IRB Verlag, 2009.

[14] Hertz Messtechnik GmbH: Handbuch BSM 100, Delmenhorst, 2008.

On The Way To Micrometer Scale: Applications Of UHPC In Machinery Construction

Bernhard Sagmeister
durcrete GmbH, Germany

The machine tools and manufacturing systems industry has a great demand for high precision cutting and grinding machines with the need for higher working speed combined with less deterioration of tools. This is possible using massive machine beds which are damping the vibrations effectively. For this purpose the use of a material with a high mass and a high damping coefficient of the material itself is required. State of the art is the application of beds made of polymer concrete, but machine beds of UHPC are produced by several precast plants in Germany. The lecture compares the possibility and limits of UHPC, ordinary concrete, polymer concrete and natural stone for machine beds. In a general way, the calculation principles and the non-cracked design are explained, also in addition with pre-stressing. The demands for accuracy and low tolerances of about 5/1000 mm, including their measurement (e.g. under climatic conditions) are demonstrated.

Keywords: machinery construction with UHPC, machine bed, accuracy of concrete, structural analysis

1 Why to use massive machine elements

Massive and monolithic machine beds and bases made of UHPC are necessary where high-speed machining is combined with the utmost of precision and strict tolerances. Machines can run with more speed and less deterioration compared with bases made of welded steel or cast iron. The components made of cementitious High-Tech-Concrete are damping vibrations effectively. The non-combustible material reacts slowly to temperature changes.

Machine building companies in the furniture industry use the new material in serial production since two years and reached a remarkable outstanding position in this sector. The special concrete is damping vibrations up to 80% faster than conventional casted constructions. The machines have a new dynamic with faster feed and accelaration. Senior engineers are enthusiastic, when they listen to the silent and smooth run of the machine. The concrete beds are produced in various prefab companies with different recipes.

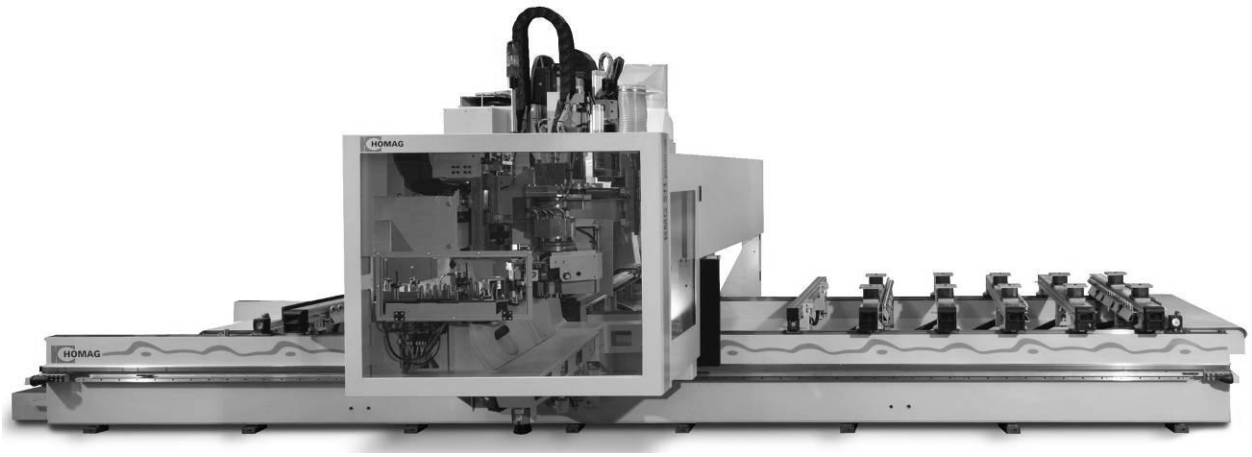

Figure 1: BMG 511 of Homag Group with SorbTech machine bed made of UHPC.

Figure 2: Concrete body of various machine beds.

2 Characteristics of UHPC for machinery industry

We use a special cement [1], which is developed and designed for UHPC applications. Due to the components of the cement, the recipe is free of microsilika. Products with this special binding agent are not designed to have a high pressure strength, but they are characterized by high flexural strength and density. So it is possible to design big machine beds without bar or fiber reinforcement. Due to the fact, that no silica fume is used, the mixture can be mixed in every mixer (even in a kitchen mixer) and can be poured very easily. With the help of a shrinkage retarder, shrinkage is reduced to 0.6 mm/mm and so embedded parts like threaded sleeves, steel rails etc. can be integrated in the concrete elements. Channels, slopes and conduits are simple to realize. The cement is delivered as a compound, where the binding agent is mixed together with stone dust, so that all fine ingredients are delivered with one truck and only one free silo is needed.

Table 1: Typical Recipe.

Materials		**amount**
Crushed aggregates 1/3 or 2/5 or 5/8 mm e.g. basalt splitt or comparable	kg/m³	880
Pit sand 0/2 mm	kg/m³	430
Nanodur Compound 5941	kg/m³	1050
Admixtures as PCE and shrinkage retarder	kg/m³	26
W/Z-value approx.		0,24-0,28
density approx.	kg/m³	2.500

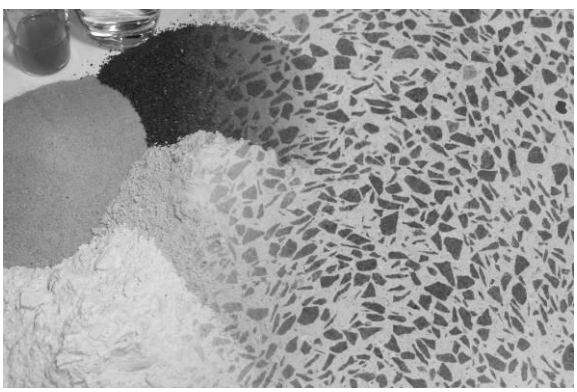

Figure 3: Ingredients.

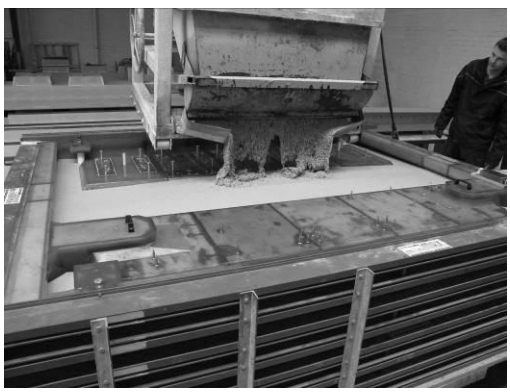

Figure 4: Pouring Concrete.

Table 2: Materials Comparison.

Materials	Density [to/m³]	Compr. Strength [MPA]	Flex. Tensile Strength [MPA]	Youngs Modulus [MPA]
UHPC for machinery	2.4 - 2.5	> 125	10 - 25	35 - 50,000
Granite	2.5 - 3.0	160 - 240	10 - 30	40 - 60,000
Polymer Concrete / PC	2.0 - 2.5	90 - 150	15 - 35	20 - 45,000
Steel / stainless steel	7.8 - 8.0	-	200 - 900	170 - 210,000

3 Design

The machinery industry needs concrete parts with a well defined stiffness, deflection and damping. So it is essential to design and produce uncracked elements. Testing procedures take care, that every machine frame is delivered without cracks and with a defined stiffness. If there is only one small crack, the machine bed has to be removed and to be demolished. This is a challenge for production, but it simplifies the design and structural calculation. The machine beds can be calculated in uncracked state, with a linear elastic FEM Calculation, using volume elements. There is no need to regard reinforcing bars or steel fibers, because these parts only really work, if the concrete is in cracked state. But if this happens, the machine bad is destroyed and out of order. So the limiting value for the design is the flexural bending strength (without any influence of fibres or reinforcing bars), which may be increased using prestressing.

Figure 5: Design possibilities.

Figure 6: Machine Base for a drilling machine.

Table 3: UHPC characteristics.

Materials	w/z-value	Compr. Strength [MPA]	Flex. Tensile Strength [MPA]	Comment
concrete used in Fig. 2	0,26	157	22,7	with fibers, with shrinkage retarder
concrete used in Fig. 6	0,27	146	19,8	no fibers, with pigment, with shrinkage retarder

Tests performed with prism 40x40x160mm, wet condition, without thermal treatment, three point bending test, pressure test with 40x40x40mm.

4 Accuracy

Fig. 6 shows and machine element for a drilling machine. Using a stiff steel form, the German prefab company reaches an accuracy of eveness of the surface less than 0,1 mm over 2 m length. The accuracy of position the embedded sleeves after shrinkage is less than 0,5 mm.

But the machinery industry needs evenness and rectangularity of rectangular and linear supports areas down to 5 micrometer/m or 0.000005 m/m and an accuracy of position of threaded sleeves of less than 0.1 mm. This can be reached by:

- embedding steel parts which are hobbed and drilled in a metall-center
- grinding and lapping the stone surface in specialiced natural stone companies
- casting/forming of epoxy against high precision models in a second pouring step.

The tolerances and deformations are so small, that they can only be measured with precise instruments under defined climatic conditions, because every change in temperature and moisture influences the result.

But all the above mentioned measures are useless, if a concrete bed with a length of some meters shrinks after the precise treatment about some millimeters. So the cement company developped an thermal treatment of the fresh poured machine elements, which stopps effectively the shrinkage of the concrete and brings it to an definite end.

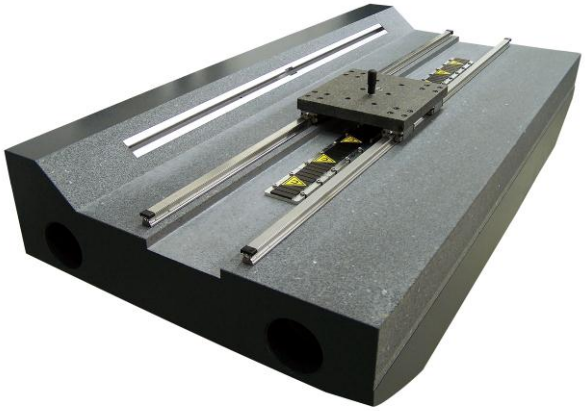

Figure 7: InnoCRETe by JFA: High Precision surface by grinding and lapping.

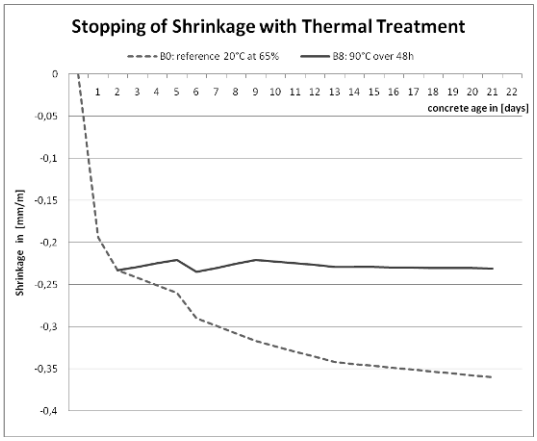

Figure 8:Stopping of shrinkage with thermal treatment.

Internal test performed at the Hochschule Reutlingen show, that the damping characteristic of the UHPC beds can be compared with polymer concrete and natural stone. The decline of the vibration is up to 10 times faster compared with welded steel constructions or casted iron [2].

5 Conclusions

This paper deals with the application of UHPC in machinery industry. The material is in competition with polymer concrete and natural stone. The technical challenge is not the strength itself, but the contour accuracy of the material and the absolute regularity and dimension tolerances of production. Several prefab companies in Germany are dealing sucessfully with different recipes in this new field of UHPC application.

6 Acknowledgement

The pictures in this paper show products and test results of the Homag-Group/Schopfloch, Johann Fischer Präzisionswerke/Aschaffenburg, Dyckerhoff AG/Wiesbaden and the production of Sudholt-Wasemann GmbH in Herzebrock-Clarholz.

References

[1] Dyckerhoff NANODUR Compound 5941 Dyckerhoff AG 05/2011.
[2] H. Nebeling: Untersuchung der Dämpfungseigenschaften von durcrete Beton, internal report of TEC Hochschule Reutlingen, 12/2011.
[3] Deuse T.; Hornung D.; Möllmann M.;: From Mikrodur to Nanodur technology. BFT Concrete Plant + Precast Technology 05/2009 volume 75, 2009.
[4] Deuse T.; Strunge J.; Parker F.: Nanostrukturierte Steuerungskomponenten in Normzement für ultrahochfeste Betone. Nanotechnologie aktuell, 2008.
[5] Ultrahochfestes Maschinenbett. maschine+werkzeug, Heft 7,Seite 302 ff, 2011.
[6] Sagmeister B., Deuse T.: Anwendungen von UHPC auf Basis eines Spezialbindemittels in Bautechnik und Maschinenbau. BWI –Betonwerk International, Heft 1, 2012.

High Strength Pervious Concrete

Kay Wille, Rui Zhong
Dept. of Civil & Environmental Engineering, University of Connecticut, USA

Pervious Concrete is a durable, sustainable, environmental friendly and economically efficient building material, which is mostly used as pavement material. Its porous structure allows the water to penetrate through, thus positively affecting our natural environment in several ways. The current hindrance of a broad and widespread application is its limited strength due to its open structure.
The objective of this research is to significantly increase the strength of pervious concrete, which will allow its application for entire urban areas including heavy weight traffic. Aimed at developing a new type of pervious concrete with enhanced strength and comparable permeability, three series of mix design have been carried out and their effects on the compressive strength and permeability investigated.

Keywords: compressive strength, pervious concrete, permeability, porosity

1 Introduction

Porous concrete is an open structured concrete with intentionally incorporated continuous voids. The porosity, generated by the elimination of fine aggregates, allows the water to penetrate through. Pervious concrete is recognized by the U.S. Environmental Protection Agency (EPA) as a Best Management Practice (BMP) in first flush pollution control and storm water management. In comparison to regular concrete, the amount of cement, which is the most expensive and the most environmentally demanding ingredient, is reduced to a minimum.

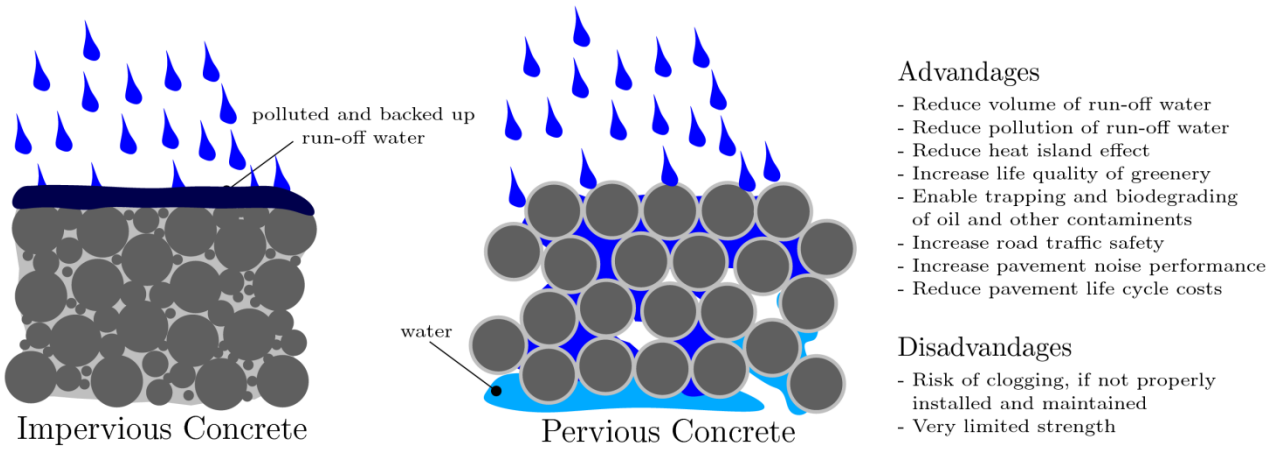

Figure.1: Comparison of impervious and pervious concrete.

Besides the ability to reduce the volume and pollution of run-off water, pervious concrete also leads to the following environmental friendly impacts:

1. Reduced heat island effect in urban areas through reduced heat absorption from solar radiation due to its light colour in comparison to dark pavements and through the open material structure, which stores less heat.
2. Increased live quality of plants and trees by increased air and water supply to the soil which facilitates the implementation of greenery in urban areas and thus helps reducing the heat island effect.
3. Trapping of oil and other contaminants with increased likelihood of biodegrading [1].
4. Water purification ability due to the large specific surface area of the pervious concrete. A porous concrete with smaller size of aggregate and a higher void content was found to have superior ability of removal of T-N and T-P in the test water [2].

Porous concrete has been used for over 30 years in Europe and the USA [3]. The material is primarily used for pavements, parking lots, footpaths, sidewalks, bicycle trails and other areas with low strength requirements, and in particular where storm water run-off is critical. The compressive strength of the material with desired porosity can currently reach about 20 to 30 MPa [4].

The limited strength is the current hindrance of a broad and widespread application of pervious concrete. Intensive research has been conducted to investigate the strength of pervious concrete. Meininger reported laboratory compressive strengths ranging from 9 to 36.5 MPa for porosity ranging from 27% down to 8% respectively using AASHTO No. 8 size aggregate [5]. A laboratory study conducted by Ghafoori and Dutta using AASHTO No. 89 size aggregate reported compressive strengths between 8.3 and 19.3 MPa for porosity of 30% down to 21% respectively [6]. ACI 211.3R shows compressive strengths of 10 to 25 MPa for AASHTO No. 8 size aggregate [7]. Tennis, Leming, and Akers report compressive strengths ranging from 3.5 to 28 MPa and state that a value of 17 MPa is typical [8]. Lian and Zhuge recommended an optimum mix design which can achieve 40 MPa. However, the porosity of such a mix design is 6.5% which is too low to be considered as pervious concrete [9].

The objective of this research is to significantly increase the strength of pervious concrete without losing its permeability. This would allow the application of high strength pervious concrete for entire urban areas including heavy weight traffic. Among numerous factors influencing the compressive strength and permeability of pervious concrete, binder and aggregate characteristics are the most important. Within this research, the combination of the use of an ultra-high strength cementitious matrix with a compressive strength of 174.3 MPa under normal laboratory curing conditions and the optimization of the amount and size of aggregate leads to an increase in strength.

Figure 2 summarizes compressive strength versus porosity test results reported by several other authors [5,9-12] and compares these to the test results achieved in the authors' current research.

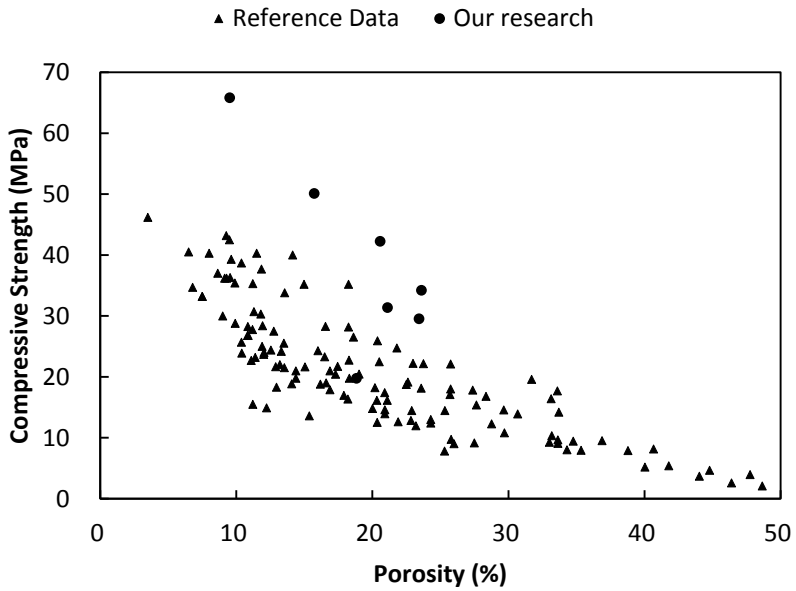

Figure.2: Overview of the relationship between compressive strength and porosity, summarized from different authors.

2 Materials and Mix Design

Based on prior research results on material design of ultra-high performance concrete [13,14] the following materials and mix proportions have been used.

Materials

1. Cement Type I with a high C_3S content (74%), a moderate fineness (3930 cm^2/g Blaine value) and a low C_3A content (<5%). It meets ASTM C150 standard specification for Portland cement.
2. Silica fume with a very low carbon content (0.3%) and a median particle size of 0.4 μm.
3. Glass powder (or silica powder or quartz powder) with a median particle size of 1.7 μm
4. Superplasticizer based on polycarboxylate ether.
5. Three different sized sands with 99% content of quartz

Mix Design

For this study, three series of tests (highlighted in bold in Table 1) have been carried out by investigating seven different pervious concrete mixtures. The first series (M1, M2, M3) was carried out to investigate the effect of matrix strength on the compressive strength and permeability of pervious concrete. The second series (M1, M4, M5) and the third series (M1, M6, M7) were carried out to investigate the effect of amount and size of aggregates, respectively.

Table 1: Series details.

	M1	M2	M3	M4	M5	M6	M7
Series Number	Ⅰ/Ⅱ/Ⅲ	Ⅰ	Ⅰ	Ⅱ	Ⅱ	Ⅲ	Ⅲ
Matrix Strength (MPa)[d]	**174.3**[a]	**133.6**[b]	**50.0**[c]	174.3[a]	174.3[a]	174.3[a]	174.3[a]
Aggregate to Binder Ratio	**3.0**	3.0	3.0	**3.5**	**2.5**	3.0	3.0
Aggregate Size (mm)	**1.19**	1.19	1.19	1.19	1.19	**4.76**	**2.38**

a: The proportion of the ultra high performance matrix (UHPM) which includes no sand or aggregate is based on [13]. The mixture proportions are given in Table 2.
b:This matrix is referred as high performance matrix (HPM) in this paper.
c:This matrix is referred as normal performance matrix (NPM) in this paper.
d:Tested with 50mm x 50xmm x 50mm cubes.

Table 2: Mix proportions used in this research.

Ingredient	Proportions By Weight						
	M1	M2	M3	M4	M5	M6	M7
Cement	1	1	1	1	1	1	1
Silica Fume	0.25	0.12	0.00	0.25	0.25	0.25	0.25
Silica Powder	0.25	0.00	0.00	0.25	0.25	0.25	0.25
Water	0.22	0.30	0.65	0.22	0.22	0.22	0.22
SP	0.036	0.005	0.000	0.036	0.036	0.036	0.036
Aggregate	3.0	3.0	3.0	3.5	2.5	3.0	3.0

3 Experimental Program

Specimen Preparation and Curing

Prior to mixing, the three different aggregates were washed to remove adhered clay and other impurities. After being dried, they were sieved to obtain three single sized aggregates. The matrix (cement, silica fume, silica powder, water and superplasticizer) was mixed first and the aggregates were added later. After mixing, the pervious concrete was poured in three layers in

cylindrical moulds to full capacity using slight vibration. Each layer was compacted by a 2.4kg hammer with three blows for 10cm by 20cm specimen and by a 1.3kg hammer for 7.5cm by 15cm specimen. After casting, the specimens were covered with plastic sheets and stored at room temperature for 24h. Then they were demoulded and stored in a water tank at 20℃ for additional 26 days. Specimens were removed from water and capped after being left to dry in laboratory environment for 12h. Specimens were tested at the age of 28 days. For each batch, a total of 6 cylinders were cast (three 7.5cm by 15cm cylinders for compressive testing, two 7.5cm by 15cm for porosity test, one 10cm by 20cm cylinder for hydraulic conductivity test).

Compressive Strength

Compressive strength was determined in accordance with ASTM C39 using sulfur mortar capping at 28 days. The reported results are an average of three tests.

Porosity

Due to the high air void content of pervious concrete typical tests such as ASTM C173 are not applicable to measure the porosity. Therefore, the porosity of pervious concrete was calculated using the difference of weight between the oven dried sample and the saturated sample under water. Test set up is shown in Fig. 3. Equation (1) was used for calculation:

$$P = \left[1 - \left(\frac{M_1 + M_2 - M_3}{\rho_w V_T}\right)\right] \times 100\% \quad (1)$$

where *P* is the porosity of the sample, M_1 is the mass of the oven dried sample, M_2 is the mass of the container filled with water, M_3 is the container with saturated sample filled with water at the same level, ρ_w is the density of water, and V_T is the volume of the sample.

Figure 3: Porosity Test Set Up.

Figure 4: Hydraulic conductivity test rig.

Hydraulic Conductivity

The constant head method was used to measure hydraulic conductivity. Equation (2) was used for calculation:

$$K = \frac{QL}{Ah} \quad (2)$$

where *K* is the hydraulic conductivity, *Q* is the flow rate of water, *L* is the length of the sample, *A* is the cross sectional area of the sample, and *h* is water head difference of the in flow and out flow. A constant head permeameter was constructed in the laboratory. The basic design of the permeameter consisted of a 10.2cm diameter clear PVC pipe “U” shape assembly as shown in Fig. 4. The specimens were sealed to only allow the water penetrating along specimen direction.

4 Results and Discussion

Effect of Matrix Strength

The effect of matrix strength on compressive strength, porosity and hydraulic conductivity are plotted in Fig. 5 (a) to (c) respectively. It can be seen from Fig. 5 (a) that compressive strength increases with the increase of the matrix strength. The averaged compressive strength values of mixtures using UHPM, HPM and NPM are 50.1 MPa, 33.7MPa and 19.8 MPa, respectively. The results show that the stronger the matrix is, the stronger the pervious concrete is in the range investigated.

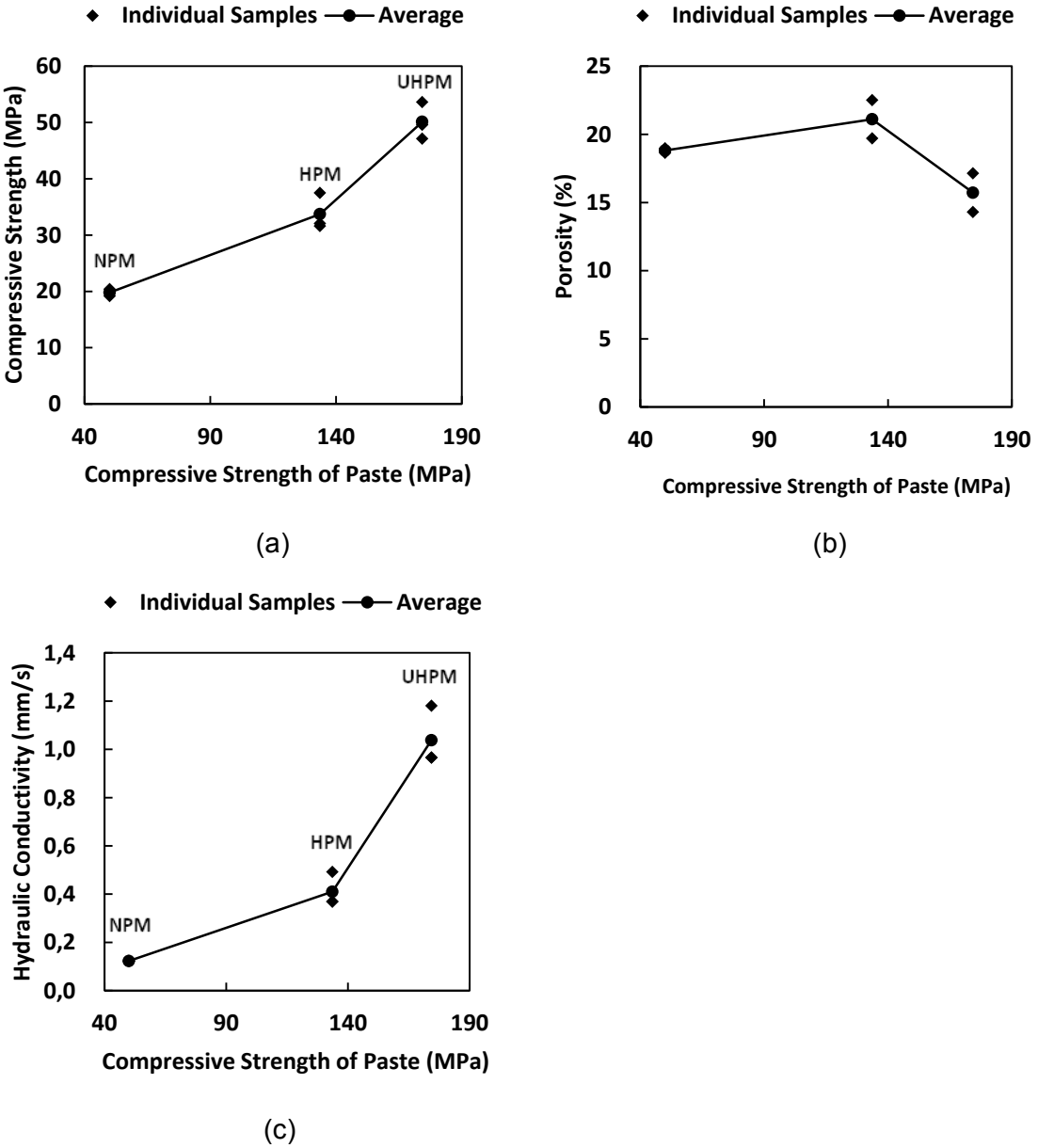

Figure 5: Effect of matrix strength on pervious concrete (a) compressive strength; (b) porosity; (c) hydraulic conductivity.

Figure 5 (b) summarizes the porosity determined from series I. It is worth noting that all porosities are larger than 15% which is within the desired void range of pervious concrete. As shown in Fig. 5 (c), the hydraulic conductivity of this series is below 1mm/s which cannot be considered pervious any more. Porosity values of larger than 15% should result into higher hydraulic conductivities. The authors see the compaction method as a dominant factor for the

low conductivity. Although the hammer with a flat surface supported the compaction of the concrete it also increased the risk of creating layers of lower porosity and thus lower hydraulic conductivity. While these layers should have very little influence on porosity they significantly influence the hydraulic conductivity, which depends on the pore connectivity. The increase of hydraulic conductivity with the increase of matrix strength might be an attribute of the different viscosities of the mixes.

Influence of Amount of Aggregate

The effect of the aggregate to binder ratio on compressive strength, porosity and hydraulic conductivity are plotted in Fig. 6 (a) to (c) respectively. As expected, the increase of the amount of aggregate leads to the reduction of strength while the porosity and hydraulic conductivity are increased. Sufficient paste is needed to cover the aggregates and ensure bonding while excessive paste will occupy the voids. It is worth noting that the mixture with A/B ratio 2.5 (M4) generates a high compressive strength of 42.3 MPa with desired hydraulic conductivity of 2mm/s.

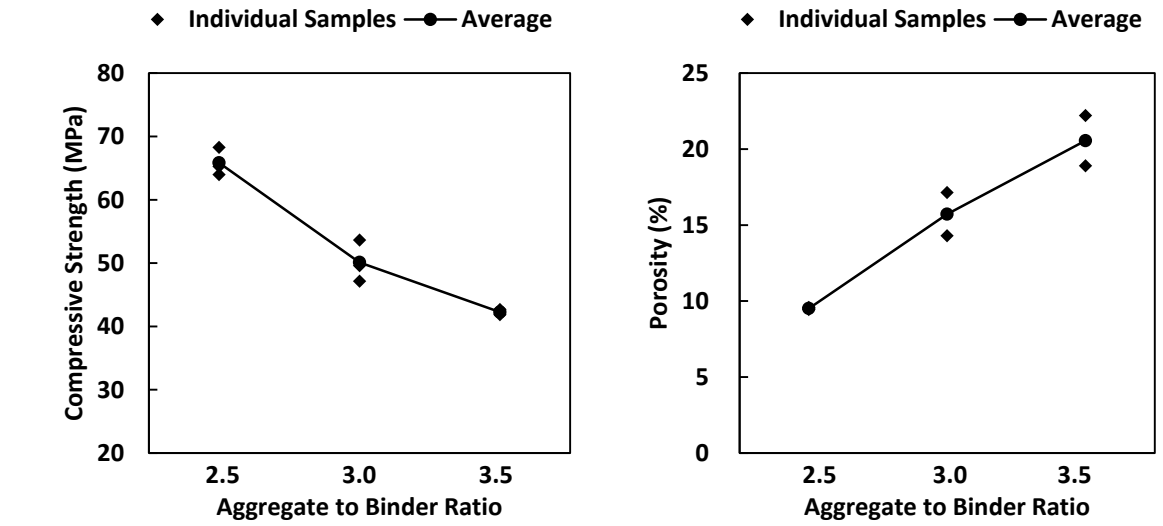

(a)

(b)

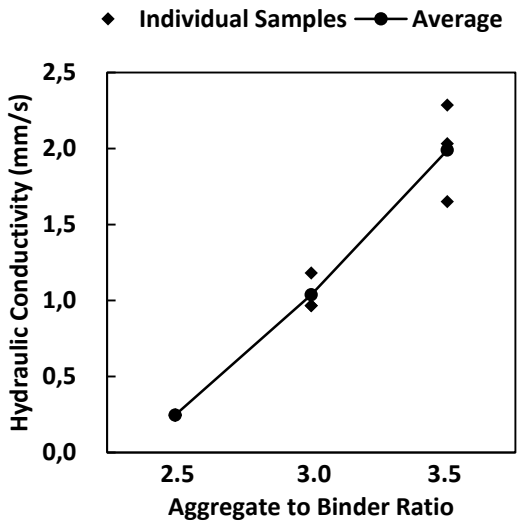

(c)

Figure 6: Effect of the ratio of the amount of aggregate to the amount of binder (A/B) on pervious concrete (a) compressive strength; (b) porosity; (c) hydraulic conductivity.

Effect of Aggregate Size

The effect of aggregate size on compressive strength, porosity and hydraulic conductivity are plotted in Fig. 7 (a) to (c) respectively.

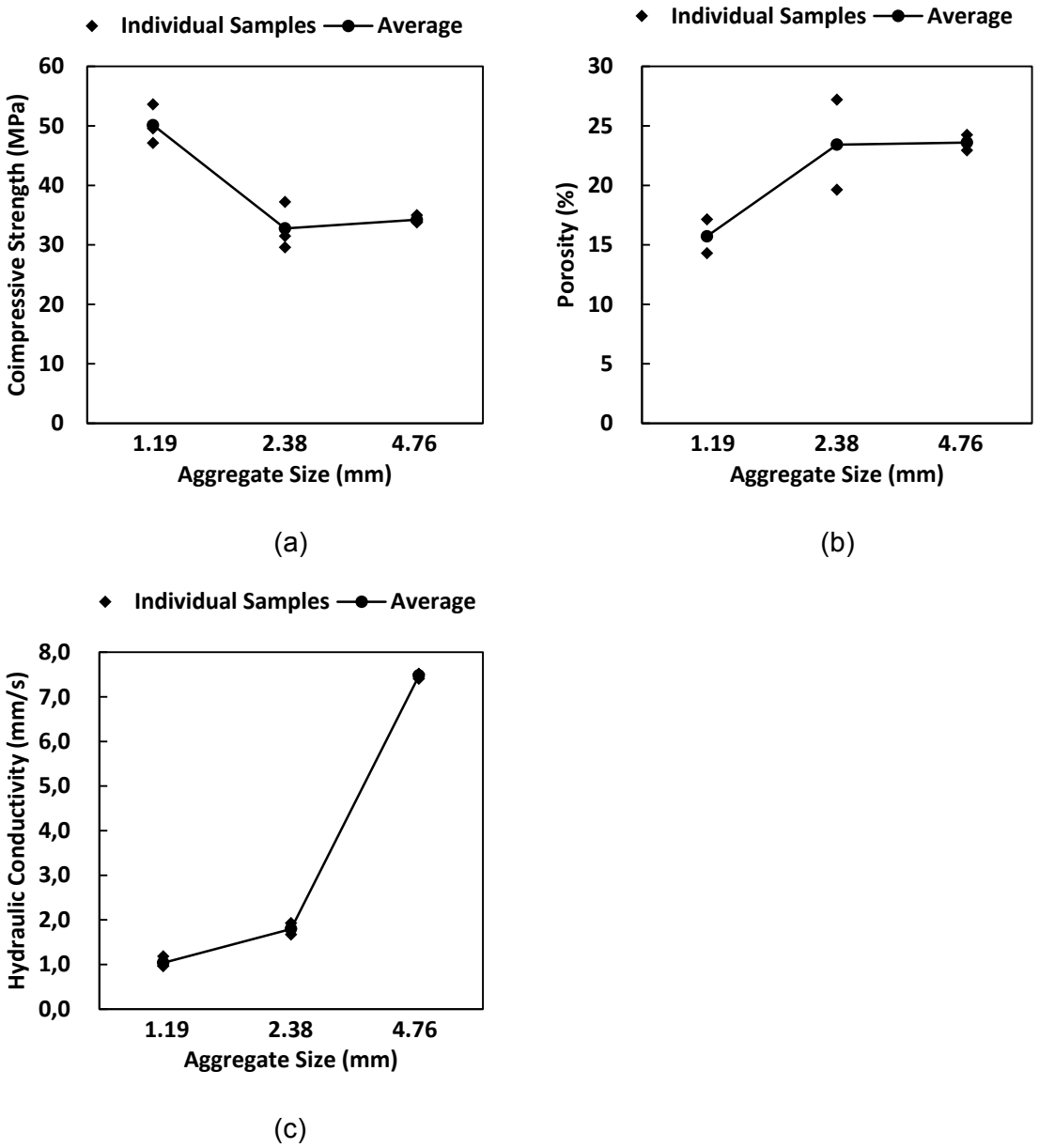

Figure 7: Effect of aggregate size on pervious concrete (a) compressive strength; (b) porosity; (c) hydraulic conductivity.

As shown in Fig. 7 (a), the compressive strength reduces significantly with the increase of aggregate size at first, then increases slightly with the increase of the aggregate size. This would suggest the existance of a critical aggregate size. At equal aggregate and matrix amount, a mixture with smaller size aggregates has more specific area than one with larger aggregates. There will be more bonding area for small size aggregates mixture leading to higher compressive strength.

Figure 7 (b) illustrates, that there also exists a critical aggregate size for porosity. At first, it seems counterintuitive that the porosity increases as the aggregate size increases. Smaller aggregate should require more matrix to cover them leaving less to fill the voids and increasing porosity. However, as mentioned before, the porosity is also affected by pore size and connectivity. The larger the aggregate size, the larger the pore size and the better the chance

pores are connected leading to a higher measured porosity. This can also be used to explain the trend shown in Fig 7 (c).

5 Conclusions

Our hypothesis that the strength of pervious concrete can be improved by using ultra-high performance matrix has been supported. More research is needed and currently carried out at the University of Connecticut to further improve the mechanical performance of pervious concrete. The following conclusions can be drawn from the current research:

1. The higher the strength of the matrix, the stronger the pervious concrete.
2. Increasing the aggregate to binder ratio of pervious concrete leads to increase of porosity and hydraulic conductivity but lower compressive strength in the range investigated (A/B=2.5 to 3.5). Sufficient matrix should be used to ensure the strength of pervious concrete while excessive matrix should be restricted.
3. With the increase of aggregate size, hydraulic conductivity is increased correspondingly due to the increase of pore size and connectivity.
4. With the combination of the use of ultra-high strength cementitious matrix and an optimum aggregate to binder ratio of 3.5, pervious concrete with high strength of 42.3 MPa and comparable permeability of 2 mm/s can be achieved.

References

[1] Pratt, C.J.; Newman, A.P.; Bond, P.C.: Mineral oil bio-degradation within a permeable pavement: long term observations. *Water Science and Technology* 39, pp. 103-109, 1999.

[2] Park, S.; Tia, M.: An experimental study on the water-purification properties of porous concrete. *Cement and Concrete Research* 34, pp 177-184, 2004.

[3] Schaefer, V.R.; Wang, K.; Sulieman, M.T.; Kevern, J.T.: Mix design development for pervious concrete in cold weather climates. Final reports, *Iowa Department of Transportation. National concrete Pavement Technology Center, Iowa Concrete Paving Association, 2006.*

[4] Yang, J.; Jiang, G.L.: Experimental study on properties of pervious concrete pavement materials. *Cement and Concrete Research 33,* pp 381-386, 2003.

[5] Meininger, R.C.:No-fines pervious concrete for paving. *Concrete International* 10 (8), pp 20-27, 1998.

[6] Ghafoori, N.; Dutta, S.: Laboratory investigation of compacted no-fines concrete for paving materials. *Journal of Materials in Civil Engineering,* 7 (3), pp 183-191, 1995.

[7] ACI 211.3-R02.: Guide for selecting proportiond for no slump concrete. *Manual of Concrete Practice 2004 CD-ROM, American Concrete Institute, Famington Hills*.

[8] Tennis, P.D.; Leming, M.L.; Akers, D.J.: Pervious concrete pavements, EB302, Portland Cement Association, Skokie, Illinoia, 2004.

[9] Lian, C.; Zhuge, Y.: Optimum mix design of enhanced permeable concrete – an experimental investigation. *Construction and Building Materials* 24, pp 2664-2671, 2010.

[10] Chindaprasirt, P.; Hatanaka, S.; Chareerat, T.; Mishima, N.; Yuasa, Y.: Cement paste characteristics and porous concrete properties. *Construction and building materials 22, pp 894-901, 2008.*

[11] Suleiman, M. T.; Kevern, J.; Schaefer, V. R.; Wang, K. : Effect of compaction energy on pervious concrete properties. Submitted to *Concrete technology forum-focus on Pervious Concrete*, National Ready Mix Concrete Association, Nashville, TN, May 23-25, 2006.

[12] Kumar, R.; Bhattacharjee, B.: Porosity, pore size distribution and in situ strength of concrete. Cement and concrete research, 33, pp 155-164, 2003.

[13] Wille, K.; Naaman, A.E.; Parra-Montesinos, G.J.: Ultra high performance concrete with compressive strength exceeding 150 Mpa (22 ksi): A simple way. *ACI Materials Journal 108 (1)*, pp 46-54, 2011.

[14] Wille, K.; Naaman, A.E.; El-Tawil, S.; Parra-Montesinos, G.J.: Ultra-high performance concrete and fiber reinforced concrete: achieving strength and ductility with no heat curing. *Materials and Structures, published online Aug. 27th 2011.*

Sewer pipes and UHPC - Development of an UHPC with earth-moist consistency

Michael Schmidt, Torsten Braun, Heiko Möller
Institute of Structural Engineering, University of Kassel, Germany

Sewer pipes and concrete have been in use since the mid-19th Century for the management of wastewater. Concrete pipes have the advantages of a large variety of possible cross-sectional shapes and they are economically producible and durable. Due to the progressive industrialization of the early to the mid 20th Century and the damaging effect of biogenic sulfuric acid in combination with a low water consumption there will be increasingly higher demands on the sewer pipes. Concrete with proper execution is in general resistant to various external influences, but has weaknesses in its resistance to acids. The protection of the sewage pipes as well as the repairs are usually very complex and expensive and presents challenges to the public sector as a carrier of the sewerage system. When using the fine-grained and slightly moist flowable UHPC in a earth-moist mixture, the acid resistance and hence the durability of concrete pipes can be increased. A UHPC has due to its low w / c ratio practically no capillary porses and its optimized packing density compared with normal concrete allows it to have a much higher structure tightness. Moreover, it is possible to achieve a reduction in the cross-sectional dimensions of the tubes, due to the high compressive strength.

Keywords: earth-moist concrete, concrete pipes

1 UHPC with earth-moist properties

Introduction

Earth-moist concrete after a vibration-press compaction is characterized by high green strength and fast direct stripping. These properties are of particular importance for the concrete products industry as the concrete products can be stripped immediately after the design. The green strength at this time must be designed so that it can hold the proper weight of the concrete products and that the shape stability is guaranteed. To achieve these properties classic earth-moist concrete has a relatively low water-cement ratio of 0.35 to 0.45 and a cement content of between 270 kg/m³ and 350 kg/m³. The paste content is between between 210 and 240 l/m [1]. These small paste content and a relatively high proportion of coarse grain in the recipe are responsible for the stiff consistency of a earth-moist concrete. The paste content, with optimal dosing, in the early hardening stage is primarily responsible for the formation of the green strength. At this stage, the paste content acts as a filler of the cavities formed between the rock grains and as an adhesive of the grain skeleton. With increasing hydration, the paste is increasingly under pressure from compression forces and combines the grain skeleton with each other. In the stage of the hardened concrete the paste is responsible for the formation of a sufficiently pressure-resistant and durable concrete. Thus the paste has two essential functions from a setting time perspective, both of which are essential features for an earth-moist concrete in the early and late stages. With the use of a fine-grain and flowable UHPC paste for the creation of earth-moist concrete, specific characteristics of traditional earth-moist concrete can be improved. This includes a denser and more closed surface that is more resistant to external influences. A further increase in efficiency in the production, transportation and handling of the pipes can be achieved by reducing the wall thickness.

Focal points of the research

The aim of the work performed was to conceive an earth-moist concrete, which contains a high proportion of coarse grain and a binders paste that is based on a UHPC. The characteristics of

this earth-moist concrete should, as with the traditional earth-moist concrete also, be a good green strength immediately after stripping. Furthermore, the results were also evaluated based on the parameters of surface integrity and of dimensional stability of the specimen. In order to achieve these conditions, the optimal relationship between the UHPC and the aggregate has been identified using a vibration proctor test developed by the University of Kassel. Following these investigations in the laboratory, the practicality of the formulations was to be documented in a concrete factory with the production of pipe demonstrators with a nominal diameter of DN 300.

Setting the UHPC paste

UHPC formulations developed at the University of Kassel are firstly fine-grain recipes with a maximum particle size of 0.5 mm and the secondly coarse-grained recipes with a maximum particle size of 8 mm. The main differences between these two recipes consist in a lower matrix fraction < 0.125 mm by 35 vol- to 40.5 vol-% and at a much lower cement content of the coarse-grained UHPC formulation [3]. During these investigations, the fine-grained and coarse-grained UHPC formulations were studied for up to a maximum particle size of 0.5 mm, in terms of fresh and hardened mortar characteristics. For the development of an earth-moist UHPC a flowable paste with a slump flow of > 30 cm should be used, and the paste should have very good compressive strength and overall porosity results. The studies were divided in fresh paste investigation with the following characteristics:

- slump flow according to DIN EN 12350 Part 3
- air content according to DIN 12 350 Part 7

and in hardened paste investigations with these characteristics:

- compressive strength after 7 - and 28 days after immersion in water
- Studies on the pore size distribution by the mercury penetration porosimetry.

Table 1: Composition of UHPC paste.

Constitutive materials	Volume [dm³]	Mass [kg]	Density [kg/dm³]
Water	158,0	175,0	1,00
Pore space	15,1	-	-
CEM I 52,5R	209,7	650	3,10
Silica fume	80,5	177,0	2,20
Superplasticizer	28,3	30,0	1,07
Quartz powder fine	122,6	325,0	2,65
Quartz powder gross	49,4	131,0	2,65
Quartz sand 0,125/0,5	133,6	354,0	2,65

Paste levels

An earth-moist concrete in the fresh state corresponds to a weakly cohesive soil [4]. The structural behavior in this early stage is not yet based on the hydration products which are being formed, but there is an interaction between paste and aggregate, which are based on known soil mechanical relationships. The cohesion of the earth-moist concrete is ensured at this point by variables such as internal friction and cohesion, and the load transfer is ensured by the grain skeleton of the rock grains [4, 5, 2, 1]. This grain structure forms a so-called load transfer chain when it comes ideally to a a grain-to-grain contact.

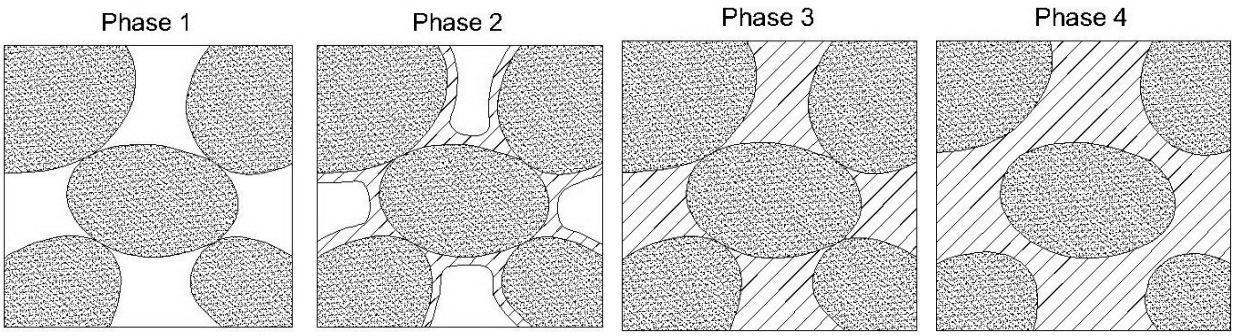

Figure 1: Four-phase model of the cavity filling.

According to [2] an optimal paste/aggregate ratio relationship exists when a grain-to-grain contact exists and when the voids are filled with paste. If the cavities are overfilled or underfilled the green strength and dimensional stability of the removed concrete products is no longer guaranteed. In Figure 1 the four-phase model of the cavitty filling is presented. It describes the increasing degree of filling of the cavities, Phase 3 is characterized by an optimal filling and with a grain-to-grain contact between the aggregate. In order to obtain the optimum filling level of a earth-moist mixture using a UHPC paste, the vibration proctor test was used. In this method the paste/aggregate ratio is graded and compressed under a steady vibration-press compaction. Through the gradual approach the paste content increases with each examination step whilst the aggregate content is decreased. This makes it possible to determine the optimal paste content of a slightly moist mixture.

Vibration proctor investigation

The proctor test [6] is a method, used in geotechnical engineering, to determine the ability of a soil compaction. With a sweeping consolidation a connection between the dry density and different water levels of the soil is created using a constant compaction work. In [2] an additional development step was created for the vibration proctor test modeled after the Proctor experiment for the use of an earth-moist sample. The apparatus consists of a steel cylinder mold (height: 300 mm, diameter 150 mm) and a load weight, which creates a constant surcharge stress of 0.016 N/mm ². The surcharge stress prevents movements of gross aggregate in the earth-moist aggregates in the sample slightly moist. The test set is fixed firmly on a vibrating table and with incipient vibrating influence stand there is a compression of the sample. Figure 2 shows the structure of vibration proctor stand. With this method it is possible to determine the maximum achievable dry density of a concrete mixture. This indicates in turn, with which level of paste content the void is completely filled.

The vibration proctor investigations were made with UHPC paste shown in Table 1. As aggregates, a gravel- (unbroken), basalt- (broken) and a basalt grain size with gap grading were used. The grain size range in each case was 0/16. In accordance with DIN 1045-2, the grain size range "cheap" was used and for the gap grading the gap grading grain size was used.

The mixing of earth-moist concrete was carried out in a compulsion mixer ZZ30 HE from the manufacturer Zyklos with a volume of 20 l at a speed of 60 rev/min with the auxiliary drive and whorl in use. The initial mixing volume was 12 l and increased with the increase of the paste content to about 20 liters. After the end of the mixing time of 10 minutes the earth-moist concrete was filled under vibration influence (60 Hz, amplitude 0.75 mm) flush with the surface in the steel cylinder mold. The load weight was placed after the filling and then it was compressed for another minute. The entire filling and compaction time was about 3 minutes.

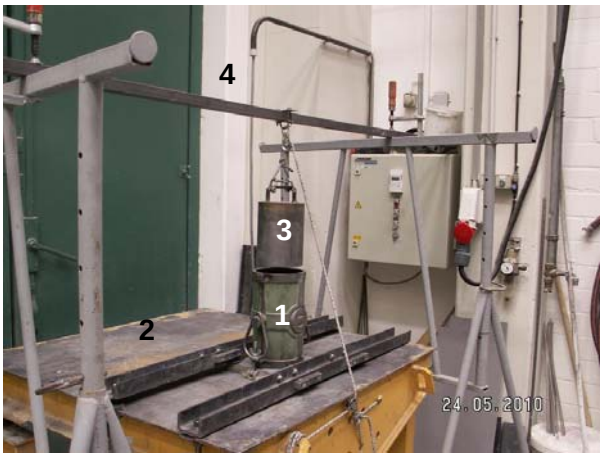

1 cylinder mold
2 vibrating table
3 load weight
4 auxiliary frame

Figure 2: Experimental setup vibration proctor test.

In Figure 3, the Proctor curve of the three test series are shown. The y-axis shows the dry density and the x-axis shows the respective paste content of the mixture. There is evidence across all three mixtures, that an optimal density is reached at about 35 vol-% paste to 65 vol-% aggregate. It can also be seen that the two basalt mixtures have almost identical patterns and overall a higher dry density than the gravel mix. In the literature it is known that with increasing fine-grain content, the dry densities also increase. The mixing quantities of basalt mixtures were larger than the mixing quantities of the gravel mixture. This is an indication that a higher void content had to be filled between the basalt graining with paste. This in turn increases the overall paste content and therefore the fine-material content of the mixture. The curve of the gravel mixture approaches saturation much more slowly, this indicates a continuous increase in the cavity saturation.

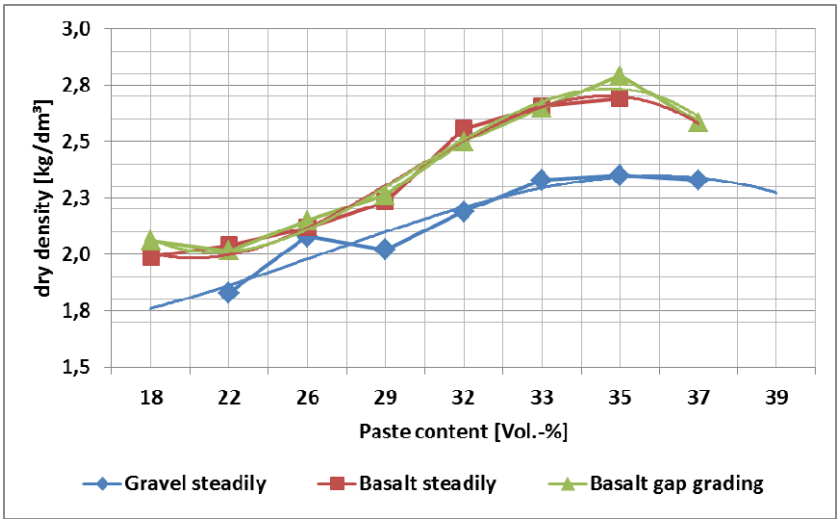

Figure 3: Determination the proctor density with three different grain compositions [7].

Critical to the selection of a suitable composition was not only the best paste/aggregate ratio, instead the surface texture of the specimens should likewise have a unified appearance.

Figure 4 shows an exemplary specimen of gravel mixture after the vibration proctor investigations. The left image shows a test specimen with the paste/aggregate ratio of 26/76, the middle image, a ratio of 35/65 and right ratio of 37/63. In the images of the specimens the phase model of the cavity filling [2] based on constructed surfaces can be seen quite clearly. The left image shows a test with too small a paste content, hence the surface is not closed. The

middle image shows an almost unbroken surface, the specimen remained stable in shape after stripping and using the Proctor curve this paste/aggregate ratio has the highest packing density. As for the right-hand specimen there was an over-filling of the cavities, this is very easily recognized by the supersaturated surface as well as the loss of form stability. In conclusion, it shows that with the vibrating proctor test the optimal density of the earth-moist mixture can be detected even with a gradual approach with regards to the paste content.

26/74 35/65 37/63

Figure 4: Specimens with different paste/aggregate ratios, gravel mixture.

2 Preparation of concrete pipes in the plant

Composition / Experimental procedure / production

In a precast concrete plant the earth-moist mixtures, which were previously examined in the laboratory, were put into practice. The plant produces steel reinforced concrete pipes for the wastewater sector in various diameters and lengths up to about 1 m. The earth-moist mixtures are manufactured in a 1.5 m³ synchronous mixer and transported via a conveyor belt to the production plant. The production of the pipes is carried out via a system with a fixed inner part and a movable and removable outer tubular casing. The filling of the formwork is done under vibrating influences, after completion of the filling the pipe is compressed under load. A total of 11 concrete pipes with a nominal diameter of DN 300, length 1100 mm were produced.

In a precast concrete plant the earth-moist mixtures, which were previously examined in the laboratory, were put into practice. The plant produces steel reinforced concrete pipes for the wastewater sector in various diameters and lengths up to about 1 m. The earth-moist mixtures are manufactured in a 1.5 m³ synchronous mixer and transported via a conveyor belt to the production plant. The production of the pipes is carried out via a system with a fixed inner part and a movable and removable outer tubular casing. The filling of the formwork is done under vibrating influences, after completion of the filling the pipe is compressed under load. A total of 11 concrete pipes with a nominal diameter of DN 300, length 1100 mm were produced.

In the practice tests in that plant the same moist mixture from the laboratory tests was used. Furthermore, a second UHPC recipe was used, which contained a different superplasticizer and silica fume. Thus conclusions about the effect of different flow agents could be drawn and this enabled a certain hedge against the possible non-success of a mixture. As the optimal paste/aggregate ratio 35/65 was also used for this second UHPC paste.

For the production of these first tube pipes made out of a earth-moist UHPC principally the following main questions should answered :

- is it possible to create and process an earth-moist UHPC in the factory given the existing mixing and compaction equipment?
- is it still possible to process the earth-moist UHPC for the duration of a production cycle which consists of a total of six tubes and a duration of about 60 minutes?
- Is it possible to obtain a closed surface (blowholes, flaws)?

A volume of 500 l was mixed using a paste/aggregate ratio of 35/65. As aggregate sand 0/2, gravel 2/8 and gravel 8/16 from the available local resources were used. The mixing time in the synchronous mixer was about 10-12 minutes. The ingredients were homogenized for 2 minutes before the water/superplasticizer mixture was added. The fresh concrete temperatures fluctuated between 24.5°C and 25.4°C. The earth-moist concrete was then transported to the pipe manufacturing plant via the conveyor belt system. Overall, the pipe fabrications were very successful, so that 5 pipes DN 300, l = 1100 mm w with bell and spigot were manufactured for each of the two recipes . The figure below shows some of the manufactured concrete pipes in the general view and the detail of the surface.

Figure 5: Manufactured concrete pipes (left) in the view, detail of surface structure UHPC pipe (middle), concrete pipe factory original (right)

The pipemanufacturing with the reformulated recipe was generally speaking a success. However, the optimum paste/aggregate ratio of the laboratory investigations of 35/65 turned out to be a bit too high for the production inside the plant system. The tubes manufactured with this ratio showed within in a shorttime a slight bulge in the middle of the tube. In a second experiment, the paste/aggregate ratio was then decreased to 30/70. These tubes could be very well produced and are shown in Figure 5.

The earth-moist concrete could be used after mixing of about 60 minutes. The surfaces shown in figures 5 indicate that that the earth-moist UHPC exhibited a similar high surface quality as the concrete tubes of the concrete plant. The surfaces of the tubes were almost cavities free except some small spots. A coarse-grained and non-closed structure was formed primarily in the folds of the spigot of those pipes that were produced at a later stage.

Post examinations

Following this production several studies of the concrete pipes were conducted. For this purpose pipes from each recipe as well as original pipes of the concrete plant were sent to the University of Kassel. The original pipes were used to generate some reference values. Several studies on the compressive strength and durability were conducted. As examples the following

figure shows the results for compressive strength according to DIN EN 12390-03 and the crown compressive strength according to DIN EN 1916.

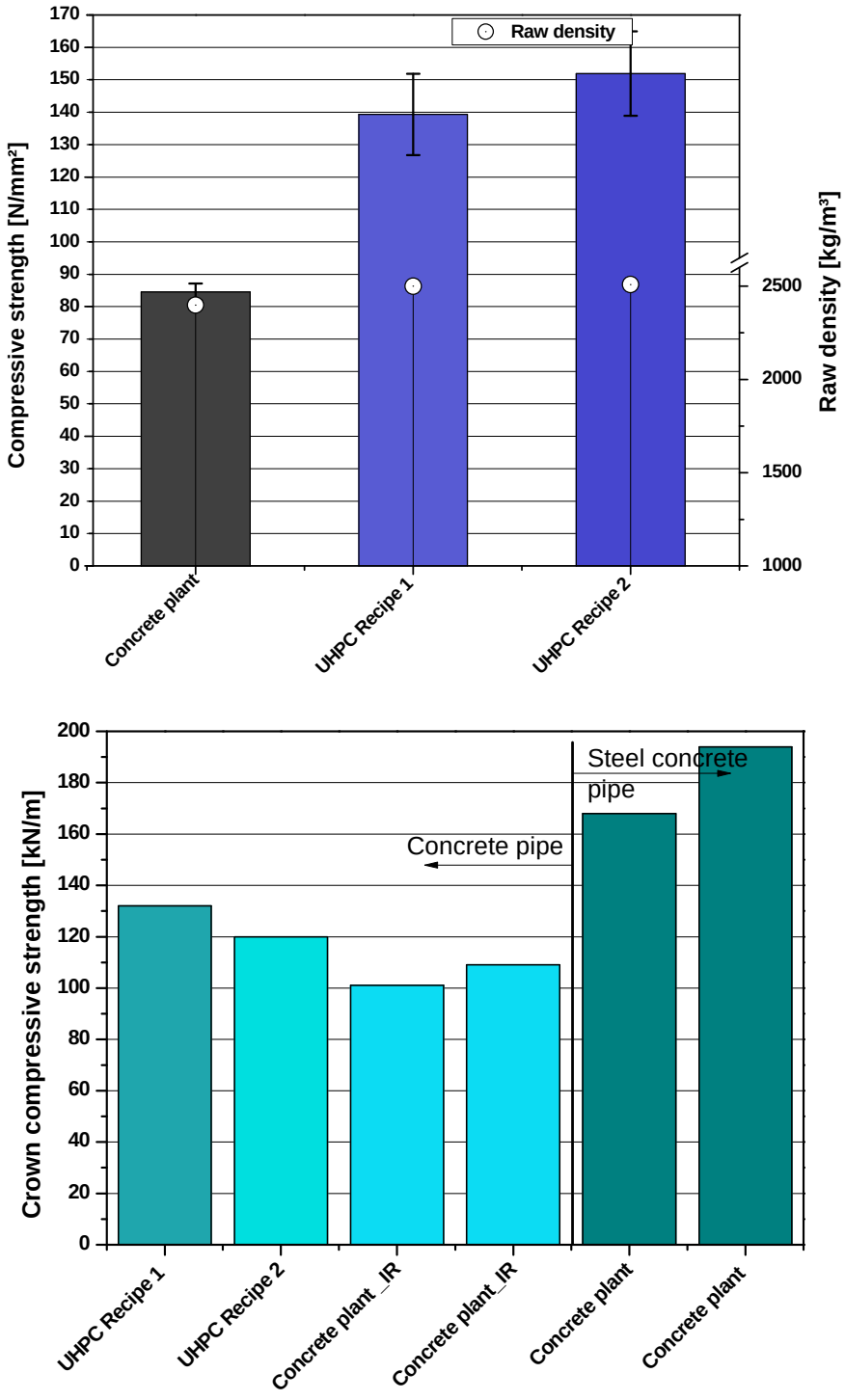

Figure 6: Compressive strength results on cores (above), results of the crown compressive strength (below)

The mixture designation Recipe 1 describes the UHPC paste that has been studied in the lab using the vibration proctor tests. The Recipe 2 is the additional recipe that was made in the concrete plant. In order to determine the compressive strength three cores were drawn from the pipes for each recipe. The ends of the cylinders were grinded so that the height and the diameter were 5 cm. The compressive strengths were determined at an age of > 56 days. The graph shows very clearly the increased strengths of a earth-moist UHPC compared with a

normal earth-moist concrete. The right figure shows the results of the crown compressive strength test after 28 days. The earth-moist UHPC pipes as well as two steel reinforced concrete pipes of the concrete plant were examined. The steel reinforced concrete pipes showed as expected, a much higher crushing strength than the concrete pipes. The two results, called concrete plant_IR show the initial cracking during the the crushing test of the steel reinforced concrete pipes. For concrete pipes the break would have occurred after the initial crack and this indicates compared to the moist UHPC pipes an increase in the crown compressive strength compared to concrete pipes made out of ordinary earth-moist concrete.

3 Summary

UHPC is typically a fine-grained, free-flowing concrete for structural applications. Its high strength and especially its much higher density structure virtually without capillary pores can also be used in other application areas. These studies with the use of UHPC in earth-moist mixtures indicate a new possible application in the field of precast concrete products. It is possible to manufacture concrete pipes with a significantly improved mechanical and chemical resistance.

The investigations showed that the optimal paste content a earth-moist mixture can be identified using a vibration proctor test. The difference to the original test procedure was that not the water content was increased gradually in the mixture but instead the UHPC paste was added as a whole in a graded fashion. Due to the dense and compact structure of the UHPC paste very good compressive strength and crushing results were obtained. For further investigations in this area, it would also be possible to reduce the wall thicknesses.

References

[1] Bornemann, R.: Untersuchungen zur Modellierung des Frisch- und Festbetonverhaltens erdfeuchter Betone; *Schriftenreihe Baustoffe und Massivbau*, Universität Kassel, Heft 4, 2005.

[2] Schmidt, M.: Stoffliche und konstruktive Eigenschaften hydraulisch gebundener Tragschichten. *Schriftenreihe der Zementindustrie*, Heft 51, 1991.

[3] Bornemann, R.; Schmidt, M.: Ultra-Hochleistungsbeton UHPC - Herstellung, Eigenschaften und Anwendungsmöglichkeiten. *Beton- und Stahlbetonbau*, 2001, S. 458-467

[4] Wierig, H.J.: Zur Frage der Theorie und Technologie des grünen Betons. *Institut für Baustoffkunde und Materialprüfwesen der Technischen Universität Hannover*, Universität Hannover, Heft 19,1971

[5] Wierig, H. J.: Einige Beziehungen zwischen den Eigenschaften von „grünen“ und „jungen“ Betonen und denen des Festbetons. *Betontechnische Berichte, Betonverlag Düsseldorf*, 1971, S. 151 – 172

[6] DIN 18127: Proctorversuch – Baugrund, Untersuchung von Bodenproben, *Deutsches Institut für Normung,* 1997

[7] Möller, H.: Konzeption und Untersuchung erdfeuchter Betone mit erhöhten Festigkeiten, *Diplomarbeit FG Werkstoffe des Bauwesens, Uni Kassel*, 2010 *unveröffentlicht*

Development of an Ultra-High Performance Concrete for precast spun concrete columns

Thomas Adam[1], Jianxin Ma[2]
1: Europoles GmbH & Co. KG, Neumarkt i.Opf., Germany
2: Inst. f. Werkstoff- und Konstruktionsentwicklung, Magdeburg, Germany

Strength Class of C100/115 is the present state of art in the field of spun concrete. Consequentially, the next step was the application of concrete above the structural capability of C100/115. Therefore EUROPOLES has started to enhance the compressive strength gradually up to 150 N/mm² during the past years. Due to the different features in compacting (spinning) process the composition and fresh propterties of this UHPC differ necessarily from that of common UHPC The volume fraction of the cementitious paste is much lower. Powders with a Blaine-fineness of about 2500 cm²/g are more favorated than ultrafine powders mostly used in common UHPC. Furthermore the spun UHPC must have a high green strength after spinning. EUROPOLES has produced prototype spun columns and poles. The whole project is undergoing.

Keywords: spun concrete, columns, UHPC

1 Introduction

It is characteristic for spun concrete, that the compaction of the fresh concrete is generated by using centrifugal forces in a rotating mould (*Figure 1*).

Figure 1: Spinning process.

Thus, the result are rod-shaped elements with a very smooth and dense concrete shell and a circular cavity in the middle of the cross section.

Applications range from light poles, telecommunication and power poles to precast columns for structural use. Logically, an increase in the compressive strength of the concrete benefit the load bearing capacity, especially of elements mainly stressed with normal forces, as columns. During the past years the compressive strength has gradually increased up to C100/115, which is the maximum strength class covered by the DIN-standard [1] and general type approval of EUROPOLES up to now. In order to stay competitive with other concrete columns and steel composite columns further progresses were needed.

Encouraged by the advances in cementious material science to Ultra High Performance Concrete (UHPC), with compressive strength up to 200 N/mm², EUROPOLES has proven the technical feasability of UHPC. The result was positive, although it turned out that the aim of 200 N/mm² is apparently too ambitious. Moreover, it became obvious that UHPC-formulas available in the scientific literature will not work as spun concrete.

In contrast to the mostly flowable consistency of UHPC, spun concrete has to have a soft plastic consitency during placing and a high green strength after the spinning is done. For that reason the content of fine material should be moderate.

For the fresh concrete properties as well as the strength the plastisicer is particularly important. The first trials showed that the so far used plastisizer, on the basis of naphthalene sulfonate, will not achieve the desired result. On the other hand, polycarboxylates, normally recommended to use in UHPC, showed some features, which made them not well suited for spun concrete. Either they led to a flowing but highly viscous mix, which was hard to work with, or the concrete maintained its soft consistency for too long. The latter led to a strong segregation during the spinning process and the liquide cement paste, so called slope, which slide down and accumulates inside the cavity (Figure 2).

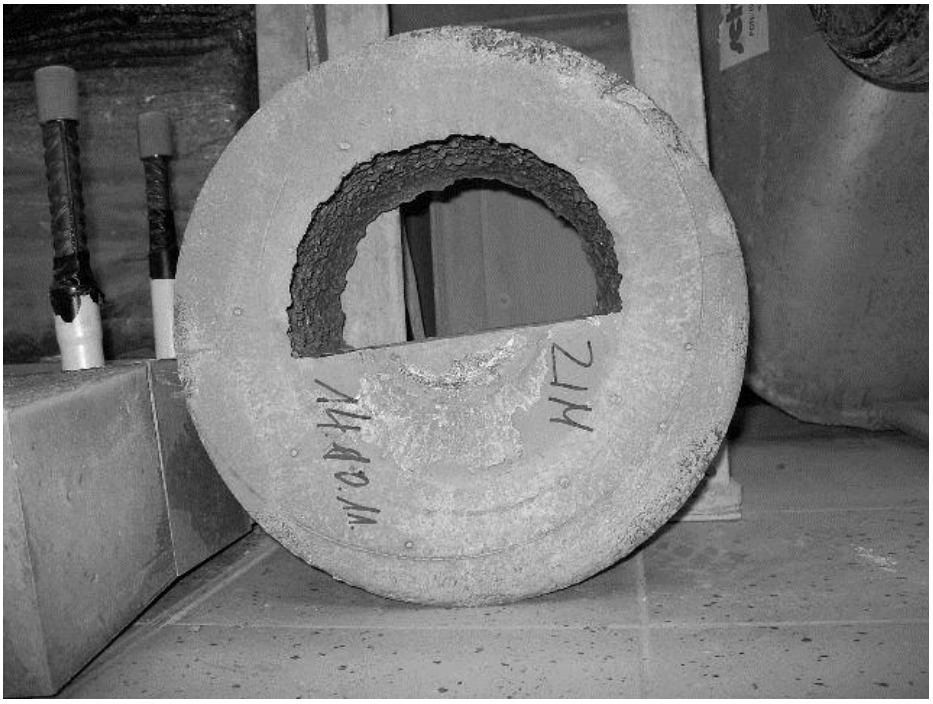

Figure 2: Cross section of a test ring with slop.

It is obvious that the choice of the plastisizer requires a compromise. This could be found in a combination of two polycarboxylates, which have shown the best results so far. The main admixture ensures the optimal liquefaction of the concrete and the other maintains a sufficient workability. The duration of workability can be controlled by means of the ratio of both admixtures. On the basis of this experiments and using standard cement, aggregates and microsilica which was in stock and everyday used in the concrete pole plant Neumarkt i.Opf. a mix design was developed and several prototypes were produced. The so-produced concrete exhibited a good workability and encouraging performance.

2 Composition of spun UHPC

Materials

The UHPC in this paper is composed of Portland cement CEM I 52,5 R according to DIN EN 196-1, silica fume, quartz powder, crushed quartz sand and basalt split with the grain size up to 5 mm. Crushed basalt sand with the grain size up to 2 mm was used in the pre-experiments. However, it showed negative affect on the concrete workability and was not used any more. In spite of its advantage in compressive strength, an ultrafine quartz powder had to be set aside, because the UHPC was too viscos and made the placing difficult.

In the laboratory experiments a PCE superplasticizer was used. In the production it was replaced by a mixure composed of two PCE superplasticizers in order to regulate the setting time of the spun concrete.

Mixture composition

The mixture composition was firstly determined in laboratory experiments and thereafter adjusted in pilot experiments at EUROPOLES. The laboratory experiments aimed to develop a basic mixture composition achieving the required compressive strength and workability. In the pilot experiments columns with different diameter and length were produced. For the pilot production the superplasticizer was adjusted to match the weather conditions.

Laboratory experiments

The design of the laboratory concept was carried out in following steps:

Step1: determination of the composition of cementitious paste, i.e. the ratio of silica fume and quartz powder to cement. The cementitious paste should meet following requirements: a compressive strength more than 170 N/mm² after heat treatment at 90°C and a slump flow more than 300 mm. The compressive strength was performed on 40×40×160 mm prism and a Haegermann table, without shock operation was used for testing the paste workability.

The volumetric ratio between water and the powders (cement, silica fume and quartz powder) in the pastes was kept constant, while the ratio of silica fume and quartz powder to cement were varied to determine the achievable compressive strength and the paste workability.

The compressive strength of the heat treated paste/concrete was affected not only by the water to powder ratio, but also by the silica fume content. Generally the compressive strength increases with the silica fume content. However, the results in [3] have shown that the silica fume above 18 wt% of the cement weight does not siginificantly improve the concrete compressive strength any more. In the laboratory experiments the silica fume content varied from 12 wt% up to 18 wt%. The results in Figure 3 show that in both series with finer and coarser quartz powder the paste strength rise with the silica fume content. In the concrete experiments the silica fume content was set at 18 wt% of the cement weight.

The superplasticizer used in the laboratory experiments was highly liquefying and exhibited a moderate retarding effect, which turned out unfavourable later. The superplasticizer dosage was adjusted to a flowablity of the paste greater than 300 mm and a compressive strength of more than 65 N/mm² after 16 hour curing at 20°C.

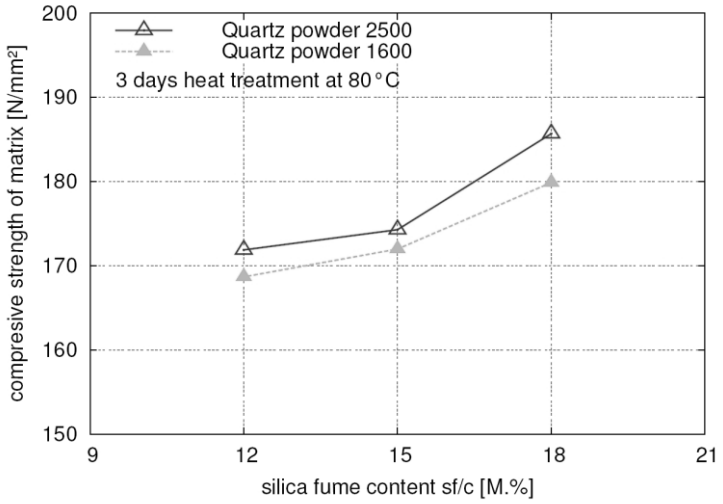

Figure 3: Compresseve strength of cementitious paste after heat treatment.

Step 2: determination of the optimal ratio between quartz sand and basalt split:
The air void among aggregate particles is affected by the sand rate. The result in *Figure 4* shows that the minimal void of 34.9 Vol.% in the aggregate mixture is reached at the optimal sand rate of 35 %. A slightly deviance from this optimal sand rate does not significantly increase the void volume in the aggregate mixture. In the later experiments the sand rate was kept at 32 %. The volume of the cementitious paste in the concrete is 380 Ltr/m³, about 10 % higher than the void volume among the aggregates.

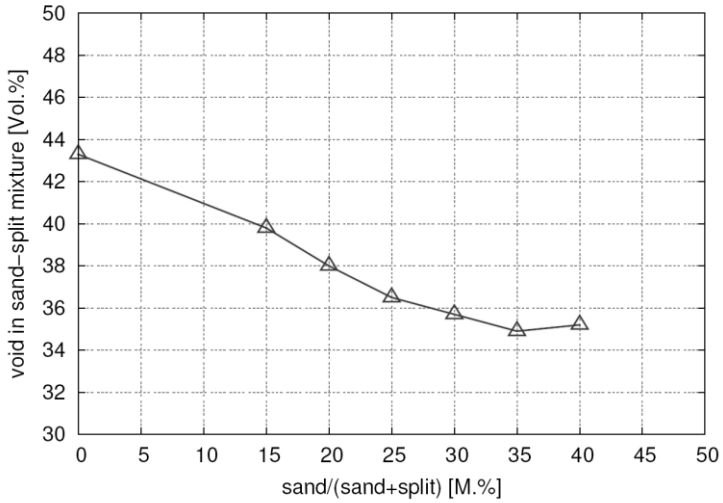

Figure 4: Void among sand-split mixture.

Densifying the concrete in laboratory
It is not easy to simulate the spinning process in laboratory. In fact the concrete during spinning process is much more intensively compacted than on a common vibration table. The concrete which is suitable to be densified on the common vibration table in laboratory is usally softer than spun concrete mixes. Conversely, the concrete consistency which fits for spinning is too stiff for laboratory experiment. For that reason using a vibration table is unfavourable. The compressive strength determined on such specimens will not be representative.

In order to simulate the spinning process the concrete was firstly vibrated in steel cylinder moulds with a diameter of 100 mm and then pressured using a testing machine. The punch,

with which the pressure was applied, had a diameter of 90 mm. The concrete was pressed in cycles with load stages between 5 und 50 kN with a rate of 0.5 N/mm²/s. After 20 cycles the upper loading of 50 kN was held for 30 seconds and then the cylinder was unloaded. During the cyclc loading the cementitious paste was queezed out.

3 Manufacture of spun concrete elements

During the last two years several test elements and prototyps were made with UHPC. Most of those were made within the scope of an extensive research program in 2011, founded by the Federal Ministry of Economics and Labour (BMWi). The project partners were the iBMB TU Braunschweig and Stahlwerk Annahuette. The iBMB has performed the load test on columns with different diameters and arrangements of reinforcement. *Figure 5* shows exemplary such columns.

Figure 5: Test columns with 350 mm diameter designated for load test.

Besides the test elements for the load tests prototypes of real columns and poles were made. This seemed to be needed to test the production of UHPC under every day conditions in normal operation and to get a feeling for the difficulties connected with it. The concreting was done with buckets, as seen in *Figure 6*.

Figure 6: Placing UHPC into mould.

The result was gratifying as can be seen in *Figure 7*. The five columns has been delivered and assembled on site. The corresponding cube strength ranged between 132,5 and 149,5 N/mm². The compressive strength of cores, taken from one element, was 157,0 N/mm².

Figure 7: UHPC-columns.

Encouraged by those results it has been decided to use UHPC for big poles as well, which might lead to thinner wall thitcknesses and therefore lighter elements. After a few smaller poles a bigger telecommunication pole (*Figure 8*) was made with UHPC. Therefore 4 batches concrete were needed, which had to be retarded decreasingly. The concrete has hardened under ambient conditions. The average core strength was 172,0 N/mm².

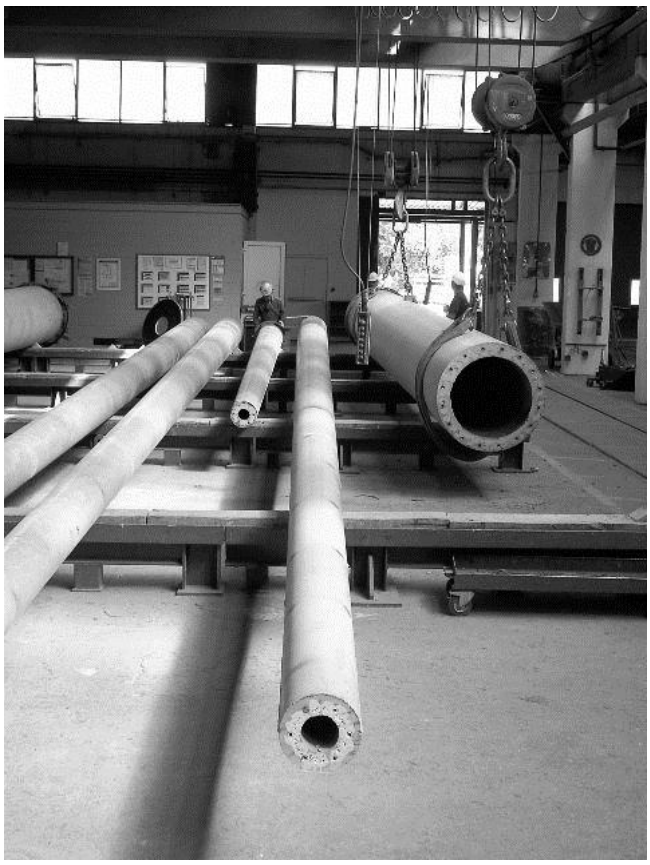

Figure 8: 22-meter telecommunication-pole.

The biggest element made up to now was a 26m-pole for overhead power line. This pole was tested in a bending test at EUROPOLES (*Figure 9*). It was not able to bend this pole until the failure of the concrete compression zone.

Figure 9: 26-meter 15KN power-pole during the bending-test.

4 Conclusions

Ultra High Performance Concrete can be applied for spun concrete. Compressive strength up to 172 N/mm² could be achieved without heat curing and the use of fibres. It could be shown that columns as well as poles can be manufactured without changing the previous production technology. Even elements consisting of several batches could be made. Most of the produced UHPC-elements were designated for load test carried out by TU Braunschweig. The results of the load test of columns are presented in a separate paper at HiPerMat2012.

References

[1] DIN 1045-1:2008-08: Tragwerke aus Beton, Stahlbeton und Spannbeton – Bemessung und Konstruktion.

[2] Deutscher Ausschuss für Stahlbeton: Ultrahochfester Beton – Sachstandsbericht. DAfStb 561, Berlin, 2008.

[3] Ma, J.: Faserfreier Ultrahochfester Beton – Entwicklung und Materialeigenschaften, Dissertation, Universität Leipzig, 2010.

Whiteman Creek Bridge – A Synthesis of Ultra High Performance Concrete and Fibre Reinforced Polymers for Accelerated Bridge Construction

Wade F. Young[1], Jasan Boparai[1], Vic Perry[2], Brent I. Archibald[3], Sameh Salib[3]

1: Ministry of Transportation Ontario, London, Ontario, Canada
2: Lafarge Canada Inc.-Ductal, Calgary, Alberta, Canada
3: Delcan, Markham, Ontario, Canada

The Whiteman Creek Bridge replacement project represents a synthesis of Ultra High Performance Concrete (UHPC) and Fibre Reinforced Polymers (FRP) to deliver Accelerated Bridge Construction (ABC) and durability at a reasonable cost. The project involves the replacement of an existing three span concrete bridge with a single 40 m span bridge, during a seven week highway closure. Prefabricated components constitute about 90% of the bridge structure including precast abutments, wingwalls, deck elements, and steel girders. The superior characterisitics of UHPC were the keys to the ABC evolution of the subject structure by down-sizing the precast elements joints and eliminating the deck formwork. Furthermore, for enhanced durability, Glass Fibre Reinforced Polymer (GFRP) bars were used as the top reinforcing mat of the precast deck elements and as the sole reinforcement of the entire new cast-in-place concrete barrier walls.

Keywords: Ultra High Performance Concrete, FRP Reinforcement, Accelerated Construction, Bridge

1 Introduction

All over the world, public and business time waste and delays due to traffic congestion and detours at infrastructure construction sites have significant impacts on the indirect cost associated with these projects. In North America, the USA Federal Highways Administration (FHWA) [1] has developed initiatives for reducing such cost by utilizing Ultra High Performance Concrete (UHPC). The superior characteristics of UHPC regarding strength, toughness and durability significantly reduce the material and labour involved in the construction process. Consequently, the construction time, initial cost, future cost, and the indirect project cost, as mentioned earlier, can be reduced as well. Also, using FRP reinforcement, with its unique non-corrosive nature and high strength to weight ratio along with UHPC, magnifies the durability and performance level of the structure. Herein, the Ministry of Transportation Ontario (MTO)-West Region completed their first ABC project utilizing both UHPC and FRP where the subject bridge, having both superstructure and substructure as prefabricated elements, was entirely replaced within seven weeks instead of several months of conventional construction.

2 Background

Highway 24 is a two-lane rural highway serving the southern portion of the Province of Ontario, Canada. The subject bridge is located near the City of Brantford at the bottom of a vertical sag curve within a natural valley with residential property and environmental constraints. The existing (replaced) bridge, with a three span concrete T-beam structure and a total length of 33.5m, was slated for replacement due to its age, condition and structural deficiencies. As a result of the site conditions and constraints of the surrounding terrain and residential properties, it was decided to replace the structure using rapid construction techniques.

The MTO Northwest Region Office in Thunder Bay pioneered the use of UHPC in Ontario. As of 2010, Northwest Region has constructed nine projects. The first project in 2006 was the CN Overhead Bridge at Rainy Lake which incorporated precast deck panels with UHPC joint fill.

Observations made to date indicate outstanding performance [2]. After 5 years of service in a northern climate, there is neither deterioration of the material nor any opening of the joints.

Since then, the MTO Northwest Region has used UHPC joint fill for the interconnection of precast bridge elements including; full depth precast deck panels; side-by-side precast girders; full depth precast approach slabs, and precast concrete deck curbs (Fig. 1).

a) Deck Prior to Receiving Asphalt Wearing Surface

b) Field Cast Joint over Pier.

Figure 1: Typical Details of Previous Projects.

Recently, during 2010 two bridge projects (Eagle River bridge and Wabigoon River bridge, Ontario) utilized UHPC field cast joints for live-load continuity over internal piers in precast girder bridges. This joint design (Fig. 1) completely eliminated the need for post-tensioning and provided for fast and simple field connections of precast bridge elements.

The MTO has also utilized UHPC field cast expansion joints as a means to provide strong and durable solutions to solve the durability problems with freeze/thaw, de-icing, the constant impact/abuse from trucks, and snow ploughs crossing the expansion joints. The use of UHPC for expansion joints eliminates the need for embedded steel edges or casting of field concrete between the precast deck and steel embed.

Also, MTO has built a number of trial projects with GFRP reinforcing utilizing their non-corrosive properties with the intent of building more durable structures [3]. The performance of these bridges is being monitored and testing to date has been very encouraging. Currently in Ontario, the cost of GFRP reinforcing is about the same as epoxy coated steel and about double that of conventional steel when calculated by length. Due to the low modulus of elasticity of GFRP reinforcing ($E \approx 40\text{-}60$ GPa vs. 200 GPa for steel) [4], crack control in concrete becomes the governing criteria for design [5]. This results in reduced bar spacing as well as increased bar size when GFRP reinforcing is used as the primary tension reinforcing. A bridge deck using only GFRP reinforcing requires an average of 60 to 70% additional reinforcing by length, when compared to a similar bridge using steel reinforcing.

3 The Project

The new bridge structure consists of a 40m single span steel plate girder structure made composite with a 225mm thick concrete deck. The bridge measures 14.5m in overall width and is supported on a single row of steel H-piles made integral with the abutments. To reduce construction time, precast concrete construction was used for all of the reinforced concrete elements, including the integral abutments, with the exception of the barrier wall, which was cast-in-place after the structure was opened to traffic. Durability was enhanced by incorporating two emerging materials into the project, namely, UHPC and GFRP reinforcing. UHPC has been proven on several projects [2] and by the FHWA [1] to be a superior material when used as a joint fill between prefabricated components in bridge decks. The non-corrosive property of GFRP reinforcing is being increasingly utilized by the MTO as a measure to build maintenance-free bridge decks [3]. In addition to its non-corrosive properties, the weight of GFRP reinforcing

is only about 30% that of steel reinforcing thus facilitating reduced labour costs. Also, in order to achieve an optimum bridge design, GFRP reinforcing was used for the top mat and conventional steel for the bottom mat which balances durability and cost.

4 UHPC Joint Fill for Precast Concrete

In terms of durability, construction joints between precast elements have traditionally been the weak link in the system, thus reducing the overall benefits of incorporating pre-cast elements. However, the use of UHPC to connect precast elements promises to eliminate this issue and in fact make the joints the strongest link. For the Whiteman creek bridge, UHPC was used to fill the voids between the precast abutments and the H-pile foundations, in joints between the precast deck panels and in joints between the precast approach slab panels. All precast elements were constructed using regular 35MPa concrete.

The UHPC technology used for the joint infill is an ultra-high strength, ductile material formulation made with constituent ingredients such as: Portland cement, silica fume, quartz flour, fine silica sand, high-range water reducer, water and steel fibres. The UHPC specified for this project was Ductal JS1000 [6] which is a proprietary product supplied by Lafarge Canada Inc, and is one of several products patented under the trademark Ductal (Table 1):

Table 1: Material Characteristics (Characteristic Design Values).

Strength		**Durabiltiy**	
Compressive (28 days)	140 MPa	Freeze/thaw (after 300 cycles)	100%
Compresive (48 hours)	100 MPa	Salt-scaling (loss of residue)	<0.10 g/m^2
Flexural	30 MPa	Carbonation depth	<0.5 mm
Young‘s Modulus (E)	50 GPa		

The ultra-high strength properties and low permeability provide for excellent protection of the rebar against corrosion and improved bond with the rebar, thereby providing short bond development lengths. To provide improved durability and crack control, steel fibres were also specified for the UHPC joint fill. For field cast UHPC, compressive strength specimens for quality control are typically 75mm x 150mm cylinders broken at 28 days. Field cast results are typically lower in compressive strength compared to lab or precast due to mix adjustments for field batching, hot weather batching and field curing (as opposed to thermally treated). While compressive strength tests are used to validate field QA/QC during casting operations, it is the short bond development length that governs the design. All testing of UHPC for joint fill has been done on specimens with a 100 MPa compressive strength inorder to validate minimum strengths for opening to traffic.

The UHPC was batched with a mini-slump flow of 200mm to 250mm and will slowly self level and fill voids without the use of any vibration. In order to ensure a complete filling of the joints and accommodate the release of any trapped air a small hydro-static head of up to 0.2m is maintained. The UHPC used is self consolidating during the initial setting of the material and also exhibits superior durability with the chloride ion permeability (<100 coulombs) being very low compared to the 1000 coulombs permeability specified for High Performance Concrete (HPC) in Ontario.

5 Integral Abutment Connection

The abutment stem was precast in four sections; the two central and the two outer sections being 3800 mm and 2575 mm wide respectively. Since the abutments were precast, and the

integral connection required the ability for the abutment to transfer both axial and flexural loads directly into the piled foundation, a suitable connection between the abutment and steel pile foundations needed to be developed. Pockets 600mm x 600mm were formed into the underside of the precast abutments to accommodate the piles and allow for allowable tolerances on the pile driving operation (See Fig. 2). UHPC was selected as the material to fill the void around the piles due to its self consolidating, permeability and shrinkage compensating properties to ensure full contact between the precast abutment and the steel piles.

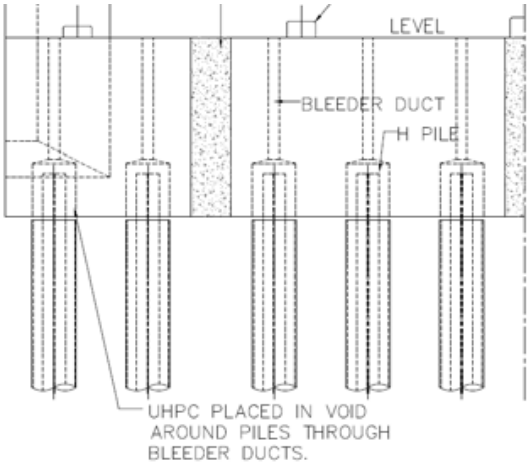

a) Precast Abutment - Elevation View.

b) Abutment Pockets Being Filled with UHPC.

Figure 2: Details of UHPC for Precast Abutments.

6 Deck Slab Connections

The outstanding strength of UHPC allows the width of joints between precast elements to be minimized due to the ability of the material to allow for reduced lap splices in the deck reinforcing. For the transverse joint, the 160 mm wide opening specified could have been further reduced; however, from a practical necessity to place the UHPC quickly, a narrower opening would slow the placement of the material. Similarly, the 350 mm wide longitudinal joint specified is quite wide to allow for the placement of the shear studs on the girders.

The deck slab consists of 16 pairs (32 total) precast panels each 225 mm thick x 2240 mm wide x 7075 mm long. Pockets in the panels were required over the girders for the shear stud connection to the girders. At the centre girder, there was a continuous longitudinal gap of 350 mm. The slabs were not post-tensioned as the performance of the UHPC joint fill provides sufficient durability, when combined with an asphalt and waterproofing system. In addition, the precast panels were detailed such that the need for formwork was eliminated, which greatly contributed to the speed of construction.

Prior to erection of the slabs, 50 mm wide strips of ethylene vinyl acetate (EVA) foam were glued to the outside edges of the top flange to contain the UHPC. The first slab was placed and adjusted to grade via 6 leveling devices (two at each girder) ensuring that proper load distribution of the precast panel to the supporting steel girders. The weight of the panel was used to compress the EVA foam strips thus resulting in a leak-proof system.

Figure 3: UHPC Being Placed into Deck Pockets for Shear Studs.

The shear pockets and haunches over the girder flanges were grouted starting at the low end, followed by the longitudinal joint along the centreline of the bridge (See Fig. 3). As grouting progressed, plywood forms were placed over the pockets and fastened down to prevent the UHPC from overflowing due to the inherent grade of the bridge, since UHPC is self-leveling. The transverse joints between the precast panels were placed subsequently (See Fig. 4).

Normal productivity for this operation was approximately 12-16 m^3/day, based on a crew of five people, and two high capacity mixers. The 21 m^3 of UHPC needed for the deck of the bridge thus required two days for placement and an additional four days for normal curing.

Figure 4: Deck Panel Layout with UHPC Placed in Pockets Over Two Girder Lines.

7 Precast Approach Slab Connections

The approach slabs consist of 6 precast panels each 250 mm thick x 2079 mm wide x 6000 mm long with 200 wide joints between the segments. After the abutments reached 20 MPa, the precast approach slab panels were installed on the finely graded subgrade and the joints filled with UHPC (See Fig. 5). The ends of the approach slabs were detailed with preformed holes to allow the slabs to be connected to the abutments using straight vertical dowels with the annular space also filled with UHPC.

Figure 5: UHPC Being Placed into Appraoch Slab Joints.

8 Testing and Development of UHPC for Joint Fill

Full Scale Cyclic and Static Loading

The FHWA [1] has been actively studying the application of UHPC in bridge decks. Slab specimens were cast in two pieces and joined together at midspan by a 150 mm UHPC joint. Various arrangements of 15M bars, some straight, some headed and some bent, were used to connect the two pieces together. Loads were applied immediately adjacent to the joint, via a 254 mm x 508 mm load patch and tested at three levels (See Fig. 6):

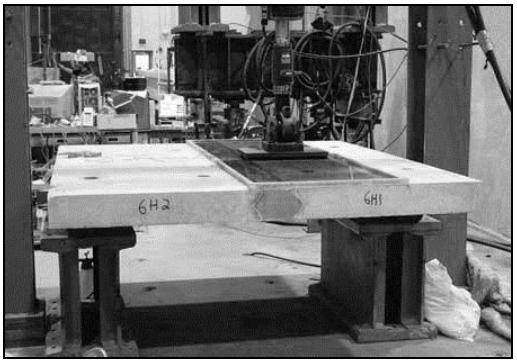

Figure 6: Load test (Courtesy of FHWA).

Testing Level	Test Type
Level A	Under cyclic load below cracking
Level B	Under cyclic load above cracking
Level C	Under static load to flexural failure

Under cyclic loading (Level A & B), there was no interface de-bonding and no leakage through the joint. Under cyclic loading (Level B), a single flexural crack in the concrete became tightly spaced micro cracks through the UHPC joint. Under ultimate loading (Level C), the panel behaved as would be expected of a monolithic concrete slab without any joint or dissimilar materials.

Pullout Tests on GFRP Reinforcing

Testing of pullout resitance of reinforcing in UHPC, namely the Ductal JS1000 [6] material have been conducted over the last several years to demonstrate the bond characteristics of the material and determine suitable development and lap lengths.

With the introduction of GFRP reinforcing, Lafarge Canada Inc undertook pullout tests in accordance with the Canadian Highway Bridge Design Code [7] in order to obtain approval for using GFRP in the UHPC deck joint fill for specific MTO projects. Pullout test specimens were manufactured with 15mm bar sizes with embedment depths of 100mm and 150mm. Failure behavior of the pullout test conducted on all samples was delamination between the GFRP core and skin of the GRFP (epoxy sand layer).

9 Future UHPC Applications for Bridges

The use of UHPC field cast connections is a relatively new solution. However, this early adoption has provided excellent field experience and validation of the methodology. It has also

provided exposure and confidence in the technology which has led to innovations for the use of UHPC for other types of field connections for precast bridge systems which the MTO will consider for future projects.

Field Cast Connections for Precast Waffle Deck Panels and Hidden Shear pockets:

The use of UHPC for Precast Waffle Deck Panels, currently under development by Lafarge North America Inc., (See Fig. 7a) provides a light weight durable bridge deck system suitable for new or the rehabilitation of bridges. Installing UHPC joint fill between the UHPC Waffle Deck panels provides an entire bridge deck made from UHPC. To further reduce dead load and improve the deck durability the waterproofing and wearing surface are removed, thereby leaving the entire UHPC deck exposed in order to provide the highest durability, where it is most needed, at the riding surface.

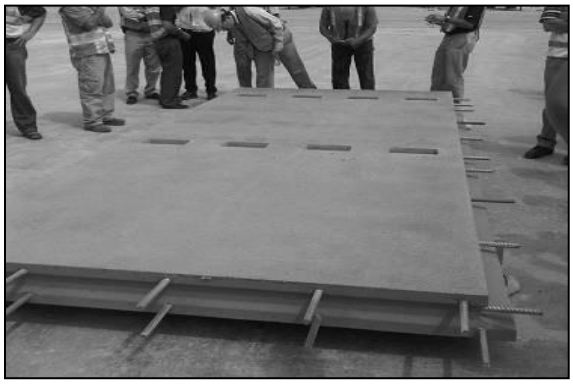

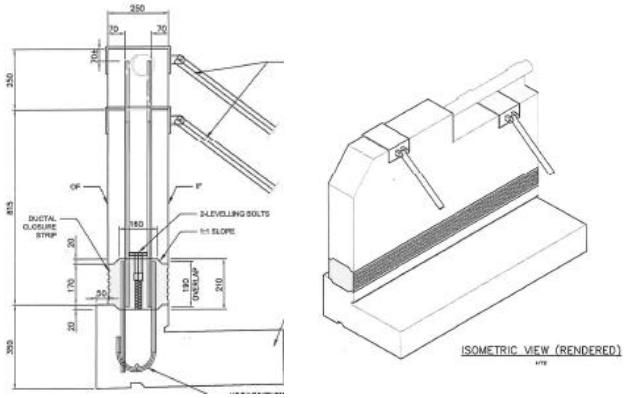

a) Waffle Deck Panels for Wapello Bridge, Iowa, USA. *b) Precast Parapet Walls Joined with UHPC.*

Figure 7: Future UHPC Applications. **Field Cast Connections for Precast Parapets / Barrier Walls:**

As an alternative to cast-in-place, precast parapets or barrier walls maybe supplied to the bridge already integral with the deck or as separate units (See Fig. 7b) to be field attached. In both cases the precast parapet units need to become fully composite with the bridge deck system in order to carry the traffic barrier loadings.

Field cast UHPC connections for precast parapets and barriers provides the integral continuity and further aids in speeding the construction of the bridge.

Field Cast UHPC for Thin bonded Overlays:

Another promising use for UHPC field cast rehabilitation is thin bonded overlays (or “Hybrid”) to re-strengthen deteriorating bridge decks. Several State DOTs cooperatively with Universities are investigating the use of UHPC as a cost effective method to significantly extend the life of bridge decks approaching their service life.

The use of this system is being investigated as both a field cast topping for in-situ deck repairs and as a precast system. The precast “Hybrid” would be cast top surface down where the UHPC is first cast in a textured form liner and then the high performance concrete (HPC) as a structural back-up. Then panels would be cured, flipped and ready for delivery to site. The precast “Hybrid” panels would be connected with field cast UHPC. Hidden shear pockets may also be used with this system.

Field Cast UHPC for Accelerated Bridge Construction:

UHPC is a family of products where the mix designs can be formulated to provide a wide range of slump flows, hardened mechanical properties and rate of strength gain. One UHPC product formulated specifically for ABC construction is being developed by Lafarge, which provides a

high early strength of 55MPa in 12 hours at normal ambient temperatures. The product has similar fluid workability to other UHPCs.

This UHPC rapid strength product is designed for ABC projects executed during week end closures or other time limited type repairs.

10 Summary and Conclusions

The bridge replacement was completed within the scheduled seven week closure of Highway 24, with the roadway reopened to two lanes of traffic using temporary concrete barriers to protect the unfinished barrier walls as planned.

Traditional reconstruction of non-complex bridges typically require a minimum of four to six months to build, or longer if the bridge work is staged to maintain traffic during construction. Alternately, using Accelerated Bridge Construction (ABC) techniques or heavy lift equipment, reconstruction of a bridge superstructure can be reduced to as little as 48 hours or one weekend. This is typically done in urban areas or on freeways, where the extra cost of using ABC can be easily justified when user costs are taken into account.

Between these two extremes are options to use more traditional equipment and maximize prefabrication, with the use of UHPC, so that with a small premium, significant savings in construction duration can be realized. The Whiteman Creek project, with only 15% premium over traditional construction, reduced construction duration to seven weeks.

This project also created a unique opportunity for a synthesis of ABC, UHPC and GFRP. The closure necessary for highway reconstruction demanded ABC. Incorporating UHPC ensures that the joints between precast elements will be durable and can be constructed quickly (no formwork). Finally, the use of GFRP for the top mat deck reinforcing eliminates corrosion of the top mat reinforcing. By synthesizing all three elements, this project is yet another step toward building more durable structures, rapidly.

11 Acknowledgements

The authors would like to thank the Whiteman Creek Bridge project team which included MTO Staff, Delcan Corporation, Lafarge Canada, and Dufferin Construction Limited for the collaborative partnership throughout the design and construction of this project.

References

[1] Graybeal, B., “Behaviour of Field-Cast Ultra-High Performance Concrete Bridge Deck Connections Under Cyclic and Static Structural Loading”, FHWA Report No. FHWA–HRT–11-023, November 2010.

[2] Perry, V., Scalzo, P., Weiss, G., “Innovative Field-Cast UHPC Joints for Pre-cast Deck Panel Bridge Superstructures – In Overhead Bridge at Rainy Lake, Ontario”, PCI – IHWA National Bridge Conference, USA 2007.

[3] Lee, J., Craig, B., Loh, P., Dimitrovski, V, “Working Towards Maintenance-Free Bridge Decks using Glass Fibre Reinforced Polymer Reinforcing Bars”, 8th International Conference on Short and Medium Span Bridges, Niagara Falls, Canada, 2010.

[4] CSA-807-10, “Specifications for Fibre-Reinforced Polymers”, Canadain Standards Association, 2010.

[5] Salib, S., “Strength of Concrete Beams Reinforced and/or Prestressed with FRP Bars”, Ph.D. thesis submittted to the Civil and Environmental Engineering Department, University of Windsor, Canada, 2001.

[6] Lafarge North America, Product Data Sheet: Ductal® JS1000, www.imagineductal.com, 2009.

[7] CHBDC-06, “Canadian Highway Bridge Design Code”, Canadain Standards Association, 2006.

Current Research on Ultra High Performance Concrete (UHPC) for Bridge Applications in Iowa

Sri Sritharan[1], Sriram Aaleti[1], Dean Bierwagen[2], Jessica Garder[1], Ahmad Abu-Hawash[2]
1: Dept. of Civil, Construction and Environmental Engineering, Iowa State University, Ames, IA 50011, USA
2: Office of Bridges and Structures, Iowa Department of Transportation, Ames, IA 50010, USA

Following the successful implementation of UHPC in bridge girders and piles, three UHPC research initiatives are currently underway. The first two initiatives focus on using UHPC for bridge decks and the third on Phase 2 of the foundation pile. In the first initiative, a prefabricated UHPC waffle deck panel was developed. Following investigation of the constructability and performance of critical connections and panels through large-scale testing, a field structure with waffle decks has been completed. The second initiative explores an innovative, cost-effective, composite deck system using UHPC and normal concrete (NC), and experimental investigations identifying the most suitable UHPC-NC interface for practical applications have been performed. For the previously developed tapered H-shaped UHPC pile, the third initiative focuses on establishing a splice and pile to abutment connection details. This paper summarizes the three initiatives, including findings from the completed experimental research.

Keywords: UHPC, deck, waffle, composite, pile, splice, connection, abutment

1 Introduction

The United States bridge infrastructure has received a 'C' grade by the American Society of Civil Engineers, which is primarily due to the structural deficiency or functional obsoleteness of one in four of the nation's bridges [1]. At the end of 2008, the estimated total number of bridges in the nation was 600,905, of which 72,868 (12.1%) were identified as structurally deficient, while 89,024 (14.8%) were listed as functionally obsolete. Unfortunately more bridges are added to this list annually, especially those from urban areas, where it is considered that one in every three bridges are deficient [1]. To overcome the nation's aging bridge infrastructure, several State Departments of Transportation (DOTs) and the Federal Highway Administration (FHWA) have engaged in the development of: a) durable, broadly applicable bridge components and systems that are cost-effective; and b) accelerated bridge construction methods to rapidly resolve the bridge deterioration problem of the nation. Due to its superior structural and durability characteristics, the use of Ultra High Performance Concrete (UHPC) for bridge applications has gained momentum in the United States over the past decade.

Through collaboration between Iowa DOT, FHWA, Iowa State University (ISU), Lafarge and Coreslab, the state of Iowa has led the nation in utilizing UHPC for bridge substructure and superstructure. The past applications include: design, testing and deployment of I-shaped girders; π-shaped girders; and design of a tapered, H-shaped precast pile. Following these successful projects, three UHPC research initiatives are currently underway in the state of Iowa with support from the Iowa Highway Research Board, FHWA, and Iowa DOT. The first two initiatives focus on using UHPC for bridge decks and the third on Phase 2 of the pile foundation program. Each of these initiatives are aimed at producing durable and longer-lasting critical bridge components that can be easily deployed. A summary of the three initiatives including the current status of each is presented in this paper.

2 UHPC waffle deck panel

By combining the advantages of UHPC and prefabricated, full-depth deck systems, a precast UHPC waffle deck system was developed as part of FHWA's Highways for LIFE program [2]. The constructability of this system and structural performance of its critical connections and

panels were investigated using large-scale laboratory tests, which applied service, fatigue, and ultimate loads. Following an exploratory study on the feasibility and structural behavior of a prestressed UHPC waffle deck system by FHWA [3], a UHPC precast waffle deck system with conventional mild steel reinforcement was developed with the intention of deploying this system on a two-lane, single-span replacement bridge in Wapello County, Iowa. This bridge, which is 10.1-m wide and 18.3-m long, was designed with five standard Iowa “B” girders, at a center-to-center distance of 2.2 m (see Figure 1).

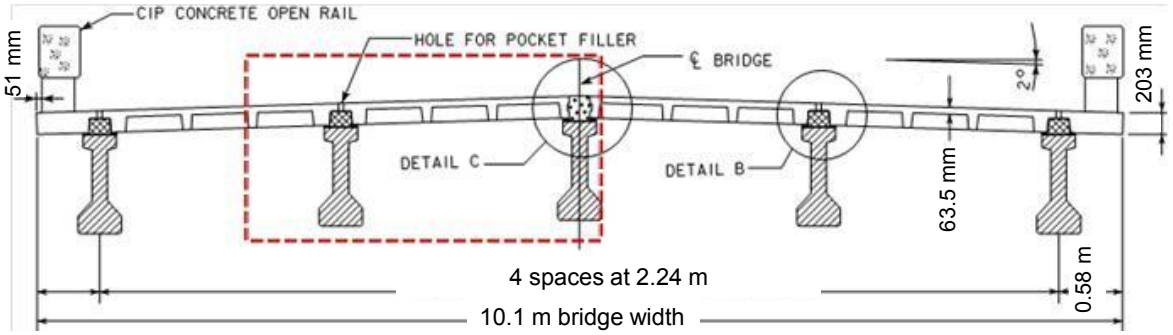

Figure 1: Cross-section of the UHPC waffle deck system bridge in Wapello County, Iowa.

Details of connections

To make the UHPC waffle deck panels fully composite with the girders, three types of connections were used, namely: 1) a pocket connection; 2) a longitudinal connection, and 3) a transverse connection. The pocket connection consisted of at least one shear hook extending from the top of the girder into a pocket in the waffle deck panel, which was filled with in-situ UHPC (see Figure 2a). This detail established the connection between the waffle panel and exterior or intermediate girders (see detail B in Figure 1). The longitudinal connection was used between the waffle panels and center girders. Dowel bars extending from the panels with shear hooks from the girders (as with detail B), and additional longitudinal mild steel reinforcement was used with in-situ UHPC (see Figure 2b) for this connection. The transverse connection joined two adjacent UHPC waffle deck panels utilizing dowel bars extended from the panels, two additional transverse reinforcement, and in-situ UHPC (see Figure 2c).

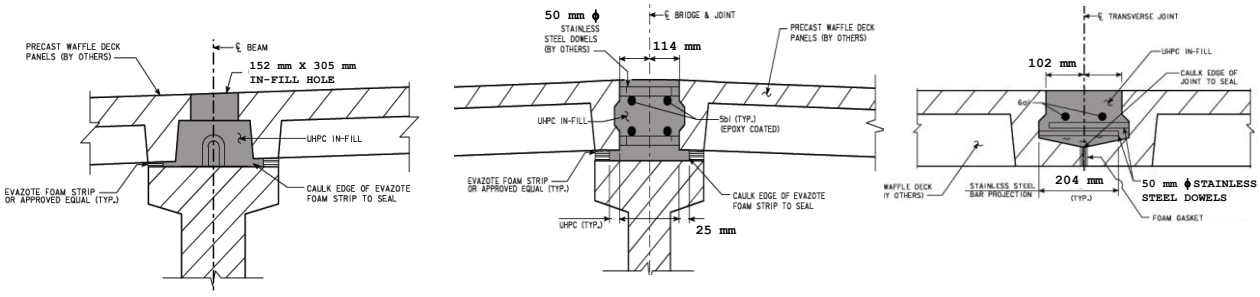

(a) Pocket connection *(b) Longitudinal connection* *(c) Transverse connection*

Figure 2: Connection details of the UHPC waffle deck bridge.

Full-scale testing

Two full-scale, full-depth, UHPC waffle deck panels connected to two precast, prestressed girders were tested to evaluate the structural characterizations of the panels and connections. In addition to subjecting a panel and connections to AASHTO [4] specified service and fatigue wheel loads, overload and ultimate load tests were also performed. The experimental investigation was complemented with a detailed finite element analysis (FEA) by assuming perfect bonding between precast panels, in-situ UHPC, and reinforcement. Figure 3 shows the construction of joints and setup.

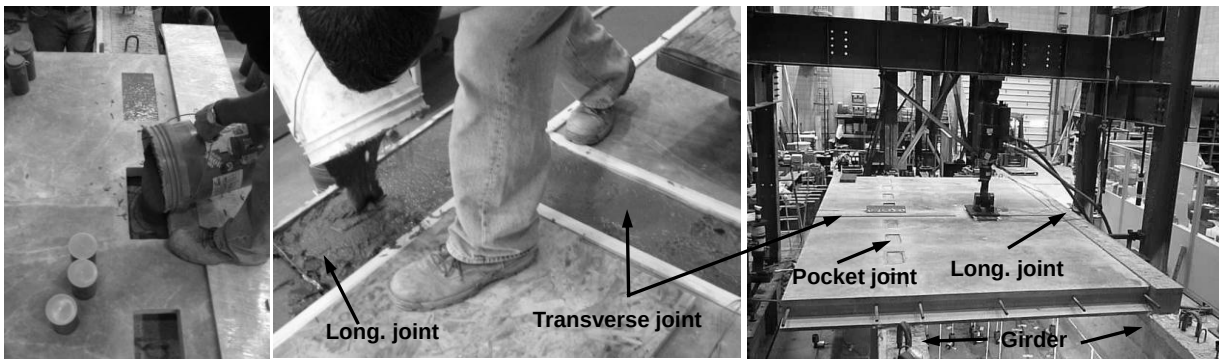

(a) Construction of connections *(b) Joint testing under simulated wheel load*

Figure 3: Construction of joints and test setup.

Key findings

As shown in Table 1, a total of eight tests were conducted in this sequence to critically evaluate the performance of the waffle panels and connections [5]. Each test produced satisfactory performance. Under service level loading, only limited micro cracking was observed on the most critical rib and the transverse joint during the panel and joint testing, respectively. When the test was repeated for more than a million cycles, no progressive degradation of the system was observed. When a panel and joints were overloaded, visible flexural cracks were noted on the transverse and longitudinal ribs. To examine the ultimate strength, a panel and joints were subjected to three to four times the service level wheel loads. Significant cracking to the ribs was observed, but no failure of the connection or the panels occurred. However, the test was terminated at this stage due to significant cracking that occurred to the bridge girders supporting the panels.

The FEA accurately predicted the load and location of the first flexural crack and the regions susceptible to increased cracking as a result of an increase in load [6]. Following successful design and performance verification, the waffle deck bridge system has been recently completed in Wapello County, Iowa (see Figure 4). Following placement of the girders, the waffle decks were installed with ease and the construction of all UHPC joints was completed without any difficulties.

Figure 4: Construction of waffle deck bridge

Table 1: Sequence and details of the tests conducted on the waffle deck system.

Test ID	Description	Load (kN)	Expected Damage from FEA
1	Service load at center of a panel	95	Micro cracking in ribs
2	Service load on transverse joint	125	Micro cracking in joint
3	Fatigue test on transverse joint	125 x 1 million cycles	No prediction was made
4	Overload on transverse joint	214	Visible flexural cracks along the joint and transverse ribs
5	Fatigue test of panel	95 x 1 million cycles	No prediction was made
6	Overload on panel	178	Visible flexural cracks along transverse ribs
7	Ultimate load on panel	712	Significant flexural cracks along transverse and longitudinal ribs
8	Ultimate load on transverse joint	689	Significant flexural cracks along transverse and longitudinal ribs

3 UHPC-NC deck interface

Following the success of the UHPC waffle deck system, the development of an innovative composite deck system using UHPC overlying normal concrete (NC) is currently underway. The ultimate goal of this project is to come up with a cost-effective UHPC-NC bridge deck system that can be used for new and existing bridge decks as a means for increasing lifespan of the superstructure. To date, the study has focused on structural characterization of different shear friction interfaces that may be appropriate for overlying UHPC on NC slabs, as well as the factors influencing the interface behavior through laboratory testing.

Test matrix and test setup

As summarized in Table 2, a test matrix that consisted of five different textures and three concrete strengths was used to examine the feasibility and effects of different interface textures, concrete strength, casting sequence, and curing condition (fully cured vs. partially cured vs. wet conditions) on the shear friction behavior of the composite deck interface. Mechanical connections between UHPC and NC such as that involving shear studs were disregarded to ensure easily constructible details.

Table 2: Summary of completed UHPC-NC interface tests.

Test type	Texture (# of specimens)	Casting sequence	Target NC Strength
UHPCw-NC5	5 textures (3 per texture)	Wet UHPC over Cured NC	34 MPa
UHPCw-NC7	5 textures (3 per texture)	Wet UHPC over Cured NC	52 MPa
UHPCw-NC10	5 textures (3 per texture)	Wet UHPC over Cured NC	69 MPa
UHPCh-NC5	5 textures (3 per texture)	Wet NC on Heat treated UHPC	34 MPa

w –wet UHPC; h-heat treated UHPC

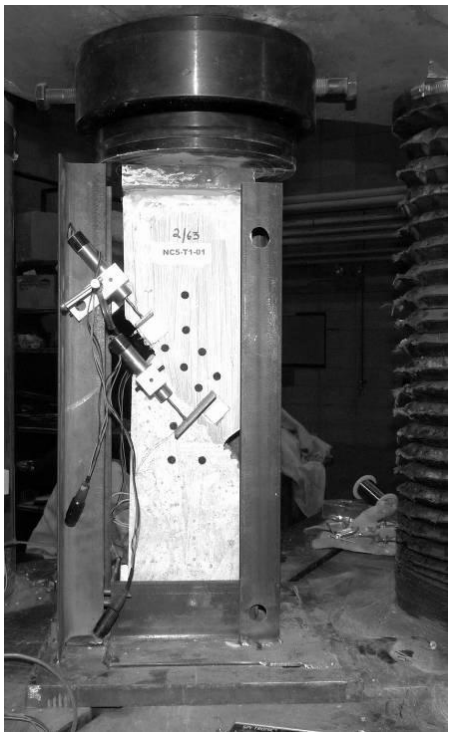

Figure 5: Slant shear test setup.

Based on the experimental study on the bond behavior of composite specimens incorporating UHPC [7] and the slant shear test concept [8], all interface tests were completed using prismatic members as shown in Figure 5. Each UHPC-NC composite specimen was 150 mm by 150 mm in cross-section, 600 mm long, and consisted of an inclined joint with different interface textures at the mid-height of the specimen. An inclination angle of 53.1 degrees was chosen for the interface based on the preliminary calculations and previous research [9]. The joint interface surface was prepared using five different form-liners with varying roughness values typically used in the precast industry for architectural panels. As the specimens were subjected to uniaxial compression at the ends, the interface was subjected to shear stresses along the inclined joint interface. Several instruments, including displacement transducers and rotation meters, were used in the joint region to adequately characterize the performance, and closely monitor the movement along the inclined shear interface. All samples were tested to failure at the interface or through splitting of the NC (see Figure 6a).

Key findings

A total of 60 slant UHPC and NC interface specimens were tested. The average depth of texture was varied from 5 mm to 1.3 mm from texture 1 to texture 5. In each case, the stress along the interface and bond strength were calculated by dividing the appropriate load along the joint by the interface area. A comparison of the average bond capacity established under shear for each surface is presented in Figure 6b. Accordingly, it was found that the bond strength developed for all textures was adequate for applications in bridge decks. The bond strength generally increased with the increase of texture roughness. The casting sequence, however, did not significantly influence the bond strength.

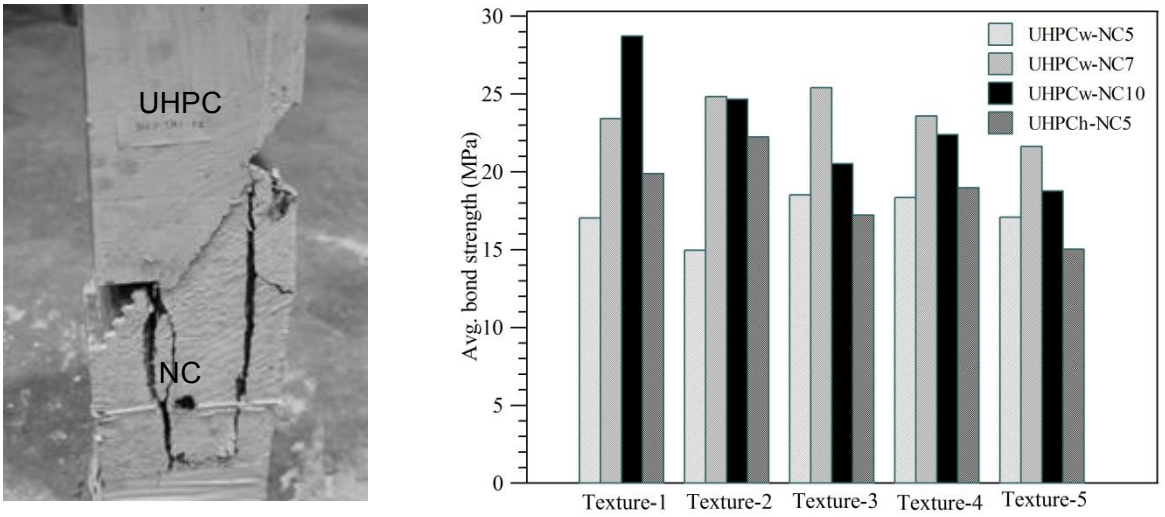

a) Compression failure of a test specimen *b) Average bond strength for different surface textures*

Figure 6: Test findings from the slant UHPC-NC concrete specimens.

4 Connections for UHPC piles

For routine bridges, the foundation can contribute up to 30% of the overall bridge cost. Furthermore, increasing the longevity of bridges requires an increase in the durability of the foundation as well. Consequently, a tapered, H-shaped, UHPC pile was previously developed at ISU as a means for increasing the longevity of bridge foundations and reducing the maintenance cost in comparison to steel and concrete piles [10]. The cross-section details of this pile and a steel H-pile, that is more commonly used in Iowa, are compared in Figure 7. The full-scale vertical and lateral load tests on UHPC piles revealed several benefits of the UHPC pile including reduced risk of damage during driving, drivability with a greater range of hammers and strokes, and use of the existing equipment for pile handling and driving. To implement the UHPC piles in bridge foundations, an investigation is currently underway that will focus on developing connection details to splice piles in the field while ensuring the UHPC piles will be adequately anchored into the pile caps and bridge abutments.

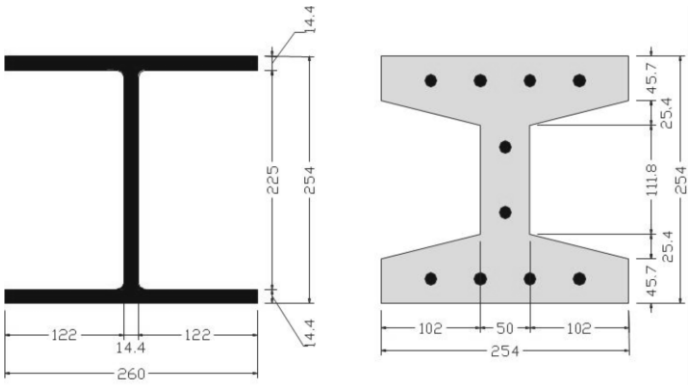

Figure 7: Cross section of HP 250x85 vs. UHPC Pile.

Splice details

With the intention of minimizing construction delays, dry connections, comprising of welding, bolting or quick-set grout, are typically preferred to extend the piles in the field during driving. It is common practice to use welding when steel piles are spliced as this is considered an efficient technique in the field. Consequently, a welded detail was preferred for the splice of the UHPC piles. Figure 8 shows the steel embedment used at the ends of UHPC piles, which facilitates welding between two H-shaped steel plates to establish the connection. This splice was designed to have a minimum of 50% of the pile capacity in tension and 100% of the pile moment capacity.

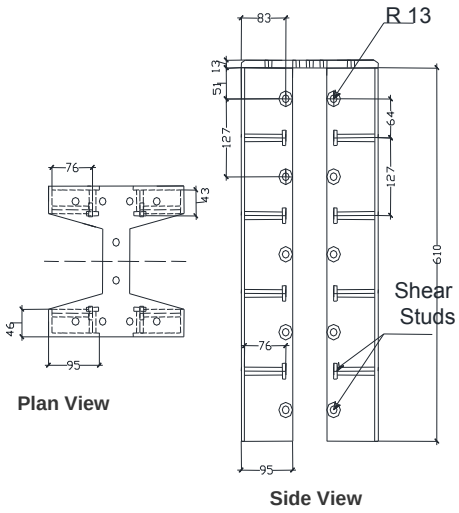

Pile-to-abutment connections

The connection of the UHPC pile-to-abutment was established using the typical Iowa DOT standard details that are routinely used for steel pile-to-abutment connection [11]. This approach was preferred in order to minimize changes to an already established construction practice due to the change in pile material.

Figure 8: Splice details.

Full-scale testing

Full-scale laboratory tests have been completed to verify the expected behavior and to ensure adequate capacity of the UHPC splice connections. The laboratory investigation included the testing of the splice region under direct tension, as well as, critical shear and flexural stresses. Two test units were used for these tests. In each case, two 1.22-m long UHPC pile segments were cast and spliced together at the ends using an 8 mm weld all around the interface at the splice. As shown in Figure 9a, the direct tension test was performed on the test unit using a self-reacting test frame supported on rollers, while the shear and flexural tests were performed using a simply supported configuration and a concentrated vertical load, as shown in Figure 9b.

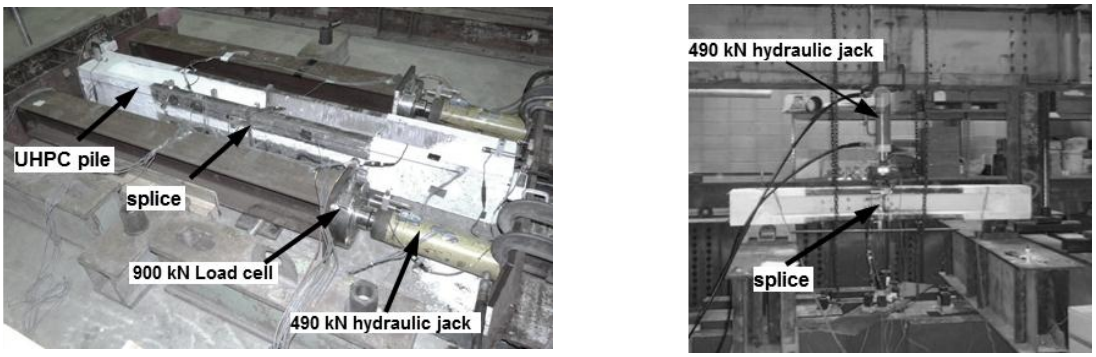

a) UHPC splice tension test setup *b) UHPC splice shear and flexure test setup*

Figure 9: UHPC splice test setup for tension, shear and moment.

The pile-to-abutment connection test was performed on a steel pile and a UHPC pile in an inverted position under combined axial and lateral loads as shown in Figure 10. For each test, a 2.4-m long pile segment was embedded into a cast-in-place concrete block, which had standard

dimensions of a bridge abutment with its length equal to typical center-to-center distance between two adjacent piles. The abutment block was suspended above the floor by post-tensioning two concrete blocks on both sides and attaching these ancillary blocks to the strong floor using high strength bars. Throughout testing, the piles were subjected to either 445 kN or 890 kN of vertical load using two post-tensioning bars and hydraulic jacks. In addition, each pile was subjected to cyclic lateral displacements using a 450 kN actuator attached at a height of 1.4 m from the top of the abutment block, to simulate the expected movement of a pile integrally connected to abutments. Based on the previous studies on the thermal movements and subsequent expansion and contraction that integral abutment bridges undergo, the piles are expected to move as much as 25 mm in the longitudinal direction, which corresponds to a 5 mm lateral displacement for the short segment of the test pile in the laboratory. The UHPC pile was tested in three phases to understand the influence of vertical load on the behavior of the pile-to-abutment connection. The load protocol used for the three phases is shown in Table 2. In a similar manner, an HP 250 x 85 steel pile was also tested to failure to provide the baseline performance of the connection.

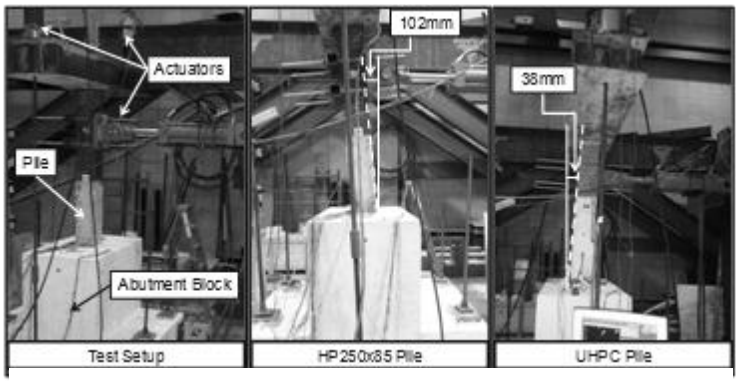

Figure 10: Pile-to-abutment connection test.

Table 2: Laboratory pile-to-abutment testing protocol for the HP 250x85 and UHPC piles.

	Axial Load (kN)	# Cycles per Step	Control	Load Step
Phase I	445	2	Force (kN)	±18, ±36, ±54, ±72
Phase II	890	2	Force (kN)	± 16, ±32, ±48, ±63
Phase III	445	3	Displacement (mm)	±13, ±19, ±25, ±38 (for steel: ±51, ±76, ±102)

Key findings

The full-scale tests on splice connection confirmed its satisfactory performance and indicated that the spice had reserve capacity in excess of 975 kN and 200 kN in tension and shear, respectively. One concern identified during the tests was that the weld quality should be assured in order for the splice to perform as quantified from the tests. The UHPC pile-to-abutment connection was also very successful. The force-displacement responses of the UHPC and steel piles are shown in Figure 11a and 11b, respectively.

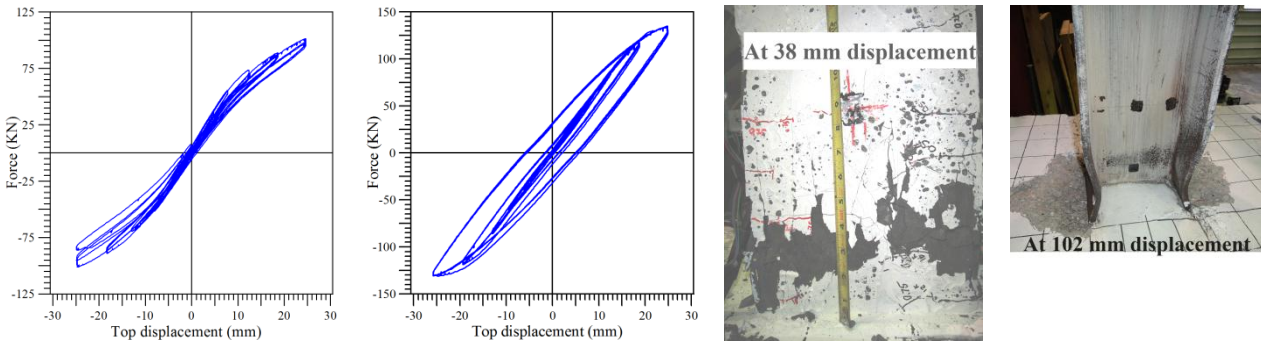

a) UHPC pile *b) Steel pile* *c) UHPC pile at failure* *d) Steel pile at failure*

Figure 11: Force vs. displacement response and failure of UHPC and HP 220 x 85 piles under lateral loads.

No cracking was observed in the UHPC pile at the expected level of lateral displacement of 5 mm. At 8 mm of lateral displacement, two hairline cracks were seen in the UHPC pile near the connection. However, these cracks were completely closed after the displacement of the pile returned to zero. The UHPC pile failed in compression at 38 mm lateral displacement (see Figure 11c). The steel pile experienced yielding in the flange tips at 13 mm of lateral displacement and buckling of flanges in the critical moment region at 102mm of lateral displacement (see Figure 11d).

5 Conclusions

Following successful use of UHPC in bridge research projects, three research initiatives are currently underway in Iowa with support from the state, FHWA and other agencies. Through these initiatives, it has been shown that 1) the UHPC waffle panel is a durable and easily constructible, full-depth precast option for bridge decks; 2) adequate shear resistance can be established between a UHPC and NC interface with minimal roughness at the interface; and 3) tapered H-shape piles can be spliced and connected to the pile caps and abutments as routinely done for steel H piles.

References

[1] American Society of Civil Engineers: Report Card for America's Infrastructure: Facts about bridges, Reston, VA, USA, 2009.

[2] Aaleti, S., Sritharan, S., Rouse, M., Wipf, T.: Phase1: The structural characterization of UHPC waffle bridge deck panels and connections. IHRB Project TR-614 Report, Iowa Department of Transportation, 2010.

[3] FHWA: Analysis of an Ultra-High Performance Concrete Two-Way Ribbed Bridge Deck Slab, TECHBRIEF, FHWA-HRT-07-055, McLean, VA, 2007.

[4] AASHTO LRFD Bridge Design Specifications. American Association of State Highway and Transportation Officials, Washington, D.C., 2007

[5] Aaleti, S., Sritharan, S., Bierwagen, D., and Wipf, T., J.: Experimental Evaluation of structural Behavior of Precast UHPC Waffle Bridge Deck Panels and Connections. Transportation Research Record: Journal of the Transportation Research Board (in press), 2011.

[6] Aaleti, S., Sritharan, S., Dean Bierwagen and Brian Moore: Precast UHPC Waffle Bridge Deck Panels and Connections for Accelerated Bridge Construction. PCI National Bridge Conference, Salt Lake City, Utah, October 2011.

[7] Harris, K., D., Sarkar, J., and Ahlborn, T.: Interface Bond Characterization of Ultra-High Performance Concrete Overlays. 90th Annual TRB Meeting, Washington D.C, January 2011.

[8] Wall, J.S. and N.G. Shrive, Factors Affecting Bond Between New And Old Concrete. ACI Materials Journal,: p. 117-125, 1988.

[9] Zilch, K.; Reinecke, R.: Capacity of Shear Joints between High-Strength Precast Elements and Normal-Strength Cast-In-Place Decks. International Symposium on High Performance Concrete", The Economical Solution for Durable Bridges and Transportation Structures, PCI / FHWA / FIB, Precast/Prestressed Concrete Institute, U.S.A., 2000.

[10] Vande Voort, T., Suleiman, M. T., and Sritharan, S.: Design and performance verification of ultra-high performance concrete piles for deep foundations. Final Report, Iowa DOT, IHRB Project TR-558, CTRE Project 06-264, Iowa Dept. of Transportation, Ames, IA, 2008.

[11] http://www.iowadot.gov/bridge/standards/english/EnglishIntegralBridges.pdf, cited on 31 October 2011.

R&D Activities and Application of Ultra High Performance Concrete to Cable Stayed Bridges

Byung-Suk Kim, Seungwook Kim, Young-Jin Kim, Sung Yong Park, Kyung-Teak Koh, Changbin Joh,

Structural Engineering Research Division, Korea Institute of Construction Technology, Korea

Ultra High Performance Concrete (UHPC) is a new kind of material that has high compressive and tensile strengths together with high durability and fluidity. This paper introduces systematic researches of Korea Institute of Construction Technology (KICT) to develop competitive bridge systems using the advantages of UHPC. KICT have developed a new kind of edge girder type cable stayed bridge system using UHPC for the main span of 200 m ~ 800 m and its feasibility study has been carried out. Various structural analyses and experiments were performed to verify the new system. Design guidelines and manufacturing specifications were prepared to design and construct innovative bridges. As a result, in 2009, UHPC pedestrian cable stayed bridge with the span length of 14 m has been design and constructed in Korea. In addition, in 2011, the first UHPC cable stayed bridge has been designed in detail for the open tender for Jobal Bridge.

Keywords: UHPC, Cable stayed bridge, edge girder system, feasibility, design guideline

1 Introduction

Ultra High Performance Concrete (UHPC) is an innovative material that has been developed to secure the ductility and strength of the structural members. UHPC exhibits significantly improved tensile strength, flexural strength, resistance to cracking, shear strength and resistance to impact through the addition of steel fibers and admixtures.

The material characteristics of UHPC can be summarized as follows: realization of ultra high strength through the exclusion of coarse aggregates, uniform material properties and satisfactory particle distribution; formation of remarkable micro-structure by high temperature steam curing; increase of toughness through the addition of steel fibers. Diminution of self weight through the reduction of the cross section and the extended lifespan of the bridge through outstanding durability can be expected from the application of UHPC to bridge structures.

Up to date, a number of bridges have been erected using UHPC. The very first application of UHPC for bridge was Sherbrooke pedestrian bridge constructed in 1997 in Canada. In Korea, Seonyu pedestrian bridge was built in 2002 but was relying completely on French technology. UHPC Highway bridges were also built. USA built several highway bridges such as Wapello County Mars Hill Bridge (2006), Cat Point Creek Bridge (2008) and Jakway Park Bridge (2008). Japan also applied UHPC to the highway bridges, Tokyo Int. Airport GSE Bridge (2010) and Kayokawa Bridge (2010). Many other UHPC bridges can be found from the reference [1].

Although UHPC pedestrian and highway bridges were built, it is difficult to say they are competitive in the bridge market. From the economic point of view, these UHPC bridges for a short or mid span are probably not competitive to conventional concrete bridges and steel composite bridges because of high initial construction cost.

On the other hand, it can be easily conceivable that the advantage of UHPC can be effective when it is applied to long span bridges such as cable stayed bridges. Application of UHPC to a concrete cable stayed bridge might lead to the reduction of self-weight by replacing heavy concrete section with compact UHPC one, which, in turn, results in the reduction of expansive cables and the size of foundation. The expensive steel sections of steel or composite cable stayed bridges might be replaced with reasonable UHPC ones without increasing the weight

excessively, which, again, results in the reduction of material cost large enough to compensate the increase of cost from the cables and foundation.

To realize this idea, however, it is not simple. Simple substitution of UHPC for concrete and steel is not enough to use maximum out of UHPC and to secure economic feasibility. A new cable stayed bridge system combined with UHPC most effectively should be developed. The realization of an UHPC cable stayed bridge, therefore, should be preceded by the systematic and intensive investigation of material, structure, construction and economic feasibility.

2 Application of UHPC to Cable Stayed Bridge: Super Bridge 200

KICT launched a 6-year research project called Super Bridge 200 from 2007. This project deals with the application of UHPC to a cable stayed bridge. The total budget is approximately 11 million USD.

The main goal of Super Bridge 200 is reducing construction and maintenance cost of cable stayed bridges by 20% respectively and extend the service life of main structural elements up to 200 years through combining UHPC and cable stayed bridge technology together.

Super Bridge 200 has developed technologies for (1) improvement of UHPC behavior, (2) design of UHPC structures such as girders and plates, (3) light and durable UHPC deck, (4) UHPC cable stayed bridge system with the main span of 200 m ~ 800 m.

UHPC Developed by KICT

The first UHPC composition developed by KICT is shown in Table 1. The water to binder ratio is 0.2 and the steel fibers of 2 volume percent are used. The steel fibers are 13 mm in length and 0.2 mm in diameter, and the tensile strength of the steel fiber is 2500 MPa. All UHPC are steam cured for 72 hours at 90 degree after 24-hour curing at room temperature. The mechanical properties of the material are summarized in Table 2.

As a result of this research, first draft of UHPC fabrication specification was proposed in 2007 and has been updated yearly to include new research.

Table 1: UHPC composition (all by weight but steel fiber).

W/B	Cement	Silica fume	Sand	Filling Power	Super plasticizer	Steel Fiber (V_f)
0.2	1	0.25	1.1	0.3	0.016	2%

Table 2: Mechanical properties of UHPC.

Design compressive strength	Design tensile strength	Elastic modulus	Poisson's ratio	Total shrinkage	Creep coefficient
180 MPa	9.5 MPa	45 GPa	0.2	600×10^{-6}	0.45

Apart from developing design technology for UHPC cable stayed bridge using first UHPC developed by KICT, the research to improve the performance and economic efficiency of UHPC itself is done in parallel.

This research is focused on both minimizing the amounts of fiber and maximizing the performance of UHPC. The large amount of the fiber increases the cost of UHPC significantly. Thus, it is important to minimize the amounts of steel fibers without scarifying the performance of UHPC.

The performance of UHPC was investigated according to the aspect ratio, shape and volume content of steel fibers. To improve the flexural and tensile characteristics of UHPC, it was found that one of the promising methods is to blend two different steel fibers together. Blending macro

fibers different in length can increase the tensile strength of UHPC while minimize the reduction in constructability due to long fibers.

The test result shows, compared to the first UHPC with 2% of steel fiber, the flexural strength increased by 27% (maximum 50%) in average for hybrid UHPC with the use of fibers of 19.5 mm and 16.3 mm in length 1% each (Fig. 1)[2]. The diameter of the fibers is 0.2 mm for both. Accordingly, the fabrication cost of hybrid UHPC can be reduced by approximately 70% compared to that of first UHPC. Direct tensile test of the hybrid UHPC reveals the tensile strength of 17 MPa, which is estimated as one of top levels of the world (Fig. 2)

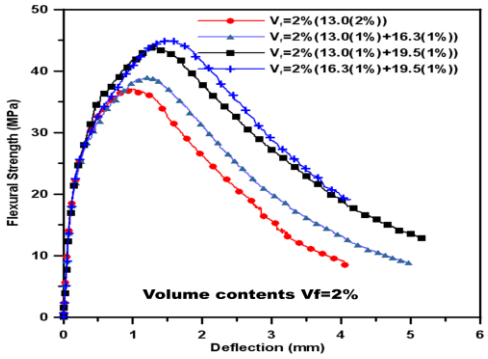

Figure 1: Flexural behavior of hybrid UHPC (v_f=2%).

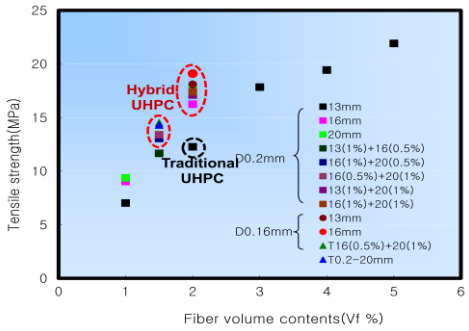

Figure 2: Tensile strength of hybrid UHPC.

Design of UHPC structures

For the structural design of UHPC, various structural tests were performed at the KICT; flexural, shear and torsional tests of UHPC girder and punching test of UHPC plates and miscellaneous tests of reinforced UHPC structural details. As a result of this research, first drafts of UHPC structural design guidelines were proposed in 2008 and have been updated yearly to include new researches.

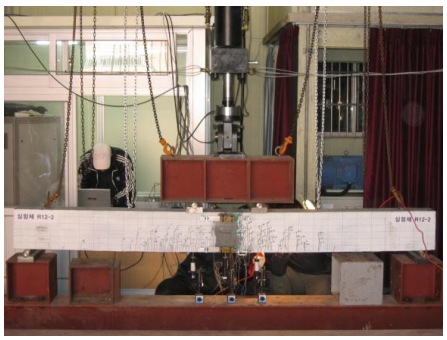

Figure 3: Flexural test of UHPC girder reinforced with rebars.

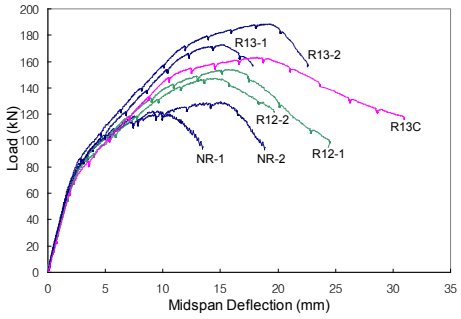

Figure 4: Load-deflection curve (UHPC girders reinforced with rebars) [3].

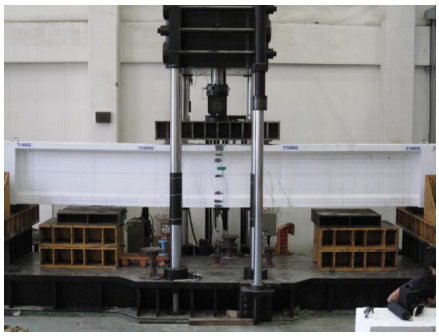

Figure 5: Flexural test of UHPC girder prestressed with tendons.

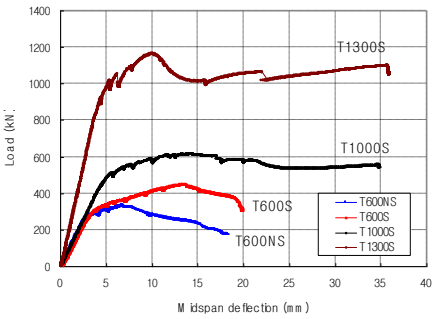

Figure 6: Load-deflection curve (UHPC girders prestressed with tendons)[4].

First, in 2008 ~2009, reinforced UHPC girders were tested to estimate the flexural strength and to find how to estimate it for the design (Fig. 3 ~ 6). The tested UHPC girder specimens were reinforced with rebars or prestressing tendons. It is because, in spite of relatively high tensile strength of UHPC compared to conventional concrete, the large difference between compressive and tensile strengths of UHPC makes it necessary to use rebars in the UHPC flexural member such as a girder.

UHPC girder test results show typical flexural behavior similar to that of a reinforced concrete girder (Fig. 4 and 6). After first cracking, according to the increase of loading, new micro-cracks started to develop between the existing cracks and most of the cracks continued to propagate toward the upper chord without visual widening of the crack width. At ultimate load, a part of the cracks showed increase of their crack widths while the other cracks exhibited practically unchanged shape until failure (Fig. 3 and 5).

Test results also show the flexural strength can be estimate reasonable well by applying stress-strain relationship with Bernoulli's assumption. In addition, the tensile behavior of UHPC together with the effect of fiber orientation should be considered in the estimation.

Second, in 2010, UHPC girders without shear stirrups were tested in shear (Fig. 7). Test results showed that, as the load was increased, initial diagonal cracks occurred in the web with degradation of stiffness (Fig. 8). However, the sudden loss of the strength was not observed and the load was gradually increased with propagation of the initial cracks to upper and lower flanges. Other diagonal cracks in the web were occurred as well. At the failure, with gradual decrease of the load, one of the diagonal cracks in the web was developed to the major diagonal crack (Fig. 7).

Test results also show that, with an additional term to consider the contribution of fibers after the initial cracks in the web, the shear strength formula for an ordinary concrete girder can be used to estimate reasonably the shear strength of UHPC girders without stirrups.

Figure 7: Shear test of UHPC girder without stirrups.

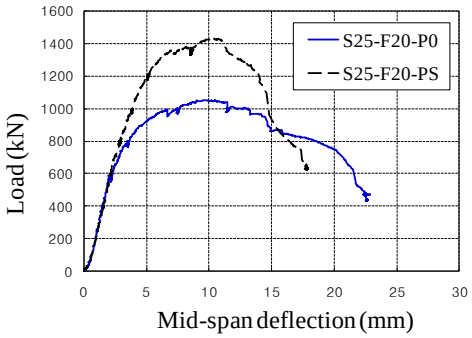

Figure 8: Load-deflection curve (UHPC girders without stirrups) [5].

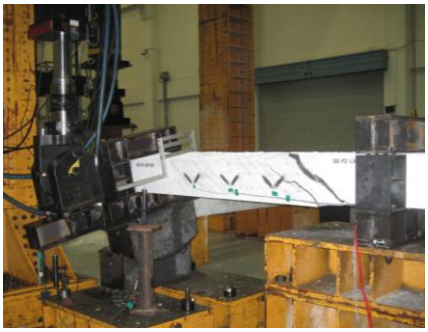

Figure 9: Torsional test of UHPC girder.

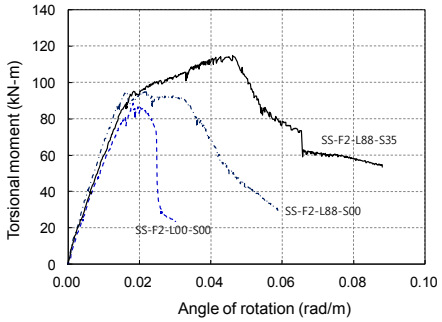

Figure 10: Torsion-rotation curve (UHPC girders with/without reinforcement) [6].

Third, UHPC square members were tested in torsion (Fig. 9). It is because the thin-walled tube theory that is currently adapted in the code seems to have no term to consider the behavior of UHPC that is different from ordinary concrete.

The test results (Fig. 10) show that the UHPC specimens with no reinforcement did not lose its torsional strength after cracking due to the ductility of UHPC, and the UHPC specimen with longitudinal rebars only also showed a ductile behavior. Those are different from the behavior of ordinary reinforced concrete members. The UHPC specimens with longitudinal rebars and stirrups showed hardening after cracking.

Comparison of test results with the design theories showed that, compared to the thin-walled theory, the skew bending theory with the tensile strength of UHPC is relatively reasonable to estimate the torsion at cracking and torsional strength of UHPC members. However, this approach also seems to have a limitation to estimate the contribution of reinforcement to the torsional strength of UHPC members.

KICT also did punching test of UHPC thin plates (Fig. 11) for punching formula and miscellaneous test to optimize structural details such as minimum cover thickness, bond-slip relation, crack width and spacing (Fig. 12), development length and etc.

Figure 11: Punching shear test of UHPC girder.

Figure 12: Miscellaneous structural tests of UHPC.

Design of UHPC structures

In long-span cable supported bridges like a cable stayed bridge, the deck contributes to the weight of the superstructure largely but does relatively small to the overall construction cost. The overall economic efficiency of the bridge, therefore, could be significantly improved by reducing the weight of the deck by the adoption of relatively expensive high-performance materials.

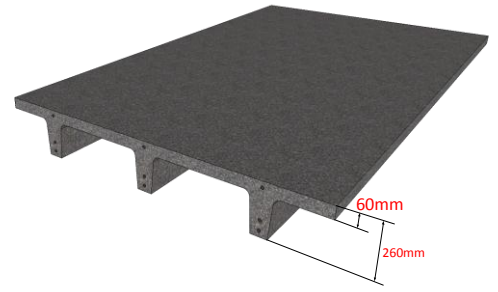

Figure 13: Shape of UHPC ribbed deck.

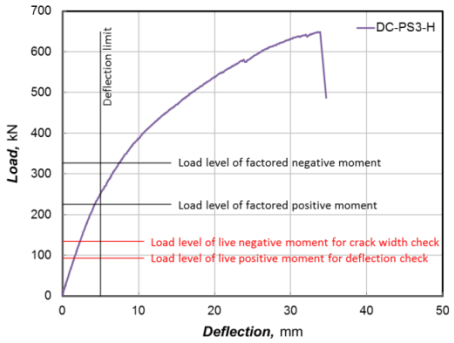

Figure 14: Load-deflection curve (UHPC ribbed deck) [7].

KICT applied this idea to the deck of an UHPC cable stayed bridge. KICT has developed the UHPC ribbed deck slab (Fig. 13) with prestressing tendons as a solution to lighten the self-weight of superstructure for cable stayed bridge. It is composed of thin plate with 60 mm in thickness and stiffening ribs with spacing 600 mm. Its weight is about half of the conventional

precast concrete deck. Optimum design and various tests were carried on to verify its behavioral characteristics and to evaluate its structural performance. Test results verified that the proposed decks satisfy the relevant design codes (Fig. 14).

UHPC cable stayed system

In the cable stayed bridge the tension in the cables produces a compression in the deck and tower. The high compressive and tensile strengths of UHPC allow for the redesign and optimization of stiffening girder and deck elements in the cable stayed bridge.

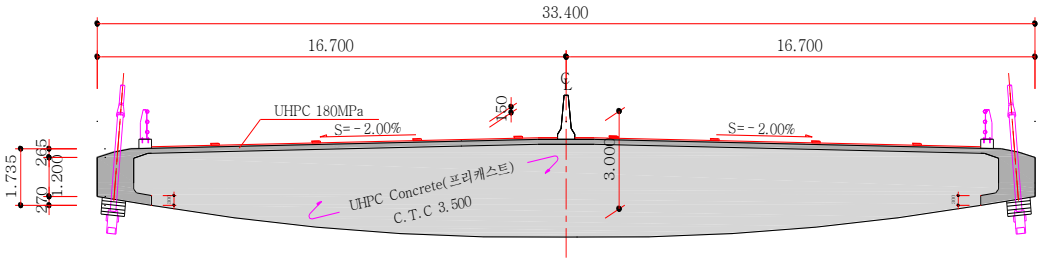

Figure 15: Cross section of UHPC edge girder system for the main span of 800 m (unit: mm).

The edge girder with parabolic cross beams (Fig. 15) was developed for the low-cost UHPC cable stayed system. This system was chosen because, first of all, considering the constructability related properties of UHPC, the edge girder system is relatively easy to fabricate compared to typical box girder system. In addition, due to the high compressive and tensile strength, the cross section and the weight of the edge girder and the thickness of deck slab can be minimized.

The typical aerodynamic difficulties of the edge girder system can be controlled by modifying the shape of the edge girder and the cross beam. The wind tunnel test partially verified the aerodynamic performance.

Figure 16: One-half model of UHPC edge girder precast segment.

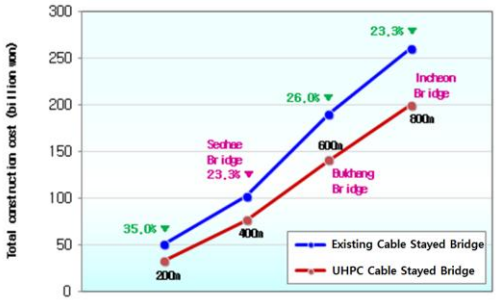

Figure 17: Cost analysis of cable stayed bridge.

The fabrication and connecting of 2 segments of 16.7 m wide one-half model of the edge girder system (Fig. 16) showed the constructability of the system. The moving wheel load fatigue test was also done to estimate the fatigue strength using the fabricated edge girder system.

Cost analyses based on detailed design shows the overall construction cost of an UHPC cable stayed bridge is lower over the main span of 200 m ~ 800 m than that of a conventional cable stayed bridge (Fig. 17). Especially, the UHPC cable stayed bridge (Super Bridge 800) with the main span length of 800 m was designed in detail and compared to recently completed Inchon Bridge, the world's 5th longest cable stayed bridge with steel deck. The cost analysis showed UHPC cable stayed bridge can save 23.3% of overall cost of Inchon Bridge (Fig. 17).

For the main span of 200 m~ 400 m, where a concrete or composite cable stayed bridge is a dominant system, the UHPC cable stayed bridge can reduce the cost by reducing the weight of

deck and, accordingly, the costs of cables and foundation. For longer span, where the cable stayed bridge with steel deck is a dominant system, UHPC cable stayed bridges reduces the cost by replacing expensive steel deck with UHPC deck. Although the weight of the deck itself is increased and the related cost is increased more or less, the overall cost is reduced due to the reasonable UHPC more than that as shown in Fig. 17.

Application of UHPC cable stayed Bridge

In 2009, Super Bridge 200 team designed and constructed UHPC pedestrian cable stayed bridge (Fig. 18), which connects two office buildings of KICT. This bridge is a full-scale test bed for Super Bridge 200.

Figure 18: UHPC pedestrian cable stayed bridge built at KICT [8].

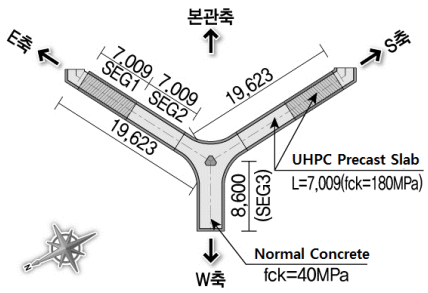

Figure 19: Plan view.

As shown in Fig. 18, the small scale edge girder is selected for the cross-section of the upper girder to exploit fully the compressive performance of UHPC. A part of the upper girder was planned as a UHPC precast girder. Two precast girders are connected using steel bar after bonding with epoxy (Fig. 19). The portion around the pylon was designed to be cast-in-place concrete considering the connection with the pylon.

In 2011, Daelim cooperation, one of the major construction companies in Korea, chose the UHPC cable stayed bridge for the biding of Jobal Bridge that is planned to connect Jobal and Dunbyung islands near south coast line of Korea.

Fig. 20 shows the bird's eye view of Jobal Bridge designed by the technologies developed from Super Bridge 200. The proposed Jobal Bridge is a three-tower UHPC cable stayed bridge (Fig. 20 and 21). The main span length is 200 m and the height of pylon is 90 m. The edge girder type superstructure (Fig. 21) was designed using UHPC. This is the first cable stayed bridge designed using UHPC for a highway bridge.

Figure 20: Bird's eye view of Jobal Bridge.

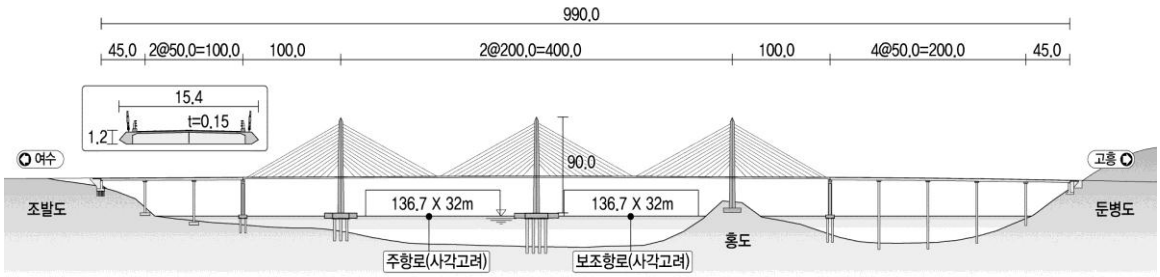

Figure 21: Jobal Bridge Plan.

3 Conclusion

This paper presented KICT's intensive and systematic development of technologies for a UHPC cable stayed bridge since 2007.

KICT launched a 6-year research project called Super Bridge 200 from 2007. The purpose was reducing construction and maintenance cost of cable stayed bridges by 20% respectively and extending the service life of main structural elements up to 200 years through combining UHPC and cable stayed bridge technology together.

As a result, Super Bridge 200 has developed technologies for (1) hybrid UHPC with tensile strength of 17 MPa, (2) design of slender and durable UHPC structures such as girders and plates based on the lots of structural tests and analyses, (3) light and durable UHPC deck based on the optimization and tests, (4) UHPC cable stayed bridge system with the main span of 200 m ~ 800 m based on the structural optimization and detailed cost analysis. The UHPC fabrication specification and UHPC structural design guideline were developed. And the Super Bridge 200 technologies were successfully applied to the design and construction of UHPC pedestrian cable stayed bridge in 2009, and design of Jobal Bridge, the UHPC cable stayed bridge.

4 Acknowledgement

This work is the result of the research project, the Super Bridge 200 of Korea Institute of Construction Technology. The authors hereby express their appreciation for the support.

References

[1] Fehling, E.; Schmidt, M; Stürwald, S.: Proceedings of the 2nd International Symposium on Ultra High Performance Concrete, Kassel, Germany, 2008.

[2] Park, S.H.; Kim, D.J.; Ryu, G.S.; Koh, K.T.: Tensile Behavior of Ultra High Performance Hybrid Fiber Reinforced Concrete, Cement and Concrete Composites, In press, 2011.

[3] Yang, I. H.; Joh. C.; Kim, B.: Structural Behavior of UHPC Beams Subjected to Bending, Engineering Structures, 32: 3478-3487, 2010.

[4] Yang, I. H.; Joh. C.; Kim, B.: Flexural Strength of Large Scale Ultra High Performance Concrete Prestressed T-Beams, Canadian J. of Civil Engineering, 38: 1185-1195, 2011.

[5] Joh, C.; Lee, J.; Yang, I.H.; Kim, B.: Shear Test of UHPC Girders without Stirrups, Proceedings of 9th Symposium on High Performance Concrete, New Zealand, 2011.

[6] Joh, C.; Lee, J.; Yang, I.H.; Kim, B.: Torsional Test of UHPC Square Members, Proceedings of 3rd International Symposium on UHPC, Kassel, Germany, 2012.

[7] Park, S.Y.; et.al.: Development of Deck systems for Cable-Stayed Bridges, 4th Year Report, Korea Institute of Construction Technology, 2010.

[8] Kim, B.; Park, H.K.; Park, S.Y.; Kim, Y.J.; Chin, W.J.; Choi, E.S.; Kim, H.H.; Kim, J.H; Kim, W.J.: Design and Construction of Innovative UHPC Pedestrian Cable Stayed Bridge in Korea, Proceedings of IABSE Conference, Bangkok, Thailand, 2009.

Structural Performance of Prestressed UHPC Ribbed Deck for Cable-Stayed Bridge

Sung Yong Park, Keunhee Cho, Jeong Rae Cho, Sung Tae Kim, Byung Suk Kim
Structural Engineering Division, Korea Institute of Construction Technology (KICT), Republic of Korea

Compared to conventional concrete, Ultra-High Performance Concrete (UHPC) develops higher tensile strength and ductility as well as very high compressive strength. The Korea Institute of Construction Technology (KICT) had succeeded in developing 200MPa class UHPC, and is now developing an economic and durable cable-stayed bridge system applying the developed UHPC since 2007. Even if the bridge deck contributes to a large proportion in the superstructure in terms of self-weight, it occupies only a small portion in the construction costs of cable-stayed bridges. Therefore, despite of their high price, applying high performance materials will improve the economics of the bridges by reducing effectively the weight of the deck. In this study, we propose the UHPC ribbed deck slab with prestressing steel as a solution to lighten the self-weight of the superstructure. Optimum design is carried out on this deck slab for a span length of 4 m. The results indicate that the optimal dimensions are a thickness of 60 mm for the plate of deck, with a height of 200 mm and width of 100 mm for the ribs. This enables a reduction of the self-weight of the deck by 50% compared to the conventional precast concrete deck slab for cable stayed bridges. Flexural tests were performed to investigate its behavioral characteristics and verify its structural performance. Test revealed that the proposed deck slab satisfies the strength and serviceability criteria required for a bridge deck..

Keywords: UHPC, ribbed deck, prestressing, flexural test, cable-stayed bridge

1 Introduction

The weight of the superstructure has significant effect on the design of cable-supported long span bridges like cable-stayed bridge. Fig. 1 illustrates the contribution of the elements of the superstructure to the weight and construction costs of a steel composite cable-stayed bridge constructed in Korea. It can be observed that the deck represents a very large proportion of 69% of the superstructure's weight while occupies only 15% of the construction costs of the superstructure [1].

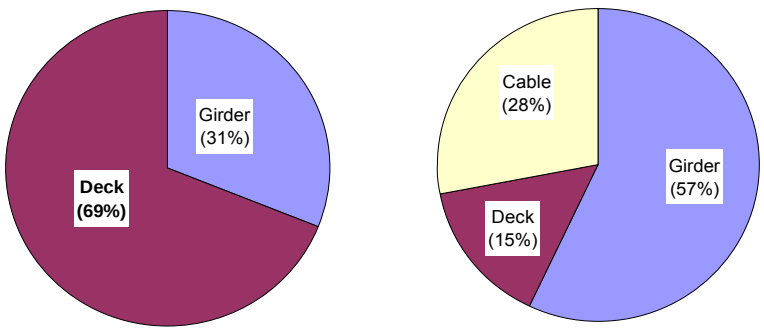

(a) Self-weight (b) Construction costs

Figure 1: Contribution of the elements constituting the superstructure of a cable-stayed bridge to the weight and construction costs.

In view of such observations, significant reduction of the weight of the deck by applying high performance materials would result in large reduction in the material quantities required for the other members and particularly the cables, and in turn, to effective reduction of the construction costs to a desirable level. Accordingly, KICT carried out research to apply UHPC to the deck of

cable-stayed bridges since 2007. To date, this research found out a highly efficient system minimizing the quantities of UHPC known to be a costly material. This system is the ribbed deck structure presented in Fig. 2.

This study intends to evaluate experimentally the behavioral characteristics of this optimized prestressed UHPC ribbed deck.

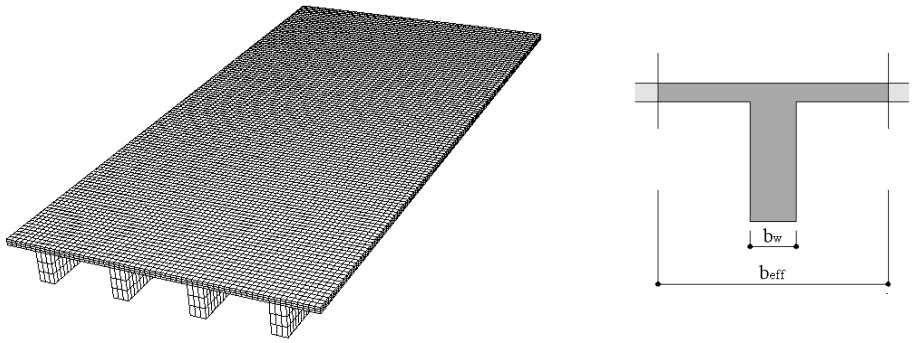

(a) Structural system (b) Sectional shape

Figure 2: Conceptual scheme of the developed UHPC ribbed deck for cable-stayed bridge.

2 Optimization of Section

UHPC develops a compressive strength reaching a value higher than conventional concrete by more than 5 times but a relatively low tensile strength. Considering such properties, it appears that introducing prestress in the tensile-loaded part of the structure will optimize the effective utilization of the material. Therefore, the following design concepts were established for the design of the ribbed deck [2].

(1) Computation of the minimum thickness of the plate member considering punching shear failure;
(2) Derivation of the maximum allowable spacing of the ribs considering the biaxial flexural behavior of the plate member; and,
(3) Determination of the dimensions of the ribs and amount of prestress considering the biaxial flexural behavior of T-shape beam with effective width.

According to these design concepts, optimization with the minimization of the quantities of UHPC as objective function and satisfying the Korean Highway Bridge Design Code [3] was conducted. The optimization led to the section shape shown in Fig. 3. Differently from normal girder bridges, the spacing of the cross-beams in a cable-stayed bridge becomes the span length of the deck. Following, the running direction of the vehicles represents the principal direction of the deck. In this study, the optimal section was derived considering a span length of 4 m for the deck.

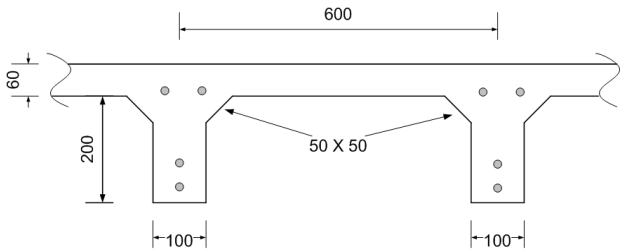

Figure 3: Shape and dimensions of the ribbed deck section resulting from optimal design.

3 Experimental Study

Design and Fabrication of Specimens

The specimens were fabricated considering the eventual introduction of prestress as shown in Table 1. The reference specimen without reinforcement was used to evaluate the material characteristics of UHPC. These characteristics compared to those of the prestressed specimen were then used to observe the effects of the disposition of the tendons. Each tendon of seven wire strand with diameter of 15.2 mm was tensioned to a force of 200 kN through pretensioning. Since the specimens were fabricated for positive moment test as shown in Fig. 4, the tendons were disposed at locations distant by 35 mm and 85 mm from the bottom of the rib. Load was applied through 4-point loading at intervals of 1.0 m.

Table 1: T-shape beam specimens of UHPC ribbed deck.

Designation	Number of strands	Number of specimens	Dimensions (length×width)	Remarks
TSST0	0	2	4 m × 0.6 m	Reference specimen
TSST2	2	2		Reinforced specimen

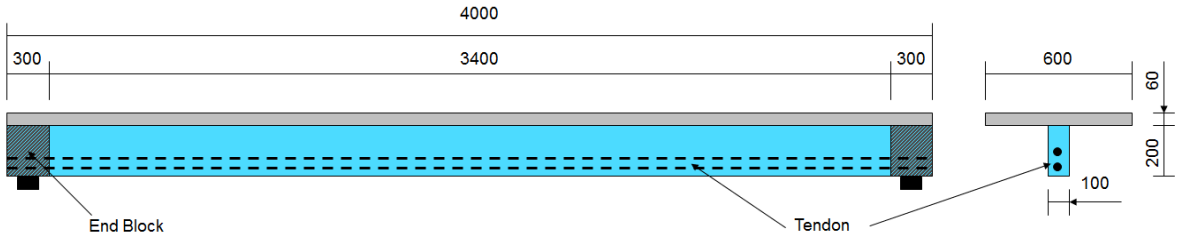

Figure 4: Shape and dimensions of the specimens.

A strong frame was assembled for the introduction of prestress. The specimens were fabricated by tensioning the tendons first followed by the placing of UHPC as shown in Fig. 5. The adopted UHPC was the one developed by KICT. Its mixing and placing were executed using the UHPC mixer fabricated in the batch plant of KICT. The capacity of the UHPC mixer shown in Fig. 6 is 1.2 m^3. Two mixers were used for the present fabrication.

Figure 5: Placing of UHPC.

Figure 6: Mixers in the batch plant of KICT.

Material Tests

Six compressive strength specimens were made in each batch. The results showed that the compressive strength averaged 194.0MPa with a standard deviation of 2.85MPa for the first batch, and a mean of 180.3MPa and standard deviation of 3.50MPa for the second batch. The slightly lower compressive strength obtained for the second batch was caused by the poor conditions of the compressive strength specimens due to shortage of the residual UHPC quantities needed.

The tensile strength of the UHPC member is significantly depending on the dispersion of the fibers. Accordingly, a separate beam specimen was fabricated to evaluate the dispersion of the fibers and its effects on the flexural tensile strength considering the fact that a small scale T-shape section should be manufactured. This spare specimen was cut at the bottom of the rib to the size of a flexural tensile strength test specimen (100 mm x 100 mm x 400 mm) as shown in Fig. 7(a). A total of 8 test specimens were sampled and subjected to flexural strength tests as shown in Fig. 7(b). Table 2 presents the corresponding results. The numbering of the specimens indicated in the table starts from the left side (#1) and is sorted in ascending order rightward with respect to the sampling sequence. Except for samples #1 and #5, the samples did not show large differences and revealed that the steel fibers are comparatively well dispersed in the longitudinal direction of the original specimen. At the exception of samples #1 and #5 which showed large discrepancies, the statistical analysis of the flexural tensile strength of the remaining six samples resulted in a mean cracking strength of 15.0 MPa with standard deviation of 1.5 MPa. Moreover, the mean and standard deviation of the flexural tensile strength were 47.5 MPa and 2.9 MPa, respectively.

(a) *Cutting of test samples for flexural strength tests.*

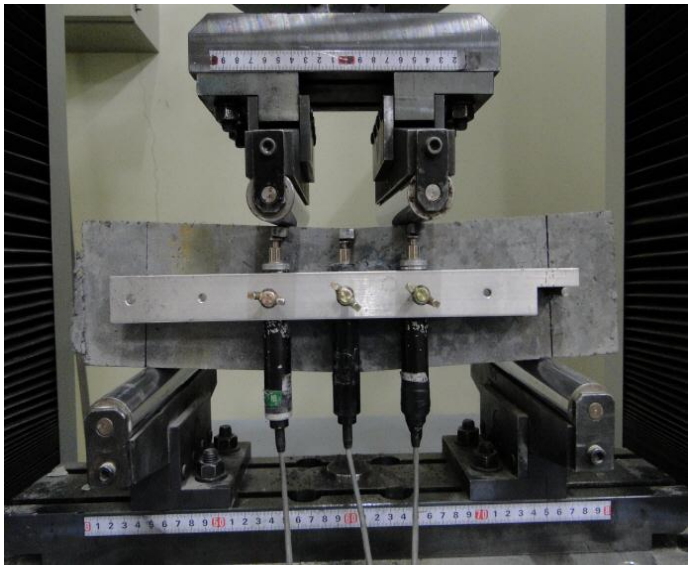

(b) Flexural strength tes.t

Figure 7: Cutting of test samples from a beam specimen and performing flexural strength tests.

Table 2: Flexural tensile strength of the test samples.

Sample number	Dimensions		Initial crack		Ultimate state	
	Width (mm)	Height (mm)	Cracking load (kN)	Cracking strength (MPa)	Failure load (kN)	Flexural tensile strength (MPa)
#1	10.4	10.0	46.2	13.3	126.3	36.4
#2	10.0	10.0	46.7	14.0	160.0	48.0
#3	10.0	10.0	57.1	17.1	172.3	51.7
#4	10.0	11.0	50.7	12.6	172.6	42.8
#5	9.8	10.0	51.0	15.6	109.5	33.5
#6	10.0	10.7	56.0	14.7	176.9	46.4
#7	10.0	10.5	59.5	16.2	183.9	50.0
#8	10.0	10.4	55.5	15.4	166.5	46.2

Test Results

Flexural tests were carried out for four simple beam specimens described in Table 1 and Fig. 4. Fig. 8 shows these flexural tests.

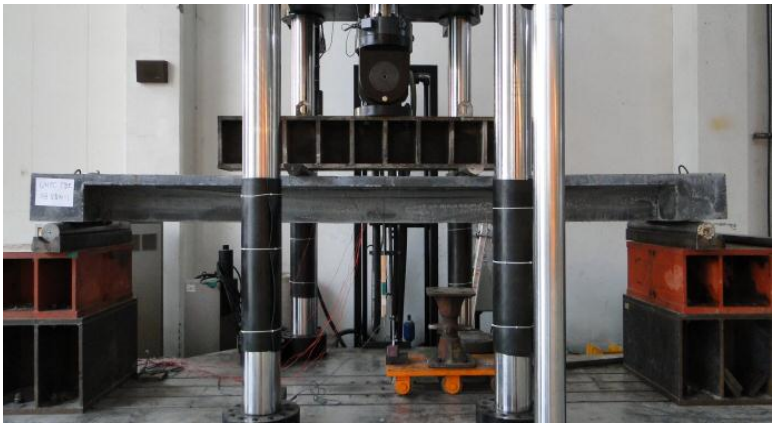

Figure 8: View of flexural tests.

Fig. 9 compares the load-deflection curves of the 4 specimens defined in Table 1. The reference specimens without reinforcement (TSST0) maintained a linear relationship until approximately 40 kN and reached a maximum of 66 kN on average before failure. As shown in Fig. 10(a), flexural crack developed at first between the loading points to slant with increasing load and turned into shear crack before final failure.

The specimens strengthened with tendons (TSST2) preserved a linear relationship until about 97 kN. The specimens reached a mean maximum load of 190kN before failure. A difference of approximately 57 kN occurred between the cracking strengths of specimens TSST0 and TSST2 and can be attributed to the effect of the introduction of prestress. As shown in Fig. 10(b), the first crack also initiated below the loading points for specimens TSST2. This crack crossed the center of the section and propagated until the flange. Thereafter, the crack continued to increase without increase of the load.

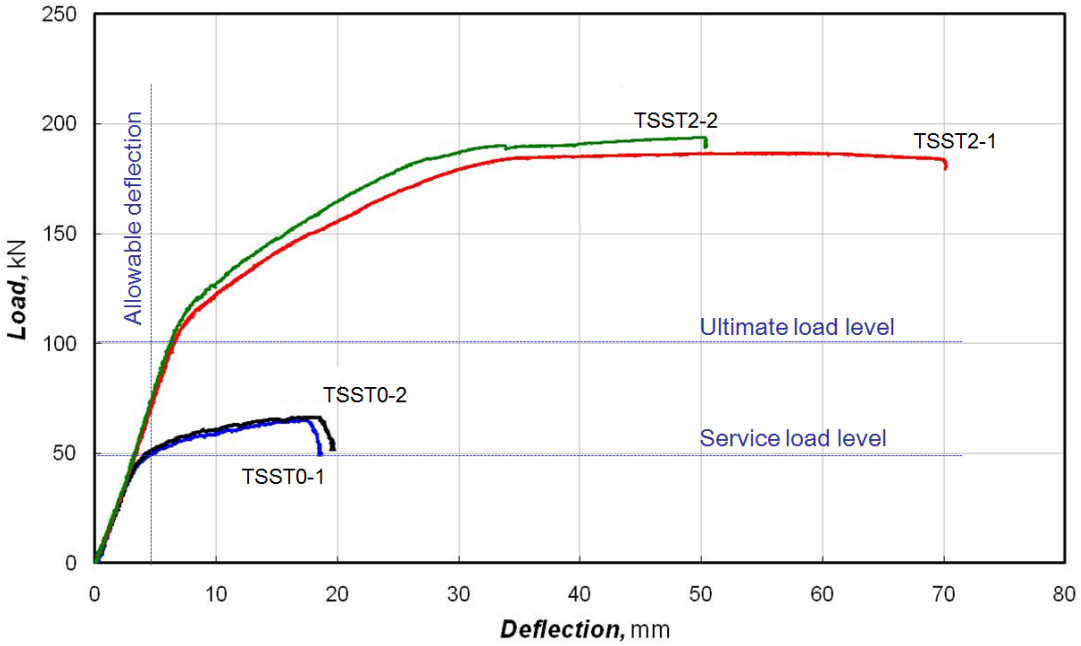

Figure 9: Comparison of load-deflection curves.

(a) Specimen without reinforcement (TSST0-1) (b) Reinforced specimen (TSST2-2)

Figure 10: Comparison of failure mode.

Table 3: Test results.

Specimens		Initial crack		Ultimate state		Failure pattern
		Crack load (kN)	Central deflection (mm)	Ultimate load (kN)	Central deflection (mm)	
Reference specimen	TSST0-1	36.6	2.60	65.1	17.48	Flexural
	TSST0-2	42.4	3.16	66.6	18.02	Flexural
Simply supported specimen	TSST2-1	95.9	6.26	186.9	55.76	Flexural
	TSST2-2	97.9	6.02	193.8	50.04	Flexural

In Fig. 9, the initial slopes of all the specimens are identical regardless of the presence or not of prestressing steels. This verifies the reliability of the fabrication of the specimens per batch as well as that of the execution of the tests. Regard to the mean failure strength of 65.9 kN obtained for the reference specimens (TSST0), the failure strength of 190.4 kN provided by the specimens TSST2 reinforced by 2 tendons at their bottom reached a value approximately larger by 2.9 times. This increase of the failure strength can be completely attributed to the tendon reinforcement. In other words, the cracking strength increased by 1.4 times due to the effect of prestress brought by the tendons, and the utlimate strength increased by 1.9 times through the action of the tendons as tensile members. Table 3 arranges these results where the initial crack corresponds to the load and deflection at the end of the initial linear part in the load-deflection curves of each specimen, and the ultimate load is the maximum load.

The strength and deflection criteria required by the Korea Highway Bridge Design Code [3] are also indicated in Fig. 9. Ultimate load level (= 48.9 kN) and service load level (= 101.0 kN) in Fig. 9 mean the required disign strength in the ultimate load state, and service load state, respectively. Allowable deflection is 4.625 mm (= L/800, L = span length of deck = 3.7 m).

The specimens without reinforcement (TSST0) failed to satisfy the strength criterion but the prestressed specimens (TSST2) exhibited a failure load 1.9 times larger than the required load.

Even if a strength reduction factor of 0.85 is applied for flexure, the developed strength remains still 1.6 times larger than the required one, which indicates that sufficient safety is secured for the positive moment. In addition, the results showed also that the deflection and crack criteria are sufficiently satisfied.

4 Conclusions

KICT is performing a project for the development of lightweight and highly durable decks using an in-house developed UHPC. A ribbed thin plate structure has been proposed as the optimal structural type for the deck. Prestress was introduced to maximize the efficient use of the material and optimization of the section was performed. This study was performed to evaluate the behavioral characteristics of this optimized structural system through tests considering the eventual presence of prestress as test variable. The test results revealed that the introduction of prestress improved the safety and serviceability by increasing the ultimate strength and cracking strength by 1.9 times and 1.4 times, respectively, for an identical section. Remarkable improvement of the ductility was also observed. Moreover, compared to the relevant design criteria, the optimal section derived in this study provided a strength larger by 1.9 times and a deflection reaching 70% of the allowable value. Accordingly, the present deck system realized by prestressing the ribbed thin plate structure is remarkably effective. Furthermore, the currently designed optimal section satisfies the safety and serviceability required for bridge decks.

5 Acknowledgement

This study has been supported through the “Development of Deck Systems for Hybrid Cable-Stayed Bridge” research project, an in-house project of the Korea Institute of Construction Technology. The authors express their gratitude for the support.

References

[1] Korea Institute of Construction Technology (KICT). 2007.: System Integration for Hybrid Cable-Stayed Bridge. Research Report (in Koran).

[2] Hwang, H.H.; Yoo, D.M.; Park, S.Y.; Kim, B.S. 2009.: Optimized Design of UHPC Bridge Deck Slab for Hybrid Cable-Stayed Girder Bridge. Proc. 13th REAAA Conference, Incheon, Korea 2009.

[3] Ministry of Land, Transport and Maritime Affairs: Korea Highway Bridge Design Code, 2010 (in Korean).

WILD-Bridge Scientific Preparation for Smooth Realisation

Bernhard Freytag[1], Günter Heinzle[1], Michael Reichel[2], Lutz Sparowitz[3]
1: Laboratory for Structural Engineering, Graz University of Technology, Austria
2: KHP-Zerna Planungsgesellschaft mbH, Leipzig, Germany
3: Institute of Structural Concrete, Graz University of Technology, Austria

Constructing with UHPFRC still strongly depends on decisions of the authorities. This limiting factor for the ongoing advance in UHPC building practice must be overcome through the development of design codes on the one hand and through pilot projects on the other hand. By means of the pilot project WILD-Bridge this paper shows that a diligent scientific preparation is an indispensable part for convincing the authorities. Large scale experiments had been necessary before the tender was opened. One focus of the paper is on the quality assurance. In particular the tolerances in flatness of contact surfaces of the dryly jointed precast elements and the non-destructive determination of the local and direction dependent post cracking tensile strength are treated. A final review on the construction process points out some innovative details and demonstrates the smooth flow of mounting.

Keywords: arch bridge, UHPFRC, flatness of surfaces in contact, non-destructive steel fibre check

1 Form Finding and Structural Philosophy

WILD is the name of a company producing electro-optic and mechatronic apparatuses. This company is resident at the eastern bound of Völkermarkt in the south of Austria. For this part of the town and especially for the company WILD a new passage to the motorway was planned. The projected road runs through a so far virgin landscape and crosses over a romantic valley. This is where the WILD Bridge was built. From an architectural as well as a structural point of view the shape of the valley offers ideal conditions for an arch bridge. The material chosen for the arch was UHPFRC, not least because of its outstanding durability. This decision made the engineer leave the traditional way of solid construction and change to a light-weight design and precast method of construction. Very slender kind of tubes form two arches side by side. These arches need a symmetrical stabilising load which is realised through a rather heavy deck concreted on site. This dead load is transferred by the columns and act as concentrated forces on the arch, which results in a polygonal thrust line. Thus, as a result of the light-weight approach, the final structure is a well-balanced and quite appreciated truss frame.

It consists of several straight hollow beam elements and also hollow node elements in between. In order to minimise the expense for formwork the arch is planned to be symmetrical accepting that the inclination of the road is not continued in the arch. A brief listing of some absolutely

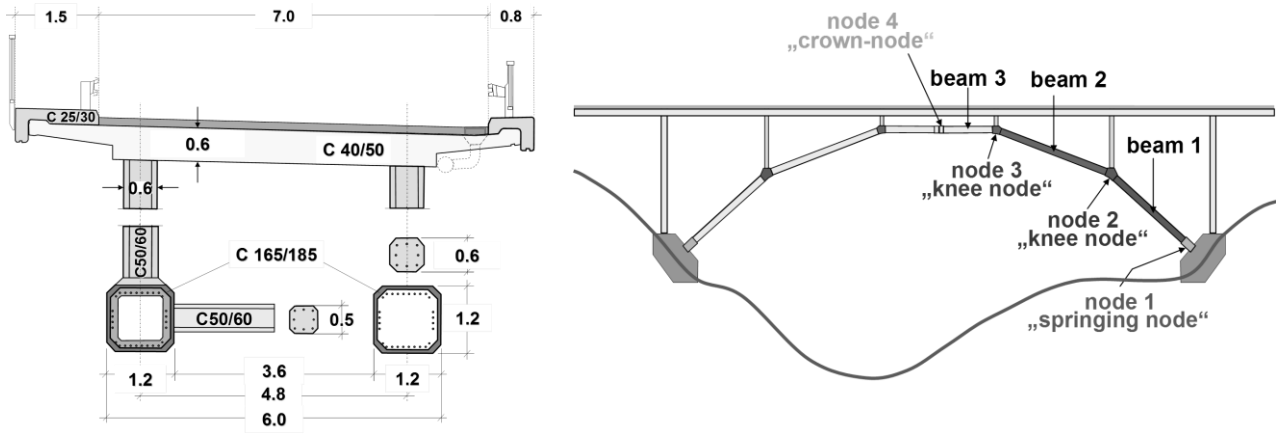

Figure 1: Cross-section and elevation.

unique key details shall give information about why the procedure of getting an admittance for construction was difficult. After that, chapter 2 illustrates the scientific preparation to overcome these understandable obstacles.

The entire arch does not contain any passive reinforcement. Except at the crown, all joints between beam and node elements are realised in form of plane dry contact joints. Axial prestress assures closed joints during erection as well as under service and provides the stiffness required for the buckling resistance under non symmetric loads. The light weight design made it possible to mount the arch by means of the swivel-in method.

2 Scientific Preparation

Required flatness of contact surfaces in dry joints

Dry joints consist of two surfaces in contact and work through a certain amount of contact pressure. Generally, the real contact takes place only in a certain number of contact points, depending on the geometric perfectness of the surface. The compressive capacity will decrease with worse accuracy. But which geometric parameter accounts for this degradation? This question will be answered by means of numerical simulations elaborated with Abaqus® using plane stress elements (CPS8R) and “hard contact”. The model simulates the worst case where the peak of one surface touches the other surface at a peak too. Thus, the model is symmetric and can consequently be simplified to a contact pair of one flat rigid body and one non perfect body made of UHPFRC specified by the wave length ***a***, the radius ***r*** and the amplitude ***s*** (see Fig. 2). These three parameters describe the occurrence, the shape and the magnitude of an idealised asperity. Nine models with various combinations of parameters are analysed.

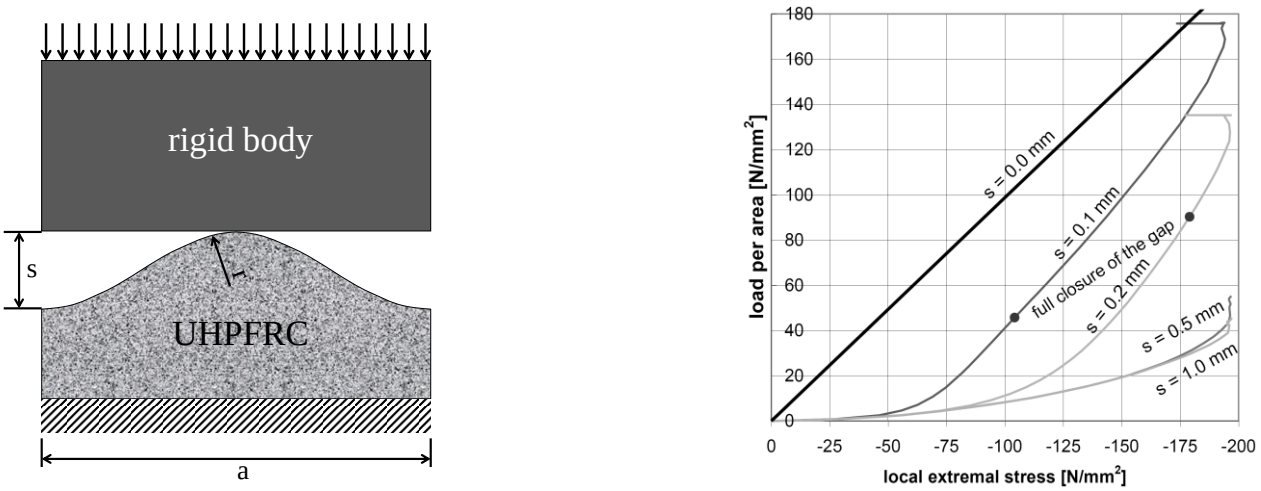

Figure 2: FE- model (left) and results of the simulation (right).

The results of the variation of ***r*** show that the shape of the contact points influence the bearing capacity only slightly. Further, the influence of the wave length ***a*** cannot be evaluated separately because geometrically affine shapes lead to the very same result. Since asperities are the subject in contrast to surface roughness, the variation of the gap width ***s*** is executed keeping ***a*** constant to 100mm. It turned out, that the gap width is the decisive parameter. Fig. 2 (right) shows the degradation of the bearing capacity with varying ***s***. A gap width of 0.1mm does not affect the bearing capacity. This value was subsequently specified as the permitted tolerance in the tender. The check of the flatness before mounting was performed with a 3D laser tracker by the manufacturer monitored by the employer.

Non destructive determination of the direction dependent post cracking tensile strength

In the pilot project WILD the required tensile strength of the hollow beams is specified separately for longitudinal and circumferential direction. Therefore, the knowledge about the

real fibre orientation all over the beams is indispensable. Equation (1) clearly shows the main parameters influencing the flexural post cracking tensile strength of UHPFRC [1] [2]. It is the basis of further developments.

$$f_{cf\,0,\,flex,x} = D \cdot \frac{l_f}{d_f} \cdot \eta_x \cdot \rho \cdot g \cdot \tau_f \qquad (1)$$

l_f ..... *fibre length*
d_f ..... *fibre diameter*
ρ ..... *fibre content*
η_x ..... *fibre orientation number related to the direction of interest (x)*
g..... effectiveness of fibres (assumed to be 1 according to [3])
τ_f ..... *bond strength between fibre and matrix*
D..... ratio between flexural strength (prism 150 mm) and axial tensile strength

η_x generally says how likely it is that a fibre of a volume -being as deep in ***x*** as the fibres are long- crosses a section perpendicular to ***x***. In the case of equation (1) η_x is an average over all fibres of a volume. The theoretical upper and lower bounds (1 and 0) result from pure uniaxial orientation. In the case of absolutely isotropic orientation η_x becomes 0.5 for each direction. In very thin building members, fibres are constrained to align nearly parallel to the mould which results in rather 2D orientation states. An isotropic 2D-orientation leads to $\eta_x = 2/\pi = 0.64$ [1].

The ferromagnetic behaviour of steel fibres allows for detecting them inside the hardened UHPC. Thus, a U-shaped core made of ferrite is provided with a spool. So, a simple inductive sensor is created (Fig. 3). This sensor changes its inductance if ferromagnetic things move to the main region of its magnetic field. In the case of steel fibres this measurable change depends on the magnetic permeability of the fibres, the fibre content and on the fibre orientation. The more a fibre is aligned to the permeating line of magnetic flux the higher is the measurable change of inductance. Thus, if we measure in several directions at one point of the structure, we will gain information about the fibre orientation state in the plane parallel to the surface. In order to transform the cluster of measured inductance values $\boldsymbol{L_i}$ to geometric (η_x, ρ) or directly to mechanical quantities ($f_{cf\,0,\,flex,x}$), it is necessary to find an adequate mathematical relationship. The project schedule did not allow for deriving sophisticated physical relations between inductance and the oriented mix of fibres. Simple empirical but physically plausible relations had to suffice. The simplest way to meet all these boundary conditions was to evaluate the inductance measurements regarding the post cracking flexural strength and to calibrate the equation of evaluation by means of bending tests.

If all directions of a measured point show the same inductance there will surely be an isotropic orientation in the plane parallel to the surface. We will call it η_{iso} which is always less than 0.64. Generally, it is assumed that analogously to principle stress directions one of the principle fibre orientation directions is always perpendicular to the surface (out of plane). We call it η_t (*t* for direction of thickness) which must obviously be less than 0.5 due to the little thickness of the beams' walls (60mm), also verified by photo-optical investigations [4].

Continuing the thoughts above, the deviation of the fibre orientation number relating to any direction ***x*** (in plane) from η_{iso} is assumed to correlate with the deviation of $\boldsymbol{L_x}$ to the mean $\boldsymbol{L_m}$. To simplify matters, a linear dependency (*B*) is proposed (see equation (3)).

$$\eta_x = (L_x - L_m) \cdot B + \eta_{iso} \qquad (3)$$

The local fibre content will mostly influence the absolute level of inductance at a measuring point. The simplest form for describing that is given in equation (4). In the project WILD-bridge four directions are considered.

$$\rho = A \cdot L_m = A \cdot \frac{L_{0°} + L_{45°} + L_{90°} + L_{135°}}{4} \tag{4}$$

Finally, all the remaining effects on the tensile strength (see equation (1)) caused by the bond strength, the slenderness of fibres and the effectiveness of fibres shall be summed up in a constant ***C***. In the project WILD a fibre cocktail is used. This is handled as follows:

$$f_{cf\,0,x} = \eta_x \cdot \left(\frac{l_{f1}}{d_{f1}} \cdot \frac{\rho_1}{\rho_{ges}} + \frac{l_{f2}}{d_{f2}} \cdot \frac{\rho_2}{\rho_{ges}} \right) \cdot g \cdot \tau_f \cdot \rho_{ges} = \eta_x \cdot C \cdot \rho_{ges} \tag{5}$$

Inserting equations (3) and (4) into equation (1) brings the final equation for the determination of the post cracking tensile strength via inductance measurements:

$$f_{cfo,\,flex,x} = A \cdot B \cdot C \cdot D \cdot \left[(L_x - L_m) + \frac{\eta_{iso}}{B} \right] \cdot L_m \tag{6}$$

Figure 3: Sensor and principle of measuring.

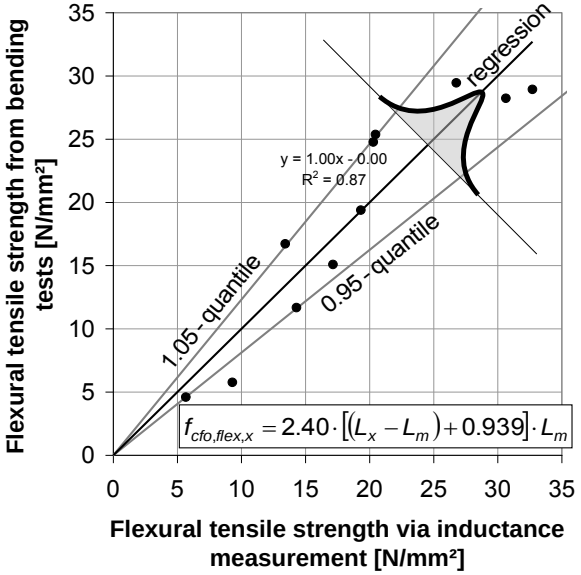

Figure 4: Individual calibration of equation (6) for the inspection of beam 2 piece 2.

If the term $A \cdot B \cdot C \cdot D$ is merged there remain only two unknown constants to be determined by the calibrating regression analysis on the basis of the minimum of the error square. For this purpose 12 prisms are sawn out from each element of the type *beam 2 and 3* (Fig. 1) which were therefore produced with extra length (see also [6]). The constants looked for are determined for each element individually (see an example in Fig. 4). So, the influence of the particular mix properties on the bond strength τ_f is also taken into account.

The beams *type 1* could not be produced with extra length, for which reason their measurements are evaluated by means of a collective calibration considering all samples taken from all beams with extra length.

In the scope of the quality assurance of the project each hollow beam is checked at 120 points. Taking into account the uncertainty of the method a 0.95-quantile is applied for the comparison with required strength values (Fig. 4). Details about the specification of required values are given in [6].

Destructive Experiments

Figure 5: Full-scale test: overview (left), instrumentation inside the beam at the joint to the node (right).

Based on findings and experience gained from many preliminary tests concerning mixing and workability, pumping, fibre segregation, fibre orientation versus casting method et. al. a costly and time-consuming full-scale experiment was conceived, prepared and carried out (Fig. 5). The specimen consisted of a hollow beam and a node element in true size. Only the length of the beam was reduced to 5m in order to make the production of the specimen easier. It was important to have one experiment which covers all interactive loads and carrying mechanisms. The dry joint between beam 1 and the springing node as well as the connection between beam 1 and the node 2 were part of the test. The load path of the test was chosen in a way that the limit states, ultimate as well as serviceability limit state, were passed in the experiment. The safety factor of the resistance (material) was shifted to the loads. Doing that, the response of the specimen in the theoretical state of the ultimate load could be demonstrated. By means of more than 50 measuring sensors the global deformation behaviour as well as local phenomena which had already been well known in theory could be verified. The accordance between theoretical predictions via finite element analysis and the measuring results was convincing [5]. Representatives of the awarding authority, the civil engineer as well as the construction company attended the experiment. Thus, the experiment not only brought about the desired technical information but it also deepened the confidence in the seemingly venturous design of the bridge.

Before the final manufacturing of the pre-cast elements could start, a further full scale test (approval test) had to be carried out. It aimed at the examination of the capability of the elements produced by the contractor. A specially developed mini anchorage for mono strands was tested according to ETAG 013. Based on the impeccable results of all tests the construction authorities gave a single approval for the construction of the WILD Bridge.

3 Practical Realisation

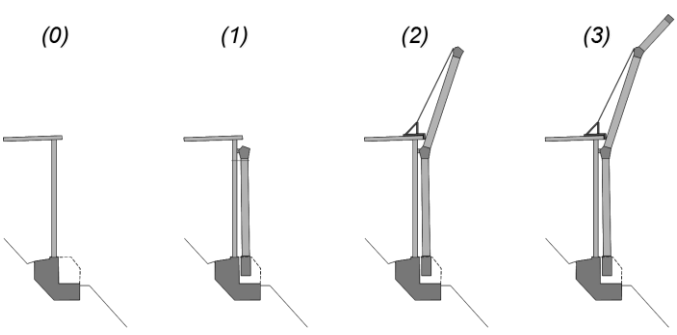

Figure 5: Mounting of arch halves.

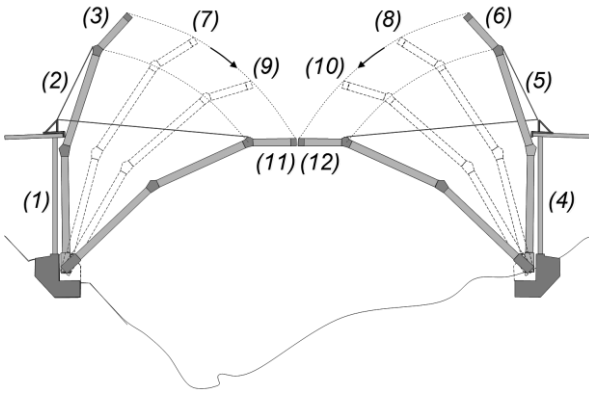

Figure 6: Process of swivelling in.

As indicated in chapter 1 there is a need of only 4 moulds for the casting of 16 node elements. The 12 beams are produced with just 1 mould. All manufacturing details are treated separately in this proceeding [7]. Corresponding node- and beam-elements are preassembled to so-called segments in the plant. Twelve segments thus created are finally shipped to the site.

Figs. 5 and 6 illustrate the final erection which only took 10 working days. The sequence is indicated by bracketed numbers, which are referred to in the following text.

Figure 7: Sinking of segment 1.

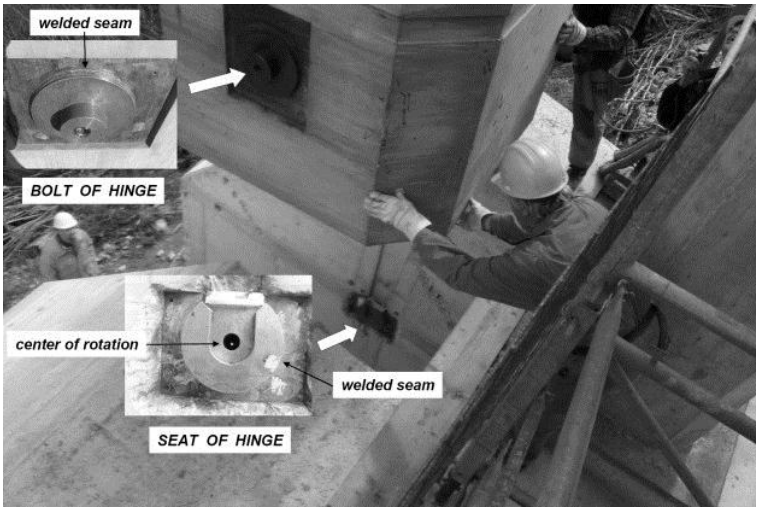

Figure 8: Details of the temporary swivelling hinge.

After the foreland bridges had been built conventionally (0), the segments were assembled to arch halves at each springing (1) to (6). The challenge at the beginning was to sink segment 1 (32 t) (Fig. 7) and to meet the seats of the hinge with the corresponding bolts (Fig 8). The 4 seats at one springing were precisely aligned to their common axis using geodetic methods. The accuracy of that was essential for a precise key stone at the end of swivelling in.

For getting an exact and total closure of the joints between the following segments a particular inclination of the hanging segments was needed (Fig. 9). For safety reasons it was not allowed to enter the inner space of the arch. Thus, the tendons had to be threaded from the top (Fig. 9) via threading ropes which had been prepared in the segments before mounting.

Figure 9: Mounting of segments 2 and 3, threading of a mono strand (above).

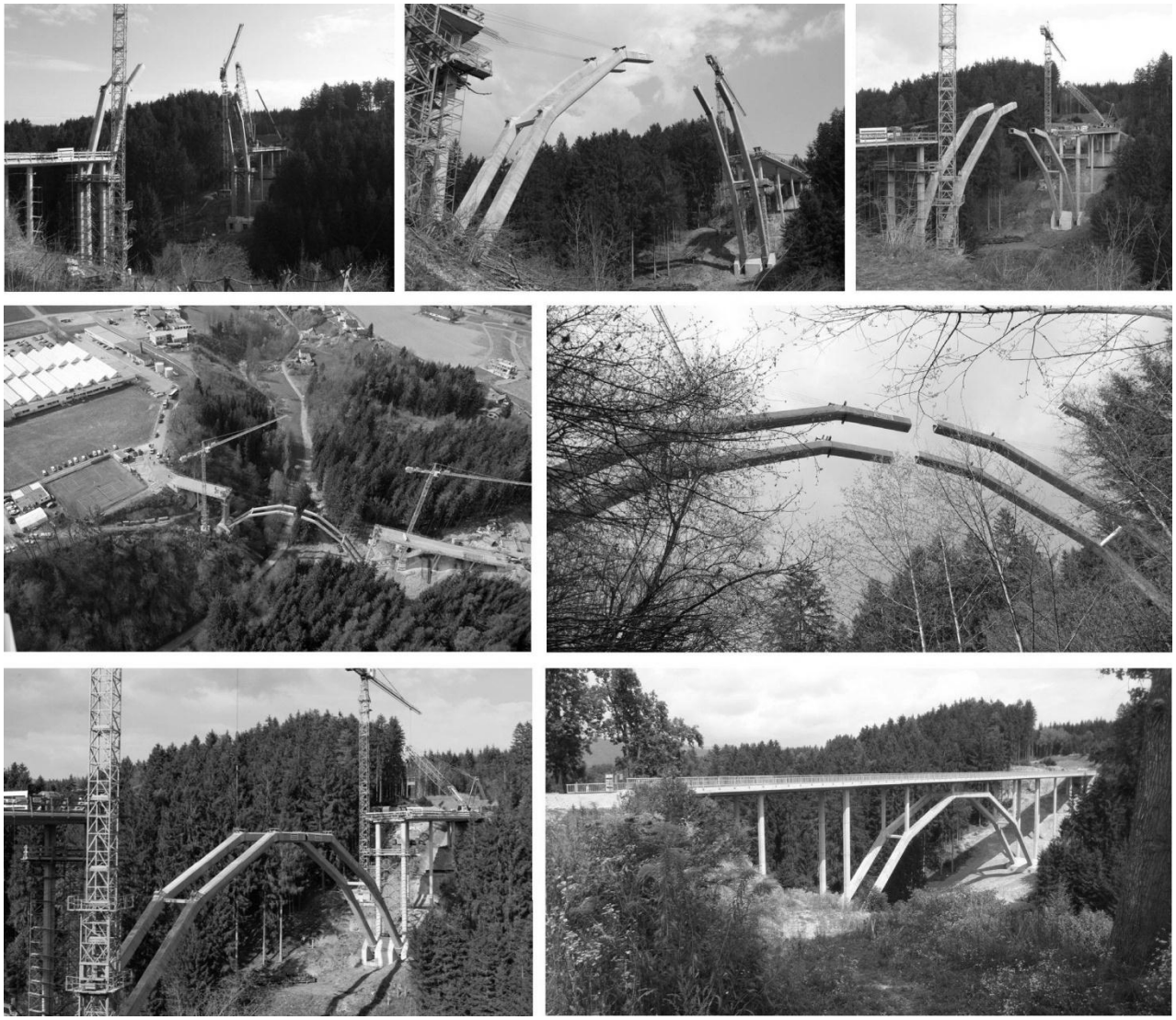

Figure 10: From mounting the last segment to the final bridge.

Fig. 10 illustrates the swivelling process which was performed by the use of 8 staying cables (mono strands) each side being fixed at the foreland bridges (7) to (12). At the crown a horizontal mismatch of just 10 cm was corrected by means of a simple steel frame, threaded bars and nuts. The next step was to stabilise the joint through load-bearing wedges (Fig. 11). Afterwards the staying cables were released, whereby the load carrying mechanism of the arch

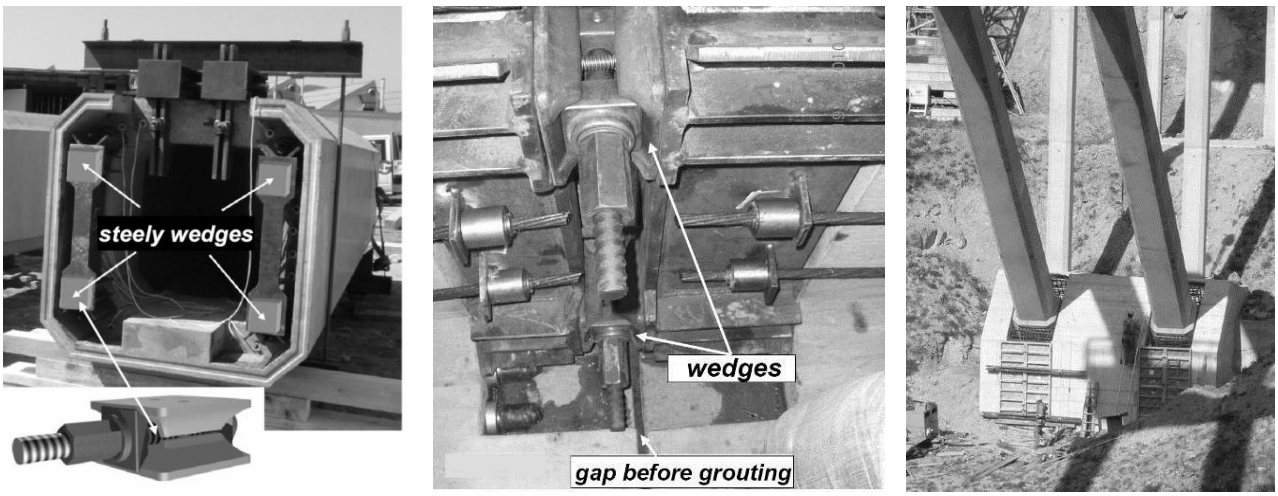

Figure 11: Details of the key stone (left, centre), fixation of the springing hinge by cast in situ concrete (right).

was activated for the very first time. Final grouting of the gap with high strength mortar can be seen as the real key stone. Eight overlapping strands coming from both sides of the crown made the crown joint bending resistant. Before the columns and the deck were built (conventionally) (Fig. 10) the springing hinges had been fixed by pouring out the space between foundation and segment 1 with concrete (Fig. 11 right). From a mechanical point of view the arch changes from a temporary two-hinged arch to the final and well-planned clamped arch.

4 Conclusions and Outlook

Many things contributed to the success of the pilot project WILD-Bridge. Beside technical innovation and scientific preparation the tight cooperation of everybody involved in the project as well as the extra visionary but responsible approach of the authorities were of greatest importance. From a technical point of view unique details and methods made the project a mile stone in the development of bridge construction and at the same time led to further research for advancing those details.

The prestressing of compressive members is currently being investigated in a fundamental research project focusing on extra slender architectural columns made of UHPFRC. This project also considers the idea of dispensing with passive reinforcement. The improvement of the non-destructive inspection method based on magnetic induction is in good progress. The project FibreScan funded by the Styrian Government deals with theoretical approaches describing general anisotropic inhomogeneous states of fibre orientation and aims at a final method without the need of destructive calibrating tests.

A mechanical monitoring system installed at the WILD -Bridge will provide information about the technical condition and allows for detailed examination of mechanical predictions.

5 Acknowledgments

The authors want to thank the following institutions for generously giving various kinds of support: Kärntner Landesregierung, Kommunalgesellschaft Völkermarkt GesmbH, STRABAG AG, FH-Kärnten, Massivbau GesmbH, SIKA Österreich, SW Umwelttechnik Österreich GmbH. We are deeply grateful.

References

[1] Behloul, M.: Les micro-bétons renforcés de fibres; De l'éprouvette aux structures; *XI-Vèmes Journées de l'AUGC*, Clermont-Ferrand. Prix Jeunes Chercheurs «René Houpert», 1996

[2] Leutbecher, T.: Rissbildung und Zugtragverhalten von mit Stabstahl und Fasern bewehrtem Ultrahochfestem Beton (UHPC); *Schriftenreihe Baustoffe und Massivbau*, Heft 9, 2007

[3] *AFGC*: Ultra High Performance Fibre-Reinforced Concretes Additional Informations for Interim Recommendations; 2002

[4] Heinzle, G.; Freytag, B.; Sparowitz, L.: Herstellungsmethoden, Faserorientierung/-verteilung und Bogenmontage der WILD-Brücke, *FFG-Projekt 819342, F-10-29-2010, TU-Graz*, 2010

[5] Freytag B. et. al.: Großversuch WILD-Brücke – Versuchsgestützte Bemessung einer UHPC-Bogenbrücke, *Beton- und Stahlbetonbau* 104 (3), p.134-144, 2009

[6] Reichel M., Sparowitz L., Freytag B.: Wildbrücke Völkermarkt – vorgespanntes Bogentragwerk aus UHFB-Segmentfertigteilen, Teil 1 – Entwurf und Bemessung, *Beton- und Stahlbetonbau* 106 (11), p.760-769, 2011

[7] Hecht, M: Practical Use of Fibre-reinforced UHPC in Construction - Production of Precast Elements for Wild-Brücke in Völkermarkt, Proceedings of the 3rd International Symposium on UHPC and Nanotechnology for Construction, Kassel University Press, 2012, Kassel 2012

Practical use of fibre-reinforced UHPC in construction - production of precast elements for Wild-Brücke in Völkermarkt

Markus Hecht
Max Boegl Group, Construction Company, Neumarkt in Upper Palatinate, Germany

The construction of the worldwide first Ultra High Performance Fibre Reinforced Concrete arched bridge, the Wild-Brücke across the Mühlgraben in Völkermarkt, Austria, required the Max Boegl Group's comprehensive concrete technology know-how. The heart of the filigree 157m long bridge (including the foreshore bridges) is comprised of the two parallel arches, both of a 70m span. Both arches consist of six components and eight joints (in the inflexion points) of a box-girder-shaped cross-section each. The thin-walled prefabricated elements were manufactured at Max Boegl prefabrication plant, Sengenthal, with an evenness of ≤ 0.1 mm in the contact areas. The developed C 165/185 UHPFRC meets all requirements regarding workability, heat development and structural demands without requiring any conventional untensioned reinforcement. The bridge was opened for traffic on 01.10.2010.

Keywords: UHPFRC, Ultra High Performance Fibre Reinforced Concrete, arched bridge

Production of precast elements for Wild-Brücke in Völkermarkt

Wild-Brücke spanning the Mühlgraben in the Austrian town of Völkermarkt (South Carinthia), smoothly integrates into the landscape thanks to its filigree arched beam structure. The name of this bridge was dedicated to the local company Wild GmbH, which is connected from Völkermarkt over this innovative bridge made of fibre-reinforced ultra-high-performance concrete. In addition to the Austrian province of Carinthia and the municipality of Völkermarkt, Wild GmbH was also involved in financing this project.

Figure 1: Wild-Brücke Völkermarkt after completion (Source: Strabag AG, engineering Austria).

The supporting structure is made of two parallel strutted arches connecting the valleysides with a clear span of approx. 70 meters. The arch crown is at a maximum level of approx. 40 meters

above the Mühlgraben. The total length of the bridge structure is approx. 157 meters including the foothills bridges – the rise of the arch is all about 18 meters.

Both bridge arches were planned as a traverse and consist of six members and eight nodes each in the salient points. The members (tubes) with up to 16 meters in length have a box-girder-shaped cross section revealing a wall thickness of only six and ten centimeters respectively in the edges. At the thicker-walled nodes which also have a box-girder cross section, the rising supporting in-situ pillars are cast into the elevated section of the track. There is a connexion to transmit load between the arch elements through externals tendons. The tendons run freely in the box-girder cross section of the members and are diverted at the arch bend through tendon ducts in the node elements. Conventional reinforcement was spared altogether. All precast elements were cast in fibre-reinforced UHPC.

The Sengenthal precasting plant of the Max Boegl Group was entrusted with the sophisticated precast elements by order of Strabag AG. The construction works were executed by the engineering division of Strabag AG, Austria. The bridge was planned and designed by Prof. L. Sparowitz, TU Graz.

Convincing Special Proposal

Both bridge arches consist of ultra-high-performance fibre reinforced concrete of a compressive strength category of C 165/185 and an elasticity module of 50.000 N/mm².

The target of such planning was to produce the construction elements of steel-fibre reinforced UHPC (UHPFRC) without using any conventional steel reinforcement.

Originally, the arch segments composed of members and nodes were to be made in a match-cast procedure. Instead, a special proposal brought forward by the Max Boegl Group was applied, to produce each member and each node for itself and to span all elements over corbel dry joints. To this effect, all contact areas between the precast elements underwent CNC milling and were ground with maximum precision to an evenness tolerance ≤ 0,1 millimeters. The evenness reached by grinding also contributes to increase the coefficient of friction in the joint which positively affects the shear force load capacity.

To ensure such precision, milling the contact joints made sense only when creep and shrinkage had largely subsided. Consequently, the components underwent heat treatment prior to CNC milling. Another positive effect of heat treatment is the increase of compressive strength and elastic modulus.

Maximum Concrete Quality

With regards to dimensions and strength category, Wild-Brücke is unique in the world and required individual acceptance for lack of standards.

The required concrete parameters necessitated the development of a new recipe through the concrete technologies of the Max Boegl Group.

The following table shows the requirements for concrete.

Table 1: Concrete parameters.

Properties	**Requirements according to Bill of Quantities**
Strength category	C 165/185
Exposure categories	XC4, XD3, XS3, XF4, XA3, XM3
Bending tensile strength	18 N/mm²
Axial tensile strength	7 N/mm²
Elasticity module	50.000 N/mm²
Equivalent bending strength (4-point, DBV)	
Deformation zone 1	18 N/mm²
Deformation zone 2	12 N/mm²
Evenness of contact surfaces	≤ 0,1mm
Frost and de-icing salt resistance (CDF)	fullfilled: 20 g/m² (≤ 1500g/m²)

In the end, a UHPFRC was developed which meets all requirements with regards to workability, heat development and statics. So the weathering rate identified by the CDF test resulting from frost and de-icing salt stress was determined to be 20 g/m².

In all arch elements (members, knee and camper notes) the same recipe was used.

The decisive factor for the recipe design were the camper nodes as they constitute the massiest building elements with 9.5 tons each. A CEM III / A 32,5 N-LH/NA was used to limit the development of hydration heat.

To harmonize the required workability, high bending tensile strengths at a marked ductile structural performance within the limit state of load-bearing capacity (equivalent tensile strength in deformation zone 2, a steel fibre mixture of short and long fibres was used.

Quality Assurance

In order to ensure a constantly high concrete quality level, increased efforts were made within the group of companies:

- To reduce the ready-mixed concrete temperature, the cement was cooled with fluid nitrogen by means of a cement cooling system.
- All base materials such as cement microsilica and steel fibre underwent a strict entrance test within the scope of quality assurance.
- A 100 % check was carried out, consequently all concreting works were carefully monitored.
- To reduce creep and shrinkage, all building elements underwent a defined temperature cycle in a heat chamber.
- To avoid cracks resulting from thermal stress, the temperatures in the building element were monitored from the start of the concreting works to the end of the heat treatment.
- The entire workforce involved in the project (ranging from the mixing plant operator to the man on the storage yard) underwent special training.

Preliminary Test at the Building Element

In the course of a large-scale test at the TU Graz a five-meter-long member element spanned on a nodal point was loaded until it broke in order to demonstrate the assumed material properties with the experiment and to compare the actually measured values with the calculated values of statics.

The building contractor extended the original requirement for an even distribution of the steel fibres by an evenly defined, homogenous steel fibre orientation. This resulted in further extensive preliminary examinations of the steel fibre orientation at the original building component cross section. Preliminary examinations were carried out at building elements of 5 m in length.

Sample bars were cut out of the tube walls and subsequently checked in bending tests.

Cores with a diameter of 50mm were extracted from the thin tube wall in longitudinal and transverse direction.

The steel fibres in the core were visualized by means of computer tomography.

Quality Check of the Building Element

At the request of the building contractor the members were produced in excess lengths. Thus, random girders could be cut out from the precast elements in excessive lengths to identify the “bending tensile strength” at the building component. In addition, an extensive testing program was made by the concrete expert assigned by the building contractor in parallel to production. After CNC milling the high-precision three-dimensional measuring of all precast elements was effected within the scope of the final check by means of the state-of-the-art measuring technology in order to verify the compliance with the required tolerances.

Production Sequence – Concreting Works

The production of the high-performance concrete used necessitated appropriate technical equipment. The concrete was mixed with a mixing unit specifically designed for high-performance concretes in the pre-casting plant Sengenthal.

All the aggregates, sands and finest substances used were dried before and filled in weather-proof daily doses and silos respectively. This ensured that no water was transported into the blend from the surface humidity through the dried base substances, which would otherwise have had to be corrected through the mixing water. The w/b-ratio to be complied with, was exclusively regulated at the mixing unit by adding water and flow agents.

The temperature of the ready-mix concrete was limited by a maximum value of 32°C. To meet such requirement even in summer temperatures, the concrete engineers worked with the cement cooling unit connected to the mixing unit. This allowed to cool an appropriate share of the cement used down to -100°C with fluid nitrogen in a counter-current process and to blend it with warm cement. Thus, the temperature of the ready-mix concrete could specifically be adjusted. 6m³ UHPFRC at 4 batches of 1,5m³ were mixed for each concreting operation.

Due to the formworks and production facilities to be kept available, the production of the members and of the nodes had to run in a production hall which could not directly be operated by the concrete mixing plant. So the UHPFRC had to be transported to the site with the ready-mix truck. The four batches were surrendered to the BMA in the pub mill of the ready-mix truck and homogenized there. Within a processing time of 120 minutes, the concrete had to be mixed and poured according to the requirements of the QA manual, which also comprised smoothing and curing the upper surface. The countdown started when water was added to batch number 1.

Within the scope of quality assurance, a random sample of the homogenized concrete from the ready-mix truck was taken prior to each concreting process. Concrete technologies of the central laboratory determined the consistency and the ready-mix temperature.

To ensure an even and homogenous mixture with the steel fibre cocktail, the steel fibre content was determined by means of electromagnetic induction measurement (measuring device BSM 100). Elution tests according to the requirements of DAfStb confirmed such measurements.

If the required ready-mix concrete parameters (temperature, consistency and steel fibre content) were observed, the concrete was released for pouring. In line with production, test specimens to identify all relevant hardened concrete parameters were produced, and the w/b value was checked. The texture was determined by a concrete flow of 58cm (+/- 2cm). The ready-mix temperature was not to exceed 32°C. The water/binder-ratio was defined at 0.23.

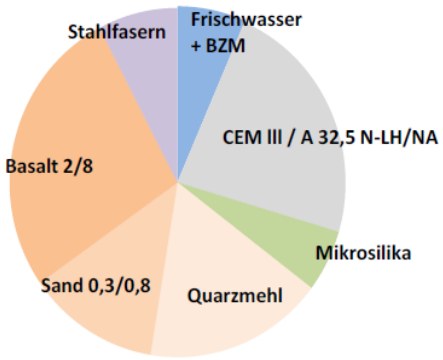

Figure 2: Composition of concrete.

Representatives of the building contractors and of the external supervisors frequently participated in the concreting works to assure themselves of the quality of production and workmanship of the concrete.

Formwork Construction and Workmanship

Choosing the appropriate production method revealed to be a particular challenge for the concrete specialists of the Max Boegl Group. In the end, the members were produced in favor of an optimized steel fibre orientation – by pouring in the mold and not, as originally intended, by equal pumping. A smart formwork system allowed extracting a core when stripping the members with box-girder profile of up to 16 meters in length.

The core designed by the formwork engineers allowed to compensate the arising shrinkage tensions. Cracks which might have arisen from the concrete shrinking up to the core, could be avoided altogether.

The high-performance concrete supplied by the ready-mix truck was divided into two crane buckets. The concrete was poured into the formwork through funnel-shaped slides arranged along the tube. The consistency of the concrete allowed a full flow of the thin-walled cross-section until it rose again on the opposite side and filled the upper surface of the formwork. The concrete in the side walls was compacted by means of form vibrators, concrete on the upper surface of the tube was compacted and planed with a vibrating beam. After the funnel-shaped slides had been removed, the concrete was protected against draught and loss of water until the concrete surface was completely smoothed. Subsequently, the building element underwent finishing treatment (curing) and thermal insulation.

The nodes were poured in concrete in a vertical position and were rather sophisticated in formwork construction, too, due to their angled geometry.

With the help of temperature measuring wires, the development of hydration heat in the building element cross sections was checked during the hardening process. The measuring sensor also helped to control and to check the heating rate in the subsequent heat treatment.

After 3.5 days the building element was lifted from the formwork with an average compressive strength of 95 MPa and prepared for thermal curing in the heating chamber, as shown in figure 3.

Figure 3: Member about 16m long, lifted out of the formwork, the inner core was already pulled out.

Heat Treatment

Heat treatment of the tubes and nodes was started on the fourth day in a heat chamber of 20m in length at a climate of 90°C and 100% r.H..

The heating and cooling rate of the chamber were permanently monitored by the inserted thermo couples connected to an automatic control system in order to avoid excessive temperature differences distributed over the concrete section – in particular in the massy camper nodes. On the one hand, this type of curing contributed to increasing the strength due to the acceleration of the puzzolanic reaction of the microsilica, on the other hand creep and shrinkage were also largely eliminated.

Shrinkage was measured with the help of a modern portable index arm which identified any alternation of length as against the previously applied gauge marks with an accuracy of +/- 0.01 mm.

A comparison between concrete that had undergone heat treatment and such concrete which had not revealed that such „artificial ageing“ helped to largely anticipate shrinkage deformation within a short time.

CNC Treatment

Subsequent to heat treatment, the individual front edge was milled at the node or at the member with an accuracy of ≤ 0.1mm. This operation ensured that an accurately fitting contact joint between node and corresponding member could be formed.

At the building contractor’s request, the members were produced in excessive lengths. Thus, sample bars could be cut out of the excessively long precast elements to identify the “bending tensile strength at the building element”. In addition, an extensive testing program was carried out by the concrete expert entrusted by the building contractor along with production. After the CNC milling process, the three-dimensional high-precision measuring of all finished elements was carried out within the scope of a final check by means of state-of-the-art measuring technology in order to verify and to document the compliance with the required tolerances.

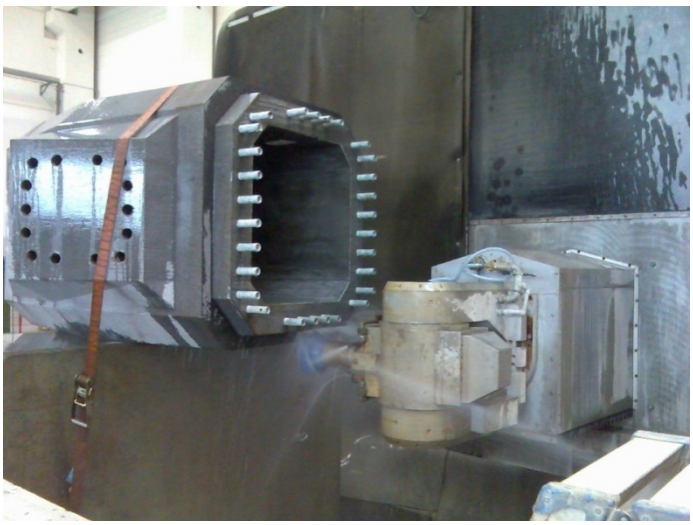

Figure 4: CNC milling process at the node.

Figure 4 shows the CNC milling of the contact joint. The small metal jacket tubes, which are encased in the concrete, can be seen at the front edge (in process). Their function is to direct the tensioning strands. Holes (for reinforcement) have been prepared to connect the in-situ concrete columns of the track elevated on the node.

Transport

To simplify the assembling process on the building site, the individual member and node elements were already tensioned to individual arch segments of up to 27 tons in weight in the factory before being delivered. Suspa DSI took over the task of prestressing the nodes and the corresponding members.

The prestressed finished elements were loaded and transported to Völkermarkt by the Max Boegl Group.

Figure 5: Loading the first arch segment (with camper and knee node).

Assembling the arch halves and folding up the semi-arches

On the building site, the arch segments were subsequently assembled by the executing company, Strabag AG. Vertical threading into the thrust bearing of the arch started with the camper node. Afterwards, the other arch segments were assembled in an almost vertical position until the semi-arches of roughly 43m in length and about 50 tons in weight were finished. The arch segments were pre-stressed over tensioning strands running in the inner part of the cross section.

After this operation, mid April 2010, the simply supported arch halves were lowered during the so-called „folding-in“ process by means of presses and steel ropes until the arch was completed. Such lowering process was alternately effected from the two valleysides.

After the successful lowering process, the arch halves were fixed and grouted at the crown. Even the camper joint was poured in concrete.

Columns out of in-situ concrete were erected above the node points (knee nodes). They are the supporting elements for the elevated track.

The bridge superstructure was made in conventional concrete construction, and the track layer was produced in asphalt.

The arches are “walkable” from inside by means of a ladder from an access at the camper. Thus, measuring technology and internal tensioning strands can be inspected.

On October 01, 2010, this unique building was solemnly opened by the Carinthia governor Mr. G. Dörfler and representatives of Messrs. Wild.

Within this building project which has been unique so far, the Max Boegl Group could impressively provide evidence of the fact that it is possible to produce and to supply precast precision elements of ultra-permanent concrete and CNC-milled contact surface in C 165/185 quality.

This high level of prefabrication resulting from milling the contact surfaces and the precision arising therefrom allowed a modular construction method as a consequence of which a lot of time could be saved during the assembling process on site.

Moreover, with the fibre-reinforced UHPC, a material was used which, due to its very compact structure results in improving the durability thus increasing the life of the building. Maintenance costs are minimized due to this sustainable and economic construction method.

“Progress is built on ideas” – Max Boegl Group

Structural Design and Preliminary Calculations of a UHPFRC Truss Footbridge

Juan Ángel López[1], Esteban Camacho[1], Pedro Serna Ros[2], Juan Navarro Gregori[3]

1: PhD student, Universitat Politècnica de València, Spain
2: University Professor, Universitat Politècnica de València, Spain
3: Assistant Professor, Universitat Politècnica de València, Spain

An innovative design of a UHPFRC footbridge of 45-metre span is presented in this paper. The resisting system consists of two identical trusses of variable depth, in which the compressed chord is also used as a railing. There is an intermediate curved ribbed slab connecting both trusses that works as the bridge deck, as well as a third truss that connects the bottom chords. The diagonals of the truss are shorter at the support than at the midspan. The design of the truss follows a wave shape that makes a reasonable transmission of the shear loads along the footbridge possible. The diagonals in tension are strongly reinforced, and second-order effects are considered in the top chord and in the compressed diagonals. The final design results in a very aesthetic, functional and safe footbridge, which may become the first UHPFRC truss pedestrian bridge. The study of alternative design solutions and preliminary calculations are presented.

Keywords: footbridge, truss, bridge, UHPFRC.

1 Introduction

The preliminary applications of UHPFRC focused on the design and construction of pedestrian bridges. Since the construction of the Sherbrooke footbridge in 1997 [1] to the most recent pedestrian bridges, the design, optimisation of UHPFRC material properties and construction methods have greatly improved. Over the years, much bolder designs have appeared thanks to a better understanding of this material and the experience gained in previous projects.

In the Sherbrooke 60-metre span footbridge, both bottom chord and diagonals are prestressed to counterbalance tension forces. In addition, diagonals consist of stainless steel with 150-mm diameter tubes filled with UHPFRC to avoid buckling and to achieve greater compression stress, confinement and ductility. As this is the first UHPC footbridge in the world, the design is quite conservative accomplishing a low dead load of around 4.4 KN/m^2 [2]. In 2002, the Sakata Mirai footbridge (49.2 m in span) achieved a dead load of 4.6 KN/m^2 with a web thickness of only 8 cm [3]. In 2007, the world record span was also recorded in Japan of a trough-girder typology with a 63.3-m span. It consists of a U-shaped prestressed section precast into segments in a precasting factory [3]. The structure, which probably best takes advantage of the UHPFRC properties, is its 69-meter span arch that supports the main span of the Wild Bridge in Austria (2011)[4]. The whole arch consists of two connected polygonal arches, each with a 6-cm thin-walled square cross-section. The arches are also prestressed to increase the flexure capacity and to make the construction system possible.

Structures are becoming increasingly slenderer, and this allows the UHPFRC structural design to come closer to steel than normal reinforced or prestressed concrete. In this way, new problems arise when using UHPFRC, such as vibrations or buckling, which are usually taken into account in steel structures.

The footbridge presented in this paper is the first to be constructed with UHPFRC in Spain and, as far as we know, it is the first truss pedestrian bridge made only of UHPFRC. It is to be located in Alicante (E Spain) very close to the sea, which justifies the use of this material given its great durability properties. A very aesthetic, innovative and slender design has been devised for the purpose of establishing a reference point, as well as a suitable connection between two

districts that are historically isolated by the Ovejas ravine. In this way, the footbridge will cover the city of Alicante's environmental and expansion needs.

2 Objectives

The main objective of this paper is the design of a 45-metre span UHPFRC footbridge. The design has to guarantee a very durable structure since it is to be located very close to the sea in a very aggressive environment. Another important requirement is slenderness and minimal visual impact. We ought not to forget the relevance of the aesthetic factor since it is an urban footbridge. Moreover, the final design must be easy to manufacture in a conventional precasting factory in order to cut costs as much as possible. Thus, the UHPFRC solution must not only be a good solution from the structural point of view, but also the best option when compared to other designs using different materials.

Given the fact that this pedestrian bridge is to be the first UHPFRC construction in Spain, the intention for the design is to show the potential of this material by making full use of all the advantages that it offers in terms of mechanical, durability and aesthetics properties.

3 Initial conditions

The design has to satisfy certain initial conditions. On the one hand, both the City Council and the Regional Government impose the following limitations:

- A 45-metre span without intermediate supports
- The upper bound deck is fixed by the maximum slope of the stairs that access the footbridge, while the bottom bound is fixed by a flood study. The distance between them is only 44 cm.
- There is no railing and the upper chord of the structure has to perform this function.
- The upper chord width has to be narrow enough to avoid people walking on it.
- Slenderness and low visual impact

On the other hand, a precasting factory established its own limitations to maintain its construction systems with only minor modifications and, in this way, to ensure an economical formwork and casting process:

- Trough-girder typology
- U-section shape
- Maximum bottom chord width of 2.90 m
- Maximum web slope of 6:1
- Use of prestressing strands must be avoided in the top chord

All these considerations have been taken into account in the design process. Despite them posing some problems, they have been overcome to ensure the safety of this pedestrian bridge.

4 Materials and design codes

The dosage used was the result of a previous study which aimed to optimise the concrete behaviour in both fresh and hardened states with 2 percent of hybrid fibres [5]. The main details of the UHPC mix design are summarised in Table 1. Using the optimal dosage, compression specimens 100x100x100 mm were cast in the laboratory at the Universitat Politècnica de València, and also in a precasting factory. A uniaxial compression test was performed on the cast specimens under both conditions. Six specimens were used for each test and the results are shown in Table 2. The average concrete compression strength is 150 MPa in both cases with a low standard deviation, which denotes good production stability. These tests confirm that

UHPFRC can be manufactured in a conventional precasting company with the same technology used until the present-date.

The tensile properties of the material were determined by means of flexural tests. In addition, a non-linear material model was used. A trilinear stress-strain curve in tension was assumed according to [6]. The parameters of the constituve law were adjusted to six flexural tests. The elastic branch had an elastic modulus of 44 GPa up to a stress of 11.5 MPa with a 5% coefficient of variation. The ultimate stress in tension was reached at a strain of 3‰ corresponding to a stress of 13 MPa with an 11% coefficient of variation.

Table 1: Details of the UHPC mix design.

	Content (Kg/m^3)		Content (Kg/m^3)
Cement	1000	Fibres OL13/0.16 (1)	78.1
Silica Fume	150	Fibres RC80/40 BP (1)	78.1
Silica Sand 0.5 mm	702	Superplasticizer (2)	9.06
Silica Sand 1.8 mm	380	w/c ratio	0.213
Total water	213	w/b ratio	0.185

(1) 1% in volume of each kind of fibre from Bekaert

(2) Solid fraction of the superplasticiser

Table 2: Concrete compression tests under lab conditions and in a precasting factory.

	Lab conditions		Precasting Factory	
Days	**Average Value (MPa)**	**Standard Deviation**	**Average Value (MPa)**	**Standard Deviation**
1	79	3.3	71	9.3
2	103	2.9	100	2.2
7	128	2	122	3.4
25	150	5	150	2.7

The actions applied to the footbridge were determined according to the Spanish Code for Actions on Bridges [7,8], which is based on Eurocodes. Table 3 shows the most important parameters considered.

Table 3: Actions considered in the footbridge design.

Dead load (KN/m^2)	**Characteristic Live Load (KN/m2)**	**Frequent Live Load (KN/m2)**	**Vertical Displacement under Frequent Live Load (cm)**
4,3	5	2	3,6
Basic Wind Velocity (m/s)	**Increase of Temperature (ºC)**	**Decrease of Temperature (ºC)**	**Horizontal/Vertical Seismic maximum acceleration (m/s^2)**
18	34,2	11,5	3,44/2,41

A 3D model was implemented into the SAP2000 software and a linear analysis was done to obtain the reinforcement requirements. Buckling problems in the top chord were studied by means of a non-linear geometric analysis. Second-order section forces were obtained, resulting in an increase of the compression diagonals reinforcement and their widths. The shear reinforcement requirement at the construction joints was also studied. Moreover, a non-linear mechanical model was developed to ensure the safety of the joints. The structural concrete design was carried out according to the Recommendations of AFGC [9] for both ultimate (ULS) and serviceability limit states (SLS).

5 Study of alternative design solutions

As mentioned earlier, the maximum vertical distance between the bottom chord and the upper bound of the deck is 44 cm. As a result, the railing is forced to be the upper chord of the structure, which makes the longitudinal shape of the footbridge very restricted. If a constant depth footbridge was to be designing, the maximum depth would be 1.34 m by considering a 0.90-m railing depth. The span-to-depth ratio would be very low (1/34) and it would be very difficult to satisfy the vertical displacement condition under live loads. Another solution would be a closed box shape, but this would result in a total depth of about 3 metres to avoid pedestrians feeling they were jailed inside the structure. As a result, the choice of a variable depth structure seems appropriate, which requires a curved top chord and also a curved deck. Thus, the railing height remains constant along the footbridge.

A maximum 6% slope in the abutments was considered to determine the curve described by the top chord. If a parabolic with a maximum depth at the midspan was used, the vertical depth at the midspan would increase by 0.675 m. If we were to assume a 0.90-m railing depth, the span-to-depth ratio at the abutments and the mid-span would be 1/34 and 1/22, respectively, which are common values for a simple supported beam.

Once the position and the curve described for the top chord and the deck has been established, the longitudinal design would be completed by defining the webs of the girder. The webs could be solid, leading to a box-girder, or they could be lightened, leading to a truss. The box girder is the commonest solution for UHPC footbridges in Japan [3] since the last six footbridges have been made with this section type. However, the Sherbrooke and Gärtnerplatz [10] pedestrian bridges tend to have a truss shape.

In our case, a truss beam is more transparent for both sight and the wind, and it enhances the sensation of the footbridge's slenderness. In addition, anyone who sees such a slender truss pedestrian bridge from a certain distance might think it is made out of steel, and it is not until they approach it that they realizes it is a actually a concrete construction. The confusion this creates gives the footbridge a good deal of aesthetic appeal. Nevertheless, a truss beam with an intermediate deck poses more buckling problems in the top chord than a box-girder since a solid web offers greater stiffness in the web-plane and in the transverse plane. Despite the fact that a box-girder is more suitable for this case with an intermediate deck, the slenderness and visual transparency have been considered to be more important than structural efficiency. The cost of this choice has resulted in greater thickness and reinforcement requirements in the diagonals and the top chord.

Truss structures have been commonly used for design purposes. The most widely used truss is the Pratt type. However, this type of truss is usually associated with industrial building solutions. Two other alternatives are the Warren or the Vierendel trusses. Six different types of trusses are presented in Figure 1. The first three examples are based on a Vierendel truss, while the others are inspired by a Warren truss. Obviously, a Warren truss is more efficient since the diagonals work alternatively in tension and compression with low flexure. However, a Vierendel truss carries the shear forces by means of flexure. The use of Vierendel trusses involves larger sized diagonals and greater reinforcement, but does not improve the aesthetics design.

Truss number four shows a common Warren solution in which all the diagonals have the same slope and length. In the fifth and sixth cases, the slope and length of the diagonals are variable. The latter solution makes sense for the shear load transfer and, therefore, axial stress is slighter at the midspan. As a result, even though the buckling length is longer, the axial load on the diagonal is lesser. Alternatives five and six offer a more pleasant longitudinal shape,

which reminds us of a wave shape, and this is most appropriate for a footbridge close to the sea.

Between solutions five and six, number five was chosen because the buckling length of the top chord is shorter, and it gives an adequate slenderness ratio resulting in more buckling stability on the truss plane.

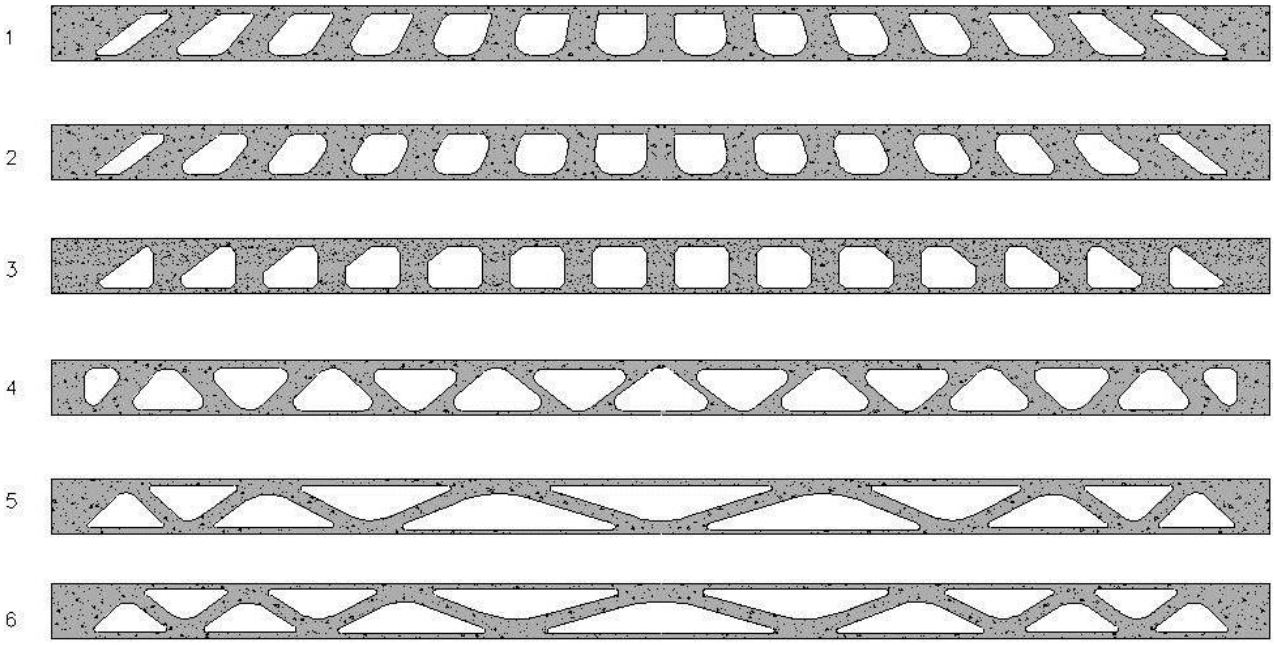

Figure 1: Different alternatives for the truss shape.

6 Final design

The final design consists of (Fig. 2 to 6) a “U”-shaped cross-section beam with a 45-metre span and a variable depth from 1.34 m at the abutments to 2.02 m at the midspan. The footbridge lateral webs are two modified Warren trusses made with a 6V:1H transverse slope, which are connected at the bottom chord with an X-shaped truss, which keeps the same wave-shape as the main truss (Fig. 3).

The truss bottom chord is 0.15 m in depth and contains a total of 18 0.6” seven-wire prestressing strands. The top chord has a constant depth and a variable width. It is narrower near the support and its width widens towards the midspan.

The deck is located in an intermediate position and connects the two trusses. It is 30 mm thick and has two longitudinal 150x240 mm cross-section ribs and transverse stiffening ribs with 1.6 m spacing. The deck is made in linear segments.

The truss diagonals members are variable in length with 150x120-mm cross-sections and are heavily reinforced. The diagonals in tension include four 20-mm diameter bars, while the diagonals in compression include four 20-mm diameter bars to bear in mind transverse bending due to the wind and to prevent the top chord from buckling on that plane. The bottom truss is formed by a 150x120-mm cross-section with four 12-mm diameter bars.

In addition, a service box is included on one of the bottom chords with three 75-mm diameter PVC tubes for water supply. A longitudinal lighting element is placed along the underside of the top chord. The holes in the truss above the deck are closed by means of transparent glass without diminishing transparency, which also make walking on the footbridge safe.

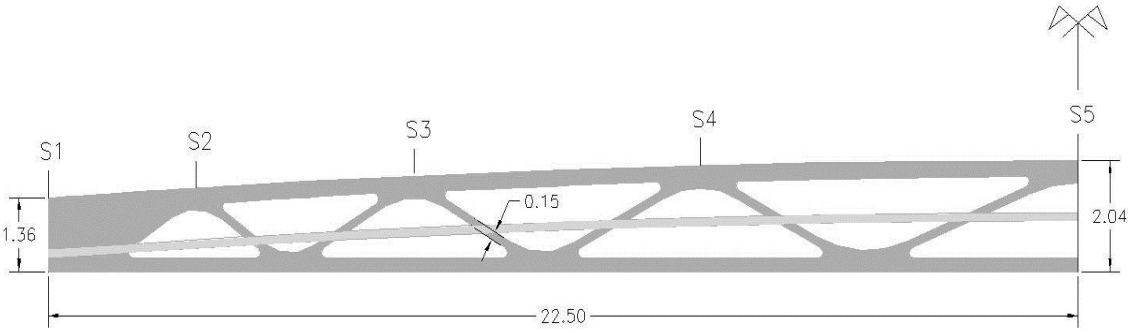

Figure 2: Longitudinal elevation of the footbridge.

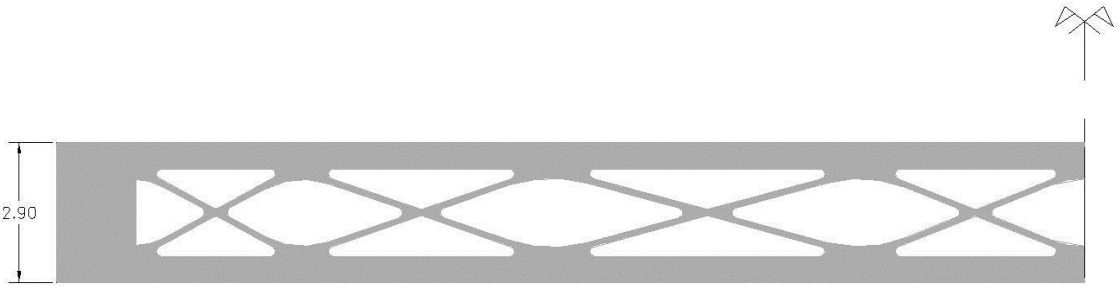

Figure 3 The X-shaped truss at the bottom chord.

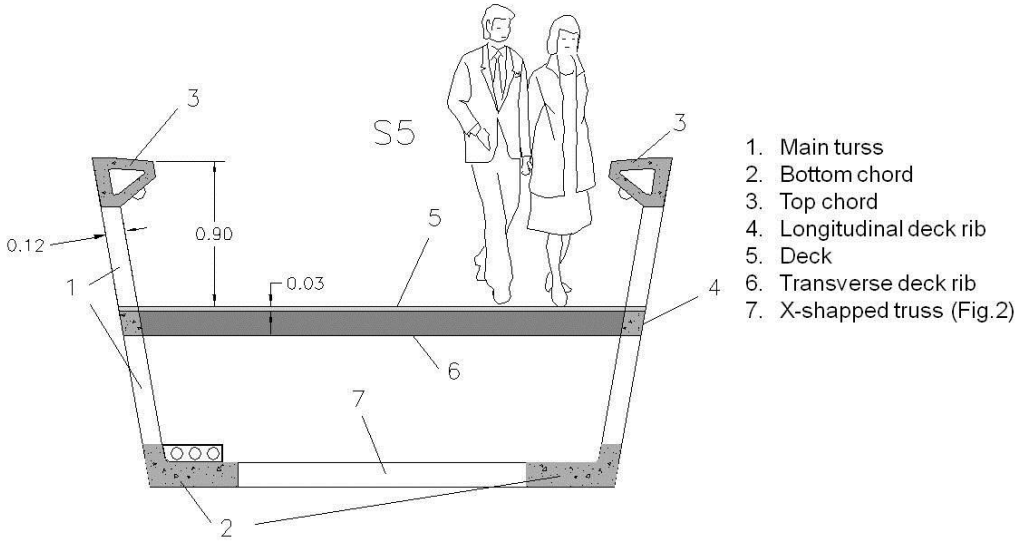

Figure 4: Cross-section at S5.

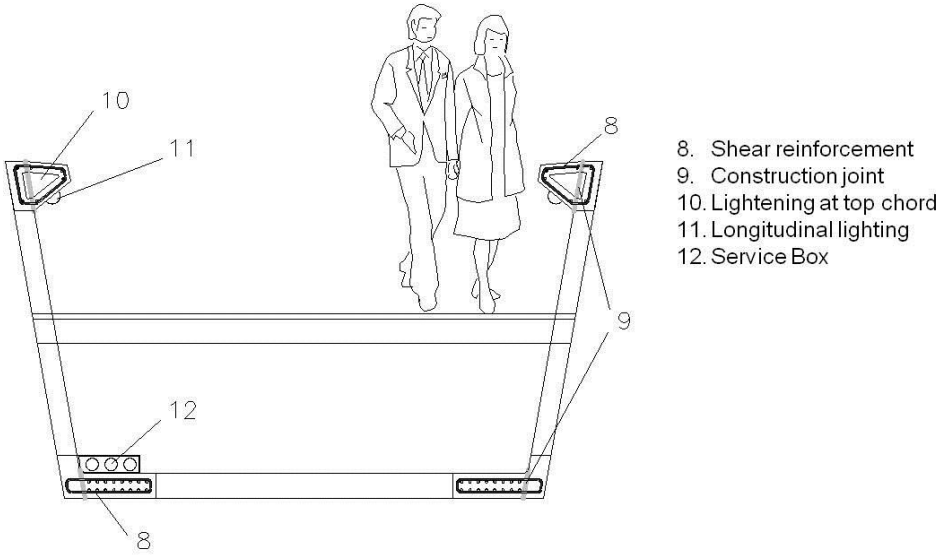

Figure 5: Cross-section at S5. Secondary elements and shear reinforcement at the construction joints.

Figure 6: Overview of the footbridge.

7 Casting process

As the footbridge has a 45-metre span, it is possible to transport the whole structure from the precasting factory to the final location by means of special transport. The whole footbridge is very difficult to cast in one segment without any joint because of the complex truss webs, the deck and the deck ribs. It was decided to cast the bridge in four steps by taking care of the construction joints generated and by taking into account the complex design.

The first elements (Fig. 8) to be cast are the two lateral trusses. These elements are cast on a horizontal position using a 45-m length, 120-mm height and variable width formwork, which follows the top chord curve. Inside the formwork, high-density polystyrene pieces of 120-mm thickness are placed. In this phase, the longitudinal deck ribs are also cast to be integrated with the truss. The truss also includes shear keys and bars to connect the top and the bottom chords and the deck.

The second elements to be cast are the top chords with their corresponding lightening and reinforcement. Once these chords are cast, both lateral trussed webs are placed with their definite slope.

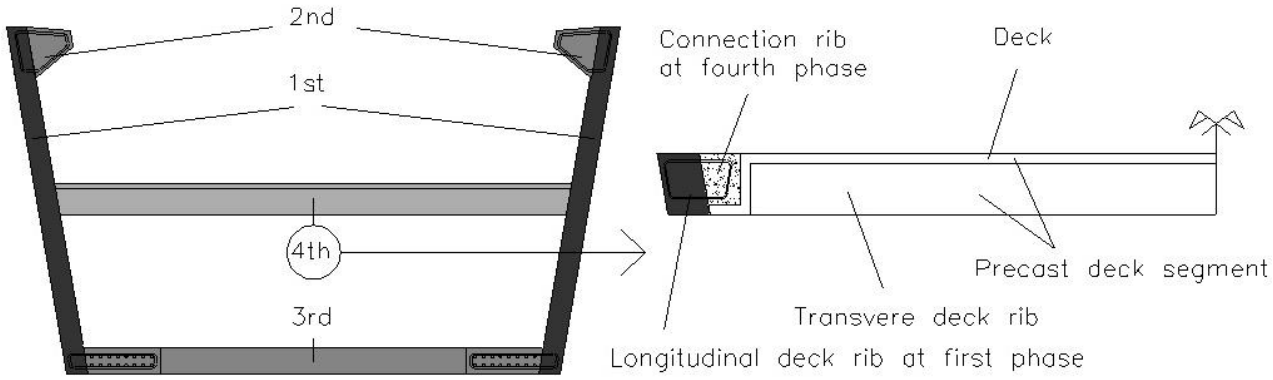

Figure 7: Casting phases. Details of the deck.

In the third phase, the bottom chord and truss are cast on the floor, following the same process used in the lateral trussed webs. The prestressing strands are previously located and tensioned.

In parallel to this process, a series of precast linear deck segments are made in a fourth phase. The precast deck segments are raised to their final position, and the bars, which were prepared in the first phase, are inclined towards the deck. Finally, the two longitudinal connection ribs are cast (Fig. 7, right).

8 Conclusions

A 45-metre span footbridge has been designed to be constructed in a neighbourhood in Alicante (E. Spain), and will be the first pedestrian bridge in Spain using UHPFRC. In addition, this footbridge will probably become the first truss pedestrian bridge only in UHPFRC. The proposed design has taken into account all the determinant factors imposed by local authorities and the precasting company. The final design consists of a slender footbridge with a total dead load of 4.3 KN/m^2, which maximises the conventional possibilities of a precasting factory and minimises the total cost; therefore, it is an economical solution if compared to other materials such as steel or normal-strength concrete.

9 Acknowledgements

The presented results were obtained in the context of the “FIBAC” research projects, with reference BIA2009-12722, supported by the Spanish Ministry of Science and Innovation. Support for this project is gratefully acknowledged. We also wish to thank the company Prevalesa S.L.

References

[1] Blais, P.Y., and M. Couture. 1999. Precast, Prestressed Pedestrian Bridge – World’s First Reactive Powder Concrete Structure. *PCI Journal,* Sept., Vol 44, No. 5: 60-71.

[2] Adeline, R., Lachemi, M., Blais, P.Y.; Design and behaviour of the Sherbrooke footbridge. Proceedings of the Internacional Symposium on High Performance and Reactive Powder Concretes, 1998. Sherbrooke University, p.59-63.

[3] Tanaka, Y., Maekawa, K., Kameyama, Y., Ohtake, A., Musha, H., Watanabe, N. 2009. Innovation and application of UFC bridges in Japan. BFUP 2009/UHPFRC2009 Proceedings.

[4] Reichel, M., Freytag, B., Sparowitz, L. 2009. Road Bridge WILD – UHPFRC for a segmental arch structure. BFUP 2009/UHPFRC2009 Proceedings, pp.88-89.

[5] López, J.A., Serna, P., Camacho, E. 2010. Diseño estructural de un muro de contención de tierras para la defensa de taludes en el puerto de Jávea (Alicante) con la utilización de hormigón de muy alto rendimiento. Final Project Degree, Universidad Politècnica de València, Spain.

[6] López, J.A., Serna, P., Camacho, E. Structural Design and Previous Tests for a retaining wall made with precast elements of UHPFRC. 6th International Conference on High Performance Fiber Reinforced Cement Composites. June 20-22, 2011, Ann Arbor, Michigan, USA.

[7] IAP2011. Instrucción sobre las acciones a considerar en el proyecto de puentes de carretera. Ministerio de Fomento. 2011. Spain.

[8] NCSP-07. Norma de construcción sismorresistente: puentes. Ministerio de Fomento. Spain.

[9] AFGC. 2002. (Association Francaise de Génie Civil). Recommendations provisoires. Bétons firbrés à ultra-hautes performances.

[10] Fehling, E., Schmidt, M., Bunje, K., Schreiber, W.; Ultra High Performance Composite Bridge across the River Fulda in Kassel – Conceptual Design, Calculations and Invitation to Tender, Proceedings of the International Symposium on Ultra High Performance Concrete, 13.-15. September, 2004, Kassel University, p.69-75.

Behaviour of an Orthotropic Bridge Deck with a UHPFRC Topping Layer

Pierre Marchand, Fernanda Gomes, Lamine Dieng, Florent Baby, Jean-Claude Renaud, Cyril Massotte, Marc Estivin, Joël Billo, Céline Bazin, Romain Lapeyrere, Dominique Siegert, François Toutlemonde

In the frame of the French national R&D project Orthoplus, an experimental program has been carried out to assess the influence of a UHPFRC topping layer on the behaviour of orthotropic decks and their fatigue resistance. This project aims at improving the design rules for orthotropic decks and developing a UHPFRC-based innovative solution to improve their durability. Bendings tests were carried out on four specimens, consisting in a realistic steel orthotropic deck model, 2.4 x 4m, with different types and thicknesses of topping layers: traditional bituminous concrete, thin layer of UHPFRC or no topping layer. The load application has been chosen as representative of real situations and of idealised cases considered in design codes. The loads were first applied through static tests with different configurations in accordance with Eurocode 1 and then through a fatigue test representative of traffic loads during bridge lifespan.

Keywords: UHPFRC, orthotropic deck, fatigue

1 Introduction

In the case of long span bridge or movable bridge, minimizing dead load becomes predominant. Despite their higher cost, orthotropic decks turn out to be competitive in these cases, because of their very low dead weight. However, one of their major weaknesses is the possible development of fatigue cracks at the junction between troughs and the upper steel plate under local repeated load due to traffic, depending on the stress level at weld toe (cf. figure 1).

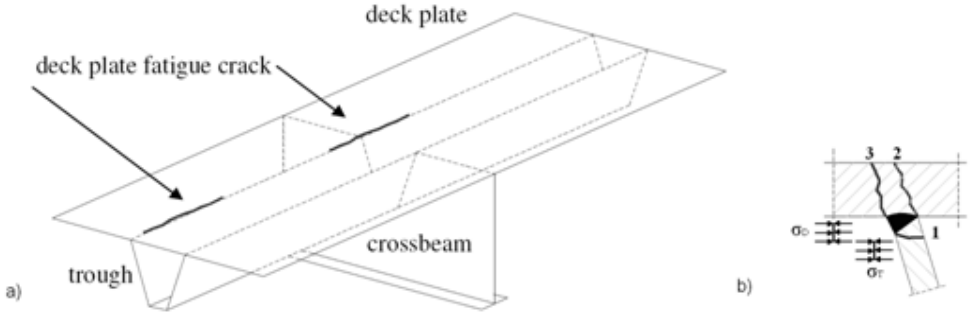

Figure 1: Possible fatigue cracks in an orthotropic deck (a) and stress level at weld toe (welded joint) on deck plate bottom side σ_D and on trough wall σ_T (b) [1].

In the frame of the National R&D project Orthoplus [2-4], tests have been carried out at LCPC (now IFSTTAR) structures laboratory, to quantify the effect of topping layers on possible fatigue cracks development. In addition of traditional bituminous concrete layer, an innovative UHPFRC topping layer was tested. This solution was inspired by some recent attempts of bridge stiffening [5].

2 Specimens

Three specimens were made by the company Eiffel, partner of the project, in Lauterbourg factory, following the same manufacturing process as for Millau viaduct (cf. figure 2).

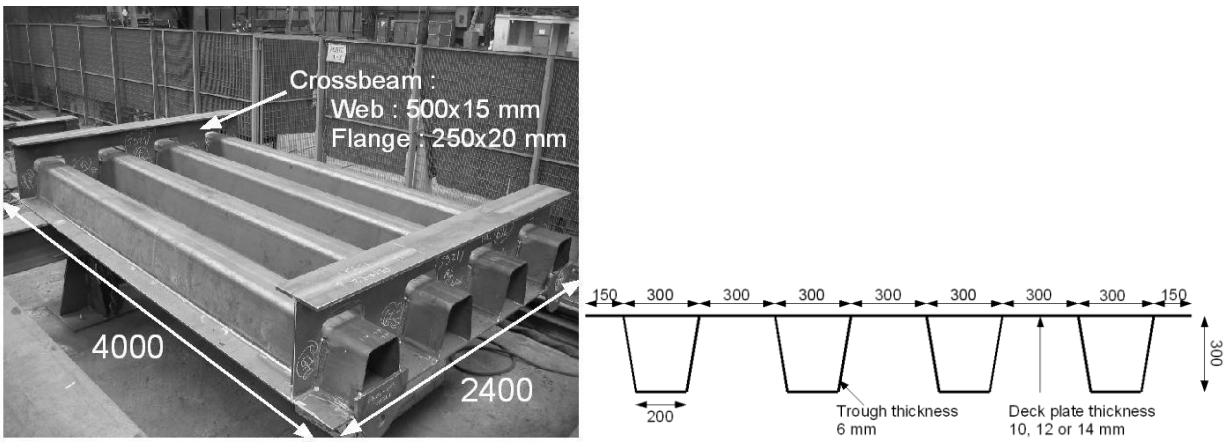

Figure 2: Test models with main dimensions : bottom side view on the left and cross section on the right.

The specimens were manufactured with deck plate thicknesses of 10, 12 and 14 mm. The 14 mm deck plate specimen was tested without topping layer and with a 70 mm-thick bituminous concrete layer. To assess the stress level under the deck plate inside the trough, a hole was made in one of central troughs, only on the 14 mm specimen. The 12 mm-thick deck plate was topped with a 35 mm UHPFRC layer connected with studs while the 10 mm deck plate was also topped with a 35 mm UHPFRC layer but connected with a welded grid mesh. The studs and welds of the grid mesh are located along the troughs axis. The connection points are hence spaced 600 mm transversally. The UHPFRC was cast directly on the steel deck plate. The UHPFRC contained steel fibres, with 2.5% volume ratio. The compressive strength was about 180 MPa, elastic limit strength in tension was about 9 MPa and Young's Modulus was about 56 GPa. The characterisation was made according to [6]. This UHPFRC was not submitted to heat treatment. The material was provided by Eiffage company, partner of the project, as well as the reference "Orthochape" bituminous concrete [7].

3 Testing conditions

Test set up

The specimens were tested under local bending at mid-span between cross-beams as shown on figure 3. Load was applied either directly with one or two real wheels or with rectangular plates representative of the fatigue load model of Eurocode 1-2 [8]. In the case of a rectangular steel plate, an elastomeric bearing was placed at the interface between the rectangular steel plate and the steel deck to distribute the load as uniformly as possible. Thereafter, we use the results corresponding to loading with a single wheel and with a rectangular steel plate with dimensions 220x320mm called plate A.

The specimens were supported on four bearings under the cross-beams, either fix or movable, to limit membrane forces inside the specimen.

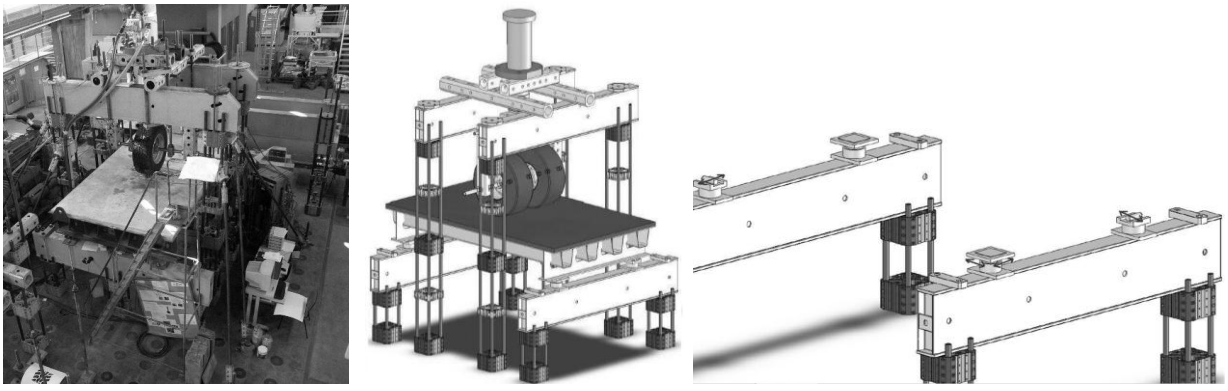

Figure 3: Testing setup and supports.

Instrumentation and stress determination at weld toe

To assess the stresses at weld toe, instrumentation with strain gauges and chains of strain gauges in the vicinity of the weld was installed. The location of gauges was determined according to ECSC report [9] and to the studies of International Institute of Welding [10] (cf. figure 4). Two stress values characterize the stress concentration critical with respect to fatigue :

σ_D at the lower side of the deck plate is the extrapolation of gauges signals located at distance t/4 and t (dD1 and dD2 on figure 4), where t is the thickness of the deck plate, following [10].

σ_T (stress at trough wall), is the extrapolation of gauges signals located at about 15 and 30 mm from weld toe or 25 and 37 mm, as recommended by [9].

The choice of extrapolating methods was made after observing that stress distribution was quite linear along the trough wall, and not linear along the deck bottom side, following transverse axis. Some displacement transducers were placed to measure the specimen deflection. In the case of specimens topped with a UHPFRC layer, some gauges were placed on the UHPFRC top side. The applied force was measured through force cells placed under the actuator and under the four bearings. Details of the tests and global analysis of the experiment are given in [11].

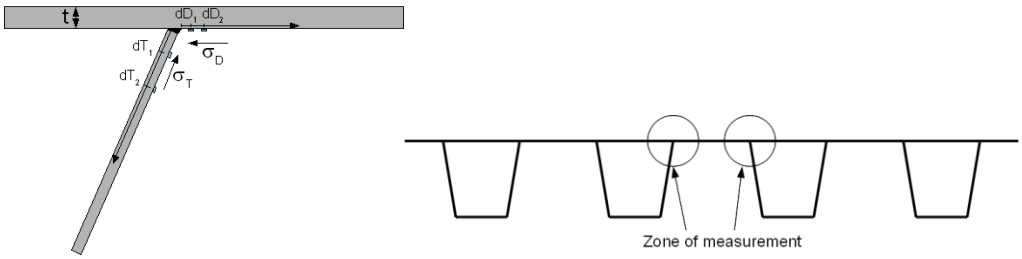

Figure 4: Gauges location to assess stress concentration at weld toe.

Loading

The force range was up to 45 kN by wheel and up to 150 kN by plate. For wheels, this corresponds to the maximum force that the wheels could take. As concerns rectangular plate, it was the maximum force at characteristic Service Limit State (SLS) given by Eurocode 1-2 (Tandem System 1 from Load Model 1).

For specimens with 10 and 12 mm deck plate thickness topped with a UHPFRC layer, a cyclic load was applied during two million cycles. The purpose was to represent 100 million cycles with 45 kN load expected in the lifetime of the bridge. Given the reduction in number of cycles, the force range was increased following the Wöhler curve for steel proposed by Eurocode 3 [12] with slope -1/3 and -1/5, which led to a cyclic loading amplitude of 111 kN.

4 Experimental results

The figure 5 shows the deflection at mid-span along the transverse axis under 45 kN centred load for different specimens loaded with plate A or real wheel.

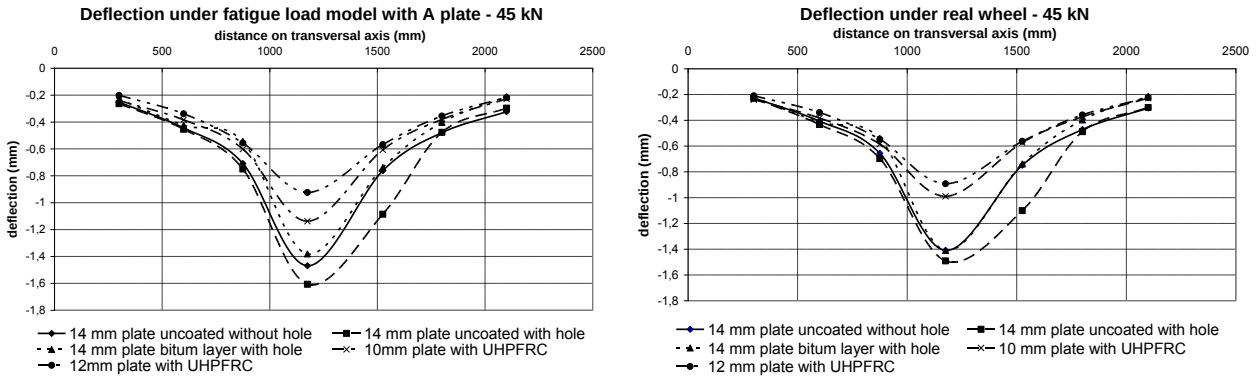

Figure 5: Deflection under steel plate A and real wheel under 45 kN load.

Despite the thinner steel deck plate, specimens with UHFRC topping layer show a lower deflection than specimens without topping layer or with bituminous concrete layer. For the 14 mm specimen, the non symmetry comes from the hole made in the third trough.

In terms of fatigue stresses at weld toe (σ_D and σ_T), the reduction is also important. Table 1 shows these results for the different configurations. The displayed figures are the mean values of results obtained on each side. For comparison, class details given by Eurocode 3 [12] and Kolstein [13] are indicated. They are the maximum stress levels admitted for the structure during 100 million cycles. Stress determination was made by multiplying the extrapolated transversal strain by steel Young's modulus, that is 210 GPa.

Table 1: Linear extrapolation for assessing fatigue stresses at weld toe.

	A-plate 45 kN		**Real wheel – 45 kN**	
Specimen	σ_D	σ_T	σ_D	σ_T
14 mm plate without coating	47 MPa	64 MPa	48 MPa	73 MPa
14 mm plate with bituminous concrete layer	37 MPa	53 MPa	44 MPa	60 MPa
10 mm plate with UHPRC topping layer	43 MPa	41 MPa	44 MPa	39 MPa
12 mm plate with UHPFRC topping layer	22 MPa	33 MPa	22 MPa	35 MPa
Class detail Eurocode 3 [7]	*100 MPa*	*71 MPa*	*100 MPa*	*71 MPa*
Class detail acc to Kolstein [8]	*125 MPa*	*90 MPa*	*125 MPa*	*90 MPa*

We can notice that either uncoated 14 mm plate orthotropic deck, or coated with an "ultra-thin" layer do not exhibit a safe enough margin on the fatigue stress at trough wall (73 MPa instead of 71 MPa according to Eurocode 3 class detail). Moreover, reference bituminous concrete layer has a significant influence on the reduction of fatigue stresses (from 15 to 20 %), and as expected, stiffness brought by UHPFRC layer enables to reduce significantly the fatigue stresses.

Non linearities and evolutions observed during static tests

During static tests, some non linearities on strain values have been noticed on specimens with UHPFRC topping layer as shown on figure 6, (transversal strains at top side of the steel deck plate).

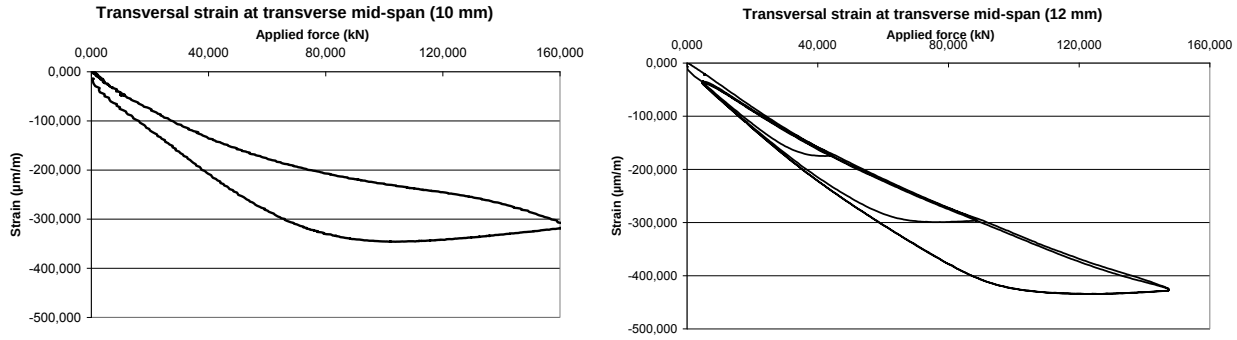

Figure 6: Transversal strain at mid-span in the middle of transversal axis for 10 mm and 12 mm deck plate.

The non linearity could be due to two phenomena. The first one is that there is some slipping at the steel-UHPFRC interface. The connexion is not perfect, and there can be some relative displacement at interface between the studs or the welds fixing the UHPFRC layer on the orthotropic steel deck. This slipping leads to the second phenomenon which is source of non linearities, that is UHPFRC cracking. If a total connexion leads to a almost total compression in UHPFRC layer, slipping at the interface leads to some tensile stress at UHPFRC bottom side. This cracking can be seen through the evolution of behaviour between the first static tests and the last ones (cf. figure 7)

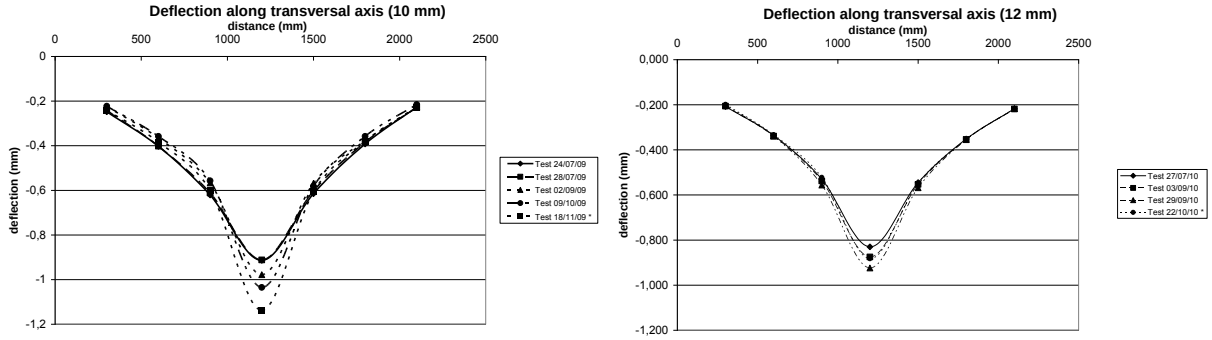

Figure 7: Deflection along transversal axis under A-plate loading (45 kN) at different dates (indicates tests which have been carried out after 2 million cycles loading).*

Figure 7 shows that the deflection significantly increased during static load tests, which certainly means an increasing cracking of the UHPFRC bottom layer. The evolution is less significant in the case of 12 mm deck plate specimen, undoubtedly due to the fact that level of stress in UHPFRC bottom layer is lower because of the thicker steel deck plate.

In the case of 12 mm deck plate specimen, the deflection decreased after cyclic loading. This clearly indicates that the damaging level is below the 111 kN cyclic loading and the decrease can result from a modification of the interface property during the 2 million cycles. In the case of 10 mm deck plate specimen, the deflection slightly increased during the 2 millions cycles which seems to indicate that the damage level is close to 111 kN.

It shall be reminded that the load applied with A-plate is more severe than Eurocode 1-2 because the loaded surface is 220x320 instead of 400x400 mm for Tandem TS1 at SLS. The 150 kN loading was consequently beyond characteristic SLS.

The nonlinearity can also be seen on linear extrapolation to assess fatigue strain and stress at weld toe, under the steel deck plate, and on the trough wall (cf. figures 8 and 9).

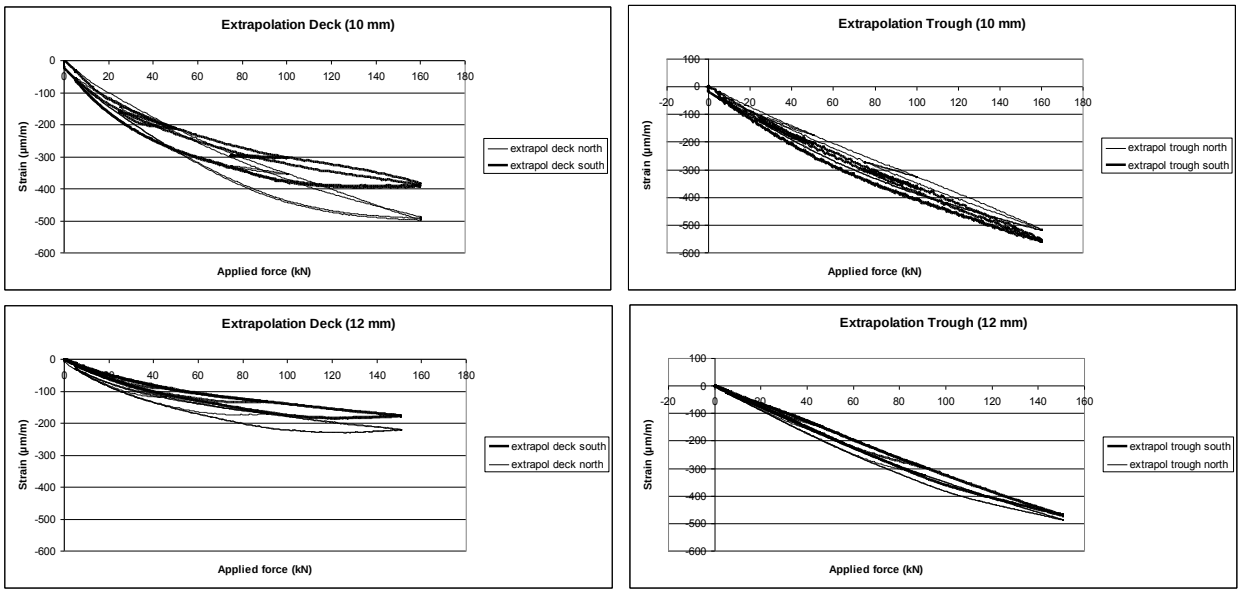

Figure 8: Strain extrapolation at weld toe under deck plate and on trough wall, versus applied force, with A-plate on 10 and 12 mm specimen topped with UHPFRC.

Cyclic loading results

Two million cycles have been applied with a force oscillating between 10 and 121 kN (ΔF=111 kN), without noticing visible damaging. The deflection slightly increased for 10 mm deck plate specimen (about 5%) and slightly decreased for 12 mm deck plate (about 1 or 2%) (cf. figure 8).

No fatigue damage was observed after fatigue test on the welds between troughs and deck plate (visual control and cutting of specimens).

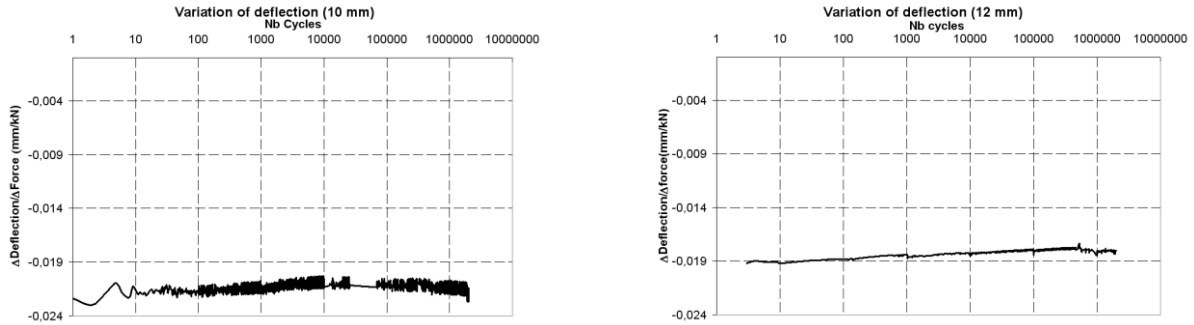

Figure 9: Variation of ratio deflection/applied force during fatigue loading (A-plate, ΔF=111 kN).

During the fatigue test with 12 mm specimen, two temperature sensors were recording temperature. One was located at midspan on the UHPFRC top side and the other one was under the deck plate, also at mid-span. During tests, we have observed a temperature systematically 3°C higher under the deck plate than on the UHPFRC layer (the temperature difference stabilized after some cycles), whatever the external temperature. This is consistent with the hypothesis of a slipping interface between the steel deck plate and the UHPFRC layer, which dissipates some energy.

5 Comparison with FEM model

Assessing stiffness brought by different topping layers

In the experimental program, the steel deck plate thickness varied between the different configurations and the specimens topped with UHPFRC layer were not tested before casting of the UHPFRC layer. Therefore, a FEM model has been developed and used to assess the

rigidity brought by the different topping layers and it will possibly help to further optimize orthotropic decks and topping layers design [14].

The used model contained 69560 quadrangular elements and 64351 nodes (Q4 : with linear interpolation) representing cross-beams, troughs, and deck plate.

For comparison, only model A rectangular plate loading at 45 kN will be considered hereafter.

Comparison between 14 mm uncoated specimens with FEM model

Table 2 compares values for 14 mm deck plate obtained by FEM model and those obtained experimentally. Fatigue stresses obtained with FEM model are extrapolation of results obtained at nodes close to the weld toe. The FEM underestimates deflection and fatigue stresses on deck plate (σ_D) of about 10% and fatigue stresses on trough wall of about 35%. The underestimation of deflection and σ_D by the model, can be explained by the unperfect modelization of bearings under the tested specimen. Although more important, the difference in σ_T is more difficult to explain.

Table 2: Values obtained with FEM Model and test results on 14 mm deck plate specimen.

	Test results	FEM model results
Deflection at mid-span	-1.44 mm	-1.36 mm
σD	45.8 MPa	39.5 MPa
σT	63.4 MPa	41.0 MPa

Comparison between 10 mm and 12 mm specimens without coating (FEM model) and with UHPFRC topping layer (test results)

We compare FEM model of uncoated specimens 10 or 12 mm thick and experimental results with UHPFRC topping layer (cf. tables 3 and 4). The ratio between coated and uncoated specimen is calculated with and without the underestimation of deflection and fatigue stress by the model obtained on the 14 mm uncoated specimen.

Table 3: Values obtained with FEM Model (uncoated specimen) and test results with UHPFRC layer on 10 mm deck plate specimens.

	FEM model results for uncoated specimen	Test results with UHPFRC layer	Ratio	Ratio taking into account model underestimation
Deflection at mid-span	-2.12 mm	-1.14 mm	46 %	51 %
σD	97.7 MPa	43.4 MPa	56 %	60 %
σT	63.2 MPa	40.5 MPa	36 %	52 %

Table 4: Values obtained with FEM Model (uncoated specimen) and test results with UHPFRC layer on 12 mm deck plate specimens.

	FEM model results for uncoated specimen	Test results with UHPFRC layer	Ratio	Ratio taking into account model underestimation
Deflection at mid-span	-1.64 mm	-0.92 mm	44 %	49 %
σD	60.7 MPa	22.0 MPa	64 %	67 %
σT	49.3 MPa	32.8 MPa	33 %	51 %

Both solutions bring similar stiffness increase. The UHPFRC layer connected with studs (applied on 12 mm deck plate specimen) seems to be consequently more efficient than UHPFRC layer connected with welded grid mesh (applied on 10 mm deck plate specimen), as

the initial rigidity is higher in the case of the 12 mm specimen. We can note that the main advantage of the 12 mm specimen is to be less critical in terms of stress σ_D.

6 Conclusions

This test campaign showed the feasability of using cast UHPFRC connected with studs or with wire mesh to bring stiffness to steel deck plate and limit the fatigue stresses. The stress reduction brought by the UHPFRC layer was shown between 30% and 60%, enabling to increase significantly lifetime of the bridge, whereas bituminous concrete layer enables a stress fatigue reduction from about 15 to 20 %, as compared to uncoated deck, or deck with ultra-thin epoxy bituminous topping layer.

Since the UHPFRC layer is not perfectly connected to the deck plate, some local slipping occurs at the interface between the two materials, which creates some non-linearities and causes some cracks at the bottom of UHPFRC under very high load (more severe than characteristic SLS).

Cyclic loadings have shown that no fatigue degradation occurred under fatigue cycles.

Next step for this kind of technical solution is now to be implemented on real bridges. A retrofitting of an existing bridge has been made recently at Illzach (France), with precast UHPFRC thin plates. [15].

References

[1] De Jong, F.B.P., Renovation techniques for fatigue cracked orthotropic steel bridge decks, PhD Thesis, TU Delft, 2006.

[2] Le Quéré C., Projet Orthoplus : ingénierie avancée des dalles orthotropes et de leur revêtement, *Revue Travaux, n° 843*, July/August 2007.

[3] Luangkhot E. et al, Orthoplus - New theoretical and methodological tools for a realistic calculation of the lifetime for orthotropic steel deck bridges, p1341, Eurosteel 2011, Budapest.

[4] Gomes F. et al, Fatigue behaviour of an orthotropic steel bridge deck – benefits of an ultra-high performance fibre reinforced concrete topping layer, p2097, Eurosteel 2011, Budapest.

[5] Braam, R., Kolstein, H., Romeijn, A., Buitelaar, P., « Concrete overlays to improve the fatigue life of movable orthotropic steel bridge », International Orthotropic Bridge Conference, Sacramento, 2008.

[6] AFGC-Sétra : Ultra-high performance Fiber-Reinforced Concretes, Interim Recommendations. Bagneux, France. 2002.

[7] Héritier B. et al, Design of a Specific Bituminous Surfacing for the World's Highest Orthotropic Steel Deck Bridge. Article, Journal of the Transportation Research Record. (2005).

[8] NF EN 1991-2, Eurocode 1, Actions on structures, Part 2: Traffic loads on bridges, March 2004.

[9] Bignonnet A., Carracilli J., Jacob B., Comportement en fatigue des ponts métalliques : application aux dalles orthotropes en acier, ECSC research report n° 7210 KD/317, LCPC, March 1990.

[10] Hobbacher A., Recommendation for fatigue design of welded joints and components, IIW document XIII-1965-03/XV-1127-03, International Institute of Welding, April 2006.

[11] Gomes F., Marchand P. et al : rapports projet ANR Orthoplus, tâche 3C, 2011.

[12] NF EN 1993-1-9, Eurocode 3, Design of steel structures, Part 1-9: fatigue, December 2005.

[13] Kolstein M.H., Fatigue classification of welded joints in orthotropic steel bridge decks, PhD Thesis, TU Delft, 2007.

[14] Dieng L., Remy C., MohammadKhani-Shali S., New numerical approach for assessing the fatigue resistance of the orthotropic steel bridge decks, Eurosteel 2011, Budapest.

[15] Hajar Z., Une cure de jouvence, La voie, Le magazine d'Eiffage Travaux Publics, n°22, septembre 2011. http://www.eiffagetravauxpublics.com/files/etp/la_voie/la_voie_22.pdf.

Application of UHPC for multifunctional road pavements

Benjamin Scheffler, Michael Schmidt
Department of Building Materials and Construction Chemistry, University of Kassel, Germany

Due to the increase of heavy traffic on German roads the serviceability and thus the service life of the pavements is more and more restricted. The challenges of modern road construction are therefore to create more durable pavement structures with prolonged service-life and reduced needs of repair and rehabilitation to be applicable not only for new roads but also allowing for a quick and inexpensive recovery of the load bearing capacity and safety of elder fatigued and damaged structures.
In addition to nowadays rehabilitation methods, a so called "Whitetopping" technique based on thin layers of high- and ultra-high performance concrete (UHPC) was developed. On top of the pavement layer a thin layer of fine grained nano-optimized UHPC is placed allowing for generating a very special surface texture to reduce the emission of tire noise.

Keywords: whitetopping, road construction, high-performance concrete pavement, noise reduction.

1 Introduction

Concrete pavements are always used when a high standard of bearing capacity and durability for road pavements is required. Nevertheless, the lifetime and service properties decrease as a result of the increasing traffic volume, especially on German highways. To take account to these problems it is necessary to develop innovative and cost effective rehabilitation procedures. They should be material-saving, but nevertheless highly loadable and durable.

A method known from the USA is “Whitetopping”. Here asphalt or concrete roads in need of rehabilitation are covered with a 15 to 25 cm thick layer of ordinary concrete. In the latest generation of “ultra-thin-whitetopping”, high- or even ultra-high-performance concrete is applied. Due to the high compressive strength of UHPC of about 150 MPa in compression and – together with steel fibres – of 15 to 35 MPa in bending tension – and due to the improved density of the microstructure durable layers of even less than 15 cm show a sufficient loadbearing capacity. In order to decouple the major requirements – sufficient load bearing characteristics, a high level of grip and low noise emissions - an advanced concrete pavement system is presented. The system consists of two different layers consisting of a combination of coarse grained UHPC and a special, nano-optimized high-performance mortar applied on top allowing for generating a very special surface texture to significantly reduce the emissions of tire noise by up to 5 dB(A).

In a first step the workability of commonly flowable UHPC used for structural elements had to be transformed to a more plastic consistency enabling to place and to sufficiently compact the coarse grained concrete by means of customary slipform pavers. Secondly the mortar of the surface layer was created. To validate the laboratory results and to further optimize the performance, the new whitetopping system was practically applied at test sections.

2 Basic concept

The results that are presented here were collected within a research project which is supported by the Federal Ministry of Education and Research (BMBF). The main aims of this project are on the one hand to deepen the findings of placing pavement layers with high performance concrete that have already been achieved in the previous BASt-study [1]. And on the other hand to transfer this knowledge to the use of ultra-high performance concrete, to answer the question if the method of whitetopping is more long-lasting and therefore more economic and

sustainable. For this purpose a highly dense structured, fibre-reinforced concrete with a compressive strength of about 150 N/mm² was used.

Figure 1 shows the method of whitetopping schematically: rehabilitation of a fatigued road pavement with a continuously reinforced layer of ultra-high performance concrete. This layer consists of an upper top layer with only 10 to 20 millimeter of thickness placed and bonded to a base layer with a height of around 100 to 130 millimeter. The existing substance of the old pavement remains in place and is used as a kind of high-quality base course.

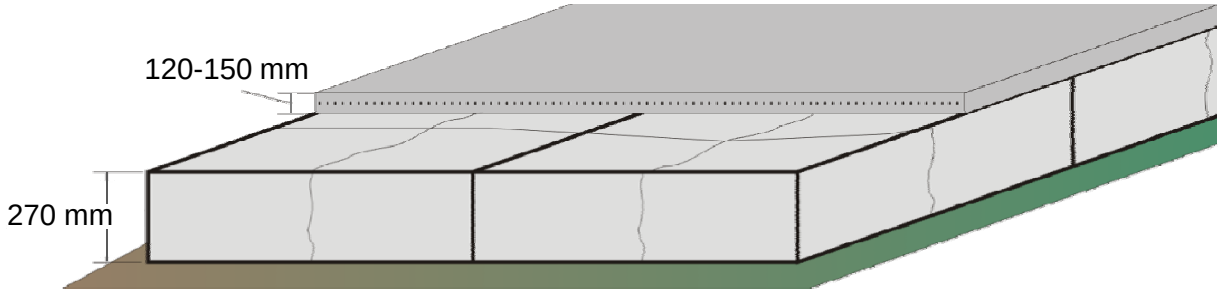

Figure 1: Whitetopping with ultra-high performance concrete.

To conceive the whitetopping-top layer the following steps were processed: at first adequate raw materials were chosen under aspects of low shrinkage, hydration heat, dense micro-structure and paver-related workability. To gain a durable microstructure, free of capillary pores and thus preventing chloride ions from accession the concrete, the packing density was optimized [2]. Subsequently, the amount of binder paste was varied in different levels to adjust it to the amount and the “skeleton” of the coarse grain structure in a way that both - a plastic consistency and a sufficient stability of the fresh concrete - was achieved after casting.

3 Experiments

Analyses on paste mixture

UHPC is usually characterized by a Portland cement content of 600 - 900 kg/m³. This leads to a high development of hydration heat and early and severe shrinkage of the concrete, the danger of undesired cracks rises. A higher demand for reinforcement in order to confine cracks is the consequence. Due to a high amount of superplasticizer and silica fume, UHPC also tends to be of a viscous consistency. The first was to reduce to content of cement and cement paste in the concrete. To reduce the heat development and shrinkage, a CEM III/A with a content of slag sand of 40 % was used. Table 1 gives an overview of the fines.

Table 1: Overview of the fine raw materials with selected characteristics.

raw materials	bulk density [kg/dm³]	max. grain size D_{95} [µm]	RRSB x‘ [µm]	RRSB n [-]	spec. surface [cm²/g]
CEM III/A 42,5 N	3.00	36.2	10.1	1.26	4000
Silica fume (Silicoll P u.)	2.20	0.5	0.3	2.12	198000 [2]
Quartz powder (Millisil W3)	2.65	256.9	84.8	0.92	1100

Besides an extraordinary compressive strength of the concrete, especially its microstructure density is essential. A higher packing density leads to a lower water demand of the grain mixture and together with a low water-binder ratio of only about 0.20, being characteristic for UHPC, a higher microstructure density of the concrete, especially against chlorides, an increased freeze-de-icing resistance (without air entrainer agents and with CEM III/A) and the

bearing capacity of the grain structure rises. The largest potential of optimization for an effective increase of the packing density lies in the holometric adjustment of the reactive and inert fine materials, smaller than 125 µm. Figure 2 shows the behavior of the granular structure by using different grain sizes and contents. In Figure 3 the grading of the fines used is given. In particular, mixtures of significantly different distributions of the fines have to have fewer voids [3].

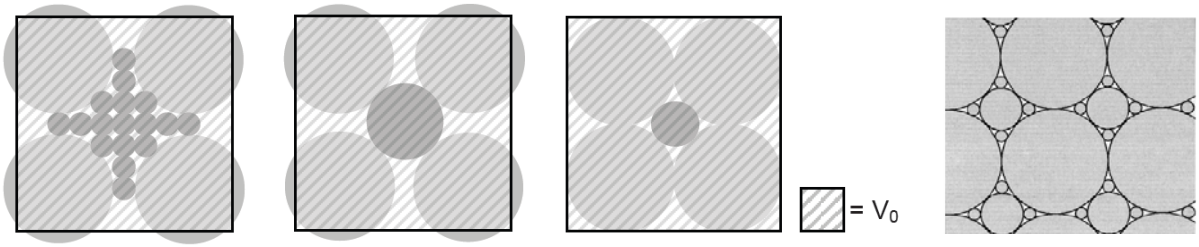

Figure 2: Left: Separation of the grain skeleton by too many fines (left), too large grains (middle) and an ideal filling of cavities (right); Right: optimum graded particle size distribution [4].

The packing density is being optimized by adding appropriate fine filling grains to fill up the pore volume between the respective larger grain fractions. The packing density was determined and theoretically pre-optimized according to a method described by Schwanda [5] and Geisenhanslüke [3]. Results of former examinations have shown that a compromise has to be found between the ideal grain composition for a high packing density of the powder and for a sufficient workability and firmness.

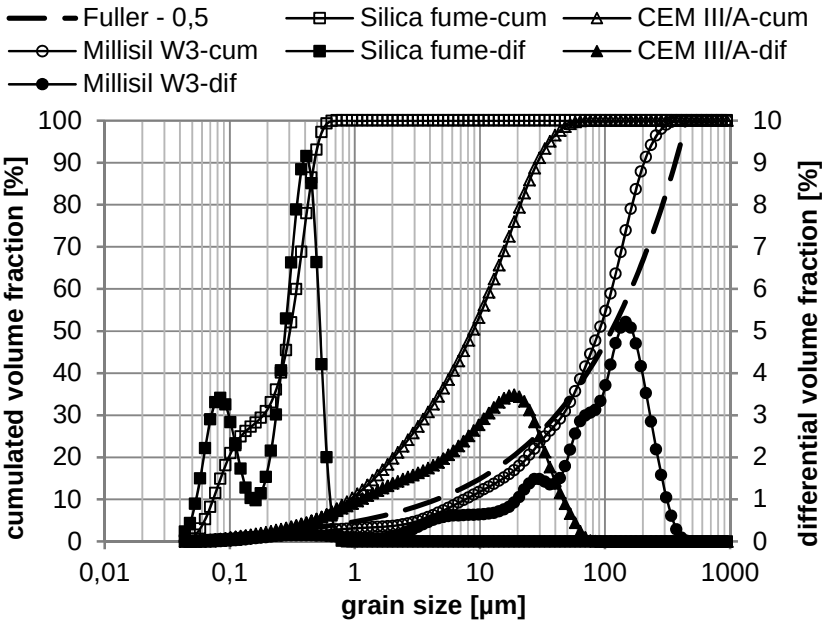

Figure 3: Cumulated und differential grading of the raw materials used.

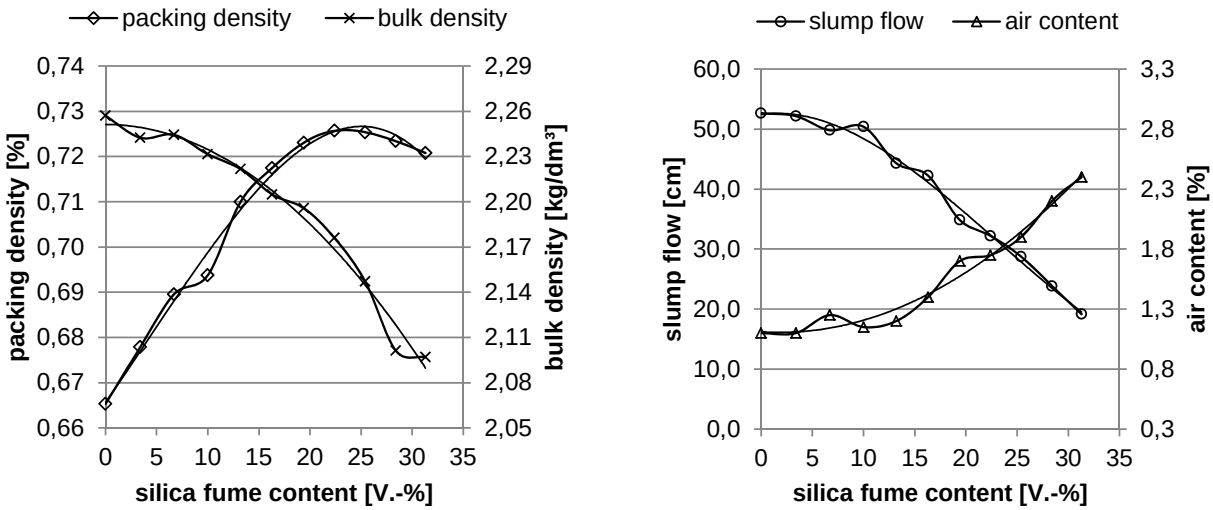

Figure 4: Left: Comparison of theoretical packing density and bulk density depending on the silica fume content; Right: Slump flow compared to air content depending on the silica fume content.

Then the laboratory tests started up with extensive paste examinations to create a flowable and ventilatable paste, to completely surround the coarse grains. The rheology of the paste is to a large extent steered by the kind and pureness silica fume due to its extreme fineness and therefore high specific surface. The amount of silica fume was increased stepwise. The spread level, the bulk density and the air content were determined, the theoretical packing density was calculated. The results are shown in Figure 4. The w-b value (water-binder) was constantly kept at 0.20 and the superplasticizer was dosed with 0.5 % (solid content based on binder b. vol.).

The left side of Figure 4 shows a significant decrease in density of the mixture, mainly due to the different densities of cement (c) and silica fume (ms). The content of silica fume was varied in steps (V.-% of binder (c+ms)). With a value of approx. 15 % the bulk density decreases disproportionately. The cause is also the higher than proportional increase of the air content at a value of 15 %. This effect can also determine the slump, which is relatively stable up to this point. In addition, it can be observed that the theoretical packing density is approaching the maximum. But also the practical measured properties assume that there is a maximum reached at the described point. With a higher content of silica fume, the packing density of the mixture increases. This generates less voids and the water demand of the mixture should decrease. However, at the point of 15 % the slump falls disproportionately - which would mean an increasing water demand. According to the practical examinations a point is reached at which the coarser grain is filled and the processing is just secured.

A silica fume content of 15 % was selected for the following analyses regarding purposes of processing. The procedure for determining the optimal proportion of quartz powder and quartz sand 0.125/0.5 was identical.

Table 2 gives an overview of the carried out measurements of the fresh and hardened fine mortar developed (prisms 40 × 40 × 160 mm³). The specimens were produced without any reinforcement and tested at the age of 28 days, stored under standard conditions.

Table 2: Overview of selected mortar measurements.

test method		**result**
slump flow [6]	[cm]	34
shear moment (yield point)	[Nmm]	0.55
density (fresh) [6]	[kg/dm³]	2.46
air content [6]	[%]	1.4
compressive strength [7]	[MPa]	144.6
flexural tensile strength [7]	[MPa]	11.6
density (hardened) [6]	[kg/dm³]	2.33
porosity (mercury intrusion porosimetry)	[V.-%]	6.5
packing density [4], [5]	[-]	0.80

Analyses on concrete

Figure 5 (left) shows a structural model of the grain skeleton of coarse aggregates with an increasing amount of fine mortar. Phase 1, characterizes the mortar free skeleton of coarse granules. In phase 2, a small volume of mortar covers the aggregates and provides the “concrete” with a certain but small strength due to the significant amount of hollow space still remaining. Regarding the deformation resistance of the freshly compacted “green” concrete and the compressive strength, phase 3 represents the optimum structure. The aggregates are still in direct contact with each other, providing the concrete with a maximum of internal transfer of compression loads. The mortar completely fills the hollow spaces in between the grains thus densifying the structure and providing it with an optimum tensile strength as well. However the workability will still be sub-optimal due to the fact that the deformability of the concrete will be hindered by the friction between the particles especially if – as usually – crushed aggregates are used. Thus phase 4 will be the optimum: A minimum surplus volume of mortar between the grains allows for a sufficient relative movement of the particles when being dynamically compacted and thus an optimum densification of the concrete on site. To ensure a sufficient

devaporation during compaction and a sufficient edge stability of the green concrete the mortar has to show an adequate viscosity and stability as describes before [8].

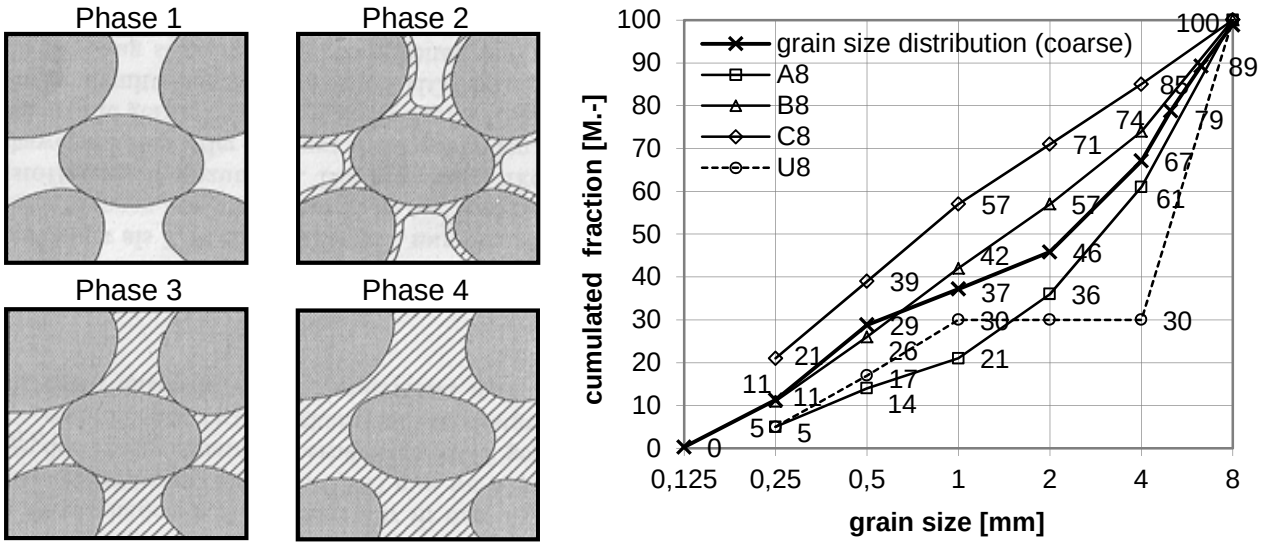

Figure 5: Left: Structural model of a bearing structure filled with fine mortar [8]; Right: Grain size distribution of coarse aggregates used.

At the right side of Figure 5 is shown the well graded and thus favorable grain size distribution of the coarse aggregates used. The amount of fine mortar with a grain size of up to 0.5 mm was increased stepwise. The ratio of paste to aggregates tested referring to the volumetric proportion of fine mortar is shown in Figure 6. For each ratio the compactability was determined according to DIN EN 12350-4 [9] and the optical appearance of the specimen was assessed, as shown in Figure 6. On the vertical axis the consistency classes according to DIN EN 206-1/DIN 1045-2 are shown [10], [11]. As a rule the consistency of ordinary concretes used for road constructions ranges between a stiff (C1) and a plastic (C2) consistency. With an increasing amount of fine mortar the compactability of the concrete steadily decreased.

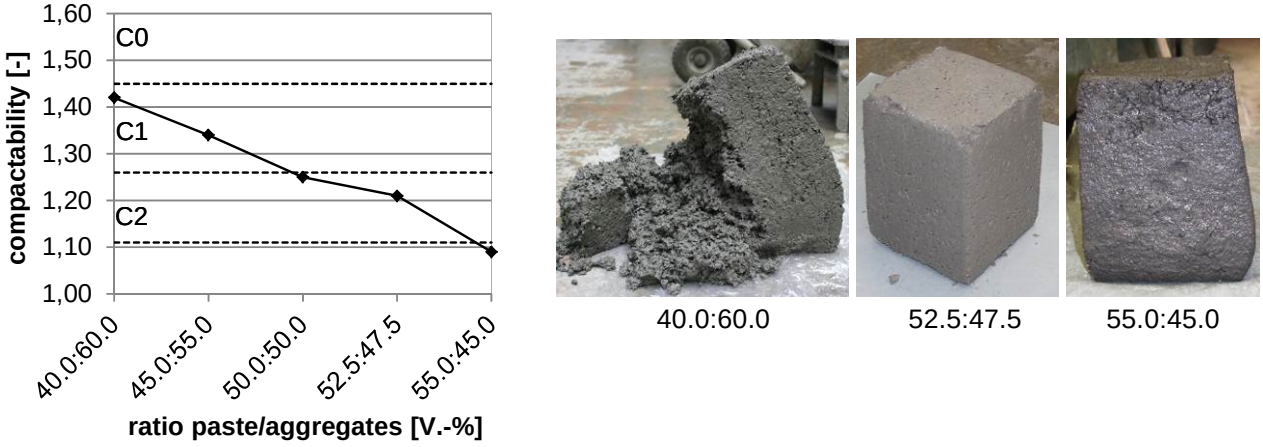

Figure 6: Left: Compactability at different ratios paste/coarse aggregates used; Right: specimens after compactability test.

To select an appropriate ratio, the stability of the compactability specimen after testing and the achieved quality of the surface was evaluated. The green strength of the concrete depending of the amount of fine mortar is shown in Figure 6 (right).

It is clearly seen that the specimen with an amount of 40 % fine mortar only falls apart. There is not enough mortar available to compact the structure, to sufficiently fill the hollows, and to build up sufficient structural cohesion to stabilize the green concrete. On the other hand an amount of 55 % by volume of the specific mortar is already too much. The green concrete specimen deforms plastically, because the mortar steers the deformation behavior and the aggregates are more or less “swimming” in the mortar.

Sufficient green strength is imperative in road construction, because the concrete must not deform after leaving the slipform. According to Figure 6 the requirements were best met at a ratio of 52.5 % b. vol. of fine mortar to 47.5 % b. vol. coarse aggregates.

Table 3: Mixture of the developed UHPC StB[1].

raw materials		**UHPC-StB[1]**
Water	kg/m³	106.0
CEM III/A 42,5 N	kg/m³	444.0
Silica fume (Silicoll P u.)	kg/m³	56.0
Quartz powder (Millisil W3)	kg/m³	34.0
Superplasticizer (PCE based)	kg/m³	8.8 [2]
Quartz sand 0.125/0.5	kg/m³	561.0
Quartz sand 0.6/2	kg/m³	272.0
Basalt 2/5	kg/m³	595.0
Basalt 5/8	kg/m³	487.0
Steel fibre 0,19/13mm (1 V.-%)	kg/m³	78.5
w/(c+ms) - ratio	-	0.22

[1] optimization in progress; [2] 54 % solid

Due to these results it can be assumed that the concrete has an adequate green strength for the following practical tests.

The mixture of the final paver adequate UHPC-StB is given in Table 3. Due to the high amount of coarse aggregate the content of cost intensive ingredients like cement, silica fume, quartz powder and superplasticizer could be significantly reduced compared to flowable UHPC mixes usually used for structural elements (cement 600 to 900 kg/m³ concrete) contributing both to a more cost effective kind of pavement construction and a reduction of the ecologic impact, for further information see [12]. The properties of the hardened UHPC, reinforced with 1 % b. vol. of steel fibres, are given in Table 4.

Table 4: Material properties of the paver adequate UHPC

test method			**result**
compressive strength [13]	7 d		110.0
	28 d	[MPa]	151.0
	56 d		162.0
flexural tensile strength [13]	7 d		13.0
	28 d	[MPa]	16.0
	56 d		17.0
apparent density [13]	28 d	[kg/dm³]	2.66
stat. modulus of elasticity [14]	28 d	[MPa]	60000
porosity [1] (cap. pores)	28 d	[V.-%]	8.0 (< 1.0)
freeze-thaw resistance [13]	28 cyc.	[g]	< 60.0
chloride penetration [15] after	120 h	[mm]	< 1.0
autogeneous shrinkage [2] after	1 d	[‰]	0.07
	60 d		0.19
carbonation depth [2] after	90 d	[mm]	< 3.0

[1] mercury intrusion porosimetry; [2] at 20 °C/65 % r. hum.

The low volume of capillary pores and the corresponding high resistance to chloride diffusion are of special interest to protect the reinforcement from corrosion even if the concrete cover is reduced to further reduce the thickness of the pavement layer.

Practical application

To validate the laboratory tests and to adjust it to the field conditions several field tests were performed as part of the research project. At first it was tested whether and with which equipment the material can be properly mixed. Due to the high content of fine materials UHPC requires a considerable mixing energy to break up agglomerations and to ensure a sufficient

homogeneity of the mixture. On the other hand the mixing time should not be too long to keep the concrete temperature within acceptable limits and to provide the building site with a steady flow of concrete to feed the paver.

The concrete was successfully mixed by means of a mobile 5 m3-mixer usually used to mix cement rich early high strength concrete being utilized to repair single concrete pavement slabs. For longer projects a stationary mixing plant provided with a normal pan mixer and additional agitators will be adequate. The concrete was placed and compacted by means of a standard concrete slipform paver as shown in Figure 7 (left). The green concrete was sufficiently compacted and stable in shape. The drill core in Figure 7 (right) demonstrates the final structure rich in coarse aggregates and provided with a minimum amount of compaction pores only.

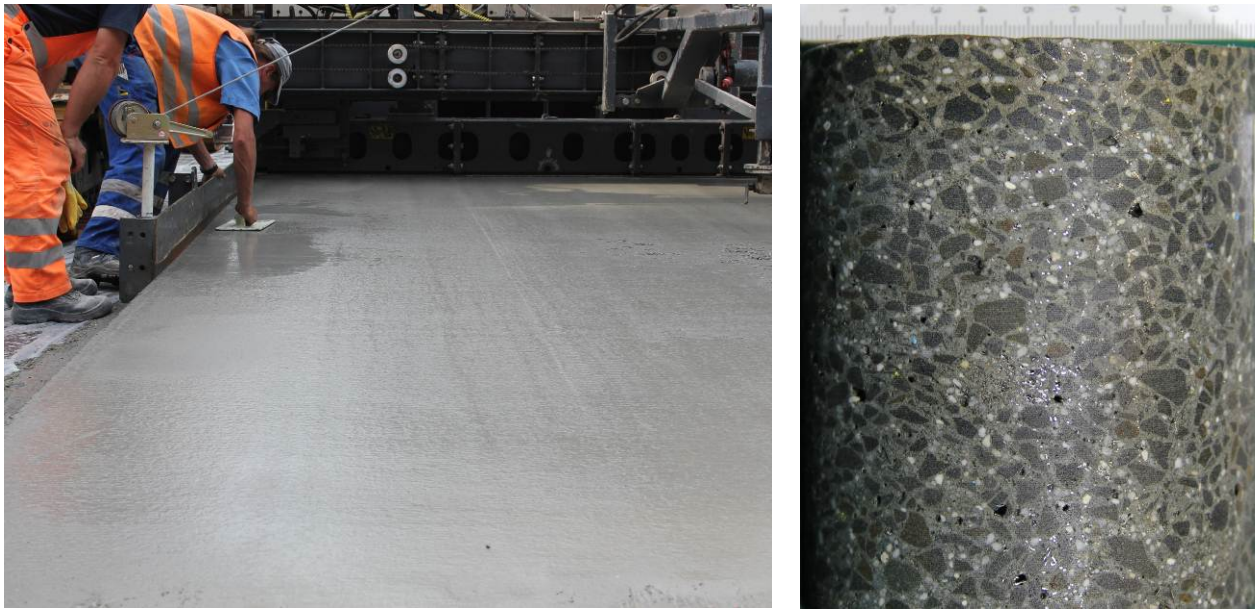

Figure 7: Left: Finishing a layer (10 cm) of UHPC with an customary slipform paver; Right: Removed drill core.

4 Conclusions and outlook

In a comprehensive research project supported by the Federal Ministry of Education and Research (BMBF) the previous experience has been processed and deepened. At the current state of development, the characteristics of the mixture can be described as follows: a low w-b ratio of 0.22, a cement content of approx. 440 kg/m³ (CEM III/A), 1 Vol.-% steel fibres and a high amount of well staggered coarse aggregates. Within these conditions a compressive strength > 150 MPa, a flexural tensile strength of > 15 MPa, a modulus of elasticity of 60000 MPa and a capillary porosity < 1 V.-% was reached. Therefor the material basis for durable and long lasting concrete pavements made of UHPC has been laid.

The workability of the concrete was adjusted to the special needs of conventional concrete slipform pavers. The field tests with customary equipment has shown that it is possible to place, compact and finish thin layers made of aggregate enriched and thus very economic UHPC. The project and research is still under progress.

The aim of further work is to optimize the processing of the mixture under real conditions and the final adaption to the road paver. In particular, the homogeneity of the mixture and the control of hydration heat development are subject to the following test series being in progress.

References

[1] Schmidt, M.; Freisinger-Schadow, S.: Dünne Deckschichten aus Hochleistungs-beton (DDHB), Schlussbericht zum Forschungsvorhaben FE-Nr. 89.0188/2007/AP, Kassel, 2009.

[2] Fehling, E.; Schmidt, M.; Teichmann, T.; Bunje, K.: Entwicklung, Dauerhaftigkeit und Berechnung Ultra-Hochfester Betone (UHPC); Forschungsbericht an die DFG, Schriftenreihe Baustoffe und Massivbau, Heft 1, kassel university press, Kassel, 2005.

[3] Geisenhanslüke, C.: Einfluss der Granulometrie von Feinstoffen auf die Rheologie von Feinstoffleimen, Schriftenreihe Baustoffe und Massivbau, Heft 13, kassel university press, Kassel, 2009.

[4] Gysau, D.: Füllstoffe. Vincentz Net-work, Hannover, 2005.

[5] Schwanda, F.: Der Hohlraumgehalt von Korngemischen, beton 9, Heft 1, S. 12-19, 1959.

[6] DIN EN 1015: Prüfverfahren für Mörtel für Mauerwerk, Beuth Verlag GmbH, Berlin, 2007.

[7] DIN EN 196: Prüfverfahren für Zement, Beuth Verlag GmbH, Berlin, 2005.

[8] Schmidt, M.: Stoffliche und konstruktive Eigenschaften hydraulisch gebundener Tragschichten, Schriftenreihe der Zementindustrie, Heft 51, Düsseldorf, 1991.

[9] DIN EN 12350: Prüfung von Frischbeton, Beuth Verlag GmbH, Berlin, 2009.

[10] DIN EN 206-1:2000: Beton – Teil 1: Festlegung, Eigenschaften, Herstellung und Konformität; Beuth Verlag GmbH, Berlin, 2000.

[11] DIN 1045: Tragwerke aus Beton, Stahlbeton und Spannbeton, Beuth Verlag GmbH, Berlin, 2001.

[12] Schmidt, C.; Schmidt, M.: "Whitetopping" of Asphalt and Concrete Pavements with thin layers of Ultra-High-Performance Concrete - Construction and economic efficiency, Proceedings of Hipermat 2012, Heft 19, kassel university press, Kassel, 2012.

[13] DIN EN 12390: Prüfung von Festbeton, Beuth Verlag GmbH, Berlin, 2000.

[14] DIN 1048: Prüfverfahren für Beton, Beuth Verlag GmbH, Berlin, 1991.

[15] Tang. L.; Nilsson, L.0.: Rapid determination of the chloride diffusivity in concrete by applying an electrical field, in: ACI Materials Journal, pp. 49-53, 1992.

“Whitetopping” of Asphalt and Concrete Pavements with thin layers of Ultra-High-Performance Concrete - Construction and economic efficiency

Cornelia Schmidt[1], Michael Schmidt[2]
1: Department of the State Northrhine-Westfalia, Gelsenkirchen, Germany
2: Institute of Structural Engineering, University of Kassel, Germany

An advanced pavement construction method, named Whitetopping was developed to improve the load-bearing capacity of underdesigned or to reconstruct damaged road pavements. A thin layer of High- or Ultra-High Performance Concrete developed at the University of Kassel reinforced with fibers and/or with steel bars is placed on top of the existing structure. Thus the existing structure must not be removed. It further on acts as a high grade base course. In a comprehensive study the technical and the economical benefits of this kind of high performance Whitetopping are compared with conventional methods to strengthen or to renew pavements by means of layers consisting of unreinforced ordinary concrete.

Keywords: UHPC, Whitetopping, economic efficiency

1 Introduction

The concept of “Whitetopping” is to strengthen or to renew underdesigned or fatigued pavement structures by applying a new concrete layer on top of the existing structure to further on take advantage of its remaining load bearing capacity.

First experiences with “Whitetopping” were made in the USA. Beginning in 1920, unreinforced jointed pavement layers out of conventional concrete were applied on damaged asphalt roads. From 1990 on, there were global developments towards so called “thin” and “ultra-thin” Whitetopping layers with a thickness of less than 150 or of 50-100 mm only respectively, still made of normal strength concrete. In Germany, particularly projects for the maintenance of intra-urban roads, industrial areas and areas of public transport were carried out, in which low-shrink fiber-modified normal- or – in few cases - high performance concretes were used.

Standard construction method for concrete pavements in Germany is a non-reinforced system with doweled transverse contraction joints at intervals of 5 m using conventional concrete of strength class C 30/37 acc. to EN 206. The thickness varies according to the intensity of the traffic between 200 (Traffic class III) und 270 mm (Traffic class SV) [1]. The base courses are bituminous or cement bound, in some cases the concrete slabs are based on layers of unbound gravel.

In some research projects performed at the University of Kassel a Whitetopping system based on specific high- and ultra-high performance pavement concretes was developed which enables to build significantly thinner layers with the same load-bearing capacity

2 High-and Ultra-high performance Pavement concretes

Ultra-High-Performance Concretes are characterized by an extremely dense microstructure free of capillary pores and a steel like compressive strength of 150 – 200 MPa. High performance concretes with a characteristic strength of up to 115 MPa are already part of the European Concrete Standard EN 206.

Different research projects performed at the Department of Building Materials of the University of Kassel together with industrial partners focused on the development of “Pavement adequate” High- and Ultra-High Performance Concretes (UHPC) made of regional raw materials

showing a sufficient workability to be placed and compacted with a conventional concrete road paver. Further requirements were a microstructure being sufficiently resistant to the diffusion of chloride and alkali ions and an improved load-bearing capacity due to a compressive strength of minimum 150 MPa and – reinforced with steel fibers - a bending tensile strength of more then approx. 15 MPa. Based on comprehensive laboratory tests mixtures were developed which already fulfilled all criteria mentioned above. Its applicability was validated by practical tests. In table 1 the optimized mixture for an UHPC pavement concrete adapted from [2] is summarized. The economical considerations presented in chapter 4 are based on this mix.

Table 1: UHPC-Pavement-Mixture.

Materials	**kg/m3 concrete**
Cement CEM III/A 42,5 N	425
Quartz sand 0,125/0,5 mm	536
Quartz sand 0,6/2 mm	285
Basalt 2/8	1132
Microsilica	53
High strength steel fibers 0.2 x 13 mm 1.5 % b. vol.	120
Quartz powder	32
Superplasticizer	6,4
Water	103
Water-cement-ratio	0.25
Water-binder-ratio	0.22

The mixture differs significantly from flowable UHPC mixtures with a maximum grain size of 0.5 to 1 mm so far used for constructive applications [3]. As can be seen from table 1 Basalt aggregate with a grain size of up to 8 mm was incorporated. As a result the volume of cement mortar was reduced from formerly 100% to approx. 45% only. Thus the amount of cost intensive ingredients was significantly reduced as well, the cement content from commonly 750 to 900 kg/m^3 to only 425 kg and the content of microsilica from regularly about 120-200 kg/m^3 to approx. 50 kg only. The average 28-days compressive strength of water cured cylinders 150/300 mm made of HPC was 122 MPa and if made of UHPC 148 MPa. The bending strengths of beams 150x150x700 mm was 13 or 16 MPa respectively.

3 Design of UHPC-Whitetopping Layers

The thickness of the Whitetopping layer being adequate to withstand both the traffic and the temperature induced stresses was calculated stepwise. Firstly the remaining load-bearing capacity of a fatigued concrete pavement was estimated. Based on the axial vertical deformations measured underneath a 60kn wheel load applied on an elder pavement structure consisting of a 260 mm concrete slab and a 100 mm asphalt base course an equivalent modulus of elasticity was iteratively calculated by means of the BISAR pavement design program [4] characterizing the deformation resistance of an assumed elastic-isotropic half-space underneath the later Whitetopping layer. The material parameters chosen are summarized in table 2.

Table 2: Characteristic values for a fatigued pavement structure; wheel load 60 kN.

Structure	**Height [mm]**	**E-mod. [N/mm²]**	**Poisson ratio [-]**	**Vertical deform. [mm]**
Concrete (fatigued)[1)]	260	6.500/ 13.500	0,50	0,130
Asphalt base layer (average)	100	3.500	0,40	0,124
FPL	340	500	0,35	0,123
Base	-	250	0,35	0,107

[1)] Precracked and thus homogenised by means of a falling weight.

Depending on the elastic modulus of the concrete layer the substitute modulus gained for the half-space amounted to min. 780 or max. 1.280 N/mm^2 respectively. With this input value, the minimum thickness of a fiber reinforced Whitetopping layer being necessary to durably withstand both the dynamic traffic loads induced by a 60kN wheel and the stresses being induced by temperature changes [5] was calculated as for a 2-layer system. Based on the material parameters of the UHPC mentioned before the minimum thickness amounted to 120 mm [4] if the static bending tensile strength of the UHPC exceeds 13 N/mm^2 verified by an adequate content of fibers. As a result it can be stated that, theoretically and without consideration of deviations in material and thickness during construction "Whitetopping" layers of HPC or UHP show a sufficient load-bearing capacity already at a thickness of 120 mm. For the economic considerations in chapter 4 however, a "safer" layer thickness of the fiber-reinforced Whitetopping layer for heavily trafficked roads (classification SV) of 150 mm was taken as a basis in order to cover possible imperfections in the execution of the construction work as well as discontinuities in the base layer. Moreover slabs with a thickness of 150 mm or more must no longer be bonded to the supporting layer to withstand the loads.

Due to construction reasons the same thickness of 150 mm was also chosen for an alternative structure consisting of a continuously reinforced layer of HPC or UHPC in combination with fiber reinforcement. According to the results of calculations performed with a three-dimensional nonlinear FE-program on the basis of the algorithms given in the technical rules and standards for the design of structural members of reinforced concrete [6] a thickness of 100 mm would have been sufficient, if the percentage of reinforcement in longitudinal and lateral direction is at least about 6 cm^2/m. For a layer of 150 mm thickness, however, a two-ply bar reinforcement of at least about 8.7 cm^2/m is necessary because of the higher temperature induced stresses. In both cases the max. crack width allowed to prevent from steel corrosion was 0.1 mm and a minimum covering of the reinforcement of only 2.5 cm instead of 5.5 cm for normal concrete was considered due to the fact that no chloride ions will penetrate into the dense concrete and thus the corrosion resistance is ensured.

4 Considerations of economic efficiency of the Whitetopping construction method

After definition of the technical conditions an overall „life cycle“ economic evaluation was executed to compare the Whitetopping system with nowadays reference structures already described in chapter 1. The criteria commonly essential for a financial decision of the road construction authorities and enterprises – primarily the initial investment, the costs of maintenance, capital- and administration cost in relation to service-life - were embedded into a total system in order to receive a valuation method for strategic decisions. Thus further targets for the preservation of the road infra-structure were considered becoming increasingly important, which can be summarized according to [7] as follows:

- *Safety* – avoiding any dangers of accidents due to bad pavement conditions
- *Trafficability* – avoiding inappropriate physical strain of the road users as well as the vehicles and their payload
- *Substance preservation* – economic preservation of the capital assets invested in the traffic areas
- *Environmental sustainability* – minimal conditioned emissions of noise / splash- / spray water and minimal optical disturbance of the street scenery

Furthermore the road user costs like vehicle operating cost, travel expenses and accident costs, have been estimated and implemented for each respective construction method. The social cost and environmental expenses play rather a minor role in this study due to the lack of basic facts.

The reference structures for the economic considerations are based on the German Catalogue of Pavement Structures RStO 01 [1]. For heavy traffic (Design class SV) as shown in figure 1 an unreinforced concrete layer of 260 mm thickness with doweled joints is applied on a 100 mm asphalt base course (ATS) resting on a 340 mm frost protection layer made of gravel. If the concrete pavement has to be renewed due to a loss of its load-bearing capacity and an insufficient rideability (“basic renewal”) either the concrete or both the concrete and the asphalt base layer are being removed and substituted.

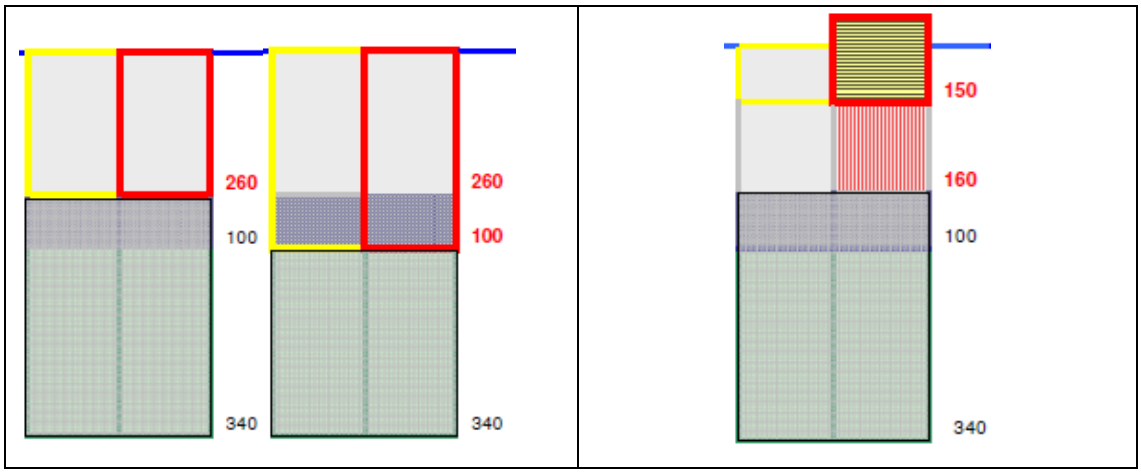

Figure 1: Reference structure and renewal (left) and renewal by Whitetopping (right) in the lifetime of 54 years.

The examination of the Whitetopping construction methods distinguishes between two cases, an 150 mm concrete overlay and a partial replacement of the existing concrete to be applied if even a thickness of only 150 mm may end up in an insufficient clearance gauge below existing bridges. Both structures apply for heavily trafficked roads (classification SV) as well as for a preventive

strengthening of roads showing an insufficient load bearing capacity, e.g. due to an increase of the traffic intensity.

Before the Whitetopping layer is placed the stability and the homogeneity of the existing concrete slabs has to be improved by means of a falling weight. In the course of the partial replacement shown in fig. 1 the existing concrete surface is milled off to a maximum of 100 mm in order not to damage the present dowels and anchors and to preserve their function. According to [8] for economic considerations the lifetime of the reference structure classified SV is 26 years. For the Whitetopping structures a lifetime of 54 years is presumed due to the higher strength and durability of the materials used together with the positive effect of the reinforcement.

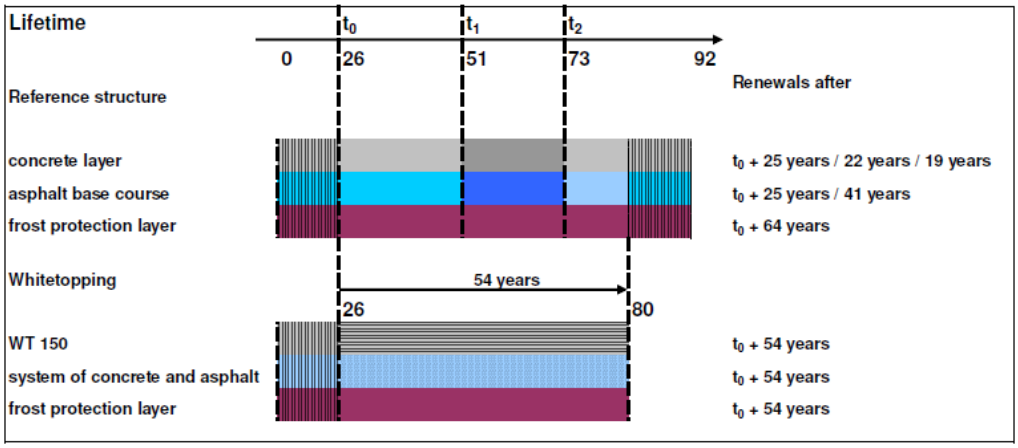

Figure 2: Lifetime according of reference structures according to [8].

At present the phD-study is not yet finished [4]. Up to now the building costs for the initial (t_o) and all further technical actions to be executed in accordance with the time schedule given in fig. 2 and the technical description given in table 3 have been calculated. The so called "net present value method" was used as a dynamic procedure of the capital expenditure budgeting, which is the most commonly used procedure for the evaluation of the profitability of investment projects. This consists of the following items as, among others, explained in [9]:

- Determination of the required rate of return
- Discounting of all payments to be effected after transacted investment at the time of the investment using the required rate of return
- Determination of the capital value
- Examination of the profitability (positive capital value)

The capital value formula for the useful life t_0 until t_n according to [10] is:

$$K_0 = \Sigma \; t_0 \text{ until } t_n \; (E_t - A_t) \times 1/(1+i)t$$

with K_0 = capital value
$(E_t - A_t)$ = cash value of all current payment balances
$1/(1+i)t = (1-i)-t$ = discount factor

All costs are capitalized to the basic year t_0 in fig. C when either the existing concrete slabs are replaced by a new conventional concrete layer or the Whitetopping layer is applied. The payments discounted to the time t_0 are the "cash values", the total of the cash values of all payments within the time of examination is called "capital value". For this calculation exclusively those expenditures are considered which occur within the time of examination of 54 years, so that the common formula of [10] presented above can be modified as follows:

$$KE = \sum_{i>0}^{b} K_i \times 1/qi = \sum_{i>0}^{b} K_i \times (1 + z/100)^{-b}$$

K_s	=Baukosten
K_E	=Kapitalisierte Erneuerungskosten, d.h. Summe aller abgezinster Erneuerungskosten, die n
b	=Bewertunszeitraum
i	=Laufzeitindex für die Jahre des Bewertungszeitraums
q	=Zinsfaktor, Berechnung mit der Formel q=1+z/100
z	=Zinssatz der Kapitalisierung, fest mit 3% anzusetzen
$1/q^b$	$=q^{-b}$ =Abzinsfaktor

The inflation-adjusted rate of interest was determined with 3% according to federal evaluation methods, as defined in [11]. The calculations were performed by means of the computer program “E-Cost” [12]. It disposes of an extensive data base covering a wide range of costs e.g. for building materials and different types of pavement structures. As the data implemented in the program still reflect the price level of 2003 they were adjusted to the level of 2010 by means of the official price index provided by the German Bureau of Statistics. To validate the data used they were compared with the effective costs of real maintenance projects performed in the state of North Rhine-Westphalia. The measures to be taken in a time period of 54 years and the total building costs evaluated for e.g. a highway section of 5 km with a width of 11.5 m are presented in table 3.

Table 3: total building costs.

Time of action acc. to fig. 2	**Conventional renewal**		**Whitetopping**	
		Building Costs [€]		**Building Costs [€]**
t_0	Replacement of original concrete layer	2.840.004,-	150 mm continuously reinforced WT-overlay	2.889.764,-
$t_{1,CR}$ (t_0 + 25)	2nd renewal: concrete and bit. base layer	3.662.304,-	-	-
$t_{2,CR}$ (t_0 + 47)	3rd renewal: concrete layer	2.840.004,-	-	-
$t_{1,WT}$ (t_0 + 54)	-		Renewal WT and bit. base	5.320.899,-
$t_{3,CR}$: (t_0,+66),	Basic renewal of the total structure	4.389.559,-		

The study will be finished completely until the time of the symposium in March 2012. But at present it can already be stated that due to the lower thickness of the UHPC-layer and to the fact that the old concrete must not be removed and despite the higher costs for the UHPC and for the reinforcement the Whitetopping method with UHPC is only marginally more expensive compared with the conventional reference method (unit price per m^2 acc. to table 3 50.25 instead of 49.39 €/m^2). Within the considered period of 54 years after the first measure (t_o in fig. 2) the concrete slabs of the reference structure have to be replaced twice after 25 and 47 years of service, once together with the bituminous base. Opposite to this, for the Whitetopping construction method only the initial application at t_0 has to be considered. The replacement of the WT-concrete layer together with the asphalt base course which becomes necessary after 54

years for the Whitetopping construction method will not be taken into consideration, neither the basic renewal of the reference structure after 66 years of service.

Over a review period of 54 years the total of the capitalized maintenance and renewal costs shows that for the Whitetopping construction method they amount only up to half of the capitalized maintenance cost of the conventional reference method. This means that in the long run, the Whitetopping construction method is economically profitable to verify the requirements of traffic and to ensure the preservation objectives. The availability of the system is increased due to little interference into the traffic flow by construction sites. The significantly longer renewal intervals lead to a further reduction of construction-, traffic congestion- and accident cost. This will be verified by further calculations to be performed in the remainder of the study.

5 Summary and Outlook

An advanced pavement construction method based on Ultra-High-Performance was developed to improve the load bearing capacity of under designed or to reconstruct damaged road pavements. A relatively thin layer of only about 150 mm of High- or Ultra-High-Performance Concrete reinforced with fibers and/or with steel bars is placed on top of the existing structure ("Whitetopping"). Thus the existing substance further on acts as a high grade base course. In a comprehensive economical study it was demonstrated that the initial costs of those high-performance Whitetopping structures are only marginally higher than for the conventional reference method based on thick unreinforced slabs of ordinary concrete. Over a review period of 54 years the capitalized costs for maintenance und renewal are only half of the reference method. Significantly longer renewal intervals lead to a further reduction of construction-, traffic congestion- and accident cost. The results will be presented at the Symposium.

References

[1] RStO 01: Richtlinien für die Standardisierung des Oberbaus, Forschungsgesellschaft für Straßen- und Verkehrswesen, 2001.

[2] Scheffler, B.: Weiterentwicklung von Ultra- Hochfestem Beton (UHPC) hinsichtlich seiner Verwendung im Straßenbau für Verbundvorhaben BMBF, unveröffentlicht, Universität Kassel, 2011

[3] Fehling, E.; Schmidt, M.; Teichmann, T.; Bunje, K.; Bornemann, R.; Middendorf, B.: Entwicklung, Dauerhaftigkeit und Berechnung Ultra-Hochfester Betone UHPC, Schriftenreihe Baustoffe und Massivbau (Structural Materials and Engineering Series) No. 1, Kassel, 2005, ISBN 3-89958-108-3.

[4] Schmidt, C.: Konstruktion und Wirtschaftlichkeit von Whitetopping aus Hochleistungsbeton für Fahrbahnen, Dissertation, unveröffentlicht, Universität Kassel, 2012

[5] Eisenmann, J. und Leykauf, G.: Betonkalender 1987, Band 1, Verlag Ernst & Sohn, 1987

[6] DIN 1045-1: Tragwerke aus Beton, Stahlbeton und Spannbeton Teil 1: Bemessung und Konstruktion Ausgabe Juli 2001 mit Berichtigung Juli 2002. Beuth Verlag, Berlin.

[7] SEP Maerschalk: Anwenderhandbuch zum Inhalt des Pavement Management System (PMS). Hrsg. Der Bundesminister für Verkehr, Berlin 2001.

[8] RPE-Stra 01: Richtlinien für die Planung von Erhaltungsmaßnahmen an Straßenbefestigungen, Forschungsgesellschaft für Straßen- und Verkehrswesen, 2001.

[9] Schmalen; Pechtl: Grundlagen und Probleme der Betriebswirtschaft, 14. Auflage 2009, Verlag Schäffer und Poeschel.

[10]Wöhe; Döring: Einführung in die Allgemeine Betriebswirtschaftslehre, 24. Auflage, Verlag Vahlen, 2010.

[11] EWS-97: Empfehlungen für Wirtschaftlichkeitsuntersuchungen an Straßen, Forschungsgesellschaft für Straßen- und Verkehrswesen, 1997.

[12] Oefner; Krmek; Nußrainer: Kostenermittlung für Erhaltungsmaßnahmen zur Bestimmung der Kosteneingangsgrößen für das PMS, Forschung Straßenbau und Straßenverkehrstechnik, Heft 896, 2004.

Application of Ultra-High Performance Concrete (UHPC) as a Thin-Topped Overlay for Concrete Bridge Decks

Sarah V. Shann[1], Devin K. Harris, Ph.D.[1], Miguel A. Carbonell[1,2], Theresa M. Ahlborn[1]
1: Michigan Technological University, United States of America
2: Polytechnic University of Valencia, Spain

As transportation infrastructure across the globe approaches the end of its service life, new innovative materials and applications are needed to sustainably repair and prevent damage to these structures. The feasibility of using Ultra-High Performance Concrete (UHPC) as a thin-bonded overlay on concrete bridge decks is investigated in this study. Design optimization of the bridge deck overlay system was examined to minimize overlay thickness, dead load, and cure time without sacrificing bond integrity or loss of protective capabilities. This was done with a 3-D finite element model of a simply supported bridge under a notional truck, the HL-93 design truck common to the United States, in the worst case loading position.

Keywords: finite element analysis, bridge decks, overlay, fibre reinforced concrete

1 Introduction

Background

A large percentage of bridges in the United States will be reaching their design service lives in the coming decades and more than 12% are currently listed as structurally deficient [1]. A major contributor to the degradation of a bridge system is the deterioration of the concrete bridge deck, as it is directly exposed to de-icing salts and serves as protection for the underlying superstructure. Concrete bridge deck degradation can be in the form of spalling, delaminations, scaling, freeze-thaw damage, or corrosion of reinforcing steel due to infiltration of chloride ions and moisture [2]. Overlays are often applied to bridge decks to protect the superstructure from these contributors, in addition to providing an improved riding surface and adequate bearing capacity. However, the maintenance, repair, and replacement of these systems are perpetual drains of the financial resources of state and national transportation agencies [2].

Feasibility of Ultra-High Performance Concrete as a Thin-Bonded Overlay

Ultra-high performance concrete (UHPC) has several properties, which make it a viable material for thin-bonded concrete bridge deck overlays. These properties include high compressive strength, post-cracking tensile capacity, high resistance to environmental and chemical attack, negligible permeability, high early strength gain, and its ability to self-consolidate [3]. A summary of representative material characteristics for various curing regimes of UHPC are presented in Table 1, however the numerous characteristics can also be found in literature [3].

Table 1: Selected Material Characteristics of UHPC [3].

	Steam	**Tempered**	**Ambient**
	90°C, 95% RH, 48 hrs	60°C, 95% RH, 14hrs	23°C, 50% RH
28-day compressive strength (MPa)	193	171	126
Direct tension cracking strength (MPa)	9.7-11.0	7.6-9.0	5.5-6.9
Scaling resistance	No scaling	No scaling	No scaling
Abrasion resistance (grams lost)	0.17	0.20	0.73
Freeze-thaw resistance (RDM)	96%	100%	112%
Chloride ion permeability (kg/m^3)	<0.06	<0.06	<0.06

Traditional bridge deck overlays include latex modified concrete, low-slump dense concrete, polymer concretes such as epoxy overlays, microsilica modified concrete, slag modified concrete, and in some cases asphalt concrete with a waterproof membrane [2]. However, each of these overlay types have their own challenges and shortcomings related to cost, cure-time, constructability, bond strength, added dead load, service life, and special equipment or experienced technician requirements [2].

2 Research Objectives

The primary objective of the ongoing research is to evaluate the feasibility of using UHPC as a thin-bonded overlay for concrete bridge decks, both from rehabilitation and new construction perspectives. The focus of the work presented in this paper is centred mainly on optimizing the thickness of the overlay layer to reduce dead load, material quantity and cost, while ensuring the integrity of the interface between the overlay and bridge deck substrate concrete. Other features investigated include the early age strength gain which relates to the opening of a rehabilitated bridge to traffic and turning beds over in a precast environment. This research is primarily a numerical investigation, using the finite element method, which evaluates the influence of overlay thickness and strength gain (or more specifically stiffness) on system behavior. In North America, multiple UHPC formulations have been developed in research environments [4], but the primary commercially available product is Ductal®, manufactured by Lafarge North America. The results presented herein are applicable to the Ductal® brand ultra-high performance concrete.

3 Bond Strength Between UHPC and Normal Strength Concrete

Combinations of optimized overlay thickness and compressive strength (stiffness) were evaluated to ensure that the interfacial stresses between the UHPC overlay and normal strength concrete (NSC) substrate were less than the bond strength determined from past and current research. Research conducted by Harris et al. [5] investigated the bond strength of UHPC to mortar by conducting slant shear tests (ASTM C882-99) and the bond strength of UHPC to NSC through splitting tensile test (modified ASTM C496). This research was used as the bounds on bond capacity. Table 2 presents the bond strength results and coefficient of variation (COV) for different surface preparations. It should be noted that these combined shear-compression and indirect tension tests are not exact characterizations of the bond strength between the two materials; however, they provide a base representation for comparison in this research. Concurrent research is being conducted to further characterize this bond strength and develop failure envelopes based concrete surface preparations.

Table 2: Bond Strength of UHPC to Deck Substrate.

Bond Surface Preparation		Slant Shear Test	Splitting Prism Test
Grooved Surface	[MPa], [COV%]	14.20, 11.7	3.28, 34.0
Smooth Surface	[MPa], [COV%]	11.07, 11.3	5.16, 16.5

4 Early Age Compression Strength

Previous research has shown that the properties of UHPC are highly influenced by curing regime [3,6]. These properties have significant implications for an overlay including strength at the time of opening, stiffness differential between overlay and substrate, and long-term compatibility of the composite deck section. Two cure methods, ambient and pre-steam/tempered steam, were included in this study with an emphasis on the stiffness ratio between the substrate and overlay. In this research, ambient curing (23°C, 50% RH) is applicable to cast-in-place, field applications of UHPC overlay, while a pre-steam treatment

(60°C, 95% RH for 14 hrs followed by ambient cure) is more applicable to the thermal and moisture capabilities of a precast plant. Figure 1 and Figure 2 show representative early age compressive strength gain characteristics of UHPC under ambient and pre-steam treatments, respectively. [6]

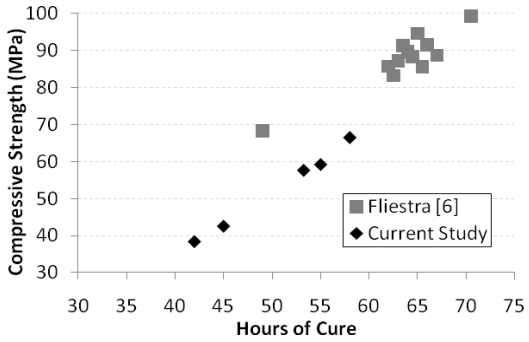

Figure 1: Ambient Cure Early Age Strength Gain.

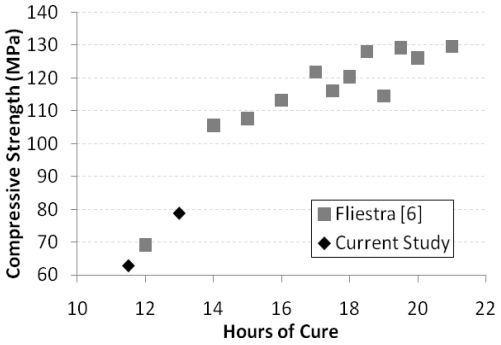

Figure 2: Pre-steam Cure Early Age Strength Gain.

UHPC compressive strengths at 24 hours of pre-steam cure and 48 hours of ambient cure were used in the finite element models described in the next section to highlight the impacts and potential benefits of early traffic openings. The compressive strengths corresponding to these cure times are shown in Table 3; however, the elastic moduli (E) for these compressive strengths at exact cure times were not available, but ranges of E between 29-50 GPa were estimated from available literature [3,5,6]. As Figure 1 and 2 illustrate, bed turnover time and traffic-opening could be shortened even further with satisfactory results.

5 Finite Element Model Methodology

The finite element method was used as the primary basis for optimizing the UHPC overlay thickness. Two model scenarios were used to evaluate the state of stress at the interface between the UHPC overlay and concrete bridge deck. The first model scenario evaluated a basic plate with variable boundary constraints intended to represent the deck region between girders in a slab-girder bridge system, while the second scenario evaluated the system response of a full bridge structure. This staged approach proved to be more computationally cost-effective due to the complexity of modeling a complete bridge. For both model scenarios, the objective was to assess the state of stress parametrically as the overlay characteristics (thickness and stiffness) varied. All models were created using ANSYS 12.0 [7] with the following assumptions: 1) perfect bond between the normal strength concrete deck and UHPC overlay, 2) perfect bond between fibres and matrix, and 3) linear-elastic materials.

Scenario 1 – Plate Model

A plate model representing the interior region between girders was created to evaluate the variation of the interfacial stress under a variety of loading scenarios based on the HL-93 design truck configuration [8]. The plate was modeling using an eight-node, layered shell element (SHELL281), which is a Mindlin-Reissner element formuled for moderately thick plates (thickness:span of 1/10-1/5). A sensitivity analysis for the plate model was conducted to select the appropriate mesh size and density and to validate results with Mindlin-Reisnner plate theory. For all of the plate models, the end restraints were assigned simple support conditions, similar to what would be observed in a simple span bridge (see Figure 3), whereas the edges labeled “girder supports” were evaluated under both simple and fully restrained conditions in order to bound the global system response. In addition to the restraint conditions, the loading configuration was varied to account for the wheel pattern position to cause peak stress

condition (Figure 3). The wheel load(s) of the HL-93 design truck were applied to the plate as a uniform pressure distributed over a patch area of 25.4 cm x 50.8 cm. To prevent the longitudinal boundary conditions from influencing the transverse behaviour, an aspect ratio of 1:3 (width:span) was used in all plate models [9].

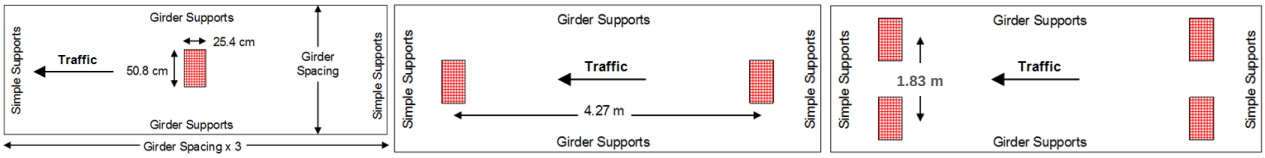

(a) One Tire. *(b) One Tire from Middle and Back Axles .* *(c) Middle and Back Axles.*

Figure 3: Loading Scenarios of Simple Plate Finite Element Model under HL-93 Design Truck.

The plate response was evaluated parametrically by changing features of the design, including overlay thickness, overlay stiffness (represtened as a ratio of the slab stiffness), girder spacing, and restraint conditions. A summary of the parameters considered are presented in Table 3 and a list of the material properties used in this analysis are shown in Table 4.

Table 3: Optimized Parameters.

		1	2	3	4	5	6
Overlay Thickness	mm	6.4	12.7	19.1	25.4	38.1	50.8
Cure Method	-	48 day Ambient	28 day Pre-steam	2 day Ambient	1 day Pre-steam	-	-
Compressive Strength of UHPC	MPa	68	69	119	147	-	-
Girder Spacing	m	1.08	2.44	3.05	-	-	-
Girder Support Conditions	-	Simple	Fixed-Fixed	-	-	-	-

Table 4: Material Properties.

		UHPC	NSC	Steel
Modulus of Elasticity (E)	GPa	29-50	24.9	200
Poisson Ratio (ν)	-	0.22	0.15	0.29

Scenario 2 – Bridge Model

To further evaluate the behavior of UHPC as a thin bonded overlay, the findings from the plate model were incorporated into a model of a complete bridge system under HL-93 truck loading. To eliminate the need for a full design, an existing 40 m long bridge (S11 – Bridge over Stanley Road) was used as the template for the analysis (Figure 4) [10]. A finite element model of the existing design was created and validated using results from field testing that was conducted in the State of Michigan [10]. Similar to the plate model, the full bridge model used layered shell elements (SHELL281) to represent the concrete bridge deck and overlay, whereas the girders and bracing members were modeled using 2-node Timoshenko beam elements (BEAM188) with composite action introduced with constraint elements (MPC184) between the deck and girders.

Variations in the design, including overlay thickness and strength (Table 3), were evaluated parametrically to assess the interfacial stresses; however, no variations in the base bridge design were considered. A summary of the material properties used in the model are presented in Table 4.

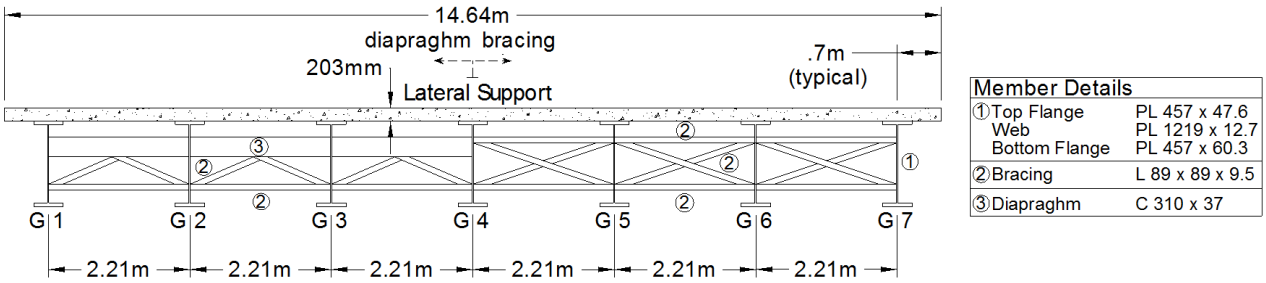

Figure 4: Cross Section of S11 – Bridge over Stanley Road.

6 Results

Interfacial stresses from the finite element analyses were used to evaluate both the plate and bridge model optimizations. These results were compared with measured results from bond tests shown in Table 2, to establish whether the various overlays were acceptable. It is again noted that the results from the bond testing do not provide a direct comparison to the complex state of 3-D stress at the interface, but do provide a basis for comparing the magnitude interface shear and principal tensile stress.

Scenario 1 – Plate Model

A summary of the variation in the interfacial stresses is presented in Figure 5 as a function of the overlay thickness, overlay stiffness, girder spacing, and boundary restraint. It was found that when girders were spaced at 1.08 m, the maximum state of stress was obtained by the loading configuration shown in Figure 3b, while the loading scenario displayed in Figure 3c produced the maximum interfacial stresses for girders spaced at 2.44 m and 3.05 m. Figure 5 displays the results from the controlling loading configuration for each given girder spacing. The maximum transverse shear stress (τ_{yz}) was higher than the longitudinal shear stress (τ_{xz}) in all plate models; therefore (τ_{yz}) is the stress presented in Figure 5. It should be noted that the scales for Figure 5 are consistent except for the principal stress results under fixed girder supports.

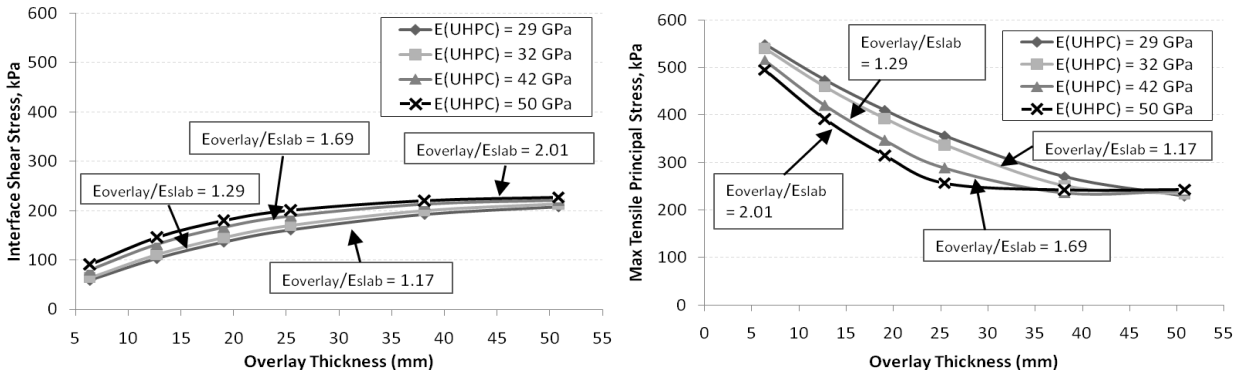

(a) Simple Girder Supports Spaced at 1.08 m.

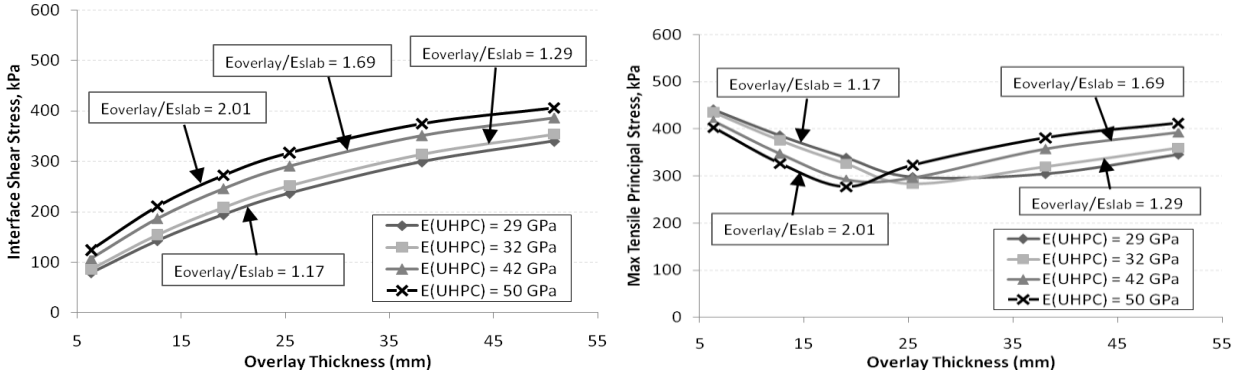

(b) Simple Girder Supports Spaced at 2.44 m.

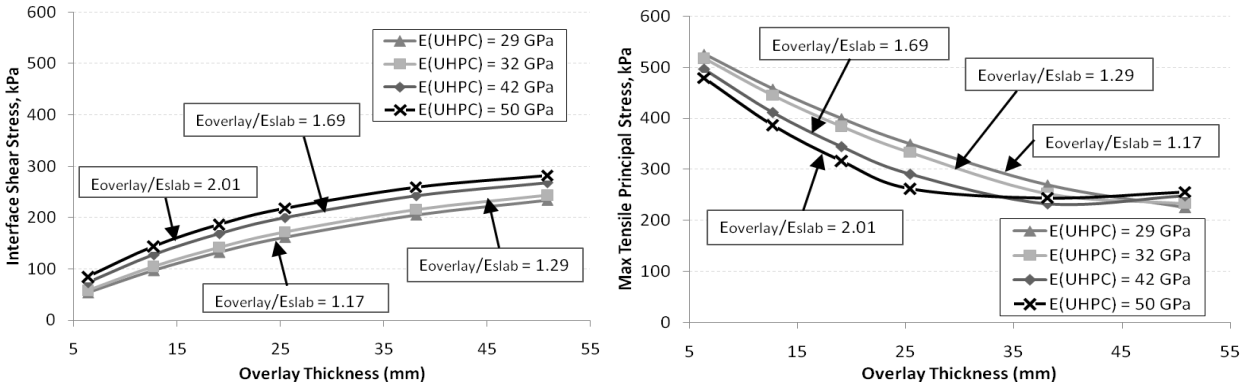

(c) Simple Girder Supports Spaced at 3.05 m.

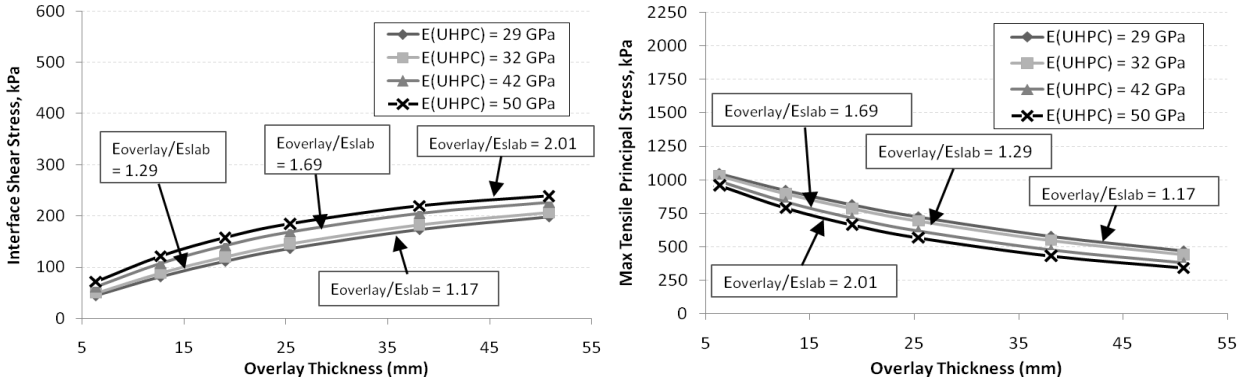

(d) Fixed Girder Supports Spaced at 1.08 m.

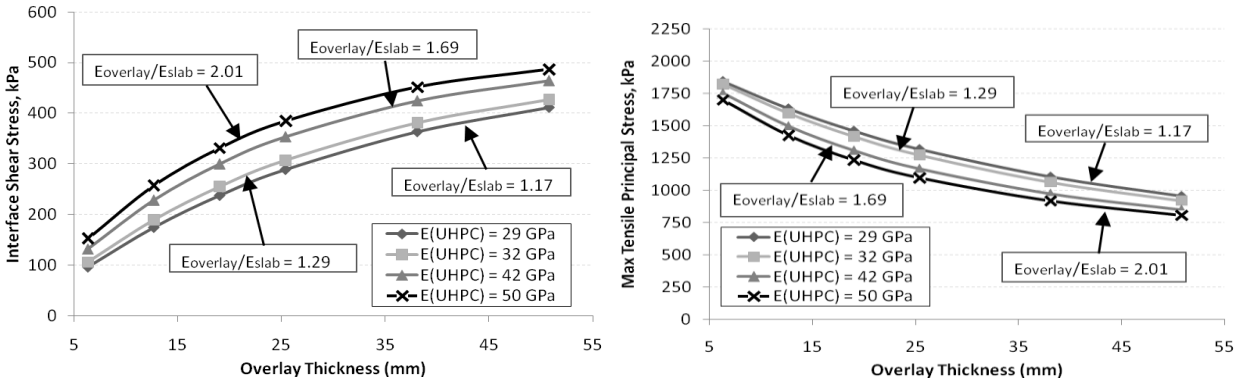

(e) Fixed Girder Supports Spaced at 2.44 m.

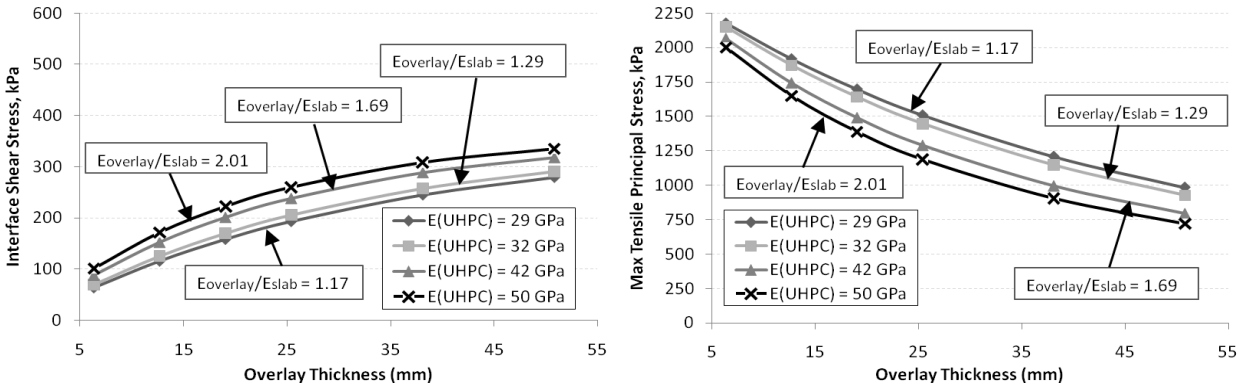

(f) Fixed Girder Supports Spaced 3.05 m.

Figure 5: State of Stress at Bond Interface using Simple Plate Finite Element Model.

In comparison to the bond test results (Table 2), all of the overlay thicknesses result in stresses below those measured. Two distinct trends include an increase in interfacial shear stress and a decrease in principal tensile stress at the interface with an increase in overlay thickness. The trends can be attributed to a shift in the location of the neutral axis, which are further confirmed

with a comparison of overlay stiffness impacts. The interfacial principal tensile stress when girders are modelled as simple supports does deviate from this trend in that it decreases with increased overlay thickness, but then plateaus and begins to increase with increased overlay thickness. This trend is not seen in cases of fixed girder supports, which indicates that the actual interfacial behaviour under a global system is somewhere in between.

Scenario 2 – Bridge Model

Figure 6 displays the variation of interfacial stresses as a function of the overlay thickness and overlay strength (stiffness) using a complete bridge system. It should be noted that while the maximum transverse shear stress (τ_{yz}) was higher than the longitudinal shear stress (τ_{xz}) in all plate models, the opposite was true in this scenario. Therefore, it is the transverse shear stress that is presented in Figure 6.

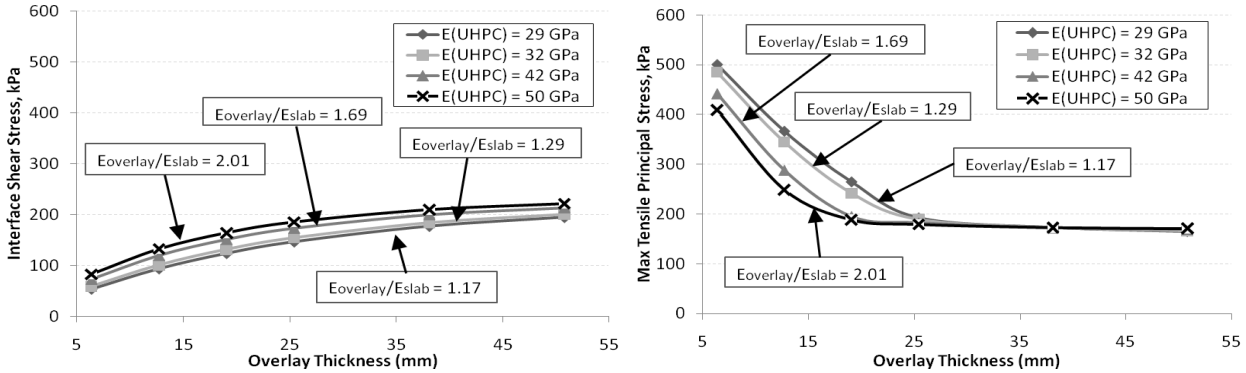

Figure 6: State of Stress at Bond Interface using Complete Bridge System.

As in Scenario 1, there continues to be an increase in interfacial shear stress and a decrease in principal tensile stress at the interface with an increase in overlay thickness. As shown in Figure 6, there is a point in which overlay thickness and stiffness no longer affect the principal tensile stress. For the S11-Bridge, this point occurs around 30 cm, however it would vary for alternative bridge configurations. The general trend of principal tensile stress shown in Figure 6 supports the trends found in Scenario 1, which are extreme bounds to the actual condition. It is again found that the stresses for all overlay thickness are below the results presented in Table 2 indicating that the minimum overlay thickness is mechanically adequate to ensure the integrity of the interfacial bond.

7 Conclusions

UHPC represents a recent advancement in the area of concrete materials due to its enhanced mechanical and durability characteristics. These characteristics make UHPC an ideal solution for a number of applications, including bridge deck overlays where the service-life of existing and new structures may be significantly extended. To evaluate the feasibility of using UHPC as a bridge deck overlay, a study was performed to optimize the appropriate thickness required to ensure integrity of the composite deck system. The optimization study was performed parametrically using the finite element method, coupled with experimental results of the bond and early-age strength in an effort to minimize the overlay thickness. From this investigation, it was determined that the state of stress at the bond interface was significantly lower than the ultimate strength determined by Harris et al [5]. Due to this considerable difference, it is reasonable that traffic could be opened earlier than 48 hours on a cast-in-place overlay or that bed-turnover time of a UHPC overlay on a precast deck panel could take place sooner than 24 hours. An overlay thickness of 6.4 mm on an uncracked concrete bridge deck is recommended

to reduce the initial cost and dead load, while ensuring the integrity of the interfacial bond. However, it is noted that constructability of a UHPC overlay will be the limiting factor in determining the required thickness, not the live load induced state of stress at the interface.

8 Future Work

Further study is needed in the following areas, which include assessing the state of interfacial stress when existing cracks in the deck are present, investigating the effect of autogeneous- and thermal-shrinkage on the interfacial bond, inspecting live load induced stresses at locations of maximum negative bending, addressing variation in early strength gain, analyze the constructability of this application, as well as a relative service-life and expense comparison between traditional overlays and a UHPC overlay.

9 Acknowledgements

The authors would like to thank Lafarge North America for providing the materials (Ductal©) for this research and also the University Transportation Center for Materials in Sustainable Transportation Infrastructure (UTC-MiSTI) at Michigan Tech for supporting the research activities.

References

[1] Federal Highway Administration (FHWA): National Bridge Inventory. Federal Highway Administration, Washington, DC, 2010.

[2] Krauss, P.; Lawler, J.; Steiner, K.: Guidelines for Selection of Bridge Deck Overlays, Sealers, and Treatments. Wiss, Janney, Elstner Associates, Inc., Northbrook, IL, 2009.

[3] Graybeal, B.: Material Property Characterization of Ultra-high Performance Concrete. Federal Highway Administration, Office of Research, Development and Technology, Turner-Fairbank Highway Research Center, McLean, VA, 2006.

[4] Astarlioglu, S.; Krauthammer, T; Felice, C.: State-of-the-art Report on Fiber Reinforced Ultra-high Performance Concrete, Technical Report to DTRA, CIPPS-TR-003-2010. Center for Infrastructure Protection and Physical Security, University of Florida, 2010.

[5] Harris, D.K.; Sarkar, J.; Ahlborn, T.M.: Interface Bond Characterization of Ultra High Performance Concrete Overlays. *Transportation Research Board (TRB) 90th Annual Meeting*, Transportation Research Board, Washington, D.C., 2011.

[6] Flietstra, J.: Creep and Shrinkage Behavior of Ultra High Performance Concrete under Compressive Loading with Varying Curing Regimes. Michigan Technological University, Houghton, MI, 2010.

[7] ANSYS Release 12.0 Documentation, Version 12.0. Swanson Analysis System, Inc., Cannonsburg, PA., 2011.

[8] American Association of State Highway and Transportation Officials (AASHTO). AASHTO LRFD bridge design specifications. American Association of State Highway and Transportation Officials, Washington D.C.

[9] Timoshenko, S; Woinowsky-Krieger, S.: Theory of plates and shells. McGraw-Hill, New York, 1959.

[10] Intelligent Engineering Limited (IE): Stanley Bridge Static and Dynamic Load Test Results, 2004.

Assessment of a UHPFRC based bridge rehabilitation in Slovenia, two years after application

Aljoša Šajna[1], Emmanuel Denarié[2], Vladimir Bras[1]

1: Slovenian National Building and Civil Engineering Institute, ZAG, Ljubljana, Slovenia.
2: Maintenance, Construction et Sécurité des ouvrages, (MCS-ENAC), Ecole Polytechnique Fédérale de Lausanne (EPFL), Suisse.

Within the framework of the EU FP6 Project ARCHES, improved Ultra High Performance Fibre Reinforced Concretes (UHPFRC) based on local components were developed and applied to the rehabilitation of an 36 years old reinforced concrete bridge in Slovenia. Two years after the rehabilitation a thorough visual inspection of the deck and kerbs was performed. During the visual inspection non-destructive and less-destructive on-site tests were performed, such as those to determine the pull-off strength of the UHPFRC layer, as well as its air permeability, the corrosion protection function and the skid resistance were performed. Additionally samples of the UHPFRC were taken for laboratory testing. The paper presents the results of the assessment, including the visual inspection and test results. Based on these, the successfulness of the UHFPRC based rehabilitation is conformed. As a conclusion the benefits and applicability of improved UHPFRC materials are discussed.

Keywords: Ultra High Performance Fibre Reinforced Concretes, bridge rehabilitation, assessment

1 Introduction

Within the framework of the EU FP6 Project ARCHES, improved Ultra High Performance Fibre Reinforced Concretes (UHPFRC) based on local components were developed and applied to the rehabilitation of a 36-year-old bridge, which is located in the Soča river valley in NW Slovenia (Figure 1a). The complete deck of this 65 m long bridge was covered by an UHPFRC overlay with a thickness of 2.5 – 3 cm. In order to perform this work successfully, various problems had to be solved, including the application of a self-compacting UHPFRC on the 5 % longitudinal slope of the bridge, the insufficient compatibility of local cement and superplasticizer, the satisfactory workability, and the surface finishing requirements set by the owner (ARCHES D14, 0). The new generation UHPFRC materials, developed at MCS/EPFL, are characterized by a significantly lower clinker content, the use of local raw materials for the UHPC matrix, adaptability to surface inclination (vertical, horizontal, inclined), and much lower global warming potential (GWP), (ARCHES D06, 0). There fibrous mix was based on the Cemtec$_{multiscale}$® concept from Rossi, 0. This full scale application confirmed the potential of cast in situ UHPFRC materials for the rehabilitation of bridges and industrial buildings, and their applicability in various countries.

This paper reports on (1) the on-site assessment, two years after the rehabilitation, of the bridge condition and (2) UHPFRC performances (protection, skid resistance, bond to the concrete substrate) both on site and in the laboratory on cores.

2 The Rehabilitation of the Log Čezsoški bridge with UHPFRC

The concept of UHPFRC, as an "everlasting UHPFRC winter coat", for the rehabilitation of structural members was proposed by Brühwiler already in 1999, 0. The use of an UHPFRC layer on bridge superstructure is to be recommended particularly in zones of severe environmental and mechanical loads (exposure classes XD2, XD3), and only where it is doing so. When a UHPFRC layer is used instead of an ordinary waterproofing membrane, this critical steps in the construction process can be eliminated together with the associated mistakes which can occur when such a membrane is used. Bituminous concrete can be applied after only

7 to 8 days of moist curing of the UHPFRC, resulting in a shorter duration of the constructions works and shorter disturbances for users. The construction process also becomes simpler, quicker, and more robust. The concept is well-suited for bridges and can also be implemented in the case of galleries, tunnels, retaining walls and buildings.

a) *b)*

Figure 1: The Log Čezsoški bridge before a), and two years after the application of the UHPFRC layer b).

Since the first on-site application of a UHPFRC during the EU project SAMARIS, in 2004 in Switzerland, various full scale applications on bridges and buildings in Switzerland have shown that UHPFRC technology is mature for cast in-situ rehabilitation applications, using standard equipments (Denarié et al. 0, 0, 0).

In 2009, during the EU project ARCHES, the concept of the rehabilitation of structures with UHPFRC was applied for the first time outside Switzerland. New materials designed predominantly from local components were used for the rehabilitation of a road bridge in Slovenia, 0. The concept of the rehabilitation of the 4.5 m wide and 65 m long bridge built in 1973 was to overlay and protect the full upper face of the bridge deck, footpath and external faces of the kerbs with a 2.5 cm to 3 cm thick layer of UHPFRC. The requirements set by the owner were the durability of the rehabilitation and as short as possible the site occupation, as well as the possibility to walking barefoot on the finished UHPFRC surfaces of the footpaths. The most challenging technical problems for the team involved the ability of the UHPFRC to maintain the longitudinal and transverse slopes of 5 % and 2.5 % respectively, and how to fill properly the formwork, which had a height of more than 50 cm and a gap of 3 cm. The application was successful and rapid (12 m^3 UHPFRC placed in 2 days in July 2009), and it demonstrated at an industrial scale that the newly designed UHPFRC mixes can respond adequately to the difficult challenges of the site, without any increase in rehabilitation costs, but to the great satisfaction of the owner, user and contractor. Since this application, slope tolerances up to 10 % are now possible in fresh state, and by means of simple surfacing techniques it is possible to achieve uniformly textured UHPFRC surfaces on which barefoot walking is possible. It is worth mentioning that the newly designed UHPFRC recipes have a dramatically reduced cement content, which makes them more economical and particularly attractive from an environmental point of view, 0.

3 Assessment of the rehabilitation

Overview

Two years after the rehabilitation of the bridge a thorough inspection of the deck and kerbs was performed. During the visual inspection non-destructive and less-destructive on-site tests, such as those top determine the pull-off strength of the UHPFRC layer, as well as its air permeability,

corrosion protection function, and the skid resistance. Additionally samples of the UHPFRC were taken for laboratory testing, e.g. for its capillary adsorption capacity.

Visual inspection

Two years after the rehabilitation the bridge was thoroughly visually assessed. During the inspection special attention was paid to the details, joints and spots of poorer quality, zones around formwork spacers, outflows, the cold joint between day 1 and day 2 casting, areas with fibres extruding from the surface, repaired zones around spacers etc.

Generally the UHPFRC layer was found to be in very good condition. Compared to the inspection performed directly after the completion of the rehabilitation works, no additional flaws or new damages could be seen. The horizontal and vertical surfaces, which were well finished using a Controlled Permeability Form liner (CPF), were still in very good shape, Figure 2a. They are still “smooth”, and the "textured" structure of the CPF “printed” on the UHPFRC surface is still undamaged. Almost no traces of corrosion or fibres protruding from the surface were observed in these zones. No new damages, compared to the inspection of 2009, were observed either on the surfaces with protruding fibres, or on the areas around the formwork spacers where UHPFRC had not penetrated properly, on the internal vertical face of the kerbs, and which were refilled with a UHPFRC. Where finishing of the UHPFRC surface by the means of the CPF was of poorer quality, the steel fibres protruding from the UHPC matrix kept corroding, resulting in a red-brownish colour, but no spalling of the UHPFRC occurred (Figure 2b). Even on the highly loaded area on the bridge turn, where traces of truck tyres are visible on the kerbs, no damage to the UHPFRC layer was observed. No cracking occurred on the joint between day 1 and day 2 casting, nor did it occur on the corners between the horizontal surface of the footpath and the vertical surfaces of the kerbs. Due to asphalt layer laid on the bridge deck, the joint between the vertical surface of the curb and the bridge deck couldn’t be inspected. The unfilled zones around formwork spacers, repaired using UHPFRC directly after the completion of the rehabilitation works, were inspected by the means of hammering. No problems with adhesion were detected. The areas around the outlets were also in unchanged condition.

Based on the results of the visual inspection it can be concluded that no damage has occurred to the UHPFRC layer since its application and that 80 % of the apparent UHPFRC surfaces are close to the visual rendering shown in Figure 2a.

On site tests

During the visual inspection some non-destructive and less-destructive in situ tests were performed, i.e. air permeability tests, pull-off strength tests, skid resistance tests, and a corrosion rate test.

a) *b)*

Figure 2: UHPFRC surface of excellent a) and poorer quality, with apparent fibres b).

The air permeability tests were performed according to the Torrent method, 0. As two different UHPFRC mixes were used on the bridge, the air permeability of both was measured, the footpath upper surface (locations F1 to F3) being coated by a mix capable of holding a 5 % slope, and on the outer, vertical surface of the kerb (locations C1 to C3) repair by a self-levelling mix. The measuring points were distributed along the whole bridge so that the results cover both casting days, and can be considered as representative. Due to the unevenness of the footpath surface, the micro-location of the tests F1 to F3 needed some attention, in order to ensure the airtightness between the UHPFRC surface and the vacuum chamber of the testing equipment. On the other hand, due to the perfect surface finishing no special attention was needed on the outer surface of the curb. The results are presented in Figure 3.

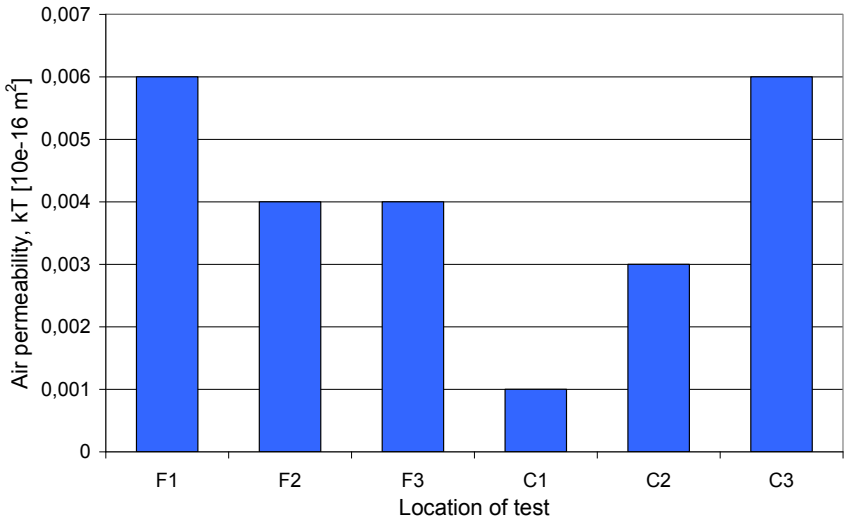

Figure 3: Results of the in situ air permeability tests.

Comparing the air permeability of the two concrete mixes it can be concluded that their air permeability is of the same order of magnitude. Furthermore, the air permeability of the in situ cast UHPFRC two years after application is very close to that of the laboratory made UHPFRC. Both UHPFRC mixes having the permeability of $0{,}004 \times 10^{-16}$ m^2 in average, can according to the quality classes of cover concrete introduced by Torrent et all 0, be classified as “very good”.

The pull-off strength of the UHPFRC was measured at three locations on the upper surface of the footpath. The tests were performed according to EN 1542, 0. The results are presented in Table 1.

Table 1: Pull-off strength of the UHPFRC layer.

	Pull-off strength [kN/m^2]	**Breaking point**
PO1	1.55	90 % contact, 10 % substrate
PO2	2.68	30 % contact, 70 % substrate
PO3	1.46	50 % contact, 50 % substrate

The pull-off strength of the UHPFRC layer is on average 1.9 kN/m^2, which is greater than the 1.5 kN/m^2 required by EN 1504-3 0 for Class R3 structural repair mortars, very close to Class R4 (2 kN/m^2). Taking into consideration that this requirement is for laboratory conditions and for a standard concrete substrate, and that the surface covered by the UHPFRC was only cleaned by water jetting, not water-blasted, the measured pull-off strength fulfil all expectations.

The safety of vehicles and pedestrians crossing the bridge is of major importance. As the road surface of the bridge is covered by an asphalt layer, skid resistance was measured only on the upper surface of the footpath. Locations without fibres protruding from the UHPC matrix were chosen for these measurements. The tests were performed according to EN 13036-4, 0, using the CEN rubber. The four SRT values obtained (70, 73, 75 and 76 respectively) were compared with the requirements to be found in the literature, such as SRT from 55 to 65 for heavy traffic and difficult driving conditions, 0, SRT > 44 – class excellent for external colonnades, walkways and pedestrian crossings, 0, or SRT > 45 for horizontal walking outside surfaces, 0. The UHPFRC surface of the footpath fulfils all these requirements.

The corrosion rate was measured below the UHPFRC layer by the means of embedded corrosion resistance sensors (CRS), patented by Legat et all, 0. Four CRSs were installed on the footpath's horizontal surface, just under the 2.5 cm thick layer of UHPFRC. The measured reduction of the sensor's thickness was 0.24 microns on average over two years, which is very low, and at the limit of the measuring accuracy.

Laboratory tests

During the inspection two cores of UHPFRC with diameters of approximately 50 mm were taken from the footpath's horizontal surface for capillary absorption tests. The core designated CA1 was taken where the UHFRC surface was, based on visual inspection, assumed to be of good quality, whereas the core designated CA2 was taken at a location where fibres were extruding from the concrete surface, representing concrete of a poorer quality, i.e. concrete where more air voids or bunches of steel fibres could be present.

The capillary absorption test results, performed according to EN 13057, 0, are presented in Figure 4. The sorption coefficient values for the cores CS1 and CS2 were 0.064 kg/m^{2}h$^{0.5}$ and 0.059 kg/m^{2}h$^{0.5}$ respectively. The difference between the two sorption coefficients, taking into account that the sample CS1 represented good quality concrete and CS2 bad concrete, is relatively small. Surprisingly, a higher sorption coefficient was measured on sample CS1, which was supposed to represent better concrete. In any case, the sorptivity S of the UHPFRC placed on the bridge footpath is one order of magnitude lower than 0.5 kg/m^{2}h$^{0.5}$, the value required by EN 1504-3 for Class R4 repair products.

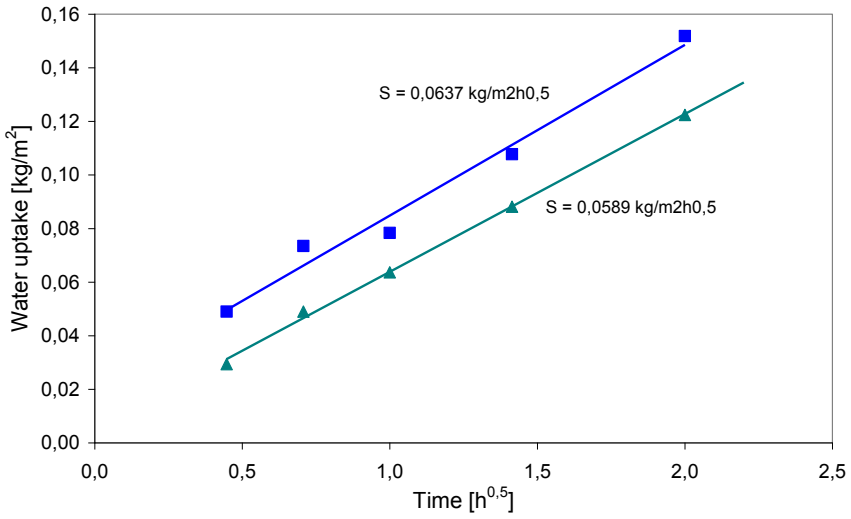

Figure 4: Capillary absorption of the UHPFRC cores.

The two capillary absorption cores (CS1 and CS2) and the three cores from the pull-off tests (PO1 to PO3) were evaluated visually. Additionally the cores PO3 and SC2 were subjected to a computer microtomography (CT) based assessment for homogeneity, i.e. for the presence of air

voids and bunches of steel fibres. The CT scan of core PO3 is presented in Figure 5 (cores are turned up-side-down). As on the core surface the concrete microstructure and especially the steel fibres are damaged during the drilling process, only the inner part of the cylinder, approx. 30 mm in diameter, but of the whole core height, which corresponds to the actual height of the UHPFRC layer, is presented. A horizontal cross-section of the core is presented on the upper left, and in the upper-right and bottom-left figures two perpendicular vertical cross-sections are shown. All three cross-sections were located through the largest air void found in the core (in the middle of the horizontal cross-section), 1.5 mm in diameter. The black spots are air voids, whereas the white colour represents the steel fibres and steel wool, and the grey-coloured part is the UHPC matrix. O the bottom-right figure the distribution of the steel fibres is presented as an 3D image.

From visual and CT assessment of the cores the following observations were made:

- The failure surface is mostly in the substrate, showing good bond between the UHPFRC layer and the substrate. Again it's worth mentioning that the substrate, in this case the footpath's upper surface, was only washed by water jetting, and not water-blasted.
- The homogeneity of the UHPFRC layer can be assessed on the curved surface of the cores. It appears that the steel fibres are well distributed in all of the cores, and that there are no bunches of steel fibres.
- Except in the case of core SC1, no air voids are visible. This is also the case for core SC2, representing the areas of poorer surface quality.
- Comparing the upper core surfaces, a significant difference in the finishing quality can be clearly seen. As already mentioned, the aim of the core sampling was to target both types of surface, i.e. concrete of good and of poorer quality. No damage was visible on the well-finished surfaces. On the surfaces of poorer quality, corrosion of fibres extruding from the cement paste was visible, but no spalling had so far occurred.
- The CT images of the cores confirm the conclusions of the visual inspection. The UHPFRC layer is homogenous, with few small pores visible, and the steel fibres are evenly distributed. Additionally the CT images confirm that all the fibres lie in the direction of the UHPFRC layer's plane, as expected.

4 Conclusions

Two years after application the UHPFRC overlay of the Log Čezsoški bridge was assessed. Based on the results of a thorough visual inspection, as well as in situ and laboratory tests, including pull-off strength, air permeability, capillary absorption and computer tomography based scanning the following conclusions can be drawn:

The concept of the rehabilitation of structures with UHPFRC was applied for the first time outside Switzerland, in Slovenia, with new materials designed predominantly from local components.

Two years after the application the UHPFRC layer was found to be in very good shape; as no damage, cracks or spalling was found during the thorough visual inspection. Areas with poorer concrete finishing, i.e. steel fibres extruding from the UHP cement matrix, continue to corrode, resulting in a red-brownish colouring of the surface, but no spalling of the concrete was recorded. The deficient areas repaired just after the application are fully functional.

The UHPFRC layer has a good bond with the substrate, and its air permeability is extremely low, within the range of an in-lab produced UHPFRC of similar composition. The capillary absorption is very low, even at the spots of (visually) poorer quality. The UHPFRC layer is homogeneous, of low porosity and with uniformly distributed fibres.

Two years after its application, the UHPFRC overlay is in good shape and fully functional.

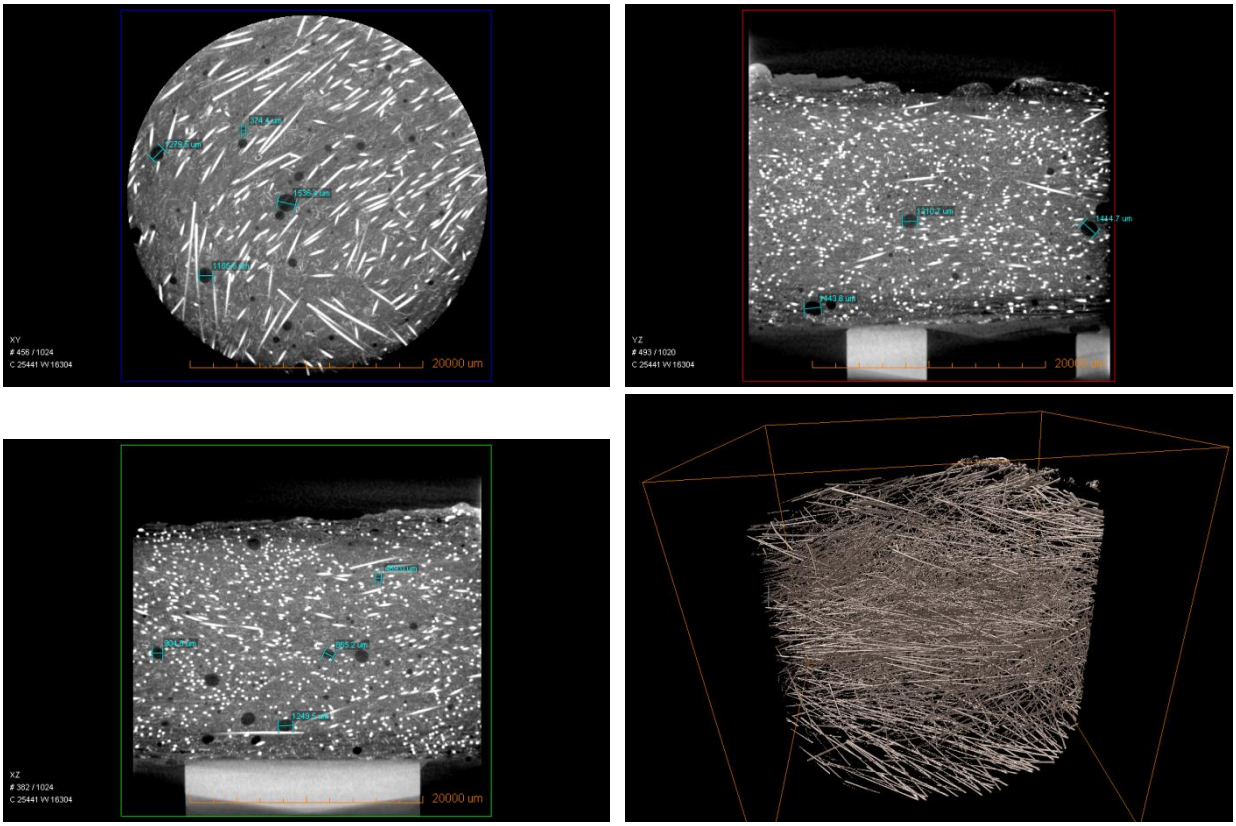

Figure 5: Computer microtomography based image of core PO3; upper-left: horizontal cross-section, upper-right and bottom-left: vertical cross-sections, and bottom-right: 3D image of the steel fibres.

5 Outlook and future possible applications

This successful example of the transfer of technology opens up very promising perspectives for the dissemination of the concepts of rehabilitation of civil engineering infrastructure not only in CEEC and New Member States (NMS), but also in practically any country.

The new generation UHPFRC materials, developed at MCS/EPFL, are characterized by a significantly lower cement content, the use of local raw materials for the UHPC matrix, adaptability to surface inclination (vertical, horizontal, inclined) and much lower global warming potential (GWP). This makes the family of UHPFRC materials cheaper, more easily adaptable to local materials and geometry challenges, more sustainable, and thus more competitive with other products for the protection and repair of concrete structures of both the infrastructure and buildings.

Nevertheless, when it is planned that UHPFRC will be used, the following concept shall be kept in mind: UHPFRC where is worth using it.

6 Acknowledgements

The ARCHES project was funded by the 6th Framework research Program from the European community. The support of the scientific and technical "UHPFRC teams" of EPFL, ZAG, LCPC, Salonit, and TKK is gratefully acknowledged. Special thanks go to the Log Čezsoški bridge owner: Municipality of Bovec and the Mayor Mr. D. Krivec, the Primorje Company and the designer Mr. B. Ipavec, the contractor CPG Nova Gorica and its director J. Brecelj for their trust and support.

References

[1] Denarié E.; Habert G.; Šajna A.: “Recommendations for the use of UHPFRC in composite structural members – rehabilitation Log Čezsoški bridge”. Deliverable ARCHES D14, http://arches.fehrl.org, 2009.

[2] Denarié E.: “Recommendations for the tailoring of UHPFRC recipes for rehabilitation”, Deliverable ARCHES D06, http://arches.fehrl.org, 2009.

[3] Rossi, P.; Arca, A.; Parant, E.; Fakhri, P.: “Bending and compressive behaviours of a new cement composite", Cement and Concrete Research, 35, 2005, pp. 27 – 33.

[4] Brühwiler E.; Denarié E.: Rehabilitation of concrete structures using Ultra-High Performance Fibre Reinforced Concrete, in Proceedings UHPC-2008: The Second International Symposium on Ultra High Performance Concrete, March 05 - 07, 2008, Kassel, Germany, Kassel University Press, pp. 895-902.

[5] Denarié, E.; Brühwiler, E.: Structural rehabilitations with Ultra High Performance Fibre Reinforced Concretes, International Journal for Restoration of Buildings and Monuments, Aedificatio, Vol. 12, No. 5 and 6, 453-467.

[6] Denarié, E. et al.: Full scale application of UHPFRC for the rehabilitation of bridges – from the lab to the field, deliverable SAMARIS D22. http://samaris.zag.si/, 2006.

[7] Denarié, E. et al. Guidance for the use of UHPFRC for rehabilitation of concrete highway structures, deliverable SAMARIS D25b http://samaris.zag.si/, 2006.

[8] ŠAJNA, A; STRUPI-ŠUPUT, J.; DENARIE, E.; BRÜHWILER, E.; HABERT, G.: ROSSI, P.; REŠČIČ, L.; WIERZBICKI, T.: Composite UHPFRC-concrete construction for rehabilitation - most recent advances and applications. V: FRANGOPOL, Dan M. (Eds.). Bridge maintenance, safety and management and life-cycle optimization: proceedings of the Fifth International conference on bridge maintenance, safety and management, Philadelphia, Pennsylvania, USA, 11-15 July 2010. Boca Raton [etc.]: CRC Press, cop. 2010, pp. 445-446.

[9] SIA 262/1 Schweizer Norm, Betonbau – Ergänzende Festlegungen, 2003.

[10] Torrent, R.J.; Frenzer, G.: The Permeability of Cover concrete. Permeability Tester Torrent, Operating Instructions, Proceq.

[11] EN 1542 Products and systems for the protection and repair of concrete structures - Test methods - Measurement of bond strength by pull-off, 1999.

[12] EN 1504-3 Products and systems for the protection and repair of concrete structures - Definitions, requirements, quality control and evaluation of conformity - Part 3: Structural and non-structural repair, 2005.

[13] EN 13036-4 Road and airfield surface characteristics - Test methods - Part 4: Method for measurement of slip/skid resistance of a surface - The pendulum test, 2004.

[14] TSC 06.620 Slovenian Technical Specification for Roads, 2003.

[15] Australian Standard HB 197: An Introductory Guide to the Slip Resistance of Pedestrian Surface Materials, 1999.

[16] SIST EN 13670/A101: Execution of concrete structures - National Annex, 2010.

[17] LEGAT, A.; KUHAR, V.;: Sensor, device and procedure for corrosion rate evaluation of steel rebar in concrete structures: patent SI 22559 A, 2008.

[18] EN 13057, Products and systems for the protection and repair of concrete structures - Test methods - Determination of resistance of capillary absorption, 2002.

Structural Health Monitoring of the Gaertnerplatz Bridge over the Fulda River in Kassel Based on Vibration Test Data and Stochastic Model Updating

Michael Link, Matthias Weiland
Institute of Structural Mechanics, University of Kassel, Germany

For structural health monitoring purposes model updating techniques are utilized for relating experimentally observed changes of the modal data (natural frequencies and mode shapes) to the changes of the physical parameters of a Finite Element model, e.g. the bending stiffness of a beam element. Such changes should indicate any significant deviation of the healthy state from the actual state of the monitored structure. Some results are reported from an application to the Gaertnerplatz Bridge in Kassel where the experimental modal data are continuously measured in the framework of a structural health monitoring project. In the contribution an extension of the classical model updating technique is presented. The extension addresses the assumption that the Finite Element modelling parameters as well as the test data are no longer treated as deterministic but as band limited stochastic variables.

Keywords: structural health monitoring, damage detection, model updating, system identification

1 Introduction

Structural monitoring of the Gaertnerplatz Bridge over the Fulda river in Kassel is aimed at evaluating the structural performance and safety. Modal data (natural frequencies and mode shapes) extracted from the dynamic bridge response due to *ambient* excitation (caused for example by pedestrians, bikers and off-bridge traffic) are used as indicators of changes of the structural performance. These data have been collected continuously since completion of the bridge construction in the year 2007 (about 500 modal data sets per year).

The construction of the Gaertnerplatz Bridge in Kassel is characterised by the first time application of Ultra High Performance Concrete (UHPC) for bridges of this size and by the application of adhesive bonded connections between the UHPC parts of the bridge, ref.[1]. Figure 1 shows a photo of the bridge shortly before it was opened together with the bridge design.

Before the continuous monitoring measurements were started experimental modal data (eigenfrequencies and mode shapes) were measured using *artificial* impact hammer excitation. It is well known that low frequency vibration test data or static response data are not very well suited for detecting and quantifying localized small size damage. Exploitable results can only be expected if high spatial resolution of the response data is available. For the Gaertnerplatz Bridge relatively high resolution modal data were obtained from the pre-monitoring test, 13 natural frequencies and mode shapes measured at 96 locations over the length of the bridge. The pre- monitoring modal test was performed by artificial impact excitation using an impact hammer instrumented by a force sensor. An impression of the impact testing is given in figure 2. The impacts were applied at the 96 locations shown in the figure. For each impact the acceleration response was measured simultaneously at 5 reference locations. These data permitted to acquire 96 frequency response functions (FRF) for each reference. The modal data (eigenfrequencies, mode shapes and modal damping values) were extracted from these FRFs for each reference using our in-house experimental modal analysis code code ISSPA [2]. From these pre-monitoring tests the reference modal data of the healthy structure were extracted. The results of these test were reported in ref.[3].

Only those modal data measured continuously from ambient excitation were retained for further evaluation which showed a strong correlation to the reference modal data coming from the pre-monitoring test. The reference modal data of the pre- monitoring test were also used to establish a reference Finite Element model calibrated to the pre- monitoring test data by computational model updating techniques as also described in ref.[3].

Figure 1(a): Gartnerplatz bridge over the Fulda river in Kassel shortly after completion of the construction

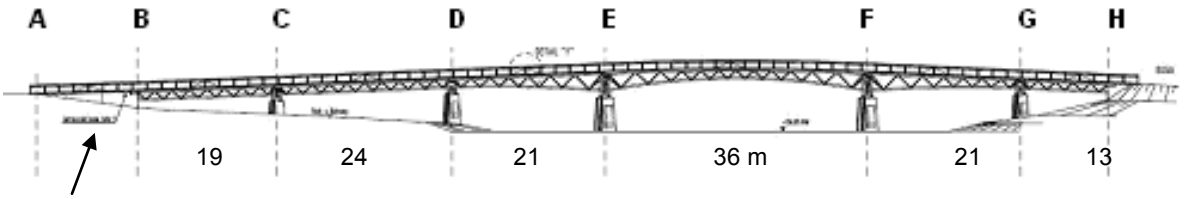

Small room in abutment for data acqusition system and internet connection1

Figure 1(b): Bridge design [1].

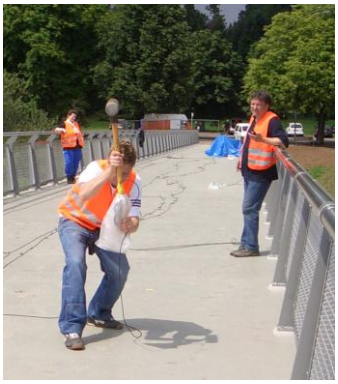

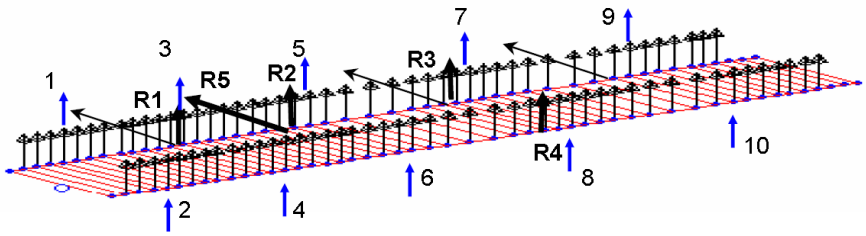

Figure 2: Impact hammer testing applied at 96 impact locations on the bridge deck using 5 reference sensors R1- R5. 10 DOFs (blue) retained for monitoring test

The Finite Element model shown in figure 3 is composed of about 200 plane shell elements for the bridge deck and the abutments and 650 beam elements for the truss and the inner piers resulting in about 3500 DOFs. Special attention was given to the adhesive bonded connection of the UHPC cord and the deck and the eccentric connections between deck and cord and cord

and truss members shown in figure 4. The bonded connection was modelled with special shear elements. The shear modulus of these elements represent important monitoring parameters.

We will present in the following the concept and some results of a structural health monitoring (SHM) procedure which is based on *continuously measured modal data (called monitoring data in the following)* taking account of the effect of unavoidable, natural variations of these data with time which might be caused by temperature and other environmental effects but not by structural damage. It is the key challenge of all vibration based SHM procedures to distinguish the natural variations of the modal data from those changes which might indicate the onset of structural degradation.

This concept leads to a set of signature parameters of the healthy structure, which might be the result of monitoring the state of the bridge over typically one year. These signature parameters are obtained from adjusting preselected characteristic parameters of the Finite Element model to the continuously measured modal data using *interval parameter identification* techniques. With this innovative technique it is not only possible to identify the mean values of the signature parameters but also their upper und lower bounds calculated from the standard deviations of the monitored modal data. It should be noted that in practice the signature parameters do not only reflect the structural properties due to damage but also due to other modelling uncertainties which makes it more difficult to distinguish the damage effects from the modelling uncertainties.

It is expected that the signature parameters of the actual monitoring state which exhibit significant deviation of the healthy state parameters shall indicate the onset of structural degradation. This would initiate another modal test and subsequent updating of the initial reference model to be used to assess the type and the severity of the degradation.

In addition to dynamic data static strain and displacement data and also physical data like temperature and humidity are also used for monitoring permitting to relate the experimental modal data to environmental conditions and to directly monitor the state of the adhesive bonded connections.

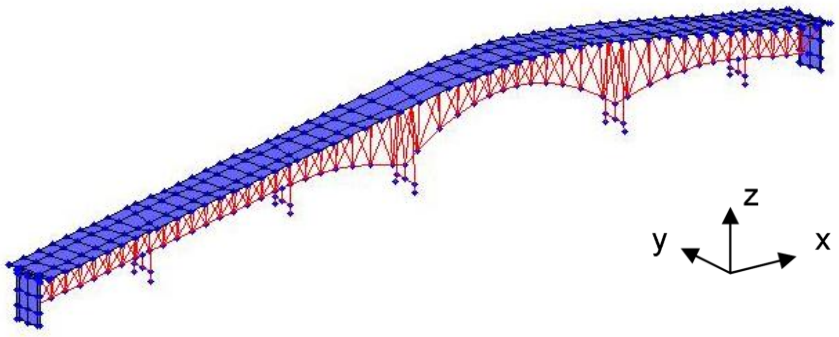

Figure 3: Finite Element model.

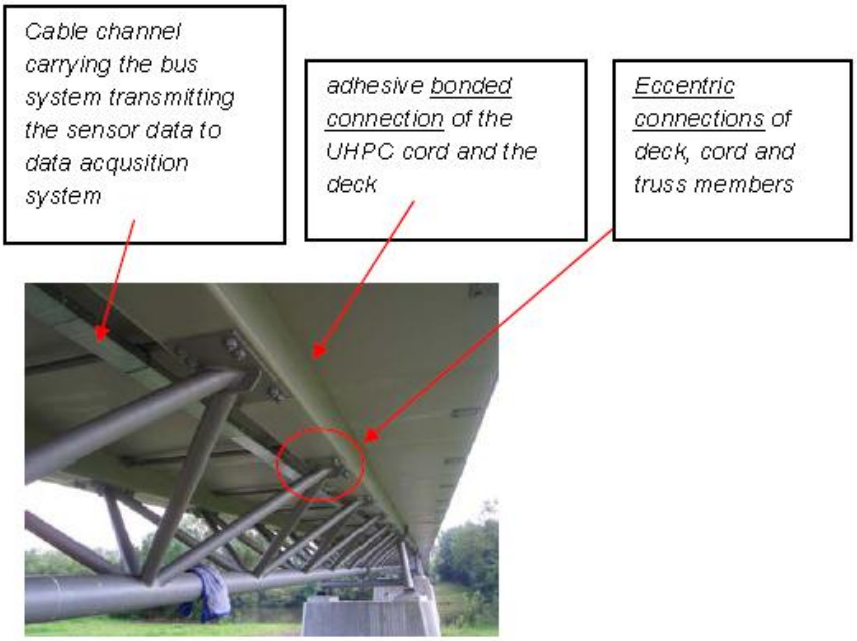

Figure 4: View on the bridge underside

2 Adjusting Finite Element (FE) model parameters to experimental test data by computational model updating

The reference FE- model represents the structure in its initial healthy state and should not only include all the parameters which are likely to change over the time either due to damage or due to changing environmental conditions but also those modelling parameters which must be assumed to be uncertain due to modelling simplifcations.

To find optimal reference values for these parameters our in-house parameter identification software UDATE_X which is based on the theory described in [4]- [6] was applied. This software permits the minimisation of an objective function

$$J = \boldsymbol{\varepsilon}_{\mathrm{w}}^{T} \boldsymbol{\varepsilon}_{\mathrm{w}} \rightarrow \min \tag{1}$$

where the residual vector

$$\boldsymbol{\varepsilon}_{\mathrm{w}} = \boldsymbol{W}_{v}\, \boldsymbol{\varepsilon} = \boldsymbol{v}_{\mathrm{m}} - \boldsymbol{v}(\boldsymbol{p})\,, \tag{2}$$

defines the weighted differences between the measured quantities $\boldsymbol{v}_m$ (in the present application we used eigenfrequencies und mode shapes, $\boldsymbol{W}_v$ denotes a weighting matrix) and their analytical counterparts $\boldsymbol{v(p)}$ which are a function of the parameters $\boldsymbol{p}$ to be updated.

For the bridge application a recently developed extension of the classical model updating technique was applied. The extension addresses the assumption that the Finite Element modelling parameters as well as the test data are no longer treated as deterministic but as band limited stochastic variables.

The technique is based on the inverse sensitivity method where in each iteration step the model parameter changes in vector $\Delta\boldsymbol{p}$ are calculated from the overdetermined equation system

$$(\boldsymbol{G}^{T}\boldsymbol{G} + \boldsymbol{W}_{p}) \cdot \boldsymbol{\Delta p} = \boldsymbol{G}^{T} (z_{exp} - z_{ana}) - w\boldsymbol{W}_{p}\boldsymbol{p} \tag{3}$$

The matrix $\boldsymbol{G} = \partial \boldsymbol{z}_{ana} / \Delta \boldsymbol{p}$ contains the sensitivities of the analytical modal data (natural frequencies and mode shapes contained in vector $\boldsymbol{z}_{ana}$) with respect to the model parameters

$\boldsymbol{p}$ in the preceding iteration step. Vector $\boldsymbol{z}_{exp}$ contains the experimental modal data corresponding to the analytical modal data. $\boldsymbol{W}_p$ represents a weighting matrix which permits to restrain the parameter changes $\boldsymbol{\Delta p}$ whereas the factor *w* permits to restrain the magnitude of the parameters over the iteration steps.

The updating parameters, $\boldsymbol{p} = [\,\boldsymbol{\alpha}\,;\,\boldsymbol{\beta}\,] = [\,\alpha_1 ... \alpha_{nK} \;\; \beta_1 ... \beta_{nM}\,]^T$ (np= nK + nM = number of parameters), are defined as dimensionless factors on selected submatrices, $\boldsymbol{K}_i$ and $\boldsymbol{M}_j$, of the overall stiffness matrix $\boldsymbol{K}$ and the overall mass matrix $\boldsymbol{M}$, so that the updated overall system matrices and parameters can be expressed by

$$\boldsymbol{K}_{up} = \boldsymbol{K}_a + \sum_{i=1}^{nK} \Delta\alpha_i \boldsymbol{K}_i \quad , \quad \boldsymbol{M}_{up} = \boldsymbol{M}_a + \sum_{j=1}^{nM} \Delta\beta_j \boldsymbol{M}_j \tag{4a}$$

The updated parameters are calculated by

$$\boldsymbol{p}_{up} = \boldsymbol{p}_a + \Delta\boldsymbol{p} \quad \text{with} \quad \boldsymbol{p}_a = [\,\boldsymbol{\alpha}_a\,;\boldsymbol{\beta}_a\,] \quad \text{and} \quad \Delta\boldsymbol{p}_a = [\,\Delta\boldsymbol{\alpha}_a\,;\Delta\boldsymbol{\beta}_a\,] \tag{4b}$$

$\boldsymbol{K}_a$ and $\boldsymbol{M}_a$ represent the system matrices and $\boldsymbol{p}_a$ the parameter vector at the actual iteration step.

The numerical method is an elementary application of interval arithmetic which does not need to make an assumption on the type of the probability functions. Instead the experimental data vector $\boldsymbol{z}_{exp}$ on the right hand side of equation (3) above is assumed to represent an interval vector defined by estimated upper and lower bounds of the experimental data.

The solution of the equation system then yields upper and lower bounds of the parameter changes, $\Delta\boldsymbol{p}^u$ and $\Delta\boldsymbol{p}^o$, which are used to calculate the central (mean) values $\Delta\boldsymbol{p}^m = (\,\Delta\boldsymbol{p}^u + \Delta\boldsymbol{p}^o\,)/2$. The central values are used to calculate the sensitivity matrix $\boldsymbol{G}$ and the analytical modal data $\boldsymbol{z}_{ana}$ used in the subsequent iteration step.

After convergence at the end of the iteration the procedure yields the central values of the parameters together with their upper and lower bounds. It should be noted that the width of the parameter bounds which characterizes the parameter uncertainties is not only affected by the experimental data uncertainties but also by the parameter sensitivities.

Finally the results are validated by calculating the analytical modal data from a number of parameter sets which were generated by Monte Carlo simulation within the identified uncertainty bounds. This simulation does not only permit to check if the generated analytical modal data fall within the experimental uncertainty bounds but also to compare the correlation of the experimental frequencies with that of the analytical frequencies.

3 Parameter identification using pre- monitoring modal test data

In ref.[3] we reported about the parameter identification for a FE model which was adjusted to the modal data obtained from the pre- monitoring test with artificial excitation. These data consisted of 13 natural frequencies and the corresponding mode shapes at 96 locations. For monitoring purposes the ambient vibration response was only measured at a subset of 10 of the 96 measurement DOFs shown in figure 2 so that the spatial resolution of the extracted mode shapes was significantly reduced. In addition the evaluation the ambient vibration response was focused on a reduced number of 6 resonance frequencies selected according to the results of

the pre- monitoring modal test. For comparison purposes with the monitoring data of the following years the pre-monitoring modal data set was reduced accordingly and used to generate a reference FE- model based on the reduced pre- monitoring modal data set. Statistical parameter identification was not possible in this case since only one modal data set was available from the pre- monitoring test.

The initial FE- model of the Gaertnerplatz Bridge was used to study the most relevant parameters to be monitored continuously over time. This study led to the selection of the following 9 parameters to be used as indicators for the structural status of the bridge:

P1: shear stiffness parameter assigned to the substructure $\boldsymbol{K}_1$ composed of the bonding elements connecting the deck and the upper cord,
P2: parameter assigned to the bending stiffness of the UHPC cords
P3: the geometrical stiffness parameter for the UHPC cords due to the prestress force
P4 - P6: parameters assigned to the longitudinal, horizontal and vertical stiffness of the pier bearings
P7: parameter for the non- structural mass (resulting from the parapet and the deck coating)
P8 - P9: parameters for the torsional and bending stiffness of the deck.

The comparison of the experimental and analytical eigenfrequencies depicted in table 1 is restricted to only those experimental modes and measurement degrees of freedom (MDOFs) which were used for monitoring purposes as mentioned before, i.e. the modal data present a subset of the full measurement set described in ref.[3].

The comparison reveals quite a satisfactory agreement. The experimental frequencies are in average a bit higher than the initial analytical frequencies with an error between 0,64 and 7,02 %. The modal assurance criterion MAC was used to compare the corresponding mode shapes (MAC = 100 % indicates perfect correlation. The MAC value is calculated from the square of the cosine of the angle between the experimental and the analytical eigenvector). In practical applications any value beyond 80% must be considered as a satisfactory agreement. After computational parameter updating the test/analysis differences of the natural frequencies were reduced significantly (max 0,16 % for the 4th frequency in table 1). An excellent agreement of the fundamental mode no.1 (MAC = 98,5%) can also be observed from the spike plot in figure 5(a) where the measured and analytical eigenvectors are plotted over the ten monitoring sensor locations shown in figure 2 . The correlation is still good for a higher mode like the torsional mode no. 6 with MAC = 87,4% in figure 6(a). The corresponding FE modes are shown in figures 5(b) and 6(b). The good convergence behaviour of the parameter identification over the iteration steps is shown in figure 7. The reference parameters identified in the last iteration step are given in the last row of table 1.

4 Parameter identification using modal data obtained from continuous monitoring

For long term monitoring sensors were installed on the bridge for recording acceleration data from ambient excitation as well as temperatures. The time domain response data are analysed after data decimation based on triggering to specified treshold values, to day time and ambient temperature. The evaluation of these data was focused on a number of resonance peaks selected according to the results of the pre- monitoring modal reference data in table 1.

Continuous recording of this data permitted to correlate the resonance frequencies to ambient temperature.

Table 1: Comparison of modal test data 2007 / analysis

Eigenfrequency number								
1	2	3	4	5	6			
Experimental eigenfrequencies [Hz] from modal test 2007 used for updating								
3.49	5.01	7.32	8.05	9.40	10.92			
Initial analytical eigenfrequencies [Hz] before parameter updating								
3.47	4.94	7.10	7.83	-	10.21			
Initial Prediction error test/analysis [%] before parameter updating								
0.64	1.31	3.13	2.77	-	7.02			
Prediction error test/analysis [%] after parameter updating								
-0.09	0.07	-0.14	0.16	-	0.05			
MAC [%] test/ initial model before parameter updating								
98.3	95.8	97.9	94.9	-	78.2			
MAC [%] after parameter updating								
98.5	96.7	87.6	99.1	-	87.4			
Identified reference parameters								
p1	p2	p3	p4	p5	p6	p7	p8	p9
1.06	0.50	0.43	0.00	-0.04	0.59	-0.52	0.36	-0.15

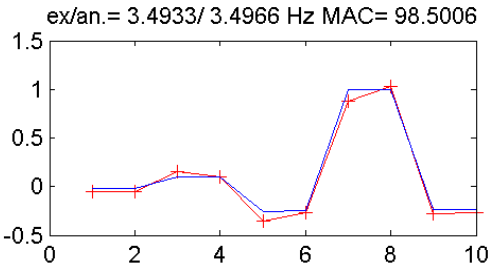

measurement DOFs for monitoring

(a) spike plot of test (+++) and FE mode

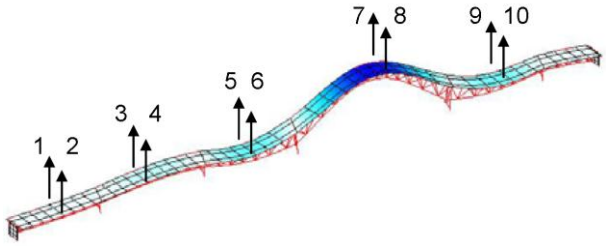

(b) monitoring DOFs on FE model mode

Figure 5: Bending mode no.1.

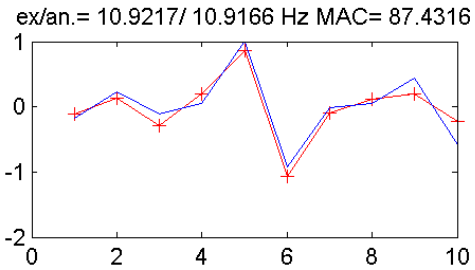

measurement DOFs for monitoring

(a) spike plot of test (+++) and FE mode

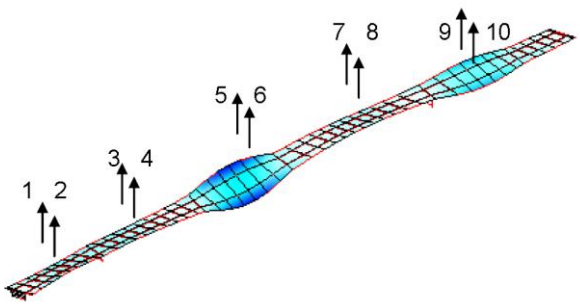

(b) monitoring DOFs on FE model mode

Figure 6: Torsional mode no. 6 .

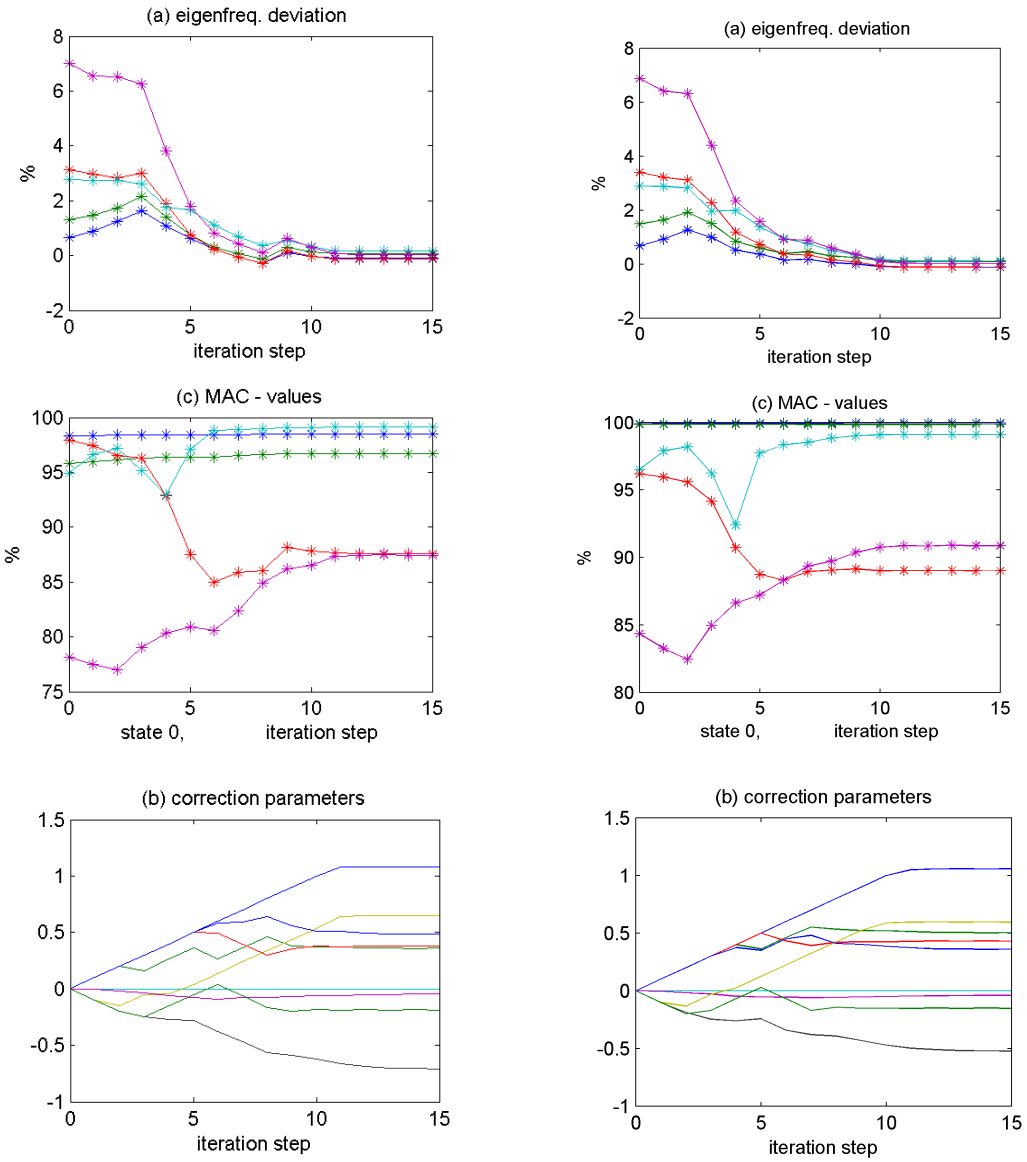

(a) modal test data 2007 *(b) monitoring test data 2008*

Figure 7: Evolution of parameter identification over iteration steps using modal test data 2007(left) and monitoring data 2008 (right).

One of the six monitored natural frequencies is plotted in figure 8 for the years 2008 – 2011 versus the bridge temperature measured below the bridge deck in the center span close to the location of the adhesive bonded connection (plots of the other monitored frequencies look very similar). The data of the years 2009 – 2011 are always plotted on top of the data of the first monitoring year 2008. The data show the systematic decrease of the resonance frequencies with temperature and their variability. In particular it is observed that the data clouds of the years 2008 - 2011 cover the clouds of the reference year 2008 and do not exhibit a systematic or a sudden decrease which is also confirmed by the evolution of the mean values over the 4 years. Also, the standard deviations are very small. Therefore, it can be concluded that no structural degradation of the bridge has happened during the monitoring period. It must be expected that the FE- model parameters identified from the monitoring test data should also reflect this conclusion.

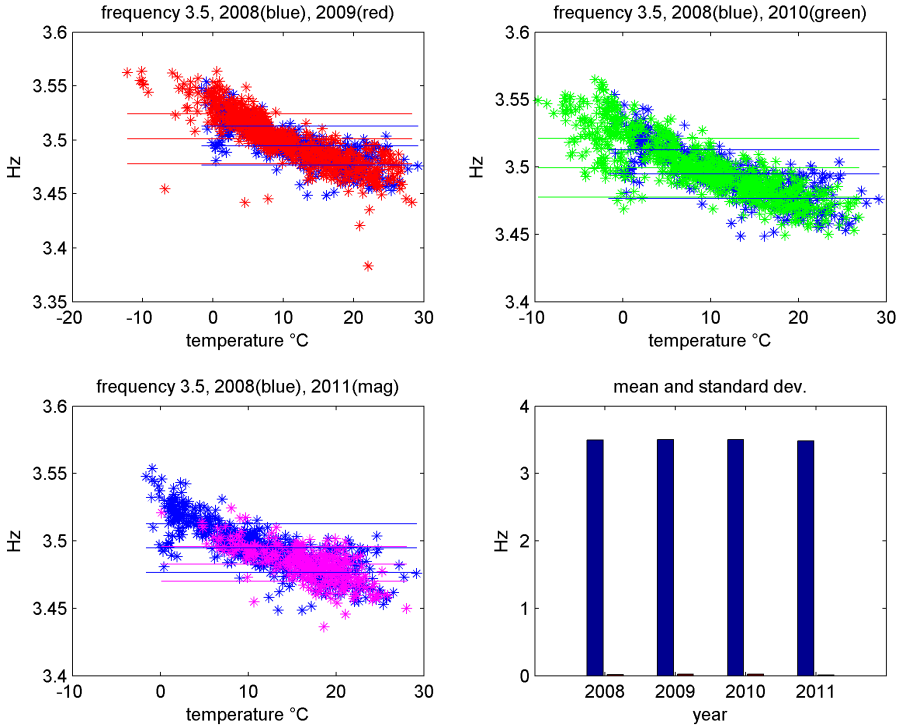

Figure 8: Natural frequency at about 3.5 Hz monitored in the years 2008 – 2011 including mean values and 1σ standard deviations (horizontal lines).

Comparison of FE- predictions and modal data obtained from continuous monitoring

Figure 7(b) shows the evolution of the parameter identification results based on the monitoring data of the year 2008 (see corresponding data clouds plotted in figure 8) in comparison with figure 7(a) where the parameter identification based on the pre-monitoring modal data of the year 2007 is shown. The differences of the identified parameters between the two years are within tolerable limits in view of the differences between the two experimental data sets caused not only by the variability of the 2008 data over the year but also by differences arising from the application of different experimental modal analysis methods used to extract the modal data from the dynamic response due to artificial excitation in 2007 and from ambient excitation over the year 2008.

Figure 10 shows the evolution of the identification for parameters p1 and p3 not only for the mean values (black) but also for the upper values (green) and lower values (red) which is the result of the extended identification technique described before in chapter 2 where we intoduced the mean values and the $\pm 2\sigma$- values of the experimental frequencies and mode shapes. This figure shows an excellent convergence behaviour of the identification procedure. In particular it can be noticed that the magnitude of the parameter bounds can be quite different depending on the magnitude of the parameter sensitivity and of the test data uncertainties. The results for all the parameters at the end of the iteration are shown in figure 11.

Applying the identification for the monitoring data of the years 2009 and 2010 gives an idea of the evolution of the parameters and their upper and lower bounds over the years which is shown in figure 12. The parameter variation is not significant except for parameters p2 (cord stiffness) and p3 (cord prestress force) which exhibit a higher band with and a trend to reduction.

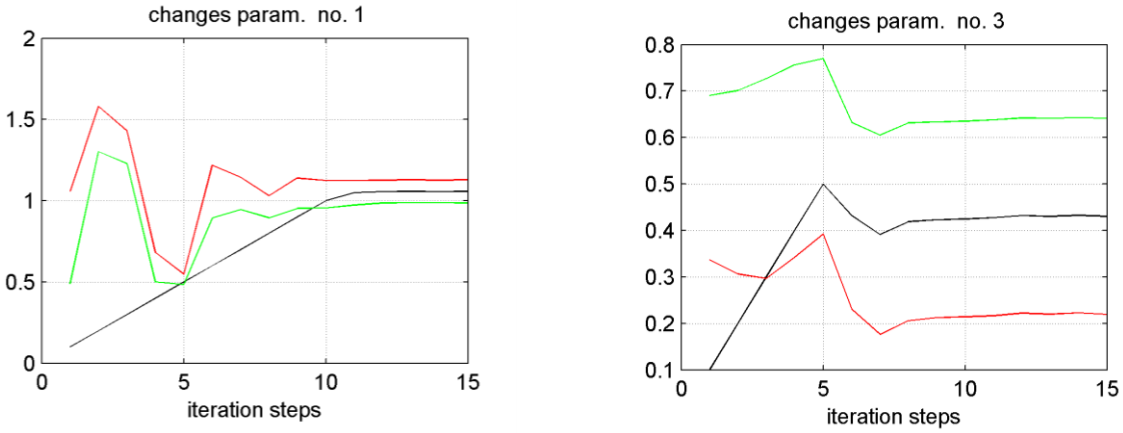

Figure 10: Evolution of parameters p1and p3 including upper and lower parameter bounds over iteration steps using monitoring data 2008.

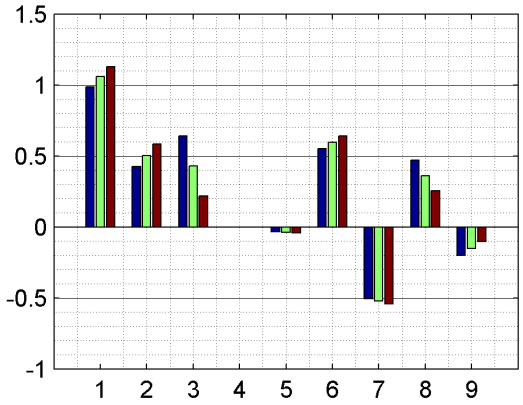

Figure 11: Parameters including parameter intervals at iteration end using monitoring data 2008.

Statistical evaluation of test and analysis data

In order to assess the parameter variability in more detail we compared the statistical properties of the Finite Element (FE) results with those of the monitoring data of the year 2008. The parameter statistics of the 9 FE parameters was generated within the identified upper and lower bounds of the parameters shown in figure 11. 200 samples were generated by Latin Hypercube sampling. The histograms of the parameter factors 1-3 and the estimated gaussian probability densities are presented in figure 13.

The 200 FE runs were performed using the 200 parameter vectors to calculate the statistics of the analytical natural frequencies and mode shapes. These data allowed a comparison of the experimental and the analytical data clouds for the frequency pairs f_i/f_j (i,j = 1,…5). Two of them, for pairs f1/f2 and f2/f5, are shown in in figure 14. These plots reveal a strong correlation of the analytical frequency pairs (blue) resulting in correlation coefficients between 88% and 100%. These strong correlation arises from the fact that the source of the analytical frequency variations was completely assigned to the stiffness and mass parameters. It is obvious that any variation of such parameters will more or less affect all natural frequencies. The experimental frequency pairs exhibit only weak correlations in the range between 21% and 56%. Therefore, it was concluded that the experimental frequency variations were *not caused* by stiffness degradations but by other sources coming from environmental effects or unavoidable measurement errors.

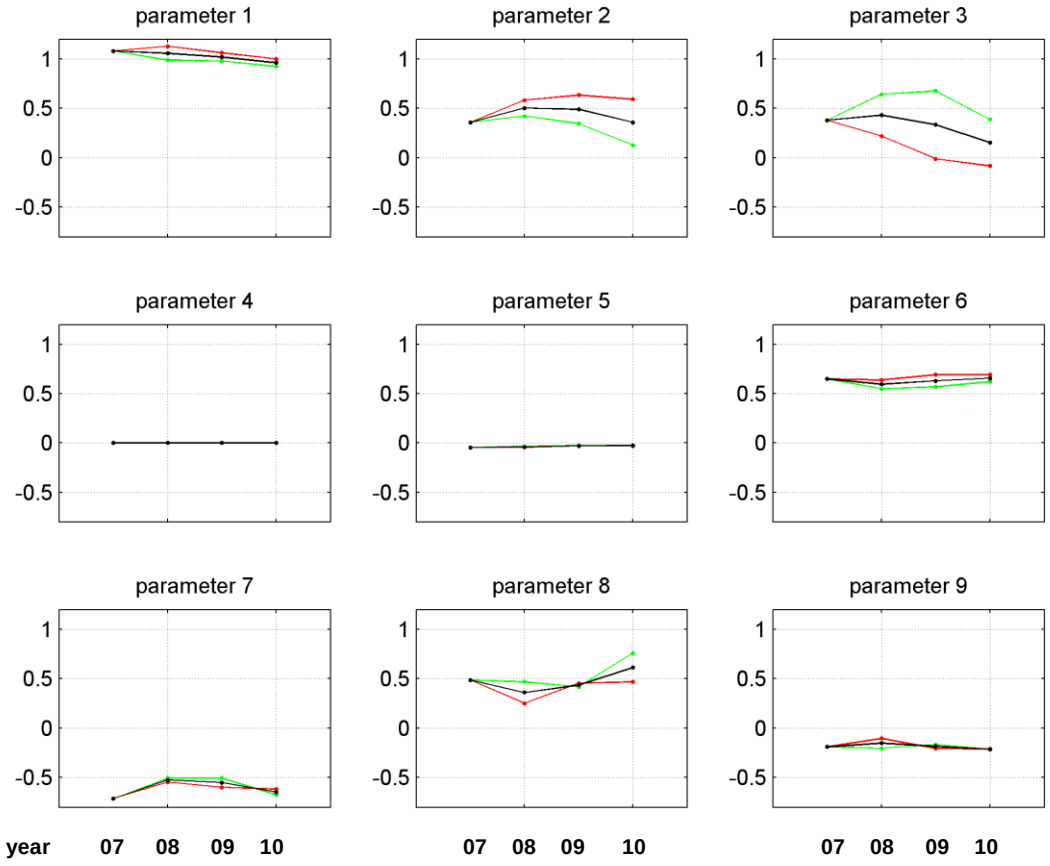

Figure 12: Evolution of parameters over the monitoring years 2007 – 2010.

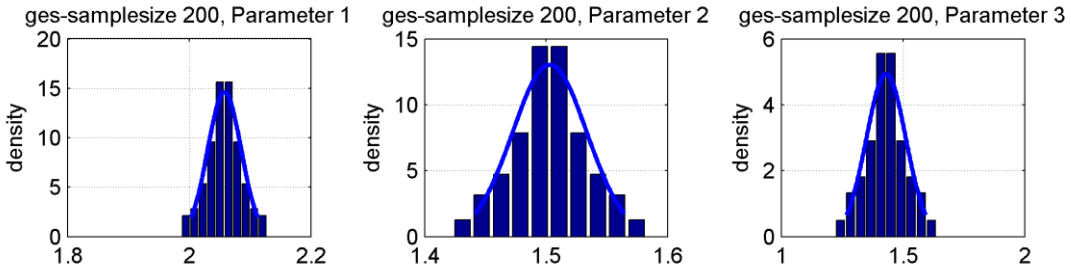

Figure 13: Probability densities of modification factors (1+p1) - (1+p3) within upper and lower parameter bounds.

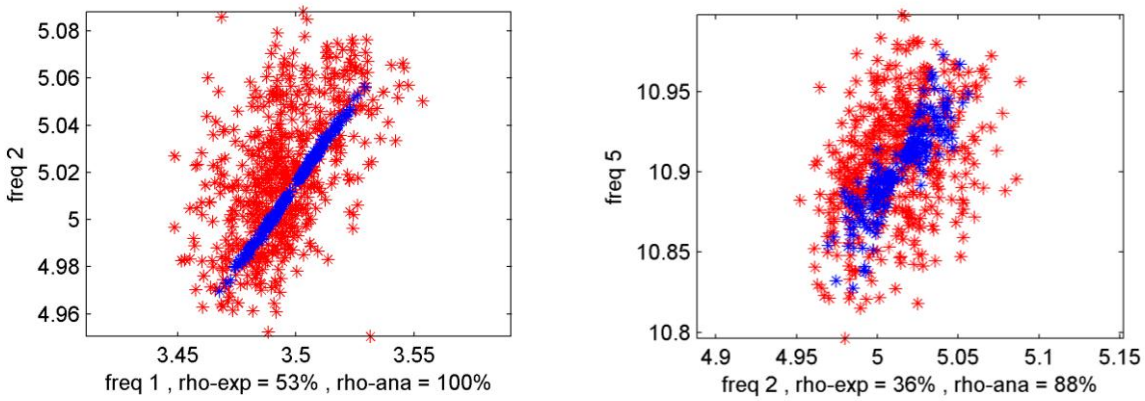

Figure 14: Comparison of test (red) and analysis (blue) for frequency pairs f1/f2 and f2/f5.

5 Summary and conclusions

In the paper we presented the methodology of vibration monitoring applied to the Gaertnerplatz Bridge in Kassel which is characterised by the following steps:

(1) Establishment of a reference FE- model representing the healthy structure in its initial state. This model was generated by computational model updating using experimental modal data obtained by artificial impact excitation of the bridge after completion of the construction. The updated model results show very good agreement with the experimental data.

(2) Bridge resonance frequencies and mode shapes were extracted from ambient excitation response over the years 2008 to 2011 and analysed with respect to their variability over the bridge temperature. These primary data did not indicate any structural degradation of the bridge over the monitoring period.

(3) The monitoring data were used to identify the parameters of a Finite Element model reflecting the variability of the test data by upper and lower parameter bounds. The identified parameters did also not give an indication of structural degradation of the bridge.

(4) A statistical correlation analysis of the Finite Element modal data and the corresponding monitoring data revealed a strong correlation of the analytical data and a weak correlation of the experimental data which led to the conclusion that the scatter of the experimental data was not caused by structural degradations.

References

[1] Fehling E., Schreiber W., Bunje K., Schmidt M.: Brücke aus Ultahochfestem Beton in Kassel über die Fulda. Bauingenieur, Bd. 79, Juli/August 2004

[2] ISSPA Manual, University of Kassel, Instiute of Statics and Dynamics, 2005

[3] Link M., Weiland M. and Hahn Th.: Structural Health Monitoring of the Gaertnerplatz Bridge over the Fulda River in Kassel. Proc. of the 2nd. International Symposium on Ultra High Performance Concrete. Structural Materials and Engineering Series, H.10, No.10, Kassel University Press, March 2008

[4] Link, M., ”Updating of Analytical Models – Basic Procedures and Extensions”. Proc. of NATO Advanced Study Institute, Sesimbra, Portugal, May 1998 in "Modal Analysis and Testing"(J.M.M. Silva and N.M.M. Maia (Eds.), Kluwer Acad. Publ., London , 1999

[5] Friswell M.I. and Mottershead J.E., Finite Element Model Updating in Structural Dynamics, Kluwer Academic Publishers, 1995

[6] Mottershead J.E., Link M. and Friswell M.I.: The sensitivity method in finite element model updating: a tutorial. Mechanical Systems and Signal Processing, Vol 25, No 7, 2011, p.2275-2296

[7] Link M. and Weiland M.: Structural Damage Identification – model based or not ? ICEDyn2011, Proc. of International Conference on Structural Engineering Dynamics, Tavira, Portugal, 2011

Life Cycle Cost Analysis of a UHPC-Bridge on Example of two Bridge Refurbishment Designs

Siemon Piotrowski, Michael Schmidt
Institute of Structural Engineering, University of Kassel, Germany

Life cycle costs of buildings, e.g. bridges, are not only determined by the costs of construction, but especially by its maintenance. The service life of bridges made of materials such as UHPC is significantly longer than that of standard bridges. The entire investment made during technical lifetime can be considerably influenced by the maintenance and user costs. The cost relationship will be exemplified in this comparative study of the Eder-Bridge in Felsberg on two alternative construction designs made of different materials. The economic advantages of UHPC lay particularly in the considerably long service life and the longer durability. In order to determine the most economical option, the material and the implementation costs must be compared to the future maintenance. However, it is important to ensure that the future investments or savings are calculated separately from the construction costs and that the future value of investment will be determined by the net present value (NPV).

Keywords: life cycle costs, UHPC-Bridge, net present value

1 Introduction

Description of the Bridge

The Eder-Bridge was built in Felsberg-Lohre in 1948. Initially, it was used by pedestrians and cyclists, and was a part of a 180 km bike path. Moreover, the bridge served agricultural traffic as well and became of great economic importance in the region. Since then the Bridge's condition has been deteriorating so that in last years the maximum vehicle weight was restricted to 6 tons and all agricultural traffic had to make detours. Municipal authorities of Felsberg decided to renovate the bridge partially.

Two different renovation designs were developed in the frames of a joint cooperation project between the engineering firm *Fehling und Jungmann* and the Department of Structural Concrete of University of Kassel. The first design was developed for normal concrete construction with external prestressing whereas the second design contains UHPC and normal concrete units. Both designs were developed allowing to use old bridge piers, i.e. three given piers and four single span beams with the total length of the bridge of 51,55 meters. The superstructure of the UHPC design significantly differs from that of normal concrete. The cross-section of the UHPC-bridge consists of UHPFRC box girders filled with lightweight concrete. The boxes are precast elements (between 10,46 and 15,7 meters long). The surface of the bridge is made of in-situ UHPC. The 2 cm thick wear layer is reinforced with PVA Fibre, whereas the 4 cm thick base course is reinforced with steel fibres. The normal concrete design, on contrary, is a traditional prestressed concrete bridge.

Preliminary Evaluation of the Life Cycle Costs: Comparative Analysis

Within the scope of this work, an economic efficiency analysis was carried out including the costs of construction. The analysis, based on the cost calculations conducted by the Engineering firm *Fehling und Jungmann,* considers only the superstructure of the bridge and compares only some single parts of the construction. The costs of the other parts of the bridge such as caps and bearings are not taken into account because they have similar traits and characteristics in both presented designs. The economic analysis considers only the prices per unit; all prices are listed in EUR netto. The imputed costs such as general business expenses or profit, etc. are not considered. The analysis assumes that no new equipment (for the UHPC produc-

tion) has to be purchased for the project; the staff is aware of both operational methods and has experience of working with both types of materials. The following table shows the masses of the UHPC-design.

Table 1: Quantities of the UHPC-design [1].

Structural element	Quantities
UHPC in the precast element	32,70 m³
In situ UHPC	11,75 m³
light-weight concrete	26,10 m³
Unbonded prestressing	4,30 t
steel bars in the precast element	6,50 t
steel bars in the in-situ concrete	3,83 t
steel bars in the light-weight concrete	0,37 t

It is necessary to exclude the named indicators in order to increase comparability of both designs. Moreover, the continually growing experience of working with the UHPC and rapid development of the high performance materials will decrease the importance of those indicators in the evaluation of life cycle costs. The restriction of the study is that UHPC costs used for the current analysis were taken from few available literature sources on structural engineering but not from the sources describing existing UHPC projects or enterprises working with ultra-high performance materials. More exact data could have enhanced the accuracy of the analysis but the novelty of the project and relatively low level of experience in this field make the precise data unavailable when dealing with UHPC.

The result of the economic efficiency analysis shows that the design applying UHPC units is approx. 23% more expensive than that of traditional concrete (costs of normal concrete: 149.359,00 €; costs of UHPC: 183.225,20 €). It is noteworthy to mention that considerably high expenditures are expected when dealing with novelty of design and material. Labour costs as well as shuttering works will increase up to 39% and 26% accordingly in relation to the total costs. These costs tent to decrease during the construction period in view of increased experience and completeness of the project [1]. The calculations of both designs are compared and summed up in the following tables.

Table 2: Calculation of the normal concrete [1].

Structural element	Costs
Concrete superstructure	41.420 €
Reinforcing steel superstructure	30.400 €
span steel superstructure	24.000 €
supporting structure (proportion of superstructure)	34.000 €
Preparing concrete area bridge deck	2.250 €
Sealing bridge deck	2.700 €
Sealing layer welded asphalt sheeting bridge deck	3.150 €
Asphalt protective layer with a thickness 3,5	6.222 €
Surface layer	5.217 €
Sum	149.359 €

Table 3: Calculation of the UHPC [1].

Structural element	Costs
Precast UHPC elements	25.210,55 €
Lightweight concrete filling	5.268,67 €
in-situ UHPC supplement	13.277,38 €
Formwork	56.957,60 €
Reinforcing steel precast elements	19.638,00 €
Reinforcement on the construction site	28.872,00 €
Transport and assembly	34.000,00 €
Sum	183.224,20 €

2 Economic Efficiency Analysis Using Life Cycle Costs of a Bridge

Life Cycle Costs of a Bridge: Basic Principles

Any decision about the bridge construction or renovation is connected to the estimations of different stages of its life cycle. The figure below (fig. 1) shows that the economic efficiency analysis, which is traditionally focused only on historical and construction costs, also includes other expenditures on the other stages of the life cycle. Usually the costs for the financing of the projects are assessed before the construction procedure. These expenditures, however, are not taken into consideration in the current study for the reason that they have minor effects on the decision-making about the choice of construction materials and therewith on the choice of the design. Apart from historical costs, consequential expenditures are also a part of the life cycle. Consequential expenditures are all costs that occur during the bridge age throughout its life cycle. User costs include expenditures on bridge preservation, maintenance and reparations [2]. The calculation of the costs must include estimations and approvals which permit the most realistic assessment of the future cash flows. Consequential expenditures also include decommissioning costs. Considering that the service life of bridges is conventionally considered to last at least one hundred years, the evaluated decommissioning costs were excluded from the current analysis for the reason that they do not influence the decision-making about construction materials.

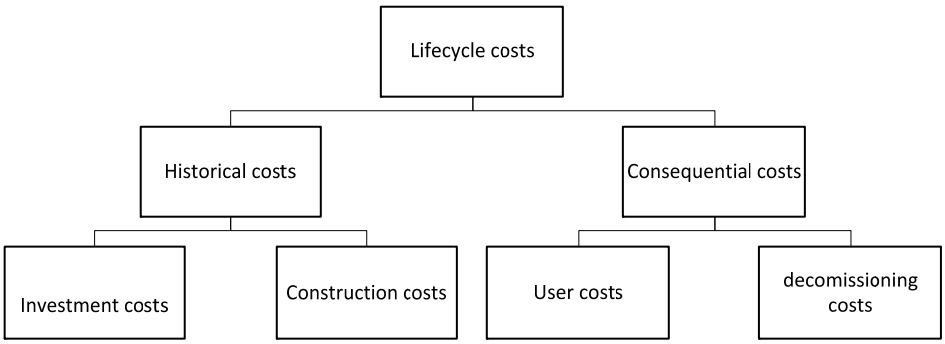

Figure 1: Cost structure [3]

Dynamic Investment Calculation

The analysis compares the sums of the final values of given designs including both construction and user costs. A method for using the time value of money to appraise this long-term project should be applied in order to compare the life cycle costs at different points of lifetime. The future cash flows should be estimated and discounted to give their present values. Theoretically,

the time period between the present moment and the future cash flows can be used for deposit accounts with capital market interest rates [4]. The net present value (NPV) method takes into account this appraisement: it considers the investments as series of cash flows and appraises their value in different periods of time. The NPV is expressed in the following formula:

$$C_0 = \sum_{t=1}^{n} \frac{D_t}{(1+i)^t} - \sum_{t=1}^{n} \frac{P_t}{(1+i)^t} \quad (1)$$

D = deposit; P = payoffs; i = permanent interest rate at perfect capital market; C_0 = cash value; t = time period; n = number of last payment

The formula may be simplified in case the payments are constant [5]:

$$C_0 = D\frac{(1+i)^n - 1}{i(1+i)^n} - P_0 \quad (2)$$

In order to use this formula in the life cycle costs analysis it has to be applied to the two given bridge designs: the deposits from the first formula turn into annual maintenance costs (Mt) and the first cash flow in the series of cash flows turn into the investment costs (I) of the bridge construction. The modified formulas for the life cycle costs analysis of a bridge is presented as follows [6]:

$$LCC_C = I + \sum_{t=1}^{n} \frac{M_t}{(1+i)^t} + \frac{P}{(1+i)^t} \quad (3) \qquad LCC_C = I + M\frac{(1+i)^n - 1}{i(1+i)^n} + P \quad (4)$$

The annuity method is another technique used to calculate the value of future cash flows. This method is related to the net present value method. The annuity is series of cash flows with equal payments at certain time intervals [5]. The formula below can be adapted to the calculation of life cycle costs as well:

$$LCC_A = \frac{LCCc}{\sum_{t=0}^{n}(1+i)^t} = LCCc\frac{(1+i)^n * i}{(1+i)^n - 1} \quad (5)$$

The annuity method makes it possible to estimate the annual user costs throughout the whole life cycle of the bridge. This method is particularly useful when comparing different lifetimes of bridges and other investment projects [6].

3 Life Cycle Cost Analysis: Case Studies

Advantages of Using High Performance Concrete in Bridge Constructions

Apart from the well-known strength of high-performance material UHPC, there are some other advantages, e.g. its durability that can lead not only to cost reduction but also increase the lifetime of constructions. The high-performance material has particular advantages over the normal concrete throughout the lifetime of the bridge: the maintenance and reparation costs of UHPC constructions are lower than those of normal concrete.

Pelke [7] marked out advantages of high-performance concrete durability:

- Improvement of freeze-thaw resistance
- Reduction of carbonation
- Improved protection against chloride contamination
- High abrasion resistance

The effects of the material durability on the lifetime and the maintenance costs of the construction units are particularly important for the life cycle analysis of the bridges. According to [8], the UHPFRC acquires waterproof protection of the surface due to its low permeability, so that the damaging chloride ions cannot easily enter into the first millimetres of the concrete body even after 100 years of exposure. Due to this feature the chlorides do not cause any corrosion of the steel [8]. Bouhaya assumes that the UHPC became an ultra-durable material because of low porosity and that it does not need any maintenance for 100 years which is considered to be the expected lifetime of a span bridge. Moreover, he supports this thesis by another statement made by Resplendino that a UHPC light construction doesn't need any maintenance or reparation throughout these years [9]. In view of the aforesaid, it is possible to assume that the UHPC gains an advantage over normal concrete in regard of the life cycle of the bridge and saving of the maintenance costs. Moreover, it makes possible to conduct scenario analysis.

Calculation of Life Cycle Costs

The most important factors for the life cycle costs calculation of a bridge besides the construction costs are the lifetime of the bridge, the annual maintenance and operational costs and the inflation-adjusted interest rate needed in order to discount the future payments. The interest rate used for the calculations is 3%, according to the Directives for the preservation of civil constructions [4]. Moreover, Heitel [6] refers to the dissertation of Radlbeck (2006) in which the calculation interest rates in state and private building projects are located between 2,5% and 3%. The life time of bridges, on contrary, varies more according to the lifetime of both bridge designs. Assuming that a bridge is a perfect construction with faultless building design then its user lifetime lasts 100 years [6]. The superstructure of the bridge which is analysed in this study has, according to [10], a lifetime of between 80 and 100 years. There is a general consensus among the experts that the lifetime of bridges is located in this timeframe. Nevertheless, it has to be mentioned that the average lifetime of the existing bridges lasts de facto for about 25 years [3]. The lifetime of the UHPC design, on contrary, will last at least for about 100 years. Moreover, in view of the aforesaid advantages of the UHPC in the bridge building and on base of the research results obtained by Dept. of Structural Materials and Construction Chemistry of the University of Kassel one of the possible scenarios is that the UHPC construction will serve twice longer than that of normal concrete. Based on construction costs, the maintenance expenditures of a bridge with 100 years lifetime make up between 0,6% p.a. [11] and 1% p.a. [12] where the superstructure of the bridge out of steel reinforced concrete makes up 0,8% p.a., and the one out of prestressed concrete makes 1,1% p.a. [2]. In view of aforesaid, it is possible to assume that the UHPC has lower maintenance costs between 0,3% p.a. and min 0,1% p.a. of construction costs. The latter percentage (0,1% p.a.) stands for the technical servicing and inspections of the bridge [13]. Based on the mentioned assumptions and using the net value method the following results were obtained:

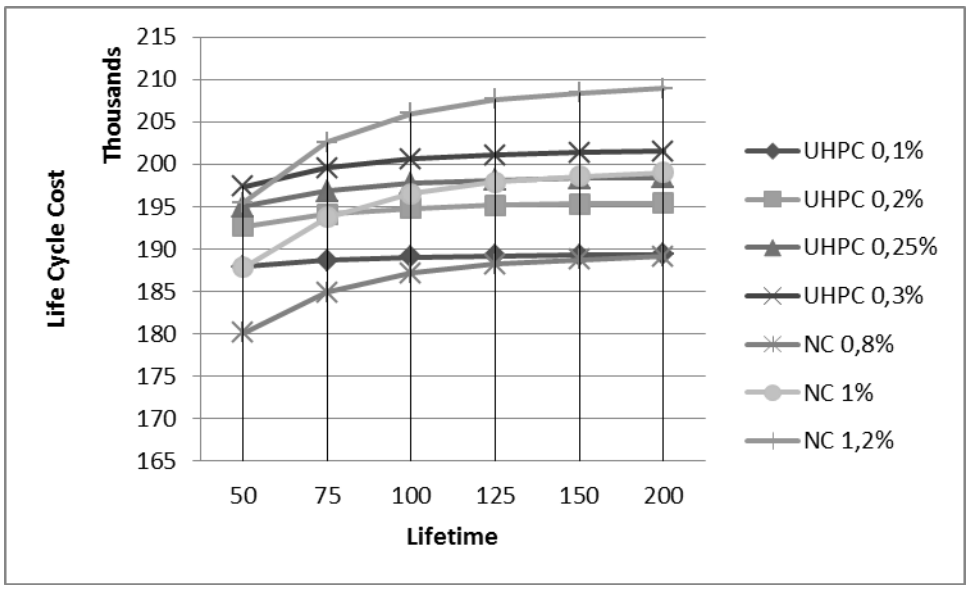

Figure 2: Capitalized life cycle costs

Figure 2 shows that the life cycle costs of the normal concrete construction are lower than those of UHPC considering short lifetime (e.g. 50 years). However, it is important to mention, that the longer the normal concrete bridge is used the more significantly increase its life cycle costs so that in the end they become much higher than those of UHPC construction. At the latest after 100 years, the UHPC construction will gain over the normal concrete under existing conditions of the bridge servicing that the UHPC maintenance costs will be 1:4 to 1:3 of the normal concrete bridge. In the later years of use (over 100 years) the UHPC design will be the most cost-efficient solution mainly because the normal concrete bridges do not reach this age and should be built again. Bearing in mind the usage costs only, the difference between the given designs is essentially bigger. The following figure (Fig. 3) shows the alteration between the two designs and their lifetimes. That shows the advantage of the usage time and lower maintenance costs of the UHPC.

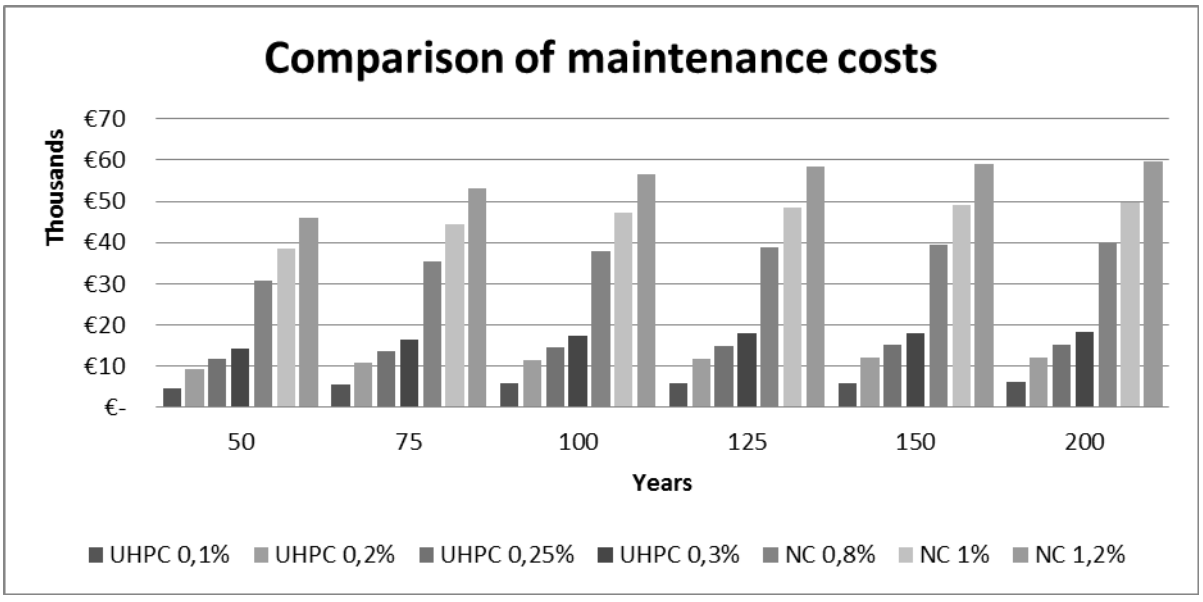

Figure 3: Comparison of maintenance costs

The annuity method is another option of life cycle costs comparison of given designs. As mentioned before, this method makes it possible to estimate the annual user costs throughout the whole life cycle of the bridge.

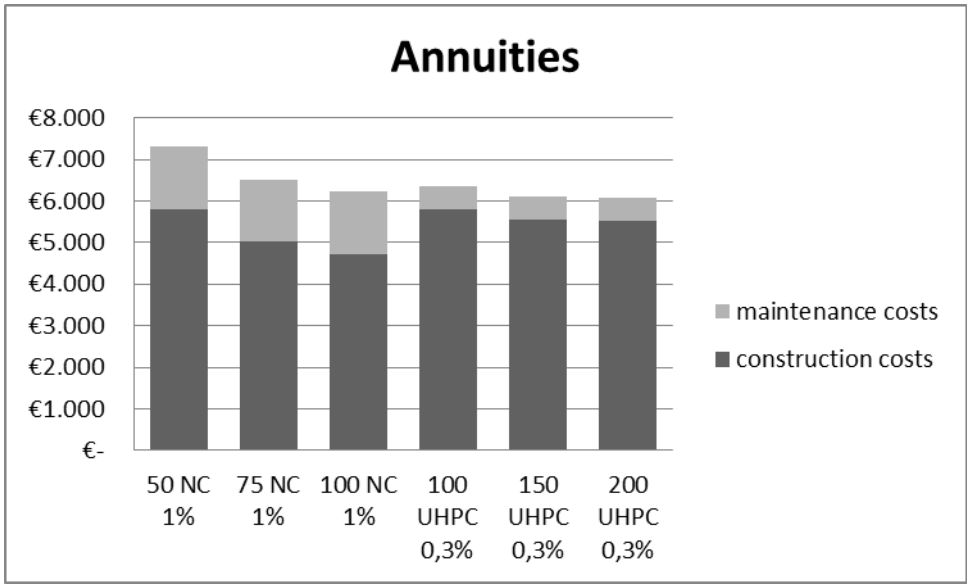

Figure 4: Annuities in life cycle

The figure above (fig. 4) shows that the annuities of UHPC in the chosen scenarios are competitive with the normal concrete. The prognosis showed that the UHPC is more cost-efficient than normal concrete in case of short-term usage of the normal concrete bridge (e.g. 50 years) and long-term usage of the UHPC bridge (over 100 years). Moreover, the UHPC has to possess higher durability so that the maintenance costs should be trice higher than those of normal concrete.

Summary and Outlook

Having compared both designs in regard of their life cycles it is possible to conclude that the UHPC-bridge is more economically efficient than the normal concrete one. Considering that the normal concrete bridge must be replaced or renovated throughout 100 years of usage or in case the bridge has average or higher maintenance costs during this timeframe, as it was expected, it is possible to conclude that the life cycle costs of a normal concrete bridge are in 100 years higher than those of UHPC. The UHPC-bridge, on contrary, has longer lifetime and significantly low maintenance costs than those of normal concrete, as it was proven in the study. Considering the average lifetime of normal concrete bridges as well as planned lifetime and the durability of the UHPC, it can be expected that the construction costs will be not only compensated but also meaningfully saved. Given that the UHPC design of the bridge is a composite construction made of both UHPC and normal concrete, not all potentials in the construction and the durability of the bridge will be reached. This type of mixed construction is still necessary for the development and the first UHPC pilot projects because otherwise the constructors will not take the risk of investment into innovative materials projects and the UHPC will not be able to gain their trust. Further optimisation of UHPC manufacturing processes, precast production as well as in-situ UHPC may increase saving potential so that the construction costs will decrease and the advantage of the user costs will be fully used.

References

[1] Hillebrandt, M: Entwurf des Überbaus einer vierfeldrigen Straßenbrücke. Master thesis. Department of Structural Concrete of the Kassel University. 2011.

[2] Kuhlmann, U.; Pelke, E.; Hauf, G.; Herrmann, T.; Steiner, J.; Aul, M.: Ganzheitliche Wirtschaftlichkeitsbetrachtungen bei Verbundbrücken unter Berücksichtigung des Bauverfahrens und der Nutzungsdauer. *Stahlbau (Stahlbau)* 76, p 105–116, 2007.

[3] Waltner, R.: Ein Brückenleben lang – Lebenszykluskosten von Brücken aus Hochleistungsbeton. Brückenbau - Fertigteile auf neuen Wegen, p 50-54, 2005.

[4] Bundesministerium für Verkehr, Bau und Stadtentwicklung: Richtlinien für die Erhaltung von Ingenieurbauten - Richtlinie zur Durchführung von Wirtschaftlichkeitsuntersuchungen im Rahmen von Instandsetzungs-/ Erneuerungsmaßnahmen bei Straßenbrücken, Ausgabe 2004.

[5] Stöttner, R.: Investition und Finanzierung, 2005.

[6] Heitel, S.; Koriath, H.; Herzog, C. S.; Specht, G.: Vergleichende Lebenszykluskostenanalyse für Fußgängerbrücken aus unterschiedlichen Werkstoffen. *Bautechnik (Bautechnik)* 85 (10), p 687–695, 2008.

[7] Pelke, E.: Neue Bauweisen im Ingenieurbau aus der Sicht der Hess. Straßen- und Verkehrsverwaltung. *Ultra-hochfester Beton - Planung und Bau der ersten Brücke mit UHPC in Europa ; Tagungsbeiträge zu den 3. Kasseler Baustoff- und Massivbautagen* Heft 2. P 69 – 77, 2003.

[8] Brühwiler, E.: Planung und Bau der ersten Brücke mit UHPC in Europa; Tagungsbeiträge zu den 3. Kasseler Baustoff- und Massivbautagen. *Der Tagungsband Seminar der Vereinigung der Straßenbau- und Verkehrsingenieure in Hessen e.V..* p 25-48, 2006.

[9] Bouhaya, L.; Le Roy, R.; Feraille-Fresnet, A. : Simplified Environmental Study on Innovative Bridge Structure. *Environmental Study on Innovative Bridge Structure* 43 (6). p 2066–2071, 2009.

[10] Empelmann, M.; Heumann, G.: Entwicklung lebensdauerorientierter Entwurfsstrategien für Brückenbauwerke. *Institut für Baustoffe, Massivbau und Brandschutz der TU Braunschweig – Materialprüfanstalt für das Bauwesen Braunschweig,* 2008.

[11] Mehlhorn, G.; Aigner, F.: Handbuch Brücken: Entwerfen, Konstruieren, Berechnen, Bauen und Erhalten. 2007.

[12] Schah, R.; Otto, J.; Häupel, M.; Fritsche, M.: Lebenszykluskosten von Brückenbauwerken. *Bauingenieur* Band 81, 2006.

[13] Graubner, C.-A.; Knauff, A.; Pelke, E.: Lebenszyklusbetrachtungen als Grundlage für die Nachhaltigkeitsbewertung von Straßenbrücken. *Stahlbau* 3, p 163–171, 2011.

Material performance control on two large projects: Jean-Bouin stadium and MUCEM museum

Dominique Corvez[1], Patrick Mazzacane[2]
1: Lafarge Ductal®, Paris, France
2: Bonna Sabla, Consolis Group, France

In 2013, two larg-scale buildings by architect R. Ricciotti and making use of UHPFRC will open in France: MUCEM museum in Marseille and Jean Bouin stadium in Paris. Industrial production of large quantities (3500 tons of UHPFRC for those two projects) requires specific material control during premix production and batching in order to lower the mechanical performance variability as required by the design specifications. In particular, post cracking behaviour assessment in design, particularly at ULS, requires suitability testing procedures to calibrate the K factor (fibre orientation factor) on full scale elements with strict industrial casting procedures and quality plan.
On those two projects, UHPFRC is used for several different structural functions: large structural prestressed columns, Pi shape prestressed footbridge girders, ribbed reinforced shells, perforated panels. It allows for a comparative presentation of the material performance control of various structural elements with different geometries and functions.
In a first part, mechanical properties of different UHPFRC mixes used for those two projects, including fire resistant UHPFRC mixes will be presented as the reference state for industrial control. Tensile properties will be extracted from a dedicated "back-analysis" software recently developed for beam and plate specimens. In a second part, suitability testings, performed to assess fibre orientation according to industrial casting procedures, will be compared according to structural functions and internal forces.

Keywords: suitability testings, fibre orientation

Figure 1: Jean Bouin stadium rendering (R. Ricciotti Architect).

Ductal® has been used for structures in infrastructures like bridges, footbridges, airport runways [1]. With Jean Bouin and MUCEM projects, both by Architect R. Ricciotti, and with Ductal® metallic fibres, LR.Ing and SICA, two innovative engineering offices, have taken the challenge of making the first large buildings in UHPFRC [2]. On both projects, Bonna Sabla [3] and Lafarge [4]. were selected by Leon Grosse and Vinci to manufacture the precast pieces.

Figure 2: MUCEM under construction (October 2011).

The structural innovations in the design phase have been thoroughly presented during the 2009 Marseille UHPC Congress [2]. This paper will focus on the material aspect during the manufacturing of the pieces.

In France, performance control of UHPFRC material is described in the "Interim Recommendations AFGC/SETRA" [5] published in 2002.

Three main phases are described:

- "Material Study" with definition for an industrial premix of an Identity Card with relevant characteristics (especially mechanical, durability, dimensional stability)
- "Suitability testings" to confirm fibre orientation through K factor
- "Routine Control" checks every 10m^3

In this paper, a focus will be made on tensile properties in the post-cracking state to emphasize fibre orientation reliability.

1 Mechanical properties in tension

Ductal® UHPFRC with metallic fibres Identity card

To assess tensile properties, a specific analysis is conducted on the premix used. This is compared with the behaviour law used during the schematic and detailed design. The post-cracking stress, after thermal treatment is constant at 7,5 MPa until a crack opening of 0,3 mm in both projects.

A back-analysis on 70 x 70 x 280 mm^3 notched specimen under three-points bending test is performed. The method developed by G. Chanvillard, P. Rossi and P. Casanova is detailed in [8 & 9]. The "bending moment versus crack opening" curve is then analysed to get the post-

cracking tensile behaviour with an “isotropic” fibre content of 2%. The results of this material study on 6 specimens confirm the value given during the design phase. (see Fig.3)

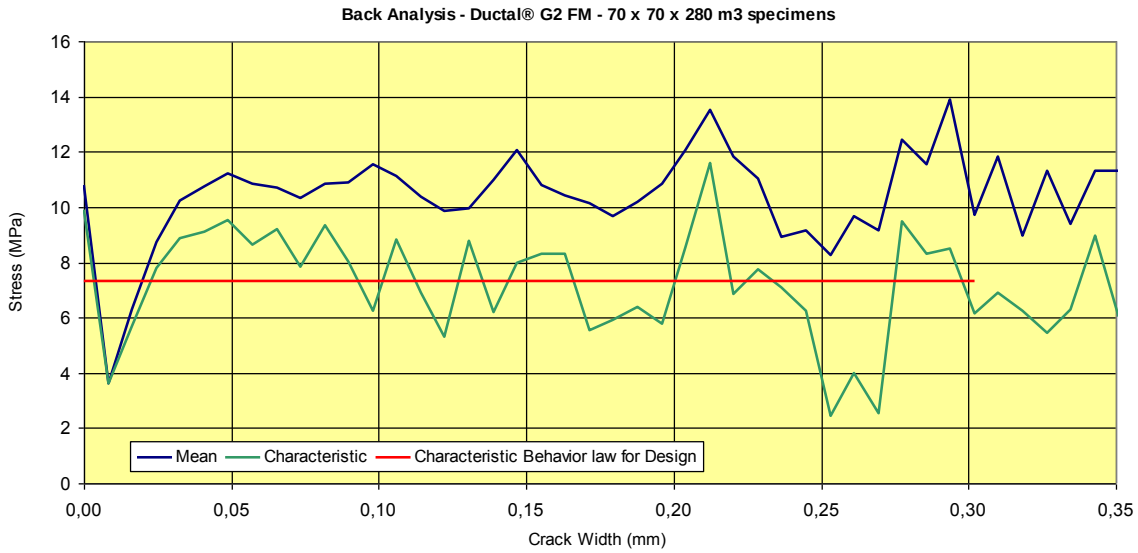

Figure 3: Back-analysis – prism according AFGC-SETRA.

For practical reasons, on site, the routine checks are done through four-points bending unotched tests compared with a “reference” and characteristic value realized on 6 specimens tested in four-points bending done during the material study.

On the MUCEM project, a specific mix called Ductal® AF (for Anti Fire), containing polypropylene fibres is used to avoid concrete spalling. The vapour entrapped in the matrix can be released through a continuous network of voids created by the melting of the polypropylene fibres. This mix is used for all the Y shape columns.

Tensile properties in case of plates

The same material has to be characterised differently for plate elements to take into account the improved properties for those type of structures. The fibre orientation is no more 3D isotropic but more 2D isotropic. This leads to better performances. A UHPFRC plate is defined as an element of thickness less than 3 L_f (L_f = fibre length). In our case, it means less than 40 mm. Plate elements are treated with a specific plate analysis developed by G. Chanvillard and S. Rigaud. The cracking concept is not introduced explicitly. The crack distribution is considered constant over the constant moment in a four point bending test. This allows developing a mechanical model based on the assumption of a constant curvature between the two loading points. Strain can be then used in replacement of crack width. The third cinematic relation in the classical back-analysis is simplified in the two Newton equations (N and M equilibrium). The resolution can be done by an iterative method [6] or by a new explicit method that will be presented in French AFGC Interim Recommendations (expected 2012). The results with this new method (with exact deflection consideration) for Jean Bouin typical plate element thickness are presented in Fig.5. done on typical equivalent bending stress vs. deflection (Fig. 4). The characteristic behaviour law for the design of “roof” plates has been chosen as an elastoplastic curve with a “plateau” of 10 MPa up to a strain of 0,4%.

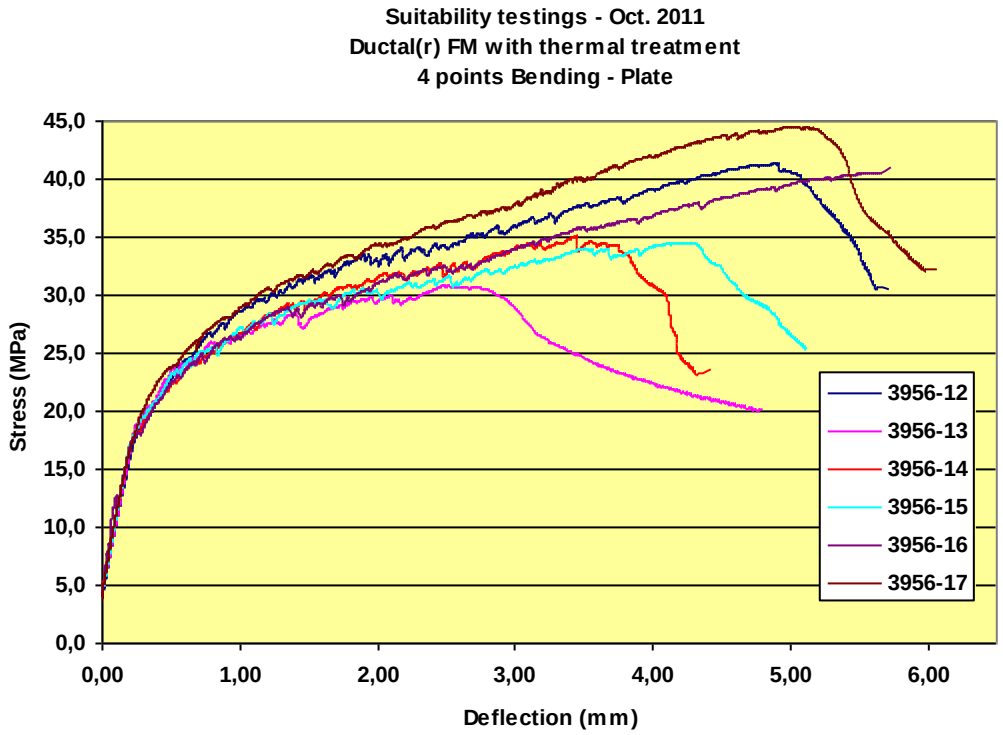

Figure 4: Flexural behaviour of Jean Bouin roof plate elements.

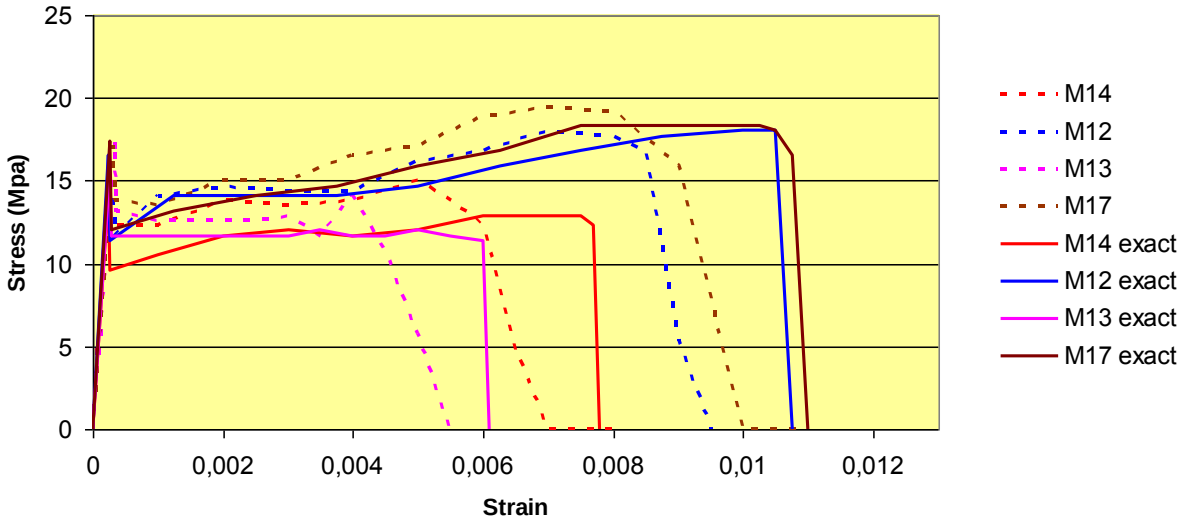

Figure 5: Direct Strain Stress Tensile curve from an explicit "back-analysis" (G. Chanvillard's method).

2 Suitability testings: key learning and particular strategies to assess fibre contribution

AFGC/SETRA interim recommendations [5] define a systematic general approach for assessing fibre orientation. This is critical because of the behaviour law defined in part 1 is related to isotropic (3D or 2D) distribution of fibres. Specimen cutting and flexural comparisons allow simple definition of the “K” factor. This approach is adapted in most cases. Nevertheless, in some parts of the projects, it is necessary to use a full testing approach.

MUCEM footbridge: process variation

The MUCEM footbridge elements have been produced with the same mold as the “Pont Du Diable” footbridge by the same contractors (Bonna Sabla, Freyssinet, Lafarge). External and internal are slightly different and prestessed cables do not allow to introduce a concrete injection pipe in the bottom of the mold. For the “MUCEM” footbridge precast elements, the introduction was performed by a pouring method using gravity. Analysis of K factor in the webs have shown an increase from K= 1.26 to K=1.65 (30%) with that pouring method using gravity compared to the injected one. Injection is actually a more efficient to maintain a 3D isotropic orientation compared to the gravity one which strongly orientates the fibres.

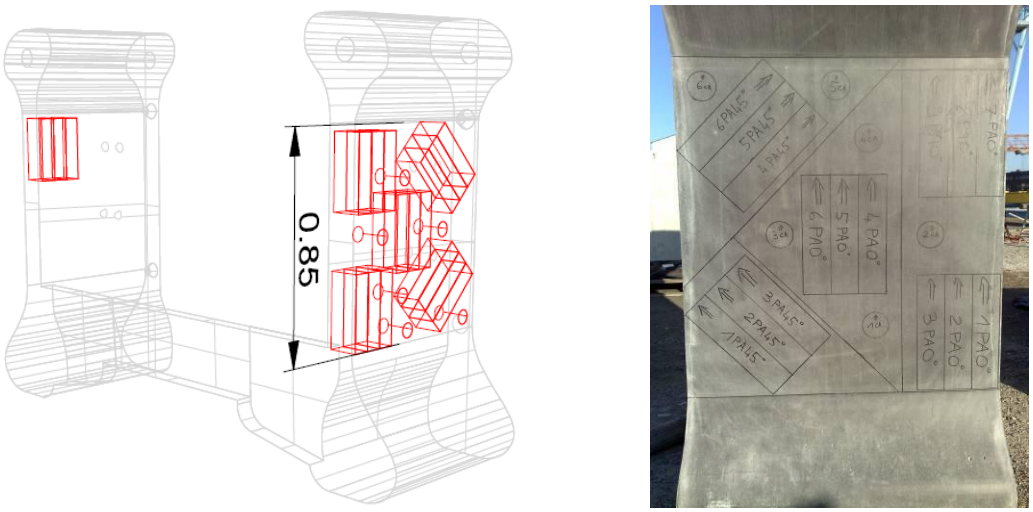

Figure 6: Specimens cutting in MUCEM footbridge precast girder.

Building Columns: Y MUCEM Columns

The Y shape columns of MUCEM are cast vertically. Fibre orientation is assessed by the “cut prismatic specimen” method. Nevertheless, due to spiral rebars near the anchorages, it was not possible to cut specimens of a regular size. In those parts, a fibre counting method was chosen with “optical data acquisition” to literally count the fibre. This complementary method was particularly relevant to check potential fibre segregation with a comparison on specimens cut at the top and bottom of the Y column.

Larger specimens have also been analysed. For instance, in the final global structural design of MUCEM project, a central concrete core carries the lateral solicitations of wind and more critical seismic lateral forces. The columns are not

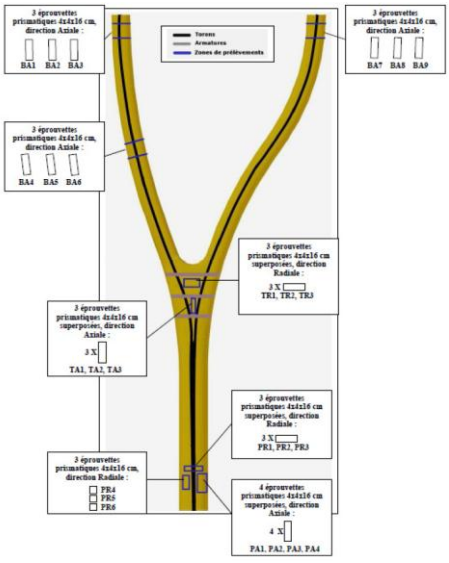

Fig. 7: Y MUCEM columns.

there to carry the lateral forces. A specific hinge have been casted to reduce lateral forces on the column. They are called “Freyssinet UHPC Hinges” since they are derived from the classical “Freyssinet Hinges”. In a small hinge area, the UHPC is highly compressed around a postensionned cable. For practical reasons, diffusion of this precast UHPC hinge, placed during the casting of the entire column is made with spiral rebars confinement. The diffusion has been checked through a dedicated compressive test.

Large Perforated cladding: MUCEM & Jean BOUIN

On both projects, vertical facades consist of perforated panels (perforation ratio: 50% or more). The fibre orientation has been checked in the branches. This have given excellent results (K<1 in longitudinal). The risk is then concentrated in the nodes where “fibre flows” can meet. In those zones, fibres from one flow do not penetrate in the other flow which leads to a drastic lack of fibres in the section defined by the meeting region of the two flows.

To correct this, a specific casting path has to be followed by the operators, especially near the nodes. On Jean Bouin, a full piece has been successfully tested in flexure to detect any weak node.

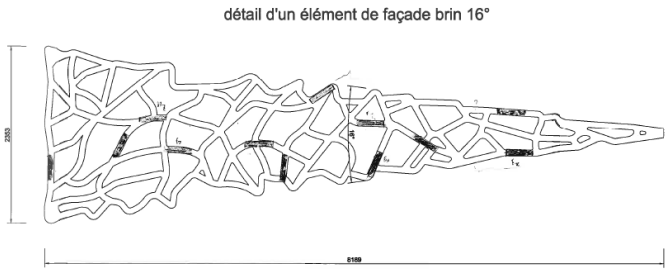

Fig. 8: Jean Bouin perforated panels.

Structural ribbed panels: Jean BOUIN roof panels

Ribbed roof thin panels are an interesting case study for which two strategies were adopted. For the planar regions, without any reinforcement, 9 plates are cut in a sacrificial piece corresponding to 9 critical zones (blue elements in Fig.8) according to structural internal forces to analyse fibre orientation. The results in flexure (4 points-bending un-notched) are then compared to the specific flexural capacity of a plate with the behaviour law defined for plates (§1) to assess K.

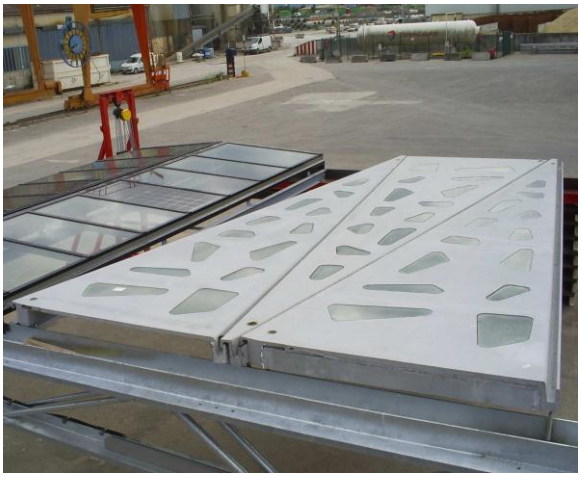

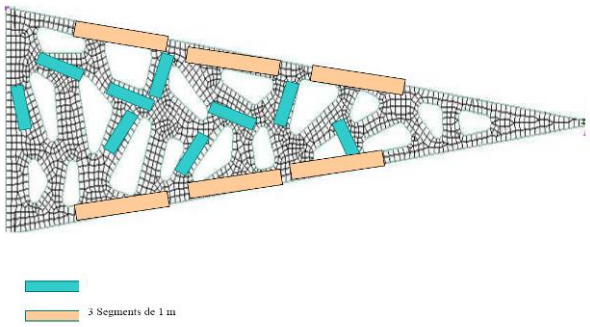

Fig. 9: Jean Bouin Roof elements an cutting pattern.

Various processes have been tested including injection in a closed mold from the top of the ribs and “opened casting process” in an “open mold” that is closed after the pouring of the material around the glass elements. With an open mold, it is possible to correct flows which is not the case in a closed mold. During trials, with close mold, K factor up to 1.7 can be observed in the flow “meeting zones” therefore it has been recommended not to use the process.

Shear strength of the reinforced ribs is assessed with short beams testings. Six portions of beams have been cut and tested in “shear» (orange elements in Fig.9) and fibre contribution in interaction with “real” rebar placing (see Fig. 10 right) can be then analysed indirectly. Safety factors is assessed directly in comparison to design internal forces. This testing has demonstrated that the design in shear with the process used will not lead to failures in shear but in flexure.

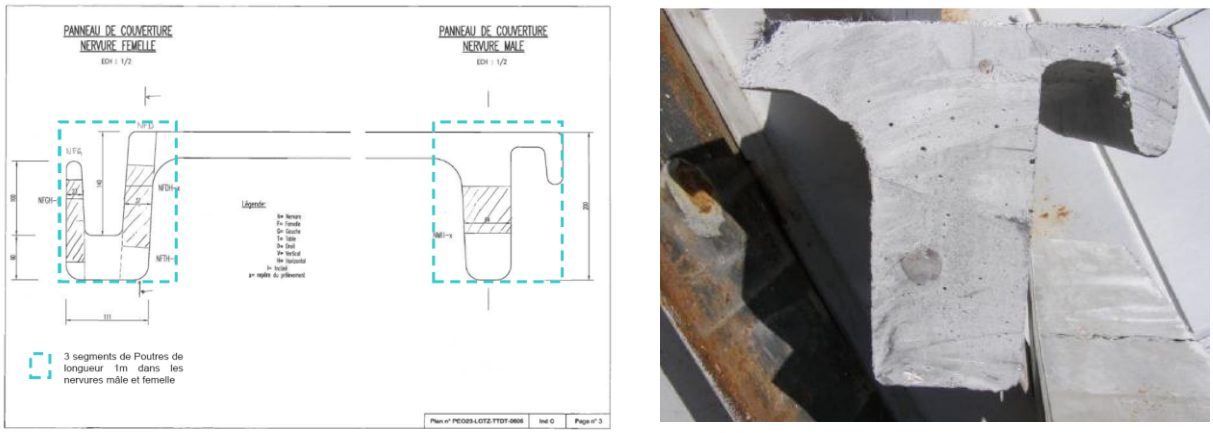

Fig. 10: Jean Bouin ribbed elements and cutting pattern.

An additional global testing was performed by the CSTB has confirmed a global safety factor of 5 for the ribs. This testing has shown a high ductile behaviour observed in Fig.11 that could be used for future projects to calibrate lower safety factors.

Fig. 11: Global testing made at CSTB.

3 Conclusions

This paper on material performance control on the two first large buildings made with structural UHPFRC in France has focused on the tensile properties in the post-cracking state. Suitability testings according to AFGC/SETRA interim Recommendations using “cut prismatic specimens” are a good and robust approach to analyse fibre distribution. It has to be strongly highlighted that a wrong placing process can lead to weak cross sections where no fibres are active. This has to be carefully avoided with a comparison between UHPFRC placing methods (injection, pouring by gravity method, etc.).

In some cases, practical approaches have been performed in addition to the “cut prismatic specimen” approach leading to global “structural “testing and global safety factor. It has been observed systematically “ductile collapse mechanism” with a high redistribution between elements (ex perforated panels). Non linear numerical software have to be systematically used during design phase to take advantage of this ductile behaviour in complex shape. Future performance based design approaches for UHPFRC components should take into account those “non fragile” behaviours to calibrate appropriately safety factors with engaged and innovative authorities.

References

[1] Batoz, J.-F.; Behloul, M.: UHPFRC development: Experience with Ductal® over the last two decades. Proceedings of Designing and Building with UHPFRC, State of the Art and Development, Marseille, France, pp. 43–62, 2009.

[2] Ricciotti, R.; Lamoureux, G.; Ricciotti, R.: The Jean-Bouin stadium. Proceedings of Designing and Building with UHPFRC, State of the Art and Development. Marseille, France, pp. 101–108, 2009.

[3] Patrick Mazzacane, Intervention Bonna Sabla, débats AFGC, juin 2011.

[4] Dominique Corvez, Intervention Lafarge, débats AFGC, décembre 2011.

[5] AFGC/SETRA, Bétons Fibrés à Ultra haute Performance, Recommandations provisoires, 2002.

[6] Rigaud, S.; Chanvillard, G.; Chen, J. J.: Characterization of bending and tensile behaviors of ultra-high performance concrete containing glass fibers. Proceedings of High Performance Fiber Reinforced Cement Composites 6, Ann Arbor, MI, USA, 2011.

[7] Behloul, M.; Bernier, G.; Cheyrezy, M. (1996): Tensile behavior of reactive powder concrete (RPC) Comportement en traction des bétons de poudres réactives (BPR). 4th International Symposium on Utilization of High-Strength/High-performance concrete, Paris, 1996.

[8] AFREM (1995):Les Bétons de fibres métalliques. Séminaire Annexe 1, 6.12.1995.

[9] Chanvillard, G.: Characterization of fibre reinforced concrete mechanical properties : A review, plenary conference, Fifth International Rilem Symposium on Fibre Reinforced Concretes, BEFIB’2000, Ed. P. Rossi and G. Chanvillard, Lyon, France, pp. 29–50, 2000.

Innovative design of bridge bearings by the use of UHPFRC

Simon Hoffmann[1], Hermann Weiher[2]
1: mageba SA, Bülach, Switzerland
2: matrics engineering GmbH, Munich, Germany

Bearings represent one of the most sensitive and demanding links for the load path in bridge structures with one of the highest requirements regarding reliability and performance in structural engineering. Therefore design in this field has been very conservative with few innovations in decades. Some manufacturers of these components worked constantly to overcome this stagnation and presented much better performing sliding materials about 5 years ago (e.g. Robo®Slide [6]). The most striking benefit of these innovative materials is its much higher durability regarding accumulated sliding path. As such this new generation of sliding bearings is able to stay in service for 50 or more years and bring into question all other elements. The paper will point out how single steel elements of sliding bearings can be substituted by UHPFRC and demonstrate their high performance. Based on extensive testing, different fiber types/ratios, bursting reinforcement and dimensions are analyzed. Requirements regarding surface quality for sliding purpose are also discussed. Particular benefits like specifically designed indication of overload and service failure are demonstrated. The presented innovation has the potential to pave the way for other mechanical engineering like components made of UHPC workshop made elements with a high degree of standardization.

Keywords: UHPFRC, bridge bearings, innovative design, durability, ductility

1 Scope

Ultra high performance (fibre reinforced) concrete as available nowadays has properties that go far beyond ordinary mass concrete (e.g. C30/37 according Eurocode 2 [1]). Especially, strength characteristics are several times higher and come close to heavier and more expensive elastic steel (e.g. S235JR according to EN 10025-2 [2]) with regard to compression. Of course, that does not apply for all properties, i.e. tensile strength, E-modulus or time-dependent behavior. However, this allows using this material for applications replacing massive steel components that are mainly exposed to compression. In addition to benefits due to material properties the concrete can be cast at ambient temperature in quite flexible shapes – and in contrast to cast iron steel that might be economic even if production numbers are small or product diversity is high.

In the civil sector there are some well suited applications of the material that fulfill the following characteristics:

- mainly stressed in very high compression
- complex geometry
- high diversity (many different sizes)
- notable numbers

These are for instance:

- anchor zones of pre-stressing cables or ground anchors
- bridge bearings

For anchor zones extremely high forces of pre-stressing or stay cables or ground anchors need to be transferred from the stressing element to the poor structure, e.g. concrete C20/25. Usually this is done by massive steel plates. Composite solutions as the “Hybridanker”-technology are combining the high compressive strength and free geometry of UHPC with different tensile materials like steel or carbon to create a prefabricated external anchor zone [3].

For bridge bearings not only high bearing compression forces need to be transferred. In addition to that movement and/or rotation need to be allowed. Especially for spherical bearings where a lot of effort is necessary for creating the shape in steel use of concrete might have a lot of benefits.

2 State of the art spherical bearings

In the sixties of the last century Fritz Leonhard, Wolfhart Andrä and Willi Bauer [4] invented the basis of modern bridge bearings, which still is applied in many aspects of current standards like EN 1337 [5]. At that time these bearings used pure PTFE as low friction sliding partner, lubricated with silicon grease and in contact with high polished austenitic steel plates.

It took about 50 years to find and establish higher performing sliding materials and apply them to modern state of the art bridge bearings. Nowadays high performance sliding material based on UHMWPE (Ultra High Molicular Weight polyethylene) is available for state of the art bridge bearings by European Technical Approvals like the one by the company mageba for spherical bearings [6]. The benefit from this new material is provided by significant higher wear resistance, combined with double pressure resistance (twice compared to PTFE), while allowing lower friction coefficients. In this way such bearings suit especially innovative and slender structures with a need for most compact and small bearings capable to resist permanent and fast movements with high accumulated sliding paths, like e.g. modern high speed railway bridges. Figure 1 shows such sliding material lubricated and installed in the calotte of a spherical bearing during assemply in the workshop.

Figure 1: ROBO®SLIDE disc installed in the calotte of a spherical bearing.

3 Basis and motivation

Low wear and low friction of the high performance sliding material requires suitable sliding partners. Austinitic steel plates and hard chrome have been used for decades for PTFE sliding bearings and have been applied successfully as well for the new high performance sliding materials. Especially hard chroming the spherical shaped calotte (used to provide the rotation capacity of the bearing) is very time consuming, cost intensive and error prone. Development aimed at alternatives to this process like powder coatings [7] have been tested within a European research project [8] and cooperated on by different European bridge bearing suppliers. In parallel the company mageba was able to test successfully another type of sliding laquere which was favourable regarding application and sliding behaviour. It is intended for coating steel surfaces which were formerly hard chromed. This coating system passed through corrosion protection tests according DIN EN ISO12944-6 [9] and has been proven during 480 h of salt spray test C4 corrosion protection performance.

Furthermore, sliding tests were conduced on test steel specimens based on general procedures provided in EN 1337-2 [10] and adapted to the high performance sliding material ROBO®SLIDE. The positive results of such tests encouraged the conduct of such tests as well on UHPFRC specimens coated with the same sliding laquere system. This gave the initiative for calottes of spherical bearings made of UHPFRC as such application of UHPFRC would have been impossible by hard chroming and impractical by powder coatings. Figure 2 shows a ROBO®SLIDE disc and sliding lacquere coated UHPFRC specimen after sliding test.

UHPFRC has been choosen for this element as other tests on non cementious and polymer only based matrix material has shown insufficient ductility and provided sufficient total load capacity, but failed in terms of service at a fraction of the desired load level. Furthermore it was expected that UHPFRC concrete can be designed to specific behaviour, which was proven in the following.

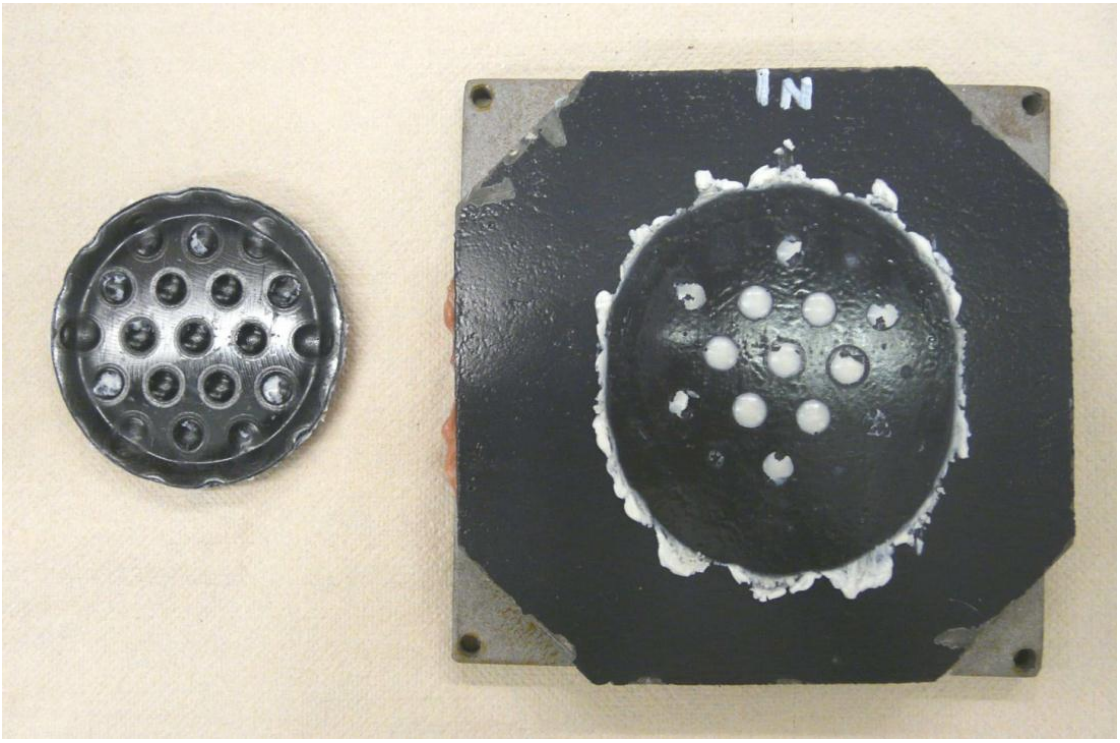

Figure 2: ROBO®SLIDE disc and sliding lacquere coated UHPFRC specimen after sliding test.

4 Test Program

All tests have been conducted at the Technische Universität München. Regular two and four columned test rigs of 6 and 10 MN maximum load capacity have been used for the testing. Experts of the Department of concrete structures of the Technische Universität München and experts in the field of sliding bearings of the Material Testing Insitute University Stuttgart (MPA Stuttgart) have surveyed the last set of tests to confirm proper testing and positive results.

All tests have been conducted with calottes only made of UHPFRC, while all other parts of the tested bearings were standard components made of S355J2+N. All made used of the high performance sliding material ROBO®SLIDE in combination with regular silicon grease according to standard application. The design and dimensions of the bearings followed basically the requirements and guideline provided by ETA-08/0115 [6].

In a total of three consecutive test series several parameters have been analysed regarding their effect on the behaviour of the overall system, which can be summarized as the following:

- different detailing and application of the sliding lacquer system
- different surface properties of the mould
- different height of the UHPFRC calotte
- different dimension and design load of the entire bearing incl. the calotte
- different ratio, shape, material and strength of the fibre reinforcement
- different ratio, shape, material, strength, location and detailing of reinforcement

During all tests the following parameters have been recorded for several load steps:

- development of compressive strength of the UHPFRC
- compressive strength of the UHPFRC (maximum 1h before test has been started)
- load applied to the bearing
- deflection measured at test rig
- deflection measured at several points on the calotte
- transversal spreading of the calotte at several points
- cracks including width, length and location

Most tests have been kept on design load level for at least one hour in order to allow evaluation of the stability of cracks on design load level and/or delayed cracking. Furthermore, some tests have been stopped before maximum load level and failure of the calotte in order to allow inspection of the sliding surface and evaluation of its integrity and serviceabilty.

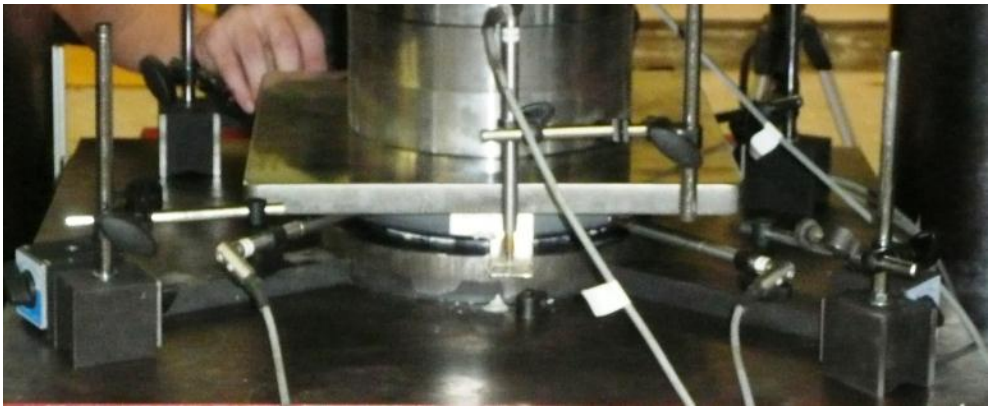

Figure 3: Spherical bearing instrumented and installed to the test rig.

5 Test Results

A profund overview of the influence of the single parameters was gained by the wide range of applied details and variations. Finally it was possible to find a stable, economical and practical combination allowing the required stiffness of the overall system crack stability and load restistance level of calotte. Figure 4 shows an example for one design adjusted almost exactly to the maximum compressive resistance of the high performance sliding material equal to 180 MPa. In this way the failure of the sliding material is on the same level as the UHPFRC calotte. The related deflection is recorded at the test rig and shows well the development of the stiffness providing allowable decrease only and sufficient ductility at the same time. It was possible to design the behaviour of the calotte very precisely by adaption of single parameters.

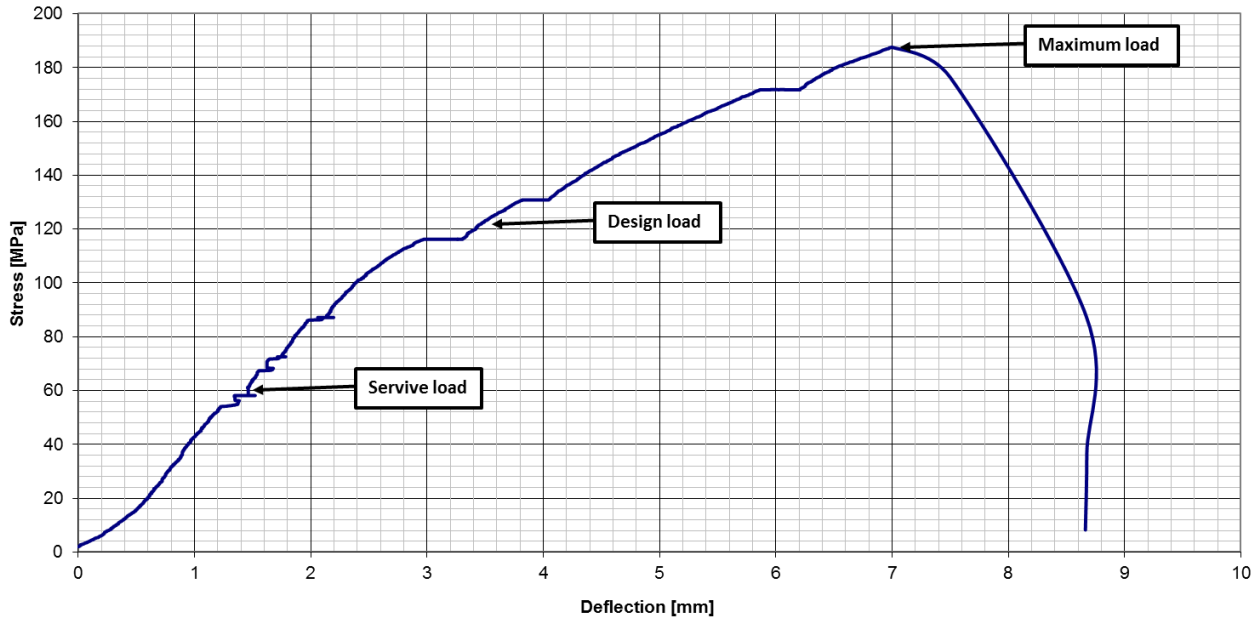

Figure 4: Load deflection curve measured at the entire bearing.

Probably more important has been a precise design of the crack behavior of the calotte. In this way crack widths could have been limited to less than 0.1 mm for certain load levels and the cracks could be used as a load indicator of the bearing. For instance, allowing cracks of more than 0.1 mm provide a permanent mark of an overload, when the calotte is designed to show such cracks at design load level. The cracks will not loose significant width when the load decreases again and keep clearly visible. In order to keep serviceability of the bearing it is important that the crack keeps at the outer vertical face of the calotte, which is easily accessible for inspection. It could be shown that a proper design of the calotte could prevent the cracks from reaching the curved and sliding lacquer coated surface of the calotte. Also, the cracks showed no influence on the performace of the sliding and service behaviour of the calotte.

Increasing the load further caused a higher number of cracks and widths of single cracks. Based on this a degree of overload could be evaluated. The sliding surface kept undamaged even at alarming crack widths at the outer vertical face of the calotte and allowed full function of the bearing.

6 Long term effects

The testing program investigated in detail the short term static behaviour of a concrete calotte. However, bearings are often used for bridges subjected to a long lasting service under heavy traffic. So it is very important to know more about fatigue and static behaviour under permanent compression.

For the latter subject reference is given to one of the latest research results published by Deutscher Ausschuss für Stahlbeton DAfStb (German Association for Reinforced Concrete), [10]. UHPC with steel fibres shows very little creep. Although there is not much experimental experience, permanent compression capacity can be taken as 90% of short-time compression capacity as usual for normal concrete (see [10], chapter 7.2.1.3.).

For fatigue behaviour reference is given to a similar product “Hybridanker”. For anchoring spherical nuts UHPC is used as bedding material surrounded by a tension ring. So the bedding UHPC is mainly stressed in multiaxial compression similar to the UHPFRC-calotte.

The contact area between steel nut and UHPC-filler is initially only a circle line. When applying load the pressure on the UHPC theoretically is infinite. Due to local platicization the contact area increases. So contact pressure is always close to compression capacity of UHPC.

Fatigue compressive testing has been done according to ETAG 013, [11], for a threaded bar with nominal tensile strength of 2,53 MN with the following conditions:

- 2 million load cycles
- upper load 65% F_{pk} = 1,65 MN
- bottom load = 52.5% F_{pk} = 1,33 MN (stress range 100 MPa)

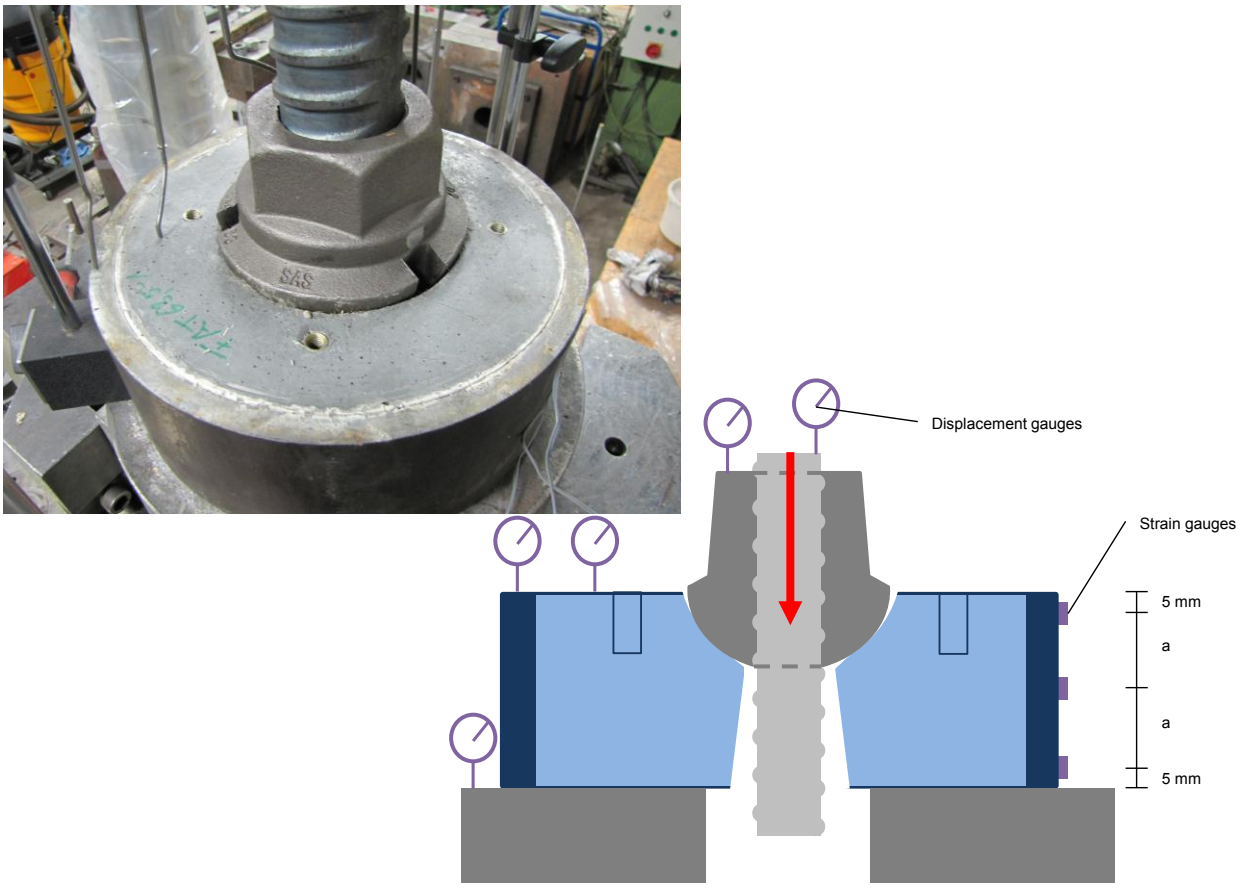

Figure 5: Set-up of fatigue test with Hybridanker for thread bar with spherical nut (courtesy of matrics engineering GmbH).

After that capacity testing has been done with the fatigue tested specimen and an identical specimen that had not been loaded before. As shown in Figure 6 no different behaviour could be detected but a slightly smaller slip for the specimen that had been loaded in fatigue prior to the capacity test.

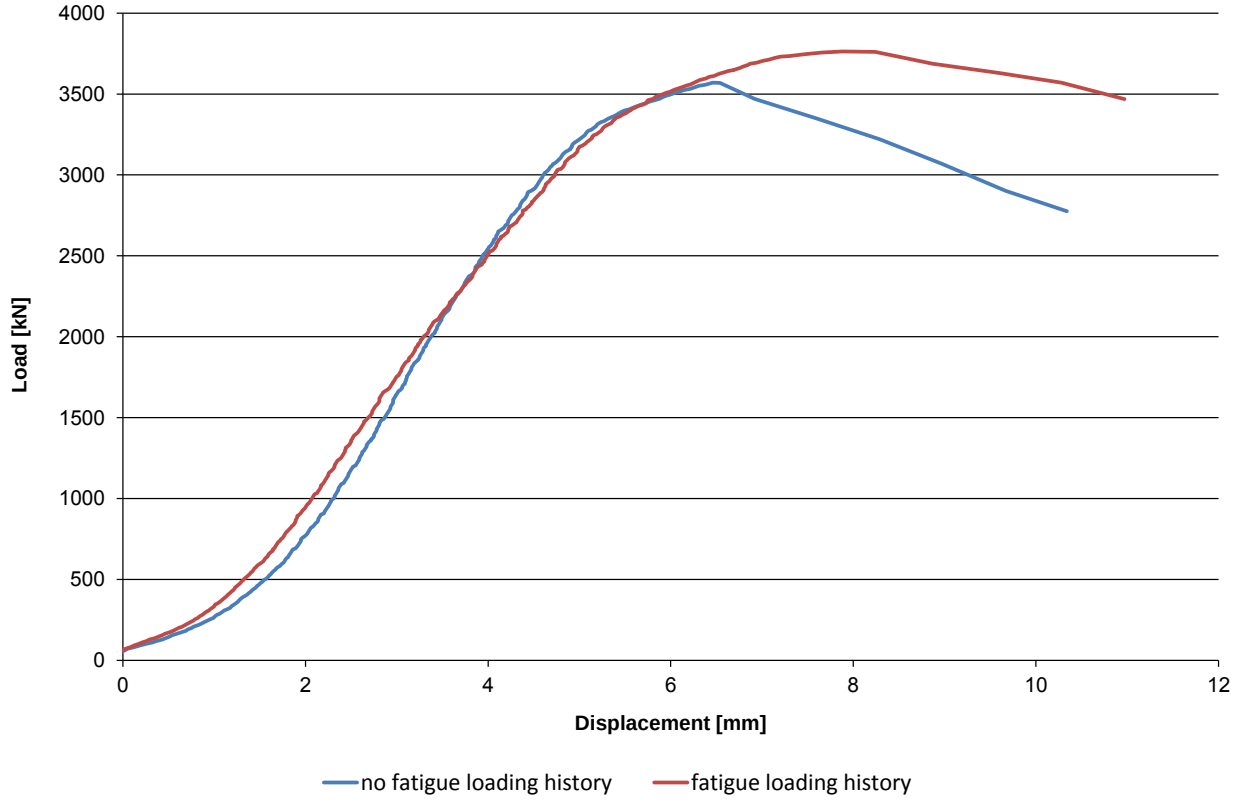

Figure 6: Load-displacement-diagramme of static compression tests with and without fatigue loading history.

7 Conclusions

The paper showed the single elements required for the design of high performance spherical bridge bearing with UHPFRC calottes. Substituting steel and hard chromed calottes with sliding lacquer coated UHPFRC elements can provide a cost effective and favourable process for the production of spherical bearings. The general performance and specific design requirements were analysed in an extensive test program. Suitable performance could be established and proven by full size tests. Long term effects as permanent static load and fatigue loading are not limiting the capacity significantly. Moreover using UHPFRC instead of steel avoids corrosion protection problems of the calotte and allows a powerful monitoring system of the bearings load history. Cracks at the calotte can be used as a clear, visible, alarming and permanent indicator of overload of the bearing. Such extra value of the bearing comes without drawbacks regarding load resistance and service performance of the bearing.

References

[1] EN 1992-1-1:2004 + AC:2010: Eurocode 2: Design of concrete structures - Part 1-1: General rules and rules for buildings.

[2] EN 10025-2:2004: Hot rolled products of structural steels - Part 2: Technical delivery conditions for non-alloy structural steels.

[3] Weiher, H.; Schulz, J.; Rohringer, M.; Zilch, K.: Concrete filled steel tubes for anchoring bars and starnds – concept and prototype testing. Proc. 3rd *fib* International Congress, Washington 2010..

[4] Andrä, W. Leonhardt, F.: New devolpments for bearings of structures, rubber- and rubber-pot bearings. *Die Bautechnik* 39 (in German), p. 37, 1967.

[5] EN 1337-1:2000: Structural bearings - Part 1: General design rules.

[6] European Technical Approval ETA-08/0115: mageba ROBO®SLIDE L2 Spherical bearing – Spherical bearing with special sliding material, issued 2008.

[7] Patent WO 2009/071051: Bearing of a structure, issued 2008.

[8] Wenzel, H.; Forstner, E.: MOBILE - Moveable Bearings Innovation Launch in Enlarged Europe. Pro. IABSE Symposium, Weimar 2007.

[9] EN ISO 12944-6:1998: Paints and varnishes - Corrosion protection of steel structures by protective paint systems - Part 6: Laboratory performance test (ISO 12944-6:1998).

[10] Deutscher Ausschuss für Stahlbeton: Heft 561, Sachstandsbericht ultrahochfester Beton, Berlin 2008.

[11] European Organisation for Technical Approval: ETAG 013 Guideline for European Technical Approval of Post-Tensioning kits for Prestressing of structures, Brussels 2010.

Study on the Application of UHPC for Precast Tunnel Segments

Norbert Randl[1], Arnold Pichler[2], Walter Schneider[1], Joachim Juhart[1]
1: Carinthia University of Applied Sciences, Austria
2: G. Hinteregger & Söhne, Baugesellschaft m.b.H., Salzburg, Austria

The use of steel-fiber reinforced Ultra-High-Performance-Concrete (UHPFRC) in the double shell segmental lining system is investigated. Serving as reference object is the Tunnel Chain Perschling (TCP) currently under construction which forms part of the four track west railway route extension between Salzburg and Vienna in Austria. The aim of the analysis is the design of an alternative UHPFRC exterior shell with minimum thickness while maintaining the deformation limit specified in the tender design with its C40/50 reinforced concrete segments. The calculation basis was an elastic foundation model, the radial foundation being represented by "compression only" springs. For the UHPFRC ("Ceracem BFM Millau" (2,5 Vol.-% of steel fibers)) a non-linear material law was used with a stress-strain curve according to the French guideline AFGC/SETRA (2002) and the material characteristics in accordance to experimental investigations carried out at CUAS.

Keywords: UHPC, UHPFRC, steel fibers, design, precast tunnel segment

1 Introduction

Segmental lining in tunneling

Tunneling in soft ground or at shallow depth (as the case is in the present study) requires immediate support by a stiff lining. For shield driven tunnels precast concrete tubbings may be used according to a single shell or a double shell segmental lining system (Fig. 1). In a single shell system precast concrete elements erected within the protection of the shield have to secure the structural stability of the tunnel as well as the serviceability (impermeability, durability) and specified quality requirements. In a double shell system the precast elements of the exterior shell only need to provide structural stability [1]. Sealing against water, i.e. waterproofing sheets, may be positioned between inner and outer ring.

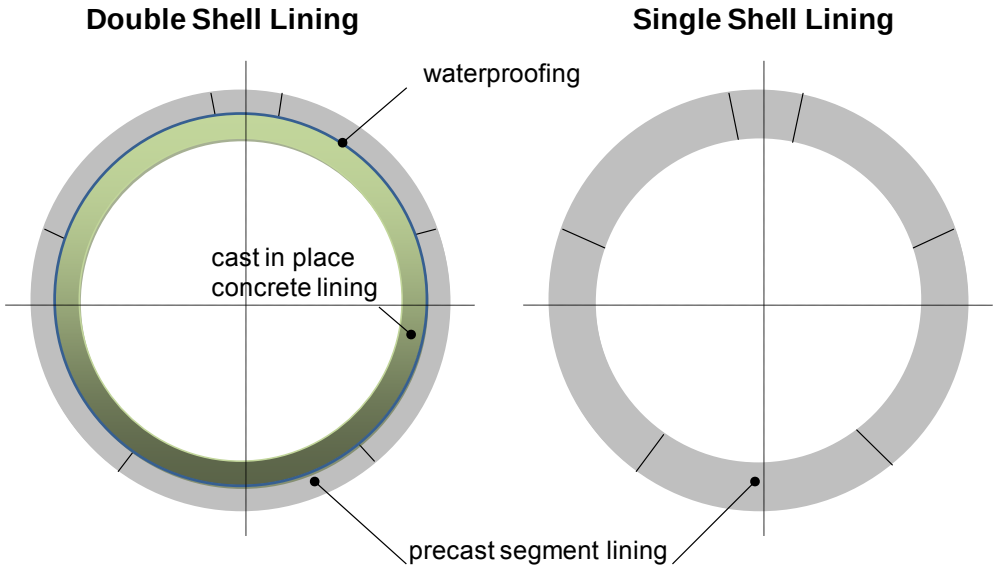

Figure 1: Segmental lining in tunneling.

Reference project Tunnel Chain Perschling

The Tunnel Chain Perschling (TCP) is part of the four track west railway route extension between Salzburg and Vienna in Austria. TCP serves as reference project for subsequent considerations. The lining of the TCP tunnel consists of a single precast element in the invert and a double shell system along the remaining circumference in which the exterior shell again consists of precast concrete elements (Fig.2). The element width measures 1,80 m. The ring is composed of 6 elements (5 regular + 1key) made of normal strength concrete (NSC) C40/50 which are placed without seal and couplers. Waterproofing towards the inner shell is provided by a double layer of impermeable membranes. The internal tunnel diameter is 11,50 m and the thickness of the precast elements 0,30 m (Fig. 3).

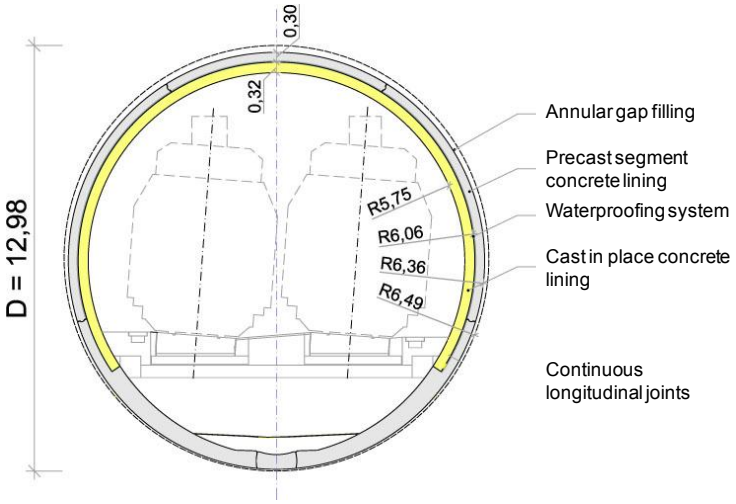

Figure 2: Standard cross-section of TCP [2].

Figure 3: Transport of tubbings at TCP.

UHPC in tunneling technology

Potential advantages of segmental lining elements made of UHPFRC are based on the enormous compression strength of approximately 200 MPa. The tensile strength of the uncracked matrix, however, compared to normal strength concrete, increases only sub-proportionally to a value between 7 and 15 MPa. The achievable tensile strength is mainly determined by the fiber content and geometry and also by the distribution of fibers in the material and their compound behavior [3, 4]. Contrary to conventional steel fiber reinforced concrete with fiber contents of around 0,5 Vol.% (or less) the fiber content in structural elements made of UHPFRC rises to 2 Vol.% and more. The use of fibers may substitute conventional steel reinforcement bars and minimize spalling risks and tensile splitting forces.

In addition, ultra high performance concrete shows extraordinary durability properties. The high material density makes UHPC particularly resistant against all kinds of external exposures. Due to reduced segment thicknesses further economical advantages (reduced excavation diameter and volume, reduced material quantity, reduced transport volume and mass with subsequent reduced construction duration) will be achieved.

2 Modeling

Static System

Computation models typically may be continuum models (FEM), bedded frame models and analytic models respectively. The continuum model computes with finite elements a perforated plate in a two or three dimensional situation. This model is preferably used for deep tunnels with a ratio h/d ≥ 3 where full compound between tunnel lining and ground is assumed. It delivers

internal force variables and deformations of ground and tunnel support as well ([5], [6], [7]). The present analysis assumes a shallow tunnel (h/d ≤ 2) with lost bedding capacity of the ground at the tunnel crown. A partially bedded model is applied where the effects of the ground are simulated in a simplified matter by applying elastic springs. Radial bedding is neglected at the tunnel crown due to local deflection of the shell and a possible subsequent loss of foundation in that area.

Contrary to the continuum model only deformations and internal force variables of the shell can be computed but not those of the enveloping ground [6, 7]. The circular profile of the statically indeterminate structural system of the lining ring is approximated by a polygonal framework consisting of 46 interconnected beams (see Fig. 7). A longitudinal twist of the joint socket is enabled constructively (convex-concave joint) and eventual rolling effects caused by eccentricity in the contact zone of the longitudinal joint may be valued as marginal. Therefore the model considers an articulated joint with a torsion stiffness of "zero" in accordance to [2]. The work analyzes a tunnel strip of 1 m width.

The radial resistance is characterized by the bedding modulus kr. It is composed of the constrained modulus E_s of the ground and the radius r of the tunnel profile. As the ground represents an inhomogeneous continuum it is difficult to define its exact characteristics. For rock mass stiffness of TCP a constrained modulus E_s = 250 MN m^{-2} was derived from ground exploration. The radial bedding modulus is approximated by:

$$k_r = E_s/r \text{ [MN m-3]} \quad \rightarrow \quad k_r = 250/6 = 41{,}7 \text{ [MN m}^{-3}\text{]} \qquad (1)$$

The radial foundation is represented by "compression only" springs. According to current experience the tangential bedding k_t can be set to $k_t = 0{,}5 * k_r$ at first estimation [5]. Neglecting the tangential component ($k_t = 0$) principally leads to a conservative result since that approach increases the bending moments. In the present case, k_t was assessed at 12,5 % (= 5,2 MNm^{-3}) of the radial bedding, a value in-between above mentioned reference values for the regular load case [2]. The tangential springs act on tension as well as on pressure forces.

Material Law for UHPFRC

For theoretic modeling of precast tunnel segments made of NSC, it is usually necessary to account for the non-linear behavior of concrete in the pressure zone, the crack development in the tension zone and the contribution of the concrete between the cracks (tension stiffening) as well as the linear elastic – ideal plastic behavior of the reinforcement steel [5, 9].

For applying a non-linear approach with UHPFRC, the stress-strain curve according to the French guideline AFGC/SETRA (2002) [10] is used. The German "Sachstandsbericht Ultrahochfester Beton" [3] also recommends the use of the stress-strain curve according to AFGC/SETRA. The present survey is based exemplarily on an UHPFRC-material called „Ceracem BFM Millau", produced by the Sika Corporation. It contains 2,5 Vol. % of steel fibers according to the formula given in [11], where test data concerning compression and bending tensile strength are published. Apart from literature, experimental investigations were undertaken by the Carinthia University of Applied Sciences in cooperation with the Graz University of Technology [12] with the aim to investigate the influence of different fiber content and of inhomogeneous fiber distribution. Tensile tests were performed at cores (Ø50 mm) drilled in two orthogonal directions (IB/QZB) from UHPC-prisms (100/100/400 mm) with 2 and 2,5 Vol.% of steel fibers, half of them afterwards being notched. Unnotched specimens are suitable to investigate the tensile strength of the cement matrix (represented by a first maximum in the stress-strain diagram after a linear-elastic ascent of the curve) due to the quite uniform stress distribution at the first crack when the load is introduced without eccentricity (Fig. 4).

Figure 4: Cracked notched and unnotched specimen after uniaxial tensile test [12].

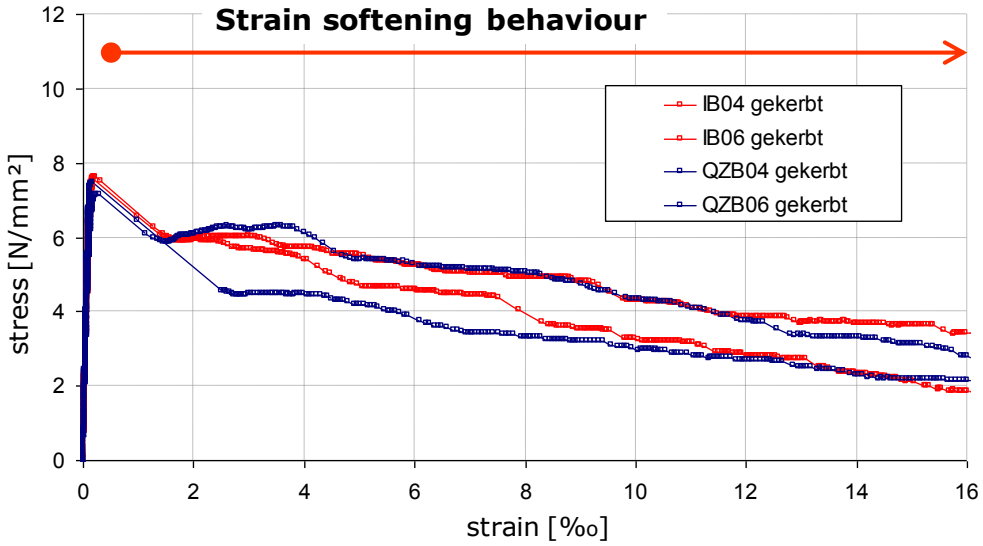

Figure 5: After-peak behavior with notched specimen (test result with 2 Vol.% of steel fibers) [12].

Notches lead to a concentration of the tensile stresses in these zones, however, the crack is well defined so that the after peak behavior, i.e. the effect of the fiber pullout, can be studied. Fig. 5 shows the results from uniaxial tensile tests with notched specimen containing 2 Vol.% of fibers, depicting a strain-softening behavior where the strength related to pull out of the fibers is lower than the matrix strength.

Based thereon and following the AFGC/SETRA guideline [10], the characteristic stress-deformation diagram for the tension and pressure zones of the „Ceracem“-UHPFRC with 2,5 Vol.% of fibers was established (Fig. 6, further details in [11, 12, 13]). The “Strain Softening Law” is used according to Fig. 6; however, the loss of strength in tension in reality is often more articulated in cracked zones than presented by the used stress-strain diagram [14]. In accordance with Fig. 6, the applied software STAB2D-NL [15] models the UHPFRC material as a polygonal framework for the tension and pressure zones. In cross sections where the load bearing capacity of the UHPFRC material is exceeded under tension forces the addition of steel reinforcement bars is envisaged. The computing program reflects a composite effect between UHPFRC material and reinforcement steel as derived from the state of the art knowledge for normal strength reinforced concrete.

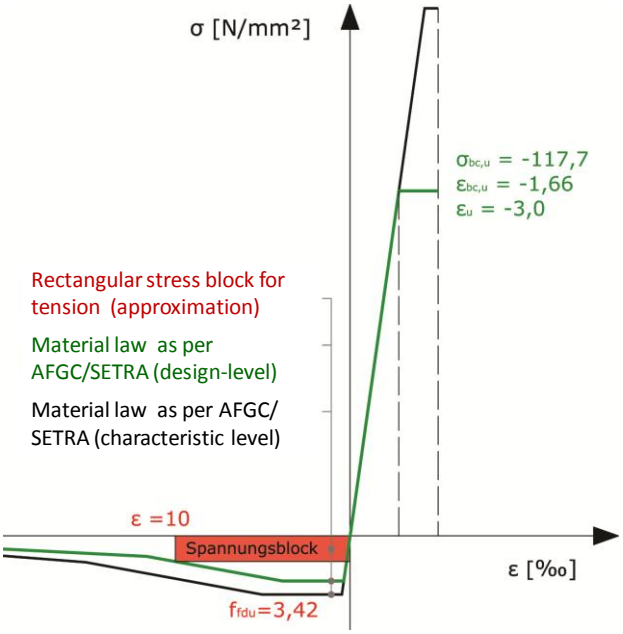

Figure 6: Used stress-strain diagrams for UHPFRC „Ceracem“.

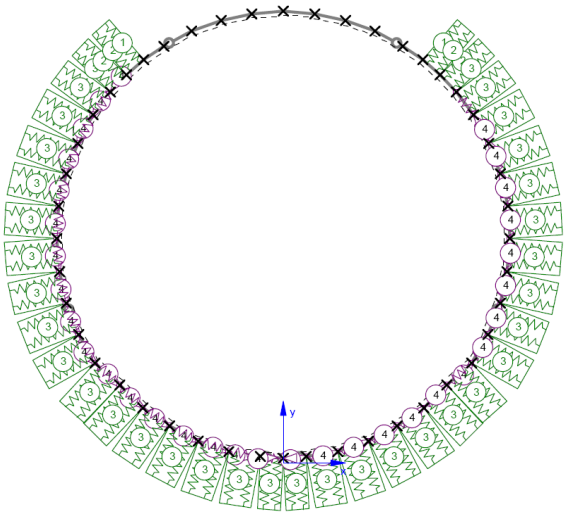

Figure 7: Structural system of tunnel ring.

Load Case approaches

During construction stage varying load case situations occur due to segment production, storage, transport and erection as well as due to feed pressure or pressure from the circular gap injection etc. [1, 8]. As permanent loads, the rock pressure, the water pressure, a possible swelling pressure and the dead load need to be taken into account. Depending on the height of the overburden also the load of buildings and live loads at the surface may require consideration. Additional impacts may be caused by structures and traffic loads acting within the tunnel, temperature changes, shrinkage, creeping and excess air pressure. Extraordinary forces due to an accident scenario within the tunnel, like fire, earthquake etc., principally need to be accounted for on a project specific basis [1, 8].

In the present case according to the reference project TCP, seven governing permanent regular load case combinations have been identified. Those comprise of load cases D1-D3 for large overburden (Fig. 8), D4-D6 for shallow overburden and load case C representing reduced ground pressure above the tunnel (Fig.9). In addition an accidental load case considering complete bursting of the ground above the tunnel at a certain critical overburden is analyzed. All of those load cases are superposed with the dead weight of the segment rings.

3 Computation and results

Computation Approaches

Three different approaches are performed for the analysis of the structural behavior, all of them based on the semi-probabilistic concept of partial safety factors. Linear and non-linear material laws are analyzed and the results compared. Approach 1 follows by approximation a linear-elastic material law. Related bending stiffness is defined as the one at non-cracked “Stage I”. Load effects are imposed at their characteristic level. Resulting internal force variables finally need to be multiplied with the relevant partial safety factors. Approach 2 reflects a non-linear material behavior according to Fig. 6 at its characteristic level. Resulting internal force variables are multiplied afterwards with relevant partial safety factors ($S_{G,k} * \gamma_G + S_{Q,k} * \gamma_Q$). Based on the non-linear material law and load effects at the characteristic level, the deformations at the limit state of serviceability have also been calculated. The deformation limit as specified at the TCP-

project was also obeyed for UHPFRC. Approach 3 follows EC 7 [16] and analyzes the load effects using the design loads (G_k * γ_G).

The bedding modulus is taken for all calculations at the characteristic level. The analysis is performed with the program STAB2D-NL [15] and is limited to a 2D-framework model. The calculation shows that due to the non-linearity, an increase of loads up to design-level results in higher bending moments compared to those derived from the analysis with loads at the characteristic level and multiplied afterwards with partial safety factors. The maximum deformation derived on the basis of approach 2 is shown in Fig. 8. The enveloping curve of internal force variables due to regular load case C by using the nonlinear approach 3 is presented in Fig. 9.

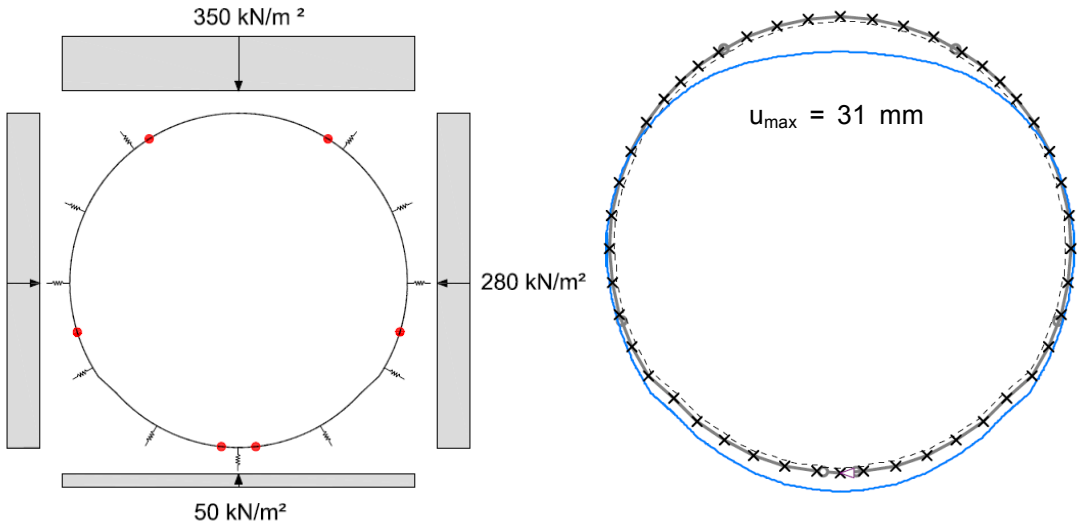

Figure 8: Load case D3 and according maximum deformation (Model 2 – characteristic level).

Design

The design value of the compression strength $\sigma_{bc,u}$ (f_{cd}) of UHFRPC for regular and extraordinary load cases is derived in accordance to AFGC/SETRA [10] and equals with its format the approach for reinforced normal strength concrete as per EC 2 [17]:

$$\sigma_{bc,u} = \frac{0{,}85}{\theta \cdot \gamma_b} \cdot f_{cj} \qquad \sigma_{bc,u} = \frac{0{,}85}{1{,}0 \cdot 1{,}3} \cdot 180 = 117{,}7 \quad MPa \qquad (2)$$

θ Coefficient for the duration of load effects (1,0 for loads acting longer than 24h)

f_{cj} Characteristic value of cylinder compression strength

γ_b Safety coefficient: 1,5 under normal condition and 1,3 for precast elements (here)

The factor 0,85 accounts for long term effects.

Cross-sectional design of the UHPFRC-segments was performed on the basis of the stress-strain diagram as per AFGC/SETRA [10]. For design purposes, the load bearing behavior under tension forces is represented by a stress-strain relation similar to the characteristic stress-deformation diagram used for the structural analysis (Fig. 6). The main difference is the introduction of partial safety factors (γ_b = 1,3 for regular load cases, 1,05 for the extraordinary load case [10]). For the sake of simplification, a rectangular stress block is introduced in the stress-deformation curve at the tension side. The same approach is used in the Austrian ÖVBB-guideline for fiber reinforced concrete [18] where the maximum tensile strain is limited to 10 ‰. Following that approach from 0 to 10 ‰ tensile strain, a constant stress value is introduced in the stress-deformation diagram at the tension side (Fig. 6). The distribution of stresses over the

cross section is then calculated by iteration with this material law, starting with a chosen strain distribution.

Results

Load case C is decisive for design (Fig. 9). Load cases D1-D6 cause mainly compression strains and therefore do not require any addition of steel reinforcement bars. Load case C however leads to the maximum related eccentricity e/h of the internal normal force which implies high bending loads at the cross section. The extraordinary load case with reduced safety levels on load- and resistance-side is evaluated separately.

For load case C, cross-sectional design leads to the requirement of additional steel bar reinforcement of 7,75 cm² for a precast element width of 1 m. For the full width of the precast element (1,8 m), this results in an amount of 13,95 cm² reinforcement. The extraordinary load case requires 14,12 cm²/m of reinforcement (further details are shown in [19]).

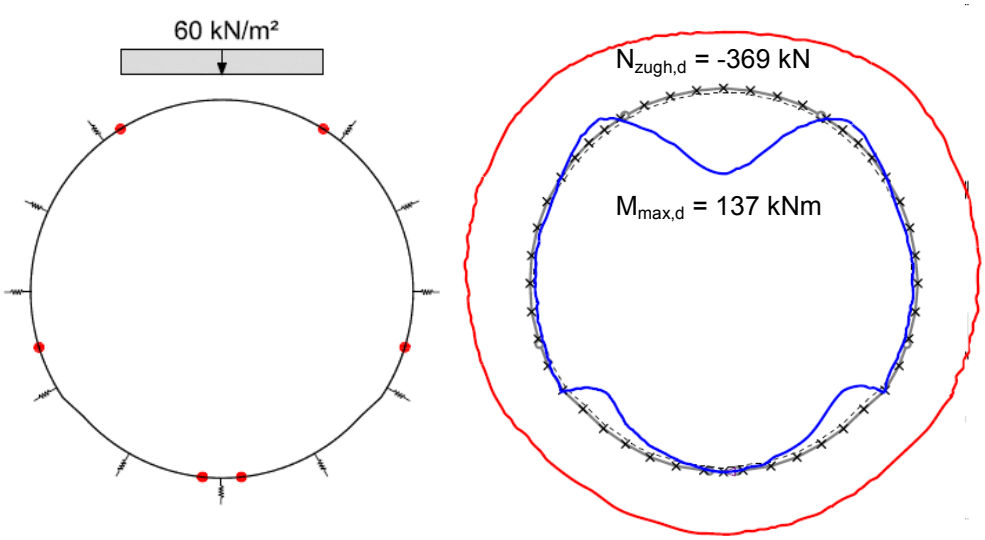

Figure 7: Load case C and enveloping design moment / corresponding normal force (Model 3).

4 Conclusions

Compared to conventional precast RC-elements of identical geometry, UHPFRC precast elements show an increased stiffness due to the higher E-modulus. In the present study, the thickness of segments made of UHPFRC is reduced until the defined deformation limit (from the reference project) is reached, thereby decreasing the segment thickness from 0,30 m to 0,22 m which corresponds to about 25%. The analysis was carried out with non-linear approaches on a partially bedded beam model.

Looking at reference objects of very long tunnels with large excavation diameters and segment thicknesses of 0,50 m and more, the authors expect even higher reduction percentages for segment thicknesses by the use of UHPFRC. The rather high material costs may be compensated for by savings in the element production and construction process. The extraordinary durability also will reduce life cycle costs, especially regarding objects built with the single shell lining system. The advantage of the increased load bearing capacity of UHPFRC elements compared to conventional precast steel reinforced segments may be used in particular where compression forces govern. Therefore smaller diameter tunnels with large overburden or shaft structures will be particularly interesting for further investigations.

5 Acknowledgements

The authors wish to extend special thanks to all those involved in the reference project TCP, in particular to the owner Österreichische Bundesbahnen (ÖBB), to the design companies ILF and VigIConsult and to the contractor STRABAG AG for the provision of information and all support granted. Further thanks are directed to Dr.–Ing. Uwe Pfeiffer for providing the computation software STAB2D-N which enabled the numerical analysis.

References

[1] ÖVBB Richtlinie 'Tübbinge aus Beton': Österreichische Vereinigung für Beton- und Bautechnik, Version 17 – Gründruck (2009).

[2] ÖBB Infrastruktur Bau AG, Baulos TKP - Tunnelkette Perschling, Documentation of 'Baulos 3' (2004-2005).

[3] DAfStb Sachstandsbericht Ultrahochfester Beton, Deutscher Ausschuss für Stahlbeton, Berlin – Wien – Zürich, Beuth Verlag GmbH, 1st Edn (2008).

[4] Fehling, E., Schmidt M. et al.: 'Entwicklung, Dauerhaftigkeit und Berechnung Ultra-Hochfester Betone (UHPC)', Forschungsbericht DFG FE 497/1-1, in: Schriftenreihe Baustoffe und Massivbau, Heft 1 (Kassel University Press, 2005).

[5] Hemmy O., 'Zum Gebrauchs- und Tragverhalten von Tunnelschalen aus Stahlfaserbeton und stahlfaserverstärktem Stahlbeton', Institut für Baustoffe, Massivbau und Brandschutz, TU Braunschweig, Vol. 170, 2003.

[6] Girmscheid G., 'Schildvorgetriebener Tunnelbau in heterogenem Lockergestein, ausgekleidet mittels Stahlbetontübbingen, Teil 2: Aspekte der Vortriebsmaschinen und Tragwerksplanung', Die Bautechnik 2/74 (1997), 85-100.

[7] Ahrens H., Lindner E., Lux K. H.: Zur Dimensionierung von Tunnelausbauten nach „Empfehlungen zur Berechnung von Tunneln im Lockergestein", Die Bautechnik 8/59 (1982), 260-273.

[8] Duddek H.: Empfehlung zur Berechnung von Tunneln im Lockergestein, Die Bautechnik 10/57 (1980), 349-356.

[9] Pfeiffer U., Quast U.: Nichtlineares Berechnen stabförmiger Bauteile, Beton- und Stahlbetonbau 9/98 (2003), 529-538.

[10] AFGC/SETRA: Bétons fibrés á ultra-hautes performances. Recommandations provisoires. Documents scientifiques et techniques. Association Francaise de Génie Civil, Setra, Bagneux Cedex (2002), 1-152.

[11] Maeder U, Lallemant- Gamboa I., Chaignon J., Lombard J. P.: Ceracem, a new high performance concrete: characterisations and applications, Schriftenreihe Baustoffe und Massivbau, Heft 3, Kassel (2004), 59-68.

[12] Juhart J., Freytag B., 'Experimentelle Bestimmung der Zug- Spannungs- Dehnungslinie an zylindrischen Proben aus UHPFRC', Research Report 2006_01, CUAS Baulabor (2007). URL: *http://www.fh-kaernten.at/bauingenieurwesen-architektur/bachelor/bauingenieurwesen/publikationen.html*

[13] Morak M., 'Design einer integralen einfeldrigen Plattenbalkenbrücke aus ultrahochfesten faserbewehrten Betonhalbfertigteilen', (Diploma Thesis TU Graz, 2005).

[14] Leutbecher T., Fehling E., 'Rissbildung und Zugtragverhalten von mit Fasern verstärktem Stahlbeton am Beispiel ultrahochfesten Betons', Beton- und Stahlbetonbau 6/104 (2009), 357-415.

[15] STAB2D-NL: Programm zur nichtlinearen Berechnung ebener Stabwerke, Version 2.80, *www.u-pfeiffer.de*, 2008.

[16] ÖNORM EN 1997-1 'EC 7: Entwurf, Berechnung und Bemessung in der Geotechnik – Teil 1: Allgemeine Regeln', Edn 2009-05-15.

[17] ÖNORM EN 1992-1-1: 'Eurocode 2- Bemessung und Konstruktion von Stahlbeton- und Spannbetontragwerken, Teil 1-1: Allgemeine Bemessungsregeln und Regeln für den Hochbau', Edn 2009-07-01.

[18] ÖVBB Richtlinie Faserbeton: Österreichische Vereinigung für Beton- und Bautechnik, 07/2008.

[19] Pichler, A., Randl, N., Juhart, J., Schneider, W.: "Untersuchungen zur Anwendung von UHPFRC-Tübbingen bei der zweischaligen Tunnelbauweise", Die Bautechnik 1/87 (2010), 19-32.

Architectural Concrete with UHPC for façades and interior design-recent application in Germany

Thomas Drössler
Benno Drössler GmbH & Co. Bauunternehmung KG, Siegen, Germany

The building company Benno Drössler has been using UHPC as a building material since 2009. This paper includes a report on three projects which are recent examples of the application of UHPC.
1. New construction of the headquarters of the Ferchau company in Gummersbach. In this project, about 900 m² of UHPC fair-faced concrete elements have been installed in a curtain wall construction. These concrete elements are about 4 cm thick and 3.0 m long, with the height spanning from floor to floor.
2. Cloakroom steles in the Bible Museum – Frankfurt, Main
These cloakroom elements, which measure 2.95 m x 1.05 m x 0.05 m, had to be clad in fair-faced concrete allround, which was achieved by casting the concrete into the vertical formwork gap from the narrow 5 cm wide side.
3. Staircase exhibit by Dyckerhoff AG made of white UHPC for the Bau 2011 trade exhibition in Munich:
The angulated structure of this staircase, which is only 29 mm thick, has been produced using white UHPC. Subsequently the precast concrete elements were bonded between two laminated safety glass cheeks using an epoxy resin adhesive.

Keywords: façades, structural analysis, design, production

1 New construction of the Ferchau headquarters in Gummersbach: fair-faced curtain wall in UHPC concrete

Design

The design for the new Ferchau headquarters on the old Steinmüller site in Gummersbach was produced by Gerber Architects, Dortmund, and features a basic rectangular footprint. The rooms are grouped around a central inner courtyard, which is open at the top, and an enclosed four-storey entrance foyer. The openness on the inside contrasts with the austere glass and fair-faced concrete element patterns of the façade. The fair-faced concrete elements consist of approx. 3.0 m high pilaster strips and approx. 1.50 m long parapet elements, with a total of about 1,120 individual parts (the area measures about 900 m² in total), forming the main design element of the outer façades as well as the façades around the open internal courtyard and the entrance foyer (see Figures 1 and 2).

Figures 1 and 2: Elevation of north façade and inner courtyard.

Concept and detailed design

The architects Ahlbrecht, Felix, Scheidt, Kasprusch were in charge of the façade design, the overall detailed design and site supervision. According to the scheme design, the façade specification called for a conventional curtain wall façade with a thickness of up to 12 cm. The grey colour of the fair-faced concrete was intended to blend in with the neighbouring buildings on the Steinmüller site, which were also built in fair-faced concrete.

However, during the initial discussions with contractors, the following difficulties emerged:

Firstly, it is very difficult to reach the inner courtyard and, especially, the covered four-storey foyer which has conventional, and hence very heavy, precast concrete components.

Secondly, the space available for the façade panels on the very slender shell structure is very limited and is further encroached upon by bonding work at the window areas. This makes the installation of precast concrete curtain wall façades with conventional fixing systems very difficult.

One solution to the problem is to minimise the thickness of the concrete panels in order to facilitate the installation in the areas with difficult access (the inner courtyard and roofed-over areas) and in order to reduce the width required for fixing the panels on the supporting structure. Having seen sample panels, the architects and the client opted for a design with 4 cm thick elements made of smooth, grey UHPC with an identical surface finish as conventional fair-faced concrete (see Figure 3).

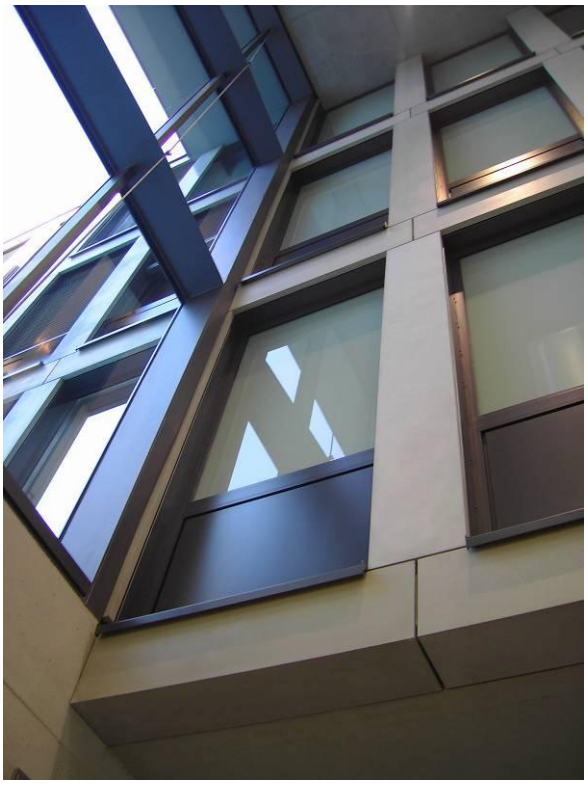

Figure 3: Elevation of roofed-over entrance area (internal).

Technical details

The façade elements are produced and monitored in accordance with DIN V 18500. The structural calculations for the façade and supporting structure are based on DIN 1055 and DIN 18516. In order to comply with structural requirements, the concrete material must have high bending tensile strength and be tested accordingly. In this case the the structural calculation demanded a present bending tensile strength >3.1 N/mm² according to DIN 18516-3, 12.99 including a 75% statement of probability and a triple factor of safety which was verified by a test

certificate according to DIN V 18500 and DIN EN 12390-5. No reinforcements or fibres were used. The elements are fixed to the shell structure using anchor pins and specially dimensioned holding and supporting brackets in stainless steel (see Figure 4).

Figure 4: Façade fixing detail.

Production

Owing to the large number of elements required it was possible to produce 20 to 30 elements per production day. The elements are cast in prefabricated forms which are placed horizontally on steel tables. Once the panels have been removed from the forms using vacuum lifting equipment, they are placed in specially designed boxes and stored where they are protected from the weather. Then they are secured for transport and shipped to the building site.

Characteristic properties of UHPC

Self-compacting UHPC is a very sensitive construction material which during mixing and in production requires nearly constant environmental conditions and production processes. The very dense surface shows a very accurate imprint of the formwork surface. Furthermore, some tests with different forming oils have revealed reactions with resulting discolourations of the concrete surface. The average tensile strength and compressive strength of the UHPC / HPC varies according to the composition of the concrete recipe and the requirements of the special projects. For the structural calculation of façades elements according to DIN V 18500 and DIN 18516-3, 12.99 the bending tensile strength and the ultimate anchor load are relevant and verified by test certificates.

Installation of elements

Once on site, the holes for the anchor pins are drilled, the elements are lifted into place on heavy-duty scaffolding, using suitable lifting apparatus, and they are then fixed manually to the shell structure with the anchor dowels. The reduced weight of the elements made it much easier to reach and clad the façades of the inner courtyard and the roofed-over four-storey entrance foyer (see Figure 5 to 7).


Figures 5 and 6: View of corner installation and completed corner.

Figure 7: View of north-western façade corner.

Project details:
Building owner: FFI Frank Ferchau Immobilien GmbH
Scheme design: Gerber Architects
Façade design, detailed design and site supervision: Ahlbrecht, Felix, Scheidt, Kasprusch
Structural calculations, production and installation: Benno Drössler GmbH & Co. Bauunternehmung KG

2 Cloakroom steles in the Bible Museum – Frankfurt, Main

Design

As part of the re-design of the new reception and cloakroom area in the Bible Museum in Frankfurt, Main, the architect Peter Harroider included 8 concrete steles measuring 2.95 x 1.05 x 0.05 m with a fair-faced finish on all surfaces (see Figures 8 and 9).

Figures 8 and 9: View of extension to the Bible Museum and Interior.

Technical details and production

The architect's requirements (thickness of only 5 cm and fair-faced finish on all sides) can only be fulfilled with self-compacting UHPC concrete. The material is filled into the vertical formwork from the 1.05 m high and 5 cm wide side. The 5.0 cm wide side, which is used for filling, is slightly larger; this makes it possible to grind down this side and thus achieve an identical appearance to the other sides with the smooth formwork pattern. Originally, the design called for a very dark, anthracite-coloured surface. During production tests it was discovered, however, that the pigmented UHPC is very prone to form pores and cavities when cast in vertical position. It was therefore decided to produce the steles with a nano-scaled white cement in natural white. The mixture does not contain reinforcements or fibres (see Figure 10).

Figure 10: Interior view of detail.

Projects details:
Building owner: Frankfurter Bibelgesellschaft e.V.
Design: Peter Harroider, Dreieich
Distribution and structural certificates: durcrete GmbH, Limburg
Production: Benno Drössler GmbH & Co. Bauunternehmung KG, Siegen

3 Staircase exhibit by Dyckerhoff AG made of white UHPC for the Bau 2011 trade exhibition in Munich

Design

The design of the staircase exhibit by Luis Ocanto-Arciniegas (Ourstudio – Architecture and Design) is intended to demonstrate the capabilities and yet lightness of the new material UHPC. The monolithic angulated structure of this filigree precast concrete staircase is only 29 mm thick. The angulated structure of the stair flight and landing have been bonded between two 20 mm thick staircase cheeks of laminated safety glass. The exhibit is 4.0 m long and 2.0 m high and comprises three parts: the lower flight, the landing and the upper flight.

Technical details and production

The intention was that, if possible, the angulated structure of the staircase and landing would have a smooth surface like that of the formwork. This meant that the steps of the staircase had to be cast in vertical position, with material poured in from the 29 mm wide side and the face on that narrow side being ground smooth afterwards. As the opening for filling in the concrete was very narrow, a new mixture of self-compacting UHPC had to be developed. Using the Nanodur Compound 5941 (white), a fine-grained mixture with a proportion of 1 volume % of micro steel fibres was developed. The micro steel fibres are intended to increase the ductility of the material and counteract stresses in case of cracking. In this fine-grain mixture, the 0/2 mm pit sand and 2/5 mm split material is replaced by < 0.5 mm quartz sand.

The material is cast monolithically in vertical formwork (see Figure 11).

Figure 11: Vertical concrete casting process.

Bonding the glass staircase cheeks

The required tensile bending strength is reached after a curing period of seven days. After that period it is possible to attach the laminated safety glass cheeks with epoxy resin in order to stabilise the staircase and provide a safety structure.

Load test

In order to verify the loadbearing capacity of the structure, which was calculated as part of a theoretical feasibility study, a load test was carried out on a test sample. For this purpose, a load of 100 kg was applied to each step and a further weight of 100 kg was suspended from the left-hand and right-hand glass cheek (see Figures 12 and 13). Once this load test had been passed successfully, a further test was carried out in which the test sample was loaded until

breaking point was reached. To do that, two precast concrete components with a total weight of approx. 7.4 tonnes were placed on a timber structure which was installed on 4 steps. Even under this weight of 7.4 tonnes, the staircase did not develop any cracks in the angulated concrete structure or the glass cheeks or show any failure of the bonded joints (see Figures 12 and 13). Meanwhile another load test was carried out at the TU Dresden where the glued connection collapsed under the weight of approx. 10.8 tonnes (approx. 2 tonnes per step). The scientific analysis is not yet completed.

Figure 12: Load test with weights.

Figure 13: Load test with precast concrete components.

Exhibit at the trade fair

The three staircase elements were assembled to form the staircase at the trade fair stand. With its combination of UHPC and glass it offers attractive design options for the future, especially using the new bonding technology for joining (see Figure 14).

Figure 14: Staircase exhibit at the trade fair.

Project details:
Idea and Nanodur Compound 5941: Dyckerhoff AG
Design: Ourstudio, Dortmund
Structural considerations: G.tecz, Kassel
White laminated safety glass: Schott AG, Mainz
Prefabricated staircase components and bonding: Benno Drössler GmbH & Co. Bauunternehmung KG, Siegen

4 Conclusions

The examples of UHPC concrete applications given here are only a small part of the visionary potential of this material. However, further research and development will be required in order to develop the full potential of UHPC and make it a realistic choice for commercial and industrial applications. Further standardisation of applications will only be possible with the close cooperation of research establishments, together with representatives from industry and users.

The First Architectural UHPC Façade Application in North America

Peter Seibert[1], Vic Perry[1], Gamal Ghoneim[2], Gerald Carson[2], Raafat El-Hacha[3], Ignacio Cariaga[4], Don Zakariasen[4]

1: Lafarge North America Inc. – Ductal®, Calgary, AB, Canada
2: DIALOG™, Calagry, AB, Canada
3: Dept. of Civil Engineering, University of Calgary, AB, Canada
4: Lafarge Canada Inc. – Precast Division, Calgary, AB, Canada

In North America, precast elements manufactured using ultra-high performance concrete (UHPC) have been in use in the bridge industry for many years. The use of UHPC is starting to enter into the building industry with "The Atrium" project in Victoria, BC as the first building in North America to have an entire architectural UHPC façade application. The close collaboration between the building owner, building architect, precast panel designer, precast manufacturer, and UHPC material supplier resulted in highly durable, attractive, thin, textured and curved UHPC panels that are part of a unitized curtain wall system. This paper will present a project overview, the impact to the building industry, fundamentals of the UHPC technology, precast element details, manufacturing, casting procedures, installation,and the importance of a strong collaborative effort when introducing highly new innovative solutions are included. The UHPC precast panel design and validation tests will be reviewed and discussed.

Keywords: UHPC, architectural precast elements, ductile, durability, fiber-reinforced, impermeability

1 Background

Ultra-High Performance Concrete (UHPC) has been in use since the mid-90's and for the last decade. In North America, it has been gaining popularity in highway and pedestrian [1] bridge applications [2] in the form of precast girders, full-depth bridge deck panels [3] and in-fill deck joints [4] [5] [6]. This paper presents "The Atrium" in Victoria, British Columbia, which is the first building in North America to have a UHPC façade. This unique project involved the close collaboration between; panel designer - DIALOG™, precast manufacturer/UHPC material ("Ductal®") supplier - Lafarge Canada Inc., and panel testing agency - Department of Civil Engineering, University of Calgary. A result of this collaboration is the customized design and creation of highly durable, attractive, ultra-thin (15 to 20 mm) UHPC cladding panels for a unitized curtain wall system.

2 Project Highlights

Comparison with the Existing & Conventional Practice

For building facades, architects, building officials and owners traditionally prefer natural materials such as stone, granite and marble or manmade materials like brick or concrete block. Exterior Insulation Finishing Systems (EIFS) are also common in the commercial sector but not suitable for buildings with openings or for integration with other wall units. Natural materials can resist compressive loads but have limited flexure resistance, no tensile resistance, and are not suitable for producing curved panels eliminating the need the assembly of multi segments of straight panels with complicated backing frames. Introducing an irregular surface texture on panels made of such materials is possible but not practical and would be labor intensive, extremely costly and result in walls about four times thicker and heavier than the UHPC cladding utilized in the Atrium project. Additionally, since this project is located in a seismic zone, the heavier panels penalize natural products.

Understanding the characteristics of UHPC; very high compressive strengths (up to 250 MPa) associated with ductility, flexural behavior and tensile properties -- in addition to its superior durability characteristics and flowability/mouldability, made UHPC the logical choice for use in the seven-storey building's cladding panels.

Collaborative Team Approach

From the early stages of this project, through to completion, it was important to establish and maintain an open, strong collaborative team approach, with a high level of trust (between the owner, architect, designer and fabricator) in order to complete prototyping, obtain approvals and avoid delays or problems with the project schedule. This team approach is "core basis" and "key requirement" to ensure a successful completion of UHPC projects especially due to the lack of design guidelines and codes in North America. From this team approach and this project, several advantages are anticipated to positively shape the North American industry.

Impact on Building and Construction Industries

In a world of increasing challenges, innovative thinking and sustainable leadership, UHPC architectural cladding provides a superior solution for The Atrium that will be appreciated by the community for generations to come. As a first of its kind in North America, this project is truly innovative and offers a positive, new approach for building and construction professionals with respect to the:

- architects' creative designs and expectations with unlimited demands on shape and form;
- structural engineers' ambition for providing safe, durable and maintenance-free structures and elements of structures;
- clients' or owner's aspiration for a building that is attractive, "Green", safe, operable, economical and profitable (including life cycle costs);
- contractor's demands for economical designs that can be constructed efficiently and safely in a timely manner and;
- precaster's/erector's concerns for ease of construction - making all the above possible.

In addition, UHPC building facades, when associated with proper choice of colors, can improve building envelope performance with increased potential for sustainability and energy efficiencies. Furthermore, UHPC will allow reduction in wall thicknesses and overall savings in material weights and quantities.

3 Project Description

The Atrium building is close to 18,600 m^2 of "Class A" commercial/retail space, located in downtown Victoria, British Columbia, Canada (see Fig.1). This seven-storey structure, with an open atrium at the building's centre, is targeted to achieve Leadership in Energy and Environmental Design (LEED) Gold rating through the Canada Green Building Council. Its high efficiency building envelope, which utilizes UHPC panels designed to be as thin as possible, is one of the major elements in this consideration.

To reflect the vibrant nature of downtown Victoria and its nearby waters, the building architect (D'Ambrosio Architecture + Urbanism) wanted to create surface texture on the panels (see Fig. 2), and curved panels at the corners of the building and into and out of the atrium perfectly utlizing the characteristics of UHPC.

Figure: 1 Atrium, Victoria.

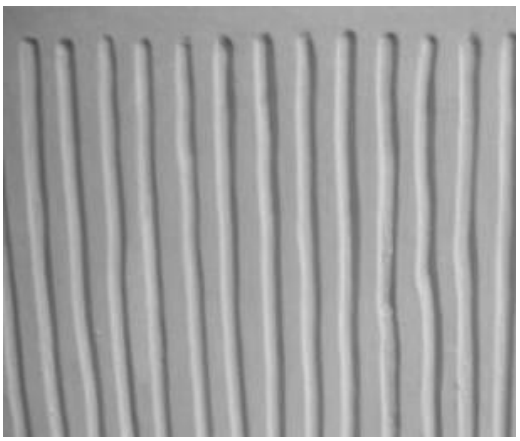

Figure 2: Surface Texture of all UHPC panels.

4 Circumstances for UHPC Selection

The following circumstances influenced the selection of UHPC for construction of the building façade:

1. Importance of sustainable construction and life cycle. Most sustainable construction projects are based on the environmental impact of the employed materials at the time of their production and construction. Some natural materials have low environmental impact at the time of production but have a short-term life. For the Atrium project, the goal was to achieve a balance between this and the life cycle. Considering that concrete is the most common manmade building material on the planet and a source of industrial emissions, minimizing the quantities of concrete is a step in the right direction. Using Fick's law for ion transportation predictive modelling (Fig. 3) and results from tests in salt water exposure, it is estimated that it would take 1,000 years for UHPC to have the same level of chloride penetration as HPC would have in less than 100 years. With the expected increase in service life, sustainable construction is obtained by utilizing minimum amount of materials for the intended function.

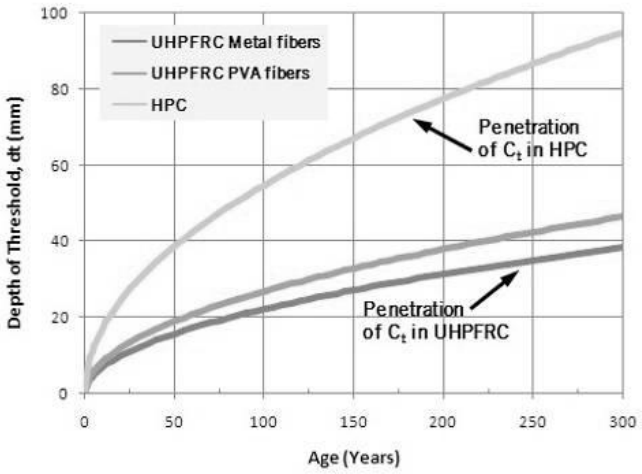

Figure 3: Predicting Service Life with Chloride Ion Transportation Predictive Modeling: UHPC vs HPC [7].

2. Minimize weight of the building exterior walls in order to:
    a. minimize initial cost as UHPC is more expensive by comparison to normal or high performance concrete;
    b. reduce the seismic forces on the support structure as the City of Victoria has one of the highest seismic ratings in Canada and;
    c. permit ease of assembly into the unitized curtain wall system at an offsite location and ease of installation on site. Conventional precast panels would have involved swinging large, heavy panels through the air to pin them on a previously erected wall system. This process was eliminated since the panels were preassembled into the wall system.

3. Maximize panel dimensions to limit the number of joints between the panels and reduce the number of bridging components to obtain a highly effective building envelope with smaller wall thickness in comparison with conventional walls.
4. Use a material at the building corners and into and out of the atrium (where curved panels are required) that allows freedom to form monolithically tight radial curves instead of smaller, segmented and stilted flat panels which would create more seams and openings, potentially reducing the building's energy efficiency.
5. Minimize potential corrosion issues and/or rust stains on the building façade by not allowing conventional reinforcing steel bars or concrete mixes with steel fibers. For this reason, a UHPC product containing polyvinyl alcohol (PVA) fibers and no metallic reinforcement was used resulting in low impermeability.
6. Use a white color UHPC mix to enhance the energy efficiencies and have the panels reflect the sun's heat energy to reduce the cooling load during service life.

5 UHPC Panel Geometry and Design

The façade design utilized 690 precast panels of flat, curved and partially curved panels. All panels were 1,300 mm high and varied in width from 750 to 2,150 mm with majority 1,300 mm wide (typical panel shape is depicted in Fig. 4). The surface texture or face ribs, which are roughly 5mm deep and vary in width (10-20 mm), are 10-20 mm apart in irregular form as shown in Figure 2.

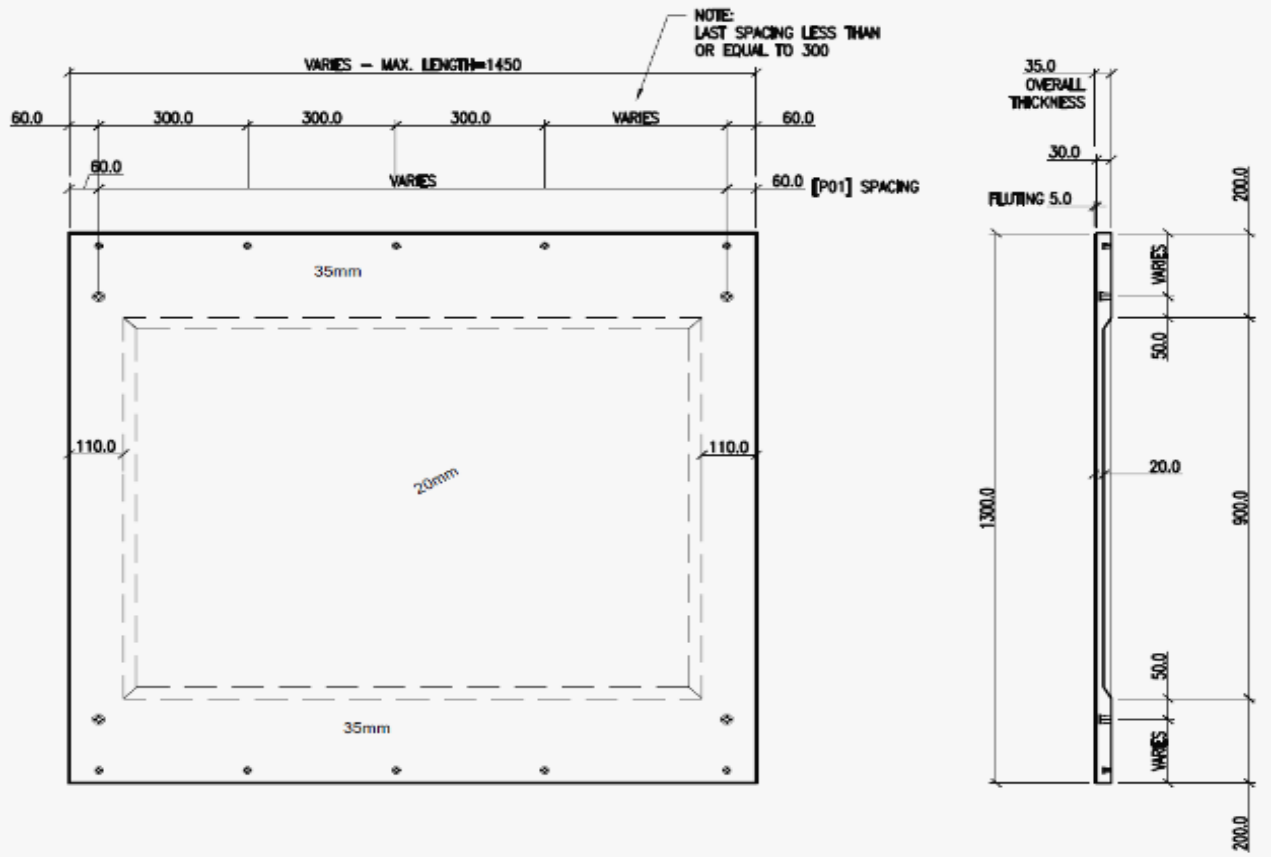

Figure 4: Typical Panel Elevation and Side View

Principal stresses and strains were used in the section design and the finite element method was used to predict the panel behavior and take into account the different thicknesses of each panel. Thin shell elements were used to model the panels and obtain the internal forces and principal stresses [8] [9], which were then. compared to the UHPC mechanical properties [10]

[11]. The lateral displacement of the panels was limited to span/600, which played a major role in selection of the panel thickness due to connections with the glass units.

Another factor that played a role in the geometry and thickness design of the panels was the need to thicken the panels around the perimeter to allow for proper sealing of the vertical joints between the precast panels and the horizontal joints between the precast and the zinc and glass panels. The increased perimeter thickness and surface texture caused a ribbing effect that enhanced the behavior of the panels after cracking and in the inelastic range of the behavior, which was apparent from the exhibited ductility during load testing.

The panels in their final position support their self weight as well as wind loads and transmit the seismic forces to the backing frame. In addition, due to the different thicknesses within the panel and the configuration of the face and back ribs, in-plane forces develop from arching action. To reduce such forces in-plane movements and volume changes due to temperature effects were accommodated in the support angles that are part of the backing frame; designed by the curtain wall manufacturer. The connections (Fig. 5) to the backing or support system were simplified through the use of bolted connections, utilizing commercially available inserts placed in the thickened perimeter of the panels. The inserts, located 30 mm from the top and bottom edges of the panel, are used for attachment of the zinc and glass panels. Fig. 6 depicts curved panels during construction and fully installed.

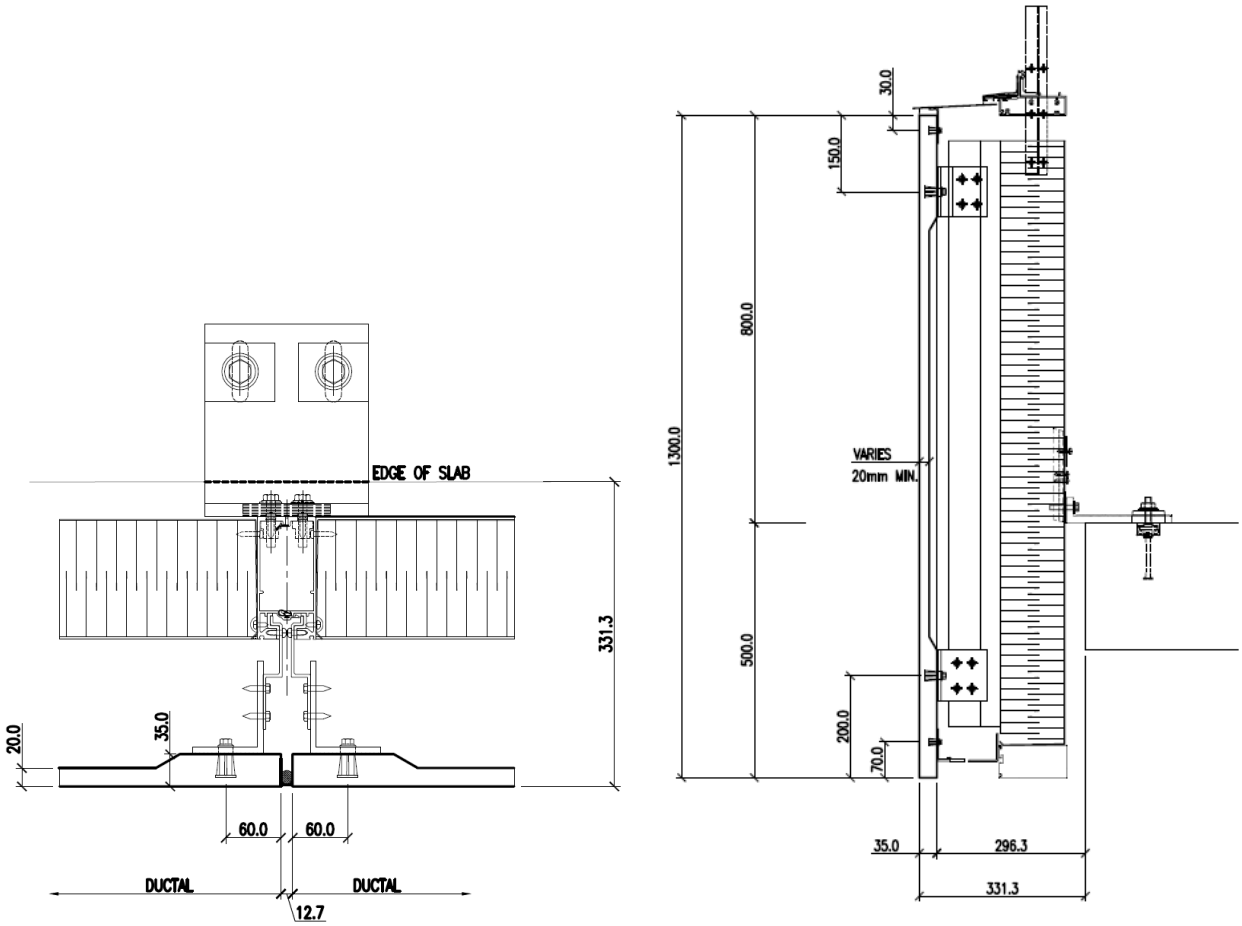

Figure 5: Precast Panel Connections.

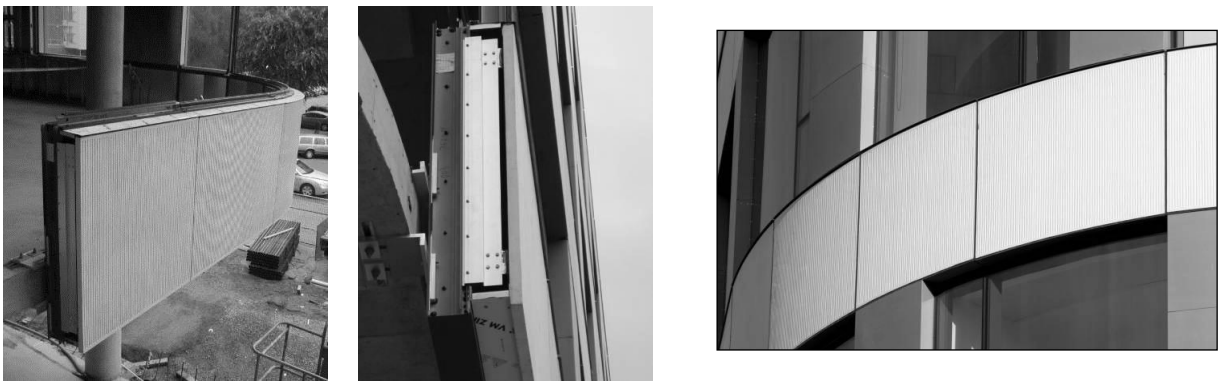

Figure 6: Curved Panels during Construction and Fully Installed.

6 Validation of UHPC Panel Design [12]

Due to the limited experience of using UHPC with PVA fibers in structural applications in North America [13], the structural design of the panels was validated via full scale testing at the University of Calgary. Fig. 7 shows a schematic of a panel testing arrangement and panel under wind pressure and under wind suction loads. After successful validation of the wind and suction loading, the panel was loaded to failure as shown in Fig. 8. The testing concluded that panel design could safely be carried out using elastic finite element and section design can be based on material models that rely on manufacturer's and published data.

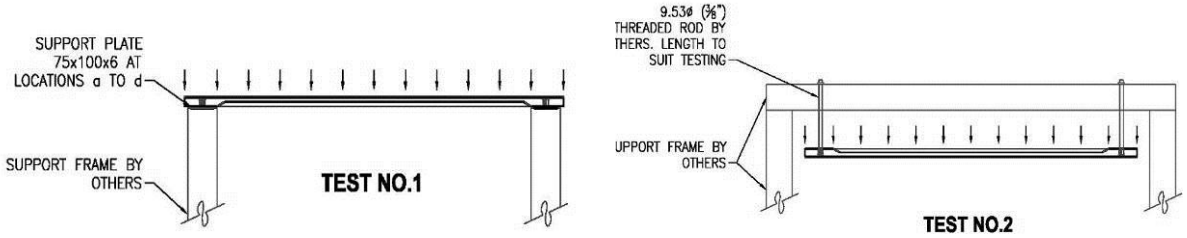

Figure 7: Testing Schematic.

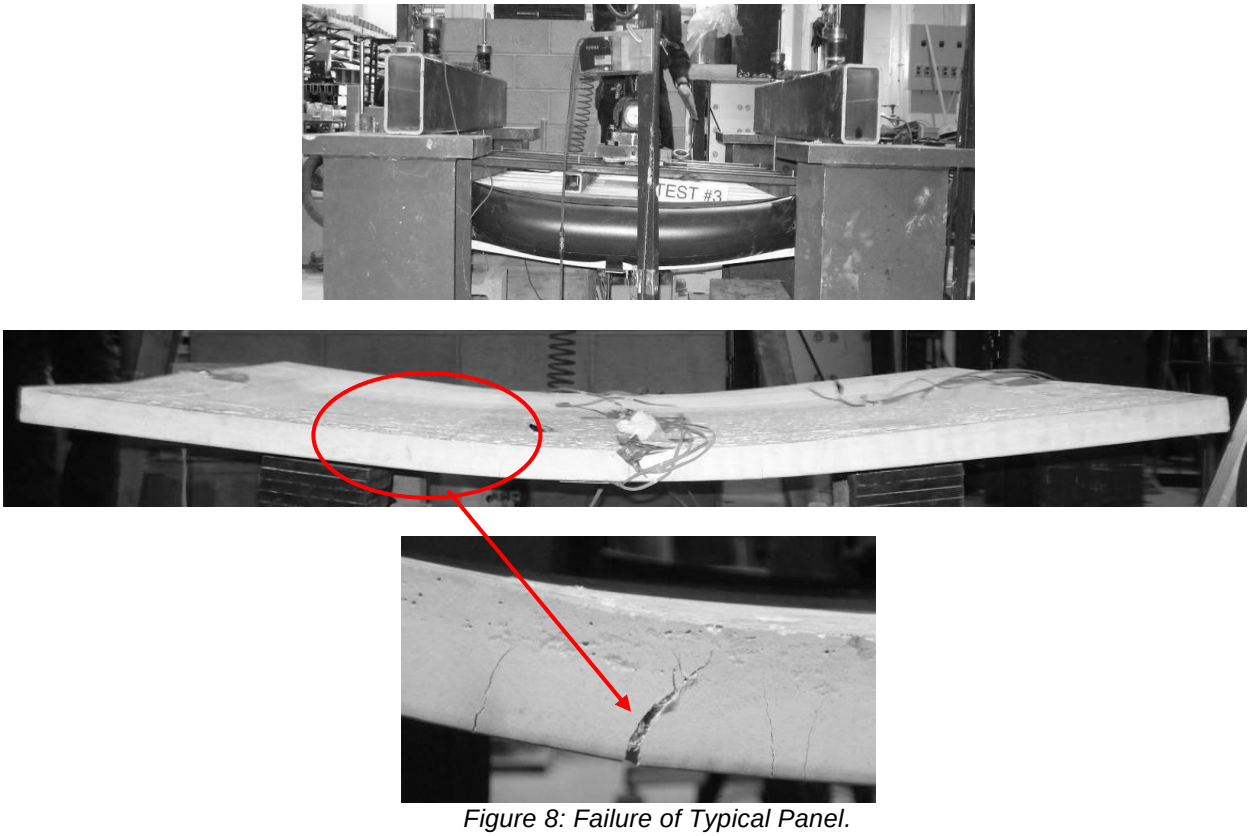

Figure 8: Failure of Typical Panel.

The amount of ductility exhibited by the panels during testing as shown in Fig. 9 indicate the panels can safely support much higher loads than required however the lateral displacement would not be acceptable for connections with the glass; one of the main factors in the selection of the panel /rib thicknesses.

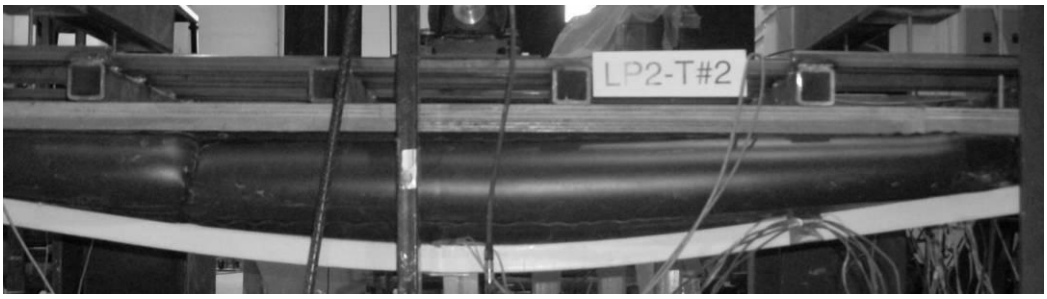

Figure 9. Lateral Displacement of 1700 mm wide Panel.

7 Manufacturing, Formulation and Casting of UHPC Panels

Manufacturing at Lafarge's precast facility in Calgary involved a displacement casting method in order to produce a total of 690 panels of flat and curved shapes. The surface texture on the panels was replicated from the architect's own hand-scored pattern in the master mould.

Lafarge's "Ductal®-AN1300FW" UHPC [14] formulation was tailored for use in manufacturing the precast façade panels. This formulation consisted of Ductal® Premix B3 (2075 kg/m^3), water (156 kg/m^3), superplasticizer (39 kg/m^3) and 12 mm Polyvinyl Alcohol (PVA) fibers (55 kg/m^3). Fine silica sand, cement, silica fume and ground quartz are blended into the Ductal® Premix B3. PVA fibers were used instead of steel fibers to avoid any possibilities for rust stains. Organic fibers were also preferred from a handling point of view for handling/safety point of view as steel fibers may cause injury and scratches. From structural point of view, UHPC with steel fibers would have been preferred as it exhibits better tension stiffening effects and increased ductility after cracking in comparison with concrete produced with PVA fibers. Fig. 10 shows one panel during casting and the PVA fibers are visible as the thin white lines in the mix.

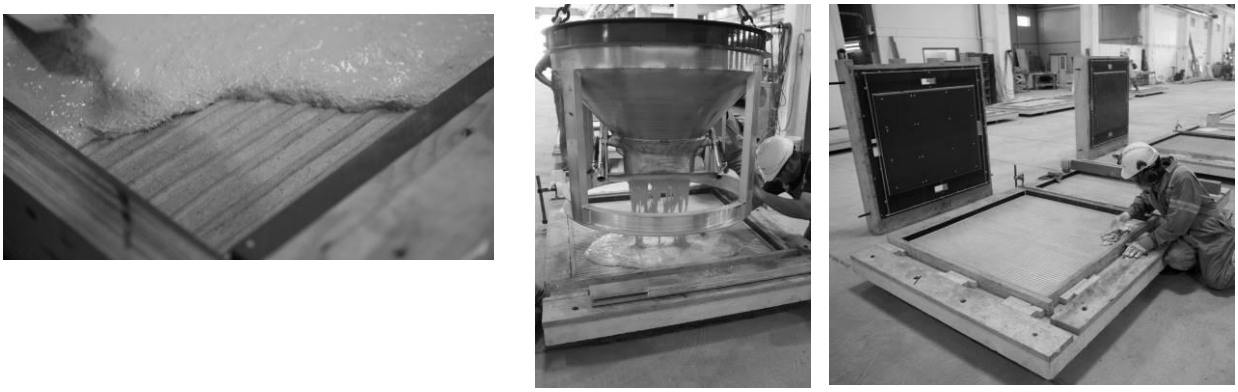

Figure 10: Panel Casting and Forms.

The front face texture of the panels was created by allowing the project architect to reflect his creativity by hand-scoring a clay panel which was then used to produce a negative plug and use as form face on all panels. This process allowed the architect to replicate his vision of the building façade into the panels. The surface texture replication was possible due to the mouldability, flowability and self consolidation properties of UHPC. Casting of the panels utilized displacement process [15] and all the panels produced on this project appear to have been hand carved (Fig. 2). For economical reasons, simple, non-complicated formworks were made

using plywood panels and rigid insulation. Steel formwork and other casting techniques have been used to successfully produce complicated shapes [16].

8 Conclusions

The innovative UHPC cladding solution, as successfully demonstrated by the Atrium, is expected to lead the way towards utilization of similar panels in future building facades and efficiently utilize UHPC material properties in architectural design. This project is the frontier in shaping the building industry and shows the required ground work required of having a close collaboration between the building owner, building architect, precast panel designer, precast manufacturer and UHPC supplier. The result will be long-lasting and sustainable structures that require less materials and unique designs with ultra-thin panel systems, complex forms, textures and shapes.

References

[1] Ghoneim, G.A.M.; Perry, V.H.; Carson, G.: Ultra-High Performance Fibre Reinforced Concrete in Footbridges. *Proceedings of 8th International Conference on Short & Medium Span Bridges, CSCE, Niagara Falls, Canada,* Paper 346, pp. 1 – 11, 2010.

[2] Perry, V.H.; Seibert, P.J.: The Use of UHPFRC (Ductal®) for bridges in North America: The Technology, Applications and Challenges Facing Commercialization. *2nd International Symposium on UHPC, Kassel, Germany,* pp. 815 – 822, 2008.

[3] Aaleti, S.R.; Sritharan, S.; Bierwagen, D.: Moore, B.P.: Precast UHPC Waffle Deck Panels and Connections for Accelerated Bride Construction. *PCI & 57th Annual National Bridge Conference, Salt Lake City, Utah,* 2011.

[4] Perry, V.H.; Weiss, G.: Innovative Field Cast UHPC Joints for Precast Bridge Decks – Design, Prototype Testing and Projects. *AFGC – Designing and Building with UHPFRC: State of the Art & Development, Marseille, France,* 2009.

[5] Rajlic, B.; Murray,P.; Dykstra, D.; Krisciunas, R.: The Eagle River Bridge Superstructure Replacement. *Proceedings of 8th International Conference on Short & Medium Span Bridges, CSCE, Niagara Falls, Canada,* Paper 105, pp. 1 – 9, 2010.

[6] Perry, V.H.; Royce, M.: Innovative Field Cast UHPC Joints for Precast Bridge Decks (Side-By-Side Bulb-Tees), Village of Lyons, NY – Design, Prototyping, Testing and Construction. *PCI & 56th Annual National Bridge Conference & 3rd fib International Congress, Washington, DC,* 2010.

[7] Thomas, M.D.A, "Performance of Reactive Powder Concrete in a Marine Environment", *ACI Annual Conference*, Chicago, IL, USA, 2010.

[8] CPCI Design Manual 4 – Precast and Prestressed Concrete, Canadian Prestressed Concrete Institute, Ottawa, Ontario, Canada, 2007.

[9] National Research Council of Canada, National Building Code of Canada, Ottawa, Canada, 2005.

[10] SETRA, Association Française de Genie Civil (AFGC), *Interim Recommendations – Ultra High Performance Fibre-Reinforced Concrete*, 2002.

[11] Gowripalan, N., and Gilbert, R.I.: Design Guidelines for RPC Prestressed Concrete Beams, School of Civil and Environmental Engineering, The University of New South Wales, 2000.

[12] Ghoneim, G., El-Hacha, R., Carson, G., and Zakariasen, D.: Precast Ultra-High Performance Concrete Replaces Stone and Granite on Building Façade, *Proceeding of the 3rd Fib Congress in Washington, D.C.*, Precast/Prestressed Concrete Institute, Chicago, IL, 2010.

[13] Vicenzino, E.; Culham, G.; Perry, V.H., Zakariasen, D., Chow, T.S: First Use of UHPFRC in Thin Precast Concrete Roof Shell for Canadian LRT Station, PCI Journal, September, 2005.

[14] D-AN1300FW, Material Data Sheet by Lafarge Precast, Calgary, Canada, 2009.

[15] Perry, V.H.; Seibert, P.J.: Equipment and Production Techniques with UHPC, CPI (Concrete Plant International), Issue 2, April, 2011.

[16] Henry, K.A., Seibert, P.J.: Manufacturing UHPC Architectural Products, CPI (Concrete Plants International), Issue 5, October, 2011.

Ultra thin Hi-Con Balconies – First Application in Holland

Rogier Friso van Nalta[1], Tommy Bæk Hansen[2]
1: Pieters Bouwtechniek Delft, The Netherlands
2: Hi-Con A/S, Denmark

The first Dutch project to be realized with Hi-Con Balconies, the housing project Amber in Delft for Woonbron Ontwikkelbedrijf by architectural firm Change.NL in cooperation with Mecanoo, introduces very thin cantilevered balconies (65 mm) made from Compact Reinforced Composite (CRC) on the Dutch market. The structural design of the balconies was made in cooperation between Pieters Bouwtechniek and the Danish producer Hi-Con, based on Hi-Cons extensive experience with thin CRC balconies in Denmark and adjusted by Pieters Bouwtechniek to fit Dutch codes and construction praxis.
The balconies are pre-fabricated in Denmark, and connected to the main structure through small consoles in-situ cast into a typical Dutch tunnel segment (walls and ceiling of an apartment cast in-place in one cast) by the contractor Era Contour. This is the first time Hi-Con CRC balconies are used in this way and the basic principles are explained.

Keywords: CRC, UHPC, balconies, full scale test

1 Introduction

The housing project Amber in Delft, consisting of 159 appartments, is the first Dutch project to be realized with Hi-Con Balconies. These are very thin balconies made from Compact Reinforced Composite (CRC). CRC is a concrete mixture designed for use in pre-cast elements, combining high amounts of conventional reinforcement with large amounts of steel fibers. This results in a concrete that is not only very strong but also very ductile and durable.

The structural design of the balconies has been made by Pieters Bouwtechniek in cooperation with the Danish producer Hi-Con who has extensive experience with thin balconies in Denmark. The Danish principles have been adjusted by Pieters Bouwtechniek to fit the Dutch building codes and construction praxis.

Compact Reinforced Composite

Compact Reinforced Composite (CRC) is an Ultra High Performance Concrete (UHPC) developed by Aalborg Portland A/S in 1986 [1]. CRC has high compressive strengths (between 100 and 400 MPa) and is extremely durable. With CRC concrete, pre-cast elements can be reinforced with high percentages of conventional reinforcement in combination with large amounts of steel fibers (between 2 and 6 vol. %). The concrete is not only very strong (hence not simply an Ultra High Strength Concrete, or UHSC), it is also very ductile and durable. CRC structures can therefore be designed with very small sections, and still provide higher safety and longer service life than conventional concrete.

The composition of CRC can be varied by applying various kinds of additives and fibers. CRC has been tested and researched in several international research projects [2,3,4,5,6,7] regarding bending, shear, fatigue, corrosion, fire, creep and shrinkage behavior. The type and amount of fibers is determined per project depending on the desired ductility and design of the elements. For the Amber housing project, corrosion resistant steel fibers were used.

Using this material, Hi-Con has more than 10 years experience in designing, manufacturing and supplying ultra-thin balconies, staircases, columns etc. in Denmark. The application outside Denmark has been limited however.

2 Dutch balcony design

Traditional Dutch balconies have drainage pipes and a slope towards the facade. However, to minimize the thickness of the balconies it was beneficial to direct the slope outwards, which is the typical design in Denmark. Although everyone was skeptical at first it turned out to be possible within the Dutch rules and resulted in some extra advantages such as the avoidance of clocked drainage pipes. Because of the inverted slope the balconies could be designed with a thickness of 90 mm at the façade and 65 mm at the balcony fronts.

Dutch building method

The structure is built using a tunnel formwork, which is one of the most widely used building methods in The Netherlands. In this building method the walls and ceiling of an apartment are cast in one cast. Then the form work is extracted the next morning. By applying heat the concrete reaches a strength of 14 N/mm^2 after approximately 8 hours.

The balconies are connected to the main structures with 600 mm wide consoles spaced approximately 1,8 m apart. The structure of the building consists of 250 mm thick concrete C28/35 walls and 300 mm thick floors spanning 7,2 m.

At first a design was made in which the balconies could be connected and adjusted after construction of the main structure. However because of the tight budget the connection was simplified to a connection that was cast directly into the floor. To create the transition from high strength to low strength concrete the consoles were designed with a CRC transition ridge. The consoles were also used to raise the balcony to the desired finished floor level (see Fig. 1).

Because of the cast in place connection, the balconies had to be cast simultaneously with the floors and walls. Usually casting stiff prefab element directly with the tunnel is avoided to make sure the floor is not supported by the prefab instead of the other way around. In this case the balcony was designed with a high stiffness in the cantilevered direction but a lower stiffness in the transverse direction. Therefore the balconies could follow the deflection of the tunnel form work and the floor after extraction of the form work without supporting the floor. The tunnel formwork was elongated to accommodate the placement of the balcony.

In this way, the Danish and Dutch construction preferences were merged into a new system suitable for application in Holland.

Two basic types of balconies were used in the project, both using the same principle of cast-in 600 mm consoles. The largest have a cantilevered length of 2.6 m.

Adapting to dutch building code

There are no codes for designing with ultra high strength concretes in The Netherlands. Even so, the balconies have been calculated according to the Eurocode including specific rules from the Dutch NAD with some exceptions because of the specific material properties of CRC. The structure of the building has been calculated according to the Dutch code NEN6720.

Translating the Danish experience from practical use into documentation acceptable to the Dutch authorites has been a major part of the work related to the process of introducing Hi-Con balconies to the Dutch market. Only through close cooperation between Hi-Con and Pieters Bouwtechniek has this been possible.

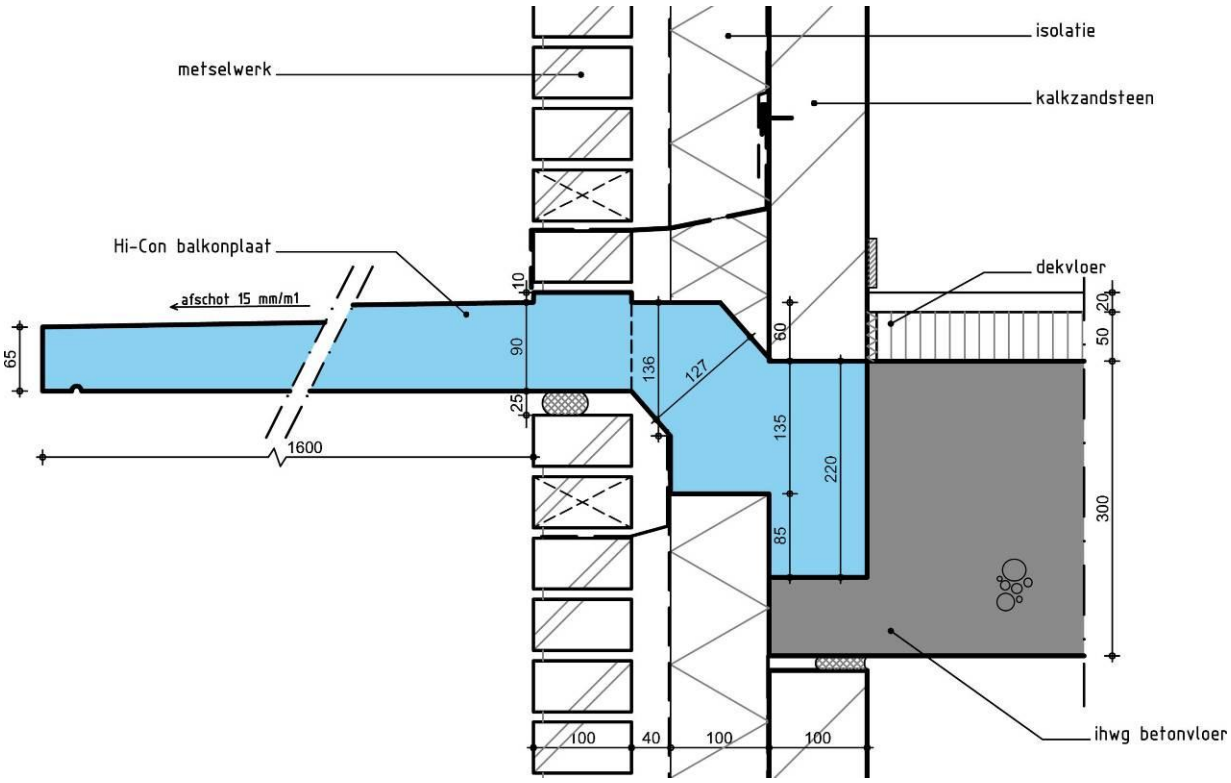

Figure 1: Principle section of the Hi-Con balconies adapted to Dutch building style.

3 Balcony Test

To practice construction of the balconies, the contractor, Era Contour, decided to make a test apartment. To have more advantage of this test it was decided to use it as a load test as well, to proof the strength, stiffness and safety of the balconies and the connection to the floor – a full scale test of the new building system and the balconies.

Two full size test balconies, each 7.2 m in length and a 1.875 m cantilevered length, were cast into a traditional Dutch tunnel segment and tested. The balconies were succesivly loaded with sand bags each weighing 1500 kg. The first balcony was loaded to 5 times the design live load of 300 kg/m^2 (see fig. 2). Then a section with a single console of the second balcony was cut free and loaded with 8 times the design live load. Even this extreme loading did not result in failure of the balcony or the connection to the tunnel segment, although cracks started to appear in the consoles and the deflection became noticeable.

Figure 2: Test balcony loaded with 12×1.5 tonnes sand bags (18 tonnes total load), or 5 times the design load.

The deflection of the floor and the balcony was measured from start of construction up unto and through the loading of the balconies. The measurements even showed how the structure deflected during construction. Because of the heating at first the floor actually deflected upwards due to the elongation of the steel formwork.

The measurements were compared to a Danish and a Dutch calculation according to the Eurocode (see fig. 3). The main difference between the two calculations is the way in which they incorporate the effect of shear force on the deflection. The measurements showed good correlation with the calculations, both regarding the general behavior of the structure and for the balconies isolated. Both methods overestimate the deflection and the Dutch method is a little more conservative then the Danish method.

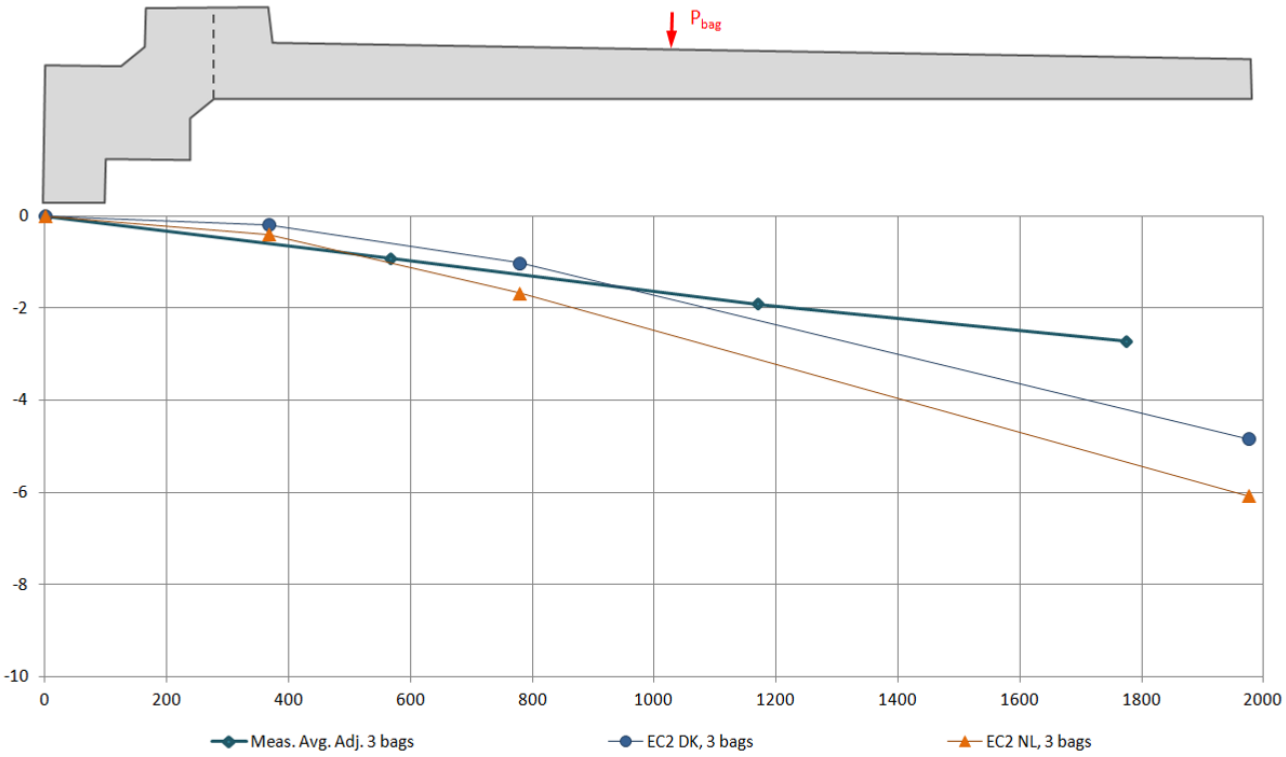

Figure 3: Comparison of measured and calculated deflection.

Balustrades

The balustrades are connected to the balconies with stainless steel inserts in the 65 mm thick front edge of the balconies. To proof the strength of these inserts a series of pull out tests were performed in connection with the full scale test of the balconies. Instead of the calculated design load of 30 kN normally applied by hi-Con, the inserts failed at app. 90 kN.

This means that even with the very limited material thickness of the balconies, balustrades can be fully and safely supported using only a few fixtures along the edges, allowing for slim and elegant balustrade designs.

4 Construction process

With different practices in Denmark and Holland, mutual expectations between Hi-Con and the contractor Era Contour had to be established. Through a constructive dialoque in the initial part of the project and continued close cooperation between Hi-Con and Pieters Bouwtechniek, solutions to the various practical obstacles that arose were found, such as maximum transport sizes of the elements, reinforcement assembly between pre-cast and in-situ cast concrete, etc.

Allignment of the balcony front edges

In typical 30 cm thick balconies in Holland, a height difference of 1 or 2 cm is hardly visible. With Hi-Con balconies of only 6.5 cm, this is accentuated because of the small thickness at the edge. To minimize height differences the balconies are therefore coupled with a steel plate right after extraction of the tunnel form work to align the balcony edges, when necessary.

Even though the tolerances are limited, the balconies are generally very well aligned directly after demoulding (see fig. 4). This precision casting is only possible due to the combined calculations of Pieters Bouwtechniek and the experienced and skilled crew of Era Contour.

Because of the creep development behavior of CRC, the forces on the foot plate relatively quickly decrease with time. After 2 to 3 months, the temporary couple plate is replaced by the permanent foot plate of the balustrade, ensuring that the balconies remain aligned throughout the service life of the building.

Figure 4: Balconies after completed casting into the tunnel segments with aligned 65 mm thin front edges.

5 Conclusions

Through close cooperation between Pieters Bouwtechniek and Hi-Con, it has been possible to adapt proven calculation and construction practices of ultra-thin Hi-Con balconies in Denmark to the current Dutch codes and building practices, and in doing so creating a new balcony system suitable for application in Holland.

Close cooperation with Dutch contractor Era Contour throughout planning and design has resulted in a successful merging of the Dutch tunnel casting system and pre-cast UHPC Hi-Con balconies.

The strength, stiffness and safety of the balconies and the system in general has been proven through full scale testing, as well as extensive calculations.

References

[1] Bache, H.H.: Compact Reinforced Composite, Basic Principles, *CBL Report No. 41*, Aalborg Portland, 87 pp., Aalborg 1987.

[2] Nielsen, C.V.: Presentation of Cyclic Load Tests of Rebars Anchored in Steel Fiber Reinforced High-Strength Composite, *Fatigue of Concrete Structures (ed. L.P. Hansen)*, Department of Building Technology and Structural Engineering, Aalborg University, pp. 65-71, Aalborg 1993.

[3] Andrade, M.C.; Frias, M.; Aarup, B.: Durability of Ultra-High Strength Concrete: Compact Reinforced Composite, BHP96 Fourth International Symposium on Utilization of High-Strength/High-Performance Concrete, Paris 1996.

[4] Nielsen, C.V.; Olesen, J.F.; Aarup, B.: Effect of fibers on the bond strength of high strength concrete; BHP96 Fourth International Symposium on Utilization of High-Strength/High-Performance Concrete, pp. 1209-1218, Paris 1996.

[5] Klinghoffer, O.; Aarup, B.: Effect of Microcracks on Durability of Ultra High Strength Concrete, 4th International Symposium on Corrosion of Reinforcement in Concrete Construction, Cambridge 1996.

[6] Aarup, B.; Jensen, B.C.: Bond Properties of High-Strength Fibre Reinforced Concrete, Bond and Development of Reinforcement, *ACI-publication SP-180*, pp. 459-472, 1998.

[7] Juvas, K.; Jumppanen, U.-M.; Aarup, B.: High Performance Concrete at High Temperatures, Proceedings of Nordic Concrete Research Meeting, Reykjavik 1999.

Precast thin shells made of UHPFRC for a large roof in a wastewater treatment plant near Paris

Gilles Delplace, Ziad Hajar, Alain Simon
Eiffage TP, Neuilly s/ Marne, France

In order to upgrade the existing waste water treatment plant of Achères, near Paris, a construction project was attributed by the owner SIAAP to the firm Eiffage TP, after a call of tender. The extension plant project includes a particular process of water biologic treatment called Biostyr®, a large tank in which water is filtered by micro-balls made of polystyrene. Due to its exceptional mechanical and durability properties, the BSI®, the UHPFRC developed by Eiffage TP, was chosen for the designing of thin architectural structures in such an aggressive area. Not less than 180 precast and pre-stressed thin shells were necessary to cover the whole 3500m² of the Biostyr® tank, according to the drawings of high waves imagined by the architect Luc Weizmann.
This article presents the main steps of the project: the designing of the different structures, the suitability tests performed to validate the casting method of the elements and to verify the K coefficients (real fibres orientation) taken into account, the concreting and pre-stressing of the elements in the precast factory, and finally the implementation methods of the structure on the construction site of the waste water treatment plant.

***Keywords**: Ultra High Performance Fibre Reinforced Concrete, thin shells, mechanical behaviour, pres-stressed elements, K factor, suitability tests, durability properties*.

1 Introduction

The Seine Aval sewage treatment plant operated by SIAAP is located on the banks of the Seine river downstream of Paris. To have it upgraded to the standards of the European Commission's UWW Directive, SIAAP awarded a design-and-build contract to a consortium made up of Eiffage TP, OTV, LWA, and BG Ingénieurs Conseils. The upgrade is based chiefly on use of the Biostyr® biological aerated filter and Biosep® separation technologies for biofiltration and treatment respectively. It will increase the plant's treatment capacity to 1,700,000 m^3 per day.

The roofing over the new tanks, totalling 3500 m², was designed to be built using ultra-high-performance fibre-reinforced concrete (UHPFRC). The post-tensioned precast shells were made with BSI®, an UHPFRC developed by Eiffage TP. Architect Luc Weitzmann chose UHPFRC because it meets three important criteria: high strength, allowing structural slenderness, superior durability, a particularly important criterion given the aggressive environment (the vapour above the Biostyr® units has high H_2S concentrations); and aesthetics, achieving a hard, mineral appearance.

This paper describes the detailed design of the roofing which consists of a large number of precast UHPFRC units: waveform shells, flat shells, framing supporting the shells, and screen elements at the sides.

2 Description of the precast units

The tank roofing consists of a total of 260 precast units: 160 curved, waveform shells, 20 flat shells, and 80 structural frames supporting the curved shells.

The plan-view dimensions of the curved shells are 11.83m x 1.8m, and their longitudinal profile is a wave form with an amplitude of 2.81 m. Structurally, their static design is that of statically determinate beams with a span of 10.63 m. In their typical cross-section (see Fig. 1) each shell consists of a thin (5 cm-thick) flange and a central rib with a downstand of 20 cm, which represents a structural slenderness of 1:42 and an equivalent depth of 81mm.

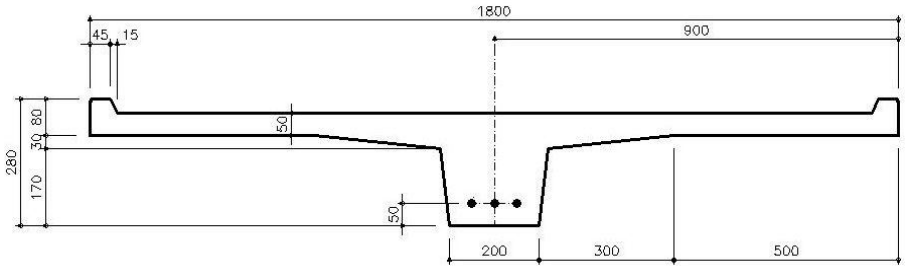

Figure 1: Cross-section of curved shell.

The inherent strength of UHPFRC, and particularly its ductility under tensile force due to the steel fibres it contains, means that no passive reinforcement is used. Moreover, each unit is prestressed longitudinally with a DSI 3T15S system comprising 3 greased and sheathed monostrand tendons wich follows the curve of the shell. The both ends of the shells, where the prestress is introduced and distributed, called for very careful study. The design of this area is particularly complex since that is also the location of the end cantilever transmitting the load of the shells to their bearings (see Fig. 2), and therefore subject to support reactions.

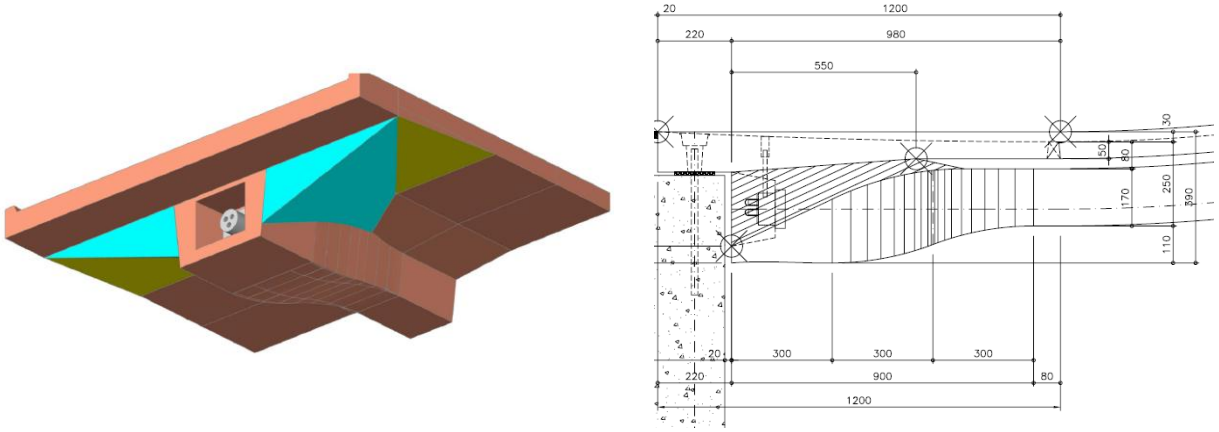

Figure 2: End block of curved shells.

The ‘top’ end of each curved shell is supported by a UHPFRC portal frame (see Photos 13 and 14). These 80 precast units contain no reinforcement, neither passive nor prestressed. The vertical members of the frames are 2.8m high, with a cross-section measuring 120x180 mm.

The 20 flat shells (slabs) are to the same plan dimensions as the curved shells and share the same static design. However, they must withstand higher service loads than the curved shells for they are trafficked by maintenance staff and machines. Their cross-section is that of a double-ribbed slab with a total depth of 370 mm and a 50 mm-thick flange (see Fig. 3), which represents an equivalent depth of 119 mm. Each rib is prestressed with the same DSI 3T15S system of greased and sheathed monostrands.

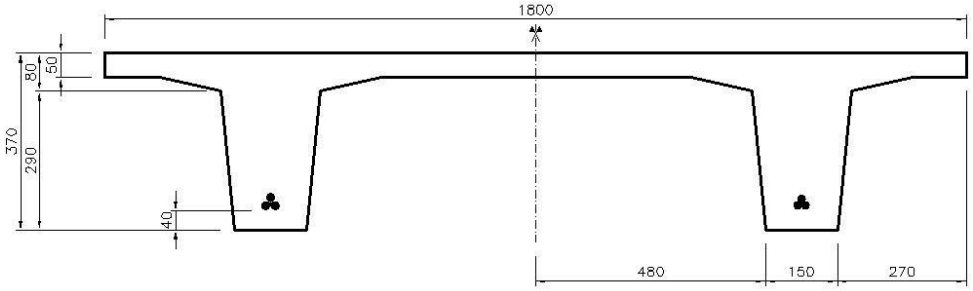

Figure 3: Cross-section of flat shell.

In addition to the elements already described, 70 white BSI® sidescreen elements were manufactured to wall in the Biostyr® building (see Fig. 4). They consist of two beams with vertical members between. Three elements are joined together to make a screen having the length of the shell elements (10.63 m). The upper beams, which carry the horizontal forces exerted on the vertical screen members, are connected by steel assemblies designed to transmit the flexural moments induced by horizontal actions, and the assembly of three units is secured at each end by the frames supporting the top ends of the curved shells. The lower beam rests directly on the perimeter wall of the tanks.

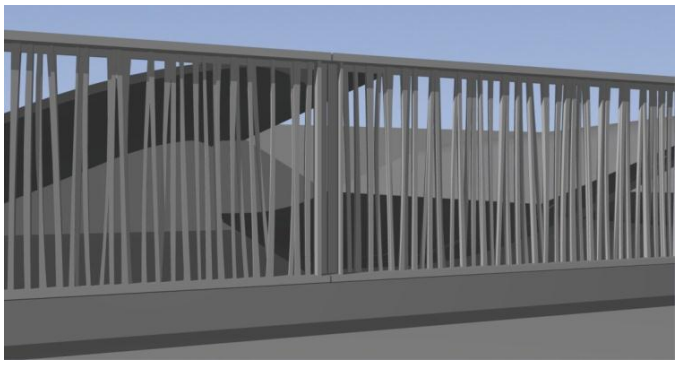

Figure 4: Layout of screen units.

It was to simplify precasting and transport that the sidescreens were divided into three panels. All three types were cast from a single mould.

3 BSI® concrete

BSI® is an UHPFRC developed and patented by the Eiffage TP group. Previous projects built with BSI® include the two pioneering Bourg-lès-Valence bridges [4], the canopy over the Millau Viaduct toll gates [5], and the Pinel and Sarcelles road bridges [6].

The main characteristics of the BSI® mix used for this application are as follows:

Ingredients of BSI® (for 1m³)		
Premix (*):	2296 kg	
Superplasticizer	39.6 kg	
Water	185 kg	
Steel fibres (L_f=20mm; Ø = 0.3mm)	195 kg	
The steel fibres are straight and made from very high tensile steel		
* The premix is a combination of all the dry ingredients (cement, silica fume, sand, coarse aggregate).		

Mechanical characteristics of the BSI® mix		
Density	ρ	2.75 t/m3
Characteristic 28-day compressive strength	f_{c28}	165 MPa
Characteristic 28-day tensile strength of concrete matrix	f_{t28}	8.8 MPa
Characteristic 28-day tensile strength of fibre-reinforced concrete	σ_{bt-28}	8.04 MPa
Mean Young's modulus at 28 days	E_{i28}	57 GPa
Autogenous shrinkage strain at infinite time	$\varepsilon_{re-\infty}$	550 µm/m
Drying shrinkage strain at infinite time	$\varepsilon_{rd-\infty}$	150 µm/m
Basic creep and drying creep (loading time t1=48h)	K_{fl}	1.00

The diagram in Figure 5 shows the design constitutive law for the UHPFRC, and how it takes account of tensile strength. It can be seen that post-cracking behaviour (after the tensile elastic phase) is expressed not as strain but as widening of the crack.

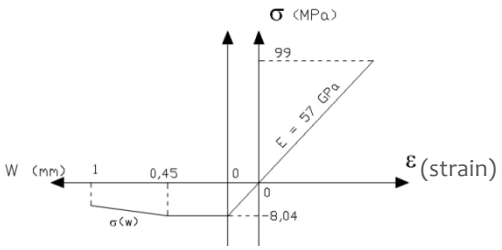

Figure 5 : Constitutive law of BSI®.

4 Construction-design studies

All the verifications of the units are based on the 2002 interim French recommendations for UHPFRC published by an AFGC-SETRA work group. In the case of the shells, since the structure is prestressed only longitudinally, different verification principles apply, depending on whether transverse or longitudinal behaviour is addressed.

The verifications for longitudinal behaviour are based on the French "BPEL" code [2] (limit state design of prestressed concrete structures), considering class II for limit stresses of the materials. Normal tensile stresses at SLS are thus limited to the tensile strength of the matrix (see Table 1).

Table 1: Prestressed elements – SLS normal stresses limited.

Interim phases	stress	σ_{max} [Mpa] =	32.17	< 81	
	● Tensile stress	σ_{min} [Mpa] =	-4.98	> -7	Top face
Rare SLS	stress	σ_{max} [Mpa] =	25.61	< 99	
	● Tensile stress	σ_{min} [Mpa] =	-6.19	> -8.8	Bottom face

The ultimate resistance bending moment (see Fig. 6) are calculated using the characteristic constitutive law of the cracked concrete, with a partial safety factor γ_{bf} = 1.3 for tensile stress.

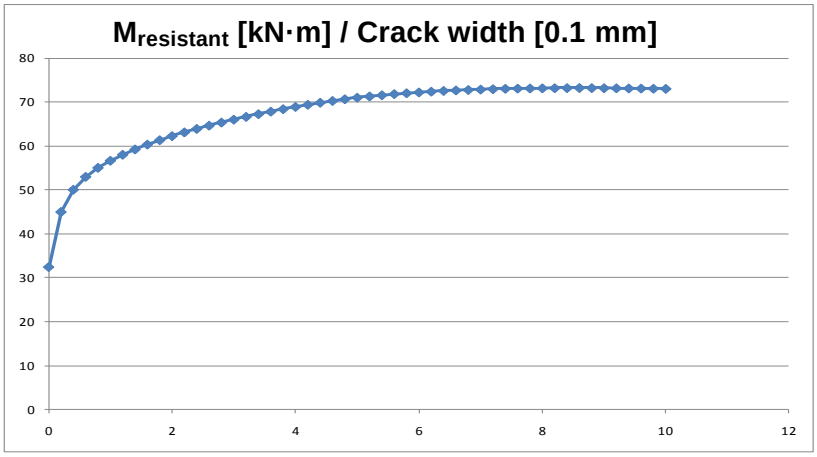

Figure 6: Resistant moment of the typical section of a shell versus crack width.

Transversally, since forces are taken solely by the fibre-reinforced concrete, the verifications refer to Class IV of French UHPFRC recommendations [1], which means the tensile behaviour of the concrete can be taken into account even if there is no active or passive reinforcing steel.

A feature of the curved shells is that they do not bear on their ribs. At each end they have an unprestressed cantilevered bearing section where the flange is simply thickened. This design, which is unusual in that there is no reinforcement at all in such a critical zone, was necessary

because of the very limited freeboard of the tank walls and the difficulty in shaping them to house the ribs. It was the strength contribution of the steel fibres which made this cantilevered bearing design possible. Verification of the cantilever included finite-element modelling of the end block. Moreover, the design was validated by laboratory tests on specimens sampled from a prototype shell as part of the suitability testing procedure.

The absence of any reinforcement in the area of introduction of prestress was validated by testing; laboratory tests on a BSI® anchor block demonstrated a safety factor of 3 for failure of the block.

Suitability testing

Application of French AFGC-SETRA recommendations [1] [3], means a number of preliminary tests must be carried out to check that the materials and equipment used under actual site conditions are consistent with the design assumptions. Consequently a representative sample of the actual structural element was built (see Fig. 7) to validate concreting methods and equipment and to measure K factors representing the distribution and orientation of fibres in the structure.

Figure 7: Trial element after test prism sampling.

Prisms sawn from the trial specimen served to verify the performance of the concrete in two characteristic zones (see Fig. 8). The principles for prism sampling are presented below.

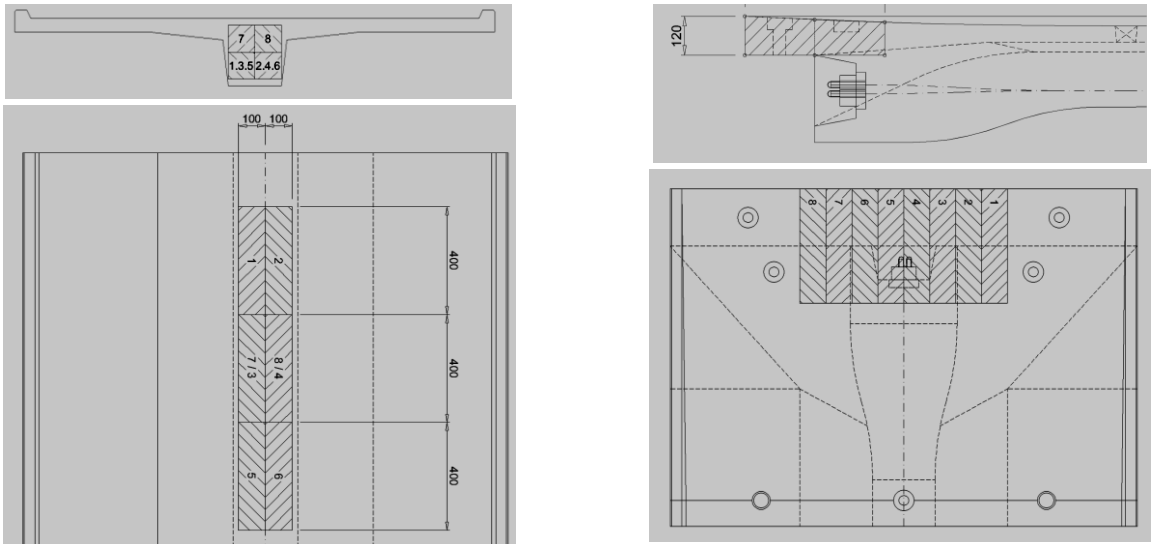

Typical section *Bearing cantilever*

Figure 8: Representative model - sempling positions.

The K factor values determined by flexural strength testing (6 tests for each zone) are given below.

	Typical section (Rib)	Bearing cantilever	Default AFGC values
Global effects	K = 1.20	K = 1.35	1.25
Local effects	K = 1.65	K = 1.55	1.75

Table 2 : K factor values.

In comparison, the default values in the AFGC-SETRA recommendations are K = 1.25 for global effects and K = 1.75 for local effects.

5 Precasting of BSI® units

The architect's desire to have a high-quality finish to both the top and bottom surfaces of the flange, the curvature of the elements, and the fact that BSI® is a self-compacting concrete meant horizontal casting was not an option for the curved shells. The units were therefore cast vertically, on edge. Given the large number of times the mould was to be used, plus the geometrical accuracy required, a steel mould was built (see Fig. 9).

The concrete was placed without vibration and was not heat treated. The mould was removed as soon as the cylinder compressive strength reached 35 MPa, i.e. after about twenty hours in cold weather. With temperatures of 20°C or more, the strength reached 60 MPa after 20 hours, so a daily casting cycle was possible.

Figure 9: Steel mould for curved units.

Figure 10: Handling after form removal.

The strength of the BSI® at the time of mould removing was sufficient for shells to be handled and moved to the storage yard (Fig. 10). The shells were prestressed in the casting yard, in the vertical position in the case of curved units (Fig. 11). The compressive strength required for prestressing was 130 MPa.

Figure 11: Storage before prestressing.

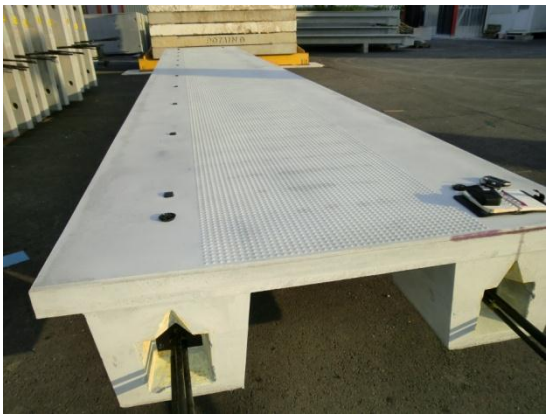

Figure 12: Flat shell with textured top face.

The flat shells were cast horizontally, but upside-down since the top surface is to be trafficked and is therefore textured. Using a turning lifting beam, they were turned over and removed from the mould once the concrete compressive strength had reached 50 MPa.

The screen panels of the Biostyr® building walls were cast in two identical polyurethane moulds cast from the same reverse mould. The panels were produced by placing stop-ends at predetermined points in the polyurethane moulds.

The moulds could be removed as soon as the compressive strength reached 75 MPa.

Figure 13: Removing a screen unit from the mould.

6 Erection of precast units

The curved shells were carried to the construction site by truck. There a cradle turned them into the horizontal position (see Fig. 14 and 15) and a crane with a special lifting beam (see Fig. 16 and 17) lifted them into place on the building.

Figure 14: Unloading from truck.

Figure 15: Curved shell on turning cradle.

Figures 16 and 17: Erection by crane with lifting beam.

The flat shells were transported face-up. The supporting frames and screen units were also transported in the horizontal position and turned to the vertical by means of a lifting sling placed around their top beams.


Figures 18 and 19: Erection of screen panels.


Figures 20 and 21: Precast BSI® shell roofing over Biostyr™ tanks.

7 Conclusion

The roofing-over of Biostyr® tanks with precast BSI® units is another pioneering development demonstrating that UHPFRC provides new solutions combining lightness, durability, and quality aspect.

References

[1] Bétons fibrés à ultra-hautes performances, Recommandations Provisoires, AFGC-SETRA, January, 2002.

[2] BPEL 91 révisé 99, Règles techniques de conception et de calcul des ouvrages et constructions en béton précontraint suivante la méthode des états limites, Fasc. 62 (Titre premier, section 2 du CCTG), avril 1999.

[3] SIMON A. : Designing and building with UHPFRC – State of the art and development, Edited by François Toulemonde and Jacques Resplendino. (ISTE and WILEY) pp.723-741, 2011.

[4] Hajar Z., Simon A., Lecointre D., Petitjean J. : Construction of the first road bridges made of UHPC, 3rd International Symposium on HPC, Orlando, 2003.

[5] Thibaux T, Hajar Z, Simon A : Thin shell structure over the Millau Viaduc tolls gates, Symposium FIB, Naples 2006.

[6] Thibaux T.: UHPFRC Prestressed beams as an alternative to composite steel-concrete decks – The example of Pinel bridge, Symposium FIB, Amesterdam 2008.

Design of Grouted Connections for Offshore Wind Energy Converters and Composite Structures using UHPC

Steffen Anders
Institute of Structural Engineering, Department Construction Materials, Universität Wuppertal, Germany

Grouted Connections are a well known connection technology for offshore applications. Design approaches of existing standards allow for a valuation of the maximal load-bearing capacity but will not answer the question about stresses in the steel members. For this reason nowadays complex finite-element calculations are made for Offshore Wind Energy Converters. The following contribution introduces a design model and compares it with experimentally determined values, allowing for the estimation of stresses in shear-keys, pile and sleeve depending on the compressive strength of the used grout materials and the connection geometry. It is discussed, which currently open questions should be addressed in order to improve new designs and which questions should be answered in order to successfully transfer this grouting technology to composite structures onshore.

Keywords: Grouted Connection, Design Model, Offshore Wind Energy, High-Performance Grout

1 Introduction

In many fields Grouted Connections are an established construction method for connecting steel tubes using grout material. The biggest field of successful application of Grouted Joints or Grouted Connections is the offshore oil- and gas industry where application started in the seventies (70s) of the last century. In comparison to the oil- and gas industry, Grouted Joints for Offshore Wind Energy Converters are firstly constructed with a lower radial stiffness of the steel-tubes and secondly the fatigue loads are more important.

In the 90s this connection technology has been transferred to Offshore Wind Energy Converters, see Figure 1. The monopile in Figure 1a) illustrates that besides axial loads the connection can be subjected to bending moments as dominating load. Due to a reduced radial stiffness compared to structures of the oil- and gas industry in combination with the slim design and low dead weight of Offshore Wind Energy Converters fatigue loads increase, specially alternating loads.

The following contribution presents an enhanced design model for grouted connections, based on experiences of the oil- and gas industry and own tests. It allows for the estimation of the stresses in the shear-keys, pile and sleeve depending on the compressive strength of the grout material.

2 Load-Bearing Behaviour of Grouted Connections

Fundamentals

The load-bearing behaviour is influenced by three major parameters: the geometry of the connection, the used grout material and the loads. As the following article presents a design model to evaluate the load-bearing capacity of statically loaded connections, the effects of fatigue loadings are not considered. Figure 2 shows different types of failures and the load-bearing behaviour of a grouted connection, depending on the design. In the connection on the left hand side without shear-keys failure is caused by exceeding the shear strength in the interface between grout material and steel tube. As the shear strength is more or less independent of the compressive strength, the quality of the grout material is of minor importance. On the right hand side of Figure 2 is shown the usual design of grouted connections for Offshore Wind Energy Converters with predominantly axial loadings. The

corresponding stresses are transferred by compression struts between the shear-keys on pile and sleeve which lead to a multiplication of the transferable loads compared to the connections without shear-keys [4]. If the multiaxial compressive strength of the grout material is exceeded on the stressed side of the shear-keys, irreversible deformations occur and a void will form behind the shear-key. This goes along with considerable relative desplacements between the steel tubes. The strength of the grout material is therefore an essential criterion for the load-bearing capacity and failure of these connections.

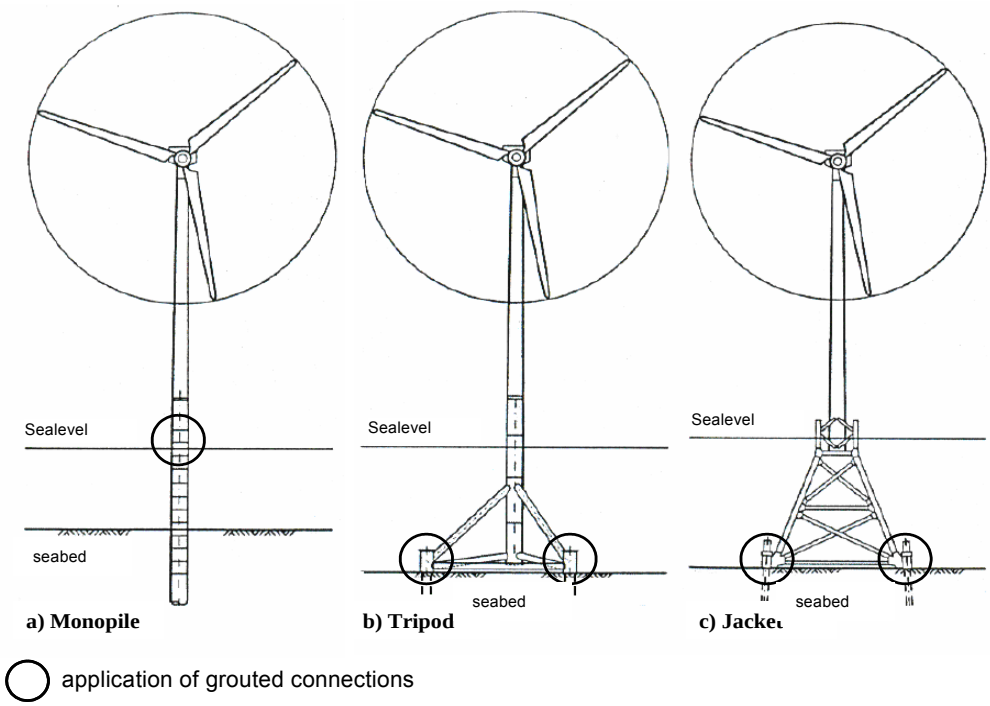

Figure 1: Examples of applications of grouted connections for Offshore Wind Energy Converters according to Schaumann [2].

Effects of shear-keys and the radial stiffness

Further influences on the load-bearing capacity are the tubes‘ radial stiffness, represented by the ratio of diameter to wall-thickness (d/t) and the geometry of the shear-keys, represented by the ratio of shear-key height to spacing, compare Figure 1. With a rising radial stiffness the confining pressure of the steel tubes on the grout material increases and activates its multiaxial compressive strength. According to [5] the load-bearing capacity of the connection increases linearly with an increasing radial stiffness.

Concerning the effect of the shear-keys a linear increase of the load-bearing capacity with an increasing h/s-ratio of the shear-keys is assumed in [5]. However, own experiments documented in [1] show that with higher h/s-ratios the increase of the connections‘load-bearing capacity is reduced. Further information on the load-bearing capacity may be found e.g. in [1, 6, 14].

The radial stiffness can be calculated according to current regulations used for the design of Grouted Connections. They are published by the American Petroleum Institute [7], Health and Safety Executives (HSE) [5] and Det Norske Veritas (DNV) [8]. As an example the radial stiffness of the connection according to HSE is given in the following equation:

$$K_{HSE} = \left(\frac{E_S}{E_g} \cdot \frac{D_g}{t_g} \right)^{-1} + \left(\frac{D_p}{t_p} + \frac{D_s}{t_s} \right)^{-1} \quad (1)$$

In this equation D denotes the diameter, t the wall-thickness of the steel tubes whereas the index p denotes the pile, the index s the sleeve and g the grout. E_s and E_g denote Young's moduli of steel and grout respectively.

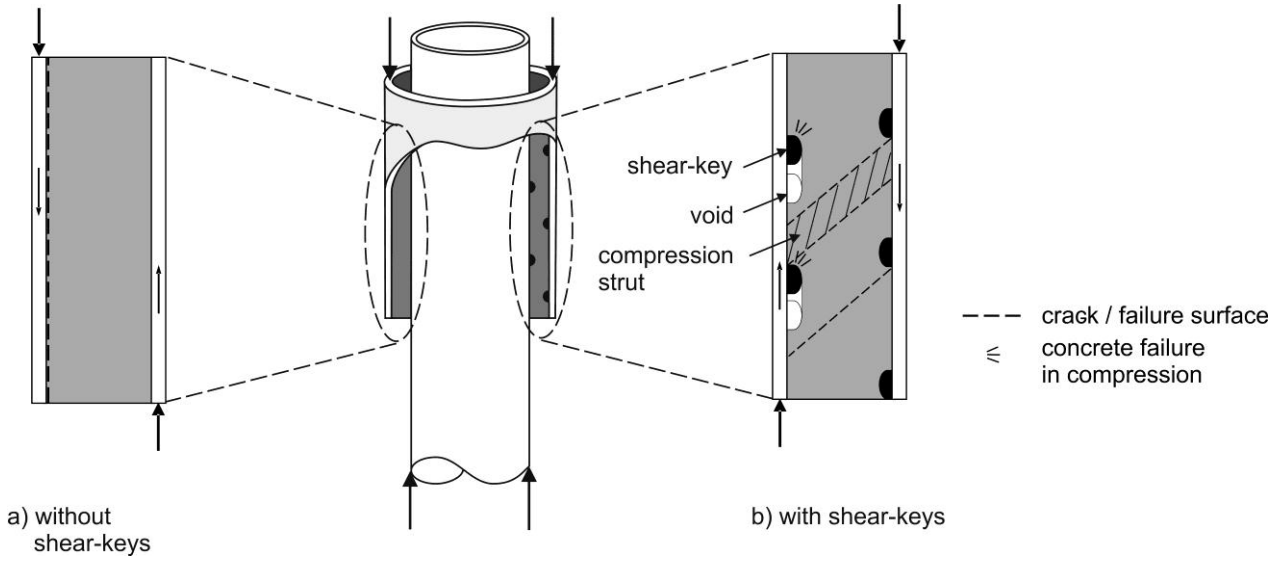

Figure 2: Types of failure of grouted connections a) without shear-keys and b) with shear-keys [1].

In Figure 3 the pile shear strength of the connection is plotted against the compressive strength of the grout. The pile shear strength is calculated by dividing the applied load by the contact area between pile and grout. Some interesting aspects concerning the radial stiffness, the shear key height and the compressive strength of the grout f_{cu} become obvious in this figure. Firstly, the pile shear strength seems to increase linearly with the grout's compressive strength, whereas the slope grows with an increasing radial stiffness. Secondly, the effects of higher shear-keys can be seen when comparing experiments with h/s-ratios of 0.056 (black rectangular symbols) and tests with h/s-ratios of 0.013 (grey triangular symbols). Again, it becomes obvious that especially a high radial stiffness offers the possibility to effectively exploit the compressive strength of the applied high-strength grout materials.

Thirdly, the effect of the radial stiffness can be seen, when comparing the tests reported in literature to the tests documented in [1]. The literature tests were conducted with specimens having a radial stiffness of K_{HSE} ranging from 0.015 to 0.025, whereas the tests in [1] had K_{HSE} values ranging from 0.07 to 0.09. If one compares the difference between the dotted lines for the tests with h/s = 0.013 of [1] to the tests in literature with h/s < 0.013 the differences in pile shear strength are caused predominantely by the radial stiffness.

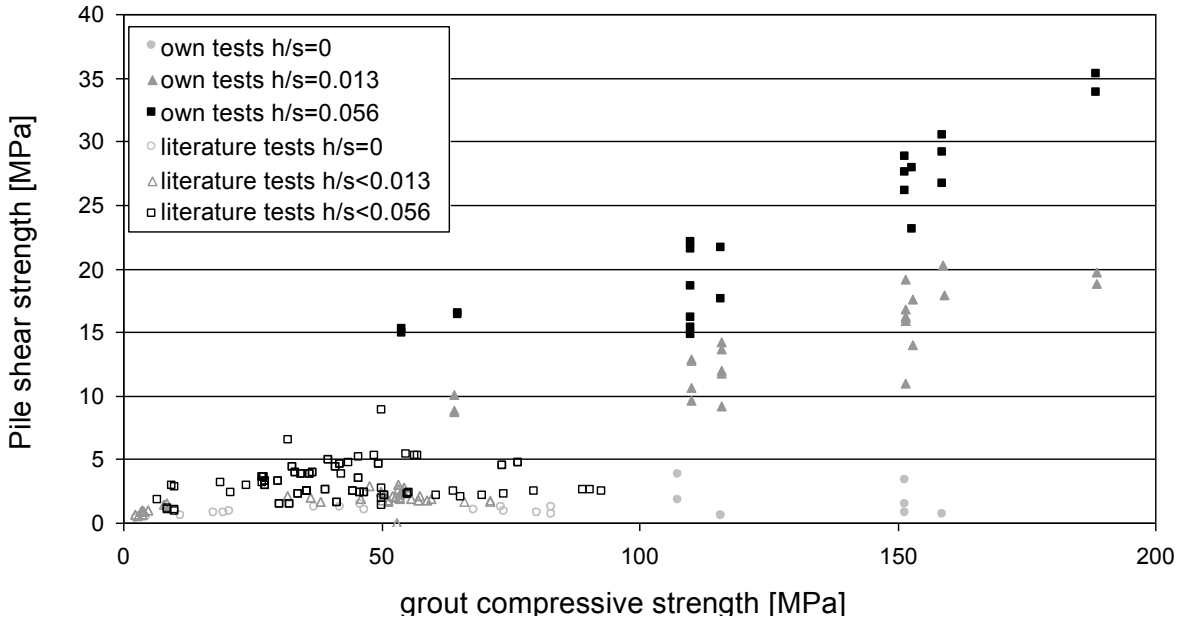

Figure 3: Pile shear strengths of experiments documented in literature e.g. [4] and in [1] plotted against the compressive strength of the grout. Effects of fibre-modifications are mathematically corrected.

3 Design models to estimate the load-bearing capacity

The existing design approaches can be divided in simplified equations for the determination of the load-bearing capacity, analytical models as well as finite element calculations. Existing regulations in the offshore oil- and gas industry are primarily based on experiments [4, 5]. Further tests especially with fatigue loading were added later in Norway. These regulations are published by [5, 7, 8]. Det Norske Veritas is the only organization having published a specific code for the design of supporting structures for Offshore Wind Energy Converters [10]. Due to recent problems with monopile connections in the North Sea this code was partially withdrawn.

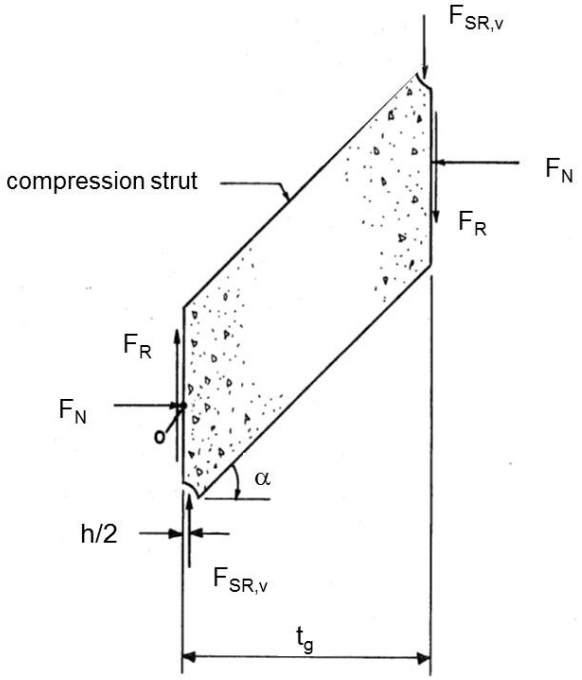

Figure 4: Mechanical model for the estimation of the normal and friction forces in a compression strut according to Lamport [6].

Analytical models are published e.g. by Paslay Inc. [11], Chilvers [12] and Lamport [6]. Lamport's model is the most developed and most accurate. He uses a plasticity based approach in order to describe the behaviour of the concrete on the stressed sides of the shear-keys. Lamport simplifies the connections to some respect. He assumes that all compression struts carry the same load, no bending moments are present and the radial stiffness is assumed to be infinite. Nevertheless, these simplifications enable Lamport to develop a mechanical model for one compression strut, as displayed in Figure 4. By assuming an infinite radial stiffness of the steel tubes the loads transferred by friction F_R (3) as well as the normal forces F_N (2) can be calculated. These forces are the reaction-forces in the connection due to the load $F_{SR,v}$.

$$F_N = \frac{F_{SR,v} \cdot (t_g - h)}{(t_g \cdot (\tan\alpha - \mu))} \qquad F_R = \mu \cdot F_N \qquad (2, 3)$$

Finite-element methods were mainly used for the calculation of grouted connections for Offshore Wind Energy Converters [14, 15]. Essential advantage is the possibility of taking into account the radial stiffness and that local stresses within steel members can be estimated. One problem of the finite-element approach is that only few experiments exist, which are appropriate for calibrating the calculations [14, 15].

4 Design model for stresses in the steel members

The advantage of the presented model is an easy estimation of the stresses in the steel members shear-keys, pile and sleeve depending on the compressive strength of the grout material. This model is based on the model published by Lamport, thus the same limitations are valid.

As input variable an expression for the maximum load transferred by the shear-keys is needed. In this case an approach published by the American Petroleum Institute [7] is chosen which defines the maximum load being 2.5 times the compressive strength of the grout f_{cu}. This factor can also be seen as a factor for the grout's multiaxial compressive strength.

$$f_{SR,v} = 2{,}5 \cdot f_{cu} \qquad (4)$$

Basing on the loading defined in equation (4) the stresses in the shear-keys as well as pile and sleeve are developed in the following.

In order to estimate the stresses in the shear-keys, the area connecting the shear-key to the steel tube has to be considered. Obviously, this area differs with the way of fixing the shear-keys to the steel tube. If the shear-keys have a circular or rectangular shape and are welded to the steel tube, the welded area has to be considered. In each case w denotes the width of the welded area. For the specimens applied in experiments in [1], the connecting area is calculated using the shear-key width (w) and the circumference of the tube. The resulting stresses σ_{SR} are then given by:

$$\sigma_{SR} = \frac{2{,}5 \cdot h \cdot (D_p + h) \cdot \sqrt{3}}{w \cdot D_p} f_{cu} \qquad (5)$$

Failure in the steel tubes, pile (index p) and sleeve (index s), is defined, as soon as the equivalent stresses in the steel tubes exceed the yield strength of the steel. Herewith the normal stresses have to be added to the hoop tensile stresses in the sleeve and the hoop compressive stresses in the pile respectively.

For the estimation of the hoop tensile stresses in the sleeve $\sigma_{r,s}$ the forces in the compression struts are used. The hoop stresses themselves are calculated in analogy to vessels subjected to inner pressure. The geometry of the connection as displayed in figure 4 is represented in the constants c_1 and c_2 which are calculated in accordance with equations 9 and 10. The hoop stresses in the pile $\sigma_{r,i}$ are calculated as follows:

$$\sigma_{r,p} = c_1 \cdot c_2 \cdot \left(\frac{D_p - t_p}{2 \cdot s \cdot D_p \cdot \pi \cdot t_p} \right) \cdot f_{cu} = c_{3,p} \cdot f_{cu} \qquad (6)$$

In these equations D_p and t_p equal the diameter and the wall-thickness of the pile respectively. The relevant normal stresses have to be taken from the structural design values. In order to be able to compare the normal stresses to the tests described in [1], a simplified equation was developed to estimate the load-bearing capacity of the tested specimens. The normal stresses are denoted $\sigma_{l,p}$ for the pile and $\sigma_{l,s}$ for the sleeve:

$$\sigma_{l,p} = c_1 \cdot (1 + c_2 \cdot \mu) \cdot \left(\frac{L}{s} - 1 \right) \cdot \left(\frac{1}{t_p \cdot \pi \cdot (D_p - t_p)} \right) \cdot f_{cu} = c_{4,p} \cdot f_{cu} \qquad (7)$$

Adding the normal stresses and the hoop stresses according to the van-Mises hypothesis, $\sigma_{v,i}$ for the pile can be defined as follows:

$$\sigma_{v,p} = f_{cu} \cdot \sqrt{c_{3,p}^2 + c_{4,p}^2 - c_{3,p} \cdot c_{4,p}} \qquad (8)$$

In the before mentioned equations c_1 und c_2 equal respectively:

$$c_1 = \frac{f_{SR,v,p}}{f_{cu}} = 2{,}5 \cdot h \cdot \pi \cdot (D_p + h) \qquad c_2 = \frac{(t_g - h)}{t_g (\tan\alpha - \mu)} \qquad (9, 10)$$

If one assumes that the forces transferred in the connection cannot exceed the forces transferred by the pile, the stresses in the sleeve can be estimated using the same equations (6 to 8). Only the geometrical values have to be changed from values for the pile D_p, t_p to the values of the sleeve D_s, t_s.

5 Comparison with Experiments

The values calculated using the model described in the previous chapter were compared to own experiments described in [1]. These experiments have the advantage that the steel tubes were stiff, compared to steel tubes used in literature. The steel used in the specimens was an S 355 grade; the measured yield stress equalled 391 MPa. The wall-thickness of the pile was 9.75 mm, with h/s = 0.056 and h = 1,25 mm.

Figure 5 shows the degree of utilization defined by the ratio of the calculated stresses in relation to the strength of the different steel members. Having a look at the calculated stresses in the pile and the shear-keys, failure is predicted at a compressive strength of the grout of about 170 MPa. However, in the experiments no yielding in pile or sleeve was observed up to grout strengths of about 190 MPa. However, when this grout material was used, one of the shear-keys failed and was sheared off.

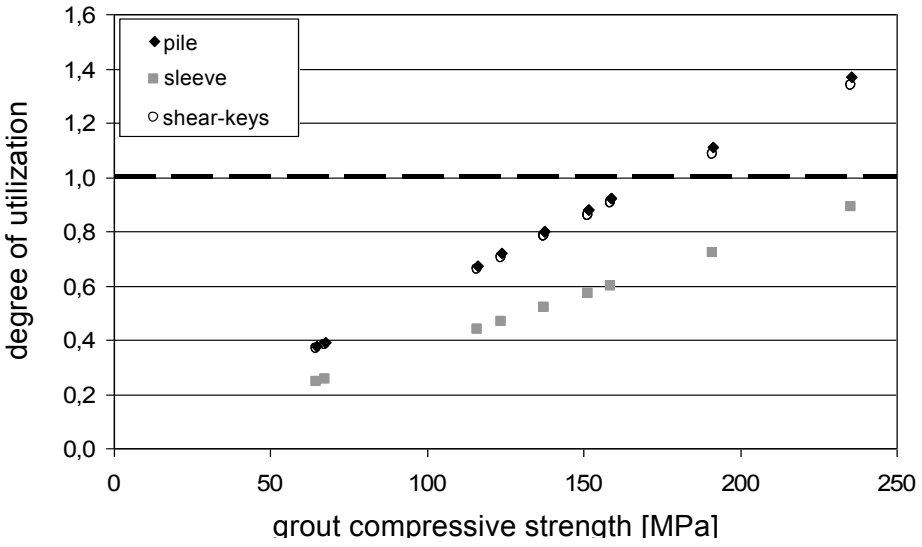

Figure 5: Degree of utilization of the shear-keys, pile and sleeve calculated for a specimen with h/s = 0,056 plotted against the compressive strength of the grout.

6 Future Research Needs

As already mentioned, in recent years problems occurred in large connections for monopile structures without shear-keys. This is one of the reasons why future research is needed on the development of improved material and design models for the grout itself and grouted connections in Offshore-Wind-Energy Converters.

Deformations as well as the load-bearing capacity of connections with shear-keys depend on compression struts, which are highly stressed close to the shear keys. A better understanding of their fatigue behaviour and the ability to describe the long-term deformations would significantly improve the design of grouted connections. Another material related question is the multiaxial compressive strength of the grout close to the shear keys. It is not known in detail in which way the confining pressure of the steel tubes affects the grout's compressive strength, which in turn is crucial for the load-bearing capacity.

At the beginning it was mentioned that the radial stiffness is one of the key-parameters for the load-bearing behaviour. It would be helpful to have a better and mechanically based understanding of its effect. Closely linked to this question are effects of bending on the load-transferring mechanisms. The existing, simplified equations do not take the corresponding stresses and deformations into account, because they were developed for axially loaded connections only. The low radial stiffnesses projected for Offshore-Wind Energy Converters demand models that take these effects into account.

Furthermore, stress concentrations at the beginning and the end of a grouted length of the connection have not been addressed in detail yet. This is especially important for long connections. One should expect stress concentrations at the ends, which are well known from welded or bolted connections in steel structures.

Besides offshore structures, conventional composite structures are assumed to be a large area of application for grouting technology with comparable open questions concerning material and design models. In addition, combinations of normal forces and bending moments vary to a greater extent. Other open questions are whether and in which way eccentricities of the load affect the radial stiffness and the load-bearing behaviour. Furthermore, the cross-sections of the steel tubes used onshore are more variable. Onshore not only circular cross-sections are used but also rectangular profiles or the cross-sections of pile and sleeve differ, meaning that forces

have to be transferred from a circular tube e.g. to a rolled I-profile. In these cases, new approaches for the characterization of the “radial stiffness” would be needed.

7 Summary

In this paper a design model for the estimation of the stresses in the steel members of grouted connections is described. It bases on the dominating effect of the shear-keys on the load-bearing capacity due to compression struts which develop between pile and sleeve. Based on an analytical approach, the equivalent stresses in the steel tubes resulting from normal stresses und hoop stresses can be estimated. Using the presented model, the stresses in the steel members can be calculated depending on the compressive strength of the used grout material.

The comparison between the design model and experiments has shown a good estimation of the stresses in the shear-keys. In contrast to the prediction of the stresses in the steel tubes in the experiments no failure or yielding of the steel tubes could be observed, The approach seems to be conservative for the design of pile and sleeve.

Finally, major open questions are addressed which should be answered for a better understanding of the load-bearing behaviour of grouted connections for Offshore Wind Energy Converters and in order to be able to transfer this technology to composite structures onshore. The most important questions are related to better material models especially for the highly stressed grout close to the shear-keys especially in fatigue loading, the effect of the radial stiffness as well as the effects of bending moments of the tube on the load-bearing behaviour.

References

[1] Anders, S.: Betontechnologische Einflüsse auf das Tragverhalten von Grouted Joints. PhD-Thesis, University of Hannover, 2008..

[2] Schaumann, P.: Bautechnische Forschung für Offshore Windenergieanlagen. Contribution to the 44. Research Kololquium of the DAfStb, 07./08.10.2004, Hannover, 2004.

[3] Schaumann, P.; Lochte-Holtgreven, S.; Lohaus, L.;Lindschulte, N.: Durchrutschende Grout-Verbindungen in OWEA – Tragverhalten, Instandsetzung und Optimierung. Stahlbau, Ernst & Sohn Verlag, 9/2010 Seiten 637-647.

[4] Department of Energy: Report of the Working Party on the Strength of Grouted Pile / Sleeve Connections for Offshore Structures – Appendix B. Offshore Technology Paper, OTP 11, 1982.

[5] Health & Security Executives: Pile / Sleeve Connections. Offshore Technology Report 2001/016, Norwich, 2002.

[6] Lamport, W.B.: Ultimate Strength of Grouted Pile-to-Sleeve Connections. PhD-Thesis, University of Texas at Houston, 1988.

[7] American Petroleum Institute (API): Planning, Designing and Constructing of Fixed Offshore Platforms. Washington 2007.

[8] Det Norske Veritas: Rules for fixed Offshore Installations. Det Norske Veritas, 1998.

[9] DIN EN ISO 19902: Erdöl- und Erdgasindustrie – Gegründete Stahlplattformen. 2007.

[10] Det norske Veritas (DnV): DNV-OS-J101 – Design of Offshore Wind Turbine Structures. Hörvik 2007.

[11] Paslay Incorporated: Development of an Analytical Model for the Ultimate Capacity of Axially Loaded Grouted Pile to Jacket Connections. Final Report to the American Petroleum Institute, 1980.

[12] Chilvers, G.A.: Analysis of the Structural Behaviour of Grouted Pile / Sleeve Connections for Offshore Structures. Ph.D.-Thesis, The City University of London, 1984.

[13] Germansicher Lloyd: Status of requirements for the certification of the Q7 Monopile Design. Research Project Opti-Pile NNE5/2001/245, Hamburg, 2004.

[14] Schaumann, P.; Wilke, F.; Lochte-Holtgreven, S.: Grout-Verbindungen von Monopile-Gründungsstrukturen – Trag- und Ermüdungsverhalten. Stahlbau, Ernst & Sohn Verlag, 9/2008, Seiten 647-658.

Compressive Strength of UHPC in Bottle-Shaped Compression Fields

Torsten Leutbecher, Ekkehard Fehling
Institute of Structural Engineering, University of Kassel, Germany

To investigate the load-bearing behavior in bottle-shaped compression fields, an extensive test program has been initiated including series on ultra high performance concrete (UHPC) as well as on high strength (HSC) and normal strength concrete (NSC). In bottle-shaped compression fields transverse compressive stresses arise directly below the concentrated load while tensile stresses act at a slightly larger distance from the load introduction area. The tensile strength may limit the bearing capacity if there is no transverse reinforcement. The experimental tests, presented in the following, showed that splitting was the governing failure mode in all cases. The fracture behavior was brittle for UHPC and HSC specimens without fibers. By using fibers, the load bearing capacity could be increased significantly. Also a more ductile behavior at ultimate load could be observed.

Keywords: bottle-shaped, stress field, biaxial, tension, compression, concentrated load, splitting

1 Introduction

Applying a concentrated load to a structural concrete member often results in a bottle-shaped compression field in the load introduction zone (see Fig. 1). By deflecting the stress trajectories, compressive stresses arise in transverse direction at the bottle neck (directly below the concentrated load) and tensile stresses in a slightly larger distance from the load introduction area. A typical example for the formation of a bottle-shaped compression field is the introduction zone of the pre-stressing force in pre-stressed concrete structures.

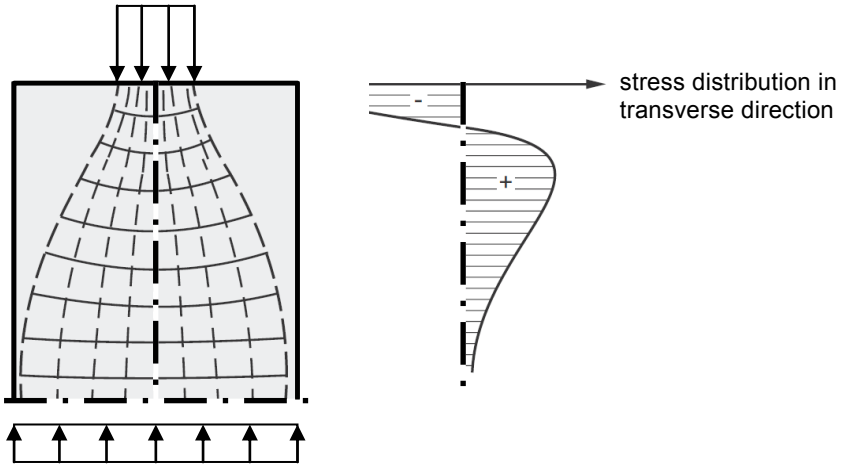

Figure 1: Bottle-shaped compression field under concentrated loads.

Usually, the transverse tensile stresses in structural concrete members are covered by transverse reinforcement. If this is not wanted or not possible, the compressive stresses under the concentrated load normally have to be limited to ensure that transverse tensile stresses do not exceed the value of the concrete tensile strength. An application is the use of high strength and ultra high strength concrete for so-called grouted connections in offshore power plants.

In these connections, the concrete makes it possible to transmit the load between the steel foundation pile(s) driven into the seabed and the upper steel structure of the tower (see Fig. 2). Compared to a pure steelwork connection, the grouting of the annular gap between these two parts with (ultra) high strength concrete offers the advantage of an easier compensation of

tolerances (especially deviations of the pile relative to the vertical axis). To prevent slippage in cylindrical connections, so-called shear keys are used. They are usually designed as circumferential weld beads. Besides the dead load, a part of the bending moment caused by wind and wave loads may be split into a couple of vertical forces and carried by the shear keys. The introduction of the concentrated forces from the steel tube into the concrete via shear keys results in a bottle-shaped compression field in the grouted connection. The question of designing these connections was responsible for initiating a test program, that is presented in the following.

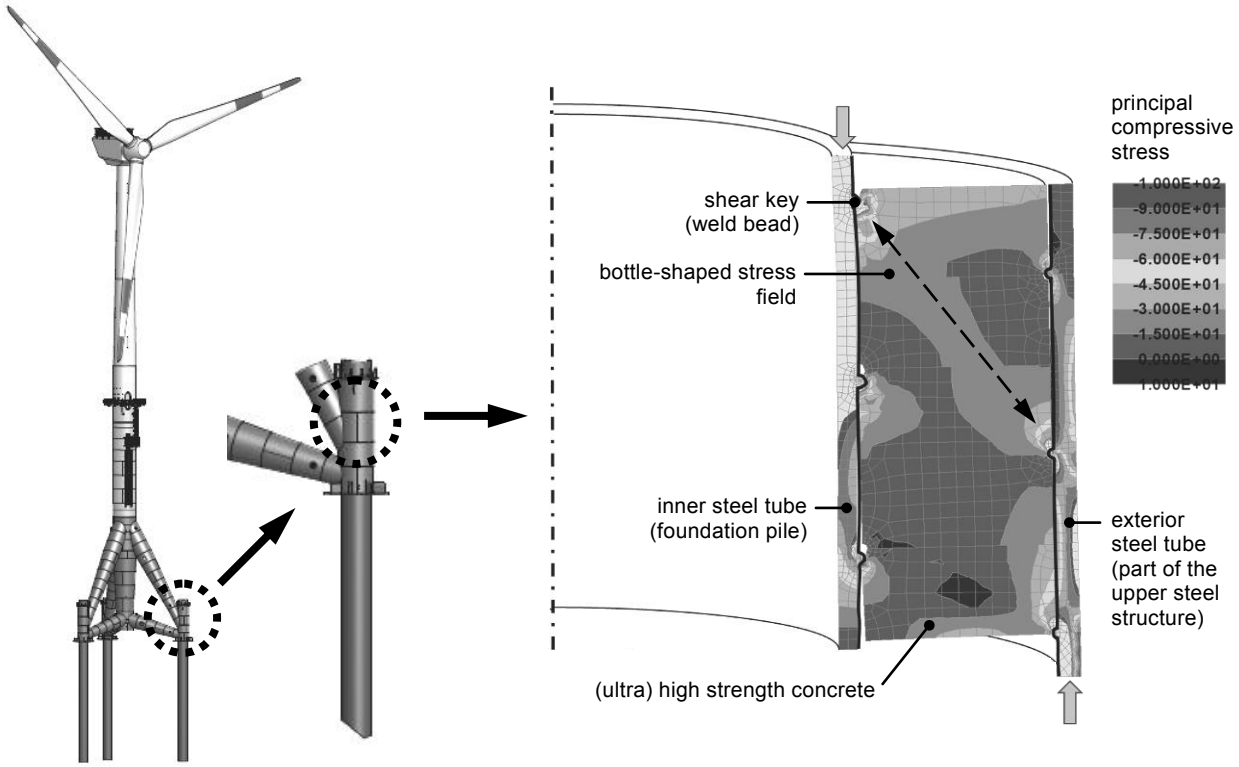

Figure 2: Offshore power plant of the wind farm Global Tech I in the Northern Sea (on the left) and FE-model of the grouted connection (on the right).

2 Cracking load of two-dimensional bottle-shaped compression fields

According to *Schlaich* and *Schäfer* [1], the cracking load represents a lower limit of the load-bearing capacity of two-dimensional bottle-shaped compression fields. The cracking forces can be determined by linear-elastic analysis using finite elements for plane stress state. It should be noted that the cracking stress may differ from the uniaxial tensile strength as a result of the biaxial tension-compression stress state within the compression field.

In Fig. 3a *Schlaich* and *Schäfer* provide a diagram for the determination of the compressive load leading to cracking of bottle-shaped compression fields. The compression field is characterized by the width *a* of the concentrated load, the maximum width *b* that is available for the compression field in the structural member, and the distance *l* between the load introduction and the section in which the stress trajectories run parallel. For structural members with very large or unlimited width, the total width *b* is to be replaced by the effective width b_{ef} according to Fig. 4 when evaluating the diagram. This takes into account that the compressive stresses acting on half-height of the compression field are not distributed equally along the total width.

As an example, the cracking load is calculated for the case that the uniaxial tensile strength f_{ct} is equal to 1/15 of the uniaxial compressive strength of the concrete f_c and for a failure criterion under tension-compression loading according to Fig. 3c. The result is represented by

the thick solid line in Fig. 3a. The further graphs in Fig. 3a are obtained for compression fields with transverse reinforcement (see Fig. 3d) depending on the mechanical reinforcement ratio ω.

As experiments have shown, the actual failure load is often higher than the cracking load [2-4] due to redistribution of the tensile stresses over the height of the compression field.

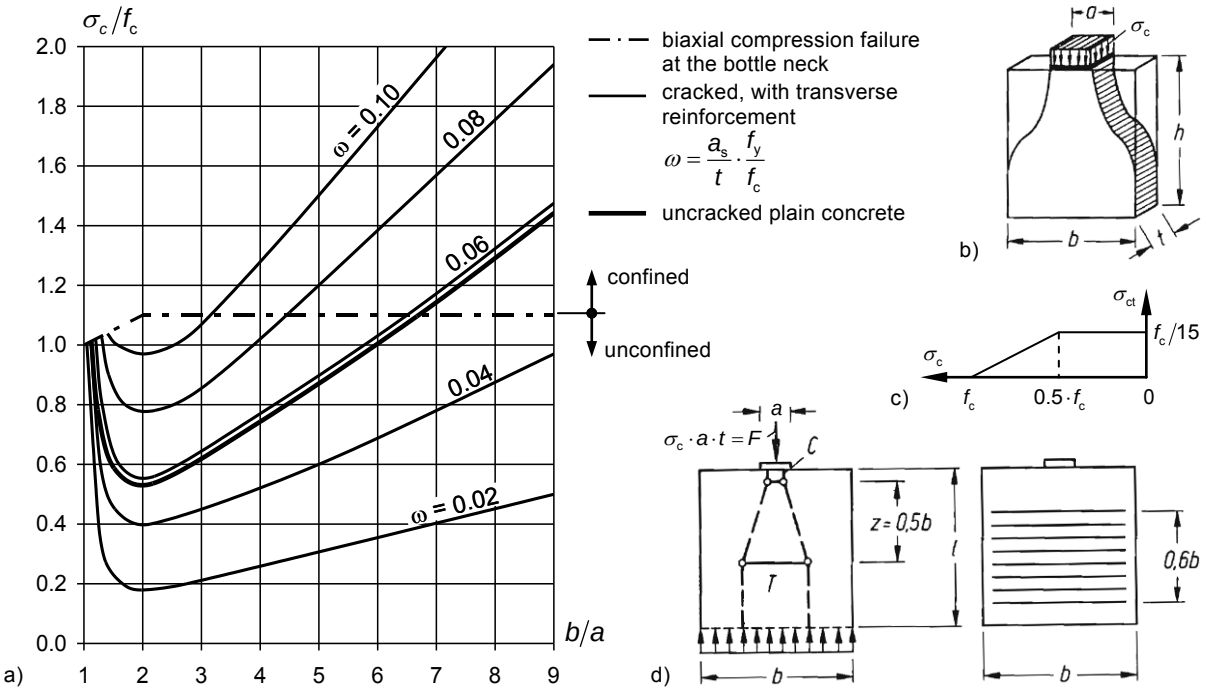

Figure 3: Two-dimensional bottle-shaped compression field according to Schlaich and Schäfer [1].
a) Compressive stress under the concentrated load causing a splitting crack (plain concrete, thick line), yielding of transverse reinforcement (thin lines) or biaxial compression failure at the bottle neck (dash-dotted line).
b) Geometry of the compression field.
c) Failure criterion under biaxial tension-compression loading.
d) Strut-and-tie model for the compression field with transverse reinforcement.

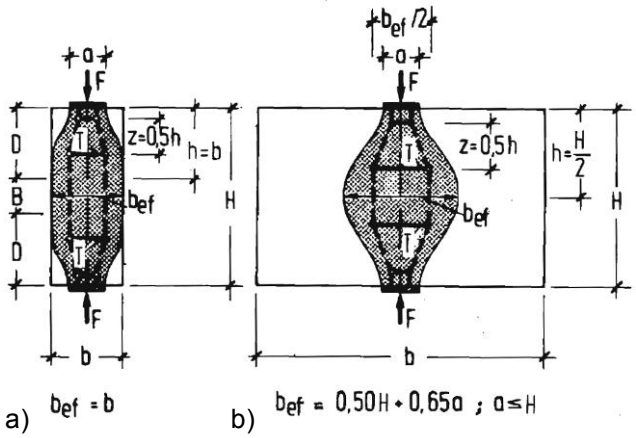

Figure 4: Effective width b_{ef} of the bottle-shaped compression field according to Schlaich and Schäfer [1]
a) structural member with small width
b) structural member with very large or unlimited width.

3 Experimental investigations

Test program and test specimens

On the one hand, high strength (HSC) and ultra high performance concretes (UHPC) differ from normal-strength concretes (NSC) in increased brittleness and mostly in the use of a relatively small maximum aggregate size. On the other hand, steel fibers, which can act as “transverse reinforcement” in bottle-shaped compression fields, are often added, especially to UHPC.

To investigate the abovementioned influences on the bearing-capacity of bottle-shaped compression fields, tests on concrete cubes with different compressive strengths were conducted. Table 1 gives an overview of the experimental program executed so far.

Table 1: Test program executed so far.

Test series	**NSC-0**	**HSC-0**	**UHPC-0-HT**	**UHPC-1-HT**	**UHPC-2-HT**
Uniaxial concrete compressive strength f_c [N/mm²]	19.7	131	194	200	201
Gross density [kg/dm³]	2.087	2.424	2.314	2.417	2.418
Maximum aggregate size [mm]	8	5	0.5	0.5	0.5
Fiber content ρ_f [% by vol.]	0	0	0	1.0	2.0
Heat treatment	no	no	yes	yes	yes

As fiber reinforcement straight steel fibers with a length of 17 mm and a diameter of 0.175 mm were used. They were added to two of the UHPC-mixtures with 1.0 % or 2.0 % by volume.

The concrete cubes had an edge length of 200 mm. They were produced in a steel mold and compacted on a vibrating table. To compact the NSC specimens, an internal vibrator was used. For each test series four concrete cubes and three cylinders (h/d = 200 mm/100 mm) were fabricated from the same mixture. The cylinders were used to determine the uniaxial concrete compressive strength. The NSC and HSC specimens were cured under room conditions after removing the formwork two days after production. The UHPC series were heat treated (labeled HT) at 90 °C for 48 hours with the result that the final strength of these specimens was achieved at the age of four days.

Test setup und test execution

The experiments were conducted in a servo-hydraulic controlled universal testing machine in the laboratory of the Institute of Structural Engineering at the University of Kassel. Fig. 5 shows the test setup.

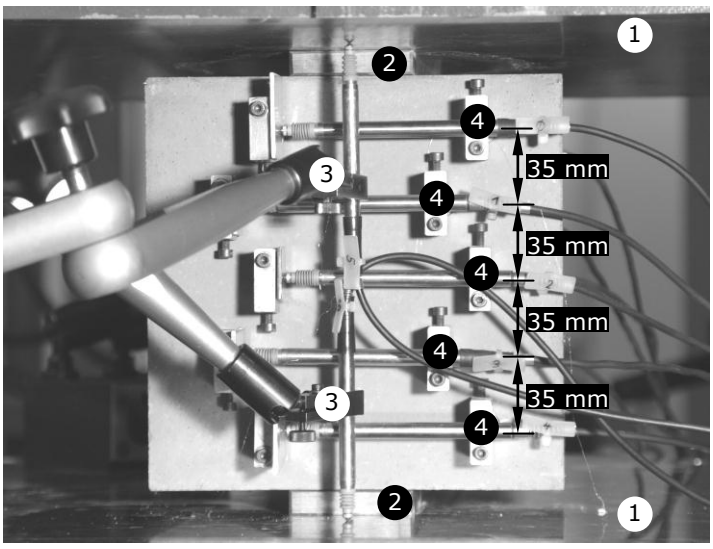

(1) Loading plates of the testing machine
(2) Steel stripes for load introduction (here: a = 60 mm)
(3) LVDTs for control of vertical displacements
(4) LVDTs for control of horizontal displacements

Figure 5: Test setup with test specimen and instrumentation.

The test specimens were placed centrically between the two loading plates of the machine. The upper loading plate was connected via a spherical hinge to the testing machine. The specimens were loaded perpendicular to the casting direction. The load was applied by means of 200 mm long steel strips, which were placed centrically at the top and at the bottom of the test

specimen. Because of the smooth concrete surface obtained by the steel mold, the steel strips could be installed without any interface layer. To obtain different geometries of the compression field b/a, steel strips with four different width values were used for load introduction (a = 10 mm, 16 mm, 25 mm, and 60 mm). This resulted in ratios $b_{(ef)}/a$ of 10.7, 6.9, 4.7, and 2.3. Hence, each ratio was applied to one of the cubes of each series.

To measure the deformations in compression direction, four LVDTs were installed, two at the front and two at the back side of the cube. They were fixed with magnetic stands and measured against the load plates of the testing machine. In addition, the displacement of the hydraulic jack was recorded.

The horizontal deformations (in tensile direction) were checked in the area in which cracking could be expected. They were measured directly by means of LVDTs mounted on the specimen. At the front and the back of the specimens five gauge lengths of 100 mm were provided. For some specimens without fibers, two gauge lengths remained vacant on each side, because it was already known from previous experiments, that meaningful data could not be gained from these specimens in the post-cracking branch due to the brittle failure.

Displacement controlled loading was performed with a constant rate of 0.01 mm/s (displacement of the hydraulic jack).

Test results

The test results are summarized in Table 2. The ultimate compressive stresses $\sigma_{c,max}$ are related to the load application area represented by the surface area of the steel strip. As expected, the ratio $\sigma_{c,max}/f_c$ increases with increasing ratio b/a. The ratio decreases significantly with increasing uniaxial concrete compressive strength f_c due to the minor ratio between tensile and compressive strength and the more pronounced brittleness of HSC and UHPC.

Table 2: Test results.

Test series	NSC-0		HSC-0		UHPC-0-HT		UHPC-1-HT		UHPC-2-HT	
	$\sigma_{c,max}$ [N/mm²]	$\sigma_{c,max}/f_c$	$\sigma_{c,max}$ [N/mm²]	$\sigma_{c,max}/f_c$	$\sigma_{c,max}$ [N/mm²]	$\sigma_{c,max}/f_c$	$\sigma_{c,max}$ [N/mm²]	$\sigma_{c,max}/f_c$	$\sigma_{c,max}$ [N/mm²]	$\sigma_{c,max}/f_c$
b/a = 2.3	17.6	0.89	79.4	0.61	78.9	0.41	173	0.87	193	0.96
b/a = 4.7	23.2	1.18	77.2	0.59	74.2	0.38	207	1.04	284	1.41
b/a = 6.9	34.6	1.75	95.3	0.73	109	0.56	256	1.28	334	1.66
b/a = 10.7	48.9	2.48	151	1.15	158	0.81	347	1.73	457	2.27

For some tests, the load-deformation curves are depicted in Fig. 6. All deformations specified in the diagrams represent mean values of the data obtained at the front and at the back side of the test specimens. In vertical direction, the elastic deformations of the steel stripes have been deducted.

Fig. 6a and 6b show the load-deformation curves for the ratio b/a = 10.7. Disregarding some nonlinearities resulting from the test setup, the load-deformation behavior of the test specimens was initially linear both in loading and transverse direction.

The HSC specimens and the UHPC specimens without fibers failed suddenly by a splitting crack (see Fig. 7c) accompanied by a load drop to zero in most cases. Also the NSC cubes did not show a pronounced nonlinear behavior before reaching the ultimate load. However, for these specimens the complete softening branch after splitting could be obtained by displacement control.

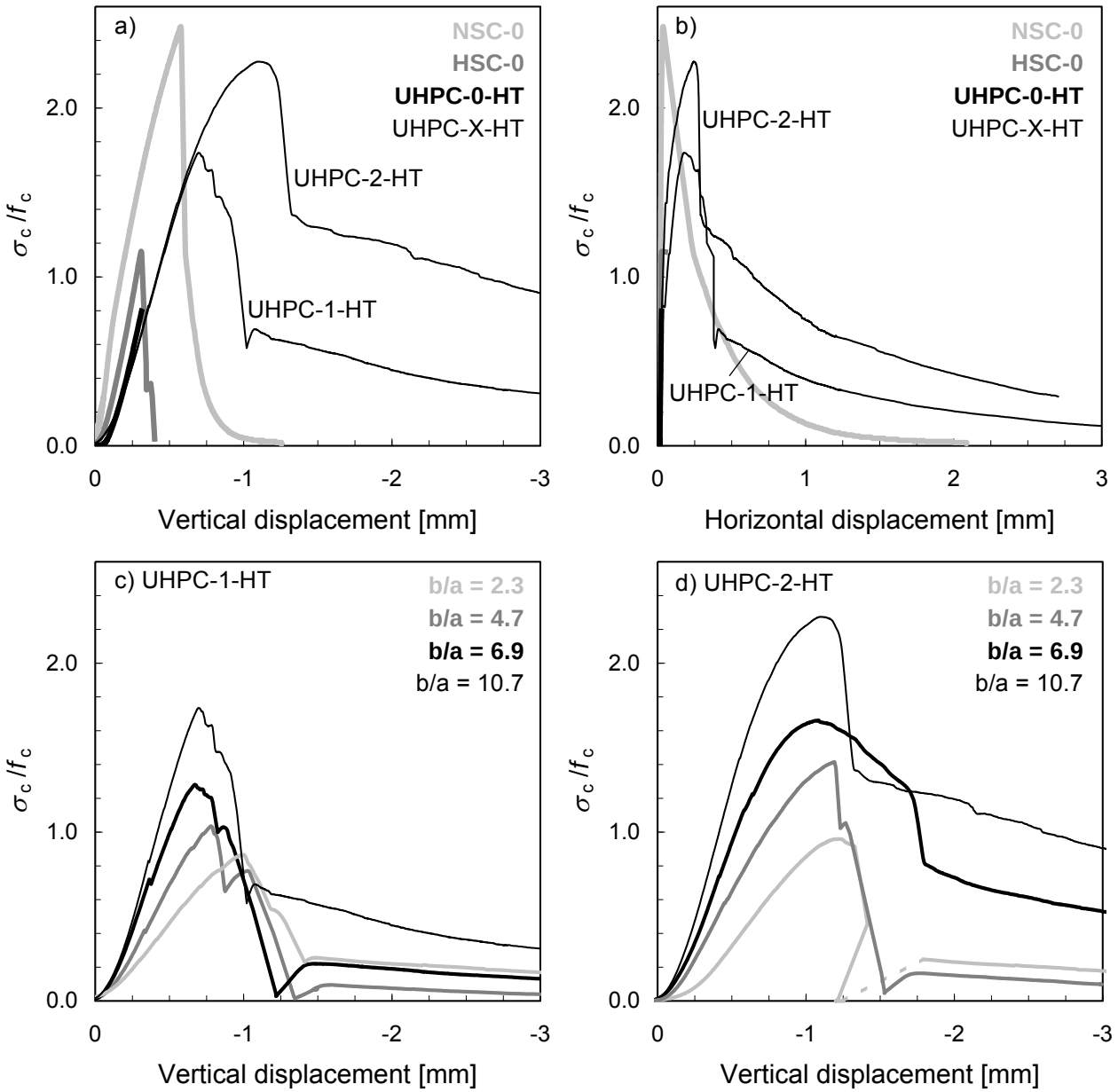

Figure 6: Load-deformation curves.
a) Load-deformation curve in loading (compression) direction for the five series and b/a = 10.7.
b) Load-deformation curve in transverse (tension) direction for the five series and b/a = 10.7.
c) Load-deformation curve in loading (compression) direction for series UHPC-1-HT and different ratios b/a.
d) Load-deformation curve in loading (compression) direction for series UHPC-2-HT and different ratios b/a.

For the fiber reinforced UHPC cubes, the load-deformation relationship initially followed almost that of the corresponding unreinforced specimens. The splitting started at about the same load level, too. However, this caused only a temporary slight drop of the load. With increasing deformation, the compressive load could be further increased, while henceforth a nonlinear relationship between load and deformation was observed. The progressive crack opening could be detected by the horizontal LVDTs very well (see Fig. 6b). The failure was announced by more or less pronounced plastic behavior before reaching the ultimate load. The specimens with large *b*/*a* ratio and higher fiber content showed in this context as well as in the post-peak branch a more ductile behavior (see Fig. 6c and 6d). For small *b*/*a* ratios the loading dropped comparatively rapidly to zero, even for the specimens with a fiber content of 2 % by volume.

Fig. 7 shows the failure pattern of split UHPC specimens. For the specimens with *b*/*a* = 2.3, splitting started from the edges of the load application area due to load concentration there. As a consequence sometimes two splitting cracks developed (see Fig. 7a).

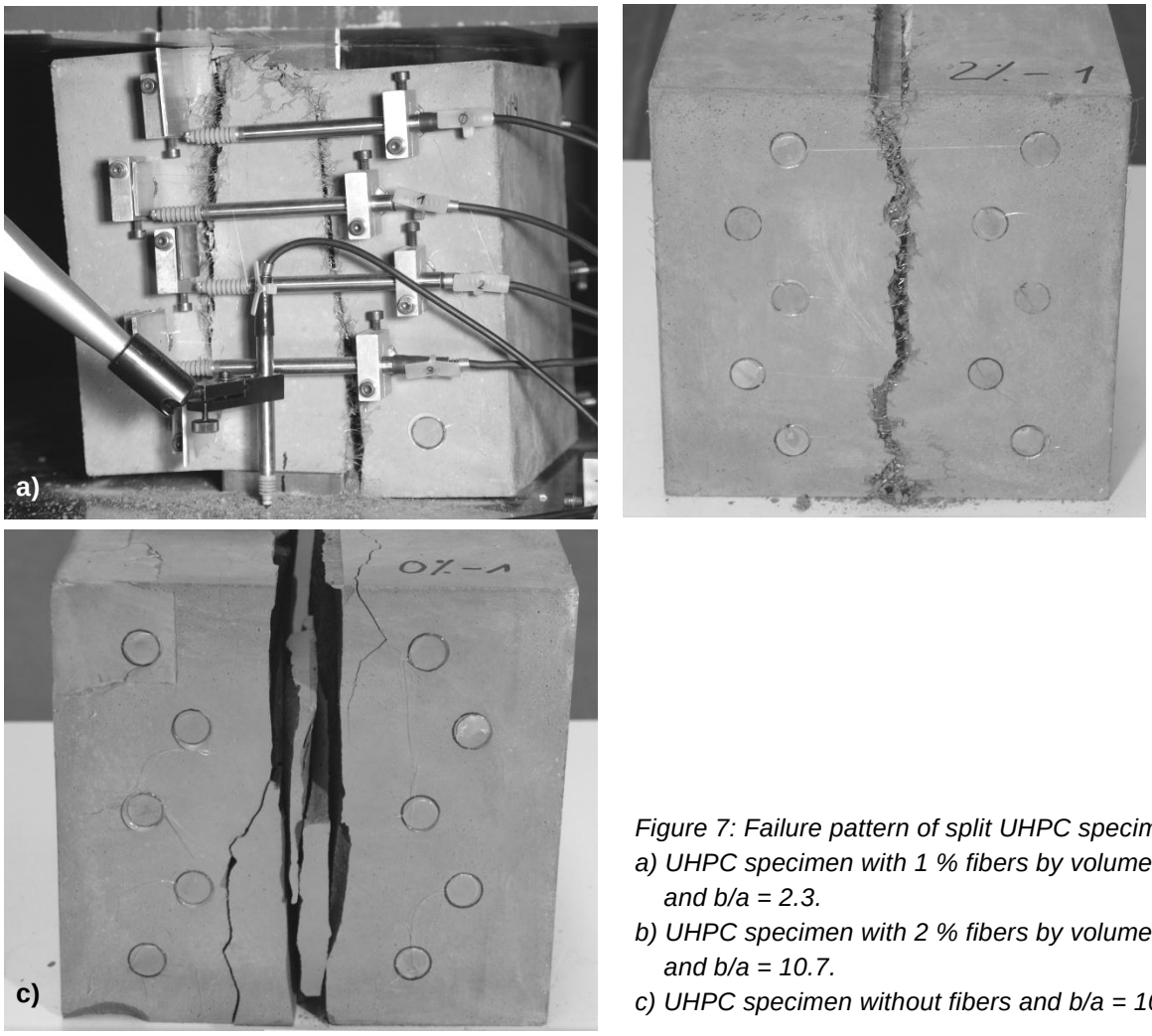

Figure 7: Failure pattern of split UHPC specimens.
a) UHPC specimen with 1 % fibers by volume and b/a = 2.3.
b) UHPC specimen with 2 % fibers by volume and b/a = 10.7.
c) UHPC specimen without fibers and b/a = 10.7.

4 Conclusions and outlook

Fig. 8 shows the ultimate compressive stresses due to concentrated load, which are related to the uniaxial concrete compressive strength. The results are depicted in dependency of the theoretical *b*/*a* ratio.

The results for the NSC specimens can be approximately related to ω = 0.09. This corresponds to a ratio between the concrete tensile strength f_{ct} and the uniaxial concrete compressive strength f_c of about 1/10, which is common for NSC. Referring the results for the HSC and UHPC specimens to the graphs ω = 0.04 and ω = 0.03, respectively, the ratios f_{ct}/f_c amount to about 1/22 and 1/29. For uniaxial compressive strengths of 131 N/mm² and 194 N/mm², respectively, the tensile strengths result in about 6.0 N/mm² and 6.7 N/mm².

By means of fiber addition to UHPC the load bearing capacity could be increased significantly. Already a fiber volume of 1 % was sufficient to achieve compressive stresses under the concentrated load that were almost equal to the uniaxial concrete compressive strength. Compared to the ultimate load, the ductility was increased at a lower rate by the addition of fibers, especially for the specimens with low *b*/*a* ratio. Despite the sometimes very high local stresses at the steel strip, splitting and not compression failure was governing in all cases.

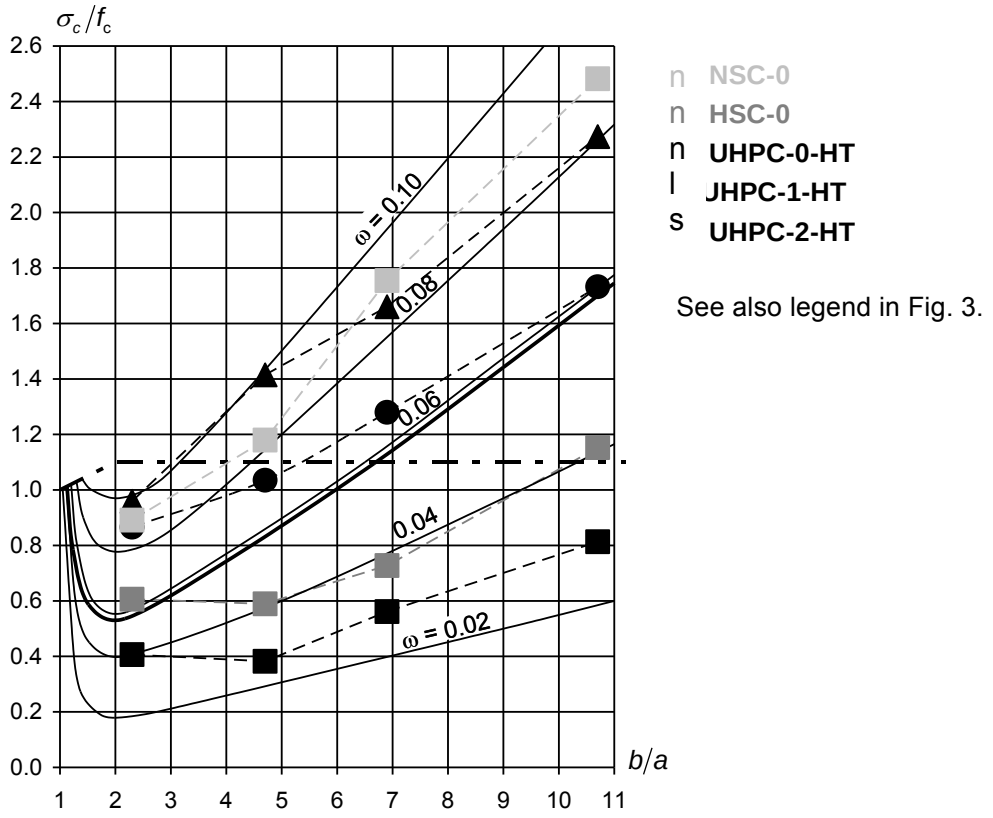

Figure 8: Test results related to the uniaxial concrete compressive strength and compared with the theoretical cracking stress according to [1] (see Fig. 3).

Further tests on HSC with fibers as well as on UHPC with low fiber content (0.5 % by volume) are scheduled. By optically analyzing the fiber orientation in the cubes and by determining the post-cracking tensile strength (fiber efficiency) in tests on notched prisms sawn from untested cubes, a relationship to concretes with different fiber content and fiber geometry may be established. The test results will also be used to calibrate a fracture model for fiber reinforced UHPC within a nonlinear finite element analysis. Afterwards, this model shall be applied to the design of grouted connections used in offshore wind turbines. For this, the fracture model is to be extended so that it is appropriate for three-dimensional stress states.

References

[1] Schlaich, J.; Schäfer, K.: Konstruieren im Stahlbetonbau. Beton-Kalender 1998, part II, Verlag Ernst & Sohn, Berlin, 1998.

[2] Fehling, E.: Zum Tragverhalten von Druckfeldern in scheibenartigen Betonbauteilen - Nichtlineare Berechnungen und Vergleich mit Versuchen. Materialmodelle und Methoden zur wirklichkeitsnahen Berechnung von Beton-, Stahlbeton- und Spannbetonbauteilen, Mehlhorn-Festschrift, Faculty of Civil Engineering, University of Kassel, 1997.

[3] Colombo, M.; Di Prisco, M.: D-zones in HPFRC. High Performance Fiber Reinforced Cement Composites 6 (Eds.: Parra-Montesinos, G. J.; Reinhardt, H. W.; Naaman; A. E.), Proceedings of the Sixth International Workshop on High Performance Fiber Reinforced Cement Composites (HPFRCC6), pp. 197-204, Ann Arbor, MI, USA, 2011.

[4] Pujol, S.; Rautenberg, J. M.; Sozen, M. A.: Compressive Strength of Concrete in Nonprismatic Elements. Concrete International 33 (9), pp. 42-49, 2011.

Schriftenreihe Baustoffe und Massivbau
Structural Materials and Engineering Series

Heft 1: **Fehling, E. / Schmidt, M. / Teichmann, T. / Bunje, K. / Bornemann, R. / Middendorf, B. (2005)**
Entwicklung, Dauerhaftigkeit und Berechnung Ultra-Hochfester Betone (UHPC). Forschungsbericht, ISBN 3-89958-108-9, € 18,00

Heft 2: **Schmidt , M. / Fehling, E. (Hrsg.) (2003)**
Ultra-Hochfester Beton - Planung und Bau der ersten Brücke mit UHPC in Europa. Tagungsbeiträge zu den 3. Kasseler Baustoff- und Massivbautagen am 10. September 2003, ISBN 978-3-89958-518-6, € 18,00

Heft 3: **Schmidt, M. / Fehling, E. / Geisenhanslüke, C. (Hrsg.) (2004)**
Ultra High Performance Concrete (UHPC), ISBN 3-89958-086-9, vergriffen

Heft 4: **Bornemann, R. (2005)**
Untersuchungen zur Modellierung des Frisch- und Festbetonverhaltens erdfeuchter Betone, ISBN 3-89958-132-6, € 24,00

Heft 5: **Solyman, M. (2006)**
Classification of Recycled Sands and their Applications as Aggregates for Concrete and Bituminous Mixtures, ISBN 978-3-89958-218-5, € 24,00

Heft 6: **Tesch, V. (2007)**
Gefügeoptimierte Instandsetzungsmörtel auf Calciumsulfat-Basis für die Anwendung im Außenbereich, ISBN 978-3-89958-333-5, € 24,00

Heft 7: **Schmidt, M. (ed.) (2007)**
Ultra High Performance Concrete (UHPC). 10 Years of research and development at the University of Kassel - 10 Jahre Forschung und Entwicklung an der Universität Kassel, ISBN 978-3-89958-347-2, € 49,00

Heft 8: **Schmidt, M. (Hg.) (2007)**
Nanotechnologie im Bauwesen Nanooptimierte Hightech-Baustoffe. 9. Mai 2007, ISBN 978-3-89958-348-9, € 22,00

Heft 9: **Leutbecher, T. (2008)**
Rissbildung und Zugtragverhalten von mit Stabstahl und Fasern bewehrtem Ultrahochfesten Beton (UHPC), ISBN 978-3-89958-374-8, € 39,00

Heft 10: **Fehling, E. / Schmidt, M. / Stürwald, S. (eds.) (2008)**
Ultra High Performance Concrete (UHPC). Second International Symposium on Ultra High Performance Concrete, March 05-07, 2008, ISBN 978-3-89958-376-2, € 79,00

Heft 11: Fehling, E. / Leutbecher, T. / Röder, F.-K. (2008)
Zur Druck-Querzug-Festigkeit von Stahlbeton und stahlfaserverstärktem Stahlbeton in scheibenförmigen Bauteilen - Biaxial Compression-Tension-Strength of Reinforced Concrete and Reinforced Steel Fibre Concrete in Structural Panels, ISBN 978-3-89958-440-0, € 39,00

Heft 12: Teichmann, T. (2008)
Einfluss der Granulometrie und des Wassergehaltes auf die Festigkeit und Gefügedichtigkeit von Zementstein, ISBN 978-3-89958-441-7, € 24,00

Heft 13: Geisenhanslüke, C. (2009)
Einfluss der Granulometrie von Feinstoffen auf die Rheologie von Feinstoffleimen, Influence of the granulometry of fine particels on the rheology of pastes, ISBN 978-3-89958-706-7, € 24,00

Heft 14: Nöldgen, M. (2010)
Modellierung von ultrahochfestem Beton (UHPC) unter Impaktbelastung. Auslegung eines Hochhauskerns gegen Flugzeuganprall,
ISBN 978-3-89958-862-0, € 29,00

Heft 15: Eden, W. (2011)
Einfluss der Verdichtung von Kalk-Sand-Rohmassen auf die Scherbenrohdichte von Kalksandsteinen,
ISBN 978-3-86219-040-9, € 29,00

Heft 16: Stephan, D. (2011)
Nanomaterialien im Bauwesen. Stand der Technik, Herstellung, Anwendung und Zukunftsperspektiven,
ISBN 978-3-86219-066-9, € 29,00

Heft 17: Emami, A. D. (2011)
Kleben von Naturfaserverbundwerkstoffen auf Mauerwerk zur nachträglichen Verstärkung erdbebengefährdeter Bauwerke – von der Werkstoffprüfung bis zur Anwendung,
ISBN 978-3-89958-558-2, € 29,00

Heft 18: Stürz, J. (2011)
Ein empirischer Ansatz zur Beschreibung der Horizontaltragfähigkeit gemauerter Wandscheiben unter Berücksichtigung der Interaktion innerhalb der Gebäudestruktur
ISBN 978-3-89958-559-9, € 29,00

Heft 19: Schmidt, M. / Fehling, E. / Glotzbach, C. / Fröhlich, S. / Piotrowski, S. (eds.) (2012)

Ultra-High Performance Concrete and Nanotechnology in Construction. Proceedings of Hipermat 2012. 3rd International Symposium on UHPC and Nanotechnology for High Performance Construction Materials, Kassel, March 7–9, 2012, ISBN 978-3-86219-236-6, € 79,00

Bestellungen: www.uni-kassel.de/upress

Ultra-High Performance Concrete (UHPC), with its high compressive strength of more than 200 MPa and an improved durability, marks a quantum leap in concrete technology. This high performance material offers a variety of interesting applications. It allows the construction of sustainable and economic buildings with an extraordinarily slim design. Its high strength and ductility makes it the ultimate building material for e.g. bridge decks, storage halls, thin-wall shell structures, and highly loaded columns. Due to its outstanding resistance against several kinds of corrosion, it is deemed suitable for new fields of application where concrete has not been considered viable before. To make use of its superior properties, special knowledge of production, construction, and design is required.

To facilitate the fruitful exchange of knowledge and experience both between international researchers and engineers in the field was the objective of the **3rd International Symposium on UHPC** that took place in Kassel on March 7–9, 2012, the proceedings of which are contained in this publication.

As an impressive amount of new knowledge could be obtained by leveraging the growing experience in the fields of nanotechnology and chemistry, the symposium was rebranded to honor this influence. It now bears the name **HiPerMat,** derived from Nanotechnology for **High Performance Materials** in Construction.

This volume thus contains about 120 contributions from many research disciplines that are influenced by High Performance Materials and UHPC in particular: material sciences, structural engineering, environmental engineering, nanotechnology, chemistry, architecture, codification, and economy.

HiPerMat
Materials Structures Design

ISBN 978-3-86219-264-9

9783862192649